Macromolecules

Perspective

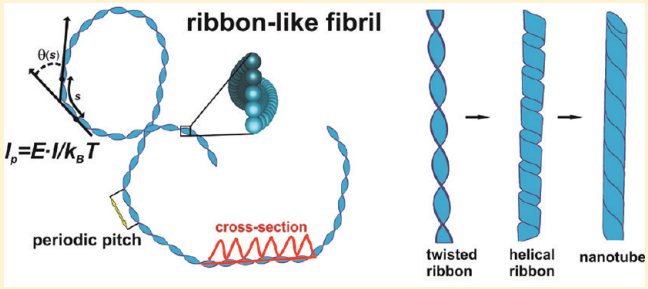
pubs.acs.org/Macromolecules

Proteins Fibrils from a Polymer Physics Perspective

Jozef Adamcik and Raffaele Mezzenga*

Food & Soft Materials Science, Institute of Food, Nutrition & Health, ETH Zürich, LFO23, Schmelzbergstrasse 9, 8092 Zürich, Switzerland

ABSTRACT: Protein fibrils resulting from assembly of proteins or peptides into long, insoluble, highly ordered fibrillar structures are emerging as one of the fastest growing scientific areas, since interest in these systems spans disciplines as broad and diverse as medicine, biology, soft condensed matter, nanotechnology, and materials science. Since the discovery of the implication of protein amyloid fibrils in neurodegenerative diseases, to their more recent applications in high-performance materials, the understanding of these intriguing macromolecular assemblies has been steadily widening and deepening. Thus, the precise characterization of structural, physical, and mechanical properties of protein fibrils is the first critical step toward our understanding of these systems not only in the context of biology and medicine but also in nanotechnology and advanced biomaterials applications. In this Perspective we wish to discuss how polymer and colloidal science concepts can be efficiently used to unravel very useful information on the mechanisms of formation, structure, and physical properties of protein fibrils and want to show, through available examples, how a soft condensed matter perspective can shed light into these fascinating systems.



1. INTRODUCTION

Proteins represent one of the most important molecules in living matter, as they accomplish a wide range of functions and play a crucial role in the maintenance of life. The protein folding is the most fundamental and universal example of biological self-assembly. The correct biological function of proteins depends on their self-assembly into well-defined highly ordered three-dimensional secondary and tertiary structures, while maintaining their native form. However, the progression from gene to a correctly folded functional protein can fail, and the incorrect protein folding can lead to the formation of disordered or highly ordered aggregates.[1−4] Protein aggregation is a widely observed phenomenon both *in vivo* and *in vitro* conditions due to its incidence in different aspects of everyday life including medicine, food processing, biotechnology, etc.[5−7] For example, *in vitro* protein aggregation in food processing might be desirable and can be used as a suitable tool to generate new forms of protein-based gelling agents, foaming agents, or emulsifiers.[5,8] On the other hand, uncontrolled and irreversible protein aggregation *in vitro* conditions can cause severe problems in the biotechnology and pharmaceutical industry during the process of expression and purification of proteins. Also in the case of *in vivo* conditions, the aggregation of proteins can be both beneficial, as in the case of blood coagulation, and detrimental, as in the case of eye cataract formation,[9,10] just to mention only two examples.

A particularly interesting case of protein aggregation occurring both *in vivo* and *in vitro* is the conversion of specific proteins from their soluble functional native form into very stable and highly ordered fibrillar structures termed as amyloid fibrils. The most widely known cases of amyloid aggregation are those related to human diseases, including numerous neurodegenerative disorders such as Parkinson's, Alzheimer's, Creutzfeldt−Jakob disease, type II diabetes, and bovine spongiform encephalopathy, and their occurrence in the body indicates the healthiness problems.[3,11−17] Generally is known that amyloid fibrils share common characteristic structural and morphological properties including a core cross-β-sheet structure in which continuous β-sheets are formed with β-strands that are stacked in the direction perpendicular to the long axis of the fibrils by hydrogen bonds.[18,19] From the morphological point of view, the amyloid fibrils typically consist of 2−6 protofilaments with 2−5 nm in diameter associated laterally or twisted together to form unbranched, several micrometer long fibrils.[20,21] Although the amyloid fibrils occurring in different diseases share structural and morphological similarities, the amyloidogenic proteins are diverse in terms of amino acid sequence and prior to fibrillation may have different compositions of β-sheet, α-helix, or natively unfolded states.[3,22] The structural similarity of these protein fibrils, their common features showing yellow−green birefringence on binding Congo red, and intense fluorescence on binding thioflavin T suggest a common mechanism of their formation. In addition to the above pathogenic examples, it has been discovered that many amyloid fibrils exist in nature, termed "functional amyloid", having a function seemingly unrelated to diseases but with normal biological activities.[23−27] The examples of such functional amyloid include bacterial coatings, catalytic scaffolds,

Received: September 23, 2011
Revised: December 6, 2011
Published: December 21, 2011

 © 2011 American Chemical Society dx.doi.org/10.1021/ma202157h | *Macromolecules* 2012, 45, 1137−1150

agents mediating epigenetic information storage and transfer, adhesives, and structures for the storage of peptide hormones.[23−27] The occurrence of functional amyloid is important because it demonstrates that the formation of amyloid fibrils is not solely connected to toxicity and diseases. This discovery further increases the relevance of this protein self-aggregating mechanism and the interest of the scientific community in the amyloid fibrils field, in general. Furthermore, another important emerging current in the amyloid fibrils is the one aiming at the *in vitro* synthesis of amyloid fibrils from nontoxic proteins and peptides to serve in a very broad spectrum of technology applications, which can rely on some of the unique amyloid fibrils physical properties. This includes, among others, food, biomedical, nanotechnology, and biomaterials applications.[28−30] Therefore, understanding the mechanisms of amyloid fibrils formation and their characterization has a great importance and may help both dealing with the diseases, that is, improving strategies toward the prevention of fibrillation processes as well as to create new application possibilities for technological purposes.

The field of amyloid fibrils has been traditionally dominated—with reasons—by molecular biology, as the protein/peptide misfolding and cross-β-sheet driven fibrillation have been tackled primarily at the molecular level. Recently, however, a soft condensed matter description of the protein aggregation and fibrillation processing is emerging as a valuable complementary approach. Following this angle of view, protein fibrils can then be studied using the same physical tools used to describe polymers, polyelectrolytes, and colloidal dispersions. While this approach obviously leads to a coarser description at the molecular level, it has the great benefit of tackling the problem from a general physics perspective, drawing common conclusions among very different protein fibrillating systems.

In this Perspective we aim at digging into the recent efforts taken in this respect, that is, to unravel the mechanisms of formation, the structure, and the physical properties of protein fibrils from a soft condensed matter approach. Some of the features discussed in the present Perspective may serve to study other nonamyloid types of protein-based fibrils. For example, biological occurrence of fibrillar structures in life is not only of amyloidal type, since extracellular matrice macromolecules have the ability to assembly into "good" structures such as fibrils, microfibrils, filaments, or network which are then used as building blocks for living matter;[31−33] collagen represents the most known example of "good" fibrillar structure,[34] but also actin and fibronectin are examples of non-amyloidal protein or peptidic-rich fibrils of prime importance in life.[33] Thus, while our main focus here is on amyloid protein fibrils, we leave the discussion sufficiently open and broad to indirectly touch on other types of protein fibrillar systems from a more general perspective, for which we believe polymer and colloidal physics approaches constitute the most solid and general toolbox of investigation.

2. MECHANISM OF FIBRILS FORMATION FROM GLOBULAR PROTEINS

For many years the ability of amyloid fibrils formation was thought to be limited to a relatively small number of proteins associated with neurodegenerative diseases. However, it is now known that many disease-unrelated proteins have the ability to aggregate into fibrils that are structurally indistinguishable from those detected in diseases, and many scientists involved in the research of amyloid fibrils formation support the idea that most proteins, perhaps all, can be forced to form amyloid fibrils under appropriate conditions.[3] Consequently, the number of studies aiming at elucidating the mechanisms of protein fibrillation has increased substantially over the past few years. The elucidation of the entire steps of fibrillation of proteins requires accessing a multitude of time and length scales and identifying all the intermediate conformational states and structures adopted by the polypeptide chains during this process. In what follows we focus on the fibrillation from globular folded proteins, due to the relevance these systems have in biology, medicine, nanotechnology, food, and pharmaceutical sciences. We select as a model globular protein undergoing fibrillation, β-lactoglobulin, as this protein has proved to be a very valuable model system in the understanding of protein fibrillation mechanisms.[35,36] β-Lactoglobulin is the major whey protein found in bovine milk and is considered as a very important functional ingredient in food processing owing to its emulsifying, structuring, and foaming activity.[8] Upon heating β-lactoglobulin solutions at high temperature such as 80−90 °C, that is above the unfolding temperature, different structural morphologies appear depending on the pH and ionic strength considered.[37] Rigid fibrillar aggregates 2−10 nm large and hundreds to thousands of nanometers long are typically found at low ionic strength ($\leq$20 mM) and pH ($\leq$2) upon heating at high temperatures ($\geq$80 °C).[38]

2.1. Protofilament Formation. From a coarse colloidal description, the protofilament can be considered as the simplest building block of the mature protein fibrils, as it shares with the final fibrils the rigid and elongated structure, but a much simpler cross section. At the molecular length scale, however, protofilaments are already highly structured supramolecular aggregates of peptides/proteins organized in a cross-β-sheet configuration and unidirectional growth. By opting for a polymeric and colloidal description of the protein fibrils, one makes the *a priori* choice to study the supramolecular assembly of protofilaments at higher length scales from the most general angle, leaving to molecular biologists the hard tasks to resolve the specific internal structure of protofilaments and their peptide-dependent structural features. We therefore review below only briefly the process leading to protofilament formation starting from globular proteins, and we leave the largest part of the discussion for the assembly of amyloid fibrils from the protofilaments upward.

In general, under normal environmental conditions, globular native proteins in solution are in equilibrium with their partially unfolded state (Figure 1). However, if environmental conditions are varied, such as for example strong departure from physiological temperature and pH, the equilibrium may be displaced between partially and completely unfolded states. It is usually accepted that that the process of amyloid fibril formation commences from partially unfolded structure of proteins. Differently from smaller, pathological peptides, globular proteins in their native form have a compact rigid structure, and therefore their fibrillation process requires the destabilization of their native rigid structure into partially unfolded conformations via robust changes of environmental conditions.[39] This conformation represent an important prerequisite for the protein fibrillation because completely unfolded proteins are devoid of ordered structure while the partially unfolded conformation of protein gives rise to specific intermolecular interactions such as hydrogen bonding, electrostatic, and hydrophobic interactions, which were minimized in the native folded state and which can then drive the oligomerization and fibrils formation. The transformation of protein into partially unfolded conformation

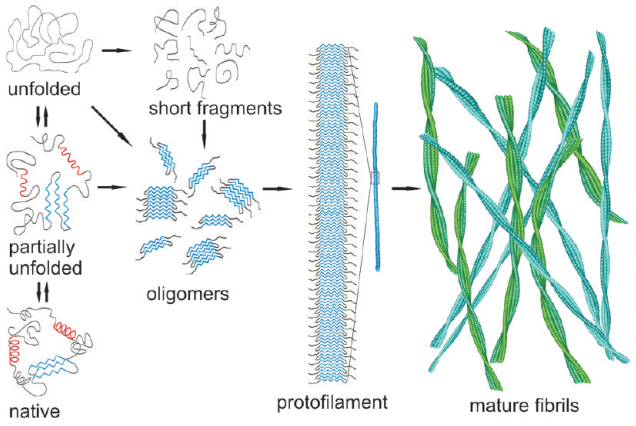


Figure 1. Scheme representing the mechanism of the conversion of globular proteins into amyloid fibrils commencing from partially unfolded conformation and proceeding through the protofibrillar structures (oligomers and protofilaments) into mature fibrils. Oligomers are assembled from either unfolded protein refolded into a cross-β-sheet or by short fragments (also folded into cross-β-sheets), which are obtained by hydrolysis of the monomeric form of the proteins.

can be induced by mutations, by changes in environmental conditions, such as increasing of incubation temperature up to 90 °C compared to physiological temperature of 37 °C and/or decreasing of pH to very acidic conditions, or by chemical modifications. However, it is not always necessary to treat the protein under so drastic conditions because the amyloid fibril formation from globular proteins can also occur under native conditions when fibril formation would initiate from locally unfolded conformation of protein which can be accessible, for instance, through thermal fluctuations of native conformation of protein.[4]

The generally accepted model for amyloid fibrils formation is the nucleation–elongation model, where the formation of a nucleus through the self-assembly of monomeric structures of protein is followed by the rapid growth through addition of monomeric structures to the nucleus leading to the formation of transiently existing protofibrillar structures, such as spherical oligomers and/or protofilaments, which are an important factor in the pathogenesis of amyloids due to the higher toxicity in the comparison with mature amyloid fibrils.[40] The protofibrillar structures are formed quite rapidly, and the mature fibrils appear upon extended incubation. In order to undergo amyloid-type fibrillation, the partially unfolded proteins have to refold (or misfold) into cross-β-sheet secondary structure, which undergoes a linear[4,16,39,41] growth orthogonal to the peptide stretched contour lengths with a characteristic interspacing of 0.47 nm, corresponding to the hydrogen-bond-mediated β-sheet distance among peptide chains (Figure 1). This early growth generates tapes that then stack laterally into protofilaments driven by interfacial energy. The steps leading a single peptide to the association into protofilaments have been considered from a statistical mechanical perspective in the work of Aggeli et al.,[42] and the reader is addressed to that paper, as we are here concerned with a coarser description of the fibrils at larger length scales (from protofilaments upward).

While the assembly scheme given above appears straightforward in short peptides, its application to globular protein must assume an unfolded and β-sheet refolded state. Recently, however, in heat-induced β-lactoglobulin fibrils, it has been shown convincingly by SDS-PAGE electrophoresis and MALDI-TOF mass spectrometry, that fibrils obtained at pH 2 and 80 °C, are not formed by the entire, unfolded proteins, but rather by smaller fragments of hydrolyzed protein.[43,44] The hydrolysis of the protein into smaller peptidic fragments would be the consequence of low pH and high temperature necessary for fibrillation. Recent results for two globular proteins as diverse as lysozyme and β-lactoglobulin under high temperature and low pH conditions further support the role of hydrolysis in globular protein fibrillation and additionally expand the findings suggesting a possible universal common unfolding–fragmentation–fibrillation mechanism for amyloidosis in globular proteins in which hydrolyzed fragments play the central role.[45] Therefore, the first step of the generalized mechanism of formation of amyloid fibrils from globular proteins consists in refolding into protofilaments, organized in cross-β-sheets, either entire unfolded proteins or short peptide fragments, obtained by the hydrolysis of the monomeric proteins. The energy required to sustain fibrillation is spent either to unfold the protein or to unfold and hydrolyze it. Which one of the two routes is followed may depend on the specific protein and on the conditions followed to promote fibrillation.

Figure 1 summarizes the different steps found in protein fibrillation from the entire native proteins to the formation of protofilaments and the subsequent assembly of protofilamnts into final mature fibrils.

2.2. Assembly of Protofilaments into Mature Fibrils. The association of individual protofilaments into mature fibrils formation is a complex multistep process, which can be tackled by performing very precise analysis of different time snapshots during the kinetics of fibrillation, with all the complications associated with the inherent heterogeneities in the assembly process. Once again, β-lactoglobulin, for which the fibrillation kinetics has been sufficiently well unveiled by combining time snapshots of reciprocal space bulk techniques such as neutron and light scattering, with single molecule atomic force microscopy, offers a valuable system to gain an understanding of the complex physics of aggregation taking place.[36]

In the very early stages of the fibrillation (after 15 min of incubation at pH 2, 90 °C), the formation of very short structures in the size range of 20 nm can be resolved. These structures correspond to the oligomeric conformation of protofibrillar structures. The growing of these oligomers to longer structures is identified by detection of very small populations (around 10%) of short protofilaments with the lengths from 100 to 300 nm. With an increase of incubation time these protofilaments further increase into longer protofilaments with average contour lengths exceeding 500 nm (Figure 2a). An important characteristic of these protofilaments is that they do not yet exhibit height fluctuations on the AFM, and as such, they can be viewed as single-strand fibrils (e.g., fibrils composed by single protofilaments).

When the length of the protofilaments is sufficiently long (500–1000 nm), individual protofilaments are locally found to align perfectly to each other (see Figure 2a). The mechanism of this alignment of protofilaments upon approaching has been explained by liquid crystalline interactions.[46,47] When individual filaments approach due to concentration fluctuations, the local density increases and the liquid crystalline interactions are mediated by the second virial coefficient, proportional to $\approx L^2D$, with L the length and D the diameter of the protofilament. Therefore, these interactions are very long range, and they span an active range, which is comparable with the contour lengths of the protofilaments and which exceeds by several orders of

dx.doi.org/10.1021/ma202157h | Macromolecules 2012, 45, 1137–1150

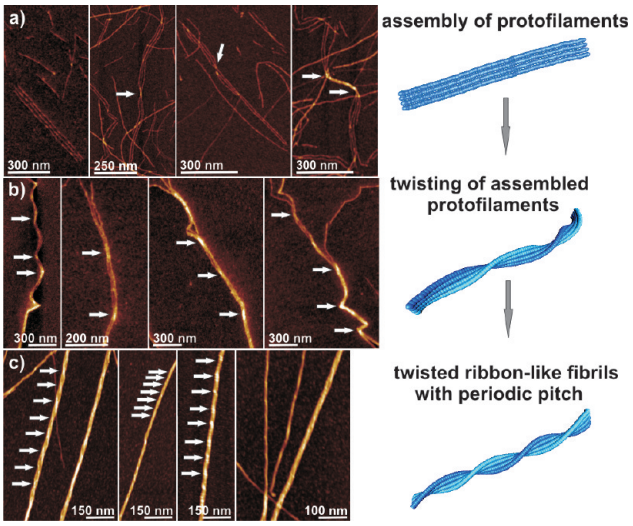


Figure 2. Set of AFM height images of heated β-lactoglobulin at pH 2 and 90 °C for the heating time of (a) 30 min, (b) 45 min, and (c) 5 h. Corresponding scheme of the assembly of protofilaments into mature fibrils of β-lactoglobulin.

magnitude the characteristic inter-protofilament distance observed for aligning protofilaments. In support of this hypothesis, there is a time-dependent development of birefringence revealing the development of liquid crystalline interactions and the widespread observation that protein fibrils with high flexibility do not exhibit multistranded nature; that is to say, they are usually formed by a single protofilament.[36] The relevance of liquid crystalline interactions in protein fibrils dispersion will be discussed in details later in this paper.

After protofilaments have aligned, they start to irreversibly aggregate and do touch at different points along the contour length (Figure 2a,b). This aggregation is observed despite the high linear charge density of the fibrils at pH 2 and without any screening of electrostatic repulsive interactions with additional salt. It has been postulated that nature of attraction inducing aggregation among likely charged protofilaments is of Lennard-Jones hydrophobic type,[35,36,47] but it has to be hoped that future works will conclusively determine the exact nature of this driving force toward aggregation.

During incubation time, the protofilaments, now aggregated into multistranded fibril precursors, undergo further structural changes. The white arrows in Figure 2a−c show the points at which the attached protofilaments cross over, as revealed by a change in the height as measured by AFM. As it can be immediately recognized, the amount of crossover points increases with incubation time, and from initially random locations along the contour length of the fibrils at the early stages (Figure 2a,b), with time they locate at well-defined positions, interspaced by a regular interval. This interval is the half-pitch of a mature fibril perfectly organized in a twisted ribbon conformation and is linearly proportional to the number of protofilaments forming the fibril. The linear proportionality of the pitch with the number of protofilaments has been predicted successfully by considering the dependence of the shear imposed by the twist at the periphery of the fibrils as a function of the number of protofilaments composing the fibrils and imposing a maximum affordable shear limited by the cohesive hydrogen-bonding energy of the fibrils.[35] More details on the cross section of the fibrils and how its geometry can be extracted from statistical polymer physics analysis and cross-sectional analysis of AFM single molecule images will be given later in this Perspective.

What is the driving force toward this observed twist? This is still a highly debated point, in which a consensus has not been yet achieved.

Some authors have suggested that twisting in the structures of amyloid fibrils results from entropic factors,[48] hydrophobic interactions,[49] or chirality.[42,50] In general, when chiral molecules assemble into fibrillar structures, chirality can be amplified and transferred to the entire supramolecular assembly, may these be rods, tapes, or tubes, which ultimately possess a right- or left-handedness with different values of chiral pitch.

In the final structural morphology of mature multistranded amyloid fibrils, handedness is indeed systematically observed. This can either be left- or right-handed, depending on the peptide composition, with a great majority being left-handed, as expected in biologically relevant fibrils which, with exception of glycine, are made exclusively of L-amino acid sequences (although exceptions and right-handed handness are also reported).[51−53] Indeed, a closer look to the model β-lactoglobulin fibrils reveals exclusively left-handed twisted ribbons. Therefore, the role of chirality is undeniable in the establishment of the final pitch, and indeed Aggeli et al.[42] have put together a pioneering model on how chirality-imposed twist and elastic energy result on well-defined pitches in amyloid fibrils. Figure 3a is a summary of the steps proposed by Aggeli et al.[42] by which the chirality of the primary β-strand constituent is transferred to the final mature amyloid fibrils made thereof, with the establishment of a defined pitch.

However, we have very recently demonstrated by performing single molecule AFM analysis on β-lactoglobulin fibrils that the periodic twisting pitch in protein amyloid fibrils can be finely tuned by exposing them, postformation, to varying ionic strengths.[54] With increasing ionic strengths, the pitch shows a continuous increase, which virtually reaches infinite values (e.g., completely untwisted fibrils) for high enough ionic strengths. These experimental finding were supported by a theoretical model in which the final pitch results by the minimization of the energy associated with the tilt of the cross section imposed by screened electrostatic interactions and the torsional elastic energy stored in the fibril.[54] Figure 3b reproduces the observed increase in the pitch for amyloid fibrils exposed at different ionic strengths and the theoretical prediction based on minimization of electrostatic and torsional elastic energy. The experimental data were fitted by eq 1:

$$Z_2 = Z_1\left[\left(\frac{\kappa_1}{\kappa_2}\right)^{1/2} + \frac{2^{3/2}\alpha_2}{4\pi}(\kappa_1 - \kappa_2){Z_1}^{3/2}\right]^{-2/3} \quad (1)$$

which is the theoretical prediction of the relationship between the periodicity of amyloid fibrils Z_2 at conditions of ionic strength 2 and corresponding Debye length ${\kappa_2}^{-1}$ as a function of the same quantities at ionic strength conditions 1, with α_2 a parameter depending on charge density, geometry, and rigidity of the fibrils.[54]

In view of the fact that most protein fibrils are charged and have an anisotropic cross section, these findings have a very high relevance and highlight the importance of electrostatic interactions in the establishment of the final pitch. We finally note that other effects may also play a role in the in formation of the amyloid fibril pitch. In the case of peptides, for example,

dx.doi.org/10.1021/ma202157h | Macromolecules 2012, 45, 1137−1150

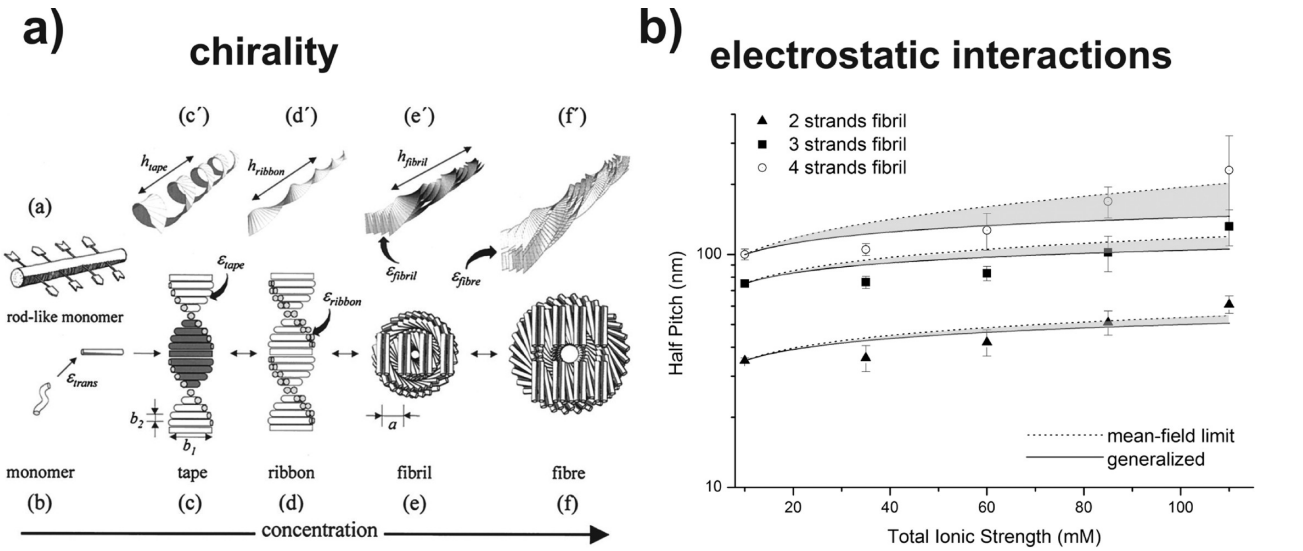


Figure 3. (a) Model of hierarchical self-assembly of chiral rodlike units, as proposed by Aggeli et al.[42] Local arrangements (c–f) and the corresponding global equilibrium conformations (c′–f′) for the hierarchical self-assembling structures formed in solutions of chiral molecules (a), which have complementary donor and acceptor groups, shown by mows, via which they interact and align to form tapes (c). The black and the white surfaces of the rod (a) are reflected in the sides of the helical tape (c) which is chosen to curl toward the black side (c′). The outer sides of the twisted ribbon (d), of the fibril (e), and of the fiber (f) are all white. One of the fibrils in the fiber (f′) is dram with darker shade for clarity. (e) and (f) show the front views of the edges of fibrils and fibers, respectively. (Reproduced with permission from ref 42. Copyright 2001 National Academy of Sciences, U.S.A.) (b) Fitting of the half-pitch versus total ionic strength of solution (NaCl concentration + pH 2 ions) by eq 1 for two, three and four-stranded β-lactoglobulin fibrils, using a classical Debye length, and the asymptotic generalized one, reveals the primary role of electrostatic interactions on the establishment of the final fibrils pitch. (Reproduced with permission from ref 54. Copyright 2011 The Royal Society of Chemistry.)

it has been shown that residue sequences differing only slightly may impose large changes in final periodicity which also supports the idea that twisting arise from a subtle ensemble of effects.[55]

To summarize this section, mature amyloid fibrils form via a complex growth and aggregation process. Current understanding of this process identifies three main critical steps: (i) when single protofilaments have reached a long enough contour length, they align on approaching, due to liquid crystalline interactions; (ii) attractive interactions of hydrophobic or Lennard-Jones nature overcome electrostatic repulsion among likewise charged protofilaments and lead to a merging of individual protofilments into multistranded fibrils precursors; (iii) the fibrils start to twist and develop with time a well-defined twisting pitch, whose handiness is settled by chirality and further amplified by electrostatic interactions.

3. STRUCTURE OF PROTEIN FIBRILS

Amyloid fibrils formed by more than one protofilament, that is to say, multistranded fibrils, can exhibit a wealth of different forms at length scales of the order of the cross section, and different packing of protofilaments can give rise to several distinct fibril morphologies and properties.[56−61] We discuss first how different packing schemes of the filaments can be identified experimentally and how this is reflected on the structure of the fibrils. In the following section we discuss the impact of different structures of the amyloid fibrils on their physical properties. Many techniques can be used to investigate the structural morphology of mature amyloid fibrils or the process of fibril formation over incubation time. The kinetics of formation is often followed by ThT analysis, but this technique being a bulk method does not allow revealing structural details at the single fibril length scales. NMR has been shown to be one of the most valuable techniques to yield information on amyloid fibril at the molecular length scales.[62−66]

From a soft condensed matter perspective, among bulk methods, scattering techniques provide a very powerful analysis.[67,36,37] Yet, the most revealing techniques to unravel the structural morphology of amyloid fibrils are undoubtedly transmission electron microscopy (TEM) techniques and atomic force microscopy (AFM). These techniques are capable to provide structural details at the single fibril length scale and via statistical analysis can yield averages over populations of hundreds to thousands of fibrils.

Beside the direct information provided in the real space on the structural conformations of amyloid fibrils, TEM, cryogenic TEM (cryo-TEM), and scanning transmission electron microscopy (STEM) can yield also other very valuable information, which are not accessible to other techniques, such as, for example the mass per unit length of amyloid fibrils. Then, if the exact peptidic sequence forming the amyloid fibrils is known, this quantity can be ideally exploited to identify and reconstruct topological models of the fibrils.[68,69] An example of how STEM and the mass per unit length can serve in the identification of twisted ribbons of Aβ(1−40) peptides is given in Figure 4.

AFM is another single-molecule technique which can provide a wealth of information about fibrils absorbed on a flat surface, but since this a surface technique, special care should be taken to discard possible surface-induced artifacts. This is however routinely done by comparing images generated on different surfaces, with a large choice of different substrates ranging from highly hydrophilic to superhydrophobic. Additionally, statistical analysis and modeling of fibrils conformations using a polymer physics approach require corrections for the apparent increased rigidity resulting from the absorption of three-dimensional objects on two-dimensional substrates. The most directly accessible significant topological details of the fibrils are the cross-sectional thickness of the fibril or the periodic pitch. Both properties are readily observable by measurements of the fibrils

dx.doi.org/10.1021/ma202157h | Macromolecules 2012, 45, 1137−1150

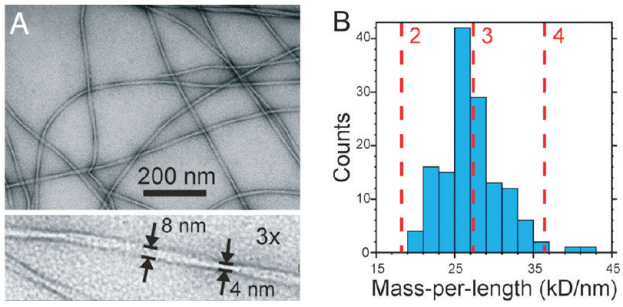


Figure 4. (A) Negatively stained TEM image of Aβ(1−40) fibrils, showing a periodically twisted morphology with apparent width modulation. (B) Mass-per-length histogram, as extracted from experimental STEM images, from which the presence of three strands composing the amyloid fibril can be deduced. (Reproduced with permission from ref 68. Copyright 2008 National Academy of Sciences, U.S.A.)

height profile and crossover distance along the contour length of the fibril (Figure 5). While the width of the fibrils obtained by AFM is usually a quantity depending on the geometry of cantilever, the height is a more relevant parameter (although values may be smaller than the real heights due to the interaction of the cantilever with fibrils during scanning) because these values do not depend on the geometry of cantilever since the force by which the cantilever is tapping is constant.

Seemingly a simple information about the fibrils, the height profile can provide crucial details on the fibril structure, as a first structural classification of amyloid fibrils can be carried out solely based on the evolution of the maximum height along the height profile. Height profiles such as that shown in Figure 5b for a double-stranded amyloid fibril yield the pitch, expressed as the periodic distance between every other maxima, and the difference between the maximum and minimum height. By comparing maximum, minimum height and the height of a single protofilament, important topological data can be extracted about the packing of the various protofilaments into fibrils. However, in case of the single protofilaments, with very small difference in maximum height, other approaches in the structural characterization of fibrils should be used.[70]

Two main packing mechanisms can be envisaged for a multistranded twisted fibril: a close-packed model (CP) and a ribbon-like packing model. We consider for both models the following parameters: the height of one protofilament (d) and the two orientations of fibrils with respect to the substrate which produce the maximum and minimum heights, h_{max} and h_{min}, respectively (Figure 6). It can easily be shown that for the

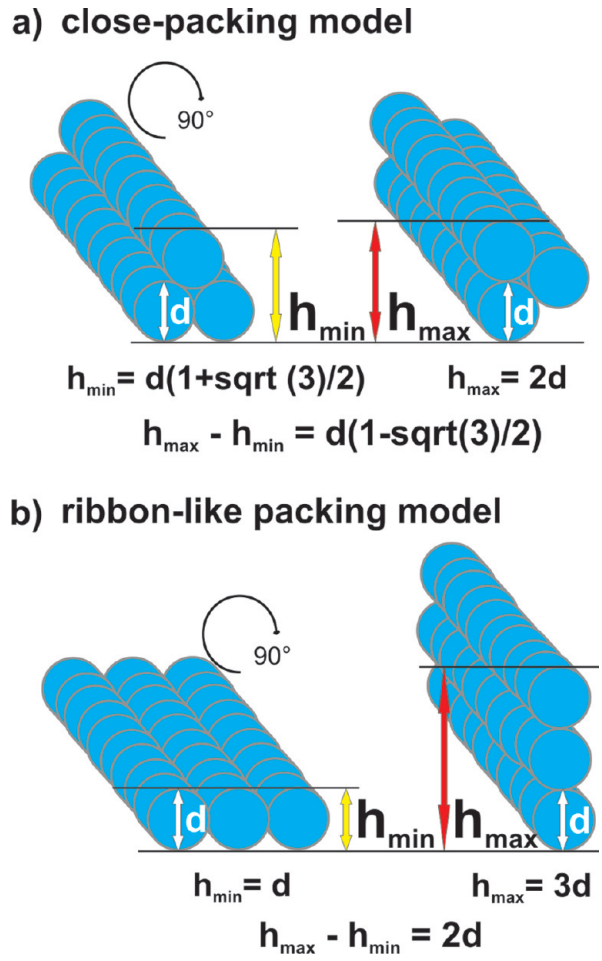


Figure 6. Scheme representing the observable differences in maximum and minimum heights from a three-stranded protein fibril with (a) closed-packed protofilaments and (b) ribbon-like packed protofilaments.

3-stranded fibril in close-packed configuration, $h_{max} - h_{min} = d(1 - \sqrt{3}/2)$, while for the 3-stranded fibril in ribbon conformation, $h_{max} - h_{min} = 2d$. Therefore, $h_{max} - h_{min}|_{ribbon} > h_{max} - h_{min}|_{CP}$. More in general, for a large enough number of protofilaments n ($n \rightarrow \infty$), it is straightforward to show

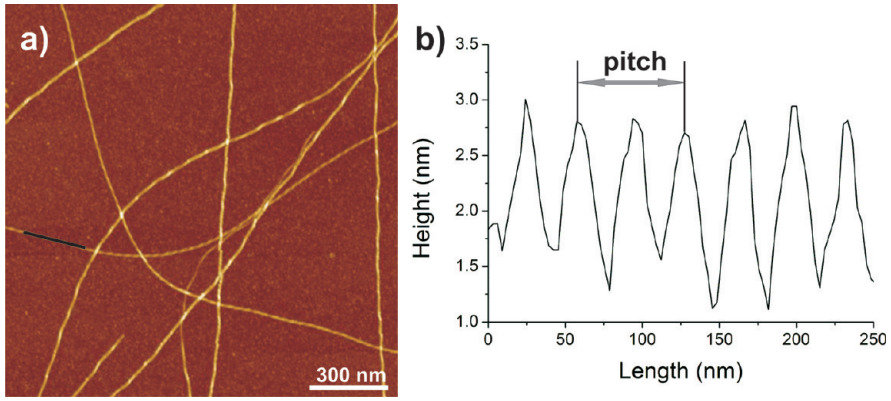


Figure 5. (a) AFM height image of β-lactoglobulin fibrils obtained after heating at pH 2 for 5 h at 90 °C and (b) corresponding height profile over contour length.

that $h_{max} - h_{min}|_{ribbon}$ = constant = $d(n - 1)$, while $h_{max} - h_{min}|_{CP} \rightarrow 0$ or, alternatively, that $h_{max}|_{CP} \rightarrow dn^{1/2}$ and that $h_{max}|_{ribbon} \rightarrow dn$. Thus, the determination of the difference between the maximum and minimum height in the height profile as a function of the number of filaments yields direct information on the packing scheme among protofilaments.

Once the packing of multiple filaments into a single fibril is accomplished, the same fibril may show several transient polymorphic states, such as twisted ribbons, helical ribbons, or nanotubes, and indeed, all these topologies have been reported in the literature.[71−78] For example, the transition of single protofilaments into multistranded twisted ribbon structures has been reported for β-lactoglobulin fibrils.[35] In the case of egg lysozyme hydrolyzed at very harsh conditions and long incubation times (90 °C, pH 2 for several days), the coexistence of both twisted and helical ribbons has also been reported.[45] This polymorphic transition is particular well observed for shorter peptide sequences. For example, the transition of twisted ribbons into the helical ribbons was observed, as a function of incubation time, for peptide amphiphiles containing three phenylalanine residues,[71] while in the case of the Aβ(16−22) fragment, the entire transition from single protofilament, to ribbons, to twisted ribbon, helical ribbon, and closed nanotubes was also resolved.[79] These results suggest the tendency of amyloid fibrils to convert from twisted ribbons to helical ribbons, while aggregation proceeds, and this mechanism might bear some generality, as its time-dependent polymorphic transition shows strong analogies with the aggregation of other surfactant systems.[74] Figure 7 summarizes the polymorphic evolution

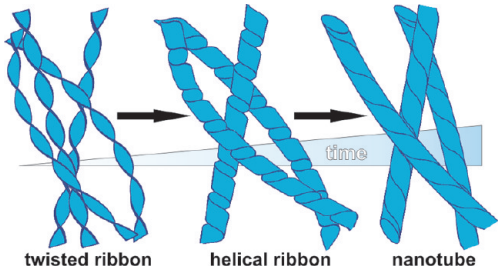


Figure 7. Scheme showing the time-dependent transformation of twisted ribbon to nanotubes through the helical ribbon intermediates.

observed upon incubation time for these three classes of amyloid fibrils.

What is the driving force for such a structural evolution? Although a conclusive answer has not yet been put together for amyloid fibrils, the work of Sawa et al.[80] on macroscopic nematic tapes might provide all the fundamental understanding necessary to unravel the twisted-helical ribbons transitions observed also on amyloids. Sawa et al. consider macroscopic tapes formed by twist nematic elastomers, in which the tendency to twist is provided by the nematic state of the tapes. This bears a direct similarity with the twist imposed to amyloid fibrils by the chirality of the amino acids. Sawa et al. find that a transition from a twisted to a helical ribbon occurs when a critical width-to-thickness ratio is reached. This results from the minimization of an energy tensor containing both in-plane elastic energy contributions (responsible for the twisting and stretching of the fibrils) and terms responsible for the out-of-plane energy of the fibrils (responsible for bending). When the width-to-thickness is small, fibrils are prone to be stretched rather than be bent and twisted ribbons, which have high Gaussian curvature but no bending, are energetically favored; when, on the other hand, the width-to-thickness is large, fibrils are easier to be bent rather than stretched, and helical ribbons are formed, which are characterized by high bending and low Gaussian curvatures, respectively. These findings seem to explain particularly well the fact that the transition from twisted ribbons to helical ribbon in amyloid fibrils is found at later stages of aggregation, when the width-to-thickness ratio has reached a sufficiently high value. More generally speaking, the chirality-induced twisted-to-helical transition mechanism may have a general validity, as even macroscopic objects as large as seed pods have been shown to follow this structural transition while opening.[81]

Once again, direct insight into the exact polymorphic state of the amyloid fibrils can be gained either by cryoTEM or via the height profile on AFM analysis. Figure 8a shows the typical

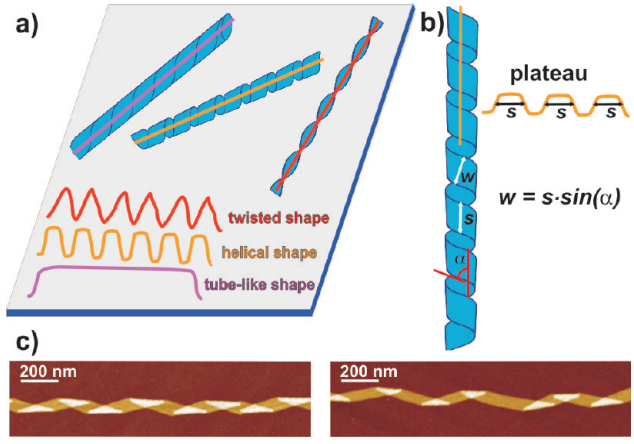


Figure 8. (a) Schematic of the characteristic height profile of twisted ribbons, helical ribbons, and nanotube structures adsorbed on a flat surface. The height profile of twisted ribbons has a sharp "zigzag" shape with sharp maxima, the height profile of helical ribbons has plateau maxima, and the height profile of nanotube shows flat, constant values. (b) Estimation of the width of helical ribbons using the height profile with a plateau of width s, where s is related to the real width of the ribbon w by $w = s \sin(\alpha)$, α being the tilt angle of the helical ribbon edges with respect to the fibril axis. (c) AFM height images of multistranded helical ribbon fibrils of lysozyme obtained after heating at pH 2 for 30 h at 90 °C and fully adsorbed on the substrate.

profiles for the three main polymorphic states of twisted ribbons, helical ribbons, and nanotubes. For the twisted ribbons the height profile has a typical "zigzag" shape with sharp maxima. When twisted ribbons transforms into helical ribbons the height profile has no longer sharp maxima but rather plateau maxima of width s, where s is related to the real width of the ribbon w by $w = s \sin(\alpha)$ and α is the tilt angle of the helical ribbon edges with respect to the fibril axis (Figure 8b). Finally, when the helical ribbons close forming nanotube-like structures, the height profile does not show any fluctuation but rather a constant plateau. Figure 8c show a typical example of AFM images of multistranded helical ribbon of lysozyme fully adsorbed on flat surface.

The other important structural parameter which can be directly extracted from AFM images is the estimation of their contour length L. Based on the measurements of L, the effects of many parameters on fibril formation have been explored. For example, the following parameters have been shown to affect

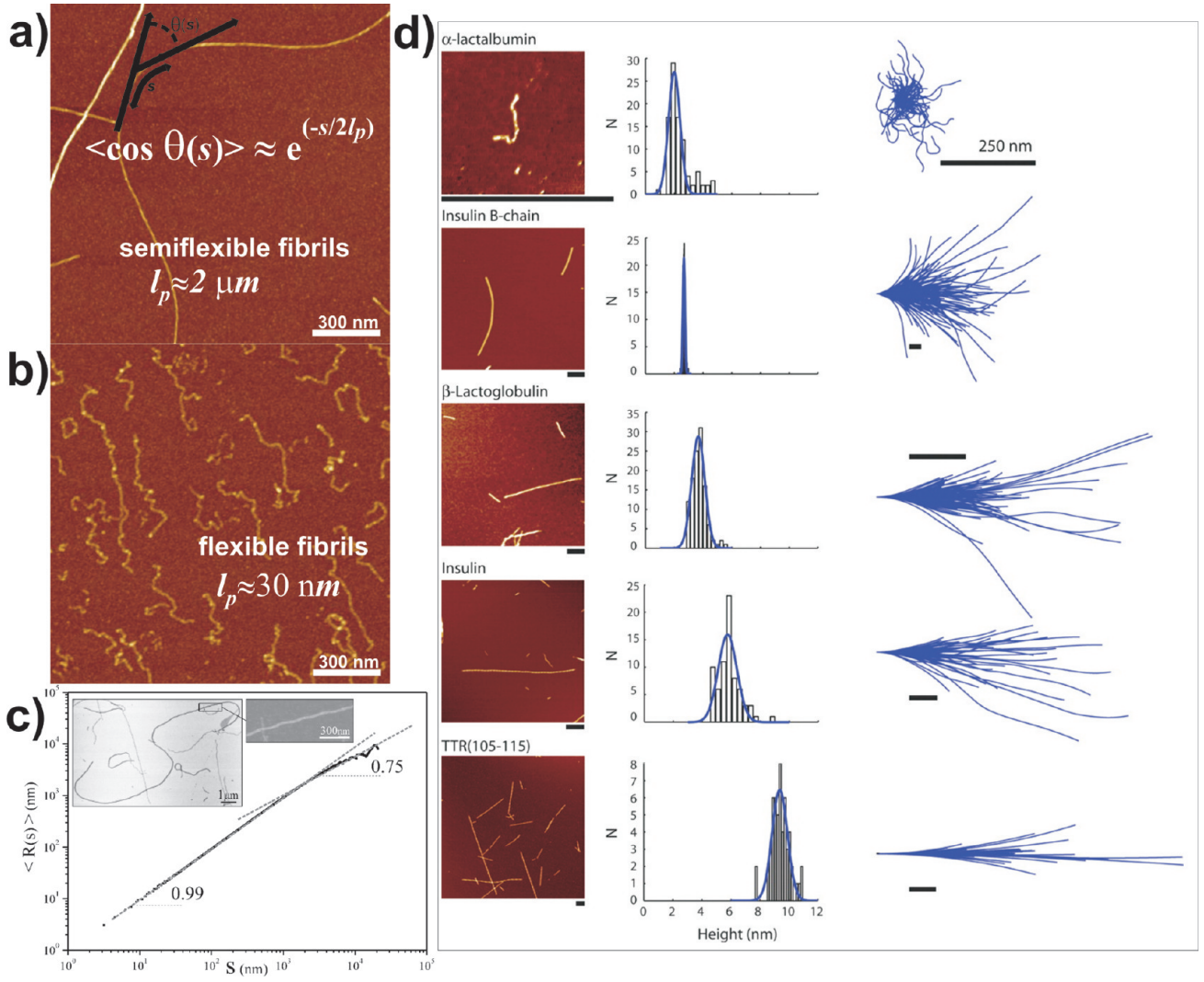


Figure 9. (a) AFM height image of β-lactoglobulin fibrils obtained after heating at pH 2 for 5 h at 90 °C representing semiflexible fibrils and schematic presentation of the estimation of the persistence length using the bond correlation function. (b) AFM height image of β-lactoglobulin fibrils after heating at pH 2 for 5 h, followed by incubation in 50% ethanol solution for 8 weeks, yielding highly flexible wormlike fibrils. (c) Mean internal end-to-end distance $\langle R(s)\rangle$ versus contour length s for lysozyme amyloid fibrils. The AFM height images of a representative lysozyme amyloid fibril are shown as high-magnification insets. (Reproduced with permission from ref 91. Copyright 2011 American Institute of Physics.) (d) Visual representation of the correlation between rigidity and diameter of amyloid fibrils (Reproduced with permission from ref 93. Copyright 2007 AAAS.) From top to bottom the protein considered are α-lactalbumin, insulin B-chain, β-lactoglobulin, insulin, and TTR(105−115). Left column: AFM images; central column: AFM height histograms; right column: amyloid fibrils from each individual protein family translated and rotated to start from a common origin and tangent. The increasing rigidity of the fibrils correlates directly with the increasing diameter of each fibril family.

the final contour length of fibrils: the shearing or stirring during fibrils formation,[82] the interaction of fibrils with charged polymer,[83] and the treatment of fibrils by sonication.[84,85]

4. PHYSICAL PROPERTIES OF PROTEIN FIBRILS

The studies on the physical properties of the amyloid fibrils have shown that fibrils exhibit remarkable mechanical properties, including high elasticity, stiffness, and resistance, with strengths comparable with other biological materials and Young's moduli E on the order of several GPa.[86] For example, insulin has been shown to possess a Young's modulus E of 3.3 ± 0.4 GPa and a tensile strength in the range 0.1−1 GPa.[87] These values are comparable to the most rigid proteinaceous materials found in nature, such as silk for example. Silk and amyloid fibrils share several similarities, such as the transition from a partially unstructured state into stable β-sheet-rich structures, the binding to Congo red and ThT, and comparable diameter of fibrils; these analogies have been considered in the literature, leading to the suggestion that amyloid fibrils and silk fibrils might represent structural subclasses of protein fibrils with a common structural core.[88]

A very convenient quantity to classify amyloid fibrils by their rigidity or flexibility is the persistence length l_p, which is the typical length at which thermal fluctuations begin to bend the polymer in different directions. A straightforward indication of the flexibility of the fibrils can be gained by comparison of contour and persistence lengths, L and l_p. A fibril is considered to be flexible when $l_p \ll L$ and rigid when the opposite holds ($l_p \gg L$).[89] The persistence length l_p can be determined directly from either AFM or cryoTEM images. In the case of AFM images, l_p can be extracted via the bond correlation function for semiflexible polymers in 2D conformations:

$$\langle \cos \theta(s) \rangle = \exp(-s/2l_p) \quad (2)$$

dx.doi.org/10.1021/ma202157h | Macromolecules 2012, 45, 1137−1150

where θ is the angle between the tangent vectors to the chain at two points separated by a contour distance s (see Figure 9a) and the factor 2 is used to rescale the exponential decay accounting for the two-dimensional nature of fibrils absorbed on a substrate.[90]

Because amyloid fibrils share many similarities with polymers, an alternative powerful way to describe fibrils flexibility is by mapping the length scales at which transitions in the scaling exponents describing the fibrils occur. This approach has been recently followed to probe lysozyme amyloid fibrils flexibility: at low length scale a scaling exponent of 1 is found, in agreement with rigid-rod-like behavior; at length scales larger than the persistence length, however, the fibrils are described by a scaling exponent of 3/4, in agreement with self-avoiding random walk (SAW) behavior in two dimensions (Figure 9c).[91]

Independently from the way by which it is determined, the persistence length encodes simultaneously the two main sources of rigidity of a fibril, that is, the intrinsic stiffness of the fibril and the geometry of its cross section, correlated by the following simple relation:[92]

$$l_p = EI/k_BT \tag{3}$$

where E is the Young's modulus of the fibril, I is the area moment of inertia of the fibril cross section, k_B is the Boltzmann constant, and T is the temperature. While E depends directly on the specific peptide sequence by which the individual protofilaments of the amyloid fibrils are formed, I depends on the form and the dimensions of the fibril cross section. In general, larger cross sections lead to large I and large persistence length. A very insightful correlation between the radius of the cross section of different amyloid fibrils and their persistence length is offered in the work of Knowles et al.,[93] where a visual representation of the persistence length is correlated to the AFM height of the fibrils or, in other words, the average diameter of their cross section, as shown in Figure 9d. From top to bottom of Figure 9d, the AFM images (left column) of α-lactalbumin, insulin B-chain, β-lactoglobulin, insulin, and TTR(105−115) are shown together with the corresponding height histogram (central column). The right column shows a visual representation of the rigidity of the fibrils, in which different fibrils of the same family have simply been translated and rotated to start with a chain end from a common origin and tangent. Although intrinsic differences in rigidity of fibrils can arise be from different Young moduli specific of the different peptidic sequences considered, the increasing stiffness of the fibrils correlates very well with the increasing diameter of the fibrils and thus with the increasing area moment of inertia, as would be expected from eq 3.

More in general, however, the sole diameter of the amyloid fibrils may not be sufficient in most of the cases to establish a first rational on the stiffness of the fibrils. Indeed, as already discussed, amyloid fibrils are often composed by a multitude of protofilaments. In the common case of fibrils constituted from several protofilaments, the area moment of inertia I depends more specifically on the packing geometry of individual protofilaments in mature fibrils (and the number of protofilaments n). Figure 10 illustrates the impact of different packing schemes of protofilaments on the persistence length of protein fibrils. It can be easily shown that for a large but constant number of protofilaments n of radius r_0 and Young's modulus E, and by neglecting lower power terms in n, the persistence length scales with the number of protofilaments as $l_p \sim nr_0^4E/k_BT$ for ribbon-like packing, $l_p \sim n^2r_0^4E/k_BT$ for close-packing, and $l_p \sim n^3r_0^4E/k_BT$ for nanotube-like packing. Therefore, for the same number of protofilaments, the ribbon-like assembly

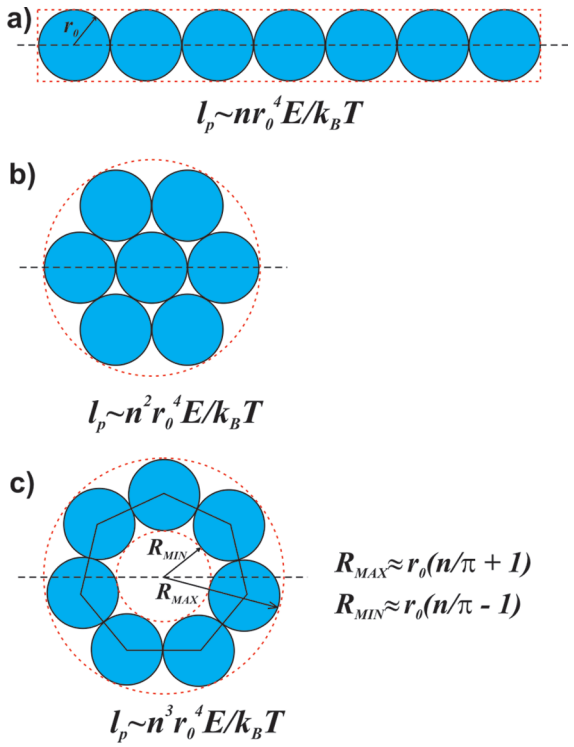


Figure 10. Possible cross sections resulting from the assembly of n (n = 7 in the case of the figure) protofilaments into a mature amyloid fibril. The different assembly schemes lead to a different area moment of inertia and therefore to differences in the persistence length. (a) Ribbon-like packing, leading to a scaling of the persistence length with n: $l_p \sim nr_0^4E/k_BT$; (b) close-packing: $l_p \sim n^2r_0^4E/k_BT$; (c) nanotube-like packing: $l_p \sim n^3r_0^4E/k_BT$. The black dashed lines represent the bending plane for the calculation of I and l_p.

yields the most flexible fibrils ($\sim n$), followed by close-packing assembly ($\sim n^2$), while the nanotube assembly yields the most rigid fibrils ($\sim n^3$). Such a scaling behavior of the persistence length versus the number of protofilaments has been already exploited in the past to resolve the exact packing scheme in multistranded amyloid fibrils.[35] Furthermore, once the exact packing scheme of the different protofilaments within the same amyloid fibrils is established, the above approach can also lead to the precise estimation of the Young's modulus of the individual protofilaments and thus of the amyloid fibril. Indeed, for a given packing scheme, the exact function relating the persistence length and the number of protofilaments, $l_p(n) = EI(n)/k_BT$, is a known expression. If the values of the persistence length, $l_p(n)$, are measured or determined for various populations of fibrils corresponding to different n, for example by using eq 1, the observed values of the persistence length $l_p(n)$ can be fitted by $l_p(n) = EI(n)/k_BT$ in which the only unknown, E, can be extracted by simple linear regression. Very recently, this approach has been successfully employed to determine the Young's modulus of β-lactoglobulin fibrils, for which the packing schemes of the protofilaments is now well-established,[35] and the values of E extracted by this procedure have been benchmarked to those measured by a new AFM tapping mode, called peak-force quantitative nano mechanical (PFQNM), showing a very good agreement.[94]

The approach discussed above requires the exact determination of the cross section of the amyloid fibrils and the known evolution of the persistence length with the number of filaments, which can both be extracted by statistical analysis of AFM

dx.doi.org/10.1021/ma202157h | Macromolecules 2012, 45, 1137−1150

images. More in general, however, AFM has emerged as one of the most suitable techniques for quantitative measurements of local elasticity of fibrils due to the individual single molecule imaging possibilities. The probing of mechanical properties of fibrils can be performed by using AFM to carry out indentation measurements with high lateral resolution: by using this method, a value of 19 GPa has been determined for the Young's modulus of phenylalanine fibrils.[95] However, for fibrils with small diameters of only a few nanometers the applicability of this method becomes challenging. Therefore, alternative methods to probe mechanical properties have been considered and applied.

The statistical analysis of fluctuations of the fibrils shape can be efficiently used to measure mechanical properties.[93] This approach is advantageous over direct mechanical probing because shape fluctuations are evaluated on accessible length scales and the knowledge of the size or shape of the AFM tip is not required to interpret the measured data. This approach is powerful and the analysis based on it has been successfully carried out for different amyloid fibril systems yielding values of E in the range 0.2−14 GPa.[93] This analysis has also suggested that the protofibrillar structures could be less ordered forms of amyloid structures, with a lower intrinsic value of E compared to mature amyloid fibrils.[93] Further detailed analysis of the shape fluctuations of protofibrillar structures indicated the existence of heterogeneous populations within the same species.[69] These findings have been successfully benchmarked to atomistic simulations, which have also shown a similar range of E values.[96,97]

What makes the fibrils so stable? Buehler and co-workers have performed very precise theoretical work to show that the strong ordering of weak hydrogen bonds is a key point for the mechanical properties of amyloid fibrils.[98,99] Recently, by using atomistic simulations, it has been found that the geometrical confinement of β-sheet in nanocrystals also results in the enhancement of the mechanical properties of fibrils.[96] These results suggest that the hydrogen bonds between β-sheet layers act as a chemical glue between the layers increasing the mechanical stability of fibrils. The structure of β-sheet is amino acid-dependent; consequently, amino acids mutation also affects the mechanical properties of amyloid fibrils.[100] This is in agreement with other experimental work where it has been shown that the important parameters encoding the intrinsic mechanical strength of amyloid fibril are the intermolecular forces between β-sheet layers.[93]

In addition, it has also been shown by studies on the failure mechanisms of amyloid fibrils under tensile loading that the amyloid fibrils ultimate strength is strongly length dependent, with amyloid fibrils with longer contour lengths becoming increasingly weak and brittle compared to shorter fibrils.[101]

Taking together these results, it is possible conclude that the mechanical properties of amyloid fibrils are dependent on a number of crucial features, including the peptide amino sequence, the way peptides assembly into protofilaments, the exact packing of protofilaments within single mature fibrils, and the contour length of the fibrils. The resulting physical properties of single amyloid fibrils ultimately determine their ensemble features and condition to a great extent their collective physical behavior and characteristics. In what follows, we therefore briefly touch on the collective colloidal behavior of amyloid fibrils in water.

5. PHASE BEHAVIOR OF PROTEIN FIBRILS IN WATER

As protein fibrils are typically semiflexible colloidal objects with a linear charge density depending on both the peptide sequence by which they are formed and the solution pH, it is natural to expect a complex phase behavior in water. Differently from ordinary colloidal particles, however, the study of the phase behavior of protein fibrils requires a number of additional precautions and extra steps to be taken into account. In practice, protein fibrils are generated *in vitro* only within a narrow window of concentrations: at too low concentrations, fibrillation may be hindered, while at high enough concentrations, fibrillation may start to coexist with other types of nonfibrillar irreversible aggregates, such as spherulites.[102,103] As a result, in order to explore regions of the phase diagram larger than those imposed by the concentration of the pristine fibrils preparation solution, the initial suspension from which they are produced needs to be adjusted in concentration by either diluting, which is straightforward, or by concentrating the solution, the last step requiring simultaneous evaporation of the solvent and readjustement of pH and ionic strength. Only such an experimental protocol allows the study of the true phase behavior of protein fibrils in which the topological characteristics of the individual fibrils are not (greatly) affected, that is to say, to keep them as constant as possible when moving from a region of the phase diagram to another. A typical phase diagram generated following such a protocol is shown in Figure 11 for β-lactoglobulin

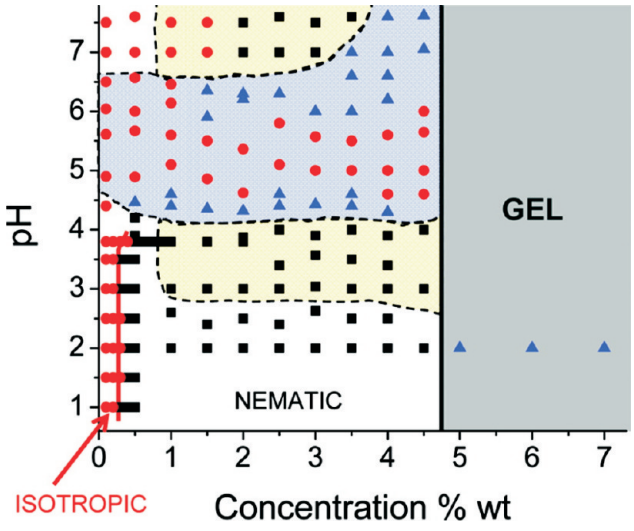


Figure 11. Phase diagram of β-lactoglobulin fibrils in water expressed as pH versus suspension concentration. Colors within the phase diagram identify regions as such: white is single-phase region; blue is two-phase regions; yellow is translucent region (aggregating dispersions which do not precipitate); gray identifies gel regions. The boundary of the sol−gel region is an extrapolation from pH 2 values only. (Reproduced from ref 47. Copyright 2010 American Chemical Society.)

fibrils.[47] As it can be recognized, at low enough concentration (e.g., below 5%), the solution is liquid and can flow, whereas beyond this concentration, fibrils start to irreversibly gel. The liquid region of the phase diagram is further divided into two main regions: a region of pH depicted in blue in Figure 11, which is centered around the isoelectric point of the β-lactoglobulin (pI = 5.1) and which indicates the precipitation of the fibrils due to the vanishing linear charge density at pH ≈ pI (or simply the tendency to aggregate in the yellow neighboring region for close enough pH and pI but with pH ≠ pI) and two regions of pH versus concentration depicted in white for pH > 6.5 and pH < 3, in which the fibrils are characterized by high enough linear charge density (positive for pH < 3 and

dx.doi.org/10.1021/ma202157h | *Macromolecules* 2012, 45, 1137−1150

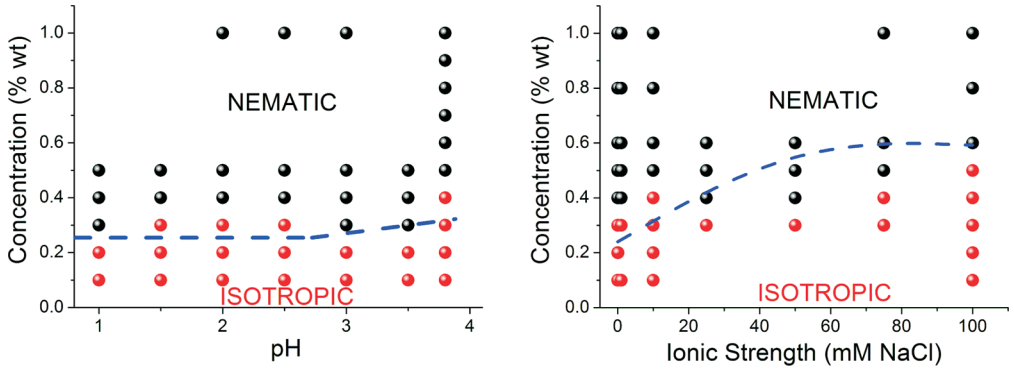


Figure 12. Isotropic–nematic transition in amyloid fibrils suspensions in water of varying pH (left) and ionic strengths (right). Black symbols identify nematic and red dots isotropic phase. The dashed blue line is the prediction of the isotropic–nematic transition using a modified Onsager theory (eq 7). (Readapted from ref 46.)

negative for pH > 6.5) to maintain a truly well-dispersed colloidal suspension of individual particles.

One of the most attractive features of this phase diagram is that the single-phase regions are further divided into an isotropic region at low concentration and a nematic phase beyond a concentration threshold which varies with pH (0.3 wt % at pH 2 and 2 wt % at pH 7). This is a feature which protein fibrils share with other rigid semiflexible biocolloidal objects: the mesoscopic features of tobacco mosaic virus[104−106] or nanocellulose[107] fibrils, for example, have been already investigated in detail. It is worth mentioning that in the case of amyloid fibrils the isotropic–nematic transition has been reported also for fibrils made by other types of proteins else than β-lactoglobulin, such as for example lysozyme[108,109] or lower molecular weight peptides.[110,111]

Attempts have been made in the past few years to rationalize the liquid crystalline behavior observed in amyloid fibrils suspensions,[47,112] but only recently, the isotropic–nematic transition in amyloid fibrils has been correctly interpreted and predicted by means of a modified Onsager theory, which accounts for the double-layer charge effects of the amyloid fibrils, their tendency to aggregate into larger bundles, and their semiflexible nature.[46]

Based on the Onsager theory, and taking as a first approximation the fibrils as fully rigid, the isotropic–nematic transition of a suspension of fibrils of diameter D and length L (the volume of a fibril is $(\pi/4)D^2L$) can be expected when the interaction among the fibrils, expressed by the second virial coefficient B_2^{iso} times their concentration, ρ, reaches a critical value[113] c^*:

$$c^* = B_2^{iso}\rho \tag{4}$$

Since the excluded volume in the nematic phase corresponds to the volume spanned by a free rotating rigid fibril polarized parallel to the nematic director, one can take in eq 4 $B_2^{iso} = (\pi/4)D_{eff}L^2$, and $\rho = N/V$ for the number density of N fibrils dispersed in a volume V. D_{eff} is larger than the geometrical D in the excluded volume to account for the double-layer electrostatic interactions associated with the linear charge density of the fibrils and is expressed as[113]

$$D_{eff} = D + k^{-1}\left(\ln A + C + \ln 2 - \frac{1}{2}\right) \tag{5}$$

with k^{-1} the Debye length, C Euler's constant, and A calculated by the following:[114]

$$A = 2\pi\nu_{eff}^2 k^{-1} Q \exp(-kD) \tag{6}$$

with ν_{eff} standing for the linear charge density and Q the Bjerrum length (≈0.7 nm in water at room temperature). By assembling everything into eq 4, it can be shown that the isotropic–nematic transition is reached at a fibrils volume fraction Φ_{IN}:[46]

$$\Phi_{IN} = c^*\frac{D^2}{D_{eff}L} \tag{7}$$

The final modification that eq 7 requires in order to become feasible for the prediction of the isotropic–nematic transition of protein fibrils is the replacement of the contour length L with the fibrils persistence length L_p, a change first proposed by Khokhlov and Semenov[115] to account for the semiflexible nature of colloidal objects and, at strong ionic strengths, a possible rescaling of D_{eff} to account for fibril aggregation.[46] Then, as soon the ionic strength of the medium and the linear charge density are known, the isotropic–nematic transition of protein fibrils can be predicted.

Figure 12 shows the comparison between the experimental isotropic–nematic transitions and those predicted as discussed above for β-lactoglobulin fibrils, when D_{eff} is altered by both means of either ionic strength or pH.[46] Increase in pH from below the pI of the fibrils has the effect of slightly decreasing the linear charge density and, thus, to decrease logarithmically D_{eff}. Increases in ionic strengths reduce the Debye length and thus also decrease D_{eff}. In both cases, the modified Onsager approach captures well the mild and stronger delay of the isotropic–nematic transition observed with increasing pH and ionic strength, respectively, as expected on the basis of the $\Phi_{IN} \sim (D_{eff})^{-1}$ behavior predicted by the excluded volume interactions.

6. CONCLUSIONS AND OUTLOOK: HIGH PERFORMANCE MATERIALS BASED ON PROTEIN FIBRILS

The very precise characterization of structural and mechanical properties of amyloid fibrils is an essential step toward our understanding of these systems in the context of not only biology and medicine but also nanotechnology and advanced biomaterials applications. The physicochemical and mechanical properties of amyloid fibrils can be tailored by modulating the amino acid sequence when synthetic peptide sequences can be used or using the different available experimental parameters such as pH, temperature, ionic strength, solvents, and pressure in the case of globular proteins.[16,116−118] Amyloid fibrils

dx.doi.org/10.1021/ma202157h | Macromolecules 2012, 45, 1137−1150

assembled from a wide range of different proteins and peptides have unique properties such as the resistance against enzymes, the ease of production, low cost, and biocompatibility. This unique combination of highly desirable features has now been recognized, and it is already forging the perception of materials scientists, which are increasingly realizing the potential of amyloid fibrils in advanced materials or high technology applications. Their ability to form highly ordered and light structures with remarkable mechanical properties, including high elasticity and strength, make them excellent candidates for the fabrication of new biomimetic materials.[119−121] Thus, the assembly of proteins into amyloid fibrils can help to create well-ordered and strong materials with suitable physical properties.[122]

Amyloid fibrils have been already used as a bioactive matrix for tissue engineering and regeneration[123] or as a novel type of carriers in drug delivery applications.[124] In food science and technology, amyloid fibrils have been shown to be efficient gelling agents[125] and outstanding interfacial stabilizers.[126,127] Hydrogels have also been successfully realized out of amyloid fibrils,[128] and by further combining protein fibrils with thermoresponsive polymers, hydrogels have been further engineered to flow at room temperature and to gel at body temperature, yielding promising injectable biocompatible scaffolds.[129] Organic−inorganic hybrids made of amyloid fibrils and metals have also been proposed for the design of metal nanowires and biomimicking self-assembled materials.[130−132] Recently, amyloid fibrils have even been used to generate materials which are at the same time printable, transparent, and twice as strong as Kevlar, showing great promise in the replacements of bulletproof glasses.[133] With only imagination as a limit in the use of proteins fibrils as a new generation of highly performing "macromolecular" building blocks, recent studies already demonstrate consistently that the ongoing change of perception of amyloid fibrils from bad to outstanding materials is more than justified and that many possibilities on the use of these systems in several aspects of life are still untouched and remain to be explored.

AUTHOR INFORMATION

Corresponding Author

*E-mail: raffaele.mezzenga@hest.ethz.ch.

Biographies



Jozef Adamcik received his master degree in Chemistry and doctoral degree in Biochemistry from P. J. Safarik University in Kosice in Slovakia. He was a postdoc at EPFL Lausanne in the Physics of Living Matter group from 2005 to 2009 working on the structural properties of DNA molecules investigated by atomic force microscopy. In December 2009 he moved to ETH Zurich in the Food and Soft Materials group. His research mainly focuses on the assembly of proteins and peptides into amyloid-like structures.



Raffaele Mezzenga received a PhD in polymer physics from EPFL Lausanne. He was a postdoc at University of California, Santa Barbara, in 2001−2002. He then moved to Nestlé Research Center to work on the self-assembly of surfactants, natural amphiphiles, and liquid crystals. In 2005, he was hired as Associate Professor in the Physics Department of the University of Fribourg, and he then joined ETH Zurich on 2009 as Full Professor. His research focuses on the fundamental understanding of self-assembly processes in polymers, liquid crystals, food, and biological colloidal systems. Prof. Mezzenga is recipient of several international awards such as the 2004 Swiss Science National Foundation Professorship Award, the 2011 Young Scientist Research Award (AOCS), and the 2011 John Dillon Medal (APS).

ACKNOWLEDGMENTS

The authors thank J. Flakowski for assistance with software graphics.

REFERENCES

(1) Dobson, C. M. *Nature* **2003**, *426*, 884−890.
(2) Selkoe, D. J. *Nature* **2003**, *426*, 900−904.
(3) Chiti, F.; Dobson, C. M. *Annu. Rev. Biochem.* **2006**, *75*, 333−366.
(4) Chiti, F.; Dobson, C. M. *Nat. Chem. Biol.* **2009**, *5*, 15−22.
(5) Mezzenga, R.; Schurtenberger, P.; Burbidge, A.; Michel, M. *Nature Mater.* **2005**, *4*, 729−740.
(6) Stradner, A.; Sedgwick, H.; Cardinaux, F.; Poon, W. C.; Egelhaaf, S. U.; Schurtenberger, P. *Nature* **2004**, *432*, 492−495.
(7) Wang, W.; Nema, S.; Teagarden, D. *Int. J. Pharm.* **2010**, *390*, 89−99.
(8) Nicolai, T.; Britten, M.; Schmitt, C. *Food Hydrocolloids* **2011**, *25*, 1945−1962.
(9) Stradner, A.; Foffi, G.; Dorsaz, N.; Thurston, G.; Schurtenberger, P. *Phys. Rev. Lett.* **2007**, *99*, 198103.
(10) Wang, Y.; Lomakin, A.; McManus, J. J.; Ogun, O.; Benedek, G. B. *Proc. Natl. Acad. Sci. U. S. A.* **2010**, *107*, 13282−13287.
(11) Caughey, B.; Lansbury, P. T. *Annu. Rev. Neurosci.* **2003**, *26*, 267−298.
(12) Taylor, J. P.; Hardy, J.; Fischbeck, K. H. *Science* **2002**, *296*, 1991−1995.
(13) Dobson, C. M. *Trends Biochem. Sci.* **1999**, *24*, 329−332.
(14) Murphy, R. M. *Annu. Rev. Biomed. Eng.* **2002**, *4*, 155−174.
(15) Lashuel, H. A.; Lansbury, P. T. Jr. *Q. Rev. Biophys.* **2006**, *39*, 167−201.
(16) Chiti, F.; Webster, P.; Taddei, N.; Clark, A.; Stefani, M.; Ramponi, G.; Dobson, C. M. *Proc. Natl. Acad. Sci. U. S. A.* **1999**, *96*, 3590−3594.

(17) Eisenberg, D.; Nelson, R.; Sawaya, M. R.; Balbirnie, M.; Sambashivan, S.; Ivanova, M. I.; Madsen, A. Ø.; Riekel, C. *Acc. Chem. Res.* **2006**, *39*, 568−575.
(18) Sunde, M.; Serpell, L. C.; Bartlam, M.; Fraser, P. E.; Pepys, M. B.; Blake, C. C. *J. Mol. Biol.* **1997**, *273*, 729−739.
(19) Nelson, R.; Sawaya, M. R.; Balbirnie, M.; Madsen, A. Ø.; Riekel, C.; Grothe, R.; Eisenberg, D. *Nature* **2005**, *435*, 773−778.
(20) Rochet, J. C.; Lansbury, P. T. Jr. *Curr. Opin. Struct. Biol.* **2000**, *10*, 60−68.
(21) Nelson, R.; Eisenberg, D. *Adv. Protein Chem.* **2006**, *73*, 235−282.
(22) Makin, O. S.; Atkins, E.; Sikorski, P.; Johansson, J.; Serpell, L. C. *Proc. Natl. Acad. Sci. U. S. A.* **2005**, *102*, 315−320.
(23) Chapman, M. R.; Robinson, L. S.; Pinkner, J. S.; Roth, R.; Heuser, J.; Hammar, M.; Normark, S.; Hultgren, S. J. *Science* **2002**, *295*, 851−855.
(24) Fowler, D. M.; Koulov, A. V.; Balch, W. E.; Kelly, J. W. *Trends Biochem. Sci.* **2007**, *32*, 217−224.
(25) Maji, S. K.; Perrin, M. H.; Sawaya, M. R.; Jessberger, S.; Vadodaria, K.; Rissman, R. A.; Singru, P. S.; Nilsson, K. P.; Simon, R.; Schubert, D.; Eisenberg, D.; Rivier, J.; Sawchenko, P.; Vale, W.; Riek, R. *Science* **2009**, *325*, 328−332.
(26) Greenwald, J.; Riek, R. *Structure* **2010**, *18*, 1244−1260.
(27) Shewmaker, F.; McGlinchey, R. P.; Wickner, R. B. *J. Biol. Chem.* **2011**, *286*, 16533−16540.
(28) Zhang, S. G. *Nature Biotechnol.* **2003**, *21*, 1171−1178.
(29) Holmes, T. C. *Trends Biotechnol.* **2002**, *20*, 16−21.
(30) Gazit, E. *Chem. Soc. Rev.* **2007**, *36*, 1263−1269.
(31) Barnhart, M. M.; Chapman, M. R. *Annu. Rev. Microbiol.* **2006**, *60*, 131−147.
(32) Hynes, R. O. *Science* **2009**, *326*, 1216−1219.
(33) Singh, P.; Carraher, C.; Schwarzbauer, J. E. *Annu. Rev. Cell. Dev. Biol.* **2010**, *26*, 397−419.
(34) Shoulders, M. D.; Raines, R. T. *Annu. Rev. Biochem.* **2009**, *78*, 929−958.
(35) Adamcik, J.; Jung, J. M.; Flakowski, J.; De Los Rios, P.; Dietler, G.; Mezzenga, R. *Nature Nanotechnol.* **2010**, *5*, 423−428.
(36) Bolisetty, S.; Adamcik, J.; Mezzenga, R. *Soft Matter* **2011**, *7*, 493−499.
(37) Jung, J. M.; Savin, G.; Pouzot, M.; Schmitt, C.; Mezzenga, R. *Biomacromolecules* **2008**, *9*, 2477−2486.
(38) Langton, M.; Hermansson, A. M. *Food Hydrocolloids* **1992**, *5*, 523−540.
(39) Uversky, V. N.; Fink, A. L. *Biochim. Biophys. Acta* **2004**, *1698*, 131−153.
(40) Bucciantini, M.; Giannoni, E.; Chiti, F.; Baroni, F.; Formigli, L.; Zurdo, J. S.; Taddei, N.; Ramponi, G.; Dobson, C. M.; Stefani, M. *Nature* **2002**, *416*, 507−511.
(41) MacPhee, C. E.; Dobson, C. M. *J. Mol. Biol.* **2000**, *297*, 1203−1215.
(42) Aggeli, A.; Nyrkova, I. A.; Bell, M.; Harding, R.; Carrick, L.; McLeish, T. C. B.; Semenov, A. N.; Boden, N. *Proc. Natl. Acad. Sci. U. S. A.* **2001**, *98*, 11857−11862.
(43) Oboroceanu, D.; Wang, L. Z.; Brodkorb, A.; Magner, E.; Auty, M. A. E. *J. Agric. Food Chem.* **2010**, *58*, 3667−3673.
(44) Akkermans, C.; Venema, P.; van der Goot, A. J.; Gruppen, H.; Bakx, E. J.; Boom, R. M.; van der Linden, E. *Biomacromolecules* **2008**, *9*, 1474−1479.
(45) Lara, C.; Adamcik, J.; Jordens, S.; Mezzenga, R. *Biomacromolecules* **2011**, *12*, 1868−1875.
(46) Mezzenga, R.; Jung, J. M.; Adamcik, J. *Langmuir* **2010**, *26*, 10401−10405.
(47) Jung, J. M.; Mezzenga, R. *Langmuir* **2010**, *26*, 504−514.
(48) Periole, X.; Rampioni, A.; Vendruscolo, M.; Mark, A. E. *J. Phys. Chem. B* **2009**, *113*, 1728−1737.
(49) van Gestel, J.; de Leeuw, S. W. *Biophys. J.* **2007**, *92*, 1157−1163.
(50) Nyrkova, I. A.; Semenov, A. N.; Aggeli, A.; Boden, N. *Eur. Phys. J. B* **2000**, *17*, 481−497.
(51) Rubin, N.; Perugia, E.; Goldschmidt, M.; Fridkin, M.; Addadi, L. *J. Am. Chem. Soc.* **2008**, *130*, 4602−4603.
(52) Koga, T.; Matsuoka, M.; Higashi, N. *J. Am. Chem. Soc.* **2005**, *127*, 17596−17597.
(53) Wadai, H.; Yamaguchi, K.; Takahashi, S.; Kanno, T.; Kawai, T.; Naiki, H.; Goto, Y. *Biochemistry* **2005**, *44*, 157−164.
(54) Adamcik, J.; Mezzenga, R. *Soft Matter* **2011**, *7*, 5437−5443.
(55) Nagarkar, R.; Hule, R. A.; Pochan, D. J.; Schneider, J. P. *J. Am. Chem. Soc.* **2008**, *130*, 4466−4474.
(56) Jimenez, J. L.; Nettleton, E. J.; Bouchard, M.; Robinson, C. V.; Dobson, C. M.; Saibil, H. R. *Proc. Natl. Acad. Sci. U. S. A.* **2002**, *99*, 9196−9201.
(57) Petkova, A. T.; Leapman, R. D.; Guo, Z. H.; Yau, W. M.; Mattson, M. P.; Tycko, R. *Science* **2005**, *307*, 262−265.
(58) Chamberlain, A. K.; MacPhee, C. E.; Zurdo, J.; Morozova-Roche, L. A.; Hill, H. A.; Dobson, C. M.; Davis, J. J. *Biophys. J.* **2000**, *79*, 3282−3293.
(59) Meinhardt, J.; Sachse, C.; Hortschansky, P.; Grigorieff, N.; Fändrich, M. *J. Mol. Biol.* **2009**, *386*, 869−877.
(60) Bauer, H. H.; Aebi, U.; Häner, M.; Hermann, R.; Müller, M.; Merkle, H. P. *J. Struct. Biol.* **1995**, *115*, 1−15.
(61) Jiménez, J. L.; Guijarro, J. I.; Orlova, E.; Zurdo, J.; Dobson, C. M.; Sunde, M.; Saibil, H. R. *EMBO J.* **1999**, *18*, 815−821.
(62) Petkova, A. T.; Ishii, Y.; Balbach, J. J.; Antzutkin, O. N.; Leapman, R. D.; Delaglio, F.; Tycko, R. *Proc. Natl. Acad. Sci. U. S. A.* **2002**, *99*, 16742−16747.
(63) Lührs, T.; Ritter, C.; Adrian, M.; Riek-Loher, D.; Bohrmann, B.; Döbeli, H.; Schubert, D.; Riek, R. *Proc. Natl. Acad. Sci. U. S. A.* **2005**, *102*, 17342−17347.
(64) Ritter, C.; Maddelein, M. L.; Siemer, A. B.; Lührs, T.; Ernst, M.; Meier, B. H.; Saupe, S. J.; Riek, R. *Nature* **2005**, *435*, 844−848.
(65) Luca, S.; Yau, W. M.; Leapman, R.; Tycko, R. *Biochemistry* **2007**, *46*, 13505−13522.
(66) Tycko, R. *Annu. Rev. Phys. Chem.* **2011**, *62*, 279−299.
(67) Aymard, P.; Nicolai, T.; Durand, D.; Clark, A. *Macromolecules* **1999**, *32*, 2542−2552.
(68) Paravastu, A. K.; Leapman, R. D.; Yau, W. M.; Tycko, R. *Proc. Natl. Acad. Sci. U. S. A.* **2008**, *105*, 18349−18354.
(69) Chen, B.; Thurber, K. R.; Shewmaker, F.; Wickner, R. B.; Tycko, R. *Proc. Natl. Acad. Sci. U. S. A.* **2009**, *106*, 14339−14344.
(70) Relini, A.; Torrassa, S.; Ferrando, R.; Rolandi, R.; Campioni, S.; Chiti, F.; Gliozzi, A. *Biophys. J.* **2010**, *98*, 1277−1284.
(71) Pashuck, E. T.; Stupp, S. I. *J. Am. Chem. Soc.* **2010**, *132*, 8819−8821.
(72) Lamm, M. S.; Rajagopal, K.; Schneider, J. P.; Pochan, D. J. *J. Am. Chem. Soc.* **2005**, *127*, 16692−16700.
(73) Lu, K.; Jacob, J.; Thiyagarajan, P.; Conticello, V. P.; Lynn, D. G. *J. Am. Chem. Soc.* **2003**, *125*, 6391−6393.
(74) Ziserman, L.; Lee, H. Y.; Raghavan, S. R.; Mor, A.; Danino, D. *J. Am. Chem. Soc.* **2011**, *133*, 2511−2517.
(75) Oda, R.; Artzner, F.; Laguerre, M.; Huc, I. *J. Am. Chem. Soc.* **2008**, *130*, 14705−14712.
(76) Castelletto, V.; Hamley, I. W.; Cenker, Ç.; Olsson, U.; Adamcik, J.; Mezzenga, R.; Miravet, J. F.; Escuder, B.; Rodríguez-Llansola, F. *J. Phys. Chem. B* **2011**, *115*, 2107−2116.
(77) Castelletto, V.; Hamley, I. W.; Cenker, C.; Olsson, U. *J. Phys. Chem. B* **2010**, *114*, 8002−8008.
(78) Castelletto, V.; Hamley, I. W.; Hule, R. A.; Pochan, D. *Angew. Chem., Int. Ed.* **2009**, *48*, 2317−2320.
(79) Adamcik, J.; Castelletto, V.; Bolisetty, S.; Hamley, I. W.; Mezzenga, R. *Angew. Chem., Int. Ed.* **2011**, *50*, 5495−5498.
(80) Sawa, Y.; Ye, F.; Urayama, K.; Takigawa, T.; Gimenez-Pinto, V.; Selinger, R. L.; Selinger, J. V. *Proc. Natl. Acad. Sci. U. S. A.* **2011**, *108*, 6364−6368.
(81) Armon, S.; Efrati, E.; Kupferman, R.; Sharon, E. *Science* **2011**, *333*, 1726−1730.
(82) Dunstan, D. E.; Hamilton-Brown, P.; Asimakis, P.; Ducker, W.; Bertolini, J. *Soft Matter* **2009**, *5*, 5020−5028.

(83) Rühs, P. A.; Adamcik, J.; Bolisetty, S.; Sánchez-Ferrer, A.; Mezzenga, R. *Soft Matter* **2011**, *7*, 3571−3579.
(84) Chatani, E.; Lee, Y. H.; Yagi, H.; Yoshimura, Y.; Naiki, H.; Goto, Y. *Proc. Natl. Acad. Sci. U. S. A.* **2009**, *106*, 11119−11124.
(85) Amar-Yuli, I.; Adamcik, J.; Lara, C.; Bolisetty, S.; Vallooran, J. J.; Mezzenga, R. *Soft Matter* **2011**, *7*, 3348−3357.
(86) Knowles, T. P.; Buehler, M. J. *Nature Nanotechnol.* **2011**, *6*, 469−479.
(87) Smith, J. F.; Knowles, T. P.; Dobson, C. M.; Macphee, C. E.; Welland, M. E. *Proc. Natl. Acad. Sci. U. S. A.* **2006**, *103*, 15806−15811.
(88) Slotta, U.; Hess, S.; Spiess, K.; Stromer, T.; Serpell, L.; Scheibel, T. *Macromol. Biosci.* **2007**, *7*, 183−188.
(89) Storm, C.; Pastore, J. J.; MacKintosh, F. C.; Lubensky, T. C.; Janmey, P. A. *Nature* **2005**, *435*, 191−194.
(90) Witz, G.; Rechendorff, K.; Adamcik, J.; Dietler, G. *Phys. Rev. Lett.* **2008**, *101*, 148103.
(91) Lara, C.; Usov, I.; Adamcik, J.; Mezzenga, R. *Phys. Rev. Lett.* **2011**, *107*, 238101.
(92) Manning, G. S. *Phys. Rev. A* **1986**, *34*, 4467.
(93) Knowles, T. P.; Fitzpatrick, A. W.; Meehan, S.; Mott, H. R.; Vendruscolo, M.; Dobson, C. M.; Welland, M. E. *Science* **2007**, *318*, 1900−1903.
(94) Adamcik, J.; Berquand, A.; Mezzenga, R. *Appl. Phys. Lett.* **2011**, *98*, 193701.
(95) Kol, N.; Adler-Abramovich, L.; Barlam, D.; Shneck, R. Z.; Gazit, E.; Rousso, I. *Nano Lett.* **2005**, *5*, 1343−1346.
(96) Paparcone, R.; Keten, S.; Buehler, M. J. *J. Biomech.* **2010**, *43*, 1196−1201.
(97) Xu, Z.; Paparcone, R.; Buehler, M. J. *Biophys. J.* **2010**, *98*, 2053−2062.
(98) Keten, S.; Buehler, M. J. *Nano Lett.* **2008**, *8*, 743−748.
(99) Keten, S.; Xu, Z.; Ihle, B.; Buehler, M. J. *Nature Mater.* **2010**, *9*, 359−367.
(100) Paparcone, R.; Pires, M. A.; Buehler, M. J. *Biochemistry* **2010**, *49*, 8967−8977.
(101) Paparcone, R.; Buehler, M. J. *Biomaterials* **2011**, *32*, 3367−3374.
(102) Krebs, M. R.; Domike, K. R.; Donald, A. M. *Biochem. Soc. Trans.* **2009**, *37*, 682−686.
(103) Domike, K. R.; Donald, A. M. *Biomacromolecules* **2007**, *8*, 3930−3937.
(104) Purdy, K. R.; Fraden, S. *Phys. Rev. E: Stat., Nonlinear, Soft Matter Phys.* **2004**, *70*, 061703.
(105) Adams, M.; Fraden, S. *Biophys. J.* **1998**, *74*, 669−677.
(106) Fraden, S.; Maret, G.; Caspar, D. L.; Meyer, R. B. *Phys. Rev. Lett.* **1989**, *63*, 2068−2071.
(107) Klemm, D.; Kramer, F.; Moritz, S.; Lindström, T.; Ankerfors, M.; Gray, D.; Dorris, A. *Angew. Chem., Int. Ed.* **2011**, *50*, 5438−5466.
(108) Muller, C.; Inganas, O. *J. Mater. Chem.* **2011**, *46*, 3687−3692.
(109) Corrigan, A. M.; Müller, C.; Krebs, M. R. *J. Am. Chem. Soc.* **2006**, *128*, 14740−14741.
(110) Hamley, I. W.; Castelletto, V.; Moulton, C. M.; Rodríguez-Pérez, J.; Squires, A. M.; Eralp, T.; Held, G.; Hicks, M. R.; Rodger, A. *J. Phys. Chem. B* **2010**, *114*, 8244−8254.
(111) Bucak, S.; Cenker, C.; Nasir, I.; Olsson, U.; Zackrisson, M. *Langmuir* **2009**, *25*, 4262−4265.
(112) Sagis, L. M.; Veerman, C.; van der Linden, E. *Langmuir* **2004**, *20*, 924−927.
(113) Vroege, G. J.; Lekkerkerker, H. N. W. *Rep. Prog. Phys.* **1992**, *55*, 1241−1309.
(114) Stroobants, A.; Lekkerkerker, H. N. W.; Odijk, Th. *Macromolecules* **1986**, *19*, 2232−2238.
(115) Khokhlov, A. R.; Semenov, A. N. *Phys. A (Amsterdam, Neth.)* **1981**, *108*, 546−556.
(116) Meersman, F.; Dobson, C. M. *Biochim. Biophys. Acta* **2006**, *1764*, 452−460.
(117) Zurdo, J.; Guijarro, J. I.; Dobson, C. M. *J. Am. Chem. Soc.* **2001**, *123*, 8141−8142.
(118) Jones, O. G.; Mezzenga, R. *Soft Matter* **2012**, DOI: 10.1039/C1SM06643A.
(119) Cherny, I.; Gazit, E. *Angew. Chem., Int. Ed.* **2008**, *47*, 4062−4069.
(120) Gras, S. L. *Adv. Chem. Eng.* **2009**, *35*, 161−209.
(121) Meier, C.; Welland, M. E. *Biomacromolecules* **2011**, *12*, 3453−3459.
(122) Buehler, M. J. *Nature Nanotechnol.* **2010**, *5*, 172−174.
(123) Holmes, T. C.; de Lacalle, S.; Su, X.; Liu, G.; Rich, A.; Zhang, S. *Proc. Natl. Acad. Sci. U. S. A.* **2000**, *97*, 6728−6733.
(124) Maji, S. K.; Schubert, D.; Rivier, C.; Lee, S.; Rivier, J. E.; Riek, R. *PLoS Biol.* **2008**, *6*, e17.
(125) Bolder, S. G.; Hendrickx, H.; Sagis, L. M. C.; van der Linden, E. *Appl. Rheol.* **2006**, *16*, 258−264.
(126) Jung, J. M.; Gunes, D. Z.; Mezzenga, R. *Langmuir* **2010**, *26*, 15366−15375.
(127) Isa, L.; Jung, J. M.; Mezzenga, R. *Soft Matter* **2011**, *7*, 8127−8134.
(128) Knowles, T. P.; Oppenheim, T. W.; Buell, A. K.; Chirgadze, D. Y.; Welland, M. E. *Nature Nanotechnol.* **2010**, *5*, 204−207.
(129) Li, C.; Alam, M. M.; Bolisetty, S.; Adamcik, J.; Mezzenga, R. *Chem. Commun.* **2011**, *47*, 2913−2915.
(130) Bolisetty, S.; Vallooran, J. J.; Adamcik, J.; Handschin, S.; Gramm, F.; Mezzenga, R. *J. Colloid Interface Sci.* **2011**, *361*, 90−96.
(131) Gazit, E. *FEBS J.* **2007**, *274*, 317−322.
(132) Reches, M.; Gazit, E. *Nature Nanotechnol* **2006**, *1*, 195−200.
(133) Adler-Abramovich, L.; Kol, N.; Yanai, I.; Barlam, D.; Shneck, R. Z.; Gazit, E.; Rousso, I. *Angew. Chem., Int. Ed.* **2010**, *49*, 9939−9942.

Macromolecules

ARTICLE

pubs.acs.org/Macromolecules

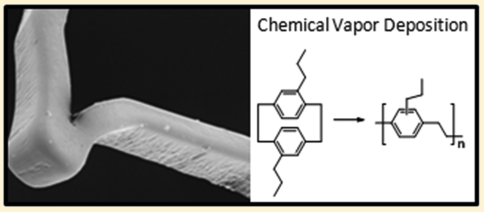
Synthesis, Structure, and Properties of Alkyl-Substituted PPXs by Chemical Vapor Deposition for Stent Coatings

Anna K. Bier, Michael Bognitzki, Jochen Mogk, and Andreas Greiner*

Fachbereich Chemie und Wissenschaftliches Zentrum für Materialwissenschaften, Philipps-Universität Marburg, Hans-Meerwein Strasse, D-35032 Marburg, Germany

Supporting Information

ABSTRACT: High-molecular-weight un-cross-linked poly(*p*-xylylene) (PPX) derivatives (**3**) with one lateral linear alkyl substituent (methyl−octyl) on each phenylene moiety were prepared by pyrolysis of corresponding paracyclophanes followed by chemical vapor deposition (CVD). Most of these PPX derivatives showed good solubility in organic solvents which allowed purification by reprecipitation, structural analysis by solution NMR techniques, and molecular weight analysis by gel permeation chromatography. High thermal stability of **3** was found by thermogravimetric analysis. The glass transition temperatures decreased systematically with increasing alkyl chain length from 53 to −23 °C. Increased elongation to break up to 380% was analyzed by stress−strain experiments for as-deposited films indicating excellent coating properties, which were proven by initial coating tests on stents.



INTRODUCTION

PPXs are of fundamental as well technical interest where they are used as coating materials for electronic or medical devices like stents or pacemakers due to their excellent barrier and insulation properties, biocompatibility, and biostability.[1] The combination of polymer synthesis and simultaneous film formation by vaporization, pyrolysis of [2.2]paracyclophanes, subsequent CVD, and polymerization of quinodimethanes under ambient conditions is unique.[2] As a result, conformal pinhole free coatings on nearly any solid substrate can be prepared.[1d] PPXs have found numerous applications as stent coatings, including drug eluting stents.[3] Although PPXs show very good performance as stent coatings, improvement of coating stability upon stent extension could be of major interest.

The properties of PPX, including its thermal and mechanical properties are governed by the substitution pattern. Unsubstituted PPX is crystalline with melting under decomposition at 420 °C. PPX is transparent and insoluble in any solvent below 220 °C and shows an elongation to break of 10−15%.[1] Only a limited number of CVD-based PPX derivatives are known. For example, PPXs with chlorine and bromine substituents at the phenylene moieties are known, which are partially crystalline and fusible. The elongation to break of the dichloro-substituted PPX amounts to 220%.[1] Only a few PPX derivatives with alkyl or phenyl substituents are known.[4,5] Methyl- and ethyl-substituted PPX were obtained by CVD as hardly soluble polymers from the corresponding [2.2]paracyclophanes. Poly(*n*-butyl-*p*-xylylene) was reported as a rubbery material with a crystallization point of 25 °C,[6] which could make such PPX promising materials for stent coating applications. The overall expectation is that the flexibility of the coatings would increase with increase in alkyl chain length combined with a drop of glass transition temperature and a loss in crystallinity. Increased solubility in organic solvents under ambient condition should allow structural proof by NMR and molecular weight and polydispersity analysis by GPC. Since the limited flexibility of stent coatings is a significant issue, it would be highly interesting to investigate alkyl-substituted PPX for such coating applications.

The aim of this work is to elaborate a versatile and highly efficient route to poly(*n*-alkyl-*p*-xylylene)s and to investigate the role of alkyl chain length of the substituent on the property profile of PPX. Further scope of this contribution is to gain an understanding of the process for achieving high molecular weights obtained by the PPX CVD route, which is not yet well developed. The concept used for achieving the aims was to synthesize poly(*n*-alkyl-*p*-xylylene)s by CVD using the corresponding di(*n*-alkyl)[2.2]paracyclophanes and to use linear alkyl substituents which do not omit the volatility of the [2.2]paracyclophanes. On the basis of this, we want to suggest suitable novel PPXs for stent coating applications based on initial coating tests.

EXPERIMENTAL SECTION

Materials. Diethyl ether was dried over phosphorus pentoxide; methanol (BASF), tetrahydrofuran (BASF), and chloroform (VWR) were distilled prior to use. 4,12-Dichloro[2.2]paracyclophane (**1**) was obtained by recrystallization of DPX C (Specialty Coating Systems) from 1,4-dioxane. Methyl iodide (Alfa Aesar, +98%), ethyl bromide (98%, Sigma-Aldrich), propyl bromide (99%, Sigma-Aldrich), butyl bromide (98%, VWR), pentyl bromide (99%, Sigma-Aldrich), hexyl bromide (99%, Sigma-Aldrich), heptyl bromide (99%, Sigma-Aldrich),

Received: October 10, 2011
Revised: November 14, 2011
Published: January 17, 2012

ACS Publications © 2012 American Chemical Society

octyl bromide (99%, Sigma-Aldrich), Ni(dppp)Cl_2 (Sigma-Aldrich and VWR), and magnesium turnings (≥99.9%, Carl Roth) were used as obtained.

Instrumentation. GC/MS measurements were done with a QP5050 A instrument from Shimadzu with a 30 m FS-SE-54-CB-0.25 column, electron ionization unit, and helium as carrier gas. A program from 100 to 280 °C with a heating rate of 10 °C and an additional 20 min at 280 °C was chosen. The injection temperature was 300 °C, and the interface temperature was maintained at 230 °C.

Elemental analysis was carried out on a Heraeus CHN-Rapid machine.

^{1}H (400 MHz), ^{13}C (100 MHz), HSQC, COSY, and HMBC spectra were recorded on a Bruker DRX 400, and ^{1}H (300 MHz) spectra were recorded on Bruker Advance 300 A at room temperature with $CDCl_3$ as solvent.

Thermogravimetric decomposition was analyzed by an 851 TG module from Mettler. In nitrogen atmosphere (flow rate: 50 mL/min) 10−12 mg of the sample was placed in an alumina crucible, which was heated to 800 °C with a rate of 10 °C/min.

For IR measurements an UMA 600 from Digilab with an ATR unit from Pike Miracle with diamond as top plate was used.

Analysis of average molecular weight and molecular weight distribution were done by GPC with chloroform and THF as eluent. For each measurement 5−10 mg of polymer (directly after pyrolysis) was dissolved in 10 mL of chloroform or THF with toluene as internal standard. For chloroform GPC the flow rate was 0.5 mL/min, and the setup included a Knauer Smartline 1000 pump, three SDV columns (pore size 1000, 100 000, 1 000 000 Å) from PSS, and a Knauer refractive index detector (RI 2300). Calibration was done versus linear PMMA purchased from PSS. THF GPC was equipped with two SDV columns (10 μm, 60 × 0.8 mm^2) from a PSS a triple detector array TDAmax 300 (RI was used); the working flow rate was 0.8 mL min^{-1}. Calibration was done versus polystyrene.

For DSC an 821 DSC module from Mettler calibrated with indium and zinc standards were used. 10−15 mg of the sample was placed into a sealed aluminum pan. In a nitrogen atmosphere (flow rate: 80 mL/min) a temperature program with a heating rate of 20 °C/min was applied. The glass transition temperature was taken as the inflection point of the observed shift of the baseline of the second heating cycle of the scan.

UV/vis measurements were performed with a Lambda 35 from Perkin-Elmer precisely.

WAXS was done with a powder diffractometer Panalytical X'Pert Pro PW3040/60 from Philips equipped with Cu Kα as a secondary monochromator.

Mechanical measurements were performed by a Zwick Roell BT-FR0.5TN.D14 equipped with a KAF-TC load sensor. The samples were prepared with a Rayran manual press with a dog-bone cutter ISO 5272-1BB.

For static contact angle measurements the Contact Angle Measurement System G10 from Krüss equipped with a CCD Video Camera Module was used. For evaluation 15−20 values where measured at different points of the sample surface.

For SEM images a CAM Scan 4 with an acceleration voltage of 5 kV was used.

General Route for Preparation of 4,12-Di(*n*-alkyl)[2.2]paracyclophanes (2). 5.0 equiv of magnesium turnings was stirred under argon to activate the surface by mechanical abrasion of the magnesium oxide layer, and then diethyl ether was added. To the mixture were given to 5.0 equiv of the alkyl bromide (methyl iodide in the case of 4,12-dimethyl-[2.2]paracyclophane) dropwise at 0 °C. In the following the reaction started and the alkyl bromide was diluted. When the reaction was finished the solution was stirred an additional hour at room temperature. The remaining magnesium residues were filtered off, and the Grignard solution was added dropwise to a suspension of 1.0 equiv of **1** and 5 mol % of [1,3-bis(dipenylphosphino)propane]nickel(II) chloride Ni((dppp)Cl_2) at 0 °C.

Table 1. Yields, Elemental Analysis, and Melting Points of 1 and 2

		elemental analysis calcd (found)		
no., formula	yield (%)	C (%)	H (%)	T_m[a] (°C)
1, $C_{16}H_{14}Cl_2$[c]		69.33 (69.35)	5.09 (5.08)	153
2a, $C_{18}H_{20}$	78	91.47 (91.20)	8.53 (8.58)	176[b,d]
2b, $C_{20}H_{24}$	83	90.85 (90.44)	9.15 (9.21)	155[e]
2c, $C_{22}H_{28}$	86	90.35 (90.13)	9.65 (9.91)	147
2d, $C_{24}H_{32}$	88	89.94 (89.70)	10.06 (10.07)	85
2e, $C_{26}H_{36}$	89	89.59 (88.89)	10.41 (10.40)	82
2f, $C_{28}H_{40}$	35	89.29 (89.21)	10.71 (10.72)	67
2g, $C_{30}H_{44}$	43	89.04 (88.69)	10.96 (10.95)	65
2h, $C_{32}H_{48}$	73	88.82 (88.32)	11.18 (11.08)	61

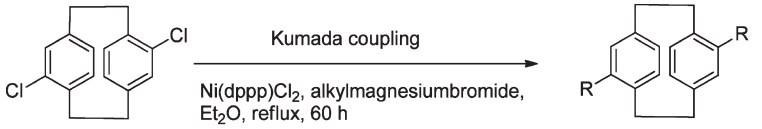
[a] Determined by DSC. Heating rate: 10 K min^{-1} for **2d**−**h**, 20 K min^{-1} for **2b**,**c**. [b] With optical microscope because vaporization starts at ∼150 °C. [c] Calcd: Cl, 25.58%. Found: Cl, 25.92%. [d] Literature value: 182−183 °C. [e] Literature value: 152−153 °C.[5c]

Then the reaction mixture was heated under reflux until the conversion was completed (GC). After cooling to 0 °C the mixture was quenched with hydrochloric acid (2 M). The organic layer was separated, and the aqueous phase was extracted twice with diethyl ether. The combined organic layers were washed with saturated sodium chloride and sodium hydrogen carbonate solution. Then the organic phase was dried over magnesium sulfate, and the solvent was removed under vacuum. The raw product was recrystallized from methanol (**2c**−**h**) or from ethanol (**2a**,**b**). The product was obtained as a colorless crystalline powder.

Analytical data and yields of the synthesized **2** are reported in Table 1 and in the Supporting Information.

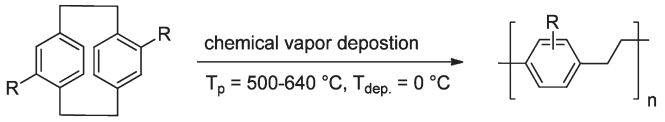
General Route for Preparation of Poly(*n*-alkyl-*p*-xylylene)s (3). For CVD process a self-constructed apparatus was used. It was composed of a tubular three zone oven (Pyrolus AT) with a total length of 115 cm and a diameter of 5.5 cm where in every zone a temperature between 25 and 1000 °C could be adjusted. Vacuum was generated with an Edwards S two-stage oil pump with base pressures between 2.0 × 10^{-3} and 3.0 × 10^{-3} mbar the pressure was controlled with an Edwards Pirani 1002 with a gauge PRL10 (DE0021-58-00). Between pump and deposition chamber three cooling traps were placed. CVD was done in a glass apparatus with vaporization chamber (*l*: 10 cm; *d*: 2.5 cm), a pyrolysis tube (fused quartz glass; *l*: 89 cm; *d*: 2.5 cm), and a deposition chamber with cooling jacket (*l*: 15 cm; *d*: 4.5 cm) maintained at 0 °C. Films of **3a**−**c** were prepared in a different chamber equipped with a cooled messing target (12.2 cm × 4.1 cm) maintained at 0 °C inside the chamber perpendicular to the monomer flow, which was wrapped with aluminum foil to facilitate removal of the film. All glass parts were connected by standard ground joint (NS 29). For a CVD run 0.50−3.00 g of the precursor was placed in the vaporization chamber under vacuum, the oven was heated to a temperature between 500 and 640 °C in the pyrolysis zone, and the transportation zone was maintained at 300 °C. When the temperatures were adjusted and the pressure was constant, the vaporization unit was heated to temperatures between 90 and 185 °C until a slight rise in pressure ((0.1−0.2) × 10^{-3} mbar) was observed. The temperature remained constant until the starting base pressure was reached again, and then the oven was cooled down; afterward, the polymer was brought into contact with air, and it was removed from the glass wall of aluminum foil by rinsing with distilled water. The polymer was dried at 40 °C for 24 h or without further purification used in GPC measurements (**3c**−**h**). For all further measurements the polymer (**3c**−**h**) was dissolved in chloroform and reprecipitated in methanol. Then it was dried for 3 days at 60 °C at a

Scheme 1. Synthesis of 2 in Kumada Coupling Reactions with 1 Used as Starting Material



1 **2 a-h**, R = CH_3 - C_8H_{17}

Scheme 2. Preperation of 3 via Chemical Vapor Deposition



R = **2a** CH_3, **2b** C_2H_5, **2c** C_3H_7, **2d** C_4H_9, **2e** C_5H_{11}, **2f** C_6H_{13}, **2g** C_7H_{15}, **2h** C_8H_{17}

R = **3a** CH_3, **3b** C_2H_5, **3c** C_3H_7, **3d** C_4H_9, **3e** C_5H_{11}, **3f** C_6H_{13}, **3g** C_7H_{15}, **3h** C_8H_{17}

Table 2. Yield, Elemental Analysis, Contact Angle Measurements, and Results for TGA and DSC of 3

					elemental analysis calcd (found)		thermal analysis		
3, molecular formula	T_{vap} (°C)	T_p (°C)	yield (%)	contact angle[d] (deg)	C (%)	H (%)	$T_{5\%}$ (%), T_{max} (%)	T_g (°C)	T_m (°C)
a, $(C_9H_{10})_n$	87	600	quant	94 ± 3[a]	91.47 (91.25)	8.53 (8.57)	469, 491	53	245
b, $(C_{10}H_{12})_n$	110	640	quant	97 ± 2[a]	90.85 (90.71)	9.15 (9.18)	463, 489	17	–[e]
c, $(C_{11}H_{14})_n$	120	550	quant (90%[c])	99 ± 2[a], 98 ± 2[b]	90.35 (90.19)	9.65 (9.73)	459, 488	2	–[e]
d, $(C_{12}H_{16})_n$	127	500	88[c]	98 ± 3[b]	89.94 (89.66)	10.06 (10.04)	444, 485	−4	118
e, $(C_{13}H_{18})_n$	130	500	64[c]	99 ± 2[b]	89.59 (89.61)	10.41 (10.46)	439, 485	−11	110
f, $(C_{14}H_{20})_n$	143	500	70[c]	98 ± 3[b]	89.29 (89.33)	10.71 (10.72)	440, 487	−21	121
g, $(C_{15}H_{22})_n$	155	500	64[c]	100 ± 2[b]	89.04 (89.21)	10.96 (10.88)	430, 486	−26	120
h, $(C_{16}H_{24})_n$	185	500	44[c]	99 ± 2[b]	88.82 (89.29)	11.18 (11.02)	428, 484	−29	117

[a] Film surface as-deposited. [b] Solvent-casted film surface. [c] Yield after reprecipitation from MeOH. [d] Contact angle measurements were realized with a distilled water droplet volume between 10 and 15 μL. [e] In a temperature region between 25 and 400 °C no melting peak was observed (heating rate: 20 °C/min), T_p: pyrolysis temperature during CVD; $T_{5\%}$: thermogravimetric decomposition of 5% of the sample; T_{max}: maximum of decomposition rate; T_g: glass transition temperature; T_m: melting peak.

pressure of 15 mbar. Samples of **3a**−**b** and **3c** prepared at 550 °C were used as deposited.

RESULTS AND DISCUSSION

4,12-Di(chloro)[2.2]paracyclophane (**1**) was isolated by recrystallization from DPX C, the commercial precursor of chlorine-substituted PPX. The synthesis of 4,12-di(*n*-alkyl)-[2.2]paracyclophanes (**2a**−**h**) as precursors for alkyl-substituted PPX (**3**) was performed in a one-step reaction by Kumada coupling of **1** and different alkylmagnesium bromides according to Scheme 1. Yields, elemental analysis data, melting points, and ^{1}H and ^{13}C NMR data of **1** and **2** are given in Table 1 and the Supporting Information and compared well to literature data as far as available.[5]

The precursors **2a**−**h** were processed to **3a**−**h** according to Scheme 2 at different pyrolysis temperatures optimized for yield and a deposition temperature of 0 °C. **3a**−**c** were obtained as clear films without impurities, whereas polymers **3d**−**h** could only be obtained as opaque films. Thermogravimetric analysis and ^{1}H NMR showed that **3d**−**h** were contaminated by low molecular weight fractions mainly precursor and cyclic trimer. However, due to the good solubility in organic solvents, reprecipitation from chloroform/methanol allowed the purification of **3d**−**h** for further analysis. The yield after reprecipitation was between 44 and 90%, showing a decrease in yield for derivatives with longer alkyl chain length (Table 2).

ATR-IR analysis of the polymers **3a**−**h** showed typical signals for sp^3 C−H stretching (2959, 2930, 2867 cm^{-1}), sp^2 C−H deformation (883, 819 cm^{-1}), and C=C ring stretching (1499, 1450 cm^{-1}) (Supporting Information).

The chemical structure of **3b**−**h** was confirmed by NMR analysis (Supporting Information and Figure 1). ^{13}C NMR spectra of **3b**−**h** reveal a "splitting" of the carbon signals (representative **3c**, Figure 2) like it was also reported for **3b**.[7] It was expected that chains with head-to-tail as well as head-to-head and tail-to-tail moieties would be formed, which can be well explained for substituted monomers as shown in Scheme 3. Similar findings were obtained with PPX derivatives prepared by the Gilch route and for the CVD route using esters of α,α′-dihydroxy-*p*-xylyenes as starting materials.[4a,8] Two-dimensional NMR techniques were applied for further structural analysis with **3c** as a representative example. ^{1}H,^{1}H−COSY showed the ^3J-couplings ($^3J_{H1H2}$, $^3J_{H2H4}$) from the side-chain atoms as expected; additionally, a ^3J-coupling between H7 and H6 or H8 was visible,

dx.doi.org/10.1021/ma202270w |*Macromolecules* 2012, 45, 1151–1157

which is important for the structure determination later on (Figure 3). The $^{1}H,^{13}C$-HSQC (consistency) spectrum permitted clear assignments for $^{1}J_{CH}$ couplings, clarifying attachment of the same hydrogen group to the multiple carbon signals (Figure 4).

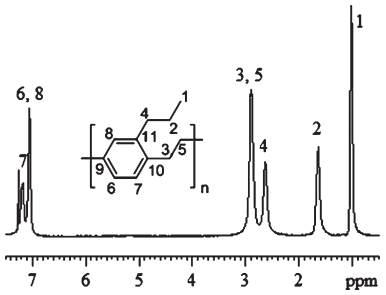


Figure 1. ^{1}H NMR of **3c** in $CHCl_3$ showing the aromatic hydrogen atoms (**6**−**8**), the backbone CH_2−groups (**3**, **5**), and the side-chain C_{arom}−CH_2 (**4**), CH_2 (**2**), and CH_3 (**1**) and structure assignment referred to in all other spectra.

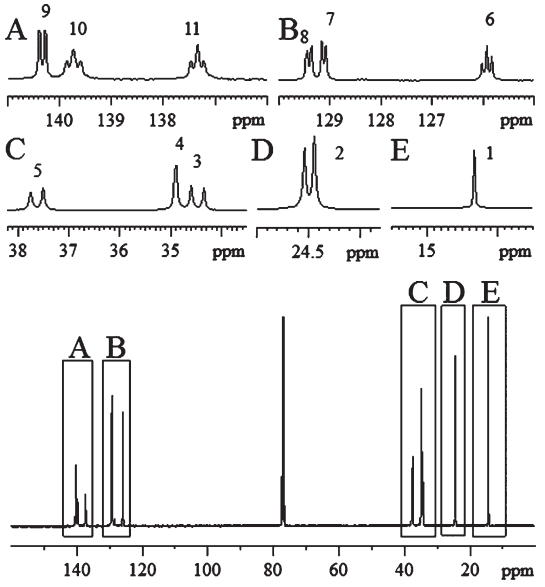


Figure 2. ^{13}C NMR of **3c** in $CDCl_3$ with magnification (A−E) showing splitting of carbon signals due to head-to-tail, head-to-head, and tail-to-tail structure of the polymer.

The HMBC spectrum showed that the structure of the polymer was not totally resolved because the different connections of the monomer units did not allow an unambiguous assignment of

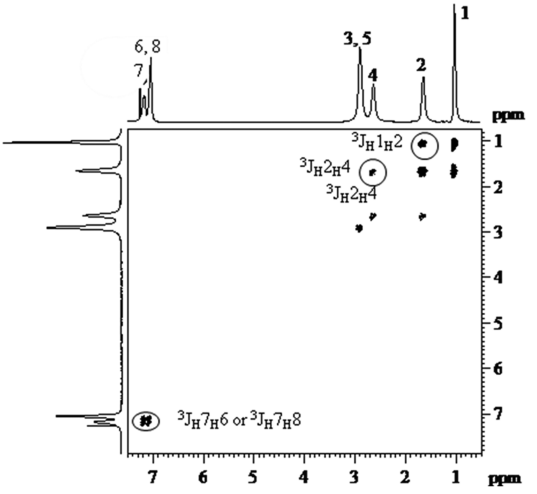


Figure 3. COSY spectrum of **3c** in $CDCl_3$ permitting the assignment of the side chain and especially important to show that hydrogen (**6**) or hydrogen (**8**) has no adjunct atom.

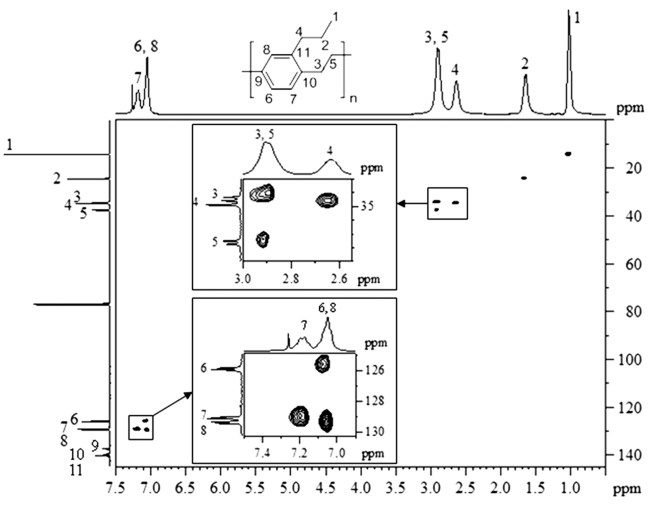
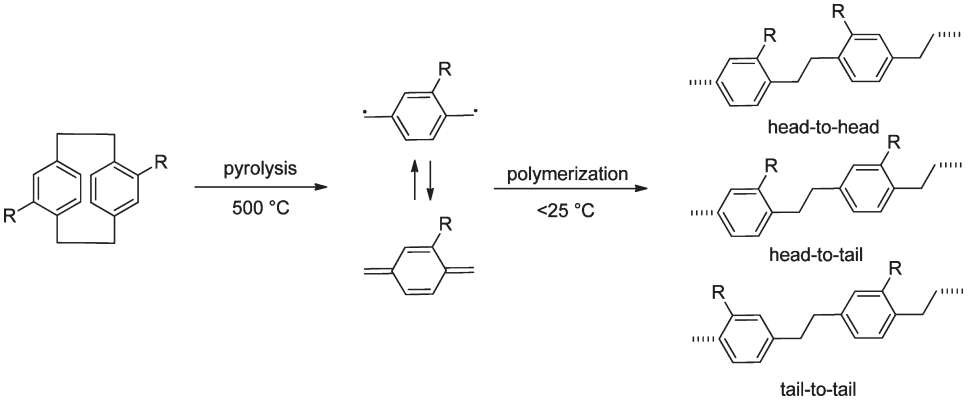


Figure 4. HSQC spectrum of **3c** in $CDCl_3$.

Scheme 3. Possible Polymer Structures Resulting from a substituted *p*-Xylylene Diradical



dx.doi.org/10.1021/ma202270w |*Macromolecules* 2012, 45, 1151–1157

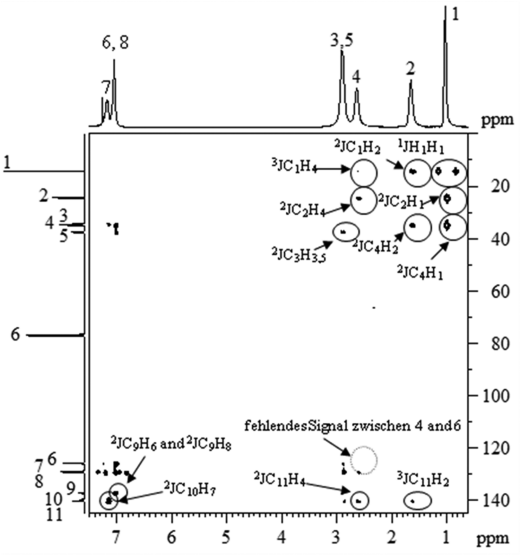


Figure 5. HMBC spectrum of **3c** in $CDCl_3$.

Table 3. GPC Results in Chloroform for Polymer Samples 3c−h Prepared at 500 °C

3	T_p	M_n	M_w	M_z	PD
c	500	227 000	598 000	1 174 000	2.6
d[a]	500	94 000	426 000	369 000	4.5
e	500	258 000	950 000	2 190 000	3.5
f	500	152 000	400 000	839 000	2.6
g	500	12 2000	477 000	129 000	3.9
h	500	64 500	228 000	65 200	3.5

[a] Sample was measured in THF, conventional calibration.

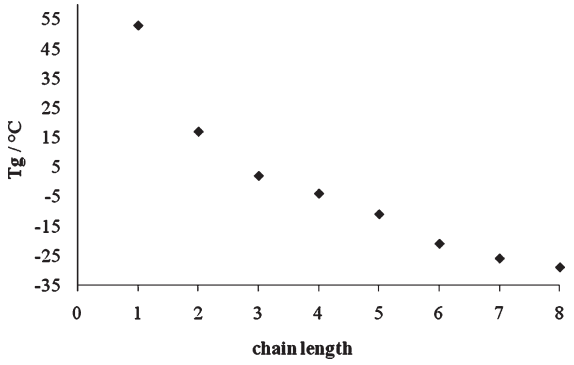


Figure 6. Glass transition temperature of **3a−h** in dependence of the carbon chain length of the alkyl side chain.

C3 and C5 (CH_2-CH_2 backbone) (Figure 5). Assignment was done for C6 by the missing coupling to H4, for H7 because of its coupling to quaternary C10, for C9 because of its coupling to H6 and H8, and for C11 because it is the only one coupling with H2 leading to the polymer assignments depicted in (Figure 1).

Molecular weights of **3c−h** ranging from 230 000 to 950 000 were obtained by GPC (Table 3). Similarly, high molecular weights recently published by us were found for siloxane-substituted PPX.[9] The polydispersities of **3c−h** were between 2.6 and 4.5.

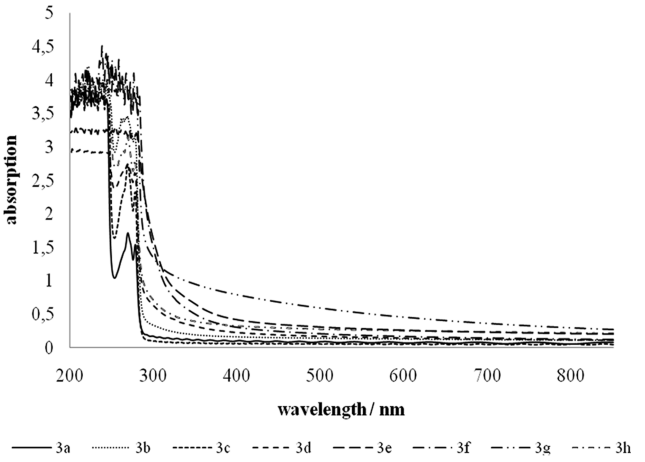


Figure 7. UV/vis spectra of **3a−h** in a region between 200 and 850 nm. The film thickness of deposited films (**3a−c**) was 2−5 μm; film thickness of solvent-casted films **3d−h** was 25−35 μm.

Table 4. Comparison of Mechanical Data of 3

3	T_p, °C	Young's modulus (lit.), GPa	Young's modulus, GPa	elongation to break (lit.), %	elongation to break, % (av film thickness, μm)
a[c]	620	2.76 (CVD[a]) 1.90 (Gilch[b])	2.51	230[a] 1−6[b]	230 (20)
b[c]	620	1.21 (CVD[a])	1.08	275[a]	235 (25)
c[c]	550		0.42		380 (40)
c[d]	530		0.31		220 (177)
d[d]	525		0.16		300 (197)
e[d]	500		0.12		250 (171)
f[d]	500		0.06		290 (72)
g[d]	500		0.06		270 (42)
h[d]	500		0.04		230 (36)

[a] **3a**: tensile strength, 9500 psi; tensile modulus, 400 000 psi; elongation to break, 230%. **3b**: tensile strength, 11 000 psi; tensile modulus, 175 000 psi; elongation to break, 275%; 10% strain per minute.[2] [b] **3a**: tensile strength, 4600 psi; tensile modulus, 275 000; elongation to break, 1−6%.[11b] [c] As-deposited. [d] Solvent-casted.

Thermogravimetric analysis showed that the **3** were highly stable ($T_{5\%}$: 428−469 °C; T_{max}: 484−491 °C) comparing well to commercial unsubstituted and chlorine substituted PPX (Table 2).[4a,10] DSC showed a decrease in glass transition temperature (T_g) with increasing length of the alkyl substituents (Figure 6). For **3a** a T_g of 53 °C and a T_m of 245 °C were found by DSC, which was in good agreement with literature (T_g: 50−60 °C,[2,11] T_m: 200−210 °C[2,11a]). For **3b** a T_g of 17 °C was found which was also confirmed by literature (T_g = 25 °C[2]), but a T_m between 160 and 180 °C[5c,6b] could not be confirmed. For **3h** a T_g of −29 °C was found.

Good transparency of visible light of **3a−c** was confirmed by absorption spectroscopy. In contrast, **3d−h** appeared to be slightly opaque even after reprecipitation as already mentioned earlier, which was confirmed by absorption measurements (Figure 7).

The crystallinity of as-deposited films of **3a−c** and solvent-casted films of **3d−h** were studied by WAXS in dependence of

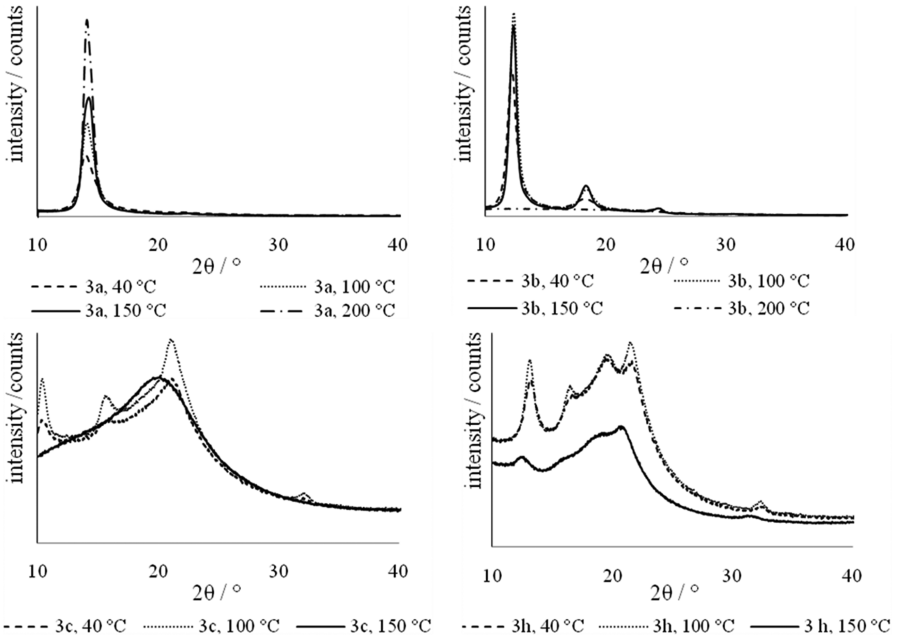


Figure 8. WAXS diagram of **3a** and **3b** as-deposited films stored at 40 °C for 24 h and **3c** and **3h** as solvent-casted film dried at 40 °C for 48 h. The annealing was done for 72 h with stepwise augmentation of temperature up to 200 °C.

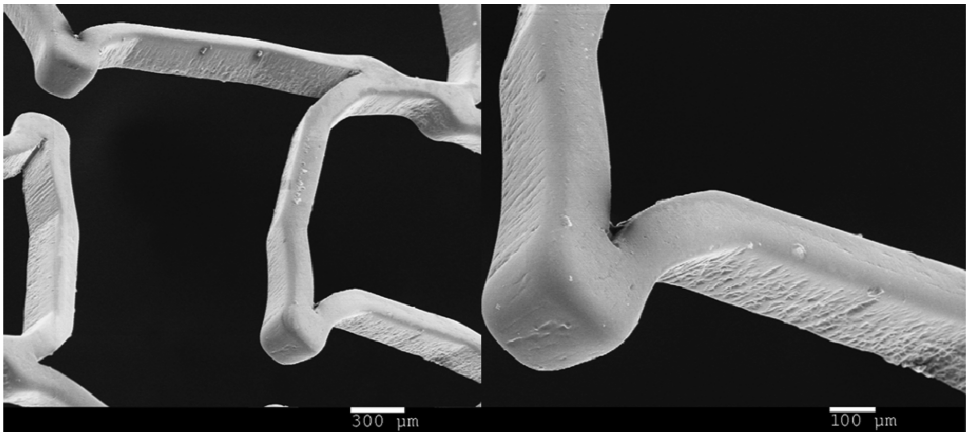


Figure 9. SEM image of CVD-coated stainless steel stent model with **3c** (film thickness: 3.1 μm) after expansion at different magnifications.

different annealing temperatures. In Figure 8 it is shown that the as-deposited films of **3a**−**b** treated at 40 °C showed distinct WAXS patterns, whereas **3c**−**h** showed a pronounced amorphous halo and broad peaks with less intensity. A possible explanation for this behavior is depicted in Scheme 3; multiple orientation possibilities of the alkyl chains in the ring have a great impact on the packing density of the polymer (e.g., favored parallel orientation of the phenylene units in the crystalline part of unsubstituted PPX could be disturbed).[12] Upon temperature treatment crystallinity of **3a** increased significantly by annealing up to 200 °C, which is still below the melting point (T_m: 245 °C) of the polymer. For **3b** an increase in crystallinity was observed for annealing up to 150 °C. The other samples (**3c**−**h**) showed a significant decrease in crystallinity (peak broadening and decreased peak intensity) upon annealing at 100 °C.

Mechanical measurements of the PPX **3** showed a decrease of the Young's modulus with increasing length of the alkyl side chain (Table 4). CVD films of **3c** showed the largest elongation to break with 380%, which is significantly higher as compared to PPX (10−15%), whereas the Young's modulus of **3c** is only 0.4 GPa (PPX Young's modulus = 2.41 GPa). For the solvent-casted films of **3d**−**h** the Young's modulus was ranging from 0.04 to 0.31 GPa, and the elongation to break was between 230 and 300%. These promising values for the elongation to break were confirmed by CVD coating of stents by **3c** followed by expansion of the stents. SEM images of the expanded stents showed conformal deposition of **3c** on the stent surface and no visible delamination or damage of the coating (Figure 9).

Contact angle measurement of as-deposited films **3a**−**c** and solution-cast films of **3c**−**h** showed contact angles against water ranging from 94° to 100°, which is not significantly higher than for unsubstituted PPX (85°) and chlorine-substituted PPX (90°) (Table 2). As far this difference in contact angle is relevant for cell

adhesion, which could play a major role in stent applications, will be the topic of an upcoming paper.

CONCLUSION

The one-step synthesis using 4,12-dichloro[2.2]paracyclophane as starting material was proven to be a versatile route to 4,12-di-(*n*-alkyl)[2.2]paracyclophanes as precursors for alkyl-substituted PPX. Poly(methyl-*p*-xylylene), poly(ethyl-*p*-xylylene), and poly(*n*-propyl-*p*-xylylene) could be prepared in quantitative yields. [2.2]-Paracyclophanes with longer alkyl substituents tolerated pyrolysis temperatures up to 500 °C. Molecular weights of **3** were high, showing that CVD polymerizations can yield high molecular weight of un-cross-linked polymers. The substitution pattern of **3** was governed by the formation of different isomeric repeating moieties and contributed to the lower crystallinity of **3** as compared to unsubstituted PPX. Glass transition temperature and crystallinity of **3** decreased with longer alkyl chain length. As a consequence, elongation to break was for all polymers >200% up to 380%, further indicating improved of mechanical properties. Initial tests on stents showed that the coatings with the alkyl-substituted PPX survive stent expansion which is an important but not the only criteria for applications on stents. Nevertheless, these results suggest alkyl-substituted PPX as promising candidates for demanding coating applications because they can be well characterized, and with this their properties can be, in contrast to present commercial PPXs, correlated with molecular parameters like the molecular weight and because their elongation to break is relatively high. The performance of this new alkyl PPX has to be verified for the demands of specific application, for example, for stent applications cell adhesion of alkyl PPX coatings, which is the topic of upcoming work.

ASSOCIATED CONTENT

Supporting Information. Tables S1 and S2. This material is available free of charge via the Internet at http://pubs.acs.org.

AUTHOR INFORMATION

Corresponding Author
*E-mail: greiner@staff.uni-marburg.de.

ACKNOWLEDGMENT

The authors are indebted to Deutsche Forschungsgemeinschaft for financial support and to Specialty Coating Systems for the donation of DPX C.

REFERENCES

(1) (a) Wolgemuth, L. The Surface Modification Properties of Parylene for Medical Applications. *Buisinessbriefing: Medical Manufacturing and Technology* **2002**, 1–4. (b) Greiner, A. Poly(p-xylylene)s (Structure, Properties, and Applications). In *The Polymeric Materials Encyclopedia*; Salamone, J. C., Ed.; CRC Press: New York, 1996; Vol. 9, pp 7171−7180. (c) Alexandrova, L.; Vera-Graziano, R. Poly(p-xylylene)s, coatings and films. In *Polymeric Materials Encyclopedia*, 2nd ed.; Salamone, J. C., Ed.; CRC Press: New York, 1996; Vol. 9, pp 7180−7189. (d) Jamin, R. Innovation in Healthcare Delivery. *Polymers for the Medical Industry 2001, Rapra Technology: Brussels, Belgium* **2001**, *17*, 1–6.

(2) Gorham, W. F. *J. Polym. Sci., Part A-1: Polym. Chem.* **1966**, *4* (12), 3027–3039.

(3) (a) Lahann, J.; Klee, D.; Pluester, W.; Hoecker, H. *Biomaterials* **2001**, *22*, 817–826. (b) Hanefeld, P.; Westedt, U.; Wombacher, R.; Kissel, T.; Schaper, A.; Wendorff, J. H.; Greiner, A. *Biomacromolecules* **2006**, *7*, 2086–90. (c) Unger, F.; Westedt, U.; Hanefeld, P.; Wombacher, R.; Zimmermann, S.; Greiner, A.; Ausborn, M.; Kissel, T. *J. Controlled Release* **2007**, *117*, 312–321. (d) Wolf, K. V.; Zong, Z.; Meng, J.; Orana, A.; Rahbar, N.; Balss, K. M.; Papandreou, G.; Maryanoff, C. A.; Soboyejo, W. *J. Biomed. Mater. Res., Part A* **2008**, *87*, 272–281. (e) Hanefeld, P.; Agarwal, S.; Kumar, R. *Macromol. Chem. Phys.* **2009**, *211*, 265–269.

(4) (a) Greiner, A.; Mang, S.; Schäfer, O.; Simon, P. *Acta Polym.* **1997**, *48*, 1–15. (b) Schäfer, O.; Brink-Spalink, F.; Smarsly, B.; Schmidt, C.; Wendorff, J. H.; Witt, C.; Kissel, T.; Greiner, A. *Macromol. Chem. Phys.* **1999**, *200* (8), 1942–1949. (c) Ishaque, M.; Wombacher, R.; Wendorff, J. H.; Greiner, A. *e-Polym.* **2001**, *5*, 1–16. (d) Ishaque, M.; Greiner, A.; Agarwal, S. *e-Polym.* **2002**, *31*, 1–10.

(5) (a) Gorham, W. F. Aklyated Di-p-xylylenes. Union Carbide Corp. U.S. Patent 3 117 168, 1964. (b) Yeh, Y. L. G.; William, F. *J. Org. Chem.* **1969**, *34* (8), 2366–2370. (c) Ying, L. Yeh, Y. Process for the preperation of alkylated Di-p-Xylylenes. Union Carbide Corp. U.S. Patent 3 349 142, 1967.

(6) (a) Gorham, W. F. Para-Xylylene Copolymers. Union Carbide Corp. U.S. Patent 3 288 728, 1966. (b) Gorham, W. F. Para-Xylylene Polymers. Union Carbide Corp. U.S. Patent 3 342 754, 1967.

(7) Loy, D. A.; Assink, R. A.; Jamison, G. M.; McNamara, W. F.; Prabakar, S.; Schneider, D. A. *Macromolecules* **1995**, *28*, 5799–5803.

(8) Simon, P.; Mang, S.; Hasenhindl, A.; Gronski, W.; Greiner, A. *Macromolecules* **1998**, *31*, 8775–8780.

(9) Bier, A. K.; Bognitzki, M.; Schmidt, A.; Greiner, A.; Gallo, E.; Klack, P.; Schartel, B. *Macromolecules* **2011**.

(10) (a) Jellinek, H. H. G.; Lipovac, S. N. *J. Polym. Sci., Part A-1* **1970**, *8* (9), 2517–2534. (b) Joesten, B. L. *J. Appl. Polym. Sci.* **1974**, *18*, 439–448.

(11) (a) Szwarc, M. *Polym. Eng. Sci.* **1976**, *16* (7), 473–479. (b) Gilch, H. G.; Wheelwright, W. L. *J. Polym. Sci., Part A-1* **1966**, *4*, 1337–1349.

(12) Miller, K. J.; Hollinger, H. B.; Grebowicz, J.; Wunderlich, B. *Macromolecules* **1990**, *23*, 3855–3859.

Macromolecules

Article

pubs.acs.org/Macromolecules

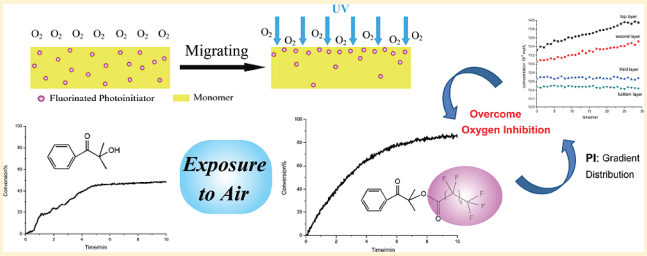
A Fluorinated Photoinitiator for Surface Oxygen Inhibition Resistance

Fei Xu, Jin-Liang Yang, Yu-Shan Gong, Gui-Ping Ma, and Jun Nie*

State Key Laboratory of Chemical Resource Engineering, Beijing University of Chemical Technology, Beijing, China, 100029

Supporting Information

ABSTRACT: A novel photoinitiator called 2-methyl-2-benzoylethanolpentadecafluorooctanote (1173-F) was synthesized and characterized. 1173-F is an efficient photoinitiator for free radical photopolymerization in the presence of oxygen and has ability of moving to the surface. The oxygen inhibition of the photopolymerization surface could be decreased because the large amount of photoinitiator at the top to be consumed by oxygen. UV absorption spectroscopy, X-ray photoelectron spectroscopy, gel permeation chromatography, and EDS-line mapping were used to prove the migratory of 1173-F in monomers. Real time FTIR analysis was taken to investigate the ability of 1173-F to overcome oxygen inhibition.



INTRODUCTION

Many products are produced via photopolymerization due to its excellent characteristics as it is economic, environmental friendly, energy saving, efficient, enabling, and rapid.[1−3] It is widely used in many regions including coatings, adhesives, dental resins, ink, paints, and microelectronics.[1−7] Free radical photopolymerization dominates most of the interest and industrial applications due to its high quantum efficiency and reactivity.[1] It is reported that the initiation rate is independently dictated by the photoinitiator and the light intensity.[8] The generation of reactive species is due to a photoinitiator absorbing the incident light and cleaving into initiating radicals.[9]

However, there are still many limitations of free radical photopolymerization, such as oxygen inhibition, volume shrinkage, light shielding.[9−12] The existent oxygen can terminate the polymerization or consume the photoinitiator by reacting with initiating radicals and growing polymer radicals to form peroxy radicals.[11] The peroxy radicals are stable that cannot reinitiate the polymerization. The effect of oxygen inhibition results in an induction period, the slowing down of the reaction, poor double bond conversion. When the sample is open to air, the conversion of polymerization is low, especially at the top of the film. The top layer remains "tacky" due to the oxygen inhibition.[9,12,13] O'Brien et al. studied the impact of oxygen on photopolymerization kinetics and polymer structure, indicating sample thickness, initiation rate and oxygen concentration result photopolymerization kinetics, respectively.[8] Several methods have been proposed to reduce the oxygen inhibition. Some traditional strategies such as using high intensity light or high cure dosage, blowing inert atmosphere, adding additives have been developed.[13−15] Higashi et al.[16]reported an alternating copolymer of alkyl sorbates was cured by photopolymerization with oxygen. Balta et al.[17] reported a thioxanthone-anthracene (TX-A) photoinitiator, which is an efficient photoinitiator for free radical polymerization of both acrylate and styrene monomers in the presence of air. El-Roz et al.[18] use silanes, germanes, and stannanes R_3XH as co-initiators and additives to overcome the oxygen inhibition.

Oxygen inhibition could be reduced by increasing the photoinitiator concentration on the surface but high concentration of photoinitiator would lead a result of light shielding and volume shrinkage. We want to find such a photoinitiator which have more content on the surface layer to be consumed by oxygen and low content in the bulk to initiate monomers. Fluorinated polymers were widely used due to the excellent properties such as low surface energy.[19] It was reported that the addition of 1−1.5 wt % of fluorine could reduce the surface energy from 45 to 20−30 mN/m.[20,21] Novel polyurethanes were prepared with fluorinated side chains attached to hard blocks. The surface of fluorinated polyurethanes was nonpolar due to migration of fluorinated side chains to the surface.[22] Ravenstein et al. reported low surface energy polymeric films from fluorinated blocked isocyanates. The fluorinated species would migrate toward the air interface to minimize the interfacial energy.[23] It was reported that oligoesters end-capped with a perfluoroalkyl group was cured with a liquid polyisocyanate cross-linker by self-stratification to prepare environmentally friendly coating system and low surface energy films. The fluorine level at the surface was many times higher than that in the bulk.[20,24] Photoinitiator containing fluorine atom was synthesized to prepare surface active coatings

Received: October 25, 2011
Revised: January 17, 2012
Published: January 27, 2012

 © 2012 American Chemical Society

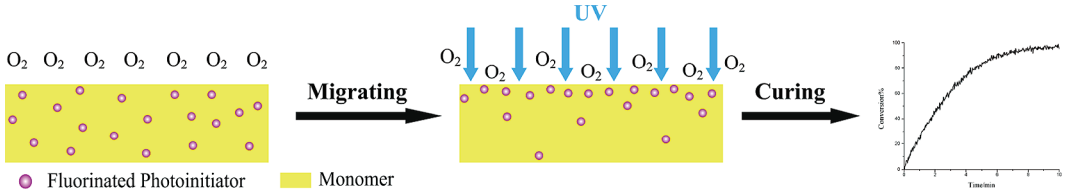
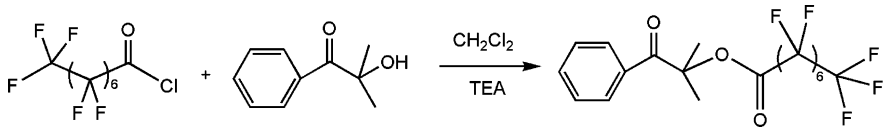


Figure 1. Scheme of 1173-F for surface oxygen inhibition resistance.

Scheme 1. Preparation of Fluorine-Containing Photoinitiator



before[25,26] but related oxygen inhibition resistance was not reported.

In this paper, we combine the advantage of fluorine molecular and 2-hydroxy-2-methylpropiophenone (1173), making a fluorinated photoinitiator for free radical photopolymerization, which could overcome oxygen inhibition efficiently without any co-initiators or additives. This photoinitiator has ability of migratory that result in aggregation of photoinitiator on the top surface. Monomer with this photoinitiator has high conversion of double bond with the presence of air, as shown in Figure 1.

EXPERIMENTAL DETAILS

Materials. 2-Hydroxy-2-methylpropiophenone (1173) was purchased from Changzhou Runtec Chemical Ltd. Pentadecafluorooctanoyl chloride (PFOC) was purchased from Alfa Aesar. Triethylamine (TEA), methylene dichloride, ethyl acetate, petroleum ether, and acetonitrile were purchased from Sinopharm Group Chemical Reagent Co. (Beijing, China). The monomers used in this paper were hexamethylene diacrylate(HDDA) and methyl methacrylate (MMA) given by Sartomer. All reagents were used as received without further purification.

Synthesis of 2-Methyl-2-benzoylethanolpentadecafluorooctanote (1173-F). First, 1.64 g (0.01 mol) 2-hydroxy-2-methylpropiophenone (1173), 1.012 g (0.01 mol) triethylamine (TEA), and 30 mL methylene dichloride (CH_2Cl_2) were added into a 100 mL round-bottom flask and stirred at room temperature by using magnetic stirring. Mixture of 4.325 g (0.01 mol) of PFOC and 20 mL of CH_2Cl_2 was dropped into the stirred solution in an ice water bath. The reaction was monitored by infrared spectroscopy. When the characteristic peaks of hydroxyl group (OH, 3465.2 cm^{-1}) was disappeared and carbonyl group (C═O, 1773.8 cm^{-1}) was generated, the reaction was stopped. The primary product was purified by silica gel column chromatography with ethyl acetate and petroleum ether as elution (1:10 v/v). ^1H NMR and ^{19}F NMR characterizations were used to observe the chemical structure of final product. The reaction of synthesis is shown in Scheme 1.

Photopolymerization. The polymerization kinetics was investigated by real time FTIR. For the sample without oxygen penetration experiment, a solution of HDDA and initiator was placed in a sealed mold made from glass slides and spacers with 10 mm in diameter and 1.2 mm in thickness. The solution was irradiated by a medium-pressure mercury lamp with incident light intensity of 10 mW/cm^2 (EXFO S1000-IB, Photonic Solutions Inc., Canada). The light intensity on the surface of sample was detected by a UV light radiometer (Beijing Normal University, China). The double bond conversion of HDDA was monitored by near FTIR spectroscopy. The absorbance change of peak area from 6100 to 6250 cm^{-1} was related to the consumption of monomers. For the sample with oxygen, the monomers and initiator with different concentrations was put into a glass container with 10 mm in length, 10 mm in width, 1.2 mm in height, and the top surface was exposed to the air. The conversion of monomers with presence of oxygen was investigated by real time FTIR with the same conditions above.

The monomer investigated in the SEM EDS-line mapping was HDDA. The sample was placed in a mold with 10 mm in length, 10 mm in width, and 3 mm in height. The light intensity was 40 mW/cm^2 and the sample was opening to air. The monomer used in GPC analysis was MMA and the monomer used in XPS test was HDDA. Both of the monomers were put into a glass tube with a diameter of 4 mm and height of 10 cm. The monomer was irradiated by a high-pressure mercury lamp with incident light intensity of 40 mW/cm^2 (FP-108EX−S1-B, Commonwealth Corporation, Taiwan). The UV light was a plane light source to guarantee the equal light intensity on each layer. The glass tube was fixed vertically on a turntable with a rotate speed of 5 r/min, in order to uniform irradiation of different location.

Surface Migratory Property. *UV Spectrophotometer.* A solution of photoinitiator (3.25×10^{-6} mol) in acetonitrile (25 mL) was prepared to study the concentration change of 1173-F. The solution was placed into a quartz cell with 10 mm in length, 10 mm in width and 12 mm in height. A black sheet with a 1 × 1 mm^2 hole was placed in front of the UV light of the UV spectrophotometer. The UV light region was controlled in 1 × 1 mm^2 by the black sheet. The thickness of layer observed was 1 mm. The absorbance of top layer and the bottom layer was investigated respectively by moving the position of the quartz cell, as shown in Figure 7A. According to the Lambert formula: $A = \varepsilon cL$, where A is the absorbance of the initiator, ε is the initiator molar absorptivity, c is the initiator concentration, and L is optical distance. The concentration could be calculated by the A, L, and ε values. The value of A could be measured by UV absorption spectroscopy directly.

GPC, XPS, EDS-Line Mapping. The polymer rod initiated by 1173-F was cut into many sheets. Five segments from top to bottom were investigated by GPC and eight segments from top to bottom were observed by XPS. The distribution of fluorine atoms in a polymer transect initiated by 1173-F was constantly observed by the EDS-line mapping with transverse direction and vertical direction, respectively.

Characterization. The chemical structure of 1173-F was investigated by FTIR (Thermo Electro Corporation, Waltham, MA), ^1H NMR, and ^{19}F NMR (Bruker AV400 unity spectrometer operated at 400 MHz with $CDCl_3$ as solvent at 23 °C). The photo absorption and photoinitiator dissociation were studied by UV absorption spectroscopy (U-3010, Hitachi High-Technologies Corporation, Tokyo, Japan). The photochemical reactivity was observed by Electron Paramagnetic Resonance (EPR, Bruker ESP300E, Germany) and laser flash photolysis experiments (355 nm, LP920, Edinburgh Instruments Ltd., England). Real time infrared spectroscopy (RTIR, Thermo Electro Corporation, Waltham, MA) was used to analysis kinetics of photopolymerization. The migration of 1173-F was studied by X-ray photoelectron spectroscopy (XPS, Thermo Electron Corporation, Escalab 250, Germany), gel permeation chromatography (GPC, Waters 1515, USA), UV Spectrophotometer (Hitachi High-

dx.doi.org/10.1021/ma2023759 | Macromolecules 2012, 45, 1158−1164

Technologies Corporation, Tokyo, Japan) and mapping energy dispersive spectroscopy (SEM EDS line mapping, Zeiss Supra 55, Germany).

RESULTS AND DISCUSSION

Synthesis and Photochemical Reactivity. 2-Methyl-2-benzoylethanolpentadecafluorooctanote (1173-F) was prepared

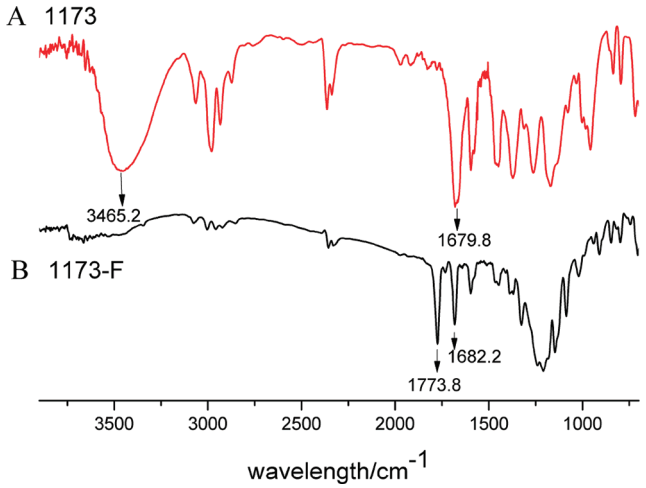


Figure 2. IR spectrum of 1173 (A) and 1173-F (B).

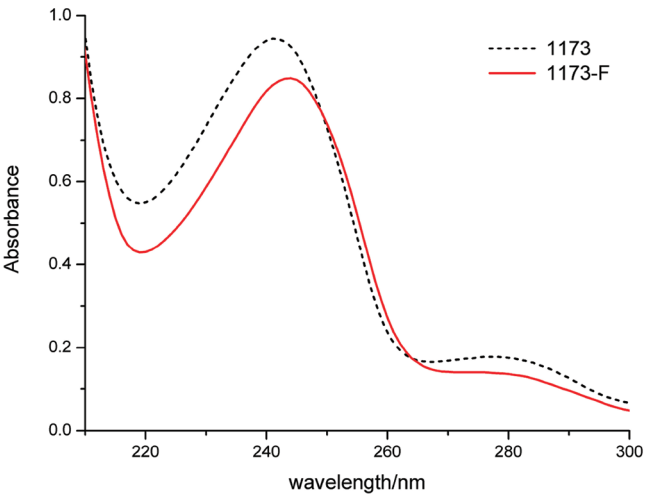


Figure 3. Absorption spectra of 1173 (dashed line) and 1173-F (solid line) in acetonitrile solution with the same concentration (5×10^{-5} mol/L) at 23 °C.

by reacting the OH of 1173 with the COCl of PFOC. The peak of hydroxyl (3645.2 cm^{-1}) disappeared after fluorination; instead a new peak of carbonyl group was shown at 1773.8 cm^{-1} (Figure 2). The change of peak at 1000 cm^{-1} to 1300 cm^{-1} was due to the stretching vibration of fluorine atom. ^{1}H NMR and ^{19}F NMR were used to monitor the chemical structure of 1173-F. ^{1}H NMR (δ, 400 MHz, ppm): 7.945–7.413 (5H, Ar–***H***), 1.849 (6H, $C(CH_3)_2$); ^{19}F NMR (δ, 400 MHz, ppm): −80.774, −117.757, −121.535, −121.969, −121.969, −122.703, −126.091. (Figure S1, Supporting Information) The UV absorption spectroscopy of 1173 and 1173-F were demonstrated in Figure 3. It could be found that 1173-F had the same UV absorption peak as 1173 at 245 and 280 nm. According to the Lambert formula: $A = \varepsilon cL$ and the L

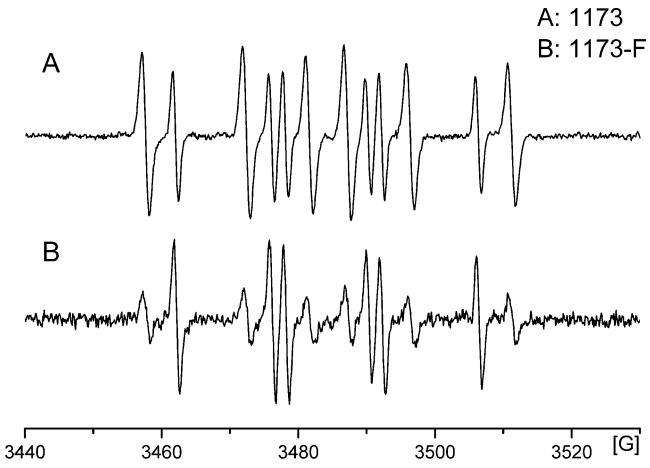


Figure 4. EPR spectrum of 1173 (A) and 1173-F (B). Photoinitiator was initiated by 355 nm laser in nitrogen saturated acetonitrile solutions at 23 °C.

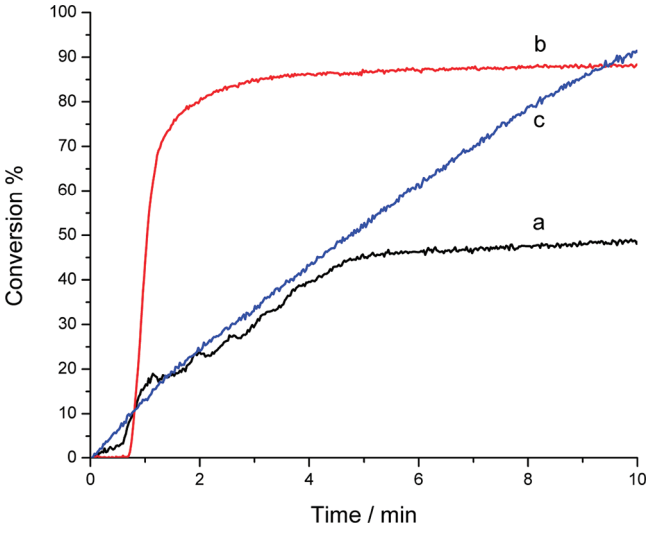


Figure 5. Polymerization kinetics of HDDA with photoinitiator: (a) 1173 with oxygen, (b) 1173 without oxygen, and (c) 1173-F, with oxygen. All the concentration of photoinitiator is 0.305 mmol/100 g. The intensity of UV light is 10 mW/cm^2.

is 1 cm, the calculated ε of 1173-F is 1040.41 L/(mol·cm). Initiated by 355 nm laser, the photoinitiator could produce radicals. The radical signal was detected by adding dimethylpyridine *N*-oxide (DMPO) as radical scavenger, as shown in Figure 4. The EPR spectra of radicals produced by 1173 and 1173-F were similar and both had 12 lines, which indicated the cleavage mechanism of 1173-F was the same as 1173. Since the triplet lifetime of 1173-F was shorter than the instrument response, an indirect method of triplet quenching was used to study the triplet lifetime by adding naphthalene.[27] The triple lifetime of 1173-F was 13 ns (Figure 2S, Supporting Information). The rate of photoinitiator dissociation (R_d) was calculated according to the following equation:

$$R_d = \frac{-\delta[\mathrm{PI}]}{\delta t} = -\left(\frac{[\mathrm{PI}]}{Ab_0}\right)\frac{\delta[\mathrm{PI}]}{\delta t} \quad (1)$$

where Ab_0 is the absorbance of 1173 and 1173-F at 245 nm before exposure to the UV light. The R_d of 1173-F was 1.46×10^{-7} $molL^{-1}s^{-1}$ and R_d of 1173 was 2.11×10^{-7} $molL^{-1}s^{-1}$.

dx.doi.org/10.1021/ma2023759 | *Macromolecules* 2012, 45, 1158–1164

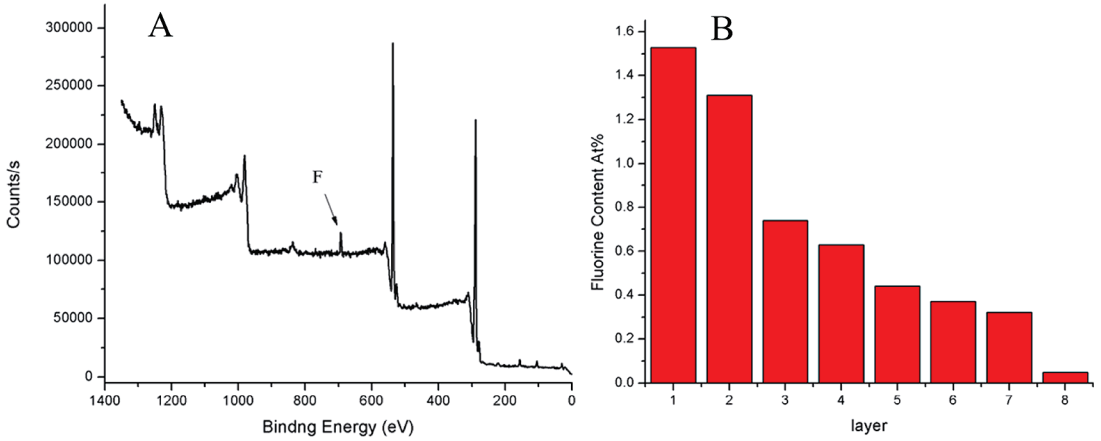


Figure 6. (A) XPS spectrum of HDDA with photoinitiator 1173-F (5 wt %). (B) Fluorine content of different layers. No. 1 is the top layer and no. 8 is the bottom layer.

Table 1. GPC Data for Different Layers Based on Polymerization of MMA

layer	M_n(1173-F)	M_w(1173-F)	D(1173-F)	M_n(1173)	M_w(1173)	D(1173)
1	7544	26 012	3.4	14 836	40 076	2.7
2	24 457	39 392	1.6	13 348	42 580	3.2
3	79 696	113 643	1.4	13 203	40 849	3.1
4	100 839	249 292	2.5	12 650	38 541	3.0
5	107 870	338 510	3.1	13 457	39 255	2.9

(Figure 3S, Supporting Information) The quantum yield was related to the dissociation rate of photoinitiator according to the equation below:[28]

$$R_d = I_0\varphi\varepsilon[\mathrm{I}]l = \varphi I_a \quad (2)$$

where I_0 is the intensity of incident light, $\varphi$is quantum yield for production of radicals, ε is molar absorption of photoinitiator, [I] is the initiator concentration, l is the path length and I_a is absorbed intensity. According to eq2, the quantum yield of 1173-F was similar to 1173 due to the uniform magnitude order of dissociation rate in the same conditions.

Photopolymerization Kinetic. As shown in Figure 5, the monomers were initiated by 1173 and 1173-F, respectively. Because of the oxygen inhibition of free radical photopolymerization, conversions of HDDA with 1173 were different when the system was with or without oxygen. It was clear that the oxygen inhibited the polymerization at the first 50 s and finally got a conversion of 45% (Figure 5a), compared to the polymerization without oxygen that the conversion got to 75% in 1 min and to 90% finally (Figure 5b). However, it was found that the conversion of HDDA with 1173-F in air (Figure 5c) was higher than HDDA with 1173 in the absence of oxygen. The conversion of HDDA with 1173-F reached to more than 90% though in the condition of opening to air and the polymerization started at the very beginning. The results indicated that the photoinitiator 1173-F had good ability to overcome the oxygen inhibition. It was initially inferred to the fluorine group that contributed to the oxygen inhibition resistance. Because of the low surface tension and low surface energy of fluorine atoms, the photoinitiator containing fluorine tended to move to the surface and gathered on the top. This movement caused high photoinitiator concentration on the top to consume the oxygen and prevented the further penetration of oxygen. The polymerization rate of monomer with 1173-F

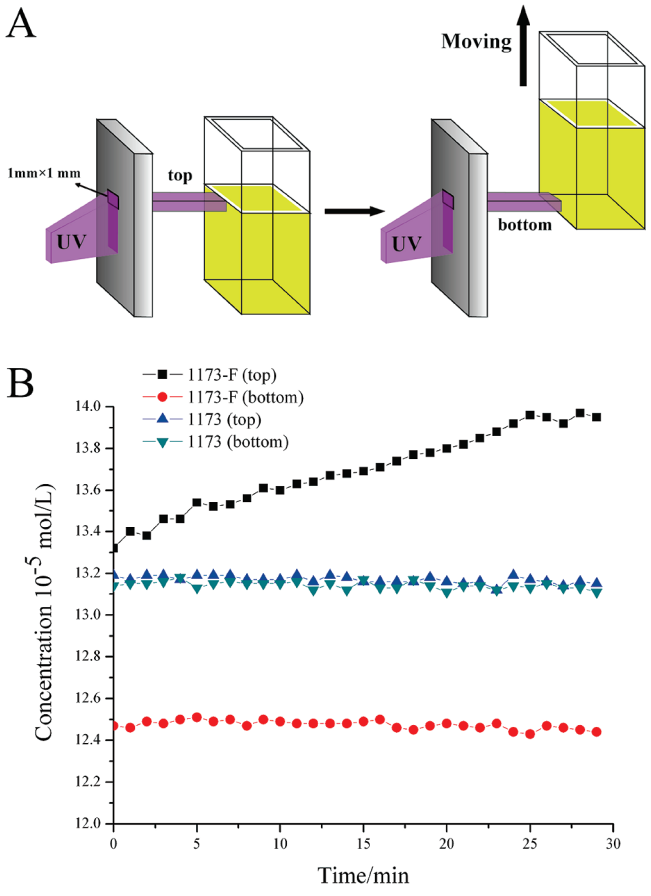


Figure 7. (A) Scheme of photoinitiator concentration in different layers by UV spectrophotometer. (B) Concentration of 1173 and 1173-F in acetonitrile solution. All the initial concentration is 1.3×10^{-4} mol/L.

was slower than that of 1173 due to the low concentration of initiator in the bulk.

Surface Migratory of 1173-F. The migratory aptitude was further supported by XPS tests with the monomer HDDA and initiator 1173-F (5 wt %). As shown the integrated spectra Figure 6A, the peak at 689.08 eV represented of fluorine. Because the only source of F in this system is 1173-F, the content of photoinitiator all through the sample could be tracked by F signal. It could be found that the fluorine atom

dx.doi.org/10.1021/ma2023759 | Macromolecules 2012, 45, 1158–1164

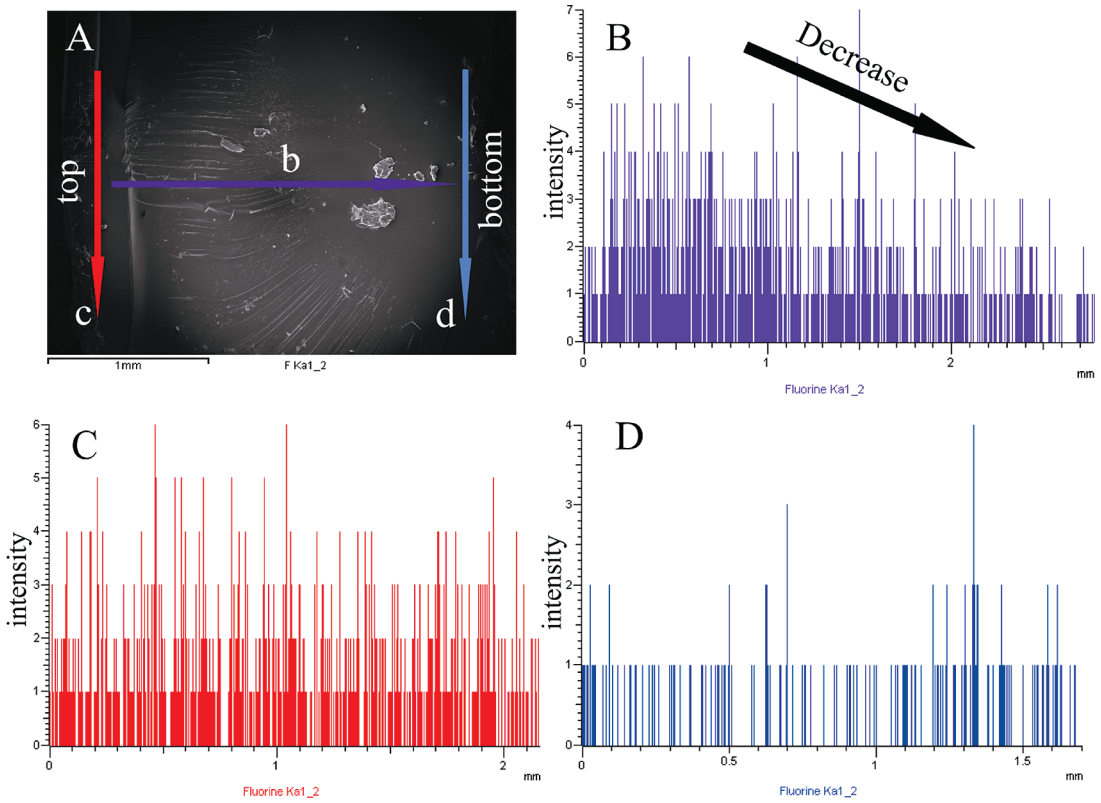


Figure 8. EDS-line mapping of HDDA with photoinitiator 1173-F, 5% wt: (A) SEM graph of polymer with 3 mm in thickness, (B) vertical direction from top to bottom, (C) transverse direction of the top layer, and (D) transverse direction of the bottom layer.

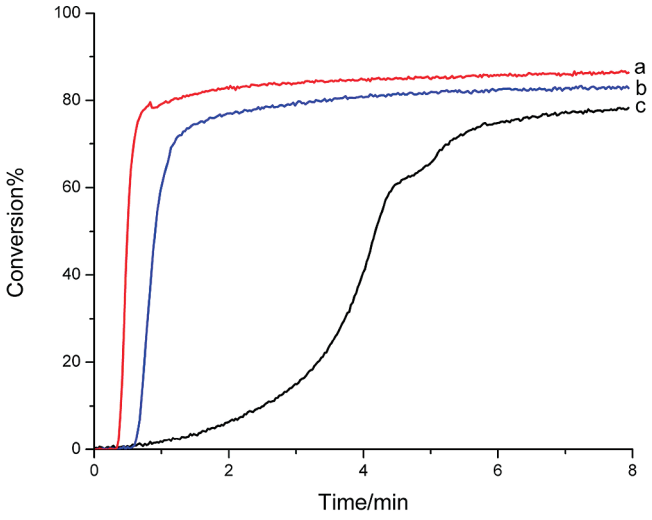


Figure 9. Polymerization kinetics of HDDA with different photoinitiator: (1) 1173, 0.305 mmol/100 g, (2) 1173, 0.1525 mmol/100 g and 1173-F, 0.1525 mmol/100 g, and (3) 1173-F, 0.305 mmol/100 g. The intensity of UV light is 10 mW/cm^2. All samples were investigated without oxygen.

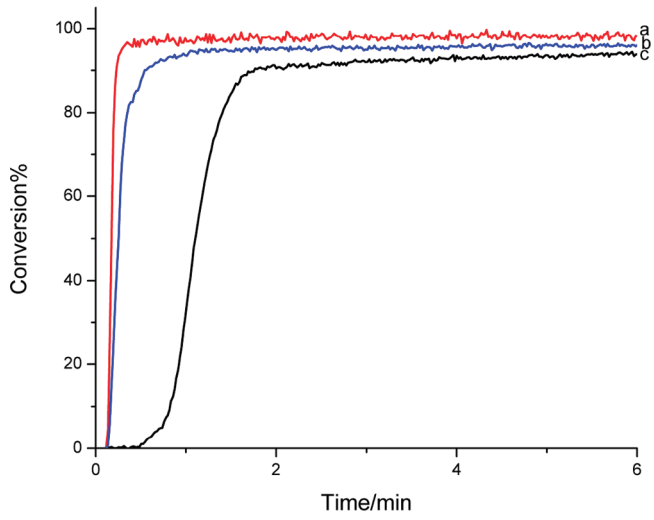


Figure 10. Polymerization kinetics of HDDA with different photoinitiator: (1) 1173, 0.305 mmol/100 g, (2) 1173, 0.1525 mmol/100 g and 1173-F, 0.1525 mmol/100 g, and (3) 1173-F, 0.305 mmol/100 g. The intensity of UV light is 40 mW/cm^2. All samples were investigated without oxygen.

content in the first layer was 1.53%, while the fluorine atom content in the eighth layer was only 0.05%, as shown in Figure 6B. No signal for fluorine element could be detected when running XPS to the very bottom layer of the sample. The distribution of F element through the sample indicated that the initiator containing fluorine had a good migratory ability leading the aggregation of the initiator to the surface. The gradient distribution was attributed to the low surface tension and the resulted movement of the fluorine atoms.

Another proof showing the migratory of 1173-F was the resultant molecular weight of polymer. Because of gradient distribution of 1173-F, the surface layer had more initiator than the bottom layer. As known to us, the molecular weight was closely related to the content of initiator. The higher of photoinitiator concentration, the lower the molecular weight is.

dx.doi.org/10.1021/ma2023759 | *Macromolecules* 2012, 45, 1158–1164

Table 2. Molar Ratio of 1173 and 1173-F in HDDA[a]

1173/1173-F	1173/10^{-4} mol	1173-F/10^{-4} mol	total/10^{-4} mol	total/g
1173	3.05	0	3.05	0.05
4/1	2.44	0.61	3.05	0.074
0.11	1.525	1.525	3.05	0.11
1/4	0.61	2.44	3.05	0.147

[a]Above HDDA = 100 g. The concentration of PI is 3.05×10^{-4} mol in 100 g monomer.

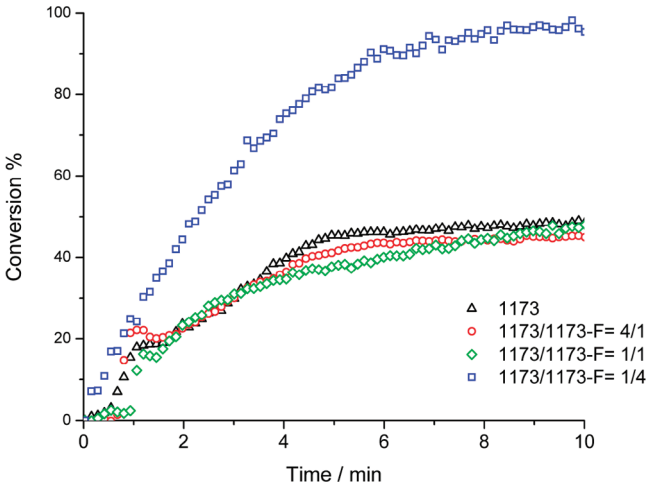


Figure 11. Conversion of HDDA with varying molor ratio of 1173 and 1173-F. The intensity of UV light is 10 mW/cm^2. All the samples are open to air.

The data from GPC was accordance well with the result from XPS, shown in Table 1. The molecular weights of the top layers were much lower than the bottom layers and increasing gradually, contrasting with the distribution of F in the system. However, the molecular weight of sample with 1173 has a uniform value from top to bottom.

In order to investigate the migration behaviors of the 1173-F, the distribution of concentration of 1173-F in the acetonitrile solution were characterized by the UV spectrophotometer. According to Figure 7, the concentration of top solution increased while the concentration of bottom solution decreased. Compared to 1173-F, the concentration of 1173 had no change all the time. The change of concentration occurred simultaneously both in top and bottom. Because of Brownian Motion, not all the 1173-F molecules could aggregate on the surface. But it was found that the concentration of the bottom was stable and the concentration of the top still increased. It might be explained that most fluorine atoms in different layers had the trend to move to the top surface with different rate. The fluorine atoms in the bottom had advantage to compete in the migratory due to attraction of low surface energy. Although the concentration of the top changed at the very beginning, it could increased because of more and more fluorine atoms moving to the top until the saturation state.

The surface migratory was investigated constantly by the EDS-line mapping, as shown in Figure 8. The height of *Y* axis indicated the intensity of fluorine signal. It was found that the amount of fluorine decreased along with the EDS-line from the top to bottom in Figure 8B. Parts C and D of Figure 8 show the amount of fluorine atom along with transverse direction on the top and bottom, respectively. It was found that the content of fluorine atom tended to be the same in the same layer. The fluorine on the top was more than that in the bottom. The trend of migration accorded with the results of XPS. Some fluorine atoms detected in the bottom were due to the molecular diffusion and Brownian motion.

Oxygen Inhibition. To further investigate the properties of photopolymerization with 1173-F, polymerization kinetics were used to investigate both in the presence of oxygen and absence of oxygen. As shown in Figure 9, all the monomers were irradiated without oxygen and the intensity of light was 10 mW/cm^2. All the samples with different photoinitiator had same molar concentration, 0.305 mmol/100 g of HDDA. It was found that the induction period of 1173-F was longer probably due to the lower concentration of initiator in the bulk and the inhomogenous photopolymerization, as show in Figure 9c. After adding 1173 to 1173-F (n(1173)/n(1173-F) = 1/1), the induction period of mixed photoinitiator decreased and the conversion was higher, as shown in Figure 9b. The molar concentration of photoinitiator in Figure 10 was the same as Figure 9 and the intensity of light was 40 mW/cm^2. But the conversion of double bond became higher due to increase of light intensity. In Figure 10, the induction period of 1173-F (Figure 10c) was decreased but was still longer than 1173 (Figure 10a). It was speculated that the inhomogenous distribution of 1173-F prevented fast polymerization of low layer. Subsequently the mixture of 1173 and 1173-F was used to initiate monomer in the presence of air. All the samples had an equal molar concentration with different ratio, as shown in Table 2. According to Figure 11, it was found that the conversion increased obviously when the ratio of 1173/1173-F was 1/4 and its induction period was less than other ratios. The results indicated that the existence of 1173-F could decrease the oxygen inhibition effect. Moreover there was a requirement of content of 1173-F to overcome the oxygen inhibition. Low concentration of 1173-F could not satisfy the consumption of oxygen on the surface.

CONCLUSION

A fluorinated photoinitiator promoted a method to overcome oxygen inhibition due to its excellent migratory. The results indicated that this fluorinated photoinitiator had better qualities in surface photopolymerization than traditional photoinitiator and could decrease oxygen inhibition effectively without any other additives or co-initiators. It dramatically increased the final conversion of HDDA to 90% with oxygen in a condition of a low light intensity and thin sample. The surface migratory was confirmed by XPS, EDS-line mapping, GPC and UV spectrophotometer. This method of relating the migratory was especially attractive to be utilized in oxygen inhibition resistance since it was simple and valid.

ASSOCIATED CONTENT

Supporting Information

^{1}H NMR and ^{19}F NMR spectra of final product, triplet time of 1173-F by flash laser photolysis, and dissociation rate of 1173 and 1173-F by UV-abs spectroscopy. This material is available free of charge via the Internet at http://pubs.acs.org.

AUTHOR INFORMATION

Corresponding Author

*E-mail: niejun@mail.buct.edu.cn. Telephone: +86 010 64421310 Fax: +86 010 64421310.

Notes

The authors declare no competing financial interest.

■ ACKNOWLEDGMENTS

The authors are grateful to the Program for Open Fund from State Key Laboratory of Chemical Resource Engineering, Beijing University of Chemical Technology.

■ REFERENCES

(1) Fouassier, J. P. *Photoinitiation, Photopolymerization, and Photocuring: Fundamentals and Applications*; Hanser/Gardner Publications: Munich, Germany, 1995.
(2) Yagci, Y.; Jockusch, S.; Turro, N. J. *Macromolecules* **2010**, *43*, 6245−6260.
(3) Bunning, T. J.; Natarajan, L. V.; Tondiglia, V. P.; Sutherland, R. L. *Annu. Rev. Mater. Sci.* **2000**, *30*, 83−115.
(4) Dickens, S. H.; Stansbury, J. W.; Choi, K. M.; Floyd, C. J. E. *Macromolecules* **2003**, *36*, 6043−6053.
(5) Shen, Y. T.; Zeng, Q. D.; Wang, C.; Gong, J. R. *Nano Lett.* **2011**, *11*, 3245−3250.
(6) Zhou, C. H.; Rajasekaran, P. R.; Wolff, J.; Li, X. L.; Kohli, P. *Langmuir* **2010**, *26* (22), 17726−17732.
(7) Griesser, T.; Kuhlmann, J. C.; Wieser, M.; Kern, W.; Trimmel, G. *Macromolecules* **2009**, *42*, 725−731.
(8) O'Brien, A. K.; Bowman, C. N. *Macromolecules* **2006**, *39*, 2501−2506.
(9) Decker, C.; Jenkins, A. D. *Macromolecules* **1985**, *18*, 1241−1244.
(10) Musto, P.; Ragosta, G.; Abbate, M.; Scarinzi, G. *Macromolecules* **2008**, *41*, 5729−5743.
(11) Shenoy, R.; Bowman, C. N. *Macromolecules* **2010**, *43*, 7964−7970.
(12) Biswal, D.; Hilt, J. Z. *Macromolecules* **2009**, *42*, 973−979.
(13) Goodnera, M. D.; Bowman, C. N. *Chem. Eng. Sci.* **2002**, *57*, 887−900.
(14) Studer, K.; Decker, C.; Beckb, E.; Schwalm, R. *Prog. Org. Coat.* **2003**, *48*, 101−111.
(15) Keskin, S.; Jockusch, S.; Turro, N. J.; Arsu, N. *Macromolecules* **2008**, *41*, 4631−4634.
(16) Matsumoto, A.; Higashi, H. *Macromolecules* **2000**, *33*, 1651−1655.
(17) Balta, D. K.; Arsu, N.; Turro, N. J. *Macromolecules* **2007**, *40*, 4138−4141.
(18) El-Roz, M.; Lalevee, J.; Allonas, X.; Fouassier, J. P. *Macromolecules* **2009**, *42*, 8725−8732.
(19) Luning, J.; Stohr, J.; Song, K. Y.; Hawker, C. J.; Iodice, P.; Nguyen, C. V.; Yoon, D. Y. *Macromolecules* **2001**, *34*, 1128−1130.
(20) Ming, W. H.; Laven, J.; van der Linde, R. *Macromolecules* **2000**, *33*, 6886−6891.
(21) Ming, W. H.; van Ravenstein, L.; van der Grampel, R.; van Gennip, W.; Krupers, M.; Niemantsverdriet, H.; van der Linde, R. *Polym. Bull. (Berlin)* **2001**, *47*, 321−328.
(22) Tan, H.; Xie, X. Y.; Li, J. H.; Zhong, Y. P.; Fu, Q. *Polymer* **2004**, *45*, 1495−1502.
(23) van Ravenstein, L.; Ming, W.; van de Grampel, R. D.; van de Linde, R.; de With, G.; Loontjens, T.; Thune, P. C.; Niemantsverdriet, J. W. *Macromolecules* **2004**, *37*, 408−413.
(24) Ming, W.; Tian, M.; Grampel, R. D.; Melis, F.; Jia, X.; Loos, J.; Linde, R. *Macromolecules* **2002**, *35*, 6920−6929.
(25) Hult, A.; Ranby, B. *Polym. Prepr. (Am. Chem. Soc. Div. Polym. Chem.)* **1984**, *25*, 329−330.
(26) Baudin, G.; Jung, T.; Husler, R. CA 2424477-A; EP 1392779-B; US 20040067311-A, CN 1235948-C; CN 1474862; JP 2004525994-A, EP 1392779-A; 2002.
(27) Jockusch, S.; Landis, M. S.; Freiermuth, B.; Turro, N. J. *Macromolecules* **2001**, *34*, 1610−1626.
(28) Rabek, J. F. *Mechanisms of Photophysical Process and Photochemical Reactions in Polymers: Theory and Applications*; John Wiley & Sons Ltd.: London, 1987; Vol. 5, p 173.

Macromolecules

Article

pubs.acs.org/Macromolecules

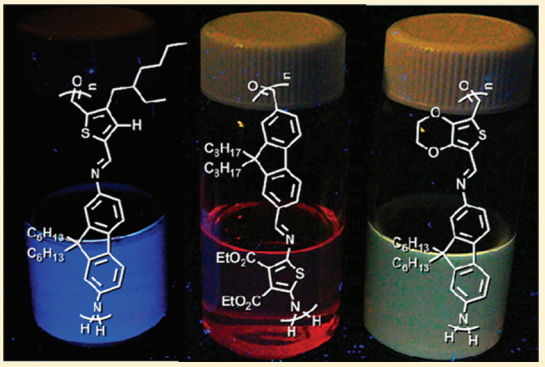
π-Conjugated Fluorescent Azomethine Copolymers: Opto-Electronic, Halochromic, and Doping Properties

Satyananda Barik, Thomas Bletzacker, and W. G. Skene*

Laboratoire de caractérisation photophysique des matériaux conjugués, Département de Chimie, Pavillon JA Bombardier, Université de Montréal, CP 6128, succ. Centre-ville, Montréal, Québec, H3C 3J7, Canada

Supporting Information

ABSTRACT: A series of new conjugated copolyazomethines consisting of alternating fluorene and thiophenes were prepared. Different thiophenes were incorporated for examining their effect on the polymer's opto-electronic properties. Blue, red, and green emissions were possible contingent on the thiophene comonomer and the placement of the azomethine nitrogen. Most notably, the polyazomethines were fluorescent both in solution and thin films with measured absolute fluorescent quantum yields (Φ_{fl}) ca. 10%. Their fluorescence could be enhanced to near unity at 77 K. High Φ_{fl} were also measured with the addition of trifluoroacetic acid (TFA). The polyazomethines' color could also be reversible altered with protonation/neutralization with TFA/triethylamine. Similar to the halochromic effect, the polyazomethines could be reversibly oxidized/neutralized with $FeCl_3$/hydrazine, resulting in reversible color changes between red and blue. The oxidation potentials and the reversibility of the anodic process were contingent on the type of thiophene incorporated into the copolymer. The stability of the electrochemically produced radical cation and the azomethine's resistance toward hydrolysis were also investigated with a model thiophene−fluorene−thiophene bisazomethine.



INTRODUCTION

Conjugated materials have drawn much attention because of their opto-electronic properties that are suitable for use in plastic electronics including organic photovoltaics, organic field effect transistors, and organic light emitting diodes (OLEDs), to name but a few.[1−10] Polyfluorene derivatives are particularity interesting. This is in part owing to their intrinsic high degree of fluorescence making them ideal for OLED applications.[11,12] As a result, much effort has been dedicated to preparing new fluorene materials with enhanced properties including high brightness[13,14] and pure color of emission.[15−17]

The preparation of polyfluorenes is possible by well established protocols, including Gilch,[18,19] Horner-Emmons,[20] Suzuki,[21] Yamamoto,[22] and Stille protocols.[23] While high conversions are possible with these methods, they require stringent reaction conditions. Additionally, pristine polymers with high color purity are obtained only after substantial product purification.

Polyazomethines are interesting alternatives to conventional coupling protocols. This is in part owing to their straightforward preparation that does not require stringent reaction conditions or coreagents. Water is also the unique reaction byproduct. Therefore, extensive purification for removing side products and coreagents is not required. In fact, pristine polymers are obtained upon solvent evaporation or by simple precipitation.

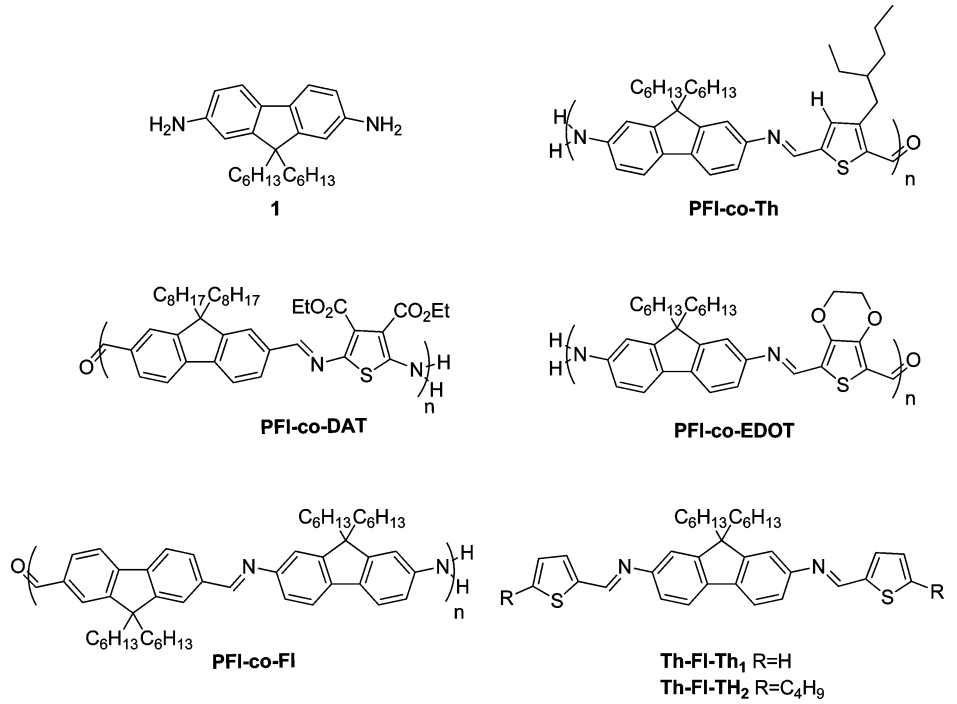
While azomethines are isoelectronic to their vinyl analogues and their preparation is synthetically advantageous relative to their carbon counterparts, they have not been pursued as functional materials for use in plastic electronics. This is partly because they are understood to be both hydrolytically and oxidatively unstable. More importantly, all previously investigated conjugated polyazomethines were nonfluorescent, despite incorporating intrinsically fluorescent monomers.[24] Accurate opto-electronic property evaluation was further problematic because of the limited solubility of previously reported polyazomethines in common organic solvents.[25−30]

We recently addressed the optical property limitations and solubility issues encountered with previously investigated polyazomethines.[31−34] This was in part owing to the use of C10 groups. This led to highly soluble polyazomethines whose molecular weight could accurately be measured using standard methods. While hydrolytically and oxidatively robust polyazomethines were possible,[31,33,35,36] they were not fluorescent. The first example of a fluorescent homopolyazomethine (**PFl-*co*-Fl**) was however possible by using the 9,9-dihexyl-2,7-diaminofluorene monomer **1**.[37] In fact, the absolute Φ_{fl} (0.4 in thin films) of the all-fluorene polyazomethine was comparable to polyfluorene prepared by common aryl coupling protocols.[38]

Received: November 2, 2011
Revised: January 6, 2012
Published: January 24, 2012

 © 2012 American Chemical Society dx.doi.org/10.1021/ma2024304 | *Macromolecules* 2012, 45, 1165−1173

Chart 1. Polyazomethines and Representative Model Azomethines Prepared and Investigated



Given the importance of tuning the emission color for a given emitting application while preserving high Φ_{fl}, copolyazomethines consisting of thiophene and fluorene derivatives were prepared. It was expected that the HOMO−HOMO energy-gap could be tailored by incorporating different electron rich and deficient thiophenes, resulting in emissions covering the RGB primary colors. Similar to emission color tailoring, the oxidation potential was also expected to be modulated contingent on the electron richness of the thiophene units in addition to the placement of the azomethine nitrogen. The copolymers reported in Chart 1 would further provide insight into the structural elements required for reducing undesired fluorescence quenching processes and for making polyazomethines fluorescent. Knowing these key structural elements is important for designing and preparing polyazomethines that are consistently fluorescent, which to date, have been elusive. The preparation and opto-electronic characterization of the new conjugated polymers illustrated in Chart 1 are herein presented. The halochromism, chemical oxidation, and electrochromism of these new copolyazomethines are also presented for demonstrating their resistance toward acid hydrolysis and oxidation.

MATERIALS AND METHODS

Reagents and solvents from commercial sources were used as received unless otherwise stated. Anhydrous and deoxygenated solvents were obtained with an activated alumina column system. ^{1}H and ^{13}C NMR spectra were recorded at room temperature on a 400 MHz spectrometer. All the samples were dissolved in deuterated solvents and the spectra were referenced to the solvent line ($CDCl_3$: ^{1}H = 7.26 and ^{13}C = 77.0 ppm) relative to TMS. $CDCl_3$ for NMR polymer analyses was purified by repeatedly passing it over a plug of activated basic alumina.

Spectroscopic Measurements. Absorption measurements were done on a Cary-500 spectrometer and fluorescence studies were carried out on an Edinburgh Instruments FLS-920 fluorimeter after deaerating the samples thoroughly with nitrogen for 20 min in Precision Glass quartz cuvettes. Relative fluorescence quantum yields were measured at 10^{-5} M by exciting the corresponding compounds at its maximum absorption in spectroscopic grade 2-methylcyclohexane solutions at room temperature relative to itself at 77 K under the same conditions. The slit widths and detector parameters were optimized for the fluorescence at 77 K. Absolute quantum yields were done at room temperature using an integrating sphere that was calibrated with fluorescein in ethanol with a calibrated excitation source. Quantum yields of the polymers in thin film were done at room temperature with the integrating sphere using a front face excitation/emission geometry. Thin films were prepared by spin coating THF solutions of the given polymer onto thin glass microscope slides.

Polymer doping was done in dichloromethane (10^{-5} M) with stock solutions of $FeCl_3$ and hydrazine that were sequentially added (5 μL). The resulting absorbance spectra after the addition of the dopant and reductant were subsequently recorded. Similarly, stock solutions of trifluoroacetic acid (TFA) and triethylamine (TEA) were sequentially added (5 μL) to the given polymer solution and the resulting absorbance spectra were recorded. The oxidation stoichiometry with $FeCl_3$ was determined via the Job method using stock solutions of known mole fractions (1.0 mM) of the polymer and ferric chloride.

Electrochemical Measurements. Cyclic voltammetry measurements were performed on a Bio Analytical Systems EC Epsilon potentiostat. Compounds were dissolved in anhydrous and deaerated dichloromethane at 10^{-4} M with 0.3 M TBAF. A platinum electrode and a saturated Ag/AgCl electrode were used as auxiliary and reference electrodes, respectively.

Molecular Weight Measurements. GPC analyses were done with a Breeze system from Waters equipped with a 717 plus autosampler, a 1525 Binary HPLC pump and a 2410 refractive index detector. Three Styragel columns HR3, HR4, and HR6 (7.8 × 300 mm) in series were used for resolving the different samples. The flow rate of the THF eluent was 1 mL/min. The temperature of the columns was 33 °C. Molecular weights were calculated relative to polystyrene standards with a SM-105 kit of 10 molecular weight standards from Shodex. The average number degree of polymerization was also determined by NMR from the ratio of the imines to the terminal aldehyde protons.

Thermal and Calorimetric Analyses. Thermogravimetric analyses (TGA) studies were carried out on a Hi-Res TGA 2950 thermogravimetric analyzer (TA Instruments) with a 10 °C/minute ramp to 700 °C (T_{dec} was defined as the onset of the decomposition

dx.doi.org/10.1021/ma2024304 | Macromolecules 2012, 45, 1165−1173

temperature). Differential scanning calorimetry (DSC) studies were carried out on a TA Instruments with a 5 °C/minute ramp from −50 to +220 °C under both N_2 and ambient atmosphere.

Syntheses. The monomers 9,9-dihexyl-fluorene-2,7-diamine (**1**), 9,9-dioctyl-fluorene-2,7-dicarbaldehyde, diethyl 2,5-diaminothiophene-3,4-dicarboxylate, and 2,3-dihydrothieno[3,4-b][1,4]dioxine-5,7-dicarbaldehyde were synthesized according to previously reported procedures.[39−42] Similarly, **PFl-*co*-Fl** was prepared according to known methods.[37]

Experimental Procedures. *3-(2-Ethylhexyl) thiophene.* In anhydrous THF (50 mL) was dissolved magnesium (2.65 g, 109 mmol) and 2-ethylhexyl bromide (15 g, 77 mmol). The reaction mixture was stirred for 30 min at 0 °C. The temperature was then gradually warmed to room temperature until most of the magnesium reacted, followed by refluxing for 2 h. In another flask was dissolved 3-bromothiophene (7.0 g, 43 mmol) to which was then added [1, 3-bis (diphenylphosphino) propane] nickel(II) chloride (200 mg, 0.4 mmol) in anhydrous THF (100 mL). Three cycles of freeze−pump−thaw were performed to ensure complete removal of oxygen. The prepared 2-ethylhexyl magnesium bromide Grignard reagent was added by cannula to the red colored solution of nickel catalyst and the resulting brown solution was then refluxed for 18 h. The reaction mixture was washed with aqueous HCl (10% w/w) after cooling to room temperature. The organic phase was extracted with ethyl acetate, dried with $MgSO_4$, and the solvent was evaporated after removing the $MgSO_4$. The crude product was chromatographed on silica with 100% hexanes to afford a colorless oil (4.9 g, 58%). ^{1}H NMR ($CDCl_3$): δ = 7.23 (d, 1H), 6.94 (d, 2H), 2.53 (t, 2H), 1.44 (m, 1H), 1.30 (bs, 8H), 0.91 (t, 6H).

*3-(2-Ethylhexyl)thiophene-2,5-dicarbaldehyde (**5**).* To a solution of 3-(2-ethylhexyl) thiophene (7.5 g, 38 mmol) and freshly distilled TMEDA (9.8 g, 84 mmol) diluted in anhydrous hexanes (50 mL) under nitrogen, was added dropwise a solution of 2 M *n*- BuLi in hexane (42 mL, 84 mmol). After refluxing for 1.5 h, THF (40 mL) was added and the solution was cooled to −50 °C. Anhydrous DMF (14 mL, 190 mmol) was then added dropwise, after which the reaction mixture was allowed to warm to room temperature. After 2.5 h at room temperature, the reaction mixture was hydrolyzed with water (60 mL) and the mixture was extracted with ether. The organic layers were dried over $MgSO_4$ and concentrated. The crude product was purified by column chromatography with hexanes/ethyl acetate (90/10 v/v) to give the product as a colorless oil (5.8 g, 61%). ^{1}H NMR ($CDCl_3$), δ, ppm: 10.09 (s, 1H), 9.56 (s, 1H), 7.16 (s, 1H), 2.61 (t, 2H), 1.59 (septet, 1H), 1.31 (qt, 2H), 1.04 (bs, 6H), 0.92 (t, 6H). HR−MS(+): calculated for $[C_{14}H_{20}O_2S + H]^+$, 253.12840; found, 253.12842.

*Poly(3-(2-ethylhexyl)thiophene)-co-9,9-dihexylfluorenylazomethine (**PFl-co-Th**).* The copolymerization was done by mixing **1** (100 mg, 0.27 mmol) and 3-(2-ethyl-hexyl)-thiophene-2,5-dicarbaldehyde (68 mg, 0.27 mmol) in $CHCl_3$ (3.0 mL) in a pressure tube. A catalytic amount of diluted TFA (30 μL) was then added. The pressure tube was sealed and heated to 90 °C for 48 h. The reaction mixture was cooled to room temperature and the polymer was precipitated from a methanol/water mixture. The resulting red solid (60%, 80 mg) was filtered and washed with methanol, water and acetone and then dried under vacuum overnight. ^{1}H NMR (400 MHz, $CDCl_3$), δ, ppm: 10.41 (m, CHO), 8.95 (m, −-*N*═CH−), 8.40 (s, −Th−H) 7.34−7.71 (m, Fl−H), 6.71 (b, NH_2), 2.82 (m, $-CH_2$), 1.31 (m, $-CH-CH_2-$), 1.93 (m, $-CH_2-$), 0.77 (m, $-CH_3$).

*Poly(thiophene-3,4-dicarboxylic acid diethyl ester)-co-9,9-dioctylfluorenylazomethine (**PFl-co-DAT**).* The copolymerization was done similar to that above with **1** (485 mg, 1.88 mmol) and 9,9-dioctyl-fluorene-2,7-dicarbaldehyde (840 mg, 1.88 mmol) in $CHCl_3$ (10 mL) in a pressure tube at 90 °C for 48 h. The reaction mixture was cooled to room temperature and it was poured into a methanol/water mixture. The resulting precipitate was filtered and it was washed with methanol, water and then acetone. The title polymer was isolated as a red solid (70%, 120 mg) after drying under vacuum overnight. ^{1}H NMR (400 MHz, $CDCl_3$) δ ppm: 10.1 (m, CHO), 8.52 (m, −*N*═CH−), 7.53−7.91 (m, Fl-H), 6.35 (b, NH_2), 4.24−4.49 (m, $O-CH_2$), 2.02 (m, $-CH_2$), 1.33 (m, $-CH_2-CH_2-$), 0.80 (m, $-CH_2-$), 0.59 (m, $-CH_3$).

*Poly(2,3-dihydrothieno[3,4-b][1,4]dioxine)-co-9,9-dihexylfluorenylazomethine (**PFl-co-EDOT**).* The copolymerization was similar to that above with 2,3-dihydrothieno[3,4-b][1,4]dioxine-5,7-dicarbaldehyde (163 mg, 0.882 mmol) and **1** (300 mg, 0.882 mmol) in $CHCl_3$ (6 mL) in a pressure tube at 90 °C for 48 h. The reaction was then cooled to room temperature and it was poured into a methanol/water mixture. The resulting red precipitate was filtered. It was then washed consecutively with methanol, water and acetone. The title polymer was isolated as a red solid (60%, 140 mg) after drying under vacuum overnight. ^{1}H NMR (400 MHz, $CDCl_3$) δ ppm: 10.01 (m, CHO), 8.75 (m, −*N*═CH−), 7.31−7.71 (m, Fl−H), 6.7 (b, NH_2), 4.44−4.47 (m, $O-CH_2$, EDOT), 1.99 (m, $-CH_2$), 1.05 (m, $-CH_2-CH_2-$), 0.78 (m, $-CH_2-$), 0.64 (m, $-CH_3$).

*9,9-Dihexyl-N,N′-bisthiophen-2-ylmethylenefluorene-2,7-diamine (**Th-Fl-Th$_1$**).* In ethanol (20 mL) were dissolved **1** (40.0 mg, 0.1 mmol) and thiophene-2-carbaxyldehyde (36 mg, 0.32 mmol) to which was then added a 1 M solution of TFA (20 μL). The solution was stirred at room temperature for 12 h, after which the solvent was evaporated and the product was extracted into ethyl acetate. The organic layer was washed with a brine solution and dried over Na_2SO_4. After filtering, the solvent was removed under reduced pressure and the crude product was purified by silica gel column chromatography with hexanes/ethyl acetate (80/20% v/v). The product was obtained as an orange solid (32 mg, 58% yield). ^{1}H NMR ($CDCl_3$), δ, ppm: 8.7 (s, 2H), 7.68 (d, 2H), 7.53 (d, 4H), 7.23−7.29 (m, 4H), 7.01 (s, 2H), 1.99 (t, 4H), 1.25 (p, 4H), 1.11 (m, 4H), 0.78 (t, 6H), 0.66 (t, 4H). ^{13}C NMR (acetone), δ, ppm: 164.9, 164.3, 161.5, 147.0, 144.1, 140.4, 133.4, 131.0, 102.2, 61.1, 60.1, 32.2, 32.0, 26.7, 22.9, 14.4, 14.1, 13.9. HR−MS (+): calculated for $[C_{35}H_{40}N_2S_2 + H]^+$, 553.27089; found, 553.27089.

*9,9-Dihexyl-N,N′-bis(5-butylthiophen-2-ylmethylene)fluorene-2,7-diamine (**Th−Fl−Th$_2$**).* In ethanol (40 mL) were dissolved **1** (110.0 mg, 0.41 mmol) and 5-butylthiophene-2-carbaxyldehyde (222 mg, 1.32 mmol) to which was then added a 1 M solution of TFA (60 μL). The solution was stirred at room temperature for 12 h. The solvent was then removed under reduced pressure and the crude product was extracted into ethyl acetate. The organic layer was washed with a brine solution and dried over Na_2SO_4. After filtering and then removing the solvent under reduced pressure, the crude product was purified by silica gel column chromatography with hexanes/ethyl acetate (70/30% v/v). The product was obtained as an orange solid (212 mg, 78% yield). ^{1}H NMR (acetone-d_6), δ, ppm: 8.78 (s, 2H), 7.78 (d, 2H), 7.46 (d, 2H), 7.37 (d, 2H), 7.25 (d, 2H), 6.94 (d, 2H), 2.88 (t, 4H), 1.73 (p, 4H), 1.30 (t, 4H), 1.08 (p, 8H), 0.95 (t, 6H), 0.74 (t, 12H). ^{13}C NMR (acetone), δ, ppm: HR−MS (+): calculated for $[C_{43}H_{56}N_2S_2 + H]^+$, 665.39840; found, 665.39751.

■ DISCUSSION AND RESULTS

The polymers presented in Chart 1 were targeted for examining the effect of incorporating different thiophenes on the polymer's opto-electronic properties. The particular properties of interest are the emission colors and fluorescence quantum yields, given that previously investigated polyazomethines were all nonfluorescent. The exception is **PFl-*co*-Fl** that fluoresces in appreciable amounts (Table 2).[37] The additional benefit of incorporating thiophene into the polymers is that significant spectral changes for both the absorbance and emission are expected relative to the all-fluorene **PFl-*co*-Fl** polymer. Significant spectral changes are additionally expected between **PFl-*co*-Th** vs **PFl-*co*-EDOT**, owing to the electronic differences of the EDOT and thiophene moieties. Meanwhile, the effect of the azomethine placement on the opto-electronic properties is expected by comparing the measured properties of **PFl-*co*-DAT** relative to both **PFl-*co*-Th** and **PFl-*co*-EDOT**.

The monomers required for synthesizing the targeted copolymers were prepared by known means as outlined in

dx.doi.org/10.1021/ma2024304 | *Macromolecules* 2012, 45, 1165−1173

the Supporting Information. Notably, the diaminothiophene was prepared in one-step from elemental sulfur via the Gewald reaction.[43−45] Meanwhile, the diaminofluorene (**1**) was prepared in three steps in 72% overall yield starting from fluorene.[37,40] It is noteworthy that the resulting **1** is not stable under ambient conditions for extended periods of time. It was therefore immediately polymerized once it was obtained in high purity. The complementary fluorene-2,7-dicarboxaldehyde was prepared from 2,7-dibromofluorene in two steps in 58% overall yield. The 3-(2-ethylhexyl)thiophene derivative was prepared from 3-bromothiophene via the Kumada reaction.[34] This monomer was chosen over 3,4-dialkylated thiophenes because the resulting polymer was expected to be soluble. Moreover, its preparation gives rise to fewer side products, in contrast when starting with 3,4-dibromothiophene.

The targeted polymers were prepared by combining stoichiometric amounts of the given monomers in chloroform in addition to a catalytic amount of trifluoroacetic acid. The homogeneous reaction mixture was subsequently heated to 90 °C in a sealed pressure tube for 48 h. In all cases, the polymers were red in color, confirming their increased degree of conjugation relative to their colorless monomers. While highly pure polymers could be obtained by simple removal of the solvent, the polymers were precipitated from a methanol/water mixture. This was to ensure that undesired low molecular weight oligomers and monomers, that would otherwise influence the opto-electronics properties, were removed. The targeted polymers were obtained in both good yields and high purity after precipitation.

Both ^{1}H NMR and GPC were used for confirming polymer formation. While formation of the desired azomethine is inferred by the change in color during the polymerization owing to an increase degree of conjugation, absolute confirmation was possible by ^{1}H NMR. The azomethine proton has a distinctive chemical shift at ca. 8.5 ppm that does not overlap with other protons. This provides a clean window for accurate integration relative to the chain-end aldehyde, which also has a distinct resonance at ca. 10 ppm. The average degree of polymerization (DP_n) was calculated by integrating imine protons relative to the terminal aldehydes (see Supporting Information). The average M_n calculated by NMR was consistent with that determined by relative GPC calibrated against polystyrene standards. This is somewhat surprising since the hydrodynamic radii of the polyazomethines and polystyrene standards are assumed to be different. This should lead to artificially higher molecular weights determined by GPC relative to those calculated by NMR. The same correlation between GPC and NMR molecular weight was also previously found for other polyazomethines.[33,37] The results suggest that GPC provides relatively accurate molecular weight for polyazomethines. This aside, the measured molecular weights and thermal properties are summarized in Table 1.

There is an appreciable difference in the degree of polymerization of **PFl-*co*-DAT** relative to **PFl-*co*-Th** and **PFl-*co*-EDOT** (Table 1). However, this was not expected to impact the opto-electronic properties. This is based on our previous work with polythiophene azomethines that showed no change in opto-electronic properties with $DP_n > 10$.[33,37] While, no attempt was made to optimize the polymerization conditions, higher molecular weights are expected with extended polymerization times and at higher concentrations. The added advantage of polyazomethines is that the terminal functional groups remain active postpolymerization. The polymers can therefore be either repolymerized resulting in increased molecular weights or reacted with other polyazomethines leading to extended block copolymers.[33]

Table 1. Molecular Weights and Thermal Properties of the Polyazomethines Studied

polymer	M_n (g/mol)[a]	M_n (g/mol)[b]	M_w (g/mol)[b]	PDI[b]	DP_n	T_d (°C)[c]	T_g (°C)[d]
PFl-*co*-Th	7 200	7 700	9 300	1.20	13	330	115
PFl-*co*-DAT	15 100	16 400	22 100	1.35	23	320	146
PFl-*co*-EDOT	6 600	6 900	11 900	1.72	13	380	148

[a]Determined by ^{1}H NMR. [b]Determined by GPC relative to polystyrene standards. [c]Determined by thermal analysis measured at 10 °C/min under N_2. [d]Determined by DSC measured at a 5 °C/min under N_2.

The thermal properties of the polyfluorenylazomethines were investigated by both thermogravimetric analysis (TGA) and differential scanning calorimetry (DSC). Interestingly, no weight loss was seen at 100 °C, confirming that the polymers are not hydroscopic and that the azomethine is not as a hydrate. This is contrast to the all-thiophene polyazomethine that was hydroscope.[34] All the polymers investigated similarly showed resolvable glass transition temperatures (T_g) between 115° and 148 °C (Figure S1, Supporting Information). **PFl-*co*-Th** has the lowest T_g as result of the branched 2-ethylhexyl side chain. Meanwhile, both **PFl-*co*-DAT** and **PFl-*co*-EDOT** were found to have similar T_g, despite having different DP_n.

Photophysical Properties. Both the absorbance and fluorescence properties of the polyazomethines were investigated. As seen in Figure 1, there are appreciable differences in the spectra that are dependent on the type of thiophene incorporated into the polymer. Taking **PFl-*co*-Fl** as the benchmark (λ_{abs} = 450 and λ_{fl} = 560 nm), both the absorbance and fluorescence of the thiophene copolymers are bathochromically shifted. This is a result of the electron richness of the heterocycle. Also, it is known that heterocycles adopt coplanar arrangements with the azomethine bond to which they are attached.[46] This further increases the degree of conjugation leading to the observed spectral changes. This is in contrast to homoaryls that are twisted by up to 65° from the azomethine bond to which they are attached.[47−51]

The absorbance of **PFl-*co*-DAT** is red-shifted by 40 nm from **PFl-*co*-EDOT**, which in turn is red-shifted by 60 nm from **PFL-*co*-Th**. The bathochromic shifts are a result of electronic effects. For example, the electron donating effect of the EDOT moiety works in concert with the electron withdrawing azomethine. The net result is an electronic *push−pull* effect. The bathochromic shift is more pronounced with **PFl-*co*-DAT** owing to the electronic *pull−pull* effect between the electron withdrawn esters and azomethines. The trend of bathochromic shifts is also observed with the fluorescence spectra shown in Figure 1B. The effect of the different thiophenes on the optical properties is further evident in the photographs in Figure 2. While subtle variations in color are visibly seen in the absorbance, the effect is more pronounced in the fluorescence. As seen in panels D−F of Figure 2, the three primary red, blue, and green emission colors are possible contingent on the thiophene incorporated into the copolymer.

Bathochromic shifts were also seen with spin coated samples of the polyazomethines deposited as thin films. The thin film

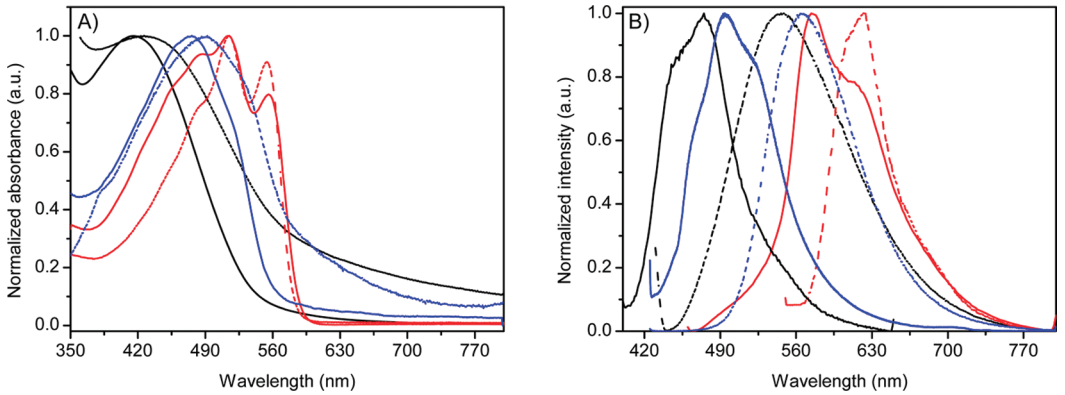


Figure 1. Normalized absorbance (A) and fluorescence (B) spectra in solution (solid line) and thin film (dashed line) of PFl-*co*-Th (black line), PFl-*co*-DAT (red line), and PFl-*co*-EDOT (blue line).

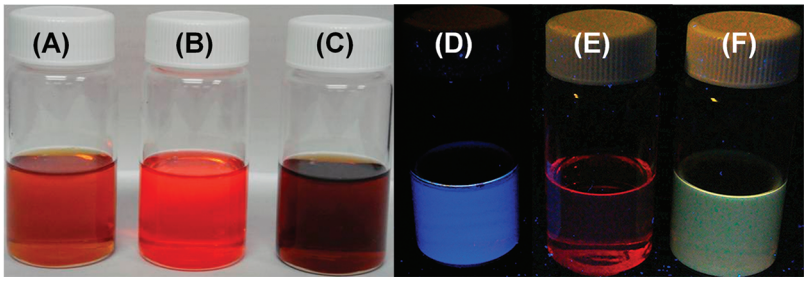


Figure 2. Photographs of PFl-*co*-Th (A), PFl-*co*-DAT (B), and PFl-*co*-EDOT (C) in dichloromethane under ambient light and PFl-*co*-Th (D), PFl-*co*-DAT (E), and PFl-*co*-EDOT (F) irradiated with a UV lamp at 350 nm.

Table 2. Photophysical and Electrochemical Properties of the Fluorenylazomethines

compound	λ_{abs} (nm)[a]	λ_{fl} (nm)[a]	λ_{abs} with added TFA (nm)	λ_{abs} with added $FeCl_3$ (nm)	E_g^{opt} (eV)[b]	E_{pa} (V)[c]	E_{pc} (V)[d]	HOMO (eV)[e]	LUMO (eV)[e]	E_g^{el} (eV)[f]	Φ_{fl} rt (H^+)[g]	Φ_{fl} 77 K[h]	Φ_{fl} (thin-film)[i]
PFl-*co*-DAT	514, 553 (516,558)	576 (622)	565	600/652	2.11	0.93	−0.98	5.16	3.47	1.7	0.13 (0.66)	3×	0.11
PFl-*co*-Th	415 (438)	473 (546)	475	440/595	1.58	0.84	−1.05	4.88	3.67	1.2	0.15	4×	0.09
PFl-*co*-EDOT	475 (493)	495 (565)	505	540	2.04	0.71	−1.11	4.98	3.63	1.3	0.26 (0.85)	3×	0.03
PFl-*co*-Fl[j]	425 (452)	551 (563)	510	531	2.20	1.54	−0.87	5.94	3.53	2.4	0.19 (0.75)	≈5×	0.4
Th-Fl-Th$_1$	388	468	440	450	2.53	0.92	-	5. 2	2.67	2.5	0.27 (0.86)	3×	-
Th-Fl-Th$_2$	395	475	460	475	2.41	0.90	-	5.16	2.7	2.4	0.12 (0.42)	2×	-

[a]In dichloromethane. Values in parentheses are for thin film samples. [b]Spectroscopically determined energy gap taken from the absorption onset (E_g = 1240/ λ_{onset}). [c]Oxidation potential relative to saturated Ag/Ag^+ electrode. [d]Reduction potential relative to Ag/Ag^+. [e]Relative to the vacuum level. [f]Electrochemically derived energy gap. [g]Absolute fluorescence quantum yield at room temperature. Values in parentheses are the room temperature absolute fluorescence quantum yield upon protonation with TFA. [h]Fluorescence enhancement at 77 K relative to room temperature and uncorrected for the change in refractive index at different temperatures. [i]Spin-coated samples. [j]From ref 37.

absorbance spectra are bathochromically shifted by ca. 20 nm while the fluorescence spectra are shifted by about 70 nm from the corresponding polyazomethine in solution.

The property of particular interest for the polyazomethines is their fluorescence quantum yield (Φ_{fl}). This is because the azomethine linkage is known to quench the fluorescence of even the most intrinsically fluorescent fluorophores.[46−54] The desired fluorescence quantum yields were measured using an integrating sphere. This method is preferred over relative methods because the absolute quantum yields can be measured independent of references whose fluorescence yields are wavelength dependent and typically contain errors up to 20%. The Φ_{fl} can therefore be accurately determined.

As seen in Table 2, the polymers fluoresce in considerable amounts. In fact, the Φ_{fl} are comparable to polyfluorene vinylenes that are used emitting devices.[29] This is in contrast to previously investigated thiophene azomethine derivatives whose fluorescence quantum yields were ca. 0.01.[46,49−51,55,56] Analogous copolyazomethines derived from 9,9-unsubstituted 2,7-diaminofluorene also do not fluoresce.[25,26] As seen in the photographs D−F in Figure 2, the polymer fluorescence can visually be detected by the naked eye. The less intense emission seen in Figure 2F,G is from the poor photoresponse of the camera's PMT and not from a low fluorescence yield. This is supported by the absolute Φ_{fl} of the polymers that are all on the order of 10%. High Φ_{fl} were even observed in thin films, suggesting that there is little self-quenching. The measured

dx.doi.org/10.1021/ma2024304 | *Macromolecules* 2012, 45, 1165−1173

absolute fluorescence quantum yields when compared to previously reported studies, confirm that 9,9-dialkylation of the diaminofluorene is a critical structural element for preserving the inherent fluorescence of the fluorene.

While the polymers' Φ_{fl} are ca. 10%, their fluorescence could be restored to near unity by two means; low temperature and acid doping. Reducing the temperature to 77 K resulted in fluorescence yield enhancement. It should be noted that the calculated values at 77 K are uncorrected for the change in solvent refractive index with temperature. Therefore, the measured values are lower limits and the true amount of fluorescence enhancement is expected to be 20% higher. Nonetheless, the increased fluorescence with temperature implies that reduced fluorescence at room temperature most likely involves bond rotation deactivation processes.

Similar to the temperature induced fluorescence changes, fluorescence enhancement was also possible by protonating the azomethine with trifluoroacetic acid. The exact mechanism responsible for fluorescence increase with protonation has not yet been confirmed. Despite this, the collective fluorescence measurements confirm that polyazomethines can me made fluorescent. Meanwhile, their fluorescence enhancement with temperature and protonation illustrate the sensor-like properties of polyazomethines.

The thiophene-fluorene triads (**Th-Fl-Th$_1$** and **Th-Fl-Th$_2$**) were prepared to investigate whether high Φ_{fl} were also possible with triads derived from **1** and having reduced degree of conjugation relative to their polymer counterparts. Equally high Φ_{fl} were observed with the model compounds. They similarly exhibited the same fluorescence enhancement at low temperature and with acid protonation. The key component for achieving fluorescent fluorene azomethine derivatives is therefore the 9,9-dialkylation derivative of 2,7-diaminofluorene. This is evident from the unalkylated derivatives of **Th-Fl-Th** that are nonfluorescent (Φ_{fl}< 0.03).[49,55] While the exact structural composition required for making highly fluorescent azomethines is currently being investigated, the collective spectroscopic data confirm that both the color and emission can be tailored as a function of the thiophene. Also, fluorescent alternating copolyazomethines that emit with the primary RGB colors are possible by adjusting the HOMO−LUMO energy levels.

Electrochemistry. The electrochemical properties of the polymers were investigated by cyclic voltammetry to further gain insight into structural effects on the oxidation potential (E_{pa}). As seen in Figure 3, the polymers all undergo an oxidation process. Both the E_{pa} and the reversibility of the anodic process are contingent on the thiophene. For example, the E_{pa} of **PFl-*co*-EDOT** is less positive than **PFl-*co*-Th** by 130 mV, as expected owing to the strong electron donating character of EDOT. Meanwhile, the E_{pa} of **PFl-*co*-DAT** is 70 mV higher than **PFl-*co*-Th**. The increased E_{pa} is expected given the strong electron withdrawing character of the thiophene esters. The measured E_{pa} of the polyazomethines confirm that the polymers are stable under ambient conditions. Meanwhile, the reversible oxidation for both **PFl-*co*-Th** and **PFl-*co*-EDOT** confirm the robustness of the heteroatomic bond under oxidation conditions.

The polymers also underwent a cathodic processes corresponding to a two-electron transfer. Interestingly, the reduction potential (E_{pc}) was less affected by the thiophene incorporated into the copolymer than the corresponding E_{pa}.

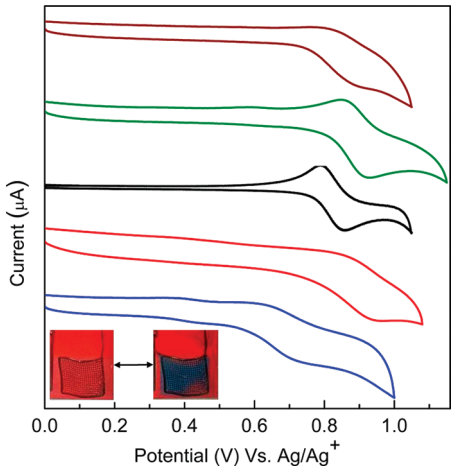


Figure 3. Cyclic voltammograms of **PFl-*co*-Th** (black line), **PFl-*co*-DAT** (red line), **PFl-*co*-EDOT** (blue line), **Th−Fl−Th$_1$** (green line), and **Th−Fl−Th$_2$** (maroon line) in dichloromethane at a scan rate of 50 mV/s under N_2. Inset: Photographs of original (left) and electrochemically oxidized (right) **PFl-*co*-DAT** by applying a potential of 1.0 V for 1 min.

Only in the case of **PFl-*co*-EDOT** (Figure S14, Supporting Information) was the cathodic process reversible.

The electrochemistry of the **Th−Fl−Th** triads was also investigated. Comparing their E_{pa} to that of **PFl-*co*-Th** would provide insight into the effect of the degree of conjugation on the oxidation potential. Furthermore, comparing the anodic behavior of **Th−Fl−Th$_2$** relative to **Th−Fl−Th$_1$** would provide information about both the stability of the radical cation and the azomethine bond. The E_{pa} of both **Th−Fl−Th** were 80 mV more positive than the corresponding polymer. While the electron withdrawing character of the azomethine should increase the oxidation potential, the high degree of conjugation of **PFl-*co*-Th** offsets this effect, leading to the observed less positive E_{pa}. As expected, there is a noticeable difference between the reversibility of the oxidation process of **Th−Fl−Th$_1$** and **Th−Fl−Th$_2$**. The oxidation process of **Th−Fl−Th$_2$** was reversible while that of **Th−Fl−Th$_1$** wass pseudoreversible. The difference in reversibility is uniquely a result of the substitution in the α,α' position. The α,α' alkylation of **Th−Fl−Th$_2$** prevents the electrochemically generated radical cation from coupling according to known means.[57−60] The observed reversible oxidation confirms that the azomethine is robust. It further confirms that heteroatomic bond does not decompose when oxidized. Meanwhile, the pseudoreversible oxidation of **Th−Fl−Th$_1$** suggests that the radical cation is not highly reactive. This is most likely a result of the high degree of conjugation of the compounds allowing the radical cation to be delocalized across the entire molecule.

The spectroscopic properties of the electrochemically generated radical cation were additionally investigated by spectroelectrochemistry in solution. From an application point of view, spectroelectrochemical studies of thin films of the polymers would be more advantageous. However, their solubility in standard electrochemical solutions precludes such studies. Spectroelectrochemical studies in solution were done by applying a potential slightly more positive than the E_{pa} of the given polymer and observing the resulting absorbance changes. In all cases, the absorbance of the generated radical cation was bathochromically shifted from the corresponding neutral form (Table 2). The most stark visible color change was with **PFl-*co*-**

dx.doi.org/10.1021/ma2024304 | *Macromolecules* 2012, 45, 1165−1173

DAT, whose color changed from red to blue upon oxidation. This is seen in the inset of Figure 3. The new absorbance occurred at 620 nm while the absorbance of the electrochemically generated radical cation for **PFl-*co*-Th** and **PFl-*co*-EDOT** was 442 and 450 nm, respectively. The original color of the polymers could be quantitatively restored by applying a potential of −100 mV. This once again illustrates the robustness of the polyazomethines.

Halochromism and Chemical Oxidation. Given that electrochemically induced color changes were possible, the chemical doping of the polymers was additionally investigated. Oxidizing the polymers in solution has the advantage that the stability of the doped state can be assessed by monitoring the reversible color changes. This is in contrast to the spectroelectrochemical studies where diffusion does not occur and the intermediates are artificially stable. Dichloromethane solutions of the copolymers were oxidized with $FeCl_3$. This is a choice oxidant because it is spectroscopically transparent in the spectral window investigated. Its reduction potential is also compatible with the oxidation potentials of the polymers investigated.

Significant color changes occurred upon adding the oxidant and the resulting absorbance shifts summarized in Table 2. A representative absorbance spectral change of **PFl-*co*-EDOT** is shown in Figure 4, illustrating a 50 nm bathochromic shift in the absorbance upon chemical doping. The oxidized species were subsequently neutralized to the original state after equilibrating for a few minutes and by adding excess hydrazine hydrate. The reversible color changes between the neutral and oxidized states are seen in the pictures of Figure 5. Both the original intensity and absorbance of the neutral azomethines were observed when reducing the oxidized states with hydrazine hydrate. It should be noted that no special precautions such as anhydrous or degassed solvents were used for the oxidation/neutralization studies. Hypsochromic shifts, decrease in intensity, and even complete disappearance of the absorbance would be observed if the polyazomethines decomposed or hydrolyzed during the oxidation/neutralization cycle. The absence of detectable change in the absorbance spectra between the original and the oxidized/neutralized azomethines (Figures 4 and 5) confirm the azomethines are both hydrolytically and oxidatively robust. The exception is **PFl-*co*-DAT** whose original color cannot be restored once neutralized with hydrazine hydrate (Figure S10, Supporting Information).

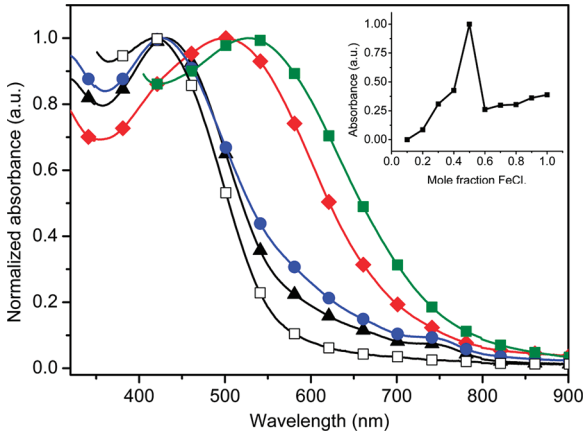


Figure 4. Normalized absorbance spectra of **PFl-*co*-EDOT** in dichloromethane (▲) with the addition of 1 equiv of TFA (red ◆), followed by the addition of 1 equiv of triethylamine (blue ●), a pristine sample of **PFl-*co*-EDOT** (▲) with the addition of 1 equiv of $FeCl_3$ (green ■), followed by the addition of 1 equiv of hydrazine hydrate (□). Inset: Absorbance of **PFl-*co*-Th** monitored at 595 nm as a function of $FeCl_3$ mole fraction.

The added advantage of oxidation studies in solution is that the stoichiometry can be spectroscopically determined via the Job method. By varying the mole fraction of the oxidant, the stoichiometry can be derived from the absorbance maximum, as seen in the inset of Figure 4. A 1:1 stoichiometry was found for the all the compounds in Chart 1. Given that ferric chloride is a one-electron oxidant taken together with the determined stoichiometry, the chemically generated intermediate is a radical cation. While this intermediate is consistent with the electrochemically produced species measured by cyclic voltammetry, there are spectroscopic differences between the chemically and electrochemically generated species (Figures S4−S6, Supporting Information). The spectroelectrochemically observed intermediates in solution for the all the polymers were hypsochromically shifted by 40 nm relative to their corresponding intermediates produced by $FeCl_3$. The observed difference may be a counteranion effect, which is currently being examined.

Azomethines are known to be halochromic with significant spectral changes occurring when protonated.[31,36,37,46,61] The advantage of the studied polyazomethines is that they absorb strongly in the visible as a result of their extended degree of conjugation. Therefore, their protonation should lead to significant visible color changes. This provides the means to spectroscopically follow the stability of the protonated form and to investigate their resistance toward acid hydrolysis. The halochromic behavior (color change with protonation) of the azomethines in Chart 1 was subsequently investigated with

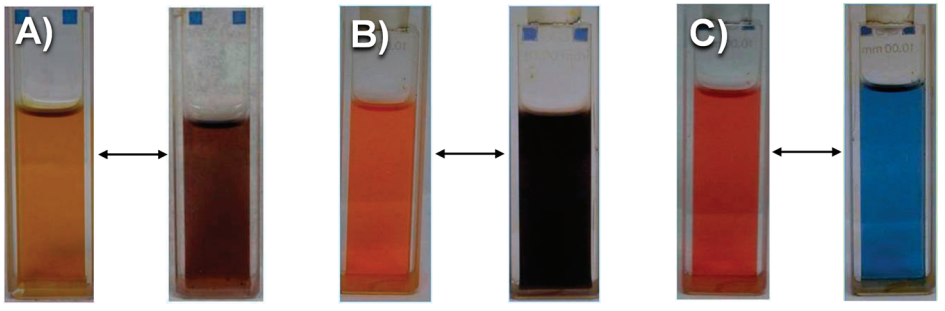


Figure 5. Pictures of PFl-*co*-Th (A), PFl-*co*-EDOT (B), and PFl-*co*-DAT (C) in dichloromethane (left), after the addition of $FeCl_3$ (right), followed by the addition of hydrazine hydrate (left).

dx.doi.org/10.1021/ma2024304 | *Macromolecules* 2012, 45, 1165−1173

trifluoroacetic acid. Exposing the polyazomethines to concentrated acid resulted in absorbance bathochromic shifts. However, the acid induced spectral changes were slightly different than those observed with ferric chloride. This is owing to the resulting cation that has weaker charge transfer effect than the radical cation that is produced by oxidation with ferric chloride (vide supra).

The protonated azomethines could be neutralized by adding triethylamine. Similar to the oxidation studies, the azomethines could be reversibly protonated and neutralized without any spectroscopically detectable decomposition. The exception being **PFl-*co*-DAT** that undergoes minor color degradation. The reversible protonation/neutralization is illustrated in Figure 4. The salient features of the absorbance spectrum are the reversible color change without color degradation after protonation and neutralization. Given that anhydrous solvents or special precautions were not used for the halochromic studies, residual water in the solvent or ambient moisture would readily hydrolyze the azomethine bond upon acid addition. However, no color degradation was observed after protonation/neutralization cycles. This demonstrates the resistance of the azomethines toward acid hydrolysis. The collective halochromic and oxidation spectroscopic studies confirm that the conjugated azomethine derivatives are robust and they resist both oxidation and acid hydrolysis.

CONCLUSION

Stable and conjugated copolyazomethines consisting of alternating fluorene and thiophenes were prepared. Both the absorbance and fluorescence of the polymers were contingent on the type of thiophene incorporated, with emission of the three primary colors being possible. The polymers were found to be consistently fluorescent with fluorescence quantum yield enhancement being possible by either protonation or with temperature decrease. The reported polymers are among the first examples of fluorescent polyazomethines. It was found that a key structural element for making polyazomethines fluorescent was the use of 9,9-dialkyl-2,7-diamino fluorene. The reasonable Φ_{fl} make the polyazomethines interesting candidates for use in emitting applications especially when considering their ease of preparation and purification. Meanwhile, the temperature and acid dependent fluorescence make the polyazomethines interesting sensor-like materials. It was further demonstrated that the polyazomethines resists both chemical and electrochemical oxidation in addition to acid hydrolysis, contrary to common belief. In fact, the stark color changes possible between their neutral and oxidized/protonated states concomitant with the chemical and hydrolytic robustness make these polyazomethines interesting materials for use in devices such as electrochromics and sensor applications.

ASSOCIATED CONTENT

Supporting Information

Synthetic schemes, absorbance, fluorescence, NMR, and doping spectra and GPC and electrochemical data. This material is available free of charge via the Internet at http://pubs.acs.org/.

AUTHOR INFORMATION

Corresponding Author

*E-mail: w.skene@umontreal.ca.

ACKNOWLEDGMENTS

The Natural Sciences and Engineering Research Council Canada is acknowledged for financial support in terms of Discovery, Strategic Research, and Research Tools and Instruments grants. The Canada Foundation for Innovation is also thanked for equipment funding. The Centre for Self-Assembled Chemical Structures is also acknowledged.

REFERENCES

(1) Szarko, J. M.; Guo, J.; Rolczynski, B. S.; Chen, L. X. *J. Mater. Chem.* **2011**, *21*, 7849.
(2) Koo, H.-J.; Chang, S. T.; Slocik, J. M.; Naik, R. R.; Velev, O. D. *J. Mater. Chem.* **2011**, *21*, 72.
(3) Xue, J. *Polym. Rev.* **2010**, *50*, 411.
(4) Wong, W.-Y.; Tang, B. Z. *Macromol. Chem. Phys.* **2010**, *211*, 2460.
(5) Gather, M. C.; Köhnen, A.; Meerholz, K. *Adv. Mater.* **2011**, *23*, 233.
(6) Kamtekar, K. T.; Monkman, A. P.; Bryce, M. R. *Adv. Mater.* **2010**, *22*, 572.
(7) Arias, A. C.; MacKenzie, J. D.; McCulloch, I.; Rivnay, J.; Salleo, A. *Chem. Rev.* **2010**, *110*, 3.
(8) Ma, H.; Yip, H.-L.; Huang, F.; Jen, A. K. Y. *Adv. Funct. Mater.* **2010**, *20*, 1371.
(9) Facchetti, A. *Chem. Mater.* **2010**, *23*, 733.
(10) Bassani, D. M.; Jonusauskaite, L.; Lavie-Cambot, A.; McClenaghan, N. D.; Pozzo, J.-L.; Ray, D.; Vives, G. *Coord. Chem. Rev.* **2010**, *254*, 2429.
(11) Wang, Y.; Tan, H.; Liu, Y.; Jiang, C.; Hu, Z.; Zhu, M.; Wang, L.; Zhu, W.; Cao, Y. *Tetrahedron* **2010**, *66*, 1483.
(12) Zhao, Q.; Liu, S.-J.; Huang, W. *Macromol. Chem. Phys.* **2009**, *210*, 1580.
(13) Wang, P.-H.; Ho, M.-S.; Yang, S.-H.; Chen, K.-B.; Hsu, C.-S. *J. Polym. Chem. A* **2010**, *48*, 516.
(14) Kucherak, O. A.; Didier, P.; Mély, Y.; Klymchenko, A. S. *J. Phys. Chem. Lett.* **2010**, *1*, 616.
(15) Wu, H. Y.; Wang, K. L.; Jiang, J. C.; Liaw, D. J.; Lee, K. R.; Lai, J. Y.; Chen, C. L. *J. Polym. Sci., Part A* **2010**, *48*, 3913.
(16) Scheler, E.; Strohriegl, P. *Chem. Mater.* **2010**, *22*, 1410.
(17) Li, K.; Liu, B. *Polym. Chem.* **2010**, *1*, 252.
(18) Wei, W.; Yu, N.; Zhu, R.; Peng, B.; Huang, W. *J. Appl. Polym. Sci.* **2008**, *108*, 2438.
(19) Jin, S.-H.; Kang, S.-Y.; Kim, M.-Y.; Chan, Y. U.; Kim, J. Y.; Lee, K.; Gal, Y.-S. *Macromolecules* **2003**, *36*, 3841.
(20) Phanichphant, S.; Anuragudom, P.; Newaz, S. S.; Lee, T. R. *Macromolecules* **2006**, *39*, 3494.
(21) Leclerc, M.; Ranger, M.; Rondeau, D. *Macromolecules* **1997**, *30*, 7686.
(22) Scherf, U.; Nothofer, H. G.; Meisel, A.; Miteva, T.; Neher, D.; Forster, M.; Oda, H.; Lieser, G.; Sainova, D.; Yasuda, A.; Lupo, D.; Knoll, W. *Macromol. Symp.* **2000**, *154*, 139.
(23) Miller, R. D.; Kreyenschmidt, M.; Klaerner, G.; Fuhrer, T.; Ashenhurst, J.; Karg, S.; Chen, W. D.; Lee, V. Y.; Scott, J. C. *Macromolecules* **1998**, *31*, 1099.
(24) Lee, T. S.; Kim, H. J.; Lee, J. H.; Lee, M. *React. Funct. Polym* **2008**, *68*, 1696.
(25) Tsai, F.-C.; Chang, C.-C.; Liu, C.-L.; Chen, W.-C.; Jenekhe, S. A. *Macromolecules* **2005**, *38*, 1958.
(26) Liu, C.-L.; Chen, W.-C. *Macromol. Chem. Phys.* **2005**, *206*, 2212.
(27) Hyun-Chul Kim, J.-S. K.; Kim, K.-S.; Park, H.-K.; Baek, S.; Ree, M. *J. Polym. Sci., Part A* **2004**, *42*, 825.
(28) Bruma, M.; Hamciuc, E.; Schulz, B.; Koepnick, T.; Kaminorz, Y.; Robinson, J. *Macromol. Symp.* **2003**, *199*, 511.
(29) Marin, L.; Perju, E.; Damaceanu, M. D. *Eur. Polym. J.* **2011**, *47*, 1284.
(30) Liu, C. L.; Chen, W. C. *Macromol. Chem. Phys.* **2005**, *206*, 2212.
(31) Barik, S.; Bishop, S.; Skene, W. G. *Mater. Chem. Phys.* **2011**, *129*, 529.

(32) Bolduc, A.; Lachapelle, V.; Skene, W. G. *Macromol. Symp.* **2010**, *297*, 87.
(33) Barik, S.; Skene, W. G. *Macromolecules* **2010**, *43*, 10435.
(34) Bourgeaux, M.; Skene, W. G. *Macromolecules* **2007**, *40*, 1792.
(35) Pérez Guarìn, S. A.; Skene, W. G. *Mater. Lett.* **2007**, *61*, 5102.
(36) Bolduc, A.; Dufresne, S.; Skene, W. G. *J. Mater. Chem.* **2010**, *20*, 4820.
(37) Barik, S.; Skene, W. G. *Polym. Chem.* **2011**, *2*, 1091.
(38) Bright, D. W.; Moss, K. C.; Kamtekar, K. T.; Bryce, M. R.; Monkman, A. P. *Macromol. Rapid Commun.* **2011**, *32*, 983.
(39) Pérez Guarìn, S. A.; Bourgeaux, M.; Dufresne, S.; Skene, W. G. *J. Org. Chem.* **2007**, *72*, 2631.
(40) Barik, S.; Friedland, S.; Skene, W. G. *Can. J. Chem.* **2010**, *88*, 945.
(41) Pérez Guarìn, S. A.; Dufresne, S.; Tsang, D.; Sylla, A.; Skene, W. G. *J. Mater. Chem.* **2007**, *17*, 2801.
(42) Tsang, D.; Bourgeaux, M.; Skene, W. G. *J. Photochem. Photobiol. A* **2007**, *192*, 122.
(43) Gewald, K. *Chem. Hetero. Comp.* **1976**, *12*, 1077.
(44) Gütschow, M.; Schröter, H.; Kuhnle, G.; Eger, K. *Monats. Chem.* **1996**, *127*, 297.
(45) Bourgeaux, M.; Vomscheid, S.; Skene, W. G. *Synth. Commun.* **2007**, *37*, 3551.
(46) Dufresne, S.; Skene, W. G. *J. Phys. Org. Chem.* **2011**, No. DOI: 10.1002/poc.1894.
(47) Dufresne, S.; Skalski, T.; Skene, W. G. *Can. J. Chem.* **2011**, *89*, 173.
(48) Dufresne, S.; Roche, I. U.; Skalski, T.; Skene, W. G. *J. Phys. Chem.* **2010**, *114*, 13106.
(49) Dufresne, S.; Guarìn, S. A. P.; Bolduc, A.; Bourque, A. N.; Skene, W. G. *Photochem. Photobiol. Sci.* **2009**, *8*, 796.
(50) Dufresne, S.; Callaghan, L.; Skene, W. G. *J. Phys. Chem. B* **2009**, *13*, 15541.
(51) Bourque, A. N.; Dufresne, S.; Skene, W. G. *J. Phys. Chem. C* **2009**, *113*, 19677.
(52) Knipping, É.; Roche, I. U.; Dufresne, S.; McGregor, N.; Skene, W. G. *Tetrahedron Lett.* **2011**, *52*, 4385.
(53) Dong, Y.; Bolduc, A. a.; McGregor, N.; Skene, W. G. *Org. Lett.* **2011**, *13*, 1844.
(54) Bolduc, A.; Dufresne, S.; Hanan, G. S.; Skene, W. G. *Can. J. Chem.* **2010**, *88*, 236.
(55) Skene, W. G.; Pérez Guarìn, S. A. *J. Fluores.* **2007**, *17*, 540.
(56) Dufresne, S.; Hanan, G. S.; Skene, W. G. *J. Phys. Chem. B* **2007**, *111*, 11407.
(57) Natera, J.; Otero, L.; Sereno, L.; Fungo, F.; Wang, N.-S.; Tsai, Y.-M.; Hwu, T.-Y.; Wong, K.-T. *Macromolecules* **2007**, *40*, 4456.
(58) Zotti, G.; Zecchin, S.; Schiavon, G.; Vercelli, B.; Berlin, A. *J. Electroanal. Chem.* **2005**, *575*, 169.
(59) Hapiot, P.; Lagrost, C.; LeFloch, F.; Raoult, E.; Rault-Berthelot, J. *Chem. Mater.* **2005**, *17*, 2003.
(60) Roncali, J. *Chem. Soc. Rev.* **2005**, *34*, 483.
(61) Dufresne, S.; Bolduc, A.; Skene, W. G. *J. Mater. Chem.* **2010**, *20*, 4861.

Macromolecules

Article

pubs.acs.org/Macromolecules

High Refractive Index Polymers Based on Thiol−Ene Cross-Linking Using Polarizable Inorganic/Organic Monomers

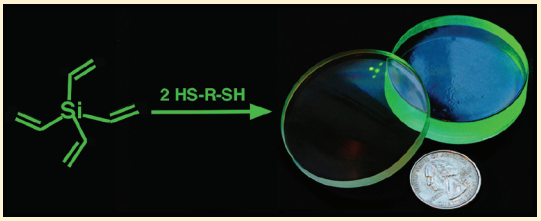
Sharad D. Bhagat,[‡] Jhunu Chatterjee,[†] Banghao Chen,[‡] and A. E. Stiegman*[,‡]

[‡]Department of Chemistry and Biochemistry, Florida State University, Tallahassee, Florida 32306, United States

[†]High Performance Materials Institute, Florida State University, Tallahassee, Florida 32306, United States

Supporting Information

ABSTRACT: The self-initiation of the thiol−ene coupling reaction of tetravinyl monomers containing main group elements and trivinyl heterocycles with alkyl and aryl dithiols resulted in the formation of highly cross-linked prepolymer gels which upon final curing at 120 °C yielded hard, monolithic polymeric materials. Because of the presence of highly polarizable main group elements such as Si, Ge, Sn, and S and the relative absence of highly electronegative elements, the resulting polymers exhibited high refractive indices ranging from 1.590 to 1.703 and Abbe numbers between 24.3 and 45.0. All of the polymers were highly transparent over the UV−vis region of the spectrum. Moreover, due to the high cross-linked density achievable in specific compositions, very hard materials capable of being ground and polished could be produced. The range of compositions produced yields important structure−property relationships, indicating the effect of monomer structure on mechanical and optical properties.



1. INTRODUCTION

Transparent optical-quality plastics are extremely important in many commercial optical applications, including camera and projector lenses, and in optometric applications, including prescription eyewear and contact lenses. These materials afford large advantages over metal oxide glasses in areas such as weight reduction and fracture resistance. A number of optical figures of merit must be achieved for a polymer to be useful for specific optical application. These include the refractive index (n), the Abbe number, and the percent transmission of light over the spectral range of interest. In addition, depending on the application, mechanical properties such as hardness, fracture toughness, and scratch resistance are also significant. Current optical polymer technology revolves principally around well-established polymers such as poly(methyl methacrylate)s, polycarbonates, polythioureas, polyvinylcarbazoles, and polyisocyanates.[1] Of the various optical properties, the refractive index is one of the most significant; as it dictates the shape and size, the lens must be to be utilized in a specific application. As such, much effort has been expended in developing high refractive index polymers. The primary approach to control the refractive index in a polymer is through the incorporation of polarizable atoms and groups, either as part of the backbone or as attached pendant groups. The basis for this approach lies in the concept of molar refractivity of the constituent monomers.[2] Constituents and monomers with high molar refractivity include aromatic and other unsaturated organic groups and groups containing polarizable main group heteroatoms, particularly sulfur. As such, polythiourethanes, polynaphthalenes, and polvinylcarbazoles exhibit refractive indices in the range of ∼1.6−1.70, which occupy the high end of the refractive index range for organic polymers.[1]

We report here the development of hybrid organic/inorganic thermoset polymers that utilize constituent monomers containing a preponderance of highly polarizable atoms such as Si, Ge, Sn, and S.[3] These polymers exhibit refractive indices that, on average, occupy the high end of the range of polymer refractive indices from 1.590 to 1.703. They also have Abbe numbers acceptable for most applications, are highly transparent, and, for many examples, are extremely hard and can be fabricated and polished into optical-quality monoliths. The repeat unit of the polymer is generated through the thiol−ene coupling reaction.[4−7] As has been noted previously, polymers formed by this reaction are particularly attractive for fabricating high index optical materials due to the fact that highly polarizable sulfur atoms are an intrinsic part of the repeat unit and that polymers can, in principle, be made which contain no highly electronegative, low-polarizability atoms such as N and O.[8,9] The problem with bulk polymers made through thiol−ene coupling reactions is that monolithic materials with the requisite strength and hardness required for optical applications are difficult to achieve due to the generally poor cross-link densities realized in this type of polymerization.[8] For this reason, thiol−ene polymers have typically been made and studied as films or in hybrid compositions with other polymers to impart strength.[8,10] We have overcome these problems by increasing the monomer functionality and through the use of a slow, self-initiation polymerization process.

Received: November 8, 2011
Revised: January 5, 2012
Published: January 20, 2012

ACS Publications © 2012 American Chemical Society

2. EXPERIMENTAL SECTION

Materials. Tetravinylsilane, tetraallylsilane, tetraallylgermanium, trimethyltrivinylcyclotrisiloxane, and tetramethyltetravinylcyclotetrasiloxane were obtained from Gelest and used as received. Tetravinyltin, triallyltriazinetrione, 1,3-benzenedithiol (99%), ethanedithiol, pentanedithiol, and azobis(isobutyronitrile) (AIBN) were purchased from Aldrich and used as received. Tetravinylgermane was synthesized using a published procedure.[11,12] It is important to note that reagent purity is extremely important in achieving hard materials. While most reagents were used as received, the highest purity was always utilized if there was a choice. In the case of tetravinylgermane, two fractional distillations were required to obtain sufficient purity to yield hard materials.

Synthesis. *Photoinitiation.* Stoichiometric solutions of vinyl and thiol monomers were mixed until homogeneous reaction mixtures were obtained; they were then transferred to quartz cuvettes. N_2 gas was bubbled through the monomer mixtures for about 15 min prior to UV exposure. The monomer solutions were then exposed to UV light using an Hg–Xe arc lamp (OREAL Instruments) to accomplish the polymerization. In order to avoid the excessive heating and thereby the boiling of the reaction mixture, they were exposed to UV light (exposure time of 2 min) in a discrete manner with 5 min intervals between two successive exposures.

Thermal Initiation. To a stoichiometric solution of vinyl and thiol monomers, AIBN (0.1 wt %) was added under constant stirring in a glass vial. Gelation was extremely rapid, occurring at room temperature (~22 °C) in ~10 min.

Self-Initiation. Fifteen different monomer mixtures were prepared by combining the polyvinyl monomers with the thiol monomers in specific mole ratio such that the number of vinyl groups equaled the number of thiol groups (e.g., for TVS–EDTH the mole ratio was 1:2). Addition of one type of monomer into another was performed in a glass vial in a dropwise fashion under constant stirring so as to achieve homogeneous reaction mixtures. The monomer mixtures were then allowed to gel at an ambient condition (temperature ~20 °C) which was accomplished in 2–48 h depending on the constituent monomers. After gelation, the prepolymers were subjected for final curing at 120 °C for 24 h in an oven to yield hard polymer samples. Samples for DMA analysis were made in Teflon molds of the appropriate dimension required for the dynamic mechanical analysis (DMA).

Characterization. The mechanical properties such as storage modulus, Young's modulus, and tan delta plots of the polymers as a function of temperature were studied using a dynamic mechanical analyzer (Q800 analyzer, TA Instruments). The measurements were performed on a thin rectangular polymer slab starting from −55 to 150 °C using a ramp rate of 3 °C/min at a constant frequency (1 Hz) and constant amplitude (15 μm).

Differential scanning calorimetry (DSC) analysis of the polymers was performed on a thermal analyzer (Model Q100, TA Instruments). Samples were scanned in the temperature range from −50 to 150 °C with a heating rate of 10 °C/min under nitrogen flow (50 mL/min). Cooling of the sample was provided RCS cooler (Model No. RCS 90, refrigerated cooling system).

Viscosity was measured on a Brookfield Model DV-II viscometer using an LV #4 spindle in an open container containing the monomer mixtures. The reported viscosities are Brookfield viscosities and not absolute viscosities.

^{29}Si solid-state MAS NMR spectra were obtained on a Varian INOVA 500WB spectrometer at the resonance frequency of 99.393 MHz (magnetic field 11.74 T). The polymer samples were ground to fine powder and were loaded into a 4 mm HXY CP/MAS probe for the analysis. A recycle delay of 5 s was used, and samples were spun at 10 kHz. The chemical shift values were referenced to TMS at 0 ppm.

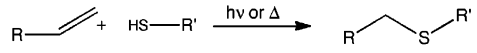
Optical transmission measurements were performed on polished polymers using a UV–vis spectrophotometer (Lambda 900, Perkin-Elmer). Sample were ground and polished to a path length of 2.5 mm. The refractive indices were obtained at 546 nm using an Abbe refractometer (NAR-4T) at 20 °C.

The bulk density of the polymers was obtained by placing dry, preweighed samples in a glass pycnometer and filling rest of the volume with distilled water at 20 °C. The densities were calculated from the weight difference and the known density of the liquid water at 20 °C. Five observations were taken for each sample, and the average was used for the density calculation.

Quantum mechanical estimates of the heat of formation were carried out using semiempirical, PM3 level of theory in the Hyperchem suite of computational software.

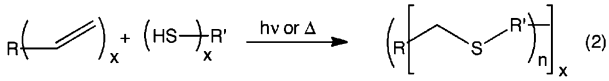
3. RESULTS AND DISCUSSION

The thiol–ene coupling reaction (reaction 1), which is typically included in the category of "click" chemistry due to its facile



(1)

nature, has been used extensively for materials and polymer applications and has been the subject of a number of thorough reviews in recent years.[4,5,7,8,10]For the generation of a polymeric material where the repeat unit is created solely through thiol–ene coupling, a functionality of 2 or higher must be present in the thiol and ene monomers, with higher functionality ($x > 2$) potentially leading to cross-linked materials (reaction 2).



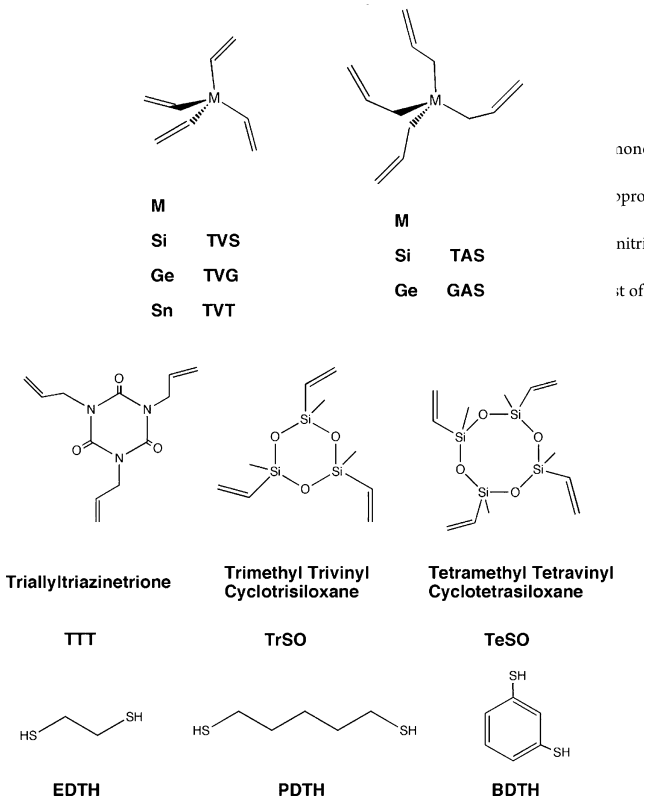
(2)

The reaction goes by a free-radical-based step-growth mechanism and is typically initiated photochemically, either through the use of molecular photoinitiators such as diaryl ketone or directly by exciting the thiol chromophore with ultraviolet light to create radicals.[5,13,14] It can also be initiated through the use of thermally activated radical initiators such as azobis(isobutyronitrile) (AIBN), as was done in earlier work on thiol–divinylbenzene polymerization.[15] As mentioned, thiol–ene polymerization has the potential to produce high refractive index materials, but the reaction typically does not produce structurally hard materials for use in optical applications due to the low amount of cross-linking often inherent in the step-growth mechanism. One route to overcoming this problem, as suggested by Fairbanks et al., is to use monomers that possess a high degree of functionality to potentially achieve higher cross-link densities.[8] The choice of vinyl monomers, which are shown in Table 1, includes tetrahedral vinyl-containing group 14 elements Si, Ge, and Sn. Along with their high functionality, it was hypothesized that the main group elements from third and lower rows would impart a higher refractive index to the bulk polymer due to the high polarizability of these elements.[3] Precedent for the choice of this group of monomers arises from studies in which tetravinylsilane has been used successfully to create dendrimeric-type structures from thiol–ene coupling chemistry.[8,16,17] In addition, several cyclic systems containing a high degree (≥3) of vinyl functionality were also utilized. The motivation for use of these heterocyclic ring systems lies in the report that triallyltriazinetrione (TTT) forms hard glassy bulk polymers with trimethylolpropane tris(3-mercaptopropionate) (TriThiol1).[5]

Synthesis. Initial attempts were made to synthesize bulk polymers starting from tretravinylsilane (TVS) and the dithiol monomers, ethanedithiol (EDTH) and benzenedithiol (BDTH). Polymerization was initially carried out using two of the established approaches: direct photoinitiation through the use of UV light and initiation using a thermally activated radical initiator, azobis(isobutyronitrile) (AIBN).[13,15]

dx.doi.org/10.1021/ma202467a | Macromolecules 2012, 45, 1174–1181

Table 1. Vinyl and Thiol Monomers



The choice of direct photoinitiation over the use of secondary initiators such as diaryl ketones was due to the fact that most of the initiators tend to remain unconsumed in the polymer, where they can potentially affect its structural and optical properties.[5]

The secondary choice of AIBN was predicated on the fact that it provided a purely thermal initiation route and that it had been used previously in making bulk thiol–ene polymers.[15] It was found that initiation by both of these methods resulted in the rapid formation of a gel, which was allowed to harden further for a period of several days. After aging and hardening, the polymer samples, while existing as free-standing monoliths, were still soft and quite flexible. In an attempt to further drive the cross-linking process and increase hardness, thermal curing of the samples was carried out by slowly heating at a rate of 0.5 °C/h to a final temperature of 120 °C. This resulted in materials that were much more robust, albeit yellow in color (Figure 1a,b). Above 120 °C, decomposition occurred, while

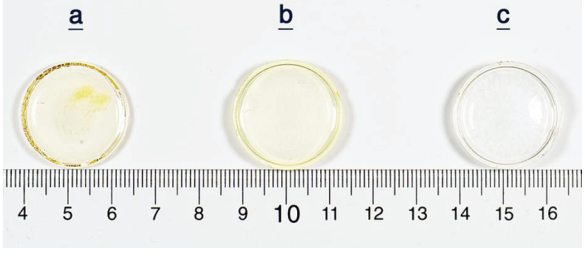


Figure 1. Monolithic TVS–EDTH samples after thermal curing at 120 °C for 24 h polymerized through (a) direct photoinitiation, (b) thermal (AIBN) initiation, and (c) room-temperature polymerization (scale in cm).

curing at lower temperatures yielded materials that were significantly softer. The density, Young's modulus, and glass transition temperature for both samples are listed in Table 2. As

Table 2. Properties of TVS–BDTH and TVS–EDTH Thiol–Ene Polymers Made through Different Initiation Methods

polymer	density (g/cm^3)	Young's modulus (MPa)	T_g (°C)
TVS–BDTH			
photoinitiation	1.40	510	63
thermal-initiation (AIBN)	1.43	530	59
self-initiation	1.43	668	69
TVS–EDTH			
photoinitiation	0.99	21	43
thermal Initiation (AIBN)	1.01	89	39
self-initiation	1.06	108	42

can be seen, the physical properties of the TVS–BDTH samples made through photoinitiation and with AIBN had similar properties, although those made with AIBN tended to be more robust. The difference between the two initiation techniques was more pronounced for the TVS–EDTH polymers, where photoinitiation yielded significantly softer materials. For reasons that will be discussed, the TVS–BDTH materials were significantly harder and had a higher glass transition temperature than did the TVS–EDTH materials.

Prior studies of free radical polymerizations in other cross-linked optical polymers have observed that high initiator concentrations tend to lower glass transition temperature in a polymer due to excess chain termination events that reduce the achievable molecular weight.[18] Since it is known that thiol–ene reactions can self-initiate without the introduction of an initiator in some systems (a property typically discussed in relation to the shelf life of thiol–ene mixtures), we hypothesized that if polymerization in our system of monomers could be carried out in the absence of initiation, polymers with better mechanical properties might be realized.[5] To test this hypothesis, stoichiometric mixtures of TVS–BDTH and TVS–EDTH were allowed to react at room temperature (~22 °C). The viscosity of the solution was monitored over time (Figure 2); initially,

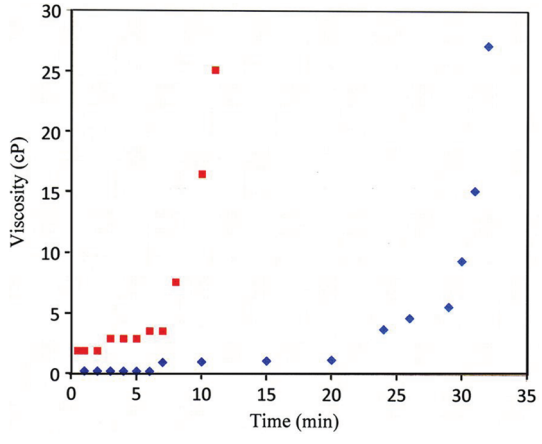


Figure 2. Viscosity changes over time for the reaction between tetravinylsilane and (■) 1,3-benzenedithiol and (◆) 1,2-ethanedithiol.

dx.doi.org/10.1021/ma202467a | *Macromolecules* 2012, 45, 1174–1181

there was a slow increase in viscosity followed by an abrupt increase, signifying gel formation. For TVS−BDTH and TVS−EDTH, gelation occurred at approximately 10 and 32 min, respectively. The origin of the self-initiation mechanism is not completely understood, although recent studies have indicated that radicals resulting from an ene−thiol charge transfer complex initiate the polymerization.[19,20] In our systems, addition of the free radical scavenger hydroquinone to the TVS−EDTH system resulted in strong inhibition of the gelation, indicating that the reaction was still proceeding through a mechanism involving free radicals. Synthesis was also carried out in the dark to verify that the reaction was not simply being initiated by adventitious light. The properties of the polymer made in darkness were unchanged, indicating that adventitious photoinitiation was not occurring. As with the samples made through the direct initiation processes, room-temperature polymerization and hardening yielded somewhat flexible materials. Further hardening of the polymer was achieved through curing at 120 °C for a period of 24 h.

The use of thermal self-initiation to drive the polymerization yielded significant improvements in the mechanical properties of the polymer. As can be seen in Table 2, the Young's modulus for the self-initiated TVS−BDTH polymers was found to be 668 MPa, which was markedly higher than the photo- and AIBN-initiated materials by 24% and 21%, respectively. Data obtained from the DMA analysis for the three methods of initiation of the TVS−BDTH system are shown in Figure 3.

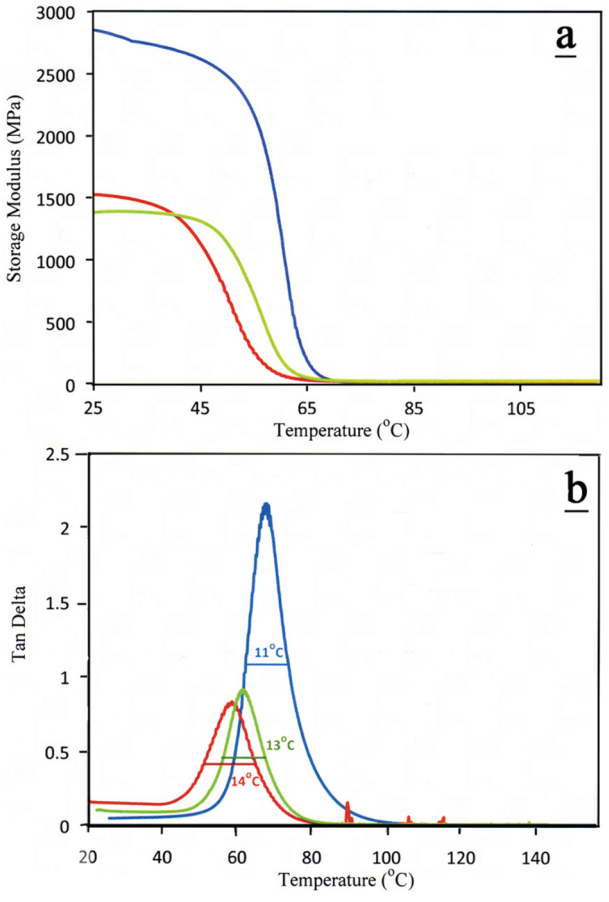


Figure 3. (a) Storage modulus and (b) tan delta plots obtained from dynamic mechanical analysis for tetravinylsilane-1,3-benzenedithiol polymers made from (red) thermal (AIBN), (green) photochemical, and (blue) self-initiation. Note: error in width ±0.5 °C.

As can be seen, the storage modulus and the glass transition temperature, as determined from the peak in the loss tangent and from DSC data, are similar for the photo- and AIBN-initiated polymers; however, both of these quantities are significantly higher for the self-initiated system. Also of interest is the effect of the different initiation protocols on the uniformity of the cross-link density, a measure of which is the width of the loss tangent measured at half height.[8,21] As can be seen (Figure 3), the photo- and AIBN-initiated materials have loss tangent widths which are, within experimental error, the same at 13 ± 0.5 and 14 ± 0.5 °C, respectively, while the width of the self-initiated materials is significantly narrower at 11 ± 0.5 °C, suggesting a more uniformly cross-linked material.

The effect of the three different initiation procedures that were explored and the effect of the thermal curing protocol on the degree of cross-linking can be seen quantitatively using ^{29}Si solid-state NMR spectroscopy. The chemical shift of the ^{29}Si nucleus is quite sensitive to the electron-donating ability of the ligands.[22,23] As such, systematic changes in the alkyl group, going from stronger to weaker electron donors, will result in an upfield shift of the Si nucleus to lower ppm values. Relative to tetramethylsilane (TMS), which is set to zero, other alkyl groups, where the silicon is bound to four methylene carbons, tend to be slightly downfield from TMS. So, for example, tetraethylsilane has a chemical shift of 7.1 ppm, while tetrallylsilane, which is less electron donating, has a chemical shift of −2.0 ppm. For tetravinylsilane, the starting monomer for our polymers, the chemical shift is well upfield at −21.5 ppm due to the weak donating ability of the vinyl groups.[24] As vinyl groups are replaced with alkyl groups, as happens during polymerizations, the ^{29}Si chemical shifts will appear systematically upfield by approximately incremental values between −21.5 and ∼7 ppm (the presence of the thioether group will shift it somewhat upfield) so that each species, $Si(CH_2CH_2S-)_{4-n}(CH{=}CH_2)_n$, as n goes from 0 to 4, will have a specific assignable resonance. Such analysis has been done extensively in studies of sol−gel polymerization of silicon alkoxides.[22,23] The solid-state ^{29}Si MAS NMR spectra of TVS−BDTH made by the three initiation methods collected after gelation and room temperature aging and after thermal processing to 120 °C are shown in Figure 4. As can be seen, different ^{29}Si resonances

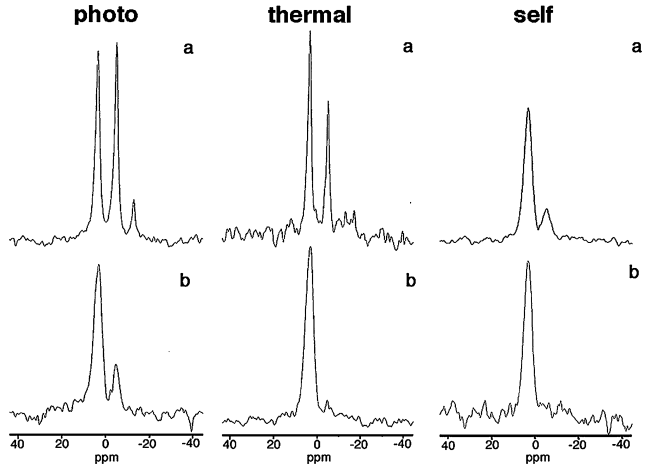


Figure 4. ^{29}Si SS CP/MAS NMR spectra of tetravinylsilane-1,3-benzenedithiol polymer made through thermal (AIBN), photochemical, and self-initiation (a) after gelation and room temperature aging and (b) after thermal curing at 120 °C.

dx.doi.org/10.1021/ma202467a | Macromolecules 2012, 45, 1174−1181

associated with different degrees of reaction are observed. In all samples, a sharp resonance is observed at 3.8 ppm, which we assign to a Si atom completely surrounded by thioalkyl groups, $Si(CH_2CH_2S-)_4$, which represents silicon atoms that are completely cross-linked. The ^{29}Si NMR for the UV-initiated materials (Figure 4a), collected after gelation and aging but before thermal curing, show three well-resolved resonances all separated by about 8 ppm. Along with the resonance at 3.8 ppm of the completely alkylated species, the two other resonances are observed downfield at −4.6 and −12.8 ppm and can be assigned to the mono- and divinylsilicon species, $Si(CH{=}CH_2)(CH_2CH_2S-)_3$ and $Si(CH{=}CH_2)_2(CH_2CH_2S-)_2$, respectively. This indicates relatively poor cross-linking, with a majority of the Si atoms still having pendant vinyl groups and, therefore, not being cross-linked. The materials made using AIBN initiation are better cross-linked, as they show only the two resonances: the fully alkylated and the monovinyl species (a very small amount of divinyl can be seen in the spectrum). Finally, as indicated by their mechanical properties, the self-initiated materials have the highest degree of cross-linking, with only a small amount of monovinyl species observed. The effect of thermal processing at 120 °C on the cross-linking can also be clearly seen in the NMR spectra (Figure 4b). In all cases, the effect of thermal processing is to greatly reduce the amount of vinyl-containing Si, leaving predominantly the fully cross-linked species. In the case of the UV-initiated polymer, unreacted vinyl groups still remain. The AIBN-initiated materials (Figure 4b) are almost fully cross-linked, although some very small amount of monovinyl species can be discerned near the baseline. The self-initiated materials appear to be fully cross-linked, within the sensitivity of the NMR experiment, as only the fully alkylated resonances remain after thermal processing. It is important to note that the NMR results are quite consistent with the DMA studies and support the conclusion that the observed mechanical properties are due to the degree of cross-linking in the polymer. In all cases, significant mechanical improvement was realized through the thermal curing to 120 °C, which it directly attributable to greater cross-link density as evidenced by the NMR data. Moreover, the mechanical properties, as measured by the Young's modulus, were highly dependent on the polymerization method, with photoinitiation yielding the least robust materials and self-initiation the most. Consistent with this, the degree of cross-linking observed in the NMR spectrum indicates that self-initiation yields the highest cross-linking density and photoinitiation the least. At this juncture, however, we do want to emphasize that there are numerous methods of initiating thiol−ene polymerization and those compared here are, necessarily, a small subset of all possible methods. As such, other approaches might well prove to be superior for making optical-quality bulk polymers from these monomers.

For the TVS−EDTH composition, the effects of the different polymerization procedures and the benefits of self-initiation appear to be more pronounced. The photoinitiated materials proved to very soft, as evidenced by the low values for the Young's modulus (Table 2). The hardness improved with AIBN initiation, although, ultimately, self-initiation yielded the hardest materials. Overall, however, the mechanical properties of these compositions, regardless of the method of synthesis, were poor relative to the TVS−BDTH materials. The DMA data (Figure S1) show a very broad loss tangent with an fwhm ≥27 °C for all methods of preparation. Moreover, as T_g is approached, the storage modulus drops rapidly (much more so than is observed for TVS−BDTH), and just above T_g the sample tends to weaken and fracture. These data indicate that this system has much more inhomogeneous cross-linking. This likely arises from the fact that these flexible groups can undergo intramolecular ring formation, which effectively limits the overall cross-linking density of the polymer (Figure 5a).

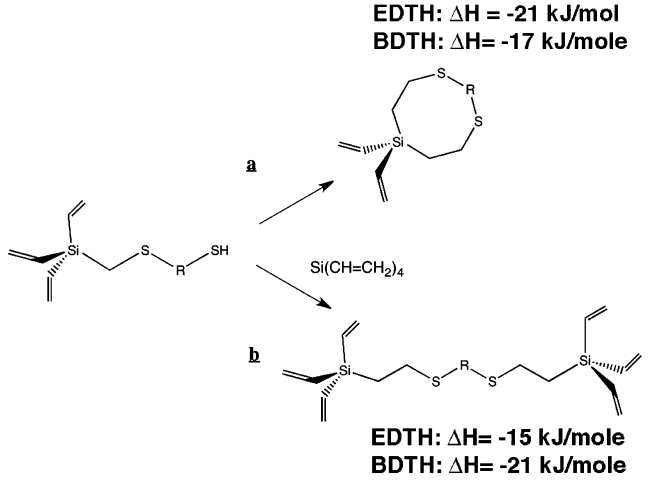


Figure 5. Cyclization (a) and cross-linking (b) pathways and associated enthalpies of thiol−ene polymerization reactions.

This effect has been discussed previously for free radical vinyl polymerizations and is likely to have a pronounced effect on the mechanical properties of the thiol−ene polymers reported here.[25] In the case of 1,3-benzenedithiol, the formation of a bond between two vinyl groups on a single silicon and the sulfur atoms on the ortho positions of the aromatic ring would create a strained ring that would be thermodynamically less favorable than intermolecular bond formation. This is supported by semiempirical PM3 calculations, which estimate the enthalpy of cyclization (Figure 5a) of EDTH to be around 4 kJ/mol more favorable than that of the BDTH. Comparing the estimated enthalpies of the cross-linking reaction (Figure 5b), the enthalpy for cross-linking of BDTH is 6 kJ/mol more exothermic than that of EDTH. In fact, the calculations suggest that for EDTH cyclization is the thermodynamically preferred route, while for BDTH, cross-linking is favored.

Finally, irrespective of their relative mechanical properties, the TVS−EDTH and TVS−BDTH polymers obtained through self-initiation were colorless after thermal processing (Figure 1c) and exhibited high transparency, with an average optical transmission across the visible region of the spectrum (400−700 nm) of ≥89%. The yellowing in samples made by the other initiation processes appears to arise, at least in part, from the oxidation of unreacted vinyl groups during heating. This can be demonstrated through polymerization and thermal processing of samples containing progressively higher TVS to EDTH mole ratios. At mole ratios above stoichiometric, which contain excess unreacted vinyl groups, progressively darker and more highly colored materials are produced (Figure S2).

Mechanical Properties. The same synthetic approach, utilizing self-initiated room temperature polymerization followed by thermal annealing, was used for the other monomer combinations. For all of the compositions, the densities, Young's moduli, and glass transition temperatures were determined (Table 3). All of the materials form free-standing monoliths

dx.doi.org/10.1021/ma202467a | Macromolecules 2012, 45, 1174−1181

Table 3. Properties of Thiol−Ene Polymer Monoliths

polymer	density (g/cm^3)	Young's modulus (MPa)	T_g (°C) DSC/DM
TVS−BDTH	1.43	668	60/69
TVG−BDTH	1.39	627	46/56
TTT−BDTH	1.53	551	59/66
TeSO−BDTH	1.75	520	51/38
TVS−EDTH	1.06	108	21/42
polymer	density (g/cm^3)	Young's modulus (MPa)	T_g (°C) DSC
TrSO−BDTH	1.36	74	26
TVS−PDTH	1.16	26	4
TVT−BDTH	1.24	26	21
TAS−EDTH	1.14	21	2
TeSO-EDTH	1.28	19	19
TAG−EDTH	1.19	18	−19
TAG−PDTH	1.23	18	−26
TrSO−EDTH	1.63	17	−2
TAG−BDTH	1.22	14	20
TAS−PDTH	1.32	13	nd[a]

[a]nd = not determined.

with high transparency and, as will be discussed, most have refractive indices that are regarded as high for polymeric materials. However, we found that the subset of materials that could be successfully ground and polished into an optical component were those with Young's moduli above ∼100 MPa. Those materials include the TVS−EDTH and TVS−BDTH polymers discussed above and the BDTH polymers of the tetravinylgermanium (TVG) and the heterocycles, triallyltriazinetrione (TTT) and trimethyltrivinylcyclotetrasiloxane (TeSO).[9,26] As a proof of concept, large monolithic examples of the TVS−EDTH and TVS−BDTH polymers were fabricated and then successfully ground and polished on commercial optical lens grinding equipment (Figure 6).



Figure 6. Monolithic sample of (left) TVS−BDTH and (right) TVS−EDTH ground and polished into optical flats (diameter = 5 cm).

Scrutiny of the data in Table 3 indicates that, in general, the mechanical properties of the polymers depend greatly on the flexibility of the constituent monomers.[5] For the systems used here, it is clear that the more flexible cross-linking groups yield materials with the lowest T_g and Young's moduli. For example, among the dithiol cross-linking groups, there is a dramatic drop in the Young's modulus and T_g in going from an ethane to a pentane in the dithiol monomer. A similar decrease in T_g and Young's modulus is also seen in going from ethylene to allene groups in the tetravinyl monomers (e.g., TVS vs TAS). This effect may arise in part from the torsional flexibility of the chains; however, the dominant factor is likely from the intramolecular cyclization processes discussed previously, which reduces the cross-link density of the polymers. One interesting series is the tetravinyl Si, Ge, and Sn monomers. Tetravinyl silane and germanium form extremely hard polymer samples with BDTH, consistent with their tendency to cross-link as opposed to cyclize. Tin, however, forms extremely soft materials with very low Young's moduli. This appears to arise from thermal instability of the polymer, in which degradation, as evidenced by the onset of strong brown coloration, occurs at the 120 °C temperature at which we typically thermally anneal the materials. As such, lower-temperature processing (40 °C) was used for these materials, resulting in a less robust, though colorless material with good transparency. The origin of this may be in the decrease in metal−ligand bond energies observed in going down a group in the p-block elements.[27] The significance of the structure−property data in Table 3 is that they suggest that the proper choice of monomers has an large effect on the mechanical properties of the polymer. This arises both due to the influence of their structural characteristics on their ability to cross-link and on their thermal stability as it relates to achieving a high cross-link density.

Optical Properties. The well-established design strategy for the production of polymeric materials with high refractive indices is the introduction of polarizable atoms or groups into the polymer network.[2] The element commonly used is sulfur, and many design strategies for increasing the refractive index involve synthetic methodologies aimed at increasing the amount of sulfur in the network. The potential for thiol−ene polymer to generate materials with high refractive indices lies in part in the fact that the repeat unit contains sulfur, but also because monomers can be chosen so that no highly electronegative atoms such as oxygen and nitrogen are present. The systems described here further extend this design strategy through the use of monomers containing other polarizable main group elements such as Si, Ge, and Sn that, in conjunction with S, add to the overall polarizability of the bulk polymer. The effect of these polarizable main group elements can be readily seen in the refractive index measurements (Table 4).

Table 4. Optical Properties of Thiol−Ene Polymers

polymer	RI (546 nm)	Abbe number	% transmission (at 633 nm)
TVT−BDTH	1.703	nd[a]	88
TVG−BDTH	1.692	nd	92
TAG−BDTH	1.690	24.3	90
TVS−BDTH	1.687	26.3	92
TrSO−BDTH	1.665	nd	91
TTT−BDTH	1.660	28.7	92
TeSO−BDTH	1.660	nd	90
TVS−EDTH	1.656	34.0	87
TrSO−EDTH	1.655	nd	89
TeSO−EDTH	1.654	nd	92
TAG−EDTH	1.620	39.9	86
TAS−EDTH	1.610	36.3	89
TVS−PDTH	1.599	41.0	90
TAG−PDTH	1.590	45.0	90
TAS−PDTH	1.570	41.5	87

[a]nd = not determined.

In going down the row from Si to Sn, the refractive index shows a steady increase, with TVT−BDTH achieving the highest refractive index we observe at 1.703. Unfortunately, as we noted

dx.doi.org/10.1021/ma202467a | Macromolecules 2012, 45, 1174−1181

previously, these materials tend to be quite soft. The best composition, in terms of both mechanical and optical properties, is TVG−BDTH, which has a Young's modulus of 627 MPa and a refractive index of 1.692. The three heterocycles, TTT, TrSe, and TeSO, have, on average, lower refractive indices than do the tetravinyl group 14 elements, although they are all above 1.6, which places them in the higher refractive index range. The lower refractive index is likely due to the presence of electronegative oxygen and nitrogen in the heterocycle.

From analysis of the data in Table 4, several significant structure−property relationships can be deduced. If we compare the refractive indices for TVS−EDTH and TVS−PDTH, they are observed to drop from 1.656 to 1.599 as the hydrocarbon chain length increases. This suggests that by reducing the relative amount of the more electronegative first-row main group atoms to the more polarizable second-row atoms, an increase in the refractive index is realized. In a similar fashion, as the vinyl monomer goes from ethylene to allene, the refractive indices drop, as can be seen by comparing TVS−EDTH and TAS−EDTH, where the refractive index goes from 1.656 to 1.610.

The Abbe numbers, for the subset of the sample for which it was measured, range from ∼24 to 45 and, consistent with prior observations, tend to decrease with increasing refractive index (Figure 7).[28,29] In these materials, the decrease in Abbe number

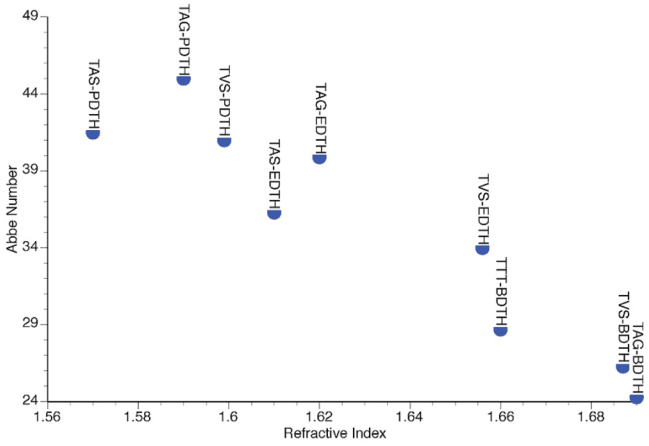


Figure 7. Refractive index dependence of the Abbe number for a selected series of thiol−ene polymers.

with increasing refractive index can be in part attributed to the fact that benzenedithiol, which is the dithiol monomer used in the highest refractive index compositions, is an aromatic species with an optical absorption in the near-UV range. The refractive index measured at 486.1 nm, which is used in the determination of the Abbe number, will be close to the absorption and, hence, will increase, thereby reducing the Abbe number. Scrutiny of the graph in Figure 7 indicates that there are two places where both the refractive index and the Abbe number increase. This occurs in going from TAS to TAG for the PDTH and EDTH dithiol monomer. In both of these cases, the dithiol is constant and the central metal in the vinyl monomer goes from Si to Ge. In going down the column, the polarizability of the metal increases, thereby increasing the refractive index. As the data indicate, however, there is not a concomitant decrease in the Abbe number, suggesting that by using main group elements from the third or lower rows as primary building blocks of optical polymers and by avoiding groups with absorption in the near-UV range, it may be possible to achieve materials with both high refractive indices and high Abbe numbers.

CONCLUSION

We have successfully synthesized a series of bulk inorganic/organic hybrid polymers utilizing the thiol−ene coupling reaction to generate the repeat unit of the polymer. This was accomplished by using vinyl monomers with a high functionality and by polymerizing the polymers through a slow self-initiation process that reduced the amount of radical species in solution. These materials exhibit, on average, high refractive indices, resulting from the fact that the thiol−ene coupling reaction contributes a highly polarizable sulfur group to the polymer chain and from the incorporation of polarizable main group elements through the use of group 14 tetravinyl-containing monomers. Very good structural properties were achieved for several of the compositions due to a high cross-link density realized through the use of monomers which inhibited intramolecular cyclization processes and facilitate intermolecular cross-linking. Taken together, the specific polymers produced and the design strategies attained from this work potentially represent a useful contribution to the field of optical polymers. Moreover, as many other suitable monomers can potentially be selected with the appropriate properties to generate both high refractive indices and structural integrity, this potentially represents a new class of high refractive index polymer.

ASSOCIATED CONTENT

Supporting Information

DMA analysis of TVS−EDTH (Figure S1) and studies showing the origin of coloration in thiol−ene materials due to excess unreacted vinyl being present (Figure S2). This material is available free of charge via the Internet at http://pubs.acs.org.

AUTHOR INFORMATION

Corresponding Author

*E-mail: stiegman@chem.fsu.edu.

ACKNOWLEDGMENTS

We are indebted to William Warner and Andre Yavourian of the Jet Propulsion Laboratory for low-temperature DMA analysis and to Dan Dang and John Bitou of Essilor for measuring the refractive index and Abbe number on some of our initial compositions. Funding for this project was initially provided by the Florida State University Research Foundation through the GAP program.

REFERENCES

(1) Jha, G. S.; Seshadri, G.; Mohan, A.; Khandal, R. K. *e-Polym.* **2007**.
(2) Liu, J. G.; Ueda, M. *J. Mater. Chem.* **2009**, *19*, 8907.
(3) Nagle, J. K. *J. Am. Chem. Soc.* **1990**, *112*, 4741.
(4) Hoyle, C. E.; Bowman, C. N. *Angew. Chem., Int. Ed.* **2010**, *49*, 1540.
(5) Hoyle, C. E.; Lee, T. Y.; Roper, T. *J. Polym. Sci., Part A* **2004**, *42*, 5301.
(6) Kade, M. J.; Burke, D. J.; Hawker, C. J. *J. Polym. Sci., Part A* **2010**, *48*, 743.
(7) Lowe, A. B. *Polym. Chem.* **2010**, *1*, 17.
(8) Fairbanks, B. D.; Scott, T. F.; Kloxin, C. J.; Anseth, K. S.; Bowman, C. N. *Macromolecules* **2009**, *42*, 211.

(9) Chan, J. W.; Zhou, H.; Hoyle, C. E.; Lowe, A. B. *Chem. Mater.* **2009**, *21*, 1579.
(10) Sangermano, M.; Colucci, G.; Fragale, M.; Rizza, G. *React. Funct. Polym.* **2009**, *69*, 719.
(11) Glockling, F.; Lyle, M. A.; Stobart, S. R. *J. Chem. Soc., Dalton Trans.* **1974**, 2537.
(12) Zhun, V. I.; Sbitneva, I. V.; Kisin, A. V.; Chernyshev, E. A. *Russ. J. Gen. Chem.* **2004**, *74*, 1130.
(13) Cramer, N. B.; Scott, J. P.; Bowman, C. N. *Macromolecules* **2002**, *35*, 5361.
(14) Cramer, N. B.; Reddy, S. K.; Cole, M.; Hoyle, C.; Bowman, C. N. *J. Polym. Sci., Part A* **2004**, *42*, 5817.
(15) Kobayashi, E.; Obata, T.; Aoshima, S.; Furukawa, J. *Polym. J.* **1990**, *22*, 803.
(16) Rissing, C.; Son, D. Y. *Organometallics* **2008**, *27*, 5394.
(17) Rissing, C.; Son, D. Y. *Main Group Chem.* **2009**, *8*, 251.
(18) Stejny, J. *Polym. Bull.* **1996**, *36*, 617.
(19) Klemm, E.; Gorski, U. *Angew. Makromol. Chem.* **1993**, *207*, 187.
(20) Kuhne, G.; Diesen, J. S.; Klemm, E. *Angew. Makromol. Chem.* **1996**, *242*, 139.
(21) Cramer, N. B.; Bowman, C. N. *Polym. Prepr.* **2003**, *44*, 17.
(22) Fyfe, C. A.; Aroca, P. P. *Chem. Mater.* **1995**, *7*, 1800.
(23) Pouxviel, J. C.; Boilot, J. P.; Beloeil, J. C.; Lallemand, J. Y. *J. Non-Cryst. Solids* **1987**, *89*, 345.
(24) Janes, N.; Oldfield, E. *J. Am. Chem. Soc.* **1985**, *107*, 6769.
(25) Elliott, J. E.; Nie, J.; Bowman, C. N. *Polymer* **2003**, *44*, 327.
(26) Li, Q.; Zhou, H.; Hoyle, C. E. *Polymer* **2009**, *50*, 2237.
(27) Skinner, H. A.; Connor, J. A. *Pure Appl. Chem.* **1985**, *57*, 79.
(28) Dislich, H. *Angew. Chem., Int. Ed.* **1979**, *18*, 49.
(29) Okutsu, R.; Ando, S.; Ueda, M. *Chem. Mater.* **2008**, *20*, 4017.

Macromolecules

Article

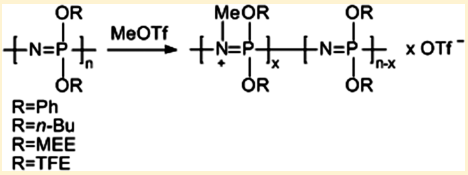
pubs.acs.org/Macromolecules

Synthesis of New Polyelectrolytes via Backbone Quaternization of Poly(aryloxy- and alkoxyphosphazenes) and their Small Molecule Counterparts

Chen Chen, Andrew R. Hess, Adam R. Jones, Xiao Liu, Greg D. Barber, Thomas E. Mallouk, and Harry R. Allcock*

Department of Chemistry, The Pennsylvania State University, University Park, Pennsylvania 16802, United States

ABSTRACT: Novel polyelectrolytes were synthesized by quaternization of the backbone of poly(alkoxy- and aryloxyphosphazenes) with strong alkylation reagents. As models for the synthesis of these polymers, similar quaternization reactions were also carried out on small-molecule alkoxy and aryloxy cyclotriphosphazenes. The quaternized small molecules and high polymers were characterized by ^{1}H NMR, ^{31}P NMR, DSC, TGA, and AC impedance studies. The quaternized poly(alkoxyphosphazenes) showed ionic conductivities of 2.58×10^{-4} S·cm^{-1} at 25 °C and 2.09×10^{-3} S·cm^{-1} at 80 °C, which are among the highest values for known solvent-free ionically conducting polymers.



INTRODUCTION

Since the first report of a solid-state polymer electrolyte composed of poly(ethylene oxide)/salt complexes by Wright et al.[1] the development of polymeric solid-state electrolytes has drawn the attention of many researchers. Solid-state polymeric electrolytes have many advantages over conventional liquid electrolytes such as high dimensional stability, excellent processability, and improved safety, which make them ideal electrolytes for solid-state electrochemical devices such as high energy density rechargeable batteries, fuel cells, electric double-layer capacitors, and electrochromic displays.[2]

Dye-sensitized solar cells (DSSCs) have been under intensive investigation as a low cost alternative to silicon solar cells.[3,4] The most important factor affecting the practicality of DSSCs is the electrolyte, which usually consists of an I^-/I_3^- redox couple in a volatile liquid organic solvent. The serious drawbacks of organic solvent based liquid electrolytes are their volatility and the possibility of leakage during extended operation, especially at elevated temperatures, together with the necessary complexity of sealing the unit. Solid-state polymeric electrolytes are a logical solution to overcome both of the problems caused by liquid organic solvent.

Polyphosphazenes are long chain macromolecules that contain an inorganic backbone composed of alternating phosphorus and nitrogen atoms joined by unusual quasi-delocalized single−double bonds, and organic side groups attached to the backbone phosphorus atoms. Many different organic side groups can be linked to the polyphosphazene backbone in variable ratios, a feature that provides this polymer platform with versatile properties and applications.[5] With appropriate side groups attached to the backbone, polyphosphazenes are known to have low glass transition temperatures (T_g) and zero crystallinity: in other words, they remain highly flexible even at low temperatures due to the unusual torsional mobility of the P═N backbone. This flexibility, which is considerably higher than in most other ionic conducting polymers including poly(ethylene oxide), allows sufficient segmental motion for the facile migration of ions through the solid electrolyte medium. Polyphosphazenes with oligoethylene oxy side chains are among the most ionically conductive polymers.[6−8] One of the disadvantages of polymer/salt complexes as polymer electrolytes is that both cations and anions are mobile, which leads to concentration polarization which significantly reduces cell performance. In addition, the mobility of both anions and cations also hampers a fundamental understanding of the ion transport mechanisms in polymer electrolytes. A solution to these problems is to covalently link anions or cations to the polymer backbone, to yield polyelectrolytes. Side groups with both cations and anions have been tethered to the polyphosphazene backbones as side groups to form polycations and polyanions.[9−13]

Functionalization of the backbone nitrogen atoms of polyphosphazenes has received far less attention than the variation of side groups at the phosphorus centers. Backbone nitrogen atoms have been shown to play key role in coordination chemistry of oligo- and polyphosphazenes.[14−19] Organo- and organoamino-substituted cyclooligophosphazenes have been quaternized at the backbone nitrogen atoms to form phosphazenium cations,[20−25] but the quaternization of organoaminophosphazene high polymer has not been studied extensively.[26]

We report the first synthesis of novel polyelectrolytes via backbone quaternization of poly(aryloxy- and alkoxyphosphazenes), in which the charge carriers are located on skeletal nitrogen atoms . These new polyelectrolytes show good ionic conductivity without the presence of plasticizers or solvents.

Received: December 2, 2011
Revised: January 10, 2012
Published: January 30, 2012

ACS Publications © 2012 American Chemical Society

dx.doi.org/10.1021/ma202619j | *Macromolecules* 2012, 45, 1182−1189

Although dealkylation reactions, which cause loss of charge carriers, were detected when these quaternized species were exposed to anions with strong nucleophilicity, the promising conductivity results reveal a new concept for the synthesis of highly conductive polyelectrolytes via backbone functionalization.

EXPERIMENTAL SECTION

Reagents and Equipment. All synthesis reactions were carried out under a dry argon atmosphere using standard Schlenk line techniques. Tetrahydrofuran (THF), 1,4-dioxane and dichloromethane (DCM) (EMD) were dried using a solvent purification system, in which the solvents pass through columns of molecular sieves under a dry argon atmosphere.[27] Di(ethylene glycol) methyl ether (Aldrich), 1-butanol (EMD), and 2,2,2-trifluoroethanol (Aldrich) were distilled over calcium hydride. Phenol was purified by sublimation under vacuum. Acetone (EMD), methanol (EMD), hexanes (EMD), *N,N*-dimethylformamide (EMD), sodium hydride (60% dispersion in mineral oil, Aldrich), sodium iodide (Aldrich), 1,2-dichloroethane (Aldrich), chorobenzene (Aldrich), sodium thiosulfate pentahydrate (Aldrich), sodium bicarbonate (EMD), triethyloxonium tetrafluoroborate (1 M solution in dichloromethane, Aldrich) and methyl trifluoromethanesulfonate (Aldrich) were used as received. Poly(dichlorophosphazene) was prepared via the thermal ring-opening polymerization of recrystallized and sublimed hexachlorocyclotriphosphazene (Fushimi Pharmaceutical Co., Japan or Ningbo Chemical Co., China) in evacuated Pyrex tubes at 250 °C.[28] Unpolymerized hexachlorocyclotriphosphazene was removed by vacuum sublimation. ^{31}P and ^{1}H NMR spectra were obtained with a Bruker 360 WM instrument operated at 145 and 360 MHz, respectively. ^{31}P NMR spectra were proton decoupled. ^{1}H shifts are reported in ppm relative to tetramethylsilane at 0 ppm. ^{31}P shifts are reported in ppm relative to 85% H_3PO_4 at 0 ppm. ^{31}P NMR spectra were simulated with SpinWorks (version 3.1.8.1). Glass transition temperatures were measured with a TA Instruments Q10 differential scanning calorimetry apparatus at a heating rate of 10 °C/min and a sample size of ca. 10 mg. Gel permeation chromatograms were obtained using a Hewlett-Packard HP 1100 gel permeation chromatograph equipped with two Phenomenex Phenogel linear 10 columns and a Hewlett-Packard 1047A refractive index detector. The samples were eluted at 1.0 mL/min with a 10 mM solution of tetra-*n*-butylammonium nitrate in THF, and the elution times were calibrated with polystyrene standards. Mass spectrometric analysis data were collected using the turbospray ionization technique with an Applied Biosystems API 150EX LC/MS mass spectrometer. Ionic conductivities were measured with a HP 4192A impedance analyzer in custom-made cells. All the ionic conductivity tests were carried out at a fixed AC level of 0.1 V, and the frequency was scanned from 5 to 6,000,000 Hz. Thermal decomposition traces were obtained using a Perkin−Elmer TGA 7 thermogravimetric analyzer. Heating occurred at a rate of 20 °C/min from 50 to 800 °C under a nitrogen atmosphere and a flow rate of 50 mL/min.

Synthesis of Unquaternized Phosphazenes. Hexa(phenoxy)cyclotriphosphazene (**2**),[29] hexa(*n*-butoxy)cyclotriphosphazene (**3**),[30] hexakis(2-(2-methoxyethoxy)ethoxy)cyclotriphosphazene (**4**),[31] hexakis(2,2,2-trifluoroethoxy)cyclotriphosphazene (**5**),[32] poly(diphenoxyphosphazene) (**13**),[28,33] poly[di(*n*-butoxy)phosphazene] (**14**),[34] poly[bis(2-(2-methoxyethoxy)ethoxy)phosphazene] (**15**)[7] and poly[bis(2,2,2-trifluoroethoxy)phosphazene] (**16**)[28,33] were synthesized by allowing sodium phenoxide or sodium alkoxides to react with hexachlorocyclotriphosphazene or poly(dichlorophosphazene) in THF or 1,4-dioxane at room temperature (25 °C) or reflux temperature. Cyclotriphosphazenes were purified by recrystallization or flash column chromatography, and polyphosphazenes were purified by reprecipitation or dialysis prior to being subjected to quaternization.

Synthesis of Cyclic Trimer Models. *Synthesis of N-Methyl Hexa(phenoxy)cyclotriphosphazenium Trifluoromethanesulfonate (**6**).* To a solution of hexa(phenoxy)cyclotriphosphazene (**2**) (2.10 g, 3.03 mmol) in 20 mL of DCM was added methyl trifluoromethanesulfonate (0.686 mL, 6.06 mmol) at room temperature dropwise, and the mixture was stirred at room temperature for 24 h. All volatiles were evaporated under vacuum and the resulting oil solidified slowly under high vacuum to yield the trimer (**6**) as a reddish waxy solid (2.42 g, 2.82 mmol), which is sufficiently pure by ^{1}H and ^{31}P NMR spectra. Yield: 93%. ^{1}H NMR (360 MHz, $CDCl_3$): δ 3.77 (t, $^{3}J_{PH}$ = 10.8 Hz, 3 H), 6.59−6.65 (m, 4 H), 6.95−7.03 (m, 8 H), 7.15−7.25 (m, 6 H), 7.28−7.47 (m, 12 H). ^{31}P NMR (145 MHz, $CDCl_3$): δ −3.60 (1 P), 1.12 (2 P), AB_2, $^{2}J_{PP}$ = 78.4 Hz. ESIMS: *m/z* 708.2 $[M - OTf]^+$.

*Attempted Quaternization of Hexa(phenoxy)cyclotriphosphazene (**2**) with Triethyloxonium Tetrafluoroborate.* To a solution of hexa(phenoxy)cyclotriphosphazene (**2**) (0.347 g, 0.500 mmol) in 5 mL of DCM was added triethyloxonium tetrafluoroborate (1 M in DCM, 1.00 mL, 1.00 mmol) at room temperature dropwise, and the mixture was stirred at room temperature for 2 days. ^{31}P NMR spectroscopy indicated that only 24% of trimer (**2**) had been quaternized. ^{31}P NMR (145 MHz, crude reaction mixture with D_2O capillary as external reference: δ −4.08 (1 P), 1.28 (2 P), AB_2, $^{2}J_{PP}$ = 77.1 Hz, 5.08 (broad, s, 76%). After quenching with saturated sodium bicarbonate solution, the broad singlet peak at 1.30 shifted back to 9.40, which could be assigned to trimer **2**.

*Synthesis of N-Methyl Hexa(n-butoxy)cyclotriphosphazenium Trifluoromethanesulfonate (**7**).* To a solution of hexa(*n*-butoxy)cyclotriphosphazene (**3**) (1.41 g, 2.46 mmol) in 25 mL of DCM was added a solution of methyl trifluoromethanesulfonate (0.334 mL, 2.95 mmol) in 10 mL of DCM dropwise at −78 °C. The mixture was allowed to warm to room temperature gradually over 1 h. The resulting mixture was diluted with 30 mL of DCM, washed with 10% sodium bicarbonate solution, dried over anhydrous sodium sulfate, and concentrated under vacuum. The residue was purified on a Sephadex LH-20 column using THF/DCM (1/1, v/v) as eluent to yield trimer (**7**) as a colorless liquid (1.57 g, 2.13 mmol). Yield: 87%. ^{1}H NMR (360 MHz, $CDCl_3$): δ 0.90−1.00 (m, 18 H), 1.35−1.50 (m, 12 H), 1.65−1.83 (m, 12 H), 2.96 (t, $^{3}J_{PH}$ = 9.3 Hz, 3 H), 3.96−4.05 (m, 4 H), 4.10−4.23 (m, 8 H). ^{31}P NMR (145 MHz, $CDCl_3$): δ 6.03 (1 P), 9.38 (2 P), AB_2, $^{2}J_{PP}$ = 72.3 Hz. ESIMS: *m/z* 588.4 $[M - OTf]^+$.

*Synthesis of N-Methyl Hexakis(2-(2-methoxyethoxy)ethoxy)cyclotriphosphazenium Trifluoromethanesulfonate (**8**).* Hexakis(2-(2-methoxyethoxy)ethoxy)cyclotriphosphazene (**4**) (1.01 g, 1.18 mmol) was quaternized to yield trimer (**8**) as a colorless liquid (1.02 g, 1.01 mmol) by following a similar procedure to the one described for the synthesis of trimer (**7**). Yield: 86%. ^{1}H NMR (360 MHz, $CDCl_3$): δ 3.00 (t, $^{3}J_{PH}$ = 9.3 Hz, 3 H), 3.36 (s, 18 H), 3.50−3.57 (m, 12 H), 3.61−3.68 (m, 12 H), 3.70−3.80 (m, 12 H), 4.18−4.25 (m, 4 H), 4.29−4.37 (m, 8 H). ^{31}P NMR (145 MHz, $CDCl_3$): δ 6.55 (1 P), 9.79 (2 P), AB_2, $^{2}J_{PP}$ = 75.5 Hz. ESIMS: *m/z* 864.4 $[M - OTf]^+$.

*Attempted Quaternization of Hexakis(2,2,2-trifluoroethoxy)cyclotriphosphazene (**5**).* To a solution of hexakis(2,2,2-trifluoroethoxy)cyclotriphosphazene (**5**) (0.365 g, 0.501 mmol) in 10 mL of DCM was added methyl trifluoromethanesulfonate (0.113 mL, 1.00 mmol) at room temperature dropwise and the mixture. After stirring for 48 h at room temperature, no quaternization could be observed based on the ^{31}P NMR spectra of the reaction mixture. The reaction mixture was then refluxed for 48 h. ^{31}P NMR spectroscopy indicated that only 26% of trimer (**5**) had been quaternized, and the presence of quaternized species (**9**) could be detected in ESIMS spectrum as well. ^{31}P NMR (145 MHz, crude reaction mixture with D_2O capillary as external reference): δ 5.24 (1 P), 9.02 (2 P), AB_2, $^{2}J_{PP}$ = 82.3 Hz, 17.24 (s, 74.5%). ESIMS: *m/z* 864.4 $[M - OTf]^+$.

*Treatment of N-Methyl Hexa(phenoxy)cyclotriphosphazenium Trifluoromethanesulfonate (**6**) with Sodium Iodide.* To a solution of *N*-methyl hexa(phenoxy)cyclotriphosphazene trifluoromethanesulfonate (**6**) (429 mg, 0.500 mmol) in 10 mL of DCM was added sodium iodide (150 mg, 1.00 mmol) and the mixture was stirred at room temperature for 48 h. Then the reaction mixture was diluted with 10 mL of DCM, washed with 5% aqueous sodium thiosulfate and brine successively, dried over anhydrous sodium sulfate, and concentrated under vacuum to yield trimer (**2**) as a yellowish solid (309 mg, 0.446

dx.doi.org/10.1021/ma202619j | *Macromolecules* 2012, 45, 1182−1189

mmol). The yield was 89%. The ^{1}H NMR and ^{31}P NMR spectra correspond well with unquaternized trimer (**2**).

*Synthesis of 1,3,3,5,5-Pentakis(n-butoxy)-1-oxo-2-methylcyclotriphosphazadiene (**10**).* To a solution of *N*-methyl hexa(*n*-butoxy)cyclotriphosphazene trifluoromethanesulfonate (**7**) (2.02 g, 2.74 mmol) in 25 mL of DCM was added sodium iodide (821 mg, 5.48 mmol) and the mixture was stirred at room temperature for 24 h. The reaction mixture was then diluted with 25 mL of DCM, washed with 5% aqueous sodium thiosulfate and brine successively, dried over anhydrous sodium sulfate, and concentrated under vacuum. The residue was purified on a Sephadex LH-20 column using methanol/DCM (1/1) as an eluent to yield compound (**10**) as a pale yellow liquid (1.16 g, 2.18 mmol). Yield: 80%. ^{1}H NMR (360 MHz, $CDCl_3$): δ 0.85−1.00 (m, 15 H), 1.33−1.47 (m, 10 H), 1.58−1.75 (m, 10 H), 2.87 (dd, $^3J_{PH}$ = 9.9, 8.2 Hz, 3 H), 3.70−4.10 (m, 10 H). ^{31}P NMR (145 MHz, $CDCl_3$): δ 1.63 (dd, $^2J_{PP}$ = 58.0, 46.4 Hz, 1 P), 7.64 (dd, $^2J_{PP}$ = 75.4, 58.0 Hz, 1 P), 15.02 (dd, $^2J_{PP}$ = 75.4, 46.4 Hz, 1 P). ESIMS: *m*/*z* 532.2 $[M + H]^+$.

*Synthesis of 1,3,3,5,5-Pentakis(2-(2-methoxyethoxy)ethoxy)-1-oxo-2-methylcyclotriphosphazadiene (**11**).* *N*-Methyl hexakis(2-(2-methoxyethoxy)ethoxy)cyclotriphosphazene trifluoromethanesulfonate (**8**) (1.90 g, 1.88 mmol) was treated with sodium iodide to form compound **11** as a colorless liquid (1.20 g, 1.58 mmol) by following a similar procedure to the one described in the synthesis of compound **10**. Yield: 84%. ^{1}H NMR (360 MHz, $CDCl_3$): δ 2.91 (dd, $^3J_{PH}$ = 9.8, 8.5 Hz, 3 H), 3.33−3.42 (m, 15 H), 3.49−3.58 (m, 10 H), 3.62−3.68 (m, 10 H), 3.68−3.76 (m, 10H), 3.95−4.22 (m, 10 H). ^{31}P NMR (145 MHz, $CDCl_3$): δ 1.44 (dd, $^2J_{PP}$ = 60.9, 47.9 Hz, 1 P), 8.22 (dd, $^2J_{PP}$ = 75.4, 60.9 Hz, 1 P), 15.15 (dd, $^2J_{PP}$ = 75.4, 47.9 Hz, 1 P). ESIMS: *m*/*z* 762.3 $[M + H]^+$.

*Treatment of Hexa(phenoxy)cyclotriphosphazene (**2**) with Iodomethane.* To a solution of hexa(phenoxy)cyclotriphosphazene (**2**) (0.347 g, 0.500 mmol) in 5 mL pf chlorobenzene was added iodomethane (0.311 mL, 5.00 mmol), and the mixture was stirred at 100 °C for 2 days. No quaternization was detected according to ^{31}P NMR spectroscopy.

*Treatment of Hexakis(2-(2-methoxyethoxy)ethoxy)-cyclotriphosphazene (**4**) with Iodomethane.* To a solution of hexakis(2-(2-methoxyethoxy)ethoxy)cyclotriphosphazene (**4**) (0.425 g, 0.500 mmol) in 8 mL of 1,2-dichloroethane was added iodomethane (0.156 mL, 2.50 mmol). No quaternization could be detected after stirring at 40 °C for 24 h. The mixture was then stirred at 60 °C for 24 h, and ^{31}P NMR indicated that 37% of trimer **5** had been converted to compound **11**, which was further confirmed by ESIMS. Quaternization at 100 °C in chlorobenzene for 24 h resulted in a complex mixture with ^{31}P NMR signals ranging from −5 to +20 ppm. The yield of compound **11** in the mixture was 54% based on the integration in the ^{31}P NMR spectrum.

Synthesis of Polymers. *Synthesis of {[NP(OPh)$_2$]$_{0.50}$[N$^+$(CH$_3$)(OTf)$^-$P(OPh)$_2$]$_{0.50}$}$_n$ (**17**).* To a suspension of poly(diphenoxyphosphazene) (**13**) (462 mg, 2.00 mmol) in 20 mL of DCM was added a solution of methyl trifluoromethanesulfonate (0.226 mL, 2.00 mmol) in 10 mL of DCM dropwise at 0 °C. The mixture was allowed to warm to room temperature gradually and was stirred for 3 days until it turned into a clear solution. The reaction mixture was then precipitated into hexanes. The precipitation was repeated twice from THF into hexanes to yield polymer **17** as a white, fibrous solid (469 mg, 1.50 mmol), which was soluble in THF and was slightly soluble in DCM and chloroform. Yield: 75%. ^{1}H NMR (360 MHz, $CDCl_3$/THF-d_8 1/1 v/v): δ 4.00 (broad, s, 1.5 H), 6.30−7.00 (m, 10 H). ^{31}P NMR (145 MHz, $CDCl_3$/THF-d_8 1/1 v/v): δ −18.0 to −16.5 (m, 11.7%), −15.55 (broad, s, 75.8%), −11.2 to −10.2 (m, 12.5%).

*Synthesis of {[NP(OBu-n)$_2$]$_{0.79}$[N$^+$(CH$_3$)(OTf)$^-$P(OBu-n)$_2$]$_{0.21}$}$_n$ (**18**).* To a solution of poly[di(*n*-butoxy)phosphazene] (**14**) (2.00 g, 10.5 mmol) in 80 mL of DCM was added a solution of methyl trifluoromethanesulfonate (1.19 mL, 10.5 mmol) in 10 mL of DCM dropwise at −78 °C. The mixture was allowed to warm to room temperature gradually and was stirred for 2 days. The mixture was dialyzed versus acetone/methanol (1/1, v/v) for 3 days (MWCO 6000−8000) to yield polymer (**18**) as a clear colorless gum (1.90 g, 8.42 mmol), which was soluble in acetone and THF and was slightly soluble in DCM and chloroform. Yield: 80%. ^{1}H NMR (360 MHz, acetone-d_6): δ 0.87−1.05 (m, 6 H), 1.48−1.55 (m, 4 H), 1.58−1.85 (m, 4 H), 3.13−3.31 (m, 0.63 H), 3.95−4.43 (m, 4 H). ^{31}P NMR (145 MHz, acetone-d_6): δ −5.8 to −3.0 (m, 60.4%), 3.0 to 5.0 (m, 39.6%).

*Synthesis of {[NP(OBu-n)$_2$]$_{0.87}$[N$^+$(CH$_3$)(OTf)$^-$P(OBu-n)$_2$]$_{0.13}$}$_n$ (**18a**).* Poly[di(*n*-butoxy)phosphazene] (**14**) (1.15 g, 6.01 mmol) was quaternized with 0.12 equiv of methyl trifluoromethanesulfonate (82 μL, 0.725 mmol) to yield polymer **18a** as a clear colorless gum (1.01 g, 4.75 mmol) by following a similar procedure to the one described for the synthesis of polymer **18**. Polymer **18a** was soluble in acetone, methanol, DCM, and chloroform. Yield: 79%. ^{1}H NMR (360 MHz, acetone-d_6): δ 0.87−1.05 (m, 6 H), 1.48−1.55 (m, 4 H), 1.58−1.85 (m, 4 H), 3.13−3.25 (m, 0.40 H), 3.95−4.43 (m, 4 H). ^{31}P NMR (145 MHz, acetone-d_6): δ −5.8 to −3.0 (m, 72.7%), 3.0−5.0 (m, 27.3%).

*Synthesis of {[NP(OCH$_2$CH$_2$OCH$_2$CH$_2$OCH$_3$)$_2$]$_{0.81}$[N$^+$(CH$_3$)(OTf)$^-$P(OCH$_2$CH$_2$OCH$_2$CH$_2$OCH$_3$)$_2$]$_{0.19}$}$_n$ (**19**).* Poly[bis(2-(2-methoxyethoxy)ethoxy)phosphazene] (**15**) (2.40 g, 8.47 mmol) was quaternized to yield polymer **19** as a clear yellow gum (2.26 g, 7.19 mmol) by following a similar procedure to the one described for the synthesis of polymer **18**. Polymer **19** was soluble in acetone, methanol, DCM, and chloroform. Yield: 85%. ^{1}H NMR (360 MHz, $CDCl_3$): δ 3.00−3.16 (m, 0.58 H), 3.34 (s, 6 H), 3.48−3.55 (m, 4 H), 3.58−3.79 (m, 8 H), 4.00−4.42 (m 4 H); ^{31}P NMR (145 MHz, $CDCl_3$) δ −8.2 to −6.0 (m, 65.6%), 0−2.5 (m, 34.4%).

*Synthesis of {[NP(OCH$_2$CH$_2$OCH$_2$CH$_2$OCH$_3$)$_2$]$_{0.88}$[N$^+$(CH$_3$)(OTf)$^-$P(OCH$_2$CH$_2$OCH$_2$CH$_2$OCH$_3$)$_2$]$_{0.12}$}$_n$ (**19a**).* Poly[bis(2-(2-methoxyethoxy)ethoxy)phosphazene] (**15**) (1.28 g, 4.52 mmol) was quaternized to yield polymer **19a** as a clear yellow gum (1.10 g, 3.63 mmol) by following a procedure similar to the one described for the synthesis of polymer **18a**. Polymer **19a** was soluble in acetone, methanol, DCM and chloroform. Yield: 80%. ^{1}H NMR (360 MHz, $CDCl_3$): δ 3.00−3.12 (m, 0.37 H), 3.35 (s, 6 H), 3.46−3.54 (m, 4 H), 3.56−3.73 (m, 8 H), 3.97−4.38 (m 4 H); ^{31}P NMR (145 MHz, $CDCl_3$) δ −8.2 to −6.0 (m, 80.5%), 0−2.5 (m, 19.5%).

*Treatment of {[NP(OPh)$_2$]$_{0.50}$[N$^+$(CH$_3$)(OTf)$^-$P(OPh)$_2$]$_{0.50}$}$_n$ (**17**) with Sodium Iodide.* To a solution of {[NP(OPh)$_2$]$_{0.50}$[N$^+$(CH$_3$)(OTf)$^-$P(OPh)$_2$]$_{0.50}$}$_n$ (**17**) (332 mg, 1.06 mmol) in 25 mL of THF was added sodium iodide (0.159 g, 1.05 mmol) at room temperature, and the mixture was stirred for 2 days, and was concentrated and precipitated from THF into water four times to yield polymer **13** as a white fibrous solid (198 mg, 0.856 mmol). The yield was 81%. The ^{1}H NMR and ^{31}P NMR spectra corresponded well to the unquaternized polymer **13**.

*Synthesis of {[NP(OBu-n)$_2$]$_{0.81}$[N(CH$_3$)P(O)(OBu-n)]$_{0.19}$}$_n$ (**20**).* To a solution of {[NP(OBu-*n*)$_2$]$_{0.81}$[N$^+$(CH$_3$)(OTf)$^-$P(OBu-*n*)$_2$]$_{0.19}$}$_n$ (**18**) (332 mg, 1.06 mmol) in 25 mL of acetone was added sodium iodide (0.159 g, 1.05 mmol) at room temperature and the mixture was stirred for 2 days. The mixture was concentrated and precipitated from acetone into water once and from THF into water twice to yield polymer **20** as a gray elastomer (380 mg, 1.93 mmol). It was soluble in THF and was slightly soluble in DCM, acetone and chloroform. Yield: 90%. ^{1}H NMR (360 MHz, THF-d_8/acetone-d_6 1/1): δ 0.96 (br, s, 5.45 H), 1.38−1.55 (m, 3.61 H), 1.58−1.85 (m, 3.58 H), 2.94−3.08 (m, 0.57 H), 3.80−4.38 (m, 3.63 H). ^{31}P NMR (145 MHz, THF-d_8/acetone-d_6 1/1) δ −6.0 to −3.0 (m, 60.2%), −3.0 to 0.5 (m, 17.2%), 6.5 to 9.0 (m, 22.6%).

*Synthesis of {[NP(OCH$_2$CH$_2$OCH$_2$CH$_2$OCH$_3$)$_2$]$_{0.81}$[N(CH$_3$)P(O)(OCH$_2$CH$_2$OCH$_2$CH$_2$OCH$_3$)]$_{0.19}$}$_n$ (**21**).* To a solution of {[NP(OCH$_2$CH$_2$OCH$_2$CH$_2$OCH$_3$)$_2$]$_{0.81}$[N$^+$(CH$_3$)(OTf)$^-$P(OCH$_2$CH$_2$OCH$_2$CH$_2$OCH$_3$)$_2$]$_{0.19}$}$_n$ (**19**) (640 mg, 2.04 mmol) in 25 mL of acetone was added sodium iodide (306 mg, 2.04 mmol) at room temperature and the mixture was stirred for 4 days. The mixture was dialyzed versus methanol for 3 days (MWCO 6000−8000) to yield polymer **21** as a clear yellow gum (500 mg, 1.88 mmol), which is soluble in acetone and THF, DCM and chloroform. Yield: 92%. ^{1}H NMR (360 MHz, $CDCl_3$): δ 2.86−2.95 (m, 0.58 H), 3.34 (s, 5.65 H), 3.45−3.53 (m, 3.94 H), 3.55−3.74 (m, 7.48), 3.95−4.35 (m, 3.6 H).

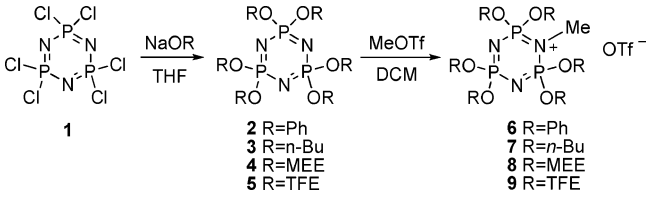
^{31}P NMR (145 MHz, $CDCl_3$) δ −7.0 to −5.0 (m, 66.9%), −4.0 to 2.5 (m, 16.4%), 4.5 to 6.2 (m, 16.7%).

*Treatment of Poly[bis(2-(2-methoxyethoxy)ethoxy)-phosphazene] (**15**) with Iodomethane.* To a solution of poly[bis-(2-(2-methoxyethoxy)ethoxy)phosphazene] (**15**) (567 g, 2.00 mmol) in 8 mL of 1,2-dichloroethane was added iodomethane (0.623 mL, 10.0 mmol) at room temperature. The mixture was stirred at 40 °C for 17 h and at 60 °C for 27 h. Then the solution was concentrated and dried under vacuum to yield a brown gum (608 mg), which is insoluble in common solvents.

RESULTS AND DISCUSSION

Quaternization of Cyclic Trimer Models. To our knowledge, the skeletal quaternization of organophosphazenes that bear P−O linked side groups has not been reported. Thus, phenoxy, *n*-butoxy, 2-(2-methoxyethoxy)ethoxy (MEEO) and 2,2,2-trifluoroethoxy (TFEO) were chosen as side groups to cover the spectrum of P−OR linked species. Reactions carried out on high polymeric phosphazenes are always more challenging than their small-molecule counterparts, especially for purification and characterization and, for this reason, small-molecule cyclic phosphazenes have played a major role as models for the development of polyphosphazene chemistry.[35] In this field, cyclotriphosphazenes (usually referred to as "trimers") are the most readily available models, and are favored for their ease of synthesis. Model reactions are shown in Scheme 1.

Scheme 1. Quaternization of Trimer Models



The syntheses of the small-molecule unquaternized trimers were carried out by the treatment of hexachlorocyclotriphosphazene **1** with an excess amount of the corresponding sodium aryloxide or alkoxides. The yields of all four trimers were over 80%. The susceptibility of the backbone nitrogen atoms in phosphazenes in the presence of alkylation reagents is controlled by their electron densities, which are ultimately determined by the substituents bonded to the neighboring phosphorus atoms. Basicity studies with small molecule cyclic phosphazenes show the ring nitrogen atoms to be the centers of greatest electron density in these molecules.[36] It is noteworthy that the basicity of a compound will not necessarily be in the same order as its nucleophilicity or electron density, because the nucleophilicity is influenced by other factors such as steric hindrance. However, the basicity of cyclotriphosphazenes with similar structures may serve as a preliminary indicator of nucleophilicity. The basicities of cyclotriphosphazenes with various substituents are reported to decrease in the order: $N_3P_3(NHR)_6$ or $N_3P_3(NR_2)_6$ (pK_a = 8.8−7.6) > $N_3P_3R_6$ (pK_a = 6.4−1.5) > $N_3P_3(OR)_6$ (pK_a = 1.4∼-5.8) > $N_3P_3Cl_6$ (pK_a < −6.0).[37−39] Fairly basic organoamino-substituted cyclooligophosphazenes are readily quaternized at the ring nitrogen atoms to form phosphazenium cations using simple alkyl halides or stronger alkylating reagents such as methyl trifluoromethanesulfonate or trimethyloxonium fluoroborate.[20−22,26] Because of the relatively lower electron densities at the ring nitrogen atoms, alkoxy or aryloxy-substituted phosphazenes are inert to iodomethane at room temperature,[26] or they undergo rearrangement of the alkoxyphosphazene to the *N*-alkyloxophosphazane at higher temperatures.[36] In this study, methyl trifluoromethanesulfonate and triethyloxonium tetrafluoroborate, two of the most aggressive alkylation reagents, were used for methyl or ethyl quaternization respectively. Dichloromethane (DCM) was chosen as the solvent because of its ability to solubilize all the trimers and its resistance to aggressive alkylation reagents. The reactions were monitored using ^{31}P NMR spectroscopy. Monoquaternization of trimer **2** was achieved at room temperature with methyl trifluoromethanesulfonate. Further quaternization did not occur even after prolonged reaction times in the presence of excess amounts of methyl trifluoromethanesulfonate. Triethyloxonium tetrafluoroborate was less reactive to trimer **2** than was methyl trifluoromethanesulfonate (see Experimental Section). Thus, only methyl trifluoromethanesulfonate was utilized for the remaining quaternization studies. For the quaternization of trimers **3** and **4**, methyl trifluoromethanesulfonate was added at −78 °C. Meanwhile, the reaction temperatures, reaction times, and the stoichiometries were carefully controlled to avoid the formation of byproduct. Only 26% of trimer **5** had been monoquaternized to form compound **9** after 48 h of refluxing. Prolonged reaction times or elevated temperatures led to the formation of a complex mixture of products. Quaternized trimer **6** could be heated at 60 °C under vacuum for drying for 1 day or stored at room temperature unsealed for a few months without detectable decomposition. Quaternized trimers **7** and **8** were found to be unstable at 60 °C while drying under vacuum. The reactivity of the trimers with different substituents corresponded well with the basicities of their skeletal nitrogen

Table 1. NMR Data for Small-Molecule Models

side group	trimer	^{31}P NMR	^{1}H NMR[a]
OPh	**2**	9.35 (s)	–
	6	−3.60 (1 P), 1.12 (2 P), AB_2, $^2J_{PP}$ = 78.4 Hz	3.77 (t, $^3J_{PH}$ = 10.8 Hz, 3 H)
	2[b]	9.34 (s)	–
OBn-*n*	**3**	18.90 (s)	–
	7	6.03 (1 P), 9.38 (2 P), AB_2, $^2J_{PP}$ = 72.3 Hz	2.96 (t, $^3J_{PH}$ = 10.8 Hz, 3 H)
	10	1.63 (dd, $^2J_{PP}$ = 58.0, 46.4 Hz, 1 P), 7.64 (dd, $^2J_{PP}$ = 75.4, 58.0 Hz, 1 P), 15.02 (dd, $^2J_{PP}$ = 75.4, 46.4 Hz, 1 P)	2.87 (dd, $^3J_{PH}$ = 9.9, 8.2 Hz, 3 H)
OMEE	**4**	19.05 (s)	–
	8	6.55 (1 P), 9.79 (2 P), AB_2, $^2J_{PP}$ = 75.5 Hz	3.00 (t, $^3J_{PH}$ = 10.8 Hz, 3 H)
	11	1.44 (dd, $^2J_{PP}$ = 60.9, 47.9 Hz, 1 P), 8.22 (dd, $^2J_{PP}$ = 75.4, 60.9 Hz, 1 P), 15.15 (dd, $^2J_{PP}$ = 75.4, 47.9 Hz, 1 P)	2.91 (dd, $^3J_{PH}$ = 9.8, 8.5 Hz, 3 H)

[a]Only the methyl groups attached to backbones are shown here. [b]Trimer **2** recovered from treatment of compound **17** with sodium iodide.

dx.doi.org/10.1021/ma202619j | *Macromolecules* 2012, 45, 1182−1189

atoms. The pK_a values of trimers **2**, **3**, **4**, and **5** are −5.8, 0.1, ∼−1 (estimated), and −6.0 respectively. The higher stability of trimer **6** than those of trimers **7** and **8** might result from a shielding effect by bulky phenoxy groups to stabilize the quaternization site, and from the resistance of the sp^2 carbons to migration and rearrangement reactions.

Because of the lack of hydrogen bonding sites and the asymmetric geometries of the quaternized trimers, quaternized trimer **6** is an amorphous solid at room temperature, whereas **7** and **8** are liquids. Thus, no X-ray crystallography data were available. The NMR spectra of unquaternized and quaternized trimers are shown in Table 1. Triplet signals at 3.77, 2.96, and 3.00 in ^{1}H NMR spectra clearly indicate the methyl groups attached to backbone nitrogen atoms in quaternized trimers **6**, **7**, and **8**. The two adjacent phosphorus atoms split the methyl groups with formally identical coupling constants ($^3J_{PH}$). The

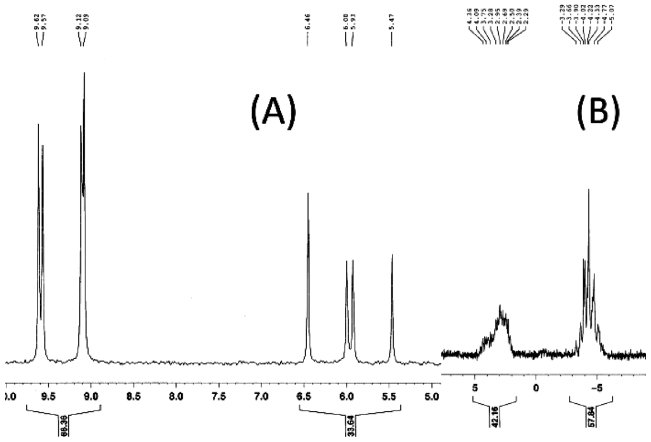
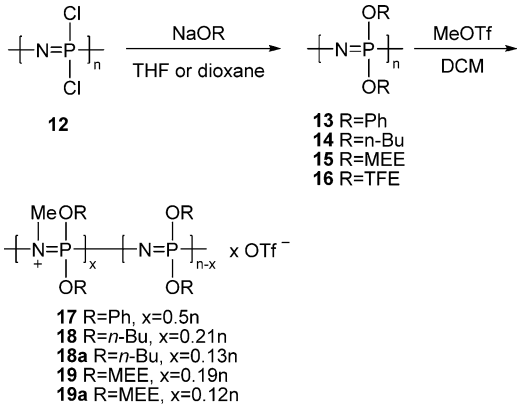


Figure 1. ^{31}P NMR spectra of quaternized phosphazenes: (A) trimer **7** and (B) polymer **18**.

^{31}P NMR spectrum of trimer **7** is shown in Figure 1A. ^{31}P NMR signals of quaternized trimers are shifted upfield compared to the singlet signals of the parent phosphazenes. Software simulation indicated that the spin systems are AB_2, similar to the reported quaternized amino-substituted trimers.[20] However, the extra splittings might be the result of the large coupling constants. Mass spectra also provide evidence for the formation of phosphazenium cations. (See Experimental Section)

Quaternization of Polymers. Following similar synthesis procedures to those employed for the small molecule models, the quaternization of polymers **13**−**16** were carried out as shown in Scheme 2. Unquaternized polymers were synthesized by replacement of the chlorine atoms in poly(dichlorophosphazene) using sodium salts of the corresponding aryloxide or alkoxide. Quaternization of the backbone nitrogen atoms of polymers **13**−**16** was attempted using methyl trifluoromethanesulfonate in dichloromethane (DCM) solutions. In all cases except for polymer **16**, the quaternization of the polymers followed the same pattern as for the small-molecule models. Quaternization of polymer **16** was unsuccessful because of its poor solubility in DCM and in other solvents which are inert to methyl trifluoromethanesulfonate and the low electron density on the backbone nitrogen atoms. The physical data for polymers **17**−**19** are shown in Table 2. Little structural information could be obtained from

Scheme 2. Quaternization of Polymers



the ^{31}P NMR data due to the inherent structural complexity of the polymers compared to those of their small-molecule models as well as the random distribution of quaternization sites along the backbone. The ^{31}P NMR spectrum of polymer **18**, as a representative, is shown in Figure 1B. Broadened peaks with ambiguous coupling in ^{1}H NMR spectra were also detected, which is also quite common for polyphosphazenes and some other polymers. These phenomena further emphasized the key role of model reactions in this chemistry. With the presence of 1 equiv of quaternization reagent per repeating unit, the percentages of quaternized backbone nitrogen atoms in polymers **17**, **18**, and **19** were 50%, 21%, and 19% respectively, with 1−2% variation from batch to batch. The surprisingly high degree of quaternization for polymer **17** can be attributed to the shielding effect of bulky phenoxy substituents as observed in the quaternization of trimer **2**. Lower degrees of quaternization were achieved by controlling the stoichiometry of the quaternization reagent. Thermogravimetric analysis (TGA) showed that the thermal stability of quaternized polymers is lower than their unquaternized counterparts, but they are considerably more stable than the small-molecule models.

Molecular weight data for quaternized polymers **17**−**19** could not be obtained by gel permeation chromatography (GPC) although they are completely soluble in THF, the mobile phase used. This is a common problem for polyelectrolytes in the absence of additional salting.[40] Because of the large quantity of alkali trifluoromethanesulfonate required to saturate the mobile phase and the solubility and possible instability of these polymers in aqueous media, we did not attempt to measure the molecular weights with the use of additional salting.

Elimination Reactions of Quaternized Phosphazenes. In order to expand the possible uses of these new materials, further attempts were conducted with the quaternized polyphosphazenes to exchange the anions from the stable trifluoromethanesulfonate ion to other anions. A motivation for this aspect was the need for an I^-/I_3^- redox couple for use in DSSC electrolytes.

Ion exchange was first studied by dialyzing polymer **19** versus 2% sodium iodide solution in methanol. The resultant polymer showed a much lower ionic conductivity. This prompted a study of the chemistry that occurs during the anion exchange. All the quaternized phophazenes were subjected to treatment with excess sodium iodide in DCM, THF, or acetone at room temperature, as shown in Scheme 3. All were found to be

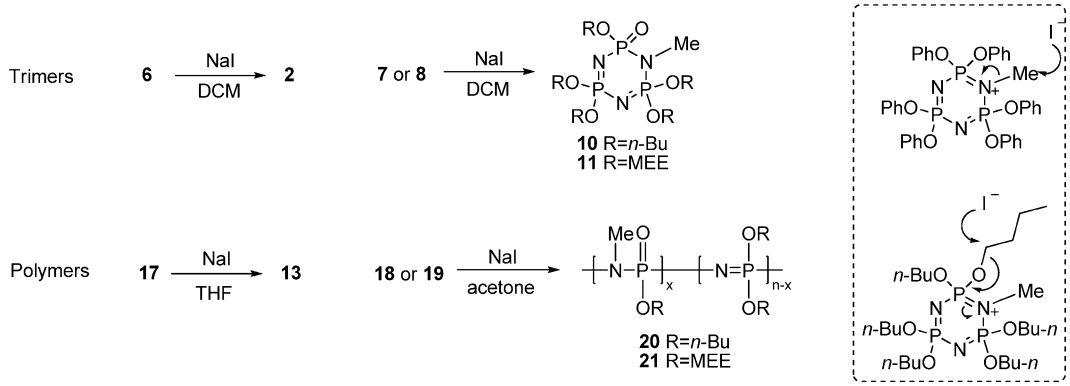
dx.doi.org/10.1021/ma202619j | Macromolecules 2012, 45, 1182−1189

Table 2. Structural and Physical Properties for Polymers

side group	polymer	^{31}P NMR	^{1}H NMR[a]	M_w (×10^3)	T_{onset} (°C)	T_g (°C)
OPh	**13**	−18.75 (s)	–	1596.2	426.6	−4.5
	17	−18.0 to −16.5 (m, 11.7%), −15.55 (br, s, 75.8%), −11.2 to −10.2 (m, 12.5%)	4.00 (br, s)	–	351.6	10.3
	13[b]	−18.81 (s)	–	345.5	372.8	−1.7
OBu-*n*	**14**	−7.32 (s)	–	2242.3	260.0	−108.7
	18	−5.8 to −3.0 (m, 57.8%), 3.0 to 5.0 (m, 42.2%)	3.13−3.32 (m)	–	157.1	−81.8
	18a	−6.0 to −3.5 (m, 72.7%), 2.2 to 4.5 (m, 27.3%)	3.13−3.24 (m)	–	192.7	−93.2
	20	−8.5 to −5.5 (m, 59.1%), −4.7 to −3.0 (m, 17.7%), 3.8 to 6.2 (m, 23.3%)	2.85−3.01	659.2	176.1	−87.7
OMEE	**15**	−7.74 (s)	–	778.0	268.7	−79.2
	19	−8.2 to −6.0 (m, 65.6%), 0 to 2.5 (m, 34.4%)	3.00−3.16 (m)	–	173.9	−70.6
	19a	−7.2 to −6.8 (m, 80.5%), 0 to 2.5 (m, 19.5%)	3.00−3.16 (m)	–	211.1	−74.2
	21	−8.5 to −5.0 (m, 66.9%), −4.0 to −2.5 (m, 16.4%), 4.3 to 6.2 (m, 23.3%)	2.85−2.95 (m)	211.0	242.5	−73.9

[a]Only the methyl groups attached to backbones are shown here. [b]Polymer **13** recovered from treatment of polymer **17** with sodium iodide.

Scheme 3. Treatment of Quaternized Phosphazenes with Sodium Iodide



susceptible to the strong nucleophilicity of iodide ion. Depending on the structures of the side groups, dealkylation of the quaternary nitrogen atoms or of the side-chain alkyl groups was detected. The progress of the elimination reactions was monitored with ^{31}P NMR spectra. For the phenoxy substituted quaternized trimer **6** or polymer **17** iodide ion attacks the methyl groups attached to the skeletal nitrogen atoms to regenerate unquaternized trimer **2** or polymer **13.** This is due to the inertness of sp^2 carbon atoms to nucleophiles. For alkoxy substituted quaternized species **7**, **8**, **18**, and **19**, iodide ion attacks the α-carbon atoms of the side groups to form oxophosphazanes **10**, **11**, **20**, and **21**, by following the mechanism proposed in Scheme 3. (see Table 1 and Table 2 for structural and physical properties and Figure 2 for ^{31}P NMR spectra) The molecular weights of the resultant polymers **13** (product by elimination), **20** and **21** were lower than the corresponding unquaternized parent polymers **13**, **14**, and **15**. This suggests that scission of the polymer backbone occurred during either the quaternization or the elimination reactions. To further investigate the mechanism of the rearrangements, unquaternized phosphazenes were treated with iodomethane. Trimer **2** was stable in the presence of 10 equiv of iodomethane at 100 °C for 2 days. In the presence of iodomethane, trimer **4** underwent rearrangement to form oxophosphazane **11** in 37% yield after being stirred at 60 °C for 24 h. Polymer **15** became an insoluble elastomer after treatment with iodomethane at 60 °C, probably due to cross-linking induced by the elevated temperature.

Ionic Conductivity and Thermal Analysis. The ionic conductivities of quaternized trimers **6**, **7**, and **8** are 3.36 × 10^{-5} S·cm^{-1}, 9.46 × 10^{-4} S·cm^{-1} and 6.21 × 10^{-4} S·cm^{-1} at 25 °C,

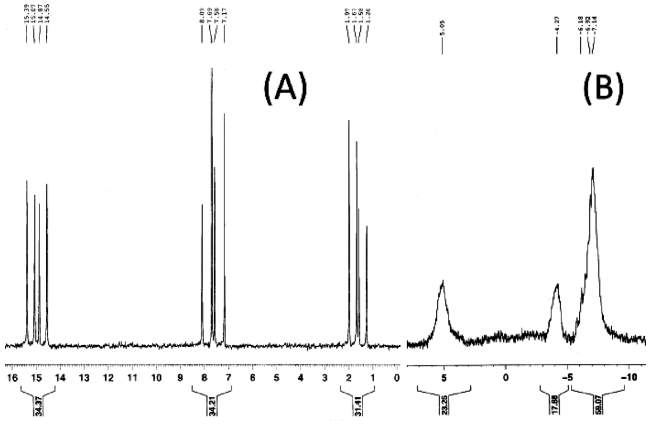


Figure 2. ^{31}P NMR spectra of dealkylization products: (A) trimer **10** and (B) polymer **20**.

values that are lower than imidazolium based ionic liquids with trifluoromethanesulfonate counterion, which usually show conductivities above 10^{-3} S·cm^{-1}.[41] This can be explained by the large sizes of the cations and the high viscosity. Polymer **17** has a low ionic conductivity of 2.53 × 10^{-9} S·cm^{-1}, due to its high T_g. No further research was carried out on these compounds.

The ionic conductivities of solvent-free quaternized polyalkoxyphosphazenes and their salt complexes with lithium trifluoromethanesulfonate and silver trifluoromethanesulfonate are shown in Table 3. For the pure quaternized polymers, a similar trend in conductivity with increasing degree of quaternization was found for all the polymers with same side

dx.doi.org/10.1021/ma202619j | Macromolecules 2012, 45, 1182−1189

Table 3. Conductivities and T_g's of Quaternized Polyphosphazenes

entry	polymer	salt (mol %)	OTf⁻/ru[a]	conductivity (S·cm^{-1})	T_g (°C)
1	**18a**	–	0.13	1.72×10^{-4}	−93.2
2		LiOTf (8%)	0.21	7.45×10^{-5}	−90.7
3		AgOTf (8%)	0.21	9.88×10^{-5}	−75.8
4	**18**	–	0.21	2.14×10^{-4}	−81.8
5		LiOTf (5%)	0.26	8.21×10^{-5}	−77.4
6		LiOTf (10%)	0.31	4.44×10^{-5}	−74.8
7		AgOTf (5%)	0.26	9.59×10^{-5}	−71.0
8		AgOTf (10%)	0.31	5.34×10^{-5}	−67.0
9	**19a**	–	0.12	1.55×10^{-4}	−74.2
10		LiOTf (7%)	0.19	1.23×10^{-4}	−69.9
11		AgOTf (7%)	0.19	2.09×10^{-4}	−70.7
12	**19**	-	0.19	2.58×10^{-4}	−70.8
13		LiOTf (5%)	0.24	1.92×10^{-4}	−67.6
14		LiOTf (10%)	0.29	1.28×10^{-4}	−63.1
15		AgOTf (5%)	0.24	2.04×10^{-4}	−66.9
16		AgOTf (10%)	0.29	1.49×10^{-4}	−61.9

[a]Repeating unit.

group. Even if only the anions are mobile, the conductivities of solvent-free quaternized polymers **18** (entry 4) and **19** (entry 12) are higher than that of a MEEP/silver trifluoromethanesulfonate complex (1.68×10^{-4} S·cm^{-1}, 12 mol %), or a MEEP/lithium trifluoromethanesulfonate complex (2.8×10^{-5} S·cm^{-1}, 17 mol %) at similar temperature.[42] The temperature dependent conductivities of polymers **18** and **19** are illustrated in Figure 3. The highest conductivities of polymer **19** of 2.58×10^{-4} S·cm^{-1} at 25 °C and 2.09×10^{-3} S·cm^{-1} at 80 °C were achieved, which are among the highest conductivities of unplasticized solid-state polymer electrolytes or polyelectrolytes. To further compare the effect of backbone-quaternization versus simple salt-complexing on conductivity, polyelectrolyte/salt complexes were formulated by drying an acetone solution of a polyelectrolyte and a salt under vacuum. Additional salt applied to polymers **18** or **19** resulted in decreased ionic conductivities (entry 5−8 and entry 13−16). Polyelectrolyte/salt complexes formulated with polymer **18a** and **19a** had lower ionic conductivities, compared to pure polymers **18** and **19** which have same ion concentrations, and even compared to polymers **18a** and **19a** which have lower ion concentrations. (entry 2−4 and entry 10−12).

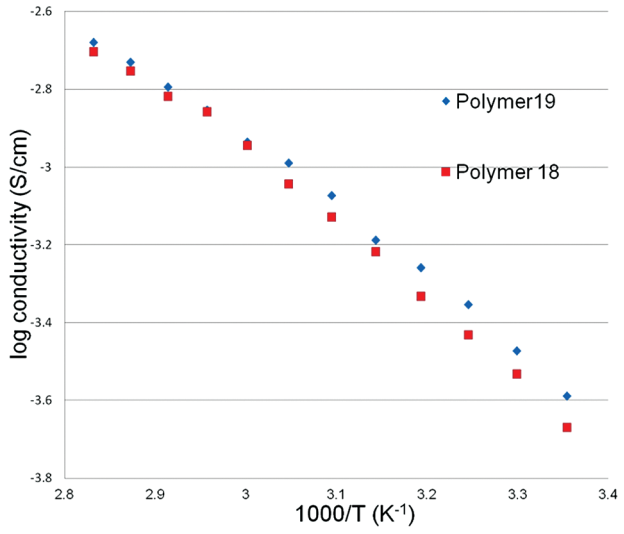


Figure 3. Arrhenius plots for the conductivity of solvent/salt-free polymers **18** and **19**.

T_g's for polyelectroytes and polyelectrolyte/salt complexes were measured by differential scanning calorimetry (DSC). All the salt/polyelectrolyte complexes underwent increases in T_g. (See Table 3.) Metal ions coordinate to the polymers to form ionic cross-links. These cross-links hinder the motion of the polymer side chains, and this is reflected in the T_g's. The elevated T_g's conform to the trend of lower conductivity of polyelectrolyte/salt complexes.

The higher conductivity and lower T_g of backbone quaternized polyelectrolytes compared to conventional polymer electrolytes can be attributed to the following factors. First, the shielding effect by side chains linked to the backbone immobilizes cations and hinders ion pairing, whereas cations and anions are more likely to pair with each other in conventional polymer electrolytes. Second, Coulombic repulsion between side-chain shielded cations is weaker compared to that in polymer electrolytes, which could help to maintain high segmental flexibility. Furthermore, ionic cross-linking is avoided or minimized in backbone quaternized polymers as there are no metal ions in the backbone quaternized species.

SUMMARY

The quaternization of poly(alkoxyphosphazenes) and poly[(bisphenoxy)phosphazene] has been accomplished. Because of the lower electron donating ability of alkoxy and aryloxy side groups than in the case of alkylamino side groups, efficient quaternization could only be achieved with methyl trifluomethanesulfonate as the reagent. This is the first report of backbone functionalization of phosphazenes that bear P−O linked side groups at both the small molecule and high polymer levels. However, the quaternized poly(alkoxyphosphazenes) are sensitive to dealkylation in the presence of nucleophilic iodide anions.

These new backbone quaternized poly(alkoxyphosphazenes) have high ionic conductivity without plasticizers or additional salts. This offers the potential for insight into the mechanism of ion transport and for the applications of polymers in solid-state electrochemical devices. The new concept of immobilizing ions onto or near to a polymer backbone may have several advantages over conventional polymer/salt complexes or side chain functionalized polyelectrolytes. The corresponding quaternization of poly(alkylaminophosphazenes) to improve the stability of polyelectrolytes is currently ongoing.

AUTHOR INFORMATION

Corresponding Author

*E-mail: hra@chem.psu.edu.

Notes

The authors declare no competing financial interest.

ACKNOWLEDGMENTS

We thank the U.S. Department of Energy for financial support (Grant DE-FG36-08GO18011) and Dr. Kirk Marat (Department of Chemistry, University of Manitoba), Dr. Wenbin Luo and Dr. Alan Benesi (Department of Chemistry, The Pennsylvania State University) for discussions on ^{31}P NMR spectra.

REFERENCES

(1) Fenton, D. E.; Parker, J. M.; Wright, P. V. *Polymer* **1973**, *14*, 589.
(2) Gray, F., *Solid Polymer Electrolytes*. VCH Publishers: New York, 1991.
(3) Oregan, B.; Gratzel, M. *Nature* **1991**, *353*, 737−740.
(4) Hagfeldt, A.; Boschloo, G.; Sun, L. C.; Kloo, L.; Pettersson, H. *Chem. Rev.* **2010**, *110*, 6595−6663.
(5) Allcock, H. R., *Chemistry and applications of polyphosphazenes*. John Wiley & Sons, Inc: Hoboken, NJ, 2003.
(6) Blonsky, P. M.; Shriver, D. F.; Austin, P.; Allcock, H. R. *J. Am. Chem. Soc.* **1984**, *106*, 6854−6855.
(7) Allcock, H. R.; Austin, P. E.; Neenan, T. X.; Sisko, J. T.; Blonsky, P. M.; Shriver, D. F. *Macromolecules* **1986**, *19*, 1508−1512.
(8) Allcock, H. R.; Pucher, S. R.; Turner, M. L.; Fitzpatrick, R. J. *Macromolecules* **1992**, *25*, 5573−5577.
(9) Ganapathiappan, S.; Chen, K.; Shriver, D. F. *Macromolecules* **1988**, *21*, 2299−2301.
(10) Ganapathiappan, S.; Chen, K. M.; Shriver, D. F. *J. Am. Chem. Soc.* **1989**, *111*, 4091−4095.
(11) Allcock, H. R.; Fitzpatrick, R. J.; Salvati, L. *Chem. Mater.* **1991**, *3*, 1120−1132.
(12) Allcock, H. R.; Welna, D. T.; Maher, A. E. *Solid State Ionics* **2006**, *177*, 741−747.
(13) Klein, R. J.; Welna, D. T.; Weikel, A. L.; Allcock, H. R.; Runt, J. *Macromolecules* **2007**, *40*, 3990−3995.
(14) Wisian-Neilson, P.; Garciaalonso, F. J. *Macromolecules* **1993**, *26*, 7156−7160.
(15) Luther, T. A.; Stewart, F. F.; Budzien, J. L.; LaViolette, R. A.; Bauer, W. F.; Harrup, M. K.; Allen, C. W.; Elayan, A. *J. Phys. Chem. B* **2003**, *107*, 3168−3176.
(16) Chandrasekhar, V.; Krishnan, V., In *Phosphazenes: A worldwide insight*, Gleria, M.; De Jaeger, R., Eds. Nova Science Pub Inc: New York, 2004; p 827.
(17) Heston, A. J.; Panzner, M. J.; Youngs, W. J.; Tessier, C. A. *Inorg. Chem.* **2005**, *44*, 6518−6520.
(18) Zhang, Y.; Huynh, K.; Manners, I.; Reed, C. A. *Chem. Commun.* **2008**, 494−496.
(19) Tun, Z. M.; Heston, A. J.; Panzner, M. J.; Medvetz, D. A.; Wright, B. D.; Savant, D.; Dudipala, V. R.; Banerjee, D.; Rinaldi, P. L.; Youngs, W. J.; Tessier, C. A. *Inorg. Chem.* **2011**, *50*, 8937−8945.
(20) Benson, M. A.; Zacchini, S.; Boomishankar, R.; Chan, Y.; Steiner, A. *Inorg. Chem.* **2007**, *46*, 7097−7108.
(21) Benson, M. A.; Boomishankar, R.; Wright, D. S.; Steiner, A. *J. Organomet. Chem.* **2007**, *692*, 2768−2772.
(22) Benson, M. A.; Steiner, A. *Chem. Commun.* **2005**, 5026−5028.
(23) Rapko, J. N.; Feistel, G. *Inorg. Chem.* **1970**, *9*, 1401−1405.
(24) Searle, H. T.; Dyson, J.; Ranganathan, T. N.; Paddock, N. L. *J. Chem. Soc., Dalton Trans.* **1975**, 203−208.
(25) Calhoun, H. P.; Trotter, J. *J. Chem. Soc., Dalton Trans.* **1974**, 377−381.
(26) Allcock, H. R.; Levin, M. L.; Austin, P. E. *Inorg. Chem.* **1986**, *25*, 2281−2288.
(27) Pangborn, A. B.; Giardello, M. A.; Grubbs, R. H.; Rosen, R. K.; Timmers, F. J. *Organometallics* **1996**, *15*, 1518−1520.
(28) Allcock, H. R.; Kugel, R. L. *J. Am. Chem. Soc.* **1965**, *87*, 4216−4217.
(29) Allcock, H. R.; Walsh, E. J. *J. Am. Chem. Soc.* **1972**, *94*, 4538−4545.
(30) Fitzsimmons, B. W.; Shaw, R. A. *J. Chem. Soc.* **1964**, 1735−1741.
(31) Fei, S. T.; Allcock, H. R. *J. Power Sources* **2010**, *195*, 2082−2088.
(32) Allcock, H. R.; Walsh, E. J. *J. Am. Chem. Soc.* **1972**, *94*, 119−124.
(33) Allcock, H. R.; Kugel, R. L.; Valan, K. J. *Inorg. Chem.* **1966**, *5*, 1709−1715.
(34) Allcock, H. R.; Connolly, M. S.; Sisko, J. T.; Alshali, S. *Macromolecules* **1988**, *21*, 323−334.
(35) Allcock, H. R. *Acc. Chem. Res.* **1979**, *12*, 351−358.
(36) Fitzsimmons, B. W.; Hewlett, C.; Shaw, R. A. *J. Chem. Soc.* **1964**, 4459−4464.
(37) Feakins, D.; Shaw, R. A.; Last, W. A. *J. Chem. Soc.* **1964**, 2387−2396.
(38) Feakins, D.; Shaw, R. A.; Last, W. A. *J. Chem. Soc.* **1964**, 4464−4471.
(39) Feakins, D.; Last, W. A.; Neemuchw, N.; Shaw, R. A. *J. Chem. Soc.* **1965**, 2804−2811.
(40) Dautzenberg, H.; Jaeger, W.; Kotz, J.; Philipp, B.; Seidel, C.; Stscherbina, D., *Polyelectrolytes: formation, characterization, and application*. Hanser: New York, 1994; pp 233−247.
(41) Holbrey, J. D.; Rogers, R. D., In *Ionic liquids in synthesis*, 2nd ed.; Wasserscheid, P.; Welton, T., Eds. Wiley-VCH: Weinheim, Germany, 2008; Vol. *1*, p 149.
(42) Allcock, H. R.; Napierala, M. E.; Olmeijer, D. L.; Best, S. A.; Merz, K. M. *Macromolecules* **1999**, *32*, 732−741.

Macromolecules

Article

pubs.acs.org/Macromolecules

Synthesis of Diverse Well-Defined Functional Polymers Based on Hydrozirconation and Subsequent Anti-Markovnikov Halogenation of 1,2-Polybutadiene

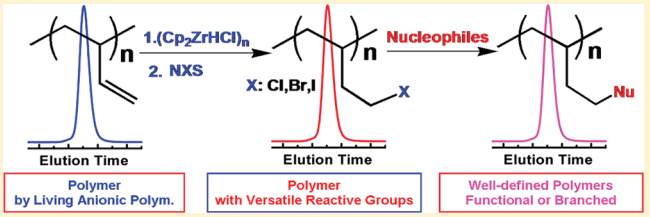
Jun Zheng,[†,‡] Feng Liu,[†,‡] Yichao Lin,[†,‡] Zhijie Zhang,[†,‡] Guangchun Zhang,[†,‡] Lu Wang,[†,‡] Yan Liu,[†] and Tao Tang*[,†]

[†]State Key Laboratory of Polymer Physics and Chemistry, Changchun Institute of Applied Chemistry, Chinese Academy of Sciences, Changchun 130022, China

[‡]Graduate School of the Chinese Academy of Sciences, Beijing 100039, China

Supporting Information

ABSTRACT: For the first time, hydrozirconation and halogenolysis of 1,2-polybutadiene (1,2-PBD, by living anionic polymerization) were studied to synthesize reactive polyhalohydrocarbons, which provide a platform for preparing well-defined functional polymers via macromolecular substitution. Hydrozirconation and halogenolysis afforded quite convenience for anti-Markovnikov hydrohalogenation of 1,2-PBD with controllable degree of functionalization. Diverse functional polymers and branched polymers were synthesized after macromolecular substitution reaction with a broad range of commercially available nucleophiles (amines, phenols, alcohols, carbanions, carboxylates, and azide) or macromolecular nucleophiles. NMR and GPC characterizations confirmed high conversion in substitution reaction and narrow molecular weight distribution of the resultant functional polymers, respectively. The methodology utilizing Schwartz's reagent for hydrozirconation of macromolecules could greatly facilitate the modification of vinyl groups containing polymers with high efficiency.



1. INTRODUCTION

Living polymerization methods (living radical and ionic polymerization) have widely been used to achieve a high degree of control over the resultant polymers and provide polymers with the narrowest molecular weight distribution.[1,2] But relatively low functional groups tolerance restricts the synthesis of functional polymers directly by living polymerization methods. To overcome such obstacles, a combination of living radical polymerization (of monomers bearing reactive moieties) and subsequent postmodification approaches[3,4] provides possibilities for preparation of various functional polymers with control over molecular weight, functionality, and tailored properties. However, living anionic polymerization seems to be extremely incompatible with most functional groups. Therefore, it is still a key challenge to prepare functional polymers directly or indirectly by living anionic polymerization. Instead of synthesis of monomers bearing reactive groups for living anionic polymerization, we try to introduce versatile reactive moieties with high efficiency into polymers for subsequent modification. By this way, a family of diverse well-defined functional polymers would be prepared indirectly by anionic polymerization, when incorporation of reactive groups was performed on an appropriate polymer precursor from living anionic polymerization.

It is known that butadiene, one of common monomers, can be polymerized by living anionic polymerization with tunable 1,4- or 1,2-microstructure. The nature of unsaturated bonds in polybutadiene (PBD) backbone or side chain offers opportunities for various modification reactions. Plenty of functional groups (e.g., hydroxyl, carbonyl, silyl, epoxy, etc.) were successfully introduced onto PBD chains via reactions with double bonds. A pioneering research has been reported on hydroboration of 1,2-PBD followed by oxidation and hydrolysis for synthesis of well-defined polyalcohol without gelation.[5] By means of hydrocarboxylation and hydroacylation, PBD could be transformed to poly(carbonyl acid) or polyaldehyde, using palladium catalyst in CO pressure[6] or by radical addition of aliphatic aldehydes.[7] Thiol−ene click chemistry was employed to introduce functional groups onto 1,2-PBD homopolymer or block polymer.[8,10] The recently reported cyclopropanation of PBD for the preparation of poly(cyclopropanyl acid) or ester would be feasible with controllable degree of functionalization.[11] Epoxidation and hydrosilylation seem to be the most popular methods used in practice due to reactive epoxy ring[12,13] and functional hydrosilanes[14,15] for possible further transformation. Different postmodification methods selectively or nonselectively toward 1,4- or 1,2-PBD successfully afford various reactive groups grafted PBDs accompanied by side reactions in some cases. Although most of grafted groups vastly expand the properties of PBD, they are not suitable for later

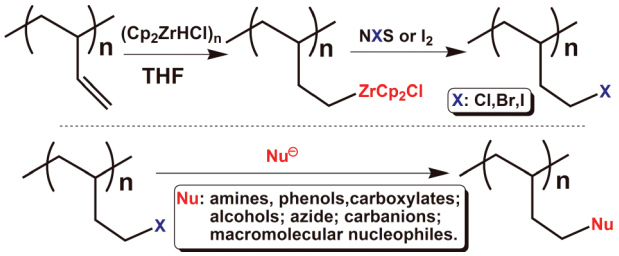
Received: December 4, 2011
Revised: January 10, 2012
Published: January 24, 2012

 © 2012 American Chemical Society dx.doi.org/10.1021/ma202628p | Macromolecules 2012, 45, 1190−1197

polymer-analogous modification due to limited reactivity toward few substrates.

It will be needed to incorporate a versatile group[14] that can be highly reactive toward a broad range of substrates for the conversion into functional groups. Halogen groups, considered as versatile groups, are quite reactive toward abundant nucleophiles (e.g., alkoxy, azide, nitrile, organometallics for C−C coupling, and so forth). Introduction of halogen onto polymers, especially primary halogen groups (in favor of substitution than elimination), would be an excellent choice for subsequent transformation of halogens into diverse functional moieties via substitution reaction. Classical hydrohalogenation by hydrogen halides usually shows limited control over anti-Markovnikov halogenation although it has been applied industrially for rubber materials.[16] Hydrozirconation and later halogenolysis are highly efficient for halogenation of alkene/alkyne in anti-Markovnikov form (high reaction rate and mild condition compared to electrophilic addition reaction with hazardous hydrohalide[17,18]). However, hydrozirconation of macromolecules with unsaturated carbon−carbon bond in the backbone or pendent chains is rarely reported to our best knowledge.[19,20] The named hydrozirconation reagent, generally referred to as "Schwartz's reagent", i.e., bis(cyclopentadienyl)-zirconium hydrochloride (Cp_2ZrHCl), is a well-known and convenient reagent in organic chemistry for functionalization of alkenes.[21,22] In this study, we demonstrate successful hydrohalogenation of 1,2-PBD (prepared by anionic polymerization) with anti-Markovnikov form by hydrozirconation and subsequent halogenolysis (Scheme 1). The synthesized well-defined halogenated 1,2-PBD was used as a platform for the preparation of diverse functional or grafted polymers via macromolecular substitution. Importantly, this method would not only produce novel well-defined polymers which could not be prepared directly by classical polymerization but also develop alternative applications of Schwartz's reagent in polymer chemistry.

Scheme 1. Hydrozirconation of 1,2-Polybutadiene and Halogenolysis Methods to Preparation of Polyhalohydrocarbon as a Platform for Diverse Functional Polymers



2. EXPERIMENTAL SECTION

2.1. Materials. All the solvents (tetrahydrofuran (THF), hexane) were distilled from sodium/potassium alloy with benzophenone. Bis(cyclopentadienyl)zirconium dichloride (99%) was purchased from Alfa Aesar. *N*-Bromosuccinimide (NBS) was recrystallized from hot water, washed with alcohol, and vacuum-dried as white flakelike crystals, while *N*-chlorosuccinimide (NCS) (98+%) and *N*-iodosuccinimide (NIS) (97%) were used as received from Alfa Aesar. The commercially available nucleophiles and other reagents used in this work were in chemically pure grade. Schwartz's reagent (Cp_2ZrHCl) was prepared[23] using diisobutylaluminum hydride (1 M in hexane) with yield 85% and stored in nitrogen-filled glovebox (used within 1 month).

2.2. Synthesis of *N,N*-Dipiperidine Ethane (DPE).[24] Piperidine (17.2 g, 0.2 mol) and 1,2-dichloroethane (9.4 g, 0.1 mol) were mixed in 60 mL of H_2O with 8.8 g of sodium hydroxide. The mixture was vigorously stirred in 80 °C oil bath for 12 h. Upper organic layer of the final immiscible mixture was separated and washed with water, vacuum distilled in the presence of sodium hydride to afford transparent oil-like liquid with yield of 70% (purity >98% GC). δ_H (300 M, $CDCl_3$): 2.48 (s, 4H, N−CH_2−CH_2−N), 2.40 (br, 8H, 2N $(CH_2)_2$), δ 1.6−1.48 (m, 8H, 2N$(CH_2CH_2)_2$), δ 1.46−1.32 (m, 4H, 2CH_2).[25]

2.3. Polymerization of Butadiene. 1,2-Polybutadiene (1,2-PBD, with vinyl content (Cv) of 98%) was prepared in hexane with DPE at −10 °C under an argon atmosphere using *sec*-butyllithium (BuLi) as initiator ([DPE]/[BuLi] > 5 (mol/mol)), while 1,2-PBD with Cv of 88% was synthesized in THF at −10 °C without DPE.

2.4. Hydrozirconation of PBD and Halogenolysis. PBD (~0.15 g) was dissolved in 20 mL of THF and stirred overnight in a N_2-filled Mbraun glovebox. Cp_2ZrHCl powder was added and vigorously stirred. The solution became dark red after all the powder dissolved, to which solid halogenation reagent (NBS, NCS, NIS, or I_2) was added for halogenolysis. The mixture was stirred for 1 h, and drops of degassed methanol were added to finish the reaction. After concentrating by rotary evaporator, the viscous product was washed with methanol and purified by dissolution−precipitation using methane dichloride/methanol for 3−5 cycles. Isolated halogenated polymers were in ca. 80% yield after dried under vacuum at 40 °C overnight.

2.5. Synthesis of Functional Polymers by Macromolecular Substitution Reaction. A typical procedure for all the selected nucleophiles was as follows: 0.18 g of iodinated PBD (92% or 80%) was dissolved in 15 mL of THF with 400−500 mol % nucleophiles and sufficient base (NaH or K_2CO_3). Tetrabutylammonium bromide was used as phase-transfer catalyst when alcohols or phenols acted as nucleophiles. The mixture was stirred at 60 °C for 24 h under an argon atmosphere, and then the mixture was filtrated and concentrated. The synthesized functional polymers were isolated by precipitation with methanol and dried at 40 °C under vacuum.

2.6. Characterization. NMR spectra were performed on a Bruker AV300 (400) spectrometer by using $CDCl_3$ as a solvent. Relative molecular weights were determined by gel permeation chromatography (GPC) on TOSOH HLC 8220 GPC at 40 °C using THF as an eluent against linear polystyrene standards. Differential scanning calorimetry (DSC, Perkin-Elmer 7 DSC instrument) was carried out in the range from −30 to 100 °C at a heating rate of 30 °C/min and then cooled down to −30 °C at a cooling rate of 30 °C/min. The secondary heating rate was 10 °C/min for glass transition temperature (T_g) determination. Thermogravimetric analysis (TGA) was performed on SDTQ600 (TA Instruments) under nitrogen flow at a heating rate of 10 °C/min.

3. RESULTS AND DISCUSSION

3.1. Hydrozirconation of 1,2-Polybutadiene. Figure 1a shows ^{1}H NMR spectra of 1,2-PBD (Cv = 88%) and hydrozirconated 1,2-PBD. It could be seen that the hydrozirconation of 1,2-PBD was realized with high conversion by using Schwartz's reagent (ZrH) in equivalent molar amount of double bonds of 1,2-PBD. The typical resonance peak at 4.9 ppm ascribed to terminal protons of CH═CH_2 almost disappeared, and a new sharp single peak at 6.0 ppm assigned to protons of Cp rings was observed. In practice, when ZrH was added to THF solution of PBD, the transparent solution turned to yellow in a minute, and ZrH was completely dissolved after 10 min when 30% of ZrH (molar ratio of [ZrH] to [C═C]) was added. If the loading of ZrH was high (70% or 100%), the solution color turned to dark red, and the reaction finished within 4 h at 30 °C (Figure 1b). Because of high reactivity of Schwartz's reagent toward terminal alkenes, quantitative

dx.doi.org/10.1021/ma202628p | *Macromolecules* 2012, 45, 1190−1197

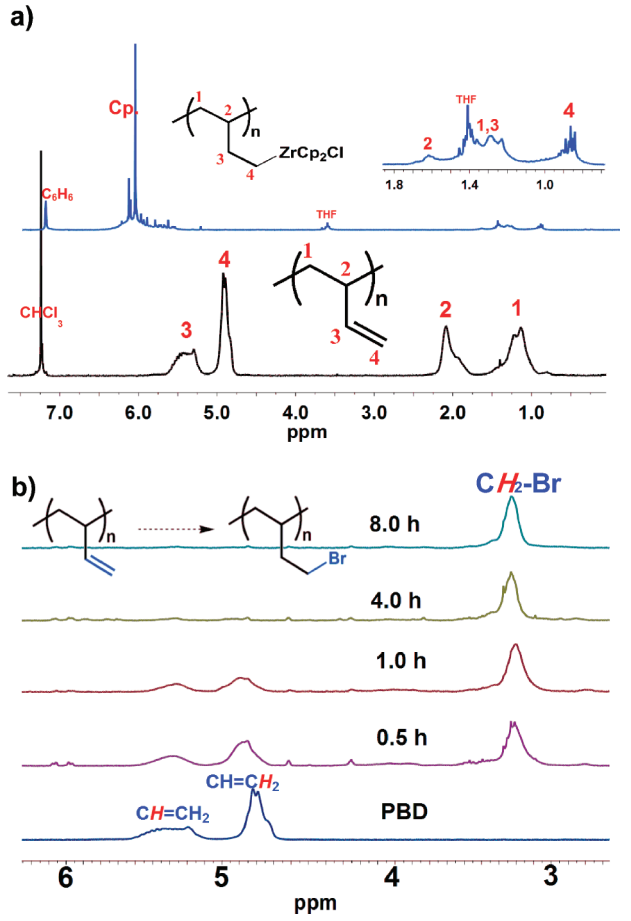


Figure 1. ^{1}H NMR (300 MHz) spectra of (a) 1,2-PBD (Cv = 88%) (in $CDCl_3$) and hydrozirconated 1,2-PBD (in C_6D_6) and (b) brominated PBDs from hydrozirconation (various reaction time) and then halogenolysis (quenched with NBS) of 1,2-PBD (Cv = 88%) at 30 °C.

conversion could take place successfully. All of the pendent vinyl groups could be hydrozircnoated, meaning no steric hindrance effect was observed. It should be mentioned that the use of THF as solvent is an important factor for such high reaction efficiency. The insolubility of Schwartz's reagent would bring kinetic hindrance for the reactions with macromolecules. Comparatively, hydrozirconation was much faster in THF than in hydrocarbon solvents due to donor capability of THF.[22] Therefore, the dissociation of ZrH cluster by THF greatly promoted the rate of hydrozirconation reaction with 1,2-PBD. Hence, hydrozirconation of PBD macromolecules is kinetically favorable in THF. Such hydrozirconated polymers are thermally stable in solution at room temperature, but sensitive to oxygen or moisture, and they can react with a variety of electrophiles including protons and halides or undergo transmetalation reactions for functional polymers.[22] (For example, our preliminary study has demonstrated that this polyorganozirconium could be reactive for initiating ethylene polymerization.) Halogenolysis is one of the examples discussed in this work for preparing reactive polymers.

3.2. Halogenolysis of Hydrozirconated 1,2-PBD for Preparing Reactive Polyhalohydrocarbons. *3.2.1. Incorporation of Halogen Atoms (Chlorine, Bromine, Iodine) via Halogenolysis.* Halogenolysis reaction was carried out with different sources of cationic halogen, such as *N*-chloro-, *N*-bromo-, and *N*-iodosuccinimide (NCS, NBS, and NIS, respectively) or molecular iodine. All of the halogens (Cl, Br, I) could be successfully incorporated onto pendent groups of PBD in anti-Markovnikov form. Figure 2 shows the ^{1}H NMR

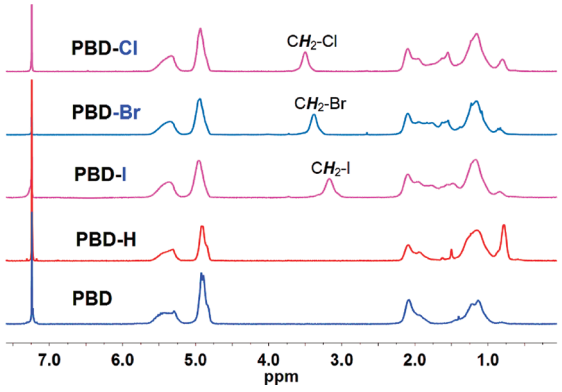


Figure 2. ^{1}H NMR spectra of halogenated (PBD-I, PBD-Cl, PBD-Br) and hydrogenated (PBD-H) of PBD with 30% degree of functionalization and pristine PBD (Cv = 88%).

spectra of chlorinated (PBD-Cl, by NCS), brominated (PBD-Br, by NBS), and iodinated (PBD-I, by NIS) PBD with about 30% degree of functionalization. The new resonance peaks centered at 3.5 (PBD-Cl), 3.4 (PBD-Br), and 3.2 ppm (PBD-I) were assigned to methylene protons of CH_2—Cl, CH_2—Br, and CH_2—I, respectively. The chemical shifts are in the order of halogen electronegativity. When hydrozirconated 1,2-PBD was treated with acidified methanol instead of succinimide, pendent vinyl groups was hydrogenated (PBD-H), resulting in the formation of methyl groups (δ 0.8 ppm in ^{1}H NMR). The functionalization degree (halogenation and hydrogenation) of 30% is consistent with the feed amount ([ZrH]/[C=C] = 0.3) of ZrH and succinimide, indicating that these reactions are almost quantitative.

3.2.2. Degree of Halogenation with Controllable Fashion. It is an interesting question whether hydrozirconation and halogenolysis were quantitatively controllable for halogenated PBDs with various functionalization degrees. Figure 3a shows ^{1}H NMR spectra of isolated brominated PBDs from varied feeding of ZrH. As the feed ratio increased, the relative intensity of peak at 3.4 ppm (CH_2—Br) increased while the intensities of peaks at 5.5 and 5.0 ppm decreased, indicating that the degree of bromination was gradually enhanced. In addition, an unexpected peak (at 0.8 ppm) was also observed, the intensity of which was increased with the intensity of CH_2—Br. This peak was assigned to protons from hydrogenated unit, meaning that the resultant polymers are a kind of copolymers of butadiene, 4-bromo-1-butene, and 1-butene. Figure 3b shows the plot of the content of each structural unit versus the feeding ratio. The formation of 1-butene structural unit was attributed to hydrolysis (with methanol in work-up) of residual alkylzirconium from incomplete halogenolysis (Figure 4 and Figure S1 in the Supporting Information). With the increase of bromination degree, glass transition temperatures (T_g) of the resultant polymers were increased according to DSC results (Table 1 and Figure S2).

Additionally, different halogenolysis reagents showed different ceiling degree of halogenations under the same reaction conditions (Figure S3). Only 50% chloronation or 77% bromination was achieved when NCS or NBS was used,

dx.doi.org/10.1021/ma202628p | *Macromolecules* 2012, 45, 1190–1197

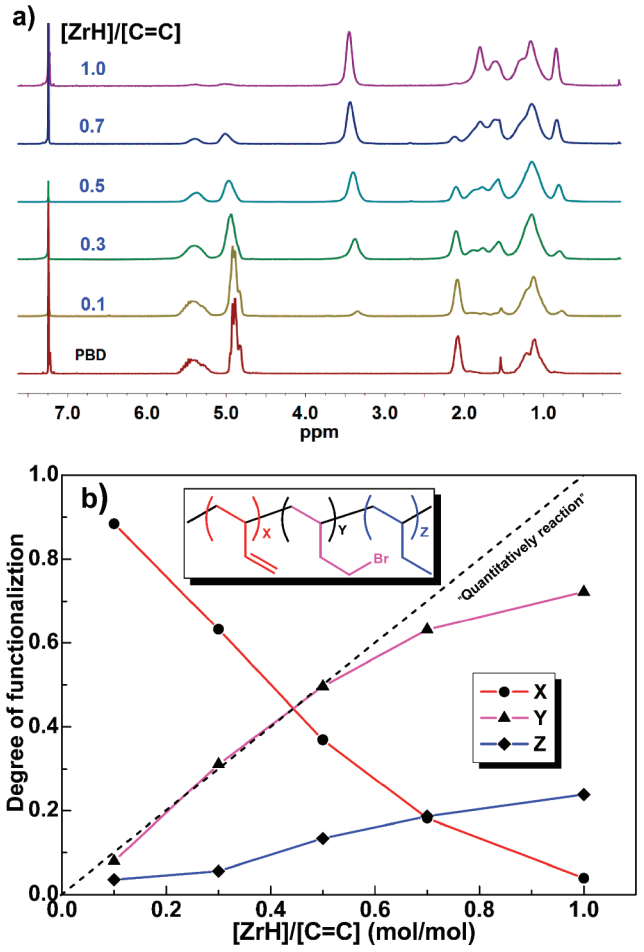


Figure 3. (a) ^{1}H NMR (300 MHz, $CDCl_3$) spectra of brominated polybutadiene from varied feeding addition and starting polybutadiene (Cv = 98%). (b) Microstructure content of brominated PBDs plotted with varied feeding addition (calculated from ^{1}H NMR (a)).

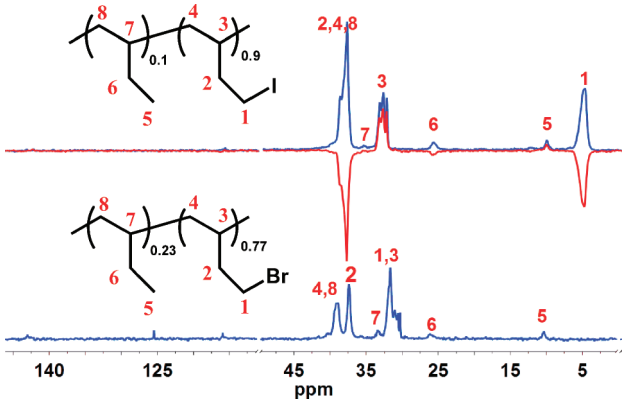


Figure 4. ^{13}C{H} NMR ($CDCl_3$, 100 MHz) spectra of brominated (77%) and iodinated (92%) PBD and DEPT135 NMR spectrum of iodinated PBD (92%).

respectively. It was helpless solely by extending halogenolysis time when succinimide was used as electrophilic halogenation reagent. However, when I_2 was used, iodinated PBD with a higher degree of halogenation (92%) was obtained. Consequently, the incomplete halogenolysis limited the complete halogenation. It is possible that the reactivity of grafted zirconium is weakened as the halogenolysis goes, resulting in

Table 1. Molecular Weights of Halogenated 1,2-PBDs (Cv of 98%)

polymers	M_n (g/mol)[a]	M_w (g/mol)[a]	PDI (M_w/M_n)[a]	T_g[b] (°C)
1,2-PBD	15800	16500	1.04	−7.4
PBD-Br(8%[c])	15400	16300	1.06	−3.1
PBD-Br(30%[c])	13500	14900	1.10	1.7
PBD-Br(51%[c])	11900	13700	1.15	4.2
PBD-Br(66%[c])	11600	13300	1.15	4.4
PBD-Br(77%[c])	10300	11700	1.13	8.0
PBD-H(99%[c])	10300	11500	1.12	−24
PBD-I(92%[c])	10200	11700	1.15	19
PBD-I(92%[c])[d]	7700	8300	1.09	
PBD-I(80%[c])[e]	2000	2200	1.07	

[a]Determined by GPC in THF vs linear PS standards. [b]Determined by DSC (Figure S2). [c]Degree of functionalization determined by ^{1}H NMR spectroscopy. [d]The number molecular weights of parental PBD was about 9600 g/mol. [e]The number molecular weights of parental PBD was about 2200 g/mol.

incomplete halogenolysis, especially when NCS is used. The low degree of chlorination was also observed in hydrozirconation of small molecular alkenes.[26] Fortunately, using molecular iodine indeed promotes halogenolysis, which leads to the formation of almost complete iodinated PBD. Moreover, another great advantage of using molecular halogen is the regeneration of bis(cyclopentadienyl)zirconium dihalide, which could be separated and reused.[26,27]

Owing to the existence of unreacted zirconium moieties on polymer chains, additional care was required for purification. Deoxygenated methanol should be used to convert all the unreacted organic zirconiums to methyl groups before exposed in air. Otherwise, possible oxygen-induced radical coupling[28] would bring a shoulder peak in GPC trace of halogenated polymer (Figure S4). Highly halogenated 1,2-PBDs were slight yellow (PBD-Br) or brown (PBD-I) solid, which were stable at room temperature in desiccator for several months (GPC traces and ^{1}H NMR spectra did not change).

3.2.3. Molecular Weight and Polydispersity of the Resulting Polyhalohydrocarbons. It is crucial to maintain lengths of parental polymers after postpolymerization modification. Thus, side reactions, such as chain-scission and cross-linking, should be avoided during polymer modification. Unfortunately, chain-scission reaction indeed happened during the hydrozirconation of 1,2-PBD with Cv of 88%. However, the chain-scission could be greatly alleviated when 1,2-PBD with Cv of 98% was used as parental materials (Figure 5), which gave the viability of the halogenation methodology based on hydrozirconation and encouraged us to make deep investigation. As we know, carbon−carbon double bond of the backbone is a key factor causing chain-scission; i.e., internal double bonds hydrozirconated compounds undergo β-alky elimination, which resulted in chain cleavage. A similar depolymerization process has been reported in hydrogenolysis of polyethylene and polypropylene.[29] Only increasing Cv content could the degree of chain scission be reduced. Increasing molecular weight of parental PBDs was useless for PBD with Cv of 88% to maintain high molecular weight after hydrozirconation and halogenolysis. The new generated end-groups from chain scission would be halogens after halogenolysis. (Systematical work related to chain scission behavior and possible mechanism will be discussed particularly in another paper.) Therefore, this method is only suitable for

dx.doi.org/10.1021/ma202628p | *Macromolecules* 2012, 45, 1190−1197

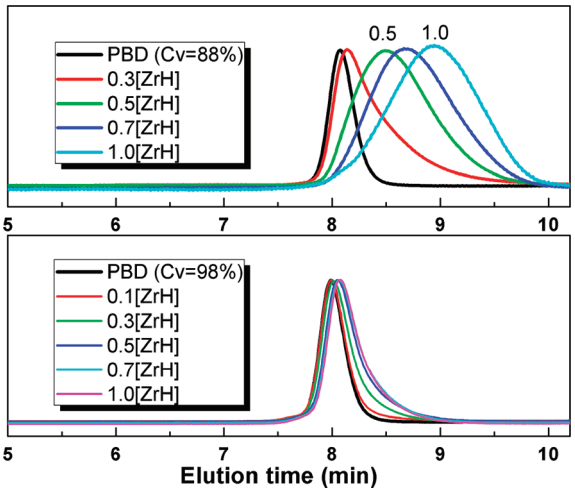


Figure 5. GPC traces of brominated 1,2-PBDs (Cv of 88% and 98%) from hydrozirconation with varied feeding ratios ([ZrH]).

the halogenation of PBDs with high Cv (>98%) for preservation of molecular weights. Although DPE is a powerful agent for synthesizing 1,2-PBD with high Cv by living anionic polymerization,[30] it failed in preparing 100% 1,2-PBD with high molecular weight. However, high iodinated PBD with preserved molecular weights and PDI would be prepared after hydrozirconation of 1,2-PBD (Cv of 98%, M_n < 15 kg/mol) and halogenolysis (Figure 6 and Table 2). In the case of 1,2-PBD

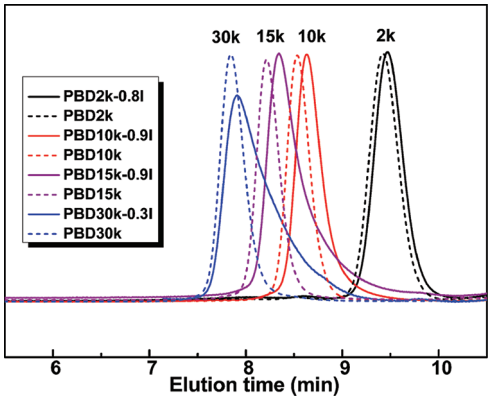


Figure 6. GPC traces of iodinated PBDs and corresponding parental PBDs.

with high molecular weight (30 kg/mol), the changes of PDI and molecular weights restricted the application of hydrozirconation of PBD (Cv = 98%) due to the existence of 1,4 structure. We speculated that hydrozirconation of 100% 1,2-PBD would be free of such molecular weight limitation and chain-scission reaction. For a special example, no chain-scission happened in the hydrozirconation of poly(*p*-(3-butenyl)-styrene) (60 kg/mol, PDI = 1.2, from living anionic polymerization) and its subsequent halogenolysis due to free double bonds in the backbone (Figure 7). As we can see, Schwartz's reagent was quite sensitive to backbone double although it was thought that terminal vinyl groups were favored for hydrozirconation than internal double bonds.[26] This phenomenon would be helpful for microstructure characterization of PBD and diagnosis of microstructure change in polymerization. Chain scission was also observed in Schwartz's

Table 2. Summary of Molecular Weights of Starting 1,2-PBDs (Cv of 98%) and the Corresponding Iodinated PBDs

polymers	M_n (g/mol)[a]	M_w (g/mol)[a]	PDI (M_w/M_n)[a]
PBD2K[b]	2200	2400	1.07
PBD2K-0.8I[c]	5800[d]	6200[d]	1.07
PBD10K[b]	9700	10000	1.04
PBD10K-0.9I[c]	24400[d]	26200[d]	1.09
PBD15K[b]	15900	16600	1.04
PBD15K-0.9I[c]	32400[d]	37900[d]	1.15
PBD30K[b]	28100	29600	1.05
PBD30K-0.3I[c]	21000[d]	26600[d]	1.27

[a]Determined by GPC in THF vs linear PS standards. [b]Parental PBDs with different molecular weights (2K, 10K, 15K, 30K) for hydrozirconation. [c]Iodinated polymers from corresponding PBD with certain degree of halogenation (0.8, 0.9, 0.9, and 0.3). [d]Calculated according to molecular weights from GPC after considering degree of halogenation.

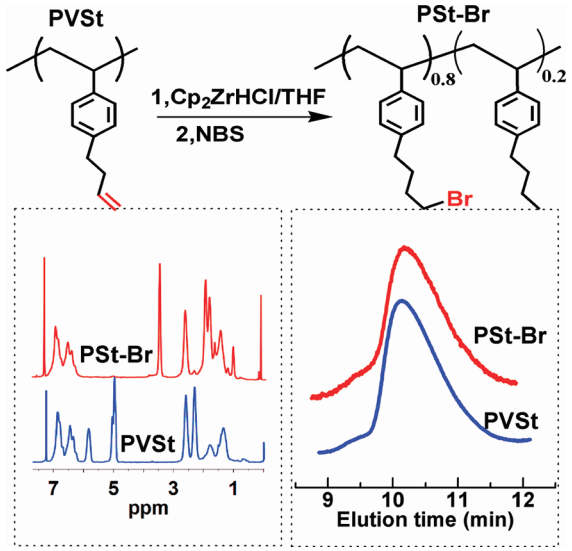


Figure 7. Hydrohalogenation of poly(*p*-(3-butenyl)styrene) by hydrozirconation and halogenolysis: ^{1}H NMR (300 MHz, $CDCl_3$) and GPC results of parental polymer (PVSt) and brominated polymer (PSt-Br).

reagent mediated hydrogenation of polybutadiene or polyisoprene.[31] However, it is believed that this chain scission will be useful on polymer recycling.

Although chain-scission took place, the halogenated polymer from 98% 1,2-PBD retained relatively high molecular weights and low polydispersity index (Tables 1 and 2). Such halogenated 1,2-PBDs could be used as reactive building blocks for functional materials and polymer architecture design (grafted or polymer brush) via macromolecular substitution reaction,[32−37] which would facilitate the preparation of polymers with low PDI described in following section.

3.3. Preparation of Functional Polymers by Macromolecular Substitution. Versatile reactivity of incorporated halogens toward various nucleophiles facilitates abundant functionality of synthesized polyhalohydrocarbon after macromolecular substitution. Typical chemical reagents (Figure 8) available in our laboratory were used to demonstrate this idea. As summarized in Table 3, the experiments with all the selected nucleophiles indicated the success of substitution reaction on versatile halogen groups to form a diverse of functional

dx.doi.org/10.1021/ma202628p | *Macromolecules* 2012, 45, 1190−1197

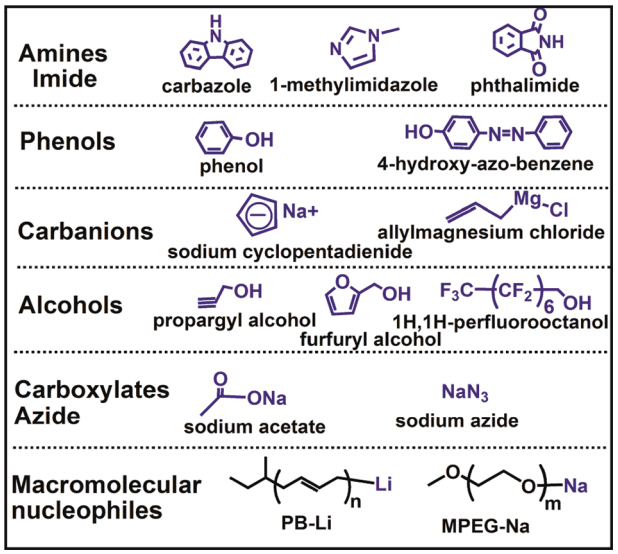


Figure 8. Chemical structures of various nucleophiles used in macromolecular substitution for functional and branched polymers.

polymers. As confirmed by ^{1}H NMR (Figure S5a and Table S1), the macromolecular substitution reaction proceeds with good conversion. Both molecular weight and molecular weight distribution were well preserved as elucidated by GPC measurement (Figure S5b). These results verified the success of the mentioned-above proposal, i.e., to prepare diverse functional polymers with controlled structure by incorporation of versatile reactive groups on well-defined polymer chains and subsequent polymer-analogy modification.

The resultant functional moieties on the 1,2-PBD would provide a potential as advanced materials. For example, poly(ionic liquid) was formed by the incorporation of methylimidazole, which could be applied in full cell alkaline anion exchange membranes[38] and antibacterial or antistatic materials. Fluororubber was made by incorporation of perfluoro-1-octanol into side chains of PBD. Cyclopentadiene containing PBD could be a kind of self-vulcanized rubber materials with thermoreversible cross-linking−de-cross-linking properties (Diels−Alder and retro-Diels−Alder reaction of grafted cyclopentadienes). Azobenzene-functionalized polymer is a kind of photoresponsive polymer[39] and also would be used in host−guest supermolecular chemistry,[40] while carbazole-modified polymers have been demonstrated to photoconductive or electric conductive polymers.[41] Alkyne, furan, and azide substituted polymers are perfect candidates for "click" reactions, especially in the combination of living anionic polymerization and click chemistry for synthesis of well-defined polymer brush or comb polymers.[42]

It is possible to use mono-end-functional polymers as macronucleophiles,[43−45] which provides a method to synthesize grafted (or branched) polymers via substitution reaction. For example, methoxypoly(ethylene glycol)s (MPEGOH) were grafted onto halogenated PBD in the presence of sodium hydride by the Williamson ether approach. PBD-*g*-PEG was synthesized with low PDI (1.05), and the graft ratio determined by GPC was about 20 mol % (Figure S6). When living polybutadienyllithium (1,4-PB-Li) was used as a macromolecular nucleophile to react with iodinated PBD, monodispersed PBD-I grafted 1,4-PBD (PBDI-*g*-PBD) was prepared with the graft ratio of 40 mol %, although dimeric products were formed[46] (Figure S7a). The length of branch chains and density of grafting would be easily adjusted by controlling the molecular weight of PB-Li and PB-Li/PBD-I ratio (Figure S7b). Hence, monohydroxyl, carboxyl, or other nucleophilic moieties terminated polymers could undoubtedly undergo similar approach to form branched or comb polymers. In these situations, living anionic macromolecular species were utilized to graft onto a well-defined polymer chain, which would be fascinating for synthesizing well-defined nonlinear polymer by living anionic polymerization. This feasibility should be attributed to the high reactivity of halogen groups toward various nucleophiles. Therefore, well-defined polyhydrohalo-

Table 3. Summary of Nucleophiles in Experiments and Degree of Conversion, Molecular Weight, and Molecular Weight Distribution of the Resultant Functional Polymers (PBD-Nu) after Macromolecular Substitution

nucleophiles (Nu)		conv[a] (%)	M_n (g/mol) (PBD-I)	M_n[b] (g/mol) (PBD-Nu)	M_w/M_n[c]
imide or amines	phthalimide[d]	80	32400	35700	1.26
	1-methylimidazole	100	24400	18400	*e*
	carbazole	100	5 800	7000	1.07
phenols	phenol	100	24400	19500	1.12
	hydroxyazobenzene	100	24400	33600	
carbanions	allylmagnesium chloride[f]	100	24400	12900	1.15
	cyclopentadienyl sodium[f]	>90[g]	24400	*h*	*h*
	1,4-polybutadienyllithium (M_n = 2200 g/mol)	40[j]	5800	25000	1.05
	1,4-polybutadienyllithium (M_n = 14300 g/mol)	47[j]	24400	863000	1.20
alcohols	propargyl alcohol	47 (48[i])	5800	3000	1.10
	furfuryl alcohol	41 (59[i])	32400	17200	1.22
	1*H*,1*H*-perfluorooctanol	39 (51[i])	5800	7100	*e*
	MPEG-OH (M_n = 2000 g/mol)	20[j]	24400	68000	1.05
carboxylates	sodium acetate	50	24400	20600	1.07
azide	sodium azide	100[k]	24400	13300	1.08

[a]Determined from ^{1}H NMR (Figure S4a); 100% for all the halogen was substituted and converted to functional groups by nucleophiles. [b]Calculated from the conversion and the characteristics of the parental polymers. [c]Determined from GPC in THF against linear PS standards (Figure S4b). [d]Phthalimide potassium was used. [e]Not measured due to insolubility of polymer in THF. [f]Reaction was carried out below 0 °C. [g]Estimated by TGA. [h]After purification, insoluble solid polymer was obtained because of D−A cross-linking. [i]Ratio of elimination reaction. [j]Graft ratio determined from GPC (Figures S6 and S7). [k]THF/DMF (v/v 4:1) was used.

dx.doi.org/10.1021/ma202628p | *Macromolecules* 2012, 45, 1190−1197

carbons provide an excellent platform for synthesis of diverse functional polymers as well as nonlinear polymers.

However, it should be noted that phase separation would happen in some case during postpolymerization reaction. For example, when 1-methylimidazole and perfluoro-1-octanol were used as nucleophiles, the precipitation of polymers was observed, which usually results in a low conversion. Despite precipitation, high conversion was still obtained for the reaction of 1-methylimidazole with polyhalohydrocarbon. Optimizing reaction conditions (such as solvents and reaction temperature) would be possible to avoid such problem. It is easy to remove excess small molecules by precipitation in methanol in most of the above experiments. Furthermore, dialysis[47] or precipitation fractionation[45] is possible for isolation of functional polymers, for example, when m-PEG or polybutadienyllithium was used for the preparation of branched polymers in this work.

4. CONCLUSIONS

First, we demonstrated a novel and quite convenient chemical modification for 1,2-PBD by hydrozirconation and halogenolysis under mild reaction conditions. Highly halogenated 1,2-PBD (up to 92% for iodination, 77% for bromination, and 50% for chlorination) was prepared with low PDI (<1.2), in which halogen atoms (chlorine, bromine, and iodine) were introduced in anti-Markovnikov form with controllable degree of functionalization. Second, the resultant halogenated 1,2-PBD was utilized as a reactive building block for polymer design. A broad range of functional or branched polymers with well-defined structure were prepared via macromolecular substitution reaction with amines or imide, phenols, alcohols, carboxylates, and carbanions. This strategy is quite versatile for controlled synthesis of functional and nonlinear polymers indirectly via living anionic polymerization, and we believe that the hydrozirconation discussed here could be extended to other vinyl groups containing polymers.[48−51] The drawback of the hydrozirconation methodology is the associated chain-scission reaction if carbon−carbon double bonds are included in polymer backbones, which can be technically suppressed by selecting high Cv content of 1,2-PBD or completely avoided by using other polymers (synthesized by living anionic polymerization), such as poly(*p*-(3-butenyl)styrene)[48] or poly(1,4-divinylbenzene).[51] On the other hand, the chain-scission reaction is being utilized in chemical recycling of diene−rubber, which will be reported in the follow-up work as another part of Schwartz's application in polymer chemistry.

■ ASSOCIATED CONTENT

Supporting Information

Related tables (Table S1 for typical ^{1}H NMR assignment of functional polymers) and figures (Figure S1−S7) mentioned in the main text. This material is available free of charge via the Internet at http://pubs.acs.org.

■ AUTHOR INFORMATION

Corresponding Author

*Tel +86 (0) 431 85262004; Fax +86 (0) 431 85262827; e-mail ttang@ciac.jl.cn.

■ ACKNOWLEDGMENTS

We thank the financial support from the National Natural Science Foundation of China for the general project (no. 51073149) and the Fund for Creative Research Groups (no. 50921062).

■ REFERENCES

(1) Webster, O. W. *Science* **1991**, *251*, 887−892.
(2) Patten, T. E.; Xia, J.; Abernathy, T.; Matyjaszewski, K. *Science* **1996**, *272*, 866−868.
(3) Gauthier, M. A.; Gibson, M. I.; Klok, H.-A. *Angew. Chem., Int. Ed.* **2009**, *48*, 48−58.
(4) Gibson, M. I.; Fröhlich, E.; Klok, H.-A. *J. Polym. Sci., Part A: Polym. Chem.* **2009**, *47*, 4332−4345.
(5) Chung, T. C.; Raate, M.; Berluche, E.; Schulz, D. N. *Macromolecules* **1988**, *21*, 1903−1907.
(6) Ajjou, A. N.; Alper, H. *Macromolecules* **1996**, *29*, 1784−1788.
(7) Podešva, J.; Hrubý, M.; Spěváček, J.; Hrdličková, M.; Netopilík, M. *J. Polym. Sci., Part A: Polym. Chem.* **2008**, *46*, 3919−3925.
(8) Ten Brummelhuis, N.; Diehl, C.; Schlaad, H. *Macromolecules* **2008**, *41*, 9946−9947.
(9) Justynska, J.; Hordyjewicz, Z.; Schlaad, H. *Polymer* **2005**, *46*, 12057−12064.
(10) Justynska, J.; Schlaad, H. *Macromol. Rapid Commun.* **2004**, *25*, 1478−1481.
(11) Urbano, J.; Korthals, B.; Diaz-Requejo, M. M.; Perez, P. J.; Mecking, S. *J. Polym. Sci., Part A: Polym. Chem.* **2010**, *48*, 4439−4444.
(12) Zuchowska, D. *Polymer* **1980**, *21*, 514−520.
(13) Nicol, M.; J. Cole-hamilton, D. *J. Mater. Chem.* **1998**, *8*, 1511−1515.
(14) Iraqi, A.; Seth, S.; Vincent, C. A.; Colehamilton, D. J.; Watkinson, M. D.; Graham, I. M.; Jeffrey, D. *J. Mater. Chem.* **1992**, *2*, 1057−1064.
(15) Chauhan, B. P. S.; Balagam, B. *Macromolecules* **2006**, *39*, 2010−2012.
(16) Otvalko, Z.; Drugov, M.; Tverdov, A.; Kuz'min, S.; Trifonova, E. *Russ. J. Appl. Chem.* **2010**, *83*, 1328−1332.
(17) Glazyrin, A. B.; Abdullin, M. I.; Muslukhov, R. R.; Kraikin, V. A. *Polym. Sci., Ser. A* **2011**, *53*, 110−115.
(18) Abdullin, M. I.; Glazyrin, A. B.; Asfandiyarov, R. N.; Muslukhov, R. R. *Polym. Sci., Ser. B* **2009**, *51*, 303−308.
(19) Bronstein, L. M.; Valetsky, P. M. *J. Inorg. Organomet. Polym.* **1994**, *4*, 415−424.
(20) Meijboom, R.; Moss, J. R.; Hutton, A. T.; Makaluza, T.-A.; Mapolie, S. F.; Waggie, F.; Domingo, M. R. *J. Organomet. Chem.* **2004**, *689*, 1876−1881.
(21) Wipf, P.; Kendall, C. In *Metallocenes in Regio- and Stereoselective Synthesis*; Takahasi, T., Ed.; Springer-Verlag: Berlin, 2005; Vol. *8*, pp 1−25.
(22) Wipf, P.; Jahn, H. *Tetrahedron* **1996**, *52*, 12853−12910.
(23) Huang, Z.; Negishi, E.-i. *Org. Lett.* **2006**, *8*, 3675−3678.
(24) Nichols, M.; Sobinsky, R.; Hunter, A.; Zeller, M. *J. Chem. Crystallogr.* **2007**, *37*, 433−438.
(25) Katritzky, A. R.; Fan, W.; Fu, C. *J. Org. Chem.* **1990**, *55*, 3209−3213.
(26) Hart, D. W.; Schwartz, J. *J. Am. Chem. Soc.* **1974**, *96*, 8115−8116.
(27) Gibson, T.; Tulich, L. *J. Org. Chem.* **1981**, *46*, 1821−1823.
(28) Labinger, J. A.; Hart, D. W.; Seibert, W. E.; Schwartz, J. *J. Am. Chem. Soc.* **1975**, *97*, 3851−3852.
(29) Dufaud, V. R.; Basset, J. M. *Angew. Chem., Int. Ed.* **1998**, *37*, 806−810.
(30) Halasa, A. F.; Lohr, D. F.; Hall, J. E. *J. Polym. Sci., Polym. Chem. Ed.* **1981**, *19*, 1357−1360.
(31) Gibler, C. J.; Chamberlain, L. R.; Kemp, R. A.; Wilson, S. E. Depolymerization of conjugated diene polymers. U.S. Patent 5162446A, Nov 10, 1992.
(32) Allcock, H. R. *Science* **1992**, *255*, 1106−1112.
(33) Kameda, T.; Fukuda, Y.; Grause, G.; Yoshioka, T. *J. Appl. Polym. Sci.* **2010**, *116*, 36−44.
(34) Church, A. C.; Pawlow, J. H.; Wagener, K. B. *Macromolecules* **2002**, *35*, 5746−5751.

(35) Guillén-Castellanos, S. A.; Parent, J. S.; Whitney, R. A. *J. Polym. Sci., Part A: Polym. Chem.* **2006**, *44*, 983−992.
(36) Yamashita, S.; Kodama, K.; Ikeda, Y.; Kohjiya, S. *J. Polym. Sci., Part A: Polym. Chem.* **1993**, *31*, 2437−2444.
(37) Yuan, J.; Ten Brummelhuis, N.; Junginger, M.; Xie, Z.; Lu, Y.; Taubert, A.; Schlaad, H. *Macromol. Rapid Commun.* **2011**, *32*, 1157−1162.
(38) Lin, B.; Qiu, L.; Lu, J.; Yan, F. *Chem. Mater.* **2010**, *22*, 6718−6725.
(39) Kumar, G. S.; Neckers, D. C. *Chem. Rev.* **1989**, *89*, 1915−1925.
(40) Taura, D.; Li, S.; Hashidzume, A.; Harada, A. *Macromolecules* **2010**, *43*, 1706−1713.
(41) Grazulevicius, J. V.; Strohriegl, P.; Pielichowski, J.; Pielichowski, K. *Prog. Polym. Sci.* **2003**, *28*, 1297−1353.
(42) Touris, A.; Mays, J. W.; Hadjichristidis, N. *Macromolecules* **2011**, *44*, 1886−1893.
(43) Ryu, S. W.; Hirao, A. *Macromolecules* **2000**, *33*, 4765−4771.
(44) Hempenius, M. A.; Michelberger, W.; Möller, M. *Macromolecules* **1997**, *30*, 5602−5605.
(45) Kempf, M.; Barroso, V. C.; Wilhelm, M. *Macromol. Rapid Commun.* **2010**, *31*, 2140−2145.
(46) Hirao, A.; Tohoyama, M.; Nakahama, S. *Macromolecules* **1997**, *30*, 3484−3489.
(47) Gromadzki, D.; Jigounov, A.; Stepánek, P.; Makuska, R. *Eur. Polym. J.* **2010**, *46*, 804−813.
(48) Zhang, H.; Ruckenstein, E. *Macromolecules* **1999**, *32*, 5495−5500.
(49) Li, Z.; Ke, Y.; Hu, Y. *J. Appl. Polym. Sci.* **2004**, *93*, 314−322.
(50) Ma, J.; Cheng, C.; Sun, G.; Wooley, K. L. *Macromolecules* **2008**, *41*, 9080−9089.
(51) Hirao, A.; Tanaka, S.; Goseki, R.; Ishizone, T. *Macromolecules* **2011**, *44*, 4579−4582.

Macromolecules

Article

pubs.acs.org/Macromolecules

Termination of Surface Radicals and Kinetic Modeling of ATRP Grafting from Flat Surfaces by Addition of Deactivator

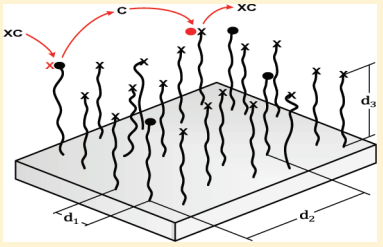
Dapeng Zhou,[†,‡] Xiang Gao,[†,§] Wen-jun Wang,[†,§] and Shiping Zhu[†,*]

[†]Department of Chemical Engineering, McMaster University, Hamilton, Ontario, Canada L8S 4L7

[‡]Department of Biochemistry and Chemical Engineering, Jiaxing University, Jiaxing, P.R. China 314001

[§]Department of Chemical and Biological Engineering, Zhejiang University, Hangzhou, P.R. China 310027

ABSTRACT: Surface-initiated controlled radical polymerization has been widely used for grafting polymers from various surfaces. However, how the surface-constrained radicals are terminated remains to be further elucidated. In this work, a simple kinetic model is developed for surface-initiated atom transfer radical polymerization (SI-ATRP) with addition of excess deactivator in solution. The model describes the development of polymer layer thickness, as well as the concentrations of radical, dormant and dead chains. A simple but accurate analytical solution is obtained for the polymer layer thickness as a function of time. The model accounts for the effects of equilibrium constant, activator/deactivator concentration ratio, monomer concentration, grafting density and rate constants of propagation and termination. The model is verified with the experimental data of 2-methacryloyloxythyl phosphorylcholine (MPC), methyl acrylate, acrylamide, and *N*-isopropylacrylamide under various conditions. In correlating thickness versus time experimental curves at different catalyst concentrations, it is clearly demonstrated that the termination of radicals on surface is facilitated by diffusion of catalyst species in solution. Although radical chains are immobilized, radical centers "migrate" and terminate through activation and deactivation reactions. The termination rate constant is therefore proportional to catalyst concentration. It is also found that the termination is influenced by chain conformation and the rate constant is grafting density dependent.



INTRODUCTION

Polymer grafting provides a powerful tool for modification and functionalization of various surfaces. There are generally two major types of grafting methods with each having advantages and shortcomings. In grafting-onto methods, polymer chains are prepared in advance so that their molecular weight distributions can be readily characterized before grafting. However, it is challenging to obtain high grafting densities (the number of graft chains per unit surface area). The reason is that the early grafted chains could impose diffusion limitations on the late chains to be grafted. In some grafting-from methods such as conventional free radical grafting polymerization, the same problem exists.[1] Individual chains are generated in seconds while the whole polymerization process takes hours. Again the early chains prevent the later chains from approach the surface. However, the recent progress of the surface-initiated controlled radical polymerization (SI-CRP) offers an excellent opportunity in overcoming this shortness. The fast initiation and slow growth in SI-CRP does not only facilitate high grafting density but also control over the microstructural properties of graft chains such as molecular weight and composition distributions.

There are three major types of CRPs: nitroxide-mediated radical polymerization (NMP), atom transfer radical polymerization (ATRP), and reversible addition−fragmentation chain transfer radical polymerization (RAFT). All the CRPs have been successfully applied to graft polymers with narrow distribution and predetermined molecular weight from various solid surfaces.[2−23] Among the CRPs, ATRP is particularly attractive surface-initiated polymerization due to its versatility in the monomer type and simple reaction conditions. With all initiator moieties RX immobilized to surface, surface-initiated ATRP (SI-ATRP) is highly efficient with every formed chain bonded to the surface. NMP is similar in terms of this efficiency; however, it usually requires high temperature, long time and is limited to styrenic type of monomers. RAFT has wonderful versatility in monomer type and favored polymerization conditions. In SI-RAFT, we face choices to immobilize initiator I or RAFT agent S═C(Z)S−R. Immobilizing initiator gives a very low efficiency with majority chains (about 90%) free in solution bearing the RAFT moieties. Immobilizing R group of S═C(Z)S−R grafts about half of the chains to surface. For high efficiency (>90%), RAFT agent must be immobilized through Z group. In this case, the grafting process becomes "grafting-onto". Radical chains would have to dive into polymer layer to access S═C(Z)S−R for addition reactions. Diffusion limitations may then play a role.

Various monomer types have been successfully grafted from surfaces by SI-ATRP, such as methyl methacrylate (MMA),[3,4] styrene,[5] 2-hydroxyethyl methacrylate (HEMA),[6] and 2-methacryloyloxyethyl phosphorylcholine (MPC).[7] In a solution ATRP process, an adequate amount of deactivator, XCu^{II}/L, is

Received: December 5, 2011
Revised: January 9, 2012
Published: January 26, 2012

 © 2012 American Chemical Society dx.doi.org/10.1021/ma202640x | *Macromolecules* 2012, 45, 1198−1207

usually generated through radical termination in RX + Cu(I)/L → $R^{\bullet}$ + XCu^{II}/L at an early stage of polymerization. In SI-ATRP, the amount of such deactivator is very small because of the small amount of immobilized initiator. This is particularly true with flat surfaces. As a result, sacrificed initiator (Method I) or extra deactivator (method II) is often added to SI-ATRP system. In method I, ATRP proceeds both in solution and on the surface. The polymer in solution provides a reference for that on surface. It is often assumed that the two polymer populations have the same molecular weight and thus grafting density can be estimated from GPC data of the solution polymer sample. Because of significant monomer consumption and radical termination in solution, Method I does not yield thick polymer layers on surface. Thicker polymer layers are normally prepared by method II.

Although numerous studies have been reported, some most fundamental issues with SI-ATRP, as well as other types of SI-CRP, remain to be answered. For examples, in method I, is the assumption of equal molecular weight of solution and surface polymers valid? If not, which is higher and it depends on what? In Method II, do termination reactions occur to the radicals constrained to surface? Their chains are not able to have translational diffusion because of the constraints. On the basis of intuition, the growth of polymer layer should be linear with reaction time because of nearly constant monomer concentration due to low monomer consumption by surface initiator.[8] However, most experimental data of polymer thickness versus time significantly deviated from linearity.[2−31] This deviation suggested that surface radicals did terminate.[2,9,10,28,29] The question is how?

Several modeling efforts have been made to interpret surface radical termination mechanism of SI-ATRP. Xiao and Wirth[28] assumed that the growth rate of polymer thickness was proportional to that of monomer consumption in solution, $[M]_0 - [M] = k_p[R^{\bullet}][M]_0$, and the surface radicals are terminated through a bimolecular reaction, $d[R^{\bullet}]/dt = -k_t[R^{\bullet}]^2$ with its initial concentration of $[R^{\bullet}]_0$ at $t = 0$. Because the monomer consumption in method II is very small, a simple analytic expression for the monomer consumption was derived as follows:

$$[M]_0 - [M] = \frac{[M]_0 k_p [R^{\bullet}]_0 t}{1 + k_t [R^{\bullet}]_0 t} \quad (1)$$

where $[M]_0$, $[M]$, $[R^{\bullet}]_0$, k_p, k_t, and t are initial monomer concentration, present monomer concentration, initial radical concentration, propagation rate constant, termination rate constant, and time, respectively. Kim et al.[3] assumed that the rate of film growth at any given time was proportional to surface radical concentration and calculated the radical concentration from the following two differential equations based on the mass balances of radical and dormant species:

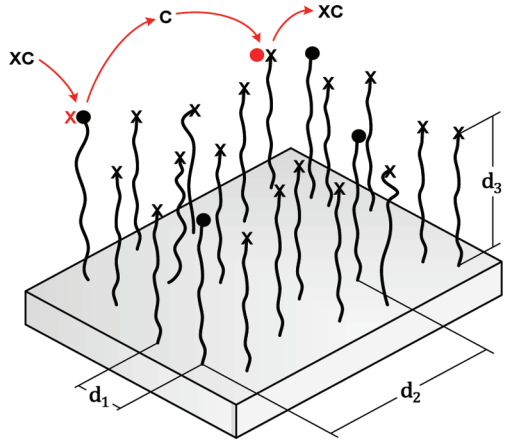
$$\frac{d[R^{\bullet}]}{dt} = k_a[RX][C] - k_d[R^{\bullet}][XC] - k_t[R^{\bullet}]^2 \quad (2)$$

$$\frac{d[RX]}{dt} = -k_a[RX][C] + k_d[R^{\bullet}][XC] \quad (3)$$

where $[R^{\bullet}]$ and $[RX]$ are the concentrations of radical and dormant chains (the latter includes initiator molecules); $[C]$ and $[XC]$ are the activator and deactivator catalyst concentrations; k_a and k_d are the rate constants of activation and deactivation, respectively. These models explained that the radical termination in solution significantly affected the rate of polymerization on surface. However, the solution-based models oversimplified the surface reactions and could not provide mechanistic insights into the surface polymerization.

Recently, Gao and Zhu proposed a new mechanism for surface radical termination, termed as "migration-termination".[29] It was argued that although polymer chains can be very crowded on surface, radical centers are sparse and are distant from each other. For example, under the condition of grafting density τ = 1 chain/nm^2 and polymer layer thickness δ = 100 nm, the average distance between neighboring chains d_1 is 1 nm. An overwhelming majority of the chains are dormant species and the fraction of radical chains is about 10^{-4} to 10^{-6}, which can be estimated from $[R^{\bullet}]/[RX] \approx k_a[C]/(k_d[XC])$. The average distance between neighboring radical chains d_2 is about 100−1000 nm. According to $\tau = \rho\delta/\bar{M}_N$ where ρ is the polymer density and $\bar{M}_N$ is the polymer number-average molecular weight, the polymer chains have an average length of 600 monomer units (assuming $\rho = 10^3$ g/L and monomer molecular weight 100 g/mol). If fully extended, the chains are 150 nm long (assuming monomer size 0.25 nm). Although radical centers are reachable in theory (fully extending two chains spans 300 nm), it is difficult to imagine how can the chains purposely extend and go through the polymer bush for termination. In the concept of "migration-termination", radical centers come together through activation and deactivation reactions. For two far away radicals on a same surface, when one radical is deactivated by a catalyst from solution, this radical chain becomes dormant. If the same catalyst activates another dormant chain adjacent to the other radical, the two radicals meet each other. This migration process of surface radicals is actually accomplished by diffusion of catalyst molecules in solution. Scheme 1 gives the quantitative picture and illustrates the "radical migration" process.

Scheme 1. SI-ATRP: How Surface Radicals Migrate toward Each Other and Terminate through Activation/Deactivation cycles[a]



[a]Key: (×) dormant chain ends; (●) radical chain ends.

Fukuda and his co-workers were the first who studied "migration termination" of surface radicals in RAFT grafting.[32] A radical reacts with a neighboring dormant chain and thus migrates to its site. While the chains have not moved, the radical center and RAFT moiety shift their positions. This "rolling migration" facilitates radical termination and is proven experimentally to be significant in the RAFT grafting (but it

dx.doi.org/10.1021/ma202640x | Macromolecules 2012, 45, 1198−1207

was unfortunately ruled out in the SI-ATRP).[32] In ATRP grafting, such "rolling migration" is absent. The migration of a surface radical from one site to another is through activation/deactivation in solution. Let us term it as "hopping migration". The fundamental difference between the "hopping migration" and the "rolling migration" is that the former goes through solution while the latter never leaves surface.

In this work, we present a simple kinetic model for the method II SI-ATRP. An analytical solution of this model is obtained and it is so simple that can be readily used for data analysis by experimentalists. Using this model, we systematically examine the effects of chemical recipes and polymerization conditions on the development of polymer layer thickness. Experimental data of various monomer systems, including methyl acrylate (MA), 2-methacryloyloxythyl phosphorylcholine (MPC), acrylamide (AM), and *N*-isopropylacrylamide (NIPAM) from flat substrate, are used for model correlation and verification. The work provides good insight into the termination mechanism of surface radicals and demonstrates catalyst concentration dependence of the termination rate. It should be pointed out that such level of mechanistic analysis becomes impossible if the simple but accurate kinetic model is not developed. The novelty of this work lies in the developed model and its use for the analysis of experimental data that provides mechanistic explanations for the effects of recipe and various kinetic parameters.

MODEL DEVELOPMENT

Numerical Model. In the SI-ATRP using method II, the initiator *RX* is immobilized onto surface, while the activator and deactivator catalysts are added to solution. The elementary reactions involved in this system are relatively simple: radical activation and deactivation,

$$\mathrm{PX}_{surf} + \mathrm{C}_{sol} \underset{k_d}{\overset{k_a}{\leftrightarrow}} \mathrm{P}^{\bullet}_{surf} + \mathrm{XC}_{sol} \tag{4}$$

monomer propagation

$$\mathrm{P}^{\bullet}_{surf} + \mathrm{M}_{sol} \overset{k_p}{\rightarrow} \mathrm{P}^{\bullet}_{surf} \tag{5}$$

and radical termination

$$\mathrm{P}^{\bullet}_{surf} + \mathrm{P}^{\bullet}_{surf} \overset{k_t}{\rightarrow} \mathrm{P}_{surf} + \mathrm{P}_{surf} \tag{6}$$

where the subscripts "surf" and "sol" indicate that the reacting species resides either on surface or in solution. There are three types of chain species (radical $\mathrm{P}^{\bullet}_{surf}$, dormant PX_{surf} and dead P_{surf}) and four types of small molecular reactants (initiator RX_{surf}, monomer M_{sol}, activator C_{sol} and deactivator XC_{sol}). The initiator RX_{surf} is included in the population of dormant chains PX_{surf}. The parameters k_a, k_d, k_p, and k_t are the rate constants of activation, deactivation, propagation and termination. The mass balances for the reacting species are as follows:

$$\frac{\mathrm{d}[\mathrm{M}]_{sol}}{\mathrm{d}t} = -k_p \varepsilon [\mathrm{P}^{\bullet}]_{surf} [\mathrm{M}]_{sol} \tag{7}$$

$$\frac{\mathrm{d}[\mathrm{P}^{\bullet}]_{surf}}{\mathrm{d}t} = k_a [\mathrm{PX}]_{surf} [\mathrm{C}]_{sol} - k_d [\mathrm{P}^{\bullet}]_{surf} [\mathrm{XC}]_{sol} - k_t ([\mathrm{P}^{\bullet}]_{surf})^2 \tag{8}$$

$$\frac{\mathrm{d}[\mathrm{PX}]_{surf}}{\mathrm{d}t} = -k_a [\mathrm{PX}]_{surf} [\mathrm{C}]_{sol} + k_d [\mathrm{P}^{\bullet}]_{surf} [\mathrm{XC}]_{sol} \tag{9}$$

$$\frac{\mathrm{d}[\mathrm{P}]_{surf}}{\mathrm{d}t} = k_t ([\mathrm{P}^{\bullet}]_{surf})^2 \tag{10}$$

$$\frac{\mathrm{d}[\mathrm{C}]_{sol}}{\mathrm{d}t} = -k_a \varepsilon [\mathrm{PX}]_{surf} [\mathrm{C}]_{sol} + k_d \varepsilon [\mathrm{P}^{\bullet}]_{surf} [\mathrm{XC}]_{sol} \tag{11}$$

$$\frac{\mathrm{d}[\mathrm{XC}]_{sol}}{\mathrm{d}t} = k_a \varepsilon [\mathrm{PX}]_{surf} [\mathrm{C}]_{sol} - k_d \varepsilon [\mathrm{P}^{\bullet}]_{surf} [\mathrm{XC}]_{sol} \tag{12}$$

Extra caution must be exercised in modeling heterogeneous polymerization systems such as SI-ATRP. Attention should be paid to the definition and unit of concentration [ ]. In this work, the solution concentrations ($[\mathrm{M}]_{sol}$, $[\mathrm{C}]_{sol}$, $[\mathrm{XC}]_{sol}$) are in mol/L, while the surface concentrations ($[\mathrm{P}^{\bullet}]_{surf}$, $[\mathrm{P}]_{surf}$, $[\mathrm{PX}]_{surf}$ and $[\mathrm{RX}]_{surf}$) are in mol/dm^2. It is essential that the mass balances use the same basis, either the surface area of substrate *S* or the volume of monomer solution *V*. This is why the surface area in dm^2 per liter of solution, ε (=S/V) in dm^{-1}, appears in eqs 7, 11, and 12. In so doing, the rate constants k_a, k_d, and k_p have the conventional unit of liter per mole per second. However, k_t is in dm^2 mol^{-1} s^{-1}. Another point worth mentioning here is that, in dealing with the reactions between surface and solution reactants, we assume the surface species experience the same environment as they were in solution. The assumption is implied in their rate expresses. However, it could be argued that in reality the environment in surface can be different from that in solution. For example, the concentrations of monomer and catalyst on surface are different from in solution and must be estimated through partitioning. Unfortunately, such 2-phase model is inevitably complex with the partitioning coefficients unknown. In deriving this model, both accuracy and simplicity are considered and balanced.

An examination of eqs 7−12 reveals that eqs 9, 11 and 12 are not independent from each other. The following conservation equations hold: First, the total number of chains on surface remains constant,

$$[\mathrm{P}^{\bullet}]_{surf} + [\mathrm{PX}]_{surf} + [\mathrm{P}]_{surf} = f[\mathrm{RX}]_{surf,0} \tag{13}$$

where *f* is the initiation efficiency and the subscript "0" denotes the concentration initially charged to the system. This conservation is also reflected in eqs 8−10 that combining the three equations gives a zero rate. In SI-ATRP experiments, the number of chains grafted is often smaller than the number of initiator molecules immobilized. For example, silicon wafer surface contains about 5 −OH groups per square nanometer, with which 4 to 5 initiator moieties can be immobilized but only 0.5 to 1 polymer chain can grow from the surface. The term $f[\mathrm{RX}]_{surf,0}$ is the total number of chains grown from surface regardless of radical, dormant or dead. Compared to dormant and dead chain concentrations, the radical concentration is negligible and eq 13 can be simplified as $[\mathrm{PX}]_{surf} + [\mathrm{P}]_{surf} \approx f[\mathrm{RX}]_{surf,0}$. Furthermore, the total number of transferable atom X and that of catalyst C remain constant,

dx.doi.org/10.1021/ma202640x | *Macromolecules* 2012, 45, 1198−1207

$$\varepsilon[\mathrm{PX}]_{surf} + [\mathrm{XC}]_{sol} = \varepsilon f[\mathrm{RX}]_{surf,0} + [\mathrm{XC}]_{sol,0} \quad (14)$$

$$[\mathrm{C}]_{sol} + [\mathrm{XC}]_{sol} = [\mathrm{C}]_{sol,0} + [\mathrm{XC}]_{sol,0} \quad (15)$$

which can also be seen from combining eqs 9 and 12 and eqs 11 and 12. It should be pointed out that the mechanism involved in surface initiation is not clear. Although it is known that only a fraction of the immobilized initiator moieties are grown to polymer chains, how the others get lost remains to be elucidated. The efficiency f is introduced into eq 13 to account for the loss. However, whether f should also be in eq 14 is questionable. Does a lost initiator RX still provide the transferable atom X that influences the equilibrium of radical activation/deactivation? In this work, we assumed not.

With the three conservations, eqs 13−15, the number of the ordinary differential equations (ODEs), i.e., eqs 7−12, can be reduced to three independent equations. Since there exist orders of magnitude differences in the monomer, polymer and radical concentrations, the ODEs are stiff. A preferred approach is to solve eq 7 for the monomer concentration, eq 9 for the dormant chain concentration and eq 10 for the dead chain concentration, together with eq 13 for the radical concentration, eq 14 for the deactivator concentration and eq 15 for the activator concentration, that is

$$\frac{\mathrm{d}[\mathrm{M}]_{sol}}{\mathrm{d}t} = -k_p\varepsilon[\mathrm{P}^\bullet]_{surf}[\mathrm{M}]_{sol} \quad (7)$$

$$\frac{\mathrm{d}[\mathrm{PX}]_{surf}}{\mathrm{d}t} = -k_a[\mathrm{PX}]_{surf}[\mathrm{C}]_{sol} + k_d[\mathrm{P}^\bullet]_{surf}[\mathrm{XC}]_{sol} \quad (9)$$

$$\frac{\mathrm{d}[\mathrm{P}]_{surf}}{\mathrm{d}t} = k_t([\mathrm{P}^\bullet]_{surf})^2 \quad (10)$$

$$[\mathrm{P}^\bullet]_{surf} = f[\mathrm{RX}]_{surf,0} - [\mathrm{PX}]_{surf} - [\mathrm{P}]_{surf} \quad (13a)$$

$$[\mathrm{XC}]_{sol} = \varepsilon f[\mathrm{RX}]_{surf,0} + [\mathrm{XC}]_{sol,0} - \varepsilon[\mathrm{PX}]_{surf} \quad (14a)$$

$$[\mathrm{C}]_{sol} = [\mathrm{C}]_{sol,0} - \varepsilon[\mathrm{RX}]_{surf,0} + \varepsilon[\mathrm{PX}]_{surf} \quad (15a)$$

The above equations can be readily solved with the following initial conditions for the three ODEs $[\mathrm{M}]_{sol} = [\mathrm{M}]_{sol,0}$, $[\mathrm{PX}]_{surf} = f[\mathrm{RX}]_{surf,0}$ and $[\mathrm{P}]_{surf} = 0$, as well as the required rate parameters ε, f, k_a, k_d, k_p, and k_t. Any commercial package with an ODE solver such as Mathcad or Matlab is adequate for the task.

The thickness of grafted polymer layer on surface (in the solid state) can be calculated from the monomer mass balance

$$\delta = \frac{m_w([\mathrm{M}]_{sol,0} - [\mathrm{M}]_{sol})}{\rho\varepsilon} \quad (16)$$

where δ is the polymer layer thickness in dm (note: nm is often used in presenting the thickness data), m_w is the monomer molecular weight in g/mol, $[\mathrm{M}]_{sol,0}$ is the initial monomer concentration in mol/L, ρ is the solid polymer density in g/L. A challenge in method II SI-ATRP is the difficulty in characterizing grafted polymer chains. Theoretically, grafted chains could be severed from surface and collected for measurements. This has been practiced in some surface-initiated controlled radical polymerization work, but mainly for grafting from particles. With a flat surface, grafted polymer is in trace amount, often not enough for characterization. However, the polymer molecular weight can be estimated from,

$$M_N = \frac{\rho\delta}{[\mathrm{PX}]_{surf} + [\mathrm{P}]_{surf}} \quad (17)$$

Analytical Model. While a numerical solution is accurate, it is not easy for most experimentalists to use. It is not straightforward to tell from the ODEs what effects of chemical recipe and experimental condition on the outcome of grafting. Therefore, a significant effort has been made to search for simple analytical solutions of the numerical model. The starting point is to apply a stationary state hypothesis to the radical population $\mathrm{P}^\bullet_{surf}$. Among the four terms in eq 8, the activation and deactivation terms on the right-hand side must be much larger than the accumulation term on the left-hand side and the termination term on the right-hand side, as long as the SI-ATRP is under control. Therefore, the radical concentration can be directly related to those of dormant, activator and deactivator,

$$[\mathrm{P}^\bullet]_{surf} = \frac{k_a[\mathrm{C}]_{sol}}{k_d[\mathrm{XC}]_{sol}}[\mathrm{PX}]_{surf} \quad (18)$$

Substituting eq 18 into eq 10 gives

$$\frac{\mathrm{d}[\mathrm{P}]_{surf}}{\mathrm{d}t} = k_t\left(\frac{k_a[\mathrm{C}]_{sol}}{k_d[\mathrm{XC}]_{sol}}\right)^2([\mathrm{PX}]_{surf})^2 \quad (19)$$

Since $[\mathrm{PX}]_{surf} \approx f[\mathrm{RX}]_{surf,0} - [\mathrm{P}]_{surf}$

$$\frac{\mathrm{d}[\mathrm{P}]_{surf}}{\mathrm{d}t} = k_t\left(\frac{k_a[\mathrm{C}]_{sol}}{k_d[\mathrm{XC}]_{sol}}\right)^2(f[\mathrm{RX}]_{surf,0} - [\mathrm{P}]_{surf})^2 \quad (20)$$

Assuming $k_t(k_a[\mathrm{C}]_{sol}/k_d[\mathrm{XC}]_{sol})^2$ independent of time and solving eq 20 with the initial condition of $[\mathrm{P}]_{surf} = 0$ at $t = 0$ yields

$$\frac{[\mathrm{P}]_{surf}}{f[\mathrm{RX}]_{surf,0}} = \frac{f[\mathrm{RX}]_{surf,0}\left(\frac{k_a[\mathrm{C}]_{sol}}{k_d[\mathrm{XC}]_{sol}}\right)^2 k_t t}{1 + f[\mathrm{RX}]_{surf,0}\left(\frac{k_a[\mathrm{C}]_{sol}}{k_d[\mathrm{XC}]_{sol}}\right)^2 k_t t} \quad (21)$$

Again $[\mathrm{PX}]_{surf} \approx f[\mathrm{RX}]_{surf,0} - [\mathrm{P}]_{surf}$,

$$\frac{[\mathrm{PX}]_{surf}}{f[\mathrm{RX}]_{surf,0}} = \frac{1}{1 + f[\mathrm{RX}]_{surf,0}\left(\frac{k_a[\mathrm{C}]_{sol}}{k_d[\mathrm{XC}]_{sol}}\right)^2 k_t t} \quad (22)$$

Substituting eq 22 into eq 18 gives

$$\frac{[\mathrm{P}^\bullet]_{surf}}{f[\mathrm{RX}]_{surf,0}} = \frac{\frac{k_a[\mathrm{C}]_{sol}}{k_d[\mathrm{XC}]_{sol}}}{1 + f[\mathrm{RX}]_{surf,0}\left(\frac{k_a[\mathrm{C}]_{sol}}{k_d[\mathrm{XC}]_{sol}}\right)^2 k_t t} \quad (23)$$

Since the change of monomer concentration in Method II SI-ATRP is very small, the present monomer concentration $[\mathrm{M}]_{sol}$ on the right-hand side of eq 7 can be approximated by its initial concentration $[\mathrm{M}]_{sol,0}$, i.e., $\mathrm{d}[\mathrm{M}]_{sol}/\mathrm{d}t = -k_p\varepsilon[\mathrm{P}^\bullet]_{surf}[\mathrm{M}]_{sol,0}$. Substituting eq 23 into eq 7 and then into eq 16 after integration with the initial condition of $[\mathrm{M}]_{sol} = [\mathrm{M}]_{sol,0}$ at $t = 0$ finally results in

dx.doi.org/10.1021/ma202640x | Macromolecules 2012, 45, 1198−1207

$$\delta = \frac{m_w k_p [M]_{sol,0}}{\rho k_t}\left(\frac{k_d[XC]_{sol}}{k_a[C]_{sol}}\right) \ln\left(1 + f[RX]_{surf,0}\left(\frac{k_a[C]_{sol}}{k_d[XC]_{sol}}\right)^2 k_t t\right) \quad (24)$$

For simplicity, let us define the following two group parameters,

$$\alpha = \frac{m_w k_p [M]_{sol,0}}{\rho k_t}\left(\frac{k_d[XC]_{sol}}{k_a[C]_{sol}}\right) \quad (25)$$

$$\beta = \tau k_t \left(\frac{k_a[C]_{sol}}{k_d[XC]_{sol}}\right)^2 \quad (26)$$

where $\tau = f[RX]_{surf,0}$ is the grafting density in mol/dm^2. eq 21−24 become

$$[P]_{surf} = \frac{\tau\beta t}{1 + \beta t} \quad (21a)$$

$$[PX]_{surf} = \frac{\tau}{1 + \beta t} \quad (22a)$$

$$[P^\bullet]_{surf} = \frac{k_a[C]_{sol}}{k_d[XC]_{sol}} \frac{\tau}{1 + \beta t} \quad (23a)$$

$$\delta = \alpha \ln(1 + \beta t) \quad (24a)$$

At $t \to 0$

$$\delta = \alpha\beta t = \frac{m_w \tau}{\rho}\left(\frac{k_a[C]_{sol}}{k_d[XC]_{sol}}\right) k_p [M]_{sol,0} t \quad (27)$$

which correlates the initial linear portion of polymer layer thickness versus time data, i.e., the initial slope of the $\delta \sim t$ curves. The linearity of thickness versus time at the early stage of SI-ATRP has been supported by many experimental data.[2−31]

RESULTS AND DISCUSSION

Comparison of Numerical and Analytical Models. In general, numerical models based on a set of differential equations are more accurate but difficult for experimentalists to use. Analytical models are often simpler and can provide straightforward analysis for the effects of various parameters on outcome. However, assumptions are inevitably employed and thus accuracy can be trade off for simplicity. In deriving the above analytical model, there were two major assumptions involved. One was the stationary state hypothesis (SSH) applied to eq 8 in order to get eq 18. The other was the time independence of $k_t(k_a[C]_{sol}/k_d[XC]_{sol})^2$ in the integration of eq 20. SSH is commonly used in conventional free radical polymerization to convert differential equations of radical population into algebra equations. It means that radical initiation rate approximately equals to radical termination rate and the rate of accumulation becomes negligible ($d[P^\bullet]/dt \approx 0$; note—radical concentrations at 10^{-7}−10^{-9} mol/L). The hypothesis was verified both theoretically by comparison between numerical simulations with and without the hypothesis and experimentally by electron spin resonance measurements of radical concentrations.[33] However, the radical concentration in controlled radical polymerization such as ATRP is not only determined by radical initiation and termination but also by radical activation and deactivation. The question is which reactions dominate. It is known that, for good controlled polymerization, radicals experience many cycles of activation and deactivation before termination. Therefore, it is the activation and deactivation reactions that determine radical concentration (see eq 18). Regarding the activator and deactivator ratio, it does not vary significantly in method II SI-ATRP because concentrations of polymer chain species are very low and their variations have little effect on catalyst concentrations.

Table 1. Kinetic Parameters and Experimental Conditions of SI-ATRP of Methyl Acrylate from the Gold Substrate Used in the Model Calculation

parameter	unit	value	reference
$[M]_{sol,0}$	mol L^{-1}	2	3
$[XC]_{sol}/[C]_{sol}$		0.3	3
k_p	L mol^{-1} s^{-1}	1580	34
k_a	L mol^{-1} s^{-1}	0.8	3
k_d	L mol^{-1} s^{-1}	10^5	3
k_t (solution)	L mol^{-1} s^{-1}	10^8	3
k_t/δ	dm^2 mol^{-1} s^{-1}	10^{14}	based on δ = 100 nm
k_t (surface)	dm^2 mol^{-1} s^{-1}	8.3×10^{13}	this work
α	nm	10	this work
β	min^{-1}	0.022	this work
m_w	g mol^{-1}	86.1	34
ρ	g cm^{-3}	1.22	34
ε	dm^{-1}	0.1	this work
τ	chains nm^{-2}	0.38	this work

Many sets of method II SI-ATRP experimental data were collected from literatures that enabled us to validate the developed model and to investigate effects of various parameters on the grafting. Table 1 lists the parameters and experimental conditions of a SI-ATRP of methyl acrylate (MA) from gold substrate. Unfortunately, the grafting density was not reported from the cited paper and it is assumed τ = 0.38 chains per nm^2 in this work. First, let us examine the accuracy of analytical model by comparison to its numerical counterpart. Figure 1 shows the variation of polymer layer thickness, as well as radical, dormant and dead chain concentrations as a function of time. The numerical and analytical models agreed very well with each other. We also checked this agreement with many other systems under various conditions. Errors introduced by the assumptions used in the derivation were all negligible. The calculations in the following sections are therefore based on the analytical model.

Rate Constant of Surface Radical Termination. Figure 2 shows model calculations against experimental data for the polymer layer thickness δ with time t of the SI-ATRP of MA with [MA] = 2 M, [CuCl/Me$_6$TREN] = 2 mM and [CuBr$_2$/Me$_6$TREN] = 0.6 mM.[3] Without termination (i.e., k_t = 0), the model gives a linear relationship. This was clearly not the case in the experiment. An examination of eq 27 reveals that possible explanations for this deviation included reduced monomer and catalyst concentrations in the polymer layer, as well as diffusion controlled reactions such as propagation, activation and deactivation. In the polymerization, the monomer and catalyst concentrations in solution remained constant. However, with polymer chains growing, their concentrations in the polymer layer could become starved.

dx.doi.org/10.1021/ma202640x | Macromolecules 2012, 45, 1198−1207

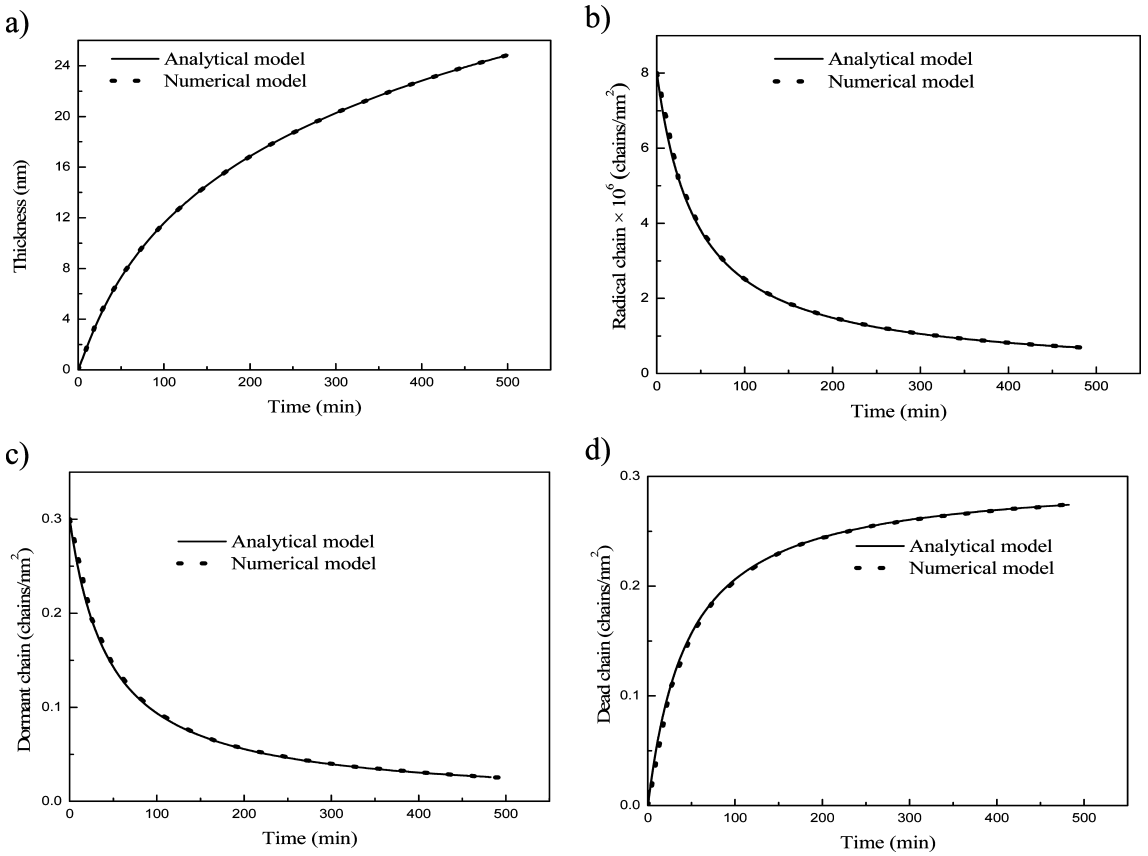


Figure 1. Comparison between analytical and numerical models for the SI-ATRP of MA as a function of time. (a) polymer layer thickness, (b) radical concentration, (c) dormant chain concentration, and (d) dead chain concentration.

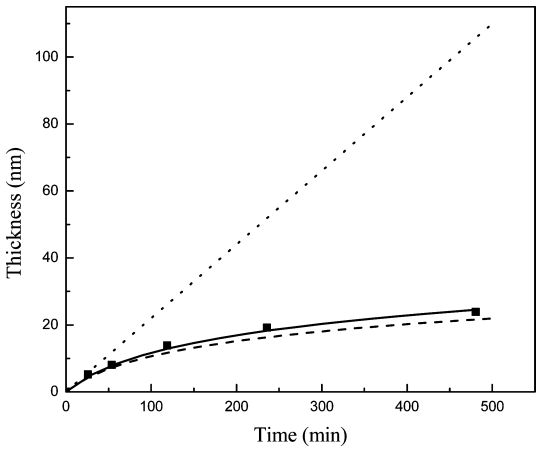


Figure 2. Polymer layer thickness versus time of the SI-ATRP of MA. Points: experimental data,[3] solid line: model result with $k_t = 8.3 \times 10^{13}$ dm^2 mol^{-1} s^{-1}, dashed line: model result with $k_t = 10^{14}$ dm^2 mol^{-1} s^{-1}, dotted line: model result with $k_t = 0$.

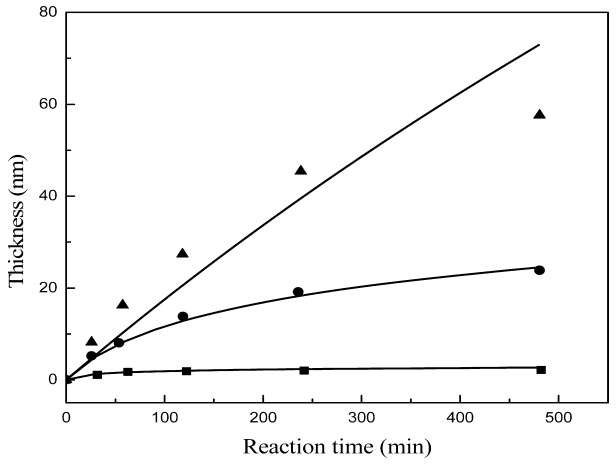


Figure 3. Dependence of polymer layer thickness on catalyst concentration in the SI-ATRP with [MA] = 2 M, [$CuBr_2$/Me_6TREN]/[CuCl/Me_6TREN] = 0.3 and three levels of [CuCl/Me_6TREN]: (■) 40 mM, (●) 2 mM, (▲) 0.1 mM. The SI-ATRP was performed in a 1:1 mixture of CH_3CN and THF at 23 °C.[3] The solid lines are model results.

The exact values of [M], [C], and [XC] on the surface might be different from solution and varied with time. A two-phase model is needed here in dealing with this situation and the reactant concentrations in the polymer layer should be estimated from their respective partition coefficients. The partition coefficients must then be correlated to polymer layer thickness to account for the observed variation with time. Such a model is out of the scope of the present work.

Reactions that readily become diffusion controlled are those involving two chain species and having high rate constants such

Table 2. α, β, and k_t Values of the SI-ATRP of MA at Various Catalyst Concentrations

catalyst concentration (mM)	α (nm)	β (min^{-1})	k_t (dm^2 mol^{-1} s^{-1})
0.1	200	0.0011	4.15×10^{12}
2	10	0.022	8.30×10^{13}
40	0.5	0.44	1.66×10^{15}

dx.doi.org/10.1021/ma202640x | *Macromolecules* 2012, 45, 1198–1207

Table 3. Experimental Conditions and Kinetic Parameters of the SI-ATRP of MPC from Silicon Wafers

parameters	unit	values	reference
$[M]_{sol,0}$	mol L^{-1}	1.33	7
$[XC]_{sol}/[C]_{sol}$		0.1	7
k_p	L mol^{-1} s^{-1}	1.6×10^3	29
k_a	L mol^{-1} s^{-1}	1	29
k_d	L mol^{-1} s^{-1}	10^6	29
k_t	dm^2 mol^{-1} s^{-1}	8.1×10^{13}	this work
α	nm	60	this work
β	min^{-1}	0.006	this work
m_w	g mol^{-1}	295	7
ρ	g cm^{-3}	1.3	7
τ	chains nm^{-2}	0.74	this work

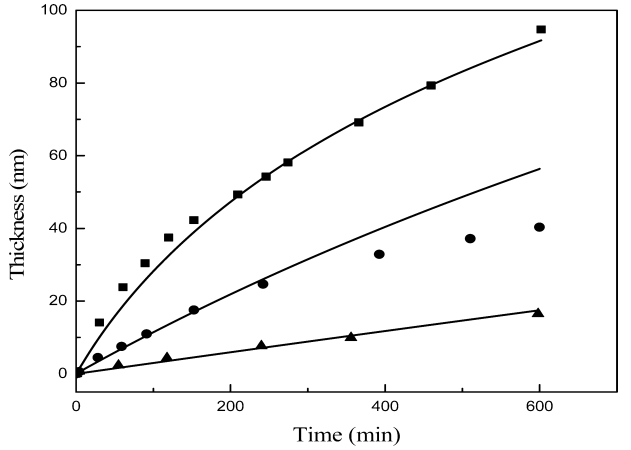


Figure 4. Polymer layer thickness versus time in the SI-ATRP of 2-methacryloyloxythyl phosphorylcholine with [MPC] = 1.33 M and [MPC]/[CuBr/2bpy] = 200 at three levels of $[CuBr_2/2bpy]/[CuBr/2bpy]$: (■) 0.1, (●) 0.2, (▲) 0.5. Solvent: methanol.[7] The solid lines are model results.

Table 4. Experimental Conditions and Kinetic Parameters of the SI-ATRP of Acrylamide from Silicon Wafers

parameters	unit	values	reference
$[M]_{sol,0}$	mol L^{-1}	3	28
$[XC]_{sol}/[C]_{sol}$		0.1	28
k_p	L mol^{-1} s^{-1}	410	34
k_a	L mol^{-1} s^{-1}	0.8	28
k_d	L mol^{-1} s^{-1}	1×10^6	28
k_t	dm^2 mol^{-1} s^{-1}	3.35×10^{14}	this work
α	nm	2.5	this work
β	min^{-1}	0.0068	this work
m_w	g mol^{-1}	71.08	34
ρ	g cm^{-3}	1.3	34
τ	chains nm^{-2}	0.32	this work

as radical termination. All propagation, activation and deactivation are bimolecular reactions between immobilized chains on surface with small molecule reactants in solution. Their rates must be limited by diffusion of the small molecules under diffusion controlled conditions. Among the three reactions, only deactivation is a fast reaction. However, a diffusion-controlled deactivation would reduce k_d and accelerate the growth of polymer thickness, which is opposite to the experimental observation. It can thus be ruled out. Since activation is much slower than deactivation, the former cannot become diffusion controlled before the latter and be responsible for the deviation either. Diffusion controlled propagation is another possibility, but it has been shown in conventional free radical polymerization that propagation becomes diffusion controlled only when polymerization system

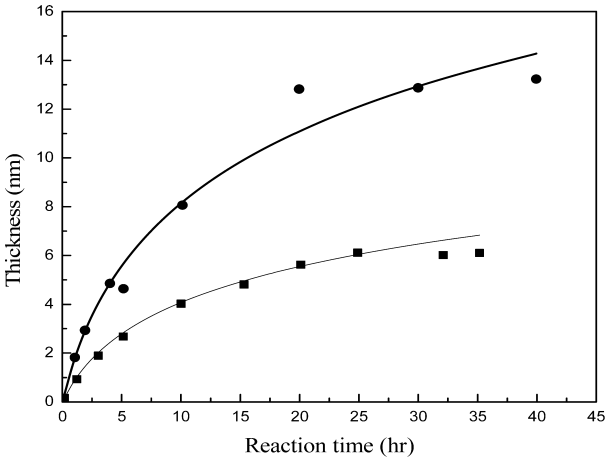


Figure 5. Polymer layer thickness versus time of the SI-ATRP of acrylamide on silicon wafers with [CuCl] = 1.08 mM and [bpy] = 3.23 mM at 130 °C. Solvent: DMF. Two acrylamide concentrations were used: (■) 3 mol/L; (●) 6 mol/L. The solid lines are model results.

Table 5. Experimental Condition and Kinetic Parameters of the SI-ATRP of *N*-Isopropylacrylamide (NIPAM) from Silicon Wafers

parameters	unit	values	reference
$[M]_{sol,0}$	mol L^{-1}	2.2	31
$[XC]_{sol}/[C]_{sol}$		0.02	31
k_p	L mol^{-1} s^{-1}	5000	34
k_a	L mol^{-1} s^{-1}	1	31
k_d	L mol^{-1} s^{-1}	10^6	31
k_t	dm^2 mol^{-1} s^{-1}	1.05×10^{14}	this work
m_w	g mol^{-1}	113.2	34
ρ	g cm^{-3}	1.269	34

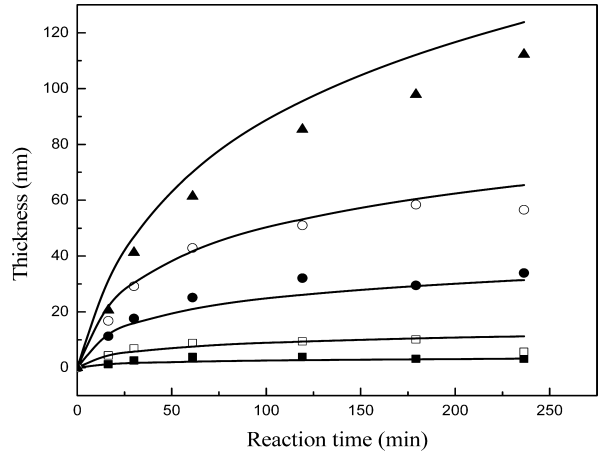


Figure 6. Polymer layer thickness versus time of the SI-ATRP of *N*-isopropylacrylamide (NIPAM) with [NIPAM] = 2.2 M, [CuCl] = 11 mM, $[CuBr_2]$ = 0.22 mM, and [PMDETA] = 55 mM in 10 mL of 1/1 (v/v) $MeOH/H_2O$ at room temperature with different grafting densities. Points are experimental data: (■) 0.04, (□) 0.13, (●) 0.33, (○) 0.52, and (▲) 0.62 chains per nm^2. Lines are model calculation results.

dx.doi.org/10.1021/ma202640x | *Macromolecules* 2012, 45, 1198–1207

Table 6. α, β, and k_t Values for the SI-ATRP of NIPAM

grafting density (chains nm^{-2})	α (nm)	β (min^{-1})	k_t (dm^2 mol^{-1} s^{-1})
0.04	0.78	0.25	2.50×10^{15}
0.13	2.80	0.23	7.00×10^{14}
0.33	7.91	0.21	2.48×10^{14}
0.52	18.69	0.14	1.05×10^{14}
0.62	45.50	0.06	4.20×10^{13}

becomes glassy (so-called "glass effect"). Such "glass effect" is unlikely in the SI-ATRP under discussion. However, it cannot be ruled out in other systems having very high grafting density and molecular weight. On the basis of intuition, in such systems, reactants (monomer catalyst and polymer chains) in the surface film would have similar experience as in bulk polymerization at high monomer conversions.

The radical termination becomes a plausible mechanism that caused the experimental $\delta \sim t$ data deviated from linearity. Termination of surface radicals is a rather complicated molecular process. Intuitively, radicals are crowded on a small area surface and their concentration can be very high. Assuming grafting density 1 chain per nm^2, polymer layer thickness 100 nm and radical/dormant ratio 10^{-5}, we estimated the volumetric radical concentration in the polymer layer 1.66×10^{-7} mol/L ($=10^{-5}/(6.023 \times 10^{23})/(100 \times 1 \times 10^{-24})$), which is comparable to solution polymerization. As the first try, we used the solution radical termination rate constant $k_t = 10^8$ L mol^{-1} s^{-1} and assumed the radicals homogeneously distributed in the 100 nm thick polymer layer. With an apparent surface radical termination rate constant $k_t/\delta = 10^{14}$ dm^2 mol^{-1} s^{-1}, we found the calculated result very close to the experimental data (see the dashed line in Figure 2). We thought we found the true mechanism for surface radical termination. However, calculations for other sets of experimental data showed all possibilities. The theoretical lines could be much higher or much lower than the experimental points. It became inconclusive. We then adjusted the surface rate constant k_t value to 8.3×10^{13} dm^2 mol^{-1} s^{-1}, giving a perfect fit to the set of experimental data (see the solid line in Figure 2). The α and β values were 10 nm and 0.022 min^{-1}, respectively.

Extra caution must be exercised in dealing with surface reactions with attention paid to their units. For the elementary reactions between surface and solution reactants such as propagation, activation and deactivation, the solution rate constants in L mol^{-1} s^{-1} can be directly used. However, for the reaction such as termination involving surface reactants only, the surface rate constant in dm^2 mol^{-1} s^{-1} must be employed.

Catalyst Concentration Dependence of Surface Radical Termination. Figure 3 shows the experimental data of polymer layer thickness versus time of the SI-ATRP of MA with [MA] = 2 M and [$CuBr_2$/Me_6TREN]/[CuCl/Me_6TREN] = 0.3 at three catalyst concentrations.[3] This set of data provoked brainstorming. The growth of polymer layer thickness with time is determined by the two group parameters α and β. It can be clearly seen from eqs 25 and 26 that both parameters depend on the activator/deactivator ratio, but not on their absolute concentrations. The effect of catalyst concentration on $\delta \sim t$ data suggested the involvement of catalyst species in surface radical termination. The radical centers "migrate" on surface through activation and deactivation reactions, as illustrated in Scheme 1. Since the rates of activation and deactivation depend on the catalyst concentration, the radical termination becomes catalyst concentration dependent. Increasing catalyst concentration make radicals "migrate" and terminate faster and thus suppress the polymer layer growth. The termination rate constant is therefore proportional to the catalyst concentration,[29]

$$k_t \propto r_{migration} \propto [C]_{sol} \tag{28}$$

where $r_{migration}$ represents the migration rate of radical centers.

On the basis of $k_t = 8.3 \times 10^{13}$ dm^2·mol^1·s^{-1} from the correlation of $[C]_{sol}$ = 2 mM data in Figure 2, the k_t values for $[C]_{sol}$ = 40 and 0.1 mM must be 20 times higher and 20 times lower than that for $[C]_{sol}$ = 2 mM, respectively, following eq 28, i.e. $k_t = 1.66 \times 10^{15}$ dm^2.mol^{-1}.s^{-1} for $[C]_{sol}$ = 40 mM and $k_t = 4.15 \times 10^{12}$ dm^2.mol^{-1}.s^{-1} for $[C]_{sol}$ = 0.1 mM. Their α and β values, together with k_t, are summarized in Table 2. Figure 3 shows the model correlation with the experimental data using the estimated α and β values. Good agreement is evident. Considering the variation of catalyst concentration over 2 orders of magnitude, this agreement is surprising. We could not think of any other mechanisms that provide so accurate qualitative description for the dependence of $\delta \sim t$ on catalyst concentration, except for the proposed "migration termination" of surface radicals.

Effect of Catalyst Ratio. From the definitions of α and β, the activator/deactivation ratio $[C]_{sol}/[XC]_{sol}$ should have strong effect on the growth of polymer layer thickness. While α is inversely proportional to this ratio, β is proportional to the

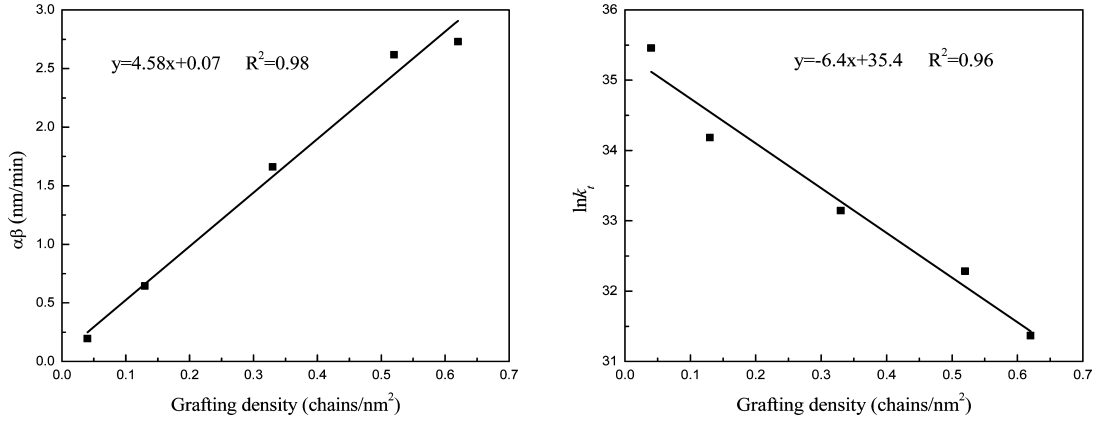


Figure 7. (a, left) Product of $\alpha\beta$ versus grafting density τ in the SI-ATRP of NIPAM. (b, right) Termination rate constant k_t versus grafting density τ in the SI-ATRP of NIPAM.

dx.doi.org/10.1021/ma202640x | Macromolecules 2012, 45, 1198–1207

square of it. Increasing the ratio increases the polymer layer growth rate. A set of experimental data of the SI-ATRP of 2-methacryloyloxythyl phosphorylcholine (MPC) was reported in literature.[7] The activator/deactivator ratio was varied while the other conditions remained constant. Table 3 lists the experimental condition and kinetic parameters. The variations of α and β at the three $[XC]_{sol}/[C]_{sol}$ levels were proportional to the ratio according to eqs 25 and 26. The α value changed five times while β varied 25 times. Figure 4 shows good agreement of the model calculation with the experimental data.

Effect of Monomer Concentration. The monomer concentration should also have an effect on the polymer layer thickness profile. The SI-ATRP of acrylamide was carried out at two monomer concentration levels while the other parameters remained constant.[28] Table 4 lists the experimental condition and kinetic rate constants. The α value varied with the monomer concentration following eq 25. The k_t and τ values were obtained through the model correlation. A good agreement between model result and experimental data is evident from Figure 5.

Effect of Grafting Density. Polymer grafting density and molecular weight are two most important parameters in surface modification and functionalization work. These parameters determine many surface application properties. A fundamental question remaining to be resolved is what is the maximum achievable grafting density? That is, how many chains can one square nanometer surface grow? Ideally, the grafting model should be able to predict the grafting density. Unfortunately, our understanding of the molecular mechanisms involved in surface initiator efficiency f is still very lacking. Many experimental studies reported grafting densities in a range of 0.1 to 1.0 chains per nm^2. Considering many more initiators can be immobilized on the same area, it is puzzling why only a small fraction of the surface initiators grow to polymer chains. What happen to the rest? Do they ever propagate with a few monomer units? If so, what causes the premature termination? Short chains constrained to surface are almost impossible to reach each other. Is it caused by crowding of chains? Are some initiated radicals thus "trapped" and could not access to monomers for propagation? There are many more questions than answers. Numerous papers were published in literatures on grafting various polymers from various surfaces under various conditions using various methods for various applications. This is particularly true in the recent years for surface initiated controlled radical polymerization. However, considerable efforts are still required in the most fundamental areas such as understanding the grafting efficiency.

In this model, the grafting density $\tau = f[RX]_{surf,0}$ is treated as a known parameter. The grafting density in SI-ATRP is often estimated from experimentally measured polymer layer thickness and molecular weight $\tau = \rho\delta/\bar{M}_N$. The challenge is the molecular weight measurement. Since the amount of graft chains on surface, even severed, is too little for characterization, initiator is often added to solution to generate free chains as reference (method I). However, method I does not yield thick polymer layers because of significant termination between surface and solution radicals and/or monomer consumption in solution. For thick layers, method II is a better choice but it does not give free chains in solution for characterization. Fortunately, a set of SI-ATRP experimental data with varying grafting density is available from the literature.[31] The grafting density data was obtained from the measured thicknesses of polyNIPAM films in the dry and swollen states based on a mean-field theory.[31] Table 5 lists the experimental condition and kinetic parameters of the SI-ATRP of NIPAM.

The grafting density τ appears in the β expression (see eq 26) but not in α (see eq 25). However, there was a lack of agreement with the experimental data by simply varying β linearly proportional to τ while remaining α constant. In order to fit the data, both α and β needed to be adjusted. Figure 6 shows the regression with adjusted α and β given in Table 6. It was found that increasing the grafting density increased α and decreased β. However, plotting the product of $\alpha\beta$ against τ gave a straight linear line, as shown in Figure 7a. The slope of the line was 4.58 nm/min, which was close to the theoretical value (4.89 nm/min) of,

$$\alpha\beta = \frac{m_w k_p [M]_{sol,0}}{\rho}\left(\frac{k_a[C]_{sol}}{k_d[XC]_{sol}}\right)\tau \tag{29}$$

This interesting observation pointed to the termination rate constant k_t be responsible for the initial lack of agreement. We therefore extracted the k_t values at the different grafting densities (see Table 6). Figure 7b plots k_t versus τ. It was found that the $k_t \sim \tau$ relationship is an exponential function,

$$k_t \sim \exp(-\gamma\tau) \tag{30}$$

where $\gamma = 6.4$.

It becomes clear that the surface radical termination is not only catalyst concentration dependent (see eq 28) but also grafting density dependent (eq 30). The former dependence can be adequately explained by "migration termination": the higher catalyst concentration, the faster activation deactivation reactions, the faster "radical migration", and thus the faster termination rate. However, the latter dependence requires further study. In general, there are three steps involved in "migration termination". First, the activator and deactivator catalyst species diffuse through solution; second, they diffuse into polymer layer, and third, they react with chain ends. It is unknown which step is rate determining. Could the catalyst diffusion through polymer layer become the rate-determining step? If so, how is this diffusion correlated to polymer grafting density and molecular weight? Chain conformation on surface can be very different from mushroom to brush, depending on these parameters. What is the influence of the chain conformation on catalyst diffusion? There are many more questions than answers in surface initiated controlled radical polymerization. After working a decade in this fascinating area, we are still puzzled with many fundamental issues and hope that this work can inspire more efforts on these issues.

■ CONCLUSION

A kinetic model has been developed for SI-ATRP from flat surfaces using Method II. A simple and accurate analytical solution was obtained. This solution allowed us to systematically analyze the experimental data of methyl acrylate (MA), 2-methacryloyloxythyl phosphorylcholine (MPC), acrylamide (AM), and *N*-isopropylacrylamide (NIPAM) on flat substrate and to examine the effects of various parameters on their grafting processes. The following conclusions were reached.

(1) The model predicts polymer layer thickness and the concentrations of radical, dormant and dead polymer chains on surface. The growth of polymer layer thickness with time follows the function of $\delta = \alpha\ln(1 + \beta t)$, which is controlled by two group parameters (i.e., eqs 25 and

dx.doi.org/10.1021/ma202640x | Macromolecules 2012, 45, 1198–1207

26), $\alpha = m_w k_p [M]_{sol,0} k_d [XC]_{sol} / (\rho k_t k_a [C]_{sol})$ and $\beta = \tau k_t (k_a [C]_{sol})^2 / (k_d [XC]_{sol})^2$. The model agreed well with the experimental data in describing the effects of various kinetic rate constants and reactant concentrations. eq 24 can be readily used by experiments for data analysis.

(2) The rate constant surface radical termination was found to be proportional to the catalyst concentration in solution (eq 28) $k_t \propto [C]_{sol}$. This catalyst concentration dependence of radical termination is caused by "migration termination". Although the chains are immobilized to surface, the radical centers "migrate" toward each other through the activation and deactivation reactions.

(3) The radical termination was also found to be grafting density dependent following $k_t \sim \exp(-\gamma\tau)$ (eq 30). While the exact mechanism is yet to be elucidated, the diffusion of catalyst species through polymer layer could have influence on the rate of termination.

AUTHOR INFORMATION

Corresponding Author

*E-mail: zhuship@mcmaster.ca.

ACKNOWLEDGMENTS

D.Z. would like to thank Jiaxing University for financially supporting his research leave and McMaster University for hosting the visit. W.W. thanks Zhejiang University for supporting his visit to McMaster University.

REFERENCES

(1) Prucker, O.; Rühe. *Macromolecules* **1998**, *31*, 592.
(2) Muhammad, E.; Kohji, O.; Yoshinobu, T.; Takeshi, F. *Macromolecules* **2000**, *33*, 2870.
(3) Kim, J.-B.; Huang, W.; Miller, D.; Baker, G. L.; Bruening, M. L. *J. Polym. Sci., Part A: Polym. Chem.* **2003**, *41*, 386.
(4) Jones, D. M.; Brown, A. A.; Huck, W. T. S. *Langmuir* **2002**, *18*, 1265.
(5) Matyjaszewski, K.; Miller, P. J.; Shukla, N.; Immaraporn, B.; Gelman, A.; Luokala, B. B.; Siclovan, T. M.; Kickelbick, G.; Vallant, T.; Hoffmann, H.; Pakula, Y. *Macromolecules* **1999**, *32*, 8716.
(6) Huang, W.; Kim, J.-B.; Bruening, M. L.; Baker, G. L. *Macromolecules* **2002**, *35*, 1175.
(7) Feng, W.; Brash, J.; Zhu., S. *J. Polym. Sci., Part A: Polym. Chem.* **2004**, *42*, 2931.
(8) Davis, K. A.; Matyjaszewski, K. *Macromolecules* **2001**, *34*, 2101.
(9) Jones, D. M.; Huck, W. T. S. *Adv. Mater.* **2001**, *13*, 1256.
(10) Kim, J.-B.; Huang, W.; Bruening, M. L.; Baker, G. L. *Macromolecules* **2002**, *35*, 5410.
(11) Bao, Z.; Bruening, M. L.; Baker, G. L. *Macromolecules* **2006**, *39*, 5251.
(12) Chen, R.; Feng, W.; Zhu, S.; Gianluigi, B.; Ong, B.; Wu, Y. *Polymer* **2006**, *47*, 1119.
(13) Jones, D. M.; Brown, A. A.; Wilhelm, T. S. H. *Langmuir* **2002**, *18*, 1265.
(14) Benetti, E. M.; Reimhult, E.; Johannes de Bruin.; Zapotoczny, S.; Textor, M.; Vansco, G. J. *Macromolecules* **2009**, *42*, 1640.
(15) Edmondson, S.; Vo, C. D.; Armes, S. P.; Unali, G. F. *Macromolecular* **2007**, *40*, 5271.
(16) Feng, W.; Chen, R.; Brash, J. L.; Zhu., S. *Macromol. Rapid Commun.* **2005**, *26*, 1383.
(17) Tsujii, Y.; Ohno, K.; Yamamoto, S.; Goto, A.; Fukuda., T. *Adv. Polym. Sci.* **2006**, *1*, 46.
(18) Borozenko, O.; Godin, R.; Lau, K. L.; Mah, W.; Cosa, G.; Skene, W. G.; Giasson, S. *Macromolecules* **2011**, *44*, 8177.
(19) Lego, B.; Skene, W. G.; Giasson, S. *Macromolecules* **2010**, *43*, 4384.
(20) Marutani, E.; S. Yamamoto, S.; Ninjbadgar, T.; Tsujii, Y.; Fukuda, T.; Takano, M. *Polymer* **2004**, *45*, 2231.
(21) Ohno, K.; Kayama, Y.; Ladmiral, V.; Fukuda, T.; Tsujii, Y. *Macromolecules* **2010**, *43*, 5569.
(22) Sheiko, S. S.; Sumerlin, B. S.; Matyjaszewski, K. *Prog. Polym. Sci.* **2008**, *33*, 759.
(23) Matyjaszewski, K.; Dong, H.; Jakubowski, W.; Pietrasik, J.; Kusumo, A. *Langmuir* **2007**, *23*, 4528.
(24) Singh, N.; Cui, X.; Boland, T.; Husson, S. *Biomaterials* **2007**, *28*, 763.
(25) Tomlinson, M. R.; Genzer, J. *Macromolecular* **2003**, *36*, 3449.
(26) Jeyaprakash, J. D.; Samuel, S.; Dhamodharan, R.; Rühe, J. *Macromol. Rapid Commun.* **2002**, *23*, 277.
(27) Renxu Chen, S. Z.; Zhu, S.; Maclaughlin, S. *Langmuir* **2008**, *24*, 6889.
(28) Xiao, D.; Wirh, M. J. *Macromolecules* **2002**, *35*, 2919.
(29) Gao, X.; Feng, W.; Zhu, S.; Heather, S.; Brash, J. L. *Macromolecular Reaction Engineering* **2010**, *4*, 235.
(30) Chen, R.; Feng, W.; Zhu, S.; Gianluigi, B.; Ong, B.; Wu., Y. *J. Polym. Sci., Part A: Polym. Chem.* **2006**, *44*, 1252.
(31) Wang, S.; Zhu., Y. *Langmuir* **2009**, *25*, 13448.
(32) Tsujii, Y.; Ejaz, M.; Sato, K.; Goto, A.; Fukuda, T. *Macromolecules* **2001**, *34*, 8872.
(33) Zhou, W.; Zhu., S. *Macromolecules* **1998**, *31*, 4335.
(34) Brandrup, J., Immergut, E. H., *Polymer Handbook*; A Wiley-Interscience Publication: NewYork, 1989.

Macromolecules

Article

pubs.acs.org/Macromolecules

Effects of π-Conjugated Bridges on Photovoltaic Properties of Donor-π-Acceptor Conjugated Copolymers

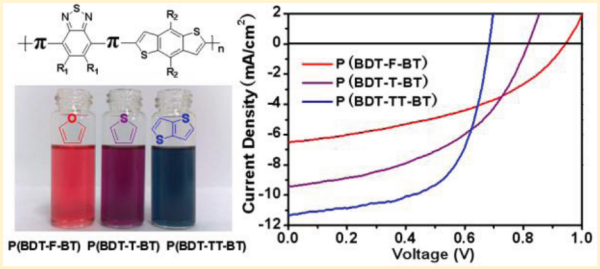
Xiaochen Wang,[†,‡] Yeping Sun,[†,‡] Song Chen,[†] Xia Guo,[‡] Maojie Zhang,[‡] Xiaoyu Li,*[,†] Yongfang Li,*[,‡] and Haiqiao Wang*[,†]

[†]State Key Laboratory of Organic−Inorganic Composites, College of Materials Science and Engineering, Beijing University of Chemical Technology, Beijing 100029, China

[‡]CAS Key Laboratory of Organic Solids, Institute of Chemistry, Chinese Academy of Sciences, Beijing 100190, China

Supporting Information

ABSTRACT: A series of conjugated donor (D)-π-acceptor (A) copolymers, **P(BDT-F-BT)**, **P(BDT-T-BT)**, and **P(BDT-TT-BT)**, based on benzodithiophene (BDT) donor unit and benzothiadiazole (BT) acceptor unit with different π-bridges, were designed and synthesized via a Pd-catalyzed Stille-coupling method. The π-bridges between the BDT donor unit and BT acceptor unit are furan (**F**) in **P(BDT-F-BT)**, thiophene (**T**) in **P(BDT-T-BT)** and thieno[3,2-*b*]thiophene (**TT**) in **P(BDT-TT-BT)**. It was found that the π-bridges significantly affect the molecular architecture and optoelectronic properties of the copolymers. With the π-bridge varied from furan to thiophene, then to thieno[3,2-*b*]thiophene, the shape of the molecular chains changed from z-shaped to almost straight line gradually. Band gaps of **P(BDT-F-BT)**, **P(BDT-T-BT)** and **P(BDT-TT-BT)** were tuned from 1.96 to 1.82 to 1.78 eV with HOMO levels up-shifted from −5.44 to −5.35 to −5.21 eV, respectively. Bulk heterojunction solar cells with the polymers as donor and $PC_{71}BM$ as acceptor demonstrated power conversion efficiency varied from 2.81% for **P(BDT-F-BT)** to 3.72% for **P(BDT-T-BT)** and to 4.93% for **P(BDT-TT-BT)**. Compared to furan and thiophene, thieno[3,2-*b*]thiophene π-bridge in the copolymers shows superior photovoltaic performance. The results indicate that the photovoltaic performance of some high efficiency D−A copolymers reported in literatures could be improved further by inserting suitable π-bridges.



INTRODUCTION

During the past decade, bulk heterojunction (BHJ) polymer solar cells (PSCs) have been the focus of both scientific research and industrial application, because of their potential applications in large area, lightweight, flexible photovoltaic devices through low-cost solution-processable techniques. Conjugated polymers with electron donor−acceptor (D−A) architecture are particularly attractive due to the facile tunability of their electronic structure of the main chain. Changing the nature of the D and A moieties combining with different side chains influences numerous properties such as absorption bands, energy levels, charge carrier mobilities, and morphology.[1−13] These properties affect the characteristics of PSCs and finally determine the power conversion efficiency (PCE) of the devices.

Many efforts have been devoted to the design and synthesis of new donor and acceptor building blocks,[14−27] in order to get efficient D−A copolymers for PSCs. But there are only a few studies focus on the bridges between D and A segments.[28−30] Recently, we designed and synthesized a furan-containing D-π-A copolymer.[28a] We found that using furan instead of thiophene as the π-bridge in the copolymer is able to significantly affect the properties of the polymer. Conjugated bridges crucially influence the electronic structure of polymer main chain and the interaction between donor and acceptor units; therefore remarkably affect stereostructure and consequently optical, electrochemical, charge transport and photovoltaic properties of the D-π-A conjugated copolymers. Thus, it is of prime importance to fully understand the effects of the π-bridges on the physicochemical and photovoltaic properties in the design of new polymers for efficient PSCs.

In this study, we designed and synthesized a series of D-π-A copolymers based on benzodithiophene (BDT) donor unit and benzodiathiazole (BT) acceptor unit bridged by different heteroaromatic rings, as shown in Figure 1. Bisalkoxy-substituted **BDT** and bis(octyloxy)-substituted **BT** were selected as donor and acceptor building blocks because they can endow polymers with broad absorption and suitable molecular energy levels[28a,31−33] to ensure sunlight harvesting and charge separation and transportation in the polymers. The properties of the polymers changed regularly from **P(BDT-F-BT)** to **P(BDT-T-BT)** and **P(BDT-TT-BT)**, corresponding to the π-bridge of furan, thiophene and thieno[3,2-*b*]thiophene. With the π-bridge units varied from furan to thiophene, then to thieno[3,2-*b*]thiophene, the shape of the molecular chains changed from z-shaped to almost straight line gradually. In this

Received: December 7, 2011
Revised: January 13, 2012
Published: January 31, 2012

 © 2012 American Chemical Society dx.doi.org/10.1021/ma202656b | *Macromolecules* 2012, 45, 1208−1216

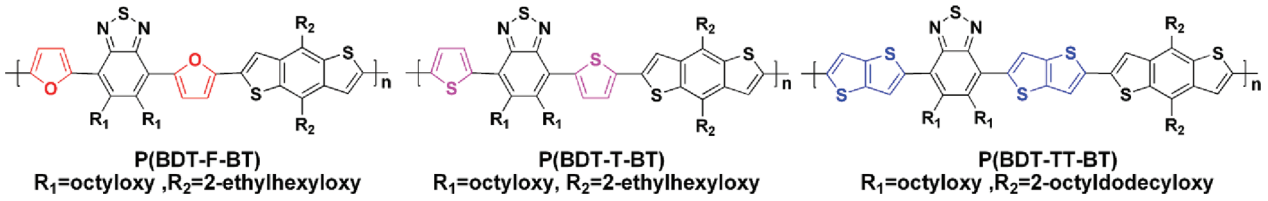
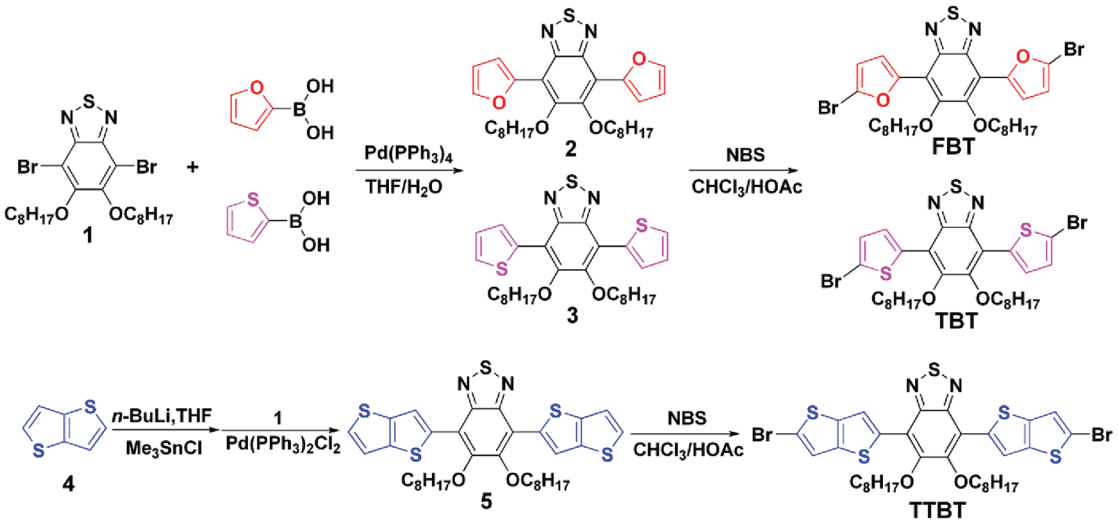


Figure 1. Molecular structures of the D-π-A conjugated copolymers with different π-bridges.

Scheme 1. Synthesis Routes of the Electron Acceptor Monomers



case, the π-orbital overlap between neighboring aromatic units was increased in turn, leading to regular changes in the frontier orbital energy levels. The absorption peak wavelengths red-shifted from 534 to 568 to 631 nm; the highest occupied molecular orbital (HOMO) energy levels increased from −5.44 to −5.35 to −5.21 eV and band gaps decreased from 1.96 to 1.82 to 1.78 eV, for **P(BDT-F-BT)**, **P(BDT-T-BT)**, and **P(BDT-TT-BT)**, respectively. The photovoltaic power conversion efficiency (PCE) of solar cells based on the polymers as donor and [6,6]-phenyl C_{71} -butyric acid methyl ester ($PC_{71}BM$) as acceptor varied from 2.81% for **P(BDT-F-BT)** to 3.72% for **P(BDT-T-BT)** to 4.93% for **P(BDT-TT-BT)**, depending on the π-bridge in the polymer backbones.

EXPERIMENTAL SECTION

Materials. 4,7-dibromo-5,6-bis(octyloxy)benzo-2,1,3-thiadiazole (**1**),[22,34] 4,8-dihydrobenzo[1,2-*b*:4,5-*b*′]dithiophen-4,8-dione(**6**)[31] and 2-octyl-1-dodecyl bromide[35] were synthesized according to the literatures. Tetrahydrofuran (THF) was dried over Na/benzophenone ketyl and freshly distilled prior to use. Other reagents and solvents were commercial grade and used as received without further purification. All reactions were performed under nitrogen atmosphere.

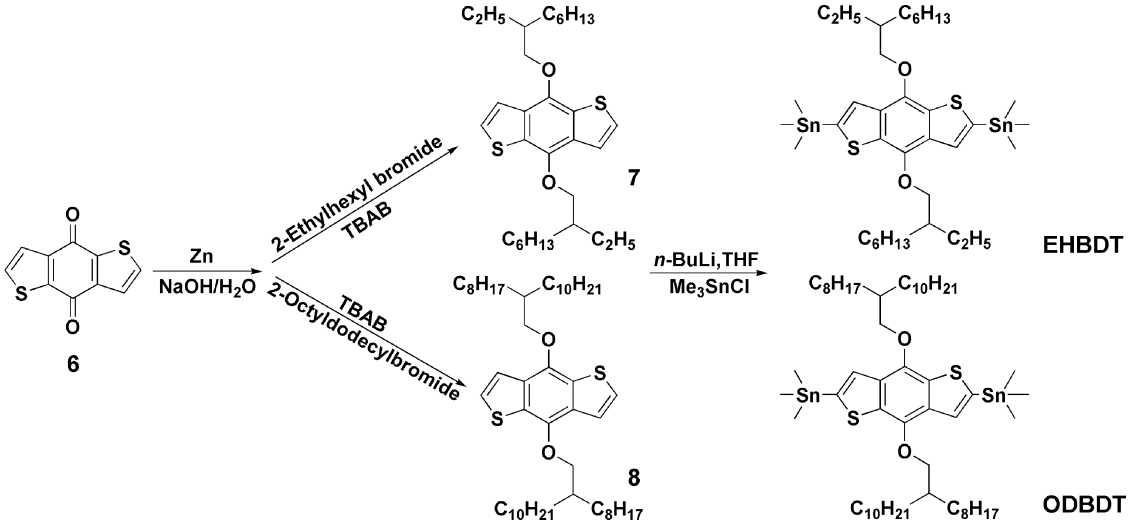
Measurements and Characterization. Molecular weights of the polymers were measured by gel permeation chromatography (GPC) method on Waters 515−2410 with polystyrenes as reference standard and tetrahydrofuran (THF) as an eluent. All new compounds were characterized by nuclear magnetic resonance spectra (NMR) recorded on a Bruker AV 600 spectrometer in $CDCl_3$ at room temperature. Chemical shifts of ^1H NMR were reported in ppm. Splitting patterns were designated as s (singlet), d (doublet), t (triplet), m (multiplet), and br (broad). Elemental analyses were performed on a Flash EA 1112 analyzer or Elementar vario EL III. Thermal gravimetric analysis (TGA, Netzsch TG209C) measurements were carried out under a nitrogen atmosphere at a heating rate of 10 °C/min. UV−vis absorption spectra were recorded on a Shimadzu spectrometer model UV-3150. Absorption spectra measurements of the polymer solutions were carried out in chloroform (analytical reagent) at 25 °C. Absorption spectra measurements of the polymer films were carried out on the quartz plates with the polymer films spin-coated from the polymer solutions in chloroform (analytical reagent) at 25 °C. The electrochemical cyclic voltammetry was conducted on a Zahner IM6e electrochemical workstation with a Pt plate, Pt wire, and Ag/Ag^+ electrode as the working electrode, counter electrode, and reference electrode, respectively, in a 0.1 mol/L tetrabutylammonium hexafluorophosphate (Bu_4NPF_6) acetonitrile solution. Polymer thin films were formed by drop-casting of polymer solutions in $CHCl_3$ (analytical reagent) on the working electrode and then dried in air. Surface morphology of films was characterized on a Digital Instruments Multimode Nanoscope IIIa atomic force microscopy (AFM) by tapping mode in an ambient atmosphere.

Fabrication of Photovoltaic Devices. PSCs were fabricated with ITO glass as a positive electrode, Ca/Al as a negative electrode, and the blend film of the polymer/$PC_{71}BM$ between them as a photosensitive layer. The ITO glass was precleaned and modified by a thin layer of PEDOT:PSS, which was spin-cast from a PEDOT:PSS aqueous solution (Clevious P VP AI 4083 H. C. Stark, Germany) on the ITO substrate, and the thickness of the PEDOT:PSS layer was about 60 nm. The photosensitive layer was prepared by spin-coating a blend solution of polymer and $PC_{71}BM$ in *o*-dichlorobenzene on the ITO/PEDOT:PSS electrode. Then, the Ca/Al cathode was deposited on the polymer layer by vacuum evaporation under 3×10^{-4} Pa. The thickness of the photosensitive layer was ca. 100 nm, measured on an Ambios Tech XP-2 profilometer. The effective area of one cell was ca. 4 mm^2. The current−voltage (*I* versus *V*) measurement of the devices was conducted on a computer controlled Keithley 236 source measure unit. A xenon lamp with an AM 1.5 filter was used as the white-light source, and the optical power at the sample was 100 mW/cm^2.

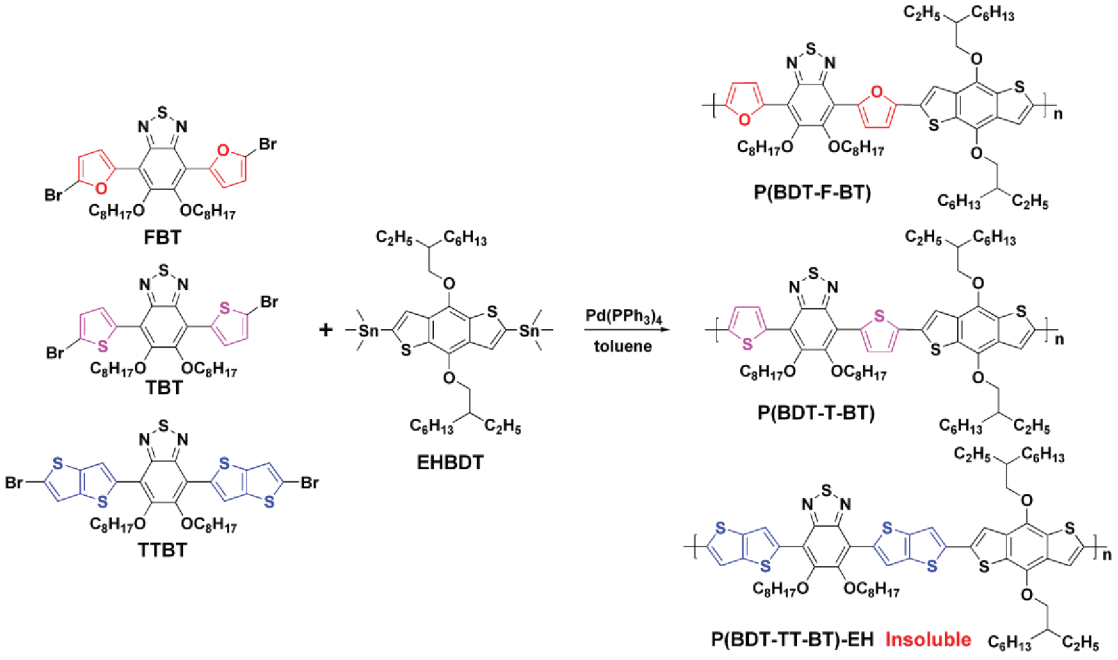
Synthesis of the Monomers. *5,6-Bis(octyloxy)-4,7-bis(thieno-[3,2-b]thiophen-2-yl)benzo-[c][1,2,5]-thiadiazole (**5**).* Thieno[3,2-*b*]-thiophene (4.8 g, 34 mmol) was dissolved in 250 mL anhydrous THF in a well-dried round flask under nitrogen atomosphere. *n*-Butyllithium (2.4 M in hexanes, 13.6 mL, 34 mmol) was added dropwise at 0 °C.

dx.doi.org/10.1021/ma202656b | *Macromolecules* 2012, 45, 1208−1216

Scheme 2. Synthesis Routes of the Electron Donor Monomers



Scheme 3. Synthetic Route of the Copolymers P(BDT-F-BT), P(BDT-T-BT) and P(BDT-TT-BT)-EH.



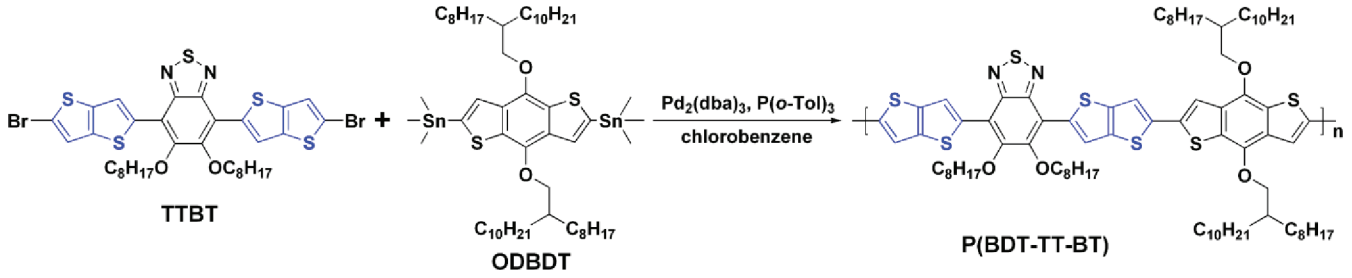
After stirring for 1 h, trimethyltinchloride (1 M in THF, 34 mL, 34 mmol) was added dropwise, and the mixture was allowed to warm to room temperature. After stirring for another 6 h, compound **1** (7.5 g, 13.6 mmol) and $PdCl_2(PPh_3)_2$ (0.42 g, 0.6 mmol) were added to this mixture. After flushing with nitrogen for 10 min, the reactant was heated to reflux for 24 h. After cooled to room temperature, the reaction mixture was poured into water. The product was extracted with ethyl acetate (3 × 150 mL). The extracts were combined and washed with water and brine then dried over anhydrous magnesium sulfate. After filtration, the solvent was removed under reduced pressure. The residue was purified by column chromatography on silica, eluting with petroleum ether/dichloromethane (from 20:0 to 20:1), to give compound **5** as a dark red liquid (7.2 g, 79%). ^{1}H NMR (600 MHz, $CDCl_3$): δ (ppm) 8.80 (s, 2H, Ar−H), 7.46 (d, 2H, Ar−H), 7.33 (d, 2H, Ar−H), 4.16 (t, 4H, CH_2), 1.98 (m, 4H, CH_2), 1.47 (m, 4H, CH_2), 1.38−1.30 (m, 16H, CH_2), 0.90 (t, 6H, CH_3)

*4,7-Bis(5-bromothieno[3,2-b]thiophen-2-yl)-5,6-bis(octyloxy)-benzo-[c][1,2,5]-thiadiazole (**TTBT**).* Compound **5** (5.89 g, 8.8 mmol) was added to a mixture of chloroform (150 mL) and acetic acid (150 mL). After *N*-bromosuccimide (NBS) (3.29 g, 18.5 mmol) was added, the mixture was stirred at room temperature in dark overnight. Then the reaction mixture was poured into water (200 mL) and extracted with chloroform (3 × 50 mL). The extracts were combined and washed with water and sat. sodium bicarbonate solution then dried over anhydrous magnesium sulfate. After filtration, the solvent was removed under reduced pressure. The residue was purified by column chromatography on silica, eluting with petroleum ether to give **TTBT** as a dark red crystal (5.9 g, 81%). Mp 109−111 °C. ^{1}H NMR (600 MHz, $CDCl_3$): δ (ppm) 8.75 (s, 2H, Ar−H), 7.33 (s, 2H, Ar−H), 4.15 (t, 4H, CH_2), 1.96 (m, 4H, CH_2), 1.46 (m, 4H, CH_2), 1.36−1.25 (m, 16H, CH_2), 0.90 (t, 6H, CH_3). ^{13}C NMR (600 MHz, $CDCl_3$): δ(ppm) 151.87, 150.65, 140.22, 139.49, 135.61, 122.47, 122.20, 117.77, 114.66,77.20, 76.99, 76.78, 74.79, 31.81, 30.33, 29.49, 29.28, 25.95, 22.66, 14.09.

*4,8-Di(2-octyldodecyloxy)benzo[1,2-b;3,4-b]dithiophene (**8**).* Compound **6** (4.4 g, 20 mmol), zinc powder (3.9 g, 60 mmol), and NaOH (24 g, 0.6 mol) were added to 100 mL of water. The mixture was well stirred and heated to reflux for 1 h. Then, 2-octyl-1-dodecyl bromide (29 g, 80 mmol) and tetrabutylammonium bromide (0.65 g, 2 mmol) were added into the flask. After being refluxed for 6 h, the

dx.doi.org/10.1021/ma202656b | *Macromolecules* 2012, 45, 1208−1216

Scheme 4. Synthetic Route of the Polymer P(BDT-TT-BT).



reactant was cooled to room temperature and added to 200 mL dichloromethane. Water was separated and extracted with dichloromethane (3 × 50 mL). The combined dichloromethane layer was dried over anhydrous magnesium sulfate. After filtration, the solvent was removed under reduced pressure. The crude product was purified by column chromatography on silica, eluting with petroleum ether to give Compound **8** as a white waxy solid (11.6 g, 75%). Mp 33−35 °C. ^{1}H NMR (600 MHz, $CDCl_3$): δ (ppm) 7.48 (d, 2H), 7.36 (d, 2H), 4.18 (d, 4H), 1.86 (m, 2H), 1.64(m, 4H), 1.51 (m, 4H), 1.43 (m, 8H),1.29 (m, 48H), 0.90 (m, 12H). ^{13}C NMR (600 MHz, $CDCl_3$): δ (ppm) 144.65, 131.47, 129.91, 125.85, 120.25, 76.38, 39.20, 31.92, 31.32, 30.06, 29.66, 29.35, 26.98, 22.69, 14.11.

*2,6-Bis(trimethyltin)-4,8-di(2-octyldodecyloxy)benzo[1,2-b;3,4-b]-dithiophene (**ODBDT**).* Compound **8** (3.9 g, 5 mmol) was dissolved in 80 mL of anhydrous THF and cooled down to −78 °C by a liquid nitrogen-acetone bath under nitrogen protection. Butyllithium solution (2.4 M, 5 mL, 12 mmol) was added dropwise with stirring. After being stirred at −78 °C for 1 h, the mixture was stirred for another 1 h without liquid nitrogen-acetone bath. When the mixture was cooled down to −78 °C again, trimethyltin chloride solution (1 M in THF, 12 mL, 12 mmol) was added and the reaction mixture was warmed to room temperature. After stirred overnight, the reactant was quenched with 50 mL of water and extracted with petroleum ether. The organic extraction was dried with anhydrous sodium sulfate and evaporated in vacuo. The crude product was purified by recrystallization in ethanol to yield the titled compound **ODBDT** as a white needle crystal (4.65 g, 84%). Mp 36−38 °C. ^{1}H NMR (600 MHz, $CDCl_3$): δ (ppm) 7.51 (s, 2H), 4.18 (d, 4H), 1.86 (m, 2H), 1.64(m, 4H), 1.54−1.42 (m, 12H),1.27 (m, 48H), 0.88 (m, 12H), 0.44(s, 18H). ^{13}C NMR (600 MHz, $CDCl_3$): δ (ppm) 143.24; 140.31, 133.84; 132.89, 127.96, 75.92, 39.20, 31.93, 31.41, 30.18, 29.76, 29.72, 29.69, 29.40, 29.37, 27.07, 22.69, 14.11.

*Synthesis of the Polymer. P(**BDT-T-BT**).* **TBT** monomer (357 mg, 0.5 mmol) and **EHBDT** monomer (386 mg, 0.5 mmol) were put into a 25 mL two-neck flask, and 10 mL of toluene was added. The mixture was stirred and purged with nitrogen for 10 min, and then $Pd(PPh_3)_4$ (30 mg, 0.025 mmol) was added. After being purged for 15 min, the mixture was heated at 110 °C for 48 h. After cooled to room temperature, the reaction mixture was added dropwise to 200 mL acidic methanol (HCl + CH_3OH), then collected by filtration and washed with methanol. The black solid was filtered into a Soxhlet funnel and extracted by methanol, hexane, and chloroform successively. The polymer recovered from chloroform was purified by preparative gel permeation chromatography. Then, the product was dried under vacuum for 1 day to recover the target polymer **P(BDT-F-BT)** as a dark red solid (yield 66%, M_n= 10.4 kDa, M_w = 23.2 kDa, PDI = 2.2). ^{1}H NMR ($CDCl_3$, 600 MHz): δ (ppm) 8.55 (br,2H), 7.71−6.95 (br, 4H), 4.23 (br, 8H), 2.06(br, 6H), 1.91−1.25 (m, 36H), 1.25−0.90 (m, 18H). Anal. Calcd for $(C_{56}H_{74}N_2O_4S_5)_n$: C, 67.23; H, 7.40; N, 2.80. Found: C, 66.85; H, 7.44; N, 2.87.

P(BDT-TT-BT)-EH. **TTBT** monomer (165 mg, 0.2 mmol) and **EHBDT** monomer (154 mg, 0.2 mmol) were put into a 25 mL two-neck flask, and 10 mL of toluene was added. The mixture was stirred and purged with nitrogen for 10 min, and then $Pd(PPh_3)_4$ (30 mg, 0.025 mmol) was added. When the mixture was heated at 110 °C for 6 h after being purged for 15 min, a great deal of dark solid precipitate appeared in the flask. After cooled to room temperature, the precipitate was collected by filtration and washed with methanol. The black solid can not be dissolved even in hot THF or chlorobenzene. This polymer can not be further purified and characterized due to its poor solubility in common organic solvents.

P(BDT-TT-BT). **TTBT** monomer (124 mg, 0.15 mmol) and **ODBDT** monomer (166 mg, 0.15 mmol) were put into a 25 mL two-neck flask, then 6 mL of chlorobenzene was added. The mixture was stirred and purged with nitrogen for 10 min, and then $Pd_2(dba)_3$ (10 mg, 0.01 mmol), $(o\text{-tol})_3P$ (25 mg, 0.08 mmol) was added. After being purged for 15 min, the mixture was heated at 140 °C for 48 h. After cooled to room temperature, the reaction mixture was added dropwise to 200 mL of methanol. The black solid was filtered into a Soxhlet funnel and extracted by methanol, hexane, and chloroform successively. The polymer recovered from chloroform solution was purified by preparative gel permeation chromatography. Then, the product was dried under vacuum for 1 day to yield the titled polymer **P(BDT-TT-BT)** as a black solid (yield 68%, M_n= 32.8 kDa, M_w = 65.0 kDa, PDI = 2.0). ^{1}H NMR ($CDCl_3$, 600 MHz): δ (ppm) 8.45 (br,2H), 6.88 (br, 4H), 4.20 (br, 8H), 1.45−1.19 (br, 90H), 0.88 (br, 18H). Anal. Calcd for $(C_{84}H_{126}N_2O_4S_7)_n$: C, 69.40; H, 8.67; N, 1.93. Found: C, 69.40; H, 8.59; N, 1.96.

RESULTS AND DISCUSSION

Synthesis and Characterization. The synthesis routes of monomers and corresponding polymers are outlined in Schemes 1−4, respectively. Monomer **FBT**, **TBT**, **EHBDT,** and polymer **P(BDT-F-BT)** were synthesized according to our previously proposed procedure.[28a,34] Polymers **P(BDT-F-BT)**, **P(BDT-T-BT)**, **P(BDT-TT-BT)-EH** and **P(BDT-TT-BT)** were synthesized by palladium-catalyzed Stille-coupling[36] polymerization. It should be mentioned that in the polymerization for the synthesis of **P(BDT-TT-BT)**, the catalyst of $Pd_2(dba)_3/(o\text{-tol})_3P$ was used instead of $Pd(PPh_3)_4$ used in the synthesis of **P(BDT-F-BT)** and **P(BDT-T-BT)**. Higher yield of **P(BDT-TT-BT)** was achieved with the catalyst of $Pd_2(dba)_3$ $/(o\text{-tol})_3P$. All starting materials, reagents, and solvents were carefully purified, and all procedures were performed under an air-free environment. **P(BDT-TT-BT)-EH** was insoluble, and can not be further characterized. To resolve this problem, **P(BDT-TT-BT)** with longer branched 2-octyldodecyloxy groups on BDT segment was designed and synthesized. All the polymers except **P(BDT-TT-BT)-EH** can be readily dissolved in common solvents, such as chloroform, toluene, THF and chlorobenzene, and processed to form smooth and pinhole-free films upon spin-coating.

The structure of **P(BDT-F-BT)**, **P(BDT-T-BT)**, and **P(BDT-TT-BT)** were confirmed by ^{1}H NMR spectroscopy and elemental analysis. Thermal properties of the polymers were determined by thermogravimetric analysis (TGA) under nitrogen atmosphere at a heating rate of 10 °C/min. The three polymers have good thermal stability with onset decomposition temperatures corresponding to 5% weight loss at 332, 327, and 320 °C, respectively, as shown in Figure 2. Obviously, the

dx.doi.org/10.1021/ma202656b | Macromolecules 2012, 45, 1208−1216

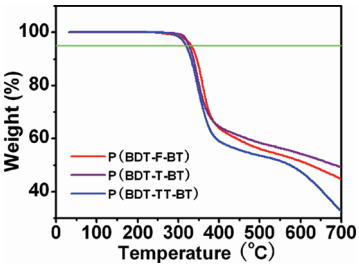


Figure 2. TGA plots of the polymers with a heating rate of 10 °C/min under an inert atmosphere.

thermal stability of these polymers is adequate for their applications in PSCs and other optoelectronic devices.

Optical Properties. Figure 3 shows absorption spectra of the polymers in chloroform solution (1 mg/100 mL) and as

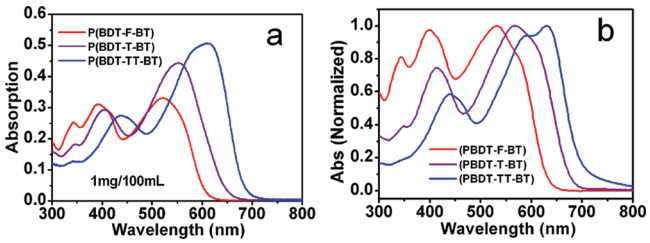


Figure 3. Absorption spectra of **P(BDT-F-BT)**, **P(BDT-T-BT)**, and **P(BDT-TT-BT)** in chloroform solution (a, concentration of 1 mg/100 mL) and solid film on a quartz plate (b).

spin-coated films on quartz substrates. Table 1 summarizes the optical data, including the absorption peak wavelengths (λ_{abs}), absorption edge wavelengths (λ_{onset}), and the optical band gap (E_g^{opt}). All of the absorption spectra recorded from dilute chloroform solutions feature three absorption bands: the first one around 345 nm, the second one at 360−480 nm, which can be assigned to localized $\pi-\pi^*$ transitions, and the third broader band from 480 to 700 nm in the long wavelength region, corresponding to intramolecular charge transfer (ICT) between donor and acceptor units. The difference in position and intensity of the absorptions are mainly duo to the different structures of the π-bridges in the polymers. The absorption spectra of the three polymers in the solid film were similar to their corresponding solution spectra, with obviously red-shifts (ca. 12−19 nm) of their absorption maxima, indicating intermolecular interactions existing in the solid state. In addition, these polymers all displayed a vibronic shoulders in films at 578, 616, and 631 nm, respectively, implying that strong $\pi-\pi$ stacking between the polymeric backbones have formed ordered arrangement in their solid films. The absorption edges for solid films of **P(BDT-F-BT)**, **P(BDT-T-BT)**, and **P(BDT-TT-BT)** increase from 632 to 680 nm and to 696 nm, corresponding to optical band gaps (E_g^{opt}) decreasing from 1.96 to1.82 to 1.78 eV, respectively, as shown in Table 1.

Electrochemical Properties. Cyclic voltammetry has been employed and considered as an effective tool in investigating electrochemical properties of conjugated oligomers and polymers.[37] From the onset oxidation and reduction potentials in the cyclic voltammogram, energy levels of the highest occupied molecular orbital (HOMO) and the lowest unoccupied molecular orbital (LUMO) energy levels can be readily estimated, which correspond to ionization potential (IP) and electron affinity (EA), respectively.[26,38]

Cyclic voltammograms of the polymer films are shown in Figure 4. The onset oxidation potential (E_{ox})/onset reduction

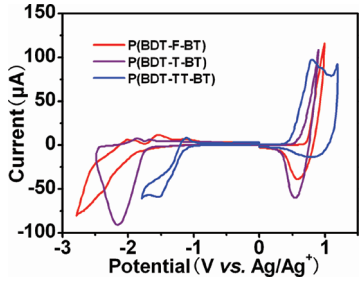


Figure 4. Cyclic voltammograms of the polymer films on Pt electrode in 0.1 mol/L Bu_4NPF_6, CH_3CN solution with a scan rate of 100 mV/s.

potential (E_{red}) of **P(BDT-F-BT)**, **P(BDT-T-BT)** and **P(BDT-TT-BT)** are 0.73/−1.33, 0.64/−1.27 and 0.50/−1.17 V vs. Ag/Ag^+ respectively. The HOMO and LUMO energy levels of the polymers were calculated from the onset oxidation potential and the onset reduction potential according to the equations:[39]

$$\text{HOMO} = -\text{IP} = -\text{e}(E_{ox} + 4.71)\ \text{(eV)} \quad (1)$$

$$\text{LUMO} = -\text{EA} = -\text{e}(E_{red} + 4.71)\ \text{(eV)} \quad (2)$$

From the value of E_{ox} and E_{red} of the polymers, the HOMO and the LUMO as well as the electrochemical bandgaps (E_g^{ec}) were calculated and also listed in Table 1. The LUMO energy levels of **P(BDT-F-BT)**, **P(BDT-T-BT)** and **P(BDT-TT-BT)** are very close. This phenomenon indicates that different π-bridges do not significantly affect the LUMO levels of the D-π-A polymers. The LUMO energy levels of the polymers are all located within a suitable range (from −3.44 to −3.54 eV, Table 1) and are significantly higher-lying than that of $PC_{71}BM$ (ca. −3.91 eV);[40] thus, efficient charge transfer (excitons dissociation) could be expected to occur in their corresponding devices.[1,2,5] From the comparison with **P(BDT-F-BT)**, it was noticed that the π-bridges of thiophene and thieno[3,2-*b*]thiophene lowered band gap of **P(BDT-T-BT)** and **P(BDT-TT-BT)** by increasing the HOMO energy level of the polymer from −5.44 eV (**P(BDT-F-BT)**) to −5.35 eV (**P(BDT-T-BT)**), and to −5.21 eV (**P(BDT-TT-BT)**). The electrochemical band gaps of the polymers are well matched with their optical band gaps within the experimental error.

Theoretical Calculations. To evaluate the impact of the different π-bridges on molecular architecture and consequently

Table 1. Optical and Electrochemical Properties of P(BDT-F-BT), P(BDT-T-BT), and P(BDT-TT-BT).

polymer	λ_{abs} in $CHCl_3$ (nm)	λ_{abs} in films (nm)	λ_{onset} in films (nm)	E_g^{opt} (eV)	HOMO (eV)	LUMO (eV)	E_g^{CV} (eV)
P(BDT-F-BT)	343, 391, 522	344, 398, 534	632	1.96	−5.44	−3.48	1.96
P(BDT-T-BT)	346, 405, 554	350, 415, 568	680	1.82	−5.35	−3.44	1.91
P(BDT-TT-BT)	343, 438, 612	346, 440, 631	696	1.78	−5.21	−3.54	1.66

dx.doi.org/10.1021/ma202656b | *Macromolecules* 2012, 45, 1208−1216

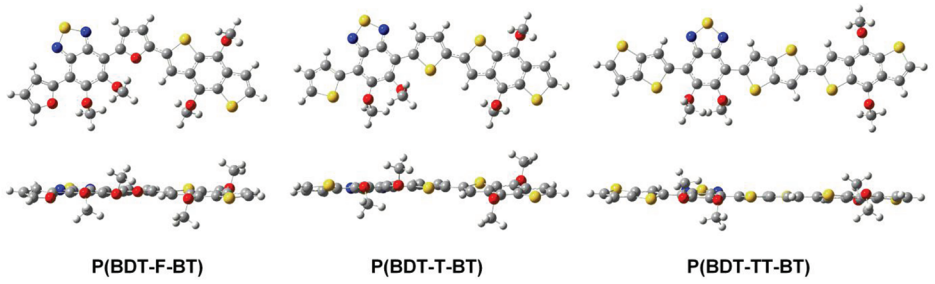


Figure 5. Top view (top) and side view (bottom) of optimized geometries of the three copolymers backbone units with a chain length n = 1. Color code: gray (C), white (H), red (O), blue (N), and yellow (S).

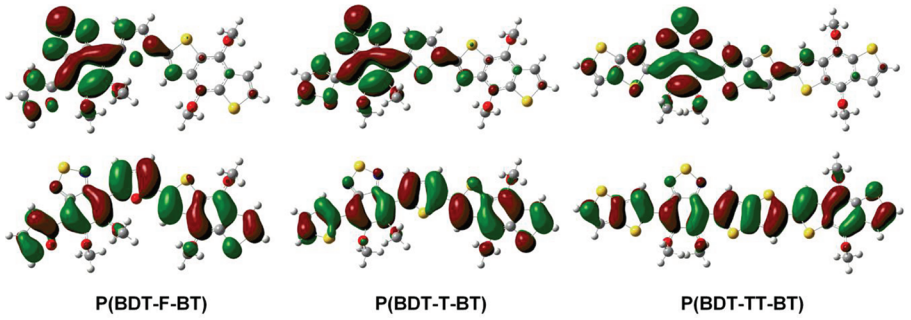


Figure 6. The frontier molecular orbital (LUMO, top; HOMO, bottom) obtained from DFT calculations on the polymers with a chain length n = 1. Color code: gray (C), white (H), red (O), blue (N), and yellow (S).

Table 2. Calculated Dihedral Angles, Bond Angle and Corresponding HOMO, LUMO Levels and Bandgaps (E_g^{cal}) of the Polymers

polymer	π-bridge	θ_1 (deg)	θ_2 (deg)	θ_3 (deg)	HOMO (eV)	LUMO (eV)	E_g^{cal} (eV)
P(BDT-F-BT)	furan	−1.02	4.88	127.50	−5.26	−2.78	2.48
P(BDT-T-BT)	thiophene	8.67	8.51	151.61	−5.21	−2.86	2.35
P(BDT-TT-BT)	thieno[3,2-*b*]thiophene	−6.16	−7.70	181.52	−5.20	−2.92	2.28

on the optoelectronic properties of the copolymers, density functional theory (DFT) calculations were performed to verify stationary points as stable states for the optimized conformations and single point energies, with a molecular main chain length n = 1, at B3LYP/6-311++G(3df, 3pd) level of theory in vacuum using the Gaussian 03 program package.[41] The final energies were calculated as the sum of single point and zero point energies. In particular, the HOMO and LUMO level positions and related electron distributions were calculated. Moreover, all the alkyl chains were replaced by methyl groups in the calculation to avoid excessive computation demand.

Optimized geometries of the three copolymers in ground state are shown in Figure 5. Calculated dihedral angles, bond angle and corresponding HOMO, LUMO levels and bandgaps (E_g^{cal}) are summarized in Table 2. The general molecules structure sketch used for the computational data is shown in Figure 7, where θ_1 is dihedral angle between **BT** unit and π-bridge, θ_2 is dihedral angles between π-bridge and **BDT** unit, θ_3 is the angle between the bonds across the π-bridge drawn in red.

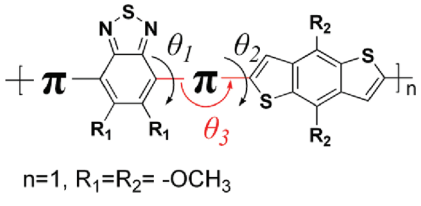


Figure 7. Molecular geometry sketch used for the computational data.

Different π-bridge units significantly affect the molecular architecture, as shown in Figure 5 and Table 2. The dihedral angles between the acceptor unit and π-bridge and between π-bridge and donor unit are all less than 10 ° in all the three polymers, indicating planar conformation of the copolymer chains. Interestingly, θ_1 and θ_2 is alternating negative and positive in furan bridged polymer, while always positive in thiophene bridged polymer and negative in thieno[3,2-*b*]thiophene bridged polymer. In other words, taking benzothiadiazole unit as reference plane, furan and BDT unit by turns deflected counterclockwise and clockwise in **P(BDT-F-BT)**; while thiophene and BDT unit deflected clockwise in turn in **PBTBDT** and thieno[3,2-*b*]thiophene and BDT unit deflected counterclockwise in turn in **P(BDT-TT-BT)**. With the π-bridge varied from furan to thiophene, then to thieno[3,2-*b*]thiophene, the shape of the molecular chains changed from *z*-shaped to almost straight line with increasing of θ_3 from 127.50° in **P(BDT-F-BT)** to 151.61 ° in **P(BDT-T-BT)**, then to 181.52 ° in **P(BDT-TT-BT)**. In this cases, the π-orbital overlap between neighboring aromatic units are increased, leading to changes in the frontier orbital energy levels and, more specifically, to decrease in band-gaps of thiophene and thieno[3,2-*b*]thiophene bridged polymers in turn. Note that due to the small number of aromatic cycles taken into account by the calculation, the absolute energy values are not reliable.

dx.doi.org/10.1021/ma202656b | *Macromolecules* 2012, 45, 1208–1216

Only relative changes of the HOMO and LUMO values with respect to the reference molecules are meaningful.

The wave functions of the frontier molecular orbital are depicted in Figure 6. As can be observed, the HOMO is delocalized along the whole π-conjugated backbone while the LUMO is mostly concentrated on the benzothiadiazole-based acceptor groups. These images provide further evidence of the formation of well-defined D-π-A structure and the intramolecular charge transfer behavior of the material (i.e., the HOMO to LUMO transition is a donor to acceptor intramolecular charge transfer).[42] The calculated HOMO and LUMO level positions and band gaps of the three polymers are listed in Table 2. As can be seen, although discrepancies exist between the calculation and experimental results, the trends of variation in the HOMO and energy gaps are similar. Compared with furan-bridged **P(BDT-F-BT)**, it was noticed that the π-bridge of thiophene and thieno[3,2-*b*]thiophene increased the HOMO energy level of the relative polymer **P(BDT-T-BT)** and **P(BDT-TT-BT)**, and as a result, lowered band gaps of the two polymers.

Photovoltaic Properties. To investigate the effects of π-conjugated bridges on the photovoltaic properties of the copolymers, bulk heterojunction PSC devices with a configuration of ITO/PEDOT:PSS/polymer:$PC_{71}BM$/Ca/Al were fabricated. Figure 8 shows the current density-potential

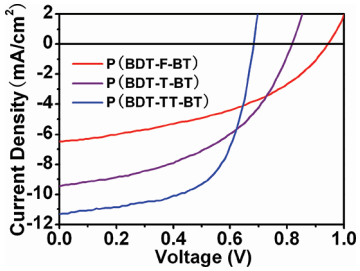


Figure 8. Current density−voltage characteristics of PSCs based on polymer:$PC_{71}BM$ blends under illumination of AM1.5G, 100 mW/cm^2.

characteristic of PSCs based on the blends of polymer:$PC_{71}BM$ under illumination of AM1.5G, 100 mW/cm^2. To further study the performance of the PSCs devices, the hole mobilities in the photosensitive layers were measured by the space charge limited current (SCLC) method using devices with structure of ITO/PEDOT:PSS/polymer:$PC_{71}BM$/Au. For unipolar transport in a trap-free semiconductor with an ohmic injecting contact, the SCLC can be approximated by the Mott-Gurney equation:[43]

$$J \cong \frac{9}{8}\varepsilon_r\varepsilon_0\mu_0 \exp\left(0.891\gamma\sqrt{\frac{V}{L}}\right)\frac{V^2}{L^3} \quad (3)$$

where J is the current density, ε_r is the dielectric constant of the polymer, ε_0 is the free-space permittivity (8.85×10^{-12} F/m), μ_0 is the charge mobility at zero field, γ is a constant, L is the thickness of the blended film layer, $V = V_{appl} - V_{bi}$, V_{appl} is the applied potential, and V_{bi} is the built-in potential which results from the difference in the work function of the anode and the cathode (in this device structure, V_{bi} = 0.2 V). Figure 9 displays $\ln(JL^3/V^2)$ versus $(V/L)^{0.5}$ curve for the measurement of the hole mobility of the copolymers by the SCLC method. As summarized in Table 3, the hole mobilities of the polymers

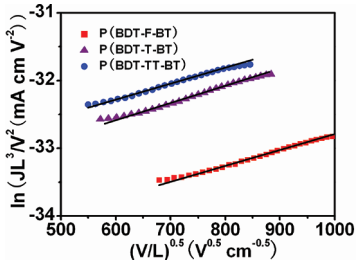


Figure 9. $\ln(JL^3/V^2)$ versus $(V/L)^{0.5}$ plots for the measurement of the hole mobility in polymer:$PC_{71}BM$ blends by the SCLC method.

Table 3. Photovoltaic Properties of the PSCs Based on P(BDT-F-BT), P(BDT-T-BT), and P(BDT-TT-BT) as Donor and $PC_{71}BM$ as Acceptor under the Illumination of AM1.5G, 100 mW/cm^2

polymer	polymer/$PC_{71}BM$ (w/w)	V_{oc} (V)	J_{sc} (mA cm^{-2})	FF	PCE (%)	mobility (cm^2 V^{-1} s^{-1})
P(BDT-F-BT)	1:2	0.94	6.50	0.46	2.81	2.1×10^{-3}
P(BDT-T-BT)	1:1.5	0.82	9.45	0.48	3.72	2.9×10^{-3}
P(BDT-TT-BT)	1:1.5	0.69	11.34	0.63	4.93	8.6×10^{-3}

calculated using eq 3 are 2.1×10^{-3} cm^2 V^{-1} s^{-1}, 2.9×10^{-3} cm^2 V^{-1} s^{-1} and 8.6×10^{-3} cm^2 V^{-1} s^{-1} for **P(BDT-F-BT)**, **P(BDT-T-BT)**, and **P(BDT-TT-BT)**, respectively. All the three polymers exhibited high hole mobilities in their respective devices (order of magnitude of 10^{-3} cm^2 V^{-1} s^{-1}).

The open-circuit voltage (V_{oc}), short-circuit current (J_{sc}), fill factor (FF), power conversion efficiency (PCE) and hole mobility of the PSCs are summarized in Table 3. The V_{oc} of PSCs based on **P(BDT-F-BT)**, **P(BDT-T-BT)**, and **P(BDT-TT-BT)** decreased from 0.94 to 0.82 to 0.69 V, which is the result of the increase of the HOMO level of the polymers. Compared to **P(BDT-F-BT)** and **P(BDT-T-BT)**, the thieno[3,2-*b*]thiophene bridged polymer showed dramatically high fill factor of 0.63, which is about one-third higher than furan and thiophene bridged polymers. The increased FF of **P(BDT-TT-BT)**-based PSCs could be ascribed to its higher hole mobility (8.6×10^{-3} cm^2 V^{-1} s^{-1}). The short-circuit currents of PSCs based on the polymers increased from 6.50 to 9.45 to 11.34 mA cm^{-2}, which is consistent with the lowered band gaps (from 1.96 to 1.82 to 1.78 eV) and enhanced extinction coefficients (from 31 to 44 to 51 cm^{-1}g^{-1} L). Although the relative low open-circuit voltage, **P(BDT-TT-BT)** exhibited the highest PCE of 4.93% in all the three aromatic rings bridged polymers. The high photovoltaic performance of thieno[3,2-*b*]thiophene bridged polymer should be benefited from its high hole mobility and broad absorption. We also checked the effect of the morphology of the active layers on the photovoltaic performance of the devices. Figure S1 in Supporting Information shows the AFM images of the active layer surfaces. The average surface roughness (R_a) of the AFM topographic images were 0.32 nm, 0.25 and 0.42 nm for the blends of **P(BDT-F-BT)**:$PC_{71}BM$, **P(BDT-T-BT)**:$PC_{71}BM$, and **P(BDT-TT-BT)**:$PC_{71}BM$, respectively, indicating smooth surface of the active layers. The uniformity of the phase image for the film of P(BDT-TT-BT):$PC_{71}BM$ is better than those of the P(BDT-F-BT):$PC_{71}BM$ and P(BDT-T-BT):$PC_{71}BM$ films. Probably, the uniform interpenetrating network in the

dx.doi.org/10.1021/ma202656b | *Macromolecules* 2012, 45, 1208−1216

P(BDT-TT-BT):$PC_{71}BM$ layer benefited the better photovoltaic performance of the corresponding PSCs.

Figure 10 shows the external quantum efficiency (EQE) curves of the PSCs based on the polymer:$PC_{71}BM$ blends.

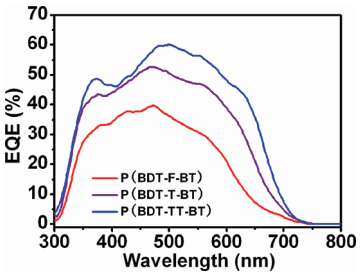


Figure 10. EQE spectra of the PSCs based on polymer:$PC_{71}BM$ blends.

These devices exhibited broad EQE responses with maximum EQE values of 40% at 472 nm, 52% at 465 nm, and 60% at 500 nm for the PSCs based on **P(BDT-F-BT)**, **P(BDT-T-BT)**, and **P(BDT-TT-BT)**, respectively. Compared to the absorption spectra of pristine polymers, the significantly broadened EQE responses in the visible region can be attributed to both the intrinsic absorptions of the polymers and the response of $PC_{71}BM$. Compared with that of **P(BDT-F-BT)**, **P(BDT-T-BT)**-based device demonstrated much higher EQE, especially in the range of 500−600 nm, and **P(BDT-TT-BT)**-based device showed the highest EQE value, especially from 500 to 700 nm. The EQE results are consistent with the J_{sc} values of the corresponding PSCs.

CONCLUSION

We designed and synthesized a series of D-π-A copolymers of BDT donor unit and BT acceptor unit with furan, thiophene and thianothiaphene π-bridges, **P(BDT-F-BT)**, **P(BDT-T-BT)**, and **P(BDT-TT-BT)**, by Pd-catalyzed Stille-coupling reaction. These polymers possess good solubility and thermal stability. The π-bridge units significantly influence the molecular architecture and consequently impact on the optoelectronic properties of the copolymers. The absorption peaks of the **P(BDT-F-BT)**, **P(BDT-T-BT)**, and **P(BDT-TT-BT)** films red-shifted from 534 to 568 to 631 nm, with the absorption edges of 632, 680, and 696 nm, respectively. The band gaps of the three polymers were tuned from 1.96 to 1.82 to 1.78 eV with the HOMO levels upshift from −5.44 to −5.35 to −5.21 eV. The PCE of the PSCs based on the polymers as donor and $PC_{71}BM$ as acceptor reached 2.81% for **P(BDT-F-BT)**, 3.72% for **P(BDT-T-BT)** and 4.93% for **P(BDT-TT-BT)**, respectively. Obviously, the PCE of the PSC based on the thieno[3,2-b]thiophene bridged polymer **P(BDT-TT-BT)** is much higher than that of the furan and thiophene-bridged polymers **P(BDT-F-BT)** and **P(BDT-T-BT)**. These results indicate that thieno[3,2-*b*]thiophene bridge is propitious to enhance the photovoltaic properties of D-π-A copolymers. Most importantly, these results provide new insights toward the design of high performance photovoltaic materials.

ASSOCIATED CONTENT

Supporting Information

AFM images of the active layers of solar cells. This material is available free of charge via the Internet at http://pubs.acs.org.

AUTHOR INFORMATION

Corresponding Author

*E-mail: wanghaiqiao@mail.buct.edu.cn (H.W.); liyf@iccas.ac.cn (Y.L.); lixy@mail.buct.edu.cn (X.L.).

Notes

The authors declare no competing financial interest.

ACKNOWLEDGMENTS

This work was supported by NSFC (Nos. 20874106, 20821120293 and 21021091), The Ministry of Science and Technology of China and Chinese Academy of Sciences.

REFERENCES

(1) Günes, S.; Neugebauer, H.; Sariciftci, N. S. *Chem. Rev.* **2007**, *107*, 1324−1338.
(2) Thompson, B. C.; Fréchet, J. M. J. *Angew. Chem., Int. Ed.* **2008**, *47*, 58−77.
(3) Peet, J.; Kim, J. Y.; Coates, N. E.; Ma, W. L.; Moses, D.; Heeger, A. J.; Bazan, G. C. *Nat. Mater.* **2007**, *6*, 497−500.
(4) Facchetti, A. *Chem. Mater.* **2011**, *23*, 733−758.
(5) Scharber, M. C.; Mühlbacher, D.; Koppe, M.; Denk, P.; Waldauf, C.; Heeger, A. J.; Brabec, C. J. *Adv. Mater.* **2006**, *18*, 789−794.
(6) Brabec, C. J.; Heeney, M.; McCulloch, I.; Nelson, J. *Chem. Soc. Rev.* **2011**, *40*, 1185−1199.
(7) Dennler, G.; Scharber, M. C.; Brabec, C. J. *Adv. Mater.* **2009**, *21*, 1−16.
(8) Boudreault, P.-L. T.; Najari, A.; Leclerc, M. *Chem. Mater.* **2011**, *23*, 456−469.
(9) Hoppe, H.; Sariciftci, N. S. *Adv. Polym. Sci.* **2008**, *214*, 1−86.
(10) Li, Y. F.; Zou, Y. P. *Adv. Mater.* **2008**, *20*, 2952−2958.
(11) Chen, J. W.; Cao, Y. *Acc. Chem. Res.* **2009**, *42*, 1709−1718.
(12) Po, R.; Maggini, M.; Camaioni, N. *J. Phys. Chem. C* **2010**, *114*, 695−706.
(13) Chochos, C. L.; Choulis, S. A. *Prog. Polym. Sci.* **2011**, *36*, 1326−1414.
(14) (a) Chen, H. Y.; Hou, J. H.; Zhang, S. Q.; Liang, Y. Y.; Yang, G. W.; Yang, Y.; Yu, L. P.; Wu, Y.; Li, G. *Nat. Photonics* **2009**, *3*, 649−653. (b) Wang, M.; Hu, X. W.; Liu, P.; Li, W.; Gong, X.; Huang, F.; Cao, Y. *J. Am. Chem. Soc.* **2011**, *13*, 9638−9641.
(15) (a) Zhou, E. J.; Nakamura, M.; Nishizawa, T.; Zhang, Y.; Wei, Q. S.; Tajima, K.; Yang, C. H.; Hashimoto, K. *Macromolecules* **2008**, *41*, 8302−8305. (b) Zhou, E. J.; Yamakawa, S.; Tajima, K.; Yang, C. H.; Hashimoto, K. *Chem. Mater.* **2009**, *21*, 4055−4061. (c) Zhou, E. J.; Cong, J. Z.; Tajima, K.; Hashimoto, K. *Chem. Mater.* **2010**, *22*, 4890−4895.
(16) (a) Huo, L. J.; Guo, X.; Zhang, S. Q.; Li, Y. F.; Hou, J. H. *Macromolecules* **2011**, *44*, 4035−4037. (b) Zhang, M. J.; Sun, Y. P.; Guo, X.; Cui, C. H.; He, Y. J.; Li, Y. F. *Macromolecules* **2011**, *44*, 7625−7631.
(17) (a) Liang, Y. Y.; Feng, D. Q.; Wu, Y.; Tsai, S. T.; Li, G.; Ray, C.; Yu, L. P. *J. Am. Chem. Soc.* **2009**, *131*, 7792−7799. (b) Zhang, M. J.; Fan, H. J.; Guo, X.; He, Y. J.; Zhang, Z. G.; Min, J.; Zhang, J.; Zhan, X. W.; Li, Y. F. *Macromolecules* **2010**, *43*, 5706−5712.
(18) Cui, C. H.; Fan, X.; Zhang, M. J.; Zhang, J.; Min, J.; Li, Y. F. *Chem. Commun.* **2011**, *47*, 11345−11347.
(19) Huo, L. J.; Hou, J. H.; Zhang, S. Q.; Chen, H. Y.; Yang, Y. *Angew. Chem., Int. Ed.* **2010**, *122*, 1542−1545.
(20) Wang, C. L.; Zhang, W. B.; Van Horn, R. M.; Tu, Y. F.; Gong, X.; Cheng, S. Z. D.; Sun, Y. M.; Tong, M. H.; Seo, J.; Hsu, B. B. Y.; Heeger, A. J. *Adv. Mater.* **2011**, *23*, 2951−2956.
(21) Zhou, H. X.; Yang, L. Q.; Stuart, A. C.; Price, S. C.; Liu, S. B.; You, W. *Angew. Chem., Int. Ed.* **2011**, *50*, 2995−2998.
(22) Qin, R. P.; Li, W. W.; Li, C. H.; Du, C.; Veit, C.; Schleiermacher, H.−F.; Andersson, M.; Bo, Z. S.; Liu, Z. P.; Inganäs, O.; Wuerfel, U.; Zhang, F. L. *J. Am. Chem. Soc.* **2009**, *131*, 14612−14613.
(23) Bronstein, H.; Chen, Z. Y.; Ashraf, R. S.; Zhang, W. M.; Du, J. P.; Durrant, J. R.; Tuladhar, P. S.; Song, K.; Watkins, S. E.; Geerts, Y.;

Wienk, M. M.; Janssen, R. A. J.; Anthopoulos, T.; Sirringhaus, H.; Heeney, M.; McCulloch, I. *J. Am. Chem. Soc.* **2011**, *133*, 3272−3275.
(24) Zou, Y. P.; Najari, A.; Berrouard, P.; Beaupré, S.; Aïch, B. R.; Tao, Y.; Leclerc, M. *J. Am. Chem. Soc.* **2010**, *132*, 5330−5331.
(25) Price, S. C.; Stuart, A. C.; Yang, L. Q.; Zhou, H. X.; You, W. *J. Am. Chem. Soc.* **2011**, *133*, 4625−4631.
(26) Wang, X. C.; Luo, H.; Sun, Y. P.; Zhang, M. J.; Li, X. Y.; Yu, G.; Liu, Y. Q.; Li, Y. F.; Wang, H. Q. *J. Polym. Sci., Part A: Polym Chem.* **2012**, *50*, 371−377.
(27) Zhang, M. J.; Guo, X.; Wang, X. C.; Wang, H. Q.; Li, Y. F. *Chem. Mater.* **2011**, *23*, 4264−4270.
(28) (a) Wang, X. C.; Chen, S.; Sun, Y. P.; Zhang, M. J.; Li, Y. F.; Li, X. Y.; Wang, H. Q. *Polym. Chem.* **2011**, *2*, 2872−2877. (b) Zhang, M. J.; Guo, X.; Li, Y. F. *Macromolecules* **2011**, *44*, 8798−8804.
(29) Baek, N. S.; Hau, S. K.; Yip, H.-L.; Acton, O.; Chen, K.-S.; Jen, A. K.-Y. *Chem. Mater.* **2008**, *20*, 5734−5736.
(30) Woo, C. H.; Beaujuge, P. M.; Holcombe, T. W.; Lee, O. P.; Fréchet, J. M. J. *J. Am. Chem. Soc.* **2010**, *132*, 15547−15549.
(31) Hou, J. H.; Park, M.-H.; Zhang, S. Q.; Yao, Y.; Chen, L. M.; Li, J. H.; Yang, Y. *Macromolecules* **2008**, *41*, 6012−6018.
(32) Helgesen, M.; Gevorgyan, S. A.; Krebs, F. C.; Janssen, R. A. J. *Chem. Mater.* **2009**, *21*, 4669−4675.
(33) Ding, P.; Chu, C. C.; Liu, B.; Peng, B.; Zou, Y. P.; He, Y. H.; Zhou, K. C.; Hsu, C. S. *Macromol. Chem. Phys.* **2010**, *211*, 2555−2561.
(34) Qing, F. Y.; Sun, Y. P.; Wang, X. C.; Li, N.; Li, Y. F.; Li, X. Y.; Wang, H. Q. *Polym. Chem.* **2011**, *2*, 2102−2106.
(35) Guo, X. G.; Watson, M. D. *Org. Lett.* **2008**, *10*, 5333−5336.
(36) Bao, Z. N.; Chan, W. K.; Yu., L. P. *J. Am. Chem. Soc.* **1995**, *117*, 12426−12435.
(37) Li, Y. F.; Cao, Y.; Gao, J.; Wang, D. L.; Yu, G.; Heeger, A. J. *Synth. Met.* **1999**, *99*, 243−248.
(38) Wang, X. C.; Wang, H. Q.; Yang, Y.; He, Y. J.; Zhang, L.; Li, Y. F.; Li, X. Y. *Macromolecules* **2010**, *43*, 709−715.
(39) (a) Sun, Q. J.; Wang, H. Q.; Yang, C. H.; Li, Y. F. *J. Mater. Chem.* **2003**, *13*, 800−806. (b) Hou, J. H.; Tan, Z. A.; Yan, Y.; He, Y. J.; Yang, C. H.; Li, Y. F. *J. Am. Chem. Soc.* **2006**, *128*, 4911−4916.
(40) (a) He, Y. J.; Li, Y. F. *Phys. Chem. Chem. Phys.* **2011**, *13*, 1970−1983. (b) He, Y. J.; Zhao, G. J.; Peng, B.; Li, Y. F. *Adv. Funct. Mater.* **2010**, *20*, 3383−3389.
(41) Frisch, M. J.; Trucks, G. W.; Schlegel, H. B.; Scuseria, G. E.; Robb, M. A.; Cheeseman, J. R.; Montgomery, J. A., Jr.; Vreven, T.; Kudin, K. N.; Burant, J. C.; Millam, J. M.; Iyengar, S. S.; Tomasi, J.; Barone, V.; Mennucci, B.; Cossi, M.; Scalmani, G.; Rega, N.; Petersson, G. A.; Nakatsuji, H.; Hada, M.; Ehara, M.; Toyota, K.; Fukuda, R.; Hasegawa, J.; Ishida, M.; Nakajima, T.; Honda, Y.; Kitao, O.; Nakai, H.; Klene, M.; Li, X.; Knox, J. E.; Hratchian, H. P.; Cross, J. B.; Adamo, C.; Jaramillo, J.; Gomperts, R.;Stratmann, R. E.; Yazyev, O.; Austin, A. J.; Cammi, R.; Pomelli, C.; Ochterski, J. W.; Ayala, P. Y.; Morokuma, K.; Voth, G. A.; Salvador, P.; Dannenberg, J. J.; Zakrzewski, V. G.; Dapprich, S.; Daniels, A. D.; Strain, M. C.; Farkas, O.; Malick, D. K.; Rabuck,A. D.; Raghavachari, K.; Foresman, J. B.; Ortiz, J. V.; Cui, Q.; Baboul, A. G.; Clifford, S.; Cioslowski, J.; Stefanov, B. B.; Liu, G.; Liashenko, A.; Piskorz, P.; Komaromi, I.; Martin, R. L.; Fox, D. J.; Keith, T.; Al-Laham, M. A.; Peng, C. Y.; Nanayakkara, A.; Challacombe, M.; Gill, P. M. W.; Johnson, B.; Chen, W.; Wong, M. W.; Gonzalez, C.; Pople, J. A. *Gaussian 03; revision C.02*; Gaussian, Inc.: Wallingford, CT, 2004.
(42) Pappenfus, T. M.; Schneiderman, D. K.; Casado, J.; López Navarrete, J. T.; Ruiz Delgado, M. C.; Zotti, G.; Vercelli, B.; Lovander, M. D.; Hinkle, L. M.; Bohnsack, J. N.; Mann, K. R. *Chem. Mater.* **2011**, *23*, 823−831.
(43) Kippelen, B., Yoo, S., Haddock, J. A., Domercq, B., Barlow, S., Minch, B., Xia, W., Marder, S. R., Armstrong, N. R. In *Organic photovoltaics: mechanism, materials, and devices*; Sun, S.-S., Sariciftci, N. S., Eds.; Taylor Francis Inc: Boca Raton, FL, 2005; Vol. *11*.

Macromolecules

Article

pubs.acs.org/Macromolecules

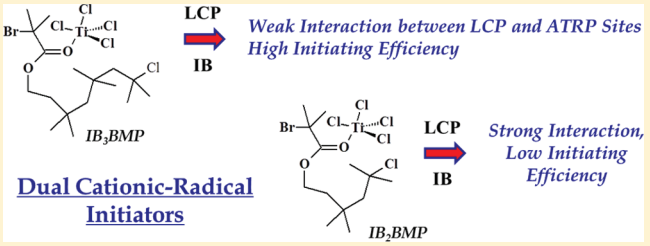
Effect of Structure on Cationic Initiation Efficiency of a Carbocatonic/ATRP Dual Initiator

Yaling Zhu and Robson F. Storey*

School of Polymers and High Performance Materials, The University of Southern Mississippi, 118 College Drive #5050, Hattiesburg, Mississippi 39406, United States

Supporting Information

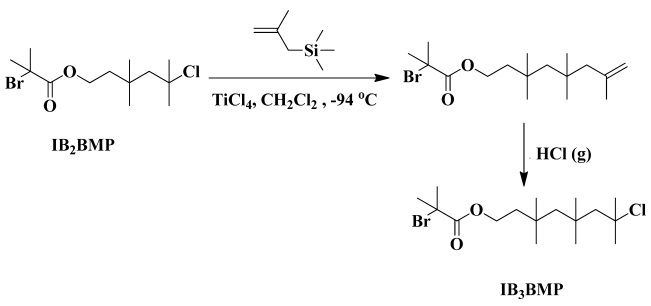
ABSTRACT: The dual initiator, 3,3,5,5,7-pentamethyl-7-chlorooctyl 2-bromo-2-methylpropionate (IB_3BMP), possessing initiating sites for both living carbocationic polymerization (LCP) and atom transfer radical polymerization (ATRP), was synthesized to overcome the low initiation efficiency of previously reported dual initiators such as 3,3,5-trimethyl-5-chlorohexyl 2-bromo-2-methylpropionate (IB_2BMP). Low initiation efficiency of the latter and similar initiators has been attributed to complexation between the Lewis acid polymerization catalyst and the ester carbonyl group of the initiator. IB_3BMP was synthesized by reacting IB_2BMP with 2-methallyltrimethylsilane at low temperature, followed by hydrochlorination. IB_3BMP, which differs from IB_2BMP by the inclusion of one additional isobutylene (IB) repeating unit, showed quantitative initiation efficiency ($I_{eff} \sim 1$) in $TiCl_4$-*co*-initiated LCP of IB under various reaction conditions, including low temperature (−70 °C) and low monomer/initiator ratios (48−164). I_{eff} and polydispersity index of the resulting polyisobutylenes were identical to those obtained with the commonly used, monofunctional cationic initiators 2-chloro-2,4,4-trimethylpentane (TMPCl) and 2-chloro-2,4,4,6,6-pentamethylheptane (PMHCl). The superiority of IB_3BMP compared to IB_2BMP in carbocationic initiation was attributed to increased separation between the *tert*-chloride initiating site and the $TiCl_4$:carbonyl complex at the ATRP initiating site. A PIB macroinitiator prepared from IB_3BMP was used to initiate ATRP of methyl acrylate. Efficiency of radical initiation was quantitative, the targeted poly(methyl acrylate) block length was obtained, and the resulting block copolymer possessed narrow polydispersity.



INTRODUCTION

In a previous publication,[1] we reported the dual initiator, 3,3,5-trimethyl-5-chlorohexyl 2-bromo-2-methylpropionate (IB_2BMP) (Scheme 1) that possesses initiating sites for both living carbocationic polymerization (LCP) and atom transfer radical polymerization (ATRP). We demonstrated that IB_2BMP is able to initiate LCP of isobutylene (IB), and that the α-bromoester headgroup is unaffected by the cationic polymerization and remains intact for subsequent ATRP initiation of, for example, an acrylate monomer. However, at low temperature (−70 °C) and relatively low monomer/initiator ratio (48−82), this initiator displayed low cationic initiation efficiencies, in the range 0.50−0.80 depending on polymerization time, catalyst concentration, and solvent polarity. Higher cationic initiation efficiencies ($0.80 < I_{eff} < 0.90$) were observed when temperature was increased to −50 °C and/or the monomer/initiator ratio was increased.

Scheme 1. Previously Reported Dual Initiator 3,3,5-Trimethyl-5-chlorohexyl 2-Bromo-2-methylpropionate (IB_2BMP) and Synthesis of 3,3,5,5,7-Pentamethyl-7-chlorooctyl 2-bromo-2-methylpropionate (IB_3BMP) Therefrom



Low I_{eff} of IB_2BMP and similar initiators such as 3,3,5-trimethyl-5-chlorohexyl acetate (TMCHA) has been attributed to complexation between the Lewis acid catalyst, $TiCl_4$, and the carbonyl oxygen of the ester group.[1−3] Complexation between Lewis acids and carbonyl groups is well-known[4−6] and nearly always characterized by a 1:1 stoichiometry.[5] In the IB_2BMP and TMCHA systems, complexation is revealed by a lower polymerization rate caused by a lower effective concentration of $TiCl_4$, $[TiCl_4]_{eff}$.[3] The effect on rate can be offset by compensating the amount of $TiCl_4$. However, we have observed that I_{eff} of IB_2BMP is unaffected by changes in $TiCl_4$ concentration.[1]

Received: December 11, 2011
Revised: January 21, 2012
Published: February 1, 2012

 © 2012 American Chemical Society dx.doi.org/10.1021/ma202682w | *Macromolecules* 2012, 45, 1217−1221

By studying the structure of IB_2BMP, we now hypothesize that low I_{eff} is not caused by complexation or the presence of the ester carbonyl within the molecule, *per se*, but rather proximity of the $TiCl_4$:carbonyl complex to the initiating center (*tert*-chloride group). In IB_2BMP, the $TiCl_4$:carbonyl complex and the *tert*-chloride group interact readily via an entropically favored cycle conformer. This interaction may substantially diminish the rate of ionization of the *tert*-chloride group, thereby reducing I_{eff}.

To test this hypothesis, in this paper we report the synthesis of 3,3,5,5,7-pentamethyl-7-chlorooctyl 2-bromo-2-methylpropionate (IB_3BMP) (Scheme 1), which preserves the same α-bromoester and *tert*-chloride functional groups as in IB_2BMP, but separates them by one additional IB repeating unit. With this structure, cyclic conformers that bring the $TiCl_4$:carbonyl complex and *tert*-chloride group into proximity are not likely and interactions between them should be disrupted. Therefore, if the hypothesis is correct, IB_3BMP should exhibit excellent initiation efficiency.

EXPERIMENTAL SECTION

Materials. 2-Methallyltrimethylsilane (MATMS) (>95%) was used as received from Gelest Inc. Ammonium hydroxide (NH_4OH) (28.0–30.0%) was used as received from Fisher Scientific. 2,4,4,6,6-Pentamethyl-1-heptene (PM1H) was generously provided by Chevron Oronite Company, LLC, and was vacuum distilled prior to use. The sources and purity of all other reagents were the same as previously reported.[1]

Instrumentation. Absolute molecular weights and polydispersity index of polyisobutylene (PIB) and poly(isobutylene-*b*-methyl acrylate) copolymer (PIB-*b*-PMA) were determined using size exclusion chromatography (SEC) (35 °C, THF) with interferometric refractometer and multiangle laser light scattering (MALLS) detectors. The dn/dc value used for PIB homopolymer was calculated from the following equation:[7] $dn/dc = 0.116(1 - 108/\bar{M}_n)$ ($\bar{M}_n$ = number-average molecular weight); the dn/dc value for PIB-*b*-PMA was calculated from the interferometric refractometer detector response and assuming 100% mass recovery from the columns. Solution ^1H and ^{13}C nuclear magnetic resonance (NMR) spectra were obtained at 22 °C using $CDCl_3$ as the solvent and tetramethylsilane as internal reference. Progress of IB polymerizations was monitored using real-time, remote-probe (light conduit type) attenuated total reflectance Fourier Transform infrared spectroscopy (FTIR) (ReactIR 4000). Detailed descriptions of the SEC, NMR, and FTIR instrumentation and corresponding procedures have been previously published.[1]

3,3,5-Trimethyl-5-chlorohexyl 2-Bromo-2-methylpropionate (IB_2BMP). IB_2BMP was prepared as previously described.[1]

3,3,5,5,7-Pentamethyl-7-chlorooctyl 2-Bromo-2-methylpropionate (IB_3BMP). As illustrated in Scheme 1, IB_3BMP was synthesized from IB_2BMP by reaction with 2-methallyltrimethylsilane (MATMS) at −94 °C with $TiCl_4$ as the catalyst, followed by hydrochlorination with anhydrous HCl (g). The procedure was analogous to that of Mayr et al.[8]

In a 250 mL round-bottom flask, MATMS (4.12 g, 3.21×10^{-2} mol) in 180 mL CH_2Cl_2 was cooled to about −94 °C using an external acetone/liquid N_2 bath. $TiCl_4$ (1.60 mL, 1.46×10^{-2} mol) was slowly added, and the color of the reaction mixture turned to dark red. Next, a solution of IB_2BMP (2.63 g, 8.03×10^{-3} mol) and MATMS (2.36 g, 1.84×10^{-2} mol) in about 10 mL of CH_2Cl_2 was dropped into the mixture during 30 min. The solution was stirred for 2 h at low temperature, and then the reaction was terminated by addition of 20 mL of NH_4OH aqueous solution. A fine, solid precipitate appeared, and the solution turned from dark orange to white. The reaction mixture was filtered, and the organic and aqueous layers were separated. The aqueous layer was extracted with CH_2Cl_2, and the combined organic fractions were dried with $MgSO_4$. The solution was filtered and vacuum stripped to yield 2.54 g (91.1%) of the crude olefin, 3,3,5,5,7-pentamethyl-7-octenyl 2-bromo-2-methylpropionate. After vacuum distillation, the pure olefin was isolated as a colorless oil in 45.3% yield (1.26 g). ^1H NMR ($CDCl_3$): δ = 1.03 (s, 6H, 5-Me), 1.05 (s, 6H, 3-Me), 1.34 (s, 2H, 3-H), 1.69 (t, 2H, 2-H), 1.78 (s, 3H, 7-Me), 1.93 (s, 6H, CH_3CBr), 2.00 (s, 2H, 6-H), 4.24 (t, 2H, 1-H), 4.64 (m, 1H, olefin), 4.86 (m, 1H, olefin) ppm. ^{13}C NMR: δ = 25.70 (7-Me), 28.97 (5-Me), 29.28 (3-Me), 30.73 (CH_3CBr), 34.26 (C3), 35.82 (C5), 42.41 (C2), 53.12 (C6), 53.59 (C4), 55.85 (CBr), 63.61 (C1), 114.53 (C8), 143.45 (C7), 171.61 (CO) ppm.

The olefin was hydrochlorinated with dry, gaseous HCl using a procedure analogous to that used for IB_2BMP,[1] and the final product, 3,3,5,5,7-pentamethyl-7-chlorooctyl 2-bromo-2-methylpropionate (IB_3BMP) was obtained in 93.5% yield (1.38 g). ^1H NMR ($CDCl_3$): δ = 1.07 (s, 6H, 3-Me), 1.18 (s, 6H, 5-Me), 1.45 (s, 2H, 4-H), 1.68 (s, 6H, CH_3CCl), 1.70 (t, 2H, 2-H), 1.93 (s, 6H, CH_3CBr), 1.95 (s, 2H, 6-H), 4.25 (t, 2H, 1-H) ppm. ^{13}C NMR: δ = 29.32 (3-Me), 29.96 (5-Me), 30.73 (CH_3CBr), 34.41 (C3), 35.18 (C8), 37.28 (C5), 42.68 (C2), 54.91 (C4), 55.85 (CBr), 58.44 (C6), 71.51 (C7), 171.61 (CO) ppm.

2-Chloro-2,4,4,6,6-pentamethylheptane (PMHCl). PMHCl was synthesized from 2,4,4,6,6-pentamethyl-1-heptene (PM1H) by hydrochlorination with dry, gaseous HCl using a procedure analogous to that used for IB_2BMP.[1] ^1H NMR ($CDCl_3$): δ = 1.00 (s, 9H, *t*-Bu), 1.15 (s, 6H, 4-Me), 1.39 (s, 2H, 5-H), 1.68 (s, 6H, CH_3CCl), 1.96 (s, 2H, 3-Me) ppm. ^{13}C NMR: δ = 29.90 (4-Me), 32.29 (6-Me), 32.48 (C6), 35.17 (CH_3CCl), 37.28 (C4), 57.07 (C5), 58.31 (C3), 71.82 (C2) ppm.

Figures A and B, Supporting Information, show ^1H and ^{13}C NMR spectra, respectively, of PM1H and PMHCl.

Polymerizations. LCPs of IB were carried out using either IB_2BMP, IB_3BMP, TMPCl, or PMHCl as initiator, $TiCl_4$ as catalyst, and 2,6-lutidine as proton trap/common ion salt precursor, in 60/40 (v/v) hexane/MeCl cosolvents at −70 °C as previously described.[1] All polymerizations were conducted within an inert atmosphere drybox equipped with a hexane/heptane cold bath using FTIR (ReactIR 4000) to monitor isobutylene conversion by observing the olefinic $=CH_2$ wag (887 cm^{-1}) of IB.

ATRP of methyl acrylate (MA) was carried out in toluene at 70 °C using IB_3BMP-initiated PIB (BMP-PIB) as macroinitiator, Cu(I)Br as catalyst, and *N,N,N′,N″,N″*-pentamethyldiethylenetriamine (PMDETA) as solvating ligand for Cu(I), in a molar ratio of 1:1:1, as previously described.[1] The concentration of BMP-PIB was 0.05 M. $\bar{M}_n$ of BMP-PIB by SEC was 4650 g/mol; the PDI was 1.02, and $\bar{X}_n$ = 77 by NMR.

RESULTS AND DISCUSSION

Synthesis of IB_3BMP. IB_3BMP cannot be prepared by reacting IB_2BMP with IB, since the desired 1:1 addition product reacts rapidly with additional IB to form polymer.[9] Instead, IB_2BMP was first reacted with MATMS in the presence of $TiCl_4$ at low temperature to yield the intermediate olefin, 3,3,5,5,7-pentamethyl-7-octenyl 2-bromo-2-methylpropionate. Then, after vacuum distillation, the olefin was hydrochlorinated to produce the final product.

Figures 1 and 2 show ^1H and ^{13}C NMR spectra, respectively, of the intermediate olefin (upper) and IB_3BMP (lower). The olefinic protons of the intermediate appear at 4.6 (peak m) and 4.9 ppm (peak n), and the methyl and methylene protons adjacent to the double bond are observed at 1.7 (peak a) and 2.0 ppm (peak b), respectively (Figure 1, upper). Upon hydrochlorination of the intermediate, the olefinic protons (peaks m and n) disappear. Peaks k, e, and l shift downfield; while peaks a and b shift slightly upfield. Integrated peak areas are consistent with the targeted structures. Likewise, in the carbon spectra (Figure 2) the olefinic carbons of the intermediate (peaks l and m) disappear upon hydrochlorination, and the new quaternary carbon bonded to chlorine appears at 72 ppm (peak m). Moreover, peaks h, i, and a move downfield after hydrochlorination.

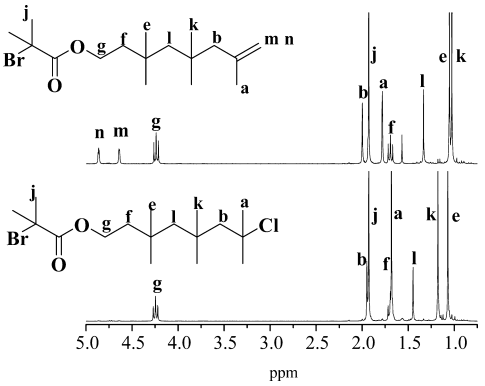


Figure 1. ^{1}H NMR spectra of 3,3,5,5,7-pentamethyl-7-octenyl 2-bromo-2-methylpropionate (upper) and IB_3BMP (lower).

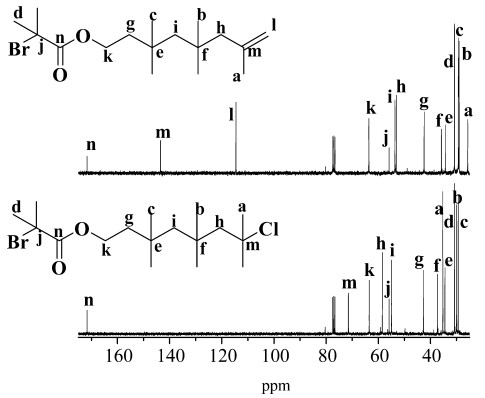


Figure 2. ^{13}C NMR spectra of 3,3,5,5,7-pentamethyl-7-octenyl 2-bromo-2-methylpropionate (upper) and IB_3BMP (lower).

IB Polymerizations. The performance of IB_3BMP as a cationic polymerization initiator was evaluated by conducting $TiCl_4$-*co*-initiated IB polymerizations at −70 °C, targeting molecular weights of 3000 (3k), 5000 (5k), and 10000 (10k) g/mol. Low target molecular weights were chosen to better judge the performance of the initiators. If IB_3BMP displays good initiation efficiency for the preparation of low molecular weight PIBs, its efficiency will be the same or higher for higher monomer/initiator ratios. IB_3BMP was directly compared to three control initiators, IB_2BMP and the two monofunctional initiators TMPCl and PMHCl (hydrochlorinated IB dimer and trimer, respectively). Faust and Mayr et al.[10] reported that, compared to the PIB *tert*-chloride chain end, TMPCl is approximately 2.5 times more slowly ionizing and PMHCl is approximately 1.4 times more slowly ionizing due to lower degrees of back strain.

Table 1 lists characterization results of PIB polymers produced from the four initiators. All results were the average of 2−5 repeated experiments. I_{eff} was calculated as $\bar{X}_{n,theo}/\bar{X}_{n,PIB}$ and $\bar{M}_{n,theo}/\bar{M}_{n,PIB}$ from NMR and SEC/MALLS data, respectively. $\bar{X}_{n,theo}$ was calculated as the molar ratio of monomer to initiator charged to the reactor; $\bar{M}_{n,theo} = (\bar{X}_{n,theo} \times M_{IB}) + M_I$, where M_{IB} and M_I are the molecular weights of isobutylene and the initiator, respectively. $\bar{X}_{n,PIB}$ was calculated from ^{1}H NMR data using eq 1

$$\bar{X}_{n,PIB} = \frac{A_{Me}/6}{A_{CE}} - i \qquad (1)$$

where, A_{Me} is the integrated peak area of the methyl protons in the PIB repeat unit, A_{CE} is defined by eq 2, and i assumes a value of 1 for IB_2BMP and TMPCl and a value of 2 for IB_3BMP and PMHCl.

Table 1. Characterization Results for PIBs Prepared from Different Initiators[a]

	NMR			SEC			
	$X_{n,PIB}$	$X_{n,theo}$	I_{eff}	$M_{n,PIB}$ (g/mol)	$M_{n,theo}$ (g/mol)	I_{eff}	PDI
TMPCl-3k	52	48	0.92	3090	2840	0.92	1.02
IB_2BMP-3k	94	48	0.51	5630	3020	0.53	1.10
IB_3BMP-3k	49	48	0.98	2880	3080	0.97	1.07
PMHCl-3k	49	48	0.98	2900	2900	1.00	1.01
TMPCl-5k	87	82	0.94	4920	4750	0.96	1.01
IB_2BMP-5k	120	82	0.64	8410	4930	0.59	1.05
IB_3BMP-5k	86	82	0.95	5070	4990	0.98	1.03
PMHCl-5k	85	82	0.97	4800	4810	1.00	1.01
TMPCl-10k	161	164	1.02	9050	9350	1.03	1.05
IB_2BMP-10k	201	164	0.82	11370	9530	0.84	1.06
IB_3BMP-10k	170	164	0.96	9580	9590	1.00	1.06
PMHCl-10k	165	164	0.99	9340	9410	1.01	1.06

[a] 60/40 Hex/MeCl cosolvents (v/v); −70 °C; $[IB]_0$ = 1.00 M; $[2,6\text{-lutidine}]_0$ = 4.00 mM. $[I]_0$ = 20.8 mM; $[TiCl_4]_0$ = 62.5 mM for 3k samples. $[I]_0$ = 12.2 mM; $[TiCl_4]_0$ = 48.8 mM for 5k samples. $[I]_0$ = 6.1 mM; $[TiCl_4]_0$ = 48.8 mM for 10k samples.

$$A_{CE} = A_{exo} + A_{endo} + A_{tert\text{-}Cl}/2 + 2A_{coupled} \qquad (2)$$

In eq 2, A_{exo} is the area of the upfield *exo*-olefinic resonance at 4.64 ppm, A_{endo} is the area of the single *endo*-olefinic resonance at 5.15 ppm, and $A_{tert\text{-}Cl}$ is the area of the resonance at 1.96 ppm due to the methylene protons of the *tert*-chloride end group. $A_{coupled}$ was calculated as follows:

$$A_{coupled} = (A_{4.75\text{-}5.0} - A_{exo}) \qquad (3)$$

Here $A_{4.75-5.0}$ is the integrated area of the convoluted peaks from 4.75 to 5.0 ppm associated with the downfield *exo*-olefinic proton and the two identical protons of the coupled product. Equation 2 accounts for all likely terminal chain end types; however, the vast majority is *tert*-Cl. Standard initiators TMPCl and PMHCl showed high initiation efficiency (~1) in all preparations. Near-monodisperse PIBs with targeted molecular weights were obtained. IB_2BMP-initiated polymers were relatively polydisperse, and I_{eff} was around 0.5 for a 3k molecular weight target, 0.6 for 5k, and 0.8 for 10k. Although I_{eff} increased with higher target molecular weight, it remained less than quantitative. In contrast, IB_3BMP was an excellent ATRP-ready cationic initiator. It consistently performed well in preparing both low and high molecular weight PIBs. NMR and SEC showed that the resulting PIBs possessed the target molecular weight and narrow PDI.

SEC elution curves of representative PIB-3k samples are shown in Figure 3. These curves dramatically demonstrate the difference between IB_2BMP and IB_3BMP. The elution curve for IB_3BMP is nearly identical to those of PMHCl and TMPCl; all are very narrow and symmetrical. On the other hand, the curve for IB_2BMP is much broader and displays a low molecular weight tail, characteristic of slow initiation.

Polyisobutylenes produced from IB_3BMP possess the desired 2-bromo-2-methylpropionate headgroup, as expected. Figure 4 shows the ^{1}H NMR spectrum of a representative PIB-3k produced from IB_3BMP. The methylene unit adjacent to the ester linkage was observed as a triplet centered at 4.2 ppm. The integrated area of this peak was approximately one-third that of the methyl groups (peak a) adjacent to the *tert*-chloride end group, indicating that the α-bromoester functionality was quantitatively

dx.doi.org/10.1021/ma202682w | *Macromolecules* 2012, 45, 1217−1221

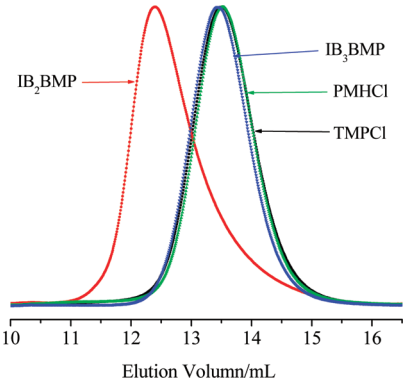


Figure 3. SEC elution curves of PIB-3k samples initiated by different initiators.

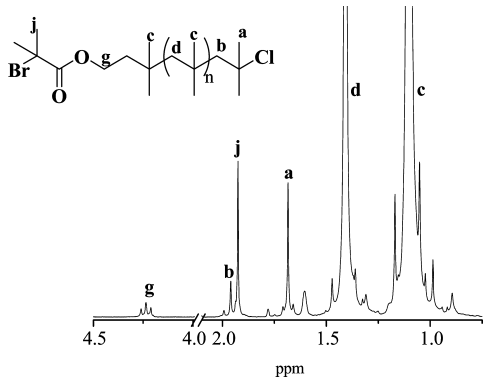


Figure 4. ^{1}H NMR spectrum of representative PIB (IB_3BMP-3k).

maintained during LCP. Thus, in addition to excellent initiating performance in cationic polymerization, this dual initiator also produces polymers that are ATRP ready.

Because of complex formation between Lewis acid and carbonyl oxygen, IB_3BMP requires a higher $TiCl_4$ concentration, compared to standard initiators TMPCl or PMHCl, to achieve a given rate of

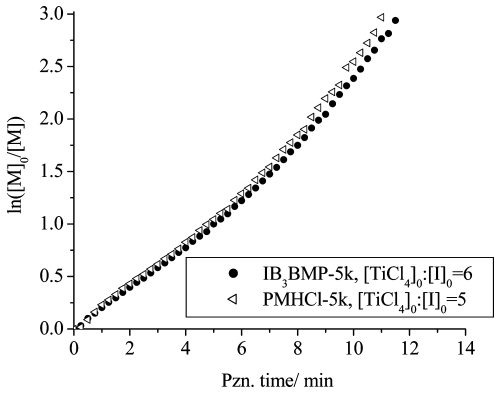


Figure 5. First-order kinetic plots for IB polymerizations at −70 °C. 60/40 Hex/MeCl cosolvents (v/v); $[IB]_0$ = 1.00 M; $[2,6\text{-lutidine}]_0$ = 4.00 mM; $[I]_0$ = 12.2 mM; $[TiCl_4]_0 = 6 \times [I]_0$ for IB_3BMP; $[TiCl_4]_0 = 5 \times [I]0$ for PMHCl.

polymerization. Figure 5 shows first-order kinetic plots as determined by *in situ* FTIR (ReactIR 4000) for IB polymerizations initiated from IB_3BMP and PMHCl. The slight deviations from linearity observed in the plots reflect shifts in the equilibrium between dormant and active chain ends, due to the rise and fall of the reaction temperature caused by the initial exotherm of polymerization. This effect has been explained in detail previously.[11] The two polymerizations depicted in Figure 5 were formulated identically except for the identity of the initiator, and the fact that one additional equivalent of $TiCl_4$ (relative to the initiator) was used for the case of IB_3BMP. The kinetic plots are identical within experimental error, indicating that $[TiCl_4]_{eff}$ was the same in the two reactions. This demonstrates the existence of complexation and shows that it is approximately 1:1.

The results in Table 1 and Figure 3 clearly show that IB_2BMP is a relatively inefficient cationic initiator compared to the standard oligoisobutylene hydrochlorides, PMHCl, and TMPCl, and also compared to IB_3BMP. Similarly disappointing results have been reported for other ester initiators derived from 5-chloro-3,3,5-trimethylhexanol, such as 3,3,5-trimethyl-5-chlorohexyl 2-bromopropionate (IB_2BP),[1] 3,3,5-trimethyl-5-chlorohexyl acetate (TMCHA),[3] 3,3,5-trimethyl-5-chlorohexyl methacrylate,[2,12] and 3,3,5-trimethyl-5-chlorohexyl isobutyrate.[12] The conclusion reached by these authors was that poor initiating performance is caused by complexation between Lewis acid and carbonyl oxygen of the ester group. However, this explanation cannot be correct in view of the essentially ideal initiating performance displayed by IB_3BMP. The latter ester is composed of the same carboxylic acid component as IB_2BMP, and the two molecules are essentially identical in the immediate environment of the ester group. Furthermore, polymerization kinetics shows that IB_3BMP and IB_2BMP tend to produce the same $[TiCl_4]_{eff}$ within the reactor, which also suggests a similar degree of complexation. This strongly supports the alternative explanation that in IB_2BMP and similar initiators the $TiCl_4$:carbonyl complex and the *tert*-chloride group interact via an entropically favorable cycle conformer. This interaction diminishes the rate of ionization of the *tert*-chloride group, thereby reducing I_{eff}. In IB_3BMP, increased separation between the two sites eliminates this interaction.

ATRP Polymerization. In our previous paper,[1] we demonstrated successful ATRP of MA from PIB macroinitiators produced from IB_2BMP. Since PIB macroinitiators prepared from IB_2BMP and IB_3BMP are identical, their behavior in subsequent ATRP initiation should also be identical. To confirm this expectation, ATRP of MA was initiated from a representative BMP-PIB macroinitiator, and the results are summarized in

Table 2. ATRP[a] of MA Initiated from a PIB Macroinitiator[b] Prepared from IB_3BMP

	NMR		SEC		
block copolymer	$X_{n\ PMA}$	wt % PMA	$M_{n\ PMA}$	PDI	wt % PMA
BMP-PIB-*b*-PMA_{40}	38	41.0	3600	1.03	43.6

[a] $[BMP\text{-}PIB]_o:[CuBr]_o:[PMDETA]_o$ = 1:1:1 ($[BMP\text{-}PIB]_o$ = 0.05 M) in toluene at 70 °C; $0.60[MA]_o/[MacroI]_o$ = 40; conversion of MA limited to 60% [b] BMP-PIB: M_n = 4650 g/mol and PDI = 1.02 (SEC); $X_{n,PIB}$ = 77 (NMR).

Table 2. The observed polymerization degree of the PMA block, $\overline{X}_{n,PMA}$, was very close to the targeted value of 40; SEC and NMR analyses indicated quantitative initiation efficiency. Figures C and D, Supporting Information, show SEC elution curves of BMP-PIB macroinitiator and resulting BMP-PIB-*b*-PMA_{40} block copolymer, and the ^{1}H NMR spectrum of BMP-PIB-*b*-PMA_{40} block copolymer, respectively.

dx.doi.org/10.1021/ma202682w | *Macromolecules* 2012, 45, 1217−1221

CONCLUSIONS

IB_3BMP, a dual initiator possessing the same radical and cationic initiating sites as the previously reported[1] dual initiator IB_2BMP, but with one more IB repeating unit in between, was shown to be an excellent cationic initiator. Structure of the new initiator was characterized using ^1H and ^{13}C NMR spectroscopy. Its initiation efficiency in LCP of IB was quantitative ($I_{eff} \sim 1$) under all polymerization conditions studied, including low temperature (−70 °C) and low monomer/initiator ratios. NMR and SEC showed IB_3BMP-initiated PIBs were the same with regard to molecular weight and PDI as those obtained from standard initiators, TMPCl and PMHCl. Since its radical initiating site is identical to that of IB_2BMP, PIB macroinitiators produced from IB_3BMP perform equally well in ATRP.

We conclude that the poor initiation efficiency of IB_2BMP, TMCHA, and related initiators derived from 3,3,5-trimethyl-5-chlorohexanol is not simply caused by complexation, but rather must be due to interactions between the $TiCl_4$:carbonyl complex and the *tert*-chloride group via an entropically favorable cyclic conformer. Therefore, it is unsurprising that differences in the carboxylic acid component of the ester, i.e., acetyl group in TMCHA, 2-bromo-2-methylpropionoyl group in IB_2BMP, etc., which might be expected to introduce different steric and/or inductive properties to the carbonyl group, do not result in any improvement in I_{eff}. However, when *tert*-chloride and ester groups are further separated, as in IB_3BMP, the interfering interaction disappears and I_{eff} approaches 100%.

ASSOCIATED CONTENT

Supporting Information

^1H and ^{13}C NMR spectra ($CDCl_3$, 22 °C) of 2,4,4,6,6-pentamethyl-1-heptene (PM1H) and 2-chloro-2,4,4,6,6-pentamethylheptane (PMHCl), SEC elution curves for BMP-PIB macroinitiator and corresponding PIB-*b*-PMA block copolymer, and ^1H NMR spectrum of PIB-*b*-PMA block copolymer. This material is available free of charge via the Internet at http://pubs.acs.org/.

AUTHOR INFORMATION

Corresponding Author

*E-mail: robson.storey@usm.edu.

Notes

The authors declare no competing financial interest.

ACKNOWLEDGMENTS

The authors of this paper would like to thank The University of Southern Mississippi Composites Center, funded by The Office of Naval Research and Northrop Grumman, Award No. N00014-07-1-1057, for partial financial support of this research.

REFERENCES

(1) Zhu, Y.; Storey, R. F. *Macromolecules* **2010**, *43*, 7048−7055.
(2) Balogh, L.; Takacs, A.; Faust, R. *ACS Div. Polym. Chem., Polym. Prepr.* **1992**, *33* (1), 958−959.
(3) Breland, L. K.; Murphy, J. C.; Storey, R. F. *Polymer* **2006**, *47*, 1852−1860.
(4) Cook, D. *Can. J. Chem.* **1963**, *41*, 522−526.
(5) Saied, O.; Bachand, B.; Wuest, J. D. *Can. J. Chem.* **1998**, *76*, 490−497.
(6) Faust, R.; Iván, B.; Kennedy, J. P. *J. Macromol. Sci.—Chem.* **1991**, *A28*, 1−13.
(7) Chance, R. R.; Baniukiewicz, S. P.; Mintz, D.; Ver Strate, G.; Hadjichristidis, N. *Int. J. Polym. Anal. Charact.* **1995**, *1*, 3−34.
(8) Mayr, H.; Roth, M.; Deters, M. *Macromolecules* **1997**, *30*, 3965−3970.
(9) Mayr, H.; Striepe, W. *J. Org. Chem.* **1983**, *48*, 1159−1165.
(10) Schlaad, H.; Kwon, Y.; Faust, R.; Mayr, H. *Macromolecules* **2000**, *33*, 743−747.
(11) Storey, R. F.; Donnalley, A. B.; Maggio, T. L. *Macromolecules* **1998**, *31* (5), 1523−1526.
(12) Faust, R. *Macromol. Symp.* **1994**, *85*, 295−306.

Macromolecules

Article

pubs.acs.org/Macromolecules

Synthesis, Characterization, and Properties of Poly(1-trimethylsilyl-1-propyne)-*block*-poly(4-methyl-2-pentyne) Block Copolymers

Eldar Yu. Sultanov,*[,†] Alexander A. Ezhov,[†,‡] Sergey M. Shishatskiy,[§] Kristian Buhr,[§] and Valeriy S. Khotimskiy[†]

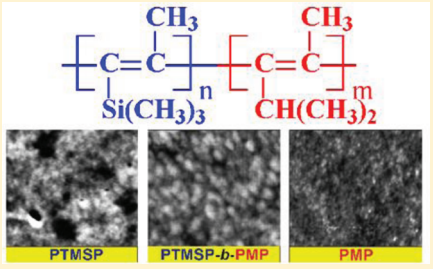
[†]A.V. Topchiev Institute of Petrochemical Synthesis, Russian Academy of Sciences, Leninsky prospect, 29, 119991 Moscow, Russia

[‡]M.V. Lomonosov Moscow State University, GSP-2, Leninskie Gory, 119992, Moscow, Russia

[§]Institute of Polymer Research, Helmholtz-Zentrum Geesthacht, Max-Planck-Str. 1, 21502 Geesthacht, Germany

Supporting Information

ABSTRACT: Poly(1-trimethylsilyl-1-propyne)-*block*-poly(4-methyl-2-pentyne) (PTMSP-*b*-PMP) block copolymers of different composition were synthesized through sequential living polymerization by catalytic systems based on niobium pentachloride with organometallic cocatalysts in cyclohexane. Mechanical, thermal, and gas transport properties of synthesized block copolymers are investigated. The morphology of PTMSP-*b*-PMP can be described as a two-phase supramolecular structure which includes regions with an increased level of ordering, distributed in an amorphous phase. The observed structure of block copolymers is explained by the presence of densely packed poly(4-methyl-2-pentyne) (PMP) blocks and less ordered poly(1-trimethylsilyl-1-propyne) (PTMSP) blocks. The correlation of morphology of block copolymers with gas transport parameters as well as with resistance toward organic solvents is discussed. As result of this study, novel polymeric materials based on PTMSP and PMP combining resistance toward aromatic and aliphatic hydrocarbons with high gas transport parameters are synthesized.



INTRODUCTION

1,2-Disubstituted polyacetylenes are nonconjugated amorphous glassy polymers with high glass transition temperatures (>200 °C) and good mechanical properties. Poly(1-trimethylsilyl-1-propyne) (PTMSP) is the most studied polymer among 1,2-disubstituted polyacetylenes due to its extremely high gas and vapor transport parameters.[1] PTMSP also has high selectivity toward condensable hydrocarbons while separating them from mixtures with noncondensable gases. However, solubility of PTMSP in higher hydrocarbons restrains wide usage of this polymer in separation processes. Therefore, investigations are conducted to improve the properties of PTMSP, for example, by synthesizing copolymers.[2−4] Another 1,2-disubstituted polyacetylene—poly(4-methyl-2-pentyne) (PMP)—has high resistance toward most of organic solvents and rather high gas and vapor transport parameters,[5,6] although these parameters are lower than that of PTMSP. Several years ago random copolymers of 1-trimethylsilyl-1-propyne (TMSP) with 4-methyl-2-pentyne (MP) were synthesized,[2] but they were not of high interest because of low molecular weights and poor mechanical properties. Block copolymers of TMSP with MP in contrast to random copolymers may combine properties of PTMSP and PMP.

Multistage or sequential polymerization of two or more monomers is one of the main methods of block copolymer synthesis. For realization of this method a living polymerization of at least one of the monomers in chosen polymerization conditions is necessary. Effective initiation of polymerization of second comonomer by active species of the first comonomer is also required. When these conditions are met for both monomers, it is possible to synthesize AB- and BA-type block copolymers.

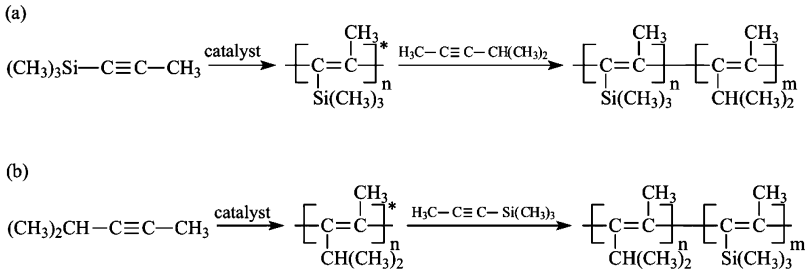
It is known that polymerization of substituted acetylenes by catalysts based on 5 and 6 group transition metals proceeds by the carbene mechanism.[7] Since the discovery of living polymerization of substituted acetylenes[8,9] many studies were carried out in this field.[10,11] Living polymerization of several substituted acetylenes was used for synthesis of their block copolymers by the sequential copolymerization method.[12−14]

Recently, we showed[15] that polymerization of TMSP and MP by the catalytic system $NbCl_5$−Ph_4Sn in cyclohexane has principal evidence of living polymerization, namely, continuation of chain propagation after addition of a new portion of the monomer, linear dependence of number-average molecular weight (M_n) on monomer conversion, and unimodal molecular weight distribution (MWD) for homopolymers obtained by sequential polymerization. It was found out[16] that the continuation of chain propagation after addition of a new portion of the same monomer is observed also when the catalyst $NbCl_5$−Ph_3SiH is used during two-stage hopolymerization of TMSP or MP. Therefore, polymerization reactions of

Received: September 21, 2011
Revised: December 22, 2011
Published: January 20, 2012

 © 2012 American Chemical Society

Scheme 1. Synthesis of AB-Type (a) and BA-Type (b) PTMSP-*b*-PMP Block Copolymers



TMSP and MP by $NbCl_5$–Ph_4Sn and $NbCl_5$–Ph_3SiH have living nature under the same conditions.

This paper reports on the synthesis of AB- and BA-type PTMSP-*b*-PMP block copolymers through sequential living polymerization of TMSP and MP by $NbCl_5$-based catalyst and the investigation of properties of these block copolymers.

EXPERIMENTAL PART

Materials. Monomers TMSP (99.9%) and MP (99.9%) were synthesized by techniques developed in cooperation with NPO OAO Yarsintez.[17,18] Monomers and cyclohexane (99%, Fluka) were distilled three times over calcium hydride under high-purity argon before polymerization experiments. Catalyst niobium pentachloride, $NbCl_5$ (99.5%, Fluka), and cocatalysts tetraphenyltin, Ph_4Sn (97%, Fluka), triphenylsilane, Ph_3SiH (97%, Fluka), triethylsilane, Et_3SiH (97%, Fluka), and tetrabutyltin, Bu_4Sn (98%, Fluka), were used as received.

Block Copolymer Synthesis. The synthesis of PTMSP-*b*-PMP was carried out by sequential polymerization according to one of the reactions in Scheme 1. The second monomer was added to the reaction mixture with living active species of the polymer being formed at the first stage of polymerization. (Here and everywhere conversion at the first stage of sequential polymerization is accepted as 100% because polymerization was carried out in conditions in which 100% yield of polymer is observed[16].)

The synthesis of AB-type PTMSP-*b*-PMP (Scheme 1a) was performed according to the following technique. A glass reactor was loaded with a solution of $NbCl_5$ (0.15 g, 0.55 mmol) and Ph_4Sn (0.24 g, 0.55 mmol) in cyclohexane (28 mL). The resulting mixture was vigorously stirred at 25 °C for 30 min in a flow of high-purity argon. Then, TMSP (3.08 g, 27.5 mmol) was added to the catalytic solution. After 24 h (during this time, 100% conversion of added TMSP was achieved) the second monomer, MP (2.26 g, 27.5 mmol), in 28 mL of cyclohexane was added to the reaction mixture. After 72 h the reaction mixture was treated with methanol (50 mL) to deactivate the catalyst. The polymer was dissolved in CCl_4 (300 mL), precipitated into methanol (1.5 L), filtered out, and dried in the air for 24 h. The resulting polymer was redissolved in CCl_4 and reprecipitated into methanol. After vacuum drying, the yield of the product was determined.

The synthesis of BA-type PTMSP-*b*-PMP was performed in a similar manner, but monomers (TMSP and MP) were added to the reactor in reversed order (Scheme 1b).

Measurements. Molecular weight characteristics were determined by gel-permeation chromatography (GPC). Measurements were performed in cyclohexane at 20 °C using a Waters chromatograph equipped with a Waters R401 refractometric detector and a system of 2 × PLgel 5 μ MiniMix-C columns. The molecular weight parameters were estimated from the calibration plot constructed on the basis of samples of PTMSP and PMP with determined molecular weights (these samples were characterized by GPC using a chromatograph equipped with light scattering and refractometric detectors).

The intrinsic viscosity of polymer solutions in CCl_4 was measured at 25 °C using an Ostwald–Ubbelohde viscometer.

The ^1H nuclear magnetic resonance (NMR) spectra of polymer solutions in $CDCl_3$ or C_6D_{12} were recorded on Bruker MSh-300 instrument operating at 300 MHz.

The infrared (IR) spectra were measured in a range 200–4000 cm^{-1} on an IFS-Bruker-113-V spectrometer. A comparison of the composition of PTMSP-*b*-PMP estimated using IR spectra and elemental analysis data revealed their good conformity.[16] Therefore, the method based on IR measurements described in ref 2 was used for calculating the composition of copolymers.

Selective extraction was performed by mixing polymer product in a sample bottle with toluene for 48 h. Then the solution was filtered and the polymer fraction insoluble in toluene was dried, whereas the filtrate with soluble in toluene fraction was reprecipitated into methanol, filtrated, and dried. The weights of fractions were determined after vacuum drying.

Polymer films used for X-ray diffraction analysis and measurement of mechanical properties and gas transport parameters were prepared by casting polymer solutions in cyclohexane onto cellophane.

The mechanical properties of polymer films were studied at 20 °C and a constant stretching rate of 10 mm/min using an Instron-1122 instrument.

The thermal properties of the polymers were investigated by differential scanning calorimetry (DSC) using a Mettler Toledo DSC-823e instrument in the temperature range 20–350 °C, thermal gravimetric analysis (TGA) using a Mettler Toledo TGA/DSC-1 instrument in the temperature range 20–1000 °C, and dynamic mechanical analysis (DMA) using a Mettler Toledo DMA/SDTA-861e instrument in the temperature range 20–300 °C. All measurements were performed under a nitrogen atmosphere.

X-ray diffraction analysis was performed at room temperature by standard DRON-1.5 diffractometer using Cu Kα radiation (λ = 0.154 nm) under transmission and reflection modes. The samples were composed of a pile of five parallel films with a surface area of 10 × 10 mm^2.

The surface of polymer films was investigated by atomic force microscopy (AFM) using scanning probe microscope SOLVER PRO-M (NT-MDT) operated in a semicontact mode with silicon cantilevers NSG10 (NT-MDT). Films were prepared by casting polymer solutions onto silicon support at room temperature and then were annealed at 150 °C in a vacuum oven.

Single gas transport properties of H_2, He, N_2, O_2, CH_4, CO_2, and *n*-C_4H_{10} gases for polymer films were determined with a constant-volume/variable-pressure (time-lag) method at 30 °C.

CH_4 and *n*-C_4H_{10} mixed gas permeation experiments were carried out with the experimental setup described by Yave et al.[19] The gas mixture was prepared directly before measurement by mixing individual gases CH_4 (purity 99.999%) and *n*-C_4H_{10} (purity 99.5%). The gas flow and pressure of feed and sweep (N_2) were measured on entrance to the measurement cell. The compositions were analyzed by an Agilent 9890N gas chromatograph.

RESULTS AND DISCUSSION

Selection of Conditions for Synthesis of PTMSP-*b*-PMP. The study of polymerization reactions of TMSP and MP in cyclohexane by common effective $NbCl_5$-based catalysts with organometallic cocatalysts showed that 100% yield of both PTMSP and PMP is observed on two catalytic systems: $NbCl_5$–Ph_4Sn and $NbCl_5$–Ph_3SiH (Table 1). Samples of

dx.doi.org/10.1021/ma202140c | Macromolecules 2012, 45, 1222–1229

Table 1. Polymerization of TMSP and MP by $NbCl_5$-Based Catalytic Systems[a]

polymer	catalyst	yield (%)	$M_n \times 10^{-5}$	M_w/M_n	$[\eta]$ (dL/g)
PTMSP	$NbCl_5$	90	2.4	1.6	0.75
PTMSP	$NbCl_5$–Bu_4Sn	50	3.2	1.8	1.0
PTMSP	$NbCl_5$–Ph_4Sn	~100	2.3	1.5	0.55
PTMSP	$NbCl_5$–Et_3SiH	65	3.5	2.4	1.2
PTMSP	$NbCl_5$–Ph_3SiH	~100	2.5	1.75	0.75
PMP	$NbCl_5$	90	6.9	2.0	3.0
PMP	$NbCl_5$–Bu_4Sn	~100	6.0	2.2	3.0
PMP	$NbCl_5$–Ph_4Sn	~100	5.1	1.9	2.7
PMP	$NbCl_5$–Et_3SiH	~100	5.1	2.15	2.8
PMP	$NbCl_5$–Ph_3SiH	~100	4.0	2.0	2.2

[a]Polymerization conditions: $[M]_0$ = 1 mol/L; [Cat.] = [Cocat.] = 20 mmol/L; solvent: cyclohexane; T = 25 °C; reaction time: 24 h.

PTMSP and PMP obtained by these catalysts have unimodal character of MWD with value $M_w/M_n \geq 1.5$. Noticeably wide MWD probably related to high molecular weights ($M_n > 2 \times 10^5$) and high intrinsic viscosities ($[\eta] > 0.5$ dL/g) of obtained polymers. Stirring and heat exchange decrease as viscosity of polymerization mixture increases, and as a result synthesis of polymer with high molecular weight and narrow MWD is complicated.[20] One more factor that influences the polydispersity is a difference in propagation and initiation rates of polymerization. Widening of MWD is observed when propagation rate is higher than initiation rate, and this effect also may take place during polymerization of TMSP and MP monomers.[8]

As shown in Table 1 at the same conditions during PMP synthesis, polymers with higher molecular weights are formed than in case of PTMSP synthesis. This is evidently related to the fact that in case of polymerization of TMSP more active species are formed. Initiation efficiency of polymerization for monomers TMSP and MP can be calculated from [P*]/[Cat.] = $[M]_{consumed}/(DP \times [Cat.])$, where [M] is the monomer concentration, DP the degree of polymerization, and [Cat.] the catalyst concentration. Polymerization initiation efficiency for TMSP is equal to 2.2% and 2.3%, while for MP is equal to 0.8% and 1.2% by catalysts $NbCl_5$–Ph_4Sn and $NbCl_5$–Ph_3SiH, respectively. So it can be concluded that efficiency of polymerization by aforementioned catalytic systems for TMSP is higher than for MP. Matson et al.[2] have also mentioned that TMSP is more active than MP due to better steric accessibility of the C≡C bond. It is worth noting that the initiation efficiency of polymerization for both TMSP and MP by $NbCl_5$-based catalysts is rather low (<5%) due to low yield of niobium carbene, which is generally accepted as active specie initiating polymerization of substituted acetylenes.[7] Low yields of metal carbenes are typical for such systems; for example, Ivin et al.[21] for a similar catalyst WCl_6–Me_4Sn have calculated that amount of formed tungsten carbene does not exceed 0.7%.

Living nature of polymerization of TMSP as well as MP by catalysts $NbCl_5$–Ph_4Sn[15] and $NbCl_5$–Ph_3SiH[16] allows synthesis of AB- and BA-type PTMSP-*b*-PMP block copolymers by the sequential polymerization method.

Synthesis and Characterization of PTMSP-*b*-PMP. Results of sequential copolymerization of TMSP and MP monomers are presented in Table 2. IR and NMR spectroscopy data indicate the presence of TMSP and MP units in copolymerization products.

IR spectra of obtained block copolymers contain analytical absorption bands at 687 and 1097 cm^{-1} characteristic of the group $-Si(CH_3)_3$ from TMSP unit and the group $-CH(CH_3)_2$ from MP unit, respectively (Figure 1).

The typical ^1H NMR spectrum of PTMSP-*b*-PMP is shown in Figure 2. The spectrum exhibits four singlets with chemical shifts at 2.98, 1.83, 1.08, and 0.23 ppm which correspond to the hydrogen atoms of elementary groups $-CH-$, $-C(CH_3)=$, $-C(CH_3)_2-$, and $-Si(CH_3)_3$. Therefore, the spectra of all studied PTMSP-*b*-PMP block copolymers contain signals characteristic of both TMSP unit (0.23 ppm) and MP unit (2.98 and 1.08 ppm).

Selective extraction also confirms formation of copolymers. Toluene is a selective solvent for the PTMSP/PMP polymer mixture because unlike PMP, PTMSP is soluble in toluene. The presence of TMSP units (together with MP units) in polymer products insoluble in toluene and the presence of MP units (together with TMSP units) in polymer products soluble in toluene indicate that copolymers (not a mix of homopolymers) are indeed formed as a result of sequential polymerization of TMSP and MP. The method of synthesis excludes formation of random copolymers, and it can be concluded that products of sequential copolymerization of TMSP and MP are block copolymers.

The synthesis of AB-type PTMSP-*b*-PMP, i.e., sequential copolymerization by addition of MP monomer to the solution of PTMSP, proceeds with 80% yield at the second stage (Table

Table 2. Results of Synthesis of PTMSP-*b*-PMP and Their Extraction in Toluene[a]

								soluble in toluene		insoluble in toluene	
run	catalyst	M_1	M_1/M_2 in feed[b]	M_1/M_2 in product[c]	yield (%)	$M_n \times 10^{-5}$	M_w/M_n	amount (%)	TMSP/MP[d]	amount (%)	TMSP/MP[d]
1	$NbCl_5$–Ph_4Sn	TMSP	50:50	60:40	79	3.1	2.1	100	60:40	0	
2	$NbCl_5$–Ph_3SiH	TMSP	50:50	60:40	80	3.5	2.2	100	60:40	0	
3	$NbCl_5$–Ph_4Sn	MP	50:50	90:10	21	5.8	2.2	0		100	10:90
4	$NbCl_5$–Ph_3SiH	MP	50:50	75:25	58	5.1	2.4	0		100	25:75
5[e]	$NbCl_5$–Ph_4Sn	TMSP	33:67	40:60	78	3.7	2.7	64	70:30	36	15:85
6[e]	$NbCl_5$–Ph_3SiH	TMSP	33:67	35:65	85	4.0	2.5	55	50:50	45	15:85
7[e]	$NbCl_5$–Ph_4Sn	MP	33:67	65:35	54	6.7	2.9	43	80:20	57	25:75
8[e]	$NbCl_5$–Ph_3SiH	MP	33:67	40:60	83	6.3	2.7	58	75:25	42	35:65

[a]Polymerization was carried out in $[M_1]_0$ = 1 mmol/L; [Cat.] = [Cocat.] = 20 mmol/L; solvent: cyclohexane; T = 25 °C; M_1 = the first monomer to the solution of which after 24 h the second monomer (M_2) was added; yield = yield of the second stage of sequential copolymerization after 72 h. [b]Molar ratio M_1:M_2 added to the reactor. [c]Molar ratio M_1:M_2 in the products of copolymerization. [d]Molar ratio TMSP:MP in the copolymer. [e]Temperature of the second stage of the sequential copolymerization equals 75 °C.

dx.doi.org/10.1021/ma202140c | Macromolecules 2012, 45, 1222–1229

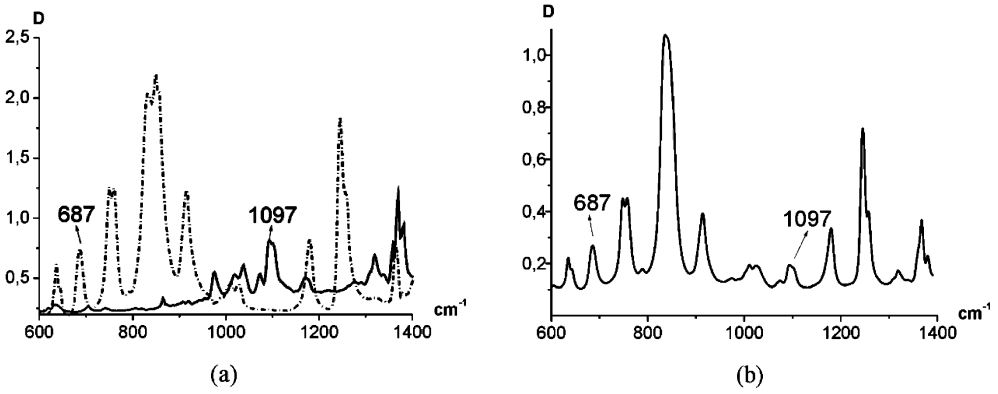


Figure 1. Typical IR spectra of (a) PTMSP (dashed line) and PMP (solid line) and (b) PTMSP-*b*-PMP.

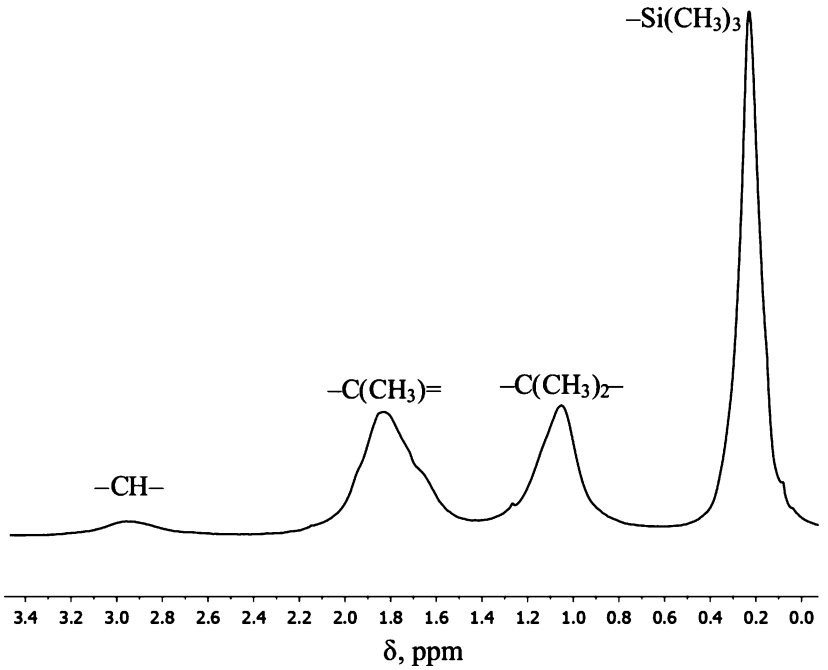


Figure 2. Typical ^{1}H NMR spectrum of PTMSP-*b*-PMP.

2, runs 1 and 2). As a result, completely soluble in toluene block copolymers containing up to 40% second block (PMP) were obtained. As seen in Figure 3a, synthesized block copolymers have higher molecular weights than PTMSP sample obtained at similar conditions.

The synthesis of BA-type PTMSP-*b*-PMP, i.e., sequential copolymerization by addition of TMSP monomer to the living PMP, proceeds with rather low yield (≤60%) at the second stage (Table 2, runs 3 and 4). Obtained block copolymers contain up to 25% second block (PTMSP), are completely insoluble in toluene, and have higher molecular weights than PMP homopolymer synthesized at similar conditions (Figure 3b).

In the case of sequential polymerization performed with double excess of second monomer and at higher temperature of second stage equal to 75 °C, it is possible to increase the yield during synthesis of both AB- and BA-type block copolymers. As a result, a mixture of copolymers with different block ratios is formed (Table 2, runs 5–8) which by extraction in toluene can be divided into two fractions: soluble fraction enriched with TMSP units and insoluble fraction enriched with MP units.

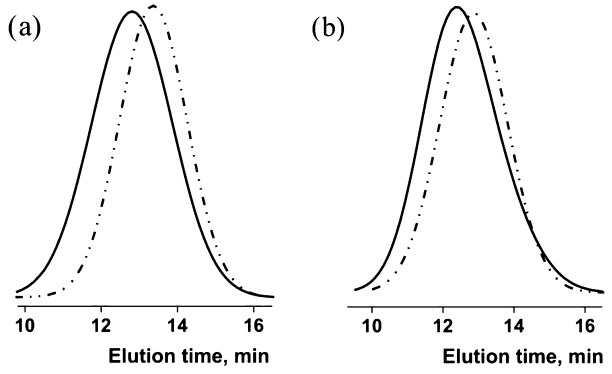


Figure 3. GPC traces of samples: (a) PTMSP (dashed line) and AB-type PTMSP-*b*-PMP (solid line); (b) PMP (dashed line) and BA-type PTMSP-*b*-PMP (solid line).

It is significant that a diffusion factor also plays a big role when polymerization proceeds in highly viscous and heterogeneous conditions as in the case of the second stage of sequential polymerization of TMSP and MP monomers. That is why we

dx.doi.org/10.1021/ma202140c | *Macromolecules* 2012, 45, 1222–1229

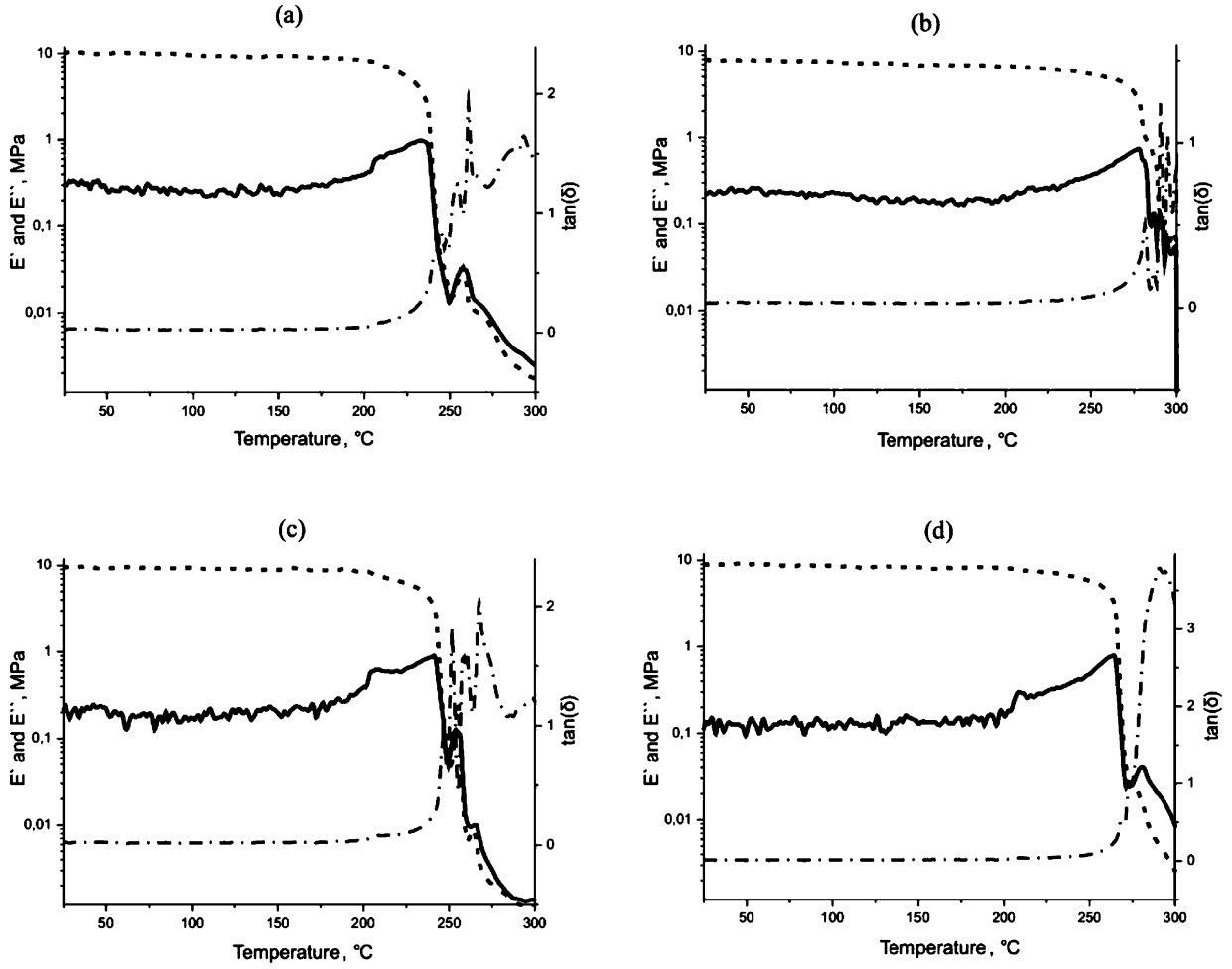


Figure 4. Behavior of storage modulus E' (dashed line), loss modulus E'' (solid line), and tan(δ) (dash-dotted line) as a function of temperature for PMP (a), PTMSP (b), and PTMSP-*b*-PMP block copolymers with the block ratio of 35:65 (c) and 60:40 (d).

suppose that the reason for broad MWD of copolymerization products as well as the cause for formation of a mixture of block copolymers with different composition is related to the high viscosity of the polymerization solutions.

Low yields of BA-type PTMSP-*b*-PMP can be also explained by high viscosity of PMP solution formed at the first stage of sequential copolymerization (intrinsic viscosity of PMP $[\eta] > 2$ dL/g). Uniform stirring and monomer diffusion are considerably hindered when TMSP is added to such viscous PMP solution at the second stage of copolymerization, and this may slow down the polymerization.

As a result of sequential copolymerization reactions, PTMSP-*b*-PMP block copolymers with different block ratios were obtained. Since the type (AB or BA) of PTMSP-*b*-PMP used for further investigations does not play a big role, only block ratios of block copolymers are undermentioned.

Properties and Morphology of PTMSP-*b*-PMP. Obtained block copolymers are colorless amorphous polymers with good film-forming and mechanical properties. Block copolymers have strength, σ = 33−42 MPa; strain break, ε = 25−60%; and Young's modulus, E = 1000−1300 MPa, depending on their composition, and these properties increase with MP content.

TGA experiments showed that decomposition of PTMSP-*b*-PMP starts at 260−280 °C and meaning high thermal stability of obtained block copolymers which is also typical for PTMSP and PMP homopolymers.

DMA data indicate that storage modulus (E') of PTMSP-*b*-PMP block copolymers falls at temperatures which are lower than decomposition temperatures of these samples. Therefore, DMA was used to determine glass transition temperatures of PTMSP-*b*-PMP, PTMSP, and PMP (Figure 4). DMA data indicate that the glass transition temperature for PTMSP-*b*-PMP with block ratios of 35:65 and 60:40 equals 245 and 265 °C, respectively, and for PMP equals 240 °C. The storage modulus of PTMSP almost does not change until its decomposition temperature equals 280 °C. So the glass transition temperature of PTMSP is higher than its decomposition temperature, and owing to this, it is not possible to determine the glass transition temperature of PTMSP and consequently the second glass transition temperature of PTMSP-*b*-PMP. It was found out glass transition temperatures of block copolymer samples are close to glass transition temperature of PMP homopolymer, which indicates the presence of PMP phase in these block copolymers. Dependence of glass transition temperature on composition of PTMSP-*b*-PMP can be related to existence of diffuse interface between PTMSP and PMP phases, which is a result of their chemical affinity.

The supramolecular structure of block copolymers was studied by X-ray diffraction analysis (Table 3). The scattering

dx.doi.org/10.1021/ma202140c | *Macromolecules* 2012, 45, 1222−1229

Table 3. X-ray Data for PTMSP-*b*-PMP, PTMSP, and PMP Samples

sample	2θ, deg	$\Delta_{1/2}$, deg	d,[b] nm
PMP	11.4	1.9	0.776
35:65[a]	10.2	2.9	0.838
60:40[a]	9.7	3.2	0.941
PTMSP	9.2	2.4	0.955

[a]PTMSP/PMP block ratio in PTMSP-*b*-PMP. [b]Interplanar spacing.

profile shows an amorphous-like pattern and displays diffuse maximum with angular position of 2Θ equal to ∼10° and with half-width ∼3°. This indicates that, although the coherent scattering region is small, it is larger than in the case of truly amorphous polymers, for which the reflection half-width is usually 5°−8°.[22] In terms of supramolecular ordering the structure of block copolymers can be defined as a certain state intermediate between liquidlike truly amorphous and ordered states (crystalline or semicrystalline). The X-ray data indicate that block copolymers possess a two-phase structure characterized by presence of less ordered regions and regions with an increased level of ordering. On the basis of the value of interplanar spacing, it can be concluded about macrochain packing. Increase of interplanar spacing with enhance of TMSP content in block copolymers indicates that packing density decreases.

The surface of PTMSP-*b*-PMP films as well as PMP and PTMSP films was studied by AFM (Figure 5). The surface of PMP and PTMSP-*b*-PMP films can be described as consisting of clusters of similar size (10−40 nm), typical for each sample (Figure 5a,c,d). The surface of PTMSP film consists of formations (Figure 5b), which have a widespread of values of the lateral size (10−100 nm), and perhaps this is due to high heterogeneity in macrochain packing. The lateral size of clusters in films from PTMSP-*b*-PMP block copolymers increases with the content of TMSP units (Figure 5c,d). It should be noted that these changes does not correlate with changes in average molecular weight. The most probable reason for increase in lateral size of clusters is decrease of average packing density with increase of TMSP content in PTMSP-*b*-PMP, and this corresponds to X-ray data. On scales of hundreds of nanometers can be seen that the inhomogeneity of the film surface increases with the content of TMSP units. At the same time the mean force of probe interaction with surface which leads to modification of the surface during AFM measurements decreases with increase of TMSP content. This fact can be interpreted as decrease of surface strength of polymer film. As a rule, the decrease of strength correlates with the decrease of the chain packing density.

Resistance of block copolymers toward organic solvents depends on composition of block copolymers (Table 4). All obtained samples can be divided into two groups: block copolymers enriched with MP units which are resistant toward aromatic and aliphatic hydrocarbons and block copolymers enriched with TMSP units which are soluble in a wide range of nonpolar and weak-polar organic solvents (for example, THF, octane, toluene, benzene, etc.). Block copolymers enriched with MP units have more ordered regions with high density of macrochain packing and as a result have high resistance toward organic solvents which is similar to PMP homopolymer. Probably, densely packed PMP blocks in PTMSP-*b*-PMP block copolymers act as physical cross-links responsible for resistance of polymer toward organic solvents. The presence of PMP phase in block copolymers enriched with MP units is confirmed

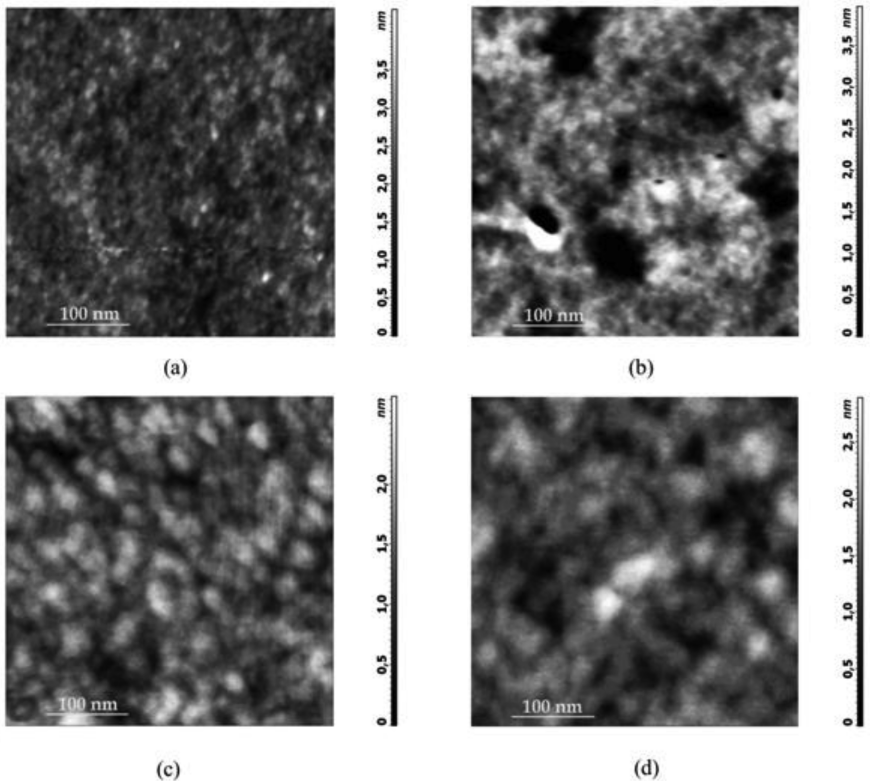


Figure 5. AFM images (topography, 400 × 400 nm) of the films from PMP (a), PTMSP (b), and PTMSP-*b*-PMP block copolymers with the block ratio of 35:65 (c) and 60:40 (d).

dx.doi.org/10.1021/ma202140c | *Macromolecules* 2012, 45, 1222−1229

Table 4. Resistance of PTMSP-*b*-PMP Block Copolymers toward Organic Solvents[a]

	solvent				
sample	heptane, octane	toluene, benzene	THF	cyclohexane	CCl_4
PMP	−	−	−	+	+
10:90[b]	−	−	−	+	+
25:75[b]	−	−	−	+	+
35:65[b]	−	−	−	+	+
50:50[b]	+	+	+	+	+
60:40[b]	+	+	+	+	+
75:25[b]	+	+	+	+	+
PTMSP	+	+	+	+	+

[a]"+", polymer is soluble at room temperature; "−", polymer is insoluble at room temperature. [b]PTMSP/PMP block ratio in PTMSP-*b*-PMP.

by DMA data since glass transition temperatures for PTMSP-*b*-PMP with block ratio of 35:65 and PMP homopolymer are almost equal (245 and 240 °C, respectively). With a rise of TMSP content the packing of block copolymers become less ordered, and it is most likely that PMP blocks are gradually transforming to an intermediate phase or a diffuse interface, i.e., a phase where both PMP and PTMSP blocks are randomly mixed. Densely packed ordered regions change into less ordered or disordered regions, and PMP blocks no longer perform the role of physical cross-links. As a result, resistance of block copolymers toward hydrocarbons is decreased, and they have solubility similar to PTMSP, despite the presence of PMP blocks. It is well-known that resistance of disubstituted polyacetylenes toward organic solvents strongly depends on the supramolecular packing.[23] In turn, supramolecular packing of PTMSP and PMP depends on their geometry, i.e., cis/trans ratios.[6,23] Therefore, cis/trans content of PTMSP, PMP, and PTMSP-*b*-PMP block copolymers was calculated using their ^{13}C NMR spectra (see Supporting Information Figures S1 and S2). Blocks of PTMSP and PMP in PTMSP-*b*-PMP block copolymers have the same cis/trans ratios as PTMSP and PMP homopolymers, which are equal to 65:35 and 50:50, respectively.

Single gas permeability through PTMSP-*b*-PMP films is presented in Table 5. (Several films were retested after 30 days, and results showed that decrease of permeabilities does not exceed 10%.) As expected, it is possible to regulate gas permeability by varying the composition of PTMSP-*b*-PMP. The presence of PTMSP blocks with high free volume provides a high level of gas permeability, and by enhancing the TMSP content in block copolymers increase of permeability coefficients is observed.

Results of separation of *n*-butane/methane mixture by films from PTMSP-*b*-PMP are presented in Table 6. Selectivity of

Table 6. *n*-Butane/Methane (2 mol %/98 mol %) Gas Mixture Permeability (*P*) and Selectivity for PTMSP-*b*-PMP, PMP, and PTMSP Samples

	P, barrer			
sample	CH_4	C_4H_{10}	mixed gas selectivity $\alpha(C_4H_{10}/CH_4)$	selectivity calcd from single gas permeability $\alpha(C_4H_{10}/CH_4)$
PMP	770	7200	9	2.5
35:65[a]	990	14000	14	2.4
60:40[a]	1100	20000	18	2.8
PTMSP	2200	68000	31	3.5

[a]PTMSP/PMP block ratio in PTMSP-*b*-PMP.

mixture separation is much higher than ideal selectivity calculated from permeability coefficients of pure gases. This is also characteristic for polymers PTMSP and PMP and can be explained as that during separation of mixture of condensable and noncondensable gases by dense polymer films the condensable vapor sorbs onto free volume elements or small "pores", eventually producing multilayer adsorption or even capillary condensation.[24] In this case the pores are partially or completely filled by adsorbed vapor and such a blockage reduces the flow of the noncondensable gases. As a result, the membrane is highly permeable to the condensable gas but significantly less permeable to noncondensable gas. Thus, during separation of *n*-butane/methane mixture transport of methane is blocked by *n*-butane condensed at the free volume elements.

The dependence of *n*-butane/methane selectivity on block ratio of the block copolymers may be due to changes in the level of free volume of PTMSP-*b*-PMP. Thus, increase in free volume contributes to the sorption of condensable molecules of *n*-butane, which leads to an increase in *n*-butane permeability.

CONCLUSION

Novel block copolymers were synthesized through sequential living polymerization of TMSP and MP by $NbCl_5$-based catalytic systems. It is possible to influence composition and properties of block copolymers by variation of monomer addition sequence and initial ratio of monomers. Furthermore, selective extraction of copolymerization products allows obtaining PTMSP-*b*-PMP in a wide range of TMSP/MP

Table 5. Pure Gas Permeability Coefficients (*P*) for PTMSP-*b*-PMP, PMP, and PTMSP Samples

	P, barrer[a]						
sample	H_2	He	N_2	O_2	CO_2	CH_4	C_4H_{10}
PMP	3500	1600	800	1700	7500	2000	5000
10:90[b]	4700	2200	1000	2300	11000	2800	6800
25:75[b]	5750	2600	1450	2750	13500	3500	8900
35:65[b]	6800	3000	1700	3300	15000	4100	10000
50:50[b]	7600	3250	2150	3800	17000	5200	14000
60:40[b]	8200	3400	2400	4100	18000	5900	17000
75:25[b]	10000	4000	3100	5100	22000	8200	26000
PTMSP	13000	5300	5200	7500	28000	14000	49000

[a]1 barrer = 1×10^{-10} cm^3 (STP) × cm × cm^{-2} × s^{-1} × $(cmHg)^{-1}$. [b]PTMSP/PMP block ratio in PTMSP-*b*-PMP.

dx.doi.org/10.1021/ma202140c | *Macromolecules* 2012, 45, 1222−1229

content ratio (from 15:85 to 80:20). Results of selective extraction, GPC, and IR and NMR spectroscopy testify formation of block copolymers of TMSP with MP.

PTMSP-*b*-PMP block copolymers have high thermal stability and good mechanical properties. The studies of supramolecular structure indicate that PTMSP-*b*-PMP possess a two-phase structure characterized by presence of regions with an increased level of ordering dispersed in amorphous polymer matrix. The macrochain packing of block copolymers enriched with TMSP units becomes less dense and less ordered. Thus, in PTMSP-*b*-PMP block copolymers gas transport parameters increase with TMSP units content, whereas resistance toward organic solvents increases with MP units content.

■ ASSOCIATED CONTENT

Supporting Information

^{13}C NMR spectra of PTMSP, PMP, and PTMSP-*b*-PMP block copolymers and calculation of their cis/trans content. This material is available free of charge via the Internet at http://pubs.acs.org.

■ AUTHOR INFORMATION

Corresponding Author

*Tel +7 495 9554205; Fax +7 495 6338520; e-mail sultanov@ips.ac.ru.

■ ACKNOWLEDGMENTS

This work was supported by the Russian Foundation of Basic Research, project 07-03-00553, and the Ministry of Education and Science of the Russian Federation (GK No. 16.516.11.6140). The authors thank G. N. Bondarenko, M. Yu. Gorshkova, and G. A. Shandryuk for their experimental help.

■ REFERENCES

(1) Nagai, K.; Masuda, T.; Nakagawa, T.; Freeman, B. D.; Pinnau, I. *Prog. Polym. Sci.* **2001**, *26*, 721−798.
(2) Matson, S. M.; Bondarenko, G. N.; Khotimskiy, V. S. *Polym. Sci., Ser. A* **2006**, *48*, 893−898.
(3) Kwak, G.; Masuda, T. *J. Polym. Sci., Part A: Polym. Chem.* **2000**, *38*, 2964−2969.
(4) Ghisellini, M.; Quinzi, M.; Baschetti, M.; Doghieri, F.; Costa, G.; Sarti, G. *Desalination* **2002**, *149*, 441−445.
(5) Morisato, A.; Pinnau, I. *J. Membr. Sci.* **1996**, *121*, 243−250.
(6) Khotimskii, V. S.; Matson, S. M.; Litvinova, E. G.; Bondarenko, G. N.; Rebrov, A. I. *Polym. Sci., Ser. A* **2003**, *45*, 740−746.
(7) Masuda, T.; Higashimura, T. *Adv. Polym. Sci.* **1987**, *81*, 121−165.
(8) Kuzler, J. F.; Percec, V. *Polym. Bull.* **1987**, *18*, 303−309.
(9) Masuda, T.; Yoshimura, T.; Fujimori, J.; Higashimura, T. *J. Chem. Soc., Chem. Commun.* **1987**, *23*, 1805−1806.
(10) Masuda, T. *J. Polym. Sci., Part A: Polym. Chem.* **2007**, *45*, 165−180.
(11) Mayershofer, M. G.; Nuyken, O. *J. Polym. Sci., Part A: Polym. Chem.* **2005**, *43*, 5723−5747.
(12) Iwawaki, E.; Hayano, S.; Nomura, R.; Masuda, T. *Polymer* **2000**, *41*, 4429−4436.
(13) Iwawaki, E.; Hayano, S.; Masuda, T. *Polymer* **2001**, *42*, 4055−4061.
(14) Akiyoshi, K.; Masuda, T.; Higashimura, T. *Makromol. Chem.* **1992**, *193*, 755−763.
(15) Sultanov, E. Yu.; Gorshkova, M. Yu.; Semenistaya, E. N.; Khotimsky, V. S. *Polym. Sci., Ser. B* **2008**, *50*, 330−333.
(16) Sultanov, E. Yu.; Khotimskiy, V. S. *Macromol. Symp.* **2010**, *296*, 72−76.
(17) Surovtsev, A. A.; Petrushanskaya, N. V.; Karpov, O. P.; Khotimskiy, V. S.; Litvinova, E. G. RF Patent 2228323, 2004.
(18) Litvinova, E. G.; Melekhov, V. M.; Petrushanskaya, N. V.; Roscheva, G. V.; Fedotov, V. B.; Feldblyum, V. Sh.; Khotimskiy, V. S. RF Patent 1823457, 1993.
(19) Yave, W.; Peinemannn, K.-V.; Shishatskiy, S.; Khotimskiy, V.; Chirkova, M.; Matson, S.; Litvinova, E.; Lecerf, N. *Macromolecules* **2007**, *40*, 8991−8998.
(20) Johnson, A. F.; Mohsin, M. A.; Meszena, Z. G.; Graves-Morris, P. *Polym. Rev.* **1999**, *39*, 527−560.
(21) Ivin, K. J.; Milligan, B. D. *Makromol. Chem., Rapid Commun.* **1987**, *8*, 269−271.
(22) Ovchinnikov, Yu. K.; Antipov, E. M.; Markova, G. S.; Bakeev, N. F. *Makromol. Chem.* **1976**, *177*, 1567.
(23) Khotimsky, V. S.; Tchirkova, M. V.; Litvinova, E. G.; Rebrov, A. I.; Bondarenko, G. N. *J. Polym. Sci., Part A: Polym. Chem.* **2003**, *41*, 2133−2155.
(24) Pinnau, I.; Toy, L. G. *J. Membr. Sci.* **1996**, *116*, 199−209.

Macromolecules

Article

pubs.acs.org/Macromolecules

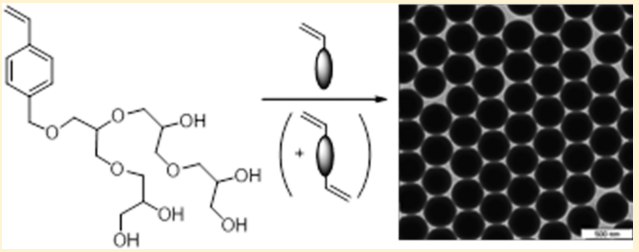
Surfactant-Free Synthesis of Polystyrene Nanoparticles Using Oligoglycidol Macromonomers

Sascha Pargen, Christian Willems, Helmut Keul, Andrij Pich,* and Martin Möller*

DWI an der RWTH Aachen e.V. and Institute of Technical and Macromolecular Chemistry, RWTH Aachen University, Forckenbeckstrasse 50, D-52056 Aachen, Germany

Supporting Information

ABSTRACT: We investigate the synthesis of functional polystyrene/oligoglycidol particles by surfactant-free emulsion polymerization. Oligoglycidol macromonomers with linear and branched oligoglycidol structure and variable oligoglycidol chain lengths were synthesized. These macromonomers were used as surfmers (surfactants and comonomers) in emulsion polymerization of styrene. Monodisperse colloidally stable polystyrene particles were obtained, decorated with oligoglycidol chains with diameters between 100 and 600 nm. The increase of the macromonomer concentration induced a decrease of the particle size and broadening of the particle size distribution. The macromonomers with branched architecture were more effective and produced monodisperse particles even at low concentrations. Due to the steric stabilization provided by the hydrophilic oligoglycidol layer on the particle surface, the emulsion of polystyrene/oligoglycidol particles obtained exhibited very good resistance against electrolytes. The chemical and enzyme catalyzed grafting polymerization of ε-caprolactone from the polystyrene/oligoglycidol particle surface was demonstrated along with formation of composite particles.



INTRODUCTION

Polymer nanoparticles are of growing interest in industry and academia. A major route to polymer nanoparticles, the so-called polymer latexes, is heterophase polymerization such as suspension, miniemulsion, or emulsion polymerization.[1] In emulsion polymerization, barely water-soluble monomers are converted in a kinetically controlled radical polymerization to yield polymer nanoparticles. Stabilization of the emulsions, which are understood as dispersed systems of (dispersed) droplets in a continuous liquid phase, is achieved sterically, or electrostatically, by addition of surfactants, such as sodium dodecyl sulfate (SDS). However, these surfactants most often lack the possibility of later functionalization or are even a hindrance in later modification of the particle surfaces. An elegant method to avoid these problems is to use reactive surfactants that are covalently linked to the particles and can be used for stabilization of the polymer latexes.[2−8] Having functional groups, these reactive surfactants are suitable for later modification reactions. Thompson et al., for example, recently reported the synthesis of polymer latexes and colloidsomes using hydroxyl functional macromonomers as reactive surfactant.[9−11] While polymer nanoparticles are usually only stable in aqueous media, cross-linked particles also offer the possibility to work in organic media. Depending on the size of particles, the core material, the shell functionality, and shell structure polymer nanoparticles, with their very high specific surface, can be used in a large variety of different applications. Cross-linked particles, for example, can be synthesized by dispersion and suspension polymerization[12−14] and are used as specific sorbents,[15−17] ion exchangers,[18,19] hydrogen storage,[20−22] or as packing in high performance liquid chromatography.[23] Furthermore, polymer nanoparticles are desirable for biomedical applications such as imaging,[24,25] drug delivery,[26,27] immobilization of bioactive compounds, e.g., protein carriers,[28,29] or as components in medical diagnostics and devices. Two of the most important requirements for polymer nanoparticles in biomedical applications are biocompatibility and functional groups suitable for efficient binding of bioactive compounds, such as proteins. From the literature poly(ethylene oxide) (PEO) is known to have excellent biocompatibility and reduced unspecific protein absorption.[30,31] However, PEO has one big disadvantage, since it bears functional groups suitable for modification or immobilization reactions only at the chain end. Polyglycidol, a polyether with hydroxymethyl side chains in each repeating unit is known to be biocompatible, too. Thus, polyglycidols represent an attractive alternative to PEO as hydrophilic part in surface active macromonomers or surfmers.[32] Additionally, linear polyglycidol can be synthesized in a controlled manner by anionic polymerization techniques, if protected glycidol monomers such as ethoxy glycidyl ether (EEGE) are used.[33−37] Polymerization of glycidol itself leads to hyperbranched structures, owing to inter- and intramolecular proton transfer from activated chain ends to free OH groups.[38−40] Recently, the synthesis of oligoglycidol macro-

Received: September 21, 2011
Revised: December 19, 2011
Published: January 17, 2012

ACS Publications © 2012 American Chemical Society

dx.doi.org/10.1021/ma2021437 | Macromolecules 2012, 45, 1230−1240

Table 1. Synthesis of Linear VBA-PEEGE Macromonomers at 80 °C

	VBA [g] ([mmol])	diglyme [mL]	KO^{t}Bu[a] [mL] ([mmol])	EEGE [g] ([mmol])	hydroquinone [mg]
1a	1.50 (11.2)	10	2.2 (2.2)	6.54 (44.7)	3
1b	3.00 (22.4)	20	4.5 (4.5)	19.65 (134.4)	5
1c	1.0 (7.5)	15	1.5 (1.5)	13.07 (89.4)	3
1d	1.0 (7.3)[b]	15	1.5 (1.5)	12.81 (87.6)	

[a]1 M solution in THF. [b]Ethylbenzyl alcohol (EBA) was used instead of VBA.

monomers, suitable as hydrophilic building block of amphiphilic copolymers, was reported by our group.[41] Linear and branched oligoglycidol macromonomers with down to 3 repeating units were accessible in this way. The oligoglycidol macromonomers themselves bear a potential amphiphilic character, with their structure consisting of a hydrophobic head and a hydrophilic oligoglycidol tail. Dworak et al. showed that such macromonomers can be used as reactive surfactants in the synthesis of polymer nanoparticles.[42] However, with their synthesis route, only linear polyglycidol macromonomers are accessible, and their hydrophobic *tert*-butyl end group might be a drawback for the amphiphilic character.

Herein we report the emulsifier-free synthesis of polystyrene nanoparticles with good colloidal stability by emulsion polymerization. In this protocol reactive, colloidally stable core−shell nanoparticles were obtained, using oligoglycidol macromonomers with linear and branched chain structures as reactive surfactants. Our aim was to explore the influence of the macromonomer type (linear or branched) and to concentrate on properties of polymer colloids. Grafting of ε-caprolactone by chemical and enzymatic catalysis is presented in a short outlook.

EXPERIMENTAL PART

Materials. Synthesis of 4-vinylbenzyl alcohol (VBA) was performed according to the literature.[41] Styrene and divinylbenzene were dried over calcium hydride and degassed by freeze−thaw cycles. Ethoxy ethyl glycidyl ether (EEGE) was obtained from 2,3-epoxypropan-1-ol (glycidol) and ethyl vinyl ether according to Fitton et al.,[43] purified by distillation, and stored under a nitrogen atmosphere over molecular sieves (4 Å). Diglyme was distilled over sodium and stored under a nitrogen atmosphere over molecular sieves (4 Å). All other chemicals were used as received. Syntheses of the oligoglycidol macromonomers and copolymers were performed in round-bottom flasks equipped with septa in a nitrogen atmosphere. Emulsion polymerizations were performed in glass reactors in a nitrogen atmosphere. For purification nitrogen (Linde 5.0) was passed over molecular sieves (4 Å).

Synthesis. *Linear VBA-PEEGE Macromonomer **1b**.* VBA (3.0 g, 22.4 mmol) and a small amount of hydroquinone were dissolved in diglyme (20 mL), a 1 M THF solution of potassium *tert*-butoxide (4.5 mL, 4.5 mmol) was added, and the solution was stirred for 30 min at room temperature. *tert*-Butanol and THF were removed in vacuum. After addition of EEGE (19.65 g, 134.4 mmol) the polymerization was carried out at 80 °C overnight. Afterward, diglyme was removed and the product was dried in a vacuum. VBA-PEEGE macromonomers **1a** and **1c** were synthesized using the same procedure (Table 1). VBA-*l*PEEGE$_6$ (**1b**): δ_H (300 MHz, $CDCl_3$) = 1.08 (t, 18 H, CH_3), 1.17 (d, 18 H, CH_3), 3.27−3.63 (m, 42 H, CH, CH_2), 4.48 (s, 2 H, CH_2), 4.64 (m, 6 H, CH), 5.35 (d, 1 H, CH_2), 5.80 (d, 1 H, CH_2), 6.68−6.76 (dd, 1 H, CH), 7.29 (d, 2 H, CH), 7.44 (d, 2 H, CH) ppm.

*Linear VBA-Oligoglycidol Macromonomer **2b**.* VBA-PEEGE macromonomer **1b** from the previous experiment was dissolved in THF (30 mL per g polymer) and aqueous HCl (35−38%) was added (1.5 mL per g polymer). The solution was stirred at room temperature for 3 h. During this time an oily phase was formed. THF was decanted, and the product was washed three times with THF. After drying in vacuum the macromonomer was isolated as viscous oil and characterized by NMR spectroscopy.

VBA oligoglycidol macromonomers **2a** and **2c** were synthesized by the same procedure. VBA-*l*PG$_6$ (**2b**): Yield: 88%. δ_H (300 MHz, DMSO) = 3.19−3.81 (m, 24 H, CH_2), 4.00−4.18 (m, 6 H, CH), 4.49−4.61 (br s, 2 H, CH_2), 4.92−5.01 (m, 1 H, OH), 5.25 (d, 1 H, CH_2), 5.82 (d, 1 H, CH_2), 6.73 (dd, 1 H, CH), 7.31 (d, 2 H, CH), 7.45 ppm (d, 2 H, CH).

*Hyperbranched VBA-Oligoglycidol Macromonomer **3**.* VBA (4.296 g, 31.88 mmol) and a small amount of hydroquinone were dissolved in DMF (5 mL), and a 1 M THF solution (6.38 mL, 6.38 mmol) of potassium *tert*-butoxide was added. After 30 min stirring at room temperature *tert*-butanol and THF were removed in a vacuum. The mixture was heated to 80 °C, and a solution of glycidol (9.40 g, 127.51 mmol) in DMF (10 mL) was added slowly over 10 h with a syringe pump. DMF was removed in a vacuum, and the crude product was dissolved in methanol. Acid ion exchanger (Amberlite 15, 1 g per g polymer) was added, and the solution was stirred for 4 h. After filtration the solvent was removed, and the product was dried in a vacuum. VBA-*b*PG$_4$ (**3**): δ_H (300 MHz, DMSO) = 3.24−3.80 (m, 20 H, CH, CH_2), 4.49 (2 H, CH_2), 4.62 (br s, 5 H, OH), 5.23 (dd, 1 H, CH_2), 5.82 (dd, 1 H, CH_2), 6.66−6.78 (m, 1 H, CH), 7.28−7.33 (m, 2 H, CH), 7.39−7.44 ppm (m, 2 H, CH).

*Polystyrene-block-oligoglycidol Copolymer **4**.* The detailed synthesis can be found elsewhere.[44] The synthesis of polystyrene-*block*-oligoglycidol block copolymers was realized in a two-step procedure. Styrene and EEGE were polymerized by sequential anionic polymerization in benzene with the initiating system *sec*-butyllithium and phophazene base (*t*-BuP$_4$). The removal of the acetal protection group was performed using acidic ion-exchange resin in THF.

*Polymer Particles **5a** Prepared from Styrene and Oligoglycidol Macromonomer **2a**.* Oligoglycidol macromonomer **2a** (5 mg, 0.1 wt %) was dissolved in degassed water (100 mL). Styrene (5.0 g) was added, and the reaction mixture was heated to 80 °C while stirring with a speed of 240 rpm. Ammonium persulfate (50 mg, 1.0 wt %) was dissolved in degassed water (2 mL) and added to the reaction mixture. The polymerization was carried out at 80 °C overnight. All other polystyrene oligoglycidol nanoparticles were prepared according to the same procedure. Starting materials are listed in Table 2.

*Cross-Linked Polymer Particles **10a** Prepared from Styrene, Divinylbenzene, and Oligoglycidol Macromonomer **2b**.* Oligoglycidol macromonomer **2b** (50 mg, 1 wt %) was dissolved in degassed water (100 mL). Styrene (5.0 g) and divinylbenzene (0.25 g, 5 wt %) were added, and the reaction mixture was heated to 80 °C while stirring with a speed of 240 rpm. Ammonium persulfate (50 mg, 1 wt %) was dissolved in degassed water (2 mL) and added to the reaction mixture. The polymerization was carried out at 80 °C overnight. All other cross-linked polystyrene oligoglycidol nanoparticles were prepared according to the same procedure. Starting materials are listed in Table 3.

*Chemically Catalyzed Grafting Reaction of ε-Caprolactone onto Polystyrene/Oligoglycidol Particles **10d**.* Cross-linked polystyrene particles **10d** with branched oligoglycidol shell were freeze-dried and afterward dried at 50 °C in vacuum overnight. Particles **10d** (135 mg) and ε-caprolactone (3 mL) were stirred 2 h at room temperature and then were heated to 130 °C to obtain a homogeneous emulsion. The catalyst Zn(oct)$_2$ (8 mg, 20 μmol) was added, and the mixture was stirred 24 h at 130 °C. Workup was performed by centrifugation and two times washing with toluene and THF each. Particles **11a** were isolated as white powder after drying in vacuum.

dx.doi.org/10.1021/ma2021437 | *Macromolecules* 2012, 45, 1230−1240

Table 2. Synthesis of Polystyrene Oligoglycidol Nanoparticles at 80 °C

	macromonomer				macromonomer		
particle		wt % (mol %)[a]	[mg]	particle		wt % (mol %)[a]	[mg]
5a	**2a**	0.1 (0.02)	5	**7a**	**2c**	0.1 (0.01)	5
5b	**2a**	0.3 (0.07)	15	**7b**	**2c**	0.3 (0.03)	15
5c	**2a**	0.5 (0.12)	25	**7c**	**2c**	0.5 (0.05)	25
5d	**2a**	1.0 (0.24)	50	**7d**	**2c**	1.0 (0.10)	50
5e	**2a**	3.0 (0.73)	150	**7e**	**2c**	3.0 (0.31)	150
5f	**2a**	5.0 (1.21)	250	**7f**	**2c**	5.0 (0.51)	250
6a	**2b**	0.1 (0.02)	5	**8a**	**3**	0.1 (0.02)	5
6b	**2b**	0.3 (0.05)	15	**8b**	**3**	0.3 (0.07)	15
6c	**2b**	0.5 (0.09)	25	**8c**	**3**	0.5 (0.12)	25
6d	**2b**	1.0 (0.18)	50	**8d**	**3**	1.0 (0.24)	50
6e	**2b**	3.0 (0.54)	150	**8e**	**3**	3.0 (0.73)	150
6f	**2b**	5.0 (0.90)	250	**8f**	**3**	5.0 (1.21)	250
				9	**4**	1.0 (0.03)[b]	268

[a]Related to styrene. [b]Related to the polyglycidol content of copolymer **4**.

Table 3. Synthesis of Cross-Linked Polystyrene Oligoglycidol Nanoparticles at 80 °C

	macromonomer					
particle		wt %[a]	[mg]	styrene [g]	DVB [mg][b]	$(NH_4)_2S_2O_8$ [mg][c]
10a	**2b**	1	50	5.0	250	50
10b	**2b**	5	250	5.0	250	50
10c	**2c**	1	50	5.0	250	50
10d	**3**	1	50	5.0	250	50

[a]Related to styrene. [b]5 wt % related to styrene. [c]1 wt % related to monomer.

Enzymatically Catalyzed Grafting Reaction of ε-Caprolactone from Polystyrene/Oligoglycidol Particles ***10a***. Cross-linked polystyrene particles **10a** with a linear oligoglycidol shell were freeze-dried and afterward dried at 50 °C in vacuum overnight. Particles **10a** (203 mg) and ε-caprolactone (5 mL) were stirred 2 h at room temperature and then heated to 90 °C to obtain a homogeneous emulsion. The catalyst Novozyme 435 (0.5 g) was added, and the mixture was stirred 24 h at 90 °C. To the product THF was added, and the Novozyme 435 was filtered off. Work-up was performed by centrifugation and two times washing with toluene and THF each. Particles **11b** were isolated as white powder after drying in vacuum.

Characterization Methods. ^{1}H NMR spectra were recorded on a Bruker AC400 FT NMR spectrometer at 400 MHz. Deuterated solvents were used, and tetramethylsilane (TMS) served as the internal standard. Molecular weights (M_n and M_w) were determined by size exclusion chromatography (SEC). For THF as the eluent high-pressure liquid chromatography pump (ERC 6420) and a refractive index detector (WGE Dr. Bures ETA 2020) were used at 30 °C, the flow rate of the eluting solvent being 1.0 mL/min. Four columns with MZ-DVB gel were applied: length of each column 300 mm, diameter 8 mm, diameter of the gel particles 5 μm, nominal pore widths 50, 100, 1000, 10 000 Å. For DMF as solvent (containing LiBr (1 mg/mL) and a flow rate of 1.0 mL/min) a high-pressure liquid chromatography pump (Bischoff HPLC Compact pump) with a RI detector (Jasco RI-2031 plus) was used. Three columns with PSS GRAM gel were applied: length of each column 300 mm, diameter 8 mm, diameter of the gel particles 5 μm, nominal pore widths 50, 100, 1000, and 10 000 Å. Calibration was achieved using poly(methyl methacrylate) (PMMA) or poly(styrene) standards. Results were evaluated using WinGPC Unity software.

Differential scanning calorimetry (DSC) measurements were carried out on a Netzsch DSC 204 differential scanning calorimeter under a nitrogen atmosphere. Samples were measured in perforated closed aluminum pans using approximately 3–6 mg of sample with a heating rate 5 °C/min. The samples were measured in the temperature range 0–200 °C. The heat flow was determined as a function of temperature. First-order transitions were reported as the maxima or minima of the endothermic or exothermic peaks during the third heating and the second cooling scans. To determine the glass transition temperature, the inflection point was taken.

Thermogravimetric analysis (TGA) measurement was performed using a Netzsch TG 209c unit operating under nitrogen atmosphere. 20–30 mg of samples were placed in standard Netzsch alumina 85 μL crucibles and heated at 10 K/min to 500 °C. Before each measurement baseline correction was performed with an empty crucible.

IR measurements were made by FTIR spectrometer: Nexus 470 (Thermo Nicolet) (spectral resolution 8 cm^{-1}). Nanogel dispersions were dried by lyophilization and pressed in KBr pellets.

Dynamic light scattering (DLS) measurements were performed with a commercial laser light scattering spectrometer (ALV/DLS/SLS-5000) equipped with an ALV-5000/EPP multiple digital time correlator and laser goniometry system ALV/CGS-8F S/N 025 with a helium–neon laser (Uniphase 1145P, output power of 22 mW and wavelength of 632.8 nm) as a light source.

The zeta-potential of the polymer particles has been measured with a Zetasizer Nano Series, (Malvern Instruments). The pH value of the solution was adjusted by addition of 0.01 M NaOH or 0.01 M HCl.

Transmission electron microscopy (TEM) was measured on Zeiss LibraTM 120 (Carl Zeiss, Oberkochen, Germany). The electron beam accelerating voltage was set at 120 kV. A drop of the sample was trickled on a piece of Formvar and carbon-coated copper grid. Before being placed into the TEM specimen holder, the copper grid was air-dried under ambient conditions. At least 100 particles have been measured, and an average value was calculated.

The surface tension on the air–liquid interface was measured for solutions of linear and hyperbranched macromonomers having four glycidol units. The aqueous solutions with variable macromonomer concentrations were prepared. Samples were investigated by the pendant drop method with DSA (Krüss, Germany) instrument. Measurements were performed at T = 25 °C.

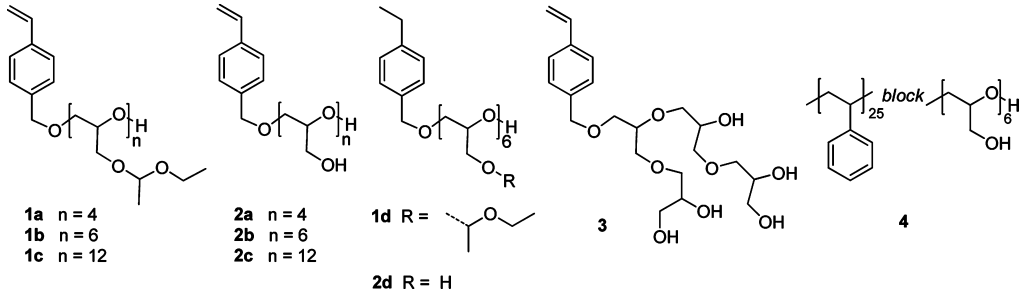


Figure 1. Oligoglycidol macromonomers and PS-*block*-oG copolymer (**4**) as surfactants for the emulsion polymerization of styrene.

dx.doi.org/10.1021/ma2021437 | *Macromolecules* 2012, 45, 1230–1240

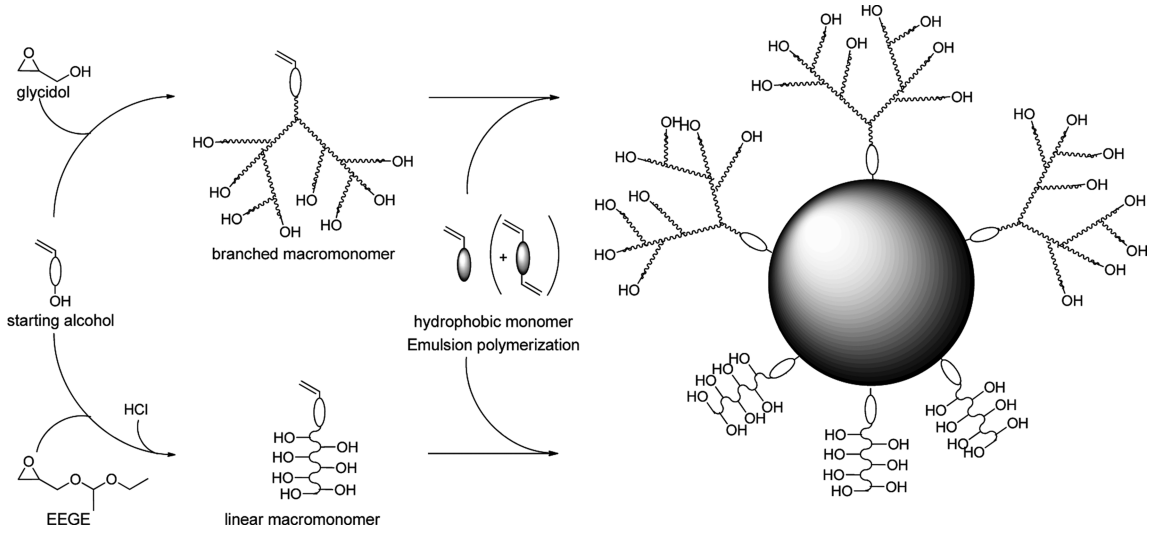


Figure 2. Synthesis of hydroxyl-functional polystyrene nanoparticles from oligoglycidol macromonomers and styrene.

RESULTS AND DISCUSSION

The objective of the experiments described here was to explore and compare the possibility of using linear and branched oligoglycidol macromonomers with the styrenic headgroup (Figure 1) as reactive surfactants in the synthesis of polystyrene nanoparticles (Figure 2).

The oligoglycidol macromonomers serve as surfmers (a combination of *surf*actant and mono*mer*) in the polymerization process and fulfill two important functions: they undergo copolymerization with styrene and stabilize growing polymer particles in continuous phase. Second, surfmers become covalently grafted to the polymer particle surface and form a hydrophilic layer providing steric stabilization for colloids (Figure 2). A direct comparison of particles decorated with linear and branched macromonomers was performed in this study. Furthermore, the influence of the oligoglycidol chain length on the particle formation was investigated. Additionally, the synthesis of polystyrene colloids decorated with oligoglycidol macromonomers was performed in the presence of divinylbenzene to obtain highly cross-linked polymer particles. The cross-linking of polystyrene particles with a functional polyglycidol shell may increase the versatility in later modification steps as well as broaden the range of possible applications.

The synthesis of linear and branched oligoglycidol macromonomers by anionic ring-opening polymerization starting from 4-vinylbenzyl alcohol (VBA) was recently published.[41]

Linear oligoglycidol macromonomers **2a−c** with 4 to 12 repeating units were obtained for this work, by anionic ring-opening polymerization of EEGE with VBA as initiator, followed by hydrolysis of the acetal protection group. The branched macromonomer **3** with four repeating units was synthesized by anionic polymerization of glycidol with VBA as initiator. The successful synthesis of these four macromonomers was proven by NMR and SEC (Table 4).

The synthesis of polymer nanoparticles was performed by emulsion polymerization in water using hydrophilic oligoglycidol macromonomers **2a−c** and **3** as reactive surfactants. No further emulsifier was added. Styrene as a commercially available monomer was chosen as core material for the polymer nanoparticles (Figure 3).

Table 4. NMR and SEC Results for Linear and Branched Oligoglycidol Macromonomers

macromonomer	P_n (th)	P_n (exp)[a]	M_n [g/mol]	M_w [g/mol]	M_w/M_n	yield [%]
VBA-*l*PEEGE$_4$ (**1a**)	4	4.1	800	900	1.13	100
VBA-*l*PEEGE$_6$ (**1b**)	6	6.3	1100[b]	1200[b]	1.09[b]	100
VBA-*l*PEEGE$_{12}$ (**1c**)	12	12.4	1800	2000	1.10	100
VBA-*b*PG$_4$ (**3**)	4	3.6	500[c]	850[c]	1.61[c]	95

[a]Determined by ^{1}H NMR. [b]Determined by size exclusion chromatography in THF using calibration with PMMA standards. [c]Determined by size exclusion chromatography in DMF with 1 g/L LiBr using calibration with PMMA standards.

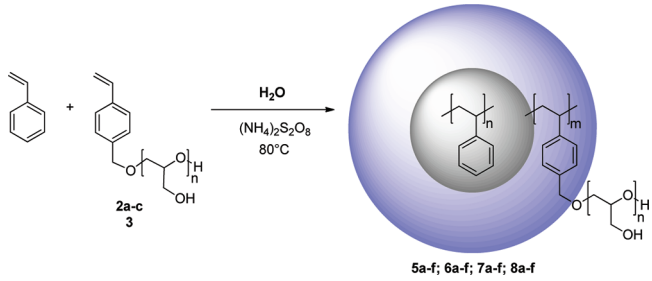


Figure 3. Emulsion copolymerization of styrene and oligoglycidol macromonomers yielding polymer nanoparticles.

A low amount of homopolystyrene coagulate was filtered off from the emulsion. No further purification was necessary before characterization. Yields were determined gravimetrically by drying 1 mL of the dispersion at 90 °C to constant weight. High yields (>75%) were achieved for all emulsion polymerizations. Stable emulsions in the whole concentration range between 0.1 and 5 wt % were obtained with all four macromonomers **2a−c** and **3**. A detailed characterization of the particle sizes obtained from the four macromonomers used in different concentrations was performed by analyzing TEM images. The detailed characterization of samples obtained with dynamic light scattering (DLS) was also performed (see example in Figure S6, Supporting Information), and we found a good correlation between two techniques. Nevertheless, we

dx.doi.org/10.1021/ma2021437 | *Macromolecules* 2012, 45, 1230−1240

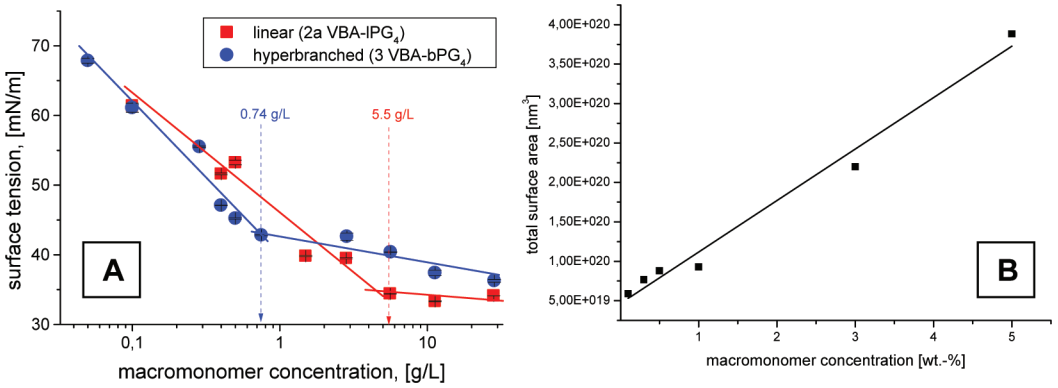


Figure 4. Surface tension vs macromonomer concentration in aqueous solution (A) and total surface area of polystyrene particles (samples **7a**–**7f**) as a function of macromonomer concentration (B) (lines are used to guide the eye).

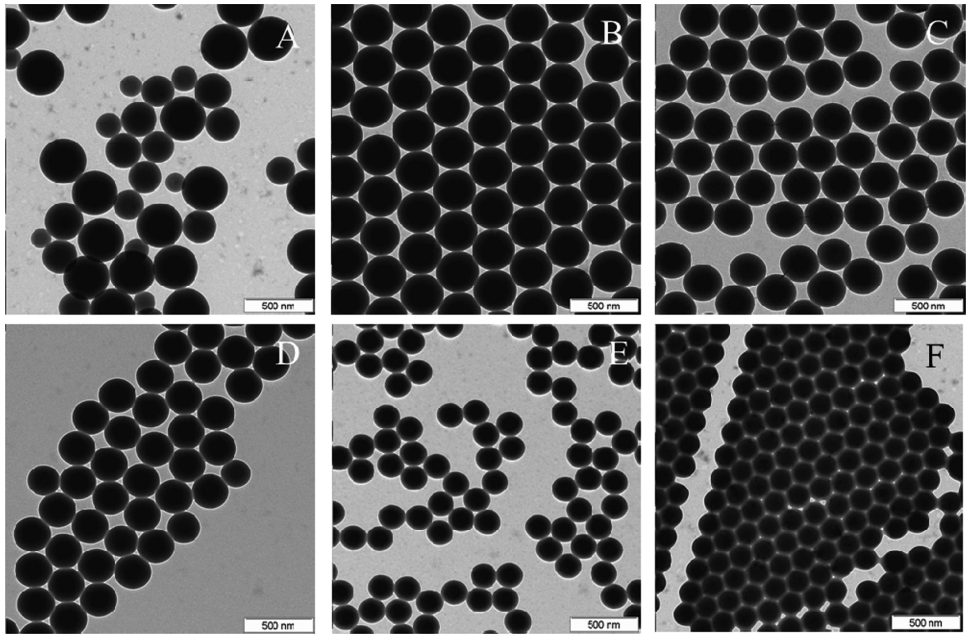


Figure 5. TEM images of polystyrene nanoparticles **5a**–**5f** synthesized with different concentrations of linear oligoglycidol macromonomer **2a** (VBA-*l*PG$_4$): A: 0.1%; B: 0.3%; C: 0.5%; D: 1%; E: 3%; F: 5% (scale bar 500 nm).

discuss here particle size determined by TEM because the DLS results for samples with broad or bimodal distribution were unsatisfactory. The experimental data for all samples presented in Table S1 (Supporting Information) indicate that an increase of the macromonomer concentration in reaction mixture reduces the size of polymer particles. This effect is observed independently from the macromonomer type.

We measured the surface tension of aqueous macromonomer solutions to investigate the ability of the macromonomers to form micellar aggregates. The experimental data for linear and hyperbranched macromonomers with four glycidol units are presented in Figure 4A. From the experimental results it was concluded that both macromonomers exhibit surface-active properties and reduce the surface tension on the water–air interface. However, the behavior of linear and hyperbranched oligoglycidol macromonomers is different from that of classical surfactants. First, the time necessary to reach the equilibrium surface tension is longer (typically each measurement was conducted for several hours). Second, the minimal surface tension (~35 mN/m) was detected at relative high concentrations (>10 g/L). These effects indicate that oligoglycidol macromonomers are not very effective surfactants, probably due to the short hydrophobic part that negatively influences the hydrophilic/lipophilic balance (HLB). Nevertheless, from the experimental data in Figure 4A—showing breakpoints in the surface tension vs macromonomer concentration curves—it can be concluded that micellar aggregates are formed. In the case of linear and hyperbranched oligoglycidol macromonomers with four glycidol units the critical concentrations are at 5.5 and 0.74 g/L, respectively. We assume that the increase of the hydrophilic oligoglycidol chain length will shift the critical concentrations to higher values. This behavior was reported for alkylated PEO-acrylate macromonomers with C_{12-14} alkyl chain length.[45] Additionally, it is known that temperature influences the aggregation of PEO-based nonionic surfactants.[46] Therefore, the influence of the temperature on the aggregate formation behavior of oligoglycidol macromonomers will be investigated in more detail. The existence of micelles and their architecture should be confirmed by light scattering techniques in our future work. Alternative methods for the determination of the critical micelle

dx.doi.org/10.1021/ma2021437 | *Macromolecules* 2012, 45, 1230–1240

concentration (cmc) such as fluorescence techniques[47] will be performed to verify these experimental data.

First of all, it is necessary to consider the mechanism of this batch polymerization process. A two-step mechanism of batch emulsion polymerization process for styrene and poly(ethylene oxide)-based macromonomer was proposed by Kawaguchi et al.[48,49] Pichot et al. confirmed this mechanism for a system based on styrene and NIPAM.[50,51] At low macromonomer concentration in the presence of a water-soluble initiator, the polymerization in water proceeds through a homogeneous nucleation mechanism because the functional monomer has a low ability to form defined micelles in water. Considering a much higher reactivity of the macromonomers compared to styrene, in the initial stage of the polymerization the formed oligomer radicals contain more macromonomer units. This will lead to the enhanced heterogeneity of the copolymers formed in water. Further addition of styrene units can provide formation of amphiphilic polymer chains that can effectively stabilize the polymerization of residual styrene in the core of the formed nuclei. So, the final particle consists of hydrophobic polystyrene-rich dense core and a more diffuse hydrophilic oligoglycidol-rich shell. Considering this mechanism, an increase of the macromonomer concentration will increase the number of nuclei and consequently the number of polymer particles. At constant monomer concentration and therefore constant monomer volume, this will induce formation of smaller polystyrene particles with a higher total surface area with an increase of macromonmer concentration. This is quantitatively shown in Figure 4B for particles **7a**−**7f** synthesized with linear oligoglycidol macromonomer **2c**.

The total surface area was calculated from the constant styrene volume used and the particle diameters determined from TEM images. The number of particles in the sample was determined from the particle diameter, the particle volume, and the overall styrene volume. The number and size of particles allowed the calculation of the total surface area in the sample. A straight line was observed for the total surface area as a function of the macromonomer concentration. Thus, a constant increase in macromonomer concentration leads to a constant increase in the total surface area and, consequently, with constant monomer volume to smaller particles. A similar behavior was observed in our previous investigation, where polystyrene particles were synthesized in the presence of a poly(ethylene glycol) methacrylate macromonomer.[52]

The morphology and size distribution of the polystyrene particles obtained have been evaluated by TEM. TEM images for particles **5a**−**5f** obtained by using the smallest linear oligoglycidol macromonomer **2a** with only four repeating units of glycidol are shown in Figure 5.

Emulsion polymerization of styrene with the lowest concentration of **2a** macromonomer (0.1 wt %) yielded particles **5a** with a bimodal size distribution. All other tested macromonomer concentrations yielded round-shaped particles with narrow size distributions (**5b**−**5f**). As expected, particle diameters decreased with increasing macromonomer (**2a**) concentration from 350 nm to about 180 nm. These results show that the size of polystyrene oligoglycidol nanoparticles can be adjusted in a wide range by the concentration of macromonomer. It should be noted that the polystyrene colloids were prepared at macromonomer concentrations below 2.5 g/L. According to Figure 4A, in this range the formation of the micellar aggregates does not take place, and the polymerization process proceeds according to the homogeneous nucleation mechanism discussed earlier.

The next step was to investigate if there is a difference in using oligoglycidol macromonomers with different chain lengths as reactive surfactants for the synthesis of polystyrene nanoparticles.

Particles **6b**−**6d** prepared with the macromonomer **2c** in concentrations between 0.3 and 1 wt % were obtained with a perfectly round shape and with narrow size distribution. In contrast, **6a** featured also smaller particles next to the main population of larger particles, with diameters of about 410 nm. It was assumed that the amount of macromonomer **2b** of 0.1 wt % was too low to form and stabilize all particles of the same size. A major difference to the particles **5a**−**5f** obtained from macromonomer **2a** with four repeating glycidol units are the particles **6e** and **6f** with 3 and 5 wt % of macromonomer **2b**, respectively. Surprisingly, both samples show larger particles with diameters of about 160 nm and also large fractions of particles with diameters in the range between 50 and 100 nm (Figure S1, Supporting Information). We assume that the formation of new nuclei is extremely fast at high macromonomer concentration. Owing to the excellent stabilization provided by the macromonomers, these nuclei do not aggregate to form larger particles but remain in the reaction mixture and may grow preferably by further additional monomer. The slow monomer diffusion may lead to the uncontrolled growth of polymer particles and finally results in the formation of different particle populations. Further attempts to obtain only the small particles of less than 100 nm by increasing the macromonomer concentration were unsuccessful.

Perfect spherical particles **7a**−**7d** with monodisperse size distribution are obtained for macromonomer concentrations between 0.1 and 1 wt % (Figure S2, Supporting Information). Further increase of the macromonomer concentration to 3 wt % still led to particles **7e** with narrow size distribution, but these particles lost the perfectly round shape. Unlike particles **6e** and **6f**, no particles with bimodal size distribution were observed for particles **7e** and **7f** with highest macromonomer concentration (3 and 5 wt %). At the highest macromonomer concentration of 5 wt %, polymer particles **7f** were obtained with a broad size distribution and without the spherical shape. Attempts to increase the macromonomer concentration further were unsuccessful, and no particles were obtained.

After testing three linear oligoglycidol macromonomers with different glycidol chain lengths, macromonomer **3** with a branched oligoglycidol structure was used as a reactive surfactant in the synthesis of polystyrene nanoparticles. Spherical particles in colloidal stable emulsions were obtained with all macromonomer concentrations. In contrast to the linear macromonomers, where only **2c** with the longest glycidol chain led to the formation of particles (**7a**) with narrow size distribution at the lowest macromonomer concentration (0.1 wt %), use of the branched macromonomer **3** with only four glycidol repeating units resulted in monodisperse particles, even at this low concentration (Figure S3, Supporting Information). In spite of this, sample **8e** with a main fraction of particles with a diameter of around 330 nm featured also smaller particles with diameters around 150 nm. Sample **8f** showed a broad size distribution with diameters between 130 and 400 nm with the highest macromonomer concentration of 5 wt % particles. It should be noted that samples **8e** and **8f** were synthesized at macromonomer concentrations 1.47 and 2.45 g/L, respectively. According to the experimental data presented in Figure 4A,

dx.doi.org/10.1021/ma2021437 | *Macromolecules* 2012, 45, 1230−1240

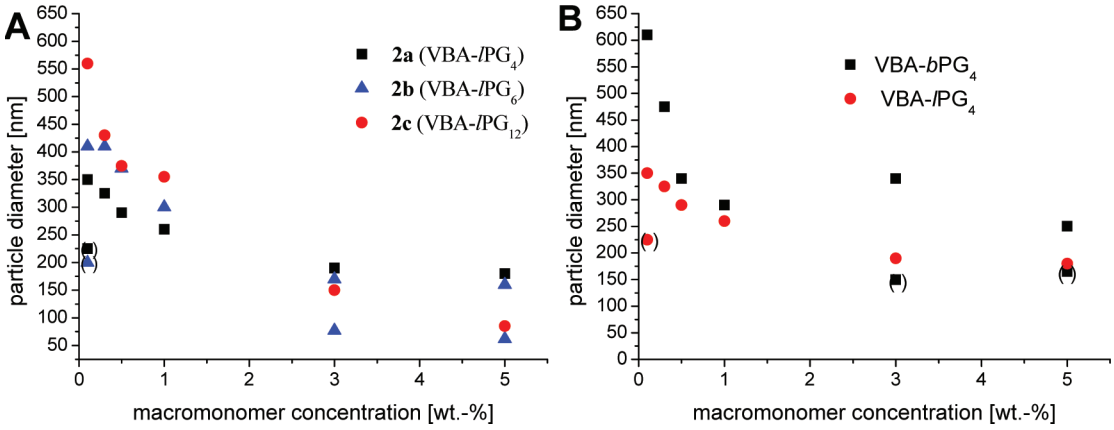


Figure 6. Size dependence of the synthesized polystyrene oligoglycidol particles **5a**−**8f** on macromonomer concentration: (A) oligoglycidol chain length and (B) oligoglycidol structure (branched or linear) as determined from TEM analysis.

these concentrations of macromonomer with a branched oligoglycidol chain are above the critical aggregation concentration. In this situation the particle formation mechanism should be different to that discussed above. Macromonomers confined in micellar aggregates can solubilize a certain amount of styrene and serve as polymerization locus leading to the formation of small polymer colloids. Simultaneously, styrene polymerizes by the homogeneous nucleation mechanism leading to the formation of larger colloids. This scenario will result in the formation of two particle populations and a bimodal size distribution.

To summarize the influence of the macromonomer type (linear or branched) and concentration, the size of all obtained polystyrene particles (samples **5a**−**8f**) are shown in Figure 6. (The small particle populations in samples with bimodal size distributions are marked in parentheses.) Especially at low macromonomer concentrations, there is a large difference in using oligoglycidol macromonomers with 4 (**2a**), 6 (**2b**), or 12 (**2c**) repeating units of glycidol. Particles of a size up to 350 and 410 nm were obtained by using macromonomers **2a** and **2b** with four and six glycidol repeating units. In comparison with the larger macromonomer **2c** with 12 glycidol repeating units, particles with diameters up to 610 nm were obtained. So, as a general trend we conclude that with an increase of the oligoglycidol molecular weight the polystyrene particle size increases.

At higher macromonomer concentrations with more than 3 wt %, only with macromonomers **2a** and **2c**, polymer particles with monomodal size distributions were obtained. As for low concentrations, the influence of the macromonomer concentration on the particle size was larger when macromonomer **2c** was used as a reactive surfactant instead of **2a**, with only four repeating units of glycidol. Another important conclusion is that the reactive surfactants with longer oligoglycidol chains allow larger variation of the particle size, depending on their concentration.

Figure 6B shows the variation of the particle size for polystyrene particles synthesized with macromonomer **2a**, exhibiting a linear oligoglycidol chain and macromonomer **3** having a branched oligoglycidol structure. The branched macromonomer **3** led at low concentrations to monodisperse particles up to 610 nm, while only particles with bimodal distribution not larger than 350 nm were obtained with the same concentration of linear macromonomer **2a**. At higher macromonomer concentration (3−5 wt %), particles show bimodal or broad size distributions when synthesized with branched macromonomer **3** as a reactive surfactant. We assumed that with the branched oligoglycidol structure a wider area of the particle surface can be covered by hydroxyl groups than with linear oligoglycidol chains. Therefore, better stabilization with branched macromonomers at lower concentration led to formation of particles with monomodal size distribution. At higher concentrations, the loss of control over size distribution might be explained by the existence of macromonomer aggregates (micelles) and particle formation by different nucleation mechanisms.

The reactions described show that various reactive polystyrene/oligoglycidol particles can be obtained by diversifying macromonomer type and concentration. However, the question was how the oligoglycidol macromonomers stabilize the polymer particles. Is there really a covalent bonding of the macromonomers to the particle core, or do they act like conventional surfactants? Because of the low oligoglycidol macromonomer concentration, NMR analysis is not an efficient tool. Therefore, macromonomer **2d** was synthesized using 4-ethylbenzyl alcohol (EBA), instead of VBA, as an initiator for the polymerization of EEGE, to yield a macromonomer with equal structure, like **2a**−**2c**, but without the reactive double bond. The amphiphilic compound **2d** was tested as a surfactant in the emulsion polymerization of styrene using the reaction conditions described before. No stable emulsion and no polymer particles were formed under these conditions. Thus, it was concluded that the reactive macromonomers are covalently bonded to the polystyrene core of the particles. It is known that there is not a static but a dynamic stabilization of the particles with constant exchange between the different SDS molecules from conventional surfactants such as SDS. From the literature, it is also known that amphiphilic copolymers can be used as surfactants. Hence, we investigated if either the oligoglycidol macromonomers form first amphiphilic copolymers with styrene that then act as a surfactant or if the macromonomers are bounded to the longer polystyrene chains of the particle core. Therefore, polystyrene-*block*-oligoglycidol (PS_{25}-*block*-PG_6) **4** was synthesized by sequential anionic polymerization of styrene and EEGE and removal of the acetal protection group afterward. Copolymer **4** was used as a surfactant in the emulsion polymerization of styrene. From the results obtained using the reactive macromonomers the amount of block copolymer **4** was chosen to yield an oligoglycidol concentration of 0.49 g/L (1 wt % relatively to styrene). A

dx.doi.org/10.1021/ma2021437 | *Macromolecules* 2012, 45, 1230−1240

colloidal stable emulsion of nanoparticles **9** was formed. However, TEM images of the particles **9** showed differences in comparison to particles **6d** with equal concentration and chain length of oligoglycidol (Figure S4, Supporting Information). The use of block copolymer **4** yielded in particles with a broad size distribution. In contrast with macromonomer **2b**, almost monodisperse particles were obtained under equal reaction conditions. Additionally, further investigations were performed using SEC to investigate the molecular weight of the polymers in particles **9** and **6d**. (SEC traces of dissolved particles **9** and **6d** are shown in Figure 7.)

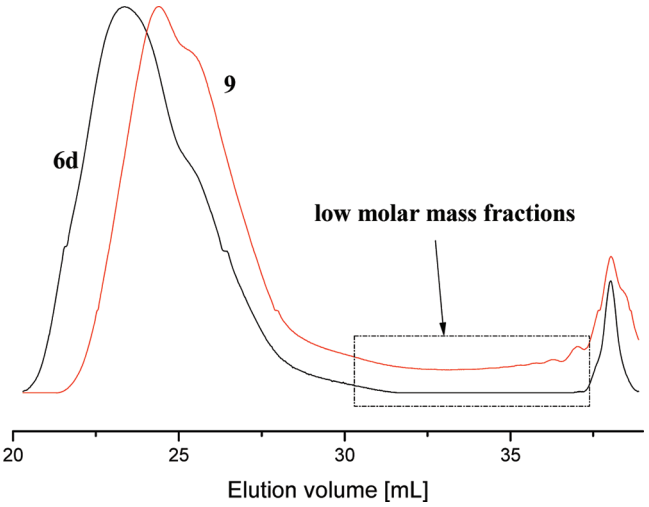


Figure 7. SEC traces in THF for the polymer of nanoparticles **9** synthesized in the presence of block copolymer **4** as surfactant and the polymer of particles **6d** synthesized in the presence of 1 wt % of macromonomer **2b** as a reactive surfactant.

The higher elution volume (lower molar mass) for polymer **9** compared to polymer **6d** is noticeable. Furthermore, larger amounts of low molar mass fractions were observed in polymer **9**. In contrast, no low molar mass components were visible in the SEC trace of polymer **6d**. On the basis of these observations, we assumed that the reactive oligoglycidol macromonomers were covalently linked to the polystyrene particle core. These experiments confirm the polymerization mechanism discussed previously and support the idea of formation of amphiphilic reactive copolymers at the early stages of polymerization process that stabilize growing polystyrene particles and become finally grafted onto the particle surface, providing efficient steric stabilization to the colloidal system. Again we stress here that this polymerization mechanism is observed at macromonomer concentrations below critical aggregate (micelle) formation.

Emulsion polymerizations described in this work showed that it was possible to synthesize various polystyrene nanoparticles with oligoglycidol macromonomers as reactive surfactants. Particles with diameters ranging from less than 100 nm to above 600 nm were obtained by changing type and concentration of macromonomer. However, these particles can be only used in aqueous medium. Particles would dissolve in organic solvents and thus be destroyed. To increase the versatility of the particles for applications in organic media, cross-linked particles were synthesized by adding 5 wt % of the cross-linker, divinylbenzene (DVB), during emulsion polymerization. Colloidal stable particle emulsions were formed, and no influence of divinylbenzene in particle formation was observed (Figure S5, Supporting Information). The successful cross-linking was proven by treatment with different organic solvents, such as DMF or THF and characterization by TEM afterward. Further characterization was performed by determining the zeta-potential (ZP) for the different polystyrene oligoglycidol nanoparticles. All particles showed a negative ZP around −40 mV, independently of the macromonomer concentration, caused by the presence of hydroxyl groups of oligoglycidol and sulfonyl groups, introduced by the initiator ammonium persulfate (Table S2, Supporting Information). The ZP was constant in a wide range of pH (Figure S7, Supporting Information).

The emulsions of the synthesized polymer nanoparticles were colloidally stable in pure water over several months. In addition, the cross-linked polymer nanoparticles were colloidally stable in various organic solvents, such as DMF of THF. However, for later applications it is important to know at which salt concentrations the particles stay colloidally stable. Therefore, particle size was analyzed by DLS in water with different salt concentrations of NaCl, $CaCl_2$, and $FeCl_3$. The salt concentration dependency was measured in the range of 10^{-5}–5 M. Particles **6c** and **8c** with a macromonomer content of 0.5 wt % were selected for these investigations. A comparison can be drawn with the choice of these two samples, if there is a difference in colloidal stability between polymer nanoparticles with a linear or a branched oligoglycidol shell. The variation of the particle size for particles **8c** with a branched oligoglycidol shell as a function of the different salt concentrations is shown in Figure 8.

A slight decrease in particle diameter was observed for NaCl with increasing salt concentration from 10^{-5} to 0.01 M. This behavior could be explained by the multidentate interaction between metal cations and polyethers which will result in a

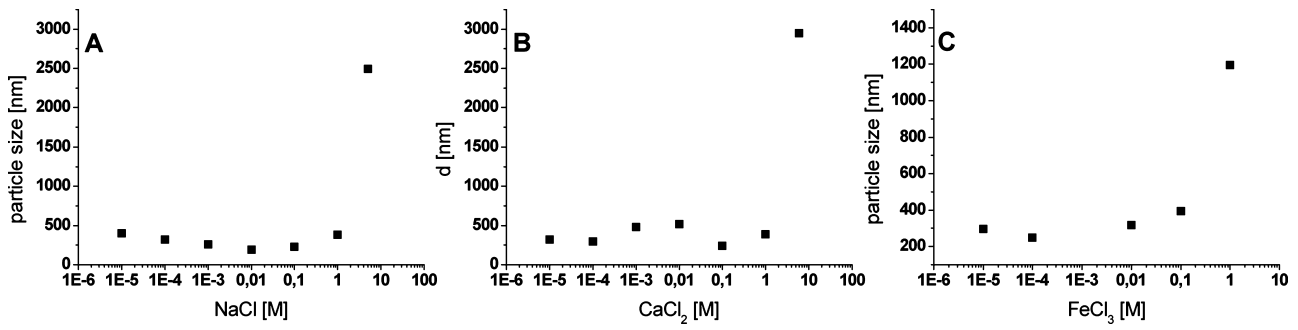


Figure 8. Variation of the size for particles **8c** synthesized with 0.5 wt % of branched macromonomer **3** at different salt concentrations.

dx.doi.org/10.1021/ma2021437 | *Macromolecules* 2012, 45, 1230–1240

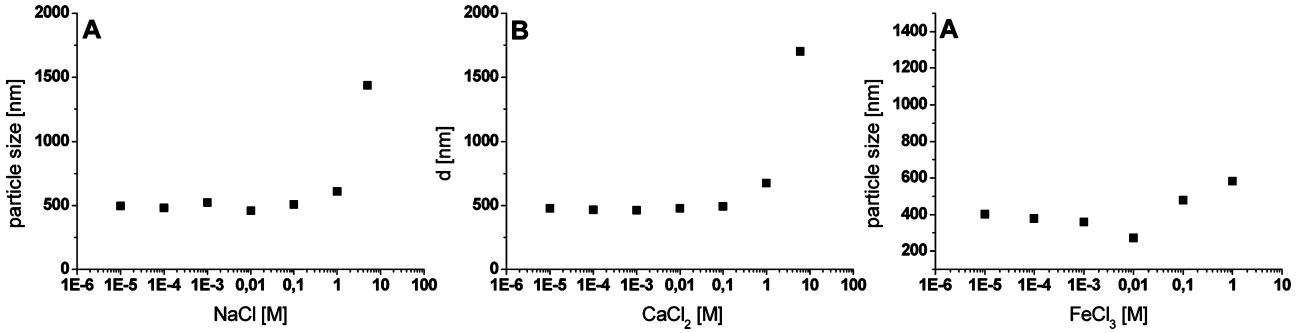


Figure 9. Variation of the size for particles **6c** synthesized with 0.5 wt % of linear macromonomer **2b** at different salt concentrations.

closer packing of the polymer segments. A further increase of the salt concentration to 1 M led to a slight increase of particle diameters. At a salt concentration of 5 M the colloidal stability was lost, and coagulates with a diameter above 2500 nm were formed. Similar behavior was found for the colloidal stability in $CaCl_2$ solutions. A small increase of the particle diameter was already observed in aqueous $FeCl_3$ solution, from 0.1 M solution. At a concentration of 1 M $FeCl_3$, particles already showed coagulate formation with diameters >1200 nm.

The determined particle sizes of polystyrene nanoparticles with linear oligoglycidol shell at different salt concentrations are shown in Figure 9 for comparison. Stable emulsions with constant particle diameters in the concentration range between 10^{-5} and 0.1 M were observed for NaCl and $CaCl_2$ solutions. This behavior was in contrast to the particles with a branched oligoglycidol shell, where a slight decrease in particle size was observed with increasing salt concentration. Therefore, the linear oligoglycidol shell showed better stabilization of polymer particles in salt-containing solutions, compared to branched oligoglycidol shells. At high concentrations of NaCl and $CaCl_2$ above, 1 M particles started to form coagulates and thus showed a similar behavior to that of particles with a branched oligoglycidol shell. In contrast, particles with a linear oligoglycidol shell showed a larger decrease in diameter by increasing the salt concentration of $FeCl_3$ from 10^{-5} to 0.01 M. Further increase of the $FeCl_3$ concentration led to coagulation of the polymer particles. In summary, polystyrene particles, with both linear and branched oligoglycidol shells, exhibit very good resistance toward electrolytes (up to 1 M for NaCl and $CaCl_2$ and up to 0.1 M $FeCl_3$ concentrations).

Finally, we discuss here a modification of the reactive polystyrene/oligoglycidol particles with another polymer to demonstrate the efficiency of the oligoglycidol surface layer for modification of polymer particles. Hans et al. reported the grafting of ε-caprolactone side chains from linear and star-shaped polyglycidols through chemical and enzymatic catalysis.[53,54] This concept was transferred to the modification of the polymer nanoparticles, and the successful grafting of ε-caprolactone was presented from cross-linked polystyrene oligoglycidol nanoparticles through chemical and enzymatic catalysis. After freeze-drying and further drying at 50 °C in vacuum, cross-linked particles were reacted with ε-caprolactone in bulk. $Zn(oct)_2$ was used as the chemical catalyst, and grafting reactions were performed at 130 °C. After several work-up steps by washing with THF and toluene and centrifugation, the particles were dried in a vacuum. For comparison, Novozyme 435 was used for the enzymatic catalysis, and the grafting reaction was performed at 90 °C in bulk. Owing to the cross-linked core of the particles, no NMR analysis could be applied to determine the successful grafting reaction. A qualitative analysis was performed using FTIR spectroscopy (Figure 10).

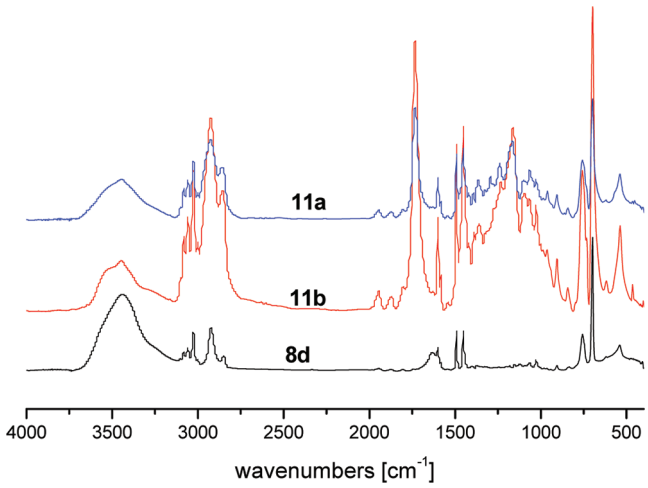


Figure 10. FTIR results for polystyrene oligoglycidol nanoparticles, after grafting ε-CL by chemical catalysis (**11a**) and after grafting ε-CL by enzymatic catalysis (**11b**).

The FTIR spectra show that grafting of ε-caprolactone on polystyrene particles was successful by chemical and by enzymatic catalysis. In both cases the FTIR showed an absorption band at 1733 cm^{-1} assigned to the carbonyl group of ε-caprolactone repeating units.

Furthermore, DSC and TGA measurements were performed to prove the successful grafting reactions. Figure 11 shows exemplarily DSC and TGA curves for particles **11a** after grafting ε-caprolactone by chemical catalysis with $Zn(oct)_2$, compared to the nonmodified polystyrene oligoglycidol particle **10a**.

A single glass transition temperature T_g = 106 °C is observed for the particle **10a** in the second heating curve of the DSC, corresponding to the polystyrene core. The T_g for the oligoglycidol shell of the polymer particles, which should be in the range of −40 °C for branched oligoglycidols with four repeating units, cannot be observed owing to its low concentration (1 wt %) in the particle. The DSC curve for PCL grafted particles **11a** showed a melting point at 45 °C with a melting enthalpy ΔH_m of 9.2 J/g, which was assigned to the poly(ε-caprolactone) grafts. The low melting point, compared to the melting temperature of homo-poly(ε-caprolactone) of about 60 °C, indicated, together with the low melting enthalpy, that only small crystallites were formed. Beside the melting

dx.doi.org/10.1021/ma2021437 | *Macromolecules* 2012, 45, 1230−1240

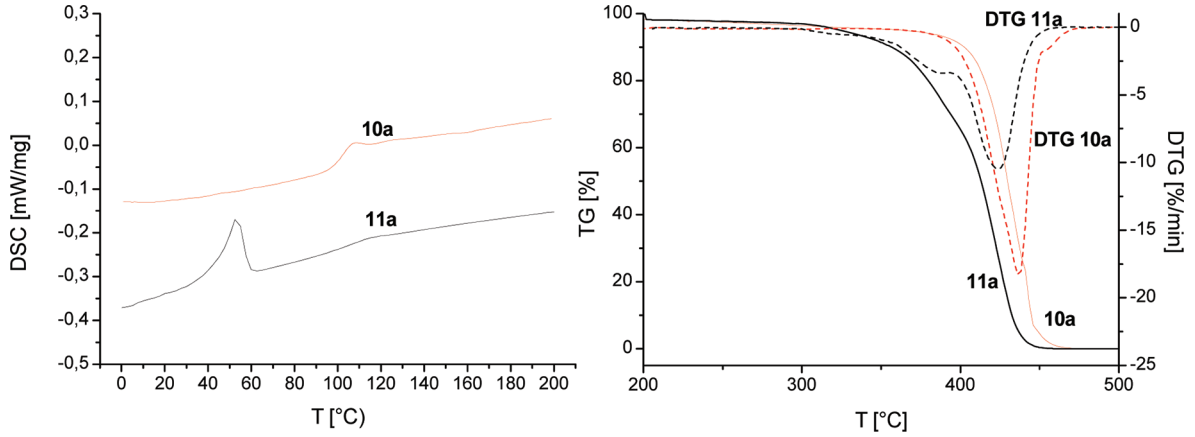


Figure 11. DSC and TGA curves for polystyrene oligoglycidol nanoparticles **10a** and PCL grafted particles **11a**.

temperature for PCL, a glass transition temperature T_g = 108 °C for the polystyrene core could be observed.

To investigate the differences in their thermal stability, thermogravimetric analysis (TGA) was conducted for polystyrene oligoglycidol nanoparticles **10a** and PCL grafted particles **11a**. Particles **10a** show one-step degradation with a significant mass loss above 400 °C. Similarly to DSC measurements, no influence of the oligoglycidol particle shell on thermal properties of polystyrene particles was detected. In comparison, the PCL grafted particles **11a** show a two-step degradation with a beginning mass loss at around 320 °C assigned to the poly(ε-caprolactone) degradation.[55] The second mass loss starting at about 400 °C was assigned to the polystyrene core. From the TGA curve the amount of PCL in particles **11a** was determined to be about 27%. This result confirms that grafting of poly(ε-caprolactone) from polystyrene oligoglycidol nanoparticles was successful. We believe that the reason for this high grafting efficiency is a high concentration of hydroxyl groups on the surface of polystyrene particles, provided by the grafted oligoglycidol layer. These results represent a short outlook for the potential use of these particles as macroinitiators for the chemical and enzymatic grafting of PCL side chains. More investigations and a more detailed analysis, especially on the polymerization efficiency, will follow.

CONCLUSIONS

The successful synthesis of functional polystyrene/oligoglycidol particles by surfactant free emulsion polymerization is presented in this work. 4-Vinylbenzyl alcohol was used for controlled synthesis of oligoglycidol macromonomers with linear and branched oligoglycidol structure and variable oligoglycidol chain lengths. These macromonomers were used as surfmers (surfactants and comonomers) in emulsion polymerization of styrene. Monodisperse polystyrene particles were obtained, decorated with oligoglycidol chains with diameters between 100 and 600 nm. The increase of the macromonomer concentration induced a decrease of the particle size. Particle size distribution becomes broad or bimodal at very low (<0.1%) or high (>3%) macromonmer concentration in the reaction mixture. The macromonomers with branched architecture were more effective and produced monodisperse particles even at low concentrations. The polystyrene particles with an oligoglycidol envelope obtained exhibited very good resistance against electrolytes owing to the steric stabilization provided by the hydrophilic oligoglycidol layer on the article surface. Finally, the chemical and enzyme catalyzed grafting of ε-caprolactone from polystyrene/oligoglycidol particles and formation of composite particles was successfully demonstrated.

ASSOCIATED CONTENT

Supporting Information

Experimental data (yield, hydrodynamic radii) for PS/PG colloids; TEM images of PS/PG colloids prepared with linear (PG: 6; 12) and branched (PG: 4) macromonomers; TEM images of PS particles prepared with PS−PG block copolymer and PS/PG colloids cross-linked with DVB; angle-dependent DLS measurement for sample **6a**; zeta-potential measurements for PS/PG particles. This material is available free of charge via the Internet at http://pubs.acs.org.

AUTHOR INFORMATION

Corresponding Author

*E-mail: moeller@dwi.rwth-aachen.de (M.M.); pich@dwi.rwth-aachen.de (A.P.).

ACKNOWLEDGMENTS

The authors thank Dr. Arthur Henke for help with DLS measurements. Financial support from VolkswagenFoundation is highly appreciated.

REFERENCES

(1) Landfester, K. *Macromol. Rapid Commun.* **2001**, *22*, 896.
(2) Meunier, F.; Elaissari, A.; Pichot, C. *Polym. Adv. Technol.* **1995**, *6*, 489.
(3) Charleux, B.; Pichot, C. *Polymer* **1993**, *34*, 195.
(4) Basinska, T. *e-Polym.* **2002**, 11.
(5) Kobayashi, S.; Uyama, H.; Choi, J. H.; Matsumoto, Y. *Polym. Int.* **1993**, *30*, 265.
(6) Herold, M.; Brunner, H. *Polym. Prepr.* **2002**, *43*, 1003.
(7) Houillot, L.; Nicolas, J.; Save, M.; Charleux, B.; Li, Y.; Armes, S. P. *Langmuir* **2005**, *21*, 6726.
(8) Amalvy, J. I.; Unali, G. F.; Li, Y.; Granger-Bevan, S.; Armes, A. P.; Binks, B. P.; Rodrigues, J. A.; Whitby, C. P. *Langmuir* **2004**, *20*, 4345.
(9) Thompson, K. L.; Armes, S. P.; York, D. W.; Burdis, J. A. *Macromolecules* **2010**, *43*, 2169.
(10) Thompson, K. L.; Armes, S. P. *Chem. Commun.* **2010**, *46*, 5274.
(11) Thompson, K. L.; Armes, S. P.; Howse, J. R.; Ebbens, S.; Ahmad, I.; Zaidi, J. H.; Yoek, D. W.; Burdis, J. A. *Macromolecules* **2010**, *43*, 10466.
(12) Davankov, V. A.; Rogozhin, S. V.; Tsyurupa, M. P. *Angew. Makromol. Chem.* **1973**, *32*, 145.

(13) Tsyurupa, M. P.; Davankov, V. A. *React. Funct. Polym.* **2006**, *66*, 768.
(14) Salek, P.; Horak, D. *e-Polym.* **2011**, 64.
(15) Azanova, V. V.; Hradil, J. *React. Funct. Polym.* **1999**, *41*, 163.
(16) Davankov, V. A.; Tsyurupa, M. P.; Tarabaeva, O. G.; Shabaeva, A. S. *Ion Exch. Dev. Appl.* **1996**, *182*, 209.
(17) Belyakova, L. D.; Schevchenko, T. I.; Davankov, V. A.; Tyyurupa, M. P. *Adv. Colloid Interface Sci.* **1986**, *25*, 249.
(18) Pan, B. C.; Xiong, Y.; Li, A. M.; Chen, J. L.; Zhang, Q. X.; Jin, X. Y. *React. Funct. Polym.* **2002**, *53*, 63.
(19) Fontanals, N.; Cormack, P. A. G.; Sherrington, D. C. *J. Chromatogr.* **2008**, *1215*, 21.
(20) Germain, J.; Hradil, J.; Fréchet, J. M. J.; Svec, F. *Chem. Mater.* **2006**, *18*, 4430.
(21) Thomas, A.; Kun, P.; Weber, J.; Titirici, M. M.; Antonietti, M. *Macromol. Rapid Commun.* **2009**, *30*, 221.
(22) Germain, J.; Fréchet, J. M. J.; Svec, F. *Small* **2009**, *5*, 1098.
(23) Kim, K.; Kim, D. *J. Appl. Polym. Sci.* **2005**, *96*, 200.
(24) Thurecht, K. J.; Blakey, I.; Peng, H.; Squires, O.; Hsu, S.; Alexander, C.; Whittaker, A. K. *J. Am. Chem. Soc.* **2010**, *132*, 5336.
(25) Raemdonck, K.; Demeester, J.; De Smedt, S. *Soft Matter* **2009**, *5*, 707.
(26) Ryu, J. H.; Jiwpanich, S.; Chacko, R.; Bickerton, S.; Thayumanavan, S. *J. Am. Chem. Soc.* **2010**, *132*, 8246.
(27) Tao, L.; Chou, W. C.; Tan, B. H.; Davis, T. P. *Macromol. Biosci.* **2010**, *10*, 632.
(28) Mantovani, G.; Lecolley, F.; Tao, L.; Haddleton, D. M.; Clerx, J.; Cornelissen, J.; Velonia, K. *J. Am. Chem. Soc.* **2005**, *127*, 2966.
(29) Heredia, K. L.; Nguyen, T. H.; Chang, C. W.; Bulmus, V.; Davis, T. P.; Maynard, H. D. *Chem. Commun.* **2008**, 3245.
(30) Li, J.; Carlsson, J.; Huang, S. C.; Caldwell, K. D. In *Hydrophilic Polymers; Performance with Environmental Acceptability*; ACS Advances in Chemistry Series 248; Glass, J. E., Ed.; American Chemical Society: Washington, DC, 1996; pp 61−78.
(31) Andrade, J. D.; Hlady, V. *Adv. Polym. Sci.* **1986**, *79*, 1.
(32) Chapek, I. *Adv. Colloid Polym. Sci.* **2000**, *88*, 295.
(33) Taton, D.; Leborgne, A.; Sepulchre, M.; Spassky, N. *Macromol. Chem. Phys.* **1994**, *195* (1), 139.
(34) Dworak, A.; Panchev, I.; Trzebicka, B.; Walach, W. *Macromol. Symp.* **2000**, *153*, 233.
(35) Hans, M.; Keul, H.; Moeller, M. *Polymer* **2009**, *50*, 1103.
(36) Walach, W.; Kowalczuk, A.; Trzebicka, B.; Dworak, A. *Macromol. Rapid Commun.* **2001**, *22*, 1272.
(37) Keul, H.; Möller, M. *J. Polym. Sci., Part A: Polym. Chem.* **2009**, *47*, 3209.
(38) Sunder, A.; Hanselmann, R.; Frey, H.; Mülhaupt, R. *Macromolecules* **1999**, *32*, 4240.
(39) Walach, W.; Trzebicka, B.; Justynska, J.; Dworak, A. *Polymer* **2004**, *45*, 1755.
(40) Wurm, F.; Nieberle, J.; Frey, H. *Macromolecules* **2008**, *41*, 1184.
(41) Pargen, S.; Keul, H.; Möller, M. *Macromol. Chem. Phys.* **2011**, *212*, 1791.
(42) Basinska, T.; Slomkowski, S.; Dworak, A.; Panchev, I.; Chehimi, M. M. *Colloid Polym. Sci.* **2001**, *279*, 916.
(43) Fitton, A. O.; Hill, J.; Jane, D. E.; Millar, R. *Synthesis (Stuttgart)* **1987**, *12*, 1140.
(44) Siebert, M.; Keul, H.; Möller, M. *Des. Monomers Polym.* **2010**, *13*, 547.
(45) Fergusson, P.; Sherrington, D. C.; Gough, A. *Polymer* **1993**, *34*, 3281.
(46) Bosch, M. Configuration of the polyoxyethylene chain in bulk. In *Non-ionic Surfactants*; Schick, M. J., Ed.; Marcel Dekker: New York, 1967; p 753.
(47) Kawaguchi, S.; Yekta, A.; Duhamel, J.; Winnik, M. A. *J. Phys. Chem.* **1994**, *98*, 7891.
(48) Hoshino, F.; Kawaguchi, H.; Ohtsuka, Y. *Polym. J.* **1987**, *19*, 1157.
(49) Kawaguchi, H.; Sugi, Y.; Ohtsuka, Y. *J. Appl. Polym. Sci.* **1981**, *26*, 1649.
(50) Duracher, D.; Sauzedde, F.; Elaissari, A.; Perrin, A.; Pichot, C. *Colloid Polym. Sci.* **1998**, *276*, 219.
(51) Duracher, D.; Sauzedde, F.; Elaissari, A.; Perrin, A.; Pichot, C. *Colloid Polym. Sci.* **1998**, *276*, 920.
(52) Pich, A.; Lu, Y.; Adler, H.-J. *Colloid Polym. Sci.* **2003**, *281*, 907.
(53) Hans, M.; Gasteier, P.; Keul, H.; Möller, M. *Macromolecules* **2006**, *39*, 3184.
(54) Hans, M.; Keul, H.; Hese, A.; Möller, M. *Macromolecules* **2007**, *40*, 8872.
(55) Mohamed, A.; Finkenstadt, V. L.; Gordon, S. H.; Biresaw, G.; Palmquist, D. E.; Rayas-Duarte, P. *J. Appl. Polym. Sci.* **2008**, *110*, 3256.

Macromolecules

Article

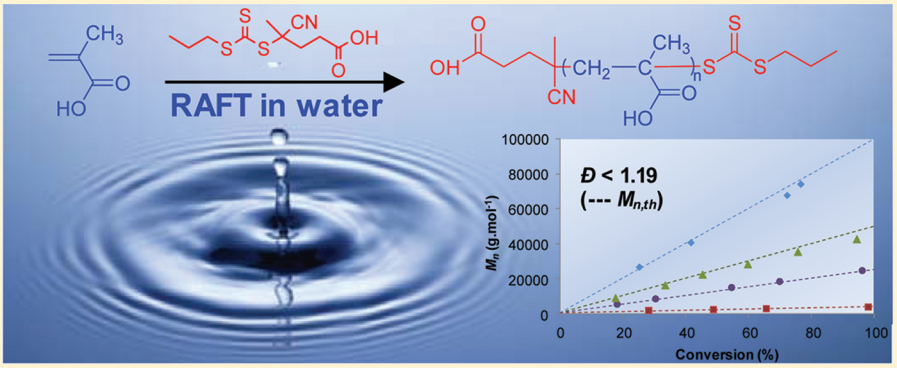
pubs.acs.org/Macromolecules

RAFT Polymerization of Methacrylic Acid in Water

Isabelle Chaduc, Muriel Lansalot,* Franck D'Agosto,* and Bernadette Charleux

Laboratoire de Chimie Catalyse Polymères et Procédés (C2P2), Université de Lyon 1, CPE Lyon, CNRS UMR 5265, Equipe LCPP Bat 308F, 43 Bd du 11 Novembre 1918, F-69616 Villeurbanne, France

Supporting Information



ABSTRACT: Reversible addition−fragmentation chain transfer (RAFT) polymerization of methacrylic acid was successfully performed in water in the presence of a trithiocarbonate, the 4-cyano-4-thiothiopropylsulfanylpentanoic acid (CTPPA), as a RAFT agent. Several parameters such as the temperature, the concentration, the pH, the targeted polymerization degree, and the initiator concentration were studied. For pH value below the pK_a of MAA, well-defined PMAA chains with different molar mass up to 92 000 g mol^{-1} exhibiting low dispersity ($Đ$ < 1.19) were obtained under a broad range of synthetic conditions.

INTRODUCTION

Water-soluble homopolymers and copolymers are of high technical importance for many applications. Poly(methacrylic acid) (PMAA) is a polyelectrolyte with aqueous solution properties that can be tuned with the pH or the ionic strength. Synthesized by free radical polymerization of a monomer commonly used in the industry, methacrylic acid (MAA), PMAA finds applications in a broad range of areas such as the coating industry[1] or drug delivery systems.[2,3] PMAA is also particularly interesting when introduced into more complex macromolecular architectures such as amphiphilic block copolymers. The corresponding syntheses require the use of controlled polymerization techniques. Direct controlled polymerization of MAA can only be achieved by the use of a free radical process. However, despite the fantastic advances made in the area of controlled radical polymerization (CRP),[4,5] only a limited number of papers report the direct CRP of MAA.[6−9] Among the different available CRP techniques, nitroxide-mediated polymerization (NMP)[10,11] is not particularly well suited for methacrylate derivatives. Indeed, the polymerization of methacrylates can only be controlled with the use of a specific nitroxide[12] or if a small amount of styrenic[13,14] or acrylonitrile[15] comonomer is employed. This has indeed been valuably applied to the polymerization of MAA in organic solution.[16,17] Very recently, we showed that MAA could be polymerized under controlled conditions in acidic water in the presence of a small fraction of styrenesulfonate as long as the polymerization time remained short enough, after which SG1 nitroxide started to degrade under the conditions employed.[18] Because of the interaction of the carboxylic acid moiety of MAA with the metallic catalyst, atom transfer radical polymerization (ATRP) failed[19,20] to control the polymerization of MAA. Armes et al.[21] circumvented this limitation by polymerizing sodium methacrylate in water. Reversible addition−fragmentation chain transfer (RAFT)[22] is probably the most monomer-compatible CRP technique and has been extensively used to control the polymerization of water-soluble monomers.[5] Surprisingly, only a limited number of papers are dealing with RAFT of MAA, which was successfully conducted in the presence of a dithiobenzoate control agent in DMF,[6] in methanol,[7,9] in dioxane,[8] and in mixtures of dioxane and water (1:4 v/v).[9] Despite the aqueous properties of MAA and PMAA and as far as we know, the use of water as a solvent for the CRP of MAA has, however, not been investigated. We recently showed that amphiphilic block copolymers could be synthesized in water using a one-pot strategy[23] starting with the successful RAFT synthesis of the hydrophilic segment—including PMAA segment—in water. While the emphasis was put on the block copolymer synthesis in that previous work, the present paper reports the first detailed study of the RAFT polymerization of MAA in water. Reactions were carried out in presence of 4-cyano-4-thiothiopropylsulfanylpentanoic acid

Received: October 25, 2011
Revised: January 6, 2012
Published: January 26, 2012

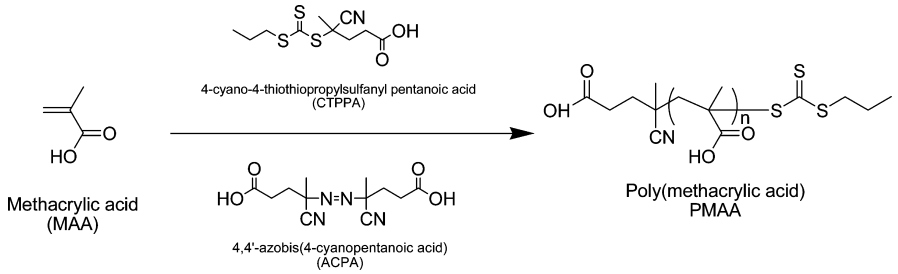
ACS Publications © 2012 American Chemical Society

Table 1. Experimental Conditions and Results for the RAFT Polymerization of MAA with [MAA]/[CTPPA] = 43[a]

entry	$[MAA]_0$ (mol L^{-1})	solvent	T (°C)	pH	time (h)	conv (%)	M_n(theo) (g mol^{-1})	M_n(exp) (g mol^{-1})	M_w/M_n
1	4.6	methanol	70		7	59	3050	3330	1.27
2	4.6	water	70	2.1	5.5	100	4000	4665	1.16
3	4.6	dioxane	70		6	91	3680	3940	1.20
4	1	water	80	2.3	4	98	3930	4020	1.15
5	1	dioxane	80		6.5	47	2010	2580	1.24
6	1	water	70	2.3	7	98	3930	4300	1.11
7	5.8	water	70	2.0	4	100	4000	4760	1.19
8	2.8	water	70	2.2	5	99	3950	4510	1.17
9	2.5	water	80	2.2	4	100	4000	4440	1.15
10[b]	2.5	water	80	4	4	99	3960	4340	1.12
11[b]	2.5	water	80	5	7	96	3515	3850	1.47
12[b]	2.5	water	80	7	6	71	3600	2925	2.59
13[c]	2.5	water	80	6.8	6	88	3560	3192	2.78

[a]MAA RAFT polymerizations were performed using ACPA as initiator and CTPPA as chain transfer agent [CTPPA]/[ACPA] = 10. [b]pH was adjusted by NaOH addition. [c]This experiment was performed with methacrylate sodium.

Scheme 1. Synthesis of Poly(methacrylic acid) by RAFT Polymerization



(CTPPA) trithiocarbonate used as chain transfer agent (CTA) and 4,4′-azobis(4-cyanopentanoic acid) (ACPA) as water-soluble initiator. Different parameters such as the temperature, the MAA concentration, the pH, the targeted polymerization degree, and the ACPA content were studied. We show that well-defined PMAA chains can be obtained under a broad range of conditions and can exhibit narrowly distributed molar masses (dispersity ($Đ$) < 1.10) up to 92 000 g mol^{-1}.

EXPERIMENTAL SECTION

Materials. Methacrylic acid (MAA, Acros, 99.5%), sodium methacrylate (Aldrich, 99%), 4,4′-azobis(4-cyanopentanoic acid) (ACPA, Fluka, >98%), 1,4-dioxane (Sigma-Aldrich, 99.5%), and methanol (Laurylab, 99%) were used as received. Water was deionized before use (Purelab Classic UV, Elga LabWater). 4-Cyano-4-thiothiopropylsulfanylpentanoic acid (CTPPA) was obtained by reaction of ACPA with bis(propylsulfanylthiocarbonyl) disulfide as described in the literature.[24,25]

Analytical Techniques. MAA conversion was determined by ^{1}H NMR spectroscopy in D_2O or DMSO (when the solvent is dioxane) at room temperature (Bruker DRX 300). Size exclusion chromatography (SEC) measurements were performed in THF at 40 °C, at a flow rate of 1 mL min^{-1}, using toluene as a flow rate marker. Before analysis, the polymers were modified by methylation of the carboxylic acid groups using trimethylsilyldiazomethane.[26] They were analyzed at a concentration of 3 mg mL^{-1} after filtration through a 0.45 μm pore-size membrane. The separation was carried out on three Polymer Laboratories columns [3 × PLgel 5 μm Mixed C (300 × 7.5 mm) and a guard column (PL gel 5 μm)]. The setup (Viscotek TDA 305) was equipped with a refractive index (RI) detector (λ = 930 nm). The average molar masses (number-average molar mass M_n and weight-average molar mass M_w) and the dispersity value ($Đ = M_w/M_n$) were derived from the RI signal by a calibration curve based on poly(methyl methacrylate) standards (PMMA from Polymer Laboratories).

RAFT Polymerizations in Water. An example of RAFT polymerization of MAA is as follows (entry 4 in Table 1). In a two-necked round-bottom flask equipped with a condenser 149 mg of CTPPA (2.29×10^{-2} mol L^{-1}) and 15 mg of ACPA (2.29×10^{-3} mol L^{-1}) were dissolved in 2 g of MAA (0.99 mol L^{-1}) and 4 mL of water. 349 mg of 1,3,5-trioxane (1.65×10^{-1} mol L^{-1}) was added as an internal reference for NMR analysis. 19.5 mL of water was finally added. After deoxygenation by nitrogen bubbling for 30 min, the resulting mixture was immersed in an oil bath thermostated at 80 °C. The regular withdrawal of samples allowed us to follow the monomer conversion as a function of time and the evolution of molar masses and molar mass distributions as a function of monomer conversion. The monomer conversion was determined by ^{1}H NMR spectroscopy in D_2O by the relative integration of the protons of 1,3,5-trioxane and the vinylic protons of MAA. Theoretical molar masses were obtained using the following equation:

$$M_n = \frac{M_{MAA}[MAA]_0 x}{[CTPPA]_0} + M_{CTPPA}$$

where M_n is the number-average molar mass, M_{MAA} and M_{CTPPA} are the molar masses of MAA and CTPPA, respectively, $[MAA]_0$ and $[CTPPA]_0$ are the initial concentrations of CTPPA and MAA, respectively, and x is the fractional conversion of MAA.

RESULTS AND DISCUSSION

In their original study, Pelet et al.[9] nicely polymerized MAA in methanol using 4-cyanopentanoic acid dithiobenzoate (CPA-DB) as RAFT agent. They investigated the potential use of a water-based solvent and performed the same polymerization in a mixture of dioxane and water (1:4, v/v). Dioxane was indeed required as a cosolvent since CPA-DB was insoluble in pure water. However, under these conditions, a remarkable increase in viscosity was observed after 90% conversion, accompanied by a deviation of the molar masses from the theoretical M_n and

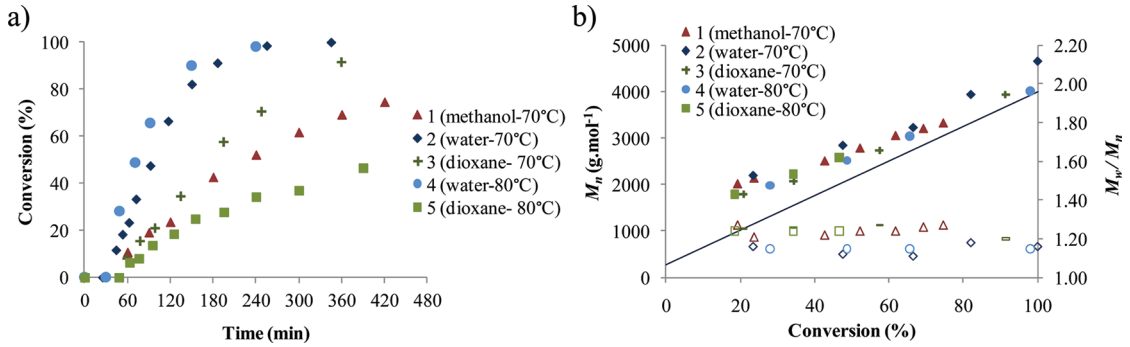


Figure 1. RAFT polymerization of MAA performed in different solvents and at different temperatures. [MAA]/[CTPPA] = 43, [CTPPA]/[ACPA] = 10, [MAA] = 4.5 mol L^{-1} at T = 70 °C, and [MAA] = 1 mol L^{-1} at T = 80 °C. Evolution of (a) monomer conversion versus time and (b) number-average molar mass M_n (full symbols) and $Đ = M_w/M_n$ (open symbols) versus conversion. Straight line is the theoretical evolution of molar masses with conversion.

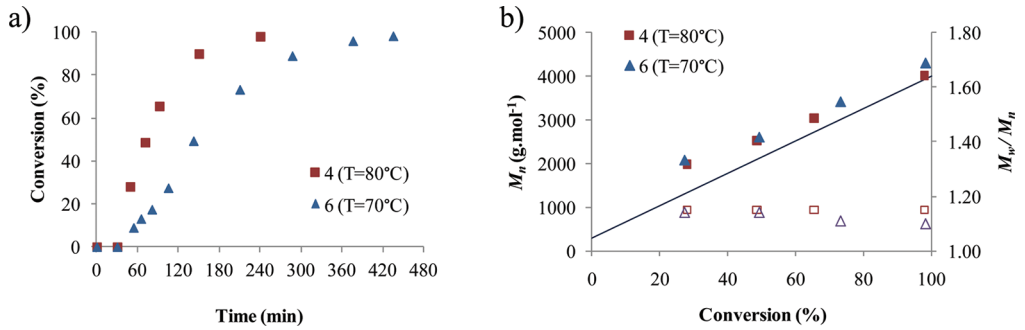


Figure 2. RAFT polymerization of MAA performed in water and at different temperatures. [MAA] = 1 mol L^{-1}, [MAA]/[CTPPA] = 43, [CTPPA]/[ACPA] = 10. Evolution of (a) monomer conversion versus time and (b) number-average molar mass M_n (full symbols) and $Đ = M_w/M_n$ (open symbols) versus conversion. Straight line is the theoretical evolution of molar masses with conversion.

with a change of color of the medium. The potential hydrolysis of the dithiobenzoate based CTA was put forward. The authors mentioned that the selection of chain transfer agents of higher solubility such as trithiocarbonates could prevent this issue. In addition, trithiocarbonate are known to be less subjected to hydrolysis.[27,28] We then selected CTPPA to perform our experiments in pure water (Scheme 1). It is worth mentioning here that CTPPA is not highly soluble in water. In all our experiments, CTPPA, ACPA, MAA, and a small amount of water were first mixed, and the resulting mixture was then added to the remaining of water. The starting polymerization medium was not homogeneous and exhibited small droplets of an organic phase suspended in water, particularly at low concentration of MAA. The rough suspension was turned into a very homogeneous but still slightly turbid solution upon heating, which quickly cleared up.

Effect of the Polymerization Solvent. The first series of experiments aimed at comparing the value that the use of water would add in terms of control compared to the solvents that were already used in the literature (Table 1, entries 1–3). RAFT polymerizations of MAA were thus performed at 70 °C with a concentration of MAA of 4.6 mol L^{-1}. An experiment carried out in water (entry 2) was compared to experiments performed in methanol (entry 1) and dioxane (entry 3) under the same conditions. In all the cases, an inhibition period was observed (Figure 1a). When methanol and dioxane were used as solvent, conversion of 59 and 91% were reached in 7 and 6 h, respectively. Quantitative conversion was reached in less than 5 h in water. Whatever the solvent, a linear increase of molar mass was observed with increasing conversion showing the controlled features of the studied systems, although molar masses were slightly higher than theoretical values particularly for low conversions (Figure 1b). The dispersity $Đ$ attained was, however, much lower in water (1.16) than in methanol or dioxane (1.30).

$[MAA]_0$ used in these experiments remained high and did not really show the advantage of using water as solvent. An experiment was then performed at much lower concentration of MAA in water (1 mol L^{-1}, Table 1, entry 4) and compared to the same experiment carried out in dioxane (entry 5). In order to keep reasonable polymerization time, the temperature was increased to 80 °C. Again, well-defined PMAA chains were formed in both cases with, however, better control features in the case of water (Table 1). In addition, the use of water as solvent allowed to reach higher conversion with a higher polymerization rate (98% in 4 h) than in dioxane (47% in 6.5 h).

As can be deduced from these first experiments, while the choice of the solvent does not dramatically impact the quality of the control, it has a great effect on the polymerization kinetics. Indeed, the propagation rate coefficient, k_p, in free-radical polymerization of MAA is dependent on the solvent. Kuchta et al.[29] studied the effect of water and organic solvents such as DMSO and methanol on the propagation rate in MAA polymerization via pulsed-laser polymerization. They showed that k_p values obtained in water were higher than those obtained in DMSO or methanol, due mainly to a lower activation energy. This was explained by a higher tendency of the monomers to be self-associated in organic solvents via

dx.doi.org/10.1021/ma2023815 | Macromolecules 2012, 45, 1241–1247

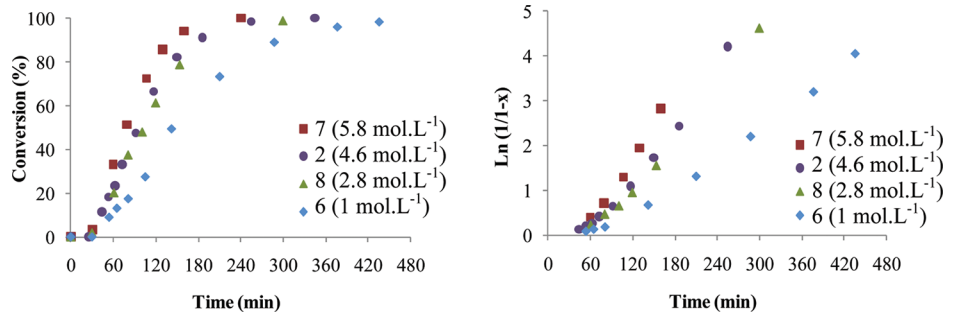


Figure 3. RAFT polymerization of MAA performed at different concentrations of MAA in water at 70 °C. [MAA]/[CTPPA] = 43 and [CTPPA]/[ACPA] = 10. Evolution of monomer conversion versus time and corresponding $\ln(1/(1-x)) = f(t)$ plots where x is MAA conversion.

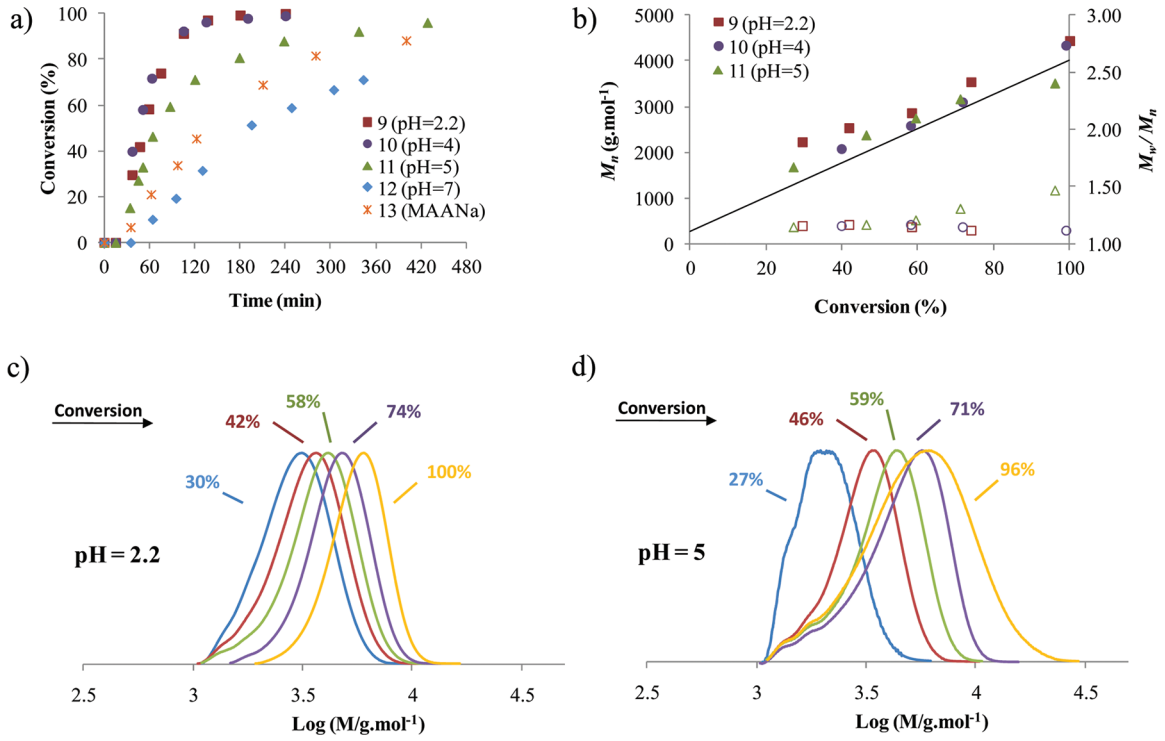


Figure 4. RAFT polymerization of MAA performed in water at 80 °C at different pH. [MAA] = 2.5 mol L^{-1}, [MAA]/[CTPPA] = 43, and [CTPPA]/[ACPA] = 10. Evolution of (a) monomer conversion versus time, (b) number-average molar mass M_n (full symbols) and $Đ = M_w/M_n$ (open symbols) versus conversion. Straight line is theoretical evolution of molar masses with conversion. Corresponding SEC chromatogram evolutions for (c) pH = 2.2 and (d) pH = 5.

hydrogen bondings, hence leading to the need for a higher energy to break these bonds for the propagation step.

Eventually, contrary to what Pelet et al.[9] observed when using dioxane/water mixture as solvent the use of pure water did not lead to the discoloration of the medium. The choice of our CTPPA trithiocarbonate and our polymerization procedure seemed thus to be a good combination to control the polymerization of MAA in pure water. To further investigate the potential of this interesting system, the influence of various parameters such as the temperature, the MAA concentration, the pH, the targeted molar mass, and the initiator content were studied.

Effect of Temperature. The effect of the temperature was further studied by performing two experiments at 70 and 80 °C under exactly the same conditions ([MAA] = 1 mol L^{-1}, entries 6 and 4, respectively, in Table 1). After a short inhibition period of about 30 min, a faster polymerization was observed when performing the reaction at 80 °C, for which 98% conversion was reached in 4 h whereas 7 h was necessary to reach the same conversion at 70 °C (Figure 2a). Nevertheless, the control features were exactly the same and well-defined PMAA chains were obtained with narrowly distributed ($Đ < 1.15$) molar masses that increased linearly with conversion. As observed previously, final molar masses were nicely matching the theoretical values (Figure 2b) although being slightly higher than expected at low conversions.

Effect of the MAA Concentration. MAA concentrations were varied from 1 up to 5.8 mol L^{-1} (entries 6, 8, 2, and 7 in Table 1). As observed by Pelet et al.,[9] the polymerization became faster when the MAA concentration was increased. Quantitative conversions were obtained in all the cases. Slightly higher dispersities were observed ($Đ$ between 1.16 and 1.19) when the [MAA] concentrations were increased (Figure 3) compared to the polymerization performed at 1 mol L^{-1} (1.11). The final molar mass values were also higher in those cases (4760 g mol^{-1}) than the ones obtained for [MAA] of 1 mol L^{-1}

dx.doi.org/10.1021/ma2023815 | Macromolecules 2012, 45, 1241−1247

Table 2. Influence of the Monomer/RAFT Agent Ratio in the RAFT Polymerization of MAA[a]

entry	$[MAA]_0/[CTPPA]_0$	$[CTPPA]_0/[ACPA]_0$	time (h)	conv (%)	M_n(theo) (g mol^{-1})	M_n(exp) (g mol^{-1})	M_w/M_n
4	43	10	4	98	3 930	4 020	1.15
14	287	10	8	96	24 040	24 880	1.07
15	578	10	8	94	47220	42 830	1.08
16	1158	10	8	77	76 620	74 410	1.11
17	1158	5	8	100	100 000	92 210	1.10
18	1158	2.5	5	96	99 000	82 370	1.15

[a]MAA RAFT polymerizations were performed in water at 80 °C using ACPA as initiator and CTPPA as chain transfer agent. [MAA] = 1 mol L^{-1}.

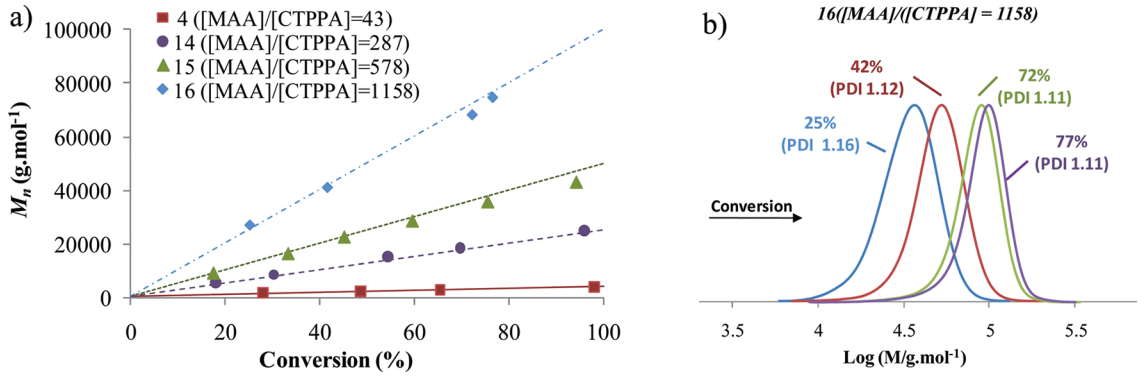


Figure 5. RAFT polymerization of MAA performed in water at 80 °C at different [MAA]/[CTPPA] ratios. [MAA] = 2.5 mol L^{-1} and [CTPPA]/[ACPA] = 10. (a) Evolution of number-average molar mass M_n versus conversion. Straight line is theoretical evolution of molar masses with conversion and (b) SEC chromatogram evolution for [MAA]/[CTPPA] = 1158.

(3930 g mol^{-1}) and higher than the expected ones (around 4000 g mol^{-1}). The increase in viscosity observed at the end of the polymerization in the experiments carried out at high concentrations of MAA may cause these variations to the theory.

Lacik et al.[30,31] performed careful studies on the propagation kinetics of free radical polymerization of MAA in aqueous solution. Using data obtained from the pulsed laser polymerization−size exclusion chromatography (PLP-SEC) technique, the authors showed that k_p may be divided by ∼4 by increasing MAA concentration from 8 to 49 wt % (range of concentrations used in the present study). Figure 3 seems however to be in contradiction with these results. The same molar masses were targeted here (ca. 4000 g mol^{-1}), and a constant molar ratio CTPPA/ACPA of 10 was employed. Thus, the concentration of initiator constantly increased when [MAA] was increased. Indeed, [ACPA] was 5.8 times higher in experiment 7 than in experiment 6. This may overcompensate the decrease of k_p suggested by Lacik et al.[30,31] and result in the observed increase of polymerization rate with MAA concentrations. Nevertheless, the control of the polymerization remained very good for the broad range of concentrations employed, showing the versatility of this robust polymerization system.

Effect of pH. As polymerizations were performed in water to produce PMAA that is a polyelectrolyte, the pH may impact the control of the polymerization. In order to assess the effect of this parameter, four experiments were carried out at pH 2.2, 4, 5, and 7 (entries 9−12, Table 1). As shown in Table 1 and in Figure 4, the ionization of MAA has a drastic impact on both the kinetics and the control of the polymerization. The higher the pH was, the slower the polymerization (Figure 4a). Like the effect of MAA concentration on kinetics, this result was already observed by Lacik et al.,[30,31] who reported a decrease of 1 order of magnitude for k_p from nonionized to fully ionized MAA. This apparently entropic effect (not temperature dependent) was related to a variation of the pre-exponential factor in the Arrhenius expression. This factor is impacted by intermolecular interactions giving rise to a hindrance of internal rotational mobility of the transition state structure, affecting the propagation step. This hindrance can be induced by both intermolecular hydrogen-bonded interactions (in nonionized MAA) and electrostatic interactions[32,33] of partially or fully ionized MAA carboxylic acid groups in the MAA moieties. Experiments carried out at pH = 2.2 or 4 reached quantitative conversion and exhibited a good control of the polymerization as shown by the low dispersity values obtained (1.15 and 1.12, respectively, entries 9 and 10 in Table 1) and by the linear increase of molar masses with conversion (Figure 4b and corresponding SEC chromatograms in Figure 4c). It is interesting to note that, in addition, the control of the polymerization seemed to be strongly affected for pH higher than the pK_a of MAA (pK_{aMAA} = 4.36[34]). In this case (pH = 5, Table 1) dispersity values started to increase ($Đ$ = 1.47, entry 11) and molar mass values escaped the linear expected evolution with conversion (pH = 5 in Figure 4b and corresponding SEC chromatograms in Figure 4d). The experiment carried out at pH 7 was not controlled anymore ($Đ$ = 2.59, entry 12).

These systems containing partially or fully ionized MAA together with partially ionized PMAA species may be rather complex due to the simultaneous occurrence of electrostatic interactions, the effects of ionic strength, the impact of electrochemical equilibria, and the action of hydrophobic forces.[30,31] In order to simplify the variety of origins of these phenomena, an additional experiment was performed with sodium methacrylate as monomer (13, Table 1) using the same conditions as the ones of the last series. As expected, the polymerization was slow compared to polymerization performed under acidic conditions. However, no control of the

dx.doi.org/10.1021/ma2023815 | Macromolecules 2012, 45, 1241−1247

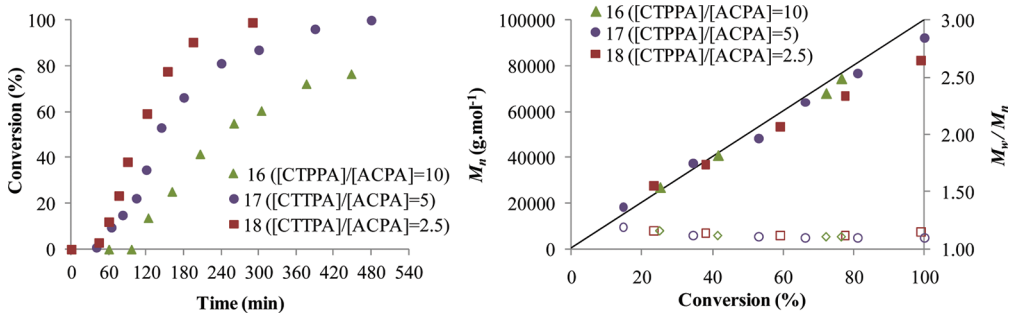


Figure 6. RAFT polymerization of MAA performed in water at 80 °C for different [CTPPA]/[ACPA] ratios. [MAA] = 1 mol L^{-1} and [MAA]/[CTPPA] = 1158. Evolution of (a) monomer conversion versus time, (b) number-average molar mass M_n (full symbols) and $Đ = M_w/M_n$ (open symbols) versus conversion. Straight line is theoretical evolution of molar masses with conversion.

polymerization was observed. Explaining the origin of the loss of control would then be risky with the experimental data obtained in this paper. The RAFT agent is less sensitive to hydrolysis in reactions performed at a low pH. However, the aforementioned hindrance effect induced by electrostatic interactions of partially or fully ionized MAA carboxylic acid groups in the MAA moieties that impact k_p may also impact in the same way the addition−fragmentation steps and thus the RAFT control. Besides, the sharp change in PMAA conformation from hypercoil to rod known to occur around pH 5[35] may also impact the reversible chain transfer kinetics.

Synthesis of Well-Defined High Molar Mass PMAA. The powerful RAFT polymerization system of MAA in water presented in this paper seemed to be an interesting way to produce well-defined PMAA chains under a broad range of conditions. In addition, the use of water as solvent strongly decreases the probability of transfer reactions that are often encountered in organic solvents. Compared to acrylic acid, the polymerization of methacrylic acid has the advantage of not involving 1,5-hydrogen shift reactions[36] that give rise to branched structures and sometimes impede the formation of high molar mass chains. Experiments were then carried out in order to target high molar mass PMAA (Table 2) by varying either [MAA]/[CTPPA] or [ACPA]. As shown in Figure 5a, whatever the final molar mass targeted, linear evolutions of experimental molar mass values versus conversion were observed in all the cases and dispersities remained lower than 1.15 (see Figure 5b and Figure S2 for SEC chromatograms corresponding to [MAA]/CTPPA] = 43, 287, and 578). An excellent agreement between experimental and theoretical molar masses was obtained (Table 2), underlining the fact that the deviations observed in previous experiments ($M_{n,targeted}$ = 4000 g mol^{-1}) particularly at low conversions were probably due to a rather low chain transfer ability of CTPPA in MAA polymerization. The time for the RAFT equilibrium to take place (up to 20% conversion),[22] the length of the inhibition period increased with [MAA]/CTPPA] ratio (30 min for [MAA]/CTPPA] = 43, 90 min for the highest [MAA]/CTPPA] = 1158; see Figure S1 in the Supporting Information), and the molar mass values were slightly higher than expected. These molar masses were then quickly reaching the expected values. Well-defined PMAA chains exhibiting molar masses up to 74 410 g mol^{-1} (Figure 5b) were obtained with dispersity as low as 1.11 (see also Figure S2).

However, reaction times were in the range of 8 h. To shorten the polymerization, experiments 17 and 18 were performed under the same conditions as experiment 16 with increasing [ACPA]. As expected (Figure 6a), polymerizations were much faster with 96% conversion reached in 8 h for experiment 17 and quantitative conversion in the case of 18 in 5 h. Besides, Figure 6b showed that a good control of the growth of the chains was maintained all over the course of the polymerization and that PMAA chains of 92 210 g mol^{-1} ($Đ$ = 1.10) could be produced.

CONCLUSION

RAFT polymerization of methacrylic acid (MAA) was performed in water in the presence of a trithiocarbonate as chain transfer agent (4-thiothiopropylsulfanylpentanoic acid, CTPPA) and 4,4′-azobis(4-cyanopentanoic acid) (ACPA) as initiator. A particular feature of this system is that CTPPA is first dissolved in MAA and then added to water. The resulting mixture is a suspension of organic droplets in water that is turned into a slightly turbid solution upon heating, which quickly cleared up. A first comparison of different experiments performed in water, in methanol, and in dioxane showed the far superiority of this aqueous polymerization system in terms of both kinetics and control of the molar masses. Then various parameters such as the temperature of the polymerization, the MAA concentration, and the pH were further studied. Over a broad range of conditions, the system obeyed to a controlled polymerization system, and well-defined PMAA chains exhibiting dispersities lower than 1.19 were obtained. However, when increasing the pH, the control features were rapidly lost above the pK_a of MAA. Eventually, the system proved to be an excellent tool to produce high molar mass PMAA (>90 000 g mol^{-1}) achieving very low dispersity ($Đ$ = 1.10).

ASSOCIATED CONTENT

Supporting Information

Conversions versus time during RAFT polymerization of MAA performed in water at 80 °C at different [MAA]/[CTPPA] ratios; SEC chromatogram evolutions for RAFT polymerizations of MAA performed in water at 80 °C at different [MAA]/[CTPPA] ratios. This material is available free of charge via the Internet at http://pubs.acs.org.

AUTHOR INFORMATION

Corresponding Author

*E-mail: lansalot@lcpp.cpe.fr (M.L.); dagosto@lcpp.cpe.fr (F.D.).

ACKNOWLEDGMENTS

The financial support from the French National Agency for Research (ANR ALGIMAT 09-CP2D-02) and the competitive-

ness cluster Axelera is acknowledged. The authors thank Olivier Boyron (C2P2, LCPP Team) for his invaluable help concerning SEC analyses and Malvern Instrument for the technical support.

REFERENCES

(1) Thomas, R. *J. Water Borne Coat.* **1989**, *12*, 8−10.
(2) Städler, B.; Price, A. D.; Zelikin, A. N. *Adv. Funct. Mater.* **2011**, *21*, 14−28.
(3) Morishita, M.; Goto, T.; Takayama, K.; Peppas, N. A. *J. Drug Delivery Sci. Technol.* **2006**, *16*, 19−24.
(4) Matyjaszewki, K.; Gnanou, Y.; Leibler, L. *Macromolecular Engineering: Precise Synthesis, Materials Properties, Applications*; Wiley-VCH: Weinheim, 2007.
(5) Braunecker, W. A.; Matyjaszewski, K. *Prog. Polym. Sci.* **2007**, *32*, 93−146.
(6) Chong, Y. K.; Le, T. P. T.; Moad, G.; Rizzardo, E.; Thang, S. H. *Macromolecules* **1999**, *32*, 2071−2074.
(7) Yang, C.; Cheng, Y. L. *J. Appl. Polym. Sci.* **2006**, *102*, 1191−1201.
(8) Hosseini Nejad, E.; Castignolles, P.; Gilbert, R. G.; Guillaneuf, Y. *J. Polym. Sci., Part A: Polym. Chem.* **2008**, *46*, 2277−2289.
(9) Pelet, J. M.; Putnam, D. *Macromolecules* **2009**, *42*, 1494−1499.
(10) Bertin, D.; Gigmes, D.; Marque, S. R. A.; Tordo, P. *Chem. Soc. Rev.* **2011**, *40*, 2189−2198.
(11) Hawker, C. J.; Bosman, A. W.; Harth, E. *Chem. Rev.* **2001**, *101*, 3661−3688.
(12) Guillaneuf, Y.; Gigmes, D.; Marque, S. R. A.; Astolfi, P.; Greci, L.; Tordo, P.; Bertin, D. *Macromolecules* **2007**, *40*, 3108−3114.
(13) Charleux, B.; Nicolas, J.; Guerret, O. *Macromolecules* **2005**, *38*, 5485−5492.
(14) Nicolas, J.; Dire, C.; Mueller, L.; Belleney, J.; Charleux, B.; Marque, S. R. A.; Bertin, D.; Magnet, S.; Couvreur, L. *Macromolecules* **2006**, *39*, 8274−8282.
(15) Nicolas, J.; Brusseau, S.; Charleux, B. *J. Polym. Sci., Part A: Polym. Chem.* **2010**, *48*, 34−47.
(16) Dire, C.; Magnet, S.; Couvreur, L.; Charleux, B. *Macromolecules* **2008**, *42*, 95−103.
(17) Brusseau, S.; Belleney, J.; Magnet, S.; Couvreur, L.; Charleux, B. *Polym. Chem.* **2010**, *1*, 720−729.
(18) Brusseau, S.; D'Agosto, F.; Magnet, S.; Couvreur, L.; Chamignon, C.; Charleux, B. *Macromolecules* **2011**, *44*, 5590−5598.
(19) Matyjaszewski, K.; Xia, J. *Chem. Rev.* **2001**, *101*, 2921−2990.
(20) Kamigaito, M.; Ando, T.; Sawamoto, M. *Chem. Rev.* **2001**, *101*, 3689−3746.
(21) Ashford, E. J.; Naldi, V.; O'Dell, R.; Billingham, N. C.; Armes, S. P. *Chem. Commun.* **1999**, 1285−1286.
(22) Barner-Kowollik, C. *Handbook of RAFT Polymerization*; Wiley-VCH: Weinheim, 2008.
(23) Chaduc, I.; Zhang, W.; Rieger, J.; Lansalot, M.; D'Agosto, F.; Charleux, B. *Macromol. Rapid Commun.* **2011**, *32*, 1270−1276.
(24) Boursier, T.; Chaduc, I.; Rieger, J.; D'Agosto, F.; Lansalot, M.; Charleux, B. *Polym. Chem.* **2010**, *2*, 355−362.
(25) Xu, X.; Smith, A. E.; Kirkland, S. E.; McCormick, C. L. *Macromolecules* **2008**, *41*, 8429−8435.
(26) Couvreur, L.; Lefay, C.; Belleney, J.; Charleux, B.; Guerret, O.; Magnet, S. *Macromolecules* **2003**, *36*, 8260−8267.
(27) Baussard, J.-F.; Habib-Jiwan, J.-L.; Laschewsky, A.; Mertoglu, M.; Storsberg, J. *Polymer* **2004**, *45*, 3615−3626.
(28) Thomas, D. B.; Convertine, A. J.; Hester, R. D.; Lowe, A. B.; McCormick, C. L. *Macromolecules* **2004**, *37*, 1735−1741.
(29) Kuchta, F.-D.; van Herk, A. M.; German, A. L. *Macromolecules* **2000**, *33*, 3641−3649.
(30) Beuermann, S.; Buback, M.; Hesse, P.; Kukučková, S.; Lacık, I. *Macromol. Symp.* **2007**, *248*, 23−32.
(31) Lacik, I.; Ucnova, L.; Kukučková, S.; Buback, M.; Hesse, P.; Beuermann, S. *Macromolecules* **2009**, *42*, 7753−7761.
(32) Mukherjee, A. K.; Schmitz, K. S.; Bhuiyan, L. B. *Langmuir* **2004**, *20*, 11802−11810.
(33) Tanaka, H.; Araki, T. *Phys. Rev. Lett.* **2000**, *85*, 1338.
(34) Katchalsky, A.; Blauer, G. *Trans. Faraday Soc.* **1951**, *47*, 1360−1370.
(35) Ruiz-Perez, L.; Pryke, A.; Sommer, M.; Battaglia, G.; Soutar, I.; Swanson, L.; Geoghegan, M. *Macromolecules* **2008**, *41*, 2203−2211.
(36) Buback, M.; Hesse, P.; Lacík, I. *Macromol. Rapid Commun.* **2007**, *28*, 2049−2054.

Macromolecules

Article

pubs.acs.org/Macromolecules

Ligands Dominate Highly Syndioselective Polymerization of Styrene by Using Constrained-geometry-configuration Rare-earth Metal Precursors

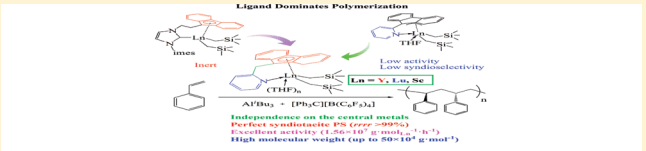
Yupeng Pan,[†,‡] Weifeng Rong,[†,‡] Zhongbao Jian,[†,‡] and Dongmei Cui*[,†]

[†]State Key Laboratory of Polymer Physics and Chemistry, Changchun Institute of Applied Chemistry, Chinese Academy of Sciences, Changchun 130022, China

[‡]Graduate School of the Chinese Academy of Sciences, Beijing 100039, China

Supporting Information

ABSTRACT: A series of novel constrained-geometry-configuration (CGC) rare-earth metal complexes $(RCH_2{-}Py)Ln(CH_2SiMe_3)_2(THF)_n$ (Py = pyridyl; Ln = Y, n = 1, R = C_5Me_4 (Cp′) (**1**); Ln = Y, n = 1, R = C_9H_6 (Ind) (**2**); Ln = Y, n = 1, R = $C_{13}H_8$ (Flu) (**3a**); Ln = Lu, n = 1, R = $C_{13}H_8$ (Flu) (**3b**); Ln = Sc, n = 0, R = $C_{13}H_8$ (Flu) (**3c**)) have been synthesized by treating rare-earth metal trisalkyls with $PyCH_2{-}Cp'$, $PyCH_2{-}$Ind, and $PyCH_2{-}$Flu compounds, respectively, and fully characterized by NMR and X-ray diffraction analyses. Complexes **1**, **2**, and **3a−b** are monomeric THF solvates while the scandium complex **3c** is solvent-free, in which all the CGC ligands adopt a η^5/κ^1 bonding mode via coordination of five carbon atoms from the cyclopentadienyl fragment and the pyridyl nitrogen atom with the central metals. Upon activation with Al^iBu_3 and $[Ph_3C][B(C_6F_5)_4]$, these complexes showed different performances toward styrene polymerization. The $Cp'CH_2{-}Py$ and $IndCH_2{-}Py$ ligated yttrium complexes **1** and **2** showed very low activity to afford syndiotactic enriched polystyrene. Strikingly, the bulky $FluCH_2{-}Py$ supported complexes **3a−c** displayed outstanding activities up to 1.56×10^7 g/(mol$_{Ln}$·h) and perfect syndioselectivity (*rrrr* > 99%), giving high molecular weight sPS; in particular, thus excellent performance was independent of the central metal type for the first time. In addition, the relationship of the ligand structure with the catalytic performances toward specific selective polymerization of styrene was reasonably revealed by comparison with the other Flu-based rare-earth metal catalysts reported previously by us. This might open a new pathway for designing catalysts for specifically selective polymerizations.



Yttrium or Lutetium or Scandium Alkyl Copmlexes bearing Flu-CH_2-pyridyl combined with Al^iBu_3 and $[Ph_3C][B(C_6F_5)_4]$ exhibited the outstanding activities on the highly syndiotactic styrene polymerization.

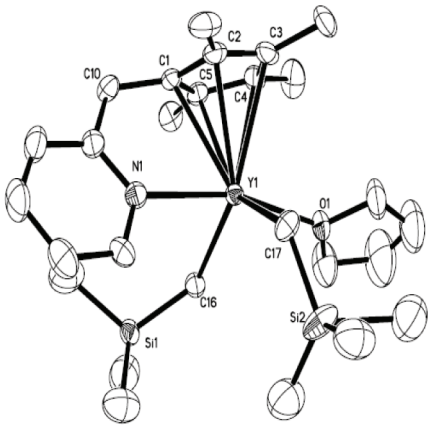
INTRODUCTION

Syndiotactic polystyrene (sPS), discovered first by Ishihara at Idemitsu in 1986 by using unlinked half-sandwich titanium catalysts,[1] is a promising engineering plastic due to its high melting point (T_m = 270 °C), rapid crystallization ability, high tensile modulus, low dielectric constant, and excellent resistance to heat and chemicals.[2] Since this breakthrough, a large number of titanium analogues generally formulated as $[LTiX_3]$, where L is an alkyl or alkoxyl- and amino-substituted cyclopentadienyl (Cp), indenyl (Ind), or fluorenyl (Flu) moiety, while X is halogen or alkoxyl group, have been extensively investigated, which exhibited obvious improvements in both catalytic activity and syndioselectivity for styrene polymerization.[3] In contrast, rare-earth metal catalysts have been noted for their inertness or low specific selectivity toward styrene polymerization.[4] In 2004, great successes were achieved by using two type of catalytic systems based on the unlinked half-sandwich cationic scandium alkyl species[5] and neutral lanthanidocene bearing $Flu{-}CMe_2{-}Cp$ ligand,[6] both displayed good activity to provide perfect sPS. Later on some derivatives supported by the substituted Cp′, hetero(B, N, P)−Cp′, oxygen-linked Cp′ and Ind′ ligands have also been reported as efficient catalysts for the syndioselective styrene polymerization.[7] Note that the common feature of these precursors is that their central metals are scandium having close electronics with titanium (only one case is based on the larger neodymium). Other rare-earth metal complexes, especially those attached to the cheapest yttrium, exhibited non or low activities.

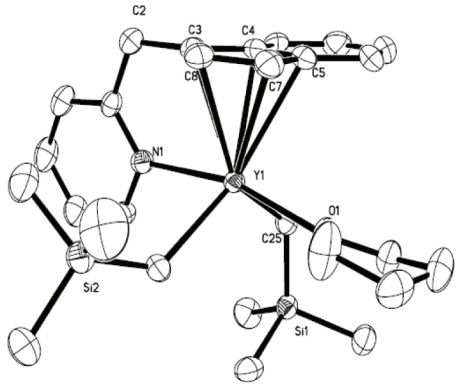
Recently, we developed a linked half-Sandwich rare-earth metal diallyl complexes $(Py{-}C_5Me_4)Ln(\eta^3\text{-}C_3H_5)_2$,[8] among which the lutetium complex for the first time showed a similar activity and perfect syndioselectivity (99%) for the polymerization of styrene to its scandium analogue, unfortunately, the performance of the congenous yttrium complex was still far less promising. Moreover, the attempts to improve the catalytic activity and to obtain high molecular weight sPS by introducing bulky indenyl or fluorenyl ligands were failed. Herein, we reported a series of rare-earth metal complexes bearing the pyridyl-methylene functionalized Cp′/Ind/Flu ligands, among

Received: November 23, 2011
Revised: January 10, 2012
Published: January 31, 2012

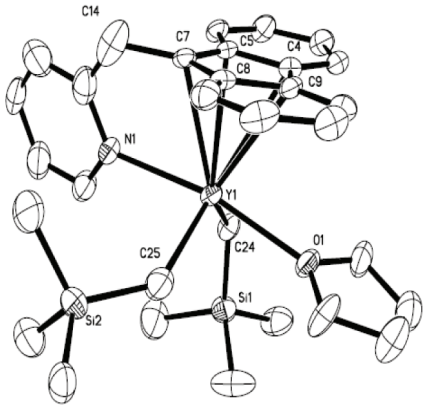
ACS Publications © 2012 American Chemical Society



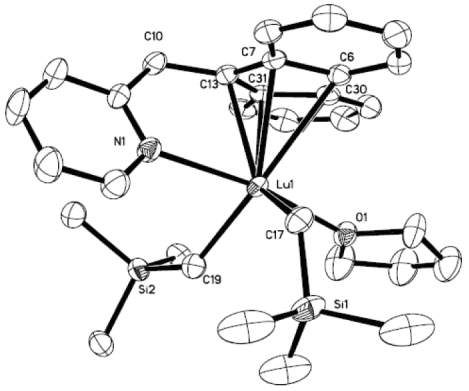
Complex 1.



Complex 2.



Complex 3a.



Complex 3b.

Figure 1. X-ray structures of complexes **1**, **2**, **3a**, **3b** with 35% probability of thermal ellipsoids. Hydrogen atoms are omitted for clarity. Selected bond distances (Å) and angles (deg): **1**, Y1−$C_{Cp'}$(av) 2.388(3), Y1−C1 2.614(6), Y1−C2 2.660(6), Y1−C3 2.724(6), Y1−C4 2.715(6), Y1−C5 2.664 (6), Y1−C17 2.434(6), Y1−C16 2.431(6), Y1−N1 2.548(5), Cp'_{cent}−Y1−N1 90.87(3), Cp'_{cent}−Y1−C16 120.56(3), Cp'_{cent}−Y1−C17 118.36(3); **2**, Y1−C_{Ind} (av) 2.410(3), Y1−C4 2.666(4), Y1−C5 2.687(4), Y1−C6 2.734(4), Y1−C7 2.710(4), Y1−C8 2.689(4), Y1−C25 2.416(4), Y1−C16 2.423(4), Y1−N1 2.512(3), Ind_{cent}−Y1−N1 91.94(3), Ind_{cent}−Y1−C16 126.43(3), Ind_{cent}−Y1−C25 117.65(3); **3a**, Y1−C_{Flu}(av) 2.465(3), Y1−C4 2.845(5), Y1−C5 2.712(4), Y1−C7 2.606(4), Y1−C8 2.845(5), Y1−C9 2.852(5), Y1−C24 2.404(5), Y1−C25 2.372(6), Y1−N1 2.513(4), Flu_{cent}−Y1−N1 92.01(3), Flu_{cent}−Y1−C24 119.53(3), Flu_{cent}−Y1−C25 121.22(3); **3b**, Lu1−C_{Flu}(av) 2.502(3), Lu1−C6 2.904(4), Lu1−C7 2.717(4), Lu1−C13 2.585(4), Lu1−C30 2.944(4), Lu1−C31 2.755(4), Lu1−C17 2.355(4), Lu1−C19 2.340(4), Lu1−N1 2.462(3), Flu_{cent}−Lu1−N1 92.16(3), Flu_{cent}−Lu1−C17 116.26(3), Flu_{cent}−Lu1−C19 136.75(3).

which those bearing bulky Flu moiety upon activation with Al^iBu_3 and $[Ph_3C][B(C_6F_5)_4]$, showed unprecedented high activities (1.56×10^7 g/(mol_{Ln}·h)) and excellent syndioselectivity (*rrrr* > 99%) to afford high molecular weight sPS irrespective with the central metal type (such as Sc, Y, or Lu) for the first time. The successful characterization of the molecular structures of these complexes allowed us to probe into the relationship between the structures of the ligands and catalytic performances of the attached central metals.

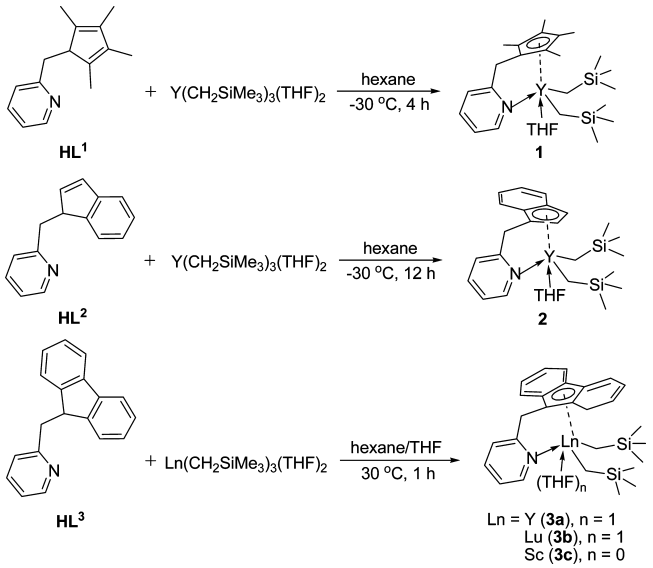
RESULTS AND DISCUSSION

Synthesis and Characterization of Complexes 1, 2, and 3a−c. The pyridyl-methylene functionalized Cp′, Ind, and Flu compounds HL^{1-3} (HL^1 = Cp′CH_2−Py; HL^2 = IndCH_2−Py; HL^3 = FluCH_2−Py) were synthesized by treatment of chloromethylpyridine hydrochloride PyCH_2Cl·HCl with Cp′, Ind, and Flu lithium salts, respectively. Deprotonation of HL^{1-3} by the corresponding rare-earth metal tris(alkyl)s, Ln-$(CH_2SiMe_3)_3(THF)_2$, with releasing $SiMe_4$ afforded the targeted bis(alkyl) complexes $L^1Y(CH_2SiMe_3)_2(THF)$ (**1**), $L^2Y(CH_2SiMe_3)_2(THF)$ (**2**), $L^3Ln(CH_2SiMe_3)_2(THF)_n$ (*n* = 1, Ln = Y (**3a**); *n* = 1, Lu (**3b**); *n* = 0, Sc (**3c**)) in high yields. ^{1}H and ^{13}C NMR spectroscopic analysis of these complexes showed the disappearance of the Cp−H proton of the ligands, and the formation of M−*σ*−C bond between the rare-earth metal ion and the methylene carbons (δ 30.38−45.27 ppm in the ^{13}C NMR).[11] The methylene protons of Y−CH_2SiMe_3 in **1** give a singlet resonance at −0.90 ppm, suggesting that they are equivalent. In contrast, the broad resonances around −1.09, −1.35, and −1.46 ppm assigned to the methylene protons arising from Y−CH_2SiMe_3 in **2** and **3a** and Lu−CH_2SiMe_3 in **3b**, respectively, suggested these metal alkyl moieties are fluxional in the solution state. The ^{1}H NMR spectrum of complex **3c** gives an AB spin (J_{H-H} = 11.2 Hz) around −0.88 ppm, indicating that the scandium methylene protons Sc−CH_2SiMe_3 are diastereotopic. The molecular structures of complexes **1**, **2**, **3a**,**b** were further confirmed by X-ray diffraction analyses, as shown in Figure 1. All the metal centers

dx.doi.org/10.1021/ma202558g | *Macromolecules* 2012, 45, 1248−1253

are bonded to one ligand unit, two alkyl groups and a THF molecule, generating a tetrahedral geometry with the center of Cp ring as the apex. Noteworthy is that all the Cp-based auxiliaries coordinate to the central metal ions in the η^5/κ^1 mode via the Cp carbons and the dangling pyridyl nitrogen atom, forming the typical constrain-geometry-configuration mode. The two alkyl species are located in *cis*-positions with one endo and the other exo with respect to the pyridyl ring. The bite angles of Cp'_{cent}–Y(1)–N(1) (90.87(3)°) in **1**, Ind_{cent}–Y(1)–N(1) (91.94 (3)°) in **2**, Flu_{cent}–Y(1)–N(1) (92.01(3)°) in **3a**, and Flu_{cent}–Lu(1)–N(1) (92.16°) in **3b** are larger than that of Flu_{cent}–Y(1)–N(1) (82.97(3)°) in (Flu–Py)Y(CH_2SiMe_3)$_2$(THF),[12] but smaller than that of Flu_{cent}–Y–C (102(3)°) in (Flu–CH_2CH_2–NHC)Y(CH_2SiMe_3)$_2$.[9] Correspondingly, the averaging bond distances between the carbon atoms of the cyclopentadienyl moieties and the central metal ions $C_{Cp'}$–Y(1) 2.388(3) Å in **1**, C_{Ind}–Y(1) 2.410(3) Å in **2**, C_{Flu}–Y(1) 2.465(3) Å in **3a**, and C_{Flu}–Lu(1) 2.502(3) Å in **3b** are longer than C_{Flu}–Lu(1) 2.357 Å in (Flu–CH_2CH_2–NHC)Lu(CH_2SiMe_3)$_2$,[9] if the difference of ionic radius of Y, Lu, and Sc central metals is ignored.[13] These crystallographic data indicate that all these complexes have a relatively opening environment around the cental metals, which allows the insertion of bulky styrene monomer.

Scheme 1. Synthesis of CGC Complexes 1, 2, and 3a–c



Syndioselective Polymerization of Styrene. All these complexes under the activation of aluminum alkyls and organoborates construct ternary systems, exhibited various catalytic activities and syndioselectivities for styrene polymerization under room temperature as shown in Table 1. Both the Cp′CH_2–Py ligated complex **1** and the IndCH_2–Py ligated complex **2** showed low activity to transfer 1000 equiv of styrene to polystyrene with low conversions (57% vs 67%) within 4 h (Table 1, runs 1, 2). The generated polystyrenes had moderate syndiotacticity of *rrrr* = 60% and 84%, respectively.[14] Surprisingly to us, when the catalytic precursors were switched to complexes **3** bearing bulky FluCH_2–Py ligand, under the same conditions, the polymerization achieved completeness in less than 1 min. Moreover, the polymerization could be performed fluently under a broad range of St-to-Y molar ratios up to 5000 within 2 min. Thus, the highest activity of the yttrium complex **3a** reached to 1.56×10^7 g·PS/(mol$_Y$·h), which ranked top of the most active catalysts, as far as we are aware (Table 1, runs 18–20). Meanwhile the molecular weight of the resultant PS increased correspondingly from $M_n = 5.4 \times 10^4$ g/mol to 49.5×10^4 g/mol close to the theoretic value (Table 1, runs 3–7), indicative of well controlled polymerization. Pleasing to us, the obtained PS was pure syndiotacticity (*rrrr* >99%) evidenced by the ^{13}C NMR spectrum[14] as well as the high melting points around 270 °C in the DSC traces. In particular, we found that the central metal type had no influence on the catalytic performances, because all the Y, Lu, and Sc complexes **3a–c** behaved in similar activity and syndioselectivity (Table 1, runs 3–17), which was in contrast to the previous results that the central metal ion is a crucial factor for governing the catalytic activity.[5] This ligand dominated catalytic performance was investigated further. We employed the similar bulky pyridyl-functionalized Flu ligated Y, Sc and Lu complexes (Chart 1, **B**), however, all showed very low activity with moderate syndioselectivity (Table 1, run 22). The difference is that the five-membered ring of the pyridyl-functionalized Flu ligand coordinates to the central metal ions in an asymmetric η^3-allyl coordination mode rather than the η^5-coordination mode of the Py–CH_2–Flu ligands in complexes **3**, which was analogous to the previous results that the coordination mode (η^5 or η^1) can show dramatic influence on the polymerization activity.[10] This η^3-allyl coordination mode may block the electron delocalization over the phenyl rings that are electron-withdrawing, and thus the ligand is more electron donating as compared with that in complexes **3**,[15] which arouse lowering of the Lewis acidity of the metal center; meanwhile the η^3-coordination mode was less steric shielding to the metal center compared with the η^5-bonding mode, resulting in low selectivity . To confirm this, we also employed our previously reported ethylene-bridged carbene modified Flu rare-earth metal complexes, (Flu–CH_2CH_2–NHC)Ln(CH_2SiMe_3)$_2$ (Chart 1A), as the precursor where the Flu moiety coordinates to the metal center in η^5-coordination mode providing enough steric shieding to the metal center by providing a living fashion with an unprecedented 3,4-selectivity (99%) toward isoprene polymerization,[9] which, unfortunately, were absolutely inert to the styrene polymerization. This could be ascribed to the highly electron-donating nature of the N-heterocyclic carbene (NHC) side arm of Flu–CH_2CH_2–NHC ligand that the Lewis acidity of the central metal ion was lowered. Moreover, the bite angle of Flu_{cent}–Y–C in **A** is much larger than those in complex **3a**, suggesting that coordination environment of the metal center is not opened enough for the insertion of the bulky monomer such as styrene (*vide supra*). These results were in consistent with those found for complexes **1–3** in this work that the catalytic activity trend followed FluCH_2–Py > IndCH_2–Py > Cp′CH_2–Py, demonstrating that a ligand of more bulky but leaving opening coordination sphere and electron less donating facilitated the attached central metals providing higher activity and syndioselectivity,[16] indicative of the crucial role of the ligand compared with that of central metal. The similar result is reported by Hou et al. that larger Cp′ ligated scandium complexes provides higher activity.[7i]

CONCLUSIONS

In summary, a series of new rare-earth metal complexes bearing pyridyl methyl functionalized Cp′ and its indenyl and fluorenyl derivatives (η^5-Cp′-CH_2Py)Y(CH_2SiMe_3)$_2$(THF), (η^5-Ind-CH_2Py) Y(CH_2SiMe_3)$_2$(THF) and (η^5-Flu-CH_2Py)Ln-

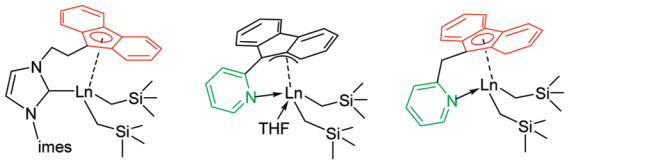
dx.doi.org/10.1021/ma202558g | Macromolecules 2012, 45, 1248–1253

Table 1. Syndiospecific Polymerization of Styrene with Rare-Earth Metal Precursors 1−3 under Various Conditions[a]

run	cat	[St]/[Ln]	t (min)	convn (%)	sPS[b] (%)	activity[c]	M_n[d] × 10^{-4}	M_w/M_n[d]	T_m (°C)[e]
1	**1**	1000	240	57	60	15	3.0	1.44	228
2	**2**	1000	240	67	84	17	3.6	1.56	234
3	**3a**	500	1	100	>99	3120	5.4	2.15	269
4	**3a**	1000	1	100	>99	6240	10.4	2.15	270
5	**3a**	2000	2	100	>99	6240	22.9	2.16	270
6	**3a**	3000	2	100	>99	9360	33.2	2.34	270
7	**3a**	5000	2	100	>99	15 600	49.5	2.58	270
8	**3b**	500	1	100	>99	3120	5.7	1.73	270
9	**3b**	1000	1	100	>99	6240	10.2	1.76	270
10	**3b**	2000	2	100	>99	6240	22.5	1.87	270
11	**3b**	3000	2	100	>99	9360	33.6	2.32	270
12	**3b**	5000	2	100	>99	15 600	48.7	2.35	270
13	**3c**	500	1	100	>99	3120	5.8	1.73	270
14	**3c**	1000	1	100	>99	6240	10.2	1.79	270
15	**3c**	2000	2	100	>99	6240	22.4	1.89	270
16	**3c**	3000	2	100	>99	9360	33.4	2.34	270
17	**3c**	5000	2	100	>99	15 600	48.5	2.38	270
18[f]	**Sc**	2500	1	87	>99	13 618	37.9	1.37	273
19[g]	**Nd**	600	5	84	>99	1710	5.4	1.73	264
20[h]	**Lu**	1000	1	>99	>99	6240	22.3	1.88	270
21[i]	**A**	500	-	-	-	-	-	-	-
22[j]	**B**	500	360	5	-	0.4	-	-	-

[a]Polymerization conditions: Ln (10 μmol), [Ln]/Al^{i}Bu$_3$/[Ph$_3$C][B(C$_6$F$_5$)$_4$] = 1/10/1 (mol/mol/mol), toluene/monomer =5/1 (v/v), T_p = 20 °C, unless otherwise noted. [b]Measured by ^{1}H NMR and ^{13}C NMR spectroscopy in tetrachloroethane-d_2 at 125 °C. [c]Given in kg of polymer/(mol$_{Ln}$·h). [d]Determined by GPC in 1,2,4-trichlorobenzene at 150 °C against polystyrene standard. [e]Determined by DSC. [f](C$_5$Me$_4$SiMe$_3$)Sc(CH$_2$SiMe$_3$)$_2$(THF), ref 5. [g](Cp−CMe$_2$−Flu)Nd(η^3-C$_3$H$_5$)(THF), ref 6. [h](C$_5$Me$_4$−C$_5$H$_4$N)Lu(η^3-C$_3$H$_5$)$_2$, ref 8. [i](Flu−CH$_2$CH$_2$−NHC)Ln(CH$_2$SiMe$_3$)$_2$, ref 9. [j](Flu−Py)Ln (CH$_2$SiMe$_3$)$_2$ (THF), ref 12.

Chart 1



$(CH_2SiMe_3)_2(THF)_n$ (Ln = Sc, n = 0; Y, Lu, n = 1) have been synthesized and well characterized. These complexes together with pyridyl fluorenyl rare-earth metal complexes (η^3-Flu-CH$_2$Py)Ln(CH$_2$SiMe$_3$)$_2$(THF) (Ln = Sc, Y, Lu) and N-heterocyclic carbene rare-earth metal complexes (NHC−CH$_2$CH$_2$−Flu)Ln(CH$_2$SiMe$_3$)$_2$ (Ln = Sc, Y, Lu) have been evaluated as precursors, upon activation with organoborates and aluminum alkyls, for the polymerization of styrene. Among these systems, the precursors bearing η^5-Flu-CH$_2$Py ligand exhibited distinguished catalytic activities up to 1.56 × 10^7 g/(mol$_{Ln}$·h) to provide pure sydiotactic sPS (*rrrr* > 99%), while those stabilized by the analogous η^5-Cp′-CH$_2$Py and η^5-Ind-CH$_2$Py and the deriative η^3-Flu-CH$_2$Py exhibited poor performances both in activity and syndioselectivity. Complexes (NHC−CH$_2$CH$_2$−Flu)Ln(CH$_2$SiMe$_3$)$_2$ were absolutely inert. This indicated that ligand played a crucial role on governing the catalytic performances of the attached metal centers while the type of the central metal ions showed almost no influence, in contrast to the previously reported results. Thus, for the first time, a yttrium based complex exhibited a competitive distinguished activity to its scandium analogue. The high activity was significantly attributed to the electron less donating nature of the η^5-Flu-CH$_2$Py ligand that increased the Lewis acidity of the central metal ion while its steric bulkiness endowed the metal center specific selectivity. This was proved by the less steric and electron donating η^5-Cp′-CH$_2$Py and η^5-Ind-CH$_2$Py supported rare-earth metal counterparts that provided poor performances, and the electron donating ethylene-carbene functionalized fluorenyl rare-earth metal complexes were completely inert. The low activity of the electron less donating pyridyl fluorenyl rare-earth metal complexes were ascribed to η^3-allyl coordination mode of the Cp fragment that inhibited the electrons delocalizing over the phenyl rings in the ligand increasing its electron donating power. This constructed relationship between catalyst structures and performances is expected to open a new route for designing more efficient and specifically selective catalysts.

EXPERIMENTAL SECTION

General Methods and Materials. All reactions were carried out under a dry and oxygen-free argon atmosphere by using Schlenk techniques or under a nitrogen atmosphere in an MBraun glovebox. All solvents were purified from an MBraun SPS system. Samples of organo rare-earth metal complexes for NMR spectroscopic measurements were prepared in the glovebox by use of NMR tubes sealed by paraffin film. ^{1}H and ^{13}C NMR spectra were recorded on a Bruker AV400 or 600 (FT, 400 or 600 MHz for ^{1}H; 100 or 150 MHz for ^{13}C) spectrometer. ^{1}H, ^{13}C NMR spectra of polymer samples were recorded on a Bruker AV400 (FT, 400 MHz for ^{1}H; 100 MHz for ^{13}C) spectrometer in tetrachloroethane-d_2. The molecular weight and molecular weight distribution of the polymers were measured by means of gel permeation chromatography (GPC) on a PL-GPC 220 type high-temperature chromatography equipped with three PL-gel 10 μm Mixed-B LS type columns at 150 °C. T_m of polystyrene samples was measured through differential scanning calorimetry (DSC) analyses, which were carried out on a Q 100 DSC from TA

dx.doi.org/10.1021/ma202558g | Macromolecules 2012, 45, 1248−1253

Instruments under nitrogen atmosphere. Elemental analyses were performed at National Analytical Research Centre of Changchun Institute of Applied Chemistry (CIAC). Styrene was dried over CaH_2 under stirring for 48 h and distilled under reduced pressure before use. ^{n}BuLi (2.5 M in hexane) was purchased from Aldrich. The pyridene methylene tetramethylcyclopentadienyl ligand HL^1 ($C_5Me_4HCH_2$–Py) was synthesized by treatment of chloromethylpyridine hydrochloride Py-CH_2Cl·HCl with C_5Me_4Li. The corresponding Ind and Flu compunds HL^2,[3] (HL^2 = $IndCH_2$–Py; HL^3 = $FluCH_2$–Py) were synthesized following the same procedure. $Ln(CH_2SiMe_3)_3(THF)_2$ were prepared according to the literature.[17] $[Ph_3C][B(C_6F_5)_4]$ was prepared following the literature procedures.[18]

X-ray Crystallographic Studies. Crystals for X-ray analysis were obtained as described in the preparations. The crystals were manipulated in a glovebox. Data collections were performed at −88.5 °C on a Bruker SMART APEX diffractometer with a CCD area detector, using graphite-monochromated Mo Kα radiation (λ = 0.71073 Å). The determination of crystal class and unit cell parameters was carried out by the SMART program package. The raw frame data were processed using SAINT and SADABS to yield the reflection data file. The structures were solved by using the SHELXTL program. Refinement was performed on F^2 anisotropically for all non-hydrogen atoms by the full-matrix least-squares method. The hydrogen atoms were placed at the calculated positions and were included in the structure calculation without further refinement of the parameters.

Synthesis of Complex ($Cp'CH_2$–Py)Y(CH_2SiMe_3)$_2$(THF) (1). Under a nitrogen atmosphere, to a hexane solution (10 mL) of $Y(CH_2SiMe_3)_3(THF)_2$ (0.451 g, 1.0 mmol), 1 equiv of HL^1 (0.213 g, 1.0 mmol) was added slowly at −30 °C. The mixture was stirred for 4 h to afford a clear red solution. Removal of dark red oily residue yielded a deep-red solution. Evaporation of the solvent left **1** as dark red crystalline solids. Recrystallization from hexane and toluene gave single crystals suitable for X-ray analysis (0.31 g, 40.0%). ^{1}H NMR (600 MHz, C_6D_6, 25 °C): δ −0.90 (br s, 4H, Y–CH_2SiMe$_3$), 0.25 (s, 18H, CH_2SiMe_3), 1.38 (br, 4H, THF), 2.01(s, 6H, $C_5H_5Me_4$), 2.04(s, 6H, $C_5H_5Me_4$), 3.75 (br, 4H, THF), 3.84 (s, 2H, $C_5H_4NCH_2$), 6.58 (d, $^3J_{H-H}$ = 6.0 Hz, 1H, C_5H_4N), 6.62 (d, $^3J_{H-H}$ = 7.8 Hz, 1H, C_5H_4N), 6.84 (t, $^3J_{H-H}$ = 7.2 Hz, 1H, C_5H_4N), 8.78 ppm (d, $^3J_{H-H}$ = 4.8 Hz, 1H, *ipso*-C_5H_4N). ^{13}C NMR (150 MHz, C_6D_6, 25 °C): δ 5.38 (s, 6C, CH_2SiMe_3), 11.82(s, 2C, C_5Me_4), 12.21(s, 2C, C_5Me_4),2 5.67 (br s, 2C, THF), 30.38 (d, J_{Y-C} = 25.5, 2C, Y-CH_2SiMe_3), 33.84 (br s, 2C,THF), 71.22(s, 2C, THF), 116.98(s, 1C, $C_5H_5Me_4$), 117.17(s, 2C, $C_5H_5Me_4$),117.74 (s, 2C, $C_5H_5Me_4$), 121.51 (s, 1C, C_5H_4N), 123.94 (s, 1C, C_5H_4N), 138.35 (s, 1C, C_5H_4N), 150.09 (s, 1C, C_5H_4N), 168.90 ppm (s, 1C, *ipso*-C_5H_4N). Anal. Calcd for $C_{27}H_{48}NOSi_2Y$ (%): C, 41.71, H, 6.22, N, 1.80. Found: C,41.61, H, 6.17, N,1 0.75.

Synthesis of Complex ($IndCH_2$–Py)Y(CH_2SiMe_3)$_2$(THF) (2). Under a nitrogen atmosphere, to a hexane solution (10 mL) of $Y(CH_2SiMe_3)_3(THF)_2$ (0.451 g, 1.0 mmol), 1 equiv of HL^2 (0.207 g, 1.0 mmol) was added slowly at −30 °C. The mixture was stirred for 12 h to afford a clear red solution. Removal of dark red oily residue yielded a deep-red solution. Evaporation of the solvent left **2** as dark red crystalline solids. Recrystallization from hexane and toluene gave single crystals suitable for X-ray analysis (0.254 g, 40.1%). ^{1}H NMR (600 MHz, C_6D_6, 25 °C): δ −1.09 (br s, 4H, Y–CH_2SiMe$_3$), 0.12 (s, 18H, CH_2SiMe_3), 1.36 (br, 4H, THF), 3.73 (br, 4H, THF), 4.15, 4.28 (AB system, J_{H-H} = 18.6 Hz, 2H, $C_5H_4NCH_2$), 6.15 (d, $^3J_{H-H}$ = 3.6 Hz, 1H, C_9H_7),6.56 (m, 1H, C_9H_7), 6.69 (d, $^3J_{H-H}$ = 7.8 Hz, 1H, C_9H_7), 6.89–6.91 (m, 1H, C_9H_7), 6.97 (d, $^3J_{H-H}$ = 3.0 Hz, 1H, C_9H_7), 7.01–7.07 (m, 3H, C_9H_7), 7.29 (d, $^3J_{H-H}$ = 7.8 Hz, 1H, C_5H_4N), 7.43 (d, $^3J_{H-H}$ = 7.8 Hz, 1H, C_5H_4N), 8.78 ppm (d, $^3J_{H-H}$ = 4.8 Hz, 1H, *ipso*-C_5H_4N). ^{13}C NMR (150 MHz, C_6D_6, 25 °C): δ 4.58 (s, 6C, CH_2SiMe_3), 25.25 (br s, 2C, THF), 35.01 (br s, 2C, Y-CH_2SiMe_3), 70.70 (br s, 2C,THF), 96.49(s, 2C, C_5H_4N) 119.83 (s, 1C, C_9H_7), 120.61 (s, 1C, C_9H_7), 121.46 (s, 1C, C_9H_7), 121.95 (s, 1C, C_9H_7), 123.51(s, 1C, C_9H_7), 126.68 (s, 1C, C_9H_7), 126.95 (s, 1C, C_9H_7), 128.32 (s, 1C, C_9H_7), 128.54 (s, 1C, C_5H_4N), 129.31 (s, 1C, C_5H_4N), 137.87 (s, 1C, C_5H_4N), 149.95 (s, 1C, C_5H_4N), 167.86 ppm (s, 1C, *ipso*-C_5H_4N). Anal. Calcd for $C_{27}H_{35}NOSi_2Y$ (%): C, 60.65, H, 6.59, N, 2.62. Found: C, 60.61, H, 6.57, N, 2.46.

Synthesis of complex ($FluCH_2$–Py)Y(CH_2SiMe_3)$_2$(THF) (3a). Under a nitrogen atmosphere, to a mixture solution of hexane with THF (10 mL) of $Y(CH_2SiMe_3)_3(THF)_2$ (0.451 g, 1.0 mmol), 1 equiv of HL^3 (0.257 g, 1.0 mmol) was added slowly at 30 °C. The mixture was stirred for 2 h to afford a clear dark yellow solution. Evaporation of the solvent left **3a** as light yellow crystalline solids (0.284 g, 48.1%). Recrystallization from hexane gave single crystals suitable for X-ray analysis. ^{1}H NMR (400 MHz, C_6D_6, 25 °C): δ −1.35 (br s, 4H, Y–CH_2SiMe$_3$), 0.06 (s, 18H, CH_2SiMe$_3$), 1.31 (br s, 4H, THF), 3.43 (br s, 4H, THF), 4.45 (s, 2H, $C_5H_4NCH_2$), 6.62 (t, $^3J_{H-H}$ = 6.0 Hz, 1H, C_5H_4N), 6.85 (d, 1H, $^3J_{H-H}$ = 8.0 Hz, C_5H_4N), 7.05 (m, 3H, $C_{13}H_9$), 7.29 (t, $^3J_{H-H}$ = 8.4 Hz, 2H, $C_{13}H_9$), 7.41 (d, $^3J_{H-H}$ = 8.4 Hz, 2H, $C_{13}H_9$), 7.93 (d, $^3J_{H-H}$ = 8.4 Hz, 2H, $C_{13}H_9$), 8.82 ppm (d, $^3J_{H-H}$ = 4.8 Hz, 1H, *ipso*-C_5H_4N). ^{13}C NMR (100 MHz, C_6D_6, 25 °C): δ 4.82 (s, 6C, CH_2SiMe_3), 25.72 (br s, 2C, THF), 33.53 (s, 2C, $C_5H_4NCH_2$), 35.36 (d, 2C, J_{Y-C} = 41.0 Hz, Y-CH_2SiMe_3), 71.13 (br s, 2C, THF), 118.38 (s, 2C, $C_{13}H_9$), 119.68 (s, 2C, $C_{13}H_9$), 121.86 (s, 2C, $C_{13}H_9$), 122.31 (s, 2C, $C_{13}H_9$), 124.38 (s, 2C, $C_{13}H_9$),125.49 (s, 1C, $C_{13}H_9$), 128.27 (s, 2C, $C_{13}H_9$), 128.51 (s, 1C, C_5H_4N), 128.75 (s, 1C, C_5H_4N), 132.23 (s, 1C, C_5H_4N), 138.82 (s, 1C, C_5H_4N), 150.63 (s, 1C, *ipso*-C_5H_4N) ppm. Anal. Calcd for $C_{31}H_{44}ONSi_2Y$ (%): C, 62.92; H, 7.49; N, 2.37. Found: C, 62.72; H, 7.47; N, 2.20.

Synthesis of complex ($FluCH_2$–Py)Lu(CH_2SiMe_3)$_2$(THF) (3b). Under a nitrogen atmosphere, to a mixture solution of hexane with THF (10 mL) of $Lu(CH_2SiMe_3)_3(THF)_2$ (0.562 g, 1.0 mmol), 1 equiv of HL^3 (0.257 g, 1.0 mmol) was added slowly at 30 °C. The mixture was stirred for 1 h to afford a clear dark yellow solution. Evaporation of the solvent left **3b** as light yellow crystalline solids (0.316 g, 46.7%). Recrystallization from hexane gave single crystals suitable for X-ray analysis. ^{1}H NMR (400 MHz, C_6D_6, 25 °C): δ −1.46 (br s, 4H, Lu–CH_2SiMe$_3$), 0.06 (s, 18H, CH_2SiMe_3), 1.30 (br s, 4H, THF), 3.41 (br s, 4H, THF), 4.42 (s, 2H, $C_5H_4NCH_2$), 6.6 (t, $^3J_{H-H}$ = 7.2 Hz, 1H, C_5H_4N), 6.8 (d, $^3J_{H-H}$ = 7.6 Hz, 1H, C_5H_4N), 6.94 (t, $^3J_{H-H}$ = 7.6 Hz, 1H, C_5H_4N), 7.10 (m, 3H, $C_{13}H_9$), 7.29 (t, 2H, $C_{13}H_9$),7.38 (d, $^3J_{H-H}$ = 8.4 Hz, 2H, $C_{13}H_9$), 7.98 (d, $^3J_{H-H}$ = 7.6 Hz, 2H, $C_{13}H_9$), 8.74 (d, $^3J_{H-H}$ = 5.2 Hz, 1H, *ipso*-C_5H_4N) ppm. ^{13}C NMR (100 MHz, C_6D_6, 25 °C): δ 4.85 (s, 6C, CH_2SiMe_3), 25.75 (br s, 2C, THF), 33.41 (s, 2C, $C_5H_4NCH_2$), 40.36 (s, 2C, Lu-CH_2SiMe_3), 71.38 (br s, 2C, THF), 118.33 (s, 2C, $C_{13}H_9$), 119.50 (s, 2C, $C_{13}H_9$), 121.15 (s, 2C, $C_{13}H_9$), 121.98 (s, 2C, $C_{13}H_9$), 122.37 (s, 1C, $C_{13}H_9$), 124.59 (s, 1C, $C_{13}H_9$), 125.64 (s, 2C, $C_{13}H_9$), 128.26 (s, 1C, $C_{13}H_9$), 128.50 (s, 1C, C_5H_4N),128.74 (s, 1C, C_5H_4N), 132.98 (s, 1C, C_5H_4N), 138.94 (s, 1C, C_5H_4N), 150.08 (s, 1C, *ipso*-C_5H_4N) ppm. Anal. Calcd for $C_{31}H_{44}$ $ONSi_2Lu$ (%): C, 62.92; H, 7.49; N, 2.37. Found: C, 62.85; H, 7.46; N, 2.35.

Synthesis of complex ($FluCH_2$–Py)Sc(CH_2SiMe_3)$_2$ (3c). Under a nitrogen atmosphere, to a mixture solution of hexane with THF (10 mL) of $Sc(CH_2SiMe_3)_3(THF)_2$ (0.450 g, 1.0 mmol), 1 equiv of HL^3 (0.257 g, 1.0 mmol) was added slowly at 30 °C. The mixture was stirred for 1 h to afford a clear dark yellow solution. Evaporation of the solvent left **3c** as light yellow crystalline solids (0.222 g, 46.7%). Recrystallization from hexane gave single crystals suitable for X-ray analysis. ^{1}H NMR (400 MHz, C_6D_6, 25 °C): δ −0.88 (AB, $^2J_{H-H}$ = 11.2 Hz, 4H, Sc–CH_2SiMe$_3$), 0.05 (s, 18H, CH_2SiMe_3), 4.14 (s, 2H, $C_5H_4NCH_2$), 6.32 (t, $^3J_{H-H}$ = 6.4 Hz, 1H, C_5H_4N), 6.61 (d, $^3J_{H-H}$ = 12.0 Hz, 1H, C_5H_4N), 6.79 (t, $^3J_{H-H}$ = 8.60 Hz, 1H, C_5H_4N), 7.10 (m, 3H, $C_{13}H_9$), 7.21 (m, 2H, $C_{13}H_9$), 7.26 (m, 4H, $C_{13}H_9$), 8.29 (d, $^3J_{H-H}$ = 8.0 Hz, 2H, $C_{13}H_9$), 8.34 (d, $^3J_{H-H}$ = 5.2 Hz, 1H, *ipso*-C_5H_4N) ppm. ^{13}C NMR (100 MHz, C_6D_6, 25 °C): δ 4.15 (s, 6C, CH_2SiMe_3), 32.18 (s, 2C, $C_5H_4NCH_2$), 45.27 (s, 2C, Sc-CH_2SiMe_3), 94.29 (s, 2C, $C_{13}H_9$), 119.15 (s, 2C, $C_{13}H_9$), 119.90 (s, 2C, $C_{13}H_9$), 120.65 (s, 2C, $C_{13}H_9$), 122.48 (s, 1C, $C_{13}H_9$),124.94 (s, 1C, $C_{13}H_9$), 125.024 (s, 2C, $C_{13}H_9$), 126.63 (s, 1C, $C_{13}H_9$), 132.18 (s, 1C, C_5H_4N), 140.12 (d, 2C, C_5H_4N),148.50 (s, 1C, C_5H_4N), 169.70 (s, 1C, *ipso*-C_5H_4N) ppm. Anal. Calcd for $C_{27}H_{36}NSi_2Sc$ (%): C, 68.17; H, 7.63; N, 2.94. Found: C, 68.15; H, 7.53; N, 2.48.

Typical Procedure for Styrene Polymerization. A typical polymerization procedure is as follows (Table 1, run 3): In a glovebox, styrene (1.04 g, 10 mmol) was added into a 25 mL flask. Then, 10 equiv Al^iBu_3 (0.20 mL, 0.5 mol/L), a toluene solution (3.0 mL) of **3a**

(5.9 mg, 10 μmol), and 1 equiv $[Ph_3C][B(C_6F_5)_4]$ (9.7 mg, 10 μmol) was added to the flask. After the reaction was stirred for 1 min, methanol was injected to terminate the polymerization. The viscous mixture was poured into a large quantity of methanol. The obtained white polymer was filtered and then dried under vacuum at 40 °C to a constant weight.

■ ASSOCIATED CONTENT

Supporting Information

NMR spectra and DSC charts of representative polymer products.This material is available free of charge via the Internet at http://pubs.acs.org. CCDC-850069 (**1**), 844680 (**2a**), 844681 (**3a**), and 844682(**3b**) contain the supplementary crystallographic data for this paper. These data can be obtained free of charge from The Cambridge Crystallographic Data Centre via www.ccdc.cam.ac.uk/data_request/cif.

■ AUTHOR INFORMATION

Corresponding Author

*E-mail: dmcui@ciac.jl.cn. Fax: (+86) 431 85262774. Telephone: +86 431 85262773.

Notes

The authors declare no competing financial interest.

■ ACKNOWLEDGMENTS

This work was partly supported by The National Natural Science Foundation of China for Project Nos. 20934006, 51073148, and 51021003. The Ministry of Science and Technology of China for Projects Nos. 2009AA03Z501 and 2011DF50650.

■ REFERENCES

(1) (a) Ishihara, N.; Seimiya, T.; Kuramoto, M.; Uoi, M. *Macromolecules* **1986**, *19*, 2464−2465. (b) Ishihara, N.; Kuramoto, M.; Uoi, M. *Macromolecules* **1988**, *21*, 3356−3360.

(2) (a) Tomotsu, N.; Ishihara, N.; Newman, T. H.; Malanga, M. T. *J. Mol. Catal. A.* **1998**, *128*, 167−190. (b) Malanga, M. *Adv. Mater.* **2000**, *12*, 1869−1872.

(3) (a) Zambelli, A.; Oliva, L.; Pellecchia, C. *Macromolecules* **1989**, *22*, 2129−2130. (b) Liguori, D.; Centore, R.; Tuzi, A.; Grisi, F.; Sessa, I.; Zambelli, A. *Macromolecules* **2003**, *36*, 5451−5460. (c) Capacchione, C.; Proto, A.; Ebeling, H.; Mullhaupt, R.; Moller, K.; Spaniol, T.; Okuda, J. *J. Am. Chem. Soc.* **2003**, *125*, 4964−4965. (d) Schellenberg, J. *Prog. Polym. Sci.* **2009**, *34*, 688−718. (e) Schellenberg, J.; Leder, H. J. *Adv. Polym. Technol.* **2006**, *25*, 141−151. (f) Schellenberg, J.; Tomotsu, N. *Prog. Polym. Sci.* **2002**, *27*, 1925−1982. (g) Averbuj, C.; This, E.; Eisen, M. S. *J. Am. Chem. Soc.* **1998**, *120*, 8640−8646. (h) Okuda, J.; Masoud, E. *Macromol. Chem. Phys.* **1998**, *199*, 543−552.

(4) (a) Yang, M.; Cha, C.; Shen, Z. *Polym. J.* **1990**, *22*, 919−923. (b) Zhang, Y.; Hou, Z.; Wakatsuki, Y. *Macromolecules* **1999**, *32*, 939−941. (c) Luo, Y.; Yao, Y.; Shen, Q. *Macromolecules* **2002**, *35*, 8670−8671. (d) Luo, Y.; Nishiura, M.; Hou, Z. *J. Organomet. Chem.* **2007**, *692*, 536−544. (e) Hou, Z.; Zhang, Y.; Tezuka, H.; Xie, P.; Tardif, O.; Take-aki., K.; Yamazaki, H.; Wakatsuki, Y. *J. Am. Chem. Soc.* **2000**, *122*, 10533−10543.

(5) Luo, Y.; Baldamus, J.; Hou, Z. *J. Am. Chem. Soc.* **2004**, *126*, 13910−13911.

(6) (a) Kirillov, E.; Lehmann, C. W.; Razavi, A.; Carpentier, J.-F. *J. Am. Chem. Soc.* **2004**, *126*, 12240−12441. (b) Rodrigues, A.-S.; Kirillov, E.; Roisnel, T.; Lehmann, C. W.; Vuillemin, B.; Razavi, A.; Carpentier, J.-F. *Chem.—Eur. J.* **2007**, *13*, 5548−5565. (c) Perrin, L.; Sarazin, Y.; Kirillov, E.; Carpentier, J.-F.; Maron, L. *Chem.—Eur. J.* **2009**, *15*, 3773−3783. (e) Perrin, L.; Kirillov, E.; Carpentier, J.-F.; Maron, L. *Macromolecules* **2010**, *43*, 6330−6336.

(7) (a) Jaroschik, F.; Shima, T.; Li, X.; Mori, K.; Ricard, L.; Le Goff, X.-F.; Nief, F.; Hou, Z. *Organometallics* **2007**, *26*, 5654−5660. (b) Nishiura, M.; Mashiko, T.; Hou, Z. *Chem. Commun.* **2008**, 2019−2021. (c) Fang, X.; Li, X.; Hou, Z.; Assoud, J.; Zhao, R. *Organometallics* **2009**, *28*, 517−522. (d) Xu, X.; Chen, Y.; Sun, J. *Chem.—Eur. J.* **2009**, *15*, 846−850. (e) Bonnet, F.; Violante, C. D. C.; Roussel, P.; Mortreux, A.; Visseaux, M. *Chem. Commun.* **2009**, 3380−3382. (f) Liu, D.; Luo, Y.; Gao, W.; Cui, D. *Organometallics* **2010**, *29*, 1916−1923. (h) Li, X.; Nishiura, M.; Hu, L.; Mori, K.; Hou, Z. *J. Am. Chem. Soc.* **2009**, *131*, 13870−13882. (i) Guo, F.; Nishiura, M.; Koshino, H.; Hou, Z. *Macromolecules* **2011**, *44*, 6335−6344. (j) Pan, L.; Zhang, K.; Nishiura, M.; Hou, Z. *Macromolecules* **2010**, *43*, 9591−9593.

(8) Jian, Z.; Tang, S.; Cui, D. *Chem.—Eur. J.* **2010**, *16*, 14007−14015.

(9) Wang, B.; Cui, D.; Lv, K. *Macromolecules* **2008**, *41*, 1983−1988.

(10) Nishiura, M.; Mashiko, T.; Hou, Z. *Chem. Commun.* **2008**, 2019−2021.

(11) (a) Liu, B.; Cui, D.; Ma, J.; Chen, X.; Jing, X. *Chem.—Eur. J.* **2007**, *13*, 834−845. (b) Liu, B.; Liu, X.; Cui, D.; Li, L. *Organometallics* **2009**, *28*, 1453−1460. (c) Yang, Y.; Li, Sh.; Cui, D.; Chen, X.; Jing, X. *Organometallics* **2007**, *26*, 671−678. (d) Li, S.; Cui, D.; Li, D.; Hou, Z. *Organometallics* **2009**, *28*, 4814−4822.

(12) Jian, Z.; Tang, S.; Cui, D. *Chem.—Eur. J.* **2011**, in press.

(13) Shannon, R. D. *Acta Crystallogr., Sect. A* **1976**, *32*, 751−767.

(14) (a) Feil, F.; Harder, S. *Macromolecules* **2003**, *36*, 3446−3448. (b) Kawamura, T.; Toshima, N.; Matsuzaki, K. *Macromol. Rapid Commun.* **1994**, *15*, 479−486. (c) Harder, S. *Angew. Chem., Int. Ed.* **2004**, *43*, 2714−2718. (d) Harder, S.; Feil, F.; Knoll, K. *Angew. Chem., Int. Ed.* **2001**, *40*, 4261−4264.

(15) Yoshizawa, K.; Yahara, K.; Taniguchi, A.; Yamabe, T.; Kinoshita, T.; Takeuchi, K. *J. Org. Chem.* **1999**, *64*, 2821−2829.

(16) Fluorenyl- (indenyl-) based ligands can adopt variable coordinationmodes, and the intermediates and active species may be stabilized;this could be another way to explain the difference of the activitiestowards styrene polymerization based on analogous Cp-like ligand.See: Kirillov, E.; Saillard, J.-Y.; Carpentier, J.-F. *Coord. Chem. Rev.* **2005**, *249*, 1221−1248.

(17) Lappert, M. F.; Pearce, R. *Chem. Commun.* **1973**, 126−127.

(18) (a) Tjaden, E. B.; Swenson, D. C.; Jordan, R. F. *Organometallics* **1995**, *14*, 371−386. (b) Chien, J. C. W.; Tsai, W. M.; Rausch, M. D. *J. Am. Chem. Soc.* **1991**, *113*, 8570−8571.

Macromolecules

Article

pubs.acs.org/Macromolecules

Automated ARGET ATRP Accelerates Catalyst Optimization for the Synthesis of Thiol-Functionalized Polymers

Daniel J. Siegwart,[†,‡,⊥] Matthias Leiendecker,[†,‡,⊥] Robert Langer,[†,‡,§] and Daniel G. Anderson*[,†,‡,§]

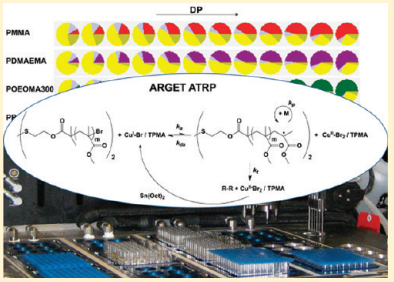
[†]Department of Chemical Engineering, Massachusetts Institute of Technology, Cambridge, Massachusetts 02139, United States

[‡]David H. Koch Institute for Integrative Cancer Research, Massachusetts Institute of Technology, Cambridge, Massachusetts 02139, United States

[§]Harvard-MIT Division of Health Sciences and Technology, Cambridge, Massachusetts 02139, United States

Supporting Information

ABSTRACT: Conventional synthesis of polymers by ATRP is relatively low throughput, involving iterative optimization of conditions in an inert atmosphere. Automated, high-throughput controlled radical polymerization was developed to accelerate catalyst optimization and production of disulfide-functionalized polymers without the need of an inert gas. Using ARGET ATRP, polymerization conditions were rapidly identified for eight different monomers, including the first ARGET ATRP of 2-(diethylamino)ethyl methacrylate and di(ethylene glycol) methyl ether methacrylate. In addition, butyl acrylate, oligo(ethylene glycol) methacrylate 300 and 475, 2-(dimethylamino)ethyl methacrylate, styrene, and methyl methacrylate were polymerized using bis(2-hydroxyethyl) disulfide bis(2-bromo-2-methylpropionate) as the initiator, tris(2-pyridylmethyl)amine as the ligand, and tin(II) 2-ethylhexanoate as the reducing agent. The catalyst and reducing agent concentration was optimized specifically for each monomer, and then a library of polymers was synthesized systematically using the optimized conditions. The disulfide-functionalized chains could be cleaved to two thiol-terminated chains upon exposure to dithiothreitol, which may have utility for the synthesis of polymer bioconjugates. Finally, we demonstrated that these new conditions translated perfectly to conventional batch polymerization. We believe the methods developed here may prove generally useful to accelerate the systematic optimization of a variety of chemical reactions and polymerizations.



INTRODUCTION

The optimization of reaction conditions is a routine and time-consuming challenge for most synthetic chemists and can often be rate-limiting in scientific progress. We developed a systematic approach to accelerate this process in the context of polymer science. The discovery of activator generated by electron transfer (AGET)[1] atom transfer radical polymerization (ATRP),[2−6] which enables polymerizations to be conducted without freeze−pump−thaw cycles,[7] has greatly simplified the setup of ATRP and poised it to reach new areas of research.[6,7] In addition to elimination of the inert gas requirement, activators regenerated by electron transfer (ARGET) ATRP[8−10] has reduced the amount of required copper catalyst to ppm levels.[11] However, the discovery of AGET and ARGET ATRP requires new polymerization conditions to optimize polymerization kinetics and control functionality. This process is typically iterative and relatively low throughput, thereby limiting the diversity and number of conditions that can be explored. Here we develop methods that can facilitate the rapid development of polymerization conditions for new monomers and accelerate the production of functional polymers of tunable length without the need of an inert gas.

Automated, high-throughput (HT) methods are important research tools for the synthesis and screening of small molecules[12−17] and polymers.[18−26] Such methods have resulted in the discovery of drugs such as sorafenib[27] and polymerization catalysts, including new polyolefin catalysts.[28] Efficient reaction optimization is a key component of chemical research, which requires significant time input. One important challenge is to adapt new chemistries such as ARGET ATRP to robotic platforms, thereby accelerating optimization. Combinatorial strategies are useful in a number of areas, including in polymer science.[18−25,28−38] Anionic[35] and cationic[39] polymerization, reversible addition−fragmentation chain transfer (RAFT) polymerization,[34] and ATRP[40−43] methods have been developed for automated platforms. However, the limiting factor is that the synthesis of narrowly distributed macromolecules by living polymerization usually requires very clean reaction conditions and an inert atmosphere. Progress in this area so far has required customized reaction setups with a continuous stream of argon or physical placement of the robot inside of a glovebox.[36,41,43]

To address these challenges, we sought to develop automated ARGET ATRP with the following aims: (1) to rapidly optimize polymerization conditions without deoxygenation, including conditions for the polymerization of new monomers, (2) to synthesize polymers of increasing lengths

Received: January 4, 2012
Published: January 20, 2012

 © 2012 American Chemical Society dx.doi.org/10.1021/ma3000219 | Macromolecules 2012, 45, 1254−1261

with disulfide functionality, and (3) validate the optimized conditions by translating automated synthesis to conventional batch polymerization. The development of ARGET ATRP in the presence of limited amounts of air (in which the oxygen is eventually consumed) allowed for automation of ATRP in sealed vials without deoxygenation. Since all of the polymers contain disulfide bridges in the center of the chains, and can be cleaved to two thiol-terminated chains, they can potentially be conjugated to other molecules such as drugs, siRNA, and proteins. The conditions developed on the robot translated to conventional batch polymerization in a chemical fume hood, suggesting that this method of reaction optimization has potential to provide valuable conditions for general purpose ARGET ATRP of various monomers.

EXPERIMENTAL SECTION

Materials. Bis(2-hydroxyethyl) disulfide, bromo-2-methylpropionic acid, *N*,*N*′-dicyclohexylcarbodiimide (DCC), 4-(dimethylamino)-pyridine (DMAP), DL-dithiothreitol (DTT), tin(II) 2-ethylhexanoate ($Sn(Oct)_2$), copper(I) bromide (99.999% trace metals basis) (CuBr), copper(II) bromide (99.999% trace metals basis) ($CuBr_2$), tetrahydrofuran (anhydrous) (THF), anisole (anhydrous), and ethanol (200 proof) were purchased from Aldrich and used as received. Tris(2-pyridylmethyl)amine (TPMA) was purchased from ATRP Solutions and used as received. Bis[2-(2-bromoisobutyryloxy)ethyl] disulfide ($(BiBOE)_2S_2$) was synthesized following a literature procedure.[44] Butyl acrylate (BA), di(ethylene glycol) methyl ether methacrylate (DEGMEMA), oligo(ethylene glycol) methacrylate 300 (OEOMA300, poly(ethylene glycol) methyl ether methacrylate, M_n = 300 g/mol), oligo(ethylene glycol) methacrylate 475 (OEOMA475, poly(ethylene glycol) methyl ether methacrylate, M_n = 475 g/mol), 2-(dimethylamino)ethyl methacrylate (DMAEMA), 2-(diethylamino)-ethyl methacrylate (DEAEMA), styrene (Sty), and methyl methacrylate (MMA) were purchased from Aldrich and passed through a short column containing basic aluminum oxide to remove the inhibitor before use. Unless otherwise noted, all other chemicals were obtained from commercial sources and used without further purification.

HTP Synthesis. Robotic polymerizations were performed on a customized Symyx Core Module equipped with four different liquid dispensing elements (a single tip, a motor driven gripper with a heated piercing tip, a positive displacement tip, and a heated parallel 4-tip). Library Studio (Symyx Discovery Tools) was used to design the polymer libraries. Automation of this process accelerated not only material handling but also data manipulations and reaction calculations. The MW, density, drawn chemical structure, and dissolved concentration were entered into Library Studio to enable rapid calculation of reaction stoichiometry, taking into account the MW, density, structure, and concentration. Polymerizations were conducted in 4 mL vials equipped with a stir bar and sealed with a rubber septum. The reactants were transferred from stock solutions in 20 mL vials into 4 mL reaction vessels using the piercing tip. The total volume of all components per vessel was fixed to 3.7 mL (0.3 mL of air). All experiments followed a set algorithm: (1) Set stirring to 300 rpm, (2) transfer monomer, (3) transfer initiator, (4) transfer catalyst (inactive, oxidized form), (5) transfer reducing agent (starts polymerization by reducing the catalyst after consumption of air), (6) set temperature to 45 °C, (7) wait 16 h, and (8) cool down to room temperature and stop stirring.

A typical polymerization was as follows: For the synthesis of PMMA with a targeted DP of 135, 1.042 mL of MMA (9.82 mmol) was added to a 4 mL vial equipped with a stir bar and rubber septum. 319.0 μL of a 100 mg/mL solution of $(BiBOE)_2S_2$ in anisole (31.9 mg, 70.57 μmol of $(BiBOE)_2S_2$) was added upon stirring. 2.014 mL of a catalyst solution of $CuBr_2$ (2.7 mmol/L, 1.19 mg, 5.32 μmol) and TPMA (6.5 mmol/L, 3.80 mg, 13.09 μmol) in anisole was transferred to the vial. 324.1 μL of a 136.4 mg/mL solution of $Sn(Oct)_2$ (44.20 mg, 109.1 μmol) was added, and the stirred mixture was heated to 45 °C for 16 h.

Optimization of the Reducing Agent Concentration. For each of the eight monomers, a polymerization was carried out at 12 different concentrations of reducing agent. The catalyst concentration was held constant in all polymerizations, which was 0.037:1 (catalyst:initiator, mol:mol). The targeted degree of polymerization (DP) was 75 for OEOMA475, 110 for OEOMA300, and 150 all other monomers. The molar ratios of $Sn(Oct)_2$ to the initiator for the OEOMA polymers were 0.30, 0.45, 0.60, 0.75, 0.90, 1.05, 1.20, 1.35, 1.50, 1.65, 1.80, and 1.95 to 1.00; for all other polymerizations 0.30, 0.60, 0.90, 1.20, 1.50, 1.80, 2,25, 3.15, 4.05, 4.95, 5.85, and 6.75 to 1.00. In total, 96 separate polymerizations were carried out to optimize the reducing agent concentration.

Optimization of the Catalyst Concentration. For each monomer, the polymerization was carried out at 12 different concentrations of catalyst. The reducing agent concentration was held constant in all reactions. The targeted DP was 75 for OEOMA475, 110 for OEOMA300, and 150 all other monomers. The molar ratios of copper(II) bromide to the initiator were 0.031, 0.037, 0.042, 0.050, 0.056, 0.062, 0.075, 0.087, 0.1, 0.112, 0.125, and 0.137 to 1.00. In total, 96 separate polymerizations were carried out to optimize the catalyst concentration.

Synthesis of Polymers with Different Chain Length. Using the results from the optimization for the concentration of catalyst and reducing agent, polymers were synthesized with different chain lengths. For POEOMA the targeted DP was 15, 30, 45, 60, 67.5, 75, 82.5, 90, 97.5, 105, 120, and 150; for all other polymers, it was 22.5, 45, 67.5, 90, 112.5, 135, 157.5, 180, 202.5, 225, 300, and 375. The concentrations of catalyst and reducing agent used are listed in Table 1. In total, 96 polymers were synthesized with various lengths.

Table 1. Optimized Molar Ratios of Catalyst and Reducing Agent Used for the Synthesis of Polymers with Different Targeted Degree of Polymerization

monomer	$[CuBr_2]/[I]$	[Red]/[I]
MMA	0.075	1.50
DEGMEMA	0.100	0.90
OEOMA300	0.062	0.75
OEOMA475	0.062	1.50
DMAEMA	0.050	1.20
DEAEMA	0.056	1.80
BA	0.062	1.50
Sty	0.050	2.25

Batch Polymerization of MMA in a Round-Bottom Flask. We equipped a standard 5 mL round-bottom flask with a standard 14/20 rubber septum and stir bar (VWR 58948-116 polygon spinbar, 1/2 in. × 5/16 in.) and measured that this flask can hold 6.6 mL of solution. We based the calculation such that the vial would contain 92.5% solution and 7.5% air (analogous to the automated polymerization condition), setting the total volume to be 6.105 mL. For the synthesis of PMMA with a targeted DP of 135, 1.695 mL of MMA (1.598 g, 15.97 mmol) was added via pipet to a 5 mL vial equipped with a stir bar. 534.6 μL of a 100 mg/mL solution of $(BiBOE)_2S_2$ in anisole (53.46 mg, 118.3 μmol of $(BiBOE)_2S_2$) was added via pipet. 3.347 mL of a catalyst solution of $CuBr_2$ (2.7 mmol/L, 1.98 mg, 8.87 μmol) and TPMA (6.5 mmol/L, 6.31 mg, 21.76 μmol) in anisole was transferred to the flask via pipet. The flask was sealed with a rubber septum and secured tightly using electrical tape. 0.527 mL of a 136.4 mg/mL solution of $Sn(Oct)_2$ (71.88 mg, 177.4 μmol) was injected via syringe to start the polymerization. The reaction was placed into a preheated oil bath set to 45 °C and stirred at 300 rpm for 16 h.

Batch Polymerization of DMAEMA in a Round-Bottom Flask. Similar to the polymerization of MMA, we set the total volume to be 6.105 mL for a standard 5 mL round-bottom flask. For the synthesis of PDMAEMA with a targeted DP of 135, 2.794 mL of DMAEMA (2.607 g, 16.58 mmol) was added via pipet to a 5 mL vial equipped with a stir bar. 555.2 μL of a 100 mg/mL solution of $(BiBOE)_2S_2$ in

dx.doi.org/10.1021/ma3000219 | Macromolecules 2012, 45, 1254−1261

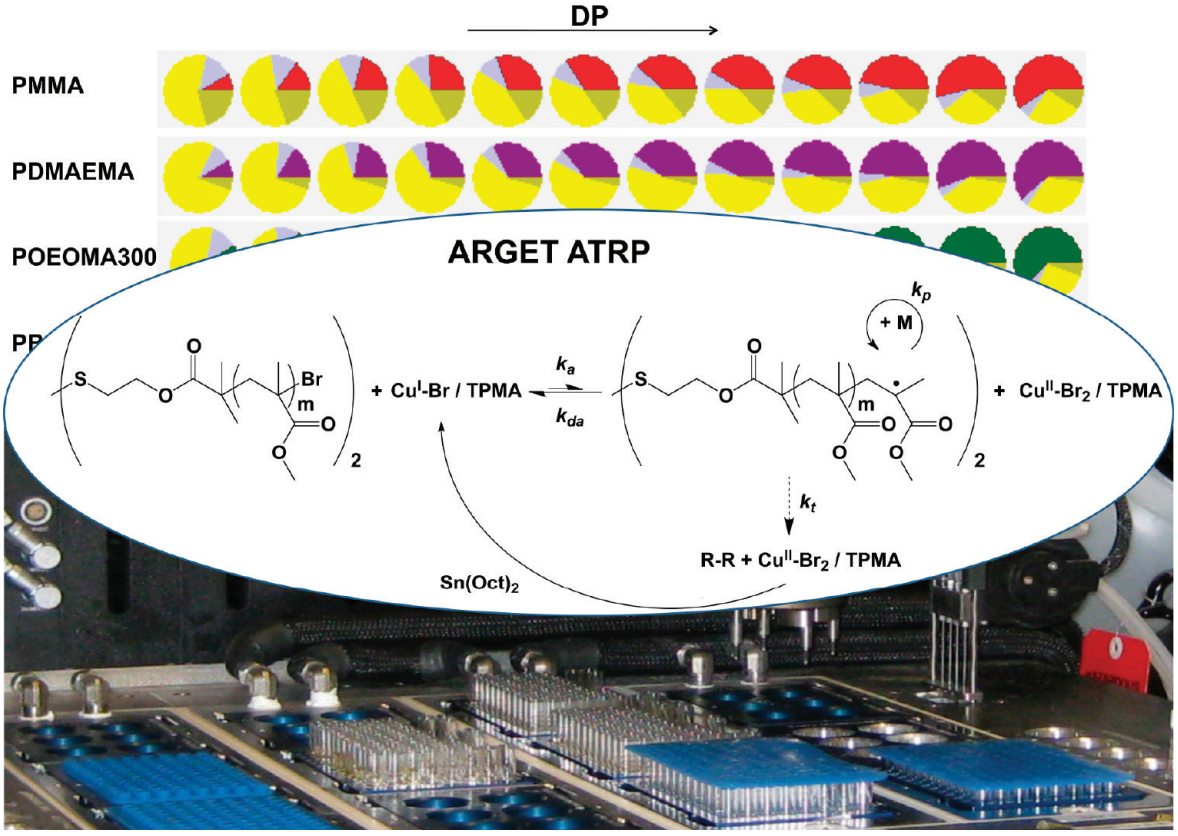


Figure 1. Automated ARGET ATRP enabled rapid catalyst optimization and efficient synthesis of a polymer library that can be tailored for specific applications.

anisole (55.52 mg, 122.8 μmol of $(BiBOE)_2S_2$) was added via pipet. 2.317 mL of a catalyst solution of $CuBr_2$ (2.7 mmol/L, 1.37 mg, 6.14 μmol) and TPMA (6.5 mmol/L, 4.36 mg, 15.06 μmol) in anisole was transferred to the flask via pipet. The flask was sealed with a rubber septum and secured tightly using electrical tape. 0.438 mL of a 136.4 mg/mL solution of $Sn(Oct)_2$ (59.71 mg, 146.6 μmol) was injected via syringe to start the polymerization. The reaction was placed into a preheated oil bath set to 45 °C and stirred at 300 rpm for 16 h.

Reduction of the Disulfide Bond Using DTT. The cleavage of the disulfide bonds was performed in THF using DTT. 1 mL of the polymer solution (3 mg/mL in THF) was transferred into a 4 mL vial. 2 mL of a DTT solution (0.1 g/mL in THF) was added. The mixture was stirred in a sealed vial for 4 days at 50 °C, and samples for GPC measurements were taken every 24 h. In a parallel control without DTT, solutions of the same polymers were stirred, heated to 50 °C, and analyzed every 24 h.

Purification. The copper catalyst and the reducing agent were removed by passing the polymer solution through a neutral alumina oxide matrix. The simultaneous purification of 24 samples was performed using a Visiprep Vacuum Manifold (Supelco). After the polymerization was finished, 0.2 mL of polymer solution was transferred into an 8 mL glass vial and diluted with 3 mL of THF. Twenty-four neutral aluminum oxide solid-phase extraction (SPE) cartridges (Waters) were placed on the manifold and filled with the diluted polymer solution. The pressure in the chamber was reduced, and the purified polymer solution was collected in 8 mL glass vials. After filtration through a 0.2 μm PTFE syringe filter, the solution was used for GPC analysis without further dilution.

GPC Analysis. All polymers were analyzed using a Waters GPC system equipped with a 2400 differential refractometer, 515 pump, and 717-plus autosampler. The flow rate was 1 mL/min, and the mobile phase was THF. The Styragel columns (Waters) and detector were thermostated at 35 °C. Linear polystyrene standards were used for calibration.

RESULTS AND DISCUSSION

Monomer and Catalyst Selection. Catalyst optimization is an important element of ATRP. In order to conduct controlled polymerizations, the molar ratios and concentrations must be systematically varied in order to determine ideal polymerization conditions. Automated ARGET ATRP aided in this process, in terms of both the calculations in Library Studio and the physical dispensing of reactants. ARGET ATRP can control the polymerization of many different kinds of monomers, and we sought to investigate polymerization conditions for a range of monomers using automated methods (Figure 1). We selected eight monomers, which were representative of acrylate, methacrylate, styrenic, PEG mimic, and cationic classes (Figure S1). For development, we used copper(II) bromide ($CuBr_2$), tris(2-pyridylmethyl)amine (TPMA) as the ligand, tin(II) 2-ethylhexanoate ($Sn(Oct)_2$) as the reducing agent, and anisole as the solvent (except for the PEG-based monomers, where ethanol was used). First, the required concentrations of reducing agent and catalyst were systematically optimized. In the second phase, various narrowly distributed polymers were synthesized using the optimized conditions. Bis[2-(2-bromoisobutyryloxy)ethyl] disulfide ($(BiBOE)_2S_2$)[44] was used as the initiator because it allows for the synthesis of disulfide-functionalized polymers that can be subsequently cleaved into two thiol-terminated chains. The choice of this initiator limited the selection of the reducing agent for ARGET ATRP. $Sn(Oct)_2$ has an appropriate redox potential, where copper(II) is reduced to copper(I), but the disulfide bridge is not cleaved during the polymerization. Preliminary experiments verified that the disulfide bond is not reduced by $Sn(Oct)_2$.

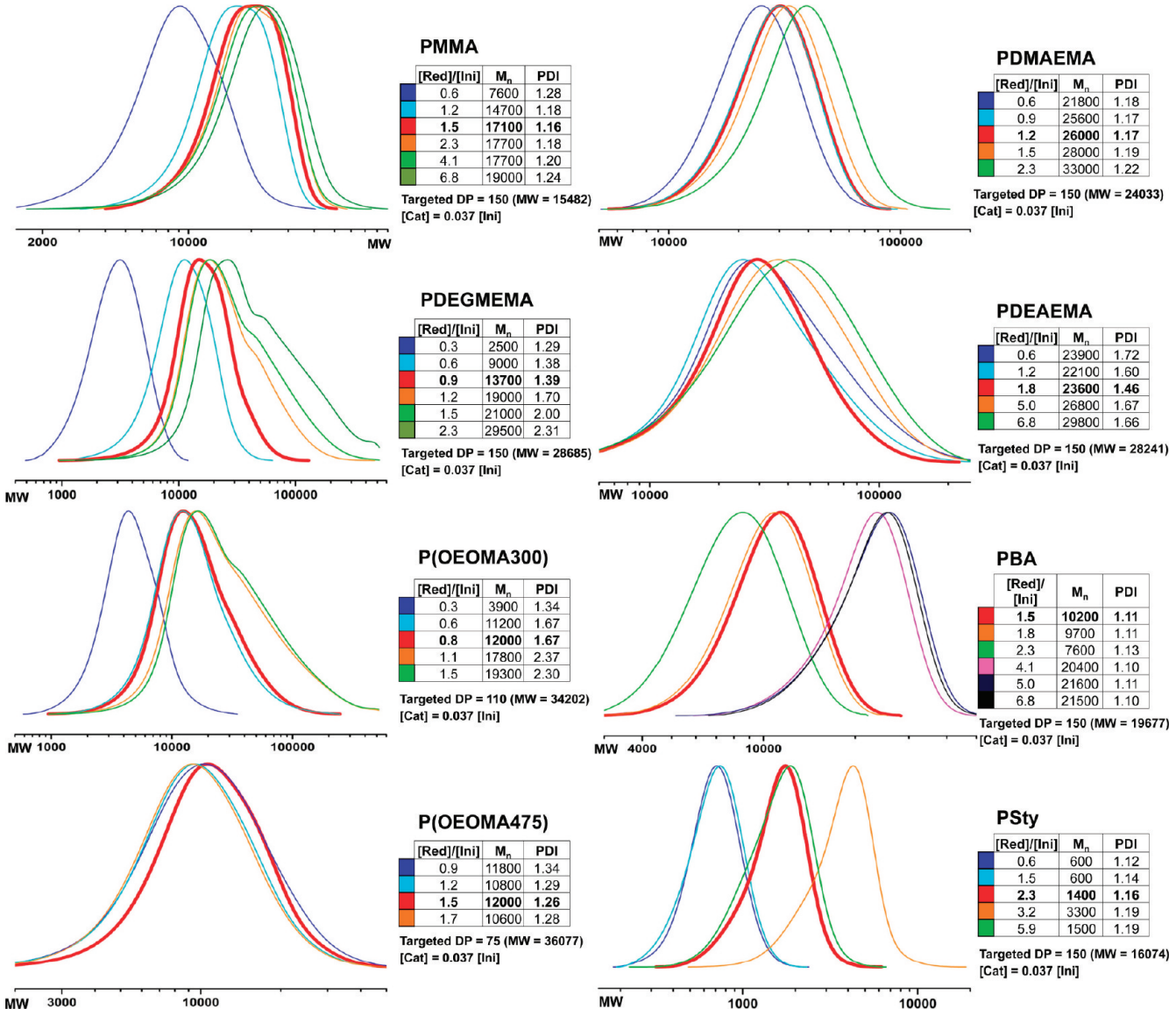


Figure 2. Optimization of the reducing agent concentration. Selected traces for the polymerization of MMA, DEGMEMA, OEOMA300, OEOMA475, DMAEMA, DEAEMA, BA, and Sty show the effect of changing the reducing agent concentration. Optimal results are indicated in red.

The process of optimization yielded information for appropriate concentrations of catalyst and reducing agent for various monomers. To the best of our knowledge, the polymerization of 2-(diethylamino)ethyl methacrylate (DEAEMA) and diethylene glycol methyl ether methacrylate (DEGMEMA) by ARGET ATRP has not yet been reported in the literature. Oligo(ethylene glycol) methyl ether methacrylate (OEOMA) has been polymerized by ATRP, RAFT, and other methods and found applications in biomedical research as free-radically polymerizable PEG mimics.[45−50] For all 288 polymerizations, the total volume was held constant at 3.7 mL (0.3 mL of air), and a single algorithm was used to standardize the results. All components were added to vials sealed with a rubber septum. After addition of the reducing agent via a piercing robotic tip, the polymerization could begin upon consumption of the air and reduction of Cu^{II} to Cu^{I}. The available amount of oxygen in the reaction vessel directly affects the required amount of reducing agent. At the beginning of the process, Cu^{II} is reduced by the reducing agent to Cu^{I}, which is immediately oxidized by oxygen in the air. However, additional reducing agent can resume the process. This cycle is repeated until all of the oxygen in the reaction vessel is completely consumed. After this induction period, the polymerization proceeds.

Optimization of the Reducing Agent Concentration. Twelve different concentrations of reducing agent were tested at constant catalyst concentration and fixed degree of polymerization (DP). All polymers were analyzed by gel permeation chromatography (GPC), and the distribution curves were plotted in the same diagram (Figure 2) (for clarity, the figure does not show all curves). The curve for the ideal concentration of reducing agent is red, where (1) the polydispersity index (PDI) was as low as possible, (2) the deviation between theoretical and experimental MW was as low as possible, and (3) the shape of the curve was most ideal (one maximum, no shoulders). (4) For similar results, the lower concentration of reducing agent was favored. In a typical ATRP process, PDI decreases with conversion and with degree of polymerization. This can be attributed to relatively slow exchange between active and dormant species (especially

dx.doi.org/10.1021/ma3000219 | *Macromolecules* 2012, 45, 1254−1261

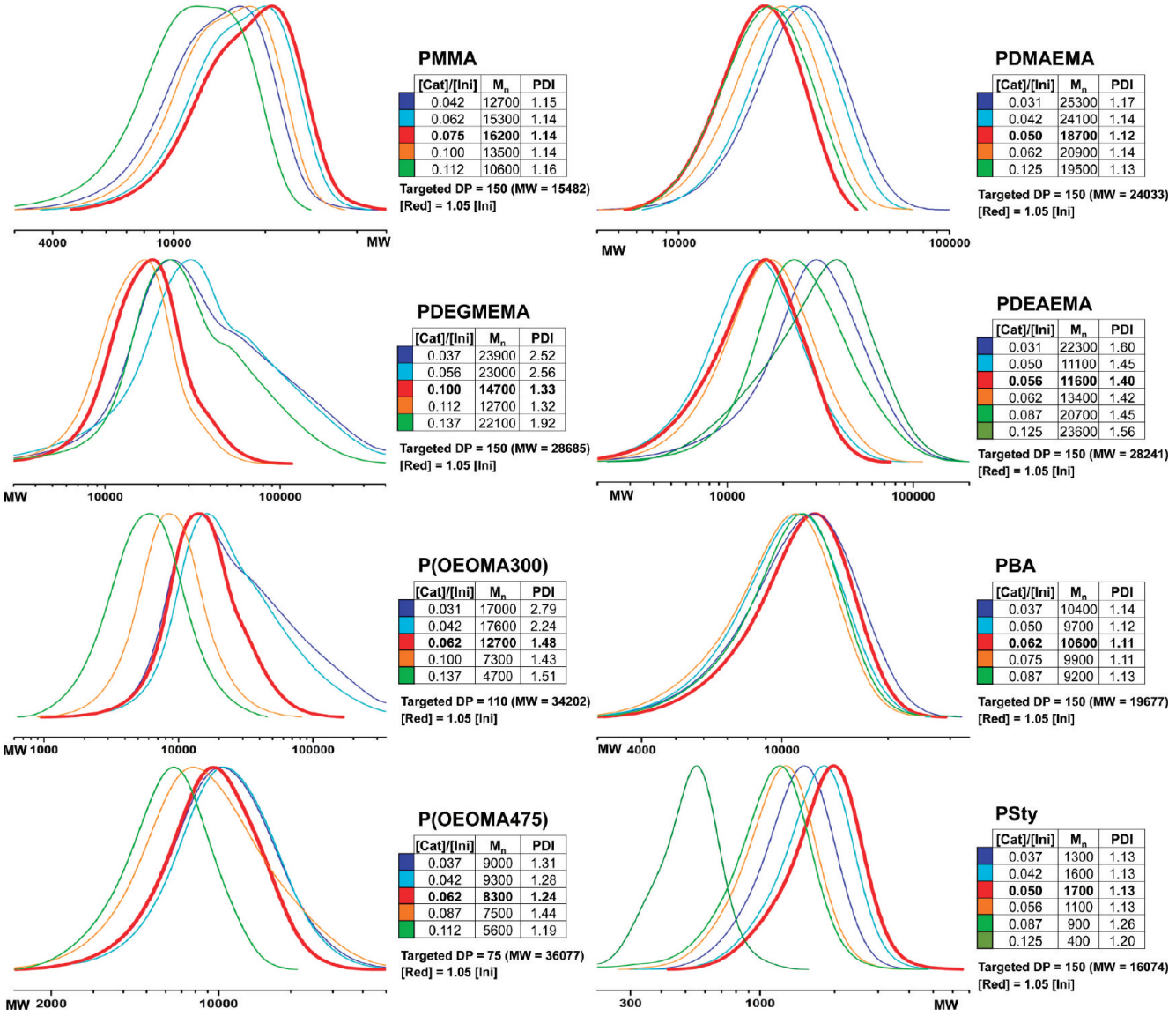


Figure 3. Optimization of the catalyst concentration for polymerization. Selected traces for the polymerization of MMA, DEGMEMA, OEOMA300, OEOMA475, DMAEMA, DEAEMA, BA, and Sty show the effect of changing catalyst concentration. Optimal results are indicated in red.

important in low Cu systems) and to slow initiation. However, PDI increases with conversion in the presence of chain breaking reactions (transfer and termination). Although conversion would be a good way to account for these differences, we focused on measurement of MW by GPC because it was more amenable to this high-throughput study. Overall, the results for these experiments were within the expected range of required reducing agent to consume all air in the vial.[7,11] In all experiments, the air volume in each reaction vessel was 300 μL, which corresponds to 0.0028 mmol of oxygen. In addition to reducing Cu^{II} to Cu^{I}, 300 μL of air requires an additional 0.0056 mmol of $Sn(Oct)_2$ because for each equivalent of oxygen, 4 equiv of Cu^{I} can be oxidized to Cu^{II}, but only 2 Cu^{II} equiv are reduced back by 1 equiv of $Sn(Oct)_2$.

The optimal ratio of reducing agent to initiator for methyl methacrylate (MMA) was determined to be 1.5:1 (mol:mol), where the resulting polymer M_n was close to theoretical and the PDI was 1.16. Increasing the reducing agent for MMA did not negatively affect the molecular weight distribution. In contrast, 1.5:1 for DEGMEMA resulted in a broad PDI and a shoulder in the GPC trace, indicating loss of control. The optimum value for DEGMEMA was 0.9:1. Polymerization of OEOMA300 showed a similar behavior, where 0.3:1 and below resulted in low M_n, and increasing the ratio to above 1.1:1 showed peak broadening. The optimum was found to be 0.8:1. When increasing the PEG side chain length of the PEG-based monomer OEOMA475, a 1.5:1 ratio was found to be optimum. Controlled polymerization of 2-(dimethylamino)ethyl methacrylate (DMAEMA) was observed over a wide range of reducing agent from 0.6 to 2.3. This may be due to the monomer's ability to serve as an intrinsic reducing agent, thereby limiting the effect of $Sn(Oct)_2$ addition.[51] Less control was observed for polymerization of DEAEMA over this range, with the lowest PDI (1.46) achieved at a 1.8:1 ratio. For butyl acrylate (BA), a higher ratio of reducing agent to initiator (3.2:1) was required to obtain a DP close to the targeted DP. However, the doubling of MW suggests the possibility of polymer chain coupling at high reducing agent concentrations. Better control was observed at 1.5:1; however, the DP reached

dx.doi.org/10.1021/ma3000219 | *Macromolecules* 2012, 45, 1254−1261

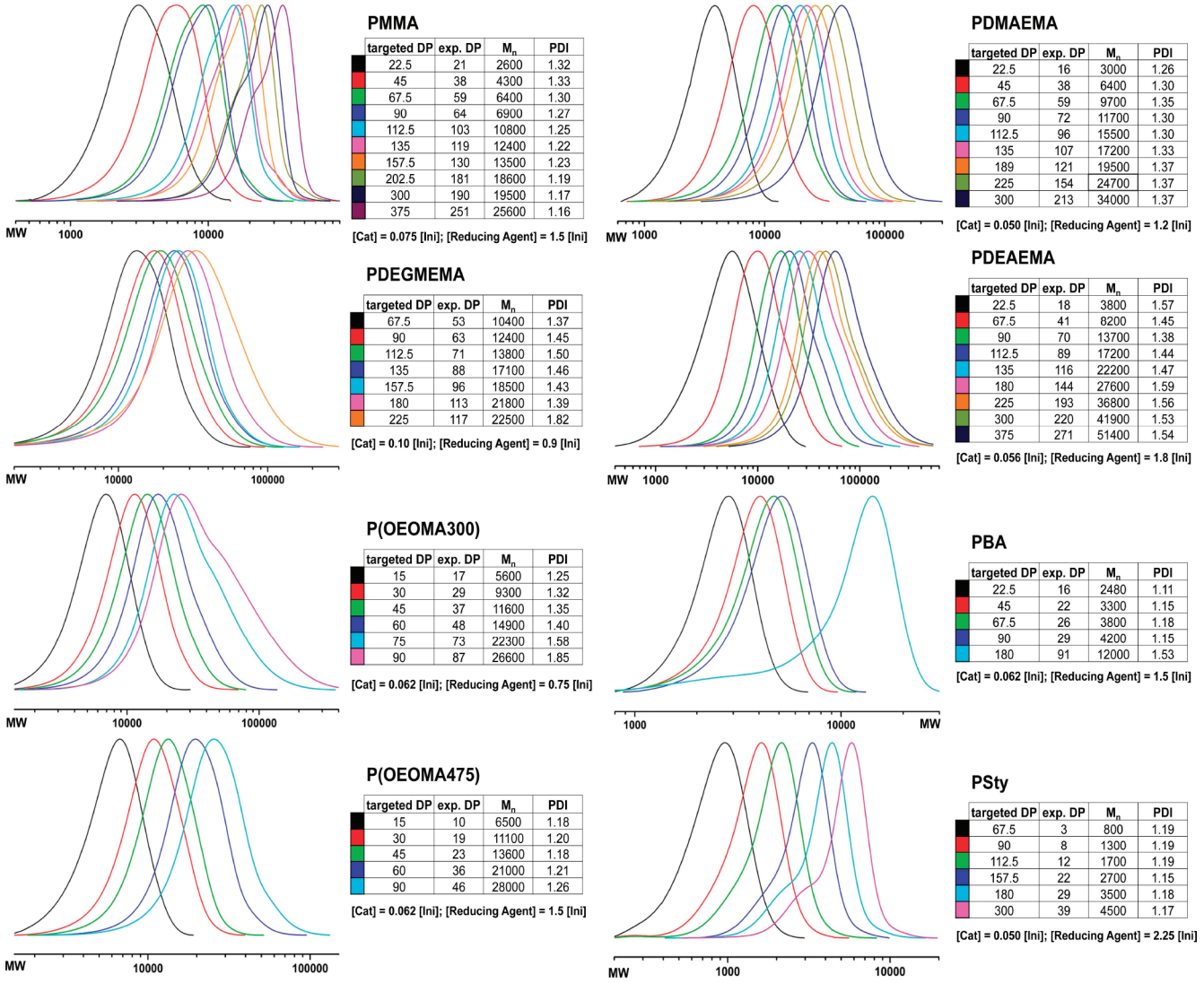


Figure 4. Using optimized concentrations of catalyst and reducing agent, a series of polymers were synthesized by automated ARGET ATRP.

was lower than theoretical. Low degrees of polymerization were also observed for polymerization of styrene (Sty).

Optimization of the Catalyst Concentration. We next optimized the catalyst concentration. Stock solutions of preformed catalyst[7] were used in all polymerizations with the molar ratio TPMA:$CuBr_2$ = 2.4:1. Twelve different concentrations of catalyst at constant concentration of reducing agent and constant DP were tested (0.031−0.137 times the initiator mole concentration) for all eight monomers. All samples were analyzed by GPC, and the distribution curves for each polymer type are shown in Figure 3. The selection of the optimal concentration was done in accordance with those criteria listed above and is shown as the red trace in all plots. Ideal catalyst concentrations for seven of the eight monomers were between 0.05 and 0.075 times the initiator concentration (mol). Although the PDI remained low for PMMA, a slightly increasing PDI was observed at higher $CuBr_2$ concentrations, with a broadening GPC trace. For DEGMEMA, the optimal value was 0.1. Nonideal curves containing shoulders were observed for values above and below 0.1. OEOMA300 and OEOMA475 polymerized similarly and required a lower amount of catalyst (0.062 or lower). Higher catalyst levels resulted in lower obtained MW. For DMAEMA and BA, the polymerizations were successful over a wide range of catalyst concentrations, with an optimal range of 0.05−0.062. DEAEMA was also polymerizable using a range of concentrations; however, the low and high concentrations of catalyst led to longer chains and higher PDI (>1.5). In theory, a catalytic amount of up to 1 mol % relative to monomer is required for ATRP.[11] In these experiments, six of the eight monomers required 5−6 mol % of catalyst relative to the initiator. In comparison, a previous study in the presence of air without robotic automation used 2−3 times less catalyst.[7] Our studies here have shown that slightly higher catalyst concentrations can lead to better controlled polymerization, at least in automated systems, where vented robotic needles may allow for more air transfer upon addition of the reducing agent.

Synthesis of Disulfide-Bridged Polymers with Different Lengths. Using optimized concentrations of catalyst and reducing agent for each monomer (Table 1), we targeted 12 different DPs for each polymer type (from 15 to 375). Optimization of the polymerization conditions yielded conditions that allowed for the controlled synthesis of various polymers with increasing lengths. In the case of MMA, the experimental DP obtained was close to the theoretical DP, with

dx.doi.org/10.1021/ma3000219 | *Macromolecules* 2012, 45, 1254−1261

a narrow MW distribution (PDI < 1.2). Polymerization of DEGMEMA resulted in the broadest distribution for polymers (PDI = 1.37−1.82). Decent control and increasing MW were observed for OEOMA300, OEOMA475, DEGMEMA, DMAEMA, and DEAEMA, which may have biomedical application. P(OEOMA475) had a PDI of 1.18−1.26 with close agreement between theoretical and experimental DP. P(OEOMA300), however, had higher PDI values and a shoulder in the curves above a length of 73 units, but all measured molecular weights were close to the theoretical. The shoulder might be due to chain transfer reactions, since we did not observe evidence for dimethacrylate impurities in LC-MS measurements. Polymerization of DMAEMA resulted in DPs from 16 to 213 units, where the PDI was 1.26−1.37. Similar results were obtained for PDEAEMA, but with slightly broader PDI. The highest experimental DPs obtained were DP 271 for PDEAEMA (M_n 51 400 g/mol; PDI 1.54) and DP 251 for PMMA (M_n 25 600 g/mol; PDI 1.16) (Figure 4). In all cases, the MW increased with higher targeted DP. A comparison between theoretical and measured M_n (calculated by GPC) verified this trend and showed that all monomers (except for Sty) could be polymerized to high DP due to successful optimization of the catalyst and reducing agent concentration. Overall, the optimization of catalyst and reducing agent concentrations allowed for the production of various polymers with increasing length and control over MW and MWD.

Polymer Cleavage to Thiol. In order to demonstrate the ability to cleave these disulfide-containing polymers into two thiol-terminated chains of half the MW, dithiothreitol (DTT) was used to cleave the disulfide bond. The resulting thiol-terminated chains have the potential for conjugation to (bio)molecules. Figure S2 shows GPC traces for selected reactions with DTT in THF at 50 °C. Cleavage of PMMA was complete within 24 h, while PBA was partially reduced after 96 h. The rate of cleavage for PSty was slower, but reduction was nevertheless observed. The MW of P(OEOMA475) also decreased, but the broader PDI and steric hindrance of this polymer resulted in slower reduction.

Translation of Automated Synthesis to Conventional Batch Synthesis. We have shown that automated methods can facilitate the rapid development of polymerization conditions for various monomers. However, most chemists synthesize polymers using traditional glassware in chemical fume hoods. To validate that these new conditions have practical utility, we investigated if these robotic conditions in glass vials would translate to conventional batch synthesis in a round-bottom flask. In our automated synthesizer, the 4 mL vials contained 92.5% solution and 7.5% air. We used that ratio of total solution volume to air when calculating the set volume for a standard 5 mL round-bottom flask. Optimized conditions for polymerization of MMA and DMAEMA (Table 1) were used in the calculation. As shown in Figure 5, the results from the automated and batch syntheses matched, proving that the automated conditions directly translated to conventional batch polymerization in standard glassware. Nearly identical experimental DP and MW were obtained.

CONCLUSION

Efficient reaction optimization is a key component of chemical research. We developed a systematic approach to accelerate reaction optimization. ARGET ATRP conditions were rapidly identified for representative monomers of acrylate, methacrylate, styrenic, PEG mimic, and cationic classes, including the first ARGET ATRP of DEAEMA and DEGMEMA. Because a functional initiator was used, all polymers were end functionalized with thiol groups after cleavage of the disulfide bond. This thiol group can be utilized for attachment to other molecules and may be useful for the synthesis of bioconjugates to drugs, proteins, and siRNA. These conditions translated to conventional batch polymerization, suggesting that these new polymerization conditions will be useful for other scientists to follow when carrying out ARGET ATRP. We therefore believe that the methods developed here may prove generally useful to accelerate the systematic optimization of a variety of reactions across the chemical disciplines.

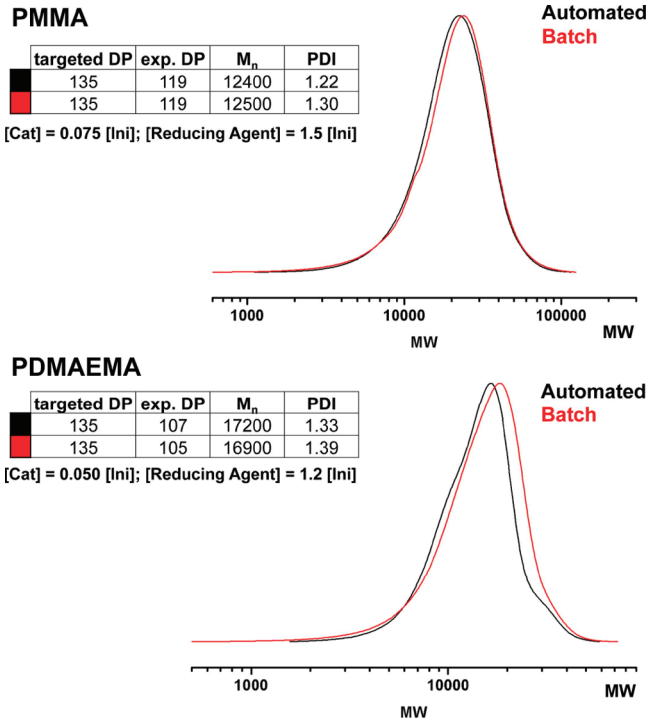


Figure 5. Using the optimized conditions determined by automated polymerization, conventional batch polymerization in round-bottom flasks closely matched robotic polymerization.

ASSOCIATED CONTENT

Supporting Information

Figures S1 and S2. This material is available free of charge via the Internet at http://pubs.acs.org.

AUTHOR INFORMATION

Corresponding Author

*E-mail: dgander@mit.edu.

Author Contributions

⊥These authors contributed equally.

ACKNOWLEDGMENTS

D.J.S. was supported by a Ruth L. Kirschstein National Research Service Award (NRSA) for Individual Postdoctoral Fellows, Award F32EB011867 from the National Institutes of Health (NIH). M.L. was supported by the Studienstiftung des deutschen Volkes and the Graduate School of Excellence MAINZ. The research was partially funded by a grant from Alnylam Pharmaceuticals. We thank Arturo Vegas, Patrick

Fenton, and Sean P. Collins for assistance with robotic automation and polymer purification.

REFERENCES

(1) Jakubowski, W.; Matyjaszewski, K. *Macromolecules* **2005**, *38*, 4139−4146.
(2) Wang, J.-S.; Matyjaszewski, K. *J. Am. Chem. Soc.* **1995**, *117*, 5614−5615.
(3) Kato, M.; Kamigaito, M.; Sawamoto, M.; Higashimura, T. *Macromolecules* **1995**, *28*, 1721−1723.
(4) Matyjaszewski, K.; Xia, J. H. *Chem. Rev.* **2001**, *101*, 2921−2990.
(5) Braunecker, W. A.; Matyjaszewski, K. *Prog. Polym. Sci.* **2007**, *32*, 93−146.
(6) Matyjaszewski, K.; Tsarevsky, N. *Nature Chem.* **2009**, *1*, 276−288.
(7) Matyjaszewski, K.; Dong, H.; Jakubowski, W.; Pietrasik, J.; Kusumo, A. *Langmuir* **2007**, *23*, 4528−4531.
(8) Matyjaszewski, K.; Jakubowski, W.; Min, K.; Tang, W.; Huang, J.; Braunecker, W.; Tsarevsky, N. *Proc. Natl. Acad. Sci. U. S. A.* **2006**, *103*, 15309−15314.
(9) Jakubowski, W.; Min, K.; Matyjaszewski, K. *Macromolecules* **2006**, *39*, 39−45.
(10) Jakubowski, W.; Matyjaszewski, K. *Angew. Chem., Int. Ed.* **2006**, *45*, 4482−4486.
(11) Pintauer, T.; Matyjaszewski, K. *Chem. Soc. Rev.* **2008**, *37*, 1087−1097.
(12) Geysen, H.; Schoenen, F.; Wagner, D.; Wagner, R. *Nat. Rev. Drug Discovery* **2003**, *2*, 222−230.
(13) Lowe, G. *Chem. Soc. Rev.* **1995**, *24*, 309−317.
(14) Thompson, L. A.; Ellman, J. A. *Chem. Rev.* **1996**, *96*, 555−600.
(15) Rohrer, S. P.; Birzin, E. T.; Mosley, R. T.; Berk, S. C.; Hutchins, S. M.; Shen, D. M.; Xiong, Y. S.; Hayes, E. C.; Parmar, R. M.; Foor, F.; Mitra, S. W.; Degrado, S. J.; Shu, M.; Klopp, J. M.; Cai, S. J.; Blake, A.; Chan, W. W. S.; Pasternak, A.; Yang, L. H.; Patchett, A. A.; Smith, R. G.; Chapman, K. T.; Schaeffer, J. M. *Science* **1998**, *282*, 737−740.
(16) Schreiber, S. L. *Science* **2000**, *287*, 1964−1969.
(17) Ramstrom, O.; Lehn, J. M. *Nat. Rev. Drug Discovery* **2002**, *1*, 26−36.
(18) Xiang, X. D.; Sun, X. D.; Briceno, G.; Lou, Y. L.; Wang, K. A.; Chang, H. Y.; Wallacefreedman, W. G.; Chen, S. W.; Schultz, P. G. *Science* **1995**, *268*, 1738−1740.
(19) Brocchini, S.; James, K.; Tangpasuthadol, V.; Kohn, J. *J. Am. Chem. Soc.* **1997**, *119*, 4553−4554.
(20) Tian, J.; Coates, G. W. *Angew. Chem., Int. Ed.* **2000**, *39*, 3626−3629.
(21) Anderson, D. G.; Lynn, D. M.; Langer, R. *Angew. Chem., Int. Ed.* **2003**, *42*, 3153−3158.
(22) Anderson, D. G.; Levenberg, S.; Langer, R. *Nature Biotechnol.* **2004**, *22*, 863−866.
(23) Hoogenboom, R.; Meier, M. A. R.; Schubert, U. S. *Macromol. Rapid Commun.* **2003**, *24*, 16−32.
(24) Meier, M. A. R.; Schubert, U. S. *J. Mater. Chem.* **2004**, *14*, 3289−3299.
(25) Hook, A.; Anderson, D.; Langer, R.; Williams, P.; Davies, M.; Alexander, M. *Biomaterials* **2010**, *31*, 187−198.
(26) Siegwart, D. J.; Whitehead, K. A.; Nuhn, L.; Sahay, G.; Cheng, H.; Jiang, S.; Ma, M. L.; Lytton-Jean, A.; Vegas, A.; Fenton, P.; Levins, C. G.; Love, K. T.; Lee, H.; Cortez, C.; Collins, S. P.; Li, Y. F.; Jang, J.; Querbes, W.; Zurenko, C.; Novobrantseva, T.; Langer, R.; Anderson, D. G. *Proc. Natl. Acad. Sci. U. S. A.* **2011**, *108*, 12996−13001.
(27) Wilhelm, S.; Carter, C.; Lynch, M.; Lowinger, T.; Dumas, J.; Smith, R. A.; Schwartz, B.; Simantov, R.; Kelley, S. *Nat. Rev. Drug Discovery* **2006**, *5*, 835−844.
(28) Boussie, T.; Diamond, G.; Goh, C.; Hall, K.; LaPointe, A.; Leclerc, M.; Lund, C.; Murphy, V.; Shoemaker, J.; Tracht, U.; Turner, H.; Zhang, J.; Uno, T.; Rosen, R.; Stevens, J. *J. Am. Chem. Soc.* **2003**, *125*, 4306−4317.
(29) Bosman, A. W.; Heumann, A.; Klaerner, G.; Benoit, D.; Frechet, J. M. J.; Hawker, C. J. *J. Am. Chem. Soc.* **2001**, *123*, 6461−6462.
(30) Hoogenboom, R.; Schubert, U. S. *J. Polym. Sci., Part A: Polym. Chem.* **2003**, *41*, 2425−2434.
(31) Hoogenboom, R.; Fijten, M. W. M.; Abeln, C. H.; Schubert, U. S. *Macromol. Rapid Commun.* **2004**, *25*, 237−242.
(32) Fijten, M. W. M.; Meier, M. A. R.; Hoogenboom, R.; Schubert, U. S. *J. Polym. Sci., Part A: Polym. Chem.* **2004**, *42*, 5775−5783.
(33) Tweedie, C. A.; Anderson, D. G.; Langer, R.; Van Vliet, K. J. *Adv. Mater.* **2005**, *17*, 2599−2604.
(34) Fijten, M. W. M.; Paulus, R. M.; Schubert, U. S. *J. Polym. Sci., Part A: Polym. Chem.* **2005**, *43*, 3831−3839.
(35) Guerrero-Sanchez, C.; Abeln, C.; Schubert, U. S. *J. Polym. Sci., Part A: Polym. Chem.* **2005**, *43*, 4151−4160.
(36) Webster, D. *Macromol. Chem. Phys.* **2008**, *209*, 237−246.
(37) Webster, D. C.; Meier, M. A. R. *Adv. Polym. Sci.* **2010**, *225*, 1−15.
(38) Becer, C. R.; Schubert, U. S. *Adv. Polym. Sci.* **2010**, *225*, 17−62.
(39) Hoogenboom, R.; Fijten, M. W. M.; Meier, M. A. R.; Schubert, U. S. *Macromol. Rapid Commun.* **2003**, *24*, 92−97.
(40) Zhang, H. Q.; Fijten, M. W. M.; Hoogenboom, R.; Reinierkens, R.; Schubert, U. S. *Macromol. Rapid Commun.* **2003**, *24*, 81−86.
(41) Zhang, H. Q.; Marin, V.; Fijten, M. W. M.; Schubert, U. S. *J. Polym. Sci., Part A: Polym. Chem.* **2004**, *42*, 1876−1885.
(42) Zhang, H. Q.; Abeln, C. H.; Fijten, M. W. M.; Schubert, U. S. *e-Polym.* **2006**, *8*, 1−9.
(43) Nasrullah, M.; Webster, D. *Macromol. Chem. Phys.* **2009**, *210*, 640−650.
(44) Tsarevsky, N. V.; Matyjaszewski, K. *Macromolecules* **2005**, *38*, 3087−3092.
(45) Oh, J. K.; Min, K.; Matyjaszewski, K. *Macromolecules* **2006**, *39*, 3161−3167.
(46) Oh, J. K.; Tang, C. B.; Gao, H. F.; Tsarevsky, N. V.; Matyjaszewski, K. *J. Am. Chem. Soc.* **2006**, *128*, 5578−5584.
(47) Oh, J. K.; Siegwart, D. J.; Matyjaszewski, K. *Biomacromolecules* **2007**, *8*, 3326−3331.
(48) Oh, J. K.; Siegwart, D. J.; Lee, H. I.; Sherwood, G.; Peteanu, L.; Hollinger, J. O.; Kataoka, K.; Matyjaszewski, K. *J. Am. Chem. Soc.* **2007**, *129*, 5939−5945.
(49) Siegwart, D. J.; Oh, J. K.; Gao, H. F.; Bencherif, S. A.; Perineau, F.; Bohaty, A. K.; Hollinger, J. O.; Matyjaszewski, K. *Macromol. Chem. Phys.* **2008**, *209*, 2180−2193.
(50) Siegwart, D. J.; Srinivasan, A.; Bencherif, S. A.; Karunanidhi, A.; Oh, J. K.; Vaidya, S.; Jin, R.; Hollinger, J. O.; Matyjaszewski, K. *Biomacromolecules* **2009**, *10*, 2300−2309.
(51) Dong, H.; Matyjaszewski, K. *Macromolecules* **2008**, *41*, 6868−6870.

Macromolecules

Article

pubs.acs.org/Macromolecules

Enhancement of Two-Photon Initiating Efficiency of a 4,4′-Diaminostyryl-2,2′-bipyridine Derivative Promoted by Complexation with Silver Ions

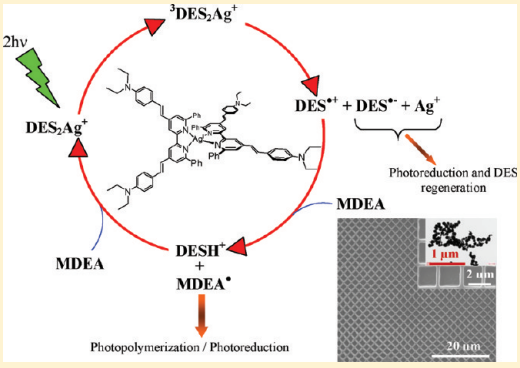
Arnaud Spangenberg,*[,†] Jean-Pierre Malval,*[,†] Huriye Akdas-Kilig,[‡] Jean-Luc Fillaut,[‡] Fabrice Stehlin,[†] Nelly Hobeika,[†] Fabrice Morlet-Savary,[†] and Olivier Soppera[†]

[†]Institut de Science des Matériaux de Mulhouse, LRC CNRS 7228, Université de Haute Alsace, 15 rue Jean Starcky, 68057 Mulhouse, France

[‡]Sciences chimiques de Rennes, UMR 6226, CNRS - Université Rennes I, Campus de Beaulieu, 263 av. du Général Leclerc, 35042 Rennes, France

Supporting Information

ABSTRACT: We report on the two-photon-induced polymerization (TPIP) ability of a new class of free radical two-photon initiator based on a cationic silver(I) complex incorporating 4,4′-diaminostyryl-2,2′-bipyridine (DES) derivatives as ligands. Coordination with Ag^+ induces a strong increase of the charge transfer character at excited state, which enhances the two-photon absorption properties of the complex with respect to that of the free ligand. A comparative analysis of the photophysical properties of DES and DES_2Ag^+ shows that the presence of silver cation increases the efficiency for the generation of radical cations ($DES^{\bullet+}$), which can be used as hydrogen abstractor in free radical photopolymerization. We show that the addition of an aliphatic amine used as hydrogen donor also opens a parallel route for the regeneration of DES. The improvement of the two-photon polymerization efficiency is then evidenced by the fabrication of microstructures. We finally demonstrate that the use of DES_2Ag^+ as two-photon initiator offers new opportunities for the fabrication of functional nanostructures composed of metal−polymer nanocomposites.



INTRODUCTION

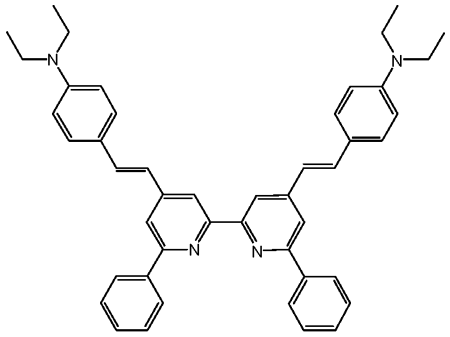
Since the past decade, two-photon-induced polymerization (TPIP) has been extensively studied due to the growing need of three-dimensional (3D) micro/nanofabrication techniques in many fields such as nanophotonics, nanoplasmonics, microfluidics, or nano- and microelectromechanical systems (NEMS/MEMS).[1−11] Among the numerous approaches for fabricating 3D microstructures, direct laser writing processes based on multiphoton polymerization provide a unique opportunity to create complex microstructures by combining both sub-100 nm resolution and relatively high throughput. In addition, various engineering materials such as polymers, ceramics, metals, and hybrid materials[12−16] have been successfully used for 3D microfabrication of micromodels,[17] micromachines,[8,18] and microdevices.[1−5] Nowadays, many efforts are focused on the development of super-resolution TPIP and on the design of new materials which can simultaneously respond to the need of higher resolution and to specific criteria such as biocompatibility for emerging fields like biosciences.[19,20] Hence, the development of new two-photon-induced initiating systems appears fundamental so as to improve the sensitivity of the materials and consequently allows the use of lower laser power and less time-consuming processes.[21−24] In this context, an elegant approach of increasing the two-photon absorption efficiency of photoinitiator (PI) is based on the complexation of PI dyes around a metal ion core. Such a geometrical organization leads to important photophysical changes, particularly a strong enhancement of the two-photon absorption cross section. Recently, we applied this strategy with 4,4′-diaminostyryl-2,2′-bipyridine series. Indeed, we showed that these "push−pull" chromophores exhibited a strong enhancement of their TPA cross sections when chelating a metal cation.[25] Several groups also demonstrated that the coordination of bypiridine ligands with transition metal results in significant enhancement of their TPA cross section,[26−31] but so far, no application to microfabrication has been attempted. It should be emphasized that even though the two-photon absorption mechanism can also refer to stepwise processes involving the absorption of an intermediate excited state, in this article the two-photon excitation of our metal-based complex leads to a simultaneous absorption of two photons.[25]

In the present study, we focus on a silver-based complex with 4,4′-bis(diethylaminostyryl)-6,6′diphenyl-2,2′-bipyridine (DES, Scheme 1) which showed very promising two-photon

Received: October 4, 2011
Revised: December 21, 2011
Published: January 25, 2012

ACS Publications © 2012 American Chemical Society

Scheme 1. Molecular Structure of DES



DES

absorption properties. In addition, Ag^+ precursors have been used recently in our group for simultaneous photoreduction and photopolymerization.[32−34] Although our first goal here is to enhance the two-photon initiating efficiency, such a strategy can be advantageously used for the production of nanocomposites in a single step by TPIP. After a short introduction about the photophysical properties of DES, the effects of complexation with Ag^+ are discussed. Through a comparative study of the photolysis of the dye and its complex, we then propose a sequential mechanism that leads to photoinitiating reaction. Finally, we demonstrate the interest of such molecular systems for TPA microfabrication by using low-power microlaser to produce microstructures by TPIP.

EXPERIMENTAL SECTION

Materials. All the solvents employed for photophysical analysis were Aldrich or Fluka spectroscopic grade. Antimony silver fluoride ($AgSbF_6$), 4-diethylaminobenzaldehyde, and *N*-methyldiethanolamine (MDEA) were purchased from Aldrich. The monomer used, namely Eb605 (bisphenol A epoxy diacrylate diluted with 25% tripropylene glycol diacrylate), was kindly provided by Sartomer. All materials were used without further purification.

Synthesis of DES. The synthesis of DES (4,4′-bis-(diethylaminostyryl)-6,6′diphenyl-2,2′-bipyridine) was already described in previous work[25] and results of a double Knoevenagel condensation between 6,6′-diphenyl-4,4′-dimethyl-2,2′-bipyridine and 4-diethylaminobenzaldehyde in dimethylformamide and tBuOK. Recrystallization from a dichloromethane−pentane mixture gave DES as an orange microcrystalline powder (230 mg, 79%). ^{1}H NMR (CD_2Cl_2, 500 MHz): δ ppm 8.68 (s, 2H, H6,6′), 8.31 (d, J = 8.3 Hz, 4H, 6H4-), 7.92 (s, 2H, H3,3′), 7.58 (m, 12H, C_6H_5− + −CH═CH−), 7.10 (d, J = 16.3 Hz, 4H, −CH═CH−), 6.75 (d, J = 9.0 Hz, 4H, C_6H_5−), 3.46 (q, J = 7.1 Hz, 8H, CH_3CH_2−), 1.24 (t, J = 7.1 Hz, 12H, CH_3CH_2−). ^{13}C NMR ($CDCl_3$, 400 MHz): δ ppm 156.8, 156.5, 148.1, 147.3, 140.0, 133.1, 128.7, 128.68, 128.64, 127.1, 123.7, 121.6, 117.0, 116.8, 111.6, 44.4, 12.6. Anal. found: C, 83.09; H, 7.05; N, 8.72. $C_{46}H_{46}N_4{\cdot}0.5H_2O$. Calcd: C, 83.22; H, 7.14; N, 8.44. m/z (Micro-TOF-Q II) 655.3793; ($[M + H]^+$, $C_{46}H_{47}N_4$ requires 655.3795).

General Techniques. The absorption measurements were carried out with a Perkin-Elmer Lambda 2 spectrometer. Steady-state fluorescence and phosphorescence spectra were collected from a FluoroMax-4 spectrofluorometer. Emission spectra were spectrally corrected. Fluorescence quantum yields include the correction due to the solvent refractive index and were determined relative to quinine bisulfate in 0.05 M sulfuric acid (Φ = 0.52).

Quantum yields of trans → cis photoisomerization were carried out under irradiation at 370 nm. The progress of the reaction was monitored via UV−vis absorption spectra. The absorbance at excitation wavelength was greater than 2 to assume a total absorption of the incident photons. The incident light intensity was measured by ferrioxalate actinometry.[35]

Phosphorescence measurements were performed in ethanol at 77 K. The samples were placed in a 5 mm diameter quartz tube inside a Dewar filled with liquid nitrogen. Phosphorescence lifetimes were measured using the FluoroMax-4 spectrofluorometer which was also equipped with a Xe-pulsed lamp operating at up to 25 Hz. The phosphorescence time decays were obtained according to a time-gated method. The emission was recorded using a control module that includes a gate-and-delay generator which allows the integration of the signal during a specific period after a flash (delay) and for a predetermined time window. The total signal was accumulated for a large number of exciting pulses.

Photolysis of photoinitiators and subsequently photoreduction of silver ions in solution were carried out under UV irradiation (P = 100 mW) via a medium-pressure mercury arc lamp (Oriel, main radiation at 365 nm) and monitored by UV−vis absorption spectroscopy. Solutions were N_2-degassed prior irradiation.

The two-photon excitable resin formulation used for microfabrication, typically DES (0.3 wt %), MDEA (1 wt %), and $AgSbF_6$ (1 wt %) in monomer, was dropped on a glass coverslip. The 3D lithographic microfabrication was performed using a Zeiss Axio Observer D1 inverted microscope equipped with a frequency-doubled Nd:YAG microlaser Nanolase from JDS Uniphase (λ_{exc} = 532 nm, pulse duration 0.61 ns, maximum pulse energy 2 μJ, repetition 11.8 kHz). The sample was mounted on a computer-controlled 3D piezoelectric stage allowing the translation relative to the laser focal point. The incident beam was focused through a 1.21 NA objective (100×) which leads to 300 nm radial spot size (1/e Gaussian). In the presence of silver ions, the average laser power and scan speeds were fixed at 130 μW and 40 μm/s, respectively. In the absence of silver ions, due to higher polymerization threshold, the average laser power was set to 732 μW. This entire lithography setup was purchased from Teemphotonics.

Transmission electron microscopy (TEM) was used to characterize the size and shape of Ag nanoparticles. Before getting their TEM images, the microgrids were cut by means of a microtome (LKB model 8800). Transmission electron microscopy measurement was carried out at 200 kV using a Philips CM20 instrument with Lab6 cathode. Energy dispersive X-ray spectroscopy (EDX) and scanning electron microscopy (SEM) were performed using a FEI-Quanta 400 model. AFM images were acquired using atomic force microscopy (PicoPlus model, Molecular Imaging AFM) in an ambient atmosphere. The characterization was obtained in resonant mode using a silicon noncontact probe (Arrow Silicon SPM Sensor; force constant: 42 N/m; resonance frequency: 285 kHz).

RESULTS AND DISCUSSION

Photophysical Properties of DES. Figure 1 depicts the absorption and the fluorescence spectra of DES in acetonitrile and hexane. The low-energy side of DES absorption spectrum is dominated by an intensive band located in the 350−450 nm

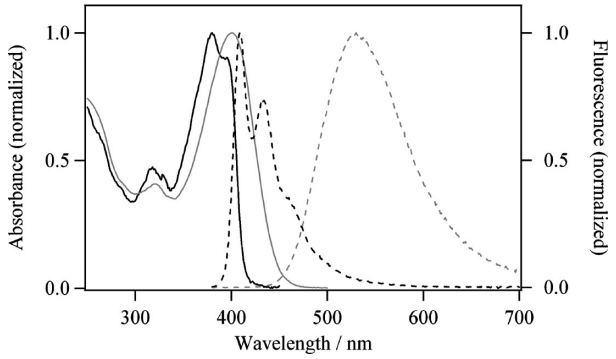


Figure 1. Normalized absorption (solid lines) and fluorescence (dashed lines) spectra of DES in acetonitrile (gray) and hexane (black). λ_{exc} = 370 nm.

dx.doi.org/10.1021/ma202224c | *Macromolecules* 2012, 45, 1262−1269

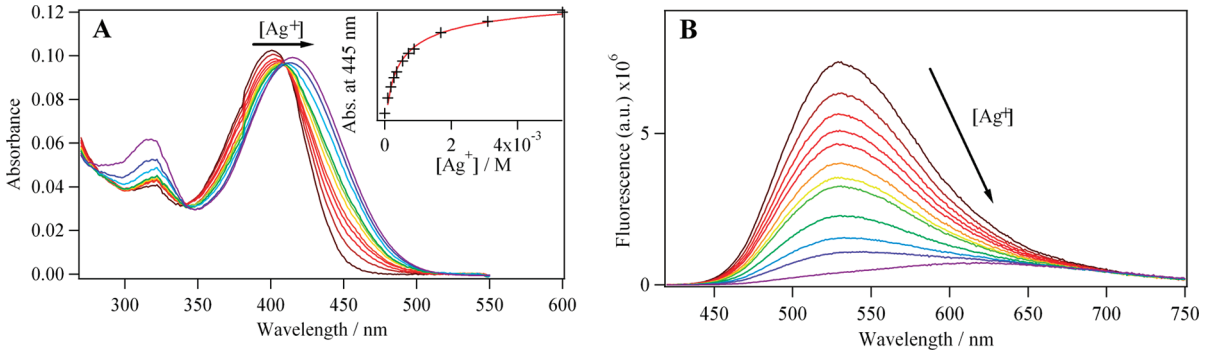


Figure 2. (A) Absorption and (B) fluorescence spectra obtained upon increasing amount of $AgSbF_6$ (from 0 to 3300 equiv). Inset: absorption−concentration profile recorded at 445 nm (solvent: acetonitrile, [DES] = 1×10^{-6} M, λ_{exc} = 415 nm).

range. This band mainly corresponds to a $\pi-\pi$ electronic transition (S_0-S_1) centered on the stilbene moieties of the chromophore and exhibits a charge transfer (CT) character from the amine (donor) to the bipyridine (acceptor) groups. At the blue side of the CT band a shoulder located at 320 nm is observed which typically corresponds to the $\pi-\pi$ transition centered in the 2,2′-bipyridine moiety.[36,37] The longest wavelength band undergoes a significant red-shift upon increasing solvent polarity. For instance, from hexane (apolar solvent) to acetonitrile (highly polar solvent), the band shifts about 20 nm. This effect clearly confirms the CT character of the S_0-S_1 transition. Such bathochromic effects are drastically enhanced when considering the fluorescence band of DES. In this case, the emission band shift is about 120 nm from apolar to polar solvent. Moreover, the vibronic structurations observed for the absorption and fluorescence bands in hexane completely disappear in polar medium. For this push−pull stilbene derivative, we have therefore a clear indication of a strong electronic relaxation at excited state which leads to the enhancement of the CT character of the emitting excited state with respect to the ground state. Even if the fluorescence spectrum of DES undergoes a strong solvent-induced spectral shift, the polarity of the solvent hardly affects the fluorescence quantum yield (Φ_{fluo}). For instance, Φ_{fluo} of DES exhibits low values of ca. 0.05 and 0.12 in hexane and acetonitrile, respectively. This weak emissivity indicates that the excited S_1 state of DES mainly undergoes nonradiative deactivation processes irrespective of the polarity of the solvent. Among these multiple deactivation channels, the photoinduced trans-to-cis isomerization should be considered as minor route since the corresponding quantum yield is very low with values of ca. 0.09 and 0.03 in hexane and acetonitrile, respectively. Hence, we propose that both S_1-S_0 internal conversion and S_1-T_n intersystem crossing constitute the main deactivation pathways of the lowest singlet excited state of DES. Figure S1 shows the emission spectrum of DES in glassy ethanol. The fluorescence band is located in the 425−550 nm range with a maximum at 455 nm. In the low-energy side of spectrum, the phosphorescence band of DES exhibits a maximum at 620 nm which leads to a T_1 energy of ca. 2.00 eV. This low T_1 state energy is similar to those previously measured for D−A stilbene derivatives.[38] Moreover, the phosphorescence lifetime has a value of 64 ms, which suggests a $\pi-\pi^*$ character for T_1 state.[39] Such an electronic configuration is in agreement with the weak reactivity of the T_1 state of DES as hydrogen abstractor which will be underlined hereafter.

Formation of the Complex DES_2Ag^+ in Solution. The formation of a DES complex with Ag^+ in acetonitrile is evidenced by both absorption and fluorescence spectroscopies. Upon gradual addition of Ag^+, the CT band of DES centered at 400 nm is progressively red-shifted (Figure 2A). This change is in agreement with a stronger electron-withdrawing character of the bipyridine group after coordination with Ag^+ cations. The complexation is confirmed by the growth of the shoulder located at 320 nm which is typical of coordination of a metal ion to the bipyridine subunit.[36,40] Three isosbestic points at 277, 342, and 408 nm confirm the occurrence of an equilibrium reaction. In order to determine the reaction constant, the absorption changes as a function of the concentration of Ag^+ have been analyzed according to the model proposed by Valeur et al.[41] The best fit is obtained with the assumption of a main formation of a 1:2 complex (metal:ligand) which is the typical complex stoichiometry observed for such bidentate chromophores.[25] The inset Figure 2A depicts the best-fitting curve of the experimental data using the method of least squares, with a calculated log $K_{1:2}$ value of ca. 9.14 ± 0.03. Figure 2B depicts the effect of gradual addition of Ag^+ on the fluorescence spectrum of DES. The presence of silver cations both induces a strong decrease of the fluorescence band of the free ligand and the progressive growth of a weak band in the 550−750 nm range. The excitation spectrum at the longer wavelength and collected at the maximum emission wavelength at 650 nm matches perfectly the longest wavelength absorption band of the silver complex which confirms that the emission at the low-energy region stems from the excited DES_2Ag^+. Upon quantitative complexation, the fluorescence quantum yield of DES is divided by a factor 8 (from 0.12 to 0.015) in acetonitrile. The very low emissivity of DES_2Ag^+ with respect to that of the free ligand should be ascribed to the occurrence of a new nonradiative deactivation channel connected to a strong increase of the CT character at S_1 state which promotes the twist of the dialkylaniline group at excited state. Such a large-amplitude motion at S_1 state has been recently proposed as the major deactivation channel in the excited-state dynamics of dialkylaminostyrylpyridinium derivatives leading to the formation of low emissive twisted internal charge transfer (TICT) state.[42] The significant increase of the charge transfer character at S_1 state is also consistent with the strong enhancement of the TPA cross section of the complex by a factor 4 as compared to that of DES.[25] This latter effect will have a strong consequence on the two-photon induced polymerization threshold as described hereafter.

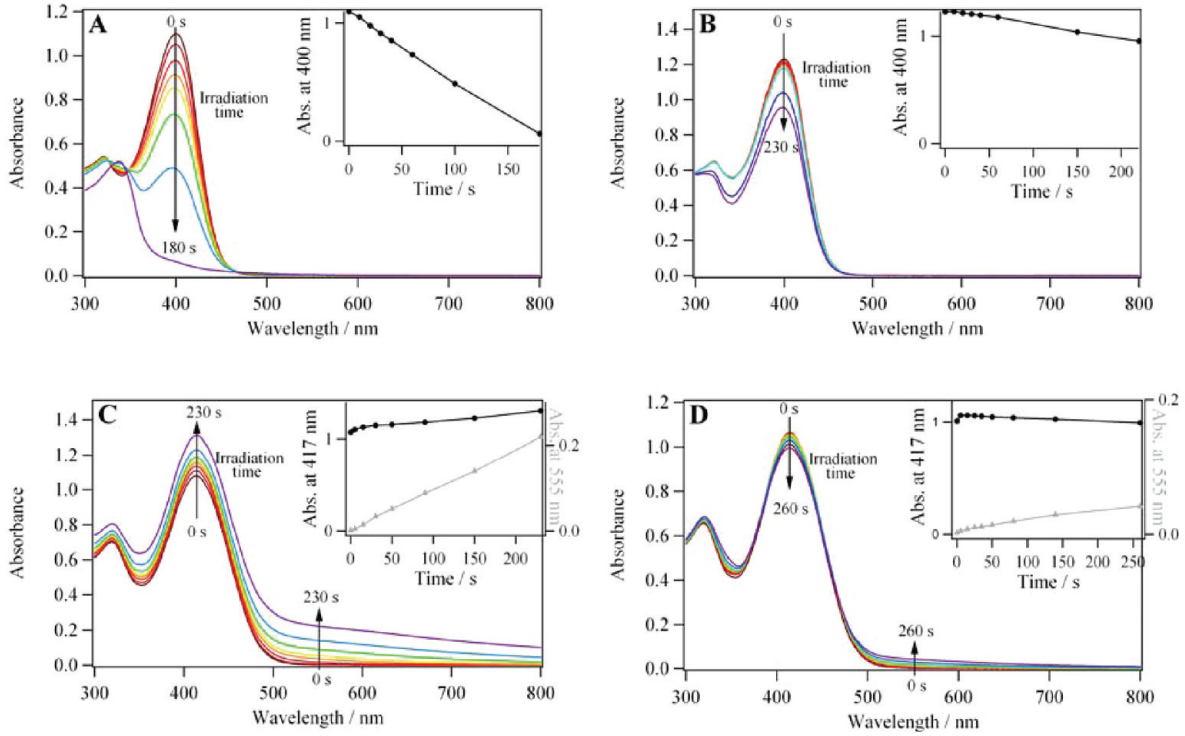


Figure 3. Absorption spectra as a function of irradiation time in different acetonitrile mixtures. Solutions were N_2-degassed prior irradiation except in case D. (A) [DES] = 1.5×10^{-5} M; (B) [DES] = 1.5×10^{-5} M and [MDEA] = 3×10^{-2} M; (C, D) [DES] = 1.5×10^{-5} M, [Ag^+] = 2×10^{-2} M and [MDEA] = 3×10^{-2} M. Insets show kinetics at λ_{max} (400 nm in A, B cases and 417 nm in C, D cases) and at 555 nm in the presence of Ag^+ upon UV irradiation of mixture. Irradiation conditions were identical in both cases (P = 100 mW).

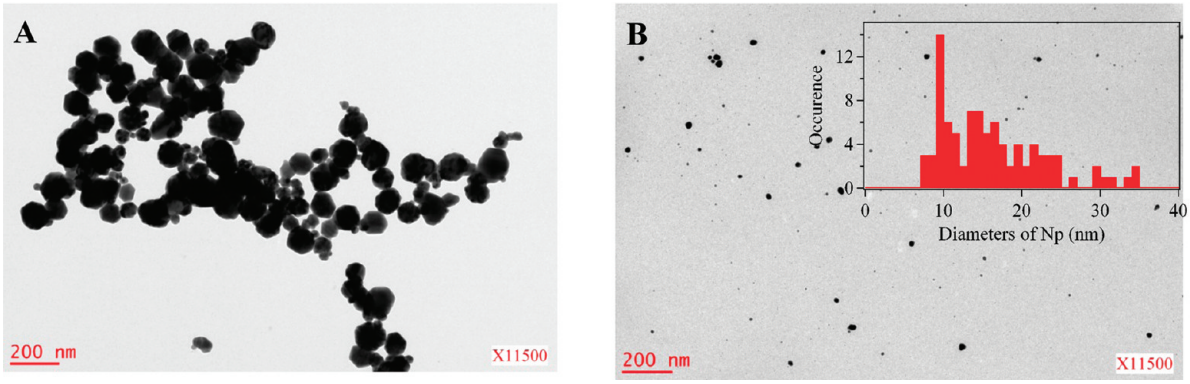


Figure 4. TEM images of Ag nanoparticles: (A) obtained by UV irradiation of acetonitrile solution N_2-degassed containing 1.5 μM DES, 20 mM Ag^+, and 30 mM MDEA (P = 100 mW); (B) embedded in microstructures obtained by 532 nm laser pulse excitation of Ebecryl 605 formulation containing 0.3 wt % DES, 1 wt % MDEA, and 1 wt % $AgSbF_6$ (power was measured after the ×100 objective (N.A. = 1.21): P = 130 μW).

Study of the Photolysis of the DES_2Ag^+ Complex. Figure 3 shows the evolution of the absorption spectra of different solutions of DES in acetonitrile in presence of Ag^+ and *N*-methyldiethanolamine (MDEA) as a function of irradiation time. Solutions are N_2-flushed prior irradiation to prevent inhibiting effect of oxygen, except in case of Figure 3D. It should be noted all these reactants will be used for TPIP; therefore, their respective role in the photoinitiating reaction should be first clarified. Figure 3A corresponds to a 1.5×10^{-5} M DES solution in acetonitrile. The main band located at 400 nm drastically decreases during irradiation process and fully collapses after 180 s of irradiation. In parallel to this photobleaching, an absorption band at 335 nm arises underlining the formation of a photoproduct. In the second solution (Figure 3B), a large excess of *N*-methyldiethanolamine (MDEA) is added (i.e., 3×10^{-2} M). In this case, the decrease of absorption band during irradiation is drastically slowed down, which indicates that the photobleaching reaction is strongly reduced in the presence of MDEA. Finally, addition of silver cations (i.e., 2×10^{-2} M) to a solution which both contains the chromophore and MDEA leads to the growth of a new band in the 350−700 nm range (Figure 3C). This large band should be assigned to the surface plasmon resonance of silver nanoparticles (NPs) that progressively aggregates during irradiation. The production of metal nanoparticles is also confirmed by TEM analysis of the sample as shown in Figure 4A. The TEM image clearly indicates a polydispersed distribution of Ag NPs with an average diameter of 50 nm. Hence, a photoreduction of the silver cation is demonstrated. Interestingly, this photoreaction is inhibited by oxygen since

dx.doi.org/10.1021/ma202224c | *Macromolecules* 2012, 45, 1262−1269

the photoreduction of Ag^+ is hardly observed when the same solution is not N_2-degassed as shown in Figure 3D. Moreover, in this case, the absorption spectrum of DES_2Ag^+ remains nearly invariant during irradiation which is ascribable to the presence of the amine as previously observed for the absorption spectrum of the free ligand in Figure 3B. Such an enhancement of the photostability observed for the dye or for its metal complex should be explained according to a regenerative pathway of the DES promoted by MDEA. In order to advance the understanding of this complex process, we propose a general mechanism susceptible to describe the photoreduction of silver ions and the regenerative pathway of DES as observed experimentally. As previously demonstrated for diaminofluorene derivatives,[33] we propose that the major route for the photobleaching of DES stems from the production of the corresponding radical cation ($DES^{\bullet+}$) and anion ($DES^{\bullet-}$). These radicals result from a self-quenching reaction of DES (eq 1) between its excited triplet state (^3DES) and its ground state (DES) as follows:

$$^3DES + DES \rightarrow DES^{\bullet+} + DES^{\bullet-} \quad \text{(self-quenching)} \tag{1}$$

$$DES^{\bullet+} + DES^{\bullet-} \rightarrow DES + DES \quad \text{(ions recombination)} \tag{2}$$

Both radical ions can either recombine (eq 2) or initiate the photobleaching process.[43] Similar reactions should also occur for the metal complex as

$$^3DES_2Ag^+ \rightarrow DES^{\bullet+} + DES^{\bullet-} + Ag^+ \tag{3}$$

$$DES^{\bullet-} + Ag^+ \rightarrow DES + Ag_0 \tag{4}$$

The self-quenching reaction for DES_2Ag^+ is not controlled by diffusion since both reactants are initially in close proximity (eq 3). In contrast with the mechanism of photobleaching involving the free ligand, the radicals recombination step for the complex should compete with the concomitant reduction of Ag^+ (eq 4). Therefore, the presence of the silver cation should indirectly contribute to the increase of the quantum yield for the generation of radical cation $DES^{\bullet+}$. This latter effect is illustrated by Figure S8 (see Supporting Information) which displays the changes of the absorption spectrum of DES_2Ag^+ upon irradiation. While the main absorption band undergoes a strong decrease with a slight red-shift, a new weakly intensive band is clearly developing in the 590−790 nm region. This band is similar to that obtain when mixing DES with $Cu(NO_3)_2$ and should be ascribed to the formation of $DES^{\bullet+}$. Indeed, it has been previously reported a simple chemical method to obtain radical cation from aromatic amine. The reaction involves the mixing of aromatic amine with $Cu(NO_3)_2$ in acetonitrile solution.[44−46] Finally, it is noteworthy that the reduction of Ag^+ by $DES^{\bullet-}$ (eq 4) constitutes a minor route for the production of NPs as compared to the major channel opened in presence of MDEA. MDEA is usually used as a co-initiator which undergoes a hydrogen abstraction from excited triplet species or radical cations.[33,47,48] This reaction then produces α-aminoalkyl radicals ($MDEA^{\bullet}$) which can both initiate free radical photopolymerization[49] and reduce silver cations.[32,33,50−52] Therefore, the sequential steps for the dye regeneration should be described as follows:

$$DES^{\bullet+} + MDEA \rightarrow DESH^+ + MDEA^{\bullet} \quad \text{(H abstraction)} \tag{5}$$

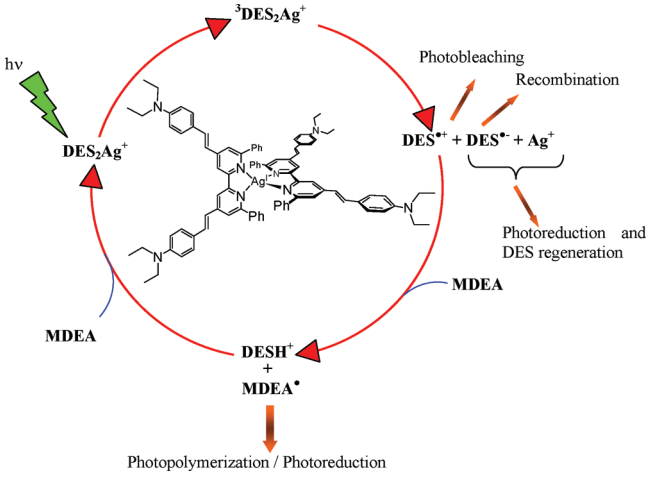
$$DESH^+ \underset{+H^+}{\overset{-H^+}{\rightleftharpoons}} DES \quad \text{(acid−base equilibrium)} \tag{6}$$

The first reaction step corresponds to the hydrogen transfer reaction which also produces the acid form of DES (eq 5). The second reaction step is a rapid acid−base equilibrium (eq 6) that regenerates DES due to the strong basicity character of MDEA which is present in large excess (i.e., 3×10^{-2} M). Finally, the presence of silver cation leads to an efficient redox reaction with $MDEA^{\bullet}$:

$$Ag^+ + MDEA^{\bullet} \rightarrow Ag_0 + MDEA^+ \quad (Ag^+ \text{ reduction}) \tag{7}$$

The efficiency of this process is strongly affected by the presence of oxygen. This effect can be correlated with the sensitivity of α-aminoalkyl radicals toward oxygen[49] and is consistent with the slight increase of the surface plasmon resonance band during the irradiation, as shown in Figure 3D. Hence, a regenerative process of the chromophore and its metal complex is observed in presence of MDEA which undergoes a hydrogen abstraction and produces a highly reducible α-aminoalkyl radical. The proposed mechanism is summarized in Scheme 2. When reactions are performed in monomer medium, photopolymerization occurs simultaneously with the photoreduction. Therefore, FTIR experiments have been performed under one photon condition to test the photoinitiation ability of DES and DES_2Ag^+. Surprisingly, no photoinitiation activity was observed. However, since these photoinitiators are specifically dedicated to TPIP, their reactivity will be probed via two-photon microfabrication. This last step will be the object of the next section.

Scheme 2. Proposed Photoinitiation Mechanism of Simultaneous Photopolymerization and Photoreduction via a Regenerative Process Leading to Higher Formation of Radical Cations $DES^{\bullet+}$



Microfabrication by Two-Photon-Induced Polymerization (TPIP) and Structural Characterizations. The potential of DES and DES_2Ag^+ as novel two-photon activable photoinitiators has been evaluated for the fabrication of

microstructures by using a 532 nm laser pulse excitation since these photoinitiator systems do not absorb at this wavelength. For each system, arrays of dots are produced to determine the energy threshold defined here as the minimum energy to observe microdots inside the photopolymer matrix (Figure 5). The microdots represent polymerized regions which can be observed by classical optical microscopy due to the difference

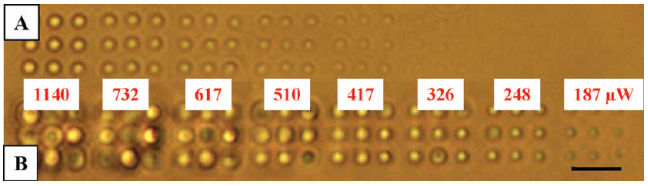


Figure 5. Determination of energy threshold by decreasing gradually the power of 532 nm laser pulse excitation source (from 1140 to 187 μW) obtained with (A) formulation A containing 0.3 wt % DES and 1 wt % MDEA in Ebecryl 605 monomer (EB605) and (B) formulation B containing 0.3 wt % DES, 1 wt % MDEA, and 1 wt % $AgSbF_6$ in Ebecryl 605 monomer. Exposure time was set to 10 ms. Scale bar: 6 μm.

of refractive index between the monomer and the polymer. The writing process is described in detail in the Experimental Section. Two types of formulation A and B have been used; both contain 0.3 wt % DES and 1 wt % MDEA in Ebecryl 605 monomer (EB605). In formulation B, 1 wt % $AgSbF_6$ is added in order to form the complex. It has to be noted that DES alone in solution can initiate the two-photon polymerization reaction, but owing to a lack of reactivity compare to that in presence of MDEA, we focused on formulations containing MDEA for microfabrication (see Figure S4). As shown in Figure 5, the energy threshold in formulation A (Figure 5A) is found to be ca. 3 times higher than that relative to formulation B (Figure 5B). Indeed, the formation of voxel induced by a minimum power is 326 and 130 μW for formulation A and B, respectively. Owing to the competition between the photoreduction and the photopolymerization in the presence of Ag^+, we would have expected to a much higher energy threshold in favor of the formulation B as demonstrated and described by Prasad et al. in the case of gold nanoparticles-doped polymeric structures.[15] In the frame of this work, this opposite effect can be explained by two distinct phenomena both resulting from the complexation of DES with Ag^+. The first point corresponds to an increase of the TPA cross section. In short, this consists in taking advantage of the complexing properties of the bipyridine functions to bond the PI around a metal ion. Indeed, metal cations can be used as 3D templates[31] which organize a set of organic ligands into a multipolar arrangement for the promotion of TPA properties. In the case of the formation of the complex DES_2Ag^+, a strong enhancement of the TPA cross section by a factor 4 was measured in ref 25. The second point concerns the formation of radical cations $DES^{\bullet+}$ which is a key step since it will affect the production of α-aminoalkyl radicals

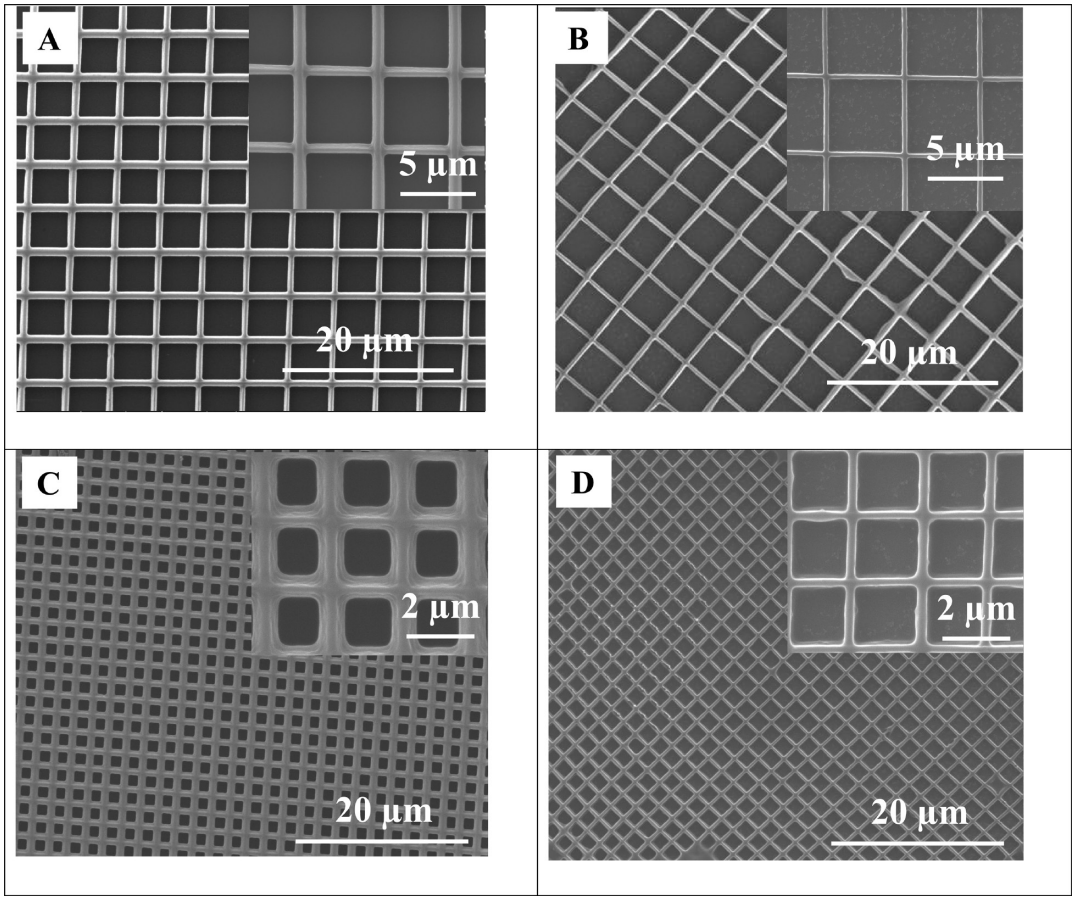


Figure 6. SEM images of the polymeric structures designed by CAD (computer-aided design). (A) and (B) correspond to a microgrid with spacing between two lines of 5 μm. (C) and (D) correspond to a microgrid with spacing between two lines of 2 μm. (A, C) EB605/DES microgrids produced at 732 μW. (B, D) EB605/DES/Ag NPs microgrids produced at 130 μW. Insets show the close-up view of the grids.

dx.doi.org/10.1021/ma202224c | *Macromolecules* 2012, 45, 1262–1269

(MDEA$^{\bullet}$) responsible of the photopolymerization and the photoreduction. On the basis of our experimental observations and the above proposed mechanism (see photolysis section), a more important yield of radical cation DES$^{\bullet+}$ is expected with DES_2Ag^+. Using this data, more complex shapes are generated, consisting in microgrids of 100 μm × 100 μm: Figures 6A and 6C exhibit the fabrication of microgrids in absence of Ag^+ with respectively a spacing between two lines of 5 and 2 μm. In order to avoid washing off the structures from the glass substrate during the development step, the power is set to 732 μW, which is almost 2 times the threshold value determined previously. The structures present submicrometric features: lines widths are measured to be ca. 780 nm. Images profiles obtained by AFM provide accurate measurements of their sizes in z dimension (1.1 μm, see Figure S2A).

Similar structures based on identical computer model have been fabricated in the presence of Ag^+. In this case, the power is set to 130 μW (Figure 6B,D), with no observation of sample delamination. The required power to write microstructures is thus divided by a factor of 5 in the presence of Ag^+. Interestingly, in this case, the value used for the polymerization threshold measurement can be used as a reference for microstructuring. This fact shows that the polymerization process initiated by the DES_2Ag^+ complex is efficient and produces a highly cross-linked polymer network compatible with applications in microfabrication. Moreover, measurements of lines widths by SEM give a value ca. 270 nm, and AFM measurement values of the heights are ca. 750 nm. The ratio between lateral and vertical size is in agreement with expected values observed in TPIP. Energy-dispersive X-ray spectroscopy (EDX) is also performed to detect the presence of Ag NPs inside the microgrids (Figure S3 in Supporting Information). According to EDX spectra, 0.3% of the material probed is composed of silver. No Ag^+ counterions, such as antimony or fluoride, have been detected by EDX, suggesting that all silver in the structure is totally reduced. Finally, the microstructure is cut by means of a microtome, and TEM image are recorded showing clearly well-isolated and spherical Ag NPs embedded in polymer matrix (Figure 4B). As depicted in inset of Figure 4B, the distribution of NPs' size exhibits wide dispersion (from 5 to 40 nm), but no noticeable aggregation effect is observed. Such a system is really interesting since it opens the doors for the fabrication of metal−polymer nanocomposites by TPA microfabrication which are highly promising materials for optical, electrical, and medical applications.

CONCLUSION

The two-photon-induced polymerization properties of a cationic silver(I) complex have been reported. We demonstrated that the presence of silver ions in the formulation influences strongly and positively the energy threshold of photopolymerization despite a potential competition with the photoreduction step of Ag^+. This paradox was explained by the formation of a strong complex between the dye DES and the silver ions which exhibits ca. 4 times higher TPA cross section and leads to an increase of the yield in radical cations DES$^{\bullet+}$. Besides, in the presence of MDEA, a regenerative pathway of the complex during photoirradiation experiments was evidenced. Our present observations allow us to propose a mechanism involving several sequential reactions. By taking benefits from a remarkable compromise between the efficiencies of the photoreduction process and the two-photon-induced polymerization, we show that this type of photoinitiator can play a crucial role in the emerging research area of 2D and 3D microfabrication of nanocomposites and metallic structures. This role is illustrated by the TPIP fabrication of microgrids with an inexpensive and low-power microlaser, leading to the observation of nanofeatures and Ag NPs embedded in a polymer matrix.

ASSOCIATED CONTENT

Supporting Information

Emission spectrum of DES in glassy ethanol; structural characterization and composition analysis of microgrids using atomic force microscopy (AFM); energy-dispersive X-ray spectroscopy (EDX); experimental evidence of DES's TPA properties; ^{1}H and ^{13}C NMR spectra; output spectrum of the UV irradiation source; experimental evidence of existence of DES$^{\bullet+}$. This material is available free of charge via the Internet at http://pubs.acs.org.

AUTHOR INFORMATION

Corresponding Author

*E-mail: arnaud.spangenberg@uha.fr (A.S.), jean-pierre.malval@uha.fr (J.-P.M.).

ACKNOWLEDGMENTS

The authors gratefully acknowledge Loïc Vidal and Stéphan Knopf for help and discussion. The authors also acknowledge financial support by Agence Nationale de la Recherche (ANR Nanoquenching, Contract 10PDOC-009 01).

REFERENCES

(1) von Freymann, G.; Ledermann, A.; Thiel, M.; Staude, I.; Essig, S.; Busch, K.; Wegener, M. *Adv. Funct. Mater.* **2010**, *20* (7), 1038−1052.
(2) Deubel, M.; Von Freymann, G.; Wegener, M.; Pereira, S.; Busch, K.; Soukoulis, C. M. *Nature Mater.* **2004**, *3* (7), 444−447.
(3) Ergin, T.; Stenger, N.; Brenner, P.; Pendry, J. B.; Wegener, M. *Science* **2010**, *328* (5976), 337−339.
(4) Ledermann, A.; Wegener, M.; von Freymann, G. *Adv. Mater.* **2010**, *22* (21), 2363−2366.
(5) Gansel, J. K.; Thiel, M.; Rill, M. S.; Decker, M.; Bade, K.; Saile, V.; von Freymann, G.; Linden, S.; Wegener, M. *Science* **2009**, *325* (5947), 1513−1515.
(6) LaFratta, C. N.; Fourkas, J. T.; Baldacchini, T.; Farrer, R. A. *Angew. Chem., Int. Ed.* **2007**, *46* (33), 6238−6258.
(7) Maruo, S.; Ikuta, K.; Korogi, H. *Appl. Phys. Lett.* **2003**, *82* (1), 133−135.
(8) Maruo, S.; Inoue, H. *Appl. Phys. Lett.* **2006**, *89* (14), 144101.
(9) Galajda, P.; Ormos, P. *Appl. Phys. Lett.* **2001**, *78* (2), 249−251.
(10) Iosin, M.; Scheul, T.; Nizak, C.; Stephan, O.; Astilean, S.; Baldeck, P. *Microfluid. Nanofluid.* **2011**, *10* (3), 685−690.
(11) Kumi, G.; Yanez, C. O.; Belfield, K. D.; Fourkas, J. T. *Lab Chip* **2010**, *10* (8), 1057−1060.
(12) Baldacchini, T.; Pons, A. C.; Pons, J.; LaFratta, C. N.; Fourkas, J. T.; Sun, Y.; Naughton, M. J. *Opt. Express* **2005**, *13* (4), 1275−1280.
(13) Vurth, L.; Baldeck, P.; Stephan, O.; Vitrant, G. *Appl. Phys. Lett.* **2008**, *92*, 17.
(14) Shukla, S.; Furlani, E. P.; Vidal, X.; Swihart, M. T.; Prasad, P. N. *Adv. Mater.* **2011**, *22* (33), 3695−3699.
(15) Shukla, S.; Vidal, X.; Furlani, E. P.; Swihart, M. T.; Kim, K. T.; Yoon, Y. K.; Urbas, A.; Prasad, P. N. *ACS Nano* **2011**, *5* (3), 1947−1957.
(16) Rill, M. S.; Plet, C.; Thiel, M.; Staude, I.; Von Freymann, G.; Linden, S.; Wegener, M. *Nature Mater.* **2008**, *7* (7), 543−546.
(17) Kawata, S.; Sun, H. B.; Tanaka, T.; Takada, K. *Nature* **2001**, *412* (6848), 697−698.
(18) Maruo, S.; Ikuta, K.; Korogi, H. *J. Microelectromech. Syst.* **2003**, *12* (5), 533−539.

(19) Tayalia, P.; Mazur, E.; Mooney, D. J. *Biomaterials* **2011**, *32* (10), 2634−2641.
(20) Tayalia, P.; Mendonca, C. R.; Baldacchini, T.; Mooney, D. J.; Mazur, E. *Adv. Mater.* **2008**, *20* (23), 4494−4498.
(21) Schafer, K. J.; Hales, J. M.; Balu, M.; Belfield, K. D.; Van Stryland, E. W.; Hagan, D. J. *J. Photochem. Photobiol., A* **2004**, *162* (2−3), 497−502.
(22) Belfield, K. D.; Schafer, K. J.; Liu, Y. U.; Liu, J.; Ren, X. B.; Van Stryland, E. W. *J. Phys. Org. Chem.* **2000**, *13* (12), 837−849.
(23) Belfield, K. D.; Ren, X. B.; Van Stryland, E. W.; Hagan, D. J.; Dubikovsky, V.; Miesak, E. J. *J. Am. Chem. Soc.* **2000**, *122* (6), 1217−1218.
(24) Belfield, K. D.; Bondar, M. V.; Yanez, C. O.; Hernandez, F. E.; Przhonska, O. V. *J. Mater. Chem.* **2009**, *19* (40), 7498−7502.
(25) Akdas-Kilig, H.; Malval, J.-P.; Morlet-Savary, F.; Singh, A.; Toupet, L.; Ledoux-Rak, I.; Zyss, J.; Le Bozec, H. *Dyes Pigm.* **2011**, *92* (1), 681−688.
(26) Coe, B. J.; Fielden, J.; Foxon, S. P.; Brunschwig, B. S.; Asselberghs, I.; Clays, K.; Samoc, A.; Samoc, M. *J. Am. Chem. Soc.* **2010**, *132* (10), 3496−3513.
(27) Coe, B. J.; Samoc, M.; Samoc, A.; Zhu, L. Y.; Yi, Y. P.; Shuai, Z. G. *J. Phys. Chem. A* **2007**, *111* (3), 472−478.
(28) Feuvrie, C.; Maury, O.; Le Bozec, H.; Ledoux, I.; Morrall, J. P.; Dalton, G. T.; Samoc, M.; Humphrey, M. G. *J. Phys. Chem. A* **2007**, *111* (37), 8980−8985.
(29) Dragonetti, C.; Balordi, M.; Colombo, A.; Roberto, D.; Ugo, R.; Fortunati, I.; Garbin, E.; Ferrante, C.; Bozio, R.; Abbotto, A.; Le Bozec, H. *Chem. Phys. Lett.* **2009**, *475* (4−6), 245−249.
(30) Mazzucato, S.; Fortunati, I.; Scolaro, S.; Zerbetto, M.; Ferrante, C.; Signorini, R.; Pedron, D.; Bozio, R.; Locatelli, D.; Righetto, S.; Roberto, D.; Ugo, R.; Abbotto, A.; Archetti, G.; Beverina, L.; Ghezzi, S. *Phys. Chem. Chem. Phys.* **2007**, *9* (23), 2999−3005.
(31) Das, S.; Nag, A.; Goswami, D.; Bharadwaj, P. K. *J. Am. Chem. Soc.* **2006**, *128* (2), 402−403.
(32) Malval, J. P.; Jin, M.; Balan, L.; Schneider, R.; Versace, D. L.; Chaumeil, H.; Defoin, A.; Soppera, O. *J. Phys. Chem. C* **2010**, *114* (23), 10396−10402.
(33) Balan, L.; Jin, M.; Malval, J. P. *Macromolecules* **2008**, *41* (23), 9359−9365.
(34) Balan, L.; Malval, J. P.; Schneider, R.; Le Nouen, D.; Lougnot, D. J. *Polymer* **2010**, *51* (6), 1363−1369.
(35) Montalti, M.; Credi, A.; Prodi, L.; Gandolfi, M. T. *Handbook of Photochemistry*, 3rd ed.; CRC Press: Boca Raton, FL, 2006.
(36) Nakamoto, K. *J. Phys. Chem.* **1960**, *64* (10), 1420−1422.
(37) Blanchet-Boiteux, C.; Friant-Michel, P.; Marsura, A.; Regnouf-de-Vains, J. B.; Ruiz-Lopez, M. F. *J. Mol. Struct.: THEOCHEM* **2007**, *811*, 169−174.
(38) Goerner, H. *J. Phys. Chem.* **1989**, *93* (5), 1826−1832.
(39) Turro, N. J. *Modern Molecular Photochemistry*; University Science Books: Sausalito, 1991.
(40) Maury, O.; Guégan, J. P.; Renouard, T.; Hilton, A.; Dupau, P.; Sandon, N.; Toupet, L.; Le Bozec, H. *New J. Chem.* **2001**, *25*, 1553−1566.
(41) Bourson, J.; Pouget, J.; Valeur, B. *J. Phys. Chem.* **1993**, *97*, 4552−4557.
(42) Martin-Gassin, G.; Villamaina, D.; Vauthey, E. *J. Am. Chem. Soc.* **2011**, *133* (8), 2358−2361.
(43) Li, X. G.; Huang, M. R.; Duan, W. *Chem. Rev.* **2002**, *103*, 2929−3030.
(44) Kirchgessner, M.; Sreenath, K.; Gopidas, K. R. *J. Org. Chem.* **2006**, *71*, 9849−9852.
(45) Sumalekshmy, S.; Gopidas, K. R. *Chem. Phys. Lett.* **2005**, *413*, 294−299.
(46) Jin, M.; Malval, J. P.; Morlet-Savary, F.; Chaumeil, H.; Defoin, A.; Batat, P.; Jonusauskas, G. *Phys. Chem. Chem. Phys.* **2009**, *11* (15), 2622−2630.
(47) Handoo, K. L.; Cheng, J. P.; Parker, V. D. *J. Chem. Soc., Perkin Trans.* **2001**, *2*, 1476−1480.
(48) Knolle, W.; Janovsky, I.; Naumov, S.; Williams, F. *J. Phys. Chem. A* **2006**, *110*, 13816−13826.
(49) Fouassier, J. P.; Rabek, J. F. *Radiation Curing in Polymer Science and Technology*; Springer-Verlag: New York, 2002; Vol. 3.
(50) Sangermano, M.; Yagci, Y.; Rizza, G. *Macromolecules* **2007**, *40*, 8827−8829.
(51) Sudeep, P. K.; Kamat, P. V. *Chem. Mater.* **2005**, *17* (22), 5404−5410.
(52) Cook, W. D.; Nghiem, Q. D.; Chen, Q.; Chen, F.; Sangermano, M. *Macromolecules* **2011**, *44* (11), 4065−4071.

Macromolecules

Article

pubs.acs.org/Macromolecules

Rotaxanes from Tetralactams

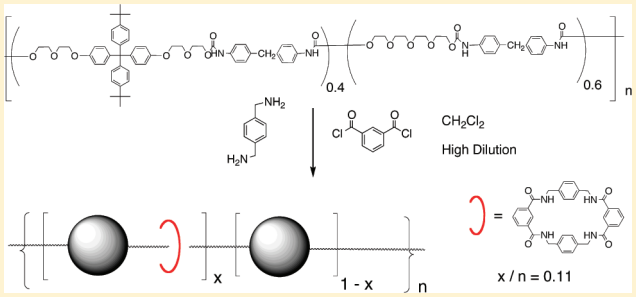
Harry W. Gibson,*[,†] Hong Wang,[†,§] Zhenbin Niu,[†] Carla Slebodnick,[†] Lev N. Zhakharov,[‡,∥] and Arnold L. Rheingold[‡,⊥]

[†]Department of Chemistry, Virginia Polytechnic Institute & State University, Blacksburg, Virginia 24060, United States

[‡]Department of Chemistry, University of Delaware, Newark, Delaware 19716, United States

Supporting Information

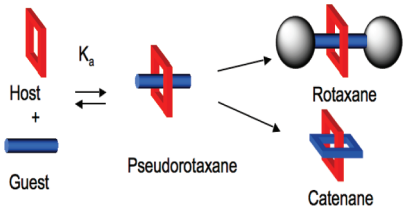
ABSTRACT: Attempts to incorporate a tetralactam (**3a**) into a side-chain polyrotaxane by formation of its complex with *p*-tritylphenolate and reaction with poly(vinybenzyl chloride) failed, probably due to steric hindrance. However, three new small molecule model rotaxanes (acetal **11a** and ethers **14a** and **14b**) were prepared based on this macrocycle, and one (**14b**) was characterized by X-ray crystallography. Attempts to prepare poly(ether rotaxane)s such as **18** and **20b** via polymerizations in the presence of this tetralactam failed because the mild conditions required for complexation (nonpolar solvent, room temperature) are not sufficient for effective step-growth polymerizations, resulting in only oligomer formation. In an alternative approach, clipping of the tetralactam **23** onto a preformed poly(urethane rotaxane) (**27**) in CH_2Cl_2 was successful, and the original biphasic segmented polymer was converted to a single-phase polyrotaxane (**28**) with a significantly lower glass transition temperature.



INTRODUCTION

Pseudorotaxanes, threaded entitities, exist in equilibrium with their linear and cyclic molecular components; attachments of bulky terminal groups on the linear molecules yield mechanically linked rotaxanes, and cyclizations of the linear component form catenanes, interlocked rings (Scheme 1), both

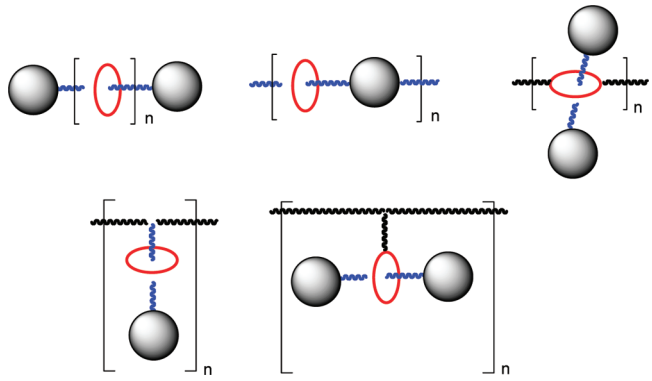
Scheme 1. Pseudorotaxanes: Precursors to Rotaxanes and Catenanes



of which can be converted to the independent species *only* by cleavage of a covalent bond.[1,2] Polyrotaxanes are polymers that include a rotaxane unit; the rotaxane unit may be in the main chain or a side chain (Scheme 2).[3,4]

We have synthesized a variety of main-chain polypseudorotaxanes and polyrotaxanes by carrying out classical step-growth[5] or free radical[6] polymerizations in the presence of cyclic components. Initially, the cyclic species were unfunctionalized aliphatic crown ethers;[7] however, functionalized crown ethers have been used by us as components of a number of types of main-chain polyrotaxanes as well.[8] Other investigators have also prepared such topologically interesting systems.[4]

Scheme 2. Polyrotaxanes: (top) Main-Chain Polyrotaxanes; (bottom) Side-Chain Polyrotaxanes

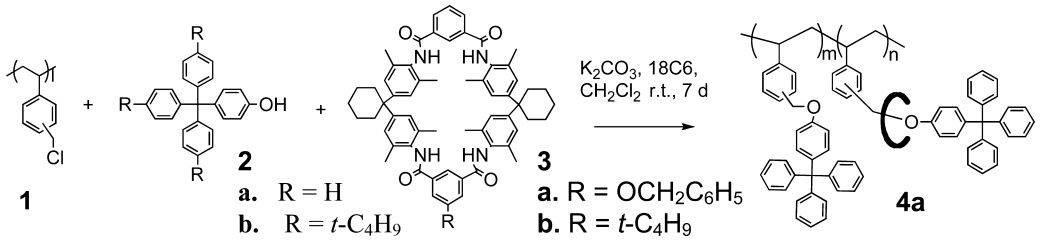


In the present work our initial aim was to prepare side-chain polyrotaxane (**4a**) from a preformed polymer, poly(vinylbenzyl chloride) (**1**), through reaction with a stopper, *p*-tritylphenol (**2a**), in the presence of tetralactam **3a** (Scheme 3). This method is based on the work of Vögtle et al.,[9] who demonstrated the formation of small molecule-based rotaxanes by initial complexation of phenolate anions with such cyclic amides, originally reported by Hunter et al.,[10] followed by alkylation with bulky stoppers in dichloromethane (Scheme 4).

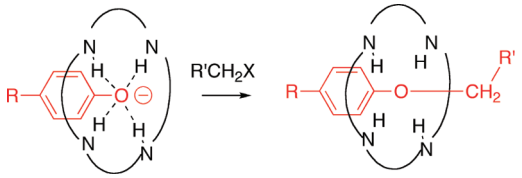
Received: October 26, 2011
Revised: December 22, 2011
Published: January 13, 2012

 © 2012 American Chemical Society dx.doi.org/10.1021/ma202373x | *Macromolecules* 2012, 45, 1270–1280

Scheme 3. Attempted Synthesis of Side-Chain Polyrotaxane 4a



Scheme 4. Schematic Illustration of Rotaxane Formation by Interaction of a Bulky Phenolate with a Tetralactam Followed by Williamson Ether Formation with a Bulky Alkyl Halide



RESULTS AND DISCUSSION

Attempted Synthesis of a Side-Chain Polyrotaxane via Threading of a Preformed Macrocycle. We prepared the known[11a] 32-membered, benzyloxy-substituted tetralactam **3a** by a process that paralleled the reported synthesis of **3b** (Scheme 5).[9a] The reported reaction[11a] that produced **3a** also produced two isomeric [2]catenanes that after deprotection were incorporated into polycatenanes.[11b,12] **3a** provides reasonable solubility in low-polarity solvents, like dichloromethane, which are required for the phenolate templation, combined with a protected functional group for later modification. The hydroxy group of dimethyl 5-hydroxyisophthalate (**5**) was protected with a benzyl moiety; **6** was obtained in 98% yield. By hydrolysis of ester **6**, diacid **7** was isolated in 89% yield; after treatment with thionyl chloride the diacid chloride **8** was isolated as a crystalline solid (72%). 1,1-Bis(4′-amino-3′,5′-dimethylphenyl)cyclohexane (**9**) was reacted with half an equivalent of isophthaloyl chloride to form the known[9,10] diamine **10** in 61% yield. Reaction of the diacid chloride **8** with diamine **10** under pseudo-high dilution conditions afforded the tetralactam **3a** in 57% yield. The composition of **3a** was confirmed by mass spectrometry; the lithium adduct was detected at *m/z* 1017.9 (theory 1017.5) in a low-resolution FAB experiment, and the macrocycle itself was detected in a high-resolution experiment at *m/z* 1011.5433 [theory for $(M + H)^+$ 1011.5424] (see Supporting Information). The ^{1}H NMR spectrum of **3a** is analogous to that of **3b**,[9a] with the exception that it lacks the *tert*-butyl methyl signals and has additional signals arising from the benzyloxy moiety. Because of its asymmetry the compound displays separate signals for protons 1 and 9 and 2 and 10 (see labeled structure in Figure 1); the signals for protons 5/5′ and

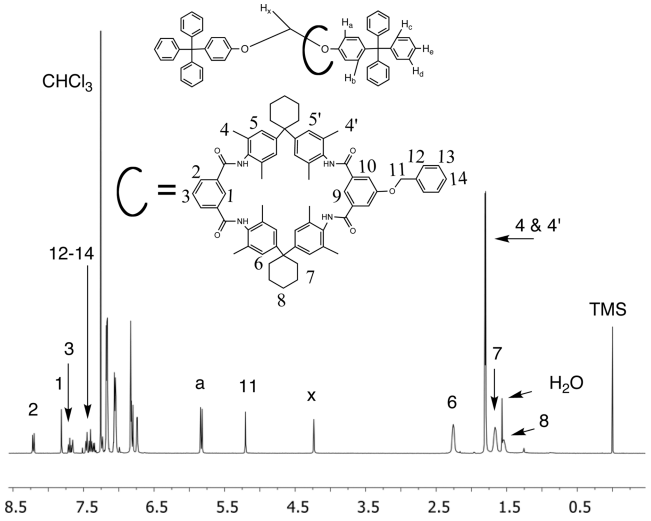
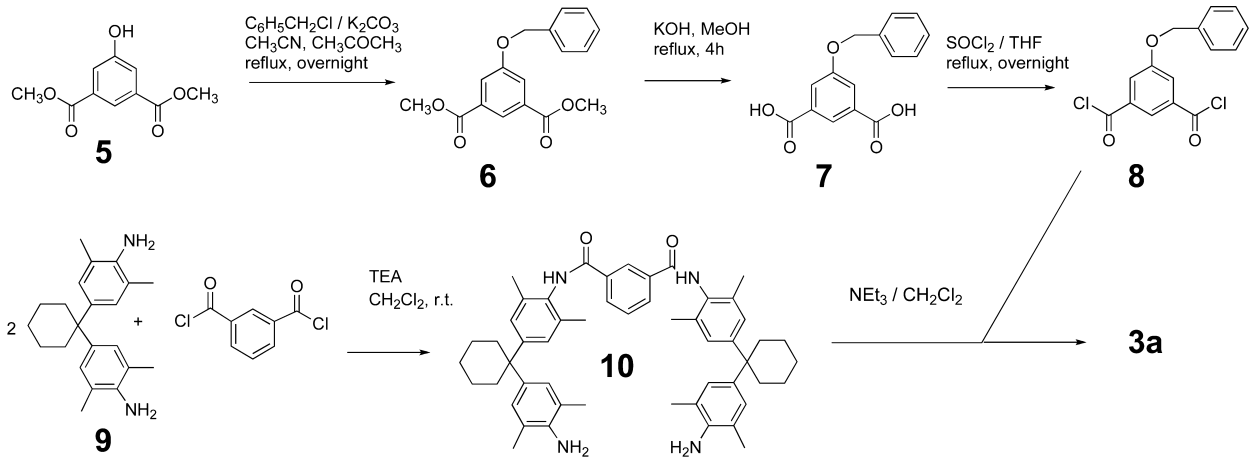


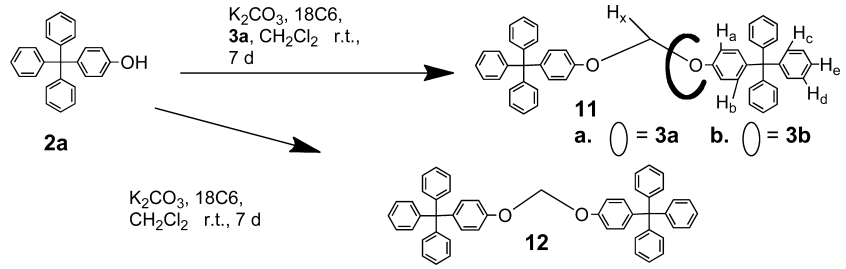
Figure 1. ^{1}H NMR spectrum (400 MHz, $CDCl_3$) of rotaxane **11a**.

Scheme 5. Synthesis of Tetralactam 3a

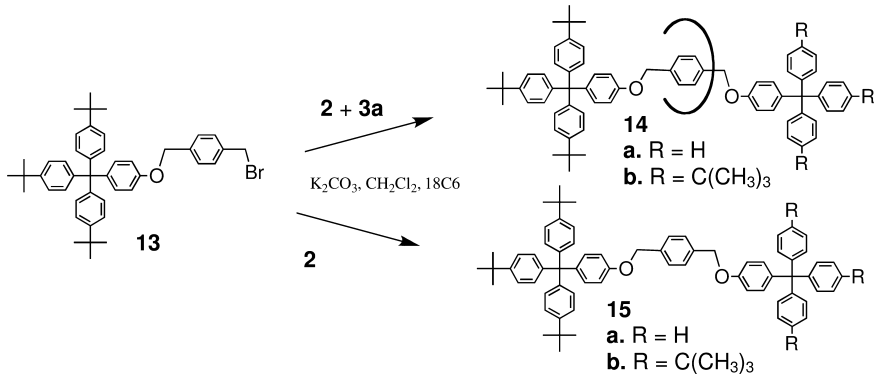


dx.doi.org/10.1021/ma202373x | Macromolecules 2012, 45, 1270−1280

Scheme 6. Synthesis of Model Rotaxanes 11a and 11b and Dumbbell 12



Scheme 7. Synthesis of Model Rotaxanes 14a and 14b and Dumbbells 15a and 15b



4/4′ overlap, yielding broad peaks in $CDCl_3$. We were also able to obtain a crystal structure of the macrocycle, although it was seriously disordered in terms of the position of the benzyloxy group (see Supporting Information); interestingly, two opposing carbonyl groups point inward and the other pair point outward.

In varied attempts to prepare the side-chain polyrotaxane under the conditions analogous to those used by Vögtle et al.,[9] the functionalized polymer **4a** was never isolated. Even an 11:1 styrene:vinylbenzyl choride copolymer, used in an attempt to reduce possible steric problems, did not react under these conditions. However, a nonpolymeric product was isolated in high yields from each of these attempts. The product was identified as the methanol-soluble rotaxane **11a** derived by reaction of the phenolate with the solvent, CH_2Cl_2, via its FAB HR MS, which displayed the $(M + Na)^+$ ion at m/z 1717.8342 (theoretical 1717.8272). This acetal rotaxane was also produced in the absence of the polymer for confirmation of its structure. Rotaxane **11a** yields an ^1H NMR spectrum (Figure 1) and displays properties that are similar to those reported by Vögtle et al. for the analogous acetal rotaxane **11b**.[9d] In particular, the signal for the acetal methylene protons H_x of **11a** appeared at 4.25 ppm in $CDCl_3$ in the present work; the reported postion for H_x of **11b** in DMF-d_7 was 4.08 ppm. Moreover, the signal for the ortho protons H_a shifted upfield from 6.7 ppm in *p*-tritylphenol to 5.85 ppm in rotaxane **11a** in $CDCl_3$, while in **11b** it appears at 6.19 ppm in DMF-d_7. A similar trityl acetal rotaxane was reported to form from a cryptand containing two amide linkages.[13] COSY experiments (see Supporting Information) confirm the assignments shown in Figure 1. ROESY and 1D NOESY experiments (see Supporting Information) indicate correlation of inner macrocyclic proton H_1 with guest proton H_x and macrocyclic methyl protons H_4 and $H_{4'}$ with guest protons H_a, consistent with the rotaxane structure. In the absence of the macrocycle the linear dumbbell molecule **12** was formed; this compound has been reported before as the linear component of rotaxanes,[9a,c−e] but not characterized itself.

Model Small Molecule Rotaxanes. Two small molecule rotaxanes **14** were synthesized from benzylic bromide precursor **13**[5h,14] and *p*-tritylphenols **2a** and **2b** in the presence of macrocycle **3a** (Scheme 7). The two dumbbell guests **15** were synthesized also. Molecular ion peaks were observed in HR MS of rotaxanes **14**: at m/z 1953.09 (theoretical 1953.07) for **14a** and at m/z 2122.25 (theoretical 2121.26) for **14b**, respectively. The ^1H NMR spectra of **14a** and **14b** (Figure 2) display signals for the central protons of the guest that are shifted upfield due to diamagnetic shielding effects of the aromatic nuclei; in rotaxane **14a** the different stoppers and the resultant unsymmetrical structure lead to doubling of some of the signals. The xylyl aromatic protons (g and g′) shift upfield from 7.38 to 5.96 ppm for **15a** vs **14a** and from 7.45 to 5.97 ppm for **15b** vs **14b**. The benzylic protons (f and f′) also shift upfield from 4.52/4.98 to 4.31/4.41 ppm for **15a** vs **14a** and from 5.04 to 4.36 ppm for **15b** vs **14b**. The aromatic protons *ortho* to the phenolic ether (a and a′) also shift upfield: from 6.77/6.79 to 6.35/6.46 ppm for **15a** vs **14a**, and from 6.85 to 6.38 ppm for **15b** vs **14b**. The integrations are all consistent with the corresponding structures.

A single crystal of rotaxane **14b** suitable for X-ray diffraction was grown from acetone by vapor diffusion of pentane. Its structure (Figure 3)[15] is triclinic with *P*1 symmetry. The tetralactam is symmetrically located between the two stoppers. The two benzylic ether moieties of the guest take on a trans disposition. The benzyloxyphenyl ring of the macrocycle is nearly perpendicular (88°) to the plane of the xylyl ring of the guest, and proton H_9 of the macrocycle is situated over the central xyly ring at a distance of 4.26 Å. Likewise, the opposing *m*-isophthaloyl ring of the host lies at an angle of 84° to the plane of the xylyl ring and H_1 is also 4.26 Å from the central xylyl ring. The phenolic rings of the stoppers are nearly coplanar (3° out) and lie at angles of 58° and 61° with respect

dx.doi.org/10.1021/ma202373x | *Macromolecules* 2012, 45, 1270−1280

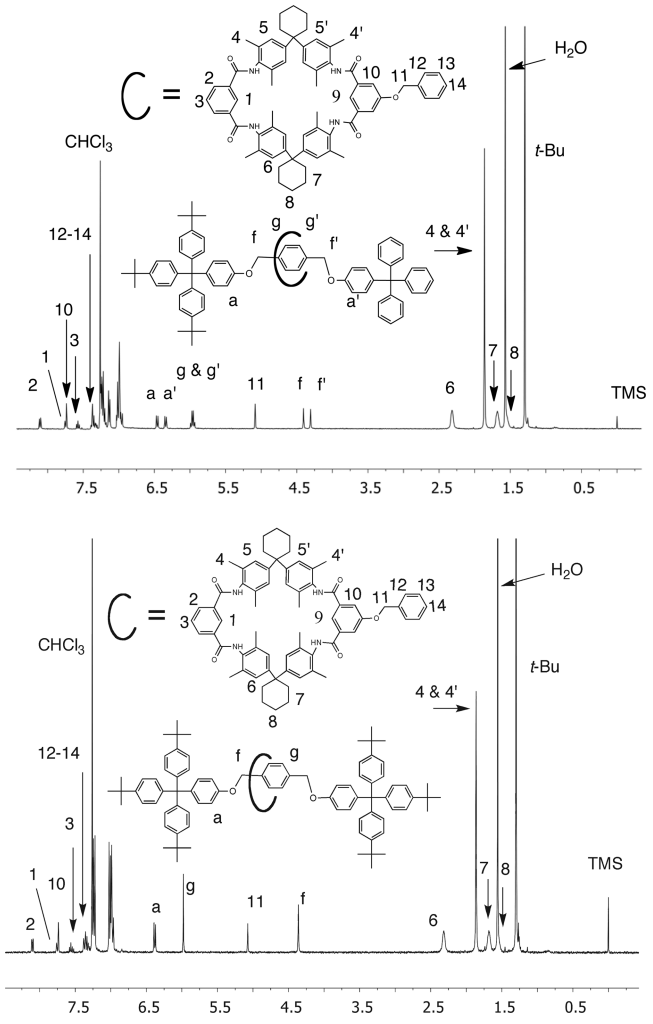


Figure 2. ^{1}H NMR spectra (400 MHz, $CDCl_3$) of rotaxanes **14a** (top) and **14b** (bottom).

to the central xylyl ring of the guest. Unlike the situation in the macrocycle itself, all of the carbonyl moieties point outward. Two of the amide NHs are hydrogen bonded to acetone molecules (O---H distances 2.10 and 2.14 Å, not shown); however, there are no close contacts between the cyclic and linear components.

These rotaxanes, **14a** and **14b**, represent a novel class in which there is little or no interaction between the linear and cyclic components; that is, there is no "memory" of the intermolecular interactions that produced the threaded structures. Such structures in polymeric systems should allow facile movement of the cyclic species along the backbone, an adaptive advantage for some applications, such as surface modification, for example.

Oligomeric Rotaxanes by Threading a Preformed Macrocycle. To take advantage of this translational freedom, the Vögtle tetralactam macrocycles have not been incorporated into analogous polymeric rotaxanes as far as we know. Thus, we thought it was of interest to extend the above small molecule model reactions to the construction of main chain polymeric analogues. We studied the reactions of bisphenol-A with difluorobenzophenone to produce a poly(ether ketone) and with difluorodiphenyl sulfone to produce a poly(ether sulfone) with no success under the mild conditions required for adequate complexation of the bisphenolate anion with the tetralactam. For example, reaction of bisphenol A (**16**) and bis(*p*-bromomethylphenyl) ether (**17**)[16] at room temperature (Scheme 8) in chloroform after precipitation from methanol produced in 71% yield only oligomeric **18**, as determined by its observed low viscosity, GPC (bimodal, M_n 610, PDI 1.3, average of three runs with universal calibration), and ^{1}H NMR spectrum; again, the nonpolar solvent and low temperature limited the molecular weight. Nonetheless, we then carried out the same reaction in the presence of cyclic tetralactam **3a**; after precipitation from methanol, the product's ^{1}H NMR spectrum indicated that it contained no cyclic component, i.e., it was identical to **18**. We concluded that in the absence of any binding interaction between the linear polymer or oligomer and the cyclic compound, the cyclic species in the presumed pseudorotaxane was removed by the precipitation process. Hence, we concluded that stoppers were necessary to form an isolable polyrotaxane.

Therefore, "bis(tritylphenol)" **19**[17] was reacted with bis(*p*-bromomethylphenyl) ether (**17**) under basic conditions in chloroform at room temperature (Scheme 9). In the absence of the cyclic species, model oligomer **20a** was formed; it had M_n 3.15 kDa and polydispersity (PDI) 2.1 by GPC analysis relative

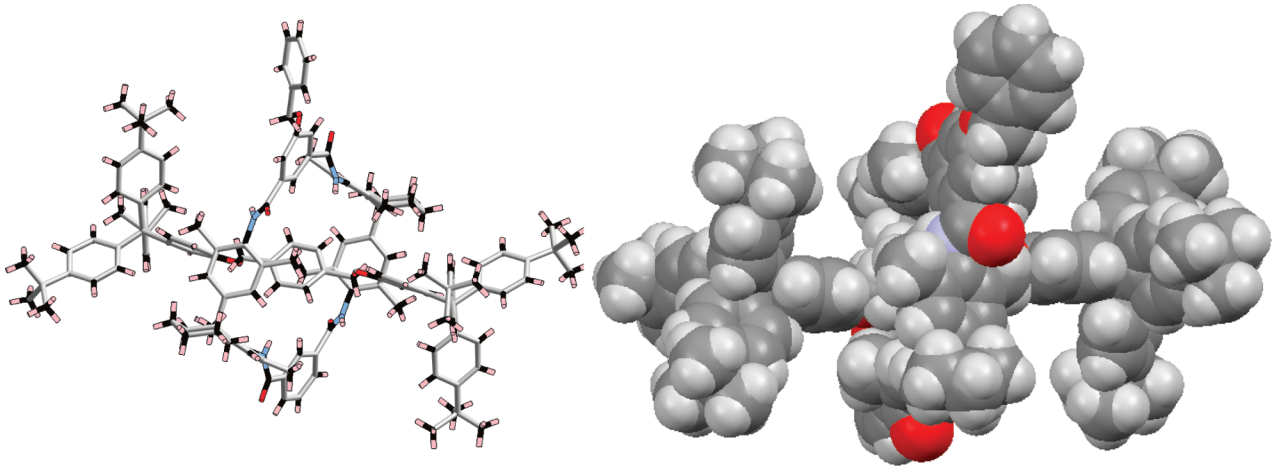
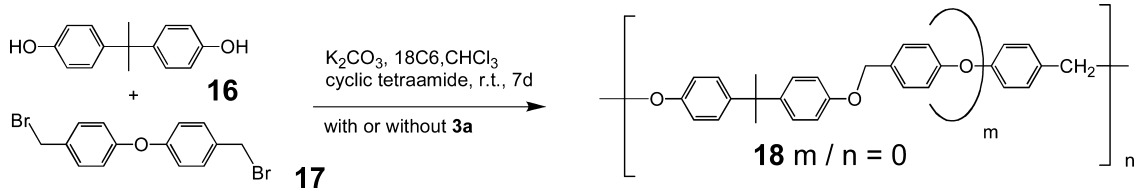


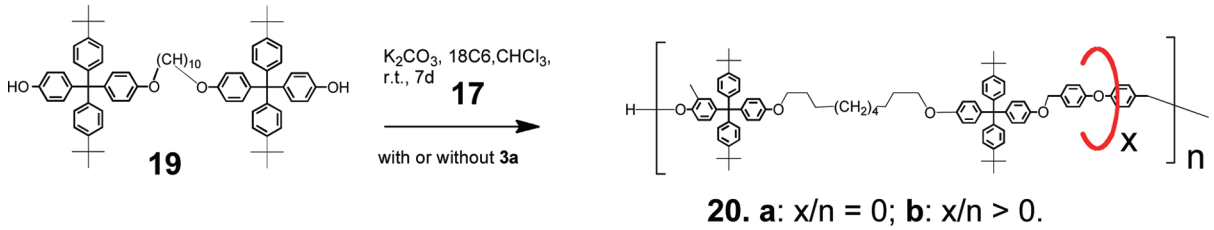
Figure 3. Structure of rotaxane **14b** as deduced from its single-crystal X-ray diffraction pattern. Left: stick figure. Right: space-filling representation. Oxygens are red, nitrogens are blue, carbons are black or dark gray, and hydrogens are white or light gray.

dx.doi.org/10.1021/ma202373x | *Macromolecules* 2012, 45, 1270–1280

Scheme 8. Attempted Synthesis of Model Polyether 18a and Polyrotaxane 18b



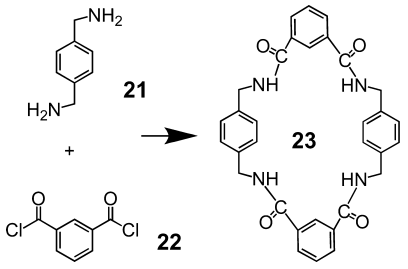
Scheme 9. Attempted Syntheses of Polyether 20a and Poly(ether rotaxane) 20b



to polystyrene standards. This corresponds to a degree of polymerization, n, of ~2.5, since the repeat unit mass is 1260 Da. When 1 equiv of cyclic tetralactam **3a** was used, **20b** resulted; the product was reprecipitated from chloroform into methanol three times before analysis. By GPC it had M_n 4.9 kDa and PDI 2.1. The ^{1}H NMR spectrum of **20b** displayed signals due to the tetralactam and a new signal for complexed benzylic protons. However, passage of this sample through a short silica gel column demonstrated the presence of unthreaded oligomer **20a** (see Supporting Information for details). Because of the low molecular weight and the mixed nature of the product, this approach was abandoned.

Main-Chain Polyrotaxanes by Clipping a Tetralactam around Preformed Polyamides. In order to prepare main-chain polyrotaxanes with tetralactams, we turned to the clipping approach, in which the cyclic component is formed around a preformed linear species.[1,18] For the cyclic species we used the 26-membered tetralactam **23** reported by Leigh et al., who demonstrated that rotaxanes could be formed by clipping its precursors, **21** and **22** (Scheme 10), around preformed small

Scheme 10. Synthesis of Leigh's Tetralactam 23



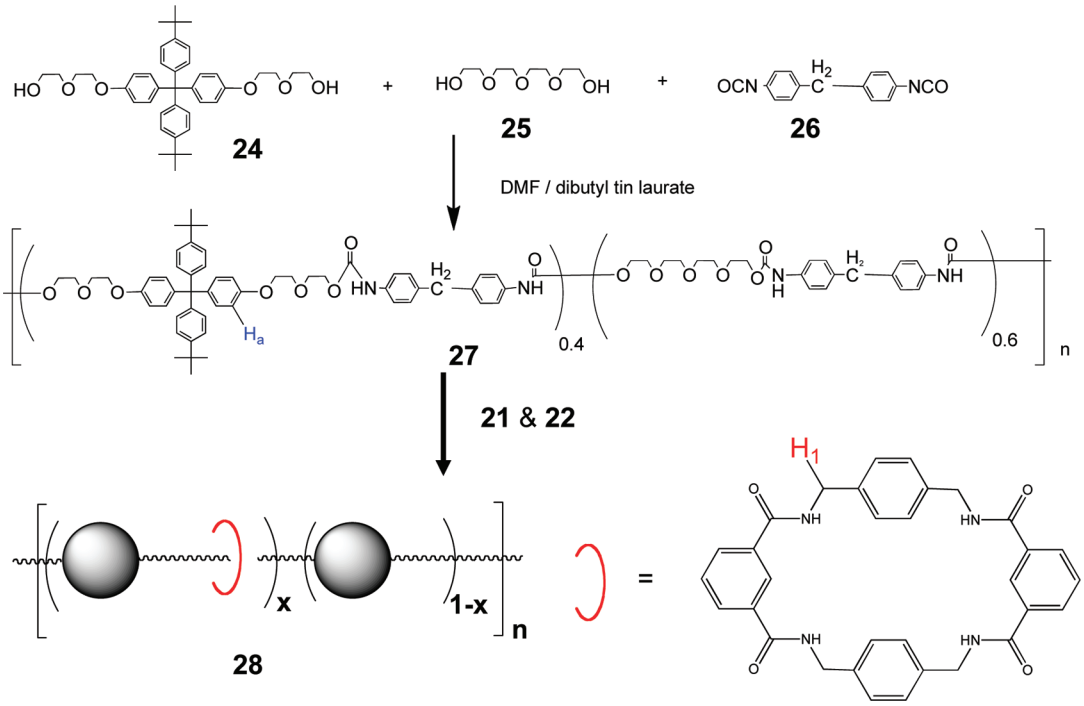
molecule amides.[19] In pursuit of our goal of incorporating Leigh's tetralactam into polyrotaxanes, we prepared a polymer that possessed suitable in-chain stoppers and solubility in nonpolar solvents. In particular, the bulky diol **24**[5i,j] was copolymerized with tetra(ethylene glycol) (**25**) (39.9:60.1 molar ratio) and MDI (**26**) to afford segmented polyurethane **27**, M_n 18.5 kDa, DP_n = 30 (Scheme 11). To bring about clipping[1,18] of the macrocycle around the polyurethane, a dilute solution of **27** in dichloromethane (1.09 g/1.5 L) was treated with diamine **21** and diacid chloride **22** by slow syringe pump addition. The resulting polymer was precipitated from dichloromethane into methanol three times until the signals due to the macrocycle no longer changed in proportion to the backbone signals. As determined by GPC, the polyrotaxane **28** had M_n 19.7 kDa. The clipping efficiency was determined to be 11 ± 1%, i.e., x/n = 0.11 ± 0.01, based on the ratio (0.55 ± 0.03) of integrals of the signals for the eight protons H_1 of the macrocycle and the four (times 0.4) aromatic protons H_a of the polymer in the NMR spectrum (Figure 4). Considering that the concentration of the urethane repeat units from **27** was 1.1 mM and only 0.8 equiv each of the building blocks **21** and **22** was applied, 14% of the theoretical yield of the macrocycle was captured in the polyrotaxane. Thus, the threading yield is impressive, and no doubt x/n could be increased by using an excess of the precursors of macrocycle **23**, analogous to our results with other polyrotaxane systems.[5c,d,h,j,n,6a,c,8e]

As shown in Figure 5, polyurethane **27** displays two glass transitions, one at 71 °C and the other at 150 °C, reflecting its phase-separated hard and soft domains. In contrast, polyrotaxane **28** has a single glass transition at 42 °C. Thus, rotaxanation of the polyurethane affects both the hard and soft phases, compatibilizing them to yield a single amorphous phase, presumably by location of the macrocycle along both segments of the copolymer through hydrogen bonding with the urethane and ether linkages, thereby interfering with interchain hydrogen bonding.

■ CONCLUSIONS

Attempts to incorporate a derivative of a tetralactam reported by Vögtle et al. into a side-chain polyrotaxane by reaction of tritylphenol with poly(vinybenzyl chloride) failed, apparently due to steric hindrance. However, three new small molecule model rotaxanes based on this macrocycle were prepared, and one was characterized by X-ray crystallography. Attempts to prepare poly(ether rotaxane)s based on this tetralactam failed because the conditions for complexation of the phenolate ion with the tetralactam (low temperature, low polarity) are not conducive to efficient step-growth polymerization. However, the first polyrotaxane **28** based on a tetralactam was synthesized by clipping Leigh's tetralactam **23** onto preformed polyurethane **27** in CH_2Cl_2. Incorporation of the macrocycle resulted in converting the two-phase segmented polyurethane **27** into a single-phase system with a significantly lower glass transition temperature in **28**.

Scheme 11. Synthesis of Segmented Polyurethane 27 and Its Conversion to Polyrotaxane 28 via Clipping of Tetralactam 23



EXPERIMENTAL SECTION

Materials. 1,4-Dioxane was freshly distilled over CaH_2; pyridine, distilled over CaH and stored over 3 Å molecular sieves; poly(vinylbenzyl chloride), Aldrich, 60/40 mixture of 3- and 4-isomers, typical M_n 55 kDa, typical M_w 100 kDa; *p*-tritylphenol, Aldrich, recrystallized from ethanol; 18C6, Aldrich, 99%; *N*,*N*-dimethylformamide (DMF), acetone, and triethylamine (TEA) were dried over 3 Å molecular sieves. K_2CO_3, tetrabutylammonium iodide (TBAI), NaOH, THF, CH_3Cl, CH_2Cl_2, toluene, HCl (36%), 1,1-bis(4′-amino-3′,5′-dimethylphenyl)cyclohexane (**9**, Aldrich), *p*-xylylenediamine (**21**, Aldrich), and isophthaloyl chloride (**22**, Aldrich) were used as received. Dimethyl 5-hydroxyisophthalate (Aldrich) was recrystallized from toluene/methanol. Compounds **13**[14a] and bis(*p*-hydroxymethylphenyl) ether[16] were prepared as previously reported.

Methods. Thin layer chromatography (TLC) utilized Whatman PE SIL G/UV254 plates. Flash column chromatography and column chromatography were carried out on silica gel. ^1H and ^{13}C NMR spectra were obtained on Varian Unity (or Inova) 400/100 MHz or JEOL Eclipse 500/125 MHz instruments instruments at ambient temperature; the usual designations of multiplicity are employed, and coupling constants (*J*) are reported in Hertz. Mass spectra (HR FAB) were obtained on a VG Quattro Fisons Instrument in positive ion mode; 3-nitrobenzyl alcohol (NBA) and poly(ethylene glycol) (PEG) matrices were employed, sometimes with other additives such as LiBr and CsI. DSC results were obtained on a TA Instruments Q2000 differential scanning calorimeter at a scan rate of 5 or 10 °C/min under a N_2 purge. Melting points (uncorrected) were observed on a Büchi B-540 apparatus at a 2 °C/min heating rate. Gel permeation chromatography (GPC) was conducted in $CHCl_3$ at 30 °C on an Alliance Waters 2690 separations module with a Viscotek T60A dual viscosity detector and laser refractometer equipped with a Waters HR 0.5 + HR 2 + HR 3 + HR 4 styragel column set and data analysis by universal calibration to obtain absolute or polystyrene equivalent molecular weights.

Dimethyl 5-Benzyloxyisophthalate (6). A mixture of 12.20 g (58.05 mmol) of dimethyl 5-hydroxyisophthalate and 9.23 g (66.8 mmol) of K_2CO_3 in CH_3CN/acetone (120 mL/100 mL) was refluxed 0.5 h to give a light yellow suspension. To this mixture was added 7.35 g (58.1 mmol) of benzyl chloride dropwise. After reaction overnight at reflux, the resulting light yellow suspension was concentrated by rotoevaporation. Water and EtOAc were added, and the water layer was extracted with EtOAc three times. The combined organic solution was washed with water to pH 7.00 and then washed with saturated NaCl solution. After drying over anhydrous Na_2SO_4, the clear solution was concentrated by rotoevaporation to give an oil, which solidified. The off-white solid was dried in vacuum (17.06 g, 98%) and recrystallized from toluene as needlelike crystals; mp 87.5–90.0 °C, lit.[20] mp 94–95 °C. ^1H NMR (400 MHz, acetone-d_6): δ 3.94 (s, 6H), 5.32 (s, 2H), 7.39 (t, J = 8 Hz, 1H), 7.44 (t, J = 8 Hz, 2H), 7.56 (d, J = 8 Hz, 2H), 7.83 (s, 2H), 8.22 ppm (s, 1H).

5-Benzyloxyisophthalic Acid (7). A solution of 3.94 g (13.1 mmol) of dimethyl 5-benzyloxyisophthalate and KOH (30.0 g, 535 mmol) in 300 mL of CH_3OH was stirred at reflux 2 h, cooled to rt, and acidified with 2 N HCl. The white precipitate was collected by filtration and dried in vacuum, 3.16 g (88%); mp 268–271 °C, lit. mp 252 °C.[21] ^1H NMR (400 MHz, acetone-d_6): δ 5.33 (s, 2H), 7.33 (t, J = 8 Hz, 1H), 7.42 (t, J = 8 Hz, 2H), 7.58 (d, J = 8 Hz, 2H), 7.92 (s, 2H), 8.33 (s, 1H), 11.6 ppm (bs, 2H).

5-Benzyloxyisophthaloyl Chloride (8). A mixture of $SOCl_2$ (55 mL, 0.75 mol), 5-benzyloxyisophthalic acid (**7**, 5.0 g, 18 mmol), and 5 drops of DMF was refluxed under N_2 protection; after 1 h a clear yellow solution formed. After 5 h of reflux, the excess $SOCl_2$ was removed by rotoevaporation. The residue was boiled with hexane, and the insoluble solid was removed by hot filtration. White crystals formed in the hexane solution as it cooled; filtration and vacuum drying afforded 4.10 g (72%) of **8**; mp 61.5–62.8 °C, lit.[10a] mp 66 °C. ^1H NMR (400 MHz, acetone-d_6): δ 5.46 (s, 2H), 7.39 (t, J = 8 Hz, 1H), 7.50 (t, J = 8 Hz, 2H), 7.57 (d, J = 8 Hz, 2H), 8.07 (s, 2H), 8.41 ppm (s, 1H).

Diamine 10. To a vigorously stirred yellow solution of 1,1-bis(4′-amino-3′,5′-dimethylphenyl)cyclohexane (**9**, 45.32 g, 139.7 mmol) in 300 mL of CH_2Cl_2 and 9.8 mL (70 mmol) of anhydrous TEA was added isophthaloyl chloride (4.53 g, 22.3 mmol) in CH_2Cl_2 (500 mL) slowly under N_2 protection. After the addition, the solution was stirred 2 days at rt. It was filtered and concentrated by rotoevaporation. The off-white solid obtained was dissolved in 200 mL of CH_2Cl_2 and added dropwise to 1.8 L of hexane. The precipitate was collected by filtration. The hexane solution was concentrated to give 7.56 g of starting diamine. The crude solid product was subjected to flash column chromatography; the eluent was changed from 1/10 v/v EtOAc/

dx.doi.org/10.1021/ma202373x | *Macromolecules* 2012, 45, 1270–1280

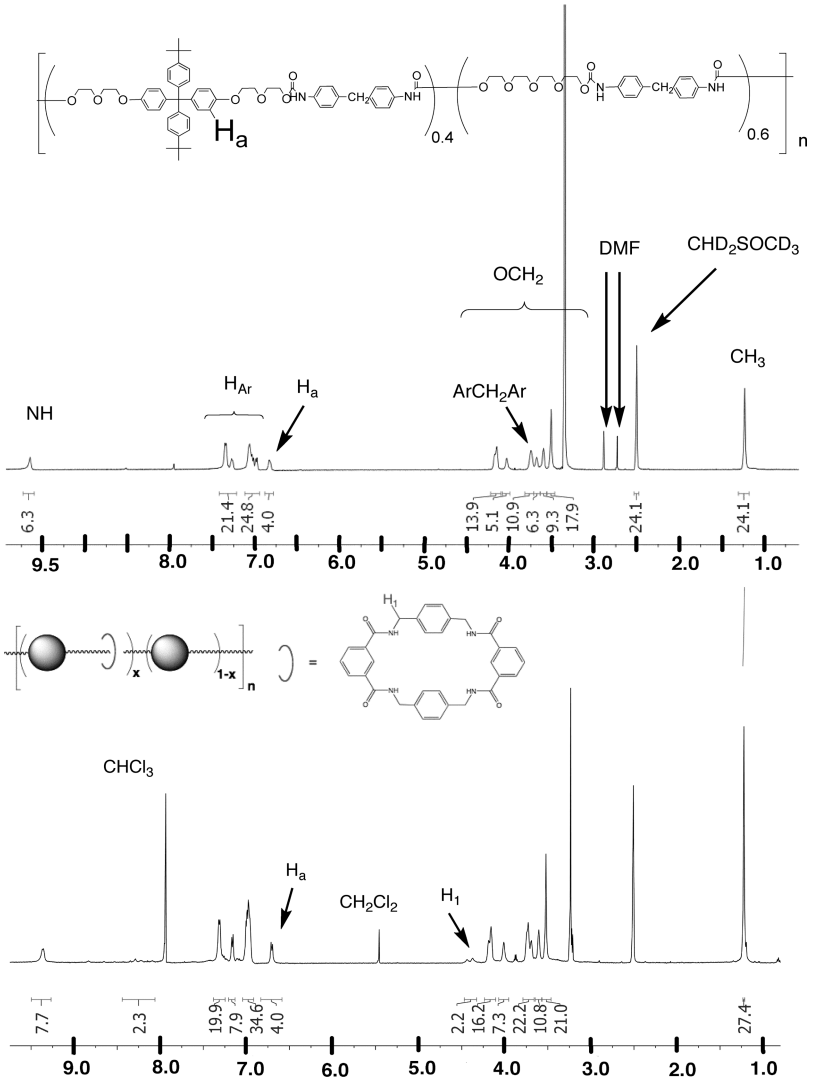


Figure 4. NMR spectra (500 MHz, 1:1 $CDCl_3$:DMSO-d_6) of polyurethane **27** (top) and polyrotaxane **28** (bottom).

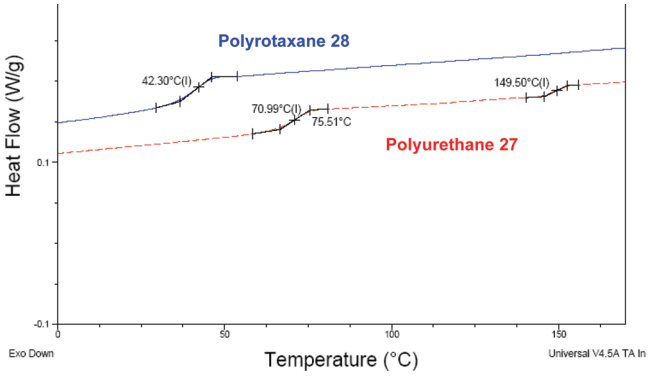


Figure 5. DSC traces of polyurethane **27** and polyrotaxane **28** (5 °C/min).

hexane to 1/3. Altogether 22.48 g of starting diamine was recovered, and 10.5 g (61%) of product **10** (mp 174–184 °C (lit.[9c] mp 179–180 °C)) was obtained. HR FAB MS (NBA PEG): m/z 775.4912 $(M + H)^+$; calcd for $C_{52}H_{63}N_4O_2$ m/z 775.4873 (error 5.0 ppm). ^{1}H NMR (400 MHz, $CDCl_3$): 1.4–1.6 (m, 12H), 2.1–2.22 (m, 8H), 2.15 (s, 12H), 2.21 (s, 12H), 3.44 (s, 4H), 6.58 (s, 4H), 7.01 (s, 4H), 7.45, (s, 2H), 7.52 (t, 1H, J = 8 Hz), 8.03 (d, 2H, J = 8 Hz), 8.44 ppm (s, 1H). ^{13}C NMR (100 MHz, $CDCl_3$): δ 165.12, 148.69, 140.03, 137.63, 134.82, 134.70, 130.65, 130.23, 129.11, 127.03, 126.91, 125.93, 121.49, 44.87, 37.14, 26.43, 22.95, 18.78, 18.04 ppm.

Tetralactam 3a. A solution of diamine **10** (1.0000 g, 1.2902 mmol) and anhydrous TEA (0.4 mL, 3 mmol) in 10 mL of CH_2Cl_2 was prepared. A separate solution of 5-benzyloxyisophthaloyl chloride (**8**, 0.3986 g, 1.289 mmol) in 10 mL of CH_2Cl_2 was prepared These two separate solutions were simultaneously added via a syringe pump over 4 h to a vigorously stirred flask containing 1.5 L of CH_2Cl_2. After the addition, the solution was stirred 2 days at rt under N_2 protection. The mixture was filtered and concentrated to give 1.6 g of off-white solid. It was combined with the crude product of two separate reactions (starting with 1.7 and 1.4 g of **10**) and subjected to flash chromatography (silica gel, v/v 99/1 $CHCl_3$/CH_3OH to 98/2). An off-white solid was obtained, 0.75 g (57%); mp 310 °C (dec), lit.[10a] mp 297 °C . LR FAB MS (NBA): m/z 1010 $(M)^+$. LR FAB MS (NBA-LiBr): m/z 1033.5 $(M + Na)^+$; 1017.9 $(M + Li)^+$; 781.7 $(M - C_{15}H_{19}NO)^+$. HR FAB MS (NBA-PEG): m/z 1011.5433 $(M + H)^+$; calcd for $C_{67}H_{71}N_4O_5$ 1011.5424 (error 0.8 ppm). ^{1}H NMR (400 MHz, $CDCl_3$): δ 1.56 (bs, 4H), 1.64 (bs + HOD, 8(?)H), 2.20 (bs, 24H), 2.33 (bs, 8H), 5.20 (s, 2H), 6.78 (s, 1H), 7.00 (s, 4H), 7.03 (s, 4H), 7.3–7.7 (m, 7H), 7.78 (bs, 1H), 7.81 (bs, 1H), 8.08 (d, J = 8, 2H), 8.14 (d, J = 8; 2H), 8.25 (s, 1H), 8.47 ppm (s, 1H).

Typical Attempted Synthesis of Polyrotaxane 4a, Producing Rotaxane 11a. A mixture of poly(vinylbenzyl chloride) (**1**, 8.23 mg, 0.064 mmol repeat units), *p*-tritylphenol (**2a**, 21.48 mg, 0.064 mmol), 18C6 (23.89 mg, 0.090 mmol), tetralactam **3a** (79.04 mg, 0.078

dx.doi.org/10.1021/ma202373x | *Macromolecules* 2012, 45, 1270–1280

mmol), and K_2CO_3 (19.68 mg, 0.142 mmol) in CH_2Cl_2 (20 mL) was stirred at rt under N_2 protection for 7 days. The solid was removed by filtration. The filtrate was evaporated, and the residue was treated with a small amount of $CHCl_3$. The insoluble solid (40.5 mg) was removed by filtration, and the filtrate was precipitated into a large amount of CH_3OH. The white precipitate was collected by filtration and dried in a vacuum: 8.28 mg, identified as unreacted **1**. The filtrate was concentrated to give a white solid, which was dissolved in $CHCl_3$ and precipitated into hexane, yielding 53.2 mg (98% based on limiting tritylphenol) of an off-white solid (crude **11a**). Flash column chromatography with $CHCl_3$ as eluent afforded 22.0 mg of purified rotaxane **11a**; mp 315 °C (color change to light brown at 245 °C, then to dark brown at 290 °C). HR FAB MS (NBA-PEGNa): *m/z* 1717.8342 $(M + Na)^+$; calcd for $C_{118}H_{110}N_4O_7Na$ 1717.8273 (error 4 ppm). ^1H NMR (400 MHz, $CDCl_3$, Figure 1): δ 1.54 (bs, 4H), 1.67 (bs, 8H), 1.79 (s, 12H), 1.83 (s, 12H), 2.26 (bs, 8H), 4.22 (s, 2H), 5.19 (s, 2H), 5.83 (d, J = 8, 4H), 6.77 (bs, 4H), 6.81 (d, J = 8, 4H), 6.82 (s, 8H), 7.05 (m, 12H), 7.16 (m, 18H), 7.24 (s, 1H), 7.36 (m, J = 8, 1H), 7.40 (t, J = 8, 2H), 7.46 (bd, J = 8, 2H), 7.65 (bs, 1H), 7.70 (t, J = 8, 1H), 7.81 (d, J = 2, 2H), 8.21 ppm (dd, J = 2, 8; 2H).

Reaction of Dichloromethane with *p*-Tritylphenol in the Presence of Tetralactam (11a). To a solution of tritylphenol (**2a**, 13.25 mg, 0.0394 mmol), tetralactam **3a** (19.54 mg, 0.0193 mmol), and 18C6 (5.21 mg, 0.0197 mmol) in CH_2Cl_2 (20 mL) was added K_2CO_3 (4.6 mg, 0.033 mmol). The mixture was stirred at rt under N_2 for 7 days. The precipitate was removed by filtration. The solution was treated as outlined above to yield a white solid identical in all respects to **11a** obtained earlier.

Formaldehyde *p*-Tritylphenyl Acetal, Dumbbell 12. To a solution of tritylphenol (**2a**, 26.68 mg, 0.0794 mmol) and 18C6 (9.64 mg, 0.0365 mmol) in CH_2Cl_2 (40 mL) was added K_2CO_3 (10.04 mg, 0.0726 mmol). It was stirred at rt under N_2 for 7 days. The solid was removed by filtration. The solution was concentrated to give a white solid (25 mg, 93%), which was subjected to column chromatography on silica, eluting with $CHCl_3$, yielding a colorless solid; mp 246.4–247.3 °C. HR ESI-MS: *m/z* 684.2991 $(M + H)^+$, 702.3318 $(M + NH_4)^+$; calcd for $C_{51}H_{40}O_2$ + H: 684.3028 (error −5.5 ppm), calcd for $C_{51}H_{40}O_2$ + NH_4: 702.3374 (error −7.9 ppm). ^1H NMR (400 MHz, $CDCl_3$): 5.69 (s, 2H), 6.97 (d, J = 8, 4H), 7.1–7.3 ppm (m, 34H).

Rotaxane 14a. To a solution of tritylphenol (**2a**, 6.62 mg, 0.0197 mmol), bromide **13** (13.65 mg, 0.0198 mmol), tetralactam **3a** (20.02 mg, 0.0198 mmol), and 18C6 (5.15 mg, 0.0195 mmol) in CH_2Cl_2 (20 mL) was added K_2CO_3 (5.02 mg, 0.0363 mmol). The suspension was stirred at rt for 7 days. Solid was removed by filtration. The filtrate was concentrated and subjected to column chromatography with $CHCl_3$ as eluent. The fractions collected from the column were: F1, 9.34 mg (bromide **13**); F2, 12.83 mg; F3, 7.20 mg; F5–F7, 7.59 mg (tetralactam **3a**); F8–F13, 8.10 mg (mainly 18C6). F2 + F3 = 20.03 mg (52%) of **14a**. Two more column chromatographic separations afforded pure **14a**; mp 291.0–292.0 °C. HR FAB MS (NBA/CsI): *m/z* 1953.20 $(M)^+$; calcd for $C_{137}H_{140}N_4O_7$ *m/z* 1953.07 (error +6.6 ppm). ^1H NMR (400 MHz, $CDCl_3$, Figure 2): δ 1.30 (s, 27H), 1.55 (bs + HOD, 4(?)H), 1.68 (bs, 8H), 1.87 (s, 24H), 2.32 (bs, 8H), 4.31 (s, 2H), 4.41 (s, 2H), 5.09 (s, 2H), 5.96 (AB q, J = 8, 4H), 6.35 (d, J = 8, 2H), 6.46 (d, J = 8, 2H), 6.90–7.30 (m, 44H), 7.30–7.35 (m, 5H), 7.58 (t, J = 8, 1H), 7.78 (m, 3H), 8.10 ppm (dd, J = 2, 8; 2H).

Rotaxane 14b. To a solution of tris(*p-tert*-butylphenyl)-4-hydroxyphenylmethane (**2b**, 10.05 mg, 0.0199 mmol), bromide **13** (13.62 mg, 0.0198 mmol), tetralactam **3a** (19.98 mg, 0.0197 mmol), and 18C6 (5.26 mg, 0.0199 mmol) in CH_2Cl_2 (20 mL) was added K_2CO_3 (5.58 mg, 0.0404 mmol). The suspension was stirred at rt for 7 days. Solid was removed by filtration. The filtrate was concentrated and subjected to column chromatography with $CHCl_3$ as eluent. The fractions collected from the column were: F1, 8.00 mg (bromide **13**); F2, 17.07 mg, F3, 7.47 mg, F5–F8, 6.68 mg (cyclic tetralactam **3a**); F8–F13, 8.03 mg (mainly 18C6). F2 + F3 = 24.54 mg (58%) of **14b**. Two more column chromatographic separations afforded pure **14b**; mp 309.5–310.6 °C. HR FAB MS (NBA): *m/z* 2122.25 $(M + H)^+$; calcd for $C_{149}H_{165}N_4O_7$ *m/z* 2122.26 (error −5 ppm). ^1H NMR (400 MHz, $CDCl_3$, Figure 2): δ 1.30 (s, 54H), 1.55 (bs + HOD, 4(?)H), 1.68 (bs, 8H), 1.86 (s, 24H), 2.32 (bs, 8H), 4.36 (s, 4H), 5.08 (s, 2H), 5.97 (s, 4H), 6.38 (d, J = 8, 4H), 6.9–7.4 (m, 47H), 7.58 (t, J = 8, 1H), 7.74 (s, 2H), 7.75 (s, 1H), 8.11 ppm (d, J = 8, 2H).

Unsymmetrical Dumbbell 15a. To a solution of *p*-tritylphenol (**2a**, 6.80 mg, 0.0202 mmol), bromide **13** (13.63 mg, 0.0198 mmol), and 18C6 (5.37 mg, 0.0230 mmol) in CH_2Cl_2 (20 mL) was added K_2CO_3 (5.05 mg, 0.0365 mmol). It was stirred at rt for 7 days. Solid in the reaction mixture was removed by filtration. The filtrate was concentrated and separated by column chromatography with a mixture of hexane and $CHCl_3$ (from 7/1 to 5/1 v/v ratio) as eluent. The expected product was a solid collected as the second fraction after the bromide starting material: 14.3 mg (76%); mp 218.6–219.3 °C. HR FAB MS (NBA-PEG): *m/z* 942.5392 $(M)^+$; calcd for $C_{70}H_{70}O_2$ *m/z* 942.5376 (error +1.6 ppm). ^1H NMR ($CDCl_3$): δ 1.30 (s, 27H), 4.55 (s, 2H), 4.96 (s, 2H), 6.76 (d, J = 8, 2H), 6.9–7.4 ppm (m, 37H).

Symmetrical Dumbbell 15b. To a solution of bromide **13** (27.84 mg, 0.0405 mmol), tris(*p-tert*-butylphenyl)-4-hydroxyphenylmethane (**2b**, 20.14, 0.0399 mmol), and 18C6 (8.33 mg, 0.032 mmol) in CH_3CN (20 mL) was added K_2CO_3 (11.2 mg, 0.0810 mmol). The suspension was stirred 7 days at rt under N_2. After reaction, the precipitate was removed by filtration. The filtrate was concentrated to give an off-white solid, which was subjected to column chromatography with a mixture of hexane and $CHCl_3$ (from 7/1 to 5/1 v/v ratio) as eluent. The expected product was a solid collected as the second fraction after the bromide starting material: 9.5 mg (40%), mp 270 °C (dec). When the reaction was carried out at 85 °C for 18 h, only 6.5% of the product was isolated. HR FAB MS (NBA-PEG): *m/z* 1110.7214 $(M)^+$; calcd for $C_{82}H_{94}O_2$ *m/z* 1110.7254 (error −3.6 ppm). ^1H NMR ($CDCl_3$): δ 1.30 (s, 54H), 5.04 (s, 4H), 6.82 (d, J = 8, 4H), 7.07–7.12 (m, 16H), 7.22 (d, J = 8, 12H), 7.45 ppm (s, 4H).

Bis(*p*-bromomethylphenyl) Ether (17). To a solution of 4.19 g (18.2 mmol) of bis(*p*-hydroxymethylphenyl) ether[16] in a mixture of THF and toluene (390 mL/775 mL) was added 6.40 mL (67.4 mmol) of PBr_3 dropwise. After the mixture had stirred overnight at rt, it was concentrated by rotoevaporation. $CHCl_3$ was added, and the resulting suspension was cooled in an ice–water bath and stirred vigorously. Water was added slowly to quench the excess PBr_3. After the organic layer was separated, the water layer was washed three times with $CHCl_3$. The combined organic layer was dried over anhydrous Na_2SO_4. After concentration, a yellow oil was obtained, which solidified upon standing. It was subjected to flash column chromatography (silica gel, 10/1 v/v hexane/ethyl acetate mixture). Three fractions were obtained. The first fraction, a white solid, 5.83 g (90%), was the expected product. It was recrystallized three times from hexanes and dried *in vacuo*; mp 84–85 °C (lit. mp 93–95,[22] 98 °C[23]). ^1H NMR ($CDCl_3$): δ 4.51 (s, 4H), 6.99 (d, J = 7, 4H), 7.38 ppm (d, J = 7, 4H).

Model Polyether 18a. To a solution of bisphenol-A (91.22 mg, 0.400 mmol), bromide **17** (142.28 mg, 0.400 mmol), and 18-crown-6 (203.30 mg, 0.769 mmol) in chloroform (10 mL) was added K_2CO_3 (106.20 mg, 0.768 mmol). The suspension was stirred at rt for 7 days. The solid was removed by filtration. The solution was precipitated into methanol to give 0.12 g (71%) of white solid. GPC (universal calibration): bimodal, M_n 610, PDI 1.3, average of three runs; see Supporting Information).

Attempted Synthesis of Polyether Pseudorotaxane 18b. To a solution of bisphenol-A (91.18 mg, 0.399 mmol), bromide **17** (142.28 mg, 0.400 mmol), tetralactam **3a** (50.85 mg, 0.05028 mmol), and 18-crown-6 (203.60 mg, 0.770 mmol) in chloroform (10 mL) was added K_2CO_3 (110.5 mg, 0.800 mmol). The suspension was stirred at rt for 7 days. After reaction, the solid was removed by filtration. The solution was precipitated into methanol to give 0.12 g of white solid. The ^1H NMR spectrum indicated that the sample was similar to model system **18a** and contained no tetralactam.

Polyether 20a. A mixture of 42.66 mg (0.0400 mmol) of diphenol **19**, 14.23 mg (0.0400 mmol) of dibromide **17**, 10.62 mg (0.077 mmol) of K_2CO_3, and 20.43 mg (0.077 mmol) of 18C6 in 10 mL of $CHCl_3$ was stirred 7 days at rt. The solid was removed by filtration. The filtrate was precipitated in CH_3OH. The off-white solid (57 mg,

~100%) was collected by filtration and reprecipitated in CH_3OH twice. A white solid was obtained, T_g 142 °C. GPC (polystyrene equivalents): M_n = 3.15 kDa, M_w = 6.54 kDa, PDI = 2.1. ^{1}H NMR (400 MHz, $CDCl_3$): δ 1.30 (s, 44H), 1.43 (bs, 4H), 1.75 (bs, 4H), 3.91 (t, J = 7, 4H), 4.96 (bs, 2.2H), 5.07 (bs, 1.2H), 6.75 (d, J = 8, 4H), 6.77−6.86 (m, 4H), 6.98−7.12 (m, 20H), 7.19−7.25 (m, 8H), 7.37 ppm (m, 4H).

Polyether Rotaxane 20b. The same procedure was applied using 40.62 mg (0.0402 mmol) of tetralactam **3a**. A white solid was obtained [70 mg (77% assuming m/n = 1, 100% for m/n = 0.49) initially and 11 mg after 3 precipitations from $CHCl_3$ into CH_3OH]. GPC (polystyrene equivalents): M_n = 4.9 kDa, M_w = 11 kDa, PDI = 2.1. ^{1}H NMR ($CDCl_3$): δ 1.30 (s), 1.35−2.00 (m), 2.30 (bs), 3.91 (bs), 4.64 (bs), 5.00 (bs), 5.07 (bs), 5.14 (bs), 6.10 (d, J = 8), 6.56 (bm); 6.6−6.8 (m), 6.9−8.25 ppm (m). See Supporting Information for further analysis.

Polyurethane 27. A solution of the bulky diol **24** (1.65 g, 2.57 mmol), 0.752 g (3.87 mmol) of tetra(ethylene glycol) (**25**), and 1.69 g (6.76 mmol) of MDI (**26**) and 2 drops of dibutyltin laurate in 20 mL of DMF was stirred at 90 °C for 24 h and precipitated into 300 mL of methanol. The pale yellow solid was filtered and dried in a vacuum oven: 4.04 g (98%). The polymer was reprecipitated twice more from the minimum amount of DMF into >10-fold excess methanol and dried in a vacuum oven: M_n 18.5 kDa (universal calibration, $CHCl_3$), PDI 8.1 (presumed to be due to aggregation). DSC: T_gs at 71 and 150 °C (Figure 5). ^{1}H NMR (400 MHz, DMSO-d_6/$CDCl_3$ = 1/1 v/v, Figure 4): δ 1.23 (s, 24 H), 3.51 (s, 18 H), 3.60 (s, 9 H), 3.68 (s, 6 H), 3.75 (s, 11 H), 4.03 (s, 5 H), 4.15 (s, 14 H), 6.83 (bs, 4 H), 6.97−7.06 (m, 25 H), 7.27−7.35 (m, 21 H), 9.25 (s, 6 H) [7.95, 2.89, 2.73 ppm (DMF)].

Polyrotaxane 28. To a solution of 1.09 g (1.76 mol of urethane moieties) of polymer **27** and 0.486 mL (3.5 mmol) of anhydrous triethylamine in 1500 mL of dichloromethane were added separately 0.190 g (1.4 mmol) of *p*-xylylenediamine (**21**) in 25 mL of dichloromethane and 0.284 g (1.4 mmol) of isophthaloyl chloride (**22**) in 25 mL of dichloromethane via two syringes at 1 mL/h. The solution was stirred for 96 h after addition, filtered, and reduced in volume to 50 mL and precipitated into 500 mL of methanol. The polymer was filtered and dried *in vacuo* (1.58 g, 78% assuming one ring per repeat unit, x/n = 1.0; theoretical yield 2.03 g) before analysis by ^{1}H NMR to determine the ratio of macrocycle (via the signal for proton H_1) to polymer repeat unit (via the signal for proton H_b). The polymer was then dissolved in the minimum amount of DMF and reprecipitated into >10-fold volume of methanol, and the filtration, drying, and analysis were repeated. The result for the third precipitation was the same as that for the second precipitation, indicating x/n = 0.11. GPC (universal calibration, $CHCl_3$): M_n 19.7 kDa, PDI 8.0 (again presumed to be due to aggregation). DSC: T_g at 42 °C (Figure 5). ^{1}H NMR (400 MHz, DMSO-d_6/$CDCl_3$ = 1/1 v/v, Figure 4): δ 1.22 (s, 27 H), 3.52 (s, 21H), 3.61 (s, 11 H), 3.73 (m, 22 H), 3.75 (s, 11.0H), 4.01 (s, 7 H), 4.15 (m, 16 H), 4.44 (m, 2.2 H), 6.71 (m, 4 H), 6.97−7.06 (m, 34 H), 7.17 (m, 8 H), 7.32 (m, 20 H), 8.09−8.35 (m, 2 H), 9.25 (s, 7 H) [plus 5.46 ppm (CH_2Cl_2)].

■ ASSOCIATED CONTENT

Supporting Information

NMR spectra and mass spectrometric traces for various intermediates and products; disordered X-ray structure of tetralactam **3a**; GPC traces for polyurethane **27** and polyrotaxane **28**. This material is available free of charge via the Internet at http://pubs.acs.org.

■ AUTHOR INFORMATION

Corresponding Author

*E-mail: hwgibson@vt.edu.

Present Addresses

[§]BIND Biosciences, Inc., 64 Sidney Street, Cambridge, MA [‖]02139.

[‖]X-ray Crystallography Facility, University of Oregon, Eugene, OR 97403.

[⊥]Department of Chemistry, University of California, San Diego, La Jolla, CA 92093.

■ ACKNOWLEDGMENTS

This work was supported by the National Science Foundation [DMR-0097126 and DMR-0704076 (H.W.G.)], to whom we are very grateful. We also acknowledge the National Science Foundation for funds to purchase the Varian Unity and Inova NMR spectrometers (DMR-8809714 and CHE-0131124) and the Oxford Diffraction SuperNova X-ray diffractometer (CHE-0131128). The authors are also grateful to Mr. Daniel Schoonover and Mr. Terry L. Price, Jr., for the chromatographic separations and related NMR spectroscopic studies of oligo(ether rotaxane) **20b**.

■ REFERENCES

(1) For reviews see: (a) Schill, G.; Zürcher, C. *Naturwissenschaften* **1971**, *58*, 40−45. (b) *Molecular Catenanes, Rotaxanes and Knots*; Sauvage, J.-P., Dietrich-Buchecker, C. O., Eds.; Wiley-VCH: Weinheim, 1999. (c) Mahan, E.; Gibson, H. W. In *Cyclic Polymers*, 2nd ed.; Semlyen, J. A., Ed.; Kluwer Publishers: Dordrecht, 2000; pp 415−560. (d) Hubin, T. J.; Busch, D. H. *Coord. Chem. Rev.* **2000**, *200−202*, 5−52. (e) Lankshear, M. D.; Beer, P. D. *Acc. Chem. Res.* **2007**, *40*, 657−668. (f) Gassensmith, J. J.; Baumes, J. M.; Smith, B. D. *Chem. Commun.* **2009**, 6329−6338. (g) Stoddart, J. F. *Chem. Soc. Rev.* **2009**, *38*, 1802−1820. (h) Thibeault, D.; Morin, J.-F. *Molecules* **2010**, *15*, 3709−3730. (i) Terao, J. *Chem. Rec.* **2011**, *11*, 269−283. (j) Beves, J. E.; Blight, B. A.; Campbell, C. J.; Leigh, D. A.; McBurney, R. T. *Angew. Chem., Int. Ed.* **2011**, *50*, 9260−9327.

(2) For recent papers *inter alia*, see: (a) Miljanic, O. S.; Stoddart, J. F. *Proc. Natl. Acad. Sci. U. S. A.* **2007**, *104*, 12966−12970. (b) Li, S.; Zhu, K.; Zheng, B.; Wen, X.; Li, N.; Huang, F. *Eur. J. Org. Chem.* **2009**, 1053−1057. (c) Li, S.; Liu, M.; Zheng, B.; Zhu, K.; Wang, F.; Li, N.; Zhao, X.; Huang, F. *Org. Lett.* **2009**, *11*, 3350−3353. (d) Ballesteros, B.; Faust, T. B.; Lee, C.-F.; Leigh, D. A.; Muryn, C. A.; Pritchard, R. G.; Schultz, D.; Teat, S. J.; Timco, G. A.; Winpenny, R. E. P. *J. Am. Chem. Soc.* **2010**, *132*, 15435−15444. (e) Roche, C.; Sauvage, J.-P.; Sour, A.; Strutt, N. L. *New J. Chem.* **2011**, *35*, 2820−2825. (f) Fang, L.; Basu, S.; Sue, C.-H.; Fahrenbach, A. C.; Stoddart, J. F. *J. Am. Chem. Soc.* **2011**, *133*, 396−399. (g) Coskun, A.; Spruell, J. M.; Barin, G.; Fahrenbach, A. C.; Forgan, R. S.; Colvin, M. T.; Carmieli, R.; Benitez, D.; Tkatchouk, E.; Friedman, D. C.; Sarjeant, A. A.; Wasielewski, M. R.; Goddard, W. A. III; Stoddart, J. F. *J. Am. Chem. Soc.* **2011**, *133*, 4538−4547. (h) Slater, B. J.; Davies, E. S.; Argent, S. P.; Nowell, H.; Lewis, W.; Blake, A. J.; Champness, N. R. *Chem.—Eur. J.* **2011**, *17*, 14746−14751.

(3) For reviews see: (a) Lipatov, Yu. S.; Lipatova, T. E.; Kosyanchuk, L. F. *Adv. Polym. Sci.* **1989**, *88*, 49−76. (b) Gibson, H. W.; Marand, H. *Adv. Mater.* **1993**, *5*, 11−21. (c) Gibson, H. W.; Bheda, M. C.; Engen, P. T. *Prog. Polym. Sci.* **1994**, 843−945. (d) Gibson, H. W. in *Large Ring Molecules*; Semlyen, J. A., Ed.; John Wiley & Sons: New York, 1996; Chapter 6, pp 191−262. (e) Raymo, F. M.; Stoddart, J. F. *Chem. Rev.* **1999**, *99*, 1643−1664. (f) Panova, I. G.; Topchieva, I. N. *Russ. Chem. Rev.* **2001**, *70*, 23−44. (g) Takata, T.; Kihara, N.; Furusho, Y. *Adv. Polym. Sci.* **2004**, *171*, 1−75. (h) Huang, F.; Gibson, H. W. *Prog. Polym. Sci.* **2005**, *30*, 982−1018. (i) Wenz, G.; Han, B.-H.; Mueller, A. *Chem. Rev.* **2006**, *106*, 782−817. (j) Loethen, S.; Kim, J.-M.; Thompson, D. H. *Polym. Rev.* **2007**, *47*, 383−418. (k) Harada, A.; Hashidzume, A.; Yamaguchi, H.; Takashima, Y. *Chem. Rev.* **2009**, *109*, 5974−6023. (l) Yui, N.; Katoono, R.; Yamashita, A. *Adv. Polym. Sci.* **2009**, *222*, 55−77. (m) Fang, L.; Olson, M. A.; Benitez, D.; Tkatchouk, E.; Goddard, W. A. III; Stoddart, J. F. *Chem. Soc. Rev.*

2010, *39*, 17−29. (n) Mayumi, K.; Ito, K. *Polymer* **2010**, *51*, 959−967. (o) Yuen, F.; Tam, K. C. *Soft Matter* **2010**, *6*, 4613−4630. (p) Li, J. J.; Zhao, F.; Li, J. *Appl. Microbiol. Biotechnol.* **2011**, *90*, 427−443.

(4) Selected recent publications from >100 per year: (a) Murayama, H.; Bin Imran, A.; Nagano, S.; Seki, T.; Kidowaki, M.; Ito, K.; Takeoka, Y. *Macromolecules* **2008**, *41*, 1808−1814. (b) Sato, T.; Takata, T. *Macromolecules* **2008**, *41*, 2739−2742. (c) Zhang, W.; Dichtel, W. R.; Stieg, A. Z.; Benitez, D.; Gimzewski, J. K.; Heath, J. R.; Stoddart, J. F. *Proc. Natl. Acad. Sci. U. S. A.* **2008**, *105*, 6514−6519. (d) Travelet, C.; Schlatter, G.; Hebraud, P.; Brochon, C.; Lapp, A.; Anokhin, D. V.; Ivanov, D. A.; Gaillard, C.; Hadziioannou, G. *Soft Matter* **2008**, *4*, 1855−1860. (e) Yamashita, A.; Kanda, D.; Katoono, R.; Yui, N.; Ooya, T.; Maruyama, A.; Akita, H.; Kogure, K.; Harashima, H. *J. Controlled Release* **2008**, *131*, 137−144. (f) Farcas, A.; Jarroux, N.; Guegan, P.; Fifere, A.; Pinteala, M.; Harabagiu, V. *J. Appl. Polym. Sci.* **2008**, *110*, 2384−2392. (g) Koopmans, C.; Ritter, H. *Macromolecules* **2008**, *41*, 7418−7422. (h) Terao, J.; Tanaka, Y.; Tsuda, S.; Kambe, N.; Taniguchi, M.; Kawai, T.; Saeki, A.; Seki, S. *J. Am. Chem. Soc.* **2009**, *131*, 18046−18047. (i) Ikeda, T.; Higuchi, M.; Kurth, D. G. *J. Am. Chem. Soc.* **2009**, *131*, 9158−9159. (j) Wang, F.; Zheng, B.; Zhu, K.; Zhou, Q.; Zhai, C.; Li, S.; Li, N.; Huang, F. *Chem. Commun.* **2009**, 4375−4377. (k) Latini, G.; Winroth, G.; Brovelli, S.; McDonnell, S. O.; Anderson, H. L.; Mativetsky, J. M.; Samori, P.; Cacialli, F. *J. Appl. Phys.* **2010**, *107*, 124509/1−124509/9. (l) Lee, Y.-G.; Koyama, Y.; Yonekawa, M.; Takata, T. *Macromolecules* **2010**, *43*, 4070−4080. (m) Isono, T.; Satoh, T.; Kakuchi, T. *J. Polym. Sci., Part A: Polym. Chem.* **2011**, *49*, 3184−3192. (n) Ishiwari, F.; Nakazono, K.; Koyama, Y.; Takata, T. *Chem. Commun.* **2011**, *47*, 11739−11741. (o) Kohsaka, Y.; Nakazono, K.; Koyama, Y.; Asai, S.; Takata, T. *Angew. Chem., Int. Ed.* **2011**, *50*, 4872−4875.

(5) (a) Wu, C.; Bheda, M. C.; Lim, C.; Shen, Y. X.; Sze, J.; Gibson, H. W. *Polym. Commun.* **1991**, *32*, 204−207. (b) Shen, Y. X.; Gibson, H. W. *Macromolecules* **1992**, *25*, 2058−2059. (c) Shen, Y. X.; Xie, D.; Gibson, H. W. *J. Am. Chem. Soc.* **1994**, *116*, 537−548. (d) Gibson, H. W.; Liu, S.; Lecavalier, P.; Wu, C.; Shen, Y. X. *J. Am. Chem. Soc.* **1995**, *117*, 852−874. (e) Loveday, D.; Wilkes, G. L.; Bheda, M. C.; Shen, Y. X.; Gibson, H. W. *J. Macromol. Sci., Chem.* **1995**, *A32*, 1−27. (f) Marand, E.; Hu, Q.; Gibson, H. W.; Veytsman, B. *Macromolecules* **1996**, *29*, 2555−2562. (g) Gong, C.; Gibson, H. W. *Macromolecules* **1996**, *29*, 7029−7033. (h) Gibson, H. W.; Liu, S.; Gong, C.; Joseph, E. *Macromolecules* **1997**, *30*, 3711−3727. (i) Gong, C.; Gibson, H. W. *Angew. Chem., Int. Ed. Engl.* **1997**, *36*, 2331−2333. (j) Gong, C.; Ji, Q.; Glass, T. E.; Gibson, H. W. *Macromolecules* **1997**, *30*, 4807−4813. (k) Gong, C.; Gibson, H. W. *Macromolecules* **1997**, *30*, 8524−8525. (l) Gong, C.; Gibson, H. W. *Macromolecules* **1998**, *31*, 308−313. (m) Mason, P. E.; Bryant, W. S.; Gibson, H. W. *Macromolecules* **1998**, *32*, 1559−1569. (n) Gong, C.; Ji, Q.; Subramaniam, C.; Gibson, H. W. *Macromolecules* **1998**, 1814−1818.

(6) (a) Gibson, H. W.; Engen, P. *New J. Chem.* **1993**, *17*, 723−727. (b) Nagapudi, K.; Leisen, J.; Beckham, H. W.; Gibson, H. W. *Macromolecules* **1999**, *32*, 3025−3033. (c) Gibson, H. W.; Engen, P. T.; Lee, S.-H. *Polymer* **1999**, *40*, 1823−1832. (d) Gibson, H. W.; Bryant, W. S.; Lee, S.-H. *J. Polym. Sci., Polym. Chem. Ed.* **2001**, *39*, 1978−1993. (e) Zhao, T.; Beckham, H. W.; Gibson, H. W. *Macromolecules* **2003**, *36*, 4833−4837. (f) Lee, M.; Moore, R. B.; Gibson, H. W. *Macromolecules* **2011**, *44*, 5987−5993.

(7) Gibson, H. W.; Bheda, M. C.; Engen, P.; Shen, Y. X.; Sze, J.; Zhang, H.; Gibson, M. D.; Delaviz, Y.; Lee, S. H.; Wang, L.; Rancourt, J.; Taylor, L. T. *J. Org. Chem.* **1994**, *59*, 2186−2196.

(8) (a) Delaviz, Y.; Gibson, H. W. *Macromolecules* **1992**, *25*, 4859−4862. (b) Gong, C.; Gibson, H. W. *J. Am. Chem. Soc.* **1997**, *119*, 5862−5866. (c) Gibson, H. W.; Nagvekar, D.; Powell, J.; Gong, C.; Bryant, W. *Tetrahedron* **1997**, *53*, 15197−15207. (d) Gong, C.; Gibson, H. W. *J. Am. Chem. Soc.* **1997**, *119*, 5862−5866. (e) Gong, C.; Gibson, H. W. *J. Am. Chem. Soc.* **1997**, *119*, 8585−8591. (f) Gibson, H. W.; Nagvekar, D. S.; Yamaguchi, N.; Wang, F.; Bryant, W. S. *J. Org. Chem.* **1997**, *62*, 4798−4803. (g) Gibson, H. W.; Nagvekar, D. S. *Can. J. Chem.* **1997**, *75*, 1375−1384. (h) Gong, C.; Gibson, H. W. *Angew. Chem., Int. Ed.* **1998**, *37*, 310−314. (i) Gong, C.; Balanda, P. B.; Gibson, H. W. *Macromolecules* **1998**, *31*, 5278−5289. (j) Yamaguchi, N.; Gibson, H. W. *Macromol. Chem. Phys.* **2000**, *201*, 815−824. (k) Gibson, H. W.; Nagvekar, D. S.; Yamaguchi, N.; Bhattacharjee, S.; Wang, H.; Vergne, M. J.; Hercules, D. M. *Macromolecules* **2004**, *37*, 7514−7529.

(9) (a) Vögtle, F.; Händel, M.; Meier, S.; Ottens-Hildebrandt, S.; Ott, F.; Schmidt, T. *Leibigs Ann.* **1995**, 739−743. (b) Hübner, G. M.; Gläser, J.; Seel, C.; Vögtle, F. *Angew. Chem., Int. Ed.* **1999**, *38*, 383−386. (c) Seel, C.; Parham, A. H.; Safarowsky, O.; Hübner, G. M.; Vögtle, F. *J. Org. Chem.* **1999**, *64*, 7236−7242. (d) Reuter, C.; Wienand, W.; Hübner, G. M.; Seel, C.; Vögtle, F. *Chem.—Eur. J.* **1999**, *5*, 2692−2697. (e) Reuter, C.; Vögtle, F. *Org. Lett.* **2000**, *2*, 593−595.

(10) (a) Hunter, C. A. *J. Chem. Soc., Chem. Commun.* **1991**, 749−751. (b) Hunter, C. A. *J. Am. Chem. Soc.* **1992**, *114*, 5303−5311. (c) Bisson, A. P.; Carver, F. J.; Eggleston, D. S.; Haltiwanger, R. C.; Hunter, C. A.; Livingstone, D. L.; McCabe, J. F.; Rotger, C.; Rowan, A. E. *J. Am. Chem. Soc.* **2000**, *122*, 8856−8868.

(11) (a) Muscat, D.; Witte, A.; Köhler, W.; Müllen, K.; Geerts, Y. *Macromol. Rapid Commun.* **1997**, *18*, 233−241. (b) Muscat, D.; Köhler, W.; Räder, H. J.; Martin, K.; Mullins, S.; Müller, B.; Müllen, K.; Geerts, Y. *Macromolecules* **1999**, *32*, 1737−1745.

(12) For a reviewof polycatenanes,see: Niu, Z.; Gibson, H. W. *Chem. Rev.* **2009**, *109*, 6024−6046.

(13) Mahoney, J. M.; Shukla, R.; Marshall, R. A.; Beatty, A. M.; Zajicek, J.; Smith, B. D. *J. Org. Chem.* **2002**, *67*, 1436−1440.

(14) (a) Gibson, H. W.; Lee, S. H.; Engen, P. T.; Lecavalier, P.; Sze, J.; Shen, Y. X.; Bheda, M. *J. Org. Chem.* **1993**, *58*, 3748−3756. (b) Liu, S.; Gibson, H. W. *Tetrahedron Lett.* **1994**, *35*, 8533−8536. (c) Liu, S.; Lee, S.-H.; Shen, Y. X.; Gibson, H. W. *J. Org. Chem.* **1995**, *60*, 3155−3162.

(15) Crystals were grown from acetone/pentane. A colorless prism (0.08 × 0.09 × 0.11 mm^3) was centered on the goniometer of an Oxford Diffraction SuperNova diffractometer operating with Cu Kα radiation. The data collection routine, unit cell refinement, and data processing were carried out with the program CrysAlisPro (CrysAlisPro v171.33.31, Oxford Diffraction: Wroclaw, Poland, 2009). The Laue symmetry was consistent with the triclinic space groups *P*1 and *P*-1. The structure was solved in both *P*-1 and *P*1 using SIR92 (Altomare, A.; Cascarano, G.; Giacovazzo, C.; Guagliardi, A. *J. Appl. Crystallogr.* **1993**, *26*, 343−350) (via WinGX: Farrugia, L. J. *J. Appl. Crystallogr.* **1999**, *32*, 837838) and the unit cell contents identified as one rotaxane complex, two acetone molecules, and additional unidentifiable and disordered solvent. The *P*-1 solution, with $Z' = 0.5$, forces apparent 50% disorder of the benzyloxy functional group. The *P*1 solution showed no disorder in the benzyloxy group, indicating the true space group is *P*1 with pseudo-*P*-1 symmetry. The structure was refined in *P*1 using SHELXL-NT (Sheldrick, G. M. *Acta Crystallogr.* **2008**, *A64*, 112−122). Because of poor data quality (e.g., mean $I/\sigma(I) = 0.93$ for 0.98−0.94 Å; $I > 2\sigma(I)$ for 34% reflections to 0.84 Å) and the absence of any heavy atoms, the absolute configuration could not be determined from the Friedel pairs; the Friedel opposites were therefore merged. All atoms were refined isotropically, and a riding model was used for all hydrogen atoms. Atoms related by pseudoinversion were restrained to have similar 1,2 and 1,3 distances (SAME) and constrained to have identical U_{iso} values (EADP) to reduce correlation instability during refinement. The residual electron density from the unidentifiable disordered solvent was subtracted out using the SQUEEZE program in PLATON (Spek, A. L. *J. Appl. Crystallogr.* **2003**, *36*, 7−13). A total of 109e^- was subtracted from a total void volume of 540 $Å^3$

(16) Yang, J.; Tyberg, C. S.; Gibson, H. W. *Macromolecules* **1999**, *32*, 8259−8268.

(17) (a) Liu, S.; Gibson, H. W. *Tetrahedron Lett.* **1994**, *35*, 8533−8536. (b) Liu, S.; Lee, S.-H.; Shen, Y. X.; Gibson, H. W. *J. Org. Chem.* **1995**, *60*, 3155−3162.

(18) Anelli, P. L.; Ashton, P. R.; Ballardini, R.; Balzani, V.; Delgado, M.; Gandolfi, M. T.; Goodnow, T. T.; Kaifer, A. E.; Philp, D. *J. Am. Chem. Soc.* **1992**, *114*, 193−218.

(19) (a) Johnston, A. J.; Leigh, D. A.; Murphy, A.; Smart, J. P.; Deegan, M. D. *J. Am. Chem. Soc.* **1996**, *118*, 10662−10663. (b) Lane, A. S.; Leigh, D. A.; Murphy, A. *J. Am. Chem. Soc.* **1997**, *119*, 11092−11093. (c) Gatti, F. G.; Leigh, D. A.; Nepogodiev, S. A.; Slawin, A. M. Z.; Teat, S. J.; Wong, J. K. Y. *J. Am. Chem. Soc.* **2001**, *123*, 5983−5989.
(20) Schwender, C. F.; Sunday, B. R.; Shavel, J. Jr.; Giles, R. E. *J. Med. Chem.* **1974**, *17*, 1112−1115.
(21) Diederich, F.; Schurmann, G.; Chao, I. *J. Org. Chem.* **1988**, *53*, 2744−2757.
(22) Beever, W. H.; Stille, J. K. *Macromolecules* **1979**, *12*, 1033−8.
(23) Golden, J. H. *J. Chem. Soc.* **1961**, 1604−1610.

Macromolecules

Article

pubs.acs.org/Macromolecules

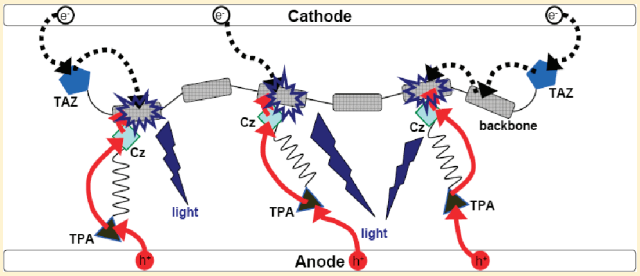
Design of Deep Blue Electroluminescent Spiro-Polyfluorenes with High Efficiency by Facilitating the Injection of Charge Carriers through Incorporation of Multiple Charge Transport Moieties

Chih-Wei Huang, Chia-Lin Tsai, Ching-Yang Liu, Tzu-Hao Jen, Neng-Jye Yang, and Show-An Chen*

Chemical Engineering Department and Frontier Research Center on Fundamental and Applied Sciences of Matters, National Tsing-Hua University, No. 101, Section 2, Kuang-Fu Road, Hsinchu, Taiwan 30013, Republic of China

Supporting Information

ABSTRACT: For polymer light-emitting diodes, developing highly efficient, stable, and saturated blue emitting polymer is essential in display and lighting applications and has long been a challenge. Here we report a concept for designing highly efficient electroluminescent polymers by introducing multiple charge transport moieties for efficient injection of charge carriers into spiro-polyfluorene (sPF). We integrate the triphenylamine (TPA) and carbazole (Cz) in the same side chain of sPF with logical spatial and energetic sequence of these moieties to establish graded route for more efficient hole injection and incorporate the electron transport moiety with strong electron-withdrawing capability, triazole (TAZ), on both chain ends to give favorable arrangement in space and energy for electron injection. These two factors allow the corresponding single layer device to exhibit deep blue (db) emission with external quantum efficiency (η_{ext}) of 7.28%, which is the highest value among the db polymer fluorescent diodes ever documented.



INTRODUCTION

For promoting the performance of polymer light-emitting diode (PLED), the key factor is to design structure of the emitting layer, which can be made by the physical method[1,2] and chemical structure tuning.[3−7] The emitting color "deep blue (db)" of interest here is defined as the summation of the x and y values in the Commission Internationale d'Enclairage (CIE_{xy}) coordinates smaller than 0.3. For the former by physical method, creating β phase (chain with extended conjugation length) via the dipping method[1] and inserting a hole blocking/electron transport layer[2] have been proposed for the poly(9,9-di-*n*-octylfluorene) (PFO)-based device, leading to the maximum luminous efficiencies (LE_{max}) 3.85 cd A^{-1} (external quantum efficiency (η_{ext}) 3.33%) and 3.5 cd A^{-1}, respectively. For the latter by chemical structure tuning, incorporating electron-deficient moieties as the end-cappers[4] and integrating bipolar transporting moieties on the structures (oxadiazole (OXD) as side chain along with triphenylamine (TPA) in main chain)[5] have been proposed on polyfluorenes (PFs), exhibiting the LE_{max} 1.67 and 2.07 cd A^{-1} (η_{ext} 1.59%), respectively. Furthermore, db PFs can also be achieved by utilizing donor−acceptor structure[6] or introducing silafluorene derivatives,[7] showing the LE_{max} 2.5 cd A^{-1} (η_{ext} 2.83%) and 2.02 cd A^{-1} (η_{ext} 3.34%), respectively. In spite of the above dbPLEDs achieving good blue color purity that is sufficient for full color displays, their device efficiencies remain ample room to be promoted. The reported η_{ext} above are still low (3.34% being the highest), mainly due to their ineffective utilization of charge carriers. To overcome such deficiency, in addition to promotion of charge balance and injection, suppressing of bypassed charge carriers through the emitting layers becomes a critical issue.

Recently, via bringing in a concept of creating a molecular-scale graded electronic profile in a single polymer, we have synthesized the sky blue and db emitting spiro-polyfluorene (sPF), TPA-carbazole (Cz)-sPF, and Cz-TPA-sPF,[8] in which TPA moieties are located away from the main chain in TPA-Cz-sPF and those in Cz-TPA-sPF are close to the main chain (in both cases, TPA and Cz moieties are on different side chains). The TPA and Cz moieties in sPFs along with main chain segments and anode notably form a downward grading sequence of HOMO levels (from anode to TPA, Cz, and finally to the main chain), leading to the promoted hole injection by factors of 1.2×10^4 (TPA-Cz-sPF) and 8.6×10^3 (Cz-TPA-sPF) relative to that of the unmodified sPF at electric field of 5×10^5 V/cm. As such, the single layer PLED fabricated with TPA-Cz-sPF gives CIE_{xy} coordinates and η_{ext} of (0.19, 0.20) and 7.53%, respectively, and those for Cz-TPA-sPF give (0.16, 0.10) and 4.54%, respectively, in which both PLEDs yield better performances over that of unmodified sPF (η_{ext} 1%). Besides, the η_{ext} of dbPLED based on Cz-TPA-sPF is superior to the best dbPLED stated above by a factor of 1.36.

For further improving the device efficiency, here we report a remarkable improvement on designing db light-emitting polymers (dbLEPs) via further manipulating the spatial and

Received: October 31, 2011
Revised: December 29, 2011
Published: January 23, 2012

ACS Publications © 2012 American Chemical Society

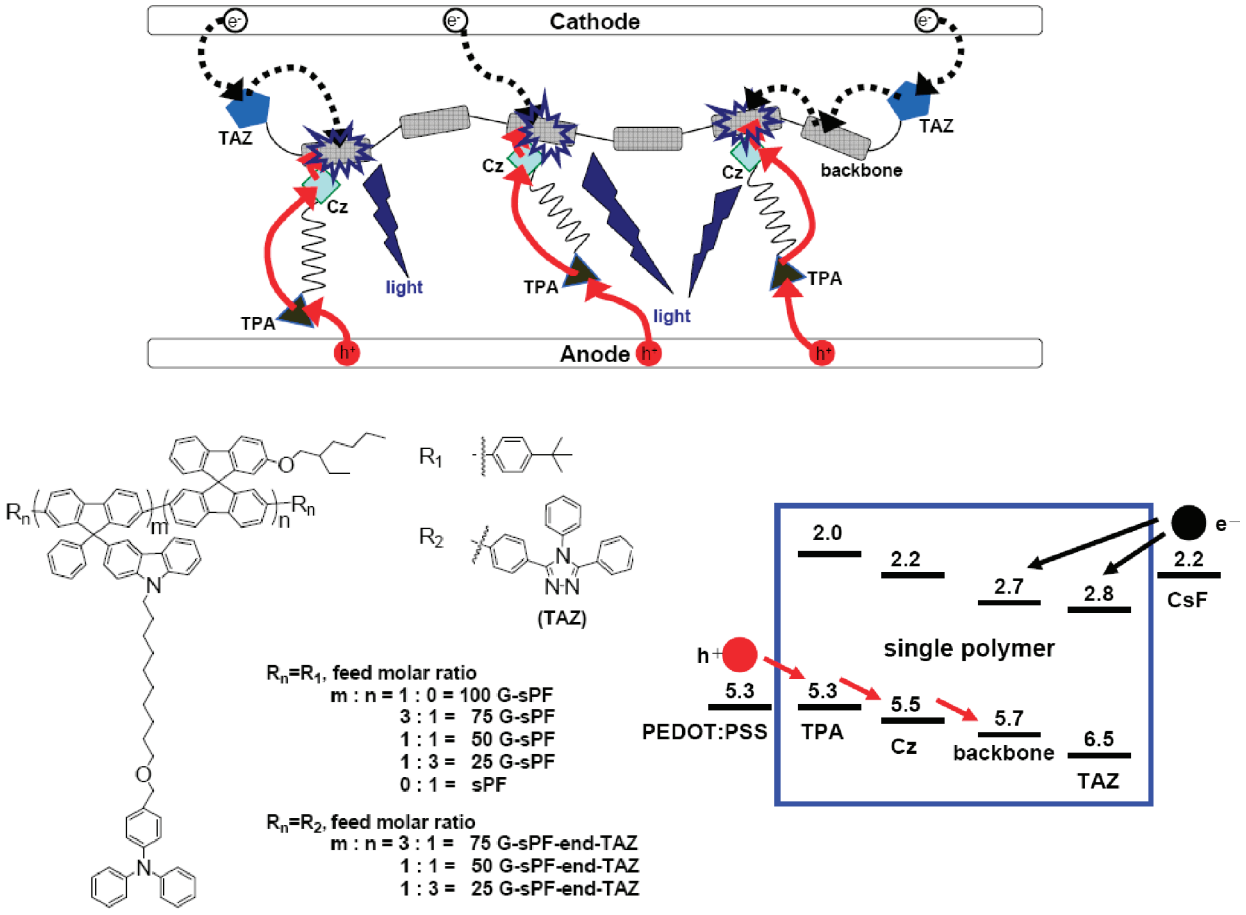


Figure 1. Schematic illustration of molecular design concept and chemical structures as well as the energy levels diagram of the materials used in this study. The polymer end-capper for G-sPFs is R_1 (*tert*-butylphenylene (TBP)), and that for G-sPFs-end-TAZ is R_2.

energetic sequence of hole transporting moieties along a side chain (i.e., integrating TPA and Cz in same side chain of sPF as TPA-flexible spacer-Cz-sPF, termed as G-sPF, as compared to the more randomly distributed arrangement in Cz-TPA-sPF or TPA-Cz-sPF[8]), giving downward grading HOMO levels along the side chain and additionally introducing the electron transport moiety (ETM) triazole (TAZ) on both chain ends to give G-sPF-end-TAZ for more effective electron injection, allowing the corresponding single layer PLED to exhibit db emission with CIE_{xy} coordinates of (0.16, 0.07) and η_{ext} of 7.28%, which is the highest value among the db fluorescent PLEDs ever documented (see the Supporting Information).

EXPERIMENTAL SECTION

Materials. The reaction routes for monomers and polymers as well as their detailed synthetic procedures and characterizations are depicted in the Supporting Information. The polymers (poly-spiros) were prepared by Yamamoto polymerization, and the energy levels are determined according to previous reports.[2,9] The actual contents of monomers are denoted in the Supporting Information.

Device Fabrication and General Instrumentation. An indium–tin oxide (ITO) glass plate was exposed on oxygen plasma at a power of 45 W for 5 min. A thin hole injection layer (25 nm) of poly(styrenesulfonic acid)-doped poly(ethylenedioxythiophene) (PEDOT:PSS, Baytron PVP. AI 4083 from Bayer, with a conductivity of 2 × 10^{-4}–2 × 10^{-3} S cm^{-1}) was spin-coated on the treated ITO as hole injection layer. On top of it, a thin layer (ca. 100 nm) of polymer was spin-cast from its solution (8 mg mL^{-1}) in the mixed solvent, tetrahydrofuran (THF):chlorobenzene (3:1 in volume). Finally, a thin layer of CsF (about 1.5 nm) and a layer of aluminum (ca. 70 nm) for bipolar device were deposited sequentially in a vacuum thermal evaporator through a shadow mask at a pressure of less than 10^{-6} Torr. The active area of the device is about 15 mm^2. Current–voltage–luminance characteristics of the devices were measured using a Keithley power supply (model 238) and luminance meter (BM8 from TOPCON), respectively; both are computer-controlled with a Labview program. The external quantum efficiencies of the devices were calculated from their corresponding current efficiencies (cd A^{-1}) using the equations described in the literature.[10] The HOMO level of PEDOT:PSS was determined by UV photoelectron spectroscopy from Thermo Electron Corp. The thickness of polymer film was measured by a Tencor P-10 surface profiler. Ultraviolet–visible (UV–vis) spectra and photoluminescent (PL) and electroluminescent (EL) spectra were measured using an UV–vis–near-IR spectrometer (Perkin-Elmer, Lambda 19) and a fluorescence spectrometer (Jobin Yvon Horiba, Fluoromax-3), respectively. No correction was made for reflection from the surface and absorption by the sample cell. For preparation of samples for time-of-flight (TOF) measurements, a thick polymer layer (thickness ca. 1.5 μm) was drop-cast on the pretreated ITO substrate from 15 mg mL^{-1} polymer solution at room temperature for 2 days in a glovebox with inert atmosphere and then baked at 50 °C under vacuum for 1 day, and an aluminum layer of 100 nm was then deposited under 10^{-6} Torr over the polymer layer through a shadow mask. The photocurrent was generated by a nitrogen-laser-pumped dye laser at 390 nm (near the absorption maxima of the polymers) with a pulse width of 500 ps through an ITO electrode. A transient current was measured across the load resistor using a 500 MHz digital oscilloscope. The carrier mobility μ is calculated from transient time t_T by the relation $\mu = d/Et_T$, where d is film thickness and E is external electric field.

dx.doi.org/10.1021/ma202413g | *Macromolecules* 2012, 45, 1281–1287

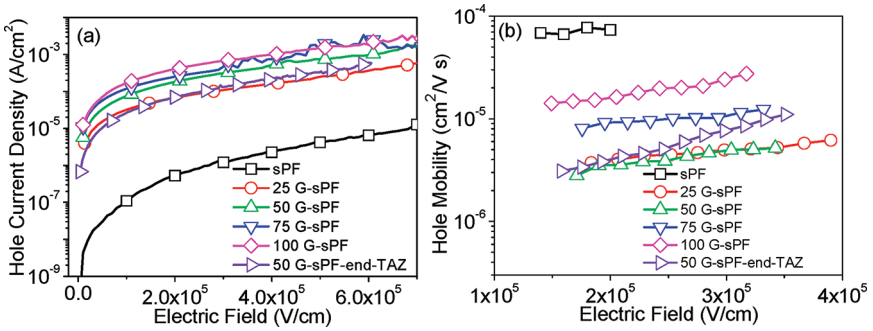


Figure 2. (a) Hole fluxes and (b) hole mobilities of poly-spiros. The structure for hole-dominated device is ITO/PEDOT:PSS/poly-spiros/Au.

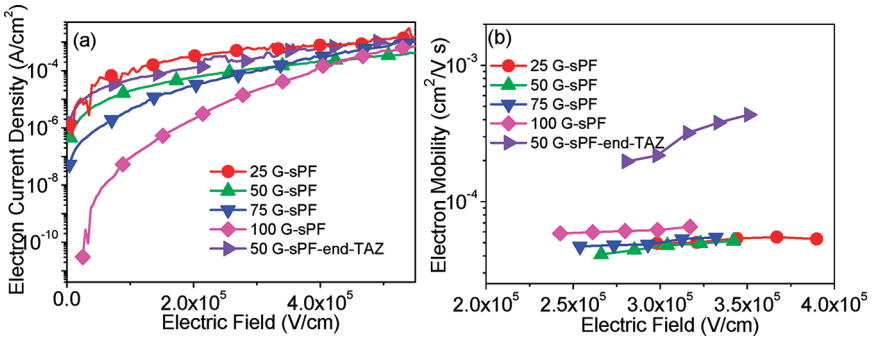


Figure 3. (a) Electron fluxes and (b) electron mobilities of poly-spiros. The structure for electron-dominated device is ITO/Al/poly-spiros/CsF/Al.

Time-Resolved Photoluminescence (TRPL) Measurement. The photoluminescence decay curves of polymers were measured by a time-correlated single photon counting (TCSPC) system with a microchannel plate photomultiplier tube (Hamamatsu Photonics R3809U-50) and a spectrometer (Edinburgh, Lifespec-ps with TCC900 data acquisition card). Excitation pulse for the TCSPC experiments was provided by a frequency-doubled output (harmonic generator, Inrad 5-050) of a mode-locked Ti–sapphire laser (Coherent Mira-900) pumped by a diode laser (Coherent Verdi-V10). The repetition rate was reduced to 4 MHz by a pulse picker (Coherent Mira 9200) between Mira-900 and In-rad 5050.

RESULTS AND DISCUSSION

Hole Injection and Transport. The chemical structures and energy levels of the poly-spirofluorenes (poly-spiros) so designed as well as the design concept are shown in Figure 1. Detailed synthesis procedures and determination of energy levels are given in the Supporting Information. To prove the proposed concept, we fabricated hole-dominated ITO/PEDOT:PSS/poly-spiros/Au) and electron-dominated (ITO/Al/poly-spiros/CsF/Al) devices separately, and their current–voltage curves are given in Figures 2a and 3a, respectively. By applying the equation $J = nq\mu E$ for the single carrier device (J is the current density, n is the carrier number, μ is the carrier mobility, and q is the charge), along with the values of charge carrier mobilities (μ) (in Figures 2b and 3b) determined by time-of-flight, the injected carrier density ratios of the modified sPFs relative to that of sPF at a specific electric field can be determined. For example, at 2.5×10^5 V cm^{-1}, the injected hole carrier density ratios relative to that of sPF for 25 G-sPF, 50 G-sPF, 50 G-sPF-end-TAZ, 75 G-sPF, and 100 G-sPF are 1.85×10^3, 6.13×10^3, 1.73×10^3, 3.09×10^3, and 2.48×10^3 (optimal at 50 G-sPF), respectively, suggesting that the designed structure can largely improve hole injection capability. The G-sPF possesses three steps of descending HOMO levels: 5.3 (for TPA), 5.5 (for Cz), and 5.7 eV (for the backbone) (Figure 1), which allows holes injected from the anode to transport through the interface to the main chain by three descending HOMO levels. The abrupt change in HOMO level from the anode to backbone in sPF (from 5.3 to 5.7 eV, i.e., 0.4 eV) can be reduced to three smaller steps: the first step (from the anode to TPA) is nearly barrier free (0.0 eV) and the second (from TPA to Cz) and the third (Cz to the backbone) steps are both 0.2 eV, which allows an easier hopping of injected holes from the anode to the main chain. Besides, we have previously shown from the TRPL that TPA has the largest hole trapping capability in TPA-Cz-sPF, followed by Cz and then main chain.[8] Therefore, similar result will be expected in the G-sPF. When hole is injected from PEDOT:PSS to G-sPF, it would hop to TPA much easier than to Cz or main chain (TPA exhibits the strongest hole trapping capability) if spatially allowed. Further hopping from TPA to Cz is much easier than to main chain due to stronger hole trapping capability of Cz. Finally, the hole in Cz would hop into the main chain. In addition to energetic considerations discussed above, G-sPF also gives favorable spatial arrangement for hole injection; that is, the TPA moieties have higher possibility to come in contact with the anode. This is because TPA moieties are located away from the main chain in both G-sPF and TPA-Cz-sPF and that more TPA moieties are on the interface in contact with the hole injection layer PEDOT:PSS than in the bulk as previously demonstrated in TPA-Cz-sPF by X-ray photoelectron spectroscopy (XPS) analysis with the aid of argon-ion etching.[8] Therefore, the same result would also be expected in G-sPF. These factors lead to an improvement in hole injection. Note that even though the energetic arrangement, spatial arrangement, and TPA content of 50 G-sPF are the same as TPA-Cz-sPF, the carrier density ratio of 50 G-sPF above is higher than that of previously reported TPA-Cz-sPF with TPA and Cz in different side chains[8] (3.57×10^3 at electric field of 2.5×10^5 V/cm) by a factor of about 1.7, implying more effective hole

dx.doi.org/10.1021/ma202413g | Macromolecules 2012, 45, 1281–1287

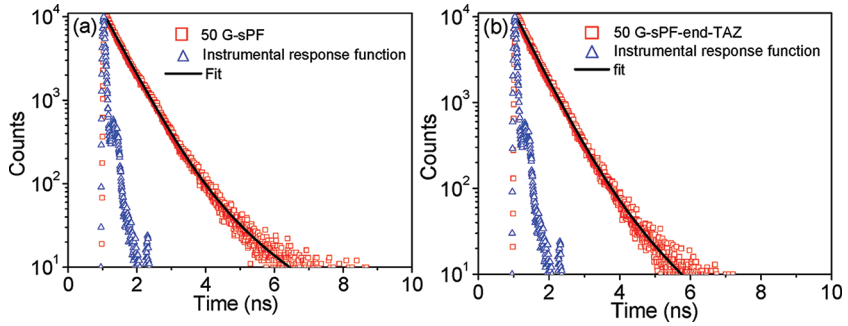


Figure 4. Luminescence decays of emission (424 nm) from (a) 50 G-sPF and (b) 50 G-sPF-end-TAZ thin films. The solid lines are double-exponential fits with fall times of 557 and 1446 ps for 50 G-sPF; those for 50 G-sPF-end-TAZ are 516 and 1116 ps, respectively.

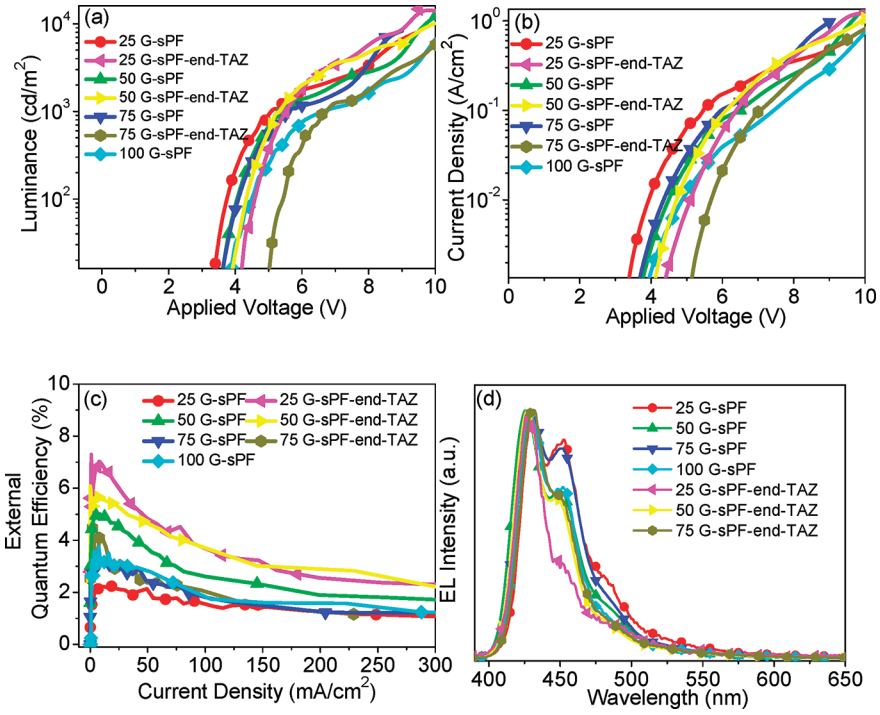


Figure 5. Device performances and EL spectra of poly-spiros with the device structure ITO/PEDOT:PSS/poly-spiros/CsF/Al. (a) Luminance–voltage curves. (b) Current density–voltage curves. (c) Efficiency–current density curves. (d) EL spectra.

injection can be achieved in 50 G-sPF. This result could be explained as shorter distance between TPA and Cz moieties in G-sPF relative to TPA-Cz-sPF facilitating hopping of hole from TPA to Cz and thus injection process.

As holes transport in the bulk, it is reasonable to conceive that holes prefer to hop to TPA or Cz moieties due to larger hole trapping capability and higher HOMO level as compared to backbone of G-sPF as mentioned above. In other words, TPA and Cz moieties can be considered as hole traps. Therefore, hole mobilities of G-sPFs are lower than that of unmodified sPF by a factor of 7–17.5 due to the trapping effect (Figure 2b). The higher mobility observed with the increasing content of hole transport moiety in G-sPFs can be explained as intermoiety transport toward counter electrode, in which holes at TPA or Cz moieties can hop to neighboring TPA or Cz sites and increase the hole mobility (Figure 2b).

Electron Injection and Transport. Also, the incorporation of TAZ on chain ends leads to an enhancement in electron injection. Taking 50 G-sPF-end-TAZ (the fraction of polymer chain ends terminated with TAZ is about 89%; see Supporting Information for detail estimation) as an example, at 3×10^5 V cm^{-1}, the injected electron carrier density ratio (versus 50 G-sPF) is 1.57 (as determined from Figure 3a,b by applying the applying the equation $J = nq\mu E$). The reason is that the TAZ can serve as an additional injection channel for electron (as compared to *tert*-butylphenylene (TBP) in 50 G-sPF). To support the above consideration, XPS analysis with the aid of argon-ion etching process was performed to investigate the distributions of moieties and main chain segments in 50 G-sPF-end-TAZ film (see Supporting Information for details). The distributions of TAZ moieties and main chain segments in 50 G-sPF-end-TAZ on the free surface are quite different from those in the bulk. On the free surface, the determined contents of C, N, and O in terms of atom % are 94.87, 2.88, and 2.25, respectively, whereas in the bulk, the corresponding contents (atom %) are 94.82, 2.61, and 2.57, respectively. The content of nitrogen atoms (TAZ moiety can be an additional source of N atom; therefore, the investigating variation of N content can provide the TAZ distribution) increases from 2.61% in the bulk to 2.88% on the surface, indicating that there are more TAZ on the surface than in the bulk by 10%, and this is possibly due to higher degree of freedom of chain end in polymer. Therefore,

dx.doi.org/10.1021/ma202413g | *Macromolecules* 2012, 45, 1281–1287

TAZ can be a possible injection route for electron from the spatial consideration.

The possibility of electron injection via TAZ moieties is also explored by TRPL. Figure 4 shows the time-resolved luminescence decay curves of 50 G-sPF and 50 G-sPF-end-TAZ (excitation at 390 nm, i.e., main chain is excited; collected wavelength is 424 nm). The luminescence decays from 50 G-sPF and 50 G-sPF-end-TAZ thin films can be fitted by a double-exponential function with fall times of 557 ps (91.13%) and 1446 ps (8.87%) for 50 G-sPF; those for 50 G-sPF-end-TAZ are 516 ps (88.56%) and 1116 ps (11.44%), respectively. The major one could be attributed to exciton relaxation from the main chain and the minor one to exciton dissociation by TPA and then recombined in the main chain.[8] As for 50 G-sPF-end-TAZ (516 ps) and 50 G-sPF (557 ps), end-capping the TAZ moiety can increase the exciton dissociation rate (in other words, shorter exciton lifetime). That is, when exciton is formed on the main chain after excitation, TAZ can dissociate exciton (i.e., trap electron) in the main chain efficiently, which could be ascribed to strong electron-withdrawing capability of the TAZ moiety. Thus, the "dissociation capability" of the TAZ can be taken as its "electron trapping capability". Therefore, from the energetic point of view, when electron injected from the cathode (CsF/Al) in the PLEDs, it would preferably hop to TAZ than to the main chain if spatially allowed. As electron injected to TAZ, further hopping from TAZ to the main chain would be favorable since very close spatial position and nearly isoenergetic LUMO levels (LUMO of TAZ is lower only by 0.1 eV than the main chain (Figure 1)) between TAZ and the main chain will facilitate electron hopping from TAZ to backbone of G-sPF and thus injection process.

As electron transport in the bulk, the TAZ moieties on the polymer chain end could facilitate intrachain electron transport; that is, when electrons hop to TAZ moieties in the bulk film, they would prefer to hop to the main chain nearby, and their transport along the polymer chain would be favorable. Take 50-GsPF for example; an enhancement in electron mobility by a factor of 4.8−8.4 in the whole range of electric field relative to that without such modification can be observed due to this reasoning (Figure 3b).

Device Performances. The performances and EL spectra of the PLEDs with the device structure ITO/PEDOT:PSS/poly-spiros/CsF/Al are shown in Figure 5, and their characteristic values are listed in Table 1. All the poly-spiros exhibit db emission (Figure 5d and Table 1), which is extremely important for high degree of color saturation. As for the performances, it has been reported that the poly-spiro without any structure modification (sPF) exhibits considerably higher electron flux than hole flux, which leads to an imbalance in charge fluxes and thus a low efficiency (η_{ext} 1%).[8] After grafting TPA and Cz in same side chain of sPF here, the G-sPFs show promoted hole fluxes by enhanced hole injection. Besides, TPA possesses a higher LUMO level than the backbone by 0.7 eV (Figure 1), which causes more difficulty for electron injection from the cathode to the bulk polymer (note that there are more TPA moieties on the surface than in the bulk as mentioned previously) as supported by the decrease in the electron fluxes in the electron-dominated devices (Figure 3a). These factors lead to a better charge balance relative to sPF, and thus device efficiencies of G-sPFs based PLEDs are superior to that of sPF by a factor of 2−5. However, high content of hole transport moieties could degrade the performances of G-sPFs-based PLEDs. As shown in Table 1, 50 G-sPF gives the best performances (maximum luminance (B_{max}) 12 100 cd m^{-2} and η_{ext} 5.00%), rather than the PLED fabricated with 100 G-sPF (B_{max} 6700 cd m^{-2} and η_{ext} 3.75%). The reason is that high content of hole transport moieties can over suppress electron flux (Figure 3a), resulting in imbalance of hole and electron fluxes and thus degrading the efficiency. Furthermore, as discussed previously, as holes transport in the bulk, it is reasonable to conceive that holes prefer to hop to TPA or Cz moieties due to larger hole trapping capability and higher HOMO level as compared to backbone of G-sPF. In other words, TPA and Cz moieties can be considered as hole traps. When the content of hole transport moiety increases, holes at TPA or Cz moieties prefer to hop to neighboring TPA or Cz sites, and those located at the main chain also prefer to hop to TPA or Cz and then to neighboring TPA or Cz, which would lead to intermoiety transport toward the counter electrode. The increasing hole mobility (Figure 2b) at higher content of hole transport moiety in G-sPFs also supports an increase in possibility of the intermoiety hole transport. As a result, the chance of hole transport following the sequence of TPA, Cz, and finally main chain (where charge recombination takes place) due to the spatially and energetically favorable binding sequence is decreased, giving lower device performances.

For the devices based on G-sPF-end-TAZs, they exhibit further remarkably enhanced performance as reflected in the increased η_{ext} 7.28% (25 G-sPF-end-TAZ), 6.08% (50 G-sPF-end-TAZ), and 4.91% (75 G-sPF-end-TAZ) as compared to those of the corresponding G-sPF (without TAZ) (Table 1), in which the η_{ext} 7.28% is the highest value among the db fluorescent PLEDs ever documented (see the Supporting Information). The reason for improvement is that TPA moieties in G-sPFs might oversuppress the electron fluxes mentioned above, leading to an imbalance in hole and electron fluxes. The TAZ introduced can serve as an additional injection route for electron toward the main chain as discussed previously, thereby improving the device efficiency as compared to G-sPFs with merely TBP as end-capper. Besides, the hole blocking capability of TAZ moiety could reduce number of injected hole in G-sPF (as supported by smaller injected hole carrier density ratio of 50 G-sPF-end-TAZ (1.73×10^3) as compared to 50 G-sPF (6.13×10^3) mentioned previously and lower HOMO level of TAZ relative to polymer backbone), leading to more balance in charge fluxes and thus performances improvement.

As discussed above, the TAZ moiety in the polymer chain ends can enhance the electron injection from the cathode, accompanying by reducing the hole injection due to its hole-blocking capability. Therefore, it is reasonable to speculate that there will be an optimized TAZ composition to obtain high EL

Table 1. Electroluminescence Data for Poly-Spiros[a]

polymer	B_{max} [cd m^{-2}]	LE_{max}; η_{ext} [cd A^{-1}]; [%]	CIE(x,y)
25 G-sPF	8100	1.81; 2.23	(0.16, 0.07)
25 G-sPF-end-TAZ	14700	4.88; 7.28	(0.16, 0.07)
50 G-sPF	12100	3.01; 5.00	(0.16, 0.06)
50 G-sPF-end-TAZ	10100	3.52; 6.08	(0.16, 0.05)
75 G-sPF	8300	1.98; 3.13	(0.16, 0.06)
75 G-sPF-end-TAZ	9800	3.11; 4.91	(0.16, 0.06)
100 G-sPF	6700	2.46; 3.75	(0.16, 0.06)

[a]Device configuration ITO/PEDOT:PSS/polymer/CsF/Al.

dx.doi.org/10.1021/ma202413g | Macromolecules 2012, 45, 1281−1287

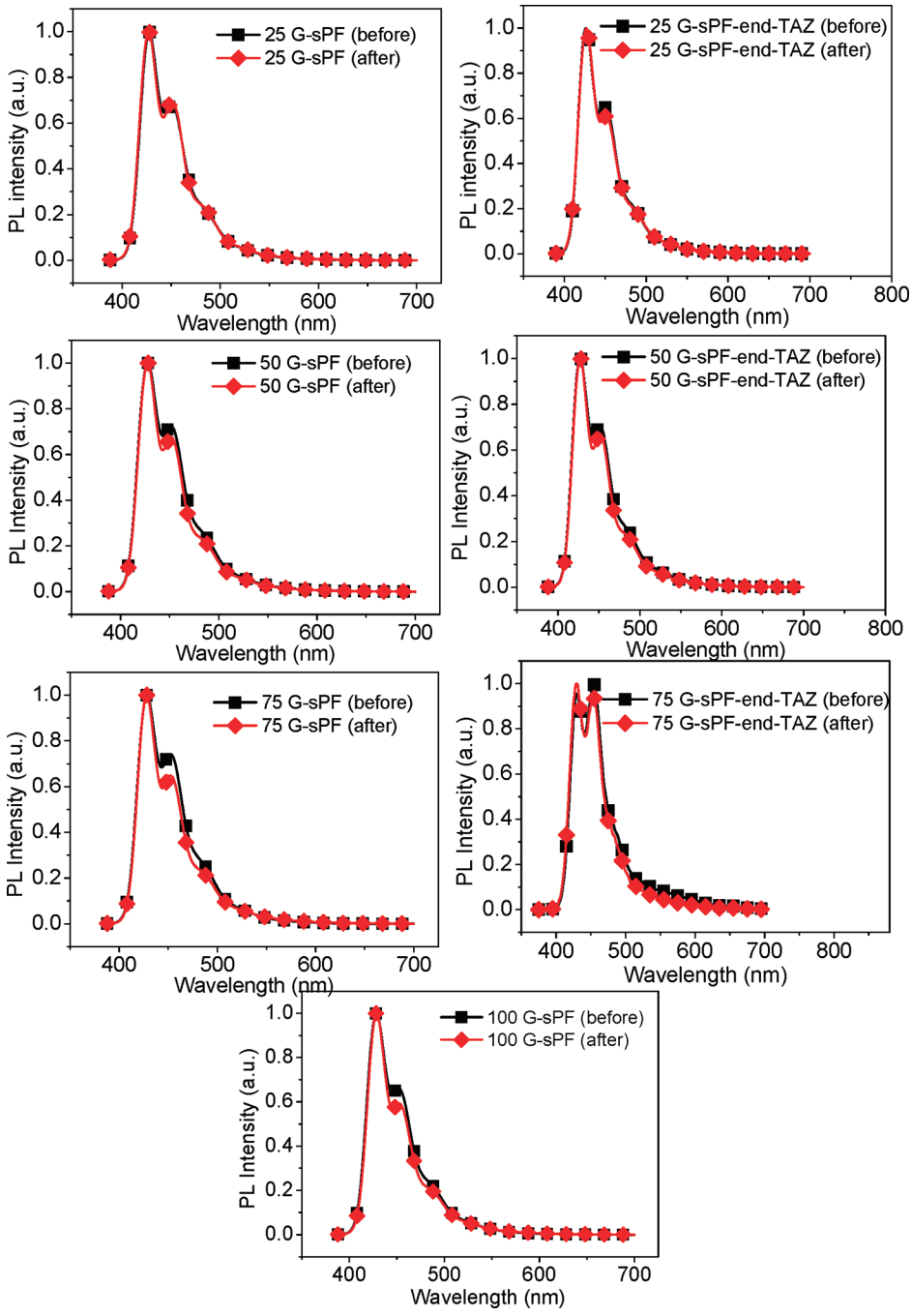


Figure 6. PL spectra of poly-spiros before and after annealing at 180 °C in air for 2 h.

efficiency as hole transport moieties (TPA and Cz) in the side chain mentioned previously. In principle, balanced hole and electron fluxes are required to obtain a highly efficient PLED. Thus, the optimized amount of TAZ moiety capping on the polymer chain end should depend on the hole and electron fluxes in the investigated PLED. If the hole flux is far higher than the electron flux, more TAZ moieties should be capped on the chain end to reduce the hole flux and increase the electron flux so that more balanced current fluxes (and thus highly efficient PLED) can be achieved.

A comparison between the performances of the present poly-spiros and TPA-Cz-sPF is not attempted since a green tail appears (which might be attributed to exciplex or excimer emission)[8] in TPA-Cz-sPF, relative to db emission in poly-spiros. However, as hole transport in the bulk of G-sPFs, the chance for hole hopping from TPA to Cz and then to the main chain (where charge recombination takes place) would be higher than that of TPA-Cz-sPF due to shorter distance between TPA and Cz moieties in G-sPF relative to TPA-Cz-sPF facilitating hole hopping following the sequence of TPA, Cz and finally main chain. As for end-capping TAZ moiety in G-sPF, more importantly, we think that incorporation of TAZ moiety on the polymer chain end can facilitate intrachain electron transport; that is, when electrons hop to TAZ moieties in the bulk film, they would prefer to hop to the main chain nearby, and their transport along the polymer chain would be favorable as evidenced by an enhancement in electron mobility by a factor of 4.8−8.4 in the whole range of electric field

dx.doi.org/10.1021/ma202413g | *Macromolecules* 2012, 45, 1281−1287

relative to that without such modification in 50 G-sPF (Figure 3b). This result would also promote the chance of charge recombination on the main chain. We also compare the performances of present poly-spiros with the dbPLEDs fabricated with Cz-TPA-sPF. As expected, the efficiencies of 50 G-sPF (η_{ext} 5%) and 50 G-sPF-end-TAZ (η_{ext} 6.08%) are higher than that of Cz-TPA-sPF (η_{ext} 4.54%) by a factor of 1.1 and 1.34, respectively. However, the brightness of 50 G-sPF (B_{max} 12 100 cd m^{-2}) and 50 G-sPF-end-TAZ (B_{max} 10 100 cd m^{-2}) is lower than that of Cz-TPA-sPF (B_{max} 22 000 cd m^{-2}) by a factor of 1.8 and 2.17, respectively. The possible reason is that different cathodes were employed in the dbPLEDs (CsF/Ca/Al for Cz-TPA-sPF and CsF/Al for present poly-spiros). In comparison with CsF/Al, it has been indicated that higher electron current can be achieved as CsF/Ca/Al is utilized as a cathode.[11] Therefore, we believe the performances (η_{ext} and B_{max}) of present poly-spiros can be further improved if more efficient cathode CsF/Ca/Al is employed.

Furthermore, all of the EL devices exhibit rather stable emission color under various operating voltages from low to high. Taking 25 G-sPF-end-TAZ as an example, the CIE values at various current densities of 1, 50, and 200 mA cm^{-2} are all identical and close to the standard pure blue emission, being x = 0.16 and y = 0.07−0.08 (details are shown in the Supporting Information). In addition to the EL stability, the poly-spiros also exhibit excellent photoluminescence thermal stability (Figure 6). After annealing at 180 °C for 2 h in air, the PL spectra of these poly-spiros remain identical to their pristine state PL spectra, in which no green-blue band emission[12] is observed after thermal treatment.

CONCLUSIONS

In conclusion, we have developed the novel molecular design strategy by introducing multiple charge transport moieties for efficient injection of charge carriers, in which the hole transport moieties, TPA and Cz, in the same side chain of sPF and the electron transport moiety TAZ on both chain ends are integrated. The ultrahigh-efficiency (7.28%) dbPLEDs with CIE_{xy} coordinates (0.16, 0.07) can be achieved, which are far superior to any db electroluminescent polymers reported in the literature. The present designing concept reveals a major advancement in electroluminescent polymers as well as provides a broad avenue for further development of illumination devices.

ASSOCIATED CONTENT

Supporting Information

Synthesis, cyclic voltammetry, X-ray photoelectron spectroscopy, EL stability at various current densities, and performances comparison of EL devices. This material is available free of charge via the Internet at http://pubs.acs.org.

AUTHOR INFORMATION

Corresponding Author

*E-mail: sachen@che.nthu.edu.tw.

ACKNOWLEDGMENTS

The authors thank the Ministry of Education and the National Science Council (Project NSC 96-2752-E-007-008-PAE, NSC 96-2752-E-007-005-PAE, and NSC 99-2221-E-007-002-MY3) for financial support.

REFERENCES

(1) Lu, H. H.; Liu, C. Y.; Chang, C. H.; Chen, S. A. *Adv. Mater.* **2007**, *19*, 2574−2579.
(2) Hsiao, C. C.; Hsiao, A. E.; Chen, S. A. *Adv. Mater.* **2008**, *20*, 1982−1988.
(3) Miteva, T.; Meisel, A.; Knoll, W.; Nothofer, H. G.; Scherf, U.; Müller, D. C.; Meerholz, K.; Yasuda, A.; Neher, D. *Adv. Mater.* **2001**, *13*, 565−570.
(4) Hung, M. C.; Liao, J. L.; Chen, S. A.; Chen, S. H.; Su, A. C. *J. Am. Chem. Soc.* **2005**, *127*, 14576−14577.
(5) Wu, F. I.; Shih, P. I.; Shu, C. F.; Tung, Y. L.; Chi, Y. *Macromolecules* **2005**, *38*, 9028−9036.
(6) Huang, F.; Zhang, Y.; Liu, M. S.; Cheng, Y. J.; Jen, A. K. Y. *Adv. Funct. Mater.* **2007**, *17*, 3808−3815.
(7) Wang, E. G.; Li, C.; Mo, Y.; Zhang, Y.; Ma, G.; Shi, W.; Peng, J.; Yang, W.; Cao, Y. *J. Mater. Chem.* **2006**, *16*, 4133−4140.
(8) Huang, C. W.; Peng, K. Y.; Liu, C. Y.; Jen, T. H.; Yang, N. J.; Chen, S. A. *Adv. Mater.* **2008**, *20*, 3709−3716.
(9) Sullivan, S. C.; Woo, W. K.; Steckel, J. S.; Bawendi, M.; Bulovic, V. *Org. Electron.* **2003**, *4*, 123−130.
(10) Forrest, S. R.; Bradley, D. D. C.; Thompson, M. E. *Adv. Mater.* **2003**, *15*, 1043−1048.
(11) Hsiao, C. C.; Chang, C. H.; Lu, H. H.; Chen, S. A. *Org. Electron.* **2007**, *8*, 343−348.
(12) Lu, H. H.; Liu, C. Y.; Jen, T. H.; Liao, J. L.; Tseng, H. E.; Huang, C. W.; Hung, M. C.; Chen, S. A. *Macromolecules* **2005**, *38*, 10829−10835.

Macromolecules

Article

pubs.acs.org/Macromolecules

Patterning Carbazole–Phenylazomethine Dendrimer Films

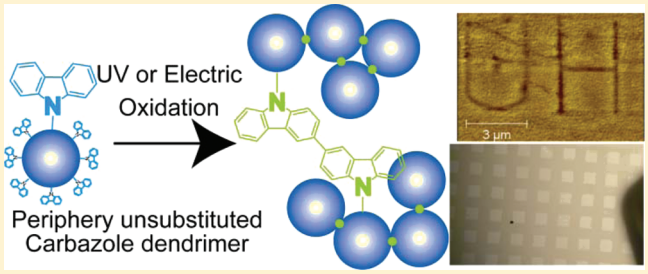
Ken Albrecht,[†] Roderick Pernites,[‡] Mary Jane Felipe,[‡] Rigoberto C. Advincula,*[,‡] and Kimihisa Yamamoto*[,†]

[†]Chemical Resources Laboratory, Tokyo Institute of Technology, 4259 Nagatsutacho, Midoriku, Yokohama 226-8503, Japan

[‡]Department of Chemistry and Department of Chemical Engineering, University of Houston, Houston, Texas 77204-5003, United States

Supporting Information

ABSTRACT: The synthesis of double-layer-type dendrimers with carbazole and phenylazomethine as the dendron with a symmetric tetraphenylmethane core is reported. Structural modeling studies showed that the G3 dendrimer has a rigid and spherical structure. These dendrimers were thermally stable ($T_{d10\%}$ over 500 °C) with the TGA-MS study revealing a degradation mechanism occurring first at the inner-layer phenylazomethine group. The metal (Lewis acid) complexation property of these dendrimers was also studied. Electrochemical measurements showed that these dendrimers have the appropriate HOMO level as a hole-transporting material with electropolymerizability on the peripheral carbazole groups. A photo-cross-linking property of the dendrimer film was also observed. Finally, electro-nanopatterning with conducting AFM and photopatterning of the dendrimer film were demonstrated. Thus, the new dendrimer is a potential hole-transporting material that is patternable through oxidation of the peripheral carbazole units by either photochemical or electrochemical methods.



INTRODUCTION

Organic electronics, which started with the discovery of charge-transfer complexes,[1] chemical doping of polymers,[2] and charge injection into organic single crystals,[3] has been of high interest for materials chemists for organic light-emitting diode (OLED) and organic photovoltaic (OPV) devices.[4] The possibility for lightweight, flexible, and low-cost electronics devices has led to a significant research effort on low to high molecular[5] weight materials for organic photoconductive devices,[6] OLED,[7] OPV,[8] OFET,[9] organic lasers,[10] organic light-emitting transistors,[11] and organic memory devices.[12] The device structure and material composition depends on the particular application. Film formation from solution (wet process), laminatability, and patternability remain important properties for the development of truly simple and low cost organic/polymer devices. However, materials that satisfy all these requirements are still rare.[13]

Dendritic molecules[14] including hyperbranched polymers[15] have been extensively studied.[16] Dendrimers have precise molecular weights and uniform structure which are suitable as model compounds to study optoelectronic properties in devices.[17] Additionally, the high solubility, amorphousness, high glass transition temperature, and low viscosity enable dendritic materials to be attractive even for practical use. To date, several dendritic materials have been developed for this purpose,[18] especially the rigid phenylene-[19] and carbazole-type[20] dendrons having potential as high-performance OLED materials.[21,22] Despite these developments, dendritic materials are not easily accessible to lamination and patterning compared to low molecular weight materials (vacuum deposition and shadow mask process).

Polymerization or cross-linking after or during film formation[23] can be a viable way to fabricate insoluble (laminable) and patternable polymer films. However, many of these cross-linkage units (especially photo-cross-linking units) are electrochemically inactive and require an initiator which can inhibit charge transfer or reduce the lifetime of the device. Adopting these units in a dendritic system is difficult. For cross-linking, the units have to be at the periphery, and this can block the charge-transfer property between dendrimers. One possible approach to solve this problem is to use peripheral units that have both cross-linking and charge-transfer abilities. As previously mentioned, carbazole units are efficient hole-transporting materials and, at the same time, known to have electrochemical and photo-cross-linking properties. In this paper, we report on a new carbazole dendrimer and demonstrate the potential for electrocemical and photo-cross-linkable (laminable and patternable) dendritic electronics materials.

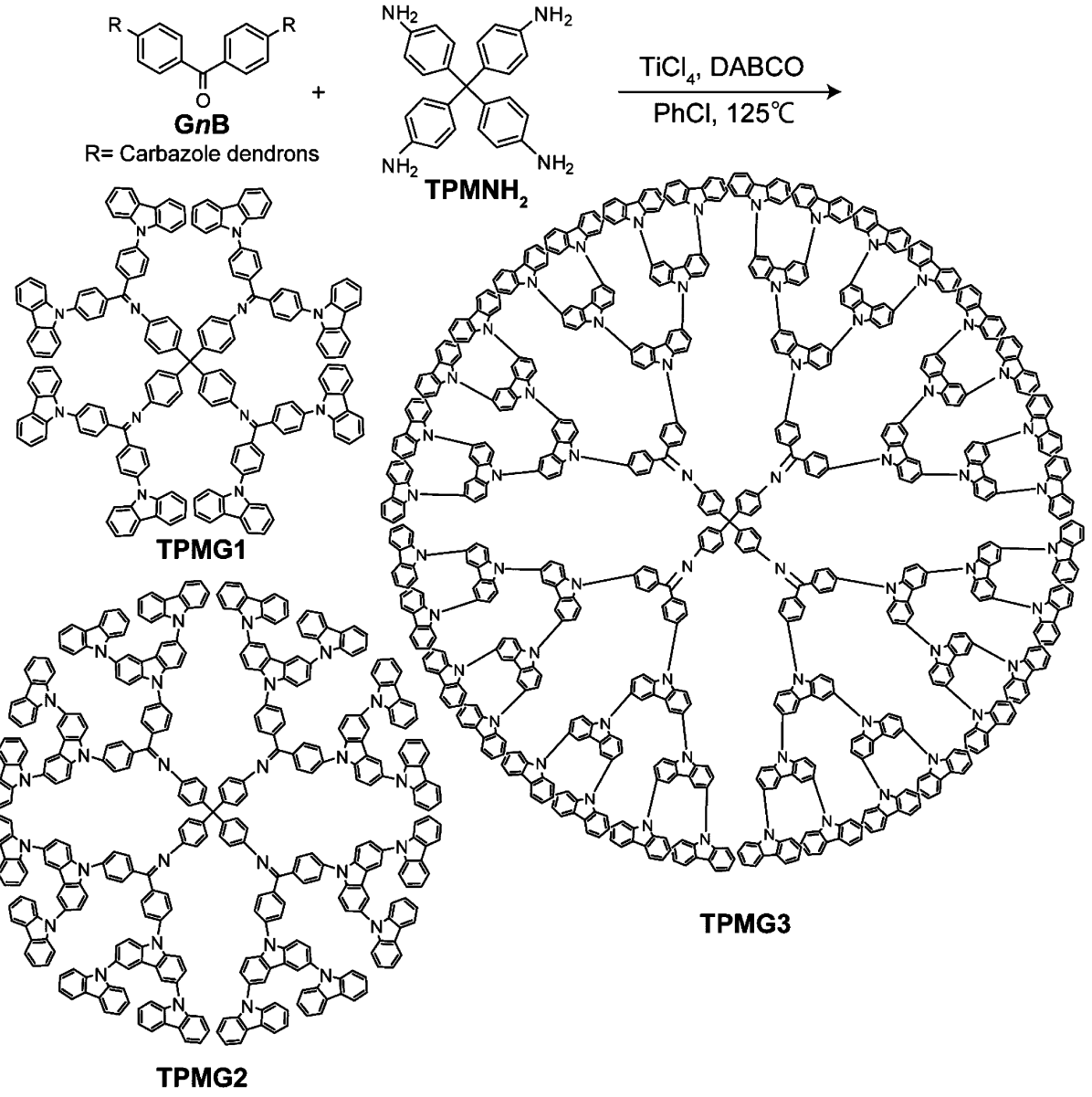
EXPERIMENTAL SECTION

Carbazole was purchased from the Kanto Kagaku Co. and recrystallized prior to use. All other reagents were purchased from Aldrich,

Received: November 10, 2011
Revised: December 27, 2011
Published: January 26, 2012

ACS Publications © 2012 American Chemical Society

Scheme 1. Synthesis of Tetraphenylmethane Core Carbazole−Phenylazomethine Double Layer-Type Dendrimers



TCI, and the Kanto Kagaku Co. and used without further purification. Solvents for the UV−vis titration and electrochemical measurements were of the dehydrated grade. The silica gel for column chromatography was of neutral grade. All the dendrimers were reprecipitated from hexane with chloroform and dried in vacuo (150 °C) before use. The NMR spectra were obtained using a JEOL JNM-GX400 (400 MHz) and a JEOL JNM-EX270 (270 MHz) with TMS as the internal standard. The MALDI TOF-MS data were obtained using a Shimadzu/Kratos AXIMA CFR plus in the linear positive ion mode. Dithranol was used as the matrix. The elemental analysis was performed at the Center for Advanced Materials Analysis, Technical Department, TIT. A preparative scale gel permeation chromatograph, LC-908 (Japan Analytical Industry Co., Ltd.), was used to isolate each compound with chloroform or THF as the eluent. The thermal analysis was performed using a Rigaku Thermoplus TG8120 with flowing nitrogen, and the temperature rate increase was 40 K/min. The thermal desorption gas analysis was performed with a Rigaku TPD type R Photo with flowing helium. The temperature rate increase was 20 K/min, and the gas was analyzed by EI (electron ionization) and PI (photoionization) MS. The UV−vis spectra were recorded using a Shimadzu UV-3150 spectrometer with a quartz cell having a 1 cm optical length at 20 °C. The electrochemical measurements were done using a conventional three-electrode configuration with an ALS Chi660 electrochemical analyzer. The working, counter, and reference electrodes were a glassy carbon (0.09 mm^2), Pt wire, and Ag/Ag^+, respectively. The solvent was 1,2-dichloroethane, the concentration of the sample was 0.5 mM, and the supporting electrolyte was 0.2 M tetra-*n*-butylammonium perchlorate (TBAP). The solution was purged with nitrogen before the measurements, and the voltage sweep rate was 0.1 V/s. The increased voltage was 0.004 V, the amplitude was 0.05 V, the pulse width was 0.06 s, the sample width was 0.02 s, and the pulse period was 0.2 s for the DPV measurements. The molecular models were calculated with the CAChe Worksystem ver. 5.04 (Fujitsu) using the MM/AM1MOZYME method. All the electro-nanopatterning experiments were done with a Picoscan AFM system and piezoscanner (Agilent Technologies). For the current-sensing AFM mode, conductive Pt/Ir-coated Si tips (Agilent Technologies) were used to pole the local nanoscale area on the dendrimer spin-coated films. Picolith software for the AFM nanolithography was used, having various options with regard to force, voltage, and speed draw the desired patterns. The UV lamp for the photopolymerization of the film was a MORITEX MUV-202U (mercury−xenon lamp), and the light intensity at the irradiation point was ca. 1.7 W/cm^2. Analytical size-exclusion chromatography (SEC) was performed using an HPLC

dx.doi.org/10.1021/ma202485h | *Macromolecules* 2012, 45, 1288−1295

(Shimadzu, LC-10AP) equipped with a TSK-GEL CMHXL (Tosoh) at 40 °C. Tetrahydrofuran (THF) was used as the eluent at the flow rate of 1 mL/min. The detection line was connected to a triple detector (refractive index, light scattering, and viscosity; Viscotek, TriSEC model 302).

Dendrons. The carbazole-substituted benzophenone derivatives (dendrons) were obtained according to the literature method (G1 to G4).[20a] The model compounds **G2A**, **G3A**, and **G3Ph** were obtained according to the literature method.[20a] Tetrakis(4-aminophenyl)-methane ($TPMNH_2$) was prepared according to the literature methods[24] from aniline and trityl chloride, and **TPMG0** was also prepared according to the literature method.[25]

TPMG1 (General Procedure for Dehydration Reaction). $TPMNH_2$ (84.0 mg, 0.221 mmol), **G1B** (1069 mg, 2.09 mmol), and DABCO (1959 mg, 17.5 mmol) were dissolved in chlorobenzene (30 mL) and heated to 75 °C. $TiCl_4$ (253 mg, 1.33 mmol) dissolved in 5 mL of chlorobenzene was dropwise added, and the addition funnel was then rinsed with 5 mL of chlorobenzene. The mixture was heated to 125 °C and stirred for 15 h under a nitrogen atmosphere. The reaction mixture was cooled to room temperature, stirred overnight in air, and then filtered through Celite. The filtrate was concentrated, and the product was isolated by silica gel column chromatography (hexane:toluene = 1:50 with 2% Et_3N) and purified by preparative GPC (eluent: chloroform). Yield: 61% (318 mg, 0.135 mmol). **TPMG1**: ^{1}H NMR (400 MHz, $CDCl_3$, TMS standard, 20.1 °C, ppm): δ 8.17 (8.0H, d, J = 7.3 Hz), 8.07 (8.0H, d, J = 7.3 Hz), 8.01 (8.0H, d, J = 8.3 Hz), 7.71 (8.0H, d, J = 8.8 Hz), 7.56 (8.0H, d, J = 8.3 Hz), 7.46 (8.0H, t, J = 7.8 Hz), 7.34 (16.0H, q, J = 7.6 Hz), 7.25−7.23 (16.0H, m), 7.18 (8.0H, d, J = 8.3 Hz), 7.05 (8.0H, d, J = 8.3 Hz), 6.96 (8.0H, d, J = 8.3 Hz), 6.55 (8.0H, d, J = 8.3 Hz). ^{13}C NMR (100 MHz, $CDCl_3$, TMS standard, 20.6 °C, ppm): δ 166.83, 149.15, 142.08, 140.36, 140.20, 140.11, 137.66, 137.58, 134.63, 131.13, 131.05, 130.80, 126.36, 126.08, 125.80, 123.62, 123.39, 120.30, 119.81, 109.76, 109.41, 63.03. MALDI TOF-MS (matrix: dithranol): calcd: 2358.9 ($[M + H]^+$); found: 2357.5. Anal. Calcd for $C_{173}H_{112}N_{12}$: C, 88.09; H, 4.79; N, 7.13. Found: C, 87.80; H, 4.65; N, 6.98.

TPMG2. As per the general procedure for the dehydration reaction, $TPMNH_2$ (41.3 mg, 0.109 mmol), **G2B** (1161 mg, 0.989 mmol), and DABCO (934 mg, 8.33 mmol) were dissolved in chlorobenzene (30 mL). $TiCl_4$ (190 mg, 1.00 mmol) was added, and the mixture was stirred for 5 h at 125 °C. The product was isolated by silica gel column chromatography (hexane:toluene = 1:10 to 1:20 with 2% Et_3N) and purified by preparative GPC (eluent: chloroform). Yield: 28% (153 mg, 0.03 mmol). **TPMG2**: ^{1}H NMR (400 MHz, $CDCl_3$, TMS standard, 22.0 °C, ppm): δ 8.26 (16.0H, dd, J = 7.6, 1.7 Hz), 8.16 (16.0H, d, J = 7.8 Hz), 8.03 (16.0H, d, J = 7.8 Hz), 7.94 (8.0H, d, J = 8.3 Hz), 7.59−7.54 (32.0H, m), 7.48 (8.0H, d, J = 8.8 Hz), 7.42−7.38 (48.0H, m), 7.30−7.28 (40.0H, m), 7.14 (16.0H, t, J = 7.3 Hz), 7.06 (8.0H, d, J = 8.3 Hz), 7.00 (8.0H, d, J = 8.3 Hz), 6.53 (8.0H, d, J = 8.3 Hz). ^{13}C NMR (100 MHz, $CDCl_3$, TMS standard, 23.1 °C, ppm): δ 166.71, 149.67, 142.10, 141.68, 141.59, 140.15, 140.00, 139.70, 137.46, 137.14, 135.65, 131.27, 131.18, 130.91, 130.80, 126.38, 126.20, 125.93, 124.33, 124.21, 123.20, 120.34, 119.92, 119.78, 111.22, 110.98, 109.63, 109.53, 63.11. MALDI-TOF-MS (matrix: dithranol): calcd: 5002.9 ($[M + H]^+$); found: 5002.5. Anal. Calcd for $C_{365}H_{224}N_{28}$: C, 87.65; H, 4.51; N, 7.84. Found: C, 87.47; H, 4.23; N, 7.84.

TPMG3. As per the general procedure for the dehydration reaction, $TPMNH_2$ (11.1 mg, 0.029 mmol), **G3B** (414 mg, 0.166 mmol), and DABCO (598 mg, 5.33 mmol) were dissolved in chlorobenzene (20 mL). $TiCl_4$ (102 mg, 0.538 mmol) was added, and the mixture was stirred for 5 h at 125 °C. The product was isolated by silica gel column chromatography (toluene with 2% Et_3N) and purified by preparative GPC (eluent: chloroform). Yield: 14% (43 mg, 0.004 mmol). **TPMG3**: ^{1}H NMR (400 MHz, $CDCl_3$, TMS standard, 19.0 °C, ppm): δ 8.47 (16.0H, d, J = 14.2 Hz), 8.28 (32.0H, d, J = 13.7 Hz), 8.15 (32.0H, d, J = 7.8 Hz), 8.00−7.94 (40.0H, m), 7.71−7.52 (80.0H, br m), 7.36−7.35 (80.0H, br m), 7.30−7.14 (128.0H, br m), 7.06−7.05 (32.0H, br m), 6.60 (8.0H, br s). ^{13}C NMR (100 MHz, $CDCl_3$, TMS standard, 19.3 °C, ppm): δ 167.53, 150.26, 142.12, 141.63, 141.49, 141.35, 141.26, 140.83, 140.03, 139.76, 136.89, 136.65, 136.46, 131.41, 130.89, 130.40, 130.24, 126.75, 126.51, 126.19, 125.81, 124.38, 124.19, 123.73, 123.06, 120.36, 120.25, 119.78, 119.64, 111.23, 110.95, 109.56, 109.32, 63.20. MALDI-TOF-MS (matrix: dithranol): calcd: 10285.7 ($[M + H]^+$); found: 10285.4. Anal. Calcd for $C_{749}H_{448}N_{60}$: C, 87.44; H, 4.39; N, 8.17. Found: C, 87.18; H, 4.19; N, 7.95.

RESULTS AND DISCUSSION

The carbazole dendrimer[20,22] with metal coordination sites (phenylazomethine[26]) on the inner layer of the dendron is expected to be an efficient hole-transporting material enhanced by metal coordination.[22a−d,27] This dendrimer was synthesized by the dehydration reaction between the carbazole dendron substituted benzophenones (**G*n*B**) and tetrakis(4-aminophenyl)methane ($TPMNH_2$) (Scheme 1). Because of the high steric hindrance (high generation dendrimers had 3-substituted products as a byproduct), the yield of the dendrimerization reaction decreased from G1 to G3 (61, 28, and 14%). All products were finally purified by preparative scale GPC and identified by ^{1}H NMR, ^{13}C NMR, MALDI-TOF MS (Figure S1), and elemental analysis, and the purity of the double layer-type dendrimers was verified by HPLC (SEC) analysis (Figure S2). Interestingly, all the dendrimers were soluble in common organic solvents, such as benzene, toluene, chloroform, and THF (at least more than 10 mg/mL), without bulky end-capping groups at the 3,6-position of the peripheral carbazole.[20b]

The intrinsic viscosity of the dendrimers and dendrons were measured and plotted versus the logarithm of the molecular weight (Mark−Houwink−Sakurada plot,[14b,28] Figure S3). The viscosity of the dendrons linearly increased with generation, but the viscosity of the dendrimer did not increase from G2 to G3. This means that the carbazole dendrons have rigid and linear molecular structures (no back-folding). On the other hand, the four-substituted tetraphenylmethane core dendrimer (G3) has a spherical structure due to the symmetric and compact core structure. This can also be confirmed by the molecular modeling (Figure S4) which verified that the peripheral carbazoles exist on the surface of the molecule.

The thermal stability of the dendrimer was evaluated by thermogravimetric analysis (TGA) measurements (Figure 1).

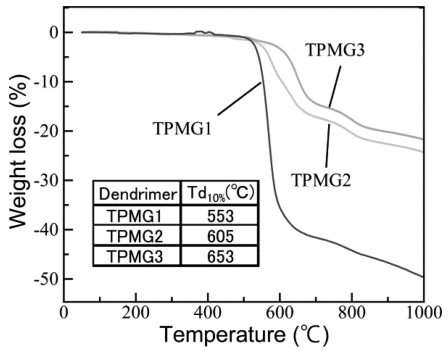


Figure 1. Temperature−weight loss plot of the dendrimers.

The 10% weight loss temperatures ($T_{d10\%}$) of the dendrimers increased when the generation increased. However, the derivative TG (DTG) plots (Figure S5) showed that all the dendrimers started to degrade at ca. 500 °C, which can be attributed to the degradation of the phenylazomethine units.[25] For further study, the EI- and PI-MS analyses of the thermal desorption gas of the model compounds[20a] (phenylazomethine substituted carbazole dendrons = one-fourth of the dendrimer;

see Chart S1 for the structure) have been performed. These data (Figures S7−S10) indicated that the model compounds (**G2A** and **G3A**) degrade at 500 °C to m/z 93 (aniline), at 540 °C to m/z 103 (benzonitrile), and at 630 °C to m/z 78 (benzene) and m/z 167 (carbazole). Additionally, the TGA curves of these compounds and the benzene-substituted carbazole dendron (**G3Ph**) showed that the degradation of the carbazole dendron occurs at ca. 600 °C (Figure S6). These results clearly show that the degradation of the dendrimer starts from the phenylazomethine units at around 500 °C followed by the degradation of the carbazole dendrons around 600 °C. When the generation of the dendrimer increases, the proportion of the phenylazomethine to total weight of the dendrimer decreases. At the same time, the molecular weight of the remaining carbazole dendrons increases and the sublimation will be suppressed. Therefore, the apparent $T_{d10\%}$ increases when the generation of the dendrimer increases. However, the degradation starting at 500 °C of all the dendrimers is still a high value which indicates the high thermal stability of these dendrimers.

The coordination chemistry of the dendrimer was confirmed by UV−vis titration with $SnCl_2$.[26a] Upon the addition of $SnCl_2$ to the dendrimer solution (benzene:acetonitrile = 4:1), the spectra gradually changed with one isosbestic point (Figure 2

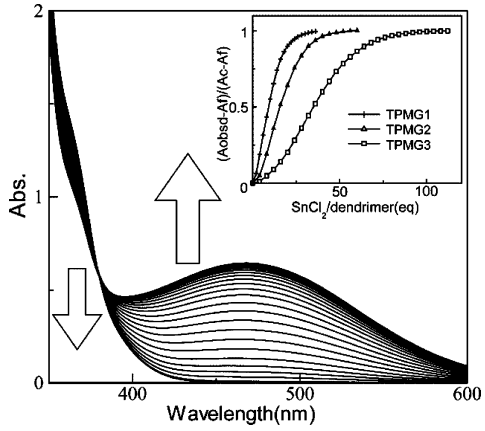


Figure 2. UV−vis spectra of **TPMG3** during the addition of $SnCl_2$ (solvent was benzene:acetonitrile = 4:1 and the concentration was 10 μM). Inset is the titration curve of three dendrimers (10 μM benzene:acetonitrile = 4:1 solution) with $SnCl_2$. A_{obsd} is the observed absorption, A_f is the final absorption, and A_c is the initial absorption.

and Figure S11). The pattern was similar to other phenylazomethine compounds[26] or the carbazole-substituted phenylazomethine compounds[20a,22a−c] which indicate the complexation of $SnCl_2$ to the inner phenylazomethine sites of the dendrimers. The equivalent amount of $SnCl_2$ that was needed until the spectral change became saturated increased when the generation increased (note that the number of binding sites and the concentration were the same for all dendrimers). The reason for this decrease in the binding constant can be twofold: the higher steric hindrance of the higher generation dendrimer and the substituent effect of the carbazole dendrons. As was noted in the Mark−Houwink−Sakurada plot, these dendrimers have an ideal "dense shell"[19b,29] structure without back-folding. It can be assumed that the increase in the steric effect is not very high. The substituent effect of the carbazole (especially when it is tilted) is reported to have a withdrawal character,[30] and the same decrease in the binding constant is reported for the carbazole-substituted phenylazomethines.[20a] Therefore, it can be concluded that the electronic density of the phenylazomethine and the binding constant decreases when the generation of the dendrimer increases due to the generation dependent withdrawal of the carbazole dendrons. This kind of Lewis acid coordination to the phenylazomethine group is reported to enhance hole-transporting property,[22a−d,27] which will be an advantage as a hole-transporting material.

The electrochemistry of the dendrimer was studied by cyclic voltammetry (CV) and differential pulse voltammetry (DPV) techniques. Cyclic voltammograms of the dendrimer (Figure 3) show a typical electropolymerization behavior due to the oxidative coupling of the peripheral carbazole units. The oxidation of the carbazole unit starts at about 0.8 V for **TPMG3** and **TPMG2** and at 1.0 V for **TPMG1** because of the difference in the oxidation potential due to the higher conjugation and substituent effect of the carbazole units[20a,d] (Figure S12). As is known,[31] the carbazole dimer will have two redox sites, and the first redox will occur at a voltage lower than the monomer. The CV of **TPMG1** from 0 to 1.5 V clearly shows this behavior; i.e., a new oxidation peak at about 0.9 V appeared during the second cycle. Additionally, the first redox peak current in the CV from −0.2 to 1.0 V of **TPMG1** was very low compared to the other generations (Figure S13) and to the CV from 0 to 1.5 V of **TPMG1**. This also suggests that the oxidative coupling occurs around 1.0 V. When the cycle is stopped at 1.0 V, the number of the formed dimers is small compared to the other generation dendrimers that have lower oxidation potentials. Other generations also show similar CV behavior, but due to the π-conjugation of several carbazole sites in the dendrimer, the redox behavior is more complicated and difficult to analyze. The peak current of the oxidation peak of the first cycle oxidation has increased although the diffusion constant of the dendrimer decreases when the generation increases (Figure S12). (Theoretically, when the diffusion constant decreases, the peak current decreases.[32]) This indicates that larger numbers of carbazole units are oxidized at once in the higher generation and reflect the higher number of peripheral carbazole units. Next, the HOMO levels of the dendrimers were estimated from the onset voltage of the oxidation in each dendrimer using DPV.[33] The HOMO levels were converted to the vacuum level using the redox potential of ferrocene,[34] and the results were **TPMG1** (5.59 eV), **TPMG2** (5.43 eV), and **TPMG3** (5.40 eV). When the generation increased, the HOMO level also increased. This can be similarly explained by the redox potential, i.e., the higher conjugation and substituent effect of the carbazole units.[20a,d] These values show that the dendrimers are suitable as hole-transporting semiconducting materials, injecting holes from ITO (4.5−5.1 eV[35]) or Au (4.6−5.2 eV[35,36]) electrodes, and also indicate that higher generation dendrimers have a better matching.

The electropolymerization and deposition that were mentioned in the last section can be certainly used to obtain patterned semiconductive films by using patterned electrodes. Moreover, this electropolymerization can be expanded to direct patterning with current-sensing AFM (CS-AFM).[37] A spin-coated film of **TPMG3** (115−130 nm thickness) on a gold-coated glass substrate was prepared, and the patterning was done by tracing a "UH" pattern at a 10 V bias and 0.5 μm/s scan rate (19 °C and 37% relative humidity). The scanning of the film was then done at a 5 V bias and 1.5 μm/s scan rate (Figure 4). The image clearly shows that the pattern is written in the dendrimer film. The negative current that was observed

dx.doi.org/10.1021/ma202485h | *Macromolecules* 2012, 45, 1288−1295

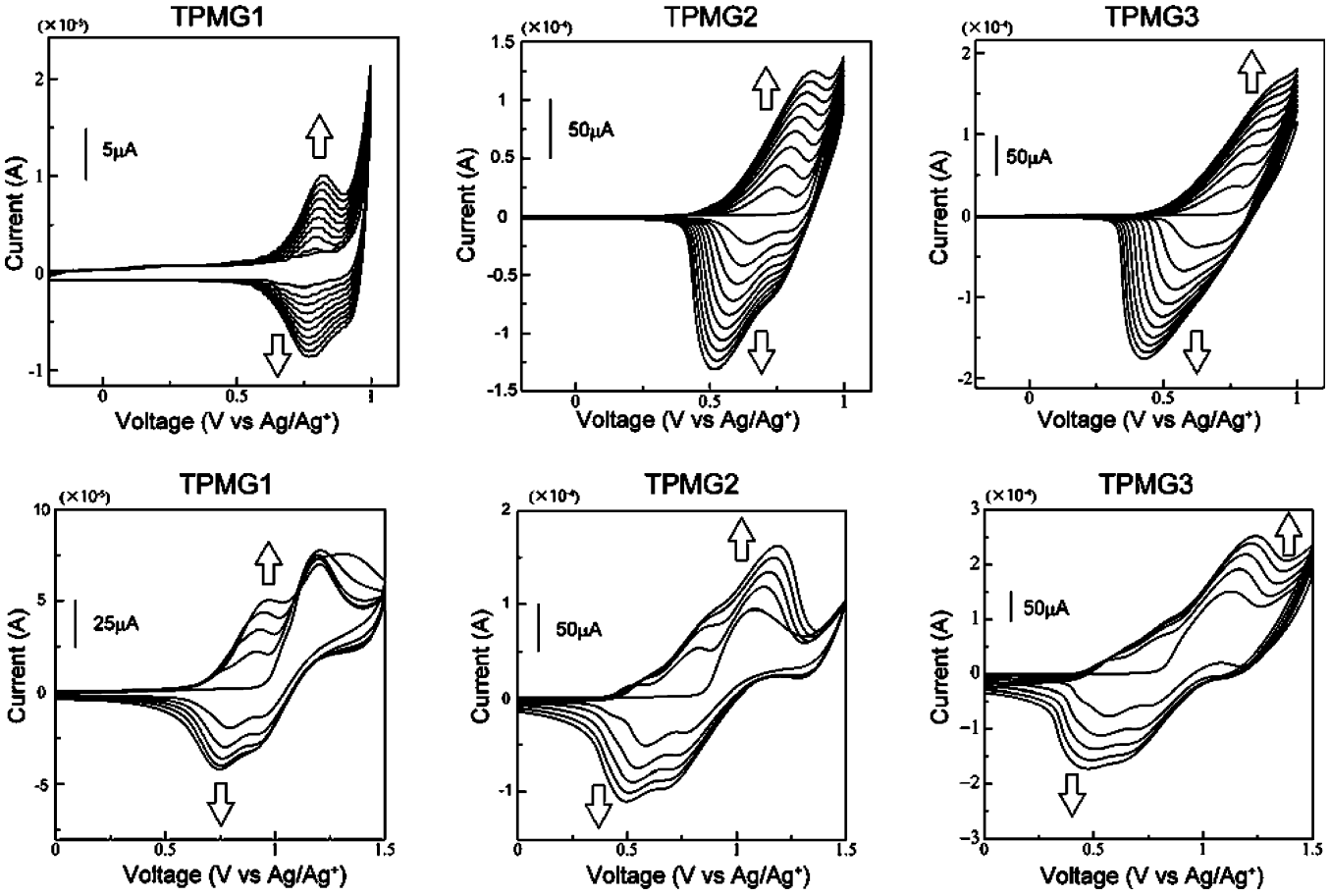


Figure 3. Cyclic voltammogram of the dendrimers during two sweeping ranges (0.5 mM with 0.2 M TBAP).

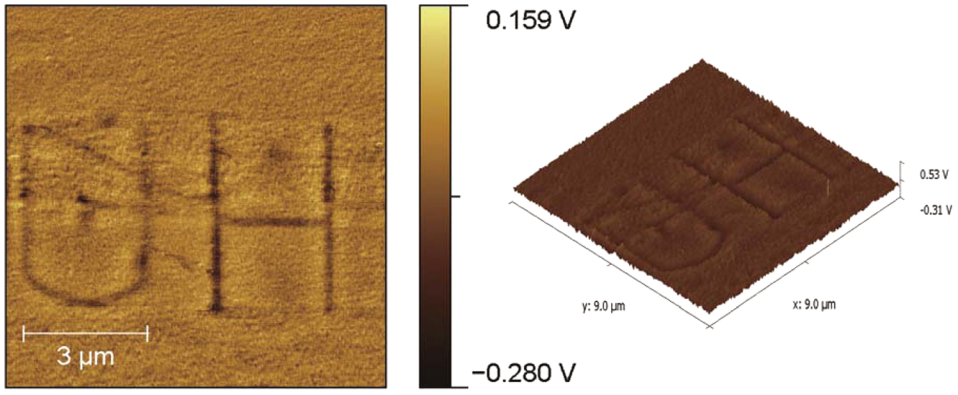


Figure 4. Electronanopatterned "UH" feature with 10 V bias and 0.5 μm/s scan rate (19 °C and 37% relative humidity) using the conducting-AFM mode.

in the pattern indicates the lower resistance of the film due to polymerization and electrodoping. On the other hand, the topographic image of the same area did not show a big change in the height (maximum 0.25 nm change). This morphological stability shows the capability of periphery unsubstituted and rigid dendrimers as patternable materials for electropolymerization.

The oxidative polymerization reaction can be possibly applied to photopolymerization reactions and for patterning with photolithography.[22d] To verify this assumption, a film of the dendrimer was formed in a quartz cell and irradiated by UV light. The spectra before and after UV irradiation in air of **TPMG3** is shown in Figure 5. After UV irradiation, a decrease in the absorption of carbazole (around 300 nm) and increase in the longer wavelength region (350−550 nm) was observed. This corresponds to the oxidative coupling of the peripheral carbazole units at the 3,6-position.[22d,38] After this UV irradiation, the film was rinsed twice with toluene (it was soluble before irradiation), and the UV−vis spectra were measured again. Indeed, no change in the UV−vis spectra was observed, which indicates that the dendrimer film has become insoluble in toluene. This experiment was performed for all three dendrimers for several irradiation times. The minimum time for insolubility to be reached (Figure 6) increased when

dx.doi.org/10.1021/ma202485h | *Macromolecules* 2012, 45, 1288−1295

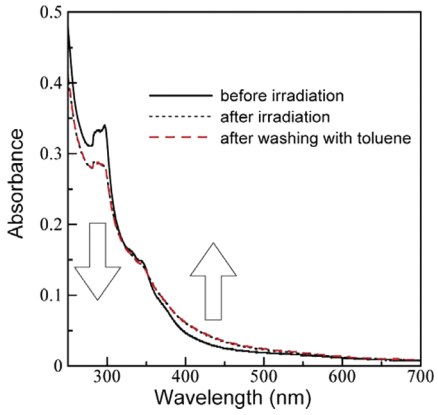


Figure 5. UV–vis spectra of the **TPMG3** film before, after a 3 min UV irradiation, and after washing with toluene.

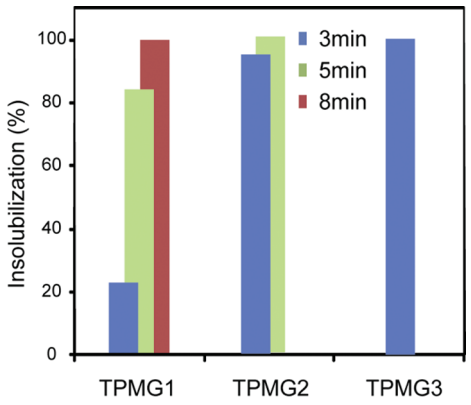


Figure 6. Rate of insolubilization of the double-layer-type dendrimers for different irradiation times.

the generation decreased. This can be explained with the next three reasons: (1) higher generation dendrimers have higher molecular weights, (2) higher generation dendrimers have more reactive units and higher density of them at the periphery, and (3) higher generation dendrimers have higher HOMO levels; i.e., higher generation dendrimers reach the molecular weight that insolubilizes the film faster than the lower generations by photopolymerization. In addition, it is reported that the dimerization reaction of 9-phenylcarbazole cation radical (intermediate of the photo-cross-linking reaction) in solution is accelerated in the presence of neutral 9-phenylacarbazole.[39] Higher generation dendrimers have higher concentration of carbazole unit at the periphery, and presumably this accelerates the photochemical reaction. Interestingly, under a nitrogen atmosphere (nitrogen was flowed through the cell) this reaction was very slow. After 10 min irradiation to **TPMG3** film the insolubilization was less than 10%. This suggests that the existence of air (oxygen) accelerates this photo-cross-linking reaction. The photo-oxidation (dimerization) reaction of carbazole and the participation of oxygen to this reaction are pointed out in some reports.[40] Electron transfer from excited carbazole group generates carbazole cation radicals that dimerize. At the same time, highly reactive oxygen anion radical is generated which can eliminate as H_2O or H_2O_2 or react with carbazole (or carbazole dimer) to produce quinones or oxygen-bridged dimer structures. In the absence of oxygen, the dimerization reaction may take place by elimination of H_2 or disproportion, similarly to the photochemical conversion of diphenylamine to carbazole.[41] However, the results indicate that the reaction without oxygen is slow and the presence of oxygen accelerates the dimerization reaction. Finally, to demonstrate photopatterning using this photoreaction, the UV irradiation through a photomask (300 mesh copper TEM grid was used) was performed. After the UV irradiation, the film was washed with toluene to remove the un-cross-linked dendrimer. A clear pattern of the 45 μm squares was observed in the optical microscope image (Figure 7), which means that the photo-

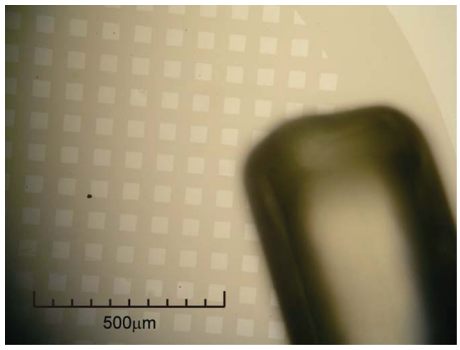


Figure 7. Optical microscope image of photopatterned **TPMG3** film. The object on the right-hand side is a 500 μm diameter wire that was inserted as a standard.

patterning of the dendrimer film has been successfully done and shows that this dendrimer can be potentially used as a photopatternable hole-transporting material.

CONCLUSION

In conclusion, periphery unsubstituted carbazole–phenylazomethine double-layer-type dendrimers with a tetraphenylmethane core were synthesized and characterized. The structure, thermal stability, and metal coordination behavior were determined. The electrochemical polymerization and application to patterning with CS-AFM and patterning with photopolymerization of the dendrimer were demonstrated. Carbazole dendrimers are well-known as an efficient hole-transporting material, and these results are promising such that this dendrimer is an efficient and patternable semiconducting to conductive (doped) material for several organic devices.

ASSOCIATED CONTENT

Supporting Information

Some chemical structures, identification data, calculations, thermal degradation analysis, UV–vis titration, and cyclic voltammograms. This material is available free of charge via the Internet at http://pubs.acs.org.

AUTHOR INFORMATION

Corresponding Author

*E-mail: yamamoto@res.titech.ac.jp (K.Y.); radvincula@uh.edu (R.C.A.).

ACKNOWLEDGMENTS

This work was supported in part by the Core Research for Evolutional Science and Technology (CREST) program of the Japan Science and Technology (JST) Agency and by an Innovative Area (Coordination Programming, Area 2107, no. 21108009) from the Ministry of Education, Culture, Sports,

Science and Technology, Japan. The authors thank the Rigaku Corp. for performing the thermal desorption gas analysis. R.C.A. thanks partial funding support of this work from the Robert A. Welch Foundation E-1551.

REFERENCES

(1) (a) Ferraris, J.; Cowan, D. O.; Walatka, V. Jr.; Perlstein, J. H. *J. Am. Chem. Soc.* **1973**, *95*, 948. (b) Coleman, L. B.; Cohen, M. J.; Sandman, D. J.; Yamagishi, F. G.; Garito, A. F.; Heeger, A. J. *Solid State Commun.* **1973**, *12*, 1125.

(2) Shirakawa, H.; Louis, E. J.; MacDiarmid, A. G.; Chiang, C. K.; Heeger, A. J. *J. Chem. Soc., Chem. Commun.* **1977**, *16*, 578.

(3) (a) Pope, M.; Kallmann, H. P.; Magnante, P. *J. Chem. Phys.* **1962**, *38*, 2042. (b) Helfrich, W.; Schneider, W. G. *Phys. Rev. Lett.* **1965**, *14*, 229.

(4) (a) Tang, C. W.; VanSlyke, S. A. *Appl. Phys. Lett.* **1987**, *51*, 913. (b) Tang, C. W. *Appl. Phys. Lett.* **1986**, *48*, 183.

(5) (a) Shirota, Y.; Kageyama, H. *Chem. Rev.* **2007**, *107*, 953. (b) Anthony, J. E. *Chem. Rev.* **2006**, *106*, 5028. (c) Logothetidis, S. *Mater. Sci. Eng., B* **2008**, *152*, 96. (d) Kanibolotsky, A. L.; Perepichka, I. F.; Skabara, P. J. *Chem. Soc. Rev.* **2010**, *39*, 2695.

(6) Strohriegel, P.; Grazulevicius, J. V. In *Handbook of Organic Conductive Molecules and Polymers*; Nalwa, H. S., Ed.; John Wiley & Sons: Chichester, 1997; Vol. *1*, Chapter 11, pp 553−620.

(7) (a) Geffroy, B.; le Roy, P.; Prat, C. *Polym. Int.* **2006**, *55*, xxxx. (b) Kido, J.; Kimura, M.; Nagai, K. *Science* **1995**, *267*, 1332. (c) Nuyken, O.; Jungermann, S.; Wiederhirn, V.; Bacher, E.; Meerholz, K. *Monatsh. Chem.* **2006**, *137*, 811. (d) Kulkarni, A. P.; Tonzola, C. J.; Babel, A.; Jenekhe, S. A. *Chem. Mater.* **2004**, *16*, 4556.

(8) (a) Brabec, C. J.; Durrant, J. R. *MRS Bull.* **2008**, *33*, 670. (b) Cheng, Y. J.; Yang, S. H.; Hsu, C. S. *Chem. Rev.* **2009**, *109*, 5868. (c) Hains, A. W.; Liang, Z.; Woodhouse, M. A.; Gregg, B. A. *Chem. Rev.* **2010**, *110*, 6689. (d) Hagfeldt, A.; Boschloo, G.; Sun, L.; Kloo, L.; Pettersson, H. *Chem. Rev.* **2010**, *110*, 6595.

(9) (a) Kudo, K.; Yamashina, M.; Moriizumi, T. *Jpn. J. Appl. Phys.* **1984**, *23*, 130. (b) Zaumseil, J.; Sirringhaus, H. *Chem. Rev.* **2007**, *107*, 1296.

(10) (a) Wallikewitz, B. H.; de la Rosa, M.; Kremer, J. H.-W. M.; Hertel, D.; Meerholz, K. *Adv. Mater.* **2010**, *22*, 531. (b) Gärtner, C.; Karnutsch, C.; Lemmer, U. *J. Appl. Phys.* **2007**, *101*, 023107. (c) Ichikawa, M.; Nakamura, K.; Inoue, M.; Mishima, H.; Haritani, T.; Hibino, R.; Koyama, T.; Taniguchi, Y. *Appl. Phys. Lett.* **2005**, *87*, 221113.

(11) (a) Muccini, M. *Nature Mater.* **2006**, *5*, 605. (b) Nakanotani, H.; Akiyama, S.; Ohnishi, D.; Moriwake, M.; Yahiro, M.; Yoshihara, T.; Tobita, S.; Adachi, C. *Adv. Funct. Mater.* **2007**, *17*, 2328. (c) Oyamada, T.; Okuyama, S.; Shimoji, N.; Matsushige, K.; Sasabe, H.; Adachi, C. *Appl. Phys. Lett.* **2005**, *86*, 093505.

(12) (a) Ling, Q. D.; Liaw, D. J.; Zhu, C.; Chan, D. S. H.; Kang, E. T.; Neoh, K. G. *Prog. Polym. Sci.* **2008**, *33*, 917. (b) Heremans, P.; Gelinck, G. H.; Müller, R.; Baeg, K. J.; Kim, D. Y.; Noh, Y. Y. *Chem. Mater.* **2011**, *23*, 341. (c) Yonekuta, Y.; Susuki, K.; Oyaizu, K.; Honda, K.; Nishide, H. *J. Am. Chem. Soc.* **2007**, *129*, 14128.

(13) Menard, E.; Meitl, M. A.; Sun, Y.; Park, J. U.; Shir, D. J. L.; Nam, Y. S.; Jeon, S.; Rogers, J. A. *Chem. Rev.* **2007**, *107*, 1117.

(14) (a) Tomalia, D. A. *Prog. Polym. Sci.* **2005**, *30*, 294. (b) Bosman, A. W.; Janssen, H. M.; Meijer, E. W. *Chem. Rev.* **1999**, *99*, 1665. (c) Fischer, M.; Vögtle, F. *Angew. Chem., Int. Ed.* **1999**, *38*, 884. (d) Tomalia, D. A.; Naylor, A. M.; Goddard, W. A. III. *Angew. Chem., Int. Ed. Engl.* **1990**, *29*, 138.

(15) (a) Voit, B. I.; Lederer, A. *Chem. Rev.* **2009**, *109*, 5924. (b) Taton, D.; Feng, X.; Gnanou, Y. *New J. Chem.* **2007**, *31*, 1097.

(16) (a) Astruc, D.; Boisselier, E.; Ornelas, C. *Chem. Rev.* **2010**, *110*, 1857. (b) Wang, Q.; Mynar, J. L.; Yoshida, M.; Lee, E.; Lee, M.; Okuro, K.; Kinbara, K.; Aida, T. *Nature* **2010**, *463*, 339.

(17) (a) Furuta, P.; Brooks, J.; Thompson, M. E.; Fréchet, J. M. J. *J. Am. Chem. Soc.* **2003**, *125*, 13165. (b) Ribierre, J. C.; Ruseckas, A.; Knights, K.; Staton, S. V.; Cumpstey, N.; Burn, P. L.; Samuel, I. D. W. *Phys. Rev. Lett.* **2008**, *100*, 017402. (c) Ribierre, J. C.; Ruseckas, A.; Samuel, I. D. W.; Staton, S. V.; Burn, P. L. *Phys. Rev. B* **2008**, *77*, 085211. (d) Namdas, E. B.; Ruseckas, A.; Samuel, I. D. W. *Appl. Phys. Lett.* **2005**, *86*, 091104.

(18) (a) Lo, S.-C.; Burn, P. L. *Chem. Rev.* **2007**, *107*, 1097. (b) Ma, C. Q.; Fonrodona, M.; Schikora, M. C.; Wienk, M. M.; Janssen, R. A. J.; Bäuerle, P. *Adv. Funct. Mater.* **2008**, *18*, 3323.

(19) (a) Berresheim, A. J.; Muller, M.; Müllen, K. *Chem. Rev.* **1999**, *99*, 1747. (b) Rosenfeldt, S.; Dingenouts, N.; Pötschke, D.; Ballauff, M.; Berresheim, A. J.; Müllen, K.; Linder, P. *Angew. Chem., Int. Ed.* **2004**, *43*, 109.

(20) (a) Albrecht, K.; Yamamoto, K. *J. Am. Chem. Soc.* **2009**, *131*, 2244. (b) Hameurlaine, A.; Dehaen, W. *Tetrahedron Lett.* **2003**, *44*, 957. (c) Zhang, Q.; Hu, Y. F.; Cheng, Y. X.; Su, G. P.; Ma, D. G.; Wang, L. X.; Jing, X. B.; Wang, F. S. *Synth. Met.* **2003**, *137*, 1111. (d) Loiseau, F.; Campagna, S.; Hameurlaine, A.; Dehaen, W. *J. Am. Chem. Soc.* **2005**, *127*, 11352. (e) Xu, T.; Lu, R.; Liu, X.; Zheng, X.; Qiu, X.; Zhao, Y. *Org. Lett.* **2007**, *9*, 797. (f) Wang, B.-B.; Li, W.-S.; Jia, X.-R.; Gao, M.; Ji, Y.; Zhang, X.; Li, Z.-C.; Jiang, L.; Wei, Y. *J. Colloid Interface Sci.* **2007**, *314*, 289. (g) Konno, T.; El-Khouly, M. E.; Nakamura, Y.; Kinoshita, K.; Araki, Y.; Ito, O.; Yoshihara, T.; Tobita, S.; Nishimura, J. *J. Phys. Chem. C* **2008**, *112*, 1244.

(21) (a) Qin, T.; Ding, J.; Wang, L.; Baumgarten, M.; Zhou, G.; Müllen, K. *J. Am. Chem. Soc.* **2009**, *131*, 14329. (b) Jaiser, F.; Neher, D.; Meisel, A.; Nothofer, H. G.; Miteva, T.; Herrmann, A.; Müllen, K.; Scherf, U. *J. Chem. Phys.* **2009**, *129*, 114901. (c) Khotina, I. A.; Lepnev, L. S.; Burenkova, N. S.; Valetsky, P. M.; Vitukhnovsky, A. G. *J. Lumin.* **2004**, *110*, 232.

(22) (a) Albrecht, K.; Kasai, Y.; Kimoto, A.; Yamamoto, K. *Macromolecules* **2008**, *41*, 3793. (b) Kimoto, A.; Cho, J. S.; Higuchi, M.; Yamamoto, K. *Macromolecules* **2004**, *37*, 5531. (c) Kimoto, A.; Cho, J. S.; Higuchi, M.; Yamamoto, K. *Macromol. Symp.* **2004**, *209*, 51. (d) Kimoto, A.; Cho, J. S.; Ito, K.; Aoki, D.; Miyake, T.; Yamamoto, K. *Macromol. Rapid Commun.* **2005**, *26*, 597. (e) Ding, J.; Gao, J.; Cheng, Y.; Xie, Z.; Wang, L.; Ma, D.; Jing, X.; Wang, F. *Adv. Funct. Mater.* **2006**, *16*, 575. (f) Zhang, Q.; Hu, Y. F.; Cheng, Y. X.; Su, G. P.; Ma, D. G.; Wang, L. X.; Jing, X. B.; Wang, F. S. *Synth. Met.* **2003**, *137*, 1111. (g) Promarak, V.; Ichikawa, M.; Meunmart, D.; Sudyoadsuk, T.; Saengsuwan, S.; Keawin, T. *Tetrahedron Lett.* **2006**, *47*, 8949. (h) Tsai, M. H.; Hong, Y. h.; Chang, C. H.; Su, H. C.; Wu, C. C.; Matoliukstyte, A.; Simokaitiene, J.; Grigalevicius, S.; Grazulevicius, J. V.; Hsu, C. P. *Adv. Mater.* **2008**, *19*, 862. (i) Jung, K. M.; Kim, K. H.; Jin, J. I.; Cho, M. J.; Choi, D. H. *J. Polym. Sci., Part A: Polym. Chem.* **2008**, *46*, 7517. (j) Gambino, S.; Stevenson, S. G.; Knights, K. A.; Burn, P. L.; Samuel, I. D. W. *Adv. Funct. Mater.* **2009**, *19*, 317. (k) Knights, K. A.; Stevenson, S. G.; Shipley, C. P.; Lo, S. C.; Olsen, S.; Harding, R. E.; Gambino, S.; Burn, P. L.; Samuel, I. D. W. *J. Mater. Chem.* **2008**, *18*, 2121.

(23) (a) Müller, C. D.; Falcou, A.; Nina Reckefuss, N.; Rojahn, M.; Wiederhirn, V.; Rudati, P.; Frohne, H.; Nuyken, O.; Becker, H.; Meerholz, K. *Nature* **2003**, *421*, 829. (b) Contoret, A. E. A.; Farrar, S. R.; O'Neill, M.; Nicholls, J. E.; Richards, G. J.; Kelly, S. M.; Hall, A. W. *Chem. Mater.* **2002**, *14*, 1477. (c) Chou, M. Y.; Leung, M.; Su, Y. O.; Chiang, C. L.; Lin, C. C.; Liu, J. H.; Kuo, C. K.; Mou, C. Y. *Chem. Mater.* **2004**, *16*, 654. (d) Zuniga, C. A.; Barlow., S.; Marder, S. R. *Chem. Mater.* **2011**, *23*, 658.

(24) (a) Laliberte, D.; Maris, T.; Wuest, J. D. *Can. J. Chem.* **2004**, *82*, 386. (b) Thaimattam, R.; Xue, F.; Sarma, J. A. R. P.; Mak, T. C. W.; Desiraju, G. R. *J. Am. Chem. Soc.* **2001**, *123*, 4432.

(25) Enoki, O.; Katoh, H.; Yamamoto, K. *Org. Lett.* **2006**, *8*, 569.

(26) (a) Yamamoto, K.; Higuchi, M.; Shiki, S.; Tsuruta, M.; Chiba, H. *Nature* **2002**, *415*, 509. (b) Yamamoto, K.; Imaoka, T. *Bull. Chem. Soc. Jpn.* **2005**, *79*, 511.

(27) (a) Cho, J. S.; Takanashi, K.; Higuchi, M.; Yamamoto, K. *Synth. Met.* **2005**, *150*, 79. (b) Satoh, N.; Cho, J. S.; Higuchi, M.; Yamamoto, K. *J. Am. Chem. Soc.* **2003**, *125*, 8104. (c) Albrecht, K.; Kimoto, A.; Cho, J. S.; Matsuura, Y.; Yamamoto, K. *J. Photopolym. Sci. Technol.* **2008**, *21*, 181.

(28) (a) Billmeyer, F. W., Jr. In *Textbook of Polymer Science*, 3rd ed.; John Wiley & Sons: New York, 1984; p 208. (b) Mourey, T. H.; Turner, S. R.; Rubinstein, M.; Fréchet, J. M. J.; Hawker, C. J. *Macromolecules* **1992**, *25*, 2401. (c) de Brabander-van den Berg, E. M. M.; Meijer, E. W. *Angew. Chem., Int. Ed. Engl.* **1993**, *32*, 1308. (d) Lyulin, A. V.; Davies, G. R.; Adolf, D. B. *Macromolecules* **2000**, *33*, 3294. (e) Naylor, A. M.; Goddard, W. A. III; Keifer, G. E.; Tomalia, D. A. *J. Am. Chem. Soc.* **1989**, *111*, 2339. (f) Striegel, A. M.; Plattner, R. D.; Willett, J. L. *Anal. Chem.* **1999**, *71*, 978. (g) Comanita, B.; Noren, B.; Roovers, J. *Macromolecules* **1999**, *32*, 1069.

(29) (a) Rosenfeldt, S.; Dingenouts, N.; Pötschke, D.; Ballauff, M.; Berresheim, A. J.; Müllen, K.; Linder, P.; Saalwächter, K. *J. Lumin.* **2005**, *111*, 225. (b) Wind, M.; Saalwächter, K.; Wiesler, U.-M.; Müllen, K.; Spiess, H. W. *Macromolecules* **2002**, *35*, 10071.

(30) (a) Schaerlaekens, M.; Hendrickx, E.; Hameurlaine, A.; Dehaen, W.; Persoons, A. *Chem. Phys.* **2002**, *277*, 43. (b) Zain, S. M.; Hashim, R.; Taylor, A. G.; Phillips, D. *J. Mol. Struct. (THEOCHEM)* **1997**, *401*, 287. (c) Zhang, X.; Matsuo, Y.; Nakamura, E. *Org. Lett.* **2008**, *10*, 4145.

(31) (a) Ambrose, J. F.; Nelson, R. F. *J. Electrochem. Soc.* **1968**, *115*, 1159. (b) Ambrose, J. F.; Carpenter, L. L.; Nelson, R. F. *J. Electrochem. Soc.* **1975**, *122*, 876.

(32) $I(t) = -(nFAD_0^{1/2}C_0)/(\pi t)^{1/2}$, where I, n, F, A, C_0, and D_0 are current, number of electrons, Faraday constant, area of the electrode, concentration of the analyte, and diffusion coefficient of the analyte, respectively. This equation is the Cottrell's equation, but in a precise sense this equation works only for reversible redox systems. See the following book: Bard, A. J.; Faulker, L. R. *Electrochemical Methods, Fundamentals and Application*, 2nd ed.; John Wiley and Sons Inc.: New York, 2001.

(33) (a) Taranekar, P.; Fulghum, T.; Patton, D.; Ponnapati, R.; Clyde, G.; Advincula, R. *J. Am. Chem. Soc.* **2007**, *129*, 12537. (b) Promarak, V.; Ichikawa, M.; Meunmart, D.; Sudyoadsuk, T.; Saengsuwan, S.; Keawin, T. *Tetrahedron Lett.* **2006**, *47*, 8949.

(34) Pommerehne, J.; Vestweber, H.; Guss, W.; Mahrt, R. F.; Bässler, H.; Porsch, M.; Daub, J. *Adv. Mater.* **1995**, *7*, 551.

(35) Adachi, C.; Oyamada, T.; Nakajima, Y. *Databook on Work Function of Organic Thin Films*, 2nd ed.; CMC: Japan, 2006; Chapter 6.

(36) (a) Tang, Q.; Li, H.; Liu, Y.; Hu, W. *J. Am. Chem. Soc.* **2006**, *128*, 14634. (b) Hirose, T.; Nagase, T.; Kobayashi, T.; Ueda, R.; Otomo, A.; Naito, H. *Appl. Phys. Lett.* **2010**, *97*, 083301. (c) Parker, I. D. *J. Appl. Phys.* **1994**, *75*, 1656.

(37) (a) Park, J. Y.; Ponnapati, R.; Taranekar, P.; Advincula, R. C. *Langmuir* **2010**, *26*, 6167. (b) Huang, C.; Jiang, G.; Advincula, R. *Macromolecules* **2008**, *41*, 4661. (c) Jiang, J.; Baba, A.; Advincula, R. *Langmuir* **2007**, *23*, 817. (d) Baba, A.; Jiang, G.; Park, K.; Park, J.; Shin, H.; Advincula, R. *J. Phys. Chem. B* **2006**, *110*, 17309. (e) Jegadesan, S.; Sindhu, S.; Advincula, R.; Valiyaveettil, S. *Langmuir* **2006**, *22*, 3807. (f) Jegadesan, S.; Sindhu, S.; Advincula, R.; Valiyaveettil, S. *Langmuir* **2006**, *22*, 780. (g) Jagadesan, S.; Advincula, R.; Valiyaveettil, S. *Adv. Mater.* **2005**, *17*, 1282.

(38) Albrecht, K.; Yamamoto, K. *J. Photopolym. Sci. Technol.* **2006**, *19*, 175.

(39) Matsui, J.; Oyama, M. *Bull. Chem. Soc. Jpn.* **2004**, *77*, 953.

(40) (a) Pfister, G.; Williams, D. J. *J. Chem. Phys.* **1974**, *61*, 2416. (b) Rivaton, A.; Mailhot, B.; Derderian, G.; Bussiere, P. O.; Gardette, J.-L. *Macromolecules* **2003**, *36*, 5815. (c) Qian, L.; Bera, D.; Holloway, P. H. *Appl. Phys. Lett.* **2008**, *92*, 053303.

(41) (a) Görner, H. *J. Phys. Chem. A* **2008**, *112*, 1245. (b) Shizuka, H.; Takayama, Y.; Tanaka, I.; Morita, T. *J. Am. Chem. Soc.* **1970**, *92*, 7270. (c) Linschitz, H.; Grellmann, K. H. *J. Am. Chem. Soc.* **1964**, *86*, 303.

Macromolecules

Article

pubs.acs.org/Macromolecules

Synthesis of a Conjugated Polymer with Broad Absorption and Its Application in High-Performance Phototransistors

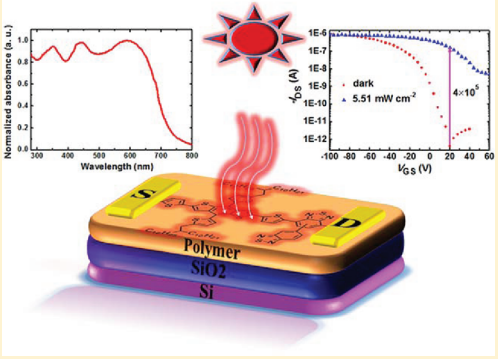
Yao Liu,[†,‡] Haifeng Wang,[†] Huanli Dong,[†] Jiahui Tan,[†,‡] Wenping Hu,*[,†] and Xiaowei Zhan*[,†]

[†]Beijing National Laboratory for Molecular Sciences and CAS Key Laboratory of Organic Solids, Institute of Chemistry, Chinese Academy of Sciences, Beijing 100190, China

[‡]Graduate School of Chinese Academy of Sciences, Beijing 100049, China

Supporting Information

ABSTRACT: An amorphous copolymer (PBDT−BBT) of 4,8-bis(2-thienyl)benzo[1,2-*b*:4,5-*b*′]dithiophene and 5,5′-bibenzo[*c*][1,2,5]thiadiazole was synthesized by Stille coupling polymerization. PBDT−BBT exhibited good solution processability, excellent thermal stability with decomposition temperature of 437 °C, broad absorption (300−800 nm), deep HOMO level (−5.7 eV), and LUMO level (−3.7 eV). The microstructure order of PBDT−BBT thin films is not susceptible to thermal annealing temperature (80−200 °C). Field-effect transistors based on this polymer exhibited a charge-carrier mobility of 6×10^{-3} cm^2 V^{-1} s^{-1}, threshold voltage of −1 V, and on/off current ratio of 10^6 without any post-treatments. Thin film phototransistors of PBDT−BBT exhibited a photoresponsivity of 3200 mA W^{-1} and photocurrent/dark current ratio of 4×10^5.



INTRODUCTION

Phototransistors, allowing additional light as the "fourth terminal" compared to common organic field-effect transistors (OFETs), are more promising as photodetectors than conventional photodiodes due to their high photosensitivity deriving from an internal amplification of the photocurrent.[1−6] Phototransistors have been widely employed for light induced switches, light triggered amplification, detection circuits, and highly sensitive image sensors.[7−9] Critical processes, which confine the realization of high-performance phototransistors, include the generation of charge carriers under light irradiation, the transfer of charge carriers, and the collection of charge carriers for signal magnification.[4,10−15]

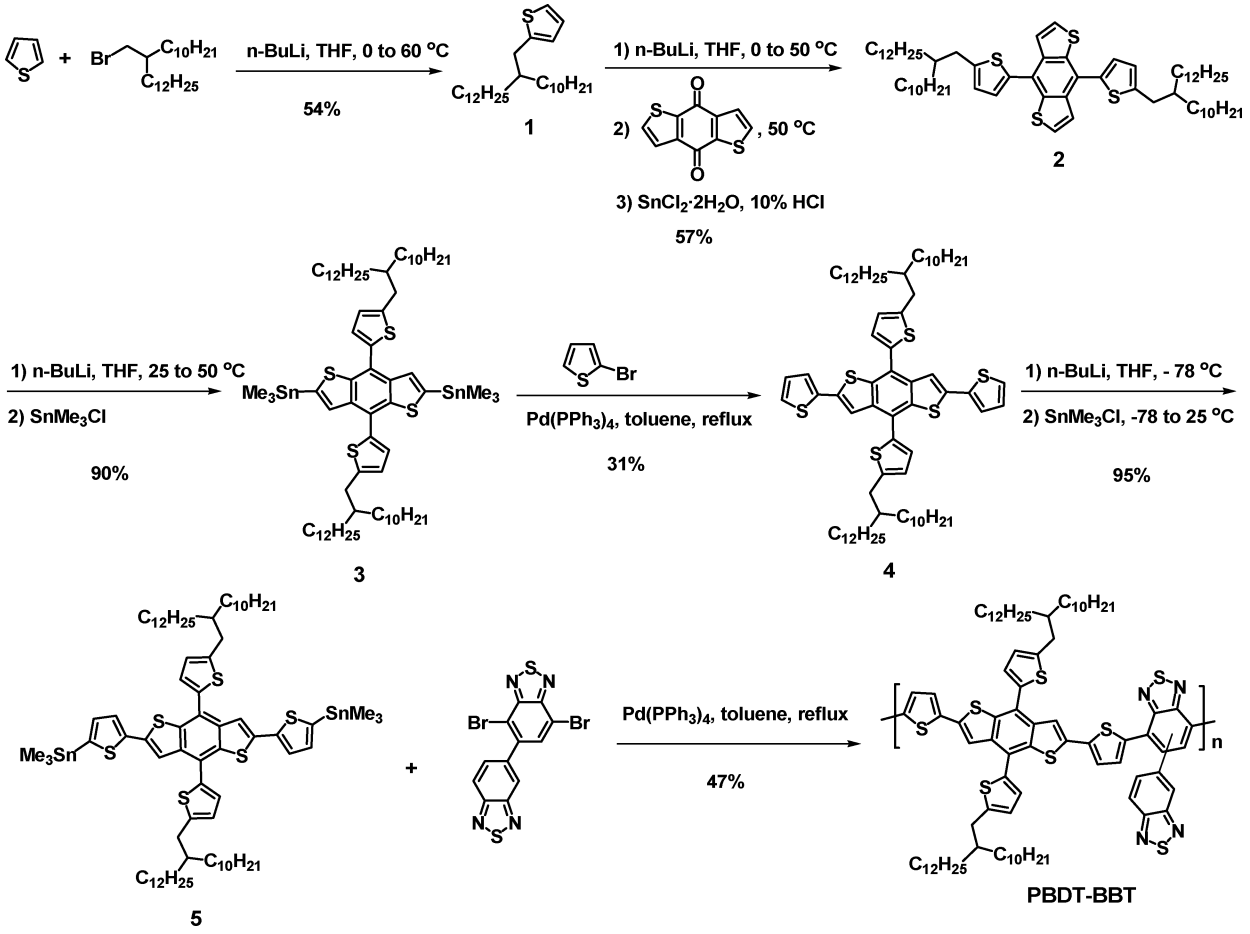
Conjugated polymers have emerged as a class of solution-processable semiconductors, and their optical and electronic properties can be tuned by chemical modification.[16−20] On one hand, the donor (D)−acceptor (A) strategy is widely used in synthetic design of narrow band gap conjugated polymers to harvest more incident photons for efficient charge-carrier generation.[17,21−23] On the other hand, to improve charge-carrier mobility and ensure broad absorption, fused-ring building blocks have been introduced into conjugated polymer backbone.[24−31] This approach can lead to more rigid and planar polymer backbone, thereby extending π-conjugated length, lowering band gap, and facilitating intermolecular charge carrier hopping and transporting.[29,32−34] Therefore, conjugated polymers are promising semiconductors for high-performance phototransistors.[11,35−37] Recently, several groups have reported their great progress in polymer thin film phototransistors. For example, Wang et al. reported phototransistors based on a polyfluorene derivative F8T2 with a photoresponsivity of 18.5 A W^{-1}.[38] The highest photoresponsivity of conjugated polymers (250 A W^{-1}) was achieved from poly(3-hexylthiophene) (P3HT)-based devices.[39] We reported a phototransistor based on a polycarbazole derivative with quite high on/off ratio of 4.6×10^4.[4]

Recently, the large planar benzo[1,2-*b*:4,5-*b*′]dithiophene (BDT) unit has emerged as an attractive building block for conjugated polymers. Copolymers of BDT and bithiophene exhibited a high mobility of 0.25 cm^2 V^{-1} s^{-1} in OFETs.[34,40] The polymer solar cells (PSCs) based on blends of BDT-based copolymers and soluble fullerene derivatives $PC_{61}BM$ or $PC_{71}BM$ afforded high power conversion efficiencies (4−8%).[41−52] In particular, 4,8-bis(2-thienyl)benzo[1,2-*b*:4,5-*b*′]dithiophene-based copolymers exhibited broad absorption and high performance as donor materials in PSCs,[48−50] However, the application of BDT-based copolymers in phototransistors has not been reported. Very recently, we reported a new n-type building block 5,5′-bibenzo[*c*][1,2,5]thiadiazole (BBT) and a BBT-based polymer for high-performance PSCs.[53] Here, we report a low band gap copolymer (PBDT−BBT, Scheme 1) of 4,8-bis(2-thienyl)benzo[1,2-*b*:4,5-*b*′]dithiophene and 5,5′-bibenzo[*c*][1,2,5]thiadiazole. PBDT−BBT has a deep highest occupied molecular orbital (HOMO) level (−5.7 eV) and a deep lowest unoccupied molecular orbital (LUMO) level (−3.7 eV) due to the stronger electron-withdrawing ability of BBT unit. In addition, BBT tends to adopt a twisted geometry, which can improve solubility of the polymer. Therefore,

Received: November 27, 2011
Revised: January 10, 2012
Published: February 1, 2012

 © 2012 American Chemical Society dx.doi.org/10.1021/ma202582n | *Macromolecules* 2012, 45, 1296−1302

Scheme 1. Synthetic Route of Polymer PBDT−BBT



PBDT−BBT could be an air-stable and solution-processable semiconducting polymer. PBDT−BBT exhibited strong absorption across the entire visible region and a relatively high hole mobility of 6×10^{-3} cm^2 V^{-1} s^{-1}. The phototransistors based on PBDT−BBT thin films exhibited a photoresponsivity of 3200 mA W^{-1} and a very high photocurrent/dark current ratio of 4×10^5.

EXPERIMENTAL SECTION

Measurements and Characterization. The ^{1}H NMR and ^{13}C NMR spectra were measured on a Bruker AVANCE 400 MHz spectrometer using tetramethylsilane (TMS; $\delta = 0$ ppm) as an internal standard. Mass spectra were measured on a GCT-MS micromass spectrometer using the electron impact (EI) mode or on a Bruker Daltonics BIFLEX III MALDI-TOF analyzer using MALDI mode. Elemental analyses were carried out using a FLASH EA1112 elemental analyzer. Thermogravimetric analysis (TGA) measurements were performed using a DTG-60 thermal analysis system under N_2 at a heating rate of 10 °C min^{-1}. Differential scanning calorimetry (DSC) measurements were performed using an SII EXSAR6000 (DSC 6220) under a nitrogen atmosphere with a heating and cooling rate of 10 °C min^{-1}. Solution (chloroform) and thin-film (on quartz substrate) UV−vis spectra were recorded on a Jasco V-570 spectrophotometer. The electrochemical measurements were carried out under nitrogen on a deoxygenated solution of tetra-*n*-butylammonium hexafluorophosphate (0.1 M) in acetonitrile with a computer-controlled CHI660C electrochemical workstation, a glassy-carbon working electrode coated with the polymer film, a platinum-wire auxiliary electrode, and an Ag wire anodized with AgCl as a pseudoreference electrode. Potentials were referenced to the ferrocenium/ferrocene ($FeCp_2^{+/0}$) couple by using ferrocene as a standard. The gel permeation chromatography (GPC) measurements were performed on a Waters 515 chromatograph connected to a Waters 2414 refractive index detector, using tetrahydrofuran (THF) as eluent and polystyrene standards as calibrants; three Waters Styragel columns (HT2, 3, 4) connected in series were used. The film morphology was analyzed in air using a Nanoscope III atomic force microscope (Digital Instruments) operated in tapping mode. X-ray diffraction (XRD) of thin films was performed in the reflection mode at 40 kV and 200 mA with Cu Kα radiation using a 2 kW Rigaku D/max-2500 X-ray diffractometer.

Device Fabrication and Characterization. All the devices based on PBDT−BBT thin films were fabricated in the bottom gate, top contact configuration under ambient atmosphere. Highly n-doped silicon and thermally grown silicon dioxide (500 nm) were used as back gate and gate dielectric, respectively. The substrates were cleaned with pure water, hot concentrated sulfuric acid−hydrogen peroxide solution (concentrated sulfuric acid/hydrogen peroxide water = 2:1), pure water, and pure isopropyl alcohol. Then vaporized octadecyltrichlorosilane (OTS) was used for surface modification of the gate dielectric layer. PBDT−BBT in *o*-dichlorobenzene (about 2 mg mL^{-1}) was drop-casted onto OTS treated substrates to form polymer films (about 100 nm). After the evaporation of solvent under dark for 48 h, polymer films were formed. Prior to thermal evaporation of top contact electrodes, the films were baked in a vacuum chamber located in the glovebox for 30 min to completely remove the residual solvent or anneal the samples. Gold contacts (25 nm) for source and drain electrodes were vacuum-deposited at a rate of 0.1 Å s^{-1} through a metal shadow mask that defined a series of transistor devices with a channel length (L) of 27 μm and a channel width (W) of 210 μm. The characterization was accomplished by a Keithley 4200 SCS with a micromanipulator 6150 probe station in a clean shielded box at ambient atmosphere. Then field-effect mobility was calculated from the standard equation for saturation region in metal−dioxide−

dx.doi.org/10.1021/ma202582n | Macromolecules 2012, 45, 1296−1302

semiconductor field effect transistors: $I_{DS} = (W/2L)\mu C_i(V_G - V_T)^2$, where I_{DS} is drain-source current, μ is field-effect mobility, W and L are the channel width and length, C_i is the capacitance per unit area of the gate insulator (C_i = 7.5 nF cm^{-2}), V_G is the gate voltage, and V_T is the threshold voltage.[54] As for the test of phototransistors, white light was irradiated directly on polymer films during the operation of field-effect transistors. To evaluate the performance of thin film phototransistors, photoresponsivity (R) and photocurrent/dark current ratio (P) are defined by the following equations:

$$R = (I_{DS,i} - I_{DS,d})/(SP_i) \quad (a)$$

$$P = (I_{DS,i} - I_{DS,d})/I_{DS,d} \quad (b)$$

where $I_{DS,i}$ and $I_{DS,d}$ are the drain-source current under illumination and in dark, P_i is the power of the incident light per unit area, and S is the effective device area.[55]

Materials. 4,7-Dibromo-5,5′-bibenzo[*c*][1,2,5]thiadiazole was synthesized according to the procedure reported by our group.[53] Toluene and THF were distilled from sodium and benzophenone under nitrogen before use. Bio-Rad Bio-Beads S-X1 is a kind of porous cross-linked polystyrene polymers used for gel permeation separations of lipophilic polymers and low molecular weight, hydrophobic materials in the presence of organic solvents. Unless stated otherwise, the other reagents were purchased from commercial sources and used without further purification.

2-(2-Decyltetradecyl)thiophene (1). A solution of thiophene (378 mg, 4.5 mmol) in dry THF (10 mL) was deoxygenated with nitrogen for 15 min, and 2 mL of *n*-butyllithium (5 mmol, 2.5 M in *n*-hexane) was added dropwise at 0 °C. After the solution was stirred at 0 °C for 30 min, 11-(bromomethyl)tricosane (2.08 g, 5 mmol) was added. Then the mixture was heated to 60 °C and was stirred for 16 h. After the reaction mixture was cooled to room temperature, it was poured into 200 mL of cool water and extracted with hexane. The organic layer was washed with water and then dried over anhydrous $MgSO_4$. After the solvent was removed under vacuum, the residue was purified by column chromatography (silica gel, hexane/CH_2Cl_2 = 1:1) to afford pale yellow oil (1.02 g, 54%). ^{1}H NMR (400 MHz, $CDCl_3$): δ 7.11 (d, J = 5.1 Hz, 1H), 6.92 (dd, J = 5.0 Hz, J = 3.1 Hz, 1H), 6.75 (d, J = 3.1 Hz), 2.77 (d, J = 6.7 Hz, 2H), 1.62 (m, 1H), 1.32−1.25 (m, 40H), 0.90 (t, J = 6.8 Hz, 6H). ^{13}C NMR (100 MHz, $CDCl_3$): δ 144.38, 126.58, 125.03, 122.97, 40.12, 34.32, 33.27, 32.07, 30.10, 30.02, 29.81, 29.51, 26.70, 22.83, 14.25. HRMS (EI): 420.3796 (calcd for $C_{28}H_{52}S$, 420.3790). Anal. Calcd for $C_{28}H_{52}S$: C, 79.92; H, 12.46. Found: C, 79.62; H, 12.42%.

4,8-Bis(5-(2-decyltetradecyl)thiophen-2-yl)benzo[1,2-*b*:4,5-*b*′]dithiophene (2). A solution of **1** (838 mg, 2 mmol) in dry THF (5 mL) was deoxygenated with nitrogen for 15 min, and 0.88 mL of *n*-butyllithium (2.2 mmol, 2.5 M in *n*-hexane) was added dropwise at 0 °C. Then the solution was allowed to warm up to 50 °C and stirred for 1.5 h; benzo[1,2-*b*:4,5-*b*′]dithiophene-4,8-dione (176 mg, 0.8 mmol) was added. The mixture was stirred at 50 °C for another 1.5 h. After the reaction mixture was cooled to room temperature, $SnCl_2{\cdot}2H_2O$ (1.44 g, 6.4 mmol) in 2.56 mL of 10% hydrochloric acid) was added, and the reaction mixture was stirred for 1.5 h. The mixture was poured into 200 mL of cool water and extracted with CH_2Cl_2. The organic layer was washed with water and then dried over anhydrous $MgSO_4$. After the solvent was removed under vacuum, the residue was purified by column chromatography (silica gel, hexane) to afford yellow oil (467 mg, 57%). ^{1}H NMR (400 MHz, $CDCl_3$): δ 7.65 (d, J = 5.7 Hz, 2H), 7.45 (d, J = 5.7 Hz, 2H), 7.30 (d, J = 3.4 Hz, 2H), 6.89 (d, J = 3.4 Hz, 2H), 2.86 (d, J = 6.7 Hz, 4H), 1.73 (m, 2H), 1.38−1.24 (m, 80H), 0.89 (t, J = 6.7 Hz, 12H). ^{13}C NMR (100 MHz, $CDCl_3$): δ 145.72, 145.05, 139.17, 137.46, 136.65, 127.81, 127.47, 125.50, 124.22, 123.54, 40.21, 34.98, 33.57, 32.17, 30.22, 29.95, 29.62, 26.88, 22.92, 14.33. MS (MALDI): m/z 1027 (M$^+$). Anal. Calcd for $C_{66}H_{106}S_4$: C, 77.13; H, 10.40. Found: C, 77.42; H, 10.42%.

(4,8-Bis(5-(2-decyltetradecyl)thiophen-2-yl)benzo[1,2-*b*:4,5-*b*′]dithiophene-2,6-diyl)bis(trimethylstannane) (3). A solution of **2** (207.4 mg, 0.2 mmol) in dry THF (5 mL) was deoxygenated with nitrogen for 15 min. 0.18 mL of *n*-butyllithium (0.45 mmol, 2.5 M in *n*-hexane) was added dropwise at room temperature. The reaction was stirred at 50 °C for 2 h. After the reaction solution was cooled to room temperature, 88 mg of trimethyltin chloride (0.44 mmol, 1 M in *n*-hexane) (*caution! very toxic!*) was added. After stirring at room temperature for 6 h, the mixture was poured into 200 mL of cool water and extracted with diethyl ether. The organic layer was washed with water and then dried over anhydrous $MgSO_4$. After the solvent was removed under vacuum, the residue was yellow oil (240 mg, 90%) and used for the next reaction without further purification due to instability of this compound. ^{1}H NMR (400 MHz, $CDCl_3$): δ 7.71 (s, 2H), 7.34 (d, J = 3.4 Hz, 2H), 6.91 (d, J = 3.4 Hz, 2H), 2.89 (d, J = 6.4 Hz, 4H), 1.75 (m, 2H), 1.38−1.22 (m, 80H), 0.90 (t, J = 6.5 Hz, 12H), 0.41 (s, 18H). Anal. Calcd for $C_{72}H_{122}S_4Sn_2$: C, 63.90; H, 9.09. Found: C, 65.55; H, 9.30%.

4,8-Bis(5-(2-decyltetradecyl)thiophen-2-yl)-2,6-bis-(thiophen-2-yl)benzo[1,2-*b*:4,5-*b*′]dithiophene (4). Compound **3** (853 mg, 0.63 mmol) and 2-bromothiophene (250 mg, 1.5 mmol) were dissolved in dry toluene (10 mL) and deoxygenated with nitrogen for 15 min. Then, $Pd(PPh_3)_4$ (60 mg, 0.05 mmol) was added under nitrogen. The mixture was stirred at reflux for 48 h. After the reaction solution was cooled to room temperature, KF (5 g) in 10 mL of water was added, and the reaction mixture was stirred for another 2 h. The mixture was poured into 200 mL of cool water and extracted with CH_2Cl_2. The organic layer was washed with 10% hydrochloric acid, saturated $NaHCO_3$ aqueous solution and then dried over anhydrous $MgSO_4$. After the solvent was removed under vacuum, the residue was purified by column chromatography (silica gel, hexane) to afford pale yellow solid (230 mg, 31%). ^{1}H NMR (400 MHz, $CDCl_3$): δ 7.65 (s, 2H), 7.31 (d, J = 3.3 Hz, 2H), 7.28 (d, J = 3.4 Hz, 2H), 7.26 (d, J = 4.8 Hz, 2H), 7.04 (dd, J = 4.8 Hz, J = 3.4 Hz, 2H), 6.91 (d, J = 3.3 Hz, 2H), 2.88 (d, J = 6.5 Hz, 4H), 1.75 (m, 2H), 1.30−1.22 (m, 80H), 0.87 (t, J = 5.2 Hz, 12H). ^{13}C NMR (100 MHz, $CDCl_3$): δ 145.93, 138.69, 137.96, 137.65, 137.32, 136.99, 127.93, 127.82, 125.59, 125.54, 125.22, 123.47, 119.17, 40.16, 34.81, 33.55, 32.06, 30.18, 29.87, 29.52, 26.85, 22.82, 14.23. MS (MALDI): m/z 1191 (M$^+$). Anal. Calcd for $C_{74}H_{110}S_6$: C, 74.56; H, 9.30. Found: C, 74.42; H, 9.42%.

(5,5′-(4,8-Bis(5-(2-decyltetradecyl)thiophen-2-yl)benzo[1,2-*b*:4,5-*b*′]dithiophene-2,6-diyl)bis(thiophene-2-yl))bis-(trimethylstannane) (5). A solution of **4** (170 mg, 0.14 mmol) in dry THF (4 mL) was deoxygenated with nitrogen for 15 min. 0.13 mL of *n*-butyllithium (0.33 mmol, 2.5 M in *n*-hexane) was added dropwise at −78 °C. After the mixture was stirred at −78 °C for 1 h, 62.6 mg of trimethyltin chloride (0.31 mmol, 1 M in *n*-hexane) (*caution! very toxic!*) was added. The reaction mixture was stirred at room temperature for 12 h. Then, the mixture was poured into 200 mL of cool water and extracted with diethyl ether. The organic layer was washed with water and then dried over anhydrous $MgSO_4$. After the solvent was removed under vacuum, a yellow oil was obtained (200 mg, 95%) and was used for polymerization without further purification due to instability of this compound. ^{1}H NMR (400 MHz, $CDCl_3$): δ 7.65 (s, 2H), 7.38 (d, J = 3.2 Hz, 2H), 7.31 (d, J = 3.3 Hz, 2H), 7.11 (d, J = 3.3 Hz, 2H), 6.91 (d, J = 3.2 Hz, 2H), 2.88 (d, J = 6.5 Hz, 4H), 1.75 (m, 2H), 1.38−1.24 (m, 80H), 0.89 (t, J = 4.7 Hz, 12H), 0.39 (s, 18H). Anal. Calcd for $C_{80}H_{126}S_6Sn_2$: C, 63.31; H, 8.37. Found: C, 62.72; H, 8.52%.

Poly{[2,6-bis(thiophene-2-yl)-4,8-bis(5-(2-decyltetradecyl)-thiophen-2-yl)benzo[1,2-*b*:4,5-*b*′]dithiophene-5,5′-diyl]-*alt*-(5,5′-bibenzo[*c*][1,2,5]thiadiazole-4,7-diyl)} (PBDT−BBT). 4,7-Dibromo-5,5′-bibenzo[*c*][1,2,5]thiadiazole (52 mg, 0.12 mmol) and compound **5** (180 mg, 0.12 mmol) were dissolved in dry toluene (4 mL) and deoxygenated with nitrogen for 15 min. Then, $Pd(PPh_3)_4$ (12 mg, 0.01 mmol) was added under nitrogen. The mixture was stirred at reflux for 3 days. After the reaction mixture was cooled to room temperature, KF (5 g) in 10 mL of water was added, and the mixture was stirred at room temperature for another 2 h. The organic phase was extracted with chloroform, washed with water, and dried over anhydrous $MgSO_4$. The polymer was precipitated by addition of 200 mL of methanol. The precipitate was filtered. Finally, the polymer was purified by size exclusion column chromatography over Bio-Rad Bio-Beads S-X1 eluting with chloroform. The polymer was recovered

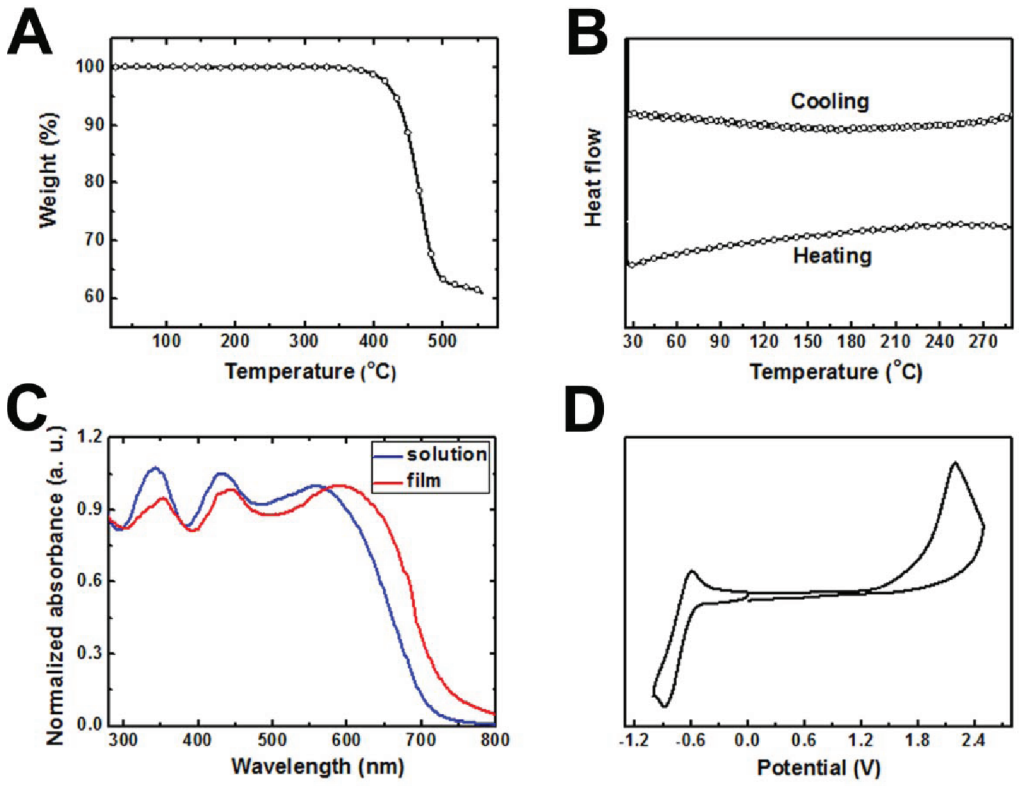


Figure 1. (A) TGA curve of PBDT−BBT under nitrogen. (B) DSC traces of PBDT−BBT under nitrogen. (C) Absorption spectra of PBDT−BBT in solution and thin film. (D) Cyclic voltammogram of PBDT−BBT.

as a red brown solid (80 mg, 47%). ^{1}H NMR (400 MHz, $CDCl_3$): δ 8.10−6.91 (br, 14H), 2.89 (br, 4H), 1.74−1.22 (br, 82H), 0.83 (br, 12H). Anal. Calcd for $(C_{86}H_{112}N_4S_8)_n$: C, 70.83; H, 7.74; N, 3.84. Found: C, 69.22; H, 7.57; N, 3.68%. M_n, 16 600, M_w, 77 700, M_w/M_n, 4.69.

RESULTS AND DISCUSSION

Synthesis and Characterization. The synthetic route of the polymer is outlined in Scheme 1. PBDT−BBT was synthesized by Stille coupling copolymerization of BBT dibromide and tetrathiophene-substituted BBT ditin. To ensure good solution processability of the resulting copolymer, long branched alky chains were symmetrically attached to thiophenes. PBDT−BBT is soluble in common organic solvents such as chloroform, THF, and dichlorobenzene. The incorporation of thiophene spacers into polymer backbone can reduce steric hindrance between BBT and BDT units, consequently leading to an extended π-conjugation. Molecular weights of PBDT−BBT were determined by gel permeation chromatography (GPC) using polystyrene standards as calibrants. PBDT−BBT has a number-average molecular weight (M_n) of 16 600, a weight-average molecular weight (M_w) of 77 700, and a polydispersity index (M_w/M_n) of 4.69.

Thermal Properties. Thermogravimetric analysis (TGA, heating ramp rate of 10 °C min^{-1} under N_2) was used to determine the thermal stability of PBDT−BBT (Figure 1A). The thermolysis onset temperature at 5% mass loss for PBDT−BBT is 437 °C, indicating that PBDT−BBT has excellent thermal stability. The thermal property of PBDT−BBT was also investigated by differential scanning calorimetry (DSC) at a scanning rate of 10 °C min^{-1} (Figure 1B). No endotherm/exotherm transition was found across the entire scanning range, suggesting that PBDT−BBT is amorphous.

Optical Properties. Figure 1C provides intensity-normalized UV−vis absorption spectra of PBDT−BBT in chloroform solution (ca. 10^{-6} M) and in thin film. The polymer film exhibited a broad and strong absorption plateau across the entire UV−vis region (300−800 nm). In film, the absorbance maximum of PBDT−BBT is 591 nm, 28 nm red shift relative to that in solution, suggesting the strong interchain interaction. The optical bandgap of PBDT−BBT estimated from the absorption edge in film is 1.72 eV.

Electrochemical Properties. To investigate the electrochemical properties of the polymer and estimate its HOMO and LUMO energy levels, cyclic voltammetry (CV) was carried out using a glassy-carbon coated with polymer film, a Pt wire, and an Ag wire coated with AgCl as the working electrode, counter electrode, and quasi-reference electrode, respectively. CV measurements were conducted in a 0.1 M Bu_4NPF_6−acetonitrile solution under N_2 at a scan rate of 50 mV s^{-1}. PBDT−BBT displays irreversible oxidation wave and reversible reduction wave. The onset oxidation and reduction potentials versus Ag are 1.4 and −0.6 V, respectively. The onset oxidation and reduction potentials versus $FeCp_2^{+/0}$ (half-wave potential of 0.5 eV) are 0.9 and −1.1 V, respectively. PBDT−BBT has a HOMO level of −5.7 eV and a LUMO level of −3.7 eV, estimated from the onset oxidation and reduction potentials, assuming the absolute energy level of ferrocene/ferrocenium to be 4.8 eV below vacuum. The deep HOMO and LUMO levels of PBDT−BBT are attributed to the strong electron-accepting ability of BBT. The HOMO level of −5.7 eV is about 0.9 eV deeper than that of P3HT (−4.8 eV), indicating the excellent ambient stability of PBDT−BBT.[56] The HOMO−LUMO gap obtained from electrochemistry is 2.0 eV, larger than the optical

dx.doi.org/10.1021/ma202582n | Macromolecules 2012, 45, 1296−1302

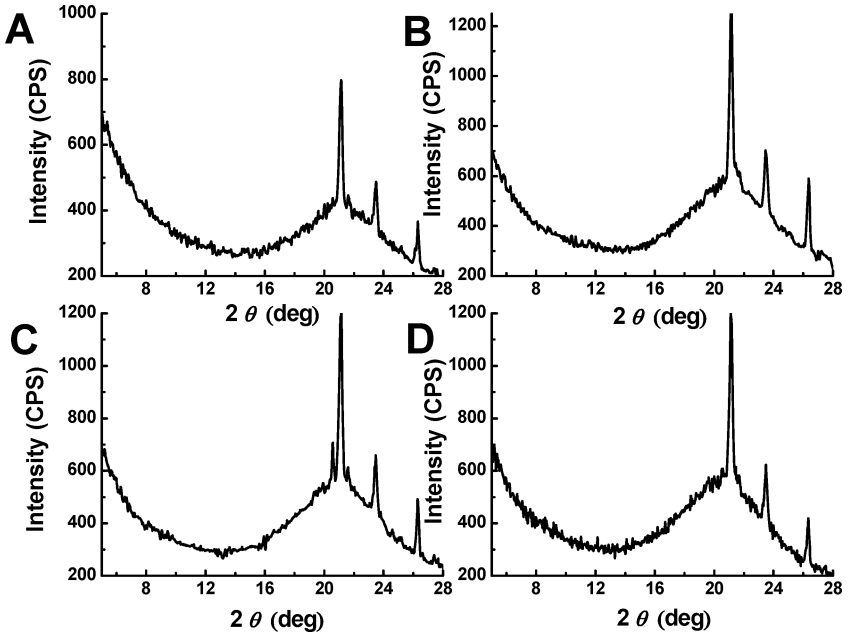


Figure 2. XRD patterns of PBDT−BBT thin films drop casted onto OTS-treated SiO_2/Si substrate after annealing at (A) 80, (B) 120, (C) 160, and (D) 200 °C for 30 min.

band gap (1.72 eV), which is a common phenomenon reported in the literature.[57−59]

Thin Film Morphology. Thin films of PBDT−BBT used in the characterization of X-ray diffraction (XRD) and atomic force microscopy (AFM) were prepared by the same procedure as device fabrication. Figure 2 shows the XRD patterns of PBDT−BBT thin films after thermal annealing at 80, 120, 160, and 200 °C. For all the XRD patterns of thin films, a broad peak accompanied by three sharp peaks appeared in 2θ = 15°−30° region corresponding to a d-spacing of 4.1 Å for 2θ = 21.2°, 3.7 Å for 2θ = 23.5°, and 3.3 Å for 2θ = 26.4°. No lamellar organization feature was found for the samples. These XRD patterns indicate that the films are amorphous collections of randomly oriented chains with a possible $\pi-\pi$ stacking distance of 3−4 Å. Figure 3 shows AFM height images of the films annealed at 80, 120, 160, and 200 °C. For all the cases, the films exhibited typical amorphous state without any crystalline domains. The root-mean-square (rms) roughness of these films is in the range of 0.6−0.9 nm. These XRD and AFM results indicate that PBDT−BBT is a thermal stable organic semiconductor, and thermal annealing has little effect on film morphology and organization of PBDT−BBT. Thus, we can expect that PBDT−BBT is a potential isotropic material in the application of OFETs and phototransistors without the use of complicated post-treatments such as thermal annealing for performance improvement.

Organic Field-Effect Transistors. Since microstructure order of PBDT−BBT thin films is not susceptible to thermal annealing temperature, we only baked the films at 80 °C to completely remove the residual solvent. Then, charge transport property of PBDT−BBT was investigated by the above-mentioned device configuration. The representative output and transfer characteristics of the devices are shown in Figures 4A and 4B. The devices exhibited typical p-type behavior with a charge-carrier mobility of 6×10^{-3} cm^2 V^{-1} s^{-1}, threshold voltage of −1 V, and on/off current ratio of 10^6. Because of the deep HOMO level of PBDT−BBT, the operation of these devices is quite stable under ambient atmosphere. Under a

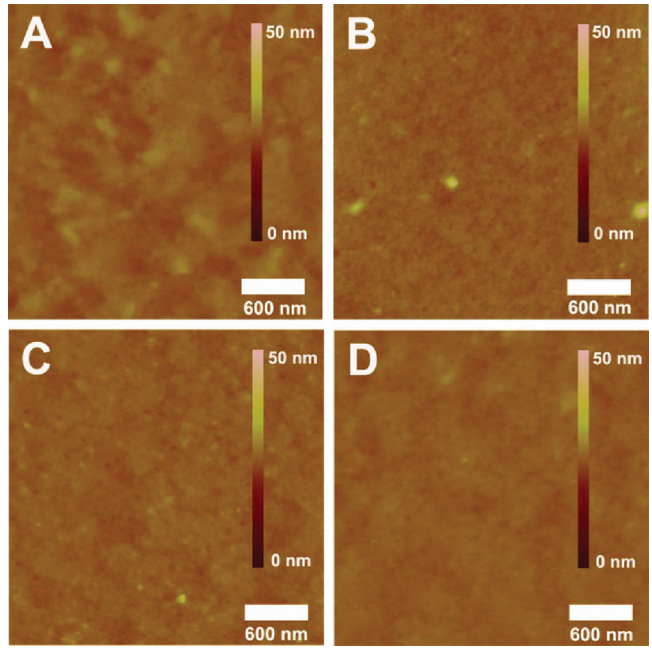


Figure 3. Tapping-mode AFM height images of PBDT−BBT drop-casted onto OTS-treated SiO_2/Si substrate after annealing at (A) 80, (B) 120, (C) 160, and (D) 200 °C for 30 min.

continuous sweep (10 cycles) of gate-source voltage (V_{GS}) with constant drain-source voltage (V_{DS}), no obvious degradation in performance was found as shown in Figure 5A. Long-term stability of the devices was investigated over one month. Figure 5B shows the transfer characteristics of the devices versus the storage time under ambient atmosphere. No obvious changes in mobility and on/off ratio were found over the period.

Thin Film Phototransistors. Thin film phototransistors based on PBDT−BBT were fabricated with a similar device configuration to that of field-effect transistors, except for a top illumination applied on the devices. Figure 6A shows the

dx.doi.org/10.1021/ma202582n | Macromolecules 2012, 45, 1296−1302

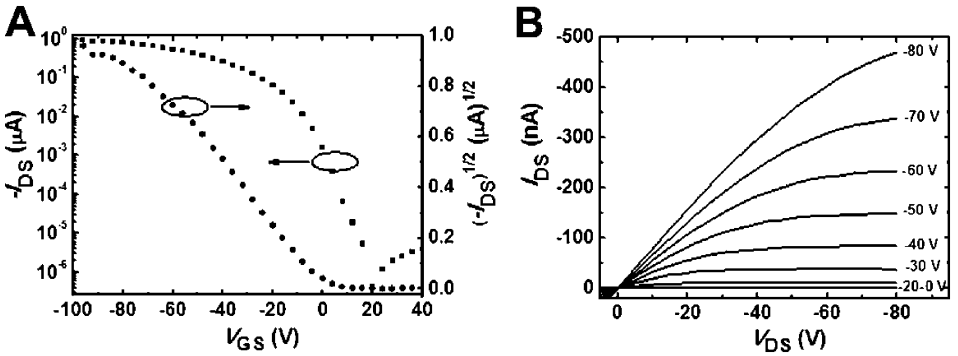


Figure 4. (A) Transfer and (B) output characteristics of drop-casted PBDT−BBT thin film transistors based on OTS-treated SiO_2/Si substrate.

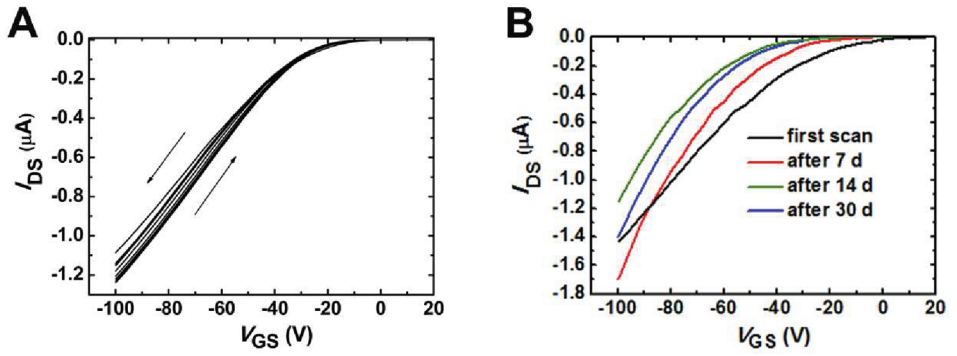


Figure 5. (A) Transfer characteristics of the devices after continuing measurement for 10 cycles in air. (B) Transfer characteristics of the devices after storage in air for 30 days.

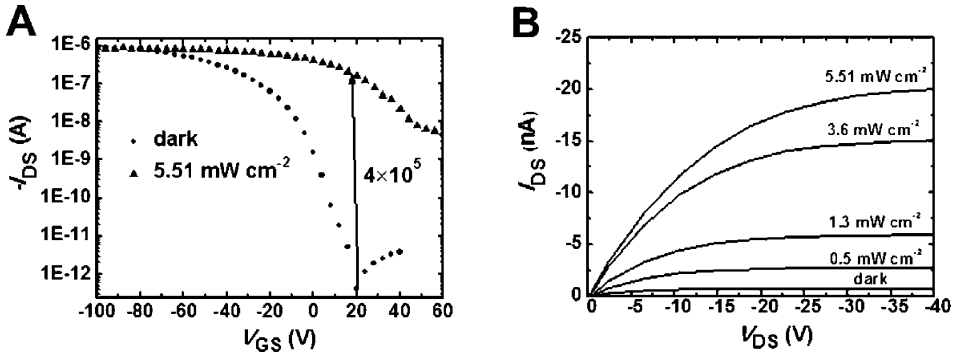


Figure 6. (A) Transfer characteristics of the polymer thin film phototransistors under dark and light irradiation. (B) Output characteristics of the polymer thin film phototransistors at different light power.

"transfer" characteristics of the phototransistor in the dark and under illumination. Under a white light irradiation of 5.51 mW cm^{-2}, these devices exhibited strong photodependence with a photoresponsivity (R) = 3200 mA W^{-1} and photocurrent/dark current ratio (P) = 4 × 10^5. The efficient charge carrier generation benefited from the broad light absorption of PBDT−BBT is the major factor for the high performance of the phototransistors. To the best of our knowledge, this is the highest on/off ratio for polymer phototransistors. The device can also work very well at low operation voltage (<40 V) under different light intensity as shown in Figure 6B. The low operation voltage together with high R and P values of the phototransistors indicates their promising application in photodetection and signal magnification in an individual device.

■ CONCLUSION

We have successfully synthesized an amorphous copolymer (PBDT−BBT) based on BDT and BBT units with good solution processability, excellent thermal stability, broad absorption (300−800 nm), and deep HOMO level (−5.7 eV). The microstructure order of PBDT−BBT thin films is not susceptible to thermal annealing temperature, indicating the potential applications of PBDT−BBT as thermal stable thin-film devices. OFETs based on this polymer exhibited a charge-carrier mobility of 6 × 10^{-3} cm^2 V^{-1} s^{-1}, threshold voltage of −1 V, and on/off current ratio of 10^6 without any post-treatments. Thin film phototransistors of PBDT−BBT exhibited a photoresponsivity of 3200 mA W^{-1} and photocurrent/dark current ratio of 4 × 10^5; the on/off ratio is the highest value for polymer phototransistors. These excellent performances combined with its long-time operational stability indicate that

dx.doi.org/10.1021/ma202582n | Macromolecules 2012, 45, 1296−1302

PBDT−BBT is promising for the application of optoelectronic devices.

■ ASSOCIATED CONTENT

Supporting Information

^{1}H NMR and ^{13}C NMR spectra of compounds **2**−**5** and PBDT−BBT. This material is available free of charge via the Internet at http://pubs.acs.org.

■ AUTHOR INFORMATION

Corresponding Author

*E-mail: xwzhan@iccas.ac.cn (X.Z.); huwp@iccas.ac.cn (W.H.).

■ ACKNOWLEDGMENTS

This material is based upon work supported in part by the NSFC (Grants 21025418 and 21021091), 973 Project (Grant 2011CB808401), and the Chinese Academy of Sciences.

■ REFERENCES

(1) Dong, H. L.; Zhu, H. F.; Meng, Q.; Gong, X.; Hu, W. P. *Chem. Soc. Rev.* **2012**, DOI: 10.1039/c1cs15205j.
(2) Narayan, K. S.; Kumar, N. *Appl. Phys. Lett.* **2001**, *79*, 1891.
(3) Saragi, T. P. I.; Pudzich, R.; Fuhrmann, T.; Salbeck, J. *Appl. Phys. Lett.* **2004**, *84*, 2334.
(4) Dong, H.; Bo, Z.; Hu, W. *Macromol. Rapid Commun.* **2011**, *32*, 649.
(5) Shockley, W.; Sparks, M.; Teal, G. K. *Phys. Rev.* **1951**, *83*, 151.
(6) Tang, Q.; Li, L.; Song, Y.; Liu, Y.; Li, H.; Xu, W.; Hu, W.; Zhu, D. *Adv. Mater.* **2007**, *19*, 2624.
(7) Soci, C.; Zhang, A.; Bao, X.-Y.; Kim, H.; Lo, Y.; Wang, D. *J. Nanosci. Nanotechnol.* **2010**, *10*, 1430.
(8) Wang, X.; Wasapinyokul, K.; Tan, W. D.; Rawcliffe, R.; Campbell, A. J.; Bradley, D. D. C. *J. Appl. Phys.* **2010**, *107*, 024509.
(9) Noh, Y. Y.; Kim, D. Y.; Yoshida, Y.; Yase, K.; Jung, B. J.; Lim, E.; Shim, H. K. *Appl. Phys. Lett.* **2005**, *86*, 04315.
(10) Yan, F.; Li, J. H.; Mok, S. M. *J. Appl. Phys.* **2009**, *106*, 074501.
(11) Xu, Y.; Berger, P. R.; Wilson, J. N.; Bunz, U. H. F. *Appl. Phys. Lett.* **2004**, *85*, 4219.
(12) Mok, S. M.; Yan, F.; Chan, H. L. W. *Appl. Phys. Lett.* **2008**, *93*, 023310.
(13) Liu, Y. R.; Peng, J. B.; Lai, P. *Thin Solid Films* **2008**, *516*, 4295.
(14) Hamilton, M. C.; Martin, S.; Kanicki, J. *IEEE Trans. Electron Devices* **2004**, *51*, 877.
(15) Hamilton, M. C.; Kanicki, J. *IEEE J. Sel. Top. Quantum Electron.* **2004**, *10*, 840.
(16) Zhao, X.; Zhan, X. *Chem. Soc. Rev.* **2011**, *40*, 3728.
(17) Gunes, S.; Neugebauer, H.; Sariciftci, N. S. *Chem. Rev.* **2007**, *107*, 1324.
(18) Pron, A.; Gawrys, P.; Zagorska, M.; Djurado, D.; Demadrille, R. *Chem. Soc. Rev.* **2010**, *39*, 2577.
(19) Mas-Torrent, M.; Rovira, C. *Chem. Rev.* **2011**, *111*, 4833.
(20) Zhan, X.; Zhu, D. *Polym. Chem.* **2010**, *1*, 409.
(21) Beaujuge, P. M.; Pisula, W.; Tsao, H. N.; Ellinger, S.; Müllen, K.; Reynolds, J. R. *J. Am. Chem. Soc.* **2009**, *131*, 7514.
(22) Zhang, Q. T.; Tour, J. M. *J. Am. Chem. Soc.* **1998**, *120*, 5355.
(23) Ajayaghosh, A. *Chem. Soc. Rev.* **2003**, *32*, 181.
(24) Zhan, X.; Tan, Z. a.; Domercq, B.; An, Z.; Zhang, X.; Barlow, S.; Li, Y.; Zhu, D.; Kippelen, B.; Marder, S. R. *J. Am. Chem. Soc.* **2007**, *129*, 7246.
(25) Zhan, X.; Tan, Z. a.; Zhou, E.; Li, Y.; Misra, R.; Grant, A.; Domercq, B.; Zhang, X.-H.; An, Z.; Zhang, X.; Barlow, S.; Kippelen, B.; Marder, S. R. *J. Mater. Chem.* **2009**, *19*, 5794.
(26) Lu, G.; Usta, H.; Risko, C.; Wang, L.; Facchetti, A.; Ratner, M. A.; Marks, T. J. *J. Am. Chem. Soc.* **2008**, *130*, 7670.
(27) Zhang, M.; Tsao, H. N.; Pisula, W.; Yang, C.; Mishra, A. K.; Müllen, K. *J. Am. Chem. Soc.* **2007**, *129*, 3472.
(28) Liu, J.; Zhang, R.; Sauvé, G. v.; Kowalewski, T.; McCullough, R. D. *J. Am. Chem. Soc.* **2008**, *130*, 13167.
(29) Rieger, R.; Beckmann, D.; Pisula, W.; Steffen, W.; Kastler, M.; Müllen, K. *Adv. Mater.* **2010**, *22*, 83.
(30) He, M.; Li, J.; Sorensen, M. L.; Zhang, F.; Hancock, R. R.; Fong, H. H.; Pozdin, V. A.; Smilgies, D.-M.; Malliaras, G. G. *J. Am. Chem. Soc.* **2009**, *131*, 11930.
(31) Osaka, I.; Abe, T.; Shinamura, S.; Miyazaki, E.; Takimiya, K. *J. Am. Chem. Soc.* **2010**, *132*, 5000.
(32) Liu, Y.; Liu, Y.; Zhan, X. *Macromol. Chem. Phys.* **2011**, *212*, 428.
(33) Osaka, I.; Sauvé, G.; Zhang, R.; Kowalewski, T.; McCullough, R. D. *Adv. Mater.* **2007**, *19*, 4160.
(34) Pan, H.; Li, Y.; Wu, Y.; Liu, P.; Ong, B. S.; Zhu, S.; Xu, G. *J. Am. Chem. Soc.* **2007**, *129*, 4112.
(35) Noh, Y.-Y.; Kim, D.-Y.; Yase, K. *J. Appl. Phys.* **2005**, *98*, 074505.
(36) Marjanovic, N.; Singh, T. B.; Dennler, G.; Günes, S.; Neugebauer, H.; Sariciftci, N. S.; Schwödiauer, R.; Bauer, S. *Org. Electron.* **2006**, *7*, 188.
(37) Dong, H.; Li, H.; Wang, E.; Nakashima, H.; Torimitsu, K.; Hu, W. *J. Phys. Chem. C* **2008**, *112*, 19690.
(38) Wang, X.; Wasapinyokul, K.; De Tan, W.; Rawcliffe, R.; Campbell, A. J.; Bradley, D. D. C. *J. Appl. Phys.* **2010**, *107*, 024509.
(39) Pal, T.; Arif, M.; Khondaker, S. I. *Nanotechnology* **2010**, *21*, 325201.
(40) Pan, H.; Wu, Y.; Li, Y.; Liu, P.; Ong, B. S.; Zhu, S.; Xu, G. *Adv. Funct. Mater.* **2007**, *17*, 3574.
(41) Liang, Y.; Wu, Y.; Feng, D.; Tsai, S.-T.; Son, H.-J.; Li, G.; Yu, L. *J. Am. Chem. Soc.* **2008**, *131*, 56.
(42) Liang, Y.; Xu, Z.; Xia, J.; Tsai, S.-T.; Wu, Y.; Li, G.; Ray, C.; Yu, L. *Adv. Mater.* **2010**, *22*, E135.
(43) Son, H. J.; Wang, W.; Xu, T.; Liang, Y.; Wu, Y.; Li, G.; Yu, L. *J. Am. Chem. Soc.* **2011**, *133*, 1885.
(44) Hou, J.; Chen, H.-Y.; Zhang, S.; Chen, R. I.; Yang, Y.; Wu, Y.; Li, G. *J. Am. Chem. Soc.* **2009**, *131*, 15586.
(45) Chen, H. Y.; Hou, J. H.; Zhang, S. Q.; Liang, Y. Y.; Yang, G. W.; Yang, Y.; Yu, L. P.; Wu, Y.; Li, G. *Nature Photonics* **2009**, *3*, 649.
(46) Price, S. C.; Stuart, A. C.; Yang, L.; Zhou, H.; You, W. *J. Am. Chem. Soc.* **2011**, *133*, 4625.
(47) Zhou, H. X.; Yang, L. Q.; Stuart, A. C.; Price, S. C.; Liu, S. B.; You, W. *Angew. Chem., Int. Ed.* **2011**, *50*, 2995.
(48) Huo, L. J.; Zhang, S. Q.; Guo, X.; Xu, F.; Li, Y. F.; Hou, J. H. *Angew. Chem., Int. Ed.* **2011**, *50*, 9697.
(49) Huo, L.; Hou, J.; Zhang, S.; Chen, H.-Y.; Yang, Y. *Angew. Chem., Int. Ed.* **2010**, *49*, 1500.
(50) Wang, M.; Hu, X.; Liu, P.; Li, W.; Gong, X.; Huang, F.; Cao, Y. *J. Am. Chem. Soc.* **2011**, *133*, 9638.
(51) Shi, Q.; Fan, H.; Liu, Y.; Chen, J.; Ma, L.; Hu, W.; Shuai, Z.; Li, Y.; Zhan, X. *Macromolecules* **2011**, *44*, 4230.
(52) Shi, Q.; Fan, H.; Liu, Y.; Hu, W.; Li, Y.; Zhan, X. *Macromolecules* **2011**, *44*, 9173.
(53) Wang, H. F.; Cheng, P.; Liu, Y.; Chen, J. M.; Zhan, X. W.; Hu, W. P.; Shuai, Z. G.; Li, Y. F.; Zhu, D. B. *J. Mater. Chem.* **2012**, DOI: 10.1039/C2JM14283J.
(54) Shirota, Y.; Kageyama, H. *Chem. Rev.* **2007**, *107*, 953.
(55) Guo, Y.; Du, C.; Yu, G.; Di, C.-a.; Jiang, S.; Xi, H.; Zheng, J.; Yan, S.; Yu, C.; Hu, W.; Liu, Y. *Adv. Funct. Mater.* **2010**, *20*, 1019.
(56) Dong, H.; Wang, C.; Hu, W. *Chem. Commun.* **2010**, *46*, 5211.
(57) Johansson, T.; Mammo, W.; Svensson, M.; Andersson, M. R.; Inganäs, O. *J. Mater. Chem.* **2003**, *13*, 1316.
(58) Chen, W. C.; Liu, C. L.; Yen, C. T.; Tsai, F. C.; Tonzola, C. J.; Olson, N.; Jenekhe, S. A. *Macromolecules* **2004**, *37*, 5959.
(59) Hou, J.; Tan, Z.; Yan, Y.; He, Y.; Yang, C.; Li, Y. *J. Am. Chem. Soc.* **2006**, *128*, 4911.

Macromolecules

Article

pubs.acs.org/Macromolecules

Synthesis and Characterization of New Selenophene-Based Donor–Acceptor Low-Bandgap Polymers for Organic Photovoltaic Cells

Woo-Hyung Lee,[†] Seon Kyoung Son,[‡] Kyoungkon Kim,[‡] Sang Kyu Lee,[§] Won Suk Shin,[§] Sang-Jin Moon,[§] and In-Nam Kang*[,†]

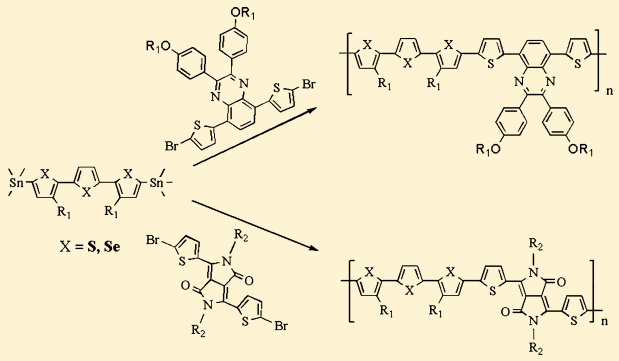
[†]Department of Chemistry, The Catholic University of Korea, Bucheon, Korea

[‡]Solar Cell Research Center, Korea Institute of Science and Technology, Seoul, Korea

[§]Energy Materials Research Division, Korea Research Institute of Chemical Technology, Daejeon, Korea

Supporting Information

ABSTRACT: A series of novel thiophene- and selenophene-based low-bandgap polymers were synthesized using a Stille cross-coupling reaction; these polymers contained quinoxaline and diketopyrrolopyrrole as acceptors. Various acceptors were introduced into the selenophene backbones, and the solubility, absorption spectra, energy levels, charge transport, blend film morphology, and photovoltaic properties of the resulting polymers were investigated. The weight-averaged molecular weights (M_w) of P3TDTQ, P3SDTQ, P3TDTDPP, and P3SDTDPP were found to be 12 300, 15 500, 13 300, and 17 200, with polydispersity indices of 1.46, 1.85, 1.58, and 1.63, respectively. Photophysical studies revealed low bandgaps of 1.70 eV for P3TDTQ, 1.63 eV for P3SDTQ, 1.27 eV for P3TDTDPP, and 1.25 eV for P3SDTDPP; the films could harvest a broad solar spectrum, covering the range from 300 to 800 nm (P3TDTQ and P3SDTQ) and from 350 to 950 nm (P3TDTDPP and P3SDTDPP). Solution-processed field-effect transistors fabricated from these polymers had p-type organic thin film transistor characteristics. The field-effect mobilities of P3TDTQ, P3SDTQ, P3TDTDPP, and P3SDTDPP were measured to be 2.8×10^{-5}, 5.0×10^{-5}, 1.0×10^{-3}, and 2.1×10^{-3} cm^2 V^{-1} s^{-1}, respectively. The novel polymers were combined with a PCBM ([6,6]-phenyl C_{71}-butyric acid methyl ester) acceptor to fabricate bulk heterojunction solar cells, which produced power conversion efficiencies of 0.64–3.18% under AM 1.5 G (100 mW/cm^2) conditions.



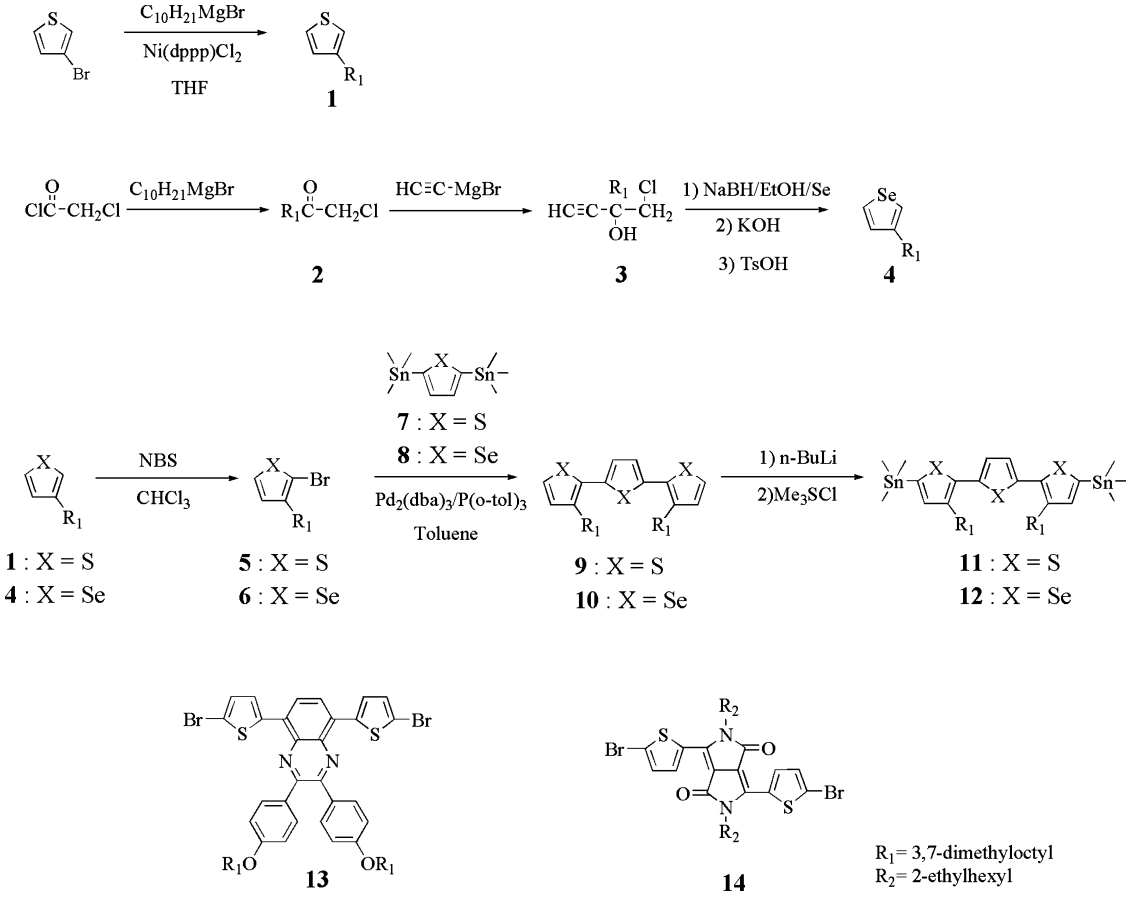
INTRODUCTION

Organic solar cells based on conjugated polymers have the potential to be applied as a clean energy source. In addition, such cells have the advantages that they can be fabricated at low cost via solution-based processing and that they have mechanical flexibility appropriate for foldable or rollable substrates.[1−4] Bulk-heterojunction (BHJ) devices—in which a donor polymer (p-type) is blended with a fullerene derivative or other acceptor (n-type) material—have emerged as the most efficient polymer solar cells (PSCs) developed to date.[5−7] One of the main factors limiting the performance of PSCs is the mismatch between their absorption and the terrestrial solar spectra. Polymer materials with low bandgaps are therefore needed to harvest solar photons at longer wavelengths, particularly in the near-IR region, and with a broader spectrum. Conjugated polymers that incorporate alternating donor and acceptor units produce significant decreases in the bandgap, due to the introduction of intramolecular charge transfer (ICT) structures.[8−10] Several types of donor–acceptor (D–A) conjugated copolymers have been synthesized for use in high-performance organic photovoltaic (OPV) applications. The use of thiophene as a donating moiety and quinoxaline (Qx) and diketopyrrolopyrrole (DPP) as accepting moieties has been closely investigated and provides a successful strategy to achieve low-bandgap materials.[11,12] Compared with their thiophene analogues, selenophene-containing polymers have been studied to a lesser extent, possibly due to the difficulties associated with their synthesis. As a class, polyselenophenes are expected to have advantages over polythiophenes. For example, interchain charge transfer should be facilitated by the intermolecular Se–Se contact, which means that polyselenophenes should have higher bulk conductivities and mobilities than polythiophenes.[13] Furthermore, selenophene substitution in conjugated polymers reduces the bandgap energy, mainly by stabilizing the lowest unoccupied molecular orbital (LUMO) level more effectively than the corresponding polythiophenes.[14−16] Poly(3-hexylselenophene) (P3HS) displays a bandgap energy (1.6 eV) lower than that of P3HT (1.9 eV).[15] The photovoltaic

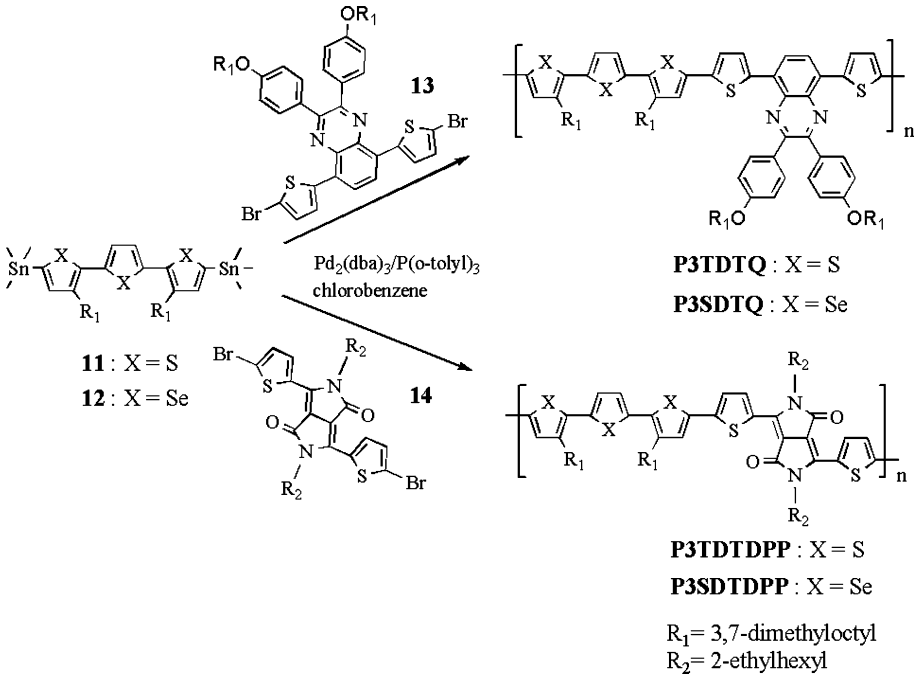
Received: September 2, 2011
Revised: December 12, 2011
Published: January 31, 2012

 © 2012 American Chemical Society dx.doi.org/10.1021/ma2020112 | *Macromolecules* 2012, 45, 1303–1312

Scheme 1. Synthetic Routes for the Monomers



Scheme 2. Synthesis of the Low-Bandgap Polymers P3TDTQ, P3SDTQ, P3TDTDPP, and P3SDTDPP



properties of P3HS:PCBM devices result in a high power conversion efficiency (2.7%) because P3HS provides a more extensive photon absorption cross section than P3HT.[14] Poly(3,3-dialkylterselenophene) (PSSS) also exhibits high charge-carrier mobilities and ambipolar behaviors in organic field effect transistor devices; the low LUMO energy levels are thought to facilitate both electron injection and transport.[16] Recently, several groups have reported the use of selenophene-

dx.doi.org/10.1021/ma2020112 | Macromolecules 2012, 45, 1303−1312

based D−A copolymers (with a selenophene donor and various acceptors) for organic transistors, but the solar cell performances of these polymers have not yet been reported.[17,18] Here, we report the synthesis, optical and physical properties, and OPV performances of novel selenophene-based D−A low-bandgap polymers. These polymers were synthesized using a Stille cross-coupling reaction, with terselenophene as a donor and quinoxaline (Qx) and diketopyrrolopyrrole (DPP) as acceptors. The Qx-containing polymers are denoted as P3SDTQ, and those containing DPP are denoted as P3SDTDPP. These polymers have lower bandgaps in π-conjugated polymers, thereby increasing the overall photon absorption by extending the spectral sensitivity. We examined the effects of the incorporation of different acceptors in the selenophene backbones on the absorption, energy levels, charge transport properties, morphologies, and photovoltaic properties of the donor/acceptor blends. In addition, terthiophene-based D−A polymers (with terthiophene as a donor and quinoxaline (Qx) (P3TDTQ) and diketopyrrolopyrrole (DPP) (P3TDTDPP) as acceptors) were also synthesized using the same polymerization method, to allow a comparison between the optoelectronic and photovoltaic properties of the terthiophene-based D−A polymers and those of the selenophene-based polymers.

RESULTS AND DISCUSSION

Synthesis and Characterization. The synthetic routes to the monomers and polymers are shown in Schemes 1 and 2, respectively. As shown in Scheme 1, a branched alkyl chain was introduced at the 3-position of the thiophene and selenophene rings to increase the solubility of the D−A copolymers. Compounds **1** and **4** were converted into the dibromo compounds **5** and **6** with *N*-bromosuccinimide (NBS) in the presence of a polar protic solvent, with good yields. Compounds **7** and **8** were synthesized according to methods described in the literature.[19,20] Compounds **9** and **10** were synthesized using the Stille coupling reaction, via the condensation of the distannyl compounds **7** and **8** and the corresponding brominated compounds **5** and **6**. Compounds **11** and **12** were synthesized from compounds **9** and **10** by distannylation, with good yields (68−91%). The P3TDTQ, P3SDTQ, P3TDTDPP, and P3SDTDPP polymers were obtained via the combinatorial Stille coupling reaction of compounds **11** and **12** with compounds **13** and **14**. The synthetic routes used to synthesize the P3TDTQ, P3SDTQ, P3TDTDPP, and P3SDTDPP polymers are also described in Scheme 2. The weight-average molecular weights (M_w) of P3TDTQ, P3SDTQ, P3TDTDPP, and P3SDTDPP were determined using gel permeation chromatography (GPC), using a polystyrene standard in a chloroform eluent; they were found to be 12 300 (PDI = 1.46), 15 500 (PDI = 1.85), 13 300 (PDI = 1.58), and 17 200 (PDI = 1.63), respectively. The polymer readily dissolved in common organic solvents such as toluene, chloroform, and THF and formed good films. Thermal analysis of the polymers was conducted using differential scanning calorimetry (DSC), and thermogravimetric analysis (TGA), as shown in Figure 1. The results showed that both polymers had good thermal stability over 300 °C, and no obvious thermal transitions were observed between 50 and 200 °C. The polymerization results for the synthesized copolymers are summarized in Table 1.

Optical and Electrochemical Properties. The UV−vis absorption spectra of the copolymers are shown in Figure 2 for

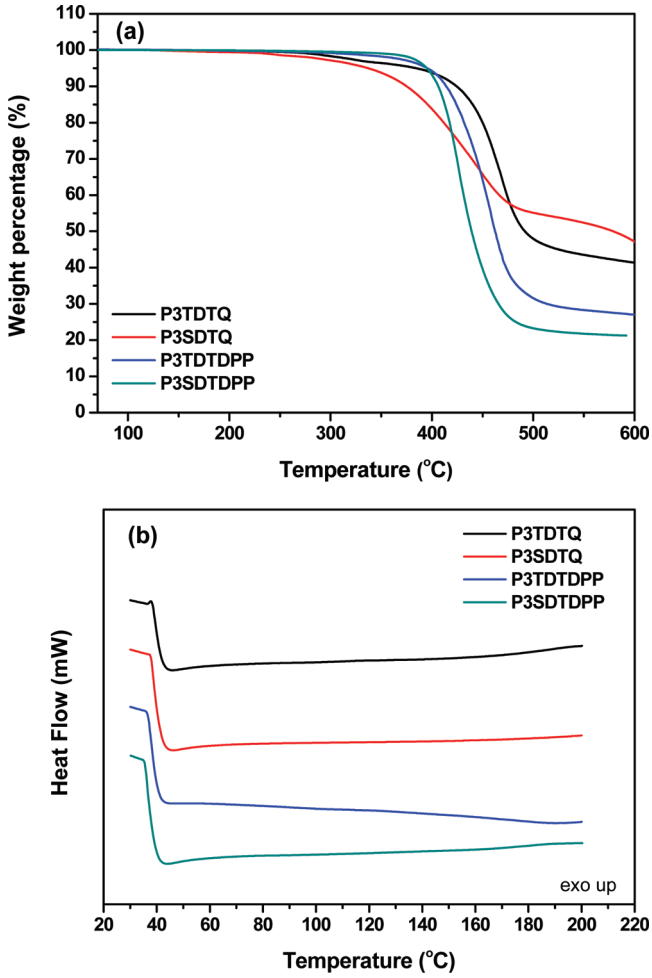


Figure 1. (a) TGA and (b) DSC of P3TDTQ, P3SDTQ, P3TDTDPP, and P3SDTDPP, performed at a heating rate of 10 °C min^{-1} under an inert atmosphere.

Table 1. Physical Properties of the Synthesized Polymers

polymer	M_n (g/mol)	M_w (g/mol)	PDI	T_d (°C)[a]
P3TDTQ	8.39K	12.3K	1.46	384
P3SDTQ	9.31K	15.5K	1.85	336
P3TDTDPP	8.43K	13.3K	1.58	395
P3SDTDPP	10.5K	17.2K	1.63	394

[a]Decomposition temperature at 5% weight loss.

copolymers in a dilute chlorobenzene solution and in thin films; the absorption data for the polymers are summarized in Table 2. The λ_{max} of P3TDTQ, P3SDTQ, P3TDTDPP, and P3SDTDPP in solution occurred at 549, 599, 679, and 702 nm, respectively, whereas those in the thin films occurred at 587, 619, 716, and 753 nm, respectively; these values were significantly red-shifted compared with those of poly(3,3-dialkylterthiophene) (PTT, $\lambda_{max,film}$ = 510 nm) and poly(3,3-dialkylterselenophene) (PSSS, $\lambda_{max,film}$ = 614 nm).[16,21] The UV−vis absorption spectra of the P3S-based polymers (P3SDTQ and P3SDTDPP) were red-shifted by about 20−50 nm with respect to those of the P3T-based polymers (P3TDTQ and P3TDTDPP), both in solution and in thin films; this resulted from the presence of selenium atoms in the polymer repeat units. Selenium atoms are more electron-rich than sulfur atoms; hence, aromatic rings containing selenium

dx.doi.org/10.1021/ma2020112 | Macromolecules 2012, 45, 1303−1312

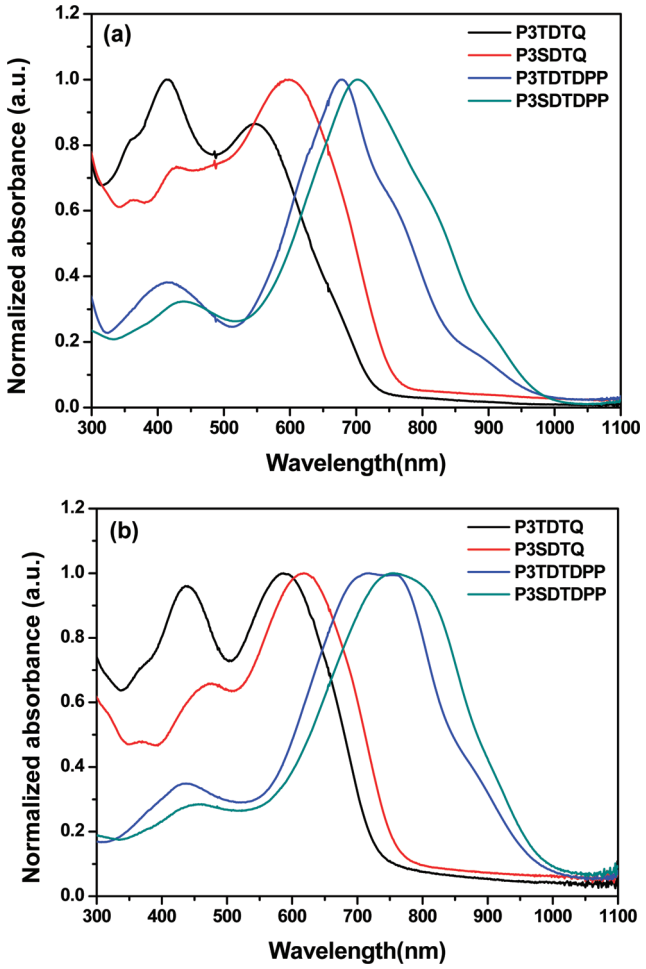


Figure 2. UV−vis spectra of P3TDTQ, P3SDTQ, P3TDTDPP, and P3SDTDPP (a) in chlorobenzene solution and (b) in thin films.

Table 2. UV−vis Maximum Absorption Wavelength (λ_{max}), Bandgap Energy (E_g), and Ionization Potential (E_{HOMO}) of P3TDTQ, P3SDTQ, P3TDTDPP and P3SDTDPP[a]

polymer	solution (λ_{max}, nm)[a]	film (λ_{max}, nm)	E_g^{opt} (eV)[b]	E_{HOMO} (eV)[c]	E_{LUMO} (eV)
P3TDTQ	431, 549	436, 587	1.70	−5.37	−3.67
P3SDTQ	428, 599	427, 619	1.63	−5.35	−3.72
P3TDTDPP	679	716	1.27	−5.21	−3.94
P3SDTDPP	702	753	1.25	−5.16	−3.91

[a]Measurements performed in chlorobenzene. [b]Estimated from the onset of the absorption in thin films (E_g = 1240/λ_{onset} eV). [c]Calculated using the optical bandgap energy.

are more easily delocalized than those containing sulfur atoms.[15,22,23] Moreover, the absorption spectra of the DPP-containing polymers (P3TDTDPP and P3SDTDPP) were red-shifted by over 130 nm compared with the spectra of the Qx-containing polymers (P3TDTQ and P3SDTQ), suggesting the presence of stronger $\pi-\pi$ interchain associations and aggregation in the solid state. Such aggregation is beneficial for improving charge mobility in thin films. The optical bandgaps of the polymer thin films were determined from the UV−vis absorption onsets in the solid state (E_g = 1240/λ_{onset} eV). The optical bandgaps (E_g) in the thin films were 1.70, 1.63, 1.27, and 1.25 eV for P3TDTQ, P3SDTQ, P3TDTDPP, and P3SDTDPP, respectively; these values were significantly lower than those found for poly(3,3-dialkylterthiophene) (PTT, 2.1 eV) and poly(3,3-dialkylterselenophene) (PSSS, 1.8 eV). This successful reduction in the bandgap was mainly due to intramolecular charge transfer (ICT) effects between the terthiophene donor or terselenophene donors and the Qx or DPP acceptor groups. The DPP moiety was a stronger acceptor than Qx, which led to a smaller E_g for P3TDTDPP and P3SDTDPP than for P3TDTQ and P3SDTQ. The low bandgaps of P3TDTDPP (1.27 eV) and P3SDTDPP (1.25 eV) may have resulted from the planarity and high degree of conjugation in the DPP acceptor, which would enhance the $\pi-\pi$ interactions and ICT among the polymer main chains.[24−26] Moreover, the optical bandgaps of the P3S-based polymer thin films were smaller than those of the P3T-based polymers because of the electron-rich selenium atoms in the core repeat units. The significant broadening in the absorption spectra of P3TDTDPP and P3SDTDPP (relative to P3TDTQ and P3SDTQ) may have indicated better ordering of the molecules in the bulk phase, which was manifested in the behavior of the external quantum efficiency (EQE).

Cyclic voltammograms (CV) are shown in Figure 3 for the polymers. These measurements were performed in an electro-

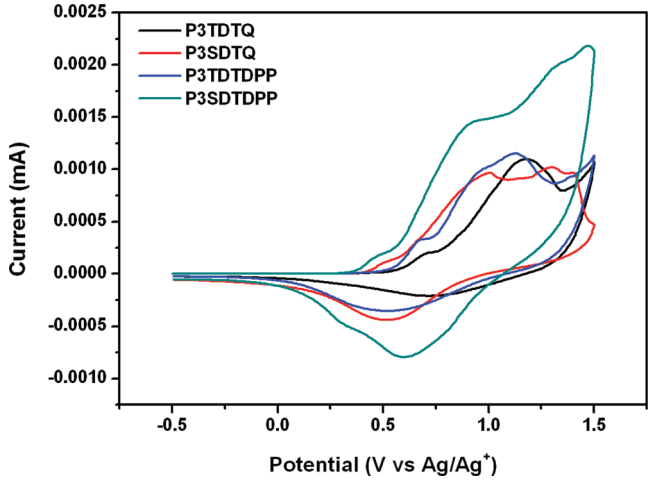


Figure 3. Cyclic voltammograms for the polymer films on ITO glass, performed at a scanning rate of 50 mV s^{-1}, in acetonitrile containing 0.1 M n-Bu_4NBF_4.

lyte solution of 0.1 M tetrabutylammonium tetrafluoroborate ($TBABF_4$) in anhydrous acetonitrile, at room temperature and under nitrogen, with a scan rate of 50 mV/s. The HOMO levels of the polymer films were estimated from the cyclic voltammograms, using the equation $E_{HOMO} = -(E_{ox} + 4.8)$ eV, where E_{ox} is the onset oxidation potential relative to the ferrocene standard material.[27] The highest occupied molecular orbital (HOMO) energy levels of P3TDTQ, P3SDTQ, P3TDTDPP, and P3SDTDPP were calculated to be −5.37, −5.35, −5.21, and −5.16 eV, respectively, using the ferrocene reference value of −4.8 eV below the vacuum level. The LUMO levels of P3TDTQ, P3SDTQ, P3TDTDPP, and P3SDTDPP were calculated to be −3.67, −3.72, −3.94, and −3.91 eV, respectively, as estimated from the optical bandgaps and HOMO energy levels. The deep HOMO levels may have contributed to the improved oxidative stability and higher open-circuit voltage (V_{oc}) compared with those of PTT (−5.2 eV) and PSSS (−4.9 eV).[16] The above results indicated that the bandgap and molecular energy levels of P3T- or P3S-based

dx.doi.org/10.1021/ma2020112 | Macromolecules 2012, 45, 1303−1312

polymers could be efficiently tuned by incorporating appropriate electron-withdrawing Qx and DPP groups. The electrochemical potentials are summarized in Table 2.

Field-Effect Transistor Characteristics. The effects of the shape and position of the side chains on the electrical transport properties of the resulting polymers were examined by measuring the field-effect transistor (FET) mobility. The field-effect carrier mobilities of the polymers were investigated by fabricating thin-film transistors with a bottom-contact geometry, using Au electrodes. The FET characteristics were determined under ambient conditions, and no precautions were taken to insulate the materials and devices from exposure to air, moisture, or light. The field-effect mobility was calculated according to the equation[28]

saturated regime ($V_D > V_G$):

$$I_D = (W/2L)\mu C_i(V_G - V_T)^2$$

where I_D is the drain current in the saturated regime, W and L are the channel width and length, respectively, μ is the field-effect mobility, C_i is the capacitance per unit area of the gate dielectric layer, and V_G and V_T are the gate and threshold voltages, respectively. The P3TDTQ, P3SDTQ, P3TDTDPP, and P3SDTDPP samples exhibited typical p-type organic semiconductor characteristics, with hole mobilities of 2.8×10^{-5}, 5.0×10^{-5}, 1.0×10^{-3}, and 2.1×10^{-3} $cm^2\ V^{-1}\ s^{-1}$, respectively. The results are plotted in Figure S1 (Supporting Information). The hole mobility values for the P3S-based polymers were ~1.5 times higher than those for the P3T-based polymers. The hole mobilities of the DPP-containing polymers (P3TDTDPP and P3SDTDPP) were 2 orders of magnitude higher than those of the Qx-containing polymers (P3TDTQ and P3SDTQ). The higher mobilities measured for P3TDTDPP and P3SDTDPP can be understood in terms of an improved intermolecular $\pi-\pi$ stacking, which corresponds well with the UV–vis results. In addition, P3TDTDPP and P3SDTDPP yielded higher hole mobilities than P3TDTQ and P3SDTQ; this was attributed to the more efficient charge extraction in the P3TDTDPP and P3SDTDPP solar cell devices (Table 3).

Table 3. PSC Performances of the Polymer/$PC_{61}BM$ Device

polymer	ratio	J_{SC} (mA/cm^2)	V_{OC} (V)	FF (%)	PCE (%)
P3TDTQ	1:1	1.29	0.68	34	0.30
	1:3	1.82	0.67	46	0.56
P3SDTQ	1:1	2.12	0.67	35	0.52
	1:3	2.48	0.63	45	0.72
P3TDTDPP	1:1	6.50	0.56	51	1.88
	1:3	5.25	0.56	51	1.49
P3SDTDPP	1:1	9.18	0.50	40	1.85
	1:3	6.45	0.51	41	1.36

Organic Photovoltaic Characteristics. Polymer solar cell devices were fabricated using the P3T- and P3S-based polymers as electron donors and [6,6]-phenyl C_{61}-butyric acid methyl ester ($PC_{61}BM$) as an electron acceptor. The device structure was ITO/PEDOT:PSS(50 nm)/polymer:$PC_{61}BM$/LiF(0.6 nm)/Al(130 nm). The photovoltaic performances of the polymer:$PC_{61}BM$ devices are summarized in Table 3 and Figure 4. The PCEs varied considerably with the polymer:PCBM blend ratio used in the devices; the details of the variation depended on the polymer backbone. Thus, the PCE

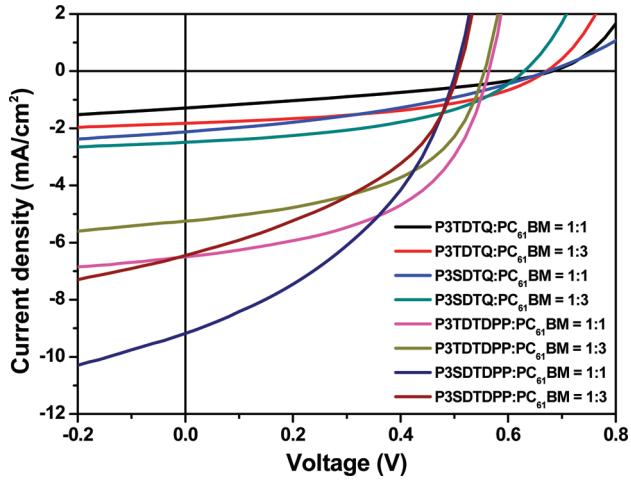


Figure 4. $J-V$ characteristics of a photovoltaic device using polymer/$PC_{61}BM$ blend films as active layers.

of the Qx-containing polymer devices was higher for a blend ratio of 1:3 than 1:1, while for DPP-containing polymer devices, the PCE was better with a 1:1 blend ratio than with a ratio of 1:3. The PCEs of the P3TDTQ, P3SDTQ, P3TDTDPP, and P3SDTDPP devices were found to be 0.30%, 0.52%, 1.88%, and 1.85%, respectively. The open-circuit voltages (V_{OC}, which is related to the difference between the HOMO level of the donor polymer and the LUMO level of the acceptor ($PC_{61}BM$)) of the P3TDTQ, P3SDTQ, P3TDTDPP, and P3SDTDPP devices were found to be 0.68, 0.67, 0.56, and 0.50 V, respectively, for a blend ratio of 1:1. The high V_{OC} values for the P3TDTQ and P3SDTQ devices could be explained by the low HOMO energy levels of P3TDTQ (−5.37 eV) and P3SDTQ (−5.35 eV) compared with those of P3TDTDPP (−5.21 eV) and P3SDTDPP (−5.16 eV). Among the devices using the P3T- and P3S-based polymers, the P3TDTDPP and P3SDTDPP devices demonstrated better photovoltaic performances than did those using P3TDTQ and P3SDTQ because the photon absorption fraction and the FET mobility were higher in the DPP-containing polymer films than in those containing Qx. The DPP-containing polymer devices therefore exhibited a high short circuit current density (J_{SC}). In the case of the Qx-containing polymer devices, the P3S-Qx devices showed higher PCE values than their thiophene analogues; however, the PCEs of the P3S-DPP devices were slightly lower than those of the P3T-DPP devices. The PCEs of the P3T-and P3S-based devices were heavily dependent on the electron-withdrawing accepting units. Interestingly, regardless of the PCE values of the devices, the P3S-based devices (Qx and DPP) always showed higher J_{SC} values than the corresponding thiophene analogues (for the same PCBM blend ratio). The increased short circuit currents of the P3S-based devices could be attributed to the increased spectral breadth of the absorbed photons and hole mobilities. To better understand the origin of the differences in the photovoltaic performances of the polymer solar cells, AFM images of the surface morphologies of each solar cell device were collected (Figure S2, Supporting Information). Generally, nanoscale phase separation should be established to allow efficient charge separation; this is true due to the short exciton diffusion length (~10 μm) of the donor polymers.[29] As can be seen in Figure S2, the P3TDTDPP:PCBM (1:1) and P3SDTDPP:PCBM (1:1) films showed a smoother and more interconnected network

dx.doi.org/10.1021/ma2020112 | Macromolecules 2012, 45, 1303–1312

of polymer−PCBM domains, which accounted for the high photocurrent density in these films. In contrast, relatively high levels of aggregation were observed in the P3TDTQ:PCBM (1:1) and P3SDTQ:PCBM (1:1) films, which reduced the area for charge separation, leading to a low photocurrent. There were no significant differences between the morphologies of the P3T-based films and those of the P3S-based films.

The performances of the solar cells based on P3TDTDPP:PCBM (1:1) and P3SDTDPP:PCBM (1:1) films were further enhanced via the use of [6,6]-phenyl C_{71}-butyric acid methyl ester ($PC_{71}BM$) as an electron acceptor and the use of a mixed chlorobenzene (CB)/1,8-diiodoctane (DIO) (97%:3% by volume) solvent. Figure 5 shows the current−

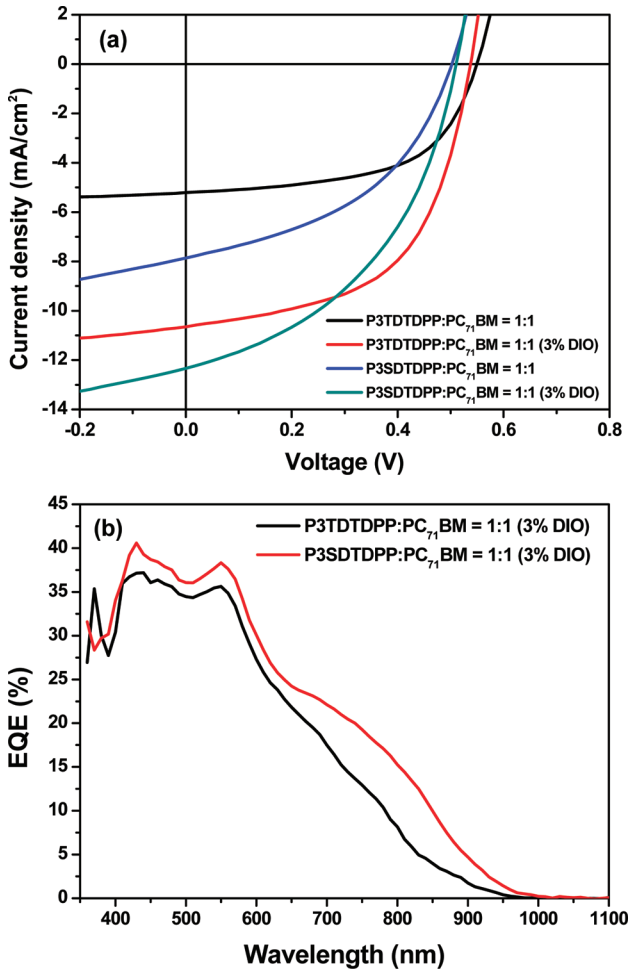


Figure 5. (a) $J-V$ characteristics of a photovoltaic device using P3TDTDPP/$PC_{71}BM$ (1:1) and P3SDTDPP/$PC_{71}BM$ (1:1) and (b) external quantum efficiency of the P3TDTDPP/$PC_{71}BM$ (1:1) and P3SDTDPP/$PC_{71}BM$ (1:1) blend films prepared from mixed CB/DIO (97/3, v/v) solvents.

voltage characteristics resulting from the use of the $PC_{71}BM$ and the mixed solvent in the polymer solar cell devices; the data are summarized in Table 4. The P3TDTDPP:$PC_{71}BM$ (1:1) and P3SDTDPP:$PC_{71}BM$ (1:1) devices showed PCE values similar to those shown by the corresponding $PC_{61}BM$ devices. In contrast, dramatic improvements were observed in the J_{SC} and PCE values for the 3% DIO-containing devices. The PCE increased from 1.88% to 3.18% for the P3TDTDPP:$PC_{71}BM$ (1:1) device and from 1.85% to 2.81% for the

Table 4. PSC Performances of the Polymer/$PC_{71}BM$ Device

polymer	ratio	J_{SC} (mA/cm^2)	V_{OC} (V)	FF (%)	PCE (%)
P3TDTDPP	1:1	5.21	0.55	58	1.65
	1:1[a]	10.65	0.54	56	3.18
P3SDTDPP	1:1	7.86	0.50	45	1.77
	1:1[a]	12.33	0.51	45	2.81

[a]3% DIO additive (v/v).

P3SDTDPP:$PC_{71}BM$ (1:1) device. In this case, the PCE of the P3SDTDPP device was slightly lower than that of the P3TDTDPP device, due to the low V_{OC} and FF; however, the J_{SC} of the P3SDTDPP device was higher than that of the P3TDTDPP device, which was attributed to the lower bandgap and higher mobility of the P3SDTDPP film (compared with the P3TDTDPP film). The improvement in the OPV performances was caused by the changes in the morphology of the blend film. AFM images (Figure. 6) clearly showed that there were large domains in the blend film prepared using only chlorobenzene; these large domains would diminish exciton migration to the donor/acceptor interface and are not favorable for charge separation. The morphology of the blend film prepared using the chlorobenzene/DIO mixed solvent was much more uniform, with no significant phase separation. Good miscibility between the donor polymer and the $PC_{71}BM$ was shown, and interpenetrating networks were formed; these factors may have led to increases in the J_{SC} value.

EQE values (which were measured to evaluate the photoresponses of the fabricated solar cells as a function of wavelength) are shown in Figure 5b for the P3TDTDPP:$PC_{71}BM$ (1:1) and P3SDTDPP:$PC_{71}BM$ (1:1) devices prepared with 3% DIO. The P3TDTDPP and P3SDTDPP devices yielded an EQE plot that was similar to the absorption spectra of P3TDTDPP and P3SDTDPP in the long wavelength region, indicating that excitons were mainly generated in the polymer phase. The spectral responses of the P3TDTDPP device showed that in the region from 350 to 950 nm photons contributed significantly to the EQE, with a maximum EQE of 35% at 550 nm. The P3SDTDPP device, however, exhibited an even better spectral response in the range 350−1000 nm, with a maximum EQE of 38% at 550 nm. The P3SDTDPP:$PC_{71}BM$ blend film exhibited a wide absorption spectrum (650−1000 nm), which resulted in a much higher J_{SC} of 12.33 mA/cm^2.

CONCLUSIONS

In summary, we successfully synthesized novel thiophene- and selenophene-based low-bandgap polymers, using the Stille coupling reaction. The P3TDTQ P3SDTQ, P3TDTDPP, and P3SDTDPP polymers showed good solubility in common organic solvents because of the presence of alkyl side chains. P3TDTQ, P3SDTQ, P3TDTDPP, and P3SDTDPP exhibited long-wavelength UV−vis absorption peaks at 587, 619, 716, and 753 nm, respectively. The P3SDTDPP:$PC_{71}BM$ blend film showed a wide absorption spectrum (650−1000 nm), which resulted in a much higher J_{SC} of 12.33 mA/cm^2. A photovoltaic device using the P3TDTDPP:$PC_{71}BM$ (1:1) and P3SDTDPP:$PC_{71}BM$ (1:1) films with added DIO as the active layer exhibited open-circuit voltages of 0.54 and 0.51 V, short-circuit current densities of 10.65 and 12.33 mA/cm^2, fill factors of 0.56 and 0.45, and power conversion efficiencies of 3.18 and 2.81% for the two films, respectively, under AM 1.5G (100 mW/cm^2) illumination. We believe that the V_{OC} and FF values

dx.doi.org/10.1021/ma2020112 | Macromolecules 2012, 45, 1303−1312

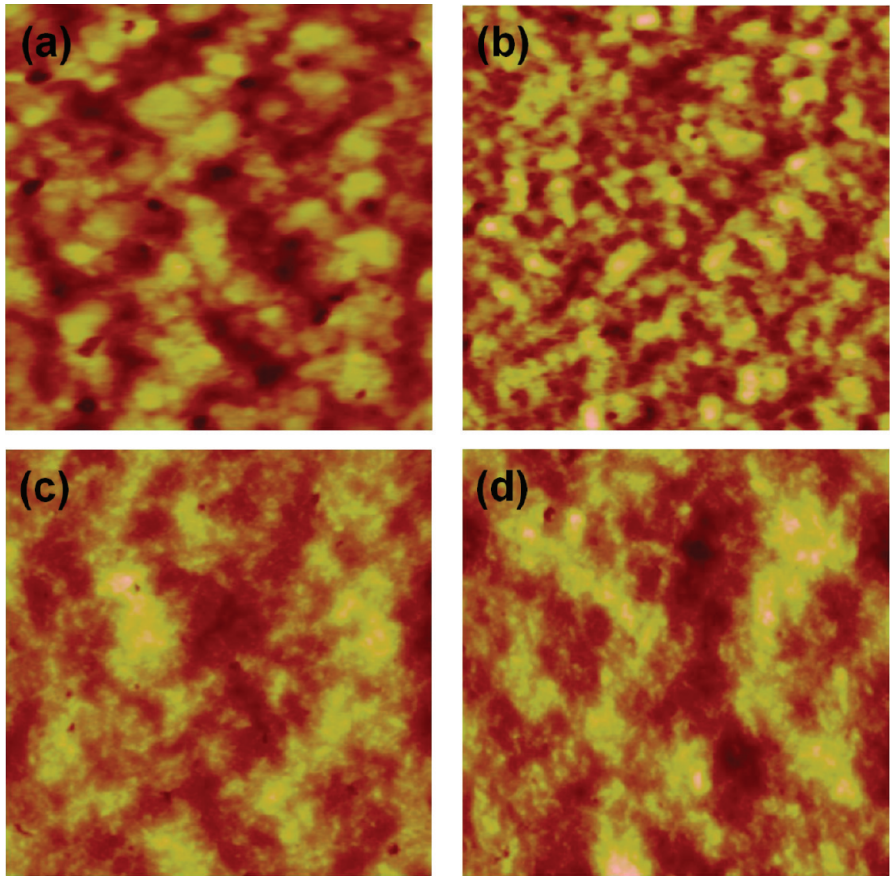


Figure 6. AFM tapping-mode height images of (a) P3TDTDPP/$PC_{71}BM$ (1:1), (b) P3SDTDPP/$PC_{71}BM$ (1:1), (c) P3TDTDPP/$PC_{71}BM$ (1:1) + 3% DIO, and (d) P3SDTDPP/$PC_{71}BM$ (1:1) + 3% DIO. The scanned area is 2 μm × 2 μm.

could be improved by the use of different solvents and/or a buffer layer. With enhanced V_{OC} and FF values, the performance of the P3S-based polymer solar cells could be improved.

EXPERIMENTAL SECTION

Instrumentation. ^{1}H and ^{13}C NMR spectra were recorded on Bruker AVANCE 400 spectrometer, with tetramethylsilane as an internal reference. The optical absorption spectra were measured by a Shimadzu UV-3100 UV−vis−NIR spectrometer. The number- and weight-average molecular weights of polymers were determined by gel permeation chromatography (GPC) on Viscotek T60A instrument, using chloroform as eluent and polystyrene as standard. The differential scanning calorimetry (DSC) and thermal gravimetric analysis were made using TA Q100 instrument and operated under a nitrogen atmosphere. Cyclic voltammetry was performed on an AUTOLAB/PG-STAT12 model system with a three-electrode cell in a solution of Bu_4NBF_4 (0.10 M) in acetonitrile at a scan rate of 50 mV/s. Polymer film coatings on ITO anode electrode were formed by the spin-coating method. Atomic force microscopy (AFM) was measured by tapping-mode using Multimode IIIa, Digital Instruments. Electrical characteristics of the TFTs were measured in ambient conditions using both Keithley 2400 and 236 source/measure units. For all measurements, we used channel lengths (L) of 12 μm and channel widths (W) of 120 μm. Field effect mobility was extracted in the saturation regime from the slope of the source-drain current.

Materials. 2,5-Bis(trimethylstannyl)thiophene (**7**),[19] 2,5-bis-(trimethylstannyl)selenophene (**8**),[20] 2,3-bis(4-(3,7-dimetyloctyloxy)-phenyl)-5,8-bis(5′-bromodithien-2-ly)quinoxaline (**13**),[30] and 3,6-bis-(5-bromothiophene-2-yl)-2,5-bis(2-ethylhexyl)pyrrolo[3,4-*c*]pyrrole-1,4(2*H*,5*H*)-dione (**14**)[31] were synthesized according to previously published procedures.

3-(3′,7′-Dimethyoctyl)thiophene (1). A 1.0 M solution 3,7-dimethyloctylmagnesium bromide (50 mL, 0.05 mol) was added dropwise to a solution of 3-bromothiophene (6.24 g, 0.04 mol) and Ni(dppp)Cl_2 (0.67 g, 1.2 mmol) in THF (60 mL) at −20 °C with stirring. The mixture was stirred at RT for 4 h and then poured into water (100 mL) and extracted with ethyl acetate. After drying over anhydrous $MgSO_4$, the solvent was evaporated and the residue was purified by column chromatography on silica gel with hexane as eluent. After drying, the product was obtained as colorless oil. Yield: 6.3 g (70%). Fab-MS: m/z = 225. ^{1}H NMR (300 MHz, $CDCl_3$, δ): 7.22 (d, 1H), 6.92 (s, 1H), 6.90 (d, 1H), 2.61 (m. 2H), 1.1−1.50 (m. 10H), 0.91 (d, 3H), 0.87 (d, 6H). ^{13}C NMR (80 MHz, $CDCl_3$, δ): 143.64, 128.48, 125.25, 119.83, 39.54, 38.05, 37.36, 32.69, 28.19, 28.19, 24.93, 22.93, 22.84, 19.79. Anal. Calcd for $C_{14}H_{24}Se$: C 74.93, H 10.78, S 41.29. Found: C 74.70, H 10.41, S 14.47.

1-Chloro-5,9-dimethyldecan-2-one (2). A 1.0 M solution 3,7-dimethyloctylmagnesium bromide (100 mL, 0.1 mol) was added dropwise to a solution of chloroacetyl chloride (16 mL, 0.2 mol) in THF (30 mL) at −78 °C with stirring. The mixture was stirred at −78 °C for 6 h and then poured into water (100 mL) and extracted with ethyl acetate. After drying over anhydrous $MgSO_4$, the solvent was evaporated. The product was used without further purification. Yield: 7.5 g (34%).

3-(Chloromethyl)-6,10-dimethylundec-1-yn-3-ol (3). A 0.5 M solution of ethynylmagnesium bromide (100 mL, 0.05 mol) was added dropwise to a solution of compound **2** (7.5 g, 0.035 mol) in THF (150 mL) at −60 °C with stirring. The mixture was stirred at −60 °C for 4 h and then poured into water (150 mL) and extracted with ethyl acetate. After drying over anhydrous $MgSO_4$, the solvent was evaporated and the residue was purified by column chromatography on silica gel with hexane as eluent. After drying, the product was obtained as colorless oil. Yield: 4.0 g (48%). Fab-MS: m/z = 243. ^{1}H NMR (300 MHz, $CDCl_3$, δ): 3.67 (d, 1H), 3.61 (d, 1H), 2.57 (s, 1H),

dx.doi.org/10.1021/ma2020112 | *Macromolecules* 2012, 45, 1303−1312

2.51 (s. 1H), 1.2−1.7 (m. 9H), 1.1 (m, 3H), 0.87 (m, 9H). ^{13}C NMR (80 MHz, $CDCl_3$, δ): 83.89, 73.88, 70.92, 53.18, 39.48, 37.28, 37.13, 36.88, 33.01, 31.23, 28.17, 24.91, 22.91, 19.83. Anal. Calcd for $C_{14}H_{25}ClO$: C 68.69, H 10.29, O 6.54. Found: C 67.76, H 10.14, O 6.9.

3-(3′,7′-Dimethyoctyl)selenophene (4). A solution selenium (2 g, 0.025 mol) and sodium borohydride (1.84 g, 0.048 mol) was dissolved in 40 mL of ethanol at 0 °C and for 1 h. Compound **3** (4 g, 0.016 mol) in 20 mL of ethanol was added to solution, and the resulting mixture was stirred at RT for 30 min. The resulting mixture was added slowly to a solution of KOH (2.73 g, 0.048 mmol) in 20 mL of ethanol−H_2O (20:1 v/v) at RT. The mixture was refluxed for 2 h at 90 °C. The reaction mixture was then poured into water and extracted with ethyl acetate. After drying over anhydrous $MgSO_4$, the solvent was evaporated. The mixture and *p*-toluenesulfonic acid monohydrate (0.1 g, 0.5 mmol) in 100 mL of hexane was refluxed for 1 h. After cooling, the mixture poured into water (100 mL) and extracted with ethyl acetate. The extract was successively washed with water, 5% sodium hydrogen carbonate aqueous solution, and brine. After drying over anhydrous $MgSO_4$, the solvent was evaporated and the residue was purified by column chromatography on silica gel with hexane as eluent. After drying, the product was obtained as yellow oil. Yield: 1.9 g (43%). Fab-MS: m/z = 273. ^{1}H NMR (300 MHz, $CDCl_3$, δ): 7.89 (d, 1H), 7.52 (s, 1H), 7.19 (d, 1H), 2.60 (m. 2H), 1.1−1.50 (m. 10H), 0.91 (d, 3H), 0.87 (d, 6H). ^{13}C NMR (80 MHz, $CDCl_3$, δ): 145.66, 131.66, 129.86, 39.54, 37.85, 37.35, 32.69, 29.70, 28.19, 24.91, 22.93, 22.84, 19.80. Anal. Calcd for $C_{14}H_{24}S$: C 61.98, H 8.92. Found: C 61.87, H 8.90.

2-Bromo-3-(3′,7′-dimethyoctyl)thiophene (5). To a stirred solution of compound **1** (3.1 g, 13.8 mmol) in chloroform−acetic acid (1:1 v/v, 150 mL), *N*-bromosuccinimide (NBS) (2.73 g, 15.3 mmol) was added. The mixture was stirred at 0 °C for 1 h and then poured into water (100 mL) and extracted with ethyl acetate. The extract was successively washed with water, 5% sodium hydrogen carbonate aqueous solution, and brine. After drying over anhydrous $MgSO_4$, the solvent was evaporated and the residue was purified by column chromatography on silica gel with hexane as eluent. After drying, the product was obtained as yellow oil. Yield: 4.00 g (95%). Fab-MS: m/z = 303. ^{1}H NMR (300 MHz, $CDCl_3$, δ): 7.16 (d, 1H), 6.79 (d, 1H), 2.60 (m. 2H), 1.12−1.54 (m. 10H), 0.91 (d, 3H), 0.87 (d, 6H). ^{13}C NMR (80 MHz, $CDCl_3$, δ): 143.64, 128.49, 125.26, 108.88, 39.53, 37.24, 37.11, 32.68, 28.20, 27.28, 24.90, 22.93, 22.85, 19.80. Anal. Calcd for $C_{14}H_{23}BrS$: C 55.44, H 7.64, S 10.50. Found: C 55.41, H 7.70, S 10.50.

2-Bromo-3-(3′,7′-dimethyoctyl)selenophene (6). The compound was synthesized using the same method as for compound **5**; using compound **3** (1.9 g, 7 mmol) in chloroform−acetic acid (1:1 v/v, 50 mL), *N*-bromosuccinimide (NBS) (1.32 g, 7.2 mmol) was added. The mixture was stirred at 0 °C for 1 h and then poured into water (100 mL) and extracted with ethyl acetate. The extract was successively washed with water, 5% sodium hydrogen carbonate aqueous solution, and brine. After drying over anhydrous $MgSO_4$, the solvent was evaporated and the residue was purified by column chromatography on silica gel with hexane as eluent. After drying, the product was obtained as yellow oil. Yield: 2.35 g (96%). Fab-MS: m/z = 351. ^{1}H NMR (300 MHz, $CDCl_3$, δ): 7.86 (d, 1H), 7.05 (d, 1H), 2.60 (m. 2H), 1.2−1.60 (m. 10H), 0.91 (d, 3H), 0.87 (d, 6H). ^{13}C NMR (80 MHz, $CDCl_3$, δ): 144.64, 131.35, 130.28, 111.20, 39.52, 37.22, 36.98, 32.70, 28.55, 28.19, 24.89, 22.94, 22.86, 19.82. Anal. Calcd for $C_{14}H_{23}BrSe$: C 48.02, H 6.62. Found: C 47.96, H 6.62.

3,3″-(3′,7′-Dimethyoctyl)-2,2′:5,2″-terthiophene (9). A solution tris(dibenzylideneacetone)dipalladium (0) (0.15 g, 0.16 mmol), tri-*o*-tolyphosphine (0.087 g, 0.28 mmol), compound **7** (0.98 g, 2.4 mmol), and compound **5** (1.52 g, 5.01 mmol) was dissolved in 40 mL of anhydrous toluene under N_2. The solution was heated at 90 °C for 3 h. The mixture was then poured into water and extracted with ethyl acetate. The extract was the successively washed with water and brine. After drying over anhydrous $MgSO_4$, the solvent was evaporated and the residue was purified by column chromatography on silica gel with hexane as eluent. After drying, the product was obtained as a yellow solid. Yield: 1.0 g (78%). Fab-MS: m/z = 528. ^{1}H NMR (300 MHz, $CDCl_3$, δ): 7.17 (d, 2H), 7.05 (d, 2H), 6.92 (s, 2H), 2.80 (m. 4H), 1.13−1.70 (m. 20H), 0.91 (d, 6H), 0.87 (d, 12H). ^{13}C NMR (80 MHz, $CDCl_3$, δ): 140.08, 136.27, 130.54, 130.23, 126.25, 124.01, 39.53, 38.21, 37.35, 33.07, 28.20, 27.18, 24.96, 22.92, 22.83, 19.84. Anal. Calcd for $C_{32}H_{48}S_3$: C 72.67, H 9.15, S 18.19. Found: C 72.70, H 9.02, S 18.14.

3,3″-(3′,7′-Dimethyoctyl)-2,2′:5,2″-terselenophene (10). The compound was synthesized using the same method as for compound **9**, using tris(dibenzylideneacetone)dipalladium(0) (0.15 g, 0.16 mmol), tri-*o*-tolyphosphine (0.087 g, 0.28 mmol), compound **8** (1.1 g, 2.39 mmol), and compound **6** (1.84 g, 5.26 mmol) was dissolved in 40 mL of anhydrous toluene under N_2. The solution was heated at 90 °C for 3 h. The mixture was then poured into water and extracted with ethyl acetate. The extract was the successively washed with water and brine. After drying over anhydrous $MgSO_4$, the solvent was evaporated and the residue was purified by column chromatography on silica gel with hexane as eluent. After drying, the product was obtained as a yellow solid. Yield: 1.2 g (82%). Fab-MS: m/z = 670. ^{1}H NMR (300 MHz, $CDCl_3$, δ): 7.88 (d, 2H), 7.21 (d, 2H), 7.14(s, 2H), 2.60 (m. 4H), 1.13−1.68 (m. 20H), 0.91 (d, 6H), 0.87 (d, 12H). ^{13}C NMR (80 MHz, $CDCl_3$, δ): 143.65, 141.41, 137.44, 133.75, 128.87, 128.83, 39.53, 38.24, 37.35, 33.15, 28.45, 24.96, 22.94, 22.85, 19.86. Anal. Calcd for $C_{32}H_{48}Se_3$: C 57.40, H 7.23. Found: C 57.35, H 7.23.

5,5″-Bis(trimethylstannyl)-3,3″-di(3′,7′-dimethyoctyl)-2,2′:5,2″-terthiophene (11). To a solution of compound **9** (0.9 g, 1.7 mmol) in THF (15 mL), a 1.6 M solution of *n*-BuLi in hexane (2.23 mL, 3.5 mmol) was added, and the mixture was stirred at −78 °C and for 1 h and then 1.0 M solution of trimethyltin chloride (3.5 mL, 3.5 mmol) was added in one portion. The solution was warmed to room temperature and stirred at room temperature for 1 h. The reaction mixture was then poured into water and extracted with ethyl acetate. After drying over anhydrous $MgSO_4$, the solvent was evaporated. The crude product was washed several times by using acetone/methanol (1/10) mixed solvents. The product was dissolved in small amount of $CHCl_3$ and precipitated in methanol at low temperature (−40 °C). Yield: 0.6 g (40%). Fab-MS: m/z = 854. ^{1}H NMR (300 MHz, $CDCl_3$, δ): 7.04 (s, 2H), 6.99 (s, 2H), 2.76 (t. 4H), 1.18−1.69 (m, 20H), 0.91 (d, 6H), 0.87 (t, 12H), 0.37 (s, 18H). ^{13}C NMR (80 MHz, $CDCl_3$, δ): 141.11, 139.98, 138.55, 136.68, 130.22, 126.29, 39.54, 38.21, 37.36, 33.23, 28.20, 27.19, 24.98, 22.84, 19.87, −8.02. Anal. Calcd for $C_{38}H_{64}S_3Sn_2$: C 53.41, H 7.15, S 11.26. Found: C 53.51, H 7.20, S 11.34.

5,5″-Bis(trimethylstannyl)-3,3″-di(3′,7′-dimethyoctyl)-2,2′:5,2″-terselenophene (12). The compound was synthesized using the same method as for compound **11**; using compound **6** (0.7 g, 1 mmol) in THF (15 mL), a 1.6 M solution of *n*-BuLi in hexane (1.3 mL, 2 mmol) was added, and the mixture was stirred at −78 °C and for 1 h and then 1.0 M solution of trimethyltin chloride (2.1 mL, 2.1 mmol) was added in one portion. The solution was warmed to room temperature and stirred at room temperature for 1 h. The reaction mixture was then poured into water and extracted with ethyl acetate. After drying over anhydrous $MgSO_4$, the solvent was evaporated. The crude product was washed several times by using acetone/methanol (1/10) mixed solvents. The product was dissolved in small amount of $CHCl_3$ and precipitated in methanol at low temperature (−60 °C). Yield: 0.41 g (52%). Fab-MS: m/z = 996. ^{1}H NMR (300 MHz, $CDCl_3$, δ): 7.37 (s, 2H), 6.81 (s, 2H), 2.73 (t. 4H), 1.18−1.69 (m, 20H), 0.91 (d, 6H), 0.87 (t, 12H), 0.36 (s, 18H). ^{13}C NMR (80 MHz, $CDCl_3$, δ): 144.01, 143.76, 143.44, 141.28, 133.73, 128.90, 39.54, 38.24, 37.36, 33.16, 28.38, 28.20, 24.98, 22.86, 19.87, −7.69. Anal. Calcd for $C_{38}H_{64}Se_3Sn_2$: C 45.86, H 6.48. Found: C 45.90, H 6.50.

P3TDTQ. A 100 mL Schlenk flask containing anhydrous chlorobenzene (10 mL), compound **11** (0.17 g, 0.2 mmol), compound **12** (0.18 g, 0.2 mmol), tris(dibenzylideneacetone)dipalladium(0) (0.01 g, 0.01 mmol), and tri(*o*-tolyl)phosphine (6 mg, 0.02 mmol) was kept under a nitrogen atmosphere at 130 °C for 72 h. When the reaction had finished, reaction mixture was precipitated from the 10 mL of HCl and 150 mL of methanol. The polymer was dissolved in

small amount of $CHCl_3$ and precipitated in methanol. The resulting polymer was further purified by Soxhlet extraction using methanol and hexane then dried in vacuum to give dark-green solid. Yield: 0.2 g (77%). ^{1}H NMR (300 MHz, $CDCl_3$, δ): 8.08 (br, 2H) 7.81 (br, 6H) 7.12 (br, 6H) 6.92 (br, 6H), 4.04 (br, 4H), 2.80 (br, 4H) 1.24−0.81 (m, 76H). Anal. Calcd for $C_{79}H_{100}N_2O_2S_5$: C 70.81, H 8.24, N 2.66, O 3.04, S 15.24. Found: C 70.72, H 8.28, N 2.66, O 3.27, S 15.21.

P3SDTQ. The compound was synthesized using the same method as for P3TDTQ, with compound **12** (0.2 g, 0.2 mmol), compound **13** (0.18 g, 0.2 mmol), tris(dibenzylideneacetone)dipalladium(0) (0.01 g, 0.01 mmol), tri(*o*-tolyl)phosphine (6 mg, 0.02 mmol), and chlorobenzene (10 mL) being kept under a nitrogen atmosphere at 130 °C for 72 h. When the reaction had finished, reaction mixture was precipitated from the 10 mL of HCl and 150 mL of methanol. The polymer was dissolved in small amount of $CHCl_3$ and precipitated in methanol. The resulting polymer was further purified by Soxhlet extraction using methanol and hexane then dried in vacuum to give dark-green solid. Yield: 0.17 g (80%). ^{1}H NMR (300 MHz, $CDCl_3$, δ): 8.09 (br, 2H) 7.81(br, 6H) 7.19 (br, 6H) 6.92 (br, 6H), 4.08 (br, 4H), 2.82 (br, 4H) 1.55−0.81 (m, 76H). Anal. Calcd for $C_{79}H_{100}N_2O_2S_2Se_3$: C 67.26, H 7.15, N 1.99, O 2.27, S 4.55. Found: C 67.19, H 7.29, N 1.84, O 2.45, S 4.16.

P3TDTDPP. The compound was synthesized using the same method as for P3TDTQ, with compound **11** (0.17 g, 0.2 mmol), compound **14** (0.136 g, 0.2 mmol), tris(dibenzylideneacetone)-dipalladium(0) (0.01 g, 0.01 mmol), tri(*o*-tolyl)phosphine (6 mg, 0.02 mmol), and chlorobenzene (10 mL) being kept under a nitrogen atmosphere at 130 °C for 72 h. When the reaction had finished, reaction mixture was precipitated from the 10 mL of HCl and 150 mL of methanol. The polymer was dissolved in a small amount of $CHCl_3$ and precipitated in methanol. The resulting polymer was further purified by Soxhlet extraction using methanol and hexane then dried in vacuum to give dark solid. Yield: 0.17 g (62%). ^{1}H NMR (300 MHz, $CDCl_3$, δ): 8.98−8.90 (br, 2H), 7.18−6.92 (br, 6H), 4.03 (br, 4H) 2.77 (br, 4H) 1.92−0.86 (m, 68H). Anal. Calcd for $C_{79}H_{100}N_2O_2S_5$: C 74.72, H 8.15, N 2.18, O 2.49, S 12.47. Found: C 74.35, H 8.04, N 2.44, O 2.37, S 12.84.

P3SDTDPP. The compound was synthesized using the same method as for P3TDTQ, with compound **12** (0.2 g, 0.2 mmol), compound **14** (0.136 g, 0.2 mmol), tris(dibenzylideneacetone)-dipalladium(0) (0.01 g, 0.01 mmol), tri(*o*-tolyl)phosphine (6 mg, 0.02 mmol), and chlorobenzene (10 mL) being kept under a nitrogen atmosphere at 130 °C for 72 h. When the reaction had finished, reaction mixture was precipitated from the 10 mL of HCl and 150 mL of methanol. The polymer was dissolved in small amount of $CHCl_3$ and precipitated in methanol. The resulting polymer was further purified by Soxhlet extraction using methanol and hexane and then dried in a vacuum to give a dark solid. Yield: 0.13 g (54%). ^{1}H NMR (300 MHz, $CDCl_3$, δ): 8.96−8.89 (br, 2H), 7.82−6.82 (br, 6H), 4.02 (br, 4H) 2.69 (br, 4H) 1.91−0.87 (m, 68H). Anal. Calcd for $C_{62}H_{86}N_2O_2S_2Se_3$: C 62.45, H 7.25, N 2.35, O 2.68, S 5.38. Found: C 62.26, H 7.28, N 2.21, O 2.91, S 5.18.

Fabrication of the Organic Thin Film Transistors (OTFTs). OTFT devices were fabricated in a bottom-contact geometry (channel length = 12 μm, width = 120 μm). The source and drain contacts consisted of gold (100 nm), and the dielectric was silicon oxide (SiO_2) with a thickness of 300 nm. The SiO_2 surface was cleaned, dried, and pretreated with a solution of 1.0 mM octyltrichlorosilane (OTS-8) in toluene at room temperature for 2 h under nitrogen to produce nonpolar and smooth surfaces onto which the polymers could be spin-coated. The polymers were dissolved to a concentration of 0.5 wt % in chlorobenzene. Films of the organic semiconductors were spin-coated at 1500 rpm for 50 s to a thickness of 50 nm, followed by an annealing process. All device fabrication procedures and measurements were carried out in air at room temperature.

Fabrication of the Polymer Solar Cells (PSCs). In this study, the devices were fabricated with the structure ITO/PEDOT:PSS/polymer:$PC_{61}BM$ or $PC_{71}BM$/LiF/Al. The procedure for cleaning the ITO surface included sonication and rinsing in deionized water, methanol, and acetone. The hole-transporting PEDOT:PSS layer was spin-coated onto each ITO anode from a solution purchased from H.C. Starck and baked for 20 min at 140 °C in a glovebox. Each polymer:$PC_{61}BM$ solution was then spin-coated onto the PEDOT:PSS layer. The polymer solution for spin-coating was prepared by dissolving the polymer (1 wt %) in chlorobenzene. Preannealing was not carried out. LiF and aluminum contacts were formed by vacuum deposition at pressures below 3×10^{-6} Torr, providing an active area of 0.09 cm^2. Solar cell efficiencies were characterized under simulated 100 mW/cm^2 AM 1.5G irradiation from a Xe arc lamp with an AM 1.5 global filter. Simulator irradiance was characterized using a calibrated spectrometer, and the illumination intensity was set using an NREL certified silicon diode with an integrated KG1 optical filter. The EQE was measured by underfilling the device are a using a reflective microscope objective to focus the light output from a 100 W halogen lamp outfitted with a monochromator and optical chopper; the photocurrent was measured using a lock-in amplifier, and the absolute photon flux was determined using a calibrated silicon photodiode. All device fabrication procedures and measurements were carried out in air at room temperature.

■ ASSOCIATED CONTENT

Ⓢ Supporting Information

IV characteristics and AFM images of the polymers. This material is available free of charge via the Internet at http://pubs.acs.org.

■ AUTHOR INFORMATION

Corresponding Author

*E-mail: inamkang@catholic.ac.kr.

■ ACKNOWLEDGMENTS

This research was supported by Basic Science Research Program through the National Research Foundation of Korea (NRF) funded by the Ministry of Education, Science and Technology (2011-0004016), also supported by the New & Renewable Energy of the Korea Institute of Energy Technology Evaluation and Planning (KETEP) grant funded by the Korea government Ministry of Knowledge Economy (2011T100200034), and by a grant from the cooperative R&D Program (B551179-08-03-00) funded by the Korea Research Council Industrial Science and Technology, Republic of Korea

■ REFERENCES

(1) Chen, H.-Y.; Hou, J. H.; Zhang, S. Q.; Liang, Y.; Yang, G. W.; Yang, Y.; Yu, L. P.; Wu, Y.; Li, G. *Nature Photonics* **2009**, *3*, 649.

(2) Yu, G.; Gao, J.; Hummelen, J. C.; Wudl, F.; Heeger, A. J. *Science* **1995**, *270*, 1789.

(3) Koetse, M. M.; Sweelssen, J.; Hoekerd, K. T.; Schoo, H. F. M.; Veenstra, S. C.; Kroon, J. M.; Yang, X.; Loos.. *J. Appl. Phys. Lett.* **2006**, *88*, 83504.

(4) Wienk, M. M.; Koon, J. M.; Verhees, W. J. H.; Knol, J.; Hummelen, J. C.; van Hal, P. L.; Janssen, R. A. J. *Angew. Chem., Int. Ed.* **2003**, *42*, 3371.

(5) Lee, S. K.; Cho, J. K.; Goo, Y.; Shin, W. S.; Lee, J.-C.; Lee, W.-H.; Kang, I.-N.; Shim, H.-K.; Moon, S.-J. *Chem. Commun.* **2011**, *47*, 1791−1793.

(6) Guänes, S.; Neugebauer, H.; Sariciftci, N. S. *Chem. Rev.* **2007**, *107*, 1324.

(7) Thompson, B. C.; Frechet, J. M. J. *Angew. Chem., Int. Ed.* **2008**, *47*, 58.

(8) Peet, J.; Kim, J. Y.; Coates, N. E.; Ma, W. L.; Moses, D.; Heeger, A. J.; Bazan, G. C. *Nature Mater.* **2007**, *6*, 497−500.

(9) Chen, H.-Y.; Hou, J.; Hayden, A. E.; Yang, H.; Houk, K. N.; Yang, Y. *Adv. Mater.* **2010**, *22*, 371−375.

(10) Kim, B.; Yeo, J. S.; Khim, D.; Kim, D.-Y. *Macromol. Rapid Commun.* **2011**, DOI: 10.1002/marc.201100327.
(11) Zou, Y.; Gendron, D.; Neagu, R.; Leclerc, M. *Macromolecules* **2009**, *42*, 6361.
(12) Wang, E.; Hou, L.; Wang, Z.; Hellström, S.; Zhang, F.; Inganäs, O.; Andersson, M. R. *Adv. Mater.* **2010**, *22*, 5240.
(13) Zade, S. S.; Zamoshchik, N.; Bendikov, M. *Chem.—Eur. J.* **2009**, *15*, 8613.
(14) Ballantyne, A. M.; Chen, L. C.; Nelson, J.; Bradley, D. D. C.; Astuti, Y.; Maurano, A.; Shuttle, C. G.; Durrant, J. R.; Heeney, M.; Duffy, W.; McCulloch, I. *Adv. Mater.* **2007**, *19*, 4544.
(15) Heeney, M.; Zhang, W.; Crouch, D. J.; Chabinyc, M. L.; Gordeyev, S.; Hamilton, R.; Higgins, S. J.; McCulloch, I.; Skabara, P. J.; Sparrowe, D.; Tierney, S. *Chem. Commun.* **2007**, *43*, 5061.
(16) Chen, Z. Y.; Lemke, H.; Albert-Seifried, S.; Caironi, M.; Nielsen, M. M.; Heeney, M.; Zhang, W. M.; McCulloch, I.; Sirringhaus, H. *Adv. Mater.* **2010**, *22*, 2371.
(17) Crouch, D. J.; Skabara, P. J.; Heeney, M.; McCulloch, I.; Sparrowe, D.; Coles, S. J.; Hursthouse, M. B. *Macromol. Rapid Commun.* **2008**, *29*, 1839−1843.
(18) Ha, J. S.; Kim, K. H.; Choi, D. H. *J. Am. Chem. Soc.* **2011**, DOI: 10.1021/ja203189h.
(19) Furuta, P.; Fréchet, J. M. J. *J. Am. Chem. Soc.* **2003**, *125*, 13173−13181.
(20) Martin, H.; Warren, D.; Iain, M.; Simon, H.; David, C.; Peter, S. EP2006/010421.
(21) Koppe, M.; Scharber, M.; Brabec, C.; Duffy, W.; Heeney, M.; McCulloch, I. *Adv. Funct. Mater.* **2007**, *17*, 1371.
(22) Patra, A.; Wijsboom, Y. H.; Zade, S. S.; Li, M.; Sheynin, Y.; Leitus, G.; Bendikov, M. *J. Am. Chem. Soc.* **2008**, *130*, 6734.
(23) Salzner, U.; Lagowski, J. B.; Pickup, P. G.; Poirier, R. A. *Synth. Met.* **1998**, *96*, 177.
(24) Cheng, Y.-J.; Wu, J.-S.; Shih, P.-I.; Chang, C.-Y.; Jwo, P.-C.; Kao, W.-S.; Hsu, C.-S. *Chem. Mater.* **2011**, *23*, 2361.
(25) Bijleveld, J. C.; Zoombelt, A. P.; Mathijssen, S. G. J.; Wienk, M. M.; Turbiez, M.; de Leeuw, D. M.; Janssen, R.A. J. *J. Am. Chem. Soc.* **2009**, *131*, 16616.
(26) Huo, L.; Hou, J.; Chen, H.-Y.; Zhang, S.; Jiang, Y.; Chen, T. L.; Yang, Y. *Macromolecules* **2009**, *42*, 6564.
(27) Rusling, J. F.; Suib, S. L. *Adv. Mater.* **1994**, *6*, 922.
(28) Dimitrakoupoulos, C. D.; Melenfant, R. M. *Adv. Mater.* **2002**, *14*, 99.
(29) Halls, J. J. M.; Pichler, K.; Friend, R. H.; Moratti, S. C.; Holmes, A. B. *Appl. Phys. Lett.* **1996**, *68*, 3120.
(30) Lee, S. K.; Lee, W.-H.; Cho, J. M.; Park, S. J.; Shin, W. S.; Lee, J.-C.; Kang, I.-N.; Moon, S.-J. *Macromolecules* **2011**, *44*, 5994−6001.
(31) Huo, L.; Hou, J.; Chen, H.-Y.; Zhang, S.; Jiang, Y.; Chen, T. L.; Yang, Y. *Macromolecules* **2009**, *42*, 6564.

Macromolecules

Article

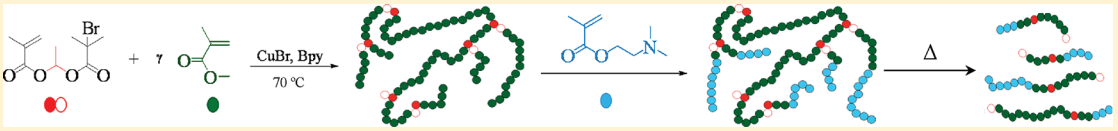
pubs.acs.org/Macromolecules

Synthesis, Characterization and Thermolysis of Hyperbranched Homo- and Amphiphilic Co-Polymers Prepared Using an Inimer Bearing a Thermolyzable Acylal Group

Maria Rikkou-Kalourkoti,[†] Krzysztof Matyjaszewski,[‡] and Costas S. Patrickios[†,*]

[†]Department of Chemistry, University of Cyprus, P.O. Box 20537, 1678 Nicosia, Cyprus

[‡]Department of Chemistry, Carnegie Mellon University, 4400 Fifth Avenue, Pittsburgh, Pennsylvania 15213, United States



ABSTRACT: Degradable hyperbranched polymers were synthesized via self-condensing atom transfer radical copolymerization of methyl methacrylate (MMA) with a novel inimer bearing a thermolyzable acylal group. This inimer was 1-(2-bromoisobutyryloxyl)ethyl methacrylate (BIB1EMA) and was synthesized in a one-step reaction between 2-bromoisobutyric acid and vinyl methacrylate at 40% yield. The inimer was subsequently used for the preparation of three degradable hyperbranched homopolymers of MMA (monomer conversion ~80%) with molecular weights in the range from 36 000 to 51 000 g mol^{-1} synthesized using initial MMA-to-inimer molar ratios between 25 and 100. The inimer was also used for the preparation of two degradable hyperbranched amphiphilic copolymers of MMA and 2-(dimethylamino)ethyl methacrylate (DMAEMA) with an MMA hydrophobic hyperbranched core and different compositions, 10 and 38 mol % DMAEMA, afforded by changing the relative loadings in the two comonomers. Both hyperbranched amphiphilic copolymers were soluble in THF: water mixtures with up to 50% w/w water content, whereas they precipitated at higher water contents. All hyperbranched (co)polymers were thermolyzed in a vacuum oven at 200 °C within 24−56 h. The molecular weights of the thermolysis products were consistent with the inimer content and the complete thermolysis of the hyperbranched (co)polymers. Hyperbranched polymers of MMA, also prepared in this investigation, but using a nondegradable inimer, isomeric to BIB1EMA, 2-(2-bromoisobutyryloxyl)ethyl methacrylate (BIB2EMA), did not present any reduction in their molecular weight when subjected to the same thermolysis conditions as those applied for the degradable hyperbranched polymers (200 °C, ~24 h).

INTRODUCTION

Hyperbranched polymers represent an interesting macromolecular architecture, with features intermediate between those of linear polymers and polymer networks. Similar to polymer networks, hyperbranched polymers are highly branched, but yet soluble as linear polymers. As mentioned in the review by Hult et al.,[1] hyperbranched polymers were first reported by DuPont in an effort to replace dendrimers, also highly branched polymers but of highly ordered structure which are difficult and time-consuming to prepare and, therefore, less appropriate for industrial use. The high degree of branching of hyperbranched polymers is responsible for their unique physical properties, such as their compact shape resulting in low viscosity in solution and in the molten state compared to their linear counterparts,[2,3] and their large number of functional groups on their periphery. Because of these properties, hyperbranched polymers[4−6] find numerous applications in surface modification,[7−12] in coatings,[13−16] in controlled drug and gene delivery,[17,18] in nonlinear optics,[19,20] and can form the cross-linking nodes in designer's hydrogels.[21−25] As mentioned before, the main advantage of hyperbranched polymers compared to dendrimers is their facile synthesis.

Hyperbranched vinyl polymers can be synthesized following three different techniques: (a) copolymerization of monovinyl with small amounts of di- or multivinyl monomers, (b) polymerization of di- or multivinyl monomers with a large excess of initiator, and (c) self-condensing vinyl polymerization of AB* initiator-monomers, known as *inimers*. Whereas the first two techniques can be applied using either controlled or conventional polymerization methods, the third technique requires the use of a controlled polymerization method. Of special interest are the different *controlled radical* polymerization methods which have been used for the preparation of hyperbranched polymers applying all three above-mentioned techniques, including atom transfer radical polymerization (ATRP),[26−32] reversible addition−fragmentation chain transfer polymerization (RAFT),[33−40] and nitroxide-mediated radical polymerization (NMP).[41−44] Furthermore, controlled/"living" ionic polymerization methods have also been used for the synthesis of hyperbranched polymers, including "living" cationic polymerization[45] and group transfer polymerization (GTP).[46−49]

In the present study, self-condensing vinyl copolymerization of a degradable inimer bearing a thermally labile acylal group

Received: September 5, 2011
Revised: December 27, 2011
Published: January 19, 2012

ACS Publications © 2012 American Chemical Society

was performed via ATRP for the preparation of hyperbranched polymers. ATRP has previously been employed several times for the preparation of hyperbranched polymers using inimers,[26−30,50] but only once did that involve degradable inimers.[31] Those degradable inimers bore disulfide or ester labile groups and were used for the preparation of degradable hyperbranched hydrophobic homopolymers of styrene.[31] In this report, we present the synthesis of thermally labile hyperbranched hydrophobic homopolymers and *amphiphilic* copolymers using a novel inimer bearing an acylal group. The successful thermolysis of these polymers and the results from the characterization of the thermolysis products are also presented. Finally, to show that the thermal cleavage of the present hyperbranched polymers was due to the thermolysis of the thermally labile inimer residue in the polymers, we also prepared similar hyperbranched polymers based on a nondegradable inimer, isomeric to the thermolyzable one. When subjected to the same thermolysis conditions as those used for the former (thermolyzable) polymers, these latter polymers did not present any reduction in their molecular weight.

EXPERIMENTAL SECTION

Materials and Methods. 2-(Dimethylamino)ethyl methacrylate (DMAEMA, 99%) and methyl methacrylate (MMA, 99%) were purchased from Aldrich, Germany. Copper(I) bromide (99%), 2,2′-bipyridine (bpy, 99%), 2-bromoisobutyric acid (98%), vinyl methacrylate (98%) and 2,2-diphenyl-1-picrylhydrazyl hydrate (DPPH, 95%) were also purchased from Aldrich and were used as received. *N*,*N*-Dimethylformamide (DMF, Merck, 99%) was dried over calcium hydride and was freshly distilled under reduced pressure. The monomers were passed through basic alumina columns to remove the polymerization inhibitor and any other acidic impurities and they were stirred overnight over calcium hydride to remove the last traces of moisture and protonic impurities. This was done in the presence of an added free radical inhibitor, DPPH, to avoid undesired thermal polymerization. The monomers were freshly distilled prior to the polymerization.

Preparation of the Degradable Acylal Inimer 1-(2-Bromoisobutyryloxyl)ethyl Methacrylate (BIB1EMA). The degradable inimer BIB1EMA was prepared by an addition reaction. In particular, to a 100 mL round-bottomed flask containing 5 mL of vinyl methacrylate (4.67 g, 0.042 mol) were added 10.42 g of 2-bromoisobutyric acid (0.062 mol) and left to react at 95 °C for 19 h until all vinyl methacrylate was consumed. As vinyl methacrylate already contained radical inhibitor, no extra inhibitor was added to this reaction. After 19 h, the mixture was allowed to cool down and was distilled under vacuum. The desired product was isolated at 40% yield as a yellowish liquid. The structure of the inimer was confirmed by ^{1}H and ^{13}C NMR spectroscopy. ^{1}H NMR (300 MHz, $CDCl_3$, δ): 6.87 (*m*, 1 × 1H, −OCH*H*(CH$_3$)O−), 6.09 (*s*, 1 × 1H, C*H*$_2$═C−, H *cis* to the carboxylate), 5.57 (*s*, 1 × 1H, C*H*$_2$═C−, H *trans* to the carboxylate), 1.87 (s, 2 × 3H, −C(C*H*$_3$)$_2$Br), 1.81 (*s*, 1 × 3H, −C(C*H*$_3$)═CH$_2$), 1.49 (*d*, 1 × 3H, −OCHH(C*H*$_3$)O−). ^{13}C NMR (300 MHz, $CDCl_3$, δ): 169.6 (1C, (CH$_3$)$_2$BrC−*C*OO−), 165.1 (1C, CH$_2$═C(CH$_3$)−*C*OO−), 135.3 (1C, CH$_2$═*C*(CH$_3$)−), 127.0 (1C, *C*H$_2$═C(CH$_3$)−), 89.9 (2C, −O*C*H(CH$_3$)O−), 55.1 (1C, −*C*(CH$_3$)$_2$Br), 30.4 (2C, −C(*C*H$_3$)$_2$Br), 19.1 (2C, −OCHH(*C*H$_3$)O−), 18.0 (1C, −C(*C*H$_3$)═CH$_2$).

Preparation of the Nondegradable Inimer 2-(2-Bromoisobutyryloxyl)ethyl Methacrylate (BIB2EMA). The nondegradable inimer BIB2EMA was prepared by an esterification reaction. In particular, to a 100 mL round-bottomed flask containing 5 mL of 2-hydroxyethyl methacrylate (5.35 g, 0.041 mol) and 34 mL of triethylamine (24.9 g, 0.25 mol) was added 7.62 mL of 2-bromoisobutyryl bromide (14.00 g, 0.062 mol). The reaction was carried out under a dry nitrogen atmosphere at 0 °C. The resulting insoluble salt of Et$_3$N·HBr was removed from the reaction mixture by filtration. Subsequently, the filtrate was passed through a column of basic alumina to remove the formed (excess) isobutyric acid. The desired product was finally obtained after vacuum distillation at 90 °C as a yellowish liquid at 43% yield. The structure of the inimer was confirmed by ^{1}H and ^{13}C NMR spectroscopy. ^{1}H NMR (300 MHz, $CDCl_3$, δ): 6.06 (*s*, 1 × 1H, C*H*$_2$═C−, H *cis* to the carboxylate), 5.52 (*s*, 1 × 1H, C*H*$_2$═C−, H *trans* to the carboxylate), 4.35 (*s*, 2 × 2H, −OCH*H*$_2$C*H*$_2$O−), 1.87 (s, 2 × 3H, −C(C*H*$_3$)$_2$Br), 1.86 (*s*, 1 × 3H, −C(C*H*$_3$)═CH$_2$). ^{13}C NMR (300 MHz, $CDCl_3$, δ): 171.4 (1C, (CH$_3$)$_2$BrC−COO−), 166.9 (1C, CH$_2$═C(CH$_3$)−COO−), 135.8 (1C, CH$_2$═*C*(CH$_3$)−), 126.1 (1C, *C*H$_2$═C(CH$_3$)−), 63.5 (1C, −O*C*H$_2$CH$_2$O−), 61.8 (1C, −OCHH$_2$*C*H$_2$O−), 55.3 (1C, −*C*(CH$_3$)$_2$Br), 30.6 (2C, −C(*C*H$_3$)$_2$Br), 18.2 (1C, −C(*C*H$_3$)═CH$_2$).

Synthesis of the Hyperbranched Homopolymers. *Polymerizations of Methyl Methacrylate Using 1-(2-Bromoisobutyryloxyl)-ethyl Methacrylate (BIB1EMA).* For the preparation of the degradable hyperbranched homopolymers of MMA, the initial monomer-to-catalyst (CuBr) molar ratio, the initial monomer concentration and the amount of the inimer loaded were kept constant at values of 100, 5 M and 5.4 × 10^{-4} mol, respectively. The initial monomer-to-inimer molar ratio was varied from 25 to 100. A typical experimental procedure for the preparation of BIB1EMA-*co*-MMA$_{25}$ was as follows. A 20 mg sample of CuBr (1.4 × 10^{-4} mol), 65.4 mg of bpy (4.2 × 10^{-4} mol), 1.44 mL of MMA (1.34 g, 0.013 mol) and 1 mL of DMF were added into a dry 25 mL Schlenk tube kept under a dry nitrogen atmosphere. The reaction mixture was degassed by two freeze−pump−thaw cycles and then 0.15 g of inimer (5.4 × 10^{-4} mol), dissolved in 0.25 mL DMF, was added to the mixture. Subsequently, the Schlenk tube was placed in a thermostated oil bath at 70 °C for 2 h until monomer conversion reached 75%. The product of the polymerization reaction was passed through a short column of neutral alumina to remove copper, was precipitated in *n*-hexane and was finally dried in a vacuum oven at room temperature for 72 h.

Polymerizations of Methyl Methacrylate Using 2-(2-Bromoisobutyryloxyl)ethyl Methacrylate (BIB2EMA). For the preparation of the nondegradable hyperbranched homopolymers of MMA, a similar procedure was followed as that employed for the preparation of the degradable hyperbranched homopolymers described above, with the only difference that the nondegradable BIB2EMA inimer was used instead of BIB1EMA.

Synthesis of the Degradable Hyperbranched Amphiphilic Copolymers. For the preparation of the degradable hyperbranched amphiphilic copolymers, copolymerizations by sequential addition of monomers were performed. A typical procedure for the preparation of BIB1EMA-*co*-MMA$_{50}$-*grad*-DMAEMA$_{50}$ is described below. To a 25 mL dry Schlenk tube kept under a dry nitrogen atmosphere were added 39.3 mg of CuBr (2.7 × 10^{-4} mol), 0.13 g of bpy (8.2 × 10^{-4} mol), 2.87 mL of MMA (2.69 g, 0.026 mol), and 2.0 mL of DMF. The mixture was degassed by two vacuum−nitrogen cycles. The reaction flask was heated to 70 °C and a deoxygenated solution of the BIB1EMA degradable inimer (0.15 g, 5.4 × 10^{-4} mol) in 0.5 mL of DMF was added. After 85 min of reaction, at a monomer conversion of 78%, samples were extracted for gel permeation chromatography (GPC) and ^{1}H NMR spectroscopy analyses (polymer relative number-average molecular weight, M_n = 11 000 g mol^{-1}, polydispersity index, PDI = M_w/M_n = 2.34; M_w is the relative weight-average molecular weight). Then, the second monomer, DMAEMA (4.5 mL, 4.20 g, 0.027 mol) was added and was allowed to react for another 120 min until the DMAEMA conversion reached 54%. As with the hyperbranched MMA homopolymers, work-up procedure involved passage through neutral alumina, precipitation in *n*-hexane and vacuum drying at room temperature for 72 h.

Thermolysis of the Hyperbranched (Co)Polymers. All hyperbranched (co)polymers were subjected to thermolysis at 200 °C to cleave the acylal group in the inimer residues. Samples (~0.5 g) of each hyperbranched polymer in glass vials were placed in a vacuum oven kept at 200 °C for about 24 h. Samples were taken out of the oven at different times during thermolysis and characterized using GPC to estimate the extent of thermolysis.

Polymer Characterization. *Gel Permeation Chromatography (GPC).* The molecular weight distributions (MWDs) of all the hyperbranched (co)polymers and their thermolysis products were recorded using GPC with single detection based on refractive index (RI), from which the relative M_n, the relative M_w, and the PDIs were calculated. This setup will be referred to as the GPC−RI system. A single Polymer Laboratories PL-Mixed "D" column (bead size =5 μm; pore sizes =100, 500, 10^3 and 10^4 Å) was used for sample analysis. The mobile phase was THF, delivered using a Waters 515 isocratic pump at a flow rate of 1 mL min^{-1}. The RI signal was measured using a Polymer Laboratories ERC-7515A RI detector. The calibration curve was based on eight narrow MW (630, 2680, 4250, 13000, 28900, 50000, 128000, and 260000 g mol^{-1}) linear polyMMA standards also supplied by Polymer Laboratories.

NMR Spectroscopy. A 300 MHz Avance Bruker spectrometer equipped with an Ultrashield magnet was used to acquire the ^{1}H NMR spectra of all the hyperbranched (co)polymers in $CDCl_3$ containing traces of $CHCl_3$ which was used as an internal reference. The same instrument was also used to collect the ^{1}H and ^{13}C NMR spectra of the two inimers synthesized.

Static Light Scattering. The absolute M_w of the hyperbranched polymers was measured using dual RI and static light scattering (SLS) detection in a GPC configuration (GPC−SLS system). To this end, a Brookhaven molecular weight analyzer (BI-*M*wA) equipped with a 30 mW red diode laser emitting at 673 nm and a multiangle detector, was used to determine the intensity of the scattered light at 7 different angles, 35°, 50°, 75°, 90°, 105°, 130°, and 145°, whereas a PL-RI 800 RI detector was used to simultaneously measure the RI signal. A Polymer Laboratories PL-LC1120 isocratic pump was used to deliver the THF mobile phase at a flow rate of 1 mL min^{-1} through a PL-Mixed "D" column, also supplied by Polymer Laboratories. The analysis for the calculation of the absolute M_w was conducted using the PSS-WinGPC 7 SLS-flow software. The hyperbranched (co)polymers were dissolved in HPLC-grade THF at a 2% w/v polymer concentration and were filtered through 0.45 μm pore size syringe filters. The RI increments (dn/dc) of the hyperbranched (co)polymer solutions in THF used for the calculation of the absolute M_w were 0.087 mL g^{-1}.

Dynamic Light Scattering (DLS). The hydrodynamic diameters of the synthesized amphiphilic hyperbranched copolymers in water/THF mixtures were measured using dynamic light scattering (DLS). A 1% w/w solution of each hyperbranched amphiphilic copolymer was prepared in the appropriate solvent mixture and was filtered three times through a PTFE syringe filter with 0.45 μm pore size diameters. The filtered solution was left to settle for about an hour, so that any air bubbles could escape before the DLS measurement. A 90Plus Brookhaven DLS spectrophotometer, equipped with a BI9000 correlator and a 30 mW red diode laser emitting at 673 nm, was used to determine the intensity of the scattered light at a 90° angle. The data were processed using multimodal size distribution (MSD) analysis based on non-negatively constrained least-squares (NNCLS).

RESULTS AND DISCUSSION

Synthesis of the Degradable Inimer. For the preparation of the degradable hyperbranched (co)polymers via the self-condensing vinyl copolymerization (SCVCP) technique and using ATRP, it was first necessary to design and synthesize the appropriate inimer. Thus, 1-(2-bromoisobutyryloxyl)ethyl methacrylate (BIB1EMA) was synthesized. This molecule consists of one polymerizable methacrylate unit (colored blue in Figure 1) and one 2-bromoisobutyrate group (in green) capable of initiating the polymerization, interconnected by one thermolyzable acylal group (in red). As shown in Figure 1, the synthesis of the inimer was performed in a simple, one-stage addition reaction between vinyl methacrylate and 2-bromoisobutyric acid. The final inimer was isolated at 40% yield and was characterized using ^{1}H and ^{13}C NMR spectroscopy. Its NMR spectra are also presented in Figure 1.

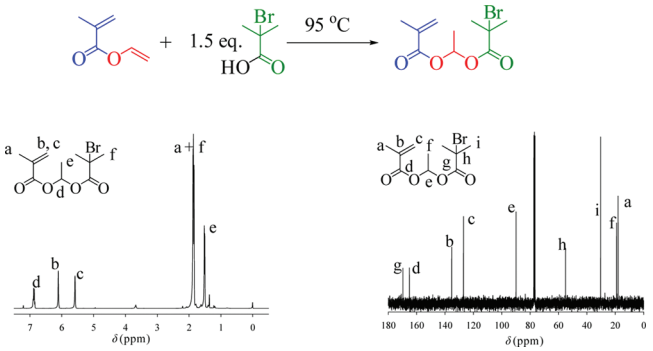


Figure 1. Reaction scheme followed for the synthesis of the degradable inimer BIB1EMA and its structure confirmation by ^{1}H and ^{13}C NMR spectroscopy.

Synthesis of the Nondegradable Inimer. As a control, the well-known nondegradable ATRP inimer 2-(2-bromoisobutyryloxyl)ethyl methacrylate (BIB2EMA) was also prepared at 43% yield following the published procedure.[51] It is noteworthy that this nondegradable inimer is isomeric to the degradable one, differing only in the arrangement of the ethyl group interconnecting the monomer and the initiator parts of the molecule. The chemical structures and the names of the two inimers and the two monomers used in this investigation are presented in Figure 2.

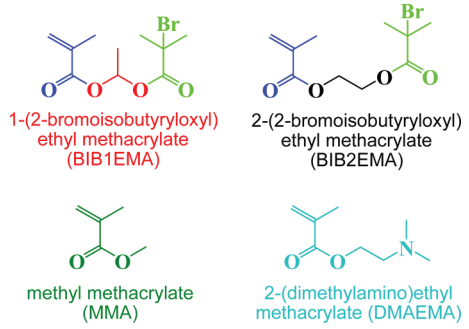


Figure 2. Chemical structures and names of the main reagents used for the preparation of the degradable and the nondegradable hyperbranched polymers using self-condensing ATRP.

Synthesis and Characterization of the Hyperbranched (Co)polymers. *Degradable Hyperbranched Homopolymers of MMA.* Before proceeding to the synthesis of the desired degradable hyperbranched polymers, a systematic study was performed to examine how important parameters, such as the initial monomer-to-inimer molar ratio and the initial monomer-to-catalyst molar ratio, influence the polymerization of MMA using the novel inimer BIB1EMA prepared for the needs of the present study. First, the effect of the initial monomer-to-catalyst molar ratio, μ, was examined by varying it in the range from 2.5 to 100, and keeping constant the initial monomer-to-inimer molar ratio, γ, at the value of 10. The polymerizations were performed at a constant initial monomer concentration of 3 M in DMF at 70 °C, and allowing a polymerization time of 2 h. Figure 3 presents the influence of the initial monomer-to-catalyst molar ratio on the M_n and the PDI values of the produced hyperbranched polymers as determined by GPC−RI.

As was expected,[52] both the M_n and the PDI values decreased as the initial monomer-to-catalyst molar ratio increased from

dx.doi.org/10.1021/ma202021y | *Macromolecules* 2012, 45, 1313−1320

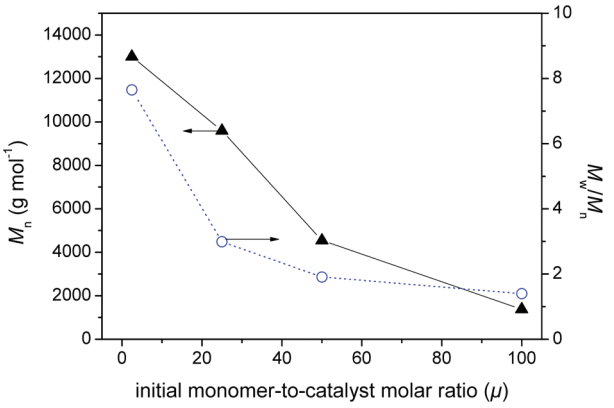


Figure 3. Dependence of number-average molecular weights (M_ns) and polydispersity indices (PDIs) on the initial monomer-to-catalyst molar ratio at an initial monomer-to-inimer molar ratio of 10 and an initial monomer concentration 3 M in DMF at 70 °C.

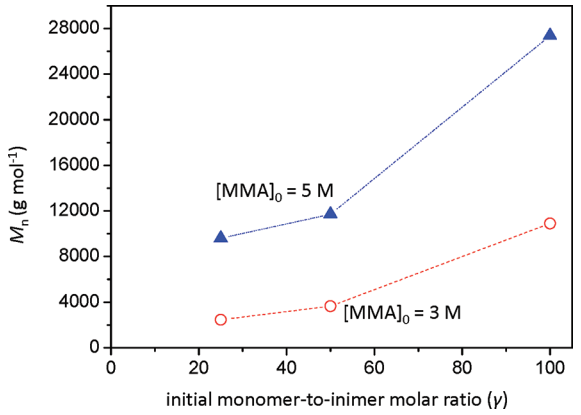


Figure 4. Dependence of the number-average molecular weights (M_ns) on the initial monomer-to-inimer molar ratio at two different initial monomer concentrations, 3 and 5 M, in DMF at 70 °C, and at constant initial monomer-to-catalyst molar ratio of 50.

2.5 to 100. A lower initial monomer-to-catalyst molar ratio corresponds to a higher catalyst concentration which leads to more extensive activation and more random initiation, resulting in the synthesis of polymers with greater branching. Higher catalyst concentrations also lead to higher polymerization rates, resulting in higher monomer conversions. These monomer conversions, as determined by ^{1}H NMR spectroscopy, along with the M_n and PDI values from GPC, are presented in Table 1.

The second parameter that was examined was the initial monomer-to-inimer molar ratio, γ. For this study, the polymerization conditions were the same as those described above ([MMA]$_0$ = 3 M in DMF at 70 °C) and the initial monomer-to-catalyst molar ratio, μ, was kept constant at μ = 50, while the initial monomer-to-inimer molar ratio was varied from 25 to 100. The M_n values of the three resulting hyperbranched MMA homopolymers are plotted against the initial monomer-to-inimer molar ratio as the open circles ([MMA]$_0$ = 3 M) in Figure 4. As shown in the figure, the M_n values increased with the initial monomer-to-inimer molar ratio, a behavior that has been described before.[52] Unlike the M_n values, the PDIs and the monomer conversion in this case were not systematically affected by the initial monomer-to-inimer molar ratio (Table 1, entries 5–7).

As shown in Table 1, all the degradable hyperbranched polymers, synthesized at [MMA]$_0$ = 3 M, presented relatively low molecular weights. To produce hyperbranched polymers of higher molecular weights, we decided to perform the rest of the syntheses at the higher initial MMA concentration of 5 rather than 3 M, at constant initial monomer-to-catalyst molar ratio equal to 50, and varied the initial monomer-to-inimer molar ratio from 25 to 100. The higher initial monomer concentration resulted in higher monomer conversion, around 80%, and also resulted in polymers with higher molecular weights, as shown in Figure 4 (closed triangles). The three degradable hyperbranched homopolymers of MMA prepared in this way were characterized in terms of their relative M_ns and PDIs using GPC–RI and also in terms of their absolute M_w using GPC–SLS, and the results are presented in Table 2.

As shown in Table 2 and in Figure 4 (closed triangles), an increase in the molecular weights was observed with an increase in the initial monomer-to-inimer molar ratio, as expected.[42] The GPC–SLS absolute M_w-values, listed in Table 2, also increased with the initial monomer-to-inimer molar ratio but were higher than the GPC–RI relative molecular weights due to the compact nature of the hyperbranched polymers compared to the linear polyMMA GPC calibration standards. In fact, hyperbranched polymers prepared via SCVCP exhibit a high degree of branching, approaching 46.5% at full monomer conversion.[53]

Nondegradable Hyperbranched Homopolymers of MMA. To compare the behavior of the novel degradable inimer with that of other inimers already reported in the literature, we performed the synthesis of nondegradable hyperbranched

Table 1. Number-Average Molecular Weights, Polydispersity Indices, Polymerization Conditions, and Monomer Conversions upon the Synthesis of the Hyperbranched Polymers Prepared from the Polymerization of MMA ([MMA]$_0$ = 3 M) Using BIB1EMA

					GPC–RI		
entry	polymer structure	γ^a	μ^b	conversion MMA (%)	M_n	M_p	M_w/M_n
1	BIB1EMA-*co*-MMA$_{10}$	10	2.5	80	13 000	12 600	7.65
2	BIB1EMA-*co*-MMA$_{10}$	10	25	76	9590	10 800	2.99
3	BIB1EMA-*co*-MMA$_{10}$	10	50	63	4550	5910	1.91
4	BIB1EMA-*co*-MMA$_{10}$	10	100	18	1380	1260	1.40
5	BIB1EMA-*co*-MMA$_{25}$	25	50	31	2450	2860	1.47
6	BIB1EMA-*co*-MMA$_{50}$	50	50	36	3660	3750	1.48
7	BIB1EMA-*co*-MMA$_{100}$	100	50	48	10 900	12 600	2.06

$^a\gamma$: initial monomer-to-inimer molar ratio; γ = [MMA]$_0$/[BIB1EMA]$_0$. $^b\mu$: initial monomer-to-catalyst molar ratio; μ = ([MMA]$_0$+[BIB1EMA]$_0$)/[CuBr]$_0$.

dx.doi.org/10.1021/ma202021y | *Macromolecules* 2012, 45, 1313–1320

Table 2. Number-Average Molecular Weights, Absolute Weight-Average Molecular Weights, Polydispersity Indices, Monomer Conversions, and Copolymer Compositions of the Hyperbranched (Co)polymers Synthesized at an Initial Monomer (MMA) Concentration of 5 M

		GPC−RI		GPC−SLS			conversion (%)		
entry	polymer structure	M_n	M_w/M_n	$M_{n(RI)}$	$M_{w(LS)}$	M_w/M_n	MMA	DMAEMA	^{1}H NMR % mol MMA
	Degradable Hyperbranched Homopolymers								
1	BIB1EMA-*co*-MMA_{25}	9600	1.71	6740	36 470	1.67	75	-	100
2	BIB1EMA-*co*-MMA_{50}	11 700	1.88	14 970	44 300	1.80	82	-	100
3	BIB1EMA-*co*-MMA_{100}	27 360	2.08	27 930	51 450	1.89	79	-	100
	Degradable Hyperbranched Amphiphilic Copolymers								
4	BIB1EMA-*co*-MMA_{50}	11 000	2.34	-	-	-	78	-	100
5	(BIB1EMA-*co*-MMA_{50})-*grad*-$DMAEMA_{50}$	16 200	1.86	19 343	40 000	1.74	89	54	62
6	BIB1EMA-*co*-MMA_{100}	16 700	2.51	-	-	-	77	-	100
7	(BIB1EMA-*co*-MMA_{100})-*grad*-$DMAEMA_{50}$	26 900	2.48	25 100	57 200	2.08	80	50	90
	Nondegradable Hyperbranched Homopolymers								
8	BIB2EMA-*co*-MMA_{25}	9450	2.25	11 700	25 480	2.32	71	-	100
9	BIB2EMA-*co*-MMA_{50}	15 700	2.67	26 540	67 670	2.17	76	-	100
10	BIB2EMA-*co*-MMA_{100}	20 900	2.54	29 720	71 970	1.90	77	-	100

homopolymers of MMA at exactly the same conditions as the degradable one. For this purpose, we chose to prepare the inimer 2-(2-bromoisobutyryloxyl)ethyl methacrylate (BIB2EMA) which is an isomer of the degradable inimer and has already been reported in the literature.[51] Three hyperbranched MMA homopolymers were synthesized using this nondegradable inimer BIB2EMA at a constant initial monomer-to-catalyst molar ratio equal to 50 and an initial monomer concentration equal to 5 M, and varied the initial monomer-to-inimer molar ratio from 25 to 100. The nondegradable hyperbranched polymers were also characterized in terms of their relative M_ns and PDIs using GPC−RI and in terms of their absolute M_ws using GPC−SLS, and the results are presented in Table 2 too, together with those for the degradable ones. As shown in the table, the polymers prepared using BIB2EMA followed the expected trends[52] and displayed similar relative M_n and PDI values to those of the degradable ones prepared using BIB1EMA.

Degradable Hyperbranched Amphiphilic MMA-DMAEMA Copolymers. The preparation of the degradable hyperbranched amphiphilic copolymers was performed in a two-step synthetic procedure, via sequential addition of monomers. In the first step, the degradable hydrophobic hyperbranched core was synthesized by the polymerization of MMA using BIB1EMA at the same conditions as those used for the synthesis of the hyperbranched MMA homopolymers described above (μ = 50, $[MMA]_0$ = 5 M, DMF, 70 °C). After allowing MMA to polymerize up to ~80% conversion, the DMAEMA hydrophilic monomer was added to the polymerization reactor (without isolating the hyperbranched MMA homopolymer and removing the unreacted MMA monomer to enhance the "livingness" of the system), resulting in the formation of the degradable hyperbranched amphiphilic copolymers with a plausible gradient composition in the second segment (although not yet reported, the reactivity ratios for the DMAEMA−MMA pair under ATRP conditions should not be exactly equal to one). Thus, two degradable hyperbranched amphiphilic copolymers were prepared, in which the length of the hydrophilic blocks was kept constant (by using the same initial DMAEMA-to-inimer molar ratio) but the size of the hydrophobic core was varied by using different initial MMA-to-inimer molar ratios. The degradable hyperbranched amphiphilic copolymers were also characterized in terms of their relative M_ns and PDIs, using GPC−RI, in terms of their absolute M_ws using GPC−SLS and in terms of their compositions using ^{1}H NMR spectroscopy, and the results are also presented in Table 2.

Figure 5 presents the GPC−RI traces of the two degradable hyperbranched amphiphilic gradient copolymers as well as

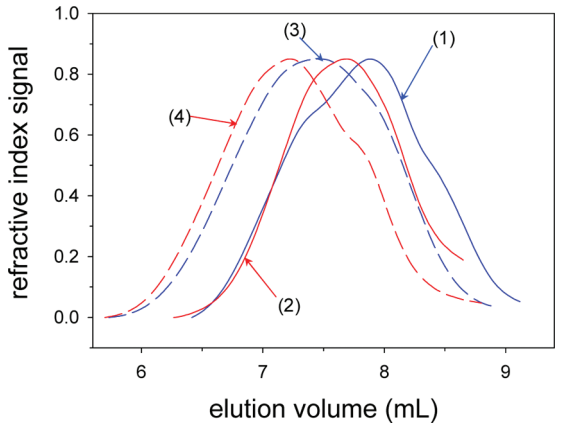


Figure 5. GPC traces of the degradable hyperbranched amphiphilic gradient copolymers, traces 2, (BIB1EMA-*co*-MMA_{50})-*grad*-$DMAEMA_{50}$, and 4, (BIB1EMA-*co*-MMA_{100})-*grad*-$DMAEMA_{50}$, along those of their hyperbranched homopolymer precursors, traces 1, BIB1EMA-*co*-MMA_{50}, and 3, BIB1EMA-*co*-MMA_{100}.

those of their hyperbranched MMA homopolymer precursors. The figure shows that the GPC traces of the copolymers were shifted to smaller elution volumes compared to the traces of the homopolymer precursors, indicating their successful synthesis. As shown in Table 2, the absolute M_ws of the hyperbranched amphiphilic copolymers determined using GPC−SLS were higher than the relative M_ns determined using GPC−RI for the same reasons explained before. The compositions of the hyperbranched amphiphilic copolymers were determined from the ^{1}H NMR spectra by ratioing the signal from the three methoxy protons (3.56 ppm) of the side group of the MMA units to the six protons in the two azamethyl groups (2.3 ppm) in DMAEMA. The thus-determined percentage of the hydrophobic units was found to be very close to that calculated on the basis of the comonomer feed ratio and monomer conversion.

dx.doi.org/10.1021/ma202021y | *Macromolecules* 2012, 45, 1313−1320

Hydrodynamic Size of the Hyperbranched Amphiphilic Copolymers. Because of the amphiphilicity of the hyperbranched copolymers, their behavior in selective solvents was investigated. In particular, DLS was employed to determine the hydrodynamic diameters of the present hyperbranched amphiphilic copolymers in THF: water mixtures as a function of the solvent composition. It was expected that larger entities would form when the percentage of the selective solvent in the solvent mixture would increase,[54] provided that the copolymer was still soluble. Thus, before proceeding to the DLS measurements, the solubility of the hyperbranched amphiphilic copolymers in solvent mixtures with water contents from 0 to 100% w/w was evaluated. It was determined that the hyperbranched amphiphilic copolymer (BIB1EMA-*co*-MMA_{50})-*grad*-$DMAEMA_{50}$ was completely soluble in solvent mixtures with up to 60% w/w water, while it precipitated at higher water contents. It was also found that the hyperbranched amphiphilic copolymer with higher MMA hydrophobic content, (BIB1EMA-*co*-MMA_{100})-*grad*-$DMAEMA_{50}$, was soluble in solvent mixtures with only up to 50% w/w water, and precipitated in mixtures richer in water.

Table 3. Hydrodynamic Diameters of the Hyperbranched Amphiphilic Copolymers in THF: Water Mixtures of Different Solvent Compositions

polymer in 1% w/w concentration	water content (% w/w) in solvent mixture	hydrodynamic diameter (nm)
(BIB1EMA-*co*-MMA_{50})-*grad*-$DMAEMA_{50}$	40	31.6
	50	31.5
	60	39.4
(BIB1EMA-*co*-MMA_{100})-*grad*-$DMAEMA_{50}$	30	27.3
	40	32.7
	50	63.0

After establishing the water-solubility of the hyperbranched amphiphilic copolymers, DLS measurements were performed for solutions with water content lower than that corresponding to the solubility limit to determine the copolymer hydrodynamic diameters. The thus-determined hydrodynamic diameters are listed in Table 3. As shown in the table, an increase in the water content led to an increase in the hydrodynamic diameters of the formed entities. Although highly branched systems like the present one do not form micelles, the observed increase in the hydrodynamic size indicates some form of weak association between these amphiphilic copolymers.

Thermolysis of the Degradable Hyperbranched (Co)-Polymers. After their characterization, all the hyperbranched (co)polymers were thermolyzed in a vacuum oven at 200 °C[55,56] for about 24 h. First, a kinetic study of the thermolysis of hyperbranched polymer BIB1EMA-*co*-MMA_{25} was performed by temporally following its thermolysis process by GPC. Figure 6a presents the GPC−RI traces of the thermolysis products at different times, whereas Figure 6b displays the temporal evolution of the relative M_ns and PDIs of the products produced during thermolysis. As shown in Figure 6, the molecular weights of the thermolysis products were gradually reduced, and the thermolysis of the hyperbranched polymer BIB1EMA-*co*-MMA_{25} was completed within 24 h. It is noteworthy that thermolysis not only confers reduction in the molecular weight but also in the PDI, due to the ultimate formation of rather homogeneous linear polymer products with monomodal MWDs.

After the thermolysis kinetic study, all hyperbranched (co)polymers were thermolyzed, and the thermolysis products were characterized in terms of their relative M_n and PDI values using GPC−RI. These results are listed in Table 4. Complete thermolysis was evidenced by reduction in M_n and PDI, arising from the formation of linear and homogeneous polymer products with a monomodal MWD. The time required for the complete thermolysis of the larger hyperbranched polymers was longer than 24 h, reaching 32 and 56 h for the hyperbranched polymers BIB1EMA-*co*-MMA_{50} and BIB1EMA-*co*-MMA_{100}. Table 4 also presents the theoretically expected molecular weights of the thermolysis products, calculated as (mass of monomer fed) × (monomer conversion)/(moles of inimer fed).

Finally, it is noteworthy that control experiments were performed by attempting the thermolysis of the three nondegradable hyperbranched polymers by subjecting them to the same cleavage conditions as those applied for the degradable ones. Molecular weight characterization using GPC−RI revealed that the relative M_n and PDI values of the processed polymers barely changed, indicating that no

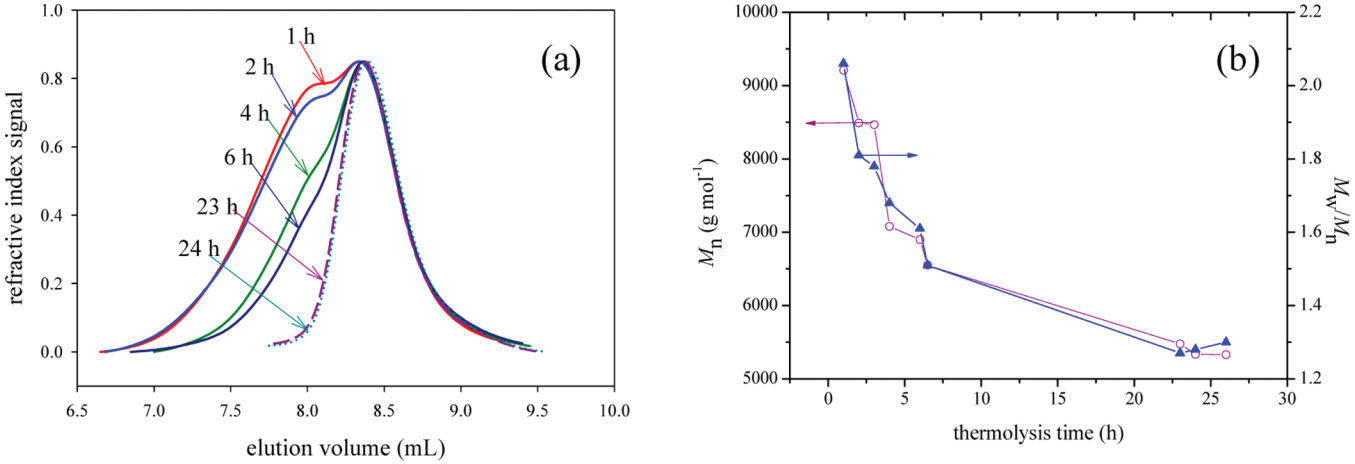


Figure 6. (a) GPC traces of the samples taken during the thermolysis of the degradable hyperberanched MMA homopolymer BIB1EMA-*co*-MMA_{25}. (b) Temporal evolution of the relative M_n and PDI values during thermolysis.

dx.doi.org/10.1021/ma202021y | *Macromolecules* 2012, 45, 1313−1320

Table 4. Molecular Weight Characteristics of the Products Formed upon Subjecting the Degradable and the Non-Degradable Hyperbranched (Co)polymers to Thermolysis Conditions (200 °C for ~24 h)

	before thermolysis		thermolysis product		
hyperbranched polymer	M_n	M_w/M_n	$MW_{theor.}$	M_n	M_w/M_n
BIB1EMA-*co*-MMA_{25}	9600	1.71	2230	2710	1.30
BIB1EMA-*co*-MMA_{50}	11 700	1.88	4460	7490	1.87
BIB1EMA-*co*-MMA_{100}	27 360	2.08	8270	12 700	1.70
(BIB1EMA-*co*-MMA_{50})-*grad*-$DMAEMA_{50}$	16 200	1.86	8510	4720	1.41
(BIB1EMA-*co*-MMA_{100})-*grad*-$DMAEMA_{50}$	26 900	2.48	12 000	6720	1.54
BIB2EMA-*co*-MMA_{25}	9450	2.25	1780	10 680	3.89
BIB2EMA-*co*-MMA_{50}	15 700	2.67	3800	16 100	2.73
BIB2EMA-*co*-MMA_{100}	20 900	2.54	7710	17 800	2.27

thermolysis took place. This also suggested that the thermolysis occurring with the degradable hyperbranched (co)polymers was the result of the thermolysis of the acylal group in these polymers.

CONCLUSION

Degradable hyperbranched (co)polymers were successfully synthesized via ATRP using a novel degradable inimer bearing acylal groups, synthesized for the purposes of this study. The behavior of this inimer during the polymerization of MMA followed the trends described in the literature. Five hyperbranched polymers were synthesized in total, from which three were hyperbranched homopolymers of MMA with different initial monomer-to-inimer molar ratios, and two were hyperbranched amphiphilic gradient copolymers with different compositions. These hyperbranched amphiphilic copolymers were soluble in THF: water mixtures with water content equal to or less than 50% w/w and exhibited hydrodynamic sizes which increased with the water content in the solvent mixture. Because of the presence of the acylal groups in their main chains, the hyperbranched polymers could be quantitatively thermolyzed to linear polymers. The time necessary for complete thermolysis of the hyperbranched polymers was found to increase with the size of the degradable hyperbranched polymers. No thermolysis was observed for similar hyperbranched polymers synthesized using a nondegradable inimer, isomeric to the degradable one. Future work will employ the present hyperbranched (co)polymers as thermolyzable cores for the preparation of cleavable[25,55−57] functional polymer conetworks.[21−24,58]

AUTHOR INFORMATION

Corresponding Author

*E-mail: costasp@ucy.ac.cy.

ACKNOWLEDGMENTS

We thank the Cyprus Research Promotion Foundation and the European Commission's Structural and Cohesion Funds for Cyprus for a Doctoral Research Grant (PENEK2008 ENISX/0308/45) to M.R.-K. Furthermore, we are grateful to the University of Cyprus Research Committee for further funding and to the A. G. Leventis Foundation for financial support in establishing the NMR spectroscopy facilities at the University of Cyprus. Finally, we thank our colleagues Dr. M. Vamvakaki and Mr. P. Falireas (University of Crete), and Dr. K. S. Pafiti (University of Cyprus) for performing for us additional DLS experiments.

REFERENCES

(1) Hult, A.; Johansson, M.; Malmström, E. *Adv. Polym. Sci.* **1999**, *143*, 1−34.
(2) Mori, H.; Müller, A. H. E. *Top. Curr. Chem.* **2003**, *228*, 1−37.
(3) Yates, C. R.; Hayes, W. *Eur. Polym. J.* **2004**, *40*, 1257−1281.
(4) Voit, B. I.; Lederer, A. *Chem. Rev.* **2009**, *109*, 5924−5973.
(5) Voit, B. *J. Polym. Sci., Part A: Polym. Chem.* **2000**, *38*, 2505−2525.
(6) Voit, B. *J. Polym. Sci., Part A: Polym. Chem.* **2005**, *43*, 2679−2699.
(7) Laibinis, P. E.; Whitesides, G. M. *J. Am. Chem. Soc.* **1992**, *114*, 9022−9028.
(8) Zhou, Y.; Bruening, M. L.; Liu, Y.; Crooks, R. M.; Bergbreiter, D. E. *Langmuir* **1996**, *12*, 5519−5521.
(9) Zhao, M.; Zhou, Y.; Bruening, M. L.; Bergbreiter, D. E.; Crooks, R. M. *Langmuir* **1997**, *13*, 1388−1391.
(10) Zhou, Y.; Bruening, M. L.; Bergbreiter, D. E.; Crooks, R. M.; Wells, M. *J. Am. Chem. Soc.* **1996**, *118*, 3773−3774.
(11) Bruening, M. L.; Zhou, Y.; Aguilar, G.; Agee, R.; Bergbreiter, D. E.; Crooks, R. M. *Langmuir* **1997**, *13*, 770−778.
(12) Johansson, M.; Malmström, E.; Hult, A. *J. Polym. Sci., Part A: Polym. Chem.* **1993**, *31*, 619−624.
(13) Shi, W. F.; Rånby, B. *J. Appl. Polym. Sci.* **1996**, *59*, 1937−1944.
(14) Shi, W. F.; Rånby, B. *J. Appl. Polym. Sci.* **1996**, *59*, 1945−1950.
(15) Shi, W. F.; Rånby, B. *J. Appl. Polym. Sci.* **1996**, *59*, 1951−1956.
(16) Claesson, H.; Malmström, E.; Johansson, M.; Hult, A.; Doyle, M.; Månson, J.-A. E. *Prog. Org. Coat.* **2002**, *44*, 63−67.
(17) Uhrich, K. *Trends Polym. Sci.* **1997**, *5*, 388−393.
(18) Roberts, J.; Bhalgat, M.; Zera, R. *J. Biomed. Mater. Res.* **1996**, *30*, 53−65.
(19) Zhang, Y.; Wang, L.; Wada, T.; Sasabe, H. *J. Polym. Sci., Part A: Polym. Chem.* **1996**, *34*, 1359−1363.
(20) Zhang, Y.; Wada, T.; Sasabe, H. *Polymer* **1997**, *38*, 2893−2897.
(21) Gudipati, C. S.; Greenlief, C. M.; Johnson, J. A.; Prayongpan, P.; Wooley, K. L. *J. Polym. Sci., Part A: Polym. Chem.* **2004**, *42*, 6193−6208.
(22) Bartels, J. W.; Cheng, C.; Powell, K. T.; Xu, J.; Wooley, K. L. *Macromol. Chem. Phys.* **2007**, *208*, 1676−1687.
(23) Lin, C.; Gitsov, I. *Macromolecules* **2010**, *43*, 10017−10030.
(24) Lin, C.; Gitsov, I. *Macromolecules* **2010**, *43*, 3256−3267.
(25) Bencherif, S. A.; Sheehan, J. A.; Hollinger, J. O.; Walker, L. M.; Matyjaszewski, K.; Washburn, N. R. *J. Biomed. Mater. Res.: Part A* **2009**, *90*, 142−153.
(26) (a) Gaynor, S. G.; Edelman, S.; Matyjaszewski, K. *Macromolecules* **1996**, *29*, 1079−1081. (b) Matyjaszewski, K.; Gaynor, S. G. *Macromolecules* **1997**, *30*, 7042−7049. (c) Matyjaszewski, K.; Gaynor, S. G.; Kulfan, A.; Podwika, M. *Macromolecules* **1997**, *30*, 5192−5194. (d) Matyjaszewski, K.; Gaynor, S. G.; Müller, A. H. E. *Macromolecules* **1997**, *30*, 7034−7041. (e) Matyjaszewski, K.; Pyun, J.; Gaynor, S. G. *Macromol. Rapid Commun.* **1998**, *19*, 665−670. (f) Yoon, J. A.; Young, T.; Matyjaszewski, K.; Kowalewski, T. *ACS Appl. Mater & Interfaces* **2010**, *2*, 2475−2480. (g) Matyjaszewski, K.; Xia, J. *Chem. Rev.* **2001**, *101*, 2921−2990.
(27) Weimer, W. M.; Frechet, J. M.; Gitsov, I. *J. Polym. Sci., Part A: Polym. Chem.* **1998**, *36*, 955−970.
(28) Cheng, C.; Wooley, K. L.; Khoshdel, E. *J. Polym. Sci., Part A: Polym. Chem.* **2005**, *43*, 4754−4770.
(29) Du, W.; Nystrom, A. M.; Zhang, L.; Powell, K. T.; Li, Y.; Cheng, C.; Wickline, S. A.; Wooley, K. L. *Biomacromolecules* **2008**, *9*, 2826−2833.
(30) Percec, V.; Barboiu, B.; Grigoras, C.; Bera, T. K. *J. Am. Chem. Soc.* **2003**, *125*, 6503−6516.
(31) Tsarevsky, N. V.; Huang, J.; Matyjaszewski, K. *J. Polym. Sci., Part A: Polym. Chem.* **2009**, *47*, 6839−6851.
(32) Isaure, F.; Cormack, P. A. G.; Graham, S.; Sherrington, D. C.; Armes, S.; Bütün, V. *Chem. Commun.* **2004**, 1138−1139.

(33) Wang, Z.; He, J.; Tao, Y.; Yang, L.; Jiang, H.; Yang, H. Y. *Macromolecules* **2003**, *36*, 7446−7452.
(34) Carter, S.; Hunt, B.; Rimmer, S. *Macromolecules* **2005**, *38*, 4595−4603.
(35) Rimmer, S.; Carter, S. R.; Rutkaite, R.; Haycock, J. W.; Swanson, L. *Soft Matter* **2007**, *3*, 971−973.
(36) Carter, S. R.; England, R. M.; Hunt, B.; Rimmer, S. *Macromol. Biosci.* **2007**, *7*, 975−986.
(37) Ishizu, K.; Kojima, T.; Ohta, Y.; Shibuya, T. *J. Colloid Interface Sci.* **2004**, *272*, 76−81.
(38) Isaure, F.; Cormack, P. A. G.; Sherrington, D. C. *Macromolecules* **2004**, *37*, 2096−2105.
(39) Baudry, R.; Sherrington, D. C. *Macromolecules* **2006**, *39*, 1455−1460.
(40) Baudry, R.; Sherrington, D. C. *Macromolecules* **2006**, *39*, 5230−5237.
(41) Hawker, C. J.; Frechet, J. M. J.; Grubbs, R. B.; Dao, J. *J. Am. Chem. Soc.* **1995**, *117*, 10763−10764.
(42) Tao, Y.; He, J.; Wang, Z.; Pan, J.; Jiang, H.; Chen, S.; Yang, Y. *Macromolecules* **2001**, *34*, 4742−4748.
(43) Li, C.; He, J.; Li, L.; Cao, J.; Yang, Y. *Macromolecules* **1999**, *32*, 7012−7014.
(44) Niu, A.; Li, C.; Zhao, Y.; He, J.; Yang, Y.; Wu, C. *Macromolecules* **2001**, *34*, 460−464.
(45) Frechet, J. M. J.; Henmi, M.; Gitsov, I.; Aoshima, S.; Leduc, M. R.; Grubbs, R. B. *Science* **1995**, *269*, 1080−1083.
(46) Bütün, V.; Bannister, I.; Billingham, N. C.; Sherrington, D. C.; Armes, S. P. *Macromolecules* **2005**, *38*, 4977−4982.
(47) Simon, P. F. W.; Radke, W.; Müller, A. H. E. *Macromol. Rapid Commun.* **1997**, *18*, 865−873.
(48) Simon, P. F. W.; Müller, A. H. E.; Pakula, T. *Macromolecules* **2001**, *34*, 1677−1684.
(49) Simon, P. F. W.; Müller, A. H. E. *Macromolecules* **2001**, *34*, 6206−6213.
(50) Bally, F.; Ismailova, E.; Brochon, C.; Serra, C. A.; Hadziioannou, G. *Macromolecules* **2011**, *44*, 7124−7131.
(51) von Werne, T. A.; Germack, D. S.; Hagberg, E. C.; Sheares, V. V.; Hawker, C. J.; Carter, K. R. *J. Am. Chem. Soc.* **2003**, *125*, 3831−3833.
(52) Mori, H.; Seng, C. D.; Lechner, H.; Zhang, M.; Müller, A. H. E. *Macromolecules* **2002**, *35*, 9270−9281.
(53) Yan, D.; Müller, A. H. E.; Matyjaszewski, K. *Macromolecules* **1997**, *30*, 7024−7033.
(54) Choucair, A.; Eisenberg, A. *Eur. Phys. J.* **2003**, *10*, 37−44.
(55) Themistou, E.; Kanari, A.; Patrickios, C. S. *J. Polym. Sci., Part A: Polym. Chem.* **2007**, *45*, 5811−5823.
(56) Themistou, E.; Patrickios, C. S. *J. Polym. Sci., Part A: Polym. Chem.* **2009**, *47*, 5853−5870.
(57) (a) Rikkou-Kalourkoti, M.; Loizou, E.; Porcar, L.; Matyjaszewski, K.; Patrickios, C. S. *Polym. Chem.* **2012**, *3*, 105−116. (b) Rikkou, M. D.; Loizou, E.; Porcar, L.; Butler, P.; Patrickios, C. S. *Macromolecules* **2009**, *42*, 9412−9421. (c) Rikkou, M. D.; Patrickios, C. S. *Macromolecules* **2008**, *41*, 5957−5959. (d) Themistou, E.; Patrickios, C. S. *Macromol. Chem. Phys.* **2008**, *209*, 1021−1028. (e) Themistou, E.; Patrickios, C. S. *Macromolecules* **2007**, *40*, 5231−5234. (f) Kafouris, D.; Themistou, E.; Patrickios, C. S. *Chem. Mater.* **2006**, *18*, 85−93. (g) Themistou, E.; Patrickios, C. S. *Macromolecules* **2006**, *39*, 73−80. (h) Themistou, E.; Patrickios, C. S. *Macromolecules* **2004**, *37*, 6734−6743.
(58) (a) Pafiti, K. S.; Philippou, Z.; Loizou, E.; Porcar, L.; Patrickios, C. S. *Macromolecules* **2011**, *44*, 5352−5362. (b) Pafiti, K. S.; Loizou, E.; Patrickios, C. S.; Porcar, L. *Macromolecules* **2010**, *43*, 5195−5204. (c) Rikkou, M. D.; Kolokasi, M.; Matyjaszewski, K.; Patrickios, C. S. *J. Polym. Sci., Part A: Polym. Chem.* **2010**, *48*, 1878−1886. (d) Rikkou, M. D.; Loizou, E.; Porcar, L.; Patrickios, C. S. *Eur. Polym. J.* **2010**, *46*, 441−449. (e) Kali, G.; Georgiou, T. K.; Iván, B.; Patrickios, C. S. *J. Polym. Sci., Part A: Polym. Chem.* **2009**, *47*, 4289−4301. (f) Hadjiantoniou, N. A.; Patrickios, C. S.; Thomann, Y.; Tiller, J. C. *Macromol. Chem. Phys.* **2009**, *210*, 942−950. (g) Kafouris, D.; Gradzielski, M.; Patrickios, C. S. *Macromolecules* **2009**, *42*, 2972−2980. (h) Achilleos, M.; Legge, T. M.; Perrier, S.; Patrickios, C. S. *J. Polym. Sci., Part A: Polym. Chem.* **2008**, *46*, 7556−7565. (i) Triftaridou, A. I.; Loizou, E.; Patrickios, C. S. *J. Polym. Sci., Part A: Polym. Chem.* **2008**, *46*, 4420−4432. (j) Georgiou, T. K.; Patrickios, C. S. *Biomacromolecules* **2008**, *9*, 574−582. (k) Vamvakaki, M.; Patrickios, C. S. *Soft Matter* **2008**, *4*, 268−276. (l) Hadjiantoniou, N. A.; Patrickios, C. S. *Polymer* **2007**, *48*, 7041−7048. (m) Kali, G.; Georgiou, T. K.; Iván, B.; Patrickios, C. S.; Loizou, E.; Thomann, Y.; Tiller, J. C. *Langmuir* **2007**, *23*, 10746−10755. (n) Vamvakaki, M.; Patrickios, C. S.; Lindner, P.; Gradzielski, M. *Langmuir* **2007**, *23*, 10433−10437. (o) Achilleos, M.; Krasia-Christoforou, T.; Patrickios, C. S. *Macromolecules* **2007**, *40*, 5575−5581. (p) Triftaridou, A. I.; Vamvakaki, M.; Patrickios, C. S. *Biomacromolecules* **2007**, *8*, 1615−1623. (q) Georgiou, T. K.; Patrickios, C. S.; Groh, P. W.; Iván, B. *Macromolecules* **2007**, *40*, 2335−2343. (r) Kali, G.; Georgiou, T. K.; Iván, B.; Patrickios, C. S.; Loizou, E.; Thomann, Y.; Tiller, J. C. *Macromolecules* **2007**, *40*, 2192−2200. (s) Triftaridou, A. I.; Kafouris, D.; Vamvakaki, M.; Georgiou, T. K.; Krasia, T. C.; Themistou, E.; Hadjiantoniou, N.; Patrickios, C. S. *Polym. Bull.* **2007**, *58*, 185−190. (t) Achilleos, D. S.; Georgiou, T. K.; Patrickios, C. S. *Biomacromolecules* **2006**, *7*, 3396−3405. (u) Karbarz, M.; Stojek, Z.; Georgiou, T. K.; Patrickios, C. S. *Polymer* **2006**, *47*, 5182−5186. (v) Krasia, T. C.; Patrickios, C. S. *Macromolecules* **2006**, *39*, 2467−2473. (w) Georgiou, T. K.; Patrickios, C. S. *Macromolecules* **2006**, *39*, 1560−1568. (x) Karbarz, M.; Stojek, Z.; Patrickios, C. S. *Polymer* **2005**, *46*, 7456−7462. (y) Georgiou, T. K.; Vamvakaki, M.; Patrickios, C. S. *Polymer* **2004**, *45*, 7341−7355. (z) Loizou, E.; Triftaridou, A. I.; Georgiou, T. K.; Vamvakaki, M.; Patrickios, C. S. *Biomacromolecules* **2003**, *4*, 1150−1160.

Macromolecules

Article

pubs.acs.org/Macromolecules

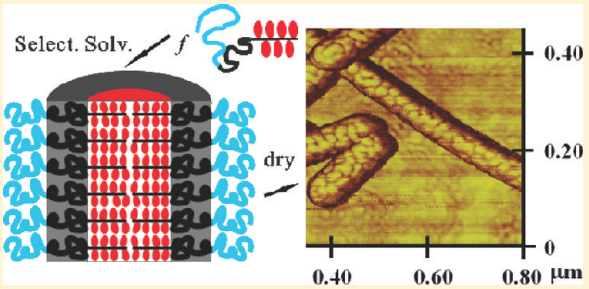
Mesogen-Driven Formation of Triblock Copolymer Cylindrical Micelles

Yang Gao, Xiaoyu Li, Liangzhi Hong, and Guojun Liu*

Department of Chemistry, Queen's University, 90 Bader Lane, Kingston, Ontario, Canada K7L 3N6

Supporting Information

ABSTRACT: Evidences were gathered to support mesogen-driven formation of cylindrical micelles from BCF and ACF triblock copolymers. Here A, B, C, and F denote poly(acrylic acid), poly(*tert*-butyl acrylate), poly(2-cinnamoyloxylethyl methacrylate), and the liquid crystalline poly(perfluorooctylethyl methacrylate) block, respectively. At room temperature (21 °C) in all tested solvents that were selective for the A or B blocks, three of the four copolymers with various compositions formed exclusively cylindrical micelles possessing an F core, a C shell, and an A or B corona. Our further analyses indicated that the F core chains were almost fully stretched, and the C shell chains were compressed relative to their unperturbed dimensions. These abnormal chain packing motifs suggest that the need to form a liquid crystalline F phase in the cores dictated micelle formation and prevailed over the needs of the shell chains to achieve their normal stretched conformations. A subsequent wide-angle X-ray scattering study of the dried cylindrical micelles confirmed smectic A phase formation for the F blocks at room temperature. The smectic A to isotropic phase transition upon raising temperature was detected by a differential scanning calorimeter for the dry cylindrical micelles and by ^{19}F NMR for the solvated micelles. This smectic A to isotropic phase transition was accompanied by a morphological transformation from cylindrical micelles at room temperature to other morphologies at 70 °C. More interestingly, this cylinder to vesicle conversion could be cycled repeatedly by temperature cycling for one ACF sample.



I. INTRODUCTION

Cylindrical micelles are useful. They are particularly suited for drug delivery applications because their circulation times, in animals, are much longer than those of spherical micelles.[1] They have also been shown to be superior to spherical micelles when used to toughen plastics.[2] Core−shell−corona cylindrical micelles of triblock terpolymers are of fundamental interest. For example, cross-linking the intermediate shell yields "permanent" nanofibers, which can be viewed as a macroscopic counterpart of polymer chains.[3] The study of the dilute solutions of block copolymer nanofibers has helped validate the classical viscosity[4,5] and light scattering theories[6,7] of wormlike polymer chains at a different size scale. The decomposition of the cores of these triblock copolymer nanofibers yields nanotubes,[8−10] whose tubular cores can be filled with magnetic and semiconducting inorganic nanoparticles yielding solvent-dispersible polymer/inorganic hybrid nanofibers.[11−13]

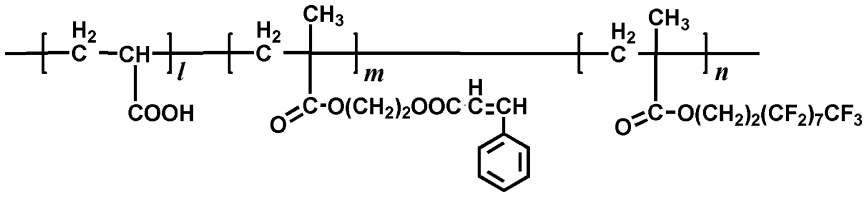
Despite their utility and interesting properties, cylindrical micelles can be difficult to obtain even from coil−coil diblock copolymers because they form only within a narrow block copolymer composition window.[14−18] Core−shell−corona cylindrical micelles are even more difficult to obtain from coil−coil−coil triblock terpolymers[19−21] because these polymers can form segmented cylinders,[22−25] looped cylinders,[26] helical cylinders,[27−29] and Janus cylinders[30−32] beside core−shell−corona cylinders. Manners, Winnik, and co-workers discovered the ready formation of cylindrical micelles[33] from block copolymers bearing crystalline blocks and many other wonderful applications[20,34−36] of this crystallization-driven micellization process. We wondered if a liquid crystalline block, possessing a weaker driving force to order than a crystalline block, could be used to direct cylindrical micelle formation and initiated this investigation. Reported in this paper is our preliminary success in this venture.

For this project four triblock copolymers were designed, synthesized, and characterized, and these were $B_{65}C_{54}F_{16}$, $B_{120}C_{100}F_{22}$, $A_{65}C_{54}F_{16}$, and $A_{120}C_{100}F_{22}$. Here A, B, C, and F denote poly(acrylic acid), poly(*tert*-butyl acrylate), poly(2-cinnamoyloxylethyl methacrylate), and poly(perfluorooctylethyl methacrylate), respectively. The subscripts refer to the repeat unit numbers for the different blocks. Evidently, the ACF polymers were derived from the BCF polymers via the selective hydrolysis of the B blocks. The F blocks were chosen because the rodlike perfluorooctyl (FO) groups were known to form a smectic A phase at room temperature.[37−40] The C blocks were used because they could be photo-cross-linked if required for later applications.[41]

Received: September 13, 2011
Revised: January 16, 2012
Published: January 31, 2012

 © 2012 American Chemical Society

Scheme 1. Chemical Structure of ACF



Our study has so far indicated that $B_{65}C_{54}F_{16}$, $A_{65}C_{54}F_{16}$, and $A_{120}C_{100}F_{22}$ readily formed cylindrical micelles in differing selective solvents for the A or B blocks. Also, various evidences suggest that liquid crystalline phase formation from the F blocks was a driving force for cylindrical micelles from these polymers under our tested conditions. Despite the preferred formation of cylindrical micelles for the three copolymers, cylindrical micelles were not the only and exclusive product from all copolymers containing an insoluble liquid crystalline block and over all compositions. $B_{120}C_{100}F_{22}$, possessing the lowest F weight fraction among the four studied copolymers and the least driving force for liquid crystalline phase formation, formed cylindrical micelles only under certain conditions. This suggests that the ultimate morphologies were governed by a balance of various energies including polymer chain stretching energy, the interfacial energy, the mesogen order energy, and others.

While core block ordering in our study of limited scope favored cylindrical micelles, Keller, Li, and co-workers studied micelles of diblock copolymers bearing pendant cholesteryl and azobenzene liquid crystalline groups and established that mesogen packing favored not only cylindrical[42,43] but also vesicular micelles,[42,44] which also have surface curvatures lower than that of spherical micelles. Vesicular micelles have also been shown by Discher and co-workers[45] to be preferred by diblock copolymers bearing an insoluble crystallizing polycaprolactone block.

We should further point out that micellization of triblock terpolymers containing fluorinated blocks has been reported by different groups.[23,40,46,47] The micellization of poly(perfluorooctylethyl methacrylate)-bearing[48] or poly(perfluorohexylethyl methacrylate)-bearing[49,50] diblock copolymers has also been studied.

II. EXPERIMENTAL SECTION

Polymer Synthesis. The precursors to BCF were prepared by sequential living anionic polymerization[51] of *tert*-butyl acrylate (tBA),[52] 2-trimethylsiloxyethyl methacrylate (HEMA-TMS),[41,53] and perfluorooctylethyl methacrylate (FOEMA)[54] in THF at −78 °C in the presence of added LiCl. The initiator used was 1,1-diphenyl-3-methylpentyllithium, which was generated *in situ* from the reaction of *sec*-butyllithium with 1.3 mol equiv of 1,1-diphenylethylene.[55] The polymerization time used for each block was 3 h. HEMA-TMS was prepared and purified following a literature method,[41,53] and tBA was initially distilled over CaH_2 and then over triethylaluminum. FOEMA was purified by distillation over CaH_2 before use. The trimethylsilyl protecting group was removed from the P(HEMA-TMS) block to yield PHEMA, poly(2-hydroxyethyl methacrylate), by stirring the resultant PtBA-*b*-P(HEMA-TMS)-*b*-PFOEMA in THF/methanol/water at v/v/v = 30/13/5 overnight. The BCF samples were obtained by reacting PtBA-*b*-PHEMA-*b*-PFOEMA with cinnamoyl chloride,[41] at 1.5 mol equiv relative to the PHEMA hydroxyl groups, and purified by precipitation in methanol containing 10% water. The selective hydrolysis of the B block was achieved by treating BCF in dichloromethane with trifluoroacetic acid,[56] yielding ACF.

Micelle Preparation. Micelles were prepared by directly dispersing a polymer at 1.0 mg/mL at 70 °C for 2 h into a mixture consisting of α,α,α-trifluorotoluene (TFT) and methanol (MeOH), ethanol (EtOH), or isopropanol (iPOH). The dispersion was then cooled stepwise by 5 °C increments and held for 30 min at each newly set temperature until it reached room temperature.

Transmission Electron Microscopy. Specimens for transmission electron microscopy (TEM) were prepared by atomizing or aero-spraying micellar solutions using a home-built device[57] onto carbon-coated copper grids. To stain the PCEMA domains, the specimens were equilibrated with OsO_4 vapor for 1 h before TEM observation. To stain the PAA domains, a specimen was equilibrated with one drop of a 20 mg/mL uranyl acetate ($UO_2(Ac)_2$) solution in MeOH for 20 min. After the residual solution was wicked off with filter paper, the excess staining agent was rinsed by MeOH droplets, which were applied by a disposable pipet and wicked off by filter paper, successively for five times. Images were recorded using a Hitachi-7000 instrument operated at 75 kV.

Wide-Angle X-ray Scattering and Differential Scanning Calorimetry. $A_{120}C_{100}F_{22}$ cylindrical micelles, 10 mL at 3.0 mg/mL, in TFT/MeOH at f_{TFT} = 44% and 10% were settled by ultracentrifugation at 17000*g* for 10 min. The settled cylinders were separated from the supernatant by decantation.

For wide-angle X-ray scattering (WAXS) measurement, the settled cylinders were transferred onto a glass holder to form a thin film. The sample was then vacuum-dried at room temperature for 48 h. WAXS analysis was performed at room temperature on a Rigaku Ru 200b instrument using the Cu Kα radiation at λ = 0.154 18 nm.

For differential scanning calorimetric (DSC) studies, the settled cylinders (~3 mg) were vacuum-dried and then transferred to a Tezo pan before measurement. A bulk $B_{120}C_{100}F_{22}$ sample was prepared by evaporating a TFT solution of the polymer in an aluminum-foil-covered Tezo pan over 3 days and then drying the sample under vacuum overnight. DSC analyses were performed on a Q2000 series TA Instruments at a heating rate of 5 °C/min from 0 to 100 °C. The traces reported were those from the first heating cycle to confirm that the liquid crystalline phase already existed in the as-prepared dried samples.

^{19}F NMR Experiments. $A_{65}C_{54}F_{16}$ was stirred for 3 h at 3.0 mg/mL in TFT/MeOH/deuterated methanol at v/v/v = 1/8/1 (f_{TFT} = 10%) and 70 °C or at v/v/v = 44/46/10 (f_{TFT} = 44%) and 75 °C, respectively. Each of the solutions was then transferred into an NMR tube and kept at their initial temperature 70 or 75 °C in the NMR instrument for 1/2 h before the data were collected using a home-built pulse sequence. The sequence included a long pulse to presaturate and suppress the TFT fluorine signal. After data collection at a given temperature, the sample was set to the next temperature and equilibrated for 1/2 h before data collection. Other experimental parameters remained the same for all the experiments.

Atomic Force Microscopy. Micellar specimens were prepared by aero-spraying solution samples onto silicon wafers using a home-built device.[57] A powdery $A_{105}C_{85}F_{19}$ cylindrical micelle sample was also analyzed. The sample was prepared analogously as those used for DSC and WAXS experiments except that the substrate used was a cleaned silicon wafer. All samples were analyzed by tapping-mode atomic force microscopy (AFM) using a Veeco multimode instrument equipped with a Nanoscope IIIa controller.

X-ray Photoelectron Spectroscopy. X-ray photoelectron spectroscopic (XPS) measurements were performed using a Thermo Instruments Microlab 310F surface analysis system (Hastings, U.K.)

Table 1. Molecular Characteristics of the BCF Samples

polymer	SEC M_n (g/mol)	SEC M_w/M_n	^{1}H NMR $l/m/n$	l	m	n	w_B (%)	w_F (%)
$B_{120}C_{100}F_{22}$	4.6×10^4	1.04	5.5/4.5/1.0	105	86	19	29	22
$B_{65}C_{54}F_{16}$	2.6×10^4	1.04	4.1/3.4/1.0	53	44	13	27	27

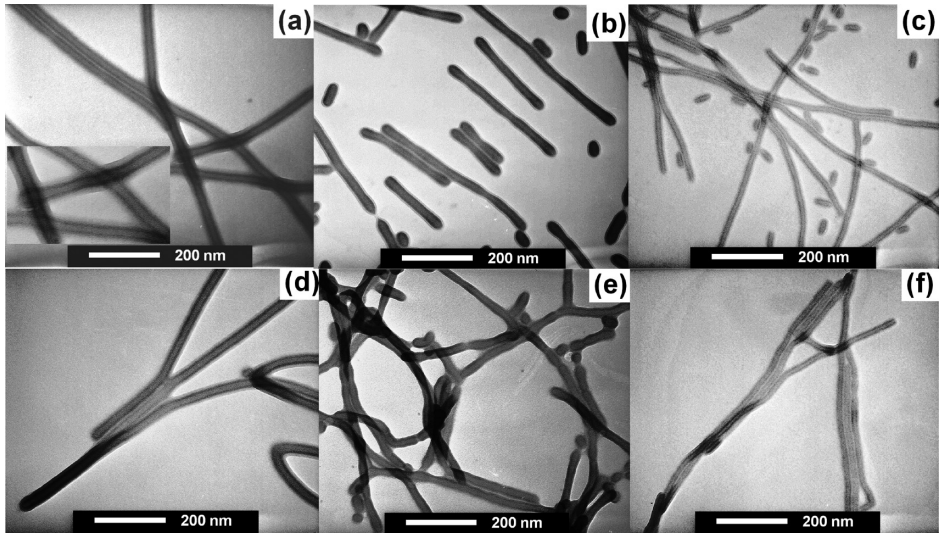


Figure 1. TEM images of ACF (a–d) and BCF (e, f) micelles aero-sprayed from TFT/MeOH (a–c and e, f) and TFT/EtOH (d): (a, b) $A_{120}C_{100}F_{22}$ micelles sprayed from TFT/MeOH at f_{TFT} = 44% and 10%, (c) $A_{65}C_{54}F_{16}$ micelles from TFT/MeOH at f_{TFT} = 30%, (d) $A_{120}C_{100}F_{22}$ micelles from TFT/EtOH at f_{TFT} = 44%, (e) $B_{120}C_{100}F_{22}$ micelles from TFT/MeOH at f_{TFT} = 10%, and (f) $B_{65}C_{54}F_{16}$ micelles from TFT/MeOH at f_{TFT} = 44%.

under ultrahigh-vacuum conditions, using a Mg Kα X-ray source (1486.6 eV) with a 15 kV anode potential and a 20 mA emission current. Scans were acquired in the fixed analyzer transmission (FAT) mode, with a pass energy of 20 eV and a surface/detector takeoff angle of 75°. All spectra were calibrated to the C 1s line at 285.0 eV.

The same method used to prepare samples for WAXS and DSC measurements was used to procure the powder samples used here. The settled cylinders (~15 mg) were transferred onto a cover glass to form a thin layer and dried under vacuum for 48 h. The cover glass was then mounted on the sample holder before analysis.

III. RESULTS AND DISCUSSION

Triblock Copolymer Characterization. Four samples—$A_{120}C_{100}F_{22}$, $A_{65}C_{54}F_{16}$, $B_{120}C_{100}F_{22}$, and $B_{65}C_{54}F_{16}$—were used in this study. Since the ACF samples were derived from BCF,[56] only $B_{120}C_{100}F_{22}$ and $B_{65}C_{54}F_{16}$ were characterized.

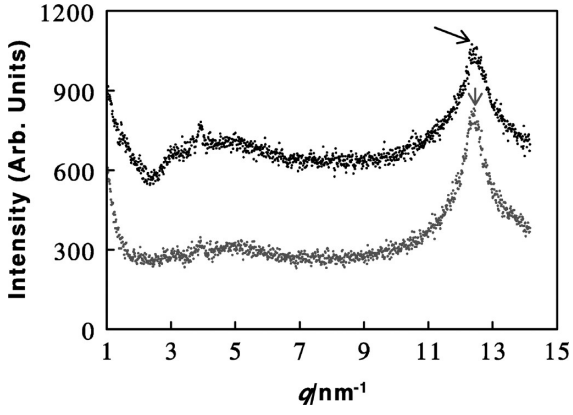


Figure 2. WAXS data of $A_{120}C_{100}F_{22}$ micelles settled from TFT/MeOH at f_{TFT} = 44% (black) and 10% (gray) and subsequently dried.

Scheme 2. Schematic Drawing of the Chain Packing in the ACF Cylindrical Micelles in the Solvated (a) and Dry (b) States; (c) the Perfluorooctyl (FO) Unit Packing in the Smectic Layers and the Average Spacing between Different FO Units

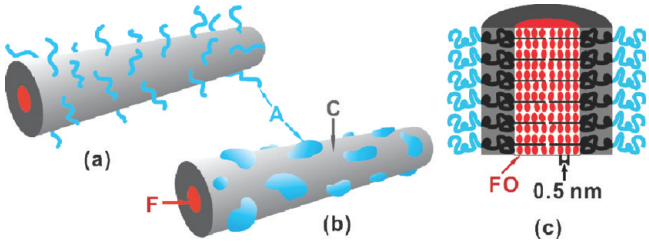


Table 1 shows the characteristics for the two polymers. The ratios between the repeat unit numbers of different blocks $l/m/n$ were obtained from ^{1}H NMR by comparing the signal integrals corresponding to the B, C, and F blocks. The weight- and number-average molecular weights (M_w and M_n) and polydispersity indices (M_w/M_n) were obtained from SEC, which was calibrated with polystyrene standards. The number-average repeat unit numbers l, m, and n for the B, C, and F blocks were calculated using the NMR $l/m/n$ values and the SEC M_n values, respectively. The SEC/NMR l, m, and n values of 105, 86, and 19 for $B_{120}C_{100}F_{22}$ and 53, 44, and 13 for $B_{65}C_{54}F_{16}$ were smaller than their targeted values, which appeared in the polymer notations, most likely due to errors introduced by using PS standards to calibrate the SEC.

We did not determine the absolute molecular weights of the BCF polymers but accepted the targeted repeat numbers as the true values for the following reasons: First, we could not find a common solvent that dissolved all of the three blocks of the copolymers. Second, even if we found such a solvent, we could

dx.doi.org/10.1021/ma202084m | Macromolecules 2012, 45, 1321–1330

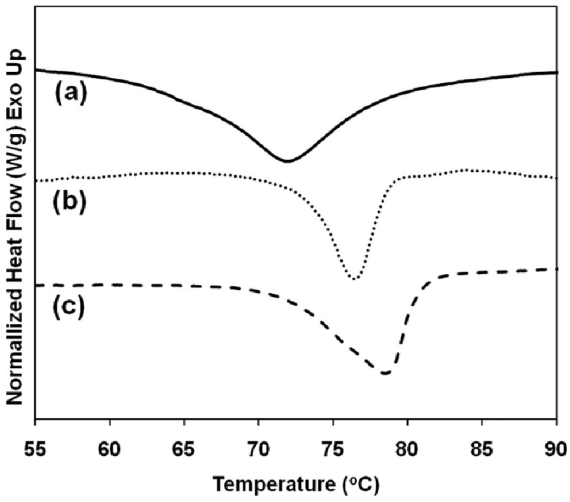


Figure 3. DSC traces of a bulk $B_{120}C_{100}F_{22}$ sample (a) and $A_{120}C_{100}F_{22}$ micelles settled from TFT/MeOH at f_{TFT} = 44% (b) and 10% (c) and vacuum-dried at room temperature.

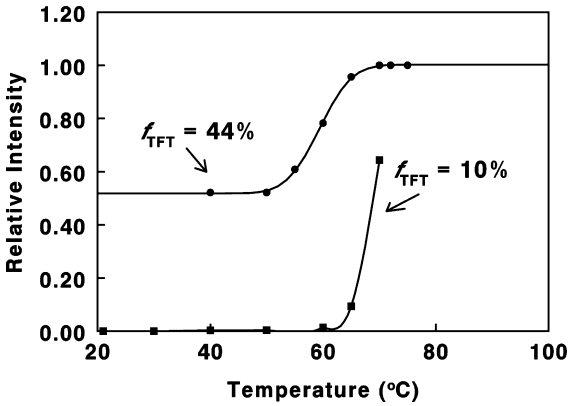


Figure 4. Variation in the integrated intensity of $A_{65}C_{54}F_{16}$ cylindrical micelles at f_{TFT} = 10% (■) and f_{TFT} = 44% (●) as a function of temperature (bottom). The intensities of the former set of data were normalized relative to that at 75 °C. The intensities of the latter set of data were divided by a number so that the relative intensity at 70 °C was at 0.64.

Table 2. TEM Diameters of Some Cylindrical Micelles Sprayed from Different TFT/Selective Solvent Mixtures

solvent	f_{TFT} (%)	core diam (nm)	shell diam (nm)	overall diam (nm)
		$A_{120}C_{100}F_{22}$ Cylindrical Micelles		
TFT/MeOH	10	11 ± 2	23 ± 2	32 ± 4
TFT/MeOH	30	11 ± 2	24 ± 2	36 ± 3
TFT/MeOH	44	12 ± 2	24 ± 2	33 ± 3
		$A_{65}C_{54}F_{16}$ Cylindrical Micelles		
TFT/MeOH	10	8 ± 2	13 ± 2	18 ± 3
TFT/MeOH	30	8 ± 1	15 ± 2	21 ± 2
TFT/MeOH	44	8 ± 1	13 ± 1	23 ± 2
		$A_{120}C_{100}F_{22}$ Cylindrical Micelles		
TFT/EtOH	44	12 ± 2	26 ± 2	
TFT/iPOH	44	12 ± 2	26 ± 2	

not have used light scattering, the only reference-free technique available to us, for an accurate determination of the molecular weights of the BCF polymers because the F block would have a negative specific refractive index increment dn_r/dc and the other two blocks would have positive dn_r/dc values in the solvent. This would greatly complicate data interpretation and introduce significant errors in the final molecular weight values. Third, we did not take samples after the polymerization of the

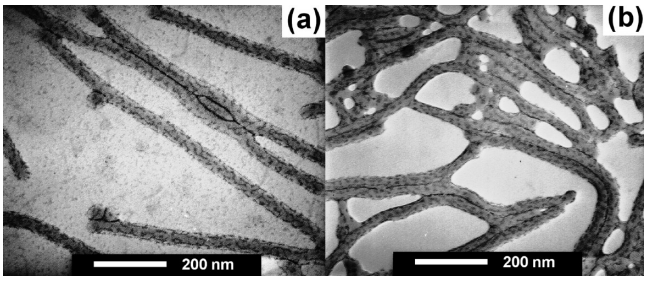


Figure 5. TEM images of $A_{120}C_{100}F_{22}$ micelles sprayed from TFT/MeOH at f_{TFT} = 30% (a) and 44% (b). The samples were stained by $UO_2(Ac)_2$.

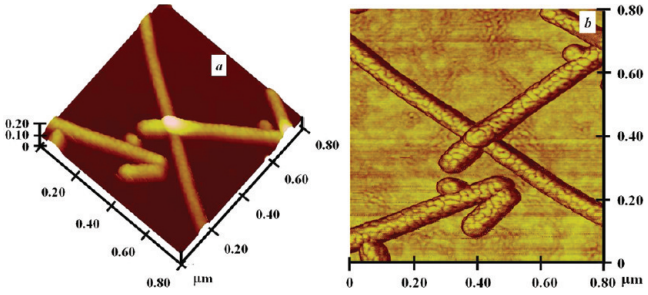


Figure 6. AFM topography (a) and phase (b) images of $A_{120}C_{100}F_{22}$ micelles sprayed from TFT/MeOH at f_{TFT} = 10%.

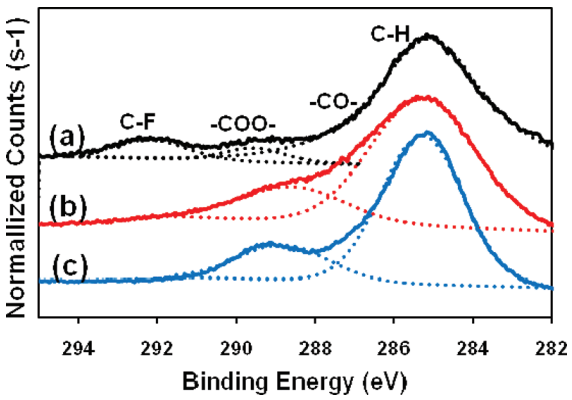


Figure 7. XPS C 1s spectra of an $A_{120}C_{100}F_{22}$ bulk sample (a), $A_{120}C_{100}F_{22}$ micelles centrifuged from TFT/MeOH at f_{TFT} = 10% (b), and 44% (c) and then dried.

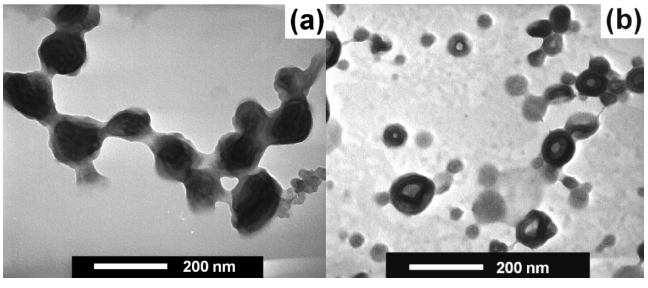


Figure 8. TEM images of $A_{120}C_{100}F_{22}$ (a) and $A_{65}C_{54}F_{16}$ micelles (b) sprayed from 70 °C TFT/MeOH at f_{TFT} = 44%. The samples were stained by OsO_4.

dx.doi.org/10.1021/ma202084m | *Macromolecules* 2012, 45, 1321–1330

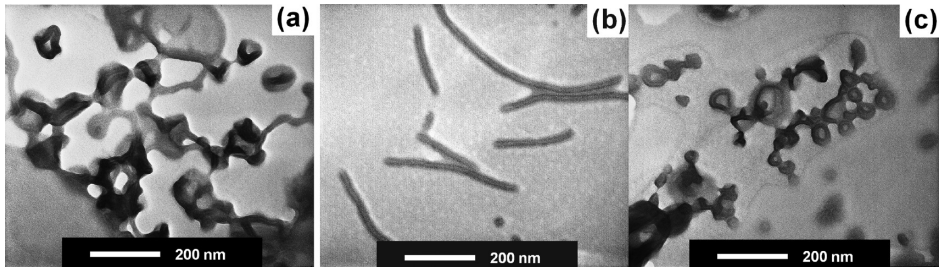


Figure 9. TEM images of $A_{65}C_{54}F_{16}$ micelles sprayed from TFT/MeOH at f_{TFT} = 44% during the second and third heating and cooling cycles: (a) sprayed the second time at 70 °C, (b) sprayed the second time at 21 °C, and (c) sprayed the third time at 70 °C.

first block because anionic polymerization has no tolerance for impurities and moisture, and we did not want to run the risk of introducing moisture into our system by adding an extra sample taking step. Fourth, at the low repeat unit numbers targeted here, the actual and targeted repeat unit numbers should be very close, e.g., within ±15%, given that anionic polymerization was used to prepare the samples. While we have not been able to confirm the molecular weights of the triblock copolymers, the targeted repeat unit ratios were 5.5/4/5/1.0 for $B_{120}C_{100}F_{22}$ and 4.1/3.1/1.0 for $B_{65}C_{54}F_{16}$. These were in exact agreement with the ratios determined from ^{1}H NMR and confirmed that the reactions did go well as we planned with all added monomers polymerized.

Using the NMR $l/m/n$ values, the B and F weight fractions (w_B and w_F, respectively) were calculated to be 29% and 22% for $B_{120}C_{100}F_{22}$ and 27% and 27% for $B_{65}C_{54}F_{16}$. For $A_{120}C_{100}F_{22}$, w_A = 19% and w_F = 25%. These values changed to 17% and 31% for $A_{65}C_{54}F_{16}$.

Facile Formation of Cylindrical Micelles. The ACF or BCF micelles were prepared by first dispersing ACF or BCF at 70 °C into a TFT/MeOH, TFT/EtOH, or TFT/iPOH mixture, which was selective toward the A or B blocks. The dispersions were then cooled in 5 °C steps and held at each new temperature for 30 min and eventually brought to room temperature. The samples were initially heated to 70 °C so that the F block was in the isotropic phase.[58] The samples were slowly cooled, providing time for the F block to form a liquid crystalline phase.

The ACF or BCF copolymers were directly dispersed into TFT/MeOH, TFT/EtOH, or TFT/iPOH rather than dissolved into a solvent that solubilized all of the blocks because such a solvent could not be found. Our further homopolymer solubility tests indicated that C was soluble in neither TFT nor MeOH, B was soluble in both TFT and MeOH, A was soluble in only MeOH, and F was soluble in only TFT. F turned insoluble in TFT/MeOH after the TFT volume fraction f_{TFT} decreased below ~74%.

We used TEM to examine the morphologies of the aero-sprayed micelles to deduce the association state of the block copolymers in their solvated state. As mentioned in the literature,[59] the morphologies of block copolymer micelles can change if a long time is allowed to evaporate solvent during TEM specimen preparation. Because of this, TEM results are frequently verified by comparing images of a sample obtained from different specimen preparation protocols.[60] Our TEM specimens were collected by swiftly passing no more than twice a carbon-covered TEM grid through an atomized spray that was generated by a home-built device.[57] Since the sprayed droplets were very fine and the distance between the spraying nozzle and the TEM grid was at least 2 feet, the solvents methanol and TFT mostly evaporated before the micellar particles landed on the grid. (Our spray of pure solvents and detection with a glove-wearing hand and eyes indicated that methanol never reached the glove, and the TFT fog managed to get to the glove but evaporated within 1 s.) Thus, given the fast solvent evaporation rate and the fact that PCEMA has an above room-temperature glass transition temperature of 69 °C,[6] we doubt that our micellar particles were able to undergo a morphological transition during our specimen preparation. In fact, this structural fidelity of aero-sprayed micelles has been verified by us many times before because our micelles normally contained a photo-cross-linkable PCEMA block and the spray of cross-linked and non-cross-linked micelles always yielded the same morphologies. We even compared the morphologies of some micelles that were observed by routine TEM after they were aero-sprayed and those that were quickly quenched in liquid ethane and then observed by cryo-TEM. No qualitative differences were observed.[61]

Despite this, we do not rule out particle deformation involving intraparticle chain motion either during specimen preparation or during specimen storage. For example, the soluble coronal chains could contract inwardly responding to solvent evaporation during their flight from the nozzle to a catching substrate or spread on a substrate due to favorable polymer/substrate interaction when plasticized by residual solvent. Even the insoluble core blocks could deform somewhat during specimen storage due to polymer creeping under gravitation. To minimize micelle structural mutation, our samples were always analyzed by TEM immediately, typically within hours, after they were prepared.

Figure 1 shows TEM images of micellar samples that were prepared using the above-mentioned aero-spraying technique and then stained by OsO_4. The insert in Figure 1a also shows a magnified view of $A_{120}C_{100}F_{22}$ micelles sprayed from TFT/MeOH at f_{TFT} = 44%. All of the micelles seemed to have a core−shell−corona structure. The core was gray, the shell was dark, and the corona was again gray and visible only in certain sections. Since OsO_4 stained selectively the PCEMA double bonds, the dark shell consisted of PCEMA. The F blocks must have formed the cores because they were insoluble under these solvation conditions. Either the A or the B blocks should have constituted the ill-defined corona.

Our examination of many TEM images concluded that cylindrical micelles were formed from $A_{120}C_{100}F_{22}$, $A_{65}C_{54}F_{16}$, and $B_{65}C_{54}F_{16}$ in TFT/MeOH at the tested f_{TFT} values of 44%, 30%, and 10%. They were also formed from $A_{120}C_{100}F_{22}$ in TFT/EtOH and TFT/iPOH at f_{TFT} = 44% (Supporting Information). The only exception was $B_{120}C_{100}F_{22}$. It yielded cylindrical micelles in TFT/MeOH at f_{TFT} = 10%. A mixture of cylindrical and spherical micelles was formed at f_{TFT} = 30% and

f_{TFT} = 44%, and the spherical micelle content increased as f_{TFT} increased (Supporting Information).

The cylindrical micelles could also be obtained by directly stirring the copolymers in TFT/MeOH at room temperature (Supporting Information). The resultant cylinders were, however, not as well-defined in block segregation and also bore more kinks probably because of their kinetic trapping in some metastable states.

Previous studies of micelles of coil−coil diblock copolymers[14,15,62] and coil−coil−coil triblock terpolymers[63] have revealed that an increase in the block-selective solvent content of a binary solvent mixture normally causes a micellar morphological transition. This happens because the interfacial tension between the solvent and the insoluble core among core−corona diblock copolymer micelles or between the solvent and the shell among triblock core−shell−corona micelles increases with the block-selective solvent content. To offset this increase, the micelles expand to decrease the interfacial area. This is, unfortunately, counterbalanced by an increase in the stretching energy of the core and coronal chains. After the micelles surpass a critical size, the stretching energy term dominates. A morphological transition eventually occurs, which is accompanied by a reduction in the interfacial and chain stretching energies.

While a morphological transition with f_{TFT} variation was indeed observed for the $B_{120}C_{100}F_{22}$ micelles prepared in TFT/MeOH, the cylindrical morphology of the other three polymers was insensitive to the f_{TFT} changes or to the replacement of MeOH by either EtOH or iPOH. Two factors could be responsible for the stability of the cylindrical micelles of these three polymers. First, the interfacial tension between the C shell and the solvent phase probably changed little among the different solvent mixtures because C dissolved in neither TFT nor any of the alcohols. Second, liquid crystalline phase formation of the F block dictated the morphology of the $A_{120}C_{100}F_{22}$, $A_{65}C_{54}F_{16}$, and $B_{65}C_{54}F_{16}$ micelles so that this morphology was not readily changed by varying the block-selective solvent composition.

We believe that the second factor was mainly responsible for the observed stability of the cylindrical micelles of $A_{120}C_{100}F_{22}$, $A_{65}C_{54}F_{16}$, and $B_{65}C_{54}F_{16}$ because f_{TFT} variation did trigger a morphological transition for the $B_{120}C_{100}F_{22}$ micelles in TFT/MeOH. This effect was unleashed in the $B_{120}C_{100}F_{22}$ system probably because this polymer had the lowest F block weight fraction and highest soluble block weight fraction and thus the lowest driving force for liquid crystalline phase formation. In this system, the other free energy terms including the interfacial and chain configuration energies had prevailed.

For coil−coil diblock copolymers, a decrease in the weight fraction of the soluble block can also trigger a morphological transition.[14,62,64] This is also true for coil−coil−coil triblock terpolymers.[21] The same cylindrical morphology was observed for $A_{65}C_{54}F_{16}$, $A_{120}C_{100}F_{22}$, and $B_{65}C_{54}F_{16}$ under all tested conditions despite the differing soluble block weight fractions of 17%, 19%, and 27%, respectively. This may be again due to mesogen-driven formation of cylindrical micelles.

Liquid Crystalline Phase Formation. Verifying liquid crystalline phase formation from F in the solvated cylindrical micelles was challenging because the micellar solutions were normally dilute at 1.0 or 3.0 mg/mL. At these concentrations techniques such as differential scanning calorimetry (DSC) were too insensitive for following the liquid crystalline to isotropic phase transition.

Because of this, we used indirect methods in combination to infer liquid crystalline phase formation from F in the solvated cylindrical micelles. The cylindrical micelles prepared at 3.0 mg/mL were settled by high-speed centrifugation and dried to yield powdery samples. We first demonstrated by atomic force microscopy (AFM) that the integrity of the cylindrical micelles was retained during this process despite some coronal chain mixing among different micelles. One of these samples was then analyzed by wide-angle X-ray scattering, WAXS, to confirm the presence of a liquid crystalline phase in the cores of these dried cylindrical micelles at room temperature. Further, DSC was used to determine the liquid crystalline to isotropic phase transition temperature. The use of solution ^{19}F NMR subsequently allowed the identification of phase transitions at similar temperatures for the F block in the solvated cylindrical micelles. These results in combination therefore strongly suggested the existence of a liquid crystalline F phase in the solvated micelles.

The BCF and ACF micelles should have survived the centrifugation step used for the preparation of the powdery micellar samples because the micelles had solid rather than hollow cores and shells. They should have also survived the solvent removal step because the C block dissolved in neither TFT nor the alcohols, and thus the preferential evaporation of either solvent would not have affected the integrity of the micelles. Unambiguous proof for the survival of these cylinders was provided by our AFM analysis of a powdery $A_{105}C_{85}F_{19}$ cylindrical micellar sample with an image shown in Figure S6 of the Supporting Information. Individual cylinders were clearly discerned in this image despite the close packing of the fibers and coronal chain mixing of different micelles.

Figure 2 shows WAXS spectra obtained for these dried $A_{120}C_{100}F_{22}$ cylindrical micelles settled from TFT/MeOH at f_{TFT} = 44% and 10%. Each sample showed a peak at q = 12.3 nm^{-1}, corresponding to a periodic distance of 0.51 nm. This was the same, within experimental error, as 0.50 nm reported by Al-Hussein et al.[39] for the average FO spacing in a smectic A layer (Scheme 2c), and this confirmed unambiguously that the F block formed a liquid crystalline phase in the dry cylindrical micelles.

Figure 3 compares the first-heating DSC traces for a bulk $B_{120}C_{100}F_{22}$ sample and the $A_{120}C_{100}F_{22}$ micelles that were centrifuged down from TFT/MeOH at f_{TFT} = 44% and 10% and subsequently dried. In every case, an endothermic peak was observed near 76 °C, which is the reported smectic A-to-isotropic phase transition temperature for the F block.[39] Therefore, the F block in the dried cylindrical micelles and the bulk existed as a liquid crystalline phase at room temperature.

Figure S7 shows the solution ^{19}F NMR spectrum of $A_{65}C_{54}F_{16}$ micelles at 70 °C in TFT/MeOH/deuterated methanol at v/v/v = 1/8/1 or f_{TFT} = 10%, where deuterated methanol was added to replace methanol to facilitate NMR magnetic field locking. Since a long pulse was used to presaturate and suppress the TFT fluorine signal, peaks of the fluorine atoms of the polymer perfluorooctyl groups were obtained free of solvent interference. After identifying all of the fluorine peaks, we focused on the CF_3 signal at −83 ppm and obtained the integrated intensity of this signal at different temperatures under otherwise identical data acquisition conditions. Figure 4 shows how this intensity changed with temperature for the above-mentioned $A_{65}C_{54}F_{16}$ micelle sample at f_{TFT} = 10% and another micellar sample in TFT/MeOH/deuterated methanol at v/v/v = 44/46/10 or f_{TFT} = 44%.

The CF_3 peak of the $A_{65}C_{54}F_{16}$ cylindrical micelles at f_{TFT} = 44% was visible at all temperatures tested between 40 and 75 °C. Between 50 and 70 °C, the signal intensity increased with temperature and leveled off above 70 °C. This intensity vs temperature variation trend was precisely what was expected for a phase transition.[65] The phase transition temperature deduced from the temperature by which a 50% increase in the intensity had occurred was 58 °C.

For the sample at f_{TFT} = 10%, no signal was detected for the CF_3 group at low temperatures. The signal appeared and increased after T exceeded ~60 °C, again suggesting the occurrence of a phase transition. Because of the higher volatile methanol content, we could not heat this system to 75 °C or higher without boiling the solvent mixture and evaporating methanol. Thus, we could not locate accurately the phase transition temperature for this sample. If the shape of the intensity vs temperature curve was similar for the samples at f_{TFT} = 10% and 44%, the phase transition temperature for this sample should be ~68 °C. While this number involved much uncertainty, what one can conclude with confidence was that the $A_{65}C_{54}F_{16}$ cylindrical micelles had a higher phase transition temperature at f_{TFT} = 10% than at f_{TFT} = 44%.

In summary, the ^{19}F NMR spectral data confirmed unambiguously the presence of a phase transition in the solvated micelles not only at the low f_{TFT} value of 10% but also at the high f_{TFT} value of 44%. Also, the phase transition temperature decreased with increasing f_{TFT}, suggesting a plasticizing effect of TFT. While the phase transition determined by NMR could have been any phase transition such as a coil−globule transition, we suspect that it was the smetic A to isotropic phase transition of the solvated micelles because the estimated phase transition temperature ~68 °C for the $A_{65}C_{54}F_{16}$ cylindrical micelles at f_{TFT} = 10% was close to ~76 °C for the smetic A to isotropic phase transition of the powdery cylindrical micelles.

Core and Shell Dimensions. The $A_{120}C_{100}F_{22}$ and $A_{65}C_{54}F_{16}$ micelles prepared from TFT/MeOH were closely investigated. We measured the core and shell diameters of more than 70 cylinders for each sample and obtained their average diameters and diameter deviations. These results are shown in Table 2 for some samples.

Table 2 shows that the core diameters of the $A_{65}C_{54}F_{16}$ or $A_{120}C_{100}F_{22}$ cylindrical micelles were constant at ~8 and ~11 nm, respectively, regardless of f_{TFT} or binary solvent combination changes. Using the core and shell diameters from Table 2, we calculated the average shell thickness of 6.0 and 3.0 nm, respectively, for the $A_{120}C_{100}F_{22}$ and $A_{65}C_{54}F_{16}$ cylindrical micelles.

At 22 and 16 repeat units and when fully stretched, the F blocks should have the end-to-end distances of 5.6 and 4.1 nm, respectively. These were the same as the TEM core radii of 5.5 and 4 nm, suggesting that the F blocks were almost fully stretched in core. We used the term "almost fully stretched" because not all chains but only the longer chains needed to reach to the core center. Thus, it appears that the formation of a liquid crystalline phase and the contour length of the polymer chains dictated the core diameters, which did not change when the solvent composition varied.

We admit that the above conclusion was reached based on the best information available to us and involved certain assumptions. First, the F repeat unit numbers were assumed to be reasonably close to the targeted numbers. Second, the cylindrical micelles were assumed not to deform extensively after they were aero-sprayed from the solvent phase.

Despite our caution, we should point out that fluorinated blocks have been previously determined by Hillmyer, Lodge, and co-workers to assume fully stretched configurations in block copolymer micelles made of miktoarm triblock terpolymers.[23] This happened because of the strong incompatibility between their fluorinated polymer block with other polymer blocks and the existence of their systems in the superstrong segregation regime.[66] Our F and C blocks should also be highly incompatible and thus a similar argument can be made for our system.

Cylinders Bearing Ridged Coronas. After aero-spraying the ACF cylindrical micelles, the dried micelles were equilibrated with a uranyl acetate ($UO_2(Ac)_2$) solution in methanol for 20 min to stain the A chains. The excess staining agent was rinsed off with methanol droplets before they were examined by TEM. Methanol was used in this staining process because it was a poor solvent for both the C and F blocks, and its use should not have perturbed the core and shell structure of the micelles. Figure 5 shows TEM images of $A_{120}C_{100}F_{22}$ micelles sprayed from TFT/MeOH at f_{TFT} = 30% and 44%, respectively. The stained A domains did not fully cover the cylinders. Rather, they appeared to consist of spherical bumps and elongated ridges decorating the cylinder surfaces.

Because of a rinsing step for unbound UO_2^{2+}, it is reasonable for one to question if these bumps and ridges were artifacts derived from the nonuniform removal of UO_2^{2+}. Also, Liu and co-workers[67,68] and Discher and co-workers[69] used divalent cations such as Cu^{2+} and Ca^{2+} to bridge different A chains and induce their segregation from other chains in the corona of block copolymer nanospheres and vesicles. Thus, one may further question if these surface ridges arose due to UO_2^{2+}-induced nonuniform gelation of the A surface chain. We reject these explanations because a uniform layer was seen by us before for the A corona of AC diblock cylindrical micelles when the A chains were stained under similar conditions.[70,71]

$A_{120}C_{100}F_{22}$ micelles were aero-sprayed from TFT/MeOH at f_{TFT} = 10% onto silicon wafers, and the resultant sample was imaged by tapping-mode AFM. Figure 6 displays the height and phase AFM images of this sample. The bumps and ridges were seen in both the height and phase images. Since this sample was not stained at all, these images clearly showed that the bumps and ridges were intrinsic features of the ACF cylinders and not artifacts from A chain staining.

We also examined by AFM the $B_{120}C_{100}F_{22}$ cylindrical micelles aero-sprayed from TFT/MeOH at f_{TFT} = 10%. The surface segregation patterns were not evident. Therefore, the surface ridges were unique of the ACF cylinders.

We further note that the ridges in Figure 6 appeared wider than those in the TEM images. This was because the AFM widths contained a contribution from the tip size. Figure 6a and images similar to Figure 6a were used also to yield an average diameter and height of 73 ± 6 and 30 ± 3 nm for the cylindrical micelles. The diameter was larger than the TEM diameter of 32 ± 4 nm (Table 2) for the overall cylinders again because of a tip contribution. The average AFM height was comparable with the TEM overall diameter because the AFM tip size did not contribute to the measured height.

Fluorinated units are known to creep toward surfaces to reduce polymer sample surface tension.[37] We ruled out the possibility of ridge formation due to phase separation between A and escaped F domains by performing an XPS study of the

cylindrical micelles that were centrifuged down and dried. Figure 7 compares the XPS spectra of the cylindrical micelles and a bulk $A_{120}C_{100}F_{22}$ sample in the C 1S spectral region. While the bulk sample exhibited a signal for C bound with fluorine atoms, this type of C was absent among the micellar samples. Since XPS is a surface technique and detects elements that are within several nanometers of a sample's surface, this result demonstrated that the F block was buried inside the cylindrical micellar core even after they were dried and thus supported our prior assertion about the structural integrity of the centrifuged and dried cylindrical micelles

Scheme 2 depicts our proposed structure for the core−shell−corona ACF cylindrical micelles. In the solvated state, the coronal A chains should stretch into the solvent phase as depicted in Scheme 2a. Upon solvent evaporation, they collapsed and aggregated into ridges (Scheme 2b). In the core, the perfluorooctyl (FO) units should pack in layers with their axes aligned, on the average, along the cylinder's axis (Scheme 2c). Evidently, this layered packing was better accommodated by the cores of the cylindrical micelles than those of the spherical micelles, for example.

We were initially puzzled by the observation of A ridges on the ACF cylinders. Our later literature search revealed that such a situation has been shown to occur by a Monte Carlo simulation study of grafted polymer brushes.[72] Polymer chains in a brush layer are stretched when solvated in a good solvent but cluster and form surface bumps and ridges when the quality of the solvent deteriorates to a theta solvent or worse due to polymer segment/segment attraction. The boiling points of TFT and methanol are 102 and 64.7 °C, respectively. When the solvents evaporated from the atomized ACF cylindrical micelle solution spray during TEM specimen preparation, methanol, the selective solvent for A, should evaporate preferentially over TFT, a poor solvent for A. This gradual deterioration of solvent quality for the mobile coronal A chains should cause them to cluster and form ridges.

Since the B chains were soluble in both TFT and methanol, the fact that the solvent did not deteriorate much for B with the preferential evaporation of methanol also explained why no obvious ridges were observed on the BCF cylindrical micelles. We should further reinforce that this preferential solvent evaporation should not have affected the core−shell structure or the morphology of the micelles because C dissolved in neither methanol nor TFT and TFT evaporated within ∼1 s.

While ridge formation from A on the ACF cylinders was in agreement with results of the Monte Carlo study mentioned above, differences existed in the details of the modeled and current systems. The substrate in the modeled system was planar and static. The substrate in the examined system consisted of the shell cylinders and was cylindrical and dynamic due to the possibility for the shell chains to move somewhat during preferential evaporation of methanol.

There have been several reports on the formation of rugged coronas from the segregation of two types of chains on the surface of block copolymer nanospheres and vesicles.[67,69,73] It is, however, rare to see bump formation from one type of chains on nanoparticle surfaces.[74] As far as we know, this is the first report on the preparation of block copolymer cylindrical micelles with nanometer-scale surface roughness. This might be useful for the creation of superhydrophobic and -oleophobic coatings[75−77] if block copolymer cylindrical micelles or nanofibers are ever to be used in such an application.

Mesogen-Driven Cylindrical Micelle Formation. To decrease the interfacial area between the core and shell and that between the shell and the solvent, the core, shell, and corona chains of coil−coil−coil triblock copolymer micelles are normally stretched radially relative to their unperturbed dimensions. As mentioned earlier, the F chains were indeed fully stretched in the cores of the ACF cylindrical micelles.

The average respective shell thicknesses were 6.0 and 3.0 nm for the $A_{120}C_{100}F_{22}$ and $A_{65}C_{54}F_{16}$ cylindrical micelles. The unperturbed root-mean-square end-to-end distances R_n for the C chains of $A_{120}C_{100}F_{22}$ and $A_{65}C_{54}F_{16}$ were calculated to be 7.7 and 5.7 nm, respectively, using the characteristic ratio of 12.6[78] and the repeat units numbers of 100 and 54 for the C chains. Thus, the C chains were compressed. We do realize that there were uncertainties in the C repeat unit numbers. Even if these numbers were 20% smaller, a highly unlikely situation, the R_n value should decrease only by ∼10% and were still much larger than the shell thickness values. These suggest that F chain or mesogen packing in the core dictated the formation of the cylindrical micelles and that the shell did not secure their normal thicknesses found in coil−coil−coil triblock copolymer micelles.

Heating the micellar solutions above the smectic A-to-isotropic transition temperature should eliminate the liquid crystalline packing of the F block, and thus the ACF micelles formed at such a high temperature should be those of coil−coil−rod triblock copolymers. The F block should remain as a rod block because of the bulky pendant FOE groups. Figure 8 shows TEM images of $A_{120}C_{100}F_{22}$ and $A_{65}C_{54}F_{16}$ micelles sprayed from 70 °C TFT/MeOH at f_{TFT} = 44%. While $A_{120}C_{100}F_{22}$ apparently formed mostly "large compound micelles",[14] $A_{65}C_{54}F_{16}$ mainly yielded vesicles. While the elucidation of the exact structure of these micelles was beyond the scope of this work, the micelles observed at 70 °C for the coil−coil−rod copolymers were certainly not cylindrical. Thus, the cylinders were formed at lower temperatures, most likely to facilitate the liquid crystalline packing of the FOE units.

More interestingly, the $A_{65}C_{54}F_{16}$ vesicles and cylinders could be repeatedly interconverted by cycling the system's temperature. After going through the heating/cooling or vesicle/cylinder cycle once for the $A_{65}C_{54}F_{16}$ micelles in TFT/MeOH at f_{TFT} = 44%, we cycled the solution temperature between 70 and 21 °C once more. The samples taken at the different temperatures in cycle 2 were analyzed by TEM, yielding images (a) and (b) in Figure 9. Analyzing a sample taken from a solution heated the third time to 70 °C yielded the image shown as Figure 9c. The vesicle−cylinder interconversion was clearly repeated by temperature cycling.

IV. CONCLUSIONS

Prepared and characterized were four F-bearing triblock terpolymers $A_{65}C_{54}F_{16}$, $A_{120}C_{100}F_{22}$, $B_{65}C_{54}F_{16}$, and $B_{120}C_{100}F_{22}$ and their micelles. The first three block copolymers readily formed cylindrical micelles at room temperature in TFT/MeOH at f_{TFT} = 44%, 30%, and 10%. $A_{65}C_{54}F_{16}$ and $A_{120}C_{100}F_{22}$ also self-assembled into cylindrical micelles in either TFT/EtOH or TFT/iPOH at f_{TFT} = 44%. The only exception was $B_{120}C_{100}F_{22}$, which had the lowest F weight fraction and the highest soluble block weight fraction among the four copolymers. $B_{120}C_{100}F_{22}$ formed cylindrical micelles in TFT/MeOH at f_{TFT} = 10%, a mixture of cylindrical and spherical micelles at f_{TFT} = 30% and 44%. The micelles all possessed an F core, a C shell, and an A or B corona. Our

detailed analysis of the TEM images indicated that the F chains in the core block were almost fully stretched and the C shell chains in the ACF cylindrical micelles were radially compressed relative to their unperturbed dimensions. These arose probably from the F-*block*-driven micellization, which yielded cylinders possessing abnormal thicknesses for the shell. Aside from the indirect evidence, the smectic layer to isotropic phase transition was confirmed by our DSC and WAXS studies of dry micelles and ^{19}F NMR studies of the solvated micelles. More interestingly, the ACF micelles underwent morphological transitions from large compound micelles or vesicles at high temperatures to cylinders when cooled below the isotropic-to-smectic A phase transition temperature for the F blocks. For $A_{65}C_{54}F_{16}$, this morphological transition was reversible via temperature cycling. This mesogen-driven process may provide a facile route for the controlled preparation of useful block copolymer cylindrical micelles.

■ ASSOCIATED CONTENT

Supporting Information

Discussion of reagents used, details of experimental techniques, more TEM images, AFM image of dried $A_{120}C_{100}F_{22}$ cylindrical micelles, ^1H NMR spectra of BCF and their SEC traces, and ^{19}F NMR spectrum of $A_{65}C_{54}F_{16}$ micelles at 70 °C at f_{TFT} = 10%. This material is available free of charge via the Internet at http://pubs.acs.org.

■ AUTHOR INFORMATION

Notes

The authors declare no competing financial interest.

■ ACKNOWLEDGMENTS

We thank the NSERC of Canada for financial support of this research. G.L. thanks the Canada Research Chairs Program for a chair position in materials science. Dr. Francoise Sauriol and Prof. Gang Wu are thanked for help with the fluorine NMR experiment. Dr. Ian Wyman is thanked for proofreading the manuscript.

■ REFERENCES

(1) Geng, Y.; Dalhaimer, P.; Cai, S. S.; Tsai, R.; Tewari, M.; Minko, T.; Discher, D. E. *Nature Nanotechnol.* **2007**, *2*, 249−255.
(2) Liu, J.; Thompson, Z. J.; Sue, H. J.; Bates, F. S.; Hillmyer, M. A.; Dettloff, M.; Jacob, G.; Verghese, N.; Pham, H. *Macromolecules* **2010**, *43*, 7238−7243.
(3) Liu, G. J. *Adv. Polym. Sci.* **2008**, *220*, 29−64.
(4) Liu, G. J.; Yan, X. H.; Duncan, S. *Macromolecules* **2003**, *36*, 2049−2054.
(5) Yan, X. H.; Liu, G. J. *Langmuir* **2004**, *20*, 4677−4683.
(6) Liu, G. J.; Ding, J. F.; Qiao, L. J.; Guo, A.; Dymov, B. P.; Gleeson, J. T.; Hashimoto, T.; Saijo, K. *Chem.—Eur. J.* **1999**, *5*, 2740−2749.
(7) Liu, G. J.; Yan, X. H.; Qiu, X. P.; Li, Z. *Macromolecules* **2002**, *35*, 7742−7747.
(8) Stewart, S.; Liu, G. *Angew. Chem., Int. Ed.* **2000**, *39*, 340−344.
(9) Liu, G. J.; Yan, X. H.; Li, Z.; Zhou, J. Y.; Duncan, S. *J. Am. Chem. Soc.* **2003**, *125*, 14039−14045.
(10) Yan, X. H.; Liu, G. J.; Li, Z. *J. Am. Chem. Soc.* **2004**, *126*, 10059−10066.
(11) Yan, X. H.; Liu, G. J.; Liu, F. T.; Tang, B. Z.; Peng, H.; Pakhomov, A. B.; Wong, C. Y. *Angew. Chem., Int. Ed.* **2001**, *40*, 3593−97.
(12) Yan, X. H.; Liu, G. J.; Haeussler, M.; Tang, B. Z. *Chem. Mater.* **2005**, *17*, 6053−6059.
(13) Li, Z.; Liu, G. J. *Langmuir* **2003**, *19*, 10480−10486.
(14) Zhang, L. F.; Eisenberg, A. *Science* **1995**, *268*, 1728−1731.
(15) Shen, H. W.; Eisenberg, A. *J. Phys. Chem. B* **1999**, *103*, 9473−9487.
(16) Srinivas, G.; Discher, D. E.; Klein, M. L. *Nature Mater.* **2004**, *3*, 638−644.
(17) Jain, S.; Bates, F. S. *Macromolecules* **2004**, *37*, 1511−1523.
(18) Jain, S.; Bates, F. S. *Science* **2003**, *300*, 460−464.
(19) Hayward, R. C.; Pochan, D. J. *Macromolecules* **2010**, *43*, 3577−3584.
(20) Qian, J. S.; Zhang, M.; Manners, I.; Winnik, M. A. *Trends Biotechnol.* **2010**, *28*, 84−92.
(21) Fustin, C. A.; Abetz, V.; Gohy, J. F. *Eur. Phys. J. E* **2005**, *16*, 291−302.
(22) Cui, H. G.; Chen, Z. Y.; Zhong, S.; Wooley, K. L.; Pochan, D. J. *Science* **2007**, *317*, 647−650.
(23) Li, Z. B.; Kesselman, E.; Talmon, Y.; Hillmyer, M. A.; Lodge, T. P. *Science* **2004**, *306*, 98−101.
(24) Dupont, J.; Liu, G. *Soft Matter* **2010**, *6*, 3654−3661.
(25) Zhu, J. T.; Jiang, W. *Macromolecules* **2005**, *38*, 9315−9323.
(26) Pochan, D. J.; Chen, Z. Y.; Cui, H. G.; Hales, K.; Qi, K.; Wooley, K. L. *Science* **2004**, *306*, 94−97.
(27) Zhong, S.; Cui, H. G.; Chen, Z. Y.; Wooley, K. L.; Pochan, D. J. *Soft Matter* **2008**, *4*, 90−93.
(28) Dupont, J.; Liu, G. J.; Niihara, K.; Kimoto, R.; Jinnai, H. *Angew. Chem., Int. Ed.* **2009**, *48*, 6144−6147.
(29) Dou, H. J.; Liu, G. J.; Dupont, J.; Hong, L. Z. *Soft Matter* **2010**, *6*, 4214−4222.
(30) Hu, J. W.; Njikang, G.; Liu, G. J. *Macromolecules* **2008**, *41*, 7993−7999.
(31) Liu, Y. F.; Abetz, V.; Muller, A. H. E. *Macromolecules* **2003**, *36*, 7894−7898.
(32) Walther, A.; Drechsler, M.; Rosenfeldt, S.; Harnau, L.; Ballauff, M.; Abetz, V.; Muller, A. H. E. *J. Am. Chem. Soc.* **2009**, *131*, 4720−4728.
(33) Massey, J. A.; Temple, K.; Cao, L.; Rharbi, Y.; Raez, J.; Winnik, M. A.; Manners, I. *J. Am. Chem. Soc.* **2000**, *122*, 11577−11584.
(34) Wang, X. S.; Guerin, G.; Wang, H.; Wang, Y. S.; Manners, I.; Winnik, M. A. *Science* **2007**, *317*, 644−647.
(35) Gadt, T.; Ieong, N. S.; Cambridge, G.; Winnik, M. A.; Manners, I. *Nature Mater.* **2009**, *8*, 144−150.
(36) Gilroy, J. B.; Gadt, T.; Whittell, G. R.; Chabanne, L.; Mitchels, J. M.; Richardson, R. M.; Winnik, M. A.; Manners, I. *Nature Chem.* **2010**, *2*, 566−570.
(37) Wang, J. G.; Mao, G. P.; Ober, C. K.; Kramer, E. J. *Macromolecules* **1997**, *30*, 1906−1914.
(38) Xiang, M. L.; Li, X. F.; Ober, C. K.; Char, K.; Genzer, J.; Sivaniah, E.; Kramer, E. J.; Fischer, D. A. *Macromolecules* **2000**, *33*, 6106−6119.
(39) Al-Hussein, M.; Serero, Y.; Konovalov, O.; Mourran, A.; Moller, M.; de Jeu, W. H. *Macromolecules* **2005**, *38*, 9610−9616.
(40) Hirao, A.; Hayashi, M.; Loykulnant, S.; Sugiyama, K. *Prog. Polym. Sci.* **2005**, *30*, 111−182.
(41) Guo, A.; Liu, G. J.; Tao, J. *Macromolecules* **1996**, *29*, 2487−2493.
(42) Xu, B.; Pinol, R.; Nono-Djamen, M.; Pensec, S.; Keller, P.; Albouy, P. A.; Levy, D.; Li, M. H. *Faraday Discuss.* **2009**, *143*, 235−250.
(43) Pinol, R.; Jia, L.; Gubellini, F.; Levy, D.; Albouy, P. A.; Keller, P.; Cao, A.; Li, M. H. *Macromolecules* **2007**, *40*, 5625−5627.
(44) Jia, L.; Cao, A.; Levy, D.; Xu, B.; Albouy, P. A.; Xing, X. J.; Bowick, M. J.; Li, M. H. *Soft Matter* **2009**, *5*, 3446−3451.
(45) Rajagopal, K.; Mahmud, A.; Christian, D. A.; Pajerowski, J. D.; Brown, A. E. X.; Loverde, S. M.; Discher, D. E. *Macromolecules* **2010**, *43*, 9736−9746.
(46) Skrabania, K.; von Berlepsch, H.; Bottcher, C.; Laschewsky, A. *Macromolecules* **2010**, *43*, 271−281.
(47) Li, Z. B.; Hillmyer, M. A.; Lodge, T. P. *Langmuir* **2006**, *22*, 9409−9417.
(48) Imae, T.; Tabuchi, H.; Funayama, K.; Sato, A.; Nakamura, T.; Amaya, N. *Colloids Surf., A* **2000**, *167*, 73−81.

(49) Lim, K. T.; Lee, M. Y.; Moon, M. J.; Lee, G. D.; Hong, S. S.; Dickson, J. L.; Johnston, K. P. *Polymer* **2002**, *43*, 7043−7049.
(50) Krupers, M. J.; Sheiko, S. S.; Moller, M. *Polym. Bull.* **1998**, *40*, 211−217.
(51) Nakahama, S.; Hirao, A. *Prog. Polym. Sci.* **1990**, *15*, 299−335.
(52) Henselwood, F.; Liu, G. J. *Macromolecules* **1997**, *30*, 488−493.
(53) Hirao, A.; Kato, H.; Yamaguchi, K.; Nakahama, S. *Macromolecules* **1986**, *19*, 1294−1299.
(54) Ishizone, T.; Sugiyama, K.; Sakano, Y.; Mori, H.; Hirao, A.; Nakahama, S. *Polym. J.* **1999**, *31*, 983−988.
(55) Hirao, A.; Sugiyama, K.; Yokoyama, H. *Prog. Polym. Sci.* **2007**, *32*, 1393−1438.
(56) Zheng, R. H.; Wang, J. D.; Liu, G. J.; Jao, T. C. *Macromolecules* **2007**, *40*, 7601−7608.
(57) Ding, J. F.; Liu, G. J. *Macromolecules* **1999**, *32*, 8413−8420.
(58) Corpart, J. M.; Girault, S.; Juhue, D. *Langmuir* **2001**, *17*, 7237−7244.
(59) Zhao, H.; Chen, Q. J.; Hong, L. Z.; Zhao, L.; Wang, J. F.; Wu, C. *Macromol. Chem. Phys.* **2011**, *212*, 663−672.
(60) Battaglia, G.; Ryan, A. J. *J. Am. Chem. Soc.* **2005**, *127*, 8757−8764.
(61) Hu, J. W.; Liu, G. J.; Nijkang, G. *J. Am. Chem. Soc.* **2008**, *130*, 3236−3237.
(62) Ding, J. F.; Liu, G. J.; Yang, M. L. *Polymer* **1997**, *38*, 5497−5501.
(63) Njikang, G.; Han, D. H.; Wang, J.; Liu, G. J. *Macromolecules* **2008**, *41*, 9727−9735.
(64) Cameron, N. S.; Corbierre, M. K.; Eisenberg, A. *Can. J. Chem.* **1999**, *77*, 1311−1326.
(65) Gent, M. P. N.; Ho, C. *Biochemistry* **1978**, *17*, 3023−3038.
(66) Semenov, A. N.; Nyrkova, I. A.; Khokhlov, A. R. *Macromolecules* **1995**, *28*, 7491−7500.
(67) Zheng, R. H.; Liu, G. J.; Yan, X. H. *J. Am. Chem. Soc.* **2005**, *127*, 15358−15359.
(68) Zhou, Z. H.; Liu, G. J.; Hong, L. Z. *Biomacromolecules* **2011**, *12*, 813−823.
(69) Christian, D. A.; Tian, A. W.; Ellenbroek, W. G.; Levental, I.; Rajagopal, K.; Janmey, P. A.; Liu, A. J.; Baumgart, T.; Discher, D. E. *Nature Mater.* **2009**, *8*, 843−849.
(70) Li, X. Y.; Liu, G. J. *Langmuir* **2009**, *25*, 10811−10819.
(71) Li, X. Y.; Liu, G. J. *Soft Matter* **2011**, DOI: 10.1039/clsm05446.
(72) Lai, P. Y.; Binder, K. *J. Chem. Phys.* **1992**, *97*, 586−595.
(73) Zhou, Z. H.; Liu, G. J.; Hong, L. Z. *Biomacromolecules* **2011**, *12*, 813−823.
(74) Xiong, D. A.; Liu, G. J.; Zhang, J. G.; Duncan, S. *Chem. Mater.* **2011**, *23*, 2810−2820.
(75) Tuteja, A.; Choi, W.; Ma, M. L.; Mabry, J. M.; Mazzella, S. A.; Rutledge, G. C.; McKinley, G. H.; Cohen, R. E. *Science* **2007**, *318*, 1618−1622.
(76) Gao, X. F.; Jiang, L. *Nature* **2004**, *432*, 36−36.
(77) Xiong, D.; Liu, G. J.; Hong, L. Z.; Duncan, E. J. S. *Chem. Mater.* **2011**, *23*, 4357−4366.
(78) Hong, L. Z.; Liu, G. J. *Macromolecules* **2010**, *43*, 3941−3946.

Macromolecules

Article

pubs.acs.org/Macromolecules

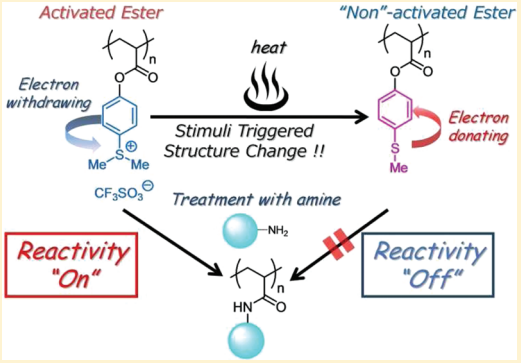
Changing the Reactivity of Polymeric Activated Esters by Temperature: On−Off Switching of the Reactivity of Poly(4-acryloxyphenyldimethylsulfonium triflate)

Ryohei Kakuchi and Patrick Theato*

Institute for Technical and Macromolecular Chemistry, University of Hamburg, Bundesstr. 45, D-20146 Hamburg, Germany

Supporting Information

ABSTRACT: RAFT polymerization of 4-acryloxyphenyldimethylsulfonium triflate (SR-AEM) using pentafluorophenyl-(4-phenylthiocarbonylthio-4-cyanovalerate) as the chain transfer agent and AIBN as a radical source in acetonitrile at 90 °C yielded poly(4-acryloxyphenyldimethylsulfonium triflate) (poly(SR-AEM))s in high yields with well-controlled molecular weights and polydispersity indices. The reactive polymer poly(SR-AEM) was converted using an excess amount of amines, e.g., isopropylamine yielding predominantly poly(*N*-isopropylacrylamide) with defects of poly(4-acryloxyphenyl methylsulfide) in a minor ration of less than 16%. Furthermore, poly(SR-AEM) could be converted by thermo-triggered release of methyl group at dimethylsulfonium ion group to afford poly(4-acryloxyphenyl methylsulfide) (poly(APM)) as proved by ^{1}H NMR measurements, which did not react with amines anymore. To the best of our knowledge, this represents the first temperature-induced "on−off switching" of the reactivity of an activated ester by using 4-dimethylsulfonim phenol as the stimuli-responsive leaving group.



INTRODUCTION

In a growing area of functional polymer science, polymers with readily clickable groups receive increasing attention because of their robust and reliable ability to yield functional materials such as bio-related polymers. Such post-polymerization processes can be conducted not only in solution but also on surfaces.[1−19] To expand the scope of click ready functional materials, many click type reactions have been utilized. This includes Cu(I)-catalyzed[12] and metal-free[2] 1,3-dipolar cycloaddition reactions between organo-azides and acetylenes as well as thiol−ene,[8] thiol−maleimide,[9] isocyanate−nucleophile,[17−19] and activated ester−amine[16] reactions, which all practically lead to quantitative conversions during the post-polymerization modification step. Although the variety in reactants, catalyst, and reaction conditions can be varied, the click reaction site itself provides only a fixed reactivity toward certain molecules. Hence, incorporation of different functionalities into a polymer by post-polymerization modifications has been achieved by orthogonal click reaction sites, which eventually leads to orthogonally functionalized block copolymers.[20−24]

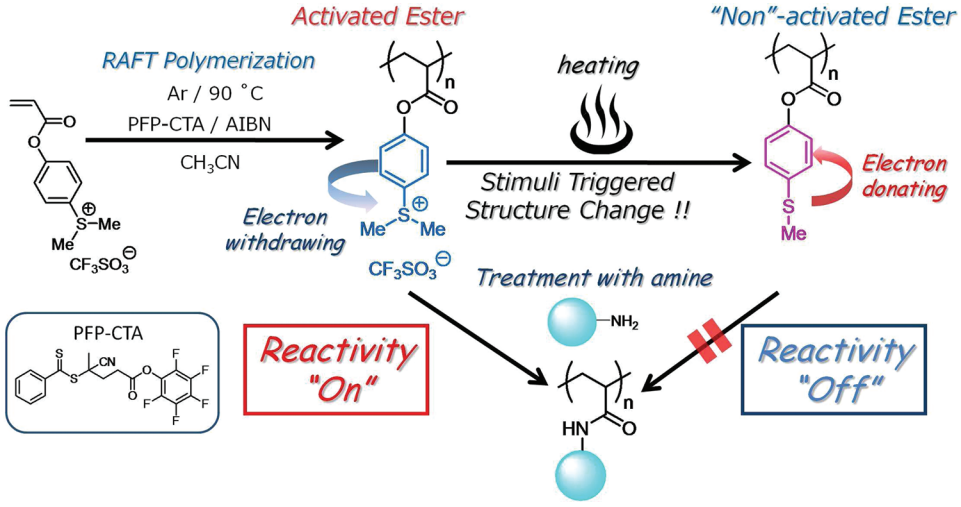
Among the number of functionalities that are potentially useful in material science, polymers with stimuli responsive properties are particular appealing.[25] When such stimuli responsive properties could be combined with a click reactivity, stimuli-induced switching of reactivity in click chemistry is rationally expected, which would lead to a new functionalization methodology for polymer scientists. Despite the great importance and potential of stimuli triggered reactivity switching for click type reactions, almost no attention has been paid to this synthetic area yet. While poly(4-vinylbenzoyl azide) could be used to generate isocyanate groups upon heating,[26] i.e., showing in principle the possibility of temperature-responsive functionalization, it was Locklin and co-workers who reported a photoresponsive polymer film consisting of cyclopropenone as a photoresponsive clickable reaction site, and they succeeded in a spatially controlled functionalization.[27] However, cyclopropenone-based click chemistry suffers from the difficulty of the monomer synthesis.[28] Furthermore, it was unfortunate that neither conversions were reported nor any reaction in solution investigated.[27]

In order to realize an external-stimuli triggered reactivity switching for click type reactions, phenoxy ester type activated ester chemistry possesses intrinsic advantages over other click type reactions: (1) no catalyst for the post-polymerization process is required, ensuring a high tolerance toward other coexisting functional groups, (2) structural diversity of the benzene ring providing a variability in solubility and reactivity, and (3) ease of chemical modification on benzene ring of phenoxy ester type activated ester because of their chemical stability other than nucleophiles. The rational requirement for stimuli-triggered reactivity switching of activated ester based on phenoxy ester type activated ester would be a switching from an electron deficient leaving group to an electron-rich leaving group triggered by external stimuli. In order to meet this

Received: September 26, 2011
Revised: January 6, 2012
Published: January 31, 2012

 © 2012 American Chemical Society dx.doi.org/10.1021/ma202175z | *Macromolecules* 2012, 45, 1331−1338

Scheme 1. Schematic Representation of Temperature-Triggered Reactivity On−Off Switching of an Activated Ester Functionality Embedded in Poly(4-acryloxyphenyldimethylsulfonium triflate)



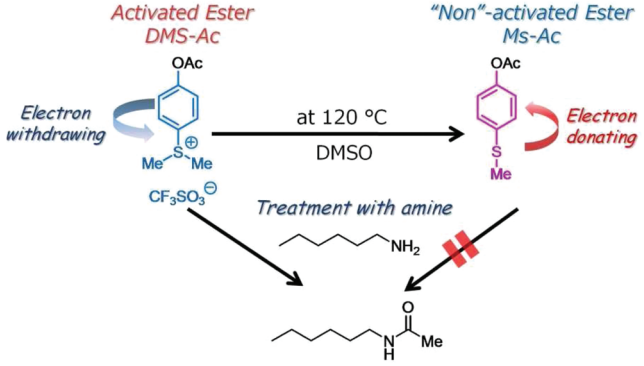
requirement, we turned our attention to the 4-dialkylsulfonium phenol as a stimuli-responsive leaving group.[29] First, 4-dialkylsulfonium phenol itself possesses highly acidic phenol proton with a $pK_a \approx 7.5$ and hence represents a good leaving group within ester derivatives because of the strong electron-withdrawing nature of sulfonium cation.[29] In addition, 4-dialkylsulfonium phenol is well-known to be decomposed applying a temperature stimuli to yield 4-alkylthiophenol, with a $pK_a \approx 10.0$, and hence its leaving-group ability of the respective ester derivatives is dramatically decreased because of electron-donating nature of the alkyl sulfide group.[29] In fact, Nagai and co-workers showed that incorporation of 4-dialkylsulfonium phenoxy ester moieties within a polymeric micelle exhibited a facile reactive site toward amines.[30−34] Furthermore, 4-acryloxyphenyldimethylsulfonium ion was revealed to possess facile radical polymerizability under both free and controlled radical polymerization conditions.[35−39] On the other hand, to the best of our knowledge, no detailed characterization about activated ester reactivity was yet reported for well-defined homopolymers featuring 4-dialkylsulfonium phenoxy ester moieties. In addition, a stimuli-triggered reactivity change of a 4-dialkylsulfonium phenoxy ester moiety within polymers has also never been examined.

Hence, in this article, we describe (i) the evaluation of our concept of external-stimuli triggered reactivity switching of 4-dialkylsulfonium phenoxy esters by means of model compounds and reactions, (ii) the RAFT polymerization of the corresponding monomer 4-acryloxyphenyldimethylsulfonium triflate to afford a polymeric activated ester, and (iii) the investigation of the post-polymerization modifications taking advantage of the switching behavior of the reactivity (Scheme 1).

RESULTS AND DISCUSSION

Monomer Design Concept of Stimuli-Responsive Activated Ester Monomer (SR-AEM). The monomer design concept in this article is comprised of the following two points: (1) a structural change of the leaving group from an electron-withdrawing state to an electron-donating group triggered by a temperature stimuli and (2) the reactivity change in the ester linkage along with the structural change in leaving group. To meet these requirements, 4-(dimethylsulfonium)phenol was selected as stimuli-responsive leaving group. First, model reactive compounds using the 4-acetoxyphenyldimethylsulfonium triflate (DMS-Ac) as an activated ester form and 4-(methysulfide)-phenoxy acetate (MS-Ac) as the corresponding deactivated ester were investigated to confirm whether the concept of reactivity change properly works or not (see Scheme 2). In order to provide

Scheme 2. Schematic Representation of Temperature-Triggered Reactivity On−Off Switching in Activated Ester Functionality for Model Compounds



a direct evidence of the structural change of the sulfonium ion group triggered by temperature, the reaction of DMS-Ac during heating was directly monitored by ^{1}H NMR. The thermal reaction of DMS-Ac was conducted in DMSO by heating to 120 °C for 1 h. As shown in Figure 1, the thermal treatment induced distinct structural changes and the observed ^{1}H NMR signals are in a perfect agreement with the peaks observed for the corresponding MS-Ac as the deactivated ester compound. To investigate the reactivity change, the model reactions between the model compounds MS-Ac or DMS-Ac with hexylamine were also directly monitored by ^{1}H NMR. As a direct consequence of the electron-donating nature of the methyl sulfide group, the deactivated ester of MS-Ac showed 0% conversion even after 1 h in the presence of 2.0 equiv of hexylamine (see Figure S-1, Supporting Information). By design, this is in a clear contrast to the results that had been obtained for the reaction of DMS-Ac in the presence of just 1.1 equiv of hexylamine. Because of the introduction of the

dx.doi.org/10.1021/ma202175z | Macromolecules 2012, 45, 1331−1338

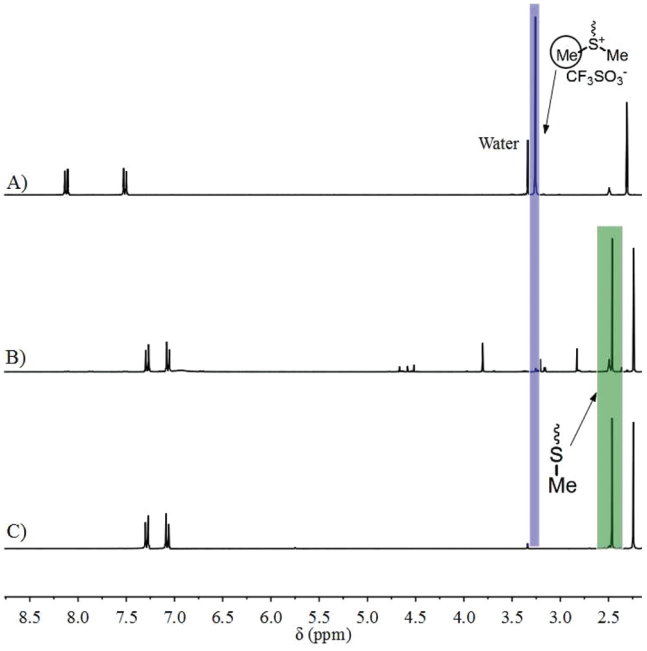


Figure 1. ^{1}H NMR spectra in DMSO-d_6 of (A) DMS-Ac, (B) DMS-Ac after thermal treatment at 120 °C in DMSO-d_6 for 1 h without purification, and (C) MS-Ac.

sulfonium ion group at the para position in the benzene ring, a drastic reactivity change was induced, resulting in over 95% conversion within 40 min (see Figure 2A). Because

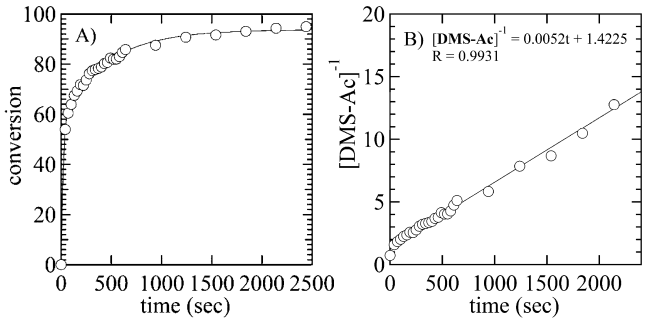


Figure 2. (A) Conversion of the DMS-Ac for the reaction between DMS-Ac and hexylamine in $CDCl_3$ (line; guidance). (B) Kinetic plots for the reaction between DMS-Ac and hexylamine in $CDCl_3$.

trialkylsulfonium ions are well-known to act as methylating agent for nucleophiles, which might cause potential side reactions, IR measurements of the reaction system were conducted to provide a direct evidence that the amidation reaction indeed took place at the carbonyl group (Figure 3). To be more precise, in the FT-IR spectrum of the DMS-Ac after reaction with hexylamine (Figure 3A) a distinct band at 1653 cm^{-1} owing to the C═O stretch of amide group developed while the band at 1763 cm^{-1} owing to the C═O stretch of activated ester group disappeared. Thus, the amidation reaction of DMS-Ac indeed took place at the carbonyl group. Furthermore, a kinetic study for the model reaction between DMS-Ac and hexylamine revealed a very fast amidation reaction at 25 °C and followed a second-order kinetic nature, which is consistent with the two component reaction of DMS-Ac with hexylamine (Figure 2). Thus, these model reactions supported that the main concept of thermally induced reactivity change can be achieved by using

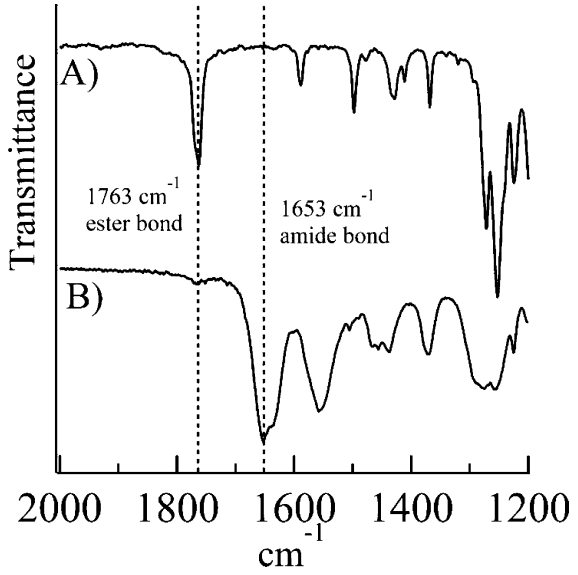


Figure 3. IR spectra of the DMS-Ac before (A) and after (B) the reaction with hexylamine in $CHCl_3$.

4-(dimethylsulfonium)phenol triflate as a thermoresponsive leaving group.

RAFT Polymerization of Stimuli-Responsive Activated Ester Monomer (SR-AEM). In order to realize the RAFT polymerization of 4-acryloxyphenyldimethylsulfonium triflate (SR-AEM), the synthetic procedure to obtain SR-AEM followed general design principles based on a methodology employed by Huck et al.[35] Briefly, 4-methylsulfide phenoxy acrylate, obtained by standard esterification chemsitry of 4-methylsulfide phenol with acryloyl chloride, was reacted with methyl triflate (MeOTf). The key step was the methylation of the sulfide linkage using MeOTf, which avoided the possibility of metal contamination and hence shows high compatibility with RAFT technique. Next, we carried out the RAFT polymerization of SR-AEM using pentafluorophenyl-(4-phenyl-thiocarbonylthio-4-cyanovalerate) as the chain transfer agent (PFP-CTA) and AIBN as a radical source in acetonitrile at 90 °C under an argon atmosphere with a ratio of $[SR\text{-}AEM]_0/[PFP\text{-}CTA]_0/[AIBN]_0$ being 50:1:0.5.[40] The SR-AEM monomer conversion reached 86% after 2 h, yielding poly(SR-AEM) with a degree of polymerization (DP_{NMR}) of 50.4 and a molecular weight distribution (M_w/M_n) of 1.32 in 70% isolated yield. The degree of polymerization of the obtained poly(SR-AEM) (DP = 50.4) was in good agreement with theoretical $DP_{theoretical}$ = 43.1, which was calculated from the initial ratio of $[SR\text{-}AEM]_0/[PFP\text{-}CTA]_0$. In addition, the SEC curve of the obtained polymer was unimodal, and its M_w/M_n value was fairly narrow,[41] indicating that the polymerization occurred in a controlled fashion. In the ^{1}H NMR spectrum of the obtained polymer, the major signals in the range both from 7.2 to 7.6 ppm and from 7.9 to 8.2 ppm were assigned to the aromatic protons and the sharp singlet signal in the range from 3.0 to 3.3 ppm was assigned to the methyl protons of disulfonium ion moiety, while the remaining broad signals appearing in the range from 1.9 to 2.5 ppm were assigned to the protons of the polyacrylate backbone (see Figure 4, upper spectrum). Thus, these results indicated that the RAFT polymerization of SR-AEM proceeded in a controlled manner with fairly good control over polymerization yielding poly(SR-AEM).

dx.doi.org/10.1021/ma202175z | Macromolecules 2012, 45, 1331−1338

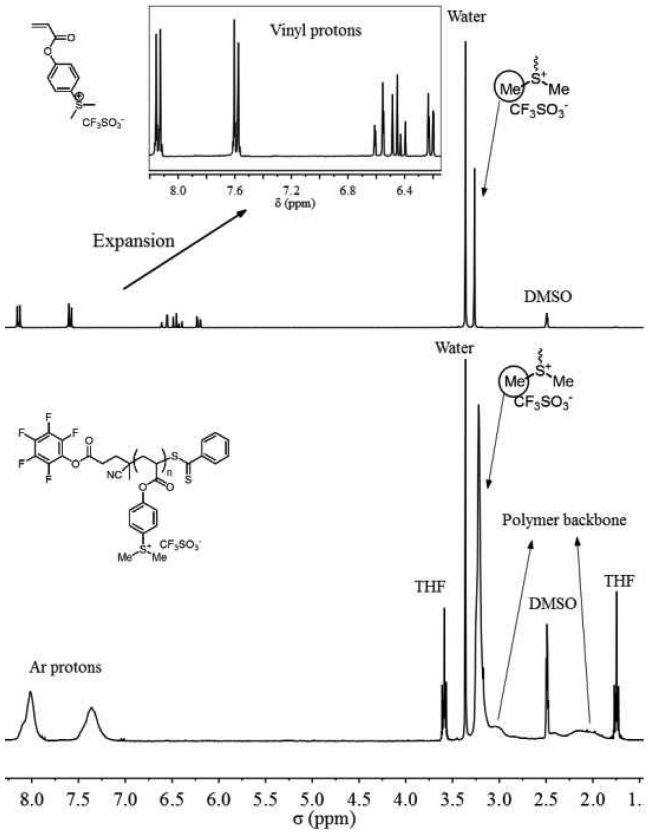


Figure 4. ^{1}H NMR spectra of the SR-AEM (upper) and poly(SR-AEM) (lower) in DMSO-d_6.

To confirm that the polymerization system proceeded in a controlled fashion, we carried out the RAFT polymerization of SR-AEM using various ratios of the $[SR\text{-}AEM]_0/[PFP\text{-}CTA]_0$ from 20 to 80 (Table 1 shows the polymerization results). As a direct consequence of the living nature of the RAFT polymerization of SR-AEM, the obtained poly(SR-AEM) had molecular weights that matched the theoretical values calculated by the $[SR\text{-}AEM]_0/[PFP\text{-}CTA]_0$ (SEC traces of runs 1, 8, and 9 in Table 1 are shown in Figure 5). It turned out, however, that a better control was obtained for smaller ratios of

Table 1. RAFT Polymerization of SR-AEM Using PFP-CTA as Chain Transfer Agent[a]

run	$[M]_0/[CTA]_0/[AIBN]_0$	time (min)	conv[b] (%)	DP_{theo}[c]	DP_{NMR}[d]	M_w/M_n[e]
1	50/1/0.5	120	86.2	43.1	48.8	1.32
2	50/1/0.5	20	0	n.d.	n.d.	n.d.
3	50/1/0.5	30	17.0	8.5	8.7	1.18
4	50/1/0.5	40	45.0	22.5	28.9	1.17
5	50/1/0.5	50	64.3	32.2	30.0	1.18
6	50/1/0.5	60	79.4	39.7	41.3	1.30
7	50/1/0.5	90	81.3	40.7	48.8	1.28
8	20/1/0.5	120	90.5	18.1	18.6	1.17
9	80/1/0.5	120	90.2	73.6	65.5	1.44

[a][M] = 0.93 mol L^{-1}; solvent, CH_3CN; temperature, 90 °C. [b]Determined by ^{1}H NMR in $CDCl_3$. [c]Calculated from $([M]_0/[I]_0) \times$ conv. [d]Determined by end-group analysis using ^{19}F NMR in DMSO-d_6. [e]Determined by SEC in THF using PSt standards. The poly(SR-AEM)s were thermally treated prior to injection to the SEC7.

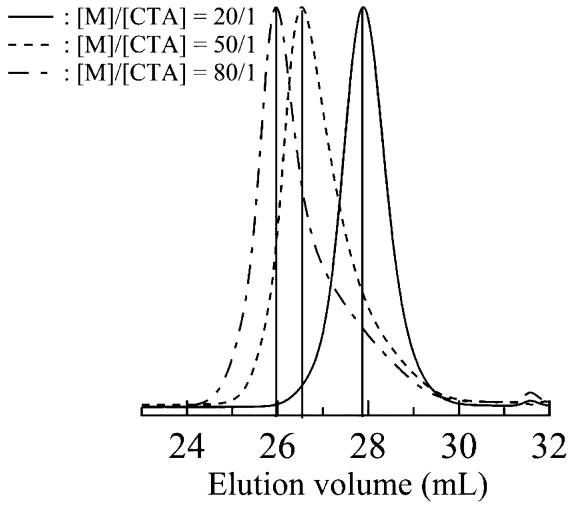


Figure 5. SEC traces of the poly(SR-AEM) (runs 1, 8, and 9; eluent, THF; flow rate, 1.0 mL min^{-1}). The poly(SR-AEM)s were thermally treated prior to injection to the SEC.

$[SR\text{-}AEM]_0$ to $[PFP\text{-}CTA]_0$ as SEC revealed a slight tailing for the ratio of 80:1. For further evidence of the controlled nature of the RAFT polymerization of SR-AEM, we carried out a kinetic investigation in acetonitrile at 90 °C under an argon atmosphere with a ratio of $[SR\text{-}AEM]_0/[PFP\text{-}CTA]_0/[AIBN]_0$ being 50:1:0.5. Although a short induction period was observed, the kinetic experiments showed a distinct first-order relationship between the reaction time and monomer conversion until the polymerization system reached around 80% monomer conversion (Figure 6A). Furthermore, the molecular weight of the obtained poly(SR-AEM) increased linearly with the reaction time (Figure 6B). It thus can be concluded that SR-AEM can be polymerized with a good control to molecular weights up to 25 kg/mol, making a very suitable candidate for a further investigation in post-polymerization modifications.

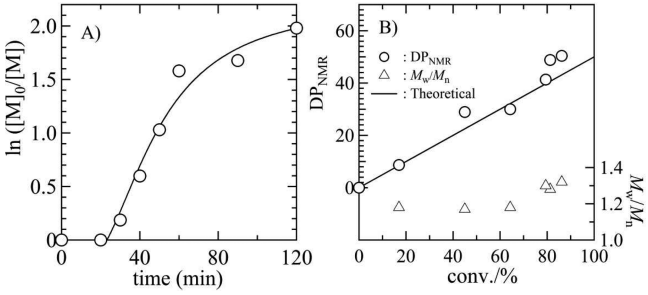


Figure 6. (A) Kinetic plots for the polymerization of SR-AEM (line; guidance). (B) Dependence of degree of polymerization (DP_{NMR}) and polydispersity (M_w/M_n) on the monomer conversion.

On−Off Reactivity Switching of the Activated Ester Moiety Embedded in Poly(SR-AEM). As a direct consequence of the successfully demonstrated preliminary model study (vide supra), the obtained poly(SR-AEM) was rationally expected to show a stimuli-responsive switching of its activated ester moiety. Hence, to verify the presence of the activated ester, the obtained polymer was reacted with an excess amount of *i*-Pr-NH_2 in CH_3CN for 19 h. After the reaction mixture was purified by dialysis in MeOH, a polymer powder was obtained in more than 83% isolated yield. The FT-IR spectrum of the obtained polymer revealed the development of a distinct band

dx.doi.org/10.1021/ma202175z | Macromolecules 2012, 45, 1331−1338

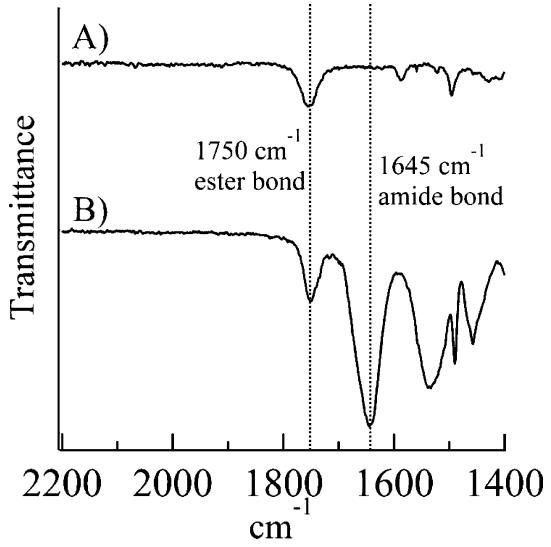


Figure 7. FT-IR spectra (ATR mode) of the poly(SR-AEM) before (A) and after (B) the reaction with *i*-Pr-NH_2 in CH_3CN.

at 1645 cm^{-1} owing to C═O stretch of amide group, while C═O stretch band of the activated ester group at 1750 cm^{-1} decreased dramatically (see Figure 7). Furthermore, in the ^1H NMR spectrum of the obtained polymer, distinct peaks due to isopropyl group appeared from 0.8 to 1.1 ppm and from 3.7 to 4.0 ppm while the peaks in the range from 7.1 to 7.6 ppm and from 7.8 to 8.2 ppm owing to the activated ester moiety disappeared (see Figure 8). Additionally, the ^1H NMR spectrum of the obtained polymer was in a good agreement with that of poly(*N*-isopropylacrylamide) synthesized by direct RAFT polymerization of *N*-isopropylacrylamide (see Figure 8B,C). The ^1H NMR spectrum of the obtained polymer revealed small but distinct peaks from 2.4 to 2.5 ppm owing to methyl sulfide linkage, showing that side reaction of methylating of amine took place in minor ratio of not more than 16%, based on ^1H NMR integration. The post-polymerization reaction took place predominantly with high efficiency. Thus, these results supported that the reaction between poly(SR-AEM) and *i*-Pr-NH_2 proceeded with high conversion affording poly(*N*-isopropylacrylamide) as a product, which showed that poly(SR-AEM) acted as a facile polymeric activated ester very similar to poly(*N*-succinimidyl acrylate) or poly(pentafluorophenyl acrylate).[16]

We next focused on the external stimuli responsive property of poly(SR-AEM). The thermal reaction of poly(SR-AEM) was conducted in DMSO at 120 °C, and the reaction progress was directly monitored by ^1H NMR measurement. As successfully demonstrated by the model reaction, poly(SR-AEM) was converted by thermo-triggered release of methyl group at dimethylsulfonium ion group to afford poly(4-acryloxyphenyl methylsulfide) (poly(APM)) as a nonactive form of poly(SR-AEM), which was directly proven by ^1H NMR measurement (see Figure 9). The signals in the ranges from 7.1 to 7.6 ppm and from 7.8 to 8.2 ppm due to phenyl ring bearing dimethylsulfonium ion group were completely shifted to the signal in the range from 6.8 to 7.3 ppm. In addition, the sharp peak in the range from 3.1 to 3.3 ppm owing to dimethylsulfonium ion group disappeared completely while a new peak appeared in the range from 2.4 to 2.5 owing to methylthio group. Furthermore, the ^1H NMR spectrum of the decomposed

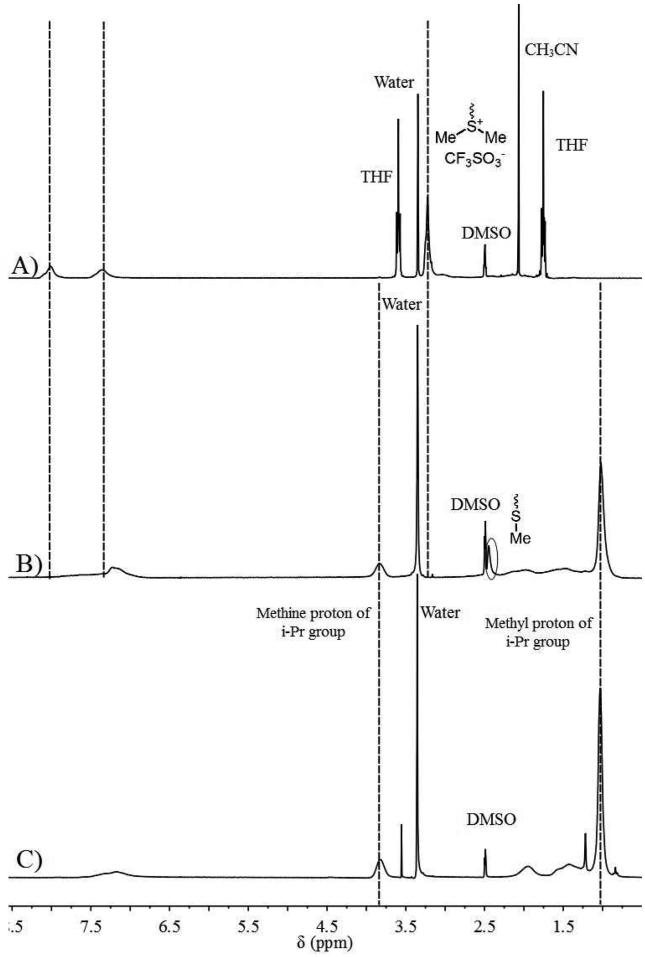


Figure 8. ^1H NMR spectra in DMSO-d_6 of (A) poly(SR-AEM), (B) poly(SR-AEM) after the treatment with *i*-Pr-NH_2 in CH_3CN overnight, and (C) poly(*N*-isopropylacrylamide) synthesized by radical polymerization.

polymer by thermo-reaction was in perfect agreement with the ^1H NMR spectrum of poly(4-methylthiophenoxy acrylate), which was prepared by direct RAFT polymerization of 4-methylthiopheoxy acrylate (see Figure 9). In addition to the spectral evidence, the solubility of the decomposed polymer differed from poly(SR-AEM). As a direct consequence of the highly ionic nature of poly(SR-AEM), poly(SR-AEM) showed a good solubility in only polar solvents such as MeOH, DMSO, DMF, and acetonitrile while it was insolubile in THF or $CHCl_3$. In a clear contrast, the nonactive form of poly(SR-AEM) was only soluble in nonpolar solvents such as THF, $CHCl_3$, CH_2Cl_2, and 1,4-dioxane, which strongly supported that the obtained polymer lost its ionic nature and thus its activated ester behavior during the decomposition. Thus, it turned out to be very clear that poly(SR-AEM) was converted to poly(4-methylthiophenoxy acrylate) by the temperature-triggered reaction, which also resulted in a solubility change from an even water-soluble polymer to nonpolar polymer by a simple thermal treatment.

We finally focused on the examination of on−off reactivity switching in poly(SR-AEM) triggered by the temperature stimulus. We evaluated the reactivity for both poly(SR-AEM) and poly(APM) using 1.1 equiv of various amines in CD_3CN and $CDCl_3$, respectively, for 1 h at room temperature, and the reactions were directly monitored by ^1H NMR measurements. It has to be noted that longer reaction times will lead in

dx.doi.org/10.1021/ma202175z | *Macromolecules* 2012, 45, 1331−1338

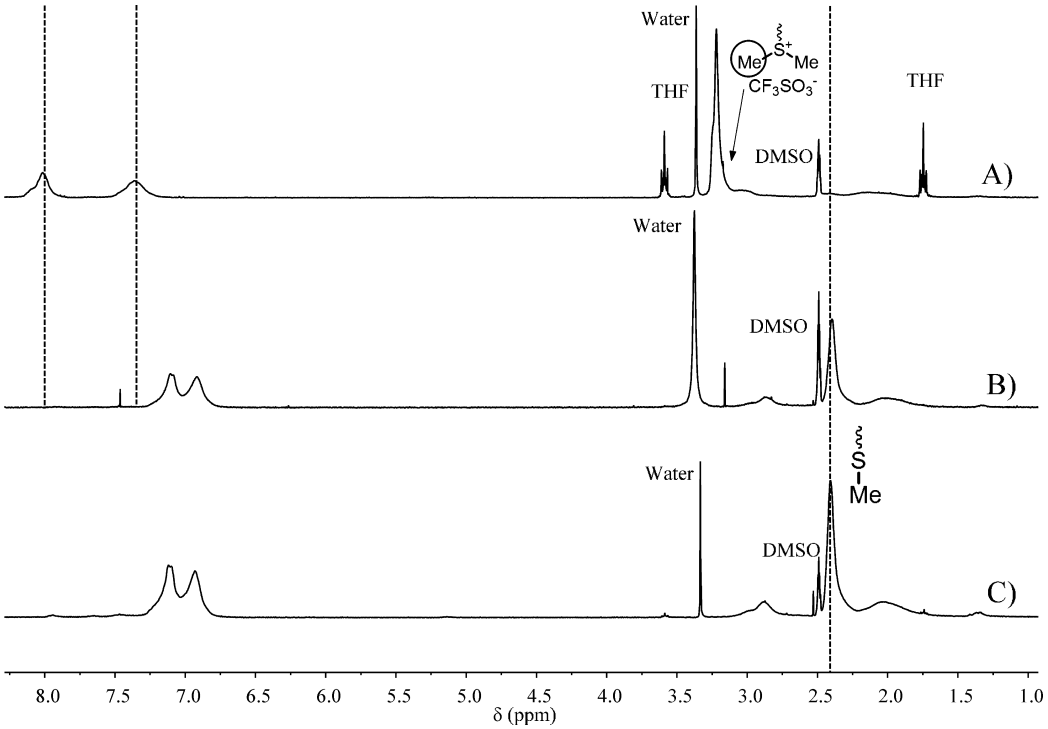


Figure 9. ^{1}H NMR spectra in DMSO-d_6 of (A) poly(SR-AEM), (B) poly(SR-AEM) after thermal treatment at 120 °C in DMSO overnight, and (C) poly(APM) synthesized by RAFT polymerization of 4-acryloxyphenyl methylsulfide.

particular for the reactive poly(SR-AEM) to higher conversions. However, to obtain comparable data, reaction times of 1 h were chosen. As shown in Figure 10, poly(SR-AEM) reacted with

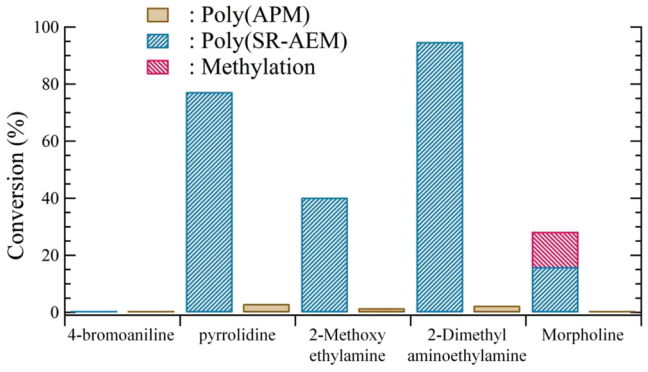


Figure 10. Reactivity comparison of poly(SR-AEM) with poly(APM) using various amines.

various amines except for aromatic amines, such as aniline. This reactivity tendency is similar to that of poly(pentafluorophenyl acrylate).[21] Thus, poly(SR-AEM) can be referred to the "on" state with respect to reactivity. On the other hand, the non-active form of poly(SR-AEM), mainly poly(APM), which was obtained after decomposition of poly(SR-AEM), showed a dramatically decreased reactivity toward various amines including even primary amines which are known to show high reactivity toward activated ester such as pentafluorophenyl ester.[21] When morpholine was used, the side reaction of methylation reaction was also observed as in the case of isopropylamine. Because of high vapor pressure of isopropylamine, it was not used in this comparative study; however, isopropylamine can successfully be used in the post-functionalization reaction for the post-modification of poly(SR-AEM) (vide supra). Interestingly, 2-methoxyethylamine showed a relatively low conversion of only 40% after 1 h. In contrast, the experiments with pyrrolidine and 2-dimethylaminoethylamine showed very high conversions of the activated ester poly(SR-AEM) after 1 h (77% and 94%, respectively), while almost no conversion of the deactivated poly(APM) could be observed.[42] This result clearly showed that decomposed state of poly(SR-AEM) can be termed as "off" state with respect to reactivity. Accordingly, this study represents the first example of a stimuli-triggered "on–off" switching in reactivity of an activated ester by utilizing 4-dimethylsulfonim phenol as stimuli-responsive leaving group.

■ CONCLUSIONS

In this study, we succeeded in the establishment of a new concept of external-stimuli triggered reactivity switching in phenoxy ester type click reaction using 4-dialkylsulfonium phenol as stimuli-responsive leaving group. The successful concept was demonstrated by means of model compounds and reactions. In addition, the RAFT polymerization of 4-acryloxyphenyldimethylsulfonium triflate was achieved using PFP-CTA as chain transfer agent affording polymeric activated ester of poly(SR-AEM) with good control over the polymerization. Obtained poly(SR-AEM) was successfully converted to deactivated ester state of poly(APM) by heating, i.e., stimulation by temperature. To the best of our knowledge, we realized the first temperature induced "on–off" switching in reactivity of activated ester by using 4-dimethylsulfonium phenol as stimuli-responsive leaving group.

■ EXPERIMENTAL SECTION

Materials. The methyltriflate was available from the Sigma-Aldrich Chemicals Co. and used as received. The 4-(methylthio)phenol was purchased from the Tokyo Kasei Kogyo Co., Ltd., and used as received. For polymerization, HPLC grade acetonitrile (>99.9%) was purchased from the VWR Co., Inc., and used without further

dx.doi.org/10.1021/ma202175z | Macromolecules 2012, 45, 1331–1338

purification. The pentafluorophenyl-(4-phenylthiocarbonylthio-4-cyanovalerate) was synthesized according to a previous report.[38] All other chemicals were commercially available and used without further purification unless otherwise stated.

Instruments. All ^{1}H and ^{13}C NMR spectra were recorded on a Bruker 300 MHz FT-NMR spectrometer in deuterated solvents and chemical shifts (δ) were given in ppm as solvent peak as internal standard. ^{19}F NMR spectra were recorded on a Bruker 400 MHz FT-NMR spectrometer in deuterated solvents. The size exclusion chromatography (SEC) was performed at room temperature using a Jasco high performance liquid chromatography (HPLC) system (PU-1580 Intelligent HPLC pump, RI-1530 Intelligent RI detector, AS-1555 Intelligent HPLC autosampler, and DG-2080-53 degasser) equipped with three MZ Analysetechnik MZ-Gel SDplus columns in THF at a flow rate of 1.0 mL min^{-1}. The number-average molecular weight (M_n) and polydispersity (M_w/M_n) of the polymers were calculated on the basis of a polystyrene calibration. IR spectra were recorded on a Bruker Vector 22 FT-IR spectrometer using an ATR unit.

Synthesis of Stimuli-Responsive Activated Ester Monomer. *Synthesis of 4-Acryloxyphenyl Methylsulfide.* To the CH_2Cl_2 solution (30 mL) of 4-methylsulfide phenol (10.0 g, 71.4 mmol) and triethylamine (7.96 g, 78.6 mmol) was added acryloyl chloride (7.12 g, 78.6 mmol) in CH_2Cl_2 (20 mL) at 0 °C for 30 min. After the reaction mixture was stirred at room temperature overnight, the mixture was filtered. The filtrate was collected and washed with 1 N HCl(aq), 1 N Na_2CO_3(aq), and water. The organic layer was dried with $MgSO_4$. The solution was evaporated to give 4-acryloxyphenyl methylsulfide as pale brown liquid. Yield: 11.3 g (58.2 mmol, 81.5%) ^{1}H NMR ($CDCl_3$, 300 MHz) δ (ppm): 7.26 (2H, d, J = 8.9 Hz), 7.05 (2H, d, J = 8.9 Hz), 6.58 (1H, dd, J = 17.3, 1.3 Hz), 6.29 (1H, dd, J = 17.3, 10.4 Hz), 5.98 (1H, dd, J = 10.4, 1.3 Hz), 2.45 (3H, s). ^{13}C NMR ($CDCl_3$, 75 MHz) δ (ppm): 164.50, 148.27, 135.72, 132.64, 127.96, 127.81, 121.97, 16.44.

Synthesis of 4-Acryloxyphenyldimethylsulfonium Triflate (SR-AEM). To a CH_2Cl_2/CH_3CN mixture solution (40/4 mL) of 4-methylsulfide phenoxy acrylate (8.0 g, 41.2 mmol) methyl triflate (7.4 g, 45.2 mmol) was slowly added at 40 °C and allowed to react for 16 h. Afterward, the reaction mixture was cooled down to room temperature, and the mixture was poured into large portion of diethyl ether. The precipitate was collected and dissolved in hot THF. The THF solution was poured into large portion of diethyl ether to yield 4-acryloxyphenyldimethylsulfonium triflate as pale yellow solid. Yield: 14.6 g (40.7 mmol, 98.8%). ^{1}H NMR (DMSO-d_6, 300 MHz) δ (ppm): 8.14 (2H, d, J = 8.9 Hz), 7.59 (2H, d, J = 8.9 Hz), 6.58 (1H, dd, J = 17.2, 1.5 Hz), 6.44 (1H, dd, J = 17.2, 10.1 Hz), 6.21 (1H, dd, J = 10.1, 1.5 Hz), 3.27 (3H, s). ^{13}C NMR (DMSO-d_6, 75 MHz) δ (ppm): 163.75, 154.18, 134.68, 131.85, 127.26, 124.14, 123.98, 120.79 (q, J = 322.2 Hz), 28.47. ^{19}F NMR (DMSO-d_6) δ (ppm): −78.1 (3F, s). FT-IR (ATR-mode): 1739 cm^{-1} (C═O reactive ester band) Anal. Calcd for $C_{12}H_{13}F_3O_5S_2$ (358.35): C, 40.22; H, 3.66. Found: C, 40.09; H, 3.57.

General Procedure for RAFT Polymerization of SR-AEM. RAFT polymerization of SR-AEM was carried out as follows: An acetonitrile solution (1.5 mL) containing SR-AEM (500 mg, 1.4 mmol), pentafluorophenyl-(4-phenylthiocarbonylthio-4-cyanovalerate) (12.5 mg, 0.028 mmol), and AIBN (2.3 mg, 0.014 mmol) was degassed with Ar at room temperature for 15 min. After degassing, the reaction mixture was stirred at 90 °C for 2 h. The reaction mixture was then cooled down and exposed to air to quench the polymerization. A portion of the reaction mixture was collected for the purpose to determine the monomer conversion, while the rest of the reaction mixture was diluted with acetonitrile. The polymer was purified by reprecipitation (acetonitrile/THF) to produce pale red solid. Yield: 368 mg (73.6%).

Synthesis of Model Compounds. *Synthesis of 4-Acetoxyphenyl Methylsulfide (MS-Ac).* To a CH_2Cl_2 solution (15 mL) of 4-methylsulfide phenol (5.0 g, 35.7 mmol) and triethylamine (3.98 g, 39.3 mmol) acetyl chloride (7.12 g, 39.3 mmol) in CH_2Cl_2 (10 mL) was added at 0 °C for 30 min. After the reaction mixture was stirred at room temperature overnight, the mixture was filtered. The filtrate was collected and washed with 1 N HCl(aq), 1 N Na_2CO_3(aq), and water. The organic layer was dried with $MgSO_4$. The solution was evaporated to give 4-acetoxyphenyl methylsulfide as pale yellow solid. Yield: 5.9 g (32.6 mmol, 91.3%). ^{1}H NMR ($CDCl_3$, 300 MHz) δ (ppm): 7.25 (d, J = 8.9 Hz, 2H), 7.00 (d, J = 8.9 Hz, 2H), 2.45 (s, 3H), 2.26 (s, 3H). ^{13}C NMR ($CDCl_3$, 75 MHz) δ (ppm): 169.47, 148.37, 135.67, 127.97, 122.03, 21.07, 16.44.

Synthesis of 4-Acetoxyphenyldimethylsulfonium Triflate (DMS-Ac). To a CH_2Cl_2/CH_3CN mixture solution (10/1 mL) containing 4-acetoxyphenyl methylsulfide (2.0 g, 11.0 mmol) methyl triflate (2.0 g, 12.1 mmol) was slowly added at 40 °C and allowed to react for 13.5 h. Afterward, the reaction mixture was cooled down to room temperature, and the mixture was poured into large portion of diethyl ether. The precipitate was collected and dissolved in acetone. The acetone solution was poured into large portion of diethyl ether to yield 4-acetoxyphenyl dimethylsulfonium triflate as white powder. Yield: 3.3 g (9.5 mmol, 86.4%). ^{1}H NMR (DMSO-d_6, 300 MHz) δ (ppm): 8.12 (2H, d, J = 8.8 Hz), 7.51 (2H, d, J = 8.8 Hz), 3.26 (6H, s), 2.31 (3H, s). ^{13}C NMR (DMSO-d_6, 75 MHz) δ (ppm): 168.91, 154.45, 131.79, 124.20, 123.71, 120.79 (q, J = 322.2 Hz), 28.48, 20.94. ^{19}F NMR (DMSO-d_6) δ (ppm): −78.1 (3F, s). FT-IR (ATR mode): 1763 cm^{-1} (C═O reactive ester band). Anal. Calcd for $C_{11}H_{13}F_3O_5S_2$ (346.34): C, 38.15; H, 3.78. Found: C, 37.86; H, 3.64.

Determination of Theoretical Degree of Polymerization for RAFT Polymerization. In a RAFT polymerization, a theoretical degree of polymerization was calculated as follows:

$$\mathrm{DP}_{\mathrm{theoretical}} = \frac{[\mathrm{monomer}]_0}{[\mathrm{CTA}]_0} \times (\mathrm{monomer\ conv})$$

The monomer conversion was directly determined from the ^{1}H NMR measurements of the polymerization mixtures.

SEC Measurements of the Polymers. Based on the fact that the obtained polymers are of highly ionic nature, the SEC measurement of the polymer was very difficult. Hence, the polymer was dissolved in DMSO and kept at 120 °C overnight in order to selectively decompose sulfonium ion structure in the polymer. The polymer solution was poured into large amount of MeOH. The obtained polymer was then used for SEC measurements in THF.

■ ASSOCIATED CONTENT

Ⓢ Supporting Information

Figure S-1. This material is available free of charge via the Internet at http://pubs.acs.org.

■ AUTHOR INFORMATION

Corresponding Author

*Tel +49 (0) 40 42838 6009; Fax +49 (0) 40 42838 6008; e-mail theato@chemie.uni-hamburg.de.

■ ACKNOWLEDGMENTS

Ryohei Kakuchi gratefully acknowledges the support by a Grant-in-Aid for the Japan Society for the Promotion of Science (JSPS) Fellows.

■ REFERENCES

(1) Barner-Kowollik, C.; Du Prez, F. E.; Espeel, P.; Hawker, C. J.; Junkers, T.; Schlaad, H.; Van Camp, W. *Angew. Chem., Int. Ed.* **2011**, *50*, 60−62.

(2) Becer, C. R.; Hoogenboom, R.; Schubert, U. S. *Angew. Chem., Int. Ed.* **2009**, *48*, 4900−4908.

(3) Chu, C.; Liu, R. *Chem. Soc. Rev.* **2011**, *40*, 2177−2188.

(4) Fournier, D.; Hoogenboom, R.; Schubert, U. S. *Chem. Soc. Rev.* **2007**, *36*, 1369−1380.

(5) Franc, G.; Kakkar, A. K. *Chem. Soc. Rev.* **2010**, *39*, 1536−1544.

(6) Fu, R.; Fu, G.-D. *Polym. Chem.* **2011**, *2*, 465−475.

(7) Golas, P. L.; Matyjaszewski, K. *Chem. Soc. Rev.* **2010**, *39*, 1338−1354.

(8) Hoyle, C. E.; Bowman, C. N. *Angew. Chem., Int. Ed.* **2010**, *49*, 1540−1573.
(9) Hoyle, C. E.; Lowe, A. B.; Bowman, C. N. *Chem. Soc. Rev.* **2010**, *39*, 1355−1387.
(10) Iha, R. K.; Wooley, K. L.; Nyström, A. M.; Burke, D. J.; Kade, M. J.; Hawker, C. J. *Chem. Rev.* **2009**, *109*, 5620−5686.
(11) Lowe, A. B. *Polym. Chem* **2010**, *1*, 17−36.
(12) Lutz, J.-F. *Angew. Chem., Int. Ed.* **2007**, *46*, 1018−1025.
(13) Qin, A.; Lam, J. W. Y.; Tang, B. Z. *Macromolecules* **2010**, *43*, 8693−8702.
(14) Qin, A.; Lam, J. W. Y.; Tang, B. Z. *Chem. Soc. Rev.* **2010**, *39*, 2522−2544.
(15) Sumerlin, B. S.; Vogt, A. P. *Macromolecules* **2009**, *43*, 1−13.
(16) Theato, P. *J. Polym. Sci., Part A* **2008**, *46*, 6677−6687.
(17) Li, H.; Yu, B.; Matsushima, H.; Hoyle, C. E.; Lowe, A. B. *Macromolecules* **2009**, *42*, 6537−6542.
(18) Li, Q.; Zhou, H.; Wicks, D. A.; Hoyle, C. E.; Magers, D. H.; McAlexander, H. R. *Macromolecules* **2009**, *42*, 1824−1833.
(19) Biedermann, F.; Appel, E. A.; del Barrio, J.; Gruendling, T.; Barner-Kowollik, C.; Scherman, O. A. *Macromolecules* **2011**, *44*, 4828−4835.
(20) Ghosh, S.; Basu, S.; Thayumanavan, S. *Macromolecules* **2006**, *39*, 5595−5597.
(21) Nilles, K.; Theato, P. *J. Polym. Sci., Part A* **2010**, *48*, 3683−3692.
(22) Li, R. C.; Hwang, J.; Maynard, H. D. *Chem. Commun.* **2007**, 3631−3633.
(23) Malkoch, M.; Thibault, R. J.; Drockenmuller, E.; Messerschmidt, M.; Voit, B.; Russell, T. P.; Hawker, C. J. *J. Am. Chem. Soc.* **2005**, *127*, 14942−14949.
(24) Yang, S. K.; Weck, M. *Macromolecules* **2007**, *41*, 346−351.
(25) Stuart, M. A. C.; Huck, W. T. S.; Genzer, J.; Muller, M.; Ober, C.; Stamm, M.; Sukhorukov, G. B.; Szleifer, I.; Tsukruk, V. V.; Urban, M.; Winnik, F.; Zauscher, S.; Luzinov, I.; Minko, S. *Nature Mater.* **2010**, *9*, 101−113.
(26) Klinger, D.; Chang, J. Y.; Theato, P. *Macromol. Rapid Commun.* **2007**, *28*, 718−724.
(27) Orski, S. V.; Poloukhtine, A. A.; Arumugam, S.; Mao, L.; Popik, V. V.; Locklin, J. *J. Am. Chem. Soc.* **2010**, *132*, 11024−11026.
(28) Jewett, J. C.; Bertozzi, C. R. *Chem. Soc. Rev.* **2010**, *39*, 1272−1279.
(29) Kouge, K.; Koizumi, T.; Okai, H.; Kato, T. *Bull. Chem. Soc. Jpn.* **1987**, *60*, 2409−2418.
(30) Nagai, K.; Ohashi, T.; Kaneko, R.; Taniguchi, T. *Colloids Surf., A* **1999**, *153*, 133−136.
(31) Takahashi, K.; Kido, J.; Kuramoto, N.; Nagai, K. *J. Colloid Interface Sci.* **1995**, *172*, 63−70.
(32) Takahashi, K.; Nagai, K. *Polymer* **1996**, *37*, 1257−1266.
(33) Takahashi, K.; Suzuki, M.; Kido, J.; Kuramoto, N.; Nagai, K. *Polymer* **1995**, *36*, 4675−4681.
(34) Yamaguchi, K.; Taniguchi, T.; Kawaguchi, S.; Nagai, K. *Colloid Polym. Sci.* **2002**, *280*, 942−948.
(35) Brown, A. A.; Azzaroni, O.; Fidalgo, L. M.; Huck, W. T. S. *Soft Matter* **2009**, *5*, 2738−2745.
(36) Kim, Y. J.; Kang, H.; Leolukman, M.; Nealey, P. F.; Gopalan, P. *Chem. Mater.* **2009**, *21*, 3030−3032.
(37) Wu, H.; Gonsalves, K. E. *Adv. Mater.* **2001**, *13*, 195−197.
(38) Wu, H.; Gonsalves, K. E. *Adv. Mater.* **2001**, *13*, 670−672.
(39) Wu, H.; Gonsalves, K. E. *Adv. Funct. Mater.* **2001**, *11*, 271−276.
(40) Although Gopalan et al. reported RAFT polymerization of 4-acryloxyphenyldimethylsulfonium triflate using 2-cyanoprop-2-yl dithiobenzoate as CTA and AIBN as radical source at 60 °C, the temperature of 90 °C was mandatory in this system. Please see ref 36.
(41) The poly(SR-AEM)s were thermally treated prior to injection to the SEC.
(42) The observed distinct discrepancy of poly(SR-AEM) reactivity toward amines might be owing to the differences in steric hindrance of utilized amines although the quantitative analysis about this reactivity discrepancy is necessary for further discussions.

Macromolecules

Article

pubs.acs.org/Macromolecules

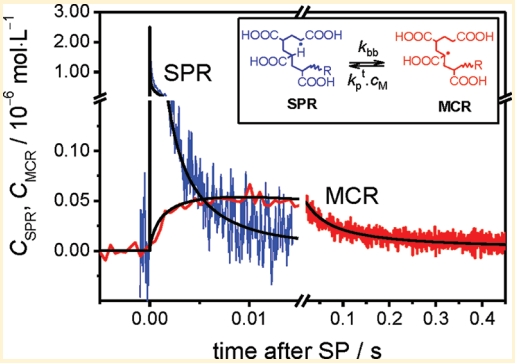
SP-PLP-EPR Study into Termination and Transfer Kinetics of Non-Ionized Acrylic Acid Polymerized in Aqueous Solution

Johannes Barth, Wibke Meiser, and Michael Buback*

Institute for Physical Chemistry, University of Göttingen, Tammannstraße 6, D-37077 Göttingen, Germany

Supporting Information

ABSTRACT: Polymerization of nonionized acrylic acid (AA) in aqueous solution has been studied via single pulse−pulsed laser polymerization in conjunction with electron paramagnetic resonance spectroscopy. Termination of two types of radicals, secondary chain-end radicals (SPRs) and midchain radicals (MCRs), as well as intramolecular chain transfer (backbiting) of SPRs have been studied between 5 and 40 °C at initial AA concentrations of 10 and 50 wt % in the presence of 15 wt % poly(AA). Predici modeling of the measured SPR and MCR concentration vs time traces after single-pulse initiation at t = 0 yields rate coefficients for backbiting, k_{bb}, and for propagation from an MCR, k_p^t. These rate coefficients increase toward lower AA-in-water concentration. Estimates for termination of two SPRs, $k_t^{s,s}$, and of an SPR and an MCR, $k_t^{s,t}$ have been obtained by assuming the reported composite-model behavior for acrylates to also hold for acrylic acid polymerization.



INTRODUCTION

Radical polymerization in aqueous phase is of considerable interest, as the solvent is cheap and environmentally friendly. Acrylic acid (AA) is extensively used for synthesis of water-soluble homo- and copolymers. The kinetics of AA polymerization is however far from being fully understood, which is due to the occurrence of backbiting reactions giving rise to the presence of tertiary midchain radicals in addition to secondary chain-end radicals, to the impact of hydrogen-bonded interactions on rate coefficients, and to difficulties met with molar mass analysis of poly(AA) via size-exclusion chromatography (SEC).[1] Nonideal polymerization kinetics are indicated by the monomer reaction order being well above unity, i.e., close to 1.5.[2] Pulsed-laser polymerization (PLP) of AA at modest laser pulse repetition rates and polymerization temperatures of and above 30 °C yields unstructured molar mass distributions, which are not suitable for deducing reliable propagation rate coefficient, k_p, data by the IUPAC-recommended PLP-SEC technique.[1,3,4] Both findings strongly indicate formation of slowly propagating tertiary midchain radicals by backbiting of secondary chain-end radicals.[5,6] Gilbert et al. were the first to detect MCRs during AA polymerization via electron paramagnetic resonance (EPR) spectroscopy using a specially designed flow reactor.[7] For polymerizations of acrylate monomers, midchain radicals have been studied in detail by several groups, mostly for butyl acrylate (BA).[5,8−10] The PLP-SEC technique has been applied at high laser pulse repetition rates for measuring accurate k_p of chain-end radicals.[9,11] Backbiting rate coefficients were first determined by ^{13}C NMR spectroscopy via the branching level of the polymeric product. This method suffers from poor signal-to-noise quality.[12] Two experimental techniques have been designed for accurately measuring rate coefficients of backbiting, k_{bb}, and of propagation from midchain radicals, k_p^t: (*i*) frequency-tuned PLP (ft-PLP) in conjunction with SEC analysis of the polymer[13] and, more recently, time-resolved EPR monitoring of SPR and MCR concentrations after single laser pulse initiation (SP-PLP-EPR). The latter method may additionally provide information about the chain-length dependence of SPR termination.[14−21] Application of a laser pulse at t = 0, produces a large amount of SPRs, which propagate and enhance SPR chain length i linearly with time t after chain start at t = 0, according to $i = k_p \cdot c_M \cdot t + 1$. The significant variation of k_p of SPRs with monomer-to-water content has already been reported.[1,22]

To the best of our knowledge, data for k_{bb}, k_p^t, and for chain-length dependent termination of two SPRs, two MCRs and for SPR-MCR cross-termination are not available for acrylic acid polymerization. Such information is however required for modeling and optimization of AA polymerization processes as well as for the fundamental understanding of the underlying reaction mechanism. The SP-PLP-EPR technique should be able to provide this data. This technique has already been successfully applied to the detailed study of butyl acrylate polymerization kinetics[21] where MCRs and SPRs are present, as with AA, and to the analysis of chain-length dependent termination in methacrylic acid (MAA) polymerization, where effects of hydrogen bonding on polymerization kinetics are operating, probably to a similar extent as with AA. The MAA experiments were carried out in EPR flat cells, which are specifically

Received: October 18, 2011
Revised: January 4, 2012
Published: January 27, 2012

 © 2012 American Chemical Society

designed for EPR experiments on polar media to overcome problems associated with dielectric loss of microwave irradiation especially at larger sample volumes as are required for polymerization reactions.

EXPERIMENTAL SECTION

Acrylic acid (AA, Aldrich, 99%) was distilled under reduced pressure prior to use. Poly(acrylic acid), (poly(AA), Aldrich, $\bar{M}_w$ = 450 000 g·mol^{-1} was used without purification. The photoinitiator 2-hydroxy-2-methylpropiophenone (Darocur, 98%, Aldrich) was used as received at initial concentrations of 1.6 × 10^{-2} mol·L^{-1}. Demineralized water was used for preparing the reaction solutions consisting of either 10 or 50 wt % AA, of water, of photoinitiator, and of 15 wt % poly(AA). The notation monomer wt % refers to the mass fraction of monomer with respect to the total reaction mixture, i.e., including monomer, water and premixed polymer. Freshly prepared solutions were filled into SQ EPR flat cells of 0.15 mL internal volume (Wilmad LabGlass). Poly(AA) has been added to favorably affect the quality factor of the EPR measurement. Moreover, termination rate data at poly(AA) contents above 15 wt % correspond to AA polymerization at relevant degrees of monomer conversion. As has been deduced from SP-PLP experiments carried out in conjunction with near-infrared spectroscopy on AA in aqueous solution at 40 °C and 2000 bar,[23] the chain-length-averaged termination rate coefficient, $\langle k_t \rangle$, at low and moderate AA concentrations is almost insensitive to polymer content up to about 70% monomer conversion. The addition of 15% poly(AA), as in the present study, is thus assumed to have no impact on the termination rate coefficient. To demonstrate the validity of this assumption, SP-PLP-EPR measurements have been performed at different conversion levels during the course of an experiment. The radical concentration vs time traces are not affected by polymer content which is enhanced upon repeated laser pulsing during the experiment.

The course of a typical SP-PLP-EPR experiment has been detailed elsewhere.[15,24] The flat cell is placed into the resonator cavity of a Bruker Elexsys E 500 series cw-EPR spectrometer and irradiated with XeF excimer laser pulses at 351 nm (Compex 102, Lambda Physik). Typical EPR settings were as follows: 3 G field modulation amplitude, 100 kHz field modulation frequency, 10 mW microwave power and a time constant of 0.01 ms. Prior to the experiment, several laser pulses were applied to the solution to remove oxygen by reaction with initiator-derived radicals. Line positions referring to SPR and MCR species, respectively, to be used for measuring EPR intensity at constant field position after laser pulse initiation were identified by taking full EPR spectra within a short 100 G field sweep of 10 s to avoid significant AA conversion prior to the SP-PLP-EPR experiment. To improve signal-to-noise quality, up to 25 individual radical concentration vs time traces were coadded. Absolute radical concentrations were obtained by calibration with TEMPOL as detailed elsewhere.[15,21] The SP-PLP-EPR experiments were carried out at 5, 12, 22, and 40 °C for 10 wt % initial AA content and at 5 and 40 °C for 50 wt % initial AA content. Monomer conversion due to laser pulsing during the experiment was measured via the AA near-infrared absorbance at 6178 cm^{-1}. Monomer conversion determined after the course of an SP-PLP-EPR experiment was typically around 30%.

Kinetic model. The following reaction steps were implemented into the PREDICI model used for fitting the experimental SPR and MCR vs time traces from SP-PLP-EPR.

The initial concentration of secondary propagating radicals, SPR_1, is obtained from the maximum concentration of SPRs, c_0(SPR), measured immediately after firing the laser pulse at $t \approx 0$ assuming a very high value for the rate coefficient of addition of an AA molecule to the primary photoinitiator fragment. The extremely fast building-up of the initial c_0(SPR) concentration may not be monitored with the presently available time resolution of the experimental setup (see Figure 2). Propagation rate coefficients as a function of temperature and monomer concentration were taken from literature.[1] Monomer concentration was determined as the arithmetic mean value obtained from the NIR-spectroscopically measured AA concentrations before and after applying a series of laser pulses. The conversion range covered during the course of a typical SP-PLP-EPR experiment was up to 30%. It was carefully checked that, within this conversion range, the time-resolved EPR signals do not change, which indicates that the underlying rate coefficients are more or less insensitive toward polymer content under the conditions of the present study. Rate coefficients for backbiting, and for propagation from MCRs were found from PREDICI fitting of the experimental SPR and MCR concentration vs time traces. Termination rate coefficients $k_t^{s,s}(i,i)$ and $k_t^{s,t}(i)$ were considered as chain-length dependent quantities. The notation $k_t^{s,t}(i)$ indicates that a dependence on chain length i is considered only for one of the radicals, whereas both SPRs contribute to the chain-length dependence of homotermination of two secondary radicals, $k_t^{s,s}(i,i)$. The variation of $k_t^{s,s}(i,i)$ with chain length is represented by the composite model:[25]

$$k_t^{i,i} = k_t^{1,1} i^{-\alpha_s}, \quad i \le i_c \tag{1}$$

$$k_t^{i,i} = k_t^{1,1}(i_c)^{-\alpha_s+\alpha_l} i^{-\alpha_l} = k_t^{0,1} i^{-\alpha_l}, \quad i > i_c \tag{2}$$

As has been reported for butyl acrylate,[21] composite-model parameters may be determined by a two-step procedure to avoid simultaneous multiparameter fitting. From SP-PLP-EPR experiments at −40 °C, where backbiting plays no significant role and SPRs are by far dominating, the composite-model parameters for acrylate SPRs, e.g., 1.5 M butyl acrylate in solution of toluene, were determined within a first step to be: α_s = 0.80, α_l = 0.16 and i_c = 30.[17,21] These numbers were assumed to be independent of temperature. The analysis of experimental SPR and MCR vs time traces recorded at higher temperature could thus be restricted to deducing $k_t(1,1)$ and the kinetic parameters referring to MCRs. This strategy can not be used with aqueous solutions of AA, as these systems solidify at temperatures where MCR concentration may be ignored. We thus adopted the SPR composite-model parameters of acrylates for AA polymerization. In order to check whether and to which extent these parameters affect PREDICI fitting, we used as a second set of SPR parameters: α_s = 0.65, α_l = 0.16 and i_c = 50, which values have been found for methacrylate bulk polymerizations and for methacrylic acid polymerization in aqueous solution.[15,24] Methacrylate polymerizations are easier to be studied, as backbiting plays no role and termination occurs exclusively between chain-end radicals.

For the present study into AA polymerization in aqueous phase, $k_t^{s,s}(1,1)$ has been obtained by PREDICI fitting. The cross-termination rate coefficient $k_t^{s,t}(i)$ was introduced into the simulation by $k_t^{s,t}(1) = a \cdot k_t^{s,s}(1,1)$, with the factor of a been varied such as to afford for an optimum fit of experimental concentration vs time curves. The composite-model parameters α_s, α_l and i_c were applied to both $k_t^{s,s}(i,i)$ and $k_t^{s,t}(i)$. An EPR spectrum recorded during pulsed-laser-initiated polymerization of AA at 5 °C is depicted in Figure 1. Time-resolved measurement of SPRs and MCRs, respectively, was carried out by monitoring EPR intensity after single laser pulse initiation at the field positions indicated by the arrows.

Fitting Procedure. PREDICI simulation reveals that extensive variation of the termination rate coefficient $k_t^{t,t}$ has no effect on the experimental SPR and MCR traces. The size of $k_t^{t,t}$ may be estimated from this experimental observation to be far below 10% of $k_t^{s,t}$.

Table 1. Kinetic Scheme Implemented into the PREDICI Model for Simulation of $c_{SPR}(t)$ and $c_{MCR}(t)$ Traces from SP-PLP-EPR

reaction step	chemical reaction	reference
single laser pulse initiation	monomer + $R_0^\bullet$ → SPR_1 (k_i)	see text
propagation of SPRs	SPR_i + monomer → SPR_{i+1} (k_p)	Lacik et al.[1]
propagation of MCRs	MCR_i + monomer → SPR_{i+1} (k_p^t)	this study
backbiting	SPR_i → MCR_i (k_{bb})	this study
termination of two SPRs	SPR_i + SPR_i → polymer ($k_t^{s,s}(i,i)$)	this study
cross-termination of an SPR and an MCR	SPR + MCR_i → polymer ($k_t^{s,t}$)	this study
termination of two MCRs	MCR + MCR → polymer ($k_t^{t,t}$)	negligible impact

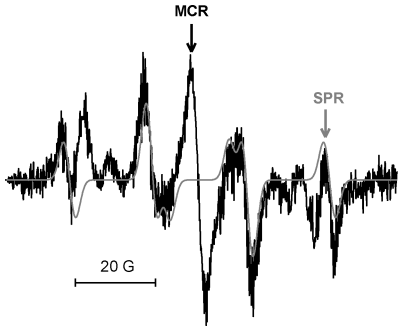


Figure 1. EPR spectrum recorded during pulsed laser polymerization of 10 wt % AA in aqueous solution at 5 °C. The arrows indicate the EPR positions used for SP-PLP-EPR monitoring of SPRs and MCRs, respectively, at constant magnetic field strength. The gray line represents the simulated EPR spectrum for SPRs. The residue arises from the MCR contribution to the experimental spectrum.

Because of the pronounced rate of cross-termination as compared to MCR termination under SP-PLP conditions, self-termination of MCRs has been neglected within the simulations. A total of three rate coefficients: k_{bb}, k_p^t and $k_t^{s,s}(1,1)$ was deduced from PREDICI fitting of the experimental SPR and MCR concentration vs time traces. Shown in Figure 2 is a typical such fit for an SP-PLP-EPR experiment

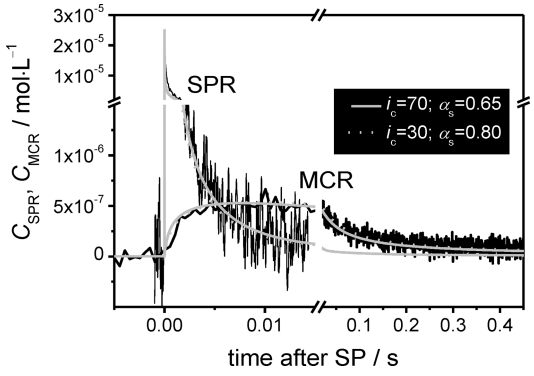


Figure 2. Comparison of experimental $c_R(t)$ data for SPRs (thin black line) and for MCRs (broad black line) with $c_R(t)$ from PREDICI modeling (dotted and full gray lines). PREDICI simulation is based on the kinetic scheme in Table 1. It is assumed that $k_t^{s,t}(1) = 0.5k_t^{s,s}(1,1)$. The comparison has been made for two sets of adopted composite-model parameters: $\alpha_s = 0.65$, $\alpha_l = 0.16$, and $i_c = 50$ (full gray lines) as well as $\alpha_s = 0.80$, $\alpha_l = 0.16$, and $i_c = 30$ (dotted gray lines).

carried out for polymerization of 10 wt % initial AA concentration in water at 15 °C in the presence of 15 wt % premixed poly(AA). For this particular fitting it has been assumed that $k_t^{s,t}(1) = 0.5k_t^{s,s}(1,1)$. Moreover, two sets of composite-model parameters, as given in the inset to Figure 2, have been used. The SPR and MCR traces obtained with $\alpha_s = 0.80$, $\alpha_l = 0.16$, and $i_c = 30$ are represented by the dotted gray lines, whereas the fits with $\alpha_s = 0.65$, $\alpha_l = 0.16$, and $i_c = 50$ are given by the full gray lines.

Inspection of the simulated data tells that the two sets of composite-model parameters result in more or less identical concentration vs time traces. The optimum values of the rate coefficients k_{bb}, k_p^t, and $k_t^{s,s}(1,1)$ obtained with the two parameter sets turn out to be identical within experimental error. In what follows, the $\alpha_s = 0.80$, $\alpha_l = 0.16$, and $i_c = 30$ set of composite-model parameters will be used for simulation of acrylic acid polymerization.

The assumed value of cross-termination rate coefficient: $k_t^{s,t}(1)/k_t^{s,s}(1,1) \approx 0.5$ is based on results obtained for butyl acrylate.[21] This $k_t^{s,t}(1)$ value may be regarded as an upper bound. Within a further fitting step, the ratio $k_t^{s,s}(1,1)/k_t^{s,t}(1)$ has been varied in order to check for k_{bb}, k_p^t, and $k_t^{s,s}(1,1)$ values associated with lower $k_t^{s,t}(1)$.

The full gray lines in Figure 3 represent data from simulation of $c_{SPR}(t)$ and $c_{MCR}(t)$ with $k_t^{s,t}(1) = 0.25k_t^{s,s}(1,1)$. The lower $k_t^{s,t}(1)$

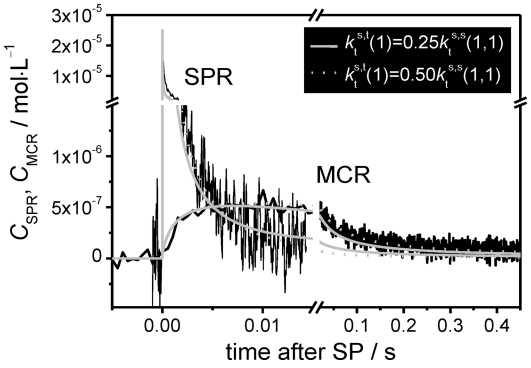


Figure 3. Comparison of experimental and simulated SPR and MCR concentration vs time traces for two adopted values of cross-termination rate coefficients: $k_t^{s,t}(1)/k_t^{s,s}(1,1) \approx 0.25$ (full gray lines) and $k_t^{s,t}(1)/k_t^{s,s}(1,1) \approx 0.50$ (dotted gray lines). Composite-model parameters $\alpha_s = 0.80$, $i_c = 30$, and $\alpha_l = 0.16$ were adopted from butyl acrylate and implemented into the simulation. The experimental SPR and MCR concentration are represented by the black lines.

affords for fits of similar quality as are achieved with $k_t^{s,t}(1) = 0.50k_t^{s,s}(1,1)$, see dotted gray lines. No adequate fits are obtained for lower $k_t^{s,t}(1)$ values than $0.25k_t^{s,s}(1,1)$. Thus, $k_t^{s,t}(1)$ should be adequately represented by the arithmetic mean value of $k_t^{s,t}(1) = (0.37 \pm 0.13)k_t^{s,s}(1,1)$. The ratio of 0.37 will be used throughout the subsequent text. Fitting by a kinetic model with chain-length dependent $k_t^{s,t}$ provides excellent results, although adopting chain-length independent cross-termination also allows for reasonable fits of the experimental data. Cross-termination predominantly occurs between long SPRs and smaller MCRs exhibiting a broad chain-length distribution. The size of the MCRs does not linearly scale with time t after laser pulsing. The associated difficulties of assigning chain lengths for both SPRs and MCRs suggests that assuming $k_t^{s,t}$ to be independent of chain length is a recommendable option.

RESULTS AND DISCUSSION

The optimized parameter values for the rate coefficients k_{bb} and k_p^t are shown in Figure 4 and Figure 5, respectively. Data for

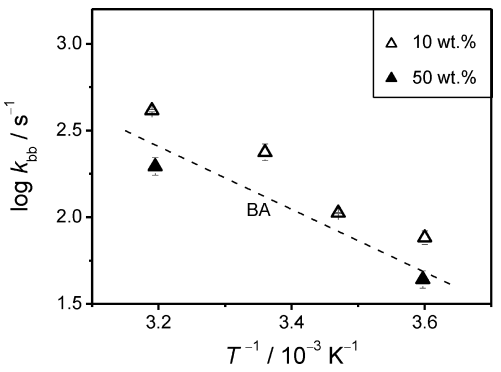


Figure 4. Rate coefficients k_{bb} from PREDICI fitting of experimental SP-PLP-EPR data for 10 wt % (open triangles) and 50 wt % (filled triangles) initial AA concentration in aqueous solution. The data points are mean values from averaging data obtained by adopting different cross-termination rate coefficients (see text). The error bars indicate the scatter associated with using these different approaches for k_{bb} analysis. The dashed line represents k_{bb} of butyl acrylate polymerization.[21]

10 wt % initial AA concentration are represented by the open symbols, whereas the filled ones refer to 50 wt % initial AA content.

dx.doi.org/10.1021/ma202322a | Macromolecules 2012, 45, 1339–1345

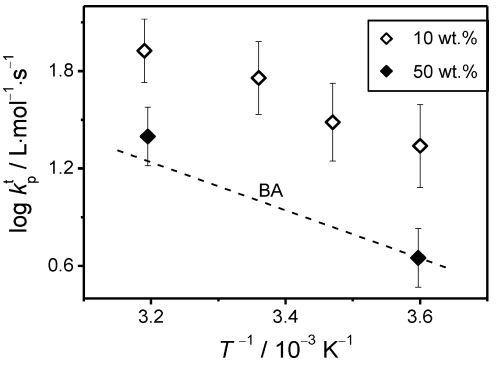


Figure 5. Rate coefficients k_p^t obtained by PREDICI fitting of experimental SP-PLP-EPR data for 10 wt % (open diamonds) and for 50 wt % (filled diamonds) initial AA concentration. The data are mean values from averaging data obtained by adopting different cross-termination rate coefficients (see text). The error bars indicate the scatter associated with applying these different approaches and with the uncertainty by which monomer concentration is accessible during the SP-PLP-EPR experiment. The dashed line represents k_p^t of butyl acrylate polymerization.[21]

The dashed line in both figures refers to butyl acrylate polymerization (1.5 M, 23 wt % in toluene).[21]

The data in Figure 4 tells that k_{bb} for 10 wt % AA is slightly, by about a factor of 2, above k_{bb} for 50 wt % AA. The backbiting rate coefficients of butyl acrylate (BA, dashed line) are in between the numbers for AA at 10 and 50 wt % AA. This close agreement is not overly surprising, as k_{bb} refers to a concerted 1,5-hydrogen shift reaction, which should be controlled by chain flexibility and thus should be similar for the two acrylate monomers acrylic acid and butyl acrylate. The enhancement of k_{bb} toward lower AA concentration may have the same origin as the reduction in branching level seen with BA polymerization in *n*-butanol solution as compared to bulk BA polymerization. This remarkable effect has been found by Hutchinson et al.[26] and has been assigned to increasing hydrogen-bonded interactions between polymer chain and solvent environment, which effect reduces chain flexibility and thus backbiting rate. That this explanation is a reasonable one could be confirmed by SP-PLP-EPR experiments, which clearly demonstrate lower k_{bb} for BA polymerization in *n*-butanol as compared to BA polymerization in toluene. The variation of k_{bb} with AA concentration illustrated in Figure 4 exhibits the same trend. At higher AA concentration, the intermolecular interactions, e.g., via hydrogen bonds between two carboxylic acid moieties, are stronger than in the case of dilute aqueous solution at 10 wt % AA. As a consequence, interactions with the molecular environment are stronger at 50 wt % AA, which should be associated with some reduction in k_{bb} as is indeed observed (Figure 4).

Arrhenius fitting of the k_{bb} data in Figure 4 yields $k_{bb} = 4.3 \times 10^8 \exp(-4331/(T/\mathrm{K}))\ \mathrm{s}^{-1}$ and $k_{bb} = 2.9 \times 10^7 \exp(-3723/(T/\mathrm{K}))\ \mathrm{s}^{-1}$ for 10 and 50 wt % AA, respectively. These two straight-line fits rest only on a few data points and thus should not be used beyond the temperature range of the underlying experiments. The pre-exponentials and activation energies are assumed to be accurate within a factor of 2 and ±10%, respectively.

It should be noted that the pre-exponential for backbiting, $A(k_{bb})$, is well below $10^{12}\ \mathrm{s}^{-1}$, which number has been reported by Toh at al.[27] as characteristic of backbiting with ethene polymerization. As these authors state, their backbiting rates from *ab initio* quantum mechanics overestimate short-chain branching and thus backbiting. Their statement is supported by experimental backbiting pre-exponentials for ethene polymerization being of the order of $10^8\ \mathrm{s}^{-1}$ (see Busch,[28] Kiparissides et al.[29] and references cited therein). That our k_{bb} pre-exponential and activation energy data for acrylic acid are reliable and no artifact due to PREDICI fitting is demonstrated by the close agreement of our numbers, $A(k_{bb}) = 2.9 \times 10^7\ \mathrm{s}^{-1}$ and $E_A(k_{bb}) = 31\ \mathrm{kJ\cdot mol}^{-1}$ for 50 wt % AA, with the backbiting parameters of butyl acrylate: $A(k_{bb}) = 3.5 \times 10^7\ \mathrm{s}^{-1}$ and $E_A(k_{bb}) = 29.3\ \mathrm{kJ\cdot mol}^{-1}$ (from ^{13}C NMR analysis, Plessis et al.[12]); $A(k_{bb}) = 4.8 \times 10^7\ \mathrm{s}^{-1}$ and $E_A(k_{bb}) = 31.7\ \mathrm{kJ\cdot mol}^{-1}$ (from frequency-tuned pulsed laser polymerization experiments, Nikitin et al.[13]); and $A(k_{bb}) = 1.6 \times 10^8\ \mathrm{s}^{-1}$ and $E_A(k_{bb}) = 34.7\ \mathrm{kJ\cdot mol}^{-1}$ (from SP-PLP-EPR experiments, Barth et al.[21]).

As compared to k_{bb}, a much larger effect of AA concentration is observed for k_p^t, the rate coefficient of propagation from an MCR (see Figure 5). Strong effects of monomer-to-water ratio on k_p of chain-end radicals (SPRs) have been reported for a series of water-soluble monomers.[1,30−32] The increase in k_p, by about 1 order of magnitude, in passing from bulk to highly dilute aqueous solution, has been assigned to an increase in the Arrhenius pre-exponential factor as a consequence of the lowering of the barrier to internal rotational mobility of the transition state structure for propagation. The reason behind the enhancement of intermolecular interactions toward higher AA concentrations is seen in the replacement of contacts between carboxylic acid groups and water molecules by the stronger interactions between two carboxylic acid moieties. For k_p^t thus the same basic effect applies as has been put forward to explain the variation of k_{bb}. The change is however weaker for the unimolecular backbiting step than for the bimolecular propagation step, in which three translational degrees of freedom are transformed into internal degrees of freedom that may be affected by interaction with the molecular environment.

It should be noted, that the increase in k_p observed for acrylic acid SPRs in aqueous phase upon dilution from 40 to 5 wt % AA monomer is similar to the one found for acrylic acid MCRs between 50 and 10 wt % AA (see Figure 5).[1] An increase in k_p by a factor of 4 to 5 has also been found for nonionized methacrylic acid within the concentration range 50 to 10 wt % MAA.[33] Because of these similarities, the variation of k_p^t with AA-to-water content is also assigned to a lowering of the barrier to internal motion of the transition-state structure for propagation of an MCR. As such variation represents a genuine kinetic effect, no reason is seen, why k_p^t should not follow the same trend as do MAA radicals and AA chain-end radicals. Arrhenius expressions for k_p^t have been deduced under the assumption that the activation energy does not depend on AA concentration. The so-obtained expressions read:

$$k_p^t = 2.2 \times 10^7 \exp(-3864/(T/\mathrm{K}))\cdot\mathrm{L\cdot mol}^{-1}\cdot\mathrm{s}^{-1}$$

(10 wt % AA)

and

$$k_p^t = 5.3 \times 10^6 \exp(-3864/(T/\mathrm{K}))\cdot\mathrm{L\cdot mol}^{-1}\cdot\mathrm{s}^{-1}$$

(50 wt % AA)

The pre-exponentials and activation energies are assumed to be accurate within a factor of 3 and ±15%, respectively. Adopting the same variation of the pre-exponential with monomer concentration as has been found for MAA radicals in aqueous solution,[23,33] the

dx.doi.org/10.1021/ma202322a | *Macromolecules* 2012, 45, 1339−1345

propagation rate coefficient for acrylic acid MCRs reads:

$$k_p^t = 3.9 \times 10^7(0.08 + 0.92\exp(-6.36\text{ wt }\%/100))\exp(-3864/(T/K))\cdot L\cdot mol^{-1}\cdot s^{-1}$$

The monomer weight percentage given above takes the 15 wt % premixed poly(acrylic acid) into account. The size of k_p^t is correlated with the monomer-to-water ratio which may be estimated from overall monomer weight fraction. It should again be mentioned that, because of the relatively small number of data points, these expressions should definitely not be used beyond the range of the underlying experiments.

Inspection of the k_p^t data in Figure 5 further suggests that the numbers for 50 wt % AA are close to the numbers reported for 23 wt % BA in toluene. According to the entropy penalty argument associated with enhanced chain mobility at lower monomer concentration, the high value of k_p^t at 10 wt % AA in aqueous solution provides an indication for significant chain mobility in dilute AA solution.

The third parameter deduced from PREDICI fitting is $k_t^{1,1}$, the rate coefficient for termination of two SPRs of chain length unity. Knowledge of $k_t^{1,1}$ together with information about the composite parameters α_s, i_c and α_l allows for a full description of termination of SPRs up to moderate degrees of AA conversion. Adopting the composite-model parameters α_s = 0.80, i_c = 30 and α_l = 0.16 from studies into BA, the $k_t^{1,1}$ values depicted in Figure 6 are obtained for AA polymerization with 10 (open circles) and with 50 wt % initial AA in aqueous solution.

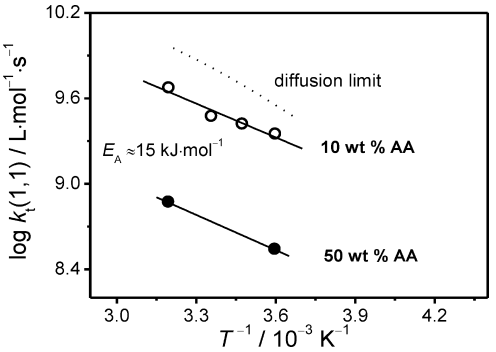


Figure 6. Rate coefficients for termination of two SPRs of chain length unity, $k_t^{1,1}$, as obtained from fitting the experimental SP-PLP-EPR data to the kinetic scheme in Table 1. Data for 10 wt % AA are represented by the open symbols. The filled symbols refer to 50 wt % initial AA. Arrhenius fitting yields an activation energy of about 15 kJ·mol^{-1} for both AA concentrations. The dotted line represents the diffusion-limited situation of maximum rate coefficient.

The $k_t^{1,1}$ values in Figure 6 may be represented by the Arrhenius straight lines: $k_t^{s,s}(1,1) = 1.5 \times 10^{12}\exp(-1819/(T/K))$ L·mol^{-1}·s^{-1} for 10 wt % AA in aqueous solution and $k_t^{s,s}(1,1) = 3.2 \times 10^{11}\exp(-1897/(T/K))$ L·mol^{-1}·s^{-1} for 50 wt % AA. The experimental rate coefficients for termination of two radicals of chain length unity are assumed to be accurate within ±20%. The $k_t^{1,1}$ value for 50 wt % AA is close to $k_t^{1,1}$ for BA in 1.5 M solution of toluene.[21] Similar numbers of $k_t^{1,1}$ are expected for the AA/water and BA/toluene systems in the case of control by center-of-mass diffusion, as both systems exhibit similar viscosity, η, and hydrodynamic monomer radius, $r_{g,1}$. At 20 °C, the viscosities are η = 1.00 mPA·s for water and η = 0.59 mPA·s for toluene. The hydrodynamic radius, on the other hand, is larger for BA than for AA. Center-of-mass diffusion is represented by the Smoluchowski eq 3 in conjunction with the Stokes–Einstein relation 4

$$k_{diff} = 4\pi N_A D_{s,i} R_c \quad (3)$$

$$D_{s,i} = \frac{k_B T}{6\pi r_{g,i}\eta} \quad (4)$$

in which R_c is the capture radius for radical termination and $D_{s,i}$ is the self-diffusion coefficient at chain length i. The latter quantity may be estimated from eq 4. Combination of eqs 3 and 4 predicts $E_a(k_t^{1,1}) \approx E_a(\eta^{-1})$. The temperature dependence of the fluidity, η^{-1}, of water[34] is $E_a(\eta^{-1}) \approx 16$ kJ·mol^{-1}, the $E_a(\eta^{-1})$ values for AA/water mixtures were determined to be 17.5 and 18.7 kJ·mol^{-1} for 10 and 50 wt % AA, respectively, (see Supporting Information) and thus are close to $E_a(k_t^{1,1}) \approx 15$ kJ·mol^{-1} obtained for polymerization of 10 and 50 wt % AA, (see Figure 6).

The surprising observation from Figure 6 is that $k_t^{1,1}$ at 10 wt % AA exceeds the value for 50 wt % initial AA content by about a factor of 5. This large difference can not be accounted for by differences in viscosity, as the η value at 50 wt % AA exceeds the one for 10 wt % AA in aqueous solution only by a factor of 2 (see viscosity data given in supporting material). The $k_t^{1,1}$ value for 10 wt % AA is close to the maximum value estimated for diffusion-controlled rate: $k_{diff}^{max} = 4RT/3\eta$. k_{diff}^{max} refers to situations where each collision of reacting species results in chemical reaction at $R_c = 2r_{g,1}$. With previously studied polymerizations, $k_t^{1,1} \ll k_{diff}^{max}$ has been observed, i.e., $R_c \ll r_{g,1}$, which suggests that the radical functionality is to a certain extent protected by unreactive molecular sites. Assuming eqs 3 and 4 to be applicable to AA termination kinetics, the question needs to be answered why the capture radius R_c increases toward low AA content such as to result in mostly successful collisions in dilute aqueous solution of AA. One explanation for approaching k_{diff}^{max} at low AA concentration may be associated with the high mobility of AA radicals, which is supported by the large values of k_{bb} (see Figure 4) and of k_p^t (see Figure 5) at 10 wt % AA. Moreover, other than with acrylates and methacrylates, the interaction via hydrogen bonding of carboxylic acid moieties may provide some glue which extends the collision period of two AA radicals and thus helps to make each collision successful. As compared to methacrylic acid, where $k_t^{1,1}$ is below k_{diff}^{max}, by almost 1 order of magnitude, termination of two small AA radicals may be much faster because of the absence of the α-methyl group which disfavors the approach of the reacting sites on two MAA radicals.

PREDICI fitting has also been carried out assuming chain-length-independent cross-termination which is accounted for by a single average value of $\langle k_t^{s,t}\rangle$. The so-obtained $\langle k_t^{s,t}\rangle$ values are listed in Table 2. At present, the accuracy of our SP-PLP-EPR experiments is not sufficiently high to reliably check for a chain-length dependence of $\langle k_t^{s,t}\rangle$, i.e., with midchain radicals being involved in the termination step.

Table 2. Rate Coefficients Obtained for $\langle k_t^{s,t}\rangle$ by Fitting the Kinetic Scheme given in Table 1 to the Experimental Data via PREDICI

	5 °C	15 °C	25 °C	40 °C
$\langle k_t^{s,t}\rangle$/L·mol^{-1}·s^{-1} in 10 wt % AA	3 × 10^7	4 × 10^7	4 × 10^7	7 × 10^7
$\langle k_t^{s,t}\rangle$/L·mol^{-1}·s^{-1} in 50 wt % AA	5 × 10^6	-	-	1 × 10^7

dx.doi.org/10.1021/ma202322a | Macromolecules 2012, 45, 1339–1345

In Figure 7, these $\langle k_t^{s,t} \rangle$ data for the two AA contents under investigation are compared to the associated $k_t^{s,s}(1,1)$ values for SPRs of chain length unity (see Figure 6).

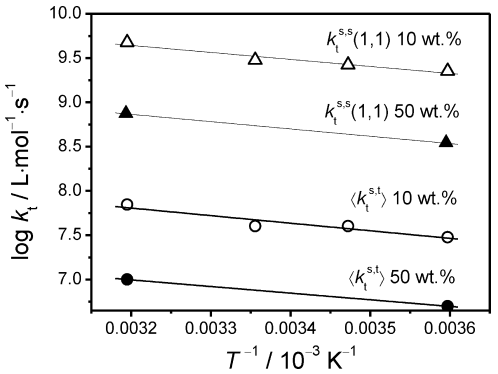


Figure 7. Rate coefficients for chain-length-independent cross-termination, $\langle k_t^{s,t} \rangle$, (circles) and rate coefficients $k_t^{s,s}(1,1)$ from Figure 6 (triangles). Filled symbols refer to 50 wt % AA and open ones to 10 wt % monomer. The straight lines represent Arrhenius fits with activation energies of $E_a(\langle k_t^{s,t} \rangle)$ = 16 and 14 kJ·mol^{-1} for 10 and 50 wt % AA, respectively.

The expressions for $\langle k_t^{s,t} \rangle$ read:

$$\langle k_t^{s,t} \rangle = 3.4 \times 10^{10} \exp(-1964/(T/\mathrm{K})) \cdot \mathrm{L} \cdot \mathrm{mol}^{-1} \cdot \mathrm{s}^{-1}$$

(10 wt % AA)

and

$$\langle k_t^{s,t} \rangle = 2.5 \times 10^{9} \exp(-1805/(T/\mathrm{K})) \cdot \mathrm{L} \cdot \mathrm{mol}^{-1} \cdot \mathrm{s}^{-1}$$

(50 wt % AA)

The experimental cross-termination rate coefficients are assumed to be accurate within ±20%. The close agreement of the activation energies of $\langle k_t^{s,t} \rangle$ and $k_t^{s,s}(1,1)$ indicates that the analysis via chain-length-independent cross-termination is reasonable and that this simplified method of analysis may be applied to the study of termination kinetics of AA in aqueous solution under conditions where both SPRs and MCRs are present. The rate coefficient $k_t^{s,s}(1,1)$ exceeds $\langle k_t^{s,t} \rangle$ by about a factor of 30, which is in the expected range. The difference will be mostly due to cross-termination occurring between larger radicals with some additional contribution from enhanced shielding with tertiary MCRs as compared to SPRs.

CONCLUSION

The SP-PLP-EPR method provides detailed kinetic insight into radical polymerization kinetics of acrylic acid in aqueous solution. This system is complicated due to two types of radicals, SPRs and MCRs, being present and due to the occurrence of strong hydrogen-bonded interactions. For nonionized acrylic acid at initial concentrations of 10 and 50 wt % AA, rate coefficients for propagation of midchain radicals, k_p^t, for backbiting of chain-end radicals, k_{bb}, and for termination of radicals of chain length unity, $k_t^{1,1}$, have been determined. All three rate coefficients are enhanced toward lower AA content, although to different extents. The increase of k_p^t occurs by the same factor as does k_p of chain-end SPR radicals. The variation of k_{bb} with AA concentration is consistent with recent findings on increased branching levels of poly(butyl acrylate) produced in a strongly interacting solvent medium, such as butanol. The termination rate coefficient $k_t^{1,1}$ of AA in dilute (10 wt %) aqueous solution is very high and approaches the maximum rate coefficient predicted for diffusion-controlled rate with almost each collision leading to reaction.

ASSOCIATED CONTENT

Supporting Information

Figures showing Arrhenius plot of viscosity and dependence of the Arrhenius pre-exponential factor and tables of rate coefficients determined via SP-PLP-EPR for acrylic acid polymerization and viscosities determined for aqueous solutions of AA. This material is available free of charge via the Internet at http://pubs.acs.org.

AUTHOR INFORMATION

Corresponding Author

*E-mail: mbuback@gwdg.de. Fax: +49 551 393144.

ACKNOWLEDGMENTS

J.B. is grateful to the *Fonds der Chemischen Industrie* for financial support. The authors acknowledge funding and stimulating discussions within an industrial collaboration with BASF SE, Ludwigshafen, Germany, as well as the scientific interaction with the groups of Professor Robin Hutchinson (Kingston, Canada) and Professor Igor Lacik (Bratislava, Slovakia).

REFERENCES

(1) Lacik, I.; Beuermann, S.; Buback, M. *Macromolecules* **2003**, *36*, 9355−9363.
(2) Cutie, S. S.; Smith, P. B.; Henton, D. E.; Staples, T. L.; Powell, C. *J. Polym. Sci. Polym. Phys.* **1997**, *35*, 2029−2047.
(3) Buback, M.; Hesse, P.; Lacik, I. *Macromol. Rapid Commun.* **2007**, *28*, 2049−2054.
(4) Lacik, I.; Beuermann, S.; Buback, M. *Macromolecules* **2001**, *34*, 6224−6228.
(5) Nikitin, A. N.; Hutchinson, R. A. *Macromolecules* **2005**, *38*, 1581−1590.
(6) Nikitin, A. N.; Castignolles, P.; Charleux, B.; Vairon, J. P. *Macromol. Rapid Commun.* **2003**, *24*, 778−782.
(7) Gilbert, B. C.; Smith, J. R. L.; Milne, E. C.; Whitwood, A. C.; Taylor, P. *J. Chem. Soc., Perkin Trans 2* **1994**, 1759−1769.
(8) Junkers, T.; Barner-Kowollik, C. *J. Polym. Sci., Polym. Chem.* **2008**, *46*, 7585−7605.
(9) Asua, J. M.; Beuermann, S.; Buback, M.; Castignolles, P.; Charleux, B.; Gilbert, R. G.; Hutchinson, R. A.; Leiza, J. R.; Nikitin, A. N.; Vairon, J. P.; van Herk, A. M. *Macromol. Chem. Phys.* **2004**, *205*, 2151−2160.
(10) Willemse, R. X. E.; van Herk, A. M.; Panchenko, E.; Junkers, T.; Buback, M. *Macromolecules* **2005**, *38*, 5098−5103.
(11) Barner-Kowollik, C.; Guenzler, F.; Junkers, T. *Macromolecules* **2008**, *41*, 8971−8973.
(12) Plessis, C.; Arzamendi, G.; Alberdi, J. M.; van Herk, A. M.; Leiza, J. R.; Asua, J. M. *Macromol. Rapid Commun.* **2003**, *24*, 173−177.
(13) Nikitin, A. N.; Hutchinson, R. A.; Buback, M.; Hesse, P. *Macromolecules* **2007**, *40*, 8631−8641.
(14) Barth, J.; Buback, M.; Hesse, P.; Sergeeva, T. *Macromolecules* **2009**, *42*, 481−488.
(15) Barth, J.; Buback, M. *Macromol. React. Eng.* **2010**, *4*, 288−301.
(16) Barth, J.; Buback, M. *Macromol. Rapid Commun.* **2009**, *30*, 1805−1811.
(17) Barth, J.; Buback, M.; Russell, G. T.; Smolne, S. *Macromol. Chem. Phys.* **2011**, *212*, 1366−1378.
(18) Buback, M.; Mueller, E.; Russell, G. T. *J. Phys. Chem. A* **2006**, *110*, 3222−3230.
(19) Buback, M.; Egorov, M.; Junkers, T.; Panchenko, E. *Macromol. Chem. Phys.* **2005**, *206*, 333−341.

(20) Buback, M.; Egorov, M.; Junkers, T.; Panchenko, E. *Macromol. Rapid Commun.* **2004**, *25*, 1004−1009.
(21) Barth, J.; Buback, M.; Hesse, P.; Sergeeva, T. *Macromolecules* **2010**, *43*, 4023−4031.
(22) Lacik, I.; Ucnova, L.; Kukuckova, S.; Buback, M.; Hesse, P.; Beuermann, S. *Macromolecules* **2009**, *42*, 7753−7761.
(23) Hesse, P. Ph.D. Thesis; University of Göttingen: Göttingen, Germany, 2008.
(24) Barth, J.; Buback, M. *Macromolecules* **2011**, *44*, 1292−1297.
(25) Smith, G. B.; Russell, G. T.; Heuts, J. P. A. *Macromol. Theory Simul.* **2003**, *12*, 299−314.
(26) Hutchinson, R. A.; Liang, K. *Macromol. Rapid Commun.* **2011**, *32*, 1090−1095.
(27) Toh, J. S. S.; Huang, D. M.; Lovell, P. A.; Gilbert, R. G. *Polymer* **2001**, *42*, 1915−1920.
(28) Busch, M. *Macromol. Theory Simul.* **2001**, *10*, 408−429.
(29) Kiparissides, C.; Verros, G.; MacGregor, J. F. *J. Macromol. Sci.—Rev. M* **1993**, *C33*, 437−527.
(30) Ganachaud, F.; Balic, R.; Monteiro, M. J.; Gilbert, R. G. *Macromolecules* **2000**, *33*, 8589−8596.
(31) Seabrook, S. A.; Tonge, M. P.; Gilbert, R. G. *J. Polym. Sci., Polym Chem.* **2005**, *43*, 1357−1368.
(32) Stach, M.; Lacik, I.; Chorvat, D.; Buback, M.; Hesse, P.; Hutchinson, R. A.; Tang, L. *Macromolecules* **2008**, *41*, 5174−5185.
(33) Beuermann, S.; Buback, M.; Hesse, P.; Lacik, I. *Macromolecules* **2006**, *39*, 184−193.
(34) Korson, L.; Drosthan., W.; Millero, F. J. *J. Phys. Chem.* **1969**, *73*, 34−39.

Macromolecules

Article

pubs.acs.org/Macromolecules

One-Pot Controlled Synthesis of Homopolymers and Diblock Copolymers Grafted Graphene Oxide Using Couplable RAFT Agents

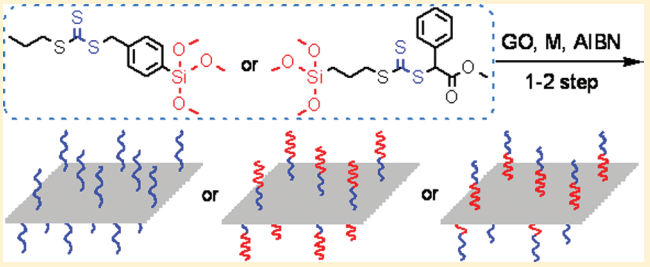
Kun Jiang,[†] Chunnuan Ye,[†] Peipei Zhang,[†] Xiaosong Wang,[‡] and Youliang Zhao[†,*]

[†]Jiangsu Key Laboratory of Advanced Functional Polymer Design and Application, Department of Polymer Science and Engineering, College of Chemistry, Chemical Engineering and Materials Science, Soochow University, Suzhou 215123, China

[‡]Department of Chemistry, University of Waterloo, 200 University Avenue West, Waterloo, Ontario, Canada N2L 3G1

Supporting Information

ABSTRACT: An original strategy is presented to synthesize homopolymers and diblock copolymers grafted graphene oxide by simultaneous coupling reaction and RAFT process. Z-functionalized *S*-methoxycarbonylphenylmethyl *S*′-3-(trimethoxysilyl)propyltrithiocarbonate (MPTT) and R-functionalized *S*-4-(trimethoxysilyl)benzyl *S*′-propyltrithiocarbonate (TBPT) were used as couplable RAFT agents to prepare the target nanocomposites. Under similar conditions, MPTT-mediated grafting reaction was liable to afford grafted chains with shorter chain length, narrower molecular weight distribution and lower grafting density than TBPT-based reaction owing to increased shielding effect and different grafting process. The grafted polymers had nearly controlled molecular weight and polydispersity ranging between 1.11 and 1.38, and the apparent molar grafting ratio was estimated to be 73.6−220 μmol/g as the molecular weights of grafted polymers were in the range of 3980−12500 g/mol. The improved solubility and dispersibility of GO−polymer composites in various solvents comprising hexane and water confirmed their amphiphilicity. The grafting process offers an opportunity to alter GO morphologies, and surface morphologies involving nanosheets, nanoparticles, and nanorods were observed as the composites were dispersed in different solvents with the aid of sonication treatment. This tandem approach is promising for surface modification of solid substrates with hydroxyl surface due to its mild conditions, straightforward synthesis and good controllability.



INTRODUCTION

Graphene is an ideal two-dimensional material with exceptional structural, chemical, and electrical properties which make it promising candidate in various fields such as microelectronics, photonic devices, composite materials and biotechniques.[1−24] Both physical and chemical modifications are utilized to increase the solubility and processability and prevent the reaggregation of graphene since it can significantly enhance the electrical, physical, mechanical, and barrier properties of polymer composites. Noncovalent routes such as $\pi-\pi$ stacking[25−30] and ionic interactions[31−34] have the advantage to maintain the structural and electrical quality of graphene-based materials, however, these structures may be unstable due to relatively weak interactions. Although the covalent modification is liable to disrupt basal plane conjugation of solid substrate, it allows for graphene oxide (GO) and graphene grafted with a variety of polymer brushes which enable multiple selective functional sites on each grafted chain and stable environments for further immobilization of functional moieties and biomolecules.

A normal route to graphene modification is to synthesize GO−polymer nanocomposites and followed by chemical or thermal reduction to fabricate polymer-tethered graphene. Surface functional groups such as hydroxyls, epoxides, and carboxylic acids are usually exploited for chemical modification of GO surface. Modification of GO nanosheets plays a vital role in tailoring the structure and properties of GO and improving the solubility and compatibility of GO sheets in polymer systems. Surface functionalization of GO also enables synthesis of novel GO−polymer nanocomposites with enhanced functionalities and properties such as improved thermal and mechanical properties.[1−24]

Stable polymer brushes with different shapes, dimensions, polymer architectures, and chemical functionalities can be prepared on substrate surface via numerous approaches. Until now, graphene and GO grafted with various functional polymers have been achieved by a variety of methods such as in situ polymerization,[35−42] coupling reaction,[43−50] ultrasonic irradiation,[51] photopolymerization,[52] and surface-initiated controlled radical polymerization (SI-CRP) such as atom transfer radical polymerization (ATRP)[53−59] and reversible addition−fragmentation chain transfer (RAFT)[60−62] polymerization. These methods have advantages and limitations. For instance, in situ polymerization, ultrasonic irradiation and photo-

Received: November 17, 2011
Revised: January 3, 2012
Published: January 20, 2012

ACS Publications © 2012 American Chemical Society

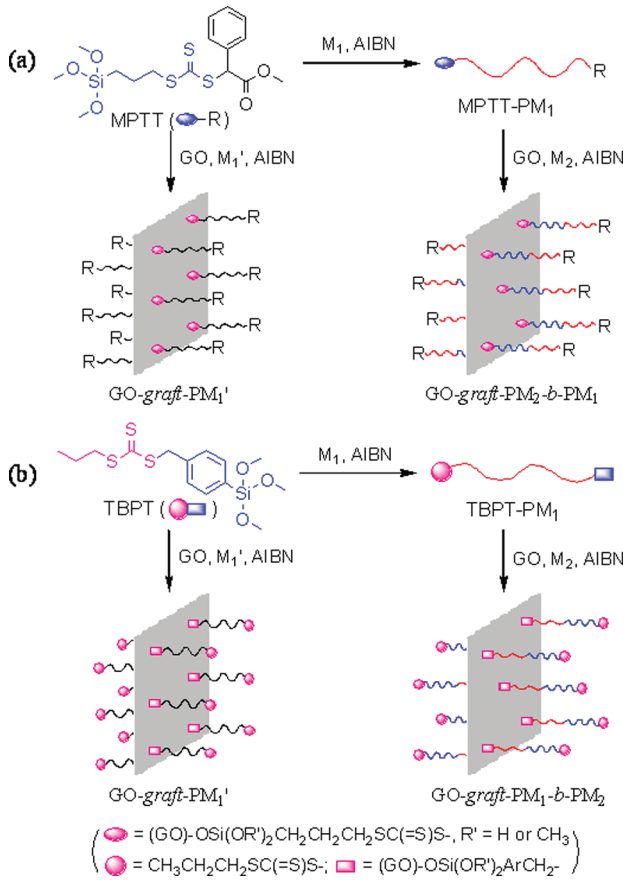
dx.doi.org/10.1021/ma2024655 | *Macromolecules* 2012, 45, 1346−1355

polymerization were easily utilized for surface modification, however, the controllability over molecular weight and polydispersity was usually poor if "living"/controlled polymerization was not used for the grafting process. Coupling reactions using as-prepared polymers afforded well-defined polymers grafted solid substrates, however, multistep syntheses were usually necessary, and the grafting density may be relatively low due to serious steric hindrance. SI-CRP techniques were liable to grow grafted polymers on solid surface with controlled functionality and adjustable grafting thickness and density, however, suitable initiators or RAFT agents should be coupled to substrate surface in advance.[63] Generally, these methods can be classified into "grafting to" and "grafting from" approaches. The former could afford well-defined homopolymers and block copolymers grafted substrate with relatively low grafting density, while the latter provided hybrid samples with high grafting density and rough control over composition and architecture although the structural defects of the tethered polymeric chains resulting from side reaction such as diradical termination and irreversible chain transfer were usually unavoidable.[64] In addition to these methods, one-pot approach such as simultaneous RAFT polymerization and click reaction was also efficiently used to synthesize silica particles grafted with polymers.[65−67] The tandem approach has significant advantages over "grafting to" and "grafting from" approaches due to saved labor, time and cost and broad applicability and is thus more promising for surface modification. So far, the examples based on the tandem approach remain limited,[65−67] thus it is very important to explore the possibility to generalize such method to surface functionalization of other substrates.

In this article, we report on the use of alkoxysilane-functionalized RAFT agents[68−73] for surface modification of GO, and homopolymers and diblock copolymers grafted GO was obtained by tandem approach comprising simultaneous hydroxyl−alkoxysilane coupling reaction and RAFT process (Scheme 1). Two kinds of RAFT agents, namely, Z-functionalized *S*-methoxycarbonylphenylmethyl *S*′-3-(trimethoxysilyl)propyltrithiocarbonate (MPTT) and R-functionalized *S*-4-(trimethoxysilyl)benzyl *S*′-propyltrithiocarbonate (TBPT), were synthesized and utilized for the synthesis of target nanocomposites. Effects of reaction processes on controllability and grafting density were investigated. The resultant GO−polymer nanocomposites were characterized by IR, Raman, XPS, TGA, SEM, and TEM, and the grafted chains were cleaved from the substrate surface to perform GPC analysis.

The purpose and novelty of this study mainly lie in three aspects. First, the tandem reaction via simultaneous RAFT process and coupling reaction was chosen to synthesize GO grafted with homopolymers and block copolymers since it required minimum steps while remained satisfactory controllability,[64−67] and a series of composites were prepared to confirm the versatility and generality of this approach. Second, the grafting density of GO−polymer composites could be adjusted by control over reaction conditions and utilization of different types of RAFT agents, and better-defined diblock copolymers with reverse sequences were tethered to the substrate surface using Z- or R-alkoxysilane-functionalized macro chain transfer agents. Last, the resultant GO−polymer composites were dispersed in a wide range of solvents with the aid of sonication treatment, and effects of solvents and grafted polymers on the apparent morphology of composites were

Scheme 1. Synthesis of Homopolymers and Diblock Copolymers Grafted GO by MPTT (a) and TBPT (b) Mediated RAFT Process and Coupling Reaction



investigated. Our preliminary results indicated that the surface modification afforded the opportunity to alter GO morphologies, and some interesting surface morphologies such as nanorods and nanoparticles could be obtained under certain conditions. To the best of our knowledge, synthesis of better-defined polymers grafted GO via a single step reaction has not been reported in literature thus far although it is of great importance. The success of this research further paves way for surface modification of GO and graphene with more complex macromolecular architectures such as polymer brushes comprising segments of functional block copolymers, V- and Y-shaped copolymers.

EXPERIMENTAL SECTION

Materials. All solvents, monomers, and other chemicals were purchased from Alfa Aesar unless otherwise stated. Graphene oxide (GO) was synthesized from natural graphite powder (40 μm in size, Qingdao Henglide Graphite Co., Ltd.) using a modified Hummers method.[74] *S*-methoxycarbonylphenylmethyl *S*′-3-(trimethoxysilyl)-propyltrithiocarbonate (MPTT) was synthesized and purified according to our previous method.[68] 3-(Mercaptopropyl)-trimethoxysilane (95%) was purchased from Lancaster. 4-(Chloromethyl)phenyltrimethoxysilane (95%) was purchased from ABCR GmbH & Co. KG, Germany. Methyl acrylate (MA, 99%), *tert*-butyl acrylate (*t*BA, 98%), *N*,*N*-dimethylacrylamide (DMA, 99%), *N*-acrylomorpholine (NAM, 97%), and styrene (St, 99%) were passed through a basic alumina column to remove the inhibitor before use. *N*-Isopropylacrylamide (NIPAM, 97%) was recrystallized twice from mixtures of hexane and toluene. 2,2′-Azobis(isobutyronitrile) (AIBN) was recrystallized twice from ethanol. *N*,*N*-Dimethyl formamide

dx.doi.org/10.1021/ma2024655 | *Macromolecules* 2012, 45, 1346−1355

(DMF) was dried over anhydrous $MgSO_4$ and distilled under reduced pressure. Other solvents with analytical grade were obtained from Sinopharm Chemical Reagent Co., Ltd., and used as received.

Synthesis of TBPT. To a stirred solution of 1-propanethiol (98%, 2.33 g, 30 mmol) in 50 mL of anhydrous methanol was added dropwise a solution of sodium methoxide in methanol (25 wt %, 6.48 g, 30 mmol) under nitrogen. CS_2 (3.05 g, 40 mmol) was added dropwise to the solution after 30 min, and the mixture was further stirred at ambient temperature for 5 h. To the yellow solution was added 4-(chloromethyl)phenyltrimethoxysilane (95%, 7.80 g, 30 mmol), and the mixture was stirred overnight under nitrogen. The mixture was concentrated, diluted with dichloromethane, filtered off, and concentrated under reduced pressure until constant weight. *S*-(4-Trimethoxysilyl)benzyl *S*′-propyltrithiocarbonate (TBPT, 10.9 g, 30 mmol) was obtained as an orange oil and used without further purification. ^{1}H NMR ($CDCl_3$): δ 7.59 and 7.38 (dd, *J* 8.0, 4H, ArH), 4.61 (s, 2H, CH_2), 3.62 (s, 9H, CH_3O), 3.35 (t, *J* 7.2, 2H, CH_2), 1.74 (m, 2H, CH_2), 1.02 (t, *J* 7.4, 3H, CH_3). ^{13}C NMR ($CDCl_3$): δ 223.5 (C═S), 137.7, 135.0, 128.7, 128.6 (PhC), 50.8, 41.2, 38.7, 21.6, 13.5. ESI-MS: m/z = 363.0564 $[M + H]^+$; theoretical value = 363.0573 (calcd for $C_{14}H_{23}O_3S_3Si$).

Synthesis of Couplable PSt Macro RAFT Agents. St (31.2 g, 300 mmol), MPTT (0.842 g, 2.0 mmol), and AIBN (33.0 mg, 0.20 mmol) were added to a glass tube with a magnetic stirring bar. The tube was sealed with a rubber septum, and the contents cooled with ice−water bath were degassed with bubbled nitrogen for 20 min. The polymerization was performed at 60 °C for 18 h, and then Z-functionalized MPTT-PSt (9.36 g, 27.3% of conversion) was obtained by concentration and precipitation into cold methanol. The molecular weight and polydispersity of PSt obtained by GPC were M_n(GPC) = 4820, PDI = 1.10 (theoretical value M_n(th) = 4690).

R-functionalized TBPT-PSt (M_n(GPC) = 5040, PDI = 1.27) was synthesized and purified according to a similar procedure using TBPT as a mediator.

Synthesis of GO Grafted with Homopolymers and Diblock Copolymers by Tandem Approach. In a typical run, 100 mg of GO and 12.0 mL of DMF in a glass tube was subjected to ultrasonic pulse for 30 min, and NIPAM (2.26 g, 20 mmol), MPTT (84.3 mg, 0.20 mmol), and AIBN (6.6 mg, 0.020 mmol) were then added and stirred until the monomer and initiator were completely dissolved. The tube was sealed with a rubber septum, and the contents cooled with ice−water bath were degassed with bubbled nitrogen for 20 min. The tube was subsequently immersed into an oil bath preheated to 60 °C and subjected to reaction for 30 h. The mixture was cooled down and subjected to reduced pressure distillation to remove most of DMF. About 5 mL of THF was added to dissolve free PNIPAM, the mixtures were then precipitated into diethyl ether twice, and monomer conversion (79.8%) was determined by gravimetry. The mixture was dispersed in DMF and filtrated, free PNIPAM was recovered by precipitation, and GO-*g*-PNIPAM crude product was subjected to redispersion, centrifugation and thoroughly washed with toluene and THF for at least five times. The composite was carefully collected and dried under vacuum at 60 °C until constant weight, and about 150 mg of GO-*g*-PNIPAM was obtained as black powders. Grafted PNIPAM was recovered by radical-induced addition−fragmentation process:[75−77] M_n(g) = 6070, PDI(g) = 1.18; free PNIPAM formed in solution: M_n(g) = 9300, PDI(g) = 1.15. The weight grafting ratio (G_r = $W_{\text{graft polymer}}$:W_{GO}, defined as weight ratio of grafted polymer to GO substrate in GO−polymer nanocomposite) and apparent molar grafting ratio (G_p) were determined by TGA or elemental analyses using the following equations to be G_r = 62.1% and G_p = 102 μmol/g.

$$G_r = (W_{100,\text{GO}-\text{polymer}} \times W_{600,\text{GO}}) / (W_{600,\text{GO}-\text{polymer}} \times W_{100,\text{GO}}) - 1 \quad (1)$$

$$G_r = \text{N\%} \times \text{MW}_m/(14 - \text{N\%} \times \text{MW}_m) \quad (2)$$

$$G_p = G_r/M_n(g) \quad (3)$$

where $W_{100,\text{GO}-\text{polymer}}$ and $W_{100,\text{GO}}$ are residual weight of polymer grafted GO and pristine GO at 100 °C, $W_{600,\text{GO}-\text{polymer}}$ and $W_{600,\text{GO}}$ are residual weight of polymer grafted GO and pristine GO at 600 °C, N% was the nitrogen content of GO-*g*-polymer determined by elemental analysis, M_n(g) was molecular weight of grafted polymer, and MW_m was molecular weight of DMA, NIPAM or NAM.

Other homopolymers and diblock copolymers grafted GO samples were synthesized and purified according to similar procedures, and MPTT, TBPT, MPTT-PSt, and TBPT-PSt were used as functional RAFT agents.

General Procedure to Cleave Grafted Chains from the Substrate Surface Using Large Excess of Thermal Initiators.[75−77] This method was used to degraft polymeric chains from GO surface where GO−polymer nanocomposites were prepared using MPTT or MPTT-PSt as a RAFT agent. In a typical run, GO-*g*-polymer (0.10 g) was dispersed in 10 mL of DMF with the aid of ultrasonic pulse, and then AIBN (328 mg, 2.0 mmol) was added. The mixture was stirred for 10 min, degassed with nitrogen for 20 min, and then heated at 80 °C for 6 h. After cooling, the samples were subjected to centrifugation, decanting, concentration and precipitation. The isolated polymers were used for GPC analysis.

General Procedure to Cleave Grafted Chains from the Substrate Surface Using HF. This method was used to degraft polymeric chains from GO surface where GO−polymer nanocomposites were prepared using TBPT or TBPT-PSt as a RAFT agent. In a typical run, GO-*g*-polymer (0.10 g) was added to a Teflon flask, and 10 mL of THF was added. The mixture was dispersed via ultrasonic pulse for 30 min, and then 0.5 mL of HF was added. The reaction was performed at room temperature in closed system overnight. The mixture was concentrated, redispersed in THF and centrifugated. The sample solution was collected and subjected to GPC analysis.

Characterization. The number-average molecular weight (M_n) and polydispersity (PDI) of polymer samples were measured on a Waters 150-C gel permeation chromatography equipped with three Ultrastyragel columns with 10 μm bead size at 35 °C. Their effective molecular weight ranges were 100−10 000 for Styragel HT2, 500−30 000 for Styragel HT3, and 5000−600 000 for Styragel HT4. The pore sizes are 50, 100, and 1000 nm for Styragels HT2, HT3, and HT4, respectively. THF was used as an eluent at a flow rate of 1.0 mL/min, polystyrene samples were calibrated with PSt standard samples; other samples were calibrated using PMMA standard samples. ^{1}H (400 MHz) and ^{13}C (100 MHz) NMR spectra were recorded on a Varian spectrometer at 25 °C using $CDCl_3$ as a solvent. Fourier transform infrared (FT-IR) spectra were recorded on a Perkin-Elmer 2000 spectrometer using KBr disks. Raman spectra were recorded on a LabRam confocal micro-Raman system. The exciting wavelength was 632.8 nm from an air-cooled He−Ne laser with a power of 16 mW and a spot of *ca* 3 μm on the surface. Thermal gravimetric analysis (TGA) was carried out using a Perkin-Elmer Pyris 6 TGA instrument with a heating rate of 20 °C/min under nitrogen. Scanning electron microscopy (SEM) images were carried on a Hitachi S-4700 field emission SEM system. Transmission electron microscopy (TEM) images were obtained through a Hitachi H-600 electron microscope. Dynamic light scattering (DLS) measurements were performed at 25 °C using Zetasizer Nano-ZS from Malvern Instruments equipped with a 633 nm He−Ne laser using backscattering detection. X-ray photoelectron spectroscopy (XPS) was recorded on a PHI 5000c ESCA photoelectron spectrometer. C, H, and N were determined by combustion followed by chromatographic separation and thermal conductivity detection using a Carlo Erba 1108 Elemental Analyzer. The electrospray ionization mass spectrometry (ESI-MS) was performed on a Bruker Daltonics micrOTOF mass spectrometer. The sonication treatment was performed on an ultrasonic instrument with a maximum output power of 90 W.

■ RESULTS AND DISCUSSION

For surface modification of graphene and GO, one-step reaction such as in situ polymerization or radical copolymeriza-

Table 1. Synthesis of GO Grafted with Homopolymers by Tandem Reaction[a]

run	M	% C[b]	M_n(th)[c]	M_n(f)[d]	PDI(f)[d]	M_n(g)[e]	PDI(g)[e]	G_r (%)[f]	G_p (μmol/g)[g]
1	St	28.5	6360	7120	1.17	3980	1.14	58.6	147
2	NIPAM	79.8	9440	9300	1.15	6070	1.18	62.1	102
3	DMA	78.7	8220	8500	1.17	5660	1.16	59.4	105
4	NAM	78.8	11500	11900	1.12	7550	1.12	69.9	92.6
5	MA	82.9	7560	8600	1.16	6120	1.15	66.1	108
6	*t*BA	86.3	11500	11600	1.15	7240	1.19	68.6	94.8
7	St	29.8	6570	6650	1.30	5860	1.33	129	220
8	NIPAM	82.4	9670	10300	1.25	9680	1.24	158	163
9	DMA	80.6	8350	8560	1.24	8020	1.26	139	173
10	NAM	81.2	11800	10900	1.21	10500	1.24	148	141
11	MA	84.5	7640	8970	1.22	8630	1.26	157	182
12	*t*BA	88.6	11700	12200	1.24	11200	1.25	145	129

[a]Reaction conditions: $[M]_0$:$[CTA]_0$:$[AIBN]_0$ = 200:1:0.2 (runs 1 and 7) or 100:1:0.2 (other runs), $[M]_0$ = 1.5 mol/L, $[CTA]_0$:W_{GO} = 2.0 mmol/g, CTA = MPTT (runs 1−6) or TBPT (runs 7−12), in DMF at 60 °C for 30 h. [b]Monomer conversion determined by gravimetry. [c]Theoretically calculated molecular weight. [d]Molecular weight and polydispersity of free polymers. [e]Molecular weight and polydispersity of grafted polymers obtained by aminolysis (runs 1−6) or HF-based decoupling reaction (runs 7−12). [f]Weight grafting ratio. [g]Apparent molar grafting ratio.

tion reported to date generally lacks good controllability although it is facile,[35−42] and CRP techniques require multistep syntheses although they usually have satisfactory controllability over molecular weight, polydispersity and grafting density. The latter usually requires step by step reactions in which functional initiators or RAFT agents are tethered to the substrate surface via linkage chemistry.[53−62] Thus, the development of facile methods to fabricate the target composites with minimal reaction steps and similar controllability is very urgent. In this study, alkoxysilane-functionalized RAFT agents MPTT (Z-functionalized) and TBPT (R-functionalized) were used to synthesize homopolymers and diblock copolymers grafted GO via one-pot reaction. The tandem approach based on simultaneous hydroxyl-alkoxysilane coupling reaction and RAFT polymerization was a straightforward synthetic route with minimum steps for surface modification, in which the functional RAFT agents acted as both coupling and RAFT agents during graft reaction. Since free RAFT agent was necessary to enhance the controllability on chain length and polydispersity, they also played a role of "sacrificial" free chain transfer agent.

Synthesis of GO Grafted with Homopolymers via Tandem Approach. MPTT- and TBPT-mediated grafting reaction was performed in DMF at 60 °C for 30 h, and GO−polymer nanocomposites such as GO grafted with polystyrene (PSt), poly(*N*-isopropyl acrylamide) (PNIPAM), poly(*N*,*N*-dimethyl acrylamide) (PDMA), poly(*N*-acrylomorpholine) (PNAM), poly(methyl acrylate) (PMA), and poly(*tert*-butyl acrylate) (P*t*BA) were obtained after thorough washing and centrifugation. Monomer conversion as listed in Table 1 was determined by gravimetry, and then theoretically calculated molecular weight (M_n(th)) was obtained. Free polymers produced in solution were isolated by concentration and precipitation, and surface-tethered polymers were degrafted from the substrate surface by radical-induced addition−fragmentation reaction (for MPTT-mediated reaction)[75−77] or HF-based cleavage reaction of Si−O bond (for TBPT-mediated reaction). As can be seen, the molecular weights of free polymers were close to the expected values, both of them were different from those of grafted polymers, and the polydispersity indices (PDI) of free and grafted polymers were always comparable. These results could be ascribed to distinct reaction processes described as follows.

MPTT-mediated reaction was similar to Z-supported graft polymerization (grafting to process),[68,69,78−80] in which the chain propagation was conducted in solution other than on surface, all the side reactions remained in reaction media, and the grafting reaction could be performed only if polymeric chain radicals participated in addition−fragmentation process on substrate surface. As a comparison, typical GPC traces of free and grafted PSt samples are shown in Figure 1a. In GPC

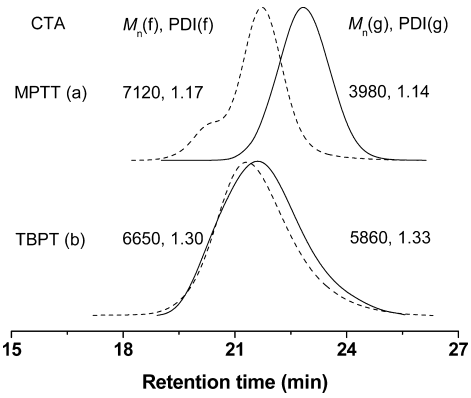


Figure 1. GPC traces of free (dashed line) and grafted (solid line) PSt samples obtained by MPTT (a) or TBPT (b) mediated one-pot grafting reaction.

traces, free MPTT-PSt exhibited significant shoulder and tailing corresponding to side reactions such as radical termination and irreversible transfer, while grafted PSt obtained by degrafting process was of symmetric distribution. The molecular weight of MPTT-PSt (M_n(f)) was significantly higher than that of grafted PSt (M_n(g)), and PDI(f) was slightly higher than PDI(g). The different molecular weights of free and grafted polymers could be ascribed to shielding effect and distinct rate of addition−fragmentation chain transfer in solution and on surface. During the tandem reaction, the shielding effect can not only slow down the polymerization rate at the surface by hindering the diffusion of monomer and polymeric chain radicals to the reactive sites, but exclude the polymeric chains with higher molecular weight from the surface to participate in the RAFT process and coupling reaction. The different rate was also liable to result in grafted chains with shorter chain length since the

dx.doi.org/10.1021/ma2024655 | *Macromolecules* 2012, 45, 1346−1355

RAFT process was usually slowed down at the surface due to heterogeneous reaction environment. The molecular weight ratio of $M_n(g)/M_n(f)$ was in the range of 0.56−0.71, and the polydispersity was typically lower than 1.2, suggesting MPTT-mediated tandem approach could afford well-defined polymers grafted GO. All the grafted chains were of reactive thiocarbonyl thio functionalities at GO surface, thus they were "living" and potentially used for the synthesis of GO grafted with diblock copolymers.

On the other hand, TBPT-mediated reaction was close to R-supported graft polymerization (grafting from process),[81−83] in which the chain propagation was conducted in solution and on surface as well, side reactions such as irreversible termination and chain transfer on substrate surface was liable to produce dead chains such as linear chains and looplike chains produced by coupling termination between surface-tethered polymeric chain radicals. Due to the presence of such dead chains, R-supported graft reaction was difficult to be further used to produce well-defined block copolymers via straightforward process. The rates of chain propagation in solution and on surface were usually close, therefore free and grafted polymers obtained by grafting from approach in the presence of sacrificial initiator or RAFT agent always possessed similar molecular weights and polydispersity indices, evident from the results as listed in runs 7−12 of Table 1. Typical GPC traces of free and grafted PSt samples are listed in Figure 1b. The molecular weight of grafted PSt was slightly lower than that of free polymer, noticeable tailing was observed in GPC traces, and grafted PSt showed broader molecular weight distribution in GPC traces, suggesting the surface graft reaction may be more complex than homogeneous polymerization in solution. The molecular weight ratio of $M_n(g)/M_n(f)$ was in the range of 0.88−0.96, indicating the chain length of free polymers was only slightly longer than that of grafted polymers. For surface-tethered polymers obtained by TBPT-mediated reaction, their molecular weights were close to theoretical values, and the polydispersity indices of grafted polymers were in the range of 1.24−1.33, suggesting TBPT-mediated tandem reaction could be also efficiently used for the synthesis of GO−polymer nanocomposites.

In Table 1, the weight grafting ratio (G_r, defined as weight ratio of grafted polymer to GO) was determined by TGA, and the apparent molar grafting ratio was estimated by equation $G_p = G_r/M_n(g)$. TGA curves of GO and polymers grafted GO obtained by TBPT-mediated grafting reaction are listed in Figure 2. For nanocomposites comprising grafted chains such as PNIPAM, PDMA and PNAM, elemental analysis results based on nitrogen content also gave G_r values similar to those calculated by TGA, and the deviation was estimated to be within ±8%, suggesting both of them could be efficiently used to determine the G_r values. By comparing results in Table 1, it can be seen that TBPT-mediated reaction could afford GO−polymer nanocomposites with higher molecular weight, broadened molecular weight distribution and increased grafting density, which was typical characteristic of graft reaction on the basis of grafting from approach. TBPT-mediated reaction was more similar to grafting from approach, in which the steric hindrance during grafting reaction was usually neglectable, and the rates of chain propagation and transfer on substrate surface were similar to those performed in solution; thus, the grafting density was relatively high. For MPTT-mediated reaction, however, the steric hindrance was usually unavoidable, the chain propagation was only conducted in solution, and the grafting reaction could happen only if addition−fragmentation chain transfer was efficiently performed on the substrate surface, therefore the grafting density was relatively low. For grafting reaction of a same monomer performed under similar conditions, the ratios of apparent molar grafting ratio of composites obtained by TBPT-mediated reaction to that originated from MPTT-mediated reaction were in the range of 1.36−1.69 even if the former could afford longer grafted chains.

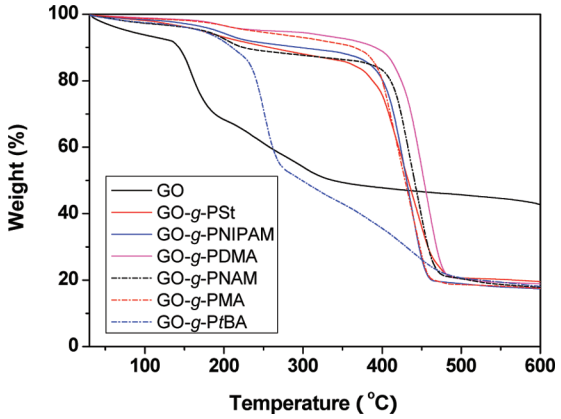


Figure 2. TGA curves of GO and polymers grafted GO obtained by TBPT-mediated grafting reaction.

Synthesis of GO Grafted with Diblock Copolymers with Reverse Sequences via Tandem Approach. The simultaneous RAFT process and coupling reaction were potentially applicable to synthesize solid substrate grafted with block copolymers with reverse sequences.[65−67] To confirm the ability to synthesize block copolymers grafted GO via one-pot method, Z- and R-functionalized macro CTAs were synthesized by RAFT polymerization mediated by MPTT or TBPT, and the resultant MPTT-PSt and TBPT-PSt were then used to mediate graft polymerization of NIPAM, MA, and *t*BA. When the reaction was performed in DMF at 60 °C for 30 h, the results are listed in Table 2. As expected, the molecular weights of free diblock copolymers were close to the theoretical values, and grafted copolymers obtained by MPTT-PSt mediated grafting reaction were usually lower than those prepared by reaction using TBPT-PSt mediator under similar conditions. The GPC traces of the resultant grafted block copolymers were completely shifted toward higher molecular weight values as compared with those of original macro CTAs, corresponding to efficient chain extension polymerization. Graft reaction mediated by MPTT-PSt afforded grafted copolymers with low polydispersity (PDI = 1.11−1.16), and no notable shoulder and tailing were observed in GPC traces (Figure 3a), suggesting well-defined diblock copolymers grafted GO were obtained by tandem approach. During MPTT-PSt mediated reaction, the resultant free diblock copolymers had enhanced polydispersity (PDI = 1.28−1.36) due to the presence of coupling termination and condensation reaction between trimethoxysilane moieties, evident from significant shoulders in GPC traces (Figure 3a). TBPT-PSt mediated reaction was liable to afford free and grafted diblock copolymers with similar polydispersity ranging between 1.32 and 1.41, and obvious shoulder and tailing were observed in GPC traces (Figure 3b), corresponding to the presence of impurities containing triblock copolymers formed by coupling termination. Meanwhile, the grafting density obtained by

dx.doi.org/10.1021/ma2024655 | *Macromolecules* 2012, 45, 1346−1355

Table 2. Synthesis of Diblock Copolymers Grafted GO by Tandem Approach Using MPTT-PSt (Runs 1−3) and TBPT-PSt (Runs 4−6) as Macro CTAs[a]

run	M	% C[b]	M_n(th)[c]	M_n(f)[d]	PDI(f)[d]	M_n(g)[e]	PDI(g)[e]	G_r (%)[f]	G_p (μmol/g)[g]
1	NIPAM	33.8	12500	12400	1.31	9830	1.16	74.9	76.2
2	MA	36.2	11800	13000	1.36	10300	1.11	79.6	77.3
3	*t*BA	34.3	13600	13300	1.28	9820	1.15	72.3	73.6
4	NIPAM	35.8	13100	13500	1.41	11900	1.38	142	119
5	MA	38.3	12400	13900	1.35	12500	1.36	155	124
6	*t*BA	36.8	14500	14200	1.33	12200	1.32	140	115

[a]Reaction conditions: $[M]_0$:[macro CTA]$_0$:[AIBN]$_0$ = 200:1:0.2, $[M]_0$ = 1.2 mol/L, $[CTA]_0$:W_{GO} = 2.0 mmol/g, macro CTAs were MPTT-PSt (runs 1−3, M_n = 4820, PDI = 1.10) or TBPT-PSt (runs 4−6, M_n = 5040, PDI = 1.27), in DMF at 60 °C for 30 h. [b]Monomer conversion. [c]Theoretical molecular weight. [d]Molecular weight and polydispersity of free polymers. [e]Molecular weight and polydispersity of grafted polymers cleaved from the substrate surface. [f]Weight grafting ratio. [g]Apparent molar grafting ratio.

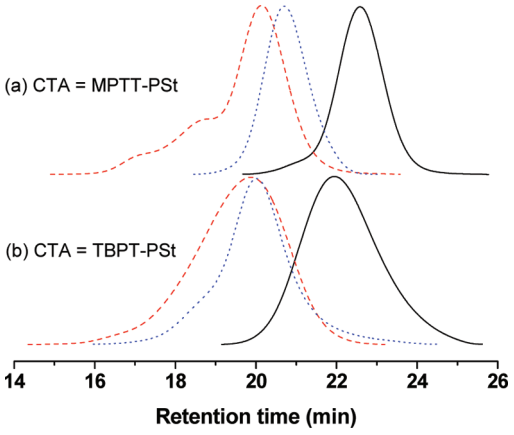


Figure 3. GPC traces of macro CTA PSt (solid line), free (dashed line), and grafted (dotted line) PSt-*b*-PMA diblock copolymers obtained by one-pot grafting reaction. PSt samples were synthesized by RAFT polymerization mediated by MPTT (a) and TBPT (b), and diblock copolymers were obtained by runs 1 and 4 of Table 2.

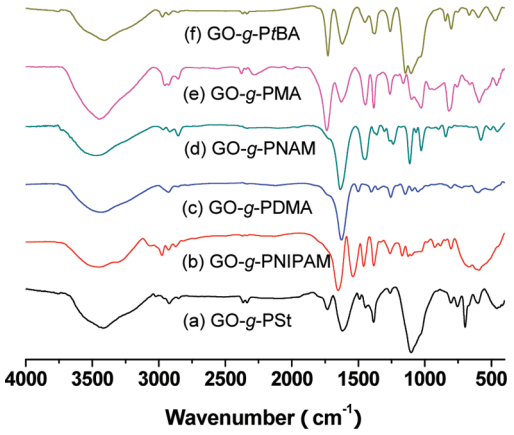


Figure 4. IR spectra of GO−polymer nanocomposites obtained by TBPT-mediated grafting reaction.

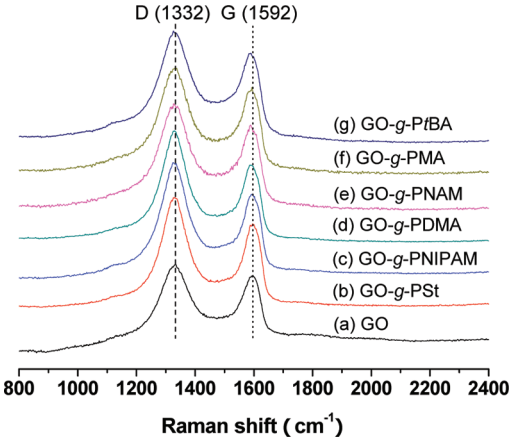


Figure 5. Raman spectra of GO (a) and various GO-*g*-polymer samples (b−g).

TBPT-PSt mediated reaction was significantly higher than that using MPTT-PSt mediator even if the grafted copolymers had longer chain length. These results demonstrated both R- and Z-functionalized macro CTAs could be efficiently used to synthesize diblock copolymers grafted GO using the versatile tandem approach, and MPTT-PSt mediated grafting reaction was liable to afford better-defined grafted copolymers at the cost of lower grafting density. These AB and BA-type diblock copolymers grafted onto GO surface are expected to exhibit different physicochemical properties due to their distinct sequence structures. In addition, functional tri- and tetrablock copolymers grafted onto GO were potentially prepared by tandem approach mediated by alkoxysilane-functionalized di- and triblock copolymers.[66,67]

Characterization of GO−Polymer Nanocomposites. Chemical structures of GO−polymer nanocomposites were confirmed by FT-IR, Raman, and XPS. In IR spectra (Figure 4), typical absorptions corresponding to characteristic groups of GO and grafted chains appeared at about 1726 ($\nu_{C=O}$, *t*BA unit, and GO sheet), 1736 ($\nu_{C=O}$, MA unit, and GO sheet), 1732 ($\nu_{C=O}$, GO sheet), 1650 ($\nu_{C=C}$ of GO sheet and $\nu_{C=O}$ of NIPAM unit), 1635 ($\nu_{C=C}$ of GO sheet and $\nu_{C=O}$ of NAM unit), 1628 ($\nu_{C=C}$ of GO sheet and $\nu_{C=O}$ of DMA unit), 1625 ($\nu_{C=C}$, St unit, and GO sheet), and 697 cm^{-1} (C−H out of plane bending, St unit). In Raman spectra (Figure 5), two representative peaks were noted at around 1332 (D band) and 1592 cm^{-1} (G band). The D/G intensity ratio increased from 1.7 (GO) to 2.0−2.5 (nanocomposite) due to increasingly disordered structures resulting from the formation of covalent bonds between GO and polymer chains.[1−20] In addition, characteristic signals for N 1s, O 1s, C 1s, S 2p, Si 2s, and Si 2p in XPS spectra also confirmed the grafted polymers were covalently tethered to GO surface. In XPS spectra of typical GO−polymer nanocomposites (Figure 6), C_{1s} peaks appeared at about 285.0 (C−C), 286.9 (C−O, C−N and C−S) and 289.0 eV (O−C═O), and other peaks corresponding to surface-tethered RAFT functional moieties were observed at about 161.8 (S 2p), 150.8 (Si 2s), and 99.8/101.5 eV (Si 2p). The silicon weight contents were determined to be 0.72% (GO-

dx.doi.org/10.1021/ma2024655 | Macromolecules 2012, 45, 1346−1355

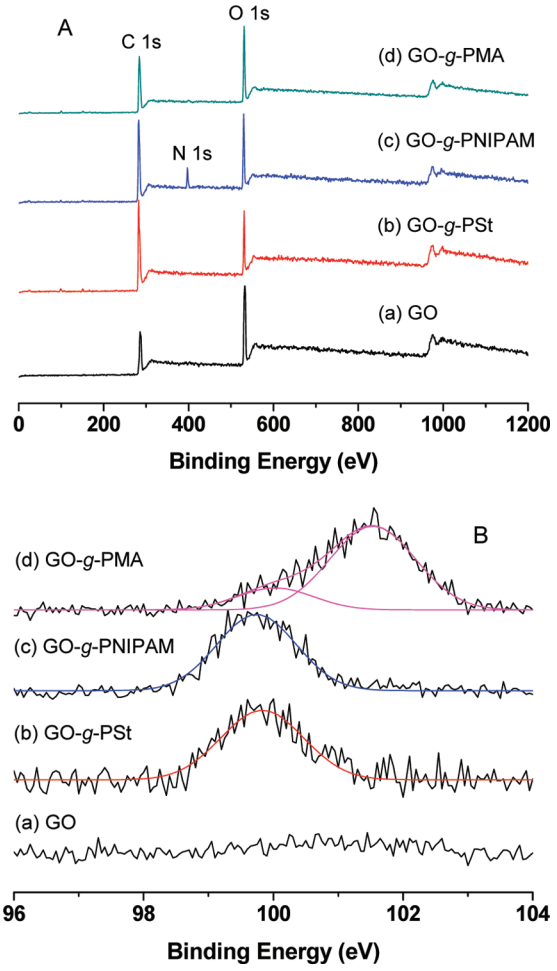


Figure 6. XPS wide-scan spectra (A) and Si 2p core-level spectra (B) of pristine GO (a) and GO grafted polymers (b–d). GO–polymer composites were synthesized by runs 7, 8, and 11 of Table 1.

g-PSt), 0.57% (GO-*g*-PNIPAM), and 0.64% (GO-*g*-PMA) by combination of XPS and elemental analyses. If all the surface-tethered RAFT agents had participated in the graft polymerization to form well-defined grafted chains, the corresponding silicon contents were estimated to be 0.27% (GO-*g*-PSt), 0.18% (GO-*g*-PNIPAM), and 0.20% (GO-*g*-PMA). The difference in silicon contents indicated that part of surface-tethered RAFT agents had not efficiently participated in the graft polymerization or only formed short grafted chains on GO surface. The weight ratio of grafted polymeric chains to GO was estimated to be in the range of 0.586–1.55 by TGA (Tables 1 and 2), and the molar grafting ratio of homopolymer and diblock copolymer grafted onto GO surface was varied between 73.6 and 220 μmol/g, suggesting about 3.7–11% of trimethoxysilane functionalities had efficiently participate in the coupling reaction to form covalently bonded grafted chains. Our study also indicated that the chemical compositions and grafting density of GO–polymer nanocomposites could be potentially adjusted by control of reaction conditions such as feed ratio, temperature, chain length and types of functionalized RAFT agents.

The resultant GO–polymer nanocomposites obtained by surface modification exhibited considerable solubility and dispersibility in a wide range of solvents, which also demonstrated the success of grafting. After sonication treatment, all the homopolymers and diblock copolymers grafted GO could be partly or completely dispersed in various solvents including hexane, toluene and water. These results indicated the composites were of more or less amphiphilicity, however, their solubility and dispersibility were usually distinct from both GO and the corresponding polymers. With the aid of sonication treatment, GO were efficiently dispersed in methanol, ethanol, THF, DMF, and water and partly dispersible in acetone, however, it could not be dispersed in hexane, toluene, and chloroform at all. Homopolymers and diblock copolymers were usually precipitated in poor solvents such as hexane and/or methanol. Because of their considerable dispersibility in a series of polar and apolar solvents, the amphiphilicity behaviors of GO–polymer composites in solvents were more like surfactants.

Table 3 lists the rough sonication time to obtain pseudo homogeneous solutions with dispersion degree close to a maximum value, after that only limited enhancement in solubility and dispersibility was observed even if much longer time was used. All the GO–polymer composites showed limited solubility lower than 50 μg/mL in hexane and had variable solubility up to 1.0 mg/mL or more in most of other solvents. For instance, with the aid of sonication treatment, GO-*g*-PSt could be completely dispersed in water within 1 h and other media in a few minutes except that it had poor dispersibility in hexane and methanol, and hydrophilic segments such as PNIPAM, PDMA, PNAM, and PAA grafted GO could be partly or completely dispersed in various solvents typically within 5–60 min. From these results, we could deduce that stable solutions were liable to form by the utilization of solvents that could dissolve the grafted chains and/or possess strong interactions with composites, in which it only took short time to form "homogeneous" solution. The resultant solutions could be stably stored at room temperature for a period of time

Table 3. Solubility and Rough Ultrasonic Time To Attain an Efficiently Dispersed Solution of GO–Polymer Nanocomposites in Various Solvents[a]

	solvent								
sample	hexane	toluene	chloroform	methanol	ethanol	acetone	THF	DMF	water
GO	>60, −	>60, −	>60, −	<5, +	<5, +	30, ±	<5, +	<5, +	20, +
GO-*g*-PSt	>60, ±	<5, +	<5, +	15, ±	<5, +	<5, +	<5, +	<5, +	60, +
GO-*g*-PNIPAM	>60, ±	30, +	40, +	30, +	30, +	15, ±	45, ±	<5, +	15, +
GO-*g*-PDMA	>60, ±	60, ±	30, +	<5, +	5, +	40, ±	30, +	<5, +	<5, +
GO-*g*-PNAM	15, ±	<5, +	50, ±	40, +	<5, +	<5, +	10, +	<5, +	<5, +
GO-*g*-PAA	60, ±	30, ±	60, ±	15, ±	15, +	15, +	<5, +	<5, +	30, +

[a]Solubility of composite in solvent: insoluble (−), partly soluble (±, with solubility less than 50 μg/mL), and completely soluble (+, with solubility higher than 50 μg/mL). GO-*g*-PAA was obtained by hydrolysis of GO-*g*-P*t*BA using trifluoroacetic acid in THF at ambient temperature.

dx.doi.org/10.1021/ma2024655 | *Macromolecules* 2012, 45, 1346–1355

(typically a few hours), and the storage time of stable solutions obtained could reach up to 1 week or longer time when DMF and 1-methyl-2-pyrrolidinone (NMP) were used as the dispersion media.

Meanwhile, we have discovered that the morphologies of GO−polymer nanocomposites are strongly dependent on the types of dispersion media because the GO−polymer nanocomposites have amphiphilicity and tend to aggregate in selective solvents. We have investigated this solution behavior using GO-*g*-PNIPAM as a typical example. DLS measurements of GO-*g*-PNIPAM in solvents such as water, methanol and ethanol were performed and compared with those of PNIPAM solutions. The results suggested that PNIPAM was molecular soluble in these solvents but GO-*g*-PNIPAM was liable to assemble into large size aggregates, and the light scattering intensities were substantially strong for the grafted samples due to the formation of self-assembled aggregates (see the Supporting Information). For the sample dispersed in DMF that is a good solvent for both GO and grafted polymers, wrinkled flakes were observed in TEM image (Figure 7a), in which the color difference between central and lateral areas may reflect the different stacking densities of grafted chains or result from stacking of single- and multilayer nanosheets with different layer numbers.[53] The distortion and deformation degree of GO nanosheet seemed lower than that of composite nanosheet (Figure 7a and Figure S10), suggesting the resultant GO−polymer composite was softer and more flexible than pristine GO. When selective solvents were used, various morphologies were observed depending on the choice of solvents. As shown in parts b and c of Figure 7, when THF and acetone were used as media, nanorods with diameter of 80−200 nm and length up to a few micrometers were observed. When methanol and chloroform were used, sphere-like aggregates with particle size in the range of 30−60 nm or larger size were noted (Figure 7, parts d and e). In addition to nanoparticles, nanosheets were also noted in Figure 7e. Other GO−polymer nanocomposites also exhibited similar solution behavior and formed various morphologies when they were dispersed in different solvents (see the Supporting Information). The observed variation in self-assembled morphologies could be ascribed to different degrees of solubility and dispersibility and changes in mode and intensity of various interactions based on van der Waals, $\pi-\pi$ stacking and hydrogen bonding between internal and external composite nanosheets in various solvents.[84] The formation of particles revealed the composites could not be efficiently unfolded in dispersion media and thus formed a collapsed morphology, the formation of flakes could be ascribed to the unfolded or layer-by-layer nanosheets similar to the original GO substrate, and the nanorods may result from curled nanosheets formed by strong internal interactions between grafted chains and GO substrate, in which the aggregates of nanoparticles and nanorods had significantly decreased surface free energies than nanosheets.

Some basic conclusions can be drawn from the above-mentioned results. First, the surface modification of GO with polymeric chains can enhance the solubility of GO in a wide range of solvents and therefore make the GO substrate more flexible. Second, sonication can induce the formation of complex aggregates such as nanorods and nanoparticles. Last, types of solvents and grafted polymers play important roles in influencing the apparent morphology of GO−polymer composites. The rich surface morphologies of the nanocomposites in various solvents possess some potential applications in smart materials and nanotechnology. Further experiments are required to give more explicit explanation on detailed process and mechanism to form nanorods and nanoparticles, and investigations on loading and release of dyes and biomolecules in these nanoobjects are under way.

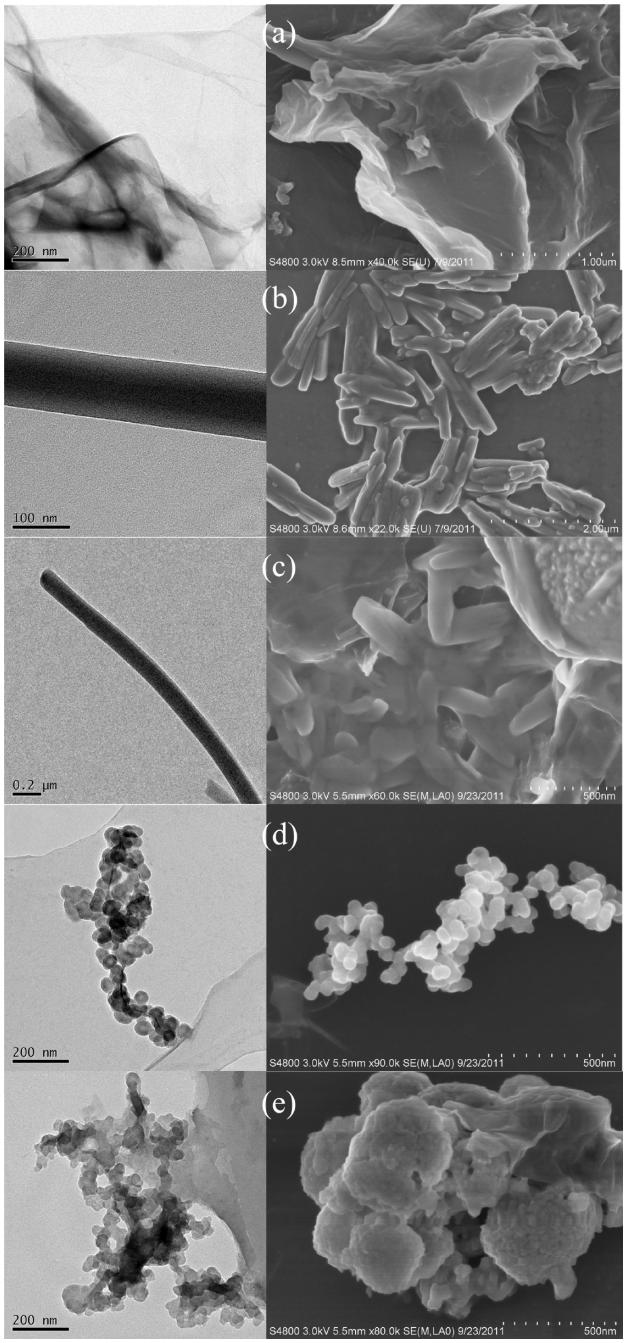


Figure 7. TEM (left) and SEM (right) images of GO-*g*-PNIPAM originally dispersed in various solvents via sonication treatment. The solvents used were DMF (a), THF (b), acetone (c), methanol (d), and chloroform (e), and the scale bar of SEM images was 500 nm (c−e), 1 μm (a) and 2 μm (b).

■ CONCLUSION

The tandem approach based on alkoxysilane-functionalized RAFT agents could be efficiently used to synthesize GO−polymer nanocomposites with nearly controlled molecular

dx.doi.org/10.1021/ma2024655 | *Macromolecules* 2012, 45, 1346−1355

weight and chemical composition, relatively low polydispersity and variable grafting density of grafted chains. Under similar conditions, simultaneous coupling reaction and RAFT process using Z-functionalized RAFT agent seemed to afford grafted chains with shorter chain length, narrower molecular weight distribution and lower grafting density than R-functionalized RAFT agent mediated reaction, which could be attributed to different grafting process and noticeable shielding effect. The resultant composites were of exfoliated morphology and enhanced solubility and dispersibility in a wide range of solvents including hexane and water. The surface modification offers an opportunity to alter GO morphologies and makes it possible to prepare GO nanoparticles. The apparent morphology of polymers grafted GO were affected by some factors such as types of solvents and grafted polymers. Some interesting surface morphologies involving nanosheets, nanoparticles and nanorods were observed in SEM and TEM images when the resultant composites were originally dispersed in various solvents with the aid of sonication treatment. Because of its mild conditions, straightforward synthesis and good controllability over molecular weight, polydispersity and grafting density, this tandem approach is of great importance for surface modification of functional solid substrates with hydroxyl surface.

■ ASSOCIATED CONTENT

Supporting Information

NMR spectra of free polymers, dependence of molar grafting ratio on chain length, photographs of GO and GO-*g*-polymer samples dispersed in various solvents, DLS curves of PNIPAM and GO-*g*-PNIPAM dissolved or dispersed in different solvents, and SEM and TEM images of GO and GO−polymer nanocomposites. This material is available free of charge via the Internet at http://pubs.acs.org.

■ AUTHOR INFORMATION

Corresponding Author

*Telephone/Fax: +86 512 65882045. E-mail: ylzhao@suda.edu.cn.

■ ACKNOWLEDGMENTS

The financial support from the National Natural Science Foundation of China (Grants 20844001, 20874067, and 21074081), the Key Project of Chinese Ministry of Education (No. 209049), the Project Funded by the Priority Academic Program Development of Jiangsu Higher Education Institutions, and Natural Science Fund for Colleges and Universities of Jiangsu Province (No. 08KJB150015) is gratefully acknowledged. The authors are grateful for helpful discussions from S. Perrier at the University of Sydney and Y. G. Yang at Soochow University.

■ REFERENCES

(1) Zhu, Y. W.; Murali, S.; Stoller, M. D.; Ganesh, K. J.; Cai, W. W.; Ferreira, P. J.; Pirkle, A.; Wallace, R. M.; Cychosz, K. A.; Thommes, M.; Su, D.; Stach, E. A.; Ruoff, R. S. *Science* **2011**, *332*, 1537−1541.
(2) Liu, M.; Yin, X. B.; Ulin-Avila, E.; Geng, B. S.; Zentgraf, T.; Ju., L.; Wang, F.; Zhang, X. *Nature* **2011**, *474*, 64−67.
(3) Li, X. L.; Wang, X. R.; Zhang, L.; Lee, S. W.; Dai, H. J. *Science* **2008**, *319*, 1229−1232.
(4) Stankovich, S.; Dikin, D. A.; Dommett, G. H. B.; Kohlhaas, K. M.; Zimney, E. J.; Stach, E. A.; Piner, R. D.; Nguyen, S. T.; Ruoff, R. S. *Nature* **2006**, *442*, 282−286.
(5) Novoselov, K.; Geim, A.; Morozov, S.; Jiang, D.; Zhang, Y.; Dubonos, S.; Grigorieva, I.; Firsov, A. *Science* **2004**, *306*, 666−669.
(6) Novoselov, K.; Geim, A.; Morozov, S.; Jiang, D.; Grigorieva, M.; Dubonos, S.; Firsov, A. *Nature* **2005**, *438*, 197−200.
(7) Zhu, Y. W.; Murali, S.; Cai, W. W.; Li, X. S.; Suk, J. W.; Potts, J. R.; Ruoff, R. S. *Adv. Mater.* **2010**, *22*, 3906−3924.
(8) Kim, H.; Abdala, A. A.; Macosko, C. W. *Macromolecules* **2010**, *43*, 6515−6530.
(9) Xu, Y. X.; Shi, G. Q. *J. Mater. Chem.* **2011**, *21*, 3311−3323.
(10) Verdejo, R.; Bernal, M. M.; Romasanta, L. J.; Lopez-Manchado, M. A. *J. Mater. Chem.* **2011**, *21*, 3301−3310.
(11) Kuilla, T.; Bhadra, S.; Yao, D. H.; Kim, N. H.; Bose, S.; Lee, J. H. *Prog. Polym. Sci.* **2010**, *35*, 1350−1375.
(12) Lee, S. H.; Lee, D. H.; Lee, W. J.; Lee, S. H.; Lee, D. H.; Lee, W. J.; Kim, S. O. *Adv. Func. Mater.* **2011**, *21*, 1338−1354.
(13) Bai, H.; Li, C.; Shi, G. Q. *Adv. Mater.* **2011**, *23*, 1089−1115.
(14) Singh, V.; Joung, D.; Zhai, L.; Das, S.; Khondaker, S. I.; Seal, S. *Prog. Mater. Sci.* **2011**, *56*, 1178−1271.
(15) Sengupta, R.; Bhattacharya, M.; Bandyopadhyay, S.; Bhowmick, A. K. *Prog. Polym. Sci.* **2011**, *36*, 638−670.
(16) Ratinac, K. R.; Yang, W. R.; Gooding, J. J.; Thordarson, P.; Braet, F. *Electroanalysis* **2011**, *23*, 803−826.
(17) Dreyer, D. R.; Park, S. J.; Bielawski, C. W.; Ruoff, R. S. *Chem. Soc. Rev.* **2010**, *39*, 228−240.
(18) Huang, L. P.; Wu, B.; Yu, G.; Liu, Y. Q. *J. Mater. Chem.* **2011**, *21*, 919−929.
(19) Cai, D. Y.; Song, M. *J. Mater. Chem.* **2010**, *20*, 7906−7915.
(20) Robinson, J. T.; Tabakman, S. M.; Liang, Y. Y.; Wang, H. L.; Casalongue, H. S.; Vink, D.; Dai, H. J. *J. Am. Chem. Soc.* **2011**, *133*, 6825−6831.
(21) Lee, S. H.; Park, J. S.; Lim, B. K.; Mo, C. B.; Lee, W. J.; Lee, J. M.; Hong, S. H.; Kim, S. O. *Soft Matter* **2009**, *5*, 2343−2346.
(22) Han, T. H.; Lee, W. J.; Lee, D. H.; Kim, J. E.; Choi, E.-Y.; Kim, S. O. *Adv. Mater.* **2010**, *22*, 2060−2064.
(23) Lee, S. H.; Kim, H. W.; Hwang, J. O.; Lee, W. J.; Kwon, J.; Bielawski, C. W.; Ruoff, R. S.; Kim, S. O. *Angew. Chem., Int. Ed.* **2010**, *49*, 10084−10088.
(24) Xu, Z.; Gao, C. *Macromolecules* **2010**, *43*, 6716−6723.
(25) Liu, J. Q.; Yang, W. R.; Tao, L.; Li, D.; Boyer, C.; Davis, T. P. *J. Polym. Sci., Part A: Polym. Chem.* **2010**, *48*, 425−433.
(26) Liu, J. Q.; Tao, L.; Yang, W. R.; Li, D.; Boyer, C.; Wuhrer, R.; Braet, F.; Davis, T. P. *Langmuir* **2010**, *26*, 10068−10075.
(27) Xu, L. Q.; Wang, L.; Zhang, B.; Lim, C. H.; Chen, Y.; Neoh, K. G.; Kang, E. T.; Fu, G. D. *Polymer* **2011**, *52*, 2376−2383.
(28) Su, Q.; Pang, S.; Alijani, V.; Li, C.; Feng, X.; Müllen, K. *Adv. Mater.* **2009**, *21*, 3191−3195.
(29) Xu, Y.; Bai, H.; Lu, G.; Li, C.; Shi, G. *J. Am. Chem. Soc.* **2008**, *130*, 5856−5857.
(30) Wang, Q. H.; Hersam, M. C. *Nat. Chem.* **2009**, *1*, 206−211.
(31) Liang, Y.; Wu, D.; Feng, X.; Müllen, K. *Adv. Mater.* **2009**, *21*, 1679−1683.
(32) Choi, E.-Y.; Han, T. H.; Hong, J.; Kim, J. E.; Lee, S. H.; Kim, H. W.; Kim, S. O. *J. Mater. Chem.* **2010**, *20*, 1907−1912.
(33) Wang, D. R.; Wang, X. G. *Langmuir* **2011**, *27*, 2007−2013.
(34) Zeng, G. H.; Xing, Y. B.; Gao, J.; Wang, Z. Q.; Zhang, X. *Langmuir* **2010**, *26*, 15022−16026.
(35) Potts, J. R.; Lee, S. H.; Alam, T. M.; An, J.; Stoller, M. D.; Piner, R. D.; Ruoff, R. S. *Carbon* **2011**, *49*, 2615−2623.
(36) Das, S.; Wajid, A. S.; Shelburne, J. L.; Liao, Y.-C.; Green, M. J. *ACS Appl. Mater. Interfaces* **2011**, *3*, 1844−1851.
(37) Wang, X.; Hu, Y.; Song, L.; Yang, H. Y.; Xing, W. Y.; Lu, H. D. *J. Mater. Chem.* **2011**, *21*, 4222−4227.
(38) Kan, L. Y.; Xu, Z.; Gao, C. *Macromolecules* **2011**, *44*, 444−452.
(39) Liu, K.; Chen, L.; Chen, Y.; Wu, J. L.; Zhang, W. Y.; Chen, F.; Fu, Q. *J. Mater. Chem.* **2011**, *21*, 8612−8617.
(40) Pramoda, K. P.; Hussain, H.; Koh, H. M.; Tan, H. R.; He, C. B. *J. Polym. Sci., Part A: Polym. Chem.* **2010**, *48*, 4262−4267.
(41) Kang, S. M.; Park, S.; Kim, D.; Park, S. Y.; Ruoff, R. S.; Lee, H. *Adv. Funct. Mater.* **2011**, *21*, 108−112.

(42) Wang, Y.; Shi, Z. X.; Fang, J. H.; Xu, H. J.; Ma, X. D.; Yin, J. *J. Mater. Chem.* **2011**, *21*, 505−512.
(43) Sun, S. T.; Wu, P. Y. *J. Mater. Chem.* **2011**, *21*, 4095−4097.
(44) Zhang, B.; Chen, Y.; Zhuang, X. D.; Liu, G.; Yu, B.; Kang, E. T.; Zhu, J. H.; Li, Y. X. *J. Polym. Sci., Part A: Polym. Chem.* **2010**, *48*, 2642−2649.
(45) Deng, Y; Li, Y. J.; Dai, J; Lang, M. D.; Huang, X. Y. *J. Polym. Sci., Part A: Polym. Chem.* **2011**, *49*, 1582−1590.
(46) Zhang, P. P.; Jiang, K.; Ye, C. N.; Zhao, Y. L. *Chem. Commun.* **2011**, *47*, 9504−9506.
(47) Vuluga, D.; Thomassin, J.-M.; Molenberg, I.; Huynen, I.; Gilbert, B.; Jérôme, C.; Alexandre, M.; Detrembleur, C. *Chem. Commun.* **2011**, *47*, 2544−2546.
(48) Cao, Y. W.; Lai, Z. L.; Feng, J. C.; Wu, P. Y. *J. Mater. Chem.* **2011**, *21*, 9271−9278.
(49) He, H. K.; Gao, C. *Chem. Mater.* **2010**, *22*, 5054−5064.
(50) Yang, X. M.; Ma, L. J.; Wang, S.; Li, Y. W.; Tu, Y. F.; Zhu, X. L. *Polymer* **2011**, *52*, 3046−3052.
(51) Xu, H. X.; Suslick, K. S. *J. Am. Chem. Soc.* **2011**, *133*, 9148−9151.
(52) Steenackers, M.; Gigler, A. M.; Zhang, N.; Deubel, F.; Seifert, M.; Hess, L. H.; Lim, C. H. Y. X.; Loh, K. P.; Garrido, J. A.; Jordan, R.; Stutzmann, M.; Sharp, I. D. *J. Am. Chem. Soc.* **2011**, *133*, 10490−10498.
(53) Fang, M.; Wang, K. G.; Lu, H. B.; Yang, Y. L.; Nutt, S. *J. Mater. Chem.* **2010**, *20*, 1982−1992 7098−7105.
(54) Lee, S. H.; Dreyer, D. R.; An, J. H.; Velamakanni, A; Piner, R. D.; Park, S.; Zhu, Y. W.; Kim, S. O.; Bielawski, C. W.; Ruoff, R. S. *Macromol. Rapid Commun.* **2010**, *31*, 281−288.
(55) Li, G. L.; Liu, G.; Li, M.; Wan, D.; Neoh, K. G.; Kang, E. T. *J. Phys. Chem. C* **2010**, *114*, 12742−12748.
(56) Gonçalves, G.; Marques, P. A. A. P.; Barros-Timmons, A.; Bdkin, I.; Singh, M. K.; Emamic, N.; Grácio, J. *J. Mater. Chem.* **2010**, *20*, 9927−9934.
(57) Yang, Y. F.; Wang, J.; Zhang, J.; Liu, J. C.; Yang, X. L.; Zhao, H. Y. *Langmuir* **2009**, *25*, 11808−11814.
(58) Iruthayaraj, J.; Chernyy, S.; Lillethorup, M.; Ceccato, M.; Røn, T.; Hinge, M.; Kingshott, P.; Besenbacher, F.; Pedersen, S. U.; Daasbjerg, K. *Langmuir* **2011**, *27*, 1070−1078.
(59) Fang, M.; Wang, K. G.; Lu, H. B.; Yang, Y. L.; Nutt, S. *J. Mater. Chem.* **2009**, *19*, 7098−7105.
(60) Zhang, B.; Chen, Y.; Xu, L. Q.; Zeng, L. J.; He, Y.; Kang, E. T.; Zhang, J. J. *J. Polym. Sci., Part A: Polym. Chem.* **2011**, *49*, 2043−2050.
(61) Etmimi, H. M.; Tonge, M. P.; Sanderson, R. D. *J. Polym. Sci., Part A: Polym. Chem.* **2011**, *49*, 1621−1632.
(62) Li, Y.; Li, X.; Dong, C. K.; Qi, J. Y.; Han, X. J. *Carbon* **2010**, *48*, 3427−3433.
(63) Barbey, R.; Lavanant, L.; Paripovic, D.; Schüwer, N.; Sugnaux, C.; Tugulu, S.; Klok, H.-A. *Chem. Rev.* **2009**, *109*, 5437−5527.
(64) *Handbook of Radical Polymerization*; Matyjaszewski, K., Davis, T. P., Eds.; Wiley: Hoboken, NJ, 2002.
(65) Ranjan, R.; Brittain, W. J. *Macromol. Rapid Commun.* **2007**, *28*, 2084−2089.
(66) Huang, Y. K.; Hou, T. T.; Cao, X. Q.; Perrier, S.; Zhao, Y. L. *Polym. Chem.* **2010**, *1*, 1615−1623.
(67) Zhao, G. D.; Zhang, P. P.; Zhang, C. B.; Zhao, Y. L. *Polym. Chem.* **2011**, DOI: 10.1039/ C1PY00396H.
(68) Zhao, Y. L.; Perrier, S. *Macromolecules* **2007**, *40*, 9116−9124.
(69) Nguyen, D. H.; Wood, M. R.; Zhao, Y. L.; Perrier, S.; Vana, P. *Macromolecules* **2008**, *41*, 7071−7078.
(70) Huang, Y. K.; Liu, Q.; Zhou, X. D.; Perrier, S.; Zhao, Y. L. *Macromolecules* **2009**, *42*, 5509−5517.
(71) Nguyen, D. H.; Vana, P. *Polym. Adv. Technol.* **2006**, *17*, 625−633.
(72) Rotzoll, R.; Vana, P. *J. Polym. Sci., Part A: Polym. Chem.* **2008**, *46*, 7656−7666.
(73) Ohno, K.; Ma, Y.; Huang, Y.; Mori, C.; Yahata, Y.; Tsujii, Y.; Maschmeyer, T.; Moraes, J.; Perrier, S. *Macromolecules* **2011**, *44*, 8944−8953.
(74) Kovtyukhova, N. I.; Ollivier, P. J.; Martin, B. R.; Mallouk, T. E.; Chizhik, S. A.; Buzaneva, E. V.; Gorchinskiy, A. D. *Chem. Mater.* **1999**, *11*, 771−778.
(75) Perrier, S.; Takolpuckdee, P.; Mars, C. A. *Macromolecules* **2005**, *38*, 6770−6774.
(76) Chen, M.; Moad, G.; Rizzardo, E. *J. Polym. Sci., Part A: Polym. Chem.* **2009**, *47*, 6704−6714.
(77) Hou, T. T.; Zhang, P. P.; Zhou, X. D.; Cao, X. Q.; Zhao, Y. L. *Chem. Commun.* **2010**, *46*, 7397−7399.
(78) Stenzel, M. H.; Davis, T. P. *J. Polym. Sci., Part A: Polym. Chem.* **2002**, *40*, 4498−4512.
(79) Hao, X. J.; Nilsson, C.; Jesberger, M.; Stenzel, M. H.; Malmström, E.; Davis, T. P.; Östmark, E.; Barner-Kowollik, C. *J. Polym. Sci., Part A: Polym. Chem.* **2004**, *42*, 5877−5890.
(80) Zhao, Y. L.; Perrier, S. *Macromolecules* **2006**, *39*, 8603−8608.
(81) Tsujii, Y.; Ejaz, M.; Sato, K.; Goto, A.; Fukuda, T. *Macromolecules* **2001**, *34*, 8872−8878.
(82) Li, C. Z.; Benicewicz, B. C. *Macromolecules* **2005**, *38*, 5929−5936.
(83) Li, C. Z.; Han, J.; Ryu, C. Y.; Benicewicz, B. C. *Macromolecules* **2006**, *39*, 3175−3183.
(84) *Macromolecular Self-Assembly*; Jiang, M., Eisenberg, A., Liu, G. J., Zhang, X., Eds.; Science Press: Beijing, 2006.

Macromolecules

Article

pubs.acs.org/Macromolecules

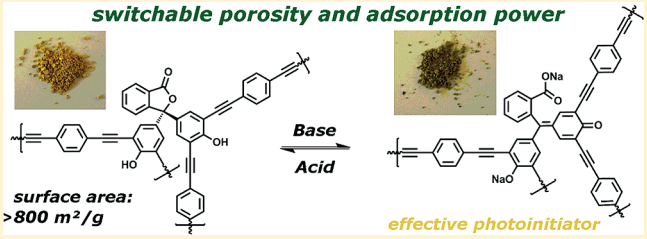
Teaching New Tricks to an Old Indicator: pH-Switchable, Photoactive Microporous Polymer Networks from Phenolphthalein with Tunable CO_2 Adsorption Power

Baris Kiskan,*,† Markus Antonietti, and Jens Weber*

Department of Colloid Chemistry, Max Planck Institute of Colloids and Interfaces, Science Park Golm, D-14424 Potsdam, Germany

Supporting Information

ABSTRACT: Switchable, organic microporous networks were synthesized by Sonogashira coupling of tetrabromophenolphthalein with 1,4-diethynylenebenzene using optimized reaction conditions. The resulting networks are microporous and have specific surface areas exceeding 800 $m^2\ g^{-1}$. The microporosity and the pore polarity are sensitive to the pH value as evidenced by nitrogen and carbon dioxide physisorption experiments. The switching between the open and closed form of the lactone ring is reversible, but some porosity is lost throughout the process. The colored, alkaline salts of these networks are photochemically active, as shown by the effective heterogeneous photosensitization of the photopolymerization of methyl methacrylate with visible light.



INTRODUCTION

Microporous polymers recently attracted a great deal of attention. Major advances have been made regarding the synthesis of various architectures, including both soluble and cross-linked polymers.[1−4] So far, stable permanent microporosity in polymers requires the use of highly rigid linkages. Consequently, most microporous polymers are based on fully aromatic, conjugated motifs (e.g., CMPs)[2,5,6] or comparable fully aromatic high-performance polymer systems (e.g., polyimides).[7−10] Such polymers were suggested for applications in various fields, e.g., gas storage, separation, and catalysis.

On top of that, there is always an interest in materials, which can change their properties by applying an external stimulus, i.e., in switchable materials. Recently, switchable microporosity has been demonstrated for molecular organic solids or metal organic frameworks,[11,12] but to the best of our knowledge there are no reports on switchable microporous polymer networks. Here we present microporous conjugated networks based on a phenolphthalein building block as the switching unit.

Phenolphthalein is a well-known, easy to synthesize indicator molecule which undergoes a structure change upon changes in pH value. A rigid, contorted molecule as such, the central carbon atom switches from a sp^3 hybridization in neutral state to a sp^2 state at high pH, going along with the formation of a more polar quinonic structure giving rise to the well-known color change from transparent to red. At high pH, the lacton ring in the phenolphthalein is opened and forms a salt. Additionally, one of the phenol groups is transformed into a phenate. The ease of access and the contorted nature were employed before by using phenolphthalein ethers as model glass builders[13] or for high gas permeation membrane polymers.[14] In those both cases, modification however involves the phenol groups, which irreversibly blocks the molecule in the nonconjugated lactone structure.

This is why it is intended to incorporate the phenolphthalein tectons keeping the phenol groups intact. We then expect the network structure to be switchable with pH, while the micropore morphology and polarity should be sensitive toward the conformation change of the central building unit. Furthermore, using bases with different counterion size (e.g., Li^+ vs Cs^+) should result in a further fine-tuning of the pore size and the pore volume as well as in the introduction of potential gas selectivities.

MATERIALS AND METHODS

Materials. All the chemicals and solvents were obtained from Sigma-Aldrich and used as received. Anhydrous grade *N,N*-dimethylformamide, triethylamine, and diisoproylamine were used throughout (Sigma-Aldrich). All chemicals used had a purity of 97% or greater.

Methods. *Gas Sorption Analysis.* Polymer surface areas and pore size distributions were measured by nitrogen adsorption and desorption at 77.3 K using Autosorb 1MP Instrument (Quantachrome Instruments). Carbon dioxide sorption isotherms were collected at 273 K using the same device. High purity gases were used. Data evaluation was performed using the AS1Win Software from Quantachrome Instruments. Pore size distributions and pore volumes were derived from the adsorption branches of the isotherms using the quenched solid density functional theory (QSDFT, N_2, assuming carbon adsorbent with slit pores) or the grand canonical Monte Carlo (GCMC) method (CO_2, assuming carbon adsorbent with slit pores). Samples were degassed at 105 °C for 24 h under high vacuum before

Received: December 9, 2011
Revised: January 23, 2012
Published: January 31, 2012

 © 2012 American Chemical Society

analysis. CO_2 heats of sorption were calculated from isotherms obtained at 273 and 283 K using the AS1Win software.

Spectroscopy. FT-IR spectra were collected in attenuated total reflection (ATR) mode on a Thermo Nicolet FT-IR Nexus 470. ^{13}C CP-MAS NMR experiments were acquired on a Bruker DMX 300WB (7 T) spectrometer using a 4 mm zirconia rotors spinning at the MAS frequency of ν_{MAS} = 11 kHz. Cross-polarization transfers were performed using adiabatic tangential ramps, the contact time was t_{CP} = 3 ms, recycle delay was 3 s, and Spinal64 decoupling was applied during signal acquisition. The FIDs were subjected to an exponential multiplication (EM) function with a line broadening value of 40 Hz prior to Fourier transform (collected by Simone Mascotto at Materials Chemistry Group, Dipartimento di Ingegneria dei Materiali e Tecnologie Industriali, Via Mesiano 77, 38123 Trento, Italy).

Scanning electron microscopy (SEM) was undertaken using a Gemini 1550 (LEO, Zeiss AG). Acceleration voltage: 3 kV; working distance: 5 mm. Samples were coated with a thin layer of Pd/C before investigation.

Molecular Modeling. Geometry optimizations were undertaken using Gaussian 03W.[15] Models of the central motif were optimized using the DFT calculations (B3LYP/6-31G). Frequency calculations were undertaken to ensure that the obtained structures are minimum structures. UV−vis spectra were calculated using the SWizard Program (S.I. Gorelsky, SWizard program) to analyze the output of the TD calculations performed using Gaussian 03. Typical input files are given in the Supporting Information.

Synthesis of Phenolphthalein-Based Networks. All of the networks were synthesized by Sonogashira−Hagihara cross-coupling condensation reaction of aryl halides and arylethynylenes. In a typical procedure, 3′,3″,5′,5″-tetrabromophenolphthalein (600 mg, 1 mmol), 1,4-diethynylbenzene (360 mg, 2.8 mmol), tetrakis-(triphenylphosphine)palladium(0) (40 mg, 0.035 mmol), and copper-(I) iodide (20 mg, 0.1 mmol) were placed in a dry 25 mL Schlenk tube. The solids were dissolved in a mixture of anhydrous *N*,*N*-dimethylformamide (DMF) (5 mL) and anhydrous diisopropylamine (DIA) (5 mL). The content was degassed by the freeze−thaw method and backfilled with argon gas three times before closing the tube. Then the tube was placed in oil bath at 90 °C and stirred for 5 days. The solid product was then collected by filtration and washed well with DMF, acetone, THF, and methanol before undergoing Soxhlet extraction with methanol for 16 h. The products were then placed in 1,4-dioxane for solvent exchange, and after three extractions all the content was freeze-dried and finally vacuum-dried at 40 °C to give insoluble yellowish solids.

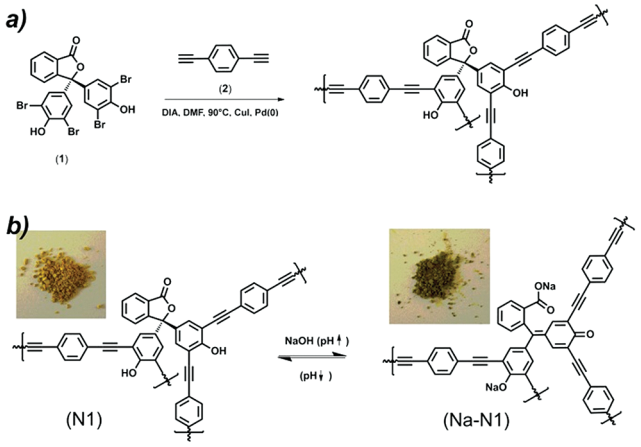
Preparation of Network Salts. All the network salts are prepared in 1 M of the corresponding methanol−water (v/v, 1:1) solutions of LiOH, NaOH, KOH, and CsOH. The solid networks treated with those solutions for 24 h; solid products were then collected by filtration and washed well with copious amounts of water, methanol, and 1,4-dioxane. The network salts are freezed and vacuum-dried subsequently.

Photopolymerization of MMA with Na-N1. Typical polymerization procedure: A stirred mixture of MMA (0.5 mL, 4.7 M), Na-N1 (10 mg), and triethylamine was irradiated in a photoreactor consisting of a 300 W xenon lamp equipped with a 420 nm cutoff filter and a water cooling system under an Ar atmosphere for 3 h. At the end of irradiation, the bulk solid was dissolved in THF, filtered, and precipitated in methanol. The collected polymers were dried under vacuum at 40 °C. Conversion: 45−82%. M_n: typically around 140 000 g mol^{-1} (GPC, eluent: THF, against PMMA standards)

RESULTS AND DISCUSSION

Network Synthesis and Switching. The synthesis of the networks starts from the commercial tetrabromo derivative (**1**). Sonogashira coupling with 1,4-diethynylbenzene (**2**) yields the microporous network (see Scheme 1). Initial experiments were undertaken following the conditions described by Cooper and co-workers.[16] The resulting networks had apparent specific surface areas (BET model) of S_{BET} = 275 m^2 g^{-1}. Changing the used base from triethylamine (TEA) to diisoproylamine (DIA), however, resulted in an increase of the maximum specific surface areas up to 813 m^2 g^{-1}. This effect was also observed for the synthesis of plain CMP-1,[17] and we consequently do not regard it as a special feature of the chosen monomer system. We suspect that this increase is due to altered solvent structures and conditions (the base makes up half of the used solvent volume),[16] thus creating some type of solvent template effect, or due to a more effective cross-coupling (DIA is typically used for Sonogashira cross-couplings in organic chemistry instead of TEA). As DIA resulted in networks of higher porosity, we restricted ourselves to its use for the rest of the study.

Scheme 1. Synthesis Pathway and pH Switch of Phenolphthalein Networks[a]



[a](a) Synthetic pathway toward phenolphthalein networks; (b) structure of network N1 and the corresponding sodium salt form Na-N1,

In order to study the switching upon pH with sufficient precision, we synthesized a single large batch of the parent network (N1), from which all switching experiments were undertaken. We are confident that this allows direct comparability of the samples.

Treatment of the network N1 with alkali bases (LiOH, NaOH, KOH, and CsOH) in methanol−water mixture (v/v, 1:1) resulted in the formation of structurally switched networks (Scheme 1b, Li-N1, K-N1, etc.). After isolation of the switched networks by filtration, their identity was confirmed by spectroscopy (FTIR, solid-state CP-MAS ^{13}C NMR). Furthermore, the color of the materials changed from yellow-orange in the lactone form to dark yellow-greenish in the salt form. This color change is very well-known from phenolphthalein derivatives and indicates already a successful transformation.

On a macroscopic scale, almost no changes in the network morphology were observed as evidenced by SEM (Figure 1). Upon freeze-drying, an open, spongelike network structure is observed, having its origin most probable in the polymerization induced phase separation. The networks feature macroporosity, which is in accordance with the nitrogen porosimetry measurements (see below). Such an open structure is beneficial for applications, which demand high mass transport, as for example catalysis. SEM analysis was also helpful in to exclude the presence of excess base. If excess base is present, it forms crystallites upon drying, which can be clearly identified (not shown). The absence of these crystallites indicates sufficient purification.

dx.doi.org/10.1021/ma202675v | *Macromolecules* 2012, 45, 1356−1361

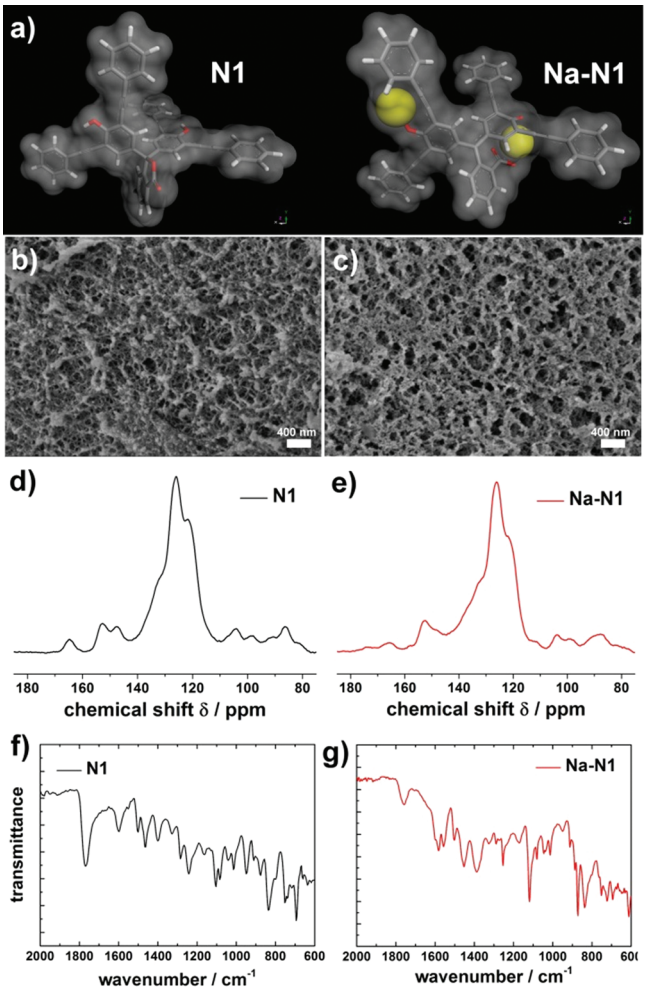


Figure 1. 3D model of the optimized geometry of the central network motif in neutral form (a, N1) and in salt form (b, Na-N1); SEM micrograph of freeze-dried N1 (b) and freeze-dried Na-N1 (c); solid-state CP-MAS ^{13}C NMR spectra of N1 (d) and Na-N1 (e); ATR-FTIR spectra of N1 (f) and Na-N1 (g).

The switch process was also analyzed on a molecular scale using spectroscopy. FTIR analysis showed a strong decrease and a slight shift of the C═O band of the lacton ring at 1774 to 1758 cm^{-1}. The band at 1600 cm^{-1} shifts to 1572 cm^{-1}; moreover, the appearance of new bands at 1553 cm^{-1} that could be attributed to carboxylate and/or conjugated C═O groups are evidence of successful transformation (Figure 1). The switch is reversible, and after switching back by acid treatment, the bands at 1758, 1572 cm^{-1} shift back to 1775, 1602 cm^{-1} and the new band at 1553 cm^{-1} disappears (see Figure S1).

Solid-state NMR could also be used to prove the change of the chemical structure. The formation of carboxylate is evidenced by the appearance of a weak peak at 174 ppm, while the intensities of peaks at 91, 147, and 169 ppm decrease due to the ring-opening of the lactone (Figure 1).

Porosity Analysis. Porosity analysis of the parent network N1 was undertaken by gas sorption analysis (N_2 at 77.3 K and CO_2 at 273 K).[18] The apparent specific surface area was found to be S_{BET} = 813 m^2 g^{-1}. The isotherm was of type I shape, indicating predominantly microporosity. At high relative pressures, we found a large additional N_2 uptake, which can be related to condensation in the macropores of the network.

Additional CO_2 sorption experiments confirmed the presence of microporosity. By comparison of the pore size distributions (PSD) obtained from CO_2 and N_2 isotherms, it is possible to estimate the predominant pore sizes. We found ultramicropores (pore diameters ~0.6 nm, from CO_2 data, see Figure S3) as well as larger pores (mean diameter ~1.1−1.3 nm, from N_2 data, see Figure 2 and Figure S3). As CO_2 at 273 K can only

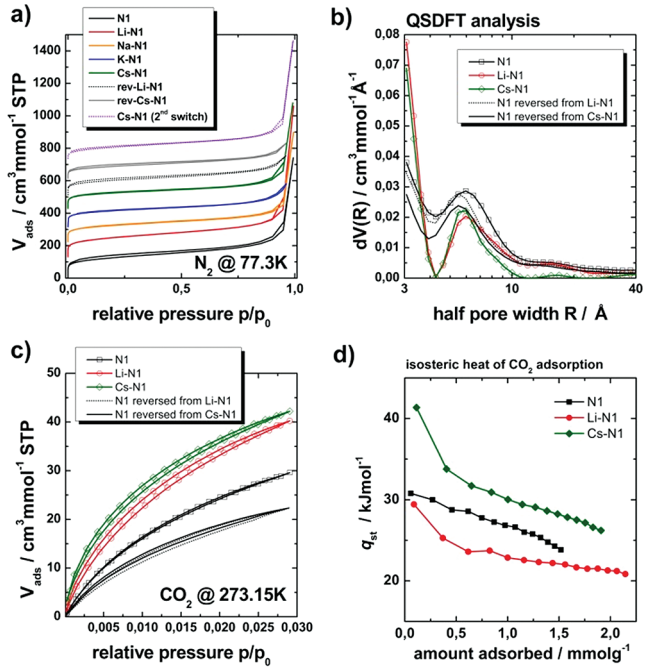


Figure 2. (a) N_2 adsorption/desorption isotherms of N1, its salt forms and networks after multiple switches, data obtained at 77.3 K, isotherms are vertically offset by 100 m^2 $mmol^{-1}$ STP for better visibility, (b) PSD of selected samples as obtained from QSDFT analysis (carbon slit pores) of the N_2physisorption isotherms, (c) CO_2 adsorption/desorption isotherms of selected samples, obtained at 273.15 K, (d) isosteric heat of CO_2 adsorption for N1, Li-N1, and Cs-N1, obtained from CO_2 adsorption isotherms at 273 and 283 K as a function of CO_2 loading.

probe ultramicropores, analysis of the N_2 adsorption isotherm resulted in higher specific surface areas compared to the results of the CO_2 analysis, the difference being due to the presence of larger micropores.

Porosity analysis of the switched polymers was again performed by N_2 and CO_2 gas adsorption/desorption (Figure 2 and Figure S3). Table 1 summarizes all data, and Figure 2 shows representative N_2 and CO_2 physisorption isotherms obtained at 77 and 273 K, respectively. In the following, we will discuss porosity parameters normalized with regard to the molecular weight of the repeating unit, i.e., surface areas are given in m^2 $mmol^{-1}$ instead of m^2 g^{-1}. Doing so, we reduce the problem of the high specific weight of the Cs^+ ion when comparing the different materials.

All salt forms show a pronounced microporosity as indicated by their N_2 adsorption behavior. Interestingly, the material Li-N1 showed a higher surface area compared to its parental network (please note that 813 m^2 g^{-1} correspond to 457 m^2 $mmol^{-1}$). The incorporation of the large Cs^+ ions also did not reduce the molar surface area. The subtle differences between the materials become visible in the CO_2 sorption. Both Cs-N1 and Li-N1 show a higher CO_2 uptake, as compared to N1. This

dx.doi.org/10.1021/ma202675v | Macromolecules 2012, 45, 1356−1361

Table 1. Porosity Parameters of the Materials

sample	S_{QSDFT} [a] (m^2 $mmol^{-1}$)	S_{BET} [b] (m^2 $mmol^{-1}$)	S_{CO_2} [b,c] (m^2 $mmol^{-1}$)	V_{micro} [b,d] (cm^3 $mmol^{-1}$)
N1	480	457	309	0.174
Li-N1	551	545	416	0.210
Na-N1	483	451	398	0.176
K-N1	401	416	n.d.	0.164
Cs-N1	467	458	429	0.180
revLi-N1	388	371	256	0.142
revCs-N1	344	321	240	0.122
Cs-N1 (2nd)	393	378	351	0.178

[a]Cumulative surface area of pores smaller 25 nm obtained from the QSDFT (quenched solid density functional theory) method. [b]Used pressure range: $0.03 < p/p_0 < 0.1$, normalized by molecular weight of the repeating unit. [c]GCMC (grand canonical Monte Carlo) model. [d]Determined from N_2 uptake at $p/p_0 = 0.1$; n.d. = not determined.

indicates that the switching mainly affects the very local structure and the related microporosity. This is also seen in the PSD, where the fraction of larger pores is diminished in the case of the salts (see Figure 2 and Figure S3).

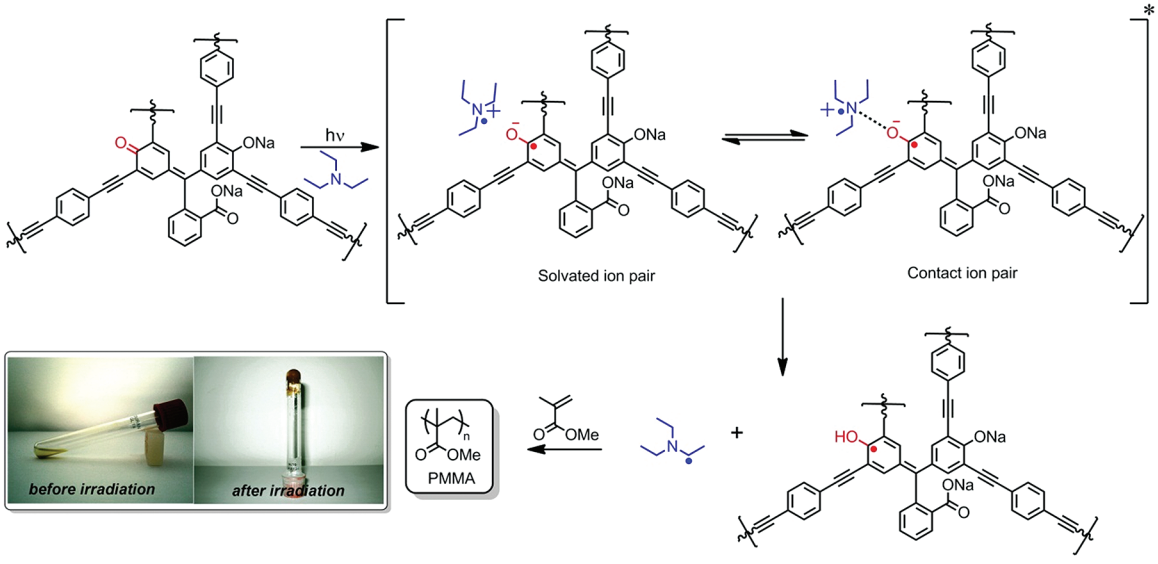
After analysis of the salt form, the samples Li-N1 and Cs-N1 were treated with aqueous HCl in order to induce the switch back to N1 (named reversed Li-N1 and reversed Cs-N1). Porosity analysis indicated that the switch back is not fully reversible as the achieved surface areas were approximately 20–25% lower than that of the original network. It is however interesting to note that the pore character was successfully switched back, as judged from the pore size distribution and the difference between the surface areas obtained from CO_2 and N_2 sorption. The fraction of large pores which were present in the parent network did reappear (Figure 2). This indicates that the structural changes induced by opening of the lacton ring and by the change of the hybridization state of the central C atom are indeed responsible for the observed differences in pore size.[19] We modeled the central motif of the polymer network (Figure 1) in the neutral and the salt form. Geometry optimization was performed using Gaussian 03 software (B3LYP/6-31G method). Frequency calculations indicated that the shown structures are indeed ground states. From the graphical representation it is obvious that rather large deformations of the polymer network must occur upon switching pH, and we speculate that these deformations may result in some irreversible changes of the network morphology as observed experimentally.

In order to see how much porosity is lost in each cycle, we switched the reversed network again to its Cs^+ form (noted as Cs-N1 (second switch)) and measured the porosity. We found that again some porosity is lost while again the pore size distribution and character was kept upon switching (higher CO_2 uptake compared to revCs-N1).

To conclude the section on porosity analysis, we shortly discuss the energetics of the CO_2 adsorption process. The isosteric heats of sorption q_{st} (i.e., a measure of the interaction strength between the polymer and CO_2 on a molecular level) were determined for N1, Li-N1, and Cs-N1 from CO_2 adsorption isotherms captured at 273 and 283 K (Figure 2). All materials show a decrease of q_{st} with increasing loading, which is commonly observed for microporous materials, as high energy adsorption sites are covered first. Interestingly, q_{st} at 1 mmol g^{-1} loading followed the order Li-N1 (23 kJ mol^{-1}) < N1 (26.8 kJ mol^{-1}) < Cs-N1 (30 kJ mol^{-1}), which implies that the interaction strength can be lowered or increased by switching of N1. This result is in agreement with reports on cation-modified zeolites, where higher interaction strength was also found for Cs^+-modified materials compared to Li^+ and partly related to a coupling to the framework.[20,21] The modification is not only described by the nature of the introduced cations, but it also induces a change in the basicity of the anions (carboxylates, hydroxylates) located at the polymer backbone. This can be interpreted as a tunable micropore polarity, a concept which might be important not only for gas sorption but also for catalytic applications.

Photocatalytic Properties. As mentioned above, quantum chemical calculations were undertaken on the central motif of the networks (see Figure 1). The salt form, as all phenolphthalein derivatives, adsorbs light in the visible range

Scheme 2. Use of Phenolphthalein Networks for Photopolymerization: Assumed Photoinitiation Mechanism[a]



[a]Inset: photographs of the mixture before and after irradiation with $\lambda > 420$ nm.

dx.doi.org/10.1021/ma202675v | Macromolecules 2012, 45, 1356–1361

(see Scheme 1 and Figure S4). Being a high surface area solid at the same time, it can be potentially used as a photosensitizer. Such molecules absorb the energy of light, use it for an electron/hole separation along the structure, and transfer one of the charges to acceptor molecules, which can use it for a variety of reactions, such as initiating a polymerization. The initiation of such a photopolymerization is called type II photoinitiated polymerization.[22] Common type II initiators include aromatic ketones, xanthenes, coumarins, and many others.

In our case, Na-N1 was exemplarily investigated for its use as photoinitiator. It can act as type II photoinitiator due to its conjugated structure with a triplet excited state which reacts with hydrogen donor triethylamine (TEA) to produce first an radical cation from TEA, which can then react via proton abstraction and electron transfer to the initiating TEA-CH radical (see Scheme 2). Deactivating processes can also occur, such as monomer and oxygen quenching, etc., which compete with the formation of radicals.[23] Hence, all our experiments were performed under argon gas to prevent quenching. The reactions were performed in bulk methyl methacrylate (MMA) in the presence of TEA under irradiation with a daylight lamp equipped with a 420 nm filter. The reaction resulted in the formation of a bulk solid poly(methyl methacrylate) (PMMA) with typical conversions of ~45−80%. The PMMA could be dissolved and analyzed by size exclusion chromatography (SEC). The obtained polymer had a number-average molecular weight (M_n) of M_n = 138 000 g mol^{-1} and a polydispersity of 4.8. As the photosensitizer is of heterogeneous nature, it can be separated very easily from the reaction product by centrifugation and filtration. That way, our heterogeneous photosensitizer prevented the coloring of the polymer, which is a common problem in dye-sensitized photopolymerizations.

Cycling of the photosensitizer Na-N1 was also performed; for the second use of the Na-N1 the conversion of the photopolymerization dropped down to 25%. The resulting PMMA had a comparable molecular weight (M_n: 146 500 g mol^{-1}). The lower conversion might be due to the consumption of the ketonic species in the first polymerization. At the moment we do not know the fate of the carbon radical left at the polymeric framework. For benzophenones in solution, they undergo recombination, which is however difficult for the cross-linked polymer. Given the lower conversion in the second run, it seems plausible that the radicals saturate during the catalysis or the work-up. This question will however be dealt with in a more detailed study on the photopolymerization mechanism. So far, the lowered conversion is still comparable with most reported conversions in homogeneous visible light free radical photopolymerizations.[24]

CONCLUSIONS

To sum up, the synthesis and characterization of a switchable, conjugated microporous network based on the phenolphthalein motif were presented. It was shown that the pH sensitivity of phenolphthalein allowed the introduction of functionality into microporous polymers, i.e., a chemical benefit above mere surface area and porosity. The networks change their porosity with regard to pH due to the well-known structural transformation of phenolphthalein. The switch has an impact on the surface area and pore size distribution. Smaller pore sizes are generally observed for the salt forms. The size of the introduced counterions is geometry-wise only of minor importance but contributes to the overall polarity and polarizability of the wall structure. This effect could also be of interest for the generation of size selective gas separation materials,[25] the switching of chemical adsorption, and many more. In this contribution, we exemplified a photoelectrochemical function of the conjugated salt form as an efficient heterogeneous photosensitizer for photopolymerization reactions.

Future studies will target a better understanding of the switch process (including the forces acting on the network) as well as a more detailed study of the heterogeneous photopolymerization process.

ASSOCIATED CONTENT

Supporting Information

Gas sorption data and analysis; details of the molecular modeling; experimental details of the photopolymerization process. This material is available free of charge via the Internet at http://pubs.acs.org.

AUTHOR INFORMATION

Corresponding Author

*E-mail jens.weber@mpikg.mpg.de (J.W.), kiskanb@itu.edu.tr (B.K.); Tel +49-331-5679569, Fax +49-331-5679502.

Present Address

†Department of Chemistry, Istanbul Technical University, 34469, Maslak, Istanbul, Turkey.

Notes

The authors declare no competing financial interest.

ACKNOWLEDGMENTS

Dr. Simone Mascotto (Materials Chemistry Group, Trento, Italy) is highly acknowledged for ^{13}C solid-state NMR measurements. We furthermore thank Prof. Y. Yagci and Prof. A. I. Cooper for helpful discussions. The Max-Planck Society is acknowledged for financial support.

REFERENCES

(1) Thomas, A.; Kuhn, P.; Weber, J.; Titirici, M.-M.; Antonietti, M. *Macromol. Rapid Commun.* **2009**, *30*, 221−236.

(2) Cooper, A. I. *Adv. Mater.* **2009**, *21*, 1291−1295.

(3) McKeown, N. B.; Budd, P. M. *Macromolecules* **2010**, *43*, 5163−5176.

(4) Thomas, A. *Angew. Chem., Int. Ed.* **2010**, *49*, 8328−8344.

(5) Weber, J.; Thomas, A. *J. Am. Chem. Soc.* **2008**, *130*, 6334−6335.

(6) Chen, L.; Honsho, Y.; Seki, S.; Jiang, D. *J. Am. Chem. Soc.* **2010**, *132*, 6742−6748.

(7) Ritter, N.; Senkovska, I.; Kaskel, S.; Weber, J. *Macromolecules* **2011**, *44*, 2025−2033.

(8) Weber, J.; Antonietti, M.; Thomas, A. *Macromolecules* **2008**, *41*, 2880−2885.

(9) Farha, O. K.; Spokoyny, A. M.; Hauser, B. G.; Bae, Y.-S.; Brown, S. E.; Snurr, R. Q.; Mirkin, C. A.; Hupp, J. T. *Chem. Mater.* **2009**, *21*, 3033−3035.

(10) Sydlik, S. A.; Chen, Z.; Swager, T. M. *Macromolecules* **2011**, *44*, 976−980.

(11) Jones, J. T. A.; Holden, D.; Mitra, T.; Hasell, T.; Adams, D. J.; Jelfs, K. E.; Trewin, A.; Willock, D. J.; Day, G. M.; Bacsa, J.; Steiner, A.; Cooper, A. I. *Angew. Chem.* **2011**, *123*, 775−779.

(12) Rabone, J.; Yue, Y.-F.; Chong, S. Y.; Stylianou, K. C.; Bacsa, J.; Bradshaw, D.; Darling, G. R.; Berry, N. G.; Khimyak, Y. Z.; Ganin, A. Y.; Wiper, P.; Claridge, J. B.; Rosseinsky, M. J. *Science* **2010**, *329*, 1053−1057.

(13) Chang, I.; Fujara, F.; Geil, B.; Heuberger, G.; Mangel, T.; Sillescu, H. *J. Non-Cryst. Solids* **1994**, *172−174*, 248−255.

(14) Pixton, M. R.; Paul, D. R. *J. Polym. Sci., Part B: Polym. Phys.* **1995**, *33*, 1353−1364.
(15) Frisch, M. J.et al. *Gaussian 03, Revision E.01*; Gaussian, Inc.: Wallingford, CT, 2004.
(16) Dawson, R.; Laybourn, A.; Khimyak, Y. Z.; Adams, D. J.; Cooper, A. I. *Macromolecules* **2010**, *43*, 8524−8530.
(17) Kiskan, B.; Weber, J. *ACS Macro Lett.* **2012**, *1*, 37−40.
(18) Weber, J.; Schmidt, J.; Thomas, A.; Böhlmann, W. *Langmuir* **2010**, *26*, 15650−15656.
(19) Whether the simultaneous formation of phenates also has an impact on the porosity based on intermolecular interactions cannot be discussed within this work as the two effects cannot be decoupled.
(20) Pirngruber, G. D.; Raybaud, P.; Belmabkhout, Y.; Čejka, J.; Zukal, A. *Phys. Chem. Chem. Phys.* **2010**, *12*, 13534.
(21) Garrone, E.; Bonelli, B.; Lamberti, C.; Civalleri, B.; Rocchia, M.; Roy, P.; Otero Areán, C. *J. Chem. Phys.* **2002**, *117*, 10274.
(22) Green, W. A. *Industrial Photoiniators*; CRC Press, Taylor and Francis Group: Boca Raton, FL, 2010.
(23) Yagci, Y.; Jockusch, S.; Turro, N. J. *Macromolecules* **2010**, *43*, 6245−6260.
(24) Tunc, D.; Yagci, Y. *Polym. Chem.* **2011**, *2*, 2557−2563.
(25) Liu, Q.; Mace, A.; Bacsik, Z.; Sun, J.; Laaksonen, A.; Hedin, N. *Chem. Commun.* **2010**, *46*, 4502−4504.

Macromolecules

Article

pubs.acs.org/Macromolecules

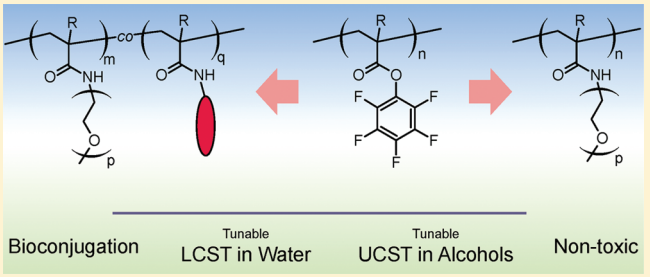
Synthesis and Thermoresponsive Solution Properties of Poly[oligo(ethylene glycol) (meth)acrylamide]s: Biocompatible PEG Analogues

Giles B. H. Chua, Peter J. Roth,* Hien T. T. Duong, Thomas P. Davis, and Andrew B. Lowe*

Centre for Advanced Macromolecular Design (CAMD), School of Chemical Engineering, University of New South Wales, Kensington, Sydney, New South Wales 2052, Australia

Supporting Information

ABSTRACT: A library of (meth)acrylamido (co)polymers was prepared by reacting poly(pentafluorophenyl (meth)-acrylate) with α-amino, ω-methoxy functionalized di(ethylene glycol), tri(ethylene glycol), and poly(ethylene glycol) (PEG)-350, PEG-750, and PEG-5k, in combination with hexylamine or thyroxine. The resulting copolymers showed an improved solubility in water (higher or absent LCST values) and in alcohols (lower or absent UCST values) than the analogous common series of poly[oligo(ethylene glycol) methyl ether (meth)acrylates]. The polyacrylamido species showed a better solubility than the corresponding polymethacrylamido derivatives of similar molecular weight with all polyacrylamides investigated being water-soluble at temperatures exceeding 90.0 °C. Tunable thermosensitive behavior could be effected by the incorporation of the hydrophobic hexylamide comonomer. Similarly, an acrylamido backbone with grafted oligo(propylene glycol 600) amides exhibited a sharp LCST-type transition around 22.0 °C. The UCST-type transitions of the (meth)acrylamido homopolymers were evaluated in 2-propanol and 1-octanol and were found to increase with an increasing ethylene glycol side chain length, but were essentially independent of the alcohol chain length with polymers exhibiting higher UCST transitions in 2-propanol vs 1-octanol. Cytotoxicity tests on MRC5 fibroblast cells of the di- and tri(ethylene glycol) methyl ether acrylamido homopolymers revealed no toxicity up to concentrations of 10.0 g/L. By employing mixtures of di(ethylene glycol) methyl ether amine and the prohormone thyroxine (T_4), water-soluble copolymers containing varying amounts of T_4 could be easily synthesized. Because of enhanced solubility, low toxicity, and higher hydrolytic stability of amides versus ester linkages, activated ester polymers in combination with amino-functionalized ethylene glycol based side chains are presented as a versatile platform for highly soluble, biocompatible, bioconjugated materials.



INTRODUCTION

The ability of certain (co)polymers in solution (aqueous or nonaqueous) to undergo conformational or phase transitions in response to a change in solution temperature, i.e., thermoresponsive polymers, are of interest as so-called "smart" materials. The response to a change in temperature can be exploited to induce self-directed assembly (micellization or vesiculation in block copolymers for example) or to promote the uptake or release of a particular molecular species and as such thermal 'triggers' have attracted significant attention.[1,2] The primary transition temperatures of interest to researchers are the lower critical solution temperature (LCST) in which a (co)polymer undergoes a coil-to-globule transition upon heating and is commonly associated with nonionic water-soluble species, and the upper critical solution temperature (UCST) whereby phase separation is induced by cooling. Examples of (co)polymers that exhibit LCST or UCST behavior are those containing, either wholly or partially, *N*-isopropylacrylamide (NIPAM, $LCST_{H2O}$ ~ 32 °C), *N*,*N*-diethylacrylamide (DEAM, $LCST_{H2O}$ ~ 32 °C),[3−5] *N*-vinylcaprolactam ($LCST_{H2O}$ ~ 32.5 °C),[6] 2-(dimethylamino)ethyl methacrylate (DMAEMA, $LCST_{H2O}$ ~ 50 °C), poly/oligo(ethylene glycol) (meth)-acrylates (OEGMA, $LCST_{H2O}$ varies depending on the degree of polymerization of the ethylene oxide side chain), methyl vinyl ether (MVE, $LCST_{H2O}$ ~ 36 °C),[7] pyrrolidone containing polymethacrylates ($LCST_{H2O}$~29−34 °C),[8] oligo(ethylene glycol) methyl ether methacrylate (OEGMA, $UCST_{ROH}$ varies from ca. 75−20 °C depending on the alcohol) and examples of polysulfopropylbetaines that can exhibit both UCST and LCST behavior.[9,10]

Of these thermoresponsive materials the PEG analogues, and especially the acrylic and methacrylic species, have attracted significant attention due in part to their LCST and UCST behaviors but also because of their well-established biocompatibility.[11−20] For example, Bebis et al.[20] recently described the effect of polymer concentration and added solutes on the LCST behavior of a series of well-defined, RAFT-synthesized, methacrylic-based oligo(ethylene glycol) species. The authors

Received: December 13, 2011
Revised: January 17, 2012
Published: February 1, 2012

ACS Publications © 2012 American Chemical Society

reported that the cloud point of such materials can increase by as much as 6 °C when polymer concentrations are decreased from 5.0 to 0.5 g/L and that the same measurements performed in bovine blood plasma indicated an additional further decrease of the cloud point (compared to water or PBS). The results, collectively, indicate that researchers should apply appropriate testing protocols for such materials when being examined for potential biomedical applications such as drug delivery. Roth, Jochum, and Theato recently detailed the behavior of poly-OEGMA (POEGMA) in a wide range of alcohols.[12] POEGMA solutions showed sharp, reversible transitions with low hystereses. The cloud points increased with an increasing alcohol chain length and were further tunable through end group structure and molecular weight. This UCST behavior in alcohols is promising because it occurs in both hydrophilic solvents such as ethanol as well as in the hydrophobic longer chain alcohols.

Reversible addition−fragmentation chain transfer (RAFT) radical polymerization is an example of a reversible deactivation radical polymerization (RDRP) process that is mediated by thiocarbonylthio compounds.[7,21−26] Since its discovery, RAFT has evolved into arguably the most robust and versatile of the RDRP systems and is now employed routinely in research laboratories worldwide. In recent years there has been significant interest in combining RDRP with a range of click and other highly efficient coupling chemistries. These include Cu-catalyzed alkyne−azide,[27−30] Diels−Alder,[31−34] and a range of thiol-based chemistries[35−41] with the aim of developing routes for the preparation of complex macromolecular architectures or facilitating the efficient postpolymerization modification of preformed (co)polymers. Indeed, RAFT has lent itself perfectly to such click and click-like chemistries in part due to the availability of a protected thiol, in the form of the thiocarbonylthio group, at the polymer chain end(s) and also due to its inherently high functional group tolerance allowing the synthesis of parent (co)polymers containing an impressive array of functionality.[42,43] Of the efficient coupling chemistries, the use of pentafluorophenyl (PFP) activated (meth)acrylic esters has proven to be particularly useful for the introduction of amine-containing species via the formation of amides.[11,44−49] For example, Gibson, Fröhlich, and Klok detailed the RAFT synthesis of three poly(pentafluorophenyl methacrylate)s with measured average molecular weights in the range 13 750−36 800 g/mol.[49] These precursor activated polymers were reacted with a range of hydrophilic primary amines including glycine, glucosamine, 2-hydroxypropylamine, and taurine yielding the corresponding functional, hydrophilic amides in generally high yields under facile conditions. The authors also demonstrated that the degree of modification was readily controlled by functional group stoichiometry (pentafluorophenyl ester:primary amine). In the case of precursor polymers modified with hydroxypropylamine cytotoxicity tests indicated no difference in the inherent toxicity of the materials via the postpolymerization route vs, for example, polymers obtained by the direct polymerization of 2-hydroxypropyl methacrylamide.

Employing a combination of RAFT radical polymerization with PFP activated ester chemistry herein we report our findings regarding the synthesis and thermal solution properties of a library of poly[oligo(ethylene glycol) *(meth)acrylamide*]s which serve as PEG analogues. While a few examples of such materials have been previously prepared there has not, to the best of our knowledge, been a systematic detailed investigation of their thermoresponsive phase behavior in water (LCST) or alcohols (UCST). We highlight how these (meth)-acrylamido-based materials represent an important addition to the family of PEG-analogues possessing fundamentally different solution properties from the corresponding (meth)acrylic species and as such may find application in areas not accessible to such (meth)acrylic derivatives.

EXPERIMENTAL PART

Instrumentation. Nuclear magnetic resonance (NMR) spectroscopic measurements were performed in $CDCl_3$ solutions on a Bruker DPX 300 instrument and evaluated using MestReC 4.7.0.0 software. The internal solvent signal was used as the reference signal (7.26 ppm). Size exclusion chromatography (SEC) was performed on a Shimadzu system with four phenogel columns in dimethylacetamide (DMAc) as eluent at a flow rate of 1.0 mL/min. Chromatograms were analyzed with Cirrus SEC software (version 3.0). The system was calibrated with a series of narrow molecular weight distribution polystyrene (PS) standards. Turbidity measurements were performed on a Varian Cary 300 Scan spectrophotometer equipped with a Cary temperature controller and a Peltier heating element in quartz cuvettes of 10 mm path length at a wavelength of 520 nm. Heating rates were 1.0 °C/min for all measurements. For clear solutions (cold water; warm alcohols), the baseline was set to zero absorbance, *A*. Transmittance, $T = 10^{-A}$, was plotted against temperature and cloud points were determined at 50% transmittance. The maximum temperature evaluated for aqueous solutions was 93.0 °C. Fourier transform infrared spectroscopy (FTIR) was performed on a Bruker IFS 66/S instrument under attenuated total reflectance (ATR) and was analyzed on OPUS software version 4.0. Differential scanning calorimetry measurements were performed with a Perkin-Elmer DSC7 instrument at a heating rate of 2.0 °C/min on 40 μL of 20 g/L solutions and were analyzed with PE Pyris software.

Synthesis. All reagents were purchased from the Aldrich Chemical Co. and used as received unless noted otherwise. 4-Cyano-4-((phenylcarbonothioyl)thio)pentanoic acid (CPADB) was prepared according to the literature.[22] 2,2′-Azobis(2-methylpropionitrile) (AIBN) was recrystallized from methanol.

Synthesis of Pentafluorophenyl (Meth)acrylate Monomers. Pentafluorophenyl acrylate and pentafluorophenyl methacrylate were synthesized according to the general procedure described by Eberhardt et al.[50]

Synthesis of Ethylene Glycol Methyl Ether Amines. Di- and triethylene glycol methyl ether amine were prepared according to the method of Clerc et al.[51] Diethylene glycol methyl ether amine: 65% overall yield; ^{1}H NMR, 300 MHz, $CDCl_3$, δ (ppm) = 3.55 (m, 2 H), 3.50−3.40 (m, 4 H), 3.32 (m, 3 H, $-OCH_3$), 2.80 (m, 2 H, $-CH_2NH_2$), 1.73 (bs, $-NH_2$). Triethylene glycol methyl ether amine: 64% overall yield; ^{1}H NMR, 300 MHz, $CDCl_3$, δ (ppm) = 3.52 (m, 6 H, PEG), 3.43/3.38 (m, 4 H, $-CH_2-$), 3.24 (m, 3 H, $-OCH_3$), 2.73 (m, 2 H, $-CH_2NH_2$), 1.50 (bs, $-NH_2$).

Poly(ethylene glycol) methyl ether amines with average molecular weights of 350, 750 and 5000 were prepared following the procedure of Mongondry and co-workers.[52] PEG-350 amine: 50% overall yield; ^{1}H NMR, 300 MHz, $CDCl_3$, δ (ppm) = 3.53 (bs, ∼ 29 H, PEG), 3.44−3.38 (m, 4 H, $-CH_2-$), 3.36 (s, 3 H, $-OCH_3$), 2.75 (bt, 2 H, $-CH_2NH_2$), 2.12 (bs, $-NH_2$). PEG-750 amine: 86% overall yield; ^{1}H NMR, 300 MHz, $CDCl_3$, δ (ppm) = 3.71−3.44 (bs, ∼ 83 H, PEG), 3.31 (bs, 3 H, $-OCH_3$), 2.81 (m, 2 H, $-CH_2NH_2$), 2.49 (bs, $-NH_2$). PEG-5000 amine: 73% overall yield; ^{1}H NMR, 300 MHz, $CDCl_3$, δ/ppm =3.75−3.40 (bs, PEG), 3.33 (bs, $-OCH_3$), 2.80 (m,$-CH_2NH_2$).

All PEG amines were of sufficient purity for the conversions of polymeric activated esters without further purification.

RAFT Homopolymerization of PFP Ester Monomers. Below is given a typical procedure for the RAFT homopolymerization of pentafluorophenyl acrylate (**PFPA**). The same general procedure was employed for the homopolymerization of pentafluorophenyl methacrylate (**PFPMA**).

PFPA (5.0 g, 21.0 mmol), CPADB (78 mg, 0.28 mmol), AIBN (9.2 mg, 0.056 mmol), and 1,4-dioxane (8.0 mL) were combined in a

dx.doi.org/10.1021/ma202700y | *Macromolecules* 2012, 45, 1362−1374

round bottomed flask equipped with a magnetic stir bar. The flask was sealed with a rubber septum and nitrogen was bubbled through the solution for 20 min. The reaction vessel was subsequently immersed in a preheated oil bath set to 70 °C. Polymerization was allowed to proceed for 12 h. The resulting **polyPFPA** was isolated via two precipitations into methanol and subsequently dried under vacuum. **PolyPFPA**: SEC 26.6 kg/mol, PDI 1.19. ^{1}H NMR, 300 MHz, $CDCl_3$, δ (ppm) = 3.40, 2.52, 2.15 (m, backbone). ^{19}F NMR, 282 MHz, $CDCl_3$, δ (ppm) = −153.1 (bs, 2 F, *ortho*), −153.7 (bs, 1 F, *para*), −162.1 (2 F, *meta*). IR, ν (cm^{-1}) = 2931 (w), 1780 (m), 1513 (s), 1218 (w), 1076 (m), 985 (s), 860 (w), 852 (w). **PolyPFPMA**: SEC 15.4 kg/mol, PDI 1.21. ^{1}H NMR, 300 MHz, $CDCl_3$, δ (ppm) = 2.44, 2.19, 1.46, 1.40 (m, backbone). ^{19}F NMR, 282 MHz, $CDCl_3$, δ (ppm) = −150.9, −151.9 (2 m, 2 F, *ortho*), −157.4 (bs, 1 F, *para*), −162.5 (2 F, *meta*). IR, ν (cm^{-1}) = 2967 (w), 1758 (m), 1515 (s), 1240 (w), 1043 (s), 989 (s), 854 (w).

Reaction of Pentafluorophenyl (Meth)acrylate Polymers with Primary Amines in the Presence of Methyl Methanethiosulfonate. Below is a typical example for the reaction of a pentafluorophenyl (meth)acrylate (**PFPMA**) polymer with an oligo(ethylene glycol) methyl ether amine.

To a glass vial equipped with a magnetic stir bar was added **polyPFPA** (214 mg, 0.9 mmol of pentafluorophenyl esters, 1 equiv) and DMF (2.0 mL). To a separate flask was added diethylene glycol methyl ether amine (273.2 mg, 2.25 mmol, 2.5 equiv), DBU (202 μL, 1.35 mmol), methyl methanethiosulfonate (22 μL, 10 equiv. with respect to polymer end groups) and DMF (0.9 mL). After complete dissolution the solutions were combined and the reaction allowed to proceed overnight at room temperature. For poly(pentafluorophenyl methacrylate) the excess of amines was increased to 5 equiv. and THF and triethylamine were used as solvent and auxiliary base, respectively. IR, ν (cm^{-1}) = 3457 (w), 3300 (m), 2865 (m), 1644 (s), 1539 (s), 1452 (m), 1093 (s), 1022 (m), 844 (w). Reaction of **polyPFPMA** with diethylene glycol methyl ether amine: IR, ν (cm^{-1}) = 3505 (w), 3352 (m), 2868 (m), 1637 (s), 1518 (s), 1452 (m), 1198 (m), 1095 (s), 845 (w).

Copolymer Synthesis. Reaction of **PFPA** with two different primary amines in the presence of methyl methanethiosulfonate. Below is a typical example for the reaction of a **polyPFPA** with an oligo(ethylene glycol) methyl ether amine (85 mol %) and hexylamine (15 mol %).

To a glass vial equipped with a magnetic stir bar was added **polyPFPA** (119 mg, 0.5 mmol of PFP esters, 1 equiv) and DMF (1.5 mL). To a separate flask was added di(ethylene glycol) methyl ether amine (60.8 mg, 0.51 mmol, 1.02 equiv, 20% excess), hexylamine (9.1 mg, 0.09 mmol, 0.18 equiv, 20% excess), methyl methanethiosulfonate (10 μL) and DMF (1.0 mL). The amine solution was quickly added to the polymer solution under vigorous stirring and allowed to react at room temperature overnight. IR, ν (cm^{-1}) = 3469 (w), 3284 (m), 2918 (m), 1641 (s), 1540 (s), 1440 (m), 1095 (s), 845 (m).

The same protocol was employed for the preparation of thyroxine (T_4) containing copolymers where ratios of 9:1 and 8:2 of di(ethylene glycol) methyl ether amine to thyroxine with an excess of 20 mol % of amines toward PFP esters were used.

General Purification Protocols. After stirring overnight, 0.2 mL of reaction mixture was withdrawn, 0.45 mL of $CDCl_3$ was added and a ^{19}F NMR measurement was made (example poly[di(ethylene glycol) methyl ether acrylamide]: ^{19}F NMR, 282 MHz, $CDCl_3$, δ (ppm) = −170.7 (m, 2 F, *ortho*), −171.7 (m, 2 F, *meta*), −189.5 (m, 1 F, *para*), pentafluorophenol). The NMR sample was combined with the remaining reaction mixture which was then placed into a dialysis membrane (regenerated cellulose, 3500 g/mol MWCO for di- and triethylene glycol amine and PEG-350 amine; MWCO 6−8 kg/mol for PEG-750 amine; MWCO 12−14 k for PEG-5000 amine) and dialyzed against methanol for 3 days with solvent changes twice per day. The solvent was removed by blowing in air; the residue was then dissolved in a small amount of water and lyophilized to obtain the final products.

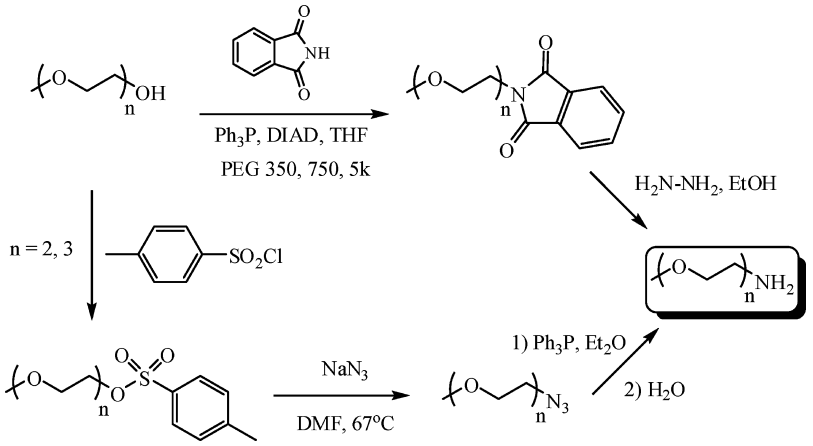
Cytotoxicity Testing. The toxicity of the prepared polymers was tested on a MRC5 fibroblast cell line. Cell culture: MRC5 fibroblast cells were cultured in growth media consisting of Dulbecco's modified Eagle's medium: Nutrient Mix F-12 (DMEM) supplemented with 10% (v/v) foetal bovine serum (FBS) in a ventilated tissue culture flask T-75 and passaged every 2−3 days when the monolayer reached around 80% confluence. The cells were used only when stable cell growth was obtained (approximately 3−4 passages). The cells were incubated at 37 °C in a 5% CO_2 humidified atmosphere. The cell density was determined by counting the number of viable cells using a trypan blue dye exclusion test. The cells were detached using 0.05% trypsin-EDTA (Invitrogen), stained using trypan blue dye, and loaded on a hemocytometer. One day prior to the treatment, the cells were seeded at required cell densities on a 96-well plate. Cell viability: The cytotoxicity of the (meth)acrylamido-based polymers was tested *in vitro* by a standard Alamar Blue assay which provides a homogeneous, fluorescent method for monitoring cell viability. The assay is based on the ability of living cells to convert a redox dye (blue resazurin) into a fluorescent end product (red resorufin). Nonviable cells rapidly lose metabolic capacity and thus do not generate a fluorescent signal. The cells were seeded in a tissue culture treated 96-well plate in 100 μL medium per well at a density of 5000 cells/well and incubated for 24 h. The medium was then replaced with fresh medium containing the polymer samples and incubated for 72 h. The final concentration of polymer in the wells was adjusted to the desired concentrations ranging from 0.005 to 10.0 g/L in DMEM media containing 10% v/v FBS. Alamar Blue dye (20 μL) was added to each well and the cells were incubated for 6 h. After the incubation step, data was recorded using a fluorescence plate reader (λ_{ex} = 540 nm; λ_{em} = 595 nm).

RESULTS AND DISCUSSION

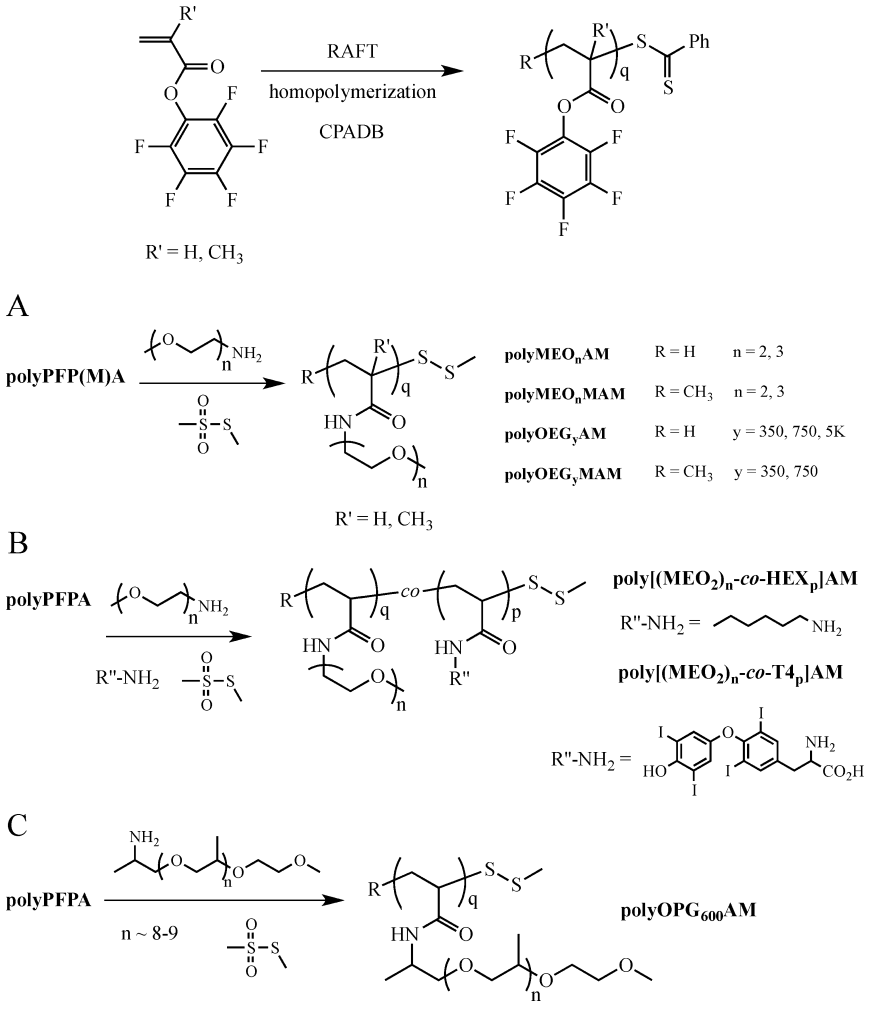
Synthesis. The desired oligo(ethylene glycol) methyl ether amines (OEGMEAs) were obtained via two different routes the choice of which was dictated by the molecular weight of the precursor oligo(ethylene glycol) methyl ether (OEGME). The di- and tri(ethylene glycol) methyl ether amines (MEO_2 and MEO_3) were prepared from the corresponding OEGME via a three step procedure involving tosylation, nucleophilic substitution with azide followed by Staudinger reduction. The higher molecular weight target OEGMEAs with average precursor molecular weights of 350, 750, and 5000 g/mol were prepared via a Mitsunobu reaction with phthalimide followed by a Gabriel synthesis-like reaction of the intermediate functional phthalimide via hydrazinolysis, Scheme 1. In all instances the target OEGMEAs were obtained in moderate to high overall yield and purity.

With the OEGMEAs in hand two different pentafluorophenyl- (PFP-) containing homopolymers (one derived from PFP-acrylate (**PFPA**) and the other from PFP-methacrylate (**PFPMA**)) were prepared under standard RAFT conditions employing 4-cyano-4-((phenylcarbonothioyl)thio)pentanoic acid (CPADB) as the mediating agent and AIBN as the source of primary radicals, Scheme 2. The RAFT (co)polymerization of **PFPA** and **PFPMA** is well-documented[46,50] and the polymerizations were allowed to proceed for a predetermined period of time yielding two homopolymers with measured number-average molecular weights (M_n) of 26 600 g/mol (**polyPFPA**) and 15 400 g/mol (**polyPFPMA**) and relatively low polydispersity indices (M_w/M_n = 1.19 and 1.21 respectively). With the **polyPFPA** and **polyPFPMA** parent homopolymers in hand a library of oligo(ethylene glycol)-based (meth)acrylamido (co)polymers were prepared via the reaction of the OEGMEAs prepared above (as well as with some commercially available primary amine species, vide infra) with the **PFPA** and **PFPMA** homopolymers, Scheme 2. The use of two simple precursor homopolymers as activated substrates thus allowed the preparation of a library of amide-based PEG analogues with identical average main-chain degrees of polymerization. It should be noted that the acyl substitution

Scheme 1. Synthetic Approaches for the Preparation of Oligo(ethylene glycol) Methyl Ether Amines



Scheme 2. Outline for the RAFT Homopolymerization of Pentafluorophenyl (Meth)acrylate Monomers and Procedures for the Subsequent Post-Polymerization Acyl Substitution Reactions with OEGMEAs



reactions were performed in the presence of *S*-methyl methanethiosulfonate (MMTS). Thiocarbonylthio functional groups (found at the ω-chain end of the RAFT-prepared **PFPA** and **PFPMA** homopolymers in the form of dithiobenzoate species) are extremely reactive towards primary and secondary amines with reactions resulting in the cleavage of the thiocarbonylthio end groups yielding the corresponding macromolecular thiol. Indeed, this represents the most commonly employed route for the removal of such end-groups in RAFT-synthesized (co)polymers with the liberated thiol being able to undergo a range of further chemical reactions.[36,43,53] However, one common problem with the formation of macromolecular thiols is their propensity to undergo oxidative coupling forming polymeric disulfides. Such

dx.doi.org/10.1021/ma202700y | *Macromolecules* 2012, 45, 1362–1374

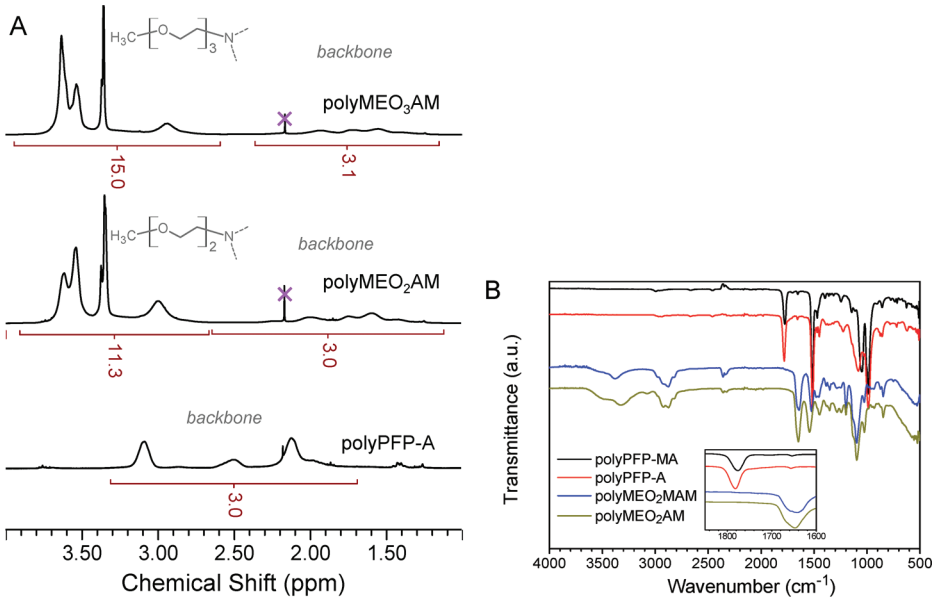


Figure 1. Monitoring the conversion of PFP esters with OEGMEAs. (A) ^{1}H NMR spectra of parent **polyPFPA** (bottom), **polyMEO$_2$AM** (middle), and **polyMEO$_3$AM** (top) showing quantitative formation (within NMR accuracy) of the PEG-amides. (B) FTIR spectra of the activated polymers **polyPFPA** and **PFPMA** and after conversion of each with di(ethylene glycol) amine, with the inset highlighting the shift of the carbonyl band.

reactions, while reversible, consume the thiol, which is clearly problematic if further modification is the goal but also results in an effective doubling of the average molecular weight or degree of polymerization. Since molecular weight is an important parameter affecting the solution phase behavior of thermoresponsive (co)polymers this precautionary step of capturing the macromolecular thiol was adopted. Indeed, it has previously been shown that MMTS, and functional derivatives thereof, are extremely effective reagents for 'trapping' liberated thiols produced during the aminolysis of end-groups in RAFT-prepared (co)polymers[12,54−57] thus negating any undesirable polymer−polymer disulfide formation.

Initially, both **polyPFPMA** and **polyPFPA** were reacted with four OEGMEAs: di(ethylene glycol) methyl ether amine, tri(ethylene glycol) methyl ether amine and two OEGMEAs with average M_n's of 350 and 750 g/mol, Scheme 2A. The resulting acrylamido (**AM**) and methacrylamido (**MAM**) analogues are denoted **polyMEO$_n$AM** and **polyMEO$_n$MAM** for the dimer and trimer ethylene glycol species (n = 2 and 3) and **polyOEG$_y$AM** and **polyOEG$_y$MAM** for those derived from the OEGMEAs with y = 350 and 750 g/mol. Conversion of the parent **polyPFPA** and **polyPFPMA** homopolymers to the corresponding PEG-amides was quantified employing a combination of ^{1}H and ^{19}F NMR spectroscopy, SEC and FTIR spectroscopy. For the acrylic activated esters quantitative conversion was achieved with 2.5 equiv of amine with regards to PFP esters. This procedure did not, however, give a full conversion of the analogous methacrylic esters to the desired amides. In case of **polyPFPMA**, ^{1}H NMR spectroscopy showed less than quantitative formation of the PEG amides and FTIR spectroscopy revealed the presence of acid groups (~1710 cm^{-1}). The nonquantitative conversion of methacrylic PFP esters with 2 equiv of amine, followed by hydrolysis of unreacted esters during work-up, has been reported.[49] Similarly, nonquantitative amidation of surface tethered poly(methacrylic acid) during the activation step with EDC/NHS (*N*-ethyl-*N*′-(3-(dimethylamino)-propyl)carbodiimide/*N*-hydroxysuccinimide) was recently described.[58] The authors detailed the formation of methacrylic acid anhydrides, as opposed to the desired activated esters, between neighboring −CO_2H groups, which subsequently formed one amide and one acid group upon exposure with amines. On the other hand, poly(acrylic acid) gave a high amide yield. While different to the current research, where the activation step took place prior to polymerization, the low amidation of methacrylic PFP derivatives and the fundamental difference compared to the polyacrylate should be noted. Here, the ratio of amine with respect to methacrylic PFP esters was increased to 5 to minimize the formation of hydrolysis byproducts. For the acrylate derivative on the other hand, as little as 1.2 equiv of amines (as used in the production of copolymers) was sufficient to achieve a quantitative conversion to the target amides as evidenced by ^{1}H, ^{19}F NMR and FTIR spectroscopies.

For example, Figure 1A shows the ^{1}H NMR spectra, plotted between 1.0 and 4.0 ppm, for the **polyPFPA** homopolymer (bottom) and the corresponding amides obtained after reaction with di(ethylene glycol) methyl ether amine (**polyMEO$_2$AM**) (middle) and tri(ethylene glycol) methyl ether amine (**polyMEO$_3$AM**) (top). The spectrum associated with **polyPFPA** is relatively simple with only backbone hydrogens visible which span the range of ~3.2−2.0 ppm. After modification with the di- and tri(ethylene glycol) amino species peaks appear in the range ~3.8−2.8 ppm which correspond to the side-chain hydrogens associated with the ethylene glycol methyl ether segments. Analysis of the integrals associated with these new peaks indicated quantitative formation of the PEG-acrylamides when compared to the integrals associated with the backbone hydrogens. Figure 1B shows the FTIR spectra for **polyPFPA**, **polyPFPMA**, **polyMEO$_2$MAM**, and **polyMEO$_2$AM**. The most distinctive feature when comparing the parent (meth)acrylic homopolymers and the resulting PEG-(meth)acrylamides, and qualitatively verifying complete reaction, relates to the C═O peak associated with the parent esters vs the product amides. In the parent homopolymers the ester C═O peak appears at ca. 1780 cm^{-1} while in the product (meth)acrylamides the amide C═O

dx.doi.org/10.1021/ma202700y | *Macromolecules* 2012, 45, 1362−1374

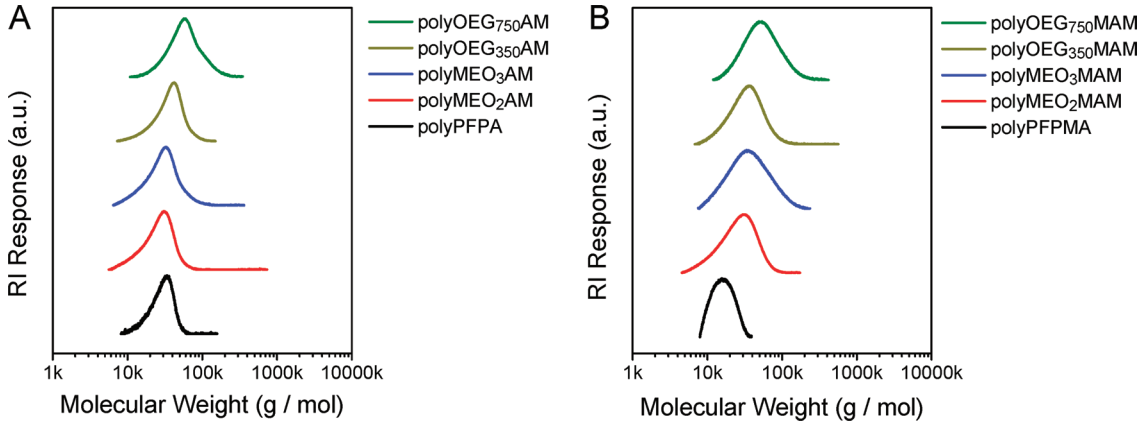


Figure 2. SEC traces of (A) the acrylamido series including the precursor **polyPFPA** and (B) the methacrylamide series with its parent polymer **polyPFPMA**.

Table 1. Summary of Prepared OEG Amide Homopolymers and Statistical Copolymers, SEC-Measured Molecular Weights, Polydispersities, and Cloud Points in Water

(meth)acrylamido (co)polymers						reference (meth)acrylates		
				cloud point (5 g/L)[b]				
entry	polymer	M_n[a] (kg/mol)	PDI[a]	heating (°C)	cooling (°C)	polymer	cloud point[b] (°C)	reference
1	**polyMEO$_2$AM**	22.5	1.22	s[c]	s	polyMEO$_2$A	38	59
2	**polyMEO$_3$AM**	24.7	1.25	s	s	polyMEO$_3$A	58	59
3	**polyOEG$_{350}$AM**	31.1	1.2	s	s	polyOEG$_{370}$A[e]	s	60
4	**polyOEG$_{750}$AM**	47.0	1.25	s	s			
5	**polyOEG$_{5k}$AM**	177.4	1.74	s	s			
6	**poly[(MEO$_2$)$_{49}$-*co*-Hex$_{51}$]AM**	19.7	1.26	ins[d]	ins			
7	**poly[(MEO$_2$)$_{76}$-*co*-Hex$_{24}$]AM**	20.7	1.24	26.0	21.1			
8	**poly[(MEO$_2$)$_{85}$-*co*-Hex$_{15}$]AM**	21.3	1.24	46.7	43.0			
9	**poly[(MEO$_2$)$_{93}$-*co*-Hex$_7$]AM**	20.7	1.25	77.7	75.9			
10	**poly[(MEO$_2$)$_{91}$-*co*-T4$_9$]AM**	42.5	1.21	s	s			
11	**poly[(MEO$_2$)$_{87}$-*co*-T4$_{13}$]AM**	49.7	1.18	s	s			
12	**polyOPG$_{600}$AM**	18.0	1.26	22.1	16.7			
13	**polyMEO$_2$MAM**	21.3	1.32	55.8	52.7	polyMEO$_2$MA	26	19
14	**polyMEO$_3$MAM**	28.2	1.38	69.3	63.2	polyMEO$_3$MA	52	19
15	**polyOEG$_{350}$MAM**	27.8	1.26	s	s	polyOEG$_{375}$MA[f]	90	17
16	**polyOEG$_{750}$MAM**	42.5	1.29	s	s			

[a]Data obtained by SEC. [b]Cloud points depend on concentration, molecular weight and polymer end groups. [c]Soluble between 0 and 93 °C. [d]Insoluble between 0 and 93 °C. [e][Poly(ethylene glycol) monomethyl ether acrylate], $M_{monomer}$ = 454 g/mol. [f][Poly(ethylene glycol) monomethyl ether methacrylate], $M_{monomer}$ = 475 g/mol.

peak appears at ca.1640 cm^{-1} with no evidence of residual ester C═O species. Additionally, we note the appearance of bands at ca. 2850 cm^{-1} that may be assigned to the C−H stretches in the CH_2 and CH_3 groups associated with the newly introduced ethylene glycol side chains and the broad bands between 3500 and 3100 cm^{-1} due to the N−H stretch of the newly introduced secondary amide functionality. Representative ^{19}F NMR spectra demonstrating the complete cleavage of the activated esters are given in Figure S1 of the Supporting Information.

Figure 2 shows the measured molecular weight distributions for the parent **polyPFPA** (Figure 2A black line) and **polyPFPMA** (Figure 2B black line) as well as the resulting (meth)acrylamides derived from reaction with the OEGMEAs. The experimentally determined molecular weight and polydispersity data is summarized in Table 1 (entries 1−4 for the acrylamides and 13−16 for the methacrylamides). In the case of the acrylamido derivatives we observe an increase in the M_n as the length of the oligo(ethylene glycol) side chain increases, as expected. In all instances the measured polydispersity indices increase slightly compared to the parent **polyPFPA** but are all between 1.20 and 1.25 with the molecular weight distributions being unimodal and essentially symmetrical. This also indicates that the macromolecular thiols were successfully trapped with MMTS since there is no evidence of high molecular weight (coupled) species in the chromatograms. The same general trends are observed in the case of the methacrylamide derivatives, with an increase in the measured M_n as side-chain degree of polymerization increases and polydispersity indices in the range 1.26−1.38.

Aqueous Solution Properties. With a library of acrylamido and methacrylamido-based PEG analogues prepared the aqueous phase behavior of the polymers was investigated at a concentration of 5.0 g/L (0.5 wt %). Consider first the range of acrylamido derivatives (entries 1−4 Table 1). In all cases, at the concentration evaluated, the PEG-based acrylamido homopolymers did not exhibit any LCST behavior in pure water and were completely soluble between 0 and 93 °C. This is in sharp contrast to acrylate derivatives in which polymers

dx.doi.org/10.1021/ma202700y | *Macromolecules* 2012, 45, 1362−1374

with di- and tri(ethylene glycol) side chains have reported LCSTs of 38 and 58 °C respectively.[59] This difference in solubility is, presumably, due to the enhanced hydrophilicity of the amide-based materials due to the H-bond donor and acceptor properties of the amide functional group and highlights how subtle functional group changes can have a marked effect on the aqueous solution properties of such PEG-containing polymers. The absence of LCST behavior for the acrylamido-based PEGs with the longer side chains is consistent with the enhanced aqueous solubility reported for analogous acrylic derivatives.[60]

It is well documented that the LCST behavior of thermoresponsive polymers may be tuned via the incorporation of a hydrophobic comonomer[61,62] or, in the case of suitably low molecular weight species, via variation of the hydrophilicity/hydrophobicity of polymer end-groups.[5,63] In an effort to induce LCST behavior the **polyPFPA** parent homopolymer was reacted with varying ratios of di(ethylene glycol) methyl ether amine and hexylamine, Scheme 2 route B, yielding, presumably, random amphiphilic copolymers containing 51, 24, 15, and 7 mol % hydrophobic hexylamide residues. Compositions were determined by ^{1}H NMR spectroscopy by a comparison of the hexyl $-CH_3$ group with the ethylene glycol $-OCH_3$ group. Both amines exhibited a similar reactivity toward the activated esters yielding polymers with essentially the same composition as the feed ratio of amines (see Figure S2, and Table S1 in Supporting Information). Molar compositions, molecular weights and polydispersity indices for these copolymers are listed in Table 1 (entries 6–9). SEC traces are shown in Figure S3. It should be noted that this yields statistical copolymers with the same degree of polymerization whose individual components are either wholly soluble in water (di(ethylene glycol) methyl ether amide residues) or completely insoluble, i.e. hydrophobic (hexylamide residues) and thus should allow for a tuning of the LCST behavior.[61,62] The LCST characteristics of these amphiphilic copolymers were evaluated under the same conditions as noted above for the acrylamide homopolymers. Two additional amphiphilic statistical copolymers were also prepared by substituting hexylamine for the prohormone thyroxine (Table 1 entries 10 and 11) and these will be discussed in the final part of this contribution.

Figure 3 shows the cloud-point curves for the **poly**-$[(\mathbf{MEO_2})_{1\text{-}x}\text{-}co\text{-}\mathbf{Hex_x}]$**AM** statistical copolymers as well as the **polyMEO$_2$AM** homopolymer. As noted above, **polyMEO$_2$AM** is completely soluble and does not exhibit a phase transition upon heating (solid blue line). With the introduction of as little as 7 mol % hexylamide residues the amphiphilic copolymer undergoes a phase transition upon heating with a measured cloud point of 77.7 °C (taken at 50% transmittance, solid red line) although the transition is not particularly sharp. Increasing the hexylamide content to 15 and 24 mol % results in a systematic lowering of the cloud point to 46.7 °C (solid black line) and 26.0 °C (solid green line) respectively and also appears to result in sharper, more distinct transitions. Increasing the hexylamide content to just above equimolar (51 mol %) yields a copolymer that is completely insoluble in water even when cooled to temperatures approaching 0 °C. Also shown in Figure 3 are the corresponding cooling curves for the three thermoresponsive copolymers, and the corresponding phase transition temperatures are listed in Table 1. Little hysteresis is observed for all three samples and in all instances the redissolution temperatures are only several degrees lower than the cloud points found for heating. This is consistent with the well-known kinetic effect and the process of rehydration of the highly compact globules and aggregates thereof. Shown inset in Figure 3 is a plot of the cloud point vs mol % hexylamide residues. It can be seen that this plot is essentially linear and indicates that the synthetic route described herein offers a simple and convenient approach to thermoresponsive copolymers with tunable, and essentially predetermined, LCST behavior simply by varying the molar content of hexylamide residues.

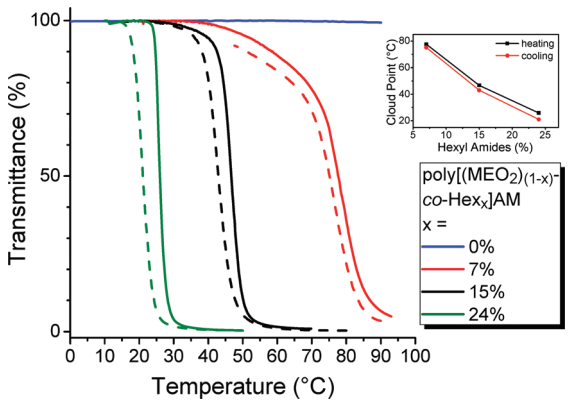


Figure 3. Turbidity curves of the **poly**$[(\mathbf{MEO_2})_{1\text{-}x}\text{-}co\text{-}\mathbf{Hex_x}]$**AM** series demonstrating tunable LCST behavior: heating curves (solid lines); cooling curves (dashed lines).

Another strategy was also investigated to induce LCST behavior into the acrylamido polymers, this time by a "hydrophobic modification" of the ethylene glycol side chains. Poly(propylene glycol) (PPG) is a well documented thermoresponsive polymer that exhibits a marked dependence of its LCST on the polymer molecular weight. For example, increasing the MW from 1000 to 2000 to 3000 results in a decrease in the LCST from 42.0 to 23.0 to 15.5 °C.[64] PPG, while not perhaps as currently widely evaluated or employed in polymer synthesis as PEG, due in part to such low thermal transitions, finds wide use as the hydrophobic middle section of the commercially important Pluronic series of surfactants.[65] To evaluate the effect of relative hydrophobicity of the oligoether side chains the **polyPFPA** homopolymer was also reacted with a commercially available oligo(propylene glycol) amine (Jeffamine) with an average molecular weight of ca. 600 g/mol. Consistent with the previous postpolymerization conjugations the reaction of the Jeffamine proceeded smoothly, quantitatively yielding a well-defined oligo(propylene glycol) methyl ether acrylamido homopolymer, **polyOPG$_{600}$AM**, entry 12 in Table 1, Figure S4 in the Supporting Information. Evaluation of the cloud point behavior of this PPG-acrylamido derivative, Figure 4, indicates a sharp phase transition upon heating at 22.1 °C with the cooling curve also indicating moderate hysteresis. Thus, the combination of PPG side-chains linked to a backbone via a hydrophilic acrylamido functional group allows for the preparation of PPG-containing polymers that exhibit distinctly different aqueous phase behavior compared to simple linear PPG materials and facilitates the preparation of water-soluble PPG-containing substrates with much higher effective molecular weights than the linear species.

The thermal phase transitions of two samples, **polyOPG$_{600}$AM** and **poly**$[(\mathbf{MEO_2})_{85}\text{-}co\text{-}\mathbf{Hex_{15}}]$**AM**, were also briefly examined by differential scanning calorimetry (DSC). Experiments were performed at 20.0 g/L, four times higher than the

dx.doi.org/10.1021/ma202700y | Macromolecules 2012, 45, 1362–1374

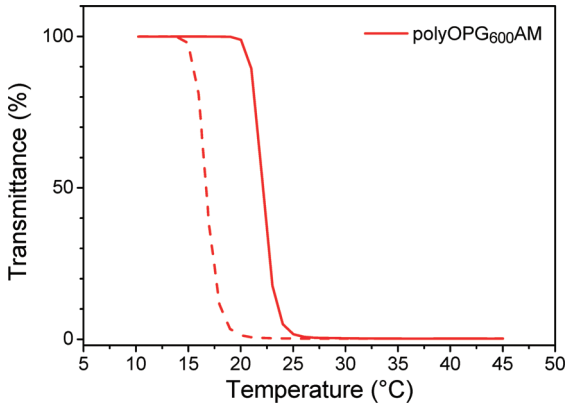


Figure 4. Turbidity measurement (dashed line cooling curve) of the Jeffamide derivative showing a sharp LCST transition.

concentration examined above in cloud point measurements. The measured transition temperatures were in agreement with turbidity measurements performed at the same concentration (Supporting Information, Figure S5). The endotherms of both polymers do however show distinct differences. **PolyOPG$_{600}$AM** shows a very broad transition occurring over a range ~10 °C with a heat of 22.94 kJ/mol monomer units calculated from the peak area, Figure 5. On the other hand, the

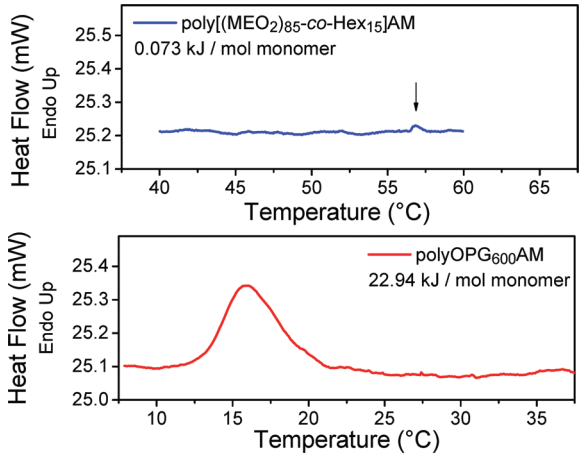


Figure 5. Heating endotherms of two samples obtained by differential scanning calorimetry showing the significant difference of the transitions of a copolymer with few hydrophobic comonomer units (blue curve, top) and a polymer with thermally responsive side chains (red curve, bottom).

poly[(MEO$_2$)$_{85}$-*co*-Hex$_{15}$]AM copolymer produced only a very small narrow peak spanning ~2 °C and an area of 0.073 kJ/mol average monomer units. The endotherms represent molecular events occurring during the phase transition and account for the loss of solvation (e.g., through hydrogen bonding) when the polymer undergoes a coil-to-globule transition. The large difference between the two observed polymers thus suggests a much larger number of hydrogen bonds are breaking during the phase transition of the OPG derivative. This is not surprising as the OPG graft homopolymer carries stronger hydrophobic side chains that are in fact thermally responsive themselves—in contrast to the **poly[(MEO$_2$)$_{85}$-*co*-Hex$_{15}$]AM** copolymer.

Next, the thermal behavior of the methacrylamido polymers, Table 1 entries 13–16, was investigated. In contrast to the **polyMEO$_2$AM** and **polyMEO$_3$AM** acrylamido homopolymers both the **polyMEO$_2$MAM** and **polyMEO$_3$MAM** species exhibit LCST behavior in water with measured cloud points of 55.8 and 69.3 °C respectively, Figure 6. Both of these values are

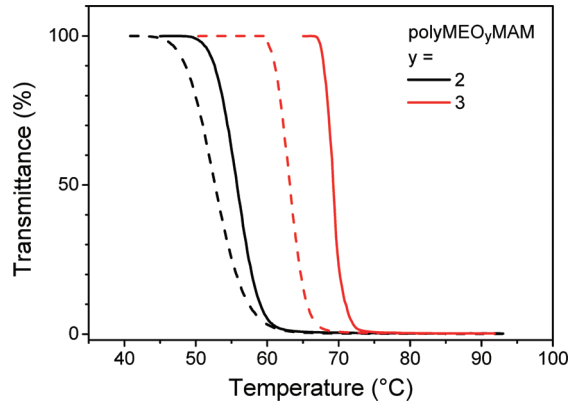


Figure 6. Turbidity curves (dashed curve cooling) for the methacrylamido polymers with 2 and 3 ethylene glycol units showing sharp transmittance decreases and low to moderate hystereses.

higher than identical methacrylic derivatives whose reported cloud points are 26.0 and 52.0 °C[19] again highlighting the enhanced hydrophilicity associated with these (meth)-acrylamido derivatives vs the corresponding (meth)acrylates. Interestingly, the observed phase transition behavior of the methacrylamido vs acrylamido species is opposite to that which has been reported for poly(*N*-isopropylacrylamide) (PNIPAM) vs poly(*N*-isopropylmethacrylamide) species (PNIPMAM).[66,67] In the case of the latter two polymers, PNIPAM has a well-documented LCST of ca. 32.0 °C whereas the methacrylamido species, PNIPMAM, has a reported higher LCST of ~47.0 °C even though a cursory examination of the structure, with the extra hydrophobic methyl group, would suggest that PNIPMAM should undergo a temperature induced phase transition at a temperature below that of PNIPAM. This interesting behavior has been attributed to the methyl group hindering the coil-to-globule transition and subsequent aggregation and phase transition. Such an effect is not, apparently, at play in the case of the ethylene glycol-based methacrylamido polymers described here. In agreement with the enhanced water solubility of amides vs esters and with an increase of OEG side chain length, **polyOEG$_{350}$MAM** and **polyOEG$_{750}$MAM** (Table 1, entries 15, 16) did not show a phase transition between 0 and 93 °C.

The effect of (co)polymer concentration on the cloud point was determined for two samples: **poly[(MEO$_2$)$_{76}$-*co*-Hex$_{24}$]AM** and **polyMEO$_2$MAM** which have cloud points of 26.0 and 55.8 °C respectively at the concentration of 5.0 g/L examined previously. The (co)polymers were also examined at concentrations of 0.5, 1.0, 2.0, and 10.0 g/L, Figure 7. Consider first the concentration effect on **poly[(MEO$_2$)$_{76}$-*co*-Hex$_{24}$]AM**. At the lowest concentration evaluated, 0.5 g/L, this amphiphilic copolymer exhibits a measured cloud point of 37.2 °C. Doubling this concentration results in a decrease of the cloud point of nearly seven degrees to 30.4 °C while increasing the concentration further to 2.0 g/L results in a further, but less pronounced decrease to 26.7 °C. Beyond this concentration

dx.doi.org/10.1021/ma202700y | *Macromolecules* 2012, 45, 1362–1374

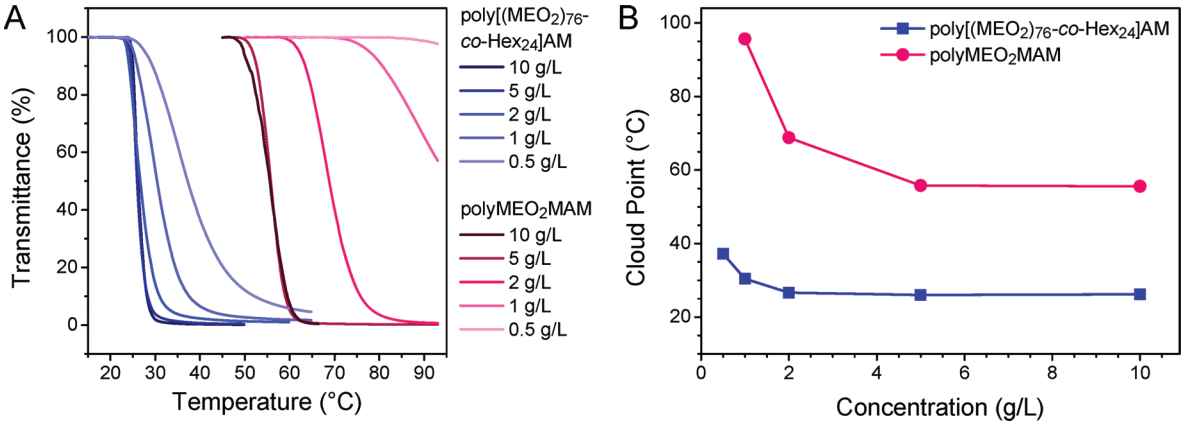


Figure 7. Influence of (co)polymer concentration on the cloud point for an acrylamido copolymer (blue curves) and a methacrylamido polymer (red curves). (A) Turbidity curves. (B) Plot of cloud point versus concentration showing the stronger increase of phase separation temperature with decreasing temperature for the methacrylamido derivative.

there appears to be little, if any, concentration dependence on the LCST with phase transitions occurring at 26.0 and 26.2 °C at concentrations of 5.0 and 10.0 g/L. The concentration dependence of the cloud point for **polyMEO$_2$MAM** is significantly more pronounced. Recall that the cloud point at a concentration of 5.0 g/L for this homopolymer was determined to be 55.8 °C. A similar value of 55.6 °C was found for a 10.0 g/L solution. At 2.0 g/L, however, the cloud point jumps by 13 to 68.8 °C, while at the a concentration of 1.0 g/L the cloud point jumps an additional ~30 to 95.7 °C (determined by extrapolation of the measured cloud point curve to 50% transmittance). Below this concentration the polymer was soluble over the entire observed temperature range. These results indicate that the acrylamido copolymer would be the better choice for applications where a larger range of, essentially, concentration independent responsiveness is desired.

Urea is a well-documented H-bond breaking molecule that can have a dramatic effect upon the solution behavior of (co)polymers in aqueous media.[68−70] For example, Sagle et al.[68] noted that the LCST of PNIPAM gradually decreases from ~32.0 to ca. 23.0 °C upon increasing the urea concentration to 7.0 M; an observation rationalized in terms of urea facilitating the hydrophobic collapse via intramolecular H-bonding to the PNIPAM amide residues. Similarly, the addition of urea can induce insoluble-to-soluble transitions upon heating (UCST-type behavior) whereby urea disrupts the inter- or intramolecular H-bonding interactions responsible for initial insolubility.[70] The effect of added urea upon the aqueous phase transitions of **polyMEO$_2$MAM** and **poly[(MEO$_2$)$_{85}$-*co*-Hex$_{15}$]** was examined with the expectation that these (meth)acrylamido-PEG species would behave in a fashion similar to that reported for PNIPAM, i.e., urea addition would result in a decrease in the LCST. As described above, **polyMEO$_2$MAM** has a measured cloud point, in pure water, of 55.8 °C at 5.0 g/L. At a urea concentration of 26.7 mM, corresponding to one molecule of urea per repeat unit, a small *increase* in the LCST is observed with the phase transition occurring at 56.5 °C. Increasing the concentration to 0.5 M urea results in a more significant increase in the LCST to 63.1 °C and finally at concentrations ≥2.0 M the LCST behavior completely vanishes and the polymer remains soluble up to temperatures in excess of 93.0 °C. This would suggest that inter- and intramolecular H-bonding associated with the amide residues is a very important factor governing the phase behavior of these materials and has a pronounced effect on the LCST. Disruption of these H-bonding associations raises the LCST by eliminating an important physical pathway by which such polymers can self-aggregate and undergo the coil-to-globule phase transition. A similar increase in the LCST was also observed for **poly[(MEO$_2$)$_{85}$-*co*-Hex$_{15}$]** upon addition of 0.5 M urea (46.7 to 48.8 °C), Figure S6 in Supporting Information.

Solution Properties in Alcohols. In addition to an evaluation of the LCST behavior in aqueous media of the (meth)acrylamido PEG derivatives their UCST behavior in 2-propanol and 1-octanol was also investigated at a concentration of 5.0 g/L. The experimentally determined UCST values are given in Table 2 and are plotted in Figure 8A. Turbidity curves measured in 2-propanol are shown in Figure 8B, curves measured in 1-octanol may be found the Supporting Information, Figure S7.

Table 2. Cloud Points (50% Transmittance) Found for (Meth)acrylamido Homopolymers in 2-Propanol and 1-Octanol

		cloud point 2-propanol (5.0 g/L)[a]		cloud point 1-octanol (5.0 g/L)[a]	
entry	polymer	cooling (°C)	heating (°C)	cooling (°C)	heating (°C)
1	**polyMEO$_2$AM**	s[b]	s	s	s
2	**polyMEO$_3$AM**	s	s	s	s
3	**polyOEG$_{350}$AM**	s	s	s	s
4	**polyOEG$_{750}$AM**	9.3	16.0	7.5	18.9
5	**pOEG$_{5k}$AM**	30.2	38.5	25.5	45.5
6	**polyMEO$_2$MAM**	s	s	s	s
7	**polyMEO$_3$MAM**	n.d.	−3[c]	n.d.	2[c]
8	**polyOEG$_{350}$MAM**	4.4	8.1	4.0	8.8
9	**polyOEG$_{750}$MAM**	13.9	17.4	9.0	18.6
10	**PEG 6k**	15.8	41.5	16.5	49.2
11	**polyMEO$_{4/5}$MA**[d]	18.7[e]			

[a]Cloud points depend on concentration, molecular weight and polymer end groups. [b]Measurements in alcohols were carried out between 0 and 70.0 °C. [c]Determined visually with a thermometer. [d][Poly(ethylene glycol) monomethyl ether methacrylate], $M_{monomer}$ = 300 g/mol. [e]Found for a 10.3 kg/mol sample at 5.0 g/L, value taken from reference[12]

dx.doi.org/10.1021/ma202700y | *Macromolecules* 2012, 45, 1362−1374

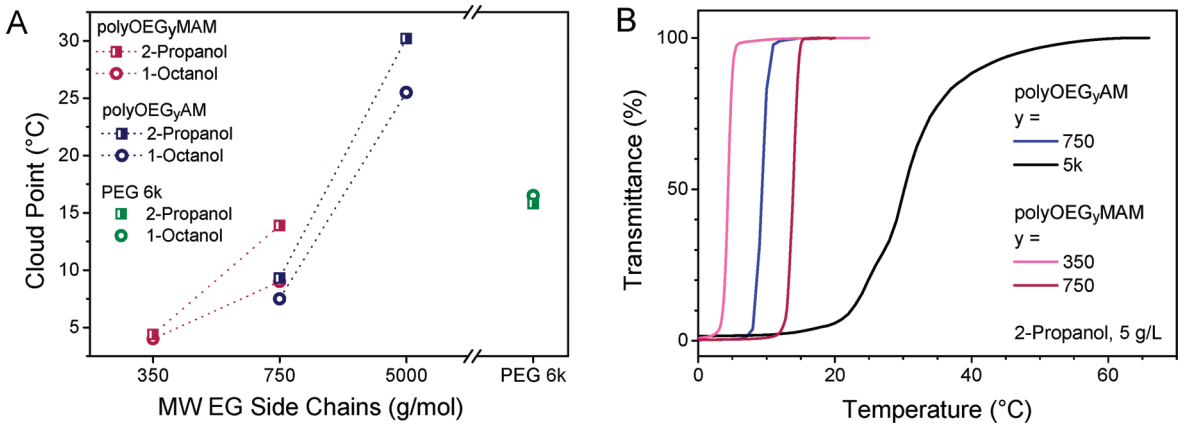


Figure 8. UCST-type behavior of OEG amide homopolymers in alcohols. (A) Cloud point values of polyacrylamides (blue), polymethacrylamides (purple), and reference PEG 6k in 2-propanol (squares) and 1-octanol (circles) in dependence of OEG side chain length (dotted lines are added to guide the eye). (B) Cooling curves of homopolymers in 2-propanol.

Several important observations were made. First, both diethylene glycol (meth)acrylamido polymers **polyMEO$_2$AM** and **polyMEO$_2$MAM** exhibit high solubility in both 2-propanol and 1-octanol with no clouding occurring when kept at −25.0 °C for several days (Table 2, entries 1 and 6). For longer EG side chains, the acrylamido derivatives showed a better solubility in both tested alcohols compared to the methacrylamido versions, very similar to the observations made on aqueous solutions. Whereas **polyMEO$_3$MAM** and **polyOEG$_{350}$MAM** (Table 2, entries 7 and 8) were found to cloud in 2-propanol at low temperatures (below −3.0 °C and at 4.4 °C, respectively), the solutions of the corresponding acrylamido polymers **polyMEO$_3$AM** and **polyOEG$_{350}$AM** (Table 2, entries 2 and 3) in both alcohols remained transparent down to −25.0 °C. In the same fashion, but significantly less pronounced, the cloud points of **polyOEG$_{750}$MAM** (Table 2, entry 9, purple symbols in Figure 8A) were found to be slightly higher (4.6 °C higher in 2-propanol, 1.5 °C higher in 1-octanol) than those of **polyOEG$_{750}$AM** (Table 2, entry 4, blue symbols in Figure 8A) indicating a decreased solubility. Second, with an increasing length of the pendant EG chains the UCST-type cloud point increases, as indicated by the dotted lines in Figure 8A. For example, in 2-propanol, the phase separation of **polyOEG$_{750}$MAM** (13.9 °C) occurred at a temperature 9.5 °C higher than that of **polyOEG$_{350}$MAM** (4.4 °C) (dotted purple lines in Figure 8A). In order to evaluate whether this was also true for acrylamido polymers and to determine the properties of a graft-copolymer with much longer PEG side chains, **polyPFPA** was reacted with PEG 5000 amine. As with the lower molecular weight amines, ^{19}F NMR of the reaction mixture indicated a complete cleavage of the activated esters. However, SEC analysis revealed a bimodal distribution with a (PS standard) molecular weight of 177.4 kg/mol and a PDI of 1.74 (Table 1, entry 5, Figure S4 in Supporting Information). This very broad distribution may be due to an incomplete conversion involving hydrolysis reactions and suggesting that this sterically challenging graft reaction poses a limitation to the PFP ester approach. It is also plausible that the PEG 5000 amine contained some diamine impurities that caused cross-linking. In spite of its broad molecular weight distribution, **polyOEG$_{5K}$AM** represented a significantly larger PEG amide analogue. As anticipated, it was found to have increased cloud points (i.e., decreased solubility) in both alcohols compared to the acrylamido polymer with shorter OEG side chains, with transitions occurring at 30.2 °C (2-propanol) and 25.5 °C (1-octanol), respectively (Table 2, entry 5, dotted blue lines in Figure 8A). It was, however, noted that the increase of transition temperature with increasing OEG side chain length also caused an increase in the hysteresis. Heating and cooling transition temperatures highlighting the hysteresis are plotted in Figure S8A, B in the Supporting Information. This effect was especially pronounced in 1-octanol, where the temperature difference between cooling and heating cycles was found to increase from 4.8 to 9.6 °C when going from **polyOEG$_{350}$MAM** to **polyOEG$_{750}$MAM** and from 11.4 to 20.0 °C when increasing the PEG chain length from **polyOEG$_{750}$AM** to **polyOEG$_{5K}$AM**. For comparison, a standard PEG 6K, with OH end groups, was measured in 2-propanol and 1-octanol giving cloud points of 15.8 and 16.5 °C, respectively, values in between those of the acrylamido OEG$_{750}$ and OEG$_{5K}$ graft polymers (Table 2, entry 10). The hystereses of PEG 6K in 2-propanol and 1-octanol were found to be very large with 25.7 and 32.7 °C, respectively, suggesting that in terms of retarded redissolution characteristics, the OEG amide polymers approach the behavior of pure PEG with an increasing OEG side chain length. Similar to the case in aqueous solutions, the amide species exhibited a better solubility than the corresponding ester analogues. As a reference, the cloud point of the polymethacrylate **polyMEO$_{4/5}$MA** in 2-propanol was found to be 18.7 °C[12] which is higher than the measured transition temperatures even for the methacrylamido polymers with longer OEG side chains, **polyOEG$_{350}$MAM** (4.4 °C) and **polyOEG$_{750}$MAM** (13.9 °C). A surprising observation was the very little difference between 2-propanol and 1-octanol, with all transition temperatures (except PEG 6K) in 2-propanol being somewhat higher than those in 1-octanol. This is in complete contrast to the behavior of the methacrylate derivatives for which a transition temperature increase of roughly 5.0 °C per additional methylene group in *n*-alcohols was found.[12] It therefore seems that the ester group plays an important role in the unfavorable interactions between an OEG-based polymer and the alcoholic solvent, that cause the polymer to lose solvation during the chain collapse. The amide group on the other hand seems to be capable of forming hydrogen bonds of similar thermal stability independent of the chain length of the alcohol. Upon exchanging the ester for an amide group, there is no decreased solubility with an increased alcohol chain length. The amide analogues therefore present an interesting

dx.doi.org/10.1021/ma202700y | *Macromolecules* 2012, 45, 1362−1374

class of materials with predictable thermal properties independent of alcohol polarity that can range from hydrophilic (2-propanol, miscible with water in all proportions) to hydrophobic (1-octanol, essentially insoluble in water).

Biocompatibility and Bioconjugation. As noted earlier, besides the interesting phase behavior exhibited by (meth)-acrylic PEG analogues, and also demonstrated herein for (meth)acrylamido species, PEG and its derivatives have attracted significant attention in the biomaterials arena due to the nontoxic, antifouling and so-called 'stealth' properties exhibited by such materials. To demonstrate the potential of these (meth)acrylamido (co)polymers in biomedical applications the cytotoxicity of two samples, **polyMEO$_2$AM** and **polyMEO$_3$AM**, were tested on MRC5 fibroblast cells at concentrations ranging from 0.005 to 10.0 g/L. These two samples were chosen since both are completely soluble in aqueous media up to temperatures in excess of 93.0 °C, in contrast to the acrylic analogues, and highlights how the (meth)acrylamido species may offer advantages in biomedical applications over the (meth)acrylic species by virtue of both enhanced solubility (higher or absent LCSTs) and significantly improved hydrolytic stability of the amide vs ester functional groups. Cell viability was determined via a fluorescence method by which living, metabolically active, MRC5 cells convert a redox dye (blue resazurin) into a fluorescent species (red resorufin). Thus, measuring the fluorescence affords a straightforward method for determining cell concentration and thus, indirectly, the cytotoxicity of the acrylamido-PEG polymers. Figure 9 shows a plot of cell viability vs polymer concentration after incubation of the MRC5 cells in the presence of **polyMEO$_2$AM** and **polyMEO$_3$AM** for 72 h. In both instances these acrylamido-based PEG analogues were found to be noncytotoxic with measured cell viability at ≥85% after 3 days even at high concentrations. These results confirm that these acrylamido-PEG derivatives exhibit desirable "biocompatible" properties which when taken in conjunction with the enhanced solubility and hydrolytic stability (vs the (meth)acrylic species) suggests that these materials may find potential application in areas not accessible to the ester-analogues.

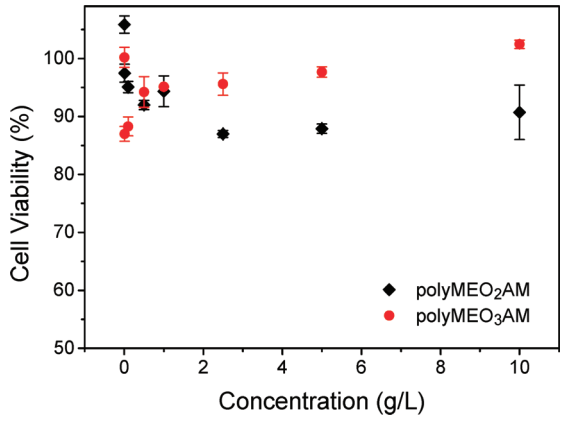


Figure 9. Cell viability after incubation of MRC5 cells with varying concentrations of acrylamido PEG polymers for 72 h.

As discussed above, the aqueous phase behavior of the acrylamido-based PEG analogues can be tuned via the incorporation of a hydrophobic comonomer. In addition to statistical copolymers containing hexylamide residues, and to demonstrate the potential of the route described herein for preparing biocompatible copolymers containing biorelevant molecules, the precursor **polyPFPA** homopolymer was treated with a mixture of di(ethylene glycol) methyl ether amine and thyroxine (T_4), Table 1 entries 10 and 11. T_4 is a prohormone serving as a precursor to triiodothyronine (T_3) secreted by the thyroid gland and is involved in controlling the rate of metabolic processes and also influences physical development.[71,72] The relevant region of T_4, where recognition and metabolic conversion into T_3 takes place, is the outer diiodophenyl ring. T_4 has been shown to selectively recognize and bind its transport protein transthyretin even when the amino group at the opposite end has been functionalized.[11,73] The synthesis was accomplished by employing a mixture of di(ethylene glycol) methyl ether amine and T_4, the incorporation ratio was verified and quantified by ^{1}H NMR spectroscopy, which showed the distinctive broad aromatic signals at 7.81 and 7.11 ppm originating from the incorporated T_4 groups. The activated esters were quantitatively cleaved, as determined by ^{19}F NMR spectroscopy, and ^{1}H NMR of the product indicated a complete presence of MEO_2 + T_4 groups in both cases (Figure S9 in Supporting Information). SEC analyses gave unimodal narrow distributions with the apparent molecular weight increasing with increasing T_4 contents which can be attributed to a conformational influence of the bulky T_4 side groups (Figure S10 in Supporting Information). Two copolymers, **poly**[(**MEO$_2$**)$_{91}$-*co*-**T4$_9$**]**AM** and **poly**[(**MEO$_2$**)$_{87}$-*co*-**T4$_{13}$**]**AM** with 9 and 13 mol % of T_4 units respectively were prepared. This demonstrates that the PFP precursors provide a versatile platform for the preparation of biofunctionalized PEG analogues. In particular, in light of specific binding of proteins to main chain bound targets, the short di(ethylene glycol) amide side chains would be at an advantage over longer, sterically more challenging, ester-bound OEG chains that would be necessary to provide a similar thermally independent water solubility. Both copolymers with 9 and 13% of T_4 were found to be totally soluble in water up to 93 °C, again highlighting the enhanced solubility provided by the OEG amides also in the presence of the biological hydrophobic comonomer.

CONCLUSIONS

Acrylamido and methacrylamido (co)polymers with ethylene glycol (EG) side chains of varying lengths were prepared from pentafluorophenyl activated ester precursor polymers with the respective ethylene glycol amines. Quantitative formation of EG amides, as well as of amide copolymers was found for the acrylic derivatives with as low as 1.2 equiv of amines per activated ester. For the methacrylate polymers a larger excess of amines was necessary to minimize the formation of acid groups. The PEG amide analogues showed an enhanced solubility in water and alcohols compared to the more commonly used ester derivatives which is attributed to the H-bond donor/acceptor properties of the amide linkage. All acrylamido species showed a better solubility (higher LCST transitions in water, lower UCST transitions in alcohols) than the corresponding methacrylamido polymers, and in contrast to the PNIPAM/PNIPMAM pair in water. Of the examined homopolymers, only the polymethacrylamides with MEO_2 or MEO_3 side groups showed LCST behavior in water, however with an unusually strong concentration dependence of the cloud point, as determined for **polyMEO$_2$MAM**. The acrylamido polymers can be rendered thermosensitive by the incorporation of hydrophobic comonomers such as *n*-hexylamide via the

dx.doi.org/10.1021/ma202700y | *Macromolecules* 2012, 45, 1362−1374

concurrent reaction of the **PFPA** precursor with a mixture of hexylamine and diethylene glycol methyl ether amine. The reactivity of hexylamine and diethylene glycol methyl ether amine toward PFP esters was found to be very similar. The cloud points of the obtained copolymers varied in a monotonically decreasing fashion with the incorporated hexylamides, providing a simple synthetic method to tune the thermal response of a library of copolymers with essentially the same degree of polymerization. An acrylamido derivative carrying stronger hydrophobic oligopropylene glycol side chains was also found to be thermally responsive with a cloud point around 22.0 °C which also exhibited a very strong endothermic transition, as determined by DSC, compared to a MEO_2/hexylacrylamide copolymer, which was attributed to a loss of hydration along the entire OPG side chains. An important finding of the study of thermal behavior in alcohols was that the strong dependence of the UCST-type transition on the alcohol chain length which was found for the ester derivatives is lost when the ester groups are exchanged for amides. With an increasing length of EG side chains, the solubility in water increased and the solubility in alcohols decreased, however, in the latter case, it was also accompanied by a strong increase of hysteresis which was also found for a linear PEG sample. **polyMEO$_2$AM** and **polyMEO$_3$AM** were nontoxic to MRC5 fibroblast cells at concentrations up to 10.0 g/L and the acrylic activated ester backbone provided a versatile platform for the incorporation of the hydrophobic prohormone thyroxine while the MEO_2 comonomers maintained an excellent solubility. The thorough investigation of the synthesis and thermal solution properties of this class of PEG analogues has provided a valuable insight into the activated ester precursor route and the significant roles comonomers, backbone methyl groups, and amide versus ester linkages play for the properties of these biocompatible materials.

■ ASSOCIATED CONTENT

Supporting Information

Representative ^{19}F NMR spectra, ^{1}H NMR spectra of hexylamide copolymers, list of feed ratios and obtained ratio for hexylamide copolymers, SEC traces of hexylamide copolymers and of **polyOPG$_{600}$AM** and **polyOEG$_{5k}$AM**, turbidity measurements of DSC samples, turbidity measurements of samples containing urea, turbidity curves of (meth)acrylamido homopolymers in 1-octanol, plot of UCST cloud points found in 2-propanol and 1-octanol showing hysteresis values, ^{1}H NMR spectra and SEC chromatograms of copolymers containing thyroxine. This material is available free of charge via the Internet at http://pubs.acs.org.

■ AUTHOR INFORMATION

Corresponding Author

*E-mail: (A.B.L.) a.lowe@unsw.edu.au; (P.J.R.) p.roth@unsw.edu.au.

Notes

The authors declare no competing financial interest.

■ ACKNOWLEDGMENTS

Dr. Anthony Granville is kindly thanked for help with the DSC measurements.

■ REFERENCES

(1) Lu, Y.; Ballauff, M. *Prog. Polym. Sci.* **2011**, *36*, 767.
(2) Shao, P.; Wang, B.; Wang, Y.; Li, J.; Zhang, Y. *J. Nanomater.* **2011**, *2011*, No. in press.
(3) Fischer, F.; Zufferey, D.; Tahoces, R. *Polym. Int.* **2011**, *60*, 1259.
(4) Idziak, I.; Avoce, D.; Lessard, D.; Gravel, D.; Zhu, X. X. *Macromolecules* **1999**, *32*, 1260.
(5) Li, H.; Yu, B.; Matsushima, H.; Hoyle, C. E.; Lowe, A. B. *Macromolecules* **2009**, *42*, 6537.
(6) Maeda, Y.; Nakamura, T.; Ikeda, I. *Macromolecules* **2002**, *35*, 217.
(7) Chiefari, J.; Chong, Y. K.; Ercole, F.; Krstina, J.; Jeffrey, J.; Le, T. P. T.; Mayadunne, R. T. A.; Meijs, G. F.; Moad, C. L.; Moad, G.; Rizzardo, E.; Thang, S. H. *Macromolecules* **1998**, *31*, 5559.
(8) Iskander, G. M.; Baker, L. E.; Wiley, D. E.; Davis, T. P. *Polymer* **1998**, *39*, 4165.
(9) Monroy Soto, V. M.; Galin, J. C. *Polymer* **1984**, *25*, 254.
(10) Kudaibergenov, S.; Jaeger, W.; Laschewsky, A. *Adv. Polym. Sci.* **2006**, *201*, 157.
(11) Roth, P. J.; Jochum, F. D.; Zentel, R.; Theato, P. *Biomacromolecules* **2010**, *11*, 238.
(12) Roth, P. J.; Jochum, F. D.; Theato, P. *Soft Matter* **2011**, *7*, 2484.
(13) Neugebauer, D. *Polym. Int.* **2007**, *56*, 1469.
(14) Lutz, J.-F.; Hoth, A. *Macromolecules* **2005**, *39*, 893.
(15) Lutz, J.-F.; Akdemir, Ö.; Hoth, A. *J. Am. Chem. Soc.* **2006**, *128*, 13046.
(16) Lutz, J.-F. *Adv. Mater.* **2011**, *23*, 2237.
(17) Lutz, J.-F. *J. Polym. Sci., Part A: Polym. Chem.* **2008**, *46*, 3459.
(18) Hu, Z.; Cai, T.; Chi, C. *Soft Matter* **2010**, *6*, 2115.
(19) Han, S.; Hagiwara, M.; Ishizone, T. *Macromolecules* **2003**, *36*, 8312.
(20) Bebis, K.; Jones, M. W.; Haddleton, D. M.; Gibson, M. I. *Polym. Chem.* **2011**, *2*, 975.
(21) Moad, G.; Rizzardo, E.; Thang, S. H. *Aust. J. Chem.* **2005**, *58*, 379.
(22) Moad, G.; Rizzardo, E.; Thang, S. H. *Aust. J. Chem.* **2006**, *59*, 669.
(23) Moad, G.; Rizzardo, E.; Thang, S. H. *Aust. J. Chem.* **2009**, *62*, 1402.
(24) Lowe, A. B.; Torres, M.; Wang, R. *J. Polym. Sci., Part A: Polym. Chem.* **2007**, *45*, 5864.
(25) Lowe, A. B.; McCormick, C. L. *Prog. Polym. Sci.* **2007**, *32*, 283.
(26) Boyer, C.; Bulmus, V.; Davis, T. P.; Ladmiral, V.; Liu, J.; Perrier, S. *Chem. Rev.* **2009**, *109*, 5402.
(27) Evans, R. A. *Aust. J. Chem.* **2007**, *60*, 384.
(28) Binder, W. H.; Sachsenhofer, R. *Macromol. Rapid Commun.* **2007**, *28*, 15.
(29) Fournier, D.; Hoogenboom, R.; S., S. U. *Chem. Soc. Rev.* **2007**, *36*, 1369.
(30) Binder, W. H.; Sachsenhofer, R. *Macromol. Rapid Commun.* **2008**, *29*, 15.
(31) Hizal, G.; Tunca, U.; Sanyal, A. *J. Polym. Sci., Part A: Polym. Chem.* **2011**, *49*, 4103.
(32) Iskin, B.; Yilmaz, G.; Yagci, Y. *Polym. Chem.* **2011**, *2*, 2865.
(33) Franc, G.; Kakkar, A. K. *Chem.—Eur. J.* **2009**, *15*, 5630.
(34) Inglis, A. J.; Sinnwell, S.; Stenzel, M. H.; Barner-Kowollik, C. *Angew. Chem., Int. Ed.* **2009**, *48*, 2411.
(35) Lowe, A. B. *Polym. Chem.* **2010**, *1*, 17.
(36) Roth, P. J.; Boyer, C.; Lowe, A. B.; Davis, T. P. *Macromol. Rapid Commun.* **2011**, *32*, 1123.
(37) Lowe, A. B.; Harvison, M. A. *Aust. J. Chem.* **2010**, *63*, 1251.
(38) Lowe, A. B.; Hoyle, C. E.; Bowman, C. N. *J. Mater. Chem.* **2010**, *20*, 4745.
(39) Hoyle, C. E.; Lowe, A. B.; Bowman, C. N. *Chem. Soc. Rev.* **2010**, *39*, 1355.
(40) Hoyle, C. E.; Bowman, C. N. *Angew. Chem., Int. Ed.* **2010**, *49*, 1540.
(41) Boyer, C.; Bulmus, V.; Davis, T. P. *Macromol. Rapid Commun.* **2009**, *30*, 493.
(42) Harvison, M. A.; Lowe, A. B. *Macromol. Rapid Commun.* **2011**, *32*, 779.

(43) Harvison, M. A.; Roth, P. J.; Davis, T. P.; Lowe, A. B. *Aust. J. Chem.* **2011**, *64*, 992.
(44) Jochum, F. D.; Roth, P. J.; Kessler, D.; Theato, P. *Biomacromolecules* **2010**, *11*, 2432.
(45) Schattling, P.; Jochum, F. D.; Theato, P. *Chem. Commun.* **2011**, *47*, 8859.
(46) Theato, P. *J. Polym. Sci., Part A: Polym. Chem.* **2008**, *46*, 6677.
(47) Zhang, X. A.; Chen, M. R.; Zhao, H.; Gao, Y.; Wei, Q.; Zhang, S.; Qin, A.; Sun, J. Z.; Tang, B. Z. *Macromolecules* **2011**, *44*, 6724.
(48) Nilles, K.; Theato, P. *J. Polym. Sci., Part A: Polym. Chem.* **2010**, *48*, 3683.
(49) Gibson, M. I.; Frohlich, E.; Klok, H.-A. *J. Polym. Sci., Part A: Polym. Chem.* **2009**, *47*, 4332.
(50) Eberhardt, M.; Mruk, R.; Zentel, R.; Théato, P. *Eur. Polym. J.* **2005**, *41*, 1569.
(51) Clerc, J.; Schellenberg, B.; Groll, M.; Bachmann, A. S.; Huber, R.; Dudler, R.; Kaiser, M. *Eur. J. Org. Chem.* **2010**, *21*, 3991.
(52) Mongondry, P.; Bonnans-Plaisance, C.; Jean, M.; Tassin, J. F. *Macromol. Rapid Commun.* **2003**, *24*, 681.
(53) Willcock, H.; O'Reilly, R. K. *Polym. Chem.* **2010**, *1*, 149.
(54) Roth, P. J.; Kessler, D.; Zentel, R.; Theato, P. *Macromolecules* **2008**, *41*, 8316.
(55) Roth, P. J.; Kessler, D.; Zentel, R.; Theato, P. *J. Polym. Sci., Part A: Polym. Chem.* **2009**, 3118.
(56) Roth, P. J.; Kim, K.-S.; Bae, S. H.; Sohn, B.-H.; Theato, P.; Zentel, R. *Macromol. Rapid Commun.* **2009**, *30*, 1274.
(57) Jochum, F. D.; Roth, P. J.; Kessler, D.; Theato, P. *Biomacromolecules* **2010**, *11*, 2432.
(58) Wang, C.; Yan, Q.; Liu, H.-B.; Zhou, X.-H.; Xiao, S.-J. *Langmuir* **2011**, *27*, 12058.
(59) Hua, F.; Jiang, X.; Li, D.; Zhao, B. *J. Polym. Sci., Part A: Polym. Chem.* **2006**, *44*, 2454.
(60) Mertoglu, M.; Garnier, S.; Laschewsky, A.; Skrabania, K.; Storsberg, J. *Polymer* **2005**, *46*, 7726.
(61) Taylor, L. D.; Cerankowski, L. D. *J. Polym. Sci., Polym. Chem. Ed.* **1975**, *13*, 2551.
(62) Steinhauer, W.; Hoogenboom, R.; Keul, H.; Moeller, M. *Macromolecules* **2010**, *43*, 7041.
(63) Roth, P. J.; Jochum, F. D.; Forst, F. R.; Zentel, R.; Theato, P. *Macromolecules* **2010**, *43*, 4638.
(64) Dai, S.; Tam, K. C. *Langmuir* **2004**, *20*, 2177.
(65) Batrakova, E. V.; Kabanov, A. V. *J. Controlled Release* **2008**, *130*, 98.
(66) Tang, Y.; Ding, Y.; Zhang, G. *J. Phys. Chem. B* **2008**, *112*, 8447.
(67) Crespy, D.; Rossi, R. M. *Polym. Int.* **2007**, *56*, 1461.
(68) Sagle, L. B.; Zhang, Y.; Litosh, V. A.; Chen, X.; Cho, Y.; Cremer, P. S. *J. Am. Chem. Soc.* **2009**, *131*, 9304.
(69) Saito, S.; Otsuka, T. *J. Colloid Interface Sci.* **1967**, *25*, 531.
(70) Longenecker, R.; Mu, T.; Hanna, M.; Burke, N. A. D.; Stöver, H. D. H. *Macromolecules* **2011**, *44*, 8962.
(71) Kendall, E. C. *J. Am. Med. Assoc.* **1915**, *64*, 2042.
(72) Walker, P.; Weichsel, M.; Fisher, D.; Guo, S. *Science* **1979**, *204*, 427.
(73) Marchesini, G. R.; Meimaridou, A.; Haasnoot, W.; Meulenberg, E.; Albertus, F.; Mizuguchi, M.; Takeuchi, M.; Irth, H.; Murk, A. J. *Toxicol. Appl. Pharmacol.* **2008**, *232*, 150.

Macromolecules

Article

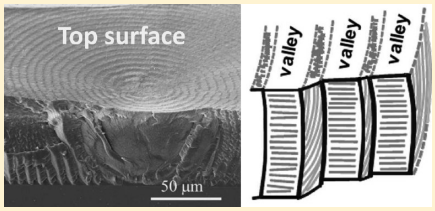
pubs.acs.org/Macromolecules

Crystal Lamellae of Mutually Perpendicular Orientations by Dissecting onto Interiors of Poly(ethylene adipate) Spherulites Crystallized in Bulk Form

E. M. Woo,* Lai-Yen Wang, and Siti Nurkhamidah

Department of Chemical Engineering, National Cheng Kung University, Tainan 701-01, Taiwan

ABSTRACT: Three-dimensional dissecting onto interior lamellar structures of spherulites in poly(ethylene adipate) (PEA) in bulk forms crystallized at 28 ± 3 °C were studied in correlation with thin-film forms. Interior morphology in bulk PEA samples revealed onion-like alternating shells. Interior spherulites clearly exposes that the lamellae within the shell interior are composed of stacked plate lamellae in radial direction while the shell surface region are arranged by tangential lamellae. Shell interior and surface correspond to the valley and ridge of ring-banded on the top surface, respectively. Morphology characterization on fracturing patterns further evidence that the shells could be cleaved apart along the shell surface, indicating weak physical connection between these two perpendicularly oriented shells. Further thermal analysis and X-ray results also supported existence of highly ordered lamellar packing into two mutually perpendicular chain orientations in the 28 °C-crystallized PEA bulks, which differed significantly from the randomly oriented lamellae in either 2 or 33 °C-crystallized PEA bulks.



INTRODUCTION

Interpretations on the formation of ring-banded morphology in polymer spherulites have been debated for decades. Lamellar twisting among all the proposed mechanisms is the most adapted model to account for the formation of the concentric ring bands in spherulites.[1−8] Explanations provided to account for lamellar twisting may be divided into two views. One view proposes that lamellar twisting is associated with features that exist during growth or are generated by the growth process itself,[9] while another describes that lamellar twisting is associated with the morphology or structures of lamellae themselves. These may be associated with screw dislocations[6,8,10] or surface stresses at the fold surface.[11] These complex issues have long been explored by some outstanding work in the literature. By following the classical work of Keith and Padden's hints,[2,3] Bassett et al.[12,13] have explored further possibilities of lamellar assembly in relation with the ring-banded patterns in polymer spherulites. If the polymer chains are tilted in the lamellae and screw dislocations are present, they have shown that the development of the lamellae in the screws can be asymmetric. In addition, if the twist of the leading lamellae is influenced by these additional lamellae in the screws, then the whole stack of leading lamellae would be asymmetrical. Lustiger and Lotz et al.[5] have further suggested that polyethylene (PE) lamellae undergo continuous twisting rather than successive misalignment of essentially untwisted segments. Crystals of C-shapes (abbreviated Cs), S-shapes (abbreviated Ss), or a combination of both of shapes can be observed on the top surface of PE ring-banded spherulites in the bulk samples depend on the projection of helicoids on a plane. It has been suggested that Cs and Ss are caused by geometrical effects as the lamellae are projected onto a surface at various angles.[5]

Microscopic observation on thin-film samples has been the most often used method to study the ring-banded morphological features. Xu et al.[14] have characterized banded spherulites of poly(3-hydroxybutyrate-*co*-hydroxyhexanoate) (P(HB-*co*-HHx) using in situ atomic force microscopy (AFM) and found that the lamellae in the banded spherulites of P(HB-*co*-HHx) exhibit complicated growth behaviors: twisting, bending, backward growth, and branching. In addition, the lamellae of P(HB-*co*-HHx) spherulites continuously twist to show alternating edge-on and flat-on views along the radial direction, and Xu et al. concluded that the lamellae of P(HB-*co*-HHx) exhibited right-handed twisting.[14] However, hypothesis of stem helical handedness may be no longer adequate, and a chiral polymer can have right- and left-handed lamellae within the same spherulites or upon blending according to Xu et al.'s later work.[15] Apart from AFM, transmission electron microscopy (TEM) has commonly been adapted to analyze the banded morphology in polymer spherulites. Ho et al.[16] have explained that the banded morphology in poly(trimethylene terephthalate) (PTT) is attributed to lamellar twisting which is evidenced by the observations of wavy morphology from reflected light microscopy and TEM. Furthermore, the lamellar twisting in PTT may be caused by the tilted chain stems which are nonorthogonal to fold surface.[16] Recently, microfocus (microbeam) wide-angle X-ray diffraction (WAXD) was used to analyze the ring-banded morphology in spherulites.[17−20] A single poly(3-hydroxybutyrate) (PHB) spherulite has been mapped by means of microbeam X-ray diffraction using a synchrotron source with 7 μm beam, and it is concluded that

Received: October 4, 2011
Revised: January 13, 2012
Published: January 24, 2012

ACS Publications © 2012 American Chemical Society

dx.doi.org/10.1021/ma202222e | *Macromolecules* 2012, 45, 1375−1383

the ringed spherulite of PHB is attributed to the lamellar twisting.[16]

Other researchers, however, propose mechanisms different from the lamellar twisting in expounding the formation of ringed spherulites.[21−23] Wang et al.[21] have proposed a nonlinear diffusion process induced rhythmic growth mechanism to interpret the concentric ring-banded structures of poly(ε-caprolactone) (PCL) produced during solvent evaporation, and the nonlinear diffusion process is due to the periodically change in the concentration gradient of the polymer solution. Ring-banded spherulites in poly(1,4-butylene adipate) (PBA) have attracted many researchers' attention, and different mechanisms have ever been provided. Poly(ethylene adipate) (PEA) also shows apparent extinction double-ring bands at a very narrow crystallization temperature range (T_c = 28 ± 3 °C), whose surface morphological characterization on the ring-banded spherulites of PEA was performed using AFM.[24] It has been revealed that the crystal species on the ridges and valley seem discrete and unrelated with each others. To be complete, the surface morphology PEA may have to be further extended by interior 3-D structural characterization. Thus, the frequently adapted lamellar twisting mechanism may have to be refined to account for the ring-banded spherulites in different polymers. Keith and Padden[25] have stated in conclusion that it needs emphasis that a supposed "unique cause" for twisting orientation in banded polymer spherulites is a chimera and that twisting can be attributed to one or other of two factors: (i) chain tilt which promotes a generation of surface stresses in lamellae and (ii) isochiral helicity. Even though these two factors have been assumed by many investigators, however, Keith had reservation that they universally account for ring bands in all polymers. In addition, the lamellar packing in thin films may differ significantly from thick/bulk polymers as growth constraints and surface stress may be completely different in the bulk state.

So far, attempts on interpreting the ring-banded spherulites of polymers have been based on the characterizations of surfaces of thin-film polymer samples. As pointed out in a preliminary study,[26] interiors of 3-D ring bands of spherulites would be essential and informative for probing more details in the complex growth mechanisms of these periodical lamellar assembly patterns in semicrystalline polymers. As cited above, interpretations on the ring banded spherulites of polymers have been mostly based on the characterization on thin-film samples, and interiors of 3-D pictures of ring bands are yet to be probed for more detailed views on understanding the fine structures of ring bands in spherulites. In this study, scanning electron microscopy (SEM), wide-angle X-ray, and differential scanning calorimetry analyses were collectively applied to observe the crystalline morphology in the interior of bulk form using PEA as a model, which is know to exhibit ring bands in thin film when crystallized at 28 °C. Furthermore, three-dimensional structures of ring bands were expounded to more fully understand complex factors in lamellar assembly in crystallization and to shed new light on the architecture or mechanisms of the ringed spherulites in semicrystalline polymers.

When crystallized at the 25−32 °C window, PEA is widely known to show ring bands on thin-film samples (nanometers to less than 10 μm),[23,24] whose ring-band mechanism has been widely discussed and was not the objective of this study. This study for the first time addresses three-dimensional dissecting into interiors of lamellar assembly in spherulites of bulk PEA samples (50−150 μm). Ring-banded patterns have conventionally been reported for the some polymers in thin films, but in this study, fractured interiors of bulk-crystallized PEA were observed instead for revealing inner lamellae in comparison with its top free-surface ring bands. In this study, using PEA as a convenient model, the crystalline morphology in the interior of bulk form was expounded by three-dimensional dissecting. There were two reasons for using PEA as a model system in this study: (1) the surface ring bands in PEA in thin-film forms have been well studied, and (2) PEA exhibits well-defined ring bands in a narrow temperature window (28 ± 3 °C); (3) PEA bulk samples could be easily fractured to expose the interiors. PEA samples were prepared in (a) films in comparison with (b) thicker bulks for stereo three-dimensional dissecting and ultimate construction of the periodical patterns underneath the surface rings. Furthermore, three-dimensional structures of ring bands were expounded to more fully understand the complex factors in lamellar assembly in crystallization and to shed new light on the architecture or mechanisms of the ring-banded spherulites in semicrystalline polymers. Correlation of surface ring bands with inner concentric 3-D shells (in fracture surface) was attempted by dissecting across several different interior spots of spherulites in bulk crystallized PEA.

EXPERIMENTAL SECTION

Materials and Procedures. Poly(ethylene adipate) (PEA), a low-melting semicrystalline polyester with T_g = −52 °C and T_m = 43 °C, was purchased as research-grade materials from Aldrich Co. The weight-average molecular weight (M_w) was nearly 10 000 g/mol, determined by gel permeation chromatography (GPC, Waters 410) using tetrahydrofuran (THF) as eluent at a flow rate of 1.0 mL/min. The polymer was purified by reprecipitation from chloroform into cold methanol (ca. −10 °C). PEA pellets/powder were heated, melted, and then brought to crystallization immediately by quenching into an isothermal bath. Alternatively, PEA was also dissolved in $CHCl_3$ (chloroform) in higher concentrations, and a few drops were repeatedly deposited on glass substrate to stacked into thick bulks. Degassing was performed at 45 °C in a vacuum oven for 24 h. Crystallization conditions were as follows. PEA in thick bulk forms (25−50 μm) was typically heated to T_{max} = 90 °C, rapidly brought to T_c = 2, 26, 28, 29, and 33 °C, etc., and held for time = 1−24 h (longer time for higher T_c) for full crystallization. Alternatively, another set of PEA samples in even thicker bulk forms were prepared by melting the PEA polymer deposited on aluminum foil or in wrapped with aluminum foil (for molding) at 90 °C for premelting, and then the molten PEA in foil was quickly dipped into water bath set precisely at controlled temperature of 2, 26, 28, 29, 33, and 35 °C for at least 2−4 h for full crystallization. During sample crystallization, the temperature of the bath was kept exactly isothermal within ±0.5 °C. For water bath, washing of samples was not needed. Bulk PEA samples had thickness from 50 to 75 μm. In this condition, nucleation was expected to initiate from (1) bottom substrate surface, (2) top surface, and (3) occasionally from interior. As cleavage across spherulites tended to be randomly initiated, fracture was performed on PEA bulk samples several times to acquire sufficient number of specimens for morphology analyses. Cleavage of samples was controlled to fracture near the poles of spherulites and across equator line of spherulites.

Apparatus. *Polarizing Optical Microscopy (POM).* A polarizing optical microscope (Nikon Optiphot-2, POM), equipped with a digital camera charge-coupled device (CCD), was used to confirm the crystal morphology as crystallized at several T_c (2, 26, 28, 29, and 33 °C) of thin-film PEA samples.

Scanning Electron Microscopy (SEM). Fractured surfaces of bulk-form PEA samples were examined and characterized using scanning electron microscopy (FEI Quanta-400F, SEM) for revealing lamellar structure in the fracture and top free surface of bulk PEA. Samples

were coated with gold vapor deposition using vacuum sputtering prior to SEM characterization.

Differential Scanning Calorimetry (DSC). Thermal transitions of bulk crystallized PEA samples were characterized with a differential scanning calorimeter (Diamond, Perkin-Elmer Corp.) equipped with an intracooler for quenching and cooling. For measurement of melting temperatures, a scanning rate of 10 °C/min was used. Prior to DSC runs, the temperature and heat of transition of the instrument were calibrated with indium or zinc standards. A continuous nitrogen flow in the DSC sample cell was maintained.

Wide-Angle X-ray Diffraction (WAXD). PEA bulk samples (crystallized at specified T_c = 2, 26, 28, 29, and 33 °C) were characterized with X-ray instrument (Shimadzu/XRD-6000) with Cu Kα radiation (30 kV and 40 mA). The scanning angle (2θ) covered a range between 10° and 30° at a rate of 2°/min.

RESULTS AND DISCUSSION

Figure 1 shows SEM graphs (8000×) on top surfaces of bulk PEA sample (50−75 μm) crystallized at T_c = 28 °C. The ridge

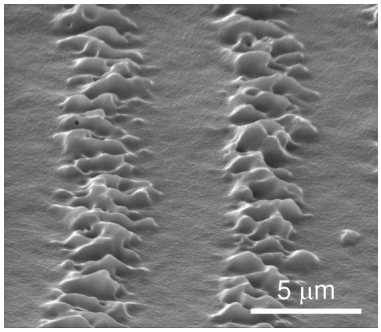


Figure 1. SEM graphs (8000×) of the top surface of bulk PEA crystallized at 28 °C.

band is packed with discrete triangular crystals, and the valley is apparently flat. It should be noted that such 3-D stereo ridge morphology with triangular protrusion crystals on the ridge band is not seen in thin-film PEA sample crystallized at the same T_c. Naturally crystallized bulk PEA would have amorphous constituents expelled to partially fill or cover up the lamellae in ridges and/or valley; i.e., the crystal plates associated with ridge and valley might both be partially or fully covered in samples as crystallized. To dig into interior of bulk lamellae, fracturing on bulk PEA samples (crystallized at T_c = 28 °C) was attempted.

Acetone-solvent vapor etching was performed on PEA bulk (50−75 μm in thickness) to induce splitting of the specimens. Splitting of specific locations of PEA samples such that the interiors of the ring-banded spherulites were exposed. SEM was then performed such that both the top surface and interior fractured surface in bulk PEA crystallized at 28 °C could be revealed simultaneously for comparison and correlation of the top surface with the interior lamellar structure. Figure 2 shows SEM graphs on partially fractured PEA bulk correlating from top surface into interior surface perpendicular to each other. By this way, correlation between the interior layered lamellae and their correspondence to the ring band pattern on top surface can be viewed in a direct way. Two interesting morphological features are critical. First of all, the SEM micrograph onto the interior PEA bulk reveals clearly that the lamellae underneath the top surface are aligned in layered and laminated cassettes resembling a corrugated board. The layer of radial lamellae is equivalent to "fluting", and the layer of tangential cilia lamellae

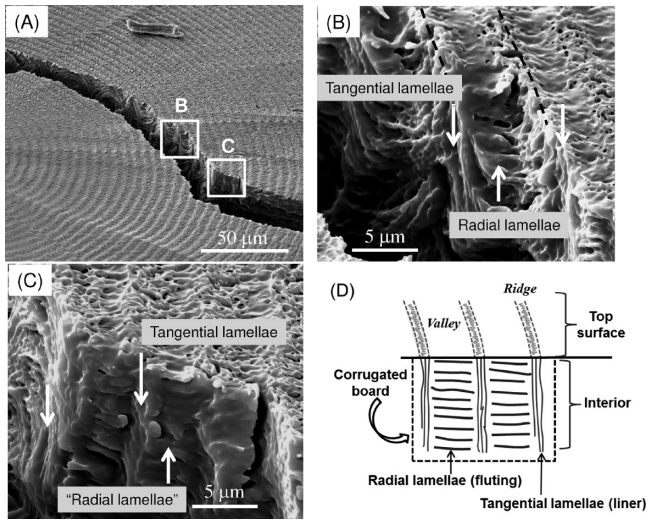


Figure 2. (A) SEM graphs for interior layered lamellae and their correspondence to top surface bands as viewed in a partially fractured bulk PEA samples, (B, C) zoom-in area as indicated in graph A, and (D) scheme for lamellar arrangement underneath the top surface.

is equivalent to "linear" of the corrugated board. In addition, each of the underneath shell cassettes corresponds to one ring band on the top surface, and the width of the interior cassette is exactly identical to the inter-ring spacing (~6 μm) on the top surface. In each cassette shell, the lamellae are structured like a laminated corrugated board, where the radial lamellae are directly underneath the valley band on the top surface and the lamellae are oriented horizontal to the top surface. In between the laminated shells of the radial lamellae, there is an interfacial layer filled with tangential lamellae, which protrude out vertically to form the ridge band on the top surface. That is, each of the corrugate boards is packed with alternating shells of radial lamellae and tangential lamellae that are oriented at 90° angle to each other. Ideally, interior morphology of ring-banded PEA would be clearer if the interfaces of the neighboring laminated cassettes could be torn off from each other. Such viewed would be further shown and discussed on following results based on PEA bulk samples that were fractured in patterns suited for this objective.

Side Views (Fracture across Thickness) on Internal Lamellae of Bulk PEA. Figure 3 shows SEM micrographs (A) top and fracture surfaces of an entire spherulite and (B) zoom-in to portion of spherulite revealing concentric tangential lamellae-stacked plate lamellae underneath the top surface ring bands. Figure 3B shows zoom-in magnification SEM graph of the top free surface and interior fracture surface morphologies of bulk PEA samples. Ridge band of the top surface ringed spherulites corresponds to the ark-shaped tangential lamellae on the fracture surface, while the valley band of the top surface corresponds to the stacked plates lamellae on the fracture surface. The top surface displays evident ring-banded patterns similar to those observed in thin cast PEA films under POM. Concentric ring bands in the spherulites of PEA appear in two-dimensional thin films, but alternating shell lamellae of two opposite orientations form in the interior of three-dimensional bulk PEA. The ring-banded patterns in top free surface of the spherulites in thick bulk PEA are quite similar to those typically seen thin-film morphology crystallized of PEA at the same T_c. However, the interior fracture exhibits a corrugate-board shell structure, which is not same as the top-surface ring but is

dx.doi.org/10.1021/ma202222e | *Macromolecules* 2012, 45, 1375−1383

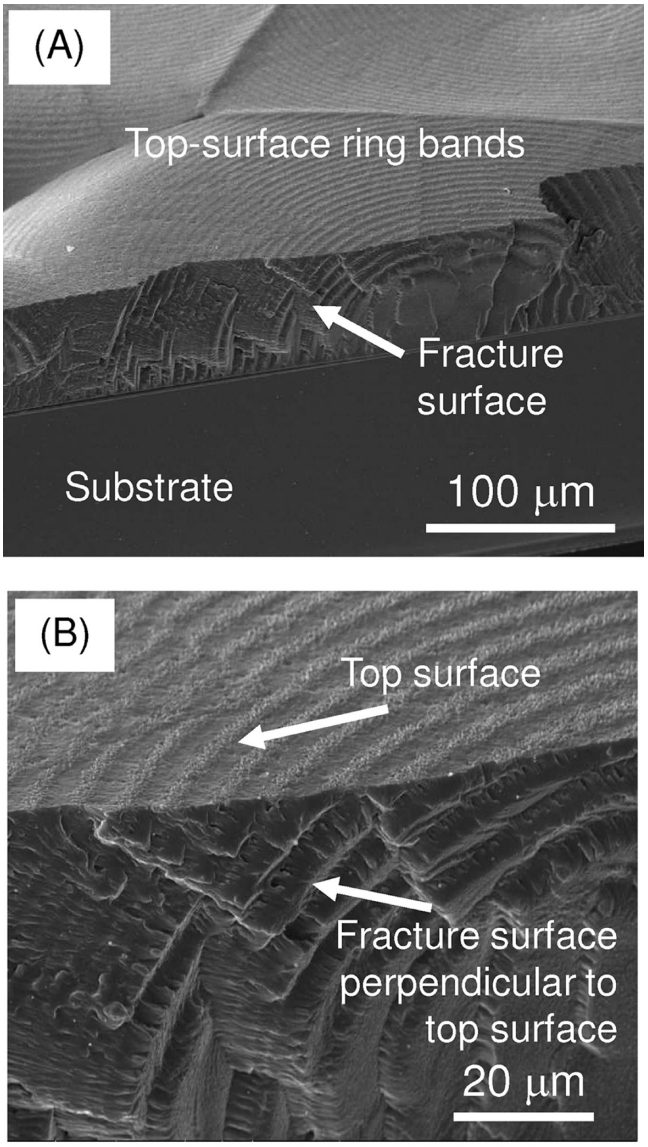


Figure 3. SEM micrographs of (A) top and fracture surfaces of entire spherulite and (B) zoom-in portion of spherulite revealing concentric tangential lamellae-stacked plate underneath the top-surface ring bands. (C) Schemes for fracture across a 3-D truncated sphere.

apparently correlated with the periodical ring-banded pattern on the outer surface. The intershell spacing in the fracture surface is about 6.4 μm, which is same as the inter-ring spacing on the top surface. Interestingly, the corrugated crystals of two opposite orientations as revealed by SEM correspond to the alternating bright (ridge region) and dark bands (valley region) observed using POM, respectively.

Figure 4 shows schemes illustrating two different nucleation sites: interior nucleation (left) and nucleation from top surface or bottom substrate (right). Top free surface nucleation leads

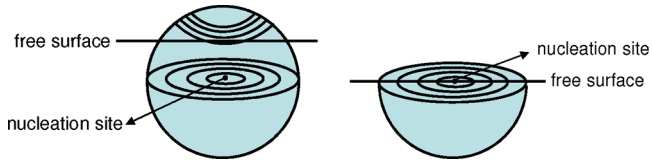


Figure 4. Schemes illustrating two different nucleation sites: interior nucleation (left) and nucleation from top surface or bottom substrate (right).

to ring bands on top surfaces and concave bowls associated with exterior surface growth and interior growth in 3-D patterns. Interior nucleation also leads to alternating shells of corrugated board structure, with a convex dome bulging out of the surface when fully grown. Both nucleation types can lead to a ring-banded structure on top surfaces, but the interior lamellae are packed differently.

Fractured surface for the interior of ringless Maltese-cross spherulites in PEA crystallized at T_c = 35 °C and was characterized using SEM for direct comparison with the alternating-shell interior of ring-banded spherulites in PEA crystallized at 28 °C. For comparison, the interiors of bulk PEA sample crystallized at T_c = 35 °C where ringless spherulites are present on top surface were compared with bulk PEA sample crystallized at T_c = 28 °C where ring-banded spherulites are present on top surface. Figure 5 shows SEM graphs on the

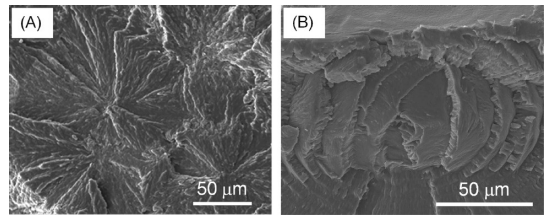


Figure 5. SEM graphs on fracture interior of (A) bulk PEA crystallized at T_c = 35 °C and (B) 28 °C-crystallized PEA.

fracture surface of (A) interiors of bulk PEA crystallized at 35 °C for 24 h (for full crystallinity) and (B) interiors of bulk PEA crystallized at 28 °C for 4 h. The SEM graph in Figure 5A (35 °C-crystallized bulk) reveals that lamellae radiate out straightly from center, but no alternating shells are seen in the fractured surface. Such interior morphology corresponds to no ring bands found in the top (outer) surface of the PEA sample crystallized at T_c = 35 °C. Lamellae go straightly from center to edge of the spherulite with no periodical turns, twists, or sudden changes in orientations. For direct comparison, 28 °C-crystallized bulk PEA samples were fractured and similarly characterized using SEM. As the fracturing would randomly cut across the 28 °C crystallized PEA samples, bulk PEA samples were fractured at several different locations for SEM examinations of interiors for dissecting a full picture of entire 3-D spherulites and lamellar structure therein. Note that depending on fracturing across poles or equators of 3-D spherulites the interiors might differ slightly. Figure 5B shows SEM graphs of 28 °C-crystallized PEA, revealing onion-like alternating shells near the center of 3-D spherulites. Corrugate-board shells of arc or hemisphere curves are clearly seen in the SEM graphs. The lamellae within the shell boundary are apparently perpendicular to the shell boundary. The shell boundary is easily fractured away, indicating that the interlayer is not interconnected by wandering chains from one layer to

dx.doi.org/10.1021/ma202222e | Macromolecules 2012, 45, 1375–1383

another. A closer look reveals that the shell surface is composed of tangential lamellae that are mostly oriented in the tangential direction. That is, within each shell of the onion structure, the lamellae are oriented in radial direction, similar to stacked plates. But the shell surface boundary reveals dramatically different lamellae, which differ from the stacked plates lamellae in shapes and orientation. The lamellae on the shell surface region are not plate-like but resemble tangential lamellae with orientation perpendicular to the stacked plates. Owing to such perpendicular orientation noninterconnecting of these two lamellae, fracturing of the interior exposes that the alternating shells are cleanly cleaved apart. Apparently, for bulk PEA (T_c = 33−35 °C) with top surface showing ringless spherulites, the corresponding interiors are dramatically different from PEA bulk crystallized at T_c = 28 °C with top surface showing apparently ring bands. The main differences are that alternate corrugate-board lamellar assembly is present only in PEA bulk crystallized with ring bands on top free surface.

Figure 6A−C shows the SEM graphs of the interior versus exposed surface of PEA spherulite crystallized at 28 °C. The

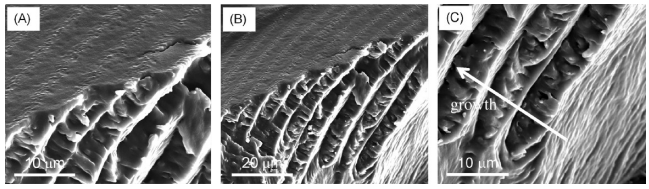


Figure 6. SEM graphs for (A, B) surface vs fractured interior; (C) close-up view of interior of ring-banded spherulites in fractured bulk PEA sample crystallized at 28 °C.

spherulite of PEA is composed of multiple shells of crystals, which appear as multiple shells of corrugated boards stacked alternately. In between the longitudinal shells of crystals, there are transverse-oriented crystal species, with these two types of crystals orienting as a "T" joint. Growth direction of the spherulites is indicated on the graph. Note that the shell surface distance of the interior corrugate-board shell structure is exactly equal to the inter-ridge distance of the surface ring bands (∼6 μm). The growth direction of the short transverse-oriented crystals is along the radial direction while that of the long longitudinal crystals is perpendicular to the growth direction. A clear correlation between interior lamellae assembly and surface ring-banded textures of PEA spherulite can be established. Closer inspection in Figure 6C reveals that the transverse-oriented crystal layers in spherulite interior correspond to the flat/valley regions in the surface and longitudinal straight-stalk crystal layers correspond to the ridge bands on the surface. Note that the 3-D periodical assembly leads to not only the noticeable ring band on exterior surfaces but also corrugate-board-like multishell structures in the interior of the spherulites. The orientations of the crystals forming the corrugated boards are discretely perpendicular to each other, with no gradual turning from one to another. These two crystal species are discrete and contact with one to the other like a "T"-shaped joint.

It is clear that the interior of bulk PEA (T_c = 28 °C) is composed of concentric multishells of two opposite lamellar directions (radial from sphere center and tangential to radial direction). Bulk PEA (T_c = 28 °C) samples were fractured in several possible locations so that some of the dissections cut through the samples to expose the tangential regions (where tangential lamellae exist). Figure 7 shows SEM graphs: (A) 1500× and (B) 3000× for fractured bulk PEA crystallized at 28

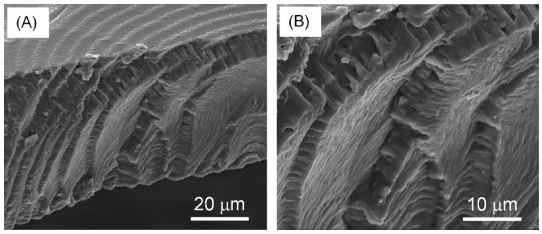


Figure 7. SEM graphs: (A) top surface and fractured cross section and (B) magnified cross section, for bulk PEA crystallized at 28 °C, revealing alternating shells (corrugated board structure).

°C, revealing interiors with alternating shells. Figure 7A (1500×) shows the top-surface morphology (upper portion) in correlation with the interior morphology by dissecting into the thickness cross section, which exhibits distinct alternating hemisphere layers with the center near bottom substrate (lower portion). As the hemisphere is confined by the thickness (∼50 μm) on the top surface, the hemisphere layers are confined into an arc shape; however, layers of two opposite orientations are clearly visible on the thickness cross section. The morphology of alternating shells on the thickness cross section is correlated to the ring bands on the top surface. On the top surface (upper portion of Figure 7A) of bulk PEA, alternating concentric ring bands are clear. The ridge band (whiter contrast) of the surface bands again is lined with tangential lamellae. Note that in thin PEA films of crystallized PEA similar ring bands are present; however, the ridge bands in thin-film PEA are not lined with tangential lamellae like those seen in the top surface of bulk PEA crystallized at same T_c = 28 °C. Albeit similar ring bands are seen, the mechanisms in bulk PEA top surface ring bands apparently are subtly different from those in thin films. This can be reasonably expounded in greater details as the interior bulk morphology is further dissected. Figure 7B (3000×) shows magnified SEM image for the morphology of the thickness cross section. Between the two alternating hemisphere shells, apparently, the outer shells of the layers were incidentally fractured and exposed in this sample for ideal SEM characterization. The SEM graph in Figure 7B clearly shows that the shell surfaces are mainly composed of the bundles of tangential lamellae that run perpendicularly to the transverse stacked plates within the shells. These tangential thin lamellae on the shell surface in the interior bulk may reach the top surface and become the discrete triangular lamellae seen on the ridge band of the top-surface rings. Thus, the tangential lamellae correspond to the ridge band on the top surface, while the stacked plates lamellae (radial from sphere center) eventually packed like stacked cards to the surface and form the valley band of the top surface.

Fractured surfaces in alternative bulk-crystallized PEA samples were examined for more thorough analysis. This was necessary as assurance of evidence should be made that the fractured interior morphology patterns in previous discussions were not sporadic or incidental. During bulk crystallization of PEA, it may be heterogeneously nucleated on the top or bottom surface or homogeneously nucleated in interior. Bulk crystallized PEA samples with nucleation near the bottom (or top) surface were fractured for SEM characterization. Figure 8 shows SEM graphs for top- or bottom-nucleated 3-D

dx.doi.org/10.1021/ma202222e | Macromolecules 2012, 45, 1375−1383

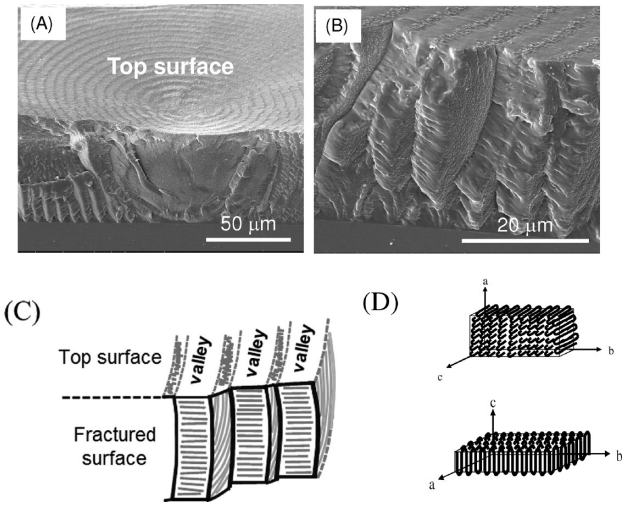


Figure 8. SEM graphs for top- or bottom-nucleated 3-D spherulites in bulk PEA crystallized at 28 °C: (A) top surface and fractured cross section, (B) magnified cross section, (C) scheme for correlation between top-surface and interior lamellar morphology, and (D) edge-on lamellae in tangential lamellae (top) and flat-on lamellae in stacked-plate (bottom).

spherulites in bulk PEA crystallized at 28 °C: (A) top surface and fractured cross section and (B) magnified cross section by zoom-in to interior spots. Again, the top-surface ring-band morphology (upper portion) is in correlation with the interior corrugate-board morphology on the fractured thickness cross section. The interior exhibits distinct alternating hemisphere shells. Shells of two opposite orientations are clearly visible on the thickness cross section. Figure 8B shows by zoom-in to interior spots the SEM graphs for the fractured interior of this PEA sample clearly evidence that the shell surface are mainly composed of the bundles of tangential lamellae that run perpendicularly to the stacked plates within the shells. Additionally, in order to vividly summarize the arc-shaped tangential lamellae-stacked plate shells in the fractured interior, Figure 8C shows a scheme for the interior corrugate-board lamellar morphology in the 3-D truncated sphere. The tangential lamellae are located in the shell surface regions sandwiched between the stacked plates. Figure 8D shows two schemes for edge-on lamellae in the tangential lamellae (bottom left) and flat-on lamellae in the stacked plate (bottom right) plate. In addition to the obvious geometric difference in these two lamellae in the mutually perpendicular tangential lamellae and stacked plates, the chain orientations in these two oppositely oriented lamellae are also different, with one being parallel and the other perpendicular to polarized light. Note that the chain orientations in these two lamellae in bulk PEA are perpendicular to each other, and this opposite orientation in the bulk PEA form would correspond to the two birefringence colors as viewed in POM if it is prepared in thin films crystallized at 28 ± 3 °C. Most evidently, thickness (50 μm) of the 3D interior lamellae shells of opposite orientations in PEA bulks as revealed in SEM perfectly agrees with the observed pitch of the thin-film ring bands (10 μm) [at T_c = 28 ± 3 °C] in POM characterization. This evidence from 3D dissecting on the bulks fully explains and justifies the quantitative birefringence rings and their pitches in POM characterization on thin films.

In addition, it has been reported by Wang et al.[27] and Chuang et al.[28] that the growth of ring-banded spherulites in thin-film polymers, such as poly(ε-caprolactone) copolymers or poly(trimethylene terephthalate), is not uniform along the radial direction, and the growth is typically faster in one band and slower in the next band, i.e., intermittent growth across the two bands of opposite birefringence They inferred that the ridge band of spherulites in thin-film samples grows more slowly than the valley bands.[27,28] The 3-D dissecting analyzed on the interior lamellae of PEA in this study could fully justify and explain this phenomenon of intermittent growth in ring-banded spherulites. Growth rates of spherulites are typically measured in plane along radial direction. The 3-D interior morphology has revealed that the growth of the radial lamellae (the fluting layer) can be measured at their true pace; however, as they turn 90° to form the tangential lamellae in the linear layer of the corrugated cassettes, they are slower as the lamellar direction is perpendicular to the radial growth measurement. In addition, the alternating ridge and valley band on top surface can be nicely explained. The interior of tangential lamellae are aligned to the top surface, and they grow and protrude outward to the top surface to form the ridged band; by contrast, the radial lamellae in the fluting layer are parallel to the top surface, and they are stacked to form the flat valley bands between two ridges on top surface.

To summarize such complex 3D views in a simpler context, Figure 9 shows a scheme for correlations between the interior

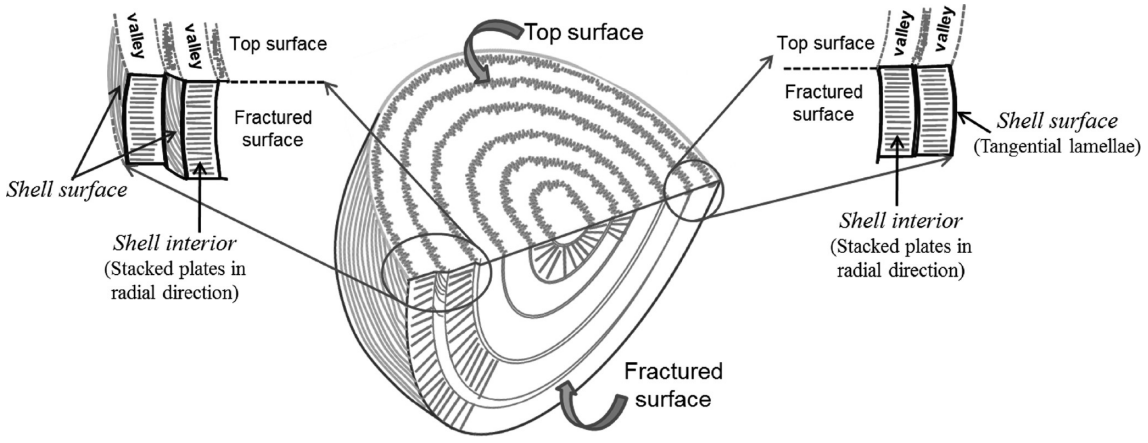


Figure 9. Schemes for correlations between the interior layered lamellae and top-surface ring bands showing onion-like alternating shell.

dx.doi.org/10.1021/ma202222e | *Macromolecules* 2012, 45, 1375–1383

layered lamellae and top-surface ring bands showing onion-like alternating shell. Brief explanations are offered. The 3-D interior morphology of bulk PEA has revealed that ring-banded spherulites are composed of onion-like alternating shells. Depending on which direction of the morphology of fractured surfaces was dissected, it shows slightly different morphology. Two regions of different view angles are of special interest: (A) Zoom-in graph in the left side, which shows alternating shells. Shell interior and surface correspond to the valley and ridge of ring-banded on the top surface, respectively. Shell interior is arranged by stacked lamellae in radial direction. The lamellae on the shell surface are perpendicular to the stacked lamellae in shell interior and ridge in the top surface. These two crystal species are discrete and contact with one to the other like a "T"-shaped joint. In addition, another view angle is (B) zoom-in graph in the right side, which shows that ridge and valley on the top surface are correlated with tangential and radial lamellae in the fractured surface. That is, 3D morphology changes and switches slightly as the lamellae grow away from the center to peripherals, and as they are viewed from different perspectives.

X-ray and Thermal Evidence for Highly Oriented Tangential Lamellae. Furthermore, preferred lamellar orientation could be discerned in WAXD diffractions peaks. PEA normally has only one crystal form of monoclinic cell, with a = 0.547 nm, b = 0.724 nm, c = 1.172 nm (fiber axis), and a monoclinic angle of α = 113.5°.[29,30] For this form of crystallized PEA, three prominent diffraction peaks for (111), (110), and (020) are generally seen at 2θ = 20.5°, 21.7°, and 24.6°, respectively.[31] Figure 10 shows WAXD diffractograms

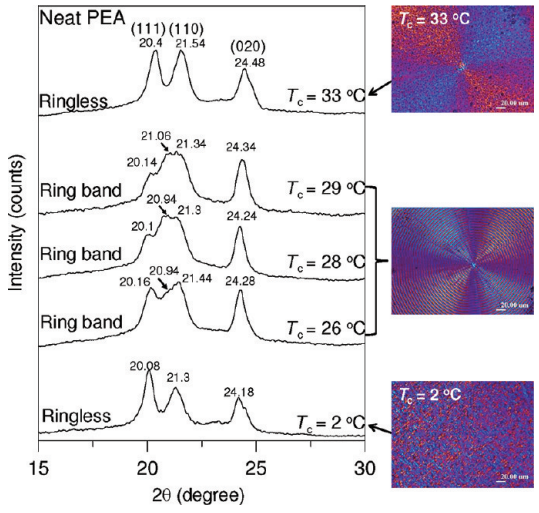


Figure 10. WAXD diffractograms for PEA bulk samples crystallized at T_c = 2, 26, 28, 29, and 33 °C.

for 2, 26, 28, 29, and 33 °C-crystallized PEA bulk samples. Again, similar to the DSC differences among the various samples, the 28 °C-crystallized PEA sample (ring-banded) exhibits a WAXD diffractogram that is distinctly different from those for the 2 and 33 °C-crystallized PEA bulk samples (ringless). The 28 °C-crystallized PEA sample, similar to 26 and 29 °C-ones, exhibits an additional peak at 21.0°, and the (111) peak intensity (2θ = 20.4°) is much lower for PEA crystallized at 26–29 °C than that for PEA crystallized outside this T_c range (2 and 33 °C). The WAXD curves for the 2 and 33 °C-crystallized PEA bulk samples (with ringless spherulites) are almost identical, but they both differ significantly from the WAXD intensity curves for the 26, 28, and 29 °C-crystallized PEA samples. All PEA samples show diffraction peaks at (111), (110), and (020) planes; however, only the 26, 28, and 29 °C-crystallized PEA samples (ring-banded) show a much weaker diffraction intensity of the (111) plane. Additionally, the 26, 28, and 29 °C-crystallized PEA samples (ring-banded on top surfaces) show much a stronger intensity at the (020) diffraction (2θ = 24.5°) than that of the 2 and 33 °C-crystallized PEA bulk samples (ringless). Furthermore, WAXD diffractograms for 28 °C-crystallized PEA show an extra peak at 2θ = 21.0°, which is absent in all PEA samples crystallized at 2 or 33 °C (i.e., outside the 28 ± 3 °C window). The WAXD diffractograms for 26 and 29 °C-crystallized PEA bulks also have this extra peak at 2θ = 21.0°. Such WAXD data of distinctly different diffraction patterns support that the highly ordered lamellar packing into two perpendicular chain orientations in the 28 °C-crystallized PEA sample differ significantly from the randomly distributed lamellae in 2 and 33 °C-crystallized PEA bulk samples. Inoue et al.[31] have pointed out that PEA of high enough M_w may exhibit different intensities of the (111) peak (2θ = 20.5°) depending on the spherulite orientations or T_c in high-molecular-weight PEA, but for low-M_w PEA, the effect of orientation is relatively less. In addition, it has been claimed that highly oriented spherulites in PEA would exhibit much less intensity of (111) WAXD diffraction. To briefly summarize, the WAXD data apparently show that 26, 28, and 29 °C-crystallized PEA bulk samples have much lower (111) diffraction intensity but slightly sharper (020) diffraction peak, indicating that the tangential lamellae may be highly oriented in a uniform direction in the bulk PEA samples that exhibit apparent corrugate-board lamellae in interior assembly and ridge-valley ring bands on exterior surfaces.

Thermal behavior of the oriented tangential lamellae in bulk PEA samples crystallized at 28 °C was investigated. The tangential lamellae, being almost fully extended into thin needle-like crystals, are supposed to have a higher T_m than the stacked plate lamellae. Thermal analysis was performed on 2, 28, and 33 °C-crystallized bulk PEA samples. It has been earlier proposed that the multiple melting peaks in crystallized PEA are associated with the different lamellae in the ring-banded spherulites.[32] Figure 11 shows DSC thermograms (10 °C/min) for 2, 28, and 33 °C-crystallized PEA bulk samples. The 28 °C-crystallized PEA sample exhibits DSC curve that is distinctly different from those for the 2 and 33 °C-crystallized PEA bulk samples. For the 28 °C-crystallized PEA sample, there are two peaks: one lower T_m (~45 °C) and one higher T_m (52 °C), not counting the minor shoulder peak. The first lower T_m melting peak (P_1) is more prominent than the second higher T_m peak (P_2) when scanned at 10 °C/min. The tangential lamellae (chain more extended with more regular re-entry) are likely associated with the higher melting peak P_2, while the lower melting P_1 lamella (T_m = 45 °C) are associated with the stacked plate lamellae (chain folding with irregular re-entry) in the spherulites. For the 28 °C-crystallized PEA, the higher melting P_2 (with T_{m2} = 52 °C) may be attributed to the more highly oriented tangential lamella in the shell surface regions. The high-melting peak (higher P_2 with T_{m2} = 52 °C) indicates that the molecular chains in the tangential crystals on the shell surface are more highly oriented than those in the stacked plates (lower P_1 with T_{m1} = 45 °C). In addition, the relatively smaller fraction of the tangential crystals in comparison to the larger fraction of the stacked plate lamellae, which is also

dx.doi.org/10.1021/ma202222e | Macromolecules 2012, 45, 1375–1383

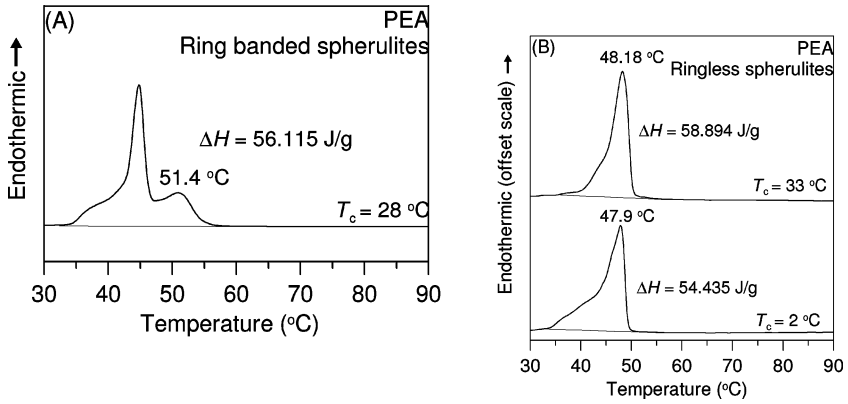


Figure 11. DSC (10 °C/min) traces for PEA bulk samples crystallized at T_c: (A) 28 °C and (B) 2 and 33 °C.

correctly reflected in the smaller melting endotherm peak area of P_2 to that of P_1. On the other hand, there is only a single melting peak (T_m = 48 °C) for the 2 or 33 °C-crystallized PEA samples, which differ significantly from the 28 °C-crystallized PEA. For the 2 or 33 °C-crystallized PEA samples, the fractured surfaces of spherulites show no alternating corrugated layers of linear and fluting and that their corresponding POM micrographs would show ringless spherulites in thin-film forms of PEA crystallized at 2 and 33 °C. The DSC curves for the 2 and 33 °C-crystallized PEA bulk samples are almost the same with a single melting peak with T_m (=48 °C) intermediate to the values of the double melting peaks of T_{m1} and T_{m2} of the 28 °C-crystallized PEA sample. The heats of fusion for all three samples are comparable at ΔH_f = 56−58 J/g, indicating that all three samples have been crystallized almost to their maximum at respective T_c's (2, 28, and 33 °C).

Such DSC results suggest that the lamellae in the 2 or 33 °C-crystallized PEA spherulites are randomly distributed to exhibit a single melting peak, but those in 28 °C-crystallized PEA sample are likely packed into two distinctly different lamellar types. Rijke and Mandelkern[33] have shown that annealed stirred crystallized polyethylene at 142 °C with a melting tail of 152 °C is an indication of a small portion of fully extended chain system in PE. Similarly, Aida et al.[34] have shown in extrusion polymerization via mesoporous silica using catalyzed synthesis of crystalline linear polyethylene, and they were able to produce PE nanofibers, which show a portion of crystals being packed in fully extended chains as evidenced by a trailing shoulder melting peak at 158 °C (in addition to the normal major melting peak at ∼140 °C). Clearly, the DSC result proves that the extra melting peak (the higher P_2 peak) is associated with the melting of the tangential lamellae that are present only in 28 °C-crystallized PEA bulk samples, but such tangential lamellae packed in shell surface are absent in the 2 and 33 °C-crystallized ones. The tangential lamellae in the corrugate-board layers of PEA 3-D spherulites serve to connect the tangentially adjacent stacked plates, and they act like the linking fibrillar crystals reported earlier in PE lamellae, which have extended chains with some imperfect folded chains.

An analogy can be drawn between the phase-separation morphology of amorphous polymer blends and ring-band spherulites of crystalline polymers or blends in thin films vs bulk states. It has been amply proven that the phase-separation morphology in polymer blends of bulk states are different with that in thin films of the same blend systems.[35−38] This study based on bulk-state PEA has yielded critical evidence that the assembly of lamellae leading to alternating morphology in bulk form of PEA can also differ from the mechanism of lamellar packing or twisting in thin-film PEA. In addition, an aryl polyester poly(nonamethylene terephthalate) (PNT), crystallized into ring-banded spherulites in bulk form, has been proven to exhibit similar interior corrugate-board shells of alternating orientations corresponding to ridge/valley of the top-surface ring bands.[39] This study, using PEA as a another model dissected parallel and vertical to the top-surface planes, further clearly proves that fine tangential lamellae are highly oriented in the tangential direction and emerge to top surface to form ridge bands.

■ CONCLUSION

For the first time, 3-D spherulites in crystallized bulk polymers were dissected in aims to correlate the interior lamellar assembly with the outer surface ring-band patterns by directly tracing the morphology patterns from top surfaces onto interior fractured surfaces. Three-dimensional dissecting on spherulites in bulk PEA (50−75 μm) crystallized at T_c = 2−35 °C was performed and analyzed. Numerous attempts were made in order to achieve that 3-D PEA bulk spherulites were cleaved in several possible planes to expose details of interior structures, and morphology analyses were performed by dissecting several fracture surfaces across the specimen thickness. The interior morphology of bulk PEA crystallized at 28 ± 3 °C exhibits distinct corrugate-board layers stacked into 3-D spherulites or truncated hemisphere, depending on sample thickness confinement. SEM evidence reveals that interior of 3-D spherulites is composed of onion-like alternating shells. The shell interior is arranged by stacked lamellae in radial direction. The lamellae on the shell surface are perpendicular to the stacked plate lamellae in shell interior and ridge in the top surface. Shell interior and surface correspond to the valley and ridge of ring-banded on the top surface, respectively. Fracturing morphology of the 3-D spherulites further proves that the stacked shells could be cleanly cleaved apart along the shell surface lamellae, exposing that these two oppositely oriented crystal species are discrete and not physically interconnected.

Thus, on the top surface, there are two types of free-surface ring band patterns depending on top-surface or interior nucleation. Both nucleation types in bulk PEA crystallization lead to multiple shell as interior of the spherulites. The interior of bulk PEA shows corrugate-board layers and the top free surface exhibits a ring-banded pattern. DSC and WAXD characterization results on PEA bulk samples crystallized at 28 °C vs 2 °C and 33 °C fully support that the lamellae in the 28

°C-crystallized PEA bulk are orderly assembled into two types of crystals with mutually perpendicular orientations, which yield distinctly different melting behavior and crystal diffractions from those in 2 or 33 °C-crystallized PEA bulks that contain only one type of randomly distributed lamellae.

AUTHOR INFORMATION

Corresponding Author

*E-mail: emwoo@mail.ncku.edu.tw; Fax: +886 6 234-4496; Tel: +886 6 275-7575 ext 62670.

Notes

The authors declare no competing financial interest.

ACKNOWLEDGMENTS

This work has been financially supported by a basic research grant (NSC-97-2221-E-006-034-MY3) for three consecutive years from Taiwan's National Science Council (NSC), to which the authors express their gratitude. The authors especially express their gratitude to Prof. B. Lotz for better and further refining the models and views in this work via many informal and casual but extremely helpful communications. Finally, this paper is dedicated to remember late Professor Jean-Jacques Point (retired from the University of Mons, Belgium, and passed away in November 2011) for his critical and original pioneering work in PEA ring bands and opening up an interesting field in polymer morphology so that others may pursue further by following his footsteps, to diversify and refine.

REFERENCES

(1) Lotz, B.; Cheng, S. Z. D. *Polymer* **2005**, *46*, 577−610.
(2) Keith, H. D.; Padden, F. J. Jr. *J. Polym. Sci.* **1959**, *39*, 101−122.
(3) Keith, H. D.; Padden, F. J. Jr. *J. Polym. Sci.* **1959**, *39*, 123−138.
(4) Keller, A. *J. Polym. Sci.* **1959**, *39*, 151−173.
(5) Lustiger, A.; Lotz, B.; Duff, T. S. *J. Polym. Sci., Part B: Polym. Phys.* **1989**, *27*, 561−579.
(6) Bassett, D. C. *J. Macromol. Sci.* **2003**, *B42*, 227−256.
(7) Schultz, J. M. *Polymer* **2003**, *44*, 433−441.
(8) Toda, A.; Arita, T.; Hikosaka, M. *Polymer* **2001**, *42*, 2223−2233.
(9) Kyu, T.; Chiu, H. W.; Guenthner, A. J.; Okabe, Y.; Saito, H.; Inoue, T. *Phys. Rev. Lett.* **1999**, *83*, 2749−2752.
(10) Bassett, D. C.; Hodge, A. M. *Polymer* **1978**, *19*, 469−472.
(11) Keith, H. D.; Padden, F. J. Jr. *Polymer* **1984**, *25*, 28−42.
(12) Bassett, D. C.; Hodge, A. M. *Proc. R. Soc. London, A* **1981**, *377*, 25−37.
(13) Bassett, D. C.; Hodge, A. M.; Olley, R. H. *Proc. R. Soc. London, A* **1981**, *377*, 39−60.
(14) Xu, J.; Guo, B.-H.; Zhang, Z.-M.; Zhou, J. -J.; Jiang, Y.; Yan, S.; Li, L.; Wu, Q.; Chen, G.-Q.; Schultz, J. M. *Macromolecules* **2004**, *37*, 4118−4123.
(15) Ye, H.-M.; Wang, J.-S.; Tang, S.; Xu, J.; Feng, X.-Q.; Guo, B.-H.; Xie, X.-M.; Zhou, J.-J.; Li, L.; Wu, Q.; Chen, G.-Q. *Macromolecules* **2010**, *43*, 5762−5770.
(16) Ho, R.-M.; Ke, K.-Z.; Chen, M. *Macromolecules* **2000**, *33*, 7529−7537.
(17) Tanaka, T.; Fujita, M.; Takeuchi, A.; Suzuki, Y.; Uesugi, K.; Doi, Y.; Iwata, T. *Polymer* **2005**, *46*, 5673−5679.
(18) Gazzano, M.; Focarete, M. L.; Riekel, C.; Ripamonti, A.; Scandola, M. *Macromol. Chem. Phys.* **2001**, *202*, 1405−1409.
(19) Nozue, Y.; Hirano, S.; Kurita, R.; Kawasaki, N.; Ueno, S.; Iida, A.; Nishi, T.; Amemiya, Y. *Polymer* **2004**, *45*, 8299−8302.
(20) Nozue, Y.; Kurita, R.; Hirano, S.; Kawasaki, N.; Ueno, S.; Iida, A.; Nishi, T.; Amemiya, Y. *Polymer* **2003**, *44*, 6397−6405.
(21) Wang, Z.; Hu, Z.; Chen, Y.; Gong, Y.; Huang, H.; He, T. *Macromolecules* **2007**, *40*, 4381−4385.
(22) Frömsdorf, A.; Woo, E. M.; Lee, L. T.; Chen, Y. F.; Förster, S. *Macromol. Rapid Commun.* **2008**, *29*, 1322−1328.
(23) Gan, Z.; Kuwabara, K.; Yamamoto, M.; Abe, H.; Doi, Y. *Polym. Degrad. Stab.* **2004**, *83*, 289−300.
(24) Meyer, A.; Yen, K. C.; Li, S. H.; Förster, S.; Woo, E. M. *Ind. Eng. Chem. Res.* **2010**, *49*, 12084−12092.
(25) Keith, H. D.; Padden, F. J. Jr. *Macromolecules* **1996**, *29*, 7776−7786.
(26) Chen, Y. F.; Woo, E. M. *Macromol. Rapid Commun.* **2009**, *30*, 1911−1916.
(27) Wang, Z.; An, L.; Jiang, B.; Wang, X. *Macromol. Rapid Commun.* **1998**, *19*, 131−133.
(28) Chuang, W.-T.; Hong, P.-D.; Chuah, H. H. *Polymer* **2004**, *45*, 2413−2425.
(29) Turner-Jones, A.; Bunn, C. W. *Acta Crystallogr.* **1962**, *15*, 105−113.
(30) Hobbs, S. Y.; Billmeyer, F. W. Jr. *J. Polym. Sci., Part A-2: Polym. Phys.* **1969**, *7*, 1119−1121.
(31) Yang, J.; Pan, P.; Dong, T.; Inoue, Y. *Polymer* **2010**, *51*, 807−815.
(32) Woo, E. M.; Wu, P. L.; Wu, M. C.; Yan, K. C. *Macromol. Chem. Phys.* **2006**, *207*, 2232−2243.
(33) Rijke, A. M.; Mandelkern, L. *J. Polym. Sci., Part A-2: Polym. Phys.* **1970**, *8*, 225−242.
(34) Kageyama, K.; Tamazawa, J.; Aida, T. *Science* **1999**, *285*, 2113−2115.
(35) Tanaka, K.; Takahara, A.; Kajiyama, T. *Macromolecules* **1996**, *29*, 3232−3239.
(36) Kajiyama, T.; Tanaka, K.; Takahara, A. *Macromolecules* **1998**, *31*, 3746−3749.
(37) Walheim, S.; Böltau, M.; Mlynek, J.; Krausch, G.; Steiner, U. *Macromolecules* **1997**, *30*, 4995−5003.
(38) Johnson, W. C.; Wang, J.; Chen, Z. *J. Phys. Chem. B* **2005**, *109*, 6280−6286.
(39) Woo, E. M.; Nurkhamidah, S.; Chen, Y. F. *Phys. Chem. Chem. Phys.* **2011**, *13*, 17841−17851.

Macromolecules

Article

pubs.acs.org/Macromolecules

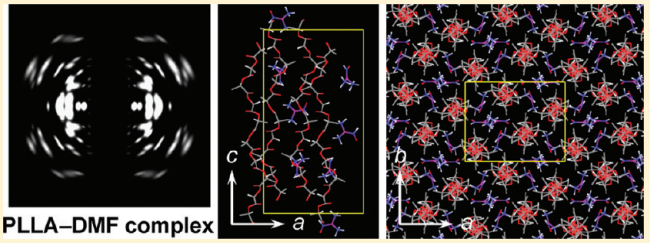
Complex Crystal Formation of Poly(L-lactide) with Solvent Molecules

Hironori Marubayashi,† Shigeo Asai,* and Masao Sumita

Department of Chemistry and Materials Science, Graduate School of Science and Engineering, Tokyo Institute of Technology, Ookayama, Meguro-ku, Tokyo 152-8552, Japan

Supporting Information

ABSTRACT: By screening examinations for a wide variety of organic solvents, we found that poly(L-lactide) (PLLA) forms the crystalline complex (ε-form) with the specific organic solvents such as tetrahydrofuran (THF) and *N*,*N*-dimethylformamide (DMF) below room temperature. It was revealed that PLLA has high selectivity for low molecular weight compounds to form the ε-crystals. By fiber diagram analyses for the ε-forms, it was found that PLLA chains take the 10_7 (left-handed 10_3) helical conformation and are packed in the orthorhombic lattice (a = 1.5−1.6 nm, b = 1.2−1.3 nm, c = 2.8−2.9 nm, and $\alpha = \beta = \gamma = 90°$). Based on *R*-factor and packing energy calculations, the plausible crystal structure of PLLA−DMF complex was proposed, in which four PLLA chains and eight guest solvents are packed in the unit cell.



INTRODUCTION

The complexation of macromolecules with low molecular weight compounds via nonbonded interactions is categorized as the supramolecular chemistry composed of macromolecules and low molecular weight compounds. There have been many studies on crystalline complexes and clathrates composed of macromolecules and low molecular weight compounds: amylose/iodine,[1] poly(vinyl alcohol)/iodine,[2] cellulose/low molecular weight compounds,[3] polymer/urea,[4] polymer/cyclodextrins,[5] poly(ethylene oxide) (PEO)/inorganic compounds,[6] syndiotactic polystyrene (sPS) /solvents,[7,8] polyethylenimine (PEI)/low molecular weight compounds,[9] syndiotactic poly(methyl methacrylate) (st-PMMA)/solvents,[10] st-PMMA/fullerenes,[11] chitosan/low molecular weight compounds,[12] etc. In particular, the complexation of amylose with iodine[1] is well-known phenomenon as the "iodo-starch reaction". The complexation of PEO with metallic salts[6] has a great effect on the ionic conductivity, which is of great importance in use of solid electrolytes. Petraccone et al. reported the nanoporous polymer crystals with pores or channels using sPS/solvents clathrates (δ- and ε-forms), which are suitable for applications such as chemical separation.[8] Kawauchi et al. found that in aromatic solvents such as toluene st-PMMA encapsulates C_{60} molecules in its helical cavity to form a supramolecular inclusion complex.[11] Uda et al. prepared the sPS clathrate containing organic dye (azulene) by the guest-exchange procedure and controlled the orientation of organic dye encapsulated in the sPS crystal.[13] In addition, coordination polymers, which are constructed from transition metal ions and bridging organic ligands, attract much attention because these polymers can adsorb gases to a remarkable extent.[14] Thus, studies on the complexation of macromolecules with low molecular weight compounds are of great importance in terms of both basic and applied researches.

Poly(L-lactide) (PLLA), one of the enantiomers of polylactide, can be synthesized from the plant-derived materials. PLLA shows the crystal polymorphism: the α-,[15,16] α' (δ)-,[17,18] α''-,[19] β-,[20] and γ-[21]forms. Sasaki et al. clearly showed that PLLA helices in the α-form (orthorhombic unit cell of parameters a = 1.066 nm, b = 0.616 nm, and c = 2.888 nm) slightly deviate from the regular 10_7 helix by the linked-atom least-squares refinements coupled with the Rietveld whole-fitting method.[16a] Wasanasuk et al. performed a detailed analysis on the PLLA α-form using 2-dimensional wide-angle X-ray diffraction (WAXD) and wide-angle neutron diffraction (WAND) for the ultradrawn sample.[16b] On the basis of X-ray fiber diagrams and polarized IR/Raman spectra, Zhang et al. proposed that the chain conformation and packing mode of the α'-form are slightly different from those of the α-form of PLLA.[17b] Marubayashi et al. revealed that the formation of disordered α (α'') crystals arises under high-pressure CO_2 (0−20 °C and 3 MPa; 0−30 °C and 7−15 MPa), and the crystal structure transition from α''- to α-forms occurs with increasing CO_2 temperature.[19] Furthermore, it was indicated that CO_2 molecules are trapped in a PLLA unit cell during CO_2-induced crystallization below room temperature. Puiggali et al. reported that stretching and stroking of PLLA give the frustrated packing of three chains with 3_2 helix in a trigonal unit cell of parameters $a = b$ = 1.052 nm and c = 0.88 nm (β-form) using electron diffraction and conformational energy analysis.[20b] Cartier et al. showed that two antiparallel chains with 3_2 helical conformation are packed in an orthorhombic unit cell of parameters a = 0.995 nm, b = 0.625 nm, and c = 0.88 nm (γ-form) by epitaxial crystallization on hexamethylbenzene

Received: October 17, 2011
Revised: December 22, 2011
Published: January 26, 2012

ACS Publications © 2012 American Chemical Society

around 140 °C using electron diffraction and packing energy analysis.[21]

There are a few studies on the complexation of PLLA, in which PLLA is a guest and low molecular weight compounds are hosts. Howe et al. succeeded in incorporating PLLA into the narrow channels of its inclusion compound with urea.[22] Ohya et al. reported that the inclusion complex of α-cyclodextrin with PLLA is preferentially formed compared to that with poly(D-lactide) (PDLA).[23] As far as we know, there are no reports that conducted an exhaustive research on solvent-induced crystallization of PLLA and the complexation of PLLA, in which PLLA acts as a host. In this article, we describe the crystalline complex formation of PLLA with the specific solvent molecules by screening examinations for a wide variety of organic solvents using WAXD mainly. It is hoped that this study gives some insights into the molecular recognition ability of not only PLLA but also bio-based polymers having the structural similarity to PLLA such as poly(hydroxyalkanoate)s and poly(amino acid)s.

EXPERIMENTAL SECTION

Samples. PLLA used in this study is Lacty #5408 with M_w of 107 000 and an optical purity of 98.6%, which was supplied from the Toyota Motor Corp. Amorphous films with a thickness of 0.45 mm were prepared by melt pressing of the pellets at 200 °C and 20 MPa for 5 min followed by quenching by ice water. The obtained films were confirmed to be completely amorphous by WAXD and differential scanning calorimetry (DSC). Oriented films were prepared by drawing the amorphous films in water at 50, 55, or 60 °C (around T_g of PLLA) by 2−5 times the original length. Drawing at 50−55 °C by 2−4 times the original length gave the oriented amorphous films (halo pattern around 2θ = 16.0° for Cu Kα), while drawing at 60 °C provided a small number of α'-crystals (e.g., strong diffraction peak at 2θ = 16.5° for Cu Kα). Organic solvents were used as received from commercial suppliers without further purification.

Solvent Exposure. A PLLA amorphous film in the unoriented state (1 cm × 2 cm) was placed in a 20 mL vial container with 5 mL of organic solvents. In the case of highly volatile solvents such as acetone and tetrahydrofuran (THF), crystallization of PLLA was conducted by exposure to solvent vapor. On the contrary, in the case of solvents that are not highly volatile such as γ-butyrolactone (GBL), PLLA was crystallized by immersion into solvent in the liquid state. In principle, 25 (room temperature), 5, and −25 °C were selected as the crystallization temperature (T_c). In the case of organic compounds having the melting temperature (T_m) higher than 25, 5, or −25 °C, such as ethylene carbonate (EC) and 1,4-dioxane (DOX), T_c's higher than T_m's of these organic compounds were selected. Organic compounds having T_m higher than the glass transition temperature (T_g) of PLLA were omitted in this study. Namely, all T_c's used in this study are lower than T_g of PLLA (ca. 60 °C) because our research interest is solvent-induced crystallization, not thermal crystallization. The periods for exposure of a film to a solvent atmosphere (i.e., crystallization periods) were changed from 1 to 60 days depending on solvent species to complete crystallization of PLLA. For the protic polar solvents such as ethanol, and hydrocarbons such as hexane, crystallization of PLLA was not finished in 60 days due to poor plasticizing effects of these solvents on PLLA. When a shape of a film was not kept due to dissolution of PLLA in organic solvents, solution casting was conducted at 25 and 40 °C for about 12 h. After taken out of a vial container, each PLLA film containing solvent molecules was weighed and sandwiched by polyimide tapes with a thickness of 50 μm to minimize volatilization of solvents. In the case of solvents that are not highly volatile, which was judged from small weight loss of the film containing solvents at room temperature, sealing by polyimide tapes was not conducted. Organic solvents used in this study are listed in Table 1. The details for solvent exposure conditions are shown in the Supporting Information. In principle, solvent desorption from each PLLA film was carried out at room temperature under atmospheric pressure. When solvents were removed to some extent and desorption became relatively slow, surrounding temperature was set to 30−40 °C (<T_g of PLLA) in order to accelerate solvent desorption. Finally, vacuum drying at 40 °C was performed to remove solvents from PLLA films completely.

The oriented films were exposed to the solvents in which PLLA in the unoriented state forms the specific crystal structure (CPO, DMF, DOL GBL, and THF, as mentioned later). The drawing and exposure conditions are shown in Table 2.

Table 1. Organic Solvents Used for Solvent-Induced Crystallization of PLLA

name	abbrev	name	abbrev
acetone		γ-valerolactone	GVL
acetonitrile		hexane	
α-methyl-γ-butyrolactone	AMGBL	isobutyraldehyde	IBA
anisole		methyl acetate	MAc
β-butyrolactone	BBL	2-methyl-1,3-dioxolane	2MDOL
chloroform		2-methyltetrahydrofuran	2MTHF
cyclohexanone	CHO	*N*-methylacetamide	NMA
cyclopentanone	CPO	*N*-methylformamide	NMF
diethyl ether	DEE	*N*-methylpyrrolidone	NMP
2,3-dihydrofuran	23DHF	*N*,*N*-diethylformamide	DEF
2,5-dihydrofuran	25DHF	*N*,*N*-dimethylacetamide	DMAc
1,4-dioxane	DOX	*N*,*N*-dimethylformamide	DMF
1,3-dioxolane	DOL	3-pentanone	3PO
ethanol		propylene carbonate	PC
ethyl acetate	EAc	2-pyrrolidone	2Py
ethylene carbonate	EC	tetrahydrofuran	THF
formamide		tetrahydrofurfuryl acrylate	THFA
furan		tetrahydrofurfuryl methacrylate	THFMA
γ-butyrolactone	GBL	toluene	

Table 2. Drawing and Subsequent Solvent Exposure Conditions

	drawing conditions		solvent exposure conditions		
solvent	T_d (°C)[a]	ratio	T_c (°C)[b]	period	state
CPO	55	4	−25	30 days	vapor
DMF	55	4	−25	30 days	liquid
DOL	60	5	−25	1 day	vapor
GBL	50	4	−25	30 days	liquid
THF	60	5	−25	2 days	vapor
air	60	4	140	5 h	vapor

[a]Drawing temperature. [b]Solvent exposure temperature. For "air", T_c means the annealing temperature in air.

Wide-Angle X-ray Diffraction. One-dimensional WAXD measurements were conducted using a RINT-2100 (Rigaku Corp.) in the symmetrical transmission mode, equipped with a graphite monochromator ($2\theta_M$ = 26.58° for Cu Kα) at the scattered X-ray position. In an operating condition at 40 kV and 40 mA using Cu Kα (λ = 0.154 18 nm) as a X-ray source, X-ray radiation time was about 90 min for a single film (2θ = 3°−50°, $\Delta(2\theta)$ = 0.05°). All measurements were carried out at room temperature under atmospheric pressure. Silicon powder was used as a standard sample. To minimize solvent evaporation, the unoriented films containing solvents were sealed by polyimide tapes during X-ray radiation. Owing to sealing by polyimide tapes, there was only a relatively small change in solvent solubility after WAXD measurements. Polyimide tapes are useful not only as sealing materials but also as low-background samples (small scattering peak at 5° for Cu Kα).

dx.doi.org/10.1021/ma202324g | Macromolecules 2012, 45, 1384−1397

Each X-ray fiber diagram was recorded on an imaging plate (Fujifilm Corp.) using a NANO-Viewer (Rigaku Corp.) with Cu Kα radiation (λ = 0.154 18 nm) and read by an R-AXIS DS3A (Rigaku Corp.). For 2−6 films laid on top of another (total thickness is ca. 0.5 mm), X-ray radiation time was 6−10 h in an operating condition at 40 kV and 20 mA. All measurements were carried out at room temperature under atmospheric pressure. Silicon powder was used as a standard sample. To minimize solvent evaporation, each oriented film containing solvents was sealed by polyimide tapes during X-ray radiation. In spite of relatively long radiation time (6−10 h), there was only a relatively small change in each diffraction pattern (intensity increased with a similar diffraction feature) and solvent solubility, which would be attributed to sealing by polyimide tapes.

To observe the reflections from the reciprocal lattice points in the blind region for the normal-beam fiber diagram, Weissenberg photographs were taken with the drawing direction (chain axis) perpendicular to the camera axis (Norman method[24]). PLLA oriented films used for Weissenberg photographs have a size of 2 mm (parallel to the drawing axis) × 4 mm (perpendicular to the drawing axis) × 0.2−0.4 mm (thickness). Sealing by polyimide tapes was also conducted during X-ray radiation (Ni-filtered Cu Kα at 40 kV and 40 mA for 4−24 h) for Weissenberg photographs.

WAXD profile analysis was performed by the handmade GUI software developed by Marubayashi using Java programming language (HerMesJ-1D[25]). X-ray fiber diagram analysis and determination of unit cell dimensions were performed by the handmade GUI software developed by Marubayashi using Java programming language (HerMesJ-2D and HerMesJ-UC, respectively[25]). The details are described in the Supporting Information.

Energy Calculations. Energy calculations were executed by the handmade GUI software developed by Marubayashi using Java language (HerMesJ-ER[25]). In the early stage of calculations, the ordered 10_7 helix model, which is the initial model of α-form by Sasaki,[16a] was used as the chain conformation of PLLA. Each methyl group in a PLLA chain was treated as a single atom in energy calculations. As the molecular conformations of organic solvents, we used the molecular structures obtained by the gas-phase electron diffraction (CPO[26] and DMF[27]).

The nonbonded interaction energy (U_{NB}) was estimated as sum of the van der Waals interaction energy (U_{vdW}) and the electrostatic interaction energy (U_{EL}). The Lennard-Jones 6−12 potential was used to describe van der Waals interactions (see Supporting Information). Electrostatic interactions were estimated by the Coulomb potential between point charges (Supporting Information). The cutoff distance was set to 1.5 nm in all the energy calculations, so that the interactions between atoms separated by a distance larger than 1.5 nm were truncated. To estimate the intramolecular nonbonded interaction energy of PLLA, U_{NB} of each atom in 10 monomeric units (60 atoms in a period) with atoms in the same PLLA chain was summed up and defined as E_H. The skeletal torsional energy was summed up over a period (10 residues) and defined as E_{tors} (see Supporting Information). In the calculation of the host−host (PLLA−PLLA) interaction energy, U_{NB} of each atom in 10 monomeric units with atoms in other PLLA chains was summed up (E_{HH}). To calculate the host−guest (PLLA−solvent) interaction energy, U_{NB} of each atom in 10 residues of PLLA with atoms in guest molecules was summed up (E_{HG}). In other words, a PLLA helix was subjected to the potential E_{HG} by surrounding guest solvents. On the contrary, to calculate the guest−host (solvent−PLLA) interaction energy, U_{NB} of each atom in guests in a period with atoms in PLLA chains was summed up (E_{GH}). Namely, guest molecules in a period were subjected to the potential E_{GH} by surrounding PLLA chains. In addition, U_{NB} of each atom in guests in a period with atoms in other guest molecules was summed up (E_{GG}).

Structure Refinements. The reliability factor R and the weighted reliability factor wR are given by the following equations:

$$R = \frac{\sum ||F_{obs}| - C|F_{cal}||}{\sum |F_{obs}|} \quad (1)$$

$$wR = \left(\frac{\sum (|F_{obs}| - C|F_{cal}|)^2}{\sum |F_{obs}|^2} \right)^{1/2} \quad (2)$$

$$|F_{cal}| = \sqrt{\sum m |F_{hkl}|^2} \quad (3)$$

$$F_{hkl} = \sum_j f_j T_j \exp[2\pi i(hx_j + ky_j + lz_j)] \quad (4)$$

where F_{obs} is the observed structure factor, C is the inverse of the scaling factor K ($C = 1/K$), F_{cal} is the calculated structure factor, m is the multiplicity of the reflection, F_{hkl} is the structure factor of the hkl plane, j is the index of constituent atom, f_j is the atomic scattering factor, T_j is the Debye−Waller factor ($T_j = \exp(-B_j \sin^2\theta/\lambda^2)$, where B_j is the isotropic atomic displacement parameter), and (x_j, y_j, z_j) is the fractional coordinate. In the case of PLLA, B was set to 13 Å^2 for a methyl group and 10 Å^2 for other constituent atoms.[16a] For all the atoms in each solvent molecule, B was assumed to be 10 Å^2. In the calculation of reliability factors, the contribution from three hydrogen atoms in each methyl group was neglected. The parameter C was roughly estimated by fitting $C\sum|F_{cal}|$ to $\sum|F_{obs}|$ and refined by minimizing wR.

Before the structure refinements, the positional parameters of PLLA chains and guest molecules were changed randomly around those optimized by the grid search algorithm. Random numbers were produced using a xorshift random number generator (xorshift RNG),[28] in which four seeds (8 bite integers) were made based on current local time in Japan.

The structure refinements were performed by the constrained least-squares method[29] using the handmade GUI software (HerMesJ-ER[25]):

$$\Theta = \sum_{m=1}^{M} (K|F_{obs}| - |F_{cal}|)^2 + \sum_{h=1}^{H} \lambda_h G_h \quad (5)$$

where m is the index of the nonequivalent reflections, h is the index of the restricting conditions, λ_h is the Lagrange's undetermined multiplier, and G_h is the restricting condition.

Thermogravimetry−Differential Thermal Analysis (TG-DTA). TG-DTA was carried out using a TG8120 (Rigaku Corp.). Measurements were conducted from room temperature to 500 °C with a heating rate of 20 °C/min in a N_2 gas atmosphere. We performed TG-DTA only for films containing the solvents with a relatively low desorption rate (CPO and GBL), as in density measurements.

Fourier Transformed Infrared (FTIR) Spectroscopy. FTIR spectra were measured using an FT/IR-620 equipped with a MICRO-20 (JASCO Corp.) with a resolution of 4 cm^{-1} and a cumulative number of 64 in air at room temperature. For PLLA films crystallized in a CPO or GBL atmosphere, thin films with a thickness of 2−4 μm were prepared from the solvent-crystallized films with a thickness of 450 μm using a rotary microtome. In the case of THF, DOL, and DMF, solvent desorption during microtoming was unable to be neglected. Therefore, for these three solvents, we were not able to use the same films as those used in WAXD measurements (450 μm thickness). Alternatively, thin films with a thickness of 1−2 μm were prepared by solution casting ($CHCl_3$). These thin films were confirmed to be the amorphous state judging from the lack of the crystalline band (≈922 cm^{-1}). Each thin film was exposed to a THF, DOL, or DMF atmosphere at −25 °C for desired periods. Just after an exposure period, FTIR spectra of these thin films were measured.

Density Measurements. Densities of various PLLA films were determined by the flotation method (water) using an SD-200 L (Alfa Mirage Co., Ltd.). In the case of PLLA films crystallized in CPO and GBL, solvent desorption during density measurements was able to be neglected. To minimize the effects of extra solvents in the PLLA amorphous region, these solvent-crystallized films were dried at room temperature under atmospheric pressure. Just before the crystal transition to the α-form starts, the drying was finished and then

density measurements were conducted. In the case of PLLA films crystallized in THF, DOL, and DMF, a solvent desorption rate was relatively high, so that density measurements for films containing these three solvents were not performed.

RESULTS AND DISCUSSION

Solvent Species Dependence of PLLA Crystal Structures. For the aprotic polar solvents with relatively low boiling point (T_b), such as acetone and THF, crystallization of PLLA was completed within 1 day even at −25 °C. On the other hand, for the aprotic polar solvents with relatively high T_b, such as GBL and PC, it took 2 months for PLLA molecules to crystallize sufficiently at −25 °C. As mentioned above, WAXD measurements were conducted for PLLA films containing solvents, which were sealed by polyimide tapes to minimize solvent desorption. For a large part of solvents such as acetone, acetonitrile, and toluene (Figure 1), it was found that PLLA molecules form the α-crystals ($2\theta_{CuK\alpha}$ = 16.7° and 19.1°),[15,16] as is the case with crystallization in air above 120 °C. The formation of α'-crystals ($2\theta_{CuK\alpha}$ = 16.5° and 18.9°)[17,18] was not observed in organic solvent atmospheres, as in crystallization of PLLA under high-pressure CO_2.[19] On the other hand, when PLLA was crystallized in some five-membered ring compounds (THF, CPO, DOL, and GBL) or DMF below room temperature (−25 °C for THF and DMF; −25−5 °C for CPO, DOL, and GBL), the specific WAXD profiles (strong diffraction peaks at $2\theta_{CuK\alpha} \approx$ 11°, 14°, 18°, and 22°) were observed (Figure 2), which are quite different from that of the α-form ($2\theta_{CuK\alpha}$ = 16.7° and 19.1°). Furthermore, these specific WAXD profiles cannot be attributed to the α' (δ)-, α''-, β-, and γ-forms;[17−21] i.e., these crystal structures have not been reported. Here, we define the crystal structure formed in the specific five-membered ring compounds (THF, CPO, DOL, and GBL) or DMF below room temperature as the "ε-form" of PLLA. For convenience, we define the ε-crystals formed in the presence of THF, CPO, DOL, GBL, and DMF as the ε_{THF}, ε_{CPO}, ε_{DOL}, ε_{GBL}, and ε_{DMF}, respectively. In addition, we name THF, CPO, DOL, GBL, and DMF the "ε-solvents". Since there are small differences in diffraction peak position and shape among these ε-crystals, it follows that the lattice spacings of ε-crystals change by solvent species, as shown later in detail. Differences in the molecular size and functional groups of solvents should be responsible for such changes in lattice spacings.

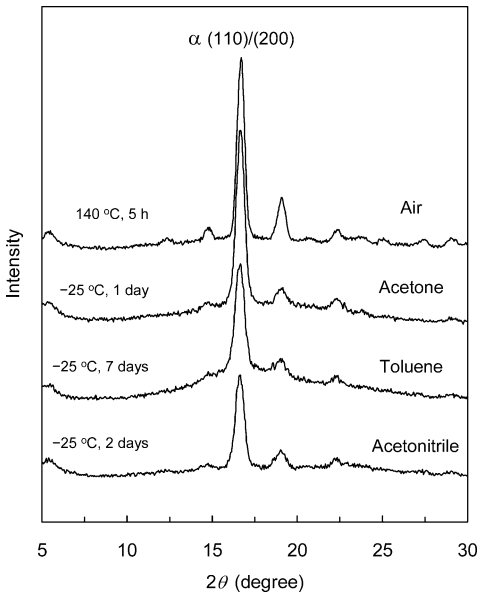


Figure 1. WAXD curves of PLLA crystallized in acetone, acetonitrile, and toluene atmosphere. WAXD curve of PLLA crystallized in air (α-form) is also shown for comparison.

Now, we discuss the effect of solvent species on the ε-crystal formation. First, the ε-solvents with the five-membered ring structure (THF, CPO, DOL, and GBL) are discussed. THF and DOL are five-membered ring ethers, CPO is a five-membered ring ketone, and GBL is a five-membered ring ester. Therefore, the five-membered ring structure, the nucleophilic oxygen, or both of them should play an important role in the formation of ε-crystals. As shown in Figure 3a, the generation of ε-form did not occur in DEE vapor, although this ether has one oxygen and four carbons as constituent elements, as is the case with THF. Similarly, PLLA molecules form only the α-crystals by crystallization in 3-pentanone, which is a ketone having same numbers of oxygen and carbon as CPO. Furthermore, a six-membered ring ketone such as CHO and a six-membered ring ether (DOX) yielded not the ε-crystals but the α-ones, as shown in Figure 3b. These results indicate that the size and shape of solvents are of great importance in the ε-crystal formation.

In spite of five-membered ring structures, cyclic carbonates (EC and PC) or pyrrolidones (2Py and NMP) gave only the α-form, as shown in Figure 3b. This result indicates that the PLLA monomer unit (LLA) makes poor interactions with the carbonate linkage and the amide bond because there are only relatively small differences in the molecular size and shape among these cyclic carbonates, pyrrolidones, and the five-membered ring ε-solvents. Namely, the carbonate linkage and the amide bond are considered to be inappropriate for intermolecular interactions with LLA, resulting in the formation of α-crystals. Thus, it was indicated that the appropriate functional groups as well as the molecular size and shape are needed for solvents to assist the ε-crystal formation.

To verify the importance of LLA−solvent interaction, we investigated the effect of unsaturated carbon bonds on the formation of ε-crystals (Figure 3c). Only the α-form was generated by casting furan (two unsaturated carbon bonds in the five-membered ring structure) solution of PLLA. Similarly, for 23DHF and 25DHF, which contain one unsaturated carbon bond in the five-membered ring structure, PLLA formed only the α-crystals. Namely, it was found that unsaturated carbon bonds in the five-membered ring hinder the formation of PLLA ε-crystals. Differences in the molecular size and shape between furan and furan hydrides are relatively small, so that hydrogenation of furan should have a great influence on intermolecular interactions with LLA, which would determine whether the formation of ε-crystals arises or not.

As shown in Figure 3d, substitution of one hydrogen atom in the second position of THF (2MTHF, THFA, and THFMA) or DOL (2MDOL) hindered the generation of ε-form. Similarly, replacement of one hydrogen atom by a methyl group for GBL (AMGBL and GVL) prohibited PLLA molecules from forming the ε-crystals. For comparison, sPS forms clathrates with both benzene and its substitutes such as toluene, xylene, and bromobenzene.[7a] Compared to sPS−solvent clathrates, there might be smaller spaces for including solvent molecules in the ε-form of PLLA, as discussed later in detail.

dx.doi.org/10.1021/ma202324g | Macromolecules 2012, 45, 1384−1397

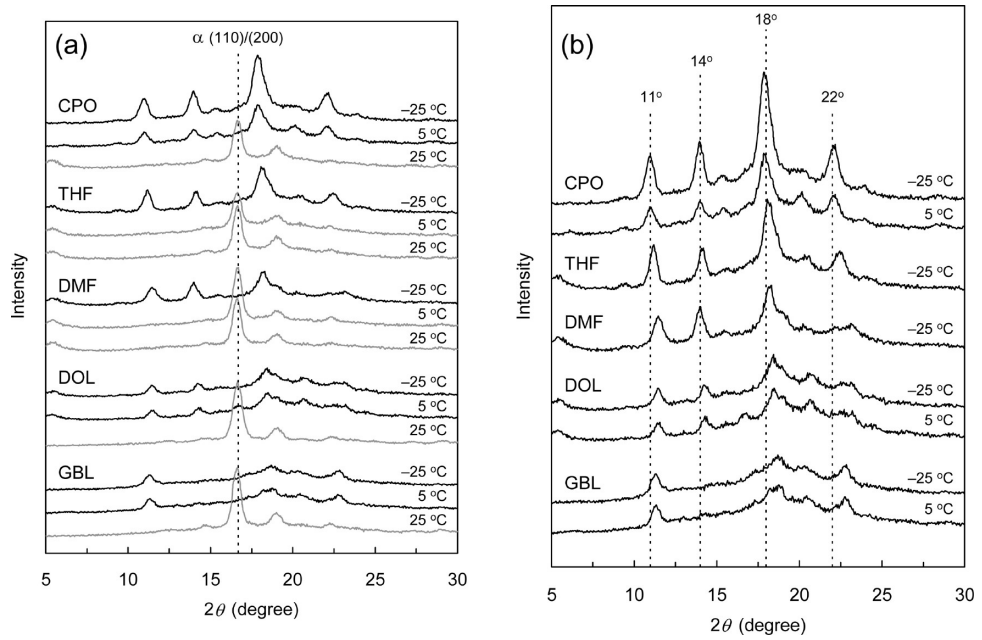


Figure 2. WAXD curves of PLLA crystallized in CPO, THF, DMF, DOL, and GBL at various temperatures: (a) total curves and (b) selected ones (ε-forms).

Next, we have a discussion on DMF. In all the DMF derivatives used in this study (DMAc, DEF, NMF, NMA, formamide, and IBA), the formation of ε-crystals did not occur, as shown in Figure 3e. In a formamide atmosphere, crystallization of PLLA was not completed even by solvent exposure at room temperature for several months, as in ethanol and hexane. Substitution of a methyl group for one aldehyde hydrogen of DMF gives DMAc, substitution of two ethyl groups for two methyl groups gives DEF, substitution of a hydrogen atom for one methyl group corresponds to NMF, substitution of a hydrogen atom for one methyl group on a nitrogen atom of DMAc corresponds to NMA, substitution of two hydrogen atoms for two methyl groups yields formamide, and substitution of a methine for a nitrogen atom corresponds to IBA. This systematic study on DMF derivatives also supports our idea that the size, shape, and functional groups of solvents play an important role in the ε-crystal formation. Since DMF is not a five-membered ring solvent, it follows that the five-membered ring structure is not necessarily essential in the formation of ε-crystals.

Figure 4 is a summary of solvent species dependence of PLLA crystal structures. Thus, it was found that PLLA has high selectivity for low molecular weight compounds to form the ε-crystals. Here, for good solvents for PLLA such as chloroform and furan, solution casting was done only at 25 and 40 °C. If one can crystallize PLLA molecules in atmospheres of such good solvents below room temperature, some new insights into the solvent species effects on PLLA crystal structures might be obtained. Of course, there is the possibility that some solvents that were not used in this study assist the formation of PLLA ε-crystals or other crystal polymorphs. In fact, we tried only one kind of four-membered ring solvents (BBL) and none of three-membered rings.

Crystal Structure Transition of PLLA by Solvent Desorption. Figure 5 shows the change of WAXD curve of PLLA with desorption of THF. Each WAXD curve is labeled with corresponding solvent solubility q (g/g$_{PLLA}$). The result of peak separation for these WAXD curves (area, intensity, and position of the selected diffraction peaks) is shown in Figure 6 as a function of solvent solubility. The *hkl* indices for the ε-form are on the basis of our indexing, as mentioned later. The diffraction peaks at $2\theta \approx 11°$ and 14° correspond to the (200) and (020) reflections for the ε-form, respectively. The diffraction peak area and intensity for the ε-form slightly increased with solvent desorption, and when solvent solubility in a PLLA film reduced to 0.3–0.4 g/g$_{PLLA}$ (0.37 g/g$_{PLLA}$ for THF, 0.29 g/g$_{PLLA}$ for DMF, 0.33 g/g$_{PLLA}$ for DOL, 0.31 g/g$_{PLLA}$ for CPO, and 0.30 g/g$_{PLLA}$ for GBL), the peak area and intensity for the ε-form started to decrease and simultaneously those of (110)/(200) reflections for the α-one appeared at 2θ = 16.7°, showing the occurrence of crystal transition from ε- to α-forms with solvent desorption. Here, since the molecular weight of each ε-solvent is comparable with that of one residue in PLLA (LLA), the solvent solubility at which the ε-to-α transition starts can be expressed by values in a molar ratio (0.25–0.37 mol/mol$_{LLA}$) similar to those in a weight ratio (0.29–0.37 g/g$_{PLLA}$). After that, the ε-to-α transition proceeded with solvent desorption. It should be noted that there were no peak position changes in ε-crystal reflections ((200) and (020)) during the ε-to-α transition. This result indicates that some drastic *d*-spacing changes (i.e., drastic rearrangement of PLLA chains in a crystal) are induced by solvent desorption.

In the case of sPS–solvent cocrystals, the formation of specific crystal structures arises by solvent desorption (γ, δ, and ε[7,8]), which does not occur by thermal annealing. The chain conformation in these emptied crystals of sPS is the same as that in cocrystals, which is different from that in crystals prepared by annealing (α and β). That is, sPS molecules can keep the history of cocrystalline phase to some extent despite solvent removal. Similarly, it was suggested that the α''-form of PLLA results from CO_2 desorption from a PLLA crystal lattice.[19] On the other hand, there were no emptied crystal phases in the ε-to-α transition of PLLA.

Figure 7 shows the result of thermogravimetric measurement for the PLLA film containing ca. 0.3 g/g$_{PLLA}$ CPO. Weight loss started to be observed around the original T_g of PLLA (60 °C).

dx.doi.org/10.1021/ma202324g | *Macromolecules* 2012, 45, 1384–1397

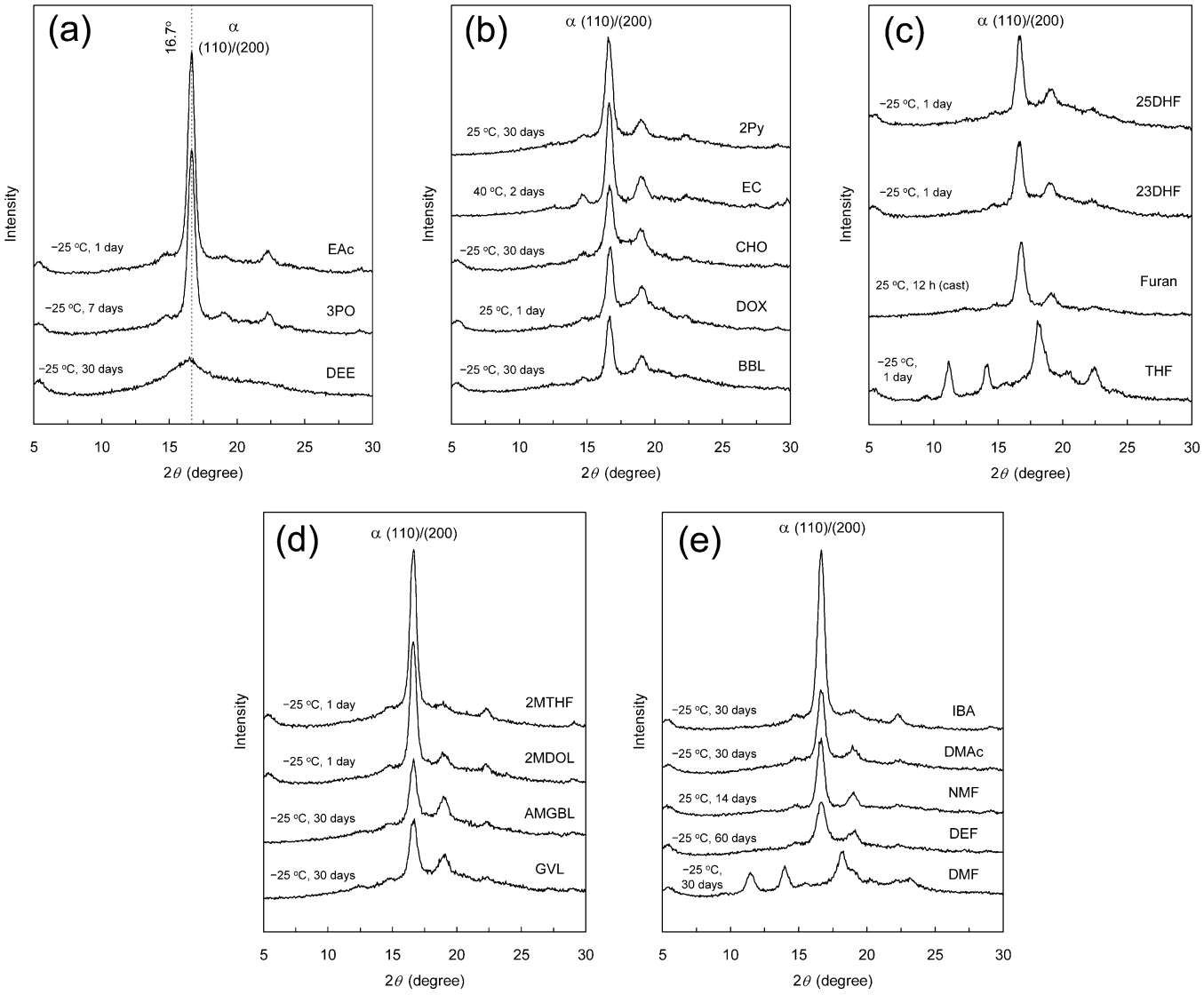


Figure 3. WAXD curves of PLLA crystallized in (a) chain molecules, (b) various ring compounds, (c) THF derivatives, (d) methyl-substituted ε-solvents, and (e) DMF derivatives.

As a result, there was 22% weight loss before the occurrence of thermal decomposition of PLLA (>300 °C). If one assumes that this weight loss is due to CPO, then the calculated CPO solubility is 0.28 g/g_{PLLA}, which is in good agreement with the value obtained from the weighing (ca. 0.3 g/g_{PLLA}). A similar result was obtained for the PLLA film containing ca. 0.3 g/g_{PLLA} GBL.

FTIR Spectra of PLLA ε-Forms. Figure 8 shows FTIR spectra of PLLA crystallized in a CPO, DMF, DOL, GBL, or THF atmosphere. The existence of solvents in PLLA films was confirmed by the solvent-derived IR bands,[30] although it was hard to determine the location of solvents (i.e., PLLA amorphous or crystalline region). In particular for CPO and GBL, one would expect that the number of the extra solvents in the amorphous region was minimized by drying in air for the desired periods (just before the diffraction peak of α-form appears). First, we focus our attention on the spectral region of 1850−1600 cm^{-1} (Figure 8a). As for the carbonyl stretching band, there were almost no differences in the peak positions (1758 cm^{-1} for gt; 1777 cm^{-1} for gg[31]) and shape among the ε-forms and α-one. This result suggests that the interaction among PLLA chains and solvent molecules is not enough to affect the C═O stretching mode of PLLA. Next, we turn our attention to the spectral region of 1000−600 cm^{-1} (Figure 8b). For the α-crystals formed in air, there is a small band around 922 cm^{-1}, attributed to the coupling of the C−C backbone stretching with the CH_3 rocking mode.[32] This band is sensitive to the helical chain conformation of PLLA, hence called the crystalline band of PLLA. The crystalline band position changes with PLLA helical sense (e.g., 912 cm^{-1} for the β-form with 3_2 helices[33]), so that we can obtain the information on PLLA helical nature from the crystalline band position. For most of the PLLA ε-forms, unfortunately, it was difficult to determine the crystalline band position because of overlapping of the crystalline band and the solvent-derived bands (913 cm^{-1} for CPO, 923 cm^{-1} for DOL, 931 cm^{-1} for GBL, and 912 cm^{-1} for THF[30]). In the case of DMF, the crystalline band was located around 921 cm^{-1}, in good agreement with the crystalline band position of the α-form.

Summarizing the points so far, we found that the specific crystal structure of PLLA (ε-form) is formed in the specific organic solvent atmosphere, and the ε-to-α transition occurs

dx.doi.org/10.1021/ma202324g | Macromolecules 2012, 45, 1384−1397

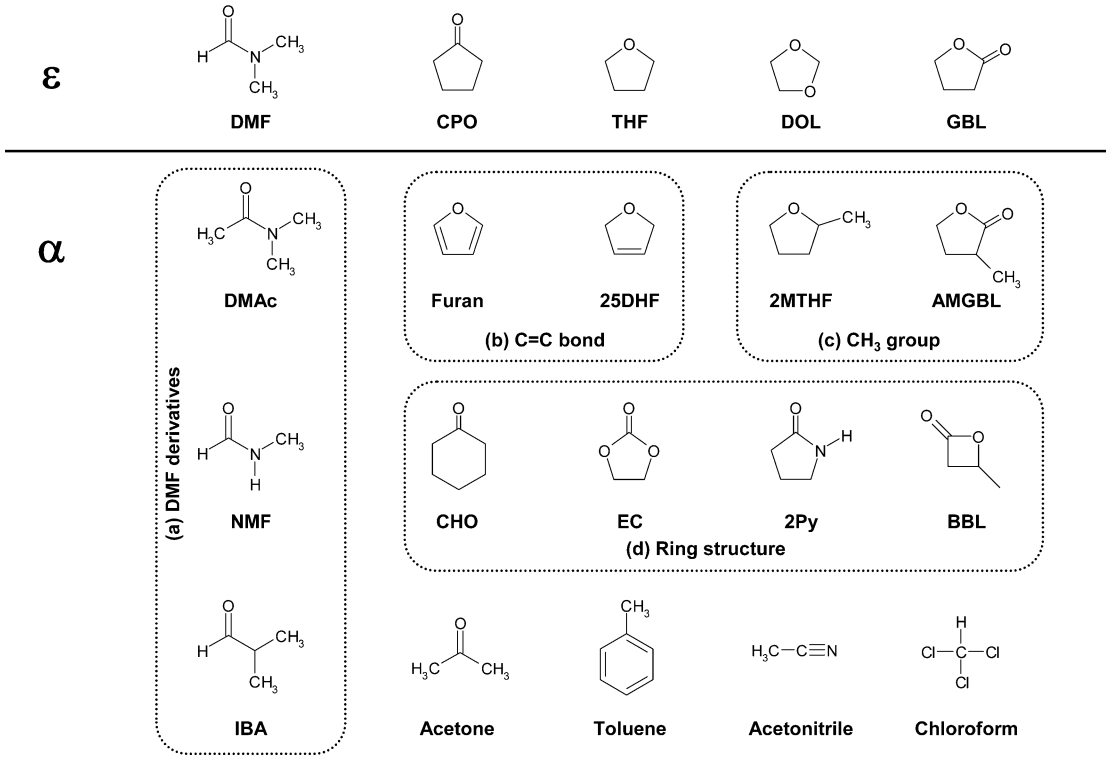


Figure 4. Effect of solvent species on ε-crystal formation of PLLA.

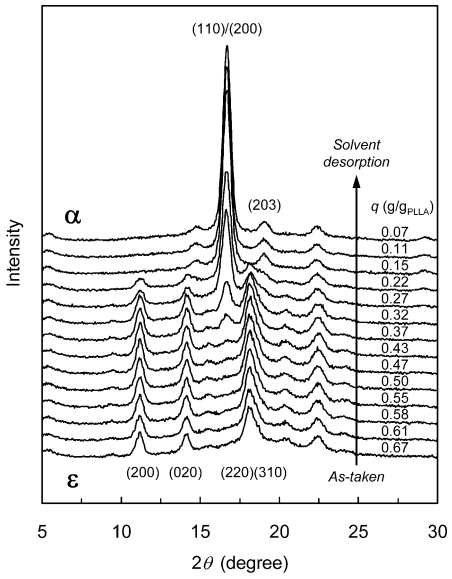


Figure 5. Change of WAXD curve for ε_{THF}-film with solvent desorption.

with solvent desorption. On the basis of these results, we move on to the next section, assuming that the ε-form is the PLLA–solvent complex crystal (cocrystal).

Unit Cells of PLLA ε-Forms. Fiber diagrams for the ε- and ε-rich PLLA films are shown in Figure 9. The corresponding ξ–ζ converted patterns of the intensity-corrected fiber diagrams and Weissenberg photographs are shown in the Supporting Information. For comparison, the data of α-form are also shown. For THF, GBL, and DOL, unfortunately, we failed to prepare the oriented crystallized films having only the ε-crystals. Namely, the oriented crystallized films for these three solvents have a small number of α-crystals as well as the ε-ones (ε-rich state). Preparing conditions of the oriented ε- and ε-rich films (Table 2) were chosen to minimize the ratio of α-form. Roughly estimated magnitude relation of the ratio of ε- to α-crystals is as follows: THF ≈ GBL > DOL. Therefore, we first analyzed the fiber diagrams of ε_{DMF}- and ε_{CPO}-films (see Supporting Information), which are almost free from the α-form. Based on results of fiber diagram analyses on ε_{DMF}-, ε_{CPO}-, and α-films, the α-derived reflections were separated from the fiber diagrams for THF, GBL, and DOL. The fiber periods of ε-forms, which were calculated from the distance between neighboring layer lines, are in the range 2.8–2.9 nm, in good agreement with that of the α-form (2.888 nm: one period for a 10_7 helix of PLLA[16a]). Furthermore, the integrated intensity was relatively high on the layer lines with l = 0 (equatorial), 1, 3, 4, 6, 7, and 10, whereas relatively low on the layer lines with l = 2, 5, 8, and 9. Such dependence of diffraction intensity on the layer line order clearly shows that PLLA chains in the ε-form take the 10_7 helical conformation and the chain axis is perpendicular to *ab* plane ($\alpha = \beta = 90°$), as in the α-form.[34] As mentioned before, FTIR spectroscopic data suggest that the PLLA–solvent interaction is not enough to affect the C=O stretching mode of PLLA. This infrared result would be linked with the diffraction result that there are almost no differences in a fiber period and helical sense among the ε- and α-forms. Namely, if solvent molecules have a great effect on the C=O stretching mode of PLLA, then some conformational changes of PLLA should be induced, resulting in the changes in helical sense and a fiber period. In some cases, the complexation with low molecular weight compounds induces the conformational changes of host polymer. The chain conformation of PEI changes from the double-standard helix to the planar zigzag by the formation of crystalline hydrates.[9] sPS takes the TTGG

dx.doi.org/10.1021/ma202324g | Macromolecules 2012, 45, 1384–1397

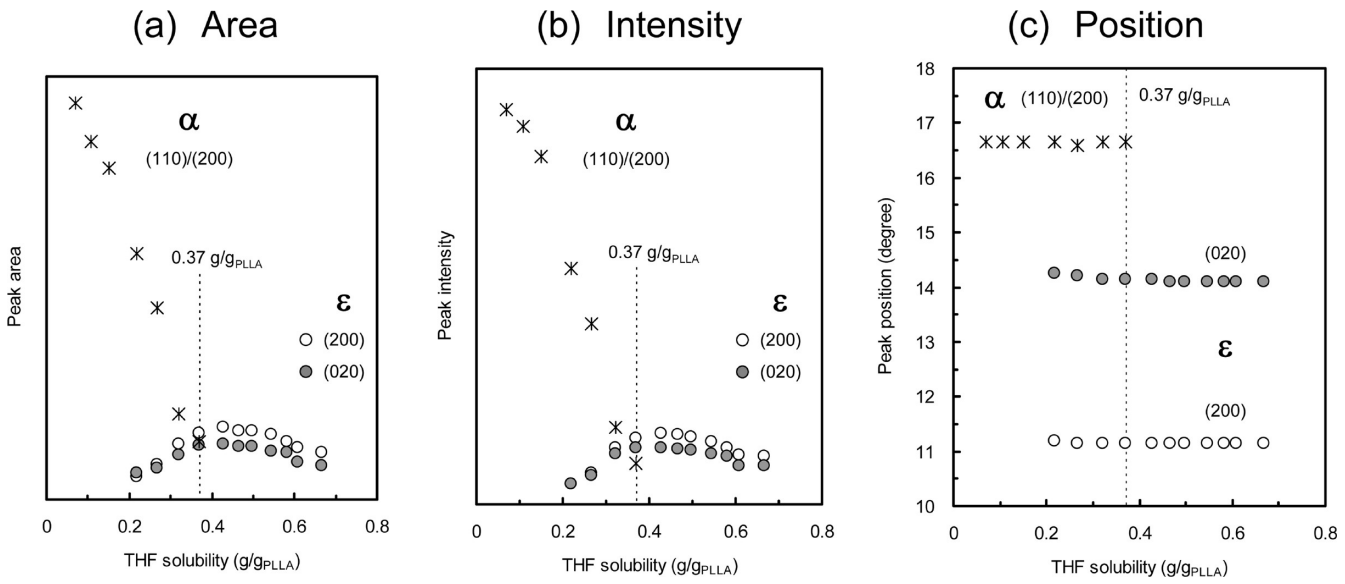


Figure 6. THF solubility dependence of (a) area, (b) intensity, and (c) position of ε-derived and α-derived diffraction peaks.

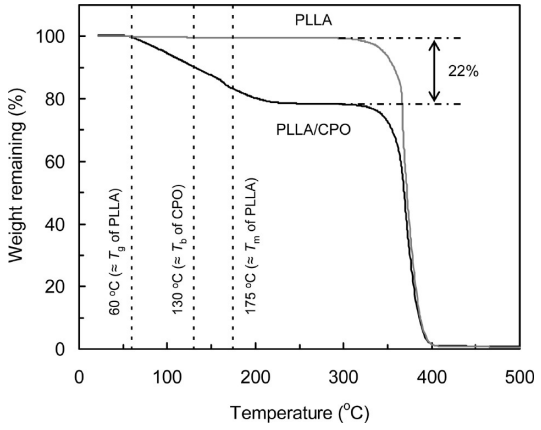


Figure 7. Thermogravimetric curve of PLLA crystallized in CPO vapor at 5 °C for 15 days and dried in air. Data of PLLA free from solvents are also shown for comparison.

helical conformation in the clathrate, whereas the planar zigzag conformation in the annealed samples (α or β).[7,8]

By the trial-and-error method taking into account the 2_1 helical symmetry of the 10_7 PLLA helix, indexing by the orthorhombic unit cell (a = 1.5−1.6 nm, b = 1.2−1.3 nm, c = 2.8−2.9 nm, and $\alpha = \beta = \gamma = 90°$) was successful for the ε-forms, as shown in Table 3. For the ε-forms, the length of a-axis is about 1.5 times that for the α-form, and the length of b-axis is about twice that for the α-form. Namely, the area of ab plane of the ε-form is about 3 times that of the α-form. The space group of ε-forms was assumed to be $P2_12_12_1$, which is same as that of the α-form, from the systematic absences of odd reflections for $h00$, $0k0$, and $00l$. It is unlikely that the chain folding direction changes during the ε-to-α transition with solvent desorption. Therefore, it should be reasonable to assume that the unit cell of each ε-form consists of parallel and antiparallel chains, as in the α-form. In the α-form, parallel chains are located in corners of the orthorhombic unit cell, and an antiparallel chain is in the center of the orthorhombic lattice. These parallel and antiparallel chains are related each other by 2_1 screw axes parallel to a- and b-axes, respectively ($P2_12_12_1$).[16]

The density of PLLA is 1.248 g/cm^3 in the amorphous state and 1.26−1.29 g/cm^3 in the crystalline state (α-form).[16,36] Therefore, the density of PLLA in the semicrystalline state (α-form) is in the range between these values. In contrast, the observed density is 1.195 g/cm^3 for the PLLA film having ε-crystals with CPO (semicrystalline state). Thus, the observed density of ε_{CPO}-film was smaller than that of the amorphous PLLA (d_{obs} = 1.254 g/cm^3). For the ε_{GBL}-film, the observed density is 1.258 g/cm^3. As mentioned in the Experimental Section, for the PLLA−solvent complexes having DMF, DOL, and THF, the density of each film was unable to be measured due to relatively fast desorption of these solvents. Since the contribution from the amorphous region needs to be considered, the observed densities were used as a rough indication, as shown later.

Packing of PLLA Chains and Solvents in ε-Crystal Unit Cell. In this study, the crystal structure analyses on PLLA−DMF and PLLA−CPO complexes were performed because the oriented ε-films containing almost no α-crystals were able to be obtained only for these solvents. As a result, we succeeded in obtaining the plausible crystal structure of ε_{DMF}. In the case of PLLA−CPO complex, however, the packing model with R < 20% and a relatively low packing energy was unable to be obtained. Therefore, the crystal structure analysis process is shown below only for the PLLA−DMF complex. First, the number of PLLA chains in the unit cell was assumed to be four. If there are 2, 4, and 6 chains in the unit cell of PLLA−DMF complex, the calculated densities are 0.440, 0.880, and 1.321 g/cm^3, respectively. For the two-chain model, the calculated density is too small (d_{cal} < 1.0), even if 20 solvent molecules are encapsulated in the unit cell (1:1 complex). In the case of the six-chain model without guests, the calculated density (1.321 g/cm^3 for the ε_{DMF}) is higher than that of the α-form (1.26−1.29 g/cm^3). If one assumes that there are four chains and some solvents in the unit cell, the calculated densities become valid values in terms of the observed densities (1.195 g/cm^3 for the ε_{CPO}-film and 1.258 g/cm^3 for the ε_{GBL}-film).

Second, values of two skeletal torsional angles—φ = (C′$_0$, O″$_1$, C$^\alpha_1$, C′$_1$) and ψ = (O″$_1$, C$^\alpha_1$, C′$_1$, O″$_2$)—were optimized with the constraints of a constant fiber period (refined value), helical periodicity (ideal 10_7 helix), and a constant torsional

dx.doi.org/10.1021/ma202324g | Macromolecules 2012, 45, 1384−1397

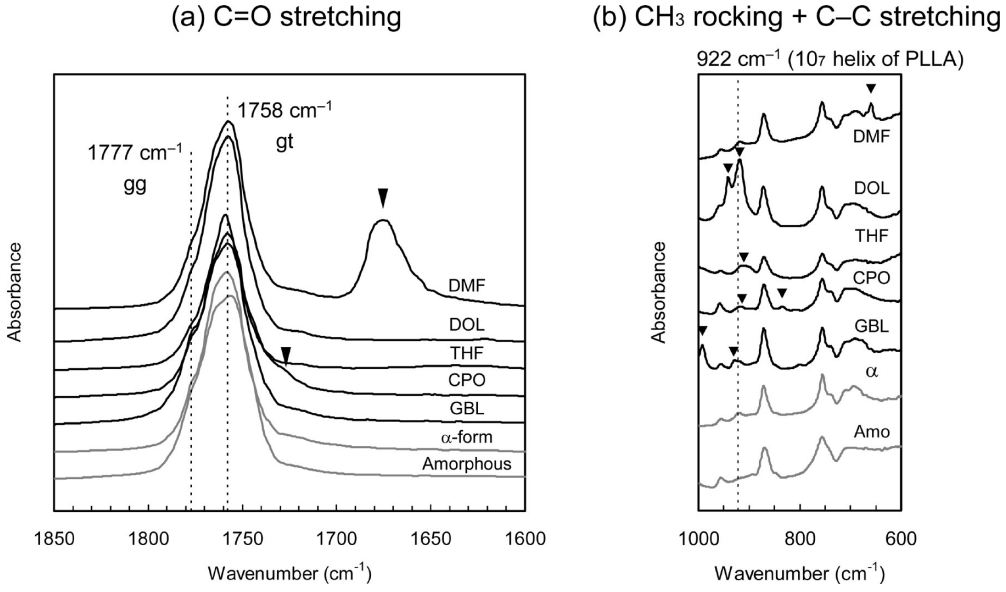


Figure 8. FTIR spectra of PLLA ε-films at (a) 1600−1850 cm^{-1} and (b) 600−1000 cm^{-1}. Solvent-derived IR bands are marked with black triangles. Data of amorphous and α-films are also shown for comparison.

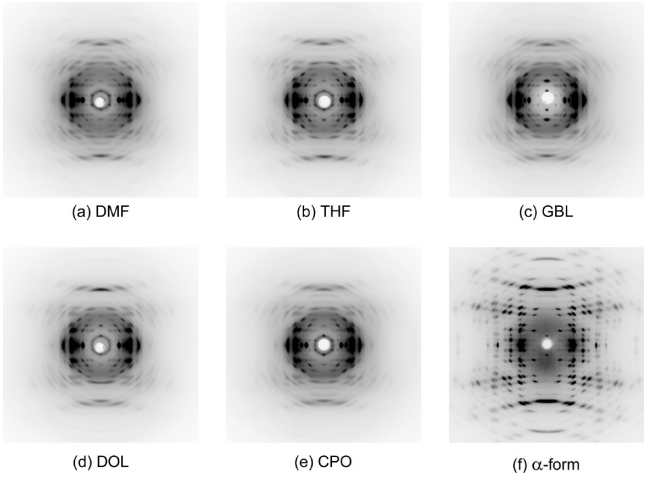


Figure 9. Observed fiber diagrams for oriented ε- and ε-rich films (a–e) and annealed one (f). Drawing direction equals the vertical direction.

Table 3. Lattice Constants of ε-Forms ($\alpha = \beta = \gamma = 90°$)

solvent	a (nm)	b (nm)	c (nm)	unique reflections[a]
CPO	1.616	1.261	2.899	30
DMF	1.551	1.227	2.857	30
DOL	1.539	1.215	2.898	29
GBL	1.558	1.242	2.891	38
THF	1.574	1.236	2.871	40
air[b]	1.066	0.616	2.888	121

[a]The number of unique reflections used for refinement of lattice constants. [b]Lattice constants of the α-form ($\alpha = \beta = \gamma = 90°$) reported by Sasaki et al.[16a]

angle (ω = (C^{α}_1, C'_1, O''_2, C^{α}_2) = 180°: ester bond) using the Miyazawa equation.[37] These two torsional angles (φ and ψ) were changed around those of α-form ($\varphi = -66.0°$ and $\psi = 150.8°$) with a range of ±10° and a step of 0.1°. The obtained results are as follows: $\varphi = -63.7°$ and $\psi = 148.5°$ for the ε_{DMF} (fiber period: 2.857 nm).

Third, energy and R-factor calculations without guest solvents were performed to save calculation time. With the conformation of PLLA fixed (rigid chain model), the chain packing style of PLLA was parametrized by four variables: (1) the translation to the a-axis direction from the center of chain (X), (2) the translation to the b-axis direction from the center of chain (Y), (3) the translation to the c-axis direction (Z), and (4) the rotation around the helix center (W). Z is a height of the ether oxygen atom in the first residue of a PLLA chain. The orientational angle (W) was determined as follows: $W = W' + 100.6°$, where W' is the angle (ab plane) between the unit vector parallel to the a-axis and the shortest vector from the center of chain to the ether oxygen in the first residue. If the position of one chain in the unit cell is determined by X, Y, Z, and W, then those of other three chains are determined automatically owing to the symmetry of $P2_12_12_1$. Each chain packing parameter was changed, as follows: $0 \le X \le 0.25$ (fractional coordinate), $0 \le Y \le 0.5$ (fractional coordinate), $0 \le Z \le 0.1$ (fractional coordinate), and $0 \le W \le 180°$. A step of each packing parameter is as follows: ca. 0.02 nm for X, ca. 0.02 nm for Y, ca. 0.03 nm for Z, and 12° for W. Here, torsional energies and nonbonded interactions between atoms in the same chain (intramolecular interactions) were constant values because of the fixed conformation. Therefore, these energies were not calculated in this stage. The mapping of R-factor and host–host interaction energy for ε_{DMF} is shown in the Supporting Information. Since (X, Y) for the minimum R-factor was not in agreement with that for the minimum energy, we selected some (X, Y) points, at which a relatively small R-factor with an attractive packing energy was obtained. Here, the discrepancy between minima of R-factor and host–host interaction energy may be attributed to the instability of PLLA crystal lattice without solvents, which can be seen from a drastic change in the unit cell dimension by solvent desorption (ε-to-α transition), as mentioned above.

Three packing models were selected for PLLA chains in the ε_{DMF} (models I_{DMF}, II_{DMF}, and III_{DMF}), in which guest solvents are not taken into consideration. The R-factor and the packing energy (E_{HH}) for these three models are shown in Table 4. For

dx.doi.org/10.1021/ma202324g | Macromolecules 2012, 45, 1384–1397

Table 4. Energy and *R*-Factor of Each Packing Model for PLLA−DMF Complex

model	E_{HH}[a]	E_{HG}[a]	E_{GH}[a]	E_{GG}[a]	E_{intra}[a]	*R* (%)
I_{DMF}	−37.2				−85.1	39.0
II_{DMF}	−39.0				−85.1	39.8
III_{DMF}	−20.7				−85.1	39.4
I_{DMF}'	−37.2	25.4	51.1	−9.2	−85.1	29.3
$I_{DMF}'_{-R}$	−32.7	46.6	79.3	−10.4	−80.3	23.3
I_{DMF}''	−36.2	10.0	18.0	−12.6	−85.1	27.5
$I_{DMF}''_{-R}$	−32.6	28.9	55.6	−14.5	−80.8	19.6

[a]Energies are given in kcal/mol.

all the selected models, there are relatively large cavities (e.g., around $(x_f, y_f) = (0.25, 0.5)$), and each cavity is surrounded by four chains. Therefore, we assumed that guest solvents are encapsulated in these cavities. By the symmetry of $P2_12_12_1$, if one puts a solvent in the cavity, another three solvents emerge automatically in the unit cell. Accordingly, the number of solvents in the unit cell is multiple of four (4, 8, 12, 16, 20, ...).

For the models I_{DMF}, II_{DMF}, and III_{DMF}, *R*-factor calculations with guests were conducted by changing the packing of solvents in the symmetry of $P2_12_12_1$ with PLLA chains fixed. To change the coordination style of guests, we used three parameters (r, z, μ) that represent the position of the selected atom in the solvent located at the lowest height (their zero point is the intersection of a 2_1 screw axis and $Z = 0$) and another three variables (φ_x, φ_y, φ_z) that determine rotation angles of the solvent around three axes in the internal coordinate system, in which a zero point is the center of mass for each solvent (see Supporting Information). For the ε_{DMF}-form, these positional parameters were changed in the following range: -0.20 nm $\leq r \leq 0.30$ nm (ca. 0.03 nm step), 0 nm $\leq z \leq 1.40$ nm (ca. 0.03 nm step), and $0° \leq \mu, \varphi_x, \varphi_y, \varphi_z \leq 315°$ (45° step). We introduced solvents by four in the unit cell and calculated the *R*-factor of each system. Bond lengths, bond angles, and torsional angles of guests were set to constant values in the following calculations. Namely, only intermolecular interactions that act guest molecules in a period (E_{GH} and E_{GG}) were considered as a measure of the packing stability.

By introducing four solvent molecules in the unit cell (a total of 4 guests), a decrease in *R*-factor was able to be obtained for some packing styles of guests. On the basis of a relatively small *R*-factor with the attractive packing energy, we selected some packing models (16 models). By introducing another four guest molecules (a total of 8 guests) to these selected models, the improvement of *R*-factor was seen for some packing models with the attractive packing energy (18 models). We tried to introduce another four guest molecules (a total of 12 guests) to these packing models, but valid models were unable to be obtained due to short contacts between the host and guest and those between guests. In the cases of 8-guest models, the calculated density is 1.059 g/cm^3. Since the ε_{DMF}-film has the complex region (d_{cal} = 1.059 g/cm^3) and the amorphous one (d_{obs} = 1.254 g/cm^3), d_{obs} of the ε_{DMF}-film (not measured) would be an intermediate value between 1.059 and 1.254 g/cm^3, which is comparable with the observed densities of ε-films (1.195 g/cm^3 for CPO and 1.258 g/cm^3 for GBL).

For the structure refinement of PLLA ε_{DMF}-form, the linked-atom least-squares method[29] was applied to the 8-guest models, which were obtained by the grid search algorithm, as mentioned above. We used three types of refinement methods (RM1, RM2, and RM3), as shown in detail in the Supporting Information. By combining these three methods, the structural refinements were performed for the PLLA−DMF complex. PLLA has relatively small side groups (CH_3 groups), so that relatively large intermolecular forces would act to the main-chain atoms, as mentioned by Takahashi and Tadokoro for PEO.[35b] As a result, helix distortion would be induced as in the α-form.[16]

One of the selected packing models having 8 DMF molecules per unit cell, which started from I_{DMF}, gave a distinct decrease in the *R*-value by the constrained least-squares method, keeping the energetically favorable state. Here, the corresponding models before and after the refinement are named the models I_{DMF}' and $I_{DMF}'_R$, respectively (Table 4 and Figure 10). In the

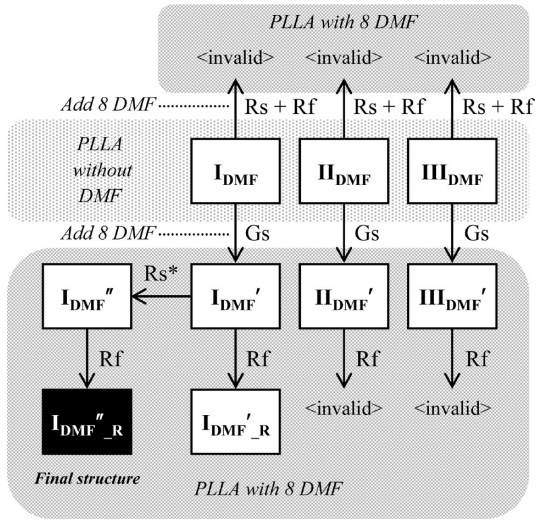


Figure 10. Flowchart of the crystal structure analysis process for PLLA−DMF complex. Gs: grid search algorithm; Rs: random search algorithm; Rs*: Rs around the optimized model (= I_{DMF}'); and Rf: refinement by the constrained least-squares method.

model $I_{DMF}'_R$, the *R*-factor was 23.3% for 30 unique reflections, with E_{HH} = −32.7 kcal/mol, E_{HG} = 46.6 kcal/mol, E_{GH} = 79.3 kcal/mol, and E_{GG} = −10.4 kcal/mol. In general, in the crystal structure analyses of polymers, the *R*-factor of 20% is a criterion. Therefore, our result (23.3%) is not enough in the current state. To reduce the *R*-factor, the positional parameters of PLLA chains and DMF molecules were changed randomly around those optimized by the grid search algorithm (I_{DMF}'). The distance parameters (X, Y, Z, r, and z) were changed ±0.01 nm, and the angular ones (W, μ, φ_x, φ_y, φ_z) were changed ±20°. In addition, the following calculations were also done as the special cases: (i) changing only the host parameters randomly with the guest ones fixed and (ii) changing only the guest ones randomly with the host ones fixed. From the obtained packing styles, valid models were selected and refined, taking into account the *R*-factor and the packing energy (E_{HH} + E_{HG} + E_{GH} + E_{GG}). For one of them, the *R*-factor of 19.6% was obtained with E_{HH} = −32.6 kcal/mol, E_{HG} = 28.9 kcal/mol, E_{GH} = 55.6 kcal/mol, and E_{GG} = −14.5 kcal/mol. Here, this model is named $I_{DMF}''_R$ (see Table 4 and Figure 10). Before the refinement, the corresponding model is I_{DMF}''. Here, the intramolecular interaction energy of PLLA chain (E_{intra} = E_H + E_{tors}) just exhibited a relatively small change by the structure refinement from the ideal 10_7 helix to the distorted helix with the 2_1 symmetry along the chain axis, as shown in Table 4. Figure 11 shows the *ab*- and *ac*-projections of $I_{DMF}''_R$. Figure

dx.doi.org/10.1021/ma202324g | *Macromolecules* 2012, 45, 1384−1397

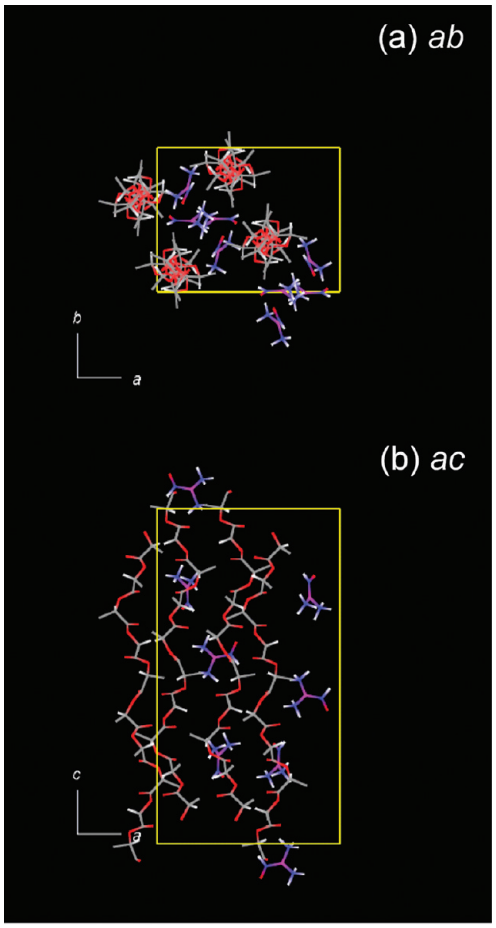


Figure 11. Packing model of PLLA chains and DMF molecules in the ε_{DMF} ($I_{DMF}''_R$): (a) *ab*- and (b) *ac*-projections. Carbon atoms in PLLA chains and DMF molecules are shown by gray and blue, respectively. The unit cell is shown by a yellow rectangle.

12 is the *ab*-projection of $I_{DMF}''_R$ to show the positions of host and guest molecules clearly and compare with the α-form. Table 5 shows the comparison of the observed and calculated values of lattice spacings and structure factors for the ε_{DMF} ($I_{DMF}''_R$). The atomic fractional coordinates of atoms in the PLLA chain (one period: 60 atoms) and DMF molecules (two molecules: 24 atoms) for $I_{DMF}''_R$ are shown in the Supporting Information. The skeletal torsional angles of PLLA in half a period (five residues) for $I_{DMF}''_R$ are also listed in the Supporting Information.

Comments on Crystal Structures of PLLA–Solvent Complexes. For the PLLA–DMF complex, the valid model $I_{DMF}''_R$ (R < 20% with a relatively low packing energy) was able to be obtained. As shown in Figures 11 and 12, PLLA chains in the PLLA–DMF complex form the channel-shaped cavities along the chain direction (*c*-axis direction), in which DMF molecules are packed. As mentioned above, PLLA has relatively high selectivity of solvents in complexation, while sPS can form clathrates with both benzene and its substitutes. The channel-shaped cavity with a relatively short diameter for the PLLA–DMF complex should be responsible for such high selectivity of solvents. For the PLLA/PDLA stereocomplex, the existence of weak hydrogen bonding (C_α–H···O and CH_3···O interactions) was reported by Sarasua et al.[38] In the case of PLLA–DMF complex, it is considered that the same kind of interactions between the host (PLLA) and guest (DMF) have an important role in stabilizing the complex structure. Judging from FTIR data (C=O stretching band), intermolecular interactions between PLLA and DMF molecules should be comparable with those between PLLA chains in the α-form. Namely, a large number of weak interactions between the host and guest should stabilize the PLLA–solvent complex. When PLLA was crystallized in the solvents that have the similar chemical structure to the ε-solvents (e.g., CH_3-substituted), it should be difficult for PLLA chains to form the weak hydrogen

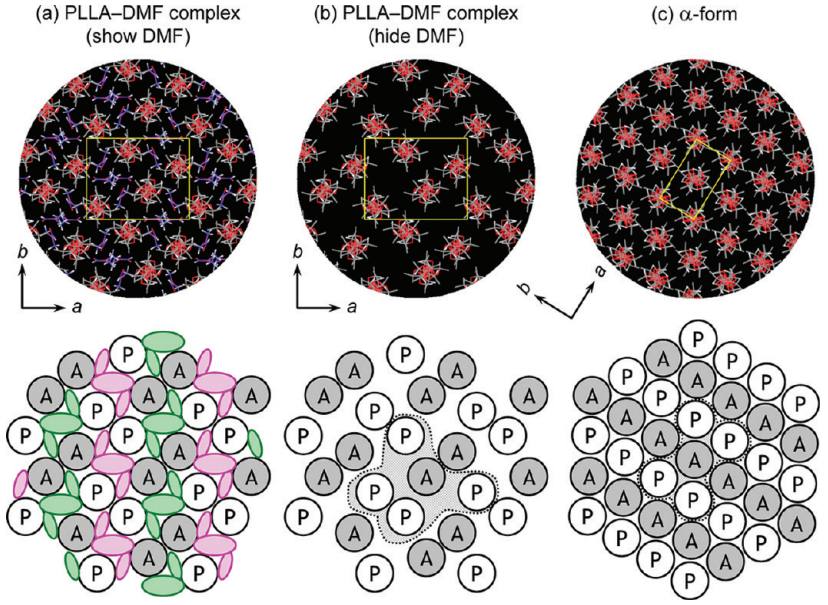


Figure 12. Comparison of *ab* projection of PLLA–DMF complex with that of α-form: (a) PLLA–DMF complex with DMF shown, (b) PLLA–DMF complex with DMF hidden, and (c) α-form.[16a] Schematic illustrations of packing of PLLA chains and DMF molecules are also shown below the corresponding *ab* projections. White circle (P) and gray one (A) mean the parallel and antiparallel chains, respectively. Four parallel and one antiparallel helices are enclosed by a dotted line for comparison (b, c). The occupied regions by DMF molecules are represented by purple and green ellipsoids (a).

dx.doi.org/10.1021/ma202324g | *Macromolecules* 2012, 45, 1384–1397

Table 5. Observed and Calculated Lattice Spacings and Structure Factors of ε-Form of PLLA with DMF ($I_{DMF}''__R$)

h	k	l	d_{obs} (nm)	d_{cal} (nm)	F_{obs}	F_{cal}
2	0	0	0.762	0.777	285	230
0	2	0	0.625	0.614	211	208
2	2	0	0.487	0.482	420	399
3	1	0		0.478		
1	3	0	0.383	0.396	609	575
3	2	0		0.396		
4	0	0		0.389		
0	4	0	0.314	0.307	108	150
5	1	0		0.301		
1	1	1	0.912	0.913	27	81
2	2	1	0.471	0.475	586	462
3	1	1		0.471		
1	3	1	0.398	0.392	385	333
3	2	1		0.392		
4	0	1		0.385		
1	1	3	0.679	0.677	46	70
2	0	3	0.587	0.602	63	112
1	2	3	0.478	0.490	288	339
2	2	3	0.434	0.430	363	370
3	1	3		0.427		
0	5	3	0.242	0.238	110	80
5	3	3		0.240		
6	1	3		0.245		
1	1	4	0.570	0.574	49	53
3	0	4	0.412	0.419	251	203
2	2	4	0.395	0.400	193	101
3	1	4		0.397		
2	4	4	0.258	0.265	224	191
4	3	4		0.262		
5	2	4		0.259		
2	1	5	0.429	0.431	151	113
2	3	5	0.309	0.306	180	157
4	1	5		0.311		
0	5	5	0.233	0.226	223	130
5	3	5		0.227		
6	1	5		0.232		
1	1	6	0.427	0.427	54	133
2	2	6	0.339	0.339	211	315
3	1	6		0.337		
1	3	6	0.306	0.304	187	228
3	2	6		0.305		
4	0	6		0.301		
1	4	6	0.254	0.255	387	371
5	1	6		0.255		
1	5	6	0.219	0.216	398	362
4	4	6		0.215		
6	2	6		0.213		
1	1	7	0.379	0.376	65	146
1	2	7	0.335	0.332	153	203
0	2	10	0.261	0.259	174	138
2	2	10	0.246	0.246	275	306
3	1	10		0.245		
2	3	10	0.226	0.224	236	233
4	1	10		0.226		

bonding with these solvents in the channel-shaped cavities, resulting in the formation of noncomplex structure (α). Here, it should be reasonable to assume that each guest goes along the channel-shaped cavity and gets out of the PLLA crystal lattice during solvent desorption. Namely, it should be assumed that solvent desorption proceeds gradually from the lamellar surface. By solvent desorption, there would remain many cavities that had been occupied by DMF molecules. In terms of the packing energy, this emptied form can be allowed ($E_{HH} < 0$). However, the ε-to-α transition proceeds directly from the ε- to the α-forms, not via the intermediate phase (e.g., emptied form). This result implies that the activation energy needed for the ε-to-α transition is relatively small. When solvent desorption proceeds to some extent (e.g., in a large part of a lamella), the chain rearrangement to the α-form should occur to fill cavities and take a more stable packing style, as shown in Figure 12. Also, other PLLA–solvent complexes (CPO, DOL, GBL, and THF) would have similar packing styles to the PLLA–DMF complex because of the similarity of these five complexes in unit cell dimensions and transition behavior to the α-form. In terms of the packing styles of hosts and guests (e.g., four chains in the $P2_12_12_1$ orthorhombic lattice and guests encapsulated in the cavity surrounded by helices), the PLLA–DMF complex has the similarity to amylose cocrystallized with water and 2-propanol.[39]

CONCLUSIONS

In this study, we investigated the crystalline complex formation of PLLA with low molecular weight compounds by screening examinations for a wide variety of organic solvents. As a result, we found that PLLA forms the crystalline complex (ε-form) with the specific five-membered ring compounds (CPO, DOL, GBL, and THF) or DMF below room temperature. In addition, the ε-to-α transition occurred with solvent desorption, in which solvent solubility of 0.3–0.4 g/g_{PLLA} is a starting point. By fiber diagram analyses, it was revealed that PLLA chains in the ε-form take the 10_7 helical conformation as in the α-form. We succeeded in indexing by the orthorhombic unit cell (a = 1.5–1.6 nm, b = 1.2–1.3 nm, c = 2.8–2.9 nm, and $\alpha = \beta = \gamma = 90°$) for the PLLA ε-forms. Considering both R-factor and packing energy (host–host, host–guest, guest–host, and guest–guest interaction energies), the plausible crystal structure of ε_{DMF} (PLLA–DMF complex) was proposed ($I_{DMF}''__R$), in which four PLLA chains and eight guest solvents are packed in the unit cell.

ASSOCIATED CONTENT

Supporting Information

Solvent exposure conditions (Table S1); the details on WAXD profile and fiber diagram analyses, details on nonbonded interaction and torsional energies, van der Waals parameters (Table S2); the calculated partial charges for PLLA, DMF, and CPO (Tables S3, S4, and S5, respectively); ξ–ζ conversion of intensity-corrected fiber diagrams (Figure S1); Weissenberg photographs (Figure S2); fiber diagram analysis processes for the oriented ε_{DMF}- and ε_{CPO}-films (Figures S3 and S4, respectively); the mapping of R-factor and host–host interaction energy for ε_{DMF} and ε_{CPO} (Figures S5 and S6, respectively); positional parameters of the guest molecule (Figure S7); refinement methods, atomic fractional coordinates for $I_{DMF}''__R$ (Table S6); and skeletal torsional angles of $I_{DMF}''__R$ (Table S7). This material is available free of charge via the Internet at http://pubs.acs.org.

dx.doi.org/10.1021/ma202324g | Macromolecules 2012, 45, 1384–1397

AUTHOR INFORMATION

Corresponding Author

*Tel +81-3-5734-2432; Fax +81-3-5734-2431; e-mail asai.s.aa@m.titech.ac.jp.

Notes

[†]Research Fellow of the Japan Society for the Promotion of Science.

ACKNOWLEDGMENTS

H.M. thanks Prof. K. Tashiro (Toyota Technological Institute), Prof. T. Ozeki (Tokyo Institute of Technology), Prof. P. D. Hong (National Taiwan University of Science and Technology), Prof. O. Tarallo (Università degli Studi di Napoli Federico II), Prof. M. Wada (The University of Tokyo), and Dr. H. Shii for giving him beneficial suggestions. H.M. thanks Prof. H. Uekusa (Tokyo Institute of Technology) for letting him use a Weissenberg camera. H.M. also thanks Prof. T. Hayakawa and Dr. Y. Ishida (Tokyo Institute of Technology) for supplying some organic solvents. We thank the Toyota Motor Corporation, Japan, for supplying the PLLA pellets. Financial support from Tokyo Institute of Technology Global COE program "Education and Research Center for Emergence of New Molecular Chemistry" is gratefully acknowledged. This work was partly supported by Grant-in-Aid for JSPS Fellows (No. 22008912) from Japan Society for the Promotion of Science.

REFERENCES

(1) (a) Rundle, R. E.; Baldwin, R. R. *J. Am. Chem. Soc.* **1943**, *65*, 554−558. (b) Rundle, R. E.; French, D. *J. Am. Chem. Soc.* **1943**, *65*, 558−561. (c) Rundle, R. E.; French, D. *J. Am. Chem. Soc.* **1943**, *65*, 1707−1710. (d) Rundle, R. E.; Edwards, F. C. *J. Am. Chem. Soc.* **1943**, *65*, 2200−2203. (e) Rundle, R. E. *J. Am. Chem. Soc.* **1947**, *69*, 1769−1772.

(2) (a) Choi, Y. S.; Miyasaka, K. *J. Appl. Polym. Sci.* **1993**, *48*, 313−317. (b) Choi, Y. S.; Miyasaka, K. *J. Appl. Polym. Sci.* **1994**, *51*, 613−618.

(3) (a) Blackwell, J.; Kurz, D.; Su, M. Y.; Lee, D. M. In *The Structures of Cellulose*; Atalla, R. H., Ed.; ACS Symposium Series 340; American Chemical Society: Washington, DC, 1987; Chapter 12. (b) Wada, M.; Nishiyama, Y.; Langan, P. *Macromolecules* **2006**, *39*, 2947−2952.

(4) (a) Chatani, Y.; Nakatani, S.; Tadokoro, H. *Macromolecules* **1970**, *3*, 481−486. (b) Chenite, A.; Brisse, F. *Macromolecules* **1991**, *24*, 2221−2225. (c) Chenite, A.; Brisse, F. *Macromolecules* **1992**, *25*, 776−782.

(5) (a) Harada, A.; Kamachi, M. *Macromolecules* **1990**, *23*, 2821−2823. (b) Harada, A.; Li, J.; Kamachi, M. *Macromolecules* **1990**, *26*, 5698−5703.

(6) (a) Chatani, Y.; Okamura, S. *Polymer* **1987**, *28*, 1815−1820. (b) Chatani, Y.; Fujii, Y.; Takayanagi, T.; Honma, A. *Polymer* **1990**, *31*, 2238−2244.

(7) (a) Chatani, Y.; Shimane, Y.; Inoue, Y.; Inagaki, T.; Ishioka, T.; Ijitsu, T.; Yukinari, T. *Polymer* **1992**, *33*, 488−492. (b) Chatani, Y.; Shimane, Y.; Inagaki, T.; Ijitsu, T.; Yukinari, T.; Shikuma, H. *Polymer* **1993**, *34*, 1620−1624. (c) Chatani, Y.; Inagaki, T.; Shimane, Y.; Shikuma, H. *Polymer* **1993**, *34*, 4841−4845. (d) De Rosa, C.; Guerra, G.; Petraccone, V.; Pirozzi, B. *Macromolecules* **1997**, *30*, 4147−4152.

(8) (a) Petraccone, V.; Ballesteros, D. R. O.; Tarallo, O.; Rizzo, P.; Guerra, G. *Chem. Mater.* **2008**, *20*, 3663−3668. (b) Tarallo, O.; Schiavone, M. M.; Petraccone, V.; Daniel, C.; Rizzo, P.; Guerra, G. *Macromolecules* **2010**, *43*, 1455−1466.

(9) (a) Chatani, Y.; Tadokoro, H.; Saegusa, T.; Ikeda, H. *Macromolecules* **1981**, *14*, 315−321. (b) Chatani, Y.; Kobatake, T.; Tadokoro, H. *Macromolecules* **1983**, *16*, 199−204. (c) Chatani, Y.; Irie, T. *Polymer* **1988**, *29*, 2126−2129. (d) Kusanagi, H.; Chatani, Y.; Tadokoro, H. *Polymer* **1994**, *35*, 2028−2039.

(10) Kusuyama, H.; Takase, M.; Higashihata, Y.; Tseng, H. T.; Chatani, Y.; Tadokoro, H. *Polymer* **1982**, *23*, 1256−1258.

(11) (a) Kawauchi, T.; Kumaki, J.; Kitaura, A.; Okoshi, K.; Kusanagi, H.; Kobayashi, K.; Sugai, T.; Shinohara, H.; Yashima, E. *Angew. Chem., Int. Ed.* **2008**, *47*, 515−519. (b) Kawauchi, M.; Kawauchi, T.; Takeichi, T. *Macromolecules* **2009**, *42*, 6136−6140.

(12) (a) Okuyama, K.; Noguchi, K.; Miyazawa, T.; Yui, T.; Ogawa, K. *Macromolecules* **1997**, *30*, 5849−5855. (b) Lertworasirkul, A.; Yokoyama, S.; Noguchi, K.; Ogawa, K.; Okuyama, K. *Carbohydr. Res.* **2004**, *339*, 825−833. (c) Lertworasirkul, A.; Noguchi, K.; Ogawa, K.; Okuyama, K. *Carbohydr. Res.* **2004**, *339*, 835−843.

(13) Uda, Y.; Kaneko, F.; Tanigaki, N.; Kawaguchi, T. *Adv. Mater.* **2005**, *17*, 1846−1850.

(14) (a) Li, H.; Eddaoudi, M.; O'Keeffe, M.; Yaghi, O. M. *Nature* **1999**, *402*, 276−279. (b) Noro, S.; Kitagawa, S.; Kondo, M.; Seki, K. *Angew. Chem., Int. Ed.* **2000**, *39*, 2081−2084.

(15) (a) Santis, P. D.; Kovacs, A. J. *Biopolymers* **1968**, *6*, 299−306. (b) Hoogsteen, W.; Postema, A. R.; Pennings, A. J.; ten Brinke, G.; Zugenmaier, P. *Macromolecules* **1990**, *23*, 634−642. (c) Aleman, C.; Lotz, B.; Puiggali, J. *Macromolecules* **2000**, *34*, 4795−4801.

(16) (a) Sasaki, S.; Asakura, T. *Macromolecules* **2003**, *36*, 8385−8390. (b) Wasanasuk, K.; Tashiro, K.; Hanesaka, M.; Ohhara, T.; Kurihara, K.; Kuroki, R.; Tamada, T.; Ozeki, T.; Kanamoto, T. *Macromolecules* **2011**, *44*, 6441−6452.

(17) (a) Zhang, J.; Duan, Y.; Sato, H.; Tsuji, H.; Noda, I.; Yan, S.; Ozaki, Y. *Macromolecules* **2005**, *38*, 8012−8021. (b) Zhang, J.; Tashiro, K.; Domb, A. J.; Tsuji, H. *Macromol. Symp.* **2006**, *242*, 274−278. (c) Zhang, J.; Tashiro, K.; Tsuji, H.; Domb, A. J. *Macromolecules* **2008**, *41*, 1352−1357. (d) Cho, T. Y.; Strobl, G. *Polymer* **2006**, *47*, 1036−1043. (e) Kawai, T.; Rahman, N.; Matsuba, G.; Nishida, K.; Kanaya, T.; Nakano, M.; Okamoto, H.; Kawada, J.; Usuki, A.; Honma, N.; Nakajima, K.; Matsuda, M. *Macromolecules* **2007**, *40*, 9463−9469. (f) Pan, P.; Kai, W.; Zhu, B.; Dong, T.; Inoue, Y. *Macromolecules* **2007**, *40*, 6898−6905. (g) Pan, P.; Zhu, B.; Kai, W.; Dong, T.; Inoue, Y. *J. Appl. Polym. Sci.* **2008**, *107*, 54−62. (h) Yasuniwa, M.; Sakamo, K.; Ono, Y.; Kawahara, W. *Polymer* **2008**, *49*, 1943−1951.

(18) (a) Wasanasuk, K.; Tashiro, K. *Polymer* **2011**, *52*, 6097−6109. (b) Wasanasuk, K.; Tashiro, K. *Macromolecules* **2011**, *44*, 9650−9660.

(19) Marubayashi, H.; Akaishi, S.; Akasaka, S.; Asai, S.; Sumita, M. *Macromolecules* **2008**, *41*, 9192−9203.

(20) (a) Eling, B.; Gogolewski, S.; Pennings, A. J. *Polymer* **1982**, *23*, 1587−1593. (b) Puiggali, J.; Ikada, Y.; Tsuji, H.; Cartier, L.; Okihara, T.; Lotz, B. *Polymer* **2000**, *41*, 8921−8930.

(21) Cartier, L.; Okihara, T.; Ikada, Y.; Tsuji, H.; Puiggali, J.; Lotz, B. *Polymer* **2000**, *41*, 8909−8919.

(22) Howe, C.; Vasanthan, N.; MacClamrock, C.; Sankar, S.; Shin, I. D.; Simonsen, I. K.; Tonelli, A. E. *Macromolecules* **1994**, *27*, 7433−7436.

(23) Ohya, Y.; Takamido, S.; Nagahama, K.; Ouchi, T.; Ooya, T.; Katoono, R.; Yui, N. *Macromolecules* **2007**, *40*, 6441−6444.

(24) Norman, N. *Acta Crystallogr.* **1954**, *7*, 462−463.

(25) If you have an interest in a series of handmade analytical programs, please contact H. Marubayashi (marubayashi.h.aa@gmail.com).

(26) Tamagawa, K.; Hilderbrandt, R. L.; Shen, Q. *J. Am. Chem. Soc.* **1987**, *109*, 1380−1383.

(27) Schultz, G.; Hargittai, I. *J. Phys. Chem.* **1993**, *97*, 4966−4969.

(28) Marsaglia, G. *J. Stat. Software* **2003**, *8*, 1−6.

(29) (a) Arnott, S.; Wonacott, A. J. *Polymer* **1966**, *7*, 157−166. (b) Okada, K.; Noguchi, K.; Okuyama, K.; Arnott, S. *Comput. Biol. Chem.* **2003**, *27*, 265−285.

(30) National Institute of Advanced Industrial Science and Technology, Spectral Database for Organic Compounds (SDBS) Web; http://riodb01.ibase.aist.go.jp/sdbs/ (accessed 2009−2010).

(31) Meaurio, E.; de Arenaza, I. M.; Lizundia, E.; Sarasua, J. R. *Macromolecules* **2009**, *42*, 5717−5727.

(32) (a) Kister, G.; Cassanas, G.; Vert, M. *Polymer* **1998**, *39*, 267−273. (b) Kang, S.; Hsu, S. L.; Stidham, H. D.; Smith, P. B.; Leugers, M. A.; Yang, X. *Macromolecules* **2001**, *34*, 4542−4548.
(33) Sawai, D.; Takahashi, K.; Sasashige, A.; Kanamoto, T.; Hyon, S. H. *Macromolecules* **2003**, *36*, 3601−3605.
(34) Such dependence of diffraction intensity on the layer line order is typical of the 10_7 or 10_3 helix, which can be understood by solving the equation $l = 7n + 10m$ or $l = 3n + 10m$ (n: the order of Bessel function; $m = 0, \pm 1, \pm 2, ...$).[35] It is well-known that a PLLA chain takes the left-handed helical conformations such as 10_7 and 3_2, whereas a PDLA chain forms the right-handed helices such as 10_3 and 3_1. Therefore, it follows that PLLA chains in the ε-form take the 10_7 helical conformation and the chain axis is perpendicular to *ab* plane ($\alpha = \beta = 90°$), as in the α-form.
(35) (a) Cochran, W.; Crick, F. H. C.; Vand, V. *Acta Crystallogr.* **1952**, *5*, 581−586. (b) Takahashi, Y.; Tadokoro, H. *Macromolecules* **1973**, *6*, 672−675.
(36) Fischer, E. W.; Sterzel, H. J.; Wegner, G. *Kolloid Z. Z. Polym.* **1973**, *251*, 980−990.
(37) Miyazawa, T. *J. Polym. Sci.* **1961**, *55*, 215−231.
(38) Sarasua, J. R.; Rodríguez, N. L.; Arraiza, A. L.; Meaurio, E. *Macromolecules* **2005**, *38*, 8362−8371.
(39) Nishiyama, Y.; Mazeau, K.; Morin, M.; Cardoso, M. B.; Chanzy, H.; Putaux, J.-L. *Macromolecules* **2010**, *43*, 8628−8636.

Macromolecules

Article

pubs.acs.org/Macromolecules

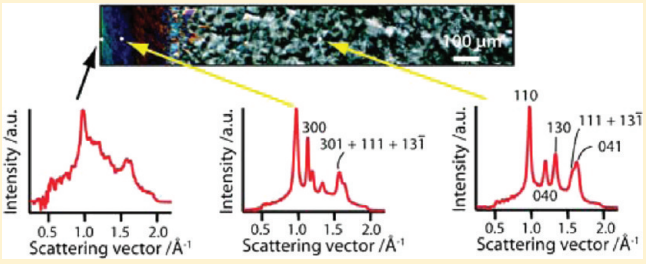
Effect of Structural Inhomogeneity on Mechanical Behavior of Injection Molded Polypropylene Investigated with Microbeam X-ray Scattering

Yuya Shinohara,*[,†] Kosuke Yamazoe,[†] Takashi Sakurai,[‡] Shuichi Kimata,[‡] Toshiya Maruyama,[‡] and Yoshiyuki Amemiya[†]

[†]Graduate School of Frontier Sciences, The University of Tokyo, 5-1-5 Kashiwanoha, Kashiwa, Chiba 277-8561, Japan

[‡]Petrochemicals Research Laboratory, Sumitomo Chemicals Co., Ltd., 2-1 Kitasode Sodegaura, Chiba 299-0295, Japan

ABSTRACT: Relationship between the structure of injection-molded isotactic polypropylene and its tensile mechanical properties, necking and fracture behaviors in particular, was investigated in terms of micrometer-scale structural inhomogeneity of nanometer- and subnanometer-scale structures. To clarify the micrometer-scale inhomogeneity, we employed scanning microbeam wide-angle X-ray diffraction and small-angle X-ray scattering technique. Four isotactic polypropylene samples were studied, produced using different injection-condition and thermal treatments. The results of scanning microbeam X-ray scattering measurements showed the presence of two types of micrometer-scale structural inhomogeneity in addition to the orientation of molecules: the distribution of polymorphs and of crystalline ordering. The results of scanning microbeam X-ray scattering of deformed sample showed the disappearance of the β-form isotactic polypropylene crystals at the outer regions accompanied by the plastic deformation. It is indicated that the inhomogeneous distribution of crystalline ordering and the existence of different polymorphs are highly related to the tensile mechanical behavior.



INTRODUCTION

Isotactic polypropylene (iPP) is widely used in industrial products. Most of the products are manufactured by polymer processing such as injection molding, fiber spinning, and extrusion and by additional processing such as annealing. Among these processing procedures, injection molding is widely employed for shaping the products. In the injection molding process, a flow field changes the chain morphology, which accelerates a nucleation rate in the subsequent crystallization process. The structure of injection molding is greatly affected by molding conditions such as injection speed, injection pressure, processing temperature, holding pressure, cooling time, and cooling temperature. Injection-molded iPP generally consists of a skin−core structure in which several layers are observed with polarized optical microscope (POM).[1−8] The skin−core structure is typically classified into three layers; a highly oriented skin layer, a shear layer with molecular chains oriented parallel to the flow direction, and a spherulitic core without chain orientation. In the surface region of the skin layer, so-called shish-kebab structure consisting of folded chain lamellae and extended chain crystals can be formed.[6,9] A lower cooling rate and a shear strain history in the core area result in the relaxation of chain molecules leading to the growth of spherulites. The molding conditions affect the formation of these layered structures and also induces the appearance of different crystallographic forms: monoclinic α-form, hexagonal β-form, orthorhombic γ-form, and smectic mesophase.[10,11] It has been reported that injection-molded iPP mainly composed of the α-form of crystallites while the β-form and the γ-form exist as minority components.[12] Significant differences in the mechanical properties between the different forms of iPP have been reported;[13−16] the β-form crystal[17−19] is thermodynamically and mechanically less stable than the α-form.[10]

The effect of molding conditions on the final morphology has been widely investigated by using POM, transmission electron microscope, infrared spectroscopy, and X-ray scattering.[20−25] It is of practical importance to investigate the mechanical properties of products with relation to the layered structures.[3,4,8,25−39] The effects of both the morphology and the nucleating agents on the mechanical properties have been studied from the industrial point of view.[8,21,35−38] The tensile mechanical behaviors depend on the morphology of injection-moldings such as the volume ratio of the skin−core layer, the degree of crystallinity, and the orientation of crystallites.[7,23,27,31,39] The thermal treatments also affect the structure and tensile mechanical properties of products;[12,26,32,37−40] for example, an increase in crystallinity and crystal size by annealing process has been reported.[40,41] Recent solid-state NMR techniques reveal that annealing treatments induce the

Received: September 27, 2011
Revised: January 4, 2012
Published: January 24, 2012

 © 2012 American Chemical Society

rearrangement process of the chain packing in melt and isothermal-crystallized iPP.[42−44] Despite a large number of studies, the relationship between the structure and tensile mechanical behavior has not been clarified. One of the reasons is the lack of the detailed structural information in terms of micrometer-scale structural inhomogeneity. It has been noticed that there are cases such that the tensile strength and stiffness does not rise as the crystallinity increases.[37] Injection moldings are by nature spatially inhomogeneous; thus spatially resolved structural study is required.

Microbeam X-ray scattering is a powerful tool to provide the structural information on local spatial inhomogeneity of nanostructure in a micrometer scale.[45,46,68] A conventional X-ray beam size for scattering experiments is approximately some hundreds micrometers; this size is too large to obtain the micrometer-scale inhomogeneity and only spatially averaged structural information is obtained. Scanning microbeam X-ray scattering measurements have been successfully applied to the structural analysis of injection molded iPP.[8,35,36,47−49] However, the inhomogeneity of the crystalline ordering as well as the crystallinity and orientation of the crystallites has not been investigated, despite its importance for discussing the relationship between tensile mechanical behaviors and morphology induced by injection molding.

In this paper, we focused on the relationship between micrometer-scale structural inhomogeneity, that of crystalline morphology and crystalline ordering in particular, and the tensile mechanical behavior of injection-molded iPP by examining the effects of difference in the skin−core morphology and annealing on the structural inhomogeneity and mechanical properties. To reveal the micrometer-scale structural inhomogeneity of nanostructure, we employed scanning microbeam wide-angle X-ray diffraction (WAXD) and small-angle X-ray scattering (SAXS). Furthermore, the structure of deformed specimens was investigated to examine the structural change accompanied by the deformation. It was found out that the inhomogeneous distributions of polymorph and that of crystalline ordering are highly related to tensile mechanical behaviors such as necking and fracture. In situ observation of structural change during a deformation process employing X-ray microbeam will be reported in another paper.

MATERIALS AND METHODS

Materials. A commercial-grade isotactic polypropylene (Sumitomo Noblen) was used as the sample. The weight-averaged molecular weight M_w was 804 000 and M_w/M_n was 3.5, where M_n is the number-averaged molecular weight. The samples were molded as tensile specimens with a thickness of 3 mm according to ASTM D638 by using an injection-molding machine (Toshiba Machine IS100EN) at a melt temperature of 260 °C and a mold temperature of 50 °C. The details of injection-molding conditions and the sample codes are listed in Table 1. An injection speed was controlled to prepare the specimens with different skin−core morphology. An injection pressure was automatically controlled to keep the injection speed constant. For the annealed samples, we kept the specimens in an oven at 155 °C for 60 min. Uniaxial tensile tests were performed at room temperature and the strain rate was 50 mm/min.

Table 1. Sample Fabrication Conditions and Sample Codes

sample code	injection speed [mm/s]	holding pressure [MPa]	annealing
PP1	1000	20	no
PP1A	1000	20	yes
PP2	1400	65	no
PP2A	1400	65	yes

All specimens were cut by using microtome with a thickness of approximately 30 μm along the transverse direction as schematically illustrated in Figure 1. Prior to the X-ray measurements, POM images were recorded to observe the structures of injection-molded iPP in micrometer-scale.

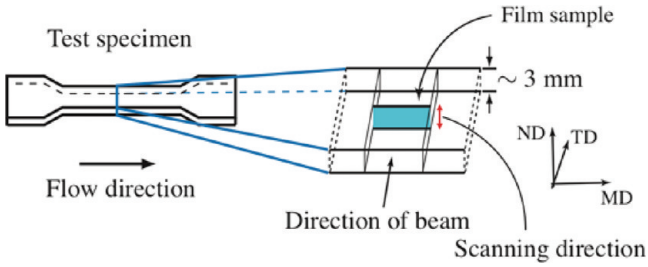


Figure 1. Schematic illustration of the specimen. The directions of flow and scanning X-rays are shown in the figure: MD, machine direction; ND, normal direction; and TD, transverse direction.

Scanning Microbeam Wide-Angle X-ray Diffraction. Scanning microbeam WAXD measurements were performed at BL-4A, Photon Factory (Japan). The X-ray beam was focused to 5 μm × 5 μm (full-width at half of maximum: fwhm) at a sample position with a Kirkpatrick-Baez mirror and the X-ray wavelength was chosen to be 0.113 nm with a multilayer monochromator. An X-ray CCD detector (C4880−50, Hamamatsu Photonics Co. Ltd.) coupled with an X-ray Image Intensifier (Hamamatsu Photonics Co. Ltd.)[50] was used to record WAXD images. The distance between the sample and the detector was approximately 170 mm. Two sets of beamstop were placed at the downstream of sample to prevent the damage of the X-ray detector and to reduce the background air-scattering. We scanned a sample with the X-ray microbeam from an edge to the other edge of the sample with a step of 10 μm as shown in Figure 1. To estimate the X-ray radiation damage, we continuously irradiated the samples with the X-ray microbeam; the sample started to be damaged after an exposure of 20 s. Thus, we set the exposure time for each WAXD measurement to be 4−6 s to avoid the radiation damage during scanning of the X-ray microbeam. The position of X-ray irradiation was monitored with a POM. For deformed samples, we selected several scanning positions to elucidate the dependence of the structural distribution on the position from a fracture front area. Each scanning was performed more than four times at different positions of the samples to confirm reproducibility.

Scanning Microbeam Small-Angle X-ray Scattering. Scanning microbeam SAXS measurements were performed at BL40XU, SPring-8. The quasi-monochromatic X-ray beam from a helical undulator was used.[51] An X-ray beam of 5 μm was produced by inserting a pinhole of 5 μm diameter. Another pinhole of 100 μm diameter was inserted to remove parasitic scattering. The exposure time was 100−3000 ms, and the X-ray wavelength was 0.10 nm. The distance between the sample and the detector was approximately 2.5 m, which was later calibrated with the diffraction peaks of silver behenate. The position of X-ray irradiation was monitored with a POM. The scanning condition was the same with that for the WAXD measurements.

RESULTS

Deformation Behavior. The tensile behaviors of PP1, PP1A, PP2, and PP2A are presented in Figure 2 and are summarized in Table 2. The photograph of deformed specimens is shown in Figure 3. Nonannealed specimens, PP1 and PP2, showed a well-defined necking behavior both in the tensile testing and the photograph. They broke at a draw ratio of approximately 2.7 and showed no strain hardening. There was no significant difference between the tensile

dx.doi.org/10.1021/ma202178r | Macromolecules 2012, 45, 1398−1407

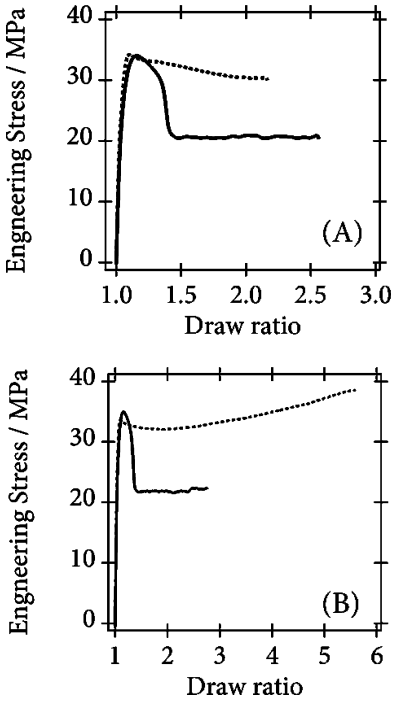


Figure 2. Macroscopic tensile behavior of (A) PP1 (solid line) and PP1A (dashed line), and (B) PP2 (solid line) and PP2A (dashed line).

Table 2. Tensile Testing Results of Injection-Molded iPP

	PP1	PP1A	PP2	PP2A
yield stress [MPa]	34.0	34.2	35.0	33.6
yield draw ratio	1.15	1.1	1.15	1.1
fracture stress [MPa]	20.2	29.4	21.2	38.0
fracture draw ratio	2.6	2.2	2.8	5.6

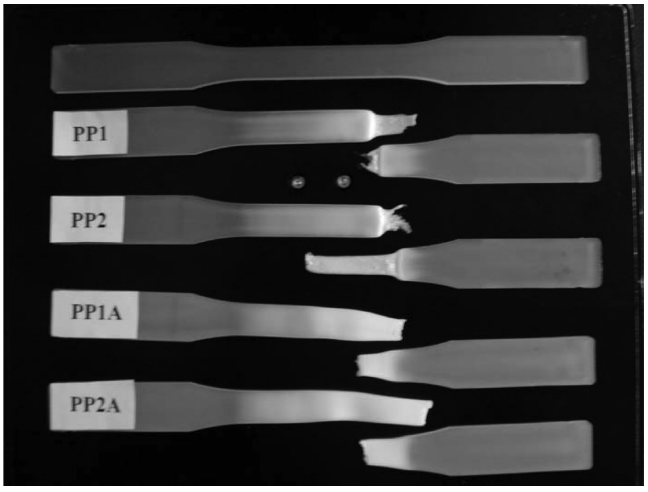


Figure 3. Photograph of the fractured specimen. The top specimen is a sample before deformation.

behaviors of PP1 and PP2. In the case of the annealed specimens, PP1A and PP2A, no distinctive necking behavior was detectable in the tensile mechanical behavior, while they show mild plastic deformation in the photograph (Figure 3). Note that PP2A specimen did not break up to a draw ratio of 5.6. Similar stress−strain behavior was reported in the previous studies.[37] All the specimens show the occurrence of whitening as shown in Figure 3; this indicates that the cavitation in the amorphous regions. The degree of whitening seems to be higher for the annealed specimens. To summarize, the necking behavior highly depends on the annealing.

POM Observation. Figure 4 shows the POM images of the cross-section of PP1, PP1A, PP2 and PP2A, which shows a

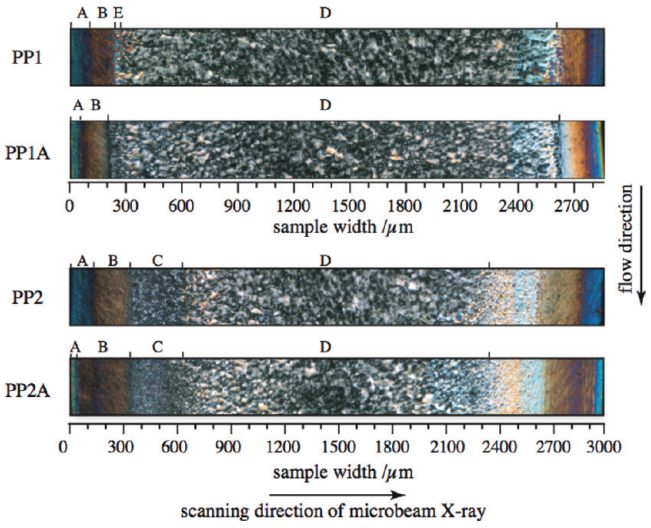


Figure 4. POM images of PP1, PP1A, PP2, and PP2A.

skin−core structure; the flow direction and the scanning direction of X-ray microbeam are vertical and horizontal in the image, respectively. The layers of a skin−core structure can be characterized by several regions from its surface to its center.[1,49] At least five types of layers were recognized by combining the POM figures with the X-ray results described later; we classified them as follows: (A) a skin layer, (B) a shear layer, (C) a fine-grained layer, (D) a core layer, and (E) a β-form rich layer. Before describing the characteristics of these layers, let us recall that we do not intend to discuss the mechanism of crystallization under flow conditions[9,20] nor the relationship between the molding conditions and the resultant structure; our focus in this study is to clarify the mechanical properties and the micrometer-scale structural inhomogeneity.

There are two types of remarkable morphology in PP1 and PP2: (1) PP2 contains a layer of small spherulite between the outer layers (A and B) and the core (D). In the present study, we call this region *fine-grained layer* (C). (2) There is another type of layer at the boundary of the skin layer and the core in PP1. This layer has peculiar crystalline polymorph, containing only the β-form crystals of iPP, the detail of which is described in the next section; thus we call this layer *β-form rich layer* (E). The thickness of outer layers including the skin layer (A) and the shear layer (B) increased with the increase of the injection speed and the holding pressure (PP2 and PP2A). The β-form rich layer (E) in PP1 disappeared by the annealing treatment, suggesting the transition of β-form crystals into α-form crystals of iPP upon annealing.

Distribution of Polymorph in Injection-Molded iPP. Figure 5 shows typical WAXD images and their corresponding one-dimensional WAXD intensity profiles that were obtained from different positions on PP1. At the point 3, four different reflections (110, 040, 130, and 041) from the α-form crystals are distinguished, while two reflections (111 and 13−1) overlap each other. No reflection from the γ-form crystals was observed in the present study. In addition to the reflections from the α-

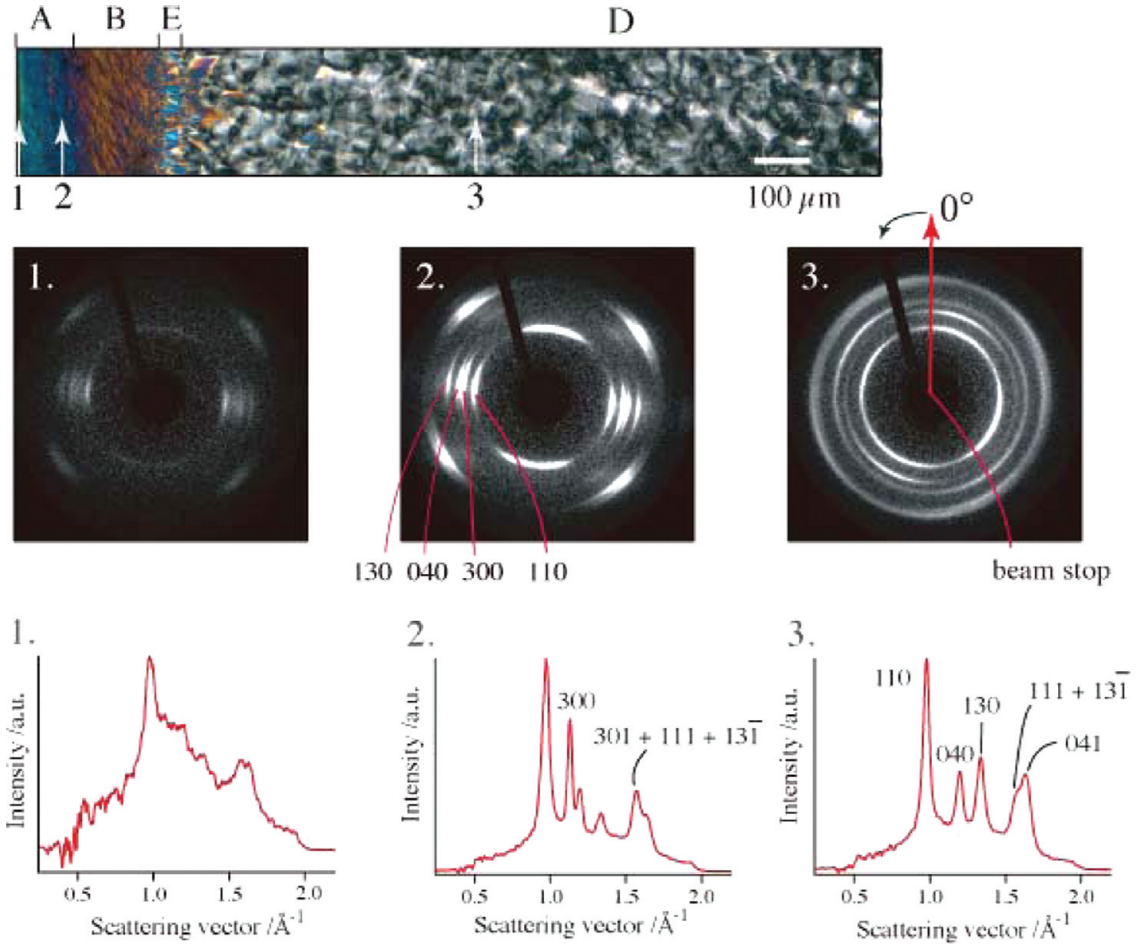


Figure 5. The WAXD images and their one-dimensional intensity profiles of PP1 at (1) the outermost region of skin layer, (2) the central part of the skin layer, and (3) the core layers. The definition of azimuthal angle is shown in the WAXD image of part 3. The positions of X-ray irradiation are shown by the white arrows in the POM images.

form crystal, those from the β-form crystals (300 and 301) were observed at the point 2. In the following, we focus on the distribution of the 110 (α-form) and the 300 (β-form) reflections.

Figure 6 shows the distribution of integrated intensity of the 110 reflection and that of the 300 reflection. The integrated intensity of diffraction can be used as the estimate of the amount of crystals. The 300 reflection was not observed in the annealed samples, PP1A and PP2A, while it was observed in PP1 and PP2 at the outer regions. The β-form crystals distributed in a wider region in PP2 than in PP1; in PP1, the 300 reflection from the β-form crystals was observed in the skin and the β-form rich layers in both of which no spherulite was observed in the POM images. In these layers, the crystals are highly oriented as shown in Figure 7, in which the azimuthal distribution of 110 reflection intensity is presented. From these results, it is concluded that the β-form crystals exist only in the layers composed of highly oriented structure in PP1. The situation is utterly different in PP2: the 300 reflection from the β-form crystals was observed in the skin, sheared, and fine-grained layers. The fine-grained layers were composed of spherulites and there was no orientation characteristic to the injection molding found in 110 refleciton. Another feature of the polymorph's distribution is that the β-form crystals are rich at around 300 and 2550 μm in PP1. In this region, the 110 reflection is hardly observed and only the 300 reflection is observed; thus, this layer is composed of only the β-form crystals. This peculiar layer is not observed in PP2.

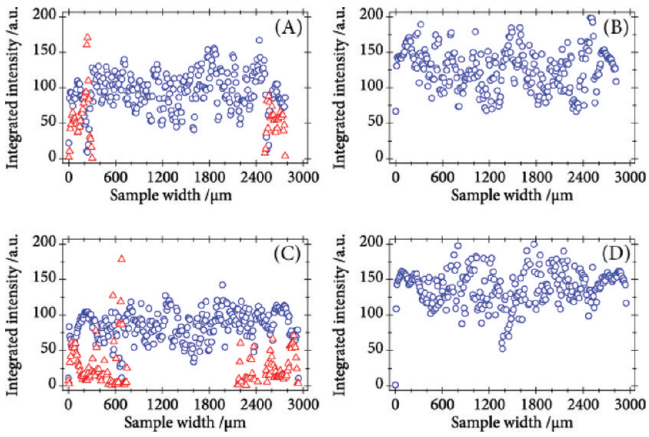


Figure 6. Distribution of WAXD integrated intensity of 110 reflection of the α-form (open circles) and 300 reflection of the β-form (open triangles). (A) PP1, (B) PP1A, (C) PP2, and (D) PP2A.

Distribution of Crystalline Orientation. Figures 7 and 8 show the distribution of azimuthal orientation of 110 and 040 reflections, respectively. At the skin layer (A) and the shear layer (B) of PP1 and PP1A, both the 110 and 040 reflections

dx.doi.org/10.1021/ma202178r | Macromolecules 2012, 45, 1398–1407

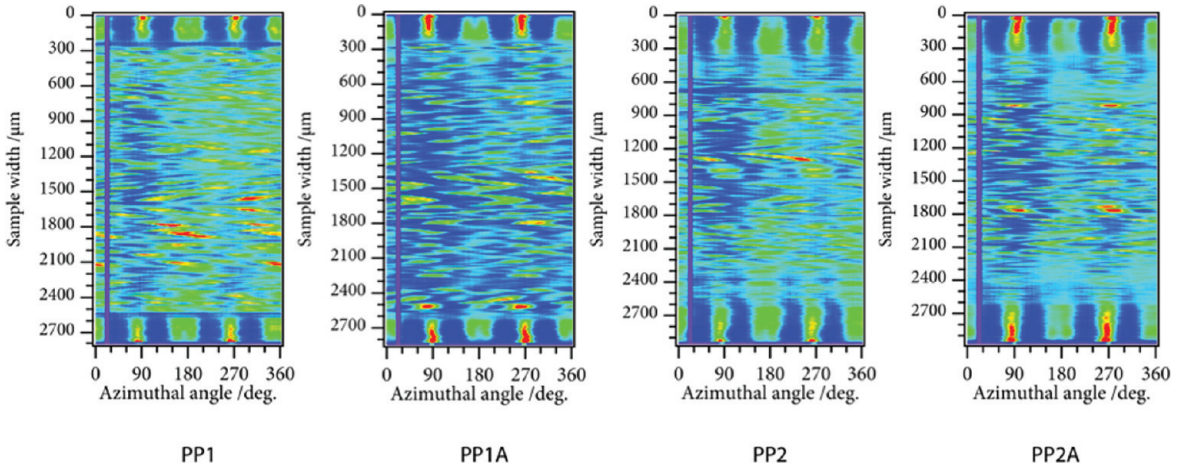


Figure 7. Azimuthal distribution of the 110 reflection of the α-form crystals.

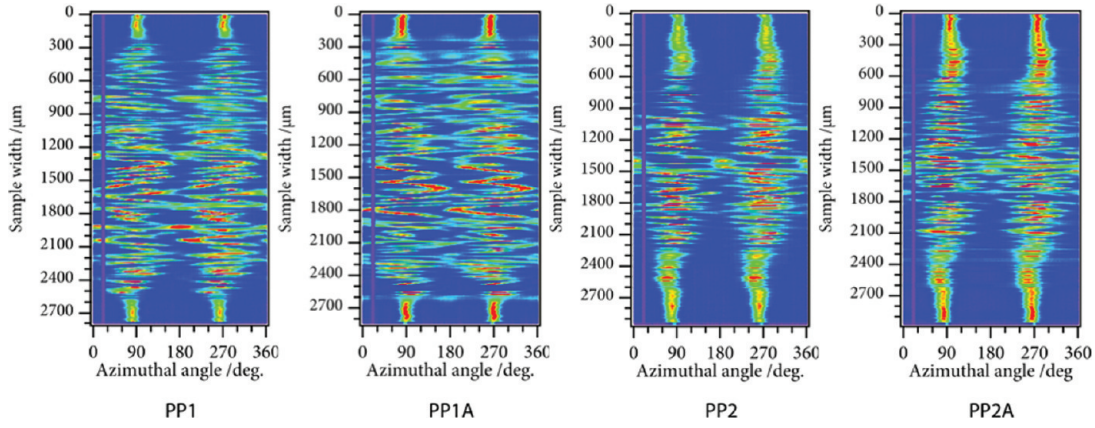


Figure 8. Azimuthal distribution of the 040 reflection of the α-form crystals.

are highly oriented, while their orientation at the core layer (D) is randomly distributed. The random distribution of the crystalline orientation originates from the fact that the core is composed of spherulites as shown in the POM images; microbeam X-ray scattering method observes the local structure of cross-hatched crystals of iPP, and the scattering attributing to the parent- and daughter-lamella is observed.[45] At the β-phase rich layer (E) of PP1, there is no reflection from the α-form crystals. PP2 and PP2A show a similar behavior: at the skin and sheared layer, both the 110 and 040 reflections are highly oriented. At the fine-grained layer (C), 110 reflection is less oriented, or randomly distributed, whereas 040 reflection is oriented. At the core region (D), both the reflection shows random orientation.

Distribution of Crystalline Ordering. The degree of crystalline ordering, which includes the packing order and the crystal size, is estimated from the fwhm of a diffraction peak by using the Scherrer's formula. Each WAXD diffraction peak was fitted with a Gaussian function and the fwhm of each diffraction peak along the radial direction in the scattering image was calculated. The results are shown in Figure 9, in which the distribution of the crystalline ordering along ⟨110⟩ is clearly observed. When annealed, the crystalline ordering along ⟨110⟩ increases in all of the layers. The distribution of the crystalline ordering along ⟨110⟩ is qualitatively preserved after annealing; this indicates that no drastic structural change occurs during annealing.

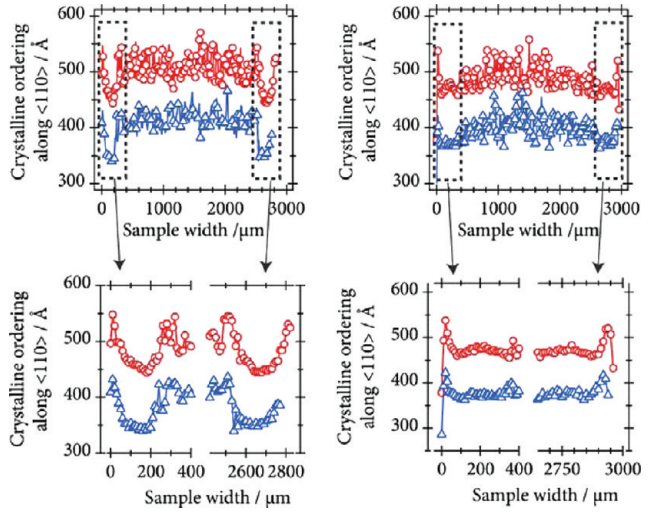


Figure 9. (Upper) Distribution of the crystalline ordering along ⟨110⟩ and (lower) its expanded views: (left) PP1 (triangles) and PP1A (circles); (right) PP2 (triangles) and PP2A (circles).

At the outermost region of the skin layers other than that at 2800 μm of PP1 and PP1A, the crystalline ordering along ⟨110⟩ is small compared to those at the neighboring parts. This indicates that the amorphous structure formed at the outermost region of the surface. This idea is supported from the fact that the scattering from amorphous structure was observed in the

dx.doi.org/10.1021/ma202178r | *Macromolecules* 2012, 45, 1398–1407

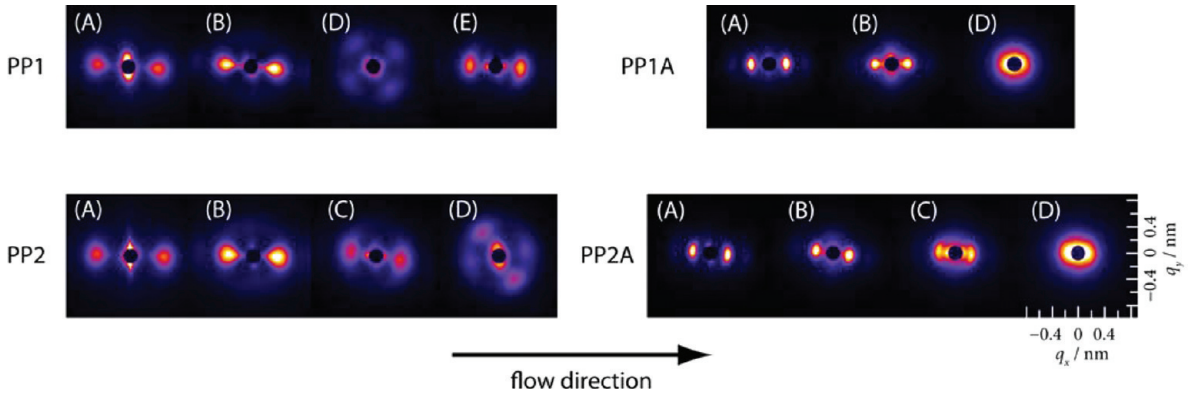


Figure 10. Typical SAXS images of PP1, PP1A, PP2, and PP2A. (A–E) Layers at which the X-ray microbeam irradiates.

WAXD intensity profile at the outermost surface region in Figure 5. The discrepancy between the values of crystalline ordering along ⟨110⟩ at the both ends of PP1 and PP1A comes from the difficulty in accurately define the position of the surface. The size of microbeam (approximately 5 μm) equaled the width of the outermost region; it was thus difficult to elucidate the detailed structure of the outermost region. In relation to the mechanical properties, the existence of amorphous structure at the outermost region does not have a large influence on the difference of tensile mechanical properties observed in Figure 2, because all the samples show a similar tendency at the outermost region. Next to the outermost region, there are regions at which the crystalline ordering along ⟨110⟩ is large. Then, the crystalline ordering along ⟨110⟩ decreases and shows minimum values at approximately 200 and 2700 μm when we scanned the inner part of the skin region. We emphasize that the crystalline ordering along ⟨110⟩ at these regions is obviously minima for PP1 and PP1A, while it is in the same order with those in the inner regions for PP2 and PP2A. In other words, PP1 and PP1A have a region where the crystalline ordering along ⟨110⟩ is particularly small; they have inhomogeneity in the crystalline ordering along ⟨110⟩ compared to PP2 and PP2A.

The crystalline ordering along ⟨110⟩ of PP1 and PP1A increased discontinuously from the innermost region of the shear layer to the outermost region of the core layer. Then, it kept a constant value in the core layer, although the values were sparsely dispersed. By contrast, the crystalline ordering along ⟨110⟩ of PP2 and PP2A gradually increased toward the central part of the core layer from the skin layer; in other words, the inhomogeneity in the crystalline ordering along ⟨110⟩ over the sample width of PP2 and PP2A is qualitatively less than PP1 and PP1A.

Results of Scanning SAXS. Figure 10 shows typical SAXS images of PP1, PP1A, PP2, and PP2A at each layer. At the skin layer (A), the shear layer (B), the fine-grained layer (C), and the β-phase rich layer (E), a spot-like pattern along the flow direction was observed. In the core layer (D), a four-point pattern characteristic to the cross-hatched crystals of iPP[45] was observed for PP1 and PP2. In the SAXS patterns at the skin, shear, and fine-grained layers of the annealed sample (PP1A and PP2A), the peaks originating from the lamellar long period existed in a lower angle; this indicates that the annealing increased a lamellar long period. At the core of the annealed sample, no distinctive pattern originating from the existence of lamellae is observed in the present SAXS resolution.

Microbeam WAXD Results of Deformed Sample. Next we discuss the structural distribution after tensile testing. Hereafter we focus on the results of PP1 and PP2A because these two samples show utterly different mechanical behaviors. Figure 11 shows an example of image plots representing the

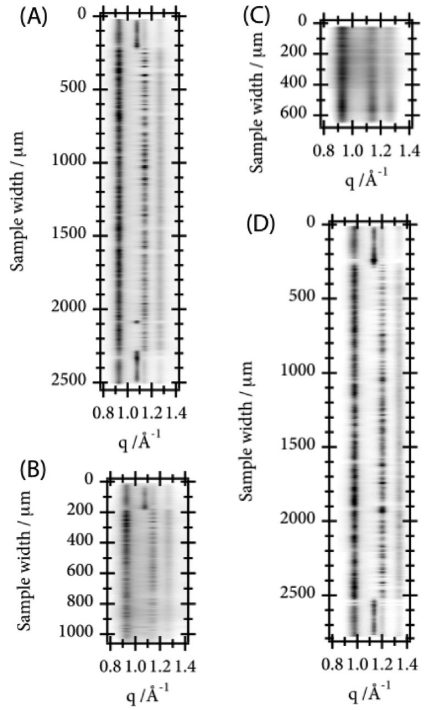


Figure 11. Distribution of WAXD intensity of PP1 at (A) 5 mm apart from the fracture point (Figure 12A), (B) the necking area (Figure 12B), (C) the fracture area (Figure 12C), and (D) for the sample without deformation.

intensity distribution of WAXD of deformed PP1 at different scanning positions. The POM images of scanning positions are shown in Figure 12. At the position where the necking did not develop (Figure 11A), the distribution of morphology was similar to that of virgin specimen (Figure 11D); the diffraction from the β-form crystals was observed only at the outer regions. At the necking point (Figure 11B), the diffraction from the β-form crystals was observed only at the upper region, which agrees with the characteristics observed in the POM image (Figure 12B); along the scanning position of X-rays, the sample was highly stretched and yielded at the lower region, while not

dx.doi.org/10.1021/ma202178r | Macromolecules 2012, 45, 1398–1407

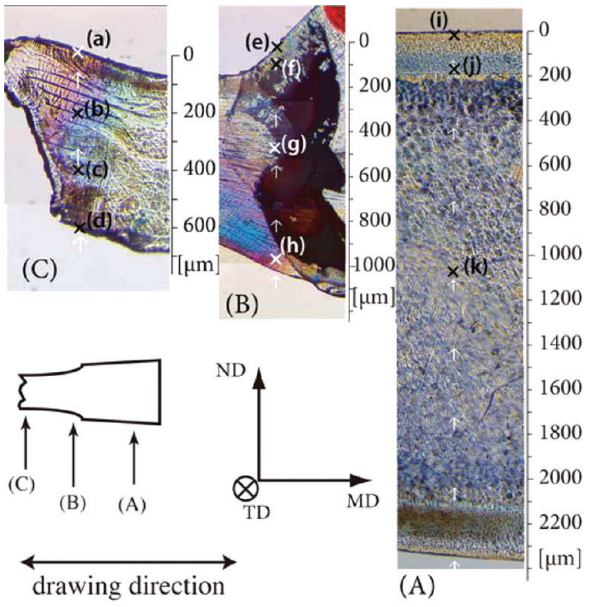


Figure 12. POM images of drawing specimen of PP1 (A) 5 mm apart from the fracture point, (B) necking region, and (C) the fracture point. The white arrows in the POM images indicate the positions of irradiation with an X-ray microbeam. The crossed marks indicated (a–k) show the positions of irradiation of microbeam SAXS experiments (Figure 15).

at the upper region. At the fracture area (Figure 11C), the fwhm of diffraction from the α-form crystals clearly increased, and the diffraction from the β-form crystals was no longer observed. It can be concluded that the disappearance of the diffraction from the β-form crystals and the disordering of the α-form crystals relate to the necking and breaking-up behaviors, respectively.

The situation is, to the contrary, different for PP2A as shown in Figures 13 and 14. In PP2A, it is hard to distinguish the differences between the image plots of the WAXD intensity distribution before (Figure 13C) and after (Figure 13A,B) deformation. Also, a clear skin–core structure can be observed in the POM image of the deformed sample (Figure 14).

Microbeam SAXS Results of Deformed Sample. Typical SAXS images of deformed specimen of PP1 and PP2A are shown in Figure 15 and 16, respectively. At the positions where the necking did not develop (Figure 15i–k), the SAXS patterns were similar to those without deformation; a two-spot pattern at the outer region and a cross-hatched pattern at the inner region. At the necking point (Figure 15e–h), remarkable changes in the SAXS pattern were observed. First, the peaks originating from the lamellar structure disappeared or weakened. Secondary, an isotropic central scattering around the beamstop drastically increased for the upper part of specimen (Figure 15e,f), while it was not observed at the lower part of specimen (Figure 15g,h). This central scattering should correspond to the formation of voids, which agrees with the whitening observed in the photograph of deformed specimen (Figure 3). At the breakup point (Figure 15a–d), further changes were observed; at each position, scattering from the lamellar structure is observed while the orientated central scattering was also observed.

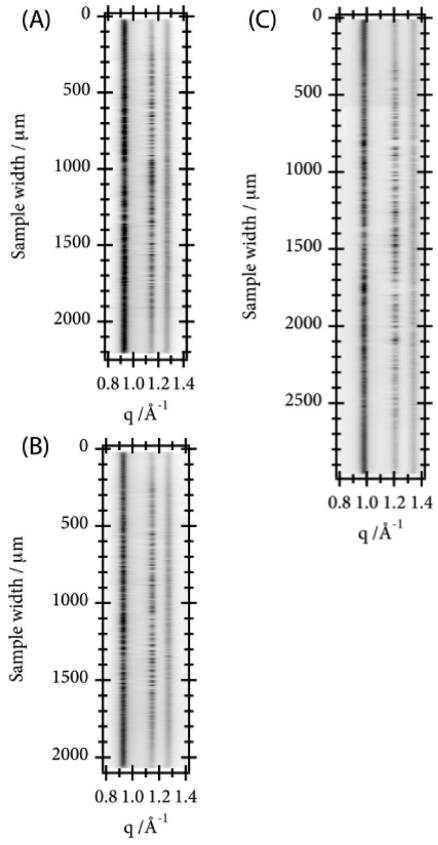


Figure 13. Distribution of WAXD intensity of PP2A at (A) 2 mm apart from the fracture point (Figure 14A), (B) the fracture point (Figure 14B), and (C) the sample without deformation.

DISCUSSION

The structural characteristics obtained in the present study can be summarized as follows:

(1) The annealing increases the size of α-form crystals irrespective of molding condition and layers.
(2) The β-form crystals exist in the skin (PP1 and PP2), shear (PP1 and PP2), and fine-grained layers (PP2), while they disappear when annealed.
(3) The distribution of crystalline ordering along ⟨110⟩ in PP2 and PP2A is rather homogeneous compared to those in PP1 and PP1A; PP1 and PP1A have a region where the crystalline ordering is particularly small.
(4) The β-form crystals disappear at necking region when deformed.
(5) All the deformed samples show whitening.

The most striking differences in the tensile mechanical behavior are found in the necking behaviors. From the tensile testing, PP2A exhibits no distinctive necking and shows tough and strong properties compared to the other samples, PP1, PP1A, and PP2. In this section, the relationship between the tensile mechanical properties and the inhomogeneity of both the crystalline ordering and the polymorph in micrometer scale is discussed.

The annealed specimen, PP1A and PP2A, show homogeneous deformation rather than strain localization (necking) observed for PP1 and PP2. Generally, there can be two different origins for the transition from necking to a more homogeneous mode of deformation. First, the deformation will become homogeneous under the condition that the deforma-

dx.doi.org/10.1021/ma202178r | Macromolecules 2012, 45, 1398–1407

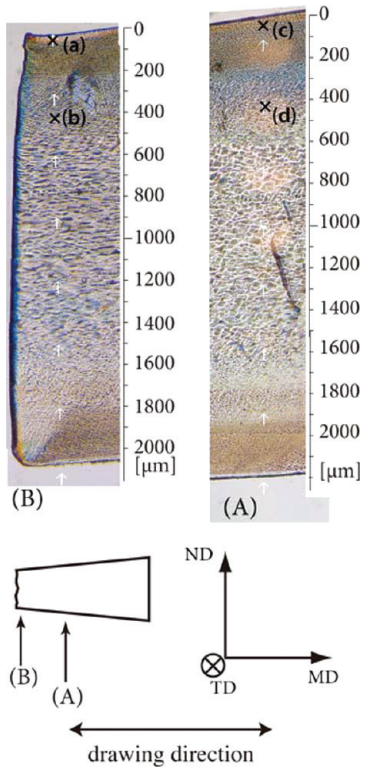


Figure 14. POM images of drawn specimen of PP2A. (A) 2 mm apart from the fracture point, and (B) the fracture point. The white arrows in the POM images indicate the positions of irradiation with an X-ray microbeam. The crossed marks indicated by parts a–d show the positions of irradiation of microbeam SAXS experiments (Figure 16).

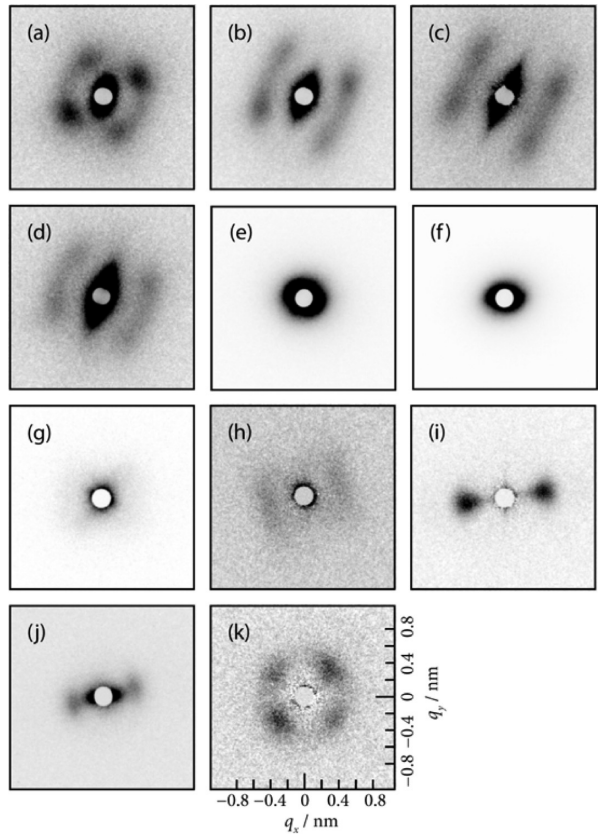


Figure 15. Typical SAXS images of drawn specimen of PP1. The positions of irradiation are shown in Figure 12. The horizontal direction along q_x is the drawing direction.

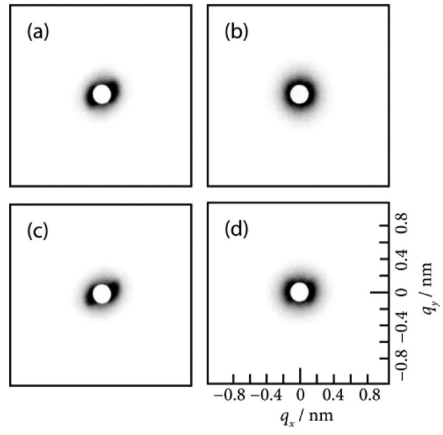


Figure 16. Typical SAXS images of drawn specimen of PP2A. The positions of irradiation are shown in Figure 14. The horizontal direction along q_x is the drawing direction.

tion proceeds under a constant volume.[52−54] The second possibility is the occurrence of stress whitening. In this case, deformation does not proceed under a constant volume since the amorphous regions cavitate. Because of this formation of voids, microscopic strain localization will take place and can proceed on the micrometer-scale, and macroscopically the deformation is fairly homogeneous.[55−58] The crystallites work as the point of action for tensile stress, and the necking stress depends on the crystallinity.[59] Usually, the deformation under a constant volume is observed in highly oriented samples,[47] which is not the case for our samples in which nonoriented spherulites form the core part. Furthermore, strong whitening was observed for the annealed specimen, PP1A and PP2A; thus it can be concluded that the occurrence of stress whitening is the origin of transform from the necking behavior to rather homogeneous deformation behavior. Unfortunately, the SAXS data of deformed specimen of PP2A shows little information about the void formation because of the present SAXS resolution, which is limited by the existence of Fraunhofer diffraction from the first pinhole producing the intense microbeam X-rays.

With regard to the structural characteristics leading to the void formation, there are two features: the disappearnace of the β-form crystals in the annealed sample and the increase in the crystalline ordering by the annealing.[70,72] As shown in Figure 9, the crystalline ordering along ⟨110⟩ increased when annealed, and at the same time, the annealing induces the disappearance of the β-form crystals; thus, it is difficult to discuss that either of them is a principal factor determining the stress whitening phenomenon. In this regard, it is interesting to see combined results of SAXS and WAXD of deformed specimen of PP1. At the necking area (Figure 12B), WAXD results show that the β-form crystals disappeared at the lower region where the sample was highly deformed while they existed at the upper region (Figure 11B). On the other hand, an isotropic central scattering around beamstop in SAXS was observed at the upper region (Figure 15e,f) while it was hardly observed at the lower region (Figure 15h). This indicates the possibility that the existence of β-form crystals prevents the voids formation and growth; the β-form crystals yield at lower stress[71] and thus the amorphous regions cannot cavitate. This discussion will be confirmed by

dx.doi.org/10.1021/ma202178r | Macromolecules 2012, 45, 1398–1407

further studies with in situ observation of structural change using microbeam X-ray diffraction.

The SAXS images of the fractured area (Figure 15a–d) show the anisotropic oriented central scattering pattern with peaks originating from lamellar structure. This central scattering would originate from either of the voids or highly oriented fibril structure. Although there are previous reports in which the voids can be oriented in the deformed sample,[73] it is reasonable to suppose that fibril structure like shish-kebab structure is formed at this region,[69] because the orientation of the central scattering corresponds to the orientation of lamellar scattering. This also supports the above discussion that the formation of voids in the annealed sample leads to the transformation from necking to rather homogeneous deformation modes; macroscopically homogeneous deformation cannot proceed in PP1 because of the absence of voids as the source of microscopic strain localization.

The disappearance of the β-form crystals at the fracture areas and the lower parts of necking areas (Figure 11B,C) indicates a mechanically induced β- to α-form crystals transition during deformation.[14,60−62] The fact that the β-form crystals are absent only at the necked region supports the idea that the β-form crystals are stable to the yield point and transform to the α-form crystals only during necking.[62]

It should be noted that the draw ratio of fracture of PP2A is considerably long. Compared to PP1A, the crystalline ordering of PP2A is in the same order but has less inhomogeneity; the crystalline ordering along ⟨110⟩ of PP1A obviously shows minima at 200 and 2700 μm while that of PP2A shows no clear minimum. It is fairly reasonable to assume that the region where the crystalline ordering along ⟨110⟩ shows minima relates to the breakdown.

One may attribute the increase in the mechanical properties to the existence of highly ordered crystallites such as α2-form of iPP. To clarify this point, the WAXD intensity profiles of PP2 and PP2A are shown in Figure 17. No diffraction from the α2-crystals (for example, 2 $\bar{3}$ 1 and 1 $\bar{6}$ 1 at $q \sim 2.24$ Å^{-1}) was observed[63,64] in both PP2 and PP2A; thus, the increase in the mechanical properties can be attributed to the absence of structural inhomogeneity.

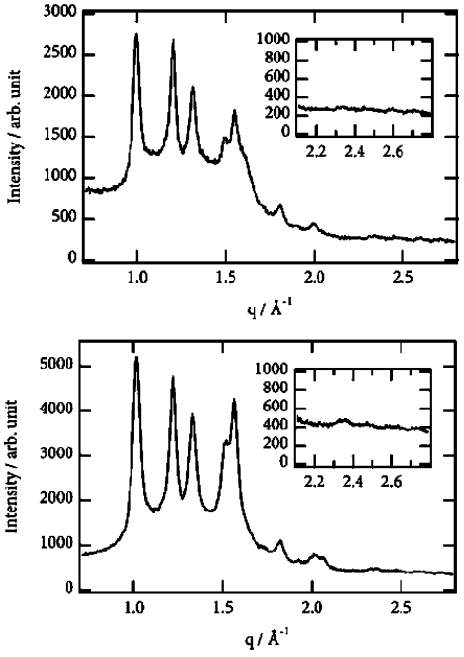


Figure 17. One-dimensional WAXD intensity profiles of PP2 (upper) and PP2A (lower).

In this study, the relationship is indicated between the inhomogeneous distribution of polymorph/crystalline ordering and the mechanical properties of injection-molded iPP. To elucidate the relationships further, a real-time monitoring of the structural change during sample deformation[45,65,66] is a powerful method. Although it is difficult to map the structural distribution during sample deformation, in situ observation of structural change at a single layer will be possible with a recent progress in the X-ray microbeam scattering technique. Also, in situ observation of structural change at each layers during the annealing of injection-molded specimen will give us a clue for understanding the nature of structural change during the annealing.[74] Furthermore, the combination of microbeam X-ray scattering technique with a WAXS pole-figure technique[67] will be important to quantify the amount of each crystalline phases and amorphous phases at each layer. These studies are now in progress and will be reported in the near future.

■ CONCLUSION

We aimed to reveal the relationship between micrometer-scale inhomogeneous distribution of subnm- and nm-scale structure of injection-molded iPP and its tensile mechanical properties. We successfully employed scanning microbeam X-ray scattering techniques to reveal the micrometer-scale inhomogeneous structural distribution. The relationship between structural inhomogeneity and tensile mechanical behavior was revealed for four types of injection-molded specimen. The annealing process leads to the increase in the crystalline ordering and the disappearance of β-form crystals, which would lead to void formation during tensile deformation. The results indicate that the inhomogeneous distribution of polymorph and crystalline ordering is related to the appearance of necking and the breakdown at relatively low strain. Further studies with in situ observation of structural evolution process during sample stretching process[45,65,66] will provide us fruitful information regarding the detailed mechanism of structural change upon elongation.

■ AUTHOR INFORMATION

Corresponding Author

*E-mail: yuya@k.u-tokyo.ac.jp.

■ ACKNOWLEDGMENTS

Microbeam WAXD experiments were performed under the approval of Photon Factory Proposal Advisory Committee (2008G700, 2010G540). Microbeam SAXS experiments were performed under the approval of SPring-8 Proposal Advisory Committee (2009B1260). We thank Drs. N. Ohta and N. Yagi (JASRI/SPring-8) for their kind help on the microbeam SAXS experiments and Prof. A. Iida (KEK) for his assistance on the microbeam WAXD experiments.

■ REFERENCES

(1) Kantz, M. R.; Newman, H. D. Jr.; Stigale, F. H. *J. Appl. Polym. Sci.* **1972**, *16*, 1249−1260.
(2) Fujiyama, M.; Kimura, S. *J. Appl. Polym. Sci.* **1978**, *22*, 1225−1241.
(3) Trotignon, J. P.; Verdu, J. *J. Appl. Polym. Sci.* **1987**, *34*, 1−18.
(4) Fujiyama, M.; Wakino, T. *J. Appl. Polym. Sci.* **1988**, *35*, 29−49.

(5) Wenig, W.; Herzog, F. *J. Appl. Polym. Sci.* **1993**, *50*, 2163−2171.
(6) Ania, F.; Baltá-Calleja, F. J.; Bayer, R. K.; Tshmel, A.; Naumann, I.; Michler, H. G. *J. Mater. Sci.* **1996**, *31*, 4199−4206.
(7) Viana, J. C.; Cunha, A. M.; Billon, N. *Polymer* **2002**, *43*, 4185−4196.
(8) Housmans, J. W.; Gahleitner, M.; Peters, G. W. M.; Meijer, H. E. H. *Polymer* **2009**, *50*, 2304−2319.
(9) Kimata, S.; Sakurai, T.; Nozue, Y.; Kasahara, T.; Yamaguchi, N.; Karino, T.; Shibayama, M.; Kornfield, J. A. *Science* **2007**, *316*, 1014−1017.
(10) Lotz, B.; Wittmann, J. C.; Lovinger, A. J. *Polymer* **1996**, *37*, 4979−4992.
(11) Iijima, M.; Strobl, G. *Macromolecules* **2000**, *33*, 5204−5214.
(12) Hedesiu, C.; Demco, D. E.; Kleppinger, R.; Poel, G. V.; Remerie, K.; Litvinov, V. M.; Blumich, B.; Steenbakkers, R. *Macromol. Mater. Eng.* **2008**, *293*, 847−857.
(13) Tordjeman, P.; Robert, C.; Marin, G.; Gerard, P. *Eur. Phys. J. E* **2001**, *4*, 459−465.
(14) Grein, C.; Plummer, C. J. G.; Kausch, H.-H.; Germain, Y.; Béguelin, Ph. *Polymer* **2002**, *43*, 3279−3293.
(15) Chen, H. B.; Karger-Kocsis, J.; Wu, J. S.; Varga, J. *Polymer* **2002**, *43*, 6505−6514.
(16) Kotek, J.; Raab, M.; Baldrian, J.; Grellmann, W. *J. Appl. Polym. Sci.* **2002**, *85*, 1174−1184.
(17) Lovinger, A. J.; Chua, J. O.; Gryte, C. C. *J. Appl. Polym. Sci.* **1977**, *15*, 641−656.
(18) Brückner, S.; Meille, S. V.; Petraccone, V.; Pirozzi, B. *Prog. Polym. Sci.* **1991**, 361−404.
(19) Meille, S. V.; Ferri, D. R.; Brückner, S.; Lovinger, A. J.; Padden, F. J. *Macromolecules* **1994**, *27*, 2615−2622.
(20) Kumaraswamy, G.; Issaian, A. M.; Kornfield, J. A. *Macromolecules* **1999**, *32*, 7537−7547.
(21) Guo, X.; Isayev, A. I.; Demiray, M. *Polym. Eng. Sci.* **1999**, *39*, 2132−2149.
(22) Mendoza, R.; Regnier, G.; Seiler, W.; Lebrun, J. L. *Polymer* **2003**, *44*, 3363−3373.
(23) Viana, J. C. *Polymer* **2004**, *45*, 993−1005.
(24) Pantani, R.; Coccorullo, I.; Speranza, V.; Titomanlio, G. *Polymer* **2007**, *48*, 2778−2790.
(25) Shen, C. Y.; Zheng, G. Q.; Liu, C. T.; Wang, Y. M.; Chen, J. B.; Peng, X. F. *J. Macromol. Sci. Part B* **2009**, *48*, 439−448.
(26) Coxon, L. D.; White, R. J. *Polym. Eng. Sci.* **1980**, *20*, 230−236.
(27) Trotignon, J. P.; Verdu, J. *J. Appl. Polym. Sci.* **1987**, *34*, 19−36.
(28) Zipper, P.; Janosi, A.; Geymayer, W.; Ingolic, E.; Fleischmann, E. *Polym. Eng. Sci.* **1996**, *36*, 467−482.
(29) Kalay, G.; Bevis, M. J. *J. Polym. Sci., Part B* **1997**, *35*, 265−291.
(30) Nitta, K.; Takayanagi, M. *J. Polym. Sci., Part B* **2000**, *38*, 1037−1044.
(31) Fujiyama, M.; Kitajima, Y.; Inata, H. *J. Appl. Polym. Sci.* **2002**, *84*, 2142−2156.
(32) Drozdov, A. D.; Christiansen, J. deC. *Eur. Polym. J.* **2003**, *39*, 21−31.
(33) Viana, J. C.; Billon, N.; Cunha, A. M. *Polym. Eng. Sci.* **2004**, *44*, 1522−1533.
(34) Viana, J. C. *Polymer* **2005**, *46*, 11773−11785.
(35) Zhu, P.; Tung, J.; Edward, G. *Polymer* **2005**, *46*, 10960−10969.
(36) Zhu, P.; Tung, J.; Phillips, A.; Edward, G. *Macromolecules* **2006**, *39*, 1821−1831.
(37) Stern, C.; Frick, A.; Weickert, G. *J. Appl. Polym. Sci.* **2007**, *103*, 519−533.
(38) Bai, H.; Wang, Y.; Zhang, Z.; Han, L.; Li, Y.; Lin, L.; Zhou, Z.; Men, Y. *Macromolecules* **2009**, *42*, 6647−6655.
(39) Yu, X.; Wu, H.; Li, J.; Guo, S.; Qiu. *J. Polym. Eng. Sci.* **2009**, *49*, 703−711.
(40) Poussin, L.; Bertin, Y. A.; Parisot, J.; Brassy, C. *Polymer* **1998**, *39*, 4261−4265.
(41) Ferrer-Balas, D.; Maspoch, M. L.; Martinez, A. B.; Santana, O. O. *Polymer* **2001**, *42*, 1697−1705.
(42) Uehara, H.; Yamanobe, T.; Komoto, T. *Macromolecules* **2000**, *33*, 4861−4870.
(43) Yao, Y. F.; Graf, R.; Spiess, H. W.; Rastogi, S. *Macromolecules* **2008**, *41*, 2541−2519.
(44) Miyoshi, T.; Mamun, A.; Hu, W. *J. Phys. Chem. B* **2010**, *114*, 92−100.
(45) Nozue, Y.; Shinohara, Y.; Ogawa, Y.; Sakurai, T.; Hori, H.; Kasahara, T.; Yamaguchi, N.; Yagi, N.; Amemiya, Y. *Macromolecules* **2007**, *40*, 2036−2045.
(46) Nozue, Y.; Shinohara, Y.; Amemiya, Y. *Polym. J.* **2007**, *39*, 1221−1237.
(47) Schrauwen, B. A. G.; Breemen, L. C. A.; Spoelstra, A. B.; Govaert, L. E.; Peters, G. W. M.; Meijer, H. E. H. *Macromolecules* **2004**, *37*, 8618−8633.
(48) Zhu, P.; Edward, G. *Polymer* **2004**, *45*, 2603−2613.
(49) Kobayashi, Y.; Kanno, H.; Hanamoto, Y.; Ando, M.; Kanai, T. *J. Appl. Polym. Sci.* **2010**, *116*, 1823−1831.
(50) Amemiya, Y.; Ito, K.; Yagi, N.; Asano, Y.; Wakabayashi, K.; Ueki, T.; Endo, T. *Rev. Sci. Instrum.* **1995**, *66*, 2290−2294.
(51) Inoue, K.; Yagi, N. *J. Nucl Instrum. Meth. Phys. Res. Sec. A* **2001**, *467−468*, 674−677.
(52) Haward, R. N. *Polymer* **1987**, *28*, 1485−1488.
(53) Haward, R. N. *Macromolecules* **1993**, *26*, 5860−5869.
(54) van Melick, H. G. H.; Govaert, L. E.; Meijer, H. E. H. *Polymer* **2003**, *44*, 3579−3591.
(55) G'Sell, C.; Hiver, J. M.; Dahoun, A. *Int. J. Solids Struct.* **2002**, *39*, 3857−3872.
(56) Bai, S.-L.; Wang, G.-T.; Hiver, J. M.; G'Sell, C. *Polymer* **2004**, *45*, 3063−3071.
(57) G'Sell, C.; Bai, S.-L.; Hiver, J. M. *Polymer* **2004**, *45*, 5785−5792.
(58) Aboulfaraj, M.; G'Sell, C. G.; Ulrich, B.; Dahoun, A. *Polymer* **1995**, *36*, 731−742.
(59) Sakurai, T.; Nozue, Y.; Kasahara, T.; Mizunuma, K.; Yamaguchi, N.; Tashiro, K.; Amemiya, Y. *Polymer* **2005**, *46*, 8846−8858.
(60) Karger-Kocsis, J.; Varga, J. *J. Appl. Polym. Sci.* **1996**, *62*, 291−300.
(61) Riekel, C.; Karger-Kocsis, J. *Polymer* **1999**, *40*, 541−545.
(62) Li, J. X.; Cheung, W. L. *Polymer* **1998**, *39*, 6935−6940.
(63) Radhakrishnan, J.; Ichikawa, K.; Yamada, K.; Toda, A.; Hikosaka, M. *Polymer* **1998**, *39*, 2995−2997.
(64) Gu, F.; Hikosaka, M.; Toda, A.; Ghosh, S. K.; Yamazaki, S.; Arakaki, M.; Yamada, K. *Polymer* **2002**, *43*, 1473−1481.
(65) Davies, R. J.; Zafeiropoulos, N. E.; Schneider, K.; Roth, S. V.; Burghammer, M.; Riekel, C.; Kotek, J. C.; Stamm, M. *Colloid Polym. Sci.* **2004**, *282*, 854−866.
(66) Nozue, Y.; Shinohara, Y.; Ogawa, Y.; Takamizawa, T.; Sakurai, T.; Kasahara, N.; Yamaguchi, N.; Yagi, N.; Amemiya, Y. *Polymer* **2010**, *51*, 222−231.
(67) Wang, Y. D.; Cakmak, M. *Polymer* **2001**, *42*, 4233−4251.
(68) Zaheiropoulos, N. E.; Davies, R. J.; Roth, S. V.; Burghammer, M.; Schneider, K.; Riekel, C.; Stamm, M. *Macromol. Rapid Commun.* **2005**, *26*, 1547−1551.
(69) Koike, Y.; Cakmak, M. *Macromolecules* **2004**, *37*, 2171−2181.
(70) Hedesiu, C.; Demco, D. E.; Kleppinger, R.; Poel, G. V.; Gijsbers, W.; Blümich, B.; Remerie, K.; Litvinov, V. M. *Macromolecules* **2007**, *40*, 3977−3989.
(71) Tjong, S. C.; Shen, J. S.; Li, R. K. Y. *Polym. Eng. Sci.* **1996**, *36*, 100−105.
(72) Zia, Q.; Radusch, H.-J.; Androsch, R. *Polymer* **2007**, *48*, 3504−3511.
(73) Li, X.; Schneider, K.; Kretzschmar, B.; Stamm, M. *Macromolecules* **2008**, *41*, 4371−4379.
(74) Martorana, A.; Piccarolo, S.; Sapoundjieva, D. *Macromol. Chem. Phys.* **1999**, *200*, 531−540.

Macromolecules

Article

pubs.acs.org/Macromolecules

Protracted Crossover to Reptation Dynamics: A Field Cycling ^{1}H NMR Study Including Extremely Low Frequencies

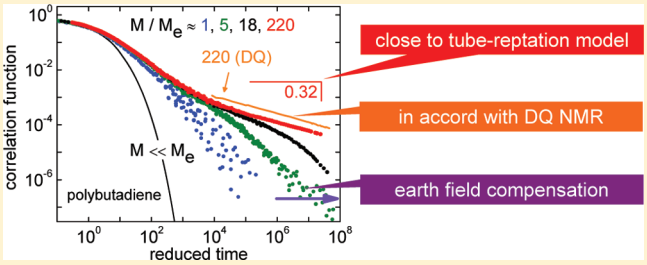
A. Herrmann,[†,‡] B. Kresse,[‡] J. Gmeiner,[‡] A. F. Privalov,[‡] D. Kruk,[†,§] F. Fujara,[‡] and E. A. Rössler*[,†]

[†]Experimentalphysik II, Universität Bayreuth, D-95440 Bayreuth, Germany

[‡]Institut für Festkörperphysik, TU Darmstadt, Hochschulstr. 6, 64289 Darmstadt, Germany

[§]University of Warmia & Mazury Olsztyn, Faculty of Mathematics & Computer Science, PL-10710 Olsztyn, Poland

ABSTRACT: The segmental dynamics of 1,4-polybutadiene is investigated by means of electronic field cycling ^{1}H NMR. The frequency dependence (dispersion) of the spin−lattice relaxation time is probed over a broad range of temperature (223−408 K), molecular mass ($355 \leq M$ (g/mol) $\leq 441\,000$), and frequency (200 Hz−30 MHz). The extremely low frequencies are accessed by employing a home-built compensation for earth and stray fields extending prior reports about 2 decades to lower frequencies. Applying frequency−temperature superposition yields master curves over 10 decades in frequency (or time), and after Fourier transform the full dipolar correlation function is traced over up to 8 decades in amplitude. Several relaxation regimes can be identified, and their power-law exponents are compared to the predictions of the Doi−Edwards tube-reptation model, namely the free Rouse (I) and the constrained Rouse regime (II). Whereas the predicted value of the power-law exponent of regime II is 0.25, we find that it depends on M and levels off at 0.32 for very high $M = 441\,000 \approx 220M_e$ (M_e: entanglement molecular mass). This is in good agreement with recent results from double quantum ^{1}H NMR and indicates that the actual onset of full reptation dynamics is strongly protracted.



1. INTRODUCTION

The dynamics of polymer melts is unremittingly subject to theoretical and experimental scientific research. The dynamical features are most often describable by the tube-reptation model of Doi and Edwards,[1] which can be considered as a combination of the Rouse model[2] for nonentangled polymer chains (with molecular mass M below the entanglement molecular mass M_e) and the essence of de Gennes' reptation model[3] for $M > M_e$. The tube-reptation model is very successful in predicting semiquantitatively the M dependence of transport coefficients like viscosity and translational diffusion coefficient. In order to account for weak deviations between model predictions and experimental or simulation findings, ongoing discussions[4−9] refine the model, e.g., by effects of contour length fluctuations (CLF)[10,11] and constraint release (CR).[12,13] The first ones are due to motions of the chain ends, and the latter are caused by the chains forming a nonstatic tube (or matrix). It remains an experimental challenge to probe the dynamics on a microscopic scale involving all the relaxation regimes forecast by the tube-reptation model. Important experimental techniques addressing these issues and revealing details of the dynamics on a molecular level are for example dielectric spectroscopy,[14,15] neutron spin echo,[16,17] and NMR,[18−23] in particular NMR relaxometry.[24,25]

Electronic (fast) field cycling (FC) NMR relaxometry has become an important tool for the investigation of collective dynamics in nonentangled and entangled polymers.[24−26] It can be applied to measure the frequency dependence (dispersion) of the spin−lattice relaxation rate $1/T_1$ over a frequency range of usually about 3 decades (10 kHz−20 MHz). In the case of ^{1}H NMR the technique probes the dipolar fluctuations of the proton spin pairs in the polymer melt, and they are usually assumed to be dominated by reorientational motion of the polymer segment. In a recent series of papers, we have investigated polymer dynamics of linear polybutadiene (PB) with systematically varied M.[27−31] Frequency−temperature superposition (FTS), commonly employed in rheology of polymers,[32] has been applied in order to extend the accessible frequency window of FC NMR. Thereby we have been able to monitor the dipolar correlation function of PB over more than 6 decades in amplitude and 8 decades in frequency, encompassing local segmental as well as collective polymer dynamics. In particular, the regimes I and II of the Doi−Edwards tube-reptation model[1] have been covered.

Vaca Chávez and Saalwächter have combined these results with their data from double quantum (DQ) ^{1}H NMR[33] which almost perfectly extend the FC ^{1}H NMR data up to even longer times into the reptation (III) and free-diffusion regimes (IV) of the tube-reptation model.[33,34] Thus, for the first time the full segmental correlation function has been disclosed over more than 10 decades in time. In the light of these joint NMR results, the long-time relaxation behavior in linear polymer melts can be

Received: November 11, 2011
Revised: December 20, 2011
Published: January 24, 2012

ACS Publications © 2012 American Chemical Society

attributed to a highly protracted transition from Rouse dynamics to almost completely established tube reptation. The latter has been reached only at $M/M_e > 200$ ($M_e \approx 2000$: entanglement molecular mass). For example, the power-law exponent ε of regime II has turned out to be M-dependent. A transition from $\varepsilon \cong 0.6$ at $M \cong M_e$ to $\varepsilon \cong 0.29$ at $M \cong 1000M_e$ has been observed. The latter exponent is quite close to the predicted value of $\varepsilon = 0.25$. In accordance with rheological[35,36] and dielectric experiments[15] as well as Monte Carlo simulations,[37,38] we have claimed that the crossover to full tube-reptation dynamics occurs only above another characteristic molecular mass $M_r \gg M_e$.[30]

So far, the necessary frequency (or time) window to probe the saturation behavior of the exponent ε at high M has only been accessible by DQ ^{1}H NMR. Yet, a field-gradient NMR study[18] revealed the crossover for the self-diffusion coefficient from regime IV to regime III coming from long times. Standard FC ^{1}H NMR as provided by utilizing, e.g., the commercial Stelar spectrometer reaches only a low-frequency bound of, say, 10 kHz. However, especially for polymers (or soft matter in general) even lower frequencies or longer times are desirable in order to investigate their slow dynamics, i.e., tracing the correlation function over as many decades as possible with one experimental method. This can be achieved by actively compensating earth and stray fields. Already Noack and coworkers[39] have reported relaxation dispersion results reaching about 100 Hz. Exploiting the possibilities of a home-built FC spectrometer, very recently Kresse et al.[40] have reached down below 100 Hz. In the present contribution we will apply this technique to measure $T_1(\nu)$ of linear PB melts for different M down to 200 Hz, which is almost 2 decades lower in frequency as compared to our previous FC ^{1}H NMR measurements.[30] Thereby we considerably extend our accessible time scales to those of DQ ^{1}H NMR, and we will show that indeed the exponent of the regime II continuously decreases down to $\varepsilon = 0.32$ for $M = 441\,000$; i.e., even at $Z > 200$ the prediction of the power-law exponent $\varepsilon = 0.25$ is not reached. On the one hand, this well confirms the results from DQ ^{1}H NMR;[34] on the other hand, this suggests that additional relaxation mechanisms may have to be taken into consideration to describe the dynamics of entangled polymers.

2. THEORETICAL BACKGROUND

Tube-Reptation Model. As thoroughly discussed in refs 1,7,25,32, 33, and 41, the dynamics of entangled polymer chains can be attributed to five relaxation regimes (0–IV) depending on the time scale of the motion and the length of the chain. Figure 1 shows schematically the mean-square displacement $\langle \mathbf{r}^2(t) \rangle$ and a rank-two reorientational correlation function $g^{(2)}(t)$ for a polymer segment as predicted by the Doi–Edwards tube-reptation model for a simple liquid, a nonentangled and an entangled polymer. At the shortest times, $t \leq \tau_\alpha \cong \tau_s$ (regime 0), the dynamics is governed by the glass transition phenomenon for which the long-time tail of $g^{(2)}(t)$ can be described by a stretched exponential decay, and the segmental correlation time τ_s can be identified with that of the α-process τ_α.[24,27,33] The absence of any slower dynamics is the characteristic of a simple liquid, e.g., a molecular glass-former. In $\langle \mathbf{r}^2(t) \rangle$ the ballistic short-time behavior ($t \ll \tau_s$) followed by a plateau signaling the cage effect is typical of glassy dynamics. Beyond the transition from oligomers to polymers at M_R (molecular mass of a Rouse unit) the chain connectivity starts to govern the segmental dynamics and is best described by the

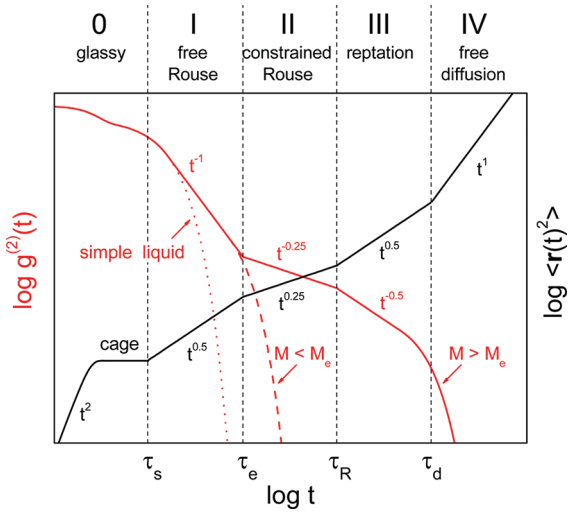


Figure 1. Schematic time dependence of the logarithm of the segmental reorientational correlation function of rank-two $g^{(2)}(t)$ (red line) and the mean-square displacement $\langle \mathbf{r}^2(t) \rangle$ (black line) as a function of logarithm of time as expected from the Doi–Edwards tube-reptation model ($M > M_e$). For $g^{(2)}(t)$ the behavior of a simple liquid (dotted line), a nonentangled polymer ($M < M_e$, dashed line), and entangled polymers ($M > M_e$, solid line) is distinguished.

Rouse model (regime I) as reflected in the power-law behavior $g^{(2)}(t) \propto t^{-1}$ or $\langle \mathbf{r}^2(t) \rangle \propto t^{0.5}$. Above the entanglement molecular mass M_e and between the entanglement time τ_e and the Rouse time τ_R the chain feels the constraints of its surrounding, i.e., a fictitious curved tube formed by its neighboring chains (regime II). At longer times the polymer chain diffuses along the primitive path of the tube (regime III), and finally free diffusion is reached after the terminal relaxation time ($t \gg \tau_d$: disengagement time, regime IV), leading at longest times to an essentially exponential cutoff in $g^{(2)}(t)$ or $\langle \mathbf{r}^2(t) \rangle \propto t^1$. Note that Ball et al.[41] have provided a joint analytical description for regimes III and IV. The mean-square displacement $\langle \mathbf{r}^2(t) \rangle$ in regime II and III is proportional to the tube survival probability and $g^{(2)}(t) \propto 1/\langle \mathbf{r}(t)^2 \rangle$ holds.[24,41] The power-laws of the individual regimes for both quantities are displayed in Figure 1, and it is a great challenge to completely identify experimentally these different relaxation regimes characterizing the microscopic dynamics of entangled polymer melts.

Field Cycling NMR, Susceptibility Representation, and Frequency–Temperature Superposition. Field cycling NMR can be applied to probe the frequency dependence of the spin–lattice relaxation time T_1 which is determined by the evolution of the nuclear magnetization toward its equilibrium value. The frequency is given by the Larmor frequency $\omega = \gamma B$ depending on the magnetic relaxation field B where γ denotes the gyromagnetic ratio of the nucleus. In the case of ^{1}H NMR fluctuations of the magnetic dipole–dipole (DD) interaction cause relaxation, and therefore the observed relaxation rate $R_1 = 1/T_1$ contains both intra- and intermolecular contributions.[24,42-44] Whereas the latter one is mainly due to translational motion among molecules, the first is due to segmental, i.e. local, reorientation dynamics and is usually assumed to be the dominating part because of the short-range nature of the DD coupling. However, Kehr et al. have shown that the intermolecular contribution to R_1 must not be ignored.[43,44]

dx.doi.org/10.1021/ma202489y | Macromolecules 2012, 45, 1408–1416

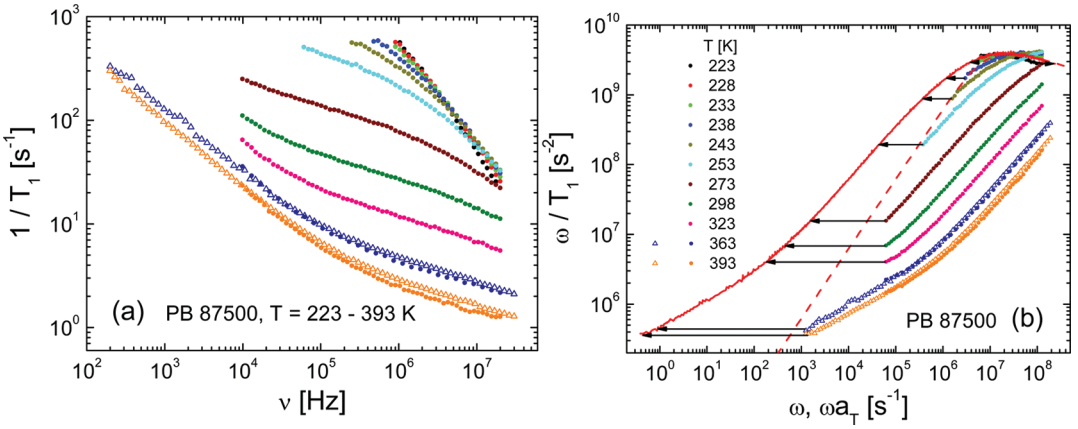


Figure 2. (a) Dispersion of the relaxation rate $1/T_1$ for 1,4-polybutadiene (PB) with M = 87500 g/mol in the temperature range as indicated measured with (open triangles) and without (circles) compensation. (b) Susceptibility representation ω/T_1 of the same data as in (a). At lowest temperatures the α-peak is discernible and fitted with Cole–Davidson function (dashed red line). Arrows illustrate frequency–temperature superposition which is applied to create a master curve (solid red line). The color for temperatures is equivalent in both figures.

Measurements in a large temperature interval (223–393 K) provide relaxation rates $1/T_1$ as shown in Figure 2a for 1,4-polybutadiene with molecular mass 87 500 g/mol (as an example). For each temperature a differently strong dispersion is observed. Rewriting the Bloembergen, Purcell, and Pound (BPP) expression[42,47] for the relaxation rate

$$R_1(\omega) \propto [J(\omega) + 4J(2\omega)] \quad (1)$$

in the susceptibility representation[25,27−31]

$$\omega/T_1(\omega) = K[\chi''(\omega) + 2\chi''(2\omega)] \equiv 3K\chi''_{DD}(\omega) \quad (2)$$

allows a direct comparison with results from other techniques. K is the NMR coupling constant, and $\chi''_{DD}(\omega)$ is subsequently called "dipolar susceptibility" probed by ^{1}H NMR. Although $\chi''_{DD}(\omega)$ is a weighted sum of susceptibilities $\chi''(\omega)$, both quantities are essentially indistinguishable for a broad relaxation dispersion on logarithmic scales. Via $\chi''(\omega) = \omega J(\omega)$ the normalized imaginary part of the susceptibility is associated with the spectral density $J(\omega)$ being the Fourier transform of the dipolar correlation function $C^{DD}(t)$ which, in turn, has to be distinguished from $g^{(2)}(t)$ being exclusively sensitive to rotational motion. We note that the susceptibility representation of NMR relaxation data has also been used by, for example, Cohen-Addad.[48] Applying this conversion to the relaxation data of Figure 2a yields the curves displayed in Figure 2b (colors used correspondingly), which exhibit a maximum (main relaxation or α-peak) at low temperatures or high frequencies, and obviously share a common shape but are shifted due to the applied temperatures.

In the susceptibility representation a master curve $\chi''_{DD}(\omega a_T)$ (solid red line) can easily be created by moving the individual curves solely in frequency (frequency–temperature superposition (FTS), illustrated by arrows) to achieve a good agreement. FTS is a principle commonly used, e.g., in rheology[32,49,50] in order to extend significantly the frequency range. After interpolating the α-peak with an appropriate function (for instance, Cole–Davidson susceptibility, dashed red line) yielding the time constant τ_s for one temperature (T = 228 K in Figure 2b), the shift factors $a_T(T)$ can be transformed to the time constants $\tau_s(T) \approx \tau_\alpha(T)$ of segmental reorientation.[27−29] Therefore, in the following the master curves are plotted as a function of the reduced frequency $\omega\tau_s$ and can be regarded as "isofrictional" spectra[50,51] in which the dynamics of polymers with different molecular masses can be evaluated because the M dependence of the glass transition temperature T_g has been taken into account which is pronounced especially at low M.[29] Finally, by Fourier transform of the susceptibility master curves the dipolar correlation function $C^{DD}(t/\tau_s)$ can be obtained (cf. Figure 6a), permitting a comparison with the power-law regimes shown in Figure 1.

Relaxation at Extremely Low Frequencies. The intrinsic assumption of the polymer theories predicting the characteristic power-laws of the spin–lattice relaxation dispersion is that the ^{1}H spin–lattice relaxation rate $R_1(\omega)$ can be described as a combination of spectral densities (eq 1). The associated exponents have been derived within the framework of the BPP theory assuming specific forms of the spectral densities. The relaxation formula stems from the second-order perturbation theory, and in consequence, its validity regime is limited.[52-54] There are two fundamental assumptions determining its applicability range. First, the relaxation time must not be shorter than (even comparable to) the correlation time τ of the dynamical process causing relaxation; second, the dipolar interaction has to be a small perturbation compared to the Zeeman interaction.[42,45,55] Both conditions are potentially violated at extremely low frequencies.

On the one hand, at lower frequencies the spin–lattice relaxation rate becomes faster (T_1 becomes shorter), while on the other hand progressively slower dynamical processes are probed. When at a given frequency ν_x the relaxation dispersion still does not reach the low-frequency plateau (i.e., the extreme narrowing condition[42,46] $2\pi\nu_x\tau \ll 1$ is not reached yet) it is obvious that $\tau \gg (2\pi\nu_x)^{-1}$. If at the same frequency the relaxation rate R_1 is larger than $2\pi\nu_x$, the condition $T_1 \gg \tau$ will be violated; such a situation is schematically depicted in Figure 3. In this regime care has to be taken when discussing the observed slopes of the apparent relaxation time in the context of the predictions of the polymer theories as the concept of the spectral density function does not apply; to describe the magnetization decay the stochastic Liouville equation (SLE) has to be employed, and this has been done up to now only for paramagnetic systems.[53,56] The relationship $T_1 \gg \tau$ is equivalent in the low-frequency range to the Redfield condition[42,46,52,55] $\omega_{DD}\tau \ll 1$, where ω_{DD} is the amplitude of the dipole–dipole coupling in angular frequency units. In the

dx.doi.org/10.1021/ma202489y | Macromolecules 2012, 45, 1408–1416

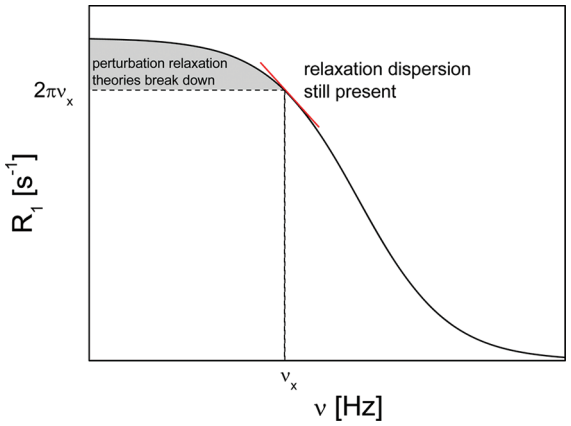


Figure 3. Schematic illustration of the validity range of the perturbation approach to relaxation. When at a frequency ν_x the relaxation rate approaches or exceeds the value of $2\pi\nu_x$, the perturbation treatment breaks down (gray area).

extreme narrowing range the relation $R_1 \propto \omega_{DD}{}^2\tau = (\omega_{DD}\tau)^2\tau^{-1}$ holds, and then $\omega_{DD}\tau \ll 1$ implies that $R_1 \ll \tau^{-1}$, i.e., $T_1 \gg \tau$.

As far as the second condition is concerned, in the low-field range ω_{DD} can approach or even exceed the Zeeman splitting frequency ω, and then the dipolar interaction which is responsible for the relaxation cannot be treated as a small perturbation of the Zeeman interactions. Then the classical relaxation formulae break down, and the SLE approach has to be applied as well.[52,53] It can also happen that residual dipolar interactions (a part of the dipolar coupling which does not vanish due to motional averaging) become comparable with the Zeeman interaction, thereby considerably altering the proton energy level structure. In such a case one can still apply the perturbation relaxation theory (if other conditions are not violated), but the resulting relaxation expressions are different from the "classical" ones[52-54,57] (eq 1) which is not taken into account in the theoretical predictions for the characteristic polymer relaxation slopes. This is a typical situation in polymer melts where a residual coupling exists due to the slow anisotropic dynamics of entangled chains. We will return to these issues in the discussion part, however, a satisfactory consideration will remain the task of future theoretical work.

3. EXPERIMENTAL SECTION

Samples of linear 1,4-polybutadiene (PB) with a narrow molecular mass distribution have been investigated over a large range of molecular masses (M). The polymers have been purchased from Polymer Standards Service, Mainz, Germany, thoroughly degassed in 5 and 10 mm NMR tubes and sealed under vacuum. Table 1 gives an overview over molecular masses and polydispersities M_w/M_n in addition to those M already studied in ref 30.

Table 1. Details on the Samples[a]

sample	M_w [g/mol]	M_w/M_n
PB 24300	24300	1.01
PB 47000	47000	1.04
PB 87500	87500	1.05
PB 143000	143000	1.02
PB 196000	196000	1.02
PB 441000	441000	1.07

[a]The sample name reflects the molecular mass M_w.

^{1}H NMR spin−lattice relaxation experiments have been performed with two different electronic field cycling (FC) relaxometers: a commercial one (Stelar Spinmaster FFC2000) at Bayreuth University and a home-built one at Darmstadt University. In Bayreuth, experiments were performed at temperatures from 223 up to 408 K; in Darmstadt, temperatures from 355 up to 393 K were measured.

Let us, at this point, mention the most important characteristics and the specific differences between the two FC relaxometers: The Bayreuth Stelar relaxometer covers a ^{1}H frequency range from $\nu = \omega/2\pi$ = 10 kHz up to 20 MHz. Times of about or less than 3 ms are achieved for switching from a high polarization field to any desired evolution field, thereby avoiding undershoots or strong field oszillations. Lower ^{1}H frequencies can only be reached at the home-built Darmstadt relaxometer[58] which, since about 10 years, has been continuously upgraded. For the present project, frequencies down to 200 Hz and up to 30 MHz have been reached. The low frequencies can be attained by utilizing a three-dimensional resistive coil arrangement for compensating for the earth field and other magnetic stray fields. For stabilizing fields corresponding to ^{1}H frequencies below 1 kHz an active field drift and fluctuation compensation tool is activated. Field switching is performed in a controlled way reaching switching times of about 3 ms if the active compensation tool is not used (above 1 kHz) and 6 ms if the compensation tool is used (below 1 kHz). For technical details the reader is referred to ref 40, where it is demonstrated that in favorable cases ^{1}H frequencies down to 12 Hz can be reached.

Spin−lattice relaxation times—especially for high-M polymers at very low fields, yet at a temperature far above T_g—may eventually become even shorter than the switching time of the employed relaxometer. As long as the magnetization decay is monoexponential, this does not cause a conflict with the finite switching time except for a corresponding signal reduction. Exemplifying magnetization decay curves are shown in Figure 4 for a couple of ^{1}H frequencies. For each

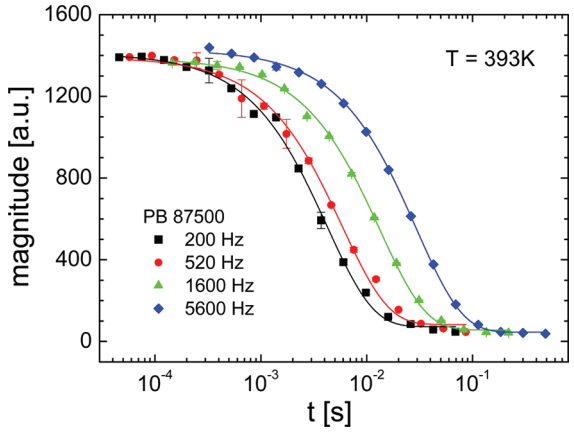


Figure 4. Magnetization decay curves of PB 87500 at T = 393 K in various relaxation fields as indicated. Solid lines: corresponding monoexponential fit.

relaxation field the magnetization decays exponentially characterized by the spin−lattice relaxation time T_1. Note that the abscissa assignment of the variable time starts from a point safely after the field switching has been done.

A comparison of the relaxation rate $1/T_1(\nu)$ and susceptibility $\chi''_{DD} = \omega/T_1$ measured with both the Stelar and the home-built spectrometer is shown in Figures 2a and 2b, respectively, for PB 87500 at T = 363 and 393 K. The curves coincide well for the two temperatures, indicating also that the temperature control agrees for both instruments. Furthermore, it demonstrates the benefit of a compensation for stray fields: almost 2 decades can be gained at low frequencies, and consequently the relaxation rate dispersion covers more than 5 decades.

dx.doi.org/10.1021/ma202489y | Macromolecules 2012, 45, 1408−1416

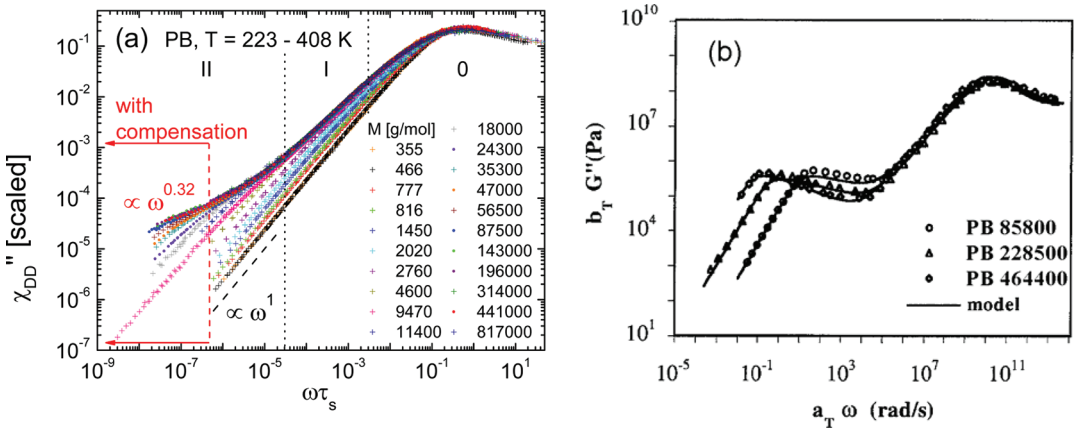


Figure 5. (a) Susceptibility master curves as a function of the reduced frequency $\omega\tau_s$ for all investigated M of PB in the temperature range as indicated. The frequency range in which T_1 has been acquired while employing the compensation for stray fields is marked by arrows. Vertical dotted lines: relaxation regimes 0, I, and II, i.e., glassy dynamics, Rouse and entanglement dynamics, respectively. (b) Loss modulus $G''(\omega)$ for PB (with M as indicated) as obtained with a mechanical rheometer and applying FTS (figure adapted with permission from ref 60).

As outlined in section 2, Fourier transform is applied to obtain the dipolar correlation function. Since many decades in frequency are involved, instead of fast Fourier transform, we utilize an algorithm based on the Filon algorithm.[59] When at low frequencies the terminal relaxation, i.e., the crossover to $\chi''_{DD} \propto \omega^1$, is reached, the susceptibility master curve can be transformed as it is. For the master curves with $M \geq 35\,300$, for which the terminal relaxation is beyond the experimentally accessible frequency window, it is essential to extend the susceptibility with the corresponding power-law $\omega^{\varepsilon(M)}$ over some decades. Otherwise, truncation errors of the algorithm would cause a misleading decay of the correlation function at longest times, which can be avoided by the described extension and subsequently discarding the previously added points. This, in contrast, is not necessary for the evaluation of the DQ ^{1}H NMR experiments measuring dipolar couplings directly in the time domain,[19,33,34] however, being able to probe the correlation function only for $t > \tau_e$. We will demonstrate that low-field FC NMR adds 2 decades to our prior results[30] in $C^{DD}(t/\tau_s)$ and also allows investigating higher M, in total providing a mutual verification of the results of both NMR techniques.

4. RESULTS

According to the procedure outlined in section 2, the T_1 dispersion data have been converted to the susceptibility representation $\chi''_{DD} = \omega/T_1$, and by merging the data of the different temperatures, a master curve of the reduced frequency $\omega\tau_s$ has been created for each M (Figure 5a). The scaling by the segmental correlation time τ_s as said yields "isofrictional" spectra and provides a common peak at $\omega\tau_s \approx 1$ representing the primary α-relaxation governed by the glass transition. At $\omega\tau_s \geq 1$ the spectral shape of the peak is independent of M. With increasing M a continuously rising excess intensity on the low-frequency side of the peak ($\omega\tau_s < 1$) is discernible which is due to the slower, M-dependent polymer dynamics. For the high-M ($M > M_e \approx 2000$) master curves three different relaxation regimes (0, I, II) can be distinguished and are phenomenologically in accordance with those from Kimmich's classification.[24] Below we will attribute them to glassy (0), Rouse (I), and constrained Rouse (II) dynamics of the Doi–Edwards tube-reptation model which is however different from Kimmich's interpretation.[24,25,30,31] At lowest frequencies in regime II, especially in the range in which the compensation tool has been employed (arrows in Figure 5a), M-dependent power-laws can be identified.

The susceptibility master curves (Figure 5a) reflect segmental ("local") as well as collective polymer dynamics and will be described in the following by going from high to low reduced frequencies. While a simple liquid (PB with $M = 466$) only exhibits glassy dynamics in form of the α-peak with a power-law ω^1 at $\omega\tau_s < 1$, at $M = 777$ the contribution of polymer dynamics begins to increase with M in regime 0 and saturates around $M = 4600$. Yet, since for frequencies $\omega\tau_s > 3 \times 10^{-3}$ and around the relaxation maximum glassy dynamics still contributes, regime 0 is designated as glassy dynamics (cf. Figure 1). Note that the frequency position of the lines separating the regimes in Figure 5a differs slightly from our previous works.[25,31] In the frequency range $3 \times 10^{-5} < \omega\tau_s < 3 \times 10^{-3}$ the susceptibility of $M = 4600 \approx 2M_e$ represents an envelope with a power-law ω^ε even for the high-M ($M \gg M_e$) systems, indicating that the dynamics remains unchanged if M is increased beyond M_e. In this regime the dispersion data can be well described by applying the Rouse model;[29] therefore, it is attributed to free Rouse dynamics (regime I). Approaching lower frequencies ($\omega\tau_s < 3 \times 10^{-5}$, regime II), a crossover to a second power-law $\omega^{\varepsilon(M)}$ with $\varepsilon < \alpha$ is observed. While increasing M the master curves progressively approach the enveloping shape constituted by the highest M. Whereas for $M \leq 11\,400$ a crossover to the power-law ω^1 (Debye limit) characterizing terminal relaxation is accessible in the frequency range of the Stelar spectrometer ($\omega\tau_s \geq 5 \times 10^{-7}$), for larger M the slowest relaxation mode is more and more shifted to lower frequencies. Together with the fact that the power-laws of the tube-reptation model (regimes II and III) are expected to be very protracted, i.e., to be disclosed only for very high M ($M > 100M_e = 200\,000$),[15,34,37] this rendered the need for low-field relaxation experiments.

Within the frequency range marked by the arrows in Figure 5a ($\omega\tau_s < 5 \times 10^{-7}$) the relaxation data have been obtained with the home-built spectrometer equipped with the active compensation system. Two limiting power-laws can be distinguished in the susceptibility of PB with different M: For $M \leq 35\,300$ the power-law ω^1 indicates that the terminal relaxation has been detected (in a $1/T_1$ plot such as Figure 2a this would manifest itself in a horizontal line, i.e., ω^0), and for $M = 441\,000$ a power-law $\omega^{0.32}$ is revealed extending over more than 1 decade at lowest frequencies. In between the power-law exponent continuously decreases for increasing M, which will be evaluated and discussed below (see also Figure 6b).

dx.doi.org/10.1021/ma202489y | Macromolecules 2012, 45, 1408–1416

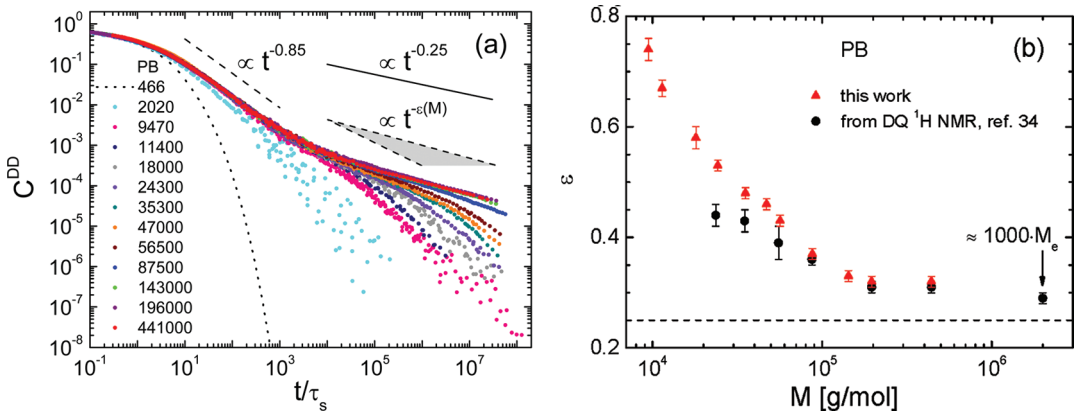


Figure 6. (a) Dipolar correlation function $C^{DD}(t/\tau_s)$ of PB for various M obtained by Fourier transforming the susceptibility master curves of Figure 5a. Dotted curve: low-M system representing glassy dynamics. Dashed lines: observed power-laws of regime I and II. Gray area illustrates variation of power-law exponent ε of regime II for 24 300 ≤ M ≤ 441 000. Solid line: predicted power-law of regime II by tube-reptation model. (b) Power-law exponent ε as a function of M obtained in the time domain. For comparison, DQ ^{1}H NMR results[34] are included. Even at $M \approx 2\,000\,000$ the prediction of the tube-reptation model $\varepsilon = 0.25$ (dashed line) is not fully approached yet.

However, this already shows that the dynamics in regime II is dependent on M even if $M \gg M_e$.

For comparison, Figure 5b contains master curves of the dynamic loss modulus $G''(\omega)$ for different high-M PB from rheological measurements.[60] In that study a mechanical spectrometer with cone−plate and torsional configuration was used in the temperature range from 158 to 353 K, and FTS has been applied as well, thereby increasing the accessible frequency range from 3 (as in FC NMR using the Stelar relaxometer) to 17 decades. The master curves of different M exhibit a common high-frequency peak and an M-dependent minor peak at lower frequencies. The first is attributed to the glassy dynamics, and the latter represents the slowest relaxation mode. Since a low-frequency peak as in the rheological data is not observed in the FC ^{1}H NMR master curves, obviously the relaxation mode spectrum is weighted differently for the two techniques. However, the susceptibility representation offers the possibility to directly compare the results from FC ^{1}H NMR (Figure 5a) and rheology (Figure 5b), i.e., microscopic and macroscopic dynamics as reflected in the $T_1(\omega)$ and $G''(\omega)$ measurements, respectively. Recently,[34] the term "molecular rheology" was coined with respect to FC and DQ ^{1}H NMR and their capability of exploring the time range from glassy dynamics to terminal relaxation in entangled polymers like "conventional" rheology.

Fourier-transforming the susceptibility master curves $\chi''_{DD}(\omega\tau_s)$ of Figure 5a allows displaying them as the full dipolar correlation function $C^{DD}(t/\tau_s)$ in Figure 6a (cf. Experimental Section). While the low-M system (PB 466, dotted line) exhibits a stretched exponential (Kohlrausch) decay typical of a simple liquid, for higher M the relaxation becomes increasingly retarded as already discussed in ref 30. Depending on M characteristic power-laws t^{α} can be identified with their exponents (above M_e) having the same absolute value than in the frequency domain (Figure 5a). In the time range up to $t/\tau_s < 10^3$ a common envelope with $\alpha = 0.85$ is found which is not altered at high M similarly to the susceptibility representation. This is close to $\alpha = 1$ predicted by the Rouse theory (cf. Figure 1), and therefore it can be regarded as the high-M envelope for the free Rouse dynamics (regime I). First, the free Rouse dynamics leads to a distribution of correlation times in the range $\tau_s < \tau < \tau_e$, and then above M_e entanglement dynamics provides relaxation on increasingly slower time scales $t > \tau_e$ (regime II), leading to a bimodal shape. Here, particularly the M-dependent power-law $t^{\varepsilon(M)}$ is recognized. Analogous to Figure 5a, ε is reduced with growing M as indicated by the gray sector (for 24 300 ≤ M ≤ 441 000) in Figure 6a.

This dependence $\varepsilon(M)$ is plotted in Figure 6b. From the correlation functions (Figure 6a) the minimum slope ε has been determined for each M by a linear fit in the double-logarithmic representation over at least 1 decade in time. A continuous decrease of ε from 0.73 to 0.32 can be noted in the M range between 9470 and 441 000. Note that our previous data[30] were restricted to M = 18 000 or $\varepsilon > 0.5$, and now the M range in the time domain is extended by a factor of about 25. The new high-M results obtained by low-field FC ^{1}H NMR agree well with those from DQ ^{1}H NMR,[34] which are included in Figure 6b for comparison. This demonstrates that low-field FC ^{1}H NMR is capable to cover the full M dependence of ε. For the highest M the power ε determined by FC and DQ ^{1}H NMR is slightly larger, yet close to the prediction $\varepsilon = 0.25$ of the tube-reptation model for regime II (cf. Figure 1). Since this theoretically expected value is still not yet reached with both NMR techniques and could possibly be attained only for $M >$ 2 000 000, it can be concluded that the crossover to full reptation dynamics is very protracted.

Figure 7 shows a direct comparison of the correlation function for several high-M PB measured by FC and DQ ^{1}H NMR plotted in a way to further test the relaxation behavior in regime II. It displays the long-time end of the FC data of Figure 6a focusing on the time window of the DQ data which have been inserted from ref 34. Samples with comparable M are displayed in the same color. The amplitude is divided by the predicted power-law $t^{-0.25}$ for regime II of the tube-reptation model illustrating how the theoretically expected behavior (horizontal line) is approached with increasing M, yet not completely attained. Whereas in the correlation function of PB with M = 9470 ≈ $5M_e$ no indication for the power-law of regime II can be seen; above M = 24 300 the curves come closer to the model prediction and trace the envelope shape of the highest M = 441 000 continuously longer with higher M before bending away at long times. Moreover, a good agreement among the FC and DQ ^{1}H NMR data can be observed. In order to achieve the best match among them, the DQ data have been scaled by a factor of 0.5 in amplitude. Vaca

dx.doi.org/10.1021/ma202489y | Macromolecules 2012, 45, 1408−1416

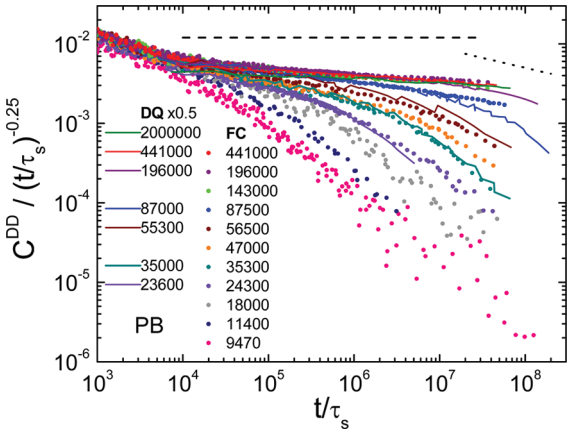


Figure 7. Correlation function for PB with M as indicated measured by FC and DQ ^{1}H NMR[34] (dots and lines, respectively) divided by the power-law $t^{-0.25}$. Dashed horizontal line and dotted line: expectation for regimes II and III of the tube-reptation model, respectively.

Chávez and Saalwächter[61] applied a factor of 0.7, ascribing it to shortcomings of their model determining the absolute value of the correlation function. We note that the investigated polymers were obtained from the same supplier and in the case of PB with M = 196 000 and 441 000 the identical polymer was examined by both NMR methods.

5. DISCUSSION

In Figure 7, a second power-law regime (II) can be clearly identified extending over 3 decades in time for $M \geq$ 143 000. While increasing M the protracted transition to almost completely established reptation dynamics is characterized by the very slow approach of the exponent ε toward ε = 0.25 predicted by the tube-reptation model (Figure 6b). The latter has been reported for the mean-square displacement by, e.g., neutron spin echo (NSE)[17] and simulations.[4,37,38] The observed exponent ε(441 000) = 0.32 corresponds in the $1/T_1$ representation to −0.68, which is larger than the value −0.42 found by Kimmich et al.[62] for PB with M = 65 500 at T = 313 K. This difference is due to the larger M investigated at both higher temperatures and lower frequencies in the present study. Concerning the identification of regime III of the tube-reptation model, the situation is less convincing. For PB with $M \leq$ 56 500 the correlation function exhibits just a smooth transition to terminal relaxation, and the predicted power-law $t^{-0.5}$ (cf. dotted line in Figure 7) may merely be assumed over 1 decade. Therefore, according to our current results, it cannot be decided whether the dynamic range of regime III is quite narrow, resulting in a smooth transition to regime IV (as observed in the DQ ^{1}H NMR study[34]), whether there is an interplay between the dynamics of different regimes, or whether the power-law would be more pronounced for higher M and at yet longer times beyond our experimentally accessible range. The first is corroborated by a theoretical work[41] yielding an analytical expression for regimes III and IV together. However, the direct comparison of the correlation functions from both NMR methods demonstrates that FC ^{1}H NMR is indeed capable of reaching the time scales which formerly have been restricted to DQ ^{1}H NMR. We emphasize the agreement among the results of DQ and FC ^{1}H NMR, since the theoretical concepts involved in these methods are quite different, i.e., coherent spin-evolution measuring dipolar correlations in the time domain and longitudinal relaxation probing a spectral density in the frequency domain, respectively.

Regarding the limitations of the perturbation-based relaxation theories (cf. Theoretical Background), we are aware that our experimental results collected at lowest frequencies need to be treated cautiously. For the high-M polymers one sees from Figure 2a that the relaxation rate still grows up at low frequencies even though it has already reached (3 ms)$^{-1}$ at ν = 200 Hz. Consequently with $\tau = (2\pi\nu)^{-1}$ = 0.8 ms the condition $T_1 \gg \tau$ is not strictly fulfilled anymore. Even more, since a relaxation dispersion is still observed the condition will be violated further as frequency decreases. In order to provide exact theoretical predictions for the characteristic polymer relaxation, a treatment based on a full (nonperturbative) solution the stochastic Liouville equation should be adopted. To our knowledge, such a general description has not been formulated yet. Therefore, we base our analysis on the second-order perturbation theory, even though we are aware of its limitation. We note that the Larmor frequencies are still above the typical residual dipolar coupling of about 100 Hz observed for high-M polymer melts which was the second condition to be fulfilled (see above).[34,63] Together with the consistency between FC and DQ ^{1}H NMR data (Figures 6b and 7) this provides some confidence that our results are still unaffected by low-frequency effects exceeding second-order perturbation theory.

When comparing the observed power-law exponents to the predicted ones, we underline that the dipolar correlation function $C^{DD}(t)$ probed by FC ^{1}H NMR does not need to be identical to the rank-two reorientational correlation function $g^{(2)}(t)$ of a polymer segment. A common assumption in the analysis of FC ^{1}H NMR experiments is that the intramolecular contribution to relaxation dominates, and therefore the influence of intermolecular relaxation can be neglected.[26,27,30,34] As mentioned, results by Kehr et al.[43,44] indicate that this is not necessarily the case at low frequencies, suggesting that ε might also be sensitive to influences of the intermolecular relaxation. However, DQ ^{1}H NMR results for isotopic dilution of PB 196000 with deuterated PB of the same M and thereby suppressing the intermolecular interaction have shown[33] that the value of ε remains the same as in the pure PB though the absolute values of $C^{DD}(t)$ are different. Very recent own measurements point into the same direction.

The ε values in Figure 6b are notably higher than 0.25 predicted by the tube-reptation model. This may be caused by the early onset of terminal relaxation for $M \leq$ 56 500 or by additional relaxation mechanisms. Even at highest M = 441 000 $\gg M_e$ the theoretical exponent is not reached. In other words, although $M \gg M_e$ a static tube appears to be not formed yet. All approaches to refine the Doi−Edwards model such as constraint release (CR) or contour length fluctuations (CLF) cause additional correlation loss, i.e., a steeper decay which results in ε being higher than expected from the original tube-reptation model, and are candidates for interpreting our findings. We note that the (twice) renormalized Rouse theory has been used by Kimmich and Fatkullin to describe the experimentally observed power-laws.[24,62] In the light of the recent DQ ^{1}H NMR results together with our data measuring a large frequency and temperature range and exploiting FTS, the applicability of the renormalized Rouse model as proposed in ref 24 can be ruled out, especially in the low-frequency range.[25,44]

dx.doi.org/10.1021/ma202489y | Macromolecules 2012, 45, 1408−1416

The protracted transition to full reptation dynamics has also been observed in Monte Carlo simulations by Kreer et al.[37] and Paul.[38] Actually, Kreer et al. seem to be the first ones to discuss this phenomenon; however, such a delayed crossover has not been recognized by more recent simulation work.[64] A possible explanation may be due to the fact that the NMR signal is averaged over all segments in the chain. Whereas the chain ends participate in forming a new tube, the inner monomers are exposed to the topological confinement of the tube to a higher degree. Therefore, their reorientation is more hindered, which is closer to the model picture of a static tube. Kremer et al.[65,66] already pointed out by means of MD simulations that the outer monomers fluctuate stronger, and in order to observe actual entanglement effects, one should inspect the innermost monomers. Zamponi et al.[67] have concluded from a NSE study of polyethylene (PE) with M = 25 000 that the dynamic structure factor of a completely protonated chain differs from that of a partially deuterated chain with protons only at the inner part due to CLF. Effects of CR were believed to be negligible.

Yet, complementing the NSE experiments, Vaca Chávez and Saalwächter[33] directly proved that ε is influenced indeed by CR effects, since diluting PB with M = 55 000 in a deuterated PB matrix with both lower and higher M changes ε. Because diluting PB with M = 196 000 in the same deuterated M does not modify ε, an influence of intermolecular relaxation on ε for the highest M can be excluded. However, a very recent study[68] combining viscoelastic and dielectric relaxation spectra claims to have proven that the dielectric spectra are determined by reptation and CLF motion only and not by CR contributions. Thus, for a final interpretation additional evidence addressing the relevance of CR, CLF, and NMR specific intermolecular relaxation effects is needed and part of ongoing work.

Whereas the above discussion implies a continuous transition to full reptation, there are several indications for a discontinuous change of the dynamics at another characteristic molecular mass $M_r \gg M_e$. For PB Colby et al.[50] disclosed at $M_r \approx 200M_e$ a departure from the viscosity power-law $\eta(M) \sim M^{3.4}$ to $M^{3.0}$, for PE Vega et al.[35] found $M_r \approx 440M_e$, and for polyisoprene (PI) Abdel-Goad et al.[36] discovered $M_r \approx 44M_e$. Therefore, the relation M_r/M_e is not constant for different polymers.[69] In a recent study[15] by dielectric spectroscopy on PI we reported a saturation behavior at $M_r \approx 20M_e$ both from the shape and time constant of the dielectric normal mode.

6. CONCLUSIONS

We have investigated the dynamics of PB melts in a series of different M by FC ^{1}H NMR focusing on the low-frequency behavior for $M > M_e$. The frequency window provided by the commercially available Stelar FC spectrometer has been extended significantly for 2 decades toward lower frequencies (Figure 2) with the aid of a home-built spectrometer[40] in order to explore polymer dynamics on even slower time scales than in our previous study.[30] The susceptibility representation of the relaxation dispersion offers a comparison with rheological data (Figures 5a and 5b). As a result of applying FTS, the susceptibility master curves and the corresponding dipolar correlation functions (Figure 5a and 6a, respectively) embrace over 10 decades in frequency or time and can be analyzed in a range which before was restricted to DQ ^{1}H NMR experiments.[33] Consequently, for all M studied FC ^{1}H NMR is now able to cover the relaxation regimes 0, I, and II (glassy, free Rouse, and constrained Rouse dynamics, respectively; cf. Figure 1) and for $M \leq$ 56 500 also regimes III and IV (reptation dynamics and free diffusion, respectively) of the tube-reptation model.

The particular goal of this contribution has been to study the transition from Rouse to fully established reptation dynamics at $M \gg M_e$. From the slow decrease of the power-law exponent $\varepsilon(M)$ in regime II from 0.73 to 0.32 with increasing M toward the predicted ε = 0.25, it can be concluded that only for very high M the characteristic dynamics of the tube-reptation model is disclosed. The M dependence of ε is very similar to the values reported by DQ ^{1}H NMR[34] for high M (Figure 6b), and a direct comparison of the correlation functions obtained by FC and DQ ^{1}H NMR shows a good agreement (Figure 7). Hence, FC NMR has turned from a complementary method to DQ NMR into a competitive one. Moreover, we anticipate that a further enhancement of the stray field compensation tool will contribute 1 more decade at low frequencies. This could further illuminate the reptation dynamics of regime III and provide the basis for a joint description of dielectric, viscoelastic, and NMR relaxometric data.

AUTHOR INFORMATION

Corresponding Author

*E-mail: ernst.roessler@uni-bayreuth.de.

ACKNOWLEDGMENTS

The financial support of Deutsche Forschungsgemeinschaft (DFG) through priority program SPP 1369 "Polymer-Solid Contacts: Interfaces and Interphases" (RO 907/16) and grant FU 308/14 is acknowledged. The authors thank F. Vaca Chávez and K. Saalwächter for valuable discussions and providing their data for Figure 7.

REFERENCES

(1) Doi, M.; Edwards, S. F. *The Theory of Polymer Dynamics*; Oxford Science Publications: Oxford, 1986.
(2) Rouse, P. E. *J. Chem. Phys.* **1953**, *21*, 1272−1280.
(3) de Gennes, P. G. *J. Chem. Phys.* **1971**, *55*, 572−579.
(4) Kremer, K.; Grest, G. S. *J. Chem. Phys.* **1990**, *92*, 5057−5086.
(5) Lodge, T. P.; Rotstein, N. A.; Prager, S. *Adv. Chem. Phys.* **1990**, *79*, 1−132.
(6) Watanabe, H. *Prog. Polym. Sci.* **1999**, *24*, 1253−1403.
(7) Binder, K.; Baschnagel, J.; Paul, W. *Prog. Polym. Sci.* **2003**, *28*, 115−172.
(8) Richter, D.; Monkenbusch, M.; Arbe, A.; Colmenero, J. *Neutron Spin Echo in Polymer Systems*; Springer: Berlin, 2005.
(9) Read, D. J.; Jagannathan, K.; Likhtman, A. E. *Macromolecules* **2008**, *41*, 6843−6853.
(10) Doi, M. *J. Polym. Sci., Polym. Lett. Ed.* **1981**, *19*, 265−273.
(11) Milner, S. T.; McLeish, T. C. B. *Phys. Rev. Lett.* **1998**, *81*, 725−728.
(12) Rubinstein, M.; Colby, R. H. *J. Chem. Phys.* **1988**, *89*, 5291−5306.
(13) Likhtman, A. E.; McLeish, T. C. B. *Macromolecules* **2002**, *35*, 6332−6343.
(14) Adachi, K.; Wada, T.; Kawamoto, T.; Kotaka, T. *Macromolecules* **1995**, *28*, 3588−3596.
(15) Abou Elfadl, A.; Kahlau, R.; Herrmann, A.; Novikov, V. N.; Rössler, E. A. *Macromolecules* **2010**, *43*, 3340−3351.
(16) Zamponi, M.; Wischnewski, A.; Monkenbusch, M.; Willner, L.; Richter, D.; Likhtman, A. E.; Kali, G.; Farago, B. *Phys. Rev. Lett.* **2006**, *96*, 238302.
(17) Richter, D.; Butera, R.; Fetters, L. J.; Huang, J. S.; Farago, B.; Ewen, B. *Macromolecules* **1992**, *25*, 6156−6164.

(18) Pahl, S.; Fleischer, G.; Fujara, F.; Geil, B. *Macromolecules* **1997**, *30*, 1414−1418.
(19) Graf, R.; Heuer, A.; Spiess, H. W. *Phys. Rev. Lett.* **1998**, *80*, 5738−5741.
(20) Pearson, D. S.; Fetters, L. J.; Graessley, W. W.; Ver Strate, G.; von Meerwall, E. *Macromolecules* **1994**, *27*, 711−719.
(21) Komlosh, M. E.; Callaghan, P. T. *J. Chem. Phys.* **1998**, *109*, 10053−10067.
(22) Klein, P. G.; Adams, C. H.; Brereton, M. G.; Ries, M. E.; Nicholson, T. M.; Hutchings, L. R.; Richards, R. W. *Macromolecules* **1998**, *31*, 8871−8877.
(23) Chernov, V. M.; Krasnopol'skii, G. S. *J. Exp. Theor. Phys.* **2008**, *107*, 320−312.
(24) Kimmich, R.; N. Fatkullin, N. *Adv. Polym. Sci.* **2004**, *170*, 1−113.
(25) Kruk, D.; Herrmann, A.; Rössler, E. A. *Prog. Nucl. Magn. Reson. Spectrosc.* **2011**, DOI: 10.1016/j.pnmrs.2011.08.001.
(26) Kimmich, R.; Anoardo, E. *Prog. Nucl. Magn. Reson. Spectrosc.* **2004**, *44*, 257−320.
(27) Kariyo, S.; Gainaru, C.; Schick, H.; Brodin, A.; Novikov, V. N.; Rössler, E. A. *Phys. Rev. Lett.* **2006**, *97*, 207803. Erratum: Kariyo, S.; Herrmann, A.; Gainaru, C.; Schick, H.; Brodin, A.; Novikov, V. N.; Rössler, E. A. *Phys. Rev. Lett.* **2008**, *100*, 109901.
(28) Kariyo, S.; Brodin, A.; Gainaru, C.; Herrmann, A.; Schick, H.; Novikov, V. N.; Rössler, E. A. *Macromolecules* **2008**, *41*, 5313−5321.
(29) Kariyo, S.; Brodin, A.; Gainaru, C.; Herrmann, A.; Hintermeyer, J.; Schick, H.; Novikov, V. N.; Rössler, E. A. *Macromolecules* **2008**, *41*, 5322−5332.
(30) Herrmann, A.; Novikov, V. N.; Rössler, E. A. *Macromolecules* **2009**, *42*, 2063−2068.
(31) Herrmann, A.; Kariyo, S.; Abou Elfadl, A.; Meier, R.; Gmeiner, J.; Novikov, V. N.; Rössler, E. A. *Macromolecules* **2009**, *42*, 5236−5243.
(32) Strobl, G. *The Physics of Polymers*; Springer: Berlin, 1996.
(33) Vaca Chávez, F.; Saalwächter, K. *Phys. Rev. Lett.* **2010**, *104*, 198305.
(34) Vaca Chávez, F.; Saalwächter, K. *Macromolecules* **2011**, *44*, 1549−1559.
(35) Vega, J. F.; Rastogi, S.; Peters, G. W. M.; Meijer, H. E. H. *J. Rheol.* **2004**, *48*, 663−678.
(36) Abdel-Goad, M.; Pyckhout-Hintzen, W.; Kahle, S.; Allgaier, J.; Richter, D.; Fetters, L. J. *Macromolecules* **2004**, *37*, 8135−8144.
(37) Kreer, T.; Baschnagel, J.; Müller, M.; Binder, K. *Macromolecules* **2001**, *34*, 1105−1117.
(38) Paul, W. *Chem. Phys.* **2002**, *284*, 59−66.
(39) Noack, F. *Prog. NMR Spectrosc.* **1986**, *18*, 171−276.
(40) Kresse, B.; Privalov, A. F.; Fujara, F. *Solid State Nucl. Magn. Reson.* **2011**, *40*, 134−137.
(41) Ball, R. C.; Callaghan, P. T.; Samulski, E. T. *J. Chem. Phys.* **1997**, *106*, 7252−7361.
(42) Abragam, A. *The Principles of Nuclear Magnetism*; Clarendon Press: Oxford, 1961.
(43) Kehr, M.; Fatkullin, N.; Kimmich, R. *J. Chem. Phys.* **2007**, *126*, 094903-1−094903-8.
(44) Kehr, M.; Fatkullin, N.; Kimmich, R. *J. Chem. Phys.* **2007**, *127*, 084911-1−084911-7.
(45) Solomon, I.; Bloembergen, N. *J. Chem. Phys.* **1956**, *25*, 261−266.
(46) Slichter, C. P. *Principles of Magnetic Resonance*; Springer: Berlin, 1990.
(47) Bloembergen, N.; Purcell, E. M.; Pound, R. V. *Phys. Rev.* **1948**, *73*, 679−715.
(48) Guillermo, A.; Dupeyre, R.; Cohen-Addad, J. P. *Macromolecules* **1990**, *23*, 1291−1297.
(49) Ferry, J. D. *Viscoelastic Properties of Polymers*; J. Wiley: New York, 1980.
(50) Rubinstein, M.; Colby, R. H. *Polymer Physics*; Oxford University Press: Oxford, 2003.
(51) Colby, R. H.; Fetters, L. J.; Graessley, W. W. *Macromolecules* **1987**, *20*, 2226−2237.
(52) Kruk, D. *Theory of Evolution and Relaxation of Multi-Spin Systems*; Arima: Bury St. Edmunds, 2007.
(53) Kruk, D.; Kowalewski, J. *J. Magn. Reson.* **2003**, *162*, 229−240.
(54) Kruk, D.; Fujara, F.; Gumann, P.; Medycki, W.; Tacke, Ch. *Solid State Nucl. Magn. Reson.* **2009**, *35*, 152−163.
(55) Redfield, A. G. In *Encyclopedia of Nuclear Magnetic Resonance*; Grant, D. M., Harris, R. K., Eds.; Wiley: Chichester, 1996; p 4085.
(56) Freed, J. H. In *Spin Labeling Theory and Applications*, 53rd ed.; Berliner, L. J., Ed.; Academic Press: New York, 1976.
(57) Kruk, D.; Nilsson, T.; Kowalewski, J. *Phys. Chem. Chem. Phys.* **2001**, *3*, 4907−4917.
(58) Lips, O.; Privalov, A.; Dvinskikh, S.; Fujara, F. *J. Magn. Reson.* **2001**, *149*, 22−28.
(59) Filon, L. N. G. *Proc. R. Soc. Edinburgh* **1929**, *49*, 38−47.
(60) Palade, L.; Verney, V.; Attané, P. *Rheol. Acta* **1996**, *35*, 265−273.
(61) Vaca Chávez, F.; Saalwächter, K. *Macromolecules* **2011**, *44*, 1560−1569.
(62) Kimmich, R.; Fatkullin, N.; Seitter, R-.O.; Gille, K. *J. Chem. Phys.* **1998**, *108*, 2173−2177.
(63) Cohen Addad, J. P. *Prog. NMR Spectrosc.* **1993**, *25*, 1−316.
(64) Meyer, H. Private communication.
(65) Kremer, K. *Macromolecules* **1983**, *16*, 1632−1638.
(66) Kremer, K.; Grest, G. S.; Carmesin, I. *Phys. Rev. Lett.* **1988**, *61*, 566−569.
(67) Zamponi, M.; Monkenbusch, M.; Willner, L.; Wischnewski, A.; Farago, B.; Richter, D. *Europhys. Lett.* **2005**, *72*, 1039−1044.
(68) Glomann, T.; Schneider, G. J.; Brás, A. R.; Pyckhout-Hintzen, W.; Wischnewski, A.; Zorn, R.; Allgaier, J.; Richter, D. *Macromolecules* **2011**, *44*, 7430−7437.
(69) Fetters, L. J.; Lohse, D. J.; Milner, S. T.; Graessley, W. W. *Macromolecules* **1999**, *32*, 6847−6851.

Macromolecules

Article

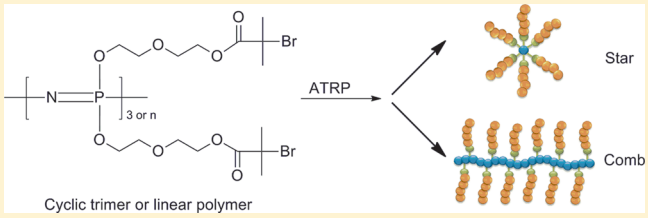
pubs.acs.org/Macromolecules

Synthesis and Characterization of Brush-Shaped Hybrid Inorganic/Organic Polymers Based on Polyphosphazenes

Xiao Liu, Zhicheng Tian, Chen Chen, and Harry R. Allcock*

Department of Chemistry, The Pennsylvania State University, University Park, Pennsylvania 16802, United States

ABSTRACT: A series of densely grafted star- and comb-shaped molecular brushes composed of polystyrene, poly(*tert*-butyl acrylate), and poly(*N*-isopropylacrylamide) were prepared by atom transfer radical polymerization (ATRP) using either cyclotriphosphazenes or polyphosphazenes as initiators. The initiators were prepared by the introduction of a free hydroxyl group into the side chains of a phosphazene cyclic trimer and polymer, followed by esterification with 2-bromopropionyl bromide. The grafting conditions were optimized for various monomers. The kinetics of the reaction were first-order with respect to the monomer concentration in both cyclotriphosphazene and polyphosphazene systems. The molecular weights of the resulting polymers were estimated by gel permeation chromatography (GPC). The side chains of the brush polymers were cleaved from the backbone and analyzed by GPC to confirm the synthesis of well-defined polymer brushes. Brushes based on poly(*tert*-butyl acrylate) were subjected to hydrolysis to yield negatively charged brushes. In addition, the lower critical solution temperature (LCST) of poly(*N*-isopropylacrylamide) brush polymers was measured by both dynamic light scattering (DLS) and differential scanning calorimetry (DSC), exhibiting a sharp phase transition at 33 °C. Furthermore, star- and comb-block copolymers with a hard polystyrene core and a soft poly(*tert*-butyl acrylate) shell were also synthesized.



INTRODUCTION

Molecular brushes consisting of multiple polymer chains grafted onto a linear polymer are among the most intriguing macromolecular structures because they have unique chemical and physical properties.[1−3] Because of competing forces between the backbone and side chains, brush polymers usually adopt a cylindrical conformation. The densely grafted side chains repel each other, but their ability to move apart is hindered by the backbone, which confines the side chains to a cylindrical volume.[4] This leads to numerous distinctive properties of molecular brushes. The most important attribute of molecular brushes is their molecular segregation. For example, unlike linear polymers, the reversible conformational changes in response to external stimuli can be limited to the single molecule identified by atomic force microscopy.[5,6] In addition, steric repulsion between the side chains generates significant mechanical tension in the backbone which can be tuned by varying the grafting density, solvent quality, and the side chain length.[7,8] Furthermore, a stable unimolecular micelle of cylindrical shape formed from amphiphilic molecular brush copolymers cannot dissociate in aqueous solution, which is one of the major disadvantages associated with polymer micelles formed from amphiphilic linear polymers.[9,10]

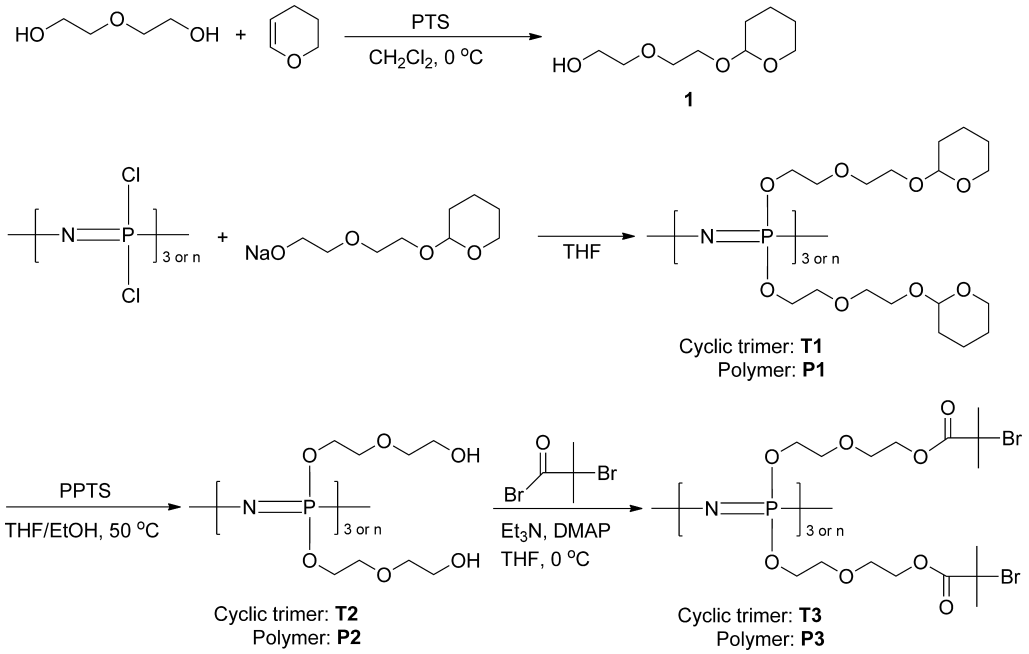
Because of their nonspherical macromolecular geometries and lengths up to a few hundred nanometers, brush polymers have afforded numerous potential applications in nanoscience, such as molecular actuators,[11] templates for inorganic particles,[9] and as precursors for nanocapsules,[12] nanotubes,[13] and other carbon nanostructures.[14] Another prominent application of molecular brushes is in the biological field, due to the similar molecular structures of their natural counterparts known as proteoglycans,[15,16] which are brushlike polyelectrolytes that consist of a protein backbone with carbohydrate side chains. Proteoglycans are found in a variety of places within the body and perform multiple biological functions such as cell signaling and cell surface protection,[17] shock absorption, lubrication,[18,19] and lung clearance.[20] Therefore, molecular brushes have been widely studied as synthetic counterparts for natural proteoglycans in order to better understand the architecture−property relationships, which could potentially lead to advances in biomedical applications.

However, even though a considerable number of molecular brushes have been synthesized and studied, most of these brush polymers are built up from backbones based on carbon−carbon polymers, such as poly(styrene),[21] poly(methacrylate) derivatives,[22,23] polynorbornenes,[24] and poly(thiophene).[25,26] A further study of molecular brushes based on novel polymer backbones offers the opportunity to extend this field in novel ways. The construction of molecular brushes based on non-carbon backbones provides a means to elucidate the effect of the backbone on molecular conformation as well as the resulting chemical and physical properties. Also, the lack of biodegradability of most molecular brushlike materials limits their applications in biological areas, some of which require degradation after fulfilling a function in the human body and allowing renal excretion of the small molecule products.[27] The lengths of molecular brushes are usually up to hundreds of nanometers,[9,11] which is too large for direct renal excretion,

Received: November 28, 2011
Revised: January 5, 2012
Published: January 18, 2012

 © 2012 American Chemical Society dx.doi.org/10.1021/ma202587z | *Macromolecules* 2012, 45, 1417−1426

Scheme 1. Synthesis of Macroinitiators T3 and P3



since it has been shown that only linear polymers with molecular weights below 40 kDa, or ~5 nm in diameter, are cleared readily through the renal system.[27] A possible solution to this specific problem is to design the backbone of molecular brush polymers to be biodegradable to release short side chain products, which are small enough to allow kidney-based excretion.

Polyphosphazenes provide a way to construct molecular brushes with a hydrolytically degradable backbone. Polyphosphazenes are hybrid organic−inorganic polymers that contain a flexible phosphorus−nitrogen backbone with various side groups, such as organic,[16,28] organometallic,[29] or inorganic units.[30] Thus, polyphosphazenes potentially offer advantages over other polymers for biomedical applications since the side groups can be changed easily by macromolecular substitution methods to target specific combinations of properties. In addition, polyphosphazenes can be designed to be hydrolyzable, in a way that liberates the side groups and converts the backbone to a pH-buffered mixture of phosphate and ammonia which can neutralize the acid degradation products from polyester segments.[31,32] The side groups can be selected to be biocompatible, the phosphate may be metabolized, and the ammonia, which is innocuous at low concentrations, can be excreted.[31,32]

The preparation of some molecular brushes based on polyphosphazenes with organic polymer grafts has been reported in earlier publications.[29,33] There are three main strategies for preparing such species. These are "grafting through" (the polymerization of macromonomers),[34,35] "grafting onto" (the addition of previously prepared side chains to a backbone),[36,37] and "grafting from" (the polymerization of side chains from a macroinitiator backbone).[29,33,38] By far, the largest effort to construct brushlike polyphosphazenes has been reported by Gleria and co-workers using the "grafting from" technique.[29,39,40] Their strategy was to use a poly(organophosphazene) with organic side groups that would generate free radical sites when treated with peroxides or when exposed to high-energy radiation. These radical sites then served as initiation species for the free radical polymerization of vinyl-type monomers. However, one of the major drawbacks of this classical free radical polymerization process is the difficulty of controlling different structural parameters, including chemical composition, grafting density, degree of polymerization of side chains, and sequential grafting of second segments. In addition, a high concentration of radical species during free radical polymerization may cause intramolecular termination resulting in pendant macrocyles and even forming intermolecular coupling and macroscopic gelation.[41]

Controlled/living radical polymerization (CRP), especially atom transfer radical polymerization (ATRP), is a versatile route for the synthesis of well-defined polymers with predetermined molecular weights, narrow molecular weight distributions, various architectures, and useful end-functionalities.[9,10,23,41] Thus, ATRP has been widely used for complete control/design of the molecular architecture of brushes, producing unique and novel molecules.[4,10,22] More importantly, ATRP can maintain a low instantaneous concentration of radical species which necessarily limits termination events and avoids macroscopic gelation from intermolecular coupling. In fact, several researchers have explored the filed of synthesis of hybrid materials based on polyphosphazenes by the ATRP technique.[42−44]

In this study, we report the preparation of nonlinear brushes with six-armed star architecture and comb structures through ATRP by using the starlike cyclotriphosphazene or a linear macroinitiator based on a polyphosphazene, with subsequent grafting-from various monomers as shown in Scheme 1. A series of six-armed star and comb brush polymers were synthesized, and their compositions were analyzed. Confirmation of the functionality of the resultant polymers has also been demonstrated. Star- and comb-block copolymers from multifunctional polymeric macroinitiators were also synthesized.

■ EXPERIMENTAL SECTION

Materials. All reactions were carried out under a dry argon atmosphere using standard Schlenk line techniques. Tetrahydrofuran (EMD) and triethylamine (EMD) were dried using solvent

dx.doi.org/10.1021/ma202587z | Macromolecules 2012, 45, 1417−1426

purification columns.[45] 3,4-Dihydro-2*H*-pyran (Acros), diethylene glycol (Sigma), *p*-toluenesulfonic acid monohydrate (Alfa Aesar), pyridinium *p*-toluenesulfonate (PPTS) (Aldrich), sodium hydride (Aldrich), 2-bromopropionyl bromide (Sigma), pentamethyldiethylenetriamine (PMDETA) (TCI), and copper(I) bromide (Sigma) were used as received. Styrene (Aldrich) and *tert*-butyl methacrylate (Aldrich) were stirred over calcium hydride for 2 days and distilled under vacuum. The distillates were stored at −54 °C before use. *N*-Isopropylacrylamide was purified by recrystallization from hexane to remove the inhibitor and dried under vacuum. Tris[2-(dimethylamino)ethyl]amine (Me_6-TREN) was synthesized according to a literature procedure.[46] Hexachlorocyclotriphosphazene (HCCTP) (Fushimi Pharmaceutical Co., Japan, or a Ningbo Chemical, China) was purified by recrystallization from hexanes and vacuum sublimation at 50 °C. Poly(dichlorophosphazene) was prepared by the thermal ring-opening polymerization of recrystallized and sublimed hexachlorocyclotriphosphazene in evacuated Pyrex tubes at 250 °C.[47]

Equipment. ^{1}H and ^{31}P NMR spectra were obtained using a Bruker AMX-360 NMR spectrometer, operated at 360 and 146 MHz, respectively. ^{1}H NMR spectra were referenced to tetramethylsilane signals while ^{31}P NMR chemical shifts were referenced to 85% phosphoric acid as an external reference, with positive shift values downfield from the reference. All chemical shifts are reported in ppm. Molecular weight distribution data were obtained using a Hewlett-Packard HP 1090 gel permeation chromatograph equipped with two Phenomenex Phenogel linaer 10 columns and a Hewlett-Packard 1047A refractive index detector. The samples were eluted at 1.0 mL/min with a 10 mM solution of tetra-*n*-butylammonium nitrate in THF. The elution times were calibrated with polystyrene standards.

Synthesis of Macroinitiators. *2-[2-(Tetrahydropyranyloxy)-ethoxy]ethanol (**1**).* At −10 °C, 3,4-dihydro-2*H*-pyran (21.3 g, 0.23 mol) was added over a period of 45 min to a mixture of 46 mg of *p*-toluenesulfonic acid (PTS) in 180 mL (1.89 mol) of diethylene glycol. The reaction mixture was stirred for 1 h at −10 °C and then for 2 h at room temperature. The mixture was poured into 500 mL of 1 M $NaOH_{(aq)}$ and extracted with dichloromethane (5 × 200 mL). The combined organic layers were dried over $MgSO_4$ and concentrated under vacuum. The crude product was distilled at reduced pressure. The colorless liquid product was obtained with yield of 30.7 g (70.0%). ^{1}H NMR ($CDCl_3$), δ: 4.55 (t, OC*H*O, 1 H, J = 3.54 Hz), 3.80−3.43 (m, OCH_2, 10 H), 1.72−1.44 (m, CH_2, 6 H).

*Hexakis[2-[2-(tetrahydropyranyloxy)ethoxy]ethoxy]-cyclotriphosphazene (**T1**).* A THF solution (50 mL) of hexachlorocyclotriphosphazene (2.0 g, 5.75 mmol) was added dropwise to a THF (50 mL) suspension of the sodium salt of **1**, prepared from 2-[2-(tetrahydropyranyloxy)ethoxy]ethanol (7.66 g, 40.3 mmol) and sodium hydride (1.73 g, 43.1 mmol). The solution was stirred for 48 h at reflux. THF was removed by rotary evaporation, and the mixture was redissolved in dichloromethane. The mixture was transferred to a separatory funnel and extracted consecutively with deionized water (100 mL × 3), $NaHCO_{3(aq)}$ (100 mL × 3), and deionized water (100 mL × 3). The organic phase was dried over $MgSO_4$ overnight then filtered, and the solvent was removed by rotary evaporation. The crude product was purified by silica column chromatography with an eluent of hexane/ethyl acetate (4:6). After evaporation of the eluent, a colorless oil was obtained with a yield of 6.2 g (84.9%). ^{1}H NMR ($CDCl_3$), δ: 4.60 (t, OC*H*O, 1 H, J = 3.44 Hz), 4.05−3.50 (m, OCH_2, 10 H), 1.83−1.51 (m, CH_2, 6 H). ^{31}P NMR ($CDCl_3$), δ: 18.5 (s).

*Hexakis[2-(2-hydroxyethoxy)ethoxy]cyclotriphosphazene (**T2**).* Hexakis[2-[2-(tetrahydropyranyloxy)ethoxy]ethoxy]cyclotriphosphazene (**T1**) (1 g, 0.79 mmol) was first dissolved in dichloromethane (5 mL), and a solution of pyridinium-*p*-toluenesulfonate (PPTS) (0.06 g, 0.24 mmol) in absolute ethanol (50 mL) was added slowly. The solution was heated at 50 °C for 1 day. The ethanol was removed by rotary evaporation and redissolved in deionized water. The crude product was purified by means of a LH 20 column. Yield: 0.2 g, 33.1%. ^{1}H NMR (D_2O), δ: 4.17 (t, POCH_2CH_2O, 2 H, J = 4.43), 3.80−3.66 (m, OCH_2, 6 H). ^{31}P NMR (D_2O), δ: 18.4 (s).

*Hexakis[2-[2-(2-bromoisobutyryloxy)ethoxy]ethoxy]-cyclotriphosphazene (**T3**).* Hexakis[2-(2-hydroxyethoxy)ethoxy]-cyclotriphosphazene (**T2**) (1 g, 1.30 mmol) was placed in a 100 mL Schlenk flask with THF (50 mL), triethylamine (1.2 g, 11.8 mmol), and 4-(dimethylamino)pyridine (DMAP) (0.48 g, 3.90 mmol). A solution of 2-bromopropionyl bromide (2.7 g, 11.8 mmol) in 20 mL of THF was added dropwise to the reaction mixture at 0 °C in an ice bath. The mixture was stirred for 2 days and allowed to warm to room temperature. The solvent was removed by rotary evaporation, and the residue was redissolved in dichloromethane. The mixture was transferred to a 200 mL separatory funnel and extracted consecutively with deionized water (100 mL × 3), $NaHCO_{3(aq)}$ (100 mL × 3), and deionized water (100 mL × 3). The organic phase was dried over $MgSO_4$ and then filtered, and the solvent was removed by rotary evaporation. The crude product was passed through a silica gel column with an eluent of dichloromethane and ethyl acetate (5:3). The solvent was removed, and the resulting light yellow oil was dried under vacuum at room temperature. Yield: 0.41 g (27.0%). ^{1}H NMR ($CDCl_3$), δ: 4.17 (t, POCH_2CH_2O, 2 H), 3.96 (t, CH_2OC(O), 2 H, J = 4.86 Hz) 3.67−3.61 (m, OCH_2, 4 H), 1.85 (s, C(Br)CH_3, 6 H). ^{31}P NMR ($CDCl_3$), δ: 18.4 (s).

*Poly[bis[2-[2-(tetrahydropyranyloxy)ethoxy]ethoxy]-phosphazene] (**P1**).* A THF solution (150 mL) of poly(dichlorophosphazene) (3.0 g, 25.9 mmol) was added to a THF (150 mL) suspension of the sodium salt of **1**, prepared from 2-[2-(tetrahydropyranyloxy)ethoxy]ethanol (12.3 g, 64.7 mmol) and sodium hydride (2.90 g, 72.5 mmol). The reaction solution was stirred for 48 h at reflux. The polymer solution was concentrated by rotary evaporation, and the residue was poured into water to obtain the precipitate of the polymeric product, which was further purified by repeated precipitation three times into water and *n*-hexane. The pure product was dried under vacuum to yield a yellow adhesive solid: 8.7 g (74.5%). ^{1}H NMR ($CDCl_3$), δ: 4.60 (br, s, OC*H*O, 1 H), 4.04−3.49 (m, OCH_2, 10 H), 1.84−1.50 (m, CH_2, 6 H). ^{31}P NMR ($CDCl_3$), δ: −7.85 (s). M_n = 165 200, PDI = 3.8.

*Poly[bis[2-(2-hydroxyethoxy)ethoxy]phosphazene] (**P2**).* Poly[bis-[2-[2-(tetrahydropyranyloxy)ethoxy]ethoxy]phosphazene] (**P1**) (9.61 g, 22.7 mmol) was first dissolved in dichloromethane (50 mL), and absolute ethanol (200 mL) was added slowly with pyridinium *p*-toluenesulfonate (0.57 g, 2.27 mmol). The solution was strired at 50 °C for 3 days. The polymeric product was purified by dialysis against methanol for 4 days. An adhesive yellow product was obtained with yield of 4.86 g (50.2%). ^{1}H NMR (D_2O), δ: 4.19 (br, s, POCH_2CH_2O, 2 H), 3.78−3.66 (m, OCH_2, 6 H). ^{31}P NMR (D_2O), δ: −5.65 (s).

*Poly[bis[2-[2-(2-bromoisobutyryloxy)ethoxy]ethoxy]-phosphazene] (**P3**).* Poly[bis[2-(2-hydroxyethoxy)ethoxy]phosphazene] (**P2**) (4.86 g, 19 mmol) was placed into a 100 mL Schlenk flask with DMF (30 mL), triethylamine (5.78 g, 57.1 mmol), and 4-(dimethylamino)pyridine (2.32 g, 19.0 mmol). A solution of 2-bromopropionyl bromide (13.1 g, 57.1 mmol) in 10 mL of DMF was added dropwise to the reaction mixture at 0 °C in an ice bath. The reaction mixture was stirred overnight and allowed to warm to room temperature. The solvent was removed by rotary evaporation, and the residue was redissolved in methanol and dialyzed against methanol for 3 days to remove the impurities. The solvent was removed, and the resulting adhesive yellow product was dried under vacuum at room temperature. Yield: 7.46 g (71.0%). ^{1}H NMR ($CDCl_3$), δ: 4.17 (br, s, POCH_2CH_2O, 2 H), 4.06 (br, s, CH_2OC(O), 2 H) 3.74−3.67 (m, OCH_2, 4 H), 1.92 (s, C(Br)CH_3, 6 H). ^{31}P NMR ($CDCl_3$), δ: −7.80 (s). M_n = 88 500, PDI = 2.06.

Polymerization. A typical polymerization was as follows: Polymeric macroinitiator **P3** (0.216 g, 0.78 mmol initiator centers), *tert*-butyl acrylate (20 g, 0.156 mol), and pentamethyldiethylenetriamine (PMDETA) (0.135 g, 0.78 mmol) were placed in a 50 mL Schlenk flask and sparged with nitrogen for 30 min. Anisole (0.5 mL) was used as an internal standard. Afterward, deoxygenated copper(I) bromide (0.056 g, 0.39 mmol) and copper(II) bromide (4.4 mg, 0.02 mmol) were added. Approximately 0.2 mL of solution was removed, and the nitrogen-filled flask was heated at 90 °C under nitrogen. Periodically, additional 0.2 mL aliquots were removed to analyze the

dx.doi.org/10.1021/ma202587z | *Macromolecules* 2012, 45, 1417−1426

conversion and molecular weight by ^{1}H NMR and GPC. The polymerization was terminated after 34.5 h at conversion 19.9% and was quenched by liquid nitrogen. The reaction mixture was then dissolved in dichloromethane and passed through a short alumina column to remove the copper catalyst. The polymer was purified by precipitation into cold methanol/water (4:1). Yield: 1.73 g (15.5%) of isolated polymer. The polymerization conditions of all other monomers are listed in Table 1.

Table 1. Characterization Data for Initiators

entry	^{31}P NMR (ppm)	M_n	PDI	RU
T1	18.5	765.6		
T2	18.4	1270.3		
T3	18.4	1659.5		
P1	−7.8	165200	3.8	390
P2	−5.6	*a*		
P3	−7.8	88500	2.06	177

[a]**P2** did not dissolve in THF.

Star- and Comb-Polystyrene-block-poly(tert-butyl acrylate) (sPS-b-PtBuA and cPS-b-PtBuA). A typical polymerization procedure is as follows: star-polystyrene (sPS) (0.2 g, 0.066 mmol initiator centers), *tert*-butyl acrylate (5.93 g, 46.3 mmol), and PMDETA (0.023 g, 0.132 mmol) were placed into a 20 mL Schlenk flask and sparged with nitrogen for 30 min. Deoxygenated copper(I) bromide (9 mg, 0.066 mmol) and copper(II) bromide (0.74 mg, 0.0033 mmol) were then added. The flask was heated at 90 °C under nitrogen. The polymerization was terminated after 24 h at a conversion of 61.6% and was quenched by liquid nitrogen. The reaction mixture was dissolved in dichloromethane and was passed through a short alumina column to remove the copper catalyst. The polymer was purified by precipitation into cold methanol/water (4:1) Yield: 2.5 g of isolated polymer.

Solvolysis of Brush Polymers. The side chains of star-poly(*tert*-butyl acrylate) (sPtBuA) and comb-poly(*tert*-butyl acrylate) (cPtBuA) were cleaved in the similar manner. Typically, 0.1 g of polymer (sPtBuA or cPtBuA) was dissolved in 5 mL of THF in a 50 mL Schlenk flask. *n*-Butanol (18 mL) was added. After the addition of 8 drops of concentrated sulfuric acid, the mixture was heated to 90 °C for 19 days. The solvent was removed under vacuum, and the remaining polymer was dissolved in dichloromethane and precipitated into cold methanol/water (4:1). The resultant polymer was dried under vacuum and analyzed by GPC.

The side chains of star-polystyrene (sPS) and comb-polystyrene (cPS) were cleaved in the similar manner. In a typical reaction, 0.1 g of polymer (sPS or cPS) was dissolved in 20 mL of THF in a 50 mL Schlenk flask, followed by the addition of 5 mL of 1 M KOH ethanol solution. The mixture was heated to 90 °C for 12 days. The solvent was removed by rotary evaporation. The crude product was redissolved in dichloromethane, extracted with deionized water, and dried over $MgSO_4$. After precipitation in methanol, the resultant polymer was analyzed by GPC.

Deprotection of Star-Poly(tert-butyl acrylate) (sPtBuA) and Comb-Poly(tert-butyl acrylate) (cPtBuA). Star-poly(acrylic acid) (sPAA) and comb-poly(acrylic acid) (cPAA) were prepared by hydrolysis of the *tert*-butyl esters of sPtBuA and cPtBuA following a literature method.[48] A typical procedure is as follows: sPtBuA (0.2 g) and iodotrimethylsilane (0.62 g, 3.12 mmol) were allowed to react in 15 mL dry dichloromethane under nitrogen for 1 day. The volatiles were then evaporated. After redissolving the mixture in methanol, the crude product was dialyzed against methanol for 2 days. The solvent was removed by rotary evaporation and dried at room temperature under vacuum overnight. Yield: 0.06 g.

Determination of Lower Critical Solution Temperature of Comb-Poly(N-isopropylacrylamide) (cPNPA). The lower critical solution temperature (LCST) of comb-poly(*N*-isopropylarylamide) (cPNPA) was evaluated by dynamic light scattering (DLS) using a particle size analyzer (Zetasizer Nano S, Malvern Instruments Ltd.) with a scattering angle of 90° and a thermostatically controlled cell having a heating rate of 1 °C min^{-1}. Aqueous samples with a concentration of 2 mg/mL were filtered through a 0.45 μm syringe filter before measurement of particle size for each sample. Also, the LCST was determined by differential scanning calorimetry (DSC) with a TA Instruments Q10 and a heating rate of 10 °C/min and a sample size of ca. 10 mg.

RESULTS AND DISCUSSION

Initiator Syntheses. In this work, the "graft-from" approach was used to construct both star-shaped and comb-shaped brush polymers. For this purpose, initiators **T3** and **P3** were synthesized as illustrated in Scheme 1 using hexachlorocyclotriphosphazene (**T1**) or poly(dichlorophosphazene) (**P1**) as starting materials. As a representative example, the following pathways were involved in the preparation of initiator **P3**. Diethylene glycol was monoprotected by dihydropyran to yield compound **1**. The sodium salt of **1** was allowed to react with poly(dichlorophosphazene) to produce polymer **P1**. The singlet resonance at −7.85 ppm in the ^{31}P NMR spectrum suggested complete chlorine replacement. In the deprotection of the pyranyl moiety, the polymer **P1** solution in THF/ethanol was treated at 50 °C in the presence of pyridinium *p*-toluenesulfonate to yield polymer **P2**. The completion of deprotection was confirmed by the ^{1}H NMR spectrum with the total disappearance of the resonances at 4.60 ppm and between 1.84 and 1.50 ppm, which were due to pyranyl groups.

The macroinitiator **P3** was synthesized by esterification of polymer **P2** with 2-bromopropionyl bromide. The ^{1}H NMR spectrum indicated 100% esterification of hydroxyl groups from the ratio between the methylene group at 4.17 ppm (2H) and the methyl groups at 1.92 ppm (6H). The initiator **T3** was synthesized by a similar approach. Characterization data for the initiators are summarized in Table 1. Both of the initiators were used to induce polymerization of various monomers.

Polymerization. A series of star- and comb-shaped brushes were synthesized by grafting styrene, *tert*-butyl acrylate, and *N*-isopropylacrylamide from the aforementioned initiators (**T3** and **P3**) by controlled atom transfer radical polymerization (ATRP) as illustrated in Scheme 2. Because the initiating groups remain at the ends of the grafted side chains, it was possible to extend the side chains in a well-defined manner.

Synthesis of Star-Shaped Brush Polymers. For each of the monomers studied, conditions were developed using **T3** as an initiator, which provided linear first-order kinetic plots typical of a controlled living polymerization (Table 2). Figure 1a shows the linear relationships of $\ln([M]_0/[M])$ vs time for these three monomers. This means that the concentration of growing radicals is constant during the polymerization in all systems, confirming the first-order in monomer concentration kinetics. However, the molecular weight vs time plot shown in Figure 1b illustrates marked deviations from the theoretical value calculated from the conversion of monomer in Table 2, which is approximately twice as high as the molecular weight measured by GPC (Table 2). For a controlled living polymerization the observed molecular weight should coincide with the theoretical value. The deviation of molecular weight from the theoretical value may be due to the highly compact nature of the polymers, which results in lower hydrodynamic volumes of star brush polymers and does not correspond well to the linear standards.[49]

During optimization of the ATRP of *tert*-butyl acrylate at 90 °C, cross-linking occurred when using higher concentrations of catalyst relative to initiator or lower monomer-to-initiator

dx.doi.org/10.1021/ma202587z | *Macromolecules* 2012, 45, 1417−1426

Scheme 2. Graft of Different Monomers from Initiators T3 and P3

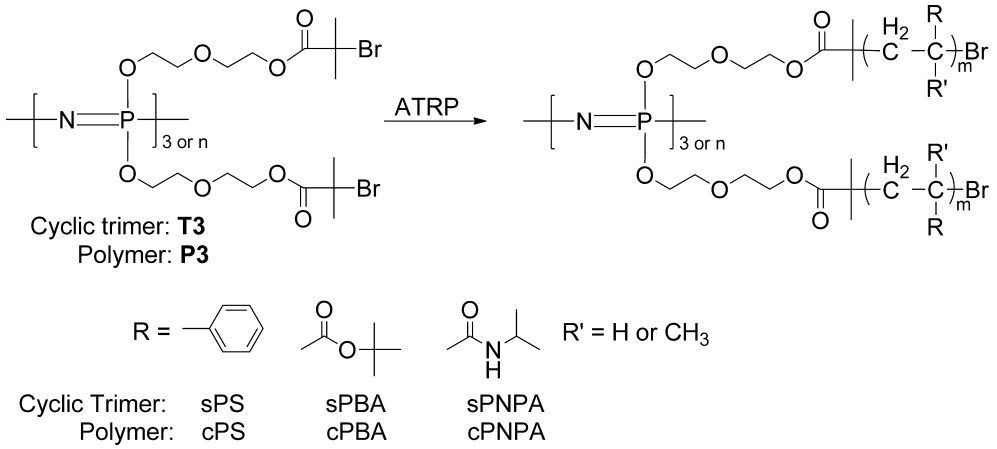


Table 2. Reaction Conditions for Grafting of Different Monomers from Initiator T3 and P3

						M_n (PDI)		
entry	M	[M]:[I]:[CuBr]:[$CuBr_2$]:[ligand]	temp (°C)	time (h)	conv (%)	GPC[a]	conv[b]	cleavage[c]
sPS	Sty	1200:1:3:0.15:6	105	31.5	38.3	27 600 (1.22)	49 200	19 700
sPBA	BA	1200:1:3:0.15:6	90	13.5	61.7	45 700 (1.10)	96 600	53 000
sPNPA	NPA	1200:1:3:0.15:6	55	25	15.4	20 400 (1.35)	22 800	
cPS	Sty	400:1:2:0.1:1	105	40	22.4	200 300 (1.94)	1 903 700	862 100
cPBA	BA	400:1:2:0.2:1	90	34.5	19.9	125 700 (1.38)	1 749 600	2 086 300
cPNPA	NPA	400:1:2:0.1:1[d]	50	96	5.2	173 900 (1.79)	1 349 000	

[a]Measured by GPC calibrated by linear polystyrene standards. [b]Calculated from conversion measured by NMR. [c]Calculated from cleaved side chains. [d]Reaction was conducted in methanol/DMF (10 mL/7 mL), and the ligand is Me_6TREN.

ratios. Even when the ratio of monomer-to-initiator increased to 150 to 1, cross-linking was still detected. One consequence of using radical polymerization to grow the side chains from the backbone is that radical−radical coupling must be significantly suppressed. When the concentration of the active species is too high, radical coupling resulted in aggregates of stars, the appearance of a high molecular weight shoulder on the GPC traces, and ultimately cross-linking.[50,51] The results showed that cross-linking can be significantly suppressed when the monomer-to-initiator ratio is increased to 200 to 1.

The temperature should also be carefully controlled in order to obtain well-defined molecular structures. For example, it has been reported that, in some cases, ATRP of *N*-isopropylacrylamide in grafting reactions when heated or at room temperature may result in gel-like products due to cross-linking.[25] However, no cross-linking was detected in the present reactions either at room temperature or when heated. In contrast, increased temperature (50 °C) is necessary to improve the grafting efficiency of *N*-isopropylacrylamide.

Also, a sufficiently low active species concentration, which is 50 mol % relative to initiator, was used in order to avoid cross-linking and obtain well-defined molecular brushes with monomodal and narrow molecular weight distributions even at high monomer conversions. In addition, the deactivation species $CuBr_2$ (2.5 mol %) was added to avoid its spontaneous formation in situ by radical termination. This established better control by anticipation of the persistent radical effect.[52] Therefore, in every case, the graft polymerization of each monomer was well controlled, and this resulted in the synthesis of polymers with low polydispersity (Figure 1c). The absence of termination reactions from recombination reactions is indicated by the absence of a small shoulder in the high molecular weight portion of the GPC trace for both sPS and sPBA (Figure 2).

Synthesis of Comb-Shaped Brush Polymers. Similarly, comb-shaped brush polymers were synthesized by grafting styrene, *tert*-butyl acrylate, and *N*-isopropylacrylamide from the **P3** macroinitiator as illustrated in Scheme 2. As in the synthesis of the star-shaped brush polymers, Figure 3 shows linear first-order kinetic plots typical of a controlled living polymerization, which indicates conservation of radicals throughout the reaction of each monomer. However, a significant difference in polymerization rate was found when compared with the star-shaped brush system. These differences are apparent from the comparison in Figure 4, especially between the polymerization of styrene and *tert*-butyl acrylate from **T3** and **P3** initiators. In general, the polymerization rate in the comb−brush system is much slower than for the star-brush system. This is probably due to the more sterically hindered conformation of macroinitiator **P3**. Thus, the presence of adjacent polymer chains in comb−brush polymers may hinder polymer chain growth from the beginning. The star−brush system may also suffer from the same problem, but the relatively wide-open core structure will allow a much faster polymerization rate than the comb−brush system. Another specific example to illustrate the steric hindrance effect is the polymerization rate of styrene and *tert*-butyl acrylate in the same system. For example, sPBA has higher polymerization rate than sPS in star−brush reactions in the cyclotrimeric system (**T3**). This is probably due to the difference in reactivity among the different monomers. However, nearly identical polymerization rates of these two monomers were found in the comb−brush system (Figure 4), probably because the reactivity difference between styrene and *tert*-butyl acrylate is dominated by the steric hindrance effect,

dx.doi.org/10.1021/ma202587z | *Macromolecules* 2012, 45, 1417−1426

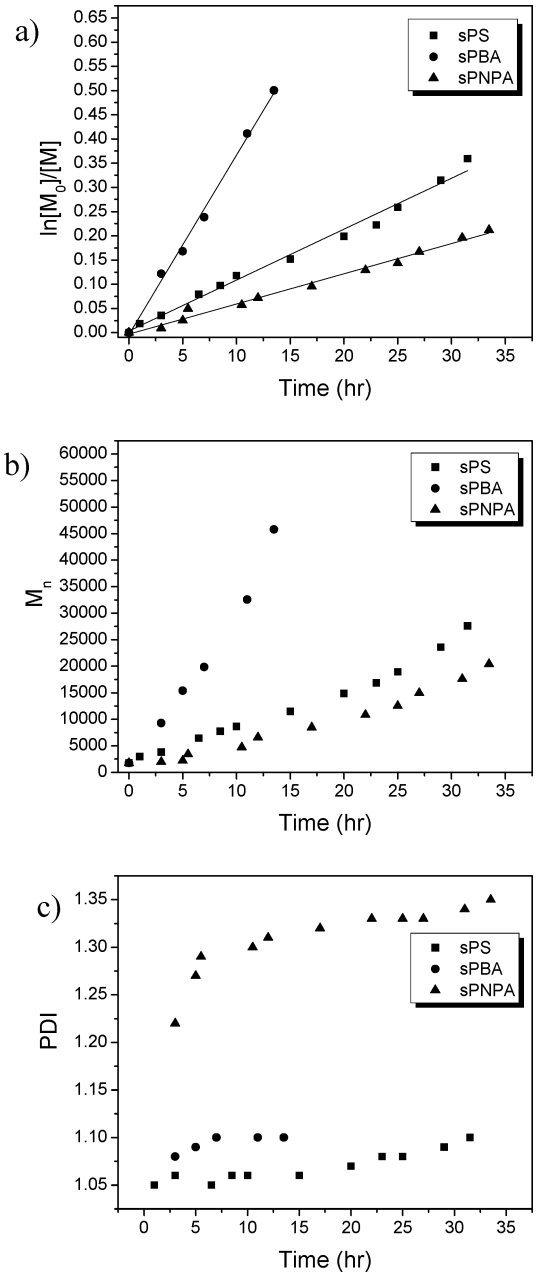


Figure 1. Dependence of (a) $\ln([M]_0/[M])$, (b) M_n, and (c) polydispersity on time in the polymerization of different monomers from **T3**.

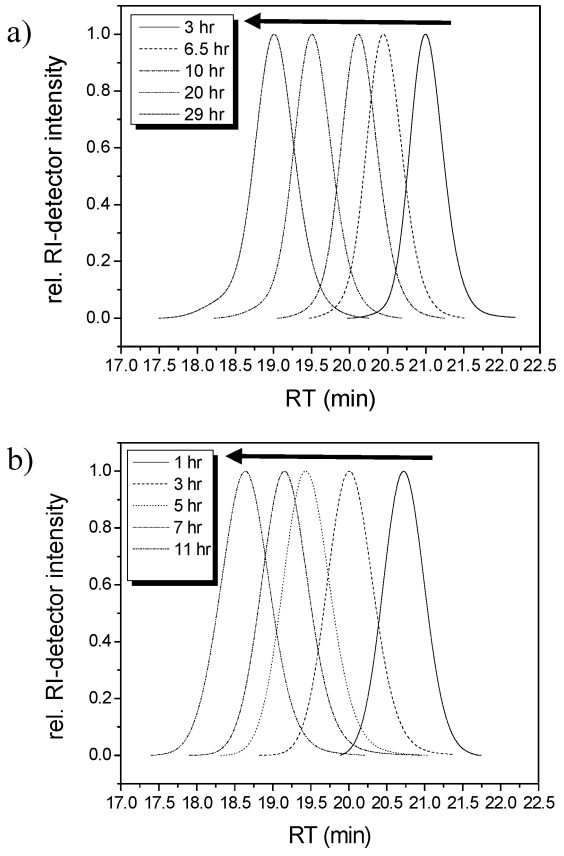


Figure 2. GPC traces of graft polymerization of (a) sPS and (b) sPBA from **T3**.

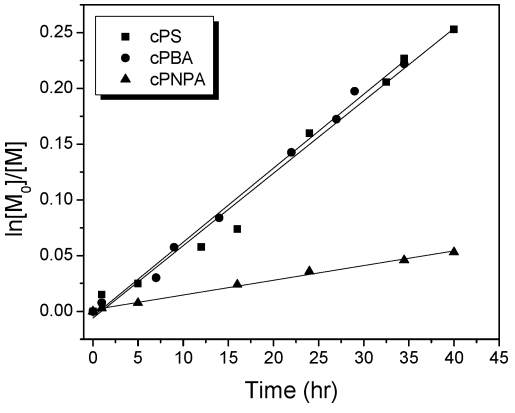


Figure 3. Dependence of $\ln([M]_0/[M])$ on time in the polymerization of different monomers from **P3**.

leading to the similar polymerization rates in the comb−brush system.

No linear increase of molecular weight was detected during the synthesis of comb−brush polymers in contrast to the structure found in the star system. The tendency of molecular weight change throughout the polymerization process is illustrated in Figure 5. During the grafting of *tert*-butyl acrylate from the macroinitiator **P3**, the GPC-derived molecular weight initially appeared to increase from 88 500 to 107 700 but was followed by a dramatic decrease down to 67 900. Later, the molecular weight increased again gradually as the polymerization progressed and reached a final value of 125 700. This abnormal result may be due to the difference in hydrodynamic radii between the macroinitiator **P3** and the resultant cPBA. In the first hour of polymerization, only 0.76% of *tert*-butyl acrylate was grafted onto the backbone of polyphosphazene **P3**. Thus, the molecular weight was still defined by the hydrodynamic radius of the polyphosphazene backbone structure, and an expected increase in molecular weight was detected by GPC. However, as more and more *tert*-butyl acrylate was grafted, the hydrodynamic radius became dominated by brush poly(*tert*-butyl acrylate) units instead of polyphosphazene, and this resulted in the initial significant decrease in measured molecular weight, followed by a gradual increase. Therefore, the actual molecular weight may be higher than the value measured by GPC. In fact, both the molecular weights calculated from conversion and from chain cleavage indicate a remarkably higher value than the one reflected by GPC (Table 2).

dx.doi.org/10.1021/ma202587z | *Macromolecules* 2012, 45, 1417−1426

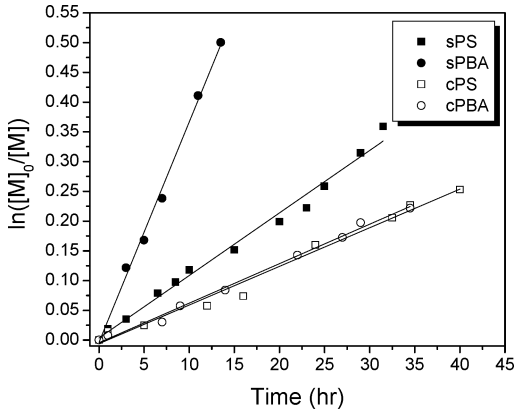


Figure 4. Comparison of dependence of $\ln([M]_0/[M])$ on time in the polymerization of Sty and BA from **T3** and **P3**.

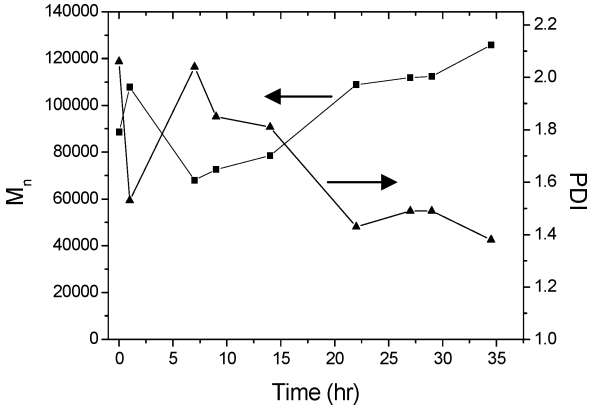


Figure 5. Dependence of M_n and PDI on time in the polymerization of BA from **P3**.

An interesting aspect is that the molecular weights of cPBA increased with polymerization time, while the molecular weight distributions decreased from 2.06 to 1.38. This decrease of the molecular weight distribution may be attributed to the formation of well-defined poly(*tert*-butyl acrylate) side chains by ATRP.[53] It should be pointed out that the molecular weight distribution of **P3** was larger than 2 since the macroinitiators were prepared by thermal ring-opening polymerization, which usually provides no control over molecular weight distribution. In addition, all the GPC traces of the polymer brushes were found to be unimodal without any trace of a shoulder, indicating that almost all the macroinitiators were converted to the corresponding polymer brushes.

Analysis of the Grafted Side Chains. In order to determine the uniformity of the grafted side chains, both the star- and comb-shaped brush polymers were subjected to solvolysis to release the grafted side chains. sPS and cPS were cleaved with potassium hydroxide in THF and ethanol to release the polystyrene side chains. On the other hand, sPBA and cPBA were cleaved using acid-catalyzed transesterfication in *n*-butanol to ensure that the *tert*-butyl ester groups of sPBA and cPBA side chains remained either intact or were replaced with *n*-butyl without formation of free carboxylic acid groups.

The GPC traces of the starting brush cPBA and the hydrolyzed product are given in Figure 6. The peak of the cPBA polymer disappeared after 10 days solvolysis. Instead, a low and a high molecular weight fraction appeared which confirmed the degradation of the polyphosphazene backbone and the release

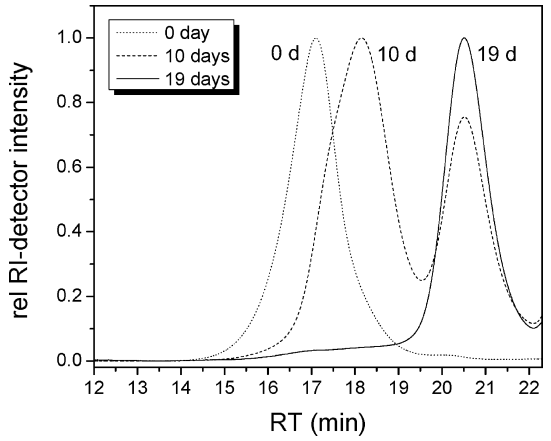


Figure 6. GPC traces of solvolysis of cPBA in *n*-butanol.

of the cleaved side chains, respectively. Complete cleavage required 19 days of reaction. The low molecular weight fraction has a symmetrical GPC trace, the number-average molecular weight is 5600, and the polydispersity is 1.16. Following a similar procedure, the side chains of sPBA, sPS, and cPS brush polymers were cleaved from the polymer backbones, and the low molecular weight fractions were analyzed by GPC. The results are listed in Table 3.

Table 3. GPC Characterization of Cleaved Brush Side Chanis

	star		comb	
	sPS	sPBA	cPS	cPBA
reaction time (days)	12	12	12	19
side chain M_n	3001	8549	2159	5617
PDI	1.16	1.19	1.21	1.16
polymer M_n	19 773	53 061	862 198	2 086 330

No significant tailing of the cleaved side chains from all four brushes was detected by GPC, and the narrow unimodal distribution of the detached poly(*tert*-butyl acrylate) and polystyrene substantiates the well-controlled ATRP reaction of *tert*-butyl acrylate and styrene initiated by **T3** and **P3**. The potential reactions that could lead to a bimodal side chain distribution such as intra- or intermolecular coupling have clearly been effectively suppressed by controlling the amount of catalyst used.

It is interesting to compare the molecular weights calculated based on the cleaved side chains with those detected by GPC (Table 2). For starlike brush polymers, no significant difference of the molecular weights was found by these two methods which is probably due to the relatively less densely grafted polymer side chains on star-shaped initiator **T3** as a consequence of its relatively open conformation. However, a significant difference in molecular weight calculated by these two methods was found for comblike polymers (cPS and cPBA). As mentioned above, the probable reason is that the densely grafted and compact side chains make the hydrodynamic radius much smaller than that of the corresponding linear polymers, so the molecular weights of comblike polymers appear to be lower when compared to the molecular weights calculated from either conversion or from the cleaved side chains.

dx.doi.org/10.1021/ma202587z | *Macromolecules* 2012, 45, 1417–1426

Moreover, no remaining backbone polymer was detected in the GPC traces. This may be because of the low proportion of backbone with respect to side chains or because of degradation of the polyphosphazene backbone into ammonium ion and phosphate.[31,32]

Hydrolysis of sPBA/cPBA. The brushes with PBA side chain were subjected to further functionalization in order to obtain a negatively charged polyelectrolyte.

sPBA and cPBA were treated with trimethylsilyl iodide to deprotect the *tert*-butyl ester group and form a carboxylic acid group.[48,54] These conditions avoid the possible cleavage of grafted side chains under harsh acidic or basic conditions. The reaction was completed within 24 h. The resultant product was 100% deprotected, as determined by ^{1}H NMR with complete disappearance of *tert*-butyl group at 1.4 ppm and was soluble in water but insoluble in tetrahydrofuran and chloroform, which is significantly different from the parent polymers, thus indicating the total cleavage of *tert*-butyl groups from the brush polymers.

Determination of Lower Critical Solution Temperature (LCST) of cPNPA. The lower critical solution temperature (LCST) of cPNPA was examined by both differential scanning calorimetry (DSC) and dynamic light scattering (DLS).

Figure 7a shows the enthalpy of transition of the grafted polymer cPNPA in water using DSC by repeatedly cycling the solution between 20 and 55 °C. An endothermic transition at 32.3 ± 0.3 °C was detected which is assigned to the enthalpy change associated with the breaking/making of hydrogen bonds between poly(isopropylacrylamide) grafts and water.[55] This result is consistent with previous studies of poly(isopropylacrylamide) and confirms that the stimuli-responsive conformational change of cPNPA is reversible and sensitive to temperature variations.

In addition, the LCST and the corresponding molecular conformation transition of polymer cPNPA were also studied by DLS, which shows a change in molecular shape after passing through the LCST at 33 °C. In Figure 7b, the variations of apparent hydrodynamic radius (R_h) and M_w with temperature are summarized. The hydrodynamic radius of brush polymer cPNPA was found to gradually decrease from 26 nm at 20 °C to 21 nm at 32.5 °C, followed by a large increase from 21 to 33 nm within a small temperature interval of 0.5 °C. The first slow decrease of R_h from 26 to 21 nm reflects the shrinkage of the individual brush polymer, where the repulsion of the densely grafted side chains represents the extension force and acts against the entropic contraction force from the phase transition due to increase of temperature. This result is similar to that reported earlier for a different system.[56] Afterward, the significant increase of R_h was detected beyond the LCST of cPNPA up to 34 nm, which indicates the aggregation of grafted copolymer molecules due to the enhanced hydrophobicity of poly(*N*-isopropylacrylamide).

Synthesis of Star- and Comb-Block Copolymers. One of the advantages of the ATRP polymerization is the preservation of chain end functionality, from which diblock or even triblock copolymers can be synthesized in a well-controlled manner.[57] Studies show that star polymers synthesized by ATRP also exhibit conservation of active species. Hence, it is possible to synthesize star-block copolymers by polymerization of another monomer from a preformed polymeric macroinitiator.[58] Therefore, both star- and comb-bush polystyrene polymers sPS and cPS were used as macroinitiators for the copper bromide/PMEDTA-mediated

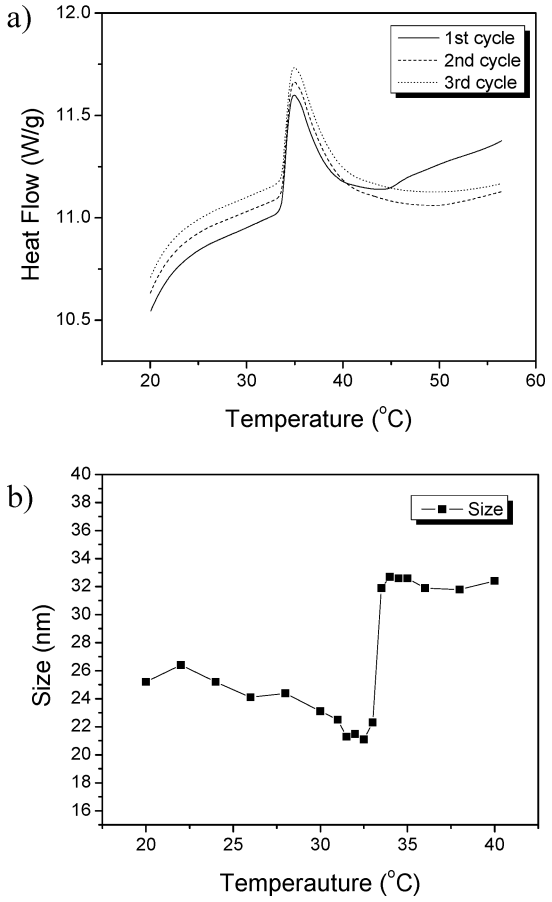


Figure 7. LCST of cPNAP determined by (a) DSC and (b) DLS.

polymerization of *tert*-butyl acrylate. Figure 8 illustrates GPC traces for the polymerizations of the homocopolymers (sPS) and block copolymers (sPS-*b*-PBA). The absence of a high

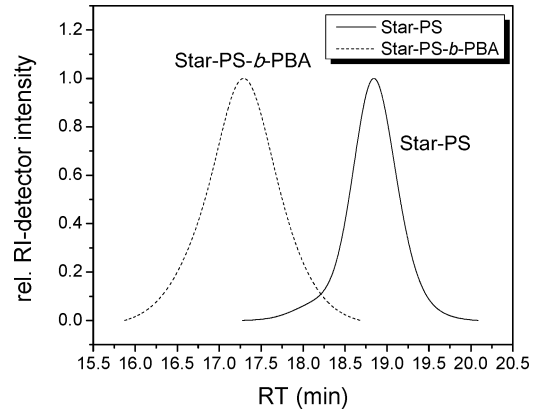


Figure 8. GPC traces of the subsequent synthesis of sPS-*b*-PBA.

molecular weight shoulder indicates no detectable brush-coupling product and a controlled polymerization reaction. The reaction was terminated at 61.6% conversion after 20 h for sPS-*b*-PBA. The GPC chromatograms shifted cleanly to higher molecular weight from 27 600 (M_w/M_n = 1.10) to 107 600 (M_w/M_n = 1.16). Furthermore, block copolymers cPS-*b*-PBA were also synthesized using cPS as a macroinitiator. The characterization data are listed in Table 4 together with sPS-*b*-PBA. Thus, a star- or comb-block copolymer consisting of a hard,

dx.doi.org/10.1021/ma202587z | *Macromolecules* 2012, 45, 1417–1426

Table 4. Molecular Weight and Polydispersity of Block Brush Copolymers

	star		comb	
	sPS	sPS-*b*-PBA	cPS	cPS-*b*-PBA
M_n	27 600	107 600	200 300	435 400
PDI	1.10	1.16	1.94	1.85

high-T_g segment in the core and a soft, low-T_g segment in the shell was confirmed, which is a promising architecture in the design of thermoplastic elastomeric materials.

CONCLUSIONS

A variety of well-defined, densely grafted molecular brushes based on polyphosphazenes were synthesized by ATRP polymerization. Three different monomers—styrene, *tert*-butyl acrylate, and *N*-isopropylacrylamide—have been grafted from cyclotriphosphazene or polyphosphazene initiators to form star- or comb-shaped brush polymers. Both systems follow first-order reaction kinetics during polymerization, exhibiting living polymerization features. The resultant polymers show well-defined structures with controlled molecular weight and low polydispersity. Also, the side chains, when cleaved from the skeleton, have a relatively low polydispersity, $M_w/M_n \leq 1.21$, which demonstrates the controlled nature of the grafting procedure. Positively charged molecular brushes were obtained through hydrolysis of *tert*-butyl groups to provide free carboxylic acid functional groups. Also, the thermal sensitivity of poly(*N*-isopropylacrylamide) brush polymers remains intact and independent of the side chain length. The interesting change of hydrodynamic radius before and after its LCST exhibits the unique properties of single cylindrical brush molecule with stimuli-responsive behavior. Furthermore, the resultant functionalized block brush polymers with a hard polystyrene core and a soft poly(*tert*-butyl acrylate) shell are promising candidates for a variety of applications in thermoplastic elastomeric materials and in the biomedical field, such as drug delivery and tissue engineering.

AUTHOR INFORMATION

Corresponding Author

*E-mail: hra@chem.psu.edu.

REFERENCES

(1) Vanhee, S.; Rulkens, R.; Lehmann, U.; Rosenauer, C.; Schulze, M.; Kohler, W.; Wegner, G. *Macromolecules* **1996**, *29*, 5136−5142.
(2) Khelfallah, N.; Gunari, N.; Fischer, K.; Gkogkas, G.; Hadjichristidis, N.; Schmidt, M. *Macromol. Rapid Commun.* **2005**, *26*, 1693−1697.
(3) Neugebauer, D.; Zhang, Y.; Pakula, T.; Sheiko, S. S.; Matyjaszewski, K. *Macromolecules* **2003**, *36*, 6746−6755.
(4) Sheiko, S. S.; Sumerlin, B. S.; Matyjaszewski, K. *Prog. Polym. Sci.* **2008**, *33*, 759−785.
(5) Sheiko, S. S.; Moeller, M. *Chem. Rev.* **2001**, *101*, 4099−4123.
(6) Sheiko, S. S.; da Silva, M.; Shirvaniants, D.; LaRue, I.; Prokhorova, S.; Moeller, M.; Beers, K.; Matyjaszewski, K. *J. Am. Chem. Soc.* **2003**, *125*, 6725−6728.
(7) Panyukov, S.; Zhulina, E. B.; Sheiko, S. S.; Randall, G. C.; Brock, J.; Rubinstein, M. *J. Phys. Chem. B* **2009**, *113*, 3750−3768.
(8) Park, I.; Sheiko, S. S.; Nese, A.; Matyjaszewski, K. *Macromolecules* **2009**, *42*, 1805−1807.
(9) Djalali, R.; Li, S. Y.; Schmidt, M. *Macromolecules* **2002**, *35*, 4282−4288.
(10) Zhang, M. F.; Breiner, T.; Mori, H.; Muller, A. H. E. *Polymer* **2003**, *44*, 1449−1458.
(11) Li, C. M.; Gunari, N.; Fischer, K.; Janshoff, A.; Schmidt, M. *Angew. Chem., Int. Ed.* **2004**, *43*, 1101−1104.
(12) Cheng, C.; Qi, K.; Khoshdel, E.; Wooley, K. L. *J. Am. Chem. Soc.* **2006**, *128*, 6808−6809.
(13) Huang, K.; Rzayev, J. *J. Am. Chem. Soc.* **2009**, *131*, 6880−6885.
(14) Tang, C.; Dufour, B.; Kowalewski, T.; Matyjaszewski, K. *Macromolecules* **2007**, *40*, 6199−6205.
(15) Iozzo, R. V. *Proteoglycans: Structure, Biology, and Molecular Interactions*; Marcel Dekker: New York, 2000.
(16) Varki, A.; Cummings, R.; Esko, J.; Freeze, H.; Hart, G.; Marth, J. *Essentials of Glycobiology*; Cold Spring Harbor Laboratory Press: Cold Spring Harbor, NY, 1999.
(17) Kaneider, N. C.; Dunzendorfer, S.; Wiedermann, C. J. *Biochemistry* **2004**, *43*, 237−244.
(18) Scott, J. E. *Biochemistry* **1996**, *35*, 8795−8799.
(19) Khalsa, P. S.; Eisenberg, S. R. *J. Biomech.* **1996**, *30*, 589−594.
(20) Bromberg, L. E.; Barr, D. P. *Biomacromolecules* **2000**, *1*, 325−334.
(21) Deffieux, A.; Schappacher, M. *Macromolecules* **1999**, *32*, 1797−1802.
(22) Sumerlin, B. S.; Neugebauer, D.; Matyjaszewski, K. *Macromolecules* **2005**, *38*, 702−708.
(23) Tsarevsky, N. V.; Matyjaszewski, K. *Chem. Rev.* **2007**, *107*, 2270−2299.
(24) Heroguez, V.; Breunig, S.; Gnanou, Y.; Fontanille, M. *Macromolecules* **1996**, *29*, 4459−4464.
(25) Balamurugan, S. S.; Bantchev, G. B.; Yang, Y. M.; McCarley, R. L. *Angew. Chem., Int. Ed.* **2005**, *44*, 4872−4876.
(26) Wang, M. F.; Zou, S.; Guerin, G.; Shen, L.; Deng, K. Q.; Jones, M.; Walker, G. C.; Scholes, G. D.; Winnik, M. A. *Macromolecules* **2008**, *41*, 6993−7002.
(27) Yokoyama, M. *J. Artif. Organs* **2005**, *8*, 77−84.
(28) Allcock, H. R.; Connolly, M. S.; Sisko, J. T.; Alshali, S. *Macromolecules* **1988**, *21*, 323−334.
(29) Gleria, M.; Bolognesi, A.; Porzio, W.; Catellani, M.; Destri, S.; Audisio, G. *Macromolecules* **1987**, *20*, 469−473.
(30) Allcock, H. R.; Nelson, C. J.; Coggio, W. D. *Organometallics* **1991**, *10*, 3819−3825.
(31) Krogman, N. R.; Singh, A.; Nair, L. S.; Laurencin, C. T.; Allcock, H. R. *Biomacromolecules* **2007**, *8*, 1306−1312.
(32) Deng, M.; Nair, L. S.; Nukavarapu, S. P.; Kumbar, S. G.; Jiang, T.; Krogman, N. R.; Singh, A.; Allcock, H. R.; Laurencin, C. T. *Biomaterials* **2008**, *29*, 337−349.
(33) Wisian-Neilson, P.; Schaefer, M. A. *Macromolecules* **1989**, *22*, 2003−2007.
(34) Allcock, H. R.; de Denus, C. R.; Prange, R.; Laredo, W. R. *Macromolecules* **2001**, *34*, 2757−2765.
(35) Prange, R.; Reeves, S. D.; Allcock, H. R. *Macromolecules* **2000**, *33*, 5763−5765.
(36) Korsak, V. V.; Vinogradova, S. V.; Tur, D. R.; Gilman, L. M. *Acta Polym.* **1980**, *31*, 85?9.
(37) Allcock, H. R.; Kuharcik, S. E.; Reed, C. S.; Napierala, M. E. *Macromolecules* **1996**, *29*, 3384−3389.
(38) Chang, J. Y.; Park, P. J.; Han, M. J. *Macromolecules* **2000**, *33*, 321−325.
(39) Gleria, M.; Minto, F.; Scoponi, M.; Pradella, F.; Carassiti, V. *Chem. Mater.* **1992**, *4*, 1027−1032.
(40) Minto, F.; Gleria, M.; Bortolus, P.; Fambri, L.; Pegoretti, A. *J. Appl. Polym. Sci.* **1995**, *56*, 747−756.
(41) Matyjaszewski, K.; Miller, P. J.; Pyun, J.; Kickelbick, G.; Diamanti, S. *Macromolecules* **1999**, *32*, 6526−6535.
(42) Liu, W.; Jin, J.; Huang, X.; Zheng, Y.; Zhang, J.; Fu, J.; Huang, Y.; Tang, X. *Polym. Int.* **2010**, *59*, 1252−1257.
(43) Cambre, J. N.; Wisian-Neilson, P. *J. Inorg. Organomet. Polym. Mater.* **2006**, *16*, 311−318.
(44) Matyjaszewski, K.; Miller, P. J.; Fossum, E.; Nakagawa, Y. *Appl. Organomet. Chem.* **1998**, *12*, 667−673.

(45) Pangborn, A. B.; Giardello, M. A.; Grubbs, R. H.; Rosen, R. K.; Timmers, F. J. *Organometallics* **1996**, *15*, 1518−1520.
(46) Britovsek, G. J. P.; England, J.; White, A. J. P. *Inorg. Chem.* **2005**, *44*, 8125−8134.
(47) Allcock, H. R.; Kugel, R. L.; Valan, K. J. *Inorg. Chem.* **1966**, *5*, 1709−1715.
(48) Jung, M. E.; Lyster, M. A. *J. Am. Chem. Soc.* **1977**, *99*, 968−969.
(49) Ueda, J.; Kamigaito, M.; Sawamoto, M. *Macromolecules* **1998**, *31*, 6762−6768.
(50) Cheng, G. L.; Boker, A.; Zhang, M. F.; Krausch, G.; Muller, A. H. E. *Macromolecules* **2001**, *34*, 6883−6888.
(51) Borner, H. G.; Duran, D.; Matyjaszewski, K.; da Silva, M.; Sheiko, S. S. *Macromolecules* **2002**, *35*, 3387−3394.
(52) Fischer, H. *Macromolecules* **1997**, *30*, 5666−5672.
(53) Ding, L.; Huang, Y. Y.; Zhang, Y. Y.; Deng, J. P.; Yang, W. T. *Macromolecules* **2011**, *44*, 736−743.
(54) Liu, G. J.; Ding, J. F. *Adv. Mater.* **1998**, *10*, 69−70.
(55) Heskins, J.; Guillet, E. *J. Macromol. Sci., Part A: Chem.* **1968**, *2*, 1441−1455.
(56) Fischer, K.; Schmidt, M. *Macromol. Rapid Commun.* **2001**, *22*, 787−791.
(57) Borner, H. G.; Beers, K.; Matyjaszewski, K.; Sheiko, S. S.; Moller, M. *Macromolecules* **2001**, *34*, 4375−4383.
(58) Strandman, S.; Zarembo, A.; Darinskii, A. A.; Lauritnmaki, P.; Butcher, S. J.; Vuorimaa, E.; Lemmetyinen, H.; Tenhu, H. *Macromolecules* **2008**, *41*, 8855−8864.

Macromolecules

Article

pubs.acs.org/Macromolecules

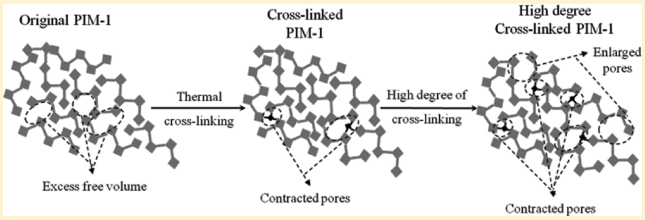
High-Performance Thermally Self-Cross-Linked Polymer of Intrinsic Microporosity (PIM-1) Membranes for Energy Development

Fu Yun Li,[†] Youchang Xiao,[‡] Tai-Shung Chung,*[,†] and Sibudjing Kawi[†]

[†]Department of Chemical & Biomolecular Engineering, National University of Singapore, 4 Engineering Drive 4, 117576 Singapore

[‡]Suzhou Faith & Hope Membrane Technology Co., Ltd., Suzhou Industrial Park, Jiangsu Province, 215123, PR China

ABSTRACT: Novel thermally self-cross-linked polymers of intrinsic microporosity (PIM-1) membranes have been prepared by postmodification of PIM-1 at the elevated temperature for a period of 0.5−2 days. The occurrence of cross-linking reaction has been verified by thermogravimetric analysis (TGA), X-ray photoelectron spectrometer (XPS) and gel content analyses. TGA analyses indicate an increase in thermal stability of membranes after the thermal cross-linking treatment. There is also an obvious drop in the maximum decomposition rate comparing to the original PIM-1when membranes are thermally treated for an extended period of time. Both FTIR and XPS results suggest that the nitrile-containing PIM-1 membranes undergo a latent cross-linking reaction, and form stable bulky triazine rings. The resultant cross-linked polymeric membranes exhibit exceptional gas separation performance that surpasses the most recent upper bound of state-of-the-art polymeric membranes for the important gas separations, such as hydrogen purification, CO_2 capture and flue gas separation. In addition, both gas permeability (attributed to the contorted nature, rearrangement and pronounced inefficient packing of PIM polymer chains) and selectivity (attributed to the decrease of chain-to-chain spacing) increase diagonally with the upper bound line when thermal soaking time increases. PIM-1 thermally treated at 300 °C for 2 days has the CO_2 permeability of 4000 barrer with CO_2/CH_4 and CO_2/N_2 ideal selectivity of 54.8 and 41.7, respectively. The thermally cross-linked PIM-1 membranes will probably provide a promising alternative in industrial energy development.



INTRODUCTION

Natural gas purification and carbon capture by membrane technology have attracted great interest in the recent years due to the simplicity, ease of scale-up and environmental friendliness of membrane processes as compared to conventional gas separation methods such as amine absorption, pressure swing adsorption or cryogenic separation.[1,2] Polymeric materials are suitable candidates for fabricating membranes owing to their low cost and ease of processability into different configurations.[3] There are many factors affecting the gas separation performance of a polymeric membrane. High permeation flux and gas-pair selectivity are regarded as two of the most important criteria for the selection of a membrane for industrial use. This is because high permeation flux is desired to minimize the membrane area required and thus reduce the production cost while high selectivity would enhance the separation efficiency and hence achieve high purity products.[4−7] Membranes fabricated from commercial polymeric materials typically have a low permeation flux. This drives researchers to develop novel materials with a higher flux. However, there exists a trade-off behavior between permeability and selectivity; namely, an increase in permeability of the more permeable gas component usually results in a decline in selectivity. This trend is depicted by the upper-bound line that Robeson has derived from many polymeric membranes.[8] Continuous research efforts have focused on developing membranes that deviate and surpass the upper bound relationship.

Recently, a novel class of polymers, termed "polymers of intrinsic microporosity" (PIMs) has emerged as a promising membrane material for gas separation.[9−17] It possesses unusually high free volume and high surface areas (i.e., ~700 $m^2\ g^{-1}$ for PIM-1), which can be mainly ascribed to its special ladder-type structures with contorted sites that prevent rotation of polymer chains and efficient space packing. Besides their high surface areas, PIMs also exhibit easy solution processability with a high degree of microporosity. Among all the PIMs synthesized, PIM-1 is one of the most well-known types for membrane gas separation.[16,17] The pristine PIM-1 membrane has demonstrated extremely high gas permeability with moderate-to-good separation factor for several important gas pairs (e.g., O_2/N_2, CO_2/N_2, and CO_2/CH_4).[10,13] Later on, several works have attempted to postmodify the PIM-1 membrane to further enhance its gas transport properties mainly with respect to gas-pair selectivity.

In the work of Du et al.,[18] the nitrile groups of PIM-1 were converted to carboxyl groups via a simple postmodification hydrolysis reaction. The degree of conversion could be controlled by the hydrolysis time and temperature. In terms of gas permeation separation performance, the hydrolyzed PIM-1 membranes revealed an evident decrease in gas

Received: December 8, 2011
Revised: January 20, 2012
Published: January 31, 2012

ACS Publications © 2012 American Chemical Society

permeability and obvious increase in gas-pair selectivity. However, the overall gas separation performance still followed the upper bound line in which an increase in gas-pair selectivity was at the expense of gas permeability. The researchers at UOP[19] proposed a UV-cross-linking approach to possibly tighten the polymer chains and reduce the interchain space for gas separation. The PIM-1 membrane under UV-cross-linking treatment for a period of 30 min exhibited O_2/N_2 selectivity of 5.4 with O_2 permeability of 147 barrer. However, no detailed scientific explanation was disclosed in this work. Recently, Du et al.[20] incorporated CO_2-philic pendant tetrazole groups into PIM-1 membranes and the resultant membranes revealed an obvious enhancement in gas permeation separation performance. It provided a viable alternative for CO_2 capture from flue gas. In another work done by Mason et al.,[21] they converted the original nitrile group to the thioamide groups in PIM-1 by using phosphorus pentasulfide as the thionating agent. The modified thioamide-PIM-1 membrane showed an increased selectivity but a reduced permeability compared to the pristine PIM-1 membrane.

In order to enhance the gas-pair selectivity and at the same time maintaining the gas permeability of PIM-1 membranes, we sought to molecularly design the cavity size of PIM-1 membrane by the cross-linking method. In this work, we report the preparation of thermally self-cross-linked PIM-1 membranes via the inherent cross-linking reaction of aromatic nitrile groups to form triazine rings at the elevated temperature with a prolonged treatment time. It is worthwhile to note that the bulky triazine rings formed in the polymer matrix might induce inefficient packing of polymer chains such that the expected decrease in gas permeability due to the cross-linking reaction may be minimized. The thermal cross-linking reaction of the nitrile containing polymers has been well documented in the literatures.[22−26] The cross-linking reaction could be either carried out at elevated temperatures with a prolonged thermal treatment time[22−24] or catalyzed at a lower temperature.[23,25,26] The detailed synthesis method and characterizations of PIM-1 polymer are reported in this work to ensure the correct base material has been used in this study. The effects of thermal cross-linking temperature and duration on gas separation properties of PIM-1 membranes have been investigated and compared with the Robeson's upper bounds.

EXPERIMENTAL SECTION

Materials. 5,5′,6,6′-Tetrahydroxy-3,3,3′,3′-tetramethyl-1,1′-spirobisindane (TTSBI, 97%) purchased from Alfa Aesar, was recrystallized from methanol. 2,3,5,6-tetrafluoroterephthalonitrile (TFTPN, 99%) supplied by Sigma-Aldrich, was sublimated under vacuum prior to use. Anhydrous potassium carbonate (K_2CO_3, ≥ 99%) from Sigma-Aldrich, methanol (MeOH, ≥ 99.9%) from Merck and HPLC grade tetrahydrofuran (THF, 99.9%) from Fisher Chemical, were used as received. Dichloromethane (DCM, 99.99%) and hydrochloric acid (HCl, 37.5%) were obtained from Fisher Scientific and also used as received. *N*-Methyl-2-pyrrolidone (NMP, > 99.5%) from Merck was further purified via distillation prior to use.

Synthesis of PIM-1. The synthesis of PIM-1 is based on polycondensation of TFTPN with TTSBI.[9,15] A stoichiometric amount of anhydrous K_2CO_3 was added to a mixture consisting of equimolar amounts of TFTPN and TTSBI dissolved in NMP under a nitrogen atmosphere with vigorous stirring. After 30 min of nitrogen purging to remove air and moisture, the reaction solution was immersed into a preheated 60 °C oil bath for 24 h. Upon cooling, the mixture was added to MeOH and the crude product was collected by filtration. The crude product was then washed with 0.1 wt % HCl at 70 °C for at least 2 h. The fluorescent yellow solid was filtered off and washed with fresh water until the solution was neutral. It was then washed with MeOH, dissolved in DCM, reprecipitated from MeOH again and vacuum-dried at 120 °C for at least 24 h, yield of approximately 87% was obtained. Surface area (N_2 adsorption, BET analysis): 726.4 m^2 g^{-1}. ^{1}H NMR (400 MHz, $CDCl_3$-d_6, δ): 1.2−1.4 (br. m, 12H; CH_3), 2.1−2.4 (br. m, 4H; CH_2), 6.4 (br. s, 2H; CH), 6.8 (br. s, 2H; CH). ^{13}C NMR (100 MHz, $CDCl_3$, δ): 109.4 (−CN). ^{19}F NMR (376 MHz, $CDCl_3$, δ): 0 (F). FTIR (ATR): 2237 cm^{-1} (−CN), 2800−3000 cm^{-1} (H−C−H); Anal. Calcd (XPS elemental analysis) for PIM-1 ($C_{29}H_{20}N_4O_2$): C, 79.10; N, 6.36; O, 14.54. Found: C, 79.23; N, 6.20; O, 14.57.

Dense Membrane Preparation. A 2% (w/w) of polymer solution was prepared by dissolving readily soluble PIM-1 powder in DCM. The polymer solution was filtered using a 1.0 μm Whatman's filter before ring casting onto a silicon wafer plate at room temperature (i.e., 25 ± 2 °C) to allow slow evaporation of the solvent. Dense membranes were formed after approximately 5 days. The nascent dense films were then soaked in MeOH to remove prior membrane formation history and any residual possible solvents and dried in a vacuum oven at 120 °C to remove the residual solvent. Membranes with the thickness of 55 ± 5 μm were used for further studies.

Thermal Cross-Linking Treatments. The thermal cross-linking treatments of PIM-1 dense films were performed using a Centurion Neytech Qex vacuum furnace. The vacuum furnace temperature was raised to between 250 and 300 °C at a rate of 10 °C/min and held for a period of 0.5 to 2 days. After the thermal cross-linking treatment process, the membranes were cooled naturally in the vacuum furnace to room temperature and stored in a drybox for further studies. A clear coloration from yellow to dark brown and black color could be observed for the thermal-treated membranes depending on the duration and temperature of thermal treatments. In addition, all membranes after thermal treatments were flexible and tough enough for characterization and gas permeation measurements. The weights before and after the thermal treatment process of each membrane were measured and no obvious weight loss was observed (i.e., <2 wt %). The membrane dense films were labeled as "PIM-temperature-duration (day)", for example, PIM-300−0.5d.

Characterizations. The molecular weight of the synthesized PIM-1 was determined by gel-permeation chromatography (GPC) measurements. It was carried out on a HP 1100 HPLC system equipped with the HP 1047A RI detector and Agilent 79911GP-MXC columns. THF was used as the solvent and the flow rate was controlled at 1.0 mL/min. The PIM-1 powder was dissolved in THF at a concentration of 0.005 wt %. The molecular weight was estimated by comparing the retention times in the column to those of polystyrene standards. The obtained GPC result for PIM-1 is as follows: M_n: 39828. M_w: 66674. PDI (=M_w/M_n): 1.67.

The gel content of the cross-linked PIM-1 membranes with respect to the cross-linking duration at 300 °C was determined by soaking the respective membranes into DCM solvent for 24 h. The remaining insoluble portions of the membranes were dried under vacuum at 120 °C for 24 h to remove residual solvent before weighing. The gel content was evaluated using eq 1

$$\%\ \text{gel content} = M_1/M_0 \times 100 \quad (1)$$

where M_0 and M_1 are the weights of the cross-linked membrane before and after soaking in DCM, respectively.

The thermal degradation of the original PIM-1 and thermally cross-linked PIM-1 membranes were monitored by thermogravimetric analysis (TGA) with a TGA 2050 themogravimetric Analyzer (TA Instruments). The analyses were carried out with a ramping rate of 10 °C/min at temperatures ranging from 50 to 800 °C. Nitrogen was used as the purge gas and its flow rate was controlled at 50 mL/min.

The FFV of the original PIM-1 and the thermally cross-linked PIM-1 membranes were calculated based on the Bondi's method using eq 2:

$$\text{FFV} = \frac{V - V_o}{V} \quad (2)$$

where V is the specific volume of the polymer calculated from the measured density. V_o is the volume occupied by the polymer molecules and equals to 1.3 times of the polymer's van der Waals volume (V_w). The estimation of van der Waals volume was based on the group contribution method.

The possible structural change before and after the thermal cross-linking process has been monitored by FTIR analyses. The FTIR measurements were performed using an attenuated total reflection mode (FTIR-ATR) with a Perkin-Elmer Spectrum 2000 FTIR spectrometer. Each sample was scanned 32 times. The characteristic band at 2350 cm^{-1} is contributed from carbon dioxide.

An X-ray photoelectron spectrometer (XPS) was utilized to monitor the chemical changes of thermally cross-linked PIM-1 membranes. They were carried out on an AXIS HSi spectrometer (Kratos Analytical Ltd., England) using a monochromatic Al Kα X-ray source (1486.6 eV photons) at a constant dwell time of 100 ms and a pass energy of 40 eV under full vacuum. The anode voltage and anode current were 15 kV and 10 mA, respectively. All core-level spectra were obtained at a photoelectron takeoff angle of 90 owith respect to the sample.

The positron annihilation lifetime (PAL) experiments were conducted for both the original PIM-1 and the thermally cross-linked PIM-1 membranes using a variable-energy positron beam with a counting rate of 100−500 counts/s and each spectrum contains one million counts. In PAL measurements, the quantitative information on free-volume size, distribution and content is mainly ascribed to so-called the pick-off annihilation of long-lived orthopositronium (o-Ps, the triplet bound state of a positron and an electron).[27] The estimated pick-off lifetime of the o-Ps (τ_3 in ns) is correlated to the mean free volume radius R (Å) by a semiempirical spherical-cavity model as follows:[27,28]

$$\tau_3^{-1} = 2\left[1 - \frac{R}{R_o} + \frac{1}{2\pi}\sin\left(\frac{2\pi R}{R_o}\right)\right] \tag{3}$$

Here R_o is the infinite spherical potential radius that is equal to $R + \Delta R$ with ΔR as an empirical parameter (= 1.66 Å). The relative fractional free volume (FFV) is calculated based on the Williams−Landel−Ferry (WFL) equation[29]

$$\mathrm{FFV} = 0.0018 I_3 \langle v_f(\tau_3)\rangle = 0.0018 I_3\left(\frac{4}{3}\pi R^3\right) \tag{4}$$

where I_3 is the o-Ps intensity (in %) for the estimated pick-off lifetime τ_3 and v_f is the mean free volume (in Å^3) of a cavity in the polymer matrix calculated based on the mean free volume radius R. The obtained PAL data were fitted into three lifetimes using the PATFIT program, which assumes a Gaussian distribution of the logarithm of the lifetime for each component. The MELT program was also adopted to observe the trend for free volume distribution of various membranes. A detailed description of PAL can be obtained elsewhere.[27−31]

Measurement of Gas Transport Properties. The host and thermally cross-linked PIM-1 dense membranes were tested in both pure gas and mixed gas systems. The pure gas permeation properties were evaluated by a variable-pressure constant-volume method. The detailed experimental design and procedures can be found elsewhere.[32] Each pure gas was tested in the sequence of H_2, O_2, N_2, CH_4, and CO_2 at 35 °C and 3.5 atm. The rate of pressure increase (dp/dt) at steady state was used for the calculation of gas permeability with accordance to the following eq:

$$P = \frac{273.15 \times 10^{10}}{760}\frac{Vl}{AT(P_2 \times 76/14.7)}\left(\frac{dp}{dt}\right) \tag{5}$$

where P is the gas permeability of a membrane in Barrer (1 barrer = 1×10^{-10} cm^3 (STP)-cm/cm^2s cmHg), V is the volume of the downstream chamber (cm^3), l is the membrane thickness (cm), A refers to the effective area of the membrane (cm^2), T is the operating temperature (K) and P_2 is the upstream operating pressure (psia).

The ideal selectivity of a membrane for pure gases A to B is defined as follows:

$$\alpha_{A/B} = \frac{P_A}{P_B} \tag{6}$$

where P_A and P_B are the pure gas permeability of gases A and B, respectively.

The mixed gas permeation properties for a selected cross-linked PIM-1 membrane were obtained from a modified pure gas permeation cell. The detailed experimental design and procedures can be found in the work of Tin et al.[33] Both CO_2/CH_4 mixture (50%/50% mole fraction) and CO_2/N_2 mixture (50%/50% mole fractions) were used in mixed gas tests and they were carried out at 35 °C and 7 atm. The gas permeability was evaluated as follows:

$$P_a = \frac{273.15 \times 10^{10}}{760}\frac{y_a Vl}{AT(76/14.7)(x_a P_2)}\left(\frac{dp}{dt}\right) \tag{7}$$

$$P_b = \frac{273.15 \times 10^{10}}{760}\frac{(1 - y_a)Vl}{AT(76/14.7)[(1 - x_a)P_2]}\left(\frac{dp}{dt}\right) \tag{8}$$

Here x_a is the mole fraction of gas component a in the feed gas and y_a denotes the mole fraction of gas component a in the permeate. All the other symbols remain the same meanings as described previously.

The selectivity of the mixed gas was evaluated by taking the ratio of permeate (y) and feed (x) mole fraction of two components with the following eq:

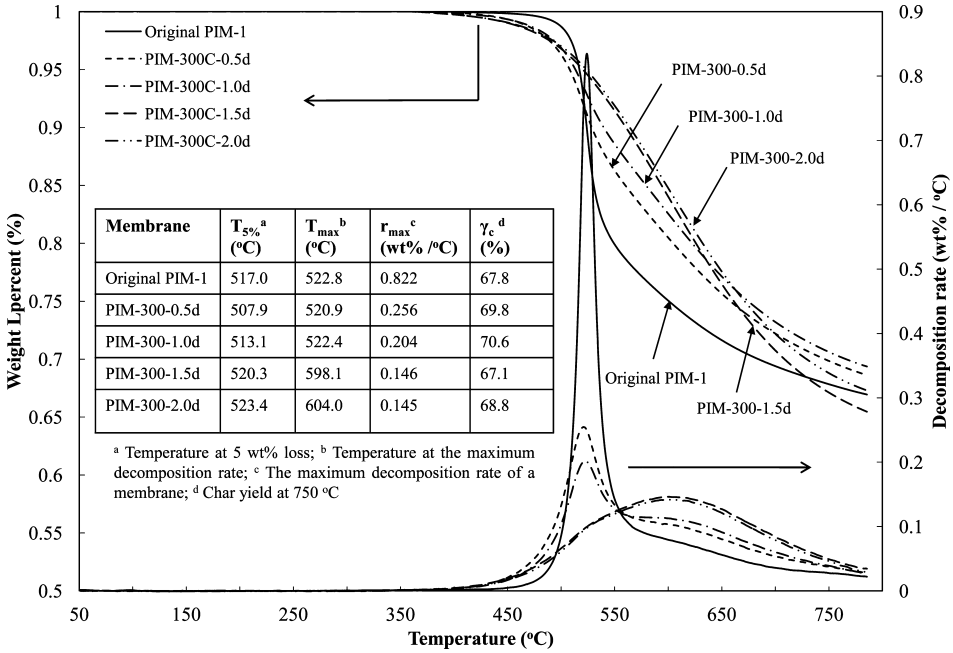
$$\alpha_{a/b} = \frac{y_a/y_b}{x_a/x_b} \tag{9}$$

The physical aging behavior of the original PIM-1 membrane and the thermally cross-linked PIM-1 membrane (i.e., PIM-300−2.0d) were preliminarily studied through a period of 240 h. H_2, O_2, N_2 and CH_4 were used in the aging test except CO_2 due to its high solubility in glassy polymers that may alter the nature of the glassy state. All membranes used in the aging study had a thickness of 55 ± 5 μm.

RESULTS AND DISCUSSION

Characterization of the Thermally Cross-Linked PIM-1 Membranes. The thermal stabilities of the original PIM-1 and the thermally cross-linked PIM-1 membranes were monitored by TGA and their degradation curves are depicted in Figure 1. As can be seen, all membranes are thermally stable up to 450 °C possibly due to the strong dipolar interactions of nitrile groups.[12] If the thermal degradation temperature is defined as a 5 wt % loss of the original weight, the longer thermal-treated PIM-1 membranes (i.e., PIM-300−1.5d and PIM-300−2d) tend to decompose at a rather later stage, which is mainly attributed to the high degree of thermal cross-linking, that stabilizes the membrane structure. Moreover, the original PIM-1 membrane exhibits the highest decomposition rate (i.e., 0.822 wt%/°C) when it starts to decompose, whereas the maximum decomposition rates of the thermally cross-linked PIM-1 membranes descend with an increase in thermal treatment time. For example, there is a clear decrease in the maximum decomposition rate from 0.822 to 0.145 wt %/°C for the original PIM-1 and the PIM-300−2d membranes, respectively. Thus, the thermally cross-linked PIM-1 membranes demonstrate much slower thermal decomposition rate when compared to the original PIM-1 membrane. Additionally, the cross-linked PIM-1 membranes show much higher weight retentions at 600 °C, which is the result of greatly enhanced thermal stability after the thermal cross-linking reaction. It is worth pointing out that all membranes contain a char yield of

dx.doi.org/10.1021/ma202667y | Macromolecules 2012, 45, 1427−1437



Membrane	$T_{5\%}$ [a] (°C)	T_{max} [b] (°C)	r_{max} [c] (wt% /°C)	γ_c [d] (%)
Original PIM-1	517.0	522.8	0.822	67.8
PIM-300-0.5d	507.9	520.9	0.256	69.8
PIM-300-1.0d	513.1	522.4	0.204	70.6
PIM-300-1.5d	520.3	598.1	0.146	67.1
PIM-300-2.0d	523.4	604.0	0.145	68.8

[a] Temperature at 5 wt% loss; [b] Temperature at the maximum decomposition rate; [c] The maximum decomposition rate of a membrane; [d] Char yield at 750 °C

Figure 1. TGA of the original and the thermally cross-linked PIM-1 membranes.

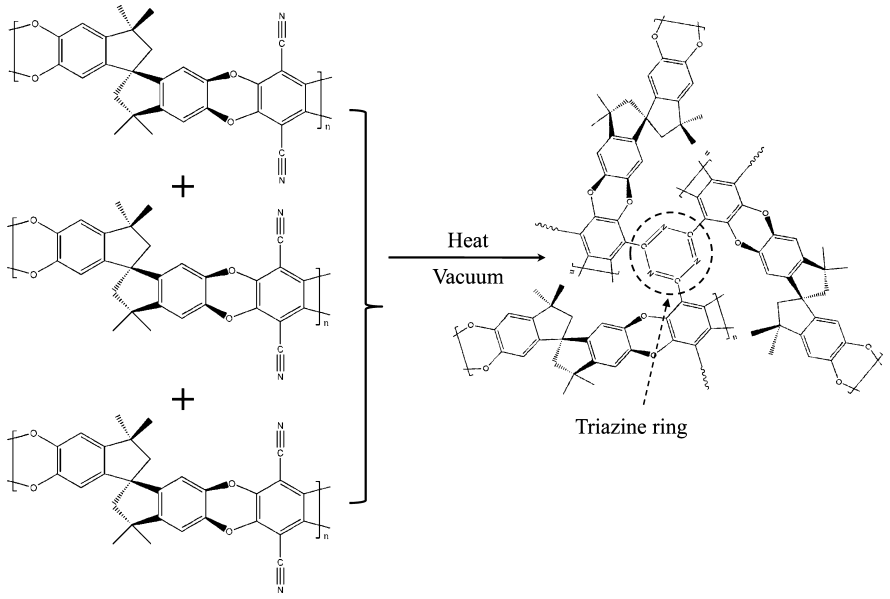


Figure 2. Proposed thermal cross-linking reaction of PIM-1.[22−24]

more than 65 wt % at 750 °C due to the unusual thermal stability of the intrinsic microporosity material.

A good indication of the occurrence and the extent of cross-linking reaction at the respective thermal treatment duration are provided by the gel content of the modified films. It is observed that there is about 86% gel content for PIM-300−0.5d, while no obvious weight loss (e.g., approximately 100% gel content) could be detected when the PIM-1 membranes are treated more than 0.5 d at 300 °C. The results from gel content reinforce the confirmation of cross-linked structure of PIM-1 membranes. It also suggests that the extent of cross-linking reaction increases with thermal treatment time.

Although both TGA and Gel content analyses demonstrate the occurrence of thermal cross-linking reaction, it is hard to know their exact chemical structure because there are many possible structures deriving from the possibly activated cyano groups.[26] According to literatures, the most likely chemical cross-linking reaction scheme is having a thermally induced trimerization of the nitriles to stable triazine rings without releasing any volatile side products, as shown in Figure 2.[22−24] However, the thermal trimerization process is slow and might be expedited by either catalyst or conducting at elevated temperature with an extended period of time.[24,25] The structural changes and the formation of triazine structures of the thermally treated PIM-1 membranes have been verified by FTIR and XPS analyses.

Figure 3 depicts the FTIR spectra for the original and the selected thermally cross-linked PIM-1 films. The FTIR spectrum of PIM-300−2.0d membrane is not showing here due to its relatively weak IR signal. This is probably caused by

dx.doi.org/10.1021/ma202667y | Macromolecules 2012, 45, 1427−1437

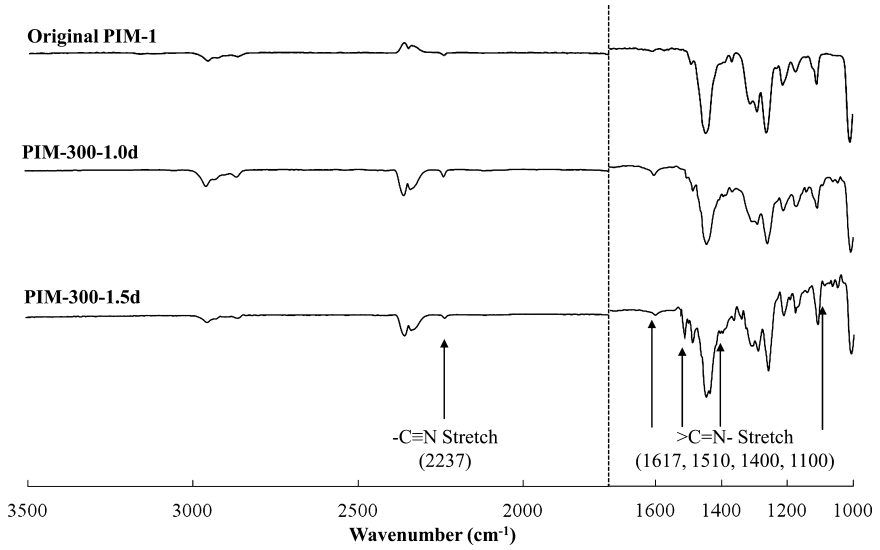


Figure 3. FTIR spectra of the original and the thermally cross-linked PIM-1 membranes.

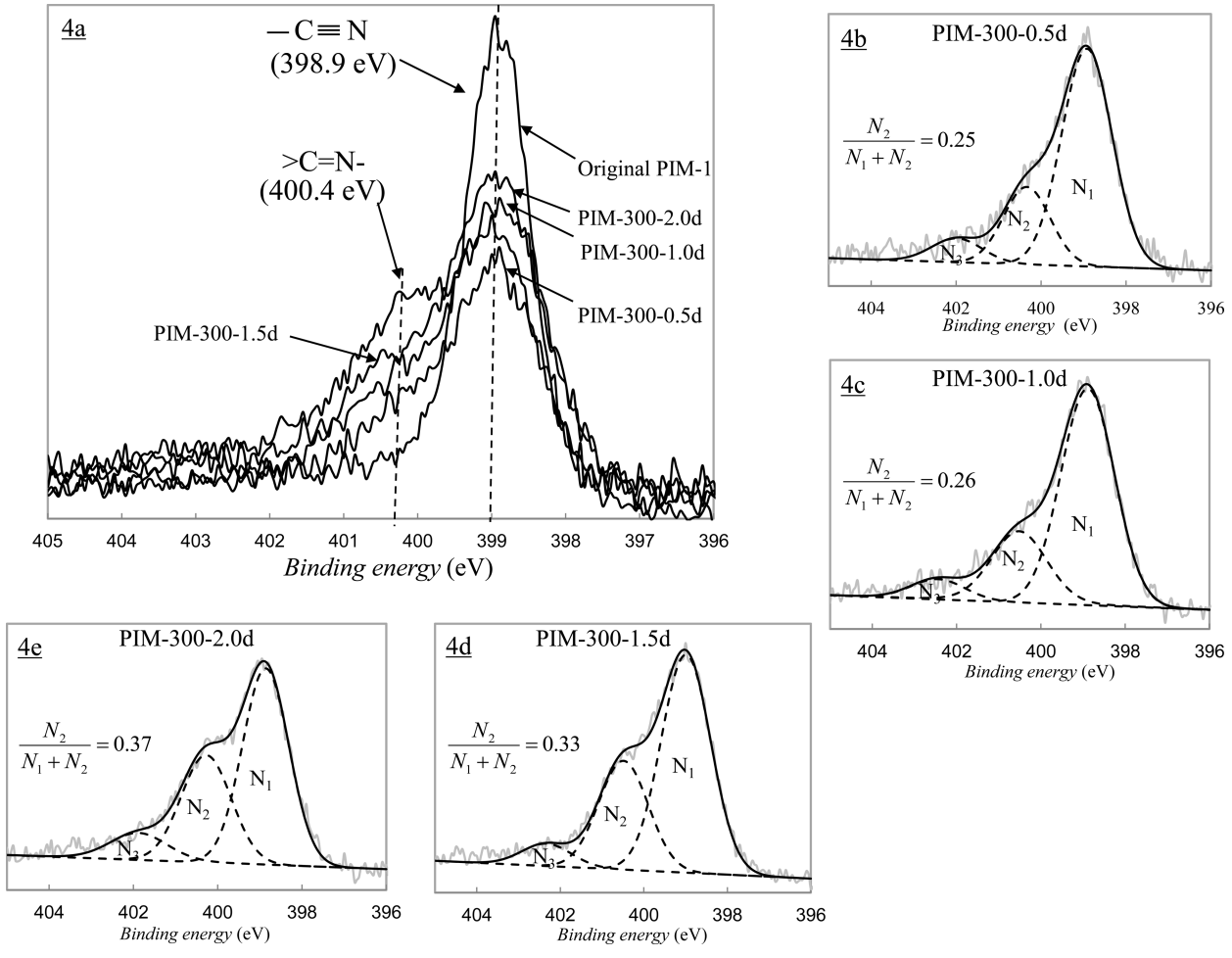


Figure 4. N_{1s} XPS analysis of the original and the thermally cross-linked PIM-1 membranes.

the weak IR reflection since this membrane is a bit dark in color. The prominent peak at 2237 cm^{-1} is attributed to the −C≡N stretching. Comparing with the original PIM-1 film, there are a few distinct new peaks near 1617, 1510, 1400, and 1100 cm^{-1}, which are characteristic peaks of >C═N− stretching and bending vibrations.[26,34] This, on the other hand, confirms the formation of triazine structure after the thermal cross-linking process. Besides, XPS analyses have been used to determine the extent of thermal cross-linking process.

Figure 4 shows the N_{1s} XPS spectrum of the host PIM-1 and the thermally cross-linked PIM-1 membranes. The original PIM-1 membrane reveals a symmetrical Gaussian-type N_{1s} core

dx.doi.org/10.1021/ma202667y | Macromolecules 2012, 45, 1427−1437

Table 1. Pure Gas Separation Performance of the Original and the Thermally Cross-Linked PIM-1 Membranes (Tested at 35 °C and 3.5 atm)

	permeability (Barrer[a])					ideal selectivity				
membranes	H_2	O_2	N_2	CH_4	CO_2	H_2/N_2	H_2/CH_4	O_2/N_2	CO_2/CH_4	CO_2/N_2
pristine PIM-1	2696	712	166	204	3375	16.3	11.7	4.3	16.6	20.4
original PIM-1[b]	3949	1257	337	472	6957	11.7	8.4	3.7	14.8	20.7
PIM-250−1.0d	1430	400	107	145	2220	13.3	9.9	3.7	15.3	20.7
PIM-250−2.0d	1360	326	76	73	1968	17.9	18.6	4.3	27.0	25.9
PIM-300−0.5d	1666	422	99	97	2496	16.9	17.2	4.3	25.9	25.3
PIM-300−1.0d	2221	483	101	91	3083	22.1	24.5	4.8	34.0	30.7
PIM-300−1.5d	2640	557	106	95	3339	24.9	31.1	5.2	39.3	31.4
PIM-300−2.0d	3872	582	96	73	4000	40.3	53.0	6.1	54.8	41.7

[a]1 barrer =1 × 10^{-10} cm^3(STP)cm/cm^2 s cmHg. [b]Soaked in MeOH.

signal with the maximum peak at 398.9 eV which is ascribed to the −C≡N (nitrile) group in the PIM-1 polymer structure. After the thermal treatments, the symmetrical N_{1s} core signal becomes broad and asymmetrical with newly formed shoulder peaks at about 400.4 eV, which belong to the nitrogen of the >C═N− (imine) group.[35−37] A positive shift of 1.5 eV of the N_{1s} core signal is consistent with a loss of a negative charge in the nitrogen of the >C═N− group from the −C≡N group.[35,36] The partial conversion of the original nitrile group in the PIM-1 structure to the imine group is indeed caused by the thermally induced cross-linking reaction of the polymer chains.

In order to quantitatively monitor the extent of cross-linking reaction, the N_{1s} XPS spectrum of each cross-linked PIM-1 membrane was deconvoluted into three peaks at 398.9, 400.4, and 402.2 eV with a fixed fwhm of 1.4 eV. The highest decomposed N_{1s} binding energy of 402.2 eV is probably attributed to the π-excitation which appears in all carbon compounds with double bonds.[38] As illustrated in Figure 4b−e, the ratio of integrated intensity >C═N−/(>C═N− + −C≡N) (i.e., $N_2/(N_1 + N_2)$) shows an increasing trend with an increase in thermal treatment time, which suggests that the extent of thermal cross-linking is more pronounced at an extended duration of thermal treatment. For example, the conversion rate of -C≡N to the triazine structure for PIM-300−0.5d is 25%, whereas, the conversion has increased to 37% when the membrane is soaked at 300 °C for 2 d. However, thermal-treating of PIM-1 for more than 2 d would lead to the subtle brittleness of the treated membranes, hence leading to difficulties in characterization and permeation test. We therefore did not continue longer thermal treatments.

A close look at the resultant cross-linked PIM-1 membranes supports the existence of cross-linking reaction. As the cross-linking duration increases, the PIM-1 membranes turn from originally yellow, to dark brown and then black in color. The coloration of cross-linked PIM-1 membranes is mainly attributed to the formation of charge-transfer complexes (CTCs) between the PIM-1 chains that having the newly formed triazine ring as the electron acceptor and benzene rings of PIM-1 as the electron donors. During the cross-linking reaction, the formation of triazine rings tends to pull the PIM-1 benzene rings approach each other closely enough to allow transfer of π−electrons, and thus generates colors.[39,40]

Pure Gas Transport Properties. The pure gas separation performance of the original and the thermally cross-linked PIM-1 membranes is shown in Table 1. As can be seen, the gas permeability of PIM-1 post-treated with methanol (i.e., original PIM-1) has increased almost 2-fold from the pristine PIM-1. Swelling might be one of the main reasons contributing to this effect.[12,13,17] A similar phenomenon has been reported by Tin et al. and Shao et al. on Matrimid and other 6FDA polyimide.[33,41,42] The original PIM-1 membrane exhibits extremely high gas permeability and moderate selectivity for all gases, which is consistent with previously reported results.[13,16,17] After 1 d thermal treatment at 250 °C under vacuum, the gas permeability for all gases decreases significantly, whereas no enhancement in gas-pair selectivity could be obtained. This is probably attributed to the mere densification of high free volume PIM-1 membrane structure at 250 °C as no cross-linking has occurred at this stage. In fact, the N_{1s} XPS spectra for PIM-250−1d (not shown here) also reveal a symmetrical Gaussian-type signal with the maximum peak at 398.9 eV, which is exactly the same as have been observed in the original PIM-1 XPS spectrum (i.e., Figure 4). As discussed previously, the thermally induced trimerization process is slow and is probably initiated at elevated temperatures with an extended period of time. The PIM-1 membrane treated at an extended duration (e.g., PIM-250−2d) reveals a further decrease in gas permeability, but a significant enhancement in gas-pair selectivity. For example, the permeability of CO_2 decreases by about 11% with an increase of 76% in CO_2/CH_4 selectivity from membrane PIM-250−1d to PIM-250−2d. This indicates that the thermal cross-linking has probably occurred at an extended duration of thermal treatment.

To further study the thermally induced trimerization process of PIM-1 membranes, the thermal cross-linking temperature was raised to 300 °C and held for a period of 0.5 to 2 d. The gas-pair selectivity of the thermally cross-linked PIM-1 membranes increases monotonically with the increase of thermal treatment time. In particular, the selectivity of CO_2/CH_4 is almost four times higher than the original PIM-1 membrane. This monotonic increase in gas-pair selectivity is mainly attributed to the thermally induced cross-linking of polymer chains that tightens polymer chains of PIM-1. The possible tightening of polymer chains with an increase in thermal treatment time has been verified by PAL experiments. Table 2 shows the PAL results of the original and the thermal-treated PIM-1 membranes under different thermal soaking durations. Generally, an increase in thermal soaking time of PIM-1 membranes decreases the τ_3 value. To be exact, this could be caused by either the physical densification of membrane structure at elevated temperatures or the chemical tightening of polymer chains due to the formation of triazine rings within the PIM-1 matrix. However, the N_{1s} XPS results indicate that the extent of thermal cross-linking increases with soaking time when the soaking temperature is fixed at 300 °C.

dx.doi.org/10.1021/ma202667y | Macromolecules 2012, 45, 1427−1437

Table 2. PAL Results of the Original and the Thermally Cross-Linked PIM-1 Membranes

membranes	τ_3 (ns)	I_3 (%)	R_3 (Å)	FFV(%)	FFV (%)[a]
original PIM-1[b]	3.08 ± 0.07	13.82 ± 0.34	3.69 ± 0.03	5.24 ± 0.26	23.9 ± 0.4
PIM-300−0.5d	2.79 ± 0.07	13.11 ± 0.50	3.49 ± 0.04	4.20 ± 0.29	16.1 ± 0.6
PIM-300−1.0d	2.59 ± 0.05	11.13 ± 0.26	3.36 ± 0.03	3.18 ± 0.16	15.9 ± 0.5
PIM-300−1.5d	2.52 ± 0.09	10.48 ± 0.64	3.29 ± 0.05	2.82 ± 0.31	16.6 ± 0.4
PIM-300−2.0d	2.44 ± 0.08	11.43 ± 0.58	3.23 ± 0.05	2.90 ± 0.27	17.1 ± 0.4

[a]Calculated based on Bondi's method. [b]Soaked in MeOH.

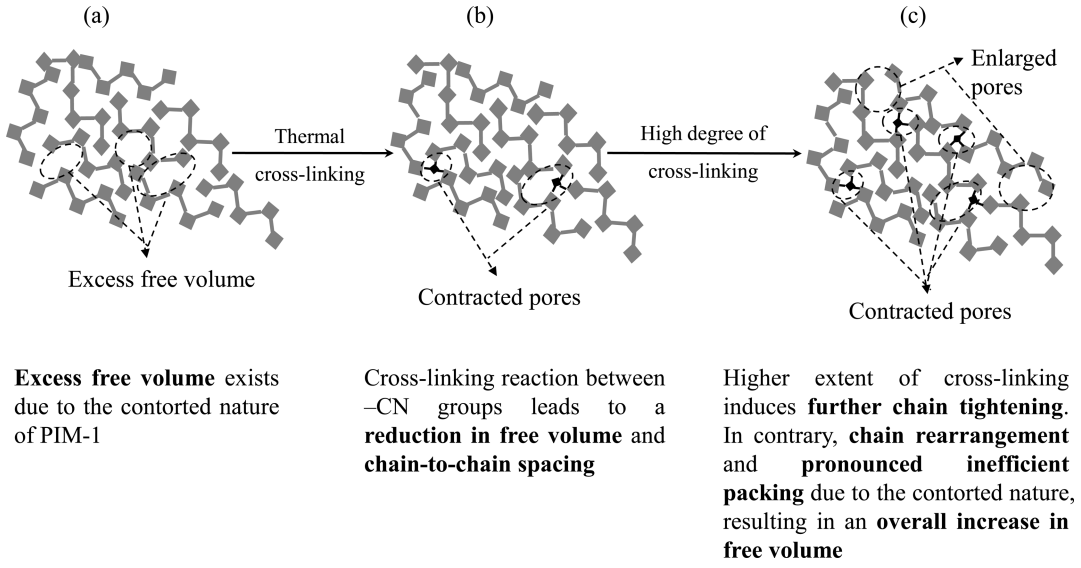


Figure 5. Two-dimensional representations of the contorted PIM-1 membrane before and after thermal cross-linking reaction with the formation of triazine rings. (a) Original PIM-1 matrix (time = 0). (b) Initiation of thermal cross-linking process (time ≫ 0). (c) Completion of thermal cross-linking process (time ≫ 0).

Hence, the decrease in o-Ps lifetime (i.e., τ_3 or corresponding mean pore size r_3) is mainly resulted from the tightening of polymer chains during the cross-linking process. A comparison between the original PIM-1and the thermal-treated PIM-300−2d membrane sees a decrease of τ_3 from 3.08 to 2.44 ns while the corresponding r_3 dwindles from 3.69 to 3.23 Å.

Generally, the calculated fractional free volume (FFV) based on τ_3 value also indicates a decrease for the thermally cross-linked PIM-1 membranes when compared to the original PIM-1 membrane. One possible reason is due to the fact that the cross-linking reaction tightens polymer chains, thereby resulting in a lower free volume. It is worthwhile to point out that the PAL calculated FFV of PIM-1 membranes is smaller than the FFV calculated based on the Bondi's method, and the calculated FFV of PIM-1 based on the Bondi's method is consistent with previously reported results.[12,14] This is because PAL experiments only consider ultrafine micropores (i.e., <4 ns in τ_3 value), while Bondi's method takes consideration of all functional groups in PIM-1 polymer structures. In fact, the long lifetimes (i.e., >4 ns in τ_4 value) of PIM-1 membranes were also observed in PAL experiments. However, due to the nature of slow positron beam, the long lifetimes of o-Ps observed results from both the positron beam itself and the large micropores in the PIM-1 membranes. To reduce complexity, only three lifetimes were adopted without consideration of long lifetimes of τ_4 value.

It has been verified that there are two kinds of pores in PIM-1 based materials: large micropores and ultrafine micropores.[12,14,43] The former is mainly attributed to the loosely packed polymer chains due to the kinked structure of PIMs, while the latter is the chain-to-chain distance of space-efficiently packed polymer chains. Generally, the loosely packed polymer chains create a large free volume in the membrane and contribute mostly to the high gas permeability, whereas the chain-to-chain spacing plays a determining role in gas-pair selectivity. With the occurrence of cross-linking reaction and formation of the bulky triazine ring with the planar structure, a synergistic effect for high permeability and high selectivity is created at one step resulting from a decrease in chain-to-chain spacing at one end of the polymer chain and an increased inefficiency of chain packing at the other end, which could be envisaged with a two-dimensional schematic illustration depicted in Figure 5.

Referring to Figure 5a, the original PIM-1 polymer chains tend to pack inefficiently due to the contorted nature of PIM backbone, which in turn generates excess free volumes. When the thermal cross-linking reaction initiates, the formation of bulky planar triazine rings tends to pull the polymer chains closer to each other at one end (i.e., site of nitrile groups) as shown in Figure 2, thus resulting in an overall decrease in FFV (e.g., Figure 5b) when compared to the host PIM-1 matrix. Additionally, the cross-linking reaction leads to a decrease in chain-to-chain spacing (i.e., verified by decreasing the τ_3 value in PAL experiments), hence increasing the gas-pair selectivity. As the cross-linking reaction continues, more bulky planar triazine rings would be formed and possibly lead to the rearrangement of polymer chains. However, due to the nature of PIM materials that do not possess rotational freedom along

dx.doi.org/10.1021/ma202667y | Macromolecules 2012, 45, 1427−1437

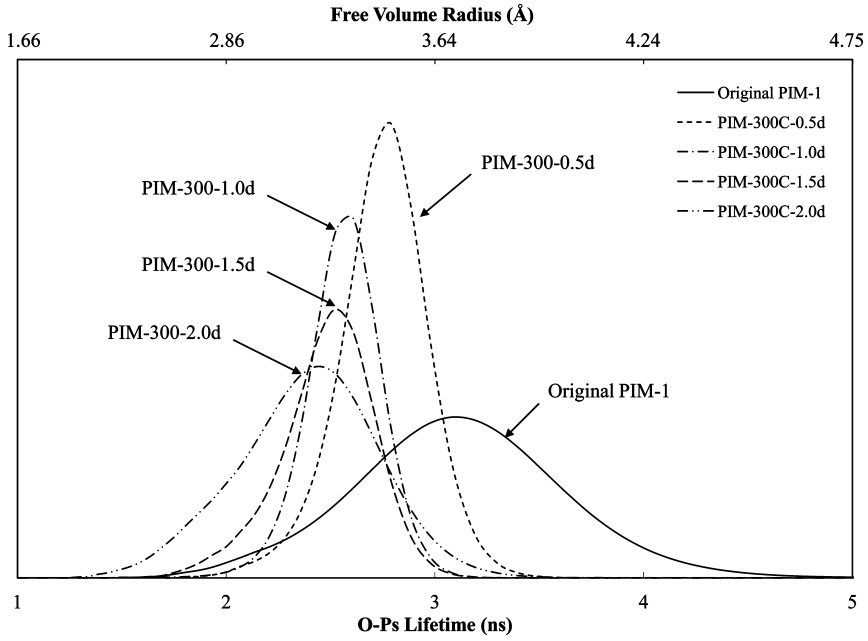


Figure 6. PAL analysis of the original and the thermally cross-linked PIM-1 membranes.

the polymer backbone,[44] the formation of bulky planar triazine rings would further constrain the movement of those polymer chains (e.g., Figure 5c). Eventually, it would induce pronounced inefficient packing, thus increases free volume and enhances gas permeability with an increase in thermal soaking duration. This is somewhat explained by the PAL data as well. As can be seen from the Table 2, there is an obvious increase in o-Ps intensity (i.e., I_3 from PAL experiments) when the PIM-1 membrane is thermally treated for a longer period of time. Although the thermal cross-linking reaction induces obvious reduction in chain-to-chain spacing, the overall FFV, which takes consideration of both τ_3 and I_3, still reveals an increase in PIM-300−2d membrane when compared to the membrane treated at a shorter period of time (i.e., PIM-300−1.5d).

To have a clearer picture of the pore size and free volume change of the thermally cross-linked PIM-1 membranes, the MELT analysis was utilized and the result is depicted in Figure 6. An increase in thermal cross-linking duration clearly shifts the peak to the left and a relatively narrower distribution is also observed. However, as the thermal cross-linking duration increases, the free volume distribution becomes broader, which suggests the various sizes of small pores have been generated when membrane is thermally treated for a longer period of time, thus the possibly more free volume and enhanced gas permeability. This is in agreement with the trend of decreasing τ_3 and increasing I_3 concluded from PATFIT results. Therefore, an effective manipulation of free volume and pore size of the PIM-1 membranes can be achieved via the thermal cross-linking reaction at the elevated temperature with an appropriate thermal soaking time. The revolution of free volume and pore size distributions toward left or become narrow indicates the thermally treated PIM-1 membranes may have higher selectivity for specific gas pair separations.

Mixed Gas Tests and Potential Applications of Thermally Cross-Linked PIM-1 Membranes. Binary CO_2/CH_4 and CO_2/N_2 tests were conducted for PIM-300−2.0d membrane at 35 °C and results are shown in Table 3. Generally, the gas permeability in mixed gas tests is lower than

Table 3. Mixed Gas Separation Performance of the Thermally Cross-Linked PIM-1 Membrane PIM-300-2.0d (Tested at 35 °C and 7.0 atm)

	permeability (Barrer[a])			selectivity	
membrane	N_2	CH_4	CO_2	CO_2/CH_4	CO_2/N_2
PIM-300−2.0d[b]	96	73	4000	54.8	41.7
Mixed Gas (CO_2/CH_4:50/50%)					
PIM-300−2.0d	--	42.9	2317	54.0	--
Mixed Gas (CO_2/N_2: 50/50%)					
PIM-300−2.0d	75.2	--	2924	--	38.9

[a]1 barrer =1 × 10^{-10}cm^3(STP)cm/cm^2 s cmHg. [b]Pure gas separation performance.

that in pure gas tests mainly ascribed to the competitive sorption in membranes.[45] Comparing the binary CO_2/CH_4 and CO_2/N_2 tests (i.e., both with the 50/50 mol % in feed) with the pure gas tests, there is an approximate 42% drop in CO_2 permeability for binary CO_2/CH_4 tests when compared to a 27% drop in CO_2/N_2 tests. This is clearly indicating a more pronounced competitive sorption in the former than the latter due to the higher condensability of CH_4 than N_2 (e.g., T_c of CH_4 is 190.6 K and T_c of N_2 is 126.2 K[4]).

Figure 7 shows gas separation performance of our cross-linked membranes in comparison with the Robeson's upper bound. It is worth noting that the gas separation performance of the original PIM-1 membrane is slightly above the upper bounds. Our synthesized PIM-1 membrane is in fact better than the most literature reported data in terms of both gas permeability and selectivity.[14−16] It is suggested that the difference in gas separation performance from the literature data is mainly caused by different film formation protocols.[12−15] When the PIM-1 film is first treated at 300 °C for 0.5 d, the gas separation performance goes along with the upper bound line, which is typically seen in most of polymeric membranes. While a longer thermal treatment time is applied, the gas separation performance goes diagonally with the upper bound line. For example, in the H_2/CH_4 upper bound plot (i.e., Figure 7a), both gas

dx.doi.org/10.1021/ma202667y | Macromolecules 2012, 45, 1427−1437

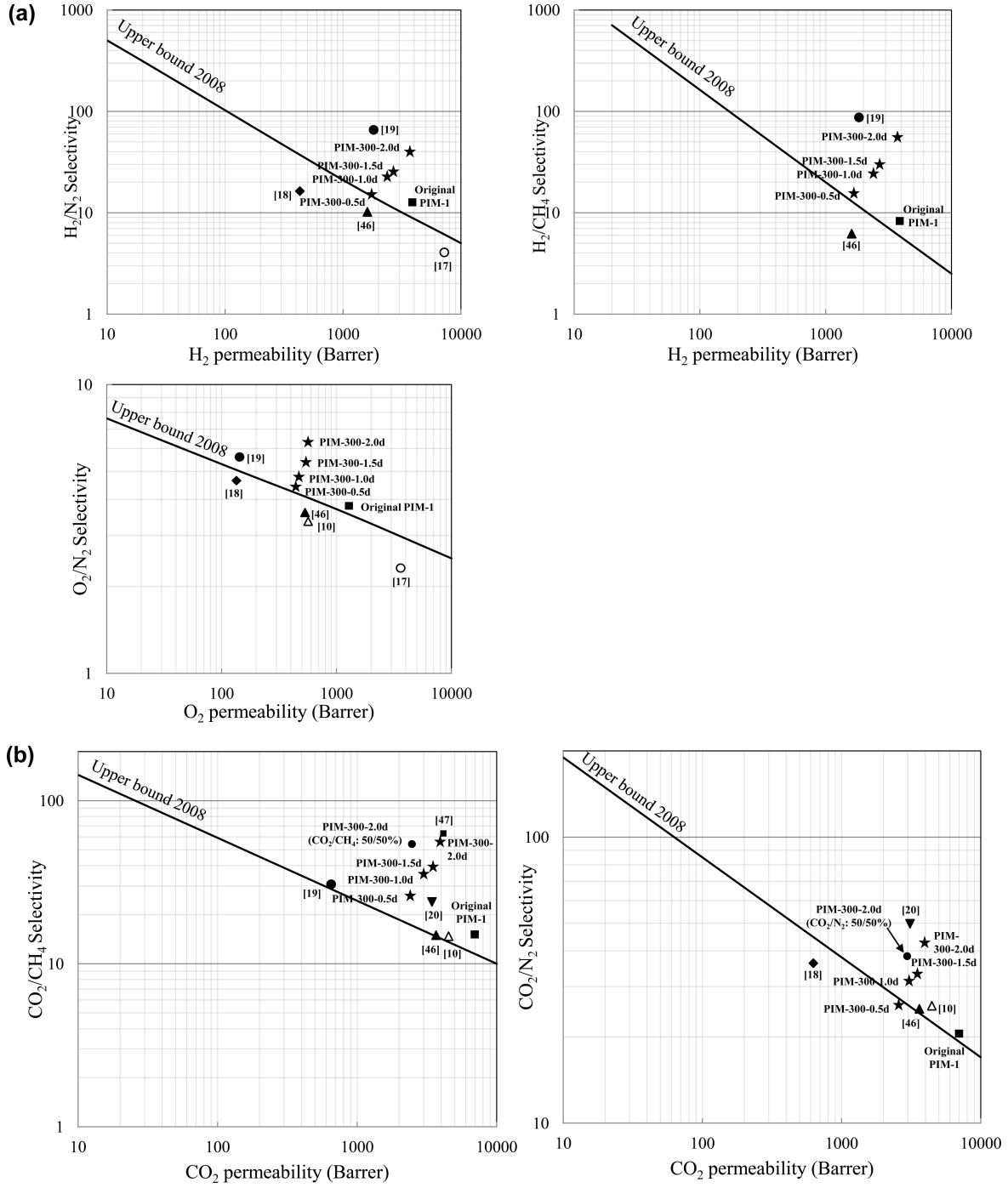


Figure 7. (a) Upper bound comparison[8] (H_2/N_2, H_2/CH_4 and O_2/N_2): PIM−PIM-8 (▲),[46] PIM-1 (Δ),[10] PIM-1/silica MMM (○),[17] carboxylated PIM-1 (♦),[18] and UV-cross-linked PIM-1 (●).[19] (b) Upper bound comparison[8] (CO_2/CH_4, and CO_2/N_2): PIM−PIM-8 (▲),[46] PIM-1 (Δ),[10] carboxylated PIM-1 (♦),[18] UV-cross-linked PIM-1 (●),[19] Tetrazole-functionalized PIM-1 (▼),[20] Thermally rearranged (TR) polymer (■).[47]

permeability and selectivity increase when PIM-1 is thermally soaked from 0.5 to 2 d at 300 °C. As discussed previously, this is resulted from a joint effect of the tightening of polymer chains and formation of bulky triazine rings. Referring to Figure 7b, the binary gas separation performance also surpasses the most recent upper bound line, which strongly suggests that the thermally cross-linked PIM-1 membranes could be used in industry gas separation. Additionally, the long-term stability test and the physical aging behavior of the selected membranes have been monitored and the results are shown in Figure 8. Compared to the original PIM-1, the thermally cross-linked membrane (i.e., PIM-300−2.0d) tends to have a better membrane stability. With consideration of the stability over a longer period, future work will be focused on physical aging over a period of at least 3 months for the thermally cross-linked membranes and ways to enhance the degree of cross-linking reaction while minimizing the thermal energy consumed.

dx.doi.org/10.1021/ma202667y | Macromolecules 2012, 45, 1427−1437

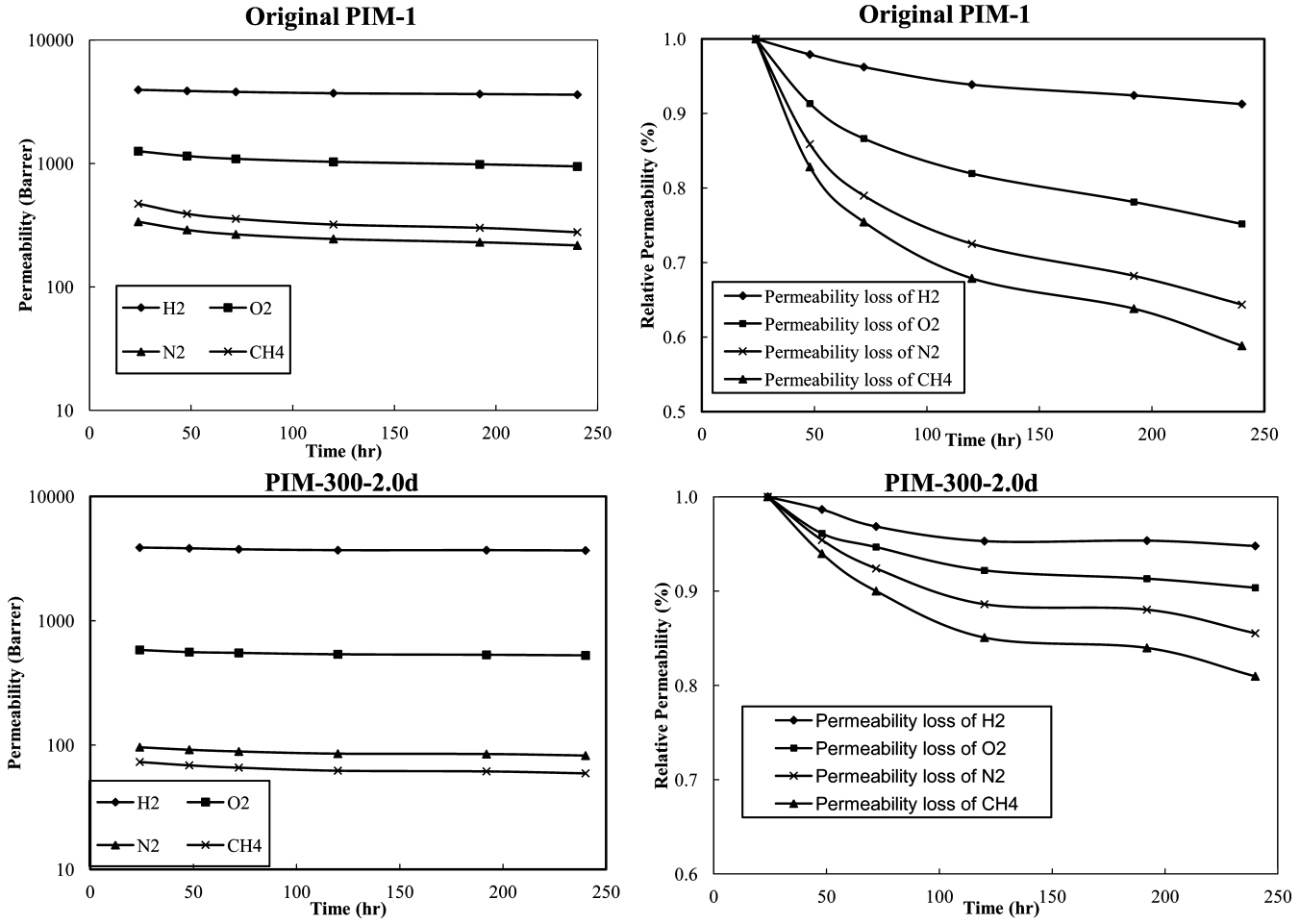


Figure 8. Aging behavior of the original and the thermally cross-linked PIM-1 membranes.

CONCLUSIONS

The high performance PIM-1 membrane has been successfully synthesized in our laboratory. The chemical structure of PIM-1 has been confirmed by XPS, FTIR and NMR analyses. After the thermal treatment of the PIM-1 film at an elevated temperature (i.e., 300 °C) for an extended period of time, the PIM-1 polymer chains tend to undergo a latent self-cross-linking reaction forming stable triazine rings. Both FTIR and XPS analyses of the resultant cross-linked PIM-1 membranes support the occurrence of cross-linking reaction and conversion of nitriles to imines. The degree of cross-linking reaction increases with an increase in thermal cross-linking time, which is also confirmed by gel content analyses. TGA analyses show an increase in thermal stability of the membrane after thermal cross-linking reaction and there is a reduction in the maximum decomposition rate when the PIM-1 membrane is thermally treated at a longer period of time. On the basis of PAL results, a clear reduction in τ_3 value with an increase in thermal treatment time suggests the chain tightening effects in the cross-linking reaction, while the formation of bulky triazine rings in the planar structure during the cross-linking reaction simultaneously constrains the polymer chains and prevents them from moving around. With the nature of the contorted structure of PIM-1 backbone, the cross-linking reaction would lead to the pronounced inefficient chain packing, thus an increase in free volume and gas permeability with the increase in thermal soaking time. In general, the thermally cross-linked PIM-1 membranes demonstrate exceptional gas separation performance that surpasses the most recent upper bounds for the important gas pairs, such as H_2/N_2, CO_2/CH_4, and CO_2/N_2. An ideal CO_2/CH_4 selectivity of 54.8, which is almost four times higher than the host PIM-1 membrane, with CO_2 permeability of 4000 barrer was obtained for PIM-1 membrane treated at 300 °C for 2 d, and mixed gas tests revealed a similar selectivity of 54. In conclusion, the thermally cross-linked PIM-1 membranes will possibly provide a promising alternative in industrial flue gas separation, natural gas purification and CO_2 capture process.

AUTHOR INFORMATION

Corresponding Author

*E-mail: chencts@nus.edu.sg.

Notes

The authors declare no competing financial interest.

ACKNOWLEDGMENTS

The authors sincerely express their gratitude to the Singapore National Research Foundation (NRF) for the financial support on the Competitive Research Programme for the project titled: "Molecular Engineering of Membrane Materials: Research and Technology for Energy Development of Hydrogen, Natural Gas and Syngas" (Grant Number R-279-000-261-281). Special thanks are also due to Miss Chua Mei Ling for her kind assistance in this work.

REFERENCES

(1) Nunes, S. P.; Peinemann, K.-V. *Membrane Technology in the Chemical Industry*; Wiley-VCH: Weinheim, Germany, 2006.
(2) Shao, L.; Samseth, J.; Hägg, M.-B. *J. Membr. Sci.* **2009**, *326*, 285−292.
(3) Car, A.; Stropnik, C.; Yave, W.; Peinemann, K.-V. *Adv. Funct. Mater.* **2008**, *18*, 2815−2823.
(4) Paul, D. R.; Yampolskii, Y. P. *Polymeric Gas Separation Membranes*; CRC Press: Boca Raton, FL, 1994.
(5) Bernardo, P.; Drioli, E.; Golemme, G. *Ind. Eng. Chem. Res.* **2009**, *48*, 4638−4663.
(6) Xiao, Y.; Chung, T. S. *Energy Environ. Sci.* **2011**, *4*, 201−208.
(7) Grainger, D.; Hägg, M.-B. *J. Membr. Sci.* **2007**, *306*, 307−317.
(8) Robeson, L. M. *J. Membr. Sci.* **2008**, *320*, 390−400.
(9) Budd, P. M.; Elabas, E. S.; Ghanem, B. S.; Makhseed, S.; McKeown, N. B.; Msayib, K. J.; Tattershall, C. E.; Wang, D. *Adv. Mater.* **2004**, *16*, 456−459.
(10) Budd, P. M.; Msayib, K. J.; Tattershall, C. E.; Ghanem, B. S.; Reynolds, K. J.; McKeown, N. B.; Fritsch, D. *J. Membr. Sci.* **2005**, *251*, 263−269.
(11) Du, N.; Song, J.; Robertson, G. P.; Pinnau, I.; Guiver, M. D. *Macromol. Rapid Commun.* **2008**, *29*, 783−788.
(12) Du, N.; Robertson, G. P.; Song, J.; Pinnau, I.; Thomas, S.; Guiver, M. D. *Macromolecules* **2008**, *41*, 9656−9662.
(13) Budd, P. M.; McKeown, N. B.; Ghanem, B. S.; Msayib, K. J.; Fritsch, D.; Starannikova, L.; Belov, N.; Sanfirova, O.; Yampolskii, Y.; Shantarovich, V. *J. Membr. Sci.* **2008**, *325*, 851−860.
(14) Staiger, C. L.; Pas, S. J.; Hill, A. J.; Cornelius, C. J. *Chem. Mater.* **2008**, *20*, 2606−2608.
(15) Song, J.; Du, N.; Dai, Y.; Roberson, G. P.; Guiver, M. D.; Thomas, S.; Pinnau, I. *Macromolecules* **2008**, *41*, 7411−7417.
(16) Thomas, S.; Pinnau, I.; Du, N.; Guiver, M. D. *J. Membr. Sci.* **2009**, *338*, 1−4.
(17) Ahn, J.; Chung, W.-J.; Pinnau, I.; Song, J.; Du, N.; Robertson, G. P.; Guiver, M. D. *J. Membr. Sci.* **2010**, *346*, 280−287.
(18) Du, N.; Robertson, G. P.; Song, J.; Pinnau, I.; Guiver, M. D. *Macromolecules* **2009**, *42*, 6038−6043.
(19) Liu, C.; Wilson, S. T.; Lesch, D. A. US Patent, 7,758,751, 2010.
(20) Du, N.; Park, H. B.; Robertson, G. P.; Dal-Cin, M. M.; Visser, T.; Scoles, L.; Guiver, M. D. *Nat. Mater.* **2011**, *10*, 372−375.
(21) Mason, C. R.; Maynard-Atem, L.; Al-Harbi, N. M.; Budd, P. M.; Bernardo, P.; Bazzarelli, F.; Clarizia, G.; Jansen, J. C. *Macromolecules* **2011**, *44*, 6471−6479.
(22) Hergenrother, P. M. *Macromolecules* **1974**, *7*, 575−582.
(23) Haddad, I. E.; Hurley, S. A.; Marvel, C. S. US Patent, 3,987,016, 1976.
(24) Idage, S. B.; Idage, B. B.; Shinde, B. M.; Vernekar, S. P. *J. Polym. Sci., Part A: Polym. Chem.* **1989**, *27*, 583−594.
(25) Mercer, F. W.; McKenzie, M. T.; Easteal, A.; Moses, S. J. *Polymer* **1994**, *35*, 5355−5363.
(26) Yu, G.; Wang, J.; Liu, C.; Lin, E.; Jian, X. *Polymer* **2009**, *50*, 1700−1708.
(27) Jean, Y. C.; Mallon, P. E.; Schrader, D. M. *Positron and Positronium Chemistry*; World Sci.: Singapore, 2003.
(28) Tao, S. J. *J. Chem. Phys.* **1972**, *56*, 5499−5510.
(29) Williams, M. L.; Landel, R. F.; Ferry, J. D. *J. Am. Chem. Soc.* **1955**, *77*, 3701−3707.
(30) Jean, Y. C. *Microchem. J.* **1990**, *42*, 72−102.
(31) Shukla, A.; Hoffmann, L.; Manuel, A. A.; Peter, M. *Mater. Sci. Forum* **1977**, *255*, 233−237.
(32) Shieh, J. J.; Chung, T. S. *J. Polym. Sci. Polym. Phys.* **1999**, *37*, 2851−2861.
(33) Tin, P. S.; Chung, T. S.; Liu, Y.; Wang, R.; Liu, S. L.; Pramoda, K. P. *J. Membr. Sci.* **2003**, *225*, 77−90.
(34) Wang, H.; Liu, S.; Chung, T. S.; Chen, H.; Jean, Y. C.; Pramoda, K. P. *Polymer* **2011**, *52*, 5127−5138.
(35) Clark, D. T. *Adv. Polym. Sci.* **1977**, *24*, 125−188.
(36) Hiraoka, H.; Lee, W.-Y. *Macromolecules* **1978**, *11*, 622−624.
(37) Rossi, F.; Andre, B.; Veen, A. V.; Mijnarends, P. E.; Schut, H.; Labohm, F.; Dunlop, H.; Delplancke, M. P.; Hubbard, K. *J. Mater. Res.* **1994**, *9*, 2440−2449.
(38) Dementjev, A. P.; de Graaf, A.; Van de Sanden, M. C. M.; Maslakov, K. I.; Naumkin, A. V.; Serov, A. A. *Diamond Relat. Mater.* **2000**, *9*, 1904−1907.
(39) Xiao, Y.; Shao, L.; Chung, T. S.; Schiraldi, D. A. *Ind. Eng. Chem. Res.* **2005**, *44*, 3059−3067.
(40) Hasegawa, M.; Kochi, M.; Mita, I.; Yokota, R. *Eur. Polym. J.* **1989**, *25*, 349−354.
(41) Tin, P. S.; Chung, T. S.; Hill, A. J. *Ind. Eng. Chem. Res.* **2004**, *43*, 6476−6483.
(42) Shao, L.; Chung, T. S.; Goh, S. H.; Pramoda, K. P. *J. Membr. Sci.* **2004**, *238*, 153−163.
(43) Du, N.; Robertson, G. P.; Pinnau, I.; Guiver, M. D. *Macromolecules* **2009**, *42*, 6023−6030.
(44) McKeown, N. B.; Budd, P. M. *Macromolecules* **2010**, *43*, 5163−5176.
(45) Coleman, M. R.; Koros, W. J. *Macromolecules* **1999**, *32*, 3106−3113.
(46) Ghanem, B. S.; McKeown, N. B.; Budd, P. M.; Selbie, J. D.; Fritsch, D. *Adv. Mater.* **2008**, *20*, 2766−2771.
(47) Park, H. B.; Jung, C. H.; Lee, Y. M.; Hill, A. J.; Pas, S. J.; Mudie, S. T.; Wagner, E. V.; Freeman, B. D.; Cookson, D. J. *Science* **2007**, *318*, 254−258.

Macromolecules

Article

pubs.acs.org/Macromolecules

Cross-Linked Benzoxazine–Benzimidazole Copolymer Electrolyte Membranes for Fuel Cells at Elevated Temperature

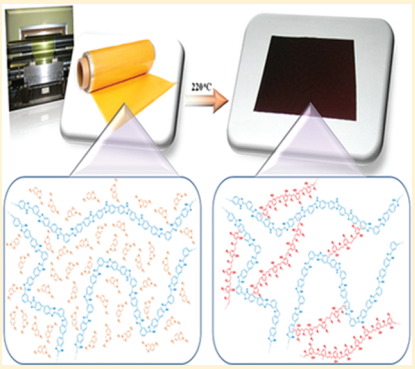
Sung-Kon Kim,[†] Seong-Woo Choi,*[,‡] Woo Seong Jeon,[‡] Jung Ock Park,[‡] Taeyun Ko,[†] Hyuk Chang,[‡] and Jong-Chan Lee*[,†]

[†]Department of Chemical and Biological Engineering, and Institute of Chemical Process, Seoul National University, 599 Gwanak-ro, Gwanak-gu, Seoul 151-744, Republic of Korea

[‡]Energy Lab., Samsung Advanced Institute of Technology, Samsung Electronics Co., Ltd., Nongseo-dong, Giheung-gu, Gyeonggi-do 446-712, Republic of Korea

Supporting Information

ABSTRACT: Here we report new H_3PO_4-doped cross-linked benzoxazine–benzimidazole copolymer membranes showing high proton conductivity and long-term durability for use in proton-exchange membrane fuel cells at elevated temperatures (>100 °C). The cross-linked copolymer membranes were prepared by mixing of poly[2,2′-(*m*-phenylene)-5,5′-bibenzimidazole] (PBI) with 3-phenyl-3,4-dihydro-6-*tert*-butyl-2*H*-1,3-benzoxazine (*p*BUa) in *N*,*N*-dimethylacetamide, with subsequent stepwise heating to 220 °C, and even large-sized films (30 cm × 140 m) could be easily prepared. The membranes showed high proton conductivities of up to 0.12 S cm^{-1} at 150 °C under anhydrous conditions. Membrane–electrode assemblies (MEAs) employing the membranes showed operating voltages of 0.71 V at 0.2 A cm^{-2}. Furthermore, the MEAs displayed long-term durability up to 1999 cycles, with much slower performance decay, −0.03 mV h^{-1}, than those prepared using the PBI membrane in *in situ* accelerated lifetime mode (load cycling testing).



INTRODUCTION

Polymer electrolyte membrane fuel cells (PEMFCs) have gained much attention as clean energy source, especially in their use at elevated temperature (generally 120–200 °C) and low-humidity conditions. However, PEMs suitable for operation at low temperature (<100 °C) in humid conditions, typified by Nafion membranes, have many weaknesses when they are used at elevated temperature or low humidity, for example, low conductivity, CO tolerance, and heat rejection.[1,2] Elevated temperature (120–200 °C) and low humidity (relative humidity (RH) < 50%) operation are desirable for surmounting these shortcomings of low-temperature PEMs[3,4] and have been sought through developing novel PEMs.[1,5−11] Much work has been focused on polybenzimidazole and its derivatives doped with phosphoric acid (PA) as a PEM in elevated temperature fuel cell process.[12−17] In particular, poly[2,2′-(*m*-phenylene)-5,5′-bibenzimidazole] (PBI, Figure 1a) is attractive as it exhibits high proton conductivity at up to 200 °C, low gas permeability, excellent oxidative and thermal stabilities, good mechanical stability, and an almost zero water drag coefficient.[11,18−21] Despite its obvious advantages, PBI has a critical drawback: the loss of its stability at large PA content.[19] Proton transport in PA-doped PBI relies on PA complexed with basic sites, imidazole units, in the PBI backbone, and the increase of PA content in PBI membranes usually increases the proton transport capability. Large PA contents degrade the chemical and mechanical stabilities of the membranes, especially at elevated temperature, hindering their use as PEMs.[19] Therefore, the development of PBI membranes that are stable at elevated temperature and pressure as well as large PA content in the membrane is important for the development of durable PEMs. Cross-linking,[22,23] blending,[24] copolymerization,[25] and hybridization with inorganic fillers[26] have been reported to improve the stability of PBI membranes. However, using the approaches mentioned above, long-term durability has not yet been achieved without decreasing proton conductivity.

Polybenzoxazines have been developed as alternatives to phenolic resins for elevated temperature application (Figure 1b).[27,28] They can be simply prepared through the ring-opening of cyclic benzoxazine monomers by heat treatment without any catalysts. Cross-linked polymeric materials with excellent thermal and dimensional stabilities are then obtained without byproducts. Various raw materials, including phenol and amine derivatives, could be used to make the benzoxazine monomer, with the final polybenzoxazine products then showing a range of chemical and physical properties because of the various linkage groups in the Mannich base bridges [−CH_2−N(R)−CH_2−]. There are very few reports of polybenzoxazines as PEMs for low-temperature application (<100 °C). Benzoxazines have been used as cross-linking agents for curing themselves, rather than for covalently bonding with a host material.[29] To the best the authors' knowledge, polybenzox-

Received: December 12, 2011
Revised: January 17, 2012
Published: January 31, 2012

 © 2012 American Chemical Society

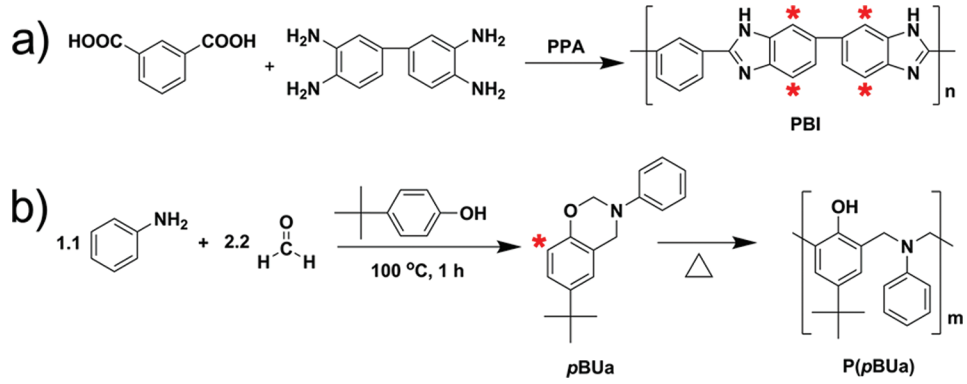


Figure 1. Synthesis of (a) PBI and (b) *p*BUa and P(*p*BUa).

azines have not previously been reported for use at elevated temperature in PEM fuel cells.

This work reports novel cross-linked copolymeric membranes based on polybenzimidazole and polybenzoxazine that show high proton conductivity, improved cell performance, and long-term durability compared with the PBI membrane. They were prepared by the solution mixing of the PBI with a benzoxazine monomer and subsequent heating.

EXPERIMENTAL SECTION

Materials. Isophthalic acid (99%, Aldrich) was purified by recrystallization in ethanol to obtain white needlelike crystals. 3,3′-Diaminobenzidine (97%, Tokyo Kasei, TCI), poly(phosphoric acid) (PPA, 116% H_3PO_4, Junsei), phosphorus pentoxide (97%, Aldrich), phosphoric acid (PA, 85 wt % aqueous solution, Aldrich), and poly(vinylidene fluoride) (PVDF, $M_n \sim 107\,000$, $M_w \sim 275\,000$, Aldrich) were used as received. 4-*tert*-Butylphenol (99%), *p*-formaldehyde (95%), and aniline (99%) were from Aldrich and used without further purification. Other solvents were used as received.

Synthetic Procedures. *3-Phenyl-3,4-dihydro-6-tert-butyl-2H-1,3-benzoxazine (pBUa).* Stoichiometric amounts of 4-*tert*-butylphenol (15.0 g, 0.100 mol), *p*-formaldehyde (6.61 g, 0.220 mol), and aniline (10.2 g, 0.110 mol) were used in benzoxazine monomer synthesis. *p*-Formaldehyde and aniline were stirred for 5 min at 60 °C in a 250 mL one-neck round-bottomed flask, 4-*tert*-butylphenol was added, and the temperature was raised to 100 °C. After 60 min, the stirring was stopped and the mixture was cooled to room temperature. The crude benzoxazine monomer was washed twice with 1 N NaOH solution and then with distilled water to give the final yellowish glassy solid product (94%). ^{1}H NMR (500 MHz, $CDCl_3$, ppm): δ 7.31−7.21 (m, 2H), 7.16−7.07 (m, 3H), 6.99 (s, 1H), 6.95−6.87 (t, J = 7.34 Hz, 1H), 6.74 (d, J = 8.4 Hz, 1H), 5.32 (s, 2H), 4.63 (s, 2H), 1.30 (s, 9H). ^{13}C NMR (125 MHz, $CDCl_3$, ppm): δ 152.0, 148.5, 143.5, 129.2, 124.8, 123.2, 121.2, 120.0, 118.1, 116.4, 76.57, 50.78, 34.08, 31.47.

Poly[2,2′-(m-phenylene)-5,5′-(bibenzimidazole)] (PBI). PBI was synthesized by the condensation polymerization of 3,3′-diaminobenzidine (DABI) with isophthalic acid (IPA) in poly(phosphoric acid) (PPA) at 200 °C. The sequence of the experimental steps applied during this polymerization procedure is as follows. PPA (90.2 g) was added to a 250 mL three-neck reactor equipped with a mechanical stirrer, nitrogen inlet, and calcium chloride drying tube and heated for 30 min at 150 °C. DABI (2.78 g, 13.0 mmol) and IPA (2.16 g, 13.0 mmol) were then added portionwise, and the solution was stirred for 1 h at 150 °C to be a homogeneous solution under a slow nitrogen stream. The reaction temperature was heated to 200 °C with constant stirring for 30 min. Finally, phosphorus pentoxide (4.84 g, 17.0 mmol) was added and heated to 200 °C for 12 h with constant stirring using a mechanical stirrer. During this time, the reaction mixture turned to a very viscous dark brown solution. The homogeneous solution was decanted into distilled water (1000 mL) to isolate the polymer, and the precipitate was neutralized with an aqueous solution of $NaHCO_3$ and rinsed several times with distilled water to remove phosphate salts. The precipitate was then dried overnight in a vacuum oven. The resulting polymer was ground using a pulverizer (A11 basic, IKA) and washed again to remove any residual phosphoric acid. Finally, the powder was dried at 70 °C in a vacuum oven for 3 days. Yield: >95%. FT-IR spectrum (KBr, cm^{-1}): 3450−3250 (ν N−H), 1640 (ν C═N). ^{1}H NMR chemical shifts (500 MHz, DMSO-d_6, ppm): δ 9.14 (s, 1H), 8.32 (d, 2H), 8.00 (s, 2H), 7.81 (d, 2H), 7.62 (br, 3H).

Preparation of PA-Doped P(*p*BUa-*co*-BI) Membranes. P(*p*BUa-*co*-BI) films were prepared by reacting different wt % of *p*BUa and PBI by solution casting, followed by stepwise heating from 60 to 220 °C for 4 h and then maintaining the temperature for an hour. PA doping was achieved by immersing dried P(*p*BUa-*co*-BI) films in 80−85 wt % PA solution at 80 °C for 4 h. The details are as follows.

When the weight ratios of *p*BUa to PBI were 65, 50, and 35, they are represented by P(*p*BUa-*co*-BI)-65, P(*p*BUa-*co*-BI)-50, and P(*p*BUa-*co*-BI)-35, respectively. The following procedure was used for the preparation of P(*p*BUa-*co*-PBI)-65. Other P(*p*BUa-*co*-PBI)s were prepared using the same procedure except the weight ratios of *p*BUa to PBI. The polymer films were prepared using solution casting techniques. 5.00 g of PBI powder and 9.28 g of *p*BUa were dissolved in 128 g of a DMAc solution at 80 °C. The blended solution was then spread onto a clean flat glass plate. The thickness of the solution was controlled using an adjustable doctor blade, and the thermal treatment of the blended solution is followed. The cast solution was heated stepwise from 60 to 220 °C for 4 h in a convection oven until no DMAc evaporation was noted, and then maintaining the temperature for an hour. After cooling to room temperature slowly, the obtained brown film, P(*p*BUa-*co*-BI), was soaked in distilled water and peeled from the substrate. The resulting film was dried at room temperature under vacuum for 2 days. The thickness of the dried films ranged from 30 to 50 μm. We found that the variation of the polymer film thickness in the range of 50−70 μm does not affect the proton conductivity if they have same PA contents. For achieving the proton conduction ability of the membrane, the dried films were immersed in 1000 mL of the PA solution with 80−85 wt % concentration at 80 °C for 4 h. The PA-doped membranes were taken out from the PA solution and then blotted with filter paper. The PA-doped membranes were dried at 70 °C under vacuum for 2 days and weighed again (W_{doped}). The PA within the membranes was intentionally removed by rinsing with an aqueous solution of $NaHCO_3$ and distilled water several times in order to measure the PA content. The films were then dried for 2 days in a vacuum oven and weighed ($W_{undoped}$). The weight difference ($W_{doped} - W_{undoped}$) was assumed to be the weight of the absorbed PA. The PA content of the membrane was then calculated as the wt % of PA absorbed in the membrane using eq 1.

$$\text{PA content (wt \%)} = (W_{doped} - W_{undoped})/W_{doped} \times 100 \quad (1)$$

The PA-doped PBI membranes was also prepared by the solution-casting method commonly used.[19,30]

dx.doi.org/10.1021/ma202694p | *Macromolecules* 2012, 45, 1438−1446

Characterization. The ^{1}H and ^{13}C nuclear magnetic resonance (NMR) spectra were collected on a Bruker Avance 500 with a proton frequency of 500 MHz. During the experiments, deuterated dimethyl sulfoxide was used as the solvent and tetramethylsilane (TMS) was used as the internal standard. Inherent viscosity was measured using an Ubbelode viscometer in a water bath at 30 °C. Polymer powder, dried under vacuum at 70 °C for 2 days, was dissolved in 96% H_2SO_4 solution at 0.3 g dL^{-1} for the viscosity tests. Gel fractions were measured by solvent extraction.[31] 2 cm × 2 cm films were dried at 70 °C under vacuum for 2 days and weighed (W_1), and then the dried films were soaked and refluxed in excess DMAc for 24 h. The solvent was changed frequently until extraction was completed. The films were then repeatedly washed with distilled water and dried for 2 days in a vacuum oven until constant weight (W_2). The gel fractions were then calculated as follows:

$$\text{gel fraction } (\%) = W_2/W_1 \times 100 \quad (2)$$

The P(*p*BUa) units per PBI repeat unit were estimated by the weight change upon PA doping. 2 cm × 2 cm films were dried at 70 °C under vacuum for 2 days, weighed (W_3), and immersed in 85 wt % PA solution at 80 °C for 4 h. They were then repeatedly washed with distilled water and dried for 2 days in a vacuum oven until constant weight (W_4). P(*p*BUa) units per PBI repeat unit were calculated as follows:

$$\begin{aligned}&\text{P}(p\text{BUa}) \text{ units per PBI repeat unit}\\ &= \{[W_3 \times \text{P}(p\text{BUa}) \text{ content}/100 - (W_3 - W_4)\\ &\quad /\text{MW}_{\text{P}(p\text{BUa})}]\}/[(W_3 \times \text{PBI content}/100)\\ &\quad /\text{MW}_{\text{PBI}}] \end{aligned} \quad (3)$$

where P(*p*BUa) content and PBI content are their wt % in the membrane and $\text{MW}_{\text{P}(p\text{BUa})}$ and MW_{PBI} are the molecular weights of the P(*p*BUa) (267.37 g mol^{-1}) and the PBI (308.34 g mol^{-1}) repeat units, respectively.

Diffusion coefficients were assessed using a 5 mm Bruker QNP or TXI probe with an actively shielded *z* gradient coil. They were extracted from ^{1}H NMR spectra measured by bipolar pulse longitudinal encode−decode (BPPLED) pulse sequences with respect to gradient amplitude. Typically, a 10 mg sample was dissolved in 0.75 mL of DMSO-d_6, and the gradient strength was logarithmically incremented in 16 steps from 2% to 95% of its maximum. Diffusion times and gradient pulse durations were optimized for each experiment to achieve a 95% decrease of resonance intensity at the largest gradient amplitude. Pulse sequences were employed with diffusion time (Δ = 0.1 s) and bipolar rectangular gradient (δ = 200 ms) pulses. After Fourier transformation and baseline correction, the diffusion dimensions of the 2D DOSY spectra were processed by Bruker Xwinnmr software (version 3.5) or Bruker Topspin software package (version 1.3). Differential scanning calorimetry (DSC) was measured on a TA Instruments 2920 modulated calorimeter at a rate of 10 °C min^{-1}. Melting transition temperature was observed at the maximum of the endothermic peak, and glass transition temperature (T_g) was taken as the point of inflection of the plot of the change in heat capacity with temperature from the DSC thermograms. Proton conductivity was measured using a four-point probe. Impedance was measured using a ZAHNER IM-6ex impedance analyzer in potentiostat mode with a perturbation amplitude of 10 mV over frequencies of 1 Hz to 1 MHz. Impedance at a controlled humidity and temperature was measured from Nyquist plots. Proton conductivity (σ) was calculated using $\sigma = d/RS$, where d is the distance between the reference and sensing electrodes and S is the cross-sectional area (thickness × width) of the doped membrane. 1 cm × 5 cm membranes were introduced to the conductivity cell and heated to 160 °C and held for 30 min. Measurements were taken as the cell then cooled to 100 °C in 10 °C steps. For large-sized scale film production (30 cm × 140 m), the mixed solution of *p*BUa and PBI in DMAc was prepared as a concentrated solution (30 wt %). The films were coated on poly(ethylene terephthalate) (PET) base film and produced continuously using a slot die coater CAG-750 (Inokin Co. Ltd., Japan) with a total length of 4 m and floating dryers. Drying zones were divided into two compartments, 100 and 130 °C, respectively. The machine speed was 0.5 m min^{-1}. The films were detached from PET base film and then transferred to an oven, followed by stepwise thermal treatment from 60 to 220 °C for 4 h.

Preparation of Membrane−Electrode Assembly (MEA). Slurry for forming catalyst layers was prepared by adding catalyst powder into PVDF in *N*-methyl-2-pyrrolidone (NMP). After the slurry was evenly spread on wet-proofed carbon using an automated doctor blade, the electrode catalyst layers were dried at 120 °C for 2 h in a ventilated oven. Catalyst layers of PtCo alloy (cathode) and PtRu (anode) were supported on carbon (Tanaka Kikinzoku Kogyo K.K., TEC36E52) and PVDF. The mean platinum loadings of catalyst layer were 0.9 mg cm^{-2} on the anode and 1.7 mg cm^{-2} on the cathode. The PA-doped membrane was mounted in a single cell, and then the electrodes and membrane without a preceding hot-pressing step were assembled in a lab-made single cell with graphite bipolar plates and gold-plated copper end plates. The active area of the MEA was 7.84 cm^2; the assembling torque was 3 N m. The MEA was operated at 150 °C with flows of hydrogen fuel and air without humidification at ambient pressure and a flow rate of 100 and 250 cm^3 min^{-1}, respectively.

Cell Performance Measurement and Acceleration Lifetime Test (ALT). The cell performance testing and *in situ* ALT were executed on a lab-made fuel cell test station. Unit cells were operated at 150 °C with hydrogen at 100 cm^3 min^{-1} and air at 250 cm^3 min^{-1} without humidification at ambient pressure. During *in situ* ALT, cell voltage was altered continuously through stepwise load circulation; it was recorded in its steady state at each load without fluctuation. Current density was increased stepwise from 0 to 1.0 A cm^{-2} for 1 h and then recurred to zero again. Such cycling was repeated until open-circuit voltage (OCV) dropped below 0.9 V.

RESULTS AND DISCUSSION

Synthesis and Characterization of Cross-Linked Benzoxazine−Benzimidazole Copolymer (P(*p*BUa-*co*-BI)) Membranes. Figure 1b shows the chemical structure of the benzoxazine monomer, 3-phenyl-3,4-dihydro-6-*tert*-butyl-2*H*-1,3-benzoxazine, abbreviated as *p*BUa used in this study, and its details are discussed in the Supporting Information (Figures S1−S3). It can easily be polymerized by heating the bulk monomer contained in a glass flask, or a DSC pan, or on a glass plate; the resulting polymer is named P(*p*BUa). PBI was prepared by condensation polymerization in a reaction medium of poly(phosphoric acid) (PPA). Its inherent viscosity (0.85 dL g^{-1}) is sufficient to produce free-standing films with reasonable physical properties for fuel cell applications.[11] PBI and *p*BUa powders were dissolved in DMAc, yielding a homogeneous solution that was solution cast to fabricate P(*p*BUa-*co*-BI)-*X* membranes,[11] where *X* represents the P(*p*BUa) to PBI wt %. The P(*p*BUa-*co*-BI) membranes with cross-liked copolymeric structures were fabricated simultaneously by spontaneous polymerization and cross-linking reactions of *p*BUa upon heating. The formation of cross-linked copolymeric structures was confirmed by 2D diffusion ordered spectroscopy (DOSY) NMR, the chemical stability of the membranes, and DSC as listed in the latter part of this paper. At P(*p*BUa) contents relative to PBI of over 65 wt %, the P(*p*BUa-*co*-BI) membranes became brittle and nonhomogeneous. Therefore, the maximum tested P(*p*BUa) content was 65 wt %.

The 2D DOSY NMR technique was used to investigate the cross-linking reactions of linear PBI with *p*BUa during casting. Figure 2a shows a spectrum obtained after heating at 140 °C for 30 min. The insolubility of the final product in any solvents forced NMR spectra to be recorded during the early stages of

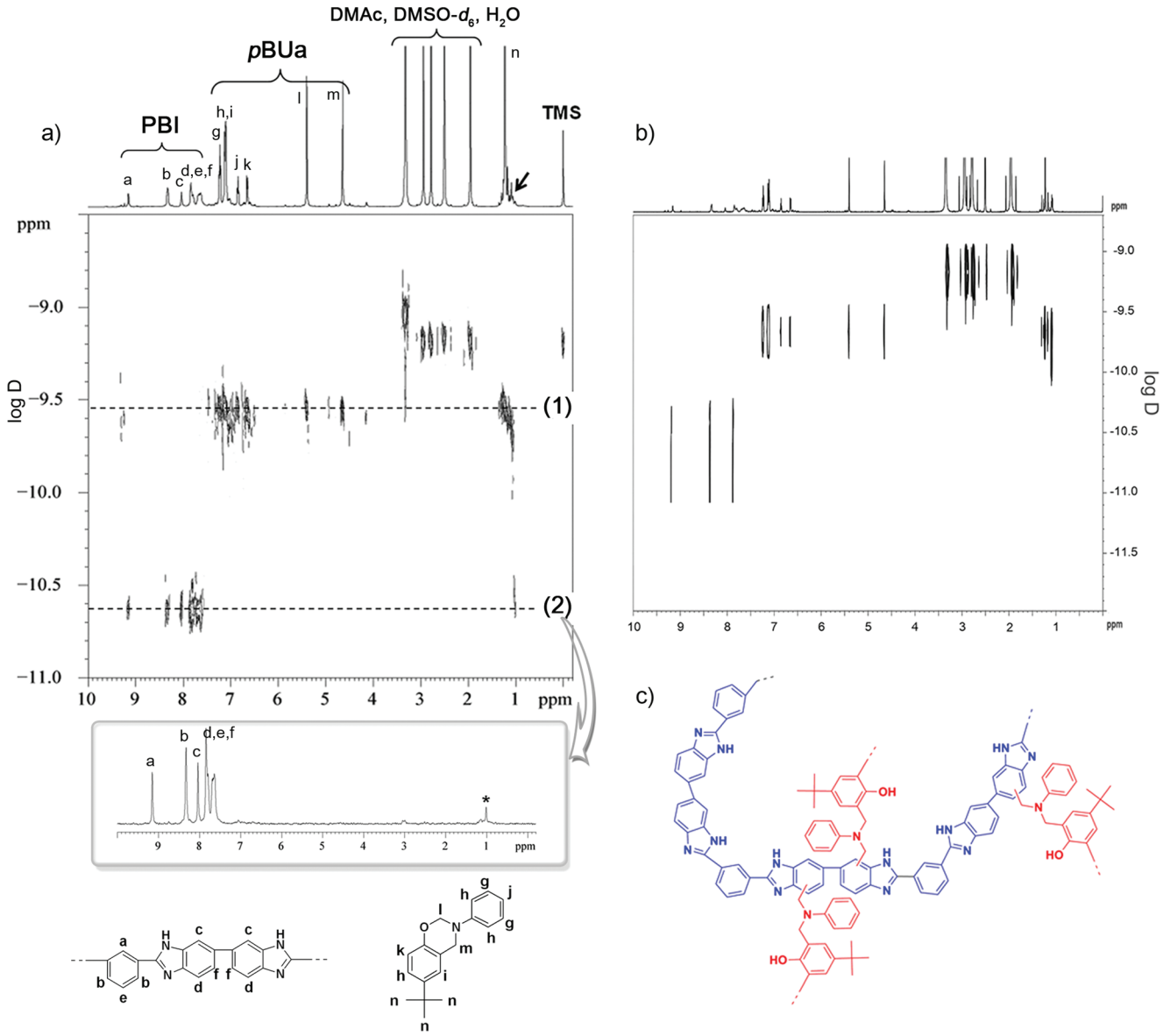


Figure 2. 2D DOSY NMR spectra of (a) *p*BUa and PBI mixture (*p*BUa:PBI = 65:35 (wt %)) obtained at 140 °C for 30 min, (inset) 1D slice ^{1}H NMR spectrum at ca. −10.6 ppm, and (b) mixture of *p*BUa obtained at 140 °C for 1 h and PBI (*p*BUa:PBI = 65:35 (wt %)). (c) Possible chemical structure of P(*p*BUa-*co*-BI)s.

polymerization, when some solubility was retained. DOSY NMR can classify the spectrum of each constituent through differences of their hydrodynamic volumes (or diffusion coefficients) in solution.[32,33] It can classify multicomponent mixtures in solution without requiring preliminary treatment. Theoretically, the same size of elements or molecules should appear in DOSY NMR spectra in the same line of the *y*-axis if they have same diffusion coefficients. Therefore, the signals in Figure 2a from the low-molecular-weight solvents like water, DMSO, and DMAc appear in similar positions at −9.0 to −9.2 ppm on the *y*-axis. The *p*BUa monomer signals and the 1.2 ppm signal from its *tert*-butyl moiety on the *x*-axis before polymerization appear at −9.5 to −9.6 ppm, as indicated by dotted line (1). On the other hand, the signals from PBI appear at ca. −10.6 ppm on the *y*-axis. By the principle of DOSY NMR, the *y*-axis coefficient, related to diffusion coefficient, becames larger minus values as molecular size increases. Therefore, it is reasonable that the signal from PBI is larger minus values than that from *p*BUa. We could also observe the small signal at 1.1 ppm in Figure 2a showing smaller intensity (marked by an arrow in Figure 2a and Figure S4) after the ring-opening (or polymerization) even at the very beginning stage of polymerization of *p*BUa. It is attributable to the *tert*-butyl moiety of *p*BUa after the ring-opening (or polymerization) of the oxazine ring from a series of ^{1}H NMR spectrum (Figure S1) of *p*BUa obtained after heating from 180 to 220 °C. The 1.1 ppm signal at −9.6 to −10.1 ppm on the *y*-axis appears more negative than the signal of the *p*BUa monomer at 1.2 ppm, indicating an increased diffusion coefficient of the *p*BUa upon polymerization. Interestingly, some of signal at 1.0 ppm appears at the same position as PBI (dotted line (2), Figure 2a) at ca. −10.6 ppm on the *y*-axis, possibly because protons in the *tert*-butyl had the same diffusion coefficient as those in PBI. The separate 1D slice NMR spectrum (inset, Figure 2a) at ca. −10.6 ppm on the *y*-axis shows *tert*-butyl protons at 1.0 ppm (marked by an asterisk in inset), which are not observed in the

dx.doi.org/10.1021/ma202694p | *Macromolecules* 2012, 45, 1438−1446

PBI or the P(*p*BUa) homopolymers. Possibly other aromatic proton signals from P(*p*BUa) homopolymers (6.0−7.7 ppm) are not clearly observed in the inset in Figure 2a, or they are in the NMR spectra while not clearly observed with the NMR resolutions we have. The *tert*-butyl group, with nine protons, is located at the side chain, so larger signal intensity is expected, while other aromatic groups located in the polymer backbone have only one or two protons and their proton signal intensity should be much smaller or they may be overlapped with those of PBI.[34] The *tert*-butyl signals at ca. −10.6 ppm on the *y*-axis were confirmed to be caused by the copolymeric structures in separate 2D DOSY NMR experiments. P(*p*BUa) homopolymer was intentionally prepared by heating the *p*BUa monomer at 140 °C for 60 min. It was mixed with PBI homopolymer at a 65 to 35 wt % ratio, and 2D DOSY NMR measurements were taken (Figure 2b). In the separate NMR spectrum, signals from *tert*-butyl protons at 1.0 ppm are not observed at ca. −10.6 ppm on the *y*-axis where the PBI signals appear. Therefore, we believe that the P(*p*BUa) signal at ca. −10.6 ppm on the *y*-axis is due to covalently bonded copolymeric structures of PBI and P(*p*BUa) moieties. The formation of cross-linked structures was further confirmed from chemical stability experiments shown at the next part of this article. The polymerization of benzoxazine has been known to proceed through reaction of the unobstructed ortho position of the benzene ring (asterisk in *p*BUa, Figure 1b) with the methylene group between oxygen and nitrogen on the oxazine ring.[35] PBI also has four carbons at the unobstructed ortho position of the benzene ring (asterisk in PBI, Figure 1a), and their reactivity should be close to or exceed that in benzoxazine due to the electron-withdrawing imidazole groups.[35,36] Therefore, we assumed that the peripheries of the carbons (marked by asterisk in Figure 1a,b) of benzene rings in PBI could covalently react with the methylene groups of *p*BUa (Figure 2c).

Chemical Stability. Figure 3 shows P(*p*BUa) powder, PBI, mixed P(*p*BUa) and PBI at 65:35 wt %, and P(*p*BUa-*co*-BI)-65

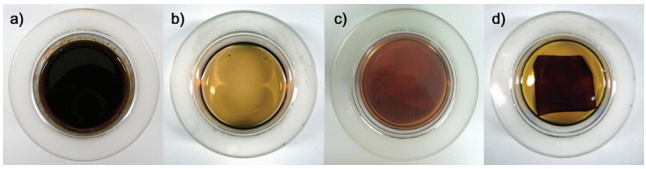


Figure 3. Chemical stability of (a) P(*p*BUa) powder, (b) PBI, (c) mixture of P(*p*BUa) (65 wt %) and PBI (35 wt %), and (d) P(*p*BUa-*co*-BI)-65 membranes after being immersed in an open flask with 85 wt % PA solution at 160 °C for 5 h.

membranes after immersion in an open flask with 85 wt % PA solution at 160 °C for 5 h. All samples dissolved in the PA solution completely, except P(*p*BUa-*co*-BI)-65, which showed some degree of swelling. The swelling was too inconsistent in its position and extent to be quantifiable.[37] The PA solution containing the P(*p*BUa-*co*-BI)-65 membrane became brown due to the dissolution of P(*p*BUa), PBI, and/or less cross-linked P(*p*BUa-*co*-BI)-65. This was confirmed by ^{1}H NMR spectroscopy (Figure S5). This result, the complete dissolution of the homopolymers (P(*p*BUa) and PBI) and their mixture while the only very low degree of swelling of P(*p*BUa-*co*-BI) membranes in the PA solution, indicates that P(*p*BUa-*co*-BI)s are cross-linked and copolymerized and not a just simple mixture of the two components, despite them possibly containing small amount of unreacted P(*p*BUa) and PBI in the film. The extents of extract and gel fractions were evaluated by solvent extraction experiment using DMAc to assess the compositions of P(*p*BUa-*co*-BI) membranes,[31] and the details will be discussed in the latter part.

Thermal and Thermooxidative Properties. Thermal and thermooxidative behaviors of the undoped polymers were examined by TGA under an air atmosphere to determine their degradation temperatures up to 800 °C. All the P(*p*BUa-*co*-BI) samples were thermally stable up to 450 °C (Figure S6). The decomposition temperatures of PBI, P(*p*BUa-*co*-BI)-65,-50,-35, and P(*p*BUa), at which they retained 90% of their initial weight, are 535, 458, 485, 483, and 330 °C, respectively. During initial heating, at around 100 °C, PBI shows a small weight loss from the evaporation of absorbed water,[38] and then its weight is maintained up to 500 °C, demonstrating its excellent thermal and thermooxidative stabilities. Since P(*p*BUa) is less hygroscopic than PBI, it shows lower initial water loss. However, the decomposition temperatures of P(*p*BUa-*co*-BI)s decrease with increasing P(*p*BUa) content because of the lower decomposition temperature of P(*p*BUa) than PBI.

Figure 4 clearly shows the glass transition temperature (T_g) of P(*p*BUa) at 115 °C, while those of P(*p*BUa-*co*-BI)s are not

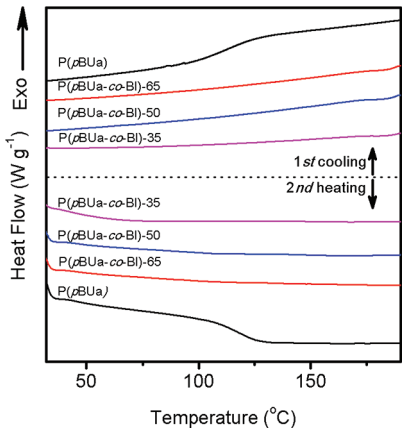


Figure 4. DSC first cooling and second heating curves of P(*p*BUa-*co*-BI)s.

detectable. Since PBI derivatives are composed of very rigid aromatic backbones, their T_g has not been easily observed by DSC.[39−41] Therefore, the reaction products, P(*p*BUa-*co*-BI)s, are not a simple mixture but a covalently bonded product, and the PA solution test at 160 °C clearly indicates that the products are cross-linked covalently. We also tried to detect T_g through dynamic mechanical thermal analyzer (DMTA). However, the detection of T_g competed with thermal degradation in air; hence, we could not obtain convincing results for T_g (Figure S7). We also measured the mechanical properties such as tensile strength, elongation at break, and modulus of the PA-doped membranes obtained after immersion in 85 wt % of PA solution at 80 °C for 4 h (Table S1). As the P(*p*BUa) content increases, the PA content in the membrane increases. As a consequence, the elongation at break increases while the tensile strength and modulus of the membranes decrease with the increase of the PA content.

Proton Conductivity. The proton conductivities of P(*p*BUa-*co*-BI) membranes with different PA content were measured at 100−160 °C under anhydrous conditions (Figure S8). In particular, the proton conductivity showed Arrhenius-type behavior ($\sigma = \sigma_0 \exp(-E_a/RT)$, where σ_0 is the pre-

dx.doi.org/10.1021/ma202694p | *Macromolecules* 2012, 45, 1438−1446

exponential factor and E_a is the activation energy for proton conduction), indicating that proton conduction in P(*p*BUa-*co*-BI) membranes follows a proton hopping dominant mechanism (Grotthuss mechanism).[25,42,43] The proton conductivity increases with increasing temperature and PA content (Table 1). Figure 5a shows the proton conductivity of P(*p*BUa-*co*-BI) membranes having close values of PA content ca. 81 wt %. Although all the membranes do not have exact 81 wt % of PA content, Figure 5a can explain the effect of P(*p*BUa) content on the conductivity behavior quite well because their PA content is not much different. It was not possible to prepare membranes to have the exact same content of PA. P(*p*BUa-*co*-BI)-20,-10 membranes were also prepared to further attest the effect of P(*p*BUa) content on proton conductivity. The proton conductivities of P(*p*BUa-*co*-BI) membranes with less than 50 wt % P(*p*BUa) content are lower than those of PBI with a similar PA content. P(*p*BUa-*co*-BI)-65 shows the highest value of ca. 0.10 S cm^{-1}. P(*p*BUa) units per PBI repeat unit and gel fractions (or degree of cross-linking) were estimated to assess how proton conductivity was influenced by P(*p*BUa) content (Table 2).

Table 1. PA Content and Proton Conductivity of P(*p*BUa-*co*-BI)s

membranes	PA content (wt %)	σ at 120 °C[a] (S cm^{-1})	σ at 150 °C[a] (S cm^{-1})
P(*p*BUa-*co*-BI)-65	88.5	0.1051	0.1206
P(*p*BUa-*co*-BI)-65	81.9	0.0942	0.1078
P(*p*BUa-*co*-BI)-50	83.9	0.0712	0.0922
P(*p*BUa-*co*-BI)-35	83.0	0.0673	0.0792
P(*p*BUa-*co*-BI)-20	87.4	0.0924	0.1073
P(*p*BUa-*co*-BI)-20	79.5	0.0528	0.0665
P(*p*BUa-*co*-BI)-10	84.5	0.0803	0.0980
P(*p*BUa-*co*-BI)-10	80.3	0.0597	0.0743
PBI	81.2	0.0832	0.0951

[a]Under anhydrous conditions.

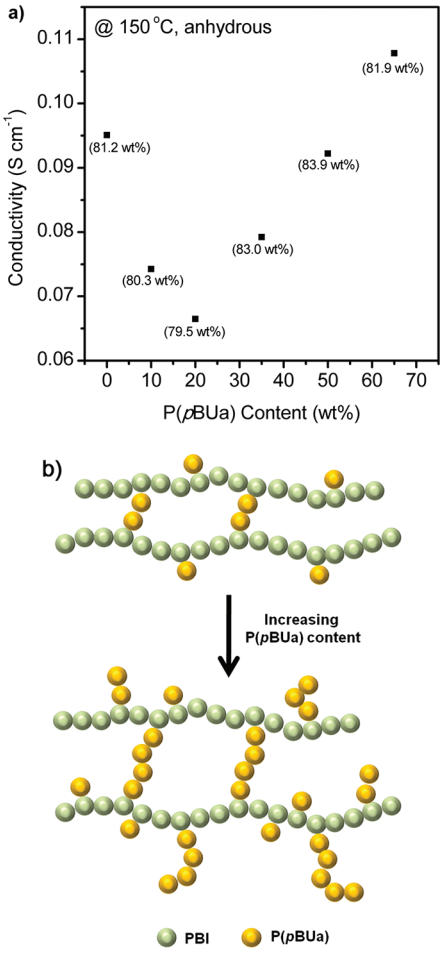


Figure 5. (a) Proton conductivities of PA-doped P(*p*BUa-*co*-BI) membranes as a function of P(*p*BUa) content (wt %) at similar PA content (ca. 81 wt %) and 150 °C under anhydrous conditions. The numbers in parentheses denote the PA content of corresponding membranes per P(*p*BUa) content. (b) Schematic view of P(*p*BUa-*co*-BI)s when P(*p*BUa) content increases.

Table 2. P(*p*BUa) Units per PBI Repeat Unit and Gel Fraction of P(*p*BUa-*co*-BI)s

membranes	P(*p*BUa) units per PBI repeat unit[a]	gel fraction (%)
P(*p*BUa-*co*-BI)-65	1.58	58.1
P(*p*BUa-*co*-BI)-50	0.84	62.7
P(*p*BUa-*co*-BI)-35	0.42	66.8
P(*p*BUa-*co*-BI)-20	0.20	53.9
P(*p*BUa-*co*-BI)-10	0.08	*b*

[a]Calculated using eq 3. [b]Dissolved completely.

First, P(*p*BUa) units per PBI repeat unit were calculated from the weight differences of P(*p*BUa-*co*-BI) films before and after immersion in 85 wt % PA solution at 80 °C for 4 h which is same as the doping conditions to measure proton conductivity and cell performance. Both P(*p*BUa) and PBI homopolymers dissolved completely in 85 wt % PA solution at 160 °C as confirmed by aforementioned PA solubility test, while ^{1}H NMR spectroscopy confirmed that immersion of P(*p*BUa-*co*-BI)s in PA solution at 80 °C resulted in the dissolution of only P(*p*BUa) moieties (Figure S9). Therefore, the amount of P(*p*BUa) moieties remaining in the P(*p*BUa-*co*-BI) membranes after PA doping could be calculated from the weight change. The remaining P(*p*BUa) moieties should be the covalent-linked component with PBI backbones and some linear chains are not extracted out possibly because they have very high molecular weights and/or they are intertwined between the polymer chains.[44,45] The P(*p*BUa) units per PBI repeat unit were calculated using eq 3 shown in the Experimental Section. The P(*p*BUa) units per PBI repeat unit increase with increasing P(*p*BUa) content (Table 2), and it was corroborated by ATR FT-IR spectroscopy (Figure S10). The increase of P(*p*BUa) content can increase the molecular weight of the polymers and also can increase the number of *p*BUa moieties bonded to the PBI; then this can increase free volume coupled with the cross-linked structures in the film as shown in Figure 5b. We believe that the functional groups, e.g. hydroxyl and *tert*-amine in the P(*p*BUa), likely provide new hopping sites, increasing acid−base interactions with PA and PBI by the Grotthuss mechanism. Therefore, the content of P(*p*BUa) units incorporated onto PBI could effect on PA content and proton transport.

Second, gel fractions of the P(*p*BUa-*co*-BI) films were estimated by measuring the weight changes after dissolving them in DMAc under reflux for 24 h.[31] P(*p*BUa), PBI, and P(*p*BUa-*co*-BI)-10 dissolved in DMAc completely, while the

dx.doi.org/10.1021/ma202694p | *Macromolecules* 2012, 45, 1438−1446

P(*p*BUa-*co*-BI) membranes with more than 10 wt % of P(*p*BUa) content remained intact. The gel fractions of the P(*p*BUa-*co*-BI) membranes initially increase with increasing P(*p*BUa) units, reach their maximum (66.8%) at 35 wt % P(*p*BUa) content, and then decrease slightly as P(*p*BUa) content further increased to 65 wt %. Cross-linked structure in membrane has been reported to decrease proton conductivities because it can restrict polymer chain mobility.[31] Therefore, the relatively low proton conductivities of the P(*p*BUa-*co*-BI) membranes with lower P(*p*BUa) contents (<50 wt %) might be due to restrictions of polymer chain mobility because P(*p*BUa) should have smaller chain lengths, and its major effect is the prevention of the chain mobility. As a result, the P(*p*BUa-*co*-BI)-35 membrane with the highest gel fraction shows a relatively low proton conductivity. On the contrary, the P(*p*BUa-*co*-BI)-65 and P(*p*BUa-*co*-BI)-50 membranes with higher P(*p*BUa) contents and lower gel fractions show the highest proton conductivities. It could be ascribed to larger content and/or longer chain length of P(*p*BUa) units in the membrane that can give the positive effect of P(*p*BUa) moiety having the various functional groups on the proton conductivity because the polymer chain mobility becomes better in the membrane. Among them, the P(*p*BUa-*co*-BI)-65 membrane shows the highest proton conductivities of ca. 0.10 and 0.12 S cm^{-1} at 120 and 150 °C, respectively.

Cell Performance and Durability Tests. Preliminary fuel cell evaluation was assessed using ca. 50 μm thick PA-doped membranes (Figure 6). PA contents of P(*p*BUa-*co*-BI)-65,-50,-35 and PBI membranes used were 88.5, 83.9, 83.0, and 81.2 wt %, respectively, which were obtained after immersion in 85 wt % of PA solution at 80 °C for 4 h. The PA-doped P(*p*BUa-*co*-BI) membranes were successfully employed in fuel cells operated at 120−180 °C without any humidification or pressure requirements. The operating voltages of P(*p*BUa-*co*-BI) membranes with larger P(*p*BUa) content (>50 wt %), P(*p*BUa-*co*-BI)-65 and P(*p*BUa-*co*-BI)-50, were found to be larger than those of PBI membrane at the same current density (>0.7 V at 0.2 A cm^{-2}, inset in Figure 6). The proton conductivities and PA contents are, undoubtedly, important determinants of fuel cell performance. Thus, P(*p*BUa-*co*-BI)-65 and P(*p*BUa-*co*-BI)-50 membranes which show higher proton conductivity than others led to high cell performance results.

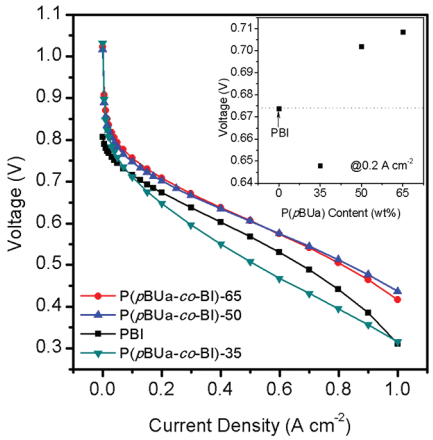


Figure 6. Cell performance of PA-doped P(*p*BUa-*co*-BI) membranes at 150 °C, nonhumidified H_2, and air (ambient pressure), cathode; 0.9 mg cm^{-2} PtRu loading, anode; 1.7 mg cm^{-2} PtCo loading. Active area is 7.84 cm^2. Inset: cell voltage as a function of P(*p*BUa) content (wt %) at 0.2 A cm^{-2}.

Recently, considerable research on the durability of PEMs has been conducted and regarded as to be realized for their widespread use. However, durability testing methods are underdeveloped and remain difficult and time-consuming processes. *In situ* acceleration lifetime test (ALT) has been proven as a reliable method to predict effectively the durability of PEMs in real operating conditions of fuel cell with time.[46−48] In this study, the severe operating conditions of dynamic mode (load changing test cycle) were employed to age cells after the complete establishment of stationary conditions. The attenuation of open-circuit voltage (OCV) below 0.9 V implies the evolution on the microstructure of membrane and was considered as a screening criterion of ALT before the failure of membranes caused by mechanical damage such as membrane thinning and pinhole formation.[46,49] The P(*p*BUa-*co*-BI)-65 membrane endured over 2000 h of ALT at 150 °C (Figure 7). Its number of load cycles was ∼1999, while that of the PBI membrane was only 1360. The lifetime loss of the P(*p*BUa-*co*-BI)-65 membrane during ALT was calculated from the variation of OCV with run time; it was at a rate of −0.03 mV h^{-1} until failure at 2003 h,[50] whereas the lifetime loss of PBI membrane was quickly increased at a rate of −0.08 mV h^{-1} and led to a rapid failing at 1360 h. Therefore, the covalent incorporation of benzoxazine (P(*p*BUa)) into PBI membranes improved the lifetime of the resulting fuel cell membrane due to the formation of cross-linked structures.

Finally, large-sized (30 cm × 140 m) films could be produced simply by mixing of PBI solution with P(*p*BUa) monomer using conventional die coating machine through the continuous process. The large-sized films containing PBI and *p*BUa monomer were coated on poly(ethylene terephthalate) (PET) base film. After drying, the films were detached from the PET base film. P(*p*BUa-*co*-BI)-65 membrane was then produced by stepwise heating from 60 to 220 °C for 4 h in an oven (Figure 8). The expected chemical structures of the films before and after the heating are also shown in the bottom part of Figure 8. The large-sized films were produced in the same way as the small-sized films (20 cm × 30 cm), making them have similar properties, including proton conductivity and cell performance. Further work assessing the practical applicability of the large-sized films is underway.[51]

CONCLUSIONS

New PEMs comprising cross-linked copolymers of polybenzoxazine (P(*p*BUa)) and PBI were developed. The cross-linked copolymeric structures were characterized by 2D DOSY NMR, solubility testing, and DSC. P(*p*BUa) contents of over 50 wt % allowed the P(*p*BUa-*co*-BI) membranes to incorporate high PA contents, with improved proton conductivity and subsequently excellent cell performance. In particular, the P(*p*BUa-*co*-BI)-65 membrane, with the largest PA content (ca. 88 wt %), showed proton conductivities of ca. 0.10 and 0.12 S cm^{-1} at 120 and 150 °C, respectively, under anhydrous conditions. Besides, its incorporation of fuel cell resulted in higher performance (0.71 V at 0.2 A cm^{-2}), durability (1999 cycles of ALT), and slower lifetime loss (−0.03 mV h^{-1}) than a cell with a PBI only membrane. Furthermore, the relative simple process for producing large-sized films and versatile molecular design through the use of benzoxazine monomers may offer a great feasibility for the use of polybenzimidazoles in solid polymer electrolytes.

dx.doi.org/10.1021/ma202694p | *Macromolecules* 2012, 45, 1438−1446

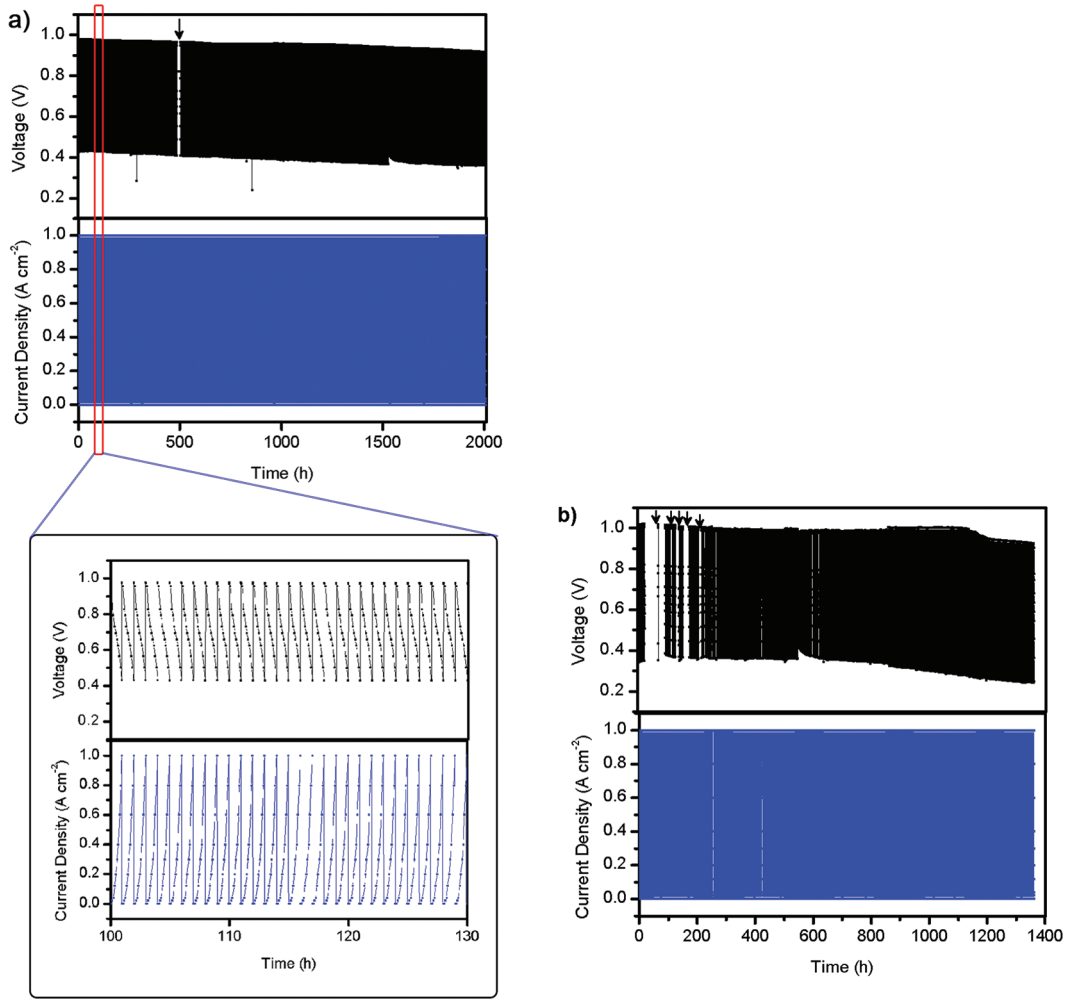


Figure 7. *In situ* acceleration lifetime test (load changing test cycle) of (a) P(*p*BUa-*co*-BI)-65 and (b) PBI membranes at 150 °C, nonhumidified H_2 and air (ambient pressure), cathode; 0.9 mg cm^{-2} PtRu loading, anode; 1.7 mg cm^{-2} PtCo loading. Active area is 7.84 cm^2. Downward arrows (↓) on figure denote the region induced by temporary recording error.

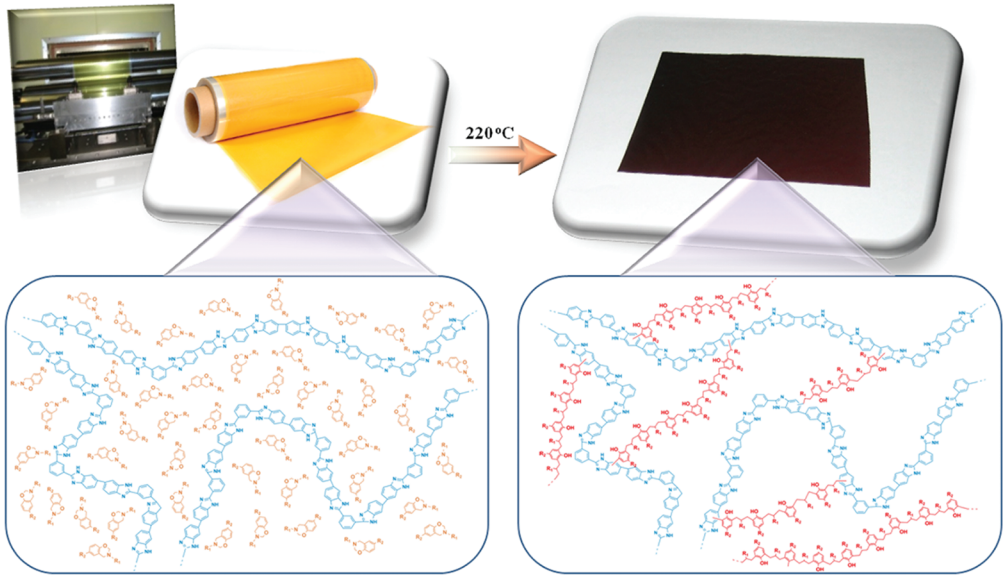


Figure 8. Large scale (30 cm × 140 m) P(*p*BUa-*co*-BI)-65 film using conventional die coating machine (the picture on top) and corresponding possible chemical structures (the picture on bottom) before (left) and after (right) heating, 220 °C.

dx.doi.org/10.1021/ma202694p | *Macromolecules* 2012, 45, 1438–1446

■ ASSOCIATED CONTENT

Supporting Information

Synthesis and characterization of benzoxazine monomer (*p*BUa) and cross-linked copolymer membranes with NMR, ATR FTIR, DSC, TGA, DMTA, mechanical properties, and proton conductivities with temperature. This material is available free of charge via the Internet at http://pubs.acs.org.

■ AUTHOR INFORMATION

Corresponding Author

*Phone +82 31 280 8162, e-mail sw0326.choi@samsung.com (S.-W.C.); phone +82 2 880 7070, Fax +82 2 888 1604, e-mail jongchan@snu.ac.kr (J.-C.L.).

Notes

The authors declare no competing financial interest.

■ ACKNOWLEDGMENTS

This research was supported by Samsung Advanced Institute of Technology, Samsung Electronics Co., Ltd., through the Brain Korea Program and the Fundamental R&D Program of World Premier Materials (WPM) funded by the Ministry of Knowledge Economy, Republic of Korea.

■ REFERENCES

(1) Kreuer, K. D. *J. Membr. Sci.* **2001**, *185*, 29−39.
(2) Shao, Y.; Yin, G.; Wang, Z.; Gao, Y. *J. Power Sources* **2007**, *167*, 235−242.
(3) Li, Q.; He, R.; Jensen, J. O.; Bjerrum, N. J. *Chem. Mater.* **2003**, *15*, 4896−4915.
(4) Zhang, J.; Xie, Z.; Zhang, J.; Tang, Y.; Song, C.; Navessin, T.; Shi, Z.; Song, D.; Wang, H.; Wilkinson, D. P.; Liu, Z.-S.; Holdcroft, S. *J. Power Sources* **2006**, *160*, 872−891.
(5) Tayouo, R.; David, G.; Améduri, B.; Roziére, J.; Roualdés, S. *Macromolecules* **2010**, *43*, 5269−5276.
(6) Kim, Y. S.; Wang, F.; Hickner, M.; McCartney, S.; Hong, Y. T.; Harrison, W.; Zawodzinski, T. A.; McGrath, J. E. *J. Polym. Sci., Part A: Polym. Chem.* **2003**, *41*, 2816−2828.
(7) Miyatake, K.; Chikashige, Y.; Higuchi, E.; Watanabe, M. *J. Am. Chem. Soc.* **2007**, *129*, 3879−3887.
(8) Savadogo, O. *J. Power Sources* **2004**, *127*, 135−161.
(9) Mustarelli, P.; Quartarone, E.; Grandi, S.; Carollo, A.; Magistris, A. *Adv. Mater.* **2008**, *20*, 1339−1343.
(10) Lee, S.-Y.; Ogawa, A.; Kanno, M.; Nakamoto, H.; Yasuda, T.; Watanabe, M. *J. Am. Chem. Soc.* **2010**, *132*, 9764−9773.
(11) Wainright, J. S.; Wang, J.-T.; Weng, D.; Savinell, R. F.; Litt, M. *J. Electrochem. Soc.* **1995**, *142*, L121−L123.
(12) Li, Q.; Jensen, J. O.; Savinell, R. F.; Bjerrum, N. J. *Prog. Polym. Sci.* **2009**, *34*, 449−477.
(13) Mader, J.; Xiao, L.; Schmidt, T. J.; Benicewicz, B. C. *Adv. Polym. Sci.* **2008**, *216*, 63−124.
(14) Mader, J. A.; Benicewicz, B. C. *Macromolecules* **2010**, *43*, 6706−6715.
(15) Yu, S.; Benicewicz, B. C. *Macromolecules* **2009**, *42*, 8640−8648.
(16) Kim, H. J.; Lim, T. H. *J. Ind. Eng. Chem.* **2004**, *10*, 1081−1085.
(17) Kim, J. H.; Kim, H. J.; Lim, T. H.; Lee, H. I. *J. Ind. Eng. Chem.* **2007**, *13*, 850−855.
(18) Weber, J.; Kreuer, K.-D.; Maier, J.; Thomas, A. *Adv. Mater.* **2008**, *20*, 2595−2598.
(19) Li, Q.; He, R.; Jenson, J. O.; Bjerrum, N. J. *Fuel Cells* **2004**, *4*, 147−159.
(20) Xiao, L.; Zhang, H.; Scanlon, E.; Ramanathan, L. S.; Choe, E. W.; Rogers, D.; Apple, T.; Benicewicz, B. C. *Chem. Mater.* **2005**, *17*, 5328−5333.
(21) Kim, S.-K.; Kim, T.-H.; Jung, J.-W.; Lee, J.-C. *Polymer* **2009**, *50*, 3495−3502.
(22) Li, Q.; Pan, C.; Jensen, J. O.; Noyé, P.; Bjerrum, N. J. *Chem. Mater.* **2007**, *19*, 350−352.
(23) Kim, S.-K.; Kim, T.-H.; Ko, T.; Lee, J.-C. *J. Membr. Sci.* **2011**, *373*, 80−88.
(24) Kerres, J.; Ullrich, A.; Meier, F.; Häring, T. *Solid State Ionics* **1999**, *125*, 243−249.
(25) Lee, H.-S.; Roy, A.; Lane, O.; McGrath, J. E. *Polymer* **2008**, *49*, 5387−5396.
(26) Miyatake, K.; Tombe, T.; Chikashige, Y.; Uchida, H.; Watanabe, M. *Angew. Chem., Int. Ed.* **2007**, *46*, 6646−6649.
(27) Ning, X.; Ishida, H. *J. Polym. Sci., Part A: Polym. Chem.* **1994**, *32*, 1121−1129.
(28) Ghosh, N. N.; Kiskan, B.; Yagci, Y. *Prog. Polym. Sci.* **2007**, *32*, 1344−1391.
(29) Ye, Y.-S.; Yen, Y.-C.; Cheng, C.-C.; Chen, W.-Y.; Tsai, L.-T.; Chang, F.-C. *Polymer* **2009**, *50*, 3196−3203.
(30) Kim, T.-H.; Lim, T.-W.; Lee, J.-C. *J. Power Sources* **2007**, *172*, 172−179.
(31) Jeong, M.-H.; Lee, K.-S.; Lee, J.-S. *Macromolecules* **2009**, *42*, 1652−1658.
(32) Antalek, B. *Concepts Magn. Reson.* **2002**, *14*, 225−258.
(33) Chen, A.; Wu, D.; Johnson, C. S. Jr. *J. Am. Chem. Soc.* **1995**, *117*, 7965−7970.
(34) Bovey, F. A.; Mirau, P. A. *NMR of Polymers*, 1st ed.; Academic Press: New York, 1996; Chapter 3.
(35) Wang, Y.-X.; Ishida, H. *Macromolecules* **2000**, *33*, 2839−2847.
(36) Leykin, A. Y.; Fomenkov, A. I.; Galpern, E. G.; Stankevich, I. V.; Rusanov, A. L. *Polymer* **2010**, *51*, 4053−4057.
(37) Wannek, C.; Lehnert, W.; Mergel, J. *J. Power Sources* **2009**, *192*, 258−266.
(38) Lobato, J.; Cañizares, P.; Rodrigo, M. A.; Linares, J. J.; Aguilar, J. A. *J. Membr. Sci.* **2007**, *306*, 47−55.
(39) Kulkarni, M.; Potrekar, R.; Kulkarni, R. A.; Vernekar, S. P. *J. Polym. Sci., Part A: Polym. Chem.* **2008**, *46*, 5776−5793.
(40) Cho, J.; Blackwell, J.; Chvalun, S. N.; Litt, M.; Wang, Y. *J. Polym. Sci., Part B: Polym. Phys.* **2004**, *42*, 2576−2585.
(41) Kim, T.-H.; Kim, S.-K.; Lim, T.-W.; Lee, J.-C. *J. Membr. Sci.* **2008**, *323*, 362−370.
(42) Bouchet, R.; Siebert, E. *Solid State Ionics* **1999**, *118*, 287−299.
(43) Bozkurt, A.; Meyer, W. H.; Wegner, G. *J. Power Sources* **2003**, *123*, 126−131.
(44) Lodge, T. P. *Phys. Rev. Lett.* **1999**, *83*, 3218−3221.
(45) Koenig, J. L. *Chemical Microstructure of Polymer Chains*, 1st ed.; John Wiley & Sons: New York, 1980; Chapter 6.
(46) Marrony, M.; Barrera, R.; Quenet, S.; Ginocchio, S.; Montelatici, L.; Aslanides, A. *J. Power Sources* **2008**, *182*, 469−475.
(47) Zhang, S.; Yuan, X.; Wang, H.; Mérida, W.; Zhu, H.; Shen, J.; Wu, S.; Zhang, J. *Int. J. Hydrogen Energy* **2009**, *34*, 388−404.
(48) Pei, P.; Chang, Q.; Tang, T. *Int. J. Hydrogen Energy* **2008**, *33*, 3829−3836.
(49) Mittal, V. O.; Kunz, H. R.; Fenton, J. M. *J. Electrochem. Soc.* **2006**, *153*, A1755−A1759.
(50) Yu, S.; Xiao, L.; Benicewicz, B. C. *Fuel Cells* **2008**, *8*, 165−174.
(51) Choi, S.-W.; Lee, J.-C.; Park, J. O. US Patent 20100273087, 2010.

Macromolecules

Article

pubs.acs.org/Macromolecules

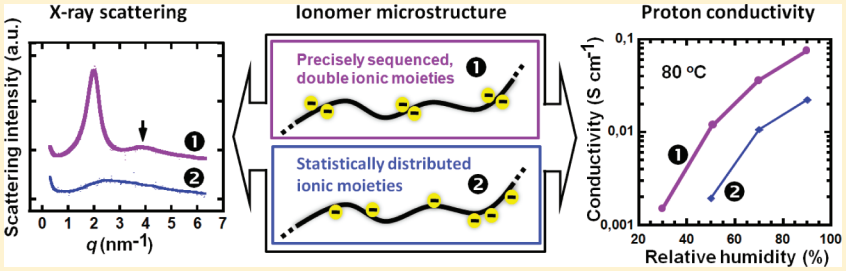
Fully Aromatic Ionomers with Precisely Sequenced Sulfonated Moieties for Enhanced Proton Conductivity

Xue-Feng Li,[†,‡] François P. V. Paoloni,[†] E. Annika Weiber,[†] Zhen-Hua Jiang,[‡] and Patric Jannasch[†,*]

[†]Polymer & Materials Chemistry, Department of Chemistry, Lund University, P.O. Box 124, SE-221 00 Lund, Sweden

[‡]Alan G. MacDiarmid Institute, Department of Chemistry, Jilin University, Qianjin Street 2699, Changchun 130012, People's Republic of China

Supporting Information



ABSTRACT: A series of six fully aromatic ionomers with precisely sequenced sulfonated sites along the polymer chains have been designed, prepared, and characterized as proton-exchange membranes. Two straightforward and efficient synthetic strategies based on Ullmann ether reactions and a Baeyer–Villiger rearrangement were devised to obtain bisphenol monomers with four or six phenylene units linked exclusively by ether bridges to avoid transetherification reactions. Polycondensations of these bisphenol monomers with mono- or disulfonated dihalide monomers gave high molecular weight poly(arylene ether), poly(arylene ether sulfone), and poly(arylene ether ketone) homopolymers having microblock-like structures with sulfonated moieties separated by monodisperse nonsulfonated oligo(ether) spacers. The nanoscale morphology and properties of solvent cast membranes were closely related to the nature of the oligo(ether) spacers. Small angle X-ray scattering (SAXS) measurements showed intense scattering and very narrow ionomer peaks with second-order features for the polymers with the six-ring spacers. This clearly indicated that the controlled ionic sequencing enabled self-assembly of ionic aggregates with a much higher degree of organization in relation to a corresponding aromatic ionomer with a statistical distribution of the sulfonate groups. At an identical ionic content, the ionomers containing *meta* ether linkages had lower glass transition temperatures than the all-*para* materials, leading to a higher water uptake and proton conductivity of the former ionomers. A membrane with an ion exchange capacity (IEC) of 2.05 mequiv g^{-1} and containing exclusively *para* linkages reached the same level of proton conductivity as Nafion at 100% relative humidity (RH), and also had an excellent dimensional stability in boiling water. Under reduced RH, the conductivity of this membrane greatly exceeded that of a membrane based on a statistical copolymer analogue with a similar ionic content.

INTRODUCTION

Sulfonated aromatic hydrocarbon polymers have attracted attention as potential candidates for membranes applied to the production of electrical power and clean water.[1] For example, sulfonated poly(aryl ether)s represent an attractive alternative to perfluorinated sulfonic acid membranes for high temperature proton-exchange membrane fuel cells (PEMFCs) because of their excellent stability and high glass transition temperature (T_g).[2] An increase of the operating temperature to above 100 °C promises crucial benefits concerning the complexity, cost and performance of automotive PEMFC systems.[3,4] However, the performance and durability of fuel cell core components such as the membrane need be further improved to meet the demands of the industry.

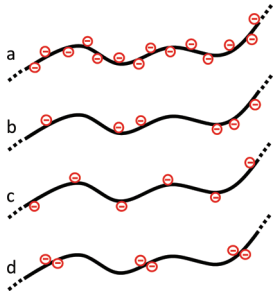
Early examples of sulfonated poly(aryl ether)s were primarily obtained by postpolymerization sulfonations.[5,6] Characteristically, membranes based on these polymers show excessive swelling in water, and even water solubility, at high acid contents, which limits their applicability. Partial sulfonations result in statistical distributions of acid groups along the polymer backbones. Unlike perfluorosulfonic acid membranes, these hydrocarbon membranes do not usually form well-connected water-filled channels that promote efficient transport of protons across the membrane.[7] Similar issues arise when sulfonated poly(aryl ether)s are prepared using a presulfonated monomer. If for example polymers are prepared by polycondensations of a presulfonated dihalide monomer with a conventional similar-sized nonsulfonated diol monomer, the acid groups will be

Received: July 13, 2011
Revised: January 4, 2012
Published: January 23, 2012

 © 2012 American Chemical Society dx.doi.org/10.1021/ma201599p | *Macromolecules* 2012, 45, 1447–1459

regularly spaced but the acid content is likely to be too high (Scheme 1). The common strategy is then to use a second non-

Scheme 1. Schematic Ionomer Structures Illustrating the Distribution of Sulfonic Acid Groups along the Backbone in Regular Homopolymers (a), in Statistical Copolymers (b), and in Homopolymers with Precisely Sequenced Singlet (c) and Doublet (d) Acid Groups



sulfonated comonomer to form statistical copolymers with reduced acid contents. However, this also leads to an irregular statistical distribution of sulfonic acid along the polymer backbone.

Several research groups have reported that synthetic strategies involving a careful control of the distribution and location of the sulfonic acid groups in the polymer structure result in well-defined hydrocarbon membrane morphologies.[8,9] This may in turn lead to the formation of well-connected water-filled channels which gives the membranes superior proton-conducting properties in relation to statistically sulfonated membranes, particularly at low relative humidity (RH). Mild methods to synthesize sulfonated multiblock copoly(aryl ether sulfone)s have been extensively used by McGrath et al.[10−13] and others.[14−17] Low-temperature coupling of oligomers mediated by a perfluorinated compound such as hexafluorobenzene or decafluorobiphenyl affords high molecular weight multiblock copolymers while limiting the extent of transetherification reaction. These multiblock copolymers typically exhibit quite well-defined morphologies, associated with high proton conductivity under reduced RH.[8,9] The length and acid density of the sulfonated blocks have a major influence on the membrane morphology and properties. This concept has been extended to copolymers which contain densely sulfonated blocks to further improve the membrane properties.[18−23] In another synthetic strategy, high local concentrations of sulfonic acid groups have been placed on pendant chains to form defined morphologies, as shown by small-angle X-ray scattering (SAXS) measurements.[24,25] The results indicated that ionic clustering was promoted by placing the sulfonic acid groups on the relatively long spacers. Increasing the number of sulfonic acid groups located on pendant chains from one to three resulted in larger ionic clusters and narrower ionomer peak widths.[24,25]

Several groups have reported on sulfonated poly(aryl ether)s composed of long hydrophobic segments combined with densely sulfonated units. For example, Hay et al. have prepared polymers containing clusters of up to 12 sulfonic acid groups statistically distributed along the backbone chain.[26] Novel bisphenols having six pendant phenyl groups were incorporated in poly(aryl ether)s by polymerization of carefully chosen comonomers. The bisphenol monomer residues underwent selective multiple sulfonations under mild conditions, resulting in statistical copolymers containing highly sulfonated moieties. The corresponding membranes had higher proton conductivity than typically observed for randomly sulfonated hydrocarbon membranes or multiblock copolymers with similar acid content.

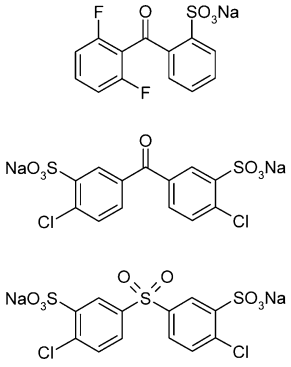
Colquhoun and co-workers have recently prepared and studied microblock ionomers, a novel class of sulfonated poly(aryl ether)s membranes.[27] In these polymers, densely sulfonated moieties are regularly spaced by monodispersed nonsulfonated segments. Essentially, these microblock copolymers are homopolymers with a very large repeat unit. The monomers were designed to yield a repeat unit composed of a long sequence of electron-poor aromatic rings, strictly alternating with a short segment composed of electron-rich phenylene units. Transetherification was avoided by excluding ether linkages activated by a sulfone or ketone bridge. Postpolymerization sulfonation under mild conditions was then selective toward electron-rich aromatic rings. The authors described a series of membranes with an ion exchange capacity (IEC, milliequivalents of H^+ per gram dry membrane) of approximately 2.1 mequiv g^{-1}.[27] Although these ionomers show attractive properties, they still suffer from two main drawbacks. First, it is often acknowledged that sulfonic acid groups located next to ether linkages are activated for desulfonation under fuel cell operation.[28,29] Second, the synthesis of the monomers used for the microblock copolymers is limited and quite complex. The monomers must be designed to eliminate the risk of transetherification reactions during the polymerization, and the bisphenol monomers must thus exclusively contain ether linkages. The number of phenylene units in these monomers will essentially determine the degree of sulfonation of the corresponding polymer. The bishalide monomers exclusively contain ketone or sulfone bridges and are often associated with poor solubility because of the high rigidity of these bonds. In addition, high local acid concentrations in the repeat unit require long dihalide monomers which are not straightforward to synthesize and purify.

In the present study, we have followed an alternative approach to sulfonated microblock poly(aryl ether)s by employing nucleophilic polycondensations of long bisphenols with sulfonated dihalide monomers. The resulting fully aromatic ionomers were composed of long hydrophobic segments, strictly alternating with singlets or doublets of sulfonic acid groups, as illustrated in Scheme 1. First, efficient methods to prepare various novel oligomeric bisphenol monomers were developed. In these monomers, the phenylene rings were exclusively connected by ether bridges in the *meta* or *para* position. Their polymerization with three different sulfonated monomers afforded six homopolymers. Two of these were composed of singlets of sulfonic acid precisely sequenced by a monodisperse oligo(ether) segment of exactly four phenylene units. The remaining four homopolymers were composed of doublets of sulfonic acid precisely sequenced by a monodisperse oligo(ether) segment of exactly six phenylene units. Solvent cast membranes were characterized with regard to ionic distribution, water uptake, thermal stability, and proton conductivity. Special attention was given to the polymer backbone structure, acid group distribution, nanostructure, and influence on the membrane properties.

RESULTS AND DISCUSSION

Synthesis of Sulfonated Monomers. The sulfonated monomers prepared and used in the present work are shown in Scheme 2. These monomers can take part in nucleophilic polycondensation via displacement of the chlorine or fluorine

Scheme 2. Sulfonated Monomers Used in the Present Study



atoms which are activated by an electron-withdrawing ketone or sulfone link. By employing presulfonated monomers, it is possible to accurately control the location of the sulfonic acid groups in the resulting polymers.

The lithium salt of 2,6-difluoro-2′-sulfobenzophenone (**1**) was conveniently synthesized in one-pot by reacting 2,6-difluorophenyllithium with 2-sulfobenzoic acid cyclic anhydride in tetrahydrofuran (THF) at −70 °C.[30] After reaction, the product readily crystallized out of solution. We have recently reported that the polymerization of this monosulfonated monomer with various bisphenols and bisthiophenols proceeds with a high reaction rate to produce corresponding high molecular weight poly(arylene ether)s.[30] 3,3′-Disulfonated-4,4′-difluorobenzophenone (**2**)[31] and 3,3′-disulfonated-4,4′-dichlorodiphenyl sulfone (**3**)[32,33] were synthesized via well-known procedures. The use of sulfonated monomers readily ensures reproducibility of the degree of sulfonation. Moreover, the side reactions and degradation[5] that are sometimes observed for sulfonation under harsh conditions are avoided. In addition, it is recognized that sulfonated polymers are most stable toward desulfonation when the sulfonic acid groups are located on electron-poor aromatic rings. The IEC of the homopolymers containing monomer **1**, **2**, or **3** can conveniently be controlled by employing monodisperse bisphenol monomers of varying molecular weight. In the case of monomer **1**, this will result in single sulfonic acid groups regularly spaced along the polymer backbone (Scheme 1c). The ionomers based on monomers **2** or **3** will consist of doublets of sulfonic acid groups, strictly alternating with hydrophobic segments (Scheme 1d).

Synthesis of Bisphenol Monomers. The bisphenol monomers will form monodisperse hydrophobic segments once incorporated in the polymer. This will result in a distribution of sulfonic acid groups that is controlled with molecular precision. As mentioned above, it is imperative that the bisphenol monomers do not contain any electron-withdrawing groups in order to exclude the possibility of transetherification during the polymerizations. Indeed, such reactions would result in chain-scrambling and introduction of defects in the sequence of the polymer backbone. Therefore, the bisphenol monomers were designed to contain aromatic rings linked exclusively by ether bonds or direct aryl−aryl bonds.

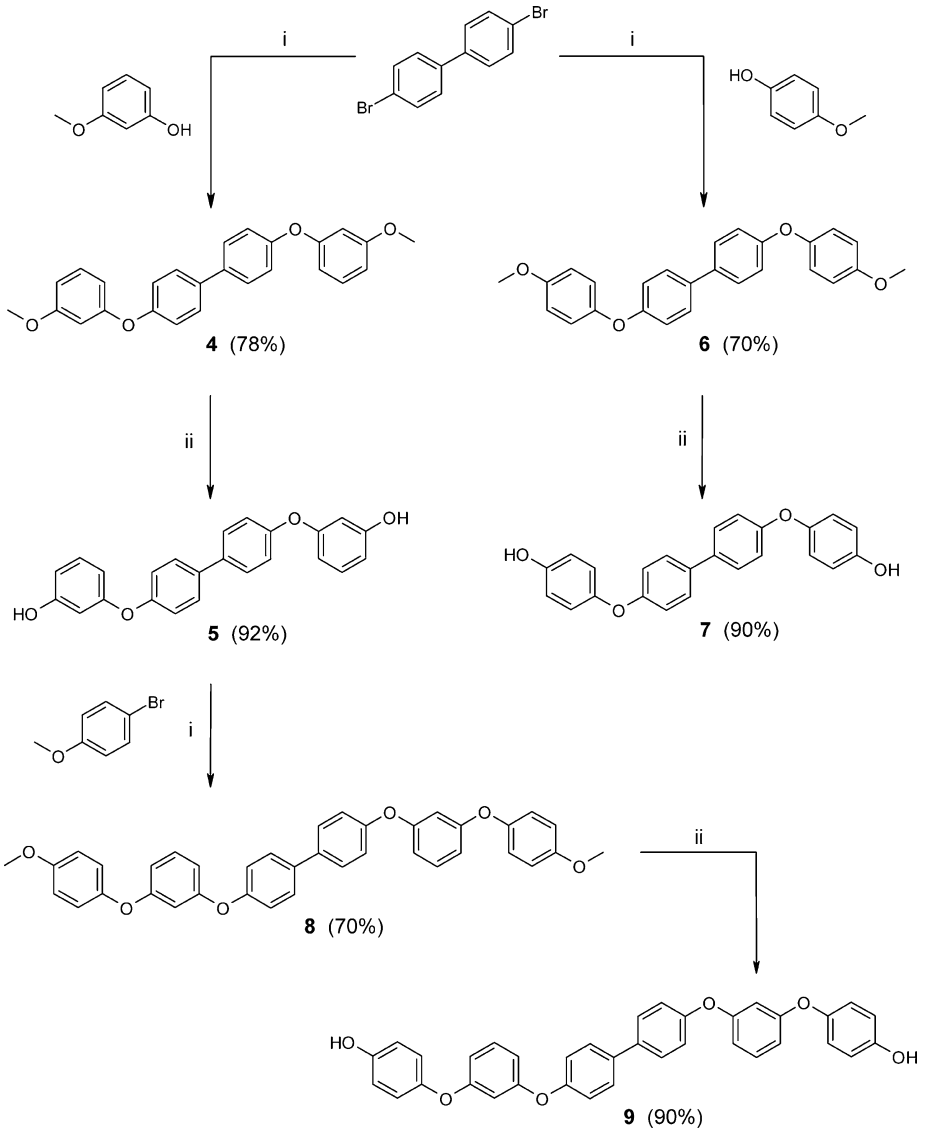
Two bisphenol monomers composed of four aromatic rings (**5** and **7**) were obtained by Ullmann ether condensation followed by hydrolysis of the methoxy protecting groups, as shown in Scheme 3. Thus, the reaction of 4,4′-dibromobiphenyl with 3-methoxyphenol gave the methoxy-terminated four-ring monomer precursor **4** in good yield. This precursor was efficiently isolated and purified by filtration through Celite to remove the copper catalyst, followed by precipitation in methanol. The highest yields were obtained under the conditions described by Song and co-workers.[34] Notably, the reaction of 4,4′-bisphenol and 1-bromo-3-methoxybenzene under identical conditions gave **4** in poor to moderate yield only. The methoxy groups of **4** were hydrolyzed by using hydrobromic acid in acetic acid, and bisphenol monomer **5** was isolated by precipitation in water and then washed extensively to remove traces of acids. The product was purified by recrystallization from hot toluene and isolated in 72% overall yield. Complete removal of the methyl groups was confirmed by the total disappearance of the resonance corresponding to the methyl group at 3.81 ppm in the ^{1}H NMR spectrum (the ^{1}H NMR spectra of all the bisphenol monomers of the present study, and their respective intermediates, are shown in the Supporting Information). The complete removal was further confirmed by the absence of resonances in the aliphatic region of the ^{13}C NMR spectrum. Formation of the phenol was finally also supported by the presence of a broad absorption band centered at 3357 cm^{-1} in the FT-IR spectra. The synthetic strategy described above is attractive because of the large variety of aromatic building blocks available and because of its simplicity. Therefore, additional bisphenol monomers with varying length and connectivity can be envisaged. Monomer **7** was synthesized in good yield by an identical method. Ullmann ether condensation of 4,4′-DBBP (4,4′-dibromobiphenyl) and 4-methoxyphenol, followed by hydrolysis of methoxy protecting groups, gave a four-ring bisphenol monomer with *para* connectivity. As expected, the connectivity had an influence on the melting point of these oligomers, and bisphenol **7** had a higher melting point (249 °C) than bisphenol **5** (168 °C). As a result, the former monomer was not soluble in chloroform and appeared to generally have a lower solubility than the latter.

The two-step method described above was also adapted to attempt the synthesis of longer bisphenol oligomers. Reaction of **5** with 4-bromoanisole gave a bismethoxy terminated oligomer **8**. Its hydrolysis with HBr afforded a six-ring oligo(ether) monomer **9** that contained both *meta* and *para* linkages. Monomer **9** was obtained in 63% yield over two steps after purification by recrystallization from hot toluene. The structure was confirmed using the same analytical techniques as mentioned previously. The monomer had a melting point similar to the shorter *meta* monomer **5**. Unfortunately, the reaction of **5** with 3-bromoanisole gave a mixture of products. Analysis by ^{1}H NMR spectroscopy indicated that the main component was the desired all-*meta* oligomer. However, it was not possible to isolate the target compound by precipitation and filtration. In addition, the reaction of **6** with 4-bromoanisole did not afford the targeted six-ring oligomers. Analysis by ^{1}H NMR spectroscopy suggested that the reaction was mostly limited to a monosubstitution that produced an oligomer composed of five aromatic units.

An alternative route involving a condensation followed by a Baeyer−Villiger oxidation[35] was utilized in order to synthesize an all *para* oligomer with six rings. As shown in Scheme 4, the reaction of bisphenol **7** with 4-fluoroacetophenone gave the six-ring oligomer **10**. In this case the fluorine atom is activated toward nucleophilic aromatic substitution by the ketone in *para* position, resulting in a higher conversion than for the Ullmann ether condensation. The oligomer was insoluble in both chloroform and dimethyl sulfoxide (DMSO). Consequently, it was characterized by NMR spectroscopy using a mixture of

dx.doi.org/10.1021/ma201599p | *Macromolecules* 2012, 45, 1447−1459

Scheme 3. Synthesis of Four-Ring Bisphenol Monomers 5 and 7 and Six-Ring Monomer 9 by Ullmann Ether Condensation Followed by Hydrolysis of the Methoxy End Groups[a]



[a]Key: (i) CuCl, Cs_2CO_3, THMD, NMP, 165 °C; (ii) HBr, AcOH, 150 °C.

$CDCl_3$ and trifluoroacetic acid. This solvent mixture is known to be a good solvent for the solubilization of fully aromatic poly(ether ketone)s.[36−39]

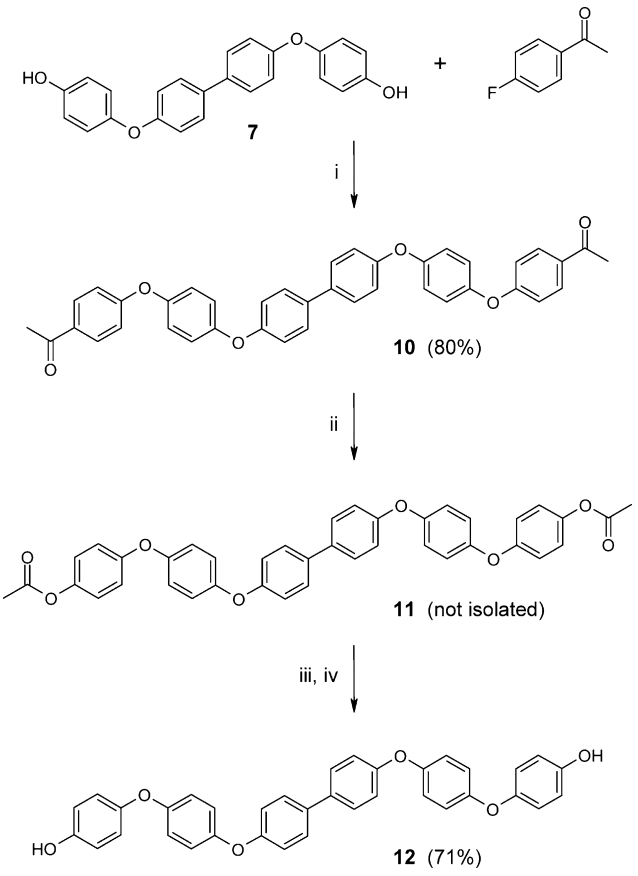
Aromatic−aliphatic ketones can be converted to arylate esters by Baeyer−Villiger rearrangements.[40] The conversion of the reaction with *m*CPBA (*m*-chloroperbenzoic acid) in chloroform was limited, even when a large excess of reactant was used because of the poor solubility of **10**. Poly(ether ketone)s can undergo homogeneous chemical modification in a mixture of chlorinated solvent and TFA (trifluoroacetic acid).[36−39] In the case of Baeyer−Villiger rearrangements, addition of a small amount of TFA has been shown to improve the conversion and to increase the reaction rate. The reaction was monitored by ^{1}H NMR spectroscopy through the progressive disappearance of the resonance at 2.73 ppm corresponding to methyl group next to the ketone, and the simultaneous appearance of a singlet at 3.63 ppm originating from the methyl ester. Excess *m*CPBA and TFA were removed by liquid extraction and oligomer **11** was immediately converted to bisphenol monomer **12** by hydrolysis. The bisphenol monomer was purified by dissolving the crude product in DMF (dimethylformamide), followed by addition of 2-propanol until a cloudy mixture was obtained. Then, the mixture was heated to give a clear solution and bisphenol **12** was recovered as a fine powder upon cooling. This monomer had the highest melting point of the series reported in the present study (274 °C).

Polycondensation and Polymer Characterization. The six sulfonated homopolymers shown in Scheme 5 were synthesized by polycondensation via nucleophilic aromatic substitutions. The monomers used for each polymer are indicated in Table 1. As seen, the polymers (ionomers) differed with regard to the connectivity and length of the hydrophobic ether segment, and the nature of the sulfonated unit.

Polymers **13** and **14** were prepared by condensation of the monosulfonated monomer **1** with bisphenol monomer **5** and **7**, respectively. These polymers contained singlets of sulfonic acid groups regularly separated by a four aromatic ring spacer, giving them a theoretical IEC of 1.5 mequiv g^{-1}. In our previous

dx.doi.org/10.1021/ma201599p | *Macromolecules* 2012, 45, 1447−1459

Scheme 4. Synthesis of Bisphenol Monomer 12 by Nucleophilic Aromatic Substitution, Followed by Baeyer–Villiger Rearrangement[a]



[a]Key: (i) K_2CO_3, DMF, 150 °C; (ii) *m*CPBA, TFA, $CHCl_3$; (iii) KOH, MeOH; (iv) HCl, H_2O.

reports on monomer **1**, polymerizations with bisphenols were carried out in dimethylacetamide (DMAc).[41,42] In the present case, the polymerizations were carried out in DMSO at 160 °C. After a 4 h dehydration period, the viscosity of the polymerization solution increased significantly after 4 and 6 h, respectively. This suggested that the polymerization of **1** with bisphenols proceeded at a higher rate in DMSO than in DMAc. Furthermore, no precipitation of the polymer was observed.

Next, four polymers were prepared by polycondensations of the six-ring bisphenol monomers **9** and **12** with the disulfonated monomers **2** and **3**. The resulting polymers were thus composed of doublets of sulfonic acid groups regularly separated by spacers containing six nonsulfonated aromatic units. The poly(arylene ether ketone)s **15** and **17** had a theoretical IEC slightly higher than the poly(arylene ether sulfone)s **16** and **18**. Indeed, monomer **2** has a lower molecular weight than monomer **3**. There are many examples of statistical copolymers of similar IEC values prepared from the sulfonated monomers **2** and **3**.[8,9] However, to the best of our knowledge, samples **15-18** are the first examples of such homopolymers with an IEC of approximately 2 mequiv g^{-1}. Polymers **15** and **17** were prepared in DMSO while polymers **16** and **18** were prepared in DMAc. Again, no precipitation of the polymers was observed during the polycondensations.

Figure 1 shows the ^{1}H NMR spectra of all polymers prepared in this study. In every case, resonances were observed exclusively in the aromatic region. The compositions of the polymers obtained by integrating and comparing the NMR signals were very close to the theoretical values predicted from the monomer feed ratios. Additional spectroscopic data were consistent with the proposed structures. The inherent viscosity (η_{inh}) of the polymers indicated that moderate to high molecular weights were systematically obtained.[43] Notably, the poly(arylene ether ketone)s **15** and **17** had significantly higher inherent viscosity than the other polymers (Table 1). This might suggest that monomer **3** was more efficient in the polycondensations than monomer **2**.

Membrane Preparation. Flexible transparent films with a thickness between 70 and 90 μm were obtained by casting the polymers from DMAc solutions in all cases but for polymer **18**. According to the inherent viscosity measurements, this polymer had a similar molecular weight as the other polymers prepared in the present work. Attempts to prepare thin films from NMP solution at different temperatures and using different casting substrates such as glass and Teflon were unsuccessful. A fragile film was obtained in every case and thus it was not possible to further evaluate the membrane properties of polymer **18**. As seen in Table 2, the IEC values of the other membranes were in very good agreement with the theoretical value calculated from the monomer feed ratios. This again confirmed the structure of the polymers prepared.

X-ray Scattering. The morphological features of the completely amorphous ionomer membranes were studied by SAXS measurements. Generally, a broad scattering peak is observed at scattering vector (q) ≈1–5 nm^{-1} in ionomers and is referred to as the "ionomer peak". This feature is widely attributed to interaggregate scattering and its position (q_{max}) can be correlated to the characteristic separation length (d) between the ionic aggregates in the polymer-rich matrix phase.[44] Because this scattering feature is usually relatively broad and weak, intraparticle interference have also been proposed to give rise to the ionomer peak.[45] However, there is now a general consensus in the community that the scattering originates from interaggregate scattering.

Shown in Figure 2 are the SAXS profiles of ionomers **13** and **14**, based on the four-ring bisphenols, and ionomers **15-17**, based on the six-ring bisphenols. Before analysis, the membranes were ion-exchanged to selectively stain the sulfonated domains of the membranes with Pb^{2+} to enhance the contrast. The values of q_{max} and d are collected in Table 2 for membranes **13–17**. For comparison, the corresponding data of Nafion NRE212 (IEC = 0.91 mequiv g^{-1}) and an archetypical post-polymerization sulfonated aromatic polymer, polyphenylsulfone (sPPSU), are included in the Pb^{2+} form. The latter polymer was obtained by polycondensation of 4,4′-biphenol and 4,4′-dichlorodiphenyl sulfone, followed by sulfonation using sulfuric acid. The fully aromatic sPPSU had an IEC of 1.84 mequiv g^{-1} and a backbone with similar structural elements as ionomers **15–17**, but with the sulfonic acid units statistically distributed along the polymer backbone in *ortho*-ether positions (Scheme 6). As seen in Figure 2, the ionomer peak of the sPPSU membrane was much broader and shifted toward a higher q-value (q_{max} = 2.4 nm^{-1}), as compared to the profile of the Nafion membrane (q_{max} = 1.65 nm^{-1}). The values of q_{max} corresponded to d = 1.65 nm for sPPSU and 3.8 nm for Nafion. The results thus indicted a smaller average interaggregate distance with a wider distribution in the sPPSU membrane. The extremely hydrophobic

dx.doi.org/10.1021/ma201599p | *Macromolecules* 2012, 45, 1447–1459

Scheme 5. Ionomers Having Poly(arylene ether) (13 and 14), Poly(arylene ether ketone) (15 and 17) and Poly(arylene ether sulfone) (16 and 18) Backbones with Precisely Sequenced Ionic Moieties

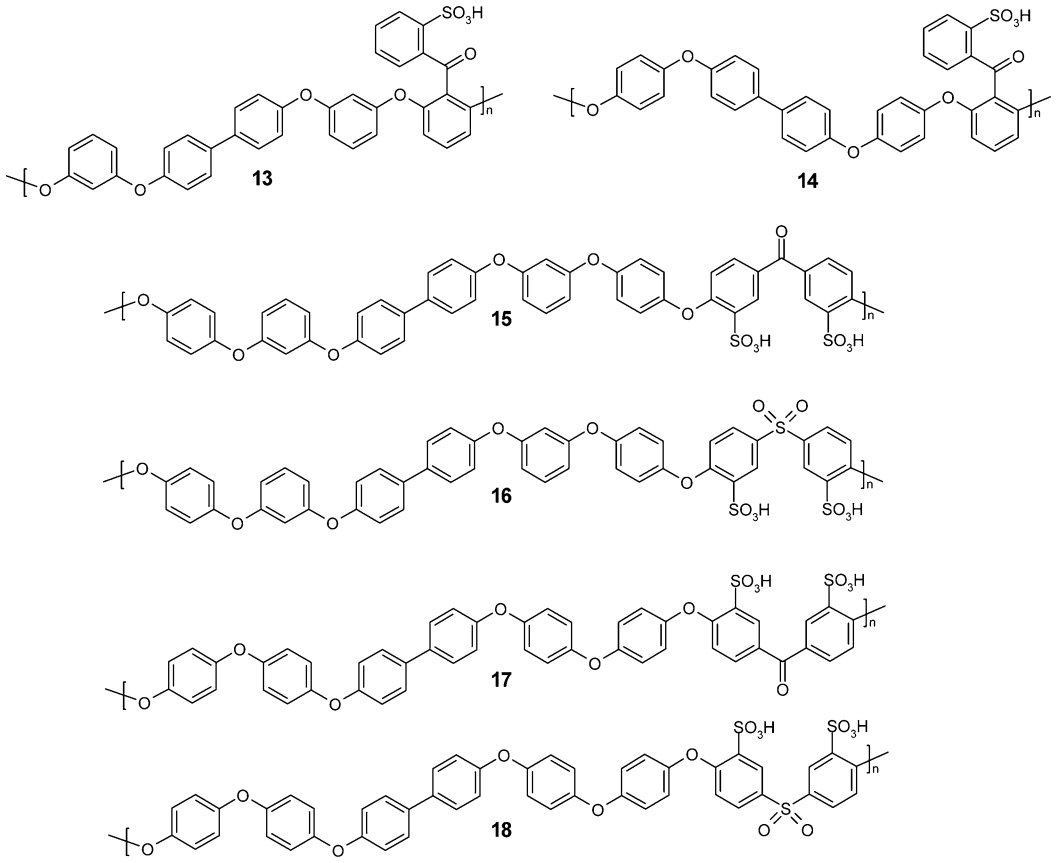


Table 1. Properties of Sulfonated Homopolymers

polymer	sulfonated monomer	bisphenol monomer	η_{inh} (dL g^{-1})[a]	T_g (°C)[b]
13	**1**	**5**	0.35	230
14	**1**	**7**	0.24	259
15	**2**	**9**	0.47	304
16	**3**	**9**	0.20	283
17	**2**	**12**	0.51	348
18	**3**	**12**	0.29	302

[a]0.5 wt % in DMF containing LiBr (0.05 M) at 25 °C. [b]Measured for polymers in the Na^+ form.

polymer backbone combined with the superacidity and hydrophilicity of the $-CF_2-SO_3H$ unit in Nafion give rise to a distinct phase separation and a quite well-defined morphology. Typically, aromatic hydrocarbon backbones are far less hydrophobic and the arylenesulfonic acid units of these ionomers are far less acidic, which leads to a morphology with a less pronounced phase separation. The morphological differences between Nafion membranes and statistically sulfonated aromatic hydrocarbon membranes have previously been extensively discussed by Kreuer on the basis of SAXS data.[7]

The SAXS profiles of membranes **13** and **14** showed ionomer peak positions at higher q_{max} in comparison with sPPSU. Moreover, the peaks were significantly narrower, with membrane **14** showing the narrowest one. Seemingly, the structure of **13** and **14** with monosulfonated sites spaced by four-ring oligo(ether) segments decreased the distributions of the interaggregate distances in relation to the statistical copolymer.

It is immediately clear from Figure 2 that membranes **15**−**17** gave rise to dramatically different scattering profiles with considerably more intense scattering and much narrower ionomer peaks than both sPPSU and Nafion. The value of q_{max} for these ionomer membranes was approximately the same as for Nafion, approximately 2 nm^{-1}. Apparently, by precisely controlling the acid group separation, and keeping it sufficiently large, the ionomer peak became much more intense and well-defined. A further strong indication of the narrow distribution in the interaggregate correlation length was the appearance of clear second order-peaks at $2q_{max}$ (indicated by arrows in Figure 2). These were similar in appearance to those only previously observed in the scattering profiles of monodisperse halato telechelic ionomers[46] and other well-defined model ionomers.[47,48] To our knowledge, this is the first report on second-order features observed for fully aromatic ionomers. There was seemingly no influence by the connectivity of the oligo(ether) spacers and the sulfonated moieties (sulfone or ketone) on the scattering peak position and width of ionomers **13**-**17**. Obviously, the precise ionomers with their evenly and sufficiently spaced ionic moieties allowed for a much more uniform self-aggregation of the ionic groups to occur. This in turn indicated an increased degree of phase separation and morphological control of the membranes. Previously, Colquhoun and co-workers have studied the morphology of microblock polymers with sulfonated moieties precisely spaced by oligo(arylene ketones) by SAXS.[27] They observed that a polymer

dx.doi.org/10.1021/ma201599p | *Macromolecules* 2012, 45, 1447−1459

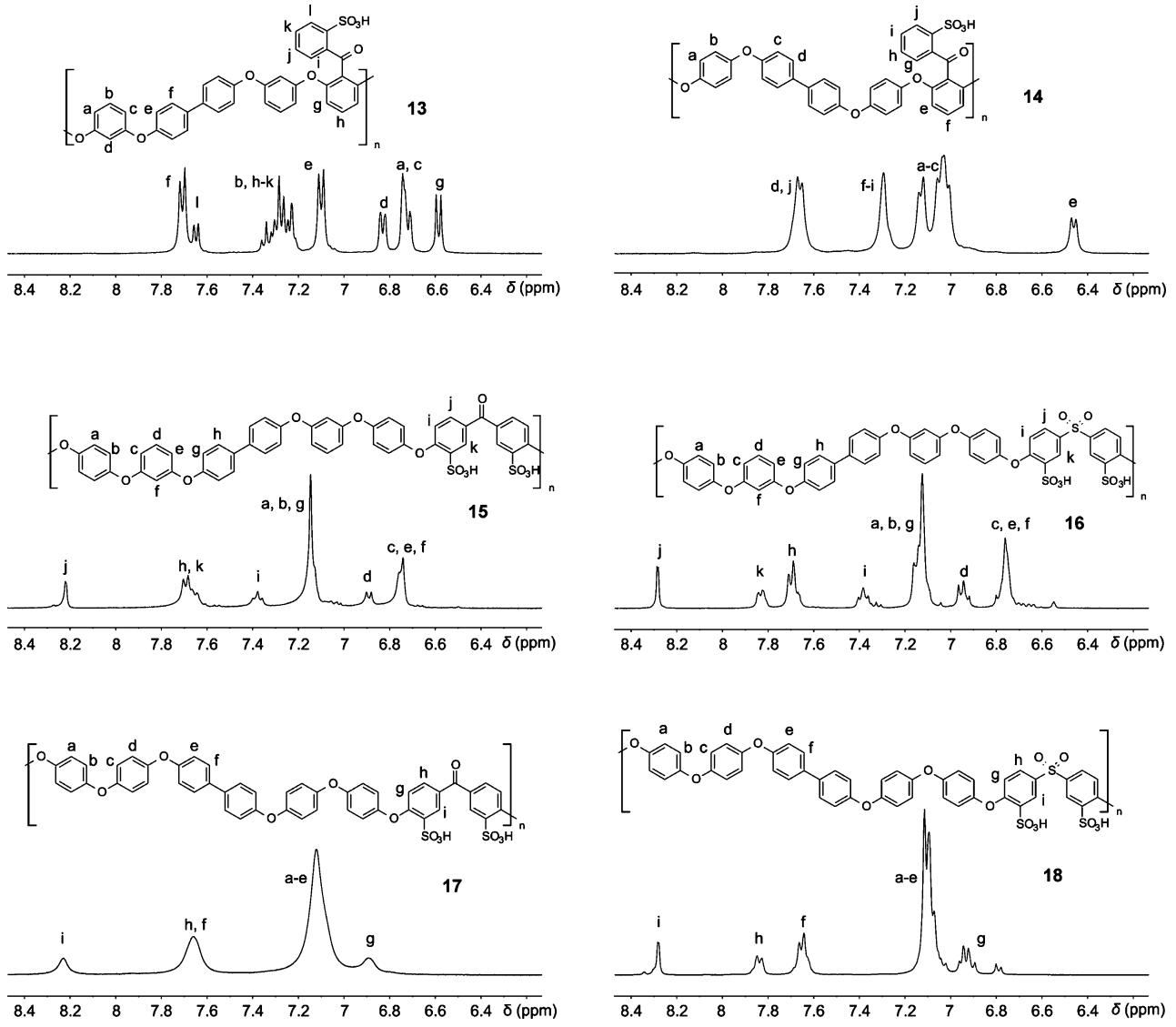


Figure 1. ^{1}H NMR spectra (DMSO-d_6) of the precisely sequenced sulfonated polymers, identified by their numerals.

Table 2. Properties of the Ionomer Membranes

polymer	theoretical IEC (mequiv g^{-1})	titrated IEC (mequiv g^{-1})	q_{max} (nm^{-1})^a	d (nm)^a	$T_{95\text{-Na}}$ (°C)^b	$T_{95\text{-H}}$ (°C)^c	water uptake (wt %)	λ
13	1.50	1.50	2.8	2.2	398	292	22	8.1
14	1.50	1.48	2.6	2.4	404	171	28	10.5
15	2.14	2.06	2.0	3.2	415	305	50	13.5
16	1.99	1.84	1.9	3.3	424	292	68	20.5
17	2.14	2.05	2.0	3.2	442	296	44	11.9

^{a}Membranes in the Pb^{2+} form. ^{b}Temperature corresponding to a 5% weight loss of membranes in their Na^+ form under nitrogen atmosphere at a heating rate of 10 °C min^{-1}. ^{c}Temperature corresponding to a 5% weight loss of membranes in their protonated form under air at a heating rate of 1 °C min^{-1}

with six-ring spacers showed a small but well-defined peak, indicating scattering at the same length-scale as that observed for Nafion. A polymer with 12-ring spacers showed a very much more intense peak, at significantly lower q, than for the one with the six-ring spacers, thus showing similar trends as observed in the present work. However, Colquhoun et al. found no second-order scattering features of their membranes. Possibly, the higher mobility of the oligo(ether) segments in relation to the oligo(ketone) segments allowed for a more efficient ionic aggregation in the present case. We have previously shown that membranes based on poly(arylene ether sulfone)s with sulfonic acid groups on short side chains gave SAXS profiles with narrow ionomer peaks at lower q_{max} than corresponding polymers with sulfonic acid groups statistically distributed along the backbone.[24,25] However, in this case no second order features were found.

The nature of the counterion have previously been reported to influence the morphology of ionomers.[49] In order to

dx.doi.org/10.1021/ma201599p | Macromolecules 2012, 45, 1447−1459

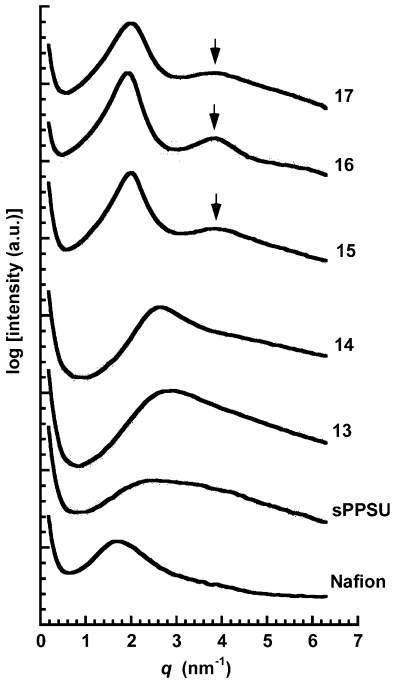
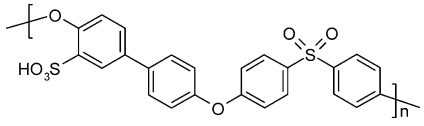


Figure 2. SAXS data recorded using ionomer membranes ion-exchanged with lead acetate to enhance the scattering intensity. The arrows indicate second-order peaks at $2q_{max}$.

Scheme 6. Structure of the sPPSU Reference Ionomer with Statistically Sequenced Ionic Groups



investigate the effect of the counterion in the present case, membranes **13** and **15** were ion-exchanged from their Pb^{2+} form to their H^+ and Na^+ form, respectively, to study the effect on the SAXS profiles. As seen in Figure 3, the position of the ionomer peak was not significantly influenced by the nature of the counterion. The reason may be that the initial membrane morphology, which is formed during the casting process, is largely retained during the ion-exchange process because of the glassy oligo(ether) segments. Perhaps a larger effect of the counterion would be observed if the membranes had been cast directly from ionomers in different ionic forms. In particular, for the series based on membrane **13**, the scattering intensity decreased with the size of the counterion. In the case of membrane **15**, the intensity of the ionomer peak did not change appreciably with the nature of the counterion. However, the intensity of the second order-peak at $2q_{max}$ decreased. It was only very slightly visible for the membrane in the Na^+ form and had disappeared for the membrane in the H^+ form.

The thermal history of ionomer membranes cast from high-T_g polymers can be expected to greatly influence the aggregation of ionic groups.[50] To study the effect of annealing on the membranes in the present case, membranes **13** and **15** in the Pb^{2+} form were kept at a temperature 20 °C above their respective T_g (Table 2). The SAXS profiles of the annealed membranes are shown together with the nonannealed (as cast) ones in Figure 4. As seen, the ionomer peak position of

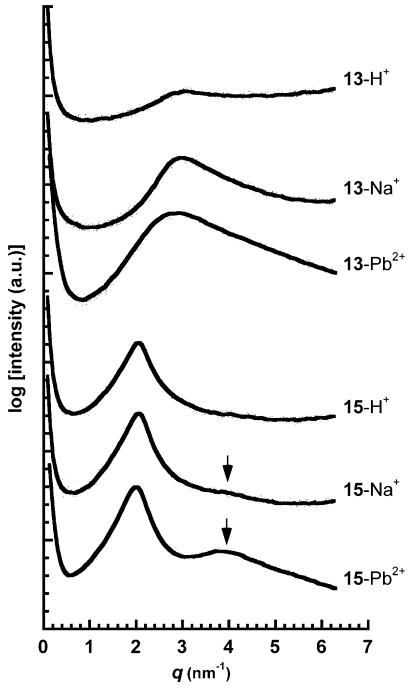


Figure 3. SAXS data recorded of ionomer membranes **13** and **15** in the H^+, Na^+, and Pb^{2+} form, respectively.

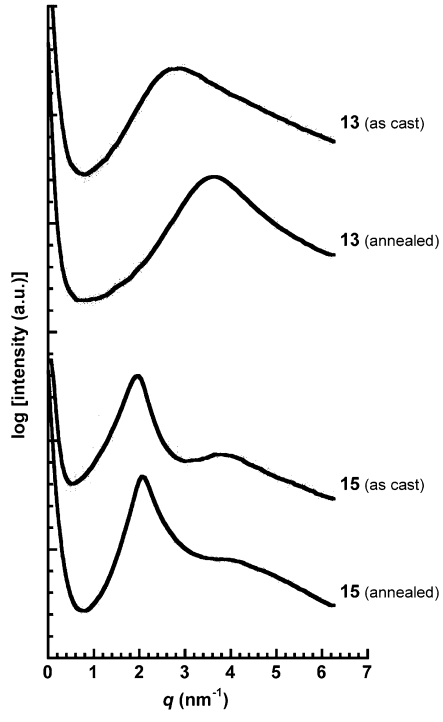


Figure 4. SAXS data of membranes **13** and **15** in the Pb^{2+} form recorded before (as cast) and after 10 min annealing 20 °C above the respective T_g.

membrane **13** increased significantly from q_{max} = 2.8 to 3.6 nm^{-1}, corresponding to a decrease in d from 2.2 to 1.7 nm. On the other hand, membrane **15** was only slightly affected by the annealing and the ionomer peak position decreased only very slightly, 0.1 nm^{-1}. This indicated that ionomer **15** with its doublet ionic moieties and longer oligo(ether) segments

dx.doi.org/10.1021/ma201599p | Macromolecules 2012, 45, 1447–1459

reached closer to an equilibrium structure during the casting process.

Thermal Properties. The thermal stability of the membranes was evaluated by thermogravimetric analysis (TGA) up to 600 °C. Measurements were performed at 10 °C min^{-1} under N_2 with the membranes in their Na^+ form. In addition, measurements were done at 1 °C min^{-1} under air with the membranes in their acid form to investigate the oxidative stability of the materials under more drastic conditions. The TGA traces are shown in Figure 5 and the

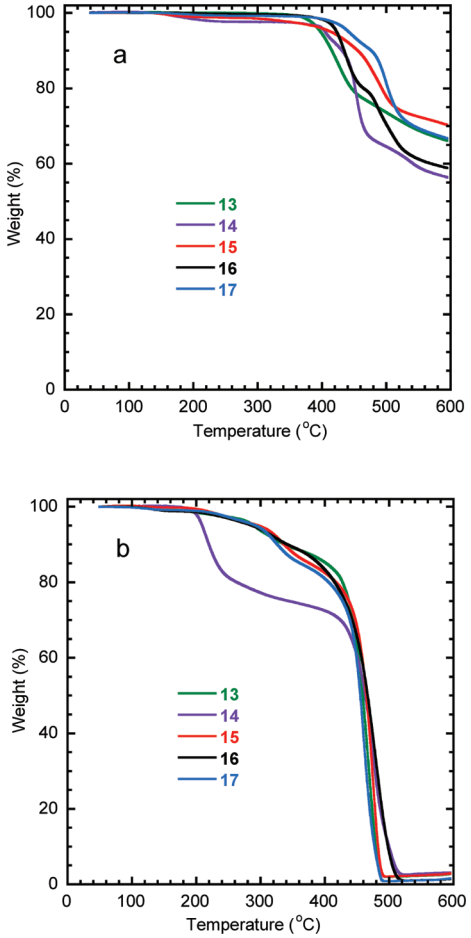


Figure 5. TGA traces of the sulfonated membranes in their Na^+ form recorded at 10 °C min^{-1} under nitrogen (a), and their acid form recorded at 1 °C min^{-1} under air (b).

temperatures corresponding to a 5% weight loss (T_{95}) are summarized in Table 2. In the Na^+ form, the polymers containing ether segments with *para* connectivity showed slightly higher T_{95} values than the corresponding polymers containing *meta* connectivity. Moreover, the polymers containing six-ring ether segments and doublets of acid units had higher T_{95} values than the polymers containing four-ring ether segments and singlets of acid units. The T_{95} values of the polymers in the Na^+ form were found between 400 and 442 °C. As expected, the thermal stability decreased after converting the membranes to the acid form. Still, the ionomers had high thermo-oxidative stability as demonstrated by their high T_{95} values above 290 °C. For some reason ionomer **14** exhibited a drastic weight loss already from 170 °C. A similar degradation has previously been observed in some cases for membranes based on monomer **1**.[41,42] For all the polymers, the degradation occurred in two steps, presumably by desulfonation followed by polymer main chain degradation.

Glass transitions were studied by differential scanning calorimetry (DSC) for the polymers in their Na^+ form and the values are found in Table 1 (the DSC traces the membranes in the Na^+ form are shown in the Supporting Information). Glass transitions were not always detected for the polymers in their acid form. However, in the cases where it was found, the T_g values recorded for the two forms were similar. The polymers containing six-ring ether segments and doublets of acid units showed higher T_g values than the polymers containing four-ring ether segments and singlets of acid units. As expected for materials based on the same sulfonated monomer, the polymer having an all-*para* connectivity in the hydrophobic polyether segment had a higher T_g than the corresponding polymer with *meta* connectivity. For example, the T_g of polymer **14** was 30 °C higher than for **13**. Also, for polymers with identical ether segment, ketone monomer **2** gave a higher T_g than polymers derived with sulfone monomer **3**. As a result, the polymer with the highest T_g in this study was **17**. In its Na^+ form, the value was found at 348 °C, close to the degradation temperature.

Water Uptake and Proton Conductivity. The water uptake plays a critical role for proton conducting polymer membranes. The presence of water is necessary to facilitate proton transport, and high proton conductivity is often associated with high IECs and high water uptake. However, excessive water uptake leads to loss of dimensional stability of the membrane. The water uptake at room temperature and the corresponding number of water molecules per sulfonic acid group (λ) are reported in Table 2. The membranes based on the polymers with the four-ring ether segments had an IEC of approximately 1.5 mequiv. g^{-1} (**13** and **14**) and showed lower water uptake values than the membranes based on polymers **15**-**17** with higher IECs. The latter membranes had water uptakes of between 44 and 68%. The membrane based on polymer **16** had a λ value of 20 which was markedly higher than for the other membranes, which most probably indicated a limited ability of this membrane to resist an excessive water uptake. There was seemingly no clear relationship between polymer chain connectivity and the water uptake at room temperature. However, the polymers containing *meta* linkages in the ether segments all swelled excessively in water at temperatures exceeding 80 °C. Substituting the *meta* linkages by *para* links in the ether segment resulted in a greatly improved dimensional stability of the membrane in hot water. For example, the all-*para* poly(arylene ether ketone) **17** with its high T_g value did not swell excessively in boiling water.

The proton conductivity of the membranes was evaluated using electrochemical impedance spectroscopy (EIS). Measurements were performed as a function of temperature at 100% RH using a 2-probe method, and also as a function of RH at 80 °C using a 4-probe method. Figure 6 shows the data collected as a function of temperature. As seen in Figure 6, the membranes based on polymers **13** and **14** showed a proton conductivity that was almost an order of magnitude lower than the other membranes under 100% RH. This was due to their lower IEC values and water uptake, as discussed above. Membrane **17** showed a conductivity in level with that of Nafion, and the conductivity of membrane **15** and **16** exceeded that of Nafion under these conditions to reach 0.2 S cm^{-1} at 80 °C. The polymer connectivity had direct influence on proton conductivity. Consistently, the *meta* homopolymers had a

dx.doi.org/10.1021/ma201599p | *Macromolecules* 2012, 45, 1447–1459

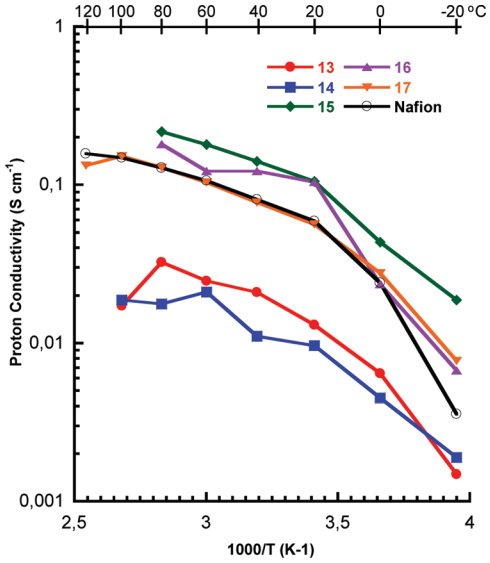


Figure 6. Arrhenius conductivity plots of data measured by electrochemical impedance spectroscopy with the membranes under 100% RH in a sealed cell. Values are given for Nafion for comparison.

higher proton conductivity than their *para* analogues. For example, membrane **13** had higher proton conductivity than membrane **14**. Similarly, membrane **15** had a higher conductivity than **17**. This may be explained by differences in the water uptake and T_g values. A lower T_g indicates a higher chain mobility which leads to higher water uptake and conductivity, especially at increasing temperatures.

Figure 7 shows the proton conductivity of **15** and **17** under reduced RH at 80 °C. Included are the corresponding data of

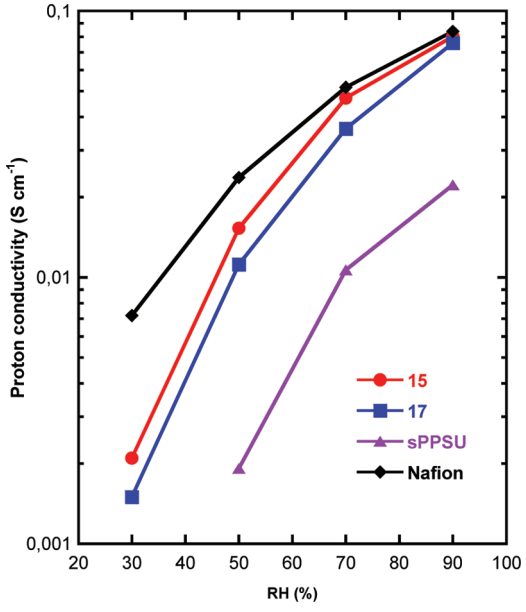


Figure 7. Conductivity data measured by electrochemical impedance spectroscopy for membranes **15** and **17** measured at 80 °C under reduced RH. Values for Nafion (IEC = 0.91 mequiv g^{-1}) and sPPSU (IEC = 1.84 mequiv g^{-1}), with statistically distributed sulfonic acid groups, are given for comparison.

Nafion and sPPSU. As seen, the conductivity of **15** and **17** reached well above that of sPPSU under reduced RH, but fell below that of Nafion in the investigated range between 30 and 90% RH. Membrane **15** had higher proton conductivity than **17** presumably because of the higher water uptake of the former membrane. The significantly higher proton conductivity of the perfectly sequenced ionic polymer membranes was likely due to the more regular ionic cluster distribution which facilitated the formation of a more efficient water pore system for proton transport.

EXPERIMENTAL SECTION

Materials. Monomer **1**,[30] **2**,[31] and **3**[32,33] were synthesized and characterized as reported previously. Cesium carbonate, magnesium sulfate, Celite, 4,4′-dibromobiphenyl (DBBP), 4-fluoroacetophenone and 4-bromoanisole were obtained from Aldrich. Dimethylformamide (DMF), *N*,*N*-dimethylacetamide (DMAc), *N*-methyl-2-pyrrolidone (NMP), 2,2,6,6-Tetramethyl-3,5-heptanedione (TMHD), copper(I) chloride, 3-methoxyphenol (*m*MP), 4-methoxyphenol (*p*MP), potassium carbonate, Hydrobromic acid 48%, acetic acid, *m*-chloroperbenzoic acid (*m*CPBA) and trifluoroacetic acid (TFA) were purchased from Acros. Methanol, 2-propanol, diethyl ether, toluene and chloroform were from Fisher. Potassium carbonate was grounded to a fine powder and dried at 120 °C prior to use. Nafion NRE212 was from Alfa Aesar.

Bismethoxy Oligomer 4. A setup consisting of a two-neck round bottomed flask heated by an oil bath and equipped with a magnetic stirrer, a N_2 inlet, and a condenser was used in the syntheses. A solution of 4,4′-dibromobiphenyl (1.560 g, 5.00 mmol), Cs_2CO_3 (1.629 g, 5.00 mmol) 3-methoxyphenol (1.862 g, 15.00 mmol), and 2,2,6,6-tetramethyl-3,5-heptanedione (0.460 g, 2.50 mmol) in NMP (10 mL) was added to the reactor and stirred at room temperature under nitrogen atmosphere. Then CuCl (0.250 g, 2.50 mmol) was added and the mixture was degassed, filled with nitrogen and heated at 165 °C. After 22 h, the solution was cooled, diluted with diethyl ether and filtered through Celite. The filtrate was washed with water, dried with magnesium sulfate, filtered and evaporated. The resulting brown solid was stirred in methanol to afford the desired product **4** that was isolated by filtration as a white powder (1.55 g, 78% yield).

Mp: 104 °C. ^{1}H NMR (400 MHz, $CDCl_3$, δ): 3.81 (6H, s, O−CH3), 6.63 (6H, m, Ar), 7.10 (4H, d, Ar), 7.27 (2H, d, Ar), 7.54 (4H, d, Ar). ^{13}C NMR (100 MHz, $CDCl_3$, δ): 55.4, 104.9, 109.1, 111.1, 119.3, 128.2, 130.2, 135.7, 156.3, 158.4, 161.1. IR (KBr): ν_{C-H} 3041 cm^{-1}, ν_{O-CH3} 2837 cm^{-1}, ν_{C-O-C} 1128 cm^{-1}.

Bisphenol Monomer 5. To a stirred solution of **4** (1.99 g, 5.0 mmol) in acetic acid (50 mL) was added 48% HBr (6 mL). After 16 h at 160 °C under air, the solution was cooled and poured in ice. The dark precipitate was washed with water, filtered, and dried under vacuum at 60 °C. Recrystallization in toluene afforded **5** as a brown solid (1.71 g, 92% yield).

Mp: 168 °C. ^{1}H NMR (400 MHz, $CDCl_3$, δ): 6.41 (6H, m, Ar), 7.07 (4H, d, Ar), 7.16 (2H, d, Ar), 7.65 (4H, d, Ar). ^{13}C NMR (100 MHz, $CDCl_3$, δ): 105.9, 109.8, 110.8, 119.6, 128.4, 130.8, 135.1, 156.4, 158.2, 159.3. IR (KBr): ν_{C-OH} 3357 cm^{-1}, ν_{C-H} 3062 cm^{-1}, ν_{C-O-C} 1128 cm^{-1}.

Bismethoxy Oligomer 6. A solution of 4,4′-dibromobiphenyl (7.800 g, 25.00 mmol), Cs_2CO_3 (9.774 g, 30.00 mmol) 4-methoxyphenol (9.310 g, 75.00 mmol), and 2,2,6,6-tetramethyl-3,5-heptanedione (2.302 g, 12.50 mmol) in NMP (50 mL) was stirred at room temperature under nitrogen atmosphere. Then CuCl (1.250 g, 12.50 mmol) was added. The mixture was degassed, filled with nitrogen and heated at 170 °C. After 22 h, the solution was cooled and filtered through Celite. The filtrate was washed with water, dried with $MgSO_4$ and evaporated. The resulting brown solid was stirred in methanol and the desired product **6** was isolated as a white powder by filtration (6.97 g, 70% yield).

Mp: 210 °C. ^{1}H NMR (400 MHz, $CDCl_3$, δ): 3.82 (6H, s, O−CH_3), 6.91 (4H, d, Ar), 7.00 (8H, AA′XX′, Ar), 7.48 (4H, d, Ar); ^{13}C NMR (100 MHz, $CDCl_3$, δ): 55.3, 114.7, 117.9, 120.8, 127.9,

dx.doi.org/10.1021/ma201599p | *Macromolecules* 2012, 45, 1447−1459

135.0, 149.9, 157.8. IR (KBr): ν_{C-H} 3040 cm^{-1}, ν_{O-CH3} 2837 cm^{-1}, ν_{C-O-C} 1132 cm^{-1}.

Bisphenol Monomer 7. To a stirred solution of **6** (1.394 g, 3.50 mmol) in acetic acid (160 mL) was added 48% HBr (12 mL). The solution was heated to 160 °C for 16 h. Then the solution was poured in ice to give a white precipitate that was filtered and washed with water. The desired product **7** was obtained as a white powder after purification by recrystallization from toluene (1.16 g, 90% yield).

Mp: 249 °C. ^{1}H NMR (400 MHz, DMSO-d_6, δ): 6.79 (4H, d, Ar), 6.91 (8H, AA'XX', Ar), 7.53 (4H, d, Ar). ^{13}C NMR (100 MHz, DMSO-d_6, δ): 116.6, 117.6, 121.5, 128.2, 134.1, 148.1, 154.3, 158.2. IR (KBr): ν_{C-OH} 3466 cm^{-1}, ν_{C-H} 3033 cm^{-1}, ν_{C-O-C} 1132 cm^{-1}.

Bismethoxy Oligomer 8. A mixture of **5** (0.926 g, 2.50 mmol), Cs_2CO_3 (1.955 g, 6.00 mmol), 4-bromanisole (1.402 g, 7.50 mmol), and 2,2,6,6-tetramethyl-3,5-heptanedione (0.921 g, 5.00 mmol) were stirred in NMP (7.5 mL) under nitrogen atmosphere. After 30 min, CuCl (0.500 g, 5.00 mmol) was added and the mixture was degassed, filled with nitrogen and heated to 170 °C. After 22 h, the solution was diluted with diethyl ether and filtered through Celite. The filtrate was washed with water, dried with magnesium sulfate, filtered and evaporated. The resulting brown solid was stirred in methanol to afford the desired oligomer **8** that was isolated by filtration (1.01 g, 70% yield).

Mp: 98 °C. ^{1}H NMR (400 MHz, $CDCl_3$, δ): 3.82 (6H, s, O−CH3), 6.68 (6H, m, Ar), 6.90 (4H, d, Ar), 7.02 (4H, d, Ar), 7.09 (4H, d, Ar), 7.24 (2H, d, Ar), 7.52 (4H, d, Ar). ^{13}C NMR (100 MHz, $CDCl_3$, δ): 55.3, 108.0, 112.1, 112.5, 114.9, 119.2, 120.8, 128.1, 130.3, 135.9, 149.3, 156.0, 158.2, 159.8. IR (KBr): ν_{C-H} 3039 cm^{-1}, ν_{O-CH3} 2834 cm^{-1}, ν_{C-O-C} 1122 cm^{-1}.

Bisphenol Monomer 9. To a stirred solution of **8** (1.16 g, 2.0 mmol) in acetic acid (20 mL) was added 48% HBr (5 mL). After 16 h at 160 °C, the solution was poured in ice. The white precipitate was then washed with water, filtered, and dried under vacuum at 60 °C. Recrystallization in toluene afforded the desired product **9** as a red powder (0.99 g, 90% yield).

Mp: 158−166 °C. ^{1}H NMR (400 MHz, DMSO-d_6, δ): 6.54 (6H, m, Ar), 6.77 (4H, d, Ar), 6.92 (4H, d, Ar), 7.09 (4H, d, Ar), 7.30 (2H, d, Ar), 7.64 (4H, d, Ar). ^{13}C NMR (100 MHz, DMSO-d_6, δ): 107.5, 112.1, 112.6, 116.6, 119.7, 121.7, 128.5, 131.3, 135.4, 147,7, 154.5, 156.1, 158.2, 160.4. IR (KBr): ν_{C-OH} 3384 cm^{-1}, ν_{C-H} 3068 cm^{-1}, ν_{C-O-C} 1122 cm^{-1}.

Bisacetophenone Oligomer 10. A solution of monomer **7** (1.111 g, 3.00 mmol), 4-fluoroacetophenone (0.967 g, 7.00 mmol), potassium carbonate (0.967 g, 7.00 mmol) in DMF (10 mL) was stirred at 150 °C under nitrogen atmosphere. After 18 h, the red solution was cooled and poured in water. The resulting white precipitate was filtered, and dried under vacuum at 80 °C (1.454 g, 80% yield).

Mp: 263 °C. ^{1}H NMR (400 MHz, $CDCl_3$/TFA 6:1, δ): 2.70 (6H, s, CO−CH3), 7.05 (16H, AA'XX', Ar), 7.58 (4H, d, Ar), 8.02 (4H, d, Ar). ^{13}C NMR (100 MHz, $CDCl_3$/TFA 6:1, δ): 25.6, 116.8, 119.0, 120.5, 122.0, 128.3, 129.9, 131.9, 136.0, 150.2, 154.2, 156.4, 164.1. IR (KBr): ν_{C-H} 3043 cm^{-1}, ν_{C-O} 1678 cm^{-1}, ν_{C-C} 1600 cm^{-1}, ν_{C-O-C} 1112 cm^{-1}.

Bisphenol Monomer 12. A suspension of **10** (0.848 g, 1.40 mmol) in chloroform (160 mL) was cooled in an ice bath. Then, *m*CPBA (2.390 g, 10.00 mmol) and trifluoroacetic acid (5 mL) were added successively. The mixture was left to warm up to room temperature and was vigorously stirred in the dark for 72 h. The reaction was then quenched by addition of a saturated solution of $NaHSO_3$. The organic layer was washed with saturated $NaHCO_3$ solution and water. It was dried with magnesium sulfate, filtered and evaporated under reduced pressure to give **11** as a white powder. Oligomer **11** was stirred in a 0.1 M solution of KOH in methanol (200 mL) under reflux condition for 90 min. Then the solvent was removed and the resulting residue was suspended in 1 M HCl. The desired bisphenol monomer **12** was isolated by filtration and was purified by adding 2-propanol to a DMF solution until a precipitate was formed. The solid was dissolved by heating and recrystallization from DMF and 2-propanol afforded **12** as a white powder.

Mp: 274 °C. ^{1}H NMR (400 MHz, DMSO-d_6, δ): 6.77 (4H, d, Ar), 6.88 (8H, AA'XX', Ar), 7.01 (8H, AA'XX', Ar), 7.60 (4H, d, Ar). ^{13}C NMR (100 MHz, DMSO-d_6, δ): 116.7, 118.5, 119.1, 121.0, 121.2, 134.7, 148.8, 151.3, 154.1, 154.8, 157.3. IR (KBr): ν_{OH} 3290 cm^{-1}, ν_{C-H} 3040 cm^{-1}, ν_{C-O-C} 1098 cm^{-1}.

Polymer 13. A mixture of potassium carbonate (0.345 g, 2.50 mmol), **5** (0.370 g, 1.00 mmol) and **1** (0.304 g, 1.00 mmol) was suspended in DMSO (3 mL) and toluene (10 mL) in a two-necked flask fitted with a nitrogen gas inlet, a Dean−Stark trap, a condenser and a calcium chloride guard. Water was removed by azeotropic distillation with toluene maintaining a reflux temperature of 140 °C for 4 h. Then, toluene was removed and the reaction temperature was increased to 160 °C. After 4 h the viscous mixture was cooled and poured into 2-propanol. The precipitate was filtered off, washed with water and dried. The solid was dissolved in DMSO and precipitated from 2-propanol to give **13** as a powder that was dried in a vacuum oven at 80 °C.

^{1}H NMR (400 MHz, DMSO-d_6, δ): 6.57 (2H, d, Ar), 6.71 (4H, m, Ar), 6.81 (2H, d, Ar), 7.09 (4H, d, Ar), 7.23 (6H, m, Ar), 7.63 (1H, d, Ar), 7.69 (4H, d, Ar). ^{13}C NMR (100 MHz, DMSO-d_6, δ): 110.7, 113.5, 113.8, 114.9, 119.5, 124.4, 127.6, 128.6, 129.1, 129.4, 130.8,132.4, 135.4, 140.2, 145.5, 156.2, 156.9, 157.7, 158.2, 193.9. IR (KBr): $\nu_{C=O}$ 1681 cm^{-1}, ν_{C-O-C} 1089 cm^{-1}, ν_{SO_3} 1022 cm^{-1}.

Polymer 14. The polymerization of **7** (0.370 g, 1.00 mmol) and **1** (0.304 g, 1.00 mmol) was carried out using an identical procedure as described for polymer **13**. The reaction was stopped after 6 h and **14** was recovered as a white powder.

^{1}H NMR (400 MHz, DMSO-d_6, δ): 6.46 (2H, br, Ar), 7.00 (12H, br, Ar), 7.31 (4H, br, Ar), 7.65 (5H, br, Ar). ^{13}C NMR (100 MHz, DMSO-d_6, δ): 112.1, 118.6, 120.7, 121.8, 123.6, 127.7, 128.4, 128.7, 129.3, 132.2, 134.8, 140.4, 145.5, 152.2, 152.7, 157.2, 157.9, 194.1. IR (KBr): $\nu_{C=O}$ 1683 cm^{-1}, ν_{C-O-C} 1089 cm-1, ν_{SO_3} 1019 cm^{-1}.

Polymer 15. A mixture of potassium carbonate (0.207 g, 1.50 mmol), **9** (0.388 g, 0.70 mmol), and **2** (0.296 g, 0.70 mmol) was suspended in DMSO (3 mL) and toluene (10 mL) in a two-necked flask fitted with a nitrogen gas inlet, a Dean−Stark trap, a condenser, and a calcium chloride guard. Water was removed by azeotropic distillation with toluene maintaining a reflux temperature of 140 °C for 4 h. Then toluene was removed and the reaction temperature was increased to 160 °C. After 21 h the viscous mixture was cooled and poured in 2-propanol. The precipitate was filtered off, washed with water and dried. The solid was dissolved in DMSO and precipitated from 2-propanol to give **15** as a powder that was dried in a vacuum oven at 80 °C.

^{1}H NMR (400 MHz, DMSO-d_6, δ): 6.73 (6H, br, Ar), 6.87 (2H, m, Ar), 7.14 (12H, br, Ar), 7.37 (2H, m, Ar), 7.68 (6H, m, Ar), 8.22 (2H, br, Ar). ^{13}C NMR (100 MHz, DMSO-d_6, δ): 108.7, 109.0, 112.8, 113.2, 118.1, 119.9, 121.5, 121,7, 122.3, 128.5, 131.1, 131.2, 131.5, 132.6, 135.4, 138.2, 152.3, 152.6, 156.0, 158.4, 159.1, 193.6. IR (KBr): $\nu_{C=O}$ 1653 cm^{-1}, ν_{SO_3} 1028 cm^{-1}.

Polymer 16. A mixture of potassium carbonate (0.207 g, 1.50 mmol), **9** (0.388 g, 0.70 mmol) and **3** (0.344 g, 0.70 mmol) was suspended in DMAc (3 mL) and toluene (10 mL) in a two-necked flask fitted with a nitrogen gas inlet, a Dean−Stark trap, a condenser and a calcium chloride guard. Water was removed by azeotropic distillation with toluene maintaining a reflux temperature of 140 °C for 4 h. Then toluene was removed and the reaction temperature was increased to 165 °C. After 22 h the viscous mixture was cooled and poured in 2-propanol. After the purification procedure described above, **16** was recovered as a powder.

^{1}H NMR (400 MHz, DMSO-d_6, δ): 6.76 (6H, br, Ar), 6.91 (2H, m, Ar), 7.12 (12H, m, Ar), 7.36 (2H, m, Ar), 7.68 (4H, m, Ar), 7.82 (2H, m, Ar), 8.28 (2H, br, Ar). ^{13}C NMR (100 MHz, DMSO-d_6, δ): 107.6, 109.0, 112.9, 113.2, 116.7, 119.1, 119.9, 121.3, 121.6, 122.3, 128.5, 130.3, 131,3 131.6, 134.4, 135.5, 139.0, 152.0, 152.7, 155.9, 158.5, 159.0. IR (KBr): $\nu_{O=S=O}$ 1163 cm^{-1}, ν_{SO_3} 1027 cm^{-1}.

Polymer 17. A mixture of potassium carbonate (0.207 g, 1.50 mmol), **12** (0.388 g, 0.70 mmol) and **2** (0.296 g, 0.70 mmol) was suspended in DMSO (3 mL) and toluene (10 mL) in a two-necked flask fitted with a nitrogen gas inlet, a Dean−Stark trap, a condenser and a calcium chloride guard. Water was removed by azeotropic distillation with toluene maintaining a reflux temperature of 140 °C for 18 h. The toluene was removed and the reaction temperature was increased

to 160 °C. After 40 min the highly viscous mixture was cooled and poured in 2-propanol. The precipitate was filtered off, washed with water and dried. The solid was dissolved in DMSO and precipitated from 2-propanol to give **17** as a powder that was dried in a vacuum oven at 80 °C.

^{1}H NMR (400 MHz, DMSO-d_6, δ): 6.89 (2H, br, Ar), 7.12 (20H, br, Ar), 7.65 (6H, br, Ar), 8.23 (2H, br, Ar). ^{13}C NMR (100 MHz, DMSO-d_6, δ): 118.1, 118.8, 120.3, 120.5, 121.0, 121.2, 121.3, 122.3, 128.4, 131.1, 132.7, 135.0, 138.2, 152.1, 152.3, 153.3, 153.6, 157.1, 158.7, 193.5. IR (KBr): $\nu_{C=O}$ 1652 cm^{-1}, ν_{SO_3} 1027 cm^{-1}.

Polymer 18. A mixture of potassium carbonate (0.207 g, 1.50 mmol), **12** (0.388 g, 0.70 mmol) and **3** (0.344 g, 0.70 mmol) was suspended in DMAc (3 mL) and toluene (10 mL) in a two-necked flask fitted with a nitrogen gas inlet, a Dean−Stark trap, a condenser and a calcium chloride guard. Water was removed by azeotropic distillation with toluene maintaining a reflux temperature of 140 °C for 4 h. Then toluene was removed and the reaction temperature was increased to 160 °C. After 7 h the mixture was cooled and poured in 2-propanol. Polymer **18** was recovered as a powder after using the same purification as described above.

^{1}H NMR (400 MHz, DMSO-d_6, δ): 6.77 (4H, m, Ar), 7.10 (16H, m, Ar), 7.64 (4H, m, Ar), 7.82 (2H, m, Ar), 8.27 (2H, br, Ar). ^{13}C NMR (100 MHz, DMSO-d_6, δ): 116.7, 118.5, 118.8, 119.0, 120.3, 120.6, 121.0, 121.2, 122.4, 128.5, 130.3, 134.3, 134.9, 138.9, 151.4, 152.4, 153.1, 154.0, 157.1, 159.2. IR (KBr): $\nu_{O=S=O}$ 1163 cm^{-1}, ν_{SO_3} 1027 cm^{-1}.

Membrane Casting. An amount of 0.300 g polymer was dissolved in DMAC (3 mL). The solution was filtered and transferred to a 1 in. Petri dish. Slow evaporation of the solvent at 80 °C under a nitrogen flow afforded transparent membranes that were washed successively with water. The membranes were ion-exchanged to the protonated form by immersion in 1 N HCl for 24 h, followed by leaching with distilled water for 2 days during which time the water was repeatedly exchanged until a neutral pH was reached.

Polymer Characterization. ^{1}H NMR spectra were recorded on a Bruker 400 MHz spectrometer using $CDCl_3$ or DMSO-d_6 solutions of the compounds. Resonances were recorded in δ (ppm) and referenced to residual solvent resonances. Fourier-transform infrared (IR) analysis was obtained with a Bruker FS66 spectrometer. Dry polymer samples were ground with potassium bromide and pressed into tablets. Inherent viscosities (η_{inh}) were determined at 25 °C for filtered 0.5 wt % polymer solutions in DMF containing 0.05 M LiBr using an Ubbelohde capillary viscometer.

Membrane Characterization. Ion exchange capacities (IECs) were determined as follow: a membrane of known weight in its protonated form was immersed overnight in an aqueous solution of sodium chloride. The quantity of protons exchanged was titrated with potassium hydroxide, using phenolphthalein as an indicator. Water uptakes were determined by immersion of membranes in their protonated form in water at room temperature. Differential scanning calorimetry (DSC) was conducted on a TA Instruments Q1000 DSC at a heating and cooling rate of 10 °C min^{-1}. Values are reported for the second heating scan of membranes in the Na^+ form. Thermogravimetric analysis was performed on a TA Instruments Q500. Samples were dried at 120 °C before analysis. Thermal stability under nitrogen atmosphere was evaluated for membranes in their Na^+ form at a heating rate of 10 °C min^{-1}. Degradation of membranes in their protonated form was assessed at a scanning rate of 1 °C min^{-1}. SAXS measurements were carried out on all membranes ion-exchanged to the Pb^{2+} form by immersion in a 1 wt % aqueous solution of lead acetate. In addition, membranes **13** and **15** were ion exchanged to their Na^+ and H^+ form to study the effect of the counterion on the scattering. Furthermore, scattering experiments were performed on membranes **13** and **15** (Pb^{2+} form) after annealing at 20 °C above their respective T_g for 10 min. All scattering experiments were performed on a SAXSess camera (Kratky, Anton Paar) equipped with a CCD detector. CuK_α radiation with a wavelength (λ) of 0.1542 nm was generated by a PANalytical PW3830 X-ray generator operating at 40 kV and 50 mA. Dry membranes were analyzed in a solid sample holder at 25 °C. The wave vector (q) was calculated by the software (SAXSquant) according to:

$$q = 4\pi\lambda^{-1}\sin(\theta) \quad (1)$$

where 2θ is the scattering angle. The characteristic separation length (d), i.e., the Bragg spacing, was calculated as:

$$d = 2\pi q^{-1} \quad (2)$$

Proton conductivity was measured by electrochemical impedance spectroscopy (EIS) using a Novocontrol V 1.01S dielectric analyzer from −20 to +120 °C under 100% relative humidity. In-plane conductivity was measured using two stainless steel electrodes. Impedance data were collected between 10^{-1} and 10^7 Hz at a voltage amplitude of 50 mV. For each temperature, the proton conductivity was taken as the real component of the conductivity corresponding to the minimum of the imaginary component of the conductivity. The humidity dependence of the proton conductivity at 80 °C from 30 to 90% RH was investigated by a four-probe method using a Gamry potentiostat/galvanostat/ZRA and a Fumatech MK3 conductivity cell, where the humidity was equilibrated by deionized water in a closed system.

■ CONCLUSIONS

The facile synthesis of a series of new aromatic oligo(ether) bisphenol monomers with four or six phenylene rings enabled the preparation of new ionic aromatic polymers with precisely sequenced ionic moieties having either one or two sulfonic acid groups along the backbone. The fully aromatic polymers thus had a microblock structure and were prepared through conventional polycondensations involving nucleophilic aromatic substitution reactions of one sulfonated dihalide and one bisphenol monomer. The polymers showed quite different properties and morphologies from analogous polymer with statistically placed sulfonic acid groups. SAXS measurements of solvent cast membranes the Pb^{2+} form showed that the precise ionomers were able to form ionic aggregates with a much more uniform distribution than a corresponding statistical ionomer with a similar backbone structure. Scattering profiles with very intense scattering, narrow ionomer peaks and second order peaks were observed for the precisely sequenced ionomers having disulfonated moieties and six-ring spacers. This indicated a significantly higher degree of morphological control in relation with the statistical ionomer. No influence of the connectivity of the oligo(ether) spacers and the nature of the sulfonated moieties (sulfone or ketone) on the scattering peak position and width was observed. Thus, ionomers with precisely and sufficiently spaced ionic moieties are required facilitate the highly uniform self-aggregation of the ionic groups. Still, the nature of the connectivity (*meta* vs *para*) of the oligo(ether) influenced the T_g, leading to higher values for the ionomers having *para* connectivity. This in turn led to lower water uptake and proton conductivities of the membranes based on these ionomers. Yet, an ionomer with disulfonated moieties perfectly alternating with a six-ring segment having exclusively *para* linkages reached a proton conductivity similar to Nafion under 100% RH at 80 °C, and had an excellent stability in boiling water. Under reduced RH, the conductivity of this membrane greatly exceeded that of a membrane based on the statistical aromatic copolymer analogue with a similar IEC, especially at low RHs. This was presumably because the more uniform distribution of the ionic aggregates in the membranes based on the precise ionomers facilitated more efficient water channels for proton transport. Even though there is increasing interest in the development of organized

polymer systems such as block copolymers, statistical copolymers are still the class of polymer primarily being used in fuel cells, especially by industry. This is due to the larger number of available synthetic techniques and their ease of synthesis in comparison with complex methods required for block and graft copolymers. Thus, developing efficient synthetic strategies to prepare precisely sequenced fully aromatic ionomers with sufficiently long sequences and appropriate IEC values may be a viable alternative for use as fuel cell membranes with controlled morphology.

■ ASSOCIATED CONTENT

Supporting Information

^{1}H NMR spectra of the bisphenol monomers and their intermediates and DSC traces of the membranes in the Na^+ form. This material is available free of charge via the Internet at http://pubs.acs.org.

■ AUTHOR INFORMATION

Corresponding Author

*E-mail: patric.jannasch@polymat.lth.se. Fax: +46-46-2224012. Telephone: +46-46-2229860.

■ ACKNOWLEDGMENTS

We gratefully acknowledge the Swedish Energy Agency for their financial support. Dr. Xuefeng Li wishes to thank the China Scholarship Council. We are also grateful to Shogo Takamuku for the synthesis of the sPPSU sample.

■ REFERENCES

(1) Hickner, M. A. *Mater. Today* **2010**, *13*, 24.
(2) Iojoiu, C.; Sanchez, J.-Y. *High Perform. Polym.* **2009**, *21*, 673.
(3) Zhang, J.; Xie, Z.; Zhang, J.; Tang, Y.; Song, C.; Navessin, T.; Shi, Z.; Song, D.; Wang, H.; Wilkinson, D. P.; Liu, Z.; Holdcroft, S. *J. Power Sources* **2006**, *160*, 872.
(4) Garland, N.; Kopasz, J. *J. Power Sources* **2007**, *172*, 94.
(5) Iojoiu, C.; Marechal, M.; Chabert, F.; Sanchez, J. Y. *Fuel Cells* **2005**, *5*, 344.
(6) Jones, D. J.; Rozière, J. *J. Membr. Sci.* **2001**, *185*, 41.
(7) Kreuer, K. D. *J. Membr. Sci.* **2001**, *185*, 29.
(8) Higashihara, T.; Matsumoto, K.; Ueda, M. *Polymer* **2009**, *50*, 5341.
(9) Peckham, T. J.; Holdcroft, S. *Adv. Mater.* **2010**, *22*, 4667.
(10) Ghassemi, H.; McGrath, J. E.; Zawodzinski, T. A. *Polymer* **2006**, *47*, 4132.
(11) Roy, A.; Lee, H. S.; McGrath, J. E. *Polymer* **2008**, *49*, 5037.
(12) Lee, H. S.; Roy, A.; Lane, O.; Dunn, S.; McGrath, J. E. *Polymer* **2008**, *49*, 715.
(13) Badami, A. S.; Lane, O.; Lee, H.-S.; Roy, A.; McGrath, J. E. *J. Membr. Sci.* **2009**, *333*, 1.
(14) Nakabayashi, K.; Matsumoto, K.; Ueda, M. *J. Polym. Sci., Polym. Chem.* **2008**, *46*, 3947.
(15) Mikami, T.; Miyatake, K.; Watanabe, M. *J. Polym. Sci., Polym. Chem.* **2011**, *49*, 452.
(16) Takamuku, S.; Akizuki, K.; Abe, M.; Kanesaka, H. *J. Polym. Sci., Polym. Chem.* **2009**, *47*, 700.
(17) Schönberger, F.; Kerres, J. *J. Polym. Sci., Polym. Chem.* **2007**, *45*, 5237.
(18) Lee, H. S.; Lane, O.; McGrath, J. E. *J. Power Sources* **2010**, *195*, 1772.
(19) Bae, B.; Yoda, T.; Miyatake, K.; Uchida, H.; Watanabe, M. *Angew. Chem., Int. Ed.* **2010**, *49*, 317.
(20) Bae, B.; Miyatake, K.; Watanabe, M. *Macromolecules* **2010**, *43*, 2684.
(21) Nakabayashi, K.; Higashihara, T.; Ueda, M. *Macromolecules* **2010**, *43*, 5756.
(22) Nakabayashi, K.; Higashihara, T.; Ueda, M. *J. Polym. Sci., Polym. Chem.* **2010**, *48*, 2757.
(23) Takamuku, S.; Jannasch, P. *Macromol. Rapid Commun.* **2011**, *32*, 474.
(24) Lafitte, B.; Jannasch, P. *Adv. Funct. Mater.* **2007**, *17*, 2823.
(25) Jutemar, E. P.; Jannasch, P. *J. Membr. Sci.* **2010**, *351*, 87.
(26) Tian, S.; Meng, Y.; Hay, A. S. *Macromolecules* **2009**, *42*, 1153.
(27) Zhu, Z.; Walsby, N. M.; Colquhoun, H. M.; Thompsett, D.; Petrucco, E. *Fuel Cells* **2009**, *9*, 305.
(28) Schuster, M.; Kreuer, K. D.; Andersen, H. T.; Maier, J. *Macromolecules* **2007**, *40*, 598.
(29) Jannasch, P. *Fuel Cells* **2005**, *5*, 248.
(30) Jutemar, E. P.; Takamuku, S.; Jannasch, P. *Macromol. Rapid Commun.* **2010**, *31*, 1348.
(31) Ueda, M.; Toyota, H.; Ouchi, T.; Sugiyama, J. I.; Yonetake, K.; Masuko, T.; Teramoto, T. *J. Polym. Sci., Polym. Chem.* **1993**, *31*, 853.
(32) Wang, F.; Chen, T.; Xu, J. *Macromol. Chem. Phys.* **1998**, *199*, 1421.
(33) Wang, F.; Li, J.; Chen, T.; Xu, J. *Polymer* **1999**, *40*, 795.
(34) Buck, E.; Song, Z. J.; Tschaen, D.; Dormer, P. G.; Volante, R. P.; Reider, P. J. *Org. Lett.* **2002**, *4*, 1623.
(35) Yeager, G. W.; Schissel, D. N. *Synthesis* **1991**, *1*, 63.
(36) Ben-Haida, A.; Colquhoun, H. M.; Hodge, P.; Lewis, D. F. *Polymer* **1999**, *40*, 5173.
(37) Ben-Haida, A.; Colquhoun, H. M.; Hodge, P.; Williams, D. J. *J. Mater. Chem.* **2000**, *10*, 2011.
(38) Colquhoun, H. M.; Paoloni, F. P. V.; Drea, M. G. B.; Hodge, P. *Chem. Commun.* **2007**, 3365.
(39) Colquhoun, H. M.; Hodge, P.; Paoloni, F. P. V.; McGrail, P. T.; Cross, P. *Macromolecules* **2009**, *42*, 1955.
(40) Ogata, Y.; Sawaki, Y. *J. Org. Chem.* **1972**, *37*, 2953. Syper, L. *Synthesis* **1989**, *3*, 167.
(41) Jutemar, E. P.; Jannasch, P. *J. Polym. Sci., Polym. Chem.* **2011**, *49*, 734.
(42) Jutemar, E. P.; Jannasch, P. *ACS Appl. Mater. Interfaces* **2010**, *2*, 3718.
(43) Daoust, D.; Godard, P.; Devaux, J.; Legras, R.; Strazielle, C. *Polymer* **1994**, *35*, 5491.
(44) Eisenberg, A.; Kim, J. S. In *Introduction to Ionomers*, 1st ed.; Wiley: New York, 1998.
(45) Fujimura, M.; Hashimoto, T.; Kawai, H. *Macromolecules* **1981**, *14*, 1309.
(46) Williams, C. E.; Russel, T. P.; Jerome, R.; Horrion, J. *Macromolecules* **1986**, *19*, 2877.
(47) Moore, R. B.; Bittencourt, D.; Gauthier, M.; Williams, C. E.; Eisenberg, A. *Macromolecules* **1991**, *24*, 1376.
(48) Seitz, M. E.; Chan, C. D.; Opper, K. L.; Baughman, T. W.; Wagener, K. B.; Winey, K. I. *J. Am. Chem. Soc.* **2010**, *132*, 8165.
(49) Batra, A.; Cohen, C.; Kim, H.; Winey, K. I. *Macromolecules* **2006**, *39*, 1630.
(50) Guo, R. L.; Lane, O.; VanHouten, D.; McGrath, J. E. *Ind. Eng. Chem. Res.* **2010**, *49*, 12125.

Macromolecules

Article

pubs.acs.org/Macromolecules

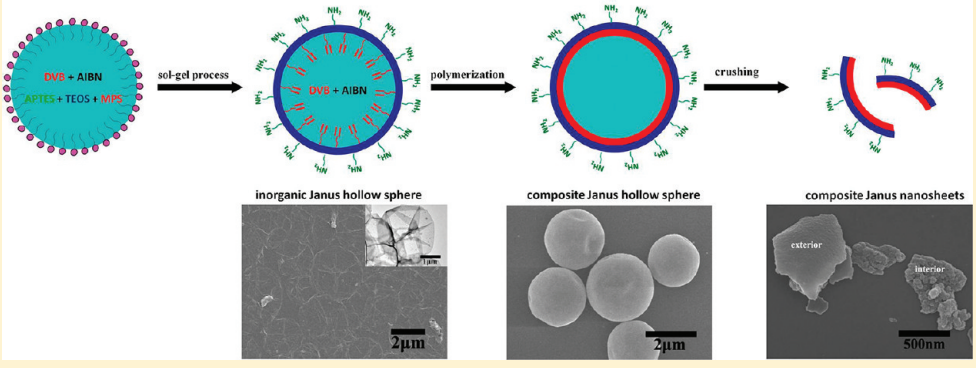
Janus Nanosheets of Polymer–Inorganic Layered Composites

Ying Chen,[†,‡] Fuxin Liang,*[,†] Haili Yang,[†] Chengliang Zhang,[†] Qian Wang,[†] Xiaozhong Qu,[†] Jiaoli Li,[†] Yuanli Cai,*[,‡] Dong Qiu,[†] and Zhenzhong Yang*[,†]

[†]State Key Laboratory of Polymer Physics and Chemistry, Institute of Chemistry, Chinese Academy of Sciences, Beijing 100190, China

[‡]College of Chemistry, Xiangtan University, Xiangtan, Hunan 411105, China

Supporting Information



ABSTRACT: Janus nanosheets of polymer–inorganic layered composites are fabricated by crushing the corresponding Janus composite hollow spheres, which are synthesized by materialization of an amphiphilic emulsion interface with self-organized sol–gel process and subsequent polymer grafting onto the lipophilic side. The Janus composite nanosheets serve as solid surfactants to stabilize emulsion droplets, which are tolerant against solvents. Janus balance of the composite nanosheets is tunable crossing from more lipophilic to hydrophilic by alteration of polymer content. Thereafter, continuous phase of the emulsions can be inverted.

1. INTRODUCTION

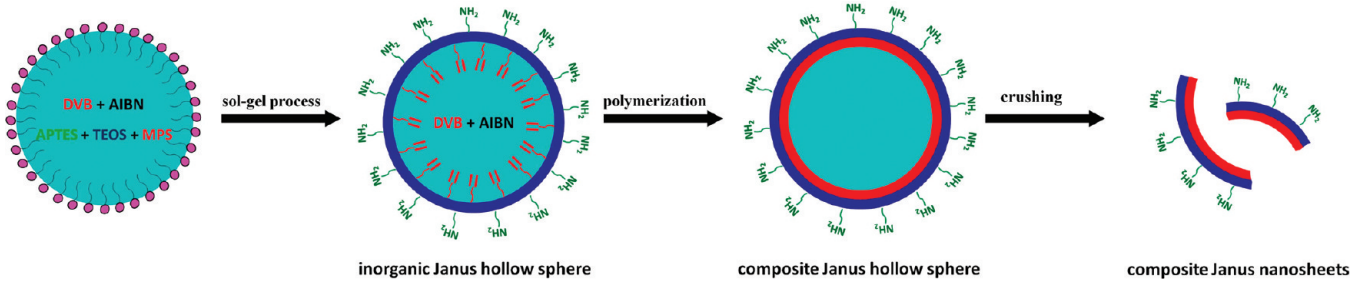
Janus particles with two different compositions compartmentalized distinctly onto the same surface[1] have gained increasing interests in both academic and industrial fields due to their diversity of promising performances.[2] For example, as solid surfactants Janus particles can easily emulsify immiscible liquids.[3,4] Besides chemical compartmentalization, anisotropic shape of the particles can endow additional dynamic gain to make emulsions more stable due to their restricted rotation at interface.[5] The currently reported morphologies mainly focus on two forms of particulate and rod.[2a−c] Recently, anisotropic organic Janus nanosized discs have been synthesized by cross-linking those supramolecular structures from block copolymers.[6] However, the polymer discs are usually swollen thus deformed in solvents. Inorganic Janus nanosheets are fabricated by multiple lithography etching onto silicon[7] or crushing modified glass hollow spheres.[8] They are tolerant to organic solvents. However, large-scale fabrication of Janus nanosheets remains challenging. We have recently developed a simple approach to large scale fabricate inorganic Janus nanosheets by crushing Janus hollow spheres with a nanosized shell. The Janus nanosheets act as solid emulsifiers, dry droplets of liquids form in air when continuous phase elutes due to their highly anisotropic shape.[9] In analogy to hydrophilic–lipophilic balance (HLB) of small surfactant molecules, the term of "Janus balance" is used to describe the hydrophilic–lipophilic balance of anisotropic particles. Janus balance of particles is usually determined by relative ratio of the two parts with varied chemistry. It is important to determine type and stability of emulsions when they serve as solid emulsifiers and to form new complex structures when as building blocks. Similar to Janus particles, it remains challenging to tune Janus balance of the nanosheets.[10] We ask if the Janus balance can be further tuned from more hydrophilic to more lipophilic.

Herein, we extend our previous synthesis of inorganic Janus nanosheets to fabricate Janus nanosheets of polymer–inorganic layered composites as illustrated in Scheme 1. First, an oil in water (O/W) emulsion forms in the presence of hydrolyzed styrene–maleic anhydride copolymer (HSMA) as a surfactant.[11] The oil internal phase is composed of *n*-decane, oil soluble monomers for example divinylbenzene (DVB), initiator azodiisobutyronitrile (AIBN), and three silanes: tetraethyl orthosilicate (TEOS), 3-methacryloxypropyltrimethoxysilane (MPS), and γ-aminopropyltriethoxysilane (APTES).

Received: October 5, 2011
Revised: December 30, 2011
Published: January 19, 2012

 © 2012 American Chemical Society

Scheme 1. Schematic Synthesis of Janus Nanosheets of Polymer−Inorganic Layered Composites



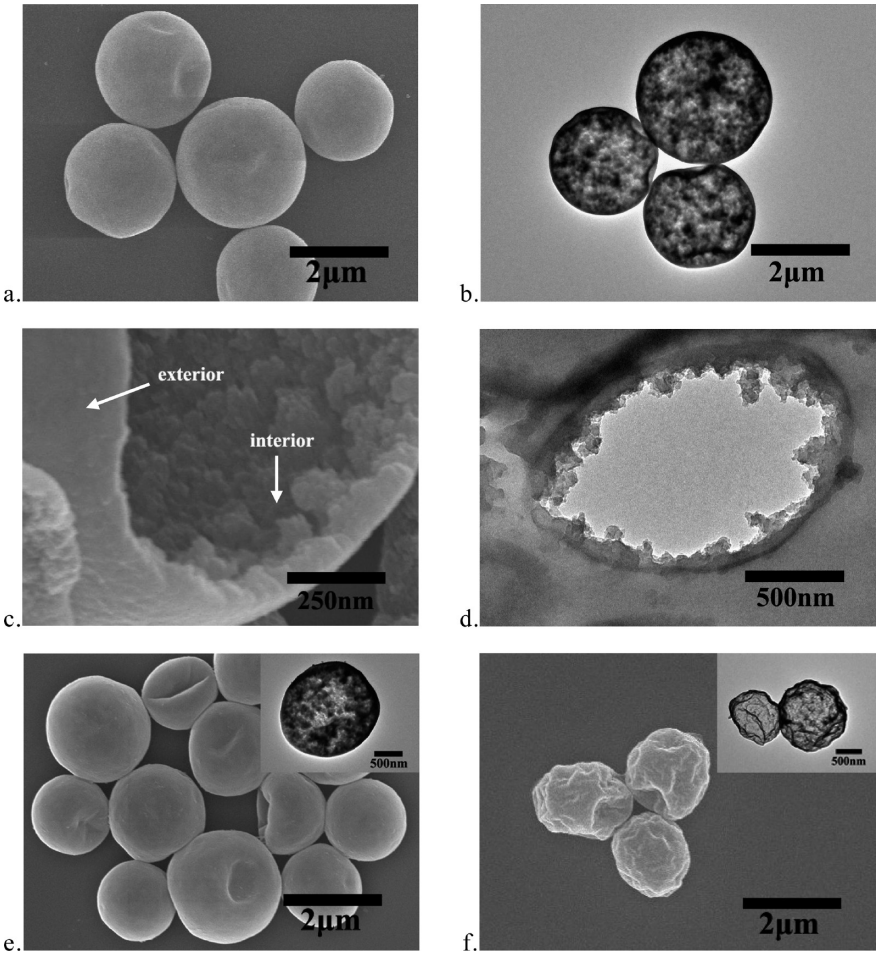


Figure 1. (a) SEM and (b) TEM images of the Janus hollow spheres with polymer−inorganic layered composite shell; (c) SEM image of a broken Janus hollow composite sphere; (d) cross-section TEM image of the Janus hollow composite sphere; (e, f) polymer and silica hollow spheres derived from the Janus hollow composite sphere after removal of silica with 10 wt % HF aqueous solution and removal of polymer by calcination at 450 °C in air, respectively.

The emulsion is kept at 25 °C for 7 h for self-organized interfacial sol−gel process under stirring. Under acidic condition, for example at pH 2.5, the sol−gel process occurs predominantly at the interface forming a smooth silica layer.[12] Onto both exterior and interior surfaces of the inorganic layer, amine- and butyl methacrylate (BMC)- groups direct external aqueous and internal oil phases, respectively. Thus, silica Janus layer forms first. Afterward, the emulsion is heated to 70 °C to initiate the polymerization of DVB onto the interior surface of the layer. While polymerization induces phase separation in the oil phase, aggregates of polydivinylbenzene (PDVB) are further grafted onto a BMC group terminated interior surface, forming a polymer layer. After dissolution of the internal oil phase, the Janus hollow composite spheres form. By crushing the hollow spheres with colloid milling creates Janus composite nanosheets.

2. EXPERIMENTAL METHODS

2.1. Materials. 3-Methacryloxypropyltrimethoxysilane (MPS, 97%) and γ-aminopropyltriethoxysilane (APTES, 98%) were purchased from Alfa Aesar. Styrene (St, AR), azodiisobutyronitrile (AIBN, CP), *n*-decane (AR), tetraethyl orthosilicate (TEOS, AR) were purchased from Sinopharm Chemical Reagent Beijing Co. Divinylbenzene (DVB, 80%) was purchased from Sigma-Aldrich. Hydrolyzed styrene−maleic anhydride (HSMA) copolymer was synthesized by free radical polymerization.[11] Au nanoparticles with an average diameter of 15 nm were prepared according to Frens method.[13] St and DVB were purified

dx.doi.org/10.1021/ma2021908 | *Macromolecules* 2012, 45, 1460−1467

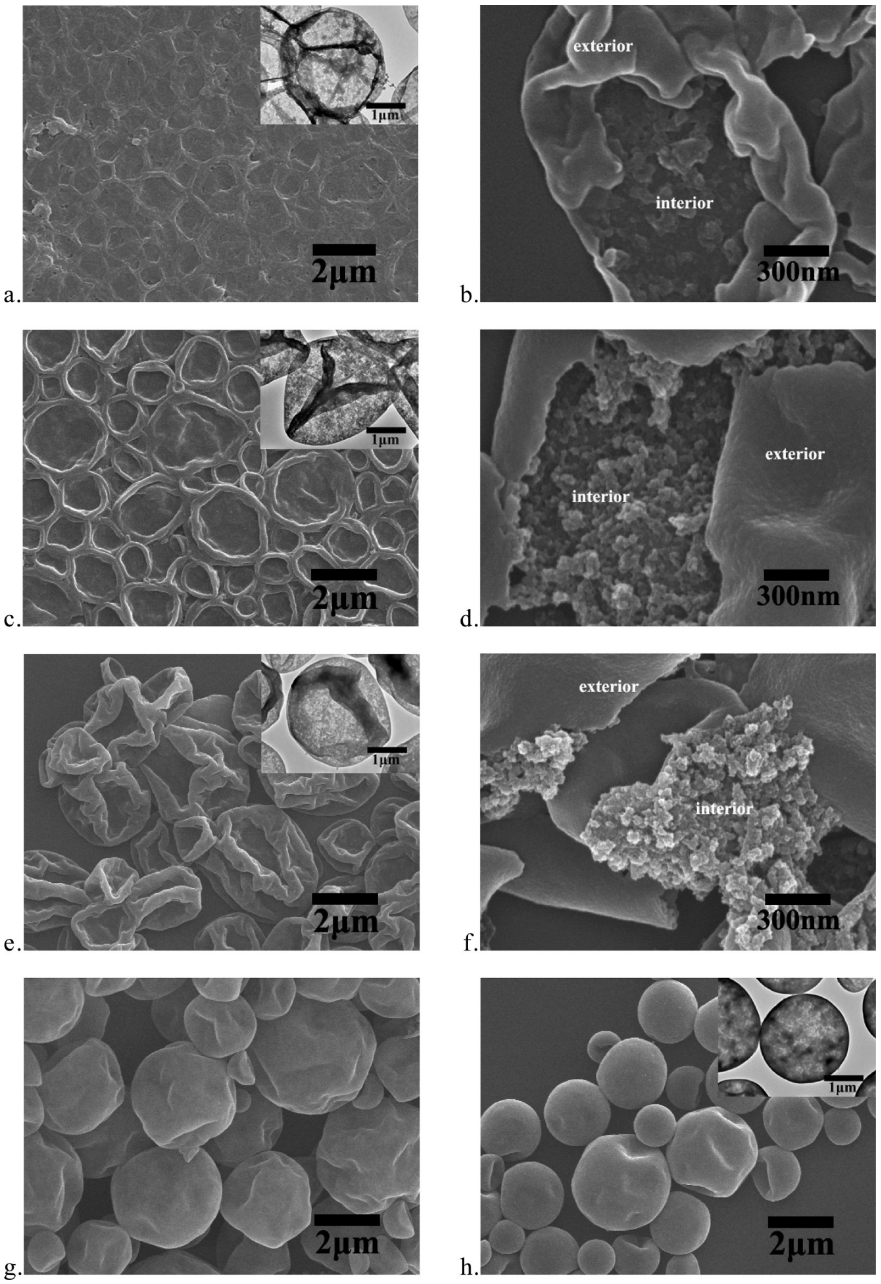


Figure 2. Morphological evolution of the Janus hollow spheres with prolonged polymerization time (h): (a, b) 0.5; (c, d) 2; (e, f) 3; (g) 8; (h) 12.

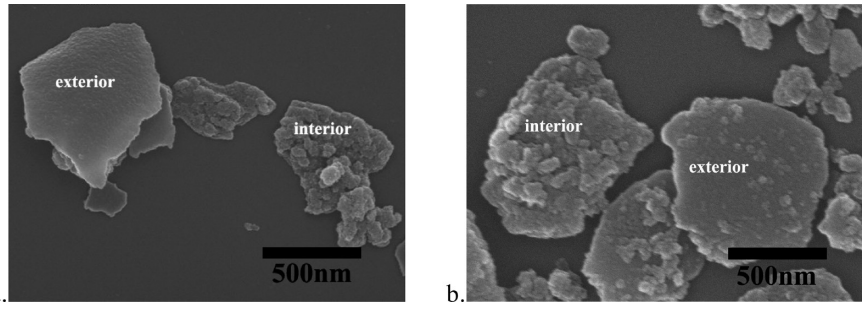


Figure 3. (a) SEM image of the Janus composite nanosheets; (b) Janus composite nanosheets after being selectively labeled with the trisodium citrate capped Au nanoparticles (about 15 nm in diameter) onto the amine-terminated side.

dx.doi.org/10.1021/ma2021908 | *Macromolecules* 2012, 45, 1460−1467

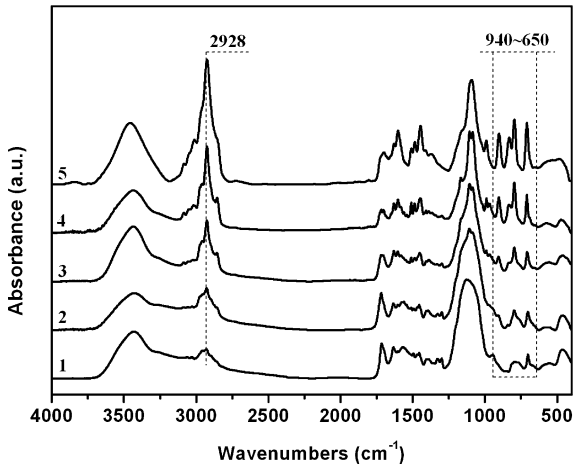


Figure 4. FT-IR spectra of some representative Janus nanosheets obtained with varied amount of DVB (g): (1) 0; (2) 5; (3) 8; (4) 10; (5) 20. Silane content is fixed at 5.2 g. The absorption peak 2928 cm^{-1} is attributed to the stretching vibration of CH_2, the multiple absorption peaks around 940–650 cm^{-1} are attributed to the C–H out-of-plane bending vibration.

over Al_2O_3 column and then stored at low temperature prior to use. All other reagents were used as received without further purification.

2.2. Synthesis of the Janus Hollow Composite Spheres and the Corresponding Janus Nanosheets. An example recipe is given as follow. A 15 mL sample of 10 wt % HSMA copolymer aqueous solution was dissolved in 75 mL of water. The pH of the mixture was adjusted to 2.5 with 2 M aqueous hydrochloric acid. Then 10 g of *n*-decane, 1.1 g of APTES, 1.24 g of MPS, 5.2 g of TEOS, 10 g of DVB and 0.1 g of AIBN were mixed. The oil mixture was dispersed into the aqueous solution with a homogenizer at a speed of 12000 rpm for 5 min forming an oil-in-water emulsion. The emulsion was held under stirring at 25 °C for 7 h for the self-organized interfacial sol–gel process of silanes. Afterward, the emulsion was heated to 70 °C to initiate the polymerization of DVB onto the interior surface of the silica layer for 12 h. Janus hollow spheres with polymer–inorganic layered composite shell were obtained. The Janus hollow spheres were crushed into Janus nanosheets by colloid milling.

2.3. Emulsification Using the Janus Nanosheets. A given amount of the Janus nanosheets was added in a glass bottle containing 4 mL of water and 2 mL of toulene. A trace of methyl orange was introduced into water for easily distinguishing water phase. After the mixture was vigorously shaken, a water-in-oil emulsion formed. At 70 °C, a given amount of Janus nanosheets was added in a glass bottle containing 4.5 g of water and 0.5 g of paraffin (T_m: 52–54 °C). After vigorously shaken, an oil-in-water emulsion formed. When the system was cooled to room temperature, the paraffin droplets were solidified. Determination of continuous phase is according to conductivity measurement.

2.4. Characterization. Morphology of the samples was characterized using transmission electron microscopy (JEOL 100CX operating at 100 kV) and scanning electron microscopy (S-4800 at 15 kV) equipped with an energy dispersive X-ray (EDX) analyzer. The samples for SEM observation were prepared by vacuum sputtering with Pt after being ambient dried. The samples for TEM observation were prepared by spreading very dilute dispersions in ethanol onto carbon-coated copper grids and dried at room temperature. FT-IR spectroscopy was performed after scanning samples for 32 times using a Bruker EQUINOX 55 spectrometer (resolution: 4 cm^{-1}) with the sample/KBr pressed pellets. Thermogravimetic analysis (TGA) was performed using the Perkin-Elmer Pyris 1 TGA under air at a heating rate of 10 °C/min. Particle size and distribution of the sample dispersions in ethanol were measured using a Zetasizer (Nano Series, Malvern Instruments). The morphology of emulsions stabilized with the Janus nanosheets was characterized using Leica DMLP microscope.

3. RESULTS AND DISCUSSION

Under acidic condition at room temperature, self-organized interfacial sol–gel process of the three silanes occurs first, forming micrometer-sized core–shell structure with the oil phase encapsulated with the silica shell. After dissolution of the internal oil phase, hollow spheres form. Both interior and exterior surfaces of the shell are smooth (Figure S1, Supporting Information). Further labeling with acidic group capped nanoparticles reveals that the silica shell is Janus with the amine group exclusively distributed onto the exterior surface. This indicates that introduction of the initiator and monomer has no influence on formation of the Janus shell at room temperature. After formation of the Janus silica shell, the emulsion was held at 70 °C for a free radical polymerization onto the interior surface for 12 h. Dynamic light scattering (DLS) measurement gives a mean diameter of the Janus spheres about 2 μm (Figure S2, Supporting Information). Although the exterior surface keeps smooth (Figure 1a), the interior surface becomes coarse (Figure 1b). Observation of a broken hollow composite sphere can further confirm that the interior surface is coarse and the exterior surface is smooth (Figure 1c). Cross-section TEM image of the hollow spheres clearly demonstrates that the double-layered shell is consisted of exterior dark smooth silica and interior coarse gray polymer (Figure 1d). The hollow spheres are dispersible in water but not in toluene. This means that the exterior shell surface is hydrophilic. When the hollow spheres were added into a toluene in water dispersion, toluene can be preferentially absorbed inside the cavity. This implies that the interior shell surface is lipophilic. Therefore, the hollow spheres are Janus. The corresponding PDVB hollow spheres (Figure 1e) were derived after silica was etched with dilute aqueous HF. The absence of the element Si in the EDX spectrum indicates the removal of silica in PDVB hollow spheres (Figure S3, Supporting Information). The exterior surface of the PDVB hollow spheres is smooth, indicating that there is no diffusion layer between polymer and silica. This confirms that the two steps forming silica shell and polymerization onto the interior surface are separated. Similarly, after removal of polymer by calcination at 450 °C in air, silica hollow spheres were derived. The characteristic peaks of polymers disappear, and only the characteristic peaks assigned to silica in FT-IR spectra remain (Figure S4, Supporting Information).

dx.doi.org/10.1021/ma2021908 | *Macromolecules* 2012, 45, 1460–1467

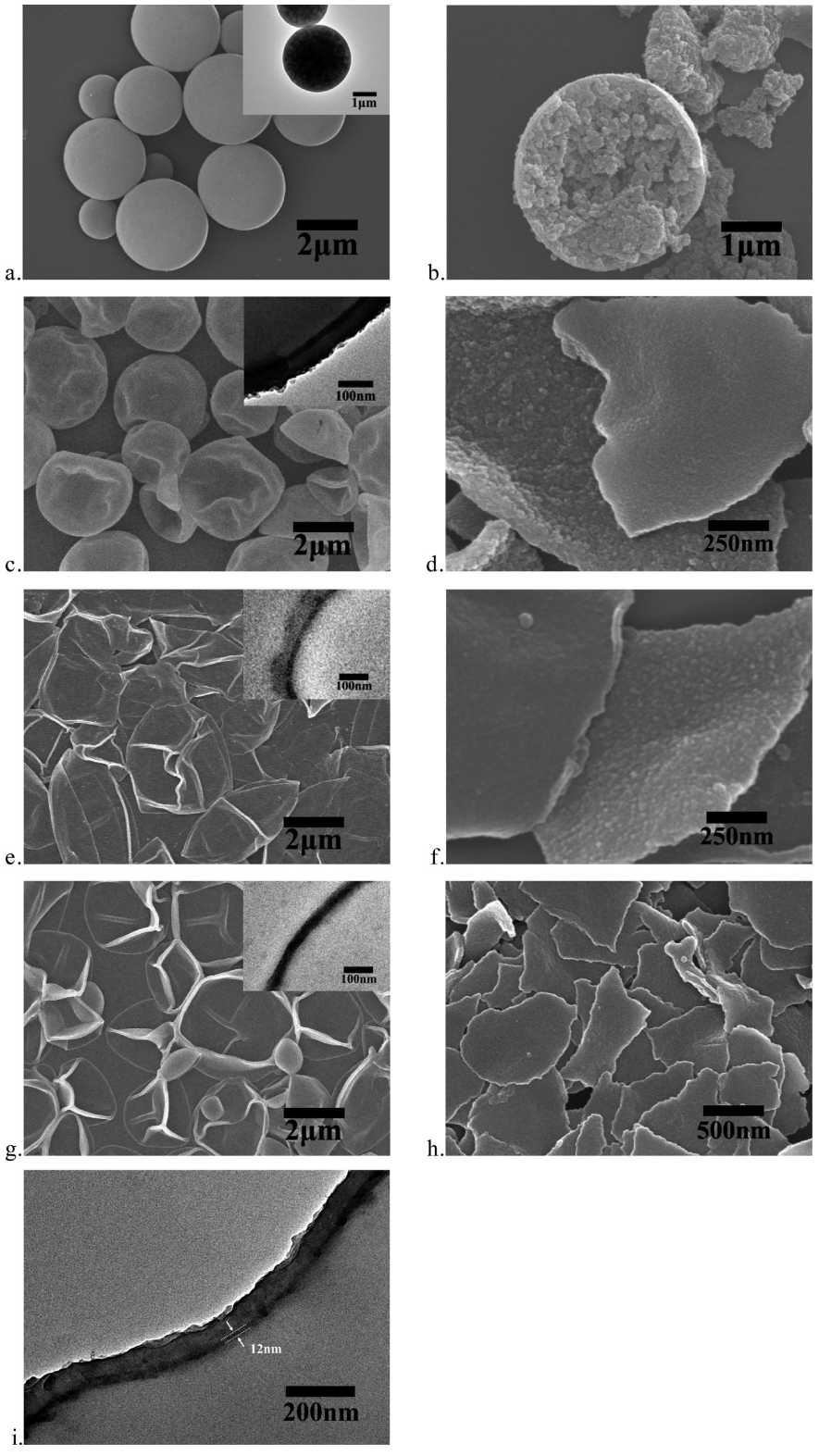


Figure 5. Some representative Janus polymer−inorganic composite hollow spheres and the corresponding Janus composite nanosheets synthesized at different DVB content (g): (a, b) 20; (c, d) 8; (e, f) 5; (g, h) 0. Silane content is fixed at 5.2 g. (i) Cross-section TEM image of the Janus hollow composite sphere at a low level of silane content (1.3 g).

Morphological evolution of the Janus hollow spheres with polymerization time was monitored (Figure 2). The interior shell surface is smooth before polymerization, meaning no polymer is grafted onto the surface of silica layer (Figure S1, Supporting Information). At an early stage of polymerization (30 min), the grafted polymer layer is thin (Figure 2b). The spherical shape is not clear after drying (Figure 2a). With polymerization proceeding, the polymer layer becomes thicker and coarse. After 2−3 h polymerization, roughness and thickness of the shell changes less, meaning that polymerization is nearly

dx.doi.org/10.1021/ma2021908 | *Macromolecules* 2012, 45, 1460−1467

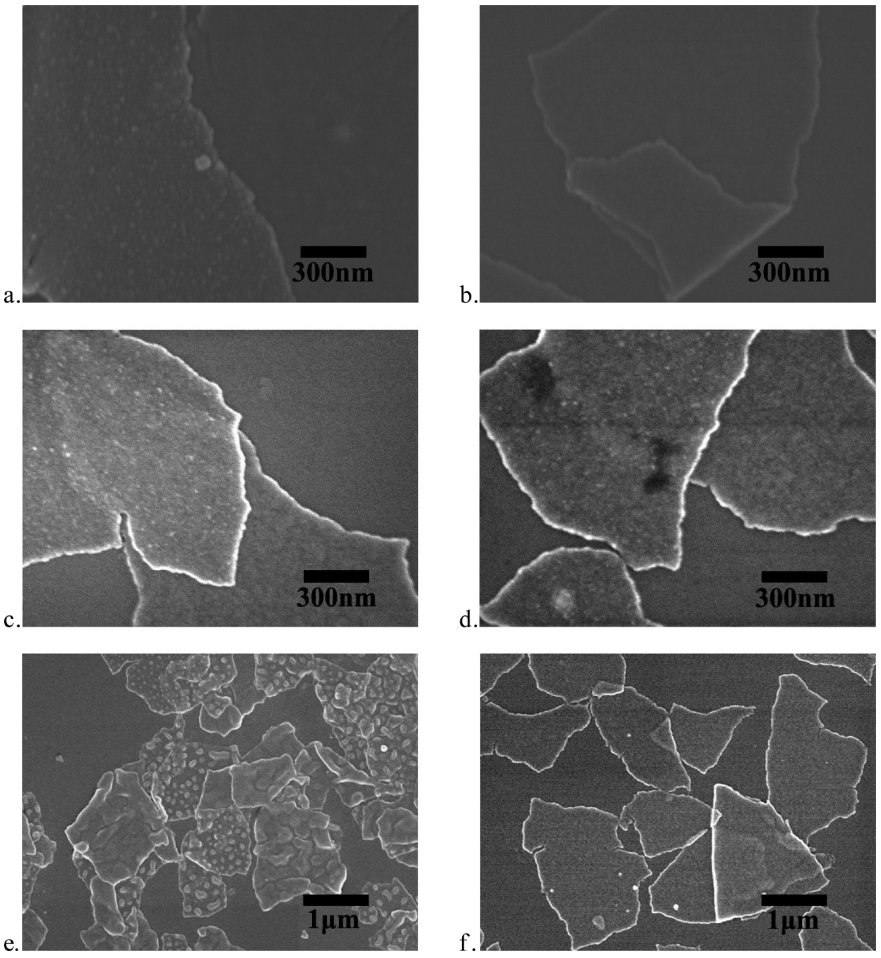


Figure 6. (a, b) SEM images of the Janus nanosheets with DVB as monomer in the absence of MPS before and after ultrasonication; (c–f) SEM images of the Janus nanosheets prepared with St as monomer: (c, d) with MPS before and after treatment with DMF; (e, f) without MPS before and after treatment with DMF.

completed (Figures 2c–f). This is consistent with kinetics of free radical polymerization. With polymerization time, the spherical contour becomes more distinct until the as-prepared hollow spheres (after 8 h polymerization) can well preserve their contour without collapse after drying (Figure 2, parts g and h). Strength enhancement of the hollow spheres is resulted from further sol–gel process of silica.[9a]

Janus composite nanosheets were achieved by crushing the as-prepared Janus hollow spheres (Figures 3a). One side of the Janus nanosheets is rough corresponding to polymer, while the other one is smooth corresponding to silica. Trisodium citrate capped Au nanoparticles (about 15 nm in diameter) were used to selectively label the amine-terminated side by electrostatic interaction. The Au nanoparticles are preferentially conjugated onto the smooth side (Figure 3b), revealing that the smooth side contains amine- group.

At a given silica shell, polymer content of the Janus composite nanosheets is tunable with monomer DVB feeding amount in the oil phase. At a fixed silane amount, intensity of the characteristic bands assigned to PDVB increases with DVB feeding amount (Figure 4), meaning the increase of polymer content of the composite nanosheets. TGA results (Figure S5a, Supporting Information) further prove that the PDVB content increases with DVB feeding content (Figure S5b, Supporting Information). PDVB/silica weight ratio is tunable across 1:1. Besides PDVB content, microstructure of the Janus composite nanosheets is controlled. At higher level of DVB (20 g) content, the interior surface of the Janus hollow spheres becomes much coarser until a polymer continuous porous network forms inside the cavity (Figure 5, parts a and b). At a low level of DVB content for example 8 g, the Janus hollow spheres partially collapse (Figure 5c). This can be explained by a weakening support of the polymer network to the shell. Cross section TEM image (inset Figure 5c) gives average thickness of the silica layer and PDVB layer about 20 and 57 nm, respectively. The PDVB surface of the Janus nanosheets becomes less coarse (Figure 5d). With further decease of DVB content for example 5 g, the PDVB layer becomes thinner from 57 nm to about 47 nm (Figure 5e) with the silica layer thickness preserved. The PDVB side of the Janus nanosheets becomes nearly smooth (Figure 5f). In the absence of DVB, the Janus hollow spheres completely collapse (Figure 5g), and both sides of the Janus nanosheets are smooth (Figure 5h). Besides the polymer layer, thickness of the silica layer is tuned with silane content. For example, the silica layer becomes thinner to 12 nm at a low silane content level, for example, 1.3 g (Figure 5i).

MPS silane plays a key role in structural control of the Janus composite nanosheets. In the absence of MPS, although a rough side of the as-prepared Janus nanosheets is observed (Figure 6a), it becomes smooth after treatment by ultrasonication (Figure 6b). This is explained by removal of physically bound PDVB particles onto the surface. In contrast, in the

dx.doi.org/10.1021/ma2021908 | *Macromolecules* 2012, 45, 1460–1467

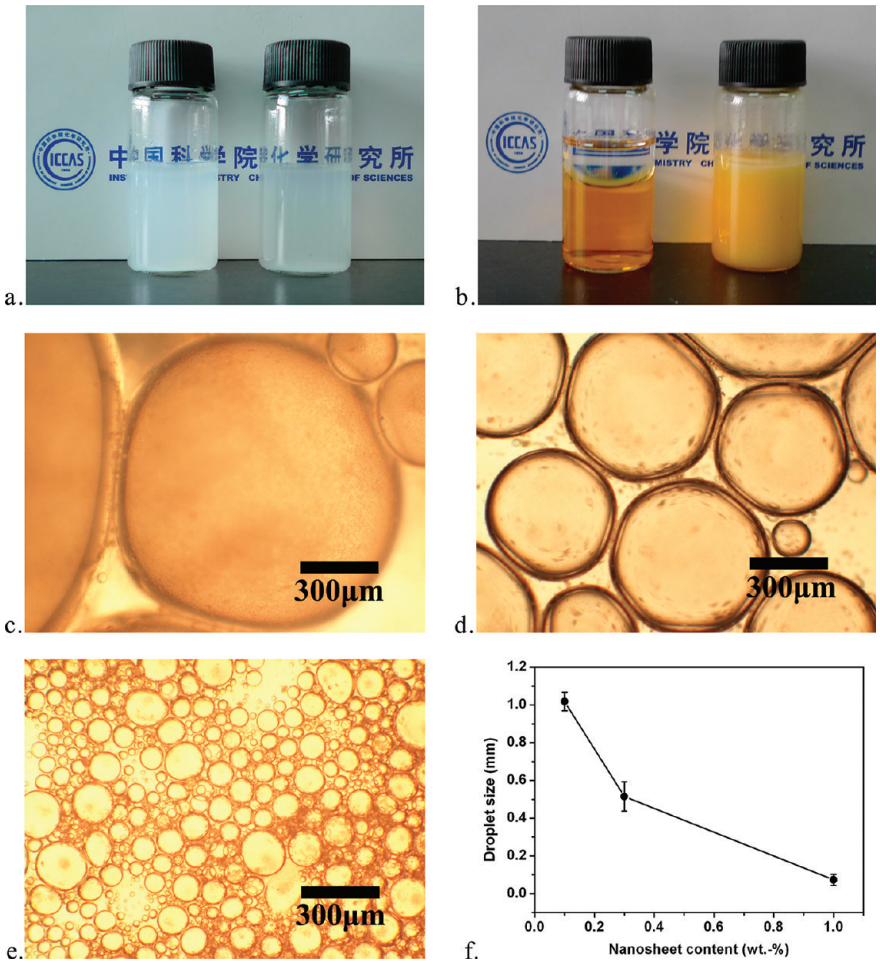


Figure 7. Emulsification of representative immiscible liquid mixture with the Janus composite nanosheets: (a) optical image of the Janus nanosheets dispersed in water (left) and toluene (right), respectively; (b) left: immiscible mixture of toluene (top) and water (bottom); right: water-in-toluene emulsion stabilized with the Janus nanosheet containing 69.6 wt % PDVB; water/toluene volume ratio is 2:1, and methyl orange is added to water as chromogenic agent; (c-e) optical microscopy image of the water-in-toluene emulsion stabilized with increasing Janus nanosheets: 0.1, 0.3, and 1.0 wt % respectively; (f) emulsion droplet diameter as a function of the Janus nanosheet content.

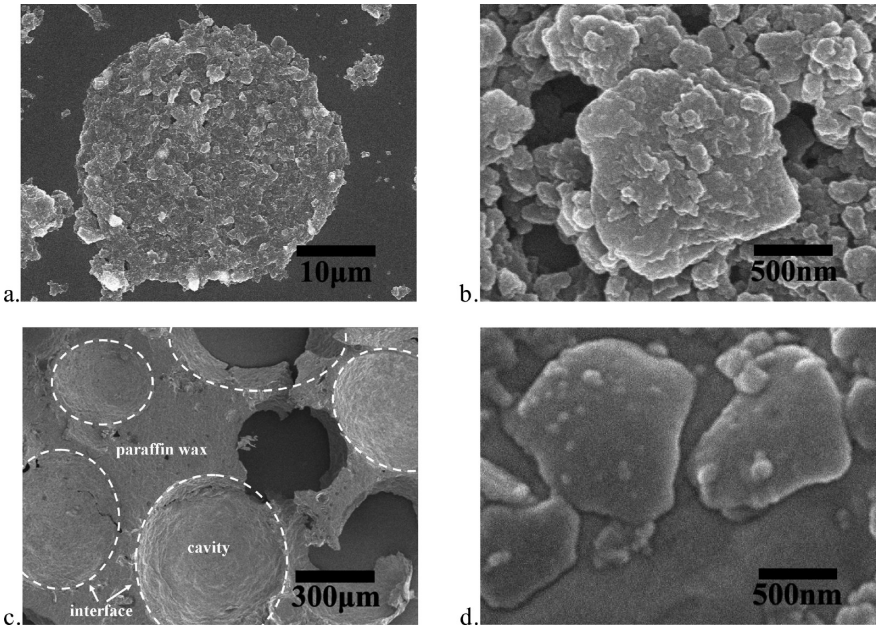


Figure 8. (a) SEM image of one emulsion drop of the water-in-toluene emulsion after drying and (b) the corresponding magnified image; (c) fracture SEM image of the cavity regions after water evaporates from the water-in-paraffin emulsion, orientation of the Janus nanosheets is frozen at the interface after paraffin is cooled to room temperature and (d) the corresponding magnified image.

dx.doi.org/10.1021/ma2021908 | *Macromolecules* 2012, 45, 1460–1467

presence of MPS, the rough surface remains, implying that PDVB is covalently bound. When styrene is used to replace DVB, the polymer side of the nanosheets remains rough, which is less influenced by treatment with DMF (Figures 6c, 6d). This means that a homogeneous PS brush has chemically grafted thereby. In comparison, in the absence of MPS, some lobes appear onto the interior surface (Figure 6e), which are easily dissolved with DMF (Figure 6f). This is explained by dewetting of PS onto silica surface. Since the side toward oil phase contains polymerizable vinyl group, the idea is universal to graft polymer brush onto the side by free radical polymerization. We have also tried to graft other polymer brushes, for instance poly(butyl acrylate) and poly(2-ethylhexyl acrylate).

The Janus composite nanosheets act as solid emulsifiers. As an example, the Janus nanosheets can be well dispersed both in water and toluene (Figure 7a), indicating that they are amphiphilic. Water and toluene are typically immiscible (Figure 7b). A trace of methyl orange was added into water phase for easy observation. In the presence of the Janus composite nanosheet containing 69.6 wt % of PDVB, a stable water-in-toluene (w/o) emulsion forms at a water/toluene volume ratio 2:1. The as-prepared emulsion keeps stable for several months. At 0.1 wt % of the nanosheet, the droplets are about 1 mm in diameter (Figure 7c). At 0.3 wt % of the nanosheet, the droplets become smaller ranging within 0.4−0.6 mm (Figure 7d). At a high level of nanosheet content for example 1.0 wt %, the droplets are about 0.1 mm (Figure 7e). The droplets become smaller with increase of Janus nanosheet content (Figure 7f).

The spherical contour is preserved after the emulsion drops are dried (Figure 8a). Magnified SEM image shows that the rough PDVB side faces the external oil phase (Figure 8b). In order to further observe orientation of the Janus nanosheet at the emulsion interface, a melt paraffin (T_m: 52−54 °C) was used instead of toluene. A water in melt-paraffin emulsion formed at 70 °C. After the paraffin was solidified upon cooling to room temperature, the Janus nanosheets were frozen at the interface. After dispersed water evaporated, some cavities were left (Figure 8c). Careful observation of the interior surface of the cavities shows that the smooth side of the Janus nanosheets faces internal water phase (Figure 8d). When water/oil volume ratio increases to higher level, for example, 9:1, continuous phase remains oil. This implies that the Janus composite nanosheets are more lipophilic. When the Janus composite nanosheet with lower PDVB content, for example, 22.1 wt %, was used, the continuous phase becomes water. In the case of lower water/toluene volume ratio, for example, 2:1, the continuous phase remains water. When water/toluene volume ratio is further decreased to 2:3, the continuous phase reverts to be oil. When the Janus silica nanosheet without PDVB was used, the continuous phase becomes water again at the water/toluene volume ratio 2:3. The fact indicates that Janus balance[10] of the composite nanosheets is tunable across from more lipophilic to more hydrophilic. It is expected to finely tune microstructure of multiple component systems using such composite nanosheets with tunable Janus balance.

4. CONCLUSION

We have proposed a facile approach to large scale fabricate polymer−inorganic layered composite Janus nanosheets. The content and thickness of both polymer layer and inorganic layer are controllable. The Janus nanosheets can be used as solid surfactants to stabilize emulsions, whose Janus balance can be greatly tunable crossing from more lipophilic to more hydrophilic. This method is general, and a huge family of polymer−inorganic composite Janus nanosheets with varied compositions and microstructures are derived.

■ ASSOCIATED CONTENT

Supporting Information

TEM and SEM Janus silica hollow spheres images, particle size and distribution of one representative as-synthesized Janus hollow sphere, EDX spectra of the Janus hollow spheres, FT-IR spectra, and thermogravimetic analysis and PDVB/silica weight ratio. This material is available free of charge via the Internet at http://pubs.acs.org/.

■ AUTHOR INFORMATION

Corresponding Author

*E-mail: (F.L.) liangfuxin@iccas.ac.cn; (Y.C.) ylcai98@xtu.edu.cn; (Z.Y.) yangzz@iccas.ac.cn.

■ ACKNOWLEDGMENTS

We thank Prof. Yunfeng Lu of UCLA for helpful discussion and careful reading of the manuscript to improve the writing. This work was supported by the NSF of China (50733004, 207201-02041, 51173191, and 50973121), MOST (2011CB933700, 2012CB933200), and CAS (KJCX2-YW-H20).

■ REFERENCES

(1) de Gennes, P. G. *Rev. Mod. Phys.* **1992**, *64*, 645.

(2) (a) Perro, A.; Reculusa, S.; Ravaine, S.; Bourgeat-Lami, E.; Duguet, E. *J. Mater. Chem.* **2005**, *15*, 3745. (b) Yang, S. M.; Kim, S. H.; Lim, J. M.; Yi, G. R. *J. Mater. Chem.* **2008**, *18*, 2177. (c) Walther, A.; Müller, A. H. E. *Soft Matter* **2008**, *4*, 663. (d) Wurm, F.; Kilbinger, A. F. M. *Angew. Chem., Int. Ed.* **2009**, *48*, 8412. (e) Wang, C.; Xu, C.; Zeng, H.; Sun, S. *Adv. Mater.* **2009**, *21*, 3045. (f) Jiang, S.; Chen, Q.; Tripathy, M.; Luijten, E.; Schweizer, K. S.; Granick, S. *Adv. Mater.* **2010**, *22*, 1060. (g) Trindade, A. C.; Canejo, J. P.; Pinto, L. F. V.; Patrício, P.; Brogueira, P.; Teixeira, P. I. C.; Godinho, M. H. *Macromolecules* **2011**, *44*, 2220. (h) Lattuada, M.; Hatton, T. A. *Nano Today* **2011**, *6*, 286.

(3) (a) Binks, B. P.; Lumsdon, S. O. *Langmuir* **2001**, *17*, 4540. (b) Vignati, E.; Piazza, R. *Langmuir* **2003**, *19*, 6650.

(4) (a) Binks, B. P.; Fletcher, P. D. I. *Langmuir* **2001**, *17*, 4708. (b) Glaser, N.; Adams, D. J.; Boker, A.; Krausch, G. *Langmuir* **2006**, *22*, 5227.

(5) (a) Nonomura, Y.; Komura, S.; Tsujii, K. *Langmuir* **2004**, *20*, 11821. (b) Nonomura, Y.; Komura, S.; Tsujii, K. *J. Phys. Chem. B* **2006**, *110*, 13124.

(6) (a) Walther, A.; André, X.; Drechsler, M.; Abetz, V.; Müller, A. H. E. *J. Am. Chem. Soc.* **2007**, *129*, 6187. (b) Walther, A.; Hoffmannc, M.; Müller, A. H. E. *Angew. Chem., Int. Ed.* **2007**, *47*, 723.

(7) (a) Dorvee, J. R.; Derfus, A. M.; Bhatia, S. N.; Sailor, M. J. *Nat. Mater.* **2004**, *3*, 896. (b) Bucaro, M. A.; Kolodner, P. R.; Taylor, J. A.; Sidorenko, A.; Aizenberg, J.; Krupenkin, T. N. *Langmuir* **2009**, *25*, 3876.

(8) Gruning, B.; Holtschmidt, U.; Koerner, G.; Rossmy, G. US 4, 715, 986, 1987.

(9) (a) Liang, F. X.; Liu, J. G.; Zhang, C. L.; Qu, X. Z.; Li, J. L.; Yang, Z. Z. *Chem. Commun.* **2011**, *47*, 1231. (b) Liang, F. X.; Shen, K.; Qu, X. Z.; Zhang, C. L.; Wang, Q.; Li, J. L.; Liu, J. G.; Yang, Z. Z. *Angew. Chem., Int. Ed.* **2011**, *50*, 2379.

(10) Jiang, S.; Granick, S. *Langmuir* **2008**, *24*, 2438.

(11) Jin, Z. G.; Wang, Y.; Liu, J. G.; Yang, Z. Z. *Polymer* **2008**, *49*, 2903.

(12) Brinker, C. J.; Scherer, G. *Sol-Gel Science: The Physics and Chemistry of Sol-Gel Processing*: Academic Press: San Diego, CA, 1990; Chapter 3.

(13) Frens, G. *Nat. Phys. Sci.* **1973**, *241*, 20.

Macromolecules

Article

pubs.acs.org/Macromolecules

Oligomeric Compatibilizers for Control of phase Separation in Conjugated Polymer Blend Films

Joanna E. Slota,[†] Einat Elmalem,[‡] Guoli Tu,[‡,§] Benjamin Watts,[⊥] Junfeng Fang,[‡,∥] Philipp M. Oberhumer,[○] Richard H. Friend,[○] and Wilhelm T. S. Huck*[,‡,▽]

[†]Nanoscience Centre, University of Cambridge, 11 JJ Thompson Avenue, Cambridge, CB3 0FF, U.K.

[‡]Melville Laboratory for Polymer Synthesis, University of Cambridge, Lensfield Road, Cambridge, CB2 1EW, U.K.

[§]Wuhan National Laboratory for Optoelectronics, Huazhong University of Science and Technology, 430074 Wuhan, P.R. China

[⊥]Swiss Light Source, Paul Scherrer Institut, Villigen 5232, Switzerland

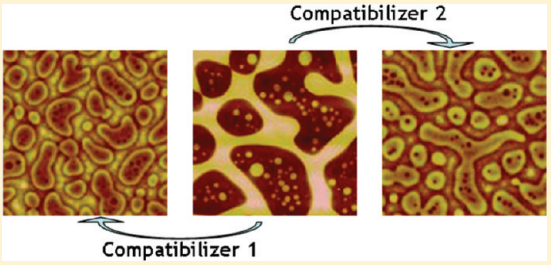
[∥]Ningbo Institute of Materials Technology and Engineering, Chinese Academy of Sciences, Ningbo, 315211 Zhejiang, P.R. China

[○]Department of Physics, Cavendish Laboratory, University of Cambridge, JJ Thompson Avenue, Cambridge, CB3 0HE, U.K.

[▽]Radboud University Nijmegen, Heyendaalseweg 135, 6525 AJ Nijmegen, The Netherlands

Supporting Information

ABSTRACT: Control over phase separation and morphology is critical to optimal function in polymer optoelectronic devices. Here, two fully conjugated oligomeric compatibilizers are introduced, and their effect on the phase separation of blends of poly(9,9′-dioctylfluorene-*co*-benzothiadiazole) (F8BT) with poly(9,9′-dioctylfluorene-*co*-bis-*N*,*N*′-(4,butylphenyl)bis-*N*,*N*′-phenyl-1,4-phenylenediamine) (PFB) are reported. AFM and STXM analysis demonstrate that the addition of compatibilizer altered the size and relative composition of phase-separated domains formed during spin-casting. Small structural differences between the two compatibilizers brought about significantly different morphological changes to the blends, suggesting that further development of compatibilizer structure could enable enhanced control toward desired blend film morphologies.



INTRODUCTION

The active layers of polymer optoelectonic devices are formed from blends of conjugated donor and acceptor polymers. Optimum performance requires, among many other parameters, control over the phase separated morphologies formed. Specifically, optimized bulk heterojunction solar cells,[1] require phase separation on a scale comparable to the exciton diffusion length (10−20 nm) for charge separation, as well as percolation pathways to each electrode to allow uninhibited charge transport. These specifications cannot easily be controlled during facile device fabrication processes, such as spin-coating.

To enhance the effectiveness of new materials, while maintaining simplicity of production, several strategies have been employed in attempts to control the morphology in functional polymer blends.[2−4] Careful regulation of the solvent evaporation rate,[5] solution concentration,[6] or material ratio[7] during thin film formation, as well as gentle thermal or solvent treatment of the cast films,[8,9] have shown some success in manipulating morphology. Particularly promising is a strategy involving solvent additives, which are understood to alter the phase separation of blends by changing the relative solubility, hence drying times of components during casting.[10,11] This method has produced some of the most efficient systems to date.[12,13] These strategies rely on influencing the complicated interplay of thermodynamic and kinetic factors controlling the nonequilibrium blend morphology arising during the film formation process.

Surface-active compatibilizers are emerging as a more stable route to morphological control. Thiophene: fullerene diblock copolymers have been used as compatibilizers in poly(3-hexylthiophene) (P3HT) and [6,6]-phenyl-C_{61}-butyric acid methyl ester (PCBM) blends, lowering surface tension and suppressing the rate of phase separation.[14−16] PV devices constructed from these blends showed lower efficiency but enhanced thermal stability with respect to standard devices containing no diblock copolymer. Similar work by Yang et al. also showed that small amounts of diblock copolymer altered the phase separation in the same blend, this time appearing to form larger phase domains, and enhancing the power conversion efficiency (PCE).[17] Control of morphology and further enhancement of the PCE (from 3.9 to 4.4%) of P3HT:PCBM-based devices was achieved by the addition of small amounts of a coil−rod−coil triblock copolymer surfactant, where the coil segment displayed selective miscibility

Received: July 6, 2011
Revised: January 11, 2012
Published: January 27, 2012

 © 2012 American Chemical Society

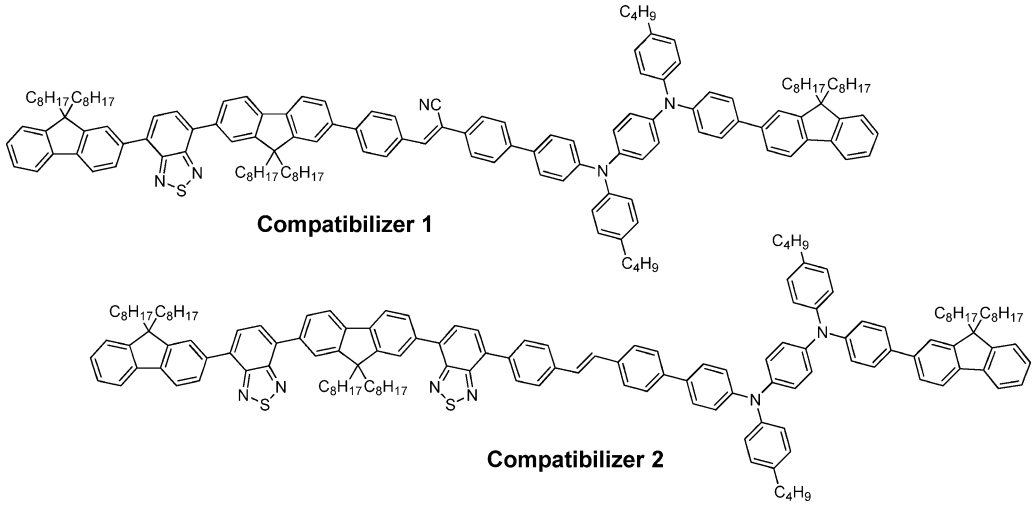


Figure 1. Chemical structures of compatibilizer **1** and compatibilizer **2**; **1** has a nitrile linker unit, and **2** has a longer F8BT block: an extra benzothiadiazole (BT) unit.

in the PCBM domain.[18] Suppressed phase separation and improved device efficiency has also been achieved by the addition of diblock copolymer to polymer−perylene bisimide devices.[19] Effective compatibilizers with alternative architectures (branched chain polymers, or bifunctional oligomers) have also been demonstrated.[20,21] Detailed morphological characterization of many of these systems, however, has generally been limited due to the small scale of phase separation.

Here we set out to investigate the morphological impact of low molecular weight oligomeric compatibilizers in a blend of two conjugated polymers. The classical compatibilizer is a diblock copolymer with blocks identical or miscible with the blend components. Although we expect that increased chain length would enhance the effect of the compatibilizer,[22] this work will demonstrate that low molecular weight compatibilizers can also change interfacial properties and direct morphology. Furthermore, shorter blocks are synthetically more accessible and reduce the likelihood of forming micelles away from the surface,[23] a morphology which would form disconnected phases and charge traps in polymer photovoltaic (PV) devices. The compatibilizers presented here are fully conjugated, which ameliorates the concern that the high amount of nonconjugated units inherent to other reported diblock copolymer compatibilizers may disrupt charge transport.[17]

Two oligomeric compatibilizers, **1** and **2**, resembling the repeat units of the conjugated homopolymers used (Figure 1), were synthesized via a procedure based on successive Suzuki-Miyaura cross-coupling reactions (full details in Supporting Information) and investigated for their effect on a 1:1 (by weight) blend of poly(9,9′-dioctylfluorene-*co*-benzo-thiadiazole) (F8BT) with poly(9,9′-dioctylfluorene-*co*-bis-*N*,*N*′-(4-butylphenyl)-bis-*N*,*N*′-phenyl-1,4-phenylene-diamine) (PFB). Although the PV characteristics of this blend are modest, the system has been extensively studied as a model system for investigations into the relationship between morphology and device performance.[24−27] The two oligomers have different molecular weights and due to the different synthetic routes a slightly different linker unit; we are interested in observing differences in the phase separation as a result of differences in structure of the oligomer as this will guide further research in this area. Since the concentration of oligomers is expected to have an impact on morphology,[28] blends including varying amounts of each compatibilizer were examined: [F8BT: PFB: compatibilizer] weight ratio (50:50:C_x), where C_x = 0, 1.25, 2.5, 5, 20, 40, or 60 (x = 1 or 2). Films were annealed at 120 °C for 60 min to allow the full morphological modifications effected by the compatibilizer to develop.[17] The resulting morphologies were characterized using tapping mode atomic force microscopy (AFM) and scanning transmission X-ray microscopy (STXM).

■ EXPERIMENTAL SECTION

Materials. PFB and F8BT homopolymers were supplied by Cambridge Display Technology Ltd. with molecular weights (M_n) of 60 kg mol^{-1} and 100 kg mol^{-1}, and PDIs of 2.8 and 2.08, respectively. Full experimental details for the synthesis of compatibilizer molecules **1** and **2** are presented in the Supporting Information.

Preparation of Polymer Blends. *m*-Xylene solutions of each material were prepared at a concentration of 15 mg mL^{-1}; blends were formed by combining an equal ratio of PFB and F8BT solutions, with varying amounts of either compatibilizer solution. These blends were spun at 2000 rpm at room temperature onto glass substrates, which had been pretreated with oxygen plasma and coated with PEDOT:PSS. Chloroform blends were prepared by combining a 1:1 weight ratio of F8BT with PFB at a total concentration of 8 mg mL^{-1}. Chloroform solutions of both compatibilizer were also prepared at a concentration of 8 mg mL^{-1} and combined with the mixed polymer solution in varying proportions. The resulting blends were spin-coated at 3000 rpm at room temperature onto glass or ITO/glass substrates, which had been pretreated with oxygen plasma and coated with PEDOT:PSS.

Morphology Characterization. Surface morphology and film thickness was measured with tapping mode AFM (Veeco 3100 Dimension AFM, using Nanoscope VI and WSxM programmes). STXM measurements were performed at the PolLux beamline of the Swiss Light Source, Paul Scherrer Institut, Villigen, Switzerland.[29,30] Sample films were floated-off the PEDOT:PSS covered, glass substrates via deionized water and mounted on copper TEM grids. Monochromated X-rays were focused onto each sample using a Fresnel zone plate to afford ≤50 nm lateral resolution. Using distinctions between the Near Edge X-ray Absorption Fine Structure (NEXAFS) spectra of F8BT and PFB (PFB displays a sharper, more intense 1s → π^* transition, with a higher onset than for F8BT; see Supporting Information), the relative composition of the two polymers was determined, following the procedure in [27]. The 5 × 5 μm 2D X-

dx.doi.org/10.1021/ma201523m | *Macromolecules* 2012, 45, 1468−1475

ray absorption images were collected in transmission mode at 284.7 and 285.1 eV (where differences in F8BT and PFB absorption are most pronounced) as well as 280 and 320 eV (where absorption is chemically indistinct, allowing calibration for absolute film thickness); these data were fitted to thickness-calibrated spectra of pristine films, producing a measure of the relative thickness of each polymer. Linescans were also recorded across each image, where the full NEXAFS spectra were collected (147 points between 275 and 355 eV with 0.1 eV resolution between 283 and 290 eV) and fitted (by least-squares) to a sum of pristine spectra. It should be noted that we were unable to include information with regard to the location of the compatibilizer molecules within the blend, because the NEXAFS spectrum observed for each compatibilizer approximated a linear combination of the F8BT and PFB spectra, which could not be separately resolved.[31]

RESULTS AND DISCUSSION

Xylene Blends. Previous studies have elucidated the phase separation regime for bulk heterojunction blends of F8BT and PFB spun from high boiling point solvents such as xylene; the binary film morphology measured here (Figure 2, top row) is consistent with previous examples.[32−36] The films display vertically depressed PFB-rich areas interspersed within a raised F8BT-rich matrix (the F8BT-rich zones having an under-layer, and partial capping-layer of PFB, and the PFB-rich zones including smaller F8BT-rich spots), a morphology driven by the immiscibility of the polymers, and the lower solubility of F8BT in xylene.[24−27]

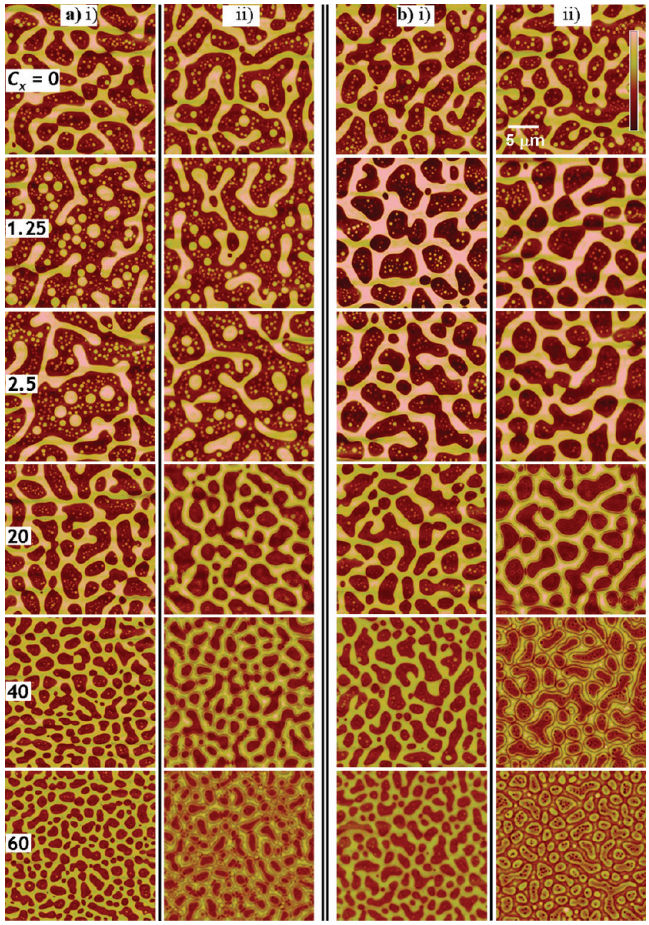


Figure 2. AFM height micrographs of (a) [F8BT:PFB:**1**] and (b) [F8BT:PFB:**2**] blends, weight ratio (50:50:C_x), (i) after spin-coating from xylene and (ii) after annealing at 120 °C for 60 min. The relative weight of compatibilizer included in each blend is indicated on the left. (The height scale represents 60 nm.)

The microscale phase separation in these films allowed morphological changes to be clearly characterized as an increasing proportion of compatibilizer was added, and as the films evolved under thermal annealing. The AFM topography micrographs presented in Figure 2 qualitatively show that significant morphological change was induced by the inclusion of even small amounts of compatibilizer, and that small structural differences between compatibilizers **1** and **2** (an extra benzothiadiazole unit on the F8BT block of 2, and a nitrile linker group on 1; Figure 1) were nonetheless sufficient to alter the blend interaction during film formation to result in differing morphologies.

The full AFM data set was summarized in terms of morphological parameters most relevant to polymer PV device performance: estimates of the amount of interface between components, size and frequency of phases and surface roughness (Figure 3).

A general decrease in surface roughness and reduction of the size of PFB-rich phases was observed upon adding large amounts of either compatibilizer ($C_x \geq 20$). Reduced size and increased frequency of PFB-rich phases led to an increase in the interface between microphases in some compatibilizer blends. The largest amount of added compatibilizer in the blends (C_1 *or* C_2 = 60) resulted in a ∼34% and ∼18% increase in the estimated interface between microphases, respectively, compared to blends containing no compatibilizer. Notably, in addition to this general trend toward finer phase separation and larger interfacial lengths, very low amounts of compatibilizer (C_x = 1.25, 2.5) had a striking impact, often contrary to this trend. For example, addition of C_1 = 1.25 led to a 424% increase in the size of PFB-rich phases; effectively the interaction of the compatibilizer in the blend altered the phase separation during film formation so as to prevent the F8BT-rich zones from forming a connecting matrix in the normal manner. This morphology also displayed a 3% increase in roughness, and an 18% increase in the estimated microphase interface. The interaction in the blend containing C_2 = 1.25 did not act in the same manner, but led to a 54% increase in roughness, raising the F8BT-rich matrix higher above the PFB-rich zones than seen for the binary blend; this morphology displayed a 19% drop in the estimated microphase interface, compared to the binary blend. These results indicate that the phase separation is sensitive to the molecular structure of the oligomeric compatibilizer.

Further qualitative changes were observed upon annealing (Figure 2, parts a(ii) and b(ii)), such as the appearance of trenches encircling the depressed phases by ∼0.3−0.4 μm. For blends including C_1 = 40 or 60, these trenches were 2 ± 0.5 nm deep, and for blends including C_2 = 20 and 40, the trenches were 4 ± 2 nm and 9 ± 1.5 nm deep, respectively. A change in relative thickness between the PFB-rich phases and the F8TBT-rich matrix was also seen (leading to an unusual morphology of raised regions within a lowered matrix for the C_2 = 60 blend after 60 min at 120 °C (Figure 2, bottom right). These unusual morphologies have not before been reported for F8BT: PFB blends,[24] or related F8BT:TFB blends.[37]

The chemical composition within the blends was investigated using STXM,[27,32] which produced 2D composition and thickness maps. Linescans corresponding to each image were also measured, which gave a more accurate analysis of the

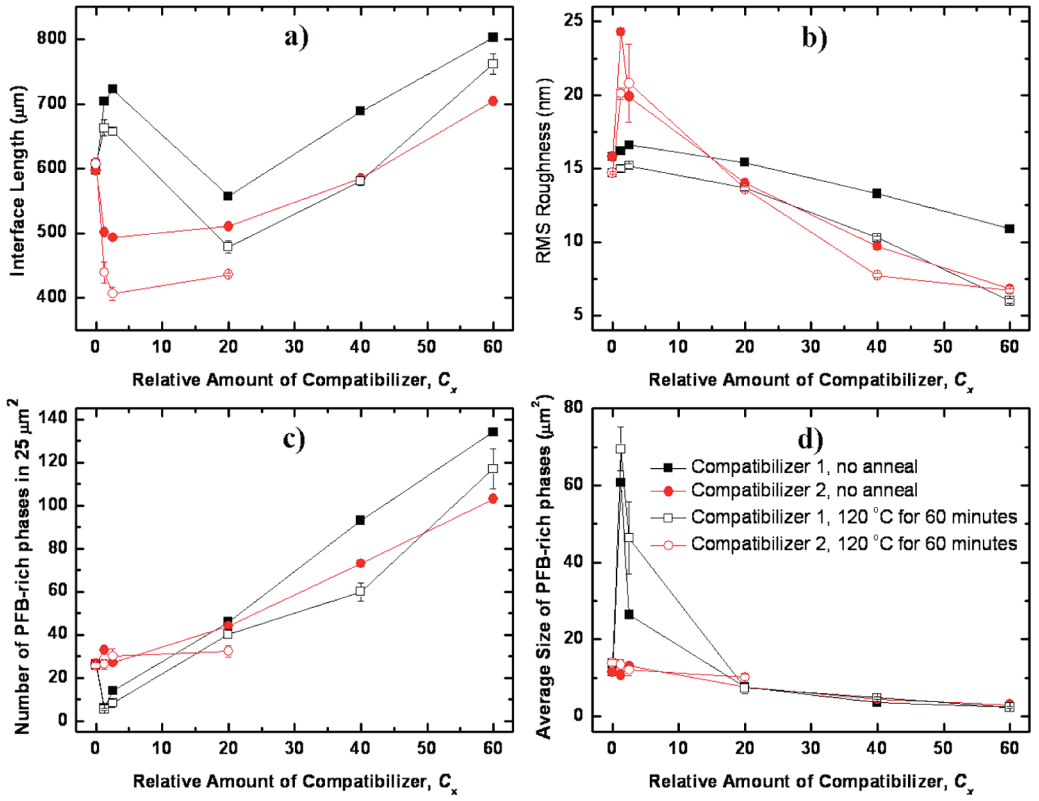


Figure 3. Analysis of AFM height data for [F8BT: PFB: compatibilizer] polymer blends, weight ratio (50:50:C_x), spun from xylene: (a) Amount of interface between PFB and F8BT rich phases, measured as a length in a 2D, 625 μm^2 slice. (b) Rms roughness of the film surfaces. (c) Number of PFB-rich phases in 625 μm^2 of film. (d) Average size of PFB-rich phases. Each data point represents average values over three 625 μm^2 AFM micrographs.

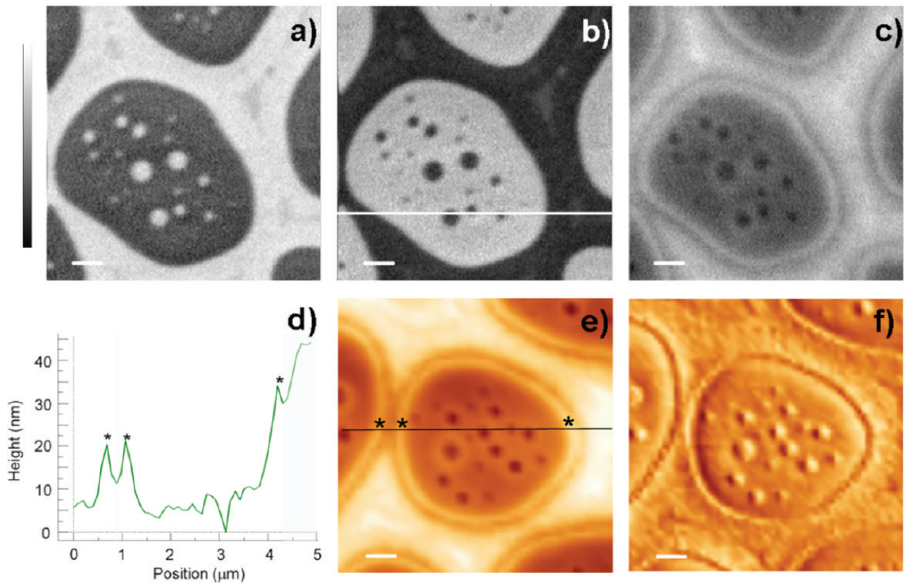


Figure 4. Characterization of [F8BT: PFB: **2**] (C_2 = 20) blends spun from xylene, after annealing at 120 °C for 60 min. STXM: (a) F8BT composition, (b) PFB composition and (c) total film thickness (height scale 68 nm). AFM: (d) height profile, (e) height micrograph, and (f) phase micrograph. (The black line in part e indicates the position of linescan d; the white line in part b indicates the position of the corresponding STXM linescan shown in Figure 6c(ii).) Scale bars indicate 500 nm.

composition and thickness within the distinct phases. Comparison of the STXM 2D composition and thickness maps with the AFM micrographs (the data for C_2 = 20 is shown in Figure 4) revealed that the observed trenches outline the edge of the PFB-rich phases, that is, the edges of the PFB-rich zones became raised (indicated with stars in Figures 4, parts d and e). Examination of the STXM linescan thickness and composition profiles (Figures 5 and 6), more fully demonstrated that upon addition of large relative amounts of compatibilizer ($C_x \geq 20$, and after annealing), the PFB-rich

dx.doi.org/10.1021/ma201523m | *Macromolecules* 2012, 45, 1468–1475

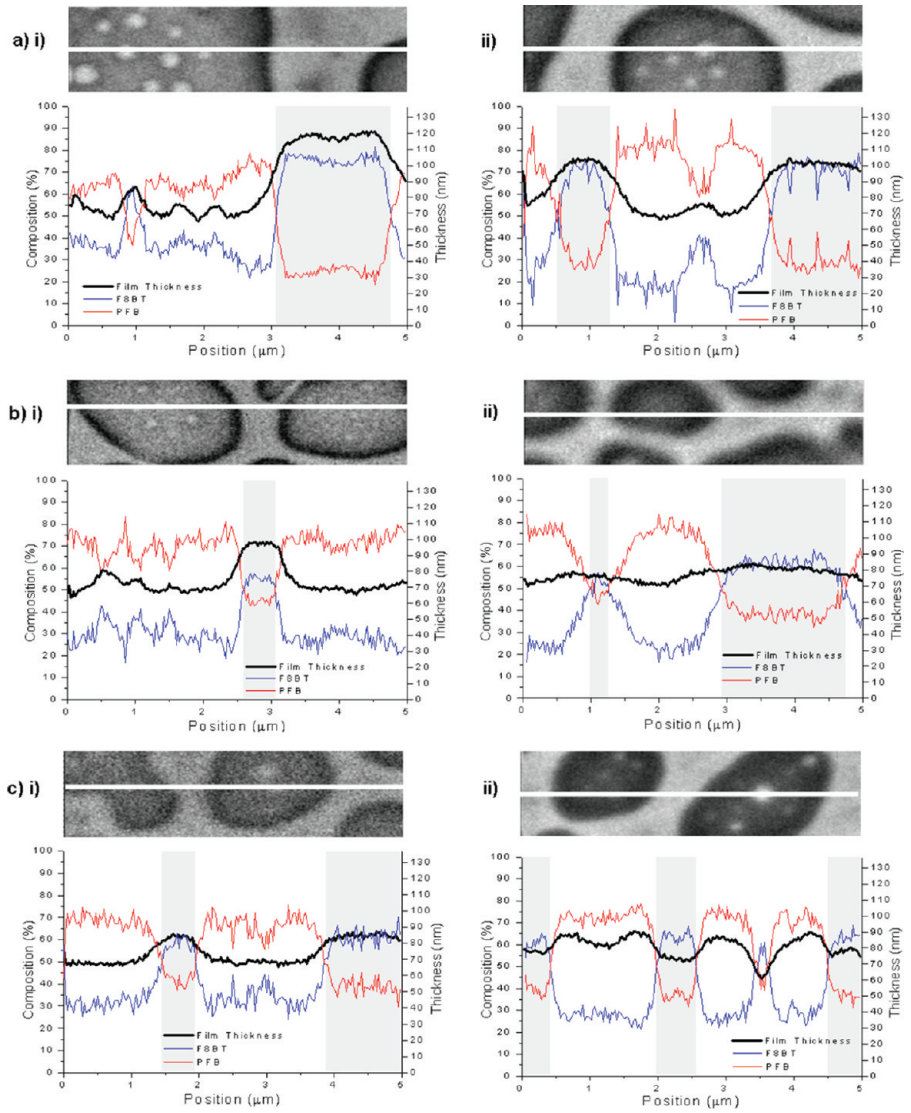


Figure 5. Composition and total film thickness profiles calculated from STXM linescans for films composed of (a) [F8BT: PFB] blends, (b) [F8BT: PFB: **1**] C_1 = 60, and (c) [F8BT: PFB: **2**] C_2 = 60, (i) after spin coating from xylene and (ii) after annealing at 120 °C for 60 min. (As a guide to the eye, areas corresponding to the F8BT-rich matrix phase are shaded.) Corresponding regions of the 2D X-ray absorption scans at 285 eV are also shown (since PFB absorbs more strongly at this wavelength, PFB-rich areas appear darker in color); white lines indicate the positions of linescans.

phases became thicker at the edges, wetting the sides of the F8BT-rich matrix. Analysis of the STXM linescans also revealed that the apparent change in relative thickness of phases on annealing (in films containing compatibilizer), was due to thinning of the F8BT-rich phase, while the average thickness of the PFB-rich phase remained relatively unchanged (Figure 7b). For large amounts of added compatibilizer **2**, the raised edges of the PFB-rich domains protruded beyond the F8BT-rich matrix, effectively reversing the regular morphology for F8BT: PFB blends of this type. These results suggest that the presence of compatibilizer may alter interactions with the solvent during film formation. Thinning of the F8BT-rich phase could be caused by an increased solubility of F8BT in xylene due to the interaction of the compatibilizer. An increased solubility would cause the F8BT phase to precipitate out of solution at a later stage of the spin-casting process, when more solvent had evaporated, hence resulting in a thinner film.

In photovoltaic devices based on this particular polymer system, photocurrent is usually generated within the intermixed microdomains, and not preferentially at the domain boundaries.[38] Therefore, we also analyzed compositional changes taking place within the microscale domains (data presented in Figures 5 and 6 are summarized in Figure 7). In the case of the binary F8BT: PFB blend with no added compatibilizer and no thermal annealing, the F8BT-rich phase shows slightly higher purity (76% F8BT) than the PFB-rich phase (66% PFB) (Figure 5a(i)); although this contrast is not as striking as seen in previous studies, perhaps due to slightly different solubilities in *m*-xylene rather than *p*-xylene[27]). After annealing at 120 °C for 60 min, the PFB-rich domain of the binary blend became the most pure (Figure 5a(ii)); 80% PFB compared to 70% F8BT). This may be due to the movement of smaller F8BT domains within the PFB-rich region toward larger F8BT-rich discrete inclusions or continuous matrix, through Ostwald ripening, as is thought to occur when the films undergo solvent annealing.[32] For the annealed samples including compatibilizer, PFB is also generally the purest phase (~66−78% PFB). This PFB purity decreases rapidly for low addition of compatibilizer ($C_x \leq 20$), but increases steadily with further addition of either compatibilizer ($C_x > 20$): Upon addition of C_2 = 2.5 to the

dx.doi.org/10.1021/ma201523m | *Macromolecules* 2012, 45, 1468−1475

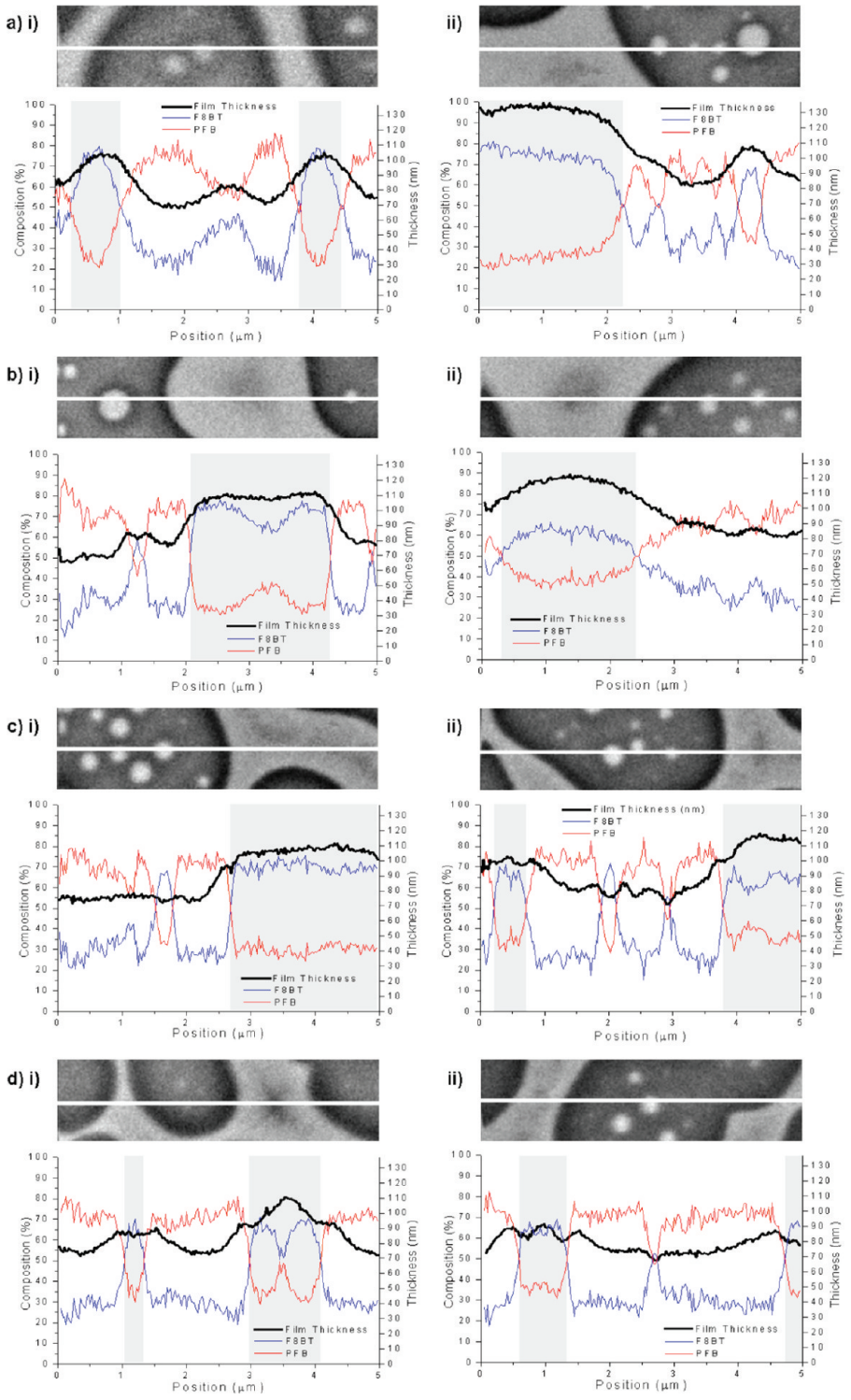


Figure 6. Composition and total film thickness profiles calculated from STXM linescans for films composed of (i) [F8BT: PFB: **1**] or (ii) [F8BT: PFB: **2**], weight ratio (50:50:C_x), spun from xylene, where C_x is (a) 1.25, (b) 2.5, (c) 20, and (d) 40; all samples were annealed at 120 °C for 60 min. (As a guide to the eye, areas corresponding to the F8BT-rich matrix phase are shaded.) Corresponding regions of the 2D X-ray absorption scans at 285 eV are also shown (since PFB absorbs more strongly at this wavelength, PFB-rich areas appear darker in color); white lines indicate the positions of linescans.

binary blend, the PFB-phase purity drops by 14% to 66%, but in the presence of C_2 = 60 the purity is raised to 74% PFB. The steady increase in PFB purity for C_x > 20 (Figure 7a) mirrors the steady reduction in domain size observed in the AFM data (Figure 3).

The F8BT-rich phases in these samples become much less pure when high amounts of compatibilizer are included, to a minimum of 55% F8BT in the case of C_1 = 40. Since the purity of F8BT-rich phases seems to decrease more than the purity of PFB-rich phases increases for high amounts of added compatibilizer (Figure 7), we expect that either the interaction

dx.doi.org/10.1021/ma201523m | *Macromolecules* 2012, 45, 1468–1475

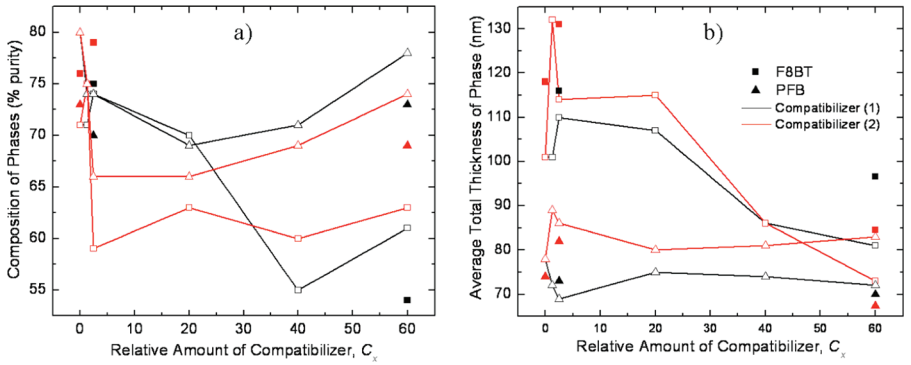


Figure 7. Summary of STXM data for [F8BT: PFB: compatibilizer] polymer blends, weight ratio (50:50:C_x), spun from xylene: (a) composition and (b) thickness of F8BT- and PFB-rich phases. Squares represent F8BT phases, triangles represent PFB phases; black or red indicates that compatibilizer **1** or compatibilizer **2** was used, respectively; filled squares/rectangles indicate no annealing, whereas open squares/rectangles indicate that the samples were annealed at 120 °C for 60 min. Lines are included as a guide to the eye.

of the compatibilizer enhances the miscibility of PFB in F8BT, or that the compatibilizer itself is located preferentially in the F8BT-rich phase.

CONCLUSIONS

Two fully conjugated oligomeric compatibilizers were synthesized and investigated for their efficacy as morphology directors within a functional blend of the corresponding homopolymers: F8BT and PFB. A combination of AFM and STXM analysis revealed that the effects of added compatibilizer were diverse and could not easily be predicted. We can draw a number of general conclusions from our experiments: (i) small amounts of C_1 resulted in large increases in interfacial area as the F8BT phase no longer formed a connected matrix; (ii) large amounts of either compatibilizer resulted in significant morphological changes in the blends spin-coated from xylene; (iii) the addition of compatibilizer influences the composition of the phases, with a general trend of lower purity with larger amounts added.

The results described here indicate that the phase separation of semiconducting polymer blends can be influenced by small molecule compatibilizers. However, the decrease in purity of the phases also strongly indicates that the compatibilizers used here are not strongly anchored at the interface and that a complex ternary system forms with increasing amounts of compatibilizer added. Future studies will study polymer blends that undergo more complete phase separation and investigate polymeric compatibilizers which will be expected to localize at the interface more strongly.

Control over blend film morphology in this manner allows the electronic performance and favorable phase separation properties of polymers to be pursued and optimized separately, thus allowing greater focus in the synthesis of new conjugated polymers for electronic device applications.

ASSOCIATED CONTENT

Supporting Information

Experiemental section giving synthesis and characterization details, including NEXAFS spectra, and AFM and EQE data. This material is available free of charge via the Internet at http://pubs.acs.org/.

AUTHOR INFORMATION

Corresponding Author

*E-mail: wtsh2@cam.ac.uk.

Notes

The authors declare no competing financial interest.

ACKNOWLEDGMENTS

The authors would like to thank Dr Chris McNeill for making arrangements with SLS and for valued discussion, the SLS for beamtime and Cambridge Display Technology Ltd. for the supply of conjugated homopolymers used in this study. PolLux is funded by the BMBF (project no. 05KS7WE1).

REFERENCES

(1) Tang, C. W. *Appl. Phys. Lett.* **1986**, *48*, 183.
(2) Yang, X.; Loos, J. *Macromolecules* **2007**, *40*, 1353.
(3) Hoppe, H.; Sariciftci, N. S. *J. Mater. Chem.* **2006**, *16*, 45.
(4) Slota, J. E.; He, X.; Huck, W. T. S. *Nano Today* **2010**, *5*, 231.
(5) Yang, X.; van Duren, J. K. J.; Rispens, M. T.; Hummelen, J. C.; Janssen, R. A. J.; Michels, M. A. J.; Loos, J. *Adv. Mater.* **2004**, *16*, 802.
(6) Hoppe, H.; Neggemann, M.; Winder, C.; Kraut, J.; Hiesgen, R.; Hinsch, A.; Meissner, D.; Sariciftci, N. S. *Adv. Funct. Mater.* **2004**, *14*, 1005.
(7) Park, S. H.; Roy, A.; Beaupre, S.; Cho, S.; Coates, N.; Moon, J. S.; Moses, D.; Leclerc, M.; Lee, K.; Heeger, A. J. *Nat. Photon.* **2009**, *3*, 297.
(8) Reyes-Reyes, M.; Kim, K.; Dewald, J.; Lopez-Sandoval, R.; Avadhanula, A.; Curran, S.; Carroll, D. L. *Org. Lett.* **2005**, *7*, 5749.
(9) Zhao, Y.; Xie, Z.; Qu, Y.; Geng, Y.; Wang, L. *Appl. Phys. Lett.* **2007**, *90*, 043504.
(10) Peet, J.; Kim, J. Y.; Coates, N. E.; Ma, W. L.; Moses, D.; Heeger, A. J.; Bazan, G. C. *Nat. Mater.* **2007**, *6*, 497.
(11) Lee, J. K.; Ma, W. L.; Brabec, C. J.; Yuen, J.; Moon, J. S.; Kim, J. Y.; Lee, K.; Bazan, G. C.; Heeger, A. J. *J. Am. Chem. Soc.* **2008**, *130*, 3619.
(12) Liang, Y.; Feng, D.; Wu, Y.; Tsai, S.-T.; Li, G.; Ray, C.; Yu, L. *J. Am. Chem. Soc.* **2009**, *131*, 7792.
(13) Liang, Y.; Xu, Z.; Xia, J.; Tsai, S.-T.; Wu, Y.; Li, G.; Ray, C.; Yu, L. *Adv. Mater.* **2010**, *22*, E135.
(14) Lee, J. U.; Jung, J. W.; Emrick, T.; Russell, T. P.; Jo, W. H. *Nanotechnology* **2010**, *21*, 105201.
(15) Sivula, K.; Ball, Z. T.; Watanabe, N.; Frechet, J. M. J. *Adv. Mater.* **2006**, *18*, 206.
(16) Lee, J. U.; Jung, J. W.; Emrick, T.; Russell, T. P.; Jo, W. H. *J. Mater. Chem.* **2010**, *20*, 3287.
(17) Yang, C.; Lee, J. K.; Heeger, A. J.; Wudl, F. *J. Mater. Chem.* **2009**, *19*, 5416.
(18) Tsai, J.-H.; Lai, Y.-C.; Higashihara, T.; Lin, C.-J.; Ueda, M.; Chen, W.-C. *Macromolecules* **2010**, *43*, 6085.
(19) Rajaram, S.; Armstrong, P. B.; Kim, B. J.; Frechet, J. M. J. *Chem. Mater.* **2009**, *21*, 1775.

(20) Economopoulos, S. P.; Chochos, C. L.; Gregoriou, V. G.; Kallitsis, J. K.; Barrau, S.; Hadziioannou, G. *Macromolecules* **2007**, *40*, 921.
(21) Kim, J. B.; Allen, K.; Oh, S. J.; Lee, S.; Toney, M. F.; Kim, Y. S.; Kagan, C. R.; Nuckolls, C.; Loo, Y.-L. *Chem. Mater.* **2010**, *22*, 5762.
(22) Jo, W. H.; Kim, S. H. *Macromolecules* **1996**, *29*, 7204.
(23) Noolandi, J.; Hong, K. M. *Macromolecules* **1982**, *15*, 482.
(24) *Organic Photovoltaics: Materials, Device Physics and Manufacturing Technologies*; Brabec, C., Scherf, U., Dyakonov, V. Wiley VCH: New York, 2008.
(25) Arias, A. C.; MacKenzie, J. D.; Stevenson, R.; Halls, J. J. M.; Inbasekaren, M.; Woo, E. P.; Richards, D.; Friend, R. H. *Macromolecules* **2001**, *34*, 6005.
(26) Halls, J. J. M.; Arias, A. C.; MacKenzie, J. D.; Wu, W.; Inbasekaran, M.; Woo, E. P.; Friend, R. H. *Adv. Mater.* **2000**, *12*, 498.
(27) McNeil, C. R.; Watts, B.; Thomsen, L.; Ade, H.; Greenham, N. C.; Dastoor, P. C. *Macromolecules* **2007**, *40*, 3263.
(28) Ni, P. H.; Zhang, M. Z.; Zhuge, L. J.; Fu, S. K. *J. Polym. Sci., Part A: Polym. Chem.* **2002**, *40*, 3734.
(29) Raabe, J.; Tzevetkov, G.; Flechsig, U.; Boge, M.; Jaggi, A.; Sarafimov, B.; Vernooij, M. G. C.; Huthwelker, T.; Ade, H.; Kilcoyne, D.; Tyliszczak, T.; Fink, R. H.; Quitmann, C. *Rev. Sci. Instrum.* **2008**, *79*, 113704.
(30) Flechsig, U.; Quitmann, C.; Raabe, J.; Booge, M.; Fink, R.; Ade, H. The PolLux microspectroscopy beamline at the Swiss Light Source In *9th International Conference on Synchrotron Radiation Instrumentation*; Choi, J. Y., Rah, S. Eds.; American Instute of Physics: Melville, NY, 2006.
(31) Analysis was aided by aXis2000 (an IDL widget available from http://unicorn.mcmaster.ca/aXis2000.html).
(32) McNeill, C. R.; Watts, B.; Thomsen, L.; Belcher, W. J.; Greenham, N. C.; Dastoor, P. C.; Ade, H. *Macromolecules* **2009**, *42*, 3347.
(33) Stevenson, R.; Arias, A. C.; Ramsdale, C.; MacKenzie, J. D.; Richards, D. *Appl. Phys. Lett.* **2001**, *79*, 2178.
(34) Chiesa, M.; Burgi, L.; Kim, J.-S.; Shikler, R.; Friend, R. H.; Sirringhaus, H. *Nano Lett.* **2005**, *5*, 559.
(35) Watts, B.; McNeill, C. R. *Macromol. Rapid Commun.* **2010**, *31*, 1706.
(36) Arias, A. C.; Corcoran, N.; Banach, M.; Friend, R. H.; MacKenzie, J. D.; Huck, W. T. S. *Appl. Phys. Lett.* **2002**, *80*, 1695.
(37) Yim, K.-H.; Zheng, Z.; Friend, R. H.; Huck, W. T. S.; Kim, J.-S. *Adv. Funct. Mater.* **2008**, *18*, 2897.
(38) Coffey, D. C.; Ginger, D. S. *Nat. Mater.* **2006**, *5*, 735.

Macromolecules

Article

pubs.acs.org/Macromolecules

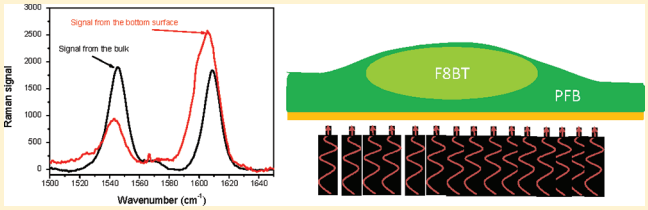
New Approach for Analyzing the Vertical Structure of Polymer Thin Films Based on Surface-Enhanced Raman Scattering

Sivan Linde, Antonio Carella, and Rafi Shikler*

Department of Electrical and Computer Engineering, Ben-Gurion University of the Negev, Beer-Sheva 84105 Israel

Supporting Information

ABSTRACT: We report on a new approach for measuring the chemical composition of the 20 nanometers at the top or bottom of a polymer film. This approach is based on a variation of the surface enhanced Raman scattering effect with laser illumination through a thin gold layer (~4 nm). We show that the introduction of the thin gold layer has little or no effect on the morphology of the film that is spin coated on top of it. We demonstrate that this technique has better than 20 nanometer vertical resolution by studying bilayers of polyfluorines with varying thicknesses and by showing the existence of top and bottom wetting layers in a polymer blend of the same polymers. We also show that the top wetting layer is thinner than the bottom one. The difference in thicknesses explains how a solar cell with an electron blocking layer at the cathode works.



INTRODUCTION

In recent years, organic optoelectronic devices based on polymers and small molecules are becoming more and more popular, ranging from organic light emitting diodes (OLED)[1−7] through organic solar cells,[8−11] organic thin film transistors (OTFT)[12,13] and more. The attractive properties of these devices that make them so popular are large versatility of the optoelectronic properties of the materials, ease of manufacturing, excellent mechanical properties and ultrathin thickness. A commonly used architecture in many devices, such as OLED and organic photovoltaic (OPV), is vertical and hence, their functionality is largely determined by the chemical structure and composition in the vertical direction. For the study of the influence of the chemical structure and composition on the optoelectronic properties, characterization techniques with better than 50 nm vertical resolution need to be developed, because the common thicknesses of these devices is around a hundred nanometer

Analysis of the vertical structure is usually performed by using either environmental scanning electron microscopy (ESEM) on a cleaved sample[14] or X-ray photoelectron spectroscopy (XPS).[15] The drawbacks of these two techniques are that they are destructive in nature and therefore, cannot be applied in situ to a working device and they both lack spatial resolution in the horizontal direction. A method that has high spatial resolution in all three directions is nanotomography.[16] This technique gives three-dimensional images with high spatial resolution of the topography of the films. However, this technique cannot give an indication on the chemical composition, unless a specific topography feature can be associated with a specific chemical structure. Moreover, because it is based on transmission electron microscope (TEM) it cannot be applied to working devices. A different approach that is short-range and sensitive to the chemical composition is the surface enhanced Raman scattering technique (SERS). The SERS effect[17−23] is a variant of the Raman effect where the Raman cross-section is considerably enhanced in the presence of plasmons in metals. The SERS effect is used to detect low quantities of materials, to study materials that have low Raman cross-section or to study the interaction between a substrate and a thin layer of metal that is gradually deposited on it. Traditionally, there are two commonly used configurations for studying materials with low Raman cross-section. In the first, a periodic structure of gold (Au) or silver (Ag) is evaporated on an opaque sample. In the second, nanoparticles (~15−20 nm in size) of the same metals are deposited on a similar substrate. In both cases, the plasmons in the metal enhance the Raman cross section by up to 7 orders of magnitude.[17−19] However, the size of the nanoparticles and the characteristics length of the periodic structure are large compared to the typical thickness of the films we aim to study and can therefore, affect their morphology. Therefore, these configurations are unsuitable for studying the morphology of thin films.

A different SERS technique is used when the aim of the study is to investigate the interaction between organic materials and metals that are evaporated on top of them as reported by Paez et al.[24,25] and by Davis and Pemberton.[26,27] In these studies, a thin layer of metal was evaporated on top of the organic layer while monitoring changes in the Raman spectra as a function of the evaporated material and its thickness. One of the findings of these studies is that when the evaporated metal is gold or silver (noble metals) and they do not chemically interact with the material the only observed effect is the enhance the Raman signal. Moreover, due to the short-range of the SERS effect, the

Received: August 17, 2011
Revised: January 20, 2012
Published: February 1, 2012

ACS Publications © 2012 American Chemical Society

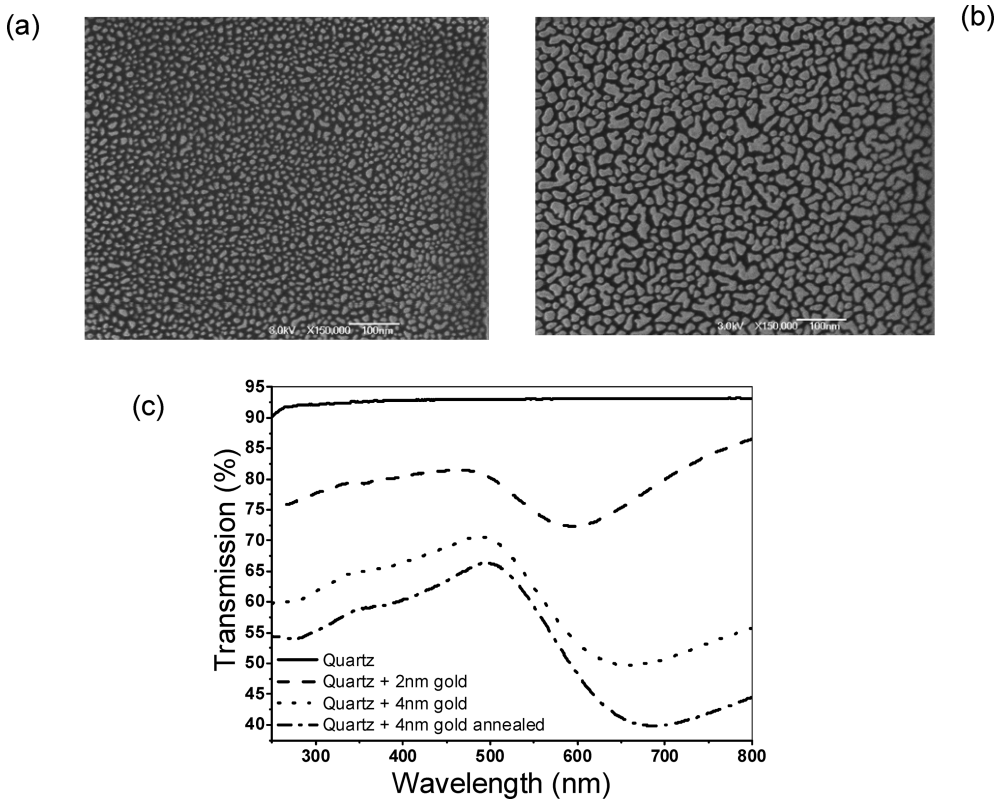


Figure 1. SEM images of 2 nm (a) and 4 nm (b) of thermally evaporated gold on silicon. UV−vis measurements of these layers on quartz substrates.

enhanced Raman signal will only come from the material that is close to the evaporated metal. This combination, of no chemical reaction and short-range interaction, is the motivation behind our idea to study the vertical chemical composition of organic structures using thermally evaporated thin layer of gold (thickness ≤4 nm) on a transparent substrate and illuminate through it using SERS technique.

EXPERIMENTAL SECTION

In all the experiments reported here we used two polyfluorenes polymers, a hole conductor Poly[(9,9-dioctylfluorenyl-2,7-diyl)-*co*-(*N*,*N*′-diphenyl)-*N*,*N*′-di(*p*-butylphenyl)-1,4-diaminobenzene)] (PFB) and an electron conductor poly[(9,9-dioctylfluorenyl-2,7-diyl)-*alt*-co-(1,4-benzo{2,1′,3}thiadiazole)] (F8BT) (American Dye Company). We chose these polymers because they have large Raman cross-section and because bilayer and blend structures made from these materials are extensively reported in the literature.[28,29,14,15] The polymers were spin-casted from a 1.5% (by weight) *p*-xylene solution. PEDOT:PSS (Clevios) was purchased from H. C. Starrck and was filtered using 0.45 μm PVDF filter. We used quartz slides that were precleaned in an ultra sonic bath using acetone, methanol and iso-propanol as substrates. The cleaning process was followed by exposure to oxygen plasma for 5 min. The cleaned substrates were then partially covered with 4 nm of gold, evaporated at 10^{-7} Torr and at a rate of 0.1 nm/s through a shadow mask. The bilayer structures were fabricated using water-floating technique to float the F8BT films that were separately prepared on a glass substrate as outlined by Xia.[30] All the Raman and topographic measurements were done on a unique set up the combines the NANOWIZARD 2 atomic force microscope (JPK GMBH) for thickness and topography measurements and iHR550 spectrograph (Horiba Jobin Yvon) for Raman measurements with laser source at 660 nm. This unique setup allows separate measurements of AFM and Raman. It also allows micro-Raman measurements using the AFM to accurately position the Raman laser at specific points across the sample. This unique combination enables us to correlate topography and Raman measurements with around 1 μm spatial resolution (defined by the numerical aperture of the lens). We used Jasco V-750 spectrophometer for UV−vis measurements.

RESULTS AND DISCUSSION

The proposed technique is based on the evaporation of a thin layer of gold (thickness ≤4 nm) on a transparent substrate and illuminates through it for SERS measurements. To this end we studied two thicknesses of gold layer, 2 and 4 nm. The SEM images of these layers along with their absorption curves are shown in Figure 1. We could not measure the film thickness directly because as seen in Figure 1, parts a and b, the film is discontinuous and therefore the reported thickness is the one measured using the evaporator thickness monitor.

We can see in Figure 1c that at the thickness of 4 nm the absorption of the gold is maximized around 660 nm (the Raman laser wavelength). This implies that the enhancement due to SERS is maximized at a thickness of 4 nm. It is also shown that upon annealing, the plasmons resonance and hence the maximum absorbance is red-shifted to 700 nm. This implies that the coupling to the surface plasmons of the gold and therefore the resulting SERS effect decrease upon annealing.

For practical and future use of this technique for the study of working organic optoelectronic devices, it is important that the thin gold layer will have minimum effect on device performance. As shown in Figure 1, parts b and c, because the gold layer is discontinuous, it has a transparency larger than 60% for wavelengths smaller than 500 nm, the wavelength region where optoelctronic devices made from these polymers absorb and emit light.[28,31] In addition, the work function of gold ∼5.0 eV[32] is similar to the work function of ITO after oxygen plasma treatment,[28] and thus it should have small effect on the

dx.doi.org/10.1021/ma201867e | *Macromolecules* 2012, 45, 1476−1482

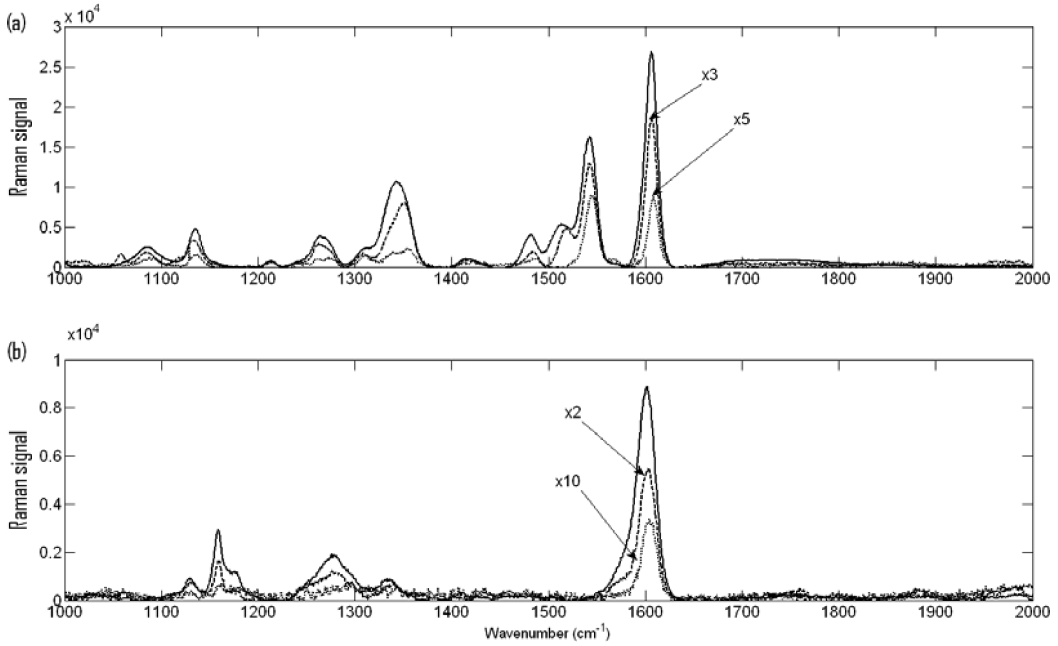


Figure 2. Raman spectra of F8BT (a) and PFB (b) under 660 nm laser. The dotted line is taken on the bare quartz, the dashed line is taken on 4 nm of gold annealed overnight, and the solid line is taken on 4 nm gold without annealing.

electrical properties of the contacts when measuring working optoelectronic devices.

We can also control the layer surface tension by varying the time between the evaporation and film deposition and therefore control the wetting properties of the gold. Through evaporation and up to 5 min the gold surface remains hydrophilic while over longer periods it becomes hydrophobic.[33]

The first step was studying the Raman spectra of the homopolymers and understands the effect of the interfacial thin gold layer. Raman spectra of 80 nm F8BT and PFB films in the region between 1000 and 2000 cm^{-1}, the region where the highest Raman peaks appear are shown in Figure 2, parts a and b, respectively.

Parts a and b of Figure 2 show three Raman spectra taken on bare quartz (dotted line), on overnight annealed (in a vacuum oven at 120 °C) polymer film on 4 nm gold layer (dashed line) and on as evaporated 4 nm gold layer (solid line). We also measured the Raman spectra of the polymer films after casting them on an annealed gold layer but without annealing the polymer film and found the results very similar to those of the annealed films (dashed line). For both homopolymers, the Raman spectra taken over the gold (with and without annealing) is enhanced in respect to the one taken on the bare quartz. As can be seen the Raman signal is smaller for the annealed samples. We assume that this change probably occurs due to the reduction in the laser-plasmon coupling as seen by the red shift in the plasmons resonance in Figure 1c. We cannot test whether or not the gold diffuses into the polymer layer but we assume that this diffusion (if exists) does not affect the chemical properties of the structure. Because the spectra of the films that were annealed with the thin gold layer and those that were casted on an annealed gold layer but were not annealed were the same. We present the measurement of the annealed sample as a basis for the next measurements in which we study the Raman spectra of a bilayer structure and the baking procedure is an inherent part of the fabrication procedure.

In Figure 2a of the Raman spectra of the F8BT, two distinguished peaks appear at ∼1546 and ∼1609 cm^{-1}.[27,28,15] The enhancement due to the SERS effect is more pronounced in the 1609 cm^{-1} peak in comparison with 1546 cm^{-1}. The ratio between these two peaks is about 0.9 when the measurement is performed on the bare quartz while it increases to about 1.5 on the gold covered area of the substrates. This is due to the different coupling strengths of the gold plasmons to the different Raman modes. Moreover, it can be seen that for the F8BT there is an additional peak that appears (∼1520 cm^{-1}) when the spectrum is taken on gold. The new peak is an IR mode that becomes active in the presence of the metal.[23,24] The second polymer, PFB, has only one peak in this region ∼1603 cm^{-1}.[15,27]

After studying the fingerprints of the SERS effect on each polymer we studied two structures that are common for organic photovoltaic devices made from polymers, namely bilayer and blend structure of F8BT and PFB. The bilayer structure provides us with vertical control on the thickness of the two homopolymer layers separately, and hence, enables us to test the vertical resolution of our technique. The blend structure cannot be controlled but previous studies by Kim et al. and us show the existence of wetting layers of PFB both on the glass and at the air interface and that the thickness of the wetting layers is in the range of 10 to 15 nm.[34,15] The existence of a PFB layer at the anode interface is beneficial as PFB is a hole conductor. The existence of the PFB at the cathode interface can degrade the device performance as PFB blocks the electrons from reaching the cathode. However, devices made from these blends work as solar cells, therefore it is assumed that the thickness of the PFB layer close to the cathode must be small but this assumption has not been proven yet.

The bilayer structures we have studied have the following architecture: thin film of constant thickness (85 ± 5 nm) of F8BT on top of a thin film with varying thicknesses (60, 50, 20 ± 5 nm) of PFB. The different thicknesses of the PFB films were obtained by controlling the spin coater spinning velocity.

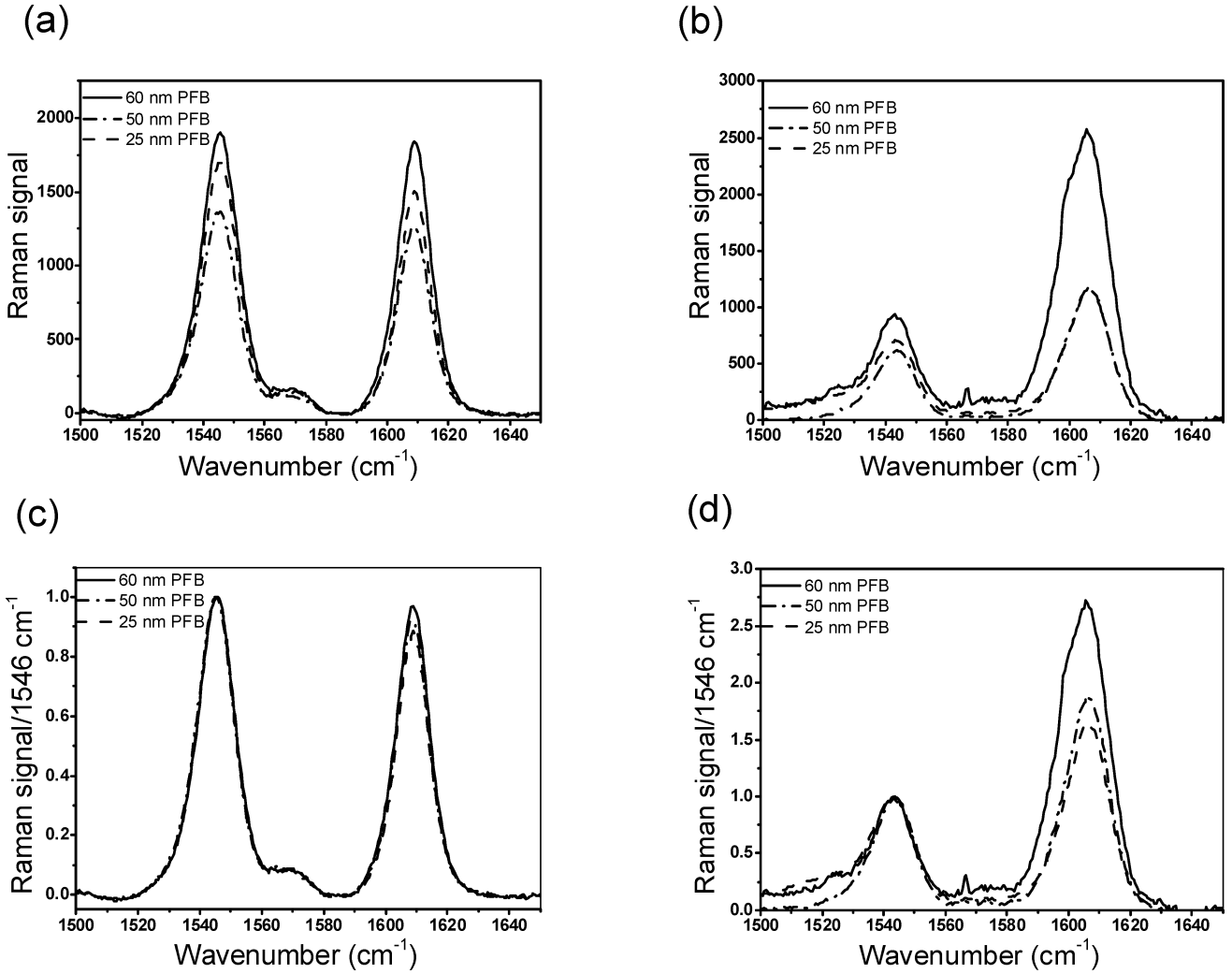


Figure 3. Raman spectra of a bilayer with different thicknesses of PFB, 60 nm 50 and 25 nm for the straight, dashed and dotted line, respectively. Spectra taken outside the gold coated area as measured (a) and normalized to by the 1546 cm^{-1} peak (c). Spectra taken on 4 nm of gold as measured (b) and normalized by the 1546 cm^{-1} peak (d).

The thicknesses of the F8BT and PFB films were measured using an atomic force microscope. We chose a constant thickness for the F8BT as we wanted the Raman signal that originates from to F8BT to be same for all samples.

Parts a and b of Figure 3 show Raman spectra measurements of the bilayers with different thicknesses of PFB films over bare quartz and over gold-coated quartz, respectively. Because the F8BT thickness is the same we have normalized the results by dividing the Raman spectrum by the height of the peak at 1546 cm^{-1} for both the bare and gold coated areas, Figure 3, parts b and d, respectively.

By comparing the spectra taken outside the gold coated area to the spectra taken on the gold area we can see that the for the same film the height of the peak which is only associated with the F8BT, i.e. the 1546 cm^{-1} peak, is smaller on the gold coated substrate compare to the uncoated areas. This complies with the fact that the intensity of the light reaching the F8BT layer should be lower after passing through the absorbing gold layer and hence should results in lower amplitude. The F8BT signal is not affected by the SERS effect as it is rather far from the gold layer. However, we do see a slight increase in the left-hand side of the 1546 cm^{-1} peak for the 25 nm thick sample, which might indicate the start of a shoulder as seen for pure F8BT samples (Figure 2a). In contrast, the ~1609 cm^{-1} peak which is common to both materials is largely enhanced on gold coated areas as expected based the larger enhancement seen for the PFB on gold sample (Figure 2b). We observe that in the measured spectra there is no direct relation between the PFB film thickness and the height of the Raman peaks. The reason is that the height of the peaks do not only dependent on the volume of the materials, i.e., the thickness of each polymer layer, but also on the magnitude of the electric field at this layer. This cannot be easily calculated as we have only a rough estimate of the thicknesses of the layers and the interface between them and we do not know the effect of gold diffusion on the optical properties of the entire structure. We then normalized the Raman spectra by the height of the 1546 cm^{-1} peak. The normalization is motivated by the constant thickness of the F8BT film. The normalized spectra are shown in Figure 3, parts c and d, for the bare and gold coated areas, respectively.

In the normalized Raman measurements taken on bare quartz, the relative height of the peak around ~1609 cm^{-1} goes down slightly with the reduction of the thickness of the PFB layer and is always smaller than one (Figure 3c). This is because the PFB Raman cross-section is twice as small as the F8BT, and Raman signal is roughly proportional to the volume of the

dx.doi.org/10.1021/ma201867e | *Macromolecules* 2012, 45, 1476–1482

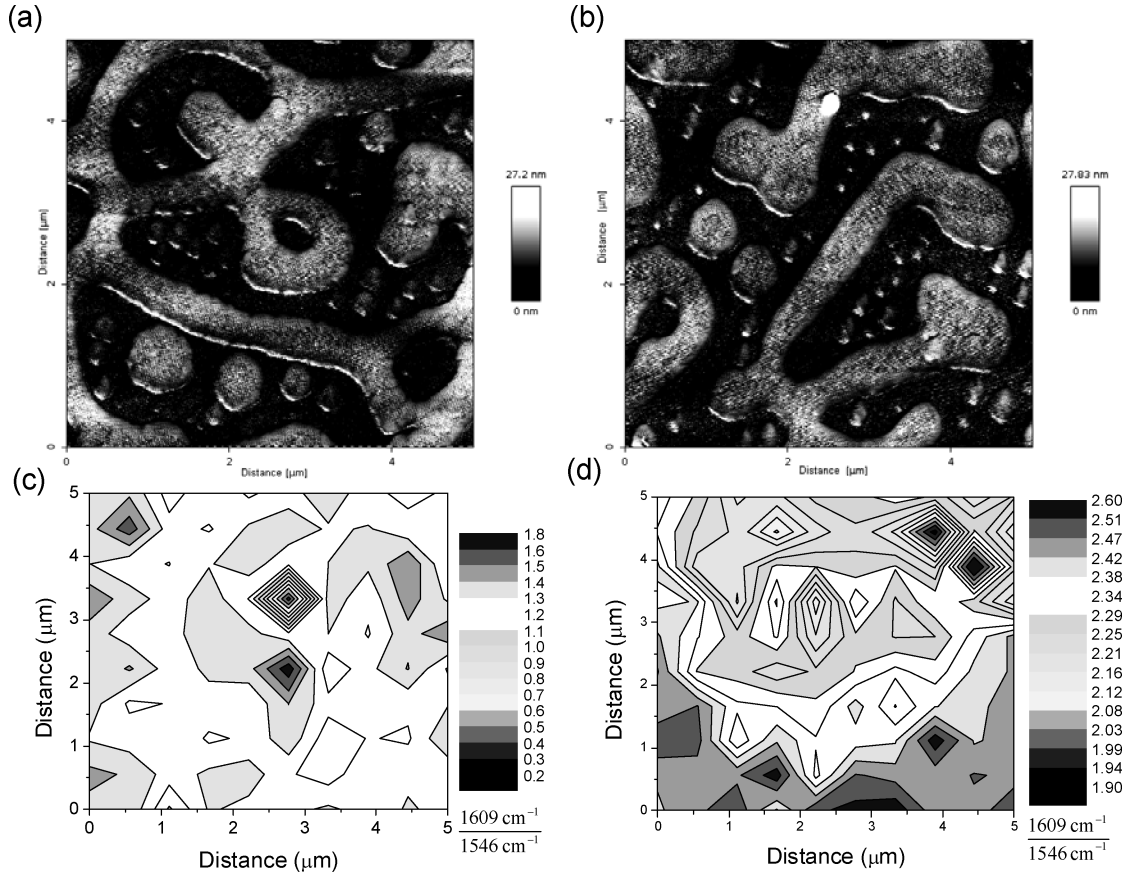


Figure 4. AFM maps of 1:1 PFB and F8BT blend on bare quartz (a) and on 4 nm gold coated quartz (b). A map of the ratio between the ~1609 cm^{-1} and the 1546 cm^{-1} peaks in the coated and bare samples (c and d), respectively.

layer.[15,30] This changes when we look at the normalized Raman spectra that were taken on the gold coated areas (Figure 3d). In this case, the peak around 1605−1609 cm^{-1} is always higher than the 1546 cm^{-1} peak (up to three times higher). A ratio larger than one was also observed for the pure F8BT structure. However, the ratio between the 1609 and 1546 cm^{-1} peaks or a pure F8BT sample in Figure 2a is less than 1.5 for the annealed sample while even for the 25 nm thick PFB sample this ratio is 1.65. This is clear evidence that the dominant part of the 1609 cm^{-1} signal comes from the PFB. This can only happen if the PFB signal is enhanced by the SERS effect because as mentioned above the Raman cross-section of PFB is smaller than F8BT

A closer inspection of the positions of the ~1609 cm^{-1} peaks for the 4 nm gold coated sample Figure 3d, shows that it moves from 1605 to 1607 cm^{-1} as the thickness of the PFB layer is reduced from 60 to 25 nm. This is an additional indication to the enhancement of the PFB signal as its peak is at 1603 cm^{-1} compared to the 1609 cm^{-1} of the F8BT. When an inverted structure with PFB on top of F8BT was measured, the measured spectrum resembled the dashed line of Figure 2a. The larger ratio between the heights of the ~1609 and 1546 cm^{-1} peaks and the lack of the shoulder at 1520 are direct evidence that our technique vertical discrimination is better than 25 nm, the smallest PFB thickness.

In the next step we have studied a 1:1 blend of F8BT and PFB. Similar blends were studied before and it was verified that the PFB wets the substrate and the air interface.[15] However, due to lack of vertical sensitivity, the thickness of the PFB has only estimated to be around 15 nm based on the testing instrument specification. We spin coated the blend on a 4 nm gold coated quartz substrate and on a bare quartz substrate. We measured the topography of the blends using atomic force microscope (AFM) as can be seen in Figure 4 (a) and (b) for the gold coated and bare areas of the substrate, respectively.

In parts a and b of Figure 4, the higher areas (the brighter colors) are the F8BT-rich phases and the lower areas are the PFB-rich phases. These two sub figures show that the thin gold layer have little or no effect on the blend morphology as shown by the similar topographic features. We used the system described above that combines an AFM and Raman for the scanning Raman measurements and took a hundred spectra over the area scanned by the AFM. The measured Raman spectra was normalized in the same manner as in the bilayer measurements to show the ratio of the 1609 and 1546 cm^{-1} peaks on the bare quartz and on the gold coated quartz are shown in Figure 4, parts c and d, respectively. Because the measured film is a blend rather than a bilayer, the value of the ratio of these peaks for the bare quartz sample indicates the relative composition of the two blend components at the measured point. The higher the ratio, the lower is the amount of F8BT at the measured point. It can be seen that there are few areas that are almost pure F8BT (ratio ~ 0.9) and there are other places when it is around 40% of F8BT (ratio ~ 1.4). However, the picture is different for similar spectra taken on the gold-coated area of the substrate (Figure 4d). In Figure 4d, we see that the minimum value of the ratio between the peaks is over 2. As we show above, for a pure F8BT sample this ratio is limited to 1.5. This is a first indication to the presence of PFB wetting layer at the gold layer. This is further supported by

dx.doi.org/10.1021/ma201867e | *Macromolecules* 2012, 45, 1476−1482

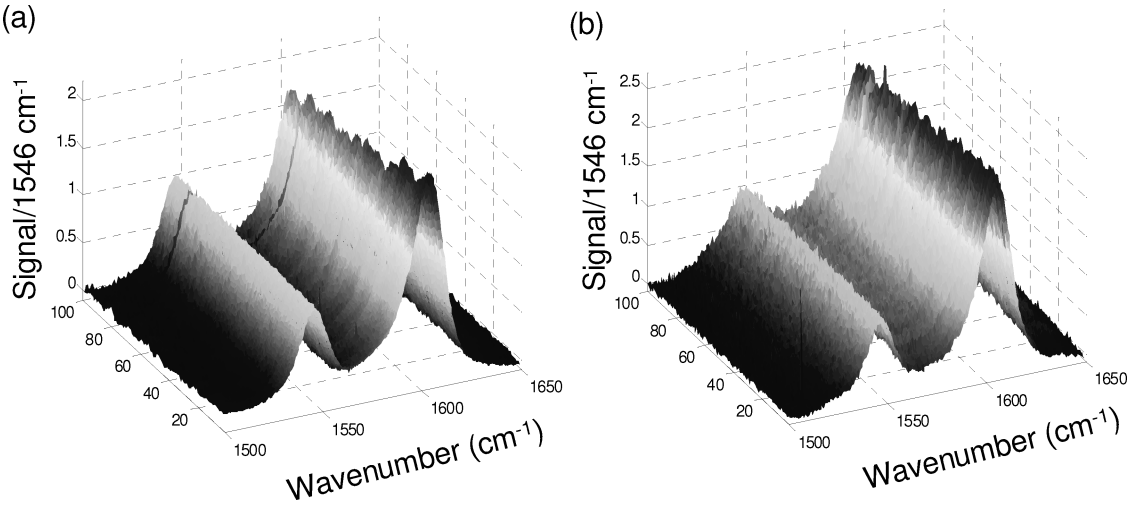


Figure 5. Combined hundred Raman spectra of an F8BT:PFB blend taken over an a region of 5 μm × 5 μm with 4 nm gold coating on top (a) and on for the same blend shown in Figure 4d.

studying what is missing from the spectra. Figure 5b shows a plot of all the normalized spectra taken at each point of the map in Figure 4d. We see that the shoulder around 1520 cm^{-1}, which appears when the F8BT is in direct contact with the gold layer (Figure 2a), is missing.

Because the effect of the Plasmon enhancement is not directional, a thin gold layer can also be evaporated on top of the structure with similar expected effects. We have repeated the same procedure we have done for coating the quartz with gold and evaporate thin gold layer on top of the films. The results are shown in Figure 5a. It is known from previous works that there are no changes in the film's structure due to the introduction of the film into vacuum.[9,14,15,34] In Figure 5a, the shoulder at 1520 cm^{-1} which is an indication of a F8BT top layer, is again absent. This is in agreement with the results of Kim et al.[15] Because the vertical resolution of the XPS used by Kim et al. was ∼15 nm, they estimated that the thicknesses of the wetting layers at the top and bottom of the blend film are similar.[15] However, our results provide additional information. The values of the normalized spectra at ∼1609 cm^{-1} are smaller, for the top gold layer, which indicate that the top wetting layer is thinner than bottom one. This explains why the presence of a top PFB wetting layer does not affect the performance of solar cells made from this blend. This result is consistent with the model presented by Chiesa et al.[34]

In many optoelectronic devices based on polymers, PEDOT:PSS is used as an electron blocking layer on the anode.[35] The thickness of this layer is around 40−50 nm, and therefore, if the semitransparent gold layer is deposited directly on the gold it cannot be used to probe the polymer layers above the PEDOT:PSS due to the short distance of the SERS effect. Therefore, we checked how we can use our technique to study polymer films that were deposited on top of the PEDOT:PSS layer. We studied the following architecture consisted of an ITO coated quartz substrate with an additional layer of PEDOT:PSS. On top of the PEDOT:PSS layer we have deposited the 4 nm gold layer. Because PEDOT:PSS is hygroscopic we did not fabricated a bilayer device but studied the Raman spectrum of F8BT that was spin coated directly on the thin gold layer. Figure 6 shows Raman spectra taken on and off the gold coated areas. It is clearly seen that the two normalized spectra are similar to the ones taken on and off the

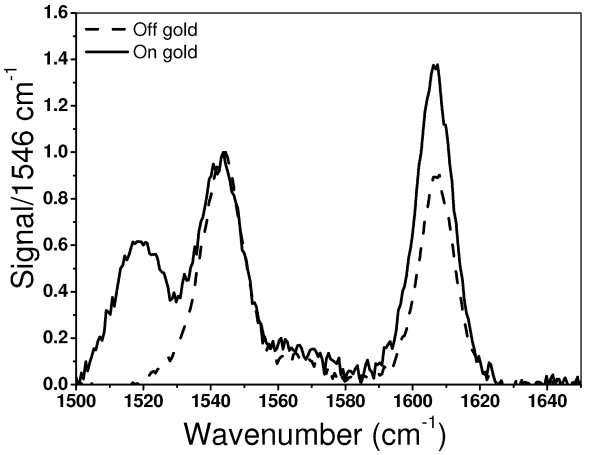


Figure 6. . Raman spectra of an F8BT layer on top of PEDOT:PSS layer with gold between the layers (solid line) and off the gold-coated area (dashed line).

gold on quartz as shown in Figure 2a with similar values for the 1609 cm^{-1} peak. This prove that our technique can by used to probe different zones in the device as long as the electrical characteristics of gold is consistent with those of the layers underneath it.

■ CONCLUSIONS

In this paper, we proposed a new method based on SERS effect for the analysis of the bottom and top 20 nm polymer films. This method is based on the evaporation of a thin layer of gold on quartz and ITO-coated quartz slides. We demonstrated the capabilities of this technique by studying bilayer structures of two polyfluorene polymers with varying bottom layer thickness. We have observed that the dominant contribution to the Raman peak around 1609 cm^{-1} comes from the SERS enhancement of the PFB signal even when the thickness of the PFB layer was only 25 nm. We also studied a 1:1 blend of the same polymers using a combination of AFM and scanning Raman and showed the existence of a wetting layer of PFB on the top and bottom of the film. From previous works, we know that the thickness of this wetting layer is around 15 nm. This proves that the vertical resolution of the proposed technique is

dx.doi.org/10.1021/ma201867e | Macromolecules 2012, 45, 1476−1482

around 20 nm. Our measurements indicate that the top layer is thinner then the bottom layer. This discovery explains why solar cells made from this blend work even when an electron blocking layer is present on the interface to the cathode. Our work can be extended to degradation studies due to the similar work functions of gold and ITO and the high transparency of the gold coated ITO (better than 65%). We are now in the process of applying this technique to study in situ working organic optoelectronic devices.

■ ASSOCIATED CONTENT

Supporting Information

Absorption spectra of F8BT and PFB on plain quartz an on 4 nm of gold. This material is available free of charge via the Internet at http://pubs.acs.org.

■ AUTHOR INFORMATION

Corresponding Author

*Telephone: 0097286472567. Fax: 0097286472949. E-mail: rshikler@ee.bgu.ac.il.

Notes

The authors declare no competing financial interest.

■ REFERENCES

(1) Burrows, P. E.; Gu, G.; Bulovic, V.; Shen, Z.; Forrest, S. R.; Thompson, M. E. *IEEE Trans. Elec. Dev.* **1997**, *32*, 1188−1203.
(2) Friend, R. H.; Gymer, R. W.; Holmes, A. B.; Burroughes, J. H.; Marks, R. N.; Taliani, C.; Bradley, D. D. C.; Dos Santos, D. A.; Bredas, J. L.; Logdlund, M.; Salaneck, W. R. *Nature* **1999**, *397*, 121−128.
(3) Morgado, J.; Friend, R. H.; Cacialli, F. *Appl. Phys. Lett.* **2002**, *80*, 2436−2438.
(4) Bernius, M. T.; Inbasekaran, M.; O'Brien, J.; Wu, W. S. *Adv. Mater.* **2000**, *12*, 1737−1750.
(5) Wilkinson, C. I.; Lidzey, D. G.; Palilis, L. C.; Fletcher, R. B.; Martin, S. J.; Wang, X. H.; Bradley, D. D. C. *Appl. Phys. Lett.* **2001**, *79*, 171−173.
(6) Lee, K. H.; You, J. N.; Kang, S.; Lee, J. Y.; Kwon, H. J.; Kim, Y. K.; Yoon, S. S. *Thin Solid Films* **2010**, *518*, 6253−6258.
(7) Seo, J. H.; Lee, K. H.; Seo, B. M.; Koo, J. R.; Moon, S. J.; Park, J. K.; Yoon, S. S.; Kim, Y. K. *Org. Elect.* **2010**, *11*, 1605−1612.
(8) Yu, G.; Gao, J.; Hummelen, J. C.; Wudl, F.; Heeger, A. J. *Science* **1995**, *270*, 1789−1791.
(9) Halls, J. J. M.; Walsh, C. A.; Greenham, N. C.; Marsegalia, E. A.; Friend, R. H.; Moratti, S. C.; Holmes, A. B. *N ature* **1995**, *376*, 498−450.
(10) Brabec, C. J.; Sariciftci, N. S.; Hummelen, J. C. *Adv. Funct. Mater* **2001**, *11*, 15−26.
(11) Liang, Y.; Xu, Z.; Xia, J.; Tsai, S. T.; Wu, Y.; Li, G.; Ray, C.; Yu, L. *Adv. Mater.* **2010**, *22*, E135−E138.
(12) Klauk, H. *Chem. Soc. Rev.* **2010**, *39*, 2643−2646.
(13) Zschieschang, U.; Ante, F.; Yamamoto, T.; Takimiya, K.; Kuwabara, H.; Ikeda, M.; Sekitani, T.; Someya, T.; Kern, K.; Klauk, H. *Adv. Mater.* **2010**, *22*, 982−985.
(14) Ramsdale, C. M.; Bache, I. C.; MacKenzie, J. D.; Thomas, D. S.; Arias, A. C.; Donald, A. M.; Friend, R. H.; Grennham, N. C. *Phys. E* **2002**, *14*, 268−271.
(15) Kim, J. S.; Ho, P. K. H.; Murphy, C. E.; Friend, R. H. *Macromolecules* **2004**, *37*, 2861−2871.
(16) Bavel, S. S.; Sourty, E.; de With, G.; Loss, J. *Nano Lett.* **2000**, *9*, 507−513.
(17) Fleischmann, M.; Hendra, P. J.; McQuillan, A. J. *Chem. Phys. Lett.* **1974**, *26*, 163−166.
(18) Moskovits, M. *Rev. Mod. Phys.* **1985**, *57*, 783−826.
(19) Moskovits, M.; Tay, L. L.; Yang, J.; Haslett, T. *Opt. Prop. Nanostruct. Random Media* **2002**, *82*, 215−226.
(20) Aroca, R. *Surface enhanced vibrational spectroscopy*. Wiley: New York, 2006.
(21) Persson, B. N. J.; Zhao, K.; Zhang, Z. Y. *Phys. Rev. Lett.* **2006**, *96*, 207401−207404.
(22) Kneipp, K.; Wang, Y.; Kneipp, H.; Perelman, L. T.; Itzkan, I.; Dasari, R.; Feld, M. S. *Phys. Rev. Lett.* **1997**, *78*, 1667−1670.
(23) Otto, A. *Phys. Status Solidi A* **2001**, *188*, 1455−1470.
(24) Paez, B. A.; Salvan, G.; Scholz, R.; Zahn, D. R. T. *Phys. Status Solidi C* **2005**, *2*, 4048−4052.
(25) Zahn, D. R. T.; Salvan, G.; Gavrila, G.; Paez, B. A.; Kramer, B. *Adv. Solid State Phys.* **2006**, *45*, 313.
(26) Davis, R. J.; Pemberton, J. E. *J. Phys. Chem. C* **2008**, *112*, 4364−4371.
(27) Davis, R. J.; Pemberton, J. E. *J. Phys. Chem. C* **2009**, *112*, 4397−4402.
(28) Ariu, M.; Lidzey, D. G.; Bradley, D. D. C. *Synth. Met.* **2000**, *111*, 607−610.
(29) Kim, J. S.; Ho, P. K. H.; Murphy, C. E.; Baynes, N.; Friend, R. H. *Adv. Mater.* **2002**, *14*, 206−209.
(30) Xia, Y.; Friend, R. H. *Appl. Phys. Lett.* **2006**, *88*, 163508−163511.
(31) Shikler, R.; Chiesa, M.; Friend, R. H. *Macromolecules* **2006**, *39*, 5393−5399.
(32) Dimitrakopoulos, C. D.; Malenfant, P. R. L. *Adv. Mater.* **2002**, *14*, 99−117.
(33) Smith, T. J. *Colloid Interface. Sci.* **1980**, *75*, 51−55.
(34) Chiesa, M.; Bürgi, L.; Kim, J. S.; Shikler, R.; Friend, R. H.; Sirringhaus, H. *Nano Lett.* **2005**, *5*, 559−563.
(35) Roman, L. S.; Mammo, W.; Petersson, L. A. A.; Andersson, M. R.; Inganas, O. *Adv. Mater.* **1998**, *10*, 774−777.

Macromolecules

Article

pubs.acs.org/Macromolecules

Block Copolymer Concentration Gradient and Solvent Effects on Nanostructuring of Thin Epoxy Coatings Modified with Epoxidized Styrene–Butadiene–Styrene Block Copolymers

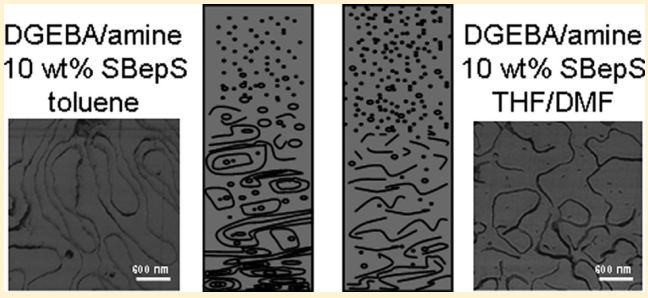
José Angel Ramos,[†] Leandro H. Espósito,[†] Raquel Fernández,[†] Iñaki Zalakain,[†] Silvia Goyanes,[‡] Apostolos Avgeropoulos,[§] Nikolaos E. Zafeiropoulos,[§] Galder Kortaberria,[†] and Iñaki Mondragon*,[†]

[†]Group "Materials + Technologies", Department of Chemical and Environmental Engineering, Polytechnic School, University of the Basque Country, Pza. Europa 1, 20018 Donostia-San Sebastian, Spain

[‡]Laboratorio de Polímeros y Materiales Compuestos, Dep Física, FCEN-UBA, Ciudad Universitaria, Pab. 1, C1428EGA, Ciudad Autónoma de Buenos Aires, Argentina

[§]Department of Materials Science and Engineering, University of Ioannina, University Campus - Dourouti, 45110 Ioannina, Greece

ABSTRACT: The gradient on block copolymer concentration through film thickness as well as the effects of casting solvents used on the nanostructuring of a thermosetting epoxy coating modified with an epoxidized poly(styrene-*b*-butadiene-*b*-styrene) (SBS) triblock copolymer was studied by means of atomic force microscopy and attenuated total reflectance infrared spectroscopy. Thin coating films based on a commercial epoxy–amine formulation consisting of diglycidyl ether of bisphenol A and a low-temperature fast curing amine were modified with several amounts of epoxidized SBS triblock copolymer. Toluene and a mixture of tetrahydrofuran and *N*,*N*-dimethylformamide were used as casting solvents. With epoxidation degrees higher than 45 mol % of polybutadiene block nanostructuring was achieved. Fast curing rate of the epoxy/amine system and the comparatively slow evaporation rate of the casting solvent led to a gradient of morphologies through the film cross section owing to the coalescence of small micelles into larger micellar domains in the case of low block copolymer content. For these reasons, different morphologies were also obtained in the midtransverse section of a film with variable thickness. Finally, pseudolamellar nanostructure at high copolymer contents was achieved as confirmed by parallel and perpendicular cuttings to the air/polymer interface.



INTRODUCTION

Nanostructured polymers are a unique class of materials that are finding an increasing number of applications.[1] Nanofoamed membranes,[2] nanoreactors,[3] nanotemplates,[4] and nanoporous structures[5] are some of the newest applications of nanostructured materials for microelectronics, nanomaterials synthesis, nanotube fabrication, and antireflection coatings. Thermosetting materials based on epoxy matrices modified with block copolymers are being used increasingly in many studies taking advantage of the capability of generating nanostructured systems as well.[6−9] In addition, the principal limitation of epoxy systems, their poor fracture toughness, can also be improved by the addition of block copolymers to the mixture.[10−13] Historically, fracture toughness improvement was achieved by epoxy modification with thermoplastics or elastomers.[14,15] However, the worsening of other properties, such as transparency, because of the generated macrophase-separated domains compromises the usefulness of those systems. Thus, recently block copolymers have been used as templates for the generation of nanostructured thermosetting matrices.[12−26] The preparation of these materials can further optimize the final properties, maintaining the transparency of the neat materials.[27−32]

Generally, to prepare nanostructured thermosetting materials using block copolymers, at least one of the blocks must be miscible with the matrix and at least one block immiscible.[33−35] However, in the case of styrene–butadiene–styrene (SBS) block copolymer both blocks tend to be immiscible with cured epoxy systems, leading to macrophase-separated material. Thus, in order to promote the compatibility of one of the blocks with the epoxy resin, polybutadiene block must be chemically modified. Serrano et al.[1] reported the synthesis and characterization of epoxidized styrene–butadiene block copolymers as templates for nanostructured thermosets, following the procedure previously reported by Jian and Hay,[36] by using hydrogen peroxide for the oxidation of the double bound of the butadiene units. Previous work of our group reported the effect of both the extent of epoxidation of polybutadiene blocks and the content of polystyrene phase on the mixture.[37,38] Thus, in general, a transition from spherical micelles to wormlike micelles and then to vesicles occurs with the decrease of the epoxy miscible

Received: August 17, 2011
Revised: January 13, 2012
Published: January 27, 2012

ACS Publications © 2012 American Chemical Society

dx.doi.org/10.1021/ma2018759 | *Macromolecules* 2012, 45, 1483–1491

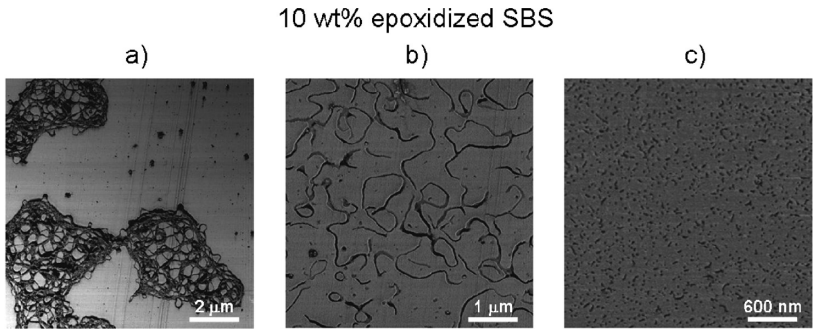


Figure 1. TM-AFM phase images of epoxy mixtures modified with 10 wt % SBS triblock copolymer, epoxidized to different extents, cast in a THF/DMF 1:1 mixture: (a) 37 mol %, image 10 × 10 μm; (b) 46 mol %, image 5 × 5 μm; (c) 52 mol %, image 3 × 3 μm. Images in the midtransverse section of a 240 μm film thickness.

block and/or the increase of the epoxy immiscible block,[27] while for epoxidation extents of the block copolymer higher than the threshold required for miscibility with the epoxy system,[37] long-range ordered nanostructures evoluting from spherical to hexagonally packed cylinders and even lamellas as copolymer content increased are achieved.[39,40]

On the other hand, in the case of thin films, the influence of both solvent used for casting and film thickness should be taken into account in the development of morphology. Hermel-Davidock et al.[26] observed morphology differences in epoxy thermosets modified with poly(ethylene oxide)-*block*-poly(ethylene-*alt*-propylene) (PEO−PEP) cast with two different solvents, acetone and tetrahydrofuran. Acetone, as poorer solvent than tetrahydrofuran for PEO block, can induce the collapse of the micelle corona chains toward the interface to minimize the interfacial tension by adopting a cylindrical morphology instead of spherical micelles. Furthermore, the influence of the amount of a selective solvent in the final morphology when a mixture of solvents is used has been reported by other authors for block copolymers showing morphology transitions from spherical micelles to vesicles.[41−44]

Because of the limited literature on the subject, the aim of this work has been the study of the gradient on copolymer segregation through film thickness and the effects of casting solvents on the resultant microphase-separated morphology achieved in the block copolymer modified epoxy thin films. In this context, the effects of the selectivity of two solvent systems, toluene and the solvent mixture tetrahydrofuran/*N*,*N*-dimethylformamide, on the nanostructured morphology have been studied.

EXPERIMENTAL SECTION

The block copolymer was a linear SBS triblock copolymer, C540, with 60 wt % PB, kindly supplied by Repsol-YPF. The number-average molar mass was 75 000 g mol^{-1}. The epoxidation reaction was carried out using hydrogen peroxide in the presence of an *in situ* prepared catalyst in a water/dichloroethane biphasic system. The details of the reaction are described elsewhere.[1,36] The degree of epoxidation is represented in mol % with respect to PB double bonds. The epoxy monomer used was a diglycidyl ether of bisphenol A (DGEBA) with epoxide equivalent weight of 184−190, supplied by Hexion. The hardener was an aliphatic fast curing amine mixture, composed by *N*-aminoethylpiperazine, *m*-xylylenediamine, and benzyl alcohol, particularly suited to low-temperature conditions, Ancamine 2500, supplied by Air Products. The mixtures were prepared with a weight ratio of 100/58 (epoxy/hardener). Toluene, tetrahydrofuran (THF), and *N*,*N*-dimethylformamide (DMF) used as casting solvents were supplied by Sigma-Aldrich. The mixtures were prepared in three steps. First, the epoxidized block copolymer and DGEBA resin were dissolved in the casting solvent with magnetic stirring. Next, the hardener was added to the mixture at room temperature for 5 min. Finally, the samples were cured in open parallelepipedic polytetrafluorethylene (PTFE) molds at 70 °C for 1 h and postcured at 135 °C for 1 h.

Atomic force microscopy (AFM) topography and phase images of the samples were recorded in tapping mode in air at room temperature by using a scanning probe microscope (Nanoscope IV, Dimension 3100 from Digital Instruments). Phosphorus (n) doped single-beam cantilever (125 μm length) silicon probes having a tip's nominal radius of curvature of 5−10 nm were used. A typical scan rate during recording was 1 Hz. Samples of cured mixtures were prepared using an ultramicrotome (Leica Ultracut R) equipped with a diamond knife.

Infrared spectra were taken using a Nicolet Nexus 670 (FTIR) spectrometer equipped with a single horizontal golden gate attenuated total reflectance (ATR) cell. The internal reflection element was ZnSe with refractive index of 2.4. Spectra were recorded using a spectral width ranging from 800 to 4000 cm^{-1}, with 4 cm^{-1} resolution and an accumulation of 32 scans.

RESULTS AND DISCUSSION

In order to promote chemical compatibilization between the block copolymer and the epoxy matrix, SBS triblock copolymer was epoxidized at different temperatures and times of reaction. Degrees of epoxidation ranging from 35 to 57 mol % of epoxidized polybutadiene units were achieved. Milder conditions produced lower percentages of modification. The degree of epoxidation was calculated by integration of signals using ^{1}H nuclear magnetic resonance (^{1}H NMR) spectra.[37]

Before curing, all the mixtures formed by DGEBA resin, hardener, randomly epoxidized SBS triblock copolymer, and the casting solvent were homogeneous and transparent or translucent, indicating that micro- or macrophase separation occurred before curing for high (>45 mol %) or low (37 mol %) degrees of epoxidation of polybutadiene block, respectively. This fact seems to be related with the degree of miscibility of the epoxidized PB block with the DGEBA/amine system, which is a function of the epoxidation extent. On the other hand, as can be shown in Figure 1 for cured systems modified with 10 wt % of epoxidized block copolymer cast with a 1:1 THF/DMF solvent mixture, a relatively low epoxidation degree (37 mol %) in the PB block led to macrophase separation in the cured system, Figure 1a, because of the larger amount of low-epoxidized PB units that provoked their phase separation before curing. As epoxidation degree increased, microphase-separated

dx.doi.org/10.1021/ma2018759 | *Macromolecules* 2012, 45, 1483−1491

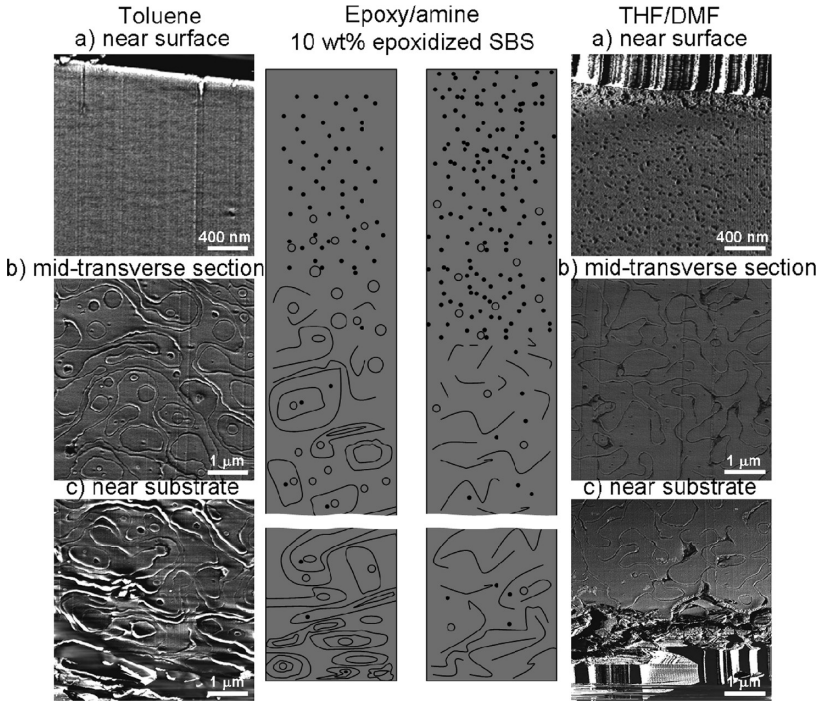


Figure 2. TM-AFM phase images for epoxy mixtures modified with 10 wt % of epoxidized SBS triblock copolymer cast in toluene and THF/DMF 1:1 mixture as a function of the location through a 240 μm film thickness: (a) near the air/polymer interface, images 2 × 2 μm; (b) in the midtransverse section of the film, images 5 × 5 μm; (c) near the polymer/substrate interface, images 5 × 5 μm.

systems could be achieved after curing. Figure 1b shows wormlike micelles corresponding to PS nanodomains (46 mol % epoxidized PB units). Compared with the epoxidation degree previously reported by Ocando et al.[37] needed to overcome the miscibility threshold between epoxidized PB block and epoxy matrix, higher degrees of epoxidation were needed to achieve microphase-separated systems, which is related with the poorer miscibility introduced by the aliphatic fast curing amine used in this work in comparison with the aromatic one in our previous studies.[37,45] Indeed, only systems with high epoxidation degrees (46 mol % or more) showed microphase-separated domains. As we previously reported,[37,45] long-range nanostructuring increased as higher miscibility of epoxidized PB block and epoxy matrix was. This fact can be seen in Figure 1c where the coexistence of spherical micelles with short wormlike micelles due to the larger epoxidation degrees (52 mol % epoxidized PB units) is shown.

With the purpose of evaluating through film thickness the gradient on copolymer segregation and the influence of solvent evaporation on the morphology, two films with constant thickness were analyzed at different regions through film thickness for samples cured with 10 wt % of epoxidized SBS copolymer and toluene and the mixture THF/DMF 1:1 as casting solvents. Ultramicrotomed samples were used for analysis. Results are shown in Figure 2. All samples used herein after have 46 mol % of epoxidation in the butadiene block. In the case of toluene as casting solvent small micelles were achieved near to the air/polymer interface, while in the midtransverse section of the film and near to the polymer/substrate interface the achieved nanostructures corresponded to large-interconnected wormlike micelles coexisting with vesicles and small micelles. The evolution of the morphology along the film thickness passed through several regions from the air/polymer interface to the polymer/substrate interface. Near the air/polymer interface, a region of about 2.2 μm without nanodomains was observed. Inside the film small micelles appeared being more noticeable at a distance of 3.7 μm in depth. At 12.1 μm in depth from the air/polymer interface, small vesicles were detected. At longer distances, up to 18.4 μm the coexistence of small micelles and vesicles, which progressively increased in size, was observed. Then, the beginning of short wormlike micelles formation took place, continuing growing in length until 42.1 μm, where the long wormlike micelles began to interconnect themselves coexisting with small micelles and vesicles. From 54.2 μm, the morphology of large-interconnected wormlike micelles coexisting with small micelles and vesicles remained constant almost up to the interface with the substrate. Finally, near the polymer/substrate interface a flattening of the large-interconnected wormlike micelles was observed. The scheme in Figure 2 simplifies the sequence of the large amount of AFM images obtained along the film thickness. For simplicity, only the regions close to the interfaces and in the mid-transverse section are shown. Similarly, in the case of the mixture with THF/DMF 1:1 as casting solvent, a gradient of morphologies was obtained along the film thickness, with some differences with respect to the case of toluene. The beginning of the nanodomains, as small micelles, started at a close, unmeasurable by AFM images, distance from the air/polymer interface. In addition, the size of these micelles was smaller than in the case of toluene but in higher concentration. This fact was the first evidence of the better solvent quality of the mixture THF/DMF with respect to toluene. Continuing with the evolution of morphology, at a distance of 9.9 μm from the air interface

dx.doi.org/10.1021/ma2018759 | *Macromolecules* 2012, 45, 1483−1491

vesicles began their appearance increasing their size until the next region. At 25.4 μm in depth the formation of short wormlike micelles coexisting with small micelles in larger amount and vesicles in smaller quantity and size than in the case of toluene started. Up to 37.5 μm, long wormlike micelles began their appearance increasing their size and coexisting with small micelles and vesicles until the formation of the morphology, at 49.2 μm in depth, morphology which remained constant until the interface with the substrate. In this case, there was no noticeable flattening of the long wormlike micelles near to the polymer/substrate interface, as in the case of toluene. The no formation of interconnected and closed wormlike micelles appears to be the second evidence of the better solvent quality of the mixture THF/DMF with respect to toluene because of the favored polymer−solvent interactions instead of polymer−polymer ones.[44] As conclusions for both solvents, it seemed that the morphology gradient could be due to the increase of copolymer concentration from the air/polymer interface to the substrate/polymer interface. The progressive increase in copolymer concentration in the region close to the air/polymer interface up to the midsection, the largest region where copolymer concentration was constant, caused the growing of the small micelles by coalescence, leading to the formation of short wormlike micelles which rapidly transformed in small vesicles to minimize the interfacial tension.[26,27] As the increase of copolymer concentration continued, larger structures were achieved. Because of the fast curing rate of the DGEBA/amine system the structures were frozen. Furthermore, the distances from the air/polymer interface to the regions of morphology transitions were similar in both cases: 12.1 and 9.9 μm for vesicles, 18.4 and 25.4 μm for wormlike micelles, 42.1 and 37.5 μm for long-wormlike, 54.2 and 49.2 μm for constant morphology for the casting solvents toluene and THF/DMF 1:1, respectively, indicating that the copolymer segregation was not due to the selected solvent. Thus, we can suggest the preparation of films by solvent evaporation does not necessarily produce the equilibrium morphology but a gradient of morphologies through the film thickness. The higher evaporation rate of solvents close to the air/polymer interface with respect to the midsection of the film decreases the possibility of the small micelles to coalesce and therefore to form larger structures. At longer distances in depth from the air/polymer interface, longer time in contact with the solvent and longer the structures that could be achieved by coalescence.[26,27] From another point of view, the fast curing rate of the used DGEBA/amine system could also freeze the structures before reaching the equilibrium state. So, the whole process of morphology formation through film thickness appears to be a competition of at least curing reaction, solvent evaporation, and coalescence of micelles.

In order to corroborate the presence of copolymer close to the interfaces and also the possible presence of residual solvent in the samples, ATR-FTIR analysis of the air/polymer and polymer/substrate interfaces was carried out. Figure 3 shows ATR-FTIR spectra of the individual components of the mixtures as well as the interfaces spectra and details of the intervals of interest. Slight variation on the bands in the region 1000−900 cm^{-1}, assigned to C═C out-of-plane bending vibration of the aromatic ring of PS block, can be seen owing to variations in block copolymer concentration. Thus, in the case of 30 wt % block copolymer and toluene as casting solvent, a noticeable decrease in the characteristic bands of PS (910 and 967 cm^{-1}) at the air/polymer interface can be seen. The band at 910 cm^{-1} is too close to the nonreacted epoxy group, and therefore it becomes difficult to distinguish this peak;[1] however, the variation in the 967 cm^{-1} band allowed confirming the variation in copolymer concentration. The depth of penetration of the infrared beam into the sample was estimated supposing a refractive index of the samples close to the neat epoxy of 1.57, as supplied by the manufacturer, and ZnSe as internal reflection element at 45°. In the wavenumbers of interest, the depth of penetration was found to be less than 3 μm (2.75 and 2.58 μm for 910 and 967 cm^{-1}, respectively), a value not sufficient to reach enough block copolymer domains to be measurable in the case of toluene as casting solvent and at the air/polymer interface. This fact supported the conclusions extracted from AFM images in Figure 2, which shows the evolution of the morphology through the film thickness, and in which the presence of the nanodomains began at a distance between 2.2 and 3.7 μm from the air interface. As wormlike micelles began from the polymer/substrate interface, they are measurable by ATR-FTIR. Some differences in FTIR spectra between samples cured with toluene or THF/DMF were observed. Thus, for the samples cured with THF/DMF as casting solvent, there were no noticeable differences in the region of 1000−900 cm^{-1} between the spectra of both interfaces, air/polymer and polymer/substrate, indicating the presence of block copolymer close to both interfaces, at a distance less than the depth of penetration of ATR-FTIR of 3 μm.

Other remarkable fact in the case of the system cast with DMF/THF was the presence of residual DMF as confirmed by means of the appearance of new bands in FTIR spectra in the region of 1800−1600 cm^{-1}, related to C═O group stretching vibration of DMF (Figure 3c).

In addition, to confirm the presence or absence of copolymer at the interfaces, Figure 4 shows the morphology at the interfaces, air/polymer and polymer/substrate, for the systems containing 10 wt % of 46 mol % epoxidized SBS triblock copolymer cured with toluene and THF/DMF as casting solvents. Both systems showed similar results. At the air/polymer interface no nanostructuring was achieved, indicating the absence of microphase-separated copolymer in that interface, far in the case of toluene, 2.2 μm, and close in the case of THF/DMF, unmeasurable. However, at the polymer/substrate interface, nanostructuring was suggested between mold imprinted lines, ensuring the presence of microphase-separated copolymer in that interface.

Thus, a conclusion that can be drawn is that AFM images and ATR-FTIR analysis revealed that the block copolymer concentration at the near air/polymer interface was much lower than in the near mold interface.

A similar effect can be observed in a film with variable thickness, from 30 to 240 μm. Figure 5 shows the morphology evolution in the midtransverse section of the film as a function of the thickness for a system containing 20 wt % epoxidized SBS triblock copolymer and cast in a 1:1 mixture of THF and DMF. Images every 10 μm from the lowest film thickness (30 μm) to the highest film thickness (240 μm) were obtained. It should be noted that images were made in the midtransverse section of each thickness of the film.

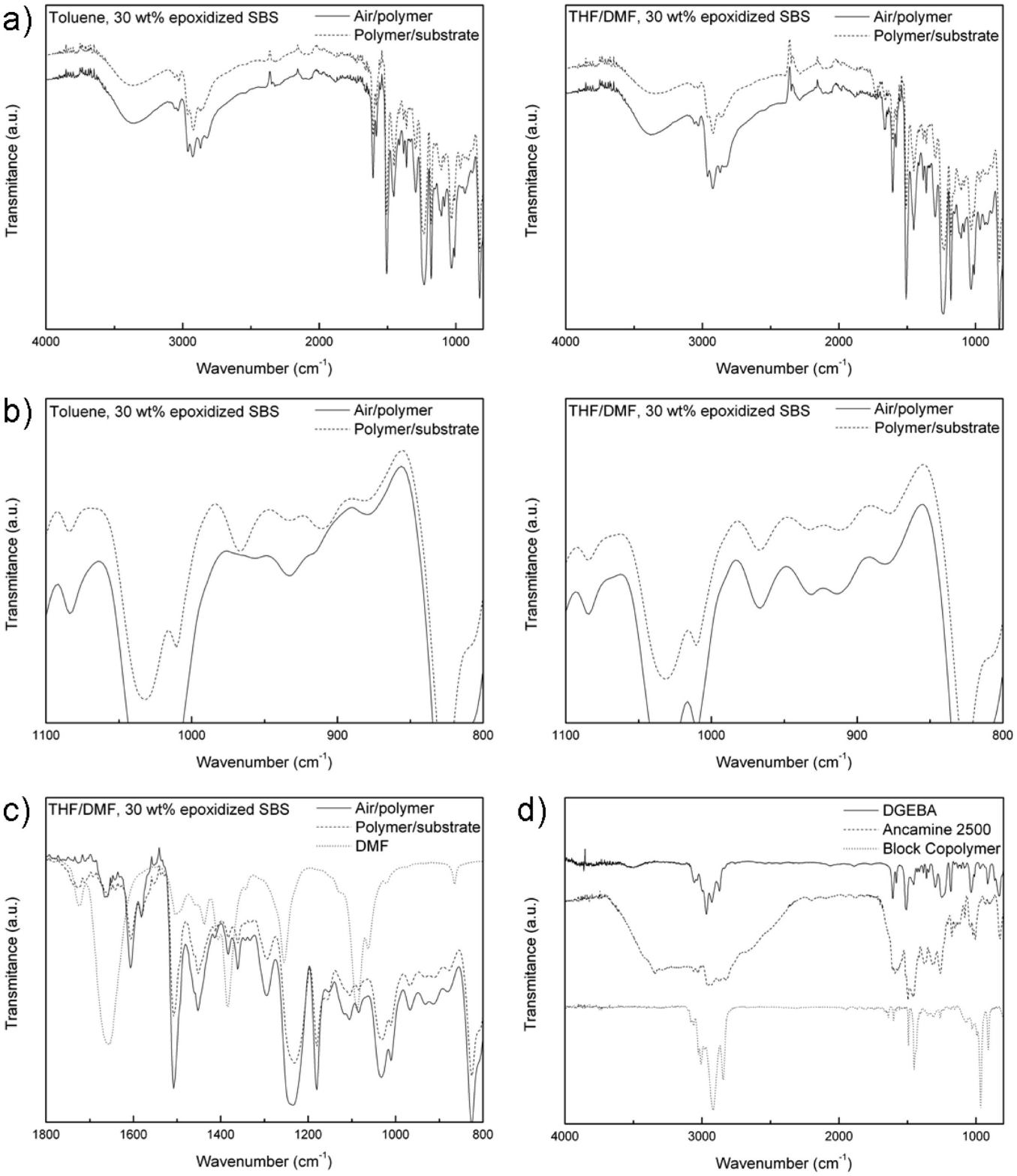


Figure 3. ATR-FTIR spectra of air/polymer and polymer/substrate interfaces of epoxy mixtures modified with 30 wt % of 46 mol % epoxidized SBS triblock copolymer cast in toluene and in THF/DMF 1:1 within the ranges (a) 4000−800, (b) 1100−800, and (c) 1800−800 cm^{-1} only cast in THF/DMF 1:1 and (d) FTIR spectra of individual components of the mixture.

Nevertheless, only four images are reported for simplicity. Spherical micelles coexisting with wormlike micelles were achieved at low thickness. With the increase in thickness, an increase in the length of the wormlike micelles, and a reduction in the amount of spherical micelles was observed. This morphological gradient seems to be due to the gradient in copolymer concentration through the film thickness and the different evaporation rate of solvents. As AFM images

dx.doi.org/10.1021/ma2018759 | *Macromolecules* 2012, 45, 1483−1491

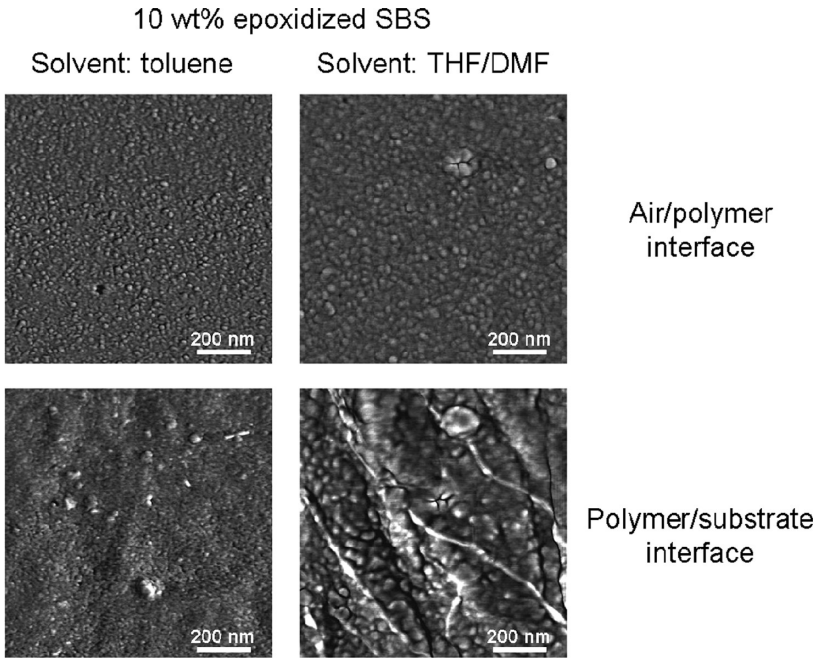


Figure 4. TM-AFM phase images of air/polymer and polymer/substrate interfaces of epoxy mixtures modified with 10 wt % of 46 mol % epoxidized SBS triblock copolymer cast in toluene and in THF/DMF 1:1. Images 1 × 1 μm.

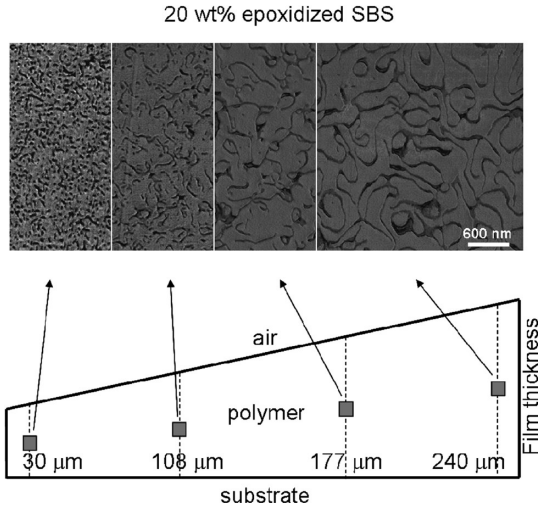


Figure 5. TM-AFM phase images in the transverse section of the film for epoxy mixtures modified with 20 wt % of 46 mol % epoxidized SBS triblock copolymer cast in THF/DMF 1:1 as a function of film thickness. Images 3 × 3 μm.

were taken in the midtransverse section of the film, the higher the film thickness the higher the depth from the air/polymer interface. Thus, the lower the film thickness the higher the influence of copolymer segregation gradient in the midtransverse section of the film. Consequently, the different morphologies due to the copolymer segregation gradient, shown in Figure 2, would be overlapped obtaining almost a unique morphology, which is shown in Figure 5 for the image corresponding to 15 μm depth from the air/polymer interface, corresponding to the midtransverse section of 30 μm film thickness. In addition, the high boiling point of DMF could ease the formation of ordered structures as the system remained longer times with low viscosity. Longer times in contact with the solvent before freezing of the nanostructure at system gelation led to minimization of the interfacial tension of nanodomains. Therefore, larger wormlike micelle morphology was developed by coalescence of spherical micelle structures.[26,27] Hence, shorter domains were achieved at low film thickness due to the faster solvent evaporation, as shown in the image of 30 μm film thickness, as occurred at low film depth in Figure 2. Thus, films thinner than 30 μm would lead to homogeneous nanostructured coatings.

On the other hand, the effect of using different casting solvents on the nanostructure of systems with different amounts of block copolymer was also studied. Figure 6 shows AFM images in the transverse section of thin films for several mixtures cast with a THF/DMF 1:1 mixture as casting solvent. The system modified with 5 wt % epoxidized SBS triblock copolymer showed a combined morphology in which spherical and wormlike micelles with vesicles did coexist. The system with 10 wt % epoxidized block copolymer exhibited the same combined morphology with longer wormlike micelles. Addition of more block copolymer resulted in the decrease of the interfacial area, which yielded to the formation of wormlike micelles by the coalescence of spherical nanodomains.[27,46] Coatings with 20 and 30 wt % epoxidized block copolymer showed interconnected wormlike micelles and more compacted nanostructures than at lower copolymer contents. Finally, microphase separation led to a pseudolamellar nanostructure for 40 wt % triblock copolymer, as the interconnected wormlike microdomains would reduce the interfacial tension by generating planar interfaces, and thereby the long-range ordered lamellar nanostructures were obtained.[35] Similar nanostructures were obtained for samples cured with toluene, as can be seen in Figure 7. However, lamellar nanostructures were achieved at lower contents, i.e., 20−30 wt % of copolymer, due to the solvent quality and the different evaporation rate of toluene and the mixture THF/DMF. In addition, interconnected wormlike micelles were also achieved at lower contents of

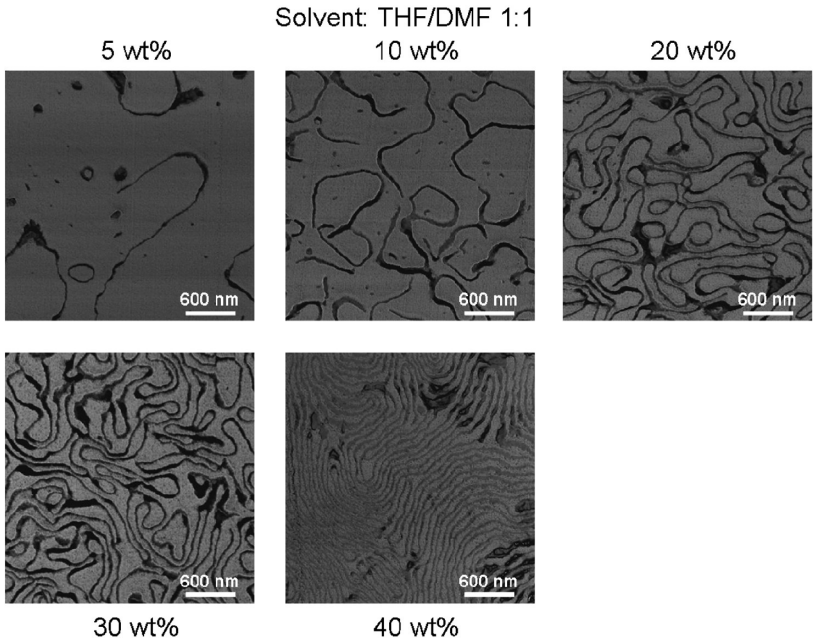


Figure 6. TM-AFM phase images for epoxy mixtures modified with 5, 10, 20, 30, and 40 wt % of 46 mol % epoxidized SBS triblock copolymer cast in THF/DMF 1:1. 3 μm × 3 μm images in the transverse section of a 240 μm film thickness.

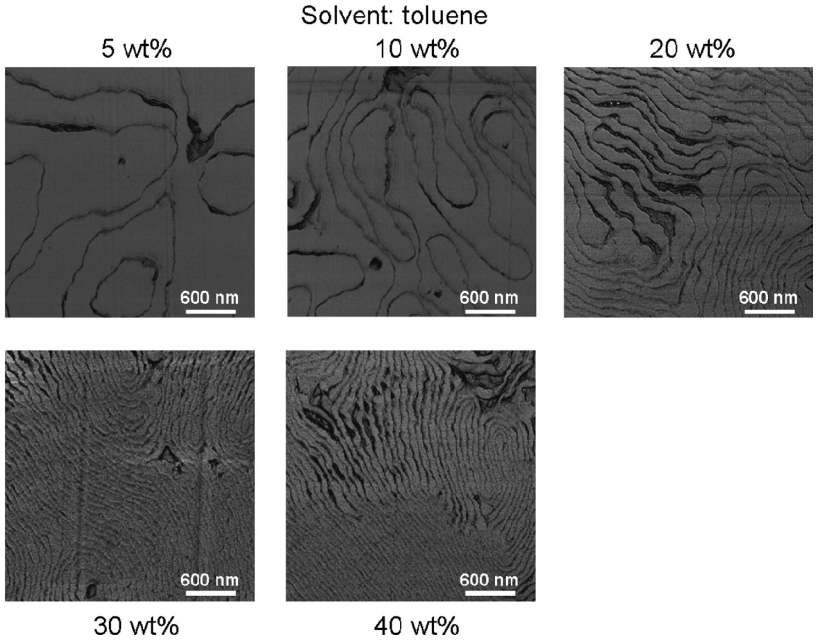


Figure 7. TM-AFM phase images for epoxy mixtures modified with 5, 10, 20, 30, and 40 wt % of 46 mol % epoxidized SBS triblock copolymer cast in toluene. Images 3 × 3 μm in the transverse section of a 240 μm film thickness.

copolymer when cured with toluene. In the mixture with THF/DMF, THF should evaporate during the first stage curing at 70 °C, whereas DMF, because of its highest boiling point, could be reserved in the coatings until the curing reaction was completed. Therefore, it is proposed that the rate of solvent evaporation could significantly affect the kinetics of curing reaction, and thus the morphologies should be influenced. However, although DMF should allow longer times to achieve ordered structures, it seemed that toluene had poorer solvent quality than the THF/DMF mixture. In this study, the individual evaluation of the effect of evaporation rate or the solvent quality was not carried out, so it is suggested that both effects increased polymer−polymer interactions instead of polymer−solvent ones, thus leading to long-range order nanostructures at lower copolymer contents.[44]

In order to analyze the formed nanostructures in all directions, films were cut in two different directions, parallel and perpendicular to the air/polymer interface, and thereafter AFM images in the transverse section of the film were obtained. Figure 8 shows similar nanostructures for two copolymer contents in both cutting directions for the system cast with toluene. Lamellar nanostructures (20 and 30 wt %) appeared in both directions, thus confirming that nanostructures were pseudolamellar instead of cylindrical.

dx.doi.org/10.1021/ma2018759 | *Macromolecules* 2012, 45, 1483−1491

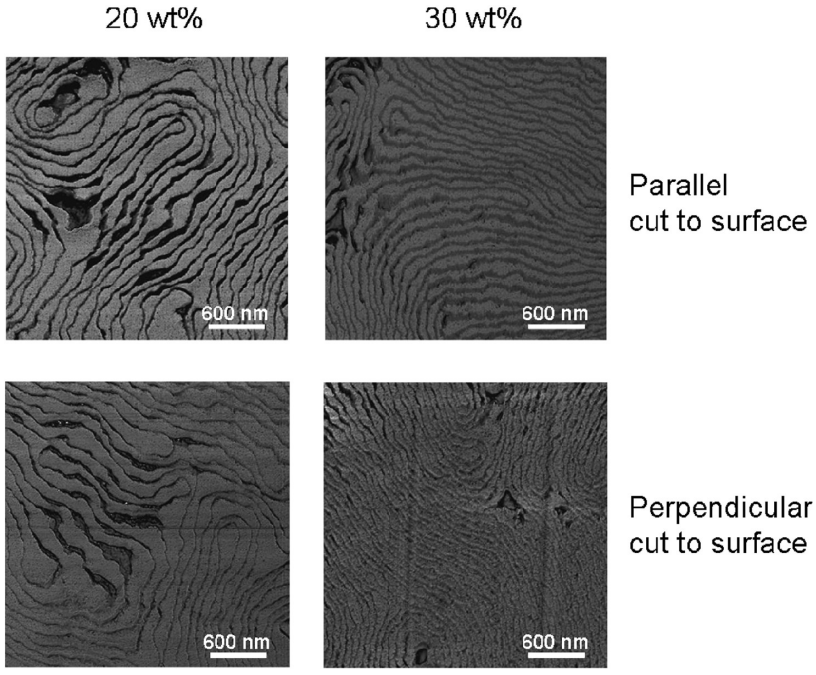


Figure 8. TM-AFM phase images for epoxy mixtures modified with 20 and 30 wt % of epoxidized SBS triblock copolymer cast in toluene as casting solvent for two different directions: top - parallel and bottom - perpendicular cuts to the air/polymer interface. Image 3 × 3 μm in the midsection of a 240 μm film thickness.

■ CONCLUSIONS

A morphological study of the gradient on block copolymer concentration through film thickness and the effects of casting solvents on nanostructuring of an epoxy thin coating system modified with a block copolymer was carried out by atomic force microscopy. A poly(styrene-*b*-butadiene-*b*-styrene) triblock copolymer was randomly epoxidized to compatibilize the butadiene block with the epoxy system. A degree of epoxidation higher than 45 mol % epoxidized polybutadiene units was needed to obtain nanostructured materials.

Owing to the differential segregation of the copolymer through the whole thickness of the film, a gradient of morphologies, which was fixed by the fast curing rate and the relatively slow evaporation rate of solvents, was obtained. By attenuated total reflectance infrared spectroscopy, the absence of block copolymer near the air/polymer interface in the system cast with toluene was verified. Analysis of a film with variable thickness revealed that for thin films morphology gradient was not evident due to the overlap of the different regions with different copolymer concentrations and the faster solvent evaporation which would lead to a homogeneous film. In addition, the poorer solvent quality of toluene in comparison with the mixture of tetrahydrofuran and *N*,*N*-dimethylformamide allowed to achieve pseudolamellar nanostructures at lower copolymer contents; these structures were confirmed by parallel cuttings to the air/polymer interface, which showed similar morphologies which dismissed cylindrical morphology.

■ AUTHOR INFORMATION

Corresponding Author

*E-mail: inaki.mondragon@ehu.es.

Notes

The authors declare no competing financial interest.

■ ACKNOWLEDGMENTS

Financial support from the EU (Carbon nanotube confinement strategies to develop novel polymer matrix composites, POCO, FP7-NMP-2007, CP-IP 213939-1), from the Basque Country Government (Inanogune IE 08-225, Inanogune IE 09-243, Grupos Consolidados IT-365-07), and from the Ministry of Education and Innovation (MAT 2009-06331) is gratefully acknowledged. Moreover, we are grateful to "Macrobehavior - Mesostructure - Nanotechnology" SGIker unit of the UPV/EHU.

■ REFERENCES

(1) Serrano, E.; Larrañaga, M.; Remiro, P. M.; Mondragon, I.; Carrasco, P. M.; Pomposo, J. A.; Mecerreyes, D. *Macromol. Chem. Phys.* **2004**, *205*, 987−996.
(2) Hong, S. M.; Hwang, S. S. *J. Appl. Polym. Sci.* **2006**, *100*, 4964−4971.
(3) Shi, X.; Shen, M.; Möhwald, H. *Prog. Polym. Sci.* **2004**, *29*, 987−1019.
(4) Fu, J.; Cherevko, S.; Chung, C.-H. *Electrochem. Commun.* **2008**, *10*, 514−518.
(5) Joo, W.; Park, M. S.; Kim, J. K. *Langmuir* **2006**, *22*, 7960−7963.
(6) Grubbs, R. B.; Dean, J. M.; Bates, F, S. *Macromolecules* **2001**, *34*, 8593−8595.
(7) Guo, Q.; Thomann, R.; Gronski, W.; Thurn-lbrecht, T. *Macromolecules* **2002**, *35*, 3133−3144.
(8) Guo, Q.; Thomann, R.; Gronski, W.; Staneva, R.; Ivanova, R.; Stühn, B. *Macromolecules* **2003**, *36*, 3635−3645.
(9) Mijovic, J.; Shen, M.; Sy, J. W.; Mondragon, I. *Macromolecules* **2000**, *33*, 5235−4244.
(10) Dean, J. M.; Lipic, P. M.; Grubbs, R. B.; Cook, R. F.; Bates, F. S. *J. Polym. Sci., Part B: Polym. Phys.* **2001**, *39*, 2996−3010.
(11) Ritzenthaler, S.; Court, F.; David, L.; Girard-Reydet, E.; Leibler, L.; Pascault, J. P. *Macromolecules* **2002**, *35*, 6245−6254.
(12) Ritzenthaler, S.; Court, F.; David, L.; Girard-Reydet, E.; Leibler, L.; Pascault, J. P. *Macromolecules* **2003**, *36*, 118−126.
(13) Dean, J. M.; Verghese, N. E.; Pham, H. Q.; Bates, F. S. *Macromolecules* **2003**, *36*, 9267−9270.

(14) Kinloch, A. J.; Shaw, S. J.; Tod, D. A.; Hunston, D. L. *Polymer* **1983**, *24*, 1341−1354.
(15) Cardwell, B. J.; Yee, A. F. *J. Mater. Sci.* **1998**, *33*, 5473−5484.
(16) Xu, Z.; Hameed, N.; Guo, Q.; Mai, Y.-W. *J. Appl. Polym. Sci.* **2010**, *115*, 2110−2118.
(17) Larrañaga, M.; Gabilondo, N.; Kortaberria, G.; Serrano, E.; Remiro, P.; Riccardi, C. C.; Mondragon, I. *Polymer* **2005**, *46*, 7082−7093.
(18) Larrañaga, M.; Arruti, P.; Serrano, E.; de la Caba, K.; Remiro, P.; Riccardi, C. C.; Mondragon, I. *Colloid Polym. Sci.* **2006**, *284*, 1419−1430.
(19) Meng, F.; Zheng, S.; Zhang, W.; Li, H.; Liang, Q. *Macromolecules* **2006**, *39*, 711−719.
(20) Ocando, C.; Serrano, E.; Tercjak, A.; Peña, C.; Kortaberria, G.; Calberg, C.; Grignard, B.; Jerome, R.; Carrasco, P. M.; Mecerreyes, D.; Mondragon, I. *Macromolecules* **2007**, *40*, 4068−4074.
(21) Meng, F.; Xu, Z.; Zheng, S. *Macromolecules* **2008**, *41*, 1411−1420.
(22) Hillmyer, M. A.; Lipic, P. M.; Hadjuk, D. A.; Almdal, K.; Bates, F. S. *J. Am. Chem. Soc.* **1997**, *119*, 2749−2750.
(23) Cicala, G.; Mamo, A.; Recca, G.; Restuccia, C. L. *Polym. Eng. Sci.* **2007**, *47*, 2027−2033.
(24) Ritzenthaler, S.; Court, F.; David, L.; Girard-Reydet, E.; Leibler, L.; Pascault, J. P. *Macromolecules* **2002**, *35*, 6245−6254.
(25) Rebizant, V.; Abetz, V.; Tournilhac, F.; Court, F.; Leibler, L. *Macromolecules* **2003**, *36*, 9889−9896 (2003).
(26) Hermel-Davidock, T. J.; Tang, H. S.; Murray, D. J.; Hahn, S. F. *J. Polym. Sci., Part B: Polym. Phys.* **2007**, *45*, 3338−3348.
(27) Dean, J. M.; Grubbs, R. B.; Saad, W.; Cook, R. F.; Bates, F. S. *J. Polym. Sci., Part B: Polym. Phys.* **2003**, *41*, 2444−2456.
(28) Rebizant, V.; Venet, A. S.; Tournilhac, F.; Girard-Reydet, E.; Navarro, C.; Pascault, J. P.; Leibler, L. *Macromolecules* **2004**, *37*, 8017−8027.
(29) Wu, J.; Thio, Y. S.; Bates, F. S. *J. Polym. Sci., Part B: Polym. Phys.* **2005**, *43*, 1950−1965.
(30) Thio, Y. S.; Wu, J.; Bates, F. S. *Macromolecules* **2006**, *39*, 7187−7189.
(31) Larrañaga, M.; Serrano, E.; Martin, M. D.; Tercjak, A.; Kortaberria, G.; de la Caba, K.; Riccardi, C. C.; Mondragon, I. *Polym. Int.* **2007**, *56*, 1392−1403.
(32) Grubbs, R. B.; Dean, J. M.; Broz, M. E.; Bates, F. S. *Macromolecules* **2000**, *33*, 9522−9534.
(33) Fan, W.; Wang, L.; Zheng, S. *Macromolecules* **2009**, *42*, 327−336.
(34) Hameed, N.; Guo, Q.; Xu, Z.; Hanley, T. L.; Mai, Y.-W. *Soft Matter* **2010**, *6*, 6119−6129.
(35) Fan, W.; Wang, L.; Zheng, S. *Macromolecules* **2010**, *43*, 10600−10611.
(36) Jian, X.; Hay, A. S. *J. Polym. Sci., Part A: Polym. Chem.* **1991**, *29*, 1183−1189.
(37) Ocando, C.; Tercjak, A.; Serrano, E.; Ramos, J. A.; Corona-Galván, S.; Parellada, M. D.; Fernández-Berridi, M. J.; Mondragon, I. *Polym. Int.* **2008**, *57*, 1333−1342.
(38) Serrano, E.; Tercjak, A.; Ocando, C.; Larrañaga, M.; Parellada, M. D.; Corona-Galván, S.; Mecerreyes, D.; Zafeiropoulos, N. E.; Stamm, M.; Mondragon, I. *Macromol. Chem. Phys.* **2007**, *208*, 2281−2292.
(39) Serrano, E.; Tercjak, A.; Kortaberria, G.; Pomposo, J. A.; Mecerreyes, D.; Zafeiropoulos, N. E.; Stamm, M.; Mondragon, I. *Macromolecules* **2006**, *39*, 2254−2261.
(40) Gutierrez, J.; Tercjak, A.; Mondragon, I. *J. Phys. Chem. C* **2010**, *114*, 22424−22430.
(41) Lazzari, M.; Scalarone, D.; Vazquez-Vazquez, C.; López-Quintela, M. A. *Macromol. Rapid Commun.* **2008**, *29*, 352−357.
(42) Choucair, A.; Eisenberg, A. *Eur. Phys. J. E* **2003**, *10*, 37−44.
(43) Bhargava, P.; Zheng, J. X.; Li, P.; Quirk, R. P.; Harris, F. W.; Cheng, S. Z. D. *Macromolecules* **2006**, *39*, 4880−4888.
(44) Cho, H.; Park, H.; Park, S.; Choi, H.; Huang, H.; Chang, T. *J. Colloid Interface Sci.* **2011**, *356*, 1−7.
(45) Ocando, C.; Tercjak, A.; Martín, M. D.; Ramos, J. A.; Campo, M.; Mondragon, I. *Macromolecules* **2009**, *42*, 6215−6224.
(46) Hameed, N.; Guo, Q.; Hanley, T.; May, Y.-W. *J. Polym. Sci., Part B: Polym. Phys.* **2010**, *48*, 790−800.

Macromolecules

Article

pubs.acs.org/Macromolecules

Dewetting-Induced Hierarchical Patterns in Block Copolymer Films

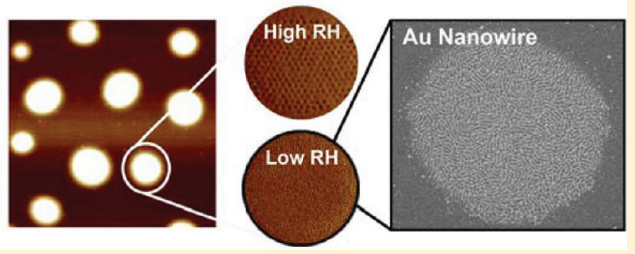
Su Yeon Choi,[†] Chansub Lee,[†] Jin Wook Lee,[†] Cheolmin Park,[‡] and Seung Hyun Kim*,[†]

[†]Division of Nano-Systems Engineering, Inha University, Incheon 402-751, South Korea

[‡]Department of Materials Science and Engineering, Yonsei University, Seoul 120-749, South Korea

Supporting Information

ABSTRACT: Thin film stability should be carefully monitored in many practical applications and at the same time can be effectively utilized to produce the surface pattern. In this work, it is demonstrated that block copolymer thin films can generate highly ordered, hierarchical surface pattern via combined process of self-assembly and film destabilization. The dewetting process generates the surface pattern of hole or island on the micrometer scale while the self-assembly produces well-ordered pattern on the nanometer scale. Highly ordered nanostructure is obtained by solvent annealing within the remaining part of dewetted film, and its orientation is systematically controlled by adjusting the relative humidity, ultimately leading to fine-tuned hierarchical surface pattern with high degree of lateral order. As a simple example, the formation of hierarchical structure containing Au nanowire along the block copolymer domains on the dewetted films illustrates that our simple approach can offer great opportunity to generate true hierarchical, complex patterns.



INTRODUCTION

The self-assembly of block copolymer (BCP) has emerged as a simple yet powerful tool to generate well-defined, well-organized nanostructures that could be utilized in a variety of applications such as nanolithography and nanoscale device fabrication.[1−5] Various shapes including spheres, cylinders, gyroids, and lamellae are generated on the nanometer scale due to the connectivity between phase-separating blocks, and their characteristic size can easily be controlled by the molecular weight of BCPs. In thin films, the situation becomes more complicated due to additional parameters and constraints that should be taken into account to control their structure and final properties. Confinement effects and surface energetics with substrate and air surfaces can lead to the formation of BCP nanostructure different from that in the bulk system and can also affect the orientation of the microdomains with asymmetric shape such as cylinders and lamellae, producing different surface patterns in thin film despite of the same components and composition. Moreover, island and hole structure can be formed at the film surface when the film thickness is not commensurate with BCP periodicity in the case of parallel orientation of microdomains. Consequently, the ability to control their phase separation behavior and nanostructure in thin films should be highly demanded in order to meet the requirements for practical applications of BCP self-assembly.[6−19]

In thin film geometry, the destabilization of films is another important technical issue that should be carefully considered for pattern formation.[20−26] Under adequate condition, the local fluctuation of film thickness is developed, and the film is retracted from the substrate to create the fragmentation of continuous films into isolated droplets. Although there are exceptional cases where dewetting process can be a route to generate the regular pattern, in most cases, the film destabilization causes detrimental problems because practical applications require stable films with uniform thickness. In contrast to homopolymer films, BCP films are known to exhibit strong stability against dewetting over wide range of film thickness due to the wetting layer by preferential interaction and the internal order within the film by phase behavior.[27,28] Nonetheless, BCP films can become unstable and dewet from the substrate below critical film thickness. In dewetting case, rather interesting behavior may be observed due to two factors that have suppressed the destabilization in BCP films. Preferential interaction of block component with the substrate forces dewetting of BCP films to proceed in an autophobic way that is different from that in homopolymer films. On the other hand, the internal order in BCP films provides an opportunity to produce hierarchical structure because film dewetting generates the patterns on the micrometer length scale while BCP self-assembly produces well-defined structure on the nanometer scale. Consequently, dewetting of BCP films can produce the surface pattern with true hierarchical structure ranging from the micrometer to nanometer scale. In spite of such expectation, the results exhibiting the hierarchical structure established by destabilization and self-assembly of BCP films in the literature are rather rare. In many cases, the film instability of BCPs has been investigated in disordered state above the order−disorder transition (ODT).[29−33] As a result, large size of droplets have been formed after dewetting,

Received: August 27, 2011
Revised: January 4, 2012
Published: January 20, 2012

ACS Publications © 2012 American Chemical Society

but no lateral order resulting from BCP self-assembly has been observed. On the other hand, BCP order has been detected after film dewetting in very limited systems where grazing incidence small-angle X-ray scattering (GISAXS) or grazing incidence small-angle neutron scattering (GISANS) were used to examine the structure of dewetted films.[28,34,35] The scattering patterns revealed the internal structure of BCP films after dewetting, but weak signals indicated ill-defined nanostructure with poor order within dewetted droplets. In other approach reported recently, the substrate was prepatterned by combining lithographic methods with chemical modification of surface to guide the dewetting process of BCP films.[36] Dewetting was controlled to occur by following the surface pattern so that it produced highly ordered pattern in the dewetted film. However, the order by BCP self-assembly was still fully not developed in such case and controlling BCP self-assembly within dewetted patterns needs to be further improved in order to realize hierarchical structure ranging from nanometer to micrometer length scale.

In this work, it is demonstrated that ideal hierarchical pattern with highly ordered lateral order can be produced by combining the dewetting process with self-assembly of BCPs in their films. The dewetting behavior of BCP films with different thickness was systematically investigated where the dewetting was triggered by solvent vapor. The order and orientation of BCP microdomains within the patterns resulting from dewetting in thin films were manipulated to realize true hierarchical structure. Moreover, the complexation with inorganic salts was utilized together with dewetting behavior to deposit inorganic materials along dewetted pattern on the nanometer scale.

EXPERIMENTAL SECTION

Cylinder-forming polystyrene-*block*-poly(ethylene oxide) (PS-*b*-PEO) diblock copolymer with a molecular weight M_n = 25.3 kg/mol and a polydispersity M_w/M_n = 1.04 was purchased from Polymer Source, Inc. Benzene was used as a solvent without further purification. BCP films were deposited on Si wafers with a native oxide layer by spin-coating, and before use, the substrates were cleaned in a piranha solution (H_2SO_4/H_2O_2 = 3/7). Film thickness was controlled by solution concentration/spinning rate and measured by using a Filmetrics interferometer Model F20-UV.

Dewetting of BCP films in our work was induced by solvent annealing where the films were put in the chamber filled with solvent vapor. Relative humidity with the chamber was controlled during solvent annealing to see its effects. After solvent annealing, the films were taken out from the chamber and quenched quickly in the air. The surface structure of films was examined with tapping-mode atomic force microscopy (AFM, MultiMode V scanning probe microscope (Digital Instruments/Veeco)) and field emission scanning electron microscope (FESEM, Hitach S-4300). For resolution, BCP films were treated with oxygen plasma for 10 s before SEM observation.

For complexation with BCP, the gold precursor, $HAuCl_4{\cdot}3H_2O$, was purchased from Sigma-Aldrich and preloaded by dissolving in THF and adding to BCP solution. The precursor concentration was set to be 16:1 molar ratio of [PEO]/[Au]. Film formation and dewetting proceeded in the same way as before without gold precursor. After solvent annealing, BCP film complexed with gold precursor was exposed to oxygen plasma for about 20 s at 20 W and a pressure of 5×10^{-1} Torr to remove BCP films and reduce the gold ions.

RESULTS AND DISCUSSION

Solvent annealing, when applied for BCP thin films, has been shown to be able to improve the degree of lateral order of microdomains and to control their orientation.[8,37] On solvent annealing, the vapor molecules of solvent are absorbed into BCP films so that they impart BCP chains with sufficient mobility to repair the structural defects and improve the lateral order in thin films. In addition, solvent molecules can mediate the interactions at substrate interface, at air surface, and between block components, which enables to manipulate the microdomain orientation by appropriate choice of solvent. Such effects appear more prominent for BCPs with stronger segregation tendency such as polystyrene-*block*-poly(ethylene oxide) (PS-*b*-PEO) and polystyrene-*block*-poly(4-vinylpyridine) (PS-*b*-P4VP).

Figure 1a exhibits solvent annealing effects where cylinder-forming PS-*b*-PEO diblock copolymer film with 30 nm thick

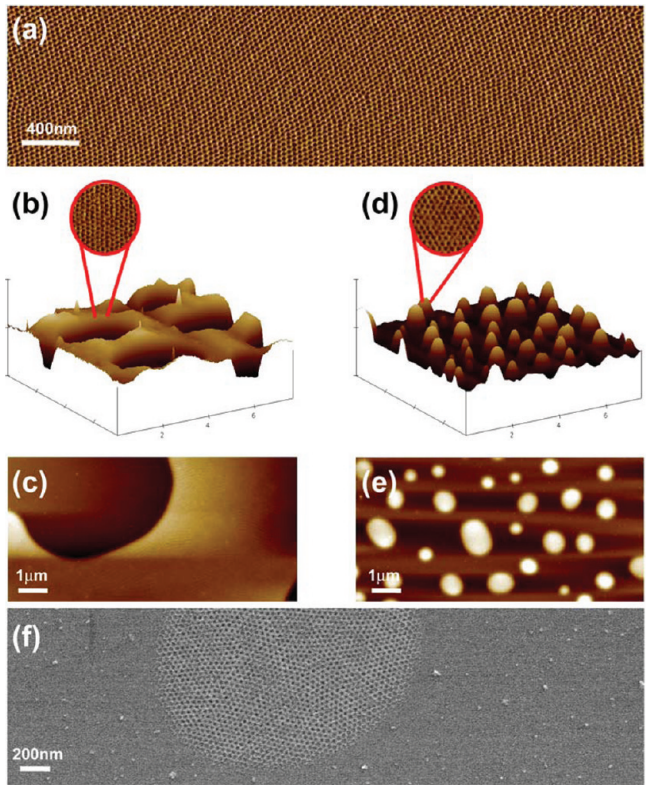


Figure 1. AFM height and SEM images of solvent-annealed PS-*b*-PEO films with different thickness: (a) 30, (b) 25, (c) 19, (d) 16, (e) and (f) 13 nm. All films were annealed under benzene vapor for 12 h at RH = 80%.

was annealed under benzene vapor for 12 h. Highly ordered array of PEO cylinders that are oriented perpendicular to the film surface is generated over large area, as seen in the previous work.[8] However, it should be borne in mind that solvent annealing can occasionally give rise to film instability, leading to catastrophic failure in controlling nanopatterns of BCP thin films. Under fully saturated vapor, copolymer films tend to be completely dewetted from the substrate and be left featureless and useless. The vapor pressure of solvents should be adjusted on annealing to prevent BCP films from dewetting and at the same time to provide sufficient chain mobility so that BCP films can take full advantage of solvent annealing. As a result, PS-*b*-PEO films thicker than 30 nm can remain stable during solvent annealing and finally produce highly ordered nanostructure after solvent annealing.

dx.doi.org/10.1021/ma2019655 | *Macromolecules* 2012, 45, 1492–1498

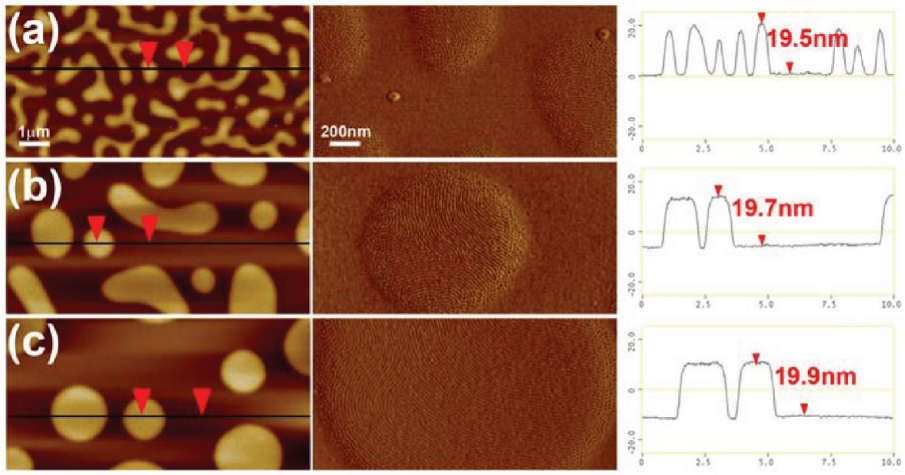


Figure 2. AFM height images and height profiles of 13 nm thick PS-*b*-PEO films annealed at RH = 43% and taken at different annealing times: (a) 30 min, (b) 1 h, and (c) 12 h. AFM images in the middle correspond to those scanned at higher magnification for PS-*b*-PEO film in the left, and each height profile corresponds to the line in the respective AFM image.

When film thickness decreases, however, BCP films suffer from instability and start to dewet from the substrate, as shown in Figure 1b–f. Figure 1b shows the surface morphology of 25 nm thick BCP film which was solvent-annealed for 12 h under the same conditions as in Figure 1a. It can be observed that BCP film destabilization is developed so that the dewetting proceeds in BCP films with thickness less than BCP periodicity. After solvent annealing, a number of holes are created at the film surface due to dewetting, and their diameter and depth are measured to be 2.7 ± 0.9 μm and 23.7 ± 2.3 nm, respectively. Closer examination of the remaining part of film reveals that highly ordered array of PEO microdomains are formed with orientation normal to the film surface, in spite of hole formation. Such highly ordered nanostructure in dewetted film is very exceptional and hard to be found in the literature. In most cases, no regular pattern or internal structure with poor order within dewetted film has been reported.[29−35] BCP film with 19 nm thickness exhibits the same hole structure, as shown in Figure 1c, except the size and number of holes in the film. With film thickness decreasing, the size of the holes increases while their number decreases. However, as thickness decreases further, dewetting in BCP films proceeds in a different way as can be seen in Figure 1d. This film with 16 nm thickness was solvent-annealed for 12 h under the same conditions, but in this case, island-like droplets with the micrometer length scale, instead of holes, are formed by dewetting during solvent annealing. In the island region, highly ordered arrays of PEO cylinders are observed while the self-assembled structure of BCP is not observed in the other region. The height of island is measured to be 28.6 ± 3.2 nm by AFM. Similar dewetting behavior is observed for thin film with thickness of 13 nm, as shown in Figure 1e. The SEM image in Figure 1f clearly shows that highly ordered PEO microdomains with perpendicular orientation are developed in the droplet region. Therefore, our results clearly indicate that dewetting process can be combined with BCP self-assembly to construct true hierarchical patterns ranging from nanometer to micrometer scales.

The orientation of PEO cylinders can be controlled by the relative humidity (RH) inside chamber during solvent annealing. When BCP film is annealed at RH less than about 60%, the orientation of PEO cylinders changes into the direction parallel to the film surface. (See Figure S1 in the Supporting Information.) This behavior can be explained by detailed balance of interaction energies between components at the interfaces. Benzene used for solvent annealing, although dissolving well both PS and PEO blocks, is a solvent slightly selective for PS blocks. Moreover, PS blocks have lower surface tension than PEO blocks and so exhibit tendency to be segregated to the films surface. However, under humid conditions, water molecules, good solvent for minor PEO component, are introduced together with benzene vapor to balance the surface interactions of PS and PEO components, which results in the neutral condition for both blocks and thus the perpendicular orientation of PEO microdomains. This balance for neutral condition will be broken at relatively low RH to produce preferential interaction at the interface, and consequently, the orientation of PEO cylinders changes from perpendicular to parallel. The same experiments were conducted on the substrate coated with hexamethyldisilazane (HMDS) which induced change in the substrate property from hydrophilic to hydrophobic. In spite of surface modification, PEO cylinders in the film are still oriented normal to the surface at high RH while parallel to the surface at lower RH, as seen in Figure S2 of the Supporting Information. These results support the explanation for the importance of balance of surface energy in controlling the microdomain orientation during solvent annealing. The same RH effects are observed in the dewetted PS-*b*-PEO films. PEO cylinders are found to be oriented parallel to the surface in the remaining part of dewetted films with hole or island patterns when annealed at RH below 60%. (See Figures 2 and 4.) It can be concluded that, in addition to the formation of hierarchical structure, the microstructure within the dewetted region can be adequately fine-tuned in dewetting process.

It may be possible that the mismatch between the film thickness and BCP periodicity causes the formation of hole or island patterns in thin film. The incommensurability of the film thickness will bring about large entropic penalty due to chain extension or contraction for compensation of mismatch between the thickness and natural periodicity and can ultimately force BCP films to be destabilized, producing holes or islands depending on the film thickness. However, such

dx.doi.org/10.1021/ma2019655 | *Macromolecules* 2012, 45, 1492−1498

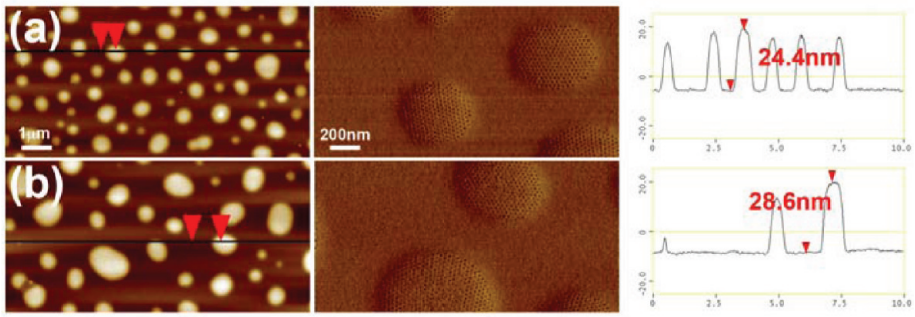


Figure 3. AFM height images and height profiles of 13 nm thick PS-*b*-PEO films annealed at RH = 80% and taken at different annealing times: (a) 30 min and (b) 12 h. AFM images in the middle correspond to those scanned at higher magnification for PS-*b*-PEO film in the left, and each height profile corresponds to the line in the respective AFM image.

behavior is usually observed in parallel orientation not perpendicular one. In the case of perpendicular orientation, the mismatch of the film thickness with the natural periodicity of BCPs is not a problem so serious as to cause the film destabilization. Therefore, the fact that the dewetting and the formation of holes or islands were observed irrespective of microdomain orientation in our work suggests that the hole or island formation is caused by different contribution from the incommensurability of thickness. On the other hand, it has been very recently reported that the asymmetry in chain dynamics due to crystallization of one component in BCP induce dewetting of the films to produce hierarchical structure.[38] In this case, the hybrid annealing that corresponds to sequential combination of thermal and solvent annealing and the presence of both components of BCP are the prerequisites for the formation of various hierarchical patterns. However, in our case, PEO blocks do not crystallize in thin films, which was confirmed by GIWAXD and DSC data.[40] This suggests that dewetting/crystallization is not the mechanism possible for production of hierarchical morphologies in our work. Several mechanisms for formation of hierarchical meso/nanoscale morphologies in polymer thin films including dewetting were discussed in the recent review paper.[39] Detailed information and related references can be found there.

The dewetting process in BCP films has been monitored as a function of time during solvent annealing, and the results are presented in Figure 2. The film with thickness of 13 nm was solvent-annealed at 43% RH, in which case island structure with parallel orientation was created after solvent annealing. As seen in Figure 2, the islands with nonspherical shape are produced at very early time of solvent annealing, but the pattern eventually evolves to form spherical islands, suggesting that BCP film dewet via the spinodal dewetting mechanism. Magnified images clearly show that highly ordered PEO cylinders with parallel orientation are produced in the island regions. In the boundary region of islands, the dot patterns, instead of lying-down cylinders, are observed due to abrupt change of film thickness, and hence the incommensurability with BCP periodicity that may lead to orientation changes of PEO cylinders or order−order transition of BCPs from cylinders to sphere.[41] On the other hand, the island height exhibits little change over the annealing time although its diameter continues to increase, as seen in the height profiles of islands obtained from AFM images. In the parallel orientation, it is important to match the film thickness with the periodicity of BCP; otherwise, BCP chains might be subject to severe entropic penalty by chain expansion or compression in the process of trying to match with film thickness. As a result, the height of islands formed at early time of dewetting remains almost constant during solvent annealing, and most of the region of isolated pattern is flat except the boundary region. In this work, it appears more appropriate to express those structures as islands rather than as droplets at the final stage of dewetting.

The results for BCP films with the same thickness but annealed at higher RH are presented in Figure 3 where a number of islands are observed to be produced during dewetting. In this case, PEO cylinders with high degree of lateral order are oriented normal to the surface in the island region. In contrast to parallel orientation, the islands that have the microdomains oriented normal to the surface show height variation with time as seen in the section analysis of Figure 3. This can be expected since there are no constraints on thickness variation in the island regions during dewetting for perpendicular orientation. Without such constraints, BCP molecules are much freer to move and dewet from the substrate. As a result, the height of islands is higher than that with parallel orientation, and their shape is even closer to droplets. Moreover, the dewetting rate seems to be faster in the perpendicular orientation, and such spinodal-like patterns as seen in Figure 2a cannot be observed even at very early annealing time. The variation of diameter and height of droplets with time is presented in Figure S4 of the Supporting Information.

Figure 4 includes AFM height images taken at different annealing times for BCP films with 22 nm thickness where the holes are produced via destabilization process. For comparison, the corresponding phase images taken at low magnification are included in Figure S5 of the Supporting Information. Here, the dewetting seems to follow the nucleation and growth dewetting mechanism. The holes form and grow with time, but their growth stops after some annealing time. Neither formation of networks of the holes nor eventual evolvement to the isolated droplets is observed. The results for longer annealing times are included in Figure S3 of the Supporting Information where the films were annealed for 18 and 100 h, respectively. Even after 100 h, the holes are still observed, and their size shows little change over annealing time. As in the case of thin films seen in Figures 2 and 3, the dewetting in the film with perpendicular orientation of microdomains (Figure 4c,d) is faster than with parallel orientation (Figure 4a,b). The holes in the films with parallel orientation exhibit no appreciable increase in their depth after formation of holes at short annealing time while small yet continuous increase in the hole depth is observed in the film with perpendicular orientation up to 12 h, and then

dx.doi.org/10.1021/ma2019655 | *Macromolecules* 2012, 45, 1492−1498

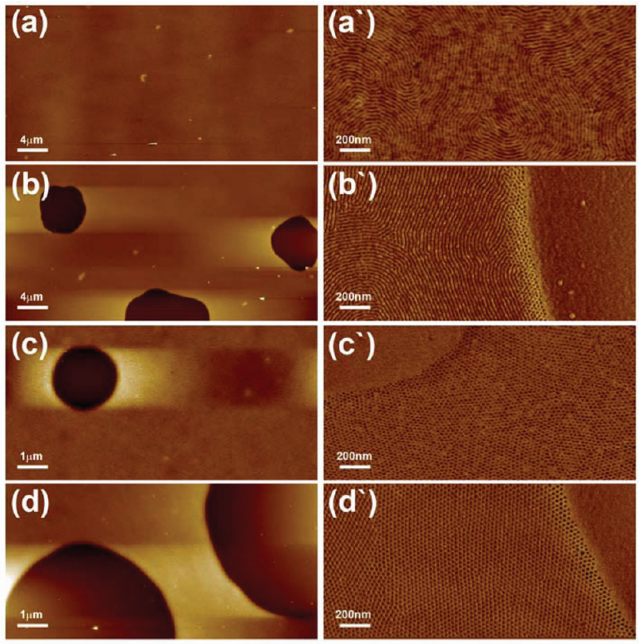


Figure 4. AFM height images of 22 nm thick PS-*b*-PEO films annealed at RH = 43% (a, b) and 80% (c, d) after annealing times of 30 min (a, c) and 12 h (b, d). AFM images in the right (a′–d′) correspond to those scanned at higher magnification for PS-*b*-PEO film in the left (a–d).

there is little change in the depth of the holes for longer annealing time. Consequently, the holes in BCP films with perpendicular orientation are wider and deeper than those with parallel orientation. Such difference results from the quantization of the film thickness due to matching with chain dimension in the case of parallel orientation.

The stability of thin polymer films is theoretically characterized by the effective interface potential that corresponds to the excess free energy per unit area required to bring two interfaces from infinity to a certain distance. It consists of two major contributions: one from strong, short-range interaction and the other from weak but long-range interaction. Short-range interaction is phenomenologically treated by the spreading coefficient that is determined by the interfacial tensions between components and substrate. Long-range interaction can be described by the van der Waals interaction, the strength of which is parametrized by the Hamaker constant. The interplay of short- and long-range interactions determines the shape of the effective interface potential as a function of film thickness and utimately the dewetting process and its mechanism. The films are stable when both short- and long-range interactions are repulsive, but in the other cases, they become unstable and dewet. For PS-*b*-PEO BCP, the effects of long-range interaction cannot be precisely determined since the Hamaker constant may be positive or negative depending on what data for the interfacial tension of copolymer components will be chosen in the literature.[36] On the other hand, short-range interaction becomes dominant as the film thickness decreases. Moreover, on solvent annealing, the short-range interaction is main factor in the film destabilization while the long-range interaction causes the film dewetting on thermal annealing.[25] In our work, no dewetting was observed to occur in PS-*b*-PEO BCP films even with thickness less than 30 nm when thermally annealed at 140 °C. The result indicates that the contribution of long-range interactions to the BCP dewetting is negligibly small. Dense packing of polymer chains at the substrate surface is also known to be able to bring about the film destabilization that is called as autophobic dewetting. Dense brush layer formed at substrate surface prevents chain molecules from penetrating into that layer, which leads to the formation of new interface between the brush layer and upper part of the film. The entropic barrier established at new interface induces the destabilization of the film, and as a result, droplets formed by dewetting reside on the remaining brush layer. In order to check whether our BCP films have such brush layer at the substrate, the region near the boundary of holes or droplets was scratched out by razor blade and the images were taken by the AFM. As shown in Figure 5, the films are not completely dewetted, but a very thin flat layer is present without any surface feature, which means that the holes or droplets are sitting on very thin brush-like layer. In both cases of holes and droplets, the thickness of such thin layer is estimated to be about 10.5 ± 0.8 nm, which exactly corresponds to half-period of characteristic length of BCPs. This layer is believed to naturally form at the substrate due to selective interaction between PEO blocks and substrate, and consequently, the dewetting of BCPs during solvent annealing proceeds in a self-phobic way, as in the case of other BCP

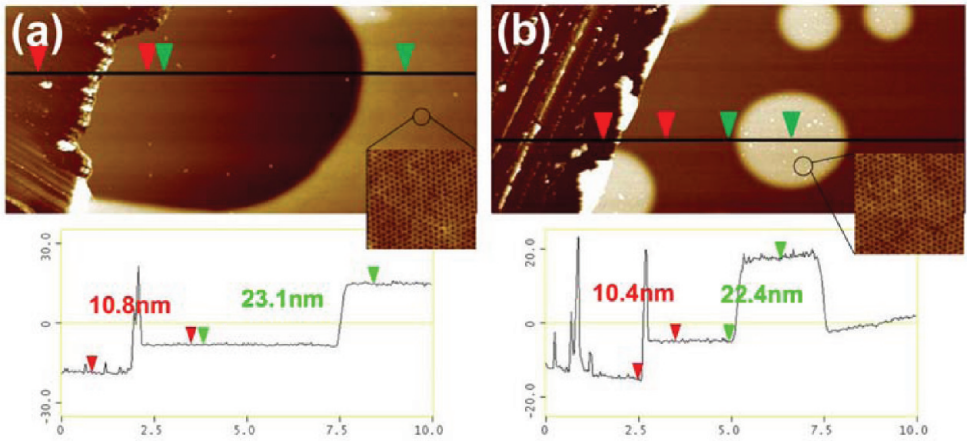


Figure 5. AFM height images and height profiles of PS-*b*-PEO films with the thickness of (a) 22 nm (a) and (b) 13 nm. The films were annealed at RH = 80%, and the height profiles correspond to the line in the AFM images. The insets are magnified images of selected regions.

dx.doi.org/10.1021/ma2019655 | *Macromolecules* 2012, 45, 1492–1498

systems presented previously. Contrary to the previous works, however, our BCP films exhibit highly ordered regular pattern on the nanometer scale within the remaining regions of the films that have been formed on the micrometer length scale via dewetting process during solvent annealing. Ultimately, well-organized hierarchical structure with high degree of lateral order which has hardly been observed before is produced in a very simple way. If the lithography techniques such as photolithography, e-beam lithography, and soft lithography could be employed to direct the dewetting process in very controlled manner, then highly ordered, well-controlled structure with hierarchical order would be obtained by combining with BCP self-assembly. We have already witnessed such possibility in a couple of remarkable examples in the literature.[36,41,42] Therefore, our ability to control the nanopatterns in dewetting process offers great opportunity to generate well-organized multifunctional nanostructure with hierarchical order.

As a simple illustrative example of practical applications, the formation of metallic nanowires on the dewetted film was demonstrated, as shown in Figure 6. BCPs are well-known to

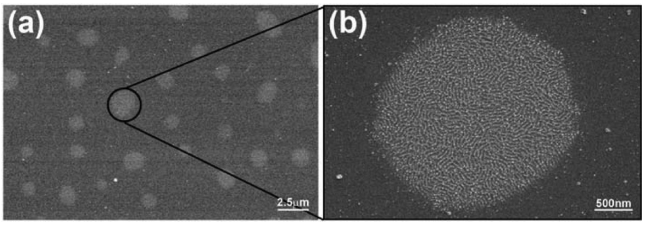


Figure 6. SEM images for Au nanowires generated by complexation with 13 nm thick PS-*b*-PEO film. The film was annealed at RH = 43% and then treated by O_2 plasma. (b) A magnified image of selected region in (a).

be able to act as a template for nanowire formation through selective interaction,[43] and in this work, PEO block was selectively complexed with $HAuCl_4$ in solution. PS-*b*-PEO complexed with gold precursor was deposited on the substrate and solvent-annealed at low humidity in the same way as described above. Finally, oxygen plasma was used to remove the BCP films and at the same time reduce the gold precursor to Au. As seen in Figure 6b, Au nanowires were generated along the PEO domains within the remaining BCP film after dewetting. The low-magnification image in Figure 6a exhibits that the Au nanowires are produced on the local area along the dewetted pattern, not on the entire substrate. These results indicate that the fabrication of functional nanostructures with hierarchical order is possible simply in terms of dewetting process of BCP films.

■ CONCLUSIONS

In this work, we demonstrate that the dewetting process of BCP films can be combined with BCP self-assembly to offer great opportunity for forming highly organized structure with hierarchical order. Controlling the film thickness and vapor pressure during solvent annealing enables to determine the hole or droplet patterns on the micrometer scale while the order and orientation of copolymer microdomains within the film can be controlled on the nanometer scale by adjusting the RH and vapor pressure on solvent annealing. As a result, fine-tuned surface patterns with highly ordered internal structure are produced that exhibit hierarchical order ranging from nanometer to micrometer scales. Such hierarchical structure looks very naive and simple compared to that observable in nature system. However, as already seen in several examples in the literature, combining with other techniques to control the structure can offer opportunity to generate more complicated hierarchical structure than can be very useful in wide range of applications. Our very simple yet robust route can be the first step toward such goals.

■ ASSOCIATED CONTENT

Supporting Information

Figure S1: AFM phase image of PS-*b*-PEO BCP film solvent-annealed at lower RH; Figure S2: AFM phase images of solvent-annealed PS-*b*-PEO films on HDMS-coated substrate; Figure S3: AFM height images showing BCP films solvent-annealed at longer times; Figure S4: diameter and height of droplets formed by dewetting in 13 nm thick film as a function of annealing time; Figure S5: AFM phase images of dewetted PS-*b*-PEO films with parallel and perpendicular orientations taken at low magnification. This material is available free of charge via the Internet at http://pubs.acs.org.

■ AUTHOR INFORMATION

Corresponding Author

*Tel +82-32-860-7493, fax +82-32-873-0181, e-mail shk@inha.ac.kr.

■ ACKNOWLEDGMENTS

This work was financially supported by the National Research Foundation of Korea (NRF) grant (No. 2010-0015541) funded by the Ministry of Education, Science and Technology (MEST).

■ REFERENCES

(1) Park, C.; Yoon, J.; Thomas, E. L. *Polymer* **2003**, *44*, 6725−6760.
(2) Hawker, C. J.; Russell, T. P. *MRS Bull.* **2005**, *30*, 952−966.
(3) Stoykovich, M. P.; Nealey, P. F. *Mater. Today* **2006**, *9*, 20−29.
(4) Darling, S. B. *Prog. Polym. Sci.* **2007**, *32*, 1152−1204.
(5) Kim, H. C.; Park, S. M.; Hinsberg, W. D. *Chem. Rev.* **2010**, *110*, 146−177.
(6) Ryu, D. Y.; Shin, K.; Drockenmuller, E.; Hawker, C. J.; Russell, T. P. *Science* **2005**, *308*, 236−239.
(7) Thurn-Albrecht, T.; Schotter, J.; Kastle, G. A.; Emley, N.; Shibauchi, T.; Krusin-Elbaum, L.; Guarini, K.; Black, C. T.; Tuominen, M. T.; Russell, T. P. *Science* **2000**, *290*, 2126−2129.
(8) Kim, S. H.; Misner, M. J.; Xu, T.; Kimura, M.; Russell, T. P. *Adv. Mater.* **2004**, *16*, 226−231.
(9) Angelescu, D. E.; Waller, J. H.; Adamson, D. H.; Deshpande, P.; Chou, S. Y.; Register, R. A.; Chaikin, P. M. *Adv. Mater.* **2004**, *16*, 1736−1740.
(10) Kimura, M.; Misner, M. J.; Xu, T.; Kim, S. H.; Russell, T. P. *Langmuir* **2003**, *19*, 9910−9913.
(11) Sundrani, D.; Darling, S. B.; Sibener, S. J. *Nano Lett.* **2004**, *4*, 273−276.
(12) Stoykovich, M. P.; Müller, M.; Kim, S. O.; Solak, H. H.; Edwards, E. W.; De Pablo, J. J.; Nealey, P. F. *Science* **2005**, *308*, 1442−1446.
(13) Ruiz, R.; Kang, H.; Detcheverry, F. A.; Dobisz, E.; Kercher, D. S.; Albrecht, T. R.; De Pablo, J. J.; Nealey, P. F. *Science* **2008**, *321*, 936−939.
(14) Bita, I.; Yang, J. K. W.; Yeon, S. J.; Ross, C. A.; Thomas, E. L.; Berggren, K. K. *Science* **2008**, *321*, 939−943.
(15) Li, H. W.; Huck, W. T. S. *Nano Lett.* **2004**, *4*, 1633−1636.

(16) Tang, C.; Tracz, A.; Kruk, M.; Zhang, R.; Smilgies, D. M.; Matyjaszewski, K.; Kowalewski, T. *J. Am. Chem. Soc.* **2005**, *127*, 6918−6919.
(17) Park, S.; Dong, H. L.; Xu, J.; Kim, B.; Sung, W. H.; Jeong, U.; Xu, T.; Russell, T. P. *Science* **2009**, *323*, 1030−1033.
(18) Tada, Y.; Akasaka, S.; Yoshida, H.; Hasegawa, H.; Dobisz, E.; Kercher, D.; Takenaka, M. *Macromolecules* **2008**, *41*, 9267−9276.
(19) Tang, C.; Lennon, E. M.; Fredrickson, G. H.; Kramer, E. J.; Hawker, C. J. *Science* **2008**, *322*, 429−432.
(20) Seemann, R.; Herminghaus, S.; Jacobs, K. *Phys. Rev. Lett.* **2001**, *86*, 5534−5537.
(21) Xue, L.; Han, Y. *Prog. Polym. Sci.* **2011**, *36*, 269−293.
(22) Sharma, A. *Langmuir* **1993**, *9*, 861−869.
(23) Reiter, G.; Sharma, A.; Casoli, A.; David, M. O.; Khanna, R.; Auroy, P. *Langmuir* **1999**, *15*, 2551−2558.
(24) Wyart, F. B.; Martin, P.; Redon, C. *Langmuir* **1993**, *9*, 3682−3690.
(25) Lee, S. H.; Yoo, P. J.; Kwon, S. J.; Lee, H. H. *J. Chem. Phys.* **2004**, *121*, 4346−4351.
(26) Liu, Y.; Rafailovich, M. H.; Sokolov, J.; Schwarz, S. A.; Zhong, X.; Eisenberg, A.; Kramer, E. J.; Sauer, B. B.; Satija, S. *Phys. Rev. Lett.* **1994**, *73*, 440−443.
(27) Müller-Buschbaum, P. *J. Phys.: Condens. Matter* **2003**, *15*, R1549−R1582.
(28) Müller-Buschbaum, P.; Gutmann, J. S.; Lorenz-Haas, C.; Wunnicke, O.; Stamm, M.; Petry, W. *Macromolecules* **2002**, *35*, 2017−2023.
(29) Limary, R.; Green, P. F. *Macromolecules* **1999**, *32*, 8167−8172.
(30) Limary, R.; Green, P. F. *Langmuir* **1999**, *15*, 5617−5622.
(31) Masson, J. L.; Limary, R.; Green, P. F. *J. Chem. Phys.* **2001**, *114*, 10963−10967.
(32) Green, P. F. *J. Polym. Sci., Part B: Polym. Phys.* **2003**, *41*, 2219−2235.
(33) Peng, J.; Xuan, Y.; Wang, H.; Li, B.; Han, Y. *Polymer* **2005**, *46*, 5767−5772.
(34) Müller-Buschbaum, P.; Bauer, E.; Wunnicke, O.; Stamm, M. *J. Phys.: Condens. Matter* **2005**, *17*, S363−S386.
(35) Sun, Y. S.; Chien, S. W.; Liou, J. Y.; Su, C. H.; Liao, K. F. *Polymer* **2011**, *52*, 1180−1190.
(36) Baralia, G. G.; Filiâtre, C.; Nysten, B.; Jonas, A. M. *Adv. Mater.* **2007**, *19*, 4453−4459.
(37) Park, S.; Kim, B.; Xu, J.; Hofmann, T.; Ocko, B. M.; Russell, T. P. *Macromolecules* **2009**, *42*, 1278−1284.
(38) Ramanathan, M.; Darling, S. B. *Soft Matter* **2009**, *5*, 4665−4671.
(39) Ramanathan, M.; Darling, S. B. *Prog. Polym. Sci.* **2011**, *36*, 793−812.
(40) Lee, J. W.; Lee., C.; Choi, S. Y.; Kim, S. H. *Macromolecules* **2010**, *43*, 442−447.
(41) Kim, T. H.; Hwang, J.; Hwang, W. S.; Huh, J.; Kim, H. C.; Kim, S. H.; Hong, J. M.; Thomas, E. L.; Park, C. *Adv. Mater.* **2008**, *20*, 522−527.
(42) Han, W.; Byun, M.; Zhao, L.; Rzayev, J.; Lin, Z. *J. Mater. Chem.* **2011**, *21*, 14248−14253.
(43) Chai, J.; Buriak, J. M. *ACS Nano* **2008**, *2*, 489−501.

Macromolecules

Article

pubs.acs.org/Macromolecules

Rationalizing Phase Transitions with Thermal Annealing Temperatures for P3HT:PCBM Organic Photovoltaic Devices

Andrew J. Pearson,* Tao Wang, Richard A. L. Jones, and David G. Lidzey*

Department of Physics and Astronomy, The University of Sheffield, Hicks Building, Hounsfield Road, Sheffield, S3 7RH, U.K.

Paul A. Staniec

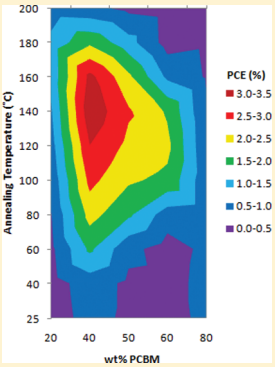
Diamond Light Source, Harwell Science & Technology Campus, Didcot Oxfordshire, OX11 0DE, U.K.

Paul E. Hopkinson and Athene M. Donald

Department of Physics, Cavendish Laboratory, University of Cambridge, JJ Thomson Avenue Cambridge, CB3 0HE, U.K.

Supporting Information

ABSTRACT: We have studied a range of organic photovoltaic devices (OPVs) based on a thin-film blend of P3HT and PCBM and show that, by comparing device studies with a characterization of the thermal transitions of the blend, we can provide a mechanistic description of the optimum annealing temperatures necessary to improve the operational efficiency of a device. For as-cast P3HT:PCBM blend thin-films we evidence two glass transition temperatures corresponding to the existence of two compositionally different amorphous states; an observation that is unreported to date. We demonstrate that an improvement in device efficiency only occurs once the film has been heated above the upper apparent glass transition temperature of the blend. If annealing is performed above the optimum temperature, excessive phase-separation and a partial reduction in film optical density leads to a general decrease in device efficiency. Both of these characteristic temperatures are dependent upon the composition of the blend. The temperature-dependent competition between such processes therefore opens a "window" within which device efficiency can be optimized and provides an opportunity to design effective annealing protocols for future polymer:fullerene blend OPVs.



INTRODUCTION

Organic photovoltaics (OPVs) are an emerging technology for renewable energy generation.[1] Such devices can be manufactured at low-cost using processes suitable for large-area deposition.[2] OPVs may also find application in niche applications where, as an example, mechanical flexibility is required.[3] Recent attention has focused on synthesizing new materials[4,5] and designing manufacturing processes[2,6] that lead to the production of efficient and stable devices. To date, the most efficient OPVs have been based on a bulk-heterojunction architecture, with power conversion efficiencies (PCEs) approaching 8% reported for low-bandgap benzodithiophene copolymer: functionalized fullerene blends.[7]

Many groups have explored the fabrication of OPVs based on a blend of the polymer poly(3-hexylthiophene) (P3HT) with the electron acceptor (6,6)-phenyl C61-butyric acid methyl ester (PCBM). While the PCE of this system is limited to between 4 and 5%[8,9] it provides a model system to probe the relations between material structure and device physics in OPVs. In particular, previous studies have focused on the effects of postdeposition treatments on photovoltaic properties.[10−12] These treatments can modify the structure of the films[13,14] permitting processes such as optical-absorption, charge-carrier generation, transport and collection to be optimized.[15] A number of studies have now shown that by thermally annealing a P3HT:PCBM device at a temperature of between 120 and 150 °C for a duration of between 10 and 120 min, device efficiency can be optimized.[8,9,16,17] Variations in material properties and device processing history provide some explanation for the range of reported temperature and time combinations. Nevertheless, a purely empirical approach to device optimization cannot provide a full understanding of this processing step, nor provide a framework in which to design annealing protocols for new blend materials.

We have recently studied the thermal transitions of P3HT:PCBM blend films using dynamic mechanical thermal analysis (DMTA).[18] Our work complements similar studies on the same system performed using different analytical techniques[19,20] with the advantage that the samples used for analysis are prepared in a manner with a greater similarity to OPV devices. In a DMTA experiment, thermal transitions are identified by peaks in a plot of tan δ vs temperature.[18] We

Received: September 9, 2011
Revised: December 9, 2011
Published: January 24, 2012

 © 2012 American Chemical Society dx.doi.org/10.1021/ma202063k | Macromolecules 2012, 45, 1499−1508

monitored the blends during the first heating cycle—thus exploring the properties of the blends during a heating process that is representative of the thermal annealing protocol used to process devices. We showed that the glass transition temperature (T_g) of the P3HT phase within the blend films increased with increasing weight fraction of PCBM (wt %), until the PCBM underwent partial phase separation in the as-cast film. Beyond this threshold concentration (which we measured at 66 wt % PCBM), a relative reduction in the T_g of the P3HT phase suggested a reduced concentration of PCBM mixed within the polymer phase.

In this paper, we apply the findings of our DMTA study to the thermal annealing protocol used to optimize the efficiency of OPVs, and characterize the properties of P3HT:PCBM blend thin-films and OPVs that have undergone a number of annealing conditions. A key technique that we use is spectroscopic ellipsometry (SE) which is used to characterize the thermal transitions of thin-film P3HT:PCBM blends by monitoring their expansion and contraction as they are heated. We confirm that the T_g of P3HT containing phases within the blend thin-films increases as the relative fraction of PCBM in the blend is increased from 20 to 60 wt %. A relative decrease is observed in T_g in a blend thin-film containing a PCBM loading of 80 wt %. We also show that for some blend compositions, two T_g transitions can be detected; an observation that is as yet unreported to date. We find that the higher temperature T_g defines the minimum annealing temperature for an OPV for which an improvement in device efficiency can occur. We show that by annealing a film above this temperature, residual casting solvent is removed, and the film is driven by phase separation between P3HT and PCBM into a nanoscale morphology that is more favorable for efficient device operation. Annealing at temperatures in excess of optimal processing conditions however results in both excessive phase separation of PCBM and a relative blue shift in the optical density of the film, limiting its ability to efficiently harvest light and transport charge. This optimum annealing temperature is dependent on the composition of the thin-film blend and decreases with increasing wt % of PCBM. We are therefore able to understand the origin of the process "window" over which thermal annealing has a beneficial effect on device efficiency. Such understanding will be of clear benefit in designing processing routes for new polymer:fullerene OPV systems.

RESULTS AND DISCUSSION

We first revisit the effects of thermal annealing on the power conversion efficiency (PCE) of a P3HT:PCBM device. Although it has been previously shown that the film composition range yielding the best devices utilizing this blend system is between 40 and 50 wt % PCBM[8,9] it is instructive to probe a broader region of parameter space to give greater insight into the thermal response of the blend thin-films. In Figure 1a, we present the measured PCE of devices having a PCBM content between 40 and 60 wt % as a function of annealing temperature. The PCE of devices containing 20 wt % and 80 wt % PCBM are shown in Figure 1b. Device metrics and external quantum efficiency spectra are provided in the Supporting Information, Figures S1 and S2.

In Figure 1a, we again demonstrate the significant improvements in device efficiency that can result from thermal annealing.[8,21] We find that power conversion efficiencies (PCEs) can be improved from less than 1% for all blend ratios, to up to 3.4% in a device containing a blend composed

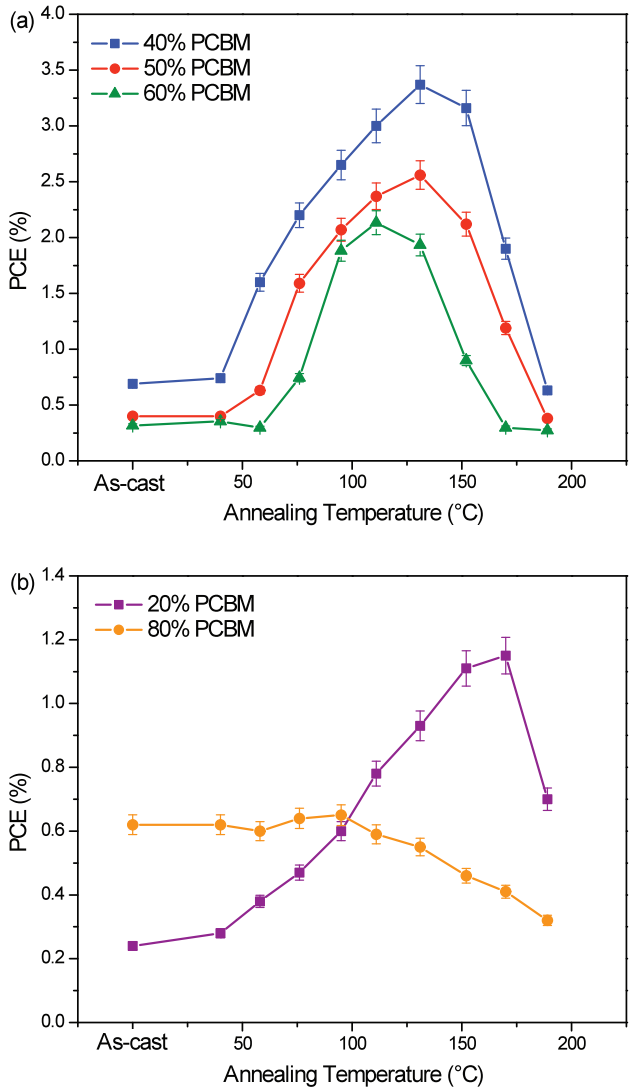


Figure 1. Power conversion efficiency (PCE) values for P3HT:PCBM blend devices as a function of annealing temperature. Data for devices having between 40 and 60 wt % PCBM in the active layer are shown in part a, while part b shows data for devices with 20 wt % and 80 wt % PCBM. Lines are provided as a guide only.

of 60:40 wt % P3HT:PCBM. The driving force for the improvements in device PCE come principally from changes in the short-circuit current density (J_{SC}), which can be seen from Figure S1, Supporting Information. We observe that the J_{sc} of each device blend composition qualitatively follows the same trend with annealing temperature as the PCE, increasing and then decreasing at temperatures that are apparently characteristic of the blend composition. We quantify this by defining T_{onset} as the temperature beyond which device efficiency is improved compared to an equivalent unannealed control. We find that T_{onset} increases from 45 ± 5 °C in devices with a film composition of 40 wt % PCBM, to 70 ± 5 °C in devices containing 60 wt % PCBM. At temperatures beyond T_{onset}, the PCE further increases, reaching an optimum value at a temperature we define as $T_{optimum}$. When annealed at a temperature above $T_{optimum}$ the PCE of devices is seen to decrease. We find that $T_{optimum}$ is also dependent on relative film composition, reducing from 130 ± 5 °C in a 40 wt % PCBM film to 110 ± 5 °C in film containing 60 wt % PCBM. Films

dx.doi.org/10.1021/ma202063k | Macromolecules 2012, 45, 1499–1508

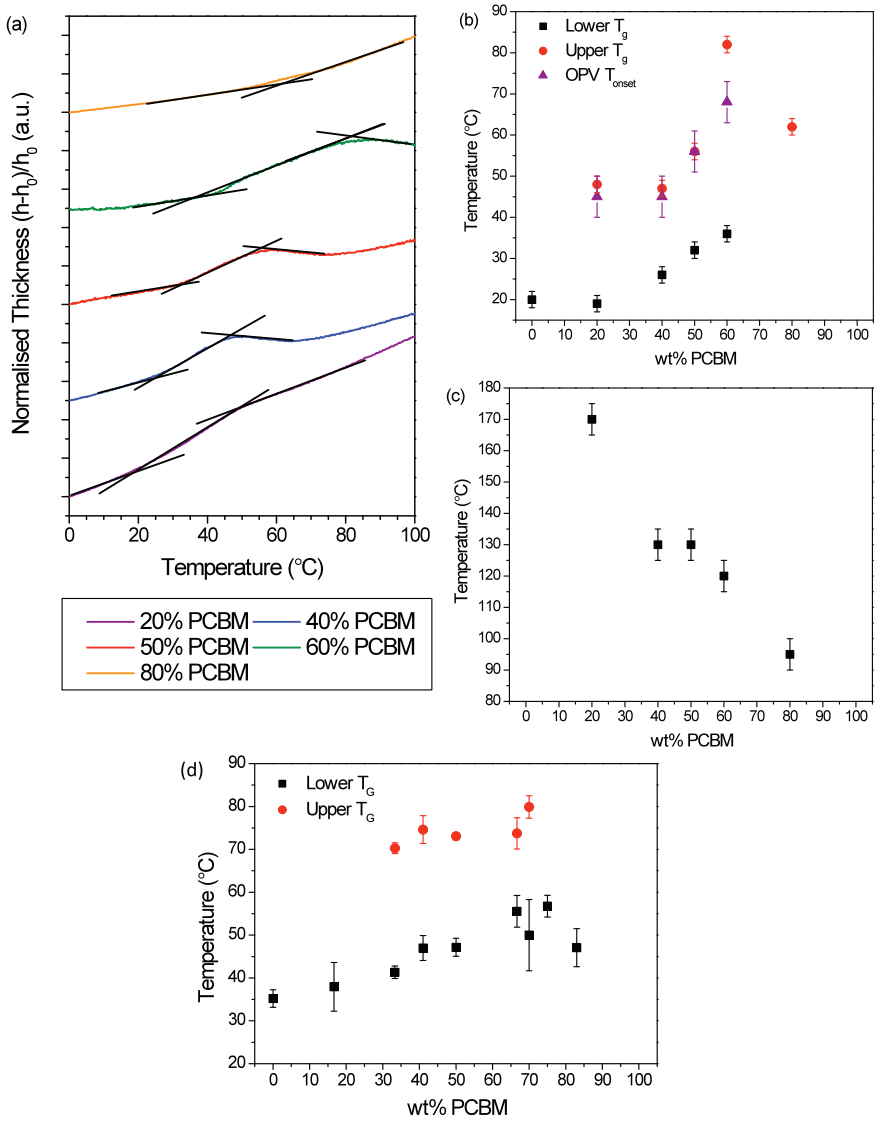


Figure 2. (a) Normalized thicknesses of P3HT:PCBM (wt %) thin films as a function of temperature during the first heating cycle. Data is offset for clarity. For each sample we fit a number of straight lines to the temperature-dependent expansion of the sample, with the intersection of such lines marking the apparent glass transitions of the blend. (b) Onset annealing temperature for PCE improvement in P3HT:PCBM OPVs as a function of the active layer composition, plotted alongside the T_g values extracted from part a. Optimum annealing temperatures for P3HT:PCBM OPVs as a function of the composition of the active layer composition are plotted in part c. T_g values for samples measured by DMTA are presented in part d.

containing a higher PCBM loading undergo a larger reduction in PCE when annealed at a temperature above $T_{optimum}$. For example, devices containing 40%, 50%, and 60% (wt %) PCBM within the active layer that have been annealed at 40 °C above $T_{optimum}$ have an efficiency that is 57, 47 and 42% of the efficiency of a device annealed at $T_{optimum}$.

In Figure 1b, we present a plot of the efficiency of devices having either a high or a low fraction of PCBM in its active layer. In both cases, we find that the PCE of the devices are low, with devices containing 20 wt % PCBM having a maximum efficiency of ~1.2%. The origin of such low efficiency is well understood,[22,23] as films composed predominantly of P3HT have favorable absorption characteristics, however exciton dissociation and extraction of electrons is inefficient due to an insufficient concentration of PCBM acceptor molecules. At high PCBM concentration however, the transport and extraction of holes becomes problematic together with a reduced absorption overlap of the active layer with the solar spectrum.[24]

For devices containing either 20% or 80 wt % PCBM, we see a change in device PCE on thermal annealing; for 20 wt % PCBM loading, we find values of T_{onset} and $T_{optimum}$ to be 50 ± 5 °C and 170 ± 5 °C respectively. When the device contains 80 wt % PCBM there is a negligible benefit from the thermal annealing process. Indeed, beyond approximately 105 °C the treatment becomes detrimental, with a monotonic decrease in PCE as the annealing temperature is increased.

From Figure S1, Supporting Information, it can also be seen that the fill-factor (*FF*) of the annealed devices is also improved by a factor of up to 2 times compared to that of the equivalent controls. We find that devices containing a high or a low fraction of PCBM undergo a smaller relative improvement compared to devices having a PCBM loading between 40 and 60 wt %. The relative magnitude of the *FF* provides an approximate measure of the relative balance between electron

dx.doi.org/10.1021/ma202063k | *Macromolecules* 2012, 45, 1499–1508

and hole mobilities,[9] with smaller *FF* indicating imbalanced charge-carrier mobility. Indeed, a number of studies have suggested that a *FF* less than ~42% indicates that charge-extraction is limited by space-charge.[25,26] The data in Figure S1 (Supporting Information) shows that for blend devices containing 20 wt % and 80 wt % PCBM, the *FF* never exceeds 37%, suggesting that such devices have highly imbalanced charge-carrier mobility.

To summarize; parts a and b of Figure 1 demonstrate that a clear composition-dependent annealing range exists. The onset temperature for improved device efficiency (T_{onset}) increases with increasing PCBM wt %, while the optimum annealing temperature ($T_{optimum}$) decreases with increasing PCBM wt %,. The effect of these two processes means that the annealing window for improving device PCE narrows with increasing PCBM wt %. Indeed, for devices containing the highest wt % of PCBM, thermal annealing is detrimental to device efficiency. We proceed to rationalize these findings on the basis of the various thermal transitions (including the apparent glass-transition temperature [T_g]) and properties of the active layer materials.

Our DMTA studies[18] indicate that when P3HT is blended with PCBM, the T_g of P3HT containing phases increase due to increased cohesive interactions between the P3HT and PCBM molecules. This observation indicates that the methanofullerene acts as an antiplastiser. Furthermore, our DMTA analysis demonstrated that this effect persists until the PCBM content becomes sufficiently high (66 wt %) whereupon the film undergoes phase-separation even within an unannealed film. This results in the formation of pure PCBM domains that lower the observed blend T_g, reflecting a reduced PCBM content in the mixed P3HT:PCBM phase.[18,27,28] Further analysis of this data shows that P3HT:PCBM blends with a PCBM composition between 33—75 wt % may actually have two T_gs, rather than a single T_g with a broad spread of values as implied previously. Either a relatively high or low T_g is observed in each sample by this technique, which we attribute to limitations in sensitivity or subtle variations in the drying time for the different samples. The general behavior of the system is shown in Figure 2d. As our spectroscopic ellipsometry data in Figure 2b show, both T_g are observed in films with 20—60 wt % PCBM, indicating that these transitions do occur in films that dry in an identical manner to OPV devices, and that therefore the two T_gs (as we will show) have an impact on the thermal annealing of OPV devices.

In the following work, we show these thermal measurements, coupled with spectroscopic ellipsometry, provide a useful framework in which to understand the effect of annealing on a P3HT:PCBM OPV device efficiency and hence be able to move away from empirically determinations of the optimum thermal treatments to apply. To do this, we have studied blend thin-films having thicknesses that are identical to those used in devices and have monitored their thermal expansion using spectroscopic ellipsometry during the first heating cycle. This method also permits us to quantify the various thermal transitions of the blend films, and permits us to reproduce the conclusions drawn from the DMTA. This is an important result, as it demonstrates that the results of our DMTA study also apply directly to device-applicable thin-films, whose thermal properties may differ from that of the bulk material.[29]

In Figure 2a, we plot the relative change in thickness of a series of blend thin-films as they are subjected to a thermal ramp. Specifically, we plot $(h - h_o)/h_o$ where h is the film thickness at temperature T and h_0 being the film thickness before thermal annealing. As shown, a number of changes occur in the thermal expansion rate as the films are annealed. We quantify the temperature at which these changes in expansion rate occur by fitting a straight line to the thermal expansion above and below each transition, a process that permits us to identify the temperature at which the transition occurs via the intersection of the fitted lines. We propose that these changes in slope occur at temperatures corresponding to the apparent glass transitions of the blends during the first heating cycle. In Figure 2b, we plot the T_g values extracted from part a, along with values for T_{onset} as determined from Figure 1, with $T_{optimum}$ values plotted in Figure 2c.

Using spectroscopic ellipsometry we have previously shown that thin-films of pure P3HT which is employed in this work have a T_g of 20 °C.[30] It can be seen in Figure 2a that in blends containing 20 wt % PCBM, there is a change in the thermal expansion rate that approximately coincides with this temperature with an additional higher temperature transition observed at 50 °C. For blend thin-films with 40−60 wt % PCBM, two transitions are again detectable, however the temperature of the T_g apparently increase as the relative content of PCBM within the blend is increased. At 80 wt % PCBM, a single transition is observed that occurs at a temperature that is relatively lower than that observed in the 60 wt % blend film. These results correlate well with the DMTA data shown in Figure 2d, again suggesting the occurrence of two T_g's across the midcomposition range.

In many cases, we find that as a film is heated above the thermal-transitions, the expansion rate remains positive. We assert that these transitions correspond to glass-transitions, with an expansion in film thickness occurring as the molecules acquire sufficient thermal energy to undergo a transition to a more mobile state and thus explore a greater free volume. A notable exception to this occurs in blends with a PCBM loading of 40−60 wt % in which the films undergo an apparent contraction in thickness when heated above the second T_g. We have previously shown in a P3HT:PCBM blend (40 wt % PCBM) that the glass transition is convoluted with the effects of the removal of residual casting solvent during first heating cycle.[30] Note that this transition is determined by the thermal properties of the blend and not the casting solvent. We are confident in this assertion as the temperature at which this process occurs is far below the boiling point of the chlorobenzene solvent used to cast the films (132 °C). It appears therefore that as the film is heated above the high temperature T_g, solvent loss occurs as the polymer chains have sufficient thermal energy to allow the expulsion of trapped solvent molecules. This loss of solvent will clearly lead to a partial self-organization of the polymer that will manifest itself by a reduction in film thickness. This volume-reduction process will dominate the competing process of thermal expansion until such a time where the majority of the solvent has been removed. At this stage the expansion rate of the sample becomes positive once more. We have estimated the volume fraction of trapped solvent by extrapolating the thermal expansion of blend thin-films below T_g to the point where the majority of solvent is presumed to have left the sample. This is defined as the local minima in the thickness-temperature data presented in Figure 2a. We estimate the volume fraction of solvent trapped in the as-cast films as 1.3%, 1.8%, and 3.2% for blends with 40, 50 and 60 wt % PCBM respectively. The increase in trapped solvent with increasing PCBM wt % is

consistent with the relatively higher T_g of these films (a blend with a higher T_g is likely to trap more solvent).

It can be seen that this solvent-loss process is not observed in blend films containing either 20 wt % or 80 wt % of PCBM. We believe that this phenomena has two different origins. First the absence of solvent loss effects in blend films containing 80 wt % PCBM blend reflects the fact the relatively low concentration of P3HT molecules within the film limits its ability to trap solvent. Second, it has been shown that as temperature difference between the temperature at which a film is cast and the T_g of film increases, a larger volume of the casting solvent is trapped.[30] As the T_g of films containing 20 wt % PCBM lies below room temperature, it suggests that the majority of casting solvent evaporates as the film is cast and thus little solvent remains to be expelled as the film is annealed.

As can be seen in Figure 2b, the T_g of P3HT:PCBM blend thin-films is larger than the T_g of the pure polymer. Furthermore this temperature increases as the relative wt % of PCBM in the blend is increased. This result is in good agreement with our previous study of this system using DMTA. It can also be seen that in the blend thin-film having the highest loading of PCBM (80 wt %), the T_g of the blend undergoes a reduction; an observation also in line with our earlier findings. The measurements presented here however indicate that in blends composed of between 20 and 60 wt % PCBM, there are in fact two distinct glass transitions. As far as we are aware, this is the first observation of such a phenomena for this system; a result we interpret in terms of the blend film comprising at least two compositionally distinct amorphous P3HT-rich phases within the blend thin-film. We emphasize that these phases coexist with the pure crystalline P3HT and PCBM phases. For many mixtures of polymers with small molecules, such phase separation is not uncommon, because of the limited solubility of the polymer in the crystalline small molecule phase.[31] However, there may be other possible explanations which will be touched on below.

To gain confidence in the existence of a phase associated with the low temperature T_g, we have measured the thermal expansion of a 50 wt % PCBM blend thin-film over the course of two heating and cooling cycles. This data is presented in Figure 3, where parts a and b correspond to the first heating and cooling respectively of the film when raised to a temperature of 50 °C. Parts c and d similarly correspond to the second heating and cooling of the same film when raised to 100 °C. We have also used SE to determine the wavelength-dependent extinction coefficient of the film as shown in part e. As can be seen in parts a–c of Figure 3, the transition around 35 °C is measurable during heating, which shifts to 25 °C as the sample is cooled. The apparent reversibility of this transition (recorded at 30 °C during the second heating cycle) within the range of heating temperatures applied suggests its origin is a glass transition within the blend. Upon cooling from a temperature above the second higher temperature T_g (see Figure 3d), we find that only a single transition at 50 °C can be detected. In Figure 3e, it can be seen that the extinction coefficient of the film remains relatively unchanged after the first heating and cooling cycle, but undergoes a significant enhancement in oscillator-strength that is accompanied by a red-shift after the second heating and cooling cycle. This suggests that heating the film above the low temperature T_g does not induce significant morphological changes within the film; an observation that we believe suggests that the phase

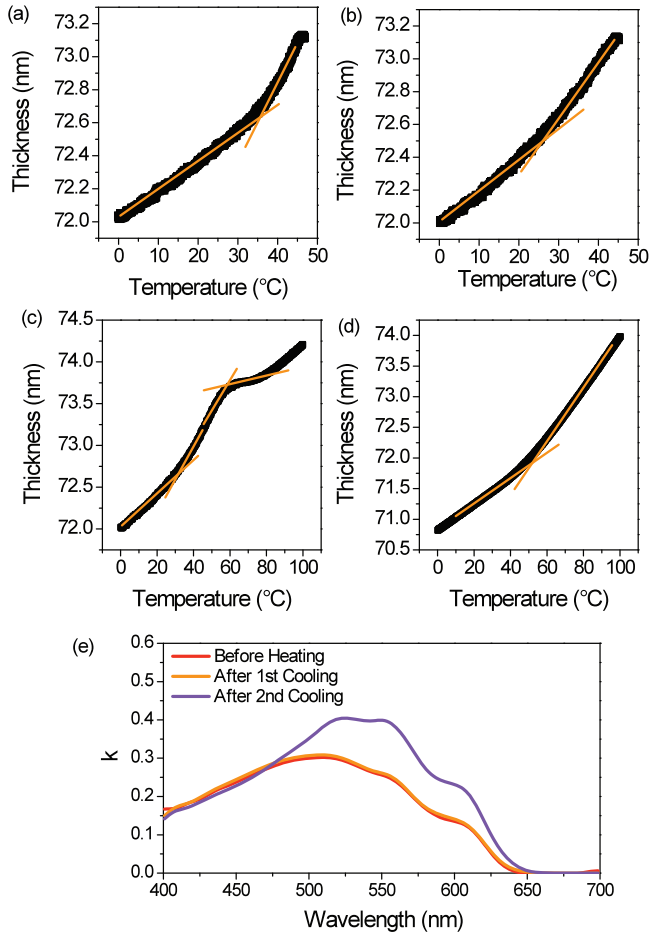


Figure 3. Thickness changes for a P3HT:PCBM (50:50 wt %) blend thin film during (a) first heating, (b) first cooling, (c) second heating, and (d) second cooling. Heating and cooling rate was kept at 5 °C/min throughout. The intersections of the orange lines mark the apparent T_g (s) of the sample. In part e, the modeled extinction coefficient spectrum for the blend before heating and after the first and second heating cycles.

associated with this transition comprises a relatively low volume-fraction of the film.

In Figure 2b, we plot the T_g values extracted from the SE data as a function of PCBM wt % in the blend, alongside the onset temperature for OPV device improvement, as determined from the data in Figure 1. Notably, a close coincidence is found between T_{onset} (for the OPVs) and the upper temperature T_g of the blends. This agreement confirms the T_g of the blend defines the minimum effective temperature for improving the photocurrent generating efficiency of the blend and, in the most efficient blend compositions, for the removal of residual solvent. The positive correlation between device data and T_g data suggests that at these annealing temperatures the major driving force for device improvement are morphological changes which occur in the bulk of the blend film, with interfacial effects playing an apparently relatively minor role.

It is important to acknowledge the differences between the samples prepared for SE and for OPVs. We have endeavored to replicate in the samples for SE as closely as possible the morphology of P3HT:PCBM blends as would exist in an OPV prior to annealing. However, for SE samples a free surface exists which is not present during the annealing process for OPVs. Additionally the films are cast onto native silicon oxide and not

dx.doi.org/10.1021/ma202063k | Macromolecules 2012, 45, 1499–1508

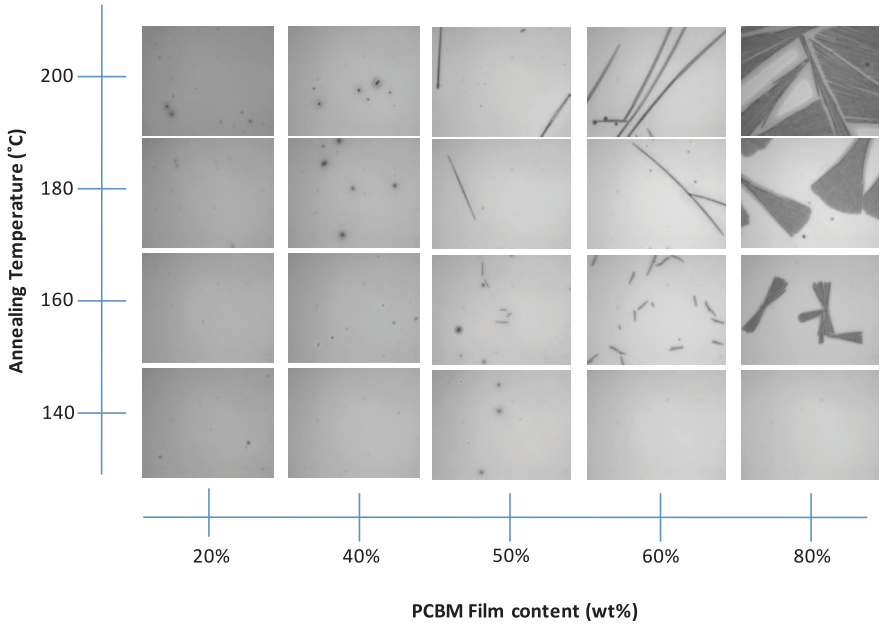


Figure 4. Optical micrographs (60 μm × 80 μm field of view) for P3HT:PCBM blend thin-films annealed and subsequently cooled from a temperature above 140 °C.

PEDOT:PSS. It is not possible to model both thickness changes and optical characteristics of films beneath 100 nm of aluminum, which would fully resemble a device and so would be the ideal sample. We have monitored a blend thin film cast onto PEDOT:PSS during heating, in addition to a control sample of PEDOT:PSS only. The modeled thicknesses, presented in the Supporting Information, Figure S3, shows that PEDOT:PSS undergoes a thickness contraction in the low temperature range up to 70 °C. For blend thin-films cast onto PEDOT:PSS this transition overlaps with the low T_g transitions identified for samples on native silicon oxide. However, it is problematic to deconvolute these two processes. A number of studies[32−34] have identified a P3HT rich surface layer in as-cast blend thin-films on PEDOT:PSS or native silicon oxide. This surface driven phase separation may be the origin of the low T_g seen in the SE sample, but at this stage this identification cannot be verified. Furthermore, the absolute volume fraction of this layer will differ depending upon the substrate used and the consequent balance of surface and interfacial energy terms, so that quantification of the volume fraction would be nontrivial. However, since the DMTA samples are much thicker, it is possible this explains why the sensitivity to detect a thin surface layer is too small reliably to see the appearance of two T_g's in a single DMTA sample.

We also note that the thin-films studied here may exhibit characteristics of optical anisotropy,[34] a consequence of the ability of P3HT chains to partially crystallize edge-on with respect to the sample substrate. However, as stated in the Experimental Section, film thicknesses are modeled in wavelength range in which the film is transparent (700−1000 nm). In this range, the absorption is close to zero, and the refractive index changes due to anisotropy are marginal. We do not expect the optical anisotropy to significantly affect the SE measurement as the phase behavior can also be determined from the raw ellipsometric data[29] (specifically Ψ, the amplitude ratio of the reflected and incident light beams). An example of identifying phase transitions using Ψ vs temperature is shown in the Supporting Information, Figure S4

We now focus our attention on the effect of annealing a blend above its T_g. With the exception of the devices based on a blend containing 80 wt % PCBM, thermal annealing at temperatures up $T_{optimum}$ increases device efficiency by driving phase separation and increasing the crystallinity of each phase.[35] Beyond $T_{optimum}$ it is possible for at least one of the materials within the film to undergo excessive phase separation or a phase-transition, resulting in a morphology that is less favorable for efficient device operation. In Figure 2c, we plot the optimum annealing temperature as a function of PCBM wt %. It can be seen that this temperature undergoes a progressive reduction as the fraction of PCBM is increased. As we discuss later, this temperature is most likely defined by the kinetics of the annealing process, rather than being associated with any one thermal transition. We note however that pure PCBM undergoes cold crystallization at around 155 °C using DMTA.[18] GIWAXS has been used to measure this transition at 148 °C for pure PCBM, with a shift to lower temperatures in P3HT:PCBM blends.[36]

To explore the apparent observation of an optimum annealing temperature, we have performed optical microscopy on a series of P3HT:PCBM blend films having a range of different relative compositions that were annealed at a series of temperatures above 140 °C and subsequently cooled rapidly to room temperature. A selection of representative images is shown in Figure 4. As can be seen, after thermal annealing at 140 °C, (a temperature that just exceeds $T_{optimum}$ for all devices with the exception of the 20:80 wt % P3HT:PCBM active layer blend) few structures are present that can be resolved optically in all of the films studied. These observations suggest that films annealed below this temperature mainly consist of nanoscale domains of P3HT and PCBM together with a molecularly mixed phase. However as the annealing temperature is raised above 140 °C, it can be seen that excessive phase separation between the blend components occurs. Indeed, aggregates having a size of 10 to 100 s of micrometers, that we identify as polycrystalline PCBM,[36] form in films composed of 80 wt % PCBM that have been annealed at a temperature above 140 °C,

dx.doi.org/10.1021/ma202063k | *Macromolecules* 2012, 45, 1499−1508

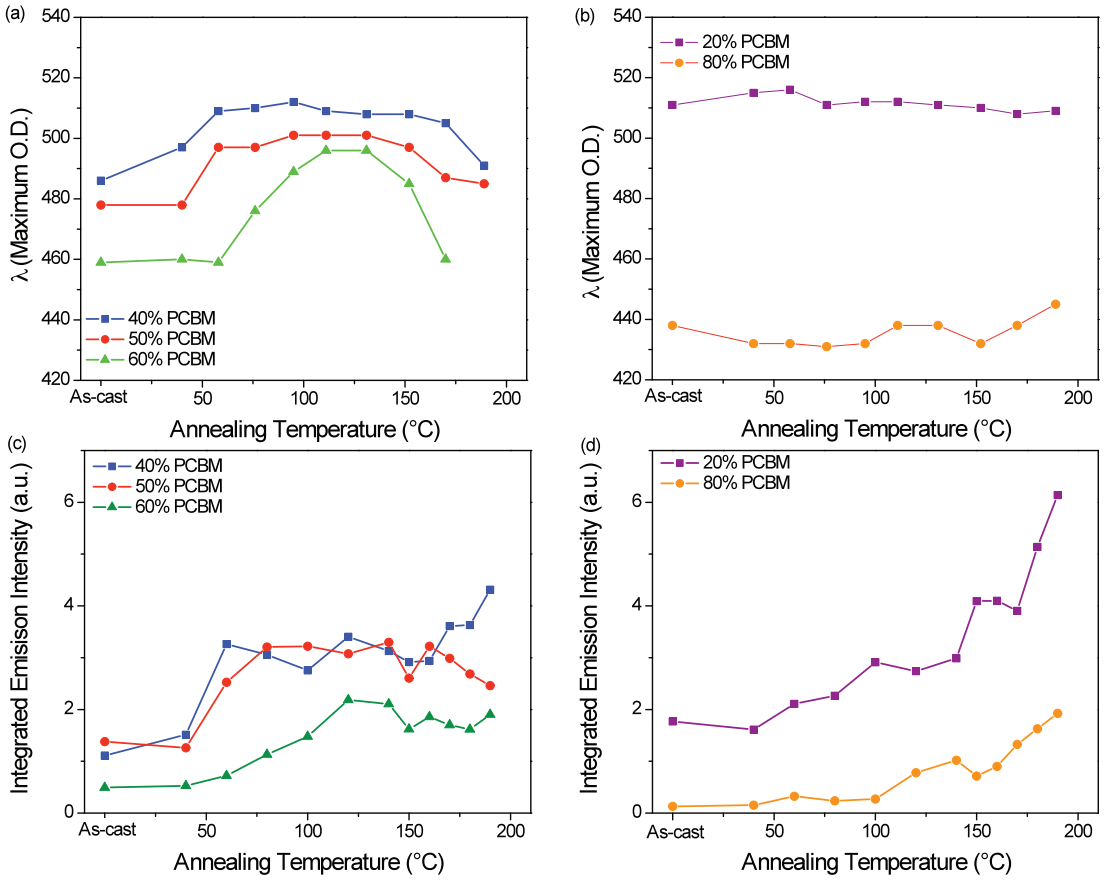


Figure 5. The wavelength at which blend thin-film optical density is maximized, λ_{max}, after thermal annealing for (a) blends with 40−60 wt % PCBM and (b) 20 wt % and 80 wt % PCBM. (c and d) Integrated photoluminescence emission from samples after annealing for blends with 40−60 wt % PCBM and 20 wt % or 80 wt % PCBM respectively. Lines are provided as a guide only.

in agreement with the PCBM solid−solid transition which we measure at 155 °C. As the relative fraction of PCBM is reduced, fewer microscopic PCBM crystallites are observed at any given annealing temperature, reflecting the fact that a smaller number of PCBM molecules are present in the sample. We believe that this observation provides a partial explanation for the relative stability of devices having a low PCBM fraction when annealed at a temperature just above $T_{optimum}$ as discussed earlier, since excessive phase separation is clearly hindered by the relatively low concentration of PCBM.

We note that the precise onset of excessive phase separation will be highly sensitive to the annealing time and exact conditions of sample preparation, including the casting solvent and the properties of the polymer (for example its molecular weight and regioregularity). However, the correlation between excessive (micrometer-scale) phase separation and the reduction in the optimum annealing temperature for devices with increasing wt % PCBM has important consequences for future polymer:PCBM blend OPVs where the optimum blend composition has not been determined. If thermal annealing is employed as a potential route for improving device efficiency with differing polymer:fullerene combinations, a range of temperatures should be employed to account for the possibility that PCBM molecules aggregate excessively when present in large weight fractions within the blend thin-film.

The existence of microscopic PCBM aggregates in P3HT:PCBM blend films is a clear indication that the film has been overannealed, resulting in reduced operational efficiency. We note that such structures may also be sufficiently large to exceed film thickness, thereby creating a short-circuit or damaging the device electrode.[37] The formation of such microscopic structures by annealing above $T_{optimum}$ will be accompanied by a relative depletion of acceptor material within the bulk of the film; an effect that will reduce both the efficiency of exciton dissociation and the extraction of electrons from the device. Nevertheless, we find that the optimum annealing temperature for OPVs occurs before the onset on PCBM micrometer-scale aggregation. To further characterize the effects of annealing on the properties of P3HT:PCBM based devices, we have measured both the optical density and relative photoluminescence efficiency of a series of representative films. Such measurements provide a useful probe to qualitatively explore structure−property relationships of the blend films at a length-scale (up to ∼10 nm) that cannot be accessed using conventional optical microscopy techniques, thereby providing a suitable compliment to the earlier discussion.

In Figure 5, we present a summary of the optical characteristics of the blend thin-films as a function of the annealing temperature. For ease of comparison, the data is split in the same manner as in Figure 1. Specifically, parts a and b of Figure 5 show the wavelength at which blend thin-films have their peak optical density (here defined as λ_{max}), while parts c and d show the integrated photoluminescence emission intensity of the same films. We also present representative spectra from which this data is extracted in the Supporting Information (Figures S5 and S6).

dx.doi.org/10.1021/ma202063k | *Macromolecules* 2012, 45, 1499−1508

It can be seen that annealing films containing between 40 and 60 wt % PCBM at a relatively low temperature results in a red-shift of λ_{max}. For example, a film containing 40 wt % PCBM undergoes a shift in λ_{max} from 485 nm to 515 nm after being annealed at 130 °C. In Figure S5, Supporting Information, it can be seen that this red-shift is also accompanied by an increase in optical density. We find this trend reverses (i.e., the optical density decreases and λ_{max} undergoes a relative blue-shift) after a film is annealed beyond a temperature approximately coincident with $T_{optimum}$. In fact, a clear correlation is found between the data in Figures 1a and 4a, showing that the increased device PCE on annealing above T_{onset} (T_g) is correlated with a red-shift of λ_{max} and an increase in OD, while annealing above $T_{optimum}$ is correlated with a blue-shift of λ_{max} and a reduction in OD. This demonstrates that annealing a P3HT:PCBM film at a temperature between T_{onset} and $T_{optimum}$, followed by cooling to room-temperature provides a driving force for P3HT crystallization, providing a partial explanation for improvements in device efficiency (for example, improved harvesting of the solar spectrum). On annealing a film above $T_{optimum}$, followed by a relatively rapid return to room temperature, the observed blue-shift of λ_{max} and relative weakening in film OD suggests that a significant fraction of the P3HT polymer is quenched into a largely amorphous state. Note that this process occurs without the film being partially melted, as the melt temperature of P3HT is expected to be above 200 °C for all the blend compositions explored in this work.[18,20] Nevertheless, this rapid return to room-temperature generates a film having poor light harvesting capability and lowered charge mobility.[38] Note however that we have previously shown that by slowly cooling blend thin-films even from relatively high (>150 °C) temperatures, polymer crystallization can be encouraged.[30]

It is apparent that the maximum OD of a film on annealing is inversely correlated with the relative PCBM concentration. As the maximum absorption wavelength λ_{max} is a measure of the degree of crystallization, this effect shows that an increased PCBM concentration hinders P3HT crystallization. Interestingly, Figure 5b demonstrates that films containing either a high or low PCBM weight fraction only undergo small changes in λ_{max} on annealing. On closer inspection of absorption spectra recorded from films containing a relatively low (20 wt %) concentration of PCBM (see Supporting Information, Figure S4a), it can be seen that even in as-cast films, there is a relative high fraction of crystalline P3HT present (as evidenced by the 0−0 vibronic peak seen around 600 nm) that is not significantly increased by subsequent thermal annealing. In films containing a high fraction (80 wt %) of PCBM, the packing and partial crystallization of P3HT is clearly restricted by the PCBM under the annealing protocol used in this work.

In parts a and b in Figure 5, we plot the integrated PL intensity from a series of thin-film blends as a function of annealing temperature. We find that the relative PL intensity is inversely proportional to the fraction of PCBM as anticipated. It can be seen that for each of the film compositions, the PL emission intensity increases once the annealing temperature exceeds a certain threshold temperature, again closely correlated to T_g and T_{onset}. The effect is particularly evident in films containing either 40 or 50 wt % PCBM, where PL emission intensity increases significantly on annealing above 50 °C, while emission from films containing 60 wt % PCBM increases in a linear fashion when annealed above 60 °C. The temperature at which the PL emission intensity increases also correlates well with observed changes in the absorption spectra (Figure 5, parts a and b) and device efficiency (Figure 1, parts a and b). Such correlated trends further suggest that annealing above T_{onset} permits the film morphology to undergo a transition from a largely mixed phase in which excitons are efficiently quenched, to a morphology in which nanoscale phase separation reduces the efficiency of exciton dissociation.

When thin films containing a relatively low fraction of PCBM are annealed at temperatures above 150 °C, we observe a marked increase in PL intensity. This increase in PL intensity is indicative of reduced exciton quenching resulting from the formation of larger (or purer) P3HT domains. In contrast, the fluorescence intensity from films containing 50 wt % by mass PCBM does not increase significantly on being annealed above 150 °C. Our measurements of the absorption spectra indicate that P3HT has limited ability to undergo self-organization in films containing a relatively high fraction of PCBM and thus such films are likely to contain a greater (relative) fraction of amorphous P3HT. We speculate therefore that the relatively small increases in P3HT PL emission intensity from films containing a relatively high fraction of PCBM on annealing results from PCBM molecules that have become mixed in regions dominated by amorphous polymer.[27,28] Such amorphous material may hinder the ability of PCBM to coalesce to form nanoscale networks upon thermal annealing, with such molecular-mixed phases being associated with relatively efficient exciton quenching.

In summary, the data presented in Figures 4 and 5 demonstrate that annealing a P3HT:PCBM film beyond $T_{optimum}$ results in both P3HT and PCBM blend fractions that have unfavorable OPV characteristics. This may arise from reduced optical density and overlap with the solar spectrum (limiting the ability of the device to harvest sunlight), as shown in Figure 4, and from the creation of microscopic PCBM aggregates, reducing its ability to disassociate excitons and transport charges as shown in Figure 3. Although we have been unable to ascribe a thermal transition to $T_{optimum}$, as we have demonstrated when correlating T_{onset} with the higher-temperature T_g of P3HT, it is likely that $T_{optimum}$ is instead determined by the kinetics of PCBM diffusion during isothermal annealing and the relative crystallinity of both P3HT and PCBM during annealing and cooling. Thus the upper bound of beneficial annealing temperatures will be sensitive to the exact conditions of sample preparation. Nevertheless, the observed trend that a relatively higher wt % of PCBM within an OPV lowers the optimum temperature range due to its propensity for excessive phase separation is likely to be general in polymer-fullerene blends and should be taken into account when exploring systems where the optimum film composition is unknown.

■ CONCLUSIONS

We have explored the impact of thermal annealing on the photovoltaic efficiency of P3HT:PCBM OPVs across a range of active layer compositions and annealing temperatures. These results are related to the phase transition behavior of the blends. Our measurements on the glass transition of the blend thin-films suggest that two distinct compositional amorphous phases exist. We demonstrate a positive correlation between the highest temperature apparent glass transition and the minimum temperature necessary to improve the efficiency of an OPV device. This confirms that annealing a film above its glass transition temperature (for that particular blend composition) will permit molecules to undergo cooperative motion, forming

a morphology that can promote efficient photocurrent generation.

We have also identified a blend-ratio dependent optimum annealing temperature for efficient device operation. This has been rationalized in terms of excessive phase separation by PCBM, and the reduced ability of the blend thin-film to harvest sunlight. As the wt % of PCBM within the blend increases, the optimum temperature decreases, from 170 °C to as low as 100 °C. We have also found that thermally annealing devices that contain a high weight fraction of PCBM apparently results in a reduction in operational efficiency only; a result that may be particularly relevant in OPVs based on amorphous low energy band gap polymers in which large relative fractions of fullerenes are often used.[39,40]

Our results demonstrate therefore that the optimum annealing temperature of an OPV device based on a polymer/fullerene blend is a function of the relative composition of the blend; an effect that we have related to the phase transition properties of the film and in particular its glass transition temperature. This is an important observation, as it indicates that phase transition characterization of unexplored polymer−fullerene systems should be performed in parallel with device optimization studies, with the glass-transition temperature of each particular polymer−fullerene blend film providing a strong indication of the minimum annealing temperature beyond which changes in device efficiency can be anticipated.

EXPERIMENTAL SECTION

Samples were prepared using P3HT (Rieke, 4002-E), PCBM (Solenne, 99% purity) and chlorobenzene (Aldrich, anhydrous, 98% purity). All materials were used as received and were not subject to additional purification protocols. All samples were prepared within an overpressure dry nitrogen glovebox. To fabricate blend solutions, P3HT and PCBM were first dissolved separately at 25 mg/mL into chlorobenzene. These solutions were then heated at 70 °C until all material was fully dissolved and then rapidly cooled to room temperature (to minimize the effects of gelation[41]), after which they were passed through a 0.45 μm PTFE filter before being blended by volume to the required composition.

OPV devices were fabricated following a method described in detail elsewhere.[42] In this work, P3HT:PCBM solutions were spin-cast forming films having a thickness of 70 ± 4 nm as measured by profilometry (Dektak 150). In all cases, spin-speed was adjusted to compensate for variations in blend solution viscosity. A series of identical control films were also prepared for spectroscopic measurements. OPV devices were subjected to thermal annealing after the vacuum deposition of a 100 nm thick aluminum cathode. This thermal anneal step was performed by placing the device substrate onto a hot plate for 10 min after which they were transferred onto a copper plate held at room temperature, facilitating rapid cooling. The PCE of encapsulated devices were determined using a Newport Solar Simulator (25 °C at 100 mW cm^{-2}) having an NREL calibrated output.

DMTA samples were drop-cast from 50 mg/mL solutions that were preheated to 70 °C onto stainless steel material pockets that were folded to enclose the film, as described previously.[18] This was performed under flowing nitrogen. Spectroscopic ellipsometry was performed on representative films cast on a silicon substrate using a M2000v, J. A. Woollam Co., ellipsometer. For measurement, films were placed on an adapted Linkam stage and heated at a rate of 5 °C/minute up to 250 °C. All measurements were performed under nitrogen. To determine film thickness from ellipsometry, a Cauchy model was applied over the spectral region where the samples were optically transparent (700−1000 nm).[43] Modeled thicknesses provided a boundary condition for the calculation of the film extinction coefficient using a b-spline model.[43] The thermal expansion of the samples during heating was used to extract the T_g using methods described elsewhere.[29] UV−vis absorption and photoluminescence (PL) of thin films were measured using a Horiba Fluoromax spectrometer. PL spectra were acquired following excitation at 500 nm and were corrected for thin-film absorption effects. Integrated PL emission values were calculated over a wavelength range of 600−800 nm.

ASSOCIATED CONTENT

Supporting Information

Device metrics for all devices fabricated (Figure S1) and characteristics of optimized devices (Figure S2). Additional ellipsometry data (Figures S3 and S4) and representative OD and PL spectra of P3HT:PCBM blend thin-films (Figures S5 and S6 respectively). This material is available free of charge via the Internet at http://pubs.acs.org.

AUTHOR INFORMATION

Corresponding Author

*E-mail: (A.J.P.) a.j.pearson@sheffield.ac.uk; (D.G.L.) d.g.lidzey@sheffield.ac.uk.

ACKNOWLEDGMENTS

We thank EPSRC for financial support via the grant "Optimization of polymer photovoltaic devices through control of phase separation" (Grant references EP/F016433/1 and EP/F019297/1). A.J.P. acknowledges an award of an EPSRC DTA Ph.D. studentship.

REFERENCES

(1) Brabec, C. J.; Gowrisanker, S.; Halls, J. J. M.; Laird, D.; Jia, S. J.; Williams, S. P. *Adv. Mater.* **2010**, *22* (34), 3839−3856.
(2) Krebs, F. C. *Sol. Energy Mater. Sol. Cells* **2009**, *93* (4), 465−475.
(3) Krebs, F. C. *Sol. Energy Mater. Sol. Cells* **2009**, *93* (4), 394−412.
(4) Boudreault, P. L. T.; Beaupre, S.; Leclerc, M. *Polym. Chem.* **2010**, *1* (2), 127−136.
(5) Allard, N.; Aich, R. B.; Gendron, D.; Boudreault, P. L. T.; Tessier, C.; Alem, S.; Tse, S. C.; Tao, Y.; Leclerc, M. *Macromolecules* **2010**, *43* (5), 2328−2333.
(6) Helgesen, M.; Sondergaard, R.; Krebs, F. C. *J. Mater. Chem.* **2010**, *20* (1), 36−60.
(7) Liang, Y. Y.; Xu, Z.; Xia, J. B.; Tsai, S. T.; Wu, Y.; Li, G.; Ray, C.; Yu, L. P. *Adv. Mater.* **2010**, *22* (20), E135−+.
(8) Ma, W. L.; Yang, C. Y.; Gong, X.; Lee, K.; Heeger, A. J. *Adv. Funct. Mater.* **2005**, *15* (10), 1617−1622.
(9) Li, G.; Shrotriya, V.; Huang, J. S.; Yao, Y.; Moriarty, T.; Emery, K.; Yang, Y. *Nat. Mater.* **2005**, *4* (11), 864−868.
(10) Li, G.; Yao, Y.; Yang, H.; Shrotriya, V.; Yang, G.; Yang, Y. *Adv. Funct. Mater.* **2007**, *17* (10), 1636−1644.
(11) Campoy-Quiles, M.; Ferenczi, T.; Agostinelli, T.; Etchegoin, P. G.; Kim, Y.; Anthopoulos, T. D.; Stavrinou, P. N.; Bradley, D. D. C.; Nelson, J. *Nat. Mater.* **2008**, *7* (2), 158−164.
(12) Clarke, T. M.; Ballantyne, A. M.; Nelson, J.; Bradley, D. D. C.; Durrant, J. R. *Adv. Funct. Mater.* **2008**, *18* (24), 4029−4035.
(13) Beal, R. M.; Stavrinadis, A.; Warner, J. H.; Smith, J. M.; Assender, H. E.; Watt, A. A. R. *Macromolecules* **2010**, *43* (5), 2343−2348.
(14) Yang, X.; Loos, J. *Macromolecules* **2007**, *40* (5), 1353−1362.
(15) Blom, P. W. M.; Mihailetchi, V. D.; Koster, L. J. A.; Markov, D. E. *Adv. Mater.* **2007**, *19* (12), 1551−1566.
(16) Li, G.; Shrotriya, V.; Yao, Y.; Yang, Y. *J. Appl. Phys.* 2005, *98*, (4), -.
(17) Kim, Y.; Cook, S.; Tuladhar, S. M.; Choulis, S. A.; Nelson, J.; Durrant, J. R.; Bradley, D. D. C.; Giles, M.; McCulloch, I.; Ha, C. S.; Ree, M. *Nat. Mater.* **2006**, *5* (3), 197−203.

(18) Hopkinson, P. E.; Staniec, P. A.; Pearson, A. J.; Dunbar, A. D. F.; Wang, T.; Ryan, A. J.; Jones, R. A. L.; Lidzey, D. G.; Donald, A. M. *Macromolecules* **2011**, *44* (8), 2908−2917.
(19) Zhao, J.; Swinnen, A.; Van Assche, G.; Manca, J.; Vanderzande, D.; Van Mele, B. *J. Phys. Chem. B* **2009**, *113* (6), 1587−1591.
(20) Muller, C.; Ferenczi, T. A. M.; Campoy-Quiles, M.; Frost, J. M.; Bradley, D. D. C.; Smith, P.; Stingelin-Stutzmann, N.; Nelson, J. *Adv. Mater.* **2008**, *20* (18), 3510−+.
(21) Padinger, F.; Rittberger, R. S.; Sariciftci, N. S. *Adv. Funct. Mater.* **2003**, *13* (1), 85−88.
(22) Baek, W. H.; Yoon, T. S.; Lee, H. H.; Kim, Y. S. *Org. Electron.* **2010**, *11* (5), 933−937.
(23) van Bavel, S. S.; Barenklau, M.; de With, G.; Hoppe, H.; Loos, J. *Adv. Funct. Mater.* **2010**, *20* (9), 1458−1463.
(24) Wienk, M. M.; Kroon, J. M.; Verhees, W. J. H.; Knol, J.; Hummelen, J. C.; van Hal, P. A.; Janssen, R. A. J. *Angew. Chem., Int. Ed.* **2003**, *42* (29), 3371−3375.
(25) Mihailetchi, V. D.; Wildeman, J.; Blom, P. W. M. *Phys. Rev. Lett.* **2005**, *94*, 12.
(26) Goodman, A. M.; Rose, A. *J. Appl. Phys.* **1971**, *42* (7), 2823−&.
(27) Treat, N. D.; Brady, M. A.; Smith, G.; Toney, M. F.; Kramer, E. J.; Hawker, C. J.; Chabinyc, M. L. *Adv. Energy Mater.* **2011**, *1* (1), 82−89.
(28) Collins, B. A.; Gann, E.; Guignard, L.; He, X.; McNeill, C. R.; Ade, H. *J. Phys. Chem. Lett.* **2010**, *1* (21), 3160−3166.
(29) Keddie, J. L.; Jones, R. A. L.; Cory, R. A. *Europhys. Lett.* **1994**, *27* (1), 59−64.
(30) Wang, T.; Pearson, A. J.; Lidzey, D. G.; Jones, R. A. L. *Adv. Funct. Mater.* **2011**, *21* (8), 1383−1390.
(31) Jones, R. A. L.; Richards, R. W., *Polymers at surfaces and interfaces*. Cambridge University Press: Cambridge, U.K., 1999.
(32) Parnell, A. J.; Dunbar, A. D.; Pearson, A. J.; Staniec, P. A.; Dennison, A. J.; Hamamatsu, H.; Skoda, M. W.; Lidzey, D. G.; Jones, R. A. *Adv. Mater.* **2010**, *22* (22), 2444−7.
(33) Tillack, A. F.; Noone, K. M.; MacLeod, B. A.; Nordlund, D.; Nagle, K. P.; Bradley, J. A.; Hau, S. K.; Yip, H.-L.; Jen, A. K. Y.; Seidler, G. T.; Ginger, D. S. *ACS Appl. Mater. Interfaces* **2011**, *3* (3), 726−732.
(34) Germack, D. S.; Chan, C. K.; Kline, R. J.; Fischer, D. A.; Gundlach, D. J.; Toney, M. F.; Richter, L. J.; DeLongchamp, D. M. *Macromolecules* **2010**, *43* (8), 3828−3836.
(35) Nguyen, L. H.; Hoppe, H.; Erb, T.; Gunes, S.; Gobsch, G.; Sariciftci, N. S. *Adv. Funct. Mater.* **2007**, *17* (7), 1071−1078.
(36) Verploegen, E.; Mondal, R.; Bettinger, C. J.; Sok, S.; Toney, M. F.; Bao, Z. A. *Adv. Funct. Mater.* **2010**, *20* (20), 3519−3529.
(37) Chirvase, D.; Parisi, J.; Hummelen, J. C.; Dyakonov, V. *Nanotechnology* **2004**, *15* (9), 1317−1323.
(38) Erb, T.; Zhokhavets, U.; Gobsch, G.; Raleva, S.; Stuhn, B.; Schilinsky, P.; Waldauf, C.; Brabec, C. J. *Adv. Funct. Mater.* **2005**, *15* (7), 1193−1196.
(39) Blouin, N.; Michaud, A.; Gendron, D.; Wakim, S.; Blair, E.; Neagu-Plesu, R.; Belletete, M.; Durocher, G.; Tao, Y.; Leclerc, M. *J. Am. Chem. Soc.* **2008**, *130* (2), 732−742.
(40) Beiley, Z. M.; Hoke, E. T.; Noriega, R.; Dacuna, J.; Burkhard, G. F.; Bartelt, J. A.; Salleo, A.; Toney, M. F.; McGehee, M. D. *Adv. Energy Mater.* **2011**, *1* (5), 954−962.
(41) Koppe, M.; Brabec, C. J.; Heiml, S.; Schausberger, A.; Duffy, W.; Heeney, M.; McCulloch, I. *Macromolecules* **2009**, *42* (13), 4661−4666.
(42) Kingsley, J. W.; Green, A.; Lidzey, D. G. *Proc. SPIE—Int. Soc. Opt. Eng.* **2009**, *7416*, 74160T.
(43) Wang, T.; Dunbar, A. D. F.; Staniec, P. A.; Pearson, A. J.; Hopkinson, P. E.; MacDonald, J. E.; Lilliu, S.; Pizzey, C.; Terrill, N. J.; Donald, A. M.; Ryan, A. J.; Jones, R. A. L.; Lidzey, D. G. *Soft Matter* **2010**, *6* (17), 4128−4134.

Macromolecules

Article

pubs.acs.org/Macromolecules

Influence of Molecular Weight Dispersity of Poly{2-(perfluorooctyl)ethyl acrylate} Brushes on Their Molecular Aggregation States and Wetting Behavior

Hiroki Yamaguchi,[†] Moriya Kikuchi,[‡,§] Motoyasu Kobayashi,[‡,§] Hiroki Ogawa,[∥] Hiroyasu Masunaga,[∥] Osami Sakata,[∥] and Atsushi Takahara*[,†,‡,§,⊥]

[†]Graduate School of Engineering, Kyushu University, 744 Motooka, Nishi-ku, Fukuoka 819-0395, Japan

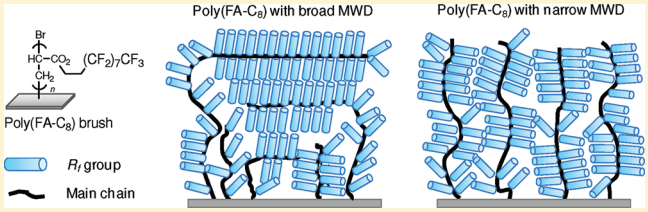
[‡]Institute for Materials Chemistry and Engineering, Kyushu University, 744 Motooka, Nishi-ku, Fukuoka 819-0395, Japan

[§] Japan Science and Technology Agency (JST), ERATO Takahara Soft Interface Project, 744 Motooka, Nishi-ku, Fukuoka 819-0395, Japan

[∥]Japan Synchrotron Research Institute, Mikazuki, Sayo, Hyogo 671-5198, Japan

[⊥]International Institute for Carbon-Neutral Energy Research (WPI-I^{2}CNER), Kyushu University, 744 Motooka, Nishi-ku, Fukuoka 819-0395, Japan

ABSTRACT: The relationships between the molecular aggregation states and water repellency of the perfluoroalkyl (R_f) groups of poly{2-(perfluorooctyl)ethyl acrylate} (poly(FA-C_8)) brush thin films with broad and narrow molecular weight dispersities (MWDs) were analyzed by grazing incidence wide-angle X-ray diffraction (GI-WAXD) and water contact angle measurements. MWD-controlled-poly(FA-C_8) brush thin films were prepared by surface-initiated atom transfer radical polymerization on a flat silicon substrate in the absence and presence of an ionic liquid. In-plane diffraction profiles of poly(FA-C_8) brush films with narrow MWD had peaks corresponding to the periodic lengths of bilayer lamellae at q_{xy} = 2−6 nm^{-1}. This indicated that the orientation of R_f groups were parallel to the surface of the silicon substrate. In contrast, the peak of the in-plane GI-WAXD for brush films with broad MWD brush was confirmed at q_{xy} = 12.5 nm^{-1}, indicating that the R_f groups were oriented perpendicular to the surface of the silicon substrate. In the case of a poly(FA-C_8) brush thin film with a narrow MWD, the receding contact angle (θ_R) and sliding contact angle (θ_S) versus water were ca. 80° and 35°, respectively, whereas θ_R and θ_S were 105° and 15°, respectively, at the surface of poly(FA-C_8) with broad MWD. These results indicated that the water repellency of poly(FA-C_8) brush surface largely depends on the molecular aggregation state and orientation of the R_f groups at the outermost surface and the MWD of the grafting polymer.



1. INTRODUCTION

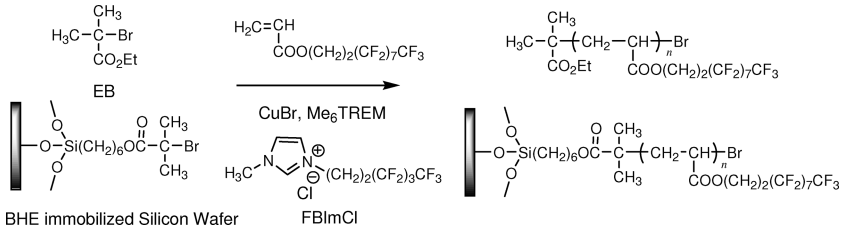
The remarkable and unique bulk properties of polymers with perfluoroalkyl (R_f) groups include excellent chemical resistance (against acids, bases, and organic solvents), thermostability, incombustibility, low dielectric constants, and low refractive index; these properties are not exhibited by conventional organic polymers. Fluoropolymers with R_f groups have excellent surface properties such as hydrophobicity, non-adhesive properties, low friction coefficients, and antifouling behaviors. The origin of these special properties of fluorinated polymers is attributed to the C−F bonds, which have a large bonding energy, quite a low surface free energy, and the intermolecular forces between R_f groups. In particular, the surface properties of fluoropolymers are influenced by the molecular aggregation states, orientation, and crystallinity of the R_f groups.[1−7] Control of the molecular aggregation structure of R_f groups is therefore an important technique for producing useful surfaces or modifying the material surfaces of fluoropolymers in industry.

Tethering the polymers on the substrate surface is a useful method for modifying surface physicochemical properties because the polymers are immobilized on the substrate surface by covalent bonds; these bonds are hardly dissociated by friction and washing with solvents. Fluoropolymer films prepared by conventional surface coating, such as dip-coating and spin-casting processes, are easily detached from the substrate because of the low surface free energies of fluoropolymers. In the past decade, various types of surface-grafted fluoropolymers have been prepared by surface-initiated controlled polymerization, so-called "polymer brush".[8] Matyjaszewski et al.[9] have prepared poly{2-(perfluorooctyl)ethyl acrylate} (poly(FA-C_8)) brush thin films of thickness with 7 nm by surface-initiated atom transfer radical polymerization (SI-ATRP) to give a surface with a 119° water contact angle against water. This value is the similar to that of the

Received: October 14, 2011
Revised: January 7, 2012
Published: January 27, 2012

ACS Publications © 2012 American Chemical Society

Scheme 1. Preparation of Poly(FA-C_8) Brush in Ionic Liquid by Surface-Initiated ATRP



corresponding spin-coated film. Brittain et al.[10] improved the solvent repellency of porous silica surfaces using diblock copolymer brushes consisting of poly(methyl acrylate)-*block*-poly(pentafluoropropyl acrylate). Surface-grafted poly(perfluoroalkyl (meth)acrylate) brushes were also prepared on silicon substrates[11,12] and cross-linked poly(dimethylsiloxane)[13] by SI-ATRP. Zhu et al.[14] have prepared poly(2,2,2-trifluoroethyl methacrylate) (poly(FMA-C_1)) brushes and poly(FMA-C_1)-*block*-poly(methyl methacrylate) (PMMA) on nickel and copper surfaces via SI-ATRP. These studies have mainly focused on physical properties such as water repellency and antifouling effect but have not investigated molecular aggregation states.

The orientations of the R_f groups of fluoropolymer films were investigated by Ober et al.[15] They prepared poly(styrene)-*block*-poly{4-(1*H*,1*H*,2*H*,2*H*-perfluorodecyl)oxymethylstyrene} brushes by nitroxide-mediated controlled radical polymerization on flat silicon surfaces. Near-edge X-ray absorption fine structure analysis showed that structures of thicker brushes had more oriented R_f groups at the surface and that surface rearrangement took place on contact with water. Previously, we prepared poly(FA-C_8) brushes with thicknesses of 4−50 nm on silicon wafers by SI-ATRP and analyzed the molecular aggregation structures of the R_f groups in the brush thin films by X-ray reflectivity (XR) and grazing incidence wide-angle X-ray diffraction (GI-WAXD) measurements.[16,17] We found that the R_f groups aggregated and oriented perpendicular to the substrate at the air/brush interface and that the molecular aggregation states of the poly(FA-C_8) brush thin films strongly depended on that thickness.

These studies mentioned above, however, used fluoropolymes with molecular weight and molecular weight dispersity (MWD) which were not well-controlled or were unclear. In general, it is still difficult to synthesize fluoropolymers with narrow MWDs, even if controlled radical polymerization of the fluoro monomers is used.[18−31] Considering the chain structure of high-density polymer brushes in which one chain end is tethered to the substrate surface, the number-average molecular weight (M_n) and MWD of the grafted polymer must greatly influence the molecular aggregation structure of the R_f groups. It is therefore fundamentally important to understand the relationship between the properties of the primary chain structure, such as M_n, MWD, branching of polymer chains, and chemical structures of repeating units, and the molecular aggregation structure and surface physicochemical properties of the brush films.

Recently, we reported the successful controlled ATRP of methacrylates bearing ionic functional groups, such as sulfobetaine and ammonium chloride, in a mixture of 2,2,2-trifluoroethanol and ionic liquids as the polymerization solvents.[32,33] We demonstrate here the SI-ATRP of FA-C_8 monomers in ionic liquids[34] to prepare fluoropolymers with predictable M_n values and narrow MWD and to achieve MWD control of the resulting polymer brush by varying the amount of ionic liquid.[32,33] Using well-defined poly(FA-C_8) brushes, we investigated the effects of the MWD of the poly(FA-C_8) brushes on the surface molecular aggregation structure of the R_f groups by GI-WAXD measurements and the surface wettability by water contact angle measurements.

2. EXPERIMENTAL SECTION

2.1. Materials. Copper(I) bromide (CuBr, Wako Pure Chemical Industries, Ltd., Osaka, Japan, 98%) was washed successively with acetic acid and ethanol and then kept under vacuum. Ethyl 2-bromoisobutyrate (EB, Tokyo Chemical Industry Co., Ltd., Tokyo, Japan, 99%) was distilled from calcium hydride before use. 4,4′-Dinonyl-2,2′-bipyridyl (C_9bpy, Aldrich, St. Louis, MO, 97%), 1-hexyl-3-methylimidazolium chloride (HMImCl, Merck, Darmstadt, Germany, 98%), sodium trifluoroacetate (Kanto Chemical Co., Inc., Tokyo, Japan), hexafluoroisopropanol (HFIP, Central Glass Co., Ltd., Yamaguchi, Japan), AK-225 (Asahi Glass Co., Tokyo, Japan), which is a mixture of 1,1-dichloro-2,2,3,3,3-pentafluoropropane and 1,3-dichloro-1,1,2,2,3-pentafluoropropane, and diiodomethane (CH_2I_2, Tokyo Chemical Industry Co., Ltd., Tokyo, Japan) were used as received. Surface initiator, (2-bromo-2-methyl)-propionyloxyhexyltriethoxysilane (BHE),[35,36] and tris(2-(dimethyl)-aminoethyl)amine (Me_6TREN)[37] were synthesized using previously reported procedures. FA-C_8 monomer (Daikin Industries Ltd., Osaka, Japan) was purified by repeated distillation under reduced pressure to remove other monomers such as 2-(perfluorodecyl)ethyl acrylate. The purity of FA-C_8 was over 99% by gas chromatography. The ionic liquid *N*-perfluorobutylethyl-*N*′-methylimidazolium chloride (FBImCl) was synthesized as follows. 1-Methylimidazole (Wako Pure Chemical Industries, Ltd., Osaka, Japan) was dissolved in toluene, treated with a slight molar deficiency of 1,1,1,2,2,3,3,4,4-nonafluoro-8-iodooctane (AZmax, Chiba, Japan), and refluxed overnight. The mixture was cooled to room temperature, and the solvent was removed under a vacuum to give *N*-perfluorobutylethyl-*N*′-methylimidazolium iodide (FBImI). The corresponding chloride salts were obtained by stirring FBImI with AgCl in aqueous NH_3 solution at room temperature for 24 h. Water for the contact angle measurements was purified using a NanoPure Water system (Millipore, Inc., Billerica, MA).

2.2. General Procedure for Surface-Initiated ATRP of FA-C_8. All procedures for the polymerization and purification of monomer were conducted under a hood to avoid health hazard because the bioaccumulation of the degraded product of poly(fluoroalkyl acrylate)s with long R_f groups at the side chains (C ≥ 8) undoubtedly have a potential risk of environmental load and health hazard.[38,39] Therefore, it is necessary to design novel fluoropolymer containing with short R_f groups. However, the aim of this study is purely scientific.

A typical procedure for SI-ATRP of FA-C_8 was performed as follows (Scheme 1). Silicon wafers were washed with piranha solution at 373 K for 1 h and then exposed to vacuum-ultraviolet rays (VUV, λ = 172 nm) for 10 min under reduced pressure (30 Pa). *Caution: piranha solution consisting of concentrated sulfuric acid and hydrogen peroxide is danger solution, which should be handled with care.* BHE was immobilized on the substrates by chemical vapor adsorption.[40] Several sheets of the BHE-immobilized silicon wafers, 1.0 g (1.93 mmol) of FA-C_8 solution, and different amounts of FBImCl were charged in a

dx.doi.org/10.1021/ma202300r | *Macromolecules* 2012, 45, 1509−1516

Table 1. Surface-Initiated ATRP of FA-C_8 in the Absence and Presence of Ionic Liquid at 333 K for 2 h[a]

run	[FA-C_8]/[EB] (molar ratio)	IL[b] (wt %)	[IL]/[CuBr] (molar ratio)	conv[c] (%)	$M_n \times 10^{-4}$ calcd[d]	$M_n \times 10^{-4}$ obsd[e]	M_w/M_n	thickness[f] (nm)
1[g]	630		0.0	64	20.8	19.4	1.97	41
2[h]	1510		0.0	29	22.7	16.4	1.62	60
3	920	FBImCl (0.011)	0.14	25	7.0	7.0	1.05	22
4	920	FBImCl (0.058)	0.75	38	11.8	11.7	1.13	24
5	920	FBImCl (0.14)	1.8	39	17.7	12.6	1.25	37
6	920	FBImCl (0.35)	4.6	37	17.6	13.5	1.37	38
7	920	FBImCl (1.1)	14.2	20	9.6	9.6	1.41	24
8	920	HMImCl (0.040)	1.2	42	20.0	18.7	1.34	37
9	920	HMImCl (0.17)	4.6	36	20.1	15.7	1.25	35
10	920	HMImCl (0.41)	9.7	33	15.8	10.8	1.23	24
11	920	HMImCl (0.79)	19.3	32	15.5	12.1	1.22	29

[a]Conditions: [CuBr]/[Me_6TREN]/[FA-C_8]/[EB] = 1/2/920/1 (molar ratio), at 333 K for 2 h. [b]IL stands for ionic liquid. Additive ratio of IL (wt %) = [weight of IL]/[weight of FA-C_8] × 100. [c]Gravity. [d]M_n(calcd) = [FA-C_8]/[EB] × conversion/100 × (MW of FA-C_8) + (MW of EB). [e]M_n(obsd) of free poly(FA-C_8) was determined by MALS-SEC calibration using an HFIP (10 mM) as an eluent. [f]Ellipsometry. [g]4,4′-Dinonyl-2,2′-bipyridyl was used as ligand at 383 K for 48 h. [h]Conditions: [CuBr]/[Me_6TREN]/[FA-C_8]/[EB] = 1/2/1510/1 (molar ratio), at 333 K for 2 h.

well-dried glass tube with a stopcock and degassed three times by the freeze−thaw process. CuBr (0.0022 mmol) and Me_6TREN (0.0042 mmol) diluted with HFIP were introduced into another glass tube, which was degassed by seven cycles of vacuum pumping and flushing with argon. A free initiator EB (0.0021 mmol) diluted with HFIP was added to the catalyst solution. After adding EB, the copper catalyst solution was stirred for 5 min to give a homogeneous solution of a characteristic light blue color. This solution of copper catalyst was degassed by repeated freeze−thaw cycles and then was injected into the monomer solution. The resulting reaction mixture was again degassed by repeated freeze−thaw cycles to remove oxygen and was then stirred in an oil bath at 333 K for 2 h under argon to simultaneously generate a poly(FA-C_8) brush from the substrate and free (unbound) poly(FA-C_8) from EB. The reaction was stopped by opening the glass vessel to the atmosphere at 273 K. The reaction mixture was poured into methanol to precipitate the free polymer and unreacted FA-C_8. The silicon wafers were washed with AK-225 using a Soxhlet apparatus for 6 h to remove the free polymer adsorbed on the surface, and they were dried under reduced pressure. All samples were annealed at 373 K for 1 h under conditions of reduced pressure and gradually cooled to room temperature at a rate of 10 K/min.

2.3. Measurements. All procedures for the size exclusion chromatography (SEC) measurements and purification of HFIP were conducted under a hood to avoid health hazard. SEC of the free soluble poly(FA-C_8) was used to determine M_n, the weight-average molecular weight (M_w), and MWD using a Waters 1515 HPLC system (Waters Corp., Milford, MA) connected to three polymethacrylate-based TSK gel columns (Tosoh Bioscience, Tokyo, Japan), α-6000, α-5000, and α-4000 and equipped with a multiangle light scattering detector (MALS; DAWN-EOS, Wyatt Technology, Santa Barbara, CA; 30 mW GaAs linearly polarized laser, wavelength: λ = 690 nm) and a refractive index detector (Waters 2414, tungsten lamp (wavelength 470−950 nm)); measurements were performed at 313 K using 10 mM sodium trifluoroacetate/HFIP as an eluent at a rate of 0.5 mL/min. The Rayleigh ratio at a scattering angle of 90° was based on that of pure toluene at a wavelength of 632.8 nm at 298 K. The sensitivities of 17 detectors at angles other than 90° and the dead volume for each detector were determined from the scattering intensities of 0.15 wt % aqueous solutions of a PMMA standard with 2.06×10^4 g/mol and M_w/M_n = 1.06. The specific refractive index increments (dn/dc) of poly(FA-C_8) in 10 mM sodium trifluoroacetate/HFIP solution were determined to be 0.0443 mL/g using an aqueous solution differential refractometer (DRM-3000, Otsuka Electronics, Osaka, Japan; wavelength λ = 632.8 nm).

The thickness of the brush thin film was determined using a spectroscopic ellipsometer (MASS-102, Five Lab Co., Ltd., Kanagawa, Japan) with a xenon arc lamp (wavelength 380−890 nm) at a fixed incident angle of 70°. The refractive index was assumed to be 1.34 as reported in the literature.[9]

X-ray photoelectron spectroscopy (XPS) measurements were carried out using an XPS-APEX (Physical Electronics Inc., Chanhassen, MN) at 1×10^{-9} Pa using a monochromatic Al K_σ X-ray source operated at 300 W. All of the XPS data were collected at a takeoff angle of 45°, and a low-energy (25 eV) electron flood gun was used to minimize sample charging. The survey spectra (0−1000 eV) and high-resolution spectra of the C_{1s}, O_{1s}, and F_{1s} regions were acquired at analyzer pass energies of 100.0 and 25.0 eV, respectively. An X-ray beam was focused on an area with a diameter of ca. 0.2 mm.

Atomic force microscopy (AFM) observations were carried out using an SPA 400 with an SPI 3800N controller (SII Nano Technology Inc., Chiba, Japan) in air at room temperature, using a Si_3N_4 integrated tip on a commercial triangular 200 μm cantilever (Olympus Co., Ltd., Tokyo, Japan) with a spring constant of 0.09 N/m.

The static contact angles against water and CH_2I_2 (volumes were 2 μL) were recorded with a drop-shaped analytical system DSA 10 Mk2 (A KRÜSS Optronic GmbH, Hamburg, Germany) equipped with a video camera. In an inclinable plane, a sample on a stage was tilted until a 50 μL water droplet began to slide down on to the sample surface. Subsequently, the advancing contact angle (θ_A), receding contact angle (θ_R), and sliding angle (θ_S) were determined. The average of five readings was used as the data.

GI-WAXD measurements were one of the very powerful surface X-ray measurements used to analyze the molecular aggregation states of the polymer thin films, and they were carried out at the BL03XU and BL13XU beamlines of SPring-8 (Japan Synchrotron Radiation Research Institute, Hyogo, Japan) using incident X-ray with wavelength λ of 0.100 nm.[41] The scattering vector, q, in specular reflectivity is defined by $q = (4\pi/\lambda) \sin\theta$, where λ and θ are the wavelength and detected angle of the X-ray beam, respectively. GI-WAXD data were obtained from the surface and deeper regions at incident angles (α_i) below and above the critical angle (α_c) with λ = 0.100 nm. The α_c for poly(FA-C_8) is calculated to be ca. 0.12°. Thus, α_i values of 0.08° and 0.16° for the surface- and bulk-sensitive measurements were chosen, respectively.[42,43] Diffractions from the sample film were detected in the in-plane and out-of-plane directions in order to change the scanning direction of the detecting element against the flat thin film. Information about the structure perpendicular to the surface is obtained from the in-plane geometry because the scattering vector (q_{xy}) is parallel to the surface. In contrast, the detected profiles reflect information on the crystalline states parallel to the brush surface in the out-of-plane geometry.

dx.doi.org/10.1021/ma202300r | Macromolecules 2012, 45, 1509−1516

3. RESULTS AND DISCUSSION

3.1. Surface-Initiated ATRP of poly(FA-C_8) Brush Thin Films on a Silicon Wafer. SI-ATRP of FA-C_8 was carried out in the presence of a free initiator EB and the initiator-immobilized substrate to produce free poly(FA-C_8) and the corresponding polymer brushes on the substrates simultaneously. Table 1 shows the M_n values and MWDs of the resulting free poly(FA-C_8)s determined by SEC-MALS, and the thicknesses of the polymer brushes measured using an ellipsometer. ATRP of FA-C_8 using CuBr and C_9bpy at 383 K for 48 h proceeded homogeneously, giving a polymer with a broad MWD in 65% yield (run 1). When Me_6TREN was used as the copper ligand, the polymer was obtained in 29% yield within 2 h by ATRP, even at the lower temperature of 333 K, although the MWD was still rather broad (run 2). Interestingly, addition of very small amounts of an ionic liquid, FBImCl, to the polymerization solution afforded poly(FA-C_8) with a narrow MWD (M_w/M_n = 1.05) and predictable M_n in 25% yield (run 3). In the case of run 3, the addition of only 0.01 wt % of FBImCl to the monomer dramatically improved control of the polymerization to give a narrow MWD. The M_n obtained in run 3 was in good agreement with the theoretical M_n calculated from the yield and feed ratio of the monomer and initiator in the polymerization. However, on increasing the amount of FBImCl added from 0.05 to 1 wt %, the MWD of poly(FA-C_8) became broader, around 1.15−1.40 (runs 4−7). The rate of polymerization of FA-C_8 also decreased with increasing of the amounts of added FBImCl (runs 3−7). A similar additive effect was also observed using HMImCl (runs 8−11) instead of FBImCl. ATRP of FA-C_8 in the presence of 0.4 and 0.8 wt % HMImCl (runs 10 and 11) gave polymers with relatively narrow MWDs M_w/M_n = 1.2, approximately.

Figure 1 shows a first-order plot of monomer conversion vs polymerization time for the ATRP of poly(FA-C_8) in the presence of an ionic liquid, i.e., FBImCl mixture, at 333 K. The logarithmic monomer conversion index calculated using $\ln([M]_0/[M])$ increased linearly with polymerization time from the initial stage to 0.15. The apparent propagation rate constant k_p^{app} at 333 K was 8.05 × 10^{-3} M^{-1} s^{-1} at the initial stage. Value of k_p^{app} at 333 K was desire from slope (dot line) of Figure 1. The plots at the middle conversion stage no longer showed a linear relationship. However, the MWD of the resulting free polymer, obtained by SEC-MALS, was relatively narrow.

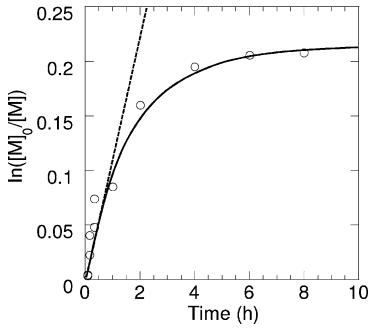


Figure 1. First-order kinetic plots of $\ln([M]_0/[M])$ versus time for the ATRP of poly(FA-C_8) at 333 K in addiotion of *N*-perfluorobutylethyl-*N*′-methylimidazorium chloride; [CuBr]/[bpy]/[FA-C_8]/[EB] = 1/2/960/1 (molar ratio), [EB] = 0.0021 mmol, where Me_6TREN, FA-C_8, and EB are tris(2-(dimethyl)aminoethyl)amine, 2-(perfluorooctyl)-ethyl acrylate, and ethyl 2-bromoisobutyrate, respectively. $\ln[M]_0/[M]$ was calculated by the gravities of synthesized poly(FA-C_8)s.

As shown in Figure 2, the M_n of poly(FA-C_8) also increased linearly, maintaining a polydispersity index narrower than 1.2 with monomer conversion until the M_n reached ca. 100 000. However, the MWDs of poly(FA-C_8)s with M_n larger than 150 000 were still lower than 1.5. This was lower value of the polymer synthesized by conventional ATRP of FA-C_8. These results indicated that the MWD of poly(FA-C_8) could be controlled by changing the molar concentration of the ionic liquid in the polymerization solution.

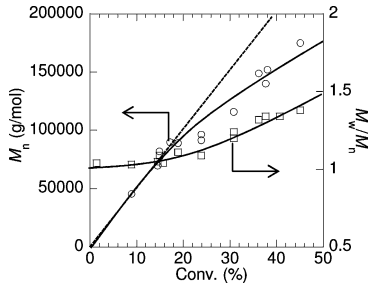


Figure 2. Evolution of the number-averaged molecular weight (M_n) (open circle and straight line) and theoretical line (dashed line) and molecular weight dispersity (M_w/M_n) (square) with conversion of ATRP of 2-(perfluorooctyl)ethyl acrylate (FA-C_8) in addition of *N*-perfluorobutylethyl-*N*′-methylimidazorium chloride at 60 °C. M_n and M_w/M_n of the poly(FA-C_8) were estimated by SEC-MALS measurement using 10 mM sodium trifluoroacetate/hexafluoroisopropanol solution.

The effects of ionic liquids on controlled polymerization of FA-C_8 are not yet understood. We supposed that imidazolium type ionic liquids affected the redox potentials of the Cu/ligands complex,[44,45] shifting the ATRP equilibrium to the dormant side to give slow propagation. Another possible explanation is halogen exchange at the propagating chain end of the polymer. The bromide atom at the chain end might be partially exchanged for chloride from the imidazolium chloride during the polymerization. A dormant species with a C−Cl bond would be more stable than one with a C−Br bond because the bonding energy of C−Cl is higher than that of C−Br. Ameduri et al.[46] have reported the kinetics of radical telomerization of vinylidene fluoride, initiated by di-*tert*-butyl peroxide, in the presence of three chain transfer agents, $HCCl_3$, CCl_4, and CCl_3Br. The values of the chain transfer constants were assessed as 35, 0.25, and 0.06 for CCl_3Br, CCl_4, and $HCCl_3$, respectively. This result implys that the C−Br bond was easy to disassociate compared with the C−Cl bond. Further experiments to explore the effects of ionic liquids on electrolyte monomers are currently in progress.

The relationship between the thickness of the poly(FA-C_8) brush and M_n of the corresponding free polymer is shown in Figure 3. A direct proportion relationship was observed between the M_n of the free polymer and brush thickness from 2 up to 35 nm. Provided that the free polymer and the brush with the same M_n are formed in the same reaction batch, the graft density σ of the polymer brush is estimated to be 0.21 chains/nm^2 based on the relationship between the thickness L (nm) and M_n:[47]

$$\sigma = \rho L N_A \times 10^{-21}/M_n \quad (1)$$

dx.doi.org/10.1021/ma202300r | *Macromolecules* 2012, 45, 1509−1516

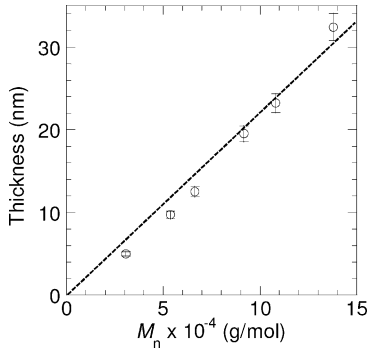


Figure 3. Thickness of poly(FA-C_8) brushes estimated by ellipsometry as a function of the number-averaged molecular weight (M_n) of the corresponding free polymer produced by ATRP in *N*-perfluorobutylethyl-*N*′-methylimidazorium chloride.

where ρ and N_A are the assumed density of the bulk polymer, i.e., 1.6 g/cm^3, and Avogadro's number, respectively. This value is lower than the typical graft density of a PMMA brush (0.60–0.70 chains/nm^2) prepared by the "grafting-from" method[35] because of the larger molecular size of the R_f groups at the side chains compared with the size of MMA. The formation of poly(FA-C_8) brushes was confirmed by XPS measurements, as shown in Figure 4. Three peaks at 688.0, 532.0, and 285.0 eV

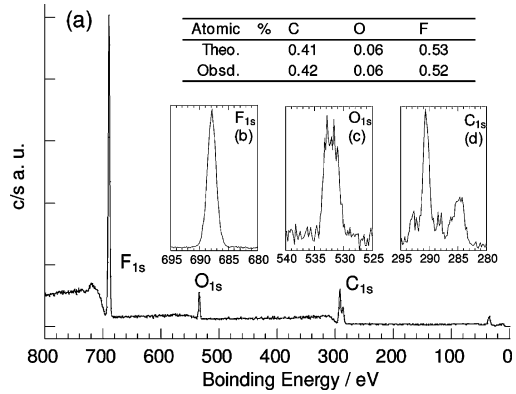


Figure 4. XPS spectra of poly(FA-C_8) brush prepared by surface-initiated ATRP of FA-C_8 in FBImCl on silicon wafer: (a) survey scan spectrum; high-resolution spectra of (b) F_{1s}, (c) O_{1s}, and (d) C_{1s} peak region.

were observed, corresponding to fluorine, oxygen, and carbon, respectively. The atomic ratios of C/O/F in the poly(FA-C_8) brush were estimated to be 0.42/0.06/0.52, which was relatively close to the theoretical values calculated from the atomic composition of FA-C_8. In the topographic AFM image of a poly(FA-C_8) brush using the tapping mode, the root-mean-square (rms) of the surface roughness was ~0.9 nm in a 5 × 5 μm^2 scanning area. No significant roughness was observed on the surfaces of the brushes by AFM in air.

3.2. Grazing Incidence X-ray Diffraction of Poly(FA-C_8) Brush. GI-WAXD is a powerful tool for characterizing the molecular aggregation states of polymer thin films containing ordered structures. Not only the bulk but also the outermost surface of the polymer thin films can be evaluated by choosing the incident angle (α_i) of the X-rays to be in the vicinity of the critical angle (α_c). When the α_i of the X-ray to the sample surface is smaller than the α_c, the incident X-rays undergo total external reflection and penetrate into the sample as evanescent waves. Under this experimental condition, using a X-ray of wavelength λ = 0.100 nm, the α_c for poly(FA-C_8) is calculated to be ca. 0.12°. Thus, α_i values of 0.08° and 0.16° for the measurements at the surface and deeper regions, respectively, were chosen.[42,43] Previously, Honda et al.[48−50] reported the molecular aggregation states of poly(FA-C_8) spin-coated thin films on silicon wafers measured by GI-WAXD. In the in-plane geometry, a diffraction peak corresponding to hexagonal packing of the R_f groups at q_{xy} = 12.5 nm^{-1} was observed at the surface and bulk regions for incident angles of 0.08° and 0.16°, respectively. In addition, the out-of-plane diffraction patterns at the surface and deeper regions gave peaks at around q_z = 2−6 nm^{-1}, attributable to the bilayer lamellar structure. Therefore, in spin-cast thin film, the R_f groups at the side chains were oriented regularly from the outermost surface to the interface between the polymer and the silicon wafer. In contrast, different molecular aggregation states of the R_f groups were observed in poly(FA-C_8) brush thin films with a thickness of ca. 40 nm.[16] In the outermost surface of the poly(FA-C_8) brush, the R_f groups were oriented perpendicular to the substrate, whereas the R_f groups at deeper regions in the brush film were in relatively random states as a result of the high graft density and restricted conformations of the brush main chains, which were covalently bonded with the substrate.

GI-WAXD measurements at the synchrotron facility SPring-8 were conducted to investigate the orientation and packing of the R_f groups at the side chains of the brush thin films to understand the effects of the MWD of the brush on the molecular aggregation states of the R_f groups. Figure 5a shows

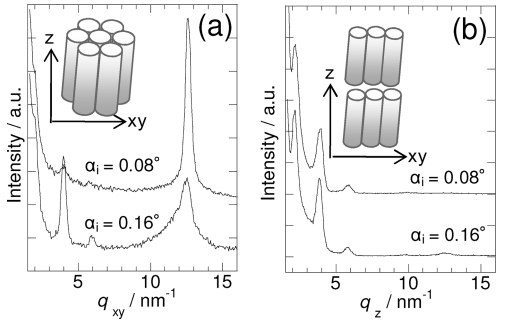


Figure 5. In-plane GI-WAXD patterns (a) and out-of-plane GI-WAXD patterns (b) of the poly(FA-C_8) brush with board MWD (thickness = 20 nm, M_n = 82 500, M_w/M_n = 1.95). The wavelength of the X-ray was 0.10 nm. The incident angle of X-ray was 0.08° and 0.16°.

the in-plane GI-WAXD profiles measured at 0.08° and 0.16° for a poly(FA-C_8) brush with a broad MWD (thickness = 20 nm, M_n = 82 500, M_w/M_n = 1.95). When α_i was 0.08°, which is below the α_c of poly(FA-C_8), sharp peaks appeared only at ca. 12.6 nm^{-1}.[51−54] The *d*-spacing calculated from the peak position was ca. 0.50 nm, which was almost the same as the intermolecular distance between the R_f groups at the side chains of poly(FA-C_8) spin-cast films (d = 0.50 nm), considering previous results for poly(FA-C_8) spin-cast thin films.[48−50] The side chains of the polymers are formed by quasi-hexagonal packing and are oriented normal to the surface. In in-plane GI-WAXD profiles with α_i = 0.16°, a peak corresponding to packing of the R_f groups was also detected. The peak top and half-width of the packing for R_f groups fitted by a Gaussian curve are slightly changed, to a low scattering vector (q_{xy} = 12.5 nm^{-1}), and broader than at the outermost

dx.doi.org/10.1021/ma202300r | *Macromolecules* 2012, 45, 1509−1516

surface. Moreover, diffraction peaks at q_{xy} = 3.95 and 5.92 nm^{-1} corresponding to the bilayer lamellar structure of the R_f groups were observed in the in-plane geometry. These results indicated that the R_f groups formed highly ordered structures at the outermost surface of the brush thin films, although in the deeper regions, the R_f groups could not form ordered molecular aggregation states because the main chains of the brush were immobilized by covalent bonding with the substrate. In a recent study,[16,17] we investigated the different molecular aggregation states of poly(FA-C_8) brushes by GI-WAXD and XR measurements. The XR profiles showed that a high-density area existed at the outermost surface of the brush thin film, indicating highly packed aggregation of the R_f groups. In the case of the GI-WAXD measurements, more ordered structures of the R_f groups, oriented perpendicular to the substrate, were also observed. These aggregation states agreed well with previously reported states. Figure 5b shows out-of-plane GI-WAXD profiles at α_i = 0.08° and 0.16° for poly(FA-C_8) brush films with broad MWDs. Sharp diffraction peaks attributed to a lamellar structure of the R_f groups were observed at q_z = 2.19, 3.95, and 5.86 nm^{-1} at the outermost surface region (α_i = 0.08°) and at q_z = 2.14, 3.84, and 5.81 nm^{-1} at bulk region (α_i = 0.16°). In symmetric reflection geometry WAXD measurements, strong diffraction peaks attributed to a lamellar structure of the R_f groups appeared for poly(FA-C_8) brushes with broad MWD.[16]

Poly(FA-C_8) brushes with narrow MWD showed different diffraction patterns from those with broad MWD in in-plane (Figure 6a) and out-of-plane (Figure 6b) GI-WAXD measurements. In the out-of-plane geometry, a poly(FA-C_8) brush film with a narrow MWD (thickness = 22 nm, M_n = 70 000, M_w/M_n = 1.05) clearly showed strong diffraction peaks at q_z = 1.94, 3.87, and 5.83 nm^{-1} in the outermost surface region and at q_z = 2.02, 3.94, and 5.92 nm^{-1} at a deeper region corresponding to a lamellar structure of R_f groups oriented parallel to the substrate. The *d*-spacings of the three peaks were calculated to be ca. 3.23, 1.62, and 1.07 nm at the outermost surface and 3.11, 1.59, and 1.06 nm at the deeper region. In the case of in-plane GI-WAXD measurement for investigating the outermost surface, packing of the R_f groups is also observed at ca. 12.6 nm^{-1}. Out-of-plane GI-WAXD profiles at 0.08° and 0.16° for poly(FA-C_8) brush films with narrow MWD are shown in Figure 6b. As mentioned above, sharp and strong diffraction peaks attributed to lamellar structure of the R_f groups were observed for the poly(FA-C_8) brush with board MWD, but no peaks appeared in the diffraction pattern of the poly(FA-C_8) brush with narrow MWD. The R_f groups attached to poly(FA-C_8) brush with narrow MWD hardly formed two-dimensional ordered packing structures because the conformations of the main chains were restricted by the densely grafted brush chain structure.

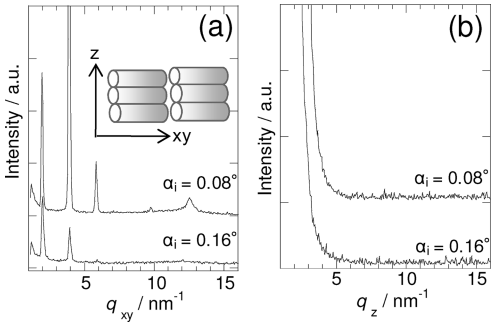


Figure 6. In-plane GI-WAXD patterns (a) and out-of-plane GI-WAXD patterns (b) of the poly(FA-C_8) brush with board MWD narrow MWD (thickness = 22 nm, M_n = 70 000, M_w/M_n = 1.05). The wavelength of the X-ray was 0.10 nm. The incident angle of X-ray was 0.08° and 0.16°.

As mentioned above, in the case of a poly(FA-C_8) brush with broad MWD such as in run 1, almost all the R_f groups at the outermost surface were oriented perpendicular to the surface. The outermost surface of the brush might be completely covered with the CF_3 groups of the R_f groups, reducing the surface free energy. In addition, the chain density at the outermost surface of the brush with large MWD is lower than that at the brush/substrate interface because polymers of various lengths were grafted on the flat surface. The main chain of the brush at the outermost surface therefore could not afford to adjust its conformation to form the most stable ordered structure of the side-chain R_f groups. The rigid-rod-like R_f groups favor formation of hexagonal packing states with directions normal to the air/polymer interface in order to reduce the surface free energy (Figure 7a).

In contrast, the chain density at the outermost surface of the brush with narrow MWD would be high enough to stretch the main chain in the perpendicular direction because polymers with well-regulated chain lengths were densely grafted on the flat substrate. The orientation of R_f groups in a brush with a narrow MWD would be governed by the nearly extended the main chain conformation in the brush state. The side chains of the R_f groups of the brush with narrow MWD would therefore be forced to orient parallel to the substrate surface. However, the side-chain R_f groups could not form a highly ordered hexagonal packing structure in the two-dimensional plane. This is the significant difference between brushes with broad and narrow MWD with respect to the orientation direction of rigid-rod-like R_f groups (Figure 7b).

We conclude that the MWD of the poly(FA-C_8) brush thin films strongly affected the molecular aggregation states of the R_f groups of the brush. This is an important result describing the relationship between the primary structure of the polymer and the molecular aggregation states in the polymer brush.

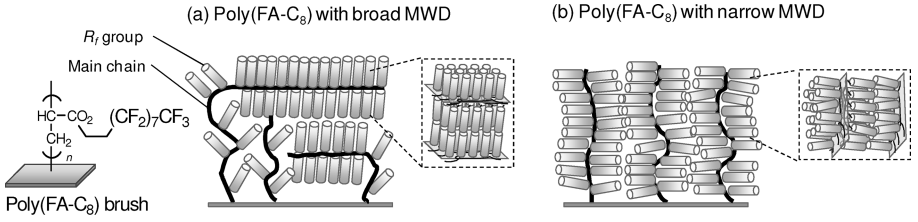


Figure 7. Schematic image of the molecular aggregation structure of R_f groups attached to poly(FA-C_8) brush with board (a) and narrow (b) MWD. The R_f group at the side chain of poly(FA-C_8) brush is represented as a small "rod" in this illustration.

dx.doi.org/10.1021/ma202300r | *Macromolecules* 2012, 45, 1509–1516

3.3. Water-Repellency Properties of Poly(FA-C_8) Brush Thin Films. Surface wettability is one of the most important properties of polymers with R_f groups and can be analyzed easily by contact angle measurements. The water repellencies of poly(FA-C_8) brushes with narrow and broad MWDs were analyzed using static and dynamic water contact angles, as shown in Table 2. The static water contact angles of broad- and narrow-MWD brushes were found to be 122° and 115°, respectively, meaning that the surfaces of poly(FA-C_8) brush thin films are hydrophobic. No significant differences were observed between the static water contact angles of poly(FA-C_8) brush with narrow MWD and those with broad MWD. The contact angles of CH_2I_2 (the volume was 2 μL) on narrow- and broad-MWD brushes were 103° and 99°, respectively. The surface free energies of both brushes were 7.7 and 9.4 mN/m, as calculated by the Owens and Wendt equation[55] with water and CH_2I_2 probing liquids. In the case of the brush with broad MWD, the value of surface free energy was relatively close to the value for CF_3 (6 mN/m). The surface roughnesses of the poly(FA-C_8) brushes with broad and narrow MWDs were the same; both rms values were 0.9−1.0 nm in a 5 × 5 μm^2 scanning area. It was clear that the surface roughness of the polymer brush does not influence the magnitude of contact angle. Photographs of dynamic contact angle with 50 μL of water are shown in Figure 8. The advancing contact angle (θ_A), receding contact angle (θ_R), and sliding contact angle (θ_S) of a poly(FA-C_8) brush with a broad MWD were 128°, 105°, and 15° and those for a narrow-MWD brush were 125°, 80°, and 35°, respectively. θ_S of the broad-MWD brush was lower than that for the narrow-MWD brush. The contact angle hysteresis, which is expressed as $\theta_A - \theta_R$ of a water droplet on a poly(FA-C_8) brush film with a broad MWD was 23° and that for a narrow MWD brush film was 45°. A sliding water droplet on a brush film with narrow MWD formed an asymmetric shape with a high θ_A and relatively low θ_R, but a water droplet on a brush film with a broad MWD began to slide maintaining a high θ_A and high θ_R, when the film was tilted to θ_S = 15° (Figure 8).

Table 2. Results of Contact Angle Measurements

sample	$M_n \times 10^{-4}$	M_w/M_n	thickness (nm)	water contact angle (deg) $\theta^{a,e}$	$\theta_A{}^{b,f}$	$\theta_R{}^{c,f}$	$\theta_S{}^{d,f}$
poly(FA-C_8) brush broad MWD	8.2	2.32	13	120	129	103	13
	9.3	1.86	20	122	128	105	15
	12.1	1.68	39	119	124	106	10
poly(FA-C_8) brush narrow MWD	3.1	1.10	9	116	128	78	36
	7.0	1.05	22	115	125	80	35
	11.7	1.13	26	118	126	80	32

[a]θ = static. [b]θ_A = advancing. [c]θ_R = receding. [d]θ_S = sliding. [e]Water volume: 2 μL. [f]Water volume: 50 μL.

As mentioned above, we found that the surface free energy and contact angle hysteresis depended strongly on the MWD of the polymer brush. These different wetting behaviors were caused by the difference in the orientations of the R_f groups of the poly(FA-C_8) brush films. GI-WAXD measurements showed that the outermost surface of a poly(FA-C_8) brush with broad MWD had a highly ordered lamellar structure of rodlike R_f groups with direction normal to the air/film interface to reduce the surface free energy effectively. In contrast, the R_f groups in a brush with narrow MWD were aligned parallel to the air/film interface and did not form highly ordered structures such as hexagonal packing in the two-dimensional plane. Surface reorientation therefore took place on contact with water, resulting in a large hysteresis in the dynamic contact angle measurements. We conclude that the water repellency of a poly(FA-C_8) brush thin film is influenced by the molecular aggregation states, which are influenced by primary structure such as MWD.

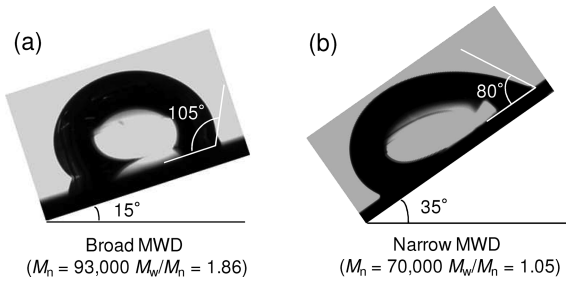


Figure 8. Optical micrograph of an water droplet on a poly(FA-C_8) film surface with broad (a) and narrow (b) MWD in dynamic contact measurements.

4. CONCLUSIONS

We carried out SI-ATRP of FA-C_8 on a flat silicon substrate in the absence and presence of an ionic liquid to give poly(FA-C_8) brush thin films with board MWD (M_w/M_n = 1.86) and narrow MWDs (M_w/M_n = 1.05). GI-WAXD revealed that the orientation of R_f groups at the side chains in the outermost surface region for poly(FA-C_8) brush thin films with broad MWDs was perpendicular to the surface. In contrast, the R_f groups were aggregated parallel to the surface in the case of poly(FA-C_8) brushes with narrow MWDs. The receding and sliding contact angles were 80° and 35°, respectively, at the surface of the poly(FA-C_8) with a narrow MWD, whereas the receding and sliding contact angles were 105° and 15°, respectively, at the surface of the poly(FA-C_8) with a broad MWD. These results indicated that the MWD of a surface-grafted poly(FA-C_8) affected the molecular aggregation state and orientation of the R_f groups, and these factors are related to the water repellency of the brush surface.

AUTHOR INFORMATION

Corresponding Author

*Tel: +81-92-802-2517; Fax: +81-92-802-2518; e-mail: takahara@cstf.kyushu-u.ac.jp.

ACKNOWLEDGMENTS

The present work is supported by a Grant-in-Aid for the Global COE Program, "Science for Future Molecular Systems", from the Ministry of Education, Culture, Science, Sports and Technology of Japan. H.Y. acknowledges the financial support of a Grant-in-Aid for JSPS Fellows. The synchrotron radiation GIWAXD measurements were performed at the BL13XU (2010B1346) and BL03XU in the SPring-8 with the approval of the Japan Synchrotron Radiation Research Institute (JASRI). We gratefully acknowledge Dr. M. Morita (Daikin Industries

Ltd.) for the generous gift of FA-C_8 monomer and Dr. Y. Okamoto (DENSO) for kindly giving us the opportunity to make the GIWAXD measurements at the BL03XU.

REFERENCES

(1) Pittman, A. G. In *Fluoropolymers*; Wall, L. A., Ed.; Wiley-Interscience: New York, 1972; p 419.
(2) Yokoyama, H.; Tanaka, K.; Takahara, A.; Kajiyama, T.; Sugiyama, K.; Hirao, A. *Macromolecules* **2004**, *37*, 939.
(3) Hikita, M.; Tanaka, K.; Nakamura, T.; Kajiyama, T.; Takahara, A. *Langmuir* **2004**, *20*, 5304.
(4) Ameduri, B.; Bongiovanni, R.; Malucelli, G.; Pollicino, A.; Priola, A. *J. Polym. Sci., Part A: Polym. Chem.* **1999**, *37*, 77.
(5) Ameduri, B.; Bongiovanni, R.; Lombardi, V.; Pollicino, A.; Priola, A.; Recca, A. *J. Polym. Sci., Part A: Polym. Chem.* **2001**, *39*, 4227.
(6) Montefusco, F.; Bongiovanni, R.; Priola, A.; Ameduri, B. *Macromolecules* **2004**, *37*, 9804.
(7) Meskini, A.; Raihane, M.; Ameduri, B. *Macromolecules* **2009**, *42*, 3532.
(8) Advincula, R. C.; Brittain, W. J.; Caster, K. C.; Rühe, J. *Polymer Brushes: Synthesis, Characterization, Applications*; Wiley-VCH: Weinheim, 2004.
(9) Matyjaszewski, K.; Miller, P. J.; Shukla, N.; Immaraporn, B.; Gelman, A.; Luokala, B. B.; Siclovan, T. M.; Kickelbick, G.; Vallant, T.; Hoffmann, H.; Pakula, T. *Macromolecules* **1999**, *32*, 8716.
(10) Granville, A. M.; Brittain, W. J. *Macromol. Rapid Commun.* **2004**, *25*, 1298.
(11) Granville, A. M.; Boyes, S. G.; Akgun, B.; Foster, N. D.; Brittain, W. J. *Macromolcules* **2004**, *37*, 2790.
(12) Granville, A. M.; Boyes, S. G.; Akgun, B.; Foster, M. D.; Brittain, W. J. *Macromolecules* **2005**, *38*, 3263.
(13) Wu, Y.; Huang, Y.; Ma, H. *J. Am. Chem. Soc.* **2007**, *129*, 7226.
(14) Chen, R.; Zhu, S.; Maclaughlin, S. *Langmuir* **2008**, *24*, 6889.
(15) Andruzzi, L.; Hexemer, A.; Li, X.; Ober, C. K.; Kramer, E. J.; Galli, G.; Chiellini, E.; Fischer, D. A. *Langmuir* **2004**, *20*, 10498.
(16) Yamaguchi, H.; Honda, K.; Kobayashi, M.; Morita, M.; Masunaga, H.; Sakata, O.; Sasaki, S.; Takahara, A. *Polym. J.* **2008**, *40*, 854.
(17) Yamaguchi, H.; Honda, K.; Kobayashi, M.; Morita, M.; Masunaga, H.; Sakata, O.; Sasaki, S.; Takata, M.; Takahara, A. *J. Phys. Conf. Ser.* **2009**, *184*, 012009.
(18) Tsubokawa, N.; Satoh, M. *J. Appl. Polym. Sci.* **1997**, *65*, 2165.
(19) Jung, D.-H.; Park, I. J.; Choi, Y. K.; Lee, S.-B.; Park, H. S.; Rühe, J. *Langmuir* **2002**, *18*, 6133.
(20) Lemieux, M.; Minko, S.; Usov, D.; Stamm, M.; Tsukruk, V. V. *Langmuir* **2003**, *19*, 6126.
(21) Yu, W. H.; Kang, E. T.; Neoh, K. G. *Ind. Eng. Chem. Res.* **2004**, *43*, 5194.
(22) Xu, F. J.; Yuan, Z. L.; Kang, E. T.; Neoh, K. G. *Langmuir* **2004**, *20*, 8200.
(23) Yu, W. H.; Kang, E. T.; Neoh, K. G. *Langmuir* **2004**, *20*, 8294.
(24) Brantley, E. L.; Jennings, G. K. *Macromolecules* **2004**, *37*, 1476.
(25) Fu, G.-D.; Shang, Z.; Hong, L.; Kang, E.-T.; Neoh, K.-G. *Adv. Mater.* **2005**, *17*, 2622.
(26) Sun, L.; Baker, G. L.; Bruening, M. L. *Macromolecules* **2005**, *38*, 2307.
(27) Xu, F. J.; Zhao, J. P.; Kang, E. T.; Neoh, K. G. *Ind. Eng. Chem. Res.* **2007**, *46*, 4866.
(28) Benedetto, A.; Viel, P.; Noël, S.; Izard, N.; Chenevier, P.; Palacin, S. *Surf. Sci.* **2007**, *601*, 3687.
(29) Gong, R.; Maclaughlin, S.; Zhu, S. *Appl. Surf. Sci.* **2008**, *254*, 6802.
(30) Li, L.; Yan, G.; Wu, J.; Yu, X.; Guo, Q. *J. Macromol. Sci., Part A* **2008**, *45*, 828.
(31) Ameduri, B. *Macromolecules* **2010**, *43*, 10163.
(32) Kobayashi, M.; Terada, M.; Terayama, Y.; Kikuchi, M.; Takahara, A. *Macromolecules* **2010**, *43*, 8409.
(33) Terayama, Y.; Kikuchi, M.; Kobayashi, M.; Takahara, A. *Macromolecules* **2011**, *44*, 104.
(34) Harrisson, S.; Mackenzie, S. R.; Haddleton, D. M. *Macromolecules* **2003**, *36*, 5072.
(35) Ohno, K.; Morinaga, T.; Koh, K.; Tsujii, Y.; Fukuda, T. *Macromolecules* **2005**, *38*, 2137.
(36) Kobayashi, M.; Takahara, A. *Chem. Lett.* **2005**, *34*, 1582.
(37) Queffelec, J.; Gaynor, S. G.; Matyjaszewski, K. *Macromolecules* **2000**, *33*, 8629.
(38) Lindstrom, A. B.; Strynar, M. J.; Libelo, E. L.; Field, J. A. *Environ. Sci. Technol.* **2011**, *45*, 7951.
(39) Houde, M.; De Silva, A. O.; Muir, D. C. G.; Letcher, R. J. *Environ. Sci. Technol.* **2011**, *45*, 7962.
(40) Kobayashi, M.; Terayama, Y.; Hosaka, N.; Kaido, M.; Suzuki, A.; Yamada, N.; Torikai, N.; Ishihara, K.; Takahara, A. *Soft Matter* **2007**, *3*, 740.
(41) Sakata, O.; Furukawa, Y.; Goto, S.; Mochizuki, T.; Uruga, T.; Takeshita, K.; Ohashi, H.; Ohata, T.; Matsushita, T.; Takahashi, S.; Tajiri, H.; Ishikawa, T.; Nakamura, M.; Ito, M.; Sumitani, K.; Takahashi, T.; Shimura, T.; Saito, A.; Takahashi, M. *Surf. Rev. Lett.* **2003**, *10*, 543.
(42) Russell, T. P. *Mater. Sci. Rep.* **1990**, *5*, 171.
(43) Yakabe, H.; Tanaka, K.; Nagamura, T.; Sasaki, S.; Sakata, O.; Takahara, A.; Kajiyama, T. *Polym. Bull.* **2005**, *53*, 213.
(44) Tang, W.; Kwak, Y.; Braunecker, W.; Tsarevsky, N. V.; Coote, M. L.; Matyjaszewski, K. *J. Am. Chem. Soc.* **2008**, *130*, 10702.
(45) Braunecker, W. A.; Tsarevsky, N. V.; Gennaro, A.; Matyjaszewski, K. *Macromolecules* **2009**, *42*, 6348.
(46) Duc, M.; Ameduri, B.; David, G.; Boutevin, B. *J. Fluorine Chem.* **2007**, *128*, 144.
(47) Husseman, M.; Malmstrom, E. E.; McNamura, M.; Mate, M.; Mecerreyes, D.; Benoit, D. G.; Hedrick, J. L.; Mansky, P.; Huang, E.; Russell, T. P.; Hawker, C. J. *Macromolecules* **1999**, *32*, 1424.
(48) Honda, K.; Morita, M.; Otsuka, H.; Takahara, A. *Macromolecules* **2005**, *38*, 5699.
(49) Honda, K.; Yakabe, H.; Koga, T.; Sasaki, S.; Sakata, O.; Otsuka, H.; Takahara, A. *Chem. Lett.* **2005**, *34*, 1024.
(50) Honda, K.; Yamaguchi, H.; Kobayashi, M.; Morita, M.; Takahara, A. *J. Phys. Conf. Ser.* **2008**, *100*, 012035.
(51) Bunn, C. W.; Howells, E. R. *Nature* **1954**, *174*, 549.
(52) Corpart, J. M.; Girault, S.; Juhué, D. *Langmuir* **2001**, *17*, 7237.
(53) Fujimori, A.; Araki, T.; Nakahara, H.; Ito, E.; Hara, M.; Ishii, H.; Ouchi, Y.; Seki, K. *Chem. Phys. Lett.* **2001**, *349*, 6.
(54) Urushihara, Y.; Nishino, T. *Langmuir* **2005**, *21*, 2614.
(55) Owens, D. K.; Wendt, R. C. *J. Appl. Polym. Sci.* **1969**, *13*, 1741.

Macromolecules

Article

pubs.acs.org/Macromolecules

The Crystallization of Confined Polymers and Block Copolymers Infiltrated Within Alumina Nanotube Templates

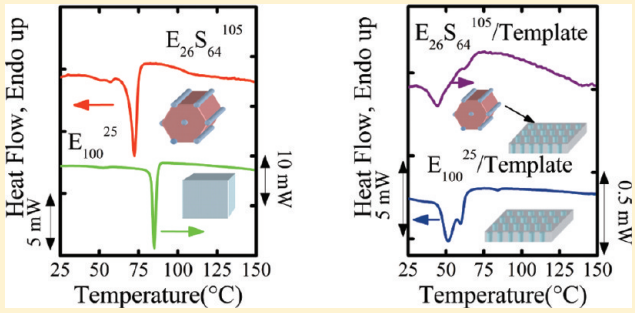
Rose Mary Michell,[†] Arnaldo T. Lorenzo,[†] Alejandro J. Müller,*[,†] Ming-Champ Lin,[‡] Hsin-Lung Chen,[‡] Iwona Blaszczyk-Lezak,[§] Jaime Martín,[§] and Carmen Mijangos[§]

[†]Grupo de Polímeros USB, Departamento de Ciencia de los Materiales, Universidad Simón Bolívar, Apartado 89000, Caracas 1080-A, Venezuela

[‡]Department of Chemical Engineering and Frontier Center of Fundamental and Applied Sciences of Matters, National Tsing Hua University, Hsin-Chu 30013, Taiwan

[§]Instituto de Ciencia y Tecnología de Polímeros, CSIC, Juan de la Cierva, 3, 28006 Madrid, Spain

ABSTRACT: Porous anodic aluminum oxide (AAO) templates with 20, 35, and 60 nm cylindrical pores were prepared and subsequently infiltrated with poly(ethylene oxide), PEO, polyethylene, PE, and polyethylene-*block*-polystyrene diblock copolymers, PE-*b*-PS, of various compositions. The crystallization of the nanocylinders within the AAO templates was studied by differential scanning calorimetry (DSC) and wide angle X-ray diffraction (WAXD). A clear change from heterogeneous to homogeneous bulk nucleation was detected in the PEO before and after infiltration within a 20 nm template, respectively. The homogeneously nucleated nanocylinders needed extreme supercooling in order to crystallize, and their low crystallization temperature was successfully correlated with the volume of the crystallizing phase. 2D-WAXD measurements demonstrated that the PEO chains within the crystals formed inside the nanocylinders, preferentially orient perpendicular to the cylinder axis. This chain orientation is probably due to the easier crystal growth propagation along the cylinder length (200 μm for the templates employed to infiltrate PEO). In the case of the infiltrated PE, although its crystallization temperature was also lowered by confinement within a large number of nanocylinders, its value is still at least 75 °C above T_g; therefore, its nucleation is probably originated at the surface of the nanocylinders and cannot be considered homogeneous bulk nucleation. Strongly segregated semicrystalline PE-*b*-PS diblock copolymers were infiltrated into AAO templates for the first time, thereby creating a nanostructured hybrid material where the PE phase experienced double confinement for some compositions (i.e, the phase-segregated confinement within a vitreous PS matrix and the physical confinement within the nanopores). Fractionated crystallization was observed for the PE block microdomains within both neat copolymers and infiltrated ones. However, in the case of the infiltrated block copolymers, the dominant crystallization was always that produced at maximum supercooling, as expected for the extreme confinement environment. In the cases of PE blocks that self-assemble to form 42 nm diameter cylinders and 24 nm spheres within the neat block copolymers, the PE phase crystallization was impossible to detect once they were infiltrated into the 35 nm templates, as opposed to the 60 nm case where the lowest crystallization and melting temperatures were recorded. The crystallization and melting temperatures decreased as the volume of the crystallizing phase decreased (i.e., with a decrease in template pore volume, for neat PE, or PE phase volume within neat of infiltrated copolymers). The nucleation of the confined PE block microdomains is probably originated at their surface.



INTRODUCTION

Nanostructured materials have attracted much scientific and technological attention.[1−7] In a semicrystalline polymer, its crystallization process and final morphology determine the end properties of the material and its application.[2,5] The confinement of the polymer within nanometer environments (e.g., ultrathin films, block copolymer nanophases and more recently, inorganic templates) can dramatically altered both the nucleation and growth processes.[8−15]

Linear diblock copolymers in the strong segregation limit undergo phase segregation to form microdomains such as spheres, cylinders, gyroids, and lamellae. If these microdomain morphologies are formed by crystalline blocks, their crystallization process can be effectively confined within the microdomains with the degree of confinement governed by their morphology.[10]

Another way to prepare 1D polymer nanostructures is through the use of porous anodic aluminum oxide (AAO) templates and subsequent infiltration of the polymer into the nanocavities of such templates. Templates of this type are prepared

Received: October 17, 2011
Revised: November 24, 2011
Published: January 31, 2012

ACS Publications © 2012 American Chemical Society

electrochemically from aluminum metal. They are highly versatile with respect to the diameter and length of the obtained 1D structure. AAO templates are characterized by uniform tailored pores with long-range ordered hexagonal symmetry in arrangement. The porous AAO templates were first synthesized by Masuda and Fukuda,[16] and further developed for the fabrication of 1D polymer nanostructures by means of nanomolding processes.[17−21] As any molding process, it consists first of the infiltration of a polymeric melt fluid into nanocavities with a well-defined shape, then the polymer is solidified within the cavities, and finally the molded polymeric material is removed (when a free polymeric nanostructure is required). The use of polymer filled inorganic templates has caused a large impact because of the versatility of these novel hybrid systems.[1,9] In this case the microdomains are formed by the material filling the pores of the template. The length and the diameter can be adjusted through the synthesis of the template.

Different polymers have been infiltrated in alumina templates, but the crystallization within the nanopores has been studied only recently.[4,5,22−30] Woo et al.[27] infiltrated polyethylene in alumina templates. They found a clear dependence of the crystallization temperature (T_c) on the pore diameter. When the diameter was smaller, T_c was lower. They also performed isothermal crystallization studies and fitted the results with the Avrami equation. They found values of the Avrami index of around 1.7.[27] Similar results have been found for infiltrated isotactic polypropylene (PP),[4] poly(vinylidene fluoride-*co*-trifluoroethylene),[24] and syndiotactic polystyrene (sPS).[23] The authors claimed that they have found homogeneous nucleation of the infiltrated materials. However, the nucleation at the pore surface was not ruled out and in some cases not even considered.

Lutkenhaus et al.[24] found that infiltration of poly(vinylidene fluoride-*co*-trifluoroethylene) within AAO pores induces the formation of a β polymorphism.[24] Similarly, Wu et al.[23,29] have shown that sPS changes its crystal modification from β in the bulk to mostly α upon infiltration.[23,29] Polyaniline (PANI) also changes its unit cell from orthorhombic to pseudo-orthorhombic after infiltration,[30] while in PVDF a change from α to γ form has been reported.[22]

In the case of block copolymers, when the crystallizable block forms cylinders, it has been shown that the chain orientation is a function of the supercooling employed during crystallization. At moderate supercoolings, the chain orientation within the cylinders is usually perpendicular to the cylinder axis.[31−37] In the templates a preferential orientation of the crystals has also been found. Shin et al.[5] studied the crystal orientation within the nanopores. They found that the chain in the crystals are perpendicular to the pore axis.[5] The same orientation of the crystals was found in sPS[28,29] and poly(vinylidene difluoride) (PVDF).[26] Steinhart et al.[25] studied the crystal orientation of the polyvinylidene fluoride (PVDF) infiltrated in an AAO template. They obtained two different situations, if the nanopores are independent and isolated no preferential orientation was found. On the other hand, if the nanopores are connected through a film on the top of the template they found a preferential orientation, the crystal grew in the fastest direction and the chain was perpendicular to the pore axis.[25] Garcia-Gutierrez et al., also found a perpendicular orientation of crystalline PDVF chains within the pores.[22]

The study of block copolymers infiltrated within AAO templates has been oriented to the study of morphological changes, but so far, not to the crystallization of such systems. The infiltration of block copolymers in AAO templates has an influence on the morphology of the microdomains.[9,38−55] The changes in the morphology depends on the relationship between the size of the microdomain and the pore diameter. For example, a nearly symmetric PMMA-*b*-PS diblock copolymer was studied by Sun et al.[38] and they found that the lamellar morphology was transformed to concentric nanotubes in pores bigger than the microdomain size. Xiang et al.[40] studied the morphology of PS-*b*-PB copolymers infiltrated in an AAO template. In this case, two different compositions were studied corresponding to lamellae and cylinders. The cylinders were aligned with the pores, while the lamellae arranged into concentric cylinders when the pore size was larger than the microdomains,[40] but when the pore diameter was similar to the MDs size, then a completely different morphology was obtained, since the cylinders transformed into helicoidal or toroidal forms.[42−51]

In this paper, we study the crystallization phenomena of crystallizable polymers and copolymers within AAO nanopores. For this purpose, three systems were selected: a PEO homopolymer, a hydrogenated polybutadiene or model polyethylene (PE) and several anionically polymerized linear PE-*b*-PS diblock copolymers. The study of the crystallization of block copolymers into AAO templates is presented here for the first time. The different confined environments generated for the crystallizable PE (i.e., AAO nanopores) and PE blocks within the copolymers upon infiltration into AAO templates are compared. We also analyze the low temperature crystallization of the infiltrated PEO and PE and consider whether the crystals originate from homogeneous bulk nuclei or surface nuclei.

EXPERIMENTAL PART

Materials. A poly(ethylene oxide) sample was purchased from Polymer Source Inc. with a number-average molecular weight of 41 000 g/mol and a polydispersity of 1.05.

The synthesis of poly(1,4-butadiene)-*block*-polystyrene diblock copolymers (PB-*b*-PS) and poly(1,4-butadiene) (PB) homopolymer was reported previously.[56] It was performed by sequential anionic polymerization of butadiene and styrene in benzene at 60 °C for butadiene (3 h) and 40 °C for styrene (5 h) using *sec*-BuLi as initiator. The reaction was terminated using isopropanol followed by precipitation in the same solvent. These block copolymers were later hydrogenated (employing a Wilkinson catalyst) in order to obtain PE-*b*-PS linear diblock copolymers. Table 1 lists the copolymers employed

Table 1. Molecular Characteristics of the Polymers and Copolymers Employed

sample	% 1,2-units	$\bar{M}_w/\bar{M}_n$
PEO[41]	-	1.05
PE[25]	11.0	1.01
$E_{79}S_{21}$[41]	12.6	1.02
$E_{53}S_{47}$[51]	11.3	1.04
$E_{26}S_{74}$[105]	11.3	1.05
$E_{11}S_{89}$[244]	11.3	1.02

with the notation $A_xB_y^m$, where the subscripts denote the mass fraction in weight percent and the superscript gives the number-averaged molecular weight M_n in kg/mol of the entire block copolymer. The synthesis process for all the diblock copolymers was designed in order to obtain a PE block within the block copolymers with the same molecular weight and approximately the same content of 1,2 units as in the PB precursor (see Table 1). After hydrogenation the PE component contains ethyl branches randomly distributed along the backbone of the chains, hence the PE component can be considered as a model ethylene/α-olefin copolymer.

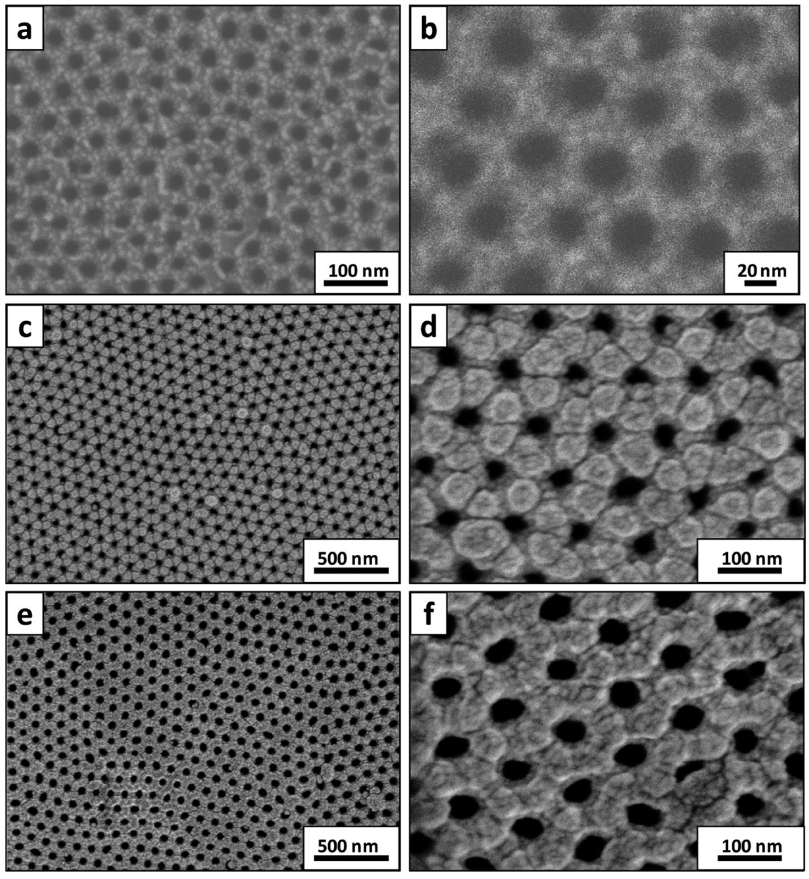


Figure 1. SEM micrographs of the surfaces of AAO templates with pores of 20 nm (a, b), 35 nm (c, d), and 60 nm (e, f).

Templates Preparation. Ordered AAO templates have been prepared by two-step electrochemical anodization of aluminum as described elsewhere.[16,57] First, ultrapure (99.999%) aluminum foils (Advent Research Materials, England) were cleaned and degreased by sonication into solvents with different polarity (acetone, isopropanol, deionized water and ethanol). Foils were then electropolished during 4 min in a solution of perchloric acid/ethanol (1/3) below 10 °C in a constant voltage of 20 V. After that, the first anodization was achieved using sulfuric acid under 19 V and at 1 °C, in order to obtain 20 nm diameter pores; and oxalic acid as electrolyte under 40 V and 1 °C for the 35 and 60 nm diameter pores. Both anodizations were performed during 24 h. Then, the first anodic layer was removed into chromic and phosphoric acid solution. Next, a second anodization was carried out under the same conditions as the first one and templates with 20 nm diameter pores (the one anodized in sulfuric acid) and 35 nm diameter pores (the one anodized in oxalic acid) were obtained. Subsequent processing under phosphoric acid (5 wt % at 30 °C) was performed to widen the pores of some of the templates from 35 to 60 nm in diameter. Pore lengths of the templates used were 200 μm for the templates with 20 nm pores, and 100 μm for the templates with 35 and 60 nm pores, respectively.

Infiltration of Polymer Melts. *Infiltrating PE-b-PS Copolymers and PE Homopolymer.* The polymer was in the molten state at a temperature well above the melting point (T_m) during infiltration. The infiltration of the PE-*b*-PS diblock copolymers into the alumina templates with 35 and 60 nm pores was carried out by placing the solid materials onto the AAO at 170 °C and then annealed at 180 °C under a nitrogen atmosphere. The high temperature was needed for complete infiltration and the nitrogen atmosphere was employed to prevent degradation. For the infiltration of the copolymer $E_{11}S_{89}$[244], the annealing time was extended to 10 h. In the case of the PE homopolymer the temperature of infiltration was 150 °C. After the infiltration process, the samples were quenched in an ice−water mixture.[19]

Infiltrating PEO Homopolymer. A PEO macroscopic film was placed onto the AAO template and annealed at 110 °C under N_2 atmosphere for 60 min. The residual PEO located outside of the pores was mechanically removed using a blade in order to induce an independent crystallization of the PEO confined within each nanopore.

Scanning Electron Microscopy (SEM) and Transmission Electron Microscopy (TEM). In order to obtain a through-hole membrane to see nanorods by SEM/TEM microscopy, the aluminum substrate and the alumina barrier layer were removed with a mixture of HCl, $CuCl_2$, and H_2O, and with 10 wt % H_3PO_4 at 30 °C, respectively.[58] The morphology of the AAO templates was characterized by SEM/TEM (Philips XL-30ESEM and FESEM Hitachi model SU8000 with TE Detector).

Differential Scanning Calorimetry (DSC). For the infiltrated and bulk PEO, sample masses of 21.6 mg (the weight includes the alumina template and the polymer, the mass of the polymer was 0.6 mg) and 2 mg were employed, respectively. The crystallization and melting temperatures of bulk and confined PEO were evaluated by DSC (Perkin-Elmer DSC-8500). Two cooling−heating cycles were applied to the sample (10 °C/min).

In the case of the infiltrated PE and PE-*b*-PS AAO templates, sample mass was 25 mg (these samples were of the alumina template plus infiltrated polymer, the exact mass of infiltrated polymer is unknown but it has been estimated by TGA to be of the order of 2% with respect to the total mass, i.e., 0.5 mg approx.). DSC standard runs were performed on a Pyris 1 Perkin-Elmer Instrument calibrated with tin and indium under an ultra high purity nitrogen atmosphere. In order to enhance the sensitivity of the experiment we employed a high cooling and heating rate of 30 °C/min. The results are compared with the PE-*b*-PS neat samples at the same scan rates and employing a mass of 2 mg.

Wide Angle X-ray Diffraction (WAXD). The WAXD measurements were performed at station BL01C at the NSRRC using an imaging plate as the detector. The X-ray beam with the wavelength of 0.954 Å was collimated into the beam size of 0.5 mm ×3 mm by two slits separated by 1.1 mm. With a sample-to-detector distance of

409.2 mm, the diffraction patterns were collected over the q range of 1 to 25 nm^{-1}.

RESULTS AND DISCUSSION

AAO Templates. Figure 1 shows SEM micrographs of the well developed structure of the neat alumina templates employed to infiltrate the polymer samples. The AAO templates used had an average diameter of 20, 35, and 60 nm. The pore lengths of the templates used was about 200 μm for the 20 nm template and 100 μm for the other two.

Confined Crystallization of PEO within the AOO Templates with 20 nm Pores. Neat PEO[41] displays a sharp crystallization exotherm, as shown in Figure 2a, with a

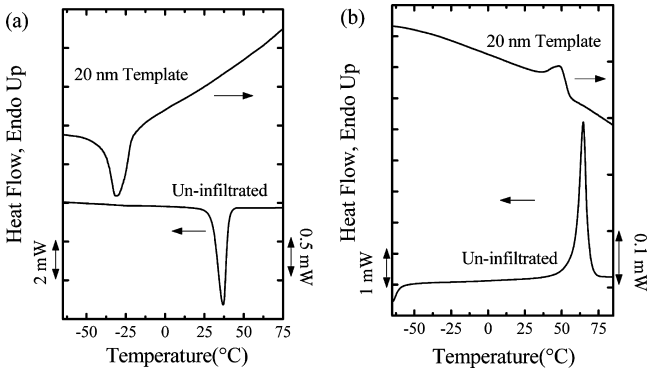


Figure 2. (a) DSC cooling curves from the melt at 10 °C/min for neat PEO[41] and the same sample infiltrated within a 20 nm AAO template (PEO[41]/20 nm). (b) Subsequent heating runs after the cooling shown in part a.

peak T_c value of 37 °C. This is the typical nonisothermal crystallization behavior of heterogeneously nucleated PEO. On the other hand, the PEO[41] that was infiltrated within the nanocylinders of 20 nm diameter only crystallizes at a T_c value of −30 °C. This is a consequence of the confinement experienced by the PEO, since it has been subdivided into isolated nanocylinders. Similar results have been found for infiltrated PVDF,[26] sPS,[28,29] PP[4] and linear PE.[5,27] It is clear that when the polymer is isolated into nanocylinders the crystallization temperature is much lower than that exhibited by the same polymer in the bulk.

The number of active heterogeneities in bulk PEO is of the order of 10^5 heterogeneities/cm^3.[8] However, the number of nanocylinders per unit volume in the 20 nm template is several orders of magnitude larger (approximately 10 orders of magnitude larger, i.e., 10^{15} nanocylinders/cm^3). Therefore, statistically speaking, the PEO nanocylinders within the AAO template are virtually heterogeneity free and must undergo either homogeneous nucleation or a heterogeneous surface nucleation on the AAO inner cylinder walls. However, homogeneous nucleation can only occur at larger supercoolings when compared with a typical heterogeneous nucleation, hence the low temperature crystallization observed.

In our case, it is difficult to ascertain whether the PEO nucleation inside the AAO template is homogeneous or heterogeneous.[8] One way to distinguish between heterogeneous and homogeneous nucleation is to determine the scaling of the time constant, associated with the nucleation event, (i.e., the particle diameter in the case of droplets) a technique that was successfully employed by Massa et al.[59] In their case, the nucleation of dewetted droplets was directly observed in an optical microscope in view of their large size. They have successfully employed a correlation analysis based on the crystallization temperatures of individual droplets for consecutive cooling runs to differentiate homogeneous from heterogeneous nucleation (see refs 59−63).

Carvalho and Dalnoki-Veress[62] have recently demonstrated that isolated PEO nanodroplets can experience homogeneous nucleation in 3, 2, or 1 dimensions (i.e., bulk, surface or edge nucleation) depending on the substrate on which they are deposited. The supercooling needed to crystallize the nanodroplets was much larger for the homogeneous bulk nucleation case than for the surface nucleation case. We will follow the terms they have employed in their work. Bulk homogeneous nucleation occurs when the polymer chains aggregate to form homogeneous nuclei that originate within the volume (or bulk) of the micro or nanodomain. This is the process that requires the largest possible supercooling. The presence of a surface during the solidification of the liquid polymer may cause some chain orientation that lowers the free energy for the formation of a homogeneous nuclei; hence, its crystallization can occur at lower supercoolings.[62]

Homogeneous bulk nucleation occurs at the maximum possible supercooling available to the material or just before vitrification, for the specific microdomain volume under consideration. The glass transition temperature of PEO is approximately −67 °C.[64] Table 2 provides a list of low temperature peak crystallization transitions reported for different types of confined PEO samples. The lowest temperature reported so far for the crystallization of PEO is −42 °C and it was observed for PEO nanospheres formed by a PEO block within PS-*b*-PEO-*b*-PCL linear triblock terpolymers.[65]

It is important to consider that the crystallization temperature after homogeneous bulk nucleation depends on the volume of the isolated crystallizable phase involved. A correlation between droplet volume and the crystallization temperature of homogeneously nucleated PEO was calculated by Müller et al. from a large number of literature data.[8] The dependence of homogeneous nucleation temperature of PEO on volume had been previously reported by Massa and Dalnoki-Veress[60] and by Chen et al.[66] Such dependence is expected since the probability of nucleation and the nucleation rate depend on sample volume. The correlation found by Müller et al.[8] in terms of the volume of the crystallizing phase was

$$T_c = -41.8 + 2.89 \log(v_d) \quad (1)$$

where T_c is the peak crystallization temperature during a DSC cooling scan in °C and v_d the volume of the PEO phase in nm. The prepared templates for PEO infiltration had a height of 200 μm. Hence the volume of one PEO cylinder (if one considers that the infiltration was 100% efficient and the entire nanopore was filled with PEO) is of the order of 6.3×10^7 nm^3. Equation 1 would then predict an experimental peak crystallization temperature during a cooling DSC run of −19.3 °C if the nucleation is homogeneous. The experimental T_c value obtained in Figure 2 for the confined PEO cylinders within the AAO template was −30 °C. Taking into consideration the experimental uncertainty in eq 1 (which can easily amount to 10 °C when experimental data dispersion is considered; see ref 8) then the nucleation process for PEO cylinders inside the AAO template is most probably homogeneous bulk in nature and not originated on the surface of the AAO nanopores.

In order to reveal the orientation of the PEO crystals within the AAO cylindrical nanopores, the samples were examined by 2-D wide-angle X-ray diffraction (WAXD). Three patterns were

Table 2. Low Temperature Crystallization Temperatures Reported for Confined PEO Micro- or Nanodomains

material	PEO content (wt %)	$T_{c\ peak}$[a] (°C)	crystallization conditions (°C/min)	morphology	particle diameter (nm)	reference
$EO_{55}B_{45}^{11}$/PB	13	−33	5	spheres	--	66, 67
$EO_{55}B_{45}^{11}$/PB	17	−33	5	spheres	--	66, 67
$B_{24}I_{56}EO_{20}^{67}$	24	−23.9	10	--	--	68−70
$B_{11}I_{70}EO_{19}^{120}$	19	−22.2	10	--	--	69, 70
$B_{17}I_{57}EO_{26}^{130}$	26	−21.0/16.1	10	--	--	69−71
$B_{19}I_{39}EO_{42}^{135}$	42	−25.0/19.8/37.5	10	--	--	70
$E_{24}I_{57}EO_{19}^{64}$	19	−26.4	10	--	--	70
$E_{11}I_{71}EO_{18}^{123}$	18	−25.4	10	--	--	70
$E_{18}I_{57}EO_{25}^{133}$	25	−21.1/26.8	10	--	--	70
$E_{19}I_{40}EO_{41}^{138}$	41	−24.0/23.6/37.6	10	--	--	70
$E_{24}EP_{57}EO_{19}^{69}$	19	−27	10	--	--	69−71
$E_{11}EP_{71}EO_{18}^{123}$	18	−25.4	10	--	--	69, 70
$E_{18}EP_{57}EO_{25}^{133}$	18	−21.1/26.8	10	--	--	70
$E_{19}EP_{40}EO_{41}^{138}$	41	−24.0/23.6/37.6	10	--	--	70
$S_{81}EO_{19}^{18.5}$	19	−40	10	--	--	65,69
$S_{63}EO_{16}C_{21}^{24}$	16	−42	10	--	--	65
EO_{17}-*b*-$B_{83}^{25.4}$	17	−25	10	spheres	--	72
PEO droplets	100	−23.3	5	droplets	83	73
PEO droplets	100	−23.9	5	droplets	83	73
PEO droplets	100	−20.5	5	droplets	120	73
$EO_{60}B_{40}^{12.5}$/PB	26	−35	5	spheres	8.8	74
$EO_{60}B_{40}^{12.5}$/PB	43	−29	5	cylinders	8.4	74
$HBd_{85}EO_{15}^{4,22}$	15	−31.4	10	--	--	75
$HBd_{76}EO_{24}^{6,44}$	24	−26.4/-7.3	10	--	--	75
$S_{74}EO_{26}^{133.3}$	26	−27	10	cylinders	13.3	33
$B_{16}S_{68}EO_{16}^{210}$	16	−33.8	10	spheres	--	76
$B_{29}S_{40}EO_{31}^{168}$	31	−27.1/37.9	10	cylinders	--	76
$B_{16}S_{40}EO_{47}^{143}$	44	−24.4/39.9	10	lamellar	--	76
$B_{19}S_{35}EO_{46}^{217}$	46	−26.4/37.2	10	lamellar	--	76
$E_{17}S_{67}EO_{16}^{211}$	16	−30.9	10	spheres	--	76
$E_{29}S_{40}EO_{31}^{170}$	31	−26.0/42.0	10	cylinders	--	76
$E_{38}S_{16}EO_{46}^{77}$	46	−27.4/39.1	10	lamellar	--	76
$E_{16}S_{40}EO_{44}^{144}$	44	−18.2/46.2	10	--	--	76
$E_{19}S_{34}EO_{47}^{143}$	47	−29.1/42.4	10	--	--	76
$E_{19}S_{35}EO_{46}^{219}$	46	−25.2/40.6	10	--	--	76
$B_{81}EO_{19}^{34}$	19	−21.1/-8.2/46.1	10	spheres	13 ± 1.3	77
$E_{82}EO_{18}^{35}$	18	−34.3/20.2/45.7	10	spheres	21 ± 1.0	77
$B_{89}EO_{11}^{102}$	11	−26.8/-11.5	10	spheres	19 ± 1.4	77
$E_{89}EO_{11}^{105}$	11	−24.3/0.5	10	spheres	31 ± 1	77
PEO/PHB	20	−27/-13	10	--	--	78
PEO droplets	100	−4.5/6/12	1	droplets	different sizes	62

[a]In some cases multiple crystallization peaks were found. All the temperatures are reported.

collected for the sample by rotating the specimen to allow for the incident X-ray to pass through the three principal axes of the specimen. That is, the PEO infiltrated template was collected by having the incident X-ray traveling along the $\hat{x}$, $\hat{y}$, and $\hat{z}$(where these three directions are orthogonal to each other), respectively, as schematically shown in Figure 3. The $\hat{x}$−$\hat{y}$ plane is corresponding to film surface and the $\hat{z}$ direction is parallel to the film normal. (i.e., cylinder axis of AAO channels).

Figure 4 shows the 2D WAXD patterns of the PEO infiltrated AAO template with 20 nm cylindrical pores. When the X-ray is traveling along the $\hat{x}$ and $\hat{y}$, similar patterns can be observed, as shown in Figure 4a and Figure 4b, respectively. The first diffraction arcs (q = 13.7 nm^{-1}) were found to locate on both the meridian and equator, which was associated with (120) diffraction of PEO crystals. On the other hand, the second quadrant (q = 16.1 nm^{-1}) was attributed to the overlap of $(\bar{1}32)$, (112), (032), $(\bar{1}24)$, $(20\bar{4})$, $(\bar{2}12)$ and (004) diffractions.

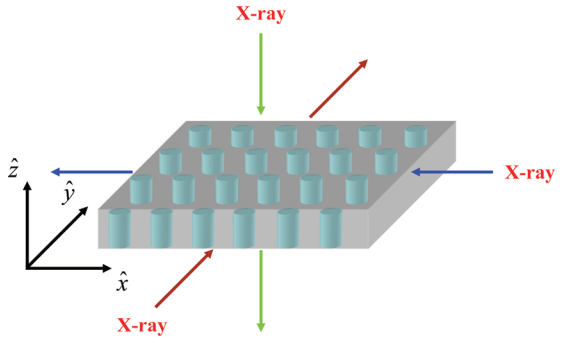


Figure 3. Schematic illustrations of the geometry employed to collect the WAXD data on the PEO infiltrated template indicating different incident directions of the X-ray beam.

In the azimuthal scans (obtained by scanning the intensity of a specific diffraction around the azimuthal angle (ψ) starting from

dx.doi.org/10.1021/ma202327f | *Macromolecules* 2012, 45, 1517−1528

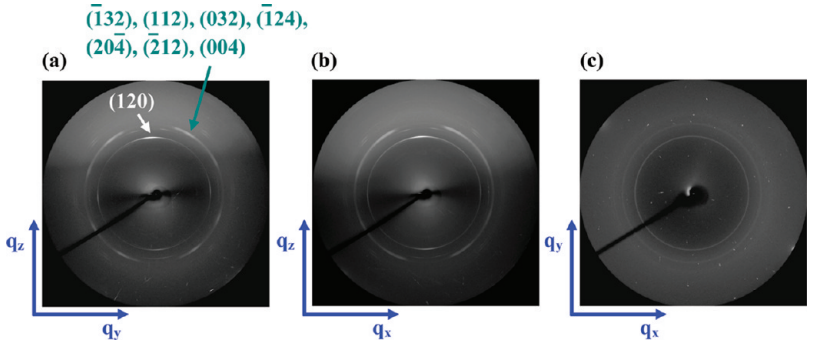


Figure 4. 2D WAXD patterns of PEO infiltrated AAO templates with 20 nm diameter cylindrical pores, collected by having the incident X-ray beam traveling along (a) $\hat{x}$, (b) $\hat{y}$, and (c) $\hat{z}$.

the vertical direction of the pattern) of the first and second diffractions, the maximum intensity of the first diffraction was found to locate at ψ = 2, 91, 182, and 273°, whereas that of second diffraction was at ψ = 35, 64, 115, 148, 213, 248, 295, and 327°, which was consistent with the reported [120] uniaxial pattern of PEO crystal.[35] Moreover, the intensity of the (120) diffraction on the meridian was stronger than that on the equator, which can also be elucidated by the PEO [120] uniaxial pattern.[79] On the basis of the fact that [120] uniaxial pattern appeared in both of the WAXD patterns when the X-ray is traveling along $\hat{x}$ (Figure 4a) and $\hat{y}$ (Figure 4b), and the ring-like pattern was obtained by having the X-ray beam traveling along $\hat{z}$ (see Figure 4c), we conclude that the crystalline stems of the PEO crystals were perpendicular to the cylindrical interface of the AAO pores but randomly oriented with respect to the $\hat{x} - \hat{y}$ plane. Such an orientation of PEO crystals was in accord with the previous results while the PEO was the minority constituent in the cylinder-forming diblock copolymer.[33,35]

Confined Crystallization of PE within PE-*b*-PS Diblock Copolymers. The materials employed for infiltration have been the subject of previous studies (refs 56, 80−82) Table 3 shows a summary of the characterization results obtained previously by SAXS and TEM. These PE-*b*-PS diblock copolymers are strongly segregated in the melt and the crystallization of the PE block occurs within the phase segregated self-assembled micro or nanodomains indicated in Table 3. These phase segregated structures will be referred to as microdomains (MDs).

Figure 5 presents the DSC cooling scans from the melt and subsequent heating runs for the neat PE and PE-*b*-PS diblock copolymer samples at a scanning rate of 30 °C/min. The results are consistent in general terms with those reported previously at 10 °C/min (see ref56).

It is important to note that the molecular weight ($M_n \approx$ 26 kg/mol) and the 1,2 units content (% 1,2-units ≈ 11%) of the PE block within the diblock copolymers as well as in the neat PE were kept constant in order to eliminate the influence of these parameters on the thermal and morphological behavior of the diblock copolymers.

The crystallization of PE^{25} displays a behavior similar to ethylene/α-olefin copolymers.[83,84] There is a sharp main crystallization process (labeled "α"), where the majority of the PE^{25} crystallizes (at T_c = 85.1 °C, see Table 4) and a much smaller exotherm at 52.1 °C. Similar small exotherms have been commonly reported in a temperature range of 40−60 °C for branched polyethylenes in general, and for linear low density polyethylene in particular. They are caused by the crystallization of short methylene sequence lengths belonging to chains whose longer methylene sequences crystallize at higher temperatures (in the exotherm α). It is well-known that such small exotherms exhibited by branched polyethylenes at 40−60 °C are due to intramolecular fractionation during crystallization produced by the distribution of branches along the chain.[84] Therefore, this exotherm has been labeled "*IF*" to indicate its origin. In Table 4, the dominant crystallization peak temperatures for each sample have been reported in bold.

Exotherm α in Figure 5 is related to the crystallization of PE chains starting from heterogeneous nuclei. In the diblock copolymers case, the T_c values for the α exotherm are shifted to lower values because of the topological restrictions imposed by the covalently bonded glassy PS phase. The observation of the α exotherm is still possible because of the percolation of the crystallizing phase, usually present through defects in the microdomain morphologies (e.g., lamellae and cylinders).

In the cases of $E_{26}S_{74}^{105}$ (PE cylinders within a glassy PS matrix) and $E_{11}S_{89}^{244}$ (PE spheres in a PS matrix) diblock copolymers, multiple crystallization exotherms are observed (more easily appreciated in the close up shown in Figure 5b). This is caused by a fractionated crystallization phenomenon that is produced as a consequence of confinement of the crystallizable phase into isolated MDs and by the existence of different types of nucleation events within such MDs[8,69,85]

Before each crystallization exotherm a specific nucleation event must occur (e.g., heterogeneous or homogeneous). The heterogeneity type present in different MDs may also vary. The fractionated behavior of the crystallization process is due to the much larger number of MDs as compared to the number of heterogeneities available to produce nucleation. According to

Table 3. Domain Size "*l*" and Spacing "*d*" of the PE-*b*-PS Diblock Copolymers As Determined by TEM and SAXS Measurements at Room Temperature,[82] with the Degree of Crystallinity Obtained by DSC also Listed

	TEM		SAXS			
sample	*l* (nm)	*d* (nm)	*d* (nm)	morphology	X_c (%)[d]	X_c (%)[e]
PE^{25}	-	-	-	bulk	35	27
$E_{79}S_{21}^{41}$	-	-	-	PS cylinders in a PE matrix	26	23
$E_{53}S_{47}^{51}$	16[a] ± 3	62 ± 3	65	lamellar	23	20
$E_{26}S_{74}^{105}$	21[b] ± 5	126[c] ± 29	99	PE cylinders	18	15
$E_{11}S_{89}^{244}$	12[b] ± 2	105[c] ± 13	108	PE spheres	15	11

[a]Thickness of the PE lamellae. [b]Radius of the microdomain. [c]Interdomain distance. [d]Obtained by DSC at 10 °C/min, data from ref 82 [e]Obtained by DSC at 30 °C/min in this work.

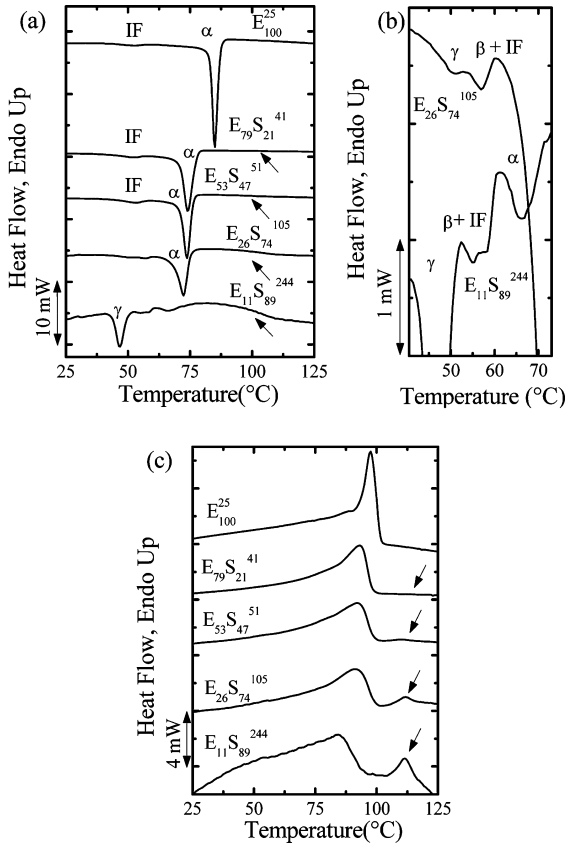


Figure 5. (a) DSC cooling curves from the melt at 30 °C/min. (b) Zoom of the $E_{26}S_{74}^{105}$ and $E_{11}S_{89}^{244}$and (c) subsequent heating runs after the cooling shown in part a. Arrows indicate the position of the T_g corresponding to the PS block.

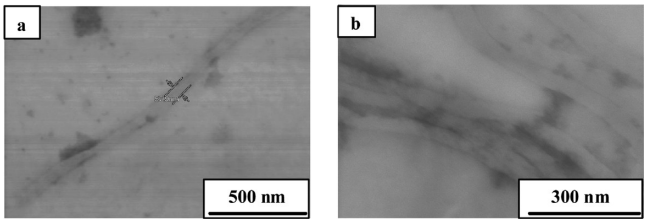


Figure 6. TEM images of nanocylinders obtained by AAO template removal. (*a*) $E_{53}S_{47}^{51}$ copolymer and (*b*) PE homopolymer.

an estimation made by measuring TEM images, there are ~10^{12} MDs/cm^3 and ~10^{15} MDs/cm^3 for $E_{26}S_{74}^{105}$ and $E_{11}S_{89}^{244}$ respectively. In contrast, the heterogeneities concentration usually present in an equivalent bulk sample of polyethylene is only ~10^9/cm^3.[53]

Fractionated crystallization will be present if there are MDs with different kinds of heterogeneities inside each population. In the present case, there could be a fraction of MDs with highly active heterogeneities (those usually present in bulk PE) that can crystallize at low supercoolings, like in the T_c range of the α exotherm. Then, a second type of heterogeneity may be present in a different fraction of MDs, that can crystallize at lower temperatures in exotherm β (for instance that produced by the remains of the Wilkinson catalyst employed for hydrogenation purposes). Finally, a clean fraction of MDs, that does not contain any heterogeneity at all, must undergo homogeneus nucleation (either surface or homogeneous bulk nucleation). The higher the heterogeneity nucleating efficiency, the lower the supercooling needed by that specific fraction of MDs to crystallize. However, the interconnection (or percolation) level in the MDs could allow the spread of secondary nucleation through out the crystallizable component.[69,86]

In Figure 5, the *IF* exotherm characteristic of branched polyethylenes may well be overlapping with the β exotherm (that originates on the crystallization provoked by the nucleation of a less efficient type of heterogeneity), hence we have labeled some exotherms as *IF* + β Figure 5. The exotherms that most probably represent the crystallization from clean or heterogeneity free MDs have been labeled γ in Figure 5.

The only block copolymer where MDs percolation is highly unlikely is $E_{11}S_{89}^{244}$, since it forms 24 nm PE spheres within a PS matrix. In fact, the number of clean droplets dominate the crystallization behavior because the most prominent crystallization event is that of exotherm γ at 46.9 °C, the lowest peak crystallization temperature for all the diblock copolymers examined. The corresponding nucleation process for this lowest temperature exotherm could be either homogeneous bulk nucleation or surface nucleation.

Table 5 presents the low temperature crystallization of PE droplets or PE MDs within block copolymers reported in the literature. The value of 46.9 °C is one of the lowest ever reported for the crystallization of confined PE phases, although even lower temperatures can be achieved by infiltration within AAO templates as will presented below.

We exclude the possibility that fractionated crystallization could be a result of a wide range of microdomain sizes (like in polyblends) since our samples were prepared by anionic polimerization and a narrow distribution of microdomains sizes was obtained. In the case of PE spheres, TEM measurements (whose experimental error due to staining could be specially large in semicrystalline samples) yielded dv/dn values (average volume diameter/average number diameter) lower than 1.5 (see ref 56).

Figure 5 also shows the DSC heating scans. The neat PE^{25} sample exhibits a peak melting temperature (T_m) of only 98.7 °C because of the influence of its short chain branching

Table 4. Peak Crystallization and Melting Temperatures Obtained from Figures 5, 7 and 8

	uninfiltrated					60 nm template				35 nm template	
	T_c					T_c				T_c	
sample	α	IF	β + IF	γ	T_m	α	β	γ	T_m	γ	T_m
E_{100}^{25}	**85.1**	52.1	--	--	**97.5**/87.5[a]	84.0	60.0	**51.5**	**96.4**	**45.2**	**88.4**
$E_{79}S_{21}^{41}$	**73.9**	51.9	--	--	**92.8**	77.0	57.0	**48.5**	**90.4**	**48.2**	**90.1**
$E_{53}S_{47}^{51}$	**73.8**	53.3	--	--	**92.3**	--	**61.0**	54.5	**91.9**	NA	NA
$E_{26}S_{74}^{105}$	**72.4**	--	56.9	49.9	**91.8**	--	--	**44.5**	**86.8**	--	--
$E_{11}S_{89}^{244}$	66.9	--	56.9	**46.9**	**85.8**	--	--	--	--	--	--

[a]Shoulder. NA = not available (the sample was not prepared).

Table 5. Low Temperature Crystallization Temperatures Reported for Confined PE Droplets or PE MDs

material	PE content (wt %)	branch content (%)	$T_{c\ peak}$[a] (°C)	crystallization conditions	morphology	particle diameter	ref
HDPE droplets/Igepal	100	---	85−87	slow cooling	droplets	<3 mm	87
HDPE droplets/dibutyl phtalate	100	---	79−81	slow cooling	droplets	<3 mm	87
HDPE droplets/dibutyl sebacate	100	---	80−82	slow cooling	droplets	<3 mm	87
HDPE droplets/phenyl carbitol	100	---	82−84	slow cooling	droplets	<3 mm	87
LDPE/PS	20	---	53.5/61.5/70/100	2 °C/min	droplets	---	88
HDPE droplets on glass treated with Natural oil	100	---	74.8	1 °C/min	droplets	---	89
HDPE droplets on glass treated with Lanolin	100	---	79.0	1 °C/min	droplets	---	89
HDPE droplets on glass treated with vacuum-evaporated carbon	100	---	127.0	1 °C/min	droplets	---	89
HDPE droplets on glass treated with other surface agents	100	---	77.6/82.0/84.9/117.0	1 °C/min	droplets	---	89
$E_{27}MB_{73}$[88]	27	7	62	---	E cylinders	---	31
LLDPE/PS	10	---	105/73	10 °C/min	droplets in blends	0.44−3.1 μm	90
LLDPE/PS	20	---	105/74	10 °C/min	droplets in blends	0.48−3.2 μm	90
LLDPE/PS	30	---	102/72	10 °C/min	droplets in blends	0.70−3.2 μm	90
LLDPE/PS	40	---	104/74	10 °C/min	droplets in blends	0.90−4.4 μm	90
HDPE/PS	10	---	115.7/100/77.2	10 °C/min	droplets in blends	0.14 μm	91
HDPE/PS	20	---	115.2/108.5/76.8/68.5	10 °C/min	droplets in blends	---	91
HDPE/PS	30	---	115.7/77.5/66.6	10 °C/min	droplets in blends	---	91
LLDPE/PS	10	---	67.3	10 °C/min	droplets in blends	0.17 μm	91
LLDPE/PS	30	---	102.9/70.4/51.2	10 °C/min	droplets in blends	0.23 μm	91
$E_{14}SEB_{86}$[54]	14	8	66−70	isothermal	E spheres	25 nm	91
$E_{18}VCH_{82}$[27]	18	7	58	10 °C/min	E spheres	---	93
$E_{18}VCH_{82}$[31]	18	7	63	10 °C/min	E cylinders	---	93
$E_{14}SEB_{86}$[64]	14	8	62	10 °C/min	E spheres	---	93
$E_{14}SEB_{86}$[74]	14	6	63	10 °C/min	E spheres	---	93
$E_{25}SEB_{75}$[70]	25	7	63	10 °C/min	E cylinders	---	93
$E_{26}S_{74}$[105]	26	11.3	71.8/56.5	10 °C/min	E cylinders	42 nm	56
$E_{11}S_{89}$[244]	11	11.3	55.6/46.6	10 °C/min	E spheres	24 nm	56
$E_{54}EP_{46}$ [53]	54		66.2	10 °C/min	lamellar	---	82
$E_{29}EP_{71}$ [99]	29		65.7	10 °C/min	lamellar	---	82
$E_{12}EP_{88}$ [238]	12		45.2/35.1	10 °C/min	---	---	82
$E_{34}S_{66}$[42]	34	3.5	71.9/75.0	5 °C/min	cylinder	16.7 nm	94
$E_{54}S_{46}$[79.3]	54	4	83/85.0	5 °C/min	lamellar	48.1 nm	94
$E_{54}S_{46}$[79.3]/PS	27	4	40	5 °C/min	cylinder	43.8 nm	94
PE nanoporous AAO template	100	0	75−99	isothermal	cylinder	15 nm	5, 95
PE nanoporous AAO template	100	0	75−99	isothermal	cylinder	20 nm	5, 95
PE nanoporous AAO template	100	0	75−99	isothermal	cylinder	33 nm	5, 95
PE nanoporous AAO template	100	0	75−99	isothermal	cylinder	41 nm	5, 95
PE nanoporous AAO template	100	0	75−99	isothermal	cylinder	48 nm	5, 95
PE nanoporous AAO template	100	0	80−84	isothermal	cylinder	62 nm	5, 95
PE nanoporous AAO template	100	0	79−83	isothermal	cylinder	110 nm	5, 95
$E_{17}S_{67}EO_{16}$[211]	17	11.5	55.9	10 °C/min	spheres	---	76
$E_{29}S_{40}EO_{31}$[170]	29	12.9	66.4	10 °C/min	cylinders	---	76
$E_{38}S_{16}EO_{46}$[77]	38	11.8	74.8	10 °C/min	lamellar	---	76
$E_{16}S_{40}EO_{44}$[144]	16	14.0	72.4	10 °C/min	---	---	76
$E_{19}S_{34}EO_{47}$[143]	19	12.8	65.1	10 °C/min	---	---	76
$E_{19}S_{35}EO_{46}$[219]	19	10.8	69.9	10 °C/min	---	---	76
PE droplets	100	---	84.0	1 °C/min	droplets	---	63

[a]In some cases multiple crystallization peaks were found. All the temperatures are reported.

content. This also impacts the degree of crystallinity degree achieved by this sample which amounts to 27%. The melting point decreases in the diblock copolymers as the PS content increases. When the PE is confined to isolated spheres where

dx.doi.org/10.1021/ma202327f | Macromolecules 2012, 45, 1517−1528

the degree of percolation is negligible as compared to the other morphologies, the T_m value decreases much more to 85.2 °C as a consequence of confinement. The degree of crystallinity also decreases markedly, a fact that affects the sensitivity of the DSC measurements, since lower latent heats of crystallization and melting are produced. The glass transition of the PS block has been indicated by arrows in Figure 5 for the PE-*b*-PS diblock copolymers and it is located around 107 °C.

Confined Crystallization of PE and PE Block within PE-*b*-PS Diblock Copolymers Infiltrated in AAO Templates. Figure 6 presents TEM micrographs of the $E_{53}S_{47}^{51}$ copolymer (*a*) and PE homopolymer (*b*) nanofibers with diameters of about 60 nm.

Figure 6 shows the nanocylinders obtained after the AAO templates were successfully removed (see Experimental Part). It is possible to observe that the nanorods can be extracted from the template and retain their approximately 60 nm diameter. On the other hand, it was not possible to obtain the morphology of the PE-*b*-PS copolymers within the nanopores. Nevertheless, since the diameter of the nanopores (especially in the case of the 35 nm templates) are very close to the sizes of some of the microdomains (see Table 3), it is possible that the morphology experiences changes as predicted by Sevink et al.[39] and demonstrated experimentally by Russell and co-workers.[41−44]

Figures 7 and 8 show the cooling and subsequent heating DSC runs that compare the uninfiltrated and infiltrated polymer samples. Table 4 lists their peak crystallization and melting temperatures.

One general feature that can be observed in Table 4 is that for nearly all infiltrated diblock copolymer samples the dominant crystallization process of the PE block corresponds to the lowest crystallization temperature or γ exotherms. Nevertheless, fractionated crystallization can still be observed in some infiltrated samples although the enthalpic signals corresponding to α or β exotherms are extremely small.

As already pointed out above, the branched PE phase employed here does not develop a high crystallization degree (as compared to linear PE) and as can be seen in Table 3, and the crystallinity is even lower for the PE block within the diblock copolymers. This fact made very difficult to detect the enthalpy of crystallization and fusion once the copolymers were infiltrated. This is one of the reasons why the DSC traces are so noisy. The other is that 98% of the sample was inert AAO and 2% was the infiltrated polymer (aprox. 0.5 mg). Therefore, it was not possible to obtain the crystal orientation of these materials due to fact that the loading amount of the infiltrated crystalline constituent was quite low. Isothermal crystallization experiments in the DSC were also impossible to achieve because of a lack of sensitivity.

Nevertheless, as far as the authors are aware, Table 4, Figure 7, and Figure 8 represent the first attempt to explore the crystallization behavior of strongly segregated copolymers within AAO templates with limiting confinement conditions, where the size of the nanopores compete with the MDs dimensions of the uninfiltrated copolymers.

Table 4 shows that as confinement increases from the uninfiltrated case to the infiltrated case, all dominant T_c and T_m temperatures decrease. When comparing the 60 nm template case with the 35 nm, the dominant crystallization temperature for the infiltrated polymers either decreases or disappears (i.e., the crystallization cannot be detected under the experimental conditions employed). PE^{25} for instance, exhibits a bulk T_c value of 85.1 °C. The dominant peak crystallization temperature decreases

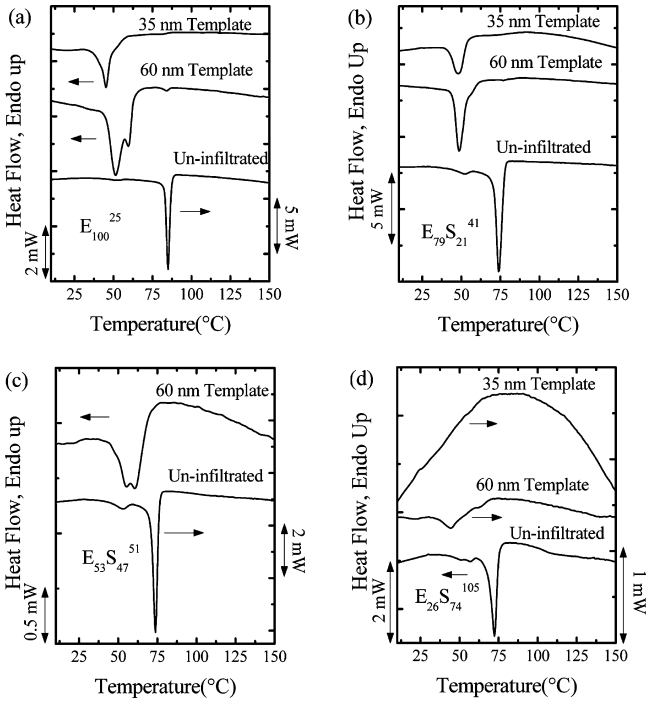


Figure 7. DSC cooling scans at 30 °C/min from the melt for the indicated samples.

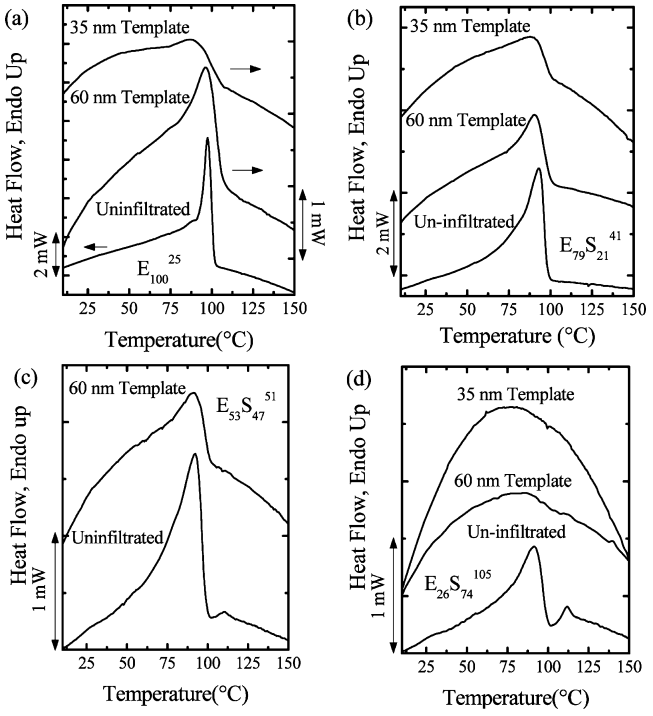


Figure 8. DSC subsequent heating scans at 30 °C/min, after the cooling shown in Figure 7, for the indicated samples.

to 51.5 °C when the sample is confined within 60 nm nanocylinders and then to 45.2 °C for the 35 nm nanocylinders. The corresponding values of T_m also decrease from 97.5 °C for bulk PE^{25} to 96.4 and 88.4 °C for the infiltrated PE^{25} nanocylinders within 60 and 35 nm AAO templates, respectively. The reduction in T_m values corresponds to the formation of thinner lamellae according to the Gibbs−Thomson equation.

dx.doi.org/10.1021/ma202327f | *Macromolecules* 2012, 45, 1517−1528

In the case of $E_{79}S_{21}$[41], where the PE phase should constitute the matrix, the behavior after infiltration was similar to that of PE[25], although in this case the change from the 60 nm template to the 35 nm did not produce a change in peak T_c values, however, the onset crystallization temperature did reduce as expected.

The most interesting result stems from the comparison of the crystallization of neat PE[25] and $E_{26}S_{74}$[105] within the templates. Neat PE[25] forms nanocylinders of 60 and 35 nm inside the 100 μm AAO pores with a corresponding volume of 28.3×10^7 nm^3 and 9.6×10^7 nm^3 respectively. This change in volume may explain the reduction in T_c values reported in Table 4 from 51 to 45.2 °C. Neat $E_{26}S_{74}$[105] diblock copolymer forms PE cylinders with a 42 nm diameter in a PS matrix. If one could produce a perfectly aligned sample of 100 μm in length with concentric PS and PE cylinders, the PE cylinders would have a volume of 13.9×10^7 nm^3. Therefore, these PE cylinders of $E_{26}S_{74}$[105] would fit within the 60 nm AAO template but the volume of the crystallizing phase would be reduced to one-half as compared to that of infiltrated neat PE[25] cylinders, a fact that may then explain the observed T_c value of 44.5 °C, which is comparable to that measured in neat PE[25] cylinders in the smaller 35 nm template (i.e., 45.2 °C).

The infiltration of $E_{26}S_{74}$[105] within the 35 nm template lead to an undetected level of crystallinity in the infiltrated material, a fact that may be related to the extreme confinement condition where the AAO nanopores are even smaller than the PE cylinders MDs in the neat diblock copolymer.

Finally, the infiltration of $E_{11}S_{89}$[244] was successful, since the material was able to completely fill the nanopores, as in all the other cases. However, because of DSC sensitivity problems (due to the low polymer mass within the template sample), no crystallinity was detected. In this case, the 24 nm PE nanospheres within the neat diblock copolymers only contain 18% crystallinity. Further confinement within the templates was probably bound to decrease this value rendering it undetectable because of the lack of sensibility in the DSC employed.

The lowest crystallization temperatures reported in Table 4 are 45.2 °C (for infiltrated PE nanocylinders within a 35 nm AAO template) and 44.5 °C (for double confined PE block cylinders within a 60 nm AAO template). These temperatures are the lowest ever reported for the crystallization of confined PE nanophases, according to a comparison with the temperatures reported in Table 5. Even though these temperatures are low, they are still much higher than the glass transition value (T_g) of PE. The T_g value of PE has been the subject of controversy, however the two most frequently quoted values are approximately −30 °C and −120 °C.[96,97] This means that in the present case, our PE MDs are crystallizing at temperatures that are at least 75 °C above T_g. This is not the case for other crystallizable polymers like PEO or poly(ε-caprolactone), which can exhibit crystallization temperatures when they are the minor components within block copolymers (e.g., nanospheres) that are very close to their respective vitrification temperatures.[64,69,98] These low values for T_c suggest that in the PEO and the PCL case true homogeneous bulk nucleation temperatures have been obtained (like in the infiltrated PEO nanocylinders presented above), since homogeneous bulk nucleation should occur at the maximum possible supercooling for the domain volume under consideration (and nucleation events below T_g would be very unlikely).

In order to emphasize the large differences encountered in relative crystallization temperatures for the cases of finely dispersed PEO and PE MDs or droplets, Table 6 lists the lowest peak crystallization temperatures reported in the literature and the difference between T_c and T_g. In the case of PEO, this difference is only 17 °C for the case of nanospheres within a block copolymer case, or 30 °C for the nanocylinders within the 20 nm template case presented here. The difference between these two values is due to the difference in volume of the crystallizing phase. However, the extremely large values reported in Table 6 for the $T_c - T_g$ difference in the case of PE, cannot be explained by difference in volumes of the phases involved. Hence, the nucleation of dispersed PE probably occurs by surface nucleation. Surface nucleation could be either heterogeneous (like for instance at the AAO pore walls) or homogeneous (at the interphase between the block copolymer microdomain boundaries, or at the surface of PE nanocylinders)[62,63]

Table 6. Comparison of Relevant Thermal Transition Temperatures for Finely Dispersed PEO and PE

polymer	T_g (°C)[a]	T_c (°C)[b]	T_m^0 (°C)[a]	$T_c - T_g$ (°C)	ref.
PEO within $S_{63}EO_{16}C_{21}$[24]	−67	−42.0	69.0	17.0	65
PEO within 20 nm AAO templates	−67	−30.0	69.0	37	this paper
HDPE	−34	66.6	145.0	100.6	92
LLDPE	−34	51.2	145.0	85.2	92
PE[25] within 35 nm AAO templates	−34	45.2	145.0	77.2	this paper
PE within $E_{26}S_{74}$[105] within 60 nm AAO templates	−34	44.5	145.0	78.5	this paper

[a]From ref 64 [b]Lowest reported.

Previous works on the crystallization of infiltrated polymers within AAO templates have claimed that a transition from heterogeneous to homogeneous nucleation has been found for PE[27] and PP[4]; however, no real demonstration has been provided. The isolation of a bulk polymer into heterogeneity free nanocylinders (or any other type of MDs) does not guarantee that the molecules will undergo homogeneous bulk nucleation, since surface nucleation requires a lower free energy to occur.

A recent key reference[63] provides further support that PE isolated MDs crystallize by surface nucleation mechanisms, hence at shallower supercoolings than that needed for homogeneous bulk nucleation. Carvalho and Dalnoki-Veress[63] prepared PE droplets by dewetting PE films deposited on a PS substrate. Using a correlation plot analysis they determined which droplet population was undergoing homogeneous nucleation. The homogeneously nucleated droplets were found to nucleate at the surface of the PE droplets, as indicated by the dependence of the nucleation rate on droplet size. As already pointed out above, in the case of PEO a quantitative dependence between domain volume and crystallization temperature has been clearly obtained, and extreme supercoolings are required as domain size is reduced into the nanoscale regime (see Tables 2 and 6). However, a much weaker temperature dependence on length scale has been observed for PE domains (see Tables 5 and 6), while reports of different crystallization temperatures for PE domains of similar size but different confining matrices can be found. Carvalho and Dalnoki-Veress[63] argued that such behavior is consistent with nucleation scaling with the surface area rather than volume, since a surface-driven homogeneous nucleation mechanism will be more sensitive to differences in interfacial energy than a volume dependent

mechanism, and thus more likely to be affected by different confining environments.

It must also be noted that a first-order crystallization kinetics (equivalent to an Avrami index of 1) is characteristic of heterogeneity free nucleation, but it can be encountered for both homogeneous bulk nucleation and surface nucleation.[8] Therefore, both the low temperature crystallization data published in the literature and that reported here can be interpreted in the case of well dispersed PE as arising from surface nucleation, since the peak crystallization temperatures observed are at least 75 °C above the T_g value.[8,56,69,90]

■ CONCLUSIONS

The synthesis and infiltration of the AAO templates with different nanopore sizes was successfully accomplished. For the PEO homopolymer a significant reduction of the crystallization temperature was obtained, also a change of heterogeneous nucleation to homogeneous bulk nucleation within the nanopores was confirmed for this system. On the contrary for the PE and PE-*b*-PS that were infiltrated in the AAO templates, a surface nucleation mechanism is more consistent with the results obtained.

On the other hand, the double confinement present in the PE blocks of the PE-*b*-PS diblock copolymer infiltrated within an alumina template further reduces the crystallization temperature. Additionally, the confinement for the PE^{25} within the alumina template with a pore diameter of 35 nm was equivalent to the confinement of a cylinder within the uninfiltrated neat block copolymer $E_{26}S_{74}^{105}$, this result indicates that the size of the MDs determine the behavior during the crystallization.

The orientation of the PEO chains within the crystal in the cylindrical nanopores is perpendicular to the nanopore axis, as evidenced by WAXD measurement. For the PE and PE-*b*-PS systems, it was not possible to obtain the crystal orientation due to the fact that the loading amount of crystalline infiltrated constituent was too low.

■ AUTHOR INFORMATION

Corresponding Author

*E-mail: amuller@usb.ve.

■ ACKNOWLEDGMENTS

The USB team acknowledges the help of Prof. Volker Abetz and Dr. Adriana Boschetti-de-Fierro in synthesizing the PE and PE-*b*-PS diblock copolymers employed here (see refs56808182,). CSIC authors acknowledge financial support from CICYT (MAT 2008-1179) and David Gómez for SEM images. I. Blaszczyk-Lezak and J Martin acknowledge support from a JAE postdoctoral fellowship (CSIC) and from a FPU AP2005-1063 (MICINN) Grant, respectively.

■ REFERENCES

(1) Steinhart, M.; Werspohn, R. B.; Gösele, U.; Wendorff, J. H. *Angew. Chem. Int.* **2004**, *43*, 1334−1344.
(2) Mundra, M. K.; Donthu, S. K.; Dravid, V. P.; Torkelson, J. M. *Nano Lett.* **2007**, *7*, 713−718.
(3) Volel, M.; Armand, M.; Gorecki, W.; Saboungi, M. L. *Chem. Mater.* **2005**, *17*, 2028−2033.
(4) Duran, H.; Steinhart, M.; Hans-Jürgen, B.; Floudas, G. *Nano Lett.* **2011**, *11*, 1671−1675.
(5) Shin, K.; Woo, E.; Jeong, Y. G.; Kim, C.; Huh, J.; Kim, K. W. *Macromolecules* **2007**, *40*, 6617−6623.
(6) Martín, J.; Mijangos, C.; Sanz, A.; Ezquerra, T. A.; Nogales, A. *Macromolecules* **2009**, *42*, 5394−5401.
(7) Martín, J.; Krutyeva, M.; Monkenbusch, M.; Arbe, A.; Allgaier, J.; Radulescu, A.; Falus, P.; Maiz, J.; Mijangos, C.; Colmenero, J.; Richter, D. *Phys. Rev. Lett.* **2010**, *104*, 197801.
(8) Müller, A. J.; Balsamo, V.; Arnal, M. L. *Adv. Polym. Sci.* **2005**, *190*, 1−63.
(9) Steinhart, M. *Adv. Polym. Sci.* **2008**, *220*, 123−187.
(10) Hamley, I. W. *The Physics of Block Copolymers*; Oxford University Press: London, 1999.
(11) Müller, A. J.; Balsamo, V.; Arnal, M. L. In *Lecture notes in physics: progress in understanding of polymer crystallization*; Reiter, G., Strobl, G., Eds.; Springer: Berlin, 2007; Vol. *714*, pp 229−259.
(12) Hamley, I. W. *Adv. Polym. Sci.* **1999**, *148*, 113−137.
(13) Loo, Y. L.; Register, R. A. In *Developments in Block Copolymer Science and Technology*; Hamley, I. W., Ed.; Wiley: New York, 2004.
(14) Nadan, B.; Hsy, J. Y.; Chen, H. L. *Polym. Rev.* **2007**, *47*, 143−172.
(15) Müller, A. J.; Arnal, M. L.; Lorenzo, A. T. In *Handbook of Polymer Crystallization*; Piorkowska, E., Rutledge, G., Eds.; Wiley: New York, 2011.
(16) Masuda, H.; Fukuda, K. *Science* **1995**, *268*, 1466−1468.
(17) Martin, C. R. *Science* **1994**, *266*, 1961−1966.
(18) Martin, C. R. *Acc. Chem. Res.* **1995**, *28*, 61−68.
(19) Martín, J.; Mijangos, C. *Langmuir* **2009**, *25*, 1181−1187.
(20) Steinhart, M.; Wendorff, J.; Greiner, A.; Wherspohn, R.; Nielsch, K.; Schilling, J.; Choi, J.; Gösele, U. *Science* **2002**, *296*, 1997.
(21) Zhang, M.; Dobriyal, P.; Chen, J. T.; Russell, T.; Olmo, J.; Merry, A. *Nano Lett.* **2006**, *6*, 1075−1079.
(22) Garcia-Gutiérrez, M. C.; Linares, A.; Hernández, J. J.; Rueda, D. R.; Ezquerra, T. A.; Poza, P.; Davies, R. *Nano Lett.* **2010**, *10*, 1472−1476.
(23) Hui, W.; Wei, W.; Huang, Y.; Wang, C.; Su, Z. *Macromolecules* **2008**, *41*, 7755−7758.
(24) Lutkenhaus, J. L.; McEnnis, K.; Serghei, A.; Russell, T. P. *Macromolecules* **2010**, *43*, 3844−3850.
(25) Steinhart, M.; Haissam, P. G.; Prabhukaran, M.; Gösele, U. *Phys. Rev. Lett.* **2006**, *97*, 1−4.
(26) Steinhart, M.; Senz, S.; Wehrspohn, R. B.; Gösele, U.; Wendorff, J. H. *Macromolecules* **2003**, *36*, 3646−3651.
(27) Woo, E.; Huh, J.; Jeong, Y. G.; Shin, K. *Phys. Rev. Lett.* **2007**, *98*, 136103.
(28) Wu, H.; Wang, W.; Huang, Y.; Su, Z. *Macromol. Rapid Commun.* **2009**, *30*, 194−198.
(29) Wu, H.; Wang, W.; Yang, H.; Su, Z. *Macromolecules* **2007**, *40*, 4244−4249.
(30) Xiong, S.; Wang, Q.; Xia, H. *Mater. Res. Bull.* **2004**, *39*, 1569−1580.
(31) Quiram, D. J.; Register, R. A.; Marchand, G. R. *Macromolecules* **1997**, *30*, 4551−4558.
(32) Quiram, D. J.; Register, R. A.; Marchand, G. R.; Adamson, D. H. *Macromolecules* **1998**, *31*, 4891−4898.
(33) Huang, P.; Guo, Y.; Quirk, R. P.; Ruan, J.; Lotz, B.; Thomas, E. L.; Hsiao, B. S.; Avila-Orta, C. A.; Sics, I.; Cheng, S. Z. *Polymer* **2006**, *47*, 5457−5466.
(34) Loo, Y. L.; Register, R. A.; Adamson, D. H. *Macromolecules* **2000**, *33*, 8361−8366.
(35) Huang, P.; Zhu, L.; Cheng, S. Z. D.; Ge, Q.; Quirk, R. P.; Thomas, E. L.; Lotz, B.; Hsiao, B. S.; Liu, L. Z.; Yeh, F. J. *Macromolecules* **2001**, *34*, 6649−6657.
(36) Nojima, S.; Ohguma., Y.; Kadena, K.; Ishizone, T.; Iwasaki, Y.; Yamaguchi, K. *Macromolecules* **2010**, *43*, 3916−3923.
(37) Hamley, I. W.; Fariclough, J. P. A.; Terrill, N. J.; Ryan, A. J.; Lipic, P. M.; Bates, F. S.; Tows-Andrews, E. *Macromolecules* **1996**, *29*, 8835−8843.
(38) Sun, Y.; Steinhart, M.; Zschech, D.; Adhikari, R.; Michler, G. H.; Gösele, U. *Macromol. Rapid Commun.* **2005**, *26*, 369−375.
(39) Sevink, G. J. A.; Zvelindovsky, A. V.; Fraaije, J. G. E.; Huinink, H. P. *J. Chem. Phys.* **2001**, *115*, 8226−8230.

(40) Xiang, H.; Shin, K.; Kim, T.; Moon, S. I.; Mccarthy, T. J.; Russell, T. P. *Macromolecules* **2004**, *37*, 5660−5664.
(41) Chen, J. T.; Zhang, M.; Yang, L.; Avallone, A.; Russell, T. P. *J. Polym. Sci., Polym. Phys.* **2007**, *45*, 2912−2917.
(42) Xiang, H.; Shin, K.; Kim, T.; Moon, S. I.; Mccarthy, T. J.; Russell, T. P. *Macromolecules* **2005**, *38*, 1055−1056.
(43) Dobriyal, P.; Xiang, H.; Kazuy, M.; Russell, T. P. *Macromolecules* **2009**, *42*, 9082−9088.
(44) Shin, K.; Xiang, H.; Moon, S. I.; Kim, T.; Mccarthy, T. J.; Russell, T. P. *Science* **2004**, *306*, 76.
(45) Maniadis, P.; Tsimpanogiannis, I. N.; Kober, E. M.; Lookman, T. *Europhys. Lett.* **2008**, *81*, 56001.
(46) Xiang, H.; Shin, K.; Kim, T.; Moon, S.; McCarthy, T. J.; Russell, T. P. *J. Polym. Sci., Part B: Polym. Phys.* **2005**, *43*, 3377−3383.
(47) Sevink, G. J. A.; Zvelindovsky, A. V. *J. Chem. Phys.* **2008**, *128*, 084901.
(48) Li, W.; Wickham, R. A. *Macromolecules* **2006**, *39*, 8492−8498.
(49) Yu, B.; Jin, Q.; Ding, D.; Li, B.; Shi, A. *Macromolecules* **2008**, *41*, 4042−4054.
(50) Yu, B.; Sun, P.; Chen, T.; Jin, Q.; Ding, D.; Li, B. *Phys. Rev. Lett.* **2006**, *96*, 138306.
(51) Wu, Y.; Cheng, G.; Katsov, K.; Sides, S. W.; Wang, J.; Tang, J.; Fredrickson, G. H.; Moskovits, M.; Stucky, G. D. *Nat. Mater.* **2004**, *3*, 816−822.
(52) Pulamagatta, B.; Yau, M. Y. E.; Gunkel, I.; Thurn-Albrecht, T.; Schröter, K.; Pfefferkorn, D.; Kressler, J.; Steinhart, M.; Binder, W. H. *Adv. Mater.* **2011**, *23*, 781−786.
(53) Wang, Q. *J. Chem. Phys.* **2007**, *126*, 024903.
(54) Li, W.; Wickham, R. A.; Garbary, R. A. *Macromolecules* **2006**, *39*, 806−811.
(55) Zhu, Y.; Jiang, W. *Macromolecules* **2007**, *40*, 2872−2881.
(56) Lorenzo, A. T.; Arnal, M. L.; Boschetti de Fierro, A.; Abetz, V. *Eur. Polym. J.* **2006**, *42*, 516−533.
(57) Li, A. P.; Muller, F.; Birner, A.; Nielsch, K.; Gösele, U. *J. App. Phys.* **1998**, *84*, 6023−6026.
(58) Vázquez, M.; Pirota, K.; Hernández-Vélez, M.; Prida, V.; Navas, D.; Sanz, R.; Batallan, F. *J. Appl. Phys.* **2004**, *95*, 6642.
(59) Massa, M.; Carvalho, J. L.; Dalnoki-Veress, K. *Eur. Phys. J.* **2003**, *12*, 111−117.
(60) Massa, M.; Dalnoki-Veress, K. *Phys. Rev. Lett.* **2004**, *92*, 255509.
(61) Massa, M.; Lee, M.; Dalnoki-Veress, K. *J. Polym. Sci., Part B: Polym. Phys.* **2005**, *43*, 3438−3443.
(62) Carvalho, J.; Dalnoki-Veress, K. *Phys. Rev. Lett.* **2010**, *105*, 237801.
(63) Carvalho, J.; Dalnoki-Veress, K. *Eur. Phys. J. E.* **2011**, *34*, 1−6.
(64) Pyda, M. ATHAS The Advanced Thermal Analysis System. http://athas.prz.edu.pl/Default.aspx?op=db (accessed Sept 30, 2011).
(65) Müller, A. J.; Arnal, M. L.; López-Carrasquero, F. *Macromol. Symp.* **2002**, *183*, 199−204.
(66) Chen, H. L.; Hsiao, S. C.; Lin, T. L.; Yamauchi, K.; Hasegawa, H.; Hashimoto, T. *Macromolecules* **2001**, *34*, 671−674.
(67) Chen, H. L.; Wu, J. C.; Lin, T. L.; Lin, J. S. *Macromolecules* **2001**, *34*, 6936−6944.
(68) Schmalz, H.; Muller, A. J.; Abetz, V. *Macromol. Chem. Phys.* **2003**, *204*, 111−124.
(69) Müller, A. J.; Balsamo, V.; Arnal, M. L.; Jakob, T.; Schmalz, H.; Abetz, V. *Macromolecules* **2002**, *35*, 3048−3058.
(70) Schmalz, H.; Knoll, A.; Müller, A. J.; Volker, A. *Macromolecules* **2002**, *35*, 10004−10013.
(71) Schmalz, H.; Abetz, V.; Müller, A. J. *Macromol. Symp.* **2002**, *183*, 179−184.
(72) Röttele, A.; Thurn-Albrecht, T.; Sommer, J. U.; Reiter, G. *Macromolecules* **2003**, *36*, 1257−1260.
(73) Taden, A.; Landfester, K. *Macromolecules* **2003**, *36*, 4037−4041.
(74) Hsu, J. Y.; Nandan, B.; Chen, M. C.; Chiu, F. C.; Chen, H. L. *Polymer* **2005**, *46*, 11837−11843.
(75) Xu, J. T.; Jin, W.; Fan, Z. Q. *J. Appl. Polym. Sci.* **2005**, *98*, 208−215.
(76) Boschetti-de-Fierro, A.; Müller, A. J.; Abetz, V. *Macromolecules* **2007**, *40*, 1290−1298.
(77) Castillo, R. V.; Arnal, M. L.; Müller, A. J.; Hamley, I. W.; Castelletto, V.; Schmalz, H.; Abetz, V. *Macromolecules* **2008**, *41*, 879−889.
(78) Pan, P.; Zhao, L.; Zhu, B.; He, Y.; Inoue, Y. *J. Appl. Polym. Sci.* **2010**, *117*, 3013−3022.
(79) Zhu, L.; Cheng, S. Z. D.; Calhoun, B. H.; Ge, Q.; Quirk, R. P.; Thomas, E. L.; Hsiao, B. S.; Yeh, F.; Lotz, B. *J. Am. Chem. Soc.* **2000**, *122*, 5957−5967.
(80) Müller, A. J.; Lorenzo, A. T.; Castillo, R. V.; Arnal, M. L.; Boschetti-de-Fierro, A.; Abetz, V. *Macromol. Symp.* **2006**, *245*−*246*, 154−160.
(81) Müller, A. J.; Lorenzo, A. T.; Arnal, M. L.; Boschetti-de-Fierro, A.; Abetz, V. *Macromol. Symp.* **2006**, *240*, 114−122.
(82) Lorenzo, A. T.; Arnal, M. L.; Müller, A. J.; Boschetti-de-Fierro, A.; Abetz, V. *Macromolecules* **2007**, *40*, 5023−5037.
(83) Müller, A. J.; Arnal, M. L. *Prog. Polym. Sci.* **2005**, *30*, 559−603.
(84) Mathot, V. *Calorimetry and Thermal Analysis of Polymers*; Hanse Publishers: New York, 1994.
(85) Frensch, H.; Harnischfeger, P.; Jungnickel, B. In *Multiphase polymers: blends and ionomers*; Utracky, L., Weiss, R., Eds.; ACS: 1989.
(86) Loo, Y. L.; Register, R. A.; Ryan, A. J. *Macromolecules* **2002**, *35*, 2365−2374.
(87) Cormia, R. L.; Price, F. P.; Turnbull, D. *J. Chem. Phys.* **1962**, *37*, 1333−1341.
(88) Baïtoul, M.; Saint-Guirons, H.; Xans, P.; Monge, P. *Eur. Polym. J.* **1981**, *17*, 1281−1287.
(89) Barham, P. J.; Jarvis, D. A.; Keller, A. *J. Polym. Sci. Polym. Phys* **1982**, *20*, 1733−1748.
(90) Arnal, M. L.; Matos, M. E.; Morales, R. A.; Santana, O.; Müller, A. J. *Macromol. Chem. Phys.* **1998**, *199*, 2275−2288.
(91) Arnal, M. L.; Müller, A. J. *Macromol. Chem. Phys.* **1999**, *200*, 2559−2576.
(92) Loo, Y. L.; Register, R. A.; Ryan, A. J. *Phys. Rev. Lett.* **2000**, *84*, 4120−4123.
(93) Loo, Y. L.; Register, R. A.; Ryan, A. J.; Dee, G. T. *Macromolecules* **2001**, *34*, 8968−8977.
(94) Takeshita, H.; Gao, Y. J.; Natsui, T.; Rodriguez, E.; Miya, M.; Takenaka, K.; Shiomi, T. *Polymer 48* **2007**, *48*, 7660−7671.
(95) Woo, E.; Huh, J.; Jeong, Y. G.; Shin, K. *Phys. Rev. Lett.* **2007**, *98*, 136103.
(96) McCrum NG, R. B. W. G. *Anelastic and dielectric effects in polymeric solids*; Dover Publications Inc.: New York, 1967.
(97) Yamamoto, K.; Kato, K.; Sugino, Y.; Hara, S.; Miwa, Y.; Sakaguchi, M.; Shimada, S. *Macromolecules* **2005**, *38*, 4737−4743.
(98) Balsamo, V.; Müller, A. J.; Gyldenfeldt, V.; Friederike.; Stadler, R. *Macromol. Chem. Phys.* **1998**, *199*, 1063−1070.

Macromolecules

Article

pubs.acs.org/Macromolecules

Nanocavitation in Carbon Black Filled Styrene–Butadiene Rubber under Tension Detected by Real Time Small Angle X-ray Scattering

Huan Zhang,[†] Arthur K. Scholz,[‡,§] Jordan de Crevoisier,[†,¶] Fabien Vion-Loisel,[∥] Gilles Besnard,[¶] Alexander Hexemer,[△] Hugh R. Brown,[#] Edward J. Kramer,*[,‡,§,⊥] and Costantino Creton*[,†]

[†]Laboratory of Soft Matter Science and Engineering, ESPCI Paristech-CNRS-UPMC, 10 rue Vauquelin, 75005 Paris, France

[‡]Materials Research Laboratory, University of California, Santa Barbara, California 93106, United States

[§]Department of Materials, University of California, Santa Barbara, California 93106, United States

[⊥]Department of Chemical Engineering, University of California, Santa Barbara, California 93106, United States

[∥]Michelin, CERL Ladoux, F-63040 Clermont Ferrand, France

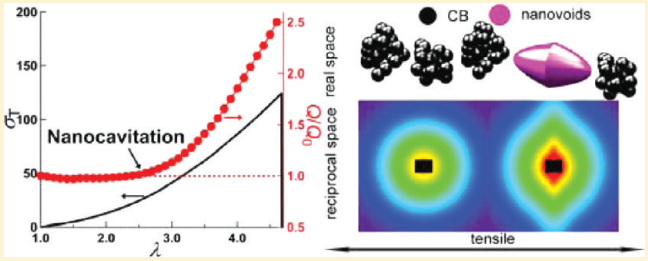
[#]University of Wollongong, Wollongong, Australia

[¶]LMT-Cachan, ENS-Cachan, 61 avenue du président Wilson, F-94230 Cachan, France

[△]Advanced Light Source, Lawrence Berkeley National Laboratory, 1 Cyclotron Road, Berkeley, California 94720, United States

Supporting Information

ABSTRACT: Nanocavitation was detected for the first time in carbon black filled styrene–butadiene rubber (CB-SBR) under uniaxial loading by real time small-angle X-ray scattering (SAXS) using synchrotron X-ray radiation. A three phase model was developed to calculate the void volume fraction from the scattering invariant Q determined from the observed SAXS patterns. The normalized scattering invariant Q/Q_0, where Q_0 is the invariant before deformation, greatly increased above a critical extension ratio λ_{onset} which we attribute to the formation of nanovoids. Analysis of the 2D scattering patterns show that voids formed are 20–40 nm in size and elongated along the tensile direction. Cavities formed beyond λ_{onset} are smaller as λ increases. Results from the scattering experiments are strongly supported by macroscopic volume change measurements on the samples under similar uniaxial strain. A nearly constant nanocavitation stress σ_{onset} (25 MPa) was observed when the filler volume fraction ϕ_{CB} was larger than 14%. This value is much higher than that predicted based on the elastic instability of small voids in an unfilled elastomer and shows only a weak dependence on the cross-linking density ν_C in heavily cross-linked samples. An energy based cavitation criterion stressing the importance of confined domains between particles or clusters of particles was adopted and found to be consistent with the observed results. The nanocavities are thought to alter the local stress state and promote local shear motion of filler particles.



1. INTRODUCTION

Elastomers are highly deformable and nearly incompressible materials that find a variety of applications where high mechanical strength needs to be combined with the accommodation of large strains. Yet to obtain these remarkable properties non-crystallizing elastomers need to be filled with nanoparticles, generally carbon black (CB) or silica. The presence of such nanoparticles introduces significant heterogeneities in the material structure and complexity in the mechanical properties of the materials. As a result the investigation of the connection between material morphology and structure, and mechanical properties has been the focus of research for decades.[1−4] Although the presence of nanoparticles has important effects on the dissipative properties at small strain, the focus of the present study is on the failure mechanisms of elastomers at large strains, mechanisms that are particularly relevant to understanding macroscopic fracture processes.

Because the bulk modulus of elastomers greatly exceeds their shear and Young's moduli, they can store large amounts of volumetric strain energy at relatively low strains if they are loaded in a confined geometry where tensile stresses are triaxial. If triaxial tensile stresses are present over a macroscopic volume, optically visible vacuoles typically appear and grow in the bulk above a critical applied stress. Such a failure process is often termed "cavitation". These cavitation phenomena have been studied in the past essentially with two experimental methods: direct optical visualization of cavities either in situ[5−9] or post mortem,[10] and measurements of volume increase of the filled elastomers during stretching using a gas or liquid dilatometer.[8,9,11,12] Such volume change experiments could be of

Received: October 22, 2011
Revised: January 5, 2012
Published: January 27, 2012

ACS Publications © 2012 American Chemical Society

course carried out equally well on unfilled elastomers or on filled elastomers with variable particle sizes and any positive change in volume was interpreted as a sign of cavitation or decohesion. Only rubbers filled with large volume fractions of micrometer size particles showed a significant volume change in uniaxial tension.[9] Criteria for the growth of such cavities (either by deformation or by fracture) under a hydrostatic tensile stress were proposed.[10,13−17] Yet individual cavities could only be detected with an optical microscope above a size of a few micrometers. The question of the nucleation of such large cavities remains therefore very much an open question.

In the case of elastomers filled with nanoparticles, in addition to the macroscopic cavities discussed above, it is reasonable to think that the presence of randomly dispersed nanoparticles and particle aggregates can create nanosized rubber domains between filler aggregates, domains that can be loaded in triaxial tension even if the macroscopic sample is deformed uniaxially. Under high tensile stresses such confined domains are prone to create nanocavities which could then act as precursors for macroscopic cracks. Yet the formation of nanovoids in filled rubbers in uniaxial tension has never been directly demonstrated. Experiments by LeCam et al.[18,19] and by Starkova and Aniskevich[20] showed indeed an increase in macroscopic volume under uniaxial tension but no direct evidence has been observed to relate it with nanovoids. A direct relationship between voids and volume changes has been convincingly demonstrated for larger particles[8,9,11] (tens of micrometers), very different from the materials of the present study. Ramier et al.[21] studied silica-filled SBR by a combination of techniques (dilatometry, light scattering, SAXS and USAXS) and only detected large cavities by small angle light scattering in a thin rubber film and qualitatively associated them with the change in macroscopic volume of the material but did not detect any nanocavities by USAXS and SAXS. In summary, no direct evidence has been observed to relate the positive changes in volume measured during uniaxial extension with the presence of nanovoids, their size or size distribution. Yet recent observations of crack propagation in filled rubbers reveal fibrillar structures at the micrometer scale at the crack tip[22,23] that suggest the genesis and development of submicrometer cavities ahead of the crack front that should be detectable by SAXS.

Thanks to the development of high flux synchrotron X-ray facilities, small-angle X-ray scattering (SAXS) has been used as a powerful tool for real time detection of changes in structure under strain. Many studies have focused on rubber toughened plastics[24,25] and on semicrystalline polymers.[26−28] However several studies have also been published for filled elastomers under uniaxial extension.[21,29−36] Most of them focused on the change of anisotropy of the system,[29,30] the changes in fractal dimension of the filler network[31−33] and the rearrangement of filler in real space under external loading.[34−36] Again, no nanocavitation was discovered in those filled systems.

The objective of the current work is to develop a methodology to *quantitatively* detect nanovoids in a noncrystallizing filled rubber and to investigate the effect of material parameters and loading parameters on such a process. All experiments were performed on a series of model filled elastomers made from an identical random copolymer of styrene−butadiene (SBR), vulcanized with a sulfur-based chemistry and filled with various proportions of the same type of carbon black. Since in carbon black filled elastomers the use of optical methods is ruled out by the absorption of light by the carbon black particles, the nanovoid formation was detected by SAXS experiments performed at synchrotron X-ray facilities during tensile tests. Our main analytical tool was the analysis of 2D scattering patterns and in particular we exploited the scattering invariant following a method proposed as far back as 1950 by Debye[37] and developed to investigate crazes in glassy polymers by Paredes, Fischer,[38,39] and Brown and Kramer.[40−42] To adapt the method to our system, a new three phase model was developed to calculate the volume fraction of nanovoids in the presence of both elastomer and filler from the 2D scattering data obtained during uniaxial extension experiments. The shape and size of the voids was then obtained from the detailed analysis of the 2D scattering pattern.

2. EXPERIMENTAL SECTION

1. Sample Preparation. Michelin prepared various samples of CB filled SBR rubber for this study. The SBR (M_n = 120 kg/mol, M_w/M_n = 1.94, T_g = −48 °C and density d_{SBR} = 0.94 g/cm^3) used was a random copolymer with 0.15 mol fraction styrene. The filler was carbon black (reference N347) with surface area (cetyltrimethylammonium bromide adsorption) of 87 ± 5 m^2/g and structure (dibutylpthlate adsorption) of 124 ± 5 mL/100 g and density d_{CB} = 1.8 g/cm^3. The amount of CB loaded in the SBR matrix was between 5 and 60 phr (parts of weight per hundred parts of rubber) which covered a range of volume fractions from 2.4% to 23.9% respectively. The cross-linking system was based on sulfur and *n*-cyclohexy1−2-benzothiazyl-sulfenamide (CBS). The antioxidant N-(1,3-dimethylbutyl)-*N*′-phenyl-p-phenylenediamine 6PPD (1.9 phr), the vulcanization activators stearic acid (2 phr) and zinc oxide (ZnO, 2.5 phr) were the same for all the samples. Elastomer and filler were mixed in a chamber at 50 °C first. Then in the second step, the CBS accelerators and sulfur were added using two-roll mills. Samples were cured at 150 °C for different times. The important parameters of the filled SBR samples are summarized in Table 1. The samples are designated as

Table 1. Characteristics of the Samples

label	SBR (phr)	CB (vol %)	sulfur (phr)	CBS (phr)	ν_c (10^{-5} mol/cm^3)	curing time (min)
2CB_8NC	100	2.3	1.6	1.6	6.5	35
14CB_8NC	100	13.5	1.6	1.6	8.2	23
17CB_8NC	100	17.3	1.6	1.6	7.4	20
21CB_8NC	100	20.7	1.6	1.6	8.3	20
24CB_8NC	100	23.9	1.6	1.6	7.7	15
17CB_0NC	100	17.3	1.6	1.6	/	/
17CB_4NC	100	17.3	1	1	3.6	41
17CB_11NC	100	17.3	2.3	2.3	10.6	18
17CB_15NC	100	17.3	4.7	4.7	15.5	15

*m*CB_*n*NC where *m* is the volume fraction of carbon black and *n* is the nominal molar density of cross-links in 10^{-5} mol/cm^3. The cross-linking density ν_c was obtained by swelling experiments analyzed using the Flory−Rehner equation[43] assuming that the filler cannot swell.

Dog-bone shaped samples were cut from rubber sheets for mechanical testing with a gauge length of 50 mm ×4 mm (width) × 2 mm (thickness). All samples were kept at −18 °C to prevent aging until shipping to the beamline.

2. Small Angle X-ray Scattering Measurement. The SAXS measurements were performed at the synchrotron beamline 7.3.3 at the Advanced Light Source, Lawrence

dx.doi.org/10.1021/ma2023606 | *Macromolecules* 2012, 45, 1529−1543

Berkeley National Laboratory, Berkeley, CA. The energy of the X-ray radiation was 10 keV, resulting in an X-ray wavelength λ_{wave} of 0.127 nm. The incident beam intensity $IC1$ (counts per second) and the transmitted beam intensity $IC2$ (counts per second) were measured by an ion chamber before the samples and a pin diode in the beam stop, respectively. Two dimensional scattering patterns were recorded by a Pilatus 1 M detector (pixel size 0.172 μm, 1043 pixels ×981 pixels). The sample to detector distance was roughly 4 m and was calibrated using an Ag-behenate standard sample. The size of the beam spot is 1 mm (horizontal) × 0.7 mm (vertical). The scattered intensity could be measured down to a minimum value of the scattering vector q ($q = 2\pi \sin(2\theta)/\lambda_{wave}$, where 2θ is the scattering angle) of 0.025 nm^{-1}.

Because $IC1$ and $IC2$ were measured by two different devices, a correlation factor R was introduced. It is defined by $R=IC1_{air}/IC2_{air}$ where $IC1_{air}$ and $IC2_{air}$ are the readings of the two devices without the sample. In practice, the correlation factor R was measured in the following way: Various aluminum foil layers were placed at the sample position and $IC1$ and $IC2$ were recorded. R^{-1} was extrapolated from the intercept on the plot of $IC2/IC1$ versus the number of layers in a semi-logarithmic scale. The air scattering pattern I_{air} was also recorded for data reduction.

To give a clear description of the experimental procedures and data reduction, we show a schematic of the main scattering setup in Figure 1. Mechanical tests were carried out with a

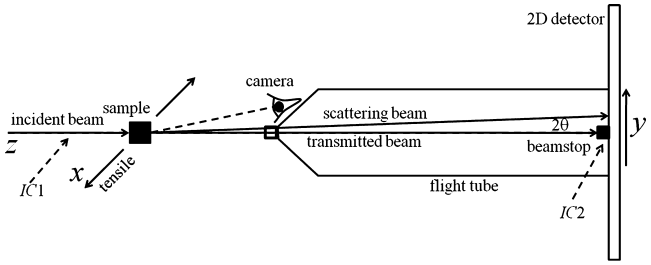


Figure 1. Schematic drawing of the experiment setup and the coordinates used in this work. The flight tube is under vacuum.

homemade tensile frame. This apparatus can stretch the sample in a symmetric fashion to guarantee the same position of the X-ray spot on the sample at all extension ratios. To measure the local strain near the region hit by the X-ray beam, an alumina powder (analytical grade) was carefully deposited on the sample surface very close to the beam spot but not inside. A camera (PixeLINK B741EF, 1280 pixel ×1024 pixel) was placed up the flight tube and tracked the displacement of the alumina particles (see Figure 1). Images were recorded every 0.5s and synchronized with the stress−strain data. After the fracture of the sample, a background optical image was captured by the PixeLINK camera. An optical standard (NT62−212, Edmund Optics) with a 50 mm ×50 mm dots pattern was placed in the clamps and the related image was also recorded for later data reduction. Samples were stretched along the x axis (horizontal direction) with an initial strain rate of 0.25/min (about 12.5 mm/min crosshead velocity). SAXS patterns were taken after each extension ratio increment $\Delta\lambda = 0.1$ with an exposure time of t (t = 1s for filled rubber samples in this work) and thus the relative change of elongation during each exposure was less than 4%. No obvious radiation damage to the filled polymer was detected during the experiment.

3. Data Reduction. *Measurement of Local Strain.* The background was first subtracted from the optical images and then each image was corrected for the nonlinear effect (due to the lens) and for the perspective effect (due to the non parallelism between the focus plane and the object plane, see Figure 1). A free particle tracking package (developed by Daniel Blair and Eric Duresne, see http://physics.georgetown.edu/matlab/) for Matlab was used to obtain the local elongation in the x direction in the vicinity of the beam spot.

SAXS Patterns. In order to obtain meaningful data when comparing materials, the measured raw intensity $I_{measure}$ (counts per second) needs to be corrected and normalized by several factors directly related both to the experimental setup and equipment being used and to the fact that during the experiment the sample thickness changed as it was strained.

The first correction to apply is the subtraction of the background which comes in two parts: the detector intensity pattern when the X-ray shutter is closed called I_{dark} and the air scattering pattern from the air between the sample and the flight tube. The air scattering measured with no sample in the beam (I_{air}) needs to be corrected by the attenuation due to the presence of the sample ($RIC2/IC1$) and by the ratio of incident beam intensity ($IC1/IC1_{air}$). The correction of air scattering is then:

$$I_{cor1} = I_{measure} - \frac{RIC2}{IC1}\frac{IC1}{IC1_{air}}(I_{air} - I_{dark}) - I_{dark} \quad (1)$$

For the Pilatus 1 M 2D detector used no signal was detected when the X-ray shutter was closed, and hence I_{dark} can be set to zero.

I_{cor1} needs to be corrected for changes in sample thickness $t_{thick} = \mu\mathrm{Ln}(IC1/RIC2)$, and transmission $T = R\ IC2/IC1$ and normalized by the incident beam intensity $IC1$.

$$I_{cor2} = \frac{I_{cor1}}{F_{Ins}IC1t_{thick}T} = \frac{I_{cor1}}{F_{Ins}\mu RIC2\ln(IC1/RIC2)} \quad (2)$$

with F_{Ins} being an instrument factor and μ the X-ray absorption coefficient of the sample. Since we always compared the intensity at a given deformation to that of the same undeformed sample and used the same instrumental setup, F_{Ins} and μ are neglected when computing the scattering pattern or scattering intensity. The scattering invariant Q, which is the integral of the corrected intensity I_{cor2} over all reciprocal space, is calculated with the assumption of cylindrical symmetry of the system along the loading direction (x axis) following the methodology developed for the analysis of crazes.

$$Q = \frac{1}{2}\int_{-\infty}^{+\infty}\int_{0}^{\infty} I_{cor2}(q_xq_y)q_y\,\mathrm{d}q_x\,\mathrm{d}q_y = \frac{1}{2}\frac{\int_{-\infty}^{+\infty}\int_{0}^{\infty} I_{cor1}(q_xq_y)q_y\,\mathrm{d}q_x\,\mathrm{d}q_y}{RIC2\ln(IC1/RIC2)} \quad (3)$$

In this work, we always use the normalized scattering invariant Q/Q_0 (eq 4). The index 0 here represents the undeformed samples.

$$\frac{Q}{Q_0} = \frac{\int_{-\infty}^{+\infty}\int_{0}^{\infty} I_{cor1}(q_xq_y)q_y\,\mathrm{d}q_x\,\mathrm{d}q_y}{\int_{-\infty}^{+\infty}\int_{0}^{\infty} I_{cor1.0}(q_xq_y)q_y\,\mathrm{d}q_x\,\mathrm{d}q_y}\frac{RIC2_0\ln(IC1_0/RIC2_0)}{RIC2\ln(IC1/RIC2)} \quad (4)$$

Notice that the thickness t_{thick} is measured by the X-ray absorption which will not be influenced by the presence of nanovoids. It will be different from the geometric thickness of

dx.doi.org/10.1021/ma2023606 | Macromolecules 2012, 45, 1529−1543

the sample when nanocavitation is present. The intensity calculated by eq 2 is actually an intensity per unit thickness of *solid material* (the size of the beam spot is constant) and so are the scattering invariants Q and Q_0.

To avoid the effect of the background noise in the high q region, a radial cutoff q value (q_{cutoff}) is introduced above which the scattering intensity is neglected for the integration of both deformed and undeformed scattering patterns. The choice of q_{cutoff} has almost no effect on the final result if a value larger than 0.8 nm^{-1} is used (see Supporting Information, SFigure 1). Thus, q_{cutoff} is set to 0.8 nm^{-1} which is already well in the Porod's law regime where the intensity decreases as a power law with q.

In the raw scattering pattern, there are horizontal and vertical black bars which are the gaps between chip arrays on the Pilatus 1 M detector (see Supporting Information, SFigure 2). We only used the right top quadrant and filled the black bars using scattering intensity in the other symmetrical positions for the calculation of Q. The scattering patterns shown in this work are also reconstructed from these right top quadrants after applying the corrections presented above.

4. The Three Phase Model. The primary goal of our scattering experiments is the detection of nanovoids during the tensile deformation of filled rubbers and for that purpose we used the scattering invariant. The scattering invariant Q is directly related to the square of the X-ray scattering length density (XSLD) contrast between each phase, and is independent of the shape of the scatterers and of their spatial arrangement.[44] The approach was originally developed to model a system containing multiple phases[42,44−46] and here we use an analogous approach. Unlike the craze structure which is a typical two phase system (polymer and void), our vulcanizate contains not only polymer and filler, but also other additives (sulfur, 6PPD, CBS, stearic acid, and ZnO). Here two important assumptions are made:

1 Additives are not taken into consideration because we assume that they are uniformly distributed in the rubber phase and while they may increase the X-ray scattering length density (XSLD) of this phase they do not give rise to a contribution to the invariant as a separate phase.
2 There are no preexisting nanocavities inside the undeformed samples, or more precisely, no preexisting nanocavities in the detectable length range via SAXS (5−250 nm in this work).

The samples were prepared under high pressure and well degassed, therefore the second assumption is reasonable and the scattering of the additives should not change during deformation. The scattering invariant for an ideal binary phase system without nanovoids is expressed by eq 5 according to small-angle X-ray scattering theory[44]

$$Q_0 = 2\pi^2 V \phi_{SBR}\phi_{CB}(\rho_{SBR} - \rho_{CB})^2 = 2\pi^2 V_{solid}\phi_{SBR}\phi_{CB}(\rho_{SBR} - \rho_{CB})^2 \quad (5)$$

where V is the volume of the scattering region and equals the volume of solid material V_{solid} if no voids are present, ϕ_{SBR} and ϕ_{CB} denote the volume fractions of the polymer matrix and of the CB particles of the virgin samples and ρ_{SBR} and ρ_{CB} are the corresponding XSLD, respectively. If, upon mechanical loading, nanocavities appear, Q is expected to increase due to the large XSLD contrast between nanovoids and their environment. For a three phase system similar to eq 5, the invariant Q can be determined via

$$Q = 2\pi^2 V[\phi_{SBR\lambda}\phi_{CB\lambda}(\rho_{SBR} - \rho_{CB})^2 + \phi_{SBR\lambda}\phi_{void}\rho_{SBR}^2 + \phi_{CB\lambda}\phi_{void}\rho_{CB}^2] = 2\pi^2 \frac{V_{solid}}{1-\phi_{void}}[\phi_{SBR\lambda}\phi_{CB\lambda}(\rho_{SBR} - \rho_{CB})^2 + \phi_{SBR\lambda}\phi_{void}\rho_{SBR}^2 + \phi_{CB\lambda}\phi_{void}\rho_{CB}^2] \quad (6)$$

where, ϕ_{SBR_λ}, ϕ_{CB_λ}, and ϕ_{void} are the volume fraction of matrix, CB particles and nanovoids under external loading, respectively.[42,45,46] Here, V is no longer equal to the volume of solid material since nanovoids appear. The XSLD of the nanovoids is zero ($\rho_{void} = 0$) and the volume fractions ϕ_{SBR_λ}, ϕ_{CB_λ}, ϕ_{void}, ϕ_{SBR}, and ϕ_{CB} are related by eqs 7a and 7b

$$\phi_{SBR\lambda} = \phi_{SBR}(1 - \phi_{void}) \quad (7a)$$

$$\phi_{CB\lambda} = \phi_{CB}(1 - \phi_{void}) \quad (7b)$$

By substituting eqs 7a and 7b into eq 6 and dividing by eq 5, an expression for the normalized invariant Q/Q_0 is obtained.

$$\frac{Q}{Q_0} = 1 + \left[\frac{\phi_{SBR}\rho_{SBR}^2 + \phi_{CB}\rho_{CB}^2}{\phi_{SBR}\phi_{CB}(\rho_{SBR} - \rho_{CB})^2} - 1\right]\phi_{void} \quad (8)$$

In this work, Q/Q_0 was calculated from the measured scattering patterns and then the void volume fractions were calculated by using eq 8.

5. Volume Variation Measurement by Digital Image Correlation. A similar dog bone shaped sample was marked with talc powder and stretched monotonically in the vertical direction with an Instron tensile machine with a cross head speed of 50 μm/s. Two cameras were placed perpendicular to the front face and to the side face of the sample. Images of a central area (7 mm × 4 mm of front face, 7 mm × 2.5 mm of side face) were recorded every 5 s and digital image correlation was then performed to calculate the macroscopic volume variation.

Digital image correlation[47] was used to obtain the displacement field on the sample between the image taken at the beginning of the test and one taken during the test. Telecentric lenses were used to reduce the effect of out-of-plane displacement on our measured displacement fields. Those effects were measured and subtracted from the measured displacements.

The strain in the tensile direction plus either the front face transverse strain or the side face transverse strain are derived from those displacement fields. As expected, there were no noticeable differences between the measured strain in the tensile direction from the front face and the side face. The full deformation gradient tensor $\boldsymbol{F}$ is diagonal in our case. Its components are deduced from the derivation of the displacement fields measured with digital image correlation (∇U).

$$\nabla U = F - I \quad (9)$$

$$F_{i,j} = \frac{\partial x_i}{\partial X_j} \quad (10)$$

where x_i are the coordinates in the deformed state and X_j the coordinates in the initial state. The relative volume change is

dx.doi.org/10.1021/ma2023606 | Macromolecules 2012, 45, 1529−1543

derived from the transformation gradient as

$$\frac{\Delta V}{V} = \frac{\det(F) - 1}{\det(F)} \quad (11)$$

where V is the volume after deformation and ΔV is the difference between the new and the initial volume V_0. The quantity $\Delta V/V$ has been selected to be comparable to the volume fraction of voids obtained by SAXS.

3. RESULTS

The results obtained from SAXS from CB-filled SBR under uniaxial tension are essentially of two kinds: the 2D scattering pattern as a function of applied elongation and the normalized scattering invariant calculated from eq 4 as a function of applied elongation. We chose to plot the data as a function of either true stress $\sigma_T = F/S$ (F is the loading force, S is the area of the cross section under deformation) or elongation $\lambda = l/l_0$ (l_0 is the initial gauge length of the sample and l is the gauge length under deformation).

1. Un-Cross-Linked Sample. To verify the validity of the data reduction procedure and the cylindrical symmetry assumption, a filled but un-cross-linked sample 17CB_0NC was tested. This sample is essentially a highly filled viscoelastic fluid and contains the same cross-linking agents as the other samples but was carefully stored to avoid any chemical cross-linking. The chain entanglements are too weak to sustain high stresses. Thus, we do not expect nanocavitation to occur upon external loading and the scattering invariant is expected to remain constant as a function of λ. The stress σ_T and the normalized invariant Q/Q_0 curves are shown in Figure 2a. The true stress σ_T increases at small elongation but reaches a plateau

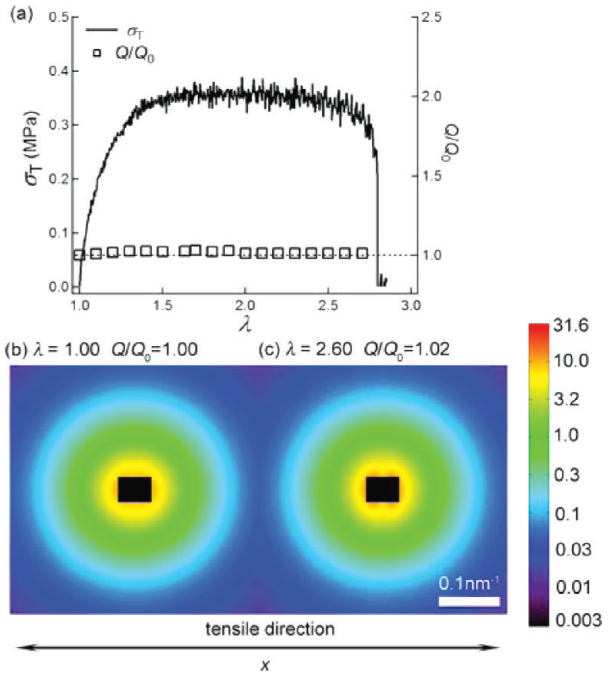


Figure 2. Results for an un-cross-linked sample 17CB_0NC. (a) True stress σ_T (line) and normalized scattering invariant Q/Q_0 (open symbols) as a function of λ. Experimental data were taken at ambient temperature (25 °C). The dashed line is just a guide to the eye. Selected scattering patterns at (b) reference state ($\lambda = 1$) and (c) close to the elongation at fracture where the log intensity (color scale) is that of intensity in arbitrary units.

when $\lambda > 1.5$. The stress–elongation curve is not very meaningful here since the sample exhibited necking at high extension. However the scattering data reveals some interesting information. In parts a and b of Figure 2, selected scattering patterns are shown. Before stretching, an isotropic pattern is observed reflecting the random dispersion of CB inside the rubber matrix. This pattern gradually changes with increasing strain to a butterfly shape in the low q region with an intensity minimum perpendicular to the tensile axis. Very close to the fracture point (in the necked region), the butterfly pattern further evolves into a four-lobe pattern (data not shown here). Similar results have been reported for other filler–polymer systems[29,30,34,48] (cross-linked or not), gels,[49−51] and polymer melts.[52] Although the detailed interpretation of such patterns is still unclear, it is generally accepted that it is the nonaffine relative displacement of the particles under deformation that accounts for the butterfly scattering pattern. CB aggregates are forced to come closer in the direction perpendicular to the tensile axis and cluster along narrow regions of higher CB particle density separated by highly deformed polymer in the direction parallel to the tensile axis. This clustering leads to a banded structure of CB aggregates lying at right angles to the tensile axis, and results in the observed butterfly scattering pattern. Yet, despite the change in the scattering pattern, Q/Q_0 remains constant at 1 which means that no new scattering phase appears during stretching as expected. Thus, our data reduction procedure and our assumption of cylindrical symmetry seem not to introduce any artifact into the analysis. To be complete one should mention that the uncertainty in Q/Q_0 for this un-cross-linked sample is ±0.02, so fluctuation of any Q/Q_0 values below this range is regarded as indicating that no new scattering phase appears.

2. Nanocavitation in Cross-Linked Samples. We now show the results for the sample 24CB_8NC that has the highest volume fraction of filler. The key data are summarized in Figures 3, 4 and 5. In Figure 3a, σ_T and Q/Q_0 are plotted as a function of λ. The true stress increases monotonically with elongation and the sample breaks at a high extension ratio that is close to 5. The invariant ratio Q/Q_0 remains equal to 1 over a rather large range of λ. Above a certain threshold value, Q/Q_0 begins to increase and reaches almost 2.5 times its original value before final fracture. This demonstrates the appearance of a third phase which exhibits a large XSLD contrast with its neighboring environment. Since SBR chains are unable to crystallize under external loading, small nanovoids represent the most probable third phase.

As shown in Figure 3b, σ_{onset} was first determined from a Q/Q_0 vs σ_T plot (Figure 3b) and used to calculate λ_{onset} from the related stress–elongation curves. For this sample, σ_{onset} = 26.0 MPa and λ_{onset} = 2.60. The Q/Q_0 vs stress curve is quite reproducible for samples from the same batch (see Supporting Information, SFigure 3) and if an error exists in determining σ_{onset}, it is mainly due to the fact that we took exposures every $\Delta\lambda$ = 0.1 which will introduce an error about ±2 MPa.

We also tried to detect the presence of nanocavities from the change in the scattering patterns. Typical scattering patterns are shown in Figure 4 and the corresponding scattering intensities along the x and y directions are also plotted in Figure 5. Without deformation, an isotropic pattern is observed, a signature of the scattering from the hierarchical structure of the CB filler aggregates in the rubber matrix (Figure 4a).[53] The scattering intensity from the CB particles is composed of a Guinier's law region coming from CB aggregates (fusion of primary particles)

dx.doi.org/10.1021/ma2023606 | Macromolecules 2012, 45, 1529–1543

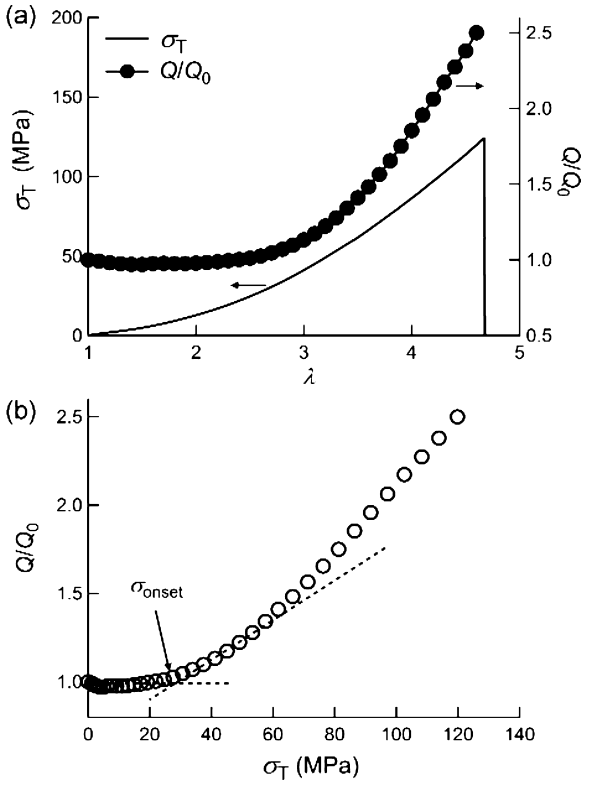


Figure 3. Scattering and tensile testing data of sample 24CB_8NC (a) σ_T (line) and Q/Q_0 (filled circle) are presented as a function of λ. (b) Q/Q_0 versus σ_T. The void onset stress σ_{onset} is determined from the intersection, indicated by the arrow, of two lines, one corresponding to $Q/Q_0 = 1$ and one tangent to the increasing Q/Q_0 curve.

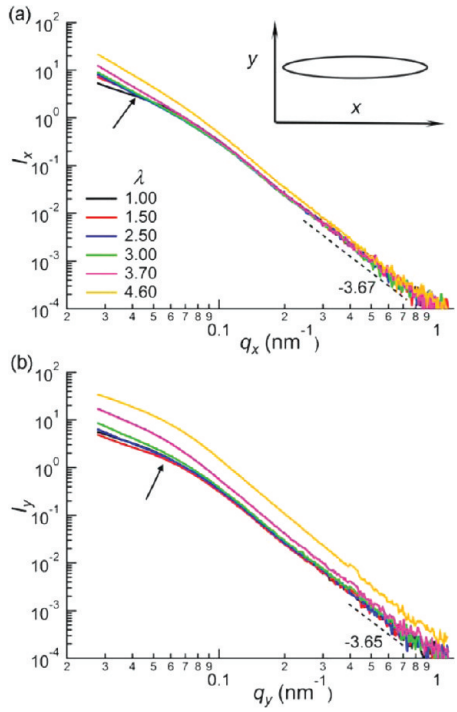


Figure 5. Scattering intensity (arbitrary units) as a function of q along the x (a) and y (b) directions at different values of λ indicated in the legend for sample 24CB_8NC. The numbers close to the dashed lines are the power law exponents in the Porod's region. Arrows indicate the q positions where scattering intensity starts to increase near σ_{onset}. The inset in part a is a schematic drawing of the elongation of nanovoids in the stretching direction.

and a Porod's law region that is due to the interface scattering between the primary particles and the matrix. Here the power law exponents are −3.67 and −3.65 in the x and y direction respectively, consistent with literature values.[53]

At small λ before nanocavitation occurs (Figure 4b), the pattern in the low q region weakly splits along the tensile direction and tends to form a faint butterfly scattering pattern. The corresponding 1-D intensity in Figure 5, parts a and b (red lines), slightly decreases in the low q region in the y direction

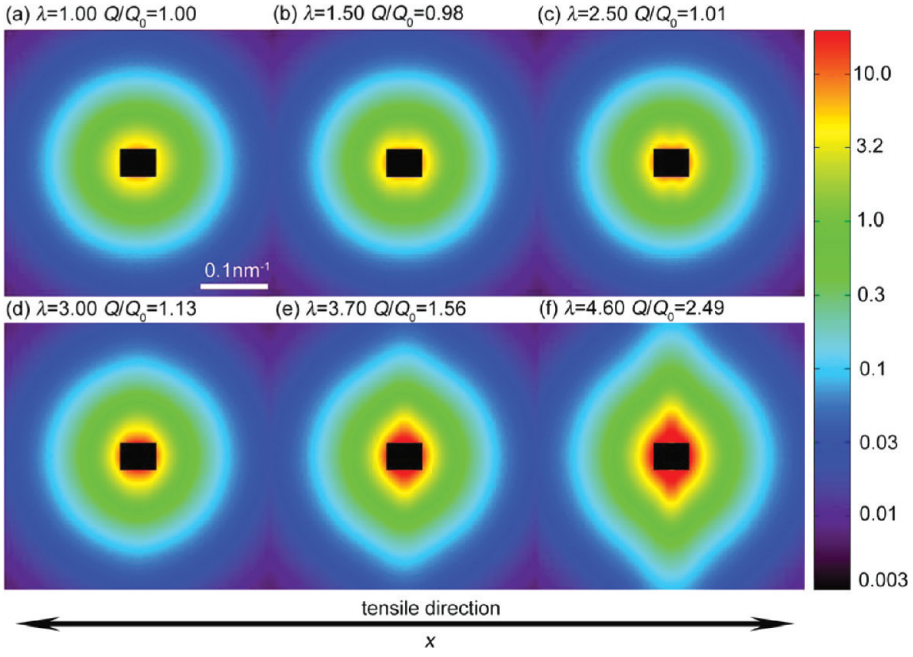


Figure 4. (a–f) Selected scattering patterns of sample 24CB_8NC at different values of λ as indicated in each frame title together with the corresponding Q/Q_0. The colors represent a logarithmic scale of scattered intensity (arbitrary units).

dx.doi.org/10.1021/ma2023606 | *Macromolecules* 2012, 45, 1529–1543

but increases in the x direction as was observed in the un-cross-linked specimen. The associated Q/Q_0 remains constant so this faint butterfly pattern is not related to the formation of nanovoids but rather to the nonaffine deformation of the filler aggregates.

At intermediate elongations before (Figure 4c) and after (Figure 4d) λ_{onset}, the valley in the y direction in the low q region is superimposed on the scattering pattern from nucleated nanocavities and gradually forms an elliptical pattern. However, this kind of change is not as sharp in other samples examined. Thus, we chose Q/Q_0 versus σ_T plots to determine the threshold stress and elongation rather than trying to directly estimate them from the SAXS patterns. In this range of λ, the intensity scattered by the nanovoids at initiation is more or less uniformly distributed along the x and y direction (blue and green lines in Figure 5) which apparently indicates that the initial shape of these nanovoids is nearly spherical. However, we think this is a false impression resulting from the superposition of the scattering from the particles and the weak scattering from the voids. As indicated by the arrows in Figure 5, the position of the crossover point is different in the x direction (~0.4 nm^{-1}) and in the y direction (~0.6 nm^{-1}) which suggests a more elongated structure in the tensile direction. Since the low q region is associated with relatively larger length scales, it is expected that the sizes of these first nanovoids is rather large. A more detailed estimate of their size and shape will be presented in the Discussion.

At higher elongation, a sharp streak develops in the high q region along the y axis (Figure 4, parts e and f) strongly suggesting the existence of highly elongated nanovoids with their major axis lying along the tensile direction (see the schematic drawing in Figure 5a). In the following we will refer to this pattern as a "flame pattern". The increase of the intensity is more pronounced in the y direction even in the very high q region though less significant in the tensile direction (x axis). This indicates the decrease of the average size of the nanovoids in both directions. Combined with the Q/Q_0 plot (Figure 3) we may deduce a broad size distribution of nanocavities (see Discussion for details). In addition, the surface fractal dimension (Porod's law region) of the CB aggregates in both directions at high q ($q > 0.3$) remains unchanged which is consistent with Schneider's observations in filled PDMS.[31]

The volume fraction of nanovoids ϕ_{void} was calculated from eq 8. The XSLD of the SBR matrix and of the CB filler particles are $\rho_{SBR} = 8.756 \times 10^{10}$ cm^{-2} and $\rho_{CB} = 15.26 \times 10^{10}$ cm^{-2}, respectively. The curve (open symbols in Figure 6) is quite similar to the Q/Q_0 plot in Figure 3a. Above λ_{onset}, ϕ_{void} grows up to 11% before fracture occurs. Such a large volume fraction of nanocavities should be easily detectable via a macroscopic volume variation measurement. This was carried out by deforming identical tensile samples to the same extension ratios while measuring the volume change with λ of a representative volume in the center of the sample with a digital image correlation (DIC) method.

A representative result is illustrated in Figure 6a. To clearly compare between the two solutions, we did not show the data points before the onset of cavitation for either curve. The similarity between both measurements is striking. The main discrepancies are the later onset of cavitation (λ_{onset}= 2.8) and a higher amount of total volume variation from macroscopic measurement, e.g., at λ = 4.00, $\Delta V/V$ = 8% while ϕ_{void} from SAXS is 6%. The difference between the two parameters can be explained by the relative advantages and limitations of the two

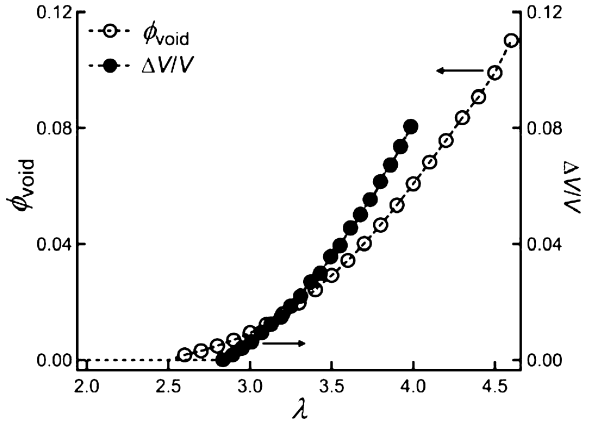


Figure 6. $\Delta V/V$ obtained from DIC measurement (right axis, filled symbols) and void volume fraction ϕ_{void} (left axis, open symbol) calculated from the three phase model are plotted as a function of elongation for comparison. The data points which are just fluctuations around zero before the onset of cavitation for both curves are not shown for clarity.

methods and by the uncertainty in our interpretation of the orientation effect at high strain.

Because of the large electron density contrast between the nanovoids and the other two phases, SAXS is more sensitive to the onset of nanocavitation but not as accurate at high deformation for the following reason: The scattering invariant is the sum of the contribution of smaller nanovoids entering into the observation window minus bigger ones exiting it; the latter scatter primarily at very low q region and can be hidden under the beamstop. The sensitivity of the detection can be estimated by eq 8 which is linear in ϕ_{void}. For example for sample 24CB_8NC 0.5% of voids results in 7% increase in Q/Q_0 which is well above our detection threshold. On the contrary, well conducted macroscopic volume variation measurements can provide the global volume change more precisely at high deformation because all cavities, regardless of their size are accounted for, but is less accurate for the λ_{onset} depending on the details of the method being used. That can explain the higher cavitation threshold value and lower amount of volume variation from the DIC measurement at the initiation of cavitation ($\lambda < 3.2$) as well as the crossing of the two curves in Figure 6. Even at higher elongations the difference between the two methods is small which quantitatively demonstrates the capability of our three phase model. In another filler−rubber systems studied by volume variation measurement alone, a value of global volume change was estimated to a similar range.[19]

3. Effect of Filler Volume Fraction. All samples shown in Figure 7 have almost the same cross-linking density but different filler volume fractions. In Figure 7a, σ_T is plotted as a function of λ for various filler volume fractions. In agreement with established data[1] the increase in filler volume fraction increases the modulus and decreases somewhat the maximum extensibility. ϕ_{void} is represented as a function of λ in Figure 7b for all four materials and λ_{onset} decreases clearly with increasing ϕ_{CB} as shown in Figure 7d. Interestingly, however, if ϕ_{void} is plotted as a function of σ_T (Figure 7c), a constant σ_{onset} of approximately 25 MPa is measured when ϕ_{CB} > 14% (Figure 7d). This value is much higher than the cavitation stress observed in bulk unfilled rubber stretched under confinement[10,14] but a similar value has also been predicted to trigger cavitation

dx.doi.org/10.1021/ma2023606 | Macromolecules 2012, 45, 1529−1543

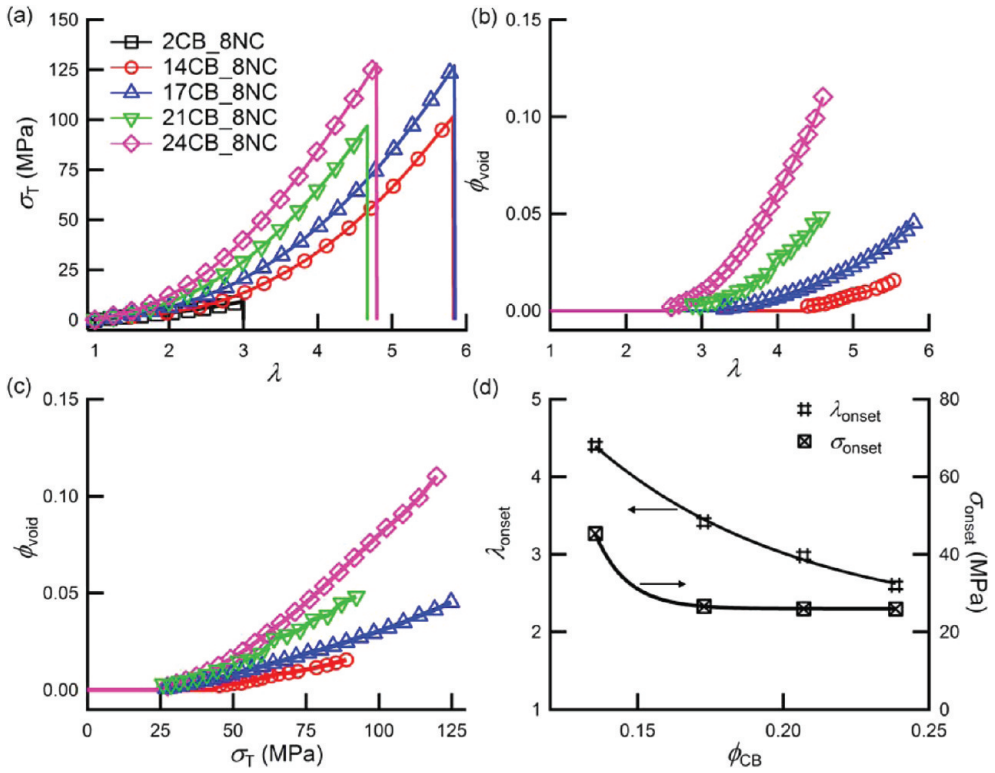


Figure 7. Effect of filler volume fraction on the nanocavitation of CB-SBR systems. (a) Stress−elongation curves. (b and c) Void volume fraction ϕ_{void} as a function of λ and σ_T respectively. (d) λ_{onset} and σ_{onset} as a function of filler volume fraction ϕ_{CB}. Lines in part d are simply guides to the eyes. The data points that are just fluctuations around zero before the onset of cavitation for all curves in parts b and c are not shown for clarity.

of the rubber phase in toughened plastics.[54,55] For 14CB_8NC, this σ_{onset} shifts to a higher value of approximately 45 MPa. After initiation, ϕ_{void} grows in a more linear fashion with σ_T. The result obtained for the sample with a very low filler content (2CB_8NC) may be representative of unfilled elastomers. For this low ϕ_{CB} sample, Q/Q_0 does not increase upon stretching and thus no significant cavitation at the nanometer length scale is detected before macroscopic fracture occurs. The fact that observable nanocavitation requires the presence of a certain amount of filler implies that the level of local confinement of the matrix induced by the filler aggregates plays a critical role.

Some additional information can be inferred from the pattern itself. In Figure 8, typical 2D scattering patterns and related Q/Q_0 are shown for different samples at different levels of elongation. In the lightly filled 2CB_8NC, an elongated scattering pattern was observed just before fracture at $\lambda = 3$. The scattering intensity increased along the y axis but decreased along the x axis, resulting in no variation in the scattering invariant ($Q/Q_0 = 0.97$). This shows that the presence of an elliptical pattern per se does not indicate the presence of nanovoids and must be combined with the measurement of Q/Q_0.

For those samples where an increase in Q/Q_0 is observed, SAXS patterns similar to those in Figure 4 are observed for both 17CB_8NC and 21CB_8NC with a transition from isotropic patterns to weak butterfly patterns and then to an elliptical shape and finally to flame patterns. As for 14CB_8NC, the weak butterfly pattern is not detected and elliptical patterns are observed directly after the onset of nanocavitation.

4. Effect of Cross-Linking Density. All samples in Figure 9 have the same filler volume fraction but different cross-linking density. Like the increase in filler volume fraction, increasing the cross-linking density results in a higher modulus of the filled rubber as shown in Figure 9a. However this increase in cross-linking density has little effect on the initiation of nanocavitation. Only a slight variation in λ_{onset} is seen in Figure 9b. If ϕ_{void} is plotted as a function of σ_T in Figure 9c, σ_{onset} has a weak dependence on the cross-linking density. Interestingly, there is no distinct difference between the 17CB_8NC and the 17CB_11NC samples in terms of nanocavitation (red and blue lines) but a notable difference in fracture elongation. An even higher cross-linking density (17CB_15NC) results in an earlier brittle rupture and hinders the nucleation of nanocavities. Probably the stress required to nucleate the nanocavities is close to or even higher than the stress to propagate a crack through the sample. Results from Figures 7 and 9 are insufficient to draw any correlations between the amount of voids just before fracture and the elongation at fracture. In some cases, the system may form many small nanovoids without coalescence thus allowing it to extend to high elongation before fracture. In other cases, the nanovoids may coalesce or develop into crack-like shapes even at low void volume fractions. In Figure 9d, λ_{onset} and σ_{onset} are summarized as a function of network cross-linking density ν_c and compared with the prediction of the macroscopic cavitation theory based on an elastic instability[10] which is indicated by the red dashed line in Figure 9d.

Concerning the scattering pattern, there are no significant differences between the two less cross-linked samples 17CB_4NC and 17CB_8NC (Figure 10 and Figure 8). The well-developed streak perpendicular to the tensile direction is observed in both cases, indicating the presence of highly elongated nanovoids parallel to the stretching axis. However, in the more cross-linked 17CB_11NC, a low eccentricity elliptical scattering pattern is present from the onset of

dx.doi.org/10.1021/ma2023606 | Macromolecules 2012, 45, 1529−1543

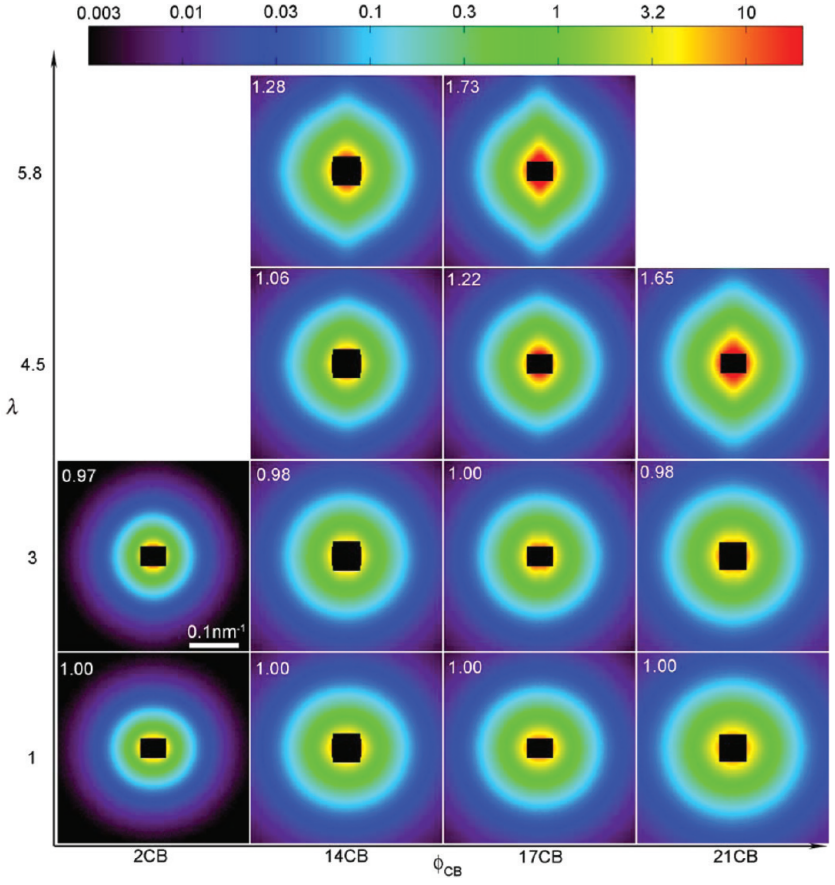


Figure 8. Effect of filler volume fraction on the scattering patterns. The vertical axis is elongation λ and the horizontal axis is filler volume fraction ϕ_{CB}. The number in each image indicates the related normalized scattering invariant Q/Q_0. Color codes are the same as in Figure 4 and are shown on a log scale.

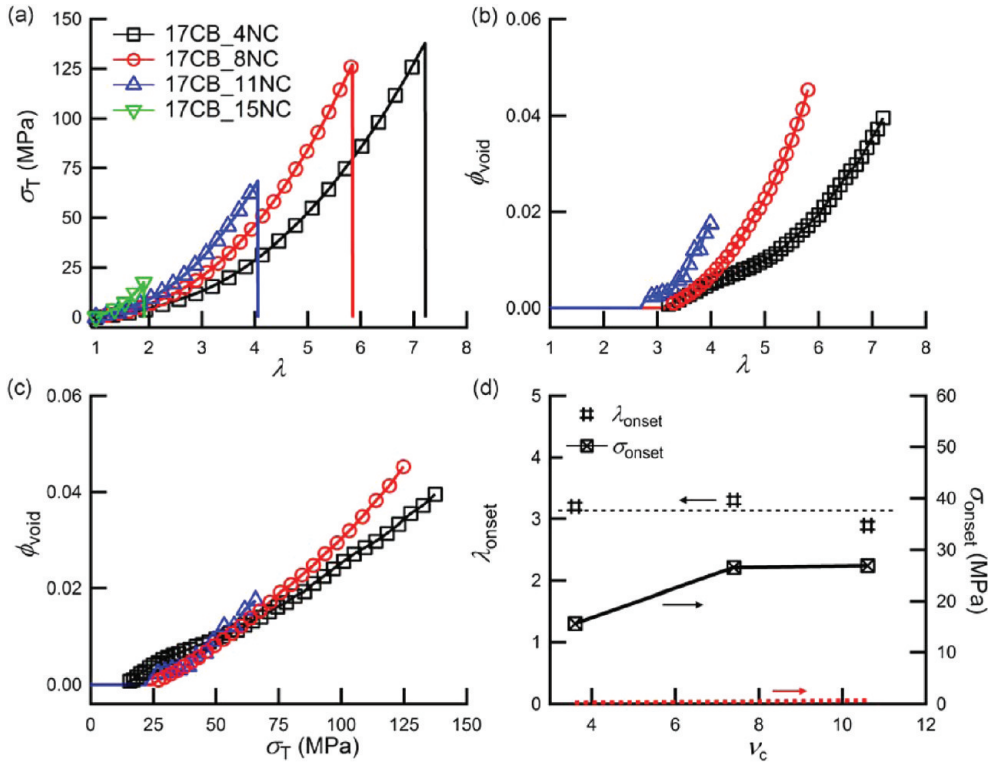


Figure 9. Effect of cross-linking density on the cavitation of CB-SBR systems. (a) Stress−elongation ratio curves. (b and c) Void volume fraction ϕ_{void} as a function of λ and σ_T respectively. (d) λ_{onset} and σ_{onset} as a function of network cross-linking density ν_c ($\times 10^{-5}$ mol/cm^3). The black dashed line in d is just a guide for the eyes while the red dashed line is the prediction of cavitation stress based on an elastic instability (eq 17 and see the Discussion for more details). The data points which are just fluctuations around zero before the onset of cavitation for all curves in parts b and c are not shown for clarity.

dx.doi.org/10.1021/ma2023606 | *Macromolecules* 2012, 45, 1529–1543

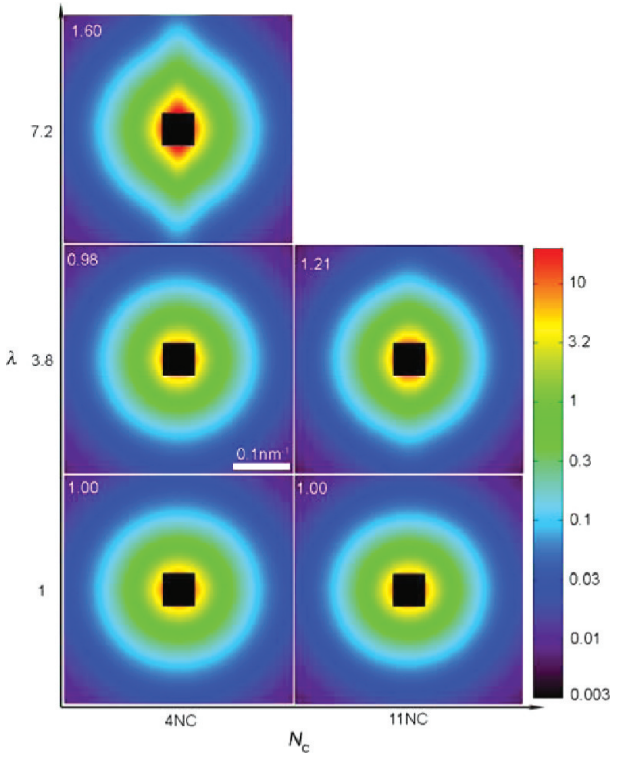


Figure 10. Effect of cross-linking on the scattering patterns. The vertical axis is the elongation λ and the horizontal axis is the network cross-linking density ν_c. The number in each pattern indicates the related normalized scattering invariant Q/Q_0. The color bar is the same as that in Figure 4.

nanocavitation to the final rupture (Figure 10). The orientation of nanovoids is moderate in this case, probably hindered by the cross-linking of the matrix, and the whole sample is quite brittle. For the even more highly cross-linked 17CB_15NC, no nanocavitation is seen before fracture and the scattering patterns are very similar to those observed for the lightly filled 2CB_8NC.

4. DISCUSSION

1. The Three Phase Model and SAXS. Possible volume changes in filled rubbers have been studied for many years[18,19,21,56] and have been reviewed by Le Cam.[18] A positive volume variation is often ascribed to cavitation or decohesion at the filler−matrix interface or to fracture of the elastomer network while a negative volume change is related with crystallization under strain. While crystallization under strain is well documented and well understood, nanocavitation in uniaxial tension has not been conclusively demonstrated and quantified. The SAXS technique and in particular the analysis of the scattering invariant using the three phase model that we have developed, offers a way to quantitatively compare the SAXS volume change measurements with macroscopic volume change measurements. A few assumptions deserve to be discussed: One may doubt the hypothesis that there are no small preexisting voids inside the sample within the size range detectable via SAXS (5−250 nm in the present work). All materials were prepared under pressure and well degassed and no evidence of preexisting nanovoids is seen from electron microscopy observations. Furthermore, if such voids were present we would expect these nanovoids to grow even at low elongation and increase Q/Q_0 which we did not observe. The main limitation of SAXS is the lack of sensitivity to large voids. Once nanovoids coalesce to form micrometer size voids at high strain, their scattering signal is hidden under the beam stop and no longer contributes significantly to the scattering invariant. So the macroscopic volume variation should always be larger than that is detected by SAXS. More consistency between the SAXS and macroscopic volume change measurements could be obtained if a much lower q region was attainable in SAXS, e.g. by using a longer sample to detector distance. Unfortunately this distance was limited in these experiments to 4 m due to the hutch dimensions at beamline 7.3.3 at ALS.

2. Size of Nanovoids. To obtain an estimate of the size of these nanovoids, the scattering from nanovoids needs to be separated from the total scattering. Perfect deconvolution is very difficult here because the formation of CB aggregates also depends on the void shape and their dispersion state inside the sample, i.e., the two forms of scatterings (from CB and from nanovoids) are coupled. But we can make an estimate based on the following assumptions:

1 The onset of nanocavitation occurs in the low q region which is associated with a length scale larger than the primary CB particles. Thus, only the CB near the boundaries of the voids modifies the scattering.
2 Except in the y-direction, the scattering changes only slightly in the high q region under external stretching, even after the appearance of nanovoids (see Figure 4, 8, and 10). It is therefore acceptable to assume an isotropic scattering from CB. Actually, CB filler clusters are believed to be relatively "stiff" at the smaller length scales,[2] consistent with a relatively unaltered scattering pattern in the high q region.

Under these two assumptions, the scattering from the voids I_{void} can be obtained from the following equation:

$$I_{void} = I_{total} - I^0_{CB} \tag{12}$$

where I_{total} is the total scattering and I^0_{CB} is the scattering from CB just before nanocavitation. In Figure 11a, the scattering patterns of I_{void} from sample 24CB-8NC are shown. Actually, the shape of the flame pattern is closer to that of a lozenge than to an ellipse. A similar lozenge shape was also observed in another sample using the same procedure. SANS "lozenge" scattering patterns are often seen in stretched polymer networks with dilute deuterated chains,[57,58] but these are thought to result from the superposition of scattering from the stretched chains between cross-links and that from relaxed dangling chain ends. Here the lozenge shape of the scattering pattern clearly results from the shape of the voids themselves. Large lozenge or diamond shaped cavities are often observed in the ductile fracture of (strain hardened and thus oriented) polycarbonate[59,60] and polyvinyl chloride.[61,62]

In order to extract size information, a classical Porod analysis[44] based on approximating the actual lozenge-of-revolution shape by an ellipsoid was applied here to I_{void} to calculate the size of the voids.

$$\frac{\langle R^3\rangle}{\langle R^2\rangle} = \frac{3\lambda_{void}{}^2}{\pi(1-\phi_{void})}\frac{Q_{void}}{K_{py}} \tag{13}$$

R is the radius of a sphere with the same volume as the ellipsoid and λ_{void} describes the deformation from a spherical shape. Q_{void} is the scattering invariant from nanovoids and K_{Py} is the Porod's constant along the y axis. Other parameters are

dx.doi.org/10.1021/ma2023606 | Macromolecules 2012, 45, 1529−1543

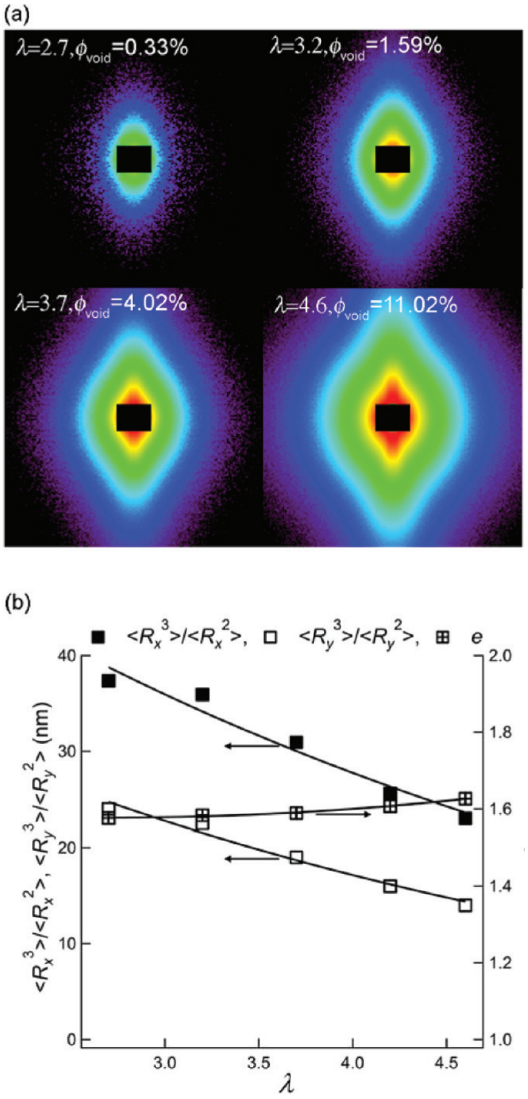


Figure 11. Estimate of the size of nanovoids for sample 24CB_8NC by eq 14 and 15. (a) Selected I_{void} (from eq 12) scattering patterns, from nanovoids at different elongations. The color scale is the same as that in Figure 4. (b) The average radius of voids in the x and y direction ($\langle R_x^3\rangle/\langle R_x^2\rangle$, filled squares) and ($\langle R_y^3\rangle/\langle R_y^2\rangle$, open squares) as well as their ratio e (eq 16, right axis) are plotted as a function of the elongation ratio λ. Black lines are just guides to the eyes.

then expressed by:

$$\frac{\langle R_x^3\rangle}{\langle R_x^2\rangle} = \frac{\langle R^3\rangle}{\langle R^2\rangle} = \lambda_{void} \tag{14}$$

$$\frac{\langle R_y^3\rangle}{\langle R_y^2\rangle} = \frac{\langle R^3\rangle}{\langle R^2\rangle}\frac{1}{\sqrt{\lambda_{void}}} \tag{15}$$

The aspect ratio e is defined as:

$$\frac{\langle R_x^3\rangle}{\langle R_x^2\rangle}\frac{\langle R_y^2\rangle}{\langle R_y^3\rangle} = \lambda_{void}^{3/2} \tag{16}$$

The detailed derivation of these expressions is in the Appendix and the result of the analysis for sample 24CB_8NC is plotted in Figure 11b.

The average size is obtained from the average volume to surface ratio ($\langle R_x^3\rangle/\langle R_x^2\rangle$ and $\langle R_y^3\rangle/\langle R_y^2\rangle$). As the elongation increases from $\lambda = 2.5$ to $\lambda = 4.5$, this average size decreases in both directions, from 37 to 25 nm in the x direction and from 24 to 15 nm in the y direction. However, the average aspect ratio e (defined by eq 16) of these nanovoids is larger than 1 (implying an elliptical shape) even at the initiation stage and remains nearly constant implying that the average shape of the nanovoids hardly changes as λ increases. If the increase of ϕ_{void} at high elongation was mainly due to the growth of existing voids, the average size in the tensile direction should have increased with elongation, which is not observed. Therefore, Figure 11b clearly confirms the appearance of additional smaller voids at larger λ, consistent with the observations in Figure 5.

3. Cavitation Criterion in CB-SBR On the basis of an Elastic Instability. Macroscopic cavitation in confined bulk unfilled elastomers is thought to originate from the unbound expansion or fracture of preexisting defects under a strong local hydrostatic tensile stress.[54] Green and Zerna[63] showed that the hydrostatic stress P_C needed to inflate a large spherical vacuole surrounded by neo-Hookean material is related to the Young's modulus E of the elastomer network by:

$$P_C = 5/6E_{network} \tag{17}$$

This result, valid for a constant applied hydrostatic true stress and for an infinitely large sample was surprisingly confirmed experimentally in Gent's early papers.[10,64] We use here the word surprisingly because the simple mechanical treatment of Green and Zerna did not include the surface tension of the rubber γ, which will introduce a closing pressure $p = 2\gamma/r$ and increase the critical expansion stress of cavities of initial ratio smaller than γ/E, and only considered reversible expansion (no fracture).

Gent and Tompkins took into account the surface tension[64] and could explain some discrepancies between experiments and predictions. However, for our materials an estimate of the initial defect size necessary to account for a surface tension controlled expansion stress of 25 MPa is around 3 nm in radius (γ is usually taken as 0.03 J/m^2 for SBR). Notice in Figure 11a, the average radius of the expanded cavities near the onset of cavitation is ~30 nm. Such an expansion would require a stretch around the nucleating defects of 10, obviously exceeding the limiting stretch of the chains. Therefore, one needs to consider irreversible fracture as a mechanism of cavitation.

Several models have been proposed to account for the expansion by irreversible fracture of a preexisting void,[13,54,65−68] which is physically reasonable for cross-linked rubbers. Gent suggested[13] that the cavitation stress should be a nonlinear function of the ratio $G_c/r_0E_{network}$, where G_c is the fracture toughness in uniaxial tension of the rubber, $E_{network}$ is the modulus of the rubber and r_0 is the radius of the initial defect.[13,14,17] In unfilled rubbers this model predicts the correct trends but the maximum measured values of the cavitation stress ($\sim 3E_{network}$) suggest the existence of large defects of the order of micrometers which are not observed experimentally prior to cavitation. In our system, we do not observe macroscopic cracks and the measured σ_{onset} of nanocavitation is at least ten times the Young's modulus of the rubbery matrix (~2 MPa) and nearly three times the best results obtained with unfilled systems relative to their modulus. We believe that the reason for this discrepancy between the threshold observed for unfilled systems (where the confined region is much larger than

dx.doi.org/10.1021/ma2023606 | Macromolecules 2012, 45, 1529−1543

the defect size) and our system (where both sizes are comparable) cannot be explained by the previously described models, which assume an infinite size for the sample, and in the following we attempt to explain the high value of nanocavitation stress and its dependence on filler volume fraction and cross-linking density (Figures 7 and 9) by a finite size effect. Although many approximations are made, we feel that the discussion following can be the basis for improvement by future experiments and simulations.

5. NANOCAVITATION IN CB-SBR BASED ON AN ENERGY BALANCE

Although the macroscopic stress we applied is uniaxial and uniform, the CB aggregates can disturb the stress field locally and create regions of radius R_{con} (presumably between filler particles) where the rubber matrix is strongly confined. As a result, a local hydrostatic expansion stress can be present in these confined regions between fillers. This local hydrostatic stress will vary spatially in magnitude and presumably depend on the spatial organization of the hard filler particles. It is difficult to quantitatively relate the macroscopic tensile stress to the distribution of local hydrostatic stresses but if the degree of local confinement remains moderate, they should have the same order of magnitude.

All models discussed in the previous section are valid for large confined volumes where the growing cavity size is much smaller than the confined volume. Yet in filled elastomer systems, the confined volumes (between particle aggregates) are of the same size as the growing nanocavities and are dispersed in a material which is predominantly in uniaxial tension. This has two consequences: First as soon as a nanocavity nucleates, its growth releases local confinement and prevents further growth by removing the driving force. This delays coalescence of the cavities and macroscopic fracture of the material. Second the growth criterion must include the size of the confined domain and not only the local stress. We propose here a model inspired from cavitation in rubber-filled thermoplastics where nanodomains under hydrostatic tension coexist with zones in uniaxial tension. In this model adapted to very small cavities, both surface tension and fracture toughness play a role.

In rubber toughened plastics, the effect of rubber particle size on particle cavitation has long been observed and discussed. Some researchers have reported that the cavitation process in rubber particles cannot occur when the diameter of the rubber particle decreases below 200 nm even if the local stress state would allow the initiation of voids. This indicates that both the local stress and the total strain energy available to drive cavitation play key roles. For example, to form a void with a radius of r_0, the local hydrostatic stress should exceed an inner pressure P_{surf} related to the surface tension of the polymer by:

$$P_{local} > P_{surf} \quad \text{with} \quad P_{surf} = 2\gamma/r_0 \quad \text{and} \quad r_0 > 2\gamma/P_{local} \tag{18}$$

The energy barrier $U_{barrier}$ used to create such a void is[69,70]

$$U_{barrier} = 4\pi\gamma {r_0}^2 > 16\pi\gamma^3/{P_{local}}^2 \tag{19}$$

Here, the $U_{barrier}$ is underestimated because the energy to fracture the cross-linked chains along the inner surface and to stretch the surrounding polymer chains should also be considered.

Several models based on an energy balance were proposed to account for cavitation of rubber particles in rubber toughened plastics or to predict cavity growth in soft adhesive layers. In those models where finite size is important, the key parameter controlling cavitation is the local volumetric strain energy rather than the hydrostatic stress (volumetric strain energy density). But none of them considered the effect of the volume fraction of fillers which will alter the dependence of the local strain energy on the external loading. To qualitatively explain nanocavitation in our CB-SBR system, we can use an energy-based model developed by Fond et al.[70] In their model, σ_{onset} is given by:

$$\sigma_{onset} = \frac{C}{f} {R_{con}}^{-3/4} K^{1/4} \gamma^{1/2} (\gamma + G_c)^{1/4} \tag{20}$$

where f is a geometrical factor relating the local hydrostatic stress to the external loading, R_{con} is the radius of the confined rubber domains (see Figure 12a), K is the bulk modulus of the rubber, γ and G_c are the surface tension and fracture toughness of the rubber, respectively. C is just a numerical factor and is not important for this qualitative description. An obvious conclusion from eq 20 is that σ_{onset} does not depend on Young's modulus but on the bulk modulus and surface tension γ which are nearly independent of the degree of cross-linking. Only G_c is indirectly related to the cross-linking density.

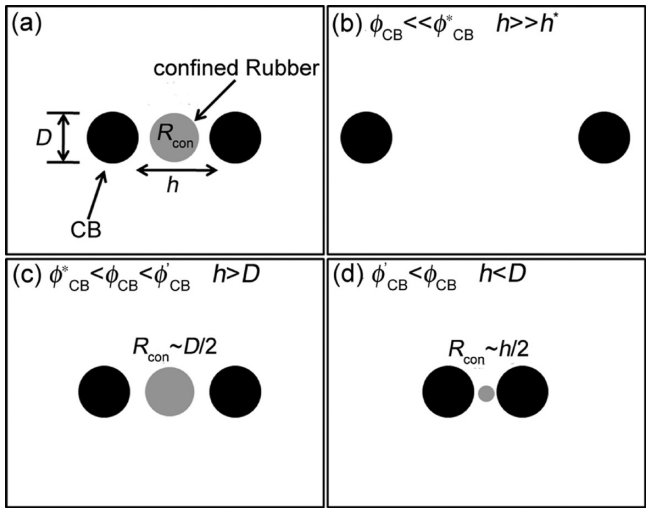


Figure 12. Schematic drawing of the filler volume fraction effect on cavitation. (a) Definition of parameters. (b) Drawing in the dilute region where there is little mechanical interaction between fillers. (c) In the moderate filler volume fraction, the volume of the confined rubber domains is unaffected. (d) In the highly filled region, the volume of the confined rubber domains depends on the interparticle distance h.

It is quite reasonable since we have mentioned that the inner pressure due to surface tension which depends on van der Waals forces rather than cross-linking density is quite important to initiate nanovoids. Equation 20 also shows that σ_{onset} depends strongly on R_{con} which implies that for very small confined rubber domains no cavitation should occur at the initial stage.

To interpret the effect of the volume fraction of filler, both the change of f and that of R_{con} with ϕ_{CB} must be described. Here we just consider the simplest situation where two filler particles (or filler aggregates) with diameter D are separated by a distance h (see Figure 12a) and the mechanical interaction

dx.doi.org/10.1021/ma2023606 | Macromolecules 2012, 45, 1529–1543

due to other fillers is not considered. Under this condition, f is a function of D and h. The increase of ϕ_{CB} always decreases the average interparticle distance h and increases the degree of confinement (i.e., larger f). Unlike in rubber toughened plastics, R_{con} in our systems also depends on the local geometry. Three regimes can be defined roughly according to the value of ϕ_{CB}. A schematic drawing is illustrated in Figure 12b–d.

(1) $\phi_{CB} \ll \phi^*_{CB}$ and interparticle distance $h \gg h^*$ (ϕ^*_{CB} and h^* relate to the point where the particle stress fields start interacting). The filler particles are so "dilute" that no mechanical interaction is present. There is no geometric confinement except very close to the particles,[7] but because the hard particle is very small as well as the associated volume of confined rubber domain, so a very large stress is required for cavitation (see Figure 12b). In this regime and in macroscopically uniaxial tension, nanocavitation, if it exists at all, is probably immediately followed by crack propagation.

(2) $\phi^*_{CB} < \phi_{CB} < \phi'_{CB}$ and interparticle distance $h > D$ (ϕ'_{CB} is the point where the $h = D$). The volume of the confined domains is almost of the order of the size of the filler particles ($R_{con} \sim D/2$) (Figure 12c) and does not change much with an increase of ϕ_{CB}. The increase of f (or of the local hydrostatic stress) dominates the nanocavitation behavior. Consequently, the local volumetric strain energy increases with ϕ_{CB} and the apparent nanocavitation stress σ_{onset} decreases with filler volume fraction.

(3) $\phi'_{CB} < \phi_{CB}$ and interparticle distance $h < D$. Now the volume of the confined rubber regions is no longer a constant value but related to the interparticle distance h ($R_{con} \sim h/2$) and has the opposite effect to the increase in f (Figure 12d). Thus, the increase of filler content in this regime does not obviously increase the local volumetric strain energy available for nanocavitation although it does increase the local volumetric strain energy density. An almost constant σ_{onset} with ϕ_{CB} is expected according to eq 20.

This simple model qualitatively explains some of our observations, but the real nanocavitation process in filled rubbers at such small scales is probably more complicated and more efforts are still required to propose a quantitative model that can predict σ_{onset}, ϕ_{void} and shape information on the nanovoids with material parameters. Nevertheless our results and analysis show that these nanocavities exist and lay the groundwork to develop such a model.

Nanocavitation itself does not absorb a lot of energy but does reduce the local confinement. Under uniaxial loading conditions, nanocavitation and the orientation of nanovoids along the tensile direction modify the local stress field from locally multiaxial to nearly uniaxial everywhere which should lead to a more effective relaxation of high stresses. The loss of local triaxiality also greatly reduces the local strain energy release rate[71] and prevents the growth of crack-like voids. It also probably promotes the reorganization of the filler particles along the direction of the maximum shear stress. A similar concept is also discussed in rubber toughened plastics where shear bands are often observed after rubber cavitation.[72] In our CB-filled materials, both nanocavitation and particle rearrangement by shear are present. Local reorganization of particles can occur before and after nanocavitation depending on the filler–filler interaction, filler–polymer interaction and organization of the aggregates. The cross-linking density of the rubber network could have an important effect on the above-mentioned scenario. For too highly cross-linked networks, the orientation of nanovoids as well as the rearrangement of filler particles could become quite difficult since stretching the highly oriented chains requires a much higher stress and involves a high risk of chain breakage.

Although the current work only focuses on uniaxial extension, it also provides clues for crack propagation. The most important role of nanovoids is to reduce the resistance of the local polymer matrix to volumetric expansion due to the hydrostatic stress field which often occurs at the crack tip. This could lead to the formation of a highly stretched zone near the crack tip over a larger volume than predicted by incompressibility.

6. CONCLUSION

We performed real-time SAXS experiments on a series of carbon black filled SBR elastomers stretched in uniaxial tension. For each value of stress and strain we recorded a 2D SAXS scattering pattern from which we extracted the scattering invariant Q as a function of σ_T or λ. A sharp increase in Q above its reference value Q_0 for the undeformed sample, was observed above a given value of λ for all materials investigated except for the fully un-cross-linked and for the cross-linked but nearly unfilled elastomer. The Q/Q_0 increased above a threshold in true stress σ_{onset} of the order of 25 MPa, which did not depend much on filler content or on the cross-link density of the elastomers. However, the subsequent increase in Q/Q_0 with σ_T beyond the threshold depended markedly on filler content and on cross-link density.

We attributed the increase in Q/Q_0 to the appearance of nanovoids and using the assumption of cylindrical symmetry and a three phase model, we computed the volume fraction of voids ϕ_{void} as a function of σ_T or λ. This volume fraction increased with λ beyond λ_{onset} and reached up to 15% at high extension ratios for the most highly filled system. The increase in volume expected from the appearance of voids and the value of σ_{onset} was confirmed by macroscopic measurements of volume variation performed by digital image correlation demonstrating for the first time unambiguously the nucleation of nanovoids (size <50 nm) in CB-filled elastomers in uniaxial extension.

The 2D scattering patterns obtained as a function of λ were further analyzed by assuming that the contribution of the CB particles and of the voids could be separated. The contribution of the voids to the scattering pattern at $\lambda > \lambda_{onset}$ displayed a lozenge shape which did not further change with λ. The average shape and size of the voids as a function of λ could be determined from the surface to volume ratio of the scattering objects and revealed that as λ increased the average size of the cavities decreased from 30 to 20 nm while their average shape remained constant. This clear result strongly suggests that new smaller cavities with similar shapes appear as λ increases. The underlying mechanism(s) for the nanocavitation is still open to discussion but we think that the cavities appear in confined regions between filler particles and an energy based nanocavitation criterion inspired by the model of Fond et al. for the cavitation of rubber nanoparticles in rubber-filled thermoplastics is consistent with our data. Two main functions of those nanocavities are to alter the local multiaxial loading to a more uniaxial loading and to promote the rearrangement of the nearby filler aggregates by shear.

dx.doi.org/10.1021/ma2023606 | Macromolecules 2012, 45, 1529–1543

APPENDIX

The deconvolution of the scattering intensity of nanovoids from the measured patterns is described below. The scattering from nanovoids I_{void} is calculated from eq 9. The classical Porod's analysis is then applied to I_{void}. If we assume that the nanovoids are ellipsoids, according to Wen Li Wu's work[73] for a single ellipsoid whose major axis is aligned with the x direction, the Porod's constants take the following form. In the x direction:

$$K_{px} = \lim_{q_x \to \infty} q_x^4 I_{void}(q_x) \cong A\rho^2(8\pi^2R^2)\lambda_{void}^{-4} \quad \text{(A1)}$$

and in the y direction,

$$K_{py} = \lim_{q_y \to \infty} q_y^4 I_{void}(q_y) \cong A\rho^2(8\pi^2R^2)\lambda_{void}^{2} \quad \text{(A2)}$$

where A is the scattering constant, ρ is the XSLD contrast between the ellipsoid and its environment, R is the radius of a sphere with the same volume as the ellipsoid and λ_{void} describes the deformation from a spherical shape. The ratios K_{Py} and K_{Px} directly give the value of λ_{void}. For a set of nanoellipsoids, eqs A1 and A2 are still applicable since the interparticle interference on the scattering intensity in the high q region is negligible,[44] but we must sum the scattering from n_{void} where:

$$n_{void} = \frac{3}{4\pi} V\phi_{void}/\langle R^3\rangle \quad \text{(A3)}$$

Similar to eq 3 and 5, the scattering invariant Q_{void} can be obtained and is related to the ϕ_{void_Bi} by:

$$Q_{void} = 2\pi^2 A\rho^2\phi_{void}(1-\phi_{void})V \quad \text{(A4)}$$

If eq A4 is divided by the product of eqs A2 and A3, one gets:

$$\frac{Q_{void}}{K_{py}} = \frac{1}{3}\pi(1-\phi_{void})\frac{\langle R^3\rangle}{\langle \lambda_{void}^2 R^2\rangle} \quad \text{(A5)}$$

If the set of nanoellipsoids have roughly the same extent of deformation, $\langle R^3\rangle/\langle R^2\rangle$ is expressed by:

$$\frac{\langle R^3\rangle}{\langle R^2\rangle} = \frac{3\lambda_{void}^2}{\pi(1-\phi_{void})}\frac{Q_{void}}{K_{py}} \quad \text{(A6)}$$

other parameters are then expressed by

$$\frac{\langle R_x^3\rangle}{\langle R_x^2\rangle} = \frac{\langle R^3\rangle}{\langle R^2\rangle} = \lambda_{void} \quad \text{(A7-1)}$$

$$\frac{\langle R_y^3\rangle}{\langle R_y^2\rangle} = \frac{\langle R^3\rangle}{\langle R^2\rangle}\frac{1}{\sqrt{\lambda_{void}}} \quad \text{(A7-2)}$$

$$\frac{\langle R_x^3\rangle}{\langle R_x^2\rangle}\frac{\langle R_y^2\rangle}{\langle R_y^3\rangle} = \lambda_{void}^{3/2} \quad \text{(A7-3)}$$

Finally, eqs A7-1−A7-3 are used as eq 14−16 in the main text to plot Figure 11.

ASSOCIATED CONTENT

Supporting Information

Influence of q_{cutoff} (radial cutoff) on the calculation of the normalized scattering invariant Q/Q_0 of sample 24CB_8NC (SFigure 1), the raw scattering pattern on the Pilatus 1 M detector with horizontal and vertical stripes of sample 24CB_8NC at λ = 4.6 (SFigure 2), and the repeatability of the measurement of the onset of cavitation (SFigure 3). This material is available free of charge via the Internet at http://pubs.acs.org.

AUTHOR INFORMATION

Corresponding Author

*E-mail: (C.C.) Costantino.Creton@espci.fr; (E.J.K.) edkramer@mrl.ucsb.edu.

ACKNOWLEDGMENTS

This work was supported by the French ANR: project AMUFISE, (MATETPRO 08-320101). A.K.S. and E.J.K. were supported by the Institute for Multiscale Materials Studies at UCSB, a collaboration with Los Alamos National Laboratory. We also appreciate the help of Eric Schaible at beamline 7.3.3 at ALS. The Advanced Light Source is supported by the Director, Office of Science, Office of Basic Energy Sciences, of U.S. Department of Energy under Contract No. DE-AC02-05CH11231. We finally specially thank Stephane Roux for his critical reading of the manuscript and for helpful discussions and we acknowledge useful discussions with Daniel Berghezan, Yannick Merckel, Julie Diani, and Mathias Brieu.

REFERENCES

(1) Heinrich, G.; Kluppel, M.; Vilgis, T. A. *Curr. Opin. Solid State Mater. Sci.* **2002**, *6* (3), 195−203.
(2) Kluppel, M. *Adv. Polym. Sci.* **2003**, *164*, 1−86.
(3) Kraus, G. *Adv. Polym. Sci.* **1971**, *8*, 155−237.
(4) Kohls, D. J.; Beaucage, G. *Curr Opin Solid State Mater. Sci.* **2002**, *6* (3), 183−194.
(5) Gent, A. N.; Park, B. *J. Mater. Sci.* **1984**, *19* (6), 1947−1956.
(6) Cho, K.; Gent, A. N. *J. Mater. Sci.* **1988**, *23* (1), 141−144.
(7) Cho, K.; Gent, A. N.; Lam, P. S. *J. Mater. Sci.* **1987**, *22* (8), 2899−2905.
(8) Oberth, A. E.; Bruenner, R. S. *Trans Soc Rheol* **1965**, *9* (2), 165−185.
(9) Oberth, A. E. *Rubber Chem. Technol.* **1967**, *40* (5), 1337−1363.
(10) Gent, A. N.; Lindley, P. B. *Proc. R. Soc. London A, Math. Phys. Sci.* **1959**, *249* (1257), 195−205.
(11) Farris, R. J. *J. Appl. Polym. Sci.* **1964**, *8* (1), 25−35.
(12) Gee, G.; Stern, J.; Treloar, L. R. G. *Trans. Faraday Soc.* **1950**, *46*, 1101−1106.
(13) Gent, A. N.; Wang, C. *J. Mater. Sci.* **1991**, *26* (12), 3392−3395.
(14) Cristiano, A.; Marcellan, A.; Long, R.; Hui, C. Y.; Stolk, J.; Creton, C. *J. Polym. Sci. Polym. Phys.* **2010**, *48* (13), 1409−1422.
(15) Gent, A. N.; Tompkins, D. A. *J. Polym. Sci. 2, Polym. Phys.* **1969**, *7* (9), 1483−1487.
(16) Horgan, C. O.; Polignone, D. A. *Appl. Mech. Rev.* **1995**, *48* (8), 471−485.
(17) Lin, Y. Y.; Hui, C. Y. *Int. J. Fract.* **2004**, *126* (3), 205−221.
(18) Le Cam, J. B. *Rubber Chem. Technol.* **2010**, *83* (3), 247−269.
(19) Le Cam, J. B.; Toussaint, E. *Mech. Mater.* **2009**, *41* (7), 898−901.
(20) Starkova, O.; Aniskevich, A. *Polym. Test.* **2010**, *29* (3), 310−318.
(21) Ramier, J.; Chazeau, L.; Gauthier, C.; Stelandre, L.; Guy, L.; Peuvrel-Disdier, E. *J. Mater. Sci.* **2007**, *42* (19), 8130−8138.
(22) Mzabi, S. Caracterisation et analyse des mecanismes de fracture en fatigue des elastomeres charges. Ph.D. Thesis, Universite Pierre et Marie Curie, Paris: 2010.
(23) Le Cam, J. B.; Huneau, B.; Verron, E.; Gornet, L. *Macromolecules* **2004**, *37* (13), 5011−5017.
(24) He, C. B.; Donald, A. M.; Butler, M. F. *Macromolecules* **1998**, *31* (1), 158−164.

(25) Magalhaes, A. M. L.; Borggreve, R. J. M. *Macromolecules* **1995**, *28* (17), 5841−5851.
(26) Humbert, S.; Lame, O.; Chenal, J. M.; Rochas, C.; Vigier, G. *Macromolecules* **2010**, *43* (17), 7212−7221.
(27) Maier, G. A.; Wallner, G.; Lang, R. W.; Fratzl, P. *Macromolecules* **2005**, *38* (14), 6099−6105.
(28) Pawlak, A.; Galeski, A. *Macromolecules* **2005**, *38* (23), 9688−9697.
(29) Ehrburger-Dolle, F.; Bley, F.; Geissler, E.; Livet, F.; Morfin, I.; Rochas, C. *Macromol. Symp.* **2003**, *200*, 157−167.
(30) Ehrburger-Dolle, F.; Hindermann-Bischoff, M.; Livet, F.; Bley, F.; Rochas, C.; Geissler, E. *Langmuir* **2001**, *17* (2), 329−334.
(31) Schneider, G. J. *J. Chem. Phys.* **2009**, *130*, 23.
(32) Schneider, G. J.; Goritz, D. *J. Chem. Phys.* **2010**, *133*, 2.
(33) Schneider, G. J.; Goritz, D. *J. Appl. Crystallogr.* **2010**, *43*, 12−16.
(34) Shinohara, Y.; Kishimoto, H.; Inoue, K.; Suzuki, Y.; Takeuchi, A.; Uesugi, K.; Yagi, N.; Muraoka, K.; Mizoguchi, T.; Amemiya, Y. *J. Appl. Crystallogr.* **2007**, *40*, S397−S401.
(35) Hagita, K.; Arai, T.; Kishimoto, H.; Umesaki, N.; Suno, H.; Shinohara, Y.; Amemiya, Y. *Rheol. Acta* **2008**, *47* (5−6), 537−541.
(36) Hagita, K.; Arai, T.; Kishimoto, H.; Umesaki, N.; Shinohara, Y.; Amemiya, Y. *J Phys, Condens. Matter* **2007**, *19*, 33.
(37) Debye, P.; Anderson, H. R.; Brumberger, H. *J. Appl. Phys.* **1957**, *28* (6), 679−683.
(38) Paredes, E.; Fischer, E. W. *Makromol. Chem.* **1979**, *180* (11), 2707−2722.
(39) Paredes, E.; Fischer, E. W. *J. Polym. Sci., Polym. Phys.* **1982**, *20* (5), 929−930.
(40) Brown, H. R.; Kramer, E. J. *J. Macromol. Sci. Phys.* **1981**, *B19* (3), 487−522.
(41) Mills, P. J.; Kramer, E. J.; Brown, H. R. *J. Mater. Sci.* **1985**, *20* (12), 4413−4420.
(42) Brown, H. R.; Kramer, E. J.; Bubeck, R. A. *J. Polym. Sci., Polym. Phys.* **1987**, *25* (8), 1765−1778.
(43) Flory, P. J. *Principles of Polymer Chemistry*; Cornell University Press: New York, 1953.
(44) Glatter, O.; Kratky, O. *Small Angle X-ray Scattering*; Academic Press: London, 1982; pp 19−51.
(45) Wu, W. *Polymer* **1982**, *23* (13), 1907−1912.
(46) Cheung, Y. W.; Stein, R. S.; Lin, J. S.; Wignall, G. D. *Macromolecules* **1994**, *27* (9), 2520−2528.
(47) Besnard, G.; Hild, F.; Roux, S. *Exp. Mech.* **2006**, *46* (6), 789−803.
(48) Le Diagon, Y.; Mallarino, S.; Fretigny, C. *Eur. Phys. J. E* **2007**, *22* (1), 77−83.
(49) Mendes, E.; Lindner, P.; Buzier, M.; Boue, F.; Bastide, J. *Phys. Rev. Lett.* **1991**, *66* (12), 1595−1598.
(50) Falcao, A. N.; Pedersen, J. S.; Mortensen, K. *J. Mol. Struct.* **1996**, *383* (1−3), 69−74.
(51) Mendes, E.; Oeser, R.; Hayes, C.; Boue, F.; Bastide, J. *Macromolecules* **1996**, *29* (17), 5574−5584.
(52) Hayes, C.; Bokobza, L.; Boue, F.; Mendes, E.; Monnerie, L. *Macromolecules* **1996**, *29* (14), 5036−5041.
(53) Koga, T.; Hashimoto, T.; Takenaka, M.; Aizawa, K.; Amino, N.; Nakamura, M.; Yamaguchi, D.; Koizumi, S. *Macromolecules* **2008**, *41* (2), 453−464.
(54) Fond, C. *J. Polym. Sci., Polym. Phys.* **2001**, *39* (17), 2081−2096.
(55) Gehant, S.; Fond, C.; Schirrer, R. *Int. J. Fract.* **2003**, *122* (3−4), 161−175.
(56) Le Cam, J. B.; Toussaint, E. *Macromolecules* **2008**, *41* (20), 7579−7583.
(57) Read, D. J.; McLeish, T. C. B. *Phys. Rev. Lett.* **1997**, *79* (1), 87−90.
(58) Straube, E.; Urban, V.; Pyckhouthintzen, W.; Richter, D.; Glinka, C. J. *Phys. Rev. Lett.* **1995**, *74* (22), 4464−4467.
(59) Donald, A. M.; Kramer, E. J. *J. Mater. Sci.* **1981**, *16* (11), 2967−2976.
(60) Cornes, P. L.; Smith, K.; Haward, R. N. *J. Polym. Sci., Polym. Phys.* **1977**, *15* (6), 955−967.
(61) Walker, N.; Haward, R. N.; Hay, J. N. *J. Mater. Sci.* **1979**, *14* (5), 1085−1094.
(62) Walker, N.; Haward, R. N.; Hay, J. N. *J. Mater. Sci.* **1981**, *16* (3), 817−824.
(63) Green, A. E.; Zerna, W. *Q. J. Mech. Appl. Math.* **1950**, *3* (1), 9−22.
(64) Gent, A. N.; Tompkins, D. A. *J. Appl. Phys.* **1969**, *40* (6), 2520−2525.
(65) Dollhofer, J.; Chiche, A.; Muralidharan, V.; Creton, C.; Hui, C. Y. *Int. J. Solids. Struct.* **2004**, *41* (22−23), 6111−6127.
(66) Diani, J. *Int. J. Fract.* **2001**, *112* (2), 151−161.
(67) Biwa, S. *Int. J. Nonlinear Mech.* **2006**, *41* (9), 1084−1094.
(68) Williams, M. L.; Schapery, R. A. *Int. J. Fracture Mech.* **1965**, *1* (1), 64−71.
(69) Lazzeri, A.; Bucknall, C. B. *J. Mater. Sci.* **1993**, *28* (24), 6799−6808.
(70) Fond, C.; Lobbrecht, A.; Schirrer, R. *Int. J. Fract.* **1996**, *77*, 141−159.
(71) Long, R.; Hui, C. Y. *Soft Matter* **2010**, *6* (6), 1238−1245.
(72) Zebarjad, S. M.; Bagheri, R.; Lazzeri, A.; Serajzadeh, S. *Mater. Design* **2004**, *25* (3), 247−250.
(73) Wu, W. *J. Polym. Sci., Polym. Phys.* **1980**, *18* (7), 1659−1661.

Macromolecules

Article

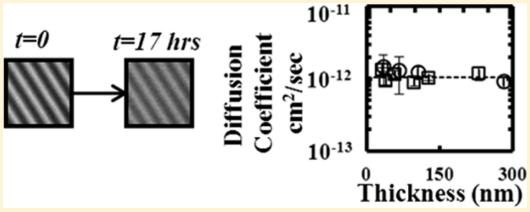
pubs.acs.org/Macromolecules

Nanoconfined Self-Diffusion of Poly(isobutyl methacrylate) in Films with a Thickness-Independent Glass Transition

Joshua M. Katzenstein, Dustin W. Janes, Haley E. Hocker, Justin K. Chandler, and Christopher J. Ellison*

Department of Chemical Engineering, The University of Texas at Austin, Austin, Texas 78712, United States

ABSTRACT: Even though the physics of nanoconfined polymers have been extensively studied for years, diffusion of polymer chains along confining interfaces has not been widely studied, likely because there are few experimental techniques available for these measurements. Here a fluorescence recovery after patterned photobleaching (FRAPP) technique is developed using an epifluorescence microscope that allows for direct, *in situ*, visualization of polymer diffusion over several periods of a photobleached array. This visualization approach is more robust compared to measuring fluorescence intensity alone and also significantly increases the experimental throughput. Using this technique, self-diffusion of poly(isobutyl methacrylate) (PiBMA) was investigated at 80 °C (29 °C above the glass transition temperature, T_g) and was found to be film thickness independent down to 30 nm (~$14R_g$, where R_g is the radius of gyration) with a diffusion coefficient well predicted by the Rouse model (1.05×10^{-12} cm^2/s). PiBMA is an ideal polymer for this study because it exhibits a film thickness-independent T_g down to 15 nm (~$7R_g$) as measured by spectroscopic ellipsometry. Since the diffusion coefficient of polymers depends strongly on the proximity of diffusion temperature to T_g, this attribute allows a straightforward measure of nanoconfined diffusion without superimposed influence from T_g nanoconfinement effects.



INTRODUCTION

Physical properties of polymers, including physical aging,[1−4] viscosity,[5−7] elastic modulus,[8−10] polymer blend stability,[11] creep compliance,[12] glass transition temperature (T_g),[13−22] polymer wrinkling,[23] adhesion,[24] and other molecular motions in glassy polymers,[25,26] are often different compared to bulk when the polymer is constrained to the ~1−100 nm size scale or nanoconfined. Considerable research has been devoted to studying polymers in thin films as a convenient means of examining interfacial effects; as film thickness decreases, the surface or interfacial area to volume ratio increases.

Unfortunately, nanoconfined polymer diffusion has not received significant experimental attention even though it is highly relevant to several important properties such as adhesion[27] and friction.[28] Nanoconfined diffusion is also important in many existing polymer technologies such as in the exfoliation of clay nanoparticles in nanocomposites, where exfoliation processes require diffusion of polymers along sheetlike filler particles and in between interparticle galleries.[29] Exfoliation of nanoparticles is key to achieving enhanced physical properties, such as increased modulus and degree of crystallinity.[30] In addition, newly emerging technologies, such as molecular transfer printing (MTP), rely on nanoconfined polymer diffusion processes in their function. In MTP, substrate-reactive polymer "inks" diffuse along polymer/polymer interfaces whose separation distance is defined by a self-assembled block copolymer.[31]

In previous work, nanoconfinement has been shown to affect the diffusion of polymer chains in a variety of ways. However, most experimental studies have examined diffusion perpendicular to the confining interfaces in thin films.[32−34] Secondary ion mass spectroscopy (SIMS) studies of entangled polystyrene films on a silicon wafer with native oxide showed changes in the molecular weight (MW) dependence of the diffusion coefficient (D) from that of bulk polymer ($D \sim MW^{-2.0}$) at both interfaces. Within a distance of ~4 times the radius of gyration (R_g) from the free interface (polymer/air), D scaled as $MW^{-2.5}$.[33] In contrast, at the supported interface (polymer/substrate) D scaled as $MW^{-1.5}$ for entangled polystyrene with dramatically slowed diffusion in films up to $10R_g$.[34] This indicates that different interfaces, at least in the case of this specific polymer film/substrate system, can have an impact on the translational mobility of the chain. Additionally, Monte Carlo simulations[35] of polymers of varying chain length confined between hard wall interfaces have revealed anisotropy to the center of mass mobility. The results suggest that the center-of-mass displacement parallel and perpendicular to the confining interfaces scaled differently with time. Such diffusion anisotropy exemplifies that studies of diffusion parallel and perpendicular to interfaces are crucial for assembling a complete understanding of nanoconfined diffusion. This is especially true given that diffusion in some applications, such as in nanocomposite exfoliation, reflects contributions from both components.

While polymer diffusion parallel to nanoconfining interfaces has important implications for a variety of applications, relatively few experimental studies have been reported to date. An early study by Frank and co-workers[36] using fluorescence recovery after patterned photobleaching (FRAPP) examined the diffusion of a single molecular weight

Received: October 22, 2011
Revised: December 29, 2011
Published: January 23, 2012

 © 2012 American Chemical Society dx.doi.org/10.1021/ma202362j | *Macromolecules* 2012, 45, 1544−1552

of polystyrene at a single temperature. This study determined that the diffusion coefficient was reduced by a factor of 2 as the film thickness was reduced below ~150 nm (about $50R_g$). Another FRAPP study of diffusion parallel to interfaces by Bae et al.,[37] subsequently extended by Wong et al.,[38] was conducted using poly(dimethylsiloxane) nanoconfined between mica sheets in a surface forces apparatus. They found, relative to bulk diffusion coefficients, a reduction in diffusion coefficients by a factor of ~40 at a film thickness of 10 nm and a reduction by a factor of ~80 at a film thickness of 2 nm. The same group had also used fluorescence correlation spectroscopy to study in-plane diffusion of adsorbed poly(ethylene glycol) chains at dilute surface coverage along the interface of a self-assembled monolayer of octadecyltriethoxysilane and water.[39] They observed the molecular weight dependence of the diffusion coefficient was much stronger ($MW^{-1.5}$) for adsorbed polymers diffusing along a surface than for the same polymer in solution ($MW^{-0.5}$). Additionally, Manias et al.[40] examined diffusion of polystyrene by small-angle neutron scattering in a 2 nm gap between atomically smooth mica sheets modified with alkyl chains of varying length on the surface. They found that not only do longer alkyl chains increase the rate of diffusion, a 10-fold increase in D going from 12 to 18 carbons, but the molecular weight dependence of the effective diffusion coefficient in these systems scaled as $MW^{-1.09}$, rather than the expected $MW^{-2.0}$ for bulk entangled polystyrene.

As for other nanoconfined polymer properties, a variety of techniques have been used to study nanoconfined polymer diffusion. Diffusion of polymers perpendicular to interfaces is most commonly studied by SIMS,[33,34] neutron scattering,[41] or elastic recoil detection.[42] However, adapting these well-established techniques to study polymer diffusion parallel to interfaces is challenging because they require a transition between isotopically different polymers that is relatively difficult to fabricate in the plane of the film. This experiment can be further complicated by the large sampling area; for example, SIMS typically uses a spot around 80 μm in diameter[27] while polymer diffusion takes place over much smaller distances during realistic experimental time scales.

In addition to isotopic techniques, other techniques to study molecular mobility in polymers rely on the presence of fluorophores. FRAPP is a popular approach, originally developed in biology,[43] for studying the diffusion of components within cell membranes[44] to quantify mobility of proteins.[45] It has been previously applied to synthetic polymers to investigate both nanoconfined polymer diffusion parallel to interfaces[36,38] and bulk diffusion of small molecule probes in a polymer matrix.[46−48] In FRAPP, select regions of a chemically homogeneous polymer film are differentiated by irreversibly photobleaching fluorophores using a photomask or a light source of well-defined shape and then monitoring diffusion by tracking the recovery of nonphotobleached fluorophores back into the bleached regions. The photobleaching step of FRAPP experiments bypasses the fabrication challenges which limit the use of isotopic approaches for in-plane diffusion studies.

A few studies of self-diffusion parallel to self-assembled block copolymer interfaces have been performed by forced Rayleigh scattering (FRS) for both lamellar[49] and cylinder forming[50] block copolymers. FRS and FRAPP have been shown to produce equivalent self-diffusion results for polystyrene, but FRAPP has the additional benefit of the photobleached product of the fluorphore being completely "dark" to the detector, whereas in FRS the fluorophore has been shown to occasionally create anomalous diffraction intensity.[51] While both FRAPP and FRS may be valid techniques for the study of in-plane diffusion, FRAPP was chosen for this study.

In this study, the self-diffusion of nanoconfined poly(isobutyl methacrylate) (PiBMA) was characterized parallel to a planar silicon oxide substrate. PiBMA was specifically chosen for this study because we determined that the T_g of this material is independent of film thickness on these substrates by spectroscopic ellipsometry. Conventionally, the bulk self-diffusion coefficient of any polymer is directly related to the proximity of the diffusion temperature to T_g.[52] By selection of a polymer with a film thickness-independent T_g, such as PiBMA, any measured trend in self-diffusion coefficient can be considered independently from changes in the self-diffusion coefficient due to T_g nanoconfinement effects. Additionally, the FRAPP procedure used here employs a periodic photobleached array of lines through which diffusion can be directly observed using a CCD camera mounted on an epifluorescence microscope. The combination of fluorescence imaging and photobleaching a periodic array improves the FRAPP method such that it should be self-referencing (e.g., diffusion measurements are not sensitive to unintended photobleaching during recovery) and enables additional statistical analysis of experimental data.

EXPERIMENTAL SECTION

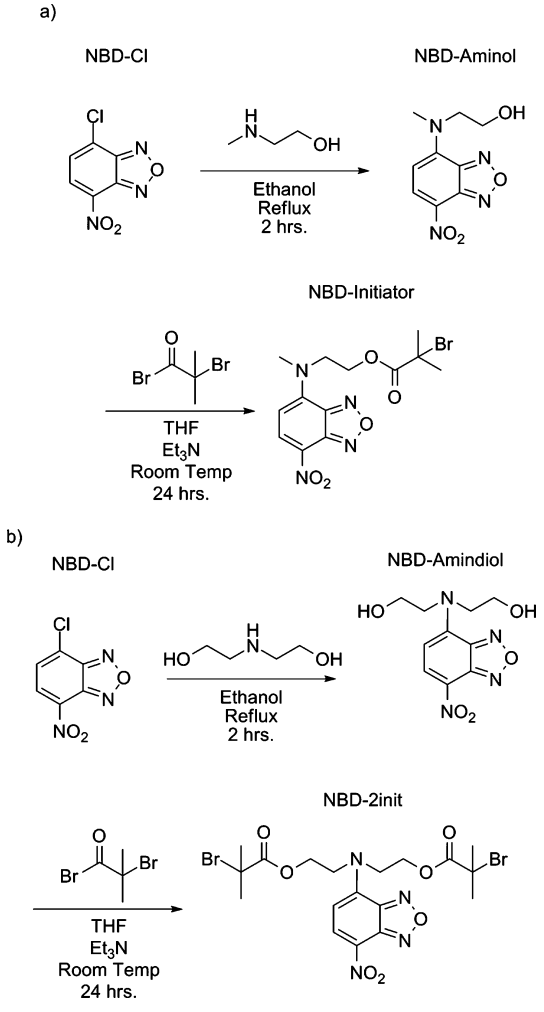
Materials. Chemicals used in this study were purchased from Fisher Scientific or Sigma-Aldrich, and all chemicals were used as received unless otherwise noted. Anisole and isobutyl methacrylate were purified by stirring with basic alumina and calcium hydride for 2 h and then filtered to remove solids. Tris(2-dimethylaminoethyl)-amine, Me_6TREN, was synthesized according to a published procedure.[53] Molecular weight and polydispersity data were measured using a Viscotek GPCMax VE 2001 gel permeation chromatography (GPC) solvent/sample module with a Viscotek Model 270 dual detector viscometer/light scattering detector and Viscotek VE 3580 refractive index detector with 2 I-Series mixed bed low MW columns. Fluorophore attachment was verified by an in-line Jasco FP-2020 Plus Intelligent Fluorescence Detector ($\lambda_{excitation}$ = 465 nm, $\lambda_{emission}$ = 520 nm, 18 nm bandpass). Molecular weights reported are relative to a conventional calibration curve created using PiBMA standards synthesized in house and absolutely characterized by Viscotek Triple Detect software combining light scattering, refractive index detection, and viscometry. Nuclear magnetic resonance (NMR) spectra were recorded on a Varian 400 MHz DirectDrive NMR with SMS sample changer. The glass transition temperature (T_g) of the bulk polymer samples was measured by differential scanning calorimetry (DSC) using a Mettler-Toledo DSC-1 with a 10 °C/min heating rate upon second heating.

Monodisperse PiBMA was synthesized using an initiator containing a covalently bound nitrobenzofurazan (NBD) fluorophore. The polymerization technique used was activators regenerated by electron transfer atom transfer radical polymerization (ARGET ATRP).[54−56] ARGET ATRP is a controlled radical polymerization technique providing a relatively simple platform for synthesis of end-functionalized polymers[57] with good control over molecular weight and PDI along with flexible monomer and initiator choice. The most significant advantage of ARGET ATRP over conventional ATRP is that the added reducing agent decreases oxygen sensitivity and the amount of copper catalyst necessary for the polymerization.

Using established literature procedures,[56,58,59] an ATRP initiator bearing an NBD fluorophore was synthesized and PiBMA-NBD was polymerized using this initiator. The monofunctional initiator was synthesized in two steps (Scheme 1a). First, 4-chloro-7-nitro-2,1,3-benzoxadiazole (NBD-Cl) was refluxed with a 3 fold molar excess of 2-(methylamino)ethanol in ethanol for 2 h, cooled, filtered, and washed with cold ethanol. The resulting orange solid was recrystallized from

dx.doi.org/10.1021/ma202362j | Macromolecules 2012, 45, 1544−1552

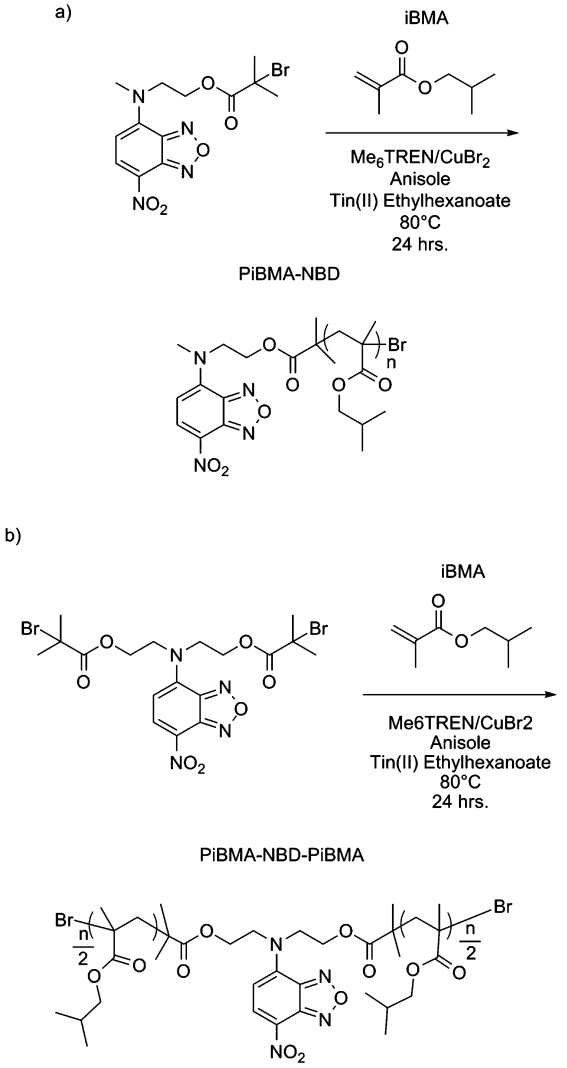
Scheme 1. (a) Synthesis of Monofunctional NBD Bearing One ATRP Initiator Site for Chain-End-Labeled Polymers; (b) Synthesis of Difunctional NBD Bearing Two ATRP Initiator Sites for Mid-Chain-Labeled Polymers



ethanol, and the solid filtrate was collected in 85% yield. The product, 2-[methyl-(7-nitro-2,1,3-benzoxadiazol-4-yl)amino]ethanol (NBD-Aminol), was dried and then dissolved in dry tetrahydrofuran and reacted with a 3 fold molar excess of dry 2-bromoisobutyryl bromide in the presence of dry triethylamine overnight at room temperature. After removing excess solvent, the product was dissolved in dichloromethane and washed with deionized water (seven times) and concentrated aqueous sodium bicarbonate (three times). Finally, the product was dried over magnesium sulfate, and the solvent removed by vacuum at 80 °C to remove solvent and excess 2-bromoisobutyryl bromide give 2-(methyl(7-nitro-2,1,3-benzoxadiazol-4-yl)amino)ethyl 2-bromo-2-methylpropanoate (NBD-Initiator) with 67% yield for this step (overall yield 57%). The procedure to synthesize the difunctional initiator 2,2′-(7-nitro-2,1,3-benzoxadiazol-4-ylazanediyl)bis(ethane-2,1-diyl)bis(2-bromo-2-methylpropanoate) (NBD-2init) (Scheme 1b), used to make polymers with the NBD fluorophore in the middle of the chain, is identical to the above procedure, except diethanolamine is used in place of 2-(methylamino)-ethanol to yield 2,2′-(7-nitro-2,1,3-benzoxadiazol-4-ylazanediyl)-diethanol (NBD-Amindiol) as an intermediate. For this case, 6 fold molar excess of triethylamine and 2-bromoisobutyryl bromide was used in the second step (Scheme 1b). All of the synthesized compounds were characterized by NMR in order to verify purity; within the limits of detection there were no remaining unreacted reagents in any of the synthesized initiators.

To synthesize the polymers (Scheme 2), the NBD containing initiator was dissolved in anisole with isobutyl methacrylate.

Scheme 2. Synthesis of (a) Chain-End-Labeled PiBMA-NBD and (b) Mid-Chain-Labeled PiBMA-NBD-PiBMA by ARGET ATRP



Copper(II) bromide was used as a catalyst, and a ligand (Me_6TREN) was incorporated to aid in copper solubility. After the reactor was sealed and sparged with dry argon for 15 min, the reducing agent, tin(II) 2-ethylhexanoate, was injected, and the reaction was allowed to proceed for 24 h at 80 °C. The resulting polymer (PiBMA-NBD or PiBMA-NBD-PiBMA) was diluted with THF and run through basic alumina to remove the copper and ligand and then dried at 100 °C under vacuum to remove residual solvents. Fluorescently labeled polymers were then repeatedly dissolved in tetrahydrofuran and precipitated in ethylene glycol seven times to remove any unreacted initiator; the absence of a small molecule fluorescence peak in GPC was used to verify removal of all unattached fluorophores. Covalent attachment of the fluorophore was verified by comparing fluorescence and refractive index detectors on GPC to show coelution of the polymer and fluorophore. For PiBMA-NBD, 100% of the polymer chains, within error, are covalently bound to a fluorophore by UV/vis absorption measurements (Hewlett-Packard 8452A diode array spectrophotometer). The fluorescently labeled PiBMA-NBD polymer was 5.8 wt % fluorophore with M_n = 8.7 kg/mol and PDI = 1.1. PIBMA-NBD-PiBMA was also synthesized (M_n = 8.3 kg/mol, PDI = 1.2), and by UV/vis absorption measurements these polymers were

dx.doi.org/10.1021/ma202362j | Macromolecules 2012, 45, 1544–1552

shown to contain two fluorophores per chain, likely due to coupling events that can be common to ARGET ATRP under some polymerization conditions. To synthesize PiBMA without a NBD fluorophore, the polymerization procedure was identical, except the initiator was ethyl 2-bromoisobutyrate (M_n = 8.6 kg/mol, PDI = 1.1). DSC measurements on both PiBMA-NBD and PiBMA confirm that the fluorophore has no measurable impact on the midpoint T_g (51 °C) of the bulk polymer for equivalent molecular weight polymers, also consistent with other bulk PiBMA samples of similar molecular weight.[60]

Sample Preparation. Films in this study were spin-coated (Specialty Coating Systems Spincoat G3-8) onto quartz (for FRAPP experiments) or silicon substrates with native oxide layers (for ellipsometry experiments) from solutions of either toluene or *n*-butanol. Quartz substrates were prepared by soaking in a piranha solution of 3:1 concentrated sulfuric acid to hydrogen peroxide and then rinsed with deionized water at least three times. Solution concentrations ranged from 0.5 to 6 wt % polymer in *n*-butanol, and spin speeds varied from 800 to 3000 rpm to control the film thickness.[61,62] The polymer in the spin-coating solution for FRAPP experiments was comprised of fluorescently labeled polymer and a molecular weight matched unlabeled polymer to mitigate fluorescence self-quenching effects. Additional experiments on films of varying ratios of labeled to unlabeled polymers confirm that, for fluorophore content under 0.18 wt %, no self-quenching is observed. After spin-coating, films were annealed under vacuum at room temperature overnight. Average thicknesses for FRAPP samples on quartz were measured using a Veeco Dektak 6M stylus profiler by recording ten measurements near the center of the film with a stylus force of 7 mg. Films prepared on silicon substrates were characterized by ellipsometry using a J.A. Woollam M-2000D spectroscopic ellipsometer.

Ellipsometry. The T_g of thin films was characterized using an established spectroscopic ellipsometry procedure.[13,16] The film is heated to 150 °C, which is well above the bulk T_g (51 °C) and the boiling point of the spin-coating solvent (118 °C for *n*-butanol, the highest boiling solvent used), and annealed for 15 min. Next, the film is cooled at 2 °C/min with an Instec mK 1000 temperature controller with a HCS 402 hot stage connected to a liquid nitrogen pump. The film thickness was plotted against sample temperature to identify T_g based on a layered model in which the only fitted parameters were the optical constants and thickness of the polymer film (WVase software, J.A. Woollam Co.).

FRAPP Experiments. For the FRAPP experiments, photobleaching was performed using a Ronchi ruling (Edmund Optics) (chrome lines deposited on a quartz substrate with 12.5 μm lines on a 25 μm pitch) as a mask for creating a periodic array of bleached and unbleached regions. The sample was photobleached using an Optical Building Blocks ScopeLite 200 (a broadband intense light source) after cooling the sample to 4 °C in order to prevent the chrome lines from forming indentations in the polymer film. Film bleaching is expected to be uniform through the film because the absorbance is 0.01 absorbance units per 100 nm of film thickness at a wavelength of 465 nm, as measured by UV/vis spectroscopy. This indicates that even for the thickest films used in this study (~280 nm), the bleaching light is attenuated a negligible amount (~5%) as it passes through the film; therefore, the photobleaching reaction takes place equally throughout the depth of the film. The film was then heated to 80 °C using a Linkham TMS91 hot stage and allowed to equilibrate for 1 h before starting to monitor the fluorescence recovery. Imaging was performed with a Hamamatsu Orca R2 camera with μManager software for camera control[63] on an Olympus BX 51 epifluorescence microscope coupled to a Photon Technologies QuantaMaster 40 fluorimeter. The excitation wavelength used was 465 nm with a 4 nm bandpass and an emission filter selected for all wavelengths greater than 520 nm. The depth of focus of the microscope is 2.9 μm, which is an order of magnitude larger than the thickest films used in this study; therefore, fluorescence from the whole depth of the film is captured in each image. Images were taken at intervals of 1 h with an automatic shutter employed to limit photobleaching during the course of the experiment. See Figure 1 for a schematic of the experimental procedure. An experiment on a film that has not been photobleached confirmed that, with the amount of cumulative exposure from a typical FRAPP experiment (~30 s total exposure at 80 °C), <5% photobleaching is caused by imaging.

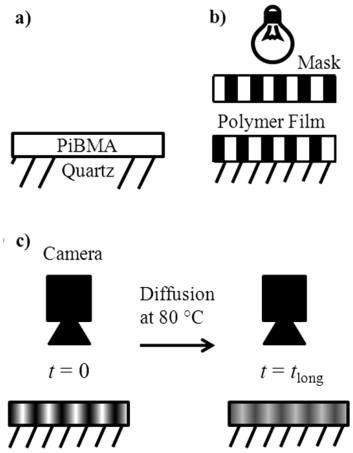


Figure 1. Schematic of the FRAPP experiment. (a) Spin-coating and annealing of a polymer film with a uniform fluorophore distribution. (b) Photobleaching with a high intensity broadband light source through a mask to initially create a periodic array of fluorescent and nonfluorescent regions. (c) Redistribution of fluorophores from the initial condition (t = 0) to long times ($t = t_{long}$) as diffusion over time causes a relaxation in the pattern monitored by an epifluorescence microscope. Light areas indicate regions of high fluorescent intensity, and dark regions indicate regions of low fluorescent intensity.

RESULTS

Nanoconfined Glass Transition Temperature. The T_g of thin polymer films can be measured by ellipsometry because the coefficient of thermal expansion (CTE) is different between the glassy and rubbery states of the polymer. Since the CTE for each polymer state is a constant, the data well above and below the T_g in a plot of film thickness against temperature can be fit with straight lines by linear regression. The intersection of these lines corresponds to the T_g of the film. Figure 2 shows a representative ellipsometric scan for a film of PiBMA with a thickness of 50.25 nm at 25 °C.

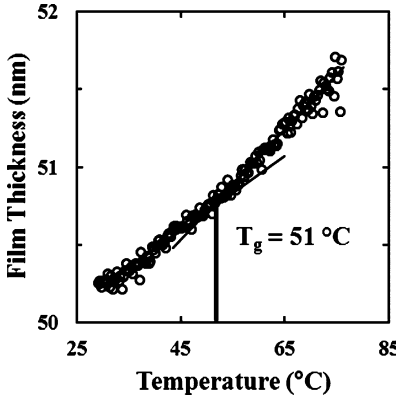


Figure 2. Representative ellipsometric scan for a 50 nm film of PiBMA. Every sixth data point collected is shown here. The linear regressions above and below the T_g uses a span of data more than 15 °C wide.

dx.doi.org/10.1021/ma202362j | Macromolecules 2012, 45, 1544–1552

The T_g of PiBMA and fluorescently labeled PiBMA-NBD was measured for films ranging from 15 to 160 nm and 18 to 125 nm, respectively, as shown in Figure 3. T_g measurements

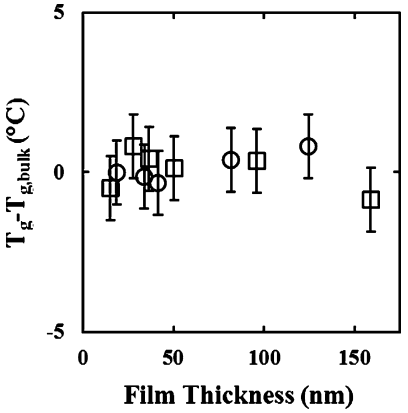


Figure 3. T_g data for PiBMA (□) and PiBMA-NBD (○) as a function of film thickness taken at 25 °C. The error bars indicate the error in ellipsometric measurements (±1 °C).[66] The bulk T_g for these materials is 51 °C, as measured by DSC and ellipsometry.

were performed by ellipsometry on silicon wafers with a native oxide layer as a substrate. However, the T_g results are expected to be similar on a quartz substrate, like those used for FRAPP experiments, due to a similar surface hydroxyl density (~5−7 hydroxyls/nm^2).[64,65] In every case, the T_g measured for the thin film was identical to the bulk T_g as measured by DSC (51 °C) within the experimental error, ±1 °C.[66] The film thickness independence of T_g for PiBMA corresponds with what has previously been reported in the literature for a different molecular weight of PiBMA.[67] Since identical T_g values are found, within error, for both labeled and unlabeled PiBMA, this is indicative that the attached fluorophore does not have significant interaction with the silicon oxide substrate. If there were a strong interaction between the NBD fluorophore and the hydroxyl groups on the silicon oxide surface, labeled polymers might be expected to show a film thickness dependent T_g due to changes in mobility at the polymer/substrate interface.

FRAPP Experiment Data Analysis. Figure 4 shows fluorescence micrographs from a characteristic FRAPP experiment for a 127 nm thick film. Micrographs were collected at 1 h intervals throughout the course of the experiment. ImageJ[68] was used to plot normalized fluorescence intensity as a function of position for the image collected at each time point. The intensity profile at each time point is well represented by a sinusoid with a characteristic amplitude (A) and wavelength (λ) as indicated in Figure 4. This figure contains an image collected (a) before photobleaching, in which fluorophore labeled polymers are uniformly distributed throughout the film, (b) after patterned photobleaching and annealing for 1 h at 80 °C, where the periodic array of lines and spaces is clearly visible, and (c) after substantial diffusion has taken place where relaxation of the array is observed as fluorophore labeled polymers are redistributed from fluorophore-labeled polymer rich to fluorophore-labeled polymer deficient regions of the film. The intensity trace of the micrograph of the prebleached film is normalized to have an average intensity of one but is shown here only for comparison and does not enter into calculation of the diffusion coefficient. Each micrograph

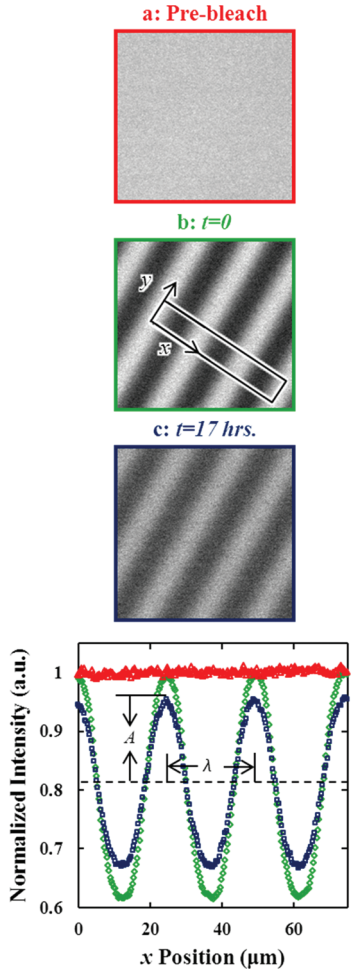


Figure 4. Fluorescence micrographs (a) before photobleaching (△), (b) at the start of the diffusion experiment after patterned photobleaching and annealing (◇), and (c) after significant recovery (□) of a 127 nm film of PiBMA-NBD. Plot shows the normalized intensity as a function of position (x) from a 300 pixel wide (in y) line integral perpendicular to the bleached pattern over several periods. A indicates the amplitude of the sinusoid, and λ indicates the wavelength.

collected during the diffusion experiment is normalized based on its own maximum intensity and then vertically shifted so each time point has the same average value as the initial condition. The region of interest over which diffusion is calculated (75 μm × 96.75 μm) in a 127 nm film contains ~7 × 10^{10} individual chains of PiBMA, which means the diffusion observed in these experiments correlates to an ensemble average diffusion coefficient.

For a polymer melt well above its T_g, Fick's second law governs one-dimensional transient polymer self-diffusion using normalized fluorescence intensity (I) to represent the concentration of unbleached fluorophores, as measured by fluorescence intensity. The initial sinusoidal shape of the intensity profiles in Figure 4b sets the initial condition and periodic boundary conditions. Equation 1 shows that the solution for $I(x,t)$ is given by

$$I(x,t) = A_0 \cos\left(\frac{2\pi x}{\lambda}\right) e^{(-4\pi^2 D/\lambda^2)t} \quad (1)$$

where A_0 is the amplitude of the sinusoid used for the initial condition, λ is the wavelength of the sinusoid, t is the diffusion

time, x is the position, and D is the diffusion coefficient. Finally, setting $I(0,t) = A(t)$ and rearranging eq 1 into a linear form with t yields eq 2

$$\ln\left(\frac{A(t)}{A_0}\right) = \frac{-4\pi^2 D}{\lambda^2} t \tag{2}$$

where $A(t)$ is the amplitude of the sinusoid at time t which decays as diffusion proceeds. The slope of the line $\ln(A(t)/A_0)$ against t is proportional to D, which can be calculated from the slope, M. Each collected intensity profile is fit with a simple sinusoid using a least-squares fitting procedure in order to calculate the amplitude, $A(t)$, and wavelength, λ, of the intensity profile for each time point.

The uncertainty in the diffusion coefficient, σ_D, is based on a propagation of error analysis of eq 2. The uncertainty in the wavelength, σ_λ, and the uncertainty in the slope M of $\ln(A(t)/A_0)$ against t, σ_M, both need to be considered. The uncertainty of the wavelength is the standard deviation of the wavelengths determined from the fit of each intensity profile and has a value of approximately one third the width of a single pixel (322.5 nm) on the camera used for imaging in all runs. The uncertainty of the slope is based on the 95% confidence limits of the linear regression. The final expression used to calculate the experimental uncertainty in the diffusion coefficient is shown in eq 3.

$$\sigma_D = \sqrt{\left(\frac{-\lambda M}{2\pi^2}\sigma_\lambda\right)^2 + \left(\frac{-\lambda^2}{4\pi^2}\sigma_M\right)^2} \tag{3}$$

Figure 5 demonstrates how the analysis technique used in this study is applied for a 127 nm film, the same film the micrographs in Figure 4 were collected from. It is clear from this figure that $\ln(A(t)/A_0)$ plotted against time forms a straight line and that the wavelength, within the resolution of the camera, is a constant. The analysis method for these experiments gives a diffusion coefficient of $(1.02 \pm 0.07) \times 10^{-12}$ cm^2/s. The diffusion coefficient was calculated using eq 2, and the uncertainty was calculated using eq 3.

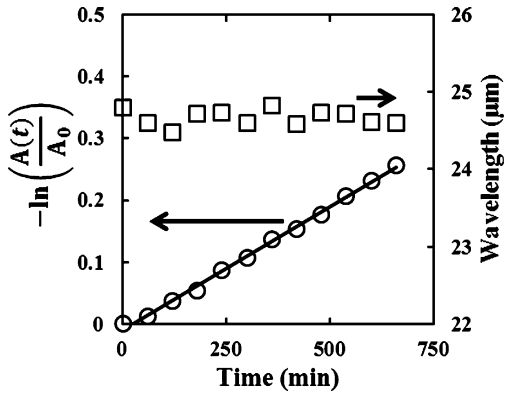


Figure 5. Results of a typical FRAPP experiment for a 127 nm film. The left axis shows the negative natural log of the amplitude normalized by the amplitude of the initial condition (A_0) (○), and the right axis contains the wavelength (□) of the best fit sinusoid against time. The solid line through the amplitude data indicates best fit line that is then used with eq 2 to calculate the diffusion coefficient. The error in the amplitude is smaller than the symbols and is less than 4% for each data point.

Since the molecular weights of the polymers used in this study (~8.7 kg/mol) are well below the entanglement molecular weight for PiBMA, ~28 kDa,[69] bulk diffusion is expected to follow the Rouse model for unentangled polymer diffusion.[70,71] The Rouse model was used to estimate the bulk diffusion coefficient for PiBMA at 80 °C as 1.05×10^{-12} cm^2/s using eq 4.[70]

$$D = \frac{\rho RT\langle R^2\rangle}{36M\eta_0} \tag{4}$$

In eq 4, ρ is the mass density, estimated at 1.071 g/cm^3 at 80 °C,[69] R is the ideal gas constant, T is the absolute temperature of the experiment, 353.15 K, $\langle R^2\rangle$ is the unperturbed mean-square end-to-end distance estimated as 8.52 nm^2,[60] M is the molecular weight, and η_0 is the zero shear viscosity. The zero shear viscosity of PiBMA was measured as 820 Pa·s by a cone and plate fixture on a TA Instruments AR-2000ex rheometer under steady shear. The diffusion coefficient for the 127 nm film represented in Figures 4 and 5 was $(1.02 \pm 0.07) \times 10^{-12}$ cm^2/s, which is identical, within uncertainty, to the value estimated from the Rouse model. Because the diffusion coefficient calculated for the thicker films corresponds well with measured values from these experiments, FRAPP clearly allows for characterization of the diffusion of polymers in thin films, and the analysis method chosen consistently yields accurate results. Additionally, this technique also allows for characterization of the uncertainty in an individual measurement as described above, which previously had only been possible by repeated measurements on similar films.

Nanoconfined Diffusion. Figure 6 displays the diffusion coefficient as a function of film thickness for PiBMA down to 30 nm. The results in this figure demonstrate that within two standard deviations, a 95% confidence interval, none of the data points are significantly different statistically from the other data points regardless of film thickness. For the PiBMA-NBD measurements, experimental uncertainty in the diffusion coefficient, as calculated by eq 3, was less than 9% of the diffusion coefficient for all film thicknesses measured. Additionally, this technique exhibits good reproducibility; for a set of three, separately prepared 61 ± 5 nm thick films the diffusion

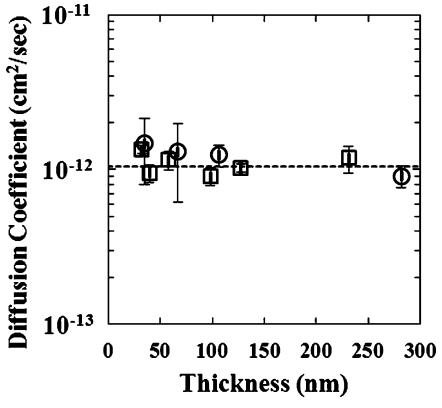


Figure 6. Diffusion coefficient at 80 °C of PiBMA-NBD (□) and PiBMA-NBD-PiBMA (○) as a function of film thickness recorded at 25 °C. The dashed line indicates the bulk diffusion coefficient estimated using the Rouse model for this molecular weight and temperature (1.05×10^{-12} cm^2/s). Error bars indicate the uncertainty as calculated from eq 3.

dx.doi.org/10.1021/ma202362j | Macromolecules 2012, 45, 1544−1552

coefficient measured was, 1.10×10^{-12}, 1.22×10^{-12}, and 1.28×10^{-12} cm^2/s. In-plane diffusion was also measured on PiBMA-NBD-PiBMA, and no deviation in the diffusion coefficient from the Rouse model prediction was observed in films as thin as 34.9 nm. Because the diffusion coefficient is invariant with the number of fluorophores per polymer chain or their position along the polymer backbone, this indicates that the presence of fluorophores in the polymer does not impact the diffusion of the polymer chains.

DISCUSSION AND CONCLUSIONS

This study has demonstrated a procedure to measure in-plane self-diffusion coefficients of polymers in thin films based on FRAPP. The relaxation of a photobleached array of lines was directly observed and imaged via an epifluorescence microscope where the rate of relaxation is directly related to the self-diffusion coefficient of PiBMA. One of the primary features of this FRAPP method is the ability to directly image the polymer film during the experiment. Many biological experiments using FRAPP use a confocal microscope with a scanning photomultiplier tube or an epifluorescence microscope with a camera to image and analyze diffusion of a target species by bleaching a single spot.[44,45] By comparison, previous polymer studies employing FRAPP utilize a photon counting technique and measure the absolute fluorescence intensity from the region of interest.[36,38,46] Through imaging with a camera and then analyzing the fluorescence intensity profile, rather than tracking absolute intensity, the results do not rely on making certain assumptions about the experiment, such as no photobleaching during imaging, because the maximum intensity of each image is referenced internally. Additionally, the ability to reliably characterize the diffusion coefficient and experimental uncertainty from a single experiment substantially reduces the need for repeated trials of each film thickness studied, leading to an increase in experimental throughput. The FRAPP procedure used in this work provides a flexible platform for the study of diffusion in thin polymer films. This approach is not specific to this polymer, substrate, or even this fluorophore, so this basic setup can be tailored to examine a wide array of parameters that will be the subject of future work.

The PiBMA diffusion results in this study show that the diffusion coefficient of PiBMA is invariant with film thickness down to 30 nm ($\sim 14R_g$). In contrast, a previous study on polystyrene indicated that D decreased for polystyrene films thinner than $\sim 50R_g$.[36] In addition, the T_g of PiBMA was measured to be independent of film thickness down to 15 nm, about $7R_g$. This T_g result is identical to that of Priestley et al. for PiBMA with M_n = 300 kg/mol.[67] In that study, additional measurements on a 14 nm thick fluorophore containing surface or substrate layer determined T_g selectively at each interface and showed that the T_g decreased by 6 °C for the 14 nm nearest the air interface and increased by 5 °C for the 14 nm closest to the substrate. This suggests the magnitude of the hydrogen-bonding interactions between the PiBMA repeat unit and the hydroxyls on the substrate are such that the increase in polymer T_g they promote balances exactly the reduction in T_g near the air interface of the film, resulting in no net change of average T_g with film thickness, as measured by ellipsometry. While the experimentally observed average T_g of PiBMA on silicon oxide substrates by ellipsometry is invariant with film thickness, the results of Priestley et al. indicate clearly that a distribution of T_g values exist within the thin film.

Examining the T_g of PiBMA in thin films is important to studies of in-plane diffusion because, at least in bulk, diffusion is related to the proximity of the diffusion temperature to the glass transition temperature ($T - T_g$). The effect of changing $T - T_g$ on D can be estimated by the Rouse model (eq 4) using a value for η_0 where T_g is adjusted by a WLF relationship[52] and the density is adjusted based on thermal expansion,[69] all other parameters constant. By this protocol, an increase in T_g leads to a decrease in the diffusion coefficient, and a decrease in T_g produces an increase in the diffusion coefficient.

Using the layered T_g data of Priestley et al.[67] and the protocol described above, diffusion coefficients near the air and substrate interfaces can be predicted. This estimation results in a PiBMA diffusion coefficient at 80 °C of 2.1×10^{-12} cm^2/s in the layer of the film closest to the air and a diffusion coefficient of 5.2×10^{-13} cm^2/s in the layer of the film closest to the substrate. Respectively, these values represent an increase by 100% and a decrease of 50% from the bulk value, well outside the experimental uncertainty of the bulk value we have measured for all film thicknesses. If the layers were significant contributors, it might be expected that there would be at least two populations of diffusing chains, one fast and one slow. More likely, however, there would be a continuous range of different diffusion coefficients, not just two populations. It is worth noting that simulations suggest that there may be different diffusion coefficients near different interfaces.[72,73] This would significantly complicate the use of Fick's law with a single diffusion coefficient and would be reflected by model predictions that fit data poorly. At this time, all our data fit the Fickian diffusion model with a single diffusion coefficient quite well. More experiments will be needed to resolve these issues.

This connection has been considered in a follow-up commentary[74] to a previous study[36] where a factor of 2 reduction in D parallel to the substrate was observed for a 50 nm thick polystyrene film[36] on a silicon oxide substrate. The associated commentary hypothesized that the thickness dependence of D could be explained by an increase in film T_g of 7 °C, using a similar analysis to that outlined in the previous paragraph.[74] However, it has most commonly been shown that T_g decreases with decreasing film thickness for polystyrene films supported on silicon or silicon oxide substrates,[18] which appears inconsistent with this argument. Using the preceding analysis and the fact that T_g typically decreases with decreasing film thickness, one would expect an increasing D with decreasing film thickness for polystyrene at any given diffusion temperature.

Finally, neutron scattering measurements indicate the chain conformations in the plane of the film (normal to the confining dimension) retain their bulk unperturbed Gaussian conformations in polystyrene films as thin as $0.5R_{g,bulk}$.[75,76] This chain conformation result suggests that D in the plane of the film should be unchanged for polystyrene films as thin as $0.5R_{g,bulk}$. Given current understanding, it is difficult to reconcile the results for polystyrene indicating decreasing D with decreasing film thickness under conditions where with the chain conformation is consistent with bulk, and more research is needed to develop a complete picture. Nonetheless, measurements of PiBMA chain conformations in nanoconfined films have not been performed, and therefore it is not possible to comment on how they may be affected at film thicknesses where D was measured in the present study.

AUTHOR INFORMATION

Corresponding Author

*E-mail: ellison@che.utexas.edu.

ACKNOWLEDGMENTS

This research was supported by the donors of the American Chemical Society−Petroleum Research Fund (Grant 49881-DNI7), the National Science Foundation CAREER Program (Grant DMR-1053293), and the Welch Foundation (grant F-1709). The authors thank Jeff Easley for providing the ligand used in this study and giving helpful comments and Paola Gonzalez for performing rheological measurements.

REFERENCES

(1) Huang, Y.; Paul, D. R. *Macromolecules* **2006**, *39*, 1554−1559.
(2) Pfromm, P. H.; Koros, W. J. *Polymer* **1995**, *36*, 2379−2387.
(3) Priestley, R. D.; Ellison, C. J.; Broadbelt, L. J.; Torkelson, J. M. *Science* **2005**, *309*, 456−459.
(4) Kawana, S.; Jones, R. A. L. *Eur. Phys. J. E* **2003**, *10*, 223−230.
(5) Khare, R.; dePablo, J. J.; Yethiraj, A. *Macromolecules* **1996**, *29*, 7910−7918.
(6) Luengo, G.; Schmitt, F. J.; Hill, R.; Israelachvili, J. *Macromolecules* **1997**, *30*, 2482−2494.
(7) Yang, Z.; Fujii, Y.; Lee, F. K.; Lam, C.-H.; Tsui, O. K. C. *Science* **2010**, *328*, 1676−1679.
(8) Stafford, C. M.; Vogt, B. D.; Harrison, C.; Julthongpiput, D.; Huang, R. *Macromolecules* **2006**, *39*, 5095−5099.
(9) Torres, J. M.; Stafford, C. M.; Vogt, B. D. *Polymer* **2010**, *51*, 4211−4217.
(10) Torres, J. M.; Stafford, C. M.; Vogt, B. D. *ACS Nano* **2009**, *3*, 2677−2685.
(11) Newby, B. M. Z.; Wakabayashi, K.; Composto, R. J. *Polymer* **2001**, *42*, 9155−9162.
(12) O'Connell, P. A.; McKenna, G. B. *Science* **2005**, *307*, 1760−1763.
(13) Beaucage, G.; Composto, R.; Stein, R. S. *J. Polym. Sci., Part B: Polym. Phys.* **1993**, *31*, 319−326.
(14) Ellison, C. J.; Kim, S. D.; Hall, D. B.; Torkelson, J. M. *Eur. Phys. J. E* **2002**, *8*, 155−166.
(15) Forrest, J. A.; DalnokiVeress, K.; Dutcher, J. R. *Phys. Rev. E* **1997**, *56*, 5705−5716.
(16) Keddie, J. L.; Jones, R. A. L.; Cory, R. A. *Faraday Discuss.* **1994**, *98*, 219−230.
(17) Ellison, C. J.; Torkelson, J. M. *Nature Mater.* **2003**, *2*, 695−700.
(18) Forrest, J. A.; Dalnoki-Veress, K. *Adv. Colloid Interface Sci.* **2001**, *94*, 167−196.
(19) Alcoutlabi, M.; McKenna, G. B. *J. Phys.: Condens. Matter* **2005**, *17*, R461−R524.
(20) Tsui, O. K. C.; Russell, T. P.; Hawker, C. J. *Macromolecules* **2001**, *34*, 5535−5539.
(21) Tsui, O. K. C.; Zhang, H. F. *Macromolecules* **2001**, *34*, 9139−9142.
(22) Roth, C. B.; Dutcher, J. R. *J. Electroanal. Chem.* **2005**, *584*, 13−22.
(23) Huang, R.; Stafford, C. M.; Vogt, B. D. *J. Aerosp. Eng.* **2007**, *20*, 38−44.
(24) Wang, X. P.; Xiao, X.; Tsui, O. K. C. *Macromolecules* **2001**, *34*, 4180−4185.
(25) Paeng, K.; Ediger, M. D. *Macromolecules* **2011**, *44*, 7034−7042.
(26) Paeng, K.; Swallen, S. F.; Ediger, M. D. *J. Am. Chem. Soc.* **2011**, *133*, 8444−8447.
(27) Russell, T. P. *Annu. Rev. Mater. Sci.* **1991**, *21*, 249−268.
(28) Green, P. F.; Palmstrom, C. J.; Mayer, J. W.; Kramer, E. J. *Macromolecules* **1985**, *18*, 501−507.
(29) Vaia, R. A.; Giannelis, E. P. *MRS Bull.* **2001**, *26*, 394−401.
(30) Gopakumar, T. G.; Lee, J. A.; Kontopoulou, M.; Parent, J. S. *Polymer* **2002**, *43*, 5483−5491.
(31) Ji, S. X.; Liu, C. C.; Liu, G. L.; Nealey, P. F. *ACS Nano* **2010**, *4*, 599−609.
(32) Schwarz, S. A.; Wilkens, B. J.; Pudenzi, M. A. A.; Rafailovich, M. H.; Sokolov, J.; Zhao, X.; Zhao, W.; Zheng, X.; Russell, T. P.; Jones, R. A. L. *Mol. Phys.* **1992**, *76*, 937−950.
(33) Pu, Y.; Rafailovich, M. H.; Sokolov, J.; Gersappe, D.; Peterson, T.; Wu, W. L.; Schwarz, S. A. *Phys. Rev. Lett.* **2001**, *87*, 206101.
(34) Zheng, X.; Rafailovich, M. H.; Sokolov, J.; Strzhemechny, Y.; Schwarz, S. A.; Sauer, B. B.; Rubinstein, M. *Phys. Rev. Lett.* **1997**, *79*, 241−244.
(35) Binder, K.; Milchev, A.; Baschnagel, J. *Annu. Rev. Mater. Sci.* **1996**, *26*, 107−134.
(36) Frank, B.; Gast, A. P.; Russell, T. P.; Brown, H. R.; Hawker, C. *Macromolecules* **1996**, *29*, 6531−6534.
(37) Bae, S. C.; Wong, J. S.; Kim, M.; Jiang, S.; Hong, L.; Granick, S. *Philos. Trans. R. Soc., A* **2008**, *366*, 1443−1454.
(38) Wong, J. S. S.; Hong, L. A.; Bae, S. C.; Granick, S. *J. Polym. Sci., Part B: Polym. Phys.* **2010**, *48*, 2582−2588.
(39) Sukhishvili, S. A.; Chen, Y.; Muller, J. D.; Gratton, E.; Schweizer, K. S.; Granick, S. *Macromolecules* **2002**, *35*, 1776−1784.
(40) Manias, E.; Chen, H.; Krishnamoorti, R.; Genzer, J.; Kramer, E. J.; Giannelis, E. P. *Macromolecules* **2000**, *33*, 7955−7966.
(41) Lin, E. K.; Kolb, R.; Satija, S. K.; Wu, W. L. *Macromolecules* **1999**, *32*, 3753−3757.
(42) Composto, R. J.; Walters, R. M.; Genzer, J. *Mater. Sci. Eng., R* **2002**, *38*, 107−180.
(43) Axelrod, D.; Koppel, D. E.; Schlessinger, J.; Elson, E.; Webb, W. W. *Biophys. J.* **1976**, *16*, 1055−1069.
(44) Johnson, M. E.; Berk, D. A.; Blankschtein, D.; Golan, D. E.; Jain, R. K.; Langer, R. S. *Biophys. J.* **1996**, *71*, 2656−2668.
(45) Zhang, F.; Schmidt, W. G.; Hou, Y.; Williams, A. F.; Jacobson, K. *Proc. Natl. Acad. Sci. U. S. A.* **1992**, *89*, 5231−5235.
(46) Smith, B. A. *Macromolecules* **1982**, *15*, 469−472.
(47) Tseng, K. C.; Turro, N. J.; Durning, C. J. *Polymer* **2000**, *41*, 4751−4755.
(48) Van Keuren, E.; Schrof, W. *Macromolecules* **2003**, *36*, 5002−5007.
(49) Hamersky, M. W.; Tirrell, M.; Lodge, T. P. *Langmuir* **1998**, *14*, 6974−6979.
(50) Cavicchi, K. A.; Lodge, T. P. *Macromolecules* **2004**, *37*, 6004−6012.
(51) Inoue, T.; Nemoto, N.; Kojima, T.; Kurata, M. *Polym. J.* **1988**, *20*, 869−874.
(52) Rubinstein, M.; Colby, R. H. *Polymer Physics*; Oxford University Press: Oxford, 2003.
(53) Fu, G. D.; Xu, L. Q.; Yao, F.; Zhang, K.; Wang, X. F.; Zhu, M. F.; Nie, S. Z. *ACS Appl. Mater. Interfaces* **2009**, *1*, 239−243.
(54) Jakubowski, W.; Min, K.; Matyjaszewski, K. *Macromolecules* **2006**, *39*, 39−45.
(55) Matyjaszewski, K.; Jakubowski, W.; Min, K.; Tang, W.; Huang, J. Y.; Braunecker, W. A.; Tsarevsky, N. V. *Proc. Natl. Acad. Sci. U. S. A.* **2006**, *103*, 15309−15314.
(56) Pintauer, T.; Matyjaszewski, K. *Chem. Soc. Rev.* **2008**, *37*, 1087−1097.
(57) Jakubowski, W.; Kirci-Denizli, B.; Gil, R. R.; Matyjaszewski, K. *Macromol. Chem. Phys.* **2008**, *209*, 32−39.
(58) Bardajee, G. R.; Li, A. Y.; Haley, J. C.; Winnik, M. A. *Dyes Pigm.* **2008**, *79*, 24−32.
(59) Kalinina, O.; Kumacheva, E. *Macromolecules* **1999**, *32*, 4122−4129.
(60) Brandrup, J.; Immergut, E. H.; Grulke, E. A. *Polymer Handbook*; Wiley and Sons: Hoboken, NJ, 1999.
(61) Hall, D. B.; Underhill, P.; Torkelson, J. M. *Polym. Eng. Sci.* **1998**, *38*, 2039−2045.
(62) Spangler, L. L.; Torkelson, J. M.; Royal, J. S. *Polym. Eng. Sci.* **1990**, *30*, 644−653.
(63) Edelstein, A.; Amodaj, N.; Hoover, K.; Vale, R.; Stuurman, N. *Computer Control of Microscopes Using μManager*; In *Current Protocols in Molecular Biology*, John Wiley & Sons, Inc.: New York, 2010.

(64) McCafferty, E.; Wightman, J. P. *Surf. Interface Anal.* **1998**, *26*, 549−564.
(65) Frankenburg, W. G. *Advances in Catalysis and Related Subjects*; Academic Press: New York, 1966.
(66) Kim, S.; Hewlett, S. A.; Roth, C. B.; Torkelson, J. M. *Eur. Phys. J. E* **2009**, *30*, 83−92.
(67) Priestley, R. D.; Mundra, M. K.; Barnett, N. J.; Broadbelt, L. J.; Torkelson, J. M. *Aust. J. Chem.* **2007**, *60*, 765−771.
(68) Abramoff, M. D.; Magelhaes, P. J.; Ram, S. J. *Biophotonics Int.* **2004**, *11*, 36−42.
(69) Bicerano, J. *Prediction of Polymer Properties*, 3rd ed.; Marcel Dekker, Inc.: New York, 2002.
(70) Doi, M.; Edwards, S. F. *The Theory of Polymer Dynamics*; Clarendon Press: Oxford, 1986.
(71) Rouse, P. E. Jr. *J. Chem. Phys.* **1953**, *21*, 1272−80.
(72) Desai, T.; Keblinski, P.; Kumar, S. K. *J. Chem. Phys.* **2005**, *122*, 134910.
(73) Torres, J. A.; Nealey, P. F.; de Pablo, J. J. *Phys. Rev. Lett.* **2000**, *85*, 3221−3224.
(74) Russell, T. P.; Kumar, S. K. *Nature* **1997**, *386*, 771−772.
(75) Jones, R. L.; Kumar, S. K.; Ho, D. L.; Briber, R. M.; Russell, T. P. *Nature* **1999**, *400*, 146−149.
(76) Jones, R. L.; Kumar, S. K.; Ho, D. L.; Briber, R. M.; Russell, T. P. *Macromolecules* **2001**, *34*, 559−567.

Macromolecules

Article

pubs.acs.org/Macromolecules

Morphology Evolution of PS-*b*-P2VP Diblock Copolymers via Supramolecular Assembly of Hydroxylated Gold Nanoparticles

Se Gyu Jang,[†] Anzar Khan,[‡] Craig J. Hawker,*[,†,§,⊥] and Edward J. Kramer*[,†,§,∥]

[†]Materials Research Laboratory, University of California, Santa Barbara, California, 93106, United States

[‡]Department of Materials, ETH-Zürich, CH-8093 Zürich, Switzerland

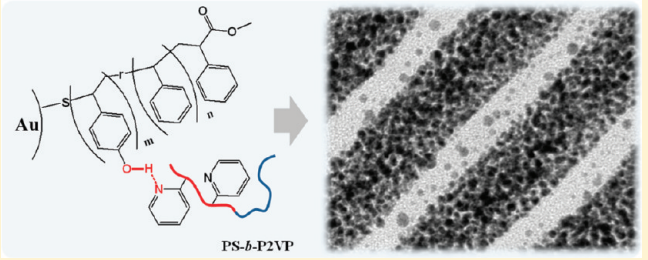
[§]Department of Materials, University of California, Santa Barbara, California, 93106, United States

[⊥]Department of Chemistry and Biochemistry, University of California, Santa Barbara, California, 93106, United States

[∥]Department of Chemical Engineering, University of California, Santa Barbara, California, 93106, United States

Supporting Information

ABSTRACT: We report on the strong segregation of core–shell Au nanoparticles, with a shell layer consisting of a random copolymer brush of styrene and vinylphenol (PS-*r*-PVPh-SH), in poly(styrene-*b*-2-vinylpyridine) (PS-*b*-P2VP) diblock copolymer. Because of the formation of multiple hydrogen bonds between the hydroxyl groups within the shell of the nanoparticles and the pyridine group in PS-*b*-P2VP, the Au nanoparticles were strongly localized into P2VP domains with a very high volume fraction of nanoparticles ($\phi_p \sim 0.53$). The spatial distribution of Au nanoparticles, observed by transmission electron microscopy (TEM), is compared with results of previous experiments where homopolymers were blended with block copolymers. If the diameter d of the nanoparticles is much less than the width D of the P2VP lamellar domains, these nanoparticles are more uniformly distributed across the P2VP domain than if d is comparable to D, in which case the nanoparticles are pushed toward the center of the P2VP domains. This behavior is similar to that observed when homopolymers are blended with block copolymers. Novel morphological transitions from spherical to cylindrical P2VP morphologies and from lamellae to cylindrical PS morphologies were observed during coassembly of these functional nanoparticles with block copolymers.



INTRODUCTION

Hydrogen bonding (H-bonding) has been widely used for supramolecular assembly of small molecules and polymers because of its molecularly specific and highly directional characteristics.[1−4] In addition, the reversible and dynamic characteristics of H-bonding enable production of self-healing materials, which is an exciting emerging theme in materials science.[5−7] In particular, block copolymers constructed using multiple H-bonding units instead of covalent linkages have been studied intensively, both theoretically and experimentally.[8−14] A judicious choice of polymers, balancing polymer interactions with the strength and directionality of H-bonding groups, opens up possibilities to create complex structures with various properties derived from simple building blocks.[4,15] Demonstrations of these possibilities include low temperature processing of materials with well-defined architectures, thermal modulation of microphase-separated domains, and development of nonconventional morphologies with nanometer-scale features such as lamellae-in-lamellae and square arrangement of cylinders.[16−19] Recently, H-bonding has also been employed to blend block copolymers and homopolymers.[20−23] The formation of multiple H-bonds between host and guest polymers significantly enhances miscibility causing swelling of the host domains of the block copolymers without macrophase separation and corresponding order–order morphology transitions.

The incorporation of inorganic nanoparticles into block copolymer matrices has been intensively studied with the aim of combining the unique physical or chemical properties of nanoparticles with hierarchical nanophase-separated self-assembly of block copolymer, which is potentially useful in high performance catalysis, sensors, optics, and electronics.[24−28] Tailoring the surface properties of nanoparticles can provide for precise control of nanoparticle segregation in block copolymers. This control has been demonstrated using nanoparticles with short aliphatic chains, homopolymers, mixed homopolymers, and random copolymers.[29−44] It is known that nanoparticles completely covered by polymeric ligands show segregation behavior similar to that of the homopolymer in blending systems.[45−52] For example, nanoparticles covered with a polystyrene (PS) homopolymer brush layer tend to segregate in PS domains of poly(styrene-*b*-2-vinylpyridine) (PS-*b*-P2VP)

Received: October 26, 2011
Revised: December 20, 2011
Published: January 20, 2012

 © 2012 American Chemical Society

diblock copolymer at low particle volume fractions. However when higher volume fractions of such particles are added, they macrophase-separate due to an increase in the entropic penalty of block copolymer chain stretching resulting from nanoparticle incorporation.[35,38,53] Most characteristic features of homopolymer addition in blending systems such as swelling of domains, morphological transitions of block copolymer, and macrophase separation of additives were observed in coassembly of nanoparticles and block copolymers. In particular, a strong segregation of nanoparticles into specific domains via H-bonding has also been reported. For example, localization of nanoparticles of cadmium selenide (CdS), Au, and silicon (Si) covered with hydroxyl groups has been observed in the poly(ethylene oxide) (PEO) or poly(4-vinylpyridine) (P4VP) domains of diblock copolymers.[54−57] Because of the strong enthalphic attraction of H-bonds, macrophase-separation of nanoparticles was significantly suppressed in favor of microphase separation and very high volume fraction of nanoparticle incorporation (~36 vol %) was demonstrated.[55] Despite the similarity between polymer blend and nanoparticle incorporation systems, according to our best knowledge, no investigation correlating these two systems in detail have been reported. Combining knowledge from both systems may allow general predictions of segregation behavior for new sets of nanoparticles or homopolymers in block copolymer matrices in order to create customized and multifunctional hybrid materials.

In this paper, Au nanoparticles covered with a brush layer of thiol-terminated random copolymers of styrene and vinylphenol (PS-*r*-PVPh-SH) were prepared and the H-bonding attraction between the hydroxyl groups on the nanoparticle ligands and pyridine rings of PS-*b*-P2VP diblock copolymers studied. The PS-*r*-PVPh-SH ligands were synthesized by reversible addition−fragmentation transfer (RAFT) polymerization of styrene and 4-acetoxystyrene (PS-*r*-PAS-RAFT) followed by hydrazinolysis to deprotect the phenol groups and to generate a thiol group at the chain end. By controlling the relative number of *p*-vinylphenol to styrene units, solubility of Au nanoparticles in nonpolar solvents could be tuned to maximize the H-bonding strength. As a result, preparation of nanoparticle/block copolymer mixtures and solvent annealing could be carried out in nonpolar solvents without any disruption or weakening of H-bonds by solvation of the phenol units by polar solvents. The random copolymer-coated nanoparticles were strongly segregated in P2VP domains of PS-*b*-P2VP block copolymer of various molecular weights and 2VP mole fractions. The spatial distribution of the nanoparticles in P2VP domains of block copolymer were compared to results of previous experiments where homopolymers were blended with block copolymers. The high incorporation of homogeneously distributed nanoparticles into P2VP domains induced morphological transitions of the PS-*b*-P2VP diblock copolymers.

EXPERIMENTAL METHODS

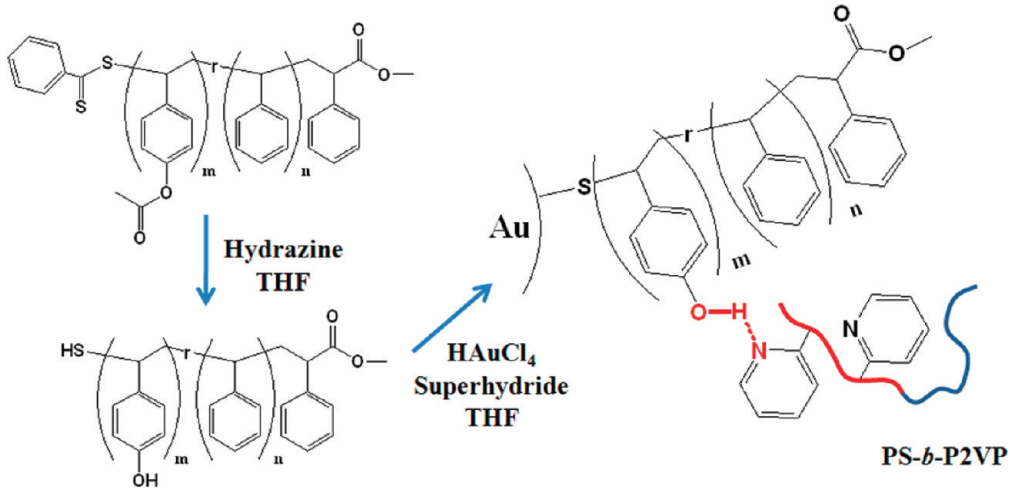
Synthesis of PS-*r*-PAS-RAFT by RAFT Polymerization. Thiol-terminated random copolymers of styrene and 4-acetoxystyrene (PS-*r*-PAS-RAFT) were synthesized via reversible addition−fragmentation transfer (RAFT) polymerization.[58,59] Dithioester-RAFT agent was prepared by the procedure described elsewhere.[34] Two PS-*r*-PAS-RAFTs were synthesized with different compositions. Styrene (Sigma-Aldrich, > 99%) and 4-acetoxystyrene (Sigma-Aldrich, 96%) were purified by passage through a basic aluminum oxide column prior to use. Styrene (6.02 g, 55.80 mmol), 4-acetoxystyrene (1.01 g, 6.20 mmol), azobis(isobutyronitrile) (AIBN, 0.01 g, 0.06 mmol), and dithioester RAFT agent (0.30 g, 0.62 mmol) were mixed and degassed by three freeze−pump−thaw cycles. The polymerization was carried out at 90 °C for 7 h under vacuum. The polymer was then precipitated in methanol and dried under vacuum. The molecular weight (M_n) and polydispersity index (PDI) of the random copolymer PS_{22}-*r*-PAS_3-RAFT as measured by gel permeation chromatography (GPC, calibrated by PS standards), were 2.6 kg/mol and 1.1, respectively. The composition of PS-*r*-PAS-RAFT calculated from ^{1}H NMR was found to be 12 mol % 4-acetoxystyrene (~3 repeating units). The M_n value of PS_{22}-*r*-PAS_3-RAFT calculated from the ratio of the peak area of RAFT agent to that of PS (broad peaks from 6.2 to 7.3 ppm) and acetoxy groups (broad peak centered at 2.3 ppm) was 3.3 kg/mol. Following the same procedure, a PS-*r*-PAS-RAFT with 26 mol % 4-acetoxystyrene (~7 repeating units, PS_{20}-*r*-PAS_7-RAFT) was synthesized. The M_n and PDI for this copolymer were 2.7 kg/mol (3.7 kg/mol by ^{1}H NMR) and 1.1, respectively.

Deprotection of PS-*r*-PAS-RAFT. The dithioester-terminus and acetoxy groups of the PS-*r*-PAS-RAFT were converted to thiol and hydroxyl groups, respectively, in a one step reaction by hydrazinolysis as reported by Lee et al.[60] PS-*r*-PAS-RAFT (1.0 g) was placed in a round-bottom flask with a magnetic stirrer. Dry THF (30 mL) was transferred into the flask via a cannula after three vacuum and argon purging cycles. Under a dry argon atmosphere, 15 mmol of hydrazine dissolved in THF (Sigma-Aldrich, 1M, 50 equiv. to dithioester-terminus) was injected by syringe (***Caution!*** *hydrazine is highly toxic and should be handled with extreme care*). The solution color changed from pink to yellow immediately. After the reaction was stirred overnight, the solvent and hydrazine were evaporated and the polymers were dissolved in dichloromethane, filtered with a syringe filter (Whatman, 200 nm pore size, PTFE) to remove insoluble species, and precipitated in cold hexane. The precipitated white polymers were dried under vacuum at room temperature for a day.

Synthesis of PS-*r*-PVPh-SH-Coated Au Nanoparticles (PS-*r*-PVPh−S-Au). Au nanoparticles coated with PS-*r*-PVPh-SH were synthesized using the THF one-phase method.[61] Au precursor ($HAuCl_4{\cdot}3H_2O$, Sigma-Aldrich, > 99.9%, 0.8 mmol) and 0.2 mmol of PS_{22}-*r*-$PVPh_3$-SH or PS_{20}-*r*-$PVPh_7$-SH polymers were placed in a round-bottom flask with a magnetic stirrer. Dry THF (20 mL) was transferred into the flask via a cannula under agitation after three vacuum and argon purging cycles. After stirring for 30 min, Au nanoparticles were synthesized by adding 2.3 mmol of the reducing agent, superhydride ($Li(C_2H_5)_3BH$, Sigma-Aldrich, 1 M in THF), dropwise under dry argon. The unbound polymer ligands were separated from the polymer brush coated Au nanoparticles by filtering, at least 5 times, with membrane centrifugal filters (Centricon-Plus 70, MWCO 100 000 Da, Millipore Inc.) using THF as the solvent. The washed Au nanoparticles in THF were filtered with a syringe filter (Whatman, 200 nm, PTFE) and precipitated in hexane.

Preparation of PS-*b*-P2VP/Au Nanoparticle Composites. A certain weight of Au nanoparticles was dissolved in a freshly prepared 1 wt % PS-*b*-P2VP diblock copolymer solution in dichloromethane (DCM) to obtain a volume fraction of nanoparticles in the range of 0.04−0.53. This volume fraction includes the volume of the polymer shell estimated from the density of the ligand (~1.05 g/cm^3) and Au (~19.3 g/cm^3) coupled with thermal gravimetric analysis (TGA) of the Au nanoparticles.[35] P2VP sphere-forming (107 kg/mol with a mole fraction of 2VP, $f_{P2VP} \sim 0.11$) and lamellae-forming (72 kg/mol with $f_{P2VP} \sim 0.40$ and 199 kg/mol with $f_{P2VP} \sim 0.48$) PS-*b*-P2VP block copolymers were used for the preparation of composites. Thick films of block copolymers and block copolymer/nanoparticle composites were prepared by drop casting the solution of nanoparticles and PS-*b*-P2VP block copolymer in DCM onto a thick Au-coated (~100 nm) sodium chloride crystal window (Sigma-Aldrich, 2 mm thick). The composites were annealed in saturated dichloromethane (DCM) vapor at room temperature for at least 2 days. After drying the composite film overnight under vacuum, a thick Au layer (~100 nm) was deposited on the sample to inhibit infiltration of the epoxy resin (Embed-812, Electron Microscopy Sciences) into the sample during TEM sample preparation. Samples of the composite film were

Scheme 1. Schematic Illustration of Synthesis of Thiol-Terminated Poly(styrene-*ran*-vinyl phenol) Copolymer Ligand[a]



[a]This was performed by hydrazinolysis of poly(styrene-*ran*-acetoxystyrene) obtained by reversible addition fragmentation chain transfer (RAFT) polymerization and hydrogen bond formation between hydroxyl groups in ligands coated on Au nanoparticles and pyridine groups on poly(styrene-*b*-2-vinylpyridine) diblock copolymer. The hydrolysis of acetoxy groups and the reduction of dithio-ester groups were carried out simultaneously by addition of hydrazine with tetrahydrofurane (THF) as a solvent. Gold nanoparticles were synthesized by reduction of chloroauric acid trihydrate with superhydride ($Li(C_2H_5)_3BH$) in the presence of random copolymer ligands dissolved in THF.

embedded into epoxy resin and sliced to a thickness of about 50−70 nm by ultramicrotoming (Leica). The sliced composite samples were exposed to iodine vapor to selectively stain the P2VP domains.

Characterization. The nanoparticles and cross-sections of the pure block copolymers and composite films were characterized by transmission electron microscopy (TEM, FEI Tecnai G2 microscope, 200 kV). The size histograms of the Au nanoparticles were determined from at least 300 nanoparticles by image analysis (Image Pro) of TEM micrographs. The mean areal chain density of polymer ligands on the Au nanoparticles was calculated from the total surface area and the weight fraction of Au and polymer ligands determined by TGA. Fourier transform infrared (FT-IR, Bruker) spectra of PS-*b*-P2VP diblock copolymer and composite samples were taken in the wavenumber range of 450−4000 cm^{-1}.

RESULTS AND DISCUSSION

Scheme 1 illustrates the strategy for synthesis of Au nanoparticles coated with random copolymer ligands containing phenolic groups and their supramolecular assembly with the pyridine groups of a poly(styrene-*b*-2-vinylpyridine) (PS-*b*-P2VP) diblock copolymer. Thiol-terminated poly(styrene-*r*-vinylphenol) (PS-*r*-PVPh-SH) ligands are obtained from the random copolymer of poly(styrene-*r*-acetoxystyrene) synthesized by reversible addition−fragmentation chain transfer (RAFT) polymerization (PS-*r*-PAS-RAFT). The hydrolysis of acetoxy groups and the reduction of thioester groups to a secondary thiol were carried out simultaneously by addition of hydrazine.[60] Then, Au nanoparticles covered with PS-*r*-PVPh-SH ligands were synthesized by reduction of a Au precursor ($HAuCl_4 \cdot 3H_2O$) with superhydride ($Li(C_2H_5)_3BH$) dissolved in THF. A key to the design of the nanoparticles is tailoring the surface properties of the polymeric shell by controlling the number of phenolic groups per polymeric ligand with enough hydroxyl groups being present to induce a strong H-bonding interaction. At the same time, the number of hydroxyl groups needs to be low enough to maintain reasonable hydrophobicity, enabling dissolution of the nanoparticles in nonpolar solvents such as dichloromethane. This avoids the need to use polar solvents, which weaken the H-bonding interaction with the P2VP by solvation of the PVPh.[20] The enthalpic gain from H-bond formation attracts the nanoparticles to the P2VP phase of microphase-separated PS-*b*-P2VP diblock copolymer domains. However the enthalphic penalty due to mixing of PS components of the polymer shell of the nanoparticles with the P2VP phase drives the nanoparticles to the PS phase. Therefore, the number ratio of styrene and phenol repeating units on the ligand determines the segregation location of nanoparticles in PS-*b*-P2VP domains as well as the solubility of nanoparticles in nonpolar solvents. To broadly define an optimum ratio, we synthesized two PS-*r*-PAS-RAFT polymers with different numbers of repeating units; PS_{22}-*r*-PAS_3-RAFT and PS_{20}-*r*-PAS_7-RAFT as shown in Table 1 (see Supporting Information, Figure S1, for ^1H NMR spectra of each polymer).

Table 1. Characterization of Poly(styrene-*r*-acetoxy styrene) Synthesized by RAFT Polymerization

	GPC		^1H NMR[a]		
	M_n (kg/mol)	PDI	M_n (kg/mol)	N_S[b]	N_{AS}[c]
PS_{22}-*r*-PAS_3-RAFT	2.6	1.1	3.3	22	3
PS_{20}-*r*-PAS_7-RAFT	2.7	1.1	3.7	20	7

[a]Calculated from the ratio of the peak area of RAFT agent to that of PS (broad peaks from 6.2 to 7.3 ppm) and acetoxy groups (broad peak centered at 2.3 ppm) by ^1H NMR. [b]Average number of styrene repeating units per chain obtained by ^1H NMR. [c]Average number of acetoxy styrene repeating units per chain obtained by ^1H NMR.

The hydrazinolysis of the random copolymers was monitored by ^1H NMR (Figure 1). Figure 1a shows the ^1H NMR spectrum of the PS_{22}-*r*-PAS_3-RAFT ($CDCl_3$) with the aromatic protons of the dithioester end group at a chemical shift of 7.8 ppm and methyl protons of the acetoxy groups at 2.3 ppm (marked by the inverse triangle), respectively.[60] After hydrazinolysis, these two peaks disappeared and a new broad peak at 9.0 ppm, corresponding to the phenolic protons, was observed (marked by the inverse triangle, Figure 1b, DMSO-d_6). This observation indicates that both the reduction of the dithioester group to a secondary thiol and hydrolysis of

dx.doi.org/10.1021/ma202391k | *Macromolecules* 2012, 45, 1553−1561

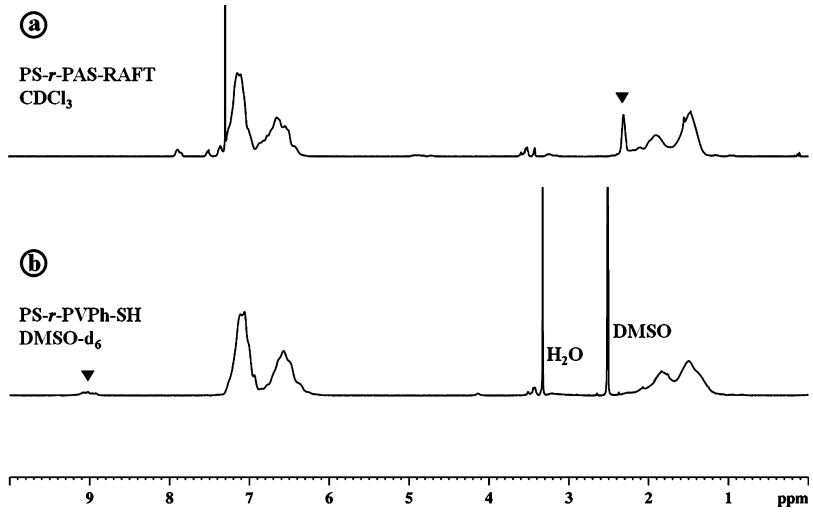


Figure 1. ^{1}H NMR spectra of a) poly(styrene-*ran*-acetoxystyrene) (PS_{22}-*r*-PAS_3-RAFT, $CDCl_3$) and b) thiol-terminated poly(styrene-*ran*-vinylphenol) (PS_{22}-*r*-$PVPh_3$-SH, DMSO-d_6) after hydrolysis of acetoxy groups and reduction of dithioester groups.

acetoxystyrene units to phenols are completed simultaneously by hydrazinolysis. The resulting PS_{22}-*r*-$PVPh_3$-SH copolymer was highly soluble in dichloromethane and toluene. On the other hand, the PS_{20}-*r*-$PVPh_7$-SH copolymer showed good solubility only in polar solvents such as THF and dimethylformamide. The synthesis of Au nanoparticles with PS_{22}-*r*-$PVPh_3$-SH copolymer ligands via the Brüst two-phase method, using toluene/water mixture, resulted in aggregated nanoparticles during the reduction of the Au precursor, maybe due to amphiphilicity of the random PS_{22}-*r*-$PVPh_3$-SH copolymer ligand. In contrast, synthesis of Au nanoparticles via the one-phase method in THF, under an argon atmosphere, was successful with no aggregated nanoparticles being observed for either copolymer. As expected, the Au nanoparticles covered with PS_{22}-*r*-$PVPh_3$-SH (PS_{22}-*r*-$PVPh_3$-S-Au) and PS_{20}-*r*-$PVPh_7$-SH (PS_{20}-*r*-$PVPh_7$−S-Au) ligands showed different solubility with the PS_{22}-*r*-$PVPh_3$-S-Au nanoparticles having high solubility in nonpolar solvents such as dichloromethane and toluene and the PS_{20}-*r*-$PVPh_7$−S-Au nanoparticles showing only limited solubility in the same solvents (about 2 mg/mL in dichloromethane).

Characterization of the PS_{22}-*r*-$PVPh_3$-S-Au nanoparticles by transmission electron microscopy (TEM) revealed their relatively narrow size distribution (histogram in the inset, see Supporting Information, Figure S2, for TEM image and size distribution of PS_{20}-*r*-$PVPh_7$−S-Au nanoparticles) with the average core diameter of the nanoparticles (d_{core}) being 3.4 ± 1.6 nm and the areal chain density of ligands on the nanoparticle surface (Σ), 1.0/nm^2 (Figure 2a). Similarly, characterization of the neat sphere-forming PS-*b*-P2VP diblock copolymer (107 kg/mol, with a mole fraction of 2VP units $f_{P2VP} \sim 0.11$) annealed in saturated dichloromethane vapor for 2 days shows regular spherical P2VP domains as dark spheres as a result of staining with iodine vapor (Figure 2b). Significantly, after adding a small volume fraction $\phi_p \sim 0.06$ of PS_{22}-*r*-$PVPh_3$-S-Au nanoparticles and solvent annealing in DCM, the nanoparticles in the PS-*b*-P2VP diblock copolymer were strongly segregated into the spherical P2VP domains as seen in Figures 2c,d. This strong segregation is due to the formation of multiple H-bonds between the large number of hydroxyl groups on the nanoparticle ligands and the pyridine rings of the 2VP units. There are about 145 phenolic hydroxyl groups per nanoparticle on average based on the number of ligands on each nanoparticle surface (see Supporting Information, Figure S3, characterized through a series of FT-IR spectra revealing multiple H-bonding formation). Synthesis of Au nanoparticles with thiol-terminated poly(styrene-*r*-acetoxystyrene) (PS-*r*-PAS-SH) ligands and investigation of their segregation behavior in PS-*b*-P2VP diblock copolymer domains are desirable as a control to further confirm the influence of hydrogen bonding on the segregation of nanoparticle. However, the synthesis of Au nanoparticles with PS-*r*-PAS-SH ligands is challenging due to difficulty in selective reduction of dithioester group without deprotection of the acetoxy groups along the backbone (see Supporting Information, Figure S4, showing deprotection of acetoxy group during reduction of dithioester and nanoparticle synthesis with superhydride). Synthesis of random copolymer ligands with polystyrene and *p*-methoxystyrene (PS-*r*-PMS-RAFT) may be an alternative way to avoid the formation of phenol group during synthesis of ligand and nanoparticles. However, the segregation behavior of the nanoparticles with PS-*r*-PMS-SH ligands cannot be directly compared to the nanoparticles with PS-*r*-PAS-SH.

A further increase in ϕ_p to 0.16 resulting in an increase in ϕ_{P+P2VP} to 0.24 and in the formation of disordered cylindrical P2VP domains (Figure 2e) with no macrophase separation of the nanoparticles from the diblock copolymer domains (Figure 2f). The morphology transition from spherical to cylindrical P2VP indicates that the Au nanoparticles have effects similar to those of a homopolymer with H-bonding donors, as demonstrated by Dobrosielska and Matsushita in the model system PS-*b*-P2VP and poly(4-hydroxystyrene).[21,22] However, the disordered cylindrical phases (Figures 1e,f) are novel and have not been observed when homopolymers are added to block copolymers. This new behavior may be due to the jamming of nanoparticles at high incorporation in the P2VP domains, such jamming of particles located at interface is known to induce metastable morphologies in the cases of immiscible polymer blends or immiscible liquids.[32,62−64]

The spatial distribution of homopolymer chains in block copolymer domains, which can control the morphology of block copolymer/homopolymer blends, is highly dependent on the relative size ratio of the block copolymer and the

dx.doi.org/10.1021/ma202391k | *Macromolecules* 2012, 45, 1553−1561

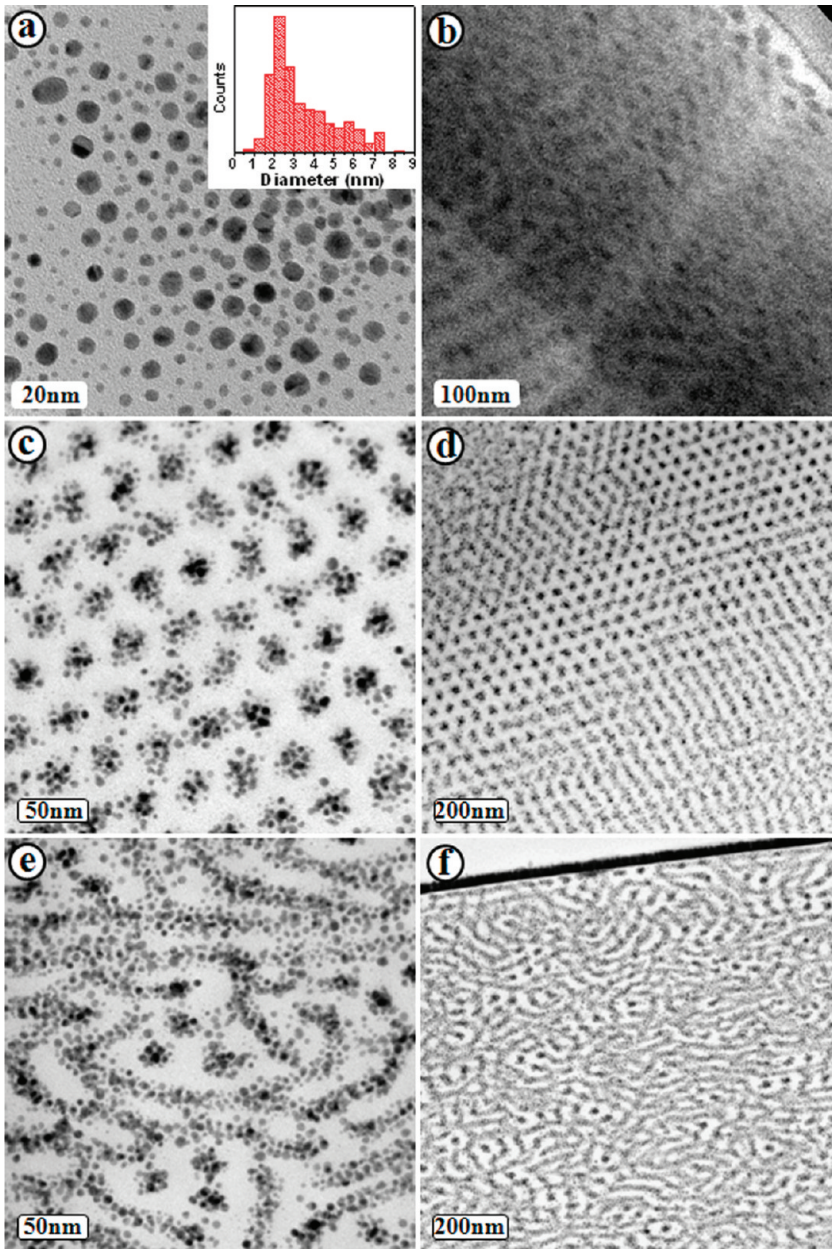


Figure 2. TEM micrographs of Au nanoparticles covered with PS-*r*-PVPh-SH ligands (PS_{22}-*r*-$PVPh_3$-S-Au) and their segregation in sphere-forming PS-*b*-P2VP diblock copolymer. (a) TEM micrograph of PS_{22}-*r*-$PVPh_3$-S-Au nanoparticles and a histogram showing their size distribution obtained from more than 300 nanoparticles by image analysis. Average diameter of nanoparticles (d_{core}) is 3.4 ± 1.6 nm. Areal chain density of ligands is ~1.0/nm^2. (b) Cross-sectional TEM micrograph of PS-*b*-P2VP diblock copolymer (107 kg/mol, $f_{P2VP} \sim 0.11$) annealed in saturated dichloromethane vapor for 2 days. P2VP domains stained by iodine vapor appear as black spheres. (c–f) Cross-sectional TEM micrographs of PS-*b*-P2VP/nanoparticle composites. The PS_{22}-*r*-$PVPh_3$-S-Au nanoparticles appearing as small black dots were strongly segregated into the spherical P2VP domains (c and d). Further increases in the volume fraction of nanoparticles (ϕ_p) resulted in the formation of disordered P2VP cylinders (e and f). A dark film on the top of the composite film in part f is a Au film deposited during the sample preparation for microsectioning to protect the composite sample from swelling by epoxy resin. ϕ_p values of c, d and e, f are 0.06 and 0.16, respectively.

homopolymer.[49−51] Homopolymers with significantly lower molecular weight than that of the host block of the block copolymer are distributed uniformly, which results in both uniform expansion of chemical junctions of block copolymer and the morphology transitions expected as the volume fraction of the host block and homopolymer increases. In contrast, homopolymers with higher molecular weight segregate to the center of the corresponding domains or are macrophase-separated. The same behavior has been observed from blending of diblock copolymer and homopolymers that have H-bonding interactions.[21,22] In order to characterize the distribution of homopolymers in such blends, small-angle X-ray scattering (SAXS) can be employed to track changes in domain spacing of block copolymer but offers only indirect evidence for the location of the homopolymer additive. An outstanding advantage of using nanoparticles instead of homopolymer is the inherent visibility of nanoparticles through TEM imaging allowing the distribution of nanoparticle additives within the block copolymer domains to be determined as shown in Figure 3. Parts a and b of Figure 3 are cross-sectional TEM

dx.doi.org/10.1021/ma202391k | *Macromolecules* 2012, 45, 1553−1561

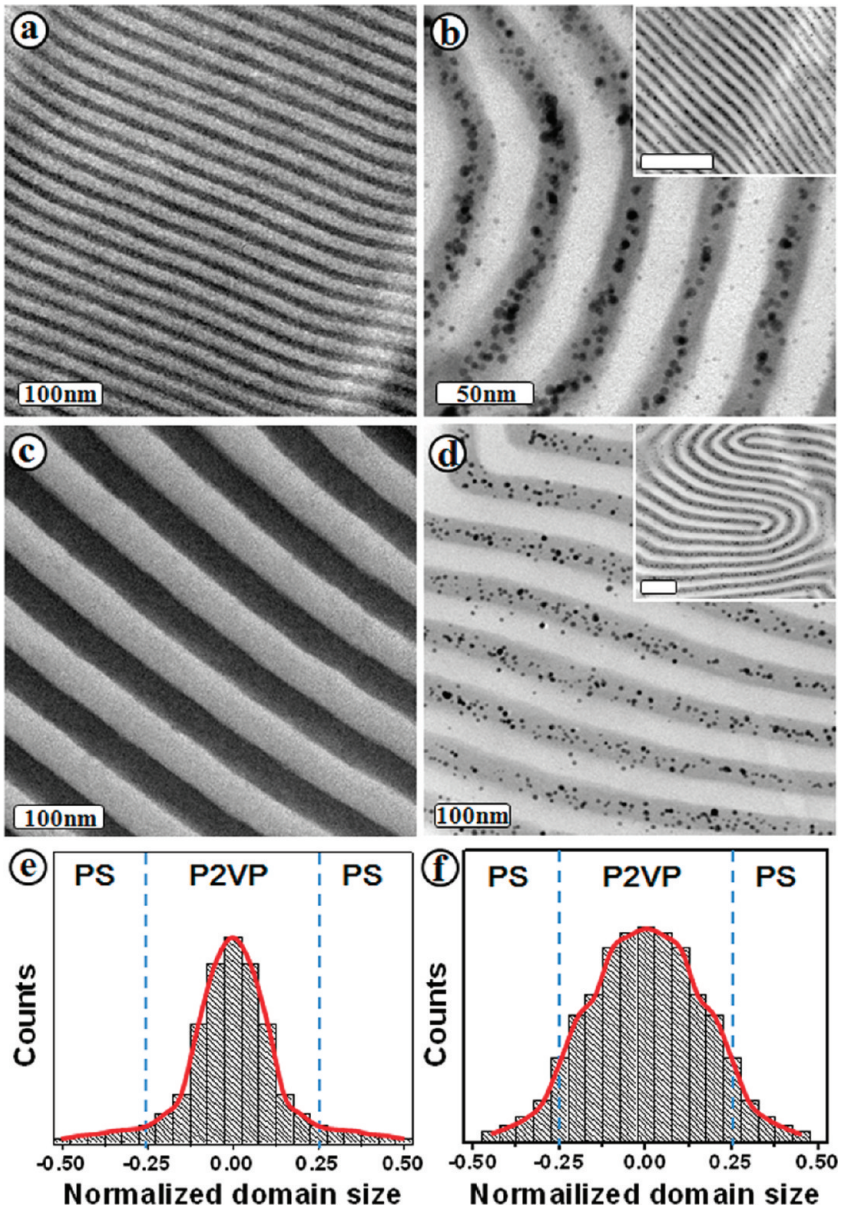


Figure 3. Cross-sectional TEM micrographs of lamellar PS-*b*-P2VP diblock copolymer: (a) 72 kg/mol ($f_{P2VP} \sim 0.40$) and (b) its composite with PS_{22}-*r*-$PVPh_3$-S-Au nanoparticles ($\phi_p \sim 0.04$). Cross-sectional TEM micrographs of lamellar PS-*b*-P2VP diblock copolymer (c) 199 kg/mol ($f_{P2VP} \sim 0.48$) and its composite with PS_{22}-*r*-$PVPh_3$-S-Au nanoparticles ($\phi_p \sim 0.04$). Inset images show lower magnification TEM micrographs of each sample. Histograms in parts e and f display the distribution of PS_{22}-*r*-$PVPh_3$-S-Au nanoparticles in the diblock copolymers shown in b and d, respectively. The normalized domain size refers to the distance of the nanoparticle from the center of the P2VP domain divided by the size of a single period of the structure formed by PS-*b*-P2VP. The blue dotted lines located at +0.25 and −0.25 represent the interfaces between PS and P2VP. PS_{22}-*r*-$PVPh_3$-S-Au nanoparticles were partially aggregated at the center of P2VP domains as shown in parts b and *e*. Meanwhile, the same nanoparticles were more homogeneously distributed in P2VP domains with larger molecular weight (d and f). Scale bars in the insets are 200 nm.

micrographs of PS-*b*-P2VP diblock copolymer (72 kg/mol, $f_{P2VP} \sim 0.40$) without and with PS_{22}-*r*-$PVPh_3$-S-Au nanoparticles, respectively. The lamellar morphology of the diblock copolymer in Figure 3a was preserved on the addition of PS_{22}-*r*-$PVPh_3$-S-Au nanoparticles with $\phi_p \sim 0.04$ (Figure 3b). Although some PS_{22}-*r*-$PVPh_3$-S-Au nanoparticles were observed in PS domains, a histogram in Figure 3e, obtained from image analysis of Figure 3b, clearly shows that most nanoparticles were segregated at the center of P2VP domains. This indicates that the size of PS_{22}-*r*-$PVPh_3$-S-Au nanoparticles, including polymeric ligands ($d_{core+ligand} \sim 6.8 \pm 2.2$ nm), is too large to be homogeneously distributed in P2VP domains having the comparable average equilibrium domain thickness measured from Figure 3a ($D_{P2VP,0} \sim 10$ nm). The average domain thickness of P2VP with PS_{22}-*r*-$PVPh_3$-S-Au nanoparticles (D_{P2VP+P}) in Figure 3b was significantly greater than the $D_{P2VP,0}$ in Figure 3a ($D_{P2VP+P}/D_{P2VP,0} \sim 1.5$), due to the confinement of nanoparticles at the center of P2VP domains and their corresponding expansion. Meanwhile, the domain thickness of PS remained the same upon addition of nanoparticles ($D_{PS}/D_{PS,0} \sim 1$), indicating that there is no expansion of the area per block copolymer chemical junction which would induce a morphology transition.[22,23,49] Interestingly, the same nanoparticles with $\phi_p \sim 0.04$ were more uniformly distributed in P2VP domains of a higher molecular weight PS-*b*-P2VP diblock copolymer (199 kg/mol, $f_{P2VP} \sim$

dx.doi.org/10.1021/ma202391k | *Macromolecules* 2012, 45, 1553–1561

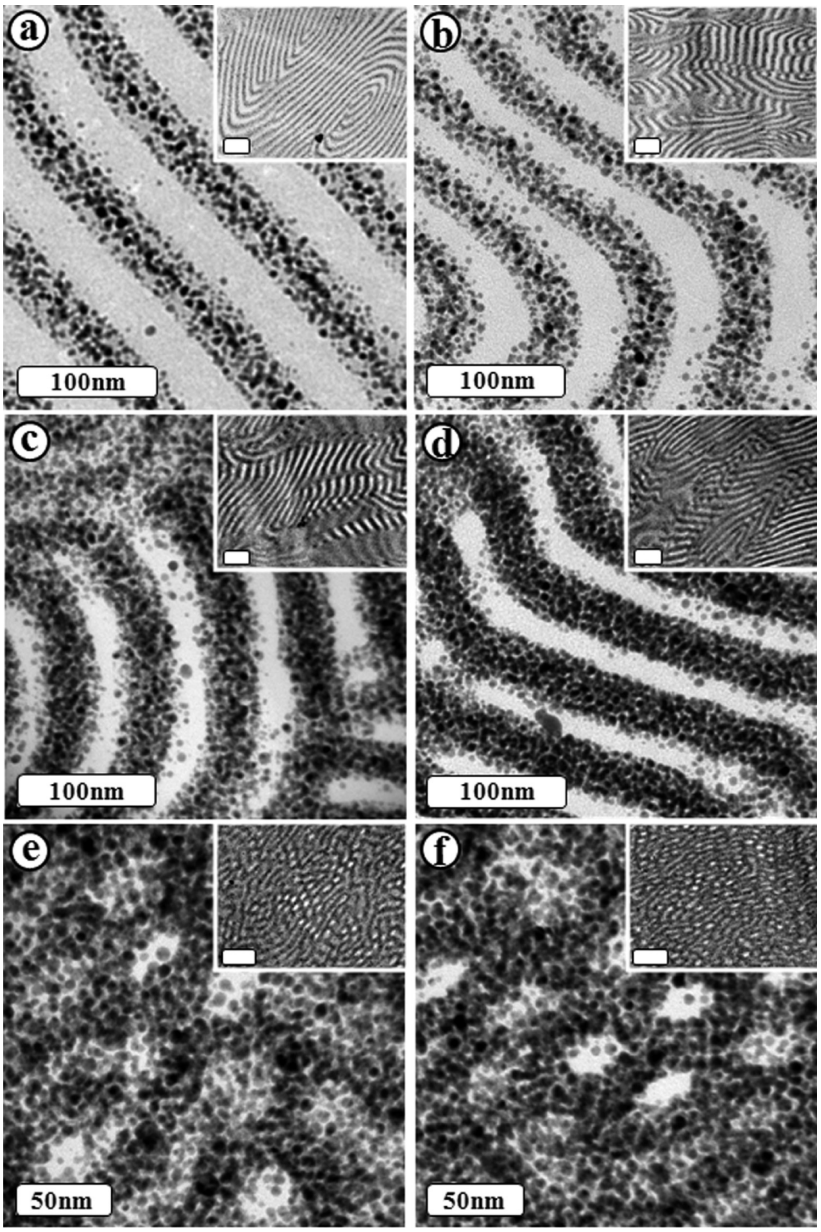


Figure 4. Cross-sectional TEM micrographs of lamellar PS-*b*-P2VP diblock copolymer (199 kg/mol, $f_{P2VP} \sim 0.48$) with various volume fractions of PS_{22}-*r*-$PVPh_3$-S-Au nanoparticles ϕ_p: (a) 0.08, (b) 0.16, (c) 0.21, (d) 0.32, (e) 0.42, and (f) 0.53. Inset images show a corresponding lower magnification TEM micrographs of each sample. Scale bars in the insets are 200 nm. The decrease in PS domain thickness by segregated nanoparticles is observed resulting from the increase in ϕ_p. The transition from lamellar to cylindrical PS was observed at $\phi_p \sim 0.32$. Calculated volume fractions of P2VP, including the volume of the nanoparticles, ϕ_{P+P2VP} are (a) 0.52, (b) 0.56, (c) 0.59, (d) 0.65, (e) 0.70, and (f) 0.76.

0.48, $M_{nP2VP} \sim 96$ kg/mol) as shown in the TEM micrograph (Figure 3d) and the histogram (Figure 3f). A decrease in average thickness of PS domains was observed upon addition of nanoparticles ($D_{PS}/D_{PS,0} \sim 0.8$) due to the expansion of chemical junctions of block copolymer chains at the interface and the corresponding relaxation of the stretched conformation of the PS chains. These results agree qualitatively with the observations from homopolymer/block copolymer blending experiments.

The decrease in average thickness for the PS domain upon addition of the PS_{22}-*r*-$PVPh_3$-S-Au nanoparticles demonstrates that morphology transitions for PS-*b*-P2VP diblock copolymer are possible by further increasing $\phi_{P+P2VP,}$ similar to that observed for uniformly distributed homopolymer in a diblock copolymer. Figure 4 shows a series of cross-sectional TEM micrographs of the PS-*b*-P2VP diblock copolymer (199 kg/mol, $f_{P2VP} \sim 0.48$) with various volume fractions (ϕ_p) ranging from 0.08 to 0.53 of PS_{22}-*r*-$PVPh_3$-S-Au nanoparticles including the volume of the ligands. Volume fraction values of the gold core on a ligand-free basis ($\phi_{P,\,core}$) for each samples in Figure 4, are (a) 0.02, (b) 0.03, (c) 0.04, (d) 0.06, (e) 0.09, and (f) 0.11. The PS_{22}-*r*-$PVPh_3$-S-Au nanoparticles are closely packed in P2VP domains regardless of ϕ_p, with no macrophase separation from block copolymer domains. The calculated volume fractions of P2VP domains, including the volume of the nanoparticles (ϕ_{P+P2VP}), are (a) 0.52, (b) 0.56, (c) 0.59, (d) 0.65, (e) 0.70, and (f) 0.76. As ϕ_{P+P2VP} increases, the lamellar structure was distorted more significantly (Figures 4a–c), and a morphological transition from one that is lamellar to one with PS cylinders was observed at $\phi_{P+P2VP} \sim 0.65$ (Figures 4d and

dx.doi.org/10.1021/ma202391k | *Macromolecules* 2012, 45, 1553–1561

4e). The long-range order of block copolymer domains was gradually suppressed upon increasing ϕ_{P+P2VP}, and finally a disordered PS cylindrical morphology was developed (Figure 4f). The variation of normalized lamellar domain thickness (D/D_0), which is the ratio of average PS (or P2VP) domain thickness D, at a volume fraction ϕ_p, to the average domain thickness D_0 for $\phi_p = 0$, is plotted versus the nanoparticle volume fraction ϕ_p in Figure 5. As reported for the polymer blend system,[23,49] the average domain thickness of PS was dramatically reduced compared to the original thickness without nanoparticle addition ($D/D_0 \sim 0.4$ at $\phi_p \sim 0.32$). Meanwhile, in contrast to the polymer blend cases that show significant swelling of the domains containing the homopolymer, the normalized domain thickness of P2VP was only slightly increased upon addition of nanoparticles. This slight increase in P2VP domain thickness may be due to the nonequilibrium structure of PS-*b*-P2VP as a result of nanoparticle jamming or due to a change in P2VP chain conformation filling the interstitial voids around the densely packed nanoparticles.

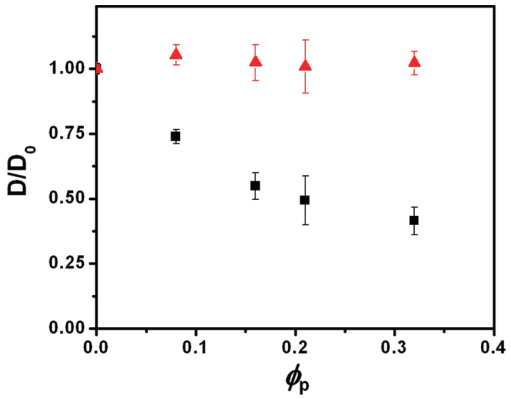


Figure 5. Normalized lamellar domain thickness (D/D_0) of PS (black squares) and P2VP (red triangles) versus the volume fraction of nanoparticles ϕ_p. The normalized domain thickness of PS decreased dramatically from the original thickness without addition of nanoparticles ($D/D_0 \sim 0.4$). Meanwhile, the average domain thickness of P2VP was slightly increased. Domain thicknesses were measured by TEM image analysis of Figures 3c and 4a–d. For accurate measurements, the samples were tilted to align the direction of the lamellar planes and electron beam of the microscope to reduce the broadening of interfaces caused by misalignment of the electron beam.

CONCLUSION

Au nanoparticles covered by PS-*r*-PVPh-SH ligands were designed to offer tunable supramolecular interactions through control of the number of phenolic groups while at the same time affording good solubility in nonpolar solvent via the styrenic repeat units. Through this design, H-bonding interactions with pyridine groups in PS-*b*-P2VP diblock copolymers can be maximized. The resulting PS_{22}-*r*-$PVPh_3$-S-Au nanoparticles showed high solubility in nonpolar solvents and strong segregation into P2VP domains while allowed a dramatic increase in the volume fraction of nanoparticles ($\phi_p \sim 0.53$) that could be blended without macrophase separation. The nanoparticles confined at the center of P2VP domains and the corresponding swelling of P2VP domains were clearly observed by TEM in the low molecular weight diblock copolymer (72 kg/mol, $f_{P2VP} \sim 0.40$). In contrast, the same nanoparticles were more homogeneously distributed in P2VP domains of a larger molecular weight diblock copolymer (199 kg/mol, $f_{P2VP} \sim 0.48$). Novel morphological transitions from spherical or lamellar to disordered cylindrical morphologies were observed as a result of strong segregation of nanoparticles into P2VP domains. These results clearly demonstrate the opportunities for nanoparticles with various functional cores (magnetic, catalytic, or fluorescent) to produce multifunctional composite materials with hierarchical nanostructures and high nanoparticle loading.

ASSOCIATED CONTENT

Supporting Information

^{1}H NMR spectra of PS_{22}-*r*-PAS_3-RAFT and PS_{20}-*r*-PAS_7-RAFT (Figure S1), TEM micrograph and size distribution of PS_{20}-*r*-$PVPh_7$–S-Au nanoparticles (Figure S2), FT-IR spectra revealing the formation of multiple H-bonding in composite (Figure S3), and ^{1}H NMR spectra showing deprotection of acetoxy groups during reduction of dithioester and nanoparticle synthesis with superhydride and cross-sectional TEM micrograph of Au–S–$PAS_{1.7}$-*r*-$PVPh_{1.3}$-*r*-PS_{22} nanoparticles in PS-*b*-P2VP microdomains (Figure S4). This material is available free of charge via the Internet at http://pubs.acs.org.

AUTHOR INFORMATION

Corresponding Author

*(C.J.H.) Telephone: 805-893-7161. Fax 805-893-8797. E-mail: hawker@mrl.ucsb.edu. (E.J.K.) Telephone: 805-893-4999. Fax: 805-893-8486. E-mail: edkramer@mrl.ucsb.edu.

ACKNOWLEDGMENTS

This work was supported by the MRSEC Program of the National Science Foundation (NSF) under Award DMR11-21053. Materials Research Laboratory Central Facilities are supported by the MRSEC Program of the NSF under Award DMR11-21053; a member of the NSF-funded Materials Research Facilities Network (www.mrfn.org).

REFERENCES

(1) Warren, S. C.; Messina, L. C.; Slaughter, L. S.; Kamperman, M.; Zhou, Q.; Gruner, S. M.; DiSalvo, F. J.; Wiesner, U. *Science* **2008**, *320*, 1748–1752.

(2) (a) Boyer, C.; Stenzel, M. H.; Davis, T. P. *J. Polym. Sci., Polym. Chem.* **2011**, *49*, 551–595. (b) Foster, E. J.; Berda, E. B.; Meijer, E. W. *J. Polym. Sci., Polym. Chem.* **2011**, *49*, 118–126. (c) Celiz, A. D.; Scherman, O. A. *J. Polym. Sci., Polym. Chem.* **2010**, *48*, 5833–5841. (d) Kurzhals, S.; Binder, W. H. *J. Polym. Sci., Polym. Chem.* **2010**, *48*, 5522–5532.

(3) Binder, W. H.; Zirbs, R. *Adv. Polym. Sci.* **2007**, *207*, 1–78.

(4) Zhao, Y.; Thorkelsson, K.; Mastroianni, A. J.; Schilling, T.; Luther, J. M.; Rancatore, B. J.; Matsunaga, K.; Jinnai, H.; Wu, Y.; Poulsen, D.; Frechet, J. M. J.; Alivisatos, A. P.; Xu, T. *Nat. Mat* **2009**, *8*, 979–985.

(5) Wojtecki, R. J.; Meador, M. A.; Rowan, S. J. *Nat. Mat.* **2011**, *10*, 14–27.

(6) Blaiszik, B. J.; Kramer, S. L. B.; Olugebefola, S. C.; Moore, J. S.; Sottos, N. R.; White, S. R. *Annu. Rev. Mat. Res.* **2010**, *40*, 79–211.

(7) Cordier, P.; Tournilhac, F.; Soulie-Ziakovic, C.; Leibler, L. *Nature* **2008**, *451*, 977–980.

(8) Feng, E. H.; Lee, W. B.; Fredrickson, G. H. *Macromolecules* **2007**, *40*, 693–702.

(9) Huh, J.; ten Brinke, G. *J. Chem. Phys.* **1998**, *109*, 789–797.

(10) Binder, W. H.; Bernstorff, S.; Kluger, C.; Petraru, L.; Kunz, M. J. *Adv. Mater.* **2005**, *17*, 2824–2828.

(11) Lee, W. B.; Elliott, R.; Katsov, K.; Fredrickson, G. H. *Macromolecules* **2007**, *40*, 8445−8454.
(12) Yang, X. W.; Hua, F. J.; Yamato, K.; Ruckenstein, E.; Gong, B.; Kim, W.; Ryu, C. Y. *Angew. Chem., Int. Ed.* **2004**, *43*, 6471−6474.
(13) Feldman, K. E.; Kade, M. J.; de Greef, T. F. A.; Meijer, E. W.; Kramer, E. J.; Hawker, C. J. *Macromolecules* **2008**, *41*, 4694−4700.
(14) Feldman, K. E.; Kade, M. J.; Meijer, E. W.; Hawker, C. J.; Kramer, E. J. *Macromolecules* **2010**, *43*, 5121−5127.
(15) Ruokolainen, J.; Makinen, R.; Torkkeli, M.; Makela, T.; Serimaa, R.; ten Brinke, G.; Ikkala, O. *Science* **1998**, *280*, 557−560.
(16) Ruokolainen, J.; Saariaho, M.; Ikkala, O.; ten Brinke, G.; Thomas, E. L.; Torkkeli, M.; Serimaa, R. *Macromolecules* **1999**, *32*, 1152−1158.
(17) Tang, C. B.; Lennon, E. M.; Fredrickson, G. H.; Kramer, E. J.; Hawker, C. J. *Science* **2008**, *322*, 429−432.
(18) Noro, A.; Matsushita, Y.; Lodge, T. P. *Macromolecules* **2008**, *41*, 5839−5844.
(19) Noro, A.; Matsushita, Y.; Lodge, T. P. *Macromolecules* **2009**, *42*, 5802−5810.
(20) Dobrosielska, K.; Takano, A.; Matsushita, Y. *Macromolecules* **2010**, *43*, 1101−1107.
(21) Dobrosielska, K.; Wakao, S.; Takano, A.; Matsushita, Y. *Macromolecules* **2008**, *41*, 7695−7698.
(22) Dobrosielska, K.; Wakao, S.; Suzuki, J.; Noda, K.; Takano, A.; Matsushita, Y. *Macromolecules* **2009**, *42*, 7098−7102.
(23) (a) Chen, S. C.; Kuo, S. W.; Jeng, U. S.; Su, C. J.; Chang, F. C. *Macromolecules* **2010**, *43*, 1083−1092. (b) Tirumala, V. R.; Romang, A.; Agarwal, S.; Lin, E. K.; Watkins, J. J. *Adv. Mater.* **2008**, *20*, 1603−1608. (c) Tirumala, V. R.; Daga, V.; Bosse, A. W.; Romang, A.; Ilavsky, J.; Lin, E. K.; Watkins, J. J. *Macromolecuels* **2008**, *41*, 7978−7985.
(24) Bockstaller, M. R.; Thomas, E. L. *J. Phys. Chem. B* **2003**, *107*, 10017−10024.
(25) Cheng, J. Y.; Ross, C. A.; Chan, V. Z. H.; Thomas, E. L.; Lammertink, R. G. H.; Vancso, G. J. *Adv. Mater.* **2001**, *13*, 1174−1178.
(26) Jaramillo, T. F.; Baeck, S. H.; Cuenya, B. R.; McFarland, E. W. *J. Am. Chem. Soc.* **2003**, *125*, 7148−7149.
(27) Mui, S. C.; Trapa, P. E.; Huang, B.; Soo, P. P.; Lozow, M. I.; Wang, T. C.; Cohen, R. E.; Mansour, A. N.; Mukerjee, S.; Mayes, A. M.; Sadoway, D. R. *J. Electrochem. Soc.* **2002**, *149*, A1610−A1615.
(28) Jang, S. G.; Khan, A.; Dimitriou, M. D.; Kim, B. J.; Lynd, N. A.; Kramer, E. J.; Hawker, C. J. *Soft Matter* **2011**, *7*, 6255−6263.
(29) Bockstaller, M. R.; Thomas, E. L. *Phys. Rev. Lett.* **2004**, *93*, 166106.
(30) Chiu, J. J.; Kim, B. J.; Kramer, E. J.; Pine, D. J. *J. Am. Chem. Soc.* **2005**, *127*, 5036−5037.
(31) Chiu, J. J.; Kim, B. J.; Yi, G. R.; Bang, J.; Kramer, E. J.; Pine, D. J. *Macromolecules* **2007**, *40*, 3361−3365.
(32) Chung, H.; Ohno, K.; Fukuda, T.; Composto, R. J. *Nano Lett.* **2005**, *5*, 1878−1882.
(33) (a) Kang, H.; Detcheverry, F. A.; Mangham, A. N.; Stoykovich, M. P.; Daoulas, K. C.; Hamers, R. J.; Muller, M.; de Pablo, J. J.; Nealey, P. F. *Phys. Rev. Lett.* **2008**, *100*, 148303. (b) Kuila, B. K.; Rama, M. S.; Stamm, M. *Adv. Mater.* **2011**, *23*, 1797−1800. (c) Daga, V. K.; Watkins, J. J. *Macromolecules* **2010**, *43*, 9990−9997. (d) Daga, V. K.; Anderson, E. R.; Gido, S. P.; Watkins, J. J. *Macromolecules* **2011**, *44*, 6793−6799. (e) Sary, N.; Richard, F.; Brochon, C.; Leclerc, N.; Leveque, P.; Audinot, J. N.; Berson, S.; Heiser, T.; Hadziioannou, G.; Mezzenga, R. *Adv. Mater.* **2010**, *22*, 763−768.
(34) Kim, B. J.; Bang, J.; Hawker, C. J.; Chiu, J. J.; Pine, D. J.; Jang, S. G.; Yang, S. M.; Kramer, E. J. *Langmuir* **2007**, *23*, 12693−12703.
(35) Kim, B. J.; Bang, J.; Hawker, C. J.; Kramer, E. J. *Macromolecules* **2006**, *39*, 4108−4114.
(36) Kim, B. J.; Chiu, J. J.; Yi, G. R.; Pine, D. J.; Kramer, E. J. *Adv. Mater.* **2005**, *17*, 2618−2622.
(37) Kim, B. J.; Fredrickson, G. H.; Hawker, C. J.; Kramer, E. J. *Langmuir* **2007**, *23*, 7804−7809.
(38) Kim, B. J.; Fredrickson, G. H.; Kramer, E. J. *Macromolecules* **2008**, *41*, 436−447.
(39) Park, S. C.; Kim, B. J.; Hawker, C. J.; Kramer, E. J.; Bang, J.; Ha, J. S. *Macromolecules* **2007**, *40*, 8119−8124.
(40) Kim, J.; Green, P. F. *Macromolecules* **2010**, *43*, 10452−10456.
(41) Hickey, R. J.; Sanchez-Gaytan, B. L.; Cui, W. H.; Composto, R. J.; Fryd, M.; Wayland, B. B.; Park, S. J. *Small* **2010**, *6*, 48−51.
(42) Costanzo, P. J.; Beyer, F. L. *Macromolecules* **2007**, *40*, 3996−4001.
(43) Böker, A.; Lin, Y.; Chiapperini, K.; Horowitz, R.; Thompson, M.; Carreon, V.; Xu, T.; Abetz, C.; Skaff, H.; Dinsmore, A. D.; Emrick, T.; Russell, T. P. *Nat. Mat.* **2004**, *3*, 302−306.
(44) Hu, Y. X.; Chen, D. A.; Park, S.; Emrick, T.; Russell, T. P. *Adv. Mater.* **2010**, *22*, 2583−2587.
(45) Bockstaller, M. R.; Mickiewicz, R. A.; Thomas, E. L. *Adv. Mater.* **2005**, *17*, 1331−1349.
(46) Balazs, A. C.; Emrick, T.; Russell, T. P. *Science* **2006**, *314*, 1107−1110.
(47) Huh, J.; Ginzburg, V. V.; Balazs, A. C. *Macromolecules* **2000**, *33*, 8085−8096.
(48) Tanaka, H.; Hasegawa, H.; Hashimoto, T. *Macromolecules* **1991**, *24*, 240−251.
(49) Hashimoto, T.; Tanaka, H.; Hasegawa, H. *Macromolecules* **1990**, *23*, 4378−4386.
(50) Semenov, A. N. *Macromolecules* **1993**, *26*, 2273−2281.
(51) Torikai, N.; Takabayashi, N.; Noda, I.; Koizumi, S.; Morii, Y.; Matsushita, Y. *Macromolecules* **1997**, *30*, 5698−5703.
(52) Mayes, A. M.; Russell, T. P.; Satija, S. K.; Majkrzak, C. F. *Macromolecules* **1992**, *25*, 6523−6531.
(53) Kim, B. J.; Fredrickson, G. H.; Bang, J.; Hawker, C. J.; Kramer, E. J. *Macromolecules* **2009**, *42*, 6193−6201.
(54) Yeh, S. W.; Chang, Y. T.; Chou, C. H.; Wei, K. H. *Macromol. Rapid Commun.* **2004**, *25*, 1680−1686.
(55) Lin, Y.; Daga, V. K.; Anderson, E. R.; Gido, S. P.; Watkins, J. J. *J. Am. Chem. Soc.* **2011**, *133*, 6513−6516.
(56) Li, Q. F.; He, J. B.; Glogowski, E.; Li, X. F.; Wang, J.; Emrick, T.; Russell, T. P. *Adv. Mater.* **2008**, *20*, 1462−1466.
(57) Yeh, S. W.; Wei, K. H.; Sun, Y. S.; Jeng, U. S.; Liang, K. S. *Macromolecules* **2003**, *36*, 7903−7907.
(58) Drockenmuller, E.; Li, L. Y. T.; Ryu, D. Y.; Harth, E.; Russell, T. P.; Kim, H. C.; Hawker, C. J. *J. Polym. Sci., Polym. Chem.* **2005**, *43*, 1028−1037.
(59) Perrier, S.; Takolpuckdee, P. *J. Polym. Sci., Polym. Chem.* **2005**, *43*, 5347−5393.
(60) Lee, C. U.; Roy, D.; Sumerlin, B. S.; Dadmun, M. D. *Polymer* **2010**, *51*, 1244−1251.
(61) Yee, C. K.; Jordan, R.; Ulman, A.; White, H.; King, A.; Rafailovich, M.; Sokolov, J. *Langmuir* **1999**, *15*, 3486−3491.
(62) Cates, M. E.; Clegg, P. S. *Soft Matter* **2008**, *4*, 2132−2138.
(63) Herzig, E. M.; White, K. A.; Schofield, A. B.; Poon, W. C. K.; Clegg, P. S. *Nat. Mat.* **2007**, *6*, 966−971.
(64) Stratford, K.; Adhikari, R.; Pagonabarraga, I.; Desplat, J. C.; Cates, M. E. *Science* **2005**, *309*, 2198−2201.

Macromolecules

Article

pubs.acs.org/Macromolecules

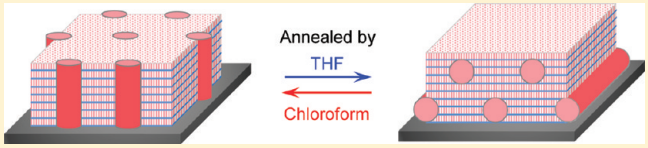
Effects of Annealing Solvents on the Morphology of Block Copolymer-Based Supramolecular Thin Films

Wei-Han Huang, Po-Yu Chen, and Shih-Huang Tung*

Institute of Polymer Science and Engineering, National Taiwan University, Taipei, 10617 Taiwan

Supporting Information

ABSTRACT: We report a strategy that combines supramolecular assembly and solvent annealing to manipulate the microdomain orientation in block copolymer thin films. In supramolecular thin films formed by polystyrene-*b*-poly(4-vinylpyridine) (PS-*b*-P4VP) with 3-pentadecylphenol (PDP) hydrogen-bonded onto P4VP blocks, where PS blocks phase-separate into cylindrical microdomains, we found that the orientation of PS cylinders can be controlled by using different types of solvents to anneal the films. As films are annealed under the vapors of solvents bearing no oxygen atoms, such as chloroform, PS cylinders are perpendicular to the surface, while under those of solvents bearing oxygen, such as THF, PS cylinders are parallel to the surface. Furthermore, the orientation is switchable upon the alternate use of different types of solvents. The ^{1}H NMR measurements showed that the strengths of hydrogen bonds between PDP and P4VP are greatly weakened in oxygen-bearing solvents due to the competition of the highly electronegative oxygen atoms. We thus suggest that the binding capability of PDP onto P4VP is the key to determine whether the supramolecules can be assembled in the vapors of different types of solvents, which in turn, regulates the orientation of PS cylinders.



INTRODUCTION

Block copolymers formed by covalently linked incompatible homopolymers phase-separate into a variety of nanoscaled microdomains, typically spherical, cylindrical, lamellar, and gyroidal.[1] For block copolymers with narrow distribution of molecular weights and under proper thermal treatments, the microdomains can be packed in a highly ordered manner, which is an effective technique for manipulating structures in nanoscale. In bulk samples, however, the orders are limited in grains and the grains are usually joined randomly, such that the overall properties are still isotropic. When block copolymers are fabricated into thin films with nanoscaled thicknesses, the effects of two additional interactions become significant, namely the polymer−substrate and polymer−air interactions.[2] The phase that interacts most strongly with the substrate prefers to stick on the substrate while the phase with the lowest surface tension tends to expose to air. Both forces regulate the alignments of the microdomains and when the thicknesses of films are thinner than the influential range of the interactions, the microdomains in the entire films will be forced to be oriented along the direction of thickness. In most cases, the cylindrical or lamellar microdomains prefer to be parallel to the surface.

The search of the approaches to obtain perpendicular microdomains in thin films has been an emerging topic recently due to its scientific merit and application potency.[3−7] To do so, the above-mentioned two interactions need be eliminated or overcome, which has been achieved by surface modifications,[3,8−15] external stimuli,[16,17] and nonequilibrium approaches.[18−21] Another strategy that has been proven to be efficient is the supramolecular assembly.[22−27] The supramolecules are formed by block copolymers with small molecules associated with one of the blocks via weak secondary bonds.[28−31] One major effect of the small molecules is that they alter the relative volume fraction of each component, therefore causing a morphological transition and creating a variety of hierarchical structures. In addition, it has been shown that there is a strong correlation between the microdomain orientation in thin films and the content of the associated small molecules.[23−26] In general, at sufficiently high ratio of small molecules, the orientation is driven to be perpendicular. This is a simple approach to tailor the microdomain orientation in block copolymer thin films since the amount of weakly bonded small molecules can be adjusted by physical means rather than chemical reaction.

Solvent annealing is usually adopted to replace thermal annealing for processing supramolecular thin films since small molecules may evaporate at high temperature and a tiny amount loss of small molecules would result in a great structural change in such thin films.[24] Different from thermal annealing, solvent molecules are extra components introduced into films and the final morphology may thus be affected by the interplays between solvents and polymers, which on one hand complicates the structural analysis and on the other hand provides opportunities to create structures that cannot be achieved by thermal annealing.[32] It has been shown that the type of solvents used for annealing plays an important role in the morphology of block copolymer thin films.[33−35] For

Received: October 31, 2011
Revised: January 1, 2012
Published: January 18, 2012

 © 2012 American Chemical Society dx.doi.org/10.1021/ma202415t | *Macromolecules* 2012, 45, 1562−1569

supramolecular thin films, the effects of annealing solvents on the morphology of polystyrene-*b*-poly(4-vinylpyridine) (PS-*b*-P4VP) with 2-(4′-hydroxybenzeneazo) benzoic acid (HABA) molecules have been reported by Minko and co-workers.[22,36,37] They found that as films were annealed by chloroform, the P4VP(HABA) cylindrical microdomains were parallel to the surface, while annealed by 1,4-dioxane, the cylinders were perpendicular to the surface, which was attributed to the different selectivity of the solvents to each phase. The previous discussions of block copolymer-based supramolecules have been generally under the presumption that the small molecules are firmly grafted on the polymer chains. However, it should be aware that the lifetimes of secondary weak bonds are much shorter than that of covalent bonds and the strength of weak interactions is subject to the influence of environments. It has been shown that hydrogen bonds, through which most supramolecules are formed, would be weakened in the presence of additional molecules with strong electronegative atoms, such as oxygen and nitrogen.[38,39] In other words, the solvents that diffuse into thin films may interfere with the original interactions in supramolecules.

For the widely studied supramolecular thin films formed by PS-*b*-P4VP with hydrogen-bonded small molecule 3-pentadecylphenol (PDP), as shown in Figure 1, the structures were usually characterized after annealing in the vapor of chloroform.[24−26,40−42] In this paper, we systematically investigated the effects of annealing solvents on the morphology of PS-*b*-P4VP(PDP) supramolecular thin films. We divide the solvents into two groups: one group contains no oxygen atom on their chemical structures, i.e., nonoxygen-bearing solvents, and the other group contains oxygen atoms, i.e., oxygen-bearing solvents. The oxygen atom is highly electronegative and capable of forming hydrogen bonds. The solvents and their properties are listed in Table 1. The classification is based on the fact that the morphologies of supramolecular thin films annealed by the solvents in each group are similar. However, nonoxygen-bearing solvents cause the PS cylindrical microdomains oriented perpendicularly while oxygen-bearing solvents lead to parallel alignment. Furthermore, the orientation is switchable when films are alternately annealed by the solvents in different groups. We provide a mechanism originated from the strengths of hydrogen bonds in the presence of different types of solvents to explain why this facile approach can be used to control the orientation of block copolymer thin films.

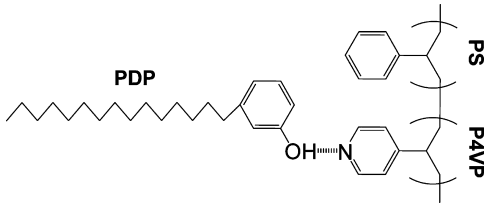


Figure 1. Chemical structure of PS-*b*-P4VP(PDP) supramolecules.

EXPERIMENTAL SECTION

Materials. PS-*b*-P4VP with $M_{n,PS}$ = 20000, $M_{n,P4VP}$ = 17000 g/mol, and PDI = 1.08 was purchased from Polymer Source Inc. P4VP homopolymer with M_w = 60000 g/mol and 3-*n*-pentadecylphenol (PDP) (95% purity) were purchased from Sigma-Aldrich. Chloroform, benzene and *n*-hexane were purchased from Sigma-Aldrich; toluene, tetrahydrofuran (THF) and *N*,*N*-dimethylformamide (DMF) were purchased from Mallinckrodt Chemicals; methanol and ethanol were purchased from ECHO chemicals; 1,4-dioxane was purchased from J.T. Baker. All the deuterated solvents used for ^{1}H NMR measurements were purchased from Sigma-Aldrich. All chemicals were used as received.

Sample Preparation. PS-*b*-P4VP was first dissolved in chloroform to form 1−2% (w/v) stock solutions. PDP in a 1:1 molar ratio to 4VP unit was also dissolved in chloroform. The PS-*b*-P4VP solution was then added dropwise to the PDP solution, followed by stirring for at least 1 week to ensure PDP molecules are hydrogen-bonded with P4VP. Thin films were prepared by spin-coating the mixed solutions onto silicon wafers at spinning speed 3000 rpm. Sample thicknesses were measured using a Filmetrics F20 interferometer. For solvent annealing, thin films were placed together with a beaker of 40 mL solvents inside an inverted dish (170 Diam × 90 H mm) on a hot plate which heated up the solvents to 30 °C. Thin films were annealed for 48 h. After annealing, the inverted dish was immediately removed and solvents were allowed to freely evaporate.

AFM and TEM Imaging. Atomic force microscopy (AFM) was performed on a MultiMode AFM system with a Nanoscope 3D controller (Digital Instruments) in tapping mode. The spring constant of the cantilever (Nanosensor PPP-NCHR) was ∼42 N/m and the resonant frequency was ∼330 kHz. To prepare thin film samples for cross-sectional transmission electron microscope (TEM) imaging, a thin layer of platinum was sputtered onto the surfaces of thin films and then the films were attached to epoxy resin and cured at room temperature for 2 weeks. The substrates were peeled off from the embedded films after the cured epoxy cubes were dipped into liquid nitrogen. The embedded films were then microtomed at room temperature. The thin sections, ∼ 80 nm in thickness, were exposed to iodine vapor for 2 h that selectively stains the P4VP blocks to enhance the contrast. TEM images were collected on a Joel JEM-1230 transmission electron microscope at an accelerating voltage of 100 kV.

GISAXS. Grazing incidence small-angle X-ray scattering (GISAXS) was conducted on beamline BL23A1 in the National Synchrotron Radiation Research Center (NSRRC), Taiwan.[43] A monochromatic

Table 1. Properties of Solvents and Resulting Thin Film Structures[a]

	Nonoxygen-bearing			Oxygen-bearing		
	Toluene	Benzene	Chloroform	THF	1,4-Dioxane	DMF
						
Solubility parameter (MPa$^{1/2}$)[44]	18.2	18.8	19.0	18.6	20.5	24.8
Boiling point (°C)[44]	111	80	61	66	102	153
Soluble components	PS, PDP	PS, PDP	PS, P4VP, PDP	PS, PDP	PS, PDP	P4VP, PDP
Orientation of PS cylinders	⊥	⊥	⊥	∥	∥	∥
Spacing of PS cylinders (nm)	35.3	35.3	35.7	33.6	34.7	32.1
Spacing of P4VP(PDP) lamellae (nm)	3.9	3.9	3.7	3.8	3.7	3.9

[a]Key: (∥) parallel to the surface; (⊥) perpendicular to the surface. See ref 44 for solubility and BP data.

dx.doi.org/10.1021/ma202415t | *Macromolecules* 2012, 45, 1562−1569

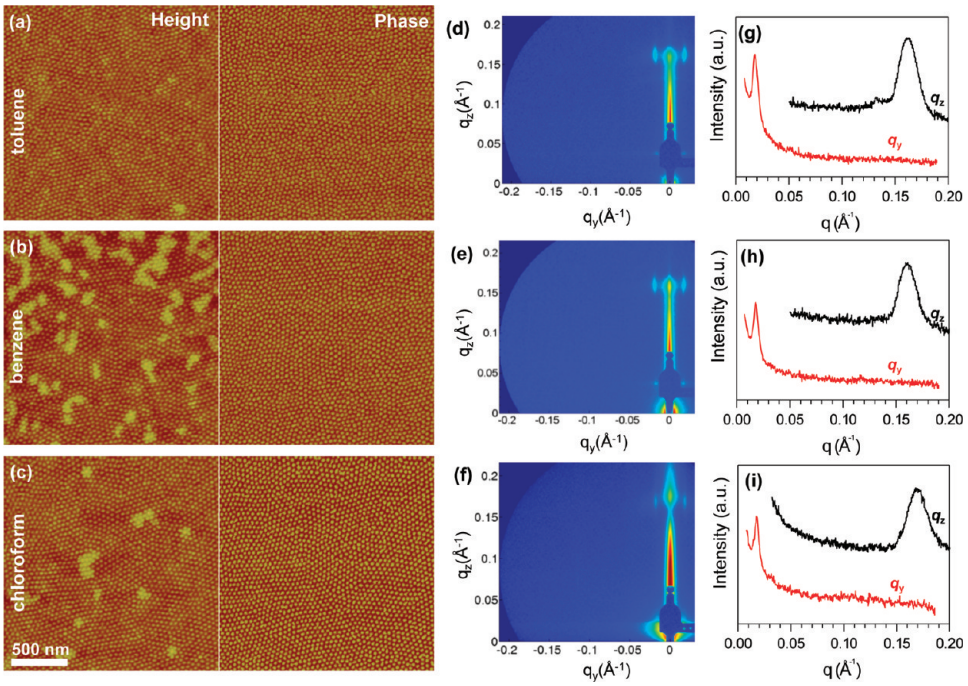


Figure 2. Structure characterization of thin films annealed by nonoxygen-bearing solvents: (a–c) AFM images, (d–f) 2-D GISAXS patterns, and (g–i) q_y and q_z scans from 2D-GISAXS patterns. (a, d, g) a ~ 41 nm thin film annealed by toluene, (b, e, h) a ~ 42 nm thin film annealed by benzene, (c, f, i) a ~ 50 nm thin film annealed by chloroform. The q_y scans were extracted at q_z = 0.160 Å^{-1} and the q_z scans were extracted at q_y = 0.018 Å^{-1}.

beam of λ = 1.240 Å was used and the incident angle was 0.2°. The scattering patterns were collected on a Mar-CCD with a diameter of 165 mm. The scattering intensity profiles were reported as the plots of the scattering intensity I vs the scattering vector q, where $q = (4\pi/\lambda)\sin(\theta/2)$ and θ is the scattering angle.

^{1}H NMR. Samples for ^{1}H NMR measurements were prepared by dissolving PDP, PS-*b*-P4VP, and PS-*b*-P4VP(PDP) in dueterated solvents, respectively, at a concentration ~0.25% (wt/v). The measurements were conducted on a Bruker DPX 400 MHz system.

RESULTS AND DISCUSSION

PS-*b*-P4VP which contains approximately symmetric blocks phase-separates into lamellar structures and when spun-cast into thin films on silicon substrate, the surface morphology probed by AFM is featureless due to the parallel lamellae driven by the preferential interaction between P4VP blocks and substrate and the lower surface tension of PS blocks that reduces the surface free energy at film–air interfaces. Upon the addition of PDP in a molar ratio of 1.0 to 4VP unit, the weight fraction of P4VP(PDP) complex in the supramolecules, denoted as PS-*b*-P4VP(PDP), is 76.8 wt %. For such supramolecules, PS blocks form cylinders embedded in P4VP(PDP) matrix where P4VP(PDP) complexes stack into small lamellae with a spacing ~4 nm, i.e., a cylinder-within-lamella hierarchical structure, as reported in our previous paper.[26]

Morphology Caused by Nonoxygen-Bearing Solvents. We first present the thin film morphologies of the supramolecules annealed by nonoxygen-bearing solvents, whose solubility parameters are usually low, as listed in Table 1. Figure 2a–c shows the AFM images of thin films, 40–50 nm in thickness, annealed in toluene, benzene, and chloroform vapors, respectively. The surface morphologies of the three samples are similar, all showing hexagonally packed dots. Such patterns imply that PS cylinders are oriented perpendicular to the surface and the dots are the cross sections of PS cylinders. To further verify the structures inside the films, the cross-sectional TEM image of a representative film, ~ 65 nm in thickness, annealed by chloroform was taken, as shown in Figure 3a. The deep black layer is the sputtered platinum and the original film–air interface is next to the platinum. The darker regions are P4VP(PDP) matrix due to the staining of iodine and the brighter pillars across the film are PS cylinders, which confirms the formation of perpendicular cylinders.

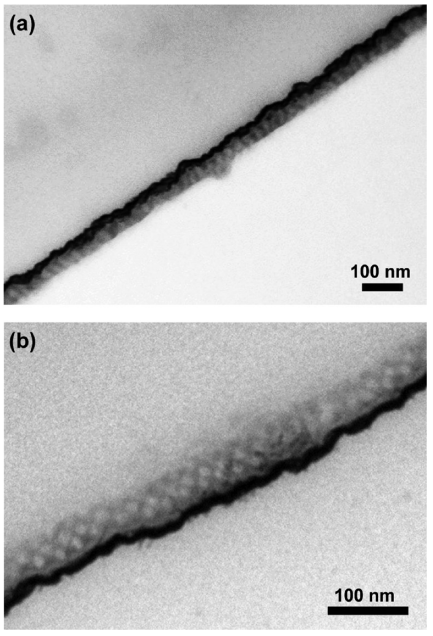


Figure 3. Cross-sectional TEM images of ~65 nm thin films annealed by (a) chloroform, a nonoxygen-bearing solvent, and (b) THF, an oxygen-bearing solvent.

dx.doi.org/10.1021/ma202415t | *Macromolecules* 2012, 45, 1562–1569

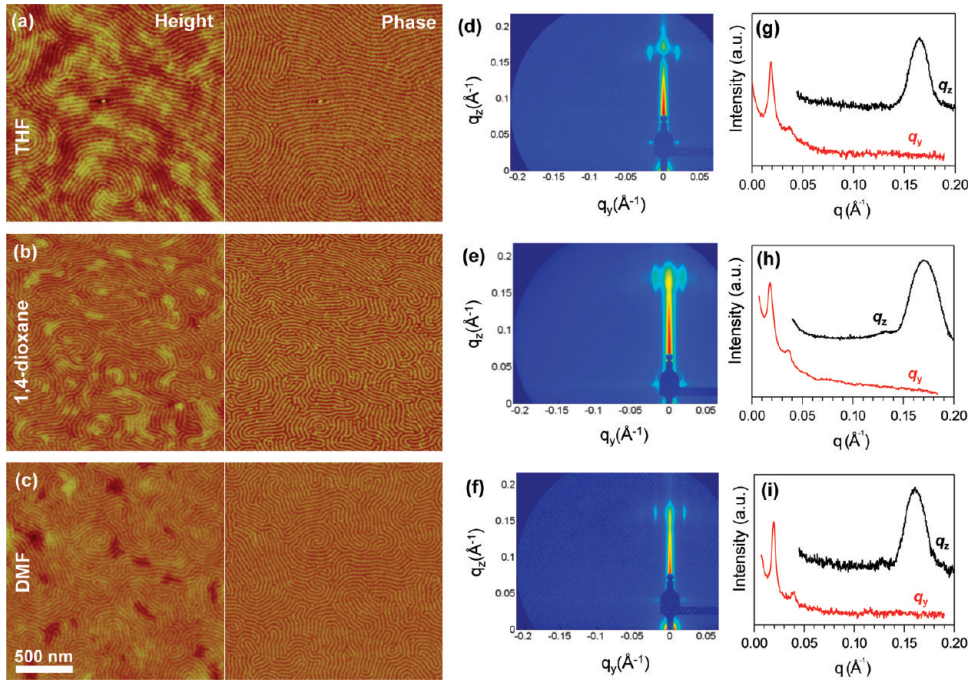


Figure 4. Structure characterization of thin films annealed by oxygen-bearing solvents: (a–c) AFM images, (d–f) 2-D GISAXS patterns, and (g–i) q_y and q_z scans from 2D-GISAXS patterns. (a, d, g) a ~ 46 nm thin film annealed by THF, (b, e, h) a ~ 41 nm thin film annealed by 1,4-dioxane, (c, f, i) a ~ 41 nm thin film annealed by DMF. The q_y scans were extracted at q_z = 0.160 Å^{-1} and the q_z scans were extracted at q_y = 0.019 Å^{-1}.

The GISAXS data of the three films are displayed in Figure 2d–i. All the 2D-patterns (Figure 2d–f) show that diffraction spots appear along both q_y and q_z axes, and the diffraction spots in q_y direction are at lower q, i.e., the large-scaled PS cylinders are perpendicular to the surface, while the diffraction spots in q_z direction are at higher q, i.e., the small-scaled P4VP(PDP) lamellae are parallel to the surface. Note that perpendicular cylinders normally show diffraction rods in q_y direction around the baseline slightly above q_z = 0.[7] However, in the present case, the diffraction spots in q_y direction at q_z ~ 0.16 Å^{-1} are stronger than those around the baselines at q_z ~ 0.03 Å^{-1}. This is because the diffraction beams produced by PS cylinders that are supposed to give bright rods on the baseline now serve as incident beams for small P4VP(PDP) lamellae and the "incident" beams are scattered again by the small lamellae to form the strong diffraction spots at q_z ~ 0.16 Å^{-1}. Similar GISAXS patterns have been found in other studies dealing with PS-*b*-P4VP(PDP) system.[24−26] q_y and q_z scans retrieved from the 2-D patterns are shown in Figure 2g-I, where the q_y scans were extracted at q_z = 0.160 Å^{-1} and the q_z scans were extracted at q_y = 0.018 Å^{-1}. The spacings of PS cylinders for the three solvents estimated from q_y scans are in the range of 35–36 nm and the spacings of small P4VP(PDP) lamellae estimated from q_z scans are 3.7–3.9 nm. The detailed data are listed in Table 1. Note that as shown in the AFM height images, particularly in parts b and c of Figure 2, islands are seen on the surfaces, with a small height ~3–4 nm close to the spacing of P4VP(PDP) lamellae. Such a terrace topography also confirms that P4VP(PDP) lamellae are oriented parallel to the surface.[42]

By combining the results of AFM, TEM and GISAXS, it is evidenced that in the vapors of nonoxygen-bearing solvents, PS cylinders in PS-*b*-P4VP(PDP) thin films are perpendicular to the surface while P4VP(PDP) lamellae are parallel to the surface, as illustrated in Figure 5a. It has been known that the orientation of microdomains in block copolymer thin films is dependent on film thickness. If the thickness and the nature period of microdomains are incommensurate, a perpendicular alignment may occur.[45] In the present case and other studies,[24−26] a series of thicknesses have been examined and the perpendicular microdomains were consistently observed, indicating that the perpendicular PS cylinders are not caused by the variation of film thickness.

Morphology Caused by Oxygen-Bearing Solvents. For thin films annealed in the vapors of oxygen-bearing solvents, the surface patterns are completely different from those annealed by nonoxygen-bearing solvents. Figure 4a–c show the AFM images of PS-*b*-P4VP(PDP) thin films, 40–50 nm in thickness, annealed by THF, 1,4-dioxane, and DMF, respectively. All the thin films show fingerprint-like patterns, which are typical of cylindrical microdomains parallel to the surface. A representative cross-sectional TEM of a film, ~ 65 nm in thickness, annealed by THF is shown in Figure 3b, where hexagonally packed dots are clearly seen. The dots are the cross sections of the parallel PS cylinders. On the surfaces shown in the AFM height images (Figure 4a–c), the formation of islands or holes with heights or depths ~3–4 nm implies that similar to thin films annealed by nonoxygen-bearing solvents, the small P4VP(PDP) lamellae here are also parallel to the surface.

The GISAXS data of thin films annealed by THF, 1,4-dioxane, and DMF are shown in Figure 4d–i. In the 2D patterns (Figure 4d–f), clear diffraction spots can be seen in q_z direction between 0.16–0.17 Å^{-1}, which confirms the P4VP-(PDP) lamellae with a spacing ~3.8 nm are parallel to the surface. Diffraction spots also appear in q_y direction at low q and interestingly, two distinct peaks with relative position 1:2 can be observed from the q_y scans shown in Figure 4g–i, which were extracted at q_z = 0.160 Å^{-1}. Such a sequence of peak positions is usually interpreted as lamellar structures but it is not the case here since TEM has demonstrated that PS phases form cylinders. It has been shown that when hexagonally

dx.doi.org/10.1021/ma202415t | *Macromolecules* 2012, 45, 1562–1569

packed cylinders are well oriented parallel to the surface in thin films, the 1:2 relative peak position may be detected in q_y axis.[46] However, since thin films with 40−50 nm thickness contain only ∼2 cylinder layers, it is more likely that the lamellar-like patterns are produced from the individual cylinder layer where the spatial arrangement of the parallel cylinders is analogous to that of perpendicular lamellae. The center-to-center distance of the cylinders are 32−35 nm estimating from the first-order peaks. The detailed spacings obtained from GISAXS data for the three annealing solvents are listed in Table 1. The proposed thin film structure annealed by oxygen-bearing solvents is schematically illustrated in Figure 5b. In sum, both PS cylinders and P4VP(PDP) lamellae are parallel to the surface.

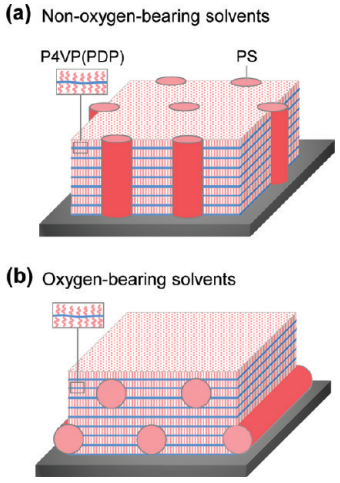


Figure 5. Schematic illustration of proposed structures. (a) Annealed by nonoxygen-bearing solvents, the PS cylinders are perpendicular to the surface while the P4VP(PDP) lamellae are parallel to the surface. (b) Annealed by oxygen-bearing solvents, both the PS cylinders and P4VP(PDP) lamellae are parallel to the surface.

The above results reveal that the orientation of cylindrical microdomains can be tuned by different annealing solvents and we now further show that the orientation is reversible. Here we used chloroform and THF as annealing solvents. As shown in Figure 6, the morphology of an as-spun film, ∼65 nm in thickness, was a mixture of perpendicular and parallel short cylinders. After annealed by chloroform, perpendicular PS cylinders were formed. We then annealed it again but in the vapor of THF and PS cylinders were driven to be parallel. Oppositely, the cylinders in thin films annealed first in the vapor of THF and subsequently in the vapor of chloroform were transformed from parallel to perpendicular. It is thus demonstrated that the supramolecular assembly is a simple and efficient approach to achieve the repeatable switch of the microdomain orientation in block copolymer thin films, which, as will be discussed later, is due to the reversible nature of supramolecules.

Morphology Caused by Other Solvents. It is apparently that the above solvents can impart mobility to supramolecules in thin films so that the supramolecules can reorganize into more ordered structures after annealing, though the mobility of each component may be in different level. In addition to the above two groups of solvents, we have also used other solvents to anneal the supramolecular thin films, including *n*-hexane, methanol and ethanol. As shown in the Supporting Information, Figure S1, the morphologies annealed by these

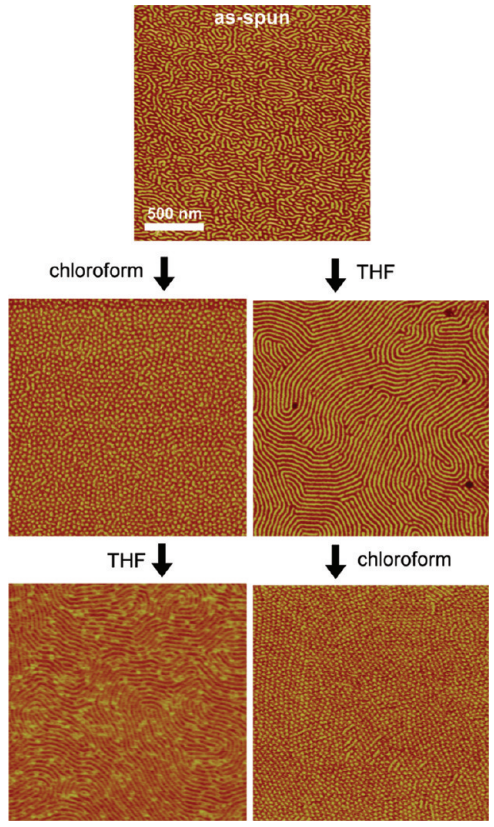


Figure 6. AFM phase images of an as-spun thin films, ∼65 nm in thickness, annealed by chloroform and THF in opposite sequence. The orientation is reversible.

three solvents are nearly identical to those of as-spun films, i.e., still a mixture of parallel and perpendicular cylinders, implying that the supramolecular chains are unable to do long-range motion under annealing. Note that all the three solvents are nonsolvent to PS while P4VP is soluble in methanol and ethanol. Although methanol and ethanol provide mobility to P4VP chains, the diffusion of the whole chains is hindered by the frozen PS chains, thereby no change caused in morphology.

Mechanism. We now discuss the mechanism by which annealing solvents cause parallel or perpendicular orientation of microdomains in supramolecular thin films. We have seen that whether the solvents are composed of oxygen or not, the small-scaled lamellae formed by P4VP(PDP) complexes are always parallel to the surface. At the bottoms of the films, the relatively hydrophilic P4VP blocks preferentially interact with the silicon substrate so that P4VP chains are attracted to the film−substrate interfaces and the tails of the associated PDP molecules are repelled from the interfaces and align normally to the substrates. On the other hand, the exposure of the hydrophobic alkyl tails of PDP to air is preferred because it prevents the high-surface-tension P4VP from contacting air, therefore a PDP brush layer formed at the film−air interfaces. Both of the forces, one from the bottom and the other from the top of the films, drive the P4VP(PDP) lamellae to be parallel to the surface and the films are so thin that the effects can propagate through the entire films.[23,26]

In our previous study, we suggested that the parallel alignment of P4VP(PDP) lamellae plays a crucial role in the formation of perpendicular alignment of PS cylinders in supramolecular thin films under annealing by chloroform.[26]

dx.doi.org/10.1021/ma202415t | *Macromolecules* 2012, 45, 1562−1569

For thin films with sufficiently high grafting density, such as the 1:1 molar ratio of PDP to 4VP as the present case, the PDP molecules prefer to orient parallel to the long axis of the cylinders to prevent the entropy loss due to the crowding effect of squeezing PDP molecules into the limit space near the nonplanar interfaces of cylinders and thus achieve interface stabilization.[47,48] As a result, PS cylinders tend to align orthogonally to the P4VP(PDP) lamellae and since the P4VP(PDP) lamellae are parallel to the surface in thin films, PS cylinders are then oriented perpendicular to the surface. As shown in the preceding section, in addition to chloroform, such alignments were also observed in thin films annealed by other nonoxygen-bearing solvents, i.e., toluene and benzene. The mechanism for perpendicular PS cylinders should be the same for all the nonoxygen-bearing solvents. Note that the mechanism during annealing is inferred from the postannealing structural analysis here. Given that the vapor pressures in the annealing setup used in this study are low, the compatibility between PS and P4VP(PDP) can only be slightly enhanced during annealing. The blocks may remain in segregation region such that the proposed alignment can reasonably occur in the swollen films.

Following this argument, the microdomain alignment in thin films annealed by oxygen-bearing solvents is in fact less stable because in such cases PS cylinders and P4VP(PDP) lamellae are both parallel to the surface. It has been shown that the selectivity of solvents to each phase[35] and the evaporation rates of solvents[21] may result in varying morphologies and orientation. However, we can find in Table 1 that the solvents in both groups are not particularly selective to PS or P4VP blocks. Furthermore, evaporation rates are generally inversely related to boiling points and the boiling points of the solvents in both groups range from 60 °C to above 100 °C. The solvents in both groups would not evaporate particularly fast or slowly at a given temperature. Therefore, there should be other factors responsible for the difference in orientation. Since the main difference between these two groups of solvents is whether their chemical structures contain oxygen atoms, we believe that it is such strong electronegative atoms that determine the orientation of PS cylinders in supramolecular thin films, which will be elaborated as follows.

The mechanism of the above proposed orthogonal alignments of PS cylinders and P4VP(PDP) lamellae is based on the assumption that the PDP molecules are grafted onto P4VP. However, the interactions between PDP and P4VP are weak hydrogen bonds whose strengths are subject to change in presence of external stimuli, unlike covalent bonds that are stable in common conditions. During solvent annealing, the solvent molecules diffuse into films and swell the films at a ratio about 1.5 to the original thicknesses.[26] In other words, there are a significant amount of solvent molecules penetrating films during annealing such that the effects of the solvent molecules on the hydrogen bonds between PDP and P4VP cannot be ignored. In the vapors of nonoxygen-bearing solvents, since the solvent molecules interact with PDP molecules and block copolymers mainly through weak van der Waals interactions, the formation of stronger hydrogen bonds between PDP and P4VP is enthalpy-favorable for lowering the system free energy. Figure 7a shows the ^{1}H NMR spectra of PDP dissolved in *d*-chloroform and the chemical shift of the hydroxyl hydrogen of PDP is 4.63 ppm. When PDP is mixed with PS-*b*-P4VP in a 1:1 molar ratio in chloroform, the peak is shifted to 5.26 ppm, confirming the formation of hydrogen bonds between PDP and P4VP.[49] The ^{1}H NMR results are similar for other nonoxygen-bearing solvents. The detailed data are listed in Table 2 and the spectra obtained in toluene and benzene are shown in the Supporting Information, Figures S2 and S3. It is thus suggested that P4VP(PDP) complexes are relatively stable in the vapors of nonoxygen-bearing solvents and PS cylinders prefer to be orthogonal to P4VP(PDP) lamellae to stabilize the interfaces of cylinders.

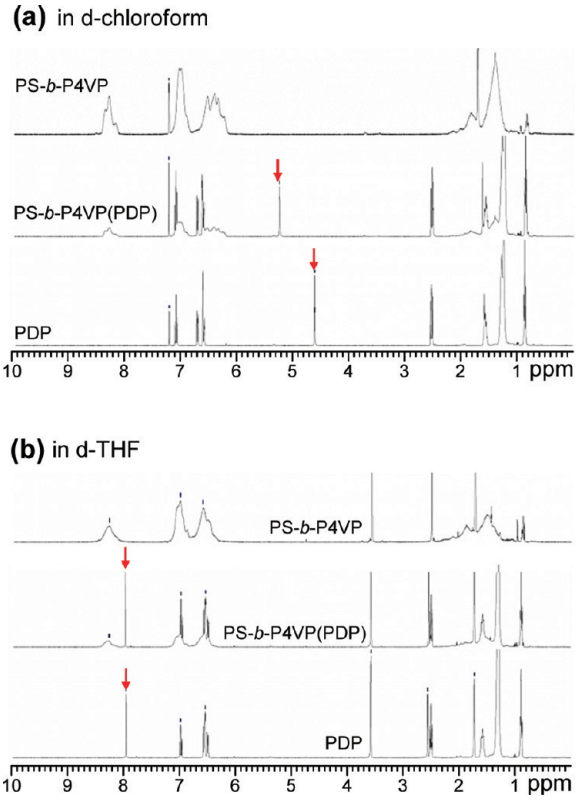


Figure 7. ^{1}H NMR spectra of PDP, PS-*b*-P4VP and PS-*b*-P4VP(PDP) dissolved in (a) *d*-chloroform and (b) *d*-THF. The arrows indicate the chemical shifts of the hydroxyl hydrogen on PDP.

Table 2. ^{1}H NMR Chemical Shifts of the Hydroxyl Hydrogen on PDP

	chemical shift (ppm)	
d-solvent	PDP	PS-*b*-P4VP(PDP)
toluene	3.98	4.30
benzene	4.10	4.47
chloroform	4.63	5.26
THF	7.97	7.99
1,4-dioxane	7.43	7.44
DMF	9.37	9.39

When thin films are annealed in the vapors of oxygen-bearing solvents, due to the competition of solvent molecules to form hydrogen bonds with PDP molecules through the highly electronegative oxygen atoms, the strength of hydrogen bonds between P4VP and PDP are greatly reduced. In Figure 7b, the chemical shift of hydroxyl hydrogen of PDP alone dissolved in *d*-THF is 7.97 ppm, which is much higher than that of PDP in nonoxygen-bearing solvents. Such a high chemical shift implies that the PDP molecules interact strongly with THF molecules. When PDP and PS-*b*-P4VP are mixed together in *d*-THF, the

dx.doi.org/10.1021/ma202415t | *Macromolecules* 2012, 45, 1562–1569

peak position is nearly unchanged, indicating that the interactions between PDP and P4VP are trivial compared to those between PDP and THF molecules. The chemical shifts of the PDP hydroxyl hydrogen in other oxygen-bearing solvents behave in a similar manner, as listed in Table 2. The spectra obtained in 1,4-dioxane and DMF can be found in the Supporting Information, Figure S4 and S5. The above results suggest that PDP molecules are unable to graft onto P4VP in the presence of oxygen-bearing solvents. During annealing, PDP molecules are relatively free so that the crowding effect near the interface of PS cylinders can be avoided and the driving force for inducing perpendicular PS cylinders is absent. Instead, the preferential interaction between P4VP and silicon substrate attracts P4VP chains to the substrate and in turn, PS cylinders are drawn to be parallel. Note that although PDP molecules are unbound during annealing, from the GISAXS data we can still see order parallel P4VP(PDP) lamellae after annealing. It is possible that most PDP molecules are still framed in their originally located P4VP domains so that they can be rapidly associated with P4VP upon solvent evaporation when films are removed from the annealing setup.

The interplays among PDP, P4VP, and solvent molecules mentioned above can be verified by the simple solubility tests of P4VP in the solvents. P4VP homopolymer with $M_w \sim 60\,000$ g/mol is insoluble in toluene, benzene, and 1,4-dioxane and only slightly swollen in THF. For nonoxygen-bearing solvents, i.e. toluene and benzene, after the addition of equimolar PDP into P4VP homopolymer solutions, P4VP becomes soluble. On the other hand, the addition of PDP is unable to enhance the solubility of P4VP homopolymer in THF and 1,4-dioxane. The results confirm that PDP molecules are hydrogen-bonded with P4VP in nonoxygen-bearing solvents and work as a compatibilizer between P4VP and the solvents, while such hydrogen bonds are missing in oxygen-bearing solvents. On the basis of what reveals here, we would like to point out the importance of the solvents used in preparing supramolecules. Supramolecules are formed through secondary bonds and the strengths of such weak interactions will be significantly affected by the types of solvents where the supramolecules are supposed to be formed. If solvents are not properly selected, the building components of supramolecules may not be successfully associated, even though each individual component can be well-dissolved. One example is P4VP and PDP mixed in DMF, where both P4VP and PDP can dissolve but the interaction between P4VP and PDP would be very weak.

CONCLUSIONS

We have demonstrated that the process of solvent annealing would greatly affect the microdomain orientation in thin films formed by PS-*b*-P4VP(PDP) supramolecules. When films are annealed by nonoxygen-bearing solvents, including toluene, benzene and chloroform, PS cylinders are perpendicular to the surface. This is due to the tendency of PS cylinders to be orthogonal to the parallel P4VP(PDP) lamellae at high molar ratio of PDP to 4VP unit and such an preferential alignment is based on the fact that PDP molecules graft onto P4VP through hydrogen bonds in the vapors of the nonoxygen-bearing solvents. PS cylinders, however, are parallel to the surface when films are annealed by oxygen-bearing solvents, such as THF, 1,4-dioxane, and DMF. From the ^{1}H NMR results, we found the PDP molecules interact strongly with the oxygen-bearing solvent molecules due to the electronegative nature of oxygen atom, while the interactions between PDP and P4VP become very weak. Such weak interactions are insufficient to lead to the formation of P4VP(PDP) complexes in oxygen-bearing solvents. As a result, the driving force for perpendicular PS cylinders disappears and the cylinders remain parallel. This work provides a simple and highly efficient approach to manipulate the microdomain orientation in block copolymer thin films, and it also emphasizes the advantage of the reversibility of supramolecules.

ASSOCIATED CONTENT

Supporting Information

AFM images of thin films annealed by other solvents and ^{1}H NMR spectra obtained in deuterated toluene, benzene, 1,4-dioxane, and DMF. This material is available free of charge via the Internet at http://pubs.acs.org/.

AUTHOR INFORMATION

Corresponding Author

*E-mail: shtung@ntu.edu.tw.

ACKNOWLEDGMENTS

This work was financially supported by the Taiwan National Science Council (NSC 99-2221-E-002-021). We acknowledge NSRRC, Taiwan, for facilitating the GISAXS experiments performed as part of this work and Dr. U-Ser Jeng, Dr. Chun-Jen Su, and Dr. Chiu-Hun Su of NSRRC for the assistance in scattering experiments.

REFERENCES

(1) Bates, F. S.; Fredrickson, G. H. *Annu. Rev. Phys. Chem.* **1990**, *41*, 525−557.
(2) Hamley, I. W. *Prog. Polym. Sci.* **2009**, *34* (11), 1161−1210.
(3) Kim, S. O.; Solak, H. H.; Stoykovich, M. P.; Ferrier, N. J.; de Pablo, J. J.; Nealey, P. F. *Nature* **2003**, *424* (6947), 411−414.
(4) van Zoelen, W.; ten Brinke, G. *Soft Matter* **2009**, *5* (8), 1568−1582.
(5) Black, C. T. *ACS Nano* **2007**, *1* (3), 147−150.
(6) Black, C. T.; Ruiz, R.; Breyta, G.; Cheng, J. Y.; Colburn, M. E.; Guarini, K. W.; Kim, H. C.; Zhang, Y. *IBM J. Res. Dev.* **2007**, *51* (5), 605−633.
(7) Park, S.; Lee, D. H.; Xu, J.; Kim, B.; Hong, S. W.; Jeong, U.; Xu, T.; Russell, T. P. *Science* **2009**, *323* (5917), 1030−1033.
(8) Ryu, D. Y.; Shin, K.; Drockenmuller, E.; Hawker, C. J.; Russell, T. P. *Science* **2005**, *308* (5719), 236−239.
(9) Huang, E.; Rockford, L.; Russell, T. P.; Hawker, C. J. *Nature* **1998**, *395* (6704), 757−758.
(10) Fasolka, M. J.; Mayes, A. M. *Annu. Rev. Mater. Res.* **2001**, *31*, 323−355.
(11) Han, E.; Stuen, K. O.; Leolukman, M.; Liu, C. C.; Nealey, P. F.; Gopalan, P. *Macromolecules* **2009**, *42* (13), 4896−4901.
(12) Ji, S.; Liu, C. C.; Son, J. G.; Gotrik, K.; Craig, G. S. W.; Gopalan, P.; Himpsel, F. J.; Char, K.; Nealey, P. F. *Macromolecules* **2008**, *41* (23), 9098−9103.
(13) Segalman, R. A.; Yokoyama, H.; Kramer, E. J. *Adv. Mater.* **2001**, *13* (15), 1152−1155.
(14) Bita, I.; Yang, J. K. W.; Jung, Y. S.; Ross, C. A.; Thomas, E. L.; Berggren, K. K. *Science* **2008**, *321* (5891), 939−943.
(15) Tang, C. B.; Lennon, E. M.; Fredrickson, G. H.; Kramer, E. J.; Hawker, C. J. *Science* **2008**, *322* (5900), 429−432.
(16) Xu, T.; Zvelindovsky, A. V.; Sevink, G. J. A.; Lyakhova, K. S.; Jinnai, H.; Russell, T. P. *Macromolecules* **2005**, *38* (26), 10788−10798.
(17) Villar, M. A.; Rueda, D. R.; Ania, F.; Thomas, E. L. *Polymer* **2002**, *43* (19), 5139−5145.
(18) Lin, Z. Q.; Kim, D. H.; Wu, X. D.; Boosahda, L.; Stone, D.; LaRose, L.; Russell, T. P. *Adv. Mater.* **2002**, *14* (19), 1373−1376.

(19) Ho, R. M.; Tseng, W. H.; Fan, H. W.; Chiang, Y. W.; Lin, C. C.; Ko, B. T.; Huang, B. H. *Polymer* **2005**, *46* (22), 9362−9377.
(20) Park, S.; Wang, J. Y.; Kim, B.; Xu, J.; Russell, T. P. *ACS Nano* **2008**, *2* (4), 766−772.
(21) Phillip, W. A.; Hillmyer, M. A.; Cussler, E. L. *Macromolecules* **2010**, *43* (18), 7763−7770.
(22) Sidorenko, A.; Tokarev, I.; Minko, S.; Stamm, M. *J. Am. Chem. Soc.* **2003**, *125* (40), 12211−12216.
(23) Albrecht, K.; Mourran, A.; Zhu, X.; Markkula, T.; Groll, J.; Beginn, U.; deJeu, W. H.; Moeller, M. *Macromolecules* **2008**, *41* (5), 1728−1738.
(24) Tung, S. H.; Kalarickal, N. C.; Mays, J. W.; Xu, T. *Macromolecules* **2008**, *41* (17), 6453−6462.
(25) Kao, J.; Tingsanchali, J.; Xu, T. *Macromolecules* **2011**, *44* (11), 4392−4400.
(26) Lee, C.-H.; Tung, S.-H. *Soft Matter* **2011**, *7* (12), 5660−5668.
(27) Lee, J. W.; Lee, C.; Choi, S. Y.; Kim, S. H. *Macromolecules* **2010**, *43* (1), 442−447.
(28) Ruokolainen, J.; Saariaho, M.; Ikkala, O.; ten Brinke, G.; Thomas, E. L.; Torkkeli, M.; Serimaa, R. *Macromolecules* **1999**, *32* (4), 1152−1158.
(29) Ikkala, O.; ten Brinke, G. *Science* **2002**, *295* (5564), 2407−2409.
(30) Ikkala, O.; ten Brinke, G. *Chem. Commun.* **2004**, *19*, 2131−2137.
(31) Valkama, S.; Ruotsalainen, T.; Nykanen, A.; Laiho, A.; Kosonen, H.; ten Brinke, G.; Ikkala, O.; Ruokolainen, J. *Macromolecules* **2006**, *39* (26), 9327−9336.
(32) Park, S.; Kim, B.; Xu, J.; Hofmann, T.; Ocko, B. M.; Russell, T. P. *Macromolecules* **2009**, *42* (4), 1278−1284.
(33) Xuan, Y.; Peng, J.; Cui, L.; Wang, H. F.; Li, B. Y.; Han, Y. C. *Macromolecules* **2004**, *37* (19), 7301−7307.
(34) Elbs, H.; Drummer, C.; Abetz, V.; Krausch, G. *Macromolecules* **2002**, *35* (14), 5570−5577.
(35) Bosworth, J. K.; Paik, M. Y.; Ruiz, R.; Schwartz, E. L.; Huang, J. Q.; Ko, A. W.; Smilgies, D.-M.; Black, C. T.; Ober, C. K. *ACS Nano* **2008**, *2* (7), 1396−1402.
(36) Tokarev, I.; Krenek, R.; Burkov, Y.; Schmeisser, D.; Sidorenko, A.; Minko, S.; Stamm, M. *Macromolecules* **2005**, *38* (2), 507−516.
(37) Nandan, B.; Vyas, M. K.; Bohme, M.; Stamm, M. *Macromolecules* **2010**, *43* (5), 2463−2473.
(38) Cordeiro, J. M. M.; Freitas, L. C. G. *Z. Naturforsch., Sect. a-a J. Phys. Sci.* **1999**, *54* (2), 110−116.
(39) Lim, W. K.; Rosgen, J.; Englander, S. W. *Proc. Natl. Acad. Sci. U.S.A.* **2009**, *106* (8), 2595−2600.
(40) Tung, S. H.; Xu, T. *Macromolecules* **2009**, *42* (15), 5761−5765.
(41) van Zoelen, W.; Asumaa, T.; Ruokolainen, J.; Ikkala, O.; ten Brinke, G. *Macromolecules* **2008**, *41* (9), 3199−3208.
(42) van Zoelen, W.; Polushkin, E.; ten Brinke, G. *Macromolecules* **2008**, *41* (22), 8807−8814.
(43) Jeng, U. S.; Su, C. H.; Su, C. J.; Liao, K. F.; Chuang, W. T.; Lai, Y. H.; Chang, J. W.; Chen, Y. J.; Huang, Y. S.; Lee, M. T.; Yu, K. L.; Lin, J. M.; Liu, D. G.; Chang, C. F.; Liu, C. Y.; Chang, C. H.; Liang, K. S. *J. Appl. Crystallogr.* **2010**, *43*, 110−121.
(44) Brandrup, J.; Immergut, E. H.; Grulke, E. A.; Abe, A.; Bloch, D. R. *Polymer Handbook*, 4th ed.; John Wiley & Sons: New York, 2005.
(45) Matsen, M. W. *J. Chem. Phys.* **1997**, *106* (18), 7781−7791.
(46) Lee, B.; Park, I.; Yoon, J.; Park, S.; Kim, J.; Kim, K. W.; Chang, T.; Ree, M. *Macromolecules* **2005**, *38* (10), 4311−4323.
(47) Osuji, C.; Zhang, Y. M.; Mao, G. P.; Ober, C. K.; Thomas, E. L. *Macromolecules* **1999**, *32* (22), 7703−7706.
(48) Verploegen, E.; McAfee, L. C.; Tian, L.; Verploegen, D.; Hammond, P. T. *Macromolecules* **2007**, *40* (4), 777−780.
(49) Wagner, G.; Pardi, A.; Wuthrich, K. *J. Am. Chem. Soc.* **1983**, *105* (18), 5948−5949.

Macromolecules

Article

pubs.acs.org/Macromolecules

Sulfonated Polyaniline Nanostructures Synthesized via Rapid Initiated Copolymerization with Controllable Morphology, Size, and Electrical Properties

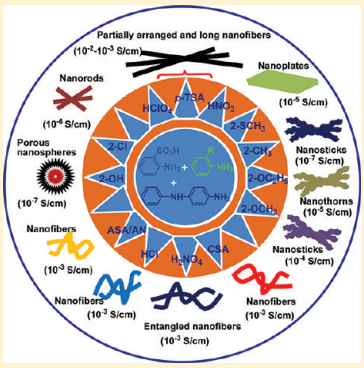
Yaozu Liao,[†,‡,§] Veronica Strong,[§] Wei Chian,[†] Xia Wang,*[,†] Xin-Gui Li,[‡] and Richard B. Kaner*[,§]

[†]School of Materials Science and Engineering, University of Shanghai for Science and Technology, 516 Jun-Gong Road, Shanghai 200093, China

[‡]Institute of Materials Chemistry, College of Materials Science and Engineering, Tongji University, 1239 Si-Ping Road, Shanghai 200092, China

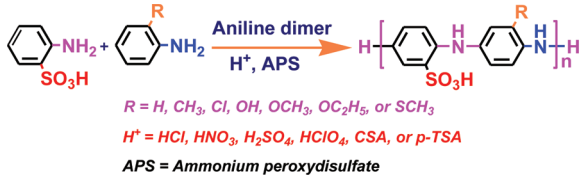
[§]Department of Chemistry and Biochemistry and California NanoSystems Institute, University of California, Los Angeles, Los Angeles, California, 90095-1569

ABSTRACT: Sulfonated polyaniline (SPANi), a self-doped conjugated polymer, has received great interest in recent years; however, controlling its shape, size, and conductivity at the nanoscale remains a significant challenge. Here, we report an initiator-assisted route to SPANi nanostructures by rapidly copolymerizing *o*-aminobenzenesulfonic acid with aniline or its derivatives in the presence of a catalytic amount of the initiator−aniline dimer. UV−vis, FT-IR, and XRD spectra reveal that the chemical compositions of the SPANi nanostructures are similar to that of conventional SPANi possessing an agglomerated morphology. By regulating the comonomer molar ratios, the aniline derivatives used and the acidic media employed, the morphology of the SPANi changes from 1-D nanofibers, nanosticks, nanothorns, and nanorods to 2-D nanoplates and 3-D porous nanospheres. The length and aspect ratio of the SPANi nanofibers can reach values up to 4.5 μm and 60, respectively. These SPANi nanostructures are readily processable in both organic and aqueous solvents and demonstrate 6 orders of magnitude enhanced conductivity at pH values of 5.5−6.0 when compared to conventional polyaniline.



Polyaniline (PANi) is one of the most widely studied conducting polymers because of its facile synthesis, excellent chemical and environmental stability and good electrical conductivity leading to many potential applications such as lightweight battery electrodes, electromagnetic shielding, anticorrosion coatings, and sensors.[1,2] Limited processability and loss of electrochemical activity at neutral pH are arguably two of the biggest problems for its utilization in fields such as bioelectrochemistry and biomaterials. Fabrication of nanostructured PANi including nanoparticles, nanowires, nanofibers, nanotubes, and nanocomposites has been well developed by chemical methods to improve its water processability.[3,4] In particular, nanostructures of PANi offer the possibility of enhanced performance wherever a high interfacial area between PANi and its environment is needed. For example, in sensor applications, PANi nanofibers display much higher sensitivities and faster time responses relative to their conventional bulk counterparts due to higher effective surface areas and shorter penetration depths for target molecules.[5] Since most biomolecules such as enzymes are only stable and bioactive at neutral pH, it is critical to develop a form of PANi that does not deprotonate and become insulating under these conditions.[6] Despite improvements in water-processability and functionalities achieved by nanofabricating PANi, maintaining electrochemical activity in solutions of pH > 4.0 has only met with limited success so far.

Scheme 1. General Chemical Route to a Variety of Sulfonated Polyanilines (SPANi)



One derivative, known as self-doped PANi, has received much interest because the dopants are bound directly to the polymer backbone, in contrast to conventional polyaniline, which uses external dopants. Self-doped PANi typically exhibits conductivity of 10^{-6}−10^{-1} S/cm,[7−12] and several advantages, including improved solubility, electrical properties and redox activity over a wide pH range. For example, unsubstituted PANi becomes insulating at pH values greater than 4, while the conductivities of 50% and 75% sulfonated PANis are pH-independent up to pHs of 7.5 and ≤14,[12] respectively. Thus, self-doped PANi is considered a promising conjugated polymer for applications in the areas of rechargeable batteries,[13]

Received: November 4, 2011
Revised: January 15, 2012
Published: January 31, 2012

ACS Publications © 2012 American Chemical Society

Table 1. Effect of ASA/Aniline Synthesized in 1.0 M HCl at Varying Molar Ratios on the Nanomorphology, Average Diameter (D_a), Average Length (L_a), Aspect Ratio (L_a/D_a), UV−Vis Absorbance Maximum (λ_{max}), Product Yield, and Conductivity of SPANi

ASA/aniline molar ratios	nanomorphology	D_a (nm)	L_a (μm)	L_a/D_a	λ_{max} (nm)	yield (%)	conductivity (S/cm)
0/100	nanofibers	50	1.0	20.0	790	45.9	3.3×10^{-8}
30/70	nanofibers	55	0.95	17.2	845	43.3	2.4×10^{-3}
50/50	nanofibers	55	0.75	13.6	856	34.5	3.0×10^{-3}
70/30	nanofibers	60	0.7	11.7	870	20.4	5.7×10^{-3}

Table 2. Effect of Acidic Media on the Nanomorphology, Average Diameter (D_a), Average Length (L_a), Aspect Ratio (L_a/D_a), UV−Vis Absorbance Maxima (λ_{max}), Product Yield, and Conductivity of SPANi When Using a 50/50 Ratio of ASA/Aniline

acidic media	nanomorphology	D_a (nm)	L_a (μm)	L_a/D_a	λ_{max} (nm)	yield (%)	conductivity (S/cm)
HCl	nanofibers	55	0.75	13.6	856	34.5	3.0×10^{-3}
HNO_3	nanofibers	55	1.8	32.7	858	28.5	1.2×10^{-2}
H_2SO_4	nanofibers	62	2.1	33.9	853	28.3	1.9×10^{-3}
CSA	nanofibers	65	1.2	18.5	853	32.4	1.9×10^{-3}
$HClO_4$	nanofibers	88	4.0	45.5	920	29.9	3.7×10^{-3}
p-TSA	nanofibers	75	4.5	60.0	873	27.1	4.5×10^{-3}

Table 3. Effect of 2-Substituents of Aniline Derivatives on the Nanomorphology, Average Diameter (D_a), Average Length (L_a), UV−Vis Absorbance Maxima (λ_{max}), Product Yield and Conductivity of SPANi Using 1.0 M HCl

2-substituents	nanomorphology	D_a (nm)	L_a (μm)	L_a/D_a	λ_{max} (nm)	yield (%)	conductivity (S/cm)
OH	nanospheres	400	–	–	418	7.8	2.9×10^{-7}
SCH_3	nanoplates	30 nm thick		–	858	22.8	1.4×10^{-5}
OCH_3	nanosticks	75	1.5	20.0	870	32.9	8.3×10^{-4}
Cl	nanorods	60	0.4	6.7	765	1.7	3.3×10^{-6}
OC_2H_5	nanothorns	63	0.8	12.7	873	30.8	6.9×10^{-5}
CH_3	nanofibers	52	0.7	13.5	825	24.2	6.0×10^{-7}

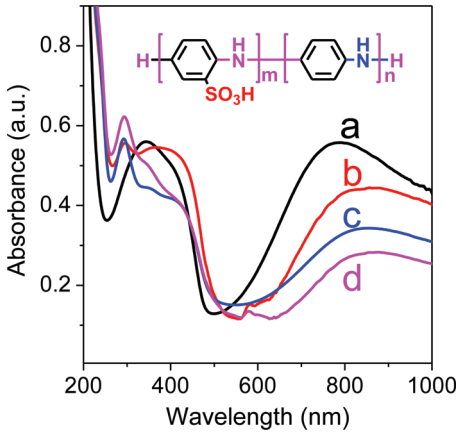


Figure 1. UV−vis spectra of SPANi synthesized with the following ASA/aniline molar ratios: (a) 0/100, (b) 30/100, (c) 50/50, and (d) 70/100 in the presence of 2.5 mol % *N*-phenyl-*p*-phenylenediamine per comonomer in 1.0 mol/L HCl.

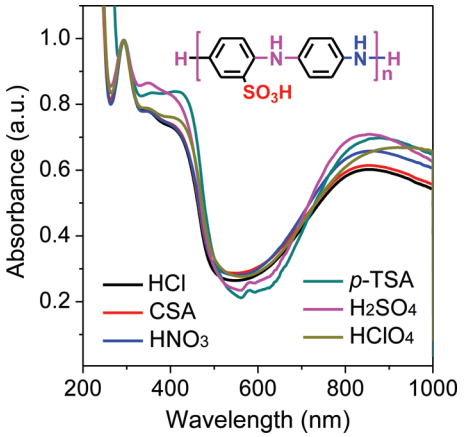


Figure 2. UV−vis spectra of SPANi synthesized in the following acidic medium: HCl (black line), HNO_3 (blue line), H_2SO_4 (magenta line), $HClO_4$ (dark yellow line), CSA (red line), or *p*-TSA (dark cyan line) in the presence of 2.5 mol % *N*-phenyl-*p*-phenylenediamine per comonomer in 1.0 mol/L HCl, at a fixed ASA/aniline molar ratio of 50/50.

light-emitting diodes,[14] biosensors,[15,16] cell scaffolds,[17] junction devices,[18] and electrochromics.[19] Examples of self-doped PANi syntheses include the introduction of sulfonic acid,[11,12,20,21] boronic acid,[22,23] carboxylic acid,[24] or phosphonic acid groups[25] into PANi either directly onto the aniline rings or on the side chains. These approaches have proved to be useful to enhance water-solubility and maintain electrochemical activity at neutral pH. Although significant progress has been made in the syntheses of self-doped PANi, there remains many limitations such as low yield, limited processability and poor mechanical, thermal and environmental stabilities. More importantly, no method has yet been developed that enables nanostructures of self-doped PANi to be varied systematically.

In this work, we report a rapid initiated copolymerization technique that produces self-doped sulfonated polyaniline (SPANi) with well-defined, controllable nanomorphologies, sizes, dimensionalities, and electric properties. Specifically, we report a new copolymerization approach using *o*-aminobenzenesulfonic acid (ASA) with aniline or aniline derivatives in the presence of a catalytic amount of the initiator *N*-phenyl-*p*-phenylenediamine (aniline dimer). The initiator accelerates the polymerization rate,

dx.doi.org/10.1021/ma2024446 | *Macromolecules* 2012, 45, 1570−1579

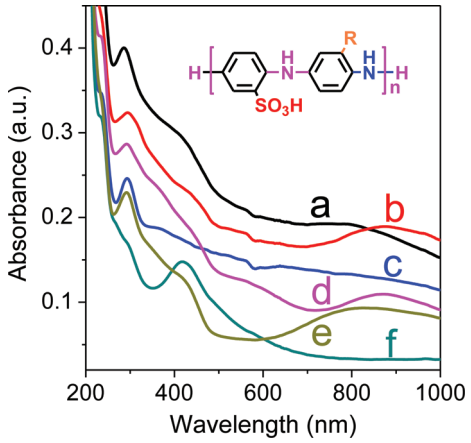


Figure 3. UV−vis spectra of SPANi synthesized with the following 2-substituted group (R) on aniline: (a) Cl, (b) OCH_3, (c) SCH_3, (d) OC_2H_5, (e) CH_3, or (f) OH in the presence of 2.5 mol % *N*-phenyl-*p*-phenylenediamine per comonomer in 1.0 mol/L HCl, at a fixed ASA/aniline molar ratio of 50/50.

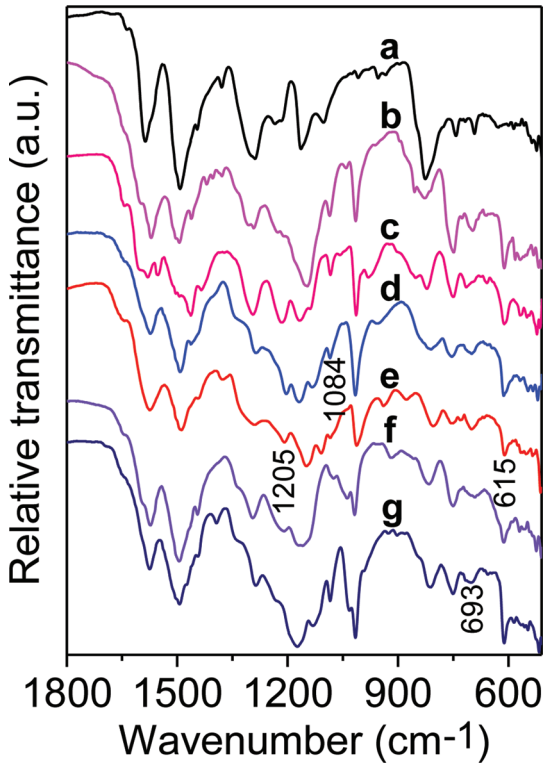


Figure 4. ATR/FT-IR spectra of (a) pristine PANi and (b−g) SPANi synthesized with the following 2-substituted group (R) on aniline: (b) Cl, (c) CH_3, (d) OH, (e), OCH_3, (f) SCH_3, or (g) OC_2H_5 in the presence of 2.5 mol % *N*-phenyl-*p*-phenylenediamine per comonomer in 1.0 mol/L HCl, at a fixed ASA/aniline ratio of 50/50.

which favors homogeneous nucleation and leads to the formation of PANi nanofibers.[2] The initiator molecules are believed to serve as nucleation centers for the growth of polymeric chains leading to the SPANi nanostructures. The effects of several important copolymerization parameters, including the comonomer ratios, aniline derivatives used and acidic media employed, on the product yields, chemical compositions, morphologies, sizes, dimensionalities, and electrical properties of the SPANi nanostructures are investigated in detail.

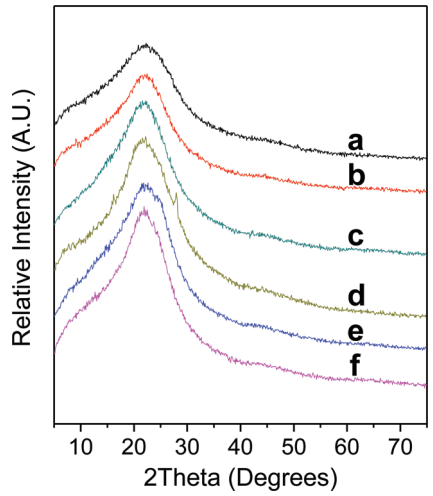


Figure 5. XRD patterns of SPANi synthesized in the following acidic media: (a) HCl, (b) HNO_3, (c) H_2SO_4, (d) $HClO_4$, (e) CSA, or (f) *p*-TSA in the presence of 2.5 mol % *N*-phenyl-*p*-phenylenediamine per comonomer in 1.0 mol/L HCl, at a fixed ASA/aniline molar ratio of 50/50.

EXPERIMENTAL SECTION

Synthesis of SPANi Nanostructures. All chemicals were of analytical grade and used as received. The SPANi nanostructures were synthesized by chemical oxidative copolymerization of ASA and aniline or aniline derivatives in the presence of 2.5 mol % (relative to the comonomers) of the aniline dimer and acidic medium. A general chemical route to a variety of SPANi derivatives is shown in Scheme 1. Typically, 2.5 mmol of ASA and 2.5 mmol of aniline were dissolved in 25 mL of 1.0 M HCl. The initiator (0.125 mmol) was predissolved in 1.0 mL of ethanol and mixed with the comonomer solution. An oxidant solution consisting of 5.0 mmol of ammonium peroxydisulfate (APS) and 25 mL of 1.0 M HCl were rapidly added to the comonomer solution. The reaction mixture was vigorously shaken for ~10 s and then left undisturbed for 24 h. The crude product of SPANi nanofibers was purified by dialysis against deionized (DI) water at a constant pH of 5.5−6.0 for approximately two months. Finally, the SPANi powder was obtained by further drying the crude product at 50 °C in a vacuum oven for 72 h. By regulating the ASA/aniline molar ratios, aniline derivatives used and acidic media employed, the rapid initiated copolymerization method produced 1-D nanofibers, nanosticks, nanothorns, and nanorods, 2-D nanoplates, and 3-D porous nanospheres of SPANi. If not specifically mentioned, all experiments were performed using 1.0 M HCl as the acidic medium.

Chemical Composition, Morphology, and Conductivity. The SPANi nanostructures dispersed in DI water and/or dried SPANi powders were utilized for characterization of chemical composition, morphology and conductivity. Ultraviolet−visible (UV−vis) absorption spectra of SPANi nanostructures dispersed in DI water were recorded on an HP 8453 spectrometer. Attenuated Total Reflection Fourier transform infrared (ATR-FT-IR) spectra of dried SPANi powders were taken with a JASCO FT-IR 420 spectrometer. X-ray diffraction (XRD) spectra of the samples were scanned on a Philips X'pert Pro powder diffractometer by using copper-monochromatized CuKα radiation (λ = 1.54178 Å). Samples for a JEOL JSM-6700 field emission scanning electron microscope (SEM) were prepared on silicon wafers. Samples for a PHILIPS CM120 transmission electron microscope (TEM) were prepared on Formvar-coated copper grids. To investigate the electrical properties, the SPANi nanostructures were cast as thin films and measured using a two-point probe technique.[26]

RESULTS AND DISCUSSION

Product Yield, Conductivity, and Dispersibility. The effect of ASA/aniline molar ratios on the morphology, size,

dx.doi.org/10.1021/ma2024446 | *Macromolecules* 2012, 45, 1570−1579

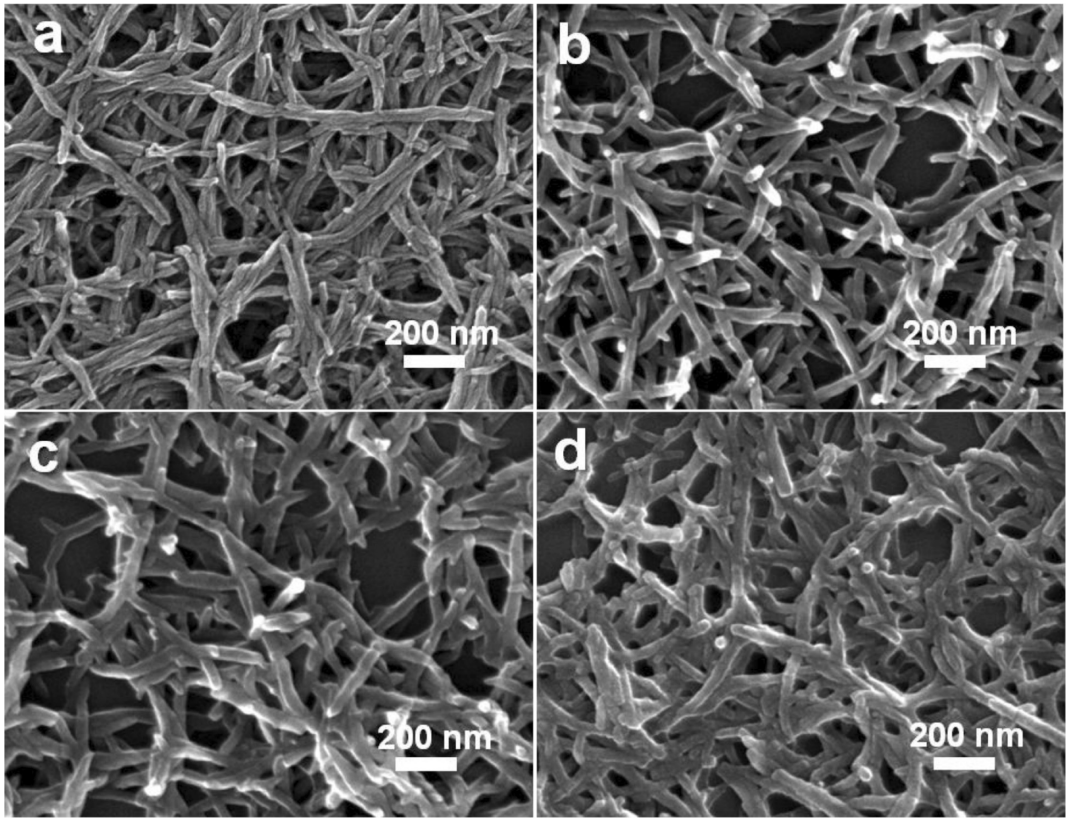


Figure 6. SEM images of SPANi synthesized with the following ASA/aniline molar ratios: (a) 0/100, (b) 30/100, (c) 50/50, and (d) 70/100 in the presence of 2.5 mol % *N*-phenyl-*p*-phenylenediamine per comonomer in 1.0 mol/L HCl.

UV−vis absorption maximum (λ_{max}), product yield, and conductivity of SPANi nanostructures, are presented in Table 1. As the ASA/aniline molar ratio is increased from 0/100 to 30/70 to 50/50 and to 70/30, the product yield of the polymers after dialysis decreased from 45.9 to 43.3 to 34.5 and to 20.4%, while the conductivity increased from 3.3×10^{-8} to 2.4×10^{-3} to 3.0×10^{-3} and to 5.7×10^{-3} S/cm, respectively. This is consistent with increasing ASA content, which results in a larger presence of sulfonic acid groups bonded to PANi, and leads to better water-solubility and higher self-doping-levels for the conjugated polymers. On the other hand, adding more ASA to copolymerize with aniline may generate copolymers with relatively low molecular weights, which would be easier to filter out during the dialysis. Both reasons may explain why the conductivities increase and the product yields of SPANi decrease.

The effect of the acidic media on the morphology, size, λ_{max}, product yield and conductivity of SPANi nanostructures is displayed in Table 2. Even when different acids are used such as hydrochloric acid (HCl), nitric acid (HNO_3), sulfuric acid (H_2SO_4), perchloric acid ($HClO_4$), camphorsulfonic acid (CSA) or *p*-toluenesulfonic acid (*p*-TSA), the obtained polymers exhibit a relatively stable product yield of 27−35%. Surprisingly, when aqueous HNO_3 is used as the polymerization medium, the self-doped SPANi also shows 6 orders of magnitude higher conductivity at neutral pH than conventional PANi with values up to 1.2×10^{-2} S/cm.

Several representative 2-substituted aniline derivatives were chosen to copolymerize with ASA in an HCl medium. The effect of the 2-substituents on the morphology, size, λ_{max}, product yield and conductivity of SPANi nanostructures is listed in Table 3. Since product yield and conductivity of SPANi largely depend on the aniline derivatives used for copolymerization, it is not surprising to find that different 2-substituents affect these characteristics. For example, when aniline derivatives like 2-chloroaniline, 2-methylaniline, 2-hydroxylaniline, 2-methoxyaniline, 2-methylthioaniline and 2-ethoxyaniline are used, the product yields of SPANi are 1.7, 24.2, 7.8, 32.9, 22.8 and 30.8%, while the conductivities achieved are 3.3×10^{-6}, 6.0×10^{-7}, 2.9×10^{-7}, 8.3×10^{-4}, 1.4×10^{-5} and 6.9×10^{-5} S/cm, respectively. Note that, the electron-donating capacities (ED) of the substituents -Cl, $-CH_3$, $-OH$, $-OCH_3$, $-SCH_3$ and $-OCH_2H_5$ follow the order: $ED_{Cl} < ED_{CH_3} < ED_{OH} < ED_{OCH_3} < ED_{SCH_3} < ED_{OC_2H_5}$, which suggests that the chain growth and elongation process readily occurs with 2-ethoxyaniline, 2-methylmercaptoaniline and 2-methoxyaniline in contrast to 2-chloroaniline, 2-methylaniline and 2-hydroxyaniline. It should also be noted that in terms of occupied volume (V), the substituents of $-Cl$, $-CH_3$, $-OH$, $-OCH_3$, $-SCH_3$ and $-OC_2H_5$ have the following order: $V_{OH} < V_{Cl} < V_{CH_3} < V_{OCH_3} < V_{SCH_3} < V_{OC_2H_5}$. The polymerization rate and $\pi-\pi$ stacking will be limited by steric hindrance as a result of increasing substituent size. This implies that the generated polymeric chains will be relatively more twisted and possess less planarity and π-conjugation in the case of 2-ethoxyaniline, thereby impairing the electron-transport properties. Both electron-donating and volume effects may be the reasons that SPANi exhibits the highest product yield and conductivity when 2-methoxyaniline is used for the reaction.

The dispersibility of SPANi nanostructures was qualitatively investigated by dispersing the products in various solvents.

dx.doi.org/10.1021/ma2024446 | *Macromolecules* 2012, 45, 1570−1579

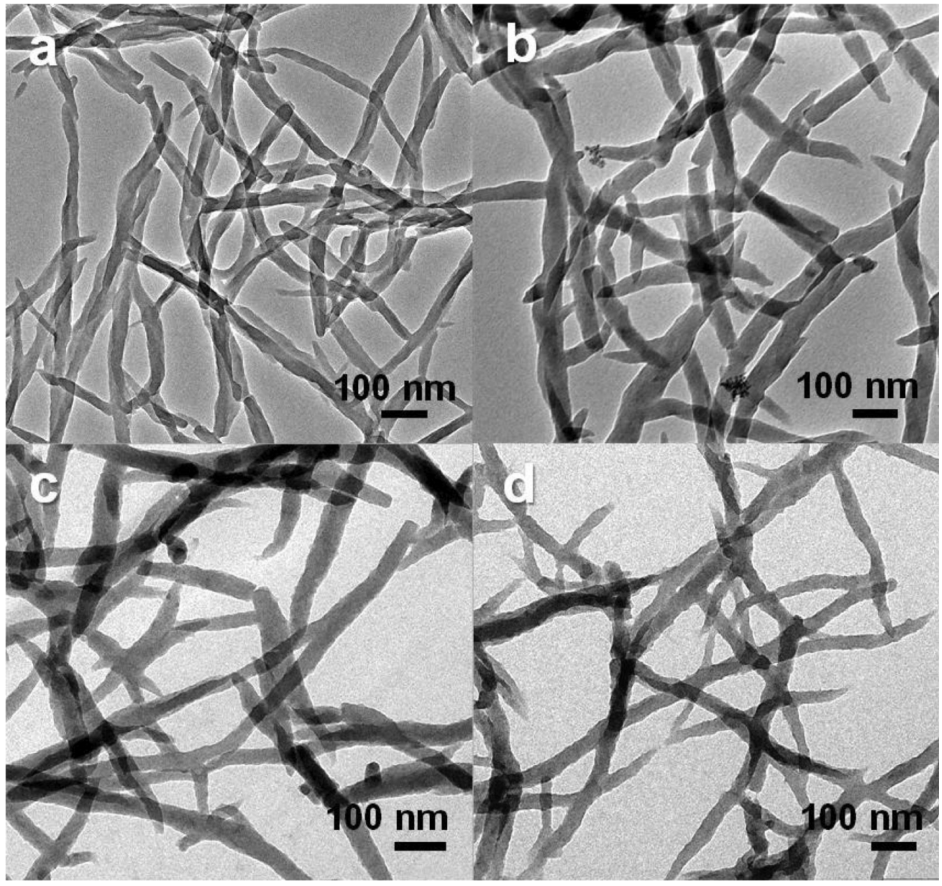


Figure 7. TEM images of SPANi synthesized with the following ASA/aniline molar ratios: (a) 0/100, (b) 30/70, (c) 50/50, and (d) 70/30 in the presence of 2.5 mol % *N*-phenyl-*p*-phenylenediamine per comonomer in 1.0 mol/L HCl.

Note that, SPANi nanostructures can be dispersed in many aqueous solvents such as DI water, alcohol, dilute acids and organic solvents such as *N*-methyl-2-pyrrolidone (NMP), *N,N*-dimethylformamide (DMF) and *N,N*-dimethylacetamide (DMAc). In particular, the nanocolloids produced can be completely stable in DI water for at least 4 weeks.

Chemical Composition. *UV–Vis Spectra.* The UV–vis spectra of aqueous dispersions of SPANi nanofibers in their acid doped salt form synthesized in HCl at variable ASA/aniline molar ratios are shown in Figure 1b–d. For comparison, the spectrum of pristine PANi nanofibers in their salt form is also presented (Figure 1a). The pristine PANi exhibits two characteristic peaks at 345 and 790 nm, while SPANi consisting of ASA and aniline exhibits two peaks at 295 and >845 nm, respectively, that can be attributed to the $\pi-\pi^*$ transition of the benzene rings and the $n-\pi^*$ transition of the quinoid rings,[5] respectively. For the emeraldine base form of oligoaniline systems, some recent theoretical work suggests that the peak at relative higher wavelength can also be attributed to the $\pi-\pi^*$ transition of the quinoid rings, according to extensive density functional theory (DFT) calculations.[27] With an increase in the ASA/aniline molar ratio from 0/100 to 30/70 to 50/50 and to 70/30, the peak due to the $n-\pi^*$ transition red shifts from 790 to 845 to 856 and to 870 nm, indicating that the ASA has been copolymerized with aniline. The exciton band near 800 nm undergoes a large red shift when more ASA is used in the copolymerization, signifying an increase in the $\pi-\pi^*$ conjugation and a decrease in the bandgap.

The UV–vis spectra of SPANi nanofibers in their salt form synthesized at an ASA/aniline molar ratio of 50/50 in the presence of different acidic media are shown in Figure 2. When using acidic media such as HNO_3, H_2SO_4, $HClO_4$, CSA, and *p*-TSA, SPANi displays $n-\pi^*$ transition peaks at 858, 853, 920, 853, and 873 nm, respectively, compared to 853 nm for the product obtained with HCl. This means that the conjugation length of SPANi depends on the acidic medium utilized. The reason may be that different acids change the solubility of the monomers and initiators, which also affect the copolymerization activity of the ASA and aniline leading to variable molecular weights of SPANi.

A series of SPANi nanostructures with various 2-substituents such as $-Cl$, $-CH_3$, $-SCH_3$, $-OCH_3$, $-OC_2H_5$, and $-OH$ were obtained by copolymerizing the ASA monomer with aniline derivatives at the same molar ratio of 50/50 in HCl. With increasing electron-donating ability of the substituents from $-Cl$ to $-CH_3$ to $-SCH_3$ to $-OCH_3$ and to $-OC_2H_5$, the λ_{max} values of the corresponding SPANi red shift from 765 to 825 to 858 to 870 and to 873 nm, respectively, as shown in Figure 3. Essentially the stronger the electron-donating substituent that is introduced, the larger the charge density that is created on the SPANi polymer backbone; as a result, the copolymer will adapt a more linear morphology, and thus increase the $\pi-\pi$ conjugation. Note that the UV–vis spectrum of the product synthesized from ASA and 2-hydroxylaniline shows a peak at a maximum wavelength of 418 nm. Generally, the more 2-hydroxylaniline monomers that are copolymerized with ASA, the greater the water-solubility of SPANi with a

dx.doi.org/10.1021/ma2024446 | *Macromolecules* 2012, 45, 1570–1579

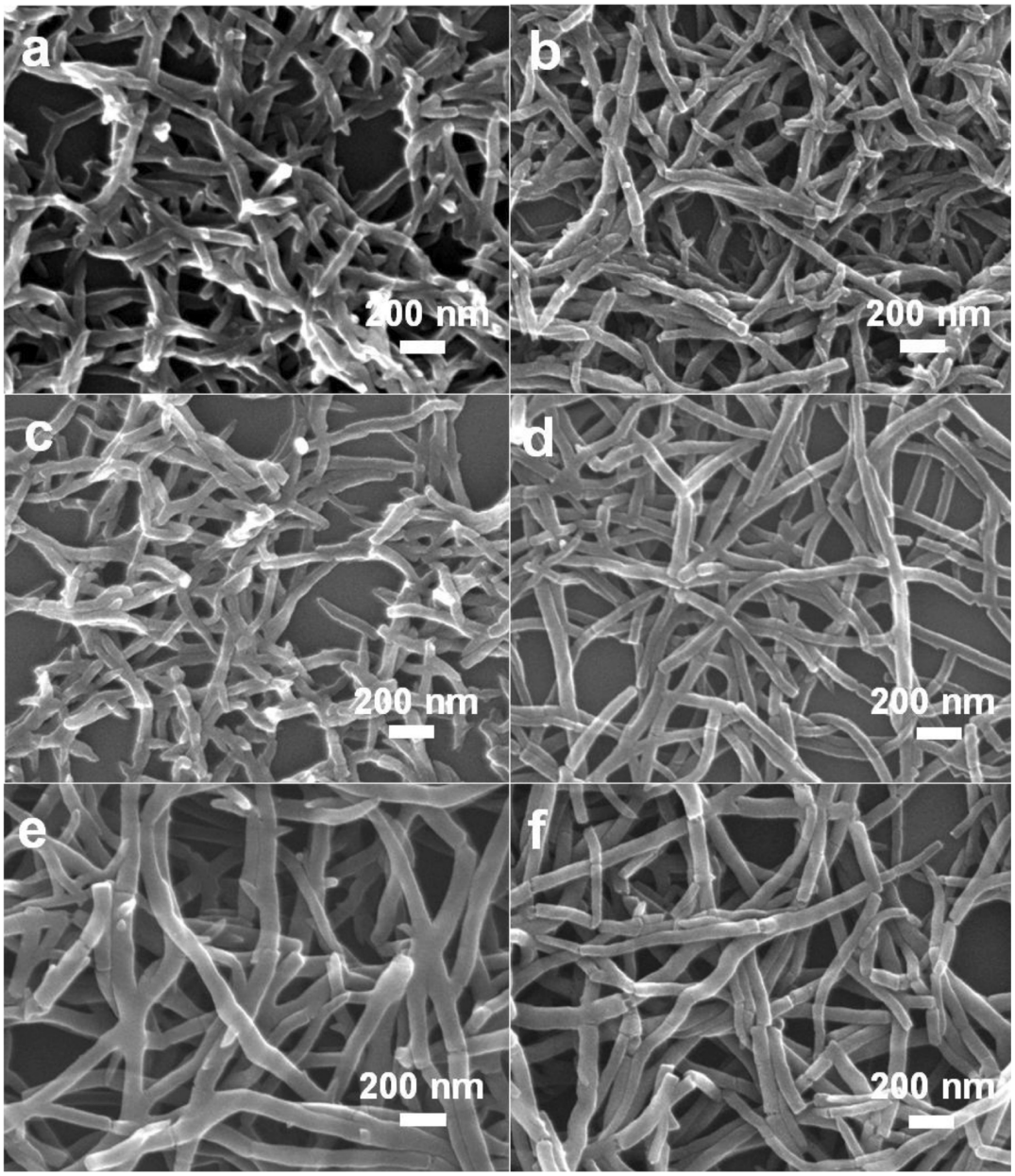


Figure 8. SEM images of SPANi synthesized in the following acidic medium: (a) HCl, (b) H_2SO_4, (c) CSA, (d) HNO_3, (e) $HClO_4$, or (f) *p*-TSA in the presence of 2.5 mol % *N*-phenyl-*p*-phenylenediamine per comonomer in 1.0 mol/L HCl, at a fixed ASA/aniline molar ratio of 50/50.

higher molecular weight. The dialysis purification used here may leave behind some sulfonated oligoaniline with a few sulfonic acid groups. This also explains why when using 2-hydroxylaniline, a higher charge density molecule than both 2-chloroaniline and 2-methylaniline, the resulting product displays far lower $\pi-\pi$ conjugation than other lower charge density molecules.

ATR-FT-IR Spectra. Figure 4b–g displays ATR-FT-IR spectra of SPANi nanostructures synthesized by copolymerizing the ASA monomer and aniline derivatives such as 2-chloroaniline, 2-methylaniline, 2-hydroxylaniline, 2-methoxyaniline, 2-methylmercaptoaniline and 2-ethoxyaniline at a comonomer ratio of 50/50 in HCl. For comparison, the spectrum of pristine PANi nanofibers in their emeraldine base form is also presented (Figure 4a). The pristine emeraldine base PANi nanofibers give characteristic IR peaks at 1587, 1493, 1289, and 1164 cm^{-1} corresponding to quinoid, benzenoid, C–N aromatic amine, and —N=quinoid=N— (electron-like band) stretching modes, respectively, which are in good agreement with a previous report.[26] The SPANi nanostructures, after dialysis in pH 5.5–6.0 for two months, show four typical IR peaks at 1205, 1084, 693, and 615 cm^{-1}, which can be assigned to the asymmetric and symmetric O–S–O stretching modes, and S–O and C–S stretching modes, respectively; these peaks do not differ significantly from that of conventional SPANi.[28,29] These characteristic bands are absent from the spectrum of pristine emeraldine base PANi, revealing that the sulfonic acid groups have been bonded to the aromatic rings in the SPANi polymeric chains.

XRD. X-ray diffraction patterns are presented in Figure 5 for SPANi nanostructures synthesized by copolymerizing ASA and aniline monomers at a molar ratio of 50/50 in acidic media of HCl, HNO_3, H_2SO_4, $HClO_4$, CSA, and *p*-TSA. The six types of SPANi powders are all nearly amorphous with

dx.doi.org/10.1021/ma2024446 | *Macromolecules* 2012, 45, 1570–1579

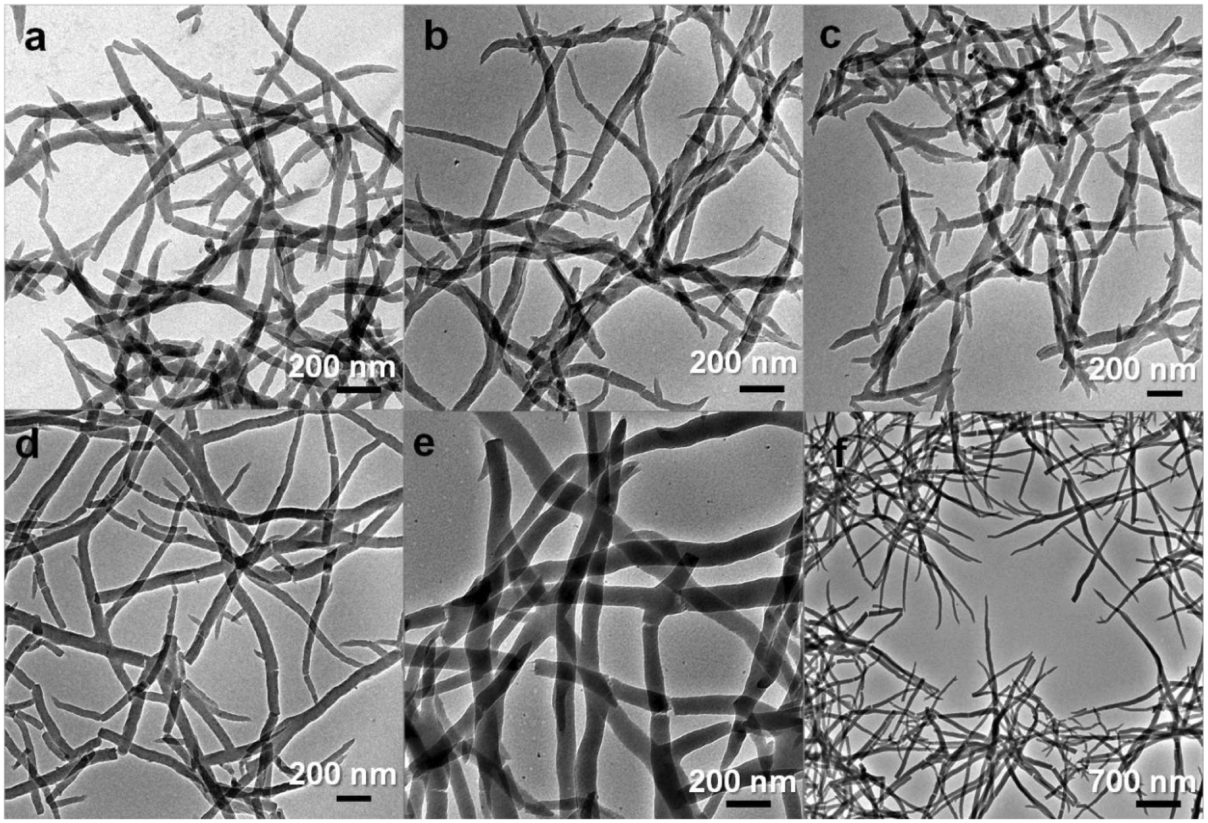


Figure 9. TEM images of SPANi synthesized in the following acidic medium: (a) HCl, (b) H_2SO_4, (c) CSA, (d) HNO_3, (e) $HClO_4$, or (f) *p*-TSA in the presence of 2.5 mol % *N*-phenyl-*p*-phenylenediamine per comonomer in 1.0 mol/L HCl, at a fixed ASA/aniline molar ratio of 50/50.

only a broad peak at 2θ = 21.5−23.1° that can be attributed to periodicity parallel and perpendicular to the semicrystalline PANi-like main chains.[30] Note that a minor peak around 2θ = 28° is observed for SPANi synthesized by $HClO_4$ (Figure 5d). This may correspond to classical $\pi-\pi$ stacking between aromatic rings of the more crystalline SPANi nanostructures. This result is consistent with rectangular nanoplates of oligoaniline induced by $HClO_4$.[31] By changing the size of the acidic dopants, the center of the peak exhibits a visible difference due to the variable supramolecular structures. Conducting polymer molecular chains are usually long and semirigid in sections. The dopant anions reside near the positively charged polymers due to ionic attractions. Thus, the dopants appear to affect the diameter of the nanofibers, and thus change their interchain packing distance and ultimately, the supramolecular structures.

Morphology, Size, and Dimensionality. Morphology, size and dimensionality control of organic nanostructures remains a significant challenge within the field of organic conductors and continues to draw much interest. SPANi synthesized by previously reported methods possesses a granular, agglomerated morphology.[28] By altering the ASA/aniline molar ratios, the aniline derivatives and the acid media, the morphology, nanosize and dimensionality of SPANi can be tuned by chemical oxidative polymerization of the monomers in the presence of the initiator, *N*-phenyl-*p*-phenylenediamine. SEM and TEM images of the resulting SPANi dispersions show that entangled nanofibers are created during this process (Figures 6 and 7). By increasing the ASA and aniline molar ratio from 0/100 to 70/30, the diameters, lengths and aspect ratios of the SPANi nanofibers change from 50 to 60 nm, 1.0 to 0.7 μm and 20.0 to 11.7 (Table 1), respectively. Increasing the number of ASA units in the SPANi chain produces shorter yet larger diameter nanofibers, which is likely due to the improved water-solubility. Note that the percentage of aniline can be as low as 10% to generate sulfonated polyaniline copolymer nanofibers. In addition, by adjusting the order in which the monomers are added, i.e. adding aniline first to form the nanofiber seeds and then ASA, we believe that the aniline and initiator will polymerize first, then the oxidant induces ASA to polymerize, finally producing PANi nanofibers doped by poly(o-aminobenzenesulfonic acid).

Previous studies have demonstrated that altering the size of the acid used is an effective method for tuning the size of polyaniline nanofibers and polypyrrole nanospheres,[32,33] and therefore, similar results were expected for SPANi nanofibers. The effect of the acidic medium on the size and nanomorphology of SPANi synthesized by an ASA/aniline molar ratio of 50/50 were examined by both SEM and TEM. When HCl, H_2SO_4 or CSA was used, entangled 1-D nanofibers formed and exhibit average diameters of 55−65 nm, lengths of 0.75−2.1 μm and aspect ratios of 13−34 (Figure 8a−c and Figure 9a−c). As the acidic medium is changed to HNO_3, $HClO_4$ or *p*-TSA, the resulting nanofibers possess average diameters and lengths with values up to 75 nm and 4.5 μm, Figure 8d−f and Figure 9d−f, respectively. These nanofibers are also less entangled and longer than nanofibers produced by HCl, H_2SO_4 or CSA. In particular, the aspect ratio of the partially arranged nanofibers is calculated to be as high as 60.0 when *p*-TSA was used (Table 2). As is well-known, when a conjugated polymer is doped with an acid, the polymeric chains become protonated and positively charged. The

dx.doi.org/10.1021/ma2024446 | *Macromolecules* 2012, 45, 1570−1579

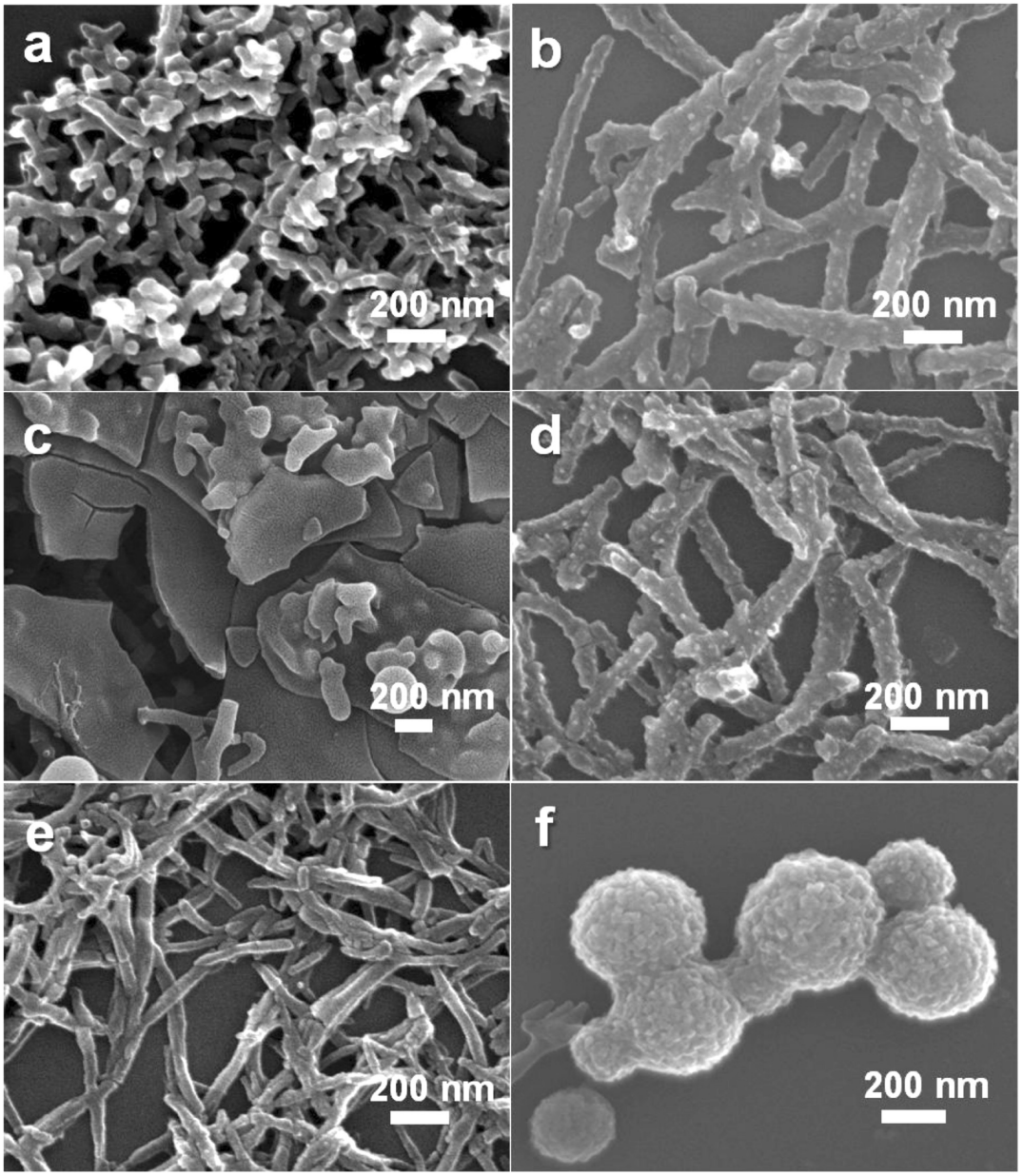


Figure 10. SEM images of SPANi synthesized with the following 2-substituted group (R) on aniline: (a) Cl, (b) OCH_3, (c) SCH_3, (d) OC_2H_5, (e) CH_3, or (f) OH in the presence of 2.5 mol % *N*-phenyl-*p*-phenylenediamine per comonomer in 1.0 mol/L HCl, at a fixed ASA/aniline ratio of 50/50.

negatively charged dopant anions reside near the positively charged polymer backbone due to ionic attractions. The size and charge density of the doping acids thus influence the interchain packing distance and ultimately the supramolecular morphology. Moreover, different acids also change the solubility of the initiator, monomers and as-formed polymers/oligomers, which also affect the diameters of the resulting nanofibers. This explains why the dopant-induced nanoscale morphology controls the size of SPANi.

In addition, the nanomorphology and dimensionality of SPANi can be readily tuned by choosing aniline derivatives with different 2-substituents. When ASA was copolymerized with aniline derivatives like 2-chloroaniliene, 2-methylaniline, 2-methoxyaniline, 2-ethoxyaniline, 2-methylmercaptoaniline, or 2-hydroxyaniline at the same molar ratio of 50/50, the SPANi formed displays drastically different morphologies of 1-D nanofibers, 1-D nanosticks, 1-D nanothorns, 1-D nanorods, 2-D nanoplates, or 3-D nanospheres (Figure 10), respectively. TEM images of SPANi confirm that the nanomorphology and dimensionality are similar to their SEM images (Figure 11). Interestingly, the TEM images show that porous nanospheres have been created by copolymerizing ASA and 2-hydroxylaniline. The substituent groups dramatically control the basic morphology of SPANi synthesized using the rapid initiated copolymerization. This phenomenon is consistent with the results reported for pristine PANi synthesized using both interfacial polymerization and rapidly mixed reactions.[34] The differences in morphology observed among these aniline derivatives when copolymerizing these monomers with ASA suggests that the basicity, solubility, redox potential and bulk volume of the monomers affect which nanostructures are observed: 1-D nanofibers, 1-D nanosticks,

dx.doi.org/10.1021/ma2024446 | *Macromolecules* 2012, 45, 1570−1579

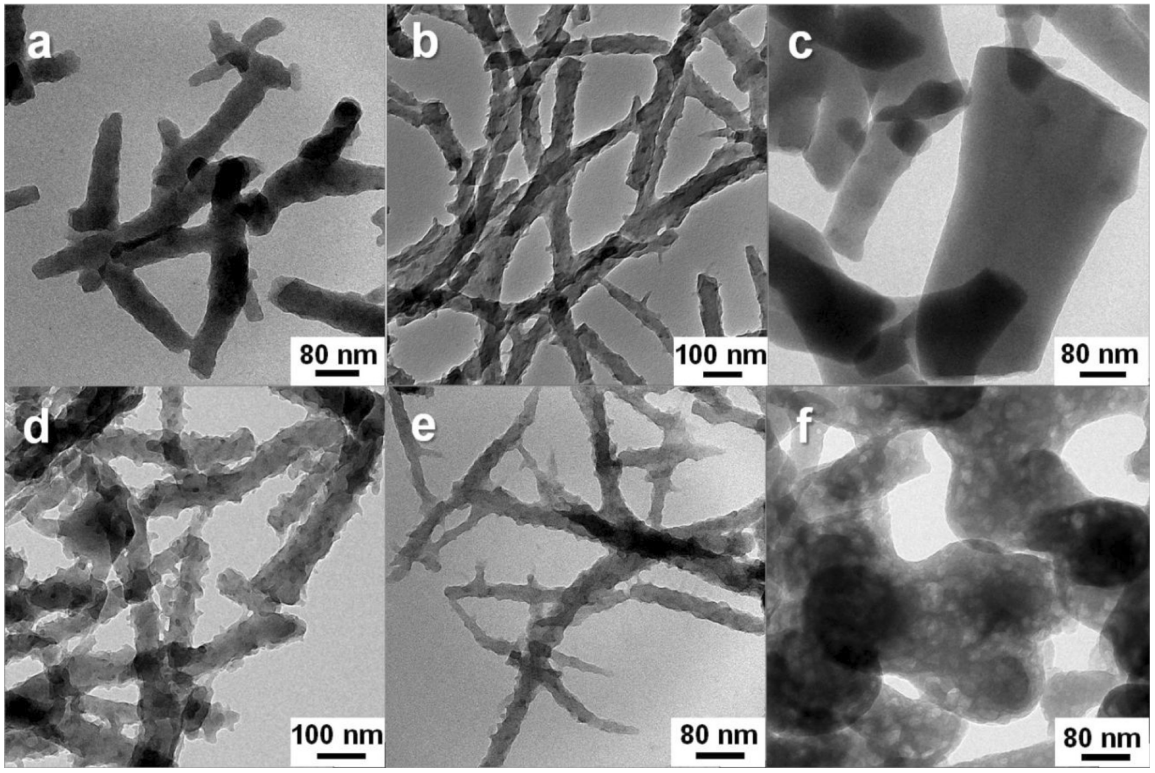


Figure 11. TEM images of SPANi synthesized with the following 2-substituted group (R) on aniline: (a) Cl, (b) OCH_3, (c) SCH_3, (d) OC_2H_5, (e) CH_3, or (f) OH in the presence of 2.5 mol % *N*-phenyl-*p*-phenylenediamine per comonomer in 1.0 mol/L HCl, at a fixed ASA/aniline derivative ratio of 50/50.

1-D nanothorns, 1-D nanorods, 2-D nanoplates, or 3-D nanospheres.

■ CONCLUSIONS

We have successfully synthesized a variety of sulfonated polyaniline (SPANi) nanostructures via rapid initiated copolymerization of *o*-aminobenzenesulfonic acid and aniline or aniline derivatives in the presence of a catalytic amount of *N*-phenyl-*p*-phenylenediamine in an acidic medium. The nanomorphology, dimensionality, chemical composition and electrical properties of SPANi were systemically characterized using SEM, TEM, UV−vis, ATR-FT-IR, XRD, and two-point probe techniques. By regulating the comonomer molar ratios, aniline derivatives used and acid media employed, 1-D nanofibers, nanosticks, nanothorns, and nanorods, 2-D nanoplates and 3-D porous nanospheres of SPANi are readily generated. In particular, the SPANi nanofibers exhibit length and aspect ratios with values up to 4.5 μm and 60, respectively, making the fabrication of single-wire devices and postsynthetic alignment possible. The SPANi nanostructures can be easily processed in many aqueous or organic solvents such as DMF, and demonstrate much better conductivity at pH values of 5.5−6.0 than their polyaniline counterparts (10^{-2} S/cm vs 10^{-8} S/cm). The SPANi nanostructures are therefore ideal candidates for electrode materials for the development of high-performance, high-power and flexible bioelectronic devices.

■ AUTHOR INFORMATION

Corresponding Author

*E-mail: (R.B.K.) kaner@chem.ucla.edu; (X.W.) wangxia@usst.edu.cn.

Notes

The authors declare no competing financial interest.

■ ACKNOWLEDGMENTS

Financial support from Abraxis Bioscience now CalCap Equity (RBK), the China Scholarship Council No. 2008626064, the Starting Fund from the University of Shanghai for Science and Technology (10-00-310-001), the Key Project of Science and Technology of Shanghai Commission (No. 10JC1411700) and the National Natural Science Foundation of China (No. 50873077) (Y.Z.L.) are gratefully acknowledged.

■ REFERENCES

(1) Li, D.; Huang, J. X.; Kaner, R. B. Polyaniline nanofibers: A unique polymer nanostructure for versatile applications. *Acc. Chem. Res.* **2009**, *42* (1), 135−145.

(2) Tran, H. D.; Li, D.; Kaner, R. B. One-dimensional conducting polymer nanostructures: Bulk synthesis and applications. *Adv. Mater.* **2009**, *21* (14−15), 1487−1499.

(3) Tran, H. D.; D'Arcy, J. M.; Wang, Y.; Beltramo, P. J.; Strong, V.; Kaner, R. B. The oxidation of aniline to produce "polyaniline": A process yielding many different nanoscale structures. *J. Mater. Chem.* **2011**, *21* (11), 3534−3550.

(4) Thiyagarajan, M.; Samuelson, L. A.; Kumar, J.; Cholli, A. L. Helical conformational specificity of enzymatically synthesized water-soluble conducting polyaniline nanocomposites. *J. Am. Chem. Soc.* **2003**, *125* (38), 11502−11503.

(5) Huang, J. X.; Virji, S.; Weiller, B. H.; Kaner, R. B. Polyaniline nanofibers: Facile synthesis and chemical sensors. *J. Am. Chem. Soc.* **2003**, *125* (2), 314−315.

(6) MacDiarmid, A. G. Synthetic metals": A novel role for organic polymers (Nobel Lecture). *Angew. Chem., Int. Ed.* **2001**, *40* (14), 2581−2590.

(7) Yue, J.; Epstein, A. J. Synthesis of self-doped conducting polyaniline. *J. Am. Chem. Soc.* **1990**, *112* (7), 2800−2801.
(8) Lee, W.; Du, G.; Long, S. M.; Epstein, A. J.; Shimizu, S.; Saitoh, T.; Uzawa, M. Charge transport properties of fully-sulfonated polyaniline. *Synth. Met.* **1997**, *84* (1−30), 807−808.
(9) Ito, S.; Murata, K.; Teshima, S.; Aizawa, R.; Asako, Y.; Takahashi, K.; Hoffman, B. M. Simple synthesis of water-soluble conducting polyaniline. *Synth. Met.* **1998**, *96* (2), 161−163.
(10) Hwang, G. W.; Chen, S. A. Structure characterization of self-acid-doped sulfonic acid ring-substituted polyaniline in its aqueous solutions and as solid film. *Macromolecules* **1996**, *29* (11), 3950−3955.
(11) Yamamoto, T.; Ushiro, A.; Yamaguchi, I.; Sasaki, S. Synthesis, structure, and chemical properties of lithium salts of poly-(2-methoxyaniline-5-sulfonic acid). *Macromolecules* **2003**, *36* (19), 7075−7081.
(12) Pornputtkul, Y.; Strounina, E. V.; Kane-Maguire, L. A. P.; Wallace, G. G. Redox behavior of poly(2-methoxyaniline-5-sulfonic acid) and its remarkable thermochromism, solvatochromism, and ionochromism. *Macromolecules* **2010**, *43* (23), 9982−9989.
(13) Rahmanifar, M. S.; Mousavi, M. F.; Shamsipur, M. Effect of self-doped polyaniline on performance of secondary Zn−polyaniline battery. *J. Power Sources* **2002**, *110* (1), 229−232.
(14) Yang, C. H.; Chih, Y. K. Molecular assembled self-doped polyaniline interlayer for application in polymer light-emitting diode. *J. Phys. Chem. B* **2006**, *110* (39), 19412−19417.
(15) Huh, P.; Kim, S. C.; Kim, Y. H.; Wang, Y. P.; Singh, J.; Kumar, J.; Samuelson, L. A.; Kim, B. S.; Jo, N. J.; Lee, J. O. Optical and electrochemical detection of saccharides with poly(aniline-co-3-aminobenzeneboronic acid) prepared from enzymatic polymerization. *Biomacromolecules* **2007**, *8* (11), 3602−3607.
(16) Ali, S. R.; Ma, Y. F.; Parajuli, R. R.; Balogun, Y.; Lai, W. Y. C.; He, H. X. A nonoxidative sensor based on a self-doped polyaniline/carbon nanotube composite for sensitive and selective detection of the neurotransmitter dopamine. *Anal. Chem.* **2007**, *79* (6), 2583−2587.
(17) Yang, Y. Y.; Min, Y.; Wu, J-C.; Hansford, D. J.; Feinberg, S. E.; Epstein, A. J. Synthesis and Characterization of Cytocompatible Sulfonated Polyanilines. *Macromol. Rapid Commun.* **2011**, *32* (12), 887−892.
(18) Silva, W. J. D.; Hümmelgen, I. A. Mello RMO. Sulfonated polyaniline/n-type silicon junctions. *J. Mater. Sci.* **2009**, *20* (2), 123−126.
(19) Yang, C. H.; Chih, Y. K.; Wu, W. C.; Chen, C. H. Molecular assembly engineering of self-doped polyaniline film for application in electrochromic devices. *Electrochem. Solid-State Lett.* **2006**, *9* (1), C5−C8.
(20) Masdarolomoor, F.; Innis, P. C.; Ashraf, S.; Kaner, R. B.; Wallace, G. G. Nanocomposites of polyaniline/poly(2-methoxyaniline-5-sulfonic acid). *Macromol. Rapid Commun.* **2006**, *27* (23), 1995−2000.
(21) Li, X. G.; Lü, Q. F.; Huang, M. R. Self-stabilized nanoparticles of intrinsically conducting copolymers from 5-sulfonic-2-anisidine. *Small* **2008**, *4* (8), 1201−1209.
(22) Deore, B. A.; Yu, I.; Freund, M. S. A switchable self-doped polyaniline: Interconversion between self-doped and non-self-doped forms. *J. Am. Chem. Soc.* **2004**, *126* (1), 52−53.
(23) Yu, I.; Deore, B. A.; Recksiedler, C. L.; Corkery, T. C.; Abd-El-Aziz, A. S.; Freund, M. S. Thermal stability of high molecular weight self-doped poly(anilineboronic acid). *Macromolecules* **2005**, *38* (24), 10022−10026.
(24) Gupta, B.; Prakash, R. Synthesis of functionalized conducting polymer "polyanthranilic acid" using various oxidizing agents and formation of composites with PVC. *Polym. Adv. Technol.* **2011**, *22* (12), 1982−1988.
(25) Chan, H. S. O.; Ho, P. K. H.; Ng, S. C.; Tan, B. T. G.; Tan, K. L. A new water-soluble, self-doping conducting polyaniline from poly(o-aminobenzylphosphonic acid) and its sodium salts: Synthesis and characterization. *J. Am. Chem. Soc.* **1995**, *117* (33), 8517−8523.
(26) Liao, Y. Z.; Zhang, C.; Zhang, Y.; Strong, S.; Tang, J. S.; Li, X. G.; Kalantar-zadeh, K.; Hoek, E. M. V.; Wang, K. L.; Kaner, R. B. Carbon nanotube/polyaniline composite nanofibers: Facile synthesis and chemosensors. *Nano Lett.* **2011**, *11* (3), 954−959.
(27) Shao, Z. F.; Rannou, P.; Sadki, S.; Fey, F.; Lindsay, D. M. Faul CFJ. Delineating poly(Aniline) redox chemistry by using tailored oligo(aryleneamine)s: Towards oligo(aniline)-based organic semiconductors with tunable optoelectronic properties. *Chem.—Eur. J.* **2011**, *17* (44), 12512−12521.
(28) Mu, S. L. Polyaniline with two types of functional groups: Preparation and characteristics. *Macromol. Chem. Phys.* **2005**, *206* (6), 689−695.
(29) Li, G. C.; Zhang, C. Q.; Peng, H. R.; Chen, K. Z.; Zhang, Z. K. Hollow self-doped polyaniline micro/nanostructures: Microspheres, aligned pearls, and nanotubes. *Macromol. Rapid Commun.* **2008**, *29* (24), 1954−1958.
(30) Wang, Y.; Tran, H. D.; Liao, L.; Duan, X.; Kaner, R. B. Nanoscale Morphology, Dimensional Control, and Electrical Properties of Oligoanilines. *J. Am. Chem. Soc.* **2010**, *132* (30), 10365−10373.
(31) Xia, H. S.; Wang, Q. Ultrasonic irradiation: A novel approach to prepare conductive polyaniline/nanocrystalline titanium oxide composites. *Chem. Mater.* **2002**, *14* (5), 2158−2165.
(32) Huang, J. X.; Kaner, R. B. A general chemical route to polyaniline nanofibers. *J. Am. Chem. Soc.* **2004**, *126* (3), 851−855.
(33) Liao, Y. Z.; Li, X. G.; Kaner, R. B. Facile synthesis of water-dispersible conducting polymer nanospheres. *ACS Nano* **2010**, *4* (9), 5193−5202.
(34) Huang, J. X.; Kaner, R. B. The intrinsic nanofibrillar morphology of polyaniline. *Chem. Commun.* **2006**, *4*, 367−376.

Macromolecules

Article

pubs.acs.org/Macromolecules

Enhanced Piezoelectricity of Nanoimprinted Sub-20 nm Poly(vinylidene fluoride−trifluoroethylene) Copolymer Nanograss

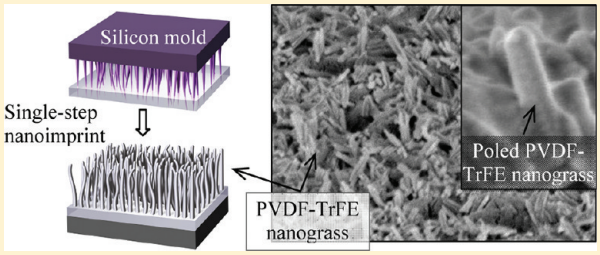
Chien-Chong Hong,*[,†] Sheng-Yuan Huang,[†] Jiann Shieh,[‡] and Szu-Hung Chen[§]

[†]Department of Power Mechanical Engineering, National Tsing Hua University, Hsinchu, Taiwan

[‡]Department of Materials Science and Engineering, National United University, Miaoli, Taiwan

[§]National Nano Device Laboratories, Hsinchu, Taiwan

ABSTRACT: In this paper, sub-20 nm ferroelectric PVDF−TrFE copolymer nanograss structures with aspect ratios up to 8.9 were developed. This study demonstrated sub-20 nm PVDF−TrFE nanograss structures that are nanoimprinted using a silicon nanograss mold in a single step. Vertically oriented PVDF−TrFE nanopillars were poled using the developed flip-stacking poling method. According to the PFM measurements, the piezoelectricity of flat thin films fabricated in this work reaches 14.0 pm/V. The maximum output voltage of the single PVDF−TrFE nanopillar was 526 mV, and the maximum piezoelectricity of the single PVDF−TrFE nanopillar was 210.4 pm/V. The piezoelectricity of the developed PVDF−TrFE nanograss structures was 5.19 times larger than that of the PVDF−TrFE flat thin films. The developed technique is simple, economical, and easy to fabricate. The developed ferroelectric PVDF−TrFE copolymer nanograss structures, which showed enhanced piezoelectricity compared to the PVDF−TrFE flat thin films, have potential applications in nanotip-based protein biosensors, nanotip-based tactile sensors, and power nanogenerators.



INTRODUCTION

For decades, ferroelectric materials, a functional material, have attracted considerable interest from scientists and engineers. The physical properties of ferroelectric inorganic materials such as polarization, piezoelectricity, and pyroelectricity have been studied extensively.[1,2] Ferroelectric inorganic materials on the nanoscale, such as zinc oxide (ZnO) nanowires, PZT nanofibers, and AlGaN nanostructures, have been developed and realized in power generation and biosensors in recent years.[3,4] In addition to fabricating devices or systems with ferroelectric inorganic materials, recent studies have focused on ferroelectric polymer materials. Ferroelectric polymers have received more attention than ferroelectric inorganic materials because of their solution processability, low processing temperature, low cost, and high flexibility.

In recent years, the piezoelectricity, ferroelectricity, and pyroelectricity of ferroelectric polymers such as poly(vinylidene fluoride) (PVDF) and its copolymers with trifluoroethylene (PVDF−TrFE) have been widely investigated.[5−9] Whereas the copolymers' unit cells are less polar than those of pure PVDF, the copolymers typically have a substantially higher crystallinity, resulting in a larger piezoelectric response. Because of its excellent ferroelectric and piezoelectric properties, PVDF−TrFE is widely used in tactile sensors, solar cells, field-effect transistors, nonvolatile memory devices, IR image sensors, pressure sensors, and acoustic sound transducers.[10−15] Surface morphology of the functional materials significantly affects transducer performance. Researchers successfully developed fabrication technologies for PVDF nanofibers, which have diameters ranging from 6.5 μm to 500 nm, using electrospinning to improve piezoelectricity because of their fiber structures.[16] In addition to performance enhancement in fiber forms, circular PVDF microstructures with a diameter of 5 μm and a height of 5 μm show 3 times more piezoelectricity than flat thin films.[17] Recently, studies have focused on feature sizes below 100 nm for polymers, and the physical and chemical properties of developed novel polymer HAR nanostructures remain under investigation. However, high-aspect-ratio (HAR) PVDF−TrFE nanostructures and PVDF−TrFEs with a feature size of below 100 nm have not yet been realized and studied.

Several techniques have been developed to realize localized polarization on PVDF−TrFE films using AFM tips to study ferroelectricity and piezoelectricity on a nano/microscale ranging from 10 nm to 10 μm.[18−22] To date, only a few studies focused on large-area fabrication and polarization for nano/microstructured ferroelectric polymers.[23−25] Among the nanofabrication techniques for polymer fabrication, nanoimprint lithography (NIL) is one of the most promising technologies for mass production on the nanoscale. NIL is often used to replicate the inverse patterns of original master structures. To date, although several studies have successfully achieved amorphous polymer nanostructures, such as cyclic olefin copolymer (COC) and poly(methyl methacrylate) (PMMA), under 20 nm using NIL,[26,27] no study has realized

Received: November 10, 2011
Revised: January 9, 2012
Published: January 30, 2012

 © 2012 American Chemical Society

and examined HAR semicrystalline polymer nanostructures under 20 nm. This study is one of the first to examine HAR ferroelectric PVDF−TrFE copolymer nanograss of less than 20 nm using the silicon nanograss mold structure created by thermal NIL.

We previously reported on morphology-controlled sub-20 nm COC plastic nanotip and nanopore arrays using an identical silicon nanograss mold.[27] The developed novel nanoimprint technique can compose positive patterns with positive master molds in only one step. It reduces the fabrication process and material costs substantially and increases the robustness of the process. We created sub-20 nm ferroelectric PVDF−TrFE copolymer nanograss structures on thin films employing a silicon nanograss master mold in one step using thermal nanoimprinting and fabricated and polarized PVDF−TrFE nanograss structures. This study investigates the piezoelectricity of vertically aligned PVDF−TrFE nanograss using piezoelectric force microscopy (PFM).

FABRICATION PROCESS

Figure 1 shows a schematic illustration of the fabrication process of PVDF−TrFE piezoelectric nanograss on PVDF−TrFE film surfaces. Thus, far, for the polarization process of ferroelectric polymer nanostructures, most studies have coated metal layers onto low-aspect-ratio PVDF−TrFE nanostructures and have poled them to obtain piezoelectricity. However, applying poling to high-aspect-ratio polymer nanostructures is a challenge. Coating thin metal layers onto polymer nanotips would not survive during polarization because of the strong electrical field, but coating thick metal layers could reduce polymer nanotip flexibility considerably, which would decrease piezoelectric performance. Here, vertically oriented PVDF−TrFE nanopillars were poled using the developed flip-stacking poling method, whereas other noncontact collapsed nanopillars were less poled, as shown in Figure 1c. No metal layer is needed to coat on polymer nanotips for polarization. We used a silicon mold to nanoimprint nanostructures on a PVDF−TrFE thin film. This study uses well-aligned silicon nanograss of sub-20 nm with high aspect ratio, fabricated on a 6 in. silicon wafer through hydrogen plasma etching alone as a thermal nanoimprinting mold. The scanning electron microscopy (SEM) pictures of the silicon nanograss master mold are shown in Figure 2.

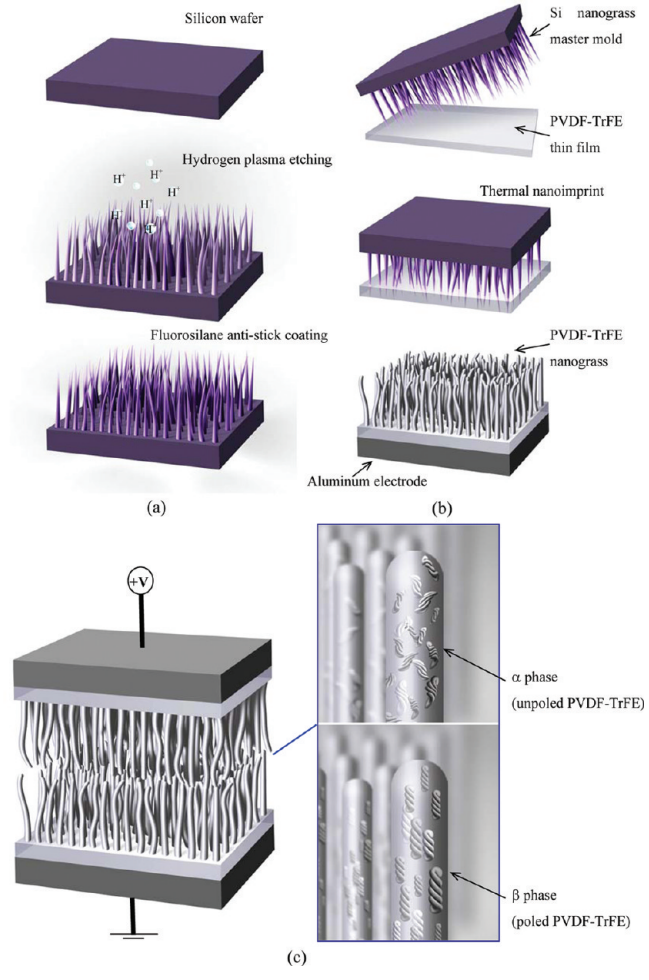
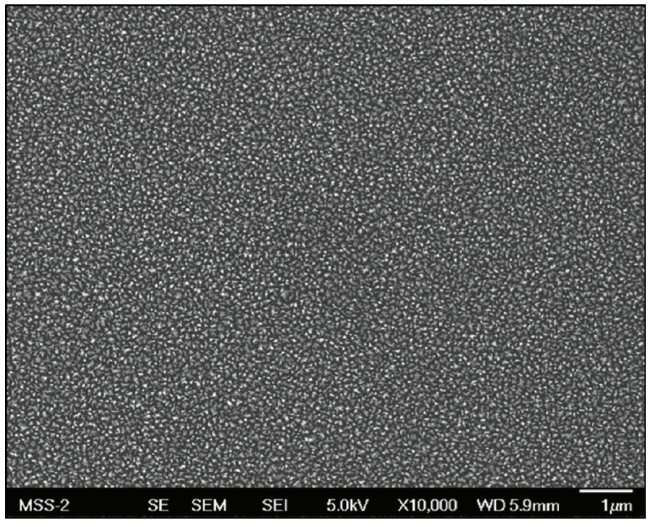
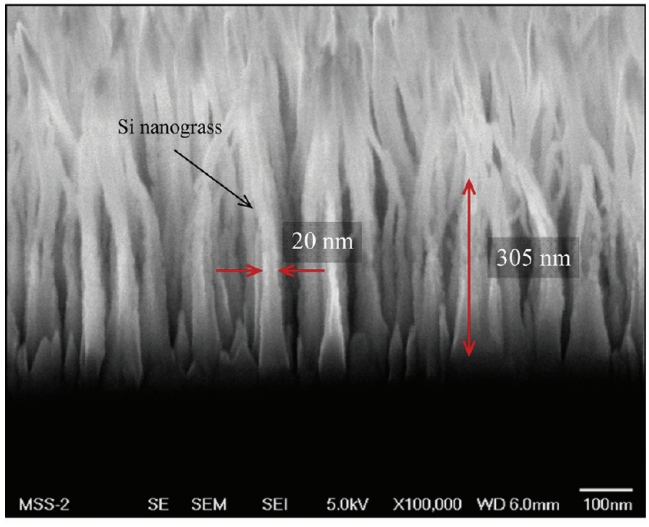


Figure 1. Schematic drawing of the fabrication process to realize PVDF−TrFE piezoelectric nanograss on polymer surfaces: (a) the fabrication steps of silicon nanograss mold, (b) the nanoimprint process of PVDF−TrFE polymer nanograss, and (c) the polarization process of PVDF−TrFE polymer nanograss.



(a)



(b)

Figure 2. SEM pictures of the silicon nanograss master mold: (a) the top view and (b) the inclined 70° view.

dx.doi.org/10.1021/ma202481t | Macromolecules 2012, 45, 1580−1586

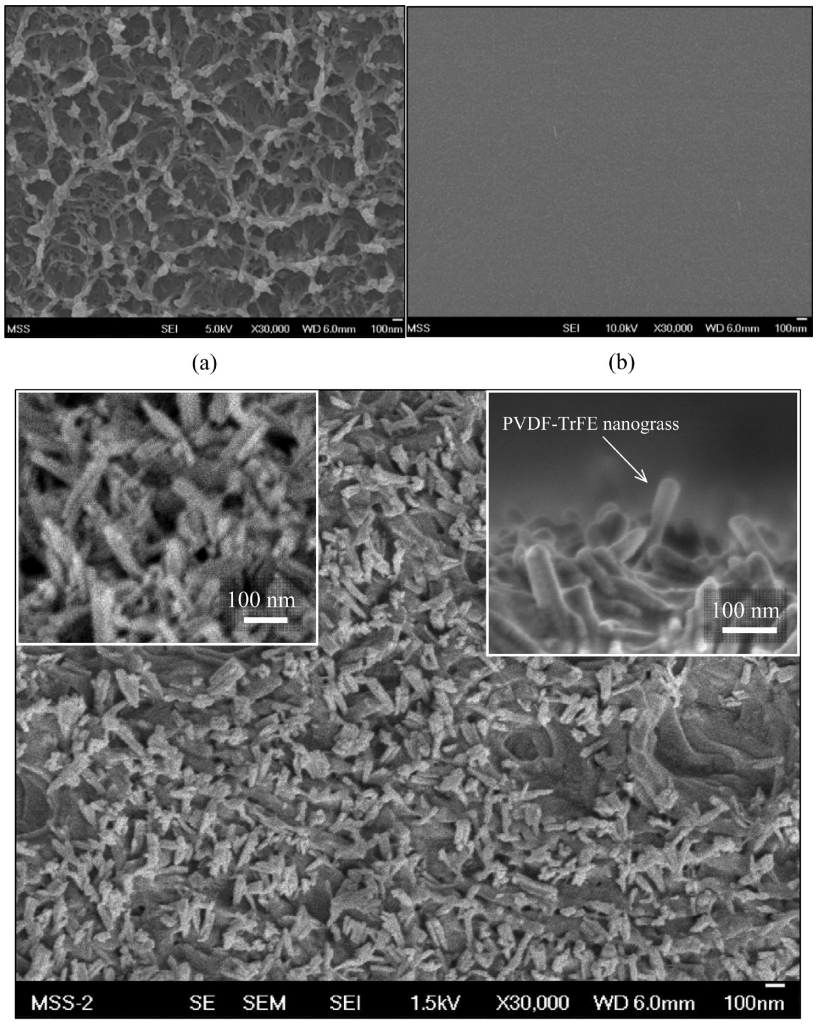


Figure 3. SEM pictures of the fabrciated PVDF−TrFE films: (a) the top view of the cast-molded PVDF−TrFE nanostructures, (b) the top view of the flat thin film before thermal nanoimprint, and (c) the top view of the PVDF−TrFE nanograss by thermal nanoimprint. The left inset image is the inclined 70° view with high magnification. The right inset image is the side view with high magnification.

The master mold was fabricated in a single step through hydrogen plasma etching without any mask or catalyst. We placed the 6 in. silicon ⟨100⟩ wafer in the plasma chamber and heated it to 400 °C before introducing hydrogen gas at a rate of 200 sccm. The 500 W RF and 300 kHz bias powers were turned on to start plasma etching. The morphologies and aspect ratio of nanograss structures can be modified by adjusting the duration of the plasma process. The detailed procedure of silicon master molds has been published in a previous paper by our coauthor, J. Shieh.[28] In this study, the silicon wafer was etched to obtain 20 nm nanotip arrays with an aspect ratio of 15 on the surface of the 6 in. silicon wafer. To reduce the surface energy of the silicon master mold for ease of demolding, chemical vapor deposition techniques were used at 250 °C for 2 h to deposit trichloro(1*H*,1*H*,2*H*,2*H*-perfluorooctyl)silane (97%, Sigma-Aldrich, St. Louis, MO) on the silicon surface. After the process, the silicon master mold was washed with hexane. The self-assembled monolayer, which had an extremely low surface energy because of its CF groups, was applied to the silicon surface. The contact angle of the fluorosilane-coated silicon nanograss surface is 158°.

PVDF−TrFE copolymer powder with a molar ratio of 77/23, obtained from Piezo Inc., was dissolved in methyl ethyl ketone (MEK) and spin-coated onto a silicon substrate, with 400 nm Al evaporated as a bottom electrode for the polarization process and PFM measurements. The concentration of PVDF−TrFE was 10% by mass fraction. The film thickness in all of our experiments was 3 μm at a spin speed of 4000 rpm for 60 s. The spin-coated films were then dried at 85 °C for 5 min. The silicon nanograss mold was used for nanoimprinting PVDF−TrFE surfaces with a molding temperature of 90 °C. We performed nanoimprinting at a fixed pressure using a hydraulic hot-press machine as a hot-embossing machine, which consisted of a heating and pressing component. The heating component used a heating coil to produce and distribute heat to the pressing component, employing a heat spreader with a proportional−integral−derivative controller to regulate the set temperature. The pressing component used hydraulic jacks to exert forces and was connected to a pressure gauge that measured the forces. First, a stack of silicon nanograss mold and PVDF−TrFE wafer were heated to specific molding temperature. When the specimen was evenly heated, an initial pressure

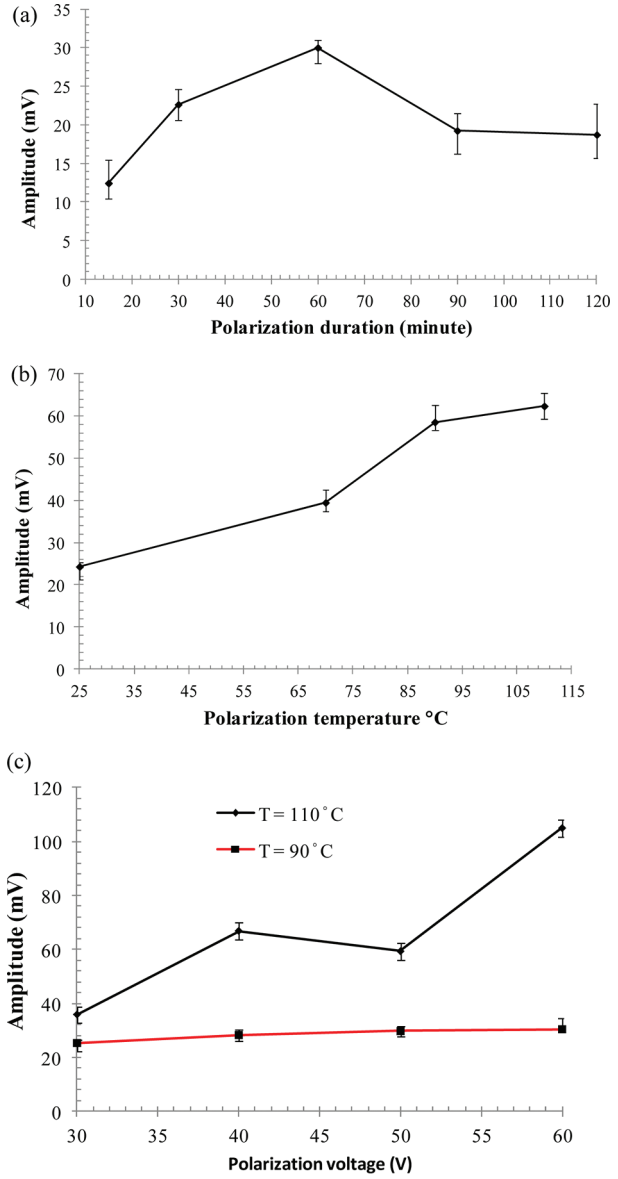


Figure 4. Polarization characterization of the fabricated PVDF−TrFE flat thin films: (a) the PFM amplitude response for different polarization durations, (b) the PFM amplitude response for different polarization temperatures, and (c) the PFM amplitude response for different polarization voltages.

of 0.1 MPa was applied to the wafer's surface to transmit the heat evenly to the wafers. This initial process lasted 5 min before reaching a steady temperature. Once the wafer temperature reached the specified level, the polymer microstructure hot-press molded it by applying a hot-press pressure of 1 MPa onto the PVDF−TrFE wafer and the silicon nanograss mold through the hydraulic rod, extruding the softened polymer material to fill the nanocavities in the mold. We maintained temperature and pressure at a fixed level, and after 30 min, thermal nanoimprinting was complete. After molding, we turned off the temperature switch to allow the temperature to cool gradually to room temperature. After removing the applied pressure, the PVDF−TrFE copolymer nanostructures were self-detached from the silicon nanograss master mold.

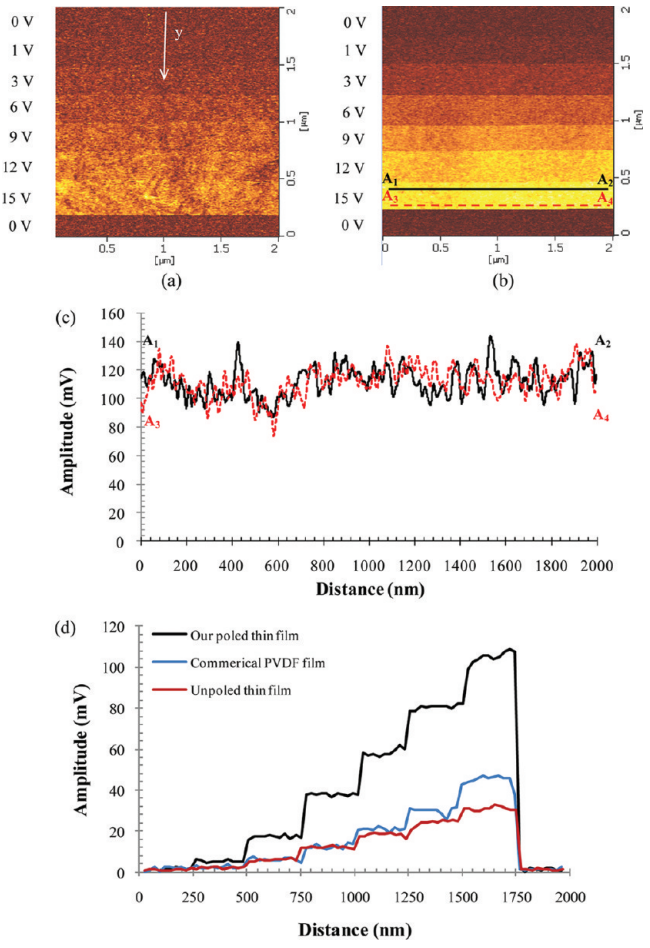


Figure 5. Polarization measurements of the fabricated PVDF−TrFE flat thin films: (a) the PFM amplitude image of the unpoled thin film, (b) the PFM amplitude image of our poled thin film for the best polarization condition, (c) the scan graphs of the PFM amplitude response along line A_1−A_2 and line A_3−A_4, and (d) the comparisons of unpoled thin film, commercial PVDF film, and our poled thin film.

RESULTS AND DISCUSSION

SEM is used to examine the morphology and side view of the nanoimprinted PVDF−TrFE thin film, with a 9 nm thick layer of platinum sputtered on the nanostructures to avoid surface charging. Figure 3a shows that on the PVDF−TrFE thin film, cast-molded on a Si nanograss mold, the PVDF−TrFE solution cannot fill the mold cavities completely to replicate negative nanostructures. Figure 3b shows the surface morphology of the PVDF−TrFE flat thin films before nanoimprinting. Figure 3c shows the SEM pictures of the top view of the nanoimprinted sub-20 nm polymer nanotips with a molding temperature of 90 °C. The SEM images show the fabricated PVDF−TrFE nanograss with a diameter of 19 nm and a length of 169 nm created using thermal nanoimprinting. We found that PVDF−TrFE nanograss structures, which have an aspect ratio of 8.9, can be replicated easily and in only one step using the silicon positive mold. The density of PVDF−TrFE nanograss structures is approximately $1 \times 10^{10}/\mathrm{cm}^2$. In the previous study, COC polymer nanotips with Young's module of 4 GPa remained vertical after the nanoimprinting. However, PVDF−TrFE copolymer nanopillars with Young's module of 2 GPa partially collapsed after the nanoimprinting.

dx.doi.org/10.1021/ma202481t | *Macromolecules* 2012, 45, 1580−1586

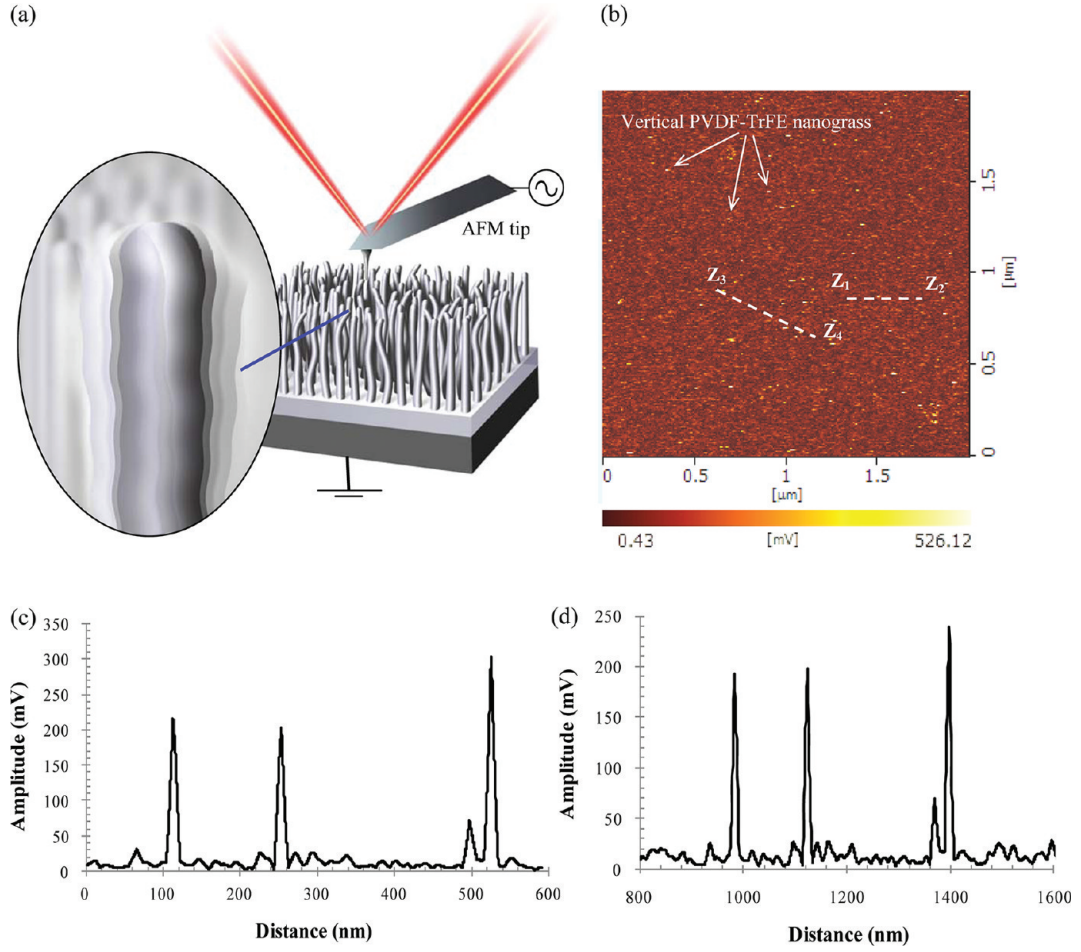


Figure 6. PFM measurements of the nanoimprinted PVDF−TrFE polymer nanograss: (a) the PFM measurement setup, (b) the image of the PFM amplitude of the PVDF−TrFE polymer nanograss, (c) the scanning graph of the piezoelectric response along the line Z_1−Z_2, and (d) the scanning graph of the piezoelectric response along the line Z_3−Z_4.

PVDF−TrFE exists in several forms: alpha (TGTG′), beta (TTTT), and gamma (TTTGTTTG′) phases, depending on the chain conformations as trans (T) or gauche (G) linkages. Processed materials are in the nonpiezoelectric alpha phase, and thus, the PVDF−TrFE requires the polarization process to reach the piezoelectric beta phase with well-oriented dipoles. To obtain a piezoelectric response, we must first pole the material in an electric field and at an elevated temperature. We performed the polarization process with PVDF−TrFE thin films, which affects the performance of PVDF−TrFE substantially. To investigate the polarization process, we examined the piezoelectric responses of the PVDF−TrFE thin films using the PFM module of AFM (SEIKO SPA-300HV) in contact mode and a ConE-G-10 cantilever composed of a platinum-coated silicon tip. The AFM tip had a spring constant of 0.2 N/m. To image the piezoelectric response, ac driving voltage at 5 kHz ranging from 0 to 15 V was applied to the AFM tip without a dc bias during the scanning. Each scanning distance for one voltage step is 250 nm.

Polarization of ferroelectric polymers had to be accomplished above the phase transition temperatures. Additionally, ferroelectric copolymer properties disappeared above the Curie point, which is 90 °C for PVDF−TrFEs. So, polarization was performed after thermal nanoimprinting. The annealing process was applied to vaporize the solvent from the polymer films and also increase the degree of crystallization, which increases poling effects. The annealing temperature was set to 120 °C for 2 h. In addition to the polarization temperatures and applied poling voltages, polarization duration plays an important role in ferroelectric polymers. An applied electrical field affects the orientation of dipoles in the polymers, and high temperatures reduce the resistance of dipole moments during poling. Completeness of rotation of dipoles is dependent on poling duration. The interval for each dipole to rotate to a specific orientation is different because of the random structure orientations of dipoles before the process. Short poling duration results in less piezoelectricity in ferroelectric polymers. However, cumulative cumbersome thermal energy caused by long poling duration could hinder dipole orientation, which would decrease the piezoelectricity of the ferroelectric polymers. Therefore, optimization of poling duration in ferroelectric polymers must be investigated. According to our study, the best duration is 60 min, which yields a piezoelectric response 50% higher than that at a poling duration of 120 min, as shown in Figure 4a. The polarization temperature is important for ferroelectric polymers. It could be applied to reduce the resistance of dipole moments, which increases poling effects. We found that polarization temperatures increase piezoelectric response efficiently when they are set above the phase-transition temperature of PVDF−TrFE (90 °C), as shown in Figure 4b. Poling temperatures and applied poling

dx.doi.org/10.1021/ma202481t | *Macromolecules* 2012, 45, 1580−1586

voltages mainly affect the poling degree of dipoles. Figure 4c shows that piezoelectric response increases with applied poling voltages, and the piezoelectric response of the PVDF−TrFE thin films at a poling temperature of 110 °C is 1.4−3.4 times larger than poling at 90 °C. According to the PFM measurements, the developed PVDF−TrFE thin films show the best inverse piezoelectricity when polarization duration, polarization temperature, and applied poling voltage are 60 min, 110 °C, and 60 V, respectively. We used the best conditions in the following experiments.

We scanned PFM images of the unpoled and poled flat thin films with an increase in applied ac voltages of 0−15 V every 250 nm in the *y* direction, as shown in Figure 5a,b. Piezoelectric response increased with applied ac voltages. The scanning graphs of the poled PVDF−TrFE thin film along the line A_1 to A_2 and the line A_3 to A_4 are plotted in Figure 5c. The average amplitude along the lines is 104.9 mV. Compared to the unpoled PVDF−TrFE thin film, the poled PVDF−TrFE thin film is 3.43 times larger. The poled 3 μm PVDF−TrFE thin film is 2.27 times larger than the commercial 40 μm PVDF film, as shown in Figure 5d, in which film thickness normalized the amplitude.

The developed, nanoimprinted PVDF−TrFE nanograss was poled using this polarization condition. Two pieces of the nanostructured PVDF−TrFE films with Al electrodes were flip-stacked together and then poled to obtain full polarization of only the vertically aligned PVDF−TrFE nanopillars on the top layer and the bottom layer, which were in contact. Other noncontact PVDF−TrFE nanopillars could only obtain partial polarization because of the air gap between them. Next, the piezoelectric responses of the PVDF−TrFE nanograss were examined using the PFM, as shown in Figure 6a. The ac driving voltage of 5 V was applied to the AFM tip during scanning. Figure 6b shows the two-dimensional piezoelectric amplitude magnitude of the output potential with a scanning area of 2 μm × 2 μm. Figures 6c and 6d show the scanning graph of the piezoelectric amplitude magnitude of the output potential along the line Z_1 to Z_2 and the line Z_3 to Z_4, respectively. Output voltage wave-shaped peaks resulted from the piezoelectric potential-driven transient flow of electrons across the load as the tip scanned across the vertically aligned PVDF−TrFE nanopillars. In the experiments, the maximum output voltage of the single PVDF−TrFE nanopillar was 526 mV, and the maximum piezoelectricity of the single PVDF−TrFE nanopillar was 210.4 pm/V. The piezoelectric response of the PVDF−TrFE nanograss structures ranges from 100 to 526 mV. The average piezoelectricity of the developed PVDF−TrFE nanograss structures was 72.7 pm/V. The piezoelectricity of the developed PVDF−TrFE nanograss structures was 5.19 times larger than that of the PVDF−TrFE flat thin films. Compared to the previous report,[25] the piezoelectricity of our developed PVDF−TrFE nanograss is 3.39 times larger. More than 40 output voltage peaks were measured in the scanned area of 2 μm × 2 μm. On the other hand, more than 10% of PVDF−TrFE nanograss structures have been poled by the flip-stacking poling method. Other output voltages on the films are less than 90 mV. These output values are substantially less than the peak output because noncontact collapse nanopillars obtained less polar.

CONCLUSION

We fabricated, poled, and characterized PVDF−TrFE nanograss structures successfully. PVDF−TrFE nanograss can self-release from silicon nanograss mold without sustaining any damage. We poled vertically oriented PVDF−TrFE nanopillars using the developed flip-stacking poling method, though other noncontact collapse nanopillars obtained less polar. Nanopillars increase the ratio of surrounding air between the electrode and polymer substrate, changing the surface capacitances and structural flexibility. The developed technique is simple, economical, and easy to fabricate. The developed ferroelectric PVDF−TrFE copolymer nanograss showed enhanced piezoelectricity compared to the PVDF−TrFE flat thin films and the previous literature. The developed PVDF−TrFE nanograss structures have potential applications in nanotip-based protein biosensors, nanotip-based tactile sensors, and power nanogenerators, which are under investigation.

AUTHOR INFORMATION

Corresponding Author

*Tel +886-3-5715131 ext 33736; fax +886-3-5722840; e-mail cchong@mx.nthu.edu.tw.

ACKNOWLEDGMENTS

This research was supported partially by the National Science Council of Taiwan (NSC 96-2221-E-007-134) and NTHU Boost Program (99N2936E1). We thank Prof. Chi-Young Lee from the Department of Material Science and Engineering, National Tsing Hua University, for help with the PFM measurements and Srikanth Ravipati for help in the preparation of the silicon nanograss mold.

REFERENCES

(1) Ahn, C. H.; Rabe, K. M.; Triscone, J.-M. *Science* **2004**, *303*, 488−491.
(2) Chen, C.-Y.; Huang, J.-H.; Song, J.; Zhou, Y.; Lin, L.; Huang, P.-C.; Zhang, Y.; Liu, C.-P.; He, J.-H.; Wang, Z.-L. *ACS Nano* **2011**, *5* (8), 6707−6713.
(3) Chen, X.; Xu, S.; Yao, N.; Shi, Y. *Nano Lett.* **2010**, *10*, 2133−2137.
(4) Xu, S.; Qin, Y.; Xu, C.; Wei, Y.; Yang, R.; Wang, Z. L. *Nature Nanotechnol.* **2010**, *5*, 366−373.
(5) Ohigashi, H.; Kagami, N.; Li, G. R. *J. Appl. Phys.* **1992**, *71* (1), 506−508.
(6) Wang, J. L.; Yuan, S. Z.; Tian, L.; Meng, X. J.; Sun, J. L.; Chu, J. H. *Appl. Phys. Lett.* **2011**, *98*, 052906.
(7) Urayama, K.; Tsuji, M.; Neher, D. *Macromolecules* **2000**, *33*, 8269−8279.
(8) Guo, S. S.; Li, W. P.; Sun, C. L.; Wang, D. H.; Zhao, X.-Z.; Lau, S. T.; Chan, H. L. W. *Mater. Chem.* **2003**, *81*, 166−173.
(9) Lu, S. G.; Rožič, B.; Zhang, Q. M.; Kutnjak, Z.; Neese, B. *Appl. Phys. Lett.* **2011**, *98*, 122906.
(10) Tien, N. T.; Seol, Y. G.; Dao, L. H. A.; Noh, H. Y.; Lee, N.-E. *Adv. Mater.* **2009**, *21*, 910−915.
(11) Zirkl, M.; Sawatdee, A.; Helbig, U.; Krause, M.; Scheipl, G.; Kraker, E.; Ersman, P. A.; Nilsson, D.; Platt, D.; Bodö, P.; Bauer, S.; Gomann, G.; Stadlober, B. *Adv. Mater.* **2011**, *22*, 2069−2074.
(12) Yuan, Y.; Reece, T. J.; Sharma, P.; Poddar, S.; Ducharme, S.; Gruverman, A.; Yang, Y.; Huang, J. *Nature Mater.* **2011**, *10*, 296−302.
(13) Kang, S. J.; Bae, I.; Shin, Y. J.; Park, Y. J.; Huh, J.; Park, S.-M.; Kim, H.-C.; Park, C. *Nano Lett.* **2011**, *11*, 138−144.
(14) Park, Y. J.; Kang, S. J.; Lotz, B.; Brinkmann, M.; Thierry, A.; Kim, K. J.; Park, C. *Macromolecules* **2008**, *41*, 8648−8654.
(15) Li, C.; Wu, P.-M.; Lee, S.; Gorton, A.; Schulz, M. J.; Ahn, C. H. *J. Microelectromech. Syst.* **2008**, *17* (2), 334−341.
(16) Chang, C.; Tran, V. H.; Wang, J.; Fuh, Y.-K.; Lin, L. *Nano Lett.* **2010**, *10*, 726−731.
(17) Xu, J.; Dapino, M. J.; Gallego-Perez, D.; Hansford, D. *Sens. Actuators, A* **2009**, *153*, 24−32.

(18) Hu, Z.; Tian, M.; Nysten, B.; Jonas, A. M. *Nature Mater.* **2009**, *8*, 62−67.
(19) Sharma, P.; Reece, T. J.; Ducharme, S.; Gruverman, A. *Nano Lett.* **2011**, *11*, 1970−1975.
(20) Bystrov, V. S.; Bdikin, I. K.; Kiselev, D. A.; Yudin, S.; Fridkin, V. M.; Kholkin, A. L. *J. Phys. D: Appl. Phys.* **2007**, *40*, 4571−4577.
(21) Tang, Q.; Shi, S.-Q.; Huang, H.; Zhou, L. M. *Superlattices Microstruct.* **2004**, *36*, 21−29.
(22) Rankin, C.; Chou, C.-H.; Conklin, D.; Bonnell, D. A. *ACS Nano* **2007**, *1* (3), 234−238.
(23) Park, Y. J.; Kang, Y. S.; Park, C. *Eur. Polym. J.* **2005**, *41*, 1002−1012.
(24) Zhang, L.; Ducharme, S.; Li, J. *Appl. Phys. Lett.* **2007**, *91*, 172906.
(25) Liu, Y.; Weiss, D. N.; Li, J. *ACS Nano* **2010**, *4* (1), 83−90.
(26) Park, H. J.; Kang, M.-G.; Guo, L. J. *ACS Nano* **2009**, *3* (9), 2601−2608.
(27) Hong, C.-C.; Huang, P.; Shieh, J. *Macromolecules* **2010**, *43*, 7722−7728.
(28) Yang, M.-C.; Shieh, J.; Hsu, C.-C.; Cheng, T.-C. *Electrochem. Solid-State Lett.* **2007**, *8*, 131−133.

Macromolecules

Article

pubs.acs.org/Macromolecules

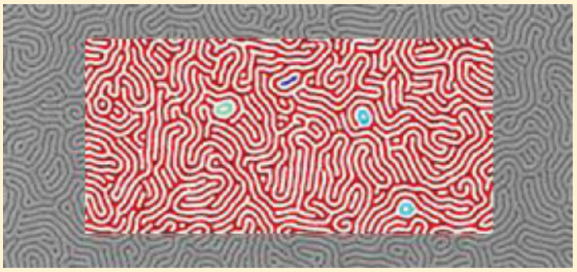
Network Connectivity and Long-Range Continuity of Lamellar Morphologies in Block Copolymer Thin Films

Ian P. Campbell, Gawain J. Lau, Jonathan L. Feaver, and Mark P. Stoykovich*

Department of Chemical and Biological Engineering, University of Colorado at Boulder, Boulder, Colorado 80309, United States

Supporting Information

ABSTRACT: The connectivity, and thus long-range continuity of the domains, in a lamellar polystyrene-*block*-poly(methyl methacrylate) copolymer in thin films depends on the volume fraction of each block and can be shifted by homopolymer addition to substrate-spanning continuity of either the polystyrene (PS) or poly(methyl methacrylate) (PMMA) domains. Essential features of the lamellar morphology were captured by a simple network analysis that quantified the number of branch points and end points in the lamellar domains. The transition in network continuity from the PS to PMMA domain as a function of copolymer volumetric composition (from f_{PMMA} = 0.45 to 0.55) was correlated with a 5-fold increase in the PMMA branch point density and a concomitant 3-fold reduction in the PMMA end point density. These results indicate that the copolymer's composition drastically impacts the self-assembled lamellar morphology in thin films and is an important design consideration when using such materials for lithographic applications, including for directed assembly to generate long-range, defect-free order.



INTRODUCTION

The directed self-assembly of block copolymers in thin films is an emerging technology with the potential to compete with traditional lithographic techniques for patterning at the nanoscale.[1−9] Self-assembling materials such as block copolymers have many advantages as lithographic materials, including tunable feature sizes below 50 nm, parallel assembly over arbitrarily large areas, and the potential for lower patterning costs.[10−15] The morphology and feature size of the nanostructures self-assembled by diblock copolymers are dictated by the overall molecular weight of the copolymer and the relative volume fraction of the components.[16−21] Morphologies commonly formed by diblock copolymers in thin films are lamellae, close-packed cylinders, spheres, and the bicontinuous gyroid.[16−18,20,22] Among these morphologies, lamellar structures have attracted interest for the patterning of integrated circuit layouts[23−26] and the fabrication of nanomeshes[27] and optical filters,[28,29] whereas cylindrical structures have been pursued for high density storage media,[30−32] photonic devices,[33−35] or filtration membranes.[36−39] Controlled orientation of the block copolymer nanostructures with respect to the substrate is also an important parameter for lithographic applications, with lamellae and cylinders in thin films being able to assemble with interfaces between domains oriented either perpendicular or parallel to the substrate. Most lithographic applications that involve pattern transfer or templating to the substrate benefit from continuous pathways through the thickness of the film; therefore, approaches such as nonpreferential wetting surfaces[40−45] and electric fields[46,47] have been developed to achieve perpendicular domain orientations in thin films.

The lamellar morphology formed by block copolymers in thin films lacks long-range order and has highly curved, tortuous, and intertwined domains when the interface between domains is oriented perpendicular to the substrate. This block copolymer morphology may be informally referred to as the "fingerprint" morphology due to structural resemblances with the loops, whorls, and arches found in human fingerprints. Although the lamellar morphology is readily recognized upon top-down imaging of the film surface by atomic force or scanning electron microscopy, the finer details of the morphology have remained unexplored, including the extent of domain continuity, the network connectivity due to branching within the domains, and the impact of the copolymer composition on the nanostructure. The continuity of block copolymer domains in bulk systems has been carefully considered for applications that require materials with three-dimensional percolating pathways for transport (e.g., material or charge transport), with bicontinuous morphologies such as gyroids,[22] perforated lamellae,[48−50] cubic bicontinuous,[35,51] and double-diamond bicontinuous[52] being of particular interest. Continuous networks of lamellar domains in thin films can also allow for long-range, in-plane transport within the nanostructured material. For example, an interconnected arrangement of metal nanowires deposited on glass using a lamellar block copolymer mask may be applied as a transparent, large area electrode.

Received: November 18, 2011
Revised: January 4, 2012
Published: January 23, 2012

 © 2012 American Chemical Society dx.doi.org/10.1021/ma2025336 | *Macromolecules* 2012, 45, 1587−1594

Directed self-assembly of lamellar-forming block copolymers into dense arrays of lines with long-range order, using chemically patterned substrates,[23,53−56] graphoepitaxy in topographic features,[57−61] or spontaneous alignment due to thickness gradients,[62] would also benefit from a better understanding of the network connectivity and continuity of the native lamellar structures. Dislocation and disclination defects that arise during directed assembly may occur with frequencies and in configurations dependent on the connectivity of the lamellar structure.[63] These properties of the defects are likely to influence their ability to be annihilated during thermal annealing processes as well as the dynamics and rates with which defect-free assembly can be achieved.[63] Furthermore, the propagation of the defect-free assemblies of lamellae away from chemically patterned substrates is limited to ∼100 nm thick films. In increasingly thick films, the directing effect of the underlying substrate is diminished, and the lamellar morphology gradually reverts to its native "fingerprint" morphology with significant branching between domains and no long-range order. The use of lamellar copolymer systems with minimal branching and domain connectivity may suppress the initial formation of such interconnected networks and allow directed assembly of defect-free arrays to be achieved in thicker films.

In this work we characterize the connectivity of block copolymer lamellae in thin films oriented perpendicular to a nonpreferential wetting substrate and present a straightforward method to control the continuity of the self-assembled network structures. Networks formed by simple block copolymer systems vary from exhibiting substrate-spanning continuity in the PS domain to substrate-spanning continuity in the PMMA domain. The density of branch points and end points in the network and the distribution of network sizes are discovered to follow trends associated solely with domain connectivity. The overall composition of the self-assembling material was systematically varied by blending a lamellar-forming diblock copolymer of polystyrene-*block*-poly(methyl methacrylate) with either polystyrene (PS) or poly(methyl methacrylate) (PMMA) homopolymer. The lamellar morphology and domain connectivity are symmetric around a volume fraction near the block copolymer blend with equal volume fractions of PS and PMMA (50 vol % PS and 50 vol % PMMA), demonstrating that the lamellar structure for this system is primarily a function of overall composition. Finally, distributions of the interfacial curvature are reported for each lamellar system, and the standard deviation of curvature is found to increase with compositional asymmetry, indicative of more highly curved networks. These results show that all lamellar morphologies formed by block copolymers in thin films are not structurally equivalent and thus will impact the selection of such materials for lithographic and templating applications, including in the directed self-assembly of microelectronics devices.

■ MATERIALS AND METHODS

Substrate Preparation. Block copolymers in thin films on substrates that are preferentially wet by one of the components self-assemble into morphologies oriented parallel to the substrate; e.g., PMMA preferentially wets the native oxide on Si wafers leading to parallel-oriented morphologies. Here, a "neutral" surface that is nonpreferentially wet by either of the block copolymer components is used to orient the assembled lamellar morphologies perpendicular to the substrate, which is the preferred orientation for templating or lithographic applications due to the domain continuity from the top to the bottom of the film. Silicon wafers were purchased from Montco Silicon and rinsed in acetone and toluene prior to any processing. Wafers were completely dried using a stream of nitrogen. A random copolymer was synthesized from styrene, methyl methacrylate, and glycidyl methacrylate by free radical polymerization (final molar composition of 58% styrene, 31% methyl methacrylate, and 1% glycidyl methacrylate).[40,44] A 0.3 wt % solution of the random copolymer in anhydrous toluene (EMD Chemicals, 99.8 wt %) was prepared and spin-coated onto dry silicon wafers. Annealing at 160 °C for 4 h cross-linked the random copolymer into a dense mat, and subsequent rinsing in a toluene bath removed unreacted polymer.

Block Copolymer Processing. Thin films of block copolymer were spun onto the prepared neutral surfaces and thermally annealed to self-assemble the characteristic lamellar morphologies. Block copolymer [polystyrene-*block*-poly(methyl methacrylate) or PS-*b*-PMMA, 53K:54K, PDI = 1.16], polystyrene homopolymer (22.2K, PDI = 1.07), and poly(methyl methacrylate) homopolymer (21.4K, PDI = 1.07) were used as purchased from Polymer Source, Inc. Individual solutions of block copolymer and homopolymer were prepared by weighing out dry polymer and adding anhydrous toluene dropwise to make solutions of 1.5 wt % polymer. Blends of block copolymer and homopolymer were prepared by mixing the stock solutions in the desired ratios. The fraction of homopolymer added varied from blend to blend and ranged from 5 wt % PS to 15 wt % PMMA. Polymer solutions were spin-coated onto Si wafers treated with the neutral surface to produce films ∼50 nm thick. The polymer films were annealed under ∼2 Torr vacuum for 10 days at 190 °C to self-assemble the block copolymer morphologies. These annealing conditions resulted in lamellar morphologies that have quantitative characteristics (i.e., periodicity and connectivity) that are reflective of thin films of block copolymers primarily undergoing defect annihilation at long times. The lamellar periodicity (L_0) ranged from 59 to 63 nm as quantified from FFT analysis of SEM images obtained after thermal annealing.

Nanostructure Imaging. The block copolymer morphology in thin films was imaged by top-down scanning electron microscopy (SEM) using a JEOL JSM-7401F operating at an accelerating voltage of 2 kV and a sample bias of 1 kV. The gun emission current was maintained at 10 mA, and all images were captured using an in-lens secondary electron detector. Each image was captured at a magnification of 25 000. The nanostructure characterized at the top surface of the film can be assumed to propagate through the entire film to the substrate, which is a reasonable assumption for perpendicular block copolymer domains in films with thicknesses less than or approximately equal to L_0 and has been shown in the literature for similar systems using cross-sectional electron microscopy[54] or scattering techniques.[64]

Characterization of the Lamellar Block Copolymer Morphology. The lamellar morphology was characterized using an in-house image analysis program coded in Matlab (v. R2011a, The Mathworks, Natick, MA). The raw SEM images were filtered and converted from grayscale to black and white in Matlab. The dark gray/black and light gray/white regions in the images represent the PMMA and PS domains, respectively. Filtering was able to approximately equalize the width of the PS and PMMA domains in the raw SEM images. Continuous networks formed by the black and white pixels were extracted and subsequently assigned a unique numerical label and distinct color.

Quantitative metrics of the network connectivity and continuity in both the PS and PMMA domains were calculated for individual images and reported as the average results from 10 distinct SEM images. The relative size of the networks was calculated by counting the number of pixels in each network. Each area was then normalized to the total number of pixels in the image. The areal density of end points and branch points in the networks was also quantified. The network structures were skeletonized (i.e., reduced to a continuous width of a single pixel) and despurred (i.e., small branches and pixels that do not contribute to connectivity were eliminated) to remove any anomalous branches produced by localized variations in domain width. Each branch point was eliminated when identified to prevent double counting and to subdivide the skeleton for the calculation of curvature.

Curvature was calculated by first fitting a fifth-order polynomial to each point and the six nearest-neighboring points on the skeleton and then by applying the curvature equation $\kappa = |y''|/(1 + y'^2)^{3/2}$, where y is the polynomial function of x at each position on the skeleton. Subdividing the skeleton into 7-point sections was determined to be sufficient to capture the local curvature of the network structure without the danger of a poor fit due to multivalued S-shaped curves. Calculations using polynomial fits based on fewer than 7 points were unable to accurately capture the behavior of highly curved structures.

RESULTS

Figure 1 shows an example of a colorized network image for lamellae assembled by a pure PS-*b*-PMMA block copolymer to demonstrate the native continuity and connectivity of the polystyrene (PS) and poly(methyl methacrylate) (PMMA) domains. Figure 1a shows the raw SEM image, and Figures 1b and 1c provide the corresponding colorized maps of the connected PS and PMMA domains, respectively. Each connected domain is shown in a separate color to provide visual information on the overall connectivity of the lamellae, but some colors are repeated in the image due to a limited color palette. Domains with a high degree of continuity produce a single network that span the entire imaged area, connect every image border, and leave very few unlinked regions. Low continuity in the lamellar domains is typified, in comparison, by a large number of distinct segments that are each relatively small compared to the overall image. The PS domain in the pure diblock copolymer characterized in Figure 1 formed large networks and was highly interconnected, as emphasized by the large red network that spans the entire imaged area (3.56 μm × 4.80 μm). There are some isolated PS features within the larger network, generally resembling small segments or loops, but their fraction of the total image area is small. On the other hand, the PMMA domain was separated into many short segments and there was no single network that connected multiple borders of the image. The composition of this block copolymer blend system is slightly asymmetric, with volume fractions (f) of 0.524 for the PS component and 0.476 for PMMA component. This slight asymmetry in composition was sufficient to produce additional connectivity in the PS domains, in the form of additional "branches" or "bridges", that generated large, continuous PS networks and concomitantly divided the PMMA domains into short, distinct segments.

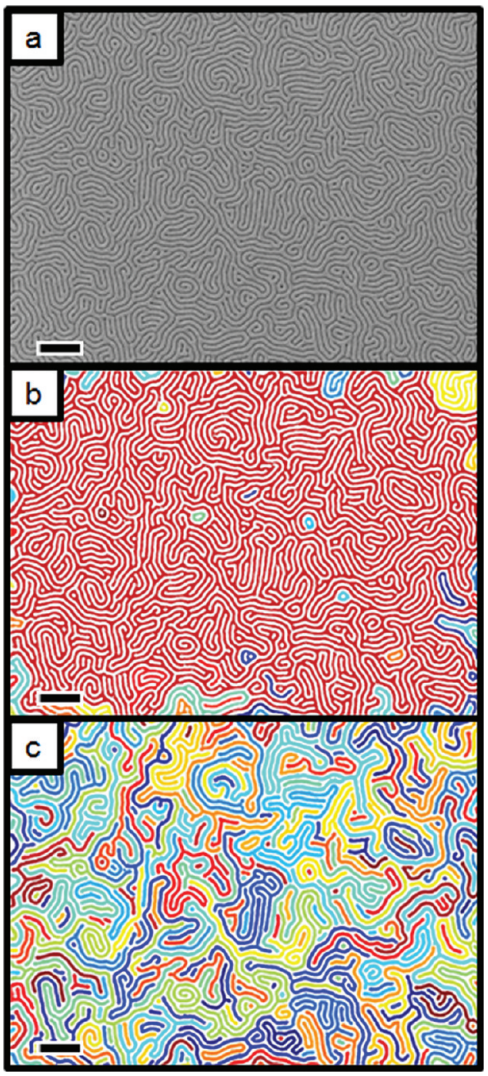


Figure 1. Network analysis of an assembled PS-*b*-PMMA (53K:54K) thin film with f_{PMMA} = 0.476. The raw SEM image is shown in (a) with colorized networks for the (b) PS and (c) PMMA domains. Images are 3.56 μm × 4.8 μm, and the scale bar corresponds to 400 nm.

The network connectivities of block copolymer blend systems with f_{PMMA} = 0.45, 0.48, 0.50, 0.52, and 0.55 are shown in Figure 2. The largest continuous PS network is shown in red for each system and the largest continuous PMMA networks are shown in blue. The largest networks in some cases span nearly the entire field of view but do not include small networks that border the image boundary. It is important to note, however, that these small features are likely connected to the primary network at some point outside the field of view. The largest and most highly interconnected networks transitioned from occurring in the PS to the PMMA domain as the volume fraction of PMMA was increased from f_{PMMA} = 0.45 to 0.55. Changes in network structure are most visible between copolymer blend systems with $0.48 \leq f_{PMMA} \leq 0.52$. A single PS network is observed over the entire field of view for f_{PMMA} = 0.48 (the corresponding PMMA domain displays short, distinct segments due to low connectivity), but conversely many short PS segments are formed when f_{PMMA} = 0.52 (now the PMMA domain forms a large-scale network). Systems with f_{PMMA} = 0.50 have high connectivity and large networks in both of the lamellar domains, with some networks spanning large areas of the field of view. The network structures are therefore qualitatively symmetric around the copolymer–homopolymer blend composition $f_{PMMA} \approx 0.50$, even though the homopolymer fractions range from 5 wt % PS to 15 wt % PMMA for f_{PMMA} = 0.45 to 0.55, respectively. This observation suggests that the homopolymer concentration primarily shifts the system composition and does not significantly influence the overall continuity and connectivity of the lamellar morphologies self-assembled by the copolymer systems. Subtle and quantitative details of the lamellar-forming blend systems, such as L_0 and the compositional symmetry point of the lamellar phase, are likely influenced by the inclusion of the homopolymer component and its concentration, but not to a significant enough extent as to be captured in the PS/PMMA system characterized here.

The highly connected networks span much larger areas than those characterized in Figures 1 and 2. Composite images covering at least 8.8 μm × 4.6 μm were stitched together from six neighboring SEM snapshots to provide large area images with a high resolution. The large area composite images, as well

dx.doi.org/10.1021/ma2025336 | *Macromolecules* 2012, 45, 1587–1594

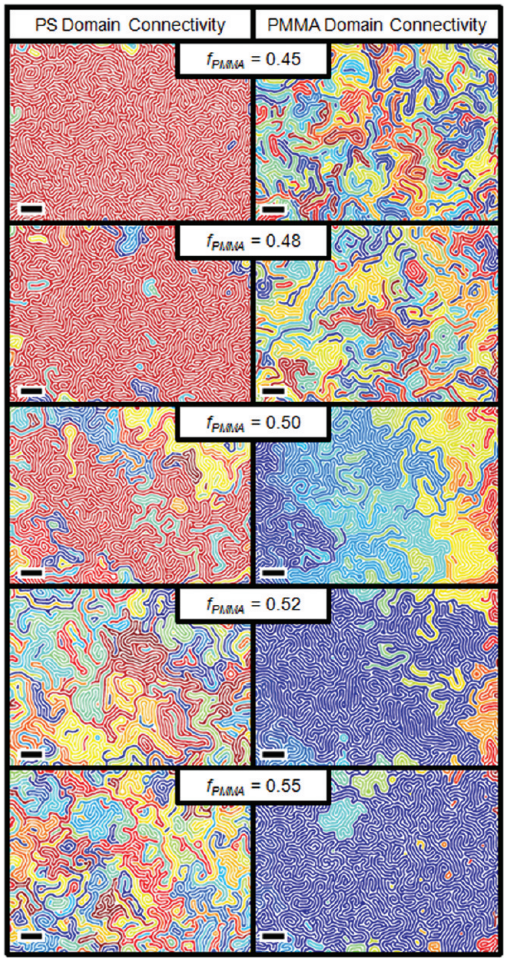


Figure 2. Network connectivity of PS (left column) and PMMA (right column) as a function of volume fraction. As the volume fraction for each component decreases, the number of connected networks increases and the average size of each network decreases. Images are 3.56 μm × 4.8 μm, and the scale bars correspond to 400 nm.

as the colorized PS and PMMA network structures of each image, for the pure block copolymer system (f_{PMMA} = 0.48) and the block copolymer–homopolymer blend system with f_{PMMA} = 0.52 are included in the Supporting Information. Continuous networks that cover the majority of these large areas are observed for the domain with the higher volumetric concentration in these asymmetric block copolymer blend systems. Some isolated networks exist within the primary network but occur with low number and areal frequency. On the basis of the analysis of these large areas, it is reasonable to conclude that continuous, interconnected lamellar networks are generated over macroscale areas for a film of block copolymers with asymmetric compositions.

Network connectivity and continuity are directly correlated to the composition of the block copolymer system. As the extent of branching increases, the continuity of the network is enhanced and the probability of forming isolated, non-interconnected domains is diminished. The areal density of branch points and end points in the lamellar morphologies are shown in Figure 3 as a function of the volume fraction of PMMA in the copolymer blend systems. Individual points in Figure 3 were averaged over 10 distinct SEM images, and the error bars correspond to one standard deviation of the measurements. The lamellar domains of the minority

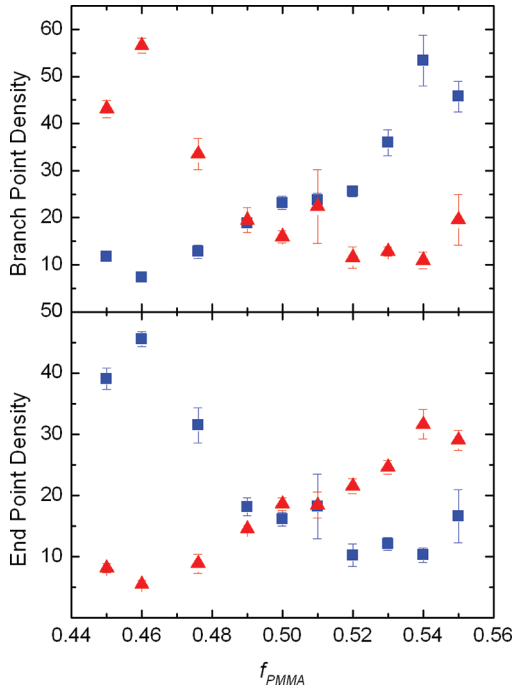


Figure 3. Branch point and end point density [number/μm^2] for PS (▲) and PMMA (■) domains over a range of blend compositions. Branch density increases with increasing volume fraction and leads to greater network connectivity. The number of end points in a domain increases as the volume fraction of that component decreases, corresponding to a more disjointed network. Error bars correspond to the standard deviation for 10 images.

component have a high density of end points and a low density of branch points. Increased concentration of one component leads directly to an increase in the number of bridges between neighboring lamellae in that domain and a concomitant decrease in the density of lamellar end points. The domain with the greater density of branch points transitions from the PS domain for $f_{PMMA} < 0.49$ to the PMMA domain for $f_{PMMA} > 0.51$. This crossover point at $f_{PMMA} \approx 0.50$ corresponds to a shift in the majority component of the copolymer blend and the formation of larger, more interconnected networks. The curves of branch point and end point density are nearly symmetric around $f_{PMMA} \approx 0.50$ for the copolymer components, which indicates that there is relatively little asymmetry in this diblock copolymer system.

A simple model of lamellar connectivity in thin films can provide insight into the long-range continuity of networks in the case of a copolymer system with a perfectly symmetric composition (f_{PMMA} = 0.50). Starting with a simple lamellar network of parallel domains, with the lamellae extended to the extremes of the film as shown in Figure 4a, the adjacent domains of PS or PMMA are not interconnected, and there is not a single network that spans the entire film. In order to form a larger PS network, an interconnection or bridge must form between adjacent PS domains. Simultaneously, the PMMA domains must also form an interconnection in order to maintain the compositional symmetry of the system (f_{PMMA} = 0.50). An example of this process is shown in Figure 4b. The formation of the PS bridge requires that two PS domains are joined into a larger continuous domain, and a PMMA domain is divided in two smaller segments. The subsequent addition of a PMMA interconnection couples two adjacent PMMA

dx.doi.org/10.1021/ma2025336 | *Macromolecules* 2012, 45, 1587–1594

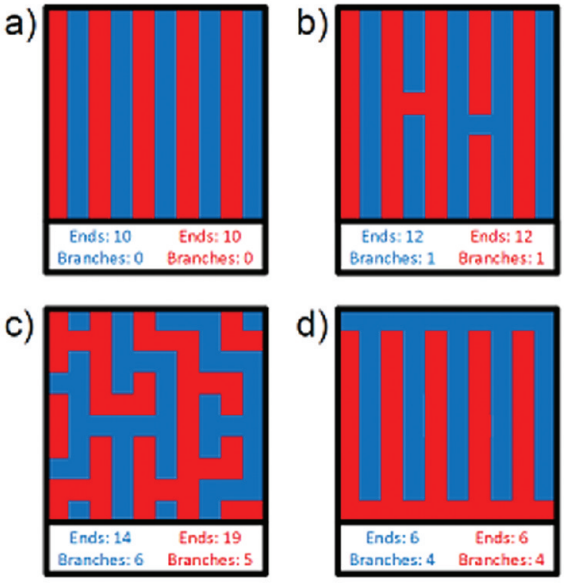


Figure 4. For $f = 0.50$: (a) Perfectly aligned lamellar block copolymer. (b) As connections form, larger networks are generated but divide other domains. (c) When assembled randomly, the networks are highly branched and interweave but still do not span the entire substrate. (d) An ideal network may be where both domains are fully connected, but neither domain connects all four substrate borders. The numbers of end points and branch points for each component are shown below the image.

domains into a single network and concomitantly subdivides a single PS domain into two separate domains. This pairwise process of adding PS and PMMA interconnections to the system can be repeated (nine times as in Figure 4c) until the lamellae resemble the network morphology observed experimentally in the self-assembled films with $f_{PMMA} = 0.50$ (see Figure 2c). Each bridge that is formed separates the opposite domain into smaller segments with end points, and therefore neither component can have substrate-spanning connectivity across an entire surface. An extreme case is shown in Figure 4d, where both the PMMA and PS domains exist as single networks but do not contact all four substrate borders.

Copolymer blend systems with asymmetric compositions ($f_{PMMA} < 0.50$ or $f_{PMMA} > 0.50$) theoretically have excess material to form a single network that reaches every substrate border. Low compositional asymmetry does not experimentally lead to long-range network connectivity, however, due to the nature of the self-assembly process and the randomness with which the branch points are located within the network. Lamellar systems with greater compositional asymmetry have a high enough spatial concentration of bridging to overcome the randomness of the self-assembly processes, such that a single network is generated that spans the entire surface of the thin film. A continuous network spanning the entire field of view can easily be observed in Figure 2 in domains for which the volume fraction is equal to 0.52. In both cases (the PS domain for $f_{PMMA} = 0.48$ and the PMMA domain for $f_{PMMA} = 0.52$) the largest network is continuous between all four borders of the image and covers a high fraction of the image area. The domain of the minority component is divided into many short segments. Lamellae in block copolymer blend systems with greater compositional asymmetry exhibit similar degrees of continuity and network sizes.

Figure 5 shows distributions of the size of the continuous networks in the PS (red) and PMMA (blue) domains. The

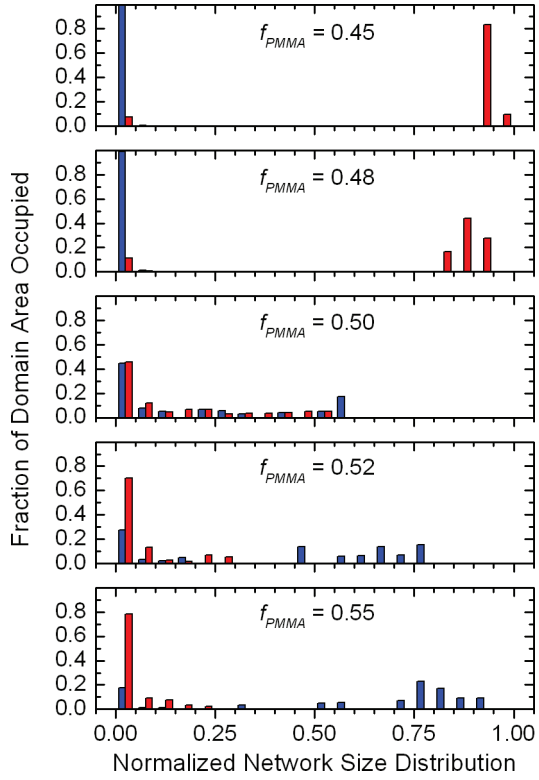


Figure 5. Normalized size distribution of connected networks of PS (red) and PMMA (blue) at different volume fractions of PMMA. The area of each connected network in an image was found and resized as a fraction either the total PS or PMMA domain size (e.g., a single connected network for PMMA or PS in an image corresponds to a size of 1) and weighted based on size (e.g., a single network at size 1 has a weight of 1). Distributions were averaged over 10 images.

normalized size of each connected network was calculated by counting the number of pixels and dividing by the total number of pixels for that domain in the entire image. The normalized network size was reported as 1.0 in the limit that only one network was present for a particular domain in an image, and each network was weighted by its size in the histogram. Distributions of network size shown in Figure 5 were averaged over 10 distinct images. The size distributions quantitatively capture the shift from small networks or segments in domains with low volumetric concentrations ($f = 0.45$) to large, nearly fully interconnected networks in domains with high volumetric concentrations ($f = 0.55$). For example, the PMMA domains formed by a copolymer blend with $f_{PMMA} = 0.45$ are all less than 5% of the image area, and there is no larger network. Copolymer blends with $f_{PMMA} = 0.55$ formed large networks such that the majority of the PMMA domains consumed between 70% and 95% of each image area. The normalized size distributions measured for the PS and PMMA domains are slightly different, with the PS domains displaying a greater propensity than the PMMA domains for forming very large networks at asymmetric copolymer blend compositions. Unlike the PMMA domain, when $f_{PS} = 0.45$ (i.e., the $f_{PMMA} = 0.55$ system), only 75% of the PS networks consume less than 5% of the image area and there is a small tail of larger networks. Similarly, when $f_{PS} = 0.55$ (i.e., the $f_{PMMA} = 0.45$ system),

dx.doi.org/10.1021/ma2025336 | *Macromolecules* 2012, 45, 1587–1594

nearly all the PS networks fill 90−100% of the PS lamellae in the field of view. Copolymer blends with the symmetric composition of f_{PMMA} = 0.50 display nearly equivalent normalized size distributions for the PS and PMMA domains; a small fraction of networks span more than 50% of the image area, many networks occupy 10−50% of image area, and most frequently short segments form that take up less than 10% of the image size.

Increasing the compositional asymmetry of lamellar-forming copolymers leads to increases in branching in the majority domain (Figure 3) and thus more interconnections and larger continuous network structures (Figure 5). These quantitative results are consistent with the lamellar structures captured in Figure 2. The greater density of end points observed in the PMMA domains than the PS domains at low volume fractions of each component (Figure 3) can explain the small differences in the normalized size distributions of the PS and PMMA networks. Copolymer systems with f_{PMMA} = 0.45 and 0.48 have more end points, and thus form more short segments, in the minority PMMA domain than observed in the minority PS domain for systems with f_{PMMA} = 0.52 and 0.55. This variation in end point density at high asymmetries in copolymer blend composition may be attributed to differences in the homopolymer concentration in the copolymer systems. Higher weight fractions of homopolymer in the majority component (15 wt % PMMA versus 5 wt % PS at f_{PMMA} = 0.55 and 0.45, respectively) perhaps allow the majority component to more readily accommodate highly connected domains of the minority component, thereby leading to the decrease in end point density and the breadth of the size distribution observed for the PS domains at f_{PMMA} = 0.55.

An additional contributing factor may be that the lamellar-forming PS/PMMA systems are unlikely to be perfectly symmetric around compositions of f_{PMMA} = 0.50. Matsen and Bates performed studies of conformationally asymmetric block copolymers and found that the ratio of the statistical segment lengths (a) between the components had a strong effect on the order−order phase boundaries.[65,66] The volume fraction at which the lamellar domain interfaces have zero spontaneous curvature, i.e., the symmetry point in a bulk A/B copolymer phase diagram, can be calculated by the equation

$$f_{A,sym} = \frac{a_A}{a_A + a_B}$$

Using the statistical segment lengths for polystyrene given by Ballard et al.[67] (a_{PS} = 6.8 Å) and for poly(methyl methacrylate) given by Kirste et al.[68,69] (a_{PMMA} = 7.4 Å), the point of zero spontaneous curvature for PS-*b*-PMMA is predicted to be $f_{PMMA} \approx 0.52$. This prediction is similar to the symmetry point $f_{PMMA} \approx 0.50$, or more broadly $0.50 < f_{PMMA} < 0.52$, measured here qualitatively in terms of the predominant network-forming domain (Figure 2) and quantitatively in terms of the crossover point in the end point/branch point densities (Figure 3). The theoretical calculation of the point of zero spontaneous curvature predicts the observed direction of asymmetry from f_{PMMA} = 0.50 toward a slightly PMMA-rich system. If the experimental symmetry point is shifted toward PMMA-rich compositions from f_{PMMA} = 0.50, this could also serve to explain some of the observed differences in domain size distributions (Figure 5) between PS and PMMA at the same volume fractions. Experimental determination of the phase diagrams of other diblock copolymer systems (e.g., polystyrene-*block*-polyisoprene and poly(oxyethylene)-*block*-poly(oxybutylene)) have shown that the symmetry points in lamellar structures can be shifted to as much as f = 0.59,[51,70] and thus the transition between the predominant network-forming domains can be anticipated to occur at substantially more asymmetric compositions for block copolymer systems other than PS-*b*-PMMA.

The curvature of the PS/PMMA interface between lamellae has been characterized as a function of the asymmetry of the copolymer blend composition. Figure 6a shows an example of the distribution of interfacial curvatures for the lamellae formed by the pure block copolymer (f_{PMMA} = 0.476), and Figure 6b shows the standard deviation of the interfacial curvature distributions as a function of copolymer composition. Each distribution of interfacial curvature was fit to a Gaussian curve from which the amplitude, mean, and standard deviation were determined. The amplitude and mean of the interfacial curvatures of the lamellae were dominated by the high fraction of linear interfaces with low curvature (radii of curvature ≥1000 nm) and were statistically independent of copolymer composition. On the other hand, the standard deviation of interfacial curvature increases with greater compositional asymmetry in the copolymer as shown in Figure 6b. The increasing width of the distribution indicates a shift in curvature away from the mean toward more highly curved lamellae and

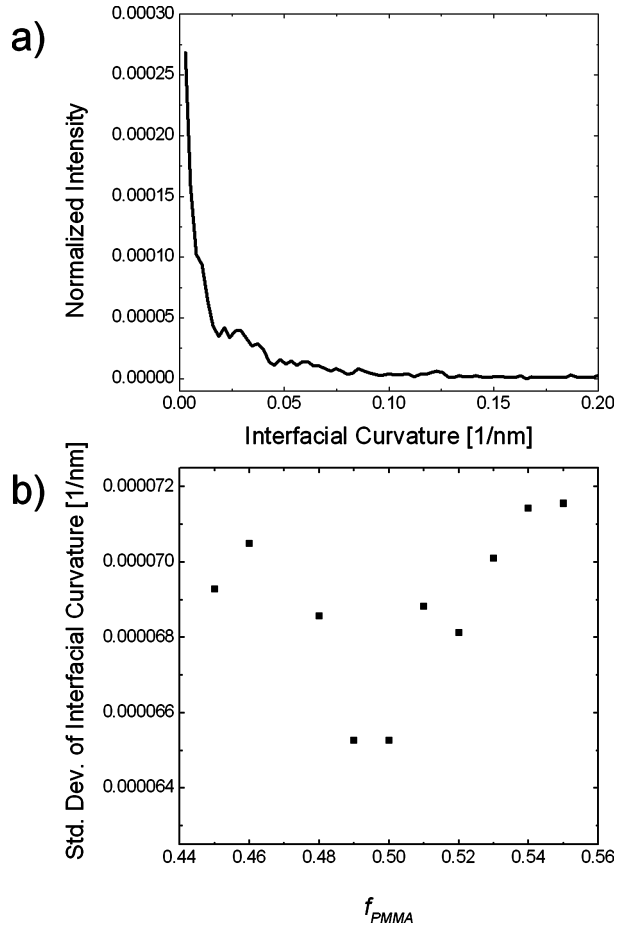


Figure 6. (a) Example of curvature distribution for f_{PMMA} = 0.48. (b) Standard deviation of interfacial curvature in PS-*b*-PMMA thin films of varying PMMA volume fraction. Larger standard deviations correspond to an increased width in the curvature distribution, indicating an increased presence of highly curved interfaces in asymmetric blends.

dx.doi.org/10.1021/ma2025336 | *Macromolecules* 2012, 45, 1587−1594

interfaces between domains. The greater curvature in asymmetric systems can be attributed in part to increased densities of branches and end points that have highly curved interfaces (radii of curvature on the order of the lamellar spacing ~25 nm or curvatures of ~0.04 nm^{-1}). The uniform broadening of the curvature distributions with greater compositional asymmetry is also observed for curvatures less than ~0.04 nm^{-1}, which indicates that variations in the branch and end point density cannot fully explain this observation and that likely there are small changes in the lamellar tortuosity that arise with copolymer composition.

In conclusion, the lamellar morphology of block copolymers self-assembled in thin films is not structurally equivalent for all systems and has been found to depend upon small variations in the compositional symmetry of the copolymer. The connectivity provided by branching and long-range continuity of the lamellar domain of the majority component increases with greater asymmetry to provide a single, continuous network that spans the entire substrate at volume fractions $f \geq 0.52$. The interwoven domains of the corresponding minority component form more end points and short, isolated segments with greater compositional asymmetry in the copolymer system. Blending homopolymer into the block copolymer system provides a simple route to fine-tune the network continuity and lamellar structure in a block copolymer thin film.

The results presented here also provide insight into the directed self-assembly of block copolymer structures with long-range order and that are defect-free over wafer-scale areas. In the case of directed assembly of dense arrays of 1:1 line:space features in thin films using chemically patterned substrates, the formation of bridges and end points in the lamellar block copolymer domains may be suppressed such that the self-assembled structures perfectly match the underlying surface pattern geometry. The total free energy required to eliminate all of the branch points and end points that occur during directed assembly, often observed in the form of dislocation and disclination defects, is dependent upon the natural concentration of such features in the block copolymer system and should therefore be greater with increasing compositional asymmetry. Block copolymer systems with high compositional asymmetry may be so mismatched from the directing surface pattern that the pattern cannot provide a sufficient energetic driving force for defect-free assembly, thereby requiring the formation of dislocation or disclination defects, interfacial roughness, and angled sidewalls between the domains. In general, the optimal conditions for defect-free directed assembly by chemically patterned surfaces occur when the volumetric composition of the block copolymer system matches the areal composition of the surface pattern, regardless of the extent of asymmetry. The directed assembly of distinct geometries in close proximity therefore presents an unaddressed challenge in the field and requires either control over the local composition of the block copolymer system or the selection of a single block copolymer system that can energetically accommodate the entire range of geometries. Finally, directed assembly of lamellar-forming block copolymers by graphoepitaxy[71,72] and density multiplication[73−79] techniques require that the self-assembly process interpolates the position and geometry of the nanostructures between sparse topographic sidewalls and chemical surface features, respectively. Defect-free, long-range assembly of lamellae between sparse chemically patterned stripes has been achieved over areas with widths 3 times the lamellar period, while block copolymer lamellae assembled in wider areas between the directing features lack long-range order (i.e., revert to the "fingerprint" morphology).[77] We believe that, based on the results presented here, the application of lamellar-forming copolymer systems optimized to have structural symmetry and thus reduced branch point and end point densities may enable defect-free directed assembly over wider areas by graphoepitaxy and density multiplication techniques.

■ ASSOCIATED CONTENT

Ⓢ Supporting Information

Figures S1 and S2. This material is available free of charge via the Internet at http://pubs.acs.org.

■ AUTHOR INFORMATION

Corresponding Author

*E-mail: mark.stoykovich@colorado.edu.

■ ACKNOWLEDGMENTS

The authors thank Chunlin He for synthesizing the random copolymer brush used to create the neutral wetting surface. This work was performed in part at the University of Colorado's Nanomaterials Characterization Facility. This research was supported in part by the NNIN at the Colorado Nanofabrication Laboratory and the National Science Foundation under Grant ECS-0335765.

■ REFERENCES

(1) Cheng, J. Y.; Ross, C. A.; Chan, V. Z. H.; Thomas, E. L.; Lammertink, R. G. H.; Vancso, G. J. *Adv. Mater.* **2001**, *13* (15), 1174.
(2) Whitesides, G. M.; Ostuni, E.; Takayama, S.; Jiang, X. Y.; Ingber, D. E. *Annu. Rev. Biomed. Eng.* **2001**, *3*, 335−373.
(3) Cheng, J. Y.; Ross, C. A.; Thomas, E. L.; Smith, H. I.; Vancso, G. J. *Appl. Phys. Lett.* **2002**, *81* (19), 3657−3659.
(4) Hawker, C. J.; Russell, T. P. *MRS Bull.* **2005**, *30* (12), 952−966.
(5) Menke, E. J.; Thompson, M. A.; Xiang, C.; Yang, L. C.; Penner, R. M. *Nature Mater.* **2006**, *5* (11), 914−919.
(6) Black, C. T.; Ruiz, R.; Breyta, G.; Cheng, J. Y.; Colburn, M. E.; Guarini, K. W.; Kim, H. C.; Zhang, Y. *IBM J. Res. Dev.* **2007**, *51* (5), 605−633.
(7) Kim, B. H.; Shin, D. O.; Jeong, S. J.; Koo, C. M.; Jeon, S. C.; Hwang, W. J.; Lee, S.; Lee, M. G.; Kim, S. O. *Adv. Mater.* **2008**, *20* (12), 2303.
(8) Ross, C. A.; Cheng, J. Y. *MRS Bull.* **2008**, *33* (9), 838−845.
(9) Tang, C. B.; Hur, S. M.; Stahl, B. C.; Sivanandan, K.; Dimitriou, M.; Pressly, E.; Fredrickson, G. H.; Kramer, E. J.; Hawker, C. J. *Macromolecules* **2010**, *43* (6), 2880−2889.
(10) Fasolka, M. J.; Mayes, A. M. *Annu. Rev. Mater. Res.* **2001**, *31*, 323−355.
(11) Park, C.; Yoon, J.; Thomas, E. L. *Polymer* **2003**, *44* (22), 6725−6760.
(12) Stoykovich, M. P.; Nealey, P. F. *Mater. Today* **2006**, *9* (9), 20−29.
(13) Hamley, I. W. *Prog. Polym. Sci.* **2009**, *34* (11), 1161−1210.
(14) Bang, J.; Jeong, U.; Ryu, D. Y.; Russell, T. P.; Hawker, C. J. *Adv. Mater.* **2009**, *21* (47), 4769−4792.
(15) Kim, H. C.; Park, S. M.; Hinsberg, W. D. *Chem. Rev.* **2010**, *110* (1), 146−177.
(16) Ohta, T.; Kawasaki, K. *Macromolecules* **1986**, *19* (10), 2621−2632.
(17) Bates, F. S.; Fredrickson, G. H. *Annu. Rev. Phys. Chem.* **1990**, *41*, 525−557.
(18) Almdal, K.; Koppi, K. A.; Bates, F. S.; Mortensen, K. *Macromolecules* **1992**, *25* (6), 1743−1751.
(19) Matsen, M. W. *Macromolecules* **1995**, *28* (17), 5765−5773.

(20) Matsen, M. W.; Bates, F. S. *Macromolecules* **1996**, *29* (4), 1091−1098.
(21) Fredrickson, G. H.; Bates, F. S. *Annu. Rev. Mater. Sci.* **1996**, *26*, 501−550.
(22) Hajduk, D. A.; Harper, P. E.; Gruner, S. M.; Honeker, C. C.; Kim, G.; Thomas, E. L.; Fetters, L. J. *Macromolecules* **1994**, *27* (15), 4063−4075.
(23) Stoykovich, M. P.; Muller, M.; Kim, S. O.; Solak, H. H.; Edwards, E. W.; de Pablo, J. J.; Nealey, P. F. *Science* **2005**, *308* (5727), 1442−1446.
(24) Daoulas, K. C.; Muller, M.; Stoykovich, M. P.; Papakonstantopoulos, Y. J.; De Pablo, J. J.; Nealey, P. F.; Park, S. M.; Solak, H. H. *J. Polym. Sci., Part B: Polym. Phys.* **2006**, *44* (18), 2589−2604.
(25) Craig, G. S. W.; Nealey, P. F. *J. Photopolym. Sci. Technol.* **2007**, *20* (4), 511−517.
(26) Stoykovich, M. P.; Kang, H.; Daoulas, K. C.; Liu, G.; Liu, C. C.; de Pablo, J. J.; Mueller, M.; Nealey, P. F. *ACS Nano* **2007**, *1* (3), 168−175.
(27) Jeong, S. J.; Xia, G. D.; Kim, B. H.; Shin, D. O.; Kwon, S. H.; Kang, S. W.; Kim, S. O. *Adv. Mater.* **2008**, *20* (10), 1898.
(28) Bockstaller, M. R.; Thomas, E. L. *J. Phys. Chem. B* **2003**, *107* (37), 10017−10024.
(29) Parnell, A. J.; Pryke, A.; Mykhaylyk, O. O.; Howse, J. R.; Adawi, A. M.; Terrill, N. J.; Fairclough, J. P. A. *Soft Matter* **2011**, *7* (8), 3721−3725.
(30) Park, S.; Lee, D. H.; Xu, J.; Kim, B.; Hong, S. W.; Jeong, U.; Xu, T.; Russell, T. P. *Science* **2009**, *323* (5917), 1030−1033.
(31) Xiao, S. G.; Yang, X. M.; Park, S. J.; Weller, D.; Russell, T. P. *Adv. Mater.* **2009**, *21* (24), 2516.
(32) Hong, A. J.; Liu, C. C.; Wang, Y.; Kim, J.; Xiu, F. X.; Ji, S. X.; Zou, J.; Nealey, P. F.; Wang, K. L. *Nano Lett.* **2010**, *10* (1), 224−229.
(33) Fink, Y.; Urbas, A. M.; Bawendi, M. G.; Joannopoulos, J. D.; Thomas, E. L. *J. Lightwave Technol.* **1999**, *17* (11), 1963−1969.
(34) Urbas, A.; Sharp, R.; Fink, Y.; Thomas, E. L.; Xenidou, M.; Fetters, L. J. *Adv. Mater.* **2000**, *12* (11), 812−814.
(35) Urbas, A. M.; Maldovan, M.; DeRege, P.; Thomas, E. L. *Adv. Mater.* **2002**, *14* (24), 1850−1853.
(36) Yang, S. Y.; Ryu, I.; Kim, H. Y.; Kim, J. K.; Jang, S. K.; Russell, T. P. *Adv. Mater.* **2006**, *18* (6), 709.
(37) Phillip, W. A.; Rzayev, J.; Hillmyer, M. A.; Cussler, E. L. *J. Membr. Sci.* **2006**, *286* (1−2), 144−152.
(38) Yang, S. Y.; Park, J.; Yoon, J.; Ree, M.; Jang, S. K.; Kim, J. K. *Adv. Funct. Mater.* **2008**, *18* (9), 1371−1377.
(39) Jackson, E. A.; Hillmyer, M. A. *ACS Nano* **2010**, *4* (7), 3548−3553.
(40) Mansky, P.; Liu, Y.; Huang, E.; Russell, T. P.; Hawker, C. J. *Science* **1997**, *275* (5305), 1458−1460.
(41) Mansky, P.; Russell, T. P.; Hawker, C. J.; Pitsikalis, M.; Mays, J. *Macromolecules* **1997**, *30* (22), 6810−6813.
(42) Huang, E.; Russell, T. P.; Harrison, C.; Chaikin, P. M.; Register, R. A.; Hawker, C. J.; Mays, J. *Macromolecules* **1998**, *31* (22), 7641−7650.
(43) In, I.; La, Y. H.; Park, S. M.; Nealey, P. F.; Gopalan, P. *Langmuir* **2006**, *22* (18), 7855−7860.
(44) Han, E.; Stuen, K. O.; La, Y. H.; Nealey, P. F.; Gopalan, P. *Macromolecules* **2008**, *41* (23), 9090−9097.
(45) Ji, S.; Liu, C. C.; Son, J. G.; Gotrik, K.; Craig, G. S. W.; Gopalan, P.; Himpsel, F. J.; Char, K.; Nealey, P. F. *Macromolecules* **2008**, *41* (23), 9098−9103.
(46) Morkved, T. L.; Lu, M.; Urbas, A. M.; Ehrichs, E. E.; Jaeger, H. M.; Mansky, P.; Russell, T. P. *Science* **1996**, *273* (5277), 931−933.
(47) Schaffer, E.; Thurn-Albrecht, T.; Russell, T. P.; Steiner, U. *Nature* **2000**, *403* (6772), 874−877.
(48) Delacruz, M. O.; Mayes, A. M.; Swift, B. W. *Macromolecules* **1992**, *25* (2), 944−948.
(49) Disko, M. M.; Liang, K. S.; Behal, S. K.; Roe, R. J.; Jeon, K. J. *Macromolecules* **1993**, *26* (11), 2983−2986.
(50) Hajduk, D. A.; Takenouchi, H.; Hillmyer, M. A.; Bates, F. S.; Vigild, M. E.; Almdal, K. *Macromolecules* **1997**, *30* (13), 3788−3795.
(51) Khandpur, A. K.; Forster, S.; Bates, F. S.; Hamley, I. W.; Ryan, A. J.; Bras, W.; Almdal, K.; Mortensen, K. *Macromolecules* **1995**, *28* (26), 8796−8806.
(52) Thomas, E. L.; Alward, D. B.; Kinning, D. J.; Martin, D. C.; Handlin, D. L.; Fetters, L. J. *Macromolecules* **1986**, *19* (8), 2197−2202.
(53) Rockford, L.; Liu, Y.; Mansky, P.; Russell, T. P.; Yoon, M.; Mochrie, S. G. J. *Phys. Rev. Lett.* **1999**, *82* (12), 2602−2605.
(54) Kim, S. O.; Solak, H. H.; Stoykovich, M. P.; Ferrier, N. J.; de Pablo, J. J.; Nealey, P. F. *Nature* **2003**, *424* (6947), 411−414.
(55) Tada, Y.; Akasaka, S.; Yoshida, H.; Hasegawa, H.; Dobisz, E.; Kercher, D.; Takenaka, M. *Macromolecules* **2008**, *41* (23), 9267−9276.
(56) Detcheverry, F. A.; Nealey, P. F.; de Pablo, J. J. *Macromolecules* **2010**, *43* (15), 6495−6504.
(57) Segalman, R. A.; Yokoyama, H.; Kramer, E. J. *Adv. Mater.* **2001**, *13* (15), 1152.
(58) Sundrani, D.; Darling, S. B.; Sibener, S. J. *Nano Lett.* **2004**, *4* (2), 273−276.
(59) Cheng, J. Y.; Mayes, A. M.; Ross, C. A. *Nature Mater.* **2004**, *3* (11), 823−828.
(60) Park, S. M.; Rettner, C. T.; Pitera, J. W.; Kim, H. C. *Macromolecules* **2009**, *42* (15), 5895−5899.
(61) Han, E.; Kang, H. M.; Liu, C. C.; Nealey, P. F.; Gopalan, P. *Adv. Mater.* **2010**, *22* (38), 4325−4329.
(62) Kim, B. H.; Lee, H. M.; Lee, J. H.; Son, S. W.; Jeong, S. J.; Lee, S.; Il Lee, D.; Kwak, S. U.; Jeong, H.; Shin, H.; Yoon, J. B.; Lavrentovich, O. D.; Kim, S. O. *Adv. Funct. Mater.* **2009**, *19* (16), 2584−2591.
(63) Kim, S. O.; Kim, B. H.; Kim, K.; Koo, C. M.; Stoykovich, M. P.; Nealey, P. F.; Solak, H. H. *Macromolecules* **2006**, *39* (16), 5466−5470.
(64) Kellogg, G. J.; Walton, D. G.; Mayes, A. M.; Lambooy, P.; Russell, T. P.; Gallagher, P. D.; Satija, S. K. *Phys. Rev. Lett.* **1996**, *76* (14), 2503−2506.
(65) Matsen, M. W.; Bates, F. S. *J. Polym. Sci., Part B: Polym. Phys.* **1997**, *35* (6), 945−952.
(66) Matsen, M. W. *J. Phys.: Condens. Matter* **2002**, *14* (2), R21−R47.
(67) Ballard, D. G. H.; Wignall, G. D.; Schelten, J. *Eur. Polym. J.* **1973**, *9* (9), 965−969.
(68) Kirste, R. G. *Makromol. Chem.* **1967**, *101*, 91.
(69) Russell, T. P.; Hjelm, R. P.; Seeger, P. A. *Macromolecules* **1990**, *23* (3), 890−893.
(70) Ryan, A. J.; Mai, S. M.; Fairclough, J. P. A.; Hamley, I. W.; Booth, C. *Phys. Chem. Chem. Phys.* **2001**, *3* (15), 2961−2971.
(71) Park, S. M.; Stoykovich, M. P.; Ruiz, R.; Zhang, Y.; Black, C. T.; Nealey, P. E. *Adv. Mater.* **2007**, *19* (4), 607.
(72) Jeong, S. J.; Kim, J. E.; Moon, H. S.; Kim, B. H.; Kim, S. M.; Kim, J. B.; Kim, S. O. *Nano Lett.* **2009**, *9* (6), 2300−2305.
(73) Ruiz, R.; Kang, H. M.; Detcheverry, F. A.; Dobisz, E.; Kercher, D. S.; Albrecht, T. R.; de Pablo, J. J.; Nealey, P. F. *Science* **2008**, *321* (5891), 936−939.
(74) Cheng, J. Y.; Rettner, C. T.; Sanders, D. P.; Kim, H. C.; Hinsberg, W. D. *Adv. Mater.* **2008**, *20* (16), 3155−3158.
(75) Tada, Y.; Akasaka, S.; Takenaka, M.; Yoshida, H.; Ruiz, R.; Dobisz, E.; Hasegawa, H. *Polymer* **2009**, *50* (17), 4250−4256.
(76) Detcheverry, F. A.; Liu, G. L.; Nealey, P. F.; de Pablo, J. J. *Macromolecules* **2010**, *43* (7), 3446−3454.
(77) Liu, G. L.; Thomas, C. S.; Craig, G. S. W.; Nealey, P. F. *Adv. Funct. Mater.* **2010**, *20* (8), 1251−1257.
(78) Kang, H. M.; Detcheverry, F.; Stuen, K. O.; Craig, G. S. W.; de Pablo, J. J.; Gopalan, P.; Nealey, P. F. *J. Vac. Sci. Technol., B* **2010**, *28* (6), C6B24−C6B29.
(79) Tang, Q. Y.; Ma, Y. Q. *Soft Matter* **2010**, *6* (18), 4460−4465.

Macromolecules

Article

pubs.acs.org/Macromolecules

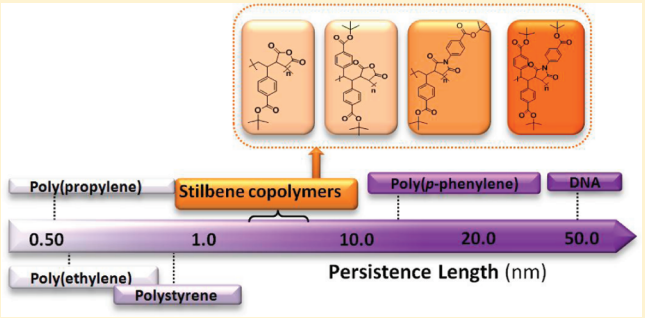
Chain Stiffness of Stilbene Containing Alternating Copolymers by SAXS and SEC

Yi Li,[†,‡] Mingqiang Zhang,[†] Min Mao,[†] S. Richard Turner,*[,†,‡] Robert B. Moore,*[,†] Thomas H. Mourey,*[,§] Lisa A. Slater,[§] and James R Hauenstein[§]

[†]Department of Chemistry and [‡]Macromolecules and Interfaces Institute, Virginia Tech, Blacksburg, Virginia 24061-0344, United States

[§]Corporate Research and Engineering, Eastman Kodak Company, 1999 Lake Avenue, Rochester, New York 14615-2136, United States

ABSTRACT: Persistence lengths of stilbene and styrene containing alternating copolymers were measured using small-angle X-ray scattering (SAXS) and size-exclusion chromatography (SEC). For SAXS measurement, a graphical approach and the Sharp and Bloomfield method of analyzing scattering data were both used to quantify the chain stiffness. For SEC measurement, the Bohdanecký linear approximation was applied to determine persistence lengths. The complementary results obtained from SAXS approaches as well as from SEC measurements characterized stilbene copolymers as a class of semirigid polymers with persistence lengths in a range of 2−6 nm. Stilbene copolymers are more rigid than their styrene analogues.



INTRODUCTION

Rigid polymers are envisioned to simplify studies of polymer interactions since the conformational changes of a flexible polymer backbone are reduced or eliminated.[1−6] The sterically crowded structures arising from the use of substituted stilbene comonomers, enchained in an alternating structure with maleic anhydride or maleimide comonomers, are anticipated to stiffen the backbone.[7−17] In addition the rich chemistry available for stilbenes makes the preparation of a variety of functional stilbene derivatives possible, which opens up interesting families of new polyelectrolytes and other functional copolymers for study. Our previous studies showed that from the solid-state NMR torsional angle measurements maleic anhydride units of *N*,*N*,*N*′,*N*′-tetraethyl-4, 4′-diaminostilbene−(TDAS−) maleic anhydride (MAH) alternating copolymer were enchained in a predominately cis configuration creating a highly contoured chain.[7] We also observed that a block copolymer containing a polyampholyte based on the TDAS−MAH comonomer and a poly(methoxy-capped oligo(ethylene glycol)methacrylate) block exhibited polyion complexes (PICs) with unusual pH and salt responsive properties similar to like-charge attraction effects in rigid polyelectrolytes.[9] In addition films of the alternating copolymer of stilbene and *N*-(2-methylphenyl)maleimide) were found to have a very strong negative birefringence while the corresponding alternating copolymer of styrene and *N*-(2-methylphenyl)maleimide did not show this effect. This significant difference is likely due to conformational constraints arising from the extra phenyl rings of enchained stilbene units.[18]

To validate the steric crowding effect and quantify the chain stiffness, a functional stilbene monomer with *tert*-butyl carboxylate in the 4,4′-position on the phenyl groups of stilbene, as well as a functional *N*-phenylmaleimide monomer with *tert*-butyl carboxylate in the 4-position on the benzene ring of maleimide have been prepared. Analogous styrenic copolymers, for direct comparison to the stilbene copolymers, have also been prepared. To obtain persistence lengths, both SEC analysis and SAXS were performed. The effect of the extra phenyl groups on the chain stiffness from the insertion of the 1, 2-diphenyl units (from stilbene) in the backbone were directly compared to the single phenyl (from styrene) in the chain.[18]

EXPERIMENTAL SECTION

Materials. Stilbene and styrenic copolymers were synthesized via free radical polymerization.[19] In Figure 1, copolymer **I** was synthesized from *tert*-butyl 4-vinyl benzoate and maleic anhydride and copolymer **III** was composed of *tert*-butyl 4-vinyl benzoate and *tert*-butyl 4-maleimidobenzoate. Copolymer **II** was synthesized from (*E*)-di-*tert*-butyl 4,4′-stilbenedicarboxylate and maleic anhydride and copolymer **IV** was prepared from (*E*)-di-*tert*-butyl 4,4′-stilbenedicarboxylate and *tert*-butyl 4-maleimidobenzoate. (*E*)-di-*tert*-butyl 4,4′-stilbenedicarboxylate was prepared from (*E*)-dimethyl 4,4′-stilbenedicarboxylate via a transesterification reaction,[19] maleic anhydride was purchased from Sigma-Aldrich, *tert*-butyl 4-maleimidobenzoate was synthesized from 4-aminobenzoic acid in 4 steps,[19,20] and *tert*-butyl 4-vinyl benzoate was

Received: October 30, 2011
Revised: January 11, 2012
Published: January 26, 2012

 © 2012 American Chemical Society dx.doi.org/10.1021/ma202406a | *Macromolecules* 2012, 45, 1595−1601

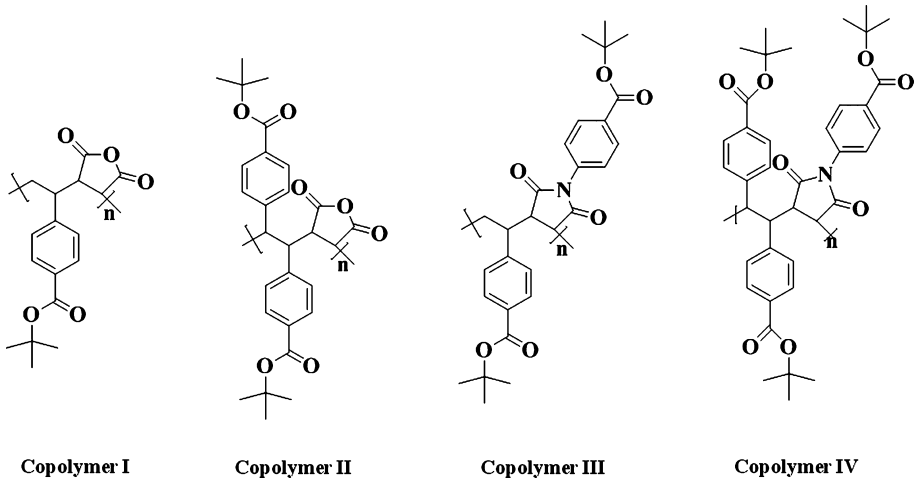


Figure 1. Chemical structure of copolymers **I**, **II**, **III**, and **IV**.

prepared from *p*-toluic acid in 6 steps.[19,21−23] Copolymers **II** and **IV** were synthesized at 110 °C with dicumylperoxide as initiator and chlorobenzene as solvent for 24 h. Copolymers **I** and **III** were prepared at 60 °C with AIBN as initiator and tetrahydrofuran (THF) as solvent for 4 h. For example, a mixture of (*E*)-di-*tert*-butyl 4,4′-stilbenedicarboxylate (3.80 g 10.00 mmol), *tert*-butyl 4-maleimidobenzoate (2.73 g, 10.00 mmol), chlorobenzene (23.5 mL, 20 wt %), DCP (0.0653 g, 1.0 wt %) was sealed in a 50 mL, septum sealed glass bottle equipped with a magnetic stirrer and was degassed by purging with argon for 20 min and polymerized for 24 h. All copolymers were recovered by precipitating into hexanes twice to remove the residue monomers and dried under vacuum at 60 °C overnight before characterization. The purity of samples was verified by ^{1}H NMR and proved to be sufficiently high for the present purpose. Molecular weights and their distributions of copolymer **I** and **II** (Table 1) were determined using *N, N*-dimethylformamide (DMF) containing 0.1 M lithium nitrate and 1% formic acid as eluent to avoid a small amount of maleic anhydride unit in acid form from interacting with the SEC columns. Molecular weights and their distributions of copolymer **III** and **IV** were determined using THF as eluent solvent. Absolute weight-average molecular weights are most accurately measured by light scattering detection, whereas absolute number-average molecular weights are normally better measured by viscometry detection and a Universal Calibration curve because the viscometry detector is more sensitive in the low-molecular weight region of chromatograms than is the light scattering detector. These molecular weight averages are provided in Table 1.

Table 1. Molecular Characteristics of Copolymers I, II, III, and IV

	M_n (g/mol)[c]	M_w (g/mol)[d]
copolymer **I**[a]	41 100	64 600
copolymer **II**[a]	73 000	163 000
copolymer **III**[b]	60 300	154 000
copolymer **IV**[b]	97 200	225 000

[a]SEC in DMF containing 0.1 M lithium nitrate and 1% formic acid. [b]SEC in THF. [c]Viscometry detection/Universal Calibration. [d]Light scattering detection.

Instrumentation. *Small-Angle X-ray Scattering.* SAXS experiments were performed using a Rigaku S-Max 3000 3 pinhole SAXS system, equipped with a copper rotating anode emitting X-rays with a wavelength of 0.154 nm (Cu Kα). Two-dimensional SAXS patterns were obtained using a fully integrated 2D gas-filled multiwire, proportional counting detector, with an exposure time of 1 h. All SAXS data was analyzed using the SAXSGUI software package to obtain radically integrated SAXS intensity versus scattering vector q (SAXS), where $q = (4\pi/\lambda)\sin(\theta)$, θ is one-half of the scattering angle and λ is the wavelength of X-rays. For all scattering experiments, the sample-to-detector distance was 1603 mm, and the q-range was calibrated using a silver behenate standard.

SAXS measurements were carried out in DMF containing 0.1 M lithium nitrate and 1% formic acid for copolymers **I**, **II**, and in DMF for copolymers **III**, **IV**. The polymer solution concentrations were 1.0 wt %. Solution samples were measured in thin-walled capillary tubes for X-ray diffraction with a diameter of 1.5 mm and wall thickness of 0.01 mm. The measured intensity was corrected for sample transmission, solvent scattering and background (capillary) scattering.

Size-Exclusion Chromatography. Copolymers **I** and **II** were examined at 35.0 °C using three 7.5 mm ×300 mm Plgel Olexis columns from Agilent Technologies. DMF containing 0.1 M lithium nitrate and 1% formic acid was used as the eluent, and the column set was calibrated with narrow-molecular-weight distribution poly(methyl methacrylate) (PMMA) standards. Instrumentation consisted of an Agilent 1100 series isocratic pump, autosampler and UV−visible absorption detector, Agilent PD2020 (formerly Precision Detectors) 15 and 90 deg elastic light scattering detector, Malvern 270 (formerly Viscotek) differential viscometry detector, and a Waters 410 differential refractive index detector plumbed in parallel with the differential viscometry detector. Uninhibited HPLC-grade THF was used as the SEC eluent for copolymers **III** and **IV** containing maleimide units. Three 7.5 mm ×300 mm Agilent PLgel mixed-C columns thermostated at 35.0 °C were calibrated with narrow-molecular-weight distribution polystyrene standards. The solvent delivery and sample management system and UV−visible detector were Waters model 2695 and 2487, respectively, and the light scattering, viscometry and refractive index detectors and their configuration were similar to those described above for the DMF system. Flow rates were nominally 1.0 mL/min and were corrected using the retention volume of acetone added to the sample solutions as a flow marker. All injection volumes were 0.1 mL and sample concentrations were between 1 and 2 mg/mL.

Persistence length can be estimated from multidetector SEC using intrinsic viscosity, $[\eta]$, and molar mass, M, conformation plots as well as from the relationship between molar mass, M, and radius of gyration, R_g. The lower measurable size limit for the 680 nm wavelength of incident light used in our SEC light scattering detector is $R_g \sim 10$ nm, which greatly restricts that range of accessible $M - R_g$ data for the polymers examined in this study. In comparison, intrinsic viscosity can be measured at lower molar masses and across a broader molar mass range than light scattering detection for these samples, making $[\eta] - M$ conformation plots a desirable alternative to $R_g - M$ plots.[24] Hence, for copolymers **I**, **II**, **III**, and **IV** intrinsic viscosity measured by the differential viscometry detector was combined with molar mass measured by light scattering detection at each data point along chromatograms to determine the persistence lengths.

dx.doi.org/10.1021/ma202406a | *Macromolecules* 2012, 45, 1595−1601

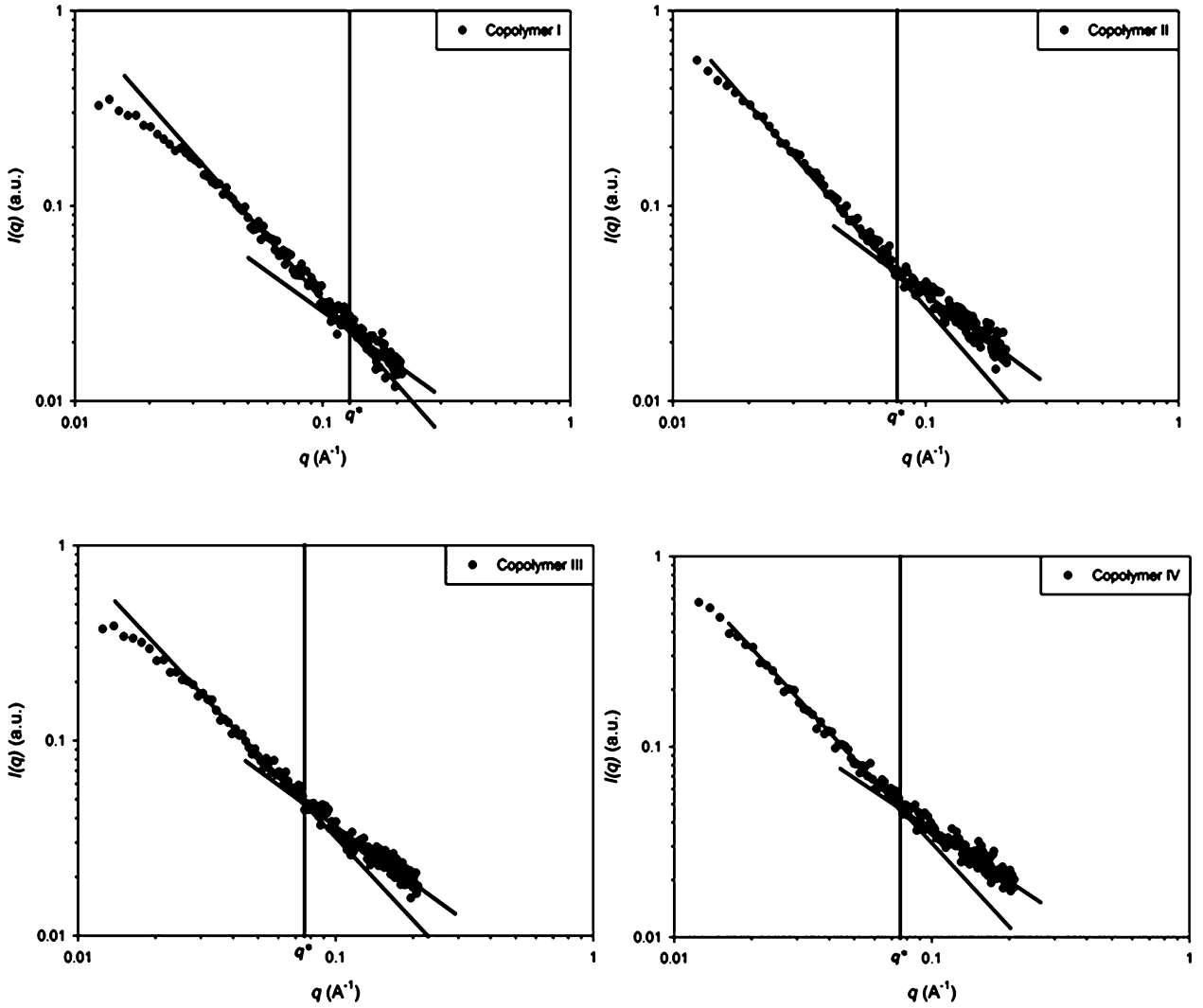


Figure 2. $I(q)$ vs q plots for copolymers **I**, **II**, **III**, and **IV**. The fit range includes all of the data points. Every fifth data point is selected to plot for clarity.

RESULTS AND DISCUSSION

Measurement of Persistence Length by SAXS. For stiff and semirigid macromolecules, Kratky and Porod proposed a chain model denoted as the "wormlike or Kratky–Porod chain model" which examines a real polymer chain in a simple way: in the smallest scale, atoms on a polymer chain are recognized; as the scale increases, a short sequence of monomeric units are exhibited; as the scale increases further, a longer sequence of the polymer chain is recognized, which resembles more or less a rigid-rod; on an even larger length scale, the whole polymer chain is recognized as behaving like a Gaussian chain.[25,26] The persistence length, l_p, was introduced in this process by Kratky and Porod to reflect the stiffness of a polymer chain. L_k is the Kuhn length, first developed by W. Kuhn in 1934.[27] In general, $2l_p = L_k$[28−30] where the persistence length, l_p, can be estimated in a SAXS experiment, as briefly discussed below. A scattering plot of $I(q)$ vs q can be divided into different regions that probe various length scales associated with different dimensions of a polymer chain. On the basis of theoretical predictions for a sufficiently long chain (a Gaussian chain),[31] two characteristic regions may be observed: at small q, the scattering pattern reflects the random coil nature of a polymer chain, and is expressed by the Debye function, where $I(q) \sim q^{-2}$ is valid;[32] as q is increased, the scattering pattern is governed by the behavior of small sections of the polymer chain and exhibits $I(q) \sim q^{-1}$ characteristic of rigid rods. An intersection of these two regions defines the persistence length. To determine the persistence length, it is customary to use a log–log plot of $I(q)$ − q where two regions are matched with lines having slopes of −2 and −1, respectively. An extrapolation of the intersection of these two linear regions at a value q^* is related to the persistence length by

$$l_p = A/q^* \tag{1}$$

where the constant A is derived from computations. Porod gave $A = 6/\pi$ for Gaussian coils.[33,34] By use of a Monte Carlo technique for coils with finite sizes (non-Gaussian coils), A = 2.3 was suggested as a more accurate approximation.[35−37] In this work, the value of 2.3 has been used for determination of persistence lengths.

In fact, for non-Gaussian coils, the ideal situation of two distinctly different linear regions having q^{-2} and q^{-1} scaling in the SAXS data is not often fulfilled. Various authors[31,38−43] have reported that the ideal slope = −2 region did not appear at small q in scattering measurements; rather, the power law was generally less than −2 in the Debye region and a change in

dx.doi.org/10.1021/ma202406a | Macromolecules 2012, 45, 1595−1601

slope of two characteristic regions was observed. This is similar to the theoretical curves described previously and the q^* at the slope change was used to define l_p.[38−43] As shown in Figure 2 in the form of an $I(q) - q$ plot, the expected −1 region was obtained from scattering measurements for copolymers **I**, **II**, **III**, and **IV**. Because of the finite molecular weights of these samples, the −2 region corresponding to the Debye function was not observed. However, changes of slopes occurred in the two expected regions. The data in common ranges both in low q range (0.030−0.052) and in high q range (0.075−0.2) were used to determine the persistence lengths of copolymers. This allows the determination of persistence lengths by eq 1, shown in Table 2.

Table 2. Results from SAXS Measurements for Copolymers I, II, III, and IV

	q^* (Å^{-1})	l_p by eq 1 (nm)
copolymer **I**	0.139	1.7
copolymer **II**	0.079	2.9
copolymer **III**	0.076	3.0
copolymer **IV**	0.075	3.1

The data in Table 2 show that copolymer **I** is less stiff than copolymer **II**. The rising trend of the chain stiffness from copolymer **III** to **IV** is not very obvious. Most of the scattering curves exhibit a gradual transition between the two regions. This makes the graphical determination of persistence lengths subject to some ambiguities.[31] To solve this problem, different analytical approaches were introduced to accurately determine the persistence length.[31,43−45] The most widely used method was developed by Sharp and Bloomfield[43,44] and corrected by Schmid[46]

$$I(q) = G_2\left\{g_D(x) + \frac{2l_p}{L}\left[\frac{4}{15} + \frac{7}{15x} - \left(\frac{11}{15} + \frac{7}{15x}\right)e^{-x}\right]\right\} \quad (2)$$

with

$$g_D(x) = 2\frac{e^{-x} + x - 1}{x^2} \quad (3)$$

where $x = (Ll_pq^2)/3$, L is the contour length, $L = 2L_pN_k$, N_k is the number of Kuhn segments per chain and G_2 in eq 2 is the Debye prefactor. A least-squares fit to the data in the entire q range was performed using Sharp and Bloomfield function (SBF). Since the scattering data were not corrected to absolute intensity values, the prefactor is treated as an undefined fitting constant, G_2' and not reported here. The results of fitting variables l_p, N_k are listed in Table 3. The fitting curves are shown in Figure 3.

Table 3. Parameters of Sharp and Bloomfield Function for Copolymers I, II, III, and IV

	N_k	l_p (nm)
copolymer **I**	7.62	2.7
copolymer **II**	11.7	3.6
copolymer **III**	7.53	3.4
copolymer **IV**	11.2	4.0

Persistence lengths obtained from both the graphical approach and the SBF approach are summarized in Table 5. The rising trends of persistence lengths observed with these two approaches with the addition of bulky phenyl rings along the polymer chains are in agreement with each other. However, because of the large error inherent in the graphical approach, it is not surprising that the absolute values of persistence lengths obtained from the graphical approach are somewhat different than the values using the SBF method. Nevertheless, by comparing the persistence lengths of copolymer **I** to copolymer **II** or copolymer **III** to copolymer **IV**, the results illustrate that the stilbene containing alternating copolymers are always stiffer than the analogous styrene containing alternating copolymers due to the addition of phenyl rings to the polymer backbone, which enhances steric conformational constraints, decreases the polymer chain mobility and thus increases chain stiffness.

Measurement of Persistence Length by SEC. SEC provides a complementary method for quantifying the stiffness of copolymer chains. The persistence length can be estimated from the relationship between M and $[\eta]$. The relationship changes in the extreme case of rigid rod-like macromolecules from $[\eta]\sim M^{1.7}$ to $[\eta]\sim M^{1/2}$ for Gaussian coils at large M, without excluded volume.[24] If a polymer sample has broad enough molecular weight distribution, the transition from a higher to lower $[\eta] - M$ power law can be used to estimate the persistence length by applying a suitable hydrodynamic chain model.

For example, the two variables $[\eta]$ and M are related according to the wormlike chain model of Yamakawa, Fujii, and Yoshizaki (Y−F−Y model) equation.[47] A popular method for obtaining the wormlike chain parameters of the Y−F−Y model is given by the Bohdanecký linear approximation[48]

$$\left(\frac{M^2}{[\eta]}\right)^{1/3} = A_\eta + B_\eta M^{1/2} \quad (4)$$

where A_η and B_η are given as

$$A_\eta = \frac{A_0 M_L}{\phi_\infty^{1/3}} \quad (5)$$

$$B_\eta = \frac{B_0}{\phi_\infty^{1/3}}\left(\frac{2l_p}{M_L}\right)^{-1/2} \quad (6)$$

$\phi_\infty = 2.87 \times 10^{23}$, and A_0 and B_0 are functions of $d/2L_p$,

$$A_0 = 0.46 - 0.53\log(d/2l_p) \quad (7)$$

$$B_0 = 1.00 - 0.0367\log(d/2l_p) \quad (8)$$

where d is the chain hydrodynamic diameter. B_0 is nearly constant and replaced by its mean value, 1.05. Values of mass per unit contour length, M_L, calculated from energy minimization in ChemBio3D Ultra, are provided in Table 4. M from light scattering detection and $[\eta]$ from the viscosity detection were used to create the plots in Figure 4 for copolymers **I**, **II**, **III**, and **IV**. A_η and B_η were determined from the slopes and intercepts of the Bohdanecký plots according to eq 4. The persistence length l_p was obtained from the intercept, B_η, $B_0 = 1.05$, and M_L values using eq 6, and are provided in Table 4. The theory underlying the linear approximation described by eq 4 neglects the effects of excluded volume on molecular dimensions, and the viscosity expansion factor may

dx.doi.org/10.1021/ma202406a | *Macromolecules* 2012, 45, 1595−1601

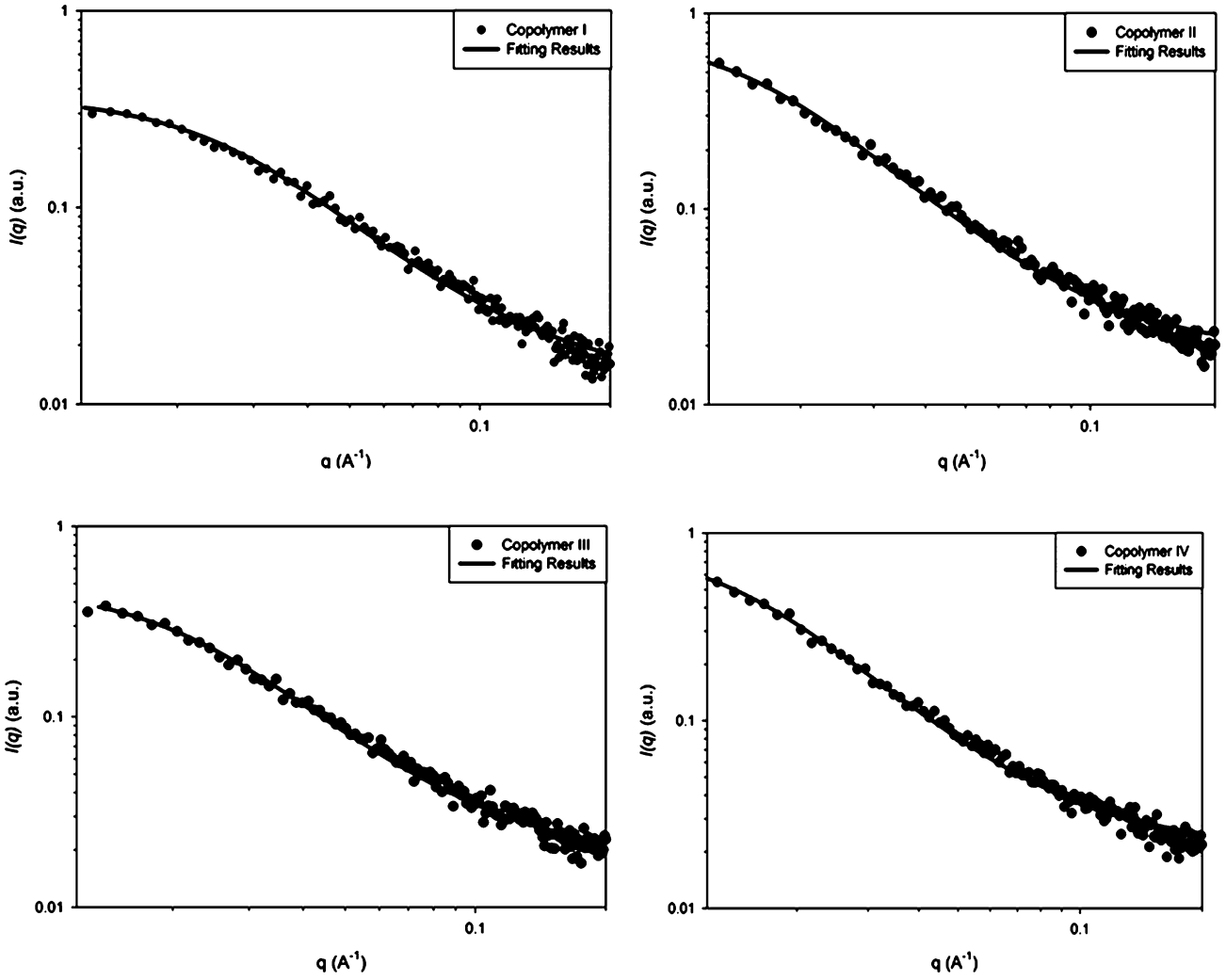


Figure 3. Sharp and Bloomfield fits to the data of Figure 2. The fit range includes all of the data points. Every fifth data point is selected to plot for clarity.

Table 4. Parameters of Bohdanecký Equation for Copolymer I, II, III, and IV

	A_η (g mol$^{-2/3}$ mL$^{-1/3}$)	B_η (g$^{1/2}$ mol$^{-1/6}$ mL$^{-1/3}$)	M_L (nm^{-1})	l_p (nm)
copolymer **I**[a]	94.4	1.74	610	2.57
copolymer **II**[a]	145	2.04	1000	3.04
copolymer **III**[b]	145	1.75	1032	4.28
copolymer **IV**[b]	240	1.69	1369	6.08

[a]SEC experiments were carried out in DMF containing 0.1 M lithium nitrate and 1% formic acid. [b]SEC experiments were carried out in THF.

Table 5. Comparison of Persistence Lengths Obtained from SAXS and SEC

	l_p by eq 1 (nm)	l_p by SBF approach (nm)	l_p by Bohdanecký approximation (nm)
copolymer **I**	1.7	2.7	2.6[a]
copolymer **II**	2.9	3.6	3.0[a]
copolymer **III**	3.0	3.4	4.3[b]
copolymer **IV**	3.1	4.0	6.1[b]

[a]l_p was determined in DM as solvent. [b]l_p was determined in THF as solvent.

not be negligible at high values of M; however, as explained by Bohdanecký in ref 48, the initial slope of the plot of $(M^{1/2}/[\eta])^{1/3}$ vs $M^{1/2}$ will not be significantly affected by expansion and the copolymers in this study fall within the valid ranges of contour lengths provided in Table 1 of ref 48.

From Table 5, the Bohdanecký linear approximation applied to the SEC data, and the graphical and SBF approaches applied to the SAXS data provided similar trends. From both SEC and SAXS measurements, the addition of the phenyl rings to the polymer backbone increases the persistence length; however, persistence length is considered a solvent-dependent quantity; hence, the SEC values for copolymers **I** and **II** in DMF/formic acid/$LiNO_3$ may not be directly comparable to those of copolymers **III** and **IV** measured in THF. Additionally, the polymer backbones with maleimide units are more rigid than the ones based on maleic anhydride units, by comparing persistence length values of copolymer **I** to its analogy, copolymer **III**, or copolymer **II** to its analogous copolymer **IV**. This is probably due to the steric hindrance caused by the bulky *tert*-butyl phenyl carboxylate functional group located on the maleimide unit. This is similar to the alternating copolymer of stilbene and *N*-(2-methylphenyl)maleimide) where a strong negative birefringence was observed due to the steric hindrance caused by the methyl substituent.[18]

dx.doi.org/10.1021/ma202406a | *Macromolecules* 2012, 45, 1595−1601

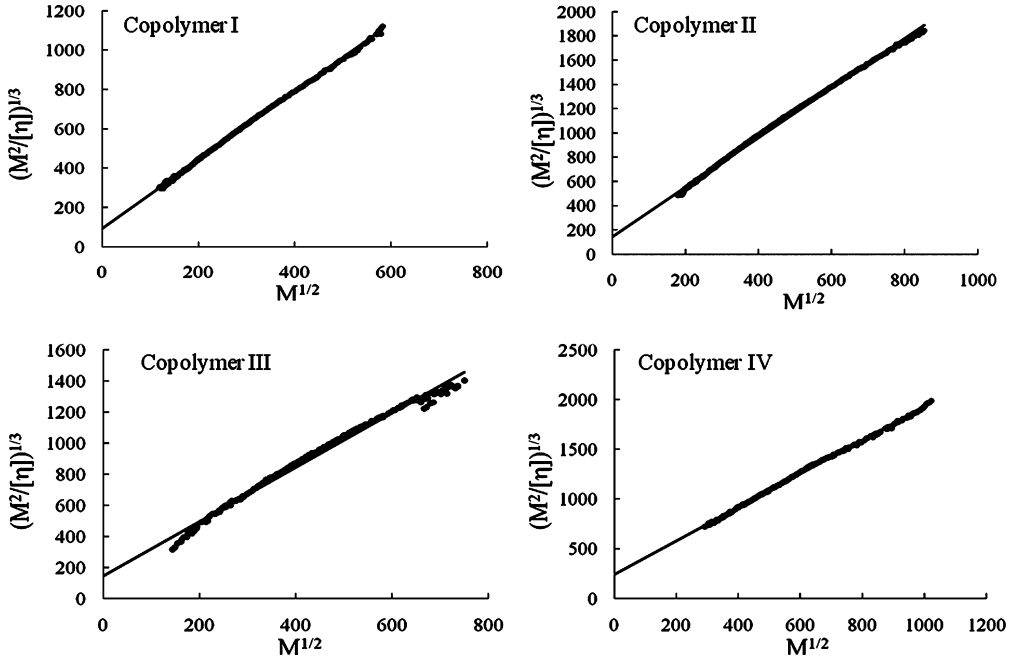


Figure 4. Bohdanecký plots of copolymer **I**, **II**, **III**, **IV**.

The results from SBF and Bohdanecký approaches showed that the added phenyl groups increase the rigidity of the polymer chains by about 30−50%. These persistence length values put these copolymers into a broadly defined "semi-rigid" category of polymers.

Table 6 provides persistence length values of different types of polymers. In comparison to rigid rod polymers such as poly(*n*-hexyl isocyanate) (l_p = 40 nm),[24,48] DNA (l_p = 50 nm),[49] and schizophyllan (l_p = 137 nm),[48] stilbene containing alternating copolymers are a class of semirigid polymers, with chain stiffness similar to ladder-type poly(*p*-phenylene) (l_p = 6.5 nm),[54] poly(*tert*-butyl crotonate) (l_p = 5.0−6.0 nm),[53] and poly(1-phenyl-1-propyne) (l_p = 3.8 nm).[55] Stilbene containing alternating copolymers with the substituted polyethylenes as the backbone are 4−10 times stiffer than most of the polymers with the successive carbons in the main chain, such as poly(*tert*-butyl methacrylate) (l_p = 0.8−1.2 nm),[56] polystyrene (l_p = 0.90 nm),[58] and polypropylene (l_p= 0.56 nm).[58] In response to these observations we have worked to obtain dilute solution properties of the stilbene and styrene polyelectrolytes through steady-state solution shear rheology to assess the effect of steric crowding with the added phenyl groups on the copolymer chain dimensions from a different perspective.

Table 6. Comparison of Persistence Lengths

	l_p (nm)	solvent	reference
schizophyllan	137	water	48
DNA	50	water	49
poly(*n*-hexyl isocyanate)	40	THF	24, 48
cellulose trinitrate	15	acetone	48
poly(*p*-phenylene) backbone with sulfonate ester and dodecyl side chains	12.6	THF	50, 51
poly(2,7-(9,9 di-*n*-hexylfluorene))	8.0	THF	24
poly(diisopropyl fumarate)	11	THF	52
poly(*tert*-butyl crotonate)	5.0−6.0	ethyl acetate	53
ladder-type poly(*p*-phenylene)	6.5	toluene	54
copolymer **IV**	6.1	THF	this work
copolymer **III**	4.3	THF	this work
poly(1-phenyl-1-propyne)	3.8	cyclohexane	55
copolymer **II**	3.0	DMF	this work
copolymer **I**	2.6	DMF	this work
poly(*tert*-butyl methacrylate)	0.8−1.2	toluene	56
poly(acrylic acid)	1.4	dioxane	57
polystyrene	0.90	melt	58
poly(ethylene)	0.69	melt	58
poly(propylene)	0.56	melt	58

SUMMARY

Measurements of SAXS and SEC on stilbene and styrenic alternating copolymers gave persistence lengths ranging from 2 to 6 nm. This characterizes these copolymers into a class of semirigid polymers. On the basis of the persistence length comparison between stilbene copolymers to their analogous styrene copolymers, the steric crowding effect of the second phenyl ring from enchainment of the stilbene units in the backbone increased the polymer chain stiffness by about 30−50%. It was also found the polymer backbones enchained with *tert*-butyl carboxylate functionalized *N*-phenyl maleimide units are more rigid than those containing maleic anhydride units. This likely originates from the steric hindrance caused by the bulky *tert*-butyl phenyl carboxylate functional group located on the maleimide unit.

AUTHOR INFORMATION

Corresponding Author

*Fax: +1-540-231-3971. E-mail: srturner@vt.edu (S.R.T.), thomas.mourey@kodak.com (T.M.), and rbmoore3@vt.edu (R.B.M.).

Notes

The authors declare no competing financial interest.

■ ACKNOWLEDGMENTS

We wish to express our gratitude to Professor R. D. Gandour for his assistance in using energy minimization in ChemBio3D Ultra and to Graduate Student G. Divoux for his assistance and helpful discussions on SAXS measurements. We also thank Professor T. E. Long's group on sharing their SEC equipment. This work was supported by the donors of the American Chemical Society Petroleum Research Fund, the National Science Foundation under Grant No. DMR-0905231 and the National Science Foundation under Grant No. DMR-0923107.

■ REFERENCES

(1) Bohrisch, J.; Eisenbach, C. D.; Jaeger, W.; Mori, H.; Müller, A. H. E.; Rehahn, M.; Schaller, C.; Traser, S.; Wittmeyer, P.; Schmidt, M., Ed.; Springer: Berlin and Heidelberg, Germany, 2004; Vol. *165*, p 277.
(2) Holm, C.; Rehahn, M.; Oppermann, W.; Ballauff, M.; Schmidt, M., Ed.; Springer: Berlin and Heidelberg, Germany, 2004; Vol. *166*, p 35.
(3) Cotts, P. M.; Berry, G. C. *J. Polym. Sci., Polym. Phys. Ed.* **1983**, *21*, 1255.
(4) Lee, C. C.; Chu, S. G.; Berry, G. C. *J. Polym. Sci., Polym. Phys. Ed.* **1983**, *21*, 1573.
(5) Roitman, D. B.; Wessling, R. A.; McAlister, J. *Macromolecules* **1993**, *26*, 5174.
(6) Roitman, D. B.; McAlister, J.; McAdon, M.; Wessling, R. A. *J. Polym. Sci. Part B: Polym. Phys.* **1994**, *32*, 1157.
(7) Mao, M.; Kim, C.; Wi, S.; Turner, S. R. *Macromolecules* **2007**, *41*, 387.
(8) Mao, M.; Turner, S. R. *Polymer* **2006**, *47*, 8101−8105.
(9) Mao, M.; Turner, S. R. *J. Am. Chem. Soc.* **2007**, *129*, 3832.
(10) Li, Y.; Turner, S. R. *Eur. Polym. J.* **2010**, *46*, 821.
(11) Wagner-Jauregg, T. *Ber. Dtsch. Chem. Ges. (A and B Ser.)* **1930**, *63*, 3213.
(12) Lewis, F. M.; Mayo, F. R. *J. Am. Chem. Soc.* **1948**, *70*, 1533−1536.
(13) Hallensleben, M. L. *Eur. Polym. J.* **1973**, *9*, 227−231.
(14) Tanaka, T.; Vogl, O. *Polym. J. (Tokyo, Jpn.)* **1974**, *6*, 522−531.
(15) Rzaev, Z. M.; Zeinalov, I. P.; Medyakova, L. V.; Babaev, A. I.; Agaev, M. M. *Vysokomol Soedin Ser A* **1981**, *23*, 614.
(16) Ebdon, J. R.; Hunt, B. J.; Hussein, S. *Br. Polym. J.* **1987**, *19*, 333−337.
(17) McNeill, I. C.; Polishchuk, A. Y.; Zaikov, G. E. *Polym. Degrad. Stab.* **1995**, *47*, 319−329.
(18) Mao, M.; England, J.; Turner, S. R. *Polymer* **2011**, *52*, 4498.
(19) Li, Y.; Mao, M.; Matolyak, L. E.; Turner, S. R. *ACS Macro Lett.* **2012**, *1*, 257.
(20) Taylor, E. C.; Fletcher, S. R.; Sabb, A. L. *Synth. Commun.* **1984**, *14*, 921.
(21) Broos, R.; Tavernier, D.; Anteunis, M. *J. Chem. Educ.* **1978**, *55*, 813.
(22) Ishizone, T.; Hirao, A.; Nakahama, S.; Tsuda, K. *Macromolecules* **1996**, *197*, 1481−1791.
(23) Rich, D. H.; Gurwara, S. K. *J. Am. Chem. Soc.* **1975**, *97*, 1575.
(24) Mourey, T.; Le, K.; Bryan, T.; Zheng, S.; Bennett, G. *Polymer* **2005**, *46*, 9033.
(25) Kratky, O.; Porod, G. *Recl. Travaux Chim. Pays-Bas* **1949**, *68*, 1106.
(26) Porod, G. *Monatsh. Chem./Chem. Monthly* **1949**, *80*, 251.
(27) Kuhn, W. *Kolloid-Z* **1934**, *68*, 2.
(28) Benoit, H.; Doty, P. *J. Phys. Chem.* **1953**, *57*, 958.
(29) Doi, M.; Edwards, S. F. *The theory of polymer dynamics*; Clarendon Press: Oxford, U.K., 1988.
(30) Gennes, P. G. *Scaling concepts in polymer physics*; Cornell University Press: Ithaca, NY, 1979.
(31) Glatter, O.; Kratky, O. *Small angle x-ray scattering*; Academic Press: San Diego, CA, 1982.
(32) Debye, P. *J. Phys. Colloid Chem.* **1947**, *51*, 18.
(33) Porod, G. *J. Polym. Sci.* **1953**, *10*, 157.
(34) Kratky, O. *Colloid Polym. Sci.* **1962**, *182*, 7.
(35) Peterlin, A. *J. Polym. Sci.* **1960**, *47*, 403.
(36) Heine, V. S.; Kratky, O.; Roppert, J. *Makromol. Chem.* **1962**, *56*, 150.
(37) Kratky, O. *Pure Appl. Chem.* **1966**, *12*, 483.
(38) Cleland, R. L. *Arch. Biochem. Biophys.* **1977**, *180*, 57.
(39) Gupta, A. K.; Cotton, J. P.; Marchal, E.; Burchard, W.; Benoit, H. *Polymer* **1976**, *17*, 363.
(40) Muroga, Y.; Noda, I.; Nagasawa, M. *Macromolecules* **1985**, *18*, 1576.
(41) Yamazaki, S.; Muroga, Y.; Noda, I. *Langmuir* **1999**, *15*, 4147.
(42) Paramita Kar, C.; et al. *J. Phys.: Condens. Matter* **2009**, *21*, 195801.
(43) Beaucage, G.; Rane, S.; Sukumaran, S.; Satkowski, M. M.; Schechtman, L. A.; Doi, Y. *Macromolecules* **1997**, *30*, 4158.
(44) Sharp, P.; Bloomfield, V. A. *Biopolymers* **1968**, *6*, 1201.
(45) Yamakawa, H.; Fujii, M. *Macromolecules* **1974**, *7*, 649.
(46) Schmid, C. W.; Rinehart, F. P.; Hearst, J. E. *Biopolymers* **1971**, *10*, 883.
(47) Yamakawa, H.; Fujii, M. *Macromolecules* **1974**, *7*, 128.
(48) Bohdanecky, M. *Macromolecules* **1983**, *16*, 1483.
(49) Wang, L.; Bloomfield, V. A. *Macromolecules* **1991**, *24*, 5791.
(50) Guilleaume, B.; Blaul, J.; Ballauff, M.; Wittemann, M.; Rehahn, M.; Goerigk, G. *Eur. Phys. J. E: Soft Matter Biol. Phys.* **2002**, *8*, 299.
(51) Vanhee, S.; Rulkens, R.; Lehmann, U.; Rosenauer, C.; Schulze, M.; Köhler, W.; Wegner, G. *Macromolecules* **1996**, *29*, 5136.
(52) Matsumoto, A.; Nakagawa, E. *Eur. Polym. J.* **1999**, *35*, 2107.
(53) Noda, I.; Imai, T.; Kitano, T.; Nagasawa, M. *Macromolecules* **1981**, *14*, 1303.
(54) Scherf, U.; Müllen, K. *Makromol. Chem., Rapid Commun.* **1991**, *12*, 489.
(55) Hirao, T.; Teramoto, A.; Sato, T.; Norisuye, T.; Masuda, T.; Higashimura, T. *Polym J* **1991**, *23*, 925.
(56) Muroga, Y.; Sakuragi, I.; Noda, I.; Nagasawa, M. *Macromolecules* **1984**, *17*, 1844.
(57) Taylor, T. J.; Stivala, S. S. *Polymer* **1996**, *37*, 715.
(58) Fetters, L.; Lohse, D.; Colby, R. In *Physical Properties of Polymers Handbook*; Mark, J. E., Ed.; Springer: New York: 2007; p 447.

Macromolecules

Article

pubs.acs.org/Macromolecules

Quantitative Measurements of the Size Scaling of Linear and Circular DNA in Nanofluidic Slitlike Confinement

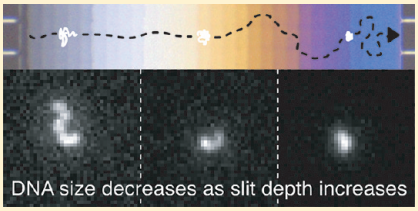
Elizabeth A. Strychalski,*[,†,§] Jon Geist,[‡] Michael Gaitan,[‡] Laurie E. Locascio,[†] and Samuel M. Stavis[‡,§]

[†]Biochemical Science Division, National Institute of Standards and Technology, Gaithersburg, Maryland 20899-1000, United States

[‡]Semiconductor and Dimensional Metrology Division, National Institute of Standards and Technology, Gaithersburg, Maryland 20899-1000, United States

Supporting Information

ABSTRACT: Quantitative size measurements of single linear and circular DNA molecules in nanofluidic slitlike confinement are reported. A novel experimental method using DNA entropophoresis down a nanofluidic staircase implemented comprehensive variation of slitlike confinement around $d \approx 2p$, where d is the slit depth and p is the persistence length, throughout the transition from strong to moderate confinement. A new numerical analysis approximated and corrected systematic imaging errors. Together, these advances enabled the first measurement of an experimental scaling relation between the in-plane radius of gyration, $R_{\parallel}$, and d, yielding $R_{\parallel} \sim d^{-1/6}$ for all DNA samples investigated. This differs from the theoretical scaling relation, $R_e \sim d^{-1/4}$, for the root-mean-square end-to-end size, R_e. The use of different labeling ratios also allowed a new test of the influence of fluorescent labels on DNA persistence length. These results improve understanding of the basic physical behavior of polymers confined to nanofluidic slits and inform the design of nanofluidic technology for practical applications.



INTRODUCTION

The size of a polymer in solution is one of its most basic physical characteristics. The scaling behavior of polymer size is therefore a central concern in polymer studies and impacts phenomena in other disciplines, such as biophysics, separation science, genetic sequencing, and lab on a chip technology.[1−3] The size of a polymer, such as a DNA molecule, changes upon confinement in nanometer scale fluidic environments. In particular, a polymer in slitlike confinement is squeezed in solution between parallel surfaces forming a shallow slit with depth d. As d is varied, a transition occurs near $d \approx 2p$, where p is the polymer persistence length, between strong[4,5] and moderate[6,7] regimes of slitlike confinement.

Despite considerable effort, and amid continuing investigation, the nature of this transition remains controversial. Over four decades, many theoretical[5,8] and numerical[8−12] studies have been performed of linear polymers in slitlike confinement. More recently, the combination of nanofabricated fluidic devices and fluorescence microscopy has enabled direct measurements of the size of single linear DNA molecules, as characterized by the component of the radius of gyration projected parallel to the slit surfaces, $R_{\parallel}$, or the in-plane radius of gyration. However, experimental studies have presented conflicting accounts of the variation of $R_{\parallel}$ with d for linear DNA in nanofluidic slits with $d \approx 2p$.[13−17] Contradictory effects of slitlike confinement have been reported and alternately validated and disputed. In particular, a recent report by Tang et al.[16] disagrees qualitatively with an earlier study by Bonthuis et al.[13] Tang et al. could not reconcile the differences between the two experimental systems and therefore concluded that the cause of this discrepancy remains unclear. This controversy prevents even a qualitative validation of the theoretical scaling relation, $R_e \sim d^{-1/4}$, for DNA size in strong and moderate confinement as characterized by the root-mean-square end-to-end size, R_e.[5,16] Moreover, none of these experimental studies has reported measured values for a size scaling exponent. In these studies, quantitative measurements of DNA size have been hindered by limited resolution in d, indeterminate or superficial analysis of systematic imaging error, and limitations associated with fluorescence detection, such as measurement errors from photobleaching and uncertainty in labeling ratios and the influence of labels on p. In summary, the effects of slitlike confinement around $d \approx 2p$ on the size of linear polymers, including linear DNA, have eluded both qualitative consensus and quantitative characterization. The size of circular polymers, such as circular DNA, in these systems remains unexplored experimentally.

Two main advances in measurement science are presented here to overcome these limitations and correctly discern the effects of nanofluidic confinement on the size scaling of DNA molecules. First, a novel experimental method using DNA entropophoresis down a nanofluidic staircase achieved comprehensive variation of slitlike confinement throughout the transition from strong to moderate confinement. Second, numerical simulations allowed the most rigorous analysis and correction of systematic imaging error to date. In addition, a judicious selection of experimental conditions eliminated measurement errors due to photobleaching, while the measurement of relative fluorescence labeling ratios allowed a new test of the effects of fluorescence labeling on p. Together, these advances

Received: November 25, 2011
Revised: January 5, 2012
Published: January 25, 2012

ACS Publications

This article not subject to U.S. Copyright. Published 2012 by the American Chemical Society

enabled a quantitative investigation of the size scaling of linear and circular DNA in nanofluidic slitlike confinement around $d \approx 2p$. Experimental size scaling exponents for both polymer morphologies are reported here for the first time. The measurements described here validate measurements by Tang et al.,[16] contradict those of Bonthuis et al.,[13] and give a different experimental size scaling relation than that derived theoretically by Odijk.[16]

The results reported here are of increasing practical importance in nanofluidic technology. For almost two decades, nanofluidic devices incorporating slits have been known to hold great promise for the analysis of long DNA molecules.[18−20] However, many aspects of polymer behavior in these systems remain poorly understood. Quantitative knowledge of the size scaling behavior, in particular, is important for DNA analysis.[2] Nanofluidic devices cannot be designed rationally for this purpose without a clear understanding of the basic physical behavior of polymers confined to nanofluidic slits.

EXPERIMENT

A nanofluidic channel with a depth profile approximated by a staircase function with many steps[21] was used to investigate the size of linear and circular DNA by entropophoresis.[22] This directed self-transport resulted in the spontaneous variation of slitlike confinement around $d \approx 2p$, enabling measurements of DNA size with unprecedented resolution in the confining depth. This new method allowed multiplexed measurements of a single DNA molecule variably confined in a single nanofluidic device during a single experiment. This is in contrast to other studies, which required separate nanofluidic devices to vary d. The nanofluidic staircase was fabricated in fused silica and consisted of 30 slitlike steps connected by vertical step edges with depths ranging from approximately 4 to 342 nm and arrayed across a 120 μm wide channel (Figure 1a,b). These depths spanned twice the native DNA persistence length, p, of 51 nm.[3,23] DNA molecules with comparable contour lengths and different morphologies (linear bacteriophage lambda DNA at 48.5 kbp and circular charomid 9−42 DNA at 42.2 kbp) were labeled with the fluorescent dye YOYO-1 at initial ratios of 5 or 20 basepairs per dye molecule for a total of four samples: linear 5:1, linear 20:1, circular 5:1, and circular 20:1. 115, 107, 59, and 129 individual DNA molecules were analyzed for linear 5:1, linear 20:1, circular 5:1, and circular 20:1 samples, respectively. These samples were dispersed in 5X tris borate ethylenediaminetetraacetic acid (TBE) buffer containing 3.0% (volume fraction) 2-mercaptoethanol (Supporting Information). As an initial condition, DNA molecules were driven electrokinetically up the staircase toward shallower steps. The applied electric field was removed. The DNA molecules then spontaneously descended the staircase by entropophoresis and were imaged by widefield epifluorescence microscopy using 40 ms exposures at 5 s intervals (Figure 1c−f).[22] Further details of the device and experiment are described elsewhere.[21,22]

At the onset of entropophoresis, a ratio of summed fluorescence intensities, $I_{5:1}/I_{20:1} \approx 3/2$, was measured for both linear and circular DNA molecules. This differs from $I_{5:1}/I_{20:1} \approx 4$ expected in the case that the 5:1 and 20:1 labeling ratios were achieved. These values show that the intended labeling ratios were not realized in the high ionic strength buffer[24] used here to isolate the steric effects of nanofluidic slitlike confinement (Supporting Information). This suggests the need to validate assumed labeling ratios in related studies. Uncertainty in the labeling ratio is not expected to affect the measurements presented here of the size scaling of DNA molecules (Supporting Information).

DNA size, as characterized by the component of the radius of gyration projected parallel to the $x-y$ plane (Figure 1), $R_{\parallel}$, was extracted from images of single molecules during entropophoresis using custom software. DNA molecules were identified in each image using a region of interest (ROI) of 40 × 40 or 18 × 18 pixels for linear and circular DNA, respectively (Figure 1). Within the ROI, Otsu's method[25] was used to differentiate fluorescence signal from background noise, and connected regions containing ≥8 pixels were identified as comprising the molecule. Fragments and concatemers of linear DNA were identified by total intensity and area and excluded from further analysis. Assuming homogeneous labeling, the mass of DNA in each pixel was proportional to the pixel intensity, which allowed calculation of the intensity weighted center of mass, $r_{cm}(t)$, and gyration tensor, $G(t)$, for each video frame at time t:

$$r_{cm}(t) = \frac{\sum r(t)I(r, t)}{\sum I(r, t)}$$

$$G(t) = \frac{\sum [r(t) - r_{cm}(t)][r(t) - r_{cm}(t)]I(r, t)}{\sum I(r, t)}$$

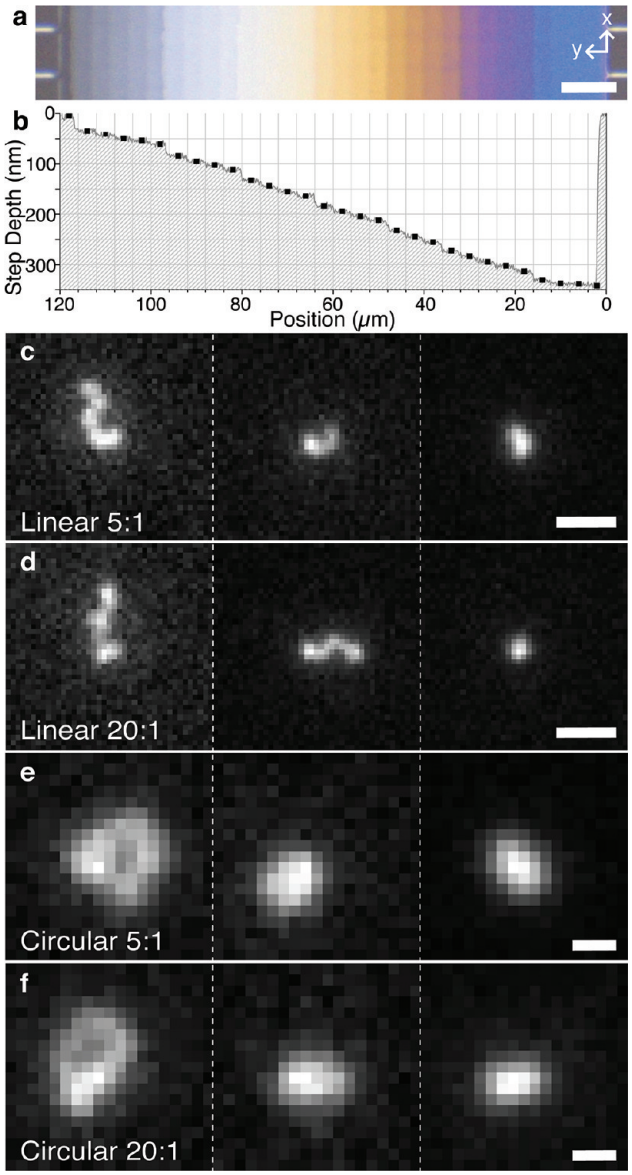


Figure 1. DNA molecules confined to a nanofluidic staircase. A bright-field optical micrograph shows the empty nanofluidic staircase with each step made evident by white light interference (scale bar: 12 μm) (a). Step depths are represented by mean values (black squares), with one standard deviation smaller than the symbols, as well as a scanned probe measurement taken nearest the location in the staircase where DNA molecules were imaged (gray line) (b). Representative fluorescence micrographs of ROIs containing individual linear 5:1 (c), linear 20:1 (d), circular 5:1 (e), and circular 20:1 (f) DNA molecules near the top, middle, and bottom of the staircase, from left to right (scale bar: 3 μm (c, d) and 1 μm (e, f)).

dx.doi.org/10.1021/ma202559k | Macromolecules 2012, 45, 1602−1611

where the sum is taken over all pixels comprising the DNA molecule and $I(r,t)$ is the intensity of the pixel at position r. The eigenvalues of this two-dimensional gyration tensor, λ_M and λ_m, with $\lambda_M > \lambda_m$, give the in-plane radius of gyration, $R_\parallel = (\lambda_M + \lambda_m)^{1/2}$.

DNA molecules confined to each step assumed a variety of conformations that can be represented in three dimensions as anisotropic ellipsoids.[10] The approximation of a two-dimensional ellipse has been used widely to characterize $R_\parallel$ for DNA molecules in slitlike confinement.[13,14,16] To interpret DNA molecules as ellipses (Figure 2), the major and minor axes were $4R_M$ and $4R_m$, respectively, where $R_M = (\lambda_M)^{1/2}$ and $R_m = (\lambda_m)^{1/2}$.

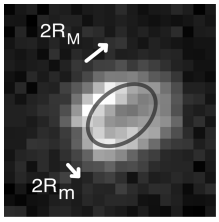


Figure 2. Elliptical interpretation of $R_\parallel$ for a DNA molecule. A fluorescence micrograph shows a circular DNA molecule labeled 20:1 in a 4.6 × 4.6 μm ROI on a step with a depth of 35 ± 4 nm (mean ± standard deviation). A representative ellipse, semimajor, $2R_M$, and seminor, $2R_m$, axes are shown schematically.

Data for unconfined DNA molecules (Supporting Information), once determined to be in focus, were analyzed similarly to data obtained using the staircase. DNA molecules in bulk solution diffused through the depth of field of the microscope objective and were considered to be in focus when the total area of the DNA molecule was small and approximately constant and $R_\parallel$ continued to fluctuate. Out of focus DNA molecules were characterized by significantly larger areas and lower signal-to-noise ratios.

For each step of the staircase and for bulk solution, R_M and R_m values were placed into 10 nm histogram bins, which were normalized and fit to probability distributions for either DNA molecules in slitlike confinement[13]

$$P_{slit}(R) = \exp[-R^2/\sigma] \exp[-R_{mod}(R_{mod} - R_{min})^3 /(\sigma(R - R_{min})^2)] \quad (1)$$

or for unconfined DNA molecules in bulk solution[7]

$$P_{bulk}(R) = \exp[-R^2/\sigma] \exp[-2R_{mod}(R_{mod} - R_{min})^4 /(3\sigma(R - R_{min})^3)]$$

where R represents R_M or R_m, the first exponential describes extended conformations, the second exponential describes compact conformations, σ depends on the physical attributes of the DNA molecule, R_{mod} gives the mode of the size distribution, and R_{min} is the smallest value of R (Figure 3). A nonlinear least-squares fitting algorithm provided statistical uncertainties for the parameters σ, R_{min}, and R_{mod}.

Although eq 1 was derived by Flory for the radius of gyration of a flexible linear polymer in two dimensions,[7] these probability distributions were used here for measurements of $R_\parallel$ for semiflexible, linear, and circular DNA molecules and slit depths that spanned the transition between two and three dimensions. On the shallowest steps of the staircase, extended conformations of circular DNA molecules were depopulated relative to linear DNA molecules (Figure 3c,d). This

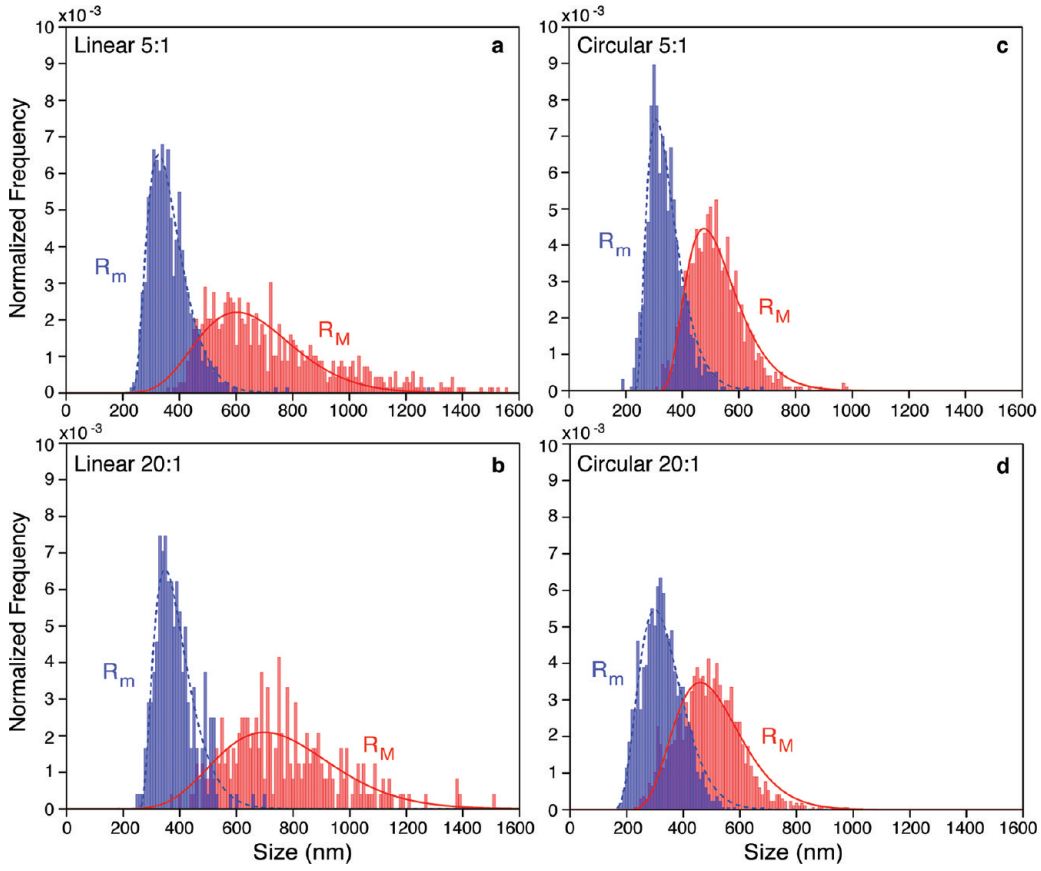


Figure 3. Size distribution measurements. Representative normalized histograms and probability distribution fits used to determine mode values for R_M (red, solid line) and R_m (blue, dash line) are shown for linear 5:1 (a), linear 20:1 (b), circular 5:1 (c), and circular 20:1 (d) DNA samples for a step depth of 35 ± 4 nm (mean ± standard deviation). A few instances of R_M values of nearly 2.3 and 1.8 μm were observed for (a) and (b), respectively, but are not plotted here.

dx.doi.org/10.1021/ma202559k | Macromolecules 2012, 45, 1602–1611

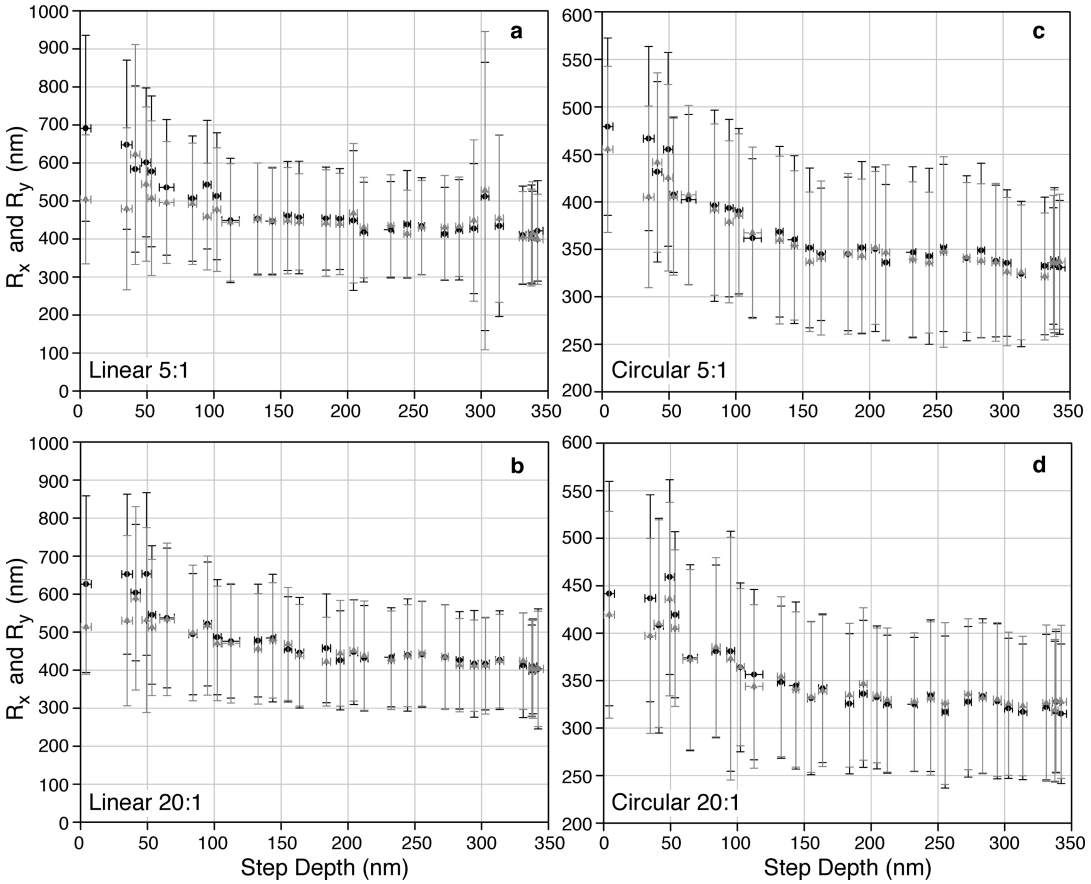


Figure 4. Orientation of DNA molecules during entropophoresis. Components of $R_{||}$ along the *x*-axis of the staircase, R_x (black circles), and along the *y*-axis of the staircase, R_y (gray triangles), as a function of step depth are shown for linear 5:1 (a), linear 20:1 (b), circular 5:1 (c), and circular 20:1 (d) DNA samples. Data points are mean values. *X*-axis bars represent one standard deviation. *Y*-axis bars represent one standard deviation and contain contributions from measurement error but are dominated by the physical fluctuation of the size of the DNA molecules. DNA molecules exhibited some tendency to orient across the staircase on the shallowest steps, especially for the linear morphology. This may be due in part to electrostatic effects at step edges or relatively long rotational relaxation times for DNA molecules in these very shallow slits.[16] In general, however, molecules entropophoresed down the staircase without a preferred orientation induced by interactions with step edges.

suggests the need for the future development of a probability distribution that more accurately models the effect of a circular morphology on the size of semiflexible polymers in slitlike confinement through this transition. For all DNA size distributions, similar trends in size variation were obtained and similar conclusions were drawn using either the fitted mode or the mean values of $R_{||}$.

During entropophoresis, DNA molecules spanned, at most, one step edge at a time, and the variation of slitlike confinement was sufficiently slow[22] to allow the DNA molecules to relax between interactions with the step edges. Components of $R_{||}$ along the *x*- and *y*-axes of the staircase showed no significant average orientation during transport (Figure 4), which would have indicated departure from equilibrium as preferential extension along a particular direction. In a test to determine whether interactions with step edges affected measured $R_{||}$ values, images with the molecular center of mass within 1.0, 0.5, or 0 μm of either side of each step edge were selectively excluded from analysis. In all cases, mode values of fits to the frequency histogram for $R_{||}$ were in good agreement. The mode was also insensitive to the relatively small number of perturbed conformations induced by interactions with step edges (Figure 5). For these reasons, and to maximize single molecule statistics, all data were included for the results presented here.

Systematic imaging errors from optical diffraction and camera pixelation of fluorescent DNA molecules in solution are intrinsic both to the measurements reported here and previous related experimental studies. These imaging errors were approximated and corrected here as an integral component of quantitative measurements of $R_{||}$ (Figure 6). Each DNA molecule remained in focus during entropophoresis down the staircase because all steps were within the depth of field of the microscope objective lens. However, the true conformations were not accessible optically, as DNA molecules fluctuated during each camera exposure, and different portions of the contour length may have been in proximity or overlapped at a length scale below the optical diffraction limit and camera pixel size. As an approximation, the most probable in-plane shapes of the DNA molecules were modeled as ellipses of uniform fluorescence intensity with a range of R_M and R_m values encompassing the measured experimental values. This enabled measurements to be related with high precision to corresponding elliptical models. A library was populated with major and minor axis values, incremented by 51 and 54 nm, respectively, which produced model ellipses of varied size and anisotropy. Imaging by wide-field epifluorescence microscopy was then simulated in two steps, as shown in Figure 6a–c. First, model ellipses representing DNA molecules were blurred with a two-dimensional Gaussian filter, which has been shown to be an accurate approximation of the Airy function for a nonparaxial wide-field fluorescence microscope.[26,27] Using the known optical properties of the fluorescent DNA molecules, the nanofluidic device, and the microscope system (Supporting Information Table 1), the standard deviation of this Gaussian distribution and the Airy radius were calculated to be 80.6 and 227 nm, respectively. These calculations were favored over an experimental determination of the point spread function, because the accuracy of such a measurement may be compromised by difficulty in obtaining a point source with an emission spectrum identical to that of YOYO-1 bis-intercalated into double-stranded DNA, as well as by large errors that may occur when a

dx.doi.org/10.1021/ma202559k | *Macromolecules* 2012, 45, 1602–1611

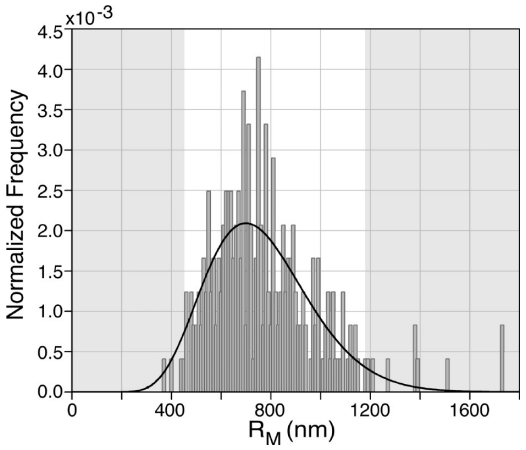


Figure 5. Robustness of fitted mode values. This plot of R_M values for linear DNA molecules labeled 20:1 on a step with a depth of 35 ± 4 nm (mean ± standard deviation) is representative of the poorest quality data analyzed in this way. These data are expected to most clearly manifest difficulties in obtaining reliable mode values, as well as the advantage of reporting mode, rather than mean, values with these small data sets. The linear morphology has the potential to become more elongated and perturbed from equilibrium than the circular morphology by interactions with step edges, which would have been most pronounced between the shallowest steps and would have shifted values of R_M and R_m in opposite directions away from the mode value. For example, a very elongated molecule transiting a step edge is represented in the data as a relatively very large R_M value and a corresponding very small R_m value. The exclusion of data in either of the gray regions from the fit to determine the mode value alters that value by <0.3%, indicating that the mode value is decidedly insensitive to data in the tails of this fitted distribution. This result underscores the robustness of the mode determination for data sets that may contain spurious data with extremely small or large values.

two-dimensional Gaussian distribution is fit to an image of a point source with a pixel size exceeding the standard deviation of the Gaussian distribution.[26] The Gaussian filter was truncated at the Airy radius and applied to the model elliptical DNA molecules. Next, the blurred model objects were binned into pixel elements of 254 × 254 nm, as obtained from the objective magnification of 63× and the camera pixel size of 16 × 16 μm. While a higher magnification objective would have resulted in a smaller effective pixel size and reduced corrections due to pixelation error, the larger field of view provided by the objective used here was necessary to image DNA molecules descending the entire 120 μm width of the staircase. The ratios of R_M and R_m values for corresponding model ellipses and simulated images provided corrections to the experimental data as a function of experimental R_M and R_m values.

As the major and minor axes of the model ellipse were incrementally increased, the corresponding imaging correction showed a rippling phenomenon with periodic peaks and troughs (Figure 6d). This rippling resulted from the fixed relationship between the model ellipses and simulated camera pixel array. To account for the random location and orientation of experimentally measured DNA molecules relative to the actual camera pixel array, this rippled imaging correction was smoothed by a polynomial fitting function. This function consisted of third-order polynomials for the major and minor axes and a first-order cross-term, which approximated the low order curvature of the imaging correction and neglected the higher order rippling effect. Thus, a smoothed imaging correction function was defined and applied to the experimental mode values of R_M and R_m for each step (Figure 6e).

In this way, systematic imaging errors were estimated to have resulted in measured values of $R_{||}$ that exceeded the actual values by 1−7% for the experimental system used here. The corresponding imaging corrections became more significant as $R_{||}$ values decreased, with measured bulk solution values of $R_{||}$ decreased by the most significant correction. This analysis has several implications. The measured $R_{||}$ value for a given d was reasonably robust against diffraction-limited

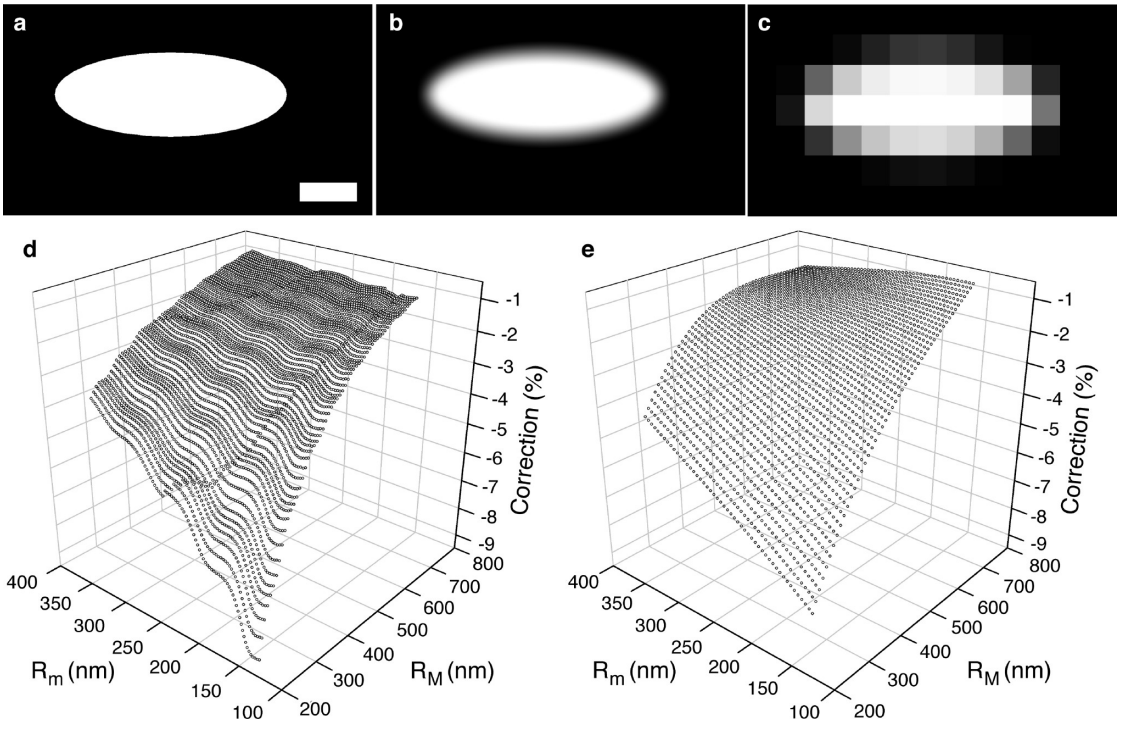


Figure 6. Systematic imaging error correction. The effects of optical diffraction and camera pixelation on measured values of $R_{||}$ were approximated, simulated, and corrected. A model ellipse (a), the ellipse blurred according to the optical point spread function (b), and the ellipse blurred and pixelated according to the finite camera pixel size (c) representing a DNA molecule are shown. These transformations enlarged the apparent size of the molecule (scale bar: 700 nm). The correction between $R_{||}$ values calculated for the original model ellipses (as in (a)) and the experimentally accessible blurred and pixelated ellipses (as in (c)) are plotted versus the experimentally accessible R_M and R_m values (d). The data in (d) were fit to provide the final correction (e).

dx.doi.org/10.1021/ma202559k | Macromolecules 2012, 45, 1602−1611

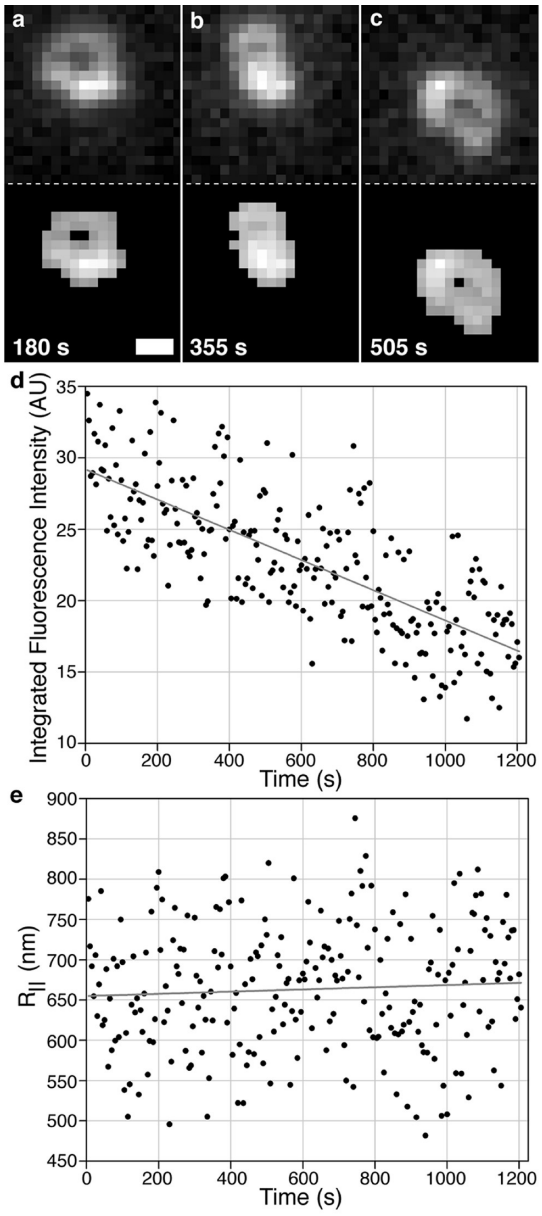


Figure 7. Effect of photobleaching on $R_{||}$ values. The size of a circular DNA molecule labeled 5:1 fluctuated on the shallowest step with a depth of 4 ± 4 nm (mean ± standard deviation) (a–c) (scale bar: 1 μm). The upper images are unprocessed fluorescence micrographs of ROIs containing a single DNA molecule, which are shown in the lower images after analysis to identify pixels comprising the molecule. The total fluorescence intensity of the molecule decreased during observation (d). However, this decrease in intensity had no significant effect on measured $R_{||}$ values (e). These data have been corrected for the diffraction-limited blurring and camera pixelation similarly to the mode values. The scatter in (e) resulted from the natural Brownian fluctuation of the molecule. Gray lines in (d) and (e) represent linear fits to the data, giving slopes of −0.0106 ± 0.0006 and 0.014 ± 0.015 (mean ± standard deviation), respectively. Each data symbol corresponds to a value obtained from a single image.

blurring and camera pixelation. However, because the systematic imaging errors varied with d, corrections for these errors had an important aggregate effect on the size scaling analysis, as described below. In contrast, normalization by the bulk solution $R_{||}$ value, and the associated imaging correction, did not influence analysis of scaling exponents due to the constant effect of normalization. This analysis supersedes a simpler correction[28] and is the most rigorous treatment to date of systematic imaging errors of DNA molecules in nanofluidic slitlike confinement.

Photobleaching is also a significant concern in single molecule fluorescence analysis.[16] However, the size measurements performed here were determined to be robust against reduction in the signal-to-noise ratio from this effect (Figure 7). Several DNA molecules paused for extended periods of time, but were not adsorbed irreversibly, on a single step near the top of the staircase. This rare behavior may have resulted from electrostatic or steric interactions that occurred between these molecules and the surfaces of the staircase structure. These immobilized DNA molecules were excluded from the analysis of size scaling but facilitated a test of the effects of dye photobleaching on the measured $R_{||}$ values. During observation, the center of mass of these DNA molecules did not descend the staircase, but the molecular conformations continued to fluctuate due to Brownian motion. Photobleaching resulted in decreased integrated fluorescence intensities of these DNA molecules but did not bias $R_{||}$ values. These results demonstrate that the signal-to-noise ratio of single molecule detection remained sufficiently high throughout the experiment for a robust analysis of single DNA molecules using the methods employed here.

RESULTS AND DISCUSSION

Together, the nanofluidic staircase and systematic imaging error corrections enabled quantitative measurements of $R_{||}$ for DNA molecules throughout the transition between strong and moderate regimes of slitlike confinement. Corrected $R_{||}$ values are presented normalized by corresponding measured bulk solution values (Figure 8), without normalization (Supporting Information Figure 1), and without correction or normalization (Supporting Information Figure 2). $R_{||}$ data for the shallowest step are shown for completeness but were excluded from further analysis, due to the relatively large surface roughness compared to d for this step.[21]

Measured sizes for all DNA samples generally decreased as d increased from strong confinement, through $d \approx 2p$, to moderate confinement. The trends in size variation observed here validate measurements reported by Tang et al.[16] and contradict those of Bonthuis et al.[13] (Figure 9 and Table 1). The previous results of Strychalski et al.[15] also do not follow the trend reported by Bonthuis et al.[13] but cannot be compared directly here, due to limited confinement resolution and lack of DNA size measurements in bulk solution for normalization. Bonthuis et al.[13] reported the abrupt onset of a saturation regime in DNA size for strong confinement near $d \approx 2p$, which was not observed here or by Tang et al.[16] In contrast to Bonthuis et al.,[13] Tang et al.[16] measured a monotonic decrease in DNA size with decreasing confinement that suggested a gradual transition between confinement regimes. Tang et al.[16] did not develop a quantitative experimental scaling relation, due to known biases from optical diffraction and photobleaching, but revisited the most recent theoretical derivation by Odijk[5] of the scaling relation $R_e \sim d^{-1/4}$. This scaling relation, which has not been verified experimentally, provides the most relevant theoretical framework to analyze the experimental results reported here.

To establish an experimental scaling relation between $R_{||}$ and d and compare this to the theoretical relation, a power law function was fit to the data presented here (Figure 8, Figure 10, and Table 2). Size scaling exponents obtained from separate fits to the uncorrected and corrected data differ significantly, emphasizing the importance of correcting for systematic imaging errors. Based on the goodness of fit parameters for fits to the corrected data (Table 2), a single power law models the system reasonably well. The size scaling relation of $R_{||} \sim d^{-1/6}$ obtained from the corrected data is in excellent agreement with

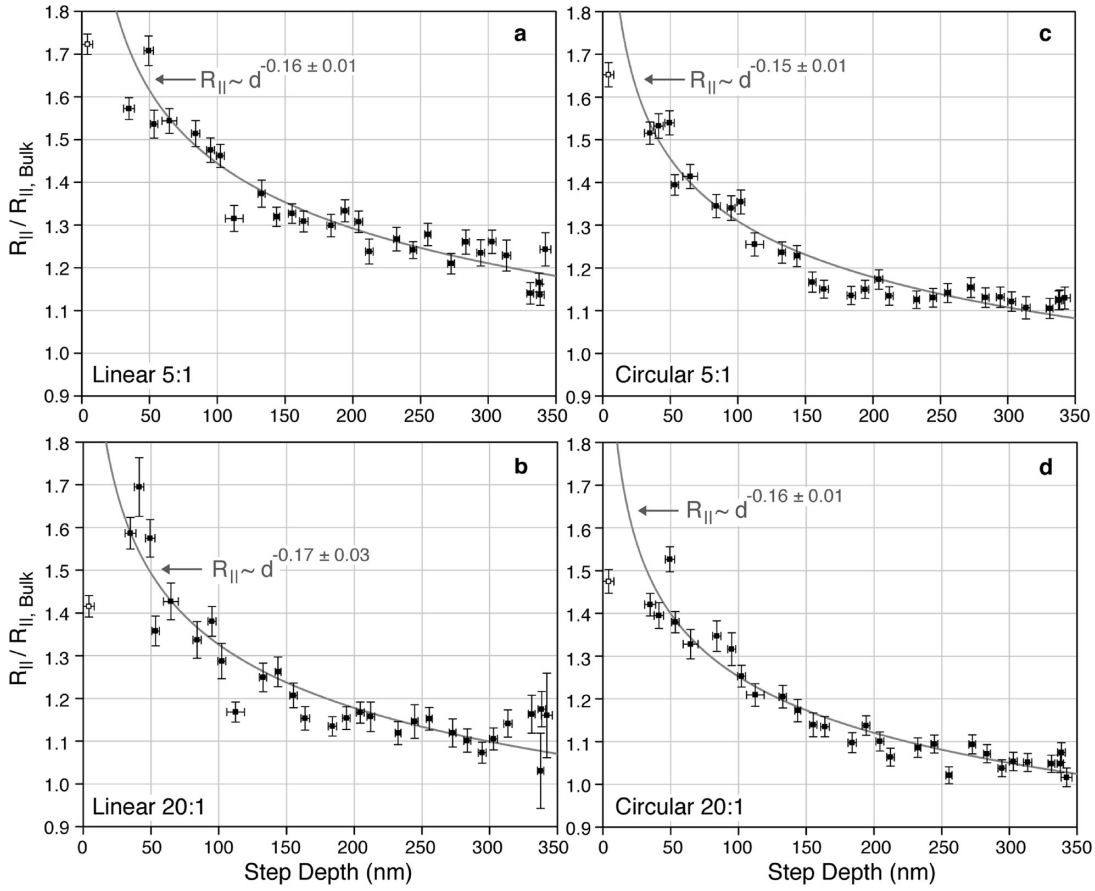


Figure 8. Size measurements. Fitted mode values of $R_{||}$ were corrected for systematic imaging error and normalized by the corresponding corrected bulk solution $R_{||}$ values, $R_{||,Bulk}$, for linear 5:1 (a), linear 20:1 (b), circular 5:1 (c), and circular 20:1 (d) DNA samples. DNA size generally decreased with increasing step depth, d. Power law fits (gray line) yielded size scaling exponents reported as mean ± standard deviation. Corrected bulk solution values of $R_{||}$ were 430 ± 5 nm (linear 5:1), 485 ± 7 nm (linear 20:1), 366 ± 6 nm (circular 5:1), and 377 ± 6 nm (circular 20:1) (mean ± standard deviation). *X*-axis bars represent one standard deviation. *Y*-axis bars represent one standard deviation of the fitted mode value and one standard deviation of the fitted bulk mode value added in quadrature and do not account for other sources of error. Data for the shallowest step (open square) were excluded from analysis.

a fit also performed here to the uncorrected data of Tang et al.[16] for $d \approx 32-565$ nm (not shown) that gave an exponent of −0.17 ± 0.01 (mean ± standard deviation). The microscope system used by Tang et al.[16] had a higher magnification objective lens with an identical numerical aperture and smaller pixel size compared to the microscope system used here. This would have reduced pixelation error but would not have reduced error from optical diffraction compared to the measurements made here. Further quantitative comparison between the corrected data reported here and the uncorrected data of Tang et al.[16] would require a full characterization of systematic errors, including photobleaching. However, in all cases, the experimental size scaling exponents fitted here to measurements of $R_{||}$ differ significantly from the theoretical value predicted for the variation of R_e with d.

The two fluorescent labeling ratios used here also enabled a new test of the equilibrium effects of YOYO-1 on p. First, consider the two linear DNA samples. The measured ratio of summed fluorescence intensities, $I_{5:1}/I_{20:1} \approx 3/2$, resulted from different numbers of dye molecules per DNA molecule. It is known that the bis-intercalation of YOYO-1 dye molecules into a DNA molecule extends its contour length, L,[3] giving different values of L for the two linear DNA samples. Despite these different L values, linear 5:1 and linear 20:1 DNA samples had nearly identical corrected $R_{||}$ values without normalization for all d (Supporting Information Figure 3). This was also measured for circular 5:1 and circular 20:1 DNA samples. Then, consider Odijk's scaling relation $R_e \sim L^{3/4}p^{1/4}w^{1/4}d^{-1/4}$, which applies throughout $d \approx 2p$ for linear DNA.[5] If this relation holds for $R_{||}$, and assuming equal scaling coefficients and effective widths, w, for the two linear DNA samples, then p decreased as labeling increased. This prediction agrees qualitatively with a nonequilibrium study of the same effect.[29] The present analysis must be viewed as approximate, however, as the size scaling exponents reported here do not validate this theoretical scaling relation. Moreover, w may vary with labeling ratio.[30] Additional study is required to understand this important effect.

■ CONCLUSION

Size scaling exponents were measured for the first time for linear and circular DNA in nanofluidic slitlike confinement around $d \approx 2p$. Size measurements of linear DNA qualitatively and semiquantitatively validate those of Tang et al.[16] and qualitatively contradict those of Bonthuis et al.[13] Specifically, power law fits to measurements of the DNA samples investigated here and the data reported by Tang et al.[16] gave size scaling relations of $R_{||} \sim d^{-1/6}$ throughout the $d \approx 2p$ transition. This experimental scaling relation differs from the

dx.doi.org/10.1021/ma202559k | *Macromolecules* 2012, 45, 1602–1611

Table 1. Comparison of Experimental Systems for Size Measurements of Linear DNA through the Transition from Strong to Moderate Slitlike Confinement

report	DNA sample	buffer system	fluorescent label	experimental temperature	buffer viscosity	surface roughness
this report	Lambda Phage, 48.5 kbp	5X TBE (650 mM tris base, 225 mM boric acid, 12.5 mM ethylenediaminetetraacetic acid), 3% (volume fraction) β-mercaptoethanol	YOYO-1, prepared at 5:1 bp:dye, measured as lower	27.0 ± 0.1 °C (mean ± limit of error)[22]	$1.254 \times 10^{-3} \pm 0.004 \times 10^{-3}$) Pa·s at 27.0 °C (mean ± std dev)[22]	eched surface: 2.9 ± 0.3 nm (mean ± std dev); cover surface: <0.5 nm[21]
Tang et al.[16]	Lambda Phage, 48.5 kbp	1.5X TBE (270 mM tris base, 270 mM boric acid, 6 mM ethylenediaminetetraacetic acid), 4% (volume fraction) β-mercaptoethanol, 12.5 mg/mL glucose, 0.16 mg/mL glucose oxidase, 9.6 μg/mL catalase	YOYO-1, prepared at 4:1 bp:dye, not measured	not reported	1.17×10^{-3} Pa·s at 22.5 °C	not reported
Bonthuis et al.[13]	Lambda Phage, 48.5 kbp	50 mM NaCl, 10 mM tris-ethylenediaminetetraacetic acid, 0.07% (volume fraction) dimethyl sulfoxide	YOYO-1, prepared at 6:1 bp:dye, not measured	not reported	not reported	not reported
Strychalski et al.[15]	Lambda Phage, 48.5 kbp	5X TBE, 2% (volume fraction) volume fraction β-mercaptoethanol	YOYO-1, prepared at 5:1 bp:dye, not measured	not reported	not reported	<1.2 nm (rms)

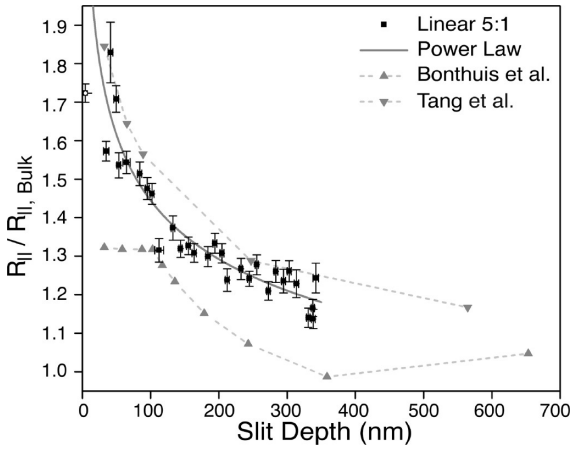


Figure 9. Interstudy comparison. Contending measurements of the size variation of lambda phage DNA molecules in nanofluidic slitlike confinement are shown, and the experimental systems are compared in Table 1. Of the four samples studied here, linear DNA labeled 5:1, corrected for systematic imaging errors and normalized by the corresponding measured bulk solution value, was selected as most directly comparable to Bonthuis et al.[13] and Tang et al.[16] Data from these studies were obtained manually from plots as published. The trend in size variation measured here contradicts that reported by Bothuis et al.[13] and validates that reported by Tang et al.[16] This interstudy comparison emphasizes the confinement resolution and quantitative measurements of the size scaling exponent achieved here.

Table 2. Comparison of Size Scaling Exponents for Fits to Corrected and Uncorrected Experimental Data[a]

DNA sample	scaling exponent for corrected data	adjusted R^2	reduced χ^2	scaling exponent for uncorrected data
linear 5:1	−0.16 ± 0.01	0.88	0.003	−0.10 ± 0.01
linear 20:1	−0.17 ± 0.03	0.86	0.004	−0.09 ± 0.01
circular 5:1	−0.15 ± 0.01	0.93	0.001	−0.10 ± 0.01
circular 20:1	−0.16 ± 0.01	0.92	0.002	−0.09 ± 0.01

[a]Adjusted $R^2$and reduced χ^2 are given for fits to the corrected data. Scaling exponents resulted from unweighted, nonlinear least-squares fitting algorithms and are reported as mean ± standard deviation. A single power law is a reasonable model for the system, as indicated by the goodness of fit parameters. However, fitted scaling exponents differ from the hypothetical scaling relation $R_{||} \sim d^{-1/4}$ in all cases.

theoretical scaling relation, $R_e \sim d^{-1/4}$, derived by Odijk.[5] The size measurements reported here also suggest a decreased persistence length as the fluorescence labeling ratio increased. These results clarify topics of enduring interest in polymer physics and increasing importance for practical applications of nanofluidic technology.

The advances reported here also highlight the need for future work in several areas. First, while a uniform ellipse is a reasonable approximation of the two-dimensional projection of the most probable shape for an ensemble of images of DNA molecules, this simple model is less accurate for an image of a single DNA molecule. Realistic numerical simulations of DNA conformations in varied slitlike confinement are needed to provide single molecule object and image distributions and give an exact imaging correction. Second, the discrepancy between the theoretical scaling relations for $R_e \sim d^{-1/4}$ and $R_{||} \sim d^{-1/6}$ could be clarified experimentally by tracking the relative positions of end labels bound to DNA molecules to measure R_e,

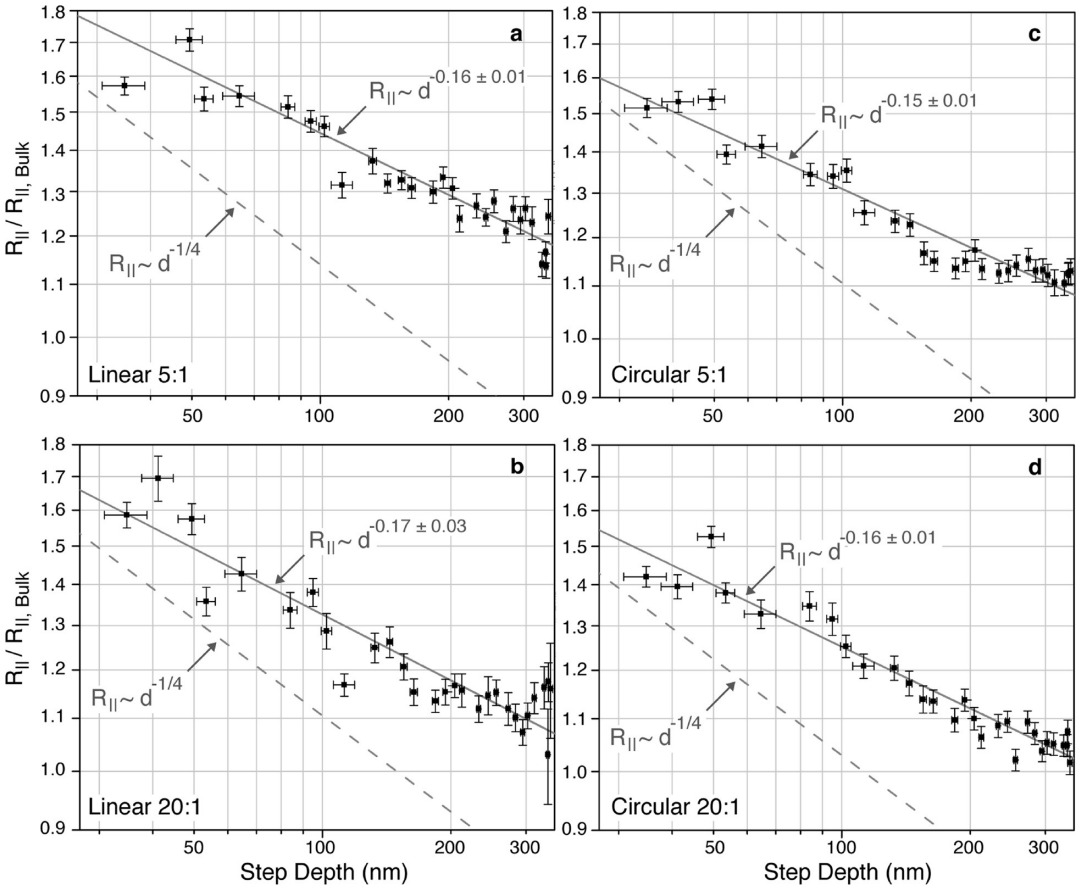


Figure 10. Corrected $R_{\|}$ values normalized by bulk solution values and plotted using log–log axes. Fitted mode values of $R_{\|}$ as a function of step depth, d, are shown for linear 5:1 (a), linear 20:1 (b), circular 5:1 (c), and circular 20:1 (d) DNA samples. The x-axis and y-axis bars represent one standard deviation. These data have been corrected for systematic optical imaging errors and normalized by corresponding corrected bulk solution values. A hypothetical scaling relation $R_{\|} \sim d^{-1/4}$ (offset dashed gray lines) differs from power law fits (solid gray lines) to the experimental data. Fitted exponents are reported as mean ± standard deviation.

theoretically by deriving a scaling relation for $R_{\|}$, or numerically by establishing a relation between R_e and $R_{\|}$. Third, a more sophisticated statistical analysis is needed to determine how accurately a single power law model describes the system and the extent to which morphology affects DNA size in slitlike confinement around $d \approx 2p$. Finally, progress is needed in measuring absolute numbers of dye molecules labeling individual DNA molecules and understanding the effects of fluorescence labeling on p.

■ ASSOCIATED CONTENT

Supporting Information

Further discussion describes the buffer solution, influence of the fluorescence labeling ratio on measurements of the size scaling exponent, size measurements in bulk solution, and optical properties of the experimental system. Additional figures show corrected size measurements without normalization, size measurements without correction or normalization, and a direct comparison of measured corrected sizes without normalization. This material is available free of charge via the Internet at http://pubs.acs.org.

■ AUTHOR INFORMATION

Corresponding Author

*E-mail: elizabeth.strychalski@nist.gov.

Author Contributions

§These authors contributed equally.

■ ACKNOWLEDGMENTS

This work was performed in part while EAS and SMS held National Research Council Research Associateship Awards. Device fabrication was performed at the Cornell Nanoscale Science and Technology Facility (CNF) and the Cornell Center for Materials Research. Device characterization was performed in part at the National Institute of Standards and Technology Center for Nanoscale Science and Technology. The authors gratefully acknowledge CNF staff for assistance with device fabrication, Andrew Rukhin and Stefan Leigh for helpful discussions, and Robert Goldberg for assistance with calculating ionic strength. Certain commercial equipment, instruments, or materials are identified to specify adequately the experimental procedure. Such identification implies neither recommendation nor endorsement by the National Institute of Standards and Technology nor that the materials or equipment identified are necessarily the best available for the purpose.

■ REFERENCES

(1) Levy, S. L.; Craighead, H. G. *Chem. Soc. Rev.* **2010**, *39*, 1133–1152.

(2) Salieb-Beugelaar, G. B.; Dorfman, K. D.; van den Berg, A.; Eijkel, J. C. T. *Lab Chip* **2009**, *9*, 2508–2523.

(3) Persson, F.; Tegenfeldt, J. O. *Chem. Soc. Rev.* **2010**, *39*, 985–999.

(4) Odijk, T. *Macromolecules* **1983**, *16*, 1340−1344.
(5) Odijk, T. *Phys. Rev. E* **2008**, *77*, 060901.
(6) Daoud, M.; de Gennes, P. G. *J. Phys. (Paris)* **1977**, *38*, 85−93.
(7) de Gennes, P.-G. *Scaling Concepts in Polymer Physics*; Cornell University Press: Ithaca, NY, 1985.
(8) Chaudhuri, D.; Mulder, B. *Phys. Rev. E* **2011**, *83*, 031803.
(9) Van Vliet, J. H.; Luyten, M. C.; ten Brinke, G. *Macromolecules* **1992**, *25*, 3802−3806.
(10) Van Vliet, J. H.; Luyten, M. C.; ten Brinke, G. *J. Chem. Phys.* **1990**, *93*, 1436−1441.
(11) Wall, F. T.; Mandel, F.; Chin, J. C. *J. Chem. Phys.* **1976**, *65*, 2231−2234.
(12) Jeon, J.; Chun, M.-S. *J. Chem. Phys.* **2007**, *126*, 154904.
(13) Bonthuis, D. J.; Meyer, C.; Stein, D.; Dekker, C. *Phys. Rev. Lett.* **2008**, *101*, 108303.
(14) Lin, P. K.; Fu, C. C.; Chen, Y. L.; Chen, Y. R.; Wei, P. K.; Kuan, C. H.; Fann, W. S. *Phys. Rev. E* **2007**, *76*, 011806.
(15) Strychalski, E. A.; Stavis, S. M.; Craighead, H. G. *Nanotechnology* **2008**, *19*, 315301.
(16) Tang, J.; Levy, S. L.; Trahan, D. W.; Jones, J. J.; Craighead, H. G.; Doyle, P. S. *Macromolecules* **2010**, *43*, 7368−7377.
(17) Uemura, H.; Ichikawa, M.; Kimura, Y. *Phys. Rev. E* **2010**, *81*, 051801.
(18) Volkmuth, W. D.; Austin, R. H. *Nature* **1992**, *358*, 600−602.
(19) Han, J.; Craighead, H. G. *Science* **2000**, *288*, 1026−1029.
(20) Cross, J. D.; Strychalski, E. A.; Craighead, H. G. *J. Appl. Phys.* **2007**, *102*, 024701.
(21) Stavis, S. M.; Strychalski, E. A.; Gaitan, M. *Nanotechnology* **2009**, *20*, 165302.
(22) Stavis, S. M.; Geist, J.; Gaitan, M.; Locascio, L. E.; Strychalski, E. A. *Lab Chip* **2012**, DOI: 10.1039/C2LC21152A.
(23) Bouchiat, C.; Wang, M. D.; Allemand, J. F.; Strick, T.; Block, S. M.; Croquette, V. *Biophys. J.* **1999**, *76*, 409−413.
(24) Gunther, K.; Mertig, M.; Seidel, R. *Nucleic Acids Res.* **2010**, *38*, 6526−6532.
(25) Otsu, N. *IEEE Trans. Syst. Man Cybern.* **1979**, *9*, 62−66.
(26) Thompson, R. E.; Larson, D. R.; Webb, W. W. *Biophys. J.* **2002**, *82*, 2775−2783.
(27) Zhang, B.; Zerubia, J.; Olivo-Marin, J. C. *Appl. Opt.* **2007**, *46*, 1819−1829.
(28) Strychalski, E. A.; Levy, S. L.; Craighead, H. G. *Macromolecules* **2008**, *41*, 7716−7721.
(29) Murade, C. U.; Subramaniam, V.; Otto, C.; Bennink, M. L. *Biophys. J.* **2009**, *97*, 835−843.
(30) Reisner, W.; Beech, J. P.; Larsen, N. B.; Flyvbjerg, H.; Kristensen, A.; Tegenfeldt, J. O. *Phys. Rev. Lett.* **2007**, *99*, 058302.

Macromolecules

Article

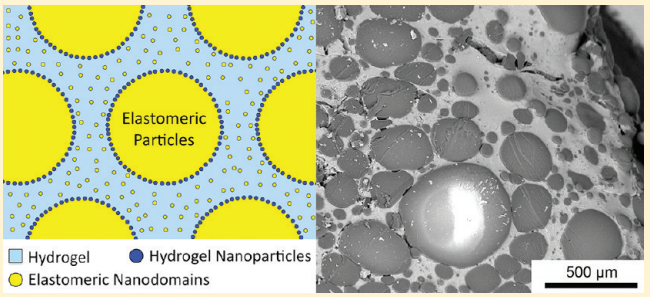
pubs.acs.org/Macromolecules

One-Pot Emulsion-Templated Synthesis of an Elastomer-Filled Hydrogel Framework

Noa Cohen and Michael S. Silverstein*

Department of Materials Engineering, Technion - Israel Institute of Technology, Haifa 32000, Israel

ABSTRACT: Sulfonated polymers are of interest as semipermeable ion-selective materials for membrane applications and as conductive materials for antistatic, electrode, and fuel cell applications. An innovative "one-pot" synthesis route was developed to produce relatively flexible systems containing a cross-linked polyacrylate elastomer within a continuous sulfonated hydrogel network. This synthesis route was based on the formation of a high internal phase emulsion (HIPE) containing an aqueous solution of styrenesulfonate and a cross-linking comonomer in the external phase and containing 2-ethylhexyl acrylate and a cross-linking comonomer in the internal phase. Both emulsifier-stabilized HIPEs and emulsifier-free polymer−nanoparticle-stabilized Pickering HIPEs were investigated using this route. A "three-step" route consisting of sulfonating a cross-linked polystyrene (xPS)-based polyHIPE in sulfuric acid and then polymerizing 2-ethylhexyl acrylate and a cross-linking comonomer within the polyHIPE was used for comparison. The chemical composition, two-phase morphology, water absorption, and mechanical properties of these materials were investigated. Unexpectedly, the walls of the materials based on cross-linked poly(styrenesulfonate) (xPSS) were found to contain cross-linked poly(2-ethylhexyl acrylate) nanodomains. Water absorption per mass sulfonated polymer was significantly greater in the xPSS-based material synthesized within a nanoparticle-stabilized HIPE.



INTRODUCTION

Emulsion templating has been used to synthesize a variety of porous polymers through the copolymerization of monomers in the external phase of high internal phase emulsions (HIPEs), emulsions containing over 74 vol % internal phase droplets.[1−6] During polymerization (or during postpolymerization processing) ruptures occur in the thin polymer walls surrounding the droplets producing continuity in the previously discrete internal phase. The internal phase is subsequently removed through drying, leaving a highly interconnected emulsion-templated porous structure. The porous polymers synthesized in this fashion have been termed polyHIPEs. Emulsion templating within HIPEs has been used to synthesize a wide variety of polyHIPE-based polymeric systems including copolymers,[7,8] interpenetrating polymer networks (IPN),[9] crystallizable side chain polymers,[10−12] biocompatible polymers,[13−18] functional surfaces,[19−21] and organic−inorganic hybrids and composites.[22−31] HIPEs are usually stabilized through the use of a relatively large amount of organic emulsifier (20−30% of the external phase). PolyHIPEs can also be synthesized using emulsifier-free particle-stabilized Pickering HIPEs.[32−39]

The characteristics of polyHIPEs that have stimulated interest for such applications as catalysis, chromatography, separation, filtration, absorption, and ion exchange include their ability to combine a fully interconnected, high porosity structure, a low bulk density, a high permeability, and a high surface area with mechanical integrity. In addition, polyHIPEs can absorb relatively large amounts of liquid through capillary action, can be used in flow-through applications, and can be produced as beads.[40,41] The most common HIPEs are based upon water-in-oil (W/O) emulsions wherein hydrophobic monomers are used to synthesize hydrophobic polyHIPEs. The unique structures and properties of polyHIPEs also make hydrophilic and hydrogel polyHIPEs of interest for such applications as synthesis supports, drug delivery, and tissue engineering.[13−15,42]

One approach to producing a hydrophilic polyHIPE takes advantage of the superior stability of W/O HIPEs as opposed to oil-in-water (O/W) HIPEs. Hydrophobic polyHIPEs are synthesized within W/O HIPEs and then modified to enhance hydrophilicity.[8,43−46] Such modifications usually take place through the addition of functionalizable comonomers such as vinylbenzyl chloride.[21,44,47] During postpolymerization functionalization the comonomer undergoes modification while the predominant monomer is not affected. A second approach is the synthesis of hydrophilic polyHIPEs directly within O/W HIPEs. Hydrophilic polyHIPEs from O/W HIPEs include those based on 2-hydroxyethyl methacrylate,[48] 2-hydroxyethyl acrylate,[49] acrylamide,[50,51] and acrylic acid.[52] Unfortunately, the poor stability of many of these O/W HIPEs can limit the internal phase content and yield polyHIPEs with low porosities and/or poor interconnectivities. A third approach is the synthesis of bicontinuous polyHIPEs through simultaneous polymerization of monomers in both the external and internal

Received: December 19, 2011
Revised: January 16, 2012
Published: January 30, 2012

 © 2012 American Chemical Society dx.doi.org/10.1021/ma2027337 | *Macromolecules* 2012, 45, 1612−1621

phases of W/O HIPEs.[53−55] The simultaneous synthesis yields a continuous hydrophobic polymer scaffold within which is a continuous hydrogel.

Sulfonated polymers are of interest as semipermeable ion-selective materials for membrane applications and as conductive materials for antistatic, electrode, and fuel cell applications.[56,57] Sulfonated polyHIPEs based on cross-linked polystyrene (xPS) have been synthesized through the use of a functionalizable monomer or through sulfonation of the xPS in sulfuric acid.[21,58,59] The direct synthesis of cross-linked poly(styrenesulfonate) (xPSS) polyHIPEs in O/W HIPEs offers an alternative to the postpolymerization functionalization used to produce sulfonated xPS (S-xPS). The micrometer-scale void dimensions in polyHIPEs are too large for proton conduction applications in which nanometer-scale hydrophilic water channels are appropriate.[56,57] It should be possible, however, to create smaller scale conductive pathways in sulfonated polyHIPEs by filling the voids with a nonconductive polymer. Filling the voids with an elastomer would provide the additional benefit of enhancing the flexibility of the polyHIPEs, as seen for other PS-based polymer systems.[60−65]

This paper will describe the one-pot emulsion-templated synthesis of xPSS frameworks filled with a cross-linked poly(2-ethylhexyl acrylate) (xPEHA) elastomer. The differences between an emulsifier-stabilized HIPE and a polymer−nanoparticle-stabilized Pickering HIPE will be discussed. In addition, the one-pot synthesis will be compared to a three-step synthesis in which an xPS polyHIPE undergoes sulfonation and is then filled with xPEHA.

EXPERIMENTAL SECTION

Materials. The monomers used for the various syntheses were 2-ethylhexyl acrylate (EHA, Aldrich), styrene (S, Fluka Chemie), and styrenesulfonate (SS, Aldrich). The cross-linking comonomers used were divinylbenzene (DVB, which contains 18% ethylstyrene, Riedel-de-Haen) for EHA and *N*,*N*-methylenebis(acrylamide) (MBAM) for SS. Styrene, DVB, and EHA were washed to remove the inhibitor (three times with a 5 wt % aqueous sodium hydroxide (NaOH, Carlo Erba) solution followed by three times with deionized water). The emulsifiers used were Triton X-405 (~70% octylphenylpolyethylene glycol ether in water, Fluka Chemie) and sorbitan monooleate (SMO, Span 80, Fluka Chemie). The water-soluble initiator was potassium persulfate (KPS, Riedel-de-Haen), and the organic-soluble initiator was benzoyl peroxide (BPO, Fluka). Poly(vinyl alcohol) (PVA 1500, Fluka Chemie) was used as a cosurfactant to stabilize the O/W HIPE. Cyclohexane (Aldrich) and deionized water were also used in the syntheses.

Nanoparticle Synthesis. The hydrogel nanoparticles (NPs) were synthesized using a W/O inverse emulsion polymerization recipe with around 4% monomer (Table 1). The SS/MBAM/S mass ratio used was 88/10/2. The aqueous phase (SS, MBAM, and water, 8.1% of the total mass) was added dropwise to the organic phase (which included S). Polymerization took place at 75 °C under nitrogen for 24 h with continuous stirring. After polymerization, cyclohexane was added to the inverse latex at a 2.5:1.0 ratio, and the diluted inverse latex was then added dropwise to an excess of acetone to precipitate the nanoparticles. The nanoparticles were removed from the acetone through filtration through glass-fiber filter paper (Whatman GF/A). The particles were washed twice in acetone to remove the emulsifier and then dried at 65 °C for 24 h.

One-Pot xPEHA-Filled xPSS PolyHIPEs. The term HIPE will be used herein for convenience, even though the internal phase contents of some of the emulsions are somewhat less than 74%. The xPSS-based polyHIPE from an emulsifier-stabilized O/W HIPE will be termed PSS-E, and its recipe is listed in Table 1. The HIPE was formed by adding the organic phase (hydrophobic monomers, initiator) dropwise to the aqueous phase (hydrophilic monomers, water, emulsifier, initiator, and PVA) with constant stirring using a magnetic stirrer. The resulting HIPE was covered with Parafilm and placed in a convection oven for polymerization at 65 °C for 24 h. The polyHIPE was then dried in a vacuum oven at room temperature for about 3 days, until a constant weight was reached. The emulsifier, cosurfactant, and initiators, which remained in the polyHIPE following drying, were removed by extraction. The polyHIPE was placed in a Soxhlet apparatus and extracted, first with water for 24 h and then with methanol for 24 h, and then it was dried in a convection oven at 60 °C for 24 h. The SS/MBAM/EHA/DVB mass ratio for PSS-E was 8.8/1.0/89.7/0.5. Based on the monomer contents, the xPSS content in PSS-E, m_s, is 9.8%.

Table 1. HIPE Recipes

		content, wt %			
phase	component	NP	PSS-E	PSS-NP	PS
organic	EHA		69.53	74.15	
	DVB		0.35	0.37	2.49
	styrene	0.08			22.51
	BPO	0.09	0.12	0.13	
	Span 80	1.83			5.00
	cyclohexane	89.90			
	total	91.90	70.00	74.65	30.00
aqueous	styrenesulfonate	3.67	6.83	7.29	
	MBAM	0.41	0.76	0.81	
	water	4.02	14.20	15.15	69.45
	Triton X-405		7.00		
	PVA		0.78	0.83	
	KPS		0.43	0.46	0.16
	potassium sulfate				0.39
	nanoparticles			0.81	
	total	8.10	30.00	25.35	70.00

The PSS-based polyHIPE from a nanoparticle-stabilized O/W Pickering HIPE will be termed PSS-NP, and its recipe is listed in Table 1. PVA was dissolved in the water, and then the nanoparticles were added. The mixture was placed in a sonicator (Branson 3510) for 2 h to break up nanoparticle agglomerates. The HIPE was formed by adding the organic phase (hydrophobic monomers, initiator) dropwise to the aqueous phase (hydrophilic monomers, initiator, PVA) with constant stirring. The polymerization and Soxhlet extractions were carried out as described above. The SS/MBAM/EHA/DVB/NP mass ratio for PSS-NP was 8.7/1.0/88.9/0.4/1.0, and therefore, PSS-NP has an m_s (xPSS content, including the NPs) of 10.7%. PSS-NP-m is a polyHIPE that was synthesized using the same PSS-NP recipe but was stirred using a high-speed mixer in an attempt to reduce the HIPE droplet size.

Three-Step xPEHA-Filled S-xPS PolyHIPE. The first step in the synthesis of an xPEHA-filled S-xPS polyHIPE was the synthesis of the xPS polyHIPE using the W/O HIPE recipe listed in Table 1. The xPS polyHIPE from the emulsifier-stabilized W/O HIPE will be termed PS-E. The W/O HIPE was formed by adding the aqueous phase (initiator) dropwise to the organic phase (hydrophobic monomers, emulsifier) with constant stirring. The polymerization and Soxhlet extractions were carried out as described above. The second step was the synthesis of a sulfonated xPS polyHIPE (termed S-PS-E) using cubes approximately 1 cm × 1 cm × 1 cm. The cubes were immersed in concentrated sulfuric acid (98%) at 70 °C for 24 h, were washed in deionized water for 24 h, underwent Soxhlet extraction with methanol for another 24 h, and then dried at 65 °C. The third step was the synthesis of an xPEHA-filled sulfonated xPS polyHIPE (termed F-S-PS-E). The S-PS-E cubes were immersed in a mixture of EHA and DVB, at a 99.5/0.5 mass ratio, and then placed in an oven at low vacuum until they sank, ~15 min. The EHA/DVB was then polymerized at 65 °C for 24 h. Based on the HIPE recipe, F-S-PS-E has an m_s (xPS content) of around 30%.

dx.doi.org/10.1021/ma2027337 | *Macromolecules* 2012, 45, 1612−1621

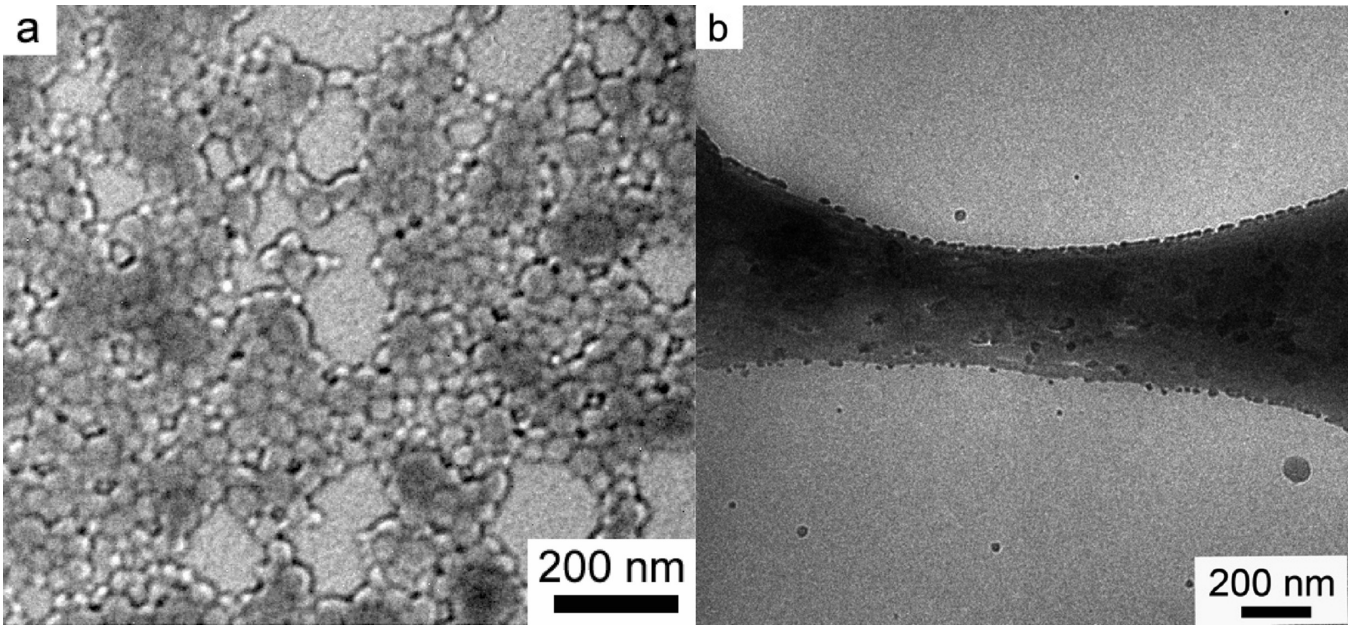


Figure 1. TEM micrographs of (a) P(SS-*co*-MBAM-*co*-S) nanoparticles and (b) PSS-NP-m wall.

Table 2. Elemental Compositions

	C	H	N	S	other	O	Na
measured, wt %							
PSS-E	69.78	10.81	0.26	0.65	18.50	NA	NA
PSS-NP	66.85	10.30	0.33	1.99	20.53	NA	NA
F-S-PS-E	67.07	10.12	0.07	2.88	19.86	NA	NA
calculated, wt %							
PSS-E	69.39	10.24	0.18	1.37	18.82	17.84	0.98
PSS-NP	69.17	10.17	0.18	1.51	18.97	17.89	1.08

Characterization. The size of the polymer nanoparticles was determined using transmission electron microscopy (TEM) and light scattering (Bl-200SM Research Goniometer System, Brookhaven Instruments, Inc.). For TEM analysis (FEI Technai G2 T20 S-Twin, operating at 200 kV) the inverse latex was diluted using cyclohexane at a ratio of 1:10, and a droplet was placed on a Si-on-Ni grid. The molecular structure was characterized using Fourier transform infrared spectroscopy (FTIR) in transmission (Equinox 55 FTIR, Bruker, from 400 to 4000 cm^{-1} at a resolution of 2 cm^{-1}) through KBr pellets (spectral grade, Riedel-de-Haen) containing 3 wt % sample.

The sulfonation of PS-E was investigated without any sample preparation using a photoacoustic attachment (MTEC Model 300) for the FTIR. The carbon, hydrogen, nitrogen, and sulfur contents were determined using chemical analysis. The multiphase polymer morphology of uncoated cryogenic facture surfaces was investigated using scanning electron microscopy (SEM, FEI Quanta 200, 20 kV) at an accelerating voltage of 20 kV combined with energy dispersive X-ray spectroscopy (EDS) for elemental analysis (INCAx-sight, Oxford Instruments). The multiphase morphology of the walls was investigated using transmission electron microscopy (TEM, monochromated FEI Titan 80-300 S/TEM operating at 300 kV) on 70−80 nm cryogenic ultramicrotomed specimens (Ultracut E, Reichert-Jung, Diatom diamond knife). The elemental mapping was obtained using the energy filtered TEM (EFTEM) mode and Gatan Digital Micrograph software.

The water uptake was determined by immersing samples in deionized water at room temperature until a constant mass was reached. The water uptake, m_w, is the ratio of the increase in mass to the original dry mass. The normalized water uptake, m_{wn}, is the water uptake divided by the xPSS or xPS mass fraction, m_s. The swelling ratio, v_s, is the ratio of the swollen hydrated volume to the original dry volume.

The compressive stress−strain measurements were carried out at 10%/min on 5 mm × 10 mm × 10 mm cubes (Instron 3345) until the sample failed or an equipment-related strain limit was reached. As the stress−strain curves for both the dry and hydrated polyHIPEs were typical of elastomers, the data were analyzed using rubber elasticity. In eq 1, the uniaxial stress, σ, in an elastomer is related to the extension ratio, λ, by the modulus, E. For convenience, the compressive stress, the absolute value of σ, was plotted versus the function of the extension ratio, $f(\lambda)$, described in eq 2. The moduli of the dry samples, E_d, and of the hydrated samples, E_h, were calculated from the linear portions of the resulting curves at low $f(\lambda)$ (low strains).

$$\sigma = \frac{E}{3}\left(\lambda - \frac{1}{\lambda^2}\right) \quad (1)$$

$$f(\lambda) = \mathrm{abs}\left(\lambda - \frac{1}{\lambda^2}\right) \quad (2)$$

RESULTS AND DISCUSSION

Nanoparticles. The somewhat broad distribution of particle sizes is seen in the TEM micrograph in Figure 1a. The number-average diameter of the dried nanoparticles, calculated from Figure 1a, was 50 nm, while the number-average diameter of the hydrated nanoparticles from light scattering was 60 nm. The as-synthesized nanoparticles exhibited an FTIR band at 1751 cm^{-1} that was associated with the Span 80 emulsifier. This band disappeared on washing

dx.doi.org/10.1021/ma2027337 | *Macromolecules* 2012, 45, 1612−1621

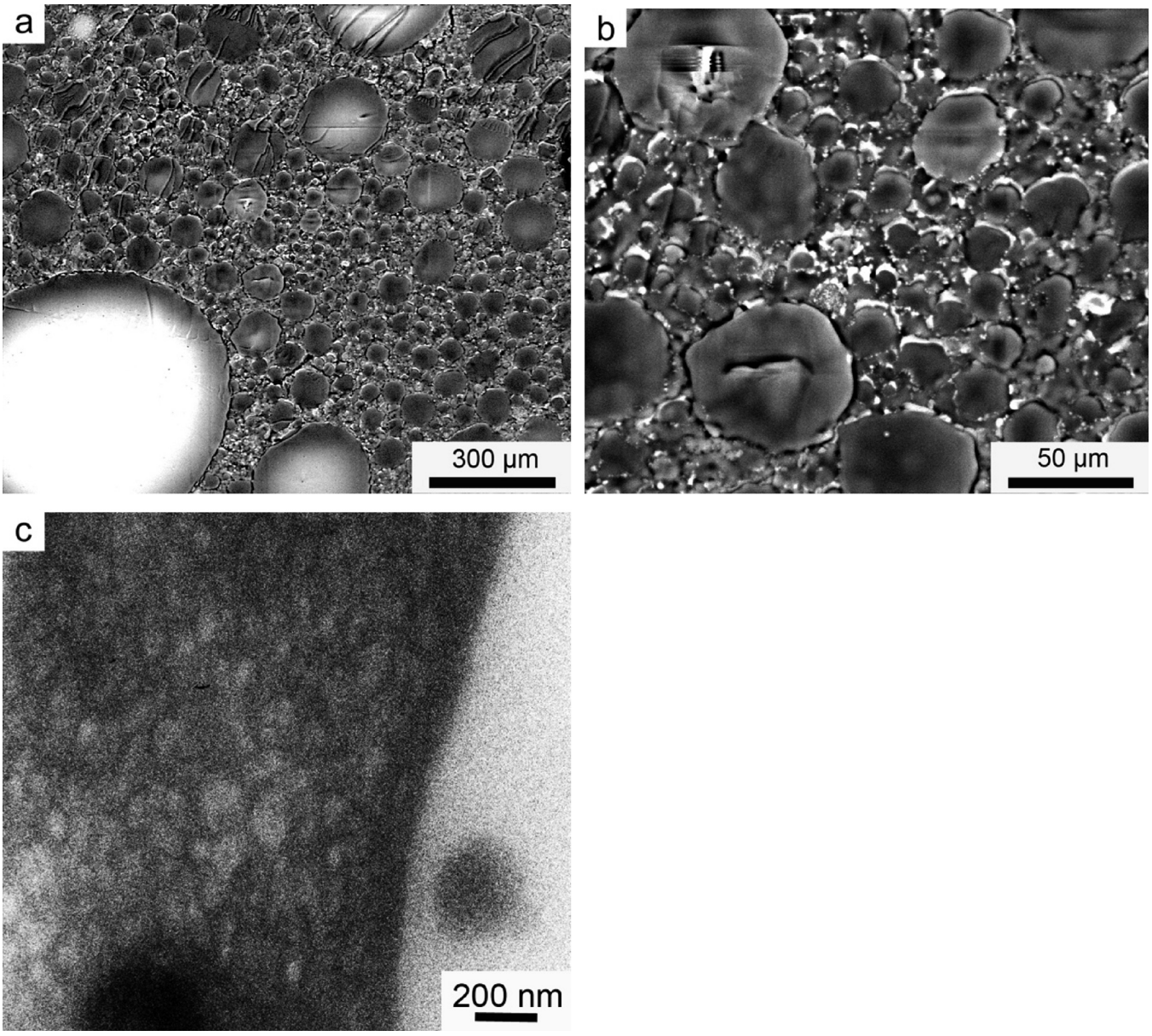


Figure 2. PSS-E: (a, b) SEM fracture surface; (c) TEM of wall.

with acetone, indicating that the emulsifier was removed. Interestingly, the nanoparticles were also observed within the TEM micrographs of PSS-NP-m (Figure 1b). Larger nanoparticles (darkest) are seen within the xPSS walls (darker), and smaller nanoparticles are seen at the interface between the xPSS walls and the xPEHA particles (lighter).

Elemental Composition. The polymerizations within the HIPEs produced white monoliths with yields of around 90%. Based on the HIPE recipes, PSS-E contained around 10 wt % xPSS, PSS-NP contained around 11 wt % xPSS, and F-S-PS-E contained around 30 wt % xPS. The remaining material in each monolith is xPEHA. The measured carbon and hydrogen contents for PSS-E and PSS-NP in Table 2 are quite similar to the values expected from the calculations based on the HIPE's monomer content (Table 1). The calculations assumed that the initiators, emulsifier, and PVA were removed through Soxhlet extraction. The unidentified mass in each case ("other" in Table 2) corresponds with the sum of the calculated oxygen and sodium contents that originate in the EHA and SS and is predominantly the oxygen from EHA. The calculated sulfur and nitrogen contents are quite small, and the discrepancies between the measured contents and the calculated contents most likely reflect experimental error and the assumption that the polyHIPE composition was identical to that in the HIPE and was not affected by the Soxhlet extraction.

The S-PS-E polyHIPE was extremely hygroscopic. The FTIR bands associated with PS were overwhelmed by the bands associated with water in the spectra from samples that were not dried thoroughly (not shown). The carbon and hydrogen contents of F-S-PS-E reflect the monomer contents in the feed, which does not include a nitrogen-containing monomer. The sulfur content of 2.88 wt % results from the sulfonation. The polyHIPE containing sulfonated xPS exhibited a somewhat higher sulfur content than those in the xPSS polyHIPEs. Here, too, the unidentified mass is predominantly oxygen from EHA.

Two-Phase Structure. The two-phase structure of PSS-E is seen in the SEM micrographs in Figure 2a,b. The xPEHA particles from polymerization in the internal phase are

dx.doi.org/10.1021/ma2027337 | *Macromolecules* 2012, 45, 1612–1621

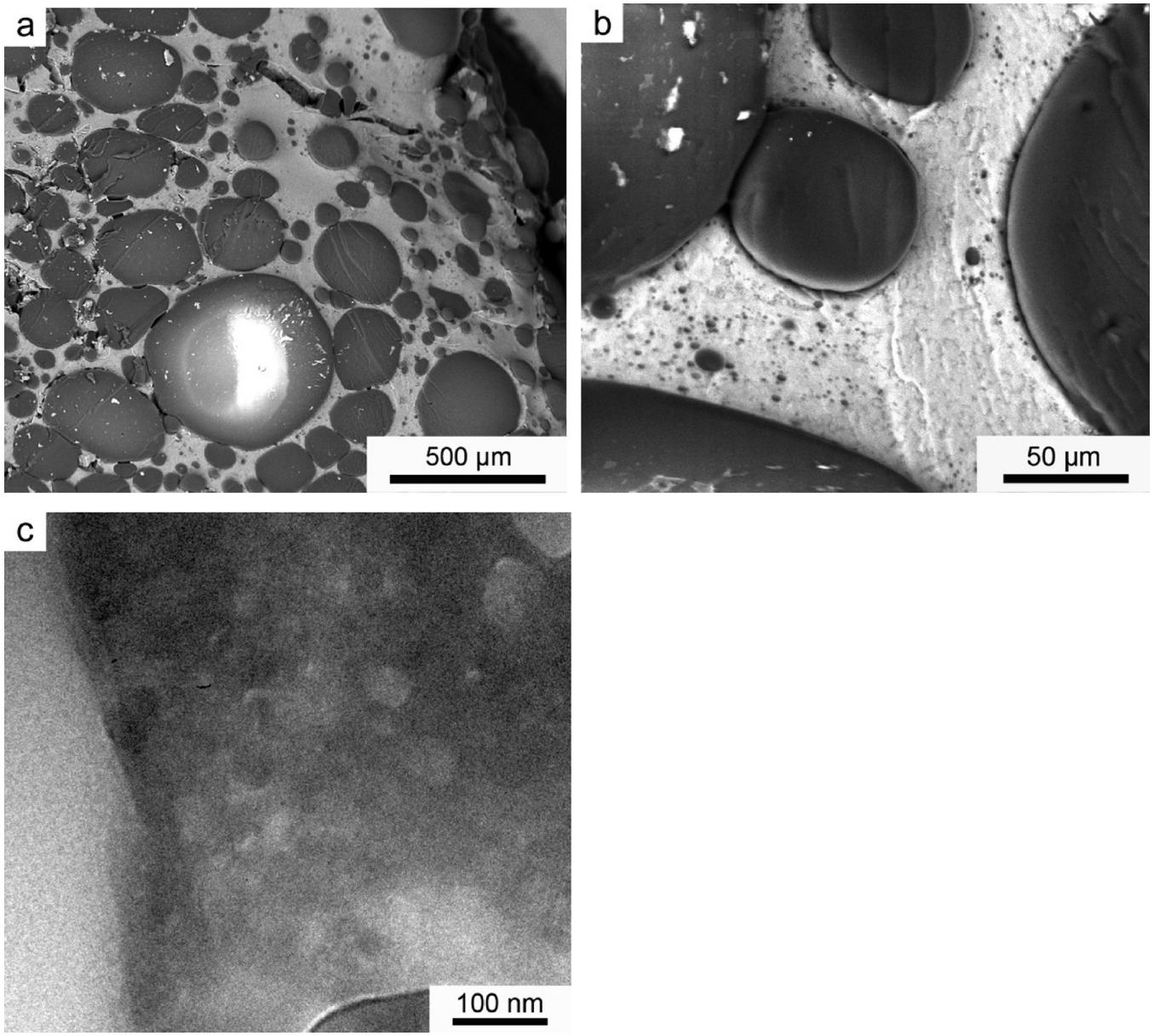


Figure 3. PSS-NP: (a, b) SEM fracture surface; (c) TEM of wall.

somewhat darker while the PSS framework from polymerization in the external phase is somewhat lighter. The origin of the contrast is the higher atomic numbers of the sulfur and sodium in the xPSS. The diameters of the xPEHA particles range from around 500 to 5 μm. EDS elemental analysis from the center of the darker domains reveals only carbon and oxygen, and the composition corresponds to that of the xPEHA. EDS elemental analysis from the lighter walls were expected to exhibit 6.9 wt % sulfur and sodium, based on the feed composition. The 4.0 and 1.8 wt % sulfur and sodium, respectively, are smaller than expected. The sodium content was smaller than the sulfur content, which may indicate that some of the sodium ions were replaced by hydrogen ions during Soxhlet extraction. The discrepancy between the experimental and calculated sulfur contents may result from the spatial resolution of EDS, which may incorporate signal from the xPEHA particles, or may result from xPEHA nanodomains within the xPSS walls (as will be discussed in the description of the wall structure).

The two-phase structure of PSS-NP in Figure 3a,b bears certain similarities to that of PSS-E in Figure 2a,b. Here, too, the diameters of the xPEHA spheres range from around 500 to 5 μm. However, there are some important differences between the two structures. PSS-E exhibits a relatively large number of smaller particles while PSS-NP exhibits a relatively small number of smaller particles. The difference in the particle size distributions is also reflected in the wall thicknesses. PSS-E, with its numerous smaller particles, exhibits thinner walls, reflecting the relatively large particle surface area. PSS-NP, with its numerous larger particles, exhibits significantly thicker walls, as seen for other polyHIPEs that are based on Pickering HIPEs.[37,39] The HIPE droplet size, and therefore the xPEHA particle size, and the xPSS wall thickness were reduced by using a high-speed mixer, as seen in Figure 4a,b. The effects of mixing speed on the structure are illustrated schematically in Figure 5. PSS-NP, and its thicker xPSS walls and larger xPEHA particles, is illustrated in Figure 5a, while PSS-NP-m, with its thinner walls and smaller particles, is illustrated in Figure 5b.

dx.doi.org/10.1021/ma2027337 | *Macromolecules* 2012, 45, 1612–1621

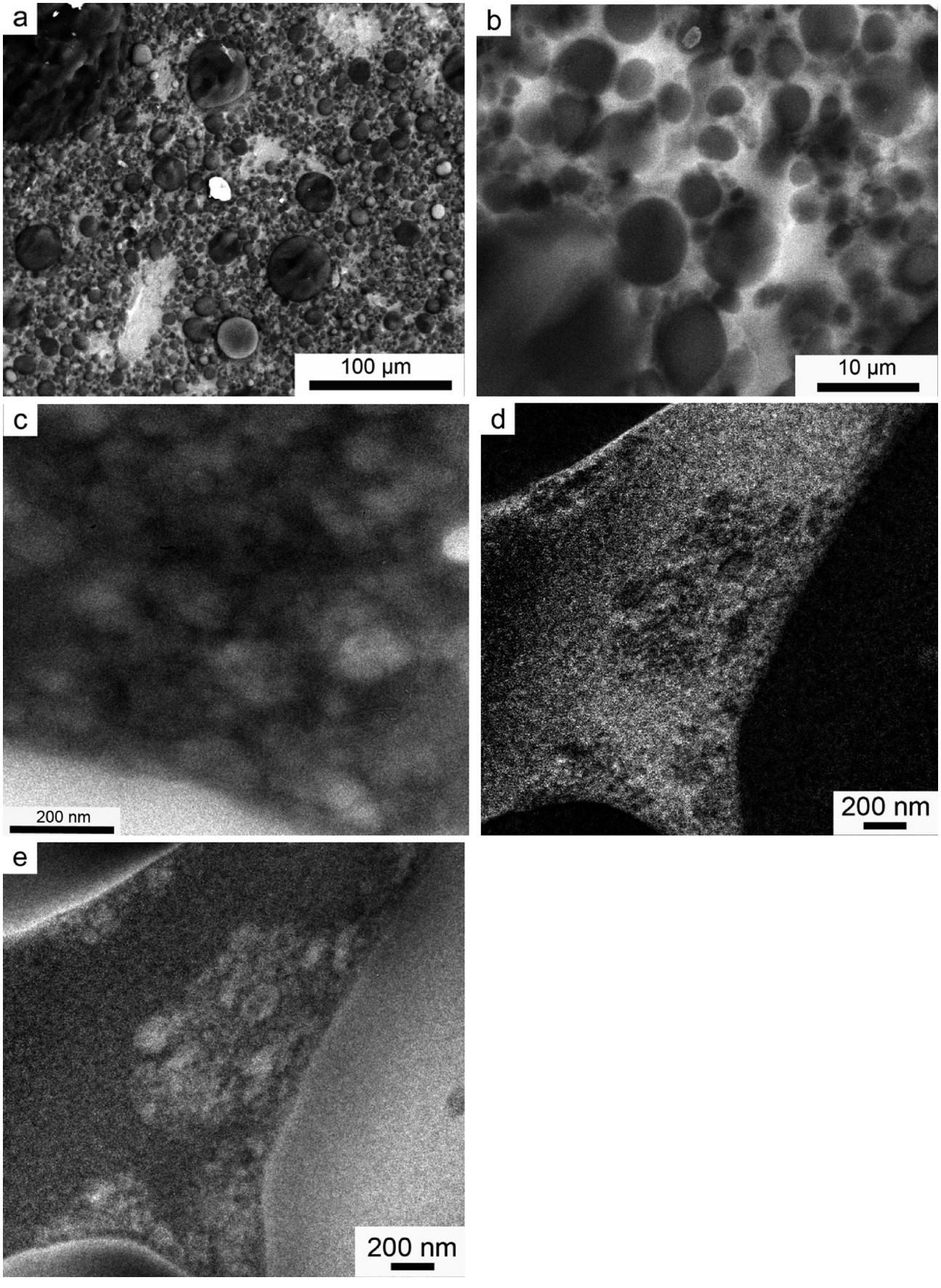


Figure 4. PSS-NP-m: (a, b) SEM fracture surface; (c) TEM of wall; (d) sulfur and (e) carbon EFTEM of wall.

dx.doi.org/10.1021/ma2027337 | *Macromolecules* 2012, 45, 1612–1621

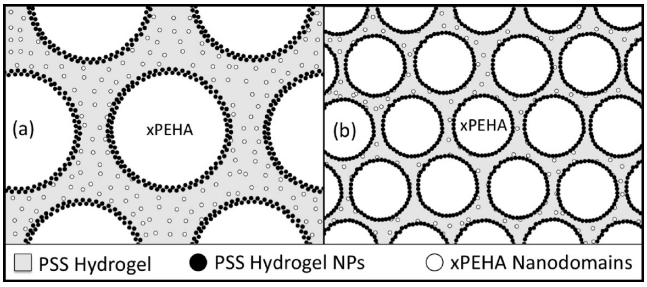


Figure 5. Schematic illustration of the xPEHA particles and nanodomains in the xPSS-based polyHIPE structure: (a) PSS-NP; (b) PSS-NP-m.

The porous xPS polyHIPE exhibits voids from 50 to 100 μm and interconnecting holes on the order of 5 μm in Figure 6a,b. The structure reflects the 30% internal phase and is different from the highly interconnected, highly porous structure typical of polyHIPEs that contain 10−20% internal phase. The darker xPEHA domains within the lighter S-xPS walls in Figure 6c,d correspond to the voids in Figure 6a,b. The structure of the F-S-PS-E framework in Figure 6c,d is similar, in many respects, to those seen in the xPSS-based polyHIPEs.

Wall Structure. The structure within the PSS-E walls is seen in the TEM micrographs in Figure 2c. The contrast between the dark sulfur-containing xPSS walls and the light xPEHA particles originates in the relatively high atomic number of the sulfur. Unexpectedly, the walls also exhibit a two-phase structure, with lighter nanodomains on the order of 50 nm within the dark walls. The walls of PSS-NP and PSS-NP-m, as seen in Figures 3c and 4c, respectively, exhibit an almost identical two-phase structure to that of PSS-E. All the xPSS-based materials exhibit xPEHA nanodomains embedded within the xPSS walls. TEM micrographs of the F-S-PS-E walls (not shown) are uniform, and there is no evidence of a multiphase structure within the S-xPS walls. The styrene was polymerized in the first stage of the synthesis, and the EHA was polymerized

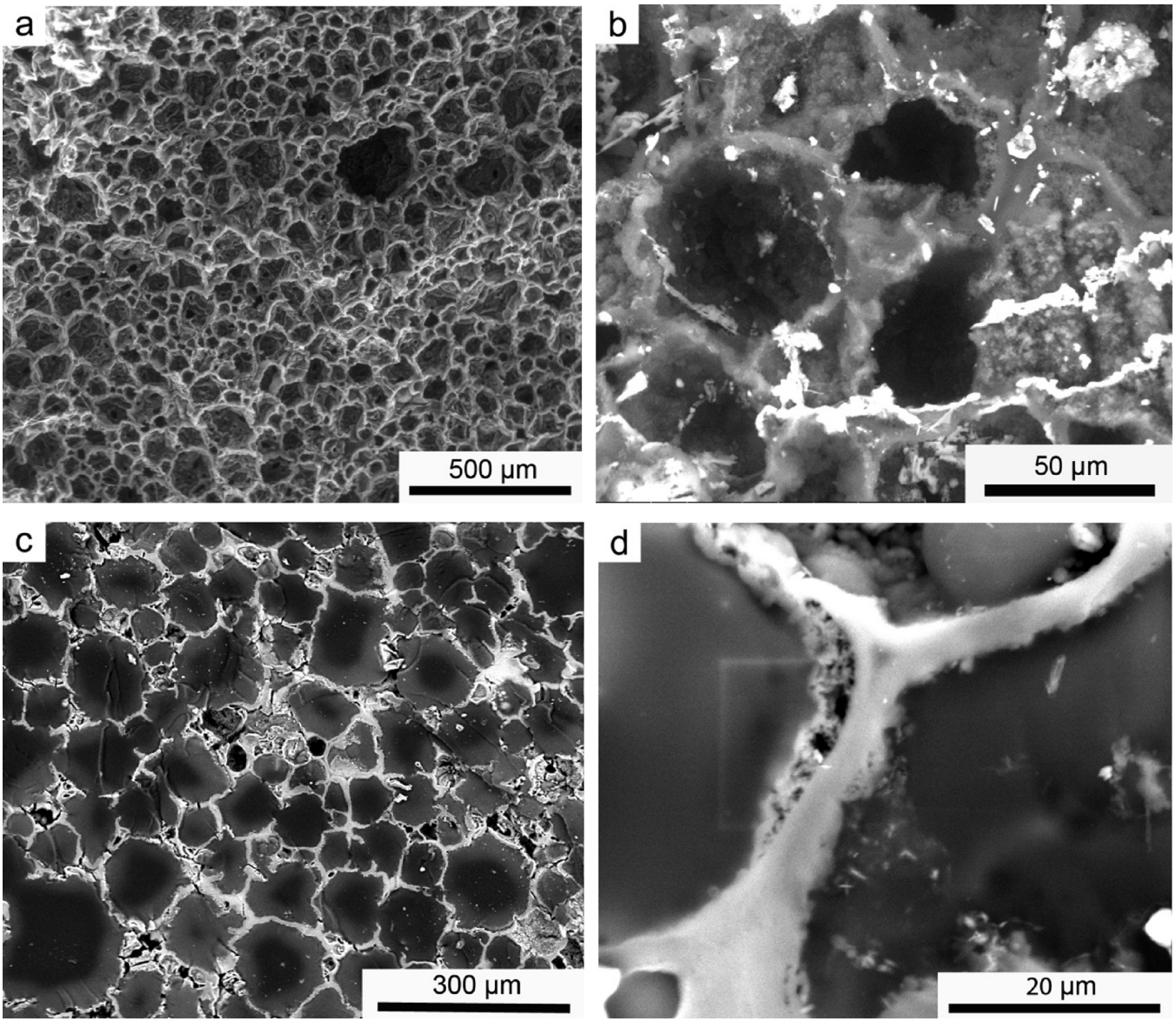


Figure 6. SEM fracture surfaces: (a, b) PS-E; (c, d) F-S-PS-E.

dx.doi.org/10.1021/ma2027337 | *Macromolecules* 2012, 45, 1612−1621

in the third stage of the synthesis, so that the absence of a multiphase structure within the S-xPS walls is not surprising.

The nature of the domains is best understood through EFTEM elemental mapping of the PSS-NP-m wall in Figure 4d,e. The bright wall in the sulfur map in Figure 4d originates in the sulfur of the xPSS. The xPEHA particles are dark since they contain no sulfur. The sulfur content within the wall is not homogeneous, and there are nanodomains with relatively low sulfur contents. These same sulfur-poor nanodomains within the wall are the carbon-rich nanodomains in the carbon mapping in Figure 4e. The carbon mapping shows that these nanodomains are richer in carbon than the surrounding areas in the wall and bear a similarity to the xPEHA particles outside the walls. These results support the contention that the xPSS walls are not porous but, rather, contain embedded xPEHA nanodomains. The wall structure most likely develops during HIPE formation. The PVA helps stabilize nanoscale EHA droplets within the continuous aqueous phase surrounding the microscale EHA droplets. The elastomeric xPEHA nanodomains within the xPSS walls are also included in the schematic illustrations in Figure 5.

Mechanical Behavior. Typical curves showing the variation of compressive stress with $f(\lambda)$ for the dry PSS-E, PSS-NP, and F-S-PS-E are presented in Figure 7. Both xPS and xPSS are glassy polymers. PSS-E, however, is unusually flexible, reaching compressive strains of over 70% and exhibiting a relatively low modulus of 0.26 MPa (Table 3). Previous work has demonstrated that extensive copolymerization can take place in emulsifier-stabilized HIPEs that contain monomers in both the external and internal phases.[53,54]

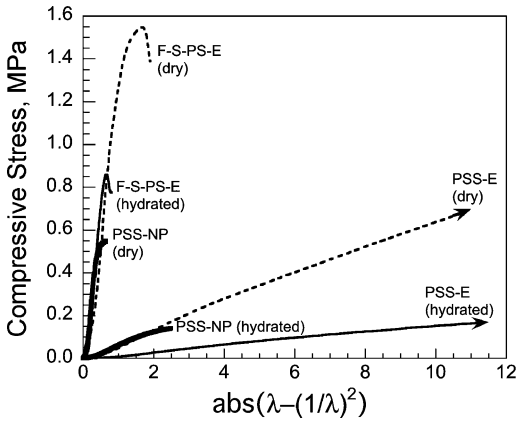


Figure 7. Compressive stress vs $f(\lambda)$ for both dry and hydrated PSS-E, PSS-NP, and F-S-PS-E.

Table 3. Scaffold Content, Compressive Modulus (Dry and Hydrated), and Water Absorption

	m_s, wt %	E_d, MPa	m_w, wt %	m_{wn}, wt %	v_s, vol %	E_h, MPa
PSS-E	9.8	0.26	53	540	144	0.08
PSS-NP	10.7	5.6	151	1410	259	0.23
F-S-PS-E	30.0	6.0	36	136	142	4.7

Copolymerization is expected to be less extensive in Pickering HIPEs due to the nanoparticle barrier around the droplets, to the higher interfacial tension between the phases in the absence of an emulsifier, and to the significantly smaller interfacial area. Indeed, the modulus is more than 20-fold higher, 5.6 MPa (Table 3), for PSS-NP. The relatively low strain at break (Figure 7) reflects the relatively low load-bearing ability of the walls. No copolymerization is expected to take place in the three-step F-S-PS-E synthesis, and therefore, the modulus is similar to that of PSS-NP. Since the walls of F-S-PS-E are solid xPS and have a superior load-bearing capability compared to xPEHA-filled xPSS, F-S-PS-E reaches a higher strain at break than does PSS-NP (Figure 7).

Water Absorption. As synthesized, PSS-E and PSS-NP contained around 15 wt % water, which was removed by drying. The water absorptions for PSS-E, PSS-NP, and F-S-PS-E are listed in Table 3. PSS-E absorbed 53% of its mass in water, and the water absorption normalized by the xPSS content is 540 wt %, more than 5 times the mass of xPSS. This water absorption is accompanied by a swelling ratio of 144%, a 44% increase in volume. F-S-PS-E absorbed 36% of its mass in water, 136% of the mass of S-xPS, and exhibited a swelling ratio of 142%. The swelling ratio of F-S-PS-E is similar to that of PSS-E since their water absorptions are of the same order of magnitude. The normalized water absorption in F-S-PS-E is significantly smaller than that in PSS-E, indicating that the S-xPS is less hydrophilic than xPSS.

The water absorption and normalized water absorption in PSS-NP are around 3 times that in PSS-E, and there is a 159% increase in volume (a swelling ratio of 259%) (Table 3). This significantly higher water absorption reflects the differences in macromolecular structure. The relatively low modulus of the dry PSS-E was attributed to the copolymerization of hydrophilic SS with hydrophobic EHA in the external phase. The incorporation of hydrophobic EHA in the macromolecular structure of the xPSS would limit its water absorption. xPSS would retain its hydrophilic nature if copolymerization was prevented by nanoparticle stabilization, and its water absorption would be significantly greater.

The variations of the compressive stress with $f(\lambda)$ for the hydrated PSS-E, PSS-NP, and F-S-PS-E are also presented in Figure 7. The compressive modulus of the hydrated PSS-E, 0.08 MPa, is about one-third that of the dry PSS-E, 0.26 MPa. This significant reduction in modulus results from the absorption of 540 wt % water within the xPSS scaffold structure. Water absorption in F-S-PS-E, which is far less significant than for PSS-E, only produces a 20% reduction in modulus. The modulus of hydrated PSS-NP is more than an order of magnitude smaller than that of dry PSS-NP (Table 3). This significantly greater decrease in modulus than that seen for PSS-E reflects the significantly greater absorption of water by PSS-NP. These results indicate that the extent of modulus reduction reflects the extent of water absorption.

CONCLUSIONS

Two different routes were successfully used to synthesize novel flexible polymer systems in which hydrogel scaffolds based on cross-linked PS bearing sulfonate groups were filled with a cross-linked PEHA elastomer. An innovative "one-pot" route was based on the formation of a HIPE containing an aqueous solution of SS (and MBAM) in the external phase and EHA (and DVB) in the internal phase. Both emulsifier-stabilized HIPEs and emulsifier-free polymer–nanoparticle-stabilized Pickering HIPEs were successfully synthesized. A "three-step" route consisted of sulfonating a cross-linked PS polyHIPE in sulfuric acid and then polymerizing and cross-linking EHA within the polyHIPE provided a reference material.

dx.doi.org/10.1021/ma2027337 | Macromolecules 2012, 45, 1612–1621

Although the sulfur contents of the different polyHIPEs were quite similar, their macromolecular structures, morphologies, and properties were quite different. Unexpectedly, the walls of the xPSS-based polyHIPEs (from both surfactant-stabilized and nanoparticle-stabilized HIPEs) contained xPEHA nanodomains. The greater flexibility and the more limited water absorption capacity of the polyHIPE from a emulsifier-stabilized HIPE seem to indicate that copolymerization of SS with EHA has taken place within the walls. Such copolymerizations have been observed in other polyHIPE systems. The thicker walls in the polyHIPE from a polymer−nanoparticle-stabilizes HIPE are typical of polyHIPEs based upon Pickering HIPEs. The higher modulus and the significantly greater water absorption capacity seem to indicate that copolymerization has not taken place during polymerization in the Pickering HIPE. The sulfonated xPS-based polyHIPE absorbed significantly less water per mass hydrophilic polymer and exhibited a relatively small decrease in modulus upon water absorption. The modulus reduction reflected the extent of water absorption.

AUTHOR INFORMATION

Corresponding Author

*E-mail: michaels@tx.technion.ac.il; Tel: 972-4-829-4582.

Notes

The authors declare no competing financial interest.

ACKNOWLEDGMENTS

The partial support of the Israel Science Foundation and of the Technion VPR Fund is gratefully acknowledged.

REFERENCES

(1) Barby, D.; Haq, Z. US Pat 4,522,953, 1985.
(2) Williams, J. M.; Wrobleski, D. A. *Langmuir* **1988**, *4*, 656−662.
(3) Williams, J. M.; Gray, A. J.; Wilkerson, M. H. *Langmuir* **1990**, *6*, 437−444.
(4) Cameron, N. R.; Sherrington, D. C. *Adv. Polym. Sci.* **1996**, *126*, 163−214.
(5) Cameron, N. R.; Krajnc, P.; Silverstein, M. S. In *Porous Polymers*; Silverstein, M. S., Cameron, N. R., Hillmyer, M. A., Eds.; John Wiley and Sons: Hoboken, NJ, 2011; Chapter 4.
(6) Silverstein, M. S.; Cameron, N. R. PolyHIPEs - Porous Polymers from High Internal Phase Emulsions. In *Encyclopedia of Polymer Science and Technology*; Wiley: New York, 2010; DOI 10.1002/0471440264.pst571.
(7) Sergienko, A.; Tai, H.; Narkis, M.; Silverstein, M. S. *J. Appl. Polym. Sci.* **2004**, *94*, 2233−2239.
(8) Leber, N.; Fay, J. D. B.; Cameron, N. R.; Krajnc, P. *J. Polym. Sci., Part A: Polym. Chem.* **2007**, *45*, 4043−4053.
(9) Tai, H.; Sergienko, A.; Silverstein, M. S. *Polym. Eng. Sci.* **2001**, *41*, 1540−1552.
(10) Livshin, S.; Silverstein, M. S. *Macromolecules* **2008**, *41*, 3930−3938.
(11) Livshin, S.; Silverstein, M. S. *Soft Matter* **2008**, *4*, 1630−1638.
(12) Livshin, S.; Silverstein, M. S. *Macromolecules* **2007**, *40*, 6349−6354.
(13) Busby, W.; Cameron, N. R.; Jahoda, C. A. B. *Biomacromolecules* **2001**, *2*, 154−164.
(14) Hayman, M. W.; Smith, K. H.; Cameron, N. R.; Przyborski, S. A. *Biochem. Biophys. Methods* **2005**, *62*, 231−240.
(15) Akay, G.; Birch, M. A.; Bokhari, M. A. *Biomaterials* **2004**, *25*, 3991−4000.
(16) Stefanec, D.; Krajnc, P. *React. Funct. Polym.* **2005**, *65*, 37−45.
(17) David, D.; Silverstein, M. S. *J. Polym. Sci., Part A: Polym. Chem.* **2009**, *47*, 5806−5814.
(18) Lumelsky, Y.; Lalush-Michael, I.; Levenberg, S.; Silverstein, M. S. *J. Polym. Sci., Part A: Polym. Chem.* **2009**, *47*, 7043−7053.
(19) Mercier, A.; Deleuze, H.; Maillard, B.; Mondain-Monval, O. *Adv. Synth. Catal.* **2002**, *344*, 33−36.
(20) Moine, L.; Deleuze, H.; Maillard, B. *Tetrahedron Lett.* **2003**, *44*, 7813−7813.
(21) Cameron, N. R. *Polymer* **2005**, *46*, 1439−1449.
(22) Normatov, J.; Silverstein, M. S. *Macromolecules* **2007**, *40*, 8329−8335.
(23) Normatov, J.; Silverstein, M. S. *Polymer* **2007**, *48*, 6648−6655.
(24) Normatov, J.; Silverstein, M. S. *J. Polym. Sci., Part A: Polym. Chem.* **2008**, *46*, 2357−2366.
(25) Normatov, J.; Silverstein, M. S. *Chem. Mater.* **2008**, *20*, 1571−1577.
(26) Menner, A.; Powell, R.; Bismarck, A. *Soft Matter* **2006**, *4*, 337−342.
(27) Haibach, K.; Menner, A.; Powell, R.; Bismarck, A. *Polymer* **2006**, *47*, 4513−4519.
(28) Menner, A.; Haibach, K.; Powell, R.; Bismarck, A. *Polymer* **2006**, *47*, 7628−7635.
(29) Tai, H.; Sergienko, A.; Silverstein, M. S. *Polymer* **2001**, *42*, 4473−4482.
(30) Silverstein, M. S.; Tai, H.; Sergienko, A.; Lumelsky, Y.; Pavlovsky, S. *Polymer* **2005**, *46*, 6682−6694.
(31) Desforges, A.; Backov, R.; Deleuze, H.; Mondain-Monval, O. *Adv. Funct. Mater.* **2005**, *15*, 1689−1695.
(32) Colver, P. J.; Bon, S. A. F. *Chem. Mater.* **2007**, *19*, 1537−1539.
(33) Menner, A.; Ikem, V.; Salgueiro, M.; Shaffer, M. S. P.; Bismarck, A. *Chem. Commun.* **2007**, 4274−4276.
(34) Menner, A.; Verdejo, R.; Shaffer, M.; Bismarck, A. *Langmuir* **2007**, *23*, 2398−2403.
(35) Ikem, V. O.; Menner, A.; Bismarck, A. *Angew. Chem., Int. Ed.* **2008**, *47*, 8277−8279.
(36) Zhang, S.; Chen, J. *Chem. Commun.* **2009**, 2217−2219.
(37) Chen, Y.; Ballard, N.; Gayet, F.; Bon, S. A. F. *Chem. Commun.* **2012**, *48*, 1117−1119.
(38) Gurevitch, I.; Silverstein, M. S. *J. Polym. Sci., Part A: Polym. Chem.* **2010**, *48*, 1516−1525.
(39) Gurevitch, I.; Silverstein, M. S. *Macromolecules* **2011**, *44*, 3398−3409.
(40) Zhang, H.; Cooper, A. I. *Chem. Mater.* **2002**, *14*, 4017−4020.
(41) Gokmen, M. T.; Van Camp, W.; Colver, P. J.; Bon, S. A. F.; Du Prez, F. E. *Macromolecules* **2009**, *42*, 9289−9294.
(42) Ciardelli, G.; Chiono, V.; Cristallini, C.; Barbani, N.; Ahluwalia, A.; Vozzi, G.; Previti, A.; Tantussi, G.; Giusti, P. *J. Mater. Sci.: Mater. Med.* **2004**, *15*, 305−310.
(43) Cameron, N. R.; Sherrington, D. C.; Ando, I.; Kurosu, H. *J. Mater. Chem.* **1996**, *6*, 719−726.
(44) Krajnc, P.; Brown, J. F.; Cameron, N. R. *Org. Lett.* **2002**, *4*, 2497−2500.
(45) Mercier, A.; Deleuze, H.; Mondain-Monval, O. *React. Funct. Polym.* **2000**, *46*, 67−79.
(46) Livshin, S.; Silverstein, M. S. *J. Polym. Sci., Part A: Polym. Chem.* **2009**, *47*, 4840−4845.
(47) Barbetta, A.; Cameron, N. R.; Cooper, S. J. *Chem. Commun.* **2000**, 221−222.
(48) Kulygin, O.; Silverstein, M. S. *Soft Matter* **2007**, *3*, 1525−1529.
(49) Butler, R.; Hopkinson, I.; Cooper, A. I. *J. Am. Chem. Soc.* **2003**, *125*, 14473−14481.
(50) Butler, R.; Davies, C. M.; Cooper, A. I. *Adv. Mater.* **2001**, *13*, 1459−1463.
(51) Zhang, H.; Cooper, A. I. *Chem. Mater.* **2002**, *14*, 4017−4020.
(52) P Krajnc, P.; Stefanec, D.; Pulko, I. *Macromol. Rapid Commun.* **2005**, *26*, 1289−1293.
(53) Gitli, T.; Silverstein, M. S. *Soft Matter* **2008**, *4*, 2475−2485.
(54) Gitli, T.; Silverstein, M. S. *Polymer* **2011**, *52*, 107−115.
(55) Kovačič, S.; Jeřabek, K.; Krajnc, P. *Macromol. Chem. Phys.* **2011**, *212*, 2151−2158.

(56) Choi, P.; Jalani, N. H. *J. Polym. Sci., Part B: Polym. Phys.* **2006**, *44*, 2183−2200.
(57) Deluca, N. W.; Elabd, Y. A. *J. Polym. Sci., Part B: Polym. Phys.* **2006**, *44*, 2201−2225.
(58) Wakeman, R. J.; Bhumgara, Z. G.; Akay, G. *Chem. Eng. J.* **1998**, *70*, 133−141.
(59) Ottens, M.; Leene, G.; Beenackers, A.; Cameron, N.; Sherrington, D. C. *Ind. Eng. Chem. Res.* **2000**, *39*, 259−266.
(60) Bucknall, C. B. *Toughened Plastics*; Applied Science Publishers: London, 1977.
(61) Rosen, S. L. *J. Appl. Polym. Sci.* **1973**, *17*, 1805−1811.
(62) Rosen, S. L. *Polym. Eng. Sci.* **1967**, *7*, 115−123.
(63) Silverstein, M. S.; Narkis, M. *Polym. Eng. Sci.* **1989**, *29*, 824−834.
(64) Silverstein, M. S.; Talmon, Y.; Narkis, M. *Polymer* **1989**, *30*, 416−424.
(65) Silverstein, M. S.; Talmon, Y.; Narkis, M. *Polymer* **1985**, *26*, 1359−1364.

Macromolecules

Article

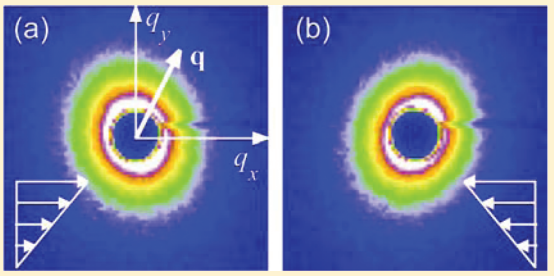
pubs.acs.org/Macromolecules

Shear-Induced Orientation in Well-Exfoliated Polystyrene/Clay Nanocomposites

Laura M. C. Dykes,[†] John M. Torkelson,[†,‡] and Wesley R. Burghardt*[,†,‡]

[†]Department of Chemical and Biological Engineering and [‡]Department of Materials Science and Engineering, Northwestern University, Evanston, Illinois 60208, United States

ABSTRACT: We report measurements of shear-induced particle orientation in highly exfoliated polystyrene/clay nanocomposites. Samples were prepared using an *in situ* polymerization technique, in which native clay is organically modified with a cationic surfactant that incoporporates a polymerizable vinylbenzyl moiety. Controlled radical polymerization was used during the synthesis to limit the molecular weight and polydispersity of the nanocomposite polymer matrix. Flow-induced orientation was measured in the flow-gradient plane of shear flow using synchrotron-based small-angle X-ray scattering. Despite the small rotational diffusivity expected for the clay particles, significant particle orientation was only observed at relatively high rates in steady shear or at high frequencies in large-amplitude oscillatory shear. Measurements of orientation upon flow cessation provided direct evidence of a structural relaxation process that was orders of magnitude faster than estimates of rotational Brownian motion. It is suggested that this fast relaxation arises from either relaxation of shear-induced distortion of partially flexible exfoliated clay sheets in a highly entangled nanoparticle network or coupling of particle and polymer dynamics.



INTRODUCTION

Polymer nanocomposites offer opportunities to engineer polymer materials with enhanced properties through introduction of modest quantities of nanometer-scale fillers. Improvements in heat distortion temperature, stiffness, flame resistance, and barrier properties have all been demonstrated in polymer/clay nanocomposites.[1−3] Use of other types of nanoparticles such as carbon nanotubes[4] or graphene sheets[5] can further expand the palette of property enhancement by imparting high electrical and/or thermal conductivity to polymers. In preparing nanocomposites, it is frequently a challenge to develop processing methods that facilitate thorough dispersion of the nanoparticles in the matrix polymer. In the case of polymer/clay nanocomposites, complete exfoliation of individual clay sheets is usually the most desired outcome, since high exfoliation maximizes the nanoparticle/polymer interfacial area. Frequently, however, conventional processing techniques like melt mixing lead to intercalated samples in which polymer penetrates into the intergallery spaces of organically modified clay, expanding but not destroying their characteristic layered structure.

Many classes of polymer nanocomposites employ highly anisotropic (rod-like or disk-like) particles. Particle orientation induced during processing of nanocomposites will have a strong impact on mechanical,[6] barrier,[7] and transport properties.[4] Flow-induced particle orientation is also frequently invoked as a possible explanation of rheological phenomena in nanocomposites.[8−10] While there is ample evidence of flow- and processing-induced orientation in polymer/clay nanocomposites, most studies have relied on *ex situ* structural studies of nanocomposites that had been quenched into the solid state.[11−15] To better anticipate how processing will impact particle orientation in nanocomposites, it is desirable to develop detailed understanding of the impact of flow on nanocomposite structure through *in situ* experiments in well-defined flows. We have recently reported detailed studies of shear flow-induced particle orientation in two different dispersions of intercalated clay particles in low-molecular-weight polymer melts that are viscous liquids at room temperature, using synchrotron-based X-ray scattering methods.[16,17] In both cases, many aspects of the observed orientation dynamics could be rationalized by appealing to concepts from the hydrodynamics of anisotropic (disk-like) Brownian particles in shear, although the propensity of clay particles to form particulate network structures also had a large impact on both particle orientation and the macroscopic rheology of these samples.

Given the strong technological interest in exfoliated polymer/clay nanocomposites, it is valuable to extend the scope of such *in situ* structural studies beyond the case of intercalated clay dispersions. Here we present studies of shear-induced orientation in highly exfoliated polystyrene (PS)/clay nanocomposites. We again employ X-ray scattering as a tool to probe particular orientation under flow. Although anisotropic wide-angle X-ray diffraction from the periodic layering within intercalated clay particles provides a direct representation of the particle orientation distribution function,[13,16,17] this option does not exist for exfoliated samples. However, the highly anisotropic shape of disk-like clay particles also induces

Received: June 6, 2011
Revised: December 21, 2011
Published: January 18, 2012

ACS Publications © 2012 American Chemical Society

anisotropy in the small-angle scattering arising from the particle as a whole, which provides an alternative route to quantify flow-induced orientation. Our earlier work included comparison between wide- and small-angle scattering as probes of particle orientation, and the methods gave generally consistent results, albeit with some quantitative differences ascribed to the difference in length scale probed in the different scattering regimes.[17] In the present study, we rely on anisotropic small-angle scattering as a probe of shear-induced orientation in exfoliated nanocomposites.

Most methods for producing well-exfoliated polystyrene/clay nanocomposites have employed *in situ* polymerization. Two general approaches have been used. In the first, an initiator is tethered to the clay surface, such that all growing polymer chains are tethered to the clay surface. This approach was first employed by Weimer et al.,[18] who used a nitroxide initiator such that the reaction proceeded via a controlled radical polymerization mechanism. Fan et al.[19,20] used thermal free radical initiators based on azobis(isobutyronitrile), to which quaternized amine groups were added to facilitate attachment to clay surfaces via ion exchange. Uthirakumar et al.[21−23] similarly employed azo-based cationic initiators in their studies of tethered radical initiators. In an alternative *in situ* polymerization approach, polymerizable surfactants are attached to the clay surface using ion exchange, providing a different route to allow direct coupling of growing polystyrene chains to the clay surface. In this strategy, initiation occurs in the bulk. Many such studies have used polymerizable surfactants employing a vinylbenzyl moiety. Tseng et al.[24] explored modifying clay surfaces with combinations of the surfactant vinylbenzyldimethylethanolammonium chloride (VBDEAC) and a long chain alkyl surfactant, cetylpyridinium chloride (CPC). Use of VBDEAC alone did not lead to well-exfoliated nanocomposites. Tseng et al. concluded that adding CPC with its longer chain helped facilitate intercalation of styrene monomer into the organically modified clay and reported optimal results at a VBDEAC:CPC ratio of 1:1.[24] A similar two-surfactant strategy was employed by Zhong et al.,[25] in which the polymerizable surfactant was based on an acrylic group. Alternatively, Fu et al.[26,27] and Zhu et al.[28] employed a single surfactant incorporating both a vinylbenzyl moiety and a long chain alkyl group; both groups had success in producing well-exfoliated nanocomposites using these polymerizable surfactants in conjunction with bulk-initiated free radical polymerization. The surfactant used by Zhu et al., dimethylhexadecylstyrylammonium chloride (denoted VB16), was subsequently used in preparation of exfoliated nanocomposites for rheological studies.[29]

In this work we have adopted the synthesis procedures of Zhu et al.[28] and Xu et al.,[29] employing the polymerizable surfactant VB16 to facilitate preparation of well-exfoliated polystyrene/clay nanocomposites. Since our ultimate goal is to study orientation dynamics in shear flow, we have deviated from their procedures by using controlled radical polymerization to limit (and better define) the degree of polymerization achieved, in order to avoid excessive "background" elasticity from the polymer melt matrix.

EXPERIMENTAL SECTION

Materials. Reactants *N,N*-dimethyl-*n*-hexadecylamine, 4-vinylbenzyl chloride, benzoyl peroxide, 2,2,6,6-tetramethylpeperidine 1-oxyl (or TEMPO), and styrene were purchased from Sigma-Aldrich. Solvents were purchased from VWR. Natural montmorillonite, trade name Cloisite NA+, was obtained from Southern Clay Products.

Synthesis. Synthesis of surfactant dimethyhexadecylstyrylammonium chloride (VB16) and its subsequent use in clay surface modification follow procedures described by Zhu et al.[28] *N,N*-Dimethyl-*n*-hexadecylamine (13.64 g) and 4-vinylbenzyl chloride (7.82 g) were mixed in equal mole ratio and stirred overnight in 50 mL of ethyl acetate. The resulting white precipitate was recrystallized using ethyl acetate, yielding 11.84 g of VB16, as confirmed by ^{1}H NMR. Ion exchange was used to modify the clay surface with the VB16 surfactant. 25 g of unmodified montmorillonite was stirred overnight in distilled water. 100 mL of a 27 mM solution of VB16 in distilled water was added dropwise to the clay suspension. The mixture was stirred for over 3 h and then filtered and vacuum-dried.

Nanocomposites of PS and VB16-modifed montmorillonite clay were synthesized via *in situ* polymerization. While Zhu et al.[28] used conventional free-radical polymerization, here we employed nitroxide-mediated controlled free-radical polymerization in order to produce samples with narrower polymer molecular weight distribution and to control the molecular weight to lower levels in order to avoid excessive viscoelasticity in the polymer melt. Polymerizations were initiated via thermal decomposition of benzoyl peroxide (BPO) in the bulk, while the concentration of propagating radicals was maintained at a low level through introduction of a stable nitroxide radical (here TEMPO).[30] 110 mL of deinhibited styrene was added to a 150 mL round-bottom flask, together with TEMPO (0.4 mol % in styrene) and BPO (TEMPO:BPO mole ratio = 3:1). VB16-modified montmorillonite was added at varying weight fractions. The flask was sealed under N_2 and stirred for at least 1 h. After three N_2/vacuum cycles, the flask was placed in an oil bath at 125 °C. The mixture was allowed to react for 72 h, resulting in a solid product that was recovered by breaking the flask. After breaking the solid polymer product into pieces, it was placed in a vacuum oven at 100 °C overnight to remove unreacted monomer.

Characterization. The clay content of the final products was determined using thermogravimetric analysis on a Mettler Toledo TGA. Samples were heated from 25 to 650 at 10 °C/min. The majority of weight loss occurred at temperatures between 350 and 450 °C. The clay content was determined from the residual mass remaining at 650 °C.

The molecular weight of the polystyrene in the nanocomposite samples was determined using gel permeation chromatography (GPC). To prevent damage to the GPC columns, the clay was first removed from the samples prior to testing using a clay stripping procedure described by Xu et al.[29] Each nanocomposite sample was refluxed for 3 h in a 1:3 volume ratio mixture of methanol and THF with 2.5 wt % LiBr. After centrifugation, the supernatant liquid was filtered with a 0.2 μm filter and the PS was precipitated in methanol. TGA was used to confirm removal of the clay. GPC was performed in tetrahydrofuran (THF) using a Waters 810 calibrated with polystyrene standards. Polystyrene/THF solutions were filtered a second time with a 0.2 μm filter prior to analysis.

Onset glass transition temperatures were determined using a Mettler Toledo Star DSC 822. Measurements were taken upon a second heating cycle, during a temperature ramp from 25 to 160 °C at a rate of 10 °C/min.

Table 1 lists composition and PS number-average molecular weight (M_n), polydispersity (M_w/M_n), and glass transition temperature (T_g) for the samples studied here. The molecular weight of the PS matrix is fairly consistent across the samples, although the 0.25 wt % clay sample has a markedly lower M_n and, correspondingly, a lower T_g.

Transmission electron microscopy (TEM) was performed using a JEOL 1230 microscope operating at 80 kV. Samples of 70 nm thickness were sectioned using a Leica Ultracut S ultramicrotome. TEM images show a well-exfoliated structure consisting mostly of individually dispersed clay layers, although layered "tactoid" structures are occasionally observed (Figure 1).

Rheological characterization was performed using a Rheometrics Scientific ARES controlled-strain rheometer. Dynamic shear testing was performed using 25 mm parallel plate fixtures, after first

Table 1. Characterization of PS/Clay Nanocomposite Samples

clay content (wt %)[a]	M_n ($\times 10^3$)[b]	M_w/M_n[b]	T_g (°C)[c]
0	24	1.28	93
0.25	16	1.55	83
1.2	26	1.16	92
2.6	20	1.49	91
4.4	23	1.39	87

[a]Determined via TGA. [b]Determined via GPC. [c]Determined via DSC.

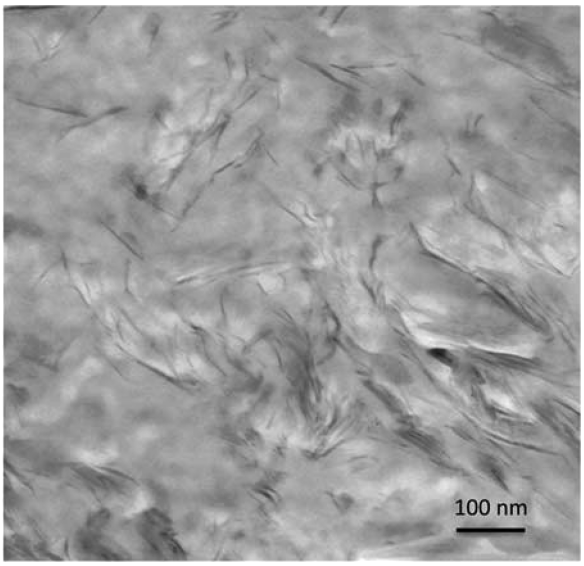


Figure 1. Transmission electron micrograph of 2.6 wt % PS/clay nanocomposite.

conducting oscillatory strain sweep experiments to determine the extent of the linear viscoelastic regime. The pure PS sample exhibits typical melt viscoelasticity for a marginally entangled polymer of relatively narrow molecular weight distribution (Figure 2). The well-

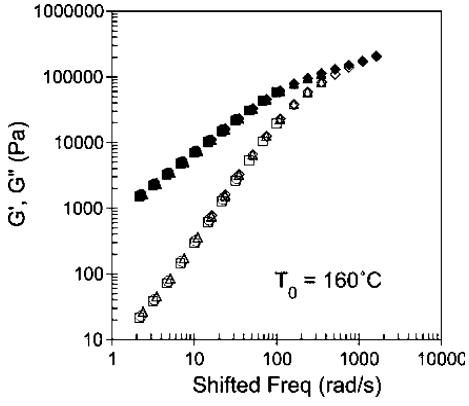


Figure 2. Linear viscoelasticity of PS homopolymer synthesized via controlled radical polymerization. Storage modulus (unfilled symbols) and loss modulus (filled symbols) data were measured at temperatures of 140 (◇, ◆), 150 (△, ▲), 160 (□, ■) and 170 °C (○,●) and shifted to a reference temperature of 160 °C.

defined terminal regime in this polymer allows extraction of an average relaxation time from the low-frequency limit of $G'/\omega G''$.[31] At a temperature of 160 °C (where melt X-ray scattering measurements were performed), the relaxation time is ~0.004 s. The fast relaxation of the polymer reduces complications associated with background elasticity from the nanocomposite matrix during shear experiments. The zero shear viscosity of the pure PS sample is 700 Pa·s at 160 °C. Using a clay platelet diameter d = 200 nm estimated from TEM images, the rotational diffusivity of an isolated particle is estimated as $D_r = 3k_BT/4\eta d^3 = 8 \times 10^{-4}$ s^{-1}. Consistent with the higher viscosity of this PS melt matrix, this estimated rotational diffusivity is substantially smaller than was the case in recent room-temperature investigations of orientation in intercalated clay dispersions in oligomeric matrices.[16,17]

Addition of clay leads to enhanced elastic character in the nanocomposite samples (Figure 3). Since each sample resulted from

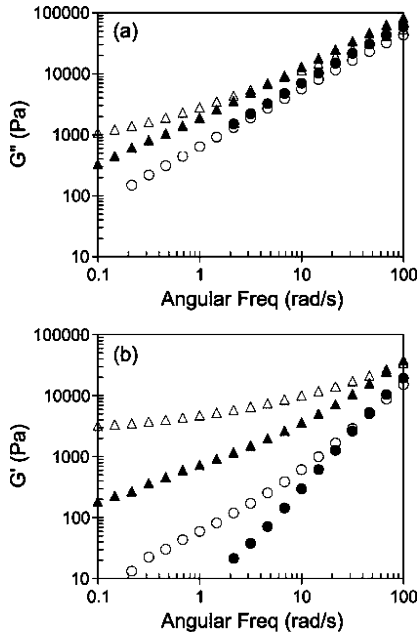


Figure 3. (a) Storage modulus and (b) loss modulus measured in PS/clay nanocomposites at a temperature of 160 °C: pure PS (●); 1.4 (○), 2.6 (▲), and 4.4 wt % clay (△) nanocomposites. (Data on 0.25 wt % clay nanocomposite not presented here, since the lower polymer molecular weight in this sample substantially reduces the matrix viscosity.)

its own polymerization, data in Figure 3 reflect variability in polymer molecular weight distribution as well as clay loading. However, the progressive increase in storage modulus with clay content, leading to a low-frequency solid-like plateau, is typical of behavior in polymer/clay nanocomposites[32−35] and is generally attributed to the development of a percolated nanoparticle network. (Data for the 0.25 wt % sample are not included here, since the combined effects of low M_n and T_g in this sample lead to a significantly lower viscosity than in the pure PS sample.[36])

The 2.6 wt % sample was subjected to more extensive rheological testing using a Paar Physica UDS rheometer equipped with an electrically heated plate temperature controller. Experiments were performed using cone and plate fixtures with a cone angle of 4°. Results of these tests are presented below.

X-ray Scattering. Flow-induced changes in PS/clay nanocomposite structure were studied using an annular cone and plate shear cell designed to facilitate small-angle X-ray scattering studies of fluid structure in the flow-gradient (1−2) plane of shear flow.[37] Experiments were conducted at 160 °C under an inert helium atmosphere. Measurements were performed at beamline 5ID-D (DND-CAT) of the Advanced Photon Source at Argonne National Laboratory, using a sample−detector distance of 0.9 m and X-ray energy of 15 keV. Two-dimensional X-ray scattering patterns were collected using a Gemstar CCD detector which allowed data acquisition at rates up to 7 frames/s; as will be seen below, this relatively high rate of data acquisition was necessary to resolve fast transient processes in the orientation dynamics of these exfoliated PS/

dx.doi.org/10.1021/ma2012738 | Macromolecules 2012, 45, 1622−1630

clay nanocomposite melts. Samples were first compression-molded at 160 °C into donut-shaped pieces, sized appropriately to fill the gap between the annular shear cell fixtures. Care was taken to minimize sample deformation during loading of the shear cell, but some deformation is inevitable as the fixtures are squeezed together. Given the possibility of incomplete structural relaxation upon cessation of shear flow, testing was performed in order of increasing shear rate (unidirectional shear) or frequency/strain (large-amplitude oscillatory shear).

Two-dimensional (2D) X-ray scattering patterns demonstrate a lack of a diffraction peak associated with clay layering (Figure 4).

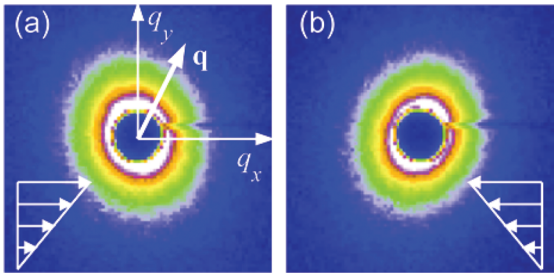


Figure 4. Two-dimensional X-ray scattering patterns measured in 2.6 wt % PS/clay nanocomposite during steady shear flow in (a) forward and (b) reverse direction at a shear rate of 6.0 s^{-1} at 160 °C. Axes used for analysis of shear-induced anisotropy are defined in part (a). The patterns cover a scattering vector range $|q_x|, |q_y| \leq 0.25$ $Å^{-1}$.

Conventional wide-angle X-ray diffraction measurements with Cu Kα radiation showed diffraction peaks at scattering angle $2\theta = 8.6°$ and 4° for respectively the native Cloisite Na+ and VB16-modified montmorillonite clays.[36] The latter feature would fall within the q-range probed in these 2D patterns; the absence of a discernible peak provides evidence of a well-exfoliated structure, consistent with previous reports using *in situ* polymerization of PS in the presence of VB16-modified clay[28,29] and with the TEM evidence presented in Figure 1.

For intercalated nanocomposites, orientation may be characterized using anisotropy in either the wide-angle diffraction peak associated with clay layering or the small-angle scattering arising from the clay particle as a whole.[17] In well-exfoliated samples, the former option is removed; however, two-dimensional small-angle scattering patterns in the PS/clay samples are clearly rendered anisotropic by application of shear flow (Figure 4). To characterize shear-induced orientation, we compute a second moment tensor of the scattered intensity distribution:

$$\langle \mathbf{qq} \rangle = \begin{bmatrix} \langle q_x q_x \rangle & \langle q_x q_y \rangle \\ \langle q_x q_y \rangle & \langle q_y q_y \rangle \end{bmatrix} = \frac{\int \mathbf{qq} I(\mathbf{q})\, dq_x\, dq_y}{\int q^2 I(\mathbf{q})\, dq_x dq_y} \quad (1)$$

where "x" denotes the flow direction and "y" denotes the velocity gradient direction. The denominator on the right-hand side of eq 1 is essentially the scattering invariant.[38] Normalization of $\langle \mathbf{qq} \rangle$ in this way accounts for frame-to-frame variability in X-ray beam intensity and also allows direct comparisons across samples with varying scattering power.

For shear flow as depicted in Figure 4a, the "shear" component, $\langle q_x q_y \rangle$, is negative due to the concentration of scattered intensity in the second and fourth quadrants. In presenting results below, we plot the positive quantity $-\langle q_x q_y \rangle$. Similarly, anisotropy in the normal components of $\langle \mathbf{qq} \rangle$ is characterized by the quantity $-\langle q_x q_x - q_y q_y \rangle$; the higher intensity observed along the gradient (y) axis is consistent with preferred alignment of thin disks along the flow direction. These two quantities are analogous to the shear stress and first normal stress difference in shear rheometry.

An alternative representation of shear-induced orientation may be obtained from the difference in the principal values of $\langle \mathbf{qq} \rangle$:

$$\text{anisotropy factor} = \sqrt{4\langle q_x q_y \rangle^2 + \langle q_x q_x - q_y q_y \rangle^2} \quad (2)$$

Defined in this way, and given the normalization used in eq 1, the anisotropy factor ranges from 0 for an isotropic scattering pattern to 1 for the hypothetical case in which all scattering is concentrated along a single direction within the 2D scattering pattern. The average particle orientation angle in the $x-y$ plane, χ, is extracted from the principal directions of $\langle \mathbf{qq} \rangle$:

$$\chi = \frac{1}{2} \tan^{-1}\left(\frac{2\langle q_x q_y \rangle}{\langle q_x q_x - q_y q_y \rangle} \right) \quad (3)$$

RESULTS

Enhanced low-frequency elasticity is polymer/clay nanocomposites is generally attributed to a percolated nanoparticle network, which may be disrupted by application of shear flow. Large-amplitude oscillatory shear (LAOS) is seen to strongly influence the elastic properties of the 2.6 wt % sample (Figure 5a). During a brief interval of LAOS with 100% strain, the storage modulus is rapidly and dramatically suppressed. Much of this reflects the intrinsically nonlinear response at large strains; data collected during this interval must be understood as "effective" storage modulus. However, upon returning to small strains in the linear viscoelastic regime, G' is much smaller than it was prior to the LAOS interval. The storage modulus gradually recovers over an extended period of time (Figure 5a) but remains well below its value prior to application of LAOS. Such gradual recovery of elasticity is frequently observed in polymer/clay systems.[9,16,39] Interestingly, a period of steady shear at a low rate (>30 strain units at 0.02 s^{-1}) leads to "rejuvenation" of the network structure (Figure 5b); the low-frequency storage modulus following steady shear at 0.02 s^{-1} is an order of magnitude larger than after LAOS. Shear stress overshoots upon flow inception are often used as another probe of elastic networks in nanocomposites.[10,16,34,39] The relative strength of elastic networks present in this 2.6 wt % sample following LAOS and steady shearing is also manifested in the transient shear stress response observed upon subsequent flow inception (Figure 5c). Following LAOS (a condition in which elasticity is considerably suppressed), the stress growth upon inception of shear flow is monotonic. Conversely, following steady shear flow at 0.02 s^{-1} (a condition with more pronounced elasticity), there is a pronounced stress overshoot upon inception of shear.

Linear viscoelastic data presented earlier in Figure 3 were all collected after first performing strain sweep experiments up to strain amplitudes of 100%. These data, then, are affected by elastic network disruption associated with LAOS. As an example, the results for the 2.6 wt % sample in Figure 3 agree closely with the post-LAOS data in Figure 5b. As a result, data in Figure 3 under-represent the true degree of elasticity present in these well-exfoliated nanocomposite samples. However, they still convey the qualitative changes associated with clay loading, since an identical shear history was used for all samples.

While shear flow at low rates leaves a robust elastic network intact, increasing prior steady shear rate does lead to a progressive suppression of elasticity measured using oscillatory shear after flow cessation (Figure 6a). Such systematic decreases in elasticity with increasing prior shear rate are commonly observed in nanocomposites[17,39,40] and attributed to

dx.doi.org/10.1021/ma2012738 | *Macromolecules* 2012, 45, 1622–1630

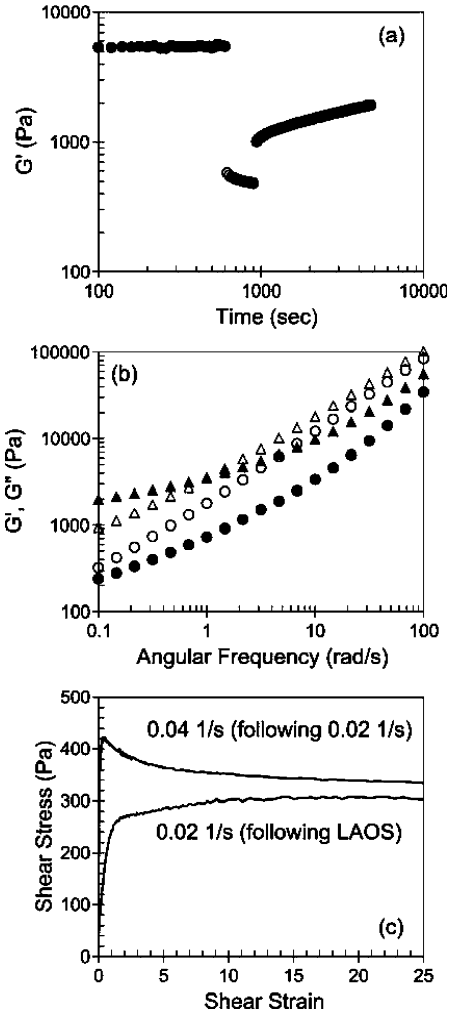


Figure 5. Impact of flow history on elastic network structure of 2.6 wt % PS/clay nanocomposite. (a) Storage modulus measured as a function of time at ω = 5 rad/s and strains of 1.0 (●) and 100% (○). (b) Storage (filled) and loss (open) moduli measured 4000 s after application of LAOS (5 rad/s, 100% strain; ○, ●) and 150 s after application of steady shear (0.02 s^{-1}; △, ▲). (c) Shear stress measured as a function of strain after inception of shear flow at 0.02 and 0.04 s^{-1}, with shear history indicated in parentheses.

progressive degradation of nanoparticle networks. Steady viscosity shows shear thinning at low rates (Figure 6b), another common manifestation of particle networks in nanocomposites[39−41] (steady data were obtained after preshearing for at least 30 strain units and using data collected in both clockwise and counterclockwise directions to guard against autozero errors associated with yield stresses). In materials where fluid structure will be a complex function of shear history, there is little reason to expect adherence to the empirical Cox−Merz rule (equivalence between steady shear viscosity $\eta(\dot{\gamma})$ and complex viscosity $|\eta^*(\omega)|$ when evaluated at $\dot{\gamma} = \omega$[31]). As is frequently observed in nanocomposites,[42,43] we find violation of the Cox−Merz rule here as well (Figure 6b).

A final manifestation of the impact of steady shear rate on fluid structure is found in measurements of shear stress relaxation following flow cessation (Figure 7). At low shear rates, a large fraction of the steady state stress is observed to relax slowly; over 20% of the steady stress remains unrelaxed after 100 s. With increasing shear rate, both the fraction of

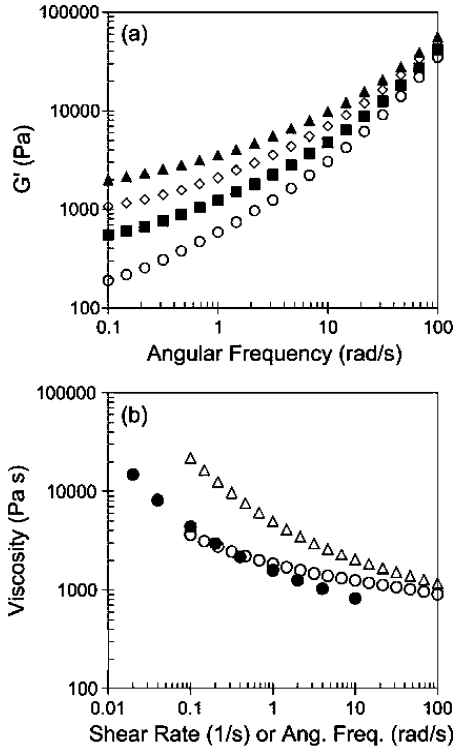


Figure 6. Effect of steady shear rate on 2.6 wt % sample rheology. (a) Effect of prior steady shear rate on storage modulus measured 150 s following flow cessation, for shear rates of 0.02 (▲), 0.1 (◇), 0.4 (■), and 2.0 s^{-1} (○). (b) Steady shear viscosity $\eta(\dot{\gamma})$ (●). Also plotted is the complex viscosity $|\eta^*(\omega)|$ measured 150 s following cessation of shear flow at 0.02 (△) and 2 s^{-1} (○).

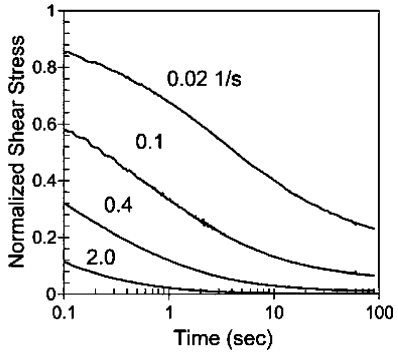


Figure 7. Normalized shear stress relaxation measured in 2.6 wt % sample upon cessation of steady shear flow at indicated rate.

"slowly relaxing" stress and the relaxation time decrease dramatically. These results closely resemble observations of Mobuchon et al.,[39] who used data of this sort to divide stress in steady shear flow into "elastic" and "viscous" contributions. The decrease in the slowly relaxing fraction with increasing shear rate is, again, attributed to progressive degradation of nanoparticle network structure in steady shear.

We turn now to measurements of clay particle orientation during shear flow. Shear rate has a significant impact on the degree of particle orientation measured in the 2.6 wt % nanocomposite sample at steady state (Figure 8). (Steady state orientation data were obtained from time-dependent results in transient shear reversal testing protocols, after at least 30 strain units had been applied.) The shear and normal components of anisotropy in the second moment tensor $\langle \mathbf{qq} \rangle$ are both

dx.doi.org/10.1021/ma2012738 | Macromolecules 2012, 45, 1622−1630

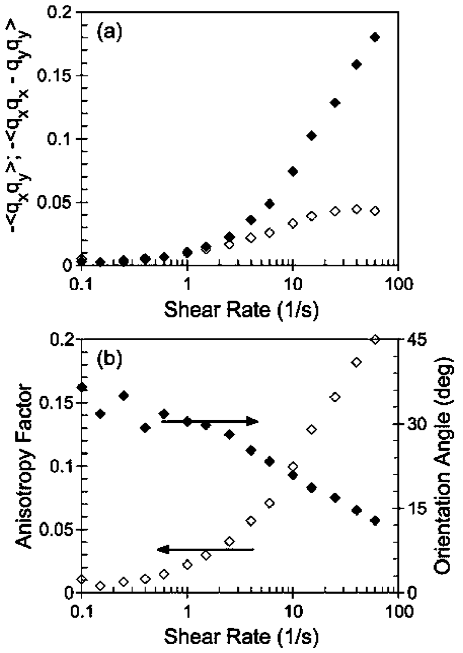


Figure 8. Shear-induced orientation measured in steady shear flow in 2.6 wt % PS/clay nanocomposite sample at 160 °C. (a) Shear (◇) and normal (◆) components of second moment tensor, defined in eq 1. (b) Anisotropy factor (◇) and orientation angle (◆), defined in eqs 2 and 3.

negligible at low rates (Figure 8a). Both $-\langle q_x q_y \rangle$ and $-\langle q_x q_x - q_y q_y \rangle$ initially increase at rates higher than ~1 s^{-1}. The normal anisotropy grows rapidly with increasing shear rate, while the shear component appears to pass through a maximum at high rates. These data may be recast as anisotropy factor and orientation angle using eqs 2 and 3 (Figure 8b). At low rates where the anisotropy factor is small, the orientation angle reaches an asymptote of ~35°, indicating substantial misalignment of clay platelets away from the flow direction, although the orientation angle does not reach the low shear rate asymptote of 45° expected for systems that relax to isotropy in the absence of flow. As anisotropy increases at higher shear rates, χ steadily decreases, indicating that particles increasingly orient toward the flow direction. However, at the highest shear rates studied, particles are still substantially misaligned relative to the flow direction, with an average orientation angle of ~12°.

Experiments on samples at various clay loadings show similar orientation behavior (Figure 9), with monotonic growth in steady state anisotropy factor with increasing shear rate. (The weak decrease in anisotropy seen in some samples at low rates is attributed to unrelaxed orientation induced by squeezing flow during sample loadings. It appears that shear flow at sufficiently low rates was actually able to progressively degrade some of this residual orientation, perhaps related to the ability of shear flow at low rates to rejuvenate elastic network structures seen in Figure 5b. Relaxation data presented below provide further insights into the incomplete relaxation of particle orientation in these samples.) In general, higher anisotropy is achieved in samples with higher clay content. Experiments on the most concentrated (4.4 wt %) sample could not be extended to high rates due to flow instabilities,[36] presumably associated with its significantly higher elasticity (Figure 3b). While constraints on available synchrotron beam time generally preclude extensive studies of reproducibility, repeated experiments using multiple

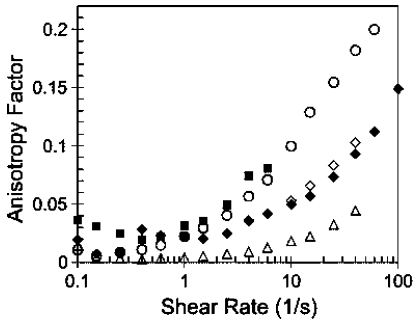


Figure 9. Anisotropy factor measured as a function of shear rate at 160 °C in PS/clay nanocomposites with clay loadings of 0.25 (△), 1.4 (◇, ◆), 2.6 (○), and 4.4 wt % (■). Multiple symbols for 1.4 wt % sample reflect duplicate X-ray scattering measurements using different sample loadings.

loadings of the 1.4 wt % sample showed good consistency. In light of the qualitative similarities in steady state orientation behavior among the samples, in the remainder of this paper we concentrate attention on the 2.6 wt % sample. More extensive orientation data on the other samples are available elsewhere.[36]

Reversal of shear flow direction leads to reorientation of the clay particles (Figure 10). Here we adopt a convention that the

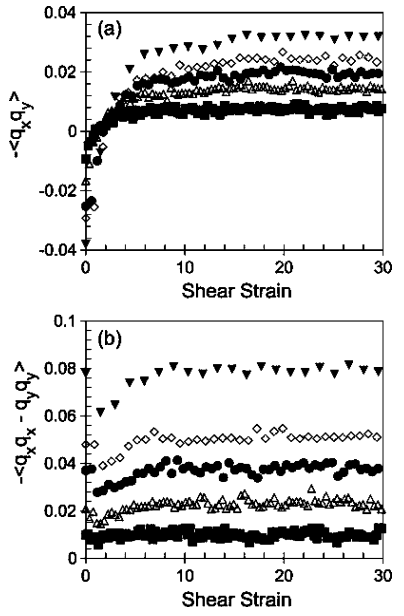


Figure 10. Transient orientation response in (a) shear and (b) normal components of second moment tensor measured in 2.6 wt % PS/clay nanocomposite following reversal of shear flow at rates of 1.0 (■), 2.5 (△), 4.0 (●), 6.0 (◇), and 10.0 s^{-1} (▼).

shear flow prior to reversal is in the negative direction. The "shear" component of the second moment tensor $-\langle q_x q_y \rangle$ changes signs, reflecting the primary reorientation process apparent in the two-dimensional scattering patterns for forward and reversed shear flow (Figure 4). During this reorientation, the normal anisotropy exhibits an undershoot, indicating that there is a transient state of lower anisotropy prior to re-establishing the steady orientation state in the reversed direction. The reorientation process is quite rapid, essentially complete within ~10 shear strain units.

dx.doi.org/10.1021/ma2012738 | Macromolecules 2012, 45, 1622–1630

Upon flow cessation there is a rapid but partial relaxation of shear-induced anisotropy (Figure 11). At higher shear rates, a

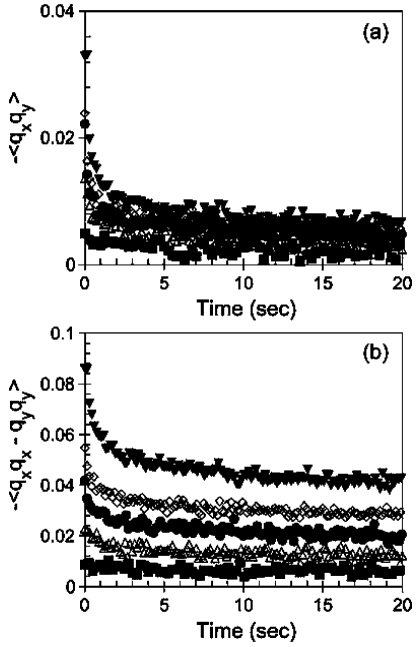


Figure 11. Transient orientation response in (a) shear and (b) normal components of second moment tensor measured in 2.6 wt % PS/clay nanocomposite following cessation of shear flow at rates of 1.0 (■), 2.5 (△), 4.0 (●), 6.0 (◇), and 10.0 s^{-1} (▼).

significant degree of relaxation is observed within the first several data points at times below 1 s, while a large fraction of the ultimate relaxation occurs within ~5 s. Particularly for the normal components, $-\langle q_x q_x - q_y q_y \rangle$, the relaxation of anisotropy is incomplete. As experiments were performed in order of increasing shear rate, there was a progressive buildup of residual orientation in the sample.

Orientation dynamics in the PS/clay nanocomposites were also studied in large-amplitude oscillatory shear (LAOS), performed with different specimens than used in unidirectional shearing experiments in order to minimize the impact of residual orientation. With the fast data acquisition afforded by the bright synchrotron source, it was possible to track time-resolved orientation dynamics during the application of oscillatory shear. At fixed strain amplitude of 200%, frequency is found to have a significant effect on the qualitative character of the orientation response (Figure 12). At low frequency, the shear component of anisotropy ($-\langle q_x q_y \rangle$) shows weak oscillations while the normal anisotropy ($-\langle q_x q_x - q_y q_y \rangle$) is essentially unaffected (Figure 12a). Increasing the frequency by an order of magnitude leads to an increase in the amplitude of the oscillatory response of $-\langle q_x q_y \rangle$ and also gives rise to perceptible fluctuations in $-\langle q_x q_x - q_y q_y \rangle$ occurring at twice the imposed frequency (Figure 12b). An even higher frequency further increased the magnitude of the $-\langle q_x q_y \rangle$ response and led to a clear dc offset in the normal anisotropy signal in addition to high-frequency fluctuations. (At these higher frequencies, these fluctuations could no longer be well-resolved with the available data acquisition rate.) The behavior of $-\langle q_x q_x - q_y q_y \rangle$ at high frequencies is analogous to the response of the first normal stress difference in viscoelastic liquids subjected to

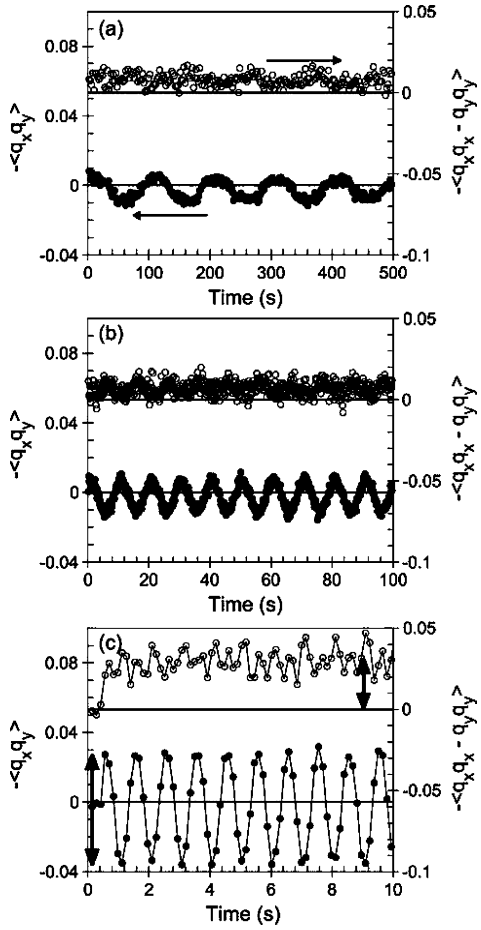


Figure 12. Time-dependent response in shear (●) and normal components (○) of second moment tensor measured in 2.6 wt % PS/clay nanocomposite during large-amplitude oscillatory shear flow at a strain amplitude of 200% and frequencies of (a) 0.01, (b) 0.1 and (c) 1 Hz. Arrows in (c) illustrate the method used to extract amplitudes of shear and normal anisotropy components.

LAOS, which oscillates at twice the input frequency, and remains positive, oscillating relative to a dc offset value.[44]

To enable a more quantitative representation of the impact oscillatory shear parameters have on orientation state, we characterize LAOS-induced orientation in terms of the peak-to-peak amplitude of oscillations in the shear component, $-\langle q_x q_y \rangle$, and the time-averaged (dc) amplitude of the normal anisotropy, $-\langle q_x q_x - q_y q_y \rangle$, as indicated by the arrows in Figure 12c. Mirroring the behavior seen in steady shear flow, only weak shear-induced orientation is found at low frequencies, while the amplitudes of both shear and normal components of $\langle \mathbf{qq} \rangle$ increase markedly at higher frequencies (Figure 13). While LAOS-induced effects in $-\langle q_x q_y \rangle$ are observable at the lowest frequencies (Figure 12a), it is likely that the low frequency asymptote in $-\langle q_x q_x - q_y q_y \rangle$ is associated with residual anisotropy induced during sample loading. At fixed frequency, higher strain amplitude leads to higher anisotropy; the effect is larger in the normal component.

■ DISCUSSION

Several features of these shear-induced orientation data in these exfoliated PS/clay nanocomposites resemble our prior observations for intercalated clay dispersions in oligomeric, room-temperature melts.[16,17] First, much of the impact of shear

dx.doi.org/10.1021/ma2012738 | Macromolecules 2012, 45, 1622−1630

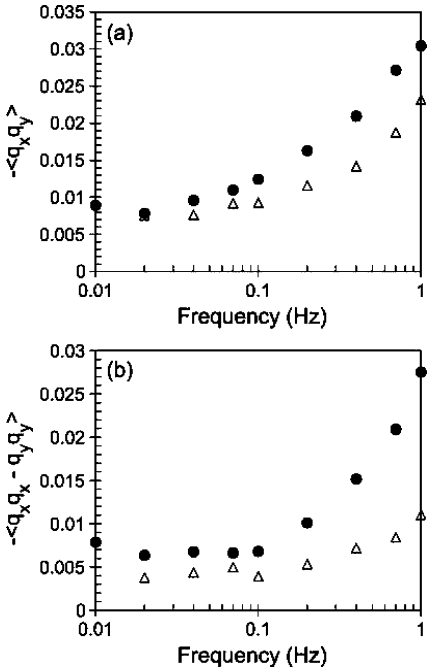


Figure 13. Frequency dependence of (a) shear and (b) normal anisotropy measured in 2.6 wt % PS/clay nanocomposite during large-amplitude oscillatory shear flow at strains of 100% (△) and 200% (●).

flow on elastic properties seems to be largely independent of particle orientation *per se*. For instance, Figures 6 and 7 show large shear-rate-dependent changes in rheological properties at rates below 2 s^{-1}, a regime in which shear-induced particle orientation is only very weak. There are also gross similarities in many aspects of the particle orientation response: (i) increase in anisotropy and decrease in orientation angle with steady shear rate; (ii) rapid reorientation upon shear flow reversal; (iii) partial relaxation of flow-induced orientation upon flow cessation; and (iv) strain dependence of shear-induced orientation in large-amplitude oscillatory shear.

Despite these similarities to earlier work, there is also a remarkable discrepancy. In the model oligomeric dispersions, many aspects of the orientation response could be qualitatively interpreted using concepts of orientation dynamics anticipated in weakly Brownian particulate dispersions. In those systems, orientation relaxed slowly, on time scales consistent with estimates of rotational diffusivities.[16,17] Similarly, the progressive increase in orientation with increasing shear rate could be rationalized in terms of increasing Peclet number ($Pe = \dot{\gamma}/D_r$), as hydrodynamic forces increasingly overwhelm the randomizing influence of Brownian motion. Translating these concepts to the present study, we first consider the hydrodynamic effects responsible for promoting particle orientation. The common expectation is that exfoliated clay platelets, with their higher aspect ratio, should be more susceptible to orient in shear than lower aspect ratio clay tactoids, owing to the characteristics of the tumbling "Jeffrey orbits" exhibited by disk-like particles in shear flow.[45] Similarly, the higher matrix viscosity in the current study—and correspondingly smaller rotational diffusivity—should make it easier for the applied flow to promote high orientation. For example, even at a shear rate of 0.1 s^{-1} (the lowest used in the X-ray orientations studies), the estimated Peclet number is 125; under all conditions studied here, Brownian effects should be minimal. Why, then, is it so difficult to obtain significant flow-induced orientation?

While the resistance of these exfoliated PS/clay nanocomposites to shear-induced particle orientation is puzzling, it is important to note that there is strong internal consistency among the results presented here. The lack of significant flow-induced anisotropy at low rates and/or frequencies implies that there must be some fast structural relaxation process, and, indeed, the relaxation data show evidence of some relaxation mechanism that is orders of magnitude faster than that expected for rotational Brownian motion. Under these conditions, the structural state of the nanocomposite melt at low shear rates will not differ appreciably from that found at equilibrium.

If Brownian motion fails to explain the fast relaxation process that underlies many of the present observations, what is its origin? In considering this question, we first note that envisioning exfoliated clays to be flat, rigid platelets is an oversimplification. Electron micrographs of exfoliated nanocomposites show ample evidence of considerable flexibility of the clay sheets.[23,26−28] In a well-exfoliated sample, the high aspect ratio of the clay sheets further means that they will be extremely crowded, a concept that is commonly invoked to relate low-frequency elasticity in polymer/clay nanocomposites to their degree of exfoliation.[33] We hypothesize that the orientation dynamics observed here may be dominated by shear-induced distortions within a highly crowded network of semiflexible clay sheets. That is, the dominant balance governing the development of orientation is not hydrodynamic vs Brownian forces, but rather hydrodynamic forces vs elastic deformation within the nanoparticle network. This line of reasoning mirrors arguments we have advanced as a possible explanation of unexpected relaxation observed in non-Brownian multiwalled carbon nanotube dispersions.[40,46] While consistent with the available evidence, this hypothesized mechanism is not the only possible origin of fast dynamics. The synthesis procedure used here should result in grafting of polymer chains to the clay particles; it is possible that this could couple the particle orientation dynamics more directly to the dynamics in the polymer matrix, providing an alternative mechanism for a fast relaxation process. To investigate this further, it would be beneficial to study shear-induced orientation dynamics in well-exfoliated polymer/clay nanocomposites that do not involve chemical tethering of polymer to the nanoparticles.

While the unexpected rapid relaxation process discovered here plays a major role in determining the nature of flow-induced particle orientation in these samples, other factors also come into play. The fact that only partial relaxation of orientation is observed upon flow cessation mirrors observations in model intercalated clay dispersions[16,17] and probably reflects the complexities of orientation dynamics within a highly crowded environment. This "hindered" relaxation may also explain the failure of the orientation angle to reach the low rate asymptote of 45° that is expected in the weak flow limit of fluids with relaxing microstructure in shear flow.

■ CONCLUSIONS

The exfoliated PS/clay nanocomposites studied here are unexpectedly resistant to shear flow-induced orientation. Despite the small magnitude of the estimated rotational diffusivity of a single clay platelet, significant orientation in steady shear flow only develops at shear rates greater than 1 s^{-1}. Similarly, flow-induced orientation in large-amplitude oscillatory shear only develops at frequencies greater than 0.1 Hz. The inability of shear at low rates and frequencies to produce

dx.doi.org/10.1021/ma2012738 | *Macromolecules* 2012, 45, 1622−1630

significant alignment suggests the existence of a structural relaxation process that is much faster than that of rotational Brownian motion of the clay particles. Direct evidence of such a fast process is found in measurements of orientation relaxation following cessation of shear flow, although the samples do not revert to a randomly oriented state as shearing at progressively higher rates leads to higher degrees of residual orientation. It is hypothesized that this fast relaxation arises from either relaxation of shear-induced distortion of partially flexible exfoliated clay sheets in a highly entangled nanoparticle network or a direct coupling of particle and polymer dynamics through the chemical tethering of particle chains that occurs during the *in situ* polymerization synthesis of these materials.

AUTHOR INFORMATION

Corresponding Author

*E-mail: w-burghardt@northwestern.edu.

ACKNOWLEDGMENTS

This work was funded by the NSF-MRSEC program (DMR-0520513) at the Materials Research Center of Northwestern University. L. Dykes acknowledges support from a GEM Fellowship. We acknowledge Dr. Charlene Wilke of Northwestern's Biological Imaging Facility for performing TEM imaging and thank Professor David Venerus for providing access to the UDS rheometer. Finally, we thank the staff of the DuPont−Northwestern−Dow Collaborative Access Team (DND-CAT) at Sector 5 of the Advanced Photon Source for their help with setup and execution of synchrotron experiments. DND-CAT is supported by the E.I. DuPont de Nemours & Co., the Dow Chemical Company, and the National Science Foundation through Grant DMR-9304725 and the State of Illinois through the Department of Commerce and the Board of Higher Education Grant IBHE HECA NWU 96. Use of the Advanced Photon Source was supported by the U.S. Department of Energy, Basic Energy Sciences, Office of Energy Research, under Contract W-31-102-Eng-38.

REFERENCES

(1) Giannelis, E. P. *Adv. Mater.* **1996**, *8*, 29−35.
(2) Alexander, M.; Dubois, P. *Mater. Sci. Eng., R* **2000**, *28*, 1−63.
(3) *Polymer-Clay Nanocomposites*; Pinnavaia, T. J., Beal, G. W., Eds.; Wiley: New York, 2000.
(4) Du, F.; Fischer, J. E.; Winey, K. I. *J. Polym. Sci., Part B: Polym. Phys.* **2003**, *41*, 3333−3338.
(5) Kim, H.; Macosko, C. W. *Polymer* **2009**, *50*, 3797−3809.
(6) Brune, D. A.; Bicerano, J. *Polymer* **2002**, *43*, 369−387.
(7) Sorrentino, A.; Gorrasi, G.; Tortora, M.; Vittoria, V. In *Polymer Nanocomposites*; Mai, Y.-W., Yu, Z.-Z., Eds.; Woodhead: Cambridge, 2006; pp 273−296.
(8) Wagener, R.; Reisinger, T. J. G. *Polymer* **2003**, *44*, 7513−7518.
(9) Ren, J.; Casanueva, B. F.; Mitchell, C. A.; Krishnamoorti, R. *Macromolecules* **2003**, *36*, 4188−4194.
(10) Letwimolnum, W.; Vergnes, B.; Ausias, G.; Carreau, P. J. *J. Non-Newtonian Fluid Mech.* **2007**, *141*, 167−179.
(11) Kojima, Y.; Usuki, A.; Kawasumi, M.; Okada, A.; Kurauchi, T.; Kamigaito, O.; Kaji, K. *J. Polym. Sci., Part B: Polym. Phys.* **1995**, *33*, 1039−1045.
(12) Varlot, K.; Reynoud, E.; Klopper, M. H.; Vigier, G.; Varlet, J. *J. Polym. Sci., Part B: Polym. Phys.* **2000**, *39*, 1360−1370.
(13) Bafna, A.; Beucage, G.; Mirabella, F.; Mehta, S. *Polymer* **2003**, *44*, 1103−1115.
(14) Fornes, T. D.; Paul, D. R. *Polymer* **2003**, *44*, 4993−5013.
(15) Galgali, G.; Agarwal, S.; Lele, A. *Polymer* **2004**, *45*, 6059−6069.
(16) Dykes, L. M. C.; Torkelson, J. M.; Burghardt, W. R.; Krishnamoorti, R. *Polymer* **2010**, *51*, 4916−4927.
(17) Pujari, S.; Dougherty, L.; Mobuchon, C.; Carreau, P. J.; Heuzey, M.-C.; Burghardt, W. R. *Rheol. Acta* **2011**, *50*, 3−16.
(18) Weimer, M. W.; Chen, H.; Giannelis, E. P.; Sogah, D. Y. *J. Am. Chem. Soc.* **1999**, *121*, 1615.
(19) Fan, X.; Xia, C.; Advincula, R. C. *Colloids Surf., A* **2003**, *219*, 75−86.
(20) Fan, X.; Xia, C.; Advincula, R. C. In *Dekker Encyclopedia of Nanoscience and Nanotechnology*; Marcel Dekker: New York, 2004; pp 2959−2971.
(21) Uthirakumar, P.; Kim, C.-J.; Nahm, K. S.; Hahn, Y. B.; Lee, Y.-S. *Colloids Surf., A* **2004**, *247*, 69−75.
(22) Uthirakumar, P.; Nahm, K. S.; Hahn, Y. B.; Lee, Y.-S. *Eur. Polym. J.* **2004**, *40*, 2437−2444.
(23) Uthirakumar, P.; Song, M.-K.; Nah, C.; Lee, Y.-S. *Eur. Polym. J.* **2005**, *41*, 211−217.
(24) Tseng, C.-R.; Wu, J.-Y.; Lee, H.-Y.; Chang, F.-C. *J. Appl. Polym. Sci.* **2002**, *85*, 1370−1377.
(25) Zhong, Y.; Zhu, Z.; Wang, S.-Q. *Polymer* **2005**, *46*, 3006−3013.
(26) Fu, X.; Qutubuddin, S. *Mater. Lett.* **2000**, *42*, 12−15.
(27) Fu, X.; Qutubuddin, S. *Polymer* **2001**, *42*, 807−813.
(28) Zhu, J.; Morgan, A. B.; Lamelas, F. J.; Wilkie, C. A. *Chem. Mater.* **2001**, *13*, 3774−3780.
(29) Xu, L.; Reeder, S.; Thopasridharan, M.; Ren, J.; Shipp, D. A.; Krishnamoorti, R. *Nanotechnology* **2005**, *16*, S514−S521.
(30) Georges, M. K.; Veregin, R. P. N.; Kazmaier, P. M.; Hamer, G. K. *Macromolecules* **1993**, *26*, 2987−2988.
(31) Macosko, C. W. *Rheology: Principles, Measurements and Applications*; Wiley-VCH: New York, 1994.
(32) Krishnamoorti, R.; Giannelis, E. P. *Macromolecules* **1997**, *30*, 4097−4102.
(33) Ren, J.; Silva, A. S.; Krishnamoorti, R. *Macromolecules* **2000**, *33*, 3739−3746.
(34) Solomon, M. J.; Asmusallam, A. S.; Seefeldt, K. F.; Somwangthanaroj, A.; Varadan, P. *Macromolecules* **2001**, *34*, 1864−1872.
(35) Wang, X. L.; Sun, P. C.; Xue, G.; Winter, H. H. *Macromolecules* **2010**, *43*, 354−361.
(36) Dykes, L. M. C. PhD Dissertation, Northwestern University, 2008.
(37) Caputo, F. E.; Burghardt, W. R. *Macromolecules* **2001**, *34*, 6684−6694.
(38) Roe, R. J. *Methods of X-ray and Neutron Scattering in Polymer Science*; Oxford University Press: New York, 2000.
(39) Mobuchon, C.; Carreau, P. J.; Heuzey, M.-C. *Rheol. Acta* **2007**, *46*, 1045−1056.
(40) Pujari, S.; Rahatekar, S.; Gilman, J. W.; Kiziol, K. K.; Windle, A. H.; Burghardt, W. R. *J. Rheol.* **2011**, *55*, 1033−1058.
(41) Galgali, G.; Ramesh, C.; Lele, A. *Macromolecules* **2001**, *34*, 852−858.
(42) Krishnamoorti, R.; Ren, J.; Silva, A. S. *J. Chem. Phys.* **2001**, *114*, 4968−4973.
(43) Ren, J.; Krishnamoorti, R. *Macromolecules* **2003**, *36*, 4443−4451.
(44) Ferry, J. D. *Viscoelastic Properties of Polymers*; Wiley: New York, 1980.
(45) Jeffrey, G. *Proc. R. Soc. London, Ser. A* **1922**, *102*, 161−179.
(46) Pujari, S.; Rahatekar, S.; Gilman, J. W.; Koziol, K. K.; Windle, A. H.; Burghardt, W. R. *J. Chem. Phys.* **2009**, *130*, 214903.

Macromolecules

Article

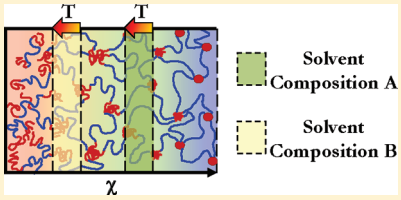
pubs.acs.org/Macromolecules

Effects of Solvent Composition on the Assembly and Relaxation of Triblock Copolymer-Based Polyelectrolyte Gels

Kevin J. Henderson and Kenneth R. Shull*

Department of Materials Science and Engineering, Northwestern University, Evanston, Illinois 60208, United States

ABSTRACT: The role of solvent selectivity has been explored extensively with regard to its role in the phase behavior of block copolymer assemblies. Traditionally, thermally induced phase separation is employed for generating micelles upon cooling a block copolymer dissolved in a selective solvent. However few amphiphilic, polyelectrolyte-containing block copolymers demonstrate a thermally accessible route of micellization, and solvent exchange routes are frequently employed instead. Here, we describe the use of mixed solvents for obtaining thermoreversible gelation behavior of poly(methyl methacrylate)-poly(methacrylic acid)-poly(methyl methacrylate) (PMMA−PMAA−PMMA) triblock copolymers. One solvent component (dimethyl sulfoxide) is a good solvent for both blocks, and the second solvent component (water) is a selective solvent for the polymer midblock. Rheological frequency sweeps at variable solvent compositions and temperatures demonstrate an adherence to time−temperature−composition superposition, so that changes in the solvent composition are analogous to changes in the Flory−Huggins interaction parameter between end block and solvent. Shift factors used for this superposition are related to the effective activation energy describing the viscosity and stress relaxation response of the triblock copolymer gels. The effectiveness of solvent exchange processes for producing hydrogels with this system is shown to originate from the ability of a small amount of added water to greatly increase the relaxation times of the self-assembled polymer gels that are formed by this process.



INTRODUCTION

The rich phase behavior of block copolymer solutions and melts has been widely reported.[1−3] In such assemblies solvent quality plays a fundamental role in the accessible phase space, defining the underlying micellar structure.[4] In many organic solvents a strong temperature dependence of the end block-solvent interaction parameter, χ, permits self-assembly of block copolymer solutions when cooled below an order−disorder transition temperature. When the polymer has an ABA-type triblock copolymer structure, this behavior results in a thermoreversible gelation behavior, as a physically associated network of midblock-bridged micelles forms a percolated structure. Examples include poly(styrene)−poly(isoprene)−poly(styrene) (SIS) block copolymers in squalane[5] and tetradecane,[6,7] poly(styrene)−poly(ethylene−butadiene)−poly(styrene) in mineral oil,[8] and acrylic polymers with poly(methyl methacrylate) end blocks in higher order alcohols.[9,10]

Amphiphilic block copolymers containing polyelectrolytes rarely demonstrate thermoreversible gelation behavior in aqueous solution. This results from the strongly disparate differences between favorable solvent conditions for the hydrophilic midblock and hydrophobic end block groups. Most commonly, micellization of block copolymers in aqueous solution is entropically driven, resulting in lower critical solution temperature (LCST) phase behavior.[11,12] In some cases solvent exchange is a useful technique for inducing micelle formation,[13] and advanced processing techniques are often employed for obtaining sophisticated morphologies for amphiphilic macromolecules in aqueous solution.[14] For the triblock copolymer-based gels of interest to us, the solvent exchange technique relies on composition-driven changes in the χ parameter characterizing the solvent/end block interaction. At the beginning of the solvent exchange process the end blocks are in good solvent conditions (low χ). Micelle formation is observed during solvent exchange when χ is increased to a critical value. The use of mixed solvents to tailor solvent selectivity in block copolymers dates back several decades[15−18] and has been the focus of more recent investigations as well.[19−22] For example, Fuse et al. have studied the formation of spherical morphologies of a unique amphiphilic copolymer in mixed solvents consisting of water and acetone.[19] In work that is particularly relevant to the work that we describe here, Krishnan et al. demonstrated that changes in solvent composition can be equivalent to changes in temperature for triblock copolymer gels formed from a midblock-selective solvent.[20]

Figure 1 illustrates the phase behavior for a physically associated triblock copolymer gel as a function of χ for the solvent/end block system. In good solvent conditions ($\chi < 0.5$) the polymer chains are fully dissolved in solution. As χ increases dynamic, solvent-swollen end block associations lead to the development of a fully percolated gel network, with successively larger χ values forming more static junctions of lower solvent content. In fully thermoreversible systems, such as acrylic block copolymers in alcohol,[10,23] a strong temperature dependence of χ enables a large χ window to be accessed with a single solvent composition, simply by changing the temperature. For the

Received: July 13, 2011
Revised: November 11, 2011
Published: January 24, 2012

 © 2012 American Chemical Society

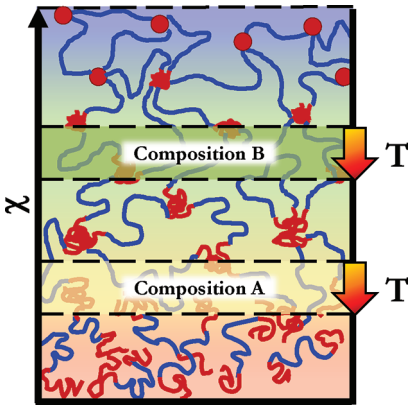


Figure 1. Schematic illustrating the effect of solvent quality and temperature on the phase behavior of physically associated triblock copolymer gel networks. Here, a narrow χ window is accessible across an experimentally accessible range of temperatures, T. Composition A and composition B represent two fixed solvent compositions, with composition B (higher χ) corresponding to a greater concentration of the poor solvent for the associating end blocks of the triblock copolymer.

mixed solvent systems described in this paper, a smaller χ window is accessible for a given solvent composition, but the location of the accessible χ window can be shifted by changing the solvent composition itself. For example, increasing the fraction of the solvent mixture that acts as a poor solvent for the end block increases the effective value of χ, shifting the χ window from "composition A" to "composition B" in Figure 1. Within each of these windows, χ can be adjusted by changing the temperature, with an increased temperature giving a decrease in χ.

The use of mixed solvents to induce micelle formation is quite general, as is the connection between micelle formation and the rheological properties of the block copolymer solution. We are interested in intermediate copolymer concentrations, where the copolymer concentration is large enough so that a one-phase, percolated network is formed,[24] but low enough so that a crystalline array of micelles is not formed.[4,25] In this regime, corresponding to all of the experiments performed here, the structural features of the micellar gel do not change significantly as χ increases, but the characteristic relaxation time of this gel increases dramatically.[23]

The process illustrated in Figure 1 can be used to form hydrogels with a well-controlled and reproducible structure, provided that water is the solvent responsible for the increase in χ for the solvent/end block system, and that water and the cosolvent are both good solvents for the midblock of the triblock copolymer. This process has been used previously to form poly(methyl methacrylate)-poly(methacrylic acid)-poly-(methyl methacrylate) (PMMA−PMAA−PMMA) triblock copolymer hydrogels, beginning with solutions in dimethyl sulfoxide (DMSO) and inducing gelation by the addition of water by vapor phase transfer.[13] With respect to Figure 1, this solvent exchange process is analogous to passing from the bottom of the figure (small χ) to the top (large χ). For a mixed solvent system, this process can be thought of in the context of ternary phase diagram in which the ratio of solvents used determines whether the polymer is present in a homogeneous solution or a micellar network of end block aggregates that are bridged by midblock chains. Such behavior has been studied previously for polyimide systems in water-DMSO,[26] though similar behavior in PMMA has not been explored. Membranes of PMMA formed by phase inversion in water/DMSO have indicated that PMMA is insoluble for solutions containing 30% water though no lower values are reported.[27] For the polyimide system in DMSO-water, a water content of only 0.3% was sufficient for phase separation of a 15% polymer solution. This result can be attributed to the fact that DMSO itself is a marginally good solvent for the polyimide. Because DMSO is a similarly marginal solvent for PMMA at room temperature (Θ temperature = 35 °C),[28] a similar trend is expected for the DMSO−water−PMMA system.

Here we explore the use of mixed solvents of DMSO−water for forming thermoreversible gels of PMMA−PMAA−PMMA triblock copolymer. Oscillatory shear rheometry is employed to dynamically define the onset of gelation induced by cooling, and frequency sweeps across regular temperature intervals are used to generate a master curve of the frequency-dependent rheological response across temperature and composition. Small angle X-ray scattering is used to characterize micelle size, and the ability to obtain reproducible hydrogels by vapor phase solvent exchange is discussed.

EXPERIMENTAL SECTION

Sample Information. The triblock copolymer was synthesized via anionic polymerization as described previously,[13] and was initially composed of a poly(*tert*-butyl methacrylate) (P*t*BMA) midblock and poly(methyl methacrylate) (PMMA) end blocks. The P*t*BMA midblock length and copolymer polydispersity (PDI = 1.12) were assessed using gel-permeation chromatography (Waters 717plus autosampler connected to a Waters 2410 refractive index detector) in HPLC grade tetrahydrofuran against polystyrene standards. The end block lengths were determined using proton nuclear magnetic resonance spectroscopy (Inova 400 MHz) by comparing integrated peak ratios of the methoxy protons in PMMA (δ = 3.60 ppm) versus the *tert*-butyl protons in P*t*BMA (δ = 1.43 ppm) of known molecular weight. The amphiphilic copolymer was obtained by hydrolysis of the *t*BMA units using a 3 times molar excess of hydrochloric acid (relative to the concentration of *t*BMA units) in 1,4-dioxane at 80 °C for 6 h. The molecular weights of each block in the final converted polymer are 43k−151k−43k, corresponding to a degree of polymerization of 430−1750−430. For these experiments, 7 wt % solutions of copolymer were dissolved in mixed solvents containing DMSO and water. DMSO(Sigma-Aldrich) was used as received, and solutions were mixed using nanopure water (18.2 MΩ·cm).

Rheological Characterization. Rheological measurements were conducted on an Anton Paar Physica Modular Compact Rheometer 300 with a double gap Couette fixture and a Peltier heating/cooling element. Gels were loaded in the liquid state (above 75 °C) into the fixture. Temperature sweep data were collected on cooling at 1 °C/min with an angular frequency of 10 s^{-1} and constant strain amplitude of 1%. Master frequency curves were generated through extension of frequency sweeps from 0.1 to 1 s^{-1} under controlled stress (1−7 Pa) in the linear range at 5 degree intervals from 20 to 75 °C, with shift factors generated by superposition of the loss angle at a reference temperature of 25 °C.

Small-Angle X-ray Scattering. SAXS measurements were taken at Sector 5ID-D of the Advanced Photon Source at Argonne National Laboratory at a sample-to-detector distance of 4.0 m and a energy of 17.0 keV with gel samples placed in nylon washers capped with polyimide sheeting. Consequent scattering patterns were fit using a Percus−Yevick hard sphere approximation[29,23] to obtain the average micelle size and spacing.

RESULTS AND DISCUSSION

Thermoreversible Gelation. The dynamic gelation behavior within these materials is readily apparent by a sharp

increase in the modulus upon cooling. Rheologically, the crossover between viscous solution behavior and elastic gel behavior can be defined as the intersection between the storage (G') and loss (G'') moduli at a specified frequency. This temperature is referred to as the gelation temperature, T_{GEL}, and corresponds to the temperature at which the relaxation time of the material approaches the inverse of the angular frequency of the measurements, in our case 0.1 s. This dynamic signature of gelation has reproducibly been used to define the onset of elastic character in thermoreversible gels in previous work.[9,23,30] For the concentration regime of interest to us, which is well above the critical concentration for gelation, this approach is more useful than the commonly used Winter–Chambon approach[31] used to detect the onset of a percolating network.[10]

Figure 2 depicts the temperature sweep rheological data upon cooling at 1 °C/min for 7 wt % polymer mixtures in 4%,

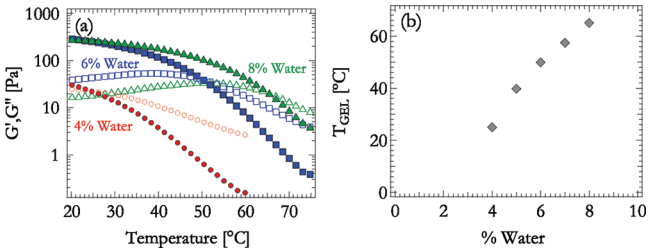


Figure 2. (a)Temperature dependence of storage (filled) and loss (unfilled) moduli at ω = 10 s^{-1} for 7 wt % gels in mixed solvents of DMSO-water containing 4% (red circles), 6% (blue squares), and 8% (green triangles) water. (b) Values of T_{GEL} for these same gels as a function of water content.

6%, and 8 wt % water solutions in DMSO and the resulting values of T_{GEL}. For the 4% water solution, the crossover between G' and G'' occurs near 30 °C, which is just above the freezing point of DMSO (~18 °C). An increase in water content to 6% results in an increase of T_{GEL} to 50 °C. A further increase to 8% water increases T_{GEL} to 65 °C. Gelation in these systems is driven by changes in the PMMA solubility associated with changes in either temperature or solvent composition. The fact that only 4% water is needed to induce gelation at temperatures above the freezing point of DMSO indicates that PMMA becomes insoluble in DMSO-water mixtures for water contents that are quite small. A similarly small composition window for solubility DMSO-water mixtures has been observed for other polymers as well, including polyimides.[26]

Master Curves. Master time–temperature superposition curves for these gels are shown in Figure 3a and elucidate the frequency dependence of the rheological response. Similar to acrylic block copolymers in 2-ethyl-1-hexanol,[23] these mixed solvent gels demonstrate the response of a viscoelastic liquid at low frequencies (high temperatures), as evidenced by the power law slopes of 1 and 2 for G'' and G', respectively. At a frequency unique to each sample, the storage and loss moduli cross, and in the limit of high frequencies (low temperature), G' approaches a plateau value (G_0) demonstrating the response of an elastic solid. This plateau modulus is most evident for the 8% water sample, which has a 45° range of accessible temperatures between T_{GEL} and the freezing point of DMSO. The 4% sample, in contrast, only has a 10° window, making the elastic plateau region inaccessible. However, as depicted by Figure 1b, while the concentration of the polymer is kept

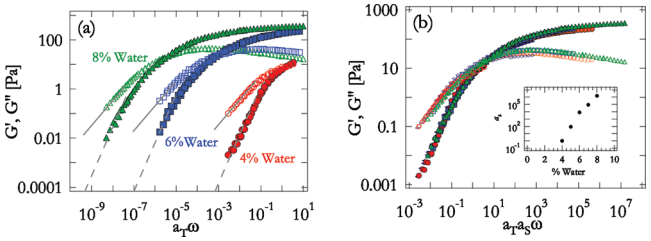


Figure 3. (a) Time–temperature superposition master curves illustrating storage (filled) and loss (unfilled) moduli for 7 wt % copolymer gels in DMSO-water mixtures containing 4% (red circles), 6% (blue squares), and 8% (green triangles) water. Reference temperature: 25 °C. Terminal slopes at low frequencies reflect $G' \propto \omega^2$ (dashed lines) and $G'' \propto \omega$ (solid line) behavior. (b) Time–temperature–composition superposition of the data from part a, obtained using the composition shift factors, a_s, denoted by the inset.

constant, changing the solvent quality is analogous to changing the temperature. As a result, each of these master curves generated through time–temperature superposition at a given solvent composition can be shifted horizontally to a reference solvent content to generate a single plot depicting the universal relaxation behavior for the polymer concentration studied. This plot is depicted in Figure 3b, and includes data for 7 wt % gels containing 4%, 5%, 6%, 7%, and 8% water in DMSO. Here, the reference composition where the composition shift factor, a_s, is equal to one is set at 4% water. These composition shift factors are plotted as a function of the solvent composition in the inset of Figure 3b.

Activation Energies. Apparent activation energies, ΔH_{app} for end block pull-out can be extracted from the temperature dependence of a_T.[32,33] The apparent activation energy is obtained by assuming that the temperature dependence across the experimentally accessible range follows a simple Arrhenius form:

$$a_T = A e^{\Delta H_{app}/RT} \quad (1)$$

While the behavior in or case is not strictly Arrhenius, we use this analysis as a means to quantify the temperature dependence of the relaxation times within the gels. Figure 4a

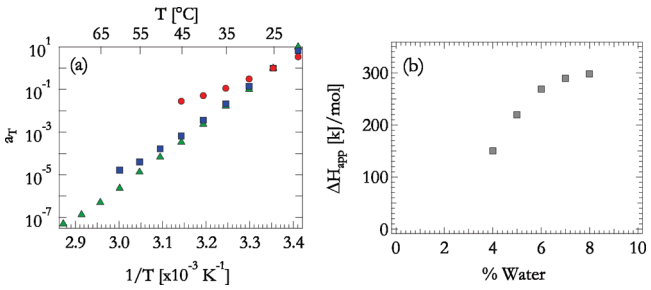


Figure 4. (a) Arrhenius plot depicting the temperature dependence of shift factors used for generating master curves in 7 wt % DMSO–water gels containing 4% (red circles), 6% (blue squares), and 8% (green triangles) water. (b) Values of the apparent activation energy, ΔH_{app}, for these same gels as a function of water content.

shows the temperature dependence of a_T for solvents with 4, 6 and 8% water, and Figure 4b shows the value of ΔH_{app} as a function of water content. For the gels studied here, ΔH_{app} ranges from 150 to 300 kJ/mol, increasing with increasing water content. These values are larger than the determined

dx.doi.org/10.1021/ma201607m | Macromolecules 2012, 45, 1631–1635

activation energies for poly(ethylene glycol) chains with alkyl end groups in aqueous solution (ΔH_{app}~ 70 kJ/mol),[34] and are comparable to SIS copolymers in squalane (ΔH_{app} ~ 200 kJ/mol).[5] Triblock copolymers with PMMA end blocks in higher alcohols show larger apparent activation energies, typically between 350 and 500 kJ/mol.[10,23] The large value of the apparent activation energy results from a changing value of the glass transition temperature as the solvent quality changes with temperature.

Relaxation Behavior. The advantage of employing a mixed solvent in these systems is the ability to tailor both the magnitude and temperature dependence of the relaxation time, while maintaining a similar network structure. The ability to superpose data obtained at different temperatures and different solvent contents is consistent with our expectation that these gels are structurally similar, with a plateaus modulus, G_0, that is determined by the gel structure. For our gels this plateau modulus is ~400 Pa (see Figure 3). The characteristic relaxation time, τ, obtained from the following equation:

$$\tau = \frac{\eta_0 a_T}{G_0} \quad (2)$$

where η_0 is the zero shear viscosity obtained from the low frequency (high temperature) data, i.e. the limiting value of G''/ω. The viscosity is proportional to the composition shift factor a_s and is strongly dependent on solvent composition, as shown in Figure 5a. Over the composition range studied(4−8 wt %

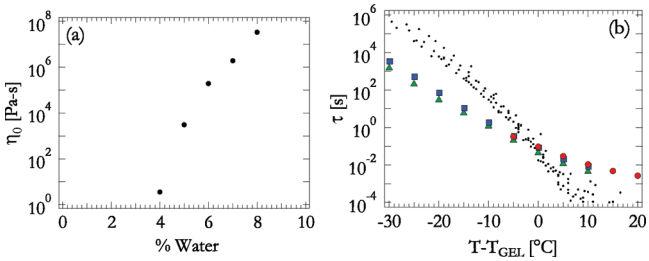


Figure 5. (a) Zero-shear viscosity, η_0, as a function of water content for 7 wt % polymer gels at the reference temperature, 25 °C. (b) Relaxation times in DMSO−water mixtures containing 4% (red circles), 6% (blue squares), and 8% (green triangles) water as a function of $T - T_{GEL}$. Data previously collected for acrylic copolymers in 2-ethyl-1-hexanol are plotted in black.[23]

water), η_0 at a reference temperature of 25 °C increases by 7 orders of magnitude as the water content is increased from 4% to 8%. Relaxation times obtained from eq 2 are plotted in Figure 5 as a function of the distance from the gel temperature. Published data for PMMA-based triblock gels in 2-ethyl hexanol are included as well. Note that the alcohol-based gels show a 10 order of magnitude difference in relaxation times over a 40 degree temperature interval, whereas the relaxation times for the DMSO-water gels change by ~5 orders of magnitude over the same range.

Small Angle X-ray Scattering. The SAXS patterns for samples of mixed solvent content ranging from 4 to 7% water are shown as the solid lines in Figure 6. Each of these patterns is consistent with the formation of a disordered array of spherical micelles, which is expected for these particular concentrations and relative copolymer block lengths.[23,35] A more detailed fit to the Percus−Yevick model[23,29] gives an average domain spacing of 65 nm that is nearly independent of

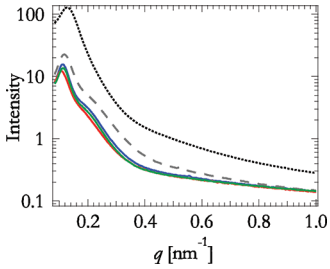


Figure 6. SAXS patterns for 7 wt % gels in mixed solvents of DMSO containing 4% (red), 6% (blue), and 7% (green) water and DMSO solutions after 3 h (dark gray, dashed) and 24 h (black, dotted) of vapor phase exchange with water.

the solvent composition. These results suggest that these samples experience similar thermodynamic conditions during cooling (though at different temperatures) before the structures of these micelles become kinetically frozen below their gelation temperatures.

These results provide important insight into the ability of a simple vapor phase solvent exchange process to produce gels with consistent properties.[13] The process involves exposing a DMSO solution of PMMA−PMAA−PMMA triblock copolymer to water vapor, with gelation occurring as water diffuses into the DMSO solution. Scattering patterns from samples after 3 and 24 h exposures to water vapor are compared to the mixed solvent samples in Figure 6. The scattering intensity for these samples is substantially higher than the samples with only small amounts of water added. This result is attributed to the deswelling of the PMMA micelle cores, which enhances the contrast with the surrounding solvent.[23] The location of the scattering peak is roughly equivalent between all mixed solvent samples and the vapor phase exchange samples, indicating little change in structure. These results suggest that during the vapor phase exchange, a homogeneous micellar structure can be obtained because only a small volume of water is necessary to induce micellization, after which the micelle size and structure are kinetically frozen. During the exchange process, a diffusion-limited water penetration front produces the nanophase structure within the gel before any substantial gel swelling from the added solvent is observed.

■ CONCLUSIONS

Here we demonstrate the thermoreversible formation of polyelectrolyte gels from DMSO/water mixtures, using triblock copolymers with poly(methyl methacrylate) endblocks and a poly(methacrylic acid) midblock. Rheological characterization at various temperatures and solvent compositions can be combined into a single master curve of the frequency-dependent storage and loss moduli. This result, in conjunction with small-angle X-ray scattering results, indicates that gels with similar structures but dramatically different relaxation times are formed for different solvent compositions. The effect of changing either temperature or solvent composition is to change the effective interaction parameter between the solvent and the end blocks. Gelation in these systems is defined dynamically, in terms of the relaxation time of the polymer gel. Specific results are as follows:

1 A water content of 4 wt % in the solvent mixture is sufficient to induce gelation at room temperature.

dx.doi.org/10.1021/ma201607m | Macromolecules 2012, 45, 1631−1635

2 The gel temperature increases by about 30 °C when the water content of the solvent is increased from 4 wt % to 8 wt %.
3 The effective activation energy describing the temperature dependence of the relaxation times increases from 100 to 300 kJ/mol as the water content of the solvent is increased from 4 wt % to 8 wt %.

These results indicate that the vapor phase exchange technique for micelle assembly and gel formation is successful because only a small amount of water is necessary to generate micelles in these networks. The micelles quickly become kinetically frozen as the viscosity-dependent relaxation behavior jumps by orders of magnitude with only a few percent increase in water content. As water is absorbed by the polymer-DMSO solutions, gel formation occurs at an overall polymer concentration that is very close to the starting polymer concentration in the original DMSO solutions.

AUTHOR INFORMATION

Corresponding Author

*E-mail: k-shull@northwestern.edu.

ACKNOWLEDGMENTS

This material is based on work supported under a National Science Foundation Graduate Research Fellowship. Support from the NSF DMR Polymers Program (DMR-0907384) and the NSF MRSEC program (DMR-0520513) is also acknowledged. Portions of this work were performed at the DuPont−Northwestern−Dow Collaborative Access Team (DND-CAT) Synchrotron Research Center located at Sector 5 of the Advanced Photon Source. DND-CAT is supported by the E.I. DuPont de Nemours & Co., The Dow Chemical Company, the U.S. National Science Foundation through Grant DMR-9304725, and the State of Illinois through the Department of Commerce and the Board of Higher Education Grant IBHE HECA NWU 96. Use of the Advanced Photon Source was supported by the U.S. Department of Energy, Office of Basic Energy Sciences, under Contract W-31-10.

REFERENCES

(1) Matsen, M. W.; Bates, F. S. *Macromolecules* **1996**, *29*, 1091−1098.
(2) Hamley, I. *The Physics of Block Copolymers*; Oxford University Press: 1998.
(3) Matsen, M. W.; Thompson, R. B. *J. Chem. Phys.* **1999**, *111*, 7139−7146.
(4) Lodge, T. P.; Pudil, B.; Hanley, K. J. *Macromolecules* **2002**, *35*, 4707−4717.
(5) Vega, D. A.; Sebastian, J. M.; Loo, Y. L.; Register, R. A. *J. Polym. Sci., Part B: Polym. Phys.* **2001**, *39*, 2183−2197.
(6) Watanabe, H.; Sato, T.; Osaki, K.; Yao, M. L.; Yamagishi, A. *Macromolecules* **1997**, *30*, 5877−5892.
(7) Watanabe, H.; Sato, T.; Osaki, K. *Macromolecules* **2000**, *33*, 2545−2550.
(8) Laurer, J. H.; Mulling, J. F.; Khan, S. A.; Spontak, R. J.; Bukovnik, R. *J. Polym. Sci., Part B: Polym. Phys.* **1998**, *36*, 2379−2391.
(9) Drzal, P.; Shull, K. *Macromolecules* **2003**, *36*, 2000−2008.
(10) Inomata, K.; Nakanishi, D.; Banno, A.; Nakanishi, E.; Abe, Y.; Kurihara, R.; Fujimoto, K.; Nose, T. *Polymer* **2003**, *44*, 5303−5310.
(11) Alexandridis, P.; Holzwarth, J. F.; Hatton, T. A. *Macromolecules* **1994**, *27*, 2414−2425.
(12) Alexandridis, P.; Lindman, B. *Amphiphilic block copolymers: self-assembly and applications*; Elsevier Science: Amsterdam, 2000.
(13) Guvendiren, M.; Shull, K. *Soft Matter* **2007**, *3*, 619−626.
(14) Hayward, R. C.; Pochan, D. J. *Macromolecules* **2010**, *43*, 3577−3584.
(15) Tuzar, Z.; Kratochv., P. *Makromol. Chem.* **1972**, *160*, 301−311.
(16) Mandema, W.; Emeis, C. A.; Zeldenrust, H. *Makromol. Chem., Macromol. Chem. Phys.* **1979**, *180*, 2163−2174.
(17) Bednar, B.; Devaty, J.; Koupalova, B.; Kralicek, J.; Tuzar, Z. *Polymer* **1984**, *25*, 1178−1184.
(18) Duval, M.; Picot, C. *Polymer* **1987**, *28*, 798−803.
(19) Fuse, C.; Okabe, S.; Sugihara, S.; Aoshima, S.; Shibayama, M. *Macromolecules* **2004**, *37*, 7791−7798.
(20) Krishnan, A. S.; Seifert, S.; Lee, B.; Khan, S. A.; Spontak, R. J. *Soft Matter* **2010**, *6*, 4331.
(21) Ando, K.; Yamanaka, T.; Okamoto, S.; Inoue, T.; Sakamoto, N.; Yamaguchi, D.; Koizumi, S.; Hasegawa, H.; Koshikawa, N. *IOP Conf. Ser.: Mater. Sci. Eng.* **2010**, *14*, 012012.
(22) Ando, K.; Yamanaka, T.; Okamoto, S.; Sakamoto, N.; Yamaguchi, D.; Koizumi, S.; Hasegawa, H.; Koshikawa, N. *J. Phys.: Conf. Ser.* **2010**, *247*, 012040.
(23) Seitz, M.; Burghardt, W.; Faber, K.; Shull, K. *Macromolecules* **2007**, *40*, 1218−1226.
(24) Mortensen, K.; Brown, W.; Jorgensen, E. *Macromolecules* **1994**, *27*, 5654−5666.
(25) Hamley, I. W.; Fairclough, J. P. A.; Ryan, A. J.; Ryu, C. Y.; Lodge, T. P.; Gleeson, A. J.; Pedersen, J. S. *Macromolecules* **1998**, *31*, 1188−1196.
(26) Kim, J. H.; Min, B. R.; Won, J.; Park, H. C.; Kang, Y. S. *J. Membr. Sci.* **2001**, *187*, 47−55.
(27) Lin, D. J.; Chang, C. L.; Lee, C. K.; Cheng, L. P. *Eur. Polym. J.* **2006**, *42*, 2407−2418.
(28) Moyses, S. *Int. J. Polym. Anal. Characteriz.* **2008**, *13*, 413−427.
(29) Percus, J. K.; Yevick, G. J. *Phys. Rev.* **1958**, *110*, 1−13.
(30) Erk, K.; Shull, K. *Macromolecules* **2011**, *44*, 932−939.
(31) Winter, H. H.; Chambon, F. *J. Rheol.* **1986**, *30*, 367−382.
(32) Tanaka, F.; Edwards, S. F. *J. Non-Newtonian Fluid Mech.* **1992**, *43*, 273−288.
(33) Tanaka, F.; Edwards, S. F. *J. Non-Newtonian Fluid Mech.* **1992**, *43*, 289−309.
(34) Annable, T.; Buscall, R.; Ettelaie, R.; Whittlestone, D. *J. Rheol.* **1993**, *37*, 695−726.
(35) Seitz, M. E.; Burghardt, W. R.; Shull, K. R. *Macromolecules* **2009**, *42*, 9133−9140.

Macromolecules

Article

pubs.acs.org/Macromolecules

Rheological Images of Dynamic Covalent Polymer Networks and Mechanisms behind Mechanical and Self-Healing Properties

Fuyong Liu,[†] Fuya Li,[‡] Guohua Deng,*[,‡] Yongming Chen,*[,§] Baoqing Zhang,[†] Jun Zhang,[†] and Chen-Yang Liu*[,†]

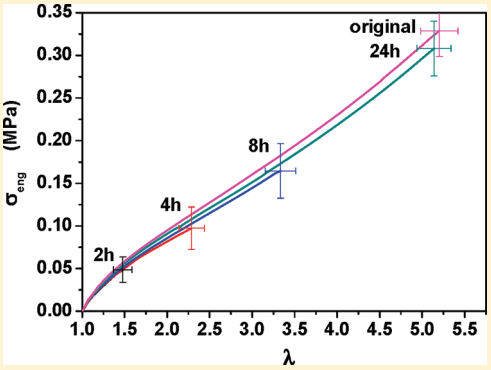
[†]Beijing National Laboratory for Molecular Sciences, CAS Key Laboratory of Engineering Plastics, Joint Laboratory of Polymer Science and Materials, Institute of Chemistry, The Chinese Academy of Sciences, Beijing 100190, China

[‡]School of Chemistry and Chemical Engineering, South China University of Technology, Guangzhou 510640, China

[§]Beijing National Laboratory for Molecular Sciences, State Key Laboratory of Polymer Physics and Chemistry, Joint Laboratory of Polymer Science and Materials, Institute of Chemistry, The Chinese Academy of Sciences, Beijing 100190, China

Supporting Information

ABSTRACT: In our previous work [*Macromolecules* **2010**, *43*, 1191−1194], we synthesized dynamic covalent cross-linked polymer gels through condensation of acylhydrazines at the chain ends of poly(ethylene oxide) (A_2) and aldehyde groups in tris[(4-formylphenoxy)methy]ethane (B_3) and reported reversible sol−gel transition and self-healing properties of the gels. For those dynamic gels, this paper examines the gelation kinetics and rheological behavior in pre- and postgelation stages and discusses the molecular mechanism underlying the mechanical and self-healing properties. The results showed that the condensation reaction before the critical gelation point can be treated as the pseudo-second-order reaction. The scaling exponent n (=0.75) for the frequency dependence of the complex moduli at the critical gel point, the exponent γ (=1.5) for the concentration dependence of the viscosity in the pregel regime, and the exponent z (=2.5) for the concentration dependence of the equilibrium modulus in the postgel regime were found to not exactly obey the relationship for covalent gels, $n = z/(z + \gamma)$, possibly because of the dynamic nature of the gels. The terminal relaxation of the dynamic gels at high temperature (125 °C) accorded with the Maxwellian model, as often observed for transient associating networks. In contrast, at low temperature (25 °C) where this transient network reorganization was essentially quenched in a time scale of experiments (~50 s), the uniaxial stress−strain behavior of the gel was well described by the classical model of rubber elasticity $\sigma_{eng} = G(\lambda - 1/\lambda^2)$ up to 300% stretch (as similar to the behavior of usual gels chemically cross-linked in a swollen state). Ultimately, the gel cut into two pieces was found to exhibit self-healing under ambient conditions in 8 and 24 h, respectively, when the edges of those pieces were coated and not coated with acid (catalyst for dynamic covalent bond formation).



1. INTRODUCTION

The dynamic covalent bond is defined as a class of chemical bonds that can break and re-form under appropriate conditions.[1−3] Dynamic covalent gels formed by such dynamic covalent bond not only have the stability of traditional covalent materials but also possess the environmental responsiveness of noncovalent supramolecular materials. The macroscopic properties of dynamic covalent gels can be tuned by adjusting the reactions involving such reversible covalent bond. Consequently, those dynamic gels are smart as supramolecular materials in response to external stimuli but have a higher stability because of the high strength of the reversible covalent bonds.[4,5]

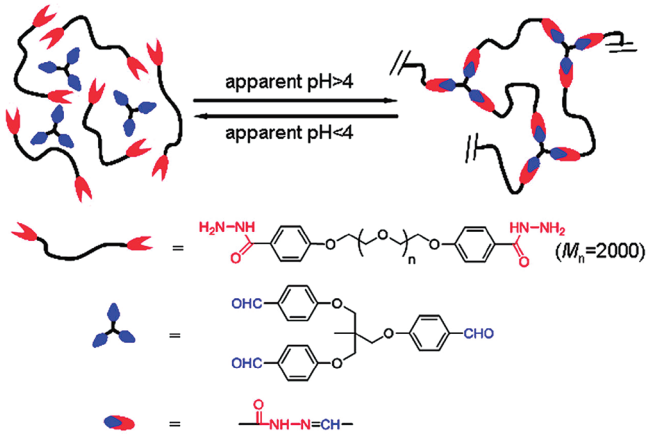
Recently, one of the dynamic covalent bonds, acylhydrazone bond formed by the condensation of hydrazide with carbonyl group, has been receiving more attention. A series of polymers having main-chain dynamic covalent based on the acylhydrazone bond have been synthesized by Lehn and coworkers.[6,7] Polyacylhydrazones, the so-called dynamers,[4,7] show the ability to exchange their components with outside monomers (to achieve spontaneous chemical modification of the original polymers).[6,8] According to this exchange, the mechanical properties[9] or the color/fluorescence[10] of the original dynamers can be modified. Very recently, glycodynamers bearing side saccharide moieties were investigated by the Lehn group.[11] In our previous work,[12] bis(acylhydrazine)-functionalized poly(ethylene oxide) (PEO) (A_2) and tris[(4-formylphenoxy)methyl]ethane (B_3) were utilized to develop three-dimensional gel sustained by the dynamic acylhydrazone covalent bond. The gel possesses self-healing ability based on

Received: November 7, 2011
Revised: January 23, 2012
Published: February 1, 2012

 © 2012 American Chemical Society

the reversible dissociation and re-formation of those bonds and undergoes reversible sol−gel transitions according to the acidity in the system, as shown in Scheme 1.

Scheme 1. Formation of Cross-Linked Polymer Gel Based on Reversible Covalent Acylhydrazone Bond



The stimuli responsiveness and mechanical properties of the dynamic covalent gels are highly dependent on the network architectures and the chemical structure of gelators. We can rheologically investigate the gelation kinetics and thermodynamics, which helps us to fully understand a relationship(s) between structure and macroscopic properties of those gels. Specifically, rheological measurements in the linear regime can detect evolution of the microstructures during the gelation process. The structure of well-developed gels can be also examined with those measurements. Thus, rheological measurements serve as a powerful tool to investigate the relationship between microstructure and macroscopic performance of the dynamic gels.[13−17] The bonding efficiency under a given set of conditions (concentration, temperature, etc.) determines the density of dynamic cross-links, thereby governing the equilibrium modulus of the well-developed gels. This efficiency is in turn determined by the bonding rate constant (k_1) and the dissociation rate constant (k_d), the parameters specifying the equilibrium constant K_{eq} (= k_1/k_d). k_1 determines the critical gelation time (t_{gel}) and can be evaluated with a rheological method. k_d can be also estimated rheologically as a dynamic relaxation frequency of the gels, as demonstrated by Craig and co-workers[15,18] for the supramolecular networks formed by metal−ligand interactions and also by Scherman and co-workers[19] for a polymeric material that utilizes the strong yet reversible cucurbit[8]uril-based 1:1:1 ternary binding motif in water.

Gels can be stretched enormously without rupture. The stress−strain behavior of the cross-linked gels (and rubbers) has been studied extensively,[20−22] and the molecular mechanism of their remarkable elasticity (of entropic origin) has been explored.[23−25] The strands of dynamic gels can pass through each other on the dissociation of dynamic cross-links and are quite different from the strands in usual cross-linked gels. The terminal relaxation of such dynamic gels in the linear regime is well described by the Maxwell model with a single relaxation time.[26−28] However, to the best of our knowledge, the rheological behavior of the dynamic gels in both linear and nonlinear regimes has not been fully characterized.

For this full characterization, we synthesized the dynamic gel utilizing acylhydrazone bonds and examined its reversible sol−gel transition and self-healing properties.[12] In this paper, we make complete rheological characterization of this gel and discuss molecular mechanism(s) underlying its rheological properties. In the remaining part of this paper, we first explain the sample preparation and experimental conditions. Then, we discuss the gelation kinetics (including the effects of the gelator concentration and temperature), the mechanical properties of well-developed dynamic gel in relation to the properties of usual covalent gels, and the quantitative aspect of self-healing of the well-developed dynamic gel. Finally, the features of the dynamic covalent gel thus discussed are summarized as the conclusion of this paper.

2. EXPERIMENTAL SECTION

2.1.1. Materials and Sample Preparation. *Materials.* Bis(acylhydrazine)-functionalized PEO polymer (A_2; M_n of PEO part = 2000 g/mol) and tris[(4-formylphenoxy)methyl]ethane (B_3) were synthesized as described in our previous work.[12] *N*,*N*-Dimethylformamide (DMF), dimethyl sulfoxide (DMSO), acetic acid (HAc), hydrochloric acid (HCl, ∼37 wt %), and triethylamine (TEA) were purchased from Beijing Chemical Reagent Factory and used as received unless specially stated.

2.1.2. Sample Preparation. The gelator mass concentration was defined as

$$c_{\text{gelator,wt\%}} = \frac{m_{A_2} + m_{B_3}}{m_{A_2} + m_{B_3} + m_s + m_{HAc}} \times 100\ (\text{wt\%}) \quad (1)$$

where m_{A_2}, m_{B_3}, m_s, and m_{HAc} are the masses of A_2, B_3, solvent, and HAc, respectively. The HAc volume fraction was defined as

$$\phi_{\text{HAc,vol\%}} = \frac{V_{HAc}}{V_s + V_{HAc}} \times 100\ (\text{vol\%}) \quad (2)$$

where V_{HAc} and V_s are the volumes of HAc and solvent, respectively.

2.1.3. Samples for Rheological Tests. A_2 and B_3 were dissolved in DMF separately, and then prescribed volumes of the two solutions containing equimolar functional groups were mixed and HAc was added subsequently. This equimolar mixture was immediately loaded on the rheometer for the rheological tests explained later.

2.1.4. Samples for Tensile Tests. The mixed solution was cast into a dumbbell-shaped mold (length 25 mm, width 10 mm, thickness 1 mm; the length and the width of the middle (neck) part of the sample are 5 and 4 mm, respectively) designed according to the size of the tensile fixture geometry of a rheometer used. The mold containing samples was kept in a sealed glass case for 12 h to obtain the stable gel samples.

2.1.5. Self-Healing. The dumbbell-shaped gel samples were mechanically cut into two pieces with a blade, and the two pieces were brought into contact in the mold. The healing automatically occurred at room temperature. To avoid evaporation of DMF from the samples, the healing was conducted in the sealed glass case saturated with DMF vapor. For comparison, the cross sections of some samples were coated with HAc (catalyst for bond formation).

2.2.1. Rheological Measurements. *Dynamic Measurements.* Dynamic measurements in the linear viscoelastic regime were carried with a stress-controlled rheometer of TA Instruments (AR-2000ex). The lower fixture incorporated a Peltier plate, providing temperature control, while the upper fixture was equipped with a parallel plate fixture of a diameter of 40 mm. Prior to the measurements, a strain-sweep test was conducted at a fixed angular frequency, ω = 6.28 rad/s. For all cases, the linear response was confirmed at the strain amplitude less than 10%. Thus, the dynamic test was performed with 5% amplitude.

For monitoring the gelation kinetics, the equimolar solutions of A_2 and B_3 were mixed and loaded in the rheometer, and the dynamic measurement at ω = 6.28 rad/s at 25 °C was started 5 min after the

dx.doi.org/10.1021/ma202461e | Macromolecules 2012, 45, 1636−1645

solution loading to measure the storage and loss moduli, G' and G'', as functions of the reaction time. In addition, for systems with the concentration in the vicinity of the critical gelation concentration c_{gel}, the dynamic frequency-sweep measurements at $\omega = 1-100$ rad/s were also made repeatedly (from low ω to high ω) during the gelation process at 25 °C. One scan lasts 50 s by controlling the number of data points per decade, and the data were interpolated to given reaction times t to construct a master plots of G' and G'' against ω for those t.

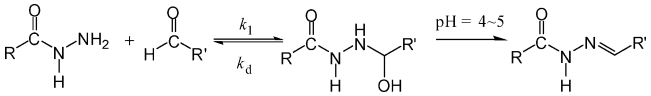
For the materials after completion of the reaction, the dynamic frequency-sweep test was made at $\omega = 0.1-100$ rad/s. In particular, for well-developed gels (having the polymer concentration well above c_{gel}), the test was made at several temperatures, T = 25, 50, 75, 100, and 125 °C. This test enabled us to examine the equilibrium modulus (G_e) that changed with T.

2.2.2. Tensile Measurement. For well-developed gels after completion of the reaction, tensile measurements were conducted at 25 °C with TA ARES-G2 rheometer utilizing its solid tensile fixture that gripped a dumbbell-shaped specimen. The deformation rate was set at 0.6 mm/s. The middle (neck) part of the dumbbell-shaped sample was prestretched to 6 mm to make sure that all samples had the same initial state. The test was made for neat (as prepared) gels and also for self-healed gels explained earlier.

3. RESULTS AND DISCUSSION

3.1. Gelation Kinetics of Dynamic Acylhydrazone Bond Gels. The condensation reaction of acylhydrazine and aldehyde groups, yielding acylhydrazone bonds, proceeds by a stepwise mechanism involving the formation of an intermediate hemiaminal.[29] At low pH (achieved with HAc), hemiaminal formation is the rate-determining step.[30] In addition, the water molecules generated by the dehydration of the hemiaminal were immediately absorbed by the HAc, so the reaction can be represented as Scheme 2.[30]

Scheme 2. Equilibrium for the Reversible Hydrazone Formation[30]



The rate equations for the above reaction can be written as

$$\frac{d[A_2]}{dt} = -k_1[A_2][B_3] + k_d[A{\cdot}B] \quad (3)$$

$$\frac{d[A{\cdot}B]}{dt} = k_1[A_2][B_3] - k_d[A{\cdot}B] \quad (4)$$

Here, $[A_2]$ and $[B_3]$ are the molar concentration of the acylhydrazine group in A_2 and molar concentration of the aldehyde group in B_3, respectively, and $[A{\cdot}B]$ is the molar concentration of the characteristic functional group in product. k_1 and k_d are the bonding and the dissociation rate constants. At equilibrium, $d[A_2]/dt = d[A{\cdot}B]/dt = 0$. Thus, the equilibrium constant K_{eq} is expressed in terms of k_1 and k_d as

$$K_{eq} = \frac{[A{\cdot}B]}{[A_2][B_3]} = \frac{k_1}{k_d} \quad (5)$$

The HAc catalyst plays an important role in the gelation kinetics. Thus, an effect(s) of its concentration on the reaction rate was examined at first, and the results are summarized in the Supporting Information. On the basis of those results, the HAc volume fraction was fixed at 13.0 vol % for the data shown in this paper.

The concentrations of gelator, $[A_2]$ and $[B_3]$, control the gelation kinetics and affects the mechanical properties of gels. This kinetics was investigated by performing dynamic time sweep for samples with the gelator concentration ranging from 5.5 to 16.2 wt %. The storage modulus (G') and loss modulus (G'') as a function of time are shown in Figure 1a. Similar time

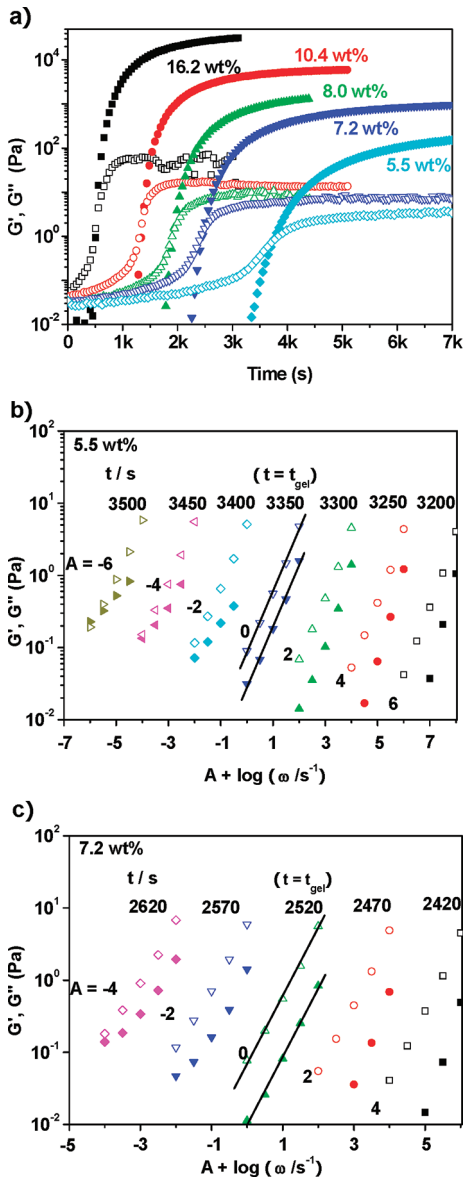


Figure 1. (a) Dynamic storage G' (solid symbol) and loss G'' (open symbol) modulus against time for samples with different gelator concentrations (5.5, 7.2, 8.0, 10.4, and 16.2 wt %). (b) Dynamic frequency spectrum at different times near the t_{gel} for the sample with 5.5 wt % gelator and (c) for the sample with 7.2 wt % gelator. HAc volume fraction is 13.0 vol %.

evolution of G' and G'' (increases of these moduli) was observed for different samples. At the beginning of the reaction, the system shows a liquidlike character, G' being much smaller than G''. As the time progresses, G'' increases gradually whereas G' shows a sharp increase in the vicinity of the gel point and becomes larger than G''. Finally, the sample shows solidlike behavior characterized with $G' \gg G''$ (G' in this zone is equivalent to the equilibrium modulus G_e). As noted in Figure 1a, a characteristic time, t_{cross}, defined as the time at which G' =

dx.doi.org/10.1021/ma202461e | Macromolecules 2012, 45, 1636–1645

G'', decreases, and the plateau of G' increases with increasing gelator concentration.

At low temperature, T = 25 °C, our gel had a very large K_{eq} (= 8000 M^{-1}), as explained later in section 3.3.1. For this case, the dissociation term $k_d[A{\cdot}B]$ in eq 3 can be safely neglected in an early stage of gelation, and the rate equation for the reaction of equimolar functional groups ($[A_2] = [B_3]$) is satisfactorily approximated as

$$\frac{d[A_2]}{dt} = -k_1[A_2][B_3] = -k_1[A_2]^2 \tag{6}$$

In fact, for such large K_{eq}, the exact and approximate rate equations (eqs 3 and 6) gave indistinguishable time evolution of $[A_2]$ in a very wide range of time (including the range of time up to critical gelation), as explained in the Appendix. Thus, we made the analysis of gelation kinetics at low T on the basis of eq 6, as explained below. (However, it should be also noted that eq 6 becomes invalid at high T where the dissociation becomes important.)

The extent of reaction is defined by

$$p = 1 - \frac{[A_2]}{[A_2]_0} \tag{7}$$

where $[A_2]_0$ is the initial molar concentration of the acylhydrazine group in A_2. Integrating eq 6, we can easily find that the time evolution of p is described by

$$\frac{1}{1-p} = k_1[A_2]_0 t + 1 \tag{8}$$

Consequently, the critical gelation time t_{gel} is specified as

$$t_{gel} = \frac{p_c}{1-p_c} k_1^{-1}[A_2]_0^{-1} \tag{9}$$

where p_c is the extent of reaction at the critical gelation point.

For the case of the equimolar functional groups examined here, p_c is estimated to be a constant independent of $[A]_0$, $p_c \cong 0.8$, because the average degree of functional groups is $\bar{f}$ = 2.4 and $p_c = 2/\bar{f}$ according to mean-field theory.[31] Thus, the simple analysis predicts that t_{gel} is proportional to $1/[A]_0$ (see eq 9). Utilizing the t_{gel} data, we examine this prediction, as explained below.

Experimentally, t_{gel} is obtained as the time where G' and G'' exhibit the critical gel behavior, $G' \propto G'' \propto \omega^n$ with n being the critical power-law exponent.[32−34] This t_{gel} was determined from the repeated frequency-sweep test as reported in the literature.[32−34] In our test, each sweep took 50 s by adequately choosing the number of data points per decade, and the data were interpolated to a given time of reaction. As an example, Figures 1b and 1c show such isochronal data of G' and G'' obtained for 5.5 and 7.2 wt % samples. The t_{gel} is estimated to be 3350 and 2520 s for the 5.5 and 7.2 wt % samples, respectively.[35]

In relation to these results, a comment is made for t_{cross}, an easily determined time at which $G' = G''$ in Figure 1a. This t_{cross} can be utilized as an apparent t_{gel},[36] although the real t_{gel} obtained for the G' and G'' ($>G'$) data exhibiting the critical power-law behavior is always shorter than the apparent t_{gel}. In fact, the difference between the two times was negligible for high concentration samples because the gelation was rapid for those samples. Nevertheless, the real and apparent t_{gel} were very different for low-concentration samples exhibiting slow gelation processes. Thus, we utilize the real t_{gel} data in the following argument for the gelation kinetics.

In Figure 2, the t_{gel} data are plotted against $1/[A_2]_0$. We note that t_{gel} is almost proportional to $1/[A_2]_0$, which suggests that

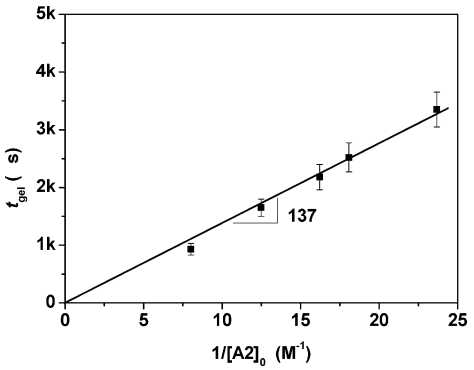


Figure 2. Dependence of t_{gel} on reciprocal of the initial molar concentration of acylhydrazine groups in A_2, $1/[A_2]_0$. The solid line is a linear fit of the data. HAc volume fraction is 13.0 vol %.

the gelation reaction up to t_{gel} is satisfactorily treated as the second-order reaction and the above analysis based on eq 6 is basically valid. At the same time, we note minor deviation from the proportionality between the t_{gel} data and $1/[A_2]_0$. This minor deviation could be attributed to a small deviation of the equimolar condition of A_2 and B_3 and also to a competing reaction that forms intramolecular loops not contributing to the gelation. (In addition, eq 6 gives a large but finite t_{gel} value even for a very small $[A_2]_0$ (cf. eq 9) while the rheologically determined t_{gel} diverges if $[A_2]_0$ is smaller than the critical gelation threshold, which could also contribute to the minor deviation from the proportionality between t_{gel} and $1/[A_2]_0$ seen in Figure 2.)

Nevertheless, the plots in Figure 2 demonstrate the basic validity of eq 6 (and eq 9) at times up to t_{gel}, as explained above. Thus, we may evaluate the bonding rate constant k_1 from those plots: $k_1 \cong 0.03\ s^{-1}\ M^{-1}$ (which corresponds to the solid line that fits the data points). For samples having 4.8−16.7 vol % HAc, k_1 changed in the range of 0.003−0.043 $s^{-1}\ M^{-1}$ (as evaluated from the t_{gel} data shown in Figure S1a of the Supporting Information), which indicates that k_1 increases with the HAc catalyst concentration. Levrand and co-workers[30,37] found that k_1 for the reaction of hydrazides and aldehydes at a fixed pH (= 2.47) varies in 0.0001−0.0012 s^{-1} according to a type of the substituting groups in hydrazides and aldehydes. In their case, the reactions between small molecules were treated as pseudo-first-order kinetics, which makes a contrast between their gel and ours, the latter containing the polymeric component.

3.2. Rheological Behavior of Gels and Sols after Full Reaction. Figures 3a and 3b show the ω dependence of the G' and G'' data at 25 °C measured for the equimolar reaction mixtures (samples) of various gelator concentrations c after a sufficiently long reaction time. We first note that well-developed gels were formed at high c (≥4.2 wt %) to exhibit ω-independent G' and much smaller G'' (not shown here for clarity of the plots). Those gels behave as elastic solids in the range of ω examined, and their G' data are regarded as the equilibrium modulus G_e. The c dependence of those G_e data is shown in Figure 3c. (Note, however, that the gel samples stored in glass vessels flowed with their own weight at 25 °C in a time

dx.doi.org/10.1021/ma202461e | Macromolecules 2012, 45, 1636−1645

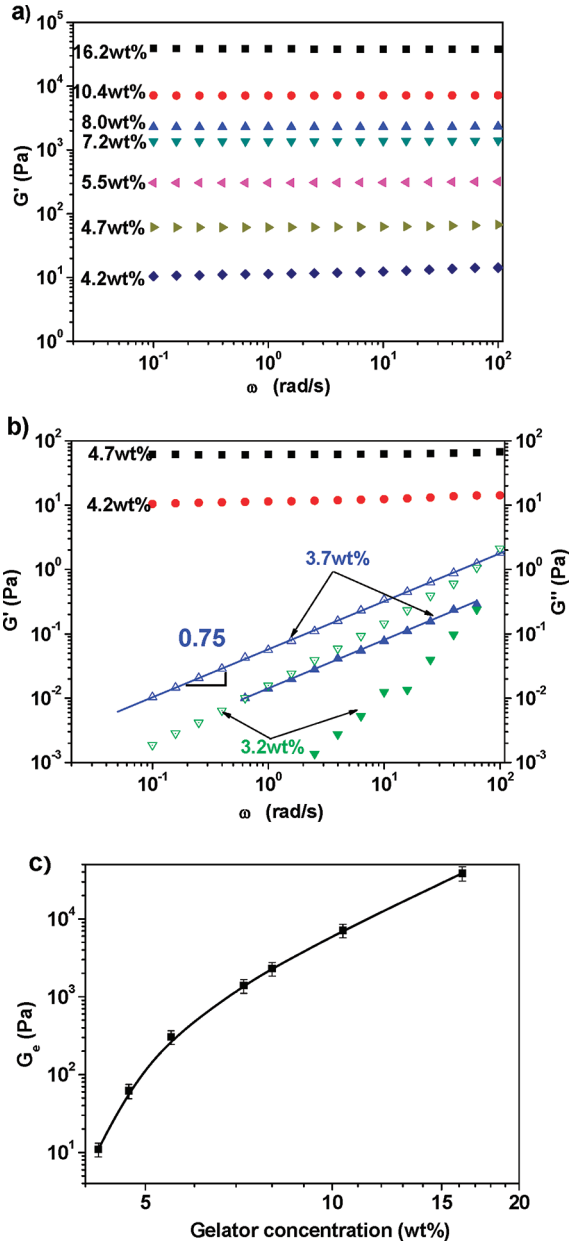


Figure 3. (a) Dynamic storage (G') modulus against frequency (ω) for the well-gelated samples with different gelator concentrations above the critical point. (b) Dynamic storage G' (solid symbol) and loss G'' (open symbol) modulus against frequency for the samples around the critical point. The samples with 3.7 and 3.2 wt % gelator have been reacted for 24 h. The solid lines are a least-squares fit of the G' and G'' data for the sample with 3.7 wt % gelator, and the slope = 0.75 was labeled. (c) Equilibrium modulus (G_e) as a function of gelator concentration. The error is estimated to be ±20%. HAc volume fraction is 13.0 vol %.

scale of a few days, which demonstrates that those samples behaved as dynamic covalent gels having a long but finite dissociation time at 25 °C, not as permanently cross-linked gels.)

In Figure 3b, we also note that the mixture with the low c (3.2 wt %) behaves as a viscoelastic fluid with a well-defined relaxation time. This behavior suggests that the network was not fully developed throughout the system at such low concentration. Finally, for c = 3.7 wt %, G' and G'' exhibit the power-law behavior (eq 11) characteristic of a critical gel.[32,33]

Typical gels are rheologically classified in three regimes characterized by the following scaling relationships.[32,33,38,39]

In the pregel regime

$$\eta_0 \propto \varepsilon^{-\gamma} \tag{10}$$

At the critical gel point

$$G'' \sim G' \sim \omega^n \tag{11}$$

$$G''(\omega)/G'(\omega) = \tan\delta = \tan(n\pi/2) \tag{12}$$

In the postgel regime

$$G_e \propto \varepsilon^z \tag{13}$$

Here, η_0 is the zero shear viscosity, ε is the relative distance of a variable q from the gel point q_g:

$$\varepsilon = |q - q_g|/q_g \tag{14}$$

q can be either the extent of reaction, the gelation time, the temperature, or the gelator concentration. γ, n, and z are the scaling exponents for the three scaling laws. In the simplest case, the exponents are expected to follow the relationship

$$n = z/(z + \gamma) \tag{15}$$

Here, we focus on the gelator concentration c and examine the above scaling relationships. The critical concentration c_g can be accurately determined by focusing on loss tangent, tan δ.[32,33] The c dependence of tan δ at various ω is shown in Figure 4a: tan δ is independent of ω for c = 3.7 wt %, and thus c_g = 3.7 wt % according to the Winter–Chambon criterion (eq 12).[32,33]

The zero-shear viscosity η_0 of the samples with $c < c_g$ (= 3.7 wt %) was obtained from steady flow measurements (cf. Figure S2 shown in the Supporting Information). Figure 4b presents the log–log plots of η_0 against $\varepsilon = |c - c_g|/c_g$. Equation 10 with γ = 1.5 describes the data well. The G_e data (Figure 3c) are replotted against ε in Figure 4c (see filled circles). Those data are well described by eq 13 with z = 2.5.

The above exponents, γ = 1.5 and z = 2.5, are close to the predictions by Martin et al. using a percolation model.[40−42] If eq 15 is applicable to our dynamic covalent gels, n is predicted to be 0.63. However, the observed n value (= 0.75 for c_g = 3.7 wt %; cf. Figure 3b) is larger than this prediction, which possibly reflected the dynamic covalent nature of our gel (that can relax through either the global motion of the self-similar gel network or slow thermal dissociation of the bonds). In relation to this point, we remember that a similar deviation from eq 15 has been noted for poly(vinyl chloride) (PVC)/bis(2-ethylhexyl) phthalate (DOP) gels systems (n = 0.75, γ = 1.5 ± 0.1, and z = 2.6 ± 0.1).[16,43,44] Thus, eq 15 is not necessary valid for all physical gels. A further study is desired for this issue.

3.3. Mechanical Properties of Well-Developed Gels with High Gelator Concentration. As noted in Figure 3a, well-developed gels were formed after sufficiently long reaction of the samples with high gelator concentration (and at the HAc catalyst volume fraction = 13.0 vol %). The 2.5th power law relationship between the G_e data and the relative gelator concentration ε (Figure 4c) reflects the gel network structure at 25 °C. The temperature dependence of G_e and the tensile behavior of gels at 25 °C are examined below to further investigate the feature of the dynamic covalent bonds.

3.3.1. Effect of Temperature on G_e. For polymer melts, an increase of temperature (T) accelerates the segment and terminal relaxation processes but hardly affects the entangle-

dx.doi.org/10.1021/ma202461e | Macromolecules 2012, 45, 1636–1645

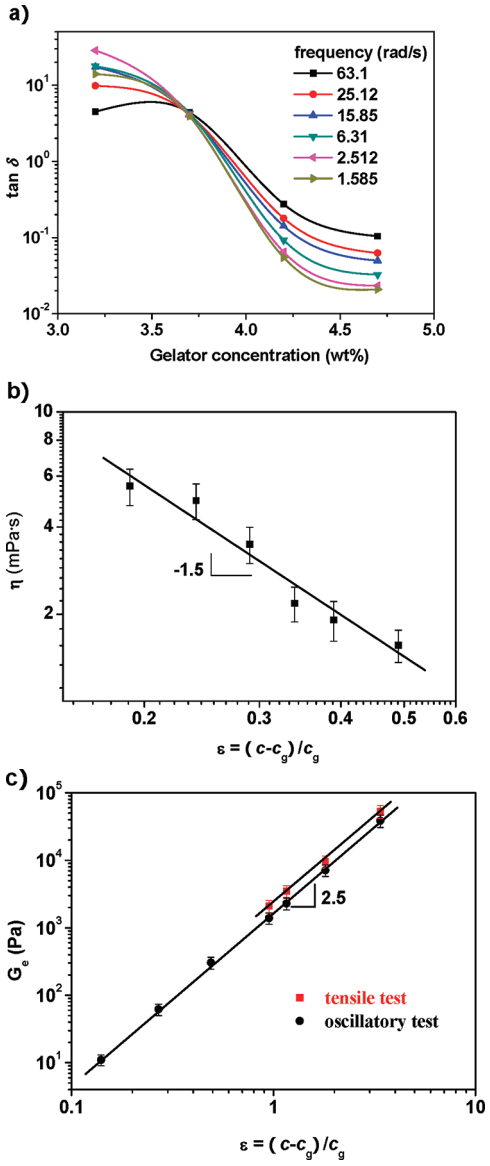


Figure 4. (a) Gelator concentration dependence of tan δ at different frequencies to determine c_g according to the Winter−Chambon criterion. (b) Viscosity (η) as a function of the relative gelator concentration ($\varepsilon = (c - c_g)/c_g$, c_g = 3.7 wt %), the error is estimated to be ±15% due to the very low viscosity. (c) Equilibrium modulus (G_e) as a function of the relative gelator concentration ($\varepsilon = (c - c_g)/c_g$, c_g = 3.7 wt %). The shear modulus (G_e) obtained from the tensile test (section 3.3.2) are compared with G_e measured by small-amplitude oscillatory shear (SAOS) test. Solid line is a least-squares fit of the data, and the slope is labeled.

ment plateau modulus. In contrast, for our dynamic covalent gels sustained by acylhydrazone bonds, the hydrolysis reaction is significantly enhanced at high T,[45,46] thereby reducing the association/dissociation equilibrium constant K_{eq} and decreasing the equilibrium modulus G_e. In fact, this decrease of G_e at high T is noted in Figure 5 where the G' and G'' data of the gel with the gelator concentration of 10.4 wt % at various T are plotted against ω. Clearly, G' decreases with increasing T (which corresponds to the decrease of G_e) and shows the flow behavior in the experimental window at $T \geq 100$ °C. G'' exhibits the corresponding behavior, the terminal peak associated with the cross with the G' curve. In particular, at

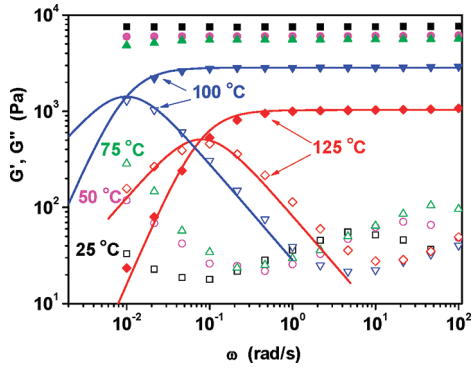


Figure 5. Dynamic storage G' (solid symbol) and loss G'' (open symbol) against frequency (ω) at different temperatures. The solid curves are the predictions of the Maxwell model. Gelator concentration is 10.4 wt %, and HAc volume fraction is 13.0 vol %.

125 °C, the crossover point of G' and G'' shifts to a higher frequency, and the well-known "terminal" regime ($G' \sim \omega^2$, $G'' \sim \omega$) is observed. The solid curves in Figure 5 show the results of Maxwellian fitting. The fit is well achieved,[27,28] as noted for transient networks relaxing on the dissociation of the cross-links.[47−49]

The flow of our dynamic gels at high T reflects the reversible nature of the acylhydrazone bond. Since the molar concentration of HAc is much higher than the gelator concentration, the water molecules generated in the reaction are mostly bounded to HAc (cf. Scheme 2). Therefore, the dissociation reaction of acylhydrazone bond can be treated as first-order, and the dissociation rate constant (k_d) can be calculated from the crossover frequency of G' and G'' (= terminal relaxation frequency for the Maxwellian relaxation) as $k_d = \omega_{cross}$ (see Figure 6a in ref 15. Thus, Figure 5 gives k_d = 0.1 and 0.01 s^{-1} for the sample with 10.4 wt % gelator at 125 and 100 °C, respectively. This decrease of k_d with decreasing T suggests that the dissociation governing the terminal relaxation becomes very slow at low T (= 25 °C, for example), which is in harmony with the observation explained earlier: The well-developed gels at 25 °C flowed with their own weight only in a time scale of a few days.

Since the flow behavior was not experimentally detected in Figure 5 at low T, k_d and the corresponding equilibrium constant K_{eq} at low T cannot be accurately determined from the rheological data. Thus, NMR experiments were conducted to determinate the equilibrium constant K_{eq} at 25 °C. (The results, ^{1}H NMR spectra of free and bonded B_3, are shown in Figures S3 and S4 of the Supporting g Information.) The K_{eq} value thus obtained, 8000 M^{-1} at 25 °C, was very large, confirming that the dissociation is negligibly slow and the cross-linking reaction approached 100% conversion at 25 °C (as discussed earlier in relation to the gelation kinetics).

3.3.2. Tensile Properties of Gels at Low T. The tensile test was performed at 25 °C for the well-developed gels with the gelator concentration ranging from 5.5 to 16.2 wt %. Figure 6a presents plots of engineering stress (σ_{eng}) against extension ratio ($\lambda = l/l_0$). The plots are similar to those seen for soft rubbers. The σ_{eng} and λ values at break increase with increasing the gelator concentration. In particular, σ_{eng} at break point reaches 0.32 MPa (true stress σ_{true} is 1.8 MPa) and λ at break exceeds 500% for the sample with 16.2 wt % gelator.

dx.doi.org/10.1021/ma202461e | Macromolecules 2012, 45, 1636−1645

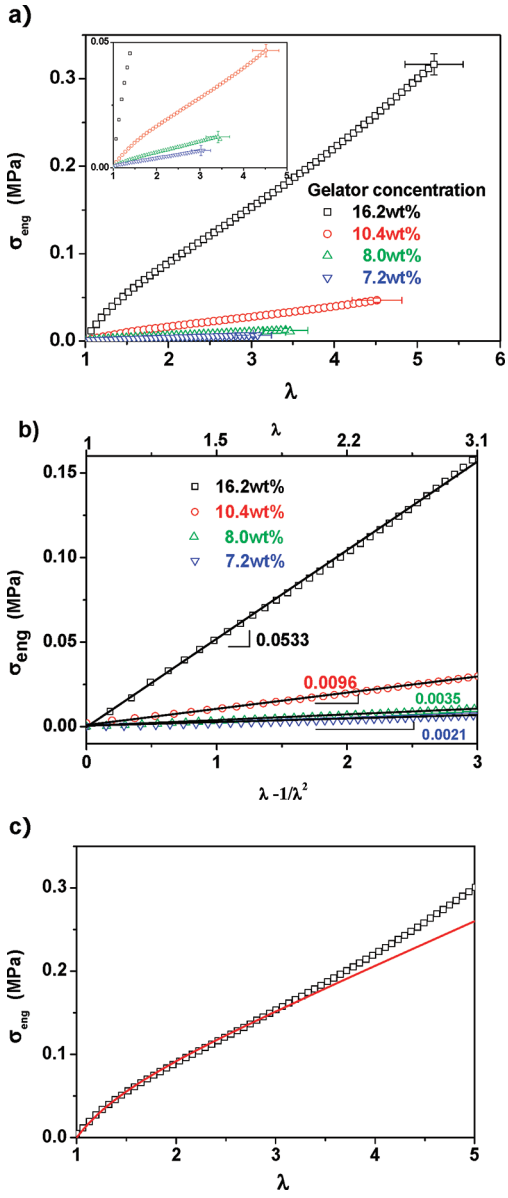


Figure 6. (a) Engineering stress (σ_{eng}) against extension ratio (λ) for the gels with different gelator concentrations. (b) σ_{eng} against $\lambda - 1/\lambda^2$ for the gels with different gelator concentrations. The slope was labeled. (c) σ_{eng} against λ for gel with 16.2 wt % gelator and 13.0 vol % HAc. The solid curve is the prediction of classical model eq 14 with G = 0.052 MPa.

In the classical theory of rubber elasticity,[31,50,51] the engineering stress in uniaxial deformation is written in terms of λ and the equilibrium shear modulus (G_e):

$$\sigma_{eng} = G_e(\lambda - 1/\lambda^2) \quad (16)$$

The data in Figure 6a are redrawn in Figure 6b as plots of σ_{eng} against $\lambda - 1/\lambda^2$. All four samples clearly obey the neo-Hookean relationship, eq 16, up to λ = 3 (300% stretch), after a moderate adjustment of the G_e value (increase, by a factor of 40%, from the G_e value obtained in the dynamic test; cf. Figure 4c). This adjustment was necessary because of unavoidable prestretching treatment in the tensile test that shifts the unstretched state. Despite the adjustment, the results seen in Figure 6b demonstrate basic validity of the neo-Hookean relationship for the dynamic gel at 25 °C where the dissociation is essentially quenched in the time scale (~50 s) of the tensile test.

In Figure 6c, the σ_{eng}–λ plot for the sample with 16.2 wt % gelator is shown in a wider range of λ (up to 5). The prediction of eq 16 with G_e = 0.052 MPa is shown with the solid curve. Clearly, the data follow the neo-Hookean relationship for $\lambda < 3$ and exhibit the hardening for $\lambda > 3$. Similar behavior has long been noted for swollen cross-linked rubbers in a wide range of λ[52−54] (for example, Figure 5 in ref 54). In fact, Urayama and co-workers[54,55] made extensive biaxial elongation tests to demonstrate that the gels showing the neo-Hookean behavior (followed by hardening at large λ) in uniaxial test do not exhibit the corresponding behavior in biaxial tests. Namely, the neo-Hookean relationship does not hold in a tensorial sense because of the interaction between the gel strands. The dynamic gel examined in this study behaves very similarly to the swollen chemical gels at least in the time scale of experiments (~50 s) because the dissociation is essentially quenched at 25 °C (K_{eq} = 8000 M^{-1}). Thus, its apparent neo-Hookean behavior (Figure 6b) is to be interpreted in the same way as for the swollen cross-linked gels.[54,55] Despite this similarity (at relatively short times) observed for our dynamic covalent gels and chemically cross-linked gels, we also note a difference in a very long time scale. This difference is most clearly demonstrated for the self-healing behavior occurring in a time scale of a day, as described below.

3.4. Self-Healing of Well-Developed Gels. In general, cracked dynamic gels can exhibit healing because of the reversibility of acylhydrazone bonds.[12,56] In fact, the dynamic gel with 10.4 wt % gelator cut into two pieces exhibited the self-healing when the two pieces are simply kept in contact for 7 h.[12] In this study, the tensile test was performed on the gel with 16.2 wt % gelator to quantitatively evaluate this self-healing ability. For this purpose, dumbbell-shaped samples were cut into two pieces with a blade, the cut surfaces were brought together to allow self-healing at 25 °C for a given time (2−24 h) and with/without HAc coating at the cut surfaces, and healed specimen was subjected to the tensile test at 25 °C. The results of this test are shown in Figure 7.

HAc works as a catalyst to accelerate the acylhydrazone bond formation. Even without this catalyst, the σ_{eng}–λ curve of the original sample (without blade-cutting) was almost recovered after self-healing for 24 h, as shown in Figure 7a. This recovery was observed in a shorter healing time, 8 h, in the presence of HAc (see Figure 7b). For both cases, the σ_{eng}–λ curves of the healed samples up to their break points were very close to that of the original sample, and the σ_{eng} and λ values at the break increased with the healing time. These results demonstrates that the acylhydrazone bonds are spontaneously reformed in a time scale of a day even at low T (25 °C), which distinguishes our dynamic covalent gels from usual chemically cross-linked gels.

Recently, Leibler and co-workers[57] designed a self-healing and thermoreversible rubber utilizing hydrogen bonds. For the supramolecular network plasticized with 11 wt % dodecane, σ_{true} at break point is about 3 MPa and strain at break exceeds 500%. The fractured material can almost recover its original properties after self-healing for 3 h at ambient temperature. Burattini and co-workers[58] obtained a dimensionally stable and flexible material utilizing π–π stacking interactions. The 100% recovery of tensile modulus of the material was achieved in 5 min after healing at 50 °C. These two systems, based on the hydrogen bonding and π–π stacking, exhibit much faster self-

dx.doi.org/10.1021/ma202461e | Macromolecules 2012, 45, 1636−1645

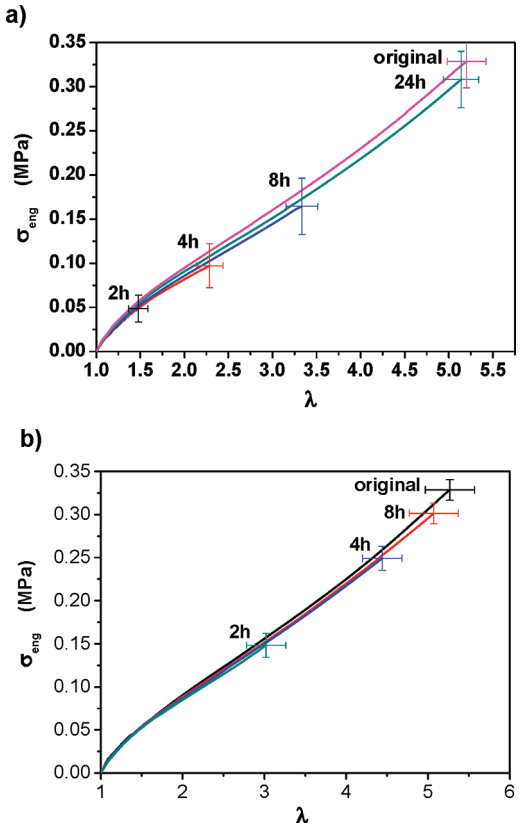


Figure 7. (a) Engineering stress (σ_{eng}) against extension ratio (λ) for the gel self-healed different times. The dumbbell-shaped gels were cut into two pieces, and the two pieces were brought into contact together in the mold immediately (waiting time less than 1 min). The tensile test was performed at room temperature on ARES-G2. (b) Engineering stress (σ_{eng}) against λ for the gel self-healed different times with the cross-section coated with HAc after cutting off. Gelator concentration is 16.2 wt %, and HAc volume fraction is 13.0 vol %.

healing compared to our dynamic gels. In addition, the bonding points in these systems are distributed along the whole backbone of polymers, and the bonding (cross-linking) density and the modulus are higher in those systems than in our gel, the latter being cross-linked only at the chain ends. Nevertheless, our dynamic covalent gels have some advantages: the gel with low solid content (16.2 wt % gelator) behaves, in a wide range of T, as a soft but tough material having a relatively high shear modulus (4.5×10^4 Pa) and a considerably large extensibility ($\lambda \sim 500\%$ at break).

4. CONCLUSIONS

Mixing tris[(4-formylphenoxy)methy]ethane (B_3) with an acylhydrazine end-capped poly(ethylene oxide) (A_2) yielded a novel dynamic covalent cross-linked polymer gel with reversible sol−gel transition and self-healing properties. Gelation kinetics, rheological behavior at pre- and postgelation, and mechanical properties of polymer gels were investigated. The gelation kinetics was highly influenced by the gelator concentration (and also by the HAc catalyst content). The reaction before the critical gelation time can be treated as the pseudo second order, and the bonding rate constant k_1 changed with the HAc content. The scaling exponent n (=0.75) for the frequency dependence of the complex moduli at the critical gel point, the exponent γ (=1.5) for the concentration dependence of the viscosity in the pregel regime, and the exponent z (=2.5) for the concentration dependence of the equilibrium modulus in the postgel regime were found to not exactly obey the relationship for covalent gels, $n = z/(z + \gamma)$, possibly because of the dynamic nature of the gels.

The terminal relaxation of dynamic gels at the high temperature (125 °C) was well described by the Maxwell model, as noted for transient associating networks. In contrast, at low temperature (25 °C) where this transient network dissociation (reorganization) was essentially quenched in the time scale of experiments (~50 s), the stress−strain behavior of the gel was close to prediction of the classical model of rubber elasticity $\sigma_{eng} = G(\lambda - 1/\lambda^2)$ up to 300% stretch, as similar to the behavior of usual chemically cross-linked gels in a swollen state.

Finally, the dynamic gel can completely recover to the original properties after self-healing for 24 h under ambient conditions. Coating HAc on two cut surfaces of gel material accelerated this healing.

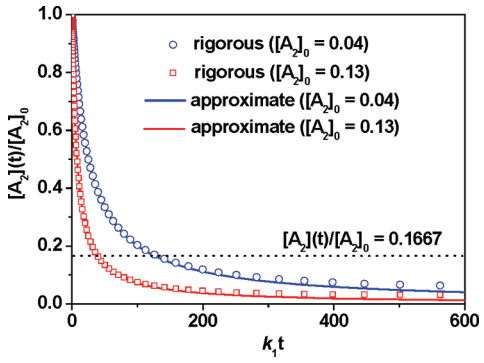


Figure 8. Evolution of $[A_2](t)/[A_2]_0$ with time.

APPENDIX. RIGOROUS AND APPROXIMATE SOLUTIONS OF THE RATE EQUATIONS OF GELATION

The rate equations for the reaction shown in the Scheme 2 are specified as

$$\frac{d[A_2]}{dt} = -k_1[A_2][B_3] + k_d[A{\cdot}B] \quad \text{(A1)}$$

$$\frac{d[A{\cdot}B]}{dt} = k_1[A_2][B_3] - k_d[A{\cdot}B] \quad \text{(A2)}$$

(Equations A1 and A2 are identical to eqs 3 and 4 in the text.) From eqs A1 and A2, we immediately find

$$\frac{d[A_2]}{dt} + \frac{d[A{\cdot}B]}{dt} = 0 \quad \text{(A3)}$$

and thus

$$[A{\cdot}B] = [A_2]_0 - [A_2] \quad \text{at any time } t \quad \text{(A4)}$$

Substituting eq A4 in eq A1, we find, for the equimolar reaction ($[A_2]_0 = [B_3]_0$)

$$\frac{dx(t)}{dt} = -k_1\{x(t)\}^2 + k_d\{[A_2]_0 - x(t)\}$$
$$\text{with } x(t) = [A_2] \text{ at } t \quad \text{(A5)}$$

dx.doi.org/10.1021/ma202461e | Macromolecules 2012, 45, 1636−1645

Equation A5 is analytically solved to give

$$\ln\left\{\frac{x(t)-x_2^*}{x(t)-x_1^*}\right\} = -(x_2^*-x_1^*)k_1 t + \ln\left\{\frac{[A_2]_0-x_2^*}{[A_2]_0-x_1^*}\right\} \quad \text{(A6)}$$

with

$$x_1^* = -\frac{1}{2}\{Q_{eq} + (Q_{eq}{}^2 + 4Q[A_2]_0)^{1/2}\} \quad \text{(A7a)}$$

$$x_2^* = \frac{1}{2}\{-Q_{eq} + (Q_{eq}{}^2 + 4Q[A_2]_0)^{1/2}\} \quad \text{(A7b)}$$

and

$$Q_{eq} = 1/K_{eq} = \frac{k_d}{k_1} \quad \text{(A8)}$$

For K_{eq} = 8000 M^{-1} (cf. section 3.3.1) and $[A_2]_0$ = 0.04, 0.13 M (in the range examined in Figure 2), the time evolution of $x(t) = [A_2](t)$ calculated from eq A6 is shown with the circles and squares in Figure 8. For comparison, the approximate solution utilized in section 3.1, $1/x(t) = k_1 t + 1/[A_2]_0$ (equivalent to eq 8 in section 3.3.1), calculated for the same parameters (K_{eq} = 8000 M^{-1} and $[A_2]_0$ = 0.04, 0.13 M) are shown with the curves. The approximate solution for those parameter values are close to the rigorous solution in the range of $[A_2](t)/[A_2]_0 \geq 0.1667$ (that corresponds to the range of $p \leq p_c = 0.8333$ focused in section 3.3.1 for discussion of t_{gel}). Thus, the discussion of t_{gel} on the basis of eq 6 in section 3.3.1 is reasonable for the above K_{eq} and $[A_2]_0$ values at 25 °C.

■ ASSOCIATED CONTENT

Supporting Information

Text giving additional experimental details for the effect of HAc catalyst concentration on gelation, for the viscosity of the samples with concentration below c_g and for the determination of the K_{eq} using NMR analysis. This material is available free of charge via the Internet at http://pubs.acs.org.

■ AUTHOR INFORMATION

Corresponding Author

*E-mail: ghdeng@scut.edu.cn (G.D.); ymchen@iccas.ac.cn (Y.C.); liucy@iccas.ac.cn (C.Y.L.).

Notes

The authors declare no competing financial interest.

■ ACKNOWLEDGMENTS

This work is supported by National Natural Science Foundation of China (Grants 20874109 and 20974034), PetroChina Innovation Foundation, and National High Technology Research, and Development Program of China (Grants 2009AA033601 and 2009AA034605).

■ REFERENCES

(1) Rowan, S. J.; Cantrill, S. J.; Cousins, G. R. L.; Sanders, J. K. M.; Stoddart, J. F. *Angew. Chem., Int. Ed.* **2002**, *41*, 898−952.
(2) Maeda, T.; Otsuka, H.; Takahara, A. *Prog. Polym. Sci.* **2009**, *34*, 581−604.
(3) Wojtecki, R. J.; Meador, M. A.; Rowan, S. J. *Nature Mater.* **2011**, *10*, 14−27.
(4) Lehn, J. M. *Chem. Soc. Rev.* **2007**, *36*, 151−160.
(5) Corbett, P. T.; Leclaire, J.; Vial, L.; West, K. R.; Wietor, J. L.; Sanders, J. K. M.; Otto, S. *Chem. Rev.* **2006**, *106*, 3652−3711.
(6) Ono, T.; Nobori, T.; Lehn, J. M. *Chem. Commun.* **2005**, 1522−1524.
(7) Lehn, J. M. *Prog. Polym. Sci.* **2005**, *30*, 814−831.
(8) Skene, W. G.; Lehn, J. M. P. *Proc. Natl. Acad. Sci. U. S. A.* **2004**, *101*, 8270−8275.
(9) Ono, T.; Fujii, S.; Nobori, T.; Lehn, J. M. *Chem. Commun.* **2007**, 46−48.
(10) Ono, T.; Fujii, S.; Nobori, T.; Lehn, J. M. *Chem. Commun.* **2007**, 4360−4362.
(11) Ruff, Y.; Buhler, E.; Candau, S. J.; Kesselman, E.; Talmon, Y.; Lehn, J. M. *J. Am. Chem. Soc.* **2010**, *132*, 2573−2584.
(12) Deng, G. H.; Tang, C. M.; Li, F. Y.; Jiang, H. F.; Chen, Y. M. *Macromolecules* **2010**, *43*, 1191−1194.
(13) Mours, M.; Winter, H. H. *Macromolecules* **1996**, *29*, 7221−7229.
(14) Winter, H. H.; Morganelli, P.; Chambon, F. *Macromolecules* **1988**, *21*, 532−535.
(15) Yount, W. C.; Loveless, D. M.; Craig, S. L. *J. Am. Chem. Soc.* **2005**, *127*, 14488−14496.
(16) Li, L.; Aoki, Y. *Macromolecules* **1997**, *30*, 7835−7841.
(17) Stadler, F. J.; Pyckhout-Hintzen, W.; Schumers, J. M.; Fustin, C. A.; Gohy, J. F.; Bailly, C. *Macromolecules* **2009**, *42*, 6181−6192.
(18) Loveless, D. M.; Jeon, S. L.; Craig, S. L. *Macromolecules* **2005**, *38*, 10171−10177.
(19) Appel, E. A.; Biedermann, F.; Rauwald, U.; Jones, S. T.; Zayed, J. M.; Scherman, O. A. *J. Am. Chem. Soc.* **2010**, *132*, 14251−14260.
(20) Dossin, L. M.; Graessley, W. W. *Macromolecules* **1979**, *12*, 123−130.
(21) Jong, L.; Stein, R. S. *Macromolecules* **1991**, *24*, 2323−2329.
(22) Ramzi, A.; Hakiki, A.; Bastide, J.; Boue, F. *Macromolecules* **1997**, *30*, 2963−2977.
(23) Deam, R. T.; Edwards, S. F. *Philos. Trans. R. Soc. London, A* **1976**, *280*, 317−353.
(24) Rubinstein, M.; Panyukov, S. *Macromolecules* **2002**, *35*, 6670−6686.
(25) Termonia, Y. *Macromolecules* **1994**, *27*, 7378−7381.
(26) Tanaka, F.; Edwards, S. F. *Macromolecules* **1992**, *25*, 1516−1523.
(27) McLeish, T. C. B. *Adv. Phys.* **2002**, *51*, 1379−1527.
(28) Cates, M. E.; Fielding, S. M. *Adv. Phys.* **2006**, *55*, 799−879.
(29) Sayer, J. M.; Peskin, M.; Jencks, W. P. *J. Am. Chem. Soc.* **1973**, *95*, 4277−4287.
(30) Levrand, B.; Ruff, Y.; Lehn, J. M.; Herrmann, A. *Chem. Commun.* **2006**, 2965−2967.
(31) Rubinstein, M.; Colby, R. H. *Polymer Physics*; Oxford University Press: New York, 2003.
(32) Winter, H. H. *Polym. Eng. Sci.* **1987**, *27*, 1698−1702.
(33) Chambon, F.; Petrovic, Z. S.; Macknight, W. J.; Winter, H. H. *Macromolecules* **1986**, *19*, 2146−2149.
(34) Takahashi, M.; Yokoyama, K.; Masuda, T.; Takigawa, T. *J. Chem. Phys.* **1994**, *101*, 798−804.
(35) The error of t_{gel} estimated is about ±10%, due to purity of A_2 and B_3 from different batches(such as the degree of functionalities, molecular weight distribution of PEO in A_2) and humidity of testing environment. It is worth noting that the apparent slope of the modulus is always bigger than the real one, since the dynamic frequency sweep was performed from the low frequency to the high frequency.
(36) Tung, C. Y. M.; Dynes, P. J. *J. Appl. Polym. Sci.* **1982**, *27*, 569−574.
(37) Levrand, B.; Fieber, W.; Lehn, J. M.; Herrmann, A. *Helv. Chim. Acta* **2007**, *90*, 2281−2314.
(38) Winter, H. H.; Chambon, F. *J. Rheol.* **1986**, *30*, 367−382.
(39) Martin, J. E.; Adolf, D.; Wilcoxon, J. P. *Phys. Rev. Lett.* **1988**, *61*, 2620−2623.
(40) Martin, J. E.; Adolf, D.; Wilcoxon, J. P. *Phys. Rev. A* **1989**, *39*, 1325−1332.
(41) Colby, R. H.; Gillmor, J. R.; Rubinstein, M. *Phys. Rev. E* **1993**, *48*, 3712−3716.
(42) Lusignan, C. P.; Mourey, T. H.; Wilson, J. C.; Colby, R. H. *Phys. Rev. E* **1995**, *52*, 6271−6280.

(43) Li, L.; Uchida, H.; Aoki, Y.; Yao, M. L. *Macromolecules* **1997**, *30*, 7842−7848.
(44) Li, L.; Aoki, Y. *Macromolecules* **1998**, *31*, 740−745.
(45) Cousins, G. R. L.; Poulsen, S. A.; Sanders, J. K. M. *Chem. Commun.* **1999**, 1575−1576.
(46) Giuseppone, N.; Schmitt, J. L.; Lehn, J. M. *Angew. Chem., Int. Ed.* **2004**, *43*, 4902−4906.
(47) Pham, Q. T.; Russel, W. B.; Thibeault, J. C.; Lau, W. *Macromolecules* **1999**, *32*, 5139−5146.
(48) Ma, S. X.; Cooper, S. L. *Macromolecules* **2002**, *35*, 2024−2029.
(49) Indei, T.; Takimoto, J. *J. Chem. Phys.* **2010**, 133.
(50) James, H. M.; Guth, E. *J. Chem. Phys.* **1943**, *11*, 455−481.
(51) Wall, F. T. *J. Chem. Phys.* **1943**, *11*, 527−530.
(52) Treloar, L. R. G. *The Physics of Rubber Elasticity*; Oxford University Press: New York, 2005.
(53) Gumbrell, S. M.; Mullins, L.; Rivlin, R. S. *Trans. Faraday Soc.* **1953**, *49*, 1495−1505.
(54) Bitoh, Y.; Urayama, K.; Takigawa, T.; Ito, K. *Soft Matter* **2011**, *7*, 2632−2638.
(55) Bitoh, Y.; Akuzawa, N.; Urayama, K.; Takigawa, T. *J. Polym. Sci., Part B: Polym. Phys.* **2010**, *48*, 721−728.
(56) Syrett, J. A.; Becer, C. R.; Haddleton, D. M. *Polym. Chem.* **2010**, *1*, 978−987.
(57) Cordier, P.; Tournilhac, F.; Soulie-Ziakovic, C.; Leibler, L. *Nature* **2008**, *451*, 977−980.
(58) Burattini, S.; Colquhoun, H. M.; Fox, J. D.; Friedmann, D.; Greenland, B. W.; Harris, P. J. F.; Hayes, W.; Mackay, M. E.; Rowan, S. J. *Chem. Commun.* **2009**, 6717−6719.

Macromolecules

Article

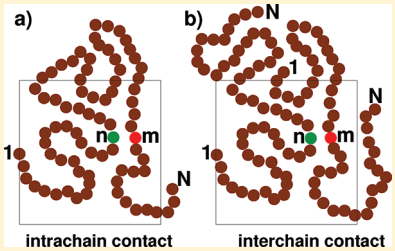
pubs.acs.org/Macromolecules

Interchain Monomer Contact Probability in Two-Dimensional Polymer Solutions

N. Schulmann, H. Meyer, J. P. Wittmer,* A. Johner, and J. Baschnagel

Institut Charles Sadron, Université de Strasbourg & CNRS, 23 rue du Loess, BP 84047, 67034 Strasbourg Cedex 2, France

ABSTRACT: Using molecular dynamics simulations of a standard bead−spring model, we investigate the density crossover scaling of strictly two-dimensional ($d = 2$) self-avoiding polymer chains without chain crossings focusing on properties related to the contact exponent θ_2 set by the intrachain subchain size distribution. With $R \sim N^{\nu}$ being the size of chains of length N, the number n_{int} of interchain monomer contacts per monomer is found to scale as $n_{int} \sim 1/N^{\nu\theta_2}$ with $\nu = 3/4$ and $\theta_2 = 19/12$ for dilute solutions and $\nu = 1/d$ and $\theta_2 = 3/4$ for $N \gg g(\rho) \approx 1/\rho^2$. Irrespective of the density ρ, sufficiently long chains are thus found to consist of compact packings of blobs of fractal perimeter dimension $d_p = d - \theta_2 = 5/4$. In agreement with the generalized Porod scattering of compact objects with fractal contour, the Kratky representation of the intramolecular form factor $F(q)$ reveals a strong nonmonotonous behavior approaching with increasing density a limiting power-law slope $F(q)q^d/\rho \approx 1/(qR)^{\theta_2}$ in the intermediate regime of the wave vector q. The demonstrated intermolecular contact probability is argued to imply an enhanced compatibility of polymer blends.



INTRODUCTION

As first suggested by de Gennes,[1] it is now generally accepted[2−15] that strictly two-dimensional (2D) self-avoiding polymer chains adopt compact and segregated conformations at high densities, i.e., the typical chain size R scales as

$$R(N, \rho) \approx (N/\rho)^{\nu} \quad \text{where } \nu = 1/d = 1/2 \tag{1}$$

with N being the chain length, ρ the monomer number density, and $d = 2$ the spatial dimension. We assume here that monomer overlap and chain intersection are strictly forbidden. Please note that relaxing the latter restriction would lead to a different universality class revealing mean-field statistics with strong logarithmic corrections.[3,16,17] Compactness obviously does not imply Gaussian chain statistics since other critical exponents with non-Gaussian values have been shown to matter.[2,3,13−15] It is thus incorrect to assume that excluded-volume effects would be screened as is approximately the case for three-dimensional (3D) melts.[18] Also, it should be emphasized that the segregation of chains (and subchains) does not impose disklike shapes minimizing the contour perimeter of the (sub)chains. Focusing on dense 2D melts, it has been shown recently[3,13−15] that the irregular chain contours are characterized in fact by a fractal perimeter of typical length

$$L \sim Nn_{int} \sim R^{d_p} \sim N^{d_p/d} \quad \text{with } d_p = d - \theta_2 = 5/4 \tag{2}$$

where n_{int} stands for the fraction of monomers of a chain interacting with monomers of other chains. The fractal line dimension d_p is set by Duplantier's contact exponent $\theta_2 = 3/4$ characterizing the size distribution of inner chain segments.[2] We remind that Duplantier's theoretical predictions obtained using conformal invariance[2] rely on both the topological constraint (no chain intersections) and the space-filling property of the melt.

Since the melt limit is experimentally extremely difficult to realize for a strictly 2D layer,[4−6] the aim of this study is to show that eq 2 holds more generally for all densities assuming that the chains are sufficiently long. This allows to view the polymer solutions as space-filling melts of "chains of blobs" following de Gennes' classical density crossover scaling.[1] The present paper is organized as follows: We recall first the computational model used for this study and turn then to our mainly numerical results starting with the characterization of the typical chain size R, focusing on the interchain monomer contact number n_{int} and ending with an experimentally relevant property, the intramolecular form factor $F(q)$. A comment on possible consequences of eq 2 for the demixing of polymer melts in strictly 2D[11,12] concludes the paper.

COMPUTATIONAL ISSUES

The aim of the present study is to clarify universal power-law scaling predictions in the limit of large chain length N and low wave vector q where the specific physics and chemistry on the monomeric level (such as the local chain stiffness) are only relevant for prefactor effects.[1] This calls for the use of a generic coarse-grained polymer model Hamiltonian which is sufficiently simple to allow the efficient computation of dense systems of large self-avoiding chains without chain intersections. As described in detail in ref 14, our numerical results are obtained by molecular dynamics simulations[19] of monodisperse and linear chains using a bead−spring model equivalent to the well-known Kremer−Grest model which has been successfully used

Received: January 12, 2012
Published: January 26, 2012

 © 2012 American Chemical Society dx.doi.org/10.1021/ma300085a | *Macromolecules* 2012, 45, 1646−1651

for a broad range of polymer physics problems.[20−22] Adjacent monomers of a chain are connected by a harmonic spring potential which is calibrated to the "finite extendible nonlinear elastic" (FENE) springs of the original Kremer−Grest model. No additional stiffness term has been included, and at variance to most experimental systems,[4−7] our chains are flexible down to monomeric scales. Lennard-Jones (LJ)[19] units are used throughout this paper and temperature is set to unity. The classical equations of motion of the multichain system are solved using a Langevin thermostat[19] with friction constant γ = 0.5. Note that monomer overlap and chain crossings are made impossible by the excluded volume interaction and the bonding potential; the chains are thus strictly 2D "self-avoiding walks" in the sense of ref 3. While our previous studies[13−15] have focused on one melt density, ρ = 0.875, we scan now over a broad range of densities ρ as may be seen from Figure 1. Chains of length N

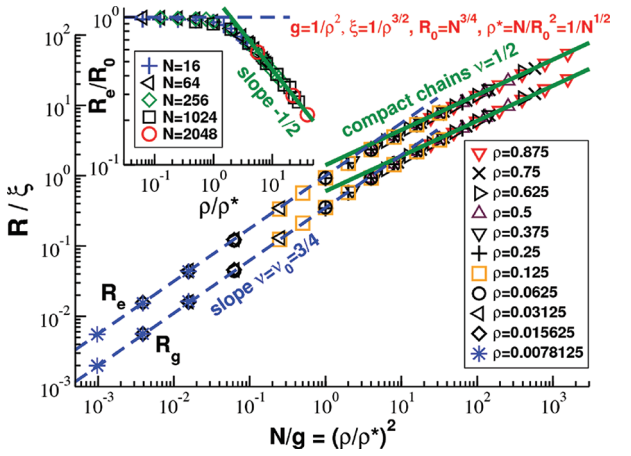


Figure 1. Average chain size R for self-avoiding polymers in d = 2 dimensions for a broad range of densities ρ and chain lengths N as indicated in the figure. The exponent $\nu = \nu_0 \equiv 3/4$ expected for the dilute swollen chain limit is given by the dashed lines and the compact chain exponent $\nu = 1/d$ by the bold lines. Main panel: root-mean square end-to-end distance R_e/ξ and radius of gyration R_g/ξ as a function of reduced chain length N/g where we set $\xi \equiv 1/\rho^{3/2}$ and $g \equiv 1/\rho^2$ as expected from standard density crossover scaling.[1] For simplicity, all prefactors related to the dilute limit are set to unity. Inset: replot focusing on the ρ-scaling for constant chain length N.

= 16 up to N = 1024 monomers have been sampled for all ρ; for ρ = 0.125, ρ = 0.5, and ρ = 0.875 we have even computed systems with N = 2048. Taken apart the latter systems with N = 2048 all chains have diffused over at least 10 times their radius of gyration,[23] providing thus high precision statistics. To avoid finite system size effects the periodic simulation boxes contain at least 96 chains for densities $\rho \geq 0.031\,25$; e.g., for N = 2048 and ρ = 0.875 we have 196 608 monomers in a box of linear length 474.02, and for N = 1024 and ρ = 0.031 25 we have 98 304 monomers in a box of length 1773.62. For lower densities, the N = 1024 systems have only 24 chains while shorter chains ($N \leq 256$) are computed for systems with 384 chains.

COMPUTATIONAL RESULTS

Compact Chains of Blobs. That sufficiently long 2D polymer chains become indeed compact for all densities, as stated by eq 1, is shown in Figure 1 presenting the overall chain size R as characterized by the root-mean-square end-to-end distance R_e and the radius of gyration R_g.[24] As one expects,[1,2] the typical chain size is found to increase with a power-law exponent $\nu = \nu_0 \equiv 3/4$ in the dilute limit (dashed lines) and with $\nu = 1/d$ for larger chains and densities in agreement with various numerical[8−10] and experimental studies.[4,5,7] Please note that the index 0 refers here as throughout this paper to the dilute swollen chain limit. The main panel of Figure 1 presents data for different densities as a function of chain length N which are successfully brought to collapse by rescaling the horizontal axis with the number of monomers

$$g(\rho) \approx \rho\xi^d \sim 1/\rho^{1/(\nu_0 d-1)} = \rho^{-2} \qquad (3)$$

spanning the semidilute blob and the vertical axis by its size $\xi \sim g^{\nu_0} \sim 1/\rho^{3/2}$. For simplicity, all prefactors related to the dilute limit are set to unity, e.g., $g \equiv 1/\rho^2$ and $\xi \equiv 1/\rho^{3/2}$. The model-dependent prefactors of ξ and g may be obtained in principle from the intercept of the dilute and compact power-law slopes. Since R_e becomes compact more rapidly than R_g, the blob size defined using R_e is slightly smaller than the one defined using R_g. Please note that due to the (generalized) Porod scattering at the chain perimeter discussed below (Figure 6), the blob size ξ should not be determined by an Ornstein−Zernike fit to the intramolecular form factor $F(q)$ as done in ref 5.

An equivalent data representation focusing on the chain size as a function of density taking as reference the dilute chain size $R_0 \equiv N^{\nu_0}$ is shown in the inset. We trace here R_e/R_0 as a function of the reduced density ρ/ρ^* with $\rho^* \equiv N/R_0^d = 1/\sqrt{N}$ being the crossover density. The typical chain size decreases indeed as $R \sim 1/\sqrt{\rho}$ with increasing density (bold line) as expected for compact chains, eq 1, in agreement with previous numerical work.[8,10] Below we refer to $N/g = (\rho/\rho^*)^2 \gg 1$ as the "compact chain limit" and to $g \to 0$ as the "melt limit".

Intrachain Subchain Size Distribution. Obviously, the mere fact that ν becomes 1/2 in the compact chain limit does not imply Gaussian chain statistics.[2,3] This can be directly seen, e.g., from the subchain size distribution $G(r,s)$ of the vector $\mathbf{r} = \mathbf{r}_m - \mathbf{r}_n$ between the monomers n and $m = n + s - 1$ on the same tagged chain presented in the main panel of Figure 2.[18] For the examples indicated we have chosen subchains of length $s = N/2$ in the middle of chains of length N = 1024.[25] The data have been binned logarithmically, and only distances $r > 2$ are presented to suppress local packing effects of the LJ beads which would superimpose and blur the expected scaling behavior. Using the measured second moment $R^2(s)$ of the distribution, we trace $R^d(s)G(r,s)$ as a function of the reduced distance $x = r/R(s)$. This is motivated by the scaling

$$R^d(s)G(r, s) = f(x) \quad \text{with } f(x) \approx x^{\theta_2} \text{ for } x \ll 1 \qquad (4)$$

observed as expected[2] in the dilute and melt limits where $R(s)$ is the only relevant length scale. Note that for $x \gg 1$ the scaling function $f(x)$ becomes a well-understood cutoff function.[26,27,14] The dashed and bold power-law slopes indicated in the figure correspond to the exponents $\theta_2 = \theta_{2,0} \equiv 19/12$ and $\theta_2 = 3/4$ predicted for both limits.[2] (We remind that for Gaussian chains $\theta_2 \equiv 0$; i.e., $G(r,s)$ decays monotonously with distance r. For good solvent chains in d = 3 dimensions it is known that θ_2 becomes $\theta_{2,0} \approx 0.815$ in the dilute limit[28] while $\theta_2 = 0$ in denser systems if distances $r \gg \xi$ are probed.[1,26]) Obviously, the scaling of $G(r,s)$ becomes more intricate for semidilute densities where the blob size ξ sets an additional length scale. For $s \gg g(\rho) \gg 1$ one expects to observe two power-law asymptotes, one scaling as $G(r,s) \sim r^{19/12}$ if the conformational properties

dx.doi.org/10.1021/ma300085a | Macromolecules 2012, 45, 1646−1651

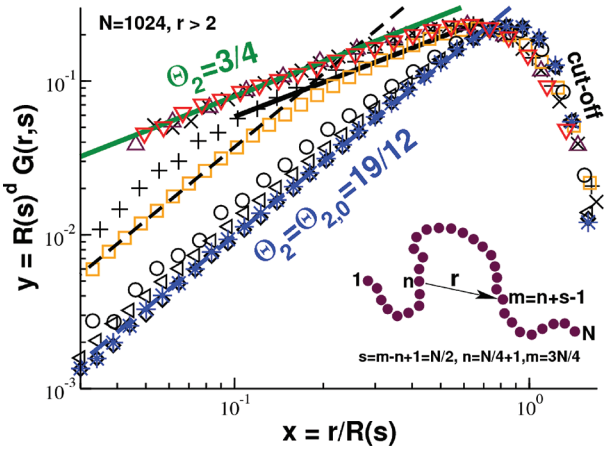


Figure 2. Subchain size distribution $G(r,s)$ between the monomers $n = N/4 + 1$ and $m = n + s - 1 = 3N/4$ obtained as illustrated by the sketch at the bottom. The histograms are logarithmically binned in r. We show data for one chain length, $N = 1024$, and various densities using the same symbols as in the main panel of Figure 1. Motivated by the scaling in the dilute and melt limits, eq 4, $R^d(s)G(r,s)$ is traced as a function of $x \equiv r/R(s)$ with $R^2(s)$ being the measured second moment of the distribution $G(r,s)$. The power-law exponent θ_2 for $x \ll 1$ is given by $\theta_2 = 19/12$ in the dilute limit (dashed lines) and by $\theta_2 = 3/4$ for $r \gg \xi$ (solid lines).

within the blob are probed ($r \ll \xi$) and one as $G(r,s) \sim r^{3/4}$ for $\xi \ll r \ll R(s)$. Although much larger blobs are certainly warranted to demonstrate this unambiguously, this expected behavior is qualitatively consistent with our data as may be seen for $\rho = 0.125$.[25]

Interchain Monomer Pair Distribution Function. As shown in Figure 3, the θ_2 exponents do not only characterize intrachain properties but are also relevant for describing the interchain monomer contacts. We have plotted here the radial pair distribution function $g_{int}(r)$ between monomers from different chains. As shown from the main panel, this distribution becomes unity (by normalization) for large reduced distances $x = r/R_g \gg 1$. The scaling of the horizontal axis is again motivated by the density limits where the chain size R is the only relevant length scale.

The power-law exponents θ_2 for $x \ll 1$ can be understood by generalizing a scaling argument given in ref 3 sketched in Figure 4. It states that it is irrelevant of whether the neighborhood at $r \ll R$ around the reference monomer is penetrated by a long loop of the same chain or by another chain with a center of mass at a typical distance R. Hence

$$g_{int}(r)\rho \approx G(r, s \approx N) \times N \times \underline{R^d \rho/N} \qquad (5)$$

where the second factor N stems from the fact that it is irrelevant which monomer of the second chain is probed.[29] Note that the underlined term characterizing the probability for having a second chain close to the reference chain drops out in the compact chain limit where eq 1 holds. Equations 4 and 5 imply

$$g_{int}(r) \approx x^{\theta_2} \sim 1/N^{\nu\theta_2} \quad \text{for } x \ll 1 \qquad (6)$$

as indicated by dashed and bold solid lines for respectively dilute and melt limits.

The scaling with respect to chain length N for small distances r indicated in eq 6 is successfully verified by comparing different chain lengths N at the same density ρ as shown in the inset of Figure 3 for $\rho = 0.875$. The distributions $g_{int}(r)$ have been sampled here using linear r-bins to emphasize that, as one expects, the standard oscillations of the monomer−monomer pair-correlations are observed for small distances r at high densities. Interestingly, the predicted N-scaling $g_{int}(r) \sim 1/N^{3/8}$ still holds in this limit. Please note that the peak structure disappears rapidly with decreasing density.

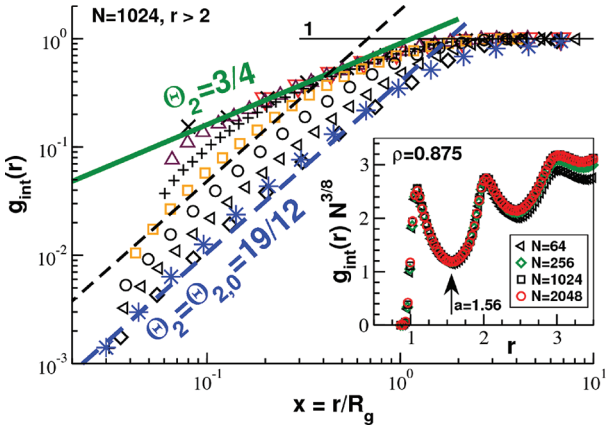


Figure 3. Monomer pair distribution function $g_{int}(r)$ between monomers from different chains using the same symbols as in Figure 1 for density ρ and chain length N. Main panel: logarithmically averaged $g_{int}(r)$ as a function of the reduced distance $x = r/R_g$ for large distances $r > 2$ with R_g being the directly measured radius of gyration. Chains of length $N = 1024$ are presented for a broad range of densities. The same exponents θ_2 are observed for $x \ll 1$ as for the intrachain subchain size distribution $G(r,s)$: $\theta_2 = 19/12$ in the dilute limit (dashed line) and $\theta_2 = 3/4$ in the compact chain limit (solid line). Because of the additional length scale $\xi(\rho)$ in the semidilute density regime data collapse is only observed for very low dilute densities and very high melt densities. Inset: perfect scaling collapse of $g_{int}(r)N^{3/8}$ for small distances r (with $g_{int}(r)$ being binned linearly in r) for one high density $\rho = 0.875$ confirming the predicted scaling $g_{int}(r) \sim 1/N^{\nu\theta_2}$ in this limit. The (essentially arbitrary) parameter $a = 1.56$ used for the determination of the typical interchain monomer contact number n_{int} is indicated by the arrow.

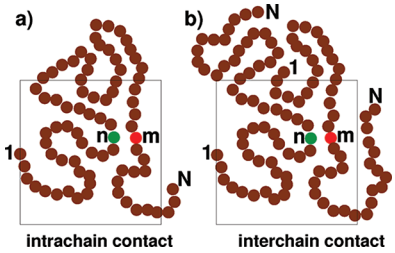


Figure 4. Key scaling argument suggested in ref 3 tested numerically in this work relating the intrachain size distribution $G(r,s \approx N)$ to the interchain pair distribution function $g_{int}(r)$. It states that it is irrelevant of whether the compactly filled neighborhood at $r \ll R$ around the reference monomer n is penetrated by a long loop of the same chain as in (a) or by another chain with a center of mass at a typical distance R as shown in (b).

Interchain Monomer Contact Probability. In order to characterize more systematically the density crossover, we focus now on $g_{int}(r \approx a)$ with a being one fixed monomeric distance for all densities. For the data presented in Figure 5 we have determined the typical number n_{int} of interchain monomer contacts for a reference monomer by integrating $g_{int}(r)\rho$ up to a cutoff $a = 1.56$. The raw data obtained for several densities is presented in panel a. The specific value of a used here is

dx.doi.org/10.1021/ma300085a | Macromolecules 2012, 45, 1646−1651

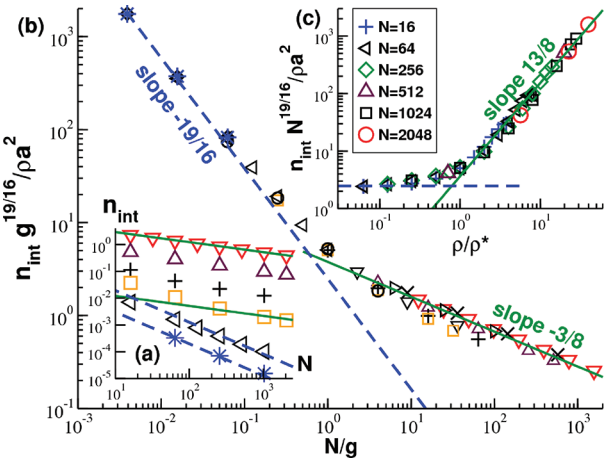


Figure 5. Average interchain monomer contact number n_{int} obtained by integrating $\rho g_{int}(r)$ up to a cutoff a = 1.56: (a) raw data vs chain length N for a few densities ρ, (b) scaling of n_{int} vs reduced chain length $N/g(\rho)$ for all densities, and (c) equivalent scaling of n_{int} vs reduced density $\rho/\rho^*(N)$. The same symbols are used in (a) and (b) as in the main panel of Figure 1. In agreement with eq 6, the dashed lines correspond to the exponent $\nu\theta_2$ = 19/16 in the dilute chain limit and the full lines to $\nu\theta_2$ = 3/8 for the compact chain limit. Considering that the raw data are spread over more than 5 orders of magnitude, the data collapse observed in (b) and (c) is remarkable. Confirming thus eq 7, this scaling is the central result of our work.

motivated by the first minimum of the pair distribution function shown in the inset of Figure 3. This minimum position varies only weakly with ρ. For not too high densities the scaling of n_{int} is found to be robust under variation of a. The quality of the ρ-scaling (but not of the scaling with respect to N) depends somewhat on a for $\rho \geq 0.75$ where additional physics due to the discrete beads becomes relevant. Note that similar scaling results have been obtained by computing the fraction of monomers of a chain with at least one monomer from another chain within a distance a following ref 14.

Using a similar representation as in Figure 1, the rescaled number of interchain contacts n_{int} is presented in panel b of Figure 5 (main panel) as a function of the reduced chain length N/g and in panel c as a function of the reduced density ρ/ρ^* for different chain lengths. The rescaling used for the vertical axes is readily obtained by matching at $N/g = (\rho/\rho^*)^2 = 1$ the power-law results implied by eq 6 for the dilute ($\nu_0\theta_{2,0}$ = 19/16) and compact ($\nu\theta_2$ = 3/8) limits. This implies for the latter limit (solid bold lines)

$$n_{int} \approx \frac{\rho a^d}{g^{\nu_0\theta_{2,0}}}(N/g)^{-\nu\theta_2} \sim \rho^{21/8}N^{-3/8} \tag{7}$$

where the first factor corresponds to the fraction of monomers of a given blob interacting with monomers from other chains given that the blob is at the chain perimeter. The second term $(N/g)^{-\nu\theta_2} = (N/g)^{-3/8}$ stands for the fraction of blobs of a chain interacting with other chains. The successful scaling presented in Figure 5 thus demonstrates that in the compact chain limit the perimeter length L scales as[30]

$$L \approx \xi(N/g)^{1-\theta_2/d} \tag{8}$$

Since, on the other hand, $L/\xi \approx (R/\xi)^{d_p} \approx (N/g)^{d_p/d}$ by definition of the fractal line dimension, this implies $d_p = d - \theta_2$ = 5/4, generalizing thus the numerical result obtained for the melt limit[14] to the broader compact chain limit.

Generalized Porod Scattering of the Intermolecular Structure Factor. Although direct real-space visualizations of 2D polymer systems are experimentally feasible,[4,5,7] allowing thus a direct computation of $G(r,s)$ and $g_{int}(r)$, it is important to note that the exponent θ_2 = 3/4 for compact chains of blobs may in principle be obtained from an analysis of the intrachain molecular form factor $F(q)$ with q being the modulus of the wave vector.[24] This point is addressed in Figure 6 where the

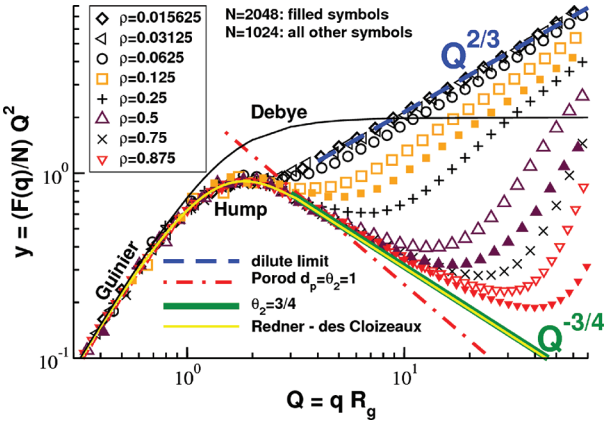


Figure 6. Kratky representation of the intramolecular form factor $F(q)$ as a function of the reduced wave vector $Q = qR_g$ for different densities ρ. Filled symbols refer to data for N = 2048 and all other symbols to N = 1024. The Debye formula is indicated by the top thin line, the dilute swollen chain limit with $F(q) \sim 1/q^{1/\nu_0}$ by the dashed line, the Porod scattering for a compact 2D object with smooth perimeter by the dash-dotted line, and the power-law exponent $-\theta_2 = -3/4$ by the bold solid line. Our complete theoretical prediction for asymptotically long chains (thin solid line) using the so-called Redner−des Cloizeaux approximation of $G(r,s)$[14] allows to fit the data starting from the Guinier regime for small wave vectors.

rescaled form factor $(F(q)/N)Q^2$ is plotted as a function of the reduced wave vector $Q = qR_g$ for different densities ρ. Filled symbols refer to data for N = 2048 and all other symbols to N = 1024. At variance to the indicated Debye formula for Gaussian chains a strong nonmonotonous behavior is revealed by our data, which approaches with increasing ρ and N a power-law exponent $-\theta_2 = -3/4$ (bold solid line). This power law limit is implied by the fact that $F(q)$ can be expressed as an integral over the Fourier transform $G(q,s)$ of the intrachain size distribution $G(r,s)$.[14,18] Using general arguments which do not depend explicitly on the density or the blob size, it has been shown[14] that as a direct consequence of eq 4 the form factor for asymptotically long chains must scale as

$$\frac{F(q)}{N}Q^d \approx \frac{1}{Q^{\theta_2}} \approx \frac{1}{Q^{d-d_p}} \quad \text{for } \frac{1}{R} \ll q \ll \frac{1}{\xi} \tag{9}$$

where we have used $d_p = d - \theta_2$. We emphasize that this result is consistent with the well-known Porod scattering expected for general compact objects of fractal surface dimension d_p.[15] Obviously, much larger chains than computationally feasible at present are required to confirm numerically the predicted perimeter dimension using eq 9.

dx.doi.org/10.1021/ma300085a | Macromolecules 2012, 45, 1646−1651

CONCLUSION

Summary. We have investigated numerically the density crossover scaling of strictly 2D self-avoiding polymer chains focusing on properties related to the θ_2 contact exponent which characterizes not only (by definition) the intrachain distribution $G(r,s)$ but also the interchain pair distribution function $g_{int}(r) \sim r^{\theta_2}$ and the monomer contact number $n_{int} \sim 1/N^{\nu\theta_2}$. The established scaling for dense melts[3,13,14] is found to remain valid for all densities if reformulated in terms of chains of blobs. As a consequence, the intramolecular form factor $F(q)$ measuring the composition fluctuations at the fractal perimeters of the compact blob chains approaches with increasing density and chain length a power-law asymptote implied by the generalized Porod scattering of compact objects of fractal perimeter dimension $d_p = d - \theta_2 = 5/4$. Note that our chains are sufficiently long to confirm d_p using the intermolecular binary contacts n_{int} (Figure 5) but not using the form factor. One reason for this is that eq 9 assumes asymptotically long chains where critical exponents other than θ_2 may be ignored. The corrections for finite N/g need still to be worked out theoretically. However, since $g_{int}(r)$ or n_{int} may be directly obtained experimentally by visualization of dilute and semidilute 2D polymer solutions,[4,5,7] our numerical results suggest that the analysis of the latter properties may allow the experimental verification of the predicted universal exponents.

Beyond the Present Study. We emphasize that at variance to most experimental systems[4,5,7] we have assumed here that the chains are flexible down to monomeric scales. As long as the persistence length remains smaller than the blob size, this should not alter the suggested scaling properties. In fact, since the blob size decreases very strongly with persistence length, i.e., N/g increases, a finite rigidity might even speed up the convergence to the predicted asymptotic behavior predicted for the compact limit, especially for the form factor. In order to bring our computational approach closer to experiment, we are currently computing systems with finite persistence length.

Finally, we point out that the scaling of the intermolecular contact probability n_{int} tested in this study is consistent with recent Monte Carlo simulations of symmetrical polymer mixtures using a version of the bond-fluctuation model in strictly two dimensions.[11,12] These simulations show that the compatibility of the chains is strongly enhanced compared to 3D blends. We remind that for the latter 3D blends the scaling of the critical temperature of unmixing $T_c \sim 1/\chi_c$ (with χ_c being the critical Flory parameter) is well described by the Flory–Huggins mean-field prediction,[1] i.e., $T_c \sim N$, and the compatibility of the blend decreases thus very strongly with chain length.[31,32] More generally, T_c is proportional to the typical interaction energy $e_{int} \sim Nn_{int}$ between different chains.[33] According to eq 7 and using eq 3, it follows thus that

$$T_c \sim Nn_{int} \approx g^{2-\nu_0\theta_{2,0}-\nu_0 d}(N/g)^{1-\nu\theta_2} \sim \rho^{21/8}N^{5/8} \quad (10)$$

in the compact chain limit.[34] The predicted exponent $5/8 = 0.625$ for the N-dependence agrees well with the value 0.65 obtained by fitting T_c for all computed chain lengths.[11] The corresponding strong power-law increase $T_c \sim \rho^{21/8}$ with density has to our knowledge not been probed yet.[35] Obviously, these theoretical predictions and numerical findings call for experimental verification.

AUTHOR INFORMATION

Notes

The authors declare no competing financial interest.

ACKNOWLEDGMENTS

We thank for generous grants of computer time by GENCI-IDRIS (Grant i2009091467) and the Pôle Matériaux et Nanosciences d'Alsace (ENIAC). N.S. acknowledges financial support by the Région Alsace. We are indebted to T. Kreer (Dresden) and M. Aichele (Frankfurt) for helpful discussions.

REFERENCES

(1) de Gennes, P. G. *Scaling Concepts in Polymer Physics*; Cornell University Press: Ithaca, NY, 1979.
(2) Duplantier, B. *J. Stat. Phys.* **1989**, *54*, 581.
(3) Semenov, A. N.; Johner, A. *Eur. Phys. J. E* **2003**, *12*, 469.
(4) Maier, B.; Rädler, J. O. *Phys. Rev. Lett.* **1999**, *82*, 1911.
(5) Maier, B.; Rädler, J. O. *Macromolecules* **2000**, *33*, 7185.
(6) Gavranovic, G. T.; Deutsch, J. M.; Fuller, G. G. *Macromolecules* **2005**, *38*, 6672–6678.
(7) Sun, F.; Dobrynin, A.; Shirvanyants, D.; Lee, H.; Matyjaszewski, K.; Rubinstein, G.; Rubinstein, M.; Sheiko, S. *Phys. Rev. Lett.* **2007**, *99*, 137801.
(8) Carmesin, I.; Kremer, K. *J. Phys. (Paris)* **1990**, *51*, 915.
(9) Nelson, P. H.; Hatton, T. A.; Rutledge, G. *J. Chem. Phys.* **1997**, *107*, 1269.
(10) Yethiraj, A. *Macromolecules* **2003**, *36*, 5854.
(11) Cavallo, A.; Müller, M.; Binder, K. *Europhys. Lett.* **2003**, *61*, 214–220.
(12) Cavallo, A.; Müller, M.; Binder, K. *J. Phys. Chem. B* **2005**, *109*, 6544.
(13) Meyer, H.; Kreer, T.; Aichele, M.; Cavallo, A.; Johner, A.; Baschnagel, J.; Wittmer, J. P. *Phys. Rev. E* **2009**, *79*, 050802(R).
(14) Meyer, H.; Wittmer, J. P.; Kreer, T.; Johner, A.; Baschnagel, J. *J. Chem. Phys.* **2010**, *132*, 184904.
(15) Meyer, H.; Schulmann, N.; Zabel, J. E.; Wittmer, J. P. *Comput. Phys. Commun.* **2011**, *182*, 1949.
(16) Nikomarov, E.; Obukhov, S. *Sov. Phys. JETP* **1981**, *53*, 328–335.
(17) Cavallo, A.; Müller, M.; Wittmer, J. P.; Johner, A.; Binder, K. *J. Phys.: Condens. Matter* **2005**, *17*, S1697–S1709.
(18) Wittmer, J.; Cavallo, A.; Xu, H.; Zabel, J.; Polin'ska, P.; Schulmann, N.; Meyer, H.; Farago, J.; Johner, A.; Obukhov, S.; Baschnagel, J. *J. Stat. Phys.* **2011**, *145*, 1017–1126.
(19) Frenkel, D.; Smit, B. *Understanding Molecular Simulation – From Algorithms to Applications*, 2nd ed.; Academic Press: San Diego, 2002.
(20) Grest, G. S.; Kremer, K. *Phys. Rev. A* **1986**, *33*, 3628.
(21) Kremer, K.; Grest, G. *J. Chem. Phys.* **1990**, *92*, 5057–5086.
(22) Plimpton, S. J. *J. Comput. Phys* **1995**, *117*, 1–19.
(23) Wittmer, J. P.; Meyer, H.; Johner, A.; Kreer, T.; Baschnagel, J. *Phys. Rev. Lett.* **2010**, *105*, 037802.
(24) Doi, M.; Edwards, S. F. *The Theory of Polymer Dynamics*; Clarendon Press: Oxford, 1986.
(25) Similar scaling plots are obtained using different monomer pairs n and $m = n + s - 1$ as long as chain end effects giving rise to different contact exponents θ_i are avoided.[2,13,14]
(26) des Cloizeaux, J.; Jannink, G. *Polymers in Solution: Their Modelling and Structure*; Clarendon Press: Oxford, 1990.
(27) Everaers, R.; Graham, I.; Zuckermann, M. *J. Phys. A* **1995**, *28*, 1271–1288.
(28) Hsu, H.-P.; Nadler, W.; Grassberger, P. *Macromolecules* **2004**, *37*, 4658.
(29) This relation between the intrachain size distribution and the interchain pair correlation function is also of relevance, e.g., for semidilute polymer solutions in $d = 3$ dimensions as may be seen from ref 36. A difference is here, however, that for $d = 3$ only the dilute limit and distances $r \ll \xi$ probing the structure within the blob are characterized by a critical exponent $\theta_{2,0} > 0$, while for $r \gg \xi$ the

intrachain and related interchain correlations are perturbative ($\theta_2 = 0$), i.e., correspond to analytic deviations with respect to the Gaussian chain model.[18] Please note also that for $r \gg \xi$ the connection between intra- and interchain correlations is implied by the incompressibility of the melt of blobs.[18]

(30) The fraction of blobs on the perimeter of the compact chains can be computed directly by partitioning the chains in curvilinear subchains of length $g \approx 1/\rho^2$ and counting the number of subchains with at least one monomer in contact with a monomer from another chain. This fraction is found to decay as $(N/g)^{-3/8}$ (not shown).

(31) Deutsch, H.; Binder, K. *J. Phys. II* **1993**, *3*, 1049.

(32) Binder, K. *Adv. Polym. Sci.* **1994**, *112*, 181.

(33) As expected from eq 7 and Figure 5, the interaction energy per chain e_{int} for our homopolymer systems is found to scale as $e_{int} \sim \rho^{21/8}N^{5/8}$ over several orders of magnitude in density and chain length. The same scaling is expected to hold close to the critical point of a polymer mixture.

(34) As discussed in ref 3, it is crucial here that the chains of the blend do not overlap or intersect as it may occur in thin films of finite width (as simulated in ref 12) where the number of monomers of a chain in contact with monomers from other chains is essentially (up to not irrelevant logarithmic corrections) proportional to N.

(35) For 3D good solvent polymer solutions it follows from eq 10 that $T_c \sim g^{-0.243}(N/g) \sim \rho^{1.626}N$ where we have used that $\nu_0 \approx 0.588$ and $\theta_{2,0} \approx 0.815$ in the dilute limit[28] and $\nu = 1/2$ and $\theta_2 = 0$ for large densities and distances ($r \gg \xi$).

(36) Müller, M.; Binder, K.; Schäfer, L. *Macromolecules* **2000**, *33*, 4568.

Macromolecules

Article

pubs.acs.org/Macromolecules

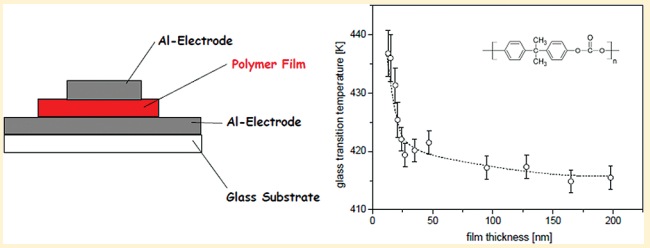
Molecular Mobility and Glass Transition of Thin Films of Poly(bisphenol A carbonate)

Huajie Yin,[†] Simone Napolitano,[‡] and Andreas Schönhals*,[†]

[†]BAM Federal Institute for Materials Research and Testing, Unter den Eichen 87, D-12200 Berlin, Germany

[‡]Department of Physics, Université Libre de Bruxelles, Boulevard du Triomphe CP 223, Bâtiment NO, B-1050 Bruxelles, Belgium

ABSTRACT: Glass transition behavior of thin poly(bisphenol A carbonate) (PBAC) films capped between two aluminum (Al) layers is investigated by means of dielectric expansion dilatometry and dielectric relaxation spectroscopy accompanied by contact angle measurements. The thermal glass transition temperature is more or less independent of the film thickness down to 20 nm. For thickness below 20 nm, an increase of T_g is observed. Meanwhile, an increase of the relaxation time at a fixed temperature is observed for the film with the thickness of 19 nm on the basis of a careful analysis of the temperature dependence of the relaxation rates. A more detailed analysis of the relaxation map reveals that the Vogel temperature increases and the fragility decreases systematically with decreasing film thickness. These properties are discussed in terms of the formation of a boundary layer with PBAC segments adsorbed onto the Al electrode due to the strong interaction between the Al and PBAC layers (2.51 mJ/m^2), which results in a reduced molecular mobility with regard to bulk PBAC behavior. As the dielectric strength is proportional to the number of segments fluctuating on the time and length scale of the dynamic glass transition, it is used as a unique probe of the deviations from bulk behavior. The temperature dependence of the penetration depth of the interfacial interactions on the structural relaxation is further quantitatively determined. The dynamic length scale of the perturbations into the chain conformations responsible for the deviation from bulk behavior is estimated to be smaller than 9 nm.



1. INTRODUCTION

Ultrathin polymer films are of considerable technological interest in a wide range of areas ranging from coatings to organic electronic devices. Their properties can be tuned at low production costs. From the scientific point of view, thin polymer films provide an ideal sample geometry for studying the effect of nanometric confinement on the structure and dynamics of polymers. Since the pioneering work of Keddie and Jones on the thickness dependence of the glass transition temperature, T_g,[1] the discussion on polymer dynamics in thin films is in the focus of scientific research and was extended to many other confinement-induced phenomena.[2] When the thickness of a polymer film is smaller than the radius of gyration of the unperturbed polymer chain, such films reveal characteristics strongly deviating from the respective bulk properties in terms of glass transition,[3] viscoelasticity,[4] crystallization kinetics,[5] diffusion,[6] etc. The glass transition of thin polymer films has been investigated for instance by X-ray reflectivity,[7−9] neutron scattering,[10,11]Brillouin light scattering,[12,13] calorimetry,[14−18] ellipsometry,[17−24] various types of fluorescence spectroscopy,[25−28] mechanical spectroscopic techniques,[29,30] positronium lifetime spectroscopy,[31,32] and especially by broadband dielectric spectroscopy.[15,17,33−37] In spite of the large amount of data, a general theory to describe confinement effects on polymer properties has not been developed yet. The question of how a solid interface influences the structure and dynamics of a polymer is still controversially discussed.

Keddie et al. reported a decrease of the glass transition temperature with decreasing film thickness for polystyrene (PS) on both gold and silicon oxide substrates.[1] However, dielectric measurements[38] on thin PS films do not show an obvious dependence of the relaxation rate on the film thickness down to few nanometers as well as the measurements performed via atomic force microscopy (AFM) based shear modulation spectroscopy,[29] ellipsometry,[17] or differential ac-chip calorimetry.[16,39] In the case of polymers like poly(2-vinylpyridine) (P2VP),[40] poly(vinyl chloride) (PVC),[41] polysulfone (PSU),[37] and poly(ethylene terephthalate) (PET),[42] which have rather strong interactions with the substrates (silicon wafers or thermally evaporated Al layers), an increase in T_g upon reduction of the film thicknesses is observed. Also, the dielectric strength, a quantity proportional to the volume fraction of segments participating in the structural relaxation, decreases strongly with decreasing film thickness,[27,42,43] which is interpreted as the effect of a reduced mobility layer.[33,44] Torkelson et al.[45] studied the glass transition behavior of styrene/methyl methacrylate (S/MMA) random copolymer films with varying S-content by intrinsic fluorescence measure-

Received: September 20, 2011
Revised: January 12, 2012
Published: January 30, 2012

 © 2012 American Chemical Society

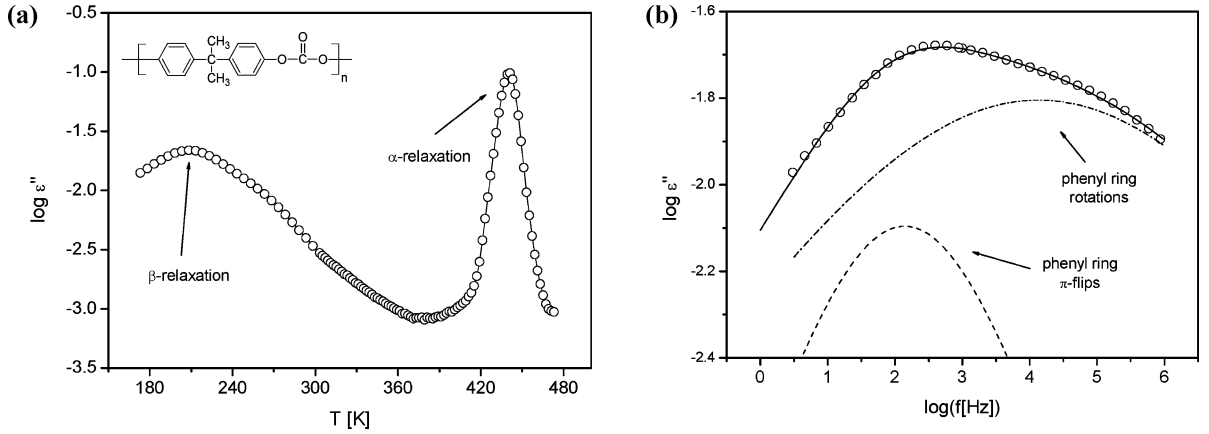


Figure 1. (a) Dielectric loss vs temperature for bulk PBAC at a frequency of 1 kHz. The line is a guide for the eyes. The inset gives the chemical structure of polycarbonate. (b) Dielectric loss versus frequency for the β-relaxation at T = 198.2 K. The solid line is a fit of two HN-functions to the data. The dashed line is the contribution of the π-flips of the phenyl rings, and the dotted-dashed line gives the contributions of the rotations of the phenyl rings.

ments to establish different polymer−substrate interactions. It was found that the glass transition temperature changes from a reduction to an increase of T_g relative to the bulk value as the S-content is reduced from 100 to 22 mol %. Such experimental observations can be discussed in terms of an interplay between confinement and surface effects. The confinement effect makes the glass transition faster compared to the bulk while the surface effect causes a decrease in segmental mobility provided that an attractive interaction of the polymers with the solid substrate is present. The existence of a solid substrate having strong interactions with the polymer film will decrease the configurational space available for the polymer chain to perform transitional motions or Brownian movements. Frictional forces between the polymer and substrate also hinder the segmental movement.[46] Fryer et al.[47] reported a direct correlation between the substrate/polymer interaction, γ_{sp}, and the change of T_g compared to the bulk. For low values of the interfacial energy (γ_{sp} < 2 mJ/m^2), the T_g of the thin polymer films is lower than the corresponding bulk value. For high values of the interfacial energy (γ_{sp} > 2 mJ/m^2), the T_g of the thin polymer films is higher than that of the bulk. On the other hand, it was also pointed out that the polymer−surface interaction energy is not the only parameter which contributes to the thickness dependence of the glass transition temperature. In addition to that, the preparation of the sample, like annealing conditions, may also affect the glass transition temperature.[48,49] Moreover, the density of the segments close to the surface and/or polymer microstructure should be taken into consideration.[50,51]

Although polycarbonate is a commercially important polymer, there are only few investigations with regard to its behavior in ultrathin films. Incoherent neutron scattering measurements were performed on thin supported (Si wafer with a native SiO_2 surface) polycarbonate films by Soles et al.[10,11] At temperatures above T_g the mean-square displacement is strongly reduced compared to the bulk and decreases with decreasing film thickness. Moreover, the localized fluctuations in the glassy state are also increasingly suppressed as the layer thickness decreases. Green et al.[52] studied thin tetramethylbisphenol-A polycarbonate (TMPC) films spin-coated on silicon substrates (with 2 nm native SiO_x layer) by ellipsometric measurement, which revealed that the T_g of TMPC films increases with decreasing film thickness. X-ray reflectivity measurements show a reduction in the glass transition temperature with decreasing film thickness for hydrophilic silicon oxide substrates (ca. −20 K).[53] This is confirmed by positron annihilation lifetime spectroscopy.[54] For hydrophobic passivated silicon substrates T_g is more or less independent of the layer thickness.[53] Torkelson et al. report a T_g reduction with decreasing film thickness by employing fluorescence spectroscopy.[55]

In this contribution, dielectric relaxation spectroscopy is employed to investigate the molecular dynamics of ultrathin polycarbonate films where polycarbonate is capped between aluminum layers in detail. In addition to that, contact angle measurements were employed to confirm the strong interaction energy between aluminum and polycarbonate.

On the basis of the experimental work, it can be concluded that the molecular mobility and glass transition of thin polycarbonate films capped between the aluminum layers show a deviation from the bulk behavior when the film thickness is smaller than 20 nm. Such deviation is caused by the formation of an interface layer with a reduced molecular mobility due to the strong interaction between polycarbonate and aluminum layers. The nonlinear reduction of the dielectric strength with thickness suggests the presence of a strong gradient of molecular mobility along the distance from the metallic interfaces.The temperature dependence of the penetration depth of the interfacial interactions on the structural relaxation is further determined. The dynamic length scale of the perturbations into the chain conformations responsible for the deviation from bulk behavior is estimated based on the broadening effect of the α-peaks with decreasing film thickness.

2. EXPERIMENTAL SECTION

Materials and Sample Preparation. Poly(bisphenol A carbonate) (PBAC, Aldrich Chemical Co.) with a molecular weight of M_w = 22 000 g/mol and a polydispersity index of 1.23 is used in this study. The chemical structure is given in the inset of Figure 1a. The glass transition temperature T_g of the bulk material determined by DSC is 153.0 °C (426.2 K; heating rate 10 K/min; second heating run).

For the dielectric measurements the thin films were prepared between two thin aluminum electrodes where glass slides with size of 10 × 10 × 1 mm were used as substrate. The procedure to clean the substrates is described in detail in ref 37. In brief, the slides were first cleaned in an ultrasound alkaline bath at 333 K for 15 min followed by a second ultrasound bath with ultrahigh purified water (Millipore,

dx.doi.org/10.1021/ma202127p | Macromolecules 2012, 45, 1652−1662

resistivity >18 MΩ/cm). Then the glass plates were first rinsed in acetone and second in chloroform (both solvents Uvasol quality). After that, the substrates were dried in a nitrogen flow. An aluminum strip (width 2 mm, height ca. 60 nm) was deposited onto the glass substrate by thermal evaporation in an ultrahigh vacuum (10^{-5} mbar). After the evaporation of this first electrode the plates were again rinsed in acetone and chloroform. Subsequently, thin films with various thicknesses were obtained by spin-coating the filtered (minipore, 0.2 μm) solutions of PBAC in dichloromethane (5000 rpm, 50 s). The film thickness was varied by changing the concentration of the polymer solution. After spin-coating, all samples were annealed at 443 K ($T_{ann} = T_{g,Bulk} + 17$ K) in an oil-free vacuum for 24 h in order to remove the residual solvent and stress induced by the spin-coating procedure[56] and, meanwhile, to ensure the same well-defined thermal histories of all samples before the experiments. AFM topography images before and after the annealing procedure further show that down to 10 nm the film had a low roughness and no sign of dewetting was observed.

The preparation of the sample capacitor was finished by the evaporation of the counter electrode on the top of the polymer film in an ultrahigh vacuum (10^{-5} mbar). In general the evaporation of metals can damage the polymer surface as discussed in ref 21. To minimize the diffusion of metal atoms into the film and to avoid a damage of the polymer, a so-called flash evaporation (>30 nm/s) was applied. It is known that under these conditions a sharp and smooth metal/polymer interface is obtained.[57] It should be noted that a thin aluminum oxide layer (1−2 nm) might be formed at the bottom electrode.[58] This layer can influence the dielectric behavior, but equivalent circuit models can be applied to estimate its influence.

The film thickness d was determined by measuring the real part of the sample capacitance C' in a temperature and frequency region rarely affected by dielectric dispersions (T = 298 K, f = 1 kHz). It holds

$$d = \frac{\varepsilon_0 \varepsilon' A}{C'} \tag{1}$$

with ε_0 the permittivity of free space and A the electrode area (4 mm^2). ε' is the permittivity of the bulk sample estimated to be 3 at T = 298 K for 1 kHz. For a few samples this procedure was checked by the absolute thickness measurements by atomic force microscopy.

The corresponding bulk sample was obtained by casting a polymer/dichloromethane solution (15 wt %) on a polished glass substrate. To control the initial evaporation of the solvent from that thick film, the glass plate was placed in a closed chamber. To remove the residual solvent, the bulk sample was annealed under the same conditions as for the ultrathin films ($T_{ann} = T_{g,Bulk} + 17$ K in an oil-free vacuum (10^{-3} mbar) for 24 h. The sample thickness was 60 μm.

Methods. A high-resolution ALPHA analyzer (Novocontrol) is used to measure the complex dielectric function $\varepsilon^*(f) = \varepsilon'(f) - i\varepsilon''(f)$ (f = frequency, ε' and ε'' = real and imaginary part of the complex dielectric function, $i = (-1)^{1/2}$) in the frequency range from 10^{-1} to 10^7 Hz. The temperature was controlled by a Quatro Novocontrol cryosystem with a stability better than 0.1 K. For more details see ref 59. During the whole measurement the sample was kept in a pure nitrogen atmosphere.

To estimate the interfacial energy between aluminum oxide AlO_x and polycarbonate, contact angle measurements were carried out. The measurements were carried out using an automated contact angle system G2 (Krüss) employing the static sessile drop method. The probe liquids used were ethylene glycol, formamide, and water. Usually 8 drops with a volume of 3 μL were dropped onto the surface of the sample or the substrate. The reported contact angles were calculated from the average of at least 6 drops.

3. RESULTS AND DISCUSSION

As known in the literature, bulk polycarbonate shows at least two relaxation processes indicated by peaks in the dielectric loss ε'' (see Figure 1a). The β-relaxation (sometimes also called γ-relaxation) at low temperatures is assigned to localized fluctuations.[60] At temperatures higher than the β-process, the α-relaxation (dynamic glass transition) takes place. The paper is organized as follows. First, the dielectric properties of bulk polycarbonate are briefly discussed. Second, the thermal and dynamic glass transition of ultrathin films of supported PBAC films are discussed in detail by employing dielectric diletometry expansion and dielectric spectroscopy. Third, the influence of a nanometer confinement on the β-process of polycarbonate is commented.

Dielectric Relaxation of Bulk Polycarbonate. Recently, the β-relaxation of polycarbonate was investigated systematically by dielectric relaxation spectroscopy and neutron scattering.[61,62] It was found that the β-relaxation consists at least of two processes.[61] (In ref 61, a third relaxation process with a weak intensity is further discussed.) This is also found for the PBAC investigated here (see Figure 1b). The carbonyl group is the only polar structure in the repeat unit of PBAC and should be therefore involved in the β-relaxation. But there are longstanding discussions that the phenyl ring should be involved in that relaxation process.[63,64] A detailed comparison of the dielectric data with the results obtained from NMR and neutron scattering yields to the conclusion that the low-frequency part of the β-process is also related to the phenylene π-flips, and the 90° rotation of the phenylene rings became dominant in the high-frequency flank of the loss peak part.[61] It was further concluded that both processes are strongly coupled.

The model function introduced by Havriliak/Negami[65] (HN function) is used to analyze the dielectric measurements quantitatively. It reads

$$\varepsilon^*_{HN}(\omega) - \varepsilon_\infty = \frac{\Delta\varepsilon}{(1 + (i\omega/\omega_0)^\beta)^\gamma} \tag{2}$$

where ω_0 is a characteristic frequency related to the frequency of maximal loss f_p (relaxation rate). $\Delta\varepsilon$ denotes the dielectric strength. ε_∞ describes the value of the real part ε' for $\omega \gg \omega_0$. β and γ are fractional parameters ($0 < \beta \leq 1$ and $0 < \beta\gamma \leq 1$) characterizing the shape of the relaxation time spectra. From the fit of the HN function to the data the relaxation rate f_p and the dielectric strength are determined and further discussed. Conduction effects are treated in the usual way by adding a contribution $\varepsilon''_{cond} = \sigma_0/[\omega^s \varepsilon_0]$ to the dielectric loss where σ_0 is related to the specific dc conductivity of the sample. The parameter s ($0 < s \leq 1$) describes for s = 1 Ohmic and for $s < 1$ non-Ohmic effects in the conductivity. If two relaxation processes are observed in the experimental frequency window, a sum of two HN functions is fitted to the experimental data. For details see ref 66. An example for that procedure is given in Figure 1b, where two HN functions are fitted to the data of the β-relaxation of polycarbonate.

Figure 2 gives the temperature dependence of the relaxation rates for the α-relaxation for bulk polycarbonate. As is known for glassy dynamics, $f_{p,\alpha}(T)$ is curved versus $1/T$ which can be described by the Vogel−Fulcher−Tammann (VFT) equation[67]

$$\log f_p = \log f_\infty - \frac{A}{T - T_0} = \log f_\infty - \frac{\ln(10) D T_0}{T - T_0} \tag{3}$$

f_∞ and A are parameters where T_0 is called ideal glass transition or Vogel temperature which is found 30−70 K below the thermal glass transition temperature. D is the so-called fragility parameter or fragility strength and provides among others a

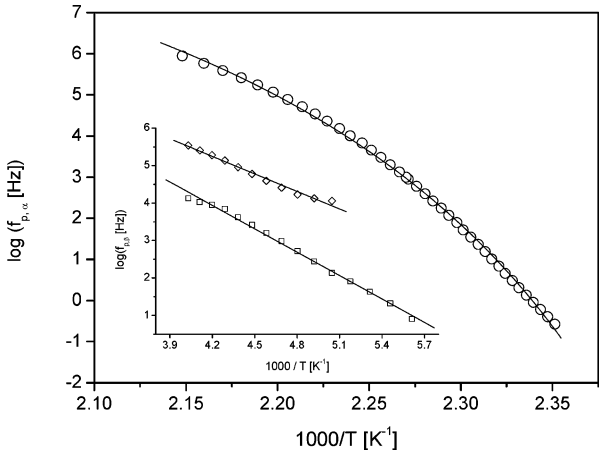


Figure 2. Relaxation rate $f_{p,\alpha}$ vs $1/T$ for the α-relaxation of bulk polycarbonate. The line is a fit of the VFT equation to the data. The inset gives $f_{p,\beta}$ vs $1/T$ for the both components of the β-relaxation of bulk PBAC: diamond, phenyl ring rotations; square, phenyl ring π-flips. The lines are fits of the Arrhenius equation to the corresponding data.

useful quantity to classify glass-forming systems.[68,69] Polymers are called "fragile" if their $f_p(T)$ dependence deviates strongly from an Arrhenius-type behavior and "strong" if $f_p(T)$ is close to the latter.

For the two components of the β-relaxation the temperature dependence of the relaxation rate obeys the Arrhenius equation (see inset of Figure 2)

$$\log f_p = \log f_\infty - \frac{\ln(10) E_A}{k_B T} \quad (4)$$

where E_A is the activation energy and k_B is the Boltzmann constant. The following activation parameters are estimated: phenyl ring rotations, E_A = 29.9 kJ/mol; $\log(f_\infty\ [\mathrm{Hz}])$ = 11.8; phenyl ring π-flips, E_A= 39.8 kJ/mol; $\log(f_\infty\ [\mathrm{Hz}])$ = 12.7. These values are in agreement with data from the literature.[61]

Dielectric Expansion Dilatometry. Dielectric expansion dilatometry relies on the analysis of the temperature dependence of the dielectric permittivity $\varepsilon'(T)$ for thin films under the assumption that no dielectric active processes take place in the selected frequency and temperature range. Its theoretical basis is considered in detail in ref 70. The real part of the permittivity can be expressed by $\varepsilon'(f_e,T) = \varepsilon_\infty(T) + \Delta\varepsilon(f_e,T)$ where $\Delta\varepsilon$ is related to a dielectric dispersion due to molecular fluctuations, ε_∞ is the real part of the permittivity in the high frequency limit, and f_e is the detection frequency. For a parallel plate capacitor in the described thin film geometry the temperature dependence of the geometrical capacitance $C_0(T) = \varepsilon_0[A/\mathrm{d}(T)] \sim \varepsilon_0(A/d_R)(1 - \alpha(T)\Delta T)$, where ΔT is a temperature change with regard to a reference temperature T_R ($T = T_R + \Delta T$), $d(T)$ is the thickness of the film in dependence of the temperature ($d_R = d(T_R)$), and A is the electrode area.[70] $\alpha(T)$ is the thermal expansion coefficient normal to the film surface. If the detection frequency f_e is set to such a value that no relaxation process is present ($\Delta\varepsilon \approx 0$), the temperature dependence of ε' is given by $\varepsilon'(T) = \varepsilon_\infty(T) \sim \varepsilon_\infty(T_R)(1 - \alpha(T)\Delta T)$. For polymers with a relatively weak dipole moment like polycarbonate this approach can be used to estimate a thermal glass transition temperature T_g from the change in the temperature dependence of ε' at sufficiently high frequencies, i.e., outside the appearance of the α-relaxation.

Figure 3 gives the temperature dependence of ε' normalized to the value at T = 380 K to get rid of temperature change due

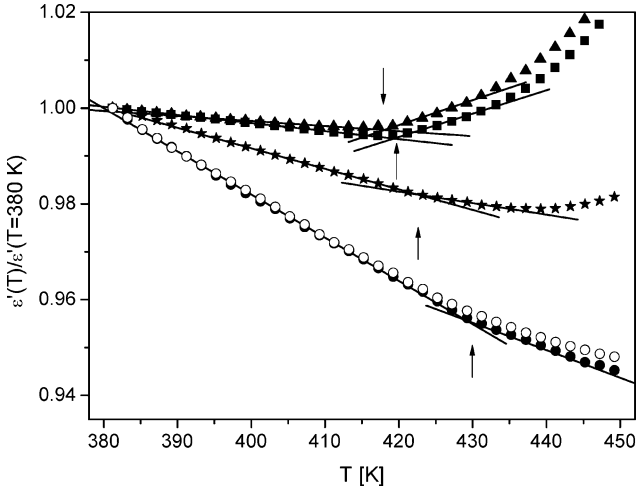


Figure 3. Temperature dependence of the dielectric permittivity ε' normalized with respect to its values at T = 380 K for a frequency of 10^5 Hz for different film thicknesses d: filled triangles, bulk; filled squares, 198 nm; filled stars, 47 nm; filled circles, 13 nm. The solid lines are linear fits of the data. The arrows indicate the values of T_g. The open circles are data for the 13 nm film measured for a frequency of 10^4 Hz. It is shown that the effect of the dielectric dispersion is quite weak above 10^4 Hz.

to the β-relaxation for several film thicknesses. For all values of the film thickness the real part of the complex permittivity decreases with increasing temperature up to a given temperature where the temperature dependence of ε' changes. This change in the temperature dependence of ε' is due to the change of the expansion coefficient at the thermal glass transition as discussed above. The initial deviation of the dielectric permittivity from a linear temperature is used to extract the thermal glass transition temperature (see Figure 3), which is plotted versus the thickness of the layer in Figure 4. The increase of ε' at higher temperatures is due to the contribution of the α-relaxation.

Figure 4 shows that down to a film thickness of ca. 20 nm T_g is more or less independent of the film thickness or increases slightly. For thicknesses lower than 20 nm an increase of T_g with decreasing d is observed. This behavior is quite similar to that found for polysulfone[37] and points to a strong interaction of polycarbonate with the aluminum substrates which leads to the formation of an adsorbed boundary layer with a reduced mobility.

Dielectric Spectroscopy on Thin Films. Different from the dielectric spectroscopy on bulk samples discussed above for the thin film geometry one has to consider that the resistance R of the Al electrodes cannot be neglected. This resistance leads to an artificial loss peak (electrode peak) on the high-frequency side of the spectra with a time constant $\tau_{Res} = RC'$ (C' = sample capacity). The electrode peak shifts to lower frequencies because with decreasing film thickness the sample capacity C' increases. The frequency dependence of the electrode peak obeys a Debye function. For optimized sample geometries the maximum position of this electrode peak $f_{Res} \sim 1/\tau_{Res}$ can be shifted outside the experimental accessible frequency window. Therefore, the Debye function can be approximated by its low-frequency tail, and the complete function reads as

dx.doi.org/10.1021/ma202127p | Macromolecules 2012, 45, 1652–1662

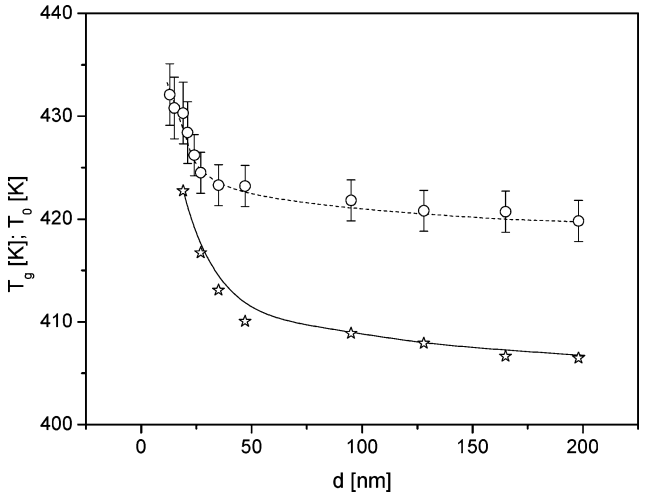


Figure 4. Circles: glass transition temperature T_g as measured by dielectric expansion dilatometry versus film thickness. The dotted line is a guide for the eyes. Stars: Vogel temperature T_0 vs film thickness. The solid line is a guide for the eyes.

$$\varepsilon^*_{\mathrm{Fit}} = \varepsilon^*_{\mathrm{HN}}(\omega) + i\frac{\sigma}{\omega^s \varepsilon_0} + iB^*\omega \tag{5}$$

where B is a fitting parameter mainly related to τ_{Res}. Figure 5 gives an example for the analysis of the dielectric spectra of a thin polycarbonate film with a thickness of 47 nm.

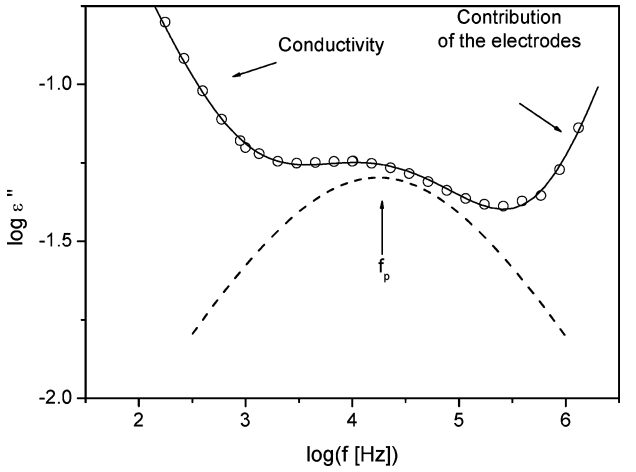


Figure 5. Dielectric loss versus frequency of a polycarbonate film with a thickness of 47 nm at T = 449 K. The solid line is a fit of eq 5 to the data. The dashed line gives the contribution of the α-relaxation.

The thin polycarbonate films show a relatively strong conductivity contribution. Therefore, the analysis of the dielectric spectra is restricted to higher frequencies and to a narrower temperature range compared to the bulk sample. The reason for the enhanced conductivity contribution might be an arrangement of the phenyl rings parallel to the electrodes.

In Figure 6, the relaxation rate $f_{p,\alpha}$ is plotted versus $1/T$ for different film thicknesses. Besides for the lowest layer thickness all other data are collapsing into one chart. This is in agreement with the results obtained by dielectric expansion dilatometry (see Figure 4). For the lowest film thickness the whole curve is shifted to higher temperatures. To analyze the temperature dependence of the relaxation rate in more detail, a derivative

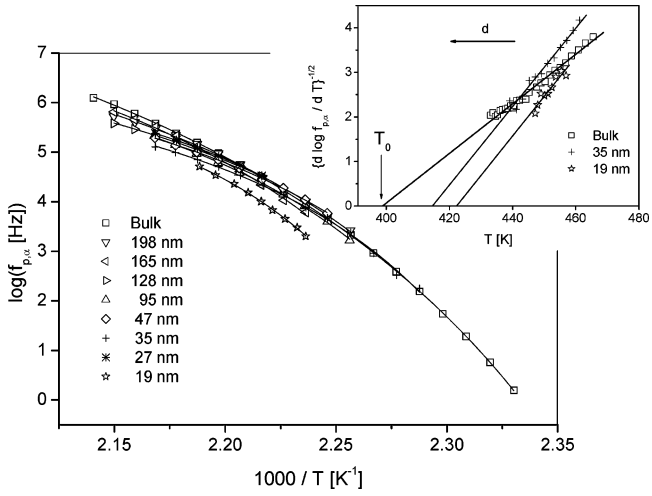


Figure 6. Relaxation rate $f_{p,\alpha}$ versus $1/T$ for the α-relaxation of polycarbonate films for the labeled film thicknesses. Lines are fits of the VFT equation to the corresponding data as described in the text. The inset gives $[(\mathrm{d}\log f_{P,\alpha})/\mathrm{d}T]^{-1/2}$ versus temperatures for labeled thicknesses. Lines are linear regressions to the data.

method is used.[71] With this method the temperature dependence of $f_{p,\alpha}$ can be analyzed in detail irrespective of the prefactor. For a temperature dependence according to the VFT equation

$$\left[\frac{\mathrm{d}\log f_p}{\mathrm{d}T}\right]^{-1/2} = A^{-1/2}(T - T_0) \tag{6}$$

is obtained. This means in a plot $[\mathrm{d}\log f_p/\mathrm{d}T]^{-1/2}$ versus T a VFT behavior shows up as a straight line (see inset of Figure 6). Besides the linearization of the data, the number of free fit parameters is reduced which increases the significance of the estimated parameters. Because all experimental data given in the inset of Figure 6 can be well described by straight lines, it is concluded that for all thicknesses the relaxation rates follow the VFT temperature dependence.

The following procedure was applied to estimate the parameters of the VFT equation and the fragility strength D for a quantitative comparison. T_0 and A were taken from the derivative technique by linear regression. The prefactors were obtained by a fit of the VFT equation to the relaxation rates keeping T_0 and A fixed. The parameters are collected in Table

Table 1. Estimated VFT Parameters and Glass Transition Temperatures T_g

thickness (nm)	log(f_∞ [Hz])	A (K)	T_0 (K)	T_g (K)	$D = A/T_0 \ln(10)$
bulk	13.22	573.4	385.0	418.5	0.646
198	9.82	242.4	406.5	419.8	0.259
165	9.68	225.3	406.6	420.7	0.240
128	8.91	190.0	407.9	420.8	0.202
95	8.95	181.9	408.8	421.8	0.193
47	8.60	169.8	410.0	423.2	0.179
35	8.24	163.8	413.1	423.3	0.172
27	8.34	131.8	416.7	424.5	0.137
19	8.20	119.4	422.7	430.3	0.122

1. As discussed above for the thin films the investigated temperature is narrower than for the bulk sample. This might

dx.doi.org/10.1021/ma202127p | Macromolecules 2012, 45, 1652–1662

complicate a direct comparison of the data point for the bulk with data for the thin films. But for the thin films a similar temperature range is analyzed where the thickness of the sample varies by more than 1 order of magnitude. Therefore, the data for the thin films can be compared directly.

The Vogel temperature T_0 shows a similar dependence on the film thickness as the glass transition temperature T_g estimated by dielectric expansion dilatometry which indicates that both data sets analyzed independently from each other are consistent. Down to a film thickness of ca. 20 nm, T_0 is more or less independent of the film thickness or increases slightly. For thicknesses lower than 20 nm an increase of T_0 with decreasing d is observed (see Figure 4). For thicknesses lower than 20 nm a strong increase of T_0 with decreasing d is observed as also found for other systems.[12,42,44] This will be discussed in detail later.

The fragility strength D is calculated from the estimated VFT parameters and plotted versus $1/d$ in Figure 7. It is shown that

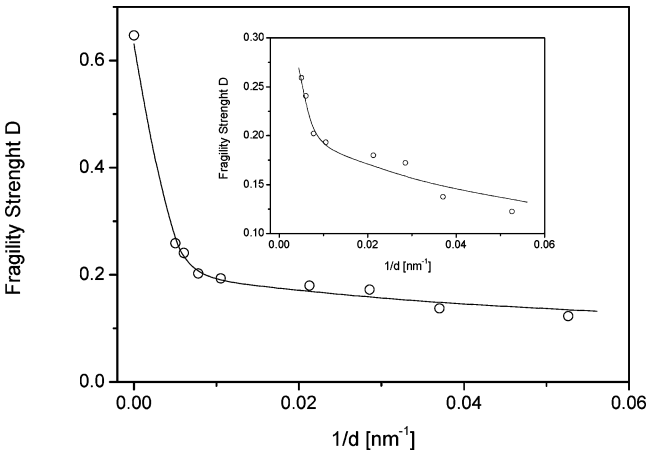


Figure 7. Fragility strength D versus inverse film thickness. The line is a guide for the eyes. The inset compares the data only for the thin films. The line is a guide for the eyes.

the fragility strength decreases with deceasing film thickness but seems to reach a plateau value for low values of d.

The dielectric strength $\Delta\varepsilon$ is obtained in addition to the relaxation rate from the fit of the HN function to the data. The Debye theory of dielectric relaxation generalized by Kirkwood and Fröhlich[72] expresses this quantity as a function of the temperature T

$$\Delta\varepsilon = \frac{1}{3\varepsilon_0} g \frac{\mu^2}{k_B T} \frac{N}{V} \tag{7}$$

The Onsager factor is omitted for sake of simplicity, ε_0 is the permittivity of the vacuum, N/V is the number density of dipoles involved in the relaxation process, and μ is the mean dipole moment of the process under consideration. g denotes the so-called Kirkwood–Fröhlich factor, which describes static correlation between the dipoles. For several layer thicknesses $\Delta\varepsilon$ is plotted versus temperature in Figure 8.

In Figure 9, $\Delta\varepsilon$ is plotted as a function of the inverse layer thickness (equivalent to the surface/volume ratio in the thin film geometry) at T = 450 K. As a general feature of the α-relaxation under confinement, the dielectric strength decreases in the thinnest films. This trend was explained in terms of chain adsorption,[73] as the dipole moment does not depend on the

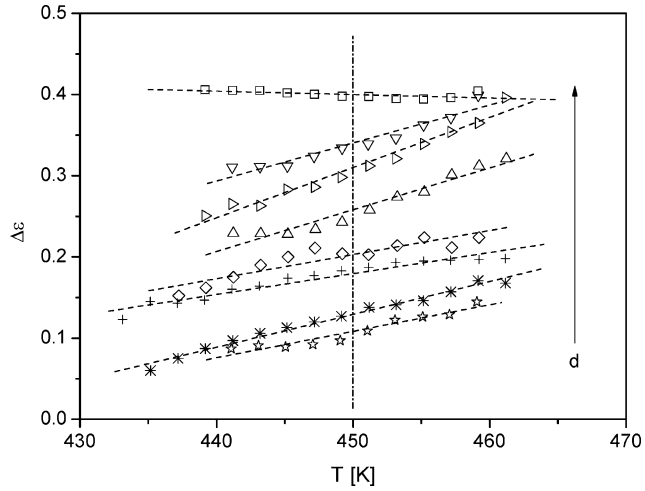


Figure 8. $\Delta\varepsilon$ versus temperature for different film thicknesses: squares, bulk; down side triangles, 198 nm; right side triangles, 128 nm; up sided triangles, 95 nm; diamonds, 47 nm; crosses, 35 nm; stars, 27 nm; full stars, 19 nm. The dashed line is a guide for the eyes. The dotted-dashed line indicates for the temperature comparison.

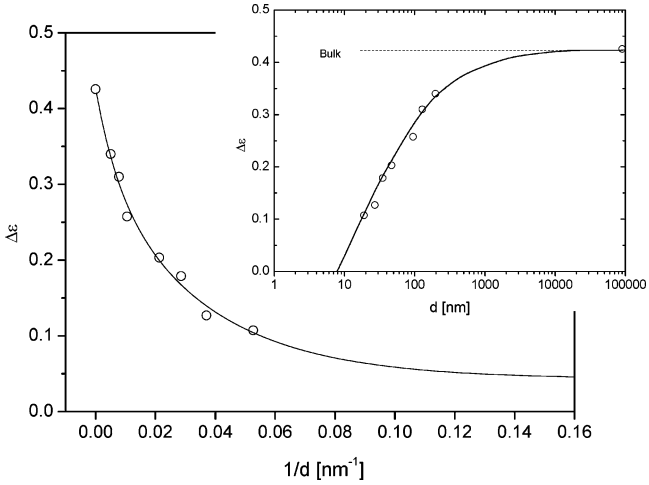


Figure 9. $\Delta\varepsilon$ vs inverse film thickness for T = 450 K. The inset gives $\Delta\varepsilon$ vs d. Lines are guides for the eyes.

film thickness. The decrease of $\Delta\varepsilon$ is due to a strong reduction of the number density of fluctuating dipoles in proximity of the interface, a hypothesis also proven by measurements of the local dielectric strength in multilayer experiments.[36] In the specific case of the polymer–metal system investigated, this idea is further confirmed by the high interfacial energy between polycarbonate and AlO_x (see below), inhibiting the motion of the segments close to the electrodes on the time and the length scale of the glass transition.

The observed pronounced nonlinear reduction of the dielectric strength upon increase of the surface-to-volume ratio suggests the presence of a strong gradient of molecular mobility along the distance from the metallic interfaces. To understand such a profile, the impact of the thickness on the temperature dependence of the dielectric strength was also analyzed (see Figure 8).

Contrary to the prediction of eq 7 valid for the structural relaxation of bulk systems, in thin films $\Delta\varepsilon$ increases with increasing temperature, a behavior was previously observed also in other polymer film of comparable thickness.[42,43] This

dx.doi.org/10.1021/ma202127p | Macromolecules 2012, 45, 1652–1662

anomalous trend is the entanglement of two different phenomena, i.e., the reduction of the number density of fluctuating dipoles in proximity of a bounding interface coupled to the impact of thermal energy on the defreezing of segmental motion.[74,75] Increasing the temperature induces a gradual release of the constraints affecting the segmental dynamics, which yields to the anomalous increase of dielectric strength upon heating.

We quantitatively determined the temperature dependence of the penetration depth of the interfacial interactions on the structural relaxation, applying an analysis recently proposed by Rotella et al.[73] The profiles of mobility, based on the density number of dipoles participating to the structural relaxation, were built up mimicking the usual dependence of density in proximity of an interface, via a function symmetric with respect to the center of the film

$$\Delta\varepsilon(x) = \Delta\varepsilon^{BULK}\left[\tanh^2\left(3\frac{x}{\phi} + \rho\right) + \tanh^2\left(3\frac{d-x}{\phi} + \rho\right) - \tanh^2\left(3\frac{d}{\phi} + \rho\right)\right] \quad (8)$$

where x is the distance from the interface, φ the length scale of the reduction of $\Delta\varepsilon$, and ρ a parameter taking account the residual polarization at the interface, as $\tanh^2(\rho) = \Delta\varepsilon(0)/\Delta\varepsilon_{bulk}$.

To obtain the best fitting parameter for each data set (i.e., $\Delta\varepsilon(d)$ in isothermal condition), the experimental data were compared to values calculated via eq 8. The procedure required the calculation of the total dielectric response of a film of thickness d, via a layer resolved approach, whose validity is supported by previous simulation work on the dielectric relaxation at the nanoscale.[76]

The film is divided into d sublayers, i.e., with a resolution of 1 nm; at each sublayer, we attributed a dielectric function reproduced by the HN equation (see eq 2). The position and the shape of the peak of each sublayer are kept constant where the dielectric strength is varied, following a profile given by discretization of eq 8 in steps of 1 nm. Considering the orientation of the electric field in our experiments (perpendicular to the polymer/metal interface), the total dielectric response was obtained summing up the contributions of all the sublayers as for capacitors in series, $C_{TOT}^{-1}(f,T) = \sum_j C_j^{-1}(f,T)$, where $C_j(f,T)$ is the capacitance of the jth sublayer. In our computation, the value of $\Delta\varepsilon_{TOT}$ was obtained directly from the real part of the dielectric function following its definition[77] as the difference between ε_S, the frequency independent value reached by the real part of the dielectric function for $\omega \ll \omega_0$, and ε_∞. We considered a frequency range broad enough to take into account the broadening of the structural peak, i.e., a larger separation between the frequency regions corresponding to ε_S and ε_∞, and the shift in the peak maximum upon confinement. Moreover, to limit the number of free parameters, we kept the shape parameters and the position of the peak in the sublayers constant. This is justified by our previous work[36,49] where we verified that in ultrathin films of amorphous polymers the dielectric strength depends on the interaction with the substrate and on the annealing conditions used. (In the samples analyzed in our work γ^{TOTAL} was constant, and samples were prepared under the same annealing conditions.) This procedure is repeated for a matrix of couples (φ^i, ρ^i) centered around physically reasonable starting parameters and found the best fitting values for the experimental values in Figure 10, upon minimization of the

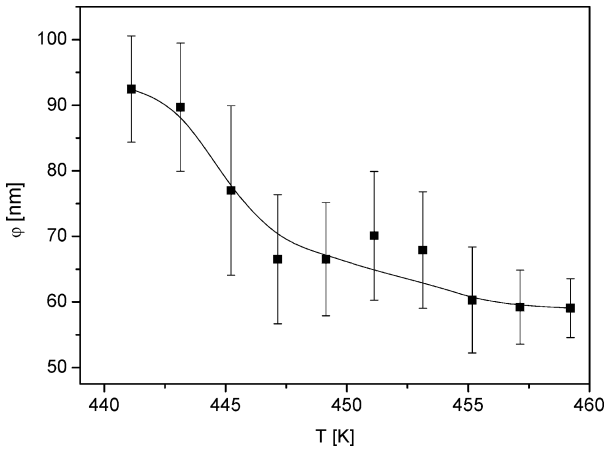


Figure 10. Temperature dependence of the penetration depth φ.

squared deviations: Err = $(1/n_{exp})\sum_{i=1}^{n_{exp}}[(\Delta\varepsilon_i^{th} - \Delta\varepsilon_i^{exp})/\Delta\varepsilon_i^{exp}]^2$, where n_{exp} is the number of the experimental data points, i.e., the number of thicknesses measured at each temperature, and $\Delta\varepsilon^{th}$ and $\Delta\varepsilon^{exp}$ are respectively the values of the dielectric strength obtained via the model and experimentally. The obtained values are plotted in Figure 10. At 443 K, φ reaches 90 nm, a value which is comparable to, although slightly larger than, that of PET in the same dynamic range. Compared to more flexible polymers, where φ does not exceed 40 nm, the relatively longer length scale reflects the rigidity of the chains of PBAC. The less flexibility combined to the previously mentioned arrangement of the phenyl rings parallel to the electrodes induces a residual polarization at the interface on the order of 20% of the bulk value, i.e., $\rho \sim 0.5$, responsible for the nonzero value of $\Delta\varepsilon$ in the thinnest films. The temperature dependence of the penetration depth of the interfacial interactions increases upon cooling with an activation energy 10-fold smaller than the structural relaxation. Such a trend is in line with what is observed in ultrathin films of polystyrene labeled with polar moieties[73] and what is predicted by molecular dynamics simulations.[78]

The presence of a profile of mobility affecting the dynamics of the film[79,80] is reflected also in the thickness dependence of the width of the α-peak, which broadens upon reduction of the thickness (see Figure 11). This broadening arises from the heterogeneity in the molecular dynamics, related to the introduction of slower modes in the distribution of relaxation times. At the polymer/metal interface, in fact, the mobility of chains is hindered down to the segmental motion, due to less available space[81] and the favorable interactions with the aluminum surface. The perturbations into the chain conformations responsible for such deviation from bulk dynamics vanish after a dynamic length scale λ. It is possible to estimate λ by an analysis of the thickness dependence of the broadening of the α-peak in capped films, based on simple considerations on samples with symmetric interfaces.[82] In thick films, $d \gg \lambda$, the volume fraction of segments relaxing like in bulk is predominant and the width is thickness independent. Upon thickness reduction, the weight of interfacial layers on the total

dx.doi.org/10.1021/ma202127p | Macromolecules 2012, 45, 1652–1662

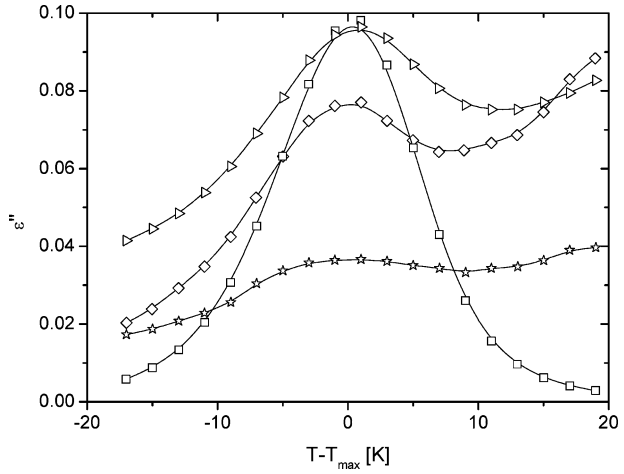


Figure 11. Dielectric loss versus normalized temperature at 1 kHz for different film thicknesses: squares, bulk; right side triangles, 95 nm; diamonds, 47 nm; full stars, 19 nm. The lines are guides for the eyes.

dielectric signal increases, and because of the different time scale of the segmental relaxation at the interface,[36] the α-peak broadens in the frequency domain. Such a confinement induced broadening reaches a maximum in proximity of 2λ, where the bulk component disappears. Further reduction of the thickness corresponds to a cutoff of those modes relaxing like in bulk, which leads to a reduction of the broadening. For PBAC, in the thickness range where it was possible to determine univocally the shape of the structural peak, i.e., down to 19 nm, only a broadening of the α-peak is observed. Consequently, we can estimate that, at each interface, the interaction with the metallic substrate affects the dynamics for a length scale $\lambda \leq 9$ nm. This critical length is in line with the trends in the thickness dependence of T_g and T_0 (see Figure 4) where no confinement effect is observed for films where the separation between the two metallic layers exceeds 20 nm.

Such a dynamic length scale is much smaller than that determined via the thickness dependence of the dielectric strength, a trend in line with the behavior of almost all polymer systems investigated at the nanoscale.[73] The origin of this apparent discrepancy stays in the different averaging rules affecting the intensity ($\Delta\varepsilon$) and the shape (peak maximum, broadness, asymmetry) of a relaxation peak,[75] which permit to observe a perturbation in the dynamics only at higher surface/volume ratios (thinner films) compared to those of interest to static properties like the dielectric strength.

To confirm the strong interaction between aluminum oxide AlO_x and polycarbonate, contact angle measurements were carried out. The angle values are given in Table 2. The contact

Table 2. Contact Angle Values of the Test Liquids with Polycarbonate[a]

	ethylene glycol	formamide	water
poly(bisphenol A carbonate)	67.6 ± 0.47	71.8 ± 0.7	93.0 ± 0.35

[a]The error bars results from the average of the measurements on 8 drops.

angle values were used as input to calculate the interfacial energy γ_{SP} in the frame of the Fowkes–van Oss–Chaudry–Good (FOCG) model.[83] The surface tension is given by $\gamma^{Total} = \gamma^{LW} + \gamma^{P} = \gamma^{LW} + 2(\gamma^{+}\gamma^{-})^{1/2}$, where γ^{LW} is the dispersive and γ^{P} the polar component. The polar component is further expressed by the electron acceptor γ^{+} and the electron donor component γ^{-}.[83,84] γ^{LW},γ^{+}, and γ^{-} were estimated by solving the system of the corresponding Young and Dupré[83] equations (system of three equations)

$$(1 + \cos\theta_i)\gamma^{PC} = 2[(\gamma_{PC}^{LW}\gamma_{L,i}^{LW})^{1/2} + (\gamma_{PC}^{+}\gamma_{L,i}^{-})^{1/2} + (\gamma_{PC}^{-}\gamma_{L,i}^{+})^{1/2}] \quad (9)$$

using the contact angles θ_i measured for each test liquid i. PC symbolizes polycarbonate and L the test liquids where the corresponding values for the test liquids were taken from ref 84 (see Table 3). The values obtained for both aluminum and

Table 3. Total Surface Energy γ^{Total} and Its Dispersive γ^{LW} and Polar Component γ^{P} for the Test Liquids According to the Data Given in Ref 84

	ethylene glycol	formamide	water
γ^{total} [mJ/m^2]	48.0	58	72.8
γ^{LW} [mJ/m^2]	29	39	26
γ^{+} [mJ/m^2]	2.60	3.1	34.2
γ^{-} [mJ/m^2]	34.8	29.1	19

Table 4. Total Surface Energy γ^{Total} and Its Dispersive γ^{LW} and Polar Component γ^{P} for Polycarbonate and Aluminum Oxide[a]

	γ^{total} [mJ/m^2]	γ^{LW} [mJ/m^2]	γ^{+} [mJ/m^2]	γ^{-} [mJ/m^2]
poly(bisphenol A carbonate)	33.21	32.95	0.03	0.56
aluminum	30.4	26.5	0.5	7.7

[a]The data for aluminium were taken from ref 42.

polycarbonate are displayed in Table 4. The combining rule of Good–Girifalco–Fowkes[85] was applied to estimate γ_{SP} between PBAC and AlO_x

$$\gamma_{SP} = (\sqrt{\gamma_S^{LW}} - \sqrt{\gamma_P^{LW}})^2 + 2[(\gamma_S^{+}\gamma_S^{-})^{1/2} + (\gamma_P^{+}\gamma_P^{-})^{1/2} - (\gamma_S^{+}\gamma_P^{-})^{1/2} - (\gamma_S^{-}\gamma_P^{+})^{1/2}] \quad (10)$$

S and P refer to the substrate and the polymer. The data for aluminum are taken from ref 42. The dispersive part of the AlO_x/PBAC is calculated to be 0.35 mJ/m^2, and the polar one is 2.16 mJ/m^2, leading to a total energy of 2.51 mJ/m^2. This value is higher than the critical value discussed in ref 47 ($\gamma^{*}_{sp} \approx$ 2 mJ/m^2 for different couples of substrates and polymers), corresponding to an increase of T_g as observed in the dielectric experiments. The real interfacial energy could be however higher than the calculated γ_{SP} due to the formation of chemical bonds or specific interaction between Al and PBAC. The interfacial chemical interaction between spin-coated polycarbonate and thermally evaporated aluminum has been studied by X-ray photoelectron spectroscopy in detail.[86] C=O and C–O entities of polycarbonate react with Al atoms to form an Al–O–C like complex. Al–C bonding also forms due to the interaction between phenyl ring and Al atoms. Aluminum oxide (O–Al) and aluminum hydroxides (HO–A1) can be detected

dx.doi.org/10.1021/ma202127p | Macromolecules 2012, 45, 1652–1662

at the Al/PBAC interface. The formation of these chemical bonds contributes to the attractive interfacial interaction between PBAC and Al layers.

To discuss the dielectric data in more detail, the loss part is plotted at a frequency of 1 kHz versus temperature for the bulk sample and for films with different thicknesses (Figure 12).

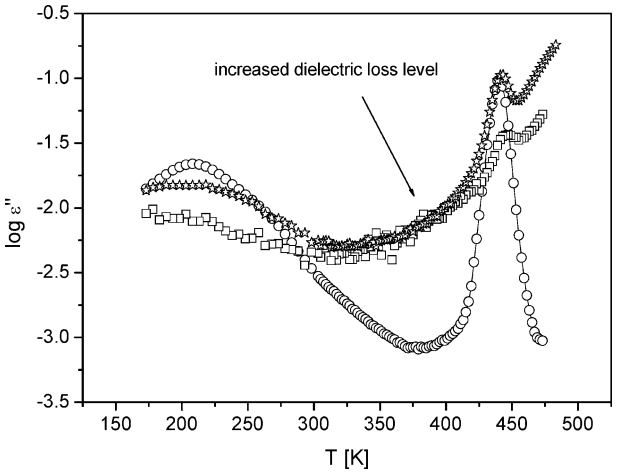


Figure 12. Dielectric loss versus temperature at a frequency of 1 kHz: circles, bulk polycarbonate; squares, 128 nm; stars, 19 nm.

Compared to the bulk sample for the thin film, the dielectric loss is significantly increased for temperatures below the α-relaxation.[87] By convention, a glass transition temperature can be defined by the maximum temperature of the α-relaxation which corresponds only to one point of the whole spectra. Any finite value of the dielectric loss corresponds to certain molecular fluctuations or motions (see ref 88). It might be that different aspects of the molecular mobility which leads to different definitions of the glass transition temperature and therefore to different thickness dependencies.

Thickness Dependence of the β-Relaxation. In addition to the facts discussed above, Figure 12 reveals also that the intensity of the β-relaxation peak decreases with the decreasing film thickness and cannot be observed for thinnest film. As discussed above, the β-relaxation is assigned to different motional modes of the phenyl ring. The observed decrease in the intensity of the β-process means that the phenyl rings are immobilized by the polymer−substrate interaction. Likely is a planar arrangement of it to the surface. A reduction of the localized fluctuation in ultrathin polycarbonate films was also observed by neutron scattering.[10] Moreover, such a depression of the β-relaxation strength is in good agreement with previous dielectric studies of PMMA.[89]

4. CONCLUSION

Ultrathin films of poly(bisphenol A carbonate) capped between two aluminum layers were studied by dielectric expansion dilatometry and dielectric spectroscopy. The thermal glass transition temperature is more or less independent of the film thickness down to 20 nm. An increase of T_g is observed when the film thickness is lower than 20 nm. This is in agreement with the thickness dependence of the Vogel temperature. It is further found that the fragility decreases with decreasing film thickness until a plateau value is reached.

To explore the interaction of polycarbonate with aluminum surface, the dielectric relaxation strength was estimated from the measurements. It is proportional to the dipole density taking part in the α-relaxation process. A pronounced nonlinear reduction of the dielectric strength with decreasing film thickness was observed, which is attributed to the formation of a reduced mobility layer at the interface. Polycarbonate chains in the proximity of the interface have adsorption to the aluminum surface due to the strong interfacial interaction. The interfacial energy between polycarbonate and aluminum layers is quantitatively determined by contact angle measurements and related calculations. With further analysis based on the impact of the thickness on the temperature dependence of the dielectric strength, the temperature dependence of the penetration depth of the interfacial interactions on the structural relaxation is determined. The broadening of the α-peak with decreasing thickness is due to the heterogeneity in the mobility induced by the interaction of the segments with the surfaces. A dynamic length scale of the surface perturbations of the chain conformations is estimated to be smaller than 9 nm. This is in agreement with the thickness dependence of the glass transition and the Vogel temperature.

AUTHOR INFORMATION

Corresponding Author

*Tel: +49 30/8104-3384; Fax: +49 30/8104-1637; e-mail: Andreas.Schoenhals@bam.de.

Notes

The authors declare no competing financial interest.

ACKNOWLEDGMENTS

The authors gratefully acknowledge the assistance of D. Neubert for his experimental help. The financial support from the German Science Foundation (Deutsche Forschungsgemeinschaft, SCHO-470/20-1) is highly acknowledged.

REFERENCES

(1) Keddie, J. L.; Jones, R. A. L.; Cory, R. A. *Faraday Discuss.* **1994**, *98*, 219−230.
(2) Alcoutlabi, M.; McKenna, G. B. *J. Phys.: Condens. Matter* **2005**, *17*, R461−R524.
(3) Fakhraai, Z.; Forrest, J. A. *Phys. Rev. Lett.* **2005**, *95*, 025701.
(4) O'Connell, P. A.; McKenna, G. B. *Science* **2005**, *307*, 1760−1763.
(5) Napolitano, S.; Wübbenhorst, M. *Macromolecules* **2006**, *39*, 5967−5970.
(6) Zheng, X.; Rafailovich, M. H.; Sokolov, J.; Strzhemechny, Y.; Schwarz, S. A.; Sauer, B. B.; Rubinstein, M. *Phys. Rev. Lett.* **1997**, *79*, 241−244.
(7) Wallace, W. E.; van Zanten, J. H.; Wu, W. L. *Phys. Rev. E* **1995**, *52*, R3329−R3332.
(8) Reiter, G. *Macromolecules* **1994**, *27* (11), 3046−3052.
(9) Weber, R.; Zimmermann, K. M.; Tolan, M.; Stettner, J.; Press, W.; Seeck, O. H.; Erichsen, J.; Zaporojtchenko, V.; Strunskus, T.; Faupel, F. *Phys. Rev. E* **2001**, *64*, 061508.
(10) Soles, C. L.; Douglas, J. F.; Wu, W. l.; Dimeo, R. M. *Phys. Rev. Lett.* **2002**, *88*, 037401.
(11) Soles, C. L.; Douglas, J. F.; Wu, W. l.; Dimeo, R. M. *Macromolecules* **2003**, *36*, 373−379.
(12) Forrest, J. A.; Dalnoki-Veress, K.; Stevens, J. R.; Dutcher, J. R. *Phys. Rev. Lett.* **1996**, *77*, 2002.
(13) Cheng, W.; Sainidou, R.; Burgardt, P.; Stefanou, N.; Kiyanova, A.; Efremov, M.; Fytas, G.; Nealey, P. F. *Macromolecules* **2007**, *40*, 7283−7290.
(14) Efremov, M. Y.; Olson, E. A.; Zhang, M.; Zhang, Z.; Allen, L. H. *Phys. Rev. Lett.* **2003**, *91*, 085703.
(15) Lupascu, V.; Huth, H.; Schick, C.; Wübbenhorst, M. *Thermochim. Acta* **2005**, *432*, 222−228.

(16) Huth, H.; Minakov, A. A.; Schick, C. *J. Polym. Sci., Part B: Polym. Phys.* **2006**, *44*, 2996−3005.
(17) Tress, M.; Erber, M.; Mapesa, E. U.; Huth, H.; Müller, J.; Serghei, A.; Schick, C.; Eichhorn, K.-J.; Voit, B.; Kremer, F. *Macromolecules* **2010**, *43*, 9937−9944.
(18) Zhou, D.; Huth, H.; Gao, Y.; Xue, G.; Schick, C. *Macromolecules* **2008**, *41*, 7662−7666.
(19) Keddie, J. L.; Jones, R. A. L.; Cory, R. A. *Europhys. Lett.* **1994**, *27*, 59.
(20) Dalnoki-Veress, K.; Forrest, J. A.; Murray, C.; Gigault, C.; Dutcher, J. R. *Phys. Rev. E* **2001**, *63*, 031801.
(21) Sharp, J. S.; Forrest, J. A. *Phys. Rev. Lett.* **2003**, *91*, 235701.
(22) Lu, H.; Chen, W.; Russell, T. P. *Macromolecules* **2009**, *42*, 9111−9117.
(23) Erber, M.; Georgi, U.; Müller, J.; Eichhorn, K. J.; Voit, B. *Eur. Polym. J.* **2010**, *46*, 2240−2246.
(24) Clough, A.; Peng, D.; Yang, Z.; Tsui, O. K. C. *Macromolecules* **2011**, *44*, 1649−1653.
(25) Ellison, C. J.; Torkelson, J. M. *Nature Mater.* **2003**, *2*, 695−700.
(26) Mundra, M. K.; Ellison, C. J.; Rittigstein, P.; Torkelson, J. M. *Eur. Phys. J.: Spec. Top.* **2007**, *141*, 143−151.
(27) Priestley, R. D.; Broadbelt, L. J.; Torkelson, J. M.; Fukao, K. *Phys. Rev. E* **2007**, *75*, 061806.
(28) Kim, S.; Roth, C. B.; Torkelson, J. M. *J. Polym. Sci., Part B: Polym. Phys.* **2008**, *46*, 2754−2764.
(29) Ge, S.; Pu, Y.; Zhang, W.; Rafailovich, M.; Sokolov, J.; Buenviaje, C.; Buckmaster, R.; Overney, R. M. *Phys. Rev. Lett.* **2000**, *85*, 2340.
(30) Dinelli, F.; Ricci, A.; Sgrilli, T.; Baschieri, P.; Pingue, P.; Puttaswamy, M.; Kingshott, P. *Macromolecules* **2011**, *44*, 987−992.
(31) Xie, L.; DeMaggio, G. B.; Frieze, W. E.; DeVries, J.; Gidley, D. W.; Hristov, H. A.; Yee, A. F. *Phys. Rev. Lett.* **1995**, *74*, 4947.
(32) DeMaggio, G. B.; Frieze, W. E.; Gidley, D. W.; Zhu, M.; Hristov, H. A.; Yee, A. F. *Phys. Rev. Lett.* **1997**, *78*, 1524.
(33) Fukao, K.; Miyamoto, Y. *Phys. Rev. E* **2000**, *61*, 1743.
(34) Lupascu, V.; Picken, S. J.; Wübbenhorst, M. *J. Non-Cryst. Solids* **2006**, *352*, 5594−5600.
(35) Serghei, A.; Huth, H.; Schick, C.; Kremer, F. *Macromolecules* **2008**, *41*, 3636−3639.
(36) Rotella, C.; Napolitano, S.; Cremer, L. D.; Koeckelberghs, G.; Wübbenhorst, M. *Macromolecules* **2010**, *43*, 8686−8691.
(37) Labahn, D.; Mix, R.; Schönhals, A. *Phys. Rev. E* **2009**, *79*, 011801.
(38) Serghei, A.; Huth, H.; Schellenberger, M.; Schick, C.; Kremer, F. *Phys. Rev. E* **2005**, *71*, 061801.
(39) Huth, H.; Minakov, A. A.; Serghei, A.; Kremer, F.; Schick, C. *Eur. Phys. J.: Spec. Top.* **2007**, *141*, 153−160.
(40) van Zanten, J. H.; Wallace, W. E.; Wu, W. l. *Phys. Rev. E* **1996**, *53*, R2053.
(41) Grohens, Y.; Sacristan, J.; Hamon, L.; Reinecke, H.; Mijangos, C.; Guenet, J. M. *Polymer* **2001**, *42*, 6419−6423.
(42) Napolitano, S.; Prevosto, D.; Lucchesi, M.; Pingue, P.; D'Acunto, M.; Rolla, P. *Langmuir* **2007**, *23*, 2103−2109.
(43) Serghei, A.; Tress, M.; Kremer, F. *Macromolecules* **2006**, *39*, 9385−9387.
(44) Napolitano, S.; Lupascu, V.; Wübbenhorst, M. *Macromolecules* **2008**, *41*, 1061−1063.
(45) Mundra, M. K.; Ellison, C. J.; Behling, R. E.; Torkelson, J. M. *Polymer* **2006**, *47*, 7747−7759.
(46) Yang, Z.; Fujii, Y.; Lee, F. K.; Lam, C.-H.; Tsui, O. K. C. *Science* **2010**, *328*, 1676−1679.
(47) Fryer, D. S.; Peters, R. D.; Kim, E. J.; Tomaszewski, J. E.; de Pablo, J. J.; Nealey, P. F.; White, C. C.; Wu, W.-l. *Macromolecules* **2001**, *34*, 5627−5634.
(48) Serghei, A.; Kremer, F. *Macromol. Chem. Phys.* **2008**, *209*, 810−817.
(49) Napolitano, S.; Wübbenhorst, M. *Nature Commun.* **2011**, *2*, 260.
(50) Tsui, O. K. C.; Russell, T. P.; Hawker, C. J. *Macromolecules* **2001**, *34*, 5535−5539.
(51) Grohens, Y.; Hamon, L.; Reiter, G.; Soldera, A.; Holl, Y. *Eur. Phys. J. E* **2002**, *8*, 217−224.
(52) Pham, J. Q.; Green, P. F. *J. Chem. Phys.* **2002**, *116*, 5801.
(53) Soles, C. L.; Douglas, J. F.; Jones, R. L.; Wu, W.-l. *Macromolecules* **2004**, *37*, 2901−2908.
(54) Soles, C. L.; Douglas, J. F.; Wu, W.-l.; Peng, H.; Gidley, D. W. *Macromolecules* **2004**, *37*, 2890−2900.
(55) Torkelson, J. M.; Priestley, R. D.; Rittigstein, P.; Mundra, M. K.; Roth, C. B. *AIP Conf. Proc.* **2008**, *982*, 192−195.
(56) Reiter, G.; Hamieh, M.; Damman, P.; Sclavons, S.; Gabriele, S.; Vilmin, T.; Raphael, E. *Nature Mater.* **2005**, *4*, 754−758.
(57) Strunskus, T.; Zaporojtchenko, V.; Behnke, K.; v. Bechtolsheim, C.; Faupel, F. *Adv. Eng. Mater.* **2000**, *2*, 489−492.
(58) Mathieu, H. J.; Datta, M.; Landolt, D. *J. Vac. Sci. Technol., A* **1985**, *3*, 331.
(59) Kremer, F.; Schönhals, A. In *Broadband Dielectric Measurement Techniques in Broadband Dielectric Spectroscopy*; Kremer, F., Schönhals, A., Eds.; Springer: Berlin, 2002; p 35.
(60) Schartel, B.; Wendorff, J. H. *Polymer* **1995**, *36*, 899−904.
(61) Alegría, A.; Mitxelena, O.; Colmenero, J. *Macromolecules* **2006**, *39*, 2691−2699.
(62) Arrese-Igor, S.; Mitxelena, O.; Arbe, A.; Alegría, A.; Colmenero, J.; Frick, B. *Phys. Rev. E* **2008**, *78*, 021801.
(63) Schaefer, J.; Stejskal, E. O.; Buchdahl, R. *Macromolecules* **1977**, *10*, 384−405.
(64) Floudas, G.; Higgins, J. S.; Kremer, F.; Fischer, E. W. *Macromolecules* **1992**, *25*, 4955−4961.
(65) Havriliak, S.; Negami, S. *J. Polym. Sci., Part C: Polym. Symp.* **1966**, *14*, 99−117.
(66) Schönhals, A.; Kremer, F. In *Analysis of Dielectric Spectra in Broadband Dielectric Spectroscopy*; Kremer, F., Schönhals, A., Eds.; Springer: Berlin, 2002; p 59.
(67) (a) Vogel, H. *Phys. Z.* **1921**, *22*, 645. (b) Fulcher, G. S. *J. Am. Ceram. Soc.* **1925**, *8*, 339. (c) Tammann, G.; Hesse, W. *Z. Anorg. Allg. Chem.* **1926**, *156*, 245.
(68) Angell, C. A. *J. Non-Cryst. Solids* **1991**, *131*−*133* (Part 1), 13−31.
(69) Angell, C. A. *J. Res. Natl. Inst. Stand. Technol.* **1997**, *102*, 171−185.
(70) Hartmann, L.; Fukao, K.; Kremer, F. In *Molecular Dynamics in Thin Polymer Films in Broadband Dielectric Spectroscopy*; Kremer, F., Schönhals, A., Eds.; Springer: Berlin, 2002; p 433.
(71) Kremer, F.; Schönhals, A. In *The Scaling of the Dynamics of Glasses and Supercooled Liquids Spectra in Broadband Dielectric Spectroscopy*; Kremer, F., Schönhals, A., Eds.; Springer: Berlin, 2002; p 99.
(72) Kremer, F.; Schönhals, A. In *Broadband Dielectric Measurement Techniques in Broadband Dielectric Spectroscopy*; Kremer, F., Schönhals, A., Eds.; Springer: Berlin, 2002; p 10.
(73) Rotella, C.; Wübbenhorst, M.; Napolitano, S. *Soft Matter* **2011**, *7*, 5260−5266.
(74) Napolitano, S.; Pilleri, A.; Rolla, P.; Wübbenhorst, M. *ACS Nano* **2010**, *2*, 841−848.
(75) Napolitano, S.; Wübbenhorst, M. *J. Phys. Chem. B* **2007**, *111*, 9197−9199.
(76) Peter, S.; Napolitano, S.; Meyer, H.; Wübbenhorst, M.; Baschnagel, J. *Macromolecules* **2008**, *41*, 7729−7743.
(77) Kremer, F.; Schönhals, A. In *The Scaling of the Dynamics of Glasses and Supercooled Liquids Spectra in Broadband Dielectric Spectroscopy*; Kremer, F., Schönhals, A., Eds.; Springer: Berlin, 2002; p 99.
(78) Baschnagel, J.; Binder, K. *Macromolecules* **1995**, *28*, 6808−6818.
(79) Lipson, J. E. G.; Milner, S. T. *Eur. Phys. J. B* **2009**, *72*, 133−137.
(80) Milner, S. T.; Lipson, J. E. G. *Macromolecules* **2010**, *43*, 9865−9873.
(81) Napolitano, S.; Rotella, C.; Wübbenhorst, M. *Macrom. Rapid Commun.* **2011**, *32*, 844−848.
(82) Napolitano, S.; Wübbenhorst, M. *Polymer* **2010**, *51*, 5309−5312.

(83) Van Oss, C. J.; Chaudhury, M. K.; Good, R. J. *Chem. Rev.* **1988**, *88*, 927−941.
(84) Lee, L.-H. *Langmuir* **1996**, *12*, 1681−1687.
(85) Good, R. J.; Girifalco, L. A. *J. Phys. Chem.* **1960**, *64*, 561−565.
(86) Massoro, C.; Le, Q. T.; Pireaux, J. J. *Surf. Interface Anal.* **1994**, *21*, 425−429.
(87) An alternative explanation to the trend in Figure 9 is the effect of the nonzero dielectric dissipation of the thin layer of oxide present on the surface of the metallic electrodes. The sum of the contribution of the inorganic layer, dielectric constant >9 and almost constant loss $\sim 10^{-3}$, to the capacitance of the polymer is more relevant in the frequency region where no molecular relaxation is active. However, considering the large value of the residual dielectric strength, the related increase in dielectric loss in between the structural relaxation and the secondary process should be observed at thicknesses 1 order of magnitude smaller.
(88) Donth, E. In *The Glass Transition: Relaxation Dynamics in Liquids and Disordered Materials*; Donth, E., Ed.; Springer: Berlin, 2001; p 269.
(89) Wübbenhorst, M.; Murray, C. A.; Forrest, J. A.; Dutcher, J. R. *Proc. 11th Int. Symp. Electrets* **2002**, 401.

Macromolecules

Article

pubs.acs.org/Macromolecules

Modeling of Intermediate Structures and Chain Conformation in Silica–Latex Nanocomposites Observed by SANS During Annealing

Anne-Caroline Genix,[†,‡,*] Mouna Tatou,[†,‡,⊥] Ainara Imaz,[§] Jacqueline Forcada,[§] Ralf Schweins,[⊥] Isabelle Grillo,[⊥] and Julian Oberdisse[†,‡,∥]

[†]Laboratoire Charles Coulomb UMR 5221, Université Montpellier 2, F-34095 Montpellier, France

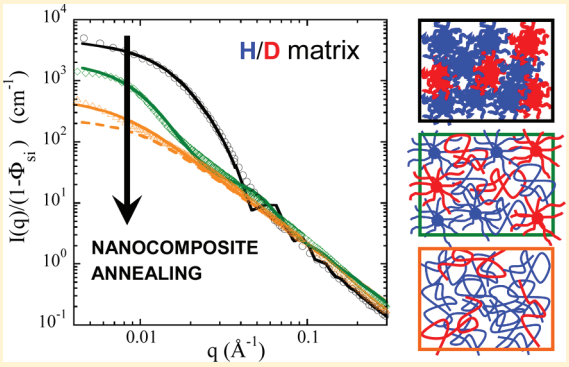
[‡]Laboratoire Charles Coulomb UMR 5221, CNRS, F-34095 Montpellier, France

[§]Grupo de Ingeniería Química, Facultad de Ciencias Químicas, The University of the Basque Country, 20080 San Sebastián, Spain

[⊥]Institut Laue-Langevin, F-38042 Grenoble, France

[∥]Laboratoire Léon Brillouin, UMR 12 CEA/CNRS, CEA Saclay, F-91191 Gif sur Yvette, France

ABSTRACT: The evolution of the polymer structure during nanocomposite formation and annealing of silica–latex nanocomposites is studied using contrast-variation small angle neutron scattering. The experimental system is made of silica nanoparticles (R_{si} ≈ 8 nm) and a mixture of purpose-synthesized hydrogenated and deuterated nanolatex (R_{latex} ≈ 12.5 nm). The progressive disappearance of the latex beads by chain interdiffusion and release in the nanocomposites is analyzed quantitatively with a model for the scattered intensity of hairy latex beads and an RPA description of the free chains. In silica-free matrices and nanocomposites of low silica content (7%v), the annealing procedure over weeks at up to T_g + 85 K results in a molecular dispersion of chains, the radius of gyration of which is reported. At higher silica content (20%v), chain interdiffusion seems to be slowed down on time-scales of weeks, reaching a molecular dispersion only at the strongest annealing. Chain radii of gyration are found to be unaffected by the presence of the silica filler.



I. INTRODUCTION

Dispersing hard filler nanoparticles in a soft polymeric matrix creates a new material, nanocomposites. Their properties may be tuned, e.g., by modifying the quality of the dispersion, or of the interfacial interactions.[1−5] Understanding how properties of nanocomposites emerge necessitates knowledge of polymer structure and dynamics, as well as of nanoparticle dispersion. General fundamental results are rare in this field, and many model systems have been investigated in the past. Focusing on chain conformation, one finds various systems, like silica particles in poly(dimethylsiloxane) (PDMS),[6] poly(styrene) (PS),[7,8] poly(isoprene)[9,10] or poly(ethylene-propylene) (PEP),[11] and cross-linked PS beads in PS.[12] The subject has also been addressed by computer simulations[13−16] and molecular theories.[17,18] The conclusion on the evolution of the chain radius of gyration with the amount of hard filler in most of these studies remains incomplete at the moment, among others due to difficulties in measuring a chain structure which is not perturbed by the filler presence. It is not clear to date, if this is a technical problem of, e.g., impossible matching of heterogeneous nanoparticles or if the chain structure is truly perturbed by obstacles.

Polymer dynamics in a hard, nanostructured filler environment is one of the intriguing problems in nanocomposites. Access to this information has been gained using fluorescence resonance energy transfer,[19] quasielastic neutron scattering,[20−23] and NMR techniques.[24−29] Reorganization of polymer molecules in melts, e.g., by following the radius of gyration of polymer chains during annealing by scattering, gives information on larger scales.[30−33] Inspired by this method, we have recently chosen a similar approach,[34] which is also used here.

A large body of experimental research has been dedicated to nanoparticle dispersions in nanocomposites.[35] A particularly interesting system is based on latex film formation. The process of formation of pure latex films has attracted considerable attention over the past two decades.[36−44] Latex beads are brought into contact by evaporation of the aqueous solvent above the minimal film formation temperature. Depending on the thermal history of the samples and the architecture of the beads, different structures may be generated. For large beads with a clearly defined shell, e.g., beads may keep their globular shape, and the shells connect into a network. In other cases, all chains may interdiffuse until the initial organization in the form of beads has completely disappeared, and the final film forms a molecularly dispersed melt of polymer chains.

Received: October 14, 2011
Revised: January 12, 2012
Published: February 1, 2012

 © 2012 American Chemical Society dx.doi.org/10.1021/ma202308c | *Macromolecules* 2012, 45, 1663−1675

Latex film formation has been used as a method to incorporate silica nanoparticles into a polymer melt, thereby forming silica−latex nanocomposites.[19] One of the advantages of the silica−latex nanocomposite system is that the silica structure in the final nanocomposites can be controlled by the physicochemical properties of the precursor solution.[34,45,46] The samples chosen in the present article have a similar silica structure at different filler volume fractions, due to a simultaneous change of solution pH and silica concentration. Another advantage is that one may mix hydrogenated (H) and deuterated (D) latex nanoparticles, and thereby create a scattering contrast for the polymer, allowing its structural analysis by neutron scattering. Under particular conditions, called zero-average contrast (ZAC),[47,48] the influence of the silica-filler may be strongly reduced. In a recent paper,[34] we have studied the rheology and silica structure of such nanocomposites. We have introduced D-latex particles, and the scattering was shown to be dominated by the polymer structure. During annealing, H- and D-latices were found to demix due to incompatibility in the physico-chemistry of the bead stabilization. The analysis of the demixing kinetics gave information on the bead dynamics in presence of the hard filler phase: low silica volume fractions (5%) had little impact on the demixing kinetics, whereas high volume fractions (15%) were sufficient to block the demixing on the time scale of observation.

In this article, the structural evolution during annealing of films made of H- and D-nanolatex beads, which are *compatible* due to the use of the same stabilization layer, is discussed. Following the ZAC-concept, it will be shown that the silica signal can be made negligible in nanocomposites. Small angle neutron scattering (SANS) then gives access to polymer structure on the nanometer scale, and to slow dynamics over time scale of weeks. This study thus opens a route to characterizing the chain structure in nanocomposites, as a function of the filler quantity and dispersion.[49] Materials, synthesis of H- and D-latices, and experimental methods are presented in section II. Experimental results are presented in section III, starting with the phenomenology of the structural evolution during annealing (section III.1). This is followed by a quantitative modeling based on a combination of the Pedersen model of hairy beads, and of the classical RPA equation for free chains. The model is applied to the experimental intensities of H−D structures both in silica-free matrices (section III.2), and in nanocomposites (section III.3). In section III.4, the impact of the silica-content on chain dynamics is discussed, before concluding with perspectives in section IV.

II. MATERIALS AND METHODS

Silica Nanoparticles. Bindzil silica nanoparticles delivered in high pH charge-stabilized aqueous suspensions (30 wt %, pH 9−9.5) were a gift from Akzo Nobel. We have checked by SANS that they are individually dispersed, and their dimensions are described by a log-normal size distribution (R_{LN} = 78.5 Å and σ = 18%) leading to an average volume of $V_{si} = 2.34 \times 10^6$ Å^3 and a volume-average radius of R_{si} = 82 Å. Contrast variation was employed to determine the scattering length density ($\rho_{si} = 3.6 \times 10^{10}$ cm^{-2}).[34] The hydrodynamic radius determined by dynamic light scattering is 120 Å.

Synthesis of Hydrogenated and Deuterated Latex Nanoparticles. Hydrogenated polymer nanoparticles (H-latex) were purpose-synthesized in San Sebastian using semicontinuous emulsion copolymerization of methyl methacrylate (MMA) and butyl acrylate (BuA). The surfactant used for stabilization was sodium dodecyl sulfate (SDS, Merck) (6 wt % with respect to the total monomer mass). The synthesis process has been described elsewhere.[34,50] Deuterated polymer nanoparticles (D-latex) were synthesized following the same protocol, with perdeuterated MMA (containing 8 D), and BuA containing 9 D and 3 H.

Characterization of Hydrogenated and Deuterated Latex Nanoparticles. The composition of both H- and D-latex beads has been checked. The molar fractions of MMA (72 ± 1%) and BuA (28 ± 1%) have been measured by ^{1}H NMR for protonated batches and by ^{13}C NMR for deuterated ones, both in $CDCl_3$. The glass-transition temperature was found to be 35 °C on average by differential scanning calorimetry. The average chain mass has been obtained by size exclusion chromatography (SEC) using hydrogenated PMMA-standards in THF, and is given, together with their polydispersity index, in Table 1. Because of limited batch size with deuterated material, four different batches were synthesized, called batches A to D. The macroscopic density was found to be $d_H = 1.16 \pm 0.02$ g.cm^{-3} for H (respectively $d_D = 1.23 \pm 0.02$ g.cm^{-3} for D) at room temperature, leading to monomer (repeat unit) volumes of $V_H = 1.54 \times 10^{-23}$ cm^3 (respectively $V_D = 1.57 \times 10^{-23}$ cm^3). The scattering length density was determined by independent contrast variation experiments (see Appendix): $\rho_H = 0.94 \times 10^{10}$ cm^{-2} (respectively $\rho_D = 6.4 \times 10^{10}$ cm^{-2}), in agreement with the macroscopic density and the composition. The index-match point of the silica nanoparticles is thereby found to be at a matrix volume fraction in hydrogenated polymer of Φ_H = 51% ($\Phi_H + \Phi_D$ = 100%). The scattering length density of the H−D-matrix is then given by $\rho_{HD} = \Phi_H\rho_H + \Phi_D\rho_D$. The nomenclature of the samples goes as follows: the letter corresponds to the batch, Φ_H is given in the index, and where appropriate, the silica volume fraction in parentheses (e.g., A_{53}(7%) for a sample made of batch A, having 53% H and 7% silica).

Table 1. Characteristics of the Different Polymer Matrices[a]

name	M_w(H)/PI (g/mol)	M_w(D)/PI (g/mol)	pH	Φ_H	χ_s
A_{53}	279 100/2.7	217 900/2.5	9	0.53	9.3×10^{-4}
A_{62}	279 100/2.7	217 900/2.5	9	0.62	10.1×10^{-4}
B_{62}	258 200/2.5	242 100/2.3	4	0.62	9.7×10^{-4}
C_{44}	305 500/3.3	240 200/2.6	7	0.44	8.3×10^{-4}
D_{51}	345 100/3.4	241 000/1.9	5	0.51	8.0×10^{-4}

[a]Chain masses of H- and D-latex were obtained by SEC, pH refers to the precursor solution, Φ_H to the volume fraction of H-latex in the matrix, and χ_s is the theoretical monomer interaction parameter on the spinodal curve calculated according to eq 7.

The size distribution of the various batches of latex beads (H and D) has been characterized by SANS in dilute suspension. The synthesis protocol gave H- and D-latex particles of typical radius $R_{Guinier} = R_g\sqrt{(3/5)} = 125$ Å. This corresponds to the average mass or dry volume measured by $I(q \to 0)$, which is 8.2×10^6 Å^3. The average mass of the H- and D-chains (280 and 230 kg/mol, respectively) of the matrices used for the annealed samples was taken to estimate the typical number of chains per latex bead: N_0 = 23.

Nanocomposite Formulation and Film Formation. Bubble-free silica−latex films were formed by slow drying in Teflon molds at 65 °C during 3 days, after deionisation and

dx.doi.org/10.1021/ma202308c | Macromolecules 2012, 45, 1663−1675

degassing of solutions, and immediate pH adjustment to the desired value using NaOH. Thermo-gravimetric analysis was used to determine the silica volume fraction in the samples. D-containing samples for scattering discussed here were thinner (0.2−0.3 mm) than the H-latex films used to determine the silica structure by SANS (cf. Appendix), to avoid multiple scattering. Annealing was performed at several temperatures well above T_g (100 to 120 °C; one test at 150 °C), over periods of 1 or 2 weeks. Cooling down samples rapidly below their glass-transition temperature T_g then freezes the structures established at high temperature. Their characterization thus conveys information on polymer structure and interactions at the annealing temperature.

Nanocomposite Film Structure Determination. The generic structure of silica nanoparticles dispersed in latex matrices has been studied previously.[34] For samples with silica, the filler structure has been checked by SANS in H-latex, and is reported in the Appendix. For all other samples discussed in this article, the silica was matched by using appropriate mixtures of H- and D-latex. The evolution of the film structure from latex nanoparticles to molecularly dispersed chains was followed by SANS, as a function of thermal history and silica content. Small angle neutron scattering was performed on beamlines D22 at Institut Laue-Langevin (ILL) (three configurations, defined by sample-to-detector distance D and incident neutron wavelength λ: D = 17 m; D = 8 m; D = 2 m, all λ = 6 Å) and PACE at Laboratoire Léon Brillouin (LLB) (D = 4.5 m, λ = 12 Å; D = 4.5 m, λ = 6 Å; D = 1 m, λ = 6 Å). Empty cell or empty beam subtraction, calibration by 1 mm light water in Hellma cuvettes, and absolute determination of scattering cross sections $I(q) = d\sum/d\Omega$ per unit sample volume in cm^{-1} were performed using standard procedures,[51] namely an incoming beam measurement for absolute units. Incoherent background was estimated using a far-point method and checked by the known high-q scattering laws of polymeric interfaces and melts.

III. RESULTS

III.1. Structural Evolution during Annealing of pure H−D-Matrices. We start with the key observations by SANS of the progressive interdiffusion of H- and D-polymer chains in pure polymer films (i.e., silica-free matrices), before modeling them quantitatively in section III.2, and studying H−D-silica nanocomposites in section III.3. In the course of the annealing procedure, the initial film structure of possibly deformed latex-beads in close contact is replaced by molecularly dispersed chains. In a scattering experiment, the two limiting cases correspond to very different signatures in q-space. Both can be seen as space-filling objects. Given that the initial bead dispersion is governed by the structure of the (drying) suspension, and that H- and D-beads contain different isotopes but are otherwise identical, there should be no preferential correlation between H- and D-beads. In particular, contrarily to our previous study,[34] both latex beads bear the same stabilizing layer. Then the theorem describing melt scattering can be applied to an ideal and incompressible mixture of H- and D-objects of normalized form factor $P(q)$:[47,48,52]

$$I(q) = \Delta\rho^2 \Phi_H \Phi_D v^* P(q) \tag{1}$$

where $\Delta\rho$ is the scattering length density difference between H- and D-objects $\Delta\rho = \rho_H - \rho_D$, Φ_i their volume fraction ($\Phi_H + \Phi_D = 1$), v* their volume, and $P(q \to 0) = 1$. The theorem simply states that in the ideal case, no bead interaction parameter χ describing possible concentration fluctuations is needed, and only form factor scattering is observed. For globular particles, the typical scattering is thus the one of beads of high mass (expressed through the volume v*), i.e., high $I_o = I(q \to 0)$. A typical radius of gyration can be identified in the Guinier regime. A Porod law $\sim 1/q^4$ in the high-q domain corresponds to its smooth interface. The other extreme − individual chains − have necessarily a lower I_o, because several chains make up one bead, and the ratio of I_o can be used to extract the average number of chains per bead. Their high-q power law is also different, proportional to $1/q^2$, which corresponds to Gaussian chain statistics in a melt[53] in our q-range. The form factor of such Gaussian chains reads:[54]

$$P_{Debye}(q) = \frac{2}{q^4 R_g^4}(\exp(-q^2 R_g^2) - 1 + q^2 R_g^2) \tag{2}$$

where R_g is the radius of gyration of the macromolecules.

While the mixture of H- and D-latex beads in solution is likely to be ideal, because it is random in the latex suspension just before the gel point, the melts of H- and D-chains are usually not ideal: a monomeric (Flory−Huggins) interaction parameter χ between H and D monomers has to be introduced.[55−57] Equation 1 is then extended to the well-known random-phase approximation (RPA).[58] In our notations, the scattering function for a mixture of H- and D-labeled chains of different masses and normalized chain form factor $P_H(q)$ ($P_D(q)$, respectively) is then given by

$$\frac{\Delta\rho^2}{I(q)} = \frac{1}{\Phi_H N_H V_H P_H(q)} + \frac{1}{\Phi_D N_D V_D P_D(q)} - \frac{2\chi}{V_M} \tag{3}$$

N_i and V_i are the number of monomeric units per chain (determined from M_w), and monomeric unit volume, for H and D isotopes, respectively. $V_M = \Phi_H V_H + \Phi_D V_D$ is the average monomer volume. The elevated number of parameters in eq 3 can be reduced significantly by fixing the volumes for both H and D chains according to independent SEC results (Table 1):

$$N_i V_i = \frac{M_i}{d N_A} \tag{4}$$

with M_i the weight-average molecular weight, d the density in g/cm^3, and N_A the Avogadro number. The number of parameters can be further limited by coupling the radii of gyration of the two species using their Gaussian statistics and identical monomeric structure:

$$R_{g,D} = R_{g,H}\sqrt{\frac{M_D}{M_H}} \tag{5}$$

There are thus only two free parameters for fits of pure chain melts with eq 3: χ, and one radius of gyration.

A plausible transition scenario between the two limiting cases—beads and individual chains—is the progressive release of chains from the beads. The average mass of the system of beads and chains thus decreases, which is detectable in the low-q scattering. Furthermore, the polymer chains probably start by interdiffusing on the surface of the beads, which generates a corona of H-chains solvated by D-chains, and vice versa. Such chains thus gain scattering contrast, and latex particles become "hairy beads". In this intermediate case, the simultaneous presence of chains and hairy beads leads to the more complex

dx.doi.org/10.1021/ma202308c | Macromolecules 2012, 45, 1663−1675

fitting procedure defined in section III.2. Equation 3 is then simplified by using only a single chain contribution:

$$\frac{\Delta\rho^2}{I(q)} = \frac{1}{\Phi_H\Phi_D N V_M P(q)} - \frac{2\chi}{V_M} \quad (6)$$

This is justified as the molecular weights of the H and D chains are altogether quite close. Note that eq 6 reduces to eq 1 for $\chi = 0$.

The existence of chain scattering, due to released or corona-chains, should result in a high-q power law with a lower exponent than the Porod law, and thus remain visible at high-q. In Figure 1, the evolution of the scattered intensity during annealing is shown for a typical silica-free sample ($A_{62}(0)$, Φ_H = 62%, see Table 1 for details). Directly after film formation at 65 °C (3 days), the highest intensity is obtained. The decay of the scattering function can be described by a Guinier law, $I = I_o \exp(-q^2R_g^2/3)$, and we find R_g = 140 Å for the typical spatial extension of the objects in the film. Given that the radius of gyration of the precursor latex beads measured independently in aqueous solution is 95 Å, its increase indicates a swelling of the beads by the chains of the surrounding beads, i.e., the beginning of chain interdiffusion. A similar behavior has been reported in the literature.[59] Following eq 1, the I_o value of 5415 cm^{-1} corresponds to a bead mass quite close to the one of the precursor latex beads (i.e., ≥ 22 chains out of 23), and in practice no chains have escaped from the beads yet. In the high-q range, however, the expected Porod-law breaks down, and a crossover to a $1/q^2$ regime is found, in close resemblance to scattering of hairy micelles.[60,61] R_g being of the same order of magnitude as the initial beads, the general structure is still a close-packed assembly of beads with a hairy corona.

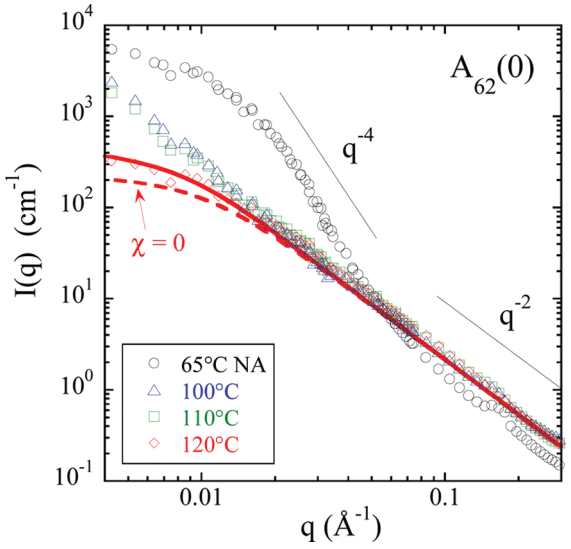


Figure 1. Structural evolution of matrix structure during annealing ($A_{62}(0)$, Φ_H = 62%). After film formation at 65 °C (no annealing), then after annealing at 100 °C (2 weeks), 110 °C (1 week), 120 °C (1 week). The solid line is the RPA description, the dotted line represents the theoretical prediction for $\chi = 0$ (Debye).

During annealing at higher temperatures −100 °C (2 weeks), 110 °C (1 week), and 120 °C (1 week), respectively − the shape of the scattering function evolves considerably in Figure 1. The limiting intensity I_o becomes smaller by more than a factor of 10, indicating vanishing of beads, and the q-range over which chain scattering (q^{-2}) is observed widens. Using the Debye formula—eq 2—together with the parameter coupling—eq 5—in eq 3 allows us to fit the scattering function after the strongest annealing in Figure 1. The resulting radii of gyration of the chains in the melt are reported in Table 2 for the different batches. The R_g values depend on the exact value of χ, the choice of which will be discussed below, but altogether their values are robust within 10%. To check consistency, the values of R_g can be compared to the average mass of the chains. Because of polydispersity in chain mass, the cloud of data points was fitted by a single relationship, $R_g = {}^1/_6 C_\infty b N_{bond}{}^{1/2}$, where C_∞ is the characteristic ratio, b the bond length (1.53 Å), and N_{bond} the number of bonds.[53] The result is $C_\infty = 12 \pm 3$, which compares favorably with other polymethacrylates, e.g., 9 for PMMA.[53] Using a Kratky-plot, a persistence length can be determined, and a Kuhn length of typically 16 ± 3 Å can be deduced (as compared to 17 Å for PMMA[53]). C_∞ deduced from the Kratky-plot method is 9 ± 2. Our chain characteristics are thus in the expected range. Note that the precursor solution pH values have been varied from 4 to 9 in the different matrices, in order to agree with those of the nanocomposites discussed later. Given the close range of observed R_g values, they seem to be unaffected by the precursor solution pH.

Table 2. RPA Fit Parameters for Chain Melts: Interaction Parameter χ and Radius of Gyration for H- and D-Chains

name	annealing	χ	R_g(H) (Å)	R_g(D) (Å)
$A_{53}(0)$	120 °C, 1 week	0.000 58	170	150
		0.0005[a]	157	139
$A_{62}(0)$	120 °C, 1 week	0.000 41	146	129
		0.0005[a]	159	140
$B_{62}(0)$	120 °C, 2 weeks	0.000 67	180	180
		0.0005[a]	166	166
$C_{44}(0)$	120 °C, 3 weeks	0.000 63	174	154
		0.0005[a]	148	131
$D_{51}(0)$	150 °C, 2 weeks	0.000 10	186	155
		0[a]	174	145

[a]This parameter was imposed as an average value compatible with all data sets.

We now turn to the choice of χ. For an ideal mixture of Gaussian chains ($\chi = 0$), the expected limiting law is shown in Figure 1. For nonzero χ values, the chain interactions lead to concentration fluctuations, which results in an increased low-q scattering, visible in Figure 1. For very high χ values, the mixture is no more homogeneous, displaying spinodal decomposition for $\chi \geq \chi_s$. The critical value can be calculated from the point of divergence of $I(q = 0)$ in eq 3 assuming identical monomer volumes:

$$\chi_s = \frac{1}{2}\left(\frac{1}{N_H\Phi_H} + \frac{1}{N_D\Phi_D}\right) \quad (7)$$

It follows from eq 7 that low molecular weights minimize the probability for the mixture to undergo phase separation. The χ_s values are reported in Table 1.

The Flory−Huggins parameter can be determined by fitting eq 3 to the SANS-data of samples annealed at sufficiently high temperatures, where chain scattering is predominantly observed. A sound strategy for χ determination is to perform the same analysis with samples of different H−D-ratio, which is what we have done with the series of samples described in

dx.doi.org/10.1021/ma202308c | Macromolecules 2012, 45, 1663−1675

Table 1. In Figure 2, the experimental scattering function of an annealed film (sample $A_{53}(0)$, 120 °C, 1 week) is compared to

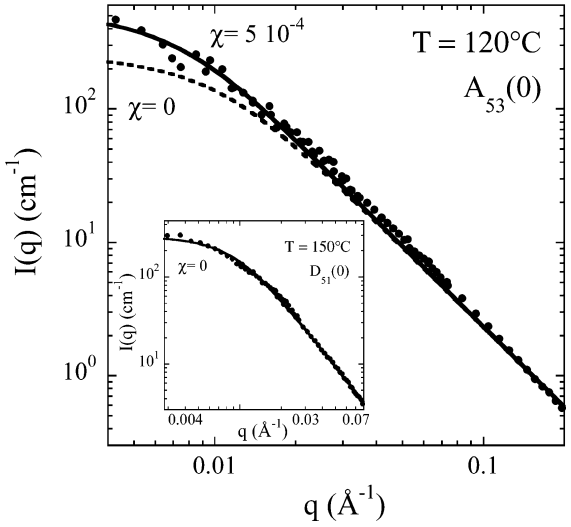


Figure 2. Single-chain form factor for the H−D matrix $A_{53}(0)$ after annealing (120 °C, 1 week). Line is a fit using the RPA description with $\chi = 5 \times 10^{-4}$ (see text for details), dashed line is the theoretical curve in the limit of ideal mixing. Inset: H−D matrix $D_{51}(0)$ after annealing at 150 °C, line is a prediction assuming $\chi = 0$.

a fit by eq 3, and good agreement is obtained for $\chi = 5 \times 10^{-4}$. The pure form factor ($\chi = 0$) is also shown for this sample. For comparison, the critical value χ_s is about twice as high (9.3×10^{-4}).

The same analysis has been performed with the complete series in Table 1, and the same χ-value (5×10^{-4}) was found to reproduce correctly all data, and will be taken from here on as the average monomeric Flory−Huggins interaction parameter of this copolymer at this temperature (120 °C). For lower annealing temperatures, only an extrapolation will be proposed. Note that again the pH has no influence on this parameter and that the same radius of gyration is found for the first two samples ($A_{53}(0)$ and $A_{62}(0)$: same batch, different Φ_H) in Table 2 with χ forced to 5×10^{-4}, which illustrates the overall coherence of the method. For completeness, slightly better fits may be obtained by letting χ evolve freely. Indeed, values between 4.1 and 6.7×10^{-4} are found, cf. Table 2, their average being close to 5×10^{-4}, with an error bar of 10^{-4}.

Upon examination of Table 2, it becomes clear that longer annealing times at 120 °C (up to 3 weeks, for different Φ_H) have no systematic effect on the interaction parameter. In an independent experiment, a single high-temperature annealing of sample $D_{51}(0)$ (150 °C, 2 weeks) has been performed, and the result is shown in the inset of Figure 2. The data are seen to be perfectly reproduced by a fit using eq 3 with $\chi = 0$. Note again that an almost imperceptibly better fit is obtained with $\chi = 10^{-4}$, which is the order of magnitude of the error bar. This suggests that the molecular dispersion obtained after stronger annealing is very close to ideal. Note that this is in qualitative agreement with the generic temperature dependence of $\chi = A + B/T$ with $B > 0$.[53,55]

III.2. Modeling of SANS data of Pure H−D-Matrices. In this section, it will be shown that the phenomenological evolution of the SANS data can be quantitatively reproduced with an additive model of free chains (RPA) and of an adaptation of the Pedersen model for hairy micelles.[60,61] The form factor of the latter is mimicked by a sphere with Gaussian chains on the surface. The model allows us to extract detailed information on the fraction and radius of gyration of free chains, as well as on the core−corona structure of the latex beads in the film.

The expression for the form factor of a hairy micelle with non interacting Gaussian corona chains[60,61] translates into the following normalized function using our notation:

$$P_{\text{hairy}}(q) = \frac{1}{V_{\text{HB}}^2}(V_{\text{core}}^2 P_{\text{core}}(q) + N_{\text{hair}} V_{\text{hair}}^2 P_{\text{hair}}(q) + 2N_{\text{hair}} V_{\text{core}} V_{\text{hair}} S_{\text{core-hair}}(q) + N_{\text{hair}}(N_{\text{hair}} - 1) V_{\text{hair}}^2 S_{\text{hair-hair}}(q)) \quad (8)$$

Here N_{hair} is the number of corona chains at the core surface, V_{hair} is the volume of one chain, and V_{core} is the volume of the polymer core. V_{HB} is the (dry) volume of the hairy bead, $V_{\text{HB}} = V_{\text{core}} + N_{\text{hair}} V_{\text{hair}}$ due to volume conservation. $P_{\text{hair}}(q)$ is the Debye function given in eq 2, and $P_{\text{core}}(q)$ is the form factor of a sphere with radius R

$$P_{\text{core}}(q) = 9\frac{(\sin(qR) - qR\cos(qR))^2}{(qR)^6} \quad (9)$$

$S_{\text{core-hair}}(q)$ is the interference cross-term between the core and a Gaussian corona chain starting at the surface with a radius of gyration R_g*

$$S_{\text{core-hair}}(q) = \frac{1 - \exp(-q^2 R_g^{*2})}{q^2 R_g^{*2}} \frac{\sin[q(R_g^* + R)]}{q(R_g^* + R)} F_{\text{sphere}}(q) \quad (10)$$

where $F_{\text{sphere}}(q)$ is the amplitude of the sphere form factor given by the square-root of eq 9. $S_{\text{hair-hair}}(q)$ is the interference between the chains forming the hairy corona

$$S_{\text{hair-hair}}(q) = \left(\frac{1 - \exp(-q^2 R_g^{*2})}{q^2 R_g^{*2}}\right)^2 \left(\frac{\sin[q(R_g^* + R)]}{q(R_g^* + R)}\right)^2 \quad (11)$$

Because of the contrast situation, only the protruding part of the chains is visible as a hair. In eqs 10 and 11, this absence of (visible) penetration in the core is mimicked by the term R_g* +R.

As we have seen in Figure 1, there is an intermediate state during annealing where the average mass of chains and beads is progressively reduced due to chain escape. Here, this is modeled with a fraction α of free chains in the bulk (out of the bead), whereas the remaining fraction of chains $(1 - \alpha)$ is still partially trapped in the latex core. α thus represents the loss of mass of the beads. A second fraction β is needed to describe the partition between core and corona: $\beta = 1$ stands for the initial bead with no chains at the surface (all is core), and $\beta = 0$ represents a Gaussian star polymer (all is corona). It follows that $V_{\text{core}} = \beta(1 - \alpha)V_0 = \beta V_{\text{HB}}$ and $V_{\text{corona}} = N_{\text{hair}} V_{\text{hair}} = (1 - \beta)(1 - \alpha)V_0 = (1 - \beta)V_{\text{HB}}$, where V_0 is the volume of the initial latex bead.

dx.doi.org/10.1021/ma202308c | Macromolecules 2012, 45, 1663−1675

To obtain the scattered intensity due to the mixture of hairy beads and free chains, we assume that one can divide our system in two independent space-filling parts: H and D core−corona beads on one side [$I_{hairy}(q)$], and H and D free chains on the other side [$I_{free}(q)$], as illustrated in Figure 3.

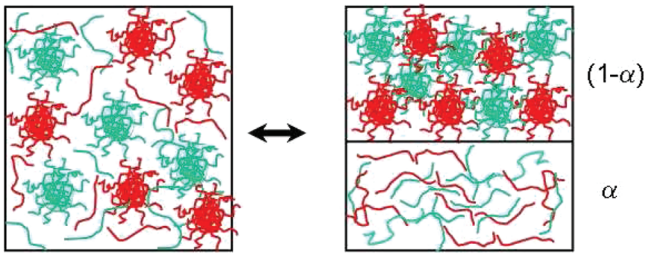


Figure 3. Right: schematic representation of the system during annealing. Deuterated components are in red and protonated ones in green. Left: decomposition in two space-filling subsystems: core−corona beads in proportion $(1 - \alpha)$ and free chains in proportion α.

Each case may be described using the formalism presented above. Equation 1 describes the scattering of the subsystem containing the ideal mixture of hairy beads, using the form factor $P_{hairy}(q)$ given in eq 8. The contrast and the fractions Φ_H and Φ_D keep their meaning, only the (dry) volume of the hairy beads, V_{HB}, needs to be used for v^*. Neglecting the cross-correlation term between the two subsystems, thus assuming that the structure of chains is not affected by the hairy beads, and vice versa, we add the intensity for each of them weighted by their proportions α (respectively $1 - \alpha$):

$$I(q) = (1 - \alpha)I_{hairy}(q) + \alpha I_{free}(q) \quad (12a)$$

$$I_{hairy}(q) = \Delta\rho^2\Phi_D\Phi_H V_{HB}P_{hairy}(q) \quad (12b)$$

$I_{free}(q)$ of the subsystem of the melt of free chains is given by the RPA expression, eq 6. The shape of the resulting signal depends on the form factor of each component, and on α. The total number of parameters seems large at first sight, but again it can be reduced to a few key parameters. Individual bead parameters (mass, density, and radius of H and D beads) are known from independent measurements, as well as chain characteristics (cf. Table 1). χ at 120 °C has been fixed to 5×10^{-4}. At lower annealing temperatures, it is higher. In this range, χ has been fixed to extrapolated values of $7.5 \pm 2 \times 10^{-4}$ at 100 °C (respectively $6.5 \pm 1.5 \times 10^{-4}$ at 110 °C), based on the relationship $\chi = A + B/T$, and vanishing χ at 150 °C. Directly after film formation at 65 °C, the extrapolated value of χ exceeds the critical value χ_s, and χ was set to χ_s. Then the free-chain intensity diverges at $q = 0$, but due to the limited number of free chains ($\alpha \leq 1/4$), only little impact on the low-q level of the fit is found. Knowing χ, the parameter α can be read off from I_0. The radius of gyration of free chains in the final melt has been reported in Table 2, and here their average over H and D chains, R_{g_free}, was imposed (150 Å for batch A), and kept fixed for all stages of annealing. This is consistent with the data, because changing R_{g_free} directly impacts the high-q prefactor. As for free chains, the radius of gyration of corona chains is coupled to their mass according to eq 5. Through the conservation of remaining bead volume, the corona chain mass is coupled to the number of corona chains, and to β. To summarize, besides α which is set independently, the remaining fit parameters are the core fraction β, and the number of corona chains N_{hair}. These two parameters have a specific impact on the medium-q data (curvature, weak oscillations), and can be determined with a relative precision of better than 5%.

The formalism of eq 12 has been applied to the scattering of the pure H−D-matrices, and the fits are superimposed to the data in Figure 4 (solid lines). All the main features, like the low-q limiting intensity, the signal curvature, and the crossover to q^{-2} chain scattering are found to be reproduced in a satisfactory manner. Note that a simple homogeneous core−shell model would follow a q^{-4} power law in the high-q range, incompatible with the data. Minor differences, like damped oscillations in the intermediate q-range of the model prediction, are due to the use of monodisperse cores and smoothing of experimental data by the spectrometer resolution function. This is shown by comparison of the individual contributions given in eqs 8−11 to a final scattered intensity, in Figure 4b. Depending on the samples, clearly either the Guinier-shoulder of the core form

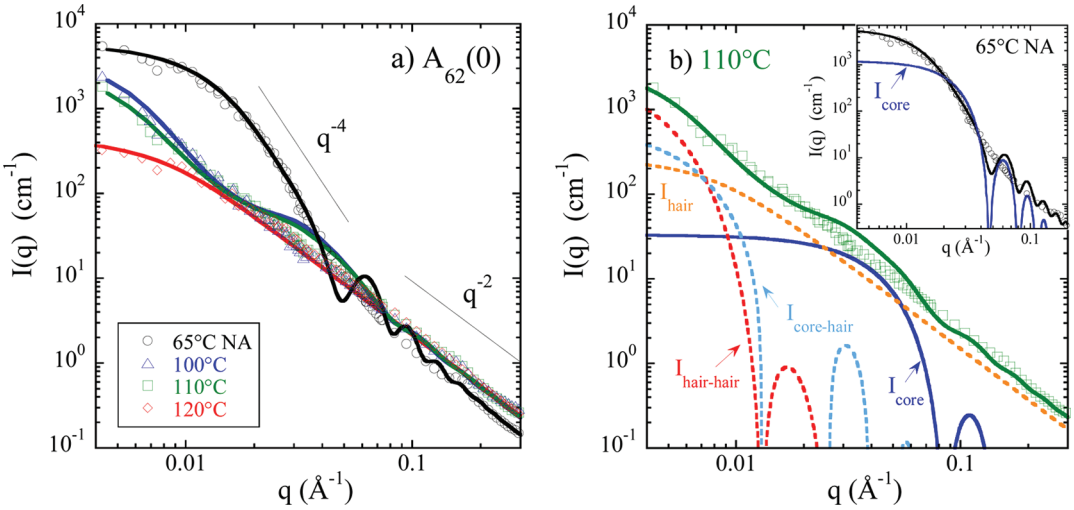


Figure 4. (a) Modeling of the structural evolution of the matrix during annealing ($A_{62}(0)$, Φ_H = 62%). After film formation at 65 °C (no annealing), then after annealing at 100 °C (2 weeks), 110 °C (1 week), 120 °C (1 week). (b) Decomposition of model fits into different contributions showing the influence of the monodispersity of the core (110 °C). Inset: same monodisperse core contribution, without annealing.

dx.doi.org/10.1021/ma202308c | Macromolecules 2012, 45, 1663−1675

Table 3. Hairy Bead Fit Parameters used in eq 12 for Analysis of Silica-Free Matrices[a]

thermal treatment	sample	α	β	N_{hair}	R_g* (Å) (corona)	R_{core} (Å)	N_{free}
65 °C, 3 days (NA), $\chi = \chi_s$	$A_{53}(0)$	0	0.55	90	51	102	0
	$A_{62}(0)$	0	0.45	90	56	96	0
100 °C, 2 weeks, $\chi = 7.5 \times 10^{-4}$	$A_{53}(0)$	0.75	0.12	8	120	39	17
	$A_{62}(0)$	0.12	0.10	14	171	56	3
110 °C, 1 week, $\chi = 6.5 \times 10^{-4}$	$A_{53}(0)$	0.75	0.12	8	120	39	17
	$A_{62}(0)$	0.25	0.10	10	187	53	6
120 °C, 1 week, $\chi = 5 \times 10^{-4}$	$A_{53}(0)$	1	-	-	-	0	23
	$A_{62}(0)$	1	-	-	-	0	23

[a]The initial number of chains per bead is $N_0 = 23$. R_{g_free} was set to its average value after annealing, 150 Å. Only α, β, and N_{hair} are fit parameters; all others are determined by coupling.

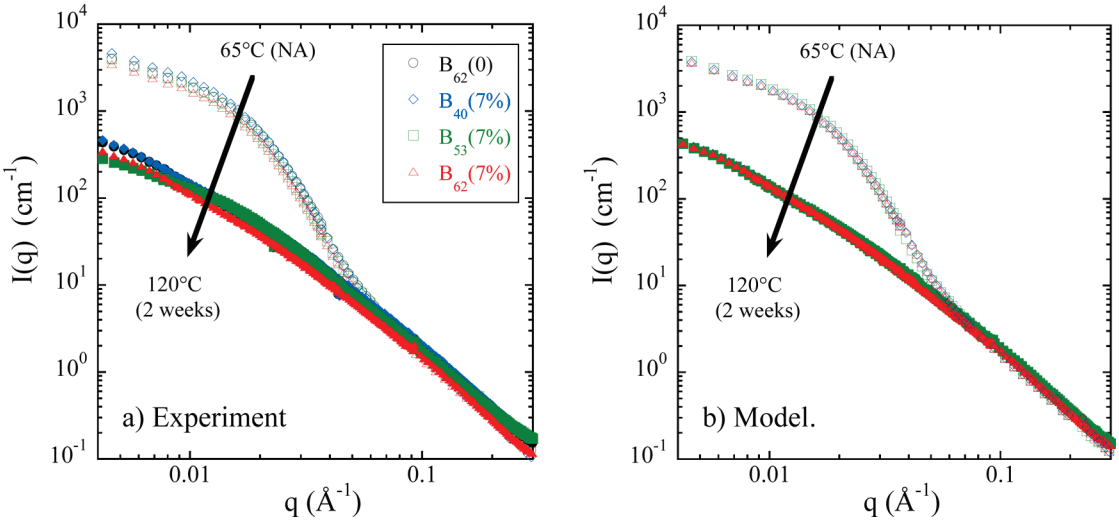


Figure 5. (a) Scattered intensities of samples $B_{62}(0)$, $B_{40}(7\%)$, $B_{53}(7\%)$, and $B_{62}(7\%)$ after film formation and after annealing. (b) Theoretical modeling for the same samples following eq 13 showing that H−D polymer scattering dominates the intensity.

factor, or the oscillations of the same function, induce a minor discrepancy between the data and the model fit.

The parameters used to fit the data are summarized in Table 3 for batch A, for two H-fractions. In the course of the annealing procedure, α is found to increase from 0 to 1 at 120 °C, where hairy beads have completely disappeared and chains are described by RPA. This is accompanied by the corresponding increase in the number of free chains escaped from each bead. Simultaneously, β decreases from an initial value of about $^1/_2$ to about $^1/_{10}$. This implies that directly after film formation at 65 °C, half of the volume of the latex particles is already "solvated" by the chains of the surrounding beads. Chain interdiffusion has already started, which is to be expected, given that such latex films possess strong mechanical properties, considerably higher than what would be found for dense assemblies of undeformed colloidal spheres. The number of corona chains, finally, is found to decrease with increasing annealing temperature. Its initial number, of the order of one hundred, is about four to five times higher than the number of chains per bead. This suggests that some chains located at the surface form loops, each being counted as an individual corona chain in the model. As the core radius goes down ($\alpha \rightarrow 1$), and the corona fraction up ($\beta \rightarrow 0$), the overall radius of gyration of the hairy beads is found to increase, as can be seen from the global shape of the curves in Figure 4a. Within our model, this swelling of the beads is described by long corona chains (cf. Table 3), which are thus more massive, and—by mass conservation—fewer. For one specific sample, their radius of gyration even exceeds the typical R_g of free chains for low-α values. This may be due to stretching (because of the star-like conformation), which is mimicked in our model by more massive chains. It may also be induced by the model which assumes all chains fixed on the core, whereas they may start from anywhere in the corona.

III.3. Modeling of SANS Data Describing the Polymer Matrix Structure of Silica−Latex Nanocomposites. The question of the microstructure of the polymer matrix in nanocomposites can be addressed by SANS.[35] Using appropriate mixtures of H- and D-latex, it is possible to index-match the silica using the method of zero-average contrast.[47,48] This is why the scattering length densities of the components have been determined with care in section II. The theoretical match point of silica by our latex is $\Phi_H = 51\%$. The small angle neutron scattering of the resulting silica-matched nanocomposites should then originate from the H−D-structure only, and this property has been searched for in the past in order to measure the chain structure in polymer nanocomposites.[6−11] In practice, the issue is more complicated, due to sometimes difficult matching, and to the question of a silica contribution via hole scattering in the matrix, i.e., holes occupied by invisible silica, which may dominate the (mostly low-q) signal at high volume fractions.

Here we start with the analysis of the matching conditions in nanocomposites through measurements around the match point. In Figure 5a, the scattering of a pure H−D-matrix (sample $B_{62}(0)$) is compared to nanocomposites at $\Phi_{si} = 7\%$:

dx.doi.org/10.1021/ma202308c | Macromolecules 2012, 45, 1663−1675

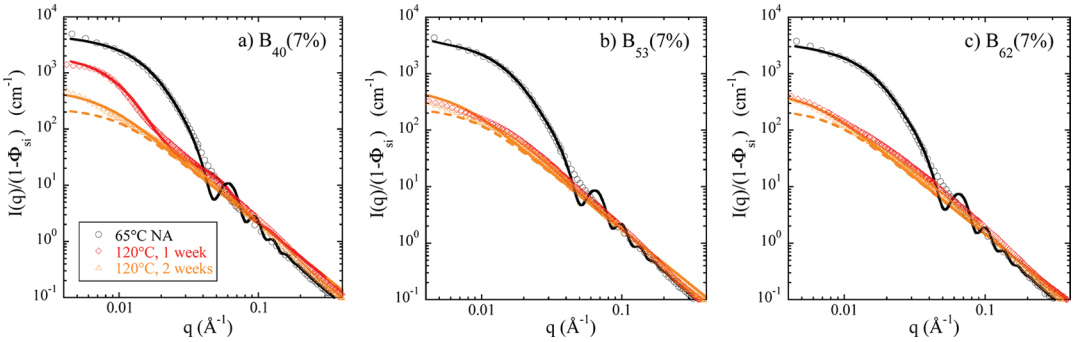


Figure 6. Structural evolution of polymer structure in nanocomposites with Φ_{si} = 7% after film formation and annealing at 120 °C for one and 2 weeks. (a) B_{40}(7%), (b) B_{53}(7%), and (c) B_{62}(7%). Solid lines are theoretical models explained in the text. The dotted line represents the theoretical prediction for χ = 0 (Debye).

Table 4. Hairy Bead Fit Parameters Used in Equation 12 for the Analysis of H−D-Nanocomposites Containing Φ_{si} = 7%[a]

thermal treatment	sample	α	β	N_{hair}	R_g* (Å) (corona)	R_{core} (Å)	N_{free}
65 °C, 3 days (NA), $\chi = \chi_s$	$B_{62}(0)$	0.24	0.57	70	54	95	6
	B_{40}(7%)	0.15	0.55	75	52	97	3
	B_{53}(7%)	0.22	0.50	90	54	91	5
	B_{62}(7%)	0.27	0.52	100	52	91	6
120 °C, 1 week, $\chi = 5 \times 10^{-4}$	$B_{62}(0)$	0.45	0.15	28	103	54	10
	B_{40}(7%)	0.43	0.10	30	95	48	10
	B_{53}(7%)	1	-	-	-	0	23
	B_{62}(7%)	1	-	-	-	0	23
120 °C, 2 weeks, $\chi = 5 \times 10^{-4}$	$B_{62}(0)$	1	-	-	-	0	23
	B_{40}(7%)	1	-	-	-	0	23
	B_{53}(7%)	1	-	-	-	0	23
	B_{62}(7%)	1	-	-	-	0	23

[a]The initial number of chains per bead is N_0 = 23. The radius of gyration of free chains is set to the average value determined for each sample after annealing: R_{g_free} = 166 Å, 152, 170, and 183 Å for matrices $B_{62}(0)$, B_{40}(7%), B_{53}(7%), and B_{62}(7%), respectively. Only α, β, and N_{hair} are fit parameters; all others are determined by coupling.

B_{40}(7%), B_{53}(7%) and B_{62}(7%), before (film formation at 65 °C) and after annealing (120 °C, 2 weeks). The scattering for different Φ_H is seen to remain very close, compared to the strong variation induced by the annealing procedure. To emphasize the satisfying matching conditions, we have calculated the theoretical intensities expected for such samples, based on rescaled additive contributions of the silica and the matrix:

$$I_{theo}(q) = \left(\frac{\Delta\rho_2}{\Delta\rho_1}\right)^2 I_{si}(q) + \frac{\Phi_H'\Phi_D'}{\Phi_H\Phi_D}(1 - \Phi_{si})I_{matrix}(q) \quad (13)$$

where $I_{si}(q)$ has been measured in a pure H-matrix with pH 4 (cf. scattering curve in Appendix), under contrast condition $\Delta\rho_1 = \rho_{si} - \rho_H$, at Φ_{si} = 7%, rescaled to contrast $\Delta\rho_2 = \rho_{si} - \rho_{HD}$; $I_{matrix}(q)$ is the scattering of the silica-free matrix measured at Φ_H = 62%, rescaled to Φ'_H (i.e., 40%, 53%, 62%). The predictions in Figure 5b are also very close for H-fractions between Φ_H = 40% and 62%, which illustrates that matching is satisfying over this range. We have checked that higher deviations (Φ_H = 70% and above) distort the intensity curves considerably, due to the then visible silica contribution. The contribution of the matched silica can thus be considered negligible, and we can apply the analysis developed in section III.2 to the scattering of the remaining matrix fraction of the samples by dividing experimental intensities by $(1 - \Phi_{si})$.

The evolution of the polymer structure with annealing of silica-containing samples with various Φ_H is shown in Figure 6, together with model fits. The data either directly after film formation at 65 °C, or after annealing of 1 or 2 weeks at 120 °C are plotted. The temperature was chosen in the light of the preceding section. In Figure 6, the scattering curves of nanocomposites show the same evolution as the pure matrices (cf. Figures 1 and 5): the low-q intensity decreases, and chain scattering progressively dominates the signal. Note that the matrix made with exactly the same batch, $B_{62}(0)$, is shown in Figure 5.

The fitting procedure of nanocomposites using eq 12 is the same as in section III.2, and fits are superimposed to the data in Figure 6. The fit parameters for all samples are given in Table 4, together with those of the corresponding silica-free matrix. The interaction parameter χ was set, as before, to χ_s after film formation and to 5×10^{-4} at 120 °C. The radius of gyration of the free chains in coexistence with the latex beads has been determined from the longest annealing (120 °C, 2 weeks) using eq 6 for each nanocomposite. These values are compatible (within 15%) with the value of the pure matrix, and have been imposed to weaker annealing (cf. caption of Table 4). The decrease in average mass is described by an increase in α from about 1/4 to 1 after 1 or 2 weeks at 120°, which implies the complete disappearance of the latex core. After 1 week, some samples (the pure matrix $B_{62}(0)$ and B_{40}(7%)) still display a

dx.doi.org/10.1021/ma202308c | Macromolecules 2012, 45, 1663−1675

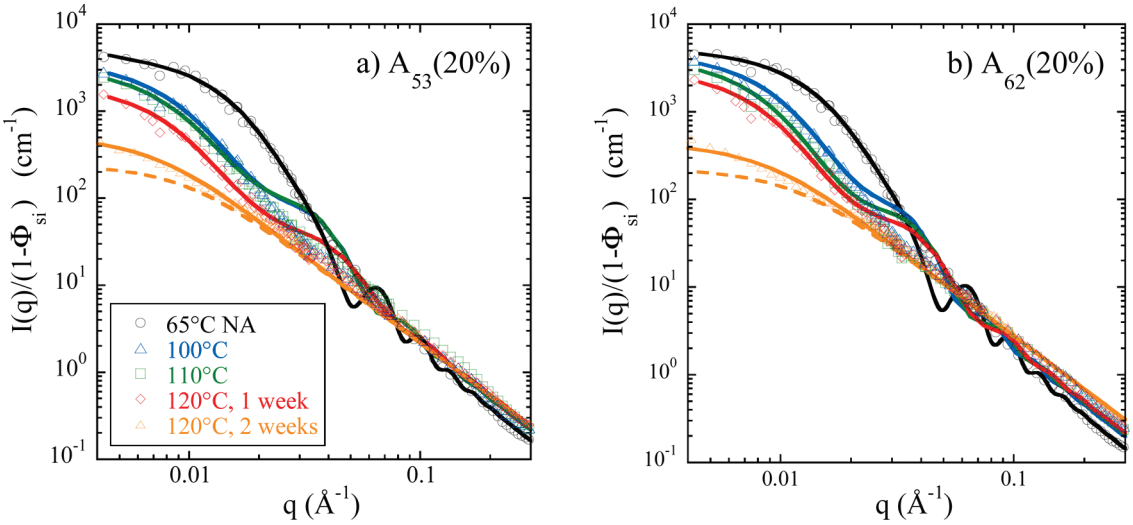


Figure 7. Structural evolution of polymer structure in nanocomposites with Φ_{si} = 20% after film formation and annealing at 100 °C (2 weeks), 110 °C (1 week), 120 °C (1 week) and 120 °C (2 weeks): (a) A_{53}(20%); (b) A_{62}(20%). Solid lines are theoretical models as explained in the text. The dotted line represents the theoretical prediction for χ = 0 (Debye). The corresponding matrix A_{62}(0) is shown in Figure 1.

Table 5. Hairy bead fit parameters used in eqs. (12) for the analysis of H−D-nanocomposites containing Φ_{si} = 20%. The initial number of chains per bead is N_0 = 23. The radius of gyration of free chains is set to the average value determined for each sample after annealing: R_{g_free} = 154 and 134 Å for A_{53}(20%) and A_{62}(20%), respectively. Only α, β, and N_{hair} are fit parameters, all others are determined by coupling

thermal treatment	sample	α	β	N_{chain} (corona)	R_g* (Å) (corona)	R_{core} (Å)	N_{free}
65 °C, 3 days (NA), $\chi = \chi_s$	A_{53}(20%)	0.14	0.46	85	53	92	3
	A_{62}(20%)	0.05	0.47	85	55	96	1
100 °C, 2 weeks, $\chi = 7.5 \times 10^{-4}$	A_{53}(20%)	0.25	0.23	28	103	70	6
	A_{62}(20%)	0.10	0.24	40	94	75	2
110 °C, 1 week, $\chi = 6.5 \times 10^{-4}$	A_{53}(20%)	0.29	0.24	22	113	69	7
	A_{62}(20%)	0.15	0.19	30	109	68	3
120 °C, 1 week, $\chi = 5 \times 10^{-4}$	A_{53}(20%)	0.45	0.15	18	116	54	10
	A_{62}(20%)	0.28	0.18	25	111	63	6
120 °C, 2 weeks, $\chi = 5 \times 10^{-4}$	A_{53}(20%)	1	-	-	-	0	23
	A_{62}(20%)	1	-	-	-	0	23

scattering function intermediate between beads and chains, which corresponds to $\alpha \approx {}^1/_2$. The core−corona parameter β—which quantifies the remaining core fraction and thus the degree of chain interdiffusion—decreases from about ${}^1/_2$ to ${}^1/_6$ for these two samples. The number of corona chains is equivalent to the one of the silica-free matrices discussed in section III.1: it decreases from about 85 to about 30. In parallel, the radius of gyration of the corona chains grows from about 50 to 100 Å. For all samples, after disappearance of the core (annealing for 2 weeks), the signal evolves to free chain RPA behavior (eq 3). The number of free chains having escaped from the beads is typically 5 directly after film formation, and reaches the maximum number N_0 = 23 after annealing.

In a previous article, we have investigated the film structure of blends of H- and D-latex beads which demix during annealing. The demixing kinetics was found to proceed during annealing for nanocomposites with low amounts of silica (Φ_{si} = 5%), and to be blocked in presence of higher amounts Φ_{si} = 15%.[34] For the present system of compatible latex beads, we have performed an analogous study with a high silica fraction (Φ_{si} = 20%). Note that the samples, A_{53}(20%) and A_{62}(20%), were designed to have a silica structure comparable to the one of the 7% samples by varying the pH. This was checked by SANS with the purely hydrogenated samples, cf. data reported in the Appendix. The evolution of the polymer structure of A_{53}(20%) and A_{62}(20%) in the course of the annealing procedure—65 °C NA, 100 °C (2 weeks), 110 °C (1 week), and 120 °C (1 week and 2 weeks)—is shown in Figure 7.

The scattering curves displayed in Figure 7 show a delayed evolution with respect to the silica-free matrices (or 7%-nanocomposites) during annealing. The initial structure directly after film formation (NA) resembles to the one previously encountered for hairy beads (cf. Figures 1 and 6). During annealing of the nanocomposites at higher T; however, the low-q intensity decreases only slowly, and longer annealing at 120 °C is needed to achieve a RPA-behavior (α = 1). The resulting radius of gyration of the free chains are R_g(H) = 163 Å (respectively 140 Å), and R_g(D) = 144 Å (respectively 124 Å) for A_{53}(20%) and A_{62}(20%) respectively, using the interaction parameter χ (fixed to 5×10^{-4}).

We have again reproduced the scattered intensities using the formalism of eq 12, based on the average (over H and D) radius of gyration of the free chains, and the fit parameters are summarized in Table 5. The NA-curve can be described by similar parameters as in Tables 3 and 4: a small α in the range 0.05−0.15, the core−corona parameter β about ${}^1/_2$ (as before in all cases), and 85 chains or loops in the corona, of typical radius of gyration R_g* ≈ 55 Å. In Figure 7, the moderate

dx.doi.org/10.1021/ma202308c | Macromolecules 2012, 45, 1663−1675

decrease in average mass is reflected by a moderate increase in α, up to 120 °C during 1 week. Contrary to the silica-poor nanocomposites, the core is thus not completely destroyed under these conditions, and as a consequence, the number of free chains having escaped from a bead is limited to 10, out of N_0 = 23 making up the initial bead. Only after 2 weeks at 120 °C, the core disappears and chain scattering is recovered. In this context, it may be noted that the RPA-fit of the chain scattering in presence of silica is empirical, as it implicitly relies on translational invariance of the system,[62] whereas some heterogeneities in chain mobility probably exist (cf. section III.4).

Simultaneously, up to annealing of 1 week at 120 °C, the core−corona parameter β decreases to $^1/_6$. This shows that interdiffusion of corona chains with chains from neighboring beads proceeds approximately in the same manner as in silica-poor samples, but does not reach the complete disappearance of the core. The number of corona chains decreases from 85 to 20, i.e., again less than with silica-poor samples. In parallel, the radius of gyration of the corona chains, R_g*, increases to 100−120 Å, i.e., to about 80% of the spatial extent of free matrix chains, as in the case of nanocomposites with 7% of silica for similar α values. The behavior seems to be different in the case of matrices, where R_g* increases above the radius of gyration of the free chains for $\alpha \approx 0.1-0.2$. This could be the signature of the impact of silica on chain interdiffusion.

To summarize, for Φ_{si} = 20%, we have found radii of gyration compatible with the pure matrix conformations, as well as with the 7%-silica nanocomposites, within error bars.

III.4. Chain Interdiffusion and Conformation. It has been shown in the preceding section that the evolution of the structure with annealing at increasing temperatures (65° up to 120 °C) is slower in the case with strong silica loading (20%v) as opposed to 7%v or silica-free samples. In all cases, the intermediate structures, which reflect the distribution of deuterated and hydrogenated polymer in the samples, could be modeled by a formalism—eq 12—based on the Pedersen model for hairy beads, and RPA for the free chains. Two robust results of the fitting procedure are α and β. Their value can be translated directly into the core volume of the latex particles V_{core}, or the corresponding radius R_{core}. Decrease of the latter illustrates the progressive interdiffusion of the latex beads. In Tables 3 and 4, the radius of the latex core can go to zero after 1 week at 120 °C for matrices and 7%-nanocomposites, whereas it never reaches zero for 20%-nanocomposites (Table 5) for the same annealing. In this case, the core vanishes only after 2 weeks. Observations of similar delay has been made in our previous study on an incompatible latex system, where the kinetics of phase-separating latex zones was investigated.[34] At high silica-content, zone-growth was impeded, but it was unclear if this could be traced back to arrested dynamics at the local scale (chains), or of larger zones (beads). Here, individual chain dispersion is quickly reached in pure matrices and low-silica nanocomposites, suggesting that it is interdiffusion of individual chain which is delayed at 20%.

This observation of delayed chain interdiffusion in presence of silica may be explained by several mechanisms, and there is some controversy in the literature. One can imagine, e.g., a sticky interaction of polymer chains on the silica nanoparticles, which would reduce chain mobility.[63,64] These authors argue that chain adsorption restricts, e.g., reptational dynamics, and thus also polymer flow around hard particles. In some sense, a zone of restricted flow may develop across the sample. Alternatively, a 'bottleneck' explanation has been put forward,[65] where the three-dimensional silica structure is thought to constrain possible motion of the polymer latex molecules. This may apply to the a priori percolated silica structure at 20%. Our observations may also be explained with NMR investigations of nanocomposite model systems developed over the past decade,[24−29] which postulate another type of zone of restricted dynamics. These authors propose the existence of a frozen polymer layer close to the filler surface, of estimated nanometric thickness (typically a few nm) at temperatures not too far above the bulk glass-transition temperature. In our case, samples are well above the bulk T_g during annealing, and the frozen layer thickness should be smaller. This layer leads to a higher volume fraction of hard matter, and thus can immobilize substantial parts of the nanocomposite sample on our time scale of observation. Exact values depend on the dispersion of the silica in the sample, as well as on the temperature-dependent layer thickness.[24] If the data shown in this article is not suitable for deciding in favor of any of the cited explanations, the existence of a delayed chain interdiffusion itself is unambiguously proven.

In the context of nanocomposite reinforcement, the conformation of macromolecules in presence of fillers has been discussed in the literature,[9,10,66] but no generally accepted trend has been found. An overview has been recently given by Nusser et al.[11] who considered both simulations and experimental aspects based on scattering experiments. They emphasized that the polymer−filler size ratio is a key parameter influencing the polymer structure. Here, we are concerned with filler particles of size comparable to the polymer chains and we will restrict the discussion of (controversial) literature results to this regime. On one hand, a decrease of the chain dimensions with respect to the unfilled polymer was observed by Nakatani[6] and Nusser[11] by means of SANS measurements. In the first case, the authors[6] used a data treatment based on the high concentration method to extract the chain radius of gyration in PDMS/polysilicate fillers blend. Note that this is a specific case because the filler is liquid at room temperature. In the second one, Nusser et al.[11] obtained the chain conformation in silica/PEP nanocomposites by the use of ZAC method. In this system, the R_g decrease was weak for high silica loading: 2% reduction at Φ_{si} = 18%v. On the other hand, various experiments using the ZAC method report that, in this regime, the chain size is not affected in the presence of silica (Sen,[8] Jouault[7]). In agreement with these findings, our results seem to indicate that there is not a strong enough tendency in the evolution of R_g with filler content in order to be detectable. Changing R_g has a direct influence on the high-q scattering, which cannot be compensated by any other parameter in our description. We have thus estimated our error bar on R_g of the free chains to ±15% using a RPA fit. For the nanocomposites with 7% silica (batch B), the R_g of the free chains stays comparable to the one of the matrix, i.e., 166 Å for $B_{62}(0)$. At 20% silica content (batch A), the average (over H and D) R_g of free chains is R_g = 154 Å (respectively 134 Å) for A_{53} (respectively A_{62}). These values can be compared to the value of the corresponding matrices (Table 2), which is about 150 Å. As mentioned before, the chain conformation thus stays within the same bounds of ±15% for the radius of gyration, i.e., chain conformation seems to be independent of silica concentration. Jouault et al.[7] draw attention to the role of the filler structure. We point out that our system has a similar aggregation state as their 5%v silica/PS nanocomposites (N_{agg}

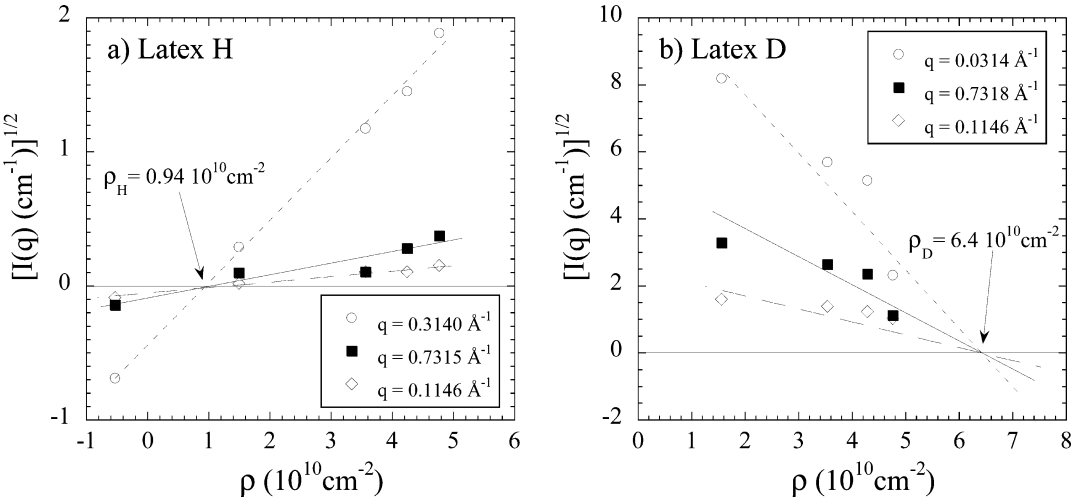


Figure 8. SANS contrast variation study of (a) protonated and (b) deuterated latex in a mixture of H_2O/D_2O.

≈ 10 versus N_{agg} ≈ 7 in our case, see Appendix), and the same unchanged R_g is observed. To summarize, using appropriate contrast-matching in a system where the scattering data are not spoiled by additional terms,[8,11] it is possible to follow the chain radius of gyration even in presence of considerable amounts of silica filler.

IV. CONCLUSION AND PERSPECTIVES

The evolving structure during annealing of silica−latex nanocomposites has been studied by SANS under zero-average contrast conditions for the silica nanoparticles. A quantitative structural model based on additive contributions of core−corona ("hairy") latex beads and of free chains in a melt has been developed. The model is demonstrated to nicely reproduce the data over the whole q-range and in absolute units, with a reduced number of free parameters describing the structure of the shrinking latex beads. Our analysis of silica-free matrices and nanocomposites with low (7%) and high (20%) silica volume fractions shows that chain interdiffusion proceeds until complete disappearance of the core, with a delay in presence of 20% of silica.

For nanocomposites, evidencing by SANS that the silica filler influences the chain dynamics is interesting for the molecular understanding of the reinforcement effect. Another relevant aspect resides in the still open question of chain conformation in hard filler environments. In this article, it has been shown that annealing at high temperature for sufficiently long times pushes the system toward individual chain dispersion. We have been able to measure chain conformation at different silica volume fractions in a given state of aggregation (typically 10 primary silica particles per aggregate, percolating at high concentration). In particular, it is found that the radius of gyration is unaffected by the silica loading under these conditions. It is now hoped that our system will allow obtaining insight in the structure of molecularly dispersed chains in nanocomposites, as a function of dispersion or aggregation, and chain mass.

APPENDIX

A. Contrast Variation

The scattering length density of both H- and D-latex was determined by external contrast variation in H_2O/D_2O mixtures (Figure 8).

B. Silica Structure at 7% and 20%

The structure of the silica filler at 7% and 20% was measured using SANS with a hydrogenated latex matrix. Following the general shape of the aggregation diagram,[34] the aggregation is expected to be similar at low Φ_{si} and low pH, and at high Φ_{si} and high pH. The data, in a normalized presentation $I(q)/\Phi_{si}$, are shown in Figure 9.

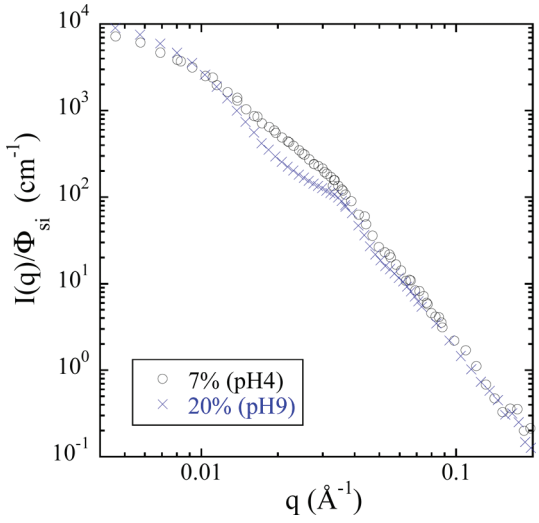


Figure 9. Normalized scattered intensity of silica−latex nanocomposites (7% with pH4, and 20% with pH9, both H-matrices) as a function of wavevector q.

As can be concluded from the overlap of large parts of the scattered intensities, the structure is indeed rather similar. A detailed analysis, however, is difficult, due to the presence of unknown, and rather featureless (no peak) structure factors in both cases. The presence of a correlation hole at intermediate q with 20% silica suggests that silica beads are aggregated, and the similar Guinier domain may indicate comparable sizes. In the case of the lower Φ_{si}, it corresponds to average aggregates (R_g = 180 Å) of about seven nanoparticles, i.e., having a compacity of about 32%. At the higher volume fraction of 20%, these aggregates come necessarily into contact, and form a network structure. To summarize, these aggregates do not change much upon simultaneous increase in concentration and decrease in

dx.doi.org/10.1021/ma202308c | Macromolecules 2012, 45, 1663−1675

pH, but approach and percolate. On the length scale probed in SANS, they have thus a comparable primary structure which is more or less diluted.

AUTHOR INFORMATION

Corresponding Author

*E-mail: acgenix@univ-montp2.fr.

Notes

The authors declare no competing financial interest.

ACKNOWLEDGMENTS

Stock solutions of silica were a gift from Akzo Nobel. Beamtime was accorded at Laboratoire Léon Brillouin (Saclay) and Institut Laue Langevin (Grenoble). This work was conducted within the scientific program of the European Network of Excellence Softcomp: "Soft Matter Composites: an approach to nanoscale functional materials", supported by the European Commission. M.T. thanks the ILL for financing her Ph.D. within the ILL international Ph.D. program. Financial support by a "chercheur d'avenir" grant (J.O.) of the Languedoc-Roussillon region is gratefully acknowledged. The authors are also very grateful to Jacques Jestin (LLB, Saclay) who performed the final measurements on the nanocomposites with high silica loading.

REFERENCES

(1) Klüppel, M. *Adv. Polym. Sci.* **2003**, *164*, 1−86.
(2) Heinrich, G.; Kluppel, M.; Vilgis, T. A. *Curr. Opin. Solid State Mater. Sci.* **2002**, *6* (3), 195−203.
(3) Mark, J. E.; Erman, B.; Eirich, F. R., *Science and Technology of Rubber*; Academic Press: San Diego, CA, 1994.
(4) Schmidt, G.; Malwitz, M. M. *Curr. Opin. Colloid Interface Sci.* **2003**, *8* (1), 103−108.
(5) Kohls, D. J.; Beaucage, G. *Curr. Opin. Solid State Mater. Sci.* **2002**, *6* (3), 183−194.
(6) Nakatani, A.; Chen, W.; Schmidt, R.; Gordon, G.; Han, C. *Polymer* **2001**, *42*, 3713−3722.
(7) Jouault, N.; Dalmas, F.; Said, S.; Di Cola, E.; Schweins, R.; Jestin, J.; Boué, F. *Macromolecules* **2010**, *43* (23), 9881.
(8) Sen, S.; Xie, Y. P.; Kumar, S. K.; Yang, H. C.; Bansal, A.; Ho, D. L.; Hall, L.; Hooper, J. B.; Schweizer, K. S. *Phys. Rev. Lett.* **2007**, *98* (12), 128302.
(9) Botti, A.; Pyckhout-Hintzen, W.; Richter, D.; Urban, V.; Straube, E.; Kohlbrecher, J. *Polymer* **2003**, *44* (24), 7505−7512.
(10) Botti, A.; Pyckhout-Hintzen, W.; Richter, D.; Straube, E. *Phys. A: . Mech. Appl.* **2002**, *304* (1−2), 230−234.
(11) Nusser, K.; Neueder, S.; Schneider, G. J.; Meyer, M.; Pyckhout-Hintzen, W.; Willner, L.; Radulescu, A.; Richter, D. *Macromolecules* **2010**, *43* (23), 9837−9847.
(12) Tuteja, A.; Duxbury, P.; Mackay, M. *Phys. Rev. Lett.* **2008**, *100*, 077801.
(13) Termonia, Y. *Polymer* **2009**, *50* (4), 1062−1066.
(14) Sharaf, M. A.; Kloczkowski, A.; Sen, T. Z.; Jacob, K. I.; Mark, J. E. *Eur. Polym. J.* **2006**, *42* (4), 796−806.
(15) Vacatello, M. *Macromol. Theory Simul.* **2002**, *11* (7), 757−765.
(16) Vacatello, M. *Macromolecules* **2002**, *35* (21), 8191−8193.
(17) Hall, L. M.; Jayaraman, A.; Schweizer, K. S. *Curr. Opin. Solid State Mater. Sci.* **2010**, *14* (2), 38−48.
(18) Hooper, J. B.; Schweizer, K. S. *Macromolecules* **2007**, *40* (19), 6998−7008.
(19) Kobayashi, M.; Rharbi, Y.; Brauge, L.; Cao, L.; Winnik, M. A. *Macromolecules* **2002**, *35* (19), 7387−7399.
(20) Triolo, A.; Celso, F. L.; Negroni, F.; Arrighi, V.; Qian, H.; Lechner, R. E.; Desmedt, A.; Pieper, J.; Frick, B.; Triolo, R. *Appl. Phys. A: Mater. Sci. Process.* **2002**, *74* (Suppl), S490−S492.
(21) Arrighi, V.; Higgins, J. S.; Burgess, A. H.; Floudas, G. *Polymer* **1998**, *39* (25), 6369−6376.
(22) Anastasiadis, S. H.; Chrissopoulou, K.; Frick, B. *Mat. Sci. Eng., B: Adv. Funct. Solid-State Mater.* **2008**, *152* (1−3), 33−39.
(23) Schneider, G. J.; Nusser, K.; Willner, L.; Falus, P.; Richter, D. *Macromolecules* **2011**, *44* (15), 5857−5860.
(24) Papon, A.; Saalwächter, K.; Schäler, K.; Guy, L.; Lequeux, F.; Montes, H. *Macromolecules* **2011**, *44* (4), 913−922.
(25) Montes, H.; Lequeux, F.; Berriot, J. *Macromolecules* **2003**, *36* (21), 8107−8118.
(26) Berriot, J.; Montes, H.; Lequeux, F.; Long, D.; Sotta, P. *Europhys. Lett.* **2003**, *64* (1), 50−56.
(27) Berriot, J.; Montes, H.; Lequeux, F.; Long, D.; Sotta, P. *Macromolecules* **2002**, *35* (26), 9756−9762.
(28) Berriot, J.; Lequeux, F.; Monnerie, L.; Montes, H.; Long, D.; Sotta, P. *J. Non-Cryst. Solids* **2002**, *307*, 719−724.
(29) Berriot, J.; Martin, F.; Montes, H.; Monnerie, L.; Sotta, P. *Polymer* **2003**, *44* (5), 1437−1447.
(30) Kim, S. D.; Klein, A.; Sperling, L. H.; Boczar, E. M.; Bauer, B. J. *Macromolecules* **2000**, *33*, 8334−8343.
(31) Kim, K. D.; Sperling, L. H.; Klein, A.; Wignall, G. D. *Macromolecules* **1993**, *26*, 4624−4631.
(32) Yousfi, M.; Porcar, L.; Lindner, P.; Boué, F.; Rharbi, Y. *Macromolecules* **2009**, *42*, 2190−2197.
(33) Summerfield, G. C.; Ullman, R. *Macromolecules* **1987**, *20*, 401−404.
(34) Tatou, M.; Genix, A. C.; Imaz, A.; Forcada, J.; Banc, A.; R., S.; Grillo, I.; Oberdisse, J. *Macromolecules* **2011**, *44*, 9029−9039.
(35) Oberdisse, J.; Pyckhout-Hintzen, W.; Straube, E. Structure Determination of Polymer Nanocomposites by Small Angle Scattering. In *Recent Advances in Polymer Nanocomposites*; Thomas, S., Zaikov, G., Valsaraj, S. V., Eds.; Brill NV: Leiden, The Netherlands, 2009; p 397.
(36) Chevalier, Y.; Pichot, C.; Graillat, C.; Joanicot, M.; Wong, K.; Maquet, J.; Lindner, P.; Cabane, B. *Colloid Polym. Sci.* **1992**, *270* (8), 806−821.
(37) Rieger, J.; Hadicke, E.; Ley, G.; Lindner, P. *Phys. Rev. Lett.* **1992**, *68* (18), 2782−2785.
(38) Hu, S. S.; Rieger, J.; Lai, Y. Q.; Roth, S. V.; Gehrke, R.; Men, Y. F. *Macromolecules* **2008**, *41* (13), 5073−5076.
(39) Rharbi, Y.; Boue, F.; Joanicot, M.; Cabane, B. *Macromolecules* **1996**, *29* (12), 4346−4359.
(40) Dingenouts, N.; Ballauff, M. *Langmuir* **1999**, *15* (9), 3283−3288.
(41) Zhang, J. Q.; Hu, S. S.; Rieger, J.; Roth, S. V.; Gehrke, R.; Men, Y. F. *Macromolecules* **2008**, *41* (12), 4353−4357.
(42) Bolze, J.; Ballauff, M.; Kijlstra, J.; Rudhardt, D. *Macromol. Mater. Eng.* **2003**, *288* (6), 495−502.
(43) Feng, J. R.; Pham, H.; Stoeva, V.; Winnik, M. A. *J. Polym. Sci., Part B: Polym. Phys.* **1998**, *36* (7), 1129−1139.
(44) Chen, X.; Fischer, S.; Men, Y. *Langmuir* **2011**.
(45) Oberdisse, J. *Soft Matter* **2006**, *2* (1), 29−36.
(46) Oberdisse, J.; Deme, B. *Macromolecules* **2002**, *35* (11), 4397−4405.
(47) Benoit, H. C.; Higgins, J. S., *Polymers and Neutron Scattering*; Oxford University Press: Oxford, U.K., 1994.
(48) Cotton, J. P. *Adv. Colloid Interface Sci.* **1996**, *69*, 1−29.
(49) Tatou, M. et al., Manuscript in preparation.
(50) Unzueta, E.; Forcada, J. *Polymer* **1995**, *36* (22), 4301−4308.
(51) Lindner, P., *Neutrons, X-ray and Light Scattering*. North Holland, Elsevier: 2002.
(52) Cotton, J. P.; Decker, D.; Benoit, H.; Farnoux, B.; Higgins, J.; Jannink, G.; Ober, R.; Picot, C.; Cloizeau, J. D. *Macromolecules* **1974**, *7* (6), 863−872.
(53) Rubinstein, M.; Colby, R. H., *Polymer Physics*; Oxford University Press: Oxford, U.K., 2003.
(54) Debye, P. *Phys. Coll. Chem.* **1947**, *51*, 18.
(55) Bates, F. S.; Wignall, G. D.; Koehler, W. C. *Phys. Rev. Lett.* **1985**, *55* (22), 2425−2428.

(56) Bates, F. S.; Fetters, L. J.; Wignall, G. D. *Macromolecules* **1988**, *21* (4), 1086−1094.
(57) Balsara, N. P.; Fetters, L. J.; Hadjichristidis, N.; Lohse, D. J.; Han, C. C.; Graessley, W. W.; Krishnamoorti, R. *Macromolecules* **1992**, *25* (23), 6137−6147.
(58) de Gennes, P. G. *Scaling Concepts in Polymer Physics*. Cornell University Press: Ithaca, NY, 1979.
(59) Hahn, K.; Ley, G.; Schuller, H.; Oberthur, R. *Colloid Polym. Sci.* **1986**, *264* (12), 1092−1096.
(60) Pedersen, J. S.; Gerstenberg, M. C. *Macromolecules* **1996**, *29* (4), 1363−1365.
(61) Pedersen, J. S.; Svaneborg, C.; Almdal, K.; Hamley, I. W.; Young, R. N. *Macromolecules* **2003**, *36* (2), 416−433.
(62) Read, D. J.; Brereton, M. G.; McLeish, T. C. B. *J. Phys. II* **1995**, *5* (11), 1679−1705.
(63) Vacatello, M. *Macromolecules* **2001**, *34* (6), 1946−1952.
(64) Robertson, C. G.; Rackaitis, M. *Macromolecules* **2011**, *44* (5), 1177−1181.
(65) Gam, S.; Meth, J. S.; Zane, S. G.; Chi, C. Z.; Wood, B. A.; Seitz, M. E.; Winey, K. I.; Clarke, N.; Composto, R. J. *Macromolecules* **2011**, *44* (9), 3494−3501.
(66) Westermann, S.; Kreitschmann, M.; Pyckhout-Hintzen, W.; Richter, D.; Straube, E.; Farago, B.; Goerigk, G. *Macromolecules* **1999**, *32* (18), 5793−5802.

Macromolecules

Article

pubs.acs.org/Macromolecules

Dynamics of Water Absorbed in Polyamides

M. Laurati,*[,†,‡,%] P. Sotta,[†] D. R. Long,[†] L.-A. Fillot,[†] A. Arbe,[‡] A. Alegrìa,[‡,§] J. P. Embs,[∥] T. Unruh,[⊥] G. J. Schneider,[#] and J. Colmenero[‡,§]

[†]Laboratoire Polymères et Matériaux Avancés (LPMA), UMR5268, CNRS and Rhodia, CRTL, 85 Rue des frères Perret, 69192 Saint-Fons, France

[‡]Centro de Física de Materiales (CSIC, UPV/EHU) and Materials Physics Center (MPC), Paseo Manuel de Lardizabal 5, E-20018 San Sebastián, Spain

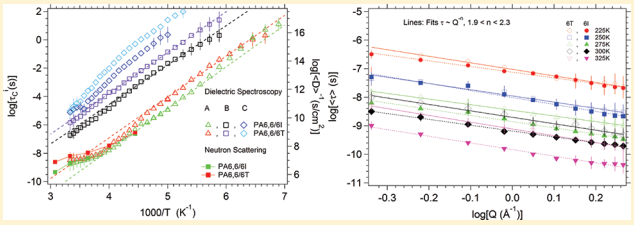
[§]Departamento de Física de Materiales, University of the Basque Country (UPV/EHU), Paseo Manuel de Lardizabal 3, E-20018 San Sebastián, Spain

[∥]Laboratory for Neutron Scattering, Paul Scherrer Institut, Villigen, Switzerland

[⊥]Forschungsneutronenquelle Heinz Maier-Leibnitz, Lichtenbergstrasse 1, D-85747 Garching, Germany

[#]Jülich Centre for Neutron Science at FRM II, Forschungszentrum Jülich GmbH, Institut für Festkörperforschung, Lichtenbergstrasse 1, D-85747 Garching, Germany

ABSTRACT: We investigate the dynamics of water absorbed in amorphous and semicrystalline aromatic polyamide copolymers. The combination of dielectric spectroscopy and quasi-elastic neutron scattering experiments allows us to characterize the water dynamics over a wide range of temperatures (dielectric spectroscopy) and at microscopic length scales (neutron scattering). The dielectric investigation evidences two relaxations associated with water motions: a fast process corresponding to motions of loosely bonded water molecules and a slower process corresponding to motions of amide−water complexes. While the slower process presents the characteristic Arrhenius temperature dependence of a secondary local relaxation over the whole temperature range, the fast process shows a crossover from Arrhenius to Vogel−Fulcher−Tamman (VFT) behavior at $T \approx 225$ K, characteristic of confined water dynamics. The microscopic investigation by neutron scattering shows than in the VFT regime of the fast process the dynamics present a diffusive nature similar to bulk water. A large distribution of diffusion coefficients indicates possible differences in the connectivity of the hydrogen bond network. Diffusive heterogeneous dynamics can arise from a nonuniform distribution of water. The confinement effect of the polymer matrix is detected as a considerable reduction of the diffusion coefficient of water with respect to bulk. The presence of a crystalline phase results in a slowing down of both the fast and slow processes involving water motions. This could give a hint to the presence of a rigid amorphous phase in the semicrystalline material.



I. INTRODUCTION

Absorption of polar solvents has a strong effect on the physical properties of polyamides,[1−3] a class of polymers intensively used in the production of engineering plastics. The principal effect of the interaction between water molecules and this hydrogen-bonded polymer is a decrease of the glass transition temperature T_g of polyamide, a phenomenon called plasticization, with the T_g shift becoming more pronounced with increasing amount of absorbed water. Such a plasticization effect has been documented by calorimetry,[2] in dielectric spectroscopy experiments,[4−8] dynamic mechanical analysis,[9−11] and NMR measurements.[12] Plasticization is a general phenomenon not exclusive for polar solvents, but in the case of wet polyamides it is often explained in terms of a loosening of the hydrogen bond network of the dry material due to the intercalation of water which binds to the amide groups, replacing the existing amide−amide H-bonds. This picture is derived from the two-step absorption model of Starkweather and co-workers.[10] Indeed, polyamide has hydrophilic absorption sites corresponding to the amide groups, but at the same time the rest of the polymer is strongly hydrophobic. This intermediate nature of polyamide may result in a peculiar structural organization of water, with a tendency to aggregate, similar to water in cavities of hydrophobic materials and polymeric aqueous solutions.[13,14] The interaction with the matrix is nevertheless significant. Simulations[15] on the structure of water absorbed in amorphous polyamide effectively indicate that at saturation water tends to form small aggregates of a limited number of molecules inside the material, with only a fraction of water molecules directly bonded to the amide groups. These structural results are compatible with the few available experimental studies on the dynamics of absorbed water, obtained by thermally stimulated depolarization and NMR experiments, which indicate the presence of two

Received: October 24, 2011
Revised: December 20, 2011
Published: January 26, 2012

 © 2012 American Chemical Society dx.doi.org/10.1021/ma202368x | *Macromolecules* 2012, 45, 1676−1687

populations of slow (tightly bonded) and fast (loosely bonded) water molecules.[4,7,16,17] Such description is also supported by simulations.[18] However, these studies do not address important questions like the nature of water dynamics in polyamides on the microscopic level, the possible confinement effect of the polymer matrix, the influence of a crystalline phase on water mobility, and the relation between dynamics and the microscopic distribution of water inside the material. Also, it is important to know on which time scale the two distinct water populations start to exchange. A better understanding of all these aspects will help the development of polyamide-based materials with improved barrier properties against polar solvents. In this study we investigate these issues by combining dielectric spectroscopy—which allows exploring a broad thermal range of the dynamics—and quasi-elastic neutron scattering, which (i) due to its spatial resolution enables us to access the microscopic details of the motions and (ii) with isotopic (H/D) labeling allows studying selectively each component. Combination of these techniques has already provided valuable results in the study of water dynamics in aqueous polymer solutions.[19]

From a different point of view, water absorbed in polyamide presents also an interesting case with respect to the dynamical behavior of water in confinement at supercooled temperatures. Dynamics of confined and interfacial water have important consequences for biological systems because they affect the properties of proteins and DNA.[20−22] The confinement effect of nanocavities does not allow for a complete development of the ice structure, and therefore crystallization is not observed even below the homogeneous crystallization temperature (235 K). This phenomenon has also been exploited to investigate on a fundamental level the dynamics of water in the supercooled regime. Regarding this topic, there is a general agreement about the existence of a pronounced crossover from low-temperature Arrhenius to high-temperature Vogel−Fulcher−Tamman (VFT) behavior of the characteristic relaxation times obtained from broadband dielectric spectroscopy (BDS) or neutron scattering, in the temperature region between 215 and 228 K.[23−27] Such crossover has been explained invoking different physical mechanisms. It has been attributed to a fragile-to-strong transition from the high density (HDL) to the low density phase (LDL) of supercooled water, based on neutron scattering experiments on water absorbed into hydrophilic and hydrophobic media and protein hydration water.[23,24,26] Alternatively, also based on neutron scattering and BDS experiments on protein hydration water and water confined in MCM-41, it has been attributed to a crossover from hydrogen-bond dynamics of water at low temperatures to the α-relaxation of water at high temperatures.[28−31] In addition, studies of aqueous polymer solutions showed that such a crossover happens in the temperature range where the mixture undergoes a glass transition.[25,27] The crossover was therefore attributed to confinement effects of the frozen matrix on water dynamics. The environment that polyamide presents to water has interesting characteristics to complement these studies. Indeed, the glass transition temperature of polyamide, even in the wet state, is considerably higher than the Arrhenius to VFT crossover, allowing eventually for a clear distinction of the two phenomena. In addition, by comparing the results obtained with an amorphous and a semicrystalline copolymer, we studied the influence of the crystalline phase on the water motions.

II. MATERIALS AND METHODS

A. Samples. The aromatic polyamide random copolymers PA6,6/6I and PA6,6/6T were provided by Rhodia. Figure 1 shows the

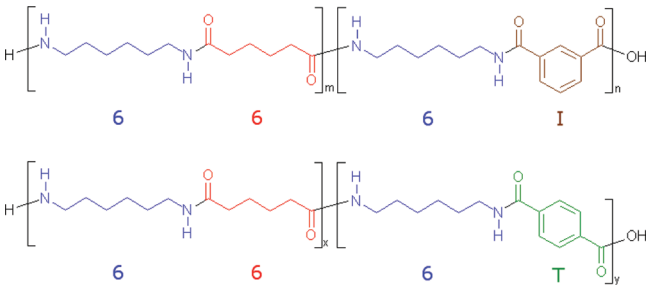


Figure 1. Chemical formulas of the copolymers PA6,6/6I (top) and PA6,6/6T (bottom).

chemical formulas of the two copolymers. The polymers are formed by copolymerization of the PA6,6 and PA6I or PA6T monomers. The monomers are obtained by condensation of hexamethylenediamine with a diacid: adipic acid for the PA6,6 monomer and isophthalic (terephthalic) acid for the PA6I (PA6T) monomers. The average molecular weight of the copolymers is M_w = 10 000 g/mol, with polydispersity M_w/M_n = 2. The fraction of PA6,6, PA6I and PA6T monomers with respect to the total are 0.4 PA6,6 and 0.6 PA6I for PA6,6/6I, 0.65 PA6,6, and 0.35 PA6T for PA6,6/6T. The PA6,6/6I copolymer is amorphous, with a T_g = 363 K as determined by differential scanning calorimetry (DSC). The PA6,6/6T copolymer is semicrystalline, with a T_g = 349 K and a melting temperature T_m = 550 K, as determined by DSC. A crystalline fraction $\chi_c \approx 0.31$ was estimated from the DSC trace by using for the melting enthalpy of a 100% crystalline PA6,6/6T sample the literature value known for a 100% crystalline PA6,6 sample (ΔH_m = 188.4 J/g).[32] We investigated the six different samples listed in Table 1. Dry samples (named PA6,6/6I and PA6,6/6T) were annealed for 16 h at T_g + 20 K under vacuum before measurement. Fully wet samples (100% relative humidity) were obtained by immersing dry films in H_2O (PA6,6/6I H_2O, PA6,6/6T H_2O) or D_2O (PA6,6/6I D_2O, PA6,6/6T D_2O). The absorption of solvent was followed by measuring the total mass of the sample as a function of immersion time. Saturation of solvent is achieved after ∼10 h. In samples PA6,6/6I D_2O and PA6,6/6T D_2O the H atoms of the amide (CONH) groups of the amorphous phase have been substituted by D atoms following the procedure described in ref 33: First, the dry samples were immersed in an excess of D_2O until fully saturated conditions were reached, and most of the NH groups of the amorphous phase were replaced by ND. Afterward, the samples were dried under vacuum (as described above) to fix the D atoms on the amide groups. After drying, samples were immersed again in D_2O until fully saturated conditions were obtained. The mass fractions of water in the wet samples are reported in Table 1. The amorphous phase fraction of the semicrystalline samples amounts to 69%. Therefore, the

Table 1. Water Mass Content (m_w) Relative to Total (m_{TOT}) and to the Mass of the Amorphous Fraction (m_{am}), Corresponding Molar Content (m_{mol}) relative to the Number of Amide groups (CONH) per Polymer Chain in the Amorphous Phase, and T_g of the Samples Investigated

sample	m_w/m_{TOT}	m_w/m_{am}	m_{mol}	T_g (K)
PA6,6/6I	0.0	0.0	0.0	363
PA6,6/6I H_2O	0.14	0.14	0.93	277
PA6,6/6I D_2O	0.143	0.143	0.95	277
PA6,6/6T	0.0	0.0	0.0	349
PA6,6/6T H_2O	0.072	0.104	0.72	273
PA6,6/6T D_2O	0.075	0.109	0.73	274

dx.doi.org/10.1021/ma202368x | Macromolecules 2012, 45, 1676−1687

water content in the amorphous phase of these samples is finally similar to that in amorphous PA6,6/6I (see Table 1), assuming homogeneous water absorption within the amorphous phase. The T_g of the wet samples was measured by DSC and is reported in Table 1.

B. Quasi-Elastic Neutron Scattering Experiments. In quasi-elastic neutron scattering experiments, the analysis of the distribution of energy changes ($\hbar\omega$) of the neutrons scattered into a solid angle comprised between Ω and Ω + dΩ allows to retrieve information on the dynamics of the sample. The double-differential scattering cross section, or scattered intensity, is given by

$$\frac{\partial^2\sigma}{\partial\Omega\,\partial\omega} = I(Q,\omega) = \frac{1}{4\pi}\frac{k_f}{k_i}[\sigma_{coh}S_{coh}(Q,\omega) + \sigma_{inc}S_{inc}(Q,\omega)] \quad (1)$$

where k_f and k_i are the momentum of the neutron after and before scattering, respectively. $Q = (4\pi/\lambda)\sin(\theta/2)$ is the modulus of the momentum transfer, with λ the wavelength of the incoming neutrons and θ the scattering angle. It determines the length scale at which the dynamics of the samples are observed in the experiment. σ_{coh} and σ_{inc} are the total coherent and incoherent scattering cross sections, respectively. $S_{coh}(Q,\omega)$ and $S_{inc}(Q,\omega)$ are the coherent and incoherent dynamic structure factors. $S_{inc}(Q,\omega)$ is related by Fourier transformation to the intermediate incoherent scattering function, $S_s(Q,t)$. The Fourier transform of this function is the self-part of the Van Hove correlation function $G_s(r,t)$. In the classical limit, $G_s(r,t)$ is the probability of a given nucleus to be at a distance r from the position where it was located at a time t before. This means that incoherent scattering gives information about the single particle dynamics of the sample. The subunits forming the random copolymers investigated in this study contain respectively a number of hydrogen H atoms equal to 22 (PA6,6) and 18 (PA6I and PA6T) per repeat unit. Given that the incoherent scattering cross section of H, σ_{inc}^{H} = 80.27 barn/atom, is much larger than all the other cross sections involved, the scattering from these polymers is largely dominated by the incoherent contributions of the hydrogens. In the experiments we therefore probe the single particle dynamics of the hydrogens in the system. In order to measure the dynamics of the water absorbed into the copolymers, for both PA6,6/6I and PA6,6/6T we performed measurements on samples fully saturated either with H_2O or D_2O. For the sample containing D_2O the contribution of water to the scattering is essentially negligible; therefore, one follows the dynamics of the polymer in presence of water at full saturation, i.e., $I(Q,\omega) \approx (1/4\pi)(k_f/k_i)\sigma_{inc}^{pol}S_{inc}^{pol}(Q,\omega)$. On the other hand, for the sample containing H_2O the contribution of water, due to its hydrogens, is significant, and the double differential cross section can be expressed as

$$I(Q,\omega) \approx \frac{1}{4\pi}\frac{k_f}{k_i}[\sigma_{inc}^{pol}S_{inc}^{pol}(Q,\omega) + \sigma_{inc}^{wat}S_{inc}^{wat}(Q,\omega)] \quad (2)$$

The incoherent dynamic structure factor corresponding to water contributions can therefore be extracted by subtracting the results of the measurements of polymer + D_2O from those of polymer + H_2O. This procedure requires good statistics of both sets of data, which is the case of data obtained from time-of-flight (TOF) measurements. Because of the lower flux of neutrons at the sample, backscattering (BS) measurements show poorer statistics, leading to an excessively large uncertainty on the results obtained with the subtraction procedure. In this case the measurements of polymer + D_2O were used to model the polymer contribution to the dynamics. The result of modeling was then used to describe the polymer contribution in the polymer + H_2O measurements, and $S_{inc}^{wat}(Q,\omega)$ could be extracted as an additional model intensity added to the polymer contribution.

Dynamics Measurements. The measurements were carried out in two dynamic windows ($\approx 2\times10^{-12}$–3×10^{-10} s and $\approx 8\times10^{-10}$–4×10^{-8} s) by means of TOF (FOCUS, Paul-Scherrer Institut, Switzerland, and TOF-TOF, FRM-II, Germany) and BS (SPHERES, JCNS, Germany) spectrometers. Samples of thickness 0.17 mm (PA6,6/6I) and 0.25 mm (PA6,6/6T) were put into flat aluminum slabs. For samples containing water the slabs were sealed using indium wire in order to avoid solvent loss. The water content of the samples was checked before and after measurements by weighing. The transmission of the samples was close to 90%; therefore, possible multiple scattering contributions were neglected. We corrected raw data for the detector efficiency, the scattering of the sample container, and absorption. In case of TOF measurements the time-of-flight was converted to energy transfer using standard programs available at PSI[34] and FRM-II.

For the TOF measurements on FOCUS we used λ = 5 Å, leading to a resolution with half-width at half-maximum (hwhm) $\delta E \approx 100$ μeV. The range of scattering angles explored goes from 10° to 130°. The energy window goes from −2 to some hundreds of meV. After applying a standard interpolation program we obtained $I_{exp}(Q,\omega)$ in the elastic Q-range $0.6 \le Q \le 1.8$ Å^{-1}. Temperatures in the range 20 K < T < 225 K were investigated. On TOF-TOF we used λ = 6 Å, leading to $\delta E \approx 65$ μeV. The range of scattering angles explored goes from 8° to 140° in an energy window similar to FOCUS. We obtained $I_{exp}(Q,\omega)$ in an elastic Q-range $0.4 \le Q \le 1.9$ Å^{-1} and in a T-range 225 K < T < 325 K. The resolution spectrum was measured at 5 K.

For the BS measurements on SPHERES (λ = 6.27 Å) the covered Q-range was $0.4 \le Q \le 1.8$ Å^{-1}. An energy window -30 μeV $\le E \le$ +30 μeV with $\delta E \approx 0.325$ μeV was explored. Temperatures in the range 225 K < T < 325 K were investigated. The resolution spectrum was measured at 4 K.

C. Dielectric Spectroscopy. A broadband high-resolution dielectric spectrometer (BDS), Novocontrol Alpha-N, was used to measure the complex dielectric function $\epsilon^*(\omega) = \epsilon'(\omega) - i\epsilon''(\omega)$ ($\omega = 2\pi f$) in the frequency range of 10^{-2}–10^7 Hz; an Agilent rf impedance analyzer 4192B covered the frequency range of 10^6–10^9 Hz. Parallel gold-plated electrodes were used, with a diameter of 40 and 10 mm for low- and high-frequency measurements, respectively. The sample thickness was 0.17 mm for PA6,6/6I and 0.25 mm for PA6,6/6T. For dry samples PA6,6/6I and PA6,6/6T the isothermal frequency scans were performed every 10 K over the temperature range of 150–170 K and every 5 K from 170 K up to 300 K. For wet samples PA6,6/6I H_2O and PA6,6/6T H_2O isothermal scans were performed every 5 K over the temperature range of 150–300 K. The maximum temperature was limited to 300 K in order to avoid significant water evaporation from samples. Water content was checked before and after measurement by weighing the sample. The sample temperature was controlled with a stability better than 0.1 K.

III. RESULTS AND DISCUSSION

A. Dielectric Spectroscopy. Results of isothermal frequency scans (BDS data) of samples in the dry (PA6,6/6I, PA6,6/6T) and fully wet states (PA6,6/6I H_2O, PA6,6/6T H_2O) are shown in Figure 2 for 180 K < T < 300 K. This is the regime where water dynamics can be observed in the frequency window accessed by BDS. In the dry state (Figure 2a,b) two relatively broad temperature-dependent relaxation processes can be distinguished, which can be identified with the γ (higher frequency) and β (lower frequency) relaxations usually observed in polyamides.[35,36] These relaxations are generally attributed to local motions of the methylene groups (γ) and rotations of the amide groups (β). The segmental α-relaxation, on the other hand, is not visible in this temperature range, as expected from the T_g values obtained by DSC for the dry copolymers. The intensity and temperature dependence of the γ and β relaxations in the amorphous PA6,6/6I (Figure 2a) and semicrystalline PA6,6/6T (Figure 2b) copolymers are comparable. In the wet state (Figure 2c,d) the overall intensity of the dielectric spectra is considerably higher due to the presence of water. A relatively broad relaxation process is seen in the temperature range where the γ relaxation is observed in the dry state. The temperature dependence of this process, which we

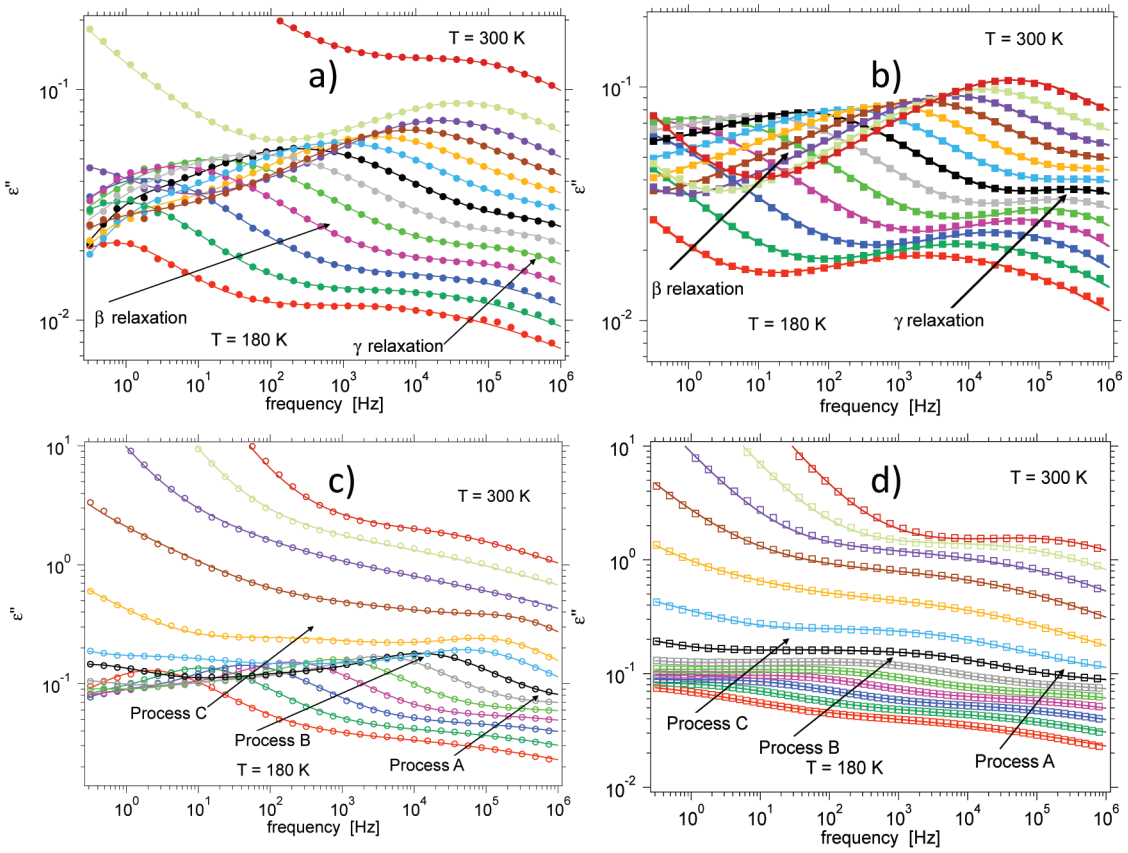


Figure 2. Imaginary part of the complex dielectric function obtained by isothermal frequency scans (ϵ'' vs frequency), measured every 10 K in the T-range from 180 K up to 300 K (from bottom to top curves). (a) PA6,6/6I in the dry state, (b) PA6,6/6T in the dry state, (c) PA6,6/6I H_2O, i.e., the fully wet state, (d) PA6,6/6T H_2O, i.e., the fully wet state. Symbols: experimental data. Full lines: best fits. Trends of the different relaxation processes contributing to ϵ'' are indicated by arrows. Error bars are smaller than symbols.

call process A, is more pronounced than that of the γ relaxation though. Moving toward lower frequencies, a process which we call process B is observed, together with another process, process C, located roughly in the same region as the β relaxation in the dry state. The different model contributions used to describe the experimental dielectric spectra are shown in Figure 3 for copolymers in the dry (a, b) and fully wet states (c, d) at $T = 240$ K. A frequency range from 1 to 10^9 Hz is shown, where local polymer motions and water motions are observed. At lower frequencies additional processes related to larger scale polymer dynamics also contribute to the dielectric signal. These processes are not discussed in this work. The relaxation processes were described by Cole−Cole functions:

$$\epsilon_i''(\omega) = \Delta\epsilon_i \frac{\sin\left(\frac{\beta_C^i \pi}{2}\right)}{1 + 2(\omega\tau_C^i)^{\beta_C^i}\cos\left(\frac{\beta_C^i \pi}{2}\right) + (\omega\tau_C^i)^{2\beta_C^i}} \quad (3)$$

where $\Delta\epsilon_i$ is the dielectric strength and τ_C^i the characteristic relaxation time of process i ($i = \gamma$ and β (A, B, and C) in the dry (wet) state). The exponent β_C^i governs the width of the peak and can assume values between 0 and 1. Also, a conductivity contribution $\epsilon_{cond}''(\omega) = \sigma_0/(\epsilon_0\omega)$, where σ_0 is the dc conductivity of the sample, was included above $T = 280$ K (240 K) in the dry (wet) state.

Figure 4 shows the values of $\Delta\epsilon_i$ obtained by fitting for the different processes described in Figure 3. In the dry state the strengths of the γ and β relaxation processes present a similar, almost T-independent behavior in the amorphous and semicrystalline polymers. In the wet state process A shows an intensity considerably larger than the γ relaxation process in the dry state (~0.45 for both wet polymers compared to 0.12 and 0.15 for the amorphous and semicrystalline dry polymers, respectively). This suggests that such process does not correspond to the γ relaxation of the dry polymer but is rather associated with water motions: The large dipole moment of water explains the larger strength of the process. However, we cannot exclude the occurrence of a γ relaxation of the polymer that could not be resolved in the dielectric data due to its low strength. In the amorphous polymer (Figure 4a) the strength of process A shows no T dependence for $T < 240$ K and a moderate increase for higher T. For the semicrystalline polymer (Figure 4b) the strength of process A remains approximately constant over the whole T range. The intensity of process B shows, for both polymers, an increase with temperature for $T <$ 260 K, considerably more pronounced for the semicrystalline material. For higher temperatures $\Delta\epsilon_B$ reaches a constant value comparable to that of process A and slightly larger than that of the β relaxation in the dry state. The strength of process C increases with temperature for both samples. The increase becomes particularly sharp in the vicinity of T_g^{wet}.

The exponents β_C^i are shown in Tables 2 and 3. For processes γ, β, B and C the exponents were found to be approximately T-independent, while β_C^A shows a pronounced T dependence which will be discussed later. All processes show a

dx.doi.org/10.1021/ma202368x | Macromolecules 2012, 45, 1676−1687

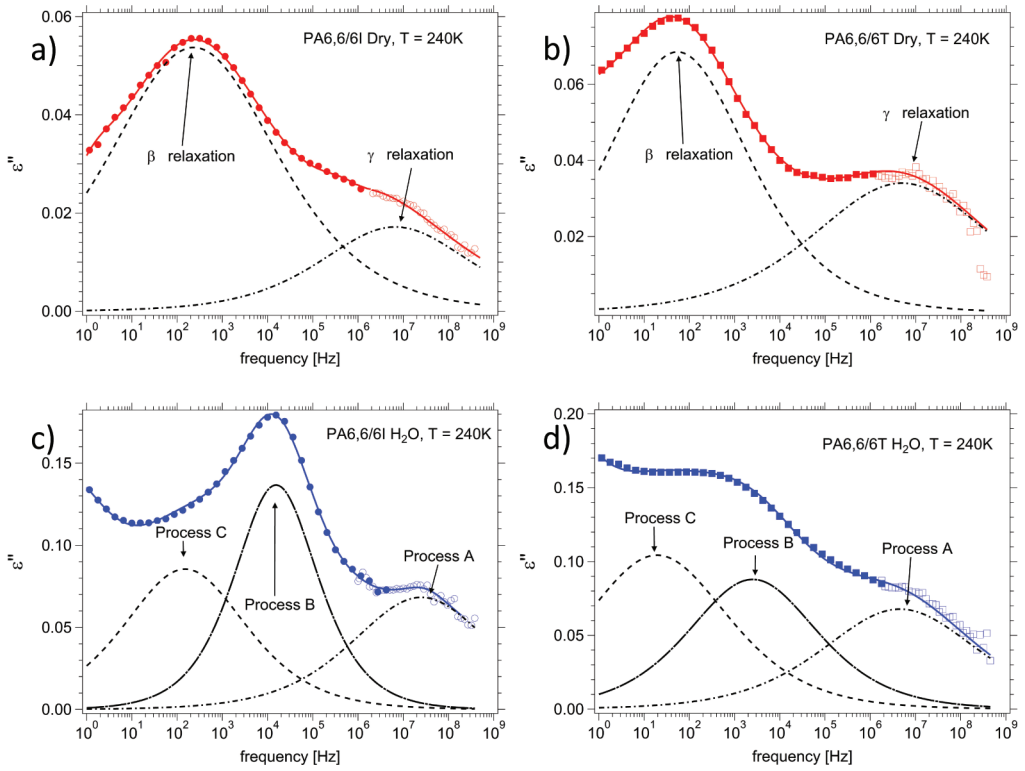


Figure 3. Results of isothermal frequency scans (ϵ'' vs frequency) at T = 240 K for samples: (a) PA6,6/6I in the dry state, (b) PA6,6/6T in the dry state, (c) PA6,6/6I H_2O, i.e., the fully wet state, (d) PA6,6/6T H_2O, i.e., the fully wet state. Full symbols: data obtained by BDS. Open symbols: data obtained using a high-frequency impedance analyzer. Full lines represent the total fit; the different contributions (dashed lines) are indicated by the annotations in the plots. Error bars are smaller than symbols.

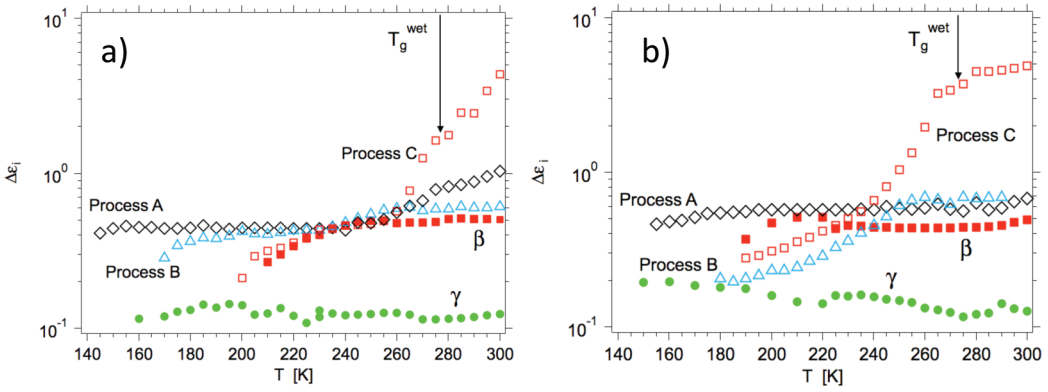


Figure 4. Dielectric strength $\Delta\epsilon$, obtained from the model fits as a function of T for the different relaxation processes described in Figure 3 and distinguished by annotations in the plots. Plot a shows results for PA6,6/6I and plot b for PA6,6/6T. The glass transition temperature of the polymers in the wet state is indicated by arrows. Filled symbols: dry samples. Open symbols: wet samples. Error bars are smaller than symbols.

large broadening reflected in the small values of β_C^i, except perhaps for process B. In the dry sample the distributions in the amorphous material are narrower than in the semicrystalline material while the opposite is observed in the wet state.

Figure 5 shows Arrhenius plots for the amorphous PA6,6/6I copolymer (a) and for the semicrystalline PA6,6/6T copolymer (c). The processes considered here are the ones described in Figure 3. In the dry state both γ and β processes show an Arrhenius dependence on T, $\tau_C^i = \tau_0^i \exp(E_i/k_BT)$, where $i = \gamma$, β. The obtained activation energies E_i and the logarithm of the time prefactors τ_0^i are reported in Table 2.

The values of E_γ, E_β, and log τ_0^β compare well with values obtained from measurements on similar polyamide materials.[4,5,7,35,37] Values of log τ_0^γ are more difficult to compare since significantly different values have been reported in the literature for different kinds of polyamides.[5,7,35,37] We note that the β-process in the amorphous sample is faster than in the semicrystalline one, in particular in the low-T range. The slightly higher value of E_β in the semicrystalline material may result from the presence of a rigid amorphous phase, as suggested for example in refs 38 and 39. A rigid amorphous phase corresponds to the amorphous fraction contained within the lamellae of the crystalline phase, its mobility being reduced by the interaction with the crystallites.[38,39]

In the wet state process A shows a particularly interesting temperature dependence, comparable for the amorphous and semicrystalline material. While τ_C^A presents similar values to τ_C^γ around 220 K, their T dependence is markedly different. At low temperatures ($1000/T > 4.4$, $T \lesssim 225$ K) the T dependence of

dx.doi.org/10.1021/ma202368x | Macromolecules 2012, 45, 1676–1687

Table 2. Samples PA6,6/6I and PA6,6/6T (Dry State): Cole–Cole Exponent β_C^i, Prefactors log τ_0^i, and Activation Energies E_i for the γ and β Relaxation Processes[a]

	γ relaxation (200 K < T < 300 K)			β relaxation (150 K < T < 290 K)		
sample	β_C^γ	log[τ_0^γ (s)]	E_γ (eV)	β_C^β	log[τ_0^β (s)]	E_β (eV)
PA6,6/6I	0.25 ± 0.06	−12.7 ± 0.2	0.39 ± 0.01	0.32 ± 0.03	−16.2 ± 0.2	0.66 ± 0.03
PA6,6/6T	0.38 ± 0.05	−12.5 ± 0.1	0.39 ± 0.01	0.40 ± 0.03	−16.5 ± 0.3	0.67 ± 0.04

[a]The T range considered is specified for each process.

Table 3. Samples PA6,6/6I H_2O and PA6,6/6T H_2O (Wet State): Cole–Cole Exponent β_C^i, Prefactors log τ_0^i, and Activation Energies E_i for Processes A, B, and C[a]

	process A (200 K < T < 300 K)			process B (160 K < T < 290 K)			process C (150 K < T < 225 K)		
sample	β_C^A	log[τ_0^A (s)]	E_A (eV)	β_C^B	log[τ_0^β (s)]	E_B (eV)	$\langle\beta_C^C\rangle$	log[τ_0^C (s)]	E_C (eV)
PA6,6/6I H_2O	0.3 ± 0.12	−16.9 ± 0.2	0.58 ± 0.01	0.64 ± 0.04	−17.3 ± 0.3	0.57 ± 0.02	0.31 ± 0.04	−15.5 ± 0.2	0.59 ± 0.04
PA6,6/6T H_2O	0.25 ± 0.1	−17.1 ± 0.1	0.60 ± 0.01	0.47 ± 0.04	−16.3 ± 0.1	0.59 ± 0.02	0.43 ± 0.05	−17.1 ± 0.4	0.59 ± 0.05

[a]The T range considered is specified for each process.

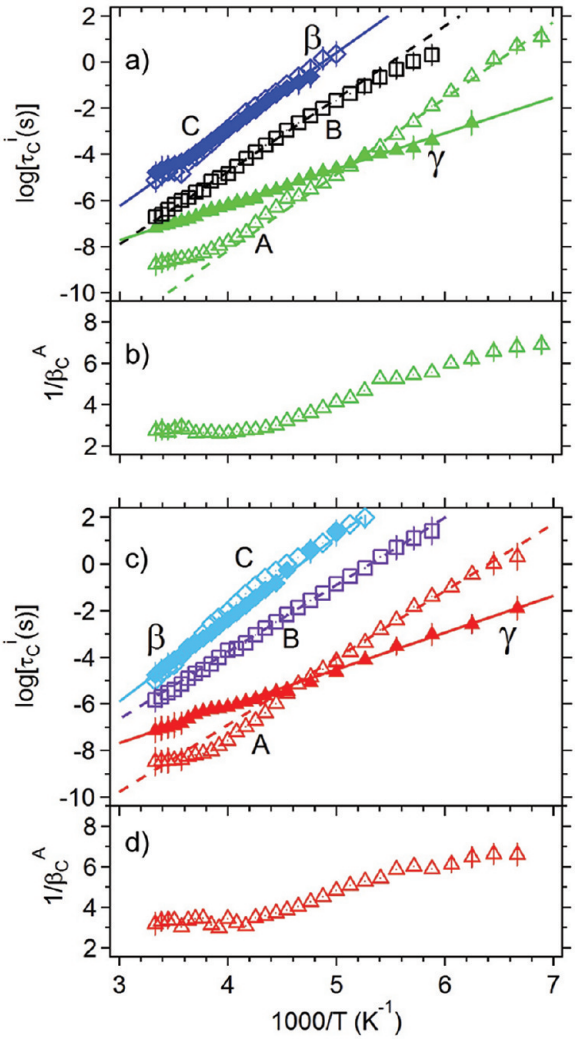


Figure 5. (a, c) Arrhenius plots of relaxation times τ_C^i vs inverse temperature for PA6,6/6I (a) and PA6,6/6T (c). Results for both the dry (full symbols) and wet (open symbols) state of the polymer are shown. Letters in the plot distinguish the different processes. Lines represent fits to Arrhenius laws. (b, d) Inverse of the Cole–Cole exponent of process A for polymers PA6,6/6I (b) and PA6,6/6T (d). Error bars are shown when bigger than symbols.

τ_C^A is Arrhenius-like, with an activation energy E_A (Table 3) considerably larger than E_γ (and rather comparable to E_β, Table 2). The prefactors log τ_0^A are also very small, much smaller than typical vibrational times. Note that the obtained values of E_A and log τ_0^A well correspond to those found for water confined in a variety of systems.[27,40,41] This observation, together with the previously discussed considerably larger dielectric strength of process A compared to the γ relaxation, supports the interpretation of process A as a relaxation associated with water motions. At high temperatures (T > 225 K) the T dependence of τ_C^A changes from Arrhenius to VFT ($\tau = \tau_0 \exp(B/(T - T_0))$ type, which is characteristic of the α relaxation in glass-forming systems. We note that this occurs in the T-range where the γ process crosses the A process. We can exclude that the change in the T dependence of the A process is an artifact due to the presence of the γ process in the wet samples given that the dielectric strength of this is negligible as compared to process A. As commented in the Introduction, such a crossover from Arrhenius to VFT behavior has been observed, in a narrow temperature range around T = 225 K, for water segregated in different media[23,24,27] and has been attributed either to confinement effects,[27] a transition from H-bond (β) to glassy (α) dynamics[31] or to a strong-to-fragile transition of water.[24,23]

Figure 5b,d shows the T dependence of the inverse of β_C^A that is a measure of the width of the spectrum. Both polymers display a crossover from T-dependent width to constant width at temperatures corresponding to the Arrhenius to VFT crossover of the relaxation times.

Process B shows, in both PA6,6/6I and PA6,6/6T, an Arrhenius T dependence, with E_B comparable to E_A and E_β (see Tables 2 and 3). The values of τ_C^B are intermediate between those of τ_C^A, associated with water motions, and those of τ_C^β. Since $\Delta\epsilon_B \approx \Delta\epsilon_\beta$, we may speculate that process B could be associated with movements of amide groups associated with water molecules by hydrogen bonding. The motions of the amide–water complex would be faster than those of the amide groups due to the faster dynamics of water. This is also supported by the values of the prefactors, which are rather comparable to those of process A.

The τ_C^C values almost overlap with those of τ_C^β. This suggests that process C can be associated with the β relaxation of the amide groups which are not forming any bond with water. Note that around 250 K the T dependence of τ_C^C shows a small kink. At the same temperature, $\Delta\epsilon_C$ starts to increase sharply. Both findings could be related to the influence of the α relaxation in the wet state, as can be seen in Figure 6. On top of this figure

dx.doi.org/10.1021/ma202368x | Macromolecules 2012, 45, 1676–1687

results of DSC measurements are presented in the form of the derivative with respect to T of the specific heat C_p vs $1000/T$, to be compared to the Arrhenius plot at the bottom of the figure. The calorimetric glass transition of the wet polymers is evidenced by a peak in dC_p/dT. The bending of τ_C^C toward faster times appears to be correlated with the occurrence of the glass transition.

Figure 6 also shows τ_C^A and τ_C^B for the amorphous and semicrystalline copolymers. In the Arrhenius regime the relaxation

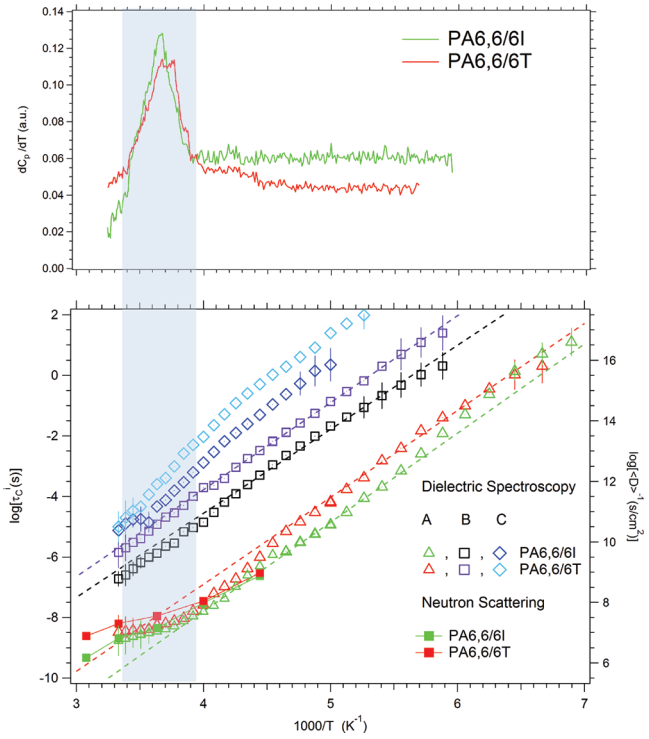


Figure 6. (bottom) Temperature dependence of the relaxation time τ_C of processes A, B, and C for the fully wet amorphous and semicrystalline copolymers observed by BDS (open symbols), compared with the corresponding temperature variation of the inverse of the diffusion coefficients obtained by quasi-elastic neutron scattering (full symbols, see section III.B). (top) dC_p/dT as a function of inverse temperature, obtained from DSC measurements for PA6,6/6I (green) and PA6,6/6T (red).

times measured for the semicrystalline copolymer are slower than for the amorphous. This could be attributed to the absorption of part of the water into the rigid amorphous phase[38,39] of the semicrystalline material, whose dynamics are slower than those of the mobile amorphous phase[38,39] (the bulk amorphous phase). Note that there are experimental evidences that water does not penetrate the crystalline phase (see ref 39 and references therein). Slower dynamics of the polymer clearly imply larger relaxation times of process B, in agreement with the interpretation of this process as the result of the movements of the water bonded to amide groups. It is more difficult to explain the slowing down of the water dynamics of process A. We would expect that τ_C^A would be determined by the strength and number of H-bonds that water molecules form with other water molecules. Therefore, one could think that in the semicrystalline material the structure of water nonbonded to the polymer could be different from that in the amorphous material due to changes in available free volume. A different water structure may result in a different (higher) degree of H-bonding per molecule in the semicrystalline material, which translates into a larger relaxation time. Note that τ_C^A in the VFT regime is also different for the amorphous and semicrystalline polymer, but the difference is considerably smaller than in the Arrhenius regime. One can speculate that in the VFT regime most of the H-bonded structure of water is disrupted due to the glass transition of water. Therefore, the relaxation times of the amorphous and semicrystalline material in this regime tend to approach each other, with some residual difference which could be arising from surface interactions with the polymer. Note that no significant peak in dC_p/dT is observed in the region of the Arrhenius to VFT crossover of process A (Figure 6, top), suggesting that in this case such crossover can hardly be associated with confinement effects imposed by the freezing of the structural relaxation of the polymer matrix. Nevertheless, we observe that the crossover takes place in the T-range where the A process crosses the γ process if the dry polymer. This could suggest that the local mobility of the polymer could play an important role in the origin of this crossover.

B. Neutron Scattering. Figure 7 presents incoherent dynamic structure factors measured by TOF. Plot a shows $S(Q,\omega)$ (we omit the suffix inc in the following) for sample PA6,6/6I H_2O, which reflect the dynamics of both the polymer and water molecules absorbed into it. Up to T = 250 K the dynamic structure factors show almost no quasi-elastic contribution and a Boson peak[42] at $E_{BP} \approx 2.5$ meV whose position does not change with T. This means that for $T < 250$ K we essentially observe localized vibrational motions. The results on the semicrystalline sample PA6,6/6T H_2O are similar (Figure 7b), with nonvibrational dynamics starting to be observed at T = 225 K.

Figures 7c (PA6,6/6I) and 7d (PA6,6/6T) show a comparison between the spectra measured for the dry polymer, the polymer saturated in D_2O and in H_2O in the range 20 K $\leq T \leq$ 225 K. In the amorphous sample (PA6,6/6I) containing D_2O the intensity of the Boson peak is reduced compared to the dry polymer, and its position is shifted to slightly higher energy. Since in the sample containing D_2O we observe the self-motions of the polymer in presence of water, the vibrational dynamics of the polymer are reduced upon addition of water. Similar results concerning the shift of the Boson peak to higher energy in relation to hydration have been found for poly(vinyl methyl ether) (PVME)[19] and for proteins in neutron scattering experiments and molecular dynamics simulations.[43−47] One possible explanation for this shift is to assume a distribution of elastic constants[48] in the wet sample. This interpretation is in agreement with the formation of water−polymer H-bonds upon hydration which are stronger than polymer−polymer H-bonds.[49] In the H_2O-saturated sample the water contribution adds an additional intensity to that of the polymer and the Boson peak shifts to slightly higher energies in the same way as with D_2O. Note that this reduced vibrational dynamics of the hydrated polymer must be clearly distinguished from the large-scale motions of the polymer, which is accelerated, thus resulting in the observed drop of T_g in the presence of water. In the semicrystalline material the Boson peak is less discernible, and its shift in the presence of water is less clear than for the amorphous sample. Nevertheless, within the uncertainties we can state that the effects of hydration are qualitatively the same in both samples.

Figure 8a,b shows dynamic structure factors of water as obtained by subtraction of the measurements with protonated and deuterated water (see Materials and Methods). Graph a

dx.doi.org/10.1021/ma202368x | Macromolecules 2012, 45, 1676−1687

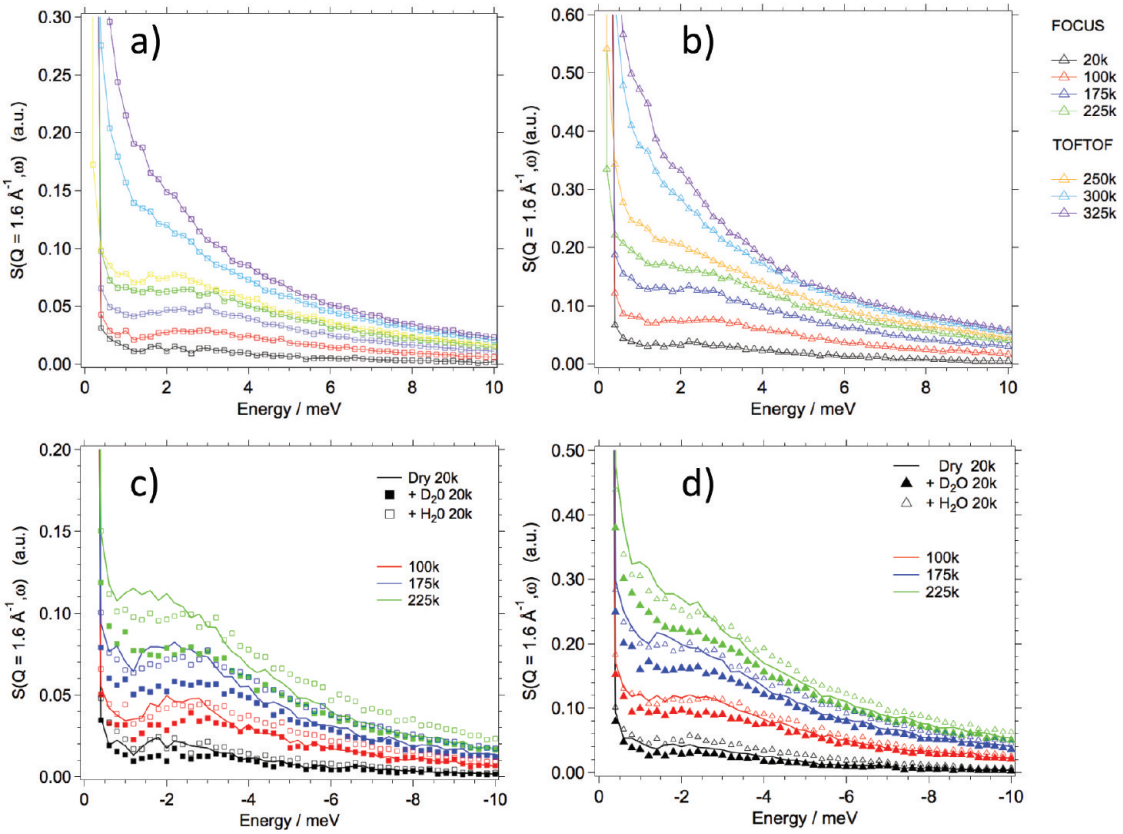


Figure 7. Dynamic structure factors measured by TOF (on FOCUS and TOFTOF, as indicated in legend) at Q = 1.6 Å^{-1}. (a) Measurements at different temperatures (indicated in legend on the right-hand side) for sample PA6,6/6I H_2O. (b) Same as in (a) for sample PA6,6/6T H_2O. (c) Comparison of the dynamic structure factors of samples PA6,6/6I (lines), PA6,6/6I H_2O (empty symbols), and PA6,6/6I D_2O (full symbols) for T = 100 K (red), 175 K (blue), 225 K (green), and 20 K (black) (FOCUS data). (d) Same as in (c) for samples PA6,6/6T, PA6,6/6T H_2O and PA6,6/6T D_2O. Error bars were omitted for clarity.

displays data obtained for water absorbed into the PA6,6/6I copolymer and graph b data obtained for water absorbed into the PA6,6/6T copolymer. In the amorphous material (a) the quasi-elastic contributions start to be significant above T = 250 K. In the semicrystalline material they are smaller, indicating that water dynamics are slower. Figure 8c presents $S(Q,t)$ obtained by Fourier transforming the dynamic structure factors of plots a and b and deconvoluted from resolution by dividing through $S(Q,t,T=0)$. A significant decay of $S(Q,t)$ is only observed for T > 250 K in both copolymers, indicating that on the TOF instruments the time scales characteristic of water dynamics are only accessible for such temperatures. The decay of $S(Q,t)$ of absorbed water is considerably more pronounced in the amorphous than in the semicrystalline polymer, confirming a higher mobility of water into the amorphous material.

For T > 250 K the time dependence of $S(Q,t)$ of water cannot be described with a single-exponential decay. Using the same approach as followed in other works on confined water dynamics as accessed by neutron scattering,[19,50,51] we used Kohlrausch–Williams–Watts (KWW) or stretched exponential functions:

$$S(Q,t) = A \exp\left[-\left(\frac{t}{\tau_w(Q,T)}\right)^{\beta_w}\right] \quad (4)$$

where A is a prefactor which accounts for the contribution of the fast dynamics, $\tau_w(Q,T)$ is the relaxation time of the dynamics, and β_w is the stretching exponent accounting for deviations from exponential behavior. It can take values between 0 and 1. As in other works, in our case, eq 4 with $\beta_w^{H_2O} \approx 0.5$ was found to properly fit the data at different Q values. Representative fits for water absorbed in the amorphous copolymer PA6,6/6I at T = 300 K are shown in Figure 9.

Backscattering results allowed us studying water dynamics down to T = 225 K. First, the data on the samples with D_2O give access to the polymer contribution $S^{\text{wet PA}}(Q,\omega)$. Figure 10a presents results for sample PA6,6/6I D_2O. At fixed Q the quasi-elastic component of the spectra moderately broadens with increasing temperature, indicating the acceleration of the polymer motions due to thermal activation. The $S(Q,\omega)$ corresponding to polymer dynamics was modeled as the Fourier transform of a KWW function (eq 4) with fixed shape parameter $\beta_w^{\text{wet PA}} = 0.5$. Fits for data of Figure 10a, obtained by convoluting the fit function with the experimental resolution, are shown as solid lines. Such a procedure was adopted for all fits.

Figure 10b presents BS results on the amorphous sample (PA6,6/6I) with H_2O at the same Q value and temperatures as in Figure 10a. Also in this case the spectra present an increasingly broadened quasi-elastic component with increasing T, now due to the thermal activation of both polymer and water dynamics. Consistently with the TOF data analysis (see above), in the BS window we also assumed a KWW (eq 4) with $\beta_w^{H_2O} = 0.5$ to describe the water contribution, $S^{H_2O}(Q,t)$. The total intermediate incoherent scattering function was therefore modeled as

$$S^{PA/H_2O}(Q,t) = f_{H_2O} S^{H_2O}(Q,t) + f_{PA} S^{\text{wet PA}}(Q,t) \quad (5)$$

dx.doi.org/10.1021/ma202368x | Macromolecules 2012, 45, 1676–1687

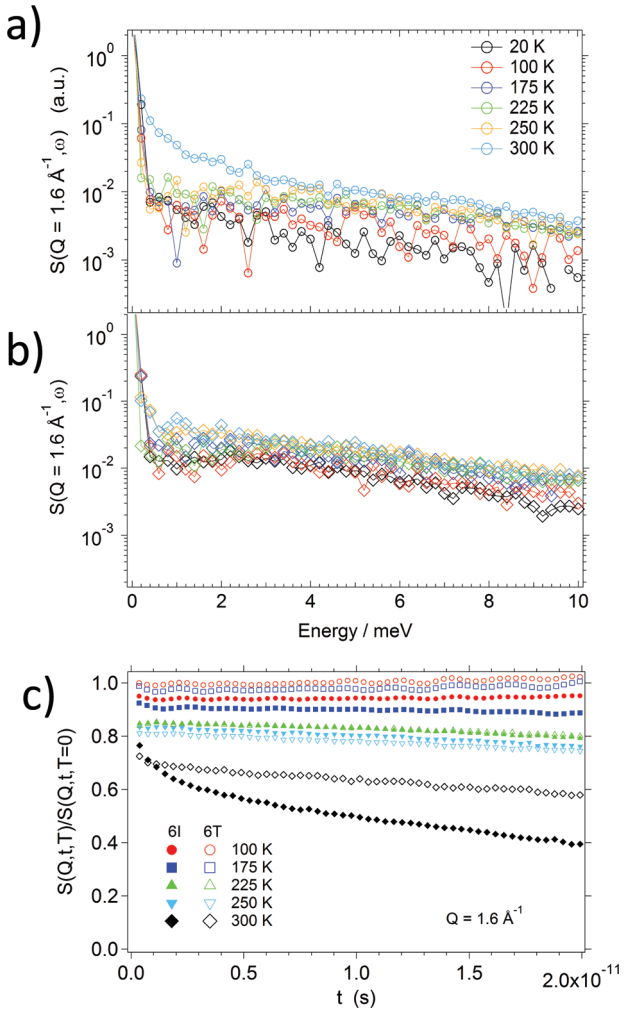


Figure 8. Dynamic structure factors of water extracted from TOF measurements (FOCUS and TOFTOF) at Q = 1.6 Å^{-1} for polymers (a) PA6,6/6I and (b) PA6,6/6T. Temperatures are indicated in legends. (c) Intermediate scattering functions obtained by Fourier transforming data of plots a and b. Solid symbols represent data of water absorbed in PA6,6/6I; open symbols represent data of water absorbed in PA6,6/6T.

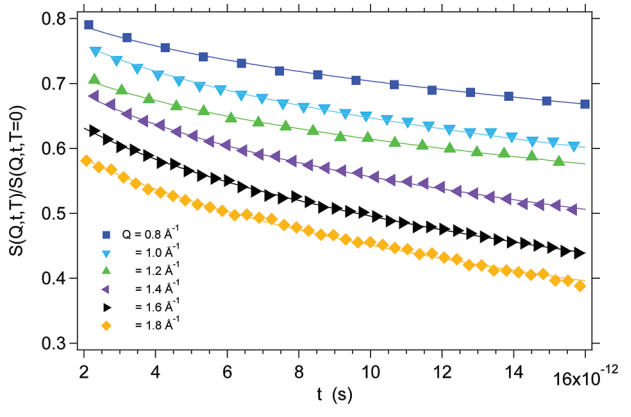


Figure 9. Intermediate scattering functions of water extracted from TOF measurements (TOFTOF), for sample PA6,6/6I at T = 300 K and different Q values (listed in legend). Lines are fits to KWW functions with $\beta_w^{H_2O} \approx 0.5$.

where the weights f_{H_2O} and f_{PA} were calculated on the basis of the corresponding cross sections: $f_{H_2O} = \sigma_{inc}^{H_2O}/\sigma_{inc}^{PA/H_2O} = 0.148$

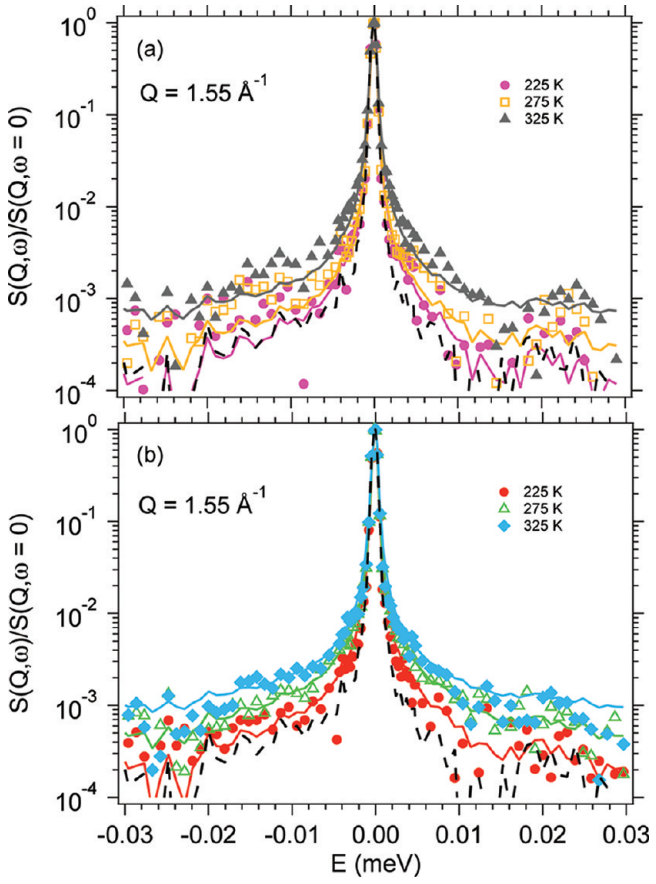


Figure 10. Normalized dynamic structure factors (symbols) measured by BS (SPHERES) at Q = 1.55 Å^{-1} and temperatures reported in legends, for samples: (a) PA6,6/6I D_2O and (b) PA6,6/6I H_2O. Solid lines are fits obtained by (a) describing the polymer dynamics using the FT of KWW functions and (b) describing the polymer dynamics using the results of (a) and using in addition the FT of KWW functions to model the water contributions. Dashed line is the measured instrument resolution.

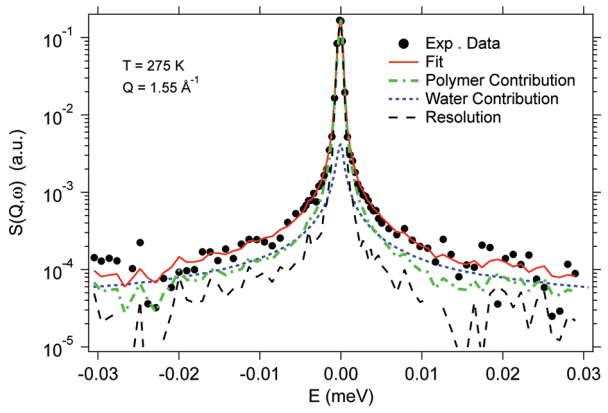


Figure 11. Dynamic structure factor of sample PA6,6/6I H_2O at T = 275 K and Q = 1.55 Å^{-1} measured by BS (symbols). The solid line represents the total fit. Dotted line: modeled water contribution. Dashed-dotted line: polymer contribution as obtained by fitting data measured for sample PA6,6/6I D_2O at the same T and Q. Dashed line: measured instrument resolution.

and $f_{PA} = \sigma_{inc}^{PA}/\sigma_{inc}^{PA/H_2O} = 0.852$. The polymer scattering function was obtained from the D_2O samples results. Figure 11 shows the so-obtained total fit and the separate contributions of the

dx.doi.org/10.1021/ma202368x | Macromolecules 2012, 45, 1676–1687

polymer and water, for sample PA6,6/6I H_2O at T = 275 K and Q = 1.55 Å^{-1}. Water contributes with a fast component affecting the spectra in the whole BS window.

Figure 12a presents the Q dependence of $S(Q,\omega)$ for sample PA6,6/6I H_2O at T = 325 K. For the total dynamic structure

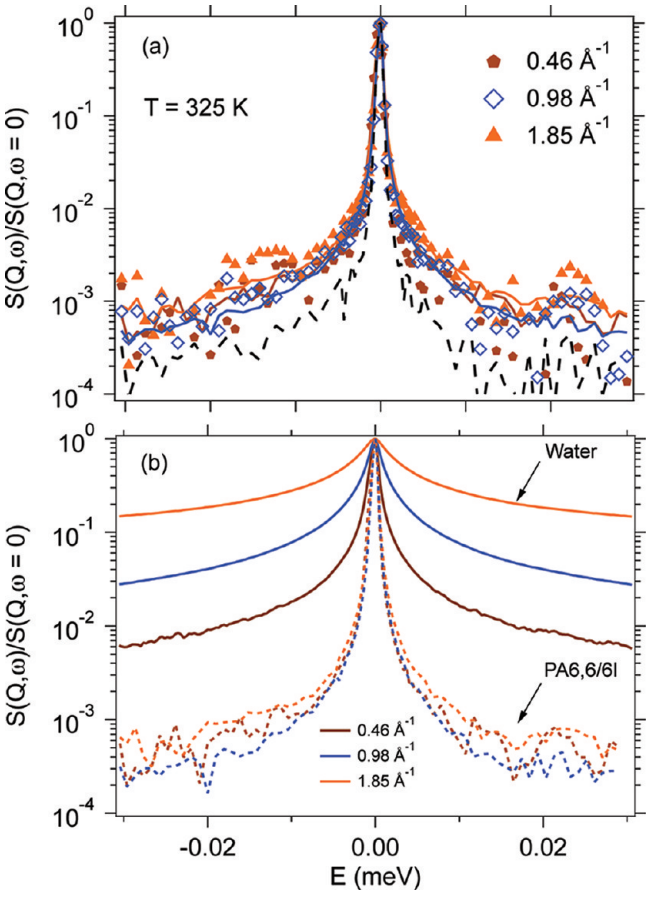


Figure 12. (a) Normalized dynamic structure factor of sample PA6,6/6I H_2O at T = 325 K and different Q values (listed in legends). Solid line: total fit. Dashed line: measured instrument resolution. (b) Single contributions of water (solid lines) and polymer (dashed lines) to the total fits of (a), illustrating the strongly different Q dependence of water and polymer dynamics.

factor, this dependence appears to be rather weak. In order to distinguish the Q dependence of the polymer and water dynamics, the relative contributions to $S(Q,\omega)$ are plotted in Figure 12b. The decomposition clearly shows that while the polymer dynamics, whose contribution dominates, are relatively insensitive to Q, the water dynamics present a pronounced Q dependence. The weak Q and T dependences (average activation energy around 0.37 eV for both amorphous and semicrystalline) of $S^{\text{wet PA}}(Q,t)$ suggest that the motions observed could be related to the γ relaxation. The relaxation times found are also in the same range of values. We recall that this process is detected by BDS in the dry sample and is associated with methylene groups but cannot be resolved in the wet sample.

The Q dependence of the characteristic relaxation times of water dynamics is illustrated in Figure 13. We have represented the average value $\langle\tau\rangle$ of the associated distribution of single relaxation times, calculated as $\langle\tau\rangle = \tau_w\Gamma(1/\beta)/\beta$ for KWW functions. It is noteworthy the consistency of the results obtained from the two different instruments and analysis

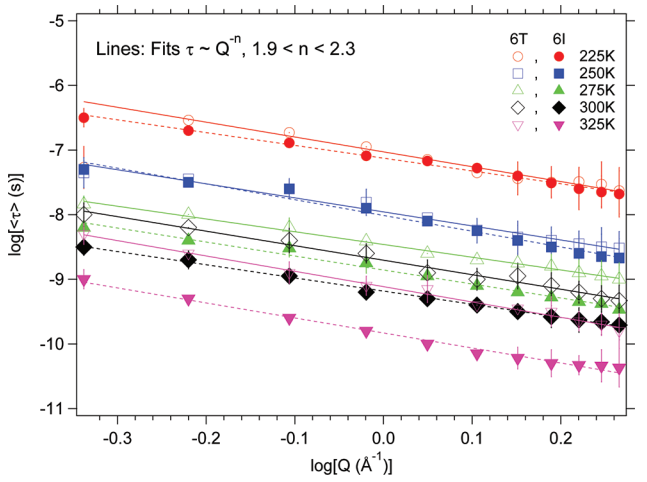


Figure 13. Average relaxation time of water, obtained from fitting TOF (T = 300 K) and BS data (all remaining temperatures), vs wave vector Q, for different temperatures (in legend). Solid symbols: water absorbed in the amorphous copolymer PA6,6/6I; open symbols: water absorbed in the semicrystalline copolymer PA6,6/6T. Lines (solid for PA6,6/6I, dashed for PA6,6/6T): power law dependencies having exponents comprised between −1.9 and −2.3.

procedures used in each case (spectra subtraction and FT vs modeling of two components and convolution with resolution). The Q dependence of $\langle\tau\rangle$ can be described using power laws $\langle\tau\rangle \propto Q^{-n}$ having exponents n in the range $1.9 < n < 2.3$, i.e., values compatible with a Q^{-2} dependence. This tells us that on average the dynamics of water absorbed in PA can be depicted as diffusive (let us remind that in simple diffusion the characteristic time τ is related with the self-diffusion coefficient D as $\tau = D^{-1}Q^{-2}$). However, the scattering function is not described by a single exponential, as expected for simple diffusion. Note also at this point that the Q range investigated corresponds to length scales at which we observe both in-cluster and intercluster motions of water. Indeed, on the basis of simulations results,[15] one can estimate a radius of 1 nm for spherical water clusters and on the basis of volumetric arguments an average distance of 0.7 nm between neighbor amide groups. We will discuss this point in the following section. It is also clear that for T > 250 K the relaxation times of absorbed water become considerably shorter in the amorphous than in the semicrystalline material. An average diffusion coefficient $\langle D\rangle$ can be obtained by fitting the Q dependence of $\langle\tau\rangle$ in Figure 13 to $\langle\tau\rangle = \langle D\rangle^{-1}Q^{-2}$. The results are presented in Figure 14 as a function of temperature T for both copolymers. The values of $\langle D\rangle$ of water absorbed in the PA copolymers are ∼2 orders of magnitude smaller than those of bulk supercooled water, which are shown as a solid line for comparison. The interaction of water with the polymer matrix considerably reduces the average mobility of the water molecules. Similar effects have been reported for water confined in different media.[24] This is usually attributed to the fact that water in layers close to the water/confining medium interface presents a different hydrogen bond structure due to bonding to the host material.[53] This different structure results in a reduction of mobility close to the interface even for molecules not directly bonded to the matrix. One can think therefore that the slower mobility of water molecules close to the interface will influence the average value of the diffusion coefficient inducing a reduction with respect to bulk water. The strong reduction observed in our case suggests that the hydrogen bond structure is significantly modified

dx.doi.org/10.1021/ma202368x | Macromolecules 2012, 45, 1676−1687

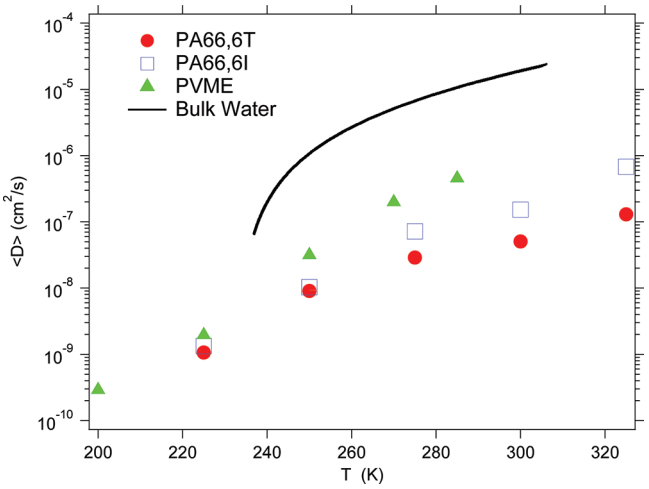


Figure 14. Average diffusion coefficients of water absorbed in the amorphous (PA6,6/6I) and semicrystalline (PA6,6/6T) copolymers vs temperature, extracted from the fitted τ vs Q dependence of Figure 13. Solid line: bulk supercooled water.[52] Green symbols: water absorbed in PVME.[19] Error bars are smaller than symbols.

as a result of the small size of water clusters. Note also that the diffusion coefficients of water absorbed in PA6,6/6I and PA6,6/6T separate for $T \geq 250$ K.

C. Discussion of the Results in a Unified Picture. Results obtained with dielectric spectroscopy (BDS) and quasi-elastic neutron scattering (QENS) can be discussed in their ensemble in order to construct a consistent picture of the dynamics of water absorbed in polyamide. BDS results indicated the presence of two well-separated dynamical processes associated with absorbed water molecules, namely A and B, which may be related to two distinct populations of water, as noted by several authors.[4,7,16,17]

Process A was interpreted in terms of motions of water molecules not directly (tightly) bonded to the polymer or confined into cavities of the polymer (at the molecular or nanometric scale). In Figure 6, the temperature dependence of the diffusion coefficient $\langle D \rangle$ obtained by QENS for absorbed water is compared to that of the relaxation times τ_C^i obtained from BDS, in both the amorphous (PA6,6/6I) and semicrystalline (PA6,6/6T) copolymers. The T dependence of $\langle D \rangle$ (from QENS) is in very good agreement with that of process A, confirming the fact that process A can be assigned to water motions (which are selectively studied in QENS experiments). In the common region of temperatures investigated by QENS and BDS (above 225 K typically) the T dependence of τ_C^A and $\langle D \rangle$ is of VFT type and could be interpreted as related to the α relaxation of confined water, which would be consistent with the Q dependence of the characteristic times indicative for diffusive-like motions obtained from the QENS experiments. Note though that in this framework the description of $S^{water}(Q,t)$ in terms of a KWW function with $\beta = 0.5$ clearly indicates a broad distribution of diffusion coefficients of water molecules, which origin would be the existence of markedly heterogeneous environments of the water molecules. This can be qualitatively understood in terms of a nonuniform degree of bonding of water molecules associated with the nonuniform distribution of water and the nonfully achieved tetrahedral structure.

We comment that in both polyamides the water dynamics is slower than in the recently investigated PVME aqueous solution,[19] as can be seen in Figure 14. In that case, however, the water concentration was significantly higher (30 wt %).

The Arrhenius to VFT crossover at $T \approx 225$ K for process A could only be observed in the BDS measurement due to the limited dynamic window accessible in the QENS experiments. It is interesting to note that this crossover occurs at a temperature considerably lower than the glass transition temperature of the hydrated polyamide, as shown in Figure 6, where the calorimetric glass transition is reported on top of the dielectric results. Note also that the calorimetric transition is relatively narrow, indicating a clear separation of the two phenomena. This suggests that confinement effects due to the frozen dynamic state of the polymer matrix cannot alone explain the Arrhenius to VFT crossover in this case. At this point it is worth noting that in the water mixtures where the Arrhenius to VFT crossover was reported to occur close to glass transition,[27] the water concentration was always above ≈30%. We can speculate that the most-likely scenario to explain the observed crossover in the case of water absorbed in polyamide is that for $T < 225$ K we are observing local hydrogen bond motions while for $T \geq 225$ K the water α process is dominating the relaxations in the BDS measurements.[28,31]

In the corresponding temperature range, process B has a much slower dynamics and is only accessed in BDS measurements. As already commented, the close similarity to the T dependence of the β relaxation of the dry polymer suggests that this process might be associated with the movements of the amide groups bonded to water molecules.

IV. CONCLUSIONS

The dynamics of water absorbed in amorphous and semicrystalline polyamide was characterized by neutron scattering experiments and broadband dielectric spectroscopy. A fast water process (A) could be observed with both techniques. The neutron scattering analysis allows to characterize such process by diffusive water motions having a broad distribution of mobilities. The diffusive nature of the motions on one hand points at similarities with bulk dynamics. The large distribution of diffusivities, on the other hand, indicates possible differences in the connectivity of the hydrogen bond network. These two features become coherent if we interpret our observations in terms of a nonuniform distribution of water molecules in terms of bonding to amide groups, with a fraction of water molecules only loosely bonded to amide groups (as reflected in process A).

Diffusive-like motions of water with a similar distribution of mobilities have also been observed for concentrated aqueous solution of PVME.[19] The average diffusion coefficients associated with these dynamics are considerably smaller than for bulk water. This clearly indicates that the interaction with the polymer matrix induces structural modifications of water.

The fast water process presents an Arrhenius to VFT crossover at $T \approx 225$ K observed by BDS. Such a crossover is well decoupled from the α relaxation of the polyamide + water system and the process presents characteristics of a local relaxation for $T < 225$ K. This suggests that the crossover could be associated with the observation in the BDS measurements of hydrogen bond dynamics for $T < 225$ K and the α relaxation of supercooled water for $T > 225$ K at least in this case.

A second slower process (B) associated with water was observed in the BDS measurements. Such process was associated with motions of hydrated amide groups. A third process at higher temperatures (C), which coincides with the

dx.doi.org/10.1021/ma202368x | Macromolecules 2012, 45, 1676–1687

β relaxation of the dry polymer, indicates that not all amide groups are bonded to water.

The presence of a crystalline phase slows down both the fast and the slow processes associated with water motions. This result might be related to the presence of some degree of motional constraint in the amorphous phase in semicrystalline material,[38,39,54] which would slow down the water dynamics in the semicrystalline copolymer. Nevertheless, it would need further investigation to be fully clarified.

Finally, the absorption of water modifies the vibrational density of polyamide deep in the glassy state. We suggest that this effect, also observed for aqueous solutions of PVME, is associated with the fact that water−amide bonds are stronger than amide−amide bonds in the dry state.

■ ACKNOWLEDGMENTS

This work is partially based on experiments performed at the Swiss spallation neutron source SINQ, Paul Scherrer Institute, Villigen, Switzerland. We thank support by the DIPC, Rhodia, the European Commission NoE SoftComp, Contract NMP3-CT-2004-502235, the projects MAT2007-63681 (Spanish Ministerio de Educacion y Ciencia) and IT-436-07 (GV) (Basque Government). M.L. acknowledges support from CNRS. We also thank Véronique Bossennec and Thierry Badel (Rhodia) for synthesizing the copolymers and for fruitful discussions. We acknowledge the funding of the Broadband Dielectric equipment in LPMA by the GRAND LYON metropolitan council.

■ AUTHOR INFORMATION

Present Address

[%]Condensed Matter Physics Laboratory, Heinrich-Heine University, Universitätsstr. 1, 40225 Düsseldorf, Germany.

■ REFERENCES

(1) Subramanian, D. R.; Venkataraman, A.; Bhat, N. V. *J. Macromol. Sci., Phys.* **1980**, *18*, 177.
(2) Ellis, T. S. *J. Appl. Polym. Sci.* **1988**, *36*, 451.
(3) Reimschuessel, H. K. *J. Polym. Sci., Part B: Polym. Phys.* **1978**, *16*, 1229.
(4) Laredo, E.; Hernandez, M. C. *J. Polym. Sci., Part B: Polym. Phys.* **1997**, *35*, 2879.
(5) Laredo, E.; Grimau, M.; Sanchez, F.; Bello, A. *Macromolecules* **2003**, *36*, 9840.
(6) Pathmanathan, K.; Cavaillé, J. Y.; Johari, G. P. *J. Polym. Sci., Part B: Polym. Phys.* **1992**, *30*, 341.
(7) Neagu, R. M.; Neagu, E.; Kyritsis, A.; Pissis, P. *J. Phys. D: Appl. Phys.* **2000**, *33*, 1921.
(8) Huy, H. M. L.; Rault, J. *Polymer* **1994**, *35*, 457.
(9) McCrum, N. G.; Read, B. E.; Williams, G. *Anelastic and Dielectric Effects in Polymer Solids*; John Wiley: New York, 1967.
(10) Starkweather, H. W. *Water in Polymers*; ACS Symposium Series Vol. 127; American Chemical Society: Washington, DC, 1980.
(11) Birkinshaw, C.; Buggy, M.; Daly, S. *Polym. Commun.* **1988**, *28*, 286.
(12) Miura, H.; Hirschinger, J.; English, A. D. *Macromolecules* **1990**, *23*, 2169.
(13) Tamai, Y.; Tanaka, H.; Nakanishi, K. *Macromolecules* **1996**, *29*, 6750.
(14) Wu, R.; Ji, Q.; Kong, B.; Yang, X. *Sci. China, Ser. B: Chem.* **2008**, *51*, 736.
(15) Goudeau, S.; Charlot, M.; Vergelati, C.; Müller-Plathe, F. *Macromolecules* **2004**, *37*, 8072.
(16) Hutchinson, J. L.; Murthy, N. S.; Samulsky, E. T. *Macromolecules* **1996**, *29*, 5551.
(17) Frank, B.; Frubing, P.; Pissis, P. *J. Polym. Sci., Part B: Polym. Phys.* **1996**, *34*, 1853.
(18) Goudeau, S.; Charlot, M.; Müller-Plathe, F. *J. Phys. Chem. B* **2004**, *108*, 1877.
(19) Capponi, S.; Arbe, A.; Cerveny, S.; Busselez, R.; Frick, B.; Embs, J. P.; Colmenero, J. *J. Chem. Phys.* **2011**, *134*, 204906.
(20) Franks, F. *Biophys. Chem.* **2002**, *96*, 117.
(21) Zhang, L.; Wang, L.; Kao, Y.-T.; Qiu, W.; Yang, Y.; Okobiah, O.; Zhong, D. *Proc. Natl. Acad. Sci. U. S. A.* **2007**, *104*, 18461.
(22) Brovchenko, I.; Oleinikova, A. *Interfacial and Confined Water*; Elsevier: Amsterdam, 2008.
(23) Chen, S. H.; Liu, L.; Fratini, E.; Faraone, A.; Mamontov, E. *Proc. Natl. Acad. Sci. U. S. A.* **2006**, *103*, 9012.
(24) Liu, L.; Chen, S. H.; Faraone, A.; Yen, C.-W.; Mou, C.-Y. *Phys. Rev. Lett.* **2005**, *95*, 117802.
(25) Cerveny, S.; Colmenero, J.; Alegria, A. *Phys. Rev. Lett.* **2006**, *97*, 189802.
(26) Faraone, A.; Liu, L.; Mou, C.-Y.; Yen, C.-W.; Chen, S. H. *J. Chem. Phys.* **2004**, *121*, 10843.
(27) Cerveny, S.; Alegria, A.; Colmenero, J. *Phys. Rev. E* **2008**, *77*, 031803.
(28) Swenson, J.; Jansson, H.; Bergman, R. *Phys. Rev. Lett.* **2006**, *96*, 247802.
(29) Pawlus, S.; Khodadadi, S.; Sokolov, A. P. *Phys. Rev. Lett.* **2008**, *100*, 108103.
(30) Teixeira, J.; Luzar, A.; Longeville, S. *J. Phys.: Condens. Matter* **2006**, *18*, S2353.
(31) Swenson, J.; Teixeira, J. *J. Chem. Phys.* **2010**, *132*, 014508.
(32) Lim, L.-T.; Britt, I. J.; Tung, M. A. *J. Appl. Polym. Sci.*, **1999**, *71*, 197.
(33) Murthy, N. S.; Stamm, M.; Sibilia, J. P.; Krimm, S. *Macromolecules* **1989**, *22*, 1261.
(34) Azuah, R. T.; Kneller, L. R.; Qiu, Y.; Tregenna-Piggott, P. L. W.; Brown, C. M.; Copley, J. R. D.; Dimeo, R. M. *J. Res. Natl. Inst. Stand. Technol.* **2009**, *114*, 341.
(35) McCrum, N. G.; Read, B. E.; Williams, G. *Anelastic and Dielectric Effects in Polymer Solids*; Dover: Mineola, NY, 1976.
(36) Hedvig, P. *Dielectric Spectroscopy of Polymers*; Wiley: New York, 1977.
(37) Beaume, F.; Laupretre, F.; Monnerie, L.; Maxwell, A.; Davies, G. *Polymer* **2000**, *41*, 2677.
(38) Rotter, G.; Ishida, H. *Macromolecules* **1992**, *25*, 2.
(39) Murthy, N. S. *J. Polym. Sci., Part B: Polym. Phys.* **2006**, *44*, 1763.
(40) Cerveny, S.; Alegria, A.; Colmenero, J. *J. Chem. Phys.* **2008**, *128*, 044901.
(41) Cerveny, S.; Colmenero, J.; Alegria, A. *Macromolecules* **2005**, *38*, 7056.
(42) Buchenau, U.; Pecharroman, C.; Zorn, R.; Frick, B. *Phys. Rev. Lett.* **1996**, *77*, 661.
(43) Diehl, M.; Doster, W.; Petry, W.; Schober, H. *Biophys. J.* **1997**, *73*, 2726.
(44) Steinback, P. J.; Loncharich, R. J.; Brooks, B. R. *Chem. Phys.* **1991**, *158*, 383.
(45) Fitter, J. *Biophys. J.* **1999**, *76*, 1034.
(46) Caliskan, G.; Kisliuk, A.; Tsai, A. M.; Soles, C. L.; Sokolov, A. P. *J. Chem. Phys.* **2003**, *118*, 4230.
(47) Paciaroni, A.; Orecchini, A.; Cinelli, S.; Onori, G.; Lechner, R. E.; Pieper, J. *Chem. Phys.* **2003**, *292*, 397.
(48) Schirmacher, W.; Diezemann, G.; Ganter, C. *Phys. Rev. Lett.* **1998**, *81*, 136.
(49) Hartikainen, J.; Lehtonen, O.; Harmia, T.; Lindner, M.; Valkama, S.; Ruokolainen, J.; Friedrich, K. *Chem. Mater.* **2004**, *16*, 3032.
(50) Chen, S.-H.; Liu, L.; Chu, X.; Zhang, Y.; Fratini, E.; Baglioni, P.; Faraone, A.; Mamontov, E. *J. Chem. Phys.* **2006**, *125*, 171103.
(51) Swenson, J.; Jansson, H.; Howells, W. S.; Longeville, S. *J. Chem. Phys.* **2006**, *122*, 084505.
(52) Prielmeier, F. X.; Lang, E. W.; Speedy, R. J.; Lüdemann, H. D. *Ber. Bunsenges. Phys. Chem.* **1988**, *92*, 1111.
(53) Gallo, P.; Rovere, M.; Chen, S.-H. *J. Phys.: Condens. Matter* **2010**, *22*, 284102.
(54) Huo, P.; Cebe, P. *Macromolecules* **2011**, *25*, 902.

Macromolecules

Article

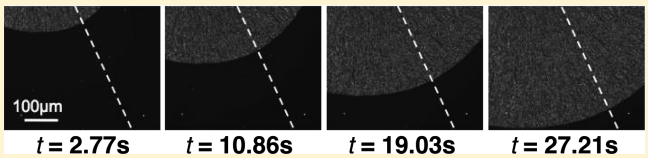
pubs.acs.org/Macromolecules

Crystal Growth Rate in a Blend of Long and Short Polymer Chains

Jessica L. Carvalho, Sara L. Cormier, Nan Lin, and Kari Dalnoki-Veress*

Department of Physics and Astronomy and the Brockhouse Institute for Materials Research, McMaster University, Hamilton, ON, Canada

ABSTRACT: Since short polymer chains have a higher mobility than long molecules, conventional expectations are that the growth rate, G, of polymer crystals should decrease as the concentration of large chains increases in a binary blend. Here we present results on G as the blend concentration, ϕ, is varied from short chains of poly(ethylene oxide) (PEO), which are well above the entanglement molecular weight, to long PEO chains. Contrary to the simple mobility argument, $G(\phi)$ is nonmonotonic—clear evidence that another mechanism can dominate. We propose a tentative model based on the simple idea that chain ends retard the crystal growth. Thus, increasing the chain end concentration with the addition of short chain molecules can reduce the crystal growth rate.



INTRODUCTION

Even though polymers are long chain molecules, typically dominated by entropy, they can form a crystalline structure. Much of the process of crystal growth is generally very well understood.[1−3] Starting from an initial crystal nucleus, segments of a chain pull out of the amorphous melt and sequentially attach to the growth front. When chains are short enough and the supercooling relatively small, crystallization proceeds slowly and extended chain crystals can form. However, with long chain systems or large supercooling, a perfectly aligned and fully extended chain arrangement is rarely realized. Such a crystal would require the chain to fully disentangle from the melt at a huge entropic cost—a cost that is too large to overcome on the time scale of growth. Instead, long chain molecules attach subchain segments to the growth front via a chain folding process to form well-defined nanoscale crystalline lamella. Defects like entanglements and chain ends are sequestered to thin amorphous layers separating the lamellae. The resulting structure is semicrystalline and driven by kinetics rather than equilibrium thermodynamics. The larger superstructures that form are round spherulites which exhibit linear growth rates, G, for a given crystallization temperature, T_c.[1−3]

There is a very extensive body of experimental and theoretical work to describe the crystallization process for monodisperse systems where the entire sample is of similar molecular weight. However, what has been generally overlooked is a means to describe the effect of polydispersity. Given the industrial importance of semicrystalline polymers, where highly polydisperse materials are the norm, this is perhaps surprising. Part of the difficulty in treating polydispersity is a lack of a solid understanding of the effect of molecular weight on crystallization kinetics. The experimental observations are complex and depend on chain length, temperature, and polymer type, to name a few, in ways that cannot be described within a single theoretical framework. For example, in a seminal study Kovacs and co-workers showed a stepwise change in growth rate as a function of temperature for short chain poly(ethylene oxide) (PEO), whereas longer chains demonstrated a continuous change.[4] This effect has been attributed to transitions from fully extended chain crystals to integer-folded crystals in the short chain systems, which contrasts with noninteger chain folding in the long chain systems. Other studies have demonstrated a complex molecular weight dependence for the growth rate of PEO spherulites, which also lacked a simple temperature dependence.[5]

One way to understand polydispersity and molecular weight effects on crystal growth is to look at blends of different monodisperse chain lengths. A large body of work exists for blends of short chain systems, like the *n*-alkanes.[6−11] These systems are ideal because perfectly monodisperse fractions have become available in recent years, making the preparation of perfectly bidisperse blends possible. Such perfectly monodisperse samples do not exist for long chains. Because simulating long chain crystallization remains very challenging, studies have focused on short chains.[12] By understanding these simpler model systems, extrapolations may be made to more complex, long-chain blends. Such studies have lent insight into chain alignment, chain-end effects, integer and noninteger chain folding, spherulite formation, etc. Work by Hosier and co-workers looked at binary blends of relatively long, monodisperse *n*-alkanes.[6−8] Differences in size between the two blend chain lengths played an important role in the resultant morphology, and growth rates were seen to decrease when small amounts of the guest molecule, whether shorter or longer, were added to the melt of the host molecule. Such nonmonotonic changes in growth rate as a function of blend composition have also been observed in simulations of short chain blend systems.[10,13]

Received: November 3, 2011
Revised: January 6, 2012
Published: January 26, 2012

ACS Publications © 2012 American Chemical Society

dx.doi.org/10.1021/ma202429q | *Macromolecules* 2012, 45, 1688−1691

A limited number of studies have explored high molecular weight blends.[14−20] These studies have mostly focused on cocrystallisation, where both chain lengths are homogeneously distributed in the crystal, contrasted with segregation, where one component is expelled from the growing crystal. Work by Cheng and co-workers thoroughly examined a large number of blends of short PEO chains (with number-averaged molecular weight ranging from $M_n \sim 3.5$ to 20 kg/mol) with much longer chains.[14−16] Segregation was seen to persist with a short chain component of 20 kg/mol. Balijepalli and co-workers examined blends of very short 5 kg/mol and long 270 kg/mol PEO molecules.[20] For temperatures where cocrystallization took place, they found a crystal lamella thickness dependence based on blend composition. Whether short or long, the majority component was responsible for templating the crystal thickness with the minority component conforming to this restriction. The authors suggested that this behavior was caused by a balance between the energy of folding long chains and the inclusion of more chain end defects for the short chains.

While nonmonotonic growth rates as a function of blend composition have been seen before in systems where integer chain folding or chain segregation are important, such effects do not play a role in high molecular weight polymers. For high molecular weight chains the expectations are more simple: increasing chain length decreases the mobility. Thus, adding a low molecular weight component should result in monotonically increasing the crystallization kinetics.

Here we present results on the spherulite growth rate, G, of high molecular weight blends of PEO. In contrast with expectations, we demonstrate a robust, *nonmonotonic change in the growth rate as a function of blend composition*. Such an effect has not been previously reported in the literature for chains of this length. From the experimental results we can only conclude that that there is a secondary mechanism, not previously accounted for, that is responsible for the nonmonotonic results. We propose a tentative model that is consistent with the experimental results.

EXPERIMENT

Three different narrow molecular weight species of PEO were used for this study. The molecules, which will be referred to as 57K, 102K, and 330K, had weight-averaged molecular weight M_w = 57, 102, and 330 kg/mol and polydispersity index M_w/M_n = 1.10, 1.08, and 1.18, where M_n is the number-averaged molecular weight (Polymer Source, Inc., Canada). Blends of the three molecular weights were dissolved in acetonitrile and spin-cast onto Si substrates to obtain uniform films with $h \sim 500$ nm. We note that all growth rates presented can be considered bulk measurements since h was chosen well above that for which thin film effects become important.[21] The films were vacuum annealed (10^{-6} Torr) about 5 °C above the melting temperature for PEO ($T_m \sim 65$ °C) for ∼24 h to remove residual solvent and relax the polymer chains. After annealing, samples were transferred to an optical microscope heating stage (Linkam, UK) and flushed with argon gas to ensure a dry environment. Samples were annealed for at least 10 min above T_m to erase thermal history and then cooled rapidly to the desired crystallization temperature, T_c, for spherulite growth measurements. Dark field optical microscopy was used to measure the spherulite growth rate, G, as shown in Figure 1.

RESULTS AND DISCUSSION

With dark field microscopy, the growing crystal appears bright with a very sharp boundary in contrast with the surrounding amorphous melt. G is readily obtained from the position of the growth front as a function of time. A plot of G as a function of the blend concentration ϕ is shown in Figure 2a for all three binary blends. We note that each composition data point represents an average of 4−8 measurements (multiple measurements of G were obtained on several individual film samples for each ϕ). Here the concentration ϕ is the number fraction of long chains in a blend. For example, for the 57K/102K blend data set, $\phi = 0$ is a film of entirely 57K PEO chains, $\phi = 0.5$ has an equal number of 57K and 102K molecules, and $\phi = 1.0$ is a film of entirely 102K PEO chains. It is important to note that the molecular weights used in this study fall in the regime of decreasing G with increasing chain length.[5] Thus, for binary blends, the mobility argument described above would predict a monotonic decrease in G for increasing ϕ. Such expectations are clearly not observed in the data. A distinct nonmonotonic change in growth rate is evident for two of the three blend compositions. While G seems to decrease monotonically with ϕ for the 102K/330K blends, the 57K/102K and 57K/330K blends exhibit an upturn in the growth rate for larger values of ϕ. The result is counterintuitive: *adding more mobile short chains to a system of long chains slows the growth kinetics of the crystals.*

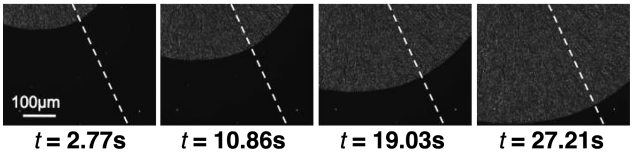


Figure 1. Dark field optical microscopy images of a growing spherulite in a PEO (57K) film at T_c = 50 °C. G is obtained from position of the growth front as a function of time.

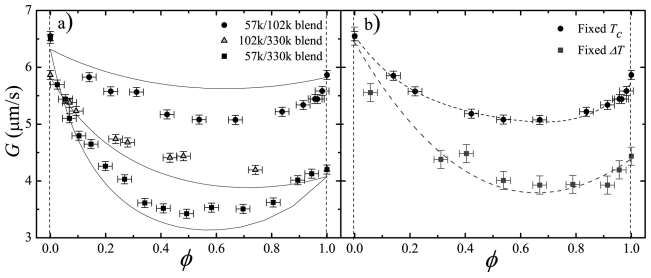


Figure 2. (a) $G(\phi)$, for three different blends crystallized isothermally at T_c = 50 °C. Nonmonotonic changes in G can be seen for two of the blends. Lines are the best fit of the model presented in the text. (b) $G(\phi)$ for 57K/102K blend as in (a) and with fixed supercooling. Lines drawn to guide the eye.

In addition to investigating binary blends, $G(\phi)$ has also been obtained for ternary systems (see Figure 3). In this ternary plot, the vertices represent films of the pure components. Each edge represents one of the binary data sets in Figure 2a, while the interior of the plot is composed of data points from the ternary blends. This plot represents hundreds of individual growth rate measurements of various blend compositions, underlining the robust nature of this anomalous nonmonotonic trend in $G(\phi)$.

From the experiments we can state with certainty that there is a second mechanism which opposes the simple mobility argument and results in an increase in the growth kinetics as the short chain component vanishes. While we cannot be certain about the cause of this mechanism, in what is to follow we speculate as to the origin and propose a simple model.

dx.doi.org/10.1021/ma202429q | *Macromolecules* 2012, 45, 1688−1691

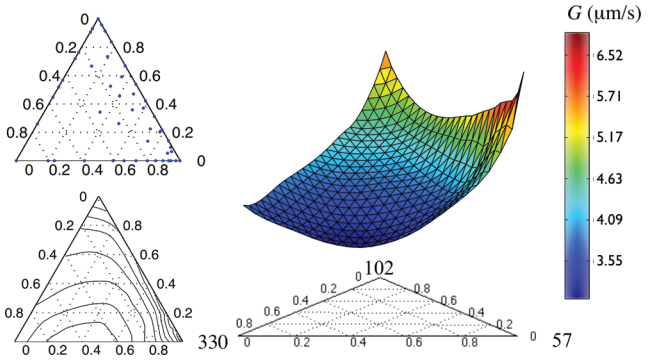


Figure 3. Ternary plot of G for all blends. Vertices represent growth rate of the pure components, edges are that of binary blends, and ternary blends fill the middle of the plot. Color scale indicates range of G values represented.

The chain lengths were chosen to be well above those where integer chain folding effects exist,[4] where chain segregation of the two components can play a role,[14] and above the entanglement molecular weight ~1.6 kg/mol.[22] For long chains, as in our system, it has been shown that the energy barrier for chain segments attaching to the crystal front is not dependent on the amount of chain left to be incorporated into the crystal.[23] Thus, from the point of view of of the growth front, the three chain lengths should be indistinguishable from one another.

Having ruled out integer chain folding and chain segregation effects, consideration must be given to the degree of supercooling in the experiments. For simplicity, all values of $G(\phi)$ were obtained at T_c = 50 °C. However, the relevant parameter for determining the growth rate is not T_c, but rather the degree of supercooling below the melting temperature, $\Delta T = T_m - T_c$. Since T_m is chain length dependent, the degree of supercooling was not identical for all measurements and hence the driving force to crystallize not equal. Experiments were carried out to ensure that the variation in the degree of supercooling is not the reason behind the nonmonotonic trends. For the three fractions considered in this work, differences in T_m were measured to be less than 1 °C, in agreement with proposed empirical relationships (see for example Figure VIII.15 in ref 24). While this is a small difference, by measuring the values of T_m for a number of 57K/102K blends, $G(\phi)$ could be obtained for fixed supercooling as shown in Figure 2b. From the data it can be seen that while the differences in T_m certainly add a correction to G, the nonmonotonic trend is still present in the fixed supercooling experiment. Thus, we can definitively conclude that the slight difference in the degree of supercooling is also not responsible for the paradoxical results. Furthermore, we have examined the morphological features of the blends both with optical microscopy and atomic force microscopy. No unusual features were noted for compositions at the minimum of the growth rate. More precisely, the morphology appears to transition from the low composition case to the high composition case in a continuous fashion.

The increase in G near ϕ = 1 suggests a mechanism that opposes the mobility argument (i.e., one would expect G to decrease with increasing ϕ because when ϕ increases, so does the fraction of longer, more sluggish, molecules). The mobility contribution modifying the growth rate can be described by a power law[3]

$$G_{\text{mobility}} \sim \left(\frac{A}{\langle M_n \rangle}\right)^{\alpha} \tag{1}$$

where A is a prefactor, $\langle M_n \rangle$ is the number-average molecular weight of the blend, and the exponent, α, is found to take a value between 0 and 1, depending on T_c. A mechanism resulting in the upturn in G with ϕ is elusive and has not been previously reported. How can one account for a reduction in the growth kinetics with the addition of *more mobile* shorter molecules? While there may well be other possible origins, we suggest that the mechanism can be explained by the increasing number of chain ends in the system with the addition of shorter molecules. In general, chain ends can be thought of as defects in the system that, because of the thermally driven entropic fluctuations, are more mobile than the midchain segments. Work by Richter and co-workers has directly verified that chain ends are much more mobile than midchain segments.[25] It is reasonable to assume that this increased motion will decrease the likelihood of a chain end attaching to the growth front compared to a stem from the midchain region. As a result, chain ends are more resistant to being folded into a compact crystalline form and are more likely to end up in the amorphous interlamellar region.[1]

We propose that the chain ends, which act as entropic defects at the crystal growth front, slow the dynamics of crystal growth. Adding short chains to a long chain system increases the concentration of chain ends or, in other words, increases the defects at the growth front. Then the increase in chain ends is responsible for the slowing of the growth rate as the concentration of small chains increases. This is consistent with the qualitative observation that the 57K/330K blend, which has the largest difference in chain lengths, also shows the greatest upturn in G near ϕ = 1. To model this mechanism, we assume that a chain end, of average length γ, has a larger time constant, τ_a, for incorporation into the growing crystal front than that for the remaining midchain, τ_b. The average time it takes for a chain of total length M to incorporate into the growth front is $t(M) \sim (M - 2\gamma)\tau_b + 2\gamma\tau_a$, which results in a growth rate contribution for a single chain given by

$$G_{\text{ends}}(M) \sim \frac{M}{(M - 2\gamma)\tau_b + 2\gamma\tau_a} \tag{2}$$

For the blend system the appropriate average of $G_{\text{ends}}(M)$ is given by the harmonic mean

$$G_{\text{ends}}(\varphi) = \left[\frac{\varphi}{G_{\text{ends}}(M_l)} + \frac{1 - \varphi}{G_{\text{ends}}(M_s)}\right]^{-1} \tag{3}$$

where M_l and M_s are the molecular weights of the long and short chains. The total contribution to the growth rate from both the mobility and our proposed chain-end mechanisms is given by the product, $G = G_{\text{mobility}}G_{\text{ends}}$. Fits to the experimental data with this functional form are shown in Figure 2a. While the fits are not in quantitative agreement, this simple model captures the observed behavior with reasonable values for the parameters: A = 1205 kg/mol, α = 0.9 (consistent with the expected range as discussed above), τ_a/τ_b = 290 (midregion of the chain is incorporated into spherulite much faster than the ends), and γ = 0.4 kg/mol. Most interesting among these parameters is the result that the chain end length, γ, which acts as a defect, corresponds to about 10 monomer units. While the model captures the qualitative features, deviations are likely due

to the need to include a more complex form of the mobility term $G_{mobility}$.[26] Furthermore, the model assumes perfectly sharp molecular weight distributions of the PEO used in the blends, but in fact the polymers are not perfectly monodisperse.

Polymer crystal growth rates are strongly dependent on temperature. Lowering T_c is equivalent to increasing the driving force for crystallization. As a last test of the model, we investigated the effect of changing the degree of supercooling on the $G(\phi)$ as shown in Figure 4. As T_c is lowered, the nonmonotonic trend weakens, with a return to the expected monotonic decrease in G with increasing ϕ for the lowest T_c. This trend is also consistent with the model we have presented. Crystals grown at larger supercoolings are typically less perfect due to the fact that they are formed under much larger growth rates.[1] It should be expected that a more imperfect crystal will be less sensitive to defects at the growth front than one formed at higher temperatures where greater crystal perfection has time to be achieved.

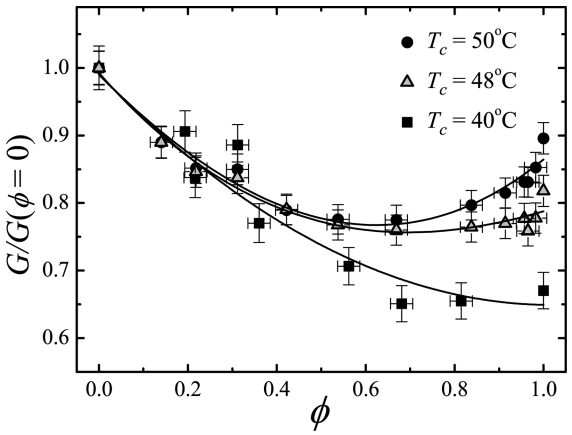


Figure 4. $G(\phi)$ for a 57K/102K blend at different values of T_c. Each data set has been normalized by $G(\phi = 0)$ to aid comparison. Lines have been drawn to guide the eye.

CONCLUSIONS

Here we have demonstrated, for the first time, that there is a nonmonotonic change in spherulite growth rate as a function of blend composition for binary and ternary blends of PEO. The conventional expectation is that as one adds short chains to a long chain system kinetics should become faster and hence the crystal growth rate should increase. This was not found to be the case, and from the experiments we can state with certainty that there is a mechanism which opposes the simple mobility argument and results in an increase in the growth kinetics as the short chain component vanishes. We suggest a tentative model based on the simple idea that the chain ends are more mobile. As a result, the ends act as defects that are more difficult to incorporate into the crystal. Thus, increasing the chain end concentration increases the defects which reduces the crystal growth rate. While the simple model fails to provide quantitative agreement, the model does capture the nonmonotonic observations in $G(\phi)$. Furthermore, from the model one would expect the chain-end retardation to become less important for greater supercooling—this expectation is also observed. The experiments provide robust proof that the conventional mobility argument is not sufficient to describe the observations. It is hoped that the simple model presented provides a starting point for more complete theoretical models.

AUTHOR INFORMATION

Corresponding Author
*E-mail: dalnoki@mcmaster.ca.

ACKNOWLEDGMENTS

We thank Dr. Michael Massa for valuable discussions. Financial support by NSERC of Canada is gratefully acknowledged.

REFERENCES

(1) Strobl, G. *The Physics of Polymers*, 2nd ed.; Springer: Berlin, 1997.
(2) Wunderlich, B. *Macromolecular Physics*; Academic Press: New York, 1973; Vol. *1*.
(3) Mandelkern, L. *Crystallization of Polymers: Kinetics and Mechanisms*; Cambridge University Press: New York, 2004.
(4) Kovacs, A. J.; Gonthier, A.; Straupe, C. *J. Polym Sci., Polym. Symp.* **1975**, *50*, 283−325.
(5) Godovsky, Y. K.; Slonimsky, G. L.; Garbar, N. M. *J. Polym. Sci., Part C: Polym. Symp.* **1972**, *38*, 1−21.
(6) Hosier, I. L.; Bassett, D. C.; Vaughan, A. S. *Macromolecules* **2000**, *33*, 8781−8790.
(7) Hosier, I. L.; Bassett, D. C. *J. Polym. Sci., Part B: Polym. Phys.* **2001**, *39*, 2874−2887.
(8) Hosier, I. L.; Bassett, D. C. *Polymer* **2002**, *43*, 307−318.
(9) Ungar, G.; Zeng, X. *Chem. Rev.* **2001**, *101*, 4157−4188.
(10) Sommer, J. U. *Polymer* **2002**, *43*, 929−935.
(11) Bassett, D. C. *Polymer* **2007**, *48*, 3384−3387.
(12) Meyer, H.; Muller-Plathe, F. *Macromolecules* **2002**, *35*, 1241−1252.
(13) Cai, T.; Ma, Y.; Yin, P.; Hu, W. *J. Phys. Chem. B* **2008**, *112*, 7370−7376.
(14) Cheng, S. Z. D.; Wunderlich, B. *J. Polym. Sci., Part B: Polym. Phys.* **1986**, *24*, 577−594.
(15) Cheng, S. Z. D.; Wunderlich, B. *J. Polym. Sci., Part B: Polym. Phys.* **1986**, *24*, 595−617.
(16) Cheng, S. Z. D.; Bu, H. S.; Wunderlich, B. *J. Polym. Sci., Part B: Polym. Phys.* **1988**, *26*, 1947−1964.
(17) Lopez, J. M.; Gedde, U. W. *Polymer* **1988**, *29*, 1037−1044.
(18) Lopez, J. M.; Braña, M. T.; Terselius, B.; Gedde, U. W. *Polymer* **1988**, *29*, 1045−1051.
(19) Hill, M. J.; Barham, P. J. *Polymer* **1995**, *36*, 1523−1530.
(20) Balijepalli, S.; Schultz, J. M.; Lin, J. S. *Macromolecules* **1996**, *29*, 6601−6611.
(21) Dalnoki-Veress, K.; Forrest, J. A.; Massa, M. V.; Pratt, A.; Williams, A. *J. Polym. Sci., Part B: Polym. Phys.* **2001**, *39*, 2615−2621.
(22) Mark, J. E., Ed.; *Physical Properties of Polymers Handbook*; American Institute of Physics: Melville, NY, 1996; pp 81−89.
(23) Hu, W.; Frenkel, D.; Mathot, V. B. F. *Macromolecules* **2003**, *36*, 8178−8183.
(24) Wunderlich, B. *Macromolecular Physics*; Academic Press: New York, 1973; Vol. *3*.
(25) Zamponi, M.; Monkenbusch, M.; Willner, L.; Wischnewski, A.; Farago, B.; Richter, D. *Europhys. Lett.* **2005**, *72*, 1039.
(26) Umemoto, S.; Okui, N. *Polymer* **2005**, *46*, 8790−8795.

Macromolecules

Article

pubs.acs.org/Macromolecules

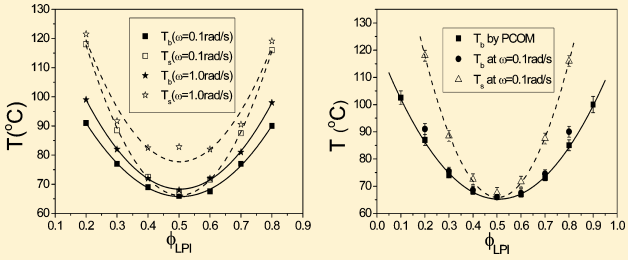
Shear Induced Phase Boundary Shift in the Critical and Off-Critical Regions for a Polybutadiene/Polyisoprene Blend

Fasheng Zou,[†] Xia Dong,*[,†] Wei Liu,[†] Jian Yang,[†] Demiao Lin,[†] Aimin Liang,[‡] Wei Li,[‡] and Charles C. Han*[,†]

[†]State Key Laboratory of Polymer Physics and Chemistry and CAS Key Laboratory of Engineering Plastics, Joint Laboratory of Polymer Science and Materials, Beijing National Laboratory for Molecular Science, Institute of Chemistry, Chinese Academy of Sciences, Beijing 100190, China

[‡]Yanshan Branch, SINOPEC Beijing Research Institute of Chemical Industry, Beijing 102500, China

ABSTRACT: The rheology of near- and off-critical elastomeric blends of polybutadiene (PB)/ low vinyl content polyisoprene (LPI) has been studied as a function of temperature, heating rate, and shear frequency. Depending on the composition, near or far away from the critical point, blends showed different behaviors in several aspects: temperature ramp curves, shift of the apparent binodal and spinodal points under oscillatory shear at the given frequency and strain amplitude. The composition dependent rheological responses are interpreted by the differences in the amplitude of the critical fluctuation near the phase boundary and in the shear induced mixing mechanisms between near- and off-critical blends. For near-critical blends, the critical fluctuation is large enough to induce a considerable extra stress when the blend is still in the miscible state. As a result, a heating rate independent upturn of G' can be observed and the apparent spinodal point can be greatly shifted through the strong suppression of the large critical fluctuations. In contrast, for off-critical blends, the critical fluctuations in the metastable region are relatively small and there is competition between the phase separation kinetics and the heating rate. Therefore, the blend displayed a heating rate dependent apparent binodal point and a large shift of the apparent binodal point but a moderate shift of the spinodal point under oscillatory shear. By lowering or extrapolating the measured frequency to a very small value (0.1 rad/s in this study) for both binodal and spinodal points, the rheologically determined phase diagram is consistent with the static results obtained by optical microscopy observations.



1. INTRODUCTION

The rheology of polymer blends has long been the interests from both fundamental and industrial viewpoints. After some important advancements were obtained in the understanding of the linear and nonlinear rheology of immiscible polymer blends in the past decades,[1−7] researchers generally turned their attention toward the miscible or partially miscible polymer blends and on the rheological responses near the boundary of the phase separation. Within the miscible region, research was mainly focused on the concentration dependence of viscosity and linear dynamic properties which can be usually determined by a simple or modified Irving relationship.[8−12] Within the phase-separated region, on one hand, the phase-separated structures like the droplet-matrix structure and bicontinuous structure in polymer blends can be reflected by rheological responses which are typically analyzed with the frequency dependence of the storage modulus.[13−16] On the other hand, the linear viscoelastic behavior of polymer blends with a droplet-matrix morphology can be described quantitatively by several emulsion models which were developed independently by Palierne, Gramespacher and Meissner, and Bousmina et al.[2−4] Besides, these models have been widely used to obtain either structure information (domain size and distribution) or interfacial tension.[17−19]

Partially miscible polymer blends in the phase transitional region also exhibit interesting rheologcial behavior. One of the most exciting results is that the rheological responses in this phase transitional region has been studied theoretically and experimentally to obtain the binodal and spinodal points of either lower critical solution temperature (LCST) or upper critical solution temperature (UCST).[10,20−25] However, recent developments[26−28] showed that rheological determination of the binodal and spinodal points may be more complicated than the traditional experimental descriptions.[20,21] Once the measured macroscopic rheological material functions are coupled with the phase separation kinetics, the temperature ramp rate effect on the determination of the binodal and/or spinodal points could occur and must be accounted for in the analysis. Besides, it has been reported that oscillatory shear flow could also affect the thermodynamics and result in shear induced mixing and/or demixing depending on the viscoelastic

Received: September 23, 2011
Revised: November 21, 2011
Published: January 23, 2012

ACS Publications © 2012 American Chemical Society

dx.doi.org/10.1021/ma2021562 | *Macromolecules* 2012, 45, 1692−1700

properties of the specific polymer blends.[27−29] Currently, it is believed that oscillatory shear does not affect the phase separation kinetics or the shift of the phase boundary if the strain rate or stress is small enough or the frequency is low enough.[20−23] However, it is not clear to what extent the coupling between thermodynamic and the applied strains and stresses can be neglected or what kind of extrapolation procedures are needed in order to obtain the real thermodynamic steady state phase boundary and unperturbed phase separation kinetics.

In this work, polybutadiene (PB)/low vinyl content polyisoprene (LPI) blends with the LCST type phase diagram are investigated by rheological measurements. There have been some reports on the PB/LPI blends about their microstructure and cross-link effects on miscibility,[30,31] phase separation kinetics under a quiescent state,[32−34] oscillatory shear,[26,35] or steady shear.[36,37] A shear induced mixing situation is always the case for PB/LPI blends under both simple shear and oscillatory shear since these are dynamically symmetrical systems we are dealing with. In addition, unlike the PS/PVME blends, no viscoelastic phase separation needs to be considered.[38−40] It is believed that PB/LPI blends can serve as a model polymer blend for studying the normal liquid−liquid phase separation (LLPS) effect on a dynamically symmetrical system by rheology. In this study, we discuss how the LLPS influences the viscoelastic properties of a dynamically symmetrical system and emphasize the basic physics of how to eliminate or extrapolate out the shear influence on the phase boundary and the phase separation kinetics.

2. THEORETICAL BACKGROUND

2.1. Rheological Determination of the Binodal and Spinodal Points. For a multicomponent polymer blend, its viscoelastic properties such as storage modulus G' and loss modulus G'' are generally related to three kinds of contributions:[27] the bulk part from the polymer chain dynamics and entanglements, G'_{bulk} or G''_{bulk}, the concentration fluctuations from thermal noise, $G'_{fluctuation}$ or $G''_{fluctuation}$, and the interfacial contribution due to the phase-separated domains, $G'_{interface}$ or $G''_{interface}$. In temperature ramp rheological measurements, when the blend is in the miscible region far from the spinodal point, its viscoelastic properties are mainly determined by the contribution from the bulk part. As the temperature approaches the spinodal point, $G'_{fluctuation}$ (or $G''_{fluctuation}$) becomes larger and larger and may cause the global storage modulus (or loss modulus) to display an observable increase. Besides, once the blend is in the two-phase region, either in the metastable region or in the unstable region, the phase-separated domains can contribute to the complex modulus as well. Thus, it is believed that a quantitative extracting of the "real" binodal point is a doable but challenging task in a temperature ramp rheological measurement.

In contrast, the determination of a spinodal point is normally based on the theoretical work of Fredrickson and Larson[41] as well as Ajji and Choplin.[42] An important expression that can be drawn from the above theories is the ratio of $G'(\omega)/G''^2(\omega)$,

$$\frac{G'(\omega)}{G''^2(\omega)} = \frac{30\pi}{k_B T}\left\{\frac{a_1^2}{36\varphi} + \frac{a_2^2}{36(1-\varphi)}\right\}^{3/2} (\chi_s - \chi)^{-3/2} \quad (1)$$

where a_i is the statistical segment length of repeated unit, χ_s designates the interaction parameter at the spinodal point, and χ is the interaction parameter. It is this expression that has been used to obtain the spinodal points. If further assuming that the interaction parameter χ is given by the form $\chi = A + B/T$, the following expression can be deduced from eq 1

$$\left[\frac{G''^2(\omega)}{G'(\omega)T}\right]^{2/3} = \frac{B}{C}\left(\frac{1}{T_s} - \frac{1}{T}\right) \quad (2)$$

where C is given by

$$C = \left(\frac{30\pi}{k_B}\right)^{2/3}\left\{\frac{a_1^2}{36\varphi} + \frac{a_2^2}{36(1-\varphi)}\right\} \quad (3)$$

Thus a linear dependence of $\{G''^2(\omega)/[G'(\omega)T]\}^{2/3}$ versus $1/T$ could be expected, which leads to an intercept at $1/T$ axis denoting the spinodal temperature, T_s. During the temperature ramp tests, the global storage and loss modulus measured generally include more than one kind of contributions.[26,27] However, in Ajji and Choplin's treatment, only the contribution from critical fluctuations is considered. Therefore, it is understandable that the phase separation kinetics will also affect the extrapolated position of the spinodal temperature as long as the contribution from the interfacial tension part is not negligible.

2.2. Shear Induced Mixing under Oscillatory Shear. In the theoretical calculation,[43−45] e.g. the kinetics equations, shear rate is normally used but not the shear frequency or the shear amplitude. Therefore, there is still no well-defined theory for the phenomenon of shear induced mixing under oscillatory shear. In this study, we will only use our basic knowledge about phase separation under steady shear and make an analogy between steady shear and oscillatory shear. For near-critical blends, a useful starting point is the mode-coupling renormalization-group (MCRG) theory of the simple binary fluids under shear.[43−45] According to MCRG theory, once $\dot{\gamma}\tau_\xi > 1$, where $\dot{\gamma}$ is the shear rate and τ_ξ is the characteristic relaxation time for concentration fluctuation, the concentration fluctuation should be distorted by the shear and shear induced mixing starts to happen. For off-critical blends, the shear induced mixing should affect the nucleation phenomena more.[46−48] For nucleation phase separation under shear flow, if the shear is strong enough to suppress the critical droplet size, that is $R_c > R^*$, where R_c is the critical radius of nucleation and R^* is the Taylor break-up size, then no nucleation phase separation could happen.[49]

3. EXPERIMENTAL SECTION

3.1. Materials. Two polymers with statistical distributed microstructures (PB and LPI) used in this study were supplied by Beijing Yanshan Petrochemical Co., Ltd. Both of them were synthesized by anionic polymerization. The number-average molecular weight (M_n), the mass-average molecular weight (M_w), and the polydispersity of the model polymers were determined by gel permeation chromatography (GPC) using polystyrene as standard in our laboratory. The composition of these materials was obtained by ^{2}H nuclear magnetic resonance (NMR). The results of the polymer characterization are summarized in Table 1. In order to make a comparison with our previous results,[18,26,27] the PB/LPI blend is labeled as LPIx, where x represents the volume fraction of LPI in the blend.

3.2. Sample Preparation. The PB/LPI blends were prepared by a solution blending method.[18] We started with a dilute solution (mass fraction of 2% of the total polymer), which contains the antioxidant

dx.doi.org/10.1021/ma2021562 | Macromolecules 2012, 45, 1692−1700

Table 1. Characterization Results of Polymers

sample code	M_n (g/mol)	M_w/M_n	density (g/cm^3)	T_g (°C)	microstructure, mol % 1,4	1,2	3,4
PB	55 000	1.10	0.877	−97	89	11	0
LPI	34 000	1.50	0.895	−63	88	0	12

butylated hydroxytoluene (BHT) with mass fraction 0.02% of the solution in a solvent of methylene chloride. Then the solution was filtered through a 0.45 μm Millipore filter, and the solvent was evaporated at 35 °C with stirring. Samples were further dried in a vacuum oven at 35 °C for a week in order to remove the residual methylene chloride.

3.3. Experiments. *3.3.1. Rheologcial Measurements.* All the rheological measurements were performed by an Advanced Rheometric Expansion System (ARES, Rheometric Scientific, Piscataway, NJ), which is a strain-controlled rheometer with a parallel plate−plate fixture (25 mm diameter), and a testing gap value of 0.5 mm between two plates was used. Temperature control in the rheometer is carried out by hot nitrogen gas with an accuracy of ±0.1 °C. Before measurements all blends were kept at 4 °C in a refrigerator and then put into a vacuum oven at 35 °C for 2 days to remove air bubbles and to ensure the same thermal history.

The following oscillatory shear experiments were carried out in the steady state region of the blends,[26] as was verified by preliminary amplitude sweep tests: (i) Dynamic temperature ramp tests were carried out by measuring storage and loss modulus at a fixed frequency and different heating rates (0.2 and 1.0 °C/min) from miscible region to the two-phase region at a constant strain (10%). (ii) Shear quench experiments were performed at a series of temperatures which included the single-phase and two-phase regions at a fixed frequency and a given strain of 10%. The detailed procedure of the shear quench experiments is as follows: first the dynamic temperature ramp tests at a frequency of 25 rad/s and strain amplitude of 10% were conducted to reach a certain temperature, and at this temperature there was no apparent phase separation at 25 rad/s. Then the temperature was held at the specified value, and the test mode was switched to a time sweep mode at a constant but lower frequency and strain amplitude of 10%. All the measurements started from 40 °C, where all blends are in the single-phase region under quiescent conditions.

3.3.2. Optical Microscopy (OM). An Olympus (BX51) phase contrast optical microscope (PCOM) was applied, and the results were recorded with an Olympus (C-5050ZOOM) camera. The experimental temperature was controlled by a Linkam (LTS 350) hot stage, and fresh nitrogen gas was circulated in the hot stage to avoid possible thermal degradation. Samples were sandwiched between a clean microscope slide and cover glass with a spacer about 30 μm in thickness. In order to obtain the static phase diagram of this polymer blend, the prepared blend was heated in 5 K increments and then annealed for a sufficient time to form observable domains, and typically the annealing time was from 2 to 24 h. Near the transitional temperature, the intervals were reduced to 2 K for better accuracy.

4. RESULTS AND DISCUSSION

4.1. Phase Diagram under Static State. Before the rheological measurements, PCOM observations have been performed to investigate the miscibility of the PB/LPI blends under the static state. As is shown in Figure 1, the PB/LPI system displayed an LCST type phase diagram with the critical temperature at about 64.0 ± 1 °C. The critical composition of LPI is about 0.5 by volume fraction, which agrees with the calculated value, 0.485, from the Flory−Huggins theory. In our studies, we simply separate our blends into two categories: off-critical blends (LPI20, LPI30, LPI70, and LPI80) and near-critical blends (LPI40, LPI50, and LPI60). As the phase diagram is rather symmetrical, more systematic studies have been focused on the compositions of the right half of the phase diagram, namely the LPI50, LPI60, LPI70, and PI80.

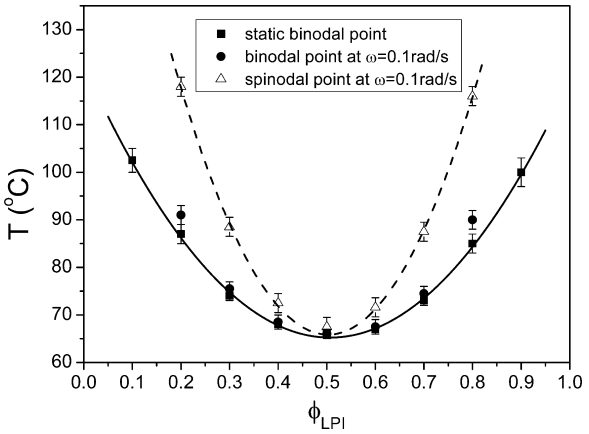


Figure 1. The static phase diagram of PB/LPI blend obtained by PCOM observations and rheological measurements. The solid and dash curves are the least-squares fit for a polynomial equation through the experimental data and are only used to guide the eye.

4.2. Temperature Ramp Experiments. Among the rheological measurements, the temperature sweep or ramp test at a fixed frequency is most widely used to investigate the binodal phase separation temperatures. There have been some papers that reported[21−24] a single shear rheological temperature ramping measurement is sufficient to determine both the binodal and spinodal curves. However, in this study, we shall demonstrate that distinguished discrepancies in temperature ramp curves can be observed between near- and off-critical blends. This indicated that the rheological determination of the binodal and spinodal points may be more complicated than the traditional experimental procedures used.[20,21] Figure 2 showed the typical temperature ramp curves of two near-critical blends (LPI50 and LPI60) and two off-critical blends (LPI70 and LPI80) at a fixed frequency of 0.25 rad/s and different heating rates of 1.0 and 0.2 °C/min. As shown in Figure 2, two near-critical blends displayed the heating rate independent initial upturn of G', while two off-critical blends displayed that the slower the heating rate the lower the temperature at which G' started to increase. By closely examining the temperatures at which G' started to increase, four temperature values (59.0 ± 1, 63.0 ± 1, 78.5 ± 1, and 95.0 ± 1 °C) were obtained for LPI50, LPI60, LPI70, and LPI80 (from the lowest heating rate), respectively. Then the first qualitative discrepancy in temperature ramp curves between near- and off-critical blends is as follows: the static binodal temperatures are higher than the apparent turning points in the rheological measurements for near-critical blends and lower than the rheological measured apparent turning points for off-critical blends. And this can be interpreted as follows. For two near-critical blends, it is believed that the initial upturn of G' is attributed to the large critical fluctuations near the critical region. Such an analysis can be proved by comparing the temperature at which G' starts to increase with its corresponding static cloud point, $T_b(0)$, which was determined by optical microscopy. It is obvious that, for either LPI50 or LPI60 blend, the static cloud point is above the temperature at which G' has encountered the fluctuation contribution and starts to increase. When the composition of G' measurements is far away from the critical composition, the critical fluctuations near the binodal phase boundary become weaker and weaker. Therefore, for off-critical blends, the initial

dx.doi.org/10.1021/ma2021562 | Macromolecules 2012, 45, 1692−1700

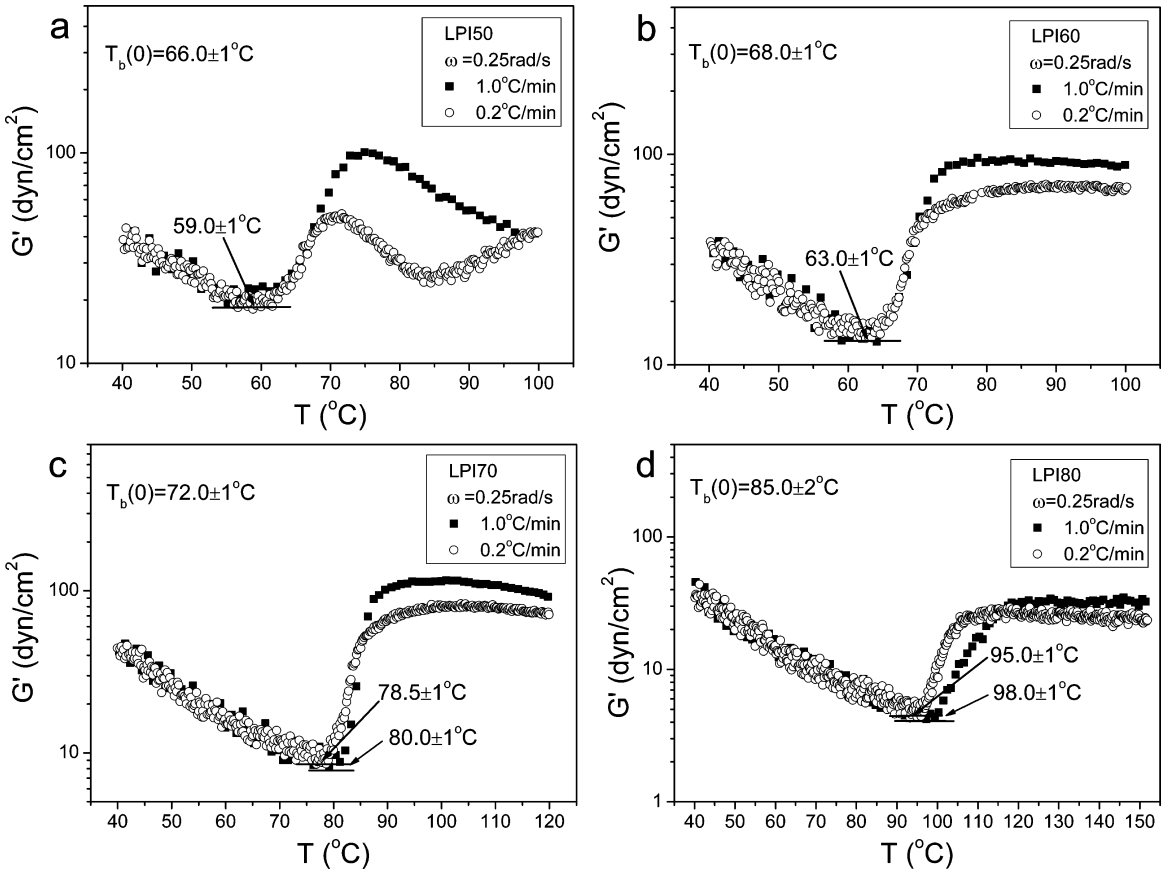


Figure 2. Temperature ramp results of G' at the fixed frequency of 0.25 rad/s and different heating rates of 1.0 and 0.2 °C/min for (a) LPI50, (b) LPI60, (c) LPI70, and (d) LPI80. $T_b(0)$ as shown in Figure 2a–d are the static cloud points which were obtained by PCOM.

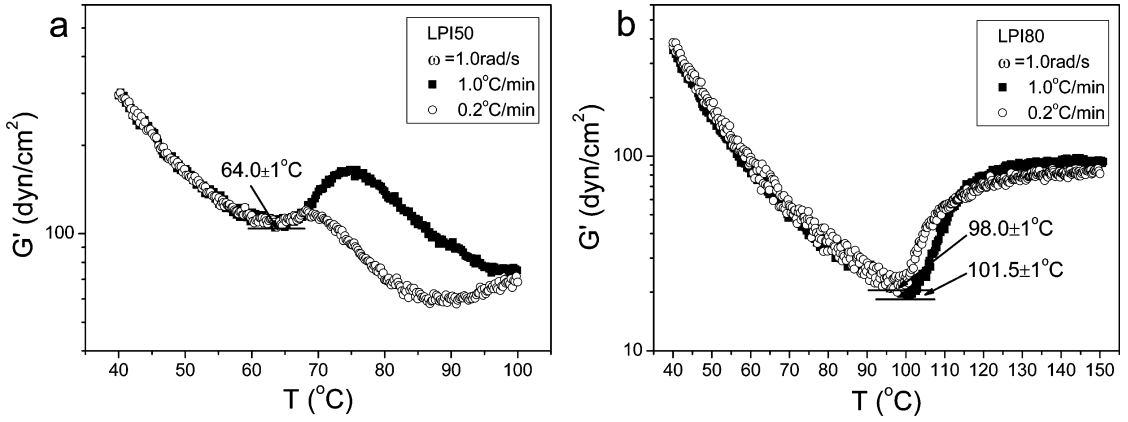


Figure 3. Temperature ramp results of G' at the fixed frequency of 1.0 rad/s and different heating rates of 1.0 and 0.2 °C/min for (a) LPI50 and (b) LPI80.

upturn of G' can come only when the nucleation phase separation process started which happens after the temperature has increased to a value higher than the binodal temperature. From Figure 2c,d, it seems that the detection of the phase-separated domains needed a rather large quench depth into the metastable region. However, what we should keep in mind is the competition between the nucleation phase separation kinetics and the heating rate. Figure 2c,d showed that a slower heating rate results in a lower apparent binodal point although they are all above the real binodal temperatures of $T_b(0)$. Another important effect we should keep in mind is that shear induced mixing can raise the apparent binodal points also. As either the two near-critical blends or the two off-critical blends should have similar rheological responses, in the next section, we mainly focus on LPI50 and LPI80. In Figure 3 we showed the temperature ramp curves of LPI50 and LPI80 at a fixed frequency of 1.0 rad/s, which is 4 times that used for the data shown in Figure 2. Again different heating rates of 1.0 and 0.2 °C/min were used. Compared with Figure 2a and d, a heating rate independent initial upturn of G' for LPI50 and a heating rate dependent apparent binodal point for LPI80 still exist at the higher frequency of 1.0 rad/s. And the rise in temperature at which G' started to increase for either LPI50 or LPI80 with higher frequency is generally believed to be the shear induced

dx.doi.org/10.1021/ma2021562 | *Macromolecules* 2012, 45, 1692–1700

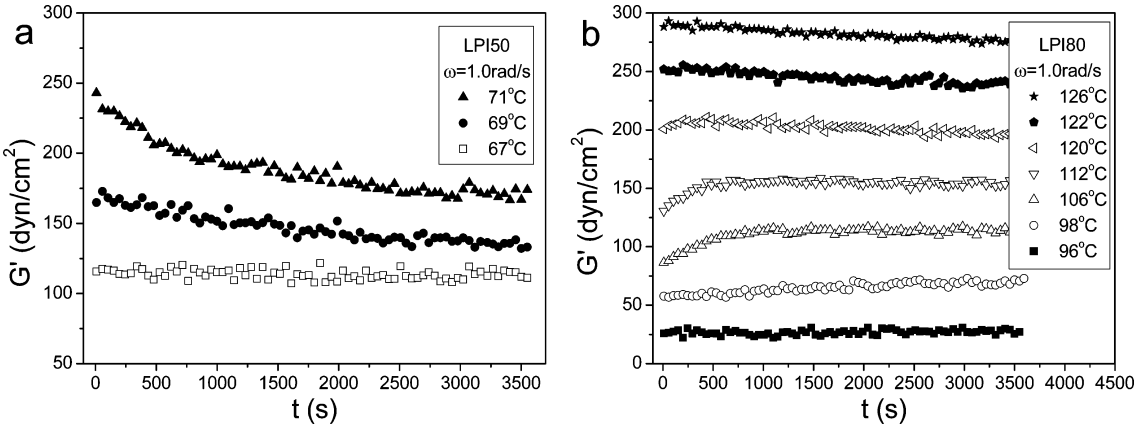


Figure 4. Time evolution of G' at the frequency of 1.0 rad/s after the shear quench from the frequency of 25 rad/s at different temperatures for (a) LPI50 and (b)LPI80. Data points are shifted vertically to avoid crossover. The experimental data for 67 and 96 °C are original data, and the shift values for each higher temperature for LPI50 and LPI80 are 40 and 30 dyn/cm^2, respectively.

mixing effect.[18,26−28] In fact, since the main contributions to the initial upturns of G' in temperature ramp curves are quite different between near- and off-critical blends, the determination of the apparent binodal points should also be treated differently. Up to now, it is believed that the apparent binodal point for near-critical blends should be higher than the temperature at which G' starts to increase in their temperature ramp curves. However, it is still not clear which point of the temperature ramp curve is more suitable for assignment as the apparent binodal point. Although the inflection point of the temperature ramp curves had been used as the apparent binodal point by several research groups,[20−22,38] they also stated that such a method had no significant physical base. Besides, as shown in Figure 3a, the LPI50 blend displayed different inflection points at different heating rates, which causes the determination of the apparent binodal point to become more confusing. For off-critical blends, although the temperature where G' starts to increase in the temperature ramp curve can be assigned as the apparent binodal point, the "real" binodal point should be obtained by extrapolating the heating rate to 0 °C/min. Since the heating rate effects on the apparent binodal point are usually very complex,[28] the heating rate extrapolation for the apparent binodal point was rarely reported. Thus, in the next section we will use the shear quench experiments to detect the phase separation temperature.

4.3. Shear Quench Experiments. Earlier studies from our group[26,27,36] and the above results of LPI50 and LPI80, both demonstrated that shear induced mixing could take place for either near- or off-critical blends. From the early work of Zhang et al.,[27] shear quench experiment can be used as an adequate technique to investigate the phase separation temperature and the phase separation kinetics of polymer blends. The details of these shear quench experiments have been described in the "Experimental Section". The basic theoretical foundation for this treatment is the assumption that the higher shear rate could shift the binodal temperature more than the lower shear rate. Figure 4 showed the time evolution of G' of LPI50 and LPI80 at the frequency of 1.0 rad/s after the shear quench from 25 rad/s at various temperatures which cover the apparent one-phase (homogeneous) and two-phase regions. It showed that both blends displayed one or two transformation temperatures below and above some temperature where the curves of G' versus scan time t are quite different. As the LPI50 blend is rather close to the critical composition, the metastable region is assumed to be quite narrow. Therefore, its time evolution curves of G' display two types which defines the critical temperature (68.0 ± 1 °C) below which G' is almost constant with scan time t. At a temperature higher than the critical temperature, a monotonous decrease of G' versus scan time t is observed, which is generally related to the structure evolutions of spinodal decomposition.[16,50,51] The simple intuitive physical explanation is that once the system is shear quenched back into the spinodal region, the spontaneous phase separation is very fast. The contribution of the growing domains (or structures) to G' becomes negative (when size is over 1 μm for this kind of system[26]) in a very short time. All the time scan observations in Figure 4a for 71 and 69 °C are due to the continuous growth of phase separating structures. In contrast, G' of the LPI80 blend displayed three types of time evolution behaviors. Except for the nearly constant G' at low temperatures and the monotonous decrease of G' at high temperatures versus scan time t, which is similar to the near-critical blend LPI50, an obvious initial increase of G' versus scan time t is observed at the intermediate temperature region. The increase of G' versus scan time t is generally related to the nucleation phase separation process.[16,27,50,51] Thus, through the above shear quench experiments, we obtained the critical temperature (namely 68.0 ± 1 °C) for LPI50 and the apparent binodal and spinodal points (namely 97.0 ± 1 and 121 ± 1 °C, respectively) for LPI80 at the given frequency of 1.0 rad/s. Compared with the results shown in Figure 3a,b, we find that these two apparent binodal points (68.0 ± 1 and 97.0 ± 1 °C) basically correspond to the temperature at which G' has increased and the temperature at which G' starts to increase in their temperature ramp curves. In other words, our shear quench experiment results are consistent with the temperature ramp results and our interpretation.

4.4. The Shift of Apparent Binodal and Spinodal Point under Oscillatory Shear. Figure 5 showed the apparent binodal points for LPI50 and LPI80 as a function of the final frequency of the shear quench experiments. Both blends displayed a relatively larger shift of the apparent binodal point in the low frequency region (from 0.1 to 1.0 rad/s) and a trend of saturation of shear induced mixing in the high frequency region (from 1.0 to 2.5 rad/s). Besides, at the frequency of 0.1 rad/s (the lowest frequency which we have used), the apparent binodal point for LPI50 has reached its static value (66.0 ± 1 °C), while the apparent binodal point for LPI80 is already well

dx.doi.org/10.1021/ma2021562 | Macromolecules 2012, 45, 1692−1700

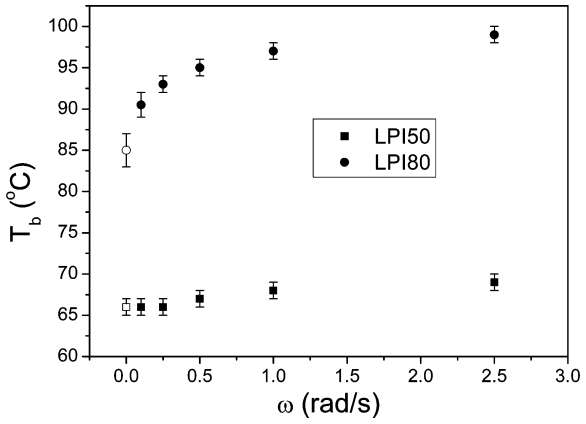


Figure 5. Shear quench experiments determined apparent binodal temperature as a function of the final frequency for LPI50 and LPI80. As a reference, the static cloud points of LPI50 and LPI80 are shown as open symbols.

above its static value (85.0 ± 2 °C). Consistent results have been obtained from other composition blends, as will be shown in Figure 8. These observed phenomena with different apparent phase boundary shifts may be rationalized by two different theories on the shear induced shift of the phase boundary between near- and off-critical blends. For near-critical blends, a useful starting point is the mode-coupling renormalization-group (MCRG) theory of the simple binary fluids under shear.[43−45] Since all the rheological measurements in this study were carried out under oscillatory shear, the maximum strain rate (for a given frequency and strain amplitude) instead of the shear rate is used, although it is understandable that the shear rate is the correct quantity which can be expressed in a kinetic equation for a theoretic analysis. However, in order to make a good comparison with many studies published on binary systems with oscillatory measurements, and also to make possible temperature and time (kinetics) dependent measurements of the system, the oscillatory measurement was selected in this study. According to MCRG theory, once $\dot{\gamma}\tau_\xi > 1$, where $\dot{\gamma}$ is the shear rate and τ_ξ is the characteristic relaxation time of concentration fluctuation, the concentration fluctuation should be distorted and shear induced mixing starts to happen. However, since $\tau_\xi \propto |T/T_c - 1|^{-3\nu}$ if we assume the symmetry in fluctuations in a two-phase region,[52,53] where T_c is the critical temperature, T is the experimental temperature, and ν is the Ising exponent, τ_ξ becomes smaller and smaller as the temperature moves away from T_c. Therefore, it is more difficult to suppress the concentration fluctuation by increasing the temperature quench depth. The maximum strain rates under an oscillatory shear of 0.1 and 2.5 rad/s are not too big, and the corresponding values are 0.01 and 0.25 s^{-1}, respectively. Consequently, we observed that the shift of the apparent binodal point is relatively small for LPI50 within our experimental conditions. For off-critical blends, the shift of the apparent binodal point under oscillatory shear should be even smaller if suppression of the concentration fluctuation effect is the main mechanism for the apparent shift of the binodal points. However, we observed a larger shift of the apparent binodal point as a function of the final frequency or shear rate. Therefore, we believe that this large shift of the apparent binodal point is due to the shear effect on the nucleation phenomena.[46−48] Generally, there exist two characteristic sizes for nucleation phase separation under shear,[49] R_c and R^*, where R_c is the critical radius of nucleation due to free energy barriers and R^* is the Taylor break-up size due to the rupture of droplets by shear flow. The observation of appreciable droplets of the new phase requires the critical droplet not to be suppressed by shear, which means $R_c < R^*$ must be satisfied. Since the critical size of nucleation, R_c, increases with deceasing quench depth and tends to infinity as the binodal point (or coexistence curve) is approached, the critical droplet can be easily suppressed by shear near the binodal phase boundary. Therefore, the oscillatory shear with low frequency may greatly shift the binodal point as shown in Figure 5.

The rheological investigation of spinodal point also showed distinct differences between near- and off-critical blends. Technically, each temperature ramp curve can be analyzed by the plot of $(G''^2/G'T)^{2/3}$ vs $1/T$ to acquire its corresponding spinodal point. In Ajji and Choplin's theory,[42] only the contribution from critical fluctuations is considered in their analysis and the shear suppression (or distortion) of critical fluctuations has been neglected. However, the global storage and loss modulus measured generally also included the contribution from the nucleation phase separation as displayed in off-critical blends. Besides, once we apply Ajji and Choplin's theory to off-critical blends, the assumption that the critical fluctuations at off-critical region are similar to that at the critical

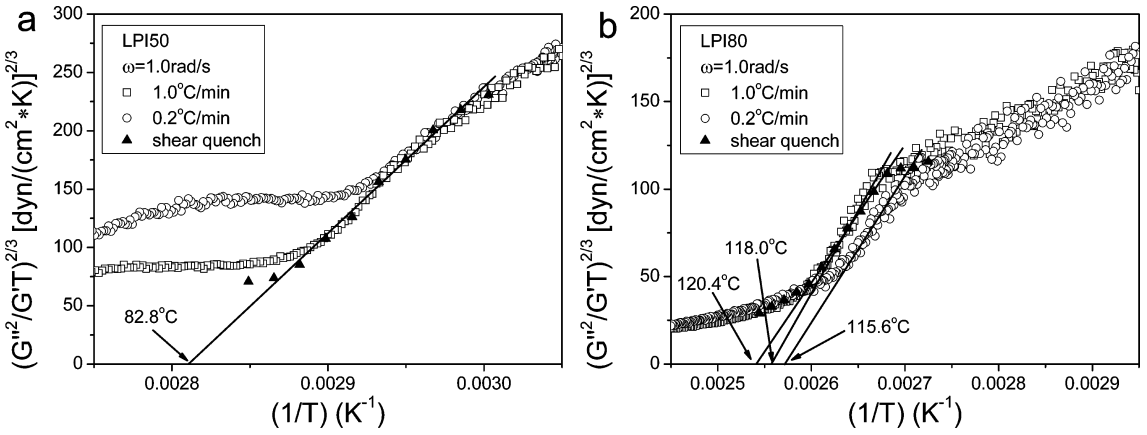


Figure 6. Plots of $\{G''^2/(G'T)\}^{2/3}$ and $\{G''^2(\omega,0)/[G'(\omega,0)T]\}^{2/3}$ versus $1/T$ in temperature ramp tests at a fixed frequency of 1.0 rad/s and different heating rates of 1.0 and 0.2 °C/min for (a) LPI50 and (b) LPI80.

dx.doi.org/10.1021/ma2021562 | Macromolecules 2012, 45, 1692−1700

region is needed. Figure 6 showed the plots of $(G''^2/G'T)^{2/3}$ vs $1/T$ for blends LPI50 and LPI80 at the frequency of 1.0 rad/s and different heating rates of 1.0 and 0.2 °C/min. In order to eliminate the influence of the contribution from nucleation phase separation on the extrapolated position of the spinodal point,[27] the shear quench experiment result $\{G''^2(\omega,0)/[G'(\omega,0)T]\}^{2/3}$, where $G'(\omega,0)^3$ and $G''(\omega,0)$ are the initial storage and loss modulus values during the dynamic time sweep after the shear quench from 25 rad/s to 1.0 rad/s at a given temperature, is also included. The essence of such a shear quench method is to measure the contribution only from critical fluctuations to the storage and loss modulus in the metastable region. For example, after the shear quench from 25 rad/s to 1 rad/s at 98 °C, the LPI80 blend will take a nucleation phase separation as shown in Figure 4b since it is in the metastable region at 1 rad/s." However, because of the slow kinetics of the nucleation phase separation, $G''(\omega,0)$ and $G'(\omega,0)$ have minimum contribution from the nucleation phase separation and are mainly affected by the critical fluctuations. From Figure 6 we observed that, for the LPI50 blend, since G' values in the linear part of the curve $(G''^2/G'T)^{2/3}$ vs $1/T$ basically come from the critical fluctuations near the critical region as shown in Figure 3a, the heating rate hardly changes the extrapolated position of the spinodal point and the shear quench method gives the same spinodal point (82.8 ± 2 °C) as shown in Figure 6a. In contrast, for LPI80 blend, both critical fluctuation and nucleation phase separation contributed to G' in the linear part of the curve $(G''^2/G'T)^{2/3}$ vs $1/T$. Furthermore, G' values which were used to estimate the spinodal point have their main contribution coming from the nucleation phase separation processes as have been discussed in Figure 3b; therefore, there is a strong heating rate (or time) dependence for the extrapolated spinodal point, and the shear quench method gives the highest spinodal point, 120.4 ± 2 °C. In fact, this value is in good agreement with the second transformation temperature (121 ± 1 °C) shown in Figure 4b. Again, it is found that the extrapolation was done mainly to the data from the temperature region between the binodal and spinodal point, which probably means that, for off-critical blends, by only going through into the metastable region and in the vicinity of the spinodal point the blend may be able to achieve a large enough concentration fluctuation. Figure 7 showed the extrapolated spinodal points from shear quench experiments as a function of the quenched final frequency for LPI50 and LPI80. The spinodal points obtained for both blends increase with frequency. Quantitatively, in the low frequency region (from 0.1 to1.0 rad/s) the shift of the spinodal point of LPI50 is more distinguished than that of LPI80, which probably means that the suppression of critical fluctuation is more serious for LPI50 than that for LPI80. For near-critical blend LPI50, the critical fluctuation near the phase boundary is rather strong so that it is more easily suppressed by the applied oscillatory shear. In contrast, for off-critical blend LPI80, the critical fluctuation in the metastable region is relatively weak; therefore, only under high frequency, e.g. 2.5 rad/s, the shift of the spinodal point is distinguishable. The composition discrepancy in the shift of the apparent binodal and spinodal points with frequency is more obvious as illustrated in Figure 8. All the data are obtained from shear quench experiments as described above. From Figure 8 we can observe that the slight shift of binodal points with frequency is accompanied by a large shift of spinodal points for three near-critical blends (LPI40, LPI50, and LPI60). In contrast, for four off-critical blends (LPI20, LPI30, LPI70, and LPI80), the shift of the binodal point with frequency is only a little larger than that of the spinodal point. Since the oscillatory shear induced shifts of the binodal point and spinodal point are quite different, especially for near-critical blends, it is found that there is no critical point at which the binodal curve contacts the spinodal curve at the frequency of 1.0 rad/s as shown in Figure 8. However, it is noteworthy to state that the rheologically determined phase boundary under the oscillatory shear frequency of 1.0 rad/s is the "apparent" value which included the coupling between the thermodynamics and the oscillatory shear flow. Due to the obvious shift of both binodal and spinodal points under oscillatory shear, we can conclude that, in order to acquire a phase diagram that can be compared with its static phase diagram of polymer blends by rheological measurements, extrapolations of both the binodal and spinodal point measurements to 0 rad/s are necessary. However, since there is no measurement if the frequency is set at 0 rad/s and there is no theory regarding the frequency extrapolation scheme of either the binodal or spinodal point, we are using the lowest frequency (0.1 rad/s) data for binodal and spinodal

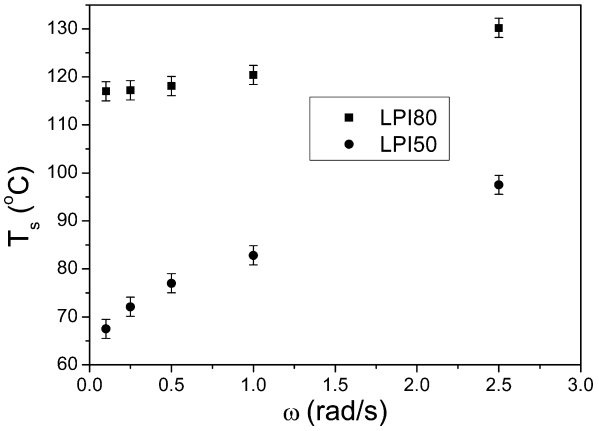


Figure 7. Frequency dependence on the extrapolated spinodal point for LPI50 and LPI80. All data are acquired by shear quench experiments.

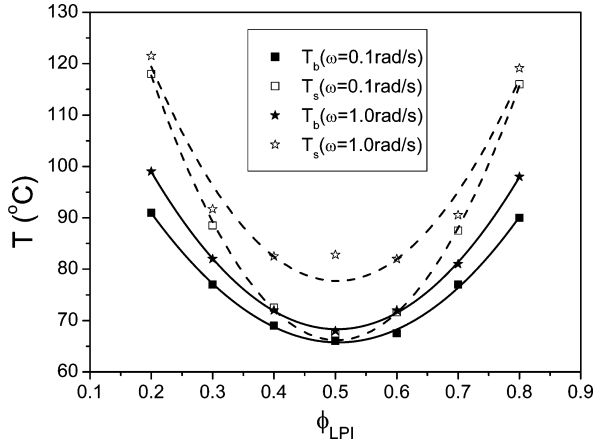


Figure 8. Shear quench experiments determined apparent binodal points (T_b) and spinodal points (T_s) at the final frequency of 0.1 and 1.0 rad/s. The dash and solid curves are the least-squares fit for polynomial equation through the experiment data and are only used to guide the eye.

dx.doi.org/10.1021/ma2021562 | Macromolecules 2012, 45, 1692–1700

points to compare with the static binodal points. Nevertheless, it is found from Figure 1 that the shifts of both the binodal and spinodal points are rather small, especially for near-critical blends, which confirms the statement that the rheologically determined phase boundary can eventually coincide with the static phase boundary determined by PCOM observations if the applied frequency is lowered.

CONCLUSION

The rheology of the elastomeric blend of PB/LPI in the miscible and immiscible region has been investigated as a function of temperature, composition, and oscillatory frequency. Our studies revealed that near- and off-critical blends displayed quite different viscoelastic properties in several aspects, such as temperature ramp curves, time evolution of storage modulus, and the shift of the apparent binodal and spinodal points under oscillatory shear. In the temperature ramp experiments, because the initial upturns of G' between near- and off-critical blends originate from different kinds of contributions, the temperature ramp curves displayed varying heating rate dependence. For near-critical blends, the basis of the upturn of G' is attributed to the increasingly large critical fluctuations near the critical region. Therefore, the heating rate independent upturn of G' can be observed. For off-critical blends, although the growing concentration fluctuations in the metastable region may elevate G' too, the main contribution to G' is the nucleation phase separation process. As a result, a slower heating rate gives a lower apparent binodal point. In the shear quench experiments, the time evolution of G' curves of near-critical blend LPI50 displayed two kinds of behaviors, which are believed to happen in the miscible and unstable region, respectively. For off-critical blend LPI80, the time evolution curves of G' displayed three different behaviors, which are believed to happen in the miscible, metastable, and unstable region, respectively. As for the shift of apparent binodal and spinodal points under the oscillatory shear, the differences in the shear induced mixing mechanism and the critical fluctuation amplitude near the binodal phase boundary should be considered. For near-critical blends, the metastable region is rather narrow and the critical fluctuation is relatively large. Therefore, the slight shift of the binodal point and large shift of the spinodal point may be interpreted by MCRG theory and by the shear induced distortion of critical fluctuations, respectively. For off-critical blends, its large shift of the binodal point and moderate shift of the spinodal point can be explained by the theory regarding nucleation under shear and by the relatively weak suppression of critical fluctuations in the metastable region, respectively. Finally, by lowering the measured frequency to a very small value (0.1 rad/s in this study) for the spinodal point, then the rheologically determined phase diagram is well consistent with the results obtained by optical microscopy observations.

AUTHOR INFORMATION

Corresponding Author

*Telephone: +86-10-82618533. Fax: +86-10-62521519. E-mail: xiadong@iccas.ac.cn; c.c.han@iccas.ac.cn.

ACKNOWLEDGMENTS

The authors are thankful for the funding support of NSFC Projects 50930002 and 51173195.

REFERENCES

(1) Utracki, L. A. *J. Rheol.* **1991**, *35*, 1615−1637.
(2) Palierne, J. F. *Rheol. Acta* **1990**, *29*, 204−214.
(3) Gramespacher, H.; Meissner, J. *J. Rheol.* **1992**, *36*, 1127−1141.
(4) Bousmina, M. *Rheol. Acta* **1999**, *38*, 73−83.
(5) Doi, M.; Ohta, T. *J. Chem. Phys.* **1991**, *95*, 1242−1248.
(6) Vinckier, I.; Moldenaers, P.; Mewis, J. *J. Rheol.* **1996**, *40*, 613−631.
(7) Chopra, D.; Vlassopoulos, D.; Hatzikiriakos, S. G. *J. Rheol.* **2000**, *44*, 27−45.
(8) Araujo, M. A.; Stadler, R. *Makromol. Chem* **1988**, *189*, 2169−2186.
(9) Mertsch, R.; Wolf, B. A. *Ber. Bunsen-Ges. Phys. Chem* **1994**, *98*, 1275−1280.
(10) Vlassopoulos, D.; Koumoutsakos, A.; Anastasiadis, S. H.; Hatzikiriakos, S. G.; Englezos, P. *J. Rheol.* **1997**, *41*, 739−755.
(11) Irving, J. B. *Viscosity of binary liquid mixtures: A survey of mixture equations; Report No. 630*. 1977, National Engineering Laboratory: East Kilbridge Glasgow, U.K.
(12) Kitade, S.; Takahashi, Y.; Noda, I. *Macromolecules* **1994**, *27*, 7397−7401.
(13) Stadler, R.; De Lucca Freitas, L.; Krieger, V.; Klotz, S. *Polymer* **1988**, *29*, 1643−1647.
(14) Mani, S.; Malone, M. F.; Winter, H. H. *J. Rheol.* **1992**, *36*, 1625−1649.
(15) Weis, C.; Leukel, J.; Borkenstein, K.; Maier, D.; Gronski, W.; Friedrich, C.; Honerkamp, J. *Polym. Bull.* **1998**, *40*, 235−241.
(16) Vinckier, I.; Laun, H. M. *Rheol. Acta* **1999**, *38*, 274−286.
(17) Friedrich, C.; Gleinser, W.; Korat, E.; Maier, D.; Weese, J. *J. Rheol.* **1995**, *39*, 1411−1425.
(18) Jeon, H. S.; Nakatani, A. I.; Han, C. C.; Colby, R. H. *Macromolecules* **2000**, *33*, 9732−9739.
(19) Niu, Y. H.; Yang, L.; Shimizu, K.; Pathak, J. A.; Wang, H.; Wang, Z. G. *J. Phys. Chem. B* **2009**, *113*, 8820−8827.
(20) Kapnistos, M.; Hinrichs, A.; Vlassopoulos, D.; Anastasiadis, S. H.; Stammer, A.; Wolf, B. A. *Macromolecules* **1996**, *29*, 7155−7163.
(21) Kapnistos, M.; Vlassopoulos, D.; Anastasiadis, S. H. *Europhys. Lett.* **1996**, *34*, 513−518.
(22) Niu, Y. H.; Wang, Z. G. *Macromolecules* **2006**, *39*, 4175−4183.
(23) Bousmina, M.; Lavoie, A.; Riedl, B. *Macromolecules* **2002**, *35*, 6274−6283.
(24) Li, R. M.; Yu, W.; Zhou, C. X. *J. Macromol. Sci. Phys* **2007**, *46*, 1051−1062.
(25) Sharma, J.; Clarke, N. *J. Phys. Chem. B* **2004**, *108*, 13220−13230.
(26) Zhang, R. Y.; Cheng, H.; Zhang, C. G.; Sun, T. C.; Dong, X.; Han, C. C. *Macromolecules* **2008**, *41*, 6818−6829.
(27) Zhang, R. Y.; Dong, X.; Wang, X.; Cheng, H.; Han, C. C. *Macromolecules* **2009**, *42*, 2873−2876.
(28) Madbouly, S. A.; Ougizawa, T. *Macromol. Chem. Phys.* **2004**, *205*, 1222−1230.
(29) Saito, S.; Koizumi, S.; Matsuzaka, K.; Suehiro, S.; Hashimoto, T. *Macromolecules* **2000**, *33*, 2153−2162.
(30) Jinnai, H.; Hasegawa, H.; Hashimoto, T.; Briber, R. M.; Han, C. C. *Macromolecules* **1993**, *26*, 182−188.
(31) Sakurai, S.; Jinnai, H.; Hasegawa, H.; Hashimoto, T.; Han, C. C. *Macromolecules* **1991**, *24*, 4839−4843.
(32) Jinnai, H.; Hasegawa, H.; Hashimoto, T.; Han, C. C. *Macromolecules* **1991**, *24*, 282−289.
(33) Laeuger, J.; Lay, R.; Gronski, W. *J. Chem. Phys.* **1994**, *101*, 7181−7184.
(34) Takeno, H.; Hashimoto, T. *J. Chem. Phys.* **1997**, *107*, 1634−1644.
(35) Matsuzaka, K.; Jinnai, H.; Koga, T.; Hashimoto, T. *Macromolecules* **1997**, *30*, 1146−1152.
(36) Kielhorn, L.; Colby, R. H.; Han, C. C. *Macromolecules* **2000**, *33*, 2486−2496.
(37) Laeuger, J.; Laubner, C.; Gronski, W. *Phys. Rev. Lett.* **1995**, *75*, 3576−3579.

(38) Khademzadeh Yeganeh, J.; Goharpey, F.; Foudazi, R. *Macromolecules* **2010**, *43*, 8670−8685.
(39) Tanaka, H. *J. Phys.: Condens. Matter* **2000**, *12*, R207−R264.
(40) Vlassopoulos, D.; Terakawa, T.; Fuller, G. G. *J. Rheol.* **2003**, *47*, 143−161.
(41) Fredrickson, G. H.; Larson, R. G. *J. Chem. Phys.* **1987**, *86*, 1553−1560.
(42) Ajji, A.; Choplin, L. *Macromolecules* **1991**, *24*, 5221−5223.
(43) Onuki, A.; Kawasaki, K. *Prog. Theor. Phys. Suppl.* **1978**, *64*, 436−441.
(44) Onuki, A.; Kawasaki, K. *Ann. Phys* **1979**, *121*, 456−528.
(45) Onuki, A.; Yamazaki, K.; Kawasaki, K. *Ann. Phys* **1981**, *131*, 217−242.
(46) Min, K. Y.; Goldburg, W. I. *Phys. Rev. Lett.* **1993**, *70*, 469−472.
(47) Min, K. Y.; Stavans, J.; Piazza, R.; Goldburg, W. I. *Phys. Rev. Lett.* **1989**, *63*, 1070−1073.
(48) Easwar, N. *Phys. Rev. Lett.* **1992**, *68*, 186−189.
(49) Onuki, A. *J. Phys.: Condens. Matter* **1997**, *9*, 6119−6158.
(50) Li, R. M.; Yu, W.; Zhou, C. X. *J. Macromol. Sci. Phys.* **2006**, *45*, 889−898.
(51) Krall, A. H.; Sengers, J. V.; Hamano, K. *Phys. Rev. E* **1993**, *48*, 357−376.
(52) Chou, Y. C.; Goldburg, W. I. *Phys. Rev. A* **1979**, *20*, 2105−2113.
(53) Knobler, C. M.; Wong, N. C. *J. Phys. Chem.* **1981**, *85*, 1972−1976.

Macromolecules

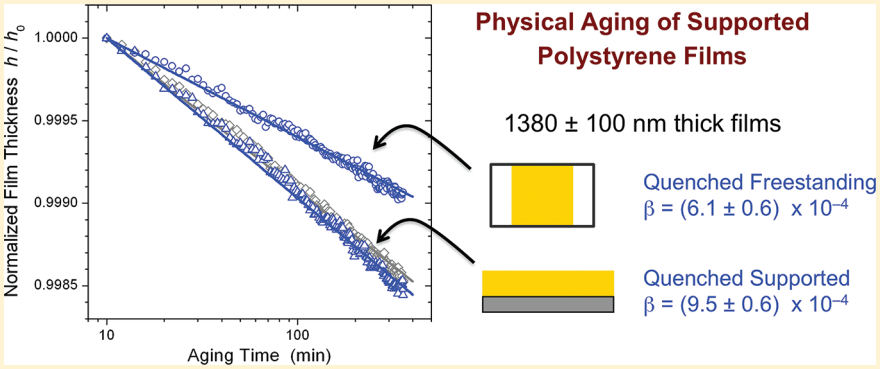
Article

pubs.acs.org/Macromolecules

Importance of Quench Conditions on the Subsequent Physical Aging Rate of Glassy Polymer Films

Laura A. G. Gray, Suk W. Yoon, William A. Pahner, James E. Davidheiser, and Connie B. Roth*

Department of Physics, Emory University, Atlanta, Georgia 30322, United States



ABSTRACT: For over a decade, research from the gas permeation community has observed faster physical aging rates with decreasing thickness of free-standing films, termed "accelerated aging". These deviations in the aging rate from bulk behavior occur at film thicknesses of several micrometers, the largest "confinement" length scale ever reported. Here we systematically address various possible causes of this phenomenon from differences in molecular structure, quench depth below T_g, experimental technique, sample preparation, and stresses on the film. We demonstrate that the physical aging of the material is strongly dependent on conditions during the formation of the glassy state. Although supported films do not display any film thickness dependence to their aging rate at this large length scale, films quenched in a free-standing state exhibit a strong thickness dependence. We suggest differing quench conditions may impose unintended stresses trapping the glassy films into different states (potential energy minima), dictating the subsequent physical aging rate.

INTRODUCTION

Glassy materials are inherently unstable, existing as "frozen liquids" below their glass transition temperature (T_g). Structurally trapped far from equilibrium, the system uses what little mobility that is available to decrease its free volume in a process called structural relaxation.[1−4] Associated with this slow densification of the material is a host of other property changes, such as increased modulus[5] and decreased permeability,[6,7] that fall under the general heading of physical aging. Within the potential energy landscape picture,[8,9] a glassy system can be viewed as being trapped within a local energy minimum with the aging process edging it deeper in toward a given minimum.[10] Numerous fundamental issues about the nature of glasses still remain unresolved:[11−13] What traps a glassy system within a particular energy minimum? What can be done to move the system within this potential energy landscape, say from one minimum to the next? For instance, what effect does stress or deformation have on the glassy material? And above all, what about the microscopic structure of the system determines the state, dynamics, and stability of the material?

Frequently, glassy systems have been studied in confined geometries as a means of probing the essential length scales and elucidating the underlying properties of the glass. Polymer thin films, with their ease of fabrication and industrial importance, have been a natural venue for such studies.[14,15] Over the past decade, several studies have been able to link various anomalous physical aging characteristics to boundary effects associated with the large surface-to-volume ratio of thin films.[16−23] For length scales of order 100 nm or less, the presence of a free surface or attractive substrate interaction can result in T_g changes near the boundary and hence concomitant changes in the physical aging rate.[20] However, there exists a second large body of work whose studies have observed deviations from bulk physical aging rates for film thicknesses already several micrometers in thickness.[6,7,24−32] The cause of these unresolved effects at this much larger length scale of several micrometers is the focus of the present study.

Since the mid-1990s, the gas permeation community has observed faster physical aging rates of micrometer thick polymer films with decreasing film thickness, a phenomenon which has been termed "accelerated" physical aging.[6,24,26−29,31] This effect has been seen for a range of high free volume, stiff backbone polymers, such as polysulfone (PSF),[6,24] polyimide,[6,24] poly(2,6-dimethyl-1,4-phenylene oxide) (PPO),[6] polynorborene,[25] and poly(1-trimethylsilyl-1-propyne)

Received: November 11, 2011
Revised: January 8, 2012
Published: January 27, 2012

 © 2012 American Chemical Society

(PTMSP).[26] These industrially relevant polymers used as gas separation membranes typically have relatively high T_gs in excess of 150 °C because they contain stiff aromatic groups within their backbone, limiting flexibility and causing poor packing that leads to the high free volume desired in these glassy films. The structural relaxation that occurs during aging of glassy materials causes only very small decreases in free volume (typically <1%);[4,30] however, because of the extreme sensitivity of gas permeability to free volume,[6] such a small decrease in free volume can easily lead to >50% decreases in permeability of gas across the membrane.[6,7] To increase gas throughput, the gas selective layer in separation membranes is made as thin as possible, easily extending below 100 nm in thickness.[7] Thus, the long-term stability of ultrathin glassy polymer membranes is of great interest.

What is most surprising about all these studies is that the accelerated physical aging behavior is observed at micrometer length scales; i.e., deviations of the aging rate from bulk behavior with decreasing film thickness occur already at film thicknesses of several micrometers.[6,24,26−29,31] This length scale is much larger than the ∼100 nm at which T_g, and other physical aging effects have been observed in polymers due to boundary effects.[16−18,20] Frequently, these studies at the smaller length scale observe reduced or suppressed physical aging, but they are typically done on flexible, C−C backbone polymers with lower T_gs and perhaps most significantly on films supported on rigid substrates. Thus, the cause of the anomalous physical aging characteristics at micrometer length scales continues to be a mystery, with numerous possibilities remaining unexplored. (1) Are there fundamental differences associated with the molecular structure of the polymer chain in how packing is frustrated in the glassy state? Do stiff backbone chains pack differently than flexible, C−C backbone polymers limited by bulky side groups leading to distinct free volume distributions that age differently? Perhaps the depth below T_g at which the material is aged plays a significant role (high vs low T_g polymers)? (2) Are there differences associated with the experimental techniques and sample preparation used? (3) Are there hidden or unintended stresses imparted to the films (e.g., spin-coating stresses)?

Here we have systematically addressed these questions and find that different quench conditions trap the glassy films into different states (potential energy minima) influencing the subsequent physical aging rate of the films. Our recently developed streamlined ellipsometry procedure[4] is able to characterize the physical aging rates of polymer films with varying chemical structure. We have found that faster physical aging rates with decreasing film thickness at large micrometer length scales can been observed in a flexible C−C backbone polymer, with a lower T_g than the polymers typical of separation membranes, when these films are quenched in a free-standing state matching the sample preparation procedure used in the gas permeation work. On the basis of process of elimination, we believe the film thickness dependence of the aging rates observed at micrometer length scales in the gas permeation studies is due to small differences in stress inadvertently applied to the free-standing films by the film support during the thermal quench. Since all thin films must be supported in some manner, understanding the unintended stresses resulting from thermal expansion mismatches between film and support are important. These studies indicate that even small stresses, only present during the formation of the glassy state, can strongly influence the subsequent stability of these films even when this stress is removed during the aging process. An improved understanding of how quench conditions affect glass formation could be used to control glassy film properties leading to materials with improved stability.

■ EXPERIMENTAL SECTION

Polystyrene (PS), M_n = 132 kg/mol and M_w = 289 kg/mol, and polysulfone (PSF), M_n = 26.9 kg/mol and M_w = 67.5 kg/mol, were purchased from Scientific Polymer Products. Films were made by dissolving PS in toluene or PSF in cyclopentanone and spin-coating the solutions onto freshly cleaved mica or silicon wafers with native oxide coatings. Unless otherwise specified, the spin speed was kept at ∼1500 rpm and the solution concentration was changed to vary the film thickness. All films were subsequently annealed for at least 12 h under vacuum at 120 °C for PS, or 150 °C for PSF,[33] in order to remove residual solvent from the films. Free-standing PS films were made by floating the films off the mica substrates onto the surface of water. The films were then captured onto either wire or rigid frames and allowed to dry thoroughly prior to measurement. Rectangular wire frames, approximately 2.0 × 2.5 cm in extent, were fashioned from 0.009 in. diameter stainless spring steel wire (0.23 mm diameter), following the description outlined in ref 28. Rigid frames with either a rectangular opening of 1.3 × 2.5 cm, or a circular opening of 1.9 cm in diameter, were punched from 0.020 in. (0.5 mm) thick nylon-6,6 or 0.004 in. (1.0 mm) thick stainless steel sheets. When capturing free-standing films onto the rectangular frames, the films were made to drape across the narrower distance, leaving the films held only from two ends. In contrast, the films captured on the circular frames were draped across the entire opening such that the film was supported on all sides.

Immediately prior to the physical aging measurements, the films, either free-standing or supported, were annealed above T_g for 30 min at a temperature T_0, typically 130 °C for PS or 215 °C for PSF, although this was varied as described in the Results and Discussion section. The films were then quenched to a temperature T_q, room temperature unless otherwise noted, by quickly removing the films from the oven and placing them in contact with a large thermal mass (aluminum block) equilibrated to T_q. To quench supported films at different controlled cooling rates, a series of base plates (all 44 cm^2 in area) were made of 1/16 in. thick copper (1.6 mm), 1/4 in. ceramic (6.4 mm), or 1/4 in. ceramic with a 0.02 in. (0.5 mm) Teflon bottom layer. For the free-standing films, rapid quenching of the film is already achieved by simply opening the door of the oven, allowing room temperature air to enter the chamber. Once quenched, the free-standing films were gently transferred to silicon wafers for the physical aging measurements by simply placing the free-standing films in contact with a wafer. Adhesion of the thin polymer film to the silicon wafer occurred immediately upon contact via van der Waals forces, allowing the film to then be cut free from the surrounding frame. Occasionally, a slow flow of dry nitrogen gas was blown over the sample to help the film make contact with the silicon wafer.

Immediately after quenching, the samples were placed on the ellipsometer hot stage (Instec HCS 302) that was pre-equilibrated at the aging temperature. The physical aging rates of the polymer films were characterized using spectroscopic ellipsometry (J.A. Woollam M-2000) by measuring the decrease in film thickness with aging time associated with the densification of the material during structural relaxation. Following the procedure we have developed in ref 4, the ellipsometric angles $\psi(\lambda)$ and $\Delta(\lambda)$ were collected every 2 min, averaging over a period of 30 s, throughout the aging measurement lasting several hours. The film thickness h and index of refraction $n(\lambda)$ were determined by fitting $\psi(\lambda)$ and $\Delta(\lambda)$, for λ = 400−1000 nm, to a layer model comprised of the polymer film, modeled as a Cauchy layer with $n(\lambda) = A + B/\lambda^2 + C/\lambda^4$, atop a silicon substrate with a 2 nm thick native oxide layer. The physical aging rate β can be determined by the slope of the normalized film thickness as a function of the logarithm of the aging time: $\beta = -1/h_0\ dh/d(\log t)$, where h_0 corresponds to the film thickness at an aging time of 10 min.[4] To minimize sample exposure to oxygen at high temperature, dry nitrogen gas (≥99.999%

purity) was continuously flowed through the sample chamber for aging runs above 80 °C.

RESULTS AND DISCUSSION

Chemical Structure: Stiff Backbone vs Flexible C−C Backbone with Bulky Side Groups. Using a common experimental technique, we compare the physical aging rate as a function of film thickness of two canonical polymers supported on silicon. Figure 1 plots the normalized film thickness, h/h_0, as a function of the logarithm of the aging time for films supported on silicon as measured by ellipsometry. Although not explicitly calculated, the aging rate is essentially the slope of the data plotted in this manner.[4] Polystyrene (Figure 1a) is a common C−C backbone polymer with a large bulky aromatic side group that limits packing (T_g = 100 °C, fractional free volume FFV = 0.176). Polysulfone (Figure 1b) is a common polymer used in gas separation membranes, whose packing is limited by the stiff aromatic groups along its backbone (T_g = 186 °C, FFV = 0.156). For each polymer, the same aging rate is observed independent of film thickness: for 570 ± 50 and 1400 ± 100 nm thick PS films aged at 65 °C for 6 h and for 400 ± 10 and 1000 ± 20 nm thick PSF films aged at 100 °C for 12 h. The aging temperature of 65 °C corresponds to the peak in aging rate for PS measured previously by our group using this ellipsometry technique,[4] while the aging temperature of 100 °C corresponds to the middle of the plateau in peak aging rate exhibited by PSF.[1]

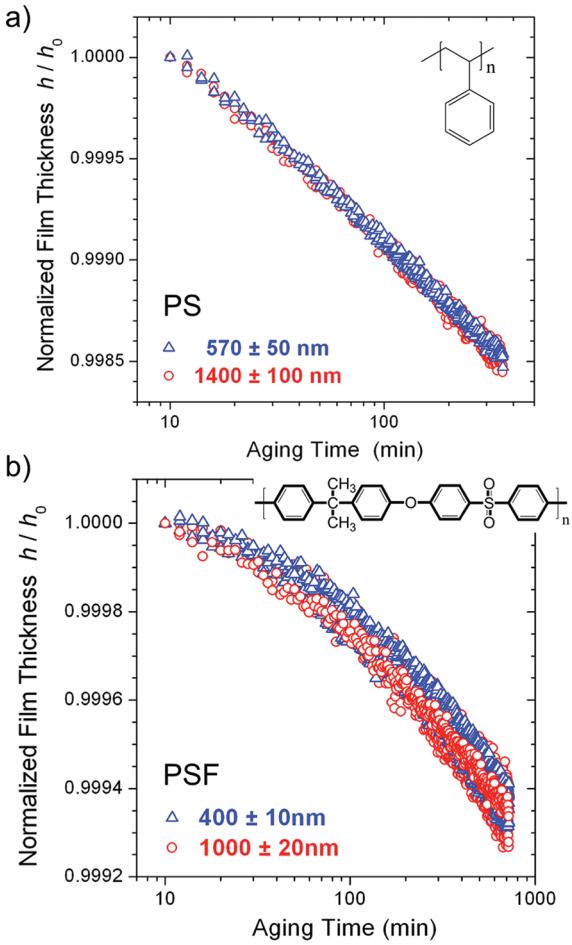


Figure 1. Semilog plot of normalized film thickness h/h_0 as a function of aging time for films supported on silicon. (a) For the PS films aged at 65 °C for 6 h, there are two data sets displayed for each film thickness range: 570 ± 50 nm (blue triangles) and 1400 ± 100 nm (red circles). (b) For the PSF films aged at 100 °C for 12 h, there are three data sets displayed for each film thickness range: 400 ± 10 nm (blue triangles) and 1000 ± 20 nm (red circles). In both cases, the data lie on top of each other, indicating no film thickness dependence to the aging rate. (These films were all quenched at a cooling rate of 50 °C/min.)

The limited data presented in Figure 1 are used to illustrate the aging behavior of supported films. We have recently published an extensive study on the film thickness and temperature dependence of the physical aging rate β for supported PS films.[20] The aging rate was found to be independent of film thickness for films between 100 and 2500 nm in thickness. Below ∼100 nm in film thickness, the aging rate was found to decrease at all aging temperatures in a manner consistent with a reduced T_g near the free surface, penetrating several tens of nanometers in from the boundary.[20] These results were consistent with other aging studies in the literature on supported films of PS,[16,18] poly(methyl methacrylate) (PMMA),[17,18,21] and poly(isobutyl methacrylate) (PiBMA).[34] As discussed above, the focus of the present study is on the thickness range of hundreds of nanometers to several micrometers and not on boundary effects in films less than ∼100 nm in thickness. The data presented in Figure 1b indicate that PSF films behave in a manner similar to that of PS films, showing no thickness dependence of the aging rate between 400 and 1000 nm in thickness when quenched and aged in a supported state.

The results presented in Figure 1 are significant when compared to those observations from the gas permeation community. Paul and co-workers have extensively characterized the aging characteristics of PSF films.[6,7,22,28−31,35] Using oxygen permeation, Huang and Paul observed faster aging rates with decreasing film thickness (i.e., accelerated aging) for PSF films below ∼4 μm in thickness measured at an aging temperature of 35 °C.[6] Similar behavior was seen with other polymers, e.g., polyimide and PPO,[6,7,29−31] and in studies by other groups.[24−27] The study that is most relevant to our results presented in Figure 1b is that by Huang and Paul, who observed the accelerated physical aging behavior using ellipsometry for PSF film thicknesses between 375 and 1000 nm,[29,31] which would appear to contradict our results. However, as we now address, these differences between our results presented in Figure 1 and those from the permeation community appear to be due to the details of sample preparation prior to the aging measurements. We note there are also recent measurements by Rowe et al.[22,35] on ultrathin PSF films that have observed decreases in the glassy relaxation time associated with physical aging for film thickness below ∼100 nm, which were linked to T_g reductions and boundary effects at these smaller length scales.

For the ellipsometry studies by Huang and Paul[29,31] in which faster physical aging rates were observed with decreasing film thickness for 375−1000 nm thick PSF films, the sample preparation procedure used was chosen to match that of the gas permeation studies as closely as possible.[6,28] Physical aging studies using gas permeation are typically initiated by annealing the films at an elevated temperature above T_g in a free-standing state held by a thin wire frame[28] and then quenching the films to room temperature prior to "masking" them for permeability measurements. The process of masking involves mounting the free-standing films onto anodized grids for support and sealing

dx.doi.org/10.1021/ma202493n | Macromolecules 2012, 45, 1701−1709

the perimeter of the films by an aluminum mask to create a well-defined surface area for exposure to the gas permeate.[6] The masking process can take ~20 min while sample mounting, conditioning, and measurement can last ~30 min. Thus, aging studies using gas permeation are typically carried out over many weeks or even months to ensure that the overall aging time is significantly longer than the individual measurement time. For the ellipsometry studies done by Huang and Paul, the PSF films were also annealed above T_g and then quenched in a free-standing state.[29,31] However, instead of masking, the films were instead gently transferred onto silicon wafers for the aging measurements in which ellipsometry was used to determine film thickness and index of refraction of the film every few days over many weeks. In between measurements, the samples were stored at the aging temperature of 35 °C. Physical aging rates determined from these ellipsometry measurements by Huang and Paul were found to be in good agreement with the gas permeation studies showing accelerated aging for thinner films.[29,31]

There are a number of important differences between our PSF aging measurements and those from Huang and Paul. We consider here which factors are important and affect the subsequent stability and mobility of the glassy state. The most significant factor, which we will demonstrate strongly affects the physical aging rate of the film, is the manner in which the films are held during the thermal quench that forms the glassy state. We discount differences in aging time and temperature because similar aging rates are obtained as a function of temperature for aging times between 6 and 24 h[4] and between 24 h and 12 days.[2]

Sample Geometry during Quench: Free-Standing vs Supported Films. By their very nature, thin films must be held in some fashion by an underlying support. Free-standing films are draped across a frame and held only by their edges, while supported films are those resting uniformly on an underlying material. Following the sample preparation procedure described by Huang and Paul,[6,28,29,31] we compare the physical aging rate of PS films quenched in a free-standing geometry held by a thin square wire frame (as described in ref 28) vs films quenched in a supported geometry on a silicon wafer. We chose to focus these studies on PS because of its ease of use in sample preparation and because it has been more extensively characterized by us[4,20] and in the literature.[2,36]

Figure 2 compares the physical aging behavior of PS films that have been thermally quenched under different conditions at the start of the aging measurement. The graphs plot the normalized film thickness, h/h_0, as a function of the logarithm of the aging time for films aged at 65 °C for 6 h. In Figure 2a, data for a 1260 nm thick PS film are shown, where the circles (upper line with slope corresponding to an aging rate $\beta = 6.0 \times 10^{-4}$) were obtained when the film was quenched in a free-standing state held by a square wire frame and then gently transferred to a silicon wafer for the aging measurement. The triangles (lower line with slope corresponding to an aging rate $\beta = 9.7 \times 10^{-4}$) were obtained when this same film was subsequently reannealed above T_g and quenched in a supported state on the silicon. For comparison, data for a 1210 nm thick PS film spin-coated directly onto silicon and quenched in a supported state are also shown (gray diamonds, $\beta = 9.2 \times 10^{-4}$). Similar measurements on multiple samples produced identical results. Physical aging rates for an average of five samples with film thicknesses of 1380 ± 100 nm gave $\beta = (6.1 \pm 0.6) \times 10^{-4}$ when quenched in a free-standing state and gently transferred onto silicon for aging, in comparison to a much faster aging rate of $\beta = (9.5 \pm 0.6) \times 10^{-4}$ for the same films reheated and quenched in a supported state. Measurements of additional films all quenched in a supported state, whether spin-coated directly onto silicon or floated from mica onto silicon and measured immediately or after multiple annealing repetitions, all resulted in the much faster aging rate of $\beta \approx 9.5 \times 10^{-4}$ when they are quenched on silicon in a supported state.

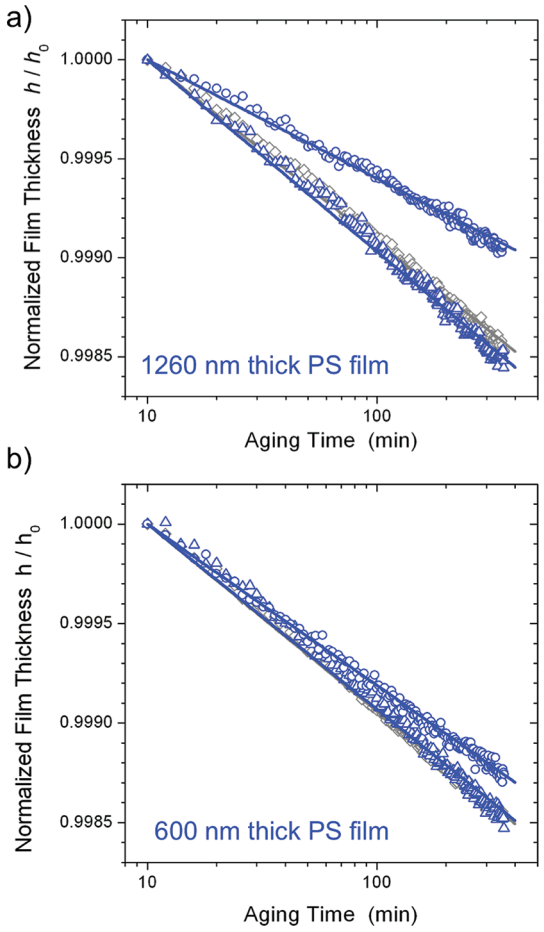


Figure 2. Semilog plot of normalized film thickness h/h_0 as a function of aging time comparing PS films quenched in a free-standing vs supported state; all films were subsequently aged in a supported state. Blue circles correspond to a 1260 nm (a) or 600 nm (b) thick PS film quenched in a free-standing state held by a wire frame and then gently transferred onto silicon for the aging measurement ($\beta = 6.0 \times 10^{-4}$ for 1260 nm and $\beta = 8.1 \times 10^{-4}$ for 600 nm). Blue triangles correspond to this same film subsequently reheated above T_g and quenched in a supported state prior to a second aging measurement ($\beta = 9.7 \times 10^{-4}$ for 1260 nm and $\beta = 9.3 \times 10^{-4}$ for 600 nm). Gray diamonds correspond to PS films spin-coated directly onto silicon and therefore also quenched in a supported state ($\beta = 9.2 \times 10^{-4}$ for 1210 nm and $\beta = 9.4 \times 10^{-4}$ for 460 nm). (The supported films were quenched at a cooling rate of 50 °C/min, while the free-standing films have an effective quench rate in excess of 30000 °C/min. See text for details.)

Figure 2b shows data corresponding to films thinner by a factor of 2. The circles (upper line, $\beta = 8.1 \times 10^{-4}$) were obtained when a 600 nm thick PS film was quenched in a free-standing state and gently placed onto a silicon wafer, while the triangles (lower line, $\beta = 9.3 \times 10^{-4}$) were obtained when the same film was subsequently reannealed above T_g and quenched in a supported state. The (barely visible) gray diamonds ($\beta =$

dx.doi.org/10.1021/ma202493n | Macromolecules 2012, 45, 1701–1709

9.4×10^{-4}) are for a 460 nm thick PS film spin-coated directly onto silicon and quenched in a supported state. An average of three samples with film thicknesses of 570 ± 50 nm gave $\beta = (8.1 \pm 0.6) \times 10^{-4}$ when quenched in a free-standing state and gently transferred onto silicon, relative to an aging rate of $\beta = (9.3 \pm 0.6) \times 10^{-4}$ for the same films reheated and quenched in a supported state. Clearly, the difference in physical aging rates between films quenched in a free-standing vs supported state is much less for the thinner (~600 nm thick) films.

The data shown in Figure 2 demonstrate that accelerated aging, i.e., faster physical aging rates for thinner films, is observed when PS films are quenched in a free-standing state, consistent with the measurements from the gas permeation community. However, no film thickness dependence to the aging rate is observed when the films are quenched in a supported state. This is consistent with oxygen permeation measurements of PMMA films by Baker et al., which saw no film thickness dependence to the aging behavior for films quenched in a supported state on mica and then floated, masked, and measured in a free-standing state.[4] Thus, the factor that affects the aging characteristics of the film is the state of the film during the thermal quench and formation of the glassy state. The state of the film in the glassy state during the aging measurement, free-standing vs supported, does not affect the physical aging rate.

Annealing Time: Residual Solvent or Relaxation of Spin-Coating Stresses? We attribute the differences in Figure 2 between the aging characteristics of films annealed and quenched in a free-standing or supported state to the thermal quenching process, and not to the annealing step, for reasons we now discuss. The adequate removal of residual solvent or relaxation of stresses from the spin-coating process has long been a concern in studies of ultrathin polymer films.[37−42] It is known that changes in T_g associated with nanoconfinement effects in films less than ~100 nm in thickness can be strongly suppressed by the presence of only a few wt % of intended (or unintended) solvent or other small molecule acting as a plasticizer.[43−45] The difference in physical aging rates observed between the free-standing and supported films cannot be attributed to the presence of residual solvent because all our films have been annealed for at least 12 h under vacuum at 120 °C, conditions which have been previously demonstrated to remove trace levels of solvent even for films as thick as 2500 nm.[4] It is also understood that spin-coating leads to extended chain conformations both globally and locally, with generally larger effects seen for larger spin speeds.[37,46,47] Previous studies have found distortions in global chain conformations to be unimportant to the T_g and physical aging behavior of ultrathin polymer films as these are local properties that are independent of chain length and molecular weight.[47−51] This is in contrast to properties such as dewetting[52,53] that depend on motion of the entire chain. Studies have found that local chain conformations can be easily relaxed by annealing films for ~20 min at T_g^{bulk} + 20 °C, resulting in samples with consistent T_g and physical aging values.[47,48,54] These are equivalent to the conditions originally proclaimed by Struik to be sufficient to erase prior thermal history and physical aging of the material, giving reproducible aging results.[1]

Regardless, we have varied the temperature and time of the annealing step above T_g prior to the aging measurements for both supported and free-standing films to further test and address these concerns. For supported PS films, we have annealed 1200 nm thick films for 25 min as low as 110 °C, $\beta = (9.2 \pm 0.6) \times 10^{-4}$, or as high as 170 °C, $\beta = (9.3 \pm 0.6) \times 10^{-4}$, and obtained physical aging rates within experimental error of the films annealed for 20 min at 120 °C, $\beta = (9.7 \pm 0.6) \times 10^{-4}$. Even PS films that have been extensively annealed at 150 °C under vacuum for 40−50 h, conditions which Napolitano and Wübbenhorst[55] have recently suggested result in chain adsorption to the substrate, did not affect the measured physical aging rate of the films.

For free-standing PS films, our ability to vary the annealing conditions was much more limited because hole formation due to thermal instability of the liquid films above T_g is prone to occur for long annealing times and higher temperatures.[56] No difference in aging rate was observed for free-standing films of the same thickness held on wire frames that were annealed above T_g between 120 and 125 °C for 15−30 min. For the free-standing films, we also investigated the influence of spin speed on the annealing step as free-standing films were found to thicken substantially overtime when held above T_g. PS films were spin-coated onto mica between 500 and 3000 rpm, using different solution concentrations, to achieve the same film thickness of 730 ± 40 nm. After annealing the films on mica at 120 °C for at least 12 h to remove residual solvent, they were floated onto wire frames and dried. The films were then further annealed at 120 °C for 20 min in a free-standing state, where they thickened to a final film thickness of 1200 ± 100 nm. Supported films, pinned to an underlying substrate, do not thicken when annealed above T_g. No clear relationship was found between spin speed and amount of film thickening that occurred in the free-standing films. For films spin coated between 500 and 3000 rpm, we obtained similar aging rates, within experimental error, for films of equivalent thickness. In summary, we observe no difference in aging rate for films of a given thickness that are annealed under different conditions, if they are all quenched to the same temperature T_q.

Thermal Quench: Differences in Heat Transfer between Free-Standing and Supported Films. From the above discussion, we conclude that the difference in aging rates between free-standing and supported films must result from the manner in which the films are held during the thermal quench. We consider now if differences in heat transfer could account for the observed effects. It is well-known, but little characterized, that cooling (quench) rate can strongly affect the glassy state formed.[2,3,9,11,57,58] At faster cooling rates, the material becomes kinetically trapped at higher temperatures forming a less stable glass. Thus, glasses formed at faster cooling rates would be expected to have faster physical aging rates, representative of the faster structural relaxation that is occurring in the material. At slower cooling rates, the more stable glasses would be expected to exhibit slower physical aging rates, with the theoretical limiting case of an equilibrium glass formed at an infinitely slow cooling rate.[3,11,59] In order to quantify this effect, we have characterized the physical aging rates of 1400 ± 45 nm thick supported PS films quenched through T_g at different rates. Figure 3 shows the effect of cooling rate on the physical aging rate of PS films held at an aging temperature of 65 °C that have been quenched at different rates: 1, 30, 75, and 135 °C/min.

Different cooling rates were obtained by changing the material and thickness of a base plate to which the silicon wafer and PS film were clamped. The entire base with the sample attached was placed in the oven at the annealing temperature of 135 °C to equilibrate the film. The temperature quench then

dx.doi.org/10.1021/ma202493n | Macromolecules 2012, 45, 1701−1709

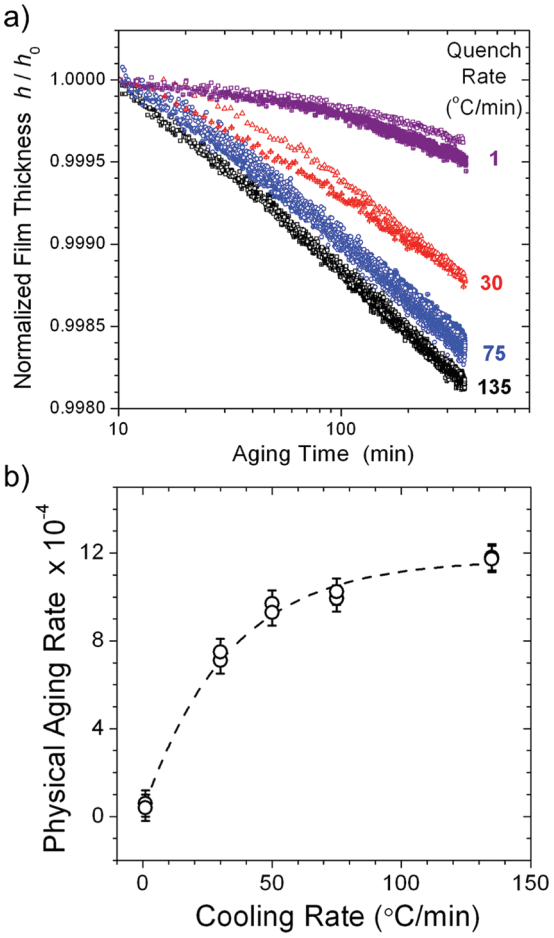


Figure 3. Supported PS films, 1400 ± 45 nm thick, aged at 65 °C for 6 h after being quenched through T_g at different cooling rates: 1, 30, 75, and 135 °C/min. (a) Semilog plot of normalized film thickness h/h_0 as a function of aging time. Two data sets are shown for each quench rate. (b) Plot of the measured physical aging rate as a function of cooling rate.

occurred by removing the base and sample from the oven and immediately placing the base in thermal contact with a large aluminum block equilibrated to 30 °C using a hot plate. Base plates were made of 1/16 in. thick copper, 1/4 in. ceramic, or 1/4 in. ceramic with a 0.02 in. Teflon bottom layer. The quench rate PS films supported on silicon experienced on each base was determined experimentally by attaching a thermocouple to the top of a bare silicon substrate. The silicon substrate was clipped to the base by a small brass clamp to ensure good thermal contact with the base. The temperature of the sample during the thermal quench was recorded every 1.0 s with the cooling rate through T_g (100 °C) defined as the slope of the recorded temperature vs time curve between 115 and 85 °C. For each base configuration, the quench rate was measured five times to obtain average cooling rates of 135 ± 13 °C/min for the copper base, 75 ± 2.5 °C/min for the ceramic base, and 30 ± 0.8 °C/min for the ceramic base with added Teflon layer. A cooling rate of 1 °C/min was obtained by doing a temperature controlled cool using our ellipsometer hot stage.

In Figure 3a, the aging rate is represented by the slope of the data in the semilog plot of normalized film thickness h/h_0 as a function of aging time. It is clear from the data that faster physical aging rates are observed for films cooled at faster rates as expected. Figure 3b plots the measured physical aging rates as a function of cooling rate, demonstrating that the aging rate saturates for quench rates in excess of ~100 °C/min. We note that the temperature T_q to which the films were cooled before being aged at 65 °C was varied between 25 and 65 °C and found to have no effect on the observed physical aging rate provided that the cooling rate was held constant. For supported films, the rate of heat transfer from the polymer film to the silicon wafer is dictated by the thermal properties of the silicon substrate and underlying base and is thus independent of polymer film thickness. Ultimately, the cooling rate of the sample is controlled by the large thermal mass of the base. For the supported film data presented in Figures 1 and 2, the underlying base during the thermal quench was actually a glass Petri dish, resulting in a reproducible quench rate of 50 °C/min for these samples.

Heat transfer to free-standing films, which have limited contact with their supports, is dominated by convection from the surrounding air. We cannot measure the cooling rate of free-standing films directly because of their fragility and that the attachment of a temperature probe would significantly alter the nature of the heat transfer to the film. However, we can use standard heat transfer methods to calculate the cooling rate of free-standing films. A lumped capacitance model, which assumes that the temperature across the entire PS film is constant at any given time, is an excellent approximation for our free-standing films because their thickness is so small. For this assumption to be valid, the Biot number, $Bi = h_{conv} L/k$, should be less than 0.1,[60] where h_{conv} is the average convective heat transfer coefficient, L is half the film thickness, and k is the thermal conductivity of PS. For the thickest films measured in the present study, $L \approx 800$ nm, and the thermal conductivity of PS at 100 °C is $k = 0.128$ W/(m K).[61] The average convective heat transfer coefficient is harder to estimate as the convective flow of the air next to the film will depend somewhat on the sample size and orientation.[60] We have estimated a value for h_{conv} by measuring the cooling rate of a 0.33 mm thick copper plate of equivalent lateral size to our free-standing films. From this we obtained a value of $h_{conv} = 10$ W/(m^2 K), which is in good agreement with expected values for natural convection of air, typically between 2 and 25 W/(m^2 K).[60] These values give a Biot number of $Bi < 0.0001$, making the lumped capacitance model an excellent approximation, even for PS films as thick as 100 μm.

For the lumped capacitance model,[60] the temperature response of the film, $T_{film}(t)$, is determined from an energy balance on the film, such that the rate of heat flux out of the film, $-h_{conv}A_{surf}(T_{flim} - T_\infty)$, is equated to the rate of heat loss in the film, $\rho(A_{surf}L)c_p\, dT_{film}/dt$. Here, A_{surf} refers to the total surface area of the free-standing film (both sides), such that the quantity $(A_{surf}L)$ is equal to the volume of the film, since L is only half the thickness. The density of the PS film (ρ = 1020 kg/m^3) and specific heat capacity at constant pressure c_p = 1838 J/(kg K) are readily found in handbooks.[61] Integrating this energy balance gives

$$\frac{T_{film}(t) - T_\infty}{T_0 - T_\infty} = \exp\left[-\frac{h_{conv}}{\rho L c_p} t\right]$$

where T_0 is the initial annealing temperature and T_∞ is the final film temperature at long times, equivalent to that of the surrounding air. We calculate an effective cooling rate through T_g for the free-standing films by determining the average slope

dx.doi.org/10.1021/ma202493n | Macromolecules 2012, 45, 1701–1709

of $T_{film}(t)$ between 115 and 85 °C, which mimics our experimental definition of cooling rate for the supported films.

If we now consider the 1260 nm thick PS film from Figure 2a and calculate an effective cooling rate for the thermal quench of the film in the free-standing state, we find that the cooling rate is of the order of 500 °C/s, i.e., 30000 °C/min. The quench rate for free-standing films is much faster than for supported films, yet films quenched in a free-standing state consistently give slower aging rates than films quenched in a supported state. Specifically for the data presented in Figure 2a, the 1260 nm thick PS film quenched in a free-standing state, with measured aging rate $\beta = 6.0 \times 10^{-4}$, had a cooling rate of ~30000 °C/min, in comparison to the same film later requenched in a supported state, which exhibited an aging rate of $\beta = 9.7 \times 10^{-4}$ and had a cooling rate of 50 °C/min. Recall that from the data shown in Figure 3, we found that faster cooling rates resulted in faster physical aging rates, up until ~100 °C/min at which the effect saturated. Thus, we can conclude that differences in cooling rate, resulting from how heat transfer occurs in free-standing and supported films, cannot explain the observed differences in physical aging rates presented in Figure 2a. For the thinner films shown in Figure 2b, the 600 nm thick free-standing film will experience a cooling rate that is basically double that of the 1260 nm thick film, while the cooling rate of the supported film will be unchanged. Thus, even though there is a film thickness dependence to the cooling rate experienced by free-standing films, with thinner films experiencing faster cooling rates, this also cannot be the cause of the faster (accelerated) aging rates observed for the thinner films quenched in a free-standing state. Even a 100 μm thick free-standing film would experience a cooling rate >400 °C/min, well above where the cooling rate dependence of the physical aging rate saturates.

Thermal Expansion Mismatch: Stresses Imparted during Thermal Quench. One final factor we have not yet considered is the effect on the physical aging rate resulting from unintended stresses imparted to the sample during the thermal quench due to differences in thermal expansion between the film and underlying support. It is well-known that thermal expansion mismatch between film and support can lead to stress buildup below T_g.[38,40,42,62,63] During a thermal cool, the PS film will try to thermally contract more than the underlying silicon because of its larger thermal expansion coefficient; α_{PS} is ~2 orders of magnitude greater than α_{Si}. The strain of the ~1 μm thick PS film is constrained to match the thermal expansion of the 500 μm thick silicon substrate:[64]

$$\frac{1-\nu_{PS}}{E_{PS}}\sigma_{PS} + \alpha_{PS}\Delta T = \alpha_{Si}\Delta T$$

This places the PS film under a biaxial tension given by

$$\sigma_{PS} = \frac{E_{PS}}{1-\nu_{PS}}(\alpha_{PS} - \alpha_{Si})\Delta T \quad (1)$$

for this plane-stress condition (no stress normal to the film plane, $\sigma_z = 0$, as the film is unconstrained in this direction).[64] In the literature, it is common to treat $\alpha_{Si} \approx 0$ such that this term is frequently omitted.[38,62] In addition, it should be explicitly recognized that the elastic modulus E_{PS} and Poisson's ratio ν_{PS} of PS, as well as α_{PS}, all depend on temperature[62] quite significantly through T_g, implying that the temperature change ΔT in eq 1 should be formally treated as an integral.[63]

The relevant temperature range to consider in eq 1 would normally be from the initial annealing temperature T_0 to the temperature the sample is quenched T_q: $\Delta T = T_0 - T_q$. However, Zhao et al. demonstrated that no stress builds up in the film above T_g, i.e., as long as the film is an equilibrium liquid.[63] This is consistent with our experimental observations, described above, in which varying the annealing temperature T_0 did not affect the measured physical aging rate. Consequently, the upper end of the temperature range in eq 1 should be replaced by a temperature close to T_g. We note that for a faster cooling rate the PS film will fall out of equilibrium sooner such that stress may start to build up in the film a few degrees earlier. The shift in T_g with cooling rate is only 3−4 °C per decade of cooling rate.[65] Because the film modulus E_{PS} is several orders of magnitude smaller near T_g than at lower temperatures in the glassy state,[62] the precise value of the upper temperature considered in eq 1 does not substantially affect the predicted stress. The lower end of the temperature range in eq 1 can also be replaced because any stress built up in the film when cooled for a short period of time to a temperature T_q below the aging temperature, T_{aging}, will be relieved when the sample is returned to T_{aging}. This reasoning is consistent with our experimental observations that varying T_q, while keeping the cooling rate constant, did not affect the measured aging rate of the film. Thus, in eq 1, the relevant temperature range to consider is $\Delta T = T_g - T_{aging}$.

On the basis of eq 1 for a temperature range $\Delta T = T_g - T_{aging}$, we calculate that the tensile stress imparted to a PS film supported on silicon during the thermal quench is ~12 MPa. This is in good agreement with the 15 MPa residual thermal stress measured by Chung et al.[40] for a PS film cooled while supported on mica. Although still below the yield stress of PS, this strong tensile stress could be expected to affect the subsequent physical aging rate of the film. We note that there is no film thickness dependence to this residual thermal stress for supported films, which is consistent with our experimental observations that the physical aging rate of PS films cooled in a supported state is independent of film thickness for films greater than 100 nm.[20]

For free-standing films held by the wire frame, the PS films are only attached on two sides, draped across the narrower width of the rectangular frame. Although it is not possible to directly calculate the stress imparted to the free-standing films by the wire frame during cooling, we can rationalize the frame's impact on the film as follows. The thin wire frame made of 0.009 in. diameter spring steel flexes slightly as the film becomes taut above T_g, an observation described by Huang and Paul.[28] As such, the wire frame effectively acts as a small spring pulling on the two ends of the film with some force $F = kx$ that will depend on the displacement x of the frame and some effective spring constant k. Unfortunately, the displacement is too small for us to characterize experimentally. The stress (uniaxial tension) applied to the film by the wire frame will be given by $\sigma = F/A = F/(hw)$, where the cross-sectional area A of the film is equal to the film thickness h times the film width w. Thus, we expect the stress imparted to free-standing films by the wire frame to depend on film thickness and get larger with decreasing thickness.

Many studies have investigated how mechanical stress and deformation enhance mobility of glassy systems. This is an active field of research with some commonalities found between polymer glasses, colloidal glasses, and jammed granular systems.[12] One of the big outstanding questions in

dx.doi.org/10.1021/ma202493n | Macromolecules 2012, 45, 1701−1709

this field is to what extent can mechanical deformations or stress act to "rejuvenate" a glass (make it appear younger) vs "overage" a glass (speed up the aging process).[10,11,13] In virtually all these studies, the initial glass is formed stress free, and then the mobility or aging behavior is investigated by subjecting the glass to various types of stresses. Very few studies, by comparison, have looked at how stress present during the formation of the glassy state affects the subsequent mobility, or physical aging, of the glass. The closest study for comparison with our free-standing films is by Shelby and Wilkes on uniaxially hot drawn PS and polycarbonate samples.[66−68] In their study, PS was elongated above T_g and cooled under tension; the physical aging rate was then measured in a stress-free state using dilatometry. The aging rate of the stressed samples was found to increase by 50% with increasing tension.[66] The effect also appeared to saturate, with further stress not increasing the aging rate beyond a certain point.

We now return to the results presented in Figure 2 and compare our physical aging rates observed for films quenched in free-standing vs supported states. The 1260 nm thick PS film quenched in a free-standing state would be expected to experience the least amount of stress. Its aging rate of $\beta = 6.0 \times 10^{-4}$ is quite close to that of (stress-free) bulk PS as measured by dilatometry, $\beta = (6.8 \pm 0.3) \times 10^{-4}$, for an aging period of ~1 day at 65 °C.[2] On average, 1380 ± 100 nm thick films quenched in a free-standing state gave aging rates of $\beta = (6.1 \pm 0.6) \times 10^{-4}$, and we have previously demonstrated in ref 4 that this ellipsometry method of measuring physical aging should be comparable to volume dilatometry. The 600 nm thick PS film quenched in a free-standing state on the wire frame is expected to be subjected to a stress that is approximately twice as large as that for 1260 nm thick films because the cross-sectional area of the film has been reduced by a factor of 2. Its aging rate of $\beta = 8.1 \times 10^{-4}$ is significantly higher and quite close to that of supported films known to experience a large (thickness independent) stress during cooling due to the thermal expansion mismatch with the substrate. On average, 570 ± 50 nm thick films quenched in a free-standing state gave aging rates of $\beta = (8.1 \pm 0.6) \times 10^{-4}$, quite close to the aging rates of supported films, $\beta = (9.4 \pm 0.6) \times 10^{-4}$, which are independent of film thickness. From our thickest free-standing quenched films, which we believe experience a sufficiently low stress to be comparable to stress-free bulk PS, to supported films, which experience the largest stress, we observe an ~50% increase in physical aging rate, in good agreement with the results by Shelby and Wilkes[66] on uniaxially hot drawn PS.

This analysis strongly suggests that the cause of the accelerated (faster) physical aging observed for thinner films quenched on free-standing wire frames is due to an increased stress experienced by the thinner films due to the springlike nature of the wire frame and arising from a decrease in the cross-sectional area of the film. To try to verify this conclusion, we have fabricated rigid frames for free-standing films that do not flex in response to the tension of the film by punching rectangular or circular openings into 0.020 in. thick nylon-6,6 and 0.004 in. thick stainless steel sheets. For this type of frame, the applied stress due to the PS film during the thermal quench can be calculated following the same procedure used to determine the stress applied to the supported films. For a free-standing film draped across the rectangular opening of a rigid frame with the film only held on two sides, the uniaxial tension applied to the PS film due to the thermal expansion mismatch between the film and the frame is given by[64]

$$\sigma_{PS} = E_{PS}(\alpha_{PS} - \alpha_{frame})\Delta T$$

For a circular opening of a rigid frame, with the film spanning the entire opening, the biaxial tension applied to the PS film is actually equivalent to that experienced by the supported films and is given by[64]

$$\sigma_{PS} = \frac{E_{PS}}{1 - \nu_{PS}}(\alpha_{PS} - \alpha_{frame})\Delta T$$

Note that, in contrast to the wire frames, the stress experienced by the PS films during cooling on either geometry of the rigid frames, due to thermal expansion mismatch between film and support, is predicted to be independent of film thickness.

After testing an extensive number of free-standing films quenched on rigid nylon or stainless steel frames with both rectangular and circular openings, we were unfortunately not able to obtain reproducible aging rates for nominally identical samples. We observed that the free-standing films supported on rigid frames wrinkled extensively, much more than the films on the wire frames. Although the free-standing films cooled through T_g in a fraction of a second as they were exposed to room temperature air, the wrinkling did not begin forming until a few seconds after the oven door had been opened. Because of their larger thermal mass, the rigid frames cooled at a slower rate and thus start to thermally contract only after the polymer film had turned glassy. As the frame thermally contracts, the glassy polymer film wrinkled and buckled extensively. In contrast, the free-standing films held on the wire frames experienced a small tension keeping the films reasonably taut during cooling. Wrinkling persisted on the rigid frames even when the samples were cooled slower, at a controlled 10 °C/min rate, using a specially designed chamber to cool the air surrounding the film and frame at this controlled rate. We believe the wrinkling and buckling that the free-standing films on the rigid frames experience lead to random stresses in the film that vary significantly from sample to sample and is likely responsible for the wide range of aging rates observed. Future efforts will focus on investigating the physical aging of glassy polymer films formed under different controlled stress conditions.

■ CONCLUSIONS

We have performed a systematic assessment of factors affecting the physical aging rate of micrometer thick polymer films and demonstrated that physical aging is dictated by conditions during the formation of the glassy state. Using ellipsometry to characterize the time-dependent decrease in film thickness that results from the increase in average film density during aging, we determined the physical aging rate of polymer films thermally quenched under different conditions. Although all films are subsequently aged in a supported state, we observed significant differences between films quenched in a free-standing compared to supported state. Films quenched in a free-standing state exhibit a strong thickness dependence to their physical aging rate at micrometer length scales, an order of magnitude or two larger than thicknesses where nanoconfinement effects of the glass transition and modulus are typically observed. In contrast, supported films do not display any film thickness dependence to their aging rate at this large length scale. This phenomenon is not affected by differences in molecular structure, annealing temperature and time above T_g,

or quench depth below T_g. Instead, we argue that different sample geometries inadvertently impose small differences in stress during vitrification that can trap the glassy films into different states (potential energy minima), strongly affecting the subsequent physical aging rate of the films.

AUTHOR INFORMATION

Corresponding Author

*E-mail: cbroth@emory.edu.

ACKNOWLEDGMENTS

We thank Justin Pye for useful discussions and acknowledge financial support from the Petroleum Research Fund (Grant PRF-48927-DN17) and Emory University.

REFERENCES

(1) Struik, L. C. E. *Physical Aging in Amorphous Polymers and Other Materials*; Elsevier Scientific Publishing Co.: Amsterdam, 1978.
(2) Greiner, R.; Schwarzl, F. R. *Rheol. Acta* **1984**, *23*, 378−395.
(3) Hutchinson, J. M. *Prog. Polym. Sci.* **1995**, *20*, 703−760.
(4) Baker, E. A.; Rittigstein, P.; Torkelson, J. M.; Roth, C. B. *J. Polym. Sci., Part B: Polym. Phys.* **2009**, *47*, 2509−2519.
(5) Simon, S. L. In *Encyclopedia of Polymer Science and Technology*; Kroschwitz, J., Ed.; Wiley: New York, 2002.
(6) Huang, Y.; Paul, D. R. *Polymer* **2004**, *45*, 8377−8393.
(7) Huang, Y.; Paul, D. R. *Ind. Eng. Chem. Res.* **2007**, *46*, 2342−2347.
(8) Stillinger, F. H. *Science* **1995**, *267*, 1935−1939.
(9) Debenedetti, P. G.; Stillinger, F. H. *Nature* **2001**, *410*, 259−267.
(10) Lacks, D. J.; Osborne, M. J. *Phys. Rev. Lett.* **2004**, *93*, 255501.
(11) McKenna, G. B. *J. Phys.: Condens. Matter* **2003**, *15*, S737−S763.
(12) Roth, C. B. *J. Polym. Sci., Part B: Polym. Phys.* **2010**, *48*, 2558−2560.
(13) Lee, H. N.; Ediger, M. D. *Macromolecules* **2010**, *43*, 5863−5873.
(14) Roth, C. B.; Dutcher, J. R. *J. Electroanal. Chem.* **2005**, *584*, 13−22.
(15) Priestley, R. D. *Soft Matter* **2009**, *5*, 919−926.
(16) Kawana, S.; Jones, R. A. L. *Eur. Phys. J. E* **2003**, *10*, 223−230.
(17) Priestley, R. D.; Ellison, C. J.; Broadbelt, L. J.; Torkelson, J. M. *Science* **2005**, *309*, 456−459.
(18) Priestley, R. D.; Broadbelt, L. J.; Torkelson, J. M. *Macromolecules* **2005**, *38*, 654−657.
(19) Koh, Y. P.; Simon, S. L. *J. Polym. Sci., Part B: Polym. Phys.* **2008**, *46*, 2741−2753.
(20) Pye, J. E.; Rohald, K. A.; Baker, E. A.; Roth, C. B. *Macromolecules* **2010**, *43*, 8296−8303.
(21) Fukao, K.; Sakamoto, A. *Phys. Rev. E* **2005**, *71*, 041803.
(22) Rowe, B. W.; Freeman, B. D.; Paul, D. R. *Polymer* **2009**, *50*, 5565−5575.
(23) Napolitano, S.; Wübbenhorst, M. *Polymer* **2010**, *51*, 5309−5312.
(24) Pfromm, P. H.; Koros, W. J. *Polymer* **1995**, *36*, 2379−2387.
(25) Dorkenoo, K. D.; Pfromm, P. H. *J. Polym. Sci., Part B: Polym. Phys.* **1999**, *37*, 2239−2251.
(26) Dorkenoo, K. D.; Pfromm, P. H. *Macromolecules* **2000**, *33*, 3747−3751.
(27) McCaig, M. S.; Paul, D. R. *Polymer* **2000**, *41*, 629−637.
(28) Huang, Y.; Paul, D. R. *J. Membr. Sci.* **2004**, *244*, 167−178.
(29) Huang, Y.; Paul, D. R. *Macromolecules* **2005**, *38*, 10148−10154.
(30) Huang, Y.; Wang, X.; Paul, D. R. *J. Membr. Sci.* **2006**, *277*, 219−229.
(31) Huang, Y.; Paul, D. R. *Macromolecules* **2006**, *39*, 1554−1559.
(32) Huang, Y.; Paul, D. R. *J. Polym. Sci., Part B: Polym. Phys.* **2007**, *45*, 1390−1398.
(33) Even though 150 °C is below the T_g of PSF (186 °C), this annealing temperature was chosen to match the work by Huang and Paul[6,28] and is sufficient to remove any residual solvent from the films.
(34) Ellison, C. J.; Kim, S. D.; Hall, D. B.; Torkelson, J. M. *Eur. Phys. J. E* **2002**, *8*, 155−166.
(35) Rowe, B. W.; Pas, S. J.; Hill, A. J.; Suzuki, R.; Freeman, B. D.; Paul, D. R. *Polymer* **2009**, *50*, 6149−6156.
(36) Simon, S. L.; Sobieski, J. W.; Plazek, D. J. *Polymer* **2001**, *42*, 2555−2567.
(37) Frank, C. W.; Rao, V.; Despotopoulou, M. M.; Pease, R. F. W.; Hinsberg, W. D.; Miller, R. D.; Rabolt, J. F. *Science* **1996**, *273*, 912−915.
(38) Richardson, H.; Carelli, C.; Keddie, J. L.; Sferrazza, M. *Eur. Phys. J. E* **2003**, *12*, 437−440.
(39) Richardson, H.; Lopez-Garcia, I.; Sferrazza, M.; Keddie, J. L. *Phys. Rev. E* **2004**, *70*, 051805.
(40) Chung, J. Y.; Chastek, T. Q.; Fasolka, M. J.; Ro, H. W.; Stafford, C. M. *ACS Nano* **2009**, *3*, 844−852.
(41) Reiter, G.; Napolitano, S. *J. Polym. Sci., Part B: Polym. Phys.* **2010**, *48*, 2544−2547.
(42) Thomas, K. R.; Steiner, U. *Soft Matter* **2011**, *7*, 7839−7842.
(43) Ellison, C. J.; Ruszkowski, R. L.; Fredin, N. J.; Torkelson, J. M. *Phys. Rev. Lett.* **2004**, *92*, 095702.
(44) Riggleman, R. A.; Yoshimoto, K.; Douglas, J. F.; de Pablo, J. J. *Phys. Rev. Lett.* **2006**, *97*, 045502.
(45) Kim, S.; Mundra, M. K.; Roth, C. B.; Torkelson, J. M. *Macromolecules* **2010**, *43*, 5158−5161.
(46) Kosbar, L. L.; Kuan, S. W. J.; Frank, C. W.; Pease, R. F. W. *ACS Symp. Ser.* **1989**, *381*, 95−111.
(47) Mundra, M. K.; Ellison, C. J.; Behling, R. E.; Torkelson, J. M. *Polymer* **2006**, *47*, 7747−7759.
(48) Fakhraai, Z.; Sharp, J. S.; Forrest, J. A. *J. Polym. Sci., Part B: Polym. Phys.* **2004**, *42*, 4503−4507.
(49) Sharp, J. S.; Forrest, J. A. *Phys. Rev. Lett.* **2003**, *91*, 235701.
(50) Prucker, O.; Christian, S.; Bock, H.; Ruhe, J.; Frank, C. W.; Knoll, W. *Macromol. Chem. Phys.* **1998**, *199*, 1435−1444.
(51) Ellison, C. J.; Mundra, M. K.; Torkelson, J. M. *Macromolecules* **2005**, *38*, 1767−1778.
(52) Reiter, G.; Hamieh, M.; Damman, P.; Sclavons, S.; Gabriele, S.; Vilmin, T.; Raphael, E. *Nature Mater.* **2005**, *4*, 754−758.
(53) Raegen, A.; Chowdhury, M.; Calers, C.; Schmatulla, A.; Steiner, U.; Reiter, G. *Phys. Rev. Lett.* **2010**, *105*, 227801.
(54) Raegen, A. N.; Massa, M. V.; Forrest, J. A.; Dalnoki-Veress, K. *Eur. Phys. J. E* **2008**, *27*, 375−377.
(55) Napolitano, S.; Wübbenhorst, M. *Nature Commun.* **2011**, *2*, 260.
(56) Roth, C. B.; Dutcher, J. R. *J. Polym. Sci., Part B: Polym. Phys.* **2006**, *44*, 3011−3021.
(57) Cangialosi, D.; Wübbenhorst, M.; Groenewold, J.; Mendes, E.; Schut, H.; van Veen, A.; Picken, S. J. *Phys. Rev. B* **2004**, *70*, 224213.
(58) Hadac, J.; Slobodian, P.; Riha, P.; Saha, P.; Rychwalski, R. W.; Emri, I.; Kubat, J. *J. Non-Cryst. Solids* **2007**, *353*, 2681−2691.
(59) Swallen, S. F.; Kearns, K. L.; Mapes, M. K.; Kim, Y. S.; McMahon, R. J.; Ediger, M. D.; Wu, T.; Yu, L.; Satija, S. *Science* **2007**, *315*, 353−356.
(60) Incropera, F. P.; Dewitt, D. P.; Bergman, T. L.; Lavine, A. S. *Fundamentals of Heat and Mass Transfer*, 6th ed.; John Wiley & Sons: Hoboken, NJ, 2007.
(61) Brandrup, J., Immergut, E. H., Grulke, E. A., Eds. *Polymer Handbook*, 4th ed.; Wiley: New York, 1999.
(62) Beaucage, G.; Composto, R.; Stein, R. S. *J. Polym. Sci., Part B: Polym. Phys.* **1993**, *31*, 319−326.
(63) Zhao, J. H.; Kiene, M.; Hu, C.; Ho, P. S. *Appl. Phys. Lett.* **2000**, *77*, 2843−2845.
(64) Benham, P. P.; Crawford, R. J.; Armstrong, C. G. *Mechanics of Engineering Materials*, 2nd ed.; Addison Wesley Longman: London, 1996.
(65) Hutchinson, J. M. *J. Therm. Anal. Calorim.* **2009**, *98*, 579−589.
(66) Shelby, M. D.; Wilkes, G. L. *Polymer* **1998**, *39*, 6767−6779.
(67) Shelby, M. D.; Wilkes, G. L. *J. Polym. Sci., Part B: Polym. Phys.* **1998**, *36*, 2111−2128.
(68) Shelby, M. D.; Hill, A. J.; Burgar, M. I.; Wilkes, G. L. *J. Polym. Sci., Part B: Polym. Phys.* **2001**, *39*, 32−46.

Macromolecules

Note

pubs.acs.org/Macromolecules

Synthesis and Photovoltaic Properties of Low Band Gap Polymers Containing Benzo[1,2-*b*:4,5-*c*′]dithiophene-4,8-dione

Jiamin Cao,[†,‡] Wei Zhang,[‡] Zuo Xiao,[‡] Lingyan Liao,[‡] Weiguo Zhu,*[,†] Qiqun Zuo,[§] and Liming Ding*[,‡]

[†]Key Lab of Environment-Friendly Chemistry and Application of the Ministry of Education, College of Chemistry, Xiangtan University, Xiangtan 411105, China

[‡]National Center for Nanoscience and Technology, No. 11 Beiyitiao, Zhongguancun, Beijing 100190, China

[§]Jiahong Optoelectronics, Suzhou 215151, China

Supporting Information

As the energy crisis is becoming a serious problem all over the world, cheap production of electricity from solar energy has attracted more and more attention. Among all the photovoltaic devices, polymer bulk heterojunction solar cells (PSCs) have shown many advantages, such as low fabrication cost, excellent mechanical flexibility and lightweight. The active layer of PSCs is based on the blend of a conjugated polymer as the electron donor and a fullerene derivative as the electron acceptor.[1] Up to now, poly(3-hexylthiophene) (P3HT) is one of the best commercialized donor materials. P3HT/$PC_{61}BM$-based PSCs have achieved power conversion efficiencies (PCE) up to ∼4−5%.[2] However, P3HT only absorbs part of the solar emission (300−600 nm) and its high-lying HOMO energy level (−4.76 eV)[3] limits the open circuit voltage (V_{oc}) of the solar cells. Therefore, design and synthesis of new conjugated polymers with deep HOMO levels for high V_{oc} and low bandgaps for broad absorption, as well as high mobilities and good solubilities, are essential for obtaining high performance PSCs.[4]

A recent strategy to satisfy these requirements above is to design conjugated copolymer containing alternating donor and acceptor units in the polymer backbone. Yu et al. reported the D−A polymers based on poly(benzo-[1,2-*b*:4,5-*b*′]-dithiophene)-*alt*-(thieno[3,4-*b*]thiophene) (PBDTTT) with efficiency up to 7.73%.[5] However, the synthesis of the monomer thieno[3,4-*b*]thiophene in PBDTTT is very tedious and with low yield. Li et al. reported a new strong electron-withdrawing unit naphtho[2,3-*c*]thiophene-4,9-dione (NTDO), which was synthesized in short route and with high yield. The copolymer with NTDO as acceptor unit has relatively lower HOMO (−5.52 eV) and gives a high PCE of 5.21%.[6] Inspired by Li's work, we designed a new acceptor unit benzo[1,2-*b*:4,5-*c*′]-dithiophene-4,8-dione (BDTD) by replacing the benzene ring of NTDO with thiophene ring because the fused thiophene ring systems are well-known to stabilize the quinoidal structure and can efficiently reduce the bandgap (Scheme 1).[7] Furthermore, BDTD unit possesses the similar structure as thieno[3,4-*b*]thiophene but more electron deficient. In this work, we synthesized two low-bandgap polymers **P1** and **P2** by copolymerization of BDTD with benzo-[1,2-*b*:4,5-*b*′]dithiophene (BDT) and dithieno[3,2-*b*:2′,3′-*d*]silole (DTS), respectively. Both **P1** and **P2** exhibit low-lying HOMO and good light-absorption properties. We further demonstrated that **P1** and **P2** are good donor materials in PSCs. Solar cells based on **P2**/$PC_{61}BM$ blend afforded a PCE of 4.33% with an impressively high V_{oc}, 0.93 V.

The synthetic routes for monomers and polymers were illustrated in Scheme 1. Thiophene-3,4-dicarboxylic was brominated by bromine in acetic acid to give 2,5-dibromothiophene-3,4-dicarboxylic acid in 50% yield. Treating 2,5-dibromothiophene-3,4-dicarboxylic acid with oxalyl chloride afforded the intermediate 2,5-dibromothiophene-3,4-dicarbonyl dichloride. The 2,5-dibromothiophene-3,4-dicarbonyl dichloride was then treated with 2-hexylthiophene in presence of $AlCl_3$ to obtain monomer BDTD in 12% yield. Monomers BDT and DTS were prepared according to the literature methods.[8,9] **P1** and **P2** were both synthesized by the Stille reaction using $Pd(PPh_3)_4$ as the catalyst. The crude products were precipitated in methanol. The impurities in the products were successively removed by methanol and hexane in a Soxhlet extractor 24 h each. Finally, the polymers were extracted with chloroform and reprecipitated in methanol and dried under vacuum. **P1** and **P2** have good solubilities in common organic solvents such as chloroform and toluene. The molecular weights of **P1** and **P2** were determined by gel permeation chromatography (GPC) against polystyrene standards in THF eluent, and the data are listed in Table 1.

Thermogravimetric analyses of **P1** and **P2** are shown in Figure 1. The temperature of 5% weight-loss was selected as the onset point of decomposition (T_d). The T_d values of **P1** and **P2** are 329 and 346 °C, respectively, indicating that they are thermally stable for organic photovoltaic applications.

The absorption spectra of the polymers in chloroform and films are shown in Figure 2. The optical properties of **P1** and **P2** are summarized in Table 2. Both polymers show strong absorption in the range of 500−650 nm. The absorption maxima of the polymers in solution are located at 551 and 586 nm for **P1** and **P2**, respectively. **P2** shows stronger absorption at the long wavelength region than **P1**, while **P1** exhibits a broader spectrum, especially in the 400−500 nm region. In solid films, both **P1** and **P2** show red shifts at the absorption maxima (576 nm for **P1** and 626 nm for **P2**), indicating the enhanced interchain π−π stacking in the solid state. The optical band gaps were calculated to be 1.78 eV for **P1** and 1.63 eV for **P2**.

Received: November 28, 2011
Revised: January 11, 2012
Published: January 23, 2012

ACS Publications © 2012 American Chemical Society

dx.doi.org/10.1021/ma202578y | *Macromolecules* 2012, 45, 1710−1714

Scheme 1. Synthesis of P1 and P2

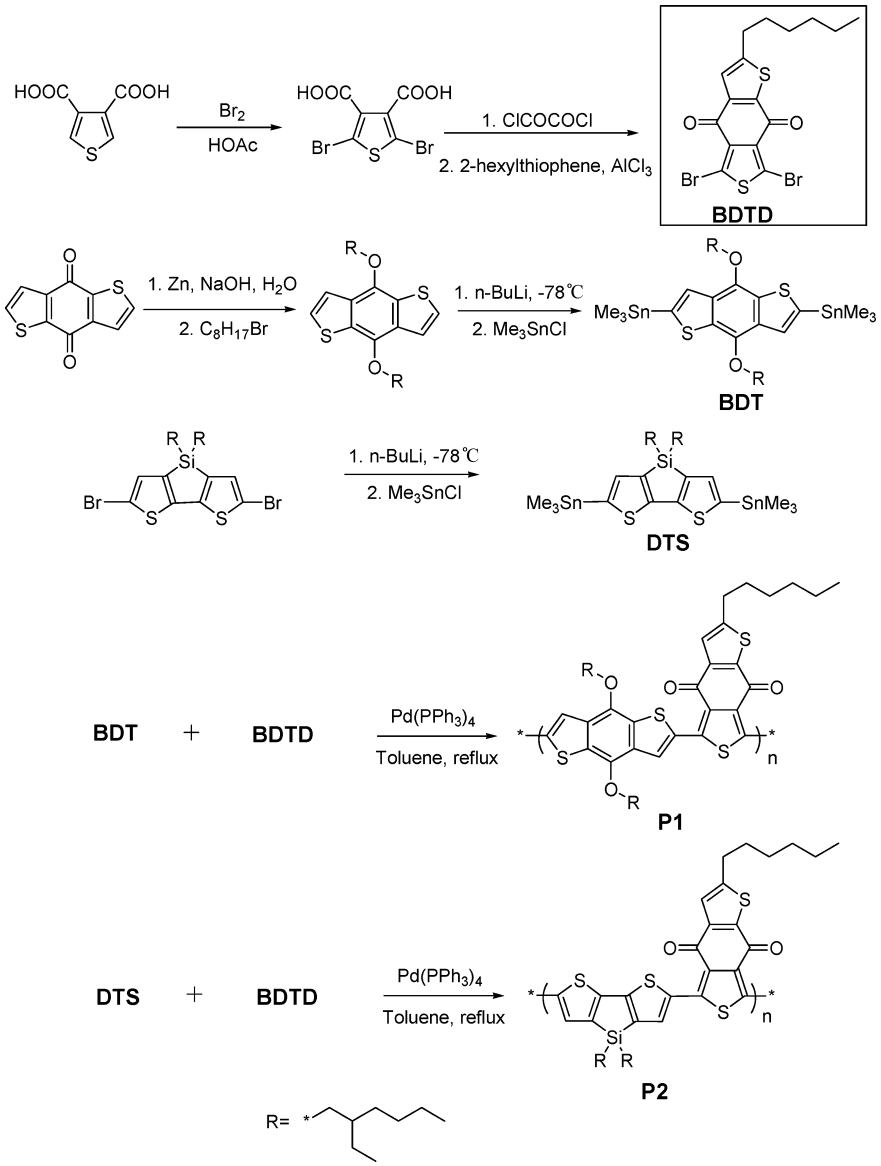


Table 1. Molecular Weights and Thermal Properties of Polymers

polymers	M_n[a]	M_w[a]	PDI[a]	T_d (°C)[b]
P1	11 490	39 382	3.43	329
P2	7037	13 384	1.90	346

[a]M_n, M_w, and PDI were determined by GPC using polystyrene standards with THF as eluent. [b]The temperature at 5% weight-loss under nitrogen.

The difference of **P1** and **P2** in optical properties reflects the different electron donating strength of their donor units (BDT and DTS).

The electrochemical properties of polymers were investigated by cyclic voltammetry (CV) method. Figure 3 shows the cyclic voltammograms of **P1** and **P2** films on glassy-carbon electrode in CH_3CN solution containing 0.1 mol/L Bu_4NPF_6. The CV data are summarized in Table 3. The onset oxidation potentials (E_{ox}) of **P1** and **P2** are 0.69 and 0.53 V, respectively, while the onset reduction potentials (E_{red}) of **P1** and **P2** are −1.27 and −1.33 V, respectively. The energy level of polymers were calculated according to the following equation: HOMO or LUMO = $-(E_{ox}$ or E_{red} + 4.8) eV. As a result, the HOMO energy levels of **P1** and **P2** are −5.49 and −5.33 eV, respectively, which are significantly deeper than that of P3HT (−4.76 eV) and close to ideal HOMO energy level (−5.4 eV).[10] Deep HOMO should render these polymers good stability against oxidization. The LUMO energy levels of **P1** and **P2** are −3.53 and −3.47 eV, respectively, and the electrochemical bandgaps of **P1** and **P2** are 1.96 and 1.86 eV, respectively. The electrochemical bandgaps of the polymers are ∼0.2 eV higher than the optical bandgaps, which might result from the interface barrier between the polymer film and the electrode surface.[11]

Solar cells with a configuration of ITO/PEDOT:PSS/polymer:$PC_{61}BM$/Ca/Al were fabricated and tested under simulated AM1.5G irradiation (86 mW/cm^2). The weight ratios of polymer to $PC_{61}BM$ for **P1** and **P2** cells were optimized from 1:1 to 1:2. $J-V$ curves for **P1** and **P2** are shown in Figure 4. The corresponding open-circuit voltage (V_{oc}), short-circuit current density (J_{sc}), fill factor (FF), and power conversion efficiency (PCE) of the cells are listed in Table 4.

dx.doi.org/10.1021/ma202578y | *Macromolecules* 2012, 45, 1710−1714

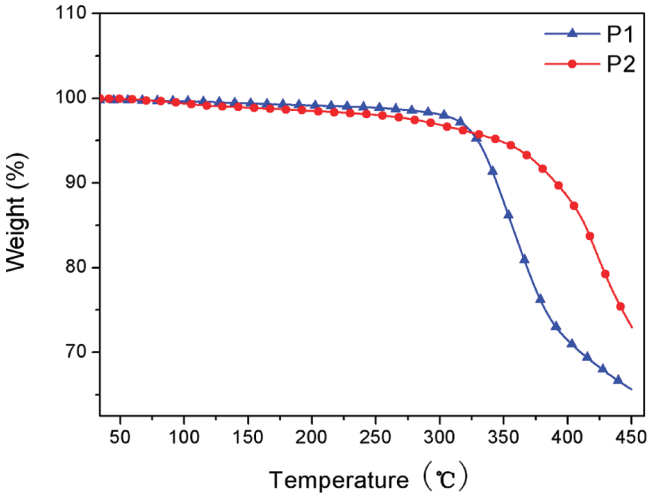


Figure 1. TGA plots of **P1** and **P2** with a heating rate of 10 °C/min under nitrogen.

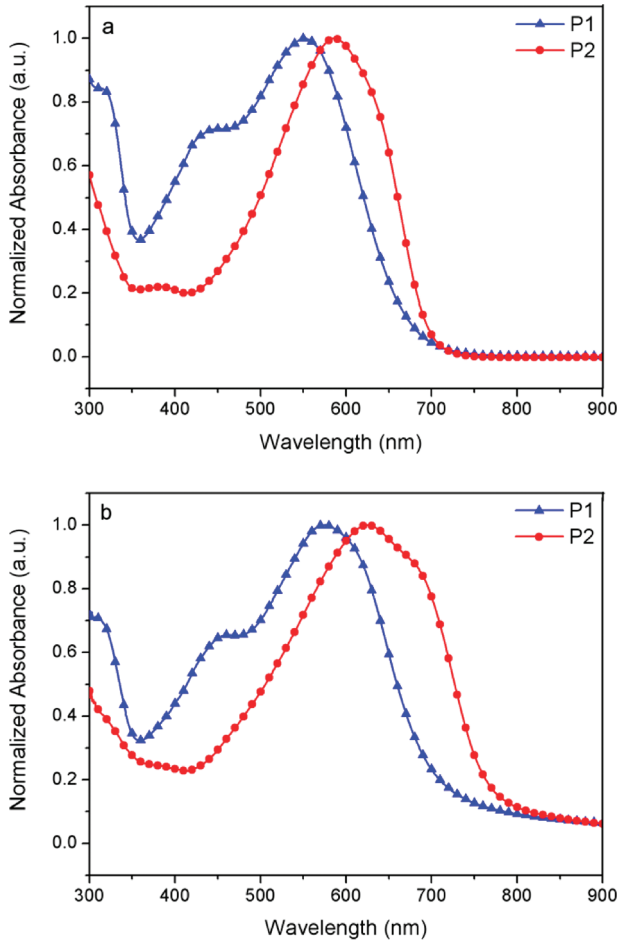


Figure 2. Normalized UV−vis absorption spectra of **P1** and **P2**: (a) in chloroform; (b) as thin film.

Cells based on **P1**/$PC_{61}BM$ and **P2**/$PC_{61}BM$ both show high V_{oc} (~0.9 V), due to the quite low HOMO levels of **P1** and **P2**. The optimized weight ratios (polymer/$PC_{61}BM$) for **P1** and **P2** both are 1:1.5. As shown in Table 4, **P2** exhibits the best PCE of 4.33% with a V_{oc} of 0.93 V, a J_{sc} of 6.66 mA/cm^2 and a FF of 60% in comparison with the best PCE of 2.18% for **P1** with a

Table 2. Optical Properties of P1 and P2

	λ_{max} (nm)		λ_{onset} (nm)	
	solution	film	film	E_g^{opt} (eV)[a]
P1	551	576	697	1.78
P2	586	626	762	1.63

[a]Calculated from the absorption band edge of the films, $E_g = 1240/\lambda_{onset}$.

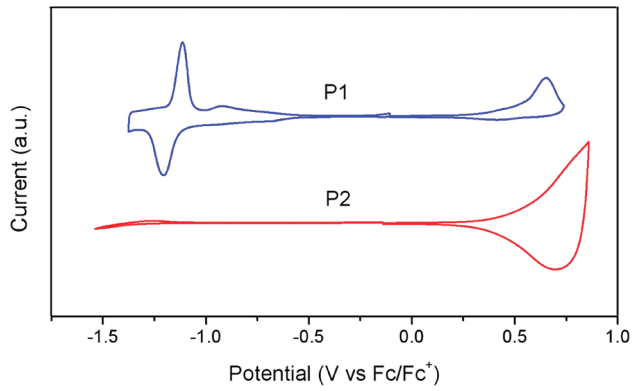


Figure 3. Cyclic voltammograms of **P1** and **P2** films in CH_3CN containing 0.1 mol/L Bu_4NPF_6.

Table 3. Electrochemical Properties of P1 and P2

	E_{ox}^{on} (V)	E_{red}^{on} (V)	HOMO (eV)	LUMO (eV)	E_g^{ec} (eV)[a]
P1	0.69	−1.27	−5.49	−3.53	1.96
P2	0.53	−1.33	−5.33	−3.47	1.86

[a]Calculated from $E_g = e(E_{ox}^{on} - E_{red}^{on})$.

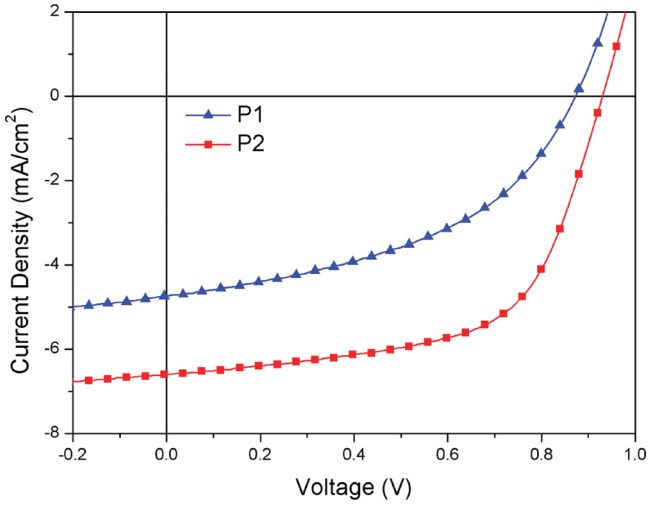


Figure 4. J−V curves for the polymer solar cells based on **P1** and **P2** under the illumination of AM1.5G, 86 mW/cm^2.

V_{oc} of 0.87 V, a J_{sc} of 4.75 mA/cm^2 and a FF of 45%. The higher performance of **P2** results from its higher J_{sc} and FF, which is probably due to its better absorption at the long wavelength region. The good hole mobility of silole moiety may account for the high J_{sc}.[12] The AFM images (tapping mode) (see Figure S1, Supporting Information) show the morphology change for the polymer/$PC_{61}BM$ composite films. The rms roughness for **P1**/$PC_{61}BM$ film decreased from 6.94 to 0.47 nm,

dx.doi.org/10.1021/ma202578y | *Macromolecules* 2012, 45, 1710−1714

Table 4. Photovoltaic Properties of the Solar Cells Based on P1 and P2

polymer	polymer:$PC_{61}BM$	V_{oc} (V)	J_{sc} (mA/cm^2)	FF (%)	PCE (%)
P1	1:1	0.91	4.03	42	1.79
	1:1.5	0.87	4.75	45	2.18
	1:2	0.89	5.23	37	1.99
P2	1:1	0.95	6.64	55	4.02
	1:1.5	0.93	6.66	60	4.33
	1:2	0.92	6.56	59	4.04

while for **P2**/$PC_{61}BM$ film from 3.85 to 2.48 nm, indicating the film morphology for **P1**/$PC_{61}BM$ film is more sensitive to thermal treatment. The molecular weight difference and structure difference could be responsible for this.

Figure 5 shows external quantum efficiency (EQE) curves for the solar cells based on **P1** and **P2**. **P1** device shows two

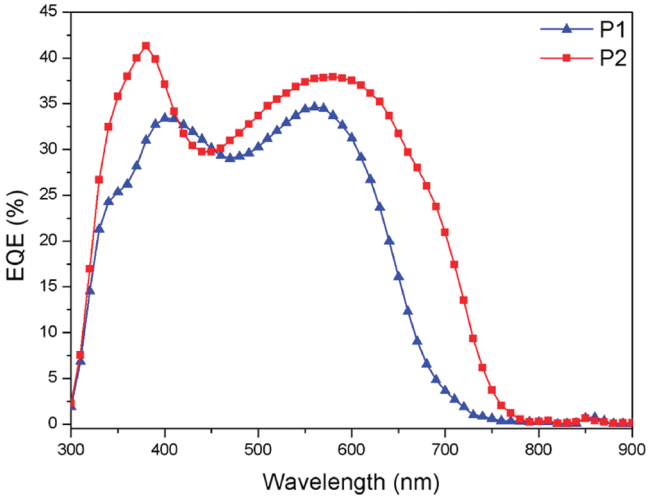


Figure 5. EQE curves for the devices based on **P1** and **P2**.

maxima at 400 and 560 nm, respectively, and **P2** device shows two maxima at 380 and 580 nm, respectively. **P2** device exhibits higher EQE than that of **P1**, which is due to stronger sunlight absorption of **P2** film (see Figure 2b).

In summary, we have synthesized two new low bandgap D−A copolymers with benzo[1,2-*b*:4,5-*c*′]dithiophene-4,8-dione as the acceptor unit. The polymers possess good light-absorption properties, thermal stability, and deep HOMO levels (−5.49 eV and −5.33 eV) due to the strong electron-withdrawing effect of BDTD unit. Solar cells based on these polymers give good PCEs and high V_{oc} indicating that BDTD is a potential building block for conjugated polymer donors. Further modification of the chemical structure of the polymer to redshift the light-absorption is currently underway.

■ ASSOCIATED CONTENT

Supporting Information

Synthetic procedures, NMR spectra, and AFM images. This material is available free of charge via the Internet at http://pubs.acs.org/.

■ AUTHOR INFORMATION

Corresponding Author

*E-mail: (L.D.) opv.china@yahoo.com; (W.Z.) zhuwg18@126.com.

Notes

The authors declare no competing financial interest.

■ ACKNOWLEDGMENTS

This work was supported by the "100 Talents Program" of the Chinese Academy of Sciences. Funding from Suzhou Jiahong Optoelectronics and the Ministry of Science and Technology of China are greatly appreciated. We thank Professor Jinsong Zhu for gifting a MBRAUN glovebox and Professor Zhong Zhang for providing lab space. We also thank Professor Jianhui Hou for his kind assistance in EQE measurements.

■ REFERENCES

(1) (a) Yu, G.; Gao, J.; Hummelen, J. C.; Wudl, F.; Heeger, A. J. *Science* **1995**, *270*, 1789. (b) Coakley, K. M.; Mcgehee, M. D. *Chem. Mater.* **2004**, *16*, 4533. (c) Scharber, M. C.; Mühlbacher, D.; Koppe, M.; Denk, P.; Waldauf, C.; Heeger, A. J.; Brabec, C. J. *Adv. Mater.* **2006**, *18*, 789. (d) Bredas, J. L.; Beljonne, D.; Coropceanu, V.; Cornil, J. *Chem. Rev.* **2004**, *104*, 4971. (e) Cheng, Y. J.; Yang, S. H.; Hsu, C. S. *Chem. Rev.* **2009**, *109*, 5868.

(2) (a) Li, G.; Shrotriya, V.; Huang, J. S.; Yao, Y.; Moriarty, T.; Emery, K.; Yang, Y. *Nat. Mater.* **2005**, *4*, 864. (b) Ma, W. L.; Yang, C. Y.; Gong, X.; Lee, K. H.; Heeger, A. J. *Adv. Funct. Mater.* **2005**, *15*, 1617.

(3) Hou, J. H.; Tan, Z. A.; Yan, Y.; He, Y. J.; Yang, C. H.; Li, Y. F. *J. Am. Chem. Soc.* **2006**, *128*, 4911.

(4) (a) Blouin, N.; Michaud, A.; Gendron, D.; Wakim, S.; Blair, E.; Neagu-Plesu, R.; Belletete, M.; Durocher, G.; Tao, Y.; Leclerc, M. *J. Am. Chem. Soc.* **2008**, *130*, 732. (b) Sun, Y.; Chien, S. -C.; Yip, H. -L.; Zhang, Y.; Chen, K. -S.; Zeigler, D. F.; Chen, F. -C.; Lin, B.; Jen, A. K. -Y. *J. Mater. Chem.* **2011**, *21*, 13247. (c) Zhang, Y.; Chien, S. -C.; Chen, K. -S.; Yip, H. -L.; Sun, Y.; Davies, J. A.; Chen, F. -C.; Jen, A. K. -Y. *Chem. Commun.* **2011**, *47*, 11026. (d) Adam, G.; Pivrikas, A.; Ramil, A. M.; Tadesse, S.; Yohannes, T.; Sariciftci, N. S.; Egbe, D. A. M. *J. Mater. Chem.* **2011**, *21*, 2594. (e) Susarova, D. K.; Khakina, E. A.; Troshin, P. A.; Goryachev, A. E.; Sariciftci, N. S.; Razumov, V. F.; Egbe, D. A. M. *J. Mater. Chem.* **2011**, *21*, 2356. (f) Xin, H.; Guo, X.; Kim, F. S.; Ren, G.; Watson, M. D.; Jenekhe, S. A. *J. Mater. Chem.* **2009**, *19*, 5303. (g) Wu, P. -T.; Bull, T.; Kim, F. S.; Luscombe, C. K.; Jenekhe, S. A. *Macromolecules* **2009**, *42*, 671. (h) Ong, K. -H.; Lim, S. -L.; Tan, H. -S.; Wong, H. -K.; Li, J.; Ma, Z.; Moh, L. C. H.; Lim, S. -H.; de Mello, J. C.; Chen, Z. -K. *Adv. Mater.* **2011**, *23*, 1409. (i) Hong, Y. -R.; Wong, H. -K.; Moh, L. C. H.; Tan, H. -S.; Chen, Z. -K. *Chem. Commun.* **2011**, *47*, 4920. (j) Duan, C. H.; Chen, K. S.; Huang, F.; Yip, -H. L.; Liu, S. J.; Zhang, J.; Jen, A. K. -Y.; Cao, Y. *Chem. Mater.* **2010**, *22*, 6444. (k) Duan, C. H.; Cai, W. Z.; Huang, F.; Zhang, J.; Wang, M.; Yang, T. B.; Zhong, C. M.; Gong, X.; Cao, Y. *Macromolecules* **2010**, *43*, 5262.

(5) (a) Liang, Y. Y.; Wu, Y.; Feng, D. Q.; Tsai, S. T.; Son, H. J.; Li, G.; Yu, L. P. *J. Am. Chem. Soc.* **2009**, *131*, 56. (b) Liang, Y. Y.; Feng, D. Q.; Wu, Y.; Tsai, S. T.; Li, G.; Ray, C.; Yu, L. P. *J. Am. Chem. Soc.* **2009**, *131*, 7792. (c) Hou, J. H.; Chen, H. Y.; Zhang, S. Q.; Chen, R. I.; Yang, Y.; Wu, Y.; Li, G. *J. Am. Chem. Soc.* **2009**, *131*, 15586. (d) Liang, Y. Y.; Yu, L. P. *Acc. Chem. Res.* **2010**, *43*, 1277. (e) Liang, Y. Y.; Xu, Z.; Xia, J. B.; Tsai, S. T.; Wu, Y.; Li, G.; Ray, C.; Yu, L. P. *Adv. Mater.* **2010**, *22*, 135. (f) Chen, H. Y.; Hou, J. H.; Zhang, S. Q.; Liang, Y. Y.; Yang, G. W.; Yang, Y.; Yu, L. P.; Wu, Y.; Li, G. *Nat. Photonics* **2009**, *3*, 649.

(6) Cui, C. H.; Fan, X.; Zhang, M. J.; Zhang, J.; Min, J.; Li, Y. F. *Chem. Commun.* **2011**, *47*, 11345.

(7) (a) Wudl, F.; Kobayashi, M.; Heeger, A. J. *J. Org. Chem.* **1984**, *49*, 3382. (b) Pomerantz, M.; Chaloner-Gill, B.; Harding, L. O.; Tseng, J. J.; Pomerantz, W. J. *J. Chem. Soc., Chem. Commun.* **1992**, 1672.

(8) (a) Hou, J. H.; Park, M. H.; Zhang, S. Q.; Yao, Y.; Chen, L. M.; Li, J. H.; Yang, Y. *Macromolecules* **2008**, *41*, 6012. (b) Zhang, G. B.; Fu, Y. Y.; Zhang, Q.; Xie, Z. Y. *Chem. Commun.* **2010**, *46*, 4997.

(9) (a) Huo, L. J.; Hou, J. H.; Chen, H. Y.; Zhang, S. Q.; Jiang, Y.; Chen, T. L.; Yang, Y. *Macromolecules* **2009**, *42*, 6564. (b) Hou, J. H.; Chen, H. Y.; Zhang, S. Q.; Li, G.; Yang, Y. *J. Am. Chem. Soc.* **2008**, *130*, 16144.

(10) Thompson, B. C.; Frechet, J. M. J. *Angew. Chem., Int. Ed.* **2008**, *47*, 58.

(11) (a) Egbe, D. A. M.; Nguyen, L. H.; Hoppe, H.; Mühlbacher, D.; Sariciftci, N. S. *Macromol. Rapid Commun.* **2005**, *26*, 1389. (b) Chen, Z. -K.; Huang, W.; Wang, L. -H.; Kang, E. -T.; Chen, B. J.; Lee, C. S.; Lee, S. T. *Macromolecules* **2000**, *33*, 9015. (c) Yamamoto, T.; Lee, B. -L. *Macromolecules* **2002**, *35*, 2993.
(12) Usta, H.; Lu, G.; Facchetti, A.; Marks, T. J. *J. Am. Chem. Soc.* **2006**, *128*, 9034.

Macromolecules

Note

pubs.acs.org/Macromolecules

Synthesis and Functionalization of Thiol-Reactive Biodegradable Polymers

Sebla Onbulak,[†] Sarah Tempelaar,[‡] Ryan J. Pounder,[‡] Ozgul Gok,[†] Rana Sanyal,[†] Andrew P. Dove,*[,‡] and Amitav Sanyal*[,†]

[‡]Department of Chemistry, University of Warwick, CV4 7AL, Coventry, U.K.

[†]Department of Chemistry, Bogazici University, Bebek 34342 Istanbul, Turkey

Supporting Information

In recent years, reactive degradable polymers have gained increased attention due to their widespread application in biomedical and materials sciences. Recent progress in efficient postfunctionalization strategies of polymeric materials have made such reactive polymers a versatile candidate for the design and synthesis of functional polymeric materials.[1] In particular, biodegradable polymeric materials that can be appropriately functionalized with biologically relevant molecules and biomolecules hold immense promise in the area of the design and fabrication of novel drug delivery systems and tissue engineering.[2] The multivalent nature of polymers allows the attachment of multiple targeting units and drugs, thus increasing the efficacy and payload. Furthermore, the degradability of polymers can be applied advantageously to allow controlled release of the drug over prolonged period of time at the disease site.

Aliphatic poly(ester)s obtained via the ring-opening polymerization (ROP) of lactides and lactones have been widely applied in these fields.[3] Such synthetic methodology allows access to poly(ester)s with good control over their molecular weight, polydispersity and end group fidelity. While historically, these polymerizations have been carried out by the ring-opening of cyclic monomers initiated by alcohols in the presence of a metal catalyst at high temperatures, metal-free organocatalytic and enzymatic processes in ROP have emerged as attractive alternatives for the "green" synthesis of polymers that are devoid of any residual metal impurities.[4] Despite the widespread utilization of poly(ester)-based materials for a variety of biomedical purposes, until recently, only a few functionalizable poly(ester)s have been available.[4,5]

Among the recently developed strategies for the synthesis of functional poly(ester)s, those based upon the highly efficient "click" reactions[6] have enabled the synthesis of biodegradable polymers that can be efficiently postfunctionalized. Functionalization of biodegradable polymers using the Cu(I) catalyzed Huisgen 1,3-dipolar cycloaddition between azide and alkyne functionalities has been applied by several groups.[7] The presence of residual metal impurities following these manipulations and concerns over polymer degradation during prolonged reaction times, provides motivation for the development of alternative approaches. A wide range of alternative metal-free "click" reactions such as strain promoted azide–alkyne cycloadditions, thiol–ene reactions and Diels–Alder cycloaddition reactions are increasingly becoming a method of choice to synthesize and functionalize polymeric materials.[8] Of these, thiol-reactive biodegradable polymers have immense potential in fabrication of functional degradable materials. Several recent reports have shown that maleimide-containing polymers can undergo mild postfunctionalization modifications.[9] Many polymers that possess a maleimide unit as a core or side-chain functionality have been synthesized due to the effective conjugation of this functional group for biological applications.[10] Notably, the nucleophilic "thiol–ene" Michael addition of thiol-containing molecules to maleimides was also demonstrated to be a highly efficient and selective methodology for the functionalization of degradable polymers in the absence of deleterious side-reactions.[11]

Cyclic carbonate monomers offer versatile methods for the incorporation of functional groups. Over the past years a number of cyclic carbonate monomers containing various pendant functional groups such as benzyl esters,[12] allyl esters,[13] azides,[14] carbamic acid benzyl ester,[15] and photolabile 2-nitrobenzoxycarbonyl groups have been reported.[16] Recently, allyl-functional poly(carbonate)s (obtained by organocatalytic ROP) were shown to be efficiently functionalized with thiol-containing molecules using the thermally initiated thiol–ene reaction in the presence of azobis(isobutyronitrile),[17] and vinyl–sulfone functionalized polymers were obtained by ROP in the presence of stannous octoate. These polymers again were shown to be reactive toward a variety of thiol-containing molecules.[18]

Herein, we describe a novel strategy to synthesize and functionalize maleimide containing thiol reactive biodegradable polymers by the organocatalyzed (co)polymerization of a novel furan-protected maleimide-functional carbonate monomer (Figure 1). Polymers obtained via ROP have pendant groups containing furan-protected maleimide units which, upon subjection to thermal cycloreversion reaction, yields maleimide groups that are ready to react with thiol containing molecules.

The furan-protected maleimide-containing cyclic carbonate monomer was synthesized using the protected diol **1** that was synthesized according to literature procedures.[19] The acetal groups were hydrolyzed using the acidic DOWEX 50W-X2 resin to generate diol **2** before ring-closure using triphosgene yielded the carbonate monomer **3** that could be readily purified either via simple precipitation in diethyl ether or column chromatography using SiO_2 (Scheme 1). The ^1H NMR spectrum (see Supporting Information, Figure S1) clearly shows the presence

Received: August 25, 2011
Revised: December 21, 2011
Published: January 17, 2012

ACS Publications © 2012 American Chemical Society

dx.doi.org/10.1021/ma2019528 | *Macromolecules* 2012, 45, 1715–1722

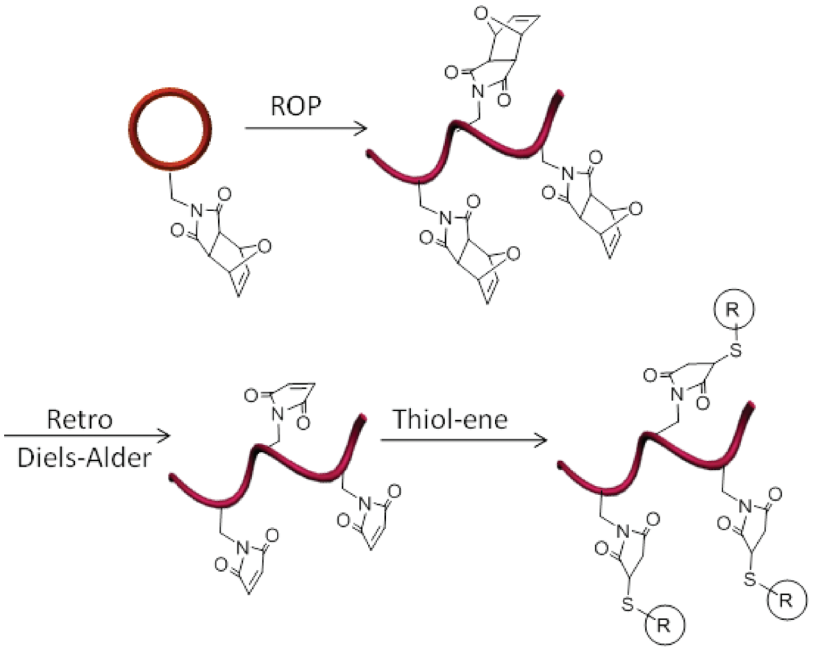


Figure 1. Illustrative scheme outlining the synthesis of maleimide containing polymers.

Scheme 1. Synthesis of Furan-Protected Maleimide-Containing Carbonate Monomer 3 and Unprotected Maleimide-Containing Monomer 4

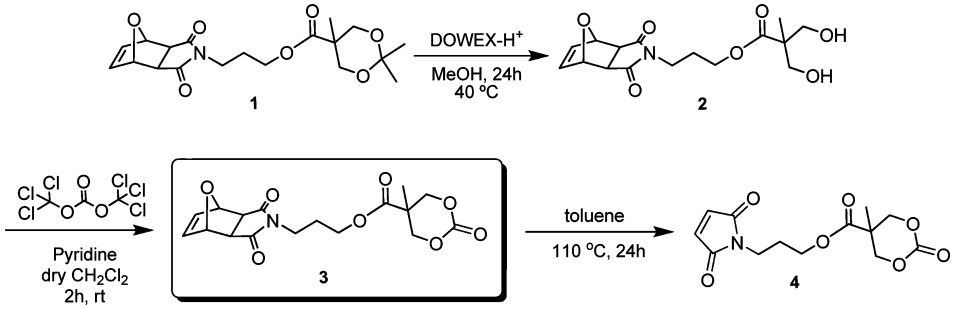


Table 1. Polymerization Conditions and Characterizations of Homopolymers of 3

item	polymer[a]	$[M]_0/[I]_0$[b]	time (h)	convn (%)	$M_{n,GPC}$ (g/mol)	M_w/M_n	$M_{n,theo}$ (g/mol)	$M_{n,NMR}$ (g/mol)
1	P1	20	192	58	5700	1.10	4300	5600
2	P2	20	24	65	2800	1.10	4800	2300
3	P3	20	4	50	2800	1.10	3800	2600
4	P4	20	117	65	3400	1.20	4800	3200
5	P5	40	27	47	5000	1.10	6900	4100
6	P6	100	27	48	5600	1.10	17 600	5000
7	P7	200	18	47	8200	1.10	34 400	8100

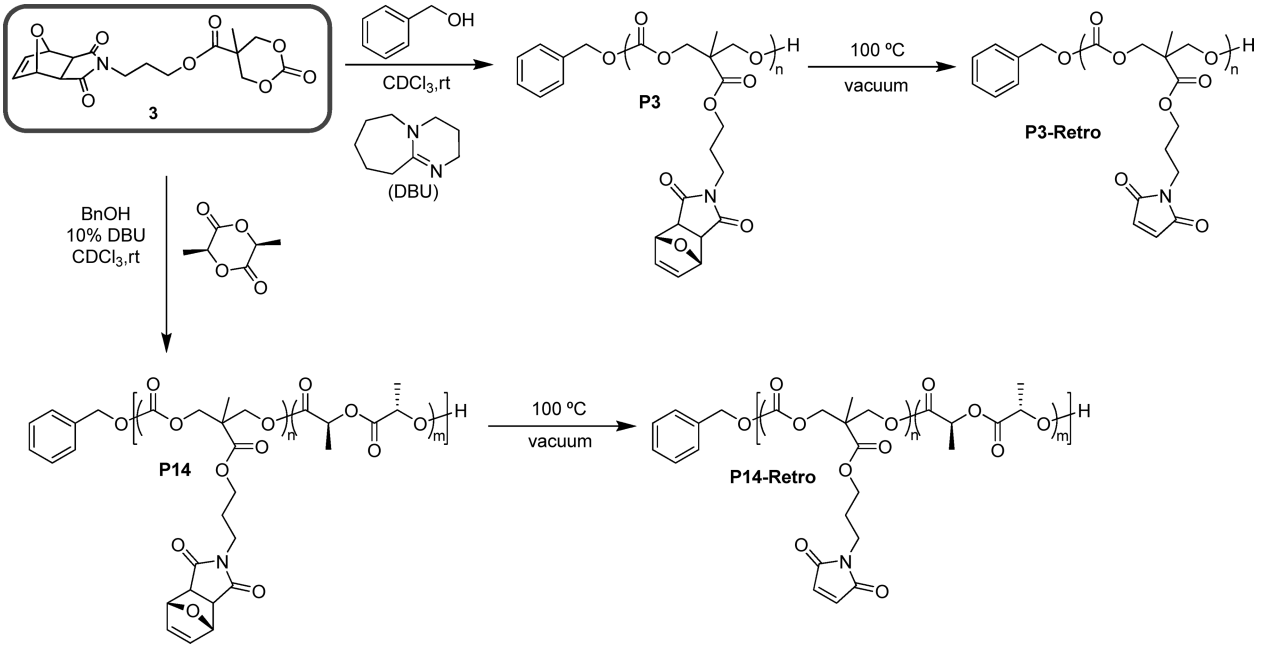
[a]Reaction conditions: 2 mol % DBU for **P1**, 20 mol % DBU for **P4** and 10 mol % DBU for all other polymers; all polymerizations were performed in $CDCl_3$ at 25 °C, [**3**] = 0.14 M using benzyl alcohol as the initiator. [b]Targeted degree of polymerization based on [M]/[I].

of the bicyclic unit composed of the furan-protected maleimide unit at δ = 2.84, 5.25, and 6.50 ppm. Additionally, the OCH_2 protons on the six membered carbonate ring appear as two doublets at δ = 4.73 and 4.20 ppm that arise as a consequence of the rigidity of the cyclic structure. The ^{13}C NMR spectrum provides further support of the monomer structure by the observation of three distinct carbonyl peaks at δ = 175.2, 169.8, and 146.6 ppm corresponding to the carbonyl carbons of ester, amide and carbonate groups respectively (see Supporting Information, Figure S2). Subsequent removal of the furan protecting group was possible by heating **3** in toluene at 100 °C for 12 h. The removal of the furan protecting group was evident by examination of the ^1H NMR spectrum of **4**, with loss of the characteristic signals at δ = 5.25 and 2.84 ppm with the concurrent observation of the shift of the vinyl resonances from δ = 6.50 to 6.70 ppm (see Supporting Information, Figure S5).

A wide range of organic catalysts have been applied in the ROP of cyclic carbonate monomers and have shown excellent

dx.doi.org/10.1021/ma2019528 | *Macromolecules* 2012, 45, 1715–1722

Scheme 2. Synthesis of Maleimide Functional Homo- and Copolymers by ROP and Activation of Maleimide Groups with Retro Diels–Alder Reaction



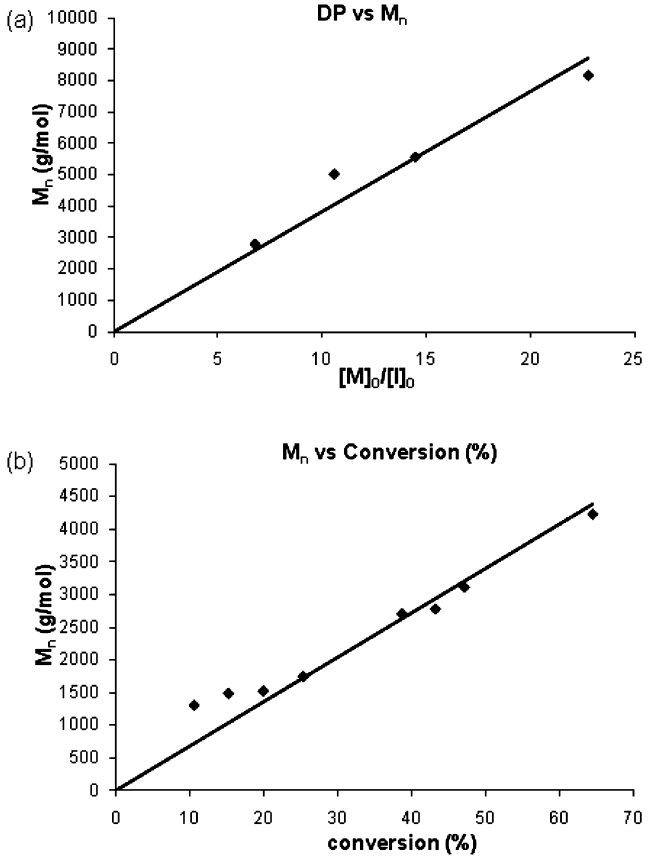


Figure 2. (a) Plot of number-average molecular weight (M_n) vs initial monomer-to-initiator ratio, $[M]_0/[I]_0$, in the ring-opening polymerization of **3**. Conditions: [**3**] = 0.14 M $CDCl_3$ at 25 °C, 10 mol % DBU using benzyl alcohol as an initiator. (b) Plot of number-average molecular weight (M_n) vs % monomer conversion in the ring-opening polymerization of **3**. Conditions: [**3**] = 0.14 M $CDCl_3$ at 25 °C, 10 mol % DBU, $[M]_0/[I]_0$ = 20 using benzyl alcohol as an initiator.

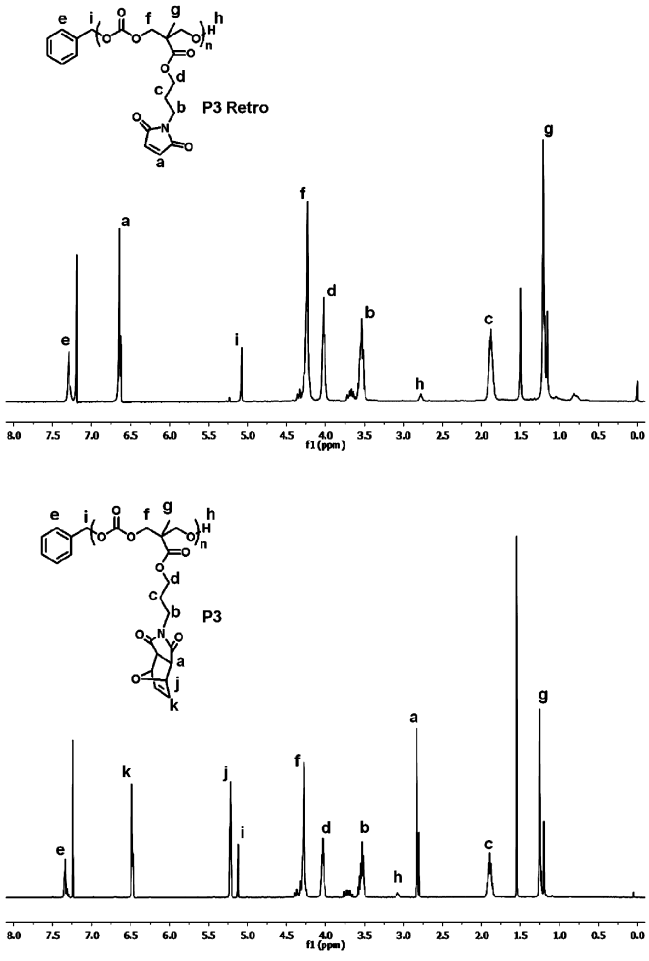


Figure 3. ^{1}H NMR of **P3** (bottom) and **P3-Retro** (top) homopolymers ($CDCl_3$, 400 MHz).

dx.doi.org/10.1021/ma2019528 | *Macromolecules* 2012, 45, 1715–1722

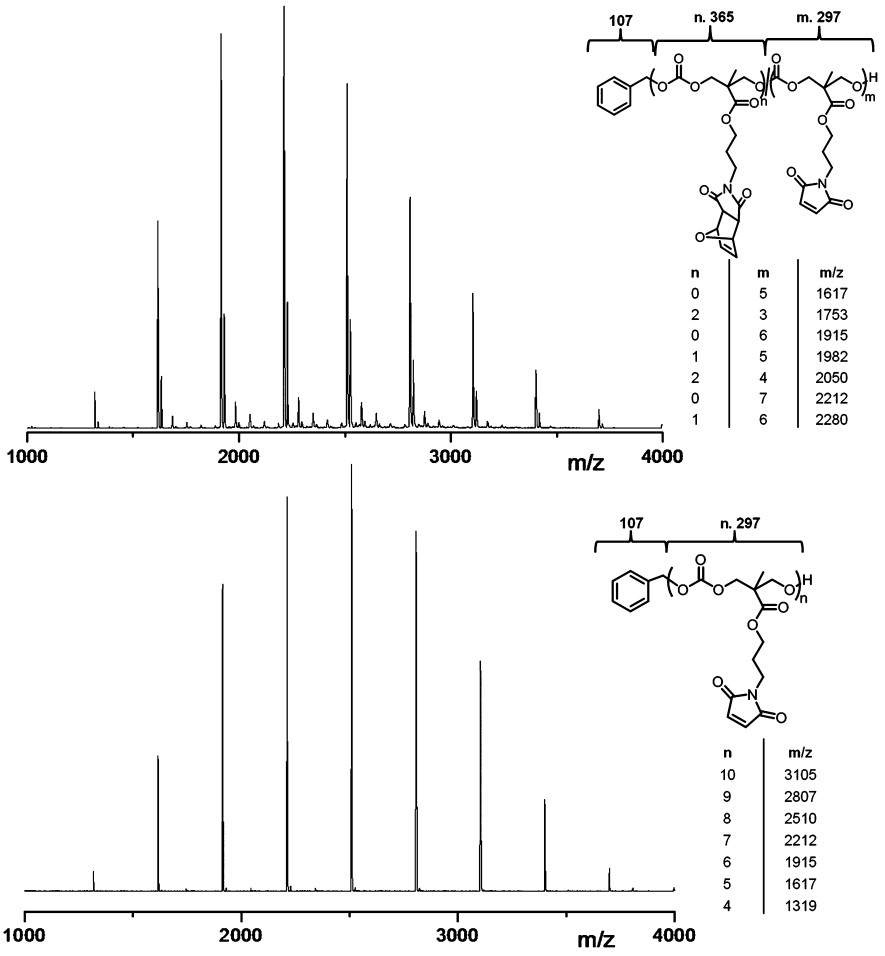


Figure 4. MALDI-TOF MS analysis of the polymer **P3** (top) and **P3** after retro DA reaction (bottom).

Table 2. Conditions and Characterizations of Carbonate Monomer 3:L-Lactide Copolymers

item	polymer[a]	time (h)	yield (%)	aimed ratio (3:LA)	obtained incorporation[b] (3:LA)	$M_{n,theo}$ (g/mol)	$M_{n,NMR}$[b] (g/mol)	$M_{n,GPC}$[c] (g/mol)	M_w/M_n
1	P8	120	90	20:80	21:79	17 100	9000	18 500	1.40
2	P9	8	95	5:95	4:96	14 800	11 100	22 000	1.10
3	P10	8	72	10:90	9:91	12 000	10 600	12 300	1.20
4	P11	24	70	25:75	17:83	13 000	7700	9800	1.10
5	P12	48	58	50:50	40:60	14 800	12 500	8300	1.20
6	P13	24	40	75:25	70:30	12 400	6500	8100	1.20
7	P14	24	85	10:90	6:94	14 200	13 300	17 000	1.20

[a]All polymerizations were performed in $CDCl_3$ at 25 °C, 2 mol % DBU, $[M]_0/[I]_0$ = 100 using benzyl alcohol as the initiator. [b]Measured by ^1H NMR spectroscopy . [c]Determined by SEC analysis in THF.

activity and selectivity.[20] DBU-catalyzed ring-opening polymerization of monomer **4** initiated with benzyl alcohol did not yield any homopolymer. Furthermore, attempts to copolymerize this unprotected monomer with L-lactide resulted in formation of a red gel. We propose that this is a consequence of cross-linking by base-catalyzed polymerization of the maleimide functionality that leads to the characteristic red color.[21] As such the furan-protected maleimide-containing carbonate monomer, **3**, was studied to provide access to biodegradable homopoly(carbonate)s bearing reactive maleimide units at their side chains via a protection/deprotection strategy (Scheme 2a). An initial survey of organocatalysts was undertaken to optimize the system with polymerizations carried out at room temperature using benzyl alcohol as an initiator in dry $CDCl_3$.[22] Polymerization using the thiourea/sparteine catalyst system resulted in very slow polymerization of **3**, hence the ROP of **3** catalyzed by 1,8-diazabicycloundec-7-ene (DBU) was studied (Table 1).

Monitoring the monomer conversion with time in the DBU-catalyzed homopolymerization of **3** revealed that the polymerization became severely retarded at ca. 60% monomer conversion,[23,20a] likely a consequence of the ring−chain equilibrium associated with sterically hindered monomers. Thereby, polymerizations were terminated at 50% monomer conversion in order to prevent possible transesterification reactions and obtain reliable data for further characterizations. Until this point, a linear relationship between conversion and molecular weight was observed. Although a discrepancy between targeted and obtained molecular weights was observed due to the

dx.doi.org/10.1021/ma2019528 | *Macromolecules* 2012, 45, 1715−1722

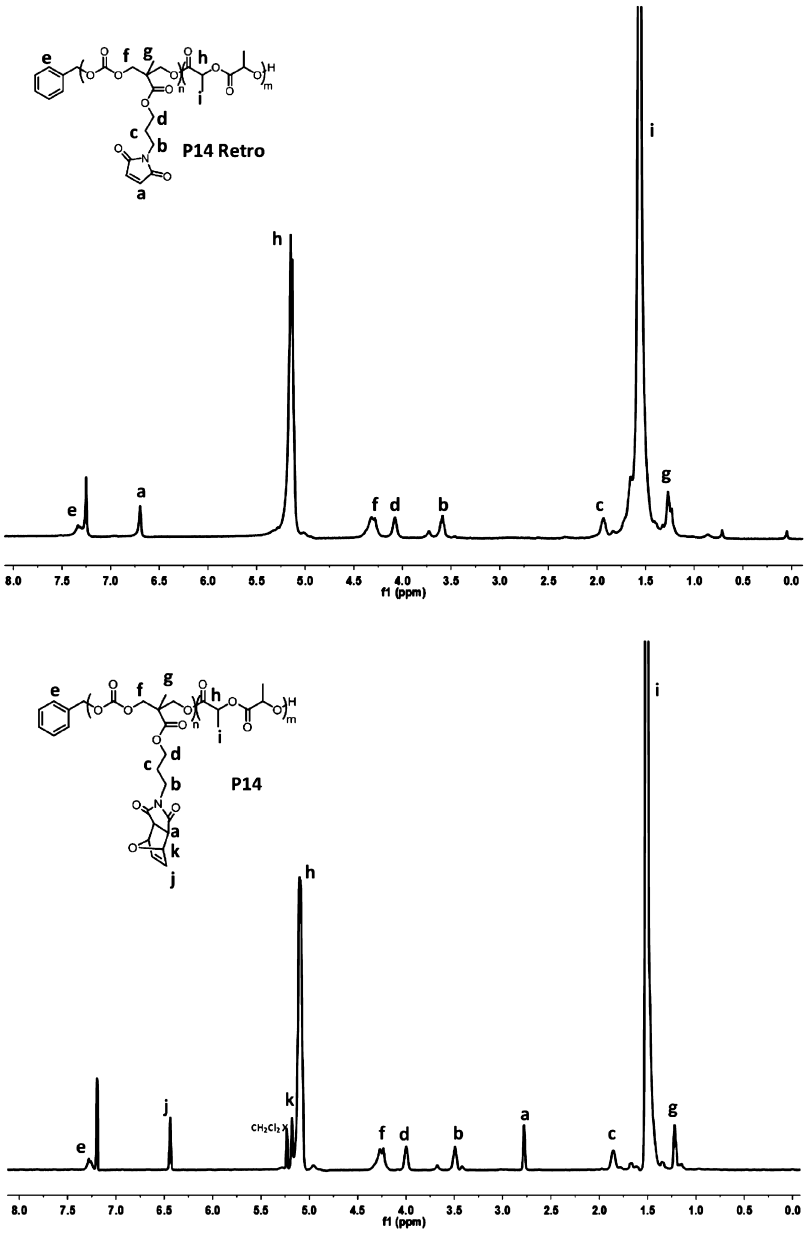


Figure 5. ^{1}H NMR spectrum of **P14** (bottom) and **P14-Retro** copolymers (top) ($CDCl_3$, 400 MHz).

extremely slow propagation of the polymer, a linear relationship between DP and obtained molecular weight was maintained (Figure 2).

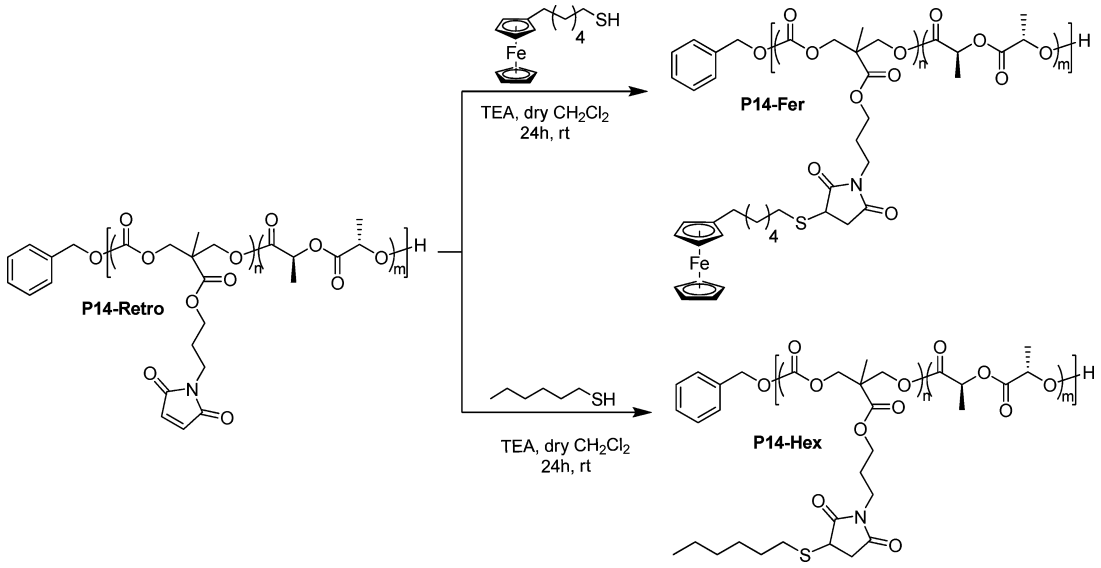
The homopolymer **P3** was subjected to the retro Diels–Alder reaction by heating to 100 °C in a vacuum oven to unmask the maleimide groups to their reactive forms. Quantitative deprotection of the maleimide functional groups by elimination of furan was evident from the disapperance of the proton resonances in the ^{1}H NMR spectrum at δ = 2.82, 5.23, and 6.47 ppm resulting from the removal of the bicyclic core, and the appearance of a new proton resonance at δ = 6.65 ppm belonging to the active double bond protons of the maleimide unit (Figure 3). As expected, a slight decrease in the molecular weight of the polymer **P3** after the retro Diels–Alder step was observed by SEC analysis (**P3**, M_n = 2800 g·mol^{-1}, PDI = 1.10; **P3-Retro**, M_n = 2700 g·mol^{-1}, PDI = 1.10). More importantly, both ^{1}H NMR and SEC analysis of the resultant polymers show that no chain scission or other side reactions occurred during this activation step (see Supporting Information, Figure S3).

The homopolymers before and after the retro Diels–Alder reaction step were also analyzed by MALDI-ToF mass spectrometry (Figure 4). The MALDI–ToF MS of the parent homopolymer **P3**, displays peaks that correspond to polymer chains that contain the deprotected maleimide functionality alongside those expected for polymer **P3** with furan protecting groups retained. These data indicate that the retro Diels–Alder reaction partially occurs upon ionization by the laser as previously observed.[11b] The MALDI-ToF spectra of the homopolymer **P3-Retro** obtained after the retro Diels–Alder step consisted solely of the polymer with the reactive maleimide side chains.

To both overcome the limitations of poor monomer polymerizability and to enable the synthesis of maleimide-functional poly(lactide)s, copolymerization of **3** with L-lactide was studied by DBU-catalyzed ROP (Scheme 2b). A range of comonomer

dx.doi.org/10.1021/ma2019528 | *Macromolecules* 2012, 45, 1715–1722

Scheme 3. Functionalization of Polymers via the Thiol−Ene Reaction



feed ratios were investigated (Table 2) with good correlation between feed ratio and comonomer incorporation being observed up to between 10 and 20% feed ratio of **3**. At higher feed ratios of **3**, lower incorporation of the carbonate comonomer into the poly(lactide) chain is observed (in comparison to that anticipated from the monomer feed ratios) which suggests that at higher overall monomer conversions the copolymers may be more accurately considered as tapered blocky copolymers, consistent with the higher rates of homopolymerization of lactide in comparison to **3**. Nonetheless, excellent control over the molecular parameters of the polymers is maintained. Following exposure of the furan-protected copolymers to high vacuum at 100 °C, the efficiency of the rDA reaction was clearly evident from the ^{1}H NMR spectra of the polymers observing a complete disappearance of the resonances at δ = 6.48, 5.28, and 2.83 ppm and appearance of a new resonance at δ = 6.69 ppm corresponding the unsaturated maleimide vinyl protons (Figure 5).

Analysis of the copolymers by thermogravimetric analysis (TGA) was also performed to probe the activation step via the rDA cycloreversion. Removal of the furan units is clearly observed between 60 and 180 °C and, as expected, different polymers containing higher maleimide incorporation displayed an increased weight loss (see Supporting Information, Figure S4).

To evaluate the efficiency of Michael type additions of thiol-containing molecules to the maleimide-functional polymers, functionalization studies were performed using two different thiols with the polymer **P14**, namely 6-(ferrocenyl)hexanethiol and 1-hexanethiol (Scheme 3). These thiols were chosen as representative examples which demonstrate the functionalization efficiency with 6-(ferrocenyl)hexanethiol providing a readily observable NMR handle as a consequence of the metalated cyclopentadienyl rings. Quantitative conjugation of thiol containing small molecules to the maleimide side chains was achieved at room temperature by using 2-fold excess of thiols per maleimide group. Using one equivalent of thiol per maleimide group led to a maximum conversion of 81%. Therefore, a thiol to maleimide ratio of 2:1 equiv was used for conjugations in order to achieve quantitative derivatization.

Examination of the ^{1}H NMR spectra of the polymer functionalized with 6-(ferrocenyl)hexanethiol revealed that the characteristic maleimide double bond resonance at δ = 6.69 ppm had disappeared and resonances corresponding to the protons on the ferrocene rings appeared at δ = 4.01 and 4.08 ppm. The proton resonances from the newly formed succinimide ring and the alkyl chain are also clearly assignable. Similarly, disappearance of maleimide proton resonances and appearance of expected proton resonances were also observed for the 1-hexanethiol conjugation reaction (see Supporting Information, Figure S7). SEC analysis of the functionalized polymers also confirmed the addition of thiol-containing species to the polymer backbones indicated by the decreased retention time in comparison to the maleimide-functional polymer precursor which indicates a change to the hydrodynamic volume of the polymer in solution as may be expected by an increase in molecular mass or a change in the polymer structure commensurate with the successful addition of thiol-containing species (Figure 6). Importantly, a narrow PDI is preserved in the polymers thus demonstrating that maleimide−thiol conjugation chemistry is an efficient method for functionalization of the copolymers without degradation of the polymer backbone.

In conclusion, a new maleimide-containing cyclic carbonate monomer has been synthesized and its homopolymerization and copolymerization behavior with L-lactide has been investigated using organocatalytic ring-opening polymerization. The side chains of these polymers were activated by retro Diels−Alder reaction to obtain reactive maleimide groups for further conjugations. Michael-addition "thiol−ene" conjugations were used to modify the pendant maleimide groups in a quantitative fashion without any noticeable degradation of the parent polymers. Further study of the copolymerization behavior of these monomers and subsequent fabrication of the resultant functional materials using this novel class of reactive polymers is underway and will be reported in due course.

dx.doi.org/10.1021/ma2019528 | *Macromolecules* 2012, 45, 1715−1722

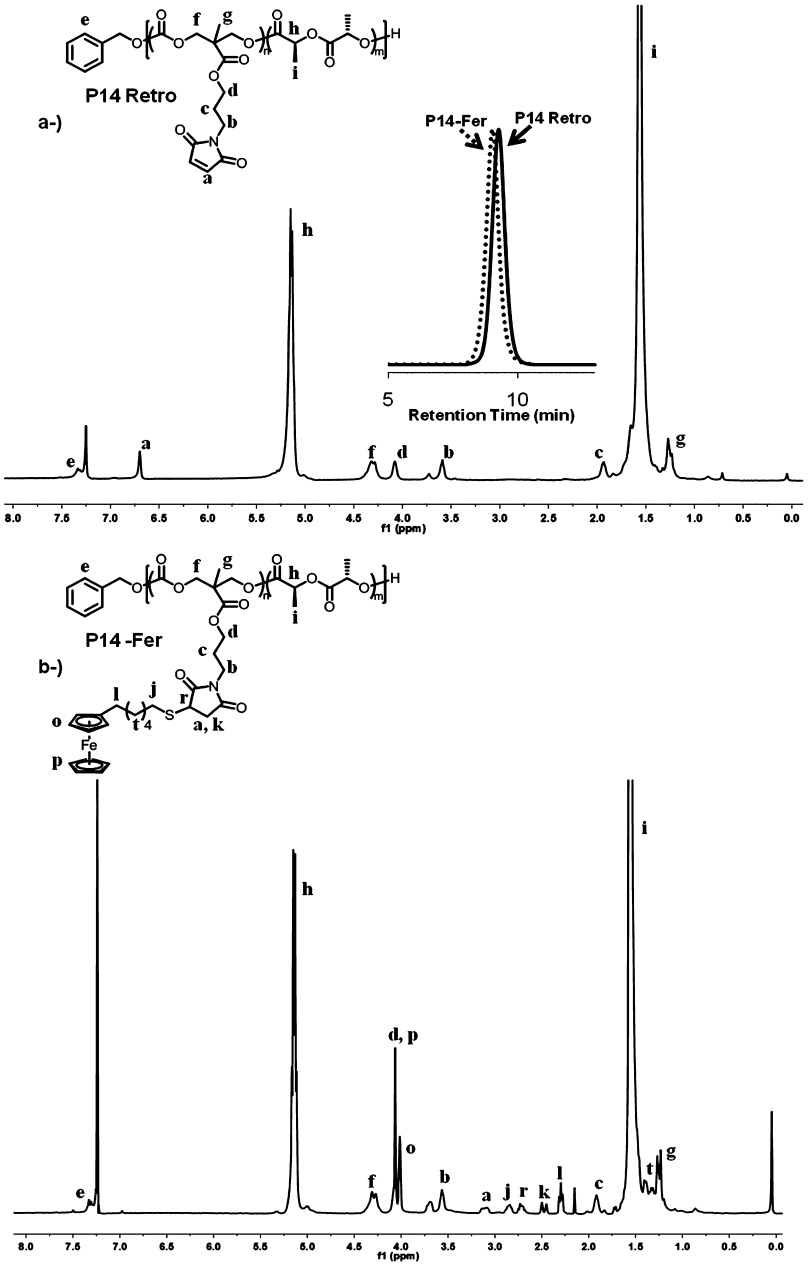


Figure 6. ^{1}H NMR in $CDCl_3$ of (a) **P14-Retro** (b) ^{1}H NMR of in $CDCl_3$ 6-(ferrocenyl)hexanethiol functionalized polymer (**P14**-Fer) and SEC traces before ($M_{n,SEC}$ = 17.0 kg/mol, M_w/M_n = 1.20) and after thiol functionalization ($M_{n,SEC}$ = 18.4 kg/mol, M_w/M_n = 1.20).

■ ASSOCIATED CONTENT

Supporting Information

Experimental section and ^{1}H and ^{13}C NMR spectra, GPC traces, and TGA thermograms. This material is available free of charge via the Internet at http://pubs.acs.org.

■ AUTHOR INFORMATION

Corresponding Author

*(A.P.D.) E-mail: a.p.dove@warwick.ac.uk. Telephone: 44-247-652-4107. Fax: 44-247-652-4112. (A.S.) E-mail: amitav.sanyal@boun.edu.tr. Telephone: 90-212-359-7613. Fax: 90-212-287-2467.

■ ACKNOWLEDGMENTS

The authors thank the Bogazici University Research Fund (BAP 6201) and Turkish Scientific and Technological Research Council (TUBITAK 110T068) for the financial support of this research. A.S. and R.S. thank the Turkish Academy for Sciences for the TUBA-GEBIP fellowship. EPSRC (EP/F068808/1 and DTA) are acknowledged for supporting a studentship (S.T. and R.J.P.) and for the purchase of the Bruker Ultraflex MALDI–ToF MS instrument (EP/C007999/1). The GPC equipment used at Warwick in this research was obtained through Birmingham Science City: Innovative Uses for Advanced Materials in the Modern World (West Midlands Centre for Advanced Materials Project 2), with support from Advantage West Midlands (AWM) and part funded by the European Regional Development Fund (ERDF).

■ REFERENCES

(1) (a) Gauthier, M. A.; Klok, H.-A. *Chem. Commun.* **2008**, 2591–2611. (b) Gauthier, M. A.; Gibson, M. I.; Klok, H.-A. *Angew. Chem., Int. Ed.* **2008**, *47*, 48–58.

(2) (a) Seyednejad, H.; Ghassemi, A. H.; van Nostrum, C. F.; Vermonden, T.; Hennink, W. E. *J. Controlled Release* **2011**, *152*, 168−176. (b) Ulery, B. D.; Nair, L. S.; Laurencin, C. T. *J. Polym. Sci., Part B: Polym. Phys.* **2011**, *49*, 832−864. (c) Albertsson, A. C.; Varma, I. K. *Adv. Polym. Sci.* **2002**, *157*, 1−40.
(3) (a) Albertsson, A. C.; Varma, I. K. *Biomacromolecules* **2003**, *4*, 1466−1486. (b) Dechy-Cabaret, O.; Martin-Vaca, B.; Bourissou, D. *Chem. Rev.* **2004**, *104*, 6147−6176. (c) Dove, A. P. *Polym. Chem.* **2010**, *1*, 260−271. (d) Jerome, C.; Lecomte, P. *Adv. Drug Delivery Rev.* **2008**, *60*, 1056−1076.
(4) (a) Kamber, N. E.; Jeong, W.; Waymouth, R. M.; Pratt, R. C.; Lohmeijer, B. G. G.; Hedrick, J. L. *Chem. Rev.* **2007**, *107*, 5813−5840. (b) Dove, A. P. *Chem. Commun.* **2008**, 6446−6470.
(5) (a) Baker, G. L.; Vogel, E. B.; Smith, M. R. *Polym. Rev.* **2008**, *48*, 64−84. (b) Bourissou, D.; Moebs-Sanchez, S.; Martin-Vaca, B. *C. R. Chim.* **2007**, *10*, 775−794.
(6) Hawker, C. J.; Wooley, K. L. *Science* **2005**, *309*, 1200−1205.
(7) (a) Parrish, B.; Breitenkamp, R. B.; Emrick, T. *J. Am. Chem. Soc.* **2005**, *127*, 7404−7410. (b) Riva, R.; Schmeits, S.; Jerome, C.; Jerome, R.; Lecomte, P. *Macromolecules* **2007**, *40*, 796−803. (c) Jiang, X.; Vogel, E. B.; Smith, M. R.; Baker, G. L. *Macromolecules* **2008**, *41*, 1937−1944.
(8) (a) Lutz, J.−F. *Angew. Chem., Int. Ed.* **2008**, *47*, 2182−2184. (b) Becer, C. R.; Hoogenboom, R.; Schubert, U. S. *Angew. Chem., Int. Ed.* **2009**, *48*, 4900−4908. (c) Hoyle, C. E.; Bowman, C. N. *Angew. Chem., Int. Ed.* **2010**, *49*, 1540−1573. (d) Hoyle, C. E.; Lowe, A. B.; Bowman, C. N. *Chem. Soc. Rev.* **2010**, *39*, 1355−1387. (e) Durmaz, H.; Colakoclu, B.; Tunca, U.; Hizal, G. *J. Polym. Sci., Part A: Polym. Chem.* **2006**, *44*, 1667−1675. (f) Gacal, B.; Durmaz, H.; Tasdelen, M. A.; Hizal, G.; Tunca, U.; Yagci, Y.; Demirel, A. L. *Macromolecules* **2006**, *39*, 5330−5336. (g) Sinnwell, S.; Inglis, A. J.; Davis, T. P.; Stenzel, M. H.; Barner-Kowollik, C. *Chem. Commun.* **2008**, 2052−2054. (h) Sanyal, A. *Macromol. Chem. Phys.* **2010**, *211*, 1417−1425. (i) Hizal, G.; Tunca, U.; Sanyal, A. *J. Polym. Sci., Part A: Polym. Chem.* **2011**, *49*, 4103−4120.
(9) Hall, D. J.; Van Den Berghe, H. M.; Dove, A. P. *Polym. Int.* **2011**, *60*, 1149−1157.
(10) (a) Lowe, A. *Polym Chem* **2010**, *1*, 17−36. (b) Kosif, I.; Park, E. J.; Sanyal, R.; Sanyal, A. *Macromolecules* **2010**, *43*, 4140−4148. (c) Mantovani, G.; Lecolley, F.; Tao, L.; Haddleton, D. M.; Clerx, J.; Cornelissen, J.; Velonia, K. *J. Am. Chem. Soc.* **2005**, *127*, 2966−2973. (d) Dispinar, T.; Sanyal, R.; Sanyal, A. *J. Polym. Sci., Part A: Polym. Chem.* **2007**, *45*, 4545−4551. (e) Bailey, G. C.; Swager, T. M. *Macromolecules* **2006**, *39*, 2815−2818. (f) Bays, E.; Tao, L.; Chang, C. W.; Maynard, H. D. *Biomacromolecules* **2009**, *10*, 1777−1781. (g) Sumerlin, B. S.; Vogt, A. P. *Macromolecules* **2010**, *43*, 1−13. (h) Boyer, C.; Bulmus, V.; Davis, T. P.; Ladmiral, V.; Liu, J.; Perrier, S. *Chem. Rev.* **2009**, *109*, 5402−5436. (i) Gok, O.; Durmaz, H.; Ozdes, E. S.; Hizal, G.; Tunca, U.; Sanyal, A. *J. Polym. Sci., Part A: Polym. Chem.* **2010**, *48*, 2546−2556.
(11) (a) Stanford, M. J.; Dove, A. P. *Macromolecules* **2009**, *42*, 141−147. (b) Pounder, R. J.; Stanford, M. J.; Brooks, P.; Richards, S. P.; Dove, A. P. *Chem. Commun.* **2008**, 5158−5160. (c) Stanford, M. J.; Pflughaupt, R. L.; Dove, A. P. *Macromolecules* **2010**, *43*, 6538−6541.
(12) (a) Bisht, K. S.; Al-Azemi, T. F. *Macromolecules* **1999**, *32*, 6536−6540. (b) Shi, M.; Wosnick, J. H.; Ho, K.; Keating, A.; Shoichet, M. S. *Angew. Chem., Int. Ed.* **2007**, *46*, 6126−6131.
(13) Mullen, B. D.; Tang, C. N.; Storey, R. F. *J. Polym. Sci., Part A: Polym. Chem.* **2003**, *41*, 1978−1991.
(14) (a) Zhang, X.; Zhong, Z.; Zhou, R. *Macromolecules* **2011**, *44*, 1755−1759. (b) Xu, J.; Prifti, F.; Song, J. *Macromolecules* **2011**, *44*, 2660−2667.
(15) Hu, X.; Chen, X.; Xie, Z.; Cheng, H.; Jing, X. *J. Polym. Sci., Part A: Polym. Chem.* **2008**, *46*, 7022−7032.
(16) Xie, Z.; Hu, X.; Chen, X.; Sun, J.; Shi, Q.; Jing, X. *Biomacromolecules* **2008**, *9*, 376−380.
(17) Tempelaar, S.; Mespouille, L.; Dubois, P.; Dove, A. P. *Macromolecules* **2011**, *44*, 2084−2091.
(18) Wang, R.; Chen, W.; Meng, F.; Cheng, R.; Deng, C.; Feijen, J.; Zhong, Z. *Macromolecules* **2011**, *44*, 6009−6016.
(19) Tonga, M.; Cengiz, N.; Kose, M. M.; Dede, T.; Sanyal, A. *J. Polym. Sci., Part A: Polym. Chem.* **2010**, *48*, 410−416.
(20) (a) Nederberg, F.; Lohmeijer, B. G. G.; Leibfarth, F.; Pratt, R. C.; Choi, J.; Dove, A. P.; Waymouth, R. M.; Hedrick, J. L. *Biomacromolecules* **2007**, *8*, 153−160. (b) Pratt, R. C.; Nederberg, F.; Waymouth, R. M.; Hedrick, J. L. *Chem. Commun.* **2008**, 114−116. (c) Suriano, F.; Coulembier, O.; Hedrick, J. L.; Dubois, P. *Polym. Chem.* **2011**, *2*, 528−533.
(21) (a) Kojima, K.; Yoda, N.; Marvel, C. S. *J. Polym. Sci., Part A-1: Polym. Chem.* **1966**, *4*, 1121−1134. (b) Hass, H. C.; Moreau, R. D. *J. Polym. Sci., Part A-1: Polym. Chem.* **1975**, *13*, 2327−2334.
(22) (a) Dove, A. P.; Pratt, R. C.; Lohmeijer, B. G. G.; Waymouth, R. M.; Hedrick, J. L. *J. Am. Chem. Soc.* **2005**, *127*, 13798−13799. (b) Lohmeijer, B. G. G.; Pratt, R. C.; Leibfarth, F.; Logan, J. W.; Long, D. A.; Dove, A. P.; Nederberg, F.; Choi, J.; Wade, C.; Waymouth, R. M.; Hedrick, J. L. *Macromolecules* **2006**, *39*, 8574−8583. (c) Pratt, R. C.; Lohmeijer, B. G. G.; Long, D. A.; Lundberg, P. N. P.; Dove, A. P.; Li, H. B.; Wade, C. G.; Waymouth, R. M.; Hedrick, J. L. *Macromolecules* **2006**, *39*, 7863−7871. (d) Pratt, R. C.; Lohmeijer, B. G. G.; Long, D. A.; Waymouth, R. M.; Hedrick, J. L. *J. Am. Chem. Soc.* **2006**, *128*, 4556−4557.
(23) Keul, H.; Bächer, R.; Höcker, H. *Makromol. Chem.* **1986**, *187*, 2579−2589.